NBS SPECIAL PUBLICATION 323

Electronic Density of States

U.S.
DEPARTMENT
OF
COMMERCE
National
Bureau
of
Standards















Institute for Materials Research Symposia

TRACE CHARACTERIZATION, CHEMICAL AND PHYSICAL
W. W. Meinke and B. F. Scribner, Editors
1st Materials Research Symposium
Held at NBS, Gaithersburg, Maryland
October 3–7, 1966

MOLECULAR DYNAMICS AND STRUCTURE OF SOLIDS
R. S. Carter and J. J. Rush, Editors
2nd Materials Research Symposium
Held at NBS, Gaithersburg, Maryland
October 16–19, 1967

ELECTRONIC DENSITY OF STATES
L. H. Bennett, Editor
3rd Materials Research Symposium
Held at NBS, Gaithersburg, Maryland
November 3–6, 1969

UNITED STATES DEPARTMENT OF COMMERCE ● MAURICE H. STANS, *Secretary*

NATIONAL BUREAU OF STANDARDS ● LEWIS M. BRANSCOMB, *Director*

Electronic Density of States

Based on Invited and Contributed Papers and Discussion
3rd Materials Research Symposium
Held at Gaithersburg, Maryland
November 3–6, 1969

Lawrence H. Bennett, Editor

Institute for Materials Research
National Bureau of Standards
Washington, D.C. 20234

U.S. National Bureau of Standards, Special Publication 323

Nat. Bur. Stand. (U.S.), Spec. Publ. 323, 834 pages (December 1971)

CODEN: XNBSA

Issued December 1971

Abstract

This volume is based on materials presented at the Third Materials Research Symposium of the National Bureau of Standards, held November 3–6, 1969. It provides a review of various experimental and theoretical techniques applied to the study of the electronic density of states in solids and liquids. The topics covered in a series of invited and contributed papers include theory of and experiments to obtain the one-electron density-of-states; many-body effects; optical properties; spectroscopic methods such as photoemission (x-ray and UV), ion neutralization, and soft x-ray; obtaining the density-of-states at the Fermi level by specific heat, magnetic susceptibility, and the Knight shift; the disordered systems of alloys, liquids, dirty semiconductors, and amorphous systems; and superconducting tunneling and the application of density of states to properties such as phase stability.

An edited discussion follows many of the papers.

Key words: Band structure; disordered systems; electronic density of states; ion neutralization; Knight shift; magnetic susceptibility; many-body effects; optical properties; photoemission; soft x-ray; specific heat; superconductivity; transport properties; tunneling.

Library of Congress Catalog Card Number 77-610600

Foreword

"Electronic Density of States," the third annual symposium of the Institute for Materials Research of the National Bureau of Standards, was held November 3–6, 1969, in the NBS laboratories at Gaithersburg, Maryland. More than 350 university, government, and industrial scientists from both the United States and abroad attended in order to take advantage of this excellent opportunity for dialogue between specialists of varying backgrounds and interests.

Proceedings of previous annual symposia sponsored by the Institute for Materials Research—the First, "Trace Characterization—Chemical and Physical," (National Bureau of Standards Monograph 100, price $4.50), and the Second, "Molecular Dynamics and Structure of Solids," (National Bureau of Standards Special Publication 301, price $4.00)—can be purchased from the Superintendent of Documents, U.S. Government Printing Office, Washington, D.C. 20402.

The purpose of these symposia is to encourage interdisciplinary cooperation by demonstrating the correlation of various experimental and theoretical techniques, and to provide a forum for the presentation and exchange of information, thereby leading to a more complete understanding of the materials of interest among the participants.

A major goal of the "Electronic Density of States" Symposium was to present a readily available treatment of a field which up to now was dealt with in widely scattered parts. This book contains the invited and contributed papers presented at the Symposium, together with the ensuing discussions.

E. Passaglia
General Chairman of the Symposium

J. D. Hoffman, *Director*
Institute for Materials Research
National Bureau of Standards

Preface

The subject matter of the third materials research symposium of the NBS Institute for Materials Research, the "Electronic Density of States" forms a central motif for the measurement and understanding of a wide variety of properties of materials. The participants at the symposium were reminded by the banquet speaker, the Honorable Lee A. DuBridge, Science Advisor to the President of the United States, that the search for the form of the electronic density of states in materials is not a recent innovation. Dr. DuBridge was among those pioneers who performed such experiments over three decades ago. Then the experimental methods were rather simpler than the sophisticated techniques described in this book, and the theoretical machinery had not progressed very far, awaiting today's high speed electronic computers. Nonetheless, the basic structure of the electronic density of states was understood.

The progress in obtaining detailed approximations to the density-of-states has been such that the time appeared ripe for a conference to review the accomplishments of the past and to assess the opportunities for the future. For in the progress there has been one unfortunate tendency; the success of independent methods of obtaining the same results has led to parallel, that is, non-intersecting schools. The main purpose of this symposium was to demonstrate and re-emphasize the correlation of the various experimental and theoretical results in obtaining a meaningful and precise measurement of the electronic density of states in solids and liquids. This volume attests to the fact that this goal was realized in some measure.

A second, and equally important, purpose of the symposium was to illustrate the possibility of application of the electronic density of states to the understanding of the properties of materials. This goal was only incompletely attained. There are several papers showing how the knowledge of the electronic density of states can be applied. We hope this volume will stimulate many more applications.

A special debt of gratitude is owed to the program committee for its selection of such outstanding speakers and writers. Appreciation is also extended to the rapporteurs who provided such faithful oral summaries, to the session chairmen especially for their ability to maximize the information exchange and to encourage useful discussions, and to the NBS Office of Technical Information and Publications for their splendid management of both the conference and this publication. I want to add my personal thanks to the large number of NBS staff members and wives who labored so hard to make the symposium a success including particularly those whose contributions remain anonymous.

The invited papers were also published in the NBS Journal of Research, Volume **74A**, Nos. 2–4 (1970).

L. H. Bennett
Editor

Contents

Page

Foreword iii
Preface iv

BAND STRUCTURE I

The Band Structure Problem*
J. M. Ziman 1
Discussion 13

BAND STRUCTURE II

Electronic Density of States of Transition, Noble, and Actinide Metals
F. M. Mueller 17
Discussion 18

Electronic Densities of States and Optical Properties of CsCl Type Intermetallic Compounds
J. W. D. Connolly and K. H. Johnson 19
Discussion 26

The Calculation of Densities of States by LCAO Interpolation of Energy Bands with Application to Iron and Chromium
J. W. D. Connolly 27

Optical Properties of Aluminum
G. Dresselhaus, M. S. Dresselhaus, and D. Beaglehole 33
Discussion 37

On the Optical Properties and the Density of States in Arsenic
R. W. Brodersen and M. S. Dresselhaus 39
Discussion 45

Density of States and Ferromagnetism in Iron
K. J. Duff and T. P. Das 47

Calculation of Density of States in W, Ta, and Mo
I. Petroff and C. R. Viswanathan 53

Adjustment of Calculated Band Structures for Calcium by Use of Low-Temperature Specific Heat Data
R. W. Williams and H. L. Davis 57
Discussion 62

Fermi Surface Properties of the Noble Metals at Normal Volume and as a Function of Pressure
W. J. O'Sullivan, A. C. Switendick, and J. E. Schirber 63
Discussion 66

Calculated Effects of Compression Upon the Band Structure and Density of States of Several Metals
E. A. Kmetko 67
Discussion 74

OPTICAL PROPERTIES; BAND STRUCTURE III

Optical Properties and Electronic Density of States*
M. Cardona 77
Discussion 90

*Invited papers.

Page

Theoretical Electron Density of States Study of Tetrahedrally Bonded Semiconductors
D. J. Stukel, T. C. Collins, and R. N. Euwema 91
Discussion 103

Electronic Density of States in Eu-Chalcogenides
S. J. Cho 105
Discussion 109

Energy Band Structure and Density of States in Tetragonal GeO_2
F. J. Arlinghaus and W. A. Albers, Jr. 111

Calculation of the Density of States and Optical Properties of PbTe from APW–LCAO Energy Bands
D. D. Buss and V. E. Schirf 115

Plasmon-Induced Structure in the Optical Interband Absorption of Free-Electron Like Metals
B. I. Lundqvist and C. Lydén 125

Theory of the Photoelectric Effect and Its Relation to the Band Structure of Metals
N. W. Ashcroft and W. L. Schaich 129
Discussion 135

PHOTOEMISSION

Optical Density of States Ultraviolet Photoelectric Spectroscopy*
W. E. Spicer 139
Discussion 158

The Density of States and Photoemission from Indium and Aluminum
R. Y. Koyama and W. E. Spicer 159

Electronic Densities of States from X-Ray Photoelectron Spectroscopy*
C. S. Fadley and D. A. Shirley 163
Discussion 179

Direct-Transition Analysis of Photoemission from Palladium
J. F. Janak, D. E. Eastman, and A. R. Williams 181
Discussion 190

Photoemission Determination of the Energy Distribution of the Joint Density of States in Copper
N. V. Smith 191

The Band Structure of Tungsten as Determined by Ultraviolet Photoelectric Spectroscopy
C. R. Zeisse 199

Photoemission Studies of Scandium, Titanium, and Zirconium
D. E. Eastman 205

Photoemission and Reflectance Studies of the Electronic Structure of Molybdenum
K. A. Kress and G. J. Lapeyre 209

Ultraviolet and X-Ray Photoemission from Europium and Barium
G. Brodén, S. B. M. Hagström, P. O. Hedén, and C. Norris 217
Discussion 221

MANY-BODY EFFECTS

What is a Quasi-Particle?*
J. R. Schrieffer 227
Discussion 232

Beyond the One-Electron Approximation: Density of States for Interacting Electrons*
L. Hedin, B. Lundqvist, and S. Lundqvist 233
Discussion 248

*Invited papers.

EXCITONS; SOFT X-RAY I

Page

Excitonic Effects in X-Ray Transitions in Metals*
G. D. Mahan 253
Discussion 259

Vibronic Exciton Density of States in Some Molecular Crystals
R. Kopelman and J. C. Laufer 261

Effect of the Core Hole on Soft X-Ray Emission in Metals
L. Hedin and R. Sjöström 269
Discussion 271

Cancellation Effects in the Emission and Absorption Spectra of Light Metals
B. Bergersen and F. Brouers 273

Photoabsorption Measurement of Li, Be, Na, Mg, and Al in the Vicinity of K and $L_{II, III}$ Edges
C. Kunz, R. Haensel, G. Keitel, P. Schreiber, and B. Sonntag 275

Optical Absorption of Solid Krypton and Xenon in the Far Ultraviolet
C. Kunz, R. Haensel, G. Keitel, and P. Schreiber 279

The Piezo Soft X-Ray Effect
R. H. Willens 281

Soft X-Ray Band Spectra and Their Relationship to the Density of States*
G. A. Rooke 287

SOFT X-RAY II; DISTRIBUTIONS IN MOMENTUM SPACE

Orbital Symmetry Contributions to Electronic Density of States of $AuAl_2$
A. C. Switendick 297
Discussion 302

Soft X-Ray Emission Spectrum of Al in $AuAl_2$
M. L. Williams, R. C. Dobbyn, J. R. Cuthill, and A. J. McAlister 303

Soft X-Ray Emission from Alloys of Aluminum with Silver, Copper, and Zinc
D. J. Fabian, G. Mc D. Lindsay, and L. M. Watson 307

Soft X-Ray Emission Spectra of Al-Mg Alloys
H. Neddermeyer 313

An L-Series X-Ray Spectroscopic Study of the Valence Bands in Iron, Cobalt, Nickel, Copper, and Zinc
S. Hanzely and R. J. Liefeld 319
Discussion 327

The Electronic Properties of Titanium Interstitial and Intermetallic Compounds from Soft X-Ray Spectroscopy
J. E. Holliday 329
Discussion 334

Soft X-Ray Emission Spectrum and Valence-Band Structure of Silicon, and Emission-Band Studies of Germanium
G. Wiech and E. Zöpf 335

Density of States in α and β Brass by Positron Annihilation
W. Triftshäuser and A. T. Stewart 339
Discussion 343

Compton Scattering from Lithium and Sodium
P. Eisenberger and P. H. Schmidt 345
Discussion 346

*Invited papers.

Page

Ion-Neutralization Spectroscopy*
H. D. Hagstrum 349
Discussion 358

Potential and Charge Density Near the Interface of a Transition Metal
E. Kennard and J. T. Waber 359
Discussion 374

Virtual Impurity Level Density of States as Investigated by Resonance Tunneling
J. W. Gadzuk, E. W. Plummer, H. E. Clark, and R. D. Young 375

What Properties Should the Density of States Have in Order That the System Undergoes a Phase Transition?
P. H. E. Meijer 381

On Deriving Density of States Information from Chemical Bond Considerations
F. L. Carter 385

Electroreflectance Observation of Band Population Effects in InSb
R. Glosser, B. O. Seraphin, and J. E. Fischer 407

Spin-Orbit Effects in the Electroreflectance Spectra of Semiconductors
B. J. Parsons and H. Piller 411

Experimental Verification of the Predictions of the Franz-Keldysh Theory as Shown by the Interference of Light and Heavy Hole Contributions to the Electroreflectance Spectrum of Germanium
P. Handler, S. Jasperson, and S. Koeppen 417

Variations of Infrared Cyclotron Resonance and the Density of States Near the Conduction Band Edge of InSb
E. J. Johnson and D. H. Dickey 423

Cyclotron Resonances of Holes in Ge at Noncentral Magnetic Critical Points
J. C. Hensel and K. Suzuki 431

Landau Level Broadening in the Magneto-Optical Density of States
B. H. Sacks and B. Lax 437

DISORDERED SYSTEMS I

The Electronic Structure of Disordered Alloys*
J. L. Beeby 453

Local Theory of Disordered Systems*
W. H. Butler and W. Kohn 465
Discussion 470

DISORDERED SYSTEMS II

Density of Electron Levels for Small Particles
L. N. Cooper and S. Hu 473
Discussion 476

One-Dimensional Relativistic Theory of Impurity States
M. Stęślicka, S. G. Davison, and A. G. Brown 477
Discussion 481

The Influence of Generalized Order-Disorder on the Electron States in Five Classes of Compound-Forming Binary Alloy Systems
E. W. Collings, J. E. Enderby, and J. C. Ho 483

*Invited papers.

Page

Localized States in Narrow Band and Amorphous Semiconductors
D. Adler and J. Feinleib ... 493
Discussion ... 504

A Cluster Theory of the Electronic Structure of Disordered Systems
K. F. Freed and M. H. Cohen ... 505
Discussion ... 508

T Matrix Theory of Density of States in Disordered Alloys – Application to Beta Brass
M. M. Pant and S. K. Joshi ... 509

On the Terms Excluded in the Multiple-Scattering Series
R. M. More ... 515
Discussion ... 519

On Non-Localization at the Centre of a Disordered Bound Band
F. Brouers ... 521

The Half-Filled Narrow Energy Band
L. G. Caron and G. Kemeny ... 527

ALLOYS; ELECTRONIC SPECIFIC HEAT I

Electronic Structure of Gold and Its Changes on Alloying
E. Erlbach and D. Beaglehole ... 545
Discussion ... 550

Density of States of AgAu, AgPd, and AgIn Alloys Studied by Means of the Photoemission Technique
P. O. Nilsson ... 551
Discussion ... 555

Density of States Information from Low Temperature Specific Heat Measurements*
P. A. Beck and H. Claus ... 557
Discussion ... 563

Electronic Density of States Determined by Electronic Specific Heat Measurements
T. Mamiya and Y. Masuda ... 565

ELECTRONIC SPECIFIC HEAT II; KNIGHT SHIFT; SUSCEPTIBILITY

Low-Temperature Specific Heats of Hexagonal Close-Packed Erbium-Thulium Alloys
A. V. S. Satya and C. T. Wei ... 571

Low Temperature Specific Heats of Face-Centered Cubic Ru-Rh and Rh-Pd Alloys
P. J. M. Tsang and C. T. Wei ... 579

Density of States of Transition Metal Binary Alloys in the Electron-to-Atom Ratio Range 4.0 to 6.0
E. W. Collings and J. C. Ho ... 587

Specific Heat of Vanadium Carbide, 1–20 K
D. H. Lowndes, Jr., L. Finegold, D. W. Bloom, and R. G. Lye ... 597
Discussion ... 598

Relevance of Knight Shift Measurements to the Electronic Density of States*
L. H. Bennett, R. E. Watson, and G. C. Carter ... 601
Discussion ... 643

Pauli Paramagnetism in Metals with High Densities of States*
S. Foner ... 645
Discussion ... 646

Calculation of the Knight Shift in Beryllium
J. Gerstner and P. H. Cutler ... 649
Discussion ... 650

*Invited papers.

Knight Shifts of the Alkali Metals — Page
A. Meyer, G. M. Stocks, and W. H. Young ... 651
Discussion ... 658

Role of Exchange Effects on the Relationship Between Spin Susceptibility and Density of States of Divalent Metals
P. Jena, T. P. Das, S. D. Mahanti, and G. D. Gaspari ... 659
Discussion ... 663

Correlation of Changes in Knight Shift and Soft X-Ray Emission Edge Height Upon Alloying
L. H. Bennett, A. J. McAlister, J. R. Cuthill, and R. C. Dobbyn ... 665

TUNNELING: SUPERCONDUCTORS: TRANSPORT PROPERTIES

Tunneling Measurements of Superconducting Quasi-Particle Density of States and Calculation of Phonon Spectra*
J. M. Rowell ... 673
Discussion ... 680

Density of States Data from Superconducting Critical Field Measurements
G. Dummer and D. E. Mapother ... 681

Temperature Dependence in Transport Phenomena and Electronic Density of States for Transition Metals
M. Shimizu ... 685
Discussion ... 691

Metal-Semiconductor Barrier Junction Tunneling Study of the Heavily Doped N-Type Silicon Density of States Function
Y. Hsia and T. F. Tao ... 693
Discussion ... 713

TRANSPORT PROPERTIES; APPLICATIONS

The Effect of Hydrostatic Pressure on the Galvano-Magnetic Properties of Graphite
I. L. Spain ... 717

Electrical Resistivity as a Function of Hydrogen Concentration in a Series of Palladium-Gold Alloys
A. J. Maeland ... 727

The Volume Dependence of the Electronic Density of States in Superconductors
R. I. Boughton, J. L. Olsen, and C. Palmy ... 731

Alloy Fermi Surface Topology Information from Superconductivity Measurements
H. D. Kaehn and R. J. Higgins ... 735

Hydrogenation Effects on Palladium Tunnel Junctions
W. N. Grant, R. C. Barker, and A. Yelon ... 737

Calculation of Thermodynamic Information Based on the Density of States Curves of Two Allotropes of Iron
D. Koskimaki and J. T. Waber ... 741
Discussion ... 753

Potential-Independent Features of Crystal Band-Structure
M. M. Saffren ... 755
Discussion ... 756

Nonlinear Optical Susceptibility of Semiconductors with Zincblende Structure
M. I. Bell ... 757

Model Density of States for High Transition Temperatures Beta-Tungsten Superconductors
R. W. Cohen, G. D. Cody, and L. J. Vieland ... 767

*Invited papers.

Summary of the Conference on Electronic Density of States* Page
H. Ehrenreich ... 775

POST-DEADLINE

Thermal Electron Effective Mass of Rubidium and Cesium
D. L. Martin ... 783

Density of States and Numbers of Carriers From the dHvA Effect
S. Hornfeldt, J. B. Ketterson, and L. R. Windmiller ... 785

A Note on the Position of the "Gold 5*d* Bands" in $AuAl_2$ and $AuGa_2$
P. D. Chan and D. A. Shirley ... 791

The Reliability of Estimating Density of States Curves From Energy Band Calculations
E. B. Kennard, D. Koskimaki, J. T. Waber, and F. M. Mueller ... 795

Appendix I. Symposium Committees ... 801
Appendix II. Session Chairmen and Rapporteurs ... 802
Appendix III. Symposium Registrants ... 804
Subject Index ... 811
Materials Index ... 815

*Invited papers.

BAND STRUCTURE I

CHAIRMEN: A. J. Freeman
E. Passaglia

The Band Structure Problem*

J. M. Ziman

H. H. Wills Physics Laboratory, Bristol, BS 8, 1TL, England

The numerical solution of the Schrödinger equation for an electron in a dense assembly of atoms (*i.e.* a solid or liquid metal or semiconductor) has made great progress in the past ten years. This is not merely a consequence of greater computing power; we now have a much better grasp of the mathematical theory of such solutions.

By 1960 a number of practical methods had been devised for the computation of the electronic structure of ordered crystals, but these lacked intuitive interpretation. The first advance was to rewrite the OPW method in terms of pseudopotentials, thus making sense of the free-electron theory of metals. This development has proved particularly valuable in semiquantitative and empirical investigations of Fermi surfaces, transport properties, lattice dynamics, cohesion, *etc.*, but we have had to wait until recently for a rigorous analysis of the criteria for convergence of the various types of model potential or pseudopotential that have been postulated.

The next step was to show that the KKR (Green function) method could also be expressed as a pseudopotential, and then to demonstrate that this was also a form of APW expansion. The relative computational power of these two methods can thus be analyzed, and questions answered concerning the fulfillment of the empty lattice test, the apparent lack of uniqueness of the expansions, the advantages of "folding" matrix elements from distant points of the reciprocal lattice, and the introduction of contributions from the interstitial potential.

At this stage, the connections between the band structure problem and the t-matrix theory of scattering were uncovered, and d-bands were seen to arise as resonances of the muffin-tin wells. The KKR matrix could now be rewritten as a mixture of pseudopotential and tight-binding elements, in harmony with the empirical model Hamiltonian representations of hybridised s-p and d-bands. This method not only permits more rapid computations, but shows clearly how the width and position of such bands should depend on the atomic potential.

Some problems still remain. For example, present techniques do not seem adequate for first-principles calculations on molecular crystals, where the anisotropy of the interstitial potential (*i.e.* easy channels along bonds, but high hills between layers or chains) is probably the dominant feature.

As for disordered systems — we know little for certain and nothing quantitatively. The linear chain model has been fully studied but is quite irrelevant to the three-dimensional case. The present theoretical confusion is exemplified by the equiconcentration substitutional alloy in the tight-binding limit; some formulae give only one band, others allow two. Again, the very possibility of producing band gaps by diffraction of free electrons in a topologically disordered system (*e.g.* amorphous Ge) has not been demonstrated mathematically with any rigor.

Key words: APW; band structure; density of states; disordered systems; KKR; pseudopotential; t-matrix; molecular crystals.

1. Algebra vs. Arithmetic

Any scientific problem or puzzle can seem interesting and significant if one gets sufficiently involved in it: the difficulty sometimes is to persuade other people of this importance. How should we defend our interest in the Electronic Density of States to an unprejudiced tribunal?

Not, surely, in terms of immediate use, but of long term understanding. Electrons being the glue of all "materials", their states within condensed matter are of fundamental importance. No quantitative estimate of any property of a metal, semiconductor, insulator, glass, liquid, mineral, *etc.*, can begin without information about these states. In fact, we want all the wave

*An invited paper presented at the 3d Materials Research Symposium, *Electronic Density of States*, November 3–6, 1969, Gaithersburg, Md.

417-156 O - 71 - 2

functions of all the electrons outside of the closed shells—a tall order, which cannot be fulfilled by direct experiment. The next best thing is the energy spectrum, or "density of states," although as we shall learn in the course of this symposium, that cannot always be deduced unambiguously from observed phenomena.

Progress in this field therefore depends on sound theoretical analysis of the hypothetical possibilities, as well as careful experimental investigation of the facts. The calculation of electronic band structure is thus the central mathematical problem of solid state physics. Every "exciting" topic or mysterious phenomenon—superconductivity, the Kondo effect, ferromagnetism, Fermi surfaces, the Gunn effect, Josephson tunnelling, *etc.*,—eventually depends for its computable parameters on this mundane task.

It is sometimes argued, by the deeply unimaginative follower of scientifc fashion, that this problem has been solved long ago, and can safely be left to the brute strength of more and more powerful computers. This is quite wrong; these elephants must be goaded and guided by experienced *mahouts*, whose skill is to see in advance the type of answer that is to be obtained, and then to deploy the minimum of force to lever away the obstacles. A ream of computer print-out is useless unless it agrees so perfectly with experiment that we need never look back and see why and how it went wrong. Our task is to devise techniques for the theoretical mastery of ever more complex systems, which requires at every stage that we know exactly what we are doing, analytically as well as numerically.

This is well illustrated by the recent history of our subject. Let me express this in personal terms. A little more than ten years ago, in gathering material for a monograph [1] of which one chapter covered this topic, I found that many techniques of band structure computation had been proposed and tried out, but that there were very few cases where the results had been confirmed experimentally, or where they gave any insight into the actual electronic structure of the materials. It was simply not obvious, for example, that almost all the calculated band structures for metals could have been derived from the free electron system by perturbation effects at the zone boundaries, because nobody had programmed his computer to print out the data in that form. We knew from the success of the free electron *model* that this could not be very far from the truth, but we had not the imagination to rewrite the algebra so as to see how this must arise within whatever method of calculation we might happen to use.

In the past decade, of course, computational techniques have improved enormously in accuracy and power, so that a whole body of expertise is now available for application in any particular case [2]. Given the exact one-electron potential of a crystalline solid, we can compute the band structure to almost any desired degree of accuracy. But the trouble is that we do not always have this potential, complete with all the electron-electron terms, spin-orbit interaction, core polarization, exchange and correlation effects and so on, so that our first-principles computations just miss the answers we are seeking. Without an appeal to the basic algebraic principles and governing features of the model, we then flounder around, trying to adjust the parameters by trial and error. Somebody else, using a different "method" may get a different answer: is this due to deep discrepancies in the fundamental assumptions, or to errors of approximation, or just numerical mistakes?

2. Pseudism

Now recall how our minds have been liberated by the pseudopotential concept. There is no need to explain this to the present audience. Let us suppose that we had tried to express the Bloch function of wave vector $\mathbf{k}$ by a sum of simple plane waves

$$\psi_{\mathbf{k}} = \sum_{\mathbf{g}} \alpha_{\mathbf{g}} e^{i(\mathbf{k}+\mathbf{g})\cdot\mathbf{r}}, \tag{1}$$

where $\mathbf{g}$ runs through the reciprocal lattice: we should have to solve the infinite set of linear equations

$$\{|\mathbf{k}+\mathbf{g}|^2 - \mathscr{E}\}\alpha_{\mathbf{g}} + \sum_{\mathbf{g}'} \mathscr{V}(\mathbf{g}-\mathbf{g}')\alpha_{\mathbf{g}'} = 0 \tag{2}$$

where $\mathscr{V}(\mathbf{g}-\mathbf{g}')$ is a Fourier component of the periodic potential in the lattice and $\mathscr{E}$ is the energy of the state we are after. By rewriting the equations in terms of orthogonalized plane waves we can show that the whole problem is equivalent to solving a very similar set of equations

$$\{|\mathbf{k}+\mathbf{g}|^2 - \mathscr{E}\}\beta_{\mathbf{g}} + \sum_{\mathbf{g}'} \Gamma_{\mathbf{g}\mathbf{g}'}\beta_{\mathbf{g}'} = 0, \tag{3}$$

in which the pseudopotential components $\Gamma_{gg'}$ are much smaller than the original set $\mathscr{V}(\mathbf{g}-\mathbf{g}')$. Thus, the whole problem is equivalent to the perturbation of free electron waves by a weak pseudopotential and can be solved by elementary computation. For a perfect Bravais lattice the value of $\mathscr{V}(\mathbf{g}-\mathbf{g}')$ or of $\Gamma_{gg'}$ is a function only of the potential associated with a single atom or ion—in the language of x-ray diffraction, it is just the "atomic form factor" in the formula for diffraction by an assembly of such objects at the appropriate Bragg angle. The band structures of most ordinary metals, and many semiconductors, can be read at a glance. Not only does this provide us with an admirable

parametrization of Fermi surfaces, optical spectra, *etc.*, in perfect crystals, but can be extended to include almost all the properties of thermally excited, impure or disordered materials—electron-phonon interactions, electrical conductivity of solid and liquid metals, lattice dynamics, phase stability of alloys, *etc.* In moments of enthusiasm [3,4,5] we may perhaps be forgiven for pretending that all the problems of the theory of metals are cured by a strong dose of "pseudism". It is a wonderful model for zeroth order calculations, and the ideal do-it-yourself kit for the enthusiastic amateur. It had the effect of turning band structure theory from a rule of thumb *technology* into an elegant *science.*

Nevertheless, the pseudopotential method is not the ultimate solution to the band structure problem. In the first place, the program of replacing the true atomic potential by a localized pseudopotential, independent of energy and momentum, cannot be fulfilled exactly. If, like Herman and his colleagues [6] one is trying to make very accurate first principles calculations, nothing is gained by rewriting the OPW equations in this form. Indeed, there is a danger that the apparent simplicity and rapid convergence of the pseudopotential equations may seduce us into further approximations which hide important effects; once having lost touch with the exact equations, we slide easily into a sloppy mess where qualitative and quantitative, first principles and parametrized, features are inextricably confused.

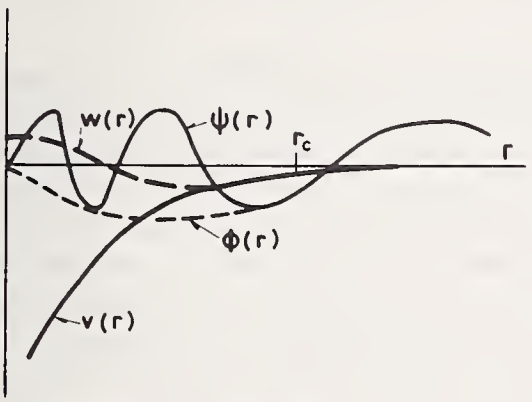

FIGURE 1. *The true wave function* $\psi(\mathbf{r})$ *in the true potential* $\theta(\mathbf{r})$ *is replaced by the pseudo wave function* $\phi(\mathbf{r})$ *in the pseudopotential* $w(\mathbf{r})$.

This type of confusion is compounded by the non-uniqueness of pseudopotentials. The original algebraic proof of this arbitrariness came as something of a surprise, but it is really quite obvious. We are asked, in effect to construct a weak potential that will reproduce the effect of a strong potential on an electron wave of given energy impinging on the atom. The boundary condition on the pseudo wave function—that it should match the true wave function on the outside—is very weak, and amounts to little more than fixing the value of a few integrals over the pseudopotential. We know, for example, that the s-wave scattering phase shift of the true potential will be reproduced at low energies if we choose the spatial average of the pseudopotential correctly—and so on. Almost any function containing a few adjustable parameters can be made to fit these conditions. Of course the problem of finding a fixed local pseudopotential that will imitate the effects of the true potential over a wide range of energy is much more difficult, and has not been solved, but that is not what we are asked to do.

This arbitrariness was exploited to the full by Heine and Abarenkov [7] who chose the most elementary pseudopotential functions so as to simplify the rest of the algebra. It was natural to reproduce the core potential of a metallic ion with a square well of depth $A_l(\mathscr{E})$, which could be continued outwards as a simple Coulomb potential; or as a screened Coulomb potential, according as one is thinking of an isolated free atom or of a "pseudo atom" in a condensed phase (fig. 2). In fact, the value of $A_l(\mathscr{E})$ for a given angular momentum can then be estimated from the optical term values, in the tradition of the quantum defect method of Kuhn and Van Vleck.

Such a "model potential" is obviously good physics, and can be more or less justified mathematically. It copes very elegantly with one of the most difficult aspects of the whole theory—the self-consistency problem for the valence electrons—about which, for reasons of brevity, I shall say very little here. According to Shaw [8], the screening corrections can be calculated accurately, although it pays to eliminate the discontinuity at the surface of the square well by treat-

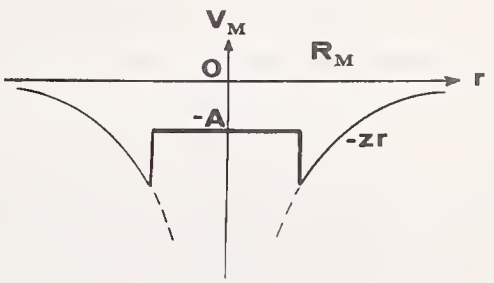

FIGURE 2*a*. *Heine-Abarenkov pseudopotential; before screening.*

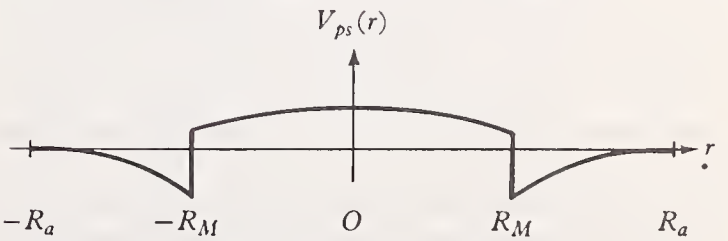

FIGURE 2*b*. *After screening (from* [5]).

ing the radius of this internal flat region as another adjustable parameter, depending also on energy and momentum (fig. 3).

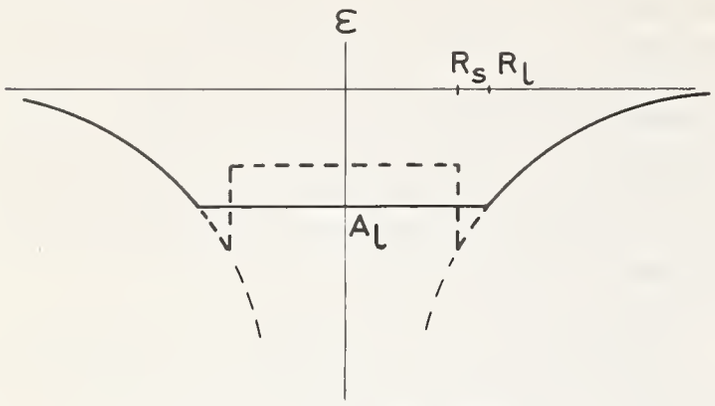

FIGURE 3. *Shaw pseudopotential.*

Notice, however, the dangers of overelaboration. An arbitrarily defined model potential in real space is valuable only in proportion to its algebraic or geometrical simplicity, and will not bear much "improvement" in the name of numerical precision or in order to get better agreement with experiment. In the event the electronic structure depends on the "form factor"—the Fourier transform of the pseudopotential—which might then just as well be derived directly from the true potential by some more powerful method, or which we could also represent by some simple empirical function [9].

From a formal point of view, the arbitrariness of the pseudopotential is certainly quite worrying. How can the electronic band structure depend uniquely on the periodic lattice potential if this arbitrary function can be interposed in the calculation? Well now, suppose we had tried to solve the equations (2) for the Bloch functions expanded in simple plane waves. Since these are an infinite set we should have had to proceed by successive approximations, just as if we are trying to sum a series term by term. But these equations really have many solutions of much lower energy than the one we are looking for, corresponding to all the narrow tight-bound bands and an expansion in powers of $\mathscr{V}(\mathbf{g}-\mathbf{g}')$ simply does not converge for energies in the valence band. We are trying to sum the Born series for scattering by one of the atomic potentials, ignoring the fact that it has numerous deep bound states. The pseudopotential trick removes all the effects of these bound states, and gives us a convergent series. It is rather like wanting to evaluate $1/(1+\chi)$ when χ is about 10: a power series in χ will not converge, but we can easily construct a new series in some new variable $y = (\chi - a)$, say, which can be made to converge in the region of interest. The actual terms in the series will depend on the value of a, which may be any arbitrary number larger than about 5—but the final answer will be independent of this choice. Thus the final value of the energy as a function of wave vector comes out the same, whatever form of pseudopotential we introduce into the equations.

This suggests a possible criterion for a "best" pseudopotential: choose the form of $\Gamma_{gg'}$ that causes the series expansion for the Bloch functions to converge most rapidly. There is a rather elaborate mathematical theory of the Born series, due to Weinberg, which can be applied to this problem [10] and which does discriminate in principle between various formulae. These investigations are not, perhaps, of very great practical value to the horny-handed programmer of computers, but they are healthy in establishing the basic mathematical foundations of the whole technique.

3. The Problem of Bound Bands

The most serious limitation of the pseudopotential concept is that it applies only to the so-called "simple" metals—those without d-states in the valence band. There is, of course, a long tradition of representing such states by the tight binding method, as a linear combination of atomic orbitals. The coefficients a_L in such combinations then have to satisfy a set of linear equations of the form

$$(\mathscr{E}_L - \mathscr{E})\, a_L + \Sigma_{L'} V_{LL'}(\mathbf{k})\, a_{L'} = 0, \qquad (4)$$

where the index L stands for different angular momentum and magnetic quantum numbers; for example, the five values of the component of angular momentum in a band of d-states. The original bound state at $\mathscr{E}_L$ is broadened into a band by the various overlap integrals $\mathscr{V}_{LL'}(\mathbf{k})$, which can in principle be evaluated, although in practice this is so complicated and inaccurate that one treats them as adjustable parameters.

It used to be thought that *all* the states in metals could be described in this way, by bringing in enough different atomic orbitals. The picture of states overlapping and broadening to make nice valence and conduction bands illustrates one of the nursery rhymes of our subject (fig. 4). Unfortunately, this is quite misleading. What happens is that as the atomic *potentials* overlap, and the barriers fall between atomic cells, most of these atomic bound-state orbitals disappear. The ordinary s and p valence levels of the atoms vanish into a nearly free-electron band which can only be described if one includes propagating wave functions from above the spectrum of bound states of the separate ions or atoms.

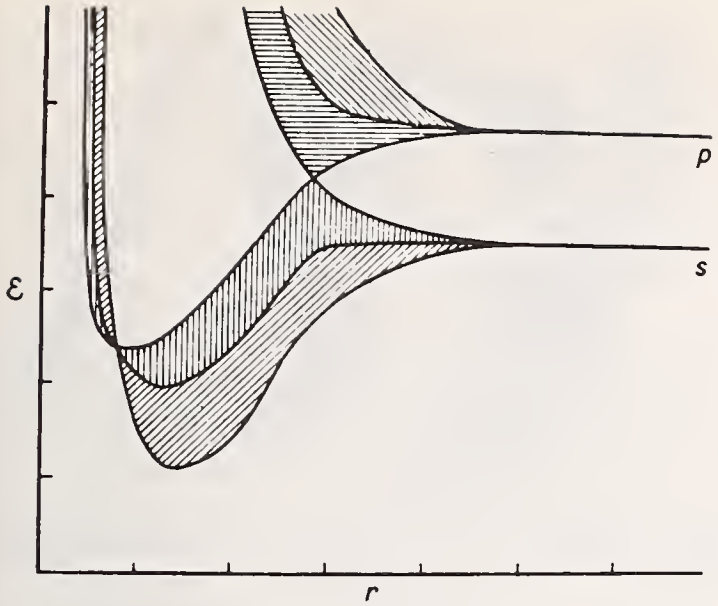

FIGURE 4. *Conventional picture of energy bands from overlap of atomic orbitals.*

We thus arrive at an impasse: we can describe ordinary s−p bands in pseudopotential language, and d-bands in tight binding language, but there seems no common tongue, even when these bands overlap and hybridize as in the transition metals.

This difficulty never seems to have worried the active calculators of band structures: they used two techniques that gave good numerical results in all cases—the augmented plane wave method and the Green function method. One of the main developments in band structure theory in the past 5 years has been to show the mathematical connections between these useful techniques and the concepts of pseudopotential and tight-binding.

The idea of an augmented plane wave is quite simple. At some given energy $\mathscr{E}$, one solves the Schrödinger equation inside a spherical potential well, of radius R_s, say. The solution is a linear combination of products or radial functions and spherical harmonics of different values of angular momentum. Now determine these coefficients so that this solution matches on to a plane wave of wave vector $\mathbf{k}$ outside the sphere. This function is still not an exact solution of the Schrödinger equation, and has a discontinuity of slope at R_s; but we can build up our Bloch function by combining a set of these with wave vectors $\mathbf{k}$, $\mathbf{k}+\mathbf{g}$, *etc.* just as in (1) and then using the variational principle for the energy. The coefficients satisfy a set of equations exactly like the pseudopotential equations (3) so that we can find

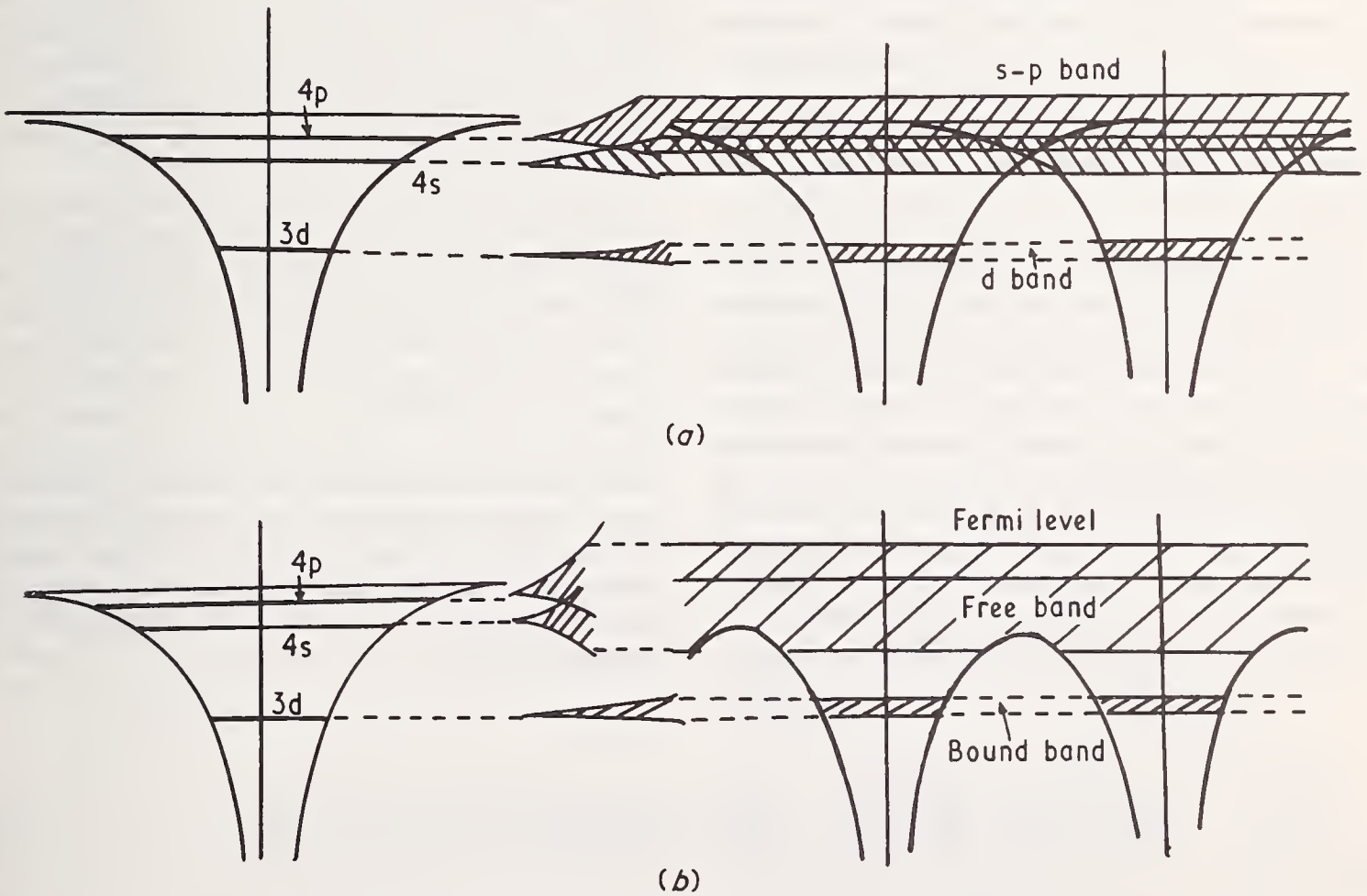

FIGURE 5. *(a) Conventional LCAO description of formation of metallic conduction band; (b) Description in terms of muffin-tin potentials.*

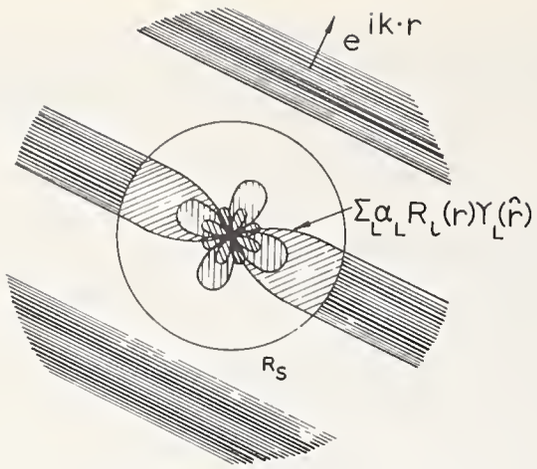

FIGURE 6. *An augmented plane wave.*

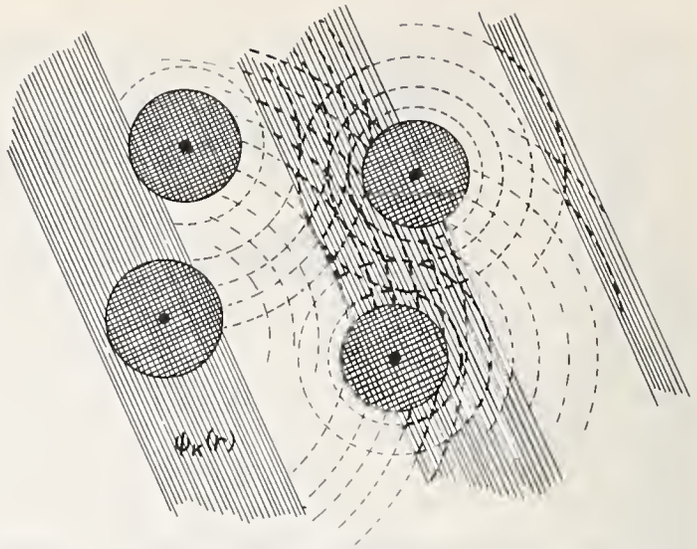

FIGURE 7. *Scattered waves recombining as plane waves in KKR method.*

the energy $\mathscr{E}$ as a function of $\mathbf{k}$ by finding the roots of the determinant in the usual way.

The actual formula for $\Gamma_{gg'}{}^{APW}$ is rather elaborate, so I will not write it down; it depends upon $\mathbf{k}$, and also upon $\mathscr{E}$ through the first derivatives of the radial solutions of the Schrödinger equation at R_s. At first sight one might have thought that this could be interpreted as an elaborate energy, and momentum-dependent form factor, derivable from a pseudopotential; but this is not the case. The difficulty is that Γ^{APW} does not vanish in the elementary case of an empty lattice—whereas we should certainly expect a pseudopotential to be zero when we remove the true potential to which it is supposed to be equivalent. The connection with the tight binding formalism appears even more obscure, even though one can compute perfectly good d-bands by this method.

In desperation, we turn to the KKR method of Korringa and of Kohn and Rostoker. This is called the Green function method because it was originally derived in that somewhat abstract language, but it really depends upon a self-consistency argument; as the Bloch wave proceeds through the crystal lattice, and encounters the various atomic spheres, it suffers scattering or diffraction—but this diffraction must be exactly what is needed to reproduce the wave and keep it on the move without loss. Again, I will spare you from the algebra, and merely report that, as in the APW method, one uses the radial solutions of the Schrödinger equation in each atomic sphere and plane waves outside. The result is yet another set of linear equations—this time for the coefficients of the mixture of solutions of various angular momentum in the sphere:

$$\kappa\{\cot \eta_l(\kappa) - i\} b_L + \Sigma_{L'} B_{LL'}(\mathbf{k}, \kappa) b_{L'} = 0. \tag{5}$$

In this formula, the energy $\mathscr{E}$ is κ^2, and $\eta_l(\kappa)$ is the phase shift that would have been produced by the atomic sphere in scattering a plane wave of this energy. The "structure constants" $B_{LL'}(\mathbf{K},\kappa)$ depend on the energy and momentum of the state being studied, but otherwise can be laboriously computed from the geometrical structure of the lattice.

This does not look very much like either of our previous formulae. Indeed, from the pseudopotential point of view it looks quite wrong, for when we apply the empty lattice test we make η_l tend to zero, which causes *cot* η_l to blow up. In fact these equations need to be turned upside down if we are to understand them physically [11]. The algebra is again a bit heavy, and depends essentially on some of the analytic properties of the structure constants, each of which is in fact a sum over reciprocal lattice vectors of products of spherical harmonics and Bessel functions *etc*. The result is a set of algebraic equations of the form of (3), with the following expression for the "matrix elements of the pseudopotential":

$$\Gamma_{gg'}^{KKR} = -\frac{4\pi N}{\kappa} \Sigma_l (2l+1) \tan \eta_l' \frac{j_l(|\mathbf{k}-\mathbf{g}|R_s) j_l(|\mathbf{k}-\mathbf{g}'|R_s)}{|j_l(\kappa R_s)|^2} P_l(\cos \theta_{gg'}) \tag{6}$$

where

$$\cot \eta_l' = \cot \eta_l - \frac{n_l(\kappa R_s)}{j_l(\kappa R_s)}. \tag{7}$$

In this formula, j_l and η_l are spherical Bessel functions, and $P_l\,(cos\theta_{gg'})$ is the ordinary Legendre polynomial for the angle between vectors $\mathbf{k}-\mathbf{g}$ and $\mathbf{k}-\mathbf{g}'$.

This formula is highly instructive, for a number of reasons.

(i) Consider an empty lattice, for which $\eta_l=0$. Then η'_l will also vanish, and with it $tan\ \eta'_l$. Thus $\Gamma_{gg'}$ is a genuine pseudopotential, which goes to zero with the true potential.

(ii) When η_l is small, the difference between, say $tan\ \eta'_l$ and $sin\ \eta_l\ exp\ (i\eta_l)$ is negligible. Ignoring the ratios of spherical Bessel functions, $\Gamma_{gg'}$ looks just like a scattering amplitude for the effect of our given potential on a single plane wave. This is good physics: the crystal is made up of an assembly of objects, each of which scatters the Bloch wave into itself.

(iii) A strong potential, with many deep bound states may, nevertheless, have quite small phase shifts, so may behave like a weak pseudopotential. Thus, the principle of subtracting away the divergences due to the bound states amounts to simply representing each phase shift as the smallest possible angle, modulo (π). This is a well-known property of phase shifts.

(iv) As shown by Lloyd [12], this form of matrix element can be derived from a simple model potential. We merely put a delta function singularity of potential over the surface of the sphere of radius R_s, of strength to match the phase shift η_l outside, for each value of l.

(v) The connection with the APW formula was discovered by Morgan [13]. Suppose we write $\Gamma^{APW}\,(0)$ for the values of the APW matrix elements in an empty lattice. Then

$$\Gamma^{APW}=\Gamma^{KKR}+\Gamma^{APW}(0). \tag{8}$$

The APW matrix elements have these extra parts to them, which do not really contribute to the band structure, and which do not vanish for any value of l, even for empty space. One can even derive Γ^{APW} from a model potential [12], but this is much more complicated in form than the one for Γ^{KKR} and does not vanish in empty space.

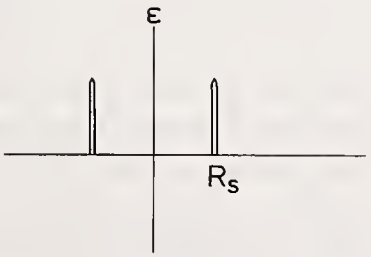

FIGURE 8. *Pseudopotential for* Γ^{KKR}.

These properties of this new form of pseudopotential suggest that it should be much easier than the APW method to use in practice for simple metals, where we need only introduce small phase shifts for a few values of angular momenta. We may also use the computational device of "folding" the determinant for large values of $\mathbf{g}-\mathbf{g}'$, as if we were treating the diffraction from distant zone boundaries as a small perturbation [14]. This form is also said to be the best for convergence of the Born series in the Weinberg sense [10], whatever that may imply. But the whole question of the relative computational efficiency of these methods and their minor variants is quite complicated; all I would say here is that the effort of comparing them is made much more fruitful when we understand the basic algebraic connections.

One further mystery needs clarification. Let us recall that the basic algebraic equations (3) are for the purpose of discovering the coefficients β_g in some expansion of the wave function in the appropriate plane waves. Thus, if we had been using Γ^{APW} in these equations, we should have been writing

$$\psi_{\mathbf{k}}=\Sigma_{\mathbf{g}}\beta_{\mathbf{g}}\phi^{APW}(\mathbf{k}+g)$$

where $\phi^{APW}\ (\mathbf{k}+\mathrm{g})$ is augmented plane wave having the form $exp\ \{i(\mathbf{k}+\mathrm{g})\cdot\mathbf{r}\}$ outside of the atomic sphere. Now it turns out [13] that the KKR equations also suppose that the wave function has been expanded in augmented plane waves—but since the matrix elements (8) are different in these equations the coefficients β_g will be different. In other words, the Bloch function ψ_k, which is supposed to be a unique solution to our band structure problem, has two entirely different representations in terms of the same set of basic functions.

This is permissible, because in fact we are only combining APW's to satisfy the Schrödinger equation *outside* the spheres; the part within each sphere is automatically determined by its adjustment to the boundary condition [15]. It is well known that a periodic function defined over only part of the unit cell can be

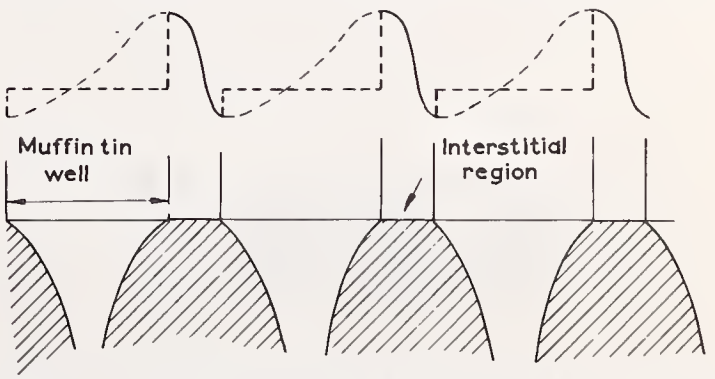

FIGURE 9. *Function defined as Bloch wave in interstitial region may have arbitrary form in muffin-tin well.*

represented by many Fourier expansions, depending on what properties it is allowed to have in the excluded region. The APW and KKR expansions both represent ψ_k correctly—yet they are not made up of exactly the same combinations of simple plane waves in the interstitial regions. This point is perhaps worth emphasizing because in either case we have a very explicit representation of the wave function of the Bloch state, in a form that is quite convenient for calculations of electron-electron interactions, self-consistency of potentials, and optical, x-ray, photoemission, and positron-annihilation matrix elements, *etc.*

It has sometimes been held against the APW & KKR methods that they can only be used for a "muffin-tin potential"—*i.e.* for a periodic lattice of spherically symmetric wells with "empty space" in between. But this is not an absolute restriction. Suppose there really is a significant nonconstant potential $\mathscr{V}_i$ in the interstitial region. Then we can take this into account by adding to $\Gamma_{gg'}$ the corresponding Fourier component $\mathscr{V}_i(\mathbf{g}-\mathbf{g}')$ of this potential—made explicit by being given a constant value across the mouths of the muffin-tin wells [16]. Thus, the level which I call the "muffin-tin zero" [17] cuts across the equipotential surfaces, producing muffin-tin wells with bound states, which are eliminated by a pseudopotential device, and ranges of weak potential hills through which the valence electrons easily tunnel, and which can be represented adequately by their Fourier transforms. If we go further, and suppose that this interstitial potential had been produced by the superposition of screened Coulomb potentials, or charge clouds, carried by the individual atoms, then we can imagine $\mathscr{V}_i$ analysed into these spherically symmetrical constituents arranged in a lattice, and reassign these to the corresponding muffin-tin wells, whose deep potentials have by now been replaced by a model potential or pseudopotential. In other words, we arrive back precisely at the sort of analysis implied by figure 2 or figure 3: the effect of the atoms on the electrons is equivalent to diffraction by an assembly of screened model potentials, whose outer fields may, within reason, be superposed without hindrance. Thus we could use $\Gamma^{KKR}+\mathscr{V}_i$ as the form factor in any calculation where model potentials are employed, *e.g.* resistivity of liquid metals, lattice dynamics, *etc.*

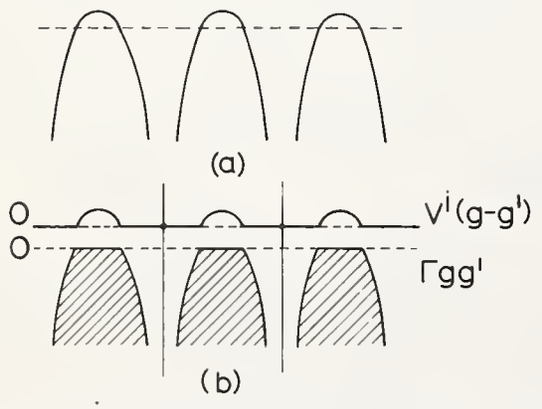

FIGURE 10. *Lattice potential (a) dissected into an interstitial potential and muffin-tin wells.*

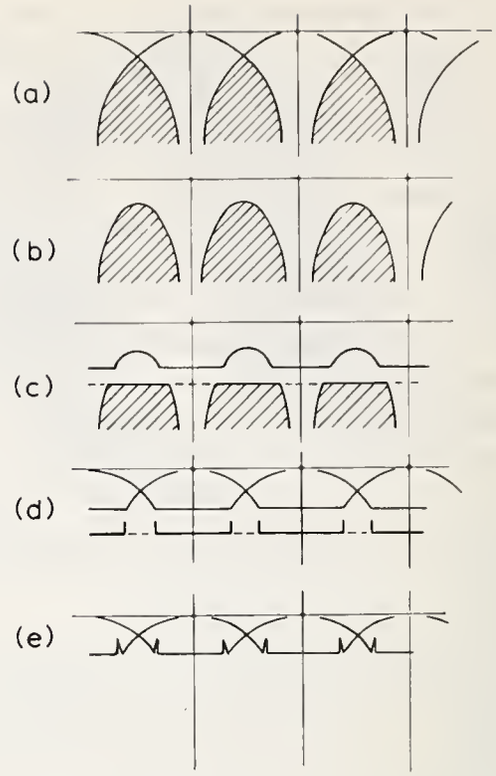

FIGURE 11. *Overlapping potentials (a), summed to make lattice potential (b), dissected into an interstitial potential and muffin-tin wells (c), redefined as pseudopotentials and overlapping external parts (d), and recombined as pseudo-atom potentials (e).*

This final demonstration of the equivalence of all three methods of band structure—OPW, APW and KKR—in the case of simple metals and semiconductors is very satisfactory, but I am now worried about one general point. Suppose we have a very anisotropic lattice—for example, the chain structure of Te, or the layer structure of graphite. The separation of the potential into muffin-tin wells and an interstitial potential must be done at a level below the lowest barriers between the atoms—for example, at the level of the potential half way between neighbors along a chain. But this may leave very high hills in the interstitial potential between the chains or layers—and the unwillingness of the electron to tunnel through such hills may not be well expressed by an expansion in plane waves in this region. Perhaps this is not a serious point after all; but I mention it to show that we are now gaining confidence to attack the electronic structure of more complex molecular crystals, a field which has up to now been dominated by an army of theoretical chemists wielding innumerable linear combinations of atomic orbitals—a

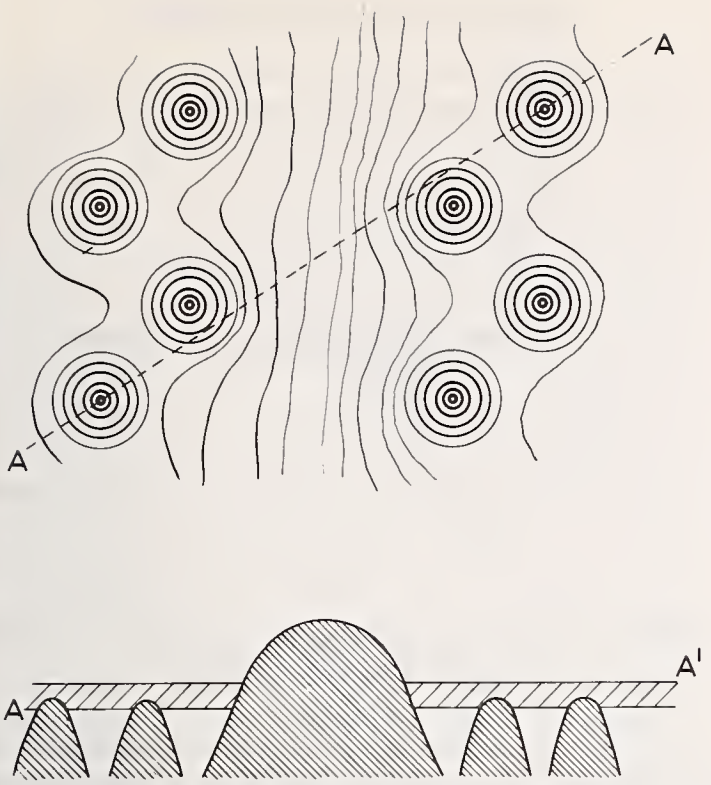

FIGURE 12. *Potentials in a crystal of long chain molecules: electrons occupy the valleys containing muffin-tin wells, separated by high potential hills.*

weapon whose fundamental efficacy I now take leave to doubt.

4. Resonance Bands

What about d-bands, which can be computed numerically by the APW and KKR method, but whose empirical description has usually been handled by the tight binding formula? The answer to this question is perhaps one of the most elegant results of the recent theory. Let us proceed from, say (5), the original KKR equations, which are not unlike the tight-binding equations (4), in that the index L, labelling the unknown coefficients, refers to various spherical harmonics, or components of angular momentum. We might ask, for example, what would happen to the phase shift $\eta_l(\kappa)$ if the energy happened to coincide exactly with a bound state $\mathscr{E}_L$ of the atomic potential. To answer this question in general, we should need to study the theory of scattering in the unphysical regions where $\mathscr{E}$ lies below the muffin-tin zero, making κ pure imaginary; but it turns out that a factor like $\mathscr{E}_L - \mathscr{E}$ then appears in $cot\ \eta_l(\kappa)$ just as we might expect. Now look at our formula (6) for the KKR pseudopotential in the reciprocal lattice representation: if $cot\ \eta'_l$ were to vanish, at any energy, then $tan\ \eta'_l$ would become infinite, and everything would go wrong. Thus, if η'_l should ever go through $\pi/2$ the band structure would be seriously affected.

Now this is a familiar situation in the general theory of scattering by atoms, molecules or nuclei: the phase shift η_l goes through $\pi/2$ in the positive energy region whenever there is a "resonance" of angular momentum. Thus, if the atomic or ionic potential has such a resonance, this will give rise to significant band effects in this neighborhood. There is a standard theory of such phenomena, which tells us that we may write

$$\tan \eta_l \sim \frac{W}{\mathscr{E} - \mathscr{E}_l} \tag{9}$$

for the phase shift of a resonance of width W centered on the energy $\mathscr{E}_l$. It is easy to show, using (6), that this has the effect of introducing a band of states of about this width, at about this energy, in the nearly-free-electron spectrum [11].

This argument can be carried further. Starting from the KKR formulae and making systematic transformations and approximations, Heine [18] showed how one could separate out a particular resonance term, and keep this in the angular momentum representation, with indices m,m' for the different components of l, while reproducing a typical pseudopotential expression in the reciprocal lattice representation $\mathbf{g},\mathbf{g}'$. The matrix of these equations can thus be written in the form

$$\begin{pmatrix} \mathscr{E}-\mathbf{k}^2 & \Gamma_{0g} & \cdots & & \gamma^{gm} \\ \Gamma_{g0} & \mathscr{E}-(\mathbf{k}+\mathbf{g})^2 & \ddots & & \\ \vdots & & \ddots & & \\ & & & \mathscr{E}-\mathscr{E}_l & V_{mm'} \cdots \\ \gamma^*_{mg} & & & V_{m'm} & \mathscr{E}-\mathscr{E}_l \ddots \\ & & & \vdots & \ddots \end{pmatrix} \tag{10}$$

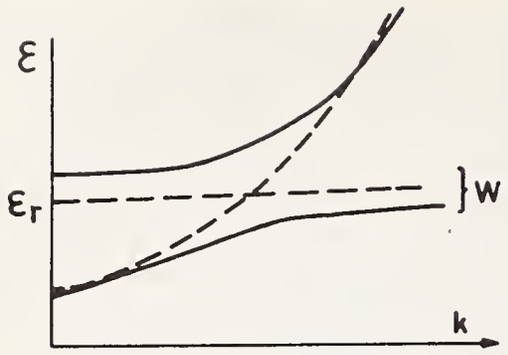

FIGURE 13. *Resonance band crossing nearly free band.*

Without the submatrices γ_{ym} *etc.*, this would factorize into a nearly-free-electron, pseudopotential matrix, such as we might expect to find in a simple metal with an s-p band, together with an ordinary tight binding matrix, corresponding to the overlapping and mixing of the 5 degenerate d-levels of the free atom. The coefficients γ_{ym} *etc.* then describe the hybridization of these two systems of states, which must necessarily occur when these bands cross one another.

As it happens (but not accidentally!) an empirical "model Hamiltonian" of just this form had already been proposed for transition and noble metals [19] before it was deduced directly from the KKR equations. We can now, therefore, justify this type of expression in principle, and even calculate the various coefficients directly from the atomic potential. In fact there are now several different versions of these equations, of varying computability, convergence and analytical simplicity [20] but all essentially equivalent of Heine's formula [5,18].

This reinterpretation of the tight-binding formalism, and its unification with the other band structure methods is very pleasing, but to my mind there is a greater gain. Let us ask how resonances actually arise? For an ordinary one-electron potential, we need to think of the effects of the centrifugal barrier term $l(l+1)/r^2$ in the radial Schrödinger equation, which becomes important for l=2. A bound d-state is really constrained to avoid the nucleus by this "potential". Now lower the ordinary potential at the outer edges of the atom: the effect may be to leave a potential dip within the core, where a "virtual", long-lived level could still exist, even though, eventually, it would have to decay as the electron tunnelled out into free space. Thus, the original bound d-state has become a d-resonance; if the potential barrier is sufficiently thick, the resonance will be sharp; it is not surprising that the language of overlapping bound states applies to the bands produced in such cases.

From this picture we can learn a lot about the gross features of the density of states of the metal. We see,

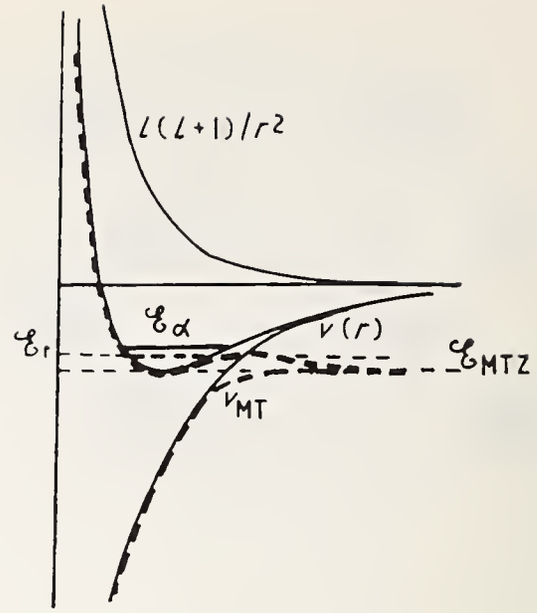

FIGURE 14. *How a bound state of the atom becomes a resonance level of the muffin-tin well (See [17]).*

for example, that although the little peaks and dips of the d-band can be derived from general tight-binding theory, especially when aided by group theory, the width of this complex of bands will depend chiefly on the width of the resonance, which is governed in turn by the potential barrier produced by the centrifugal force in the outer part of each muffin-tin well. Again, the actual position of this band will be determined mainly by the energy of the original d-state from which it derives—and this is fixed on a scale relative to, say, some deep state of the core. On this scale, however, the position of the ordinary conduction band does not depend on any atomic orbitals, but is determined mainly by the muffin-tin zero, which can only be calculated correctly by taking very careful account of screening, correlation energy, overlaps of potential, *etc.* We thus discover the reason for a well-known difficulty in band structure calculations—that the width of the d-band, and its position relative to the Fermi level is very sensitive to the model, and cannot apparently be calculated with the precision we would like.

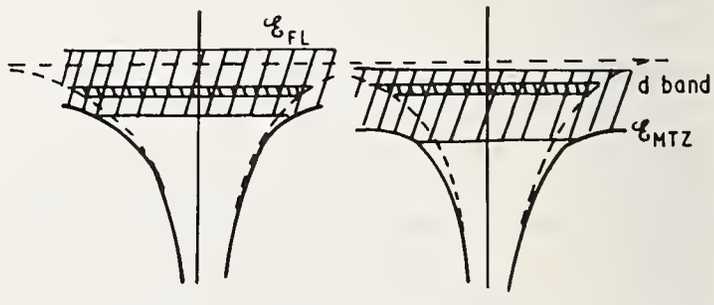

FIGURE 15. *How the position of the d-band within the conduction band depends on the muffin-tin zero (See [17]).*

5. Some Thoughts in Disorder

Now that we understand the electronic structure of crystalline solids so very well, we are tempted to attack disordered materials—liquids, alloys, amorphous and glassy substances. This campaign has been actively waged now for about a decade, but I am not sure that it has yielded many great prizes. The major difficulty, of course, is that we must abandon Bloch's theorem, which reduces the complexity of the problem in the perfect lattice by a divisor of the order of 10^{23}. Without crystal momentum as a good quantum number, we flounder about in a mixture of approximate algebra and incomplete intuition, hoping to find some clearcut concepts that will guide the interpretation of complicated experiments on messy materials.

It is true that the spectrum of the disordered linear array is now well understood [21]—and turns out to be much more spiky than one would have guessed from simple statistical considerations. Some of these features may persist in three-dimensional systems, but unfortunately the mathematical methods used in the one-dimensional case seem ill-adapted to generalization. In particular, real solid systems have two properties that cannot be simulated at all by a linear chain. In three dimensions, a localized defect or impurity can be avoided by a detour, so that it does not present an absolute barrier to an incident particle or excitation. In three dimensions, also we may have "structural disorder", which is no longer topologically equivalent to any regular lattice, whereas in a linear chain the mere succession of atoms prescribes an ordering, however wildly we vary the properties of the individual potential wells.

Let me give two examples of simple cases where our present theory is inadequate. It is obvious enough that a disordered transition metal—*e.g.* liquid iron—should have a d-band arising from the d-resonance, just as in any crystalline phase of about the same atomic volume [22]. The mathematical theory of such a band is still rather uncertain [23], but there is no doubt about the physics. Suppose, however, that we make an alloy—*e.g.* of Ag and Au—whose constituent atoms have their resonance at different energies; how far apart would these energies need to be to give us two distinct d-bands, and how would this depend on the relative concentrations and relative ordering of the constituents? The model can be made extremely elementary—equal numbers of A and B type atoms, with a single bound s-state on each, substituted at random on a regular lattice with a constant overlap integral V between nearest neighbors. Some highly respected statistical theories which rely upon defining an average propagator in such a medium, seem to insist that the bands will be drawn out into a continuous broad spectrum as the two levels move apart; others would allow a split to occur when the spacing is rather larger than the width of either band [24]. I feel sure, myself, that the latter prediction is correct, but we have still a great deal to do before we can calculate the width of each band the shape of the tails into the gap, and the nature of any levels in these regions. How far, for example, do these bands depend upon the possibilities of "percolation", from one atom to another of the same type, through large distances—a property that depends peculiarly on the dimensionality of the lattice and the relative concentrations of the components?

Another contradiction between mathematical theories and physical intuition occurs in the case of

FIGURE 16. *Does a mixed crystal have one bound band or two?*

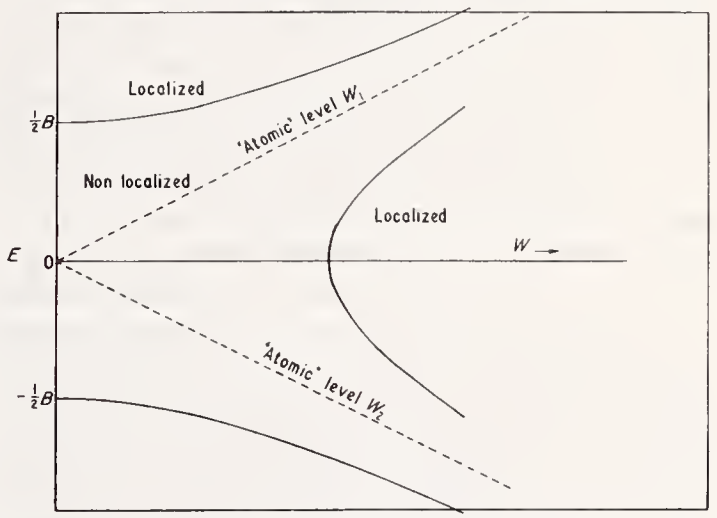

FIGURE 17. *Regions of localized and non-localized states for an "equiconcentration alloy".*

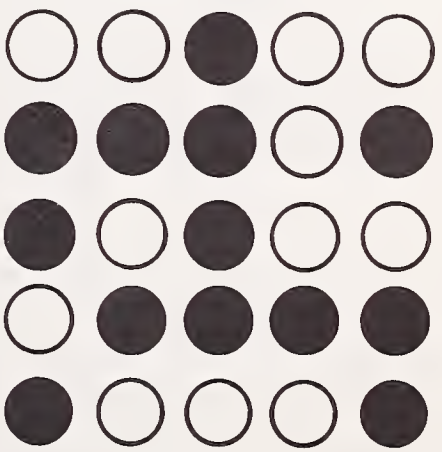

FIGURE 18. *A percolation chain in an equiconcentration alloy.*

amorphous semiconductors. Let it be granted, for the sake of argument, that amorphous Ge and Si are "tetrahedral glasses"; each atom has four neighbors, arranged more or less in the regular tetrahedral orientation, just as in the regular diamond lattice, but the connectivity of the structure has been altered in a random way, so that there is no long-range order. From the point of view of a chemist, this system is a single covalently bonded molecule: the saturation of all the bonds implies that some energy of excitation is required to create a carrier, so we should expect the material to be a semiconductor. The substantial gap in the optical spectrum of amorphous Ge supports this reasonable interpretation. But suppose we were to treat this by the conventional pseudopotential procedure, assigning a model potential to each atom and then calculating the diffraction effect on a free electron gas. In the absence of long-range order, there would be no strong Bragg reflections from well-defined lattice planes, and thus no proper band gaps at the zone boundaries, *etc.*; from the point of view of solid-state theory, this material ought to be a metal. This antinomy needs to be resolved if we are to understand the theory of disordered systems—or even the theory of the chemical bond. There is some evidence—as yet merely qualitative [27]—that the diffraction approach can be made to give a band gap if one takes into account the higher-order particle correlations. Thus, a glass differs from a liquid in that three neighboring atoms may have a strong tendency to be oriented so as to make a good bond angle; this is a form of short-range order, implying a strong constraint on the three-and four-body statistical distributions of atoms. At the same time, the relationship between the localized molecular orbitals of the chemical bonds and the delocalized "Bloch states" of the crystal or amorphous solid needs to be clarified [28]. But these are only two of the numerous unsolved problems in this field.

The above account of the band structure problem is obviously very sketchy and incomplete—especially in the total neglect of all electron-electron effects. We shall obviously learn much more about it as this conference proceeds. But I think it is good to look back and see what progress has been achieved—and even better to look forward to whole Alps of ignorance still to be surmounted.

6. References

[1] **Electrons and Phonons:** (Oxford, Clarendon Press 1960).

[2] **Methods in Computational Physics: Vol. 8: Energy Bands of Solids:** Edited by B. Alder, S. Fernbach, M. Rotenberg (New York: Academic Press 1968).

[3] Ziman, J. M., Advances in Physics, **13**, 89 (1964).

[4] Harrison, W. A., **Pseudopotentials in Metals** (New York: Benjamin 1966).

[5] Heine, V., **The Physics of Metals** (ed. J. M. Ziman: Cambridge, University Press, 1969) Chap. 1.

[6] Herman, F., R. L. Kortum, C. D. Kuglin, J. P. Van Dyke and S. Skillman in Ref. 1, p. 193.

[7] Heine, V. and I. V. Abarenkov, Phil. Mag., **9**, 451, (1964).

[8] Shaw, R. W. and W. A. Harrison, Phys. Rev. **163**, 604 (1967). R. W. Shaw, Phys. Rev. **174**, 769 (1968).

[9] Ashcroft, N. W., J. Phys. C. **1**, 232 (1968).

[10] Rubio, J. and F. Garcia-Moliner, Proc. Phys. Soc. **91**, 739; **92**, 206 (1967). J. B. Pendry, J. Phys. C. **1**, 1065 (1968).

[11] Ziman, J. M., Proc. Phys. Soc. **86**, 337 (1965).

[12] Lloyd, P., Proc. Phys. Soc. **86**, 825 (1965).

[13] Morgan, G. J., Proc. Phys. Soc. **89**, 365 (1966). K. H. Johnson, Phys. Rev. **150**, 429 (1966).

[14] Lawrence, M. J., Thesis, Bristol University (1969).

[15] Slater, J. C., Phys. Rev. **145**, 599 (1966).

[16] Scholsser, H. C. and P. M. Marcus, Phys. Rev. **131**, 2529 (1963). F. Beleznay and M. J. Lawrence, J. Phys. C. **1**, 1288 (1968).

[17] Ziman, J. M., Proc. Phys. Soc. **91**, 701 (1967).

[18] Heine, V., Phys. Rev. **153**, 673 (1967).

[19] Hodges, L. and H. Ehrenreich, Phys. Letters **16**, 203 (1965). F. M. Mueller, Phys. Rev. **153**, 659 (1967).

[20] Hubbard, J., Proc. Phys. Soc. **92**, 921 (1967). R. L. Jacobs, J. Phys. C. **1**, 492 (1968).

[21] See, *e.g.* J. Hori, **Spectral Properties of Disordered Chains and Lattices** (Oxford: Pergamon Press 1968).

[22] Anderson, P. W. and W. L. McMillan, **Teoria del magnetisino nei metalli di transizione:** Verenna Summer School XXXVII (1967).

[23] Lloyd, P., Proc. Phys. Soc. **90**, 207, 217 (1967). G. J. Morgan, J. Phys. C. **2**, 1446, 1454 (1969).

[24] Ziman, J. M., J. Phys. C. **2**, 1230 (1969) (II).

[25] Ziman, J. M., J. Phys. C. **2**, 1532 (1968) (I). D. F. Holcomb and J. J. Rehr (to be published).

[26] Tauc, J., R. Grigorivici and A. Vancu, Phys. Stat. Solid **15**, 627 (1966).

[27] Fletcher, N. H., Proc. Phys. Soc. **91**, 724; **92**, 265 (1967). J. M. Ziman, J. Phys. C. (1969) (III).

[28] Anderson, P. W., Phys. Rev. Letters **21**, 13, (1968).

Discussion on "The Band Structure Problem" by J. M. Ziman (University of Bristol)

F. Herman *(IBM Res. Center, San Jose):* I very much enjoyed Prof. Ziman's remarks. I think that Prof. Ziman's approach to the problem is in the spirit of someone who tries to give a unified picture. I think, though, it is unfair to neglect appropriate mention of all the work that has been done numerically which in fact had led and has been a stimulus for the very elegant mathematical models that you describe. As long as the subject of band structure remained in the hands of text book writers the subject did not progress very far. But as soon as computers became available, people rolled up their sleeves and began to do actual calculations. Enough empirical progress was made so that the theoretically inclined could make their contributions also. I think it is important to see both sides of the picture.

J. W. Gadzuk *(NBS):* Due to the role of inelastic electron processes at energies far (~ 20-100 eV) above the Fermi energy, (for instance as emphasized in current LEED theories) what do you feel is the situation with regards to a marriage of band structure and inelastic many-body effects for the excited states of a solid.

J. M. Ziman *(Univ. of Bristol):* I don't know the answer to this question.

P. M. Marcus *(IBM Res. Center, New York):* In reply to the question as to the validity of band structure concepts at energies above the Fermi energy, I can comment that observation of LEED spectra indicates that some remnant of a band structure persists to high energies. Reflection maxima in LEED spectra correspond to energy ranges with lowered densities of propagating states, as occur in band gaps, and such maxima are observed hundreds of volts above the Fermi energy. The effect of inelastic scattering of electrons is to wipe out any sharp band edges so that the density of the corresponding propagating states does not drop sharply to zero as it would at the Fermi energy (in fact, all states now attenuate, but do so more strongly in the ranges of the energy gaps) and the diffraction peaks become lower, smoother and, eventually, more spread out in energy.

A. J. Freeman *(Northwestern Univ.):* The complementary question, "How good are band calculations well above the Fermi energy?" is one we can answer only after we get more experiments such as those now being performed in photoemission at high energies and we have more optical experiments of that type.

A. R. Williams *(IBM, New York):* One of the great virtues of the pseudopotential method is the ease with which it permits one to go beyond Hartree-Fock theory by means of the RPA dielectric function. Is there any way of implementing the same or a similar screening approximation in KKR and APW calculations?

J. M. Ziman *(Univ. of Bristol):* We can in fact carry through a complete self consistent calculation. We have the wave function explicitly and we can go through the hard work and really slog it all out. I think you have to do this anyway. The RPA dielectric function is only an approximation and there is no theorem saying under what circumstances you may legitimately divide the pseudopotential by the dielectric function and say that is the screened core potential.

P. M. Marcus *(IBM Res. Center, New York):* How important is the interstitial potential between the spheres in these methods?

J. M. Ziman *(Univ. of Bristol):* KKR and APW are equivalent in being able to treat an interstitial potential. All you need to do in either case is to add in the Fourier components of the interstitial potential to the matrix elements in the determinants. In metals the difference between a muffin tin potential with a flat interstitial region and a real potential is probably very small because they are relatively close packed. But in the case of the semi-conductors you get very large interstitial potentials indeed, with valleys along which electrons are essentially free and hills in other directions in which the electrons are bound. I am even prepared to conjecture that these are characteristic features of semiconductors. The concept of chemical bonding implies a system with certain directions in which the electrons can travel freely without barriers, and other directions where they have to go over or tunnel through the hills. I think we must face this seriously and one of the problems that I hinted at in my talk was how to deal with that case.

A. J. Freeman *(Northwestern Univ.):* D. D. Kelling, F. M. Mueller and I have included the "warped muffin

tin" into our Symmeterized Relativistic APW Calculations (cf. Phys. Rev., Feb. 15, 1970). The formalism is identical to the muffin tin case and is readily included into the programs. From actual calculations on Pd, Pt and bcc U we find that the effect of the warping is indeed small. We are carrying out calculations for intermetallic compounds where the warped muffin tin is necessary in view of the inadequacies of using a muffin tin potential.

J. M. Ziman *(Univ. of Bristol):* I have a student working on long chain hydrocarbon structures which you can pack formally into a crystal. There this is the dominant feature. The question is not whether you can do the calculations by this method, which is exactly the same as yours, but whether it is a reasonably convergent method which does not seem to have been proved. But we have to test it out and see.

BAND STRUCTURE II

CHAIRMEN: F. Herman
R. C. Casella

RAPPORTEUR: R. E. Watson

Electronic Density of States of Transition, Noble, and Actinide Metals*

F. M. Mueller

Argonne National Laboratory, Argonne, Illinois 60439

Key words: Electronic density of states: histogram representations; QUAD scheme.

In this paper we consider recent calculations of the electronic density of states of nickel [1], palladium [2], platinum [3], scandium [4], iron [5], gold [6], and plutonium [7], as produced by the QUAD [8] scheme from histogram representations of width 0.001 Ry filled by sampling the appropriate Brillouin zone at more than 1,000,000 random points. Comparisons with the experimental data will be made where appropriate.

[1] Zornberg, E. I., and Mueller, F. M., Bull. Am. Phys. Soc. **13**, 441 (1968), and Zornberg, E. I., (to be published).

[2] Mueller, F. M., Freeman, A. J., Dimmock, J. O., and Furdyna, J. K., (to be published).

[3] Mueller, F. M., Ketterson, J. B., Windmiller, L. R., and Hornfeldt, S., (to be published).

[4] Koelling, D. D., Freeman, A. J., Mueller, F. M., and Goroff, I., Bull. Am. Phys. Soc. **14**, 360 (1969).

[5] Preston, R. S., Goroff, I., and Mueller, F. M., Bull. Am. Phys. Soc. **14**, 386 (1969).

[6] Sommers, C. B., Goroff, I., and Mueller, F. M., (to be published).

[7] Mueller, F. M., and Goroff, I., Bull. Am. Phys. Soc. **13**, 364 (1968).

[8] Mueller, F. M., Garland, J. W., Cohen, M. H., and Bennemann, K. H., The QUAD Scheme (ANL-7556) and (to be published).

*Work performed under the auspices of the U.S. Atomic Energy Commission.

417-156 O - 71 - 3

Discussion on "Electronic Density of States of Transition, Noble, and Actinide Metals" by F. M. Mueller (Argonne National Laboratory)

D. J. Fabian *(Univ. of Strathclyde):* Dr. Mueller, I noticed that in your calculation for platinum you calculated for *s*-states only; I believe you subtracted all the *d*-states leaving just a plane wave. You found a very sharp peak at the bottom of the band. Do you really attribute that totally to the *s*-states?

F. M. Mueller *(Argonne National Lab.):* The term *s*-states is a misnomer. That was why I was trying to be very careful in the beginning of the talk. This is the lowest part of the plane wave structure. If you want an *s*-like structure you have to include an additional projection operator to project out the j_0 part of the plane wave. Here we have included all of the lowest part of the plane wave and this, in terms of the interpolation scheme we have used here, represents an orthogonalized plane wave. So we have included a lot of structure in there. That is the lowest basis function. I call it an *s*-state because that is what it is called in the literature. People understand that to be a plane-wave-like structure.

F. J. Blatt *(Michigan State Univ.):* In your calculation of alpha iron, do you use the magnetization as a parameter?

F. M. Mueller *(Argonne National Lab.):* The magnetization has been put in as a parameter. We have included a sufficient amount of exchange to split the bands up and down so that the resulting number difference in the up and down structure conforms to the observed moment for iron.

Electronic Densities of States and Optical Properties of CsCl Type Intermetallic Compounds

J. W. D. Connolly and K. H. Johnson*

**Advanced Materials Research and Development Laboratory, Pratt and Whitney Aircraft Corp.
Middletown, Connecticut 06457**

The electronic band structures and densities of states have been calculated from first principles for two intermetallic compounds having the CsCl structure. The nonrelativistic augmented plane wave method has been used in conjunction with an LCAO interpolation technique to determine the band structure and density of states of β' NiAl to a high degree of accuracy. These theoretical results are in excellent agreement with the measured optical properties if **k**-conserving (direct) interband transitions are assumed to be dominant. A similar study has been carried out for β' AuZn, using as a basis the energy bands determined by the relativistic Korringa-Kohn-Rostoker method. The band profiles and density of states of β' AuZn are qualitatively similar to those of β' NiAl, except for the appearance of relativistic effects in the former alloy and differences in the relative positions and widths of the respective Au and Ni *d*-bands. The β' AuZn results have also been compared with the measured optical properties and are again consistent with these measurements if direct interband transitions are assumed.

Key words: AuZn; CsCl-type intermetallic compounds; direct interband transitions; electronic density of states; NiAl; optical properties.

1. Introduction

Theoretical energy-band calculations are not restricted, in principle, to pure monatomic crystals. In practice, however, comparatively few applications have been made to compounds, except for ionic and semiconducting cases. Aside from their intrinsic interest, an understanding of the band structures and Fermi surfaces of intermetallic compounds is of considerable importance to the theories of alloy phase stability. Traditional research on alloy formation has been primarily of two types: (1) studies which attempt to correlate a large amount of data on interatomic spacings, magnetic moments, etc., and (2) the determination of crystal structures and the correlation of certain recurring structures with electron concentration, i.e., the Hume-Rothery [1] rules for electron compounds. The theory of alloy phase stability formulated by Jones [2] and Konobejewski [3] is based on a nearly-free electron approximation and on the thermodynamic principle of minimum free energy. Implicit in the theory is the rigid-band approximation in which the density of states remains fixed as the solute concentration is increased. The newer theories, [4] while challenging the rigid band model, are themselves still only semi-quantitative in nature. While conventional energy-band techniques rigorously permit us to determine the electronic structure of ordered alloys only at exact stoichiometric proportions, it is nevertheless true that this information is quite important as a starting point for understanding the properties of neighboring concentrations of disordered solid solution alloys.

As an illustration of these ideas, we may cite earlier work on the IB-IIB ordered beta-phase compounds. The results of detailed DHVA [5] and HFMR [6] measurements together with fundamental KKR [7] and APW [8] band calculations on this system have indicated that the Fermi surface contacts the second Brillouin zone boundary. This is in accord with Jones' [2] interpretation in which the beta phase occurs at an electron-to-atom ratio of 1.5, when the Fermi sphere touches the second zone boundary. Furthermore, the use of the band profiles in conjunction with the composition dependence of the optical properties [9] has given some support for rigid-band behavior within the narrow composition limits of the ordered beta phase.

*Permanent Address: Center for Materials Science and Engineering, Massachusetts Institute of Technology.

The problem of ultimately predicting the particular structure an assembly of atoms will assume as a function of composition, pressure, volume, and temperature is a very complex one. It has not been solved satisfactorily even for the simplest pure metals, although recently there has been some quantitative research directed to that end [10,11]. We feel that the accurate determination of the Fermi surfaces and band structures of a number of specific intermetallic compounds is an important step toward the goal of being able to predict or explain features of the many alloy phase diagrams which have been established.

2. Results for AuZn

Like the other IB-IIB beta-phase alloys mentioned above, the ordered beta phase of AuZn is stable over a relatively narrow range of atomic composition bracketing stoichiometric $\beta'Au_{50}Zn_{50}$, which has the ideal CsCl-type crystal structure. At room temperature, the atomic composition limits are $\beta'Au_{48}Zn_{52}$ and $\beta'Au_{52.5}Zn_{47.5}$, the phase boundaries widening in the usual fashion with increasing temperature [12]. Unlike the alloys, β'CuZn, β'AgZn, and β'AgCd, the present system does not disorder appreciably below the melting temperature.

For our band studies of $\beta'Au_{50}Zn_{50}$, we have generated a crystal potential in the familiar "muffin-tin" representation from a superposition of neutral atomic Au and Zn charge densities determined originally by Liberman et al. [13]. The key physical parameters, e.g., atomic configurations, lattice constant, etc., adopted for this work are given in table 1.

TABLE 1. *Constants used in the first principles calculations*

AuZn	NiAl
Atomic configuration (Au) : $(5d)^{10}(6s)^1$	Atomic configuration (Ni) : $(3d)^9(4s)^1$
Atomic configuration (Zn) : $(3d)^{10}(4s)^2$	Atomic configuration (Al) : $(3s)^2(3p)^1$
Lattice constant, $a=6.028$ a.u.[a]	Lattice constant, $a=5.442$ a.u.[a]
Muffin-tin radius, R(Au) = 2.586 a.u.	Muffin-tin radius, R(Ni) = 2.262 a.u.
Muffin-tin radius, R(Zn) = 2.586 a.u.	Muffin-tin radius, R(Al) = 2.451 a.u.
Zero of potential, $V_0=-0.866$ Ry.	Zero of potential, $V_0=-1.6000$ Ry.
Maximum angular momentum used in KKR wave function expansions, $l_{max}=3$	Maximum angular momentum used in APW wave function expansion, $l_{max}=6$
	Maximum reciprocal vector magnitude used in APW wave function expansion, $\lvert\mathbf{k}+\mathbf{k}\rvert_{max}=\frac{5\pi}{2a}$

[a] R. W. G. Wyckoff, *Crystal Structures*, (Interscience Publishers, New York, 1948).

There are two principal errors in a model crystal potential of this type (relative to the exact Hartree-Fock solution), namely the lack of self-consistency and the over-estimation of the exchange effects through the use of the Slater approximation [14,15]. Recent self-consistent band calculations on transition [16] and noble [17] metals have shown that these two errors tend to cancel each other. In any case, for these metals and their alloys, the errors have the primary effect of merely shifting in opposite energy directions the positions and widths of the d-bands with respect to the conduction bands. Thus we can be reasonably confident in adopting the usual Slater-type exchange approximation in non-self-consistent band calculations on intermetallics, provided that we allow ourselves the option of using the d-band position and width as empirically adjustable parameters.

We have used the symmetrized, relativistic KKR method to determine the bands of β'AuZn along five principal symmetry directions of the simple cubic Brillouin zone. Five **k**-points were determined between the end points of each of the symmetry directions, for a total of 29 nonequivalent points in 1/48 of the zone. This corresponds to 227 points in the full zone, weighting each nonequivalent point properly. The results are illustrated in figure 1. Double group notation has been used to label the bands.

The broad conduction bands are intersected by a relatively flat and narrow set of d-bands arising principally from the $5d$ electrons of Au, but with considerable conduction s- and p-state admixture. The Au d-bands are approximately twice as wide as the Cu d-bands are in β'CuZn [7,8]. Immediately below the bottom of the conduction bands is an extremely narrow set of d-bands originating from the Zn $3d$ electrons. These bands are so flat and narrow on the chosen energy scale that we have merely indicated their boundaries by the shaded profile in figure 1.

This same relativistic KKR program has been used to determine the energy band structure of Au. The width of the d-bands and position below the Fermi level are the same as for β'AuZn. Also, the width is approxi-

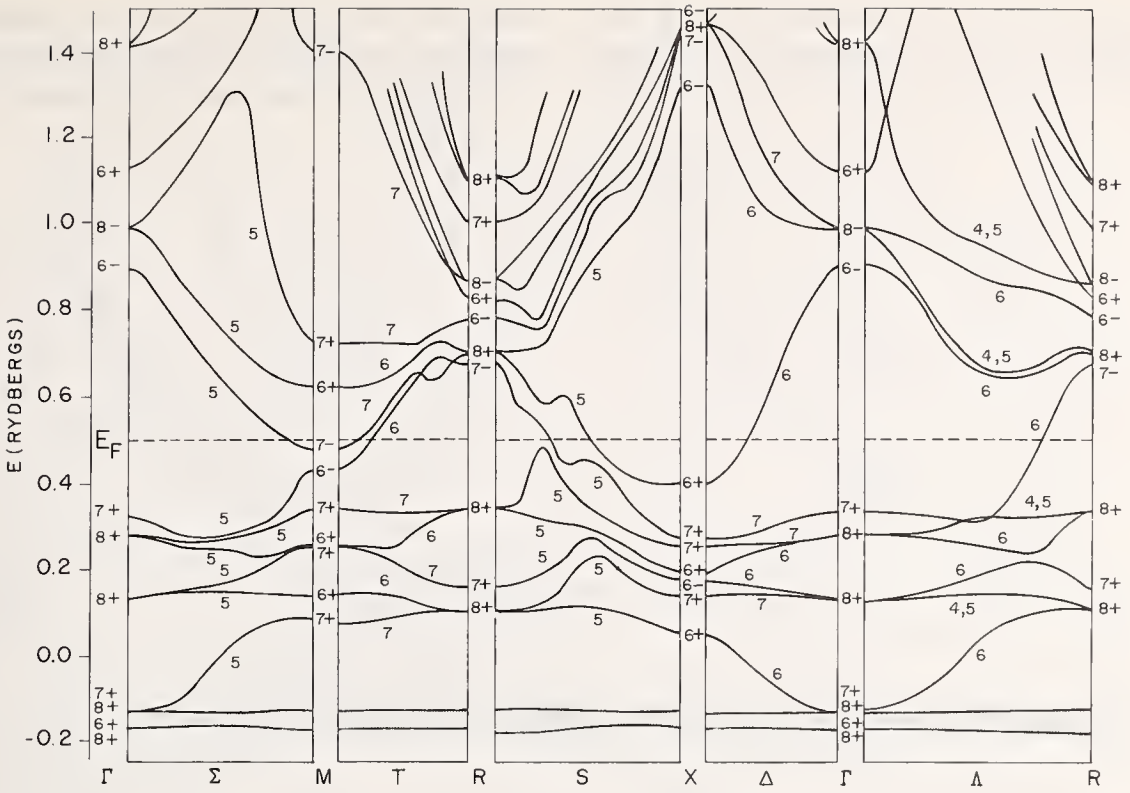

FIGURE 1. *The electronic energy bonds for β′ AuZn along the mojor symmetry directions, calculated by the relotivistic KKR method. Double group notation has been used to label the bands.*

mately twice that of the *d*-bands in pure Cu. A previous calculation for Au by Amar and Sommers [18] had the *d*-bands approximately 1 eV wider and 2 eV higher with respect to the Fermi level. This appears to be due to the use of a smaller exchange [2/3 of the Slater value] in a non-self-consistent calculation, which would tend to put the *d*-bands too high (for the reasons mentioned above).

The dominant feature of the measured optical properties of β' AuZn is a rapid rise in optical absorption in the spectral range of 2 eV to 3 eV [9,19]. This absorption is responsible for the color of the alloy at room temperature. The calculated Au *d*-bands lie between 2.5 eV and 5.5 eV below the Fermi level. However, we must regard the *d*-band position and width as uncertain by as much as ±0.5 eV, because of the aforementioned uncertainties in the crystal potential. The present band structure is therefore only semiquantitatively consistent with the optical data, in that we would expect electronic transitions between the top of the Au *d*-bands and the Fermi level to contribute to the initial rise in absorption. Another possible source of interband transitions in this spectral range are the occupied conduction states at and immediately below the Fermi level in the vicinity of the symmetry point M. Possible **k**-conserving transitions from these states to unoccupied levels just above the Fermi energy, along with the computed energy gaps are $M_{7-}(E_F) \rightarrow M_{6+} = 2.0 \pm 0.1$ eV, and $T_7(E_F) \rightarrow T_6 = 1.6 \pm 0.1$ eV. Similar interband transitions seem to be responsible for the colors of the other beta-brass-type alloys, β'CuZn, β'AgZn, and β'AgCd [7,9,19]. Additional optical absorption between 4 and 5 eV and between 7.3 and 7.8 eV is very likely due to transitions from the lower parts of the Au *d*-bands to the Fermi energy and to unoccupied conduction states, respectively. Finally, the calculated position of the center of the Zn *d*-band is approximately 9.0 eV below the Fermi energy. This agrees closely with a measured peak in optical absorption at 8.6 eV.

3. Results for NiAl

Ordered beta-phase NiAl, like β'AuZn, is a Hume-Rothery [1] electron compound of the "3/2" type. In comparison to β' AuZn, however, the composition range of phase stability is much wider for β'NiAl. At room temperature the composition limits are $\beta' Ni_{45}Al_{55}$ and $\beta' Ni_{60}Al_{40}$ [12].

We have used the symmetrized, nonrelativistic APW method to determine the bands of stoichiometric $\beta' Ni_{50}Al_{50}$. The crystal potential has been generated in an identical fashion to that described above for β'AuZn, except for the use, in this case, of nonrelativistic Hartree-Fock-Slater atomic charge densities calculated by Herman and Skillman [20]. The various physical parameters adopted for this calculation are given in table 1.

The bands have been determined at 35 points lying on a cubic grid of spacing $\pi/4a$ in 1/48 of the Brillouin zone. This grid is equivalent to 512 points in the full zone. The band profiles are shown along six symmetry directions in figures 2 and 3. Single-group notation is used. The nonrelativistic KKR method has also been

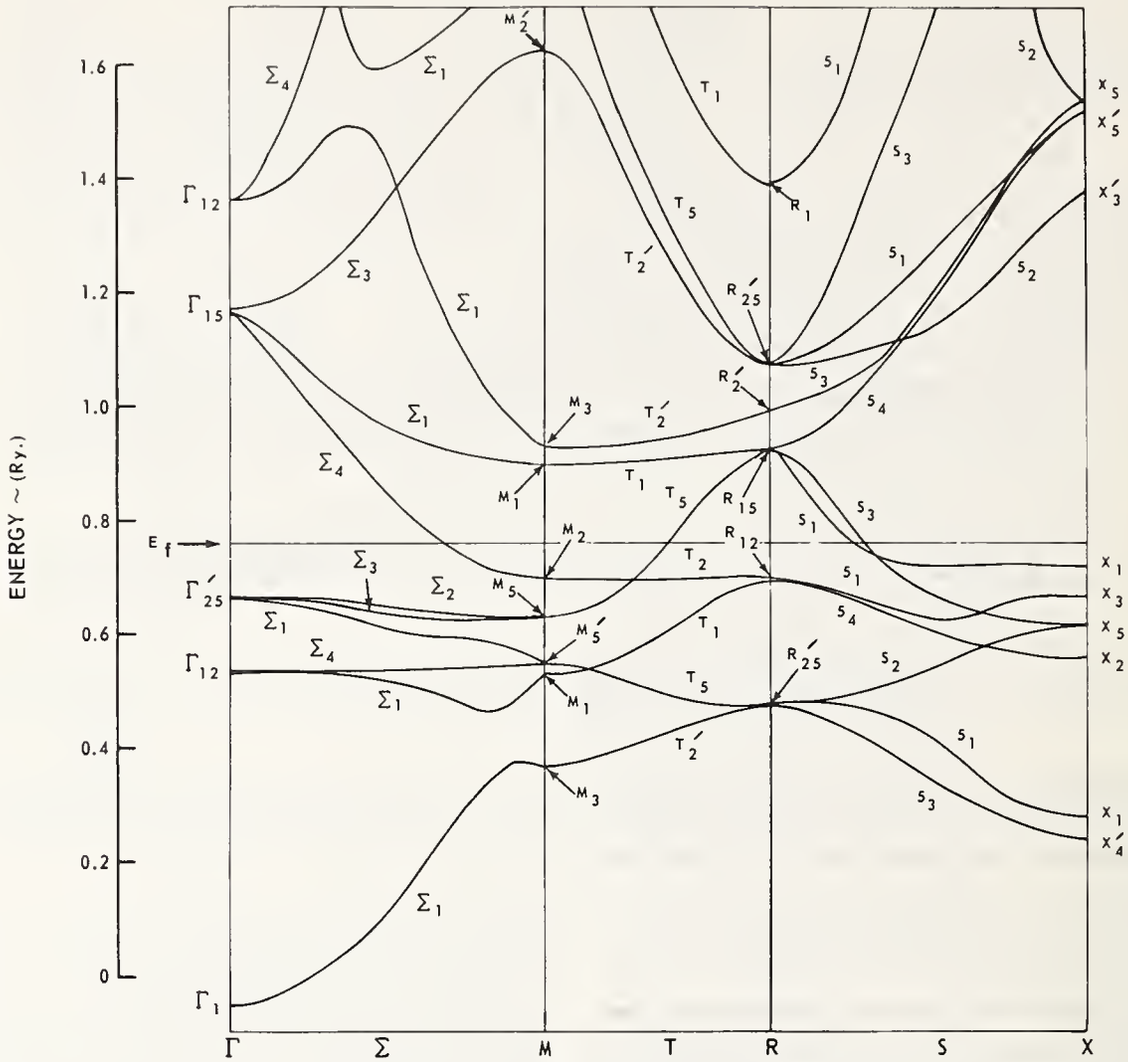

FIGURE 2. *The electronic energy bands for* β'NiAl *along the* Σ, T *and* M *directions, calculated by the nonrelativistic APW method.*

applied to β'NiAl. The disagreement is never more than a few thousandths of a Rydberg, supporting previous evidence that the KKR and APW techniques give essentially identical results when applied to the same material for identical crystal potentials.

The bands of β'NiAl are qualitatively similar to those described for β'AuZn (in the nonrelativistic limit). They are also qualitatively similar to the bands obtained earlier for β'CuZn [7,8]. The primary difference is the closer proximity of the Ni *d*-bands to the Fermi energy (indicated in figs. 2 and 3 by the solid line), relative to the locations of the *d*-bands in β'AuZn and β'CuZn, respectively. There is no narrow *d*-band below the conduction bands of β'NiAl which is analogous to the Zn *d*-band in β'AuZn and β'CuZn.

A density-of-states profile has also been generated for β'NiAl and is illustrated in figure 4. To obtain a sufficiently reliable density of states, it has been necessary to interpolate the energy bands to a much finer wavevector mesh in the Brillouin zone than the 512-point mesh calculated directly with the APW method. This has been accomplished by setting up an 18×18 LCAO type Hamiltonian matrix, the elements of which have been obtained by a least squares fitting to the APW energies at symmetry points in the zone [21]. The interaction integrals between atomic orbitals which occur in this fitting scheme have been used as parameters in the manner suggested originally by Slater and Koster [22]. With this procedure, it has been possible to determine the bands of β'NiAl on a mesh of 32,768 points in the full zone (969 nonequivalent points). The resulting histogram for the density of states has been smoothed to eliminate statistical scatter.

The sharp peaks in the energy range between 0.5 and 0.7 Ry are due to the flat *d*-bands in this region. The shoulder between .90 and .95 Ry is not due to *d*-band

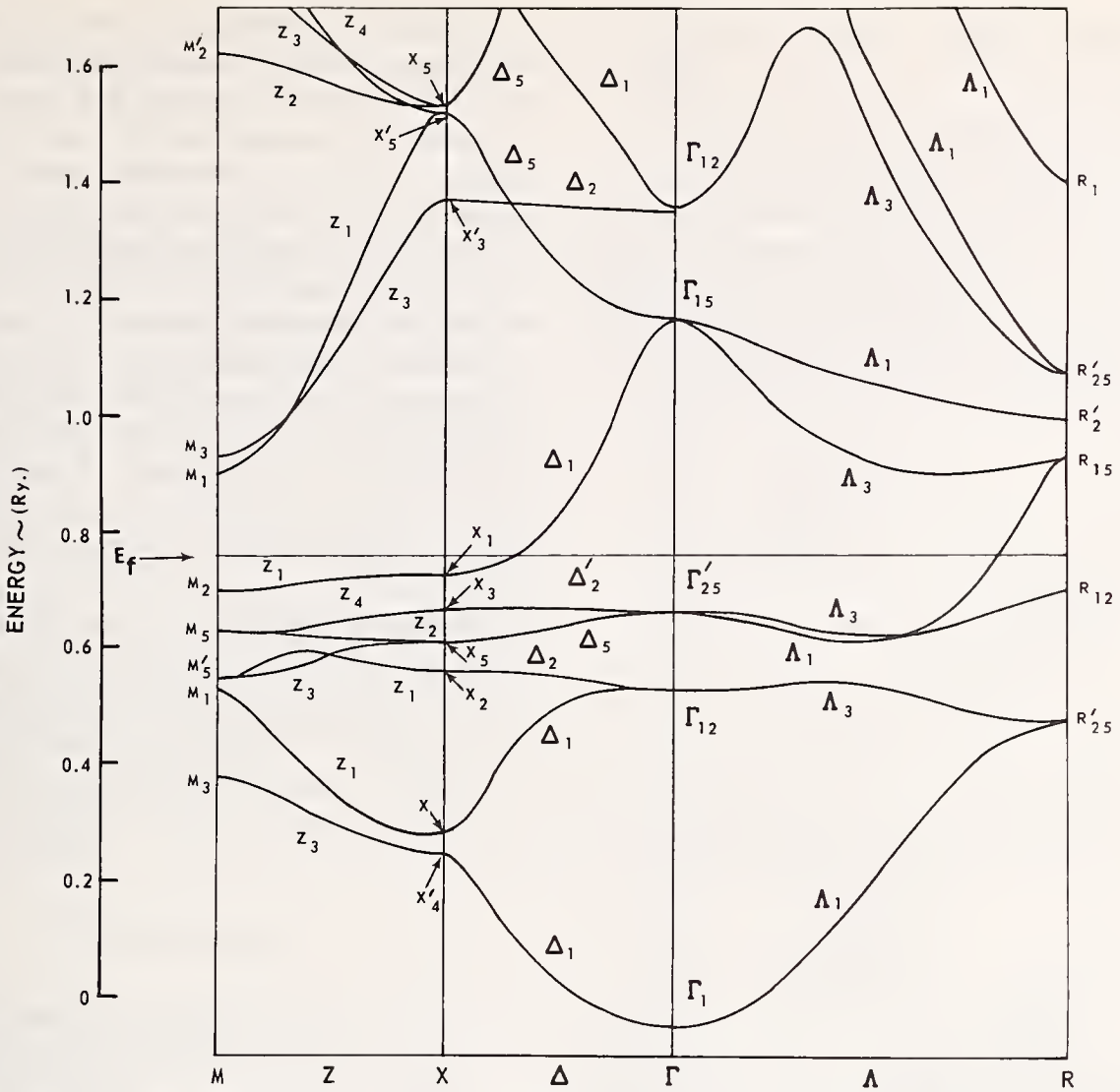

FIGURE 3. *The electronic energy bands for* β'NiAl *along the* Z, Δ, *and* Λ *directions, calculated by the nonrelativistic APW method.*

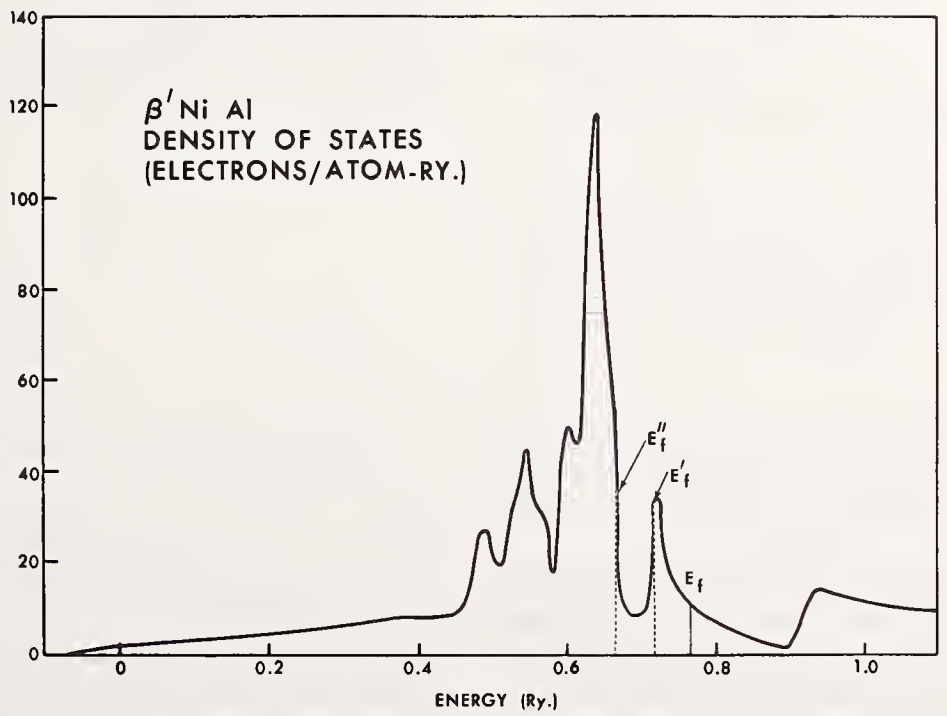

FIGURE 4. *The electronic density of states for* β'NiAl.
E_f indicates the Fermi level. E_f' and E_f'' are the Fermi levels for CoAl and FeAl respectively.

structure, but is part of the unoccupied conduction band associated with the critical points M_1 and M_3 (see fig. 2).

In addition to the ordinary density of states, in order to compare with optical experiments [23-26] two *joint* density of states curves have been generated, assuming direct and nondirect transitions. The results are shown in figure 5. Under the assumptions of (1) a long relaxation time and (2) a constant matrix element, the imaginary part of the dielectric function ϵ_2 is proportional to

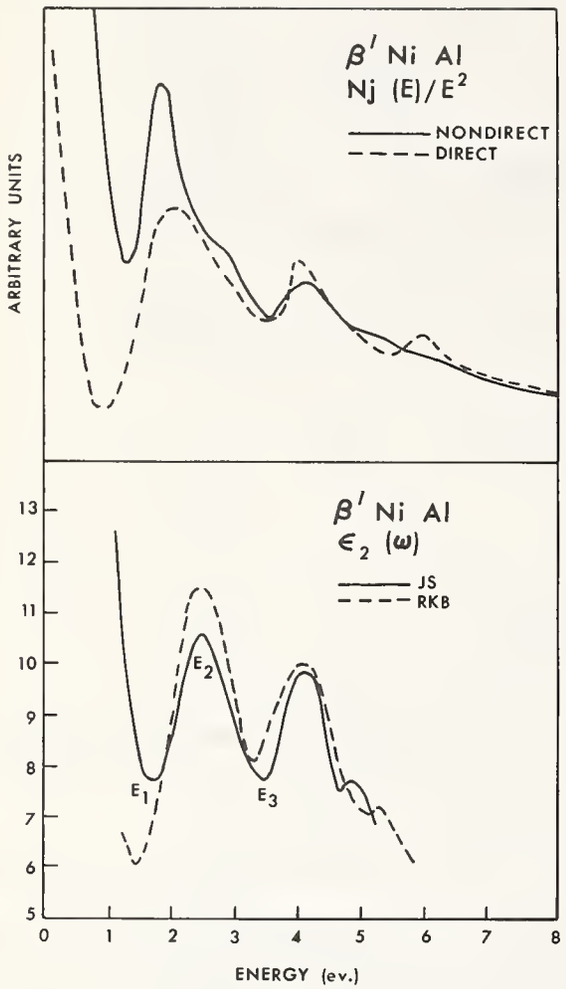

FIGURE 5. *(a) The joint density of states for* β'NiAl *divided by the energy* E *squared, as calculated assuming indirect and direct transitions. (b) The imaginary part of the dielectric function for* β'NiAl.

JS indicates the data of Jacobi and Stahl [24] and RKB indicates the data of Rechtien, Kannewurf, and Brittain [23].

the joint density divided by the square of the energy. The ϵ_2 curves have been taken from the optical data of Rechtien et al. [23] and Jacobi and Stahl [24], and are also shown in figure 5.

Because of the flatness of the *d*-bands, the direct and nondirect joint density of states curves are qualitatively similar. However, the former has slightly more structure than the latter, since the nondirect transitions effectively average out any sharp peaks. There are three main peaks in the direct curve, i.e., at 2.1, 4.0 and 5.9 eV, which compares well with the experimental structure in the dielectric function [23] at 2.5, 4.0 and 5.3 eV. The nondirect curve has structure at 1.9 and 4.2 eV, with no pronounced peak at a higher energy, although there is a weak shoulder near 5.4 eV. In both curves there is a shoulder near 3.0 eV. If we denote the structure in the conduction bands between .90 and .95 Ry by C, the major peak in the *d*-bands at .63 Ry by D_1 and the two subsidiary peaks at .72 and .50-.54 Ry by D_2 and D_3, then the following assignments can be made: (1) the structure in the joint density of states at 2.1 eV is due to transitions from the Fermi level to C ($E_f \rightarrow C$), (2) at 3.0 eV is $D_2 \rightarrow C$, (3) at 4.0 eV is $D_1 \rightarrow C$, and (4) at 5.9 eV is $D_3 \rightarrow C$. Thus, the structure in the ϵ_2 curve is mostly a reflection of the structure in the *d*-band density of states.

It is also informative to study the variation of the structure in the optical data as a function of composition, as shown in figure 6. According to the x-ray analysis [27], on the Al rich side of stoichiometry, β'NiAl

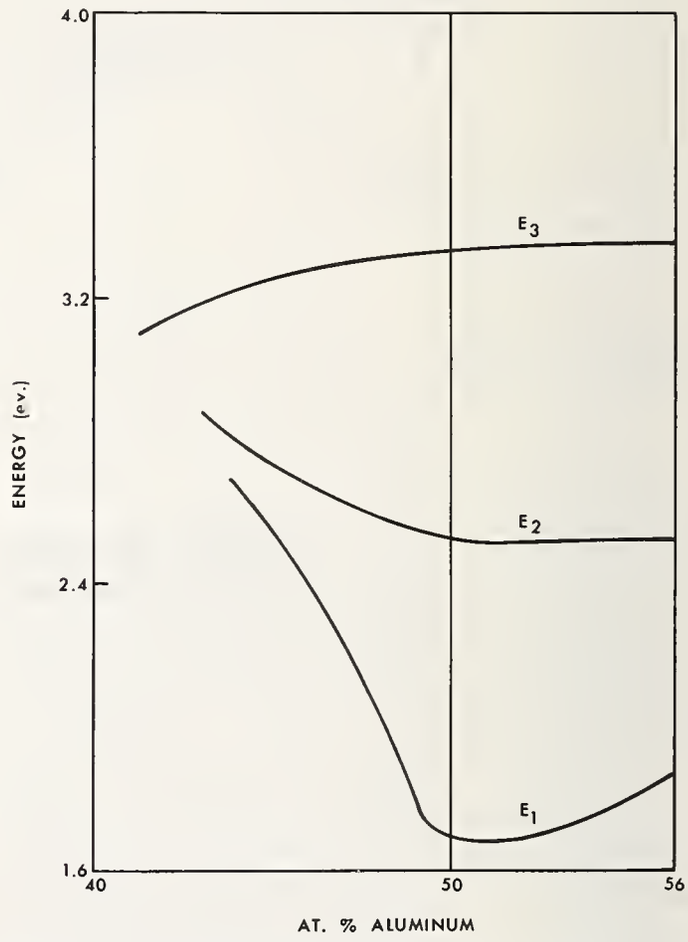

FIGURE 6. *The variation of the structure in the* ϵ_2 *function for* β'NiAl *as a function of composition.*

E_1, E_2, and E_3 are defined in figure 5. This figure is taken from ref. [24].

forms a defect structure in which there are vacancies at the Ni sites, whereas on the other side of stoichiometry, the Ni atoms occur substitutionally. Using this information, it is a simple matter for the

energy band structure to explain the variation seen in figure 6. A charge analysis of the LCAO eigenvectors shows that the density of states at the Fermi level is almost entirely due to Al s- and p-functions so that the number of Al atoms determines the position of the Fermi level. Therefore, on the Ni rich side of stoichiometry, the number of Al atoms decreases and the Fermi level is lowered, thereby increasing the energy of structure (1) while leaving that of (2), (3) and (4) relatively constant. On the other side of stoichiometry, however, the number of Al atoms stays constant and, therefore, the optical structure stays constant. Both of these conclusions are confirmed by the experimental data [23,24].

Another confirmation of the band structure presented here is given by a comparison of the optical structure in CoAl with that of NiAl [25]. Referring to figure 4, since CoAl has one less electron, the Fermi level for CoAl decreases from E_f to E_f' which is below D_2 so that structure (1) is eliminated. The experimental data shows that this is indeed the case, i.e., the 2.5 eV structure is missing in CoAl, whereas the 4.0 eV peak is still present [25].

4. References

[1] Hume-Rothery, W., J. Inst. Metals **35,** 309 (1926).

[2] Jones, H., Proc. Roy. Soc. (London) **A144,** 225 (1934); **A147,** 396 (1934); **A49,** 250 (1937).

[3] Konobejewski, S. T., Ann. Phys. **26,** 97 (1936).

[4] Cohen, M. H., and Heine, V., Advances in Physics, N. F. Mott, Editor (Taylor and Francis Ltd., London, 1958), Vol. **7,** p. 395; Hume-Rothery, W., and Roaf, W., Phil. Mag. **6,** 55 (1961).

[5] Jan, J.-P., Canad. J. Phys. **44,** 1787 (1966); Jan, J.-P., Pearson, W. B., and Saito, Y., Proc. Roy. Soc. (London) **A297,** 275 (1967).

[6] Sellmyer, D. J., Ahn, J., and Jan, J.-P., Phys. Rev. **161,** 618 (1967).

[7] Johnson, K. H., and Amar, H., Phys. Rev. **139,** A760 (1965); Amar, H., Johnson, K. H., and Wang, K. P., Phys. Rev. **148,** 672 (1966); Johnson, K. H., in Energy Bands in Metals and Alloys, L. H. Bennett and J. T. Waber, Editors (Gordon and Breach Science Publishers Inc., New York, 1968), p. 105.

[8] Arlinghaus, F. J., Phys. Rev. **157,** 491 (1967); Intern. J. Quantum Chem. **1S,** 605 (1967).

[9] Muldawer, L., Phys. Rev. **127,** 1551 (1962); Muldawer, L., and Goldman, H. J., in Optical Properties and Electronic Structure of Metals and Alloys, F. Abeles, Editor (North-Holland Publishing Company, Amsterdam, 1966), p. 574.

[10] Harrison, W. A., Pseudopotentials in the Theory of Metals, (W. A. Benjamin Inc., New York, 1966).

[11] Deegan, R. A., J. Phys. C. (Proc. Phys. Soc.) (London) **1,** 763 (1968).

[12] Hansen, M., Constitution of Binary Alloys (McGraw-Hill Book Company Inc., New York, 1958).

[13] Liberman, D., Waber, J. T., and Cromer, D. T., Phys. Rev. **137,** A27 (1965).

[14] Slater, J. C., Phys. Rev. **18,** 385 (1951).

[15] Slater, J. C., Wilson, T. M., and Wood, J. H., Phys. Rev. **179,** 28 (1969).

[16] Connolly, J. W. D., Phys. Rev. **159,** 415 (1967).

[17] Snow, E. C., and Waber, J. T., Phys. Rev. **157,** 570 (1967).

[18] Sommers, C. B., and Amar, H., Bull. Am. Phys. Soc. Ser. II, **13,** 57 (1968) (unpublished).

[19] Jan, J.-P., and Vishnubhatla, S. S., Canad. J. Phys. **45,** 2505 (1967).

[20] Herman, F., and Skillman, S., Atomic Structure Calculations (Prentice-Hall Inc., Englewood, New Jersey, 1963).

[21] Connolly, J. W. D., these Proceedings, p. 27.

[22] Slater, J. C., and Koster, G., Phys. Rev. **94,** 1498 (1954).

[23] Rechtien, J. J., Kannewurf, C. R., and Brittain, J. O., J. Appl. Phys. **38,** 3045 (1967).

[24] Jacobi, H., and Stahl, R., Z. Metallkunde **60,** 106 (1969).

[25] Sambongi, T., Hagiwara, R., and Yamadaya, T., J. Phys. Soc. Japan **21,** 923 (1966).

[26] Jacobi, H., Vassos, B., and Engell, H. J., J. Phys. Chem. Solids **30,** 1261 (1969).

[27] Bradley, A. J., and Taylor, A., Proc. Roy. Soc. **A159,** 62 (1937).

Discussion on "Electronic Densities of States and Optical Properties of CsCl Type Intermetallic Compounds" by J. W. D. Connolly (Pratt and Whitney Aircraft) and K. H. Johnson (MIT)

W. E. Spicer *(Stanford Univ.):* The rise in the density of states above the Fermi level in the nickel-aluminum alloys is quite striking. There is nothing like it in either nickel or aluminum. I wonder if you can say anything about the physics producing this? Is it mixing?

J. W. D. Connolly *(Pratt and Whitney Aircraft):* The conduction electrons in that region are definitely combinations of *s* and *p* type electrons from aluminum.

W. E. Spicer *(Stanford Univ.):* But there is no way of telling why it comes in the alloy and not the aluminum?

K. H. Johnson *(MIT):* The energy bands in that region are fairly densely clustered and to some degree parallel. When that happens, the density of states can become relatively large. You don't have this sort of behavior in aluminum or nickel separately. As to why they cluster, it seems to be true generally for the cesium-chloride system of alloys we have studied. It probably results more from the crystal symmetry than from the component atoms.

J. W. D. Connolly *(Pratt and Whitney Aircraft):* You might think of it in terms of the hybridization effect tending to push the bands up.

S. J. Cho *(National Res. Council):* I did a similar calculation for the ordered palladium-indium system recently. I have found very similar structures near the Fermi surface with one peak right above the Fermi level from the hybridization as you said.

The Calculation of Densities of States by LCAO Interpolation of Energy Bands with Application to Iron and Chromium

J. W. D. Connolly

Advanced Materials Research and Development Laboratory, Pratt and Whitney Aircraft Corp.
Middletown, Connecticut 06457

The LCAO (linear combination of atomic orbitals) interpolation method is described as a means of calculating the density of states curves of a crystalline solid. This method is shown to be more straightforward and convenient to use than the composite (LCAO-OPW) techniques that have recently been proposed for transition metals. A computer program is described which determines the LCAO interaction integrals from an *ab initio* energy band calculation by a nonlinear least squares procedure, and then uses these parameters to sample the Brillouin zone at a large number of points in order to calculate the density of states curve to a high degree of accuracy. As examples of the application of this program, the results of calculations on chromium (in both the nonmagnetic and antiferromagnetic states) and iron (nonmagnetic and ferromagnetic) are presented and compared with the recent photoemission data.

Key words: Chromium; electronic density of states; interpolation method; iron; photoemission.

1. Introduction

One of the primary computational difficulties in the theoretical determination of the physical properties of a crystalline solid is the evaluation of a three-dimensional integral over a complicated (usually nonanalytic) region of momentum space. A simple example of this type of integral is found in the expression for the electronic density of states, as a function of the energy ϵ,

$$n(\epsilon) = \frac{d}{d\epsilon} \sum_n \int_{T_n(\epsilon)} d\mathbf{k} \qquad (1)$$

where $T_n(\epsilon)$ is that region of $\mathbf{k}$ space where $E_n(\mathbf{k}) < \epsilon$. $E_n(\mathbf{k})$ is the energy of an electron in the n^{th} energy band. The problem of calculating these integrals arises from the nature of $E_n(\mathbf{k})$. This is usually available only numerically at a limited number of $\mathbf{k}$ points, as the results of an *ab initio* energy band calculation, such as by the APW or KKR methods. Since it is a costly procedure for an *ab initio* calculation to provide enough $E_n(\mathbf{k})$ values for an accurate numerical evaluation of the integral, a straightforward solution is to apply some interpolation scheme to obtain values of $E_n(\mathbf{k})$ between those provided. A modified LCAO technique to do this was suggested fifteen years ago by Slater and Koster [1]. This method is sometimes called the "tight-binding approximation," although this is really a misnomer, since the method is quite general and applicable to many types of crystals having wide bands which would not normally be considered to be tightly bound. For example, it has been recently shown by Dresselhaus and Dresselhaus [2] that this method is capable of satisfactory results for germanium and silicon.

It was this belief that this method was applicable only to narrow band electrons which led to the proposal of using composite schemes [3,4], in which the narrow band electrons are treated by the LCAO approximation and the wide band electrons by an OPW (orthogonalized plane wave) or pseudopotential approximation. These approaches were designed to handle the energy bands of transition and noble elements and are able to reproduce their energy band structure (as determined by APW calculations) quite well. It is a purpose of this paper to show that such composite schemes are unnecessary for the description of the electronic structure of transition and noble elements, and that the electrons which are described by OPW wave functions in the composite schemes can equally well be described by combinations of *s*- and *p*-type atomic orbitals. The LCAO method has the advantages of being more

straightforward and convenient, without sacrificing either speed or accuracy. The method has been applied to the calculation of the density of states curves for many materials. The resultant curves for two of them, ferromagnetic iron and antiferromagnetic chromium, are presented in section 4 of this paper.

2. The LCAO Method

In a periodic potential, the one-electron wave function can be expressed as a linear combination of Bloch sums Φ_n of atomic orbitals;

$$\Phi_n(\mathbf{k}, \mathbf{r}) = \frac{1}{\sqrt{N}} \sum_{\mathbf{R}_i} \psi_n(\mathbf{r} - \mathbf{R}_i) \exp(i\mathbf{k}\cdot\mathbf{R}_i) \quad (2)$$

where the sum is over the N lattice vectors $\mathbf{R}$ in the crystal, $\mathbf{k}$ is the reciprocal vector and $\mathbf{r}$ the position vector. The functions $\psi_n(\mathbf{r}\text{-}\mathbf{R}_i)$ are atomic orbitals centered on an atom at lattice vector $\mathbf{R}_i$. In actual practice, it is more convenient to use Löwdin functions [5] as basis functions. These are combinations of atomic orbitals which are orthogonal to each other,

$$\Phi_n(\mathbf{r} - \mathbf{R}_i) = \sum_{m, \mathbf{R}_j} \psi_m(\mathbf{r} - \mathbf{R}_j)(\Delta^{-1/2})mj;\ ni \quad (3)$$

where $\Delta mj,ni$ is the overlap matrix between the atomic orbitals. This eliminates the need to consider the overlap integrals between basis functions, leaving to be determined only the interaction integrals between the Löwdin orbitals, i.e.,

$$\alpha_{mj;\,ni} = \int \phi_n^*(\mathbf{r} - \mathbf{R}_i) \mathscr{H} \phi_m(\mathbf{r} - \mathbf{R}_j) \quad (4)$$

where $\mathscr{H}$ is the one-electron Hamiltonian operator. It can then be shown [1] that the electron energies are simply the eigenvalues ϵ_n of the matrix,

$$H_{mn}(\mathbf{k}) = \sum_{\mathbf{R}_j} e^{i\mathbf{k}\cdot(\mathbf{R}_j - \mathbf{R}_i)} \alpha_{mj;\,ni} \quad (5)$$

where $\mathbf{R}_i$ is the position of the atom in the unit cell on which the orbital ϕ_n is located. The size of the H-matrix defined in (5) is determined by the number of atoms per unit cell and the number of atomic orbitals taken on each atomic site. For example, for a transition element with one atom per unit cell, the electronic structure can be adequately described by a 9×9 H-matrix, corresponding to one s function, three p functions and five d functions. For a crystal with two atoms per unit cell like antiferromagnetic chromium or hexagonal cobalt, the size of the matrix is doubled to 18×18.

Symmetry further simplifies the problem by reducing the number of independent interaction integrals, $\alpha mj;ni$. The relationships between them can easily be generated by applying operations of the symmetry group to the integrand in definition (5). Therefore, the higher the symmetry of the crystal, the less are the number of integrals to be determined. For example, there are only four independent *(d-d)* integrals between nearest neighbors in the bcc structure. Tables of these integrals can be found in reference 1.

The integrals are now treated as adjustable parameters to be determined from an *ab initio* calculation by a nonlinear least squares procedure described in the next section.

3. Determination of the Interaction Integrals

In the least squares procedure, we are required to minimize the following expression;

$$\sum_n \int d\mathbf{k} [\epsilon_n(\mathbf{k};\ \boldsymbol{\alpha}) - E_n(\mathbf{k})]^2 \quad (6)$$

where the $E_n(\mathbf{k})$ are the calculated *(ab initio)* energy band eigenvalues at wave vector $\mathbf{k}$, as from an APW or KKR calculation, and $\epsilon_n(\mathbf{k};\alpha)$ are the eigenvalues of the Hamiltonian matrix of eq (5) which is dependent on a number M of parametric integrals α_i, which we denote by a vector $\boldsymbol{\alpha}$. The eigenvalues ϵ_n and the corresponding eigenvectors $c_j^{(n)}$ satisfy the following equation:

$$\sum_j H_{ij}(\mathbf{k}, \boldsymbol{\alpha}) c_j^{(n)}(\mathbf{k}) = \epsilon_n(\mathbf{k}, \boldsymbol{\alpha})\ c_i^{(n)}(\mathbf{k}) \quad (7)$$

The minimization of expression (6) involves the solution of the set of equations;

$$\sum_n \int d\mathbf{k} \left\{ \epsilon_n(\mathbf{k}, \boldsymbol{\alpha}) - E_n(\mathbf{k}) \right\} \frac{\partial}{\partial \alpha_i} \epsilon_n(\mathbf{K}, \boldsymbol{\alpha}) = 0,$$

$$i = 1, 2 \ldots M \quad (8)$$

These are a set of nonlinear equations which cannot be solved directly, and must be solved by iteration. We first assume an initial approximate set of parameters $\boldsymbol{\alpha}_0$ and that ϵ_n is approximately linear in $\boldsymbol{\alpha}$. This leads to a set of equations;

$$\sum_j A_{ij} \{\alpha_j - \alpha_j^0\} = b_i \qquad i = 1, 2 \ldots M \quad (9)$$

where

$$A_{ij} = \sum_n \int d\mathbf{k} \left[\frac{\partial \epsilon_n}{\partial \alpha_i} \cdot \frac{\partial \epsilon_n}{\partial \alpha_j} \right]_{\alpha = \alpha_0}$$

and

$$b_i = \sum_n \int d\mathbf{k} \left[(E_n(\mathbf{k}) - \epsilon_n) \frac{\partial \epsilon_n}{\partial \alpha_i} \right]_{\alpha = \alpha_0}$$

Equation (9) is to be solved by matrix inversion for α_j until convergence is achieved.

The key quantities in the definition of the A-matrix and the b-vector are the derivatives of the eigenvalues ϵ_n with respect to the parameters. These are conveniently found by an application of the Hellman-Feynman theorem (see, for example, ref. 6), which in terms of our variables takes the form;

$$\frac{\partial \epsilon_n}{\partial \alpha} = \sum_{l,m} c^{(n)} \frac{\partial H_{lm}}{\partial \alpha} C_m^{(n)} \tag{10}$$

In the LCAO method the quantities $\partial H_{im}/\partial \alpha_i$ are particularly simple, as can be seen from eq (5) and the eigenvectors $C_m{}^{(n)}$ can be easily determined at the same time as the ϵ_n, so that there is no difficulty in evaluating the required derivatives.

The Hellman-Feynman theorem is also a useful tool for calculating derivatives with respect to other variables, such as the **k**-vector. The first derivative with respect to **k** is the velocity function, and its zeros are critical points which contribute discontinuities to the energy derivative of the density of states curve. There is also a formula for the second derivative [6] which although not as simple as the first derivative is still easily evaluated in terms of derivatives of the Hamiltonian matrix elements, i.e.,

$$\frac{\partial^2 \epsilon_n}{\partial \alpha^2} = \sum_{l,m} C_l^{(n)} D_{lm} C_m^{(n)}$$

$$D_{lm} = \frac{\partial^2 H_{lm}}{\partial \alpha^2} - \sum_{rs} \left[\frac{\partial M_{lr}}{\partial \alpha} m_{rs}^{-1} \frac{\partial M_{sm}}{\partial \alpha} \right] \tag{11}$$

where

$$M_{lr} = H_{lr} - E\delta_{lr}$$

and m^{-1} is the "partitioned inverse" of M, in which the n^{th} eigenvalue is partitioned off.

The second derivatives with respect to the **k**-vector are of course important in the evaluation of the electronic effective masses.

A summary of the calculational procedure is as follows:

(1) The parametric interaction integrals are determined by the nonlinear least squares procedure described by eqs (9), using the derivatives defined by eq (10). The number of *ab initio* eigenvalues $E_n(\mathbf{k})$ used in this procedure is small, on the order of 10^2.

(2) These integrals so determined are used in eq (5) to define the H-matrix, which is diagonalized to give the electronic energies $\epsilon_n(\mathbf{k})$ at a large number of **k**-points, typically on the order of $10^4 - 10^5$.

(3) The density of states curve is calculated from the energy function $\epsilon_n(\mathbf{k})$. This is done by means of an ordinary histogram method. Others have suggested the use of secondary interpolation, either linear [7] or quadratic [8], in order to save computational time. However, the linear scheme does not give the correct behavior around critical points and the quadratic scheme is in error near band crossings. The errors introduced may be small, but they are as yet unknown, and until a more satisfactory interpolation scheme is developed, we feel that the histogram method is adequate for our purposes, and not likely to introduce any errors other than statistical.

4. Application of the Method to the Density of States Curves for Chromium and Iron

As a first example, the method was applied to the Fe energy bands calculated by Wood [9], who used the APW method. The calculation of the Fe density of states based on these bands has been done before in two different ways, (1) by Mattheiss [10] who used a linear interpolation method and (2) by Cornwell et al., [11] who used the LCAO technique. The resultant curve, shown on figure 1, is qualitatively similar to these two previous calculations. The discrepancy between the three calculations is never more than 10% over the whole energy range, which gives us a reasonable degree of confidence in the accuracy of the method. The LCAO integrals calculated by the procedure described in section 3 are close to those of reference 11. The d integrals do not differ by more than .01 Ry. The discrepancy in the s and p integrals is larger, between .01 and .1 Ry, but these do not contribute strongly to density of states, so that this discrepancy is not reflected in a large discrepancy in the curve.

Taking a total of 84 eigenvalues from reference 9 (representing 6 energy bands on a cubic k-point mesh of spacing $\pi/2a$), a fit was obtained whose rms deviation was approximately .003 Ry. For all the calculations done on transition metals, the rms deviations were always of this order or better. (See table 1 for the details of the other calculations.) The LCAO matrix for the bcc structure is of order 9, since there are 5 d-type basis functions, 3 p-type and one s-type. All the interaction integrals are included up to the second nearest neighbors for a total of 27 different parameters. The density of states curve is a smoothed histogram over 1,785 nonequivalent points in 1/48 of the Brillouin zone (representing a cubic mesh of spacing $\pi/8a$, and

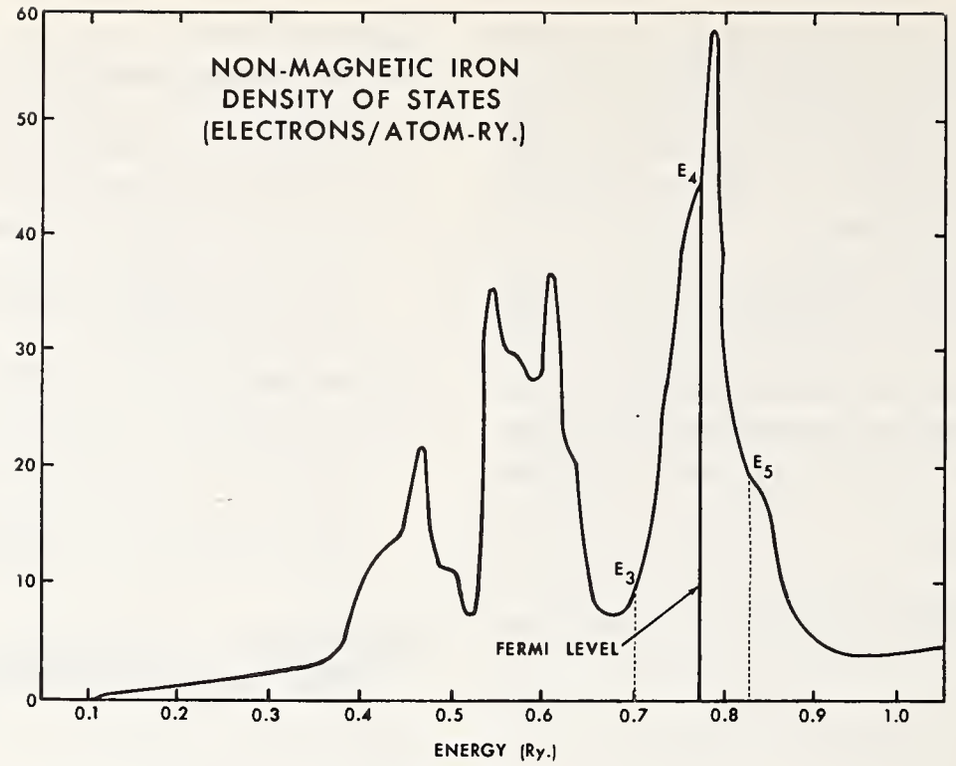

FIGURE 1. *The density of states for iron in its nonmagnetic state derived from the bands of ref.* [9].

E_3, E_4, and E_5 are the energies where the integral of the density of states equals 3, 4, and 5 respectively. E_4 is, therefore, the nonmagnetic Fermi level. E_3 and E_5 would be the minority and majority spin Fermi levels assuming a rigid band exchange splitting.

equivalent to 65,536 points in the entire zone).

A calculation was also done on ferromagnetic iron, in which the same method with the same number of parameters was applied to the energy bands calculated by the KKR method by Wakoh and Yamashita [12]. This calculation has also been done using the self-consistent APW method [13] and found to give virtually identical results. The resultant density of states curve is shown in figure 2. This was derived by doing two separate calculations on the two spin bands of reference 12, and superimposing the results. The density of states curve shown here is quite different from that shown in reference 12, due to the greater accuracy used in this calculation.

TABLE 1. *Parameters of the LCAO Calculations*

		Fe		Cr	
		Ferromagnetic			
	Non-magnetic	α	β	Non-magnetic	Antiferro-magnetic
Number of parameters	27	27	27	27	48
Number of energy eigenvalues used in least squares fit	84	84	84	154	83
RMS deviation (Ry.)	0.0034	0.0039	0.0014	0.0012	0.0009
Ab Initio bands taken from Ref. No.	9	12	12	15	15
Density of states at the Fermi level: Theoretical	47	18		12	9
Experimental (states/atom—Ry.)		[a]28		[b]13.4	[b]9.2

[a] Quoted in Ref. 12.
[b] Quoted in Ref. 15.

The photoemission data for Fe [14], which should provide a measure of the density of states curve, shows three peaks at energies .5, 1.1 and 2.1 eV below the Fermi level. These agree approximately with structure in the theoretical curve at .5, 1.0, and 2.4 eV. However, the other structure in the theoretical curve is not seen. The discrepancies with the experimental data are most likely due to a transition probability which is variable over the Brillouin zone, which is neglected in the analysis. This should be the subject of further investigation. Also, the structure is much sharper in the theoretical curve than in the experimental data, which may be a reflection of the effect of lifetime broadening.

The second example of the application of the LCAO method is a calculation on paramagnetic and antiferromagnetic chromium using the bands of Asano and Yamashita [15]. The calculation has been repeated using the self-consistent APW method [13] and found to give virtually identical results. The paramagnetic bands were fit using the 9×9 LCAO bcc matrix with the 27 first and second nearest neighbor integrals. In

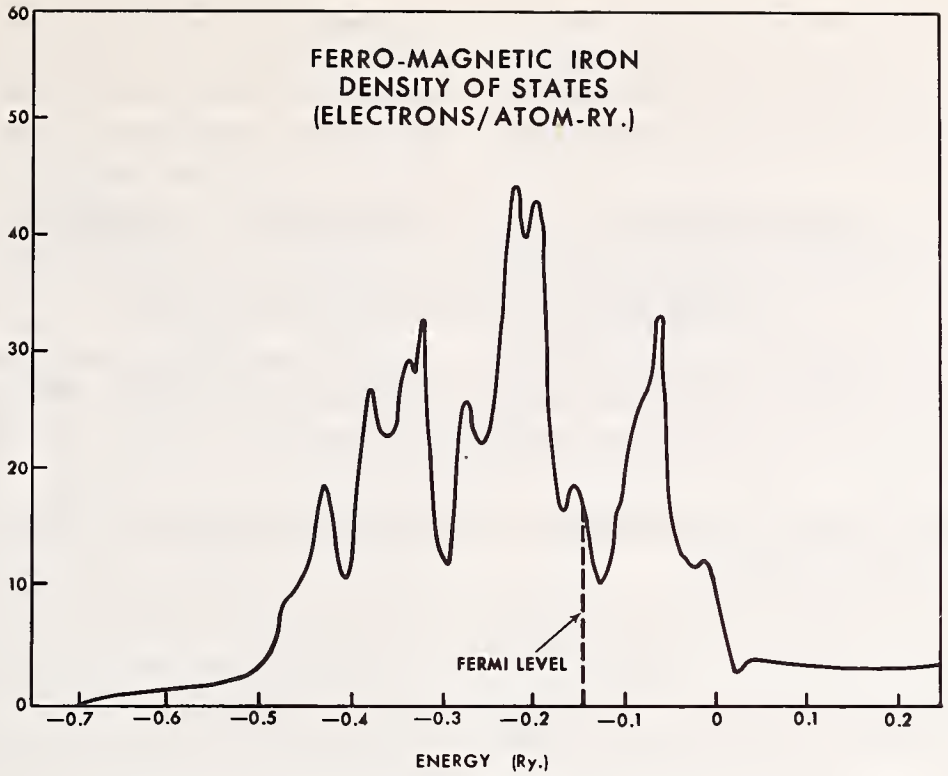

FIGURE 2. *The density of states for iron in its ferromagnetic state derived by superimposing the two spin bands of ref.* [12].

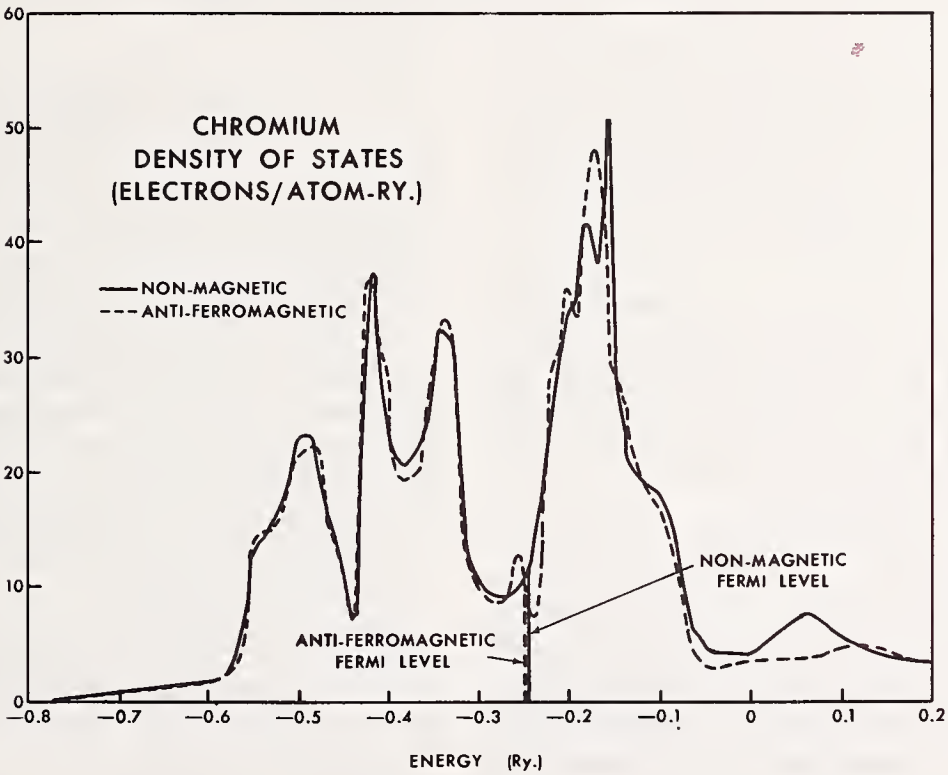

FIGURE 3. *The density of states for chromium in its nonmagnetic and antiferromagnetic states, derived from the bands of ref.* [15].
Note the drop in the density of states at the Fermi level due to the formation of the antiferromagnetic gap.

the antiferromagnetic state, the LCAO matrix doubles in size to accommodate two atoms per unit cell, one of each spin, the space group changes from body centered to simple cubic, identical to that for CsCl, and the number of integrals increases to 48. The two density of states curves are shown in figure 3. The main feature to be noted is that the two curves are virtually identical for the occupied electronic states, with the exception of the region immediately around the Fermi level. Because of the formation of an antiferromagnetic energy gap in the

bands on either side of the Fermi energy, the density of states is decreased. In this case, the decrease amounts to 25%, which compares favorably to the 30% decrease seen in the experimental electronic specific heat coefficients (cf. table 1).

The optical density of states derived from the photoemission data [14] shows structure at .4, 1.2 and 2.3 eV below the Fermi energy. The 0.4 eV structure is not seen in the theoretical curve, but the two agree with the theoretical peaks at 1.2 and 2.2 eV below the Fermi energy. Again, the discrepancies between the experimental and theoretical curves may be due to a variable transition matrix and lifetime broadening effects.

5. Discussion and Comparison with Other Interpolation Schemes

We have tried to show in the previous sections that the LCAO interpolation scheme is a straightforward, convenient and accurate way of representing an energy band structure, even when the electrons are not tightly bound.

Alternate methods, proposed by Hodges et al. [3] and Mueller [4], have assumed that the loosely bound conduction electrons must be described by orthogonalized plane wave (OPW's). This unnecessary dichotomy leads to difficulties in the hybridization terms in the Hamiltonian matrix. These terms involve interaction integrals between Bessel functions and atomic wave functions, which are not easily parametrized in terms of simple functions over **k**-space.

In reference 3, this difficulty was circumvented by the use of drastic approximation, i.e., by assuming the atomic *d*-orbitals were extremely localized (effectively δ-functions) and that the one-electron potential was constant over the unit cell. These two assumptions have the effect of eliminating the integral, but both of them are completely unjustifiable.

Another difficulty with the composite LCAO-OPW schemes is the large number of OPW's required to reproduce the conduction energy levels. Going just to nearest neighbors in bcc reciprocal space involves taking 13 OPW's, i.e., corresponding to $\mathbf{k}=(0,0,0)$ and 12 vectors of the type (1,1,0). Hodges et al., [3] found that for the fcc structure (which is the only structure to which the composite methods have as yet been applied) it was necessary to go to *second* nearest neighbors in reciprocal space, which would make a total of 15 OPW's. This difficulty, which would have required the solution of an unreasonably large secular equation, was avoided in reference 3 by using those 4 OPW's which have the lowest free-electron energies. However, by omitting the other 11, the symmetry of the eigenvectors is destroyed, thereby lifting the degeneracy of some of the eigenvalues. The introduction of arbitrary functions, referred to as "symmetrizing factors," which restores the proper degeneracies, still does not correct the errors in the eigenvectors. This is not too serious for the description of the energy band structure, but might lead to errors in the calculation of properties which depend on the wave functions. An accurate description of the OPW wave functions would also require a knowledge of the atomic core functions, since they determine the orthogonalization terms in the OPW.

Besides being free of the above difficulties, the LCAO method has other advantages: (1) It is easily extendable to more complicated structures with more than one atom per unit cell. Examples are the applications of the method to the intermetallic alloy β'NiAl [16] and the transition metal oxide ReO_3 [17]; (2) Spin-orbit effects can be inserted in a simple way [18], by the introduction of only one extra parameter for each nonzero *l*-value used in the basis functions; (3) The wave functions are easily calculable, since all that is necessary are the atomic valence orbitals without any need for the core functions, so that it may be possible to determine properties like the charge density and transition matrix elements from the results of an LCAO calculation.

6. References

[1] Slater, J. C., and Koster, G. F., Phys. Rev. **94**, 1498 (1954).
[2] Dresselhaus, G., and Dresselhaus, M. S., Phys. Rev. **160**, 649 (1967).
[3] Hodges, L., Ehrenreich, H., and Lang, N. D., Phys. Rev. **152**, 505 (1966); Ehrenreich, H., and Hodges, L., Methods in Computational Physics **8**, 149 (1968).
[4] Mueller, F. M., Phys. Rev. **153**, 659 (1967).
[5] Löwdin, P.-O., J. Chem. Phys. **18**, 365 (1950).
[6] Löwdin, P.-O., J. Mol. Spectry. **13**, 326 (1964).
[7] Gilat, G., and Raubenheimer, L. J., Phys. Rev. **144**, 390 (1966); Raubenheimer, L. J., and Gilat, G., Oak Ridge National Laboratory Report No. **TM-1425** (1966).
[8] Mueller, F. M., Garland, J. W., Cohen, M. H., and Benneman, K. H., (to be published).
[9] Wood, J. H., Phys. Rev. **126**, 517 (1962).
[10] Mattheiss, L. F., Phys. Rev. **139**, A1893 (1965). The Fe density of states curve is shown in his figure 11.
[11] Cornwell, J. F., Hum, D. M., and Wong, K. G., Phys. Letters **26A**, 365 (1968).
[12] Wakoh, S., and Yamashita, J., J. Phys. Soc. Japan **21**, 1712 (1966).
[13] Connolly, J. W. D., Intern. J. Quant. Chem. **S2**, 257 (1968).
[14] Eastman, D. E., J. Appl. Phys. **40**, 1387 (1969).
[15] Asano, S., and Yamashita, J., J. Phys. Soc. Japan **23**, 714 (1967).
[16] Connolly, J. W. D., and Johnson, K. H., these Proceedings, p. 19.
[17] Mattheiss, L. F., Phys. Rev. **181**, 987 (1969).
[18] Friedel, J., Lenglart, P., and Leman, G., J. Phys. Chem. Solids **25**, 781 (1963).

Optical Properties of Aluminum*

G. Dresselhaus and M. S. Dresselhaus**

Lincoln Laboratory, Massachusetts Institute of Technology, Lexington, Massachusetts 02173

D. Beaglehole***

Department of Physics and Astronomy, University of Maryland, College Park, Maryland 20742

The Ashcroft energy band model which provides a good representation of the measured Fermi surface of aluminum is used here to calculate the optical properties. New reflectivity measurements in aluminum have also been carried out between 2μ and 3000 A using a sensitive continuous frequency scanning technique. A Kramers-Kronig analysis of the reflectivity data yields a frequency dependent dielectric constant which is essentially in agreement with the results of the calculation. This comparison suggests that the optical properties of aluminum can be described in terms of a one-electron energy band model.

Key words: Aluminum (Al); dielectric constant; electronic density of states; interband transition; optical properties; pseudopotential.

The electronic properties of aluminum are in many ways among the simplest and best understood of all the common metals. In particular, the optical properties of aluminum can be accounted for over a wide energy range; below 0.1 eV the Drude theory works well [1] while at higher energies interband transitions become important. The dominant optical structure is a peak in ϵ_2 at $\sim$1.5 eV [2] for which the various experiments give values of 40 and higher [3]. Although the different measurements disagree on the magnitude of this main peak in ϵ_2, they agree on the energy at which ϵ_2 is a maximum. The existence of optical structure at 1.5 eV is also consistent with the various band models for aluminum [4,5]. In the intervening photon energy range $0.1 < \hbar\omega < 1.5$ eV, the Drude model has not been found to fit the data unless a frequency dependent relaxation time τ is introduced [1]. There is, however, no theoretical justification for this procedure.

This investigation was undertaken to determine whether these optical properties could be correlated with the extensive Fermi surface data that exist for aluminum [6,7]. The aim has been to achieve a quantitative fit to the measured optical constants, and to better understand the difficulties of the Drude model in the 0.1 to 1.5 eV range. Since there exist discrepancies in the literature concerning the magnitude of the peak in ϵ_2 at 1.5 eV and since the difficulty with the Drude model could arise from low energy interband transitions, careful reflectivity experiments were carried out, from which a Kramers-Kronig analysis gave the dielectric constant.

The correlation of these reflectivity measurements with Fermi surface data was aided by the pseudopotential energy band model of Ashcroft [8] which provides a good representation of the Fermi surface as determined by the de Haas-van Alphen measurements [7]. From the Ashcroft Hamiltonian, the frequency dependent dielectric constant for aluminum was calculated using k-dependent momentum matrix elements and a finite, though constant interband relaxation time. It has been found that for other materials such as germanium [9] and copper [10], phenomenological band models, which provide good agreement with experimental data at or near the Fermi energy, can be made to fit the measured $\epsilon(\omega)$ for photon energies within a few electron volts of the Fermi level. Such studies have shown that the dielectric constant is not only sensitive to the joint density of states but also to the k dependence of the momentum matrix elements.

For aluminum, there are two factors which make such a phenomenological approach attractive. First of all, the major optical structure occurs for low photon

*This work was sponsored by the Department of the Air Force.

**Also at Department of Electrical Engineering, MIT.

***Present address: Victoria University of Wellington, Wellington, New Zealand.

417-156 O - 71 - 4

energies, so that the bands near the Fermi surface are emphasized. Secondly, the electronic properties of aluminum seem to be well described by a nearly free electron band model; thus, a pseudopotential calculation requires a very small number of Fourier coefficients of the potential, while the Fourier expansion method requires only interacting s and p bands. For these reasons, aluminum appears to be a good candidate for studying the applicability of a one-electron theory to the optical properties of a metal.

In the present experimental study, greater sensitivity was achieved by a continuous reflectivity scanning technique [11], which provided reflectivity data between 2μ and 3000 Å. These data are very similar to those analyzed by Ehrenreich, Philipp and Segall [2], except for the presence of a reproducible shoulder at 1.2 eV and a small kink at 1.45 eV. A Kramers-Kronig analysis of the reflectivity data was carried out to yield the frequency dependent ϵ_1 and ϵ_2 curves. To extend the frequency range of the reflectivity data to be used in the Kramers-Kronig analysis, the present measurements were matched to Bennett's infrared data [1] and to Madden's ultraviolet data [12]. Finally, the high energy reflectivity slope beyond 20.0 eV was adjusted to agree with ellipsometry measurements in the neighborhood of 2.0 eV [13]. The results of the Kramers-Kronig analysis of the reflectivity data are shown for ϵ_2 and $\sigma_1 = \epsilon_2\omega/4\pi$ as the uppermost solid curves in figures 1 and 2 respectively. In order to display more clearly the low energy structure it is also convenient to plot the conductivity σ_1. To analyze these experimental results in terms of an energy band model, it is necessary to separate the total ϵ_2 or σ_1 into intraband and interband contributions. The results of one such separation are also shown in figures 1 and 2; it is this interband contribution to ϵ_2 and σ_1 that is directly compared with a dielectric constant calculation. With the intraband-interband separation shown here, the experimental interband peak in ϵ_2 at 1.5 eV has a magnitude of $\epsilon_2 = 52.0$.

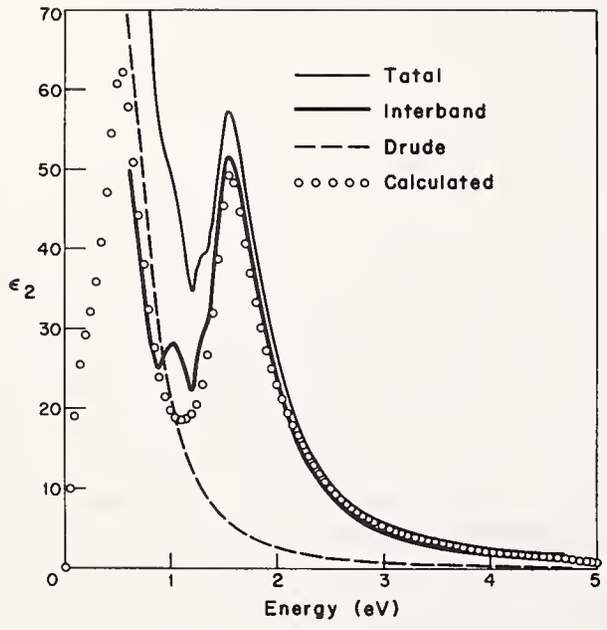

FIGURE 1. *Imaginary part of the dielectric constant ϵ_2 versus photon energy.*

The total ϵ_2 curve is obtained from a Kramers-Kronig analysis of the experimental reflectivity. The Drude contribution using the parameters $m_{opt} = 1.5$ and $\tau_{opt} = 0.5 \times 10^{-14}$ s is shown as a dashed curve. The resulting subtraction gives an experimental interband ϵ_2 shown as a dark solid curve. The open circles represent a calculation of the interband dielectric constant based on the Ashcroft model using an interband $\tau = 0.484 \times 10^{-14}$ s.

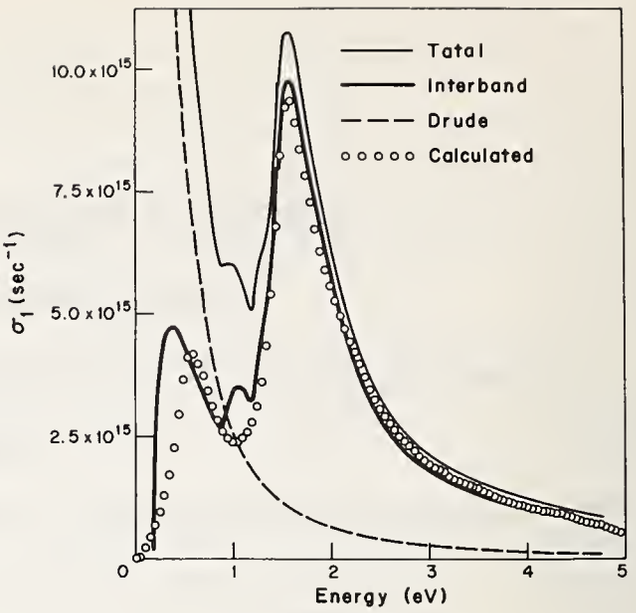

FIGURE 2. *Real part of the conductivity σ_1 versus photon energy.*

The decomposition of the total experimental σ_1 curve into the Drude and interband contributions is shown. The open circles represent the calculated interband conductivity and all parameters are the same as for figure 1.

An explicit dielectric constant calculation was carried out using the RPA expression for $\epsilon(\omega)$ [14]. Such a calculation involves an integration over the Brillouin zone of an expression depending on energy bands n and n' separated at wave vector k by $\hbar\omega_{nn'}$ and coupled through a momentum matrix element $P_{nn'}(k)$. Because of the difficulty in evaluating this integral, the computation must be carried out on a high speed electronic computer and a special effort must be made to calculate the energy levels $E_n(k)$ and momentum matrix elements $P_{nn'}(k)$ as rapidly and accurately as possible. This is efficiently accomplished through use of a model Hamiltonian. The momentum matrix elements $P_{nn'}(k)$ at every point k are calculated by differentiation of the model Hamiltonian with respect to k [9, 10]. Thus, the matrix elements are consistent with the energy band curvatures as expressed by the effective mass sum rule.

In this work, two model Hamiltonians were employed: the Ashcroft pseudopotential model [8] and the Fourier expansion band model [15]. The Ashcroft model for aluminum is based on 4 plane waves, result-

ing in a (4 × 4) model Hamiltonian involving 3 parameters which are evaluated to yield an accurate representation of the Fermi surface data. The model Hamiltonian for the Fourier expansion method also leads to a (4 × 4) matrix representing interacting s and p bands, and the Fourier expansion coefficients here are evaluated from Fermi surface data; these data are most conveniently expressed by the Ashcroft band model at the Fermi level. Because of the free electron character of the energy bands in aluminum, the Fourier expansion is not as rapidly convergent as it is for germanium [9] and copper [10] and third neighbor terms in the Fourier expansion were retained in order to achieve a good fit to the Fermi surface data. In the case of aluminum, the major advantage of the Fourier expansion technique in correlating very diverse experimental data over a wide range of energy and wave vector is not significantly exploited, since very scanty information is available away from the Fermi surface. Thus, the Fourier expansion technique mainly serves to re-express the Ashcroft band model so as to treat the symmetry properties of the Hamiltonian more correctly without increasing the size of the matrix. However, the proper use of symmetry is important in calculating matrix elements at a high symmetry point such as W. Therefore, it is of interest that the results of the dielectric constant calculation based on the Fourier expanded model Hamiltonian are in many ways similar to those based on the Ashcroft model Hamiltonian. In fact, this calculation demonstrates that the Fourier expansion technique can be made to work not only for energy bands amenable to a tight binding treatment, but also to nearly free electron energy bands.

Because of the greater simplicity of the Ashcroft Hamiltonian, a detailed comparison with the experimental data is given in this paper only for $\epsilon(\omega)$ based on the Ashcroft model. In the case of the Ashcroft band model, the momentum matrix elements were also calculated by differentiating the model Hamiltonian. This method is fully equivalent to taking matrix elements of the momentum operator between the plane wave basis states of the Ashcroft model. Because of the large contributions to the calculated $\epsilon_2(\omega)$ in the range $0.1 < \hbar\omega < 0.6$ eV (see the open circles in fig. 1), it was found more convenient to deal with $\sigma(\omega)$ rather than with $\epsilon(\omega)$. The results calculated for σ_1 are shown as open circles in figure 2. A value of $\tau_{interband} \cong 0.5 \times 10^{-14}$ sec for the interband relaxation time yielded good agreement with the observed magnitude of the peak in ϵ_2 (or σ_1) at 1.5 eV. This peak in ϵ_2 arises from interband transitions in the vicinity of the K or U points in the Brillouin zone. In addition, the calculation exhibits a low energy peak in ϵ_2 below 0.8 eV, arising from interband transitions occurring near the W point. Because of the large uncertainty in the experimental determination of the low energy interband contribution to σ_1, it is difficult to compare theory and experiment in this region. At slightly higher energies, a small shoulder is found in the experimental data at 1.2 eV and a small kink at 1.45 eV. In this work, the Monte Carlo dielectric constant calculation was carried out to sufficient accuracy to show that the Ashcroft band model yields no such structures at 1.2 and 1.45 eV.

The intraband contributions to the conductivity were treated in terms of the Drude model. A satisfactory overall fit to both $\sigma_1(\omega)$ and $\sigma_2(\omega)$ could be accomplished using a constant relaxation time τ_{opt} in the Drude model, with τ_{opt} in the range, $\tau_{opt} = (0.5 \pm 0.2) \times 10^{-14}$ sec; the range of values found for the optical mass was $m^*_{opt} = 1.5 \pm 0.15$. An example of the kind of fit that was obtained for the interband contribution to σ_1 and σ_2 is shown in figures 2 and 3 respectively where the curves are derived from the experimental data and the open circles from the energy band model. Because of the very large amplitude of the intraband contribution to σ_2, it is not convenient to display both the intraband and interband contributions to σ_2 in the same figure. The quoted errors in Drude parameters reflect the range over which the parameters could be varied without significantly changing the quality of the fit to the experimental data. The availability of more accurate experimental data in the difficult energy range $0.1 < \hbar\omega < 0.6$ eV in aluminum would serve to narrow the uncertainty in the Drude parameter determination. The strong interband absorption that appears below 1 eV in both figures 2 and 3 provides the reason for the failure

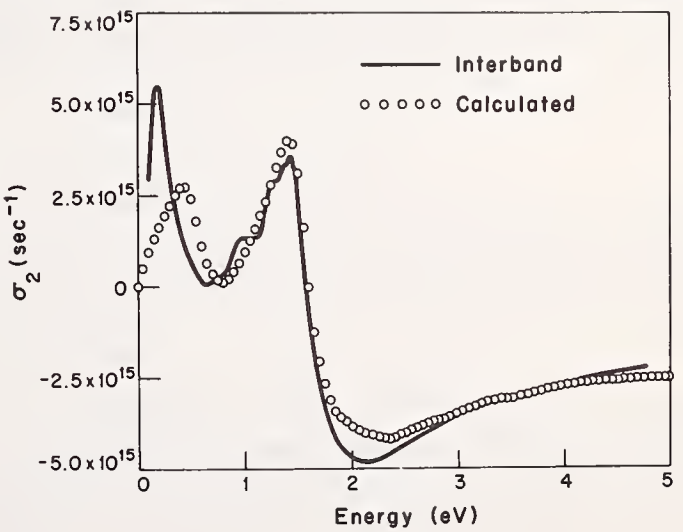

FIGURE 3. *Imaginary part of the conductivity, σ_2 versus photon energy.*

The curve represents the experimental interband contribution whereas the open circles are corresponding calculated values. All parameters are the same as for figure 1.

of a model based only on intraband contributions to the conductivity in this energy range.

The approximate equality of τ_{opt} and $\tau_{interband}$ is also of interest. Since the dominant contributions to the interband conductivity arise from states near the Fermi surface, it is largely the same states which participate in both the intraband and interband transitions. Thus, a temperature dependence of both τ_{opt} and $\tau_{interband}$ could be anticipated. It is also of interest to note that $\tau_{interband}$ for aluminum is significantly smaller than the corresponding room temperature value $\tau_{interband} = 2 \times 10^{-14}$ sec found for silicon and germanium through a similar dielectric constant calculation [9].

One outstanding puzzle which remains in this analysis is the value of $m^*_{opt} = 1.5$. Because of the nearly free electron character of the aluminum energy bands, a value close to unity would be expected for m^*_{opt}. One estimate for m^*_{opt} based on a one-electron energy band model has been made by Ehrenreich et al. [2] yielding $m^*_{opt} = 1.2$ as an upper limit. Even with this maximum value of m^*_{opt}, it is not possible to satisfactorily reproduce the reflectivity data.

In summary, the 4 plane wave Ashcroft energy band model for aluminum [8] has been used to calculate the optical properties in the energy range below 5 eV. Our recent experimental measurements are generally in good agreement with the calculated dielectric constant above 1.4 eV. In the range $0.8 < \hbar\omega < 1.4$ eV, structure is found experimentally, but is not well correlated with any structure in the theoretical curves. In the region below 0.8 eV, the band model suggests additional structure; however, the experimental data are not sufficiently accurate either to corroborate or to conflict with predictions of the band model. The free electron or intraband contribution to $\epsilon(\omega)$ is satisfactorily fit by the Drude expression with constant τ_{opt} over the entire energy range of the dielectric constant calculation; however, the optical mass parameter m^*_{opt} though consistent with other experimental determinations [2], is too large to be understood simply on the basis of a nearly free electron model.

On the basis of this dielectric constant calculation, it is concluded that the optical properties of aluminum can well be described by a one-electron energy band model for this material.

Acknowledgment

The authors would like to thank Dr. W. J. Scouler for many useful discussions.

References

[1] Bennett, H. E., Silver, M., and Ashby, E. J., J. Opt. Soc. Am. **53**, 1089 (1963).
[2] Ehrenreich, H., Philipp, H. R., and Segall, B., Phys. Rev. **132**, 1918 (1963).
[3] Beaglehole, D. (unpublished).
[4] Beeferman, L. W., and Ehrenreich, H. (to be published).
[5] Hughes, A. J., Jones, D., and Lettington, A. H., J. Phys. C. **2**, 102 (1969).
[6] Moore, T. W., and Spong, F. W., Phys. Rev. **125**, 846 (1962); **126**, 2261 (E) (1962); Kamm, G., and Bohm, H. V., Phys. Rev. **131**, 111 (1963).
[7] Priestley, M. G., Phil. Mag. **7**, 1205 (1962).
[8] Ashcroft, N. W., Phil. Mag. **8**, 2055 (1963).
[9] Dresselhaus, G., and Dresselhaus, M. S., Phys. Rev. **160**, 649 (1967).
[10] Dresselhaus, G., Solid State Communications **7**, 419 (1969).
[11] Beaglehole, D., Applied Optics **7**, 2218 (1968).
[12] Madden, R. P., Canfield, L. R., and Hass, G., J. Opt. Soc. Am. **53**, 620 (1963).
[13] Hass, G., and Waylonis, J. E., J. Opt. Soc. Am. **51**, 719 (1961).
[14] Ehrenreich, H., and Cohen, M. H., Phys. Rev. **115**, 786 (1959).
[15] Dresselhaus, G., and Dresselhaus, M. S., "Optical Properties of Solids," Proceedings of the International School of Physics "Enrico Fermi," J. Tauc, Editor (Academic Press, N.Y., 1966).

Discussion on "Optical Properties of Aluminum" by G. Dresselhaus, M. S. Dresselhaus (MIT), and D. Beaglehole (University of Maryland)

K. H. Johnson *(MIT):* Is it possible that the anomalous skin effect could account for some of the deviation from the Drude theory in the low energy region?

M. Dresselhaus *(MIT):* If that were an important effect, one would also expect significant departures from the Drude approach below 0.1 eV; but it works very well there. It is only in the energy region about 0.5 eV, where we think there is a low energy interband transition, that there is a breakdown in the Drude picture.

C. Powell *(NBS):* What is the reason for the difference in the magnitude of the interband ϵ_2 calculated here and that calculated by Ehrenreich, Phillipp and Segall in 1963?

M. Dresselhaus *(MIT):* For one thing, they used a different energy band model. But more important is the second factor. In the early days, when people did this type of calculation, they did not realize the importance of included **k** dependence in the momentum matrix elements. In the meantime, we have learned how important this **k** dependence is and it is very important for aluminum. I should like to add that when this calculation was first made by Ehrenreich et al. it represented an important contribution to the understanding of the optical properties of metals.

G. W. Pratt *(MIT):* I gather you choose the relaxation time to give you a best fit to the data?

M. Dresselhaus *(MIT):* I assume that you are talking about the interband relaxation time. The choice of that quantity regulates the height of the peaks in the dielectric constants. You have the liberty of adjusting one relaxation time and with this value of the interband relaxation time you have to fit all the peaks in both ϵ_1 and ϵ_2. You don't have as much freedom as you might think. The relaxation time is the only adjustable parameter in the whole interband dielectric constant calculation. All parameters of the Ashcroft band model are determined by the Fermi surface data.

G. W. Pratt *(MIT):* How sensitive is it to the choice of the relaxation time?

M. Dresselhaus *(MIT):* If you change the relaxation time by an order of magnitude, you will perhaps change the height of the peaks by about a factor of 2.

F. M. Mueller *(Argonne National Lab.):* You used the local pseudopotential model of Ashcroft. How important are non-local corrections far away from the Fermi surface?

M. Dresselhaus *(MIT):* The dielectric constant of aluminum in this energy range is not very sensitive to energy bands far from the Fermi surface. Aluminum is one material for which you would not expect large non-local corrections to the pseudopotential near the Fermi surface. I should also like to say that if you use a model with the proper symmetry (which the Ashcroft model does not display), the electron bands far from the Fermi level change somewhat. However, with his values of the parameters, the details of the energy bands at very high energies do not seem to be very important for the determination of the optical constants in the energy range below 5 eV. For aluminum, we find that if you have a good fit to the Fermi surface you also get a good fit for the optical data. I don't say that this will hold for all other materials. Aluminum has this nice property and for this reason is an attractive material for testing the validity of a one-electron energy band model.

F. Herman *(IBM):* We did a self-consistent OPW calculation for aluminum. We found remarkable agreement with the Ashcroft model for the entire region below the Fermi surface extending up to 5 volts above. For energies greater than 5 volts above the Fermi surface significant deviations arose.

M. Dresselhaus *(MIT):* At high energies, where $E(k)$ is free-electron like in the Ashcroft model, something is clearly wrong. However, the optical constants below 5 eV are not sensitive to the energy bands far from the Fermi energy.

J. R. Anderson *(Univ. of Maryland):* We have completed dHvA experiments in aluminum primarily on the 2nd band hole surface and determined slightly different parameters for the Ashcroft model. It appears as if we can exhibit 1.2 eV and 1.4 eV structure from our energy bands.

M. Dresselhaus *(MIT):* Our calculations showed little or no theoretical evidence for such structure.

On the Optical Properties and the Density of States in Arsenic*

R. W. Brodersen and M. S. Dresselhaus*****

Department of Electrical Engineering and Center for Materials Science and Engineering, Massachusetts Institute of Technology, Cambridge, Massachusetts 02139

The infrared reflectivity of arsenic is calculated and correlated with Fermi surface, magnetoreflection and optical reflectivity measurements. These infrared properties are strongly affected by interband transitions across a small spin-orbit induced bandgap. The unusually large intensity of this interband transition for light incident along the trigonal direction is due to the simultaneous occurrence of a strong interband momentum matrix element and a large density of states. By considering this interband transition explicitly, good agreement is obtained with the experimental data of Riccius.

Key words: Arsenic (As); electronic density of states; Fermi surface; interband transition; Landau levels; magneto-reflection.

The optical properties of arsenic have been studied over most of the photon energy range $0.02 < \hbar\omega < 21$ eV [1,2]. Because of the difficulty in preparing suitable optical faces, these studies have been mainly confined to measurements on the trigonal face, which is a cleavage plane in arsenic. The experimental reflectivity results for this face are plotted in figure 1 as a function of log $(\hbar\omega)$ in order to clearly illustrate the dominant structure at infrared frequencies. The data in this figure below 0.32 eV were taken by Riccius [2] and above 1 eV by Cardona and Greenaway [1]; data have not been reported in the region $0.32 < \hbar\omega < 1$ eV. These measurements are also incomplete with respect to crystal orientation because the rhombohedral symmetry of arsenic results in anisotropic optical constants.

Although the optical measurements are still incomplete, very extensive Fermi surface studies have been carried out [3-10]. Based on these Fermi surface measurements, Lin and Falicov have constructed an energy band model [11] which characterizes the Fermi surface very well. Their Fermi surface for the holes around the T point in the Brillouin zone is shown in figure 2. The large turnip-shaped pockets of this figure are designated as the α carriers while the 6 necks connecting the turnips contain the γ carriers. To achieve the charge compensation characteristic of semimetals, an equal number of β carriers is required, and the Lin-Falicov model places these in 3 nearly ellipsoidal pockets about the L points of the Brillouin zone.

Additional information on the energy bands near the Fermi surface has been obtained from a series of magnetoreflection experiments [12,13]. These experiments

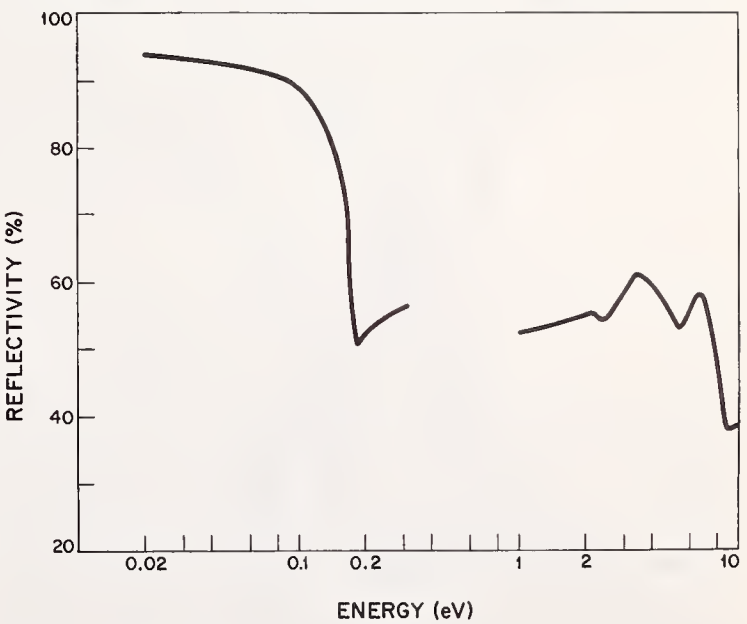

FIGURE 1. *Reflectivity data of arsenic for the trigonal face versus photon energy.*

The data between $0.02 < \hbar\omega < 0.32$ eV is from Riccius (ref. [2]) and between $1 < \hbar\omega < 10$ eV from Cardona and Greenaway (ref. [1]).

*Work supported in part by the Advanced Research Projects Agency under Contract No. SD-90.

**NSF graduate fellow.

***Also at MIT Lincoln Laboratory, which is supported by the U.S. Air Force, and a visiting scientist, Francis Bitter National Magnet Laboratory, Massachusetts Institute of Technology, Cambridge, Mass., with support from the U.S. Air Force Office of Scientific Research.

indicate that spin-orbit interaction might be important in understanding certain features of the infrared properties of arsenic [13]. In the magnetoreflection experiment, interband Landau level transitions are observed across a small bandgap of 0.172 eV attributed to the spin-orbit splitting of two bands which could otherwise cross. The symmetry properties of these transitions together with the values of the observed bandgap and cyclotron effective mass (**H** || trigonal direction) all contribute to the identification of this series of interband Landau level transitions with the γ carriers of the hole Fermi surface. The energy extrema for both the conduction and valence bands are along the Q or binary axis, but close to the T point [11]. Because of the low symmetry on the Q axis, the energy extrema for these strongly coupled bands need not occur at the same Q point as is indicated on figure 3. The magnetoreflection data associated with this small bandgap are well explained by the Lax two-band model [13].

Since the dominant structure in the optical reflectivity of figure 1 occurs at ~0.18 eV, it is of interest to seek a connection between this edge and the interband transition across the 0.172 eV bandgap. The present work explores this connection. For many small gap materials (e.g. InSb, Ge), the frequency dependent dielectric constant is only slightly affected by interband transitions across bandgaps in the infrared. The reason for this is closely related to the small density of states usually associated with these small bandgaps. In semiconductors like InSb and Ge, the strong interband coupling and small bandgaps result in small effective masses (large band curvatures) and a small density of states. Thus, only a small volume of the Brillouin zone is involved in these low photon energy transitions and only a small effect on the optical properties results. At larger photon energies, large volumes of the Brillouin zone participate in interband transitions and these interband transitions have a much larger influence on the optical properties.

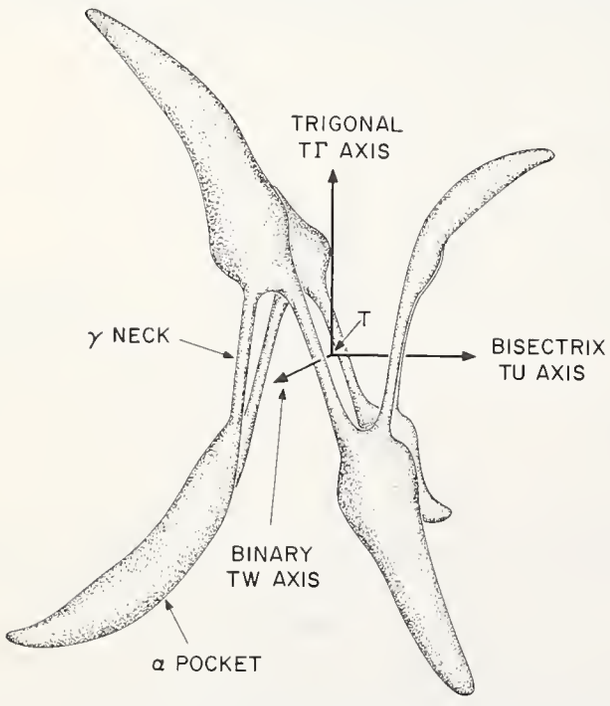

FIGURE 2. *Hole Fermi surface of arsenic as determined by Lin and Falicov (ref. [11]).*

The situation in arsenic is somewhat different from that in most small bandgap materials. Magnetoreflection measurements show that strong band coupling occurs for momentum matrix elements in the binary-bisectrix plane; however, these two bands are expected to be only weakly coupled through momentum matrix elements in the trigonal direction [14]. The strong coupling in the binary-bisectrix plane produces a large oscillator strength for interband transitions when light is incident along the trigonal direction. On the other hand, the weak coupling in the trigonal direction results in large effective mass components m_{zz} for both the valence and conduction bands. In fact, instead of repelling one another, the energy bands in this direction are nearly parallel for a small range of k values around the critical point. It is this feature of the energy bands that gives rise to a large increase in the joint density of states and makes arsenic different from other small gap materials. The unusual occurrence of both a large oscillator strength and a large density of states serves to emphasize this low frequency interband transition in the optical properties of arsenic.

The joint density of states is thus of great importance in determining the magnitude of interband contributions to the dielectric constant. Fermi surface measurements provide some information on the density of states for the occupied bands. The electrons which have a total concentration of $2.1 \times 10^{20}/\text{cm}^3$ are contained in 3 nearly ellipsoidal surfaces around the L points in the Brillouin zone. Using the cyclotron effec-

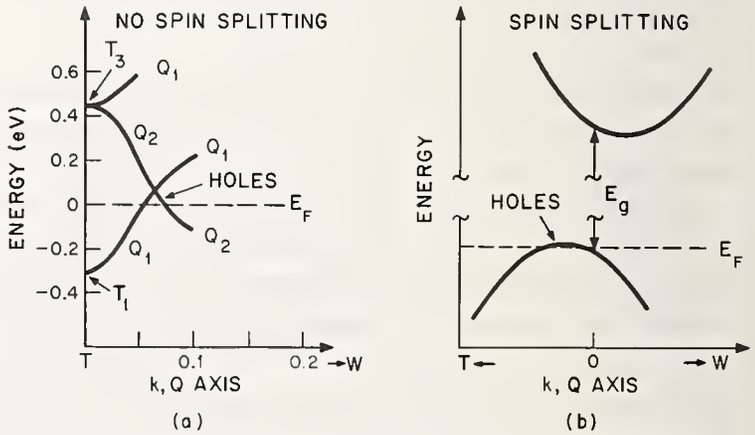

FIGURE 3. *Energy bands along the binary or Q-axis near the γ carriers.*

(a) The energy bands calculated by Lin and Falicov, not including the spin-orbit interaction. (b) An enlarged view of the region near the accidental degeneracy with spin-orbit coupling taken into account.

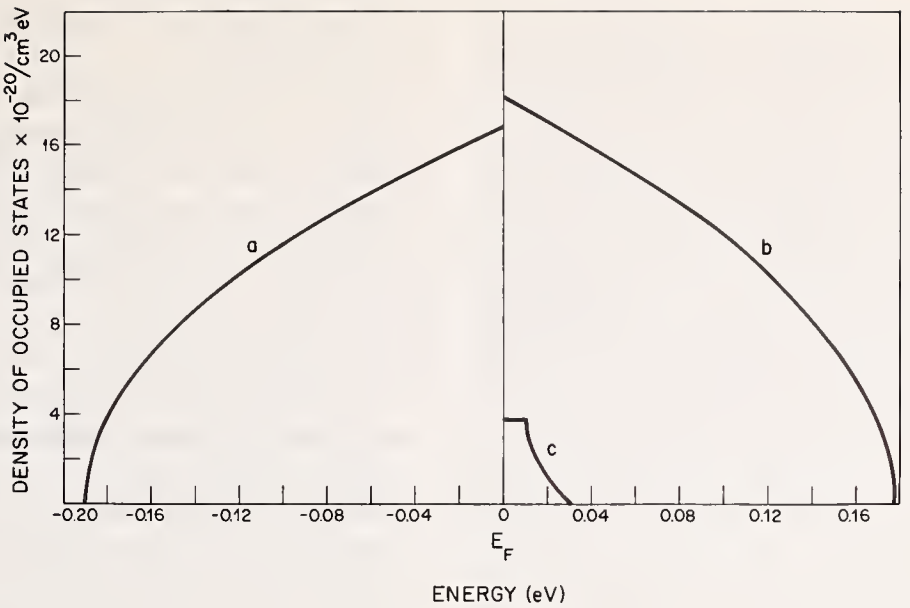

FIGURE 4. *Density of states for the various carrier pockets versus energy measured from the Fermi level.*

Curve *a* is for the electrons at the *L* points, curve *b* is for the α hole pockets and curve *c* is for the hyperboloidal γ necks.

tive mass parameters obtained from de Haas-van Alphen data [8], and assuming an ellipsoidal Fermi surface, the density of states curve shown in figure 4 is obtained. A qualitative density of states curve for the holes can be constructed by approximating the turnip-shaped hole constant energy surfaces by ellipsoids. The best ellipsoidal fit is determined from the de Haas-van Alphen data by taking the best extrapolated values of the extremal periods as the principal ellipsoids, even though the former are not 90° apart [8]. Finally, the density of states for the minority holes, the γ carriers, can be found by approximating the constant energy surfaces by hyperboloids as shown in figure 2. The boundary between the α and γ carriers provides a cutoff for the γ-carrier hyperboloids. An explicit value of k_z for this cutoff is found from the pseudopotential calculation of Lin-Falicov [11]. The density of states curves for the hole carriers are shown in figure 4. Although the number of carriers in the γ necks is only ~ 2% of the total hole carrier concentration of $2.1 \times 10^{20}/\text{cm}^3$, their relatively large density of states near the Fermi surface results in a greater importance than their relatively small numbers would seem to indicate.

In the present work an attempt is made to correlate the infrared measurements with the Fermi surface data, the magnetoreflection data and the optical data beyond 1 eV. The frequency-dependent dielectric constant is calculated using the expression of Ehrenreich and Cohen [15]:

$$\epsilon_{\alpha\beta} = \epsilon_{\text{core}} + \epsilon_{\text{intraband}} + \epsilon_{\text{interband}}$$

where

$$\epsilon_{\text{interband}} = -m_0^{-1}\left(\frac{e}{\pi}\right)^2 \times \int d\mathbf{k} \sum_{n,n'}{}' f_n(\mathbf{k}) f_{\alpha\beta n'n}\left(\omega - \omega_{nn'} + \frac{i}{\tau_{nn'}}\right)^{-1}\left(\omega + \omega_{nn'} + \frac{i}{\tau_{nn'}}\right)^{-1}. \quad (1)$$

In this expression $f_n(\mathbf{k})$ is the Fermi distribution function, $\tau_{nn'}$ is an interband relaxation time, and the oscillator strength $f_{\alpha\beta n'n}$ is related to the momentum matrix elements $P_{nn'}{}^i$ coupling bands n and n' by

$$f_{\alpha\beta n'n} = \left(\frac{2}{m_0 \hbar \omega_{n'n}}\right) P^{\alpha}_{n'n} P^{\beta}_{nn'}$$

where $\hbar\omega_{nn'}$ is the energy separation between bands n and n'. The integration is over all k states in the Brillouin zone; because of the presence of the Fermi function, the summation over band indices n,n' involve only transitions from occupied to unoccupied states. The intraband contribution $\epsilon_{intraband}$ is treated by a Drude model for the α, β and γ carriers. An explicit evaluation of the intraband term then depends on the various carrier densities, optical effective masses, relaxation times and core dielectric constant. Most of these quantities are known from other measurements on arsenic.

As a first approximation to the arsenic infrared reflectivity calculation, all interband transitions were

treated as frequency independent through a core dielectric constant. This would be a good approximation if all the important interband transitions occurred at photon energies much greater than 0.32 eV, the upper limit of the available infrared data. With this very simple treatment, the core dielectric constant is estimated from the optical reflectivity at high energies. From the reflectivity data of figure 1, we would estimate ϵ_{core} to be in the range $60 \lesssim \epsilon_{core} \lesssim 80$. The effective mass tensors and carrier densities for the various carriers are known from Fermi surface data [8]. Thus, only the relaxation times in the Drude theory remained to be determined. These intraband relaxation times were found by fitting to the reflectivity data below 0.08 eV. Using these parameters in the Drude model, the reflectivity curve (b) of figure 5 is calculated which is in rough agreement with the infrared measurements of Riccius [2].

A somewhat better fit to the experimental data is obtained by carrying out a least squares fit to the parameters of the Drude model and the results are shown as curve (c) in figure 5. The relaxation times used for the α, β and γ carriers in constructing this figure are $\tau_\alpha = 1 \times 10^{-14}$ sec and $\tau_\beta = 2 \times 10^{-14}$ sec with $\tau_\gamma = \tau_\alpha$. The fit is not significantly altered by also constraining τ_α to equal τ_β. These relaxation times are consistent with room temperature values for τ found in other materials. Because of the high reactivity of the arsenic surfaces, the possibility of the formation of an oxide layer was considered. A slightly better fit to the reflectivity data, particularly in the low photon energy range, was found for an oxide layer reducing the reflectivity by 2.5%, and the three calculated curves in figure 5 include this 2.5% reduction.

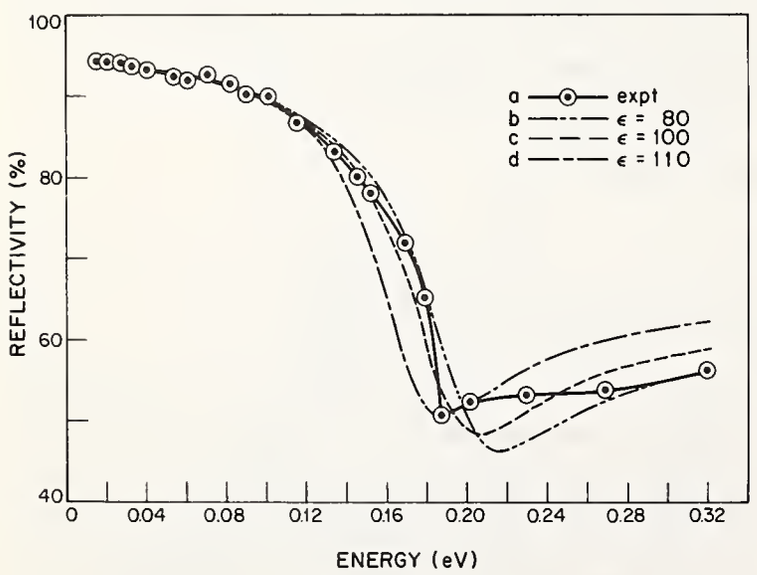

FIGURE 5. *Reflectivity of arsenic for a trigonal face versus photon energy.*

Curve (a) is the line drawn through the data of Riccius (ref. [2]). Curves (b), (c), and (d) show the calculated reflectivity including only the Drude and core contributions to the dielectric constant for several values of ϵ_{core}.

The most sensitive parameter in the least squares fitting procedure used to construct figure 5 is the core dielectric constant. It determines the photon energy of the reflectivity minimum and the magnitude of the reflectivity above $\approx$0.25 eV. The best least squares fit was found for a core dielectric constant of 100, which is the value used in curve (c) of figure 5. On the other hand, to yield a reflectivity minimum at $\hbar\omega = 0.19$ eV a value of $\epsilon_{core} = 110$ is required and the resulting reflectivity curve is shown in figure 5 as curve (d). These values of ϵ_{core} are considerably larger than that suggested by the high frequency reflectivity data and indicate that other interband transitions have been neglected that are, in fact, important at infrared frequencies. Furthermore, the three calculated curves of figure 5 show that by a judicious choice of ϵ_{core} it is possible to fit some particular feature of the reflectivity but that no values of the Drude parameters can be found to fit the shape of the reflectivity curve near the reflectivity minimum. It is clear from this figure that the interband transition across the spin-orbit induced bandgap at the Q point must be included explicitly in order to yield the sharp structure observed experimentally.

In order to calculate $\epsilon_{interband}$ associated with the interband transitions across the small bandgap at Q, several additional parameters must be evaluated; they are the energy bandgap E_g, the interband momentum matrix element coupling these bands $P^{\alpha}_{nn'}$, the unoccupied conduction band effective mass tensor, the Fermi energy and the interband relaxation time $\tau_{interband}$. Many of these parameters are either known from other measurements or can at least be estimated. For example, the magnetoreflection experiments not only provide a value for $E_g = 0.172$ eV, but also show that the two strongly coupled bands at the Q point can be described by a Lax model [13]. Therefore, the interband momentum matrix elements of eq (1) and the effective mass tensor for the unoccupied conduction band can be found from Fermi surface effective mass data. This type of approach is expected to yield reliable values for the large momentum matrix elements and for the light mass components of the unoccupied band. However, only estimates can be obtained for the small momentum matrix elements and the heavy mass components [16].

The effective mass tensor for the valence band is known from Fermi surface measurements [8]. This tensor, or more conveniently the valence band inverse effective mass tensor α^{v}_{ij}, can be related to the momen-

tum matrix elements with Q point symmetry through the two-band model, yielding

$$\alpha^v_{xx} = 1 - 2|P^x_{c1,v1}|^2/m_0E_g \tag{2a}$$

$$\alpha^v_{yy} = 1 - 2|P^y_{c1,v2}|^2/m_0E_g \tag{2b}$$

$$\alpha^v_{zz} = 1 - 2|P^z_{c1,v2}|^2/m_0E_g \tag{2c}$$

$$\alpha^v_{yz} - 2\,\mathrm{Re}\,(P^y_{c1,v2}\,P^z_{v2,c1})/m_0E_g \tag{2d}$$

$$\alpha^v_{xz} = \alpha^v_{xy} = 0 \tag{2e}$$

in which the momentum matrix elements employ a superscript to denote the direction of the momentum operator, subscripts v and c to denote valence and conduction bands, respectively, along with indices 1 and 2 to denote the two spin states. In these equations, all quantities are evaluated at the band extrema and the x, y and z directions correspond to the binary, bisectrix and trigonal axes, respectively. Since both α^v_{zz} and α^v_{yz} depend upon the same matrix element $P^z_{v2,c1}$ (and similarly for α^v_{yy} and α^v_{yz} which depend on $P^y_{c1,v2}$), an experimental determination of the effective mass tensor of the occupied valence band tests the validity of the two-band model in both the strong and weak coupling directions. Fermi surface data for the γ necks [8] indicate that the Lax two-band model is applicable in both strong and weak coupling directions.

From eqs (2), the momentum matrix elements about the Q point are evaluated. However, completely analogous equations can be written for the conduction band inverse effective mass parameters α^c_{ij} under the transformation $c \leftrightarrow v$, and the $-$ sign in eqs (2a), (2b) and (2c) into a $+$ sign. In this way, all momentum matrix elements as well as the conduction band effective mass tensor can be estimated. Explicit values used for these momentum matrix elements are $|P^x_{c1,v1}|^2 = 10\,m_0E_g$, $|P^y_{c1,v2}|^2 = 30\,m_0E_g$, and $|P^z_{c1,v2}|^2 = 0.8\,m_0E_g$.

The evaluation of the dielectric constant involves an integration over k space. This integration was carried out in the volume of k space for which the two-band model is valid. Contributions from other regions of the Brillouin zone are treated through a core dielectric constant ϵ_{core}. In the z direction, the limit of integration is taken as the boundary of the γ neck with the α pocket, which is at $\sim 5.2 \times 10^{-2}$ a.u. [11]. In the x-y plane, the limit of integration is taken as the midpoint between adjacent γ necks, leading to a cutoff energy of $\sim$0.3 eV. Over the volume of the k space integration, the nonparabolic enhancement of the momentum matrix elements as given by the two-band model is never greater than 15%. Therefore, the k dependence of these momentum matrix elements can be neglected. Furthermore, the small displacement in k space of the two-band extrema was neglected in accordance with the Lax model approximation [13].

An estimate for the remaining parameter $\tau_{interband}$ is available from the width of the magnetoreflection resonances, yielding $\tau_{interband} \approx 10^{-13}$ sec at low temperatures [13]. The shape of the calculated reflectivity curve is rather insensitive to the precise value of $\tau_{interband}$ provided that the condition $\omega\tau_{interband} \gg 1$ is satisfied [17]. This condition does seem to be satisfied according to the results of this reflectivity calculation. Because of the scanty data available near the reflectivity minimum only an estimate for $\tau_{interband}$ can be made from the reflectivity data.

To carry out the integration over $\mathbf{k}$ space explicitly, nonparabolic effects in the energy were also neglected. This is a valid approximation because of the small size of the volume of integration and the small range of band energies that are involved. Thus, the valence band energy E_v in the vicinity of the band extremum at Q can be expressed in terms of the principal axis coordinate system of the hyperboloidal constant energy surfaces as

$$E_v = -\frac{\hbar^2}{2m_0}\,(\alpha_{x'}k^2_{x'} + \alpha_{y'}k^2_{y'} - \alpha^v_{z'}k^2_{z'}) \tag{3}$$

in which the k vector is measured relative to the critical Q point and the inverse effective mass tensor $\alpha_{i'}$ is written in the principal axis coordinate system. For simplicity, a similar expression was assumed for the constant energy surfaces in the conduction band, characterized by the same inverse effective mass components $\alpha_{x'}$ and $\alpha_{y'}$ in the light mass directions, but a different $\alpha_{z'}{}^c$ parameter in the heavy mass direction. However, the constant energy surfaces for the conduction band are ellipsoids not hyperboloids. With these simplifications, the integration of eq (1) can be carried out explicitly yielding an analytic, though complicated, expression in closed form. The real and imaginary parts of the dielectric constant $\epsilon_{interband}$ obtained in this way are shown in figure 6.

With this determination of $\epsilon_{interband}$, the infrared reflectivity of arsenic was calculated, yielding good agreement with the experimental data [2]. In this case, a reasonable value of $\epsilon_{core} = 80$ produced a reflectivity minimum at 0.19 eV and a much better fit to the reflectivity lineshape was achieved. It is in fact $\epsilon_{interband}$ that provides the difference between this value of ϵ_{core} and the larger values of ϵ_{core} that were required to fit particular features of the experimental data in figure 5. Once again, the measurements could be brought into better agreement with the Drude model at very low

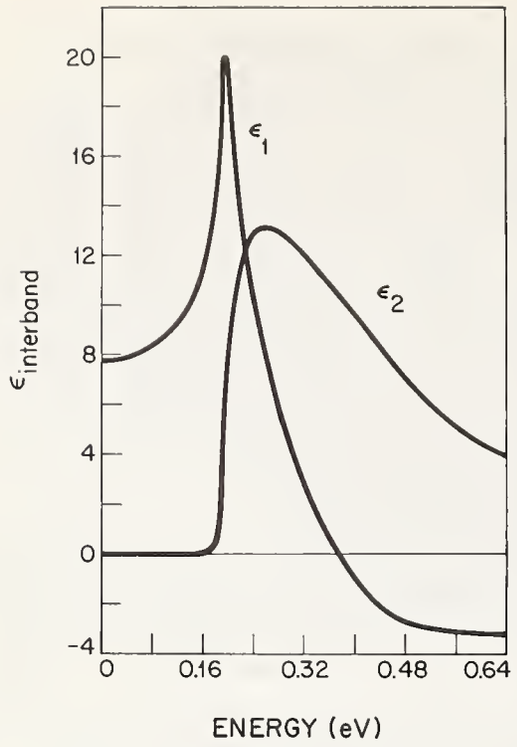

FIGURE 6. *Real and imaginary parts of $\epsilon_{interband}$ versus photon energy.*

In this figure $\tau_{interband} = 5 \times 10^{-13}$ s and values for the other pertinent parameters are given in the text.

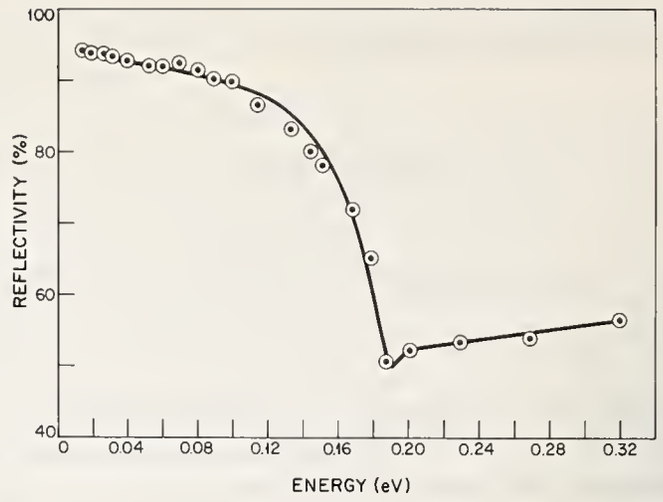

FIGURE 7. *Reflectivity of arsenic for a trigonal face versus photon energy.*

The data points are from Riccius (ref. [2]). The curve is the calculated reflectivity including the interband transition associated with the γ necks as well as the intraband and core contributions to the dielectric constant.

photon energies through correction for an oxide layer reducing the reflectivity by $\sim 3\%$. A least squares fitting procedure was also tried, but it was found that the values for these parameters determined or estimated from other experiments provided the best fit, with the exception of $\alpha^c_{z'}$. For this parameter the least squares fitting procedure yielded $\alpha^c_{z'} \cong 5$ in rough agreement with the two-band model estimate. However, the determination of $\alpha^c_{z'}$ depends strongly on the shape of the reflectivity curve close to the reflectivity minimum. Since the available data in this region are rather scanty, the quoted value of $\alpha^c_{z'} \cong 5$ is only an estimate.

The results of the reflectivity calculation including the interband transitions explicitly are shown in figure 7 as the solid curve; a comparison is also made in this figure with the measured reflectivity points [2]. It is thus found that the infrared properties of a trigonal arsenic face are strongly correlated with Fermi surface [8], magnetoreflection [13] and optical [1] measurements. The two-band model is also found to work surprisingly well for the spin-orbit split bands at Q.

References

[1] Cardona, M., and Greenaway, D. L., Phys. Rev. **133**, A1685 (1964).

[2] Riccius, H. D., Proc. Ninth Intern. Conf. on the Physics of Semiconductors, Moscow, 1968, p. 185.

[3] Berlincourt, T. G., Phys. Rev. **99**, 1716 (1955).

[4] Ketterson, J. B., and Eckstein, Y., Phys. Rev. **137**, A1777 (1965), and references quoted therein.

[5] Shapira, Y., and Williamson, S. J., Phys. Letters **14**, 73 (1965).

[6] Datars, W. R., and Vanderkooy, J., Proc. Intern. Conf. on the Physics of Semiconductors, Kyoto, 1966; J. Phys. Soc. of Japan **21**, suppl. 657 (1966).

[7] Vanderkooy, J., and Datars, W. R., Phys. Rev. **156**, 671 (1967).

[8] Priestley, M. G., Windmiller, L. R., Ketterson, J. B., and Eckstein, Y., Phys. Rev. **154**, 671 (1967).

[9] Ishizawa, Y., J. Phys. Soc. of Japan **25**, 160 (1968).

[10] Fukase, T., J. Phys. Soc. of Japan **26**, 964 (1969).

[11] Lin, P. J., and Falicov, L. M., Phys. Rev. **142**, 441 (1966).

[12] Maltz, M., and Dresselhaus, M. S., Phys. Rev. Letters **20**, 919 (1968).

[13] Maltz, M., and Dresselhaus, M. S., Phys. Rev. **182**, 741 (1969).

[14] Maltz, M., Ph. D. Thesis, Massachusetts Institute of Technology, 1968 (unpublished).

[15] Ehrenreich, H., and Cohen, M. H., Phys. Rev. **115**, 786 (1959).

[16] The effective mass data in reference 8 is consistent with the two-band model even in the weak coupling (z) direction, despite the possibility of a stronger coupling to bands outside the two-band model.

[17] The magnetoreflection linewidths were found to be relatively insensitive to temperature between liquid nitrogen and liquid helium temperatures. See reference 14.

Discussion on "On the Optical Properties and the Density of States in Arsenic" by R. W. Brodersen and M. S. Dresselhaus (MIT)

N. W. Ashcroft *(Cornell Univ.):* How sensitive are your results to the value of m^* used? In principle an effective mass derived from dHvA or other low temperature galvanometric data should not be used in the transport problem. Corrections due to electron-phonon interaction enhancements are quite substantial.

R. W. Brodersen *(MIT):* The values of m^* for the α and β carriers used in our calculation affect only the Drude contribution and not the interband transition; thus the reflectivity is not strongly dependent on the exact values of these masses. The effective masses of the γ carriers are important and these have been calculated from both dHvA and magnetoreflection data. The m^* values obtained for the γ carriers from these two measurements agree to within experimental error, showing that the mass corrections for this carrier due to the electron-phonon interaction are quite small.

Density of States and Ferromagnetism in Iron*

K. J. Duff

Scientific Laboratory, Ford Motor Company, Dearborn, Michigan 48121

T. P. Das

Department of Physics, University of Utah, Salt Lake City, Utah 84112

The band structure of ferromagnetic iron has been calculated by a variational method using a basis of tight-binding functions and orthogonalized plane waves. Exchange matrix elements are evaluated without approximation by a local potential. Correlation effects are explicitly included. Histograms for the density of states are constructed and compared with photoemission and optical reflection and x-ray emission data. The calculation leads self-consistently to the observed magnetic moment. The relative importance of intra-atomic exchange and itinerancy to the origin of iron's ferromagnetism is discussed.

Key words: Electronic density of states; ferromagnetism; iron; optical reflection; photoemission; x-ray emission.

1. Methodology of Band Structure Calculation

The aim of the present work is to explore the magnetic properties of iron via a new band structure calculation in which particular care is given to the exchange interaction, which in turn requires that the wave functions of the electronic states be as realistic as possible. For this purpose a variational method was chosen, and the trial wave function [1] was taken in the form

$$\psi = \sum_{m=1}^{5} \lambda_m u_d^m(\bar{r}) + \sum_{i=1}^{19} \mu_i u_{\mathrm{OPW}}^i(\bar{r}) \qquad (1)$$

The γ_m and μ_i are the expansion coefficients determined from the variational procedure. The functions $u_d{}^m(\mathbf{r})$ are tight-binding (TB) wave functions formed from atomic $3d$ wave functions calculated for the $3d^7 4s$ configuration [2]. The $u_{OPW}{}^i$ are orthogonalized plane wave (OPW) functions, and the sum over i extends to second nearest neighbors in reciprocal lattice space.

The presence of the OPW functions in (1) serves three purposes: (1) the diffuse $4s/4p$ . . . states are well approximated by OPW states; (2) the OPW functions can contribute some d component to the d wave functions thus making the radial part of the d wave function fully state dependent; (3) hybridization is built into the wave function. If γ_m are large and μ_i are small, a pure $3d$ state results; if the μ_i are large and γ_m are small we have a $4s/4p$ . . . state; if γ_m and μ_i are comparable, the wave function is a hybrid.

The secular equation to be solved is

$$|H - ES| = 0 \qquad (2)$$

where H and S are nondiagonal Hermitian matrices of the Hamiltonian and of unity respectively and each is of the form

$$\begin{pmatrix} \mathrm{TB} & \mathrm{hybrid} \\ \mathrm{hybrid} & \mathrm{OPW} \end{pmatrix} \qquad (3)$$

For the submatrix labelled TB, matrix elements are of the standard TB form; two center integrals only were retained. Similarly the OPW submatrix consists of standard OPW matrix elements. For a local operator $V(r)$ the hybrid matrix elements take the form

$$\sum_n \int u_{\mathrm{OPW}} V(r) u_d(r - R_n) \qquad (4)$$

and these were calculated by expanding the function $u_d(r-R_n)$ about the origin and carrying out summations as far as necessary.

Because of the radically different spatial behavior of the $3d$ and $4s$ wave functions, different methods of incorporating correlation effects were used for each. For the $4s$ states the "screened exchange plus coulomb hole" approach of Hedin [3] was used. Here, in the cal-

*Supported by a National Science Foundation Grant at University of California, Riverside, California 92503.

culation of matrix elements, a screened coulomb interaction $e^{-\alpha r_{12}}/r_{12}$ is used, and in our case α was a static, wave number independent screening constant. For an electron gas of uniform density the coulomb hole potential is a constant and has the value

$$V_{\mathrm{CH}}(r) = \frac{1}{2}\int \frac{d^3q}{(2\pi)^3} v(q)\left[\frac{1}{\epsilon(q,0)} - 1\right] \qquad (5)$$

where $v(q)$ is the Fourier component of the coulomb potential. For our choice of dielectric function the coulomb hole energy reduces to $-\alpha/2$.

Correlation among d electrons has been shown by Kanamori [4] and by Hubbard [5] to introduce localization properties into otherwise itinerant electrons, and to considerably weaken the exchange from the value calculated from Bloch wave functions. We adapt an expression given by Hubbard for the effective self exchange interaction

$$-V_{\mathrm{eff}} = -V_c \frac{\frac{1}{4}\Delta}{\sqrt{(\frac{1}{2}V_c + \frac{1}{4}\Delta)^2 - \frac{1}{4}n\Delta V_c}} \qquad (6)$$

where V_c is the usual self coulomb energy, Δ is the band width of the d electrons and n is the average occupation per atom of a single band, that is, n is taken as $1/10\,(n\uparrow + n\downarrow)$. This expression was used for the one center self exchange energy, and the total one center coulomb plus exchange energy weighted according to population was

$$(n\uparrow + n\downarrow - 1)V_c - (n\uparrow - 1)V_0/4 + (1 - n\uparrow/5)V_{\mathrm{eff}} \qquad (7)$$

where V_0 is a spherically averaged exchange interaction due to the other d electrons. Two complete band structures were calculated corresponding to assumed values of Δ of .4 Ry and .55 Ry.

2. Results of the Band Structure Calculation

Energies were calculated at 110 points in 1/48 of the Brillouin zone (BZ). The energy bands for $\Delta = .55$ Ry are depicted in figures 1 and 2. The most striking feature is the greater width found here and the appearance of a definite spin dependent component of the width. For example, at Γ we can separate out a non-spin component of the doublet-triplet splitting of .12 Ry (cf. 0.10 Ry for APW or KKR methods [6]), whereas the spin contributions are 0.11 Ry and 0.06 Ry for majority and minority spin respectively. Both the greater width and the spin dependent width found here are due to the inclusion of two-center exchange matrix elements for d-states. Clearly, assumptions made about the efficacy of screening of interatomic exchange have important consequences for the band width.

The density of states histograms for majority spin, minority spin and total electrons are given in figures 3, 4, and 5 respectively. Peaks in the total density of states occur at about 0.19 Ry, 0.39 Ry and 0.54 Ry below the Fermi level, and the occupied width of the d levels is about 0.8 Ry. The optical density of states as

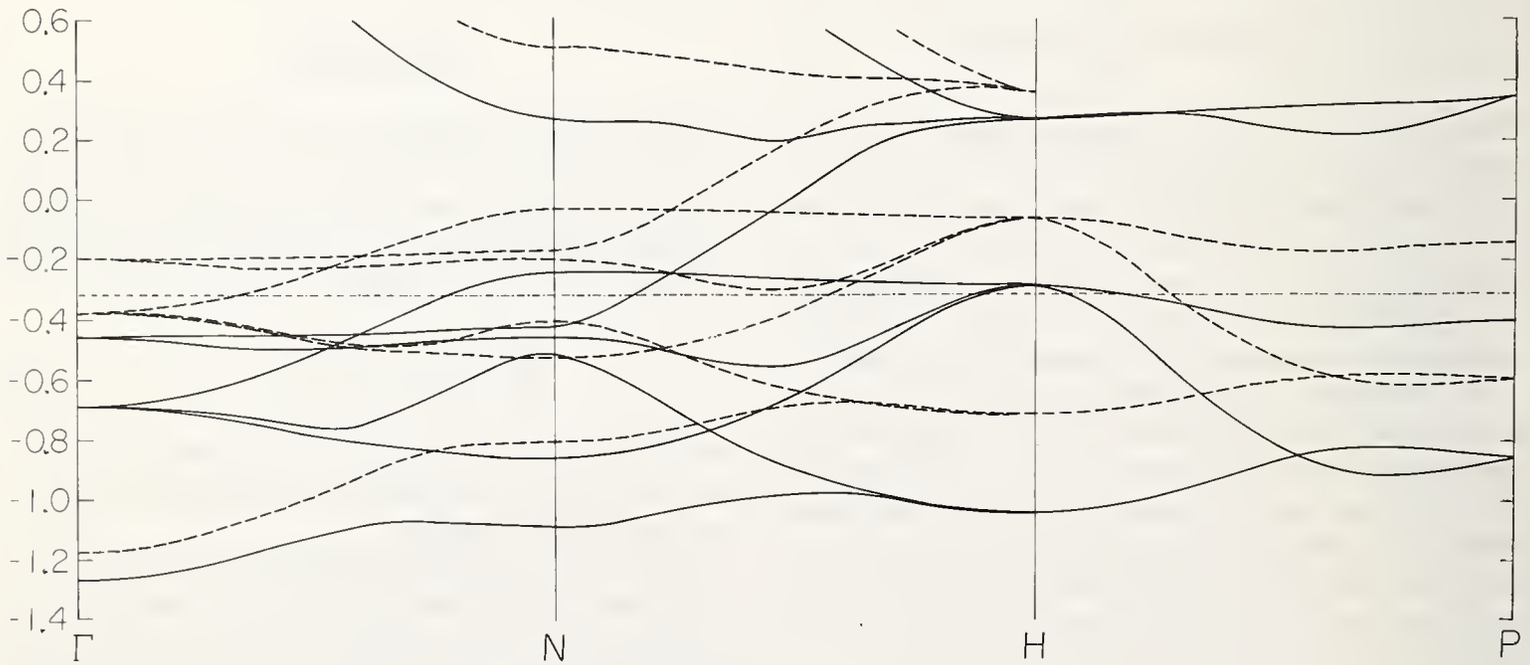

FIGURE 1. *Calculated bands for ferromagnetic iron.*

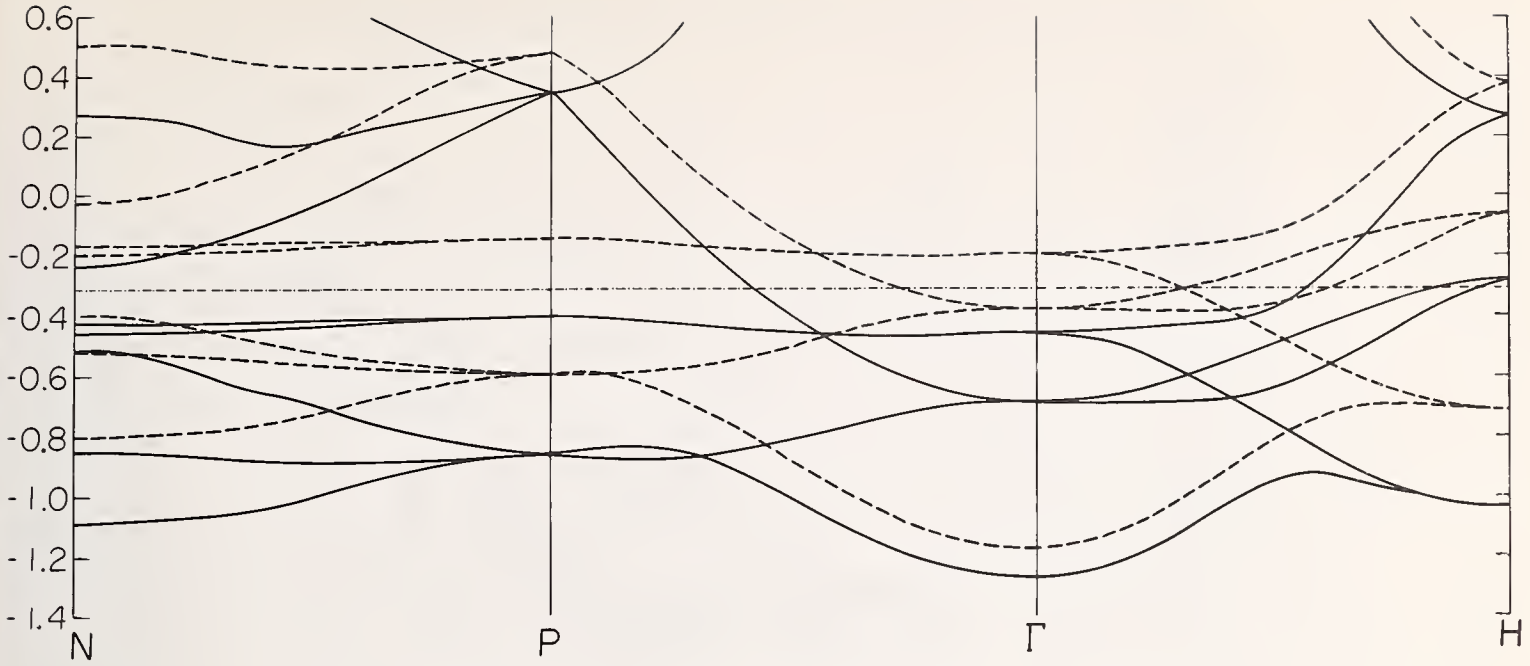

FIGURE 2. *Calculated bands for ferromagnetic iron.*

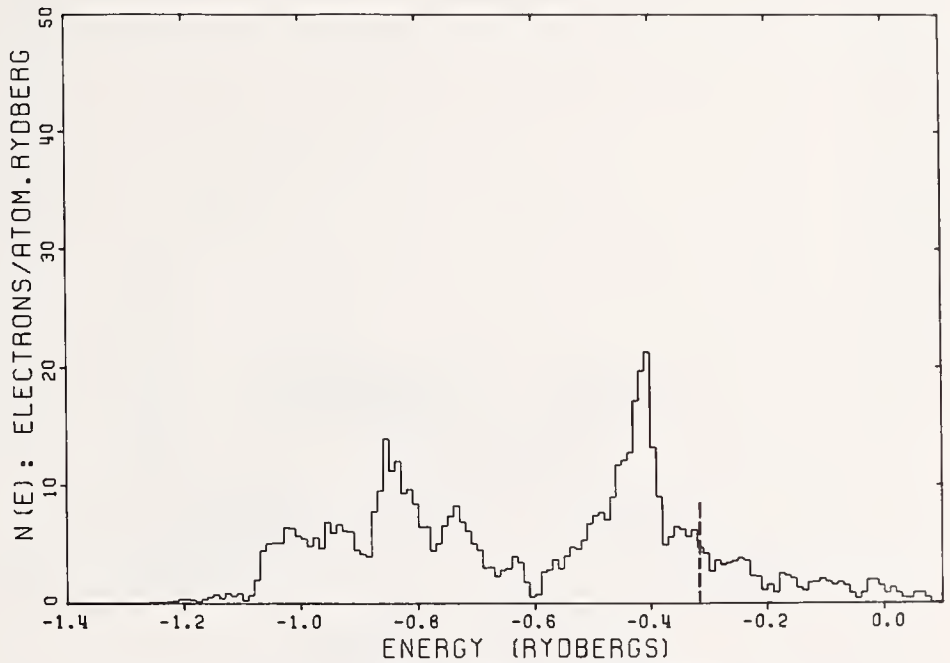

FIGURE 3. *Density of states histogram for majority spin electrons.*

measured by Blodgett and Spicer [7] indicates three peaks, one of which is now attributed to surface contamination [8]. A second peak of small amplitude appears just under the Fermi surface and has no counterpart in the theoretical density of states presented here. The remaining experimental peak coincides with the total density of states maxima between -0.4 and -0.6 Ry. Eastman [8] likewise shows a peak of about this width in his experimental optical density of states, but his peak lies closer to the Fermi surface than the

417-156 O - 71 - 5

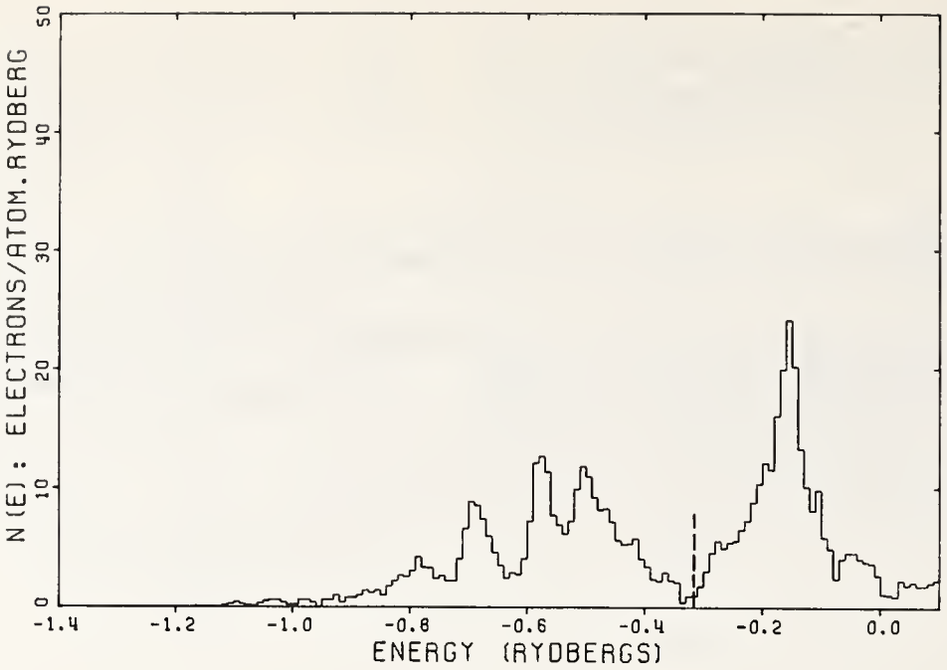

FIGURE 4. *Density of states histogram for minority spin electrons.*

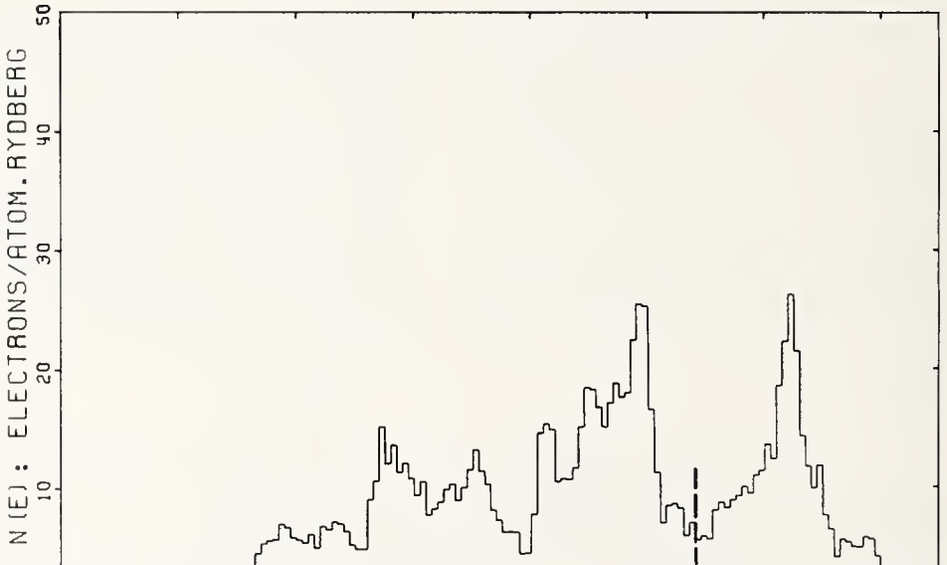

FIGURE 5. *Total density of states histogram.*

present theory depicts. However, some latitude exists for adjustment of the theoretical position of the Fermi energy, as discussed below.

Unfortunately, the optical experiments are not definitive in the overall width of the occupied portion of the *d* bands, although they do give some support to the idea of wider bands than had previously been obtained theoretically. Support for this point of view also comes from x-ray emission spectra. Figure 6 represents schematically the results of Tomboulian and Bedo [9] (their fig. 5, M_3 emission band). They assumed the band width to be given by the interval *ED* of figure 6, i.e., about 8

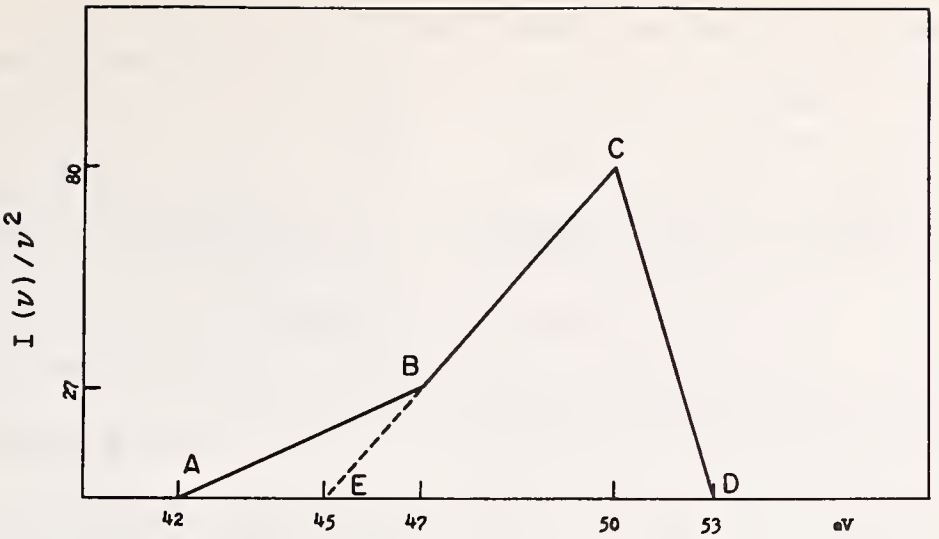

FIGURE 6. *Schematic representation of the* M_3 *x-ray emission spectra reported by Tomboulian and Bedo* [8].

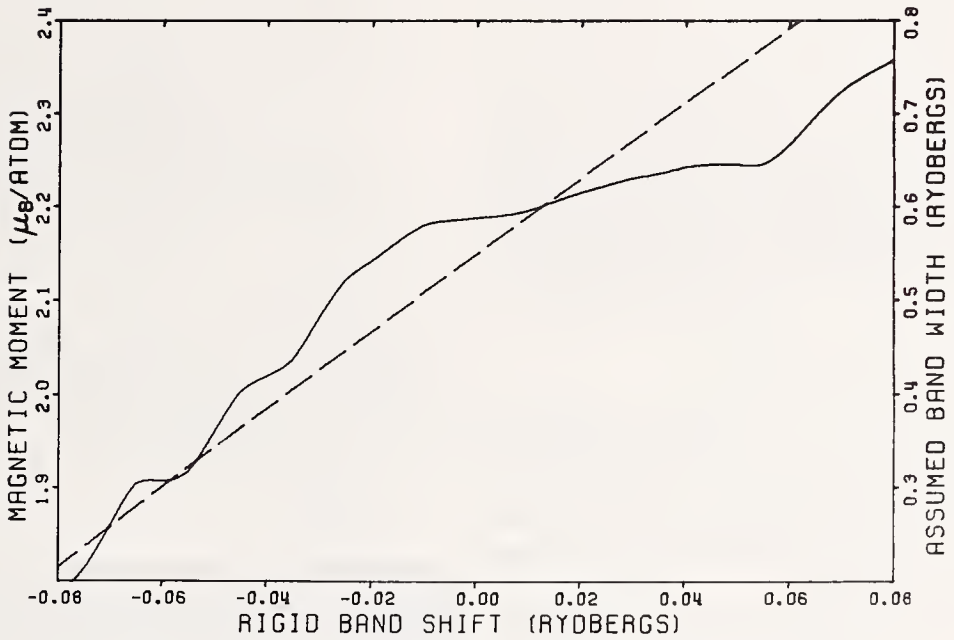

FIGURE 7. *The solid line graphs the magnetic moment as a function of rigid band displacement of majority spin states with respect to the minority spin states.*

The dotted line gives the rigid band shift calculated from eq 6 as a function of the band width parameter Δ.

eV. If we accept at least part of the previously ignored spectra, the band width could be as large as 11 eV (*AD* on fig. 6). Moreover, if the kink at *B* is interpreted as a point of superposition of two curves, one for spin up and the other for spin down, the energy interval from *A* to *B* would give the magnetic splitting at the bottom of the band of about 5 eV in good agreement with our theoretical value of 4.5 eV at the point *H*, which also happens to be the point where the magnetic splitting is largest. Further experimental clarification of this is desirable.

3. The Magnetic Moment and the Origin of Ferromagnetism

As remarked above, two band structures were calculated, with the band width Δ of eq (6) equal to 0.4 Ry and 0.55 Ry. The second value of Δ seems more appropriate to the wider *d* bands found here. In each case the magnetic moment was obtained from the density of states histograms. The moments were 2.06 μ_B/atom and 2.19 μ_B/atom respectively. Thus, within the limitations of assuming Hubbard's formula, a first principles

derivation of the magnetic moment has been achieved.

To explore the role of correlation further, the band width Δ was regarded as an adjustable parameter and the corresponding values of the effective exchange calculated. Using this to produce a rigid band shift of the spin states relative to one another, an approximate estimate of the dependence of the magnetic moment on Δ is found. The solid curve of figure 7 is the magnetic moment which results from given rigid band displacements, and the dotted curve graphs the rigid band shift as a function of Δ. The magnetic moment is characterized by a steep rise to about 2.18 μ_B/atom and then a broad plateau to 2.25 μ_B/atom followed by another steep rise. The plateau is produced when both spin states have minima of their density of states at the Fermi surface, and conversely the steep sections are characterized by a maximum of the density of states of either spin (or maxima for both spins) at the Fermi surface. Over the plateau region very large changes in Δ produce only minor changes in the magnetic moment, so in this range the choice of Δ or the accuracy of Hubbard's formula is not critical. However, its dominant role in producing the ferromagnetic moment is revealed by the rapid decrease in moment for Δ less than about .5 Ry. For $\Delta = 0$, the magnetic moment would be 1.3 μ_B/atom, implying that the remaining 0.9 μ_B/atom comes from itinerancy of the d electrons.

We therefore suggest the following mechanism for the origin of ferromagnetism in iron. Hund's rule at a given site is responsible for initially polarizing the electrons at that site. This is amplified by some itinerant ferromagnetism of the d states, and the itinerancy couples the moments on different sites.

Finally we note from figure 7 that there is latitude for some arbitrary displacement of the two density of states curves without altering the magnetic moment appreciably. Thus the total density of states at the Fermi surface can be adjusted over a wide range from a small value ($\approx$ 5 electrons/atom Ry) on the plateau to a large value ($\approx$ 20 electrons/atom Ry) on the upper parts of the steep section. Thus no reliable prediction of the electronic specific heat or susceptibility can be made, particularly in view of the uncertainty in the orbital contribution to the magnetic moment.

4. References

[1] For a discussion of the adequacy of the model of overlapping s and d bands see F. M. Mueller, Phys. Rev. **153,** 659 (1967), V. Heine, Phys. Rev. **153,** 673 (1967), and J. Hubbard, Proc. Phys. Soc. **92,** 921 (1967); pseudopotential formalisms based on this model have been given by L. Hodges, H. Ehrenreich and N. D. Lang, Phys. Rev. **152,** 505 (1966) and Walter A. Harrison, Phys. Rev. **181,** 1036 (1969); a first principles calculation of this type has been performed by R. A. Deegan and W. D. Twose, Phys. Rev. **164,** 993; combined tight-binding-OPW calculations not utilizing d states have been reported by W. Schneider, L. Jansen and L. Etienne-Amberg. Physica **30,** 84 (1964), and A. Barry Kunz, Phys. Rev. **180,** 934 (1969).

[2] We thank Dr. T. Gilbert of the Argonne National Laboratory for supplying us with the wave functions for the $3d^7 4s$ configuration.

[3] Hedin, L., Phys. Rev. **139A,** 796 (1965).

[4] Kanamori, J., Prog. Theoret. Phys. **30,** 275 (1963).

[5] Hubbard, J., Proc. Roy. Soc. (London) **A276,** 238 (1963); **A277,** 237 (1963); **A281,** 401 (1964).

[6] Wakoh, S., and Yamashita, J., J. Phys. Soc. Japan **21,** 1712 (1966); DeCicco, P. D., and Kitz, A., Phys. Rev. **162,** 486 (1967).

[7] Blodgett, A. J., and Spicer, W. E., Phys. Rev. **158,** 514 (1967).

[8] Eastman, D. E., J. Appl. Phys. **40,** 1387 (1969).

[9] Tomboulian, D. H., and Bedo, D. E., Phys. Rev. **121,** 146 (1961).

Calculation of Density of States in W, Ta, and Mo

I. Petroff and C. R. Viswanathan

Department of Electrical Sciences and Engineering, School of Engineering and Applied Sciences
University of California, Los Angeles 90024

Density of states curves were calculated for tungsten, tantalum and molybdenum from corresponding energy band structures obtained by a nonrelativistic APW calculation. The Fermi energy and the density of states at the Fermi energy were obtained for each material. The calculations were part of a study intended to calculate theoretical photoemission yield curves which could be compared with experimental results.

Key words: Electronic density of states; Fermi energy; molybdenum; photoemission; tantalum; tungsten.

1. The Band Structure

The APW method [1,2] consists in solving Schroedinger's equation

$$H\psi = E\psi \tag{1}$$

by expanding the wave function ψ in terms of augmented plane waves in the presence of a crystal potential $V(r)_{APW}$ which is spherically symmetric around each atom site up to a radius R_s, while constant for $r > R_s$. This pattern is repeated in each Wigner-Seitz cell. The augmented plane waves are functions ψ_i such that:

$$\psi_i = e^{ik_i \cdot r} \text{ for } r > R_s \text{ and} \tag{2}$$

$$\psi_i = \sum_{l=0}^{\infty} \sum_{m=-l}^{l} (2l+1) i^l \frac{j_l(k_i \cdot R_s)}{u_l(R_s)} u_l(r) \frac{(l-|m|)!}{(l+|m|)!} P_l^{|m|}(\cos\theta) P_l^{|m|}(\cos\theta_{k_i}) \exp \text{im}(\phi - \phi_{k_i}) \tag{3}$$

for $r < R_s$.

The eigenvalues E at various points in the Brillouin zone are obtained by setting up the system of equations for obtaining the expansion coefficients, and then evaluating the secular determinant of this system as a function of E. The eigenvalues are those values of E for which the determinant goes to zero.

All the three materials have a bcc crystal structure. The energy eigenvalues were determined at 55 points in 1/48 of the Brillouin zone as shown in figure 1. The points are distributed uniformly on a cubic mesh throughout the zone. Each point is located at the corner of a cubic subzone having edge dimensions $\pi/4a$ with the edges being oriented parallel to the coordinate axes k_x, k_y and k_z. There are 1024 points in the entire zone.

2. The Density of States

Density of states curves based on the 1024 points at which the energy eigenvalues are actually calculated show poor resolution. The contribution to the density of

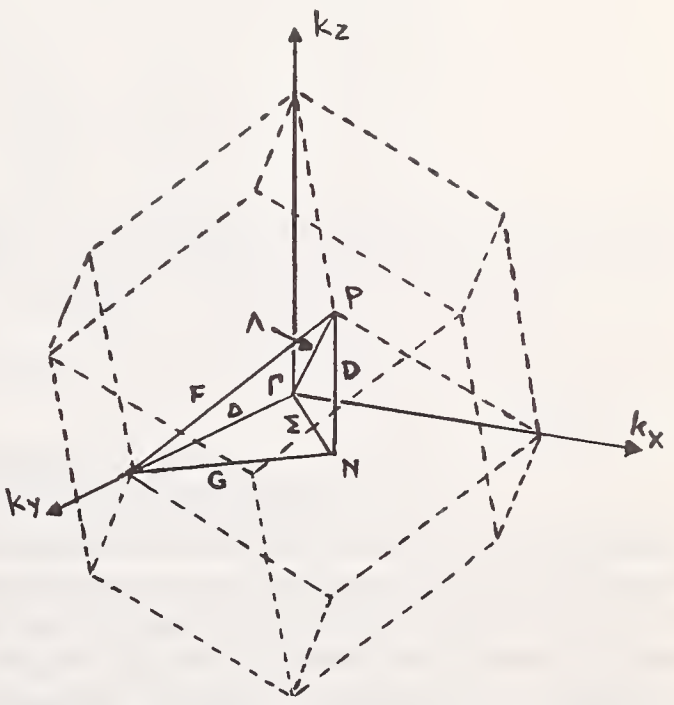

FIGURE 1. *Brillouin zone for body-centered cubic structure.*

states function from points of high symmetry where the energy eigenvalues converge from several directions is not apparent unless the band structure is known at intervals that are smaller than those used in solving for the eigenvalues. Additional points in the band structure were obtained by reducing the mesh by a factor of 4 by means of interpolation. The resulting number of points in the Brillouin zone at which energy eigenvalues are available increases from 1024 to 65,536.

The interpolation scheme is carried out in the wedge representing 1/48 of the Brillouin zone, which contains the original 55 points for which the band structure was calculated. Values at the midpoints of the edges of the cubic subzones are obtained by linear interpolation. Values at the center of the cube faces are obtained by interpolating between previously obtained midpoints. Only one pair of opposite edges is required for the interpolation since a two-way interpolation using midpoints at all four edges of the cube face would give the same result. Values at the cube centers are obtained by interpolating between previously obtained cube face centers. Again, only one pair of faces is needed. At the wedge boundaries where the symmetry planes cut the cubic subzones along face or body diagonals, as in the case of the NPΓ, NPH, or ΓHP planes, reflection properties in the appropriate symmetry plane are used to complete the cubes in order to apply the interpolation scheme described. In order to reduce the Brillouin zone mesh by a factor of four, the interpolation procedure must be applied twice. This results in 1785 points in 1/48 of the Brillouin zone. Reflection properties are again applied to extend the results throughout the entire zone.

The density of states is plotted in units of electrons per atom per rydberg. Each energy eigenvalue can accommodate two electrons, and the number of eigenvalues in a band is equal to the number of cubic subzones into which the Brillouin zone has been subdivided. In k-space, there are two electrons per atom per band. The following relation is thus established:

$$x = \frac{2N}{\text{no. of subzones}} \text{ electrons per atom per } \Delta E \qquad (4)$$

where N is the number of eigenvalues in some energy interval ΔE, and x is the corresponding number of electrons per atom in the same interval ΔE. To obtain x in units of electrons per atom per rydberg the right side of eq (4) should be divided by ΔE:

$$x = \frac{2N}{\Delta E \times \text{no. of subzones}} \text{ electrons per atom per rydberg} \qquad (5)$$

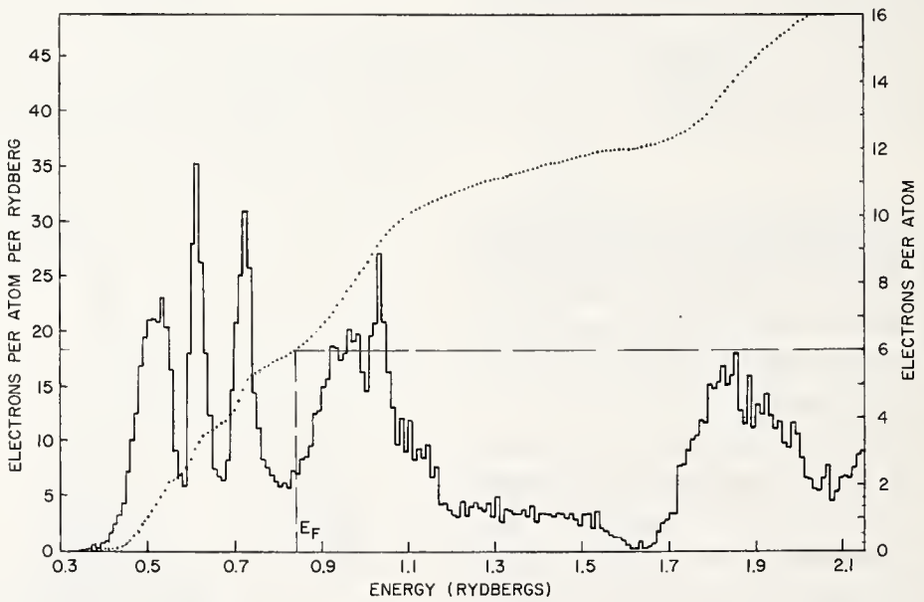

FIGURE 2. *Density of states curve for tungsten.*
The dotted line is the integrated density of states, with corresponding units to the right. The zero of energy corresponds to the constant potential for $r > R_s$.

To find the Fermi level, the density of states curve is integrated. This curve shows the number of electrons per atom as a function of energy. The Fermi level is that energy at which all the valence electrons for the given material are accounted for. In tungsten and molybdenum this energy will correspond to six electrons/atom, and in tantalum to five electrons/atom.

The density of states histograms are presented in figures 2, 3 and 4. In each case the integral of the density of states is graphed in the same figure. The energy range considered includes the bands occupied by the valence electrons, and the unoccupied states above the

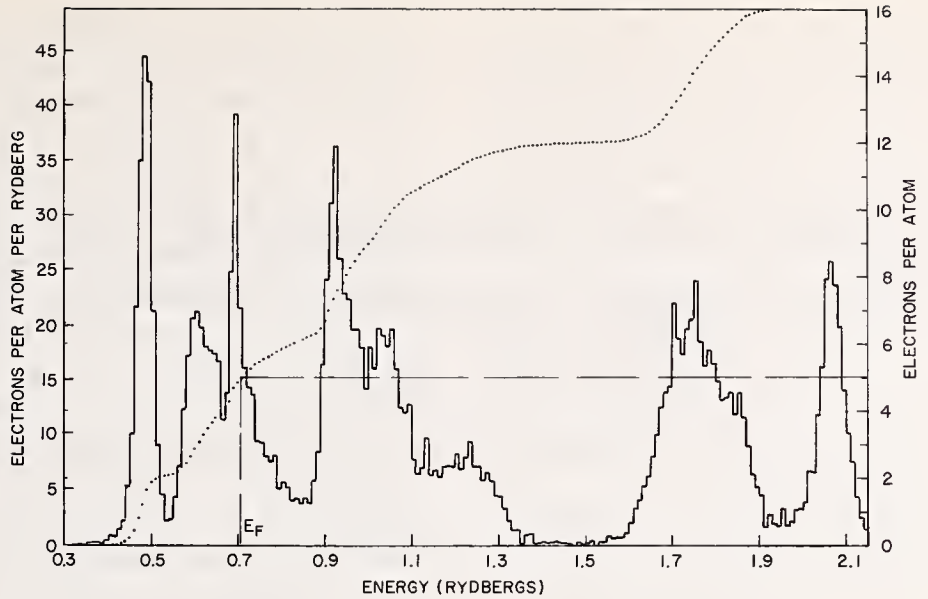

FIGURE 3. *Density of states curve for tantalum.*

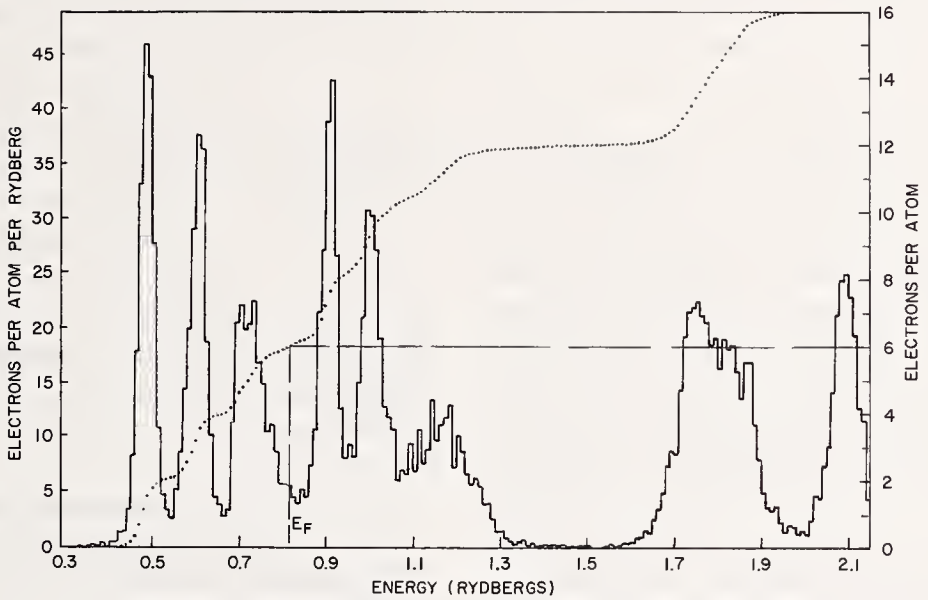

FIGURE 4. *Density of states curve for molybdenum.*

Fermi level; a total span of approximately 1.8 Ry. The resulting Fermi energy and density of states at the Fermi energy for each material are shown in table 1.

3. Discussion

The density of states curve for tungsten is in good agreement with the corresponding results obtained by Mattheiss [3] for this metal. The calculation by Mattheiss extends to 1.3 rydbergs on the energy scale.

The curve for tungsten has lower peaks and higher minima than the curves for tantalum and molybdenum, where high peaks alternate with deep minima. In other words, in tungsten, the electronic states do not group themselves into "bands" as much as in the other two metals.

TABLE 1. *Results obtained from the density of states calculation. The Fermi energy is given in rydbergs as measured from the bottom of the lowest band.*

Material	Fermi energy	Density of states at Fermi energy
	Rydbergs	
Tungsten	0.4988	7.41 electrons/atom Ry
Tantalum	0.4077	17.9 electrons/atom Ry
Molybdenum	0.4978	5.0 electrons/atom Ry

The group VI elements tungsten and molybdenum exhibit three peaks below the Fermi level. Tungsten shows a broad peak above the Fermi level and in molybdenum the peak splits into two peaks. For the higher energy states, two peaks are present in the vicinity of 1.8 and 2.1 Ry. These peaks are much more apparent in molybdenum than in tungsten.

There are three peaks in tantalum at positions corresponding to the first three peaks in tungsten and molybdenum, but in this case the second peak is broad and flat and almost merges with the third peak which is narrow and sharp. The Fermi energy falls within the range of the third peak slightly below the $\Gamma_{25'}$ level as predicted by Mattheiss [3] on the basis of a rigid-band model. There is an asymmetric broad peak above the Fermi level beginning with a maximum at about 0.9 Ry and tapering off over a range of 0.4 Ry. The two peaks at higher energies are also present and are very similar to the corresponding peaks in molybdenum.

In all three cases, there is a low density region beginning beyond the top of the *d*-band and extending over a span of approximately 0.4 Ry.

It should be noted that in the case of the group VI metals, the Fermi energy coincides with a slowly varying part of the density of states curve, such that a small variation in the band structure should not affect the magnitude of the density of states at the Fermi energy to a great extent. In tantalum, the group V metal, the Fermi energy coincides with a peak in the density of states curve, and a small variation in the band structure could have a drastic effect on the density of states at the Fermi level in view of the steepness of the curve in that region.

Relativistic as well as nonrelativistic APW calculations of the energy band structure of tungsten are found in the literature in connection with Fermi surface studies [3,4]. It appears that the relativistic and nonrelativistic calculations tend to lie on either side of the experimental results [4]. A basic problem in this respect is that in addition to relativistic effects there is an uncertainty in the APW potential which is due to the exchange term. The contribution of the exchange interaction to the crystal potential is evaluated by means of an approximation. This is necessary in order to convert the potential into a one-electron potential. A 30% reduction in the magnitude of the exchange contribution to the potential was shown by Mattheiss [3] to produce significant changes in the band structure of tungsten, comparable in magnitude with relativistic corrections. In molybdenum, relativistic effects are expected to be less pronounced because it is a lighter metal, and a comparison of the theoretical photoemission with experimental results should provide a more direct indication of the role of exchange effects.

The modified tungsten band structure obtained by Mattheiss [3] by reducing the exchange contribution to the potential by 30% results in density of states curve which is very similar in character to the curve obtained from the unmodified calculation except for a general displacement toward higher energies. The height of the peaks relative to each other remains the same, as well as their relative widths. When the band structures for tantalum and molybdenum are calculated without reducing the corresponding exchange potentials, the differences in the resulting band structures are not of such a nature as to produce relative shifts along the energy axis in the density of states curves. When the results for tungsten, tantalum and molybdenum are compared to each other, no displacement along the energy axis is found, but the relative magnitudes and widths of the peaks vary considerably from one material to the next.

4. Acknowledgments

The authors are grateful to J. H. Wood for providing APW computer programs which were used in the energy band calculations.

5. References

[1] Slater, J. C., Phys. Rev. **51**, 846 (1937).
[2] Wood, J. H., Phys. Rev. **126**, 517 (1962).
[3] Mattheiss, L. F., Phys. Rev. **139**, A1893 (1965).
[4] Loucks, T. L., Phys. Rev. **143**, 506 (1966).

Adjustment of Calculated Band Structures for Calcium by Use of Low-Temperature Specific Heat Data*

R. W. Williams and H. L. Davis

Metals and Ceramics and Solid State Divisions, Oak Ridge National Laboratory, Oak Ridge, Tennessee 37830

The electronic band structure of calcium has been studied theoretically by employing the Korringa-Kohn-Rostoker method. The crystal potentials used in our calculation were obtained by means of a standard superposition of free-atom charge densities. E_k vs $\mathbf{k}$ curves and the density of states at the Fermi energy were calculated for various potentials, with the measured low-temperature electronic specific heat coefficient, γ, being used as an empirical aid to adjust the exchange portion of the crystal potential. The important feature of the potentials used is that they all give band structures which have definite d-band character in the vicinity of the Fermi surface. These d bands or their corresponding d scattering resonances vary rapidly in energy for small changes in the exchange, resulting in values of γ which are extremely sensitive to exchange.

Key words: Calcium; de Haas-van Alphen; electronic density of states; low-temperature specific heat; pseudopotential; transition-metal behavior.

1. Introduction

The first band theoretical calculation on metallic calcium was made by Manning and Krutter in 1937 [1]. They carried out a Wigner-Seitz cellular calculation in an attempt to explain a number of electronic properties of metallic calcium, including the conductivity. This early band calculation demonstrated that calcium's metallic behavior is probably due to the overlap of an s-band with a d-band. Their calculations further implied that the density of states, as a function of energy, should be rather s-like up to the vicinity of the Fermi energy where the d-bands would then contribute a narrow, sharp bump. It is interesting to note from these conclusions that metallic calcium would have some d-like electronic character which does not appear in the free atom, thereby implying certain transition-metal-type behavior for metallic calcium.

Also, there have been several, more recent band structure calculations pertaining to metallic calcium. Some of these attempts have employed different calculational techniques such as the OPW method and the pseudopotential method [2-5]. However, there are basic disagreements between all of these calculations, either when compared to experiment or to one another. For example, there is no agreement among the presently available calculations concerning detailed features of calcium's Fermi surface, with which experimental, de Haas-van Alphen results, the most direct verification of metallic band structure calculations, could eventually be compared. At present such differences between the calculations have not been resolved by comparison with experiment, since the only available de Haas-van Alphen data [6-8] is sketchy. Furthermore, the only data available was apparently obtained from microcrystalline-aggregate-type samples, and can be misinterpreted. At the same time, no reliable calculations have appeared for the low-temperature specific heat coefficient, γ, which is a measure of the density of states at the Fermi energy. This is surprising, since such calculations would allow some comparison with experiment. This point is especially valid for calcium, since possible effects, which could enhance the band structural density of states, are expected to be small. Thus, a comparison between calculated and experimental γ should provide a more direct test of a calculated band structure for calcium than would be possible for other metals where enhancement effects are expected to be larger and cause a greater degree of quantitative uncertainty.

In an attempt to clarify some of the present circumstances mentioned above, we have decided to carry out a rather complete calculational study on metallic calcium with the aim of obtaining an experimentally verifia-

*Research sponsored by the U.S. Atomic Energy Commission under contract with Union Carbide Corporation.

ble band structure. To this end, due to possible uncertainties connected with the available de Haas-van Alphen data, we have decided to use the low-temperature specific heat coefficient as a means of experimentally testing our band structure calculations. Then, provided our calculations would lead to a reasonable agreement between calculated and measured γ, it was hoped that they would provide a quantitative prediction of calcium's Fermi surface, which could be eventually verified by an exhaustive de Haas-van Alphen study. While our projected study is not yet complete in all phases of desired detail, we have found many interesting features caused by the presence of a *d*-band in the vicinity of the Fermi energy. Also, we feel these features are of general enough interest that they should be presented at this stage of development of our study.

2. Discussion of Calculational Details

All of the band structure calculations reported here were performed by use of computer codes based upon the nonrelativistic form of the Korringa-Kohn-Rostoker (KKR) method of band theory [9-11]. Throughout, exclusive use has been made of muffin-tin potentials. The resulting accuracy then obtainable with the KKR method is governed by the highest ℓ value, denoted by ℓ_{max}, present in the spherical harmonic expansion of the wave functions inside the muffin-tin spheres. Since previous work has shown for the transition metal region of the periodic table that use of $\ell_{max}=2$ introduces calculational errors of at most a few thousandths of a rydberg in energy eigenvalues [11-13], we have used this value of ℓ_{max} in the present work. All results were then obtained by direct numerical solution of the one-particle, band-theoretic eigenvalue problem, with the restrictions mentioned above, without recourse to any interpolative scheme.

The necessary one-electron potentials were obtained by use of the heuristic prescription outlined by Mattheiss [14]. In this prescription a potential is approximated as $V(r)=V_{e.s.}(r)+V_{ex.}(r)$. Both the electrostatic coulomb contribution, $V_{e.s.}(r)$, and the exchange contribution, $V_{ex.}(r)$, are calculated using free-atom charge densities. At a given lattice site, $V_{e.s.}(r)$ is equated to the sum of, (1) the Coulomb potential centered at the site due to the free-atom charge density, and, (2) the contributions from the tails of the same Coulomb potential when centered on neighboring sites. The exchange contribution is obtained using a Slater-type approximation: $V_{ex.}(r)=-6\beta[3\rho(r)/8\pi)]^{1/3}$. $\rho(r)$ is the spherically symmetric lattice superposition of the atomic charge densities and obtained analogously to the calculation of $V_{e.s.}(r)$. β is a parameter which, in present terminology, equals one for full Slater exchange [15]. This prescription, as stated, still contains two unspecified quantities. First, what charge densities are to be used? Also, what atomic configurations are to be used? Second, given the charge densities, what value of β is to be used? Determining the answers to these questions is presently an active research field; however, such is not the main topic of the present undertaking. Rather, in a practical attempt to avoid these questions, we have adopted the approach of arbitrarily using the analytical Hartree-Fock wave functions of Synek et al. [16] for the atomic configuration $3p^6 4s^2$, and then allowing β to vary as a parameter in attempting to determine the most experimentally plausible calculated band structure.

To obtain the Fermi energy for a given potential, KKR constant-energy-search techniques [13] were used to obtain points on constant-energy surfaces within the Brillouin zone of the fcc lattice. Such points allow numerical evaluation of the volume contained by a constant-energy surface, and hence the integrated density of states for an energy is directly obtained. The Fermi energy is obtained by adjusting the energy until the proper integrated density of states is found. For all constant-energy surfaces calculated in this investigation, of the order of 25,000 points were calculated on each surface. This number of points enables the integrated density of states, for a given energy, to be obtained to an accuracy of about four significant figures. Such accuracy is not redundant but required in order to obtain an accurate value, for a given potential, of the density of states at the Fermi energy, $n(E_F)$, which we obtain by direct numerical differentiation of the integrated density of states information. This point is especially valid in the present study where $n(E_F)$ falls in an energy region where the density of states is rapidly changing. Of course, the calculated low-temperature electronic specific heat coefficient, for a given potential, directly follows from $n(E_F)$.

3. Results and Discussion

Our first calculation was made with $\beta=1.00$ and the $E_{\mathbf{k}}$ vs $\mathbf{k}$ curves for various symmetry directions are given in figure 1. The notable feature of figure 1 is the nearly filled *s-p* band intersecting with a *d*-like band in the vicinity of the Fermi energy. This is qualitatively the same as has been proposed previously by Manning et al. [1]. Our resulting density of states is 13.2 millijoules/mole-K^2. This value of γ is very much higher than the reported experimental value of 3.08 milli-

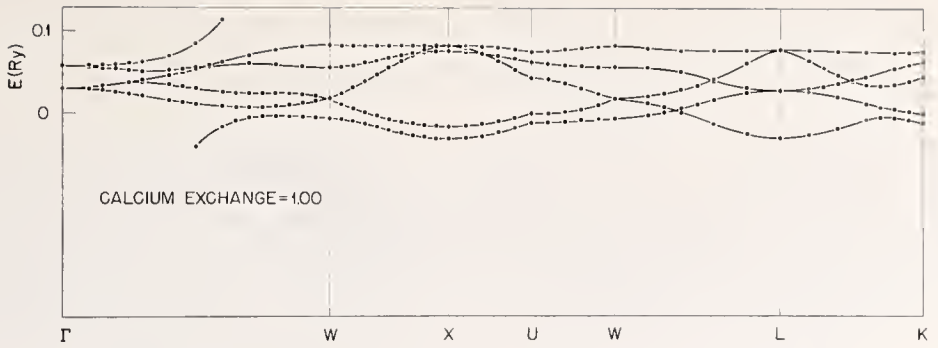

FIGURE 1. *Energy bands for calcium calculated using the potential with exchange parameter $\beta = 1.00$.*

The energies are expressed in rydbergs measured relative to the constant value of the potential between the muffin-tin spheres.

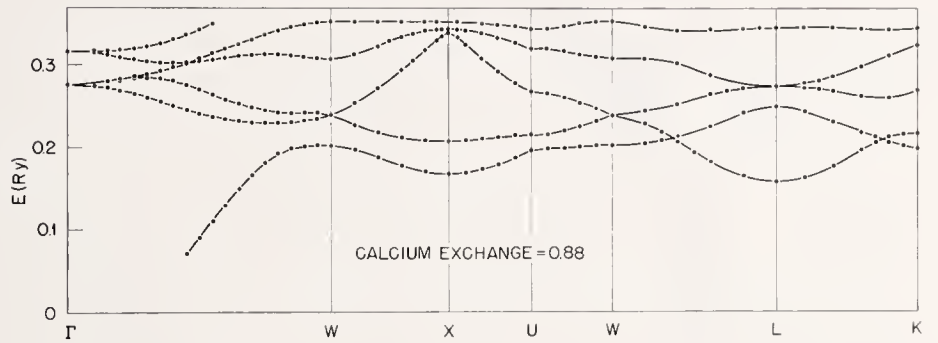

FIGURE 2. *Energy bands for calcium calculated using the potential with exchange parameter $\beta = 0.88$.*

The energies are expressed in rydbergs measured relative to the constant value of the potential between the muffin-tin spheres.

joules/mole-K² [17]. Since the electron-phonon enhancement of γ is expected to be small and since the γ obtained from a band structure calculation should be less than or equal to the γ obtained from a specific heat measurement, it is apparent that some adjustment of the crystal potential is required. Consequently, we carried out a series of calculations of γ for several different potentials. These potentials were generated by changing the exchange contribution, and the resulting values of γ as a function of β are given in table 1. As is noticed by this table, γ is extremely sensitive to the assumed potential.

We give the $E_{\mathbf{k}}$ vs $\mathbf{k}$ curves for $\beta = 0.88$ in figure 2. This particular value of β at least gives a reasonable value of γ. This figure should be compared to the $E_{\mathbf{k}}$ vs $\mathbf{k}$ curves for $\beta = 1.00$ given in figure 1. The essential features are the same, namely, a narrow d-like band intersecting an s-p band in the vicinity of the Fermi energy. However, it is seen from a comparison of the two figures that there has been a very rapid rise in the d bands from $\beta = 1.00$ to $\beta = 0.88$. Furthermore, there has been a broadening of these same bands. The Fermi energy of both sets of energy bands lies slightly in the bump of the d band density of states. Since the bump moves in energy and changes in width as β is varied, this results in a rapid change of the density of states at the Fermi energy with β. To illustrate further this effect we have treated the d band as a d scattering resonance and computed its movement in energy as a function of exchange. The results are given in table 2. Note how

TABLE 1. *Results of the calculations for the low-temperature specific heat coefficient, γ, as a function of exchange parameter, β*

β	Calculated γ (mjoules/mole-K²)
1.00	13.20
0.90	6.14
.89	3.62
.88	2.02

TABLE 2. *The numerical results showing the change in energy of the* d *resonance as a function of β. ΔE_{sd} equals the difference in energy in rydbergs between the bottom of the* s − p *conduction band, Γ_1, and the* d *resonance,* E_d

$\beta =$	1.00	0.90	0.88
$\Delta E_{sd} =$	0.174	.280	.300

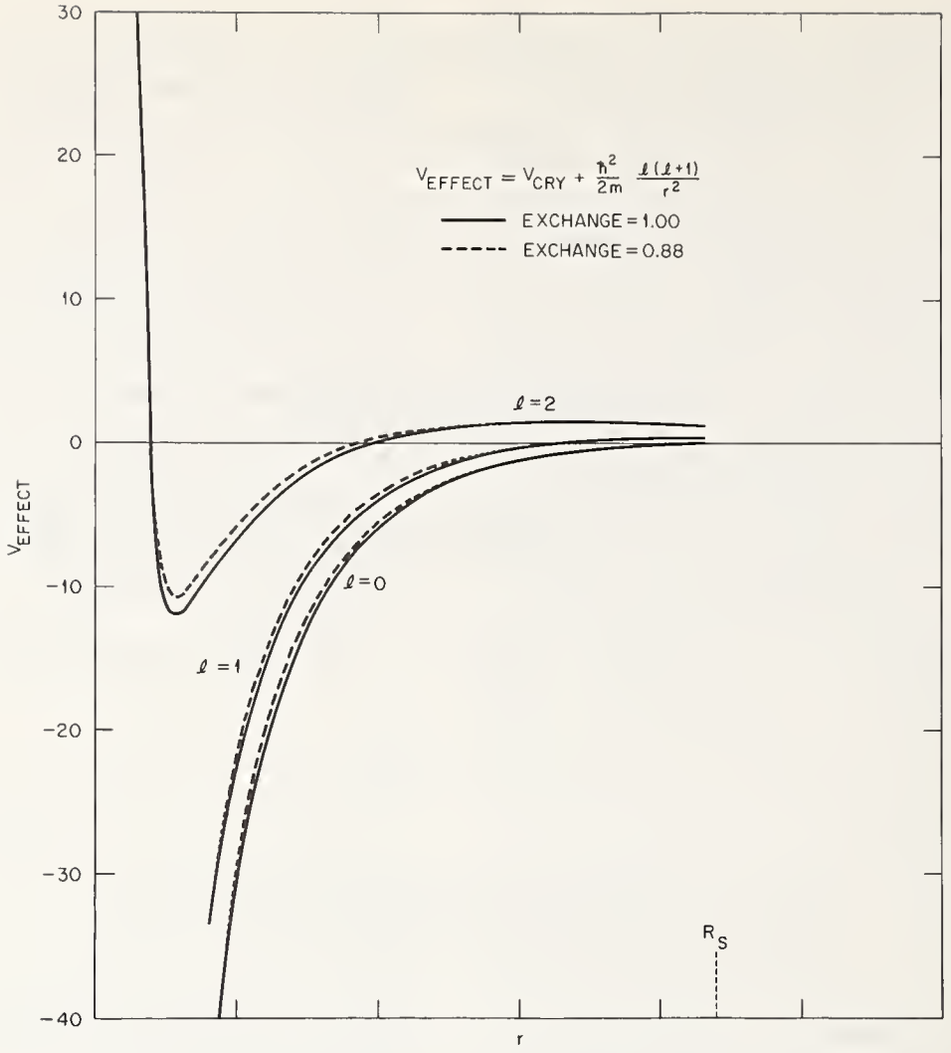

FIGURE 3. *The effective potentials, as a function of radial distance, for $\beta = 1.00$ and 0.88.*

The effective potential is the sum of the crystal potential and the centrifugal potential. R_s is the radius of the muffin-tin sphere.

rapidly the d resonance is moving in energy away from the bottom of the s-p band as a function of exchange.

We can also consider the graph of the effective potential, shown in figure 3. The $\ell = 2$ portion of the effective potential for $\beta = 1.00$ shows a "well" and, thus, a tendency to "bind" the d electron. However, for $\beta = 0.88$ it is seen that there is a tendency to push the bottom of the "well" up, or "unbind" the d electron.

Physically speaking, for these potentials metallic calcium attempts to "bind" a d electron but is only partially successful. If one considers scandium, which has one more conduction electron, he sees that it has a free atom configuration $4s^2 3d^1$. This configuration should not be far different from that of metallic scandium. Scandium apparently manages to "collect" this d electron.

4. Summary

It has been shown that consideration of the low-temperature electronic specific heat coefficient, γ, can provide insight into the problems that exist in doing a first-principle band calculation for metallic calcium. While the calculations are as yet incomplete, it is felt that the d electron, or the extreme sensitivity of the location of the d resonance to small changes in the effective crystal potential, may have a rather important role in the electronic properties of calcium. For example, one might expect very interesting effects from calcium conditions of pressure or alloying, depending on how the d band is "filled" or the d resonance is moved about.

5. Acknowledgments

The authors are grateful to Dr. J. S. Faulkner and Dr. Jan Linderberg for many helpful comments and discussions concerning this work.

6. References

[1] Manning, M. F., and Krutter, H. M., Phys. Rev. **51**, 761 (1937).
[2] Harrison, W. A., Phys. Rev. **118**, 1190 (1960).

[3] Harrison, W. A., Phys. Rev. **131**, 2433 (1963).
[4] Altmann, S. L., and Cracknell, A. P., Proc. Phys. Soc. **84**, 761 (1964).
[5] Vasvari, B., Animalu, A. O. E., and Heine, V., Phys. Rev. **154**, 535 (1967).
[6] Berlincourt, T., Proc. 7th Int. Conf. Low Temperature Physics (University of Toronto Press, Toronto, 1960), p. 231.
[7] Condon, J. H., and Marcus, J. A., Bull. Am. Phys. Soc. **6**, 145 (1961).
[8] Condon, J. H., and Marcus, J. A., Phys. Rev. **134**, A446 (1964).
[9] Korringa, J., Physica **13**, 392 (1947).
[10] Kohn, W., and Rostoker, N., Phys. Rev. **94**, 1111 (1954).
[11] Ham, F. S., and Segall, B., Phys. Rev. **124**, 1786 (1961).
[12] Segall, B., Phys. Rev. **125**, 109 (1962).
[13] Faulkner, J. S., Davis, H. L., and Joy, H. W., Phys. Rev. **161**, 656 (1967).
[14] Mattheiss, L. F., Phys. Rev. **133**, A1399 (1964).
[15] Slater, J. C., Phys. Rev. **81**, 385 (1951).
[16] Synek, M., Rainis, A. E., and Roothaan, C. C. J., Phys. Rev. **141**, 174 (1966).
[17] Griffel, M., Vest, R. W., and Smith, J. F., J. Chem. Phys. **27**, 1267 (1957).

Discussion on "Adjustment of Calculated Band Structures for Calcium by Use of Low-Temperature Specific Heat Data" by R. W. Williams and H. L. Davis (Oak Ridge National Laboratory)

W. Kohn *(Univ. of California):* The Rapporteur (R. E. Watson) mentioned some work in which the magnitude of the exchange was estimated from the atomic data. I don't know the details of this but I can understand in principle the rationale of such a procedure. But the Rapporteur also mentioned other work in which this parameter was adjusted. That I have never understood. May I elaborate on my lack of understanding here: If you are interested in electrons near the Fermi surface and if you are courageous enough to say that in some way they should be like free electrons then there is a definite value of the exchange there. Of course, they are not very much like free electrons but the fact they are not very much like free electrons affects everything about them, not just the exchange constant. So I would very much like to have some explanation of what is the rationale of saying, if we don't get a good fit with our simplified theory we are going to adjust that one parameter rather than, for example, trying to do some serious work on correlation effects and try to fit the data that way.

H. Davis *(Oak Ridge National Lab.):* From my point of view, we consider the resultant potential as a model potential and nothing more. You look at the phase shifts. Let's say you are trying to compare an electron calculation of Fermi surface parameters with single particle data such as the de Haas-van Alphen effect. You adjust to get proper phase shifts at that energy and these are the basic parameters of the theory. The result is just a model potential.

R. E. Watson *(Brookhaven National Lab.):* I believe that the screening is responsible for about half the upward *d*-shift in gold.

F. Herman *(IBM):* I would like to comment on Professor Kohn's question. My own feeling really is that the adjustment of the Slater exchange is a passing phase influenced by pseudism. You try to adjust things to make theory and experiments agree. My own present feeling is the important criterion in a first principle calculation is not really the comparison between the energy eigenvalue spectrum and experiment because if you think very carefully about the question you will be very hard put to provide a theoretical basis for demonstrating that there is any direct connection between an energy eigenvalue spectrum and the optical excitation spectrum using the approximate Hamiltonian. My own feeling at the present time is that if one really wants to do a first principles calculation one should use that exchange approximation which would give the lowest total energy for the crystal in the Hartree-Fock spirit. Now people are just beginning to try to calculate total energy in band calculations. I have a paper which will appear shortly in the International Journal of Quantum Chemistry which discusses this question and tries to reconcile the problem by indicating that what one should do is use the Gaspar-Kohn-Sham exchange approximation, perhaps also including inhomogeneous corrections, and after getting an energy eigenvalue spectrum this way, introduce corrections which hopefully give better estimates of levels whose differences correspond to optical excitations.

Fermi Surface Properties of the Noble Metals at Normal Volume and as a Function of Pressure*

W. J. O'Sullivan, A. C. Switendick, and J. E. Schirber**

Sandia Laboratories, Albuquerque, New Mexico 87107

We present the results of nonrelativistic KKR calculations of the Fermi surface properties of Cu, Ag, and Au at normal volume and as a function of pressure. In particular we compare electronic specific heats, effective masses and the associated pressure shifts with the corresponding experimental results for the noble metals. In contrast to the results of previous calculations we find that the Herman-Skillman-Mattheiss crystal potential is an excellent effective potential for both Cu and Ag.

Key words: Crystal potential; effective masses; electronic density of states; electronic specific heat; noble metals; pressure effects.

1. Introduction

Several attempts [1-4] have been made to estimate the contributions of low energy electron-phonon and electron-electron interactions to the Fermi surface properties of the noble metals by comparing calculated band effective masses m_B^* with experimental values. This approach can be understood within the context of the Landau Fermi liquid theory, in which the effective mass enhancement from combined electron-phonon and electron-electron interactions is given approximately by [5,6]

$$m^*_{\text{experimental}} \cong m_B^*(1+\alpha_e+\alpha_{ph}). \tag{1}$$

The coefficients α_e and α_{ph} correspond to specific Landau coefficients for the electron-electron and electron-phonon interactions and m_B^* is the result of a one-electron calculation of the effective mass in which effects of the static periodic lattice potential are included. The experimental and band values of the electronic specific heat are related by the same combination of enhancement factors. Although the theory assumes an isotropic Fermi surface, it is possible to gain an estimate of the effects of anisotropy by comparing the values of the lumped enhancement factor

$$\alpha=\alpha_e+\alpha_{ph} \tag{2}$$

determined by applying eq (1) to the cyclotron effective masses associated with the selected orbits about different sections of the Fermi surface.

Using this approach, Mueller and Zornberg [1] determined a value of α in Cu of about 0.25, while Faulkner, Davis, and Joy [2] (FDJ) and Dresselhaus [4] inferred a significantly smaller value. Christensen [3] has estimated an α for Ag of about 0.05, by comparing band effective masses calculated using the APW method with experiment.

In this paper we present the results of nonrelativistic KKR calculations of several band effective masses and the linear electronic specific heat coefficients for the noble metals at normal volume and as a function of pressure. Estimates of the total enhancement factors for the noble metals are derived from comparison between the calculated results and experiment.

2. The Band Calculations

The band effective masses and the electronic specific heat coefficients for the noble metals were calculated with the KKR method using a maximum angular momentum contribution, $l_{max}=3$.

The potentials used in these calculations were derived from Hartree-Fock-Slater atomic charge densities obtained from a slightly modified version of Herman and Skillman's [7] program. The superposition procedure described by Mattheiss [8] was used to obtain the spherically symmetric Coulomb and exchange potentials within the "muffin-tin" spheres. For both the atomic and crystal exchange potentials the unmodified Slater free-electron exchange approximation was used.

The effect of lattice dimension change on the crystal potential is incorporated in the variation of the con-

*This work was supported by the U.S. Atomic Energy Commission.
**Present address: University of Colorado, Boulder, Colorado.

tributions from neighboring atoms as the lattice varies in size, and in the scaling of the muffin-tin sphere radius with the lattice. Since we choose the muffin-tin radius so that the muffin-tin spheres make contact, the latter effect is determined unambiguously.

The results of the energy band calculations and the calculated Fermi surface dimensions for the noble metals at normal volume and as a function of pressure will be published [9,10] elsewhere.

Germane to this paper, however, is the fact that the calculated energy band structure for Cu is in essential quantitative agreement with that calculated by Burdick [11] with the Chodorow potential, and the experimental and calculated Fermi surface cross-sectional areas agree to about 1%. A comparison of our calculated bands for Ag with the bands calculated by Christensen [3] using Dirac-Slater wave functions, suggests that our d-bands are about 0.03 Ry too high. However, the calculated and experimental Fermi surface cross-sections agree to $\sim 1\%$ except in the case of the "neck" cross-section for $H||$ [111] where the calculated area underestimates the experimental value by about 10%.

The effective masses reported here were calculated from

$$m^* = \frac{\hbar^2}{2\pi}\left(\frac{\partial \Lambda}{\partial E}\right)_{E_F} \tag{3}$$

and the electronic specific heat coefficients, γ, were derived from

$$\gamma = \tfrac{1}{3}\pi^2 k^2 \rho(E_F), \tag{4}$$

where $\rho(E_F)$ is the calculated density of states at the Fermi energy. In these calculations, $\rho(E_F)$ was determined by a straight line fit of the derivative with respect to energy of the number of occupied states. The calculations were carried out over an energy range of $E_F \pm 0.002$ Ry, with a fixed energy increment of 0.0002 Ry. A mesh density corresponding to 561 **k** vectors in 1/48th of the Brillouin zone was used. This represents the same mesh used by Faulkner, Davis and Joy [2], and with it one can determine the Fermi energy for a noble metal to about 0.0002 Ry.

3. Comparison of Experimental and Calculated Results

The Fermi surface topology of the noble metals is simple enough that measurements of the effective masses corresponding to a small number of orbits constitute a reasonable sampling of the entire surface. The Fermi surfaces of the noble metals consist of essentially spherical electron surfaces centered at Γ with interconnecting necks in the [111] directions. With the magnetic field in the [111] direction a "belly" ($B(111)$) and "neck" ($N(111)$) orbit are observed. With the field along [110] a hole orbit made up of a combination of necks and spheres resembling a "dogbone" ($D(110)$) is observed. A similar fourfold symmetric hole orbit known as the "rosette" is observed for fields in a [100] direction in addition to another belly orbit about the spherical body of the surface ($B(100)$).

The calculated results for the band effective masses associated with all but the rosette orbit are compared with experiment in table 1. In table 2 we list the calculated electronic specific heat coefficients for the noble metals along with the corresponding experimental values.

The enhancement factor for Cu is about 0.10 ± 0.02 if we accept the lower value for the dogbone effective mass measured by Koch, Stradling and Kip [12]. In any case, α for Cu is about 0.1, in agreement with the observations of FDJ [2] and Dresselhaus [4]. The consistency of the values for α in Ag is, of course, fortuitous. We estimate α in Ag to be 0.03 ± 0.02, in essential agreement with the results of Christensen [3]. The combination of electron-electron and electron-phonon

TABLE 1. *A comparison between the calculated and experimental values of the effective masses for specific noble metal orbits*

Cu	m^*/m_0 (calculated)	m^*/m_0 (experimental)	α
N(111).....	0.412	0.46 ± 0.02 [a].....	0.12
B(111).....	1.28	$(1.410 \pm 0.005, 1.385 \pm 0.005)$ [a]..	.10
B(100).....	1.24	1.370 ± 0.005 [a].....	.10
D(100).....	1.11	1.290 ± 0.005 [a]$1.225 \pm 0.005)$ [a]...	.15(0.10)
Ag			
N(111).....	0.38	0.39 ± 0.02 [b].....	0.03
B(111).....	.902	$.93 \pm 0.01$ [c].....	.03
B(100).....	.896	$.93 \pm 0.01$ [c].....	.03
D(110).....	1.00	1.03 ± 0.01 [c].....	.03
Au			
N(111).....	0.321	0.29 [d](0.44)[e].....	< 0(0.37)
B(111).....	.844	1.14 ± 0.03 [f].....	0.28
B(100).....	.842	1.08 ± 0.03 [f].....	.28
D(100).....	.830	1.00 ± 0.03 [f].....	.20

[a] Reference 12.
[b] Reference 14.
[c] Reference 15.
[d] Reference 16.
[e] Reference 17.
[f] Reference 18.

TABLE 2. *Calculated and experimental linear electronic specific heat coefficients for the noble metals. The estimated relative error in the calculated* γ(mJ/mole-deg^2) *values is about 1 percent.*

	Calculated	Experiment [a]	α
Cu	0.641	0.698	0.09
Ag	.624	.644	.03
Au	.564	.727	.29

[a] Reference 19.

effects in Ag is much reduced over that in Cu. It is difficult to assess the effects of our neglect of relativistic contributions in the case of Au. The enhancement factor we find for Au is about 0.28.

Although effective pressures of up to 100 kbar were "applied" in these calculations, no significant variations in the calculated band effective masses were observed, with one possible exception. The calculated effective mass for the $N(111)$ orbit in Ag decreases with increasing pressure. Calculated values for $(\partial \ ln \ \gamma/\partial \ ln \ V)_T$ were obtained, although the large uncertainty in the calculated derivatives makes them of doubtful value for comparison with experiment. These results are listed in table 3. The experimental values for Cu were determined by inserting measured values for the electronic part of the linear thermal expansion coefficient in the relation

$$(\partial \ ln \ \gamma/\partial \ ln \ V)_T = 3\beta_e VB/(\gamma T) \qquad (5)$$

where β_e is the electronic linear thermal expansion coefficient, V is the molar volume and B is the bulk modulus. The uncertainty in the calculated volume derivatives of the specific heat could be reduced if we were to increase the **k** space mesh density used in the volume calculations.

While our calculated values for $\partial \ ln \ \gamma/\partial \ ln \ V$ seem to agree with the free electron value of 2/3 and the measured values of Carr et al. [13], our treatment neglects any volume dependence of the enhancement factor.

In conclusion we find that the Herman-Skillman atomic calculation with full Slater exchange provides an excellent starting point for detailed energy band and Fermi surface properties both at normal volume and as a function of pressure.

TABLE 3. *Calculated and experimental values for* $(\partial \ ln \ \gamma/\partial \ ln \ V)_T$

Metal	Calculated	Experimental
Cu	0.65 ($\pm$0.25) [a].43	[b] 0.63 ($\pm$0.06) [c] 1.21 ($\pm$0.13) [d] 1.12 ($\pm$0.05)
Ag	.83 ($\pm$0.30)	
Au	.38 ($\pm$0.25)	

[a] Reference 20.
[b] Reference 13.
[c] Reference 21.
[d] Reference 22.

4. References

[1] Zornberg, E. I., and Mueller, F. M., Phys. Rev. **151**, 557 (1966).
[2] Faulkner, J. S., Davis, H. L., and Joy, H. W., Phys. Rev. **161**, 656 (1967).
[3] Christensen, N. E., Phys. Stat. Sol. **31**, 635 (1969).
[4] Dresselhaus, G., Solid State Comm. **7**, 419 (1969).
[5] Ashcroft, N. W., and Wilkins, J. W., Phys. Letters **14**, 285 (1965).
[6] Peris, D., and Nozieres, P., The Theory of Quantum Liquids, (W. A. Benjamin, Inc., N.Y., 1966), p. 338.
[7] Herman, F., and Skillman, S., Atomic Structure Calculations, (Prentice Hall, Inc., Englewood Cliffs, N.J., 1963).
[8] Mattheiss, L. F., Phys. Rev. **133**, A1399 (1964).
[9] Schirber, J. E., and O'Sullivan, W. J., Proc. Colloque International Du C.N.R.S., Sur Les Proprietes Physiques Des Solides Sous Pression, Grenoble, France, to be published.
[10] O'Sullivan, W. J., Switendick, A. C., and Schirber, J. E., Phys. Rev., to be published.
[11] Burdick, G. A., Phys. Rev. **129**, 138 (1963).
[12] Koch, J. F., Stradling, R. A., and Kip, A. F., Phys. Rev. **133**, A240 (1964).
[13] Carr, R. H., McCammon, R. D., and White, G. K., Proc. Roy. Soc. (London) **A280**, 72 (1964).
[14] Joseph, A. S., Thorsen, A. C., and Blum, F. A., Phys. Rev. **140**, A2046 (1965).
[15] Howard, D. G., Phys. Rev. **140**, 1705 (1965).
[16] Joseph, A. S., Thorsen, A. C., and Blum, F. A., Phys. Rev. **140**, A2046 (1965).
[17] Shoenberg, D., Phil. Trans. Roy. Soc. (London) **A255**, 85 (1962).
[18] Langenberg, D. N., and Marcus, S. M., Phys. Rev. **136**, A1383 (1964).
[19] Martin, D. L., Phys. Rev. **141**, 576 (1966).
[20] Davis, H. L., Faulkner, J. S., and Joy, H. W., Phys. Rev. **167**, 601 (1968).
[21] Shapiro, J. M., Taylor, D. R., and Graham, G. M., Canad. J. Phys. **42**, 835 (1964).
[22] McLean, K. O., and Swenson, C. A., private communication.

417-156 O - 71 - 6

Discussion on "Fermi Surface Properties of the Noble Metals at Normal Volume and as a Function of Pressure" by W. J. O'Sullivan, A. C. Switendick, and J. E. Schirber (Sandia Labs.)

K. H. Johnson *(MIT):* The deviation you find in the Fermi surface of gold at the hexagonal face of the zone is, I believe, due to relativistic effects which you have not considered. We have carried out fully relativistic band calculations on gold, and we find the relativistic contributions very important.

W. J. O'Sullivan *(Sandia Labs.):* We are of course aware of this. In the paper we make no bones about our calculations on gold being more than qualitative. We just constructed a potential, carried out the calculation, and accepted the results. We made no attempt to adjust the potential in order to provide better agreement with Fermi surface data. Christensen [1] has included relativistic effects to some extent in silver by constructing a potential from the relativistic atomic Hartree-Fock-Slater wave functions. He also gets very good agreement with the Fermi surface data.

R. E. Watson *(Brookhaven National Lab.):* [In the course of reviewing the papers, the Rapporteur (R. E. Watson) had noted that there appears to be a subtle feature in the *shape* of the noble metal Fermi surface necks which has not been reproduced by either numerical or analytic band descriptions to date. The following comment refers to this.]

F. M. Mueller *(Argonne National Lab.):* Details of the noble metal Fermi surfaces will be affected by whether the potential outside the muffin tin sphere is kept constant or not. A non-constant potential will affect things because the belly orbit is largely of s-like symmetry and one would anticipate that it will sample the outside differently than the p-like levels. That is, the outside potential is different for states of odd symmetry than for states of even symmetry, and you go continuously from s-like to p-like states as you go around toward L_2'. I think this might be the source of the Fermi surface deviation. It is something left out of the calculations up until now.

J. Waber *(Northwestern Univ.):* The relativistic effects to which Dr. Keith Johnson alluded, are perhaps more important than may generally be realized. There is an interaction between two forces. The direct relativistic effect causes the s and p electrons to be attracted in toward the nucleus and concomitantly, there is a movement of the d bands outward radially because the nuclear charge is screened more effectively by the s and p electrons. I think that to a large extent this is one reason why one sees the d-bands in copper near the Fermi surface, but one finds them well below the Fermi level in silver. Finally, because of two relativistic effects, the d-bands are near the Fermi level in gold; they are driven up in energy by this indirect relativistic effect. In addition, they are separated and broadened by spin-orbit coupling. These comments will illustrate the importance of including relativistic effects in studying metals with large atomic number, like gold.

[1] Christensen, N. E., Phys. Stat. Sol. **31**, 635 (1969).

Calculated Effects of Compression Upon the Band Structure and Density of States of Several Metals*

E. A. Kmetko

University of California, Los Alamos Scientific Laboratory, Los Alamos, New Mexico 87544

Energy bands were obtained self-consistently by the augmented plane wave method for the following metals: Li, Cs, Ca, Sr, Ba, La, Ce, U, Pu, W and Fe. The density of states and the electronic charge were resolved into *s*-, *p*-, *d*-, and *f*-like components. Under compression the charges associated with the higher values of ℓ increase, mainly at the expense of the *s*-like component, and a more compact overall distribution is thereby achieved. The present results indicate that such "electronic transitions" are of general occurrence and probably play a significant role in determining the compressibility of metals.

Key words: Alkali and alkaline earth metals; augmented plane wave method (APW); cerium; compressibility; electronic density of states; lanthanides.

1. Introduction

This work is concerned with the band structure changes caused by compression and with the consequent effects upon the components of the density of states (and associated band charge) as characterized by the quantum number ℓ. The present report is preliminary inasmuch as only twelve metals, all of them cubic, have so far been investigated. They are: Li (bcc), Cs (bcc), Ca (fcc), Sr (fcc), Ba (bcc), La (fcc), Ce (fcc), U (bcc), Pu (fcc), Pb (fcc), W (bcc) and Fe (bcc). Because of the large number of graphs that would be required if complete results were to be presented for all twelve of these metals, only the results for the five underlined above will be given in detail. However, comparisons will be drawn between each of the others and the most appropriate one of the five selected for detailed presentation, and the analyzed charge distributions for all will be given in tables. Slater's augmented plane wave (APW) method [1] was used in a self-consistent manner to obtain the bands. The present investigation is not greatly concerned with details of the band structure in the vicinity of the Fermi surface, but rather with the overall or gross features that are pertinent to the interatomic interactions, elastic properties, and the electronic transitions which occur under compression. Thus, the nonrelativistic nature of the calculations is likely to be of only minor consequence except, perhaps, for U and Pu where the spin-orbit splitting of the 5*f* levels is of the order of 0.1 Ry and the velocity and Darwin corrections are far from negligible. Comparison of the present results for Pb with those of Louck's relativistic APW calculation [2] gives credence to this notion.

There have been several investigations into the effects of compression upon the electronic structure. Ham [3], using the quantum defect method, calculated bands at different interatomic distances for the alkali metals. Sternheimer [4], using Wigner-Seitz boundary conditions, numerically solved the Hartree-Fock equation for Cs in an investigation of a possible *s* to *d* electronic transition thought to cause the isomorphic collapse observed at high pressure. Recently Berggren [5], using the statistical atom model, found increases in *d*-character resulting from compression of the metals K through V. Royce [6] made what is probably the most extensive investigation of the effects of compression upon electronic structure; he compared the dependence of various calculated atomic orbital radii upon the atomic number, Z, with the Z dependence of corresponding empirical radii at different stages of compression. The observed compressibilities were thereby correlated with the degree of stability of the electronic structure under pressure. In particular, the low compressibilities of the transition metals seemed to result from the stability of the *d*-orbitals.

In the present work no attempt to obtain a quantitative correlation between the stability of the electronic bands and compressibility was made. Nevertheless, as

*Work performed under the auspices of the U.S. Atomic Energy Commission.

TABLE 1. *Lattice constants, exchange scale factors and charge distributions as analyzed into* s, p, d *and* f *components.*

Metal and structure	Linear compression %	Unit cell dimension A	Charge inside APW sphere				Plane wave charge outside APW sphere					Total charge per atom				Exchange potential scale factor
			s	*p*	*d*	*f*	Total	*s*	*p*	*d*	*f*	*s*	*p*	*d*	*f*	
Li bcc...	0.00	3.502	0.350	0.294	0.015	0.001	0.340	0.170	0.155	0.014	0.001	0.520	0.449	0.029	0.003	0.820
Li bcc...	5.0	3.326	0.336	0.302	0.015	0.001	0.346	0.170	0.160	0.014	0.001	0.506	0.462	0.029	0.002	
Cs bcc...	0.0	6.13	0.406	0.122	0.107	0.001	0.364	0.213	0.092	0.053	0.001	0.619	0.213	0.160	0.002	0.690
Cs bcc...	5.0	5.82	0.384	0.115	0.125	0.001	0.375	0.219	0.093	0.062	0.001	0.602	0.208	0.187	0.003	
Ca fcc...	0.0	5.565	0.635	0.419	0.397	0.007	0.545	0.214	0.212	0.113	0.006	0.849	0.631	0.509	0.013	0.717
Ca fcc...	5.0	5.287	0.596	0.371	0.467	0.007	0.559	0.223	0.199	0.132	0.006	0.818	0.569	0.598	0.013	
Sr fcc ...	0.0	6.0726	0.650	0.322	0.459	0.008	0.560	0.230	0.178	0.1452	0.007	0.879	0.500	0.604	0.015	0.703
Sr fcc ...	5.0	5.7690	0.624	0.287	0.512	0.008	0.569	0.226	0.168	0.168	0.007	0.850	0.455	0.680	0.015	
Ba bcc...	0.0	5.010	0.490	0.081	0.691	0.014	0.763	0.371	0.044	0.287	0.014	0.807	0.325	0.978	0.028	0.690
Ba bcc...	15.0	4.008	0.133	0.062	1.083	0.059	0.654	0.105	0.025	0.481	0.043	0.238	0.088	1.565	0.103	
β La fcc.	0.0	5.285	0.286	0.113	1.341	0.547	0.669	0.161	0.066	0.389	0.053	0.447	0.179	1.730	0.600	0.693
β La fcc.	5.0	5.021	0.230	0.126	1.657	0.384	0.651	0.098	0.059	0.462	0.032	0.328	0.185	2.120	0.416	
γ Ce fcc.	0.0	5.1612	0.281	0.103	1.294	1.653	0.662	0.155	0.057	0.375	0.075	0.436	0.159	1.669	1.730	0.696
α'Ce fcc.	10.0	4.660	0.150	0.109	1.673	1.280	0.775	0.090	0.041	0.547	0.120	0.240	0.150	2.210	1.400	
γ U bcc..	0.0	3.524	0.057	0.079	1.159	3.757	0.895	0.040	0.009	0.539	0.318	0.097	0.088	1.695	4.092	0.690
γ U bcc..	5.0	3.418	0.054	0.108	1.060	3.829	0.923	0.034	0.005	0.529	0.340	0.088	0.113	1.589	4.169	
δ Pu fcc.	0.0	4.637	0.057	0.068	0.847	6.309	0.624	0.031	0.009	0.325	0.257	0.088	0.078	1.172	6.567	0.690
δ Pu fcc.	5.0	4.405	0.059	0.053	0.811	6.407	0.575	0.037	0.013	0.304	0.221	0.095	0.066	1.115	6.627	
Pb fcc...	0.0	4.9057	1.428	1.550	0.224	0.063	0.705	0.164	0.395	0.103	0.043	1.592	1.945	0.350	0.106	0.699
Pb fcc...	5.0	4.6603	1.351	1.513	0.256	0.076	0.795	0.183	0.421	0.140	0.051	1.530	1.934	0.396	0.127	
W bcc...	0.0	3.15	0.350	0.352	3.914	0.069	1.3643	0.232	0.247	0.816	0.069	0.582	0.600	4.730	0.138	0.706
W bcc...	5.0	2.84	0.306	0.322	3.783	0.106	1.460	0.211	0.188	0.956	0.104	0.517	0.510	4.730	0.210	
Fe bcc...	0.0	2.8606	0.397	0.375	6.286	0.031	0.902	0.200	0.243	0.434	0.033	0.597	0.618	6.719	0.063	0.733
Fe bcc...	5.0	2.7178	0.378	0.379	6.230	0.036	0.967	0.203	0.254	0.471	0.039	0.580	0.632	6.701	0.075	

will be seen, considerable insight concerning the mechanisms underlying compressibility, beyond what has been provided by the work of Royce and particularly with respect to metals of the rare-earth type, seems to have been gained.

2. Method

The calculations for either 256 or 128 **k**-vectors in the reduced Brillouin zone, depending upon whether the structure was fcc or bcc, were made through use of a modified version of an APW program developed by Wood [7] and adapted to the self-consistent field method by DeCicco [8]. The self-consistency criterion was 0.002 Ry. For most of the metals the core charge was held fixed through the calculations, but in metals where the band charge contains about a tenth, or more of an *f* electron, it was found imperative to use a "soft" core. The charge distribution in such a core is atomic, and the configuration used in generating it is derived from the analyzed charge distribution appearing in the previous iteration (see below). This treatment is necessitated by the sensitivity of the core states as well as of the band states to even slight charges in *f*-character. The sensitivity is also illustrated in another way. In generating a potential for the $(N+1)$-st iteration, only about 10% of the potential from the N-th iteration can be used without causing instability where *f*-electrons

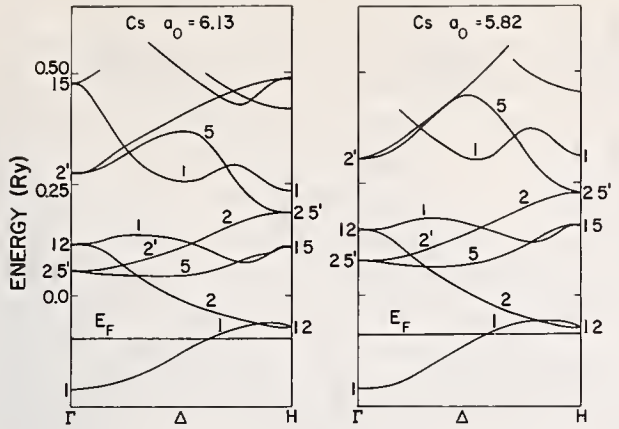

FIGURE 1. *Energy bands along [002] direction for bcc* Cs *in the normal state and under 5% linear compression.*
Energies are not absolute.

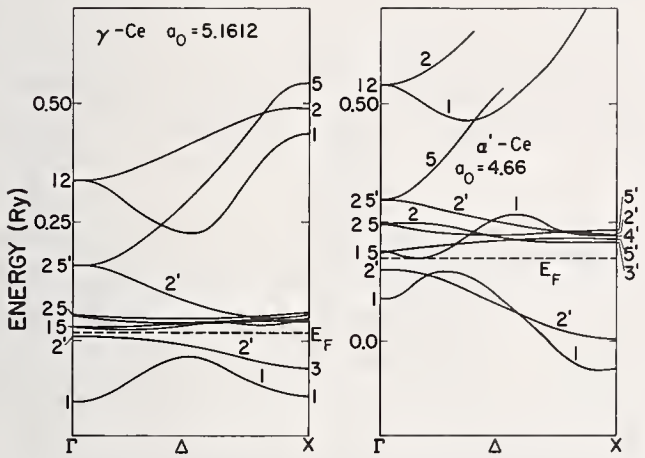

FIGURE 2. *Energy bands along [002] direction for fcc* γ-Ce *and* α'-Ce, *for which lattice constants are 5.16 A and 4.66 A, respectively.*
Energies are not absolute.

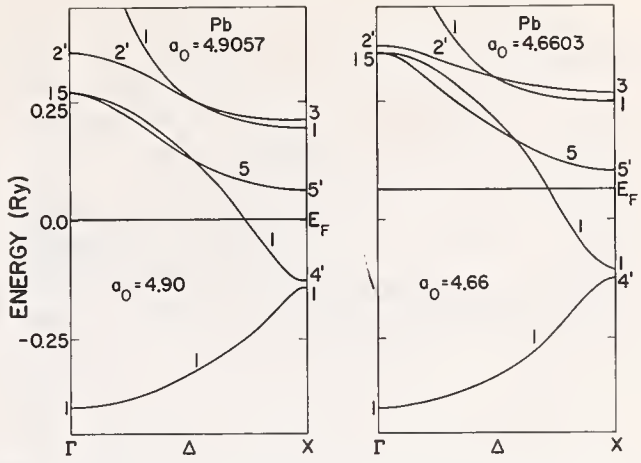

FIGURE 3. *Energy bands along [002] direction for fcc* Pb *in the normal state and under 5% linear compression.*
Energies are not absolute.

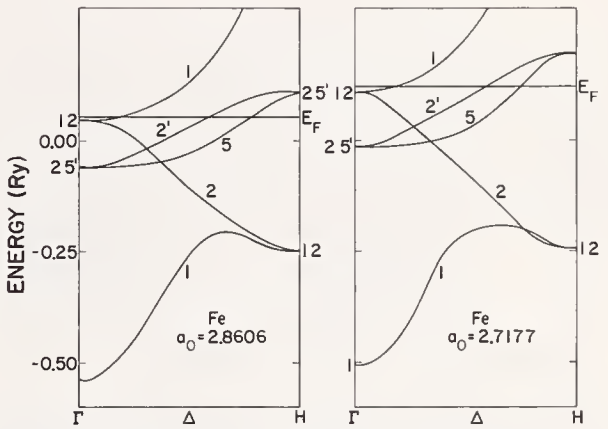

FIGURE 4. *Energy bands along [002] direction for* δ-Pu *in the normal state and under 5% linear compression.*
Energies are not absolute.

are involved. In most metals a feedback of 50% causes no difficulty. The number of iterations necessary to achieve self-consistency is variable, from three to as many as ten, and depends upon several factors which will not be mentioned here.

Starting potentials were obtained from a superposition of free atomic charge distributions by using the Löwdin technique [9]; the distributions were calculated from Hartree-Fock-Slater solutions obtained by using a variant of the program written by Herman and Skillman [10]. The local exchange potential was a scaled version of the Slater approximation [11], in which the scale factor, α, was used as a variational parameter in minimizing the total energy of the free atom. For all atoms through *Lw*, α lies between 1.0 and about 0.68 [12]. The values of α used for the metals in this study are given in table 1.

Even in free atoms the approximation of the local exchange by a single-parameter expression is questionable. In a crystal the use of such an exchange, which is optimized for the free atom, is subject to even greater criticism because of the moderate sensitivity of α to changes in potential near the "edge" of the atom when the latter self-energy correction [13] is switched on or off [12]. Nevertheless, its use seems justifiable if only because of its improved character; the virial theorem is satisfied in the case of the free atom [14] for a value of α only slightly smaller than that which minimized the Hartree-Fock total energy. The use of the original Slater exchange ($\alpha = 1.0$) causes the 4*f* band in both La and Ce to lie several tenths of a Ry below the bottom of the 6*s* band whereas the optimized exchange places this band at a physically realistic position, i.e., above the 6*s* band.

Since the APW's used have associated values of ℓ as high as 12, it is possible to resolve the band charge, and the density of states as well, into components corresponding to different values of ℓ. The plane wave

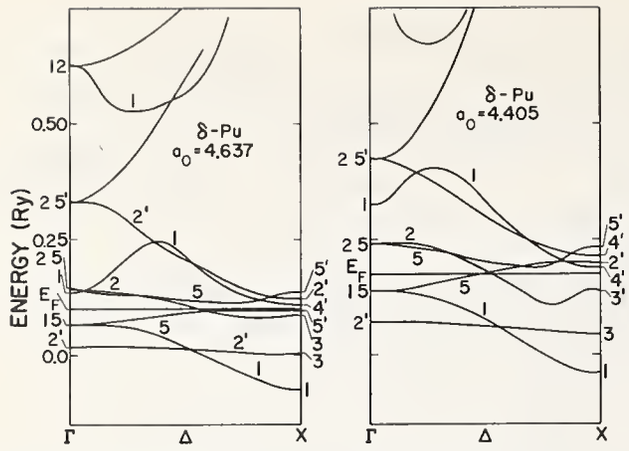

FIGURE 5. *Energy bands along* [002] *direction for bcc* Fe *in the normal state and under 5% linear compression.*
Energies are not absolute.

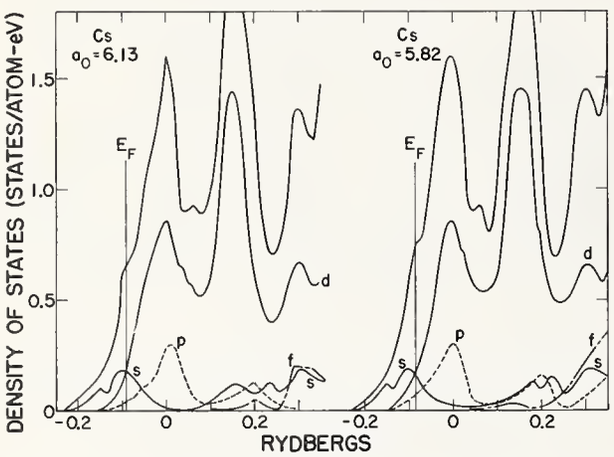

FIGURE 6. *Density of states* in toto *and as resolved into* s, p, *and* d *components for charge inside the APW sphere, shown for the normal and compressed bcc* Cs *crystal.*

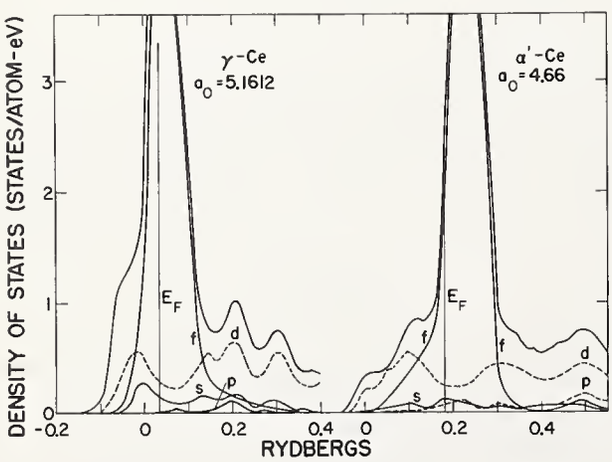

FIGURE 7. *Density of states* in toto *and as resolved into* s, p, d, *and* f *components for charge inside the APW sphere, shown for normal* (γ) *and compressed* (α') *fcc* Ce.

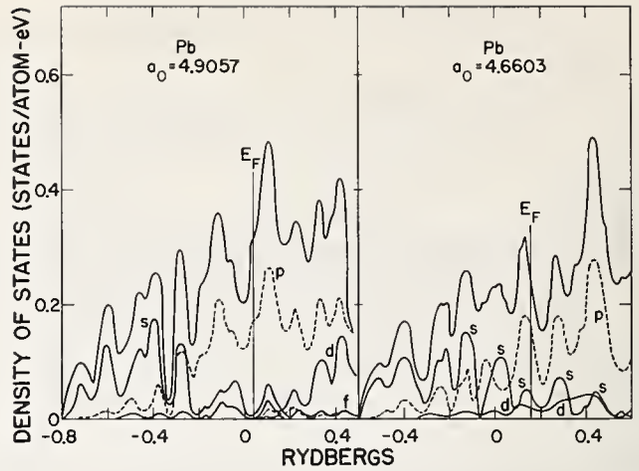

FIGURE 8. *Density of states* in toto *and as resolved into* s, p, d, *and* f *components for charge inside the APW sphere, shown for normal and compressed* Pb.

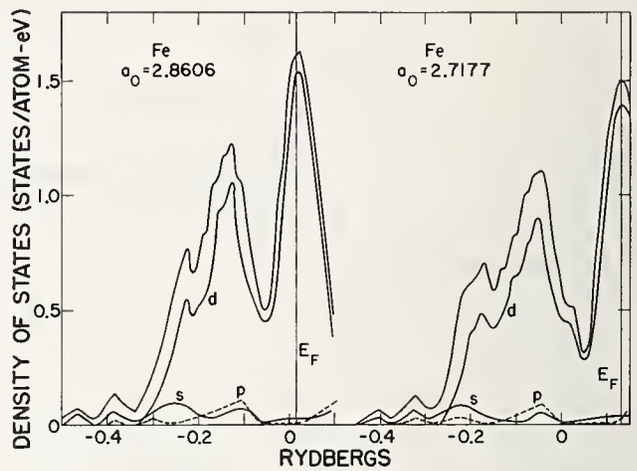

FIGURE 9. *Density of states* in toto *and as resolved into* s, p, *and* d *components for bcc* Fe *in normal and compressed crystals.*

charge can also be analyzed as to its *s*, *p*, *d* and *f*-character, as will be discussed later.

Smoothing of the density of states curves was achieved by averaging over five histograms, the origin of each having been shifted slightly relative to those of the others.

3. Results

The energy bands for both the normal lattice constants and for those decreased as indicated are shown along the [002] direction in figures 1 through 5, for Cs, Ba, Pb, Fe and Pu, respectively. The corresponding densities of states *in toto* as well as resolved into *s*, *p*, *d*, *f* and plane wave components are given in figures 6 through 9. Table 1 contains the resolved band charges for all the metals listed. In addition, table 1 includes the *s*, *p*, *d* and *f* content for the plane wave charges. The

analysis was achieved by assuming that the ℓ components in the plane waves are mixed in the proportions as are the charge distributions on the APW sphere surface, where the external plane waves are joined onto the interior wave functions.

The effects of compression upon the band charges, as shown in table 1, may be summarized as follows: (1) The components for which $\ell > 0$ generally grow at the expense of the s-like charge, the d component gaining the most except in Li, U and Pu; (2) In La and Ce f character is weakened while in U and Pu it is strengthened; (3) Where the f character is rather trivial, i.e., amounts of less than about 0.1 electron per atom, it remains so; (4) The total d character in W and Fe is very stable as indicated by the small absolute changes.

The density of states in figures 6 through 9 show how the total as well as the resolved charges are distributed in energy for both normal and compressed states. The densities shown for the s, p, d and f components pertain only to the wave functions inside the sphere inasmuch as it was not possible to analyze the plane wave functions.

For Cs we see in figure 6 that the d character falls off rapidly below the Fermi energy. This reflects the interaction between the $6s$ and $5d$ bands which is partly due to the symmetry requirement that the bands actually touch at point $H(002)$ as well as at other points on the zone boundary. The increase in d character under compression is caused by the slight band broadening apparent in figure 1.

Referring to Li in table 1, it is clear that, because the interaction is between the $2s$ and $2p$ bands, the very small d character is unchanged by the compression; here it is the p-like charge which gains. The changes calculated for the alkaline earths Ca and Sr are somewhat similar to that occurring in Cs. In both of these metals there is a comparatively large d component which is enhanced by pressure, the amounts of the other types of charge being roughly similar to the corresponding ones in the alkalis. In Ba the f-character becomes significant at a much higher compression, due to the broadening of the $4f$ band.

In La the $4f$ band lies between the $6s$ and $5d$ bands (not shown), the symmetry requirement at (002) causing strong interactions to occur between all three bands. Consequently there is over a half of an f electron in the band charge. Compression causes the f-like charge to diminish. A similar effect occurs in Ce (fig. 2). Here the $4f$ and $6s$ bands are closer together than in La and there is no double degeneracy at (002) to tie them together. As shown, when Ce is compressed the $5d$ band broadens so as to strongly perturb the lowest member of the $4f$ band and by distorting this branch, impart d-character at the expense of f-character. The situation with respect to band interaction in La is similar [15]. It is possible that this mechanism will remain valid even in the presence of magnetic interactions which are not included here. On the other hand, in both U and Pu the f-character which is very strong increases under compression. The bands for Pu are shown in figure 5.

Fe has a very stable band structure, as is quite obvious in figures 4 and 8 and in table 1. A similar result is found for W. In both of these metals, most of the charge is d-like and very stable. The relative changes in the other charge components with pressure follows the general pattern.

Pb under compression gains some d and f-character at the expense of the very large s and p-character. The s and p components in the normal metal (including that in the plane waves) are only slightly smaller than in the free atom. Consequently, self-consistency was reached very rapidly for this metal. The instability which does occur seems to be attributable to the proximity of the $6d$ and $5f$ bands. At a linear compression of 15% (not shown), the density of states is drastically altered and looks much like a serrated parabola, as might be found in a metal having free electrons [16].

4. Discussion and Conclusions

As a metal is squeezed, the charge distribution in each atomic cell necessarily becomes more compact. This occurs in two ways: (1) by simple distortion of the radial wave functions, and (2) by redistribution of charge among the various component distributions corresponding to different values of the quantum numbers n and ℓ. The results presented herein clearly demonstrate the general features of charge redistribution under compression. How each individual component is affected is determined by details of the band structure. In general, those bands which contain the valence electrons and those which lie close enough in energy to perturb them differ by no more than 1 in their values of $n + \ell$. Thus the degree of compactness of the corresponding atomic-like charge distributions increases with ℓ. In Ce, for example, the values of $n + \ell$ for the $4f$, $5d$, and $6s$ bands are 7, 7, and 6, respectively.

In metals beginning at about K, the presence of d-bands begins to be felt. Such bands are either occupied to some extent or act perturbatively to produce d-character in other bands. Probably the d-bands are responsible for the much greater compressibilities observed for K, Rb and Cs than for Li and Na [17]. In Pb, one of the most compressible metals, the high distorta-

TABLE 2. *Calculated exchange splittings and relativistic corrections for atoms of* Ce *and* U.

	Ce$(6s\alpha)(6s\beta)(4f\beta)^2$		U$(7s\alpha)(7s\beta)(6d\beta)(5f\beta)^3$		
	$4f$	$6s$	$5f$	$6d$	$7s$
Spin-orbit splitting (Ry)[a]	0.0295		0.0914	0.0549	
Velocity correction (Ry)[a]	+.0300	−0.0839	−.1127	−.0662	−0.2432
Darwin correction (Ry)[a]	−.0011	−.0465	−.0022	−.0007	+.1328
Exchange splitting (Ry)[b]	−.1540	−.0104	−.2019	−.1297	−.05332

[a] Perturbation calculations by Herman and Skillman [10].

[b] Calculated by the author in Hartree-Fock-Slater approximation with optimized statistical exchange potential [12].

bility of the very plentiful *s*-like charge plus the availability of *d* and *f*-like states probably act together to produce the large compressibility.

Only two of the transition metals, Fe and W, have so far been considered. However, the stability of their band structures is probably characteristic of transition metals, apparently stemming from the large *d*-component in the charge distribution, and is illustrated in their rather small compressibilities. This stability probably results from the difficulty of significantly altering charge distributions that are already quite compact due to their large *d*-character.

The alteration of *f*-character by compression requires special consideration. In metals lying below La the *f*-character is very small, of the order of 0.01 electron per atom or less, and is usually increased rather trivially by compression. Inasmuch as there are no *f*-bands involved in these metals, this behavior merely reflects the use of APW's having associated values of ℓ as high as 12.

The behavior of the two lanthanides, La and Ce, is diametrically opposed to that of the actinides, U and Pu, regarding the way *f*-character is altered by compression. Considering first the case of $4f$ electrons, it seems paradoxical that, under compression, charge flows out of a very compact *f*-like distribution into a more extended *d*-like one. This is deceptive, however. The effective radius of the atom is quite sensitive to the amount of $4f$ charge. As the charge is expelled, the atom shrinks. The empirical radii of rare-earth atoms are roughly 20% greater in the divalent than in the trivalent form, because of the difference in screening by $4f$ electrons. The effect of the change in *f*-character upon the atomic radius, as calculated for Ce metal, is large enough to account for a major part of the observed compressibility. This was shown by calculating for a free atom, the effect of a change in configuration from $(4f)^{1.73}\ (5d)^{1.67}\ (6s)^{0.44}\ (6p)^{0.16}$ to $(4f)^{1.40}\ (5d)^{2.21}\ (6s)^{0.24}\ (6p)^{0.15}$ which correspond to the calculated charge distributions in table 1. The radius of the outermost $5d$ maximum is reduced at the rate of 14.8% per *f*-electron removed. Thus, the band structural changes and the high compressibilities of La and Ce are apparently caused by the softness of the atom, which in turn stems from instability of the $4f$ orbitals under compression. To extend this mechanism to the other lanthanides is quite tempting, but is inadvisable inasmuch as little is known concerning band structures in those metals.

The results presented here for La and Ce are only tentative, inasmuch as exchange splitting and relativistic effects are not included. As table 2 shows, the exchange splitting of the $4f$ state in the Ce atom is of far more consequence than the relativistic corrections. Assuming that all of the corrections shown will be of similar magnitude in the metal, there should be a separation between the $4f\alpha$ and $4f\beta$ bands of about 1 eV. The perturbing, or hybridizing, effect of the $5d$ band should be similar to that indicated by the present results for Ce in spite of the large exchange splitting effect, though the band change distributions will be somewhat different.

U and Pu gain *f*-character under compression, as is indicated by these calculations. The relative change is small and the *d*-character loses correspondingly. In actinides, at least through Am, the $5f$ orbital is not so well buried as the $4f$ orbital in a lanthanide. This is illustrated as follows: If we denote by RS the APW sphere radius (approximately equal to the effective atomic radius in a metal) and by r_f the radius of the calculated principal maximum of the *f*-orbital, RS/r_f is 4.87 for Ce, 2.90 for U, and 3.2 for Pu. In U and Pu the $6d$ and $7s$ principal maxima lie outside the APW sphere, whereas

in Ce the 5*d* orbital has its maximum just inside the sphere. Consequently, (1) the 5*f* screening in actinides is not nearly so effective as that of the 4*f* charge in the lanthanides, and (2) the Coulomb interaction energy involved in squeezing the 6*d* and 7*s* charge into an atomic cell is so large that the corresponding bands lie well above the 5*f* bands in both metals. These calculations indicate that the 6*d* and 7*s* interactions with the 5*f* band diminish under compression because both the 6*d* and the 7*s* rise relative to the 5*f*. The compressibility of δ-Pu is about three times as large as that of γ-U [18], so that this property does not seem to reflect band structural changes here as well as in many other metals.

The effects of exchange and relativity in the lower actinides U and Pu will be somewhat different than in Ce, inasmuch as the 5*f* band is several times broader than the 4*f* band in Ce and the spin-orbit splitting is also much greater (table 2). The actinides beyond Am are chemically similar to the lanthanides, presumably because the 5*f* shell is more deeply buried in them than in the lower actinides. Thus, one might anticipate that the calculated compressive effects among the higher actinides would resemble those obtained for La and Ce.

These results and conclusions compare with those of Royce [6] as follows: (1) In both cases the transition metals show a high degree of stability under compression; (2) The present work suggests that the $f \rightarrow d$ rather than the $d \rightarrow f$ transitions are probably responsible for the high compressibilities of lanthanide metals; (3) Rather than an absence of 5*f* electrons in U and Pu, as suggested by Royce, the present results show large 5*f* band charges, which, because of their larger spatial extension relative to that of the 4*f* charge in the lanthanides, are actually augmented under compression at the expense of *d* charge.

The present work also indicates that charge redistribution under compression is of general occurrence and must be considered in conjunction with orbital stability in discussing compressibility.

5. Acknowledgments

The author is grateful to the following: J. H. Wood and A. M. Boring for enlightening discussions, E. C. Snow for generously making available his recent improvements in APW programming, Mrs. A. Lindstrom for her assistance in the calculational work, and to William N. Miner for editing the manuscript.

6. References

[1] Slater, J. C., Phys. Rev. **51**, 846 (1937).
[2] Loucks, T. L., Phys. Rev. Letters **14**, 1072 (1965).
[3] Ham, F. S., Phys. Rev. **128**, 82 (1962).
[4] Sternheimer, R., Phys. Rev. **78**, 235 (1950).
[5] Berggren, K. F., Phys. Letters **27A**, 125 (1968).
[6] Royce, E. B., Phys. Rev. **164**, 929 (1967).
[7] Wood, J. H., Phys. Rev. **126**, 517 (1962).
[8] De Cicco, P. D., Phys. Rev. **153**, 931 (1967).
[9] Löwdin, P. O., Phil. Mag. **5**, 1 (1956).
[10] Herman, F., and Skillman, S., Atomic Structure Calculations (Prentice-Hall Inc., Englewood Cliffs, N.J., 1963).
[11] Slater, J. C., Phys. Rev. **81**, 385 (1951).
[12] Kmetko, E. A., Phys. Rev. (to be published 1970).
[13] Latter, R., Phys. Rev. **99**, 510 (1955).
[14] Berrondo, M., and Goscinski, O., Quantum Theory Group, University of Uppsala, Report No. **198** (1967), Phys. Rev. (to be published 1969).
[15] Kmetko, E. A., Bull. Am. Phys. Soc., Ser. II, **14**, 358 (1969).
[16] Kmetko, E. A., to be published.
[17] See for example K. A. Gschneidner, Jr., Solid State Physics **16**, 275 (Academic Press, N.Y., 1964).
[18] Private communication of unpublished results by J. F. Andrew and S. Marsh of this laboratory.

Discussion on "Calculated Effect of Compression Upon the Band Structure and Density of States of Several Metals" by E. A. Kmetko (Los Alamos Scientific Laboratory)

D. J. Fabian *(Univ. of Strathclyde):* Willens and coworkers have studied the effect of pressure on soft x-ray emission from copper. They conclude that the variation of deformation potential throughout the band will give a particular effect at certain critical points, such as the Fermi surface and Van Hove singularities. Would Dr. Kmetko like to comment on this?

E. A. Kmetko *(Los Alamos Scientific Lab.):* I believe the effect could be quite serious at the Fermi level. However, I was specifically directing my attention to the overall change in hybridization which occurs under pressure. The main effect there on copper would be similar to iron. Very little overall change would occur in dehybridization.

OPTICAL PROPERTIES; BAND STRUCTURE III

CHAIRMEN: E. A. Stern
J. R. Cuthill

RAPPORTEUR: G. W. Pratt, Jr.

Optical Properties and Electronic Density of States*[1]

M. Cardona[2]

Brown University, Providence, Rhode Island and DESY, Hamburg, Germany

The fundamental absorption spectrum of a solid yields information about critical points in the optical density of states. This information can be used to adjust parameters of the band structure. Once the adjusted band structure is known, the optical properties and the density of states can be generated by numerical integration. We review in this paper the parametrization techniques used for obtaining band structures suitable for density of states calculations. The calculated optical constants are compared with experimental results. The energy derivative of these optical constants is discussed in connection with results of modulated reflectance measurements. It is also shown that information about density of empty states can be obtained from optical experiments involving excitation from deep core levels to the conduction band.

A detailed comparison of the calculated one-electron optical line shapes with experiment reveals deviations which can be interpreted as exciton effects. The accumulating experimental evidence pointing in this direction is reviewed together with the existing theory of these effects.

A number of simple models for the complicated interband density of states of an insulator have been proposed. We review in particular the Penn model, which can be used to account for response functions at zero frequency, and the parabolic model, which can be used to account for the dispersion of response functions in the immediate vicinity of the fundamental absorption edge.

Key words: Critical points; density of states; dielectric constant; modulated reflectance; optical absorption.

1. Optical Properties and One-Electron Density of States

The optical behavior of semiconductors and insulators in the near infrared, visible, and ultraviolet is determined by electronic interband transitions. An additional intraband or free electron contribution to the optical properties has to be considered for metals. We shall discuss here the relationship between the interband contribution and the density of states. The interband contribution to the imaginary part of the dielectric constant can be written as (in atomic units, $\hbar = 1$, m = 1, e = 1):

$$\epsilon_i(\omega) = \frac{1}{4\pi\omega} \iint_{\omega_{ef}=\omega} \frac{\mathbf{F}^{ef}}{|\nabla_{\mathbf{k}}\omega_{ef}|}\, dS_k \qquad (1)$$

where $\omega_{ef} = \omega_e - \omega_f$ is the difference in energy between the empty bands (e) and the filled bands (f). The spin multiplicity must be included explicitly in eq (1). The oscillator strength tensor $\mathbf{F}^{ef}$ is related to the matrix elements of $\mathbf{p}$ through $\mathbf{F}^{ef} = 2 < \mathrm{f}|\mathbf{p}|\mathrm{e} >< \mathrm{e}|\mathbf{p}|\mathrm{f} > \omega_{ef}^{-1}$. The Bloch functions are normalized over unit volume. Degenerate statistics have been assumed in eq (1) and spatial dispersion effects have been neglected.

It is customary to take the slowly varying oscillator strength out of the integral sign in eq (1) and thus write:

$$\epsilon_i(\omega) = \frac{2\pi^2}{\omega} \bar{F} N_d(\omega) \qquad (2)$$

where $\bar{F}$ is an average oscillator strength and N_d the combined optical density of states.

Structure in $\epsilon_i(\omega)$ (eq (1)) appears in the neighborhood of critical points, where $\nabla_{\mathbf{k}}\omega_{ef} = 0$. Such critical points can be localized in a small region of $\mathbf{k}$ space or can extend over large portions of the Brillouin zone over which filled and empty bands are parallel (sometimes only nearly parallel). Once the critical points which correspond to observed optical structure are identified in terms of the band structure through various devious and sometimes dubious arguments, their energies can

*An invited paper presented at the 3d Materials Research Symposium, *Electronic Density of States*, November 3–6, 1969, Gaithersburg, Md.

[1]Supported by the National Science Foundation and the Army Research Office, Durham.

[2] John Simon Guggenheim Foundation Fellow.

be used to adjust parameters of semiempirical band structure calculations.

Four different parametric techniques of calculating band structures have been used for this purpose: the empirical pseudopotential method (EPM) [1], the $\mathbf{k}\cdot\mathbf{p}$ method [2], the Fourier expansion technique (FE) [3], and the adjustable orthogonalized plane waves method (AOPW) [4].

Once reasonably reliable band structures are known it is important to calculate from them the imaginary part of the dielectric constant $\epsilon_i(\omega)$ and to compare it with experimental results so as to confirm or disprove the initial tentative assignment of critical points and thus the accuracy of the band structures. Rich structure is obtained in both experimental and calculated spectra and hence a rather stringent test of the accuracy of the available theoretical band structure is in principle possible.

In order to calculate numerically the integral of eq (1) it is necessary to sample eigenvalues and eigenfunctions at a large number of points in the Brillouin zone. The amount of computer time required for solving the band structure problem with first-principles methods (OPW, APW, KKR) at a general point of the Brillouin zone makes such methods impractical for evaluating eq (1). The parametric methods (EPM, $\mathbf{k}\cdot\mathbf{p}$, FE, but not AOPW) require only the diagonalization of a small matrix (typically 30×30) and hence it is possible to sample the band structure at about 1000 points with only a few hours of computer time. Cubic materials, in particular those with T_d, O, and O_h point groups, are simple in this respect: symmetry reduces the sampling required for the evaluation of eq (1) to only 1/48 of the Brillouin zone. Hexagonal and tetragonal materials have relatively larger irreducible zones and hence a larger number of sampling points is necessary if the resolution of the calculation is not to suffer. Once the band structure problem has been solved for all points of a reasonably tight regular mesh, the bands and matrix elements at arbitrary points can be obtained by means of linear or quadratic interpolation.

The method of Gilat and coworkers [5] has become rather popular for the numerical evaluation of eq (1) [4,6]. In the case of a cubic material the Brillouin zone is divided into a cubic mesh and the band structure problem solved at the center of these cubes (sometimes a finer mesh is generated by quadratic interpolation from the coarser mesh [6]). Within each cube of the mesh the bands are linearly interpolated and approximated by their tangent planes. The areas of constant energy plane within each cube corresponding to a given ω_{ef} are added after multiplying them by the corresponding oscillator strength and thus the integral of eq (1) is obtained.

The real part of the dielectric constant ϵ_r can be obtained from ϵ_i by using the Kramers-Kronig relations. It is also possible to obtain ϵ_r and ϵ_i simultaneously by calculating the integral:

$$\epsilon(\omega)=1-\frac{1}{2\pi^2}\iiint\frac{\mathbf{F}^{ef}\omega_{ef}}{[\omega_{ef}^2-(\omega+i\eta)^2]}\,dV_{\mathbf{k}} \qquad (3)$$

with η small and positive. For $\eta\rightarrow+$ o the imaginary part of eq (3) coincides with eq (1). Equation (3) can be evaluated with a Monte Carlo technique. Points are generated at random in $\mathbf{k}$ space within the Brillouin zone and the average value of the integrand for these points calculated. The process can be interrupted when reasonable convergence as a function of the number of random points is achieved [7,8].

We show in figure 1 the results of a calculation of ϵ_i from the $\mathbf{k}\cdot\mathbf{p}$ band structure of InAs with the method of Gilat and Raubenheimer [6]. The band structure problem, including spin-orbit effects, was solved at about 200 points of the reduced zone (1/48 of the BZ). We have indicated in this figure the symmetry of the critical points (or of the approximate regions of space) where the structure in ϵ_i originates. The experimental ϵ_i spectrum, as obtained from the Kramers-Kronig analysis of the normal incidence reflectivity [9], is also shown. The agreement between calculated and experimental spectra is good, with regards to both position and strength of the observed structure, with the excep-

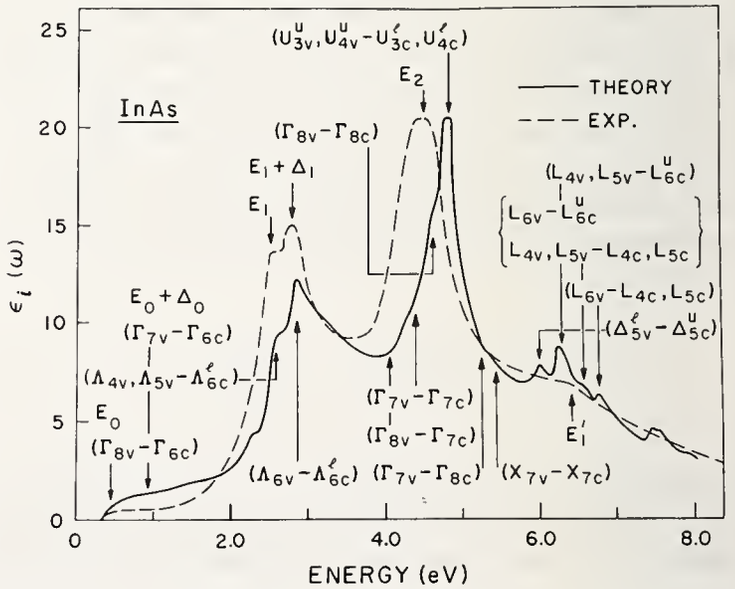

FIGURE 1. *Imaginary part of the dielectric constant of InAs as calculated from the* $\mathbf{k}\cdot\mathbf{p}$ *method* (——) [6] *and as determined experimentally* (----) [9]. *The group theoretical symmetry assignments were made with the help of the calculated isoenergy plots.*

tion of the position of the E_2 peak. This is to be attributed to an improper assignment of the E_2 peak when the 6 adjustable band structure parameters were determined. The E_2 peak had been attributed, following the tradition, to an X critical point while it is actually due to an extended region of **k** space centered around the U points [8]. It should be a simple matter to readjust the band structure parameters to lower the energy of the calculated E_2 peak by about 0.5 eV; in view of the large amount of computer time required to recalculate the energy bands this has not been done. The structure calculated around 6 eV, due mostly to spin-orbit splitting of the L_3 levels, has not yet been observed experimentally.

The conventional experimental determination of ϵ_i from normal incidence reflection data [9] suffers from considerable inaccuracy: to the experimental error produced by possible improper surface treatment and contamination one has to add the uncertainty in the high-energy extrapolation of the experimental data required for the Kramers-Kronig analysis. Some of these difficulties are avoided by comparing the *calculated* reflectivity spectra (obtained from ϵ with Fresnel's equation) with the experimental results. This is done in figure 2 for GaSb: the experimental data [10] have not been Kramers-Kronig analyzed because of the small range of the energy scale. Two calculated spectra have been plotted in this figure: one obtained from the $\mathbf{k} \cdot \mathbf{p}$ band structure [6] and the other obtained from a non-local pseudopotential calculation with 14 adjustable parameters [11]. The discrepancy between experimental and calculated curves at high energy, a common feature of many zincblende-type materials [12], has two origins: the measured reflectivity should be low because of increased diffuse reflectance at small wavelengths while the calculated one should be high because of the finite number of bands included in the calculation. In this region where $\epsilon_r - 1$ is small, the contribution to ϵ_r of transitions not included should lower the calculated reflectivity.

During the past few years a lot of activity has been devoted to the measurement and analysis of differential reflection spectra obtained with modulation techniques [13-15]. The wavelength (or photon energy) derivative spectra [14] should permit an accurate analysis of the line shapes of the spectra of figures 1 and 2. We show in figure 3 the temperature modulated reflection spectrum (thermoreflectance) of GaSb [15]: it has been shown that for the III–V materials [15] this spectrum is very similar to the photon energy derivative spectrum, difficult to obtain experimentally. The corresponding photon energy derivative spectrum obtained from the calculation of figure 2 is also shown in figure 3. The calculated and experimental shapes of the E_1, $E_1 + \Delta_1$ peaks show discrepancies of the type attributed in section 2 to exciton interaction. Derivative spectra for other germanium- and zincblende-type materials have been calculated by Walter and Cohen [12] and by Higginbotham [16].

The methods to calculate band structures from first principles, without or with only a few adjustable parameters (one [17] or three [4]) have recently achieved considerable success. However the calcula-

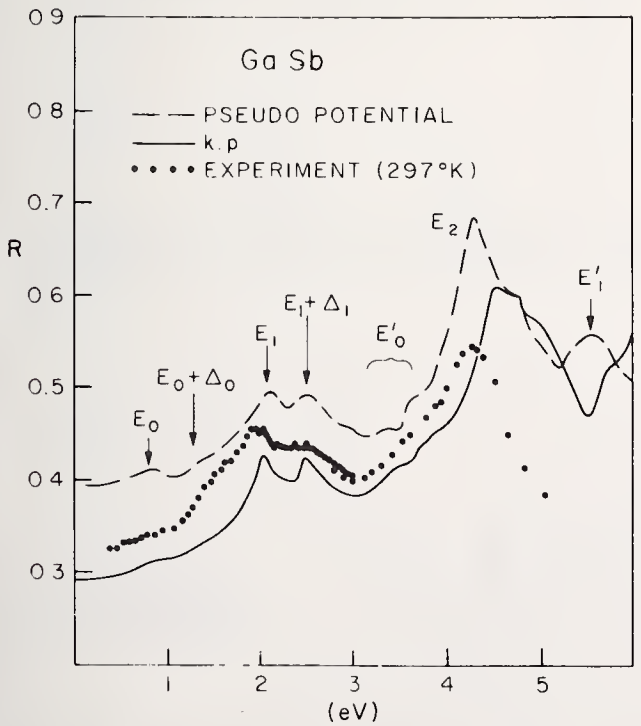

FIGURE 2. *Reflectivity of GaSb calculated from the* $\mathbf{k} \cdot \mathbf{p}$ [6] *and from a pseudopotential band structure* [11]. *Also, experimental reflectivity* [10].

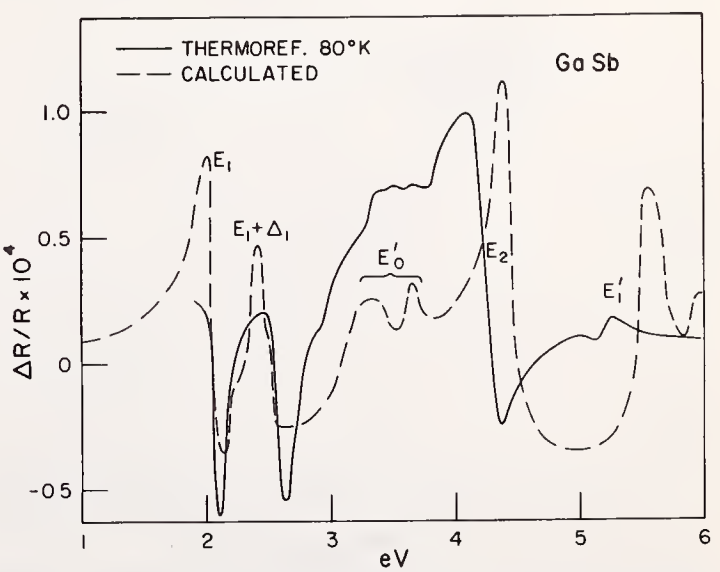

FIGURE 3. *Measured thermoreflectance spectrum of GaSb* [15] *compared with the energy derivative of the spectrum of figure 2* [16].

tion of energy bands at one general point of the BZ requires a lot of time so as to make density of states calculations prohibitive. Moreover, the evaluation of the matrix elements required for eq (1) is difficult with first principles techniques. It is nevertheless possible to use first principles calculations at a few high-symmetry points of the Brillouin zone to adjust the parameters of semiempirical band structures from which the large number of sampling points required for the evaluation of eq (1) can be obtained with relative ease. The $\mathbf{k} \cdot \mathbf{p}$ technique has proved particularly useful in this respect [2,18,19]. Matrix elements of $\mathbf{p}$ can be easily evaluated from the eigenvectors in the $\mathbf{k} \cdot \mathbf{p}$ representation. Spin-orbit interaction can also be easily included. This $\mathbf{k} \cdot \mathbf{p}$ procedure has been applied to the relativistic OPW band structure calculated by Herman and Van Dyke for gray tin [19]. Figure 4 shows the reflectivity of gray tin calculated by this procedure with the method of Gilat and Raubenheimer together with experimental results [20]. Comparison with other experimental results for the germanium family suggests that the high-energy end of the measured spectrum is too low, probably due to surface imperfections in the delicate crystals, grown from mercury solution, which were used for this experiment.

The $\mathbf{k} \cdot \mathbf{p}$ fitting procedure has also been applied to a first principles relativistic APW calculation of the band structure of PbTe by Buss and Parada [7]. Figure 5 shows the reflectivity of PbTe obtained by this method with a Monte Carlo sampling technique and figure 6 the absorption coefficient, both compared with experimental data [7,21,22]. In both cases the semiquantitative agreement between experimental and calculated data is remarkably good in view of the absence of the adjustable parameters. The calculated reflectivity is, at high energies, considerably higher than the experimental one, as discussed earlier for other materials. The E_1 peak of the experimental reflectivity spectrum appears split in the calculated spectrum, possibly because of inaccuracies in the first-principles band structure. The calculated E_1 structure appears due mostly to transitions along the Σ direction. The experimental E_1 structure has been assigned [23] to the lowest gap along Σ. The calculated E_2 peak corresponds to an extended region of the BZ without definite symmetry, as inferred from electroreflectance measurements [23].

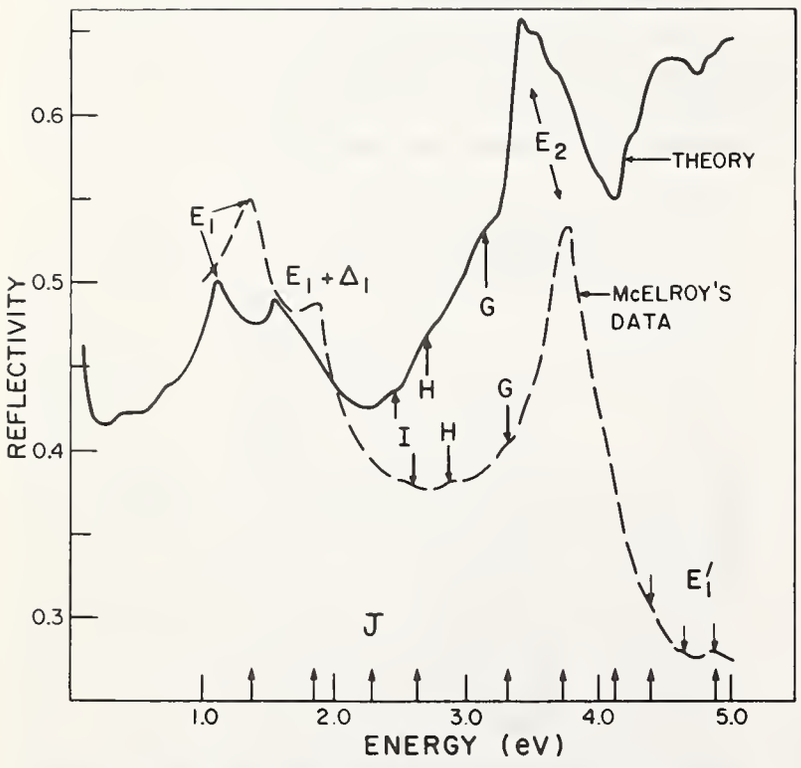

FIGURE 4. *Reflectivity of gray tin calculated from a first principles OPW band structure fitted with the* $\mathbf{k} \cdot \mathbf{p}$ *method* [19]. *Also experimental results* [20].

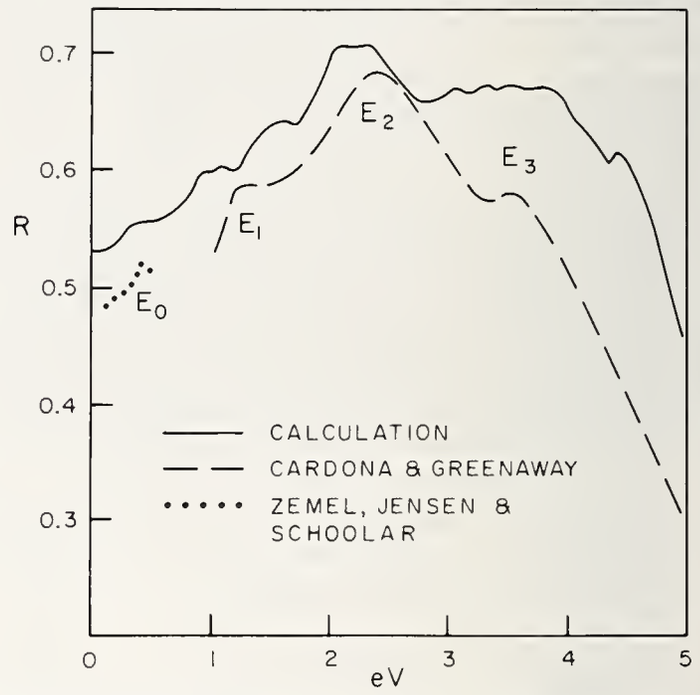

FIGURE 5. *Reflectivity of PbTe calculated from the APW-*$\mathbf{k} \cdot \mathbf{p}$ *band structure* [7], *compared with experimental results* [21].

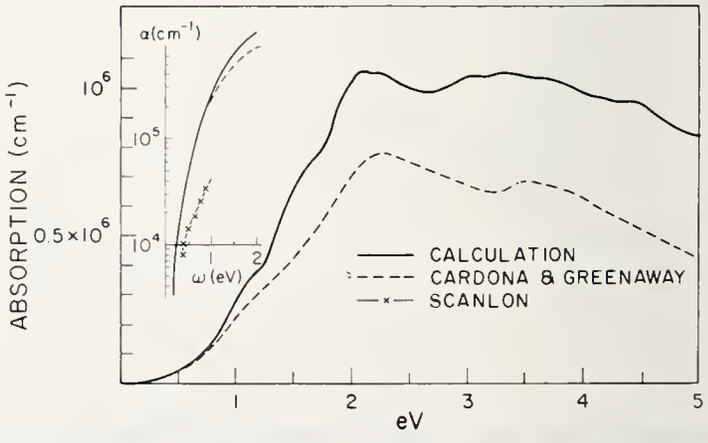

FIGURE 6. *Absorption coefficient PbTe calculated from the APW-*$\mathbf{k} \cdot \mathbf{p}$ *band structure, compared with experimental results* [21, 22].

We have so far discussed optical constants for cubic materials. While calculations for materials with lower symmetry require more computer time, one has the extra reward of being able to predict the experimentally observed anisotropy. Figure 7 shows the two principal components of ϵ_i for trigonal Se as calculated by Sandrock [24] from the pseudopotential band structure. The similarity between calculated and experimental results [25], also shown in figure 7, is especially remarkable in view of the method used to determine the pseudopotential parameters: they were determined from the pseudopotential parameters required to fit the optical structure of ZnSe. Only a small adjustment was performed so as to bring the calculated fundamental gap (1.4 eV) into agreement with the experimental one (2.0 eV). The dielectric constant of antimony (trigonal) for the ordinary and the extraordinary ray has also been calculated by a similar procedure [26].

The reasonable agreement obtained between experimental and calculated optical constants suggests the use of the corresponding band structure to determine the individual density of states D(ω): the main work, that of diagonalizing the Hamiltonian at a large number of points, has already been done. The programs required to calculate individual density of states are very similar to those used for the evaluation of eq (1): ω_{ef} must be replaced by the single band energies and F^{ef} must be removed. As an example we show in figure 8 the individual density of states of the 3 highest valence bands (six including spin) and the 3 lowest conduction bands of gray tin [19]. Direct information about the individual density of states can be obtained by a number of methods discussed in this conference. We mention, in particular, optical techniques involving transitions from deep core levels to the conduction band or from the valence band to temporarily empty core levels (soft x-ray emission) [27]. If the sometimes questionable assumption of constant matrix elements is made, the corresponding spectra represent the conduction (for absorption spectra) and the valence (for emission spectra) density of states because of the small width of the core bands. We show in figure 9 the densi-

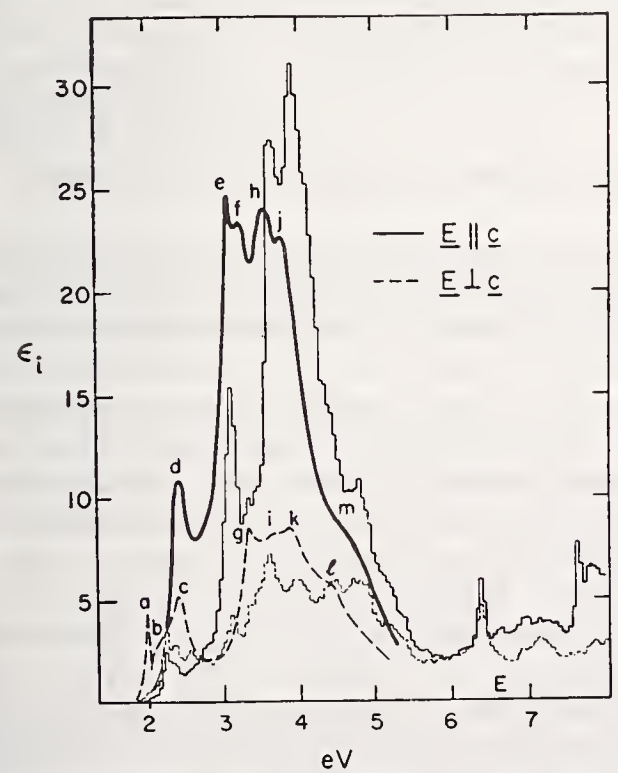

FIGURE 7. *Imaginary part of the dielectric constant of trigonal selenium for both principal directions of polarization of the electric field vector* **E** *as calculated from the pseudopotential band structure (histograms) [24] and as determined experimentally [25].*

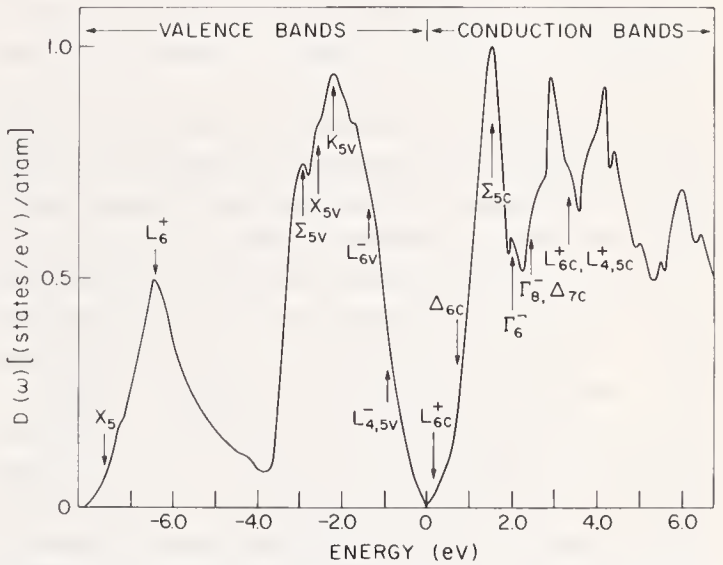

FIGURE 8. *Individual density of states for gray tin, obtained from the OPW-*$\mathbf{k}\cdot\mathbf{p}$ *band structure [19]. The top of the valence band is at 0 eV. The lowest valence band is not included.*

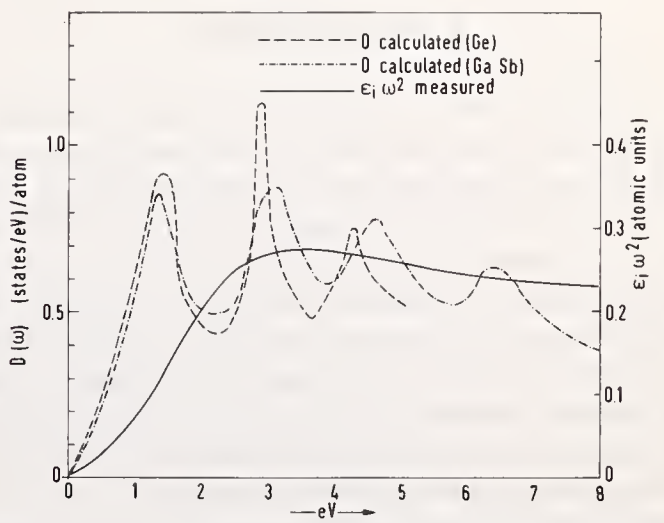

FIGURE 9. *Conduction density of states calculate for Ge [4] and for GaSb [6] together with the function* $\epsilon_i\omega^2$ *obtained from experimental data in the vacuum uv [28] (the horizontal scale for the* $\epsilon_i\omega^2$ *curve has been shifted by 29.5 eV).*

417-156 O - 71 - 7

ty of states of the conduction band of Ge calculated by Herman, *et al.* [4] and the corresponding density of states for GaSb as obtained by the $\mathbf{k} \cdot \mathbf{p}$ method [6]. The densities of states for both materials are very similar because of the similarity of their band structures. We also show in figure 9 the quantity $\epsilon_i\omega^2$ obtained by Feuerbacher *et al.* [28] for Ge in the region of the $M_{4,5}$ edge. The origin of energies has been shifted so as to make a comparison with the conduction density of states possible: $\epsilon_i\omega^2$ should be proportional to $D(\omega)$ under the assumption of constant matrix elements of $\mathbf{p}$. While the rich structure of the calculated density of states is not seen in the $\epsilon_i\omega^2$ curve, this curve is reproduced quite well if the density of states is broadened so as to remove the fine structure. The required lifetime broadening of about 1 eV is not unreasonable for the $M_{4,5}$ transitions. Using eq (2) with N_d replaced by the conduction density of states we obtain an average oscillator strength at the maximum of $\epsilon_i\omega^2\mathbf{F} = 0.15$. This oscillator strength corresponds to the 20 4d electrons per unit cell and hence it should be divided by 20 to obtain the average oscillator strength per d-band. If one reasons that the transitions from 10 of the 20 d bands to a given conduction band are forbidden because of the spin flip involved while transitions from 5 of these 10 bands are forbidden or nearly forbidden by parity, one finds for the average oscillator strength of each one of the 5 allowed bands $\overline{F} = 0.03$, which corresponds to a matrix element of $p = 0.13$ (in atomic units): this value is quite reasonable in view of the fact that the typical valence-conduction matrix element is 0.6. The small value of this matrix element explains why the d core electrons are negligible in the $\mathbf{k} \cdot \mathbf{p}$ analysis of the valence and conduction masses.

2. Exciton Effects

We have devoted section 1 to a comparison of experimental optical spectra with calculations based on the one-electron band structure. Exciton effects, *i.e.* the final state Coulomb interaction between the excited electron and the hole left behind, are known to modify substantially the fundamental edge of semiconductors and insulators [29]. Exciton-modified interband spectra seem also to occur in metals at interband edges which have the final state on the Fermi surface [30]. Experimental evidence for these effects is reported at this conference in the paper by Kunz *et al.*

We shall now discuss the question of exciton effects above the fundamental edge of insulators and semiconductors with special emphasis on the zincblende family. As mentioned in section 1 the gross features of these spectra are explained by the one-electron theory. The exciton interaction is responsible, at most, for small details concerning the observed line shapes. It is generally accepted [31,32] that the exciton interaction suppresses structure in the neighborhood of M_3 critical points: the Coulomb attraction with negative reduced masses is equivalent to a repulsion with positive masses. Such a repulsion smooths out critical point structure: no M_3 critical point has been conclusively identified in the experimental spectra. The E_1 and $E_1 + \Delta_1$ critical points of figures 1—3 are of the M_1 variety. Hence the line shape of the corresponding ϵ_i spectrum should be characterized by a steep low-energy side and a broader high-energy side. Figure 10 shows the shape of the E_1 peak observed at low temperature by Marple and Ehrenreich [33] and by Cardona [34]. In order to avoid effects due to the overlap of the E_1 and the $E_1 + \Delta_1$ peaks it has been assumed that they have exactly the same shape but shifted by 0.55 eV. The contribution of

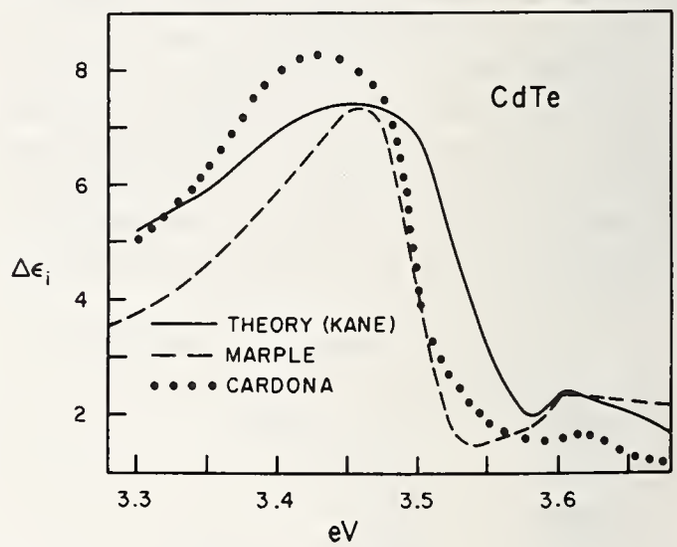

FIGURE 10. *Contribution of the* E_1 *gap to* ϵ_i *in CdTe as measured at low temperatures by Marple and Ehrenreich* [33] *and by Cardona* [34]. *Also calculation by Kane* [32] *using the adiabatic approximation.*

only E_1 has been extracted from the measured ϵ_i spectrum and displayed in figure 10. It is clear from this figure that the E_1 peak is steeper at high energies than at low energies, against the expectations for an M_1 peak. Also in figure 10 we show the results of a calculation by Kane [32] of the effect of Coulomb interaction on the E_1 line shape for CdTe, using the effective mass approximation. The solution of the effective mass Hamiltonian with non-positive-definite mass is made easier by the fact that the negative mass (along the Λ direction) has a magnitude much larger (about ten times) than the two equal positive masses. It is possible to use the adiabatic approximation [31], *i.e.*, to solve the two-dimensional hydrogen atom problem with the

third coordinate as a parameter and then solve the adiabatic equation for the third coordinate. The agreement between the calculated and the experimental line shapes of figure 10 is excellent.

Attempts have been made to calculate the dielectric constant including exciton interactions at an arbitrary point of **k** space, independently of the stringent restrictions of the effective mass approximation [35,36]. Such calculation is possible if one truncates the Coulomb interaction between electron and hole Wannier packets to extend to a finite number of neighboring cells. The extreme and simplest case of a δ-function (Koster-Slater) interaction can be solved by hand [31,35] and gives around an M_1 critical point the shapes of ϵ_r and ϵ_i shown in figure 11: for an M_i critical point the Koster-Slater interaction mixes the M_i one-electron line shape with the M_{i+1}. The high energy side of the ϵ_i peak becomes steeper, in agreement with figure 10. The line shape observed for the $E_1 - E_1 + \Delta_1$ peaks in the reflectivity spectrum is composed almost additively of the ϵ_i and ϵ_r line shape: at the energies of these peaks $dR/d\epsilon_i$ and $dR/d\epsilon_r$ are almost equal. We also show in figure 11 the line shapes expected for the reflectivity spectra of the $E_1 - E_1 + \Delta_1$ peaks and for the corresponding differential spectra ($dR/d\omega$). We show in figure 12 the photon energy derivative spectrum of these peaks in HgTe [37]: the observed line shapes disagree with those expected from the one-electron theory (equal positive and negative peaks) but agree with those predicted in the presence of a Koster-Slater interaction (fig. 11). Similar results have been found for other zincblende-type materials [37].

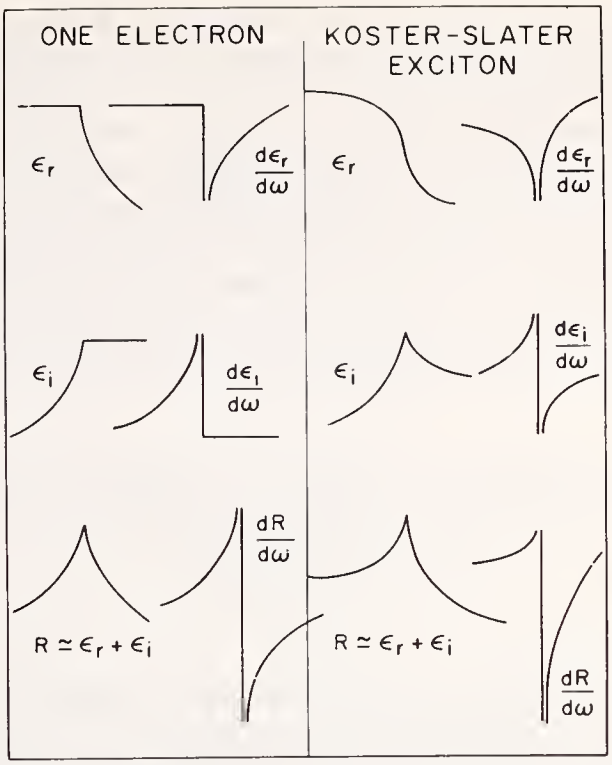

FIGURE 11. *Modification in ϵ_r and ϵ_i introduced by the Koster-Slater exciton interaction in the neighborhood of an M_1 critical point. Also, effect on the reflectivity under the assumption of an equal contribution of $\Delta\epsilon_r$ and $\Delta\epsilon_i$ to the reflectivity line shape.*

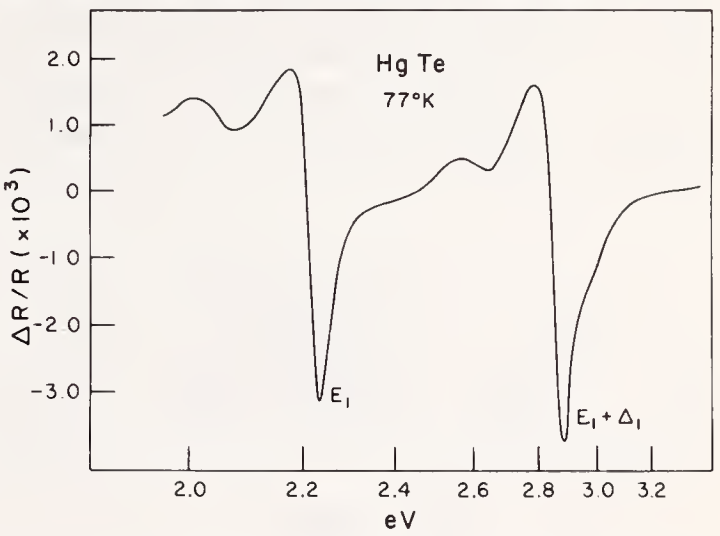

FIGURE 12. *Photon energy derivative spectrum of the reflectivity of HgTe in the neighborhood of the E_1 and $E_1 + \Delta_1$ structure* [37].

3. Simplified Models for the Density of States

As seen in section 1 the optical density of states, and thus the dielectric constant, is a complicated function of frequency and its calculation requires lengthy numerical computation. For some purposes, however, it can be approximated by simple functions. In the vicinity of a critical point of the M_i variety, for instance, the singular behavior of the dielectric constant can be approximated by:

$$\epsilon \propto i^{r+1}(\omega - \omega_g)^{1/2} + \text{constant} \qquad (4)$$

if exciton effects are neglected. Exciton interaction can be included, within the Koster-Slater model, by multiplying eq (4) by a phase factor $e^{i\phi}$ with ϕ small and positive.

As shown in figure 1, ϵ_i for the zincblende-type materials has a strong peak (E_2) in the neighborhood of which most of the optical density of states is concentrated. The corresponding transitions occur over a large region of the BZ, close to its boundaries. In order to represent this fact, Penn [38] suggested the model of a non-physical spherical BZ with an isotropic gap at its boundaries. The complex energy bands of the material are then replaced by those of a free electron with an isotropic gas ω_g at the boundary of a spherical BZ. This gap should occur in the vicinity of the E_2 optical structure. While this model represents rather poorly the rich

structure of ϵ_i (fig. 1), it is expected that it should give a good picture of ϵ_r at zero frequency. The reshuffling of density of states involved in the case of the isotropic model should not affect $\epsilon_r(\omega = o)$ very much because of the large energy denominators which appear in eq (3) for $\omega = o$: the lowest gap ω_o, usually much smaller than ω_g, accounts only for a very small fraction of the optical density of states. Penn obtained with this model the static dielectric constant for a finite wavevector $\mathbf{q}$. The result can be approximated by the analytic expression [38]:

$$\epsilon(\omega = o,\ q) = 1 + \left(\frac{\omega_p}{\omega_g}\right)^2 \mathcal{F} \left\{1 + \frac{\omega_F}{\omega_g}\frac{q}{k_F}\mathcal{F}^{1/2}\right\}^{-2} \quad (5)$$

with $$\mathcal{F} = 1 - \frac{\omega_g}{4\omega_F} + \frac{1}{3}\left(\frac{\omega_g}{\omega_F}\right)^2$$

In eq (5) ω_p is the plasma frequency obtained for the density of valence electrons and ω_F and k_F the corresponding free electron Fermi energy and wave number. The dimensionless quantity $\mathcal{F}$ is usually close to one.

Figure 13 shows eq (5) for Si compared with the exact results of the Penn model [39]. These results are obviously independent of the direction of $\mathbf{q}$. A small dependence on this direction is found from a complete pseudopotential calculation by Nara [40] (see also fig. 13). The function $\epsilon(o,\mathbf{q})$ is of interest for the treatment of dielectric screening.

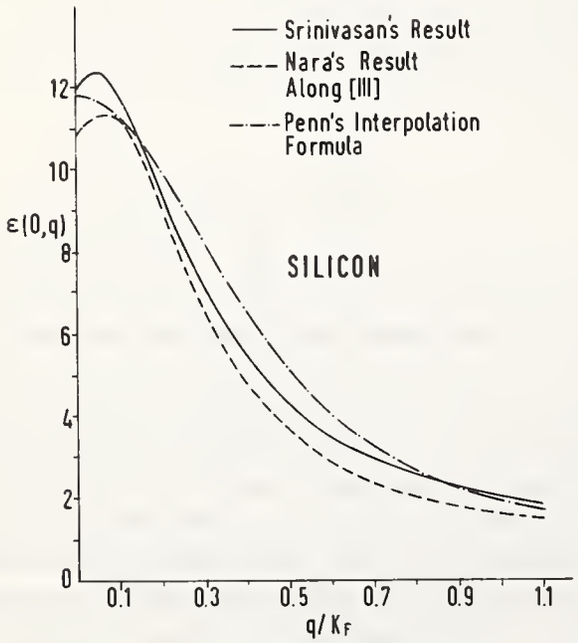

FIGURE 13. *Static dielectric constant $\epsilon(o, \mathbf{q})$ obtained by Srinivasan [39] for Si with the Penn model compared with the interpolation formula of eq (5) and with the results of a pseudopotential calculation by Nara [40] for $\mathbf{q}$ along (111).*

Equation (5) yields for $\mathbf{q} = o$ the electronic contribution to the static dielectric constant:

$$\epsilon_o = 1 + \mathcal{F}\left(\frac{\omega_p}{\omega_g}\right)^2 \simeq 1 + \left(\frac{\omega_p}{\omega_g}\right)^2 \quad (6)$$

The experimental values of ϵ_o agree reasonably well with the results of eq (6) using for ω_g the energy of the E_2 peak [34]. Equation 6 has gained recent interest as the basis of Phillips and Van Vechten's theory of covalent bonding [41,42,43]. These authors use eq (6) and the experimental values of ϵ_o to define the average gap ω_g. With this gap and the corresponding gap of the isoelectronic group IV material they can interpret a wide range of properties such as crystal structure [42], binding energy [43], energies of interband critical points [41], non-linear susceptibilities [44], *etc.* As an example we discuss the hydrostatic pressure (*i.e.* volume) dependence of ϵ_o for germanium and silicon. According to Van Vechten [41], ω_g for C, Ge, Si, and $\alpha-$Sn is proportional to $(a_o)^{-2.5}$ where a_o is the lattice constant. If one makes the assumption that this law gives also the change in ω_g with lattice constant for a given material when hydrostatic stress is applied one can calculate the volume dependence of ϵ_o [41]. Neglecting the one in eq (6), a valid approximation for Ge and Si, one finds:

$$\frac{1}{\epsilon_o}\frac{d\epsilon_o}{dV} = 2\left(\frac{d\ \ln\ \omega_p}{dV} - \frac{d\ \ln\ \omega_g}{dV}\right)$$

$$= 2[0.83 - 0.50] = 0.66 \quad (7)$$

Equation (7) explains the sign and the small magnitude observed for $(1/\epsilon_o)(d\epsilon_o/dV)$. The experimental values of this quantity are 1.0 for Ge and 0.6 for Si [41,45].

According to eq (6) the average gap ω_g determines the electronic dielectric constant for $\omega = o$. As the lowest gap ω_o is approached ($\omega_o \ll \omega_g$ usually), ϵ_r exhibits strong dispersion. This dispersion is due, in the spirit of eq (3), to the density of states in the vicinity of ω_o. For the purpose of calculating the dispersion of ϵ_r immediately below ω_o, the density of states can be approximated by that of parabolic bands with a reduced mass equal to the reduced mass μ at ω_o. These bands are assumed to extend to infinity in $\mathbf{k}$ space: the unphysical contribution to ϵ_r for $|k| \to \infty$ should be small for $\omega \leqslant \omega_o$, because of the large energy denominators of eq (3). We thus obtain for a cubic material the following contribution of the ω_o gap to the scalar dielectric constant below ω_o (under the assumption of a constant matrix element of $\mathbf{p}$ equal to $\mathbf{P}$) [46]:

$$\Delta\epsilon_r = 2(2\mu)^{3/2}\omega_0^{-3/2}|P|^2 f(\omega/\omega_0) = C_0'' f(\omega/\omega_0)$$

with (8)

$$f(x) = 2-(1+x)^{1/2}-(1-x)^{1/2}.$$

Equation (8) represents quite well the behavior of ϵ_r immediately below ω_o for the lead chalcogenides [47] and a number of other semiconductors [48]. As an example we show in figure 14 the observed dispersion of ϵ_r below ω_o at room temperature [49] together with a fit based on eq (8) [48]. For the sake of completeness we have included in the fitting equations not only the effect of ω_o (E_o) but also that of its spin-orbit-split mate $E_o+\Delta_o$ (also represented by an expression similar to eq (8)), the dispersion due to the E_1 and $E_1+\Delta_1$ gaps, and that due to the main ω_g gap assuming $\omega_g \equiv E_2$. Thus the fitting equation with three adjustable parameters C_0'', C_1'', C_2'' is [48]:

$$\epsilon_r(\omega) = 1 + C_o''\left\{f(x_o) + \frac{1}{2}\left(\frac{\omega_o}{\omega_{os}}\right)^{3/2} f(x_{os})\right\} + C_1''\left\{h(x_1) + \left(\frac{\omega_1}{\omega_{1s}}\right) h(x_{1s})\right\} + C_2''(1+2x_2^2) \quad (9)$$

where:

$$\omega_{os} = \omega_o + \Delta_o, \qquad x_{os} = \frac{\omega}{\omega_{os}}, \qquad x_1 = \frac{\omega}{\omega_1}$$

$$\omega_{1s} = \omega_1 + \Delta_1, \qquad x_{1s} = \frac{\omega}{\omega_{1s}}, \qquad x_2 = \frac{\omega}{\omega_g}$$

$$h(x_1) = 1 + \frac{x_1^2}{2}.$$

The fitting values of C_0'' (6.602) and C_1'' (2.791) are in qualitative agreement with those calculated from the band parameters [48].

The parabolic model density of states can also be used to interpret the strong dispersion in the piezobirefringence observed near the lowest direct gap of

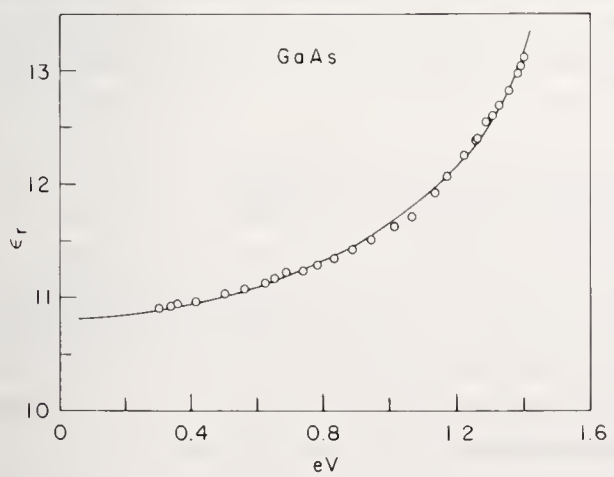

FIGURE 14. *Experimental results for ϵ_r in GaAs below the fundamental edge at room temperature [49] (circles) and fitted curve based on a model density of states.*

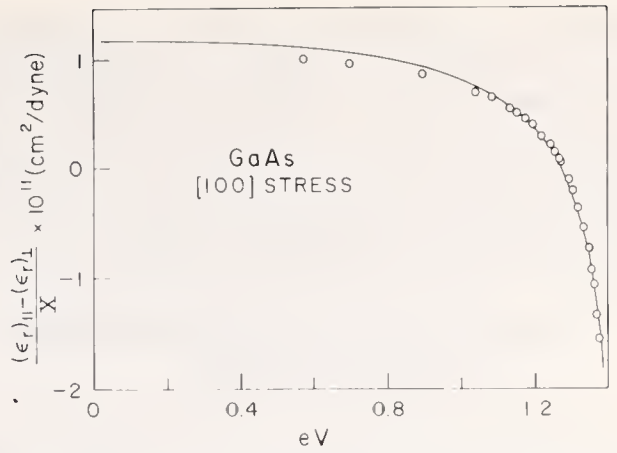

FIGURE 15. *Piezobirefringence in GaAs for an extensive stress along (100) (room temperature). The circles are experimental points. The solid line is a fit based on the model of eq (5) [48].*

Ge, GaAs [48], and other III–V semiconductors [50,51]: uniaxial stress splits the top valence band state (Γ_8) and a birefringence in the contribution of E_o to ϵ_r results because of the selection rules for transitions from the split bands. The main contribution to this piezobirefringence is expected to be proportional to f′(x), which diverges like $(\omega-\omega_0)^{-1/2}$ for $\omega \to \omega_o$. Such behavior can be seen in the experimental results (circles) of figure 15 obtained for GaAs at room temperature. Included in this figure is the corresponding fit based on the model of eq (9) [48].

The long-wavelength, non-dispersive contribution to the piezobirefringence of figure 15 can be interpreted, at least qualitatively, in terms of the Penn model of eqs (6) and (7). Equation (7) yields two contributions to the change in ϵ_r one due to the change in plasma frequency (*i.e.* carrier density) with stress and the other due to the change in the isotropic gap. The first contribution should not exist for a pure shear stress. For a hydrostatic stress the second contribution can be written in tensor form as:

$$\frac{1}{\epsilon_0}\Delta\epsilon_0 = 5\mathbf{e} \quad (10)$$

where **e** is the strain tensor. We postulate that eq (8) remains valid for pure sheer stress. This crude generalization has a clear physical meaning in terms of the Penn model. The spherical BZ becomes ellipsoidal under a sheer stress and the energy gap at an arbitrary point of the BZ boundary k_F becomes anisotropic. The gap at k_F is assumed to become larger as k_F becomes larger (k_F is the distance between atomic planes per-

pendicular to k_F). Equation (8) gives the right sign for the long wavelength contribution to the piezobirefringence of figure 15 but a magnitude about five times larger. The agreement becomes better if the contribution of the E_o edge to the long wavelength piezobirefringence, of opposite sign to that predicted by eq (10), is subtracted from the experimental results.

4. Third Order Susceptibility and Model Density of States

It has been recently suggested [52] that the third order susceptibility of Ge, Si, and GaAs at long wavelengths is related to the Franz-Keldysh effect (*i.e.* the intraband coupling by the field) of interband critical points [53]. We discuss now the Franz-Keldysh contribution of the ω_g, E_o, and E_1 gaps to $\chi^{(3)}_{1111}$.

4.1. Average Gap ω_g

In the spirit of Penn's model [38] we represent the long-wavelength dielectric constant by eq (6) with $\mathcal{F}=1$. The corresponding imaginary part of the dielectric constant is, for $\omega > \omega_g$ [47]:

$$\epsilon_i = A_\omega^{-2}(\omega-\omega_g)^{-1/2}$$

with $$A=\frac{4}{3}\,\omega_p^2\omega_g^{1/2} \tag{11}$$

The Franz-Keldysh effect for the one-dimensional absorption edge of eq (11) can be expressed in terms of the Airy functions Ai and Bi [54]. One must mention, however, that the isotropic gap problem in the presence of an electric field would only be completely equivalent to the one-dimensional problem if the field experienced by every electron were along the direction of the corresponding **k**. The fact that the field $\mathscr{E}$ is the same for all electrons, regardless of **k**, can be taken into aecount by using an average field:

$$\langle \mathscr{E}^2 \rangle = \frac{\langle \cos^4\beta\rangle}{\langle \cos^2\beta\rangle}\,\mathscr{E}^2 = \frac{3}{5}\,\mathscr{E}^2 \tag{12}$$

where β is the angle between **k** and $\mathscr{E}$. The long-wavelength expression for $\chi^{(3)}_{1111}$ thus is [54]:

$$\chi^{(3)}_{1111}=\frac{3A}{20\pi\omega^2}\lim_{\substack{\mathscr{E}\to 0\\ \omega\to 0}}\mathscr{E}^{-2}\theta^{-1/2}\left(G_1\left(\frac{\omega_g+\omega}{\theta}\right)\right. \tag{13}$$

$$\left. +G_1\left(\frac{\omega_g-\omega}{\theta}\right)-G_1\left(\frac{\omega_g}{\theta}\right)\right),$$

where the one-dimensional electro-optic function $G_1(\eta)$ is given by [54]:

$$G_1(\eta)=2\pi Ai(\eta)Bi(\eta)-H(\eta)\eta^{-1/2}$$

$$\theta=\left(\frac{\mathscr{E}^2}{2\mu}\right)^{1/3} \tag{14}$$

In eq (14) H (η) is the unit step function and μ the reduced mass of the Penn model, given by $\mu=\omega_g(2k_F)^{-2}$. The Fermi momentum of the valence electrons is related to the plasma frequency ω_p through $k_F{}^3=(3/4)\pi\omega_p{}^2$.

The limit for $\mathscr{E}\to 0$ in eq (14) is easily found using the asymptotic expansions of Ai (η) and Bi (η) for $\eta\to+\infty$ [55]. By subsequently performing the limit for $\omega\to 0$ one finds:

$$\chi^{(3)}_{1111}=\frac{287}{256\pi}\left(\frac{3}{4}\,\pi\right)^{2/3}(\epsilon_o-1)\,\frac{\omega_p^{4/3}}{\omega_g^4} \tag{15}$$

Or, for ease of evaluation, with $\chi^{(3)}_{1111}$ in e.s.u., and the energies in eV:

$$\chi^{(3)}_{1111}=1.45\cdot 10^{-11}\,(\epsilon_0-1)\,\frac{\omega_p^{4/3}}{\omega_g^4} \tag{16}$$

We list in table I the values of ω_g, ω_p and $\epsilon_o - 1$ for Ge, Si and GaAs. The values of $\chi^{(3)}_{1111}$ calculated with eq (16) are then listed in table II. This table shows agreement in sign and magnitude between the values of $\chi^{(3)}_{1111}$ predicted from ω_g and the experimental ones. An increase in the polarizability with field ($\chi^{(3)}_{1111} > 0$) is to be expected for the Franz-Keldysh effect since the intraband coupling by the electric field produces a decrease in the energy gap.

We shall consider now the contribution to $\chi^{(3)}_{1111}$ of the interband coupling by the electric field across the isotropic gap ω_g. This coupling produces an increase in energy gap, and thus its contribution to $\chi^{(3)}_{1111}$ is negative. This contribution to $\chi^{(3)}_{1111}$ is readily found from eq (6):

$$\Delta\chi^{(3)}_{1111}=-\frac{3}{5\pi}\,(\epsilon_o-1)\,\frac{1}{\omega_g}\,\frac{d\omega_g}{d(\mathscr{E}^2)}$$

$$=-\frac{3(\epsilon_0-1)}{5\pi}\left(\frac{3\pi}{4}\right)^{2/3}\frac{\omega_p^{4/3}}{\omega_g^2} \tag{17}$$

In eq (17) we have made use of the second-order perturbation expression:

$$\frac{d\omega_g}{d(\mathscr{E}^2)}=2\,\frac{|<v|\mathbf{r}|c>|^2}{\omega_g}=\frac{2k_F^2}{\omega_g^3} \tag{18}$$

Equation (18) is in agreement with the results of ref. [44]. Comparison of this equation with eq (15) shows that the magnitude of the interband contribution to $\chi^{(3)}_{1111}$ is smaller than the intraband contribution. Its consideration does not change the sign of $\chi^{(3)}_{1111}$ as found with eq (16) but introduces a numerical factor of the order of unity. In view of the uncertainties of this type of calculation we shall henceforth neglect this factor.

4.2. Lowest Gap E_o

We use for the contribution of an isotropic M_o critical point to the real part of the dielectric constant the result of eq (8). A calculation similar to that performed above yields for an M_o critical point the following Franz-Keldysh contribution to $\chi^{(3)}_{1111}$ [52]:

$$\Delta\chi^{(3)}_{1111} = 0.06 \frac{P^2 \mu_o^{1/2}}{\omega_o^{9/2}} \left(1 + 1.85 \left(\frac{\omega}{\omega_o}\right)^2 + \ldots\right) \quad (19)$$

or, transforming $\Delta\chi^{(3)}_{1111}$ to e.s.u. and ω_o to eV (P^2 and μ_o are left in atomic units for ease of computation):

$$\Delta\chi^{(3)}_{1111}(\omega) = 6 \cdot 10^{-10} \frac{C_0^2 \mu_0^{1/2}}{\omega_o^{9/2}} \times \left(1 + 1.85 \left(\frac{\omega}{\omega_o}\right)^2 + \ldots\right) \quad (20)$$

We have included in eqs (19) and (20) the first term in the dispersion of $\Delta\chi^{(3)}_{1111}$ since it may be possible to observe it experimentally in small band gap materials. This dispersion is given exactly by the function:

$$\frac{\omega_o^2}{\omega^2}\left(\left(1+\frac{\omega}{\omega_o}\right)^{-2.5} + \left(1-\frac{\omega}{\omega_o}\right)^{-2.5} - 2\omega_o^{-2.5}\right) \quad (21)$$

Equation (21) is not immediately valid for the E_o edge because of the degeneracy of the valence band. However, one can apply it to the E_o edge if one neglects the field coupling between degenerate valence bands and uses appropriate average values of P^2 and μ_o. Each one of the three valence bands can be assumed to have a mass equal to three times the conduction band mass and a corresponding matrix element equal to $\frac{1}{3}p^2$ [48]. Hence eq (20) must be used with the matrix element P^2 and $\mu_o = \frac{3}{4}m_e$ if the three valence bands are to be included. The spin-orbit splitting Δ_o of the valence band is taken into account, if $\Delta_o \ll E_o$, by replacing ω_o by its average value $E_o + \frac{\Delta_o}{3}$. Since P^2 is almost the same for all materials of the germanium family, we can replace it by a typical value ≈ 0.4 (in atomic units). The values of μ_o and $\omega_o = E_o + \frac{\Delta_o}{3}$ for Ge, Si and GaAs are listed in table I. Using these numbers, eq (20) yields the values of $\chi^{(3)}_{1111}(\omega=0)$ listed in table 2. While this contribution is zero for Si and is not excessive in GaAs (it may, therefore, be assumed as included in the average gap calculation given above), it is dominant in Ge. In first approximation it may be added to the average gap calculation: excellent agreement with the experimental results is then found.

TABLE 1. *Values of the parameters required for the evaluation of the Franz-Keldysh contributions to $\chi^{(3)}_{1111}$. Frequencies in eV, a_0 in Bohr radii, μ_0 in units of the free electron mass. P^2 has been taken equal to 0.4 for all materials.*

	Ge	Si	GaAs
ω_g	4.3	4.8	5.2
ω_p	15.5	17.35	15.5
$\epsilon_0 - 1$	11	15	10
μ_o	0.03	0.04	0.05
ω_o	0.9	4	1.5
a_o	10.7	10.3	10.7
ω_1	2.2	3.3	3.0

TABLE 2. *Contribution of the various Franz-Keldysh effects discussed here to $\chi^{(3)}_{1111}$ and $\chi^{(3)}_{\xi\xi\xi\xi}$. In units of 10^{-10} e.s.u. Also, experimental values of the bound carrier contributions to $\chi^{(3)}_{1111}$ and $\chi^{(3)}_{\xi\xi\xi\xi}$.*

		E_g contribution	E_0 contribution	E_1 contribution	Experiment[57]
Ge	$\chi^{(3)}_{1111}$	0.26	0.67	0.20	1.0
	$\chi^{(3)}_{\xi\xi\xi\xi}$	0.26	0.67	0.26	1.5
Si	$\chi^{(3)}_{1111}$	0.22	0.00	0.027	0.06
	$\chi^{(3)}_{\xi\xi\xi\xi}$	0.22	0.00	0.036	0.08
GaAs	$\chi^{(3)}_{1111}$	0.12	0.087	0.045	0.12
	$\chi^{(3)}_{\xi\xi\xi\xi}$	0.12	0.087	0.060	0.10

For InAs, with $\omega_o = 0.5$ eV and $\mu = 0.02$, we find from eq (20) $\Delta\chi^{(3)}_{1111}(\omega=0) = 7 \cdot 10^{-10}$, which is of the order of the free-carrier contribution for the samples with the lowest electron concentrations measured ($N = 2 \cdot 10^{16}$ cm^{-3}) [57]. This is contrary to the statement found in the literature that for these carrier concentrations in InAs $\chi^{(3)}_{1111}$ is dominated by the free-carrier contribution [56,57,58].

The interband contribution of E_o to $\chi^{(3)}_{1111}$ for $\omega=0$ is easily obtained from the expression (see eq (8)):

$$\Delta\epsilon_r(\omega=0)=\frac{(2\mu_0)^{3/2}P^2}{2}\omega_g^{-3/2} \tag{22}$$

If one assumes that the repulsion produced by the field affects μ_o in the manner predicted by the $\mathbf{k}\cdot\mathbf{p}$ expression with constant matrix elements of $\mathbf{p}(\mu_o \propto \omega_g)$, the corresponding interband contribution to $\chi^{(3)}_{1111}$ vanishes. If, on the other hand, one assumes μ_o to be field independent one also finds a negative contribution to $\chi^{(3)}_{1111}$ but smaller than the Franz-Keldysh contribution, and hence we shall neglect it.

4.3. E_1 Critical Points

The E_1 optical structure is usually attributed to M_1 critical points along the {111} directions. While M_1 critical points are known to yield no contribution to $\chi^{(3)}_{1111}$ [52], there are M_o critical points of the same symmetry slightly below the M_1 critical points. This combination of M_o and M_1 critical points with a very large longitudinal mass, can actually be approximated by two-dimensional minima [48]. The contribution of one of these two-dimensional minima to the long-wavelength dielectric constant is (we assume four, and not eight equivalent {111} directions):

$$\Delta\epsilon_r=\frac{4\sqrt{3}\mu_{\perp}P^2}{a_o\omega_1^2} \tag{23}$$

where a_o is the lattice constant and P^2 the appropriate square matrix element. We have tried to calculate the Franz-Keldysh contribution to $\chi^{(3)}_{1111}$ of these two-dimensional critical points in a way similar to that used above, but we have run into difficulties when evaluating the limits of the two-dimensional electro-optic functions for $\eta\rightarrow+\infty$. In view of this we have instead evaluated the effect of the three-dimensional M_o critical points, with the longitudinal effective mass replaced by the value required to give at long wavelengths a contribution to ϵ_r equal to that in eq (23).

Under these conditions, and because of the large longitudinal mass, only fields transverse to the critical point axis contribute to $\chi^{(3)}_{1111}$. When summing the contributions of the four equivalent valleys, it is found that the effect becomes anisotropic: the ratio of the third order susceptibility for $\mathscr{E}$ along {111} ($\chi^{(3)}_{\xi\xi\xi\xi}$), to that for $\mathscr{E}$ along {100} is 4/3. This argument is independent of the specific model chosen for the {111} transitions, provided $\mu_{||}\gg\mu_{\perp}$. It gives the type of anisotropy ($\chi^{(3)}_{\xi\xi\xi\xi}>\chi^{(3)}_{1111}$) observed for Ge and Si, but not for GaAs [57]. The Franz-Keldysh contribution of E_1 to $\chi^{(3)}_{1111}$ as found by the procedure sketched above, is:

$$\Delta\chi^{(3)}_{1111}=0.52\frac{P^2}{a_o\omega_1^5} \tag{24}$$

or, with ω_1 in eV and $\chi^{(3)}_{1111}$ in e.s.u.:

$$\Delta\chi^{(3)}_{1111}=2.7\cdot10^{-8}\frac{P^2}{a_o\omega_1^5} \tag{25}$$

(a_o in Bohr radii and P^2 in atomic units.)

The matrix element P should have approximately the same value as for the E_o gap. In order to take care of the spin-orbit splitting Δ_1 of E_1 we substitute ω_1 by $E_1+\Delta_1/2$. The approximate values of a_o, and ω_1 for Ge, Si and GaAs are listed in table I. The values calculated for the Franz-Keldysh contribution to E_1 to $\chi^{(3)}_{1111}$ and $\chi^{(3)}_{\xi\xi\xi\xi}$ are listed in table 2. While the calculated anisotropy has, for Ge and Si, the sign observed experimentally, its magnitude is far too small to explain the experimental anisotropy, especially after the E_o and the E_g contributions are added. There is a possibility that the E_1 contribution of eq (25) may have been underestimated. Exciton quenching effects [59,60], not included in our calculation, may increase this contribution.

We cannot offer even a qualitative explanation of the sign of the $\chi^{(3)}$ anisotropy observed for GaAs. It would be interesting to determine, through measurements of other III–V or II–VI compounds, whether it is connected with the lack of inversion symmetry in these materials.

The interband contribution of the E_1 edges can be evaluated in a manner analogous to that used for the E_o and the ω_g gaps. We also find that this contribution is negative and smaller than the Franz-Keldysh contribution.

5. Acknowledgments

I am indebted to Drs. Buss, Kane, Phillips, Van Vechten, and Aspnes for sending preprints of their work, prior to publication and to the staff of DESY for their hospitality.

I would like to dedicate this work to the memory of Rolf Sandrock, of whose untimely death I heard while this paper was in print.

6. References

[1] Cohen, M. L., and Bergstresser, T. K., Phys. Rev. **141**, 789 (1966).

[2] Cardona, M., and Pollak, F. H., Phys. Rev. **142**, 530 (1966).

[3] Dresselhaus, G., and Dresselhaus, M. S., Phys. Rev. **160**, 649 (1967).

[4] Herman, F., Kortum, R. L., Kuglin, C. D., and Shay, J. L., in "II–VI Semiconducting Compounds," D. G. Thomas, ed., (W. A. Benjamin, New York, 1967), p. 503.
[5] Gilat, G., and Dolling, G., Phys. Letters **8**, 304 (1964); Gilat, G., and Raubenheimer, L. J., Phys. Rev. **144**, 390 (1966).
[6] Higginbotham, C. W., Pollak, F. H., and Cardona, M., Proceedings of the IX International Conference on the Physics of Semiconductors, Moscow 1968 (Publishing House Nauka, Leningrad, 1968) p. 57.
[7] Buss, D. D., and Parada, N. J., private communication; see also article by D. D. Buss and V. E. Shirf in these proceedings.
[8] Kane, E. O., Phys. Rev. **146**, 558 (1966).
[9] Philipp, H. R., and Ehrenreich, H., Phys. Rev. **129**, 1550 (1963).
[10] Cardona, M., Z. Physik **161**, 99 (1961).
[11] Zhang, H. I., and Callaway, J., Phys. Rev. **181**, 1163 (1969).
[12] Walter, J. P., and Cohen, M. L., Phys. Rev., to be published.
[13] Seraphin, B. O., and Bottka, N., Phys. Rev. **145**, 628 (1966).
[14] Shaklee, K. L., Rowe, J. E., and Cardona, M., Phys. Rev. **174**, 828 (1968).
[15] Matatagui, E., Thompson, A. G., and Cardona, M., Phys. Rev. **176**, 950 (1968).
[16] Higginbotham, C. W., Ph. D. Thesis, Brown University, 1969.
[17] Eckelt, P., Madelung, O., and Treusch, J., Phys. Rev. Letters **18**, 656 (1967).
[18] Brinkman, W., and Goodman, B., Phys. Rev. **149**, 597 (1966).
[19] Pollak, F. H., Cardona, M., Higginbotham, C. W., Herman, F., and Van Dyke, J. P., Phys. Rev., to be published.
[20] McElroy, P., Ph. D. Thesis, Harvard University, 1968.
[21] Cardona, M., and Greenaway, D. L., Phys. Rev. **133**, A1685 (1964).
[22] Scanlon, W. W., J. Phys. Chem. Solids **8**, 423 (1959).
[23] Aspnes, D. E., and Cardona, M., Phys. Rev. **173**, 714 (1968).
[24] Sandrock, R., Phys. Rev. **169**, 642 (1968).
[25] Tutihasi, S., and Chen, I., Phys. Rev. **158**, 623 (1967).
[26] Lin, P. J., and Phillips, J. C., Phys. Rev. **147**, 469 (1966).
[27] Wiech, G., in "Soft X-Ray Spectra," D. J. Fabian, ed., (Academic Press, New York, 1968) p. 59.
[28] Feuerbacher, B., Skibowski, M., Godwin, R. P., and Sasaki, T., JOSA **58**, 1434 (1968).
[29] See for instance R. S. Knox, "Theory of Excitons," (Academic Press, N.Y., 1963).
[30] Mahan, G. D., Phys. Rev. Letters **18**, 448 (1967).
[31] Velicky, B., and Sak, J., Phys. Status Solidi **16**, 147 (1966).
[32] Kane, E. O., Phys. Rev. **180**, 852 (1969).
[33] Marple, D. T. F., and Ehrenreich, H., Phys. Rev. Letters **8**, 87 (1962).
[34] Cardona, M., J. Appl. Phys. **36**, 2181 (1965).
[35] Inoue, M., Okazaki, M., Toyozawa, Y., Inui, T., and Nanamura, E., Proc. Phys. Soc. Japan **21**, 1850 (1966).
[36] Hermanson, J., Phys. Rev. **150**, 660 (1966).
[37] Shaklee, K. L., Ph. D. Thesis, Brown University, 1969.
[38] Penn, D., Phys. Rev. **128**, 2093 (1962).
[39] Srinivasan, G., Phys. Rev. **178**, 1244 (1969).
[40] Nara, H., J. Phys. Soc. Japan **20**, 778 (1965).
[41] Van Vechten, J. A., Phys. Rev. **182**, 891 (1969). In this reference a correction factor of the order of unity is added to eq (6) so as to take the polarizability of the core d electrons into account.
[42] Phillips, J. C., Phys. Rev. Letters **20**, 550 (1968).
[43] Phillips, J. C., Covalent Bonding in Molecules and Solids (University of Chicago Press, Chicago) to be published.
[44] Phillips, J. C., and Van Vechten, J. A., Phys. Rev. **183**, 709 (1969); Levine, B. F., Phys. Rev. Letters **22**, 787 (1968).
[45] Cardona, M., Paul, W., and Brooks, H., J. Phys. Chem. Solids **8**, 204 (1959).
[46] Korovin, L. I., Soviet Phys. Solid State **1**, 1202 (1959).
[47] Cardona, M. in "High Energy Physics, Nuclear Physics, and Solid State Physics," I. Saavedra, ed., (W. A. Benjamin, New York, 1968).
[48] Higginbotham, C. W., Cardona, M., and Pollak, F. H., Phys. Rev. **184**, 821 (1969).
[49] De Meis, W. M., Technical Report No. HP-15 (ARPA-16), Harvard University (1965).
[50] Shileika, A. Yu., Cardona, M., and Pollak, F. H., Solid State Communications **7**, 1113 (1969).
[51] Yu, P. Y., to be published.
[52] Van Vechten, J. A., and Aspnes, D. E., Phys. Letters, in press.
[53] Aronov, A. G., and Pikus, G. E., Proceedings of the IX International Conference on the Physics of Semiconductors, Moscow, 1968, (Publishing House Nauka, Leningrad, 1968), p. 390.
[54] Cardona, M., "Modulation Spectroscopy," F. Seitz, D. Turnbull, and H. Ehrenreich, eds., (Academic Press Inc., New York, N.Y.).
[55] Antonsiewicz, H. A., in "Handbook of Mathematical Functions," (M. Abramowitz and I. A. Stegun, eds.) (Dover Pub. Inc., New York, N.Y., 1965) p. 448.
[56] Wolff, P. A., and Pearson, G. A., Phys. Rev. Letters **17**, 1015 (1966).
[57] Wynne, J. J., Phys. Rev. **178**, 1295 (1969).
[58] Patel, C. K. N., Slusher, R. F., and Fleury, P. A., Phys. Rev. Letters **17**, 1011 (1966).
[59] Hamakawa, Y., Germano, F. A., and Handler, P., J. Phys. Soc. Japan, Suppl. **21**, 111 (1966).
[60] Shaklee, K. L., Rowe, J. E., and Cardona, M., Phys. Rev. **174**, 828 (1968).

Discussion on "Optical Properties and Electronic Density of States" by M. Cardona (Brown University)

M. S. Dresselhaus *(MIT):* Introduction of a finite relaxation time does not always help to achieve good agreement between the experimental and calculated dielectric constant curves. For example, in the first slide you showed on indium-arsenide, you have the experimental ϵ_2 curve which is higher than the calculated curve. For a situation like that, introduction of a finite relaxation time can only make matters worse.

M. Cardona *(Brown Univ.):* I wanted to mention this point and the fact that you had done calculations of dielectric constants with a finite phenomenological scattering time. Such procedure may sometimes improve the agreement between theory and experiment.

M. S. Dresselhaus *(MIT):* It will not improve this particular fit in InAs. In general, I think that for most of the curves that you have shown, the agreement between theory and experiment would be improved with a finite relaxation time. The second point I would like to make is the following: I am not exactly convinced that in calculating the differential reflectivity, it is correct just to simply differentiate the reflectivity with respect to frequency because the various differential techniques emphasize different features of the energy band structure. For example, if you do a thermal reflectance measurement on a metal, it is those bands that are very close to the Fermi level that are emphasized; for example, different bands are emphasized in a piezo-reflectance measurement.

M. Cardona *(Brown Univ.):* This is correct and a very good point. Of course, one type of modulation experiment one does is simply wavelength or photon energy modulation. Your comment does not apply to this type of measurement which, however, is very difficult from the experimental point of view. It is much simpler to modulate the sample temperature (thermo-reflectance) or the electric field applied to it (electro-reflectance). An electro-reflectance spectrum, of course, should not be compared with the calculated derivative of the reflectivity. The thermo-reflectance spectra of zinc-blende semiconductors, however, should be very similar to the frequency modulation spectra since broadening is much smaller than frequency shift and the temperature coefficients of all gaps are practically the same. For metals, of course, transitions involving portions of the Fermi surface are greatly enhanced in temperature modulation spectra.

J. Tauc *(Bell Telephone Labs.):* It is a very poor approximation to compare the x-ray spectra with the band state densities. Even if one neglects the many electron effects it is necessary to compare the x-ray spectra with the densities of approximately projected states according to the symmetry of their ground states. Such calculations by J. Klima (private communication) on Ge gave a very good agreement with experiment.

M. Cardona *(Brown Univ.):* The question was whether one could improve agreement between theory and experiment for the $3d \rightarrow$ conduction transitions in germanium by including the appropriate matrix elements. This can be done, at least in part, by projecting the p component of the conduction band wave functions. The answer is yes. Actually, I notice that the paper by G. Weich and E. Zöpf contains some rather nice work along these lines.

B. H. Sacks *(Univ. of Calif.):* Is there any indication that the application of pressure (either uniaxial or hydrostatic) to GeO_2 could preferentially shift the band edges so as to give a direct gap material for use in ultraviolet laser?

G. W. Pratt *(MIT):* There is a great possibility of this.

M. Cardona *(Brown Univ.):* In connection with Dr. Pratt's statement that 200 points is a very small number of points for an ϵ_2 calculation, I would like to point out that with such a coarse mesh, one can get tremendous resolution if one derives from it a much finer mesh by quadratic interpolation. Such interpolation can cut down very considerably on the computer time required for good resolution.

J. Janak *(IBM, New York):* I would like to refute what Dr. Cardona just said. We have done some calculations for palladium and we find that to get the error down using quadratic interpolation, we have to go to about 3000 points in the reduced zone. That is to get an error of 5 millirydbergs. That is a particular case, it is true, but it is not always true that a few hundred will do.

Theoretical Electron Density of States Study of Tetrahedrally Bonded Semiconductors

D. J. Stukel, T. C. Collins, and R. N. Euwema

Aerospace Research Laboratories, Wright-Patterson Air Force Base, Ohio 45433

The electron density of states has been calculated using a self-consistent orthogonalized plane wave (SCOPW) model for compounds in the isoelectronic sequences Si-AlP and Ge-GaAs-ZnSe. The valence and conduction band density of states are presented. The location of the core states is also given. The effect upon the density of states of using the exchange approximations of Slater, Kohn-Sham, and Liberman is displayed.

Key words: Aluminum phosphide (AlP); electronic density of states; exchange potential; gallium arsenide (GaAs); germanium; self-consistent orthogonalized plane wave model (SCOPW); semiconductors, tetrahedrally bonded; silicon; zincblende; ZnSe.

1. Introduction

The purpose of this paper is (1) to present the electron density of states calculated using our self-consistent orthogonalized plane wave (SCOPW) model for compounds in the isoelectronic sequences, Si-AlP and Ge-GaAs-ZnSe and (2) to show the effect on the density of states of using different exchange approximations. The exchange approximations considered are those of Slater [1], Kohn-Sham [2], Gaspar [3], and Liberman [4].

In the past few years, a great deal of success has been attained in calculating the energy band structures of Groups III-V, II-VI and IV compounds using the first principles self-consistent unadjusted OPW model developed here at ARL. The SCOPW programs used to calculate the electronic band structure have given very good one-electron band energies for compounds such as CdS [5], ZnS and ZnSe [6], GaAs [7], Si [8], AlAs [9], and AlP [10]. These unadjusted band energies fit the known experimental facts very well when Slater's exchange is used [11].

Our SCOPW programs are described in section 2. The treatment of exchange is also discussed as is the method of calculating the density of states. The results are presented in section 3.

2. Methods of Calculations

2.1. Self-Consistent OPW Calculations

The orthogonalized plane wave (OPW) method of Herring [12] is used to calculate the electron energies. In the OPW model [5,6], the electronic states are divided into tightly bound core states and loosely bound valence states. The core states must have negligible overlap from atom to atom. They are calculated from a spherically symmetrized crystalline potential.

The valence states must be well described by a modified Fourier series

$$\Psi_{k_0}(r)=\sum_{\mu} B_{\mu}\left[\frac{1}{\sqrt{\Omega_0}}e^{ik_{\mu}\cdot r}-\sum_{a} e^{ik_{\mu}\cdot R_a}\sum_{c} A^{a}_{c\mu}\Psi_c(r-R_a)\right]$$

where $k_\mu = k_0 + K_\mu$, k_0 locates the electron within the first Brillouin zone, K_μ is a reciprocal lattice vector, R_a is an atom location, ψ_c is a core wave function and Ω_0 is the volume of the crystalline unit cell. The coefficients $A^a_{c\mu}$ are determined by requiring $\psi_{k_0}(r)$ be orthogonal to all core state wave functions. The variation of B_μ to minimize the energy then results in the valence one-electron energies and wave functions.

The dual requirements of no appreciable core overlap and the convergence of the valence wave function expansion with a reasonable number of OPW's determines the division of the electron states into core and

valence states. For Al, Si and P the $3s$ and $3p$ states (for Zn, Se, Ga, As and Ge the $4s$ and $4p$ states) are taken as the valence states. Very good convergence is obtained for ZnSe, GaAs, Ge, Si and AlP when 229 OPW's are used in the series expansion.

The calculation is self-consistent in the sense that the core and valence wave functions are calculated alternately until neither changes appreciably. The Coulomb potential due to the valence electrons and the valence charge density are both spherically symmetrized about each inequivalent atom site. With these valence quantities frozen, new core wave functions are calculated and iterated until the core wave functions are mutually self-consistent. The total electronic charge density is calculated at 650 crystalline mesh points covering 1/24 of the unit cell, and the Fourier transform of $\rho(r)^{1/3}$ is calculated. The new crystal potential is calculated from the old valence charge distribution and the new core charge distribution. Then new core-valence orthogonality coefficients, $A^{\alpha}_{c\mu}$, are calculated. The iteration cycle is completed by the calculation of new valence energies and wave functions. The iteration process is continued until the valence one-electron energies change less than 0.01 eV from iteration to iteration.

The appropriate charge density to use for the self-consistent potential calculation is the average charge density of all the electrons in the Brillouin zone. In the present self-consistent calculations, this average is approximated by a weighted mean over electrons at the Γ, X, L and W high symmetry points of the zincblende Brillouin zone shown in figure 1. The weights are taken to be proportional to the volumes within the first Brillouin zone closest to each high symmetry point. The adequacy of this approximation has been tested and the error in the energy eigenvalues has been shown to be less than 0.1 eV [8].

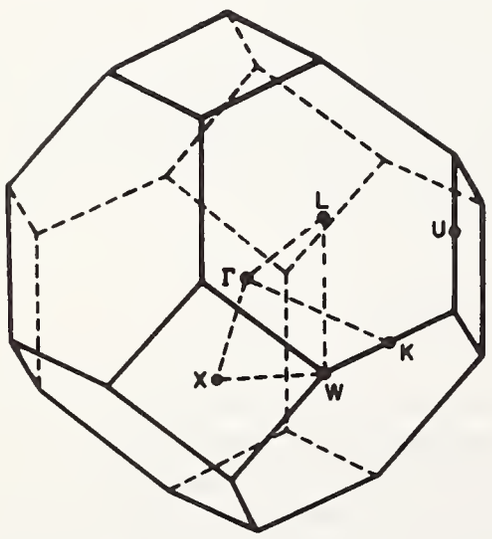

FIGURE 1. *The zincblende Brillouin zone.*

2.2. Treatment of Exchange

The nonlocal Hartree-Fock (HF) exchange term is so complicated that approximations are necessary in crystalline calculations. The best known approximations to the HF exchange terms are due to Slater, Kohn-Sham-Gaspar, and Liberman. Slater's and Kohn-Sham-Gaspar's approximations (energy independent) result in different constant coefficients multiplying the density to the one-third power whereas Liberman's approximation yields a coefficient which is a function of r and the energy of the state being considered.

a. Energy Independent Exchange Approximation

The first simplified one-electron operator which replaces the exchange operator in the HF equation was suggested by Slater [1,13]. If one multiplies and divides the exchange term in the HF equations by $\phi_i^*(x_1)\phi_i(x_1)$ one has [14]

$$\left\{-\sum_{j=1}^{N}\int \frac{d\tau_2\phi_j^*(x_2)\phi_i^*(x_1)\phi_j(x_1)\phi_i(x_2)}{\phi_i^*(x_1)\phi_i(x_1)}\frac{2}{r_{12}}\right\}\phi_i(x_1) = V_x\phi_i(x_1)$$

In this expression Slater then made the free electron gas approximation that the ϕ_i's are plane waves and obtained

$$V_x(r)|_{\mathrm{FEG}} = -8\left\{\frac{3}{8\pi}\rho(r)\right\}^{1/3} F(k/kp)$$

$$F(\eta) = \frac{1}{2} + \frac{1-\eta^2}{\tau\eta}\ln\left|\frac{1+\eta}{1-\eta}\right|$$

$\rho(r)$ is the electron density of the system. Here it has been assumed that all states are filled for $|\mathbf{k}| < |\mathbf{k}_F|$, the Fermi momentum, and all states are empty for $|\mathbf{k}| > |\mathbf{k}_F|$. The wave vector, $\mathbf{k}$ and the Fermi wave vector $\mathbf{k}_F$ were taken to be

$$k_\mu(r) = [E_\mu - V(r)]^{1/2} \qquad (1)$$

where $V(r)$, the total electronic potential, includes both Coulomb (nuclear and electron) and exchange contributions,

$$k_F(r) = [3\pi^2\rho(r)]^{1/3} \qquad (2)$$

and E_μ is the energy of the state being calculated. This definition of $\mathbf{k}_F$ is derivable from phase space considerations. Slater then averaged $F(\eta)$ over the occu-

pied states of the free electron gas and obtained the value 3/4. Hence

$$V_{xs}(r) = -6\left[\frac{3}{8\pi}\rho(r)\right]^{1/3} \tag{3}$$

If one makes Slater's approximation in the exchange term of the HF expression for the total energy and then varies the total energy, one obtains the Kohn-Sham-Gasper exchange approximation

$$V_{xKs} = \tfrac{2}{3} V_{xs} \tag{4}$$

b. Energy Dependent Exchange Coefficient

Liberman investigated $V_x(r)|_{FEG}$ with $\mathbf{k}$ and $\mathbf{k}_F$ given by eqs (1) and (2). Hence

$$V_{xL,i} = -8\left\{\frac{3}{8\pi}\rho(r)\right\}^{1/3} F(\eta_i) \tag{5}$$

Slater, Wilson and Wood [15] modified Liberman's approximation by using

$$k_F(r) = \left\{E_F - V_{\text{coulomb}}(r) + 4\left[\frac{3}{8\pi}\rho(r)\right]^{1/3}\right\}^{1/2} \tag{6}$$

instead of eq (2) so that $\eta = 1$ at the top of the Fermi distribution. We found it advantageous to calculate k_F both ways and always use the larger value. This approach gives results slightly closer to the HF results for atomic calculations. The Fermi energy, E_F, that was used in the SCOPW crystalline calculation was taken at the middle of the fundamental gap, defined by the top of the valence band and the bottom of the conduction band.

2.3. Density of States Calculations

To calculate the density of states, one must know the energy levels at an arbitrary point in the Brillouin zone. Since the SCOPW energy levels are only calculated at the Γ, X, L and W high symmetry points, one must somehow interpolate these energies throughout the Brillouin zone. We have determined the band structure in the remainder of the zone by fitting a pseudopotential-type interpolation model to the SCOPW energy levels calculated at the high symmetry points. Using this interpolation scheme, the band energies and band-energy gradients at each of 155 course mesh points in the irreducible sector (1/48th) of the reduced zone are evaluated. A fine mesh consisting of 512 points is then centered at each coarse mesh point. The band energies at each of the fine mesh points are calculated from a knowledge of the band energies and band-energy gradients at the coarse mesh points. The density of states is then calculated by summing over all bands

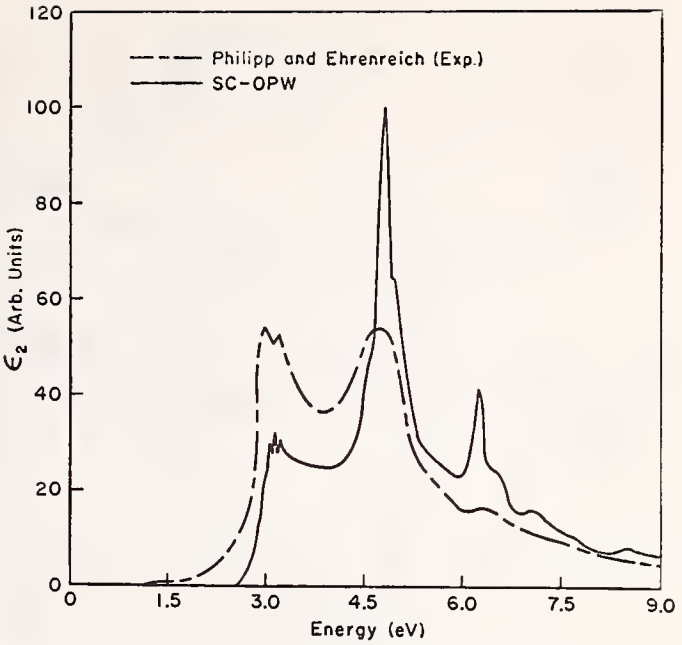

FIGURE 2. *The theoretical SCOPW (solid line) and the experimental (ref. [18] dashed curve) ϵ_2 curves for* GaAs.

(valence or conduction) at each of the 512 × 155 fine mesh points.

We use the same technique to calculate the SCOPW ϵ_2 curves [16]. The joint valence−conduction density of states is combined with pseudopotential transition matrix elements to produce the resulting ϵ_2 curve.

A typical comparison of experimental and SCOPW ϵ_2 curves is shown in figure 2. We have found that the SCOPW ϵ_2 peaks usually match experiment to within 0.2 eV. However, the shape of the ϵ_2 peaks has not matched experiment at all closely. The lack of agreement as to shape may be due to the use of pseudopotential matrix elements and to exciton assisted transitions which we have not taken into account.

3 Discussion of Results

3.1. Energy Independent Exchange Approximation

a. Valence Bands

The general structure of the SCOPW results is very similar in appearance to the adjusted non-self-consistent OPW results of Herman, Kortum, Kuglin and Shay [17]. A typical SCOPW band structure (ZnSe) is shown in figure 3. Density of states results for the valence bands are presented in figure 4. One has three regions for all the compounds studied. This is true for both Slater's and Kohn-Sham's exchange terms. The first region consists of the "s-like" bands which start around 12 eV and has a width which varies in these materials between 1 to 4 eV. This region has two main features; one is associated with the $L_{2'V}$ or L_{1V}

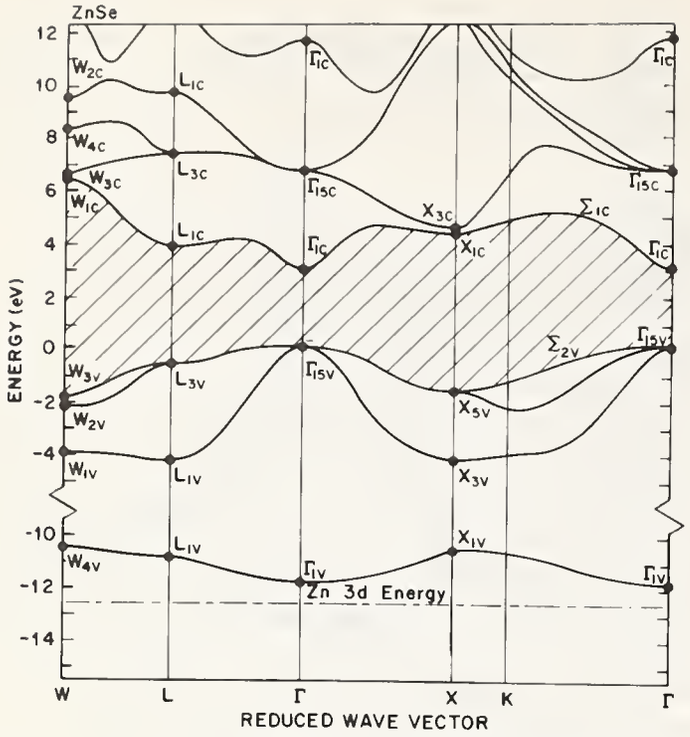

FIGURE 3. ZnSe *calculated energy bands using the SCOPW model plus the position of the* Zn 3d *core energy.*

The SCOPW high symmetry point values are indicated by heavy dots. A pseudopotential interpolation scheme was used to generate the lines.

symmetry point and the other is the high energy structure associated with the K point region of the Brillouin zone.

The second region is relatively narrow ranging from 1 to 2 eV in width over the five compounds, and is located from −8 eV to −3.5 eV. Its structure consists of a large peak which has in some compounds a shoulder or small peak on the low energy side. This large peak arises from the K point region. The source of these energy states is the "light-hole p-like" bands ($W_{1v}-L_{1v}-\Gamma_{15v}-X_{3v}$ in fig. 3). This band is nearly flat throughout the Brillouin zone except near the Γ point. There, it rises in energy very fast and becomes degenerate with the top valence band. However, there are so few states outside region two that no appreciable structure is found in region three from this band.

The third region is the one which contributes most to the calculations and to investigations involving the band gap and the imaginary part of the dielectric constant ϵ_2. The width of this region is well defined as can be seen in figure 4. The width varies in these compounds from 4.9 eV to 2.7 eV. This region has three distinct features. The low energy structure in this region comes again from the K point. The middle peak is located at the energy of the X_{4v} or X_{5v}, and the high energy shoulder or peak is associated with the L_{3v}. The electron states which form this region are derived from the "heavy-hole p-like" bands (top valence bands in fig. 3). This region contains twice as many electrons as region one or region two.

The most striking differences in going from the Group IV compounds to the III-V and then to the II-VI is that the width of the regions becomes smaller and there is a gap between the "s-like" and "p-like" bands in III-V's and II-VI's. For example, in Ge, region one has a width of 3.8 eV; in GaAs, this region's width is 2.4 eV; and in ZnSe, this region has a width of only 1.2 eV (see table 1). Thus, as one goes from a covalent bonding

TABLE 1. *The band widths of the valence bands plus the energy regions where the "*s*-like" band (region 1), the "light-hole* p*-like" bands (region 2), and the "heavy-hole* p*-like" bands (region 3) contribute to the density of states using Slater's and Kohn-Sham's approximations in the SCOPW model. The energy of the top of the valence band is set equal to zero.*

Compound	Exchange approximations	Total band width (eV)	Region 1 (eV)	Region 2 (eV)	Region 3 (eV)
Si	Slater	11.75	−11.75 to −7.68	−7.68 to −6.24	−4.16 to 0.00
	Kohn-Sham	12.05	−12.05 to −7.78	−7.78 to −6.56	−4.86 to 0.00
Ge	Slater	11.91	−11.91 to −8.17	−8.17 to −6.21	−3.69 to 0.00
	Kohn-Sham	12.12	−12.12 to −8.26	−8.26 to −6.14	−4.44 to 0.00
AlP	Slater	11.46	−11.46 to −9.04	−5.42 to −4.48	−3.44 to 0.00
	Kohn-Sham	11.66	−11.66 to −8.95	−6.09 to −4.67	−4.07 to 0.00
GaAs	Slater	11.81	−11.81 to −9.42	−6.22 to −5.45	−3.27 to 0.00
	Kohn-Sham	11.94	−11.94 to −9.14	−6.58 to −5.88	−4.06 to 0.00
ZnSe	Slater	11.82	−11.82 to −10.59	−4.47 to −3.76	−2.71 to 0.00
	Kohn-Sham	11.83	−11.83 to −10.30	−4.86 to −4.08	−3.06 to 0.00

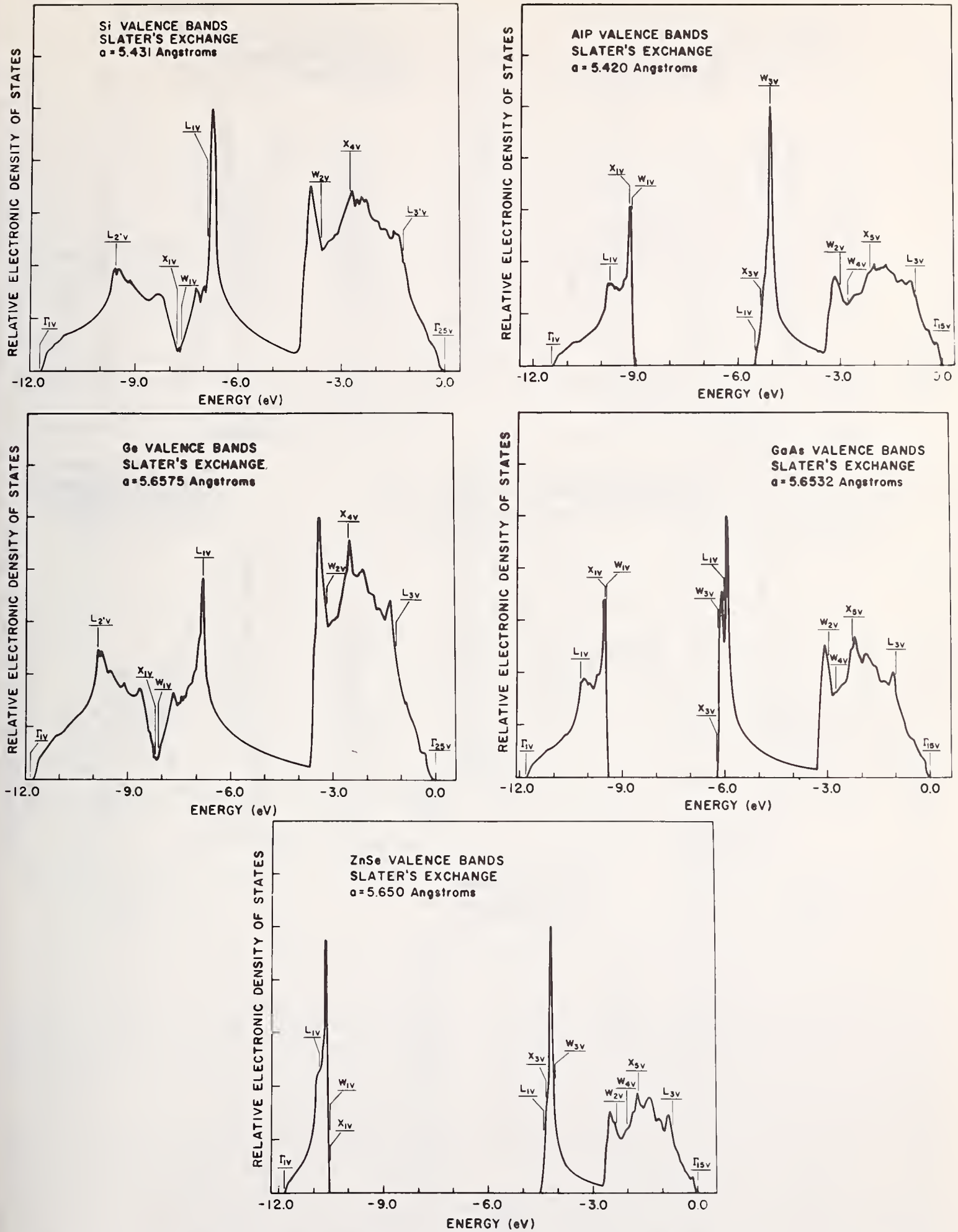

FIGURE 4. *The density of states of the valence bands of* Si, Ge, AlP, GaAs, *and* ZnSe *calculated using the SCOPW model with Slater's exchange.*

417-156 O - 71 - 8

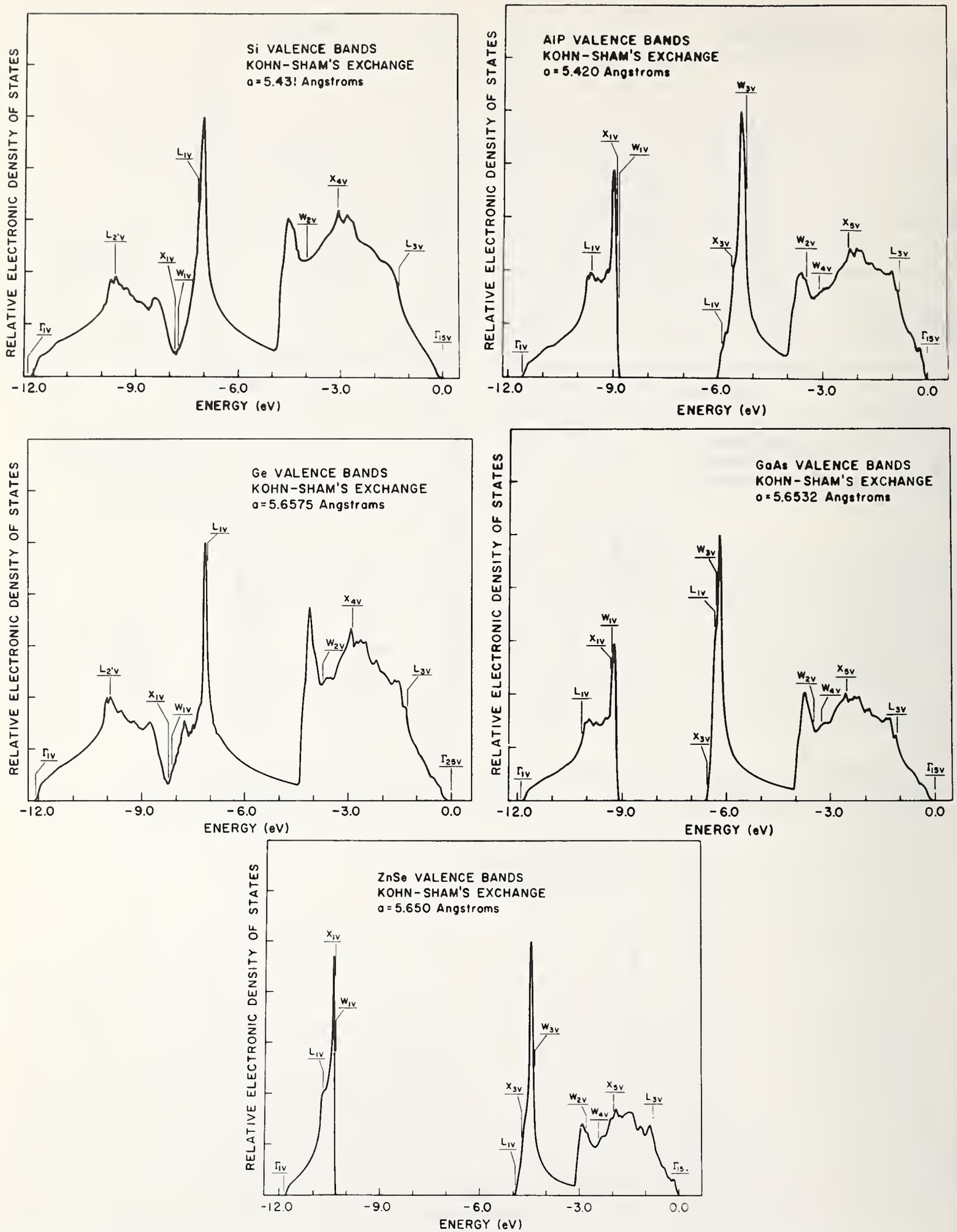

FIGURE 4. *The density of states of the valence bands of* Si, Ge, AlP, GaAs, *and* ZnSe *calculated using the SCOPW model with Kohn-Sham's exchange.*

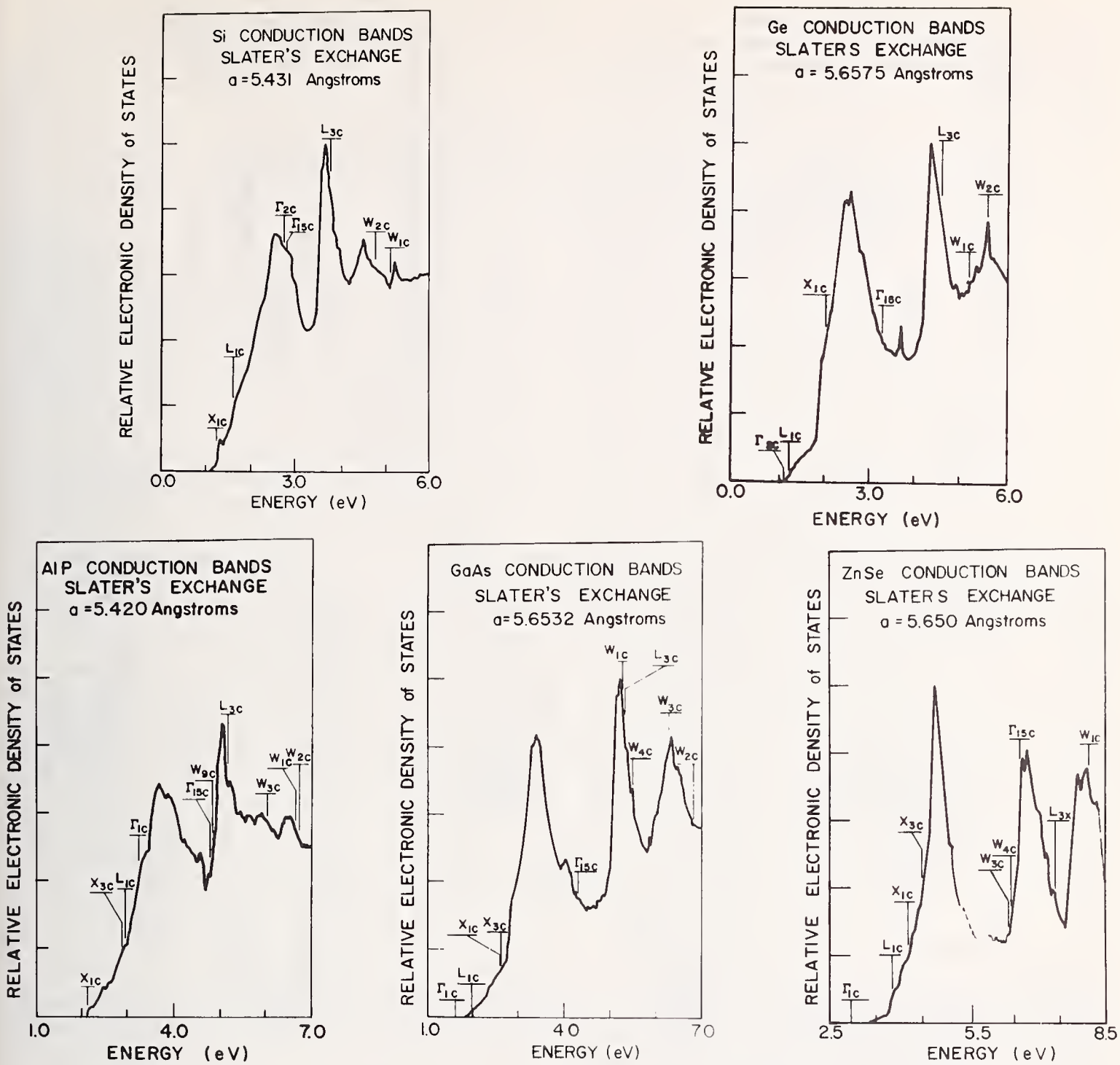

FIGURE 5. *The density of states of the lower part of the conduction bands of* Si, Ge, AlP, GaAs, *and* ZnSe *calculated using the SCOPW model with Slater's exchange.*

crystal to a more ionic bonding crystal the widths of the valence "*s*-like" and "*p*-like" bands decrease. However, the overall bandwidth from the bottom of the "*s*-like" band to the top of the "*p*-like" bands changes less than 1 eV.

In comparing the SCOPW results obtained using Slater's exchange approximation to those obtained using Kohn-Sham's approximation and to experiment, one notes that the fundamental band gaps of all of the compounds calculated except Ge match experiment when Slater's approximation is used (see table 2). This is also true when comparing the peak positions of the calculated ϵ_2 curves with experiments. In this case, Ge using Slater's approximation also matches closely the experimental results. In no case are the results obtained using the Kohn-Sham exchange approximation closer to experiment than those obtained using Slater's. Another observation is that the fundamental band gaps obtained using superposition of overlapping free atomic potential (non-self-consistent) results with Kohn-Sham's exchange is close to the SCOPW results using Slater's exchange in some crystals. Thus, if one does

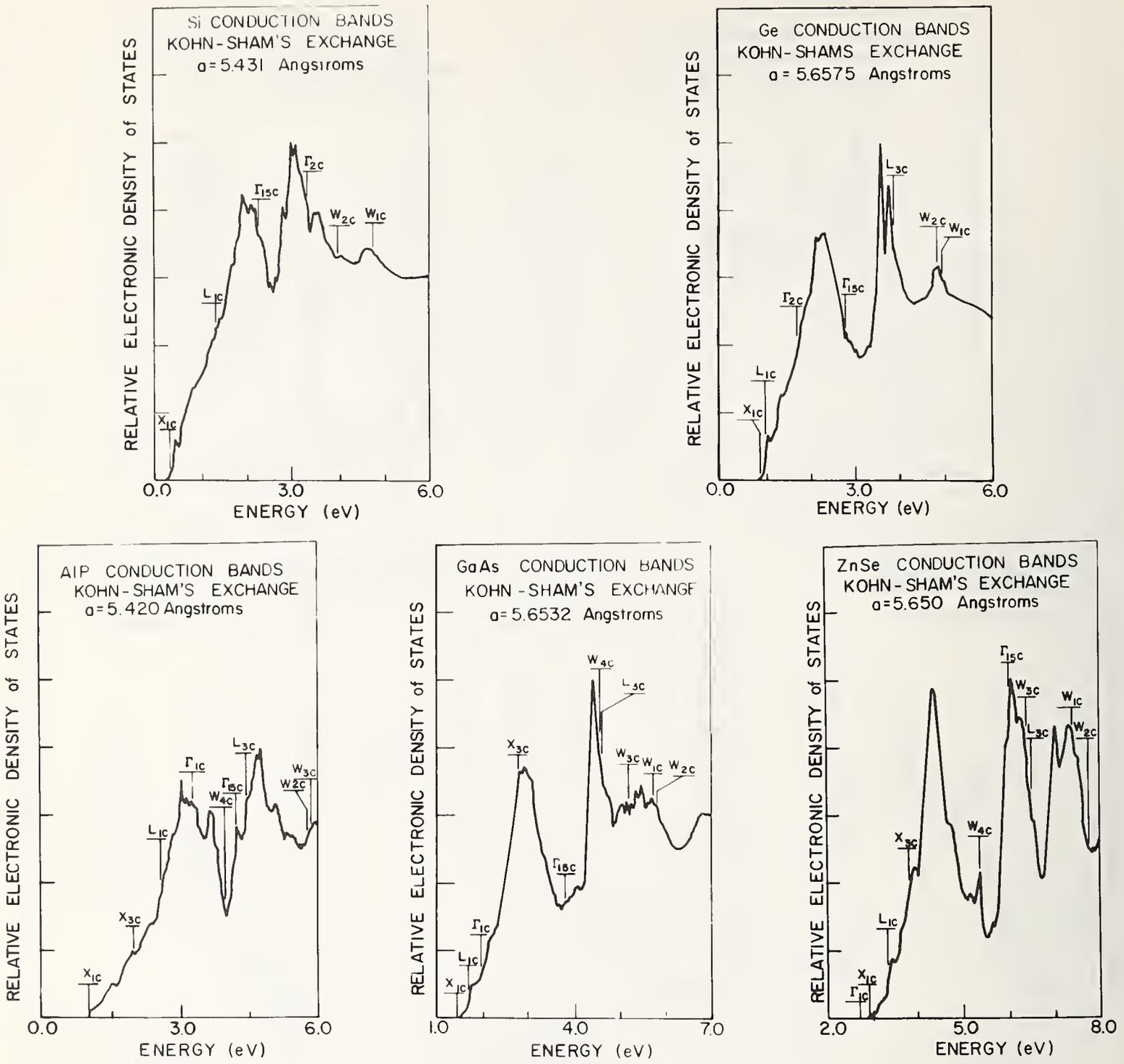

FIGURE 5. *The density of states of the lower part of the conduction bands of* Si, Ge AlP, GaAs, *and* ZnSe *calculated using the SCOPW model with Kohn-Sham's exchange.*

not carry his calculations to self-consistency, he could be lead to the incorrect conclusion that Kohn-Sham's approximation matches experiment better than Slater's approximation for these materials.

The most noticeable difference between the results using Slater's approximation and those obtained using Kohn-Sham's approximation is that region three has become wider for Kohn-Sham's approximation. In going from Slater's approximation results to those of Kohn-Sham's, the width of region three increases from 0.35 eV to 0.79 eV while the overall energy difference between the bottom of the "*s*-like" band to the top of the "*p*-like" band changes by an amount varying between 0.1 and 0.3 eV for all the crystals studied. Also region one's width shows a smaller increase in going from Slater's results to Kohn-Sham's.

b. Conduction Bands

The general structure of the SCOPW results are again similar to the non-self-consistent results of Herman, et al. [17]. One does not have the separation into

TABLE 2. *The fundamental band gaps calculated from the SCOPW model using different exchange approximations.*

Compound	Energy (eV) Slater exchange	Energy (eV) Kohn-Sham exchange	Energy (eV) experiment
Si ($\Delta_{1c}-\Gamma_{25v}$)	1.10	0.10	[a] 1.12
Ge ($L_{1c}-\Gamma_{25v}$)	1.27	1.01	[b] 0.66
($\Gamma_{2'c}-\Gamma_{25v}$)	1.18	1.73	[b] 0.80
AlP ($X_{1c}-\Gamma_{15v}$)	2.14	0.97	
GaAs ($\Gamma_{1c}-\Gamma_{15v}$)	1.61	1.97	[c] 1.54
($X_{1c}-\Gamma_{15v}$)	2.57	1.46	
ZnSe ($\Gamma_{1c}-\Gamma_{15v}$)	2.94	2.68	[d] 2.83

[a] A. Frova and P. Handler, Phys. Rev. Letters **14**, 178 (1965).
[b] G. G. MacFarlane, T. P. McLean, J. E. Quarrington and V. Roberts, Proc. Phys. Soc. (London) **71**, 863 (1958).
[c] M. Cardona, K. L. Shaklee and F. H. Pollak, Phys. Rev. **154**, 696 (1967).
[d] M. Aven, D. Marple, and B. Segall, J. Appl. Phys. Suppl. **32**, 226 (1961).

well-defined regions as in the valence band. For example, the first four electron conduction states at the Γ point are lower in energy than any of the first four conduction states at the W point. However, calculations for the five crystals give like results. In the first 6 or 7 eV of the conduction band, there are three main peaks; the lowest peak comes from the K point region; the middle peak from the L point region, and the third peak again from the K region (see fig. 5).

The onset of the conduction band changes from crystal to crystal in these examples. The reason for this is that the density of states associated with the $\Gamma_{2'c}$ or Γ_{1c} is very small compared with the L_{1c} or Δ_{1c} minimums of the conduction band. Thus, one sees that the density of states at the band edge for ZnSe or GaAs using Slater's exchange approximation does not appear in figure 5 using this scale.

The main difference between the SCOPW results using Slater's and Kohn-Sham's approximation is that the X point and L point eigenvalues move to lower energy relative to the Γ point energies. This, of course, is similar to the behavior found in region three of the valence bands. This can cause quite a change in the description of the calculated crystal. For example, the GaAs results using Slater's approximation gives a direct fundamental gap of 1.61 eV at the Γ point. When Kohn-Sham's approximation is used, both the X_{1c} and L_{1c} energy states are lower than the Γ_{1c}. This gives an indirect fundamental gap of 1.46 eV between Γ_{15v} and X_{1c}.

c. d-States

At this time a wealth of information is being obtained experimentally about the energy location and interaction with other states of the so-called "core" electrons in these materials. It is therefore interesting to examine the top d-state (which is the highest energy "core" state in Ge, GaAs, and ZnSe) that these calculations predict. In GaAs and ZnSe the non-self-consistent results (the potential is formed from a supposition of free atomic potentials) result in the d-states above the "s-like" valence band close to the "p-like" valence band. For example, in ZnSe, the Zn $3d$ state is 5.3 eV below the top of the valence band. However, the SCOPW results (using Slater's exchange) show this state to be below the "s-like" band at an energy of 12.6 eV below the top of the valence band. In the case of GaAs, the SCOPW results give the location of the Ga $3d$ state some 16 eV below the top of the valence band, and in the case of Ge, the SCOPW results give the location of the Ge $3d$ state 33 eV below the top of the valence band. In fact, the relative location of the Ge $3d$ state is close to the As $3d$ state which is 34 eV below the top of the valence band. A point of speculation as to the effective number of electrons per atom, η_{eff}, versus energy is added. Philipp and Ehrenreich [18] found a break in the η_{eff} curve of III-V compounds which was not found in the smooth curve of Ge. Their interpretation of the cause of this effect was that they had reached the onset of the d band. In looking at the results of our model, we could hypothesize that this break was caused by the fact that the "s-like" and "p-like" valence bands are separated. Thus, the break in the η_{eff} curve could be caused by the onset of the "s-like" valence band.

3.2. Energy Dependent Exchange Approximation

In all of this work, the effort has been made to simulate a Hartree-Fock crystal. That is, we have made approximations to the exchange term. And as pointed out in the previous section, the Slater approximation of the exchange term gives SCOPW results which are very close to experimental results except for Ge. However, this does not insure that the results are the same as a true Hartree-Fock calculation. In fact, if one looks at a simple metallic model [19], the Hartree results match experiment for metals. When one adds the exchange term, the bands become too wide. Thus, one does not expect a Hartree-Fock crystal to match experiment for these compounds.

In the atomic case, the authors [11] have been able to match Hartree-Fock eigenvalues by using Liberman's approximation for the exchange term. Ex-

TABLE 3. *The band gap and valence band widths of* Si, Ge, AlP, GaAs *and* ZnSe *calculated using Liberman's approximation in the SCOPW model. The energy of the top of the valence band is set equal to zero.*

Compound	Total band width (eV)	*s*-band width (eV)	*p*-band width (eV)	Band gap (eV)
Si	18.5	−18.5 to −12.3	−12.3 to 0.0	0.9
Ge	17.1	−17.1 to −12.5	−12.5 to 0.0	1.5
AlP	17.5	−17.5 to 14.6	−9.3 to 0.0	2.8
GaAs	16.8	−16.8 to 14.0	−9.9 to 0.0	2.8
ZnSe	15.5	−15.5 to 14.1	−9.2 to 0.0	5.0

tending these calculations to the crystal case, one finds the results of the SCOPW model given in table 3. In comparing the band gaps with the experimental results given in table 2, it is easily seen that Liberman's approximation results are not as good as the results using Slater's approximation. However, comparing valence band widths, one finds that Liberman's results give bands which are too broad compared to experiment, and this is what is expected from a Hartree-Fock description of these crystals.

4. Conclusion

It is concluded from this study that the SCOPW results using Slater's approximation for the exchange give a good description of the electron density of states. This good description was a result of the SCOPW model. That is, there was no empirical adjustment (or any other kind) made after the fact. The inputs to the model consist of lattice constants and the number of electrons.

It is also noted from this study that although the SCOPW results using Liberman's exchange approximation are further away from matching experiment, the results appear to be closer to the Hartree-Fock description for these materials. Thus, if one wishes to improve upon the Hartree-Fock method, such as adding Coulomb hole and screened exchange terms as investigated by Pratt [20], Hedin and Lundqvist [21,22], it is better to start from Liberman's exchange approximation rather than Slater's exchange approximation.

5. References

[1] Slater, J. C., Phys. Rev. **81,** 385 (1951).
[2] Kohn, W., and Sham, L. J., Phys. Rev. **140,** A1133 (1965).
[3] Gaspar, R., Acta Phys. Acad. Sci. Hung. **3,** 263 (1954).
[4] Liberman, D. A., Phys. Rev. **171,** 1 (1968); Sham, L. J., and Kohn, W., Phys. Rev. **145,** 56 (1966).
[5] Euwema, R. N., Collins, T. C., Shankland, D. G., and DeWitt, J. S., Phys. Rev. **162,** 710 (1967).
[6] Stukel, D. J., Euwema, R. N., Collins, T. C., Herman, F., and Kortum, R. K., Phys. Rev., March 1969.
[7] Collins, T. C., Stukel, D. J., and Euwema, R. N., (Phys. Rev. in press).
[8] Stukel, D. J., and Euwema, R. N., (to be published).
[9] Stukel, D. J., and Euwema, R. N., (Phys. Rev. in press).
[10] Stukel, D. J., and Euwema, R. N., (Phys. Rev. in press).
[11] Stukel, D. J., Euwema, R. N., Collins, T. C., and Smith, V., (Phys. Rev. in press).
[12] Herring, C., Phys. Rev. **57,** 1169 (1940).
[13] Slater, J. C., Quantum Theory of Atomic Structure, **Vol. II,** Ch. 17, App. 22.
[14] See also the derivation of P. O. Löwdin, Phys. Rev. **97,** 1590 (1955).
[15] Slater, J. C., Wilson, T. M., and Wood, J. H., Phys. Rev. **179,** 28 (1969).
[16] Euwema, R. N., Stukel, D. J., Collins, T. C., DeWitt, J. S., and Shankland, D. G., Phys. Rev. **178,** 1419 (1969).
[17] Herman, F., Kortum, R. L., Kuglin, C. D., and Shay, J. L., II-VI Semiconducting Compounds, 1967 International Conference, D. G. Thomas, Editor (W. A. Benjamin Inc., N.Y., 1967), pp. 503-551.
[18] Philipp, H. R., and Ehrenreich, H., Phys. Rev. **129,** 1550 (1963).
[19] Lundqvist, S., International Conference of Optical Properties of Solids, July 1969, (International Center for Advanced Studies, Chania, Crete, Greece).
[20] Pratt, G., Phys. Rev. **118,** 462 (1960).
[21] Hedin, L., Phys. Rev. **139,** A796 (1965).
[22] Hedin, L., and Lundqvist, S., Quantum Chemistry Group, Uppsala, Sweden, Technical Report **T III** (1960).

Discussion on "Theoretical Electron Density of States Study of Tetrahedrally Bonded Semiconductors" by D. J. Stukel, T. C. Collins, and R. N. Euwema (Aerospace Research Laboratories, Wright Patterson Air Force Base)

F. Herman *(IBM Res. Center, San Jose):* I would like to comment on the first paper by Stukel, Collins and Euwema. I really think that the reason they find the results they do is that they have not asked the right question. There is no theoretical basis for there to be a connection between an energy eigenvalue spectrum based on an approximate Hamiltonian and an optical excitation spectrum. If one does calculations using different exchange approximations and simply compared the eigenvalues with experiment there is simply no reason to expect agreement. This point prompts one to either use an empirically adjusted first principles method or else to change the question which is "How does one take an energy eigenvalue spectrum and from that with suitable modification find a spectrum that does correspond to an optical spectrum?"

T. C. Collins *(Aerospace Res. Lab.):* What I would like to point out is that there is theoretical basis for using eigenvalues. First of all, the eigenvalues using Slater's [1] exchange term match experiment within 0.2 eV. We do have one failure, germanium, which is off by half a volt in the indirect gap. All the rest fit to within that limit. There is no empirical adjustment needed or used in these calculations.

In these calculations one wants binding or excitation energies of an electron. One generally sets up the equation for the total energy. At this point you can substitute $\rho^{1/3}$ for the exchange term and vary. In this case you come out with 2/3 the value for the coefficient [2] in front of the exchange term in the effective Hamiltonian. Or, you can vary the total energy, then substitute $\rho^{1/3}$ for the exchange term. In this case you get Slater's value. Now where do you go to find binding energies? The way to find binding energies is to calculate the total energy of the N electron system and the N-1 electron system, then take the difference between the two. In the calculations, where does one substitute the exchange approximation? Making the approximation before the difference is taken one finds the eigenvalues obtained with the 2/3 approximation match the value for the binding energy. Likewise, if the substitution is made after the difference is taken, the eigenvalues obtained with Slater's value of the exchange approximation match the binding energy. So essentially your eigenvalues, in either case, represent binding energies.

We have also tried a "better" approximation, that of Liberman [3], for the exchange term. We derived the wave functions using all three values for the exchange term and calculated binding energies with Liberman's approximation—we still got bad results. The only thing that matches experiment are the eigenvalues obtained using Slater's $\rho^{1/3}$ value substituted for the exchange term.

The same thing happens in the atom. For example, we looked at Kr. Eigenvalues obtained using Slater's value for the exchange matched experiment where Hartree-Fock eigenvalues did not. But, when we took the N and N-1 total energy difference the Hartree-Fock answers were in very close agreement with experiment. This was true all the way down the line from the 1*s* value to the 4*p* value.

So it is just "magic" that $\rho^{1/3}$ values of Slater's works. We are trying to find out why. One of our purposes in this study is to develop a method to get the proper term.

E. T. Arakawa *(Oak Ridge National Lab.):* We have measured [4] the ϵ_2 absorption of Na and K. Although we have some scattering of points, it does appear that there definitely is a plasmon contribution in the absorption starting right around 6 eV for sodium.

[1] Slater, J. C., Phys. Rev. **81**, 385 (1951).
[2] Kohn, W., and Sham, L. J., Phys. Rev. **140**, A1133 (1965).
[3] Liberman, D. H., Phys. Rev. **171**, 1 (1968).
[4] Sutherland, J. C., Hamm, R. N., and Arakawa, E. T., J. Opt. Soc. Am. **59**, 1581 (1969).

Electronic Density of States in Eu-Chalcogenides

S. J. Cho

Division of Physics, National Research Council of Canada, Ottawa, Canada

The spin-polarized energy bands and the electronic density of states in the Eu-chalcogenides have been obtained by the augmented-plane-wave (APW) method. The results show that the f bands are extremely sensitive to the exchange potential used, and the $f(\uparrow)$ bands become the highest valence bands with a band width of the order of 0.5 eV. Our results have been compared with the recent photoemission spectroscopy data. The UPS data show too large f band width and too small relative peak intensities of the f bands, which disagree with our results. The $4f$ bands in the Eu and Gd could be located within 3.0 eV below their Fermi energies.

Key words: Augmented plane wave method (APW); electronic density of states; europium-chalcogenides; exchange potential; f bands; photoemission.

In the last few years a number of authors have studied the density of states $N(E)$, mainly for the transition and noble metals, by various experimental methods: UV photoemission spectroscopy (UPS), ion neutralization spectroscopy (INS), soft x-ray spectroscopy (SXS), and x-ray photoemission spectroscopy (XPS). Such measurements can provide useful information for understanding the electronic band structures in solids, and can be used as a tool to justify the theoretical energy band calculations. As far as transition and noble metals (Ni, Fe, Cu, and Co) are concerned there appears to be qualitative agreement between theory and experimental results obtained by various methods [1-4] (except for early UPS reports [5]). A probable exchange splitting ΔE_{ex} of the energy bands in Ni at or near the Fermi level E_f has been reported to be about 0.35 eV [6].

There are few theoretical and experimental studies on the density of states for the rare earth metals and their alloys. Müller [7] has studied room temperature reflectivity and transmission for Eu and Ba metals (up to 4 eV), which have isoelectronic structures. He has found almost identical optical behavior for Eu and Ba metals, and has concluded that the $4f$ electrons do not influence the optical spectrum, and that the $4f$ levels might be located far below E_f. Schüler [8] has studied temperature dependent transmission of Gd and Lu thin films, from which he has found that the transmission maximum of Lu is located at 0.75 eV which is independent of temperature. The transmission maximum of Gd is located at 0.6 eV at room temperature and is split into two peaks below the Curie temperature T_c, at 0.8 eV and 0.45 eV respectively. The extra peak is due to the spin-polarized exchange splitting of the bands, which is estimated to be about 0.4 eV for Gd. However he has not obtained any information on the possible f band positions. Blodgett et al. [9] have made UPS studies for Gd, and reported that a possible $f(\uparrow)$ band location is about 6 eV below E_f with a work function of 3.1 eV, and that a possible ΔE_{ex} is less than 0.1 eV from their temperature dependent photoemission measurements. On the other hand several authors [10,11] have studied theoretically the energy bands in the rare earth elements. However, they have found it difficult to locate the f band positions properly because of its sensitive dependence on the exchange potential used.

Recently both Busch et al. [12] and Eastman et al. [13] have studied UPS for the Eu-chalcogenides. Their results are reproduced in figure 1. In this work we have studied the spin-polarized energy bands in the Eu-chalcogenides in terms of the augmented-plane-wave (APW) method. We have found that the f band positions are extremely sensitive to the exchange potential used. In our work the $\rho^{1/3}$ exchange potential [14] for the magnetic Eu^{2+} ions has been reduced by a factor of 3/4, which has produced proper energy gaps and relative f band positions for the Eu-chalcogenides. According to our calculations the $f(\uparrow)$ bands are located in between the anion p band and the $5d$ conduction band X_3. The calculated $f(\uparrow)$ band width is about 0.5 eV and

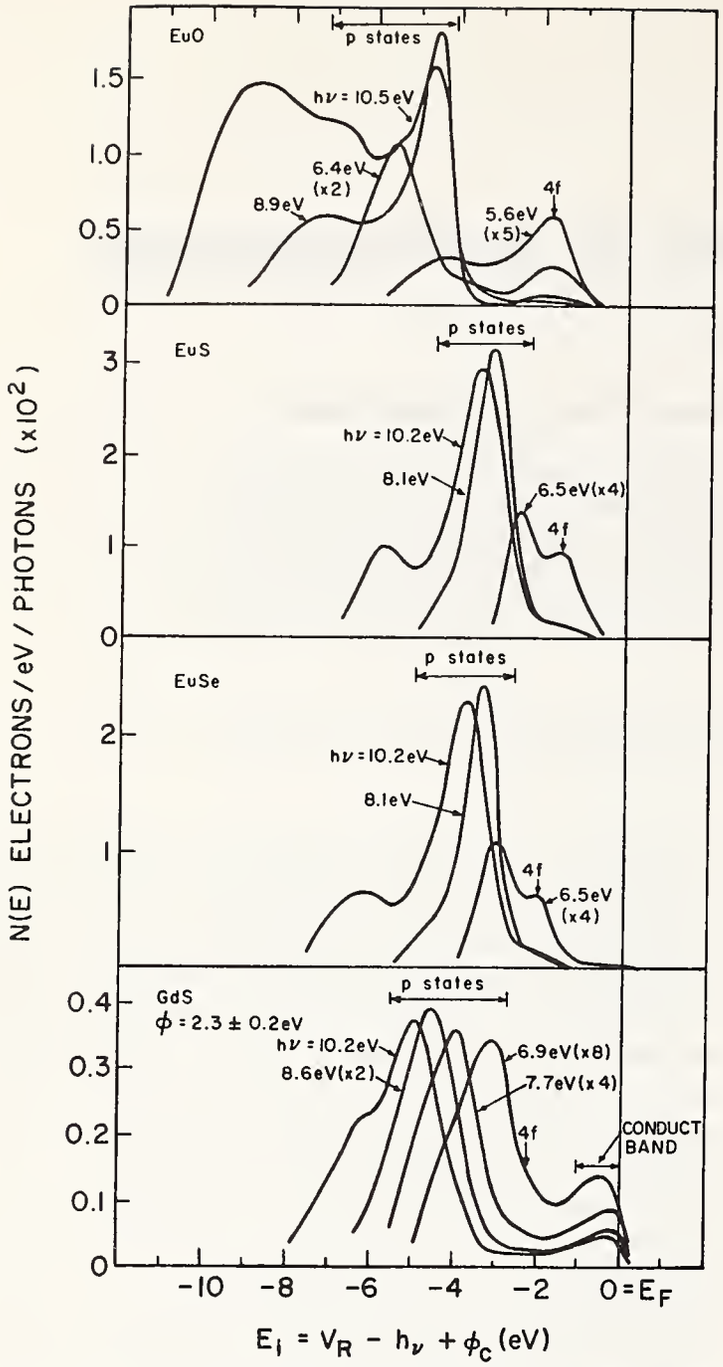

FIGURE 1. *Experimental density of states curves for* EuO, EuS EuSe, *and* GdS (*ref.* [13]).

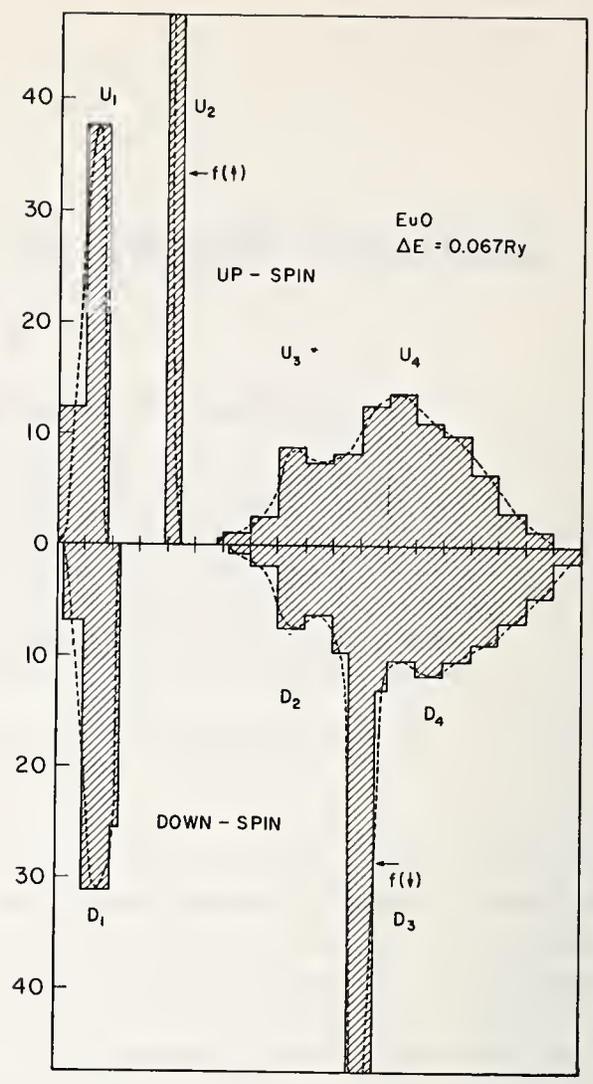

FIGURE 2. *Theoretical density of states curve for* EuO (N(E)/*Ry./unit cell*).

the up- and down-spin f band separation is about 6.0 eV. We have obtained the electronic density of states for the Eu-chalcogenides for 256 points in the Brillouin zone, and the results for EuO are shown in figure 2. Normally a knowledge of energy structures at more than 256 points is required in order to obtain reliable $N(E)$ curves in solids. In our case the valence bands are well isolated from each other and present work should give us fairly reliable information. On the other hand the conduction bands are quite complex and our results might not represent detailed structures which could exist. According to our results for the conduction bands there are two peaks which are mainly derived from the t_{2g} and e_g d bands for the up-spin electrons, and three peaks for the down-spin electrons which are due to the t_{2g} and e_g d bands and the $f(\downarrow)$ bands. Both calculated and experimental data are tabulated in table 1.

We can immediately notice from figures 1 and 2 that the experimentally observed density of states of f electrons $N(E, f)$ is considerably smaller than the density of states of the p electrons $N(E, p)$, that experimental f band widths are larger than expected for the f^7 (Eu^{2+}) band width, and that the experimental p band width of EuO is relatively larger than the corresponding p band widths for EuS and EuSe. These experimental results are in contrast to the theoretical results of a ratio of $N(E, f):N(E, p) = 7.6$, of about 0.5 eV for the f band width, and of an almost constant p band width of about 2 eV for all Eu-chalcogenides.

It is not clearly known why the measured $N(E, f)$ is so small. It might be related to the difficulty of releasing more than one f electron because it takes much larger ionization energies for subsequent f electrons from the

TABLE 1. *Theoretical and experimental data* (eV) *of the valence band structures*

		EuO	EuS	EuSe	GdS
f band width	[a]	0.57	0.54	0.70	
	[b]	1.6		1.1	
	[c]	2.0	1.3	1.5	1.0
p band width	[a]	2.12	2.19	2.33	
	[b]	2.0		1.3	
	[c]	3.0	2.3	2.4	2.9
f-p separation	[a]	1.41	0.44	−0.15	
	[b]	1.7		−0.4	
	[c]	2.5	0.5	−0.8	< 0
Average f-p separation	[a]	2.00	1.20	0.50	
	[b]	2.5		0.8	
	[c]	3.5	2.0	1.8	1.9
p to conduction band	[a]	3.61	3.04	2.37	
	[b]	3.8		2.4	
	[c]	4.3	3.1	3.1	3.0

[a] Present work.
[b] Ref. 12.
[c] Ref. 13.

same Eu atom. Another possibility would be a small transition probability for the transitions from the $f(\uparrow)$ bands to the vacuum level due to the small density of states at or near the vacuum level, or that transitions are nondirect [15].

In principle the dominant transitions from the flat $f(\uparrow)$ bands should be direct transitions. However, the f electrons have one of the heaviest effective masses and their velocity should be very small. Accordingly the f electrons involve multiple scattering with phonons and electrons before reaching the surface, or some of them are captured by existing Eu^{3+} ions which are either impurity centers or created from the Eu^{2+} ions. In this case the observed $N(E, f)$ should become considerably broader and different from the initial $N(E, f)$ which we are attempting to measure.

Another possible origin of the large f band width observed could be related to the $F_J(f^6)$ multiplets of Eu^{3+} ions (atomic F_J multiplets have a band width of 0.6 eV [16]). Both Busch et al. [12] and Eastman et al. [13] have interpreted such possible F_J multiplets as arising from the Eu^{3+} ions created from Eu^{2+} ions. We expect that there are about 0.1% concentrations of Eu_2O_3 impurities in the samples. Therefore if F_J multiplets are involved, they would be more likely from Eu^{3+} impurities rather than from Eu^{3+} ions created from Eu^{2+} ions. However, we cannot rule out the possibility of F_J multiplets of Eu^{3+} being created from Eu^{2+} ions. This problem could be resolved from the similar studies with excess Eu^{3+} impurities in the sample. In any case experiments by both Busch et al. [12] and Eastman et al. [13] do not give us proper information on the $N(E, f)$. Busch et al. have reported a linear variation of the f band position with incident photon energies, and Eastman et al. have shown f band positions independent of photon energies. According to the above UPS experiments the possible F_J multiplets of Eu^{3+} ions are located just below the $f^7(^8S_{7/2})$ bands.

The considerably larger f band width of EuO comparing with the corresponding values observed for EuS and EuSe seem to indicate that the possible F_J multiplet width decreases with increasing lattice constant, or that there is a larger amount of scattering for EuO than for EuS and EuSe due to the smaller lattice constant of EuO. As we can see from table 1, not only the experimental data of EuO disagree with theory, but two experimental results also disagree with each other. It appears that the experimental data of EuO by Busch et al. show better agreement with theoretical results than the results by Eastman et al. On the other hand the $4p$ band width of EuSe by Busch et al. is too small. In the case of EuS and EuSe there is reasonable agreement between theory and experiments, except for the f band width. It is interesting to note that the relative positions of the top of the f and p bands among EuO, EuS, and EuSe show good agreement between theory and the experiments (see table 2).

Eastman et al. [13] have also studied UPS for GdS, (see fig. 1), in which they have found that the overall situation is not much different from EuS, except for a partially filled valence $5d$ band, and that the possible $N(E, f)$ is further weakened and has no sign of $4f^7 \rightarrow 4f^6 5d$ transitions. These experimental results are interesting because they tell us that any reflectivity or absorp-

TABLE 2. *Energy differences of the highest* f *and* p *bands among* Eu-*Chalcogenides* (eV)

		p bands	f bands
EuO-EuSe	[a]	3.0	1.3
	[b]	2.9	1.1
	[c]	3.1	1.0
EuS-EuSe	[a]	0.4	0.06
	[c]	0.7	0.04

[a] Present work.
[b] Ref. 12.
[c] Ref. 13.

tion peaks from the $4f$ bands in GdS are difficult to observe. In the reflectivity or transmission experiments for Eu [7] and Gd [8] we have not observed any possible interband transitions from $4f$ bands, which could be related to almost negligible transition probability from the $f(\uparrow)$ bands.

According to the photoemission measurements for Gd metal by Blodgett et al. [9], there is a large d band peak at or near E_f and a broad peak at about 6 eV below E_f. In addition there is a small peak at about 2.8 eV below E_f. They have not elaborated to discuss a small peak at 2.8 eV. The same authors [5] have also reported a large peak at about 5 eV below E_f for Co, Fe, and Ni, which has been found to be spurious. Referring to experimental data in table 1 for the Eu-chalcogenides and GdS, it is reasonable to expect that the possible $f(\uparrow)$ band positions in Eu and Gd metals could be located at less than 3 eV below E_f, and that a small peak at about 2.8 eV below E_f in Gd observed could be the possible $f(\uparrow)$ band position.

ΔE_{ex} for Gd and the Eu-chalcogenides should be larger than the coresponding values of 0.35 eV for Ni because the magnetic moments of Gd and the Eu-chalcogenides are more than 11 times that of Ni. The ΔE_{ex} of about 0.4 eV for Gd estimated from transmission data [8] is a reasonable value. We have also obtained the ΔE_{ex} values of about $0.4 \sim 0.5$ eV for the Eu-chalcogenides [17].

Because of the exchange splitting of energy bands below T_c, the up-spin electrons have lower energy than corresponding down-spin electrons by the amount of ΔE_{ex}. Therefore, it takes more energy to lift up-spin electrons than down-spin electrons under the same experimental conditions. Accordingly, in principle, we should be able to observe such band width broadening of ΔE_{ex} in the temperature dependent studies of $N(E)$. However, practically constant $N(E)$ with variable temperatures reported for Fe and Co by XPS [1], for Ni by UPS [5] and INS [3], and for Gd by UPS [9] are in contradiction to above physical phenomena. At present various experimental methods to study $N(E)$ have shown poor energy resolution. Therefore further experimental work could elucidate this problem.

UPS data for Eu-chalcogenides [12,13], GdS [13], and Gd [9] mentioned above are based on an assumption of equal transition probability from various occupied bands throughout the Brillouin zone, which is certainly not a reasonable assumption for the case of f electrons because of the small number of transitions from f band density of states observed. It would be worthwhile to carry out more experimental studies by using other techniques such as SXS, INS, or XPS to see whether we can obtain more realistic information on the $N(E,f)$.

References

[1] Fadley, C. S., and Shirley, D. A., Phys. Rev. Letters **21**, 980 (1968).

[2] Cuthill, J. R., McAlister, A. J., Williams, M. L., and Watson, R. E., Phys. Rev. **164**, 1006 (1967).

[3] Hagstrom, H. D., and Becker, G. E., Phys. Rev. **159**, 572 (1967).

[4] Eastman, D. E., J. Appl. Phys. **40**, 1387 (1969).

[5] Blodgett, A. J., Jr., and Spicer, W. E., Phys. Rev. **146**, 390 (1966); **158**, 514 (1967); Yu, A. Y.-C. and Spicer, W. E., Phys. Rev. **167**, 674 (1968).

[6] Wohlfarth, E. P., 1964 International Magnetism Conference (Institute of Physics, London, 1965), p. 51.

[7] Müller, W. E., Phys. Kondens. Mat. **6**, 243 (1967).

[8] Schüler, C. C., Optical Properties and Electronic Structure of Metals and Alloys, p. 221, North-Holland, 1966.

[9] Blodgett, A. J., Jr., Spicer, W. E., and Yu, A. Y.-C., Optical Properties and Electronic Structures of Metals and Alloys, p. 246, North-Holland, 1966.

[10] Fleming, G. S., Liu, S. H., and Loucks, T. L., Phys. Rev. Letters **21**, 1524 (1968).

[11] Dimmock, J. O., and Freeman, A. J., Phys. Rev. Letters **13**, 750 (1964).

[12] Busch, G., Cotti, P., and Munz, P., Solid State Commun. **7**, 795 (1969).

[13] Eastman, D. E., Holzberg, F., and Methfessel, S., Phys. Rev. Letters **23**, 226 (1969).

[14] Slater, J. C., Phys. Rev. **81**, 385 (1951).

[15] Berglund, C. N., and Spicer, W. E., Phys. Rev. **136**, A1030 (1964).

[16] Dieke, G. H., and Crosswhite, H. M., Appl. Optics **2**, 675 (1963).

[17] Cho, S. J., (to be published).

Discussion on "Electronic Density of States in Eu-Chalcogenides" by S. J. Cho (National Research Council of Canada, Ottawa)

D. E. Eastman *(IBM, New York):* With regard to a "band" description of the 4*f* electrons in the Eu-chalcogenides, there is considerable experimental evidence that the 4*f* electrons are very localized (with important correlation effects), e.g., a band description appears to be inadequate.

S. J. Cho *(National Res. Council):* I have already discussed this subject elsewhere in this Conference (see "Ultraviolet and X-Ray Photoemission from Europium and Barium" by G. Broden et al.).

Energy Band Structure and Density of States in Tetragonal GeO_2

F. J. Arlinghaus and W. A. Albers, Jr.

Research Laboratories, General Motors Corporation, Warren, Michigan 48090

The electronic energy bands of tetragonal GeO_2 have been calculated and correlated with optical properties of single crystals of this material. The agreement between theory and experiment is sufficiently good to warrant calculations of densities of states and conduction band effective masses preparatory to the determination of the dielectric constant as a function of energy. The calculated energy bands, density of states, and the experimental optical absorption edge data are presented and discussed.

Key words: Augmented plane wave method (APW); electron density of states; GeO_2; indirect transition; optical properties; Slater exchange; vacuum ultraviolet reflectance spectra.

The dioxide of germanium exhibits a polymorphism which is rather unique in nature. The commonly occurring form is the α-quartz hexagonal structure which is relatively reactive and is the thermodynamically unstable phase at ordinary temperatures. The form that does not occur naturally is the rutile tetragonal structure, and it has until recently been prepared only by conversion from the hexagonal phase. In the last few years, methods have been developed for the growth of single crystals of the tetragonal material, enabling the determination of optical and electronic properties. This tetragonal form has proven to exhibit chemical properties which are consistent with possible applications as masks and protective coatings for germanium semiconductor devices. It also exhibits interesting optical properties in the near ultraviolet region of the electromagnetic spectrum. For these reasons, tetragonal GeO_2 warrants some attention, and we have determined the energy band structure in order to aid the design and interpretations of optical and electrical experiments aimed at a better fundamental understanding of the physical nature of this material. The results of these preliminary investigations are reported herein.

Tetragonal GeO_2 possesses the rutile structure with space group D_{4h}^{14} [1]. The unit cell is tetragonal, with a c/a ratio of 0.65, and contains six atoms, two germanium and four oxygen. The Brillouin zone is also simple tetragonal.

A self-consistent APW (augmented plane wave) energy band calculation was performed for GeO_2. Sphere radii were chosen as follows: the oxygen spheres were made to touch, giving as large an oxygen radius as possible; then the germanium spheres were made to touch these. Thus chosen, the spheres fill 55% of the space in the crystal.

The starting potential was derived from Ge^{+4} and $O^{=}$ ionic potentials. The Ge^{+4} ionic potential was calculated by the Herman-Skillman procedure [2]; the $O^{=}$ potential is that of Watson [3]. An Ewald problem is solved to obtain the average potential for the region outside the spheres [4]; exchange is included by means of the Slater $\rho^{1/3}$ approximation [5].

At each stage of the calculation, bands are obtained and a new trial potential obtained from the calculated charge distribution. Ten iterations were required before the eigenvalues were stable to within 0.005 Rydberg. It was found necessary to include the higher core states (the oxygen $2s$- and germanium $3d$-bands). The band structure is shown in figure 1. The main features are the broad conduction band with a parabolic minimum at Γ and the profusion of valence bands, the higher ones quite flat, arising principally from oxygen $2p$ levels.

The direct gap is at Γ; its magnitude is calculated to be 5.52 eV, for transition $\Gamma_5^+ \rightarrow \Gamma_1^+$, allowed for light polarized $\perp$ to the c-axis. The value of 6.04 eV is cal-

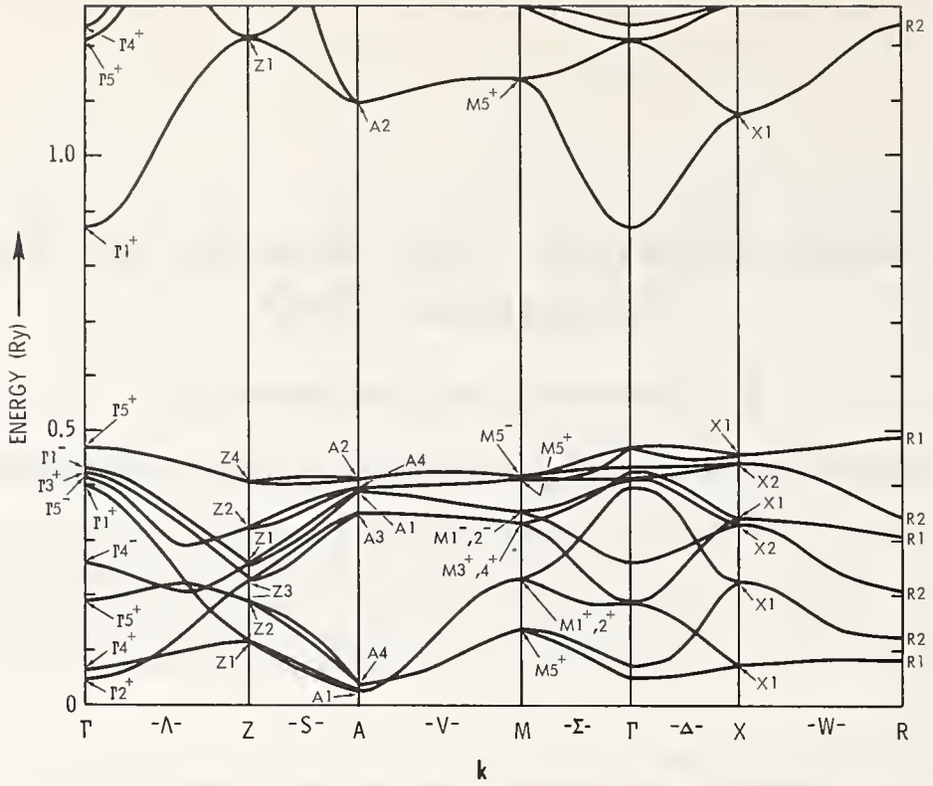

FIGURE 1. *Electronic energy band structure of tetragonal* GeO_2.

culated for transition $\Gamma_1^- \rightarrow \Gamma_1^+$, allowed for polarization. A basic feature of the calculated bands is the presence of an indirect edge. The direct gap $\Gamma_5^+ \rightarrow \Gamma_1^+$ is 5.52 eV; however, the valence band state R_1, on the top edge of the zone, is slightly higher than the Γ_5^+ state, so that the indirect transition $R_1 \rightarrow \Gamma_1^+$ is only 5.25 eV. This indirect edge is different from that of germanium, in that the valence band comes up away from the zone center: in all other cases of an indirect edge known at present, the conduction band comes down.

The numbers resulting from these calculations are in good agreement with the somewhat limited experimental data available to date. The fundamental optical absorption edge has been studied in some detail in tetragonal GeO_2 single crystals at room temperature. The resulting data are summarized in figure 2. The rather large dichroism observed at the absorption edge is consistent with the $\Gamma_5^+ \rightarrow \Gamma_1^+$ and the $\Gamma_1^- \rightarrow \Gamma_1^+$ transitions discussed above. The experimentally determined energy gaps, assuming α, the absorption coefficient, proportional to $(h\nu - E_g)^{1/2}$ at high absorption coefficients (see inset of fig. 2), are 4.99 and 5.10 eV [6]. These values are somewhat lower than those predicted by the energy band calculations, but the agreement is considered quite satisfactory in view of the preliminary nature of the calculations.

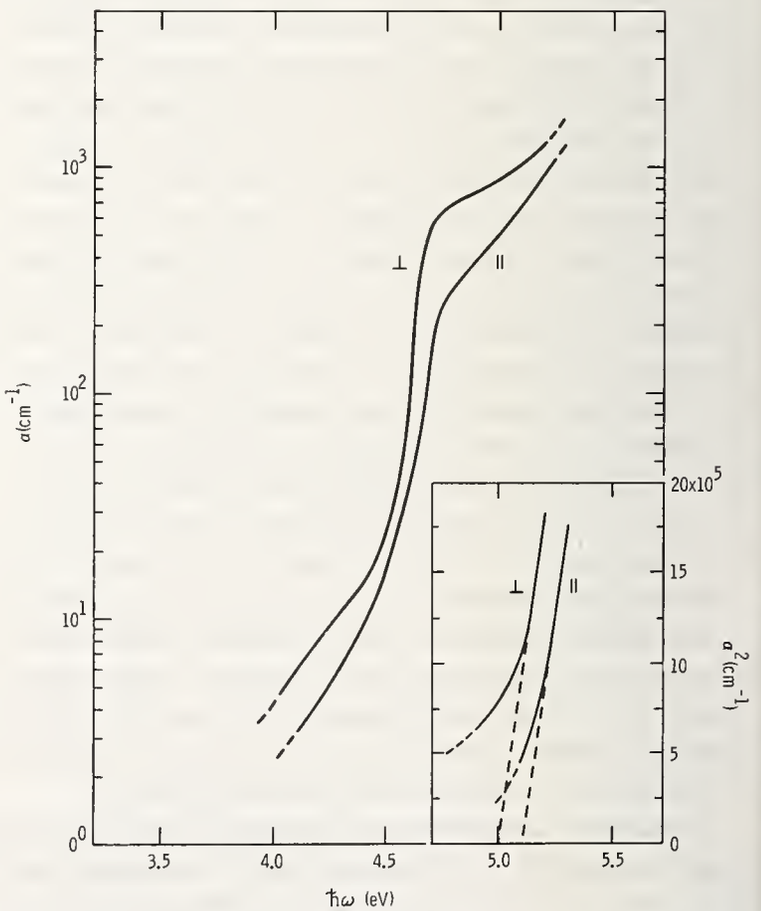

FIGURE 2. *Room temperature optical absorption edge of tetragonal* GeO_2.

The data of figure 2 indicates considerable contributions to the absorption coefficient at energies lying below the fundamental direct gaps. This is consistent with the possibility of an indirect transition as predicted by the band calculations ($R_1 \rightarrow \Gamma_1^+$). However, also possible are exciton and impurity state transitions in this same range of energy, and it has not been possible to sort out the relative contributions in order to ascertain the existence of the indirect transition unambiguously. We are currently studying the absorption edge at low temperatures in an effort to clarify this point.

Preliminary vacuum ultraviolet reflectance spectra on single crystals of tetragonal GeO_2 at room temperature have been obtained by William Scouler at MIT's Lincoln Laboratory. His results suggest a possible transition occurring in the region of 7.5−8.0 eV. The calculated band structure predicts a direct transition at the X-point ($X1 \rightarrow X1$ in fig. 1) at about 8.4 eV. Since the band calculations predict slightly larger direct gaps at Γ than experimentally observed, we feel justified in tentatively assigning the 7.5−8.0 eV structure in the reflectivity to the X-point transition.

On the basis of the above discussion, we conclude that the band calculations presented here are reasonably representative of the true electronic energy structure of tetragonal GeO_2. We have therefore determined the density of states, effective masses, and momentum matrix elements preparatory to a calculation of the dielectric constant as a function of energy. The density of states is shown in figure 3. This was obtained by summing states in 0.02 Rydberg energy intervals over a 64-point mesh in the Brillouin zone and smoothing the resulting data. Although more refined density of states could be obtained with a finer mesh, we feel that the basic structure of figure 3 will not be grossly altered by the inclusion of various other points of the Brillouin zone.

Effective masses of the anisotropic conduction band electron have been calculated to be 0.42 m perpendicular to the c-axis and 0.47 m parallel to the c-axis. These values are consistent with rather crude estimates of the electron effective mass from the optical data.

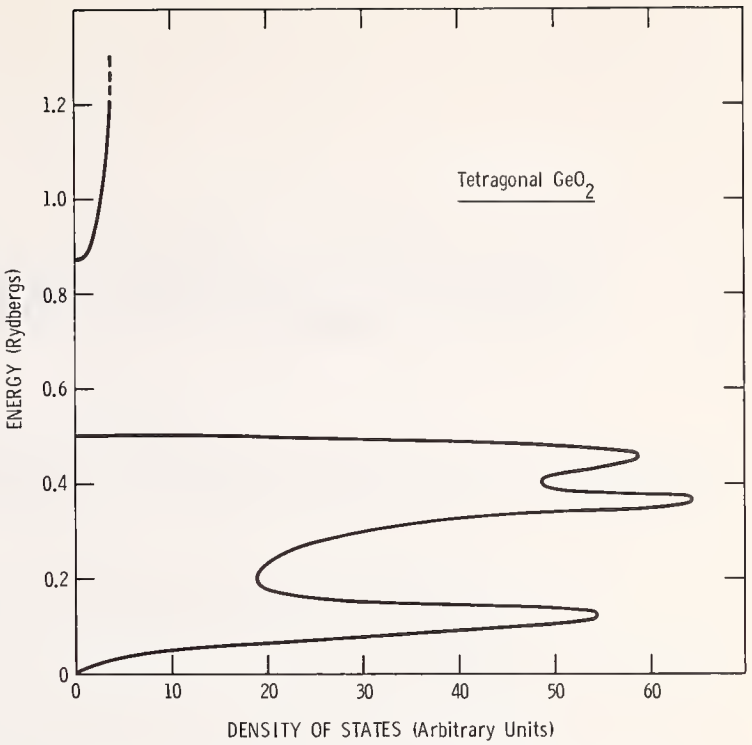

FIGURE 3. *Calculated density of states for tetragonal* GeO_2.

We conclude that the energy bands of tetragonal GeO_2 presented herein constitute a good basis for the prediction and analysis of experiments related to the optical and electronic properties of this material.

References

[1] Gay, J. G., Albers, W. A., Jr., and Arlinghaus, F. J., J. Phys. Chem. Sol. **29**, 1449 (1968).

[2] Herman, F., and Skillman, S., Atomic Structure Calculations (Prentice-Hall Inc., Englewood Cliffs, N.J., 1963).

[3] Watson, R. E., Phys. Rev. **111**, 1108 (1958).

[4] Slater, J. C., and DeCicco, P. D., M.I.T. Solid State and Molecular Theory Group Quarterly Progress Report No. 50, p. 46 (October 1963).

[5] Slater, J. C., Phys. Rev. **81**, 385 (1951).

[6] Smith, R. A., Semiconductors (Cambridge University Press, London, 1959).

Calculation of the Density of States and Optical Properties of PbTe from APW-LCAO Energy Bands*

D. D. Buss and V. E. Schirf****

Department of Electrical Engineering and Center for Material Science and Engineering, Massachusetts Institute of Technology, Cambridge, Massachusetts 02139

The overlap integrals in the tight-binding secular equation for the relativistic p-bands in PbTe have been adjusted to give the best representation of the APW results at high symmetry points. The resulting LCAO bands have been used to calculate the density of states in energy and the optical constants of PbTe. The calculated density of states is found to have peaks which correspond closely to the four peaks measured by Spicer and Lapeyre. However, the assignment of peaks to bands is found to be different from that proposed previously. The method of Dresselhaus and Dresselhaus has been used to obtain the oscillator strengths for optical transitions, and these are found to agree with previous calculations. The interband electronic contribution to the optical constants has been calculated for photon energy less than 5 eV.

Key words: Augmented plane wave method (APW); electronic density of states; k · p method; LCAO; lead telluride (PbTe); optical properties; pseudopotential; random phase approximation; tight-binding.

1. Introduction

The Augmented Plane Wave (APW) method has been applied to PbTe by Conklin, Johnson, and Pratt [1] who have obtained the relativistic energy bands at nine points of high symmetry in the Brillouin Zone (BZ). In this work we have used these energy bands to calculate the electronic density of states in energy and the interband electronic contribution to the optical constants of PbTe.

The direct absorption edge, which is most commonly used to test the validity of an energy band picture, is .3 eV in PbTe at room temperature. This is smaller than the expected accuracy of even the most optimistic first principles calculation. However, the density of states provides a less stringent test of the validity of an energy band picture, because the density of states depends upon general features of the bands over a large region of **k**-space and not upon the details of the bands at any one point in the BZ. The optical properties, on the other hand, do depend critically on the energy difference between regions of high density of states and for this reason provide a more exacting test of the validity of an energy band picture.

For both calculations, one must know the energy bands everywhere in **k**-space, and, because APW calculations are long and tedious, they can be performed only at a small number of points of high symmetry. Therefore, one is forced to use an interpolation scheme to obtain the bands in between points where the APW results are known.

Three interpolation methods are in common use today. The Linear Combination of Atomic Orbitals (LCAO) or tight binding method was first proposed by Slater and Koster [2] and has been employed extensively by Dresselhaus and Dresselhaus [3]. The **k** · **p** method has been in use for a long time but was first used to represent a large number of bands over the entire BZ by Cardona and Pollak [4]. More recently this method has been applied to PbTe [5]. The pseudopotential method is the most widely used of the three, and has been used extensively to study the optical properties of the IV, the III-V, and the II-VI materials [6]. More recently the optical properties of PbTe and related compounds have been calculated using this method [7].

In this work an LCAO representation of the bands in PbTe was obtained by adjusting the band parameters

*This work was supported in part by the National Science Foundation and in part by the Army Research Office (Durham).

**Present address: Physics Research Laboratory, Texas Instruments Incorporated, Dallas, Texas.

***Present address: Itek Corporation, Lexington, Massachusetts.

to give agreement with the APW energies as discussed in section 2 and appendix A. The density of electron states in energy was calculated from these bands, and the results are compared with photoemission data [8] in section 3. Section 4 describes the calculation of optical properties and compares the calculation with experiment [9] and with previous calculations [5]. Oscillator strengths for optical transitions have been obtained directly from the energy bands using the method of Dresselhaus and Dresselhaus [3].

2. LCAO Energy Bands

Following the method proposed in reference 2, we have expressed the crystal wavefunctions as linear combinations of Bloch sums of Löwdin functions. The Löwdin functions resemble free atom wavefunctions, but they have the property that such functions located on neighboring atomic sites in a crystal are orthogonal. For this application Löwdin functions were chosen to resemble the Pb $6p$ and the Te $5p$ free atom wavefunctions. The former are located on the Pb atom sites $\mathbf{R}$ and the latter are located on the Te atom sites $\mathbf{R}+\boldsymbol{\tau}$ where $\boldsymbol{\tau}=a/2(100)$. The orbital portion of the Löwdin functions can be written as $a_\alpha^{Pb}(\mathbf{r}-\mathbf{R})$ and $a_\alpha^{Te}(\mathbf{r}-\mathbf{R}-\boldsymbol{\tau})$ where $\alpha=x, y, z$. The orbital part of the Bloch sums is

$$b^{\pm}_{\alpha,\mathbf{k}}(\mathbf{r})=\frac{1}{\sqrt{N}}\sum_{\mathbf{R}}\frac{1}{\sqrt{2}}\left[a_\alpha^{Pb}(\mathbf{r}-\mathbf{R})\right.$$
$$\left.\pm a_\alpha^{Te}(\mathbf{r}-\mathbf{R}-\boldsymbol{\tau})e^{\,i\mathbf{k}\cdot\boldsymbol{\tau}}\right]e^{\,i\mathbf{k}\cdot\mathbf{R}} \qquad (1)$$

where N is the number of unit cells in the crystal.

When the crystal Hamiltonian is separated into a spin-independent part and a spin-orbit part

$$H=H_{\mathrm{si}}+H_{\mathrm{so}} \qquad (2)$$

the six Löwdin functions of eq (1) form a six-dimensional basis for H_{si}. In this basis, matrix elements of H_{si} take the form of a Fourier series in $\mathbf{k}$-space [3] in which the Fourier coefficient for the nth term in the expansion involves matrix elements of H_{si} between Löwdin functions which are nth neighbors, and, since Löwdin functions are localized, the expansion converges rapidly. In this work the series has been truncated with fourth neighbor terms, giving 16 independent Fourier coefficients.

When spin is included into the problem, the number of basis states doubles, but Kramer's theorem assures us that each level has at least a two-fold degeneracy. Every term in the Hamiltonian which does not explicitly involve electron spin is included in H_{si} so that

$$H_{\mathrm{so}}=\frac{\hbar}{4m^2c^2}\boldsymbol{\sigma}\cdot[(\boldsymbol{\nabla}V)\times\mathbf{p}]. \qquad (3)$$

This term is quite important in PbTe [1], but since ∇V is large only near the nucleus, it is reasonable to assume that the only matrix elements of H_{so} which are important are those between Löwdin functions on the same lattice site, and in this work, all other matrix elements are taken to be zero. This simplification is equivalent to the approximation, suggested by atomic theory, that

$$\langle a_\alpha^{Pb}(r-R),s\,|H_{\mathrm{so}}|\,a_\beta^{Pb}(r-R'),s'\rangle=\tfrac{1}{2}\lambda^{Pb}\langle a_\alpha^{Pb}(r),s\,|L\cdot\sigma\,|a_\beta^{Pb}(r),s'\rangle\delta_{R,R'}$$
$$\langle a_\alpha^{Te}(r-R-\tau),s\,|H_{\mathrm{so}}|\,a_\beta^{Te}(r-R'-\tau),s'\rangle=\tfrac{1}{2}\lambda^{Te}\langle a_\alpha^{Te}(r),s\,|L\cdot\sigma\,|a_\beta^{Te}(r),s'\rangle\delta_{R,R'}$$
$$\langle a_\alpha^{Pb}(r-R),s\,|H_{\mathrm{so}}|\,a_\beta^{Te}(r-R'-\tau),s'\rangle=\langle a_\alpha^{Te}(r-R-\tau),s\,|H_{\mathrm{so}}|\,a_\beta^{Pb}(r-R'),s'\rangle=0 \qquad (4)$$

where s and s' designate spin coordinates ($s, s'=\uparrow,\downarrow$), and λ^{Pb} and λ^{Te} are constants. Thus H_{so} introduces two additional parameters into the tight binding Hamiltonian, and, to the extent that the approximations made here are justified, λ^{Pb} and λ^{Te} should resemble the spin-orbit parameters which pertain to the free atom.

The 18 band parameters were obtained from the APW calculation in the following way. Reference 1 gives the intermediate results which were obtained by first solving the nonrelativistic problem and by subsequently including the Darwin and Mass-velocity corrections. The two spin-orbit parameters were set equal to zero, and the remaining 16 band parameters were adjusted to minimize the r.m.s. difference between the LCAO bands and the intermediate APW results given in table 1 [10]. The band parameters are defined in appendix A and their values obtained are given in table 4. These bands reproduce the 48 data points of table 1 to within an r.m.s. error of 0.014 Ry, and the size of the band parameters falls off rapidly with increasing order as it must for the scheme to have physical meaning.

The 16 nonspin-orbit parameters so determined were then fixed, and the two spin-orbit parameters were adjusted to give the best r.m.s. fit to the final results of

TABLE 1. *APW results of Ref. 1 (see Ref. 10). The LCAO band parameters were adjusted to these energies*

Γ(0, 0, 0)				Δ(1, 0, 0)				X(2, 0, 0)				Σ(1/2, 1/2, 0)			
Intermediate		Final		Intermediate		Final		Intermediate		Final		Intermediate		Final	
−0.305	Γ_{15}	−0.262	Γ_8^-	−0.274	Δ_5	−0.226	Δ_7	−0.136	X_4'	−0.132	X_6^-	−0.309	Σ_3	−0.309	Σ_5
−.305		−.262		−.274		−.311	Δ_6	−.215	X_5'	−.143	X_7^-	−.410	Σ_4	−.387	Σ_5
−.305		−.390	Γ_6^-	−.401	Δ_1	−.405	Δ_6	−.215		−.283	X_6^-	−.431	Σ_1	−.453	Σ_5
−.684	Γ_{15}	−.659	Γ_8^-	−.697	Δ_1	−.700	Δ_6	−.780	X_5'	−.747	X_7^-	−.607	Σ_1	−.599	Σ_5
−.684		−.659		−.742	Δ_5	−.706	Δ_7	−.780		−.816	X_6^-	−.661	Σ_4	−.670	Σ_5
−.684		−.735	Γ_6^-	−.742		−.788	Δ_6	−.910	X_4'	−.914	X_6^-	−.723	Σ_3	−.723	Σ_5

Σ(1, 1, 0)				K(3/2, 3/2, 0)				Λ(1/2, 1/2, 1/2)				L(1, 1, 1)			
Intermediate		Final		Intermediate		Final		Intermediate		Final		Intermediate		Final	
−0.274	Σ_3	−0.274	Σ_5	−0.200	K_3	−0.200	K_5	−0.406	Λ_3	−0.372	Λ_4, Λ_5	−0.432	L_3'	−0.394	L_4^-, L_5^-
−.452	Σ_4	−.426	Σ_5	−.320	K_4	−.299	K_5	−.406		−.397	Λ_6	−.432		−.426	L_6^-
−.461	Σ_1	−.486	Σ_5	−.335	K_1	−.361	K_5	−.436	Λ_1	−.478	Λ_6	−.472	L_2'	−.519	L_6^-
−.631	Σ_1	−.624	Σ_5	−.730	K_1	−.718	K_5	−.631	Λ_1	−.619	Λ_6	−.546	L_1	−.539	L_6^+
−.672	Σ_4	−.680	Σ_5	−.752	K_4	−.775	K_5	−.674	Λ_3	−.651	Λ_4, Λ_5	−.623	L_3	−.602	L_4^+, L_5^+
−.811	Σ_3	−.811	Σ_5	−.886	K_3	−.886	K_5	−.674		−.709	Λ_6	−.623		−.652	L_6^-

table 1. The spin-orbit effects were found to be extremely well characterized by only two constants and the values of these constants ($\lambda^{Pb} = 0.06447$ $\lambda^{Te} = 0.05396$) are reasonably close to the free atom spin-orbit parameters [11].

The final LCAO bands along the three principle axes are shown together with the APW results in figure 1. The r.m.s. error between these bands and the final APW results is 0.020 Ry.

3. Density of States

The density of states in energy was calculated from the bands of figure 1 in the following manner. The BZ was divided into cubes .4 π/a on a side, and 24 of these cubes were found to lie at least partly within the reduced BZ, i.e., within the region having 1/48th of the BZ volume which is defined by the relations $0 \leq k_z \leq k_y \leq k_x \leq 2\pi/a$ and $k_x + k_y + k_z \leq 1.5\pi/a$. Within each box i, N_i points were generated at random, the energies were obtained at each point, and the average number of states in each energy range was determined. Finally the results of each box were weighted by how much of that box lay within the reduced BZ and summed.

In all, the secular equation was solved at 4900 points. Convergence of the density of states result was guaranteed by the fact that the answer after 2450 points differed from the final answer by about 4%.

A histogram of the density of states is shown in figure 2. The calculation is not valid above the dashed line because d-bands, which have been ignored in this calculation, become important here. The arrows in figure 2 indicate the energies at which photoemission experiments [8] predict peaks in the density of states. These peaks are labeled c, v_1, v_2, v_3 and are associated with corresponding peaks in the calculated density of states as shown in the figure.

Spicer and Lapeyre [8] have identified the peaks c, v_1 and v_2 with the L point band edges of the 2nd conduction band, the 2nd valence band and the 3rd valence band respectively (bands are numbered going away from the gap), and they have presented evidence that the v_3 peak results from states elsewhere in the zone.

In the present calculation, the contribution to the density of states from each region of the zone was calculated separately. It was found that the region around L does not make the major contributions to these peaks. Instead the bands proved to be flat over a relatively large region of **k**-space which includes the point of minimum gap on the Δ- and Σ-axes. This region can be thought of as being formed by six surfaces which are approximately planar and are perpendicular to the six Δ-axes. In this calculation the surfaces intersect the Δ-axis at $\pi/a(.7, .0, .0)$, the Σ-axis at $\pi/a(.8, .8, .0)$, and the Λ-axis at $\pi/a(1.0, 1.0, 1.0)$ (the L point). In addition, the calculation reveals that the c, v_1, and v_2 peaks result from states in the principal conduction band, the principal valence band and the 2nd valence band respectively, and that they occur .08 Ry, .04 Ry, and .02 Ry away from their respective band edges.

The v_3 peak is found to result from the coincidence of maxima from two bands; the third valence band near Γ and the primary valence band near X. The fact that this peak receives contributions from two quite dif-

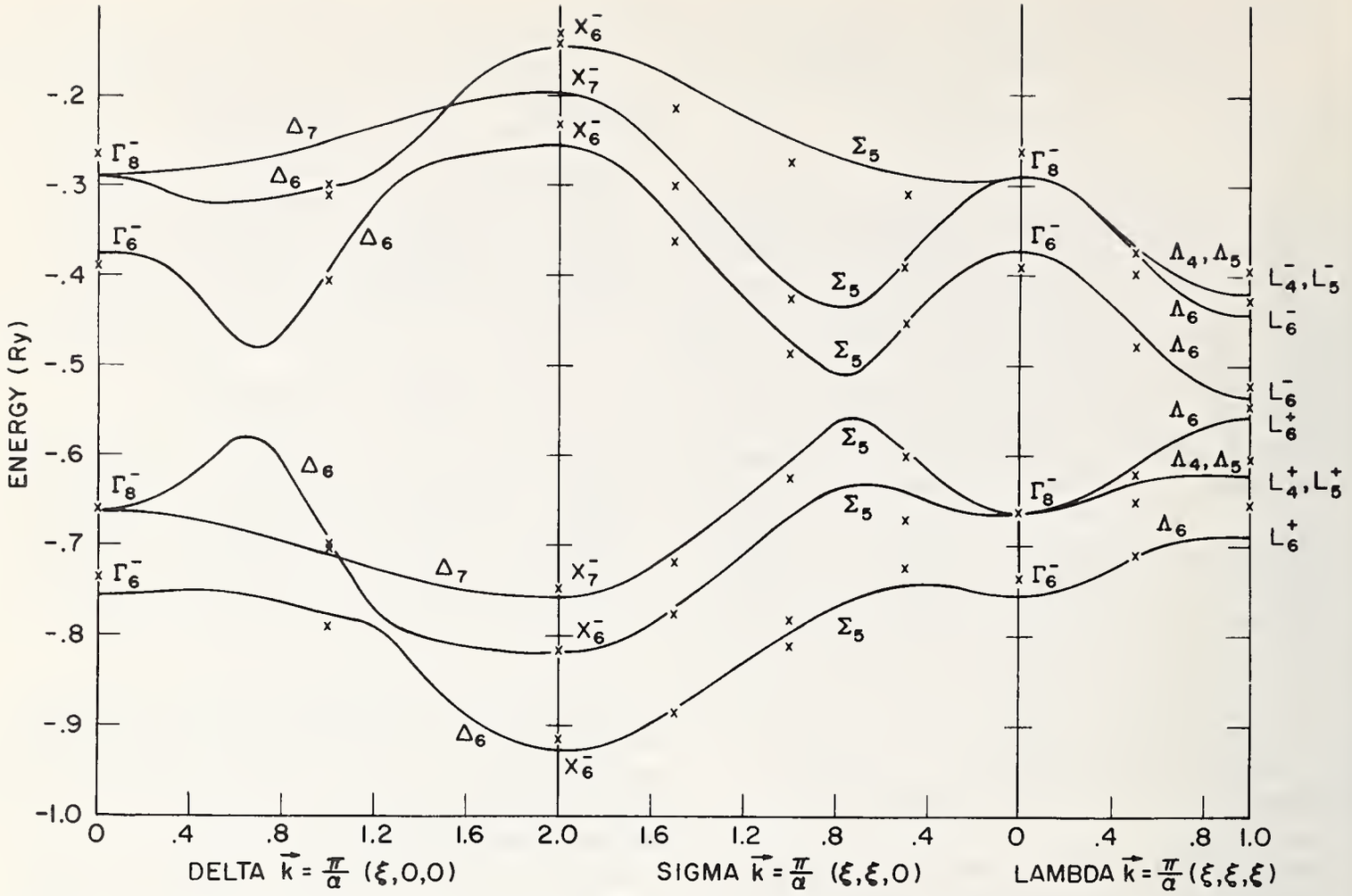

FIGURE 1. *The relativistic LCAO bands of* PbTe *on the three principle axes. The crosses give the APW results to which the bands were fit.*

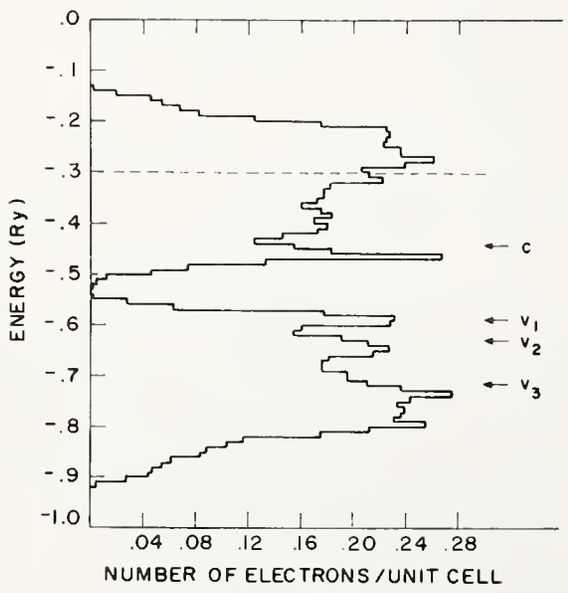

FIGURE 2. *A histogram of the density of electron states calculated from the bands of figure 1.*

The arrows indicate the positions of the peaks found in ref. [8]. The calculation is not valid above the dashed line.

ferent regions of **k**-space could explain why the peak does not disappear sharply with increasing photon energy even if the transitions causing this peak are direct [8].

In reference 8, the v_1, v_2, and v_3 peaks were observed directly in the photoemission spectrum, but the c peak was inferred indirectly using the optical measurements of reference 9. This was done by associating a joint density of states maximum with the 2.2 eV peak in the measured reflectivity and thereby placing the c peak 2.2 eV above the v_1-v_2 doublet. Joint density of states maxima are, however, most closely related to maxima in the imaginary part of the dielectric constant, $\epsilon_2(\omega)$, and peaks in $\epsilon_2(\omega)$ can be shifted by as much as .4 eV from peaks in the reflectivity [6]. The $\epsilon_2(\omega)$ calculated from the reflectivity in reference 9 and the $\epsilon_2(\omega)$ calculated in reference 5 show a shoulder at 1.8 eV and no structure at 2.2 eV. We interpret this shoulder as arising from transitions between the v_1 and c density of states

maxima, which, in our calculation, are separated by 1.7 eV. This interpretation is confirmed by the observation that the v_1 and c maxima both result from states in the same region of **k**-space and that this region of **k**-space contributes strongest to $\epsilon_2(\omega)$ at this energy [5]. Furthermore, the v_2 and c maxima do not form a joint density of states maximum because the states contributing to those peaks are in different regions of **k**-space, and hence no peak in $\epsilon_2(\omega)$ occurs at 2.5 eV.

The peak at low electron energy which begins to appear in the high photon energy results of reference 8 is interesting. If it could be resolved by going to higher photon energy, and if it could be shown to result from a density of states maximum (and not from scattered electrons [8]), then it would give information about the s-bands in PbTe. A previous calculation has indicated a sharp peak in the density of states located 7.6 eV below the valence band edge [12]. This is too low to be resolved by the maximum photon energy used in reference 8 (11.5 eV), but perhaps the tail of this peak is being observed.

4. Optical Constants

In order to calculate the optical properties of a material, it is necessary to know the oscillator strengths as well as the resonant frequencies for each transition. That is to say, at every value of **k** one must know the momentum matrix element coupling the occupied bands with the unoccupied bands as well as the energy of each band.

Momentum matrix elements can be calculated from the wavefunctions obtained from any energy band calculations. However, one can often estimate the momentum matrix elements directly from the energy bands. If two bands are quite close together in energy, it is often reasonable to assume that the bands interact (in the sense of a $\mathbf{k}\cdot\mathbf{p}$ expansion) only with one another and that the band curvature is determined only by the momentum matrix element coupling those two bands. When this is true, the Taylor expansion of $H(\mathbf{k})$ through terms linear in **k** can be identified with the $\mathbf{k}\cdot\mathbf{p}$ Hamiltonian matrix, and matrix elements of momentum can be related to the coefficients in the expansion. This method was first used by Dresselhaus and Dresselhaus [3], and the conditions for its validity seem to be well satisfied in PbTe [13]. Following reference 3 we express the ν component of the momentum matrix element coupling bands i and j as

$$p^{\nu}_{ij}(\mathbf{k}) = \frac{m}{\hbar}\sum_{l,n} U^{*}_{l,i}(\mathbf{k})\frac{\partial H_{l,n}(\mathbf{k})}{\partial k_{\nu}}U_{n,j}(\mathbf{k}) \tag{5}$$

where $U(\mathbf{k})$ is the unitary matrix which diagonalizes $H(\mathbf{k})$.

$$\sum_{l,n} U^{*}_{l,i}(\mathbf{k})H_{l,n}(\mathbf{k})U_{n,j}(\mathbf{k}) = E_i(\mathbf{k})\delta_{ij} \tag{6}$$

The interband contribution to the complex dielectric constant $\epsilon(\omega) = \epsilon_1(\omega) + i\epsilon_2(\omega)$ is given in the random phase approximation by [14]

$$\epsilon(\omega) = 1 - \frac{4\pi e^2}{\Omega}\sum_{\mathbf{k}}\sum_{i,j}\frac{|p^{\nu}_{ij}(\mathbf{k})|^2}{m^2\omega^2_{ij}(\mathbf{k})}\frac{\{f_0[E_j(\mathbf{k})] - f_0[E_i(\mathbf{k})]\}}{[E_j(\mathbf{k}) - E_i(\mathbf{k}) - \hbar\omega - ih/\tau]}. \tag{7}$$

This expression has been evaluated for intrinsic PbTe at temperatures sufficiently low that the Fermi functions $f_0(E)$ are one or zero. Ω is the unit cell volume, $\hbar\omega_{ij}(\mathbf{k}) = E_i(\mathbf{k}) - E_j(\mathbf{k})$, and τ, taken to be 6×10^{-14} sec ($h/\tau = .005$ Ry), gives a linewidth to each transition. The summation on the **k** values within the BZ is simplified to a summation over the reduced BZ (sec. 3). This is accomplished by replacing $|p^{\nu}_{ij}(\mathbf{k})|^2$ in eq (7) by

$$\frac{1}{3}|\mathbf{p}_{ij}(\mathbf{k})|^2 \equiv \frac{1}{3}\sum_{\mu}|p^{\mu}_{ij}(\mathbf{k})|^2 \tag{8}$$

This substitution is valid because the bands have cubic symmetry.

The magnitude squared $|\mathbf{p}_{ij}(\mathbf{k})|^2$ of the matrix element between the principal conduction and valence bands, calculated from the bands of section 2, is plotted in figure 3 along the three principal axes in **k**-space together with the results of reference 5. Analysis of the approximations involved in eq (5) suggests that this method should work best on the Δ-axis and worst at L. This conclusion is born out by figure 3. On the Δ-axis, the $\mathbf{k}\cdot\mathbf{p}$ and the LCAO results agree to within 20%. APW calculations at L give .331 (a.u.)^2 for this quantity [15].

The summation on the reduced BZ was carried out by dividing this region into boxes as in section 3. Within each box, a Monte Carlo integration was performed [3], and the results were weighted and added as in section 3. It was found that certain boxes contribute strongly to $\epsilon(\omega)$ and the integration was performed more accurately in these boxes than in the boxes which con-

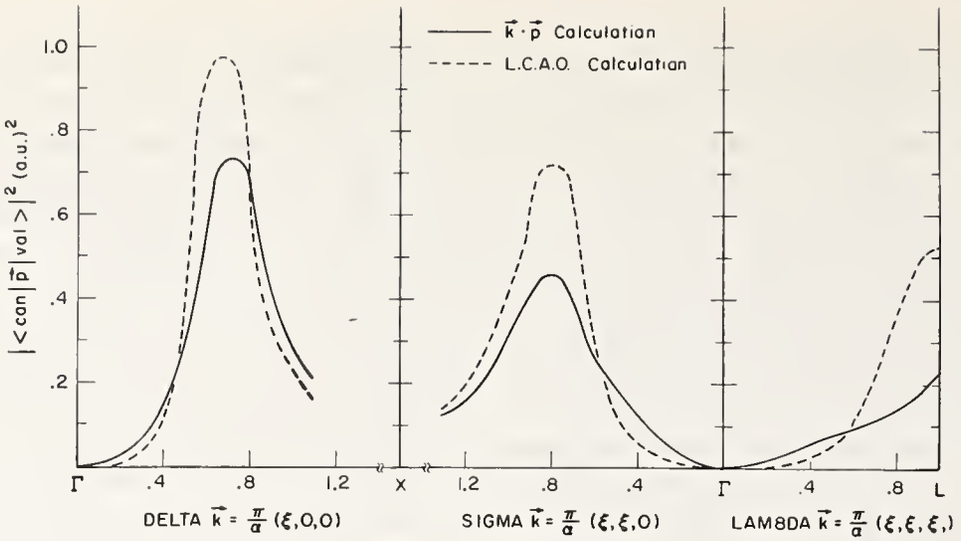

FIGURE 3. *The magnitude squared of the momentum matrix element coupling the principle conduction band with the principle valence band.*

The present calculation is compared with the $\mathbf{k}\cdot\mathbf{p}$ results of ref. [5].

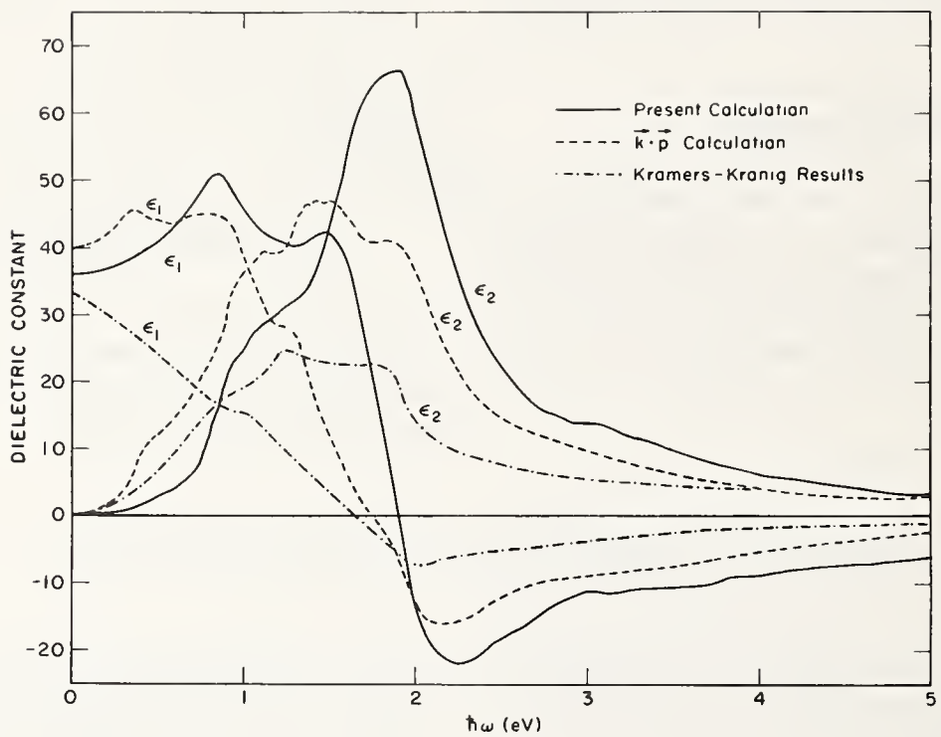

FIGURE 4. *The real and imaginary parts of the calculated interband electronic dielectric constant together with the results of ref.* [5] *and ref.* [9].

tribute less strongly. To insure convergence, the number of random points N_i within the ith box was chosen to be sufficiently large that the final result for $\epsilon_2(\omega)$ differed by a maximum of .1 or less from the intermediate result calculated with $N_i/2$ points. 11,850 points were required to obtain convergence using this criterion.

To facilitate the calculation, the eigenvalue problem was not solved at every random point. Instead it was solved on a mesh of points $\mathbf{k}=\pi/5a\ (l, m, n)$ (l, m, and n are integers), and the energies and momentum matrix elements were obtained between the mesh points by linear interpolation.

The real and imaginary parts of $\epsilon(\omega)$ calculated in this way are shown in figure 4 together with the Kramers-Kronig results of reference 9 and the $\mathbf{k}\cdot\mathbf{p}$ results of reference 5. The overwhelmingly dominant feature of this calculation of $\epsilon_2(\omega)$ is the peak at 1.9 eV which

results from transitions between the v_1 and c density of states maxima. Even though the present calculation is based on the same APW results as that of reference 5, the energy differences between the principal conduction band and the principal valence band are slightly larger causing the present result to be smaller at low energies and larger at high energies. In addition the momentum matrix elements are consistently larger.

In spite of the apparent inability of the present calculation to reproduce the experimental $\epsilon_2(\omega)$ [16], $\epsilon_1(\omega = 0) = 36.2$ is surprisingly close to the measured optical dielectric constant $\epsilon_\infty = 31.8$ [17]. This quantity is not as sensitive to small inaccuracies in the energy bands as are the optical constants at higher frequencies. Instead it reflects an average gap and an average oscillator strength.

5 Conclusion

The calculation of density of states and optical constants was undertaken primarily to test in a general way the accuracy of the APW-LCAO energy bands and secondly to test the validity of eq (5) for approximating interband oscillator strengths.

The good agreement between the calculated density of states and the photoemission data indicates that the bands are sufficiently accurate to justify unambiguous assignment of observed peaks in the valence band density of states with features of the band model. We conclude that agreement between the calculated peak in the conduction band density of states and that deduced from optical properties in reference 8 is largely fortuitous, but that a reinterpretation of the measured optical properties is consistent with the calculated position of this peak.

Based on the success of the density of states calculation, the calculation of $\epsilon(\omega)$ is disappointing indeed. It is tempting to blame this lack of success on the oscillator strengths, but this is not necessarily the case. The differences between the present calculation and that of reference 5 are due as much to small differences in the energy bands as to differences in the oscillator strengths and we have not been able to draw any conmusions about the validity of eq (5) beyond what is shown in figure 3.

This calculation illustrates an important difference between PbTe and the wider gap materials. In the former, even small changes in the bands represent large percentage changes and can drastically affect both the size and shape of the calculated $\epsilon_2(\omega)$ whereas in the latter this is not the case [18]. Considerable refinements will have to be made in the band picture of PbTe before agreement as good as that obtained in better known materials is achieved.

6. Acknowledgments

The authors are grateful to George Pratt, Gene Dresselhaus and Mildred Dresselhaus for their advice and assistance in carrying out this work and to Sahrab Rabii for making available to us his energy band calculations. We are also grateful to Prof. Marvin Cohen and Yvonne Tsang for sending us the results of their calculations of the optical constants of PbTe prior to publication.

7. References

[1] Conklin, L. B., Jr., Johnson, L. E., and Pratt, G. W., Jr., Phys. Rev. **137**, A1282 (1965).

[2] Slater, J. C., and Koster, G. F., Phys. Rev. **94**, 1498 (1954).

[3] Dresselhaus, G., and Dresselhaus, M. S., Phys. Rev. **160**, 649 (1967); Dresselhaus, G., Solid State Communications **7**, 419 (1969).

[4] Cardona, M., and Pollak, F. H., Phys. Rev. **142**, 530 (1966).

[5] Buss, D. D., and Parada, N. J., to be published.

[6] See for example: M. L. Cohen, II-VI Semiconducting Compounds, 1967 International Conference (W. A. Benjamin Inc., 1967), p. 462; F. Herman, R. L. Kortrum, C. D. Kuglin and J. L. Shay, ibid., p. 503.

[7] Lin, P. J., Saslow, W., and Cohen, M. L., Solid State Communications **5**, 893 (1967); Tung, Y. W., and Cohen, M. L., Phys. Rev. **180**, 823 (1969); Tsang, Y., and Cohen, M. L., to be published.

[8] Spicer, W. E., and Lapeyre, G. J., Phys. Rev. **139**, A565 (1965).

[9] Cardona, M., and Greenaway, D. L., Phys. Rev. **133**, A1685 (1964).

[10] The APW calculation finds the valence and conduction band edges at L to have L_6^- and L_6^+ symmetry respectively (see table 3 of ref. 1) whereas experimental evidence indicates that the symmetry of these two levels should be reversed (see ref. 1). The constant potential in the plane wave region was chosen somewhat arbitrarily to be -0.80138 Ry and it was found that increasing this potential had the effect of changing the relative ordering of the bands around the gap at L without significantly affecting the bands elsewhere. (J. B. Conklin, Jr., Ph. D. thesis, E. E. Department, M.I.T., June 1954, p. 71.) S. Rabii has recalculated the bands at L using a potential in the plane wave region of -0.59140 Ry (private communication) and his results are given in table 1 for the L point. This adjustment represents the only departure we have made from "first principles." Moreover, the density of states and optical properties do not depend critically on the position of the band edge (see secs. 3 and 4) and are quite insensitive to the adjustment.

[11] Free atom Hartree-Fock calculations for Pb and Te indicate that the $^3P_{3/2}$ level lies 0.09356 Ry and 0.06176 Ry above the $^3P_{1/2}$ giving spin orbit parameters of $\lambda^{Pb} = 0.06238$ and $\lambda^{Te} = 0.04118$ Ry, F. Herman and S. Skillman, Atomic Structure Calculations (Prentice-Hall Inc., 1963).

[12] Schirf, V. E., S. M. Thesis, E. E. Department, M.I.T., 1966.

417-156 O - 71 - 9

[13] The general applicability of this method will be discussed elsewhere.
[14] Ehrenreich, H., and Cohen, M. H., Phys. Rev. **115**, 786 (1959).
[15] Bailey, P. T., O'Brien, M. W., and Rabii, S., Phys. Rev. **179**, 735 (1969).
[16] Although the $\epsilon(\omega)$ found in reference 9 is not directly measured, we assume it is correct for the purposes of evaluating the validity of our calculation.
[17] Walton, A. K., and Moss, T. S., Proc. Phys. Soc. 81, 509 (1963).
[18] See for example: Herman et al. cited in reference 6, p. 522.

8. Appendix A

This appendix defines the parameters used in the tight binding secular equation which is discussed in section 2 and gives their value.

The 6×6 secular equation obtained by taking matrix elements of the spin independent part, H_{si}, of the crystal Hamiltonian between Bloch sums having the symmetry of eq (1) is expanded in the most general Fourier series consistent with this symmetry. The result of the expansion through fourth order terms is given in table 2. The Fourier coefficients in this table are regarded simply as adjustable parameters, but they can be related to overlap integrals of H_{si} between Löwdin functions as shown in table 3. The 16 Fourier coefficients were adjusted until the r.m.s. difference between the eigenvalues of the LCAO secular equation and the nonspin-orbit energies of table 1 is a minimum. The values so obtained are given in table 4.

When spin-orbit interaction is added, the basis states of eq (1) are multiplied by a spin state, $|\uparrow\rangle$ or $|\downarrow\rangle$. The 12×12 matrix equation which results from writing H_{so} in this basis is Fourier expanded as before, but the expansion is terminated with zeroth order. Table 5 gives the form of spin-orbit matrix in terms of the two parameters λ^{Pb} and λ^{Te} which were adjusted holding the other 16 parameters fixed as discussed in section 2.

TABLE 2. *Most general Fourier expansion in* **k***-space of the matrix elements of* H_{si} *of eq (2) between the Bloch sums of eq (1). The abbreviation* $\langle \alpha \pm | \beta \pm \rangle$ *means* $\langle b^{\pm}_{\alpha,\mathbf{k}}(\mathbf{r}) | H_{si} | b^{\pm}_{\beta,\mathbf{k}}(\mathbf{r}) \rangle$. *Other matrix elements may be obtained by pairwise interchange of* x, y, z.

$$\langle x+|x+\rangle,\ \langle x-|x-\rangle = X_0 \pm X_1 c_x \pm Y_1(c_y+c_z) + X_2(c_x c_y + c_x c_z) + Y_2 c_y c_z \pm X_3 c_x c_y c_z + X_4 c_{2x} + Y_4(c_{2y}+c_{2z})$$

$$\langle x+|y+\rangle,\ \langle x-|y-\rangle = -Z_2 s_x s_y \mp Y_3 s_x s_y c_z$$

$$\langle x+|x-\rangle,\ \langle x-|x+\rangle = Q_0 + Q_2(c_x c_y + c_x c_z) + R_2 c_y c_z + Q_4 c_{2x} + R_4(c_{2y}+c_{2z})$$

$$\langle x+|y-\rangle = \langle x-|y+\rangle = -S_2 s_x s_y$$

$$c_\alpha = \cos(k_\alpha a/2) \qquad s_\alpha = \sin(k_\alpha a/2) \qquad c_{2\alpha} = \sin(k_\alpha a)$$

TABLE 3. *The Fourier coefficients of table 1 expressed in terms of tight binding overlap integrals*

Zeroth	X_0, Q_0	$\frac{1}{2}[\langle a_x^{Pb}(\mathbf{r})\|H_{si}\|a_x^{Pb}(\mathbf{r})\rangle \pm \langle a_x^{Te}(\mathbf{r}-\boldsymbol{\tau})\|H_{si}\|a_x^{Te}(\mathbf{r}-\boldsymbol{\tau})\rangle]$
First	X_1	$\langle a_x^{Pb}(\mathbf{r})\|H_{si}\|a_x^{Te}(\mathbf{r}-\boldsymbol{\tau})\rangle$
	Y_1	$\langle a_y^{Pb}(\mathbf{r})\|H_{si}\|a_y^{Te}(\mathbf{r}-\boldsymbol{\tau})\rangle$
Second	X_2, Q_2	$2[\langle a_z^{Pb}(\mathbf{r})\|H_{si}\|a_z^{Pb}(\mathbf{r}-\mathbf{R}_1)\rangle \pm \langle a_z^{Te}(\mathbf{r}-\boldsymbol{\tau})\|H_{si}\|a_z^{Te}(\mathbf{r}-\mathbf{R}_1-\boldsymbol{\tau})\rangle]$
	Y_2, R_2	$2[\langle a_x^{Pb}(\mathbf{r})\|H_{si}\|a_x^{Pb}(\mathbf{r}-\mathbf{R}_1)\rangle \pm \langle a_x^{Te}(\mathbf{r}-\boldsymbol{\tau})\|H_{si}\|a_x^{Te}(\mathbf{r}-\mathbf{R}_1-\boldsymbol{\tau})\rangle]$
	Z_2, S_2	$2[\langle a_y^{Pb}(\mathbf{r})\|H_{si}\|a_z^{Pb}(\mathbf{r}-\mathbf{R}_1)\rangle \pm \langle a_y^{Te}(\mathbf{r}-\boldsymbol{\tau})\|H_{si}\|a_z^{Te}(\mathbf{r}-\mathbf{R}_1-\boldsymbol{\tau})\rangle]$
Third	X_3	$8\langle a_x^{Pb}(\mathbf{r})\|H_{si}\|a_x^{Te}(\mathbf{r}-\mathbf{R}_1-\mathbf{t})\rangle$
	Y_3	$8\langle a_x^{Pb}(\mathbf{r})\|H_{si}\|a_y^{Te}(\mathbf{r}-\mathbf{R}_1-\boldsymbol{\tau})\rangle$
Fourth	X_4, Q_4	$\frac{1}{2}[\langle a_x^{Pb}(\mathbf{r})\|H_{si}\|a_x^{Pb}(\mathbf{r}-2\boldsymbol{\tau})\rangle \pm \langle a_x^{Te}(\mathbf{r}-\boldsymbol{\tau})\|H_{si}\|a_x^{Te}(\mathbf{r}+\boldsymbol{\tau})\rangle]$
	Y_4, R_4	$\frac{1}{2}[\langle a_y^{Pb}(\mathbf{r})\|H_{si}\|a_y^{Pb}(\mathbf{r}-2\boldsymbol{\tau})\rangle \pm \langle a_y^{Te}(\mathbf{r}-\boldsymbol{\tau})\|H_{si}\|a_y^{Te}(\mathbf{r}+\boldsymbol{\tau})\rangle]$

$$\boldsymbol{\tau} = \frac{a}{2}(100) \qquad \mathbf{R}_1 = \frac{a}{2}(011)$$

TABLE 4. *The values of the band parameters which were used to obtain the bands of Fig. 1.*

Zeroth Order.....	$X_0=-0.52918$ $Q_0=-0.04498$
First Order.....	$X_1=-0.26730$ $Y_1=\ 0.04363$
Second Order.....	$X_2=\ 0.00798$ $Y_2=-0.00673$ $Z_2=-0.00661$ $Q_2=-0.06518$ $R_2=-0.03403$ $S_2=-0.02059$
Third Order.....	$X_3=\ 0.01203$ $Y_3=-0.02042$
Fourth Order.....	$X_4=\ 0.01110$ $Y_4=\ 0.00178$ $Q_4=\ 0.03742$ $R_4=-0.00274$
Spin Orbit.....	$\lambda^{Pb}=\ 0.06447$ $\lambda^{Te}=\ 0.05396$

TABLE 5. *Matrix elements of* H_{so} *between Bloch sums. This matrix is of course Hermitian.*

		$b_a^+\uparrow$			$b_a^-\uparrow$			$b_a^+\downarrow$			$b_a^-\downarrow$		
		x	y	z	x	y	z	x	y	z	x	y	z
$b_a^+\uparrow$	x	0	$-i\lambda^+$	0	0	$-i\lambda^-$	0	0	0	λ^+	0	0	λ^-
	y		0	0	$i\lambda^-$	0	0	0	0	$-i\lambda^+$	0	0	$-i\lambda^-$
	z			0	0	0	0	$-\lambda^+$	$i\lambda^+$	0	$-\lambda^-$	$i\lambda^-$	0
$b_a^-\uparrow$	x				0	$-i\lambda^+$	0	0	0	λ^-	0	0	λ^+
	y					0	0		0	$-i\lambda^-$	0	0	$-i\lambda^+$
	z						0	$-\lambda^-$	$i\lambda^-$	0	$-\lambda^+$	$i\lambda^+$	0
$b_a^+\downarrow$	x							0	$i\lambda^+$	0	0	$i\lambda^-$	0
	y								0	0	$-i\lambda^-$	0	0
	z									0	0	0	0
$b_a^-\downarrow$	x										0	$i\lambda^+$	0
	y											0	0
	z												0

$\lambda^{\pm}=\frac{1}{4}(\lambda^{Te}\pm\lambda^{Pb})$

Plasmon-Induced Structure in the Optical Interband Absorption of Free-Electron Like Metals*

B. I. Lundqvist and C. Lydén

Chalmers University of Technology, Göteborg, Sweden**

We have extended Butcher's method to include the spectrum of interacting electrons, which contains satellite structure. The calculated optical conductivity shows a weak additional absorption, starting at about the frequency $\omega_l + \omega_p$, where ω_l is the interband threshold frequency and ω_p the plasma frequency.

Key words: Electronic density of states; free-electron like metals; interband absorption; optical properties; plasmon; pseudopotential; quasi-particle; satellite structure.

The common description of optical properties of free-electron like metals in terms of Drude and interband contributions [1] is in qualitative agreement with experiment. In some cases there is even a quantitative agreement, as for instance the Drude absorption due to phonon-aided processes in the infrared [2]. What concerns the magnitude and shape of the interband absorption as calculated in the one-electron approximation there seems still to be deviations from the experimental values [3]. Further, the slow increase of the effective number of electrons [4], difficulties to fit data to an effective oscillator formula [5], and difficulties to fit high- and low-frequency optical masses [3], suggest the possible existence of further structure in the absorption at photon energies above the ordinary interband transition range.

A recent investigation of the one-electron spectrum of the electron gas, considering effects to the lowest order in the coupling to the density fluctuations, and in particular to the plasmons, indicates an important satellite structure in the spectrum [6]. Due to the interaction the quasi-particle branch gets reduced spectral weight and is accompanied by a pronounced plasmon-induced satellite structure for both occupied and unoccupied states (see fig. 3 of the paper by Hedin, Lundqvist and Lundqvist in this volume). The energy separation between the two branches is somewhat larger than the plasma frequency ω_p. As the source of this effect is the existence of plasma oscillations, we consider it reasonable to expect this kind of structure to be important for free-electron like metals as well.

A satellite structure in the one-electron spectrum may produce structure in the optical absorption spectrum. From a simple-minded point of view there should not only be the ordinary band-to-band transitions, which start at the threshold energy E_G. There might also be additional absorption processes, due to transitions from the occupied satellite branch, starting at about the photon energy $\hbar\omega = E_G + \hbar\omega_p$. The purpose of this note is to present an estimate of the relative importance of these kinds of absorption contributions in the ultraviolet region. We have made a numerical calculation of the optical conductivity of sodium.

The optical interband absorption at the photon frequency ω is in the one-electron approximation given by the conductivity [7,8].

$$\sigma(\omega) = \frac{e^2\hbar^3}{12\pi^2 m^2 \omega} \sum_{l,\,l'} \int_{-\hbar\omega}^{0} d\epsilon d^3k \,|M_{ll'}(\mathbf{k})|^2 \delta(\epsilon - E_l(\mathbf{k}))\,\delta(\epsilon + \hbar\omega - E_{l'}(\mathbf{k}')), \tag{1}$$

where $M_{ll'}(\mathbf{k})$ is an interband dipole matrix element and $E_l(\mathbf{k})$ a band energy in the band indicated by 1. To get our rough estimate we have used the dipole matrix element from the nearly-free-electron approximation [7],

$$|M_{ll'}(\mathbf{k})|^2 = \frac{|GV_G|^2}{(\epsilon(\mathbf{k}-\mathbf{G}) - \epsilon(\mathbf{k}))^2 + 4|V_G|^2};\ \mathbf{G} = \frac{2\pi}{a}\{1,1,0\}. \tag{2}$$

*Work supported by the Swedish Natural Science Research Council.

**Mailing Address: Foch, S-402 20 Göteborg 5, Sweden.

where V_G is the screened pseudopotential, G the smallest reciprocal lattice vector and $\epsilon(\mathbf{k})$ the free-electron energy. Because the integration will include k-values at the Brillouin zone boundary, the expression of reference 7 is modified by the $4|V_G|^2$-term in the denominator.

To describe the continuous one-electron spectrum for interacting electrons [6], we replace the sharp excitation energies in the first equation by the spectral function and get [8]

$$\sigma(\omega)=\frac{8e^2|V_G|^2G\hbar^3}{\pi\omega m^2}\int_0^\infty kdk\int_{|G-k|}^{G+k}\frac{pdp}{(\epsilon(p)-\epsilon(k))^2+4|V_G|^2}\int_{-\hbar\omega}^{0}d\epsilon A(k,\epsilon)A(p,\epsilon+\hbar\omega). \tag{3}$$

This expression has been evaluated numerically using the values of the spectral function from reference 6 at the density of sodium (electron gas parameter $r_s = 4$) and $V_G = 0.323$ eV [7].

The resulting absorption power is shown in figure 1 in order to illustrate the relative importance of the transitions between satellite and quasi-particle states.

The highest value of $\sigma(\omega)$ is roughly one half of Butcher's result [7]. The reason for this is that due to the dynamic interaction between the electrons the quasi-particles get reduced weight. This reduction is typically 30 percent. Estimations of some electron-hole scattering processes, e.g. virtual exchange of plasmons, show that there are mechanisms able to give a compensating enhancement of the absorption near the threshold $\hbar\omega = E_G$ [9-11].

The figure indicates that there is a weak contribution to the absorption power, starting at about $\hbar\omega = E_G + \hbar\omega_p$ (≈ 8 eV for Na), which is caused by the plasmon-induced satellite structure in the one-electron spectrum. As this contribution is of roughly the same size as the one from transitions between quasi-particle states, we expect it to be measurable.

In the ultraviolet region another kind of structure has been proposed [12]. In a pseudopotential treatment, the screening in the effective potential V_G should be dynamic in nature. The plasmon resonance in the screening function gives rise to a structure, which should be in the measurable range [12,13]. However, this additional absorption starts at $\omega = \omega_p$ (≈ 6 eV for Na) with a distinct onset, and it should be possible to separate it from the structure proposed in this note.

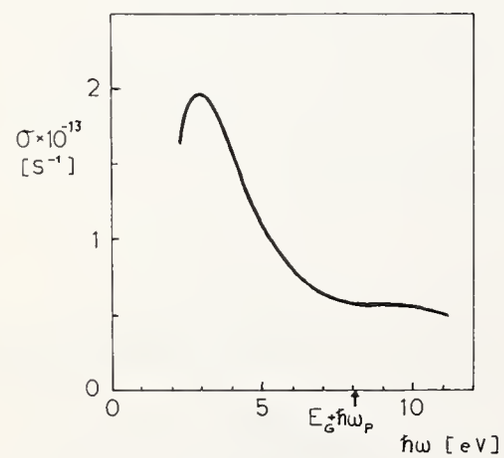

FIGURE 1. *The calculated optical absorption of sodium.*

There have been several papers on the optical absorption of an electron gas, where the process leading to a final state consisting of an electron-hole pair and a plasmon is taken into account [14-19]. This intraband absorption process is different from the interband process discussed in this note. Besides, as stressed by Hopfield [12], there is no optical absorption in a homogeneous electron gas in the long-wavelength limit due to the lack of momentum sinks. The same conclusion follows, when a proper set of diagrams in the perturbation expansion of the optical conductivity is considered [19,20].

The formula, which we have used for the conductivity, does not satisfy the sum rule for oscillator strengths. Certain vertex corrections, describing the final state interactions, ought to be included. Preliminary estimates indicate that processes, where real plasmons are exchanged, give a positive contribution to the absorption power in the photon energy region of interest here. We are presently performing numerical calculations of vertex corrections.

The experimental information about the optical constants of sodium in the ultraviolet region available in the literature concerns only the real part of the dielectric function [21]. As this quantity is so dominated by the free-electron behavior, the weak absorption mechanism proposed in this note should have a negligible effect on it. To conclude, we stress the desirability of accurate measurements of the optical absorption by free-electron like metals in the photon frequency range around and above the plasma frequency.

References

[1] Phillips, J. C., Solid State Physics **18**, 56 (Academic Press, New York 1966).

[2] Miskovsky, N. M. and Cutler, P. H., Solid State Comm. **7**, 253 (1969); see also Nettel, S. J., Phys. Rev. **150**, 421 (1966); and Haga, E., and Aisaka, T., J. Phys. Soc. Japan **22**, 987 (1967).

[3] Smith, N. V., Phys. Rev. **183,** 634 (1969).
[4] Ehrenreich, H., Philipp, H. R., and Segall, B., Phys. Rev. **132,** 1918 (1963).
[5] Powell, C. J., Phys. Rev. (to be published).
[6] Lundqvist, B. I., Phys. kondens, Materie **7,** 117 (1968).
[7] Butcher, R. N., Proc. Phys. Soc. **381A,** 765 (1951).
[8] Brust, D., and Kane, E. O., Phys. Rev. **176,** 894 (1968).
[9] Mahan, G. D., Phys. Letters **24A,** 708 (1967).
[10] Watabe, M., and Yasuhara, H. (to be published).
[11] Young, C.-Y., Phys. Rev. **183,** 627 (1969).
[12] Hopfield, J. J., Phys. Rev. **139,** A419 (1965).
[13] Foo, E. N., Phys. Rev. (to be published).
[14] Tzoar, N., and Klein, A., Phys. Rev. **124,** 1297 (1961).
[15] Matsudaira, M., J. Phys. Soc. Japan **17,** 1563 (1962).
[16] DuBois, D. F., Gilinsky, V., and Kivelson, M. G., Phys. Rev. **129,** 2376 (1963).
[17] Esposito, R. J., Muldawer, L., and Bloomfield, P. E., Phys. Rev. **168,** 744 (1968).
[18] Bose, S. M., Phys. Letters **29A,** 555 (1969).
[19] Ron, A., and Tzoar, N., Phys. Rev. **131,** 12 (1963).
[20] DuBois, D. F., and Kivelson, M. G., Phys. Rev. (to be published).
[21] Sutherland, J. C., Arakawa, E. T., and Hamm, R. N., J. Opt. Soc. Am. **57,** 645 (1967).

Theory of the Photoelectric Effect and its Relation to the Band Structure of Metals*

N. W. Ashcroft and W. L. Schaich**

Laboratory of Atomic and Solid State Physics, Cornell University, Ithaca, New York 14850

We develop the theory of the external photoelectric effect in terms of quadratic response to the incident electromagnetic field. Electrons in the solid are in states determined by their interactions with themselves, the ions and the surface. We denote by H_0 the Hamiltonian for this part. In the presence of the electromagnetic field we have a coupling term:

$$H_1=-\frac{1}{c}\int d\mathbf{r}\mathbf{A}(r,\,t)\cdot\mathbf{J}(\mathbf{r})e^{\eta t},\qquad(\eta=0^+)$$

where $\mathbf{A}(\mathbf{r},\,t)$ is the vector potential, and $\mathbf{J}(\mathbf{r})$ is the current density operator for the electrons. Let $\mathbf{R}$ be a point exterior to the solid. Then the expectation value of the operator measuring the external current density at $\mathbf{R}$ in the states of (H_0+H_1) is, to second order:

$$\langle J_\alpha(\mathbf{R},\,t)\rangle=\left(\frac{1}{\hbar c}\right)^2\int_{-\infty}^{\infty}d\tau_1\theta(t-\tau_1)\int_{-\infty}^{\infty}d\tau_2\theta(t-\tau_2)\cdot\sum_{\mu,\,\nu}\int d^3x_1\int d^3x_2A_\mu(\mathbf{x}_1,\,\tau_1)A_\nu(\mathbf{x}_2,\,\tau_2).$$
$$\langle\langle J_\mu(\mathbf{x}_1,\,\tau_1)J_\alpha(\mathbf{R},\,t)J_\nu(\mathbf{x}_2,\,\tau_2)\rangle\rangle.$$

There is no linear response and no other terms to order A^2 giving a measurable result. We show that $\langle J_\alpha(\mathbf{R},\,t)\rangle$ may be related to the expectation value of the time ordered product of the three current operators. This alternative description can be evaluated in the independent particle model (no scattering) and leads to a compact formulation of photoemission. There need not be a simple dependence of $\langle J_\alpha(\mathbf{R},\,t)\rangle$ or of its spectral reduction $\langle J_\alpha(\mathbf{R},\,t,\,e)\rangle$ (corresponding to measured electron distribution curves) on the joint density of states. Rather $\langle J_\alpha(\mathbf{R},\,t,\,E)\rangle$ depends on the density of bound states but is not at all simply related to the density of states above the vacuum level. This emerges quite clearly from an analysis carried out in the well known constant matrix element approximation. A careful examination of the terms appearing in the photoelectric current shows that it is not always correct to interpret photoemission in terms of a "volume effect" or a "surface effect." The contributions from these two interfere. The usual explanations of the processes involved (i.e., the sequential operations of excitation, transport, and transmission) are also somewhat blurred.

The effect of electron-electron scattering is well known to be important and will be discussed both in terms of its manifestation in the observed electron distribution curves and its ability to limit the contribution of the conventional volume effect.

Key words: Electronic density of states; electron-electron scattering; electrons in a box; joint density of states; Kronig-Penney model; photoelectric effect.

1. Introduction

The external photo effect can be viewed, for moderate amplitudes of the incident photon field, as the quadratic current response of a system to an applied electromagnetic field. This statement is based on the experimental fact that the photocurrent is proportional to the intensity of the incident field over at least 8 orders of magnitude of the latter [1]. We use this observation to develop a quadratic response theory of photoemission similar in spirit to the theory of linear response. A general expression for the photocurrent is derived in the next section, and in succeeding sections is analyzed in various approximations to determine its dependence on the underlying equilibrium electronic structure. Specifically we are interested in whether the photocurrent or its spectral reduction is proportional to a density of states and whether (or rather to what degree) inelastically scattered electrons retain useful information about single particle band structures. Some preliminary thoughts along these lines are given in section 4.

*Work supported by the National Science Foundation under Grant GP-7198.

**NSF Predoctoral Fellow.

417-156 O - 71 - 10

2. Quadratic Response Theory

We consider a solid (or liquid) located in the half space $x < 0$. In the presence of the incident light the Hamiltonian of the system is written

$$H = H_0 + H_1 \quad \text{with} \quad H_0 = h + H_e \tag{1}$$

Here h describes the kinetic energy of the electrons and the interaction between electrons and ions and electrons and surface, while H_e describes the interaction between electrons and electrons. For simplicity we shall invoke an adiabatic approximation in order to consider the ions as static. The interaction of the system with the electromagnetic field is represented by H_1:

$$H_1 = -\frac{1}{c}\int d\mathbf{r} \sum_{\mu} A_\mu(\mathbf{r}, t) J_\mu(\mathbf{r}) e^{\eta t}, \qquad \eta = 0^+ \tag{2}$$

where

$$J_\mu(\mathbf{r}) = \frac{e}{2m}\sum_i \{p_\mu^i \delta(\mathbf{r}-\mathbf{x}^i) + \delta(\mathbf{r}-\mathbf{x}^i) p_\mu^i\} \tag{3}$$

The scalar potential is zero by choice of gauge; we are thinking of a plane wave for the vector potential $\mathbf{A}(\mathbf{r},t)$. By using the Hamiltonian (1) we have assumed that initially (in the distant past) there were no electromagnetic fields present. Note that we ignore contributions from the diamagnetic current,

$$J_\mu^d(r, t) = -\frac{e^2}{mc}\int d\mathbf{r} \sum_i \delta(\mathbf{r}-\mathbf{x}^i) A_\mu(\mathbf{r}, t), \tag{4}$$

both here and below because it contributes only in orders higher than A^2. (Similar considerations apply to possible terms in H_1 proportional to A^2.)

In the photoemission process we are faced with the problem of determining the time independent electronic current far away (say 1 cm) from the surface which is established long after (say 10^{-8} sec) the perturbation H_1 has been applied to the equilibrium ensemble. Putting this another way, for $\mathbf{R}\cdot\hat{x} \gg 0$ and $t \sim 0$ we seek $\langle J_\alpha(\mathbf{R},t)\rangle$ where figuratively [2]

$$\langle J_\alpha(\mathbf{R}, t)\rangle = \frac{1}{Z}\sum_n e^{-\beta E_n^0}{}_0\langle n| e^{\frac{iHt}{\hbar}} J_\alpha(\mathbf{R}) e^{\frac{-iHt}{\hbar}} |n\rangle_0 \tag{5}$$

and

$$H_0|n\rangle_0 = E_n^0 |n\rangle_0, \qquad \beta = 1/k_B T \tag{6}$$

Here the $|n\rangle_0$ are those many-particle eigenstates of the equilibrium ensemble which existed before the application of H_1. To reduce (5) we work in the interaction representation and obtain to first order in the vector potential:

$$e^{\frac{-iHt}{\hbar}} \approx e^{\frac{-iH_0 t}{\hbar}}\left(1 + \frac{1}{i\hbar}\int_{-\infty}^{t} ds H_1(s) + \ldots\right) \tag{7}$$

This approximate evaluation is sufficient to determine the photocurrent to second order in the applied field. Substituting (7) in eq (5) we find the quadratic response to be:

$$\langle J_\alpha(\mathbf{R}, t)\rangle = \frac{1}{c^2\hbar^2}\int_{-\infty}^{\infty} d\tau_1 \int_{-\infty}^{\infty} d\tau_2 \theta(t-\tau_1)\theta(t-\tau_2) \int d^3\mathbf{x}_1 \int d^3\mathbf{x}_2 \sum_{\mu,\nu} A_\mu(\mathbf{x}_1\tau_1) A_\nu(\mathbf{x}_2\tau_2) \langle\langle J_\mu(\mathbf{x}_1\tau_1) J_\alpha(\mathbf{R}, t) J_\nu(\mathbf{x}_2\tau_2)\rangle\rangle \tag{8}$$

The double brackets refer to the ensemble average shown explicitly in eq (5). In deriving eq (8) we have neglected terms of the same or lower order in A on the assumption that $J_\alpha(\mathbf{R},t)$ gives a negligible contribution when it acts on an unperturbed state near (within several k_BT) the ground state. This approximation follows from the physical notion that those states favorably weighted by the thermal factor $e^{-\beta E_n^0}$ contain no electrons *outside* the metal. Equation (8) forms the basis for all further discussion; it represents a general expression for the photocurrent which we shall evaluate for specific systems in order to determine how the photocurrent depends on the electronic structure.

3. Independent Particle Model

By performing the time integrations indicated in eq (8) we find:

$$\langle J_\alpha(\mathbf{R}, t)\rangle = \frac{1}{4c^2}\sum_{\substack{\omega=\pm\Omega \\ \omega'=\pm\Omega}} e^{i(\omega-\omega')t}\int d^3x_1 \int d^3x_2 \sum_{\mu,\nu} A_\mu(\mathbf{x}_1) A_\nu(\mathbf{x}_2) \left\langle\left\langle J_\mu(\mathbf{x}_1) \frac{1}{E_0+\hbar\omega-H_0-i\delta'} J_\alpha(\mathbf{R}) \frac{1}{E_0+\hbar\omega'-H_0+i\delta} J_\nu(\mathbf{x}_2)\right\rangle\right\rangle \qquad \delta, \delta' = 0^+ \tag{9}$$

To arrive at (9) we have assumed the electromagnetic field to have a time dependence given by $\cos \Omega t$. If we now ignore the Coulomb interaction between electrons (i.e., neglect H_c), further simplifications follow immediately. Extracting the term for the observed steady photocurrent; i.e., omitting those terms that correspond to stimulated emission or that are time dependent, we find for the independent particle model

$$\langle J_\alpha(\mathbf{R}, t)\rangle = \frac{1}{4c^2}\int d^3x_1 \int d^3x_2 \sum_{\mu,\nu} A_\mu(\mathbf{x}_1)A_\nu(\mathbf{x}_2) \sum_{u,u,v} f^-(\epsilon_u)\cdot$$

$$\langle n|j_u(\mathbf{x}_1)|u\rangle \frac{f^+(\epsilon_u)}{\epsilon_u+\hbar\Omega-\epsilon_u-i\delta'} \langle u|j_\alpha(\mathbf{R})|v\rangle \frac{f^+(\epsilon_v)}{\epsilon_u+\hbar\Omega-\epsilon_v+i\delta} \langle v|j_\nu(x_2)|n\rangle \qquad (10)$$

where $|n\rangle$, $|u\rangle$, and $|v\rangle$ are single particle states with energies ϵ_n, ϵ_u, and ϵ_v, the j's refer to single particle current operators, and $f^-(\epsilon)=\{1+e^{\beta(\epsilon-\mu)}\}^{-1}$ and $f^+(\epsilon)=1-f^-(\epsilon)$ are state occupation factors. The interpretation of this expression is that it describes those electrons that escape without any reduction in their energy or any lifetime effects. Note that the photocurrent is not simply related to a product of an excitation probability and a transmission factor.

We have evaluated eq (10) for two specific examples of the independent particle Hamiltonian h. The first example is the model used by Mitchell [3]: free electrons in a semi-infinite box. The states $|n\rangle$, $|u\rangle$, $|v\rangle$ are easily evaluated and Mitchell's results follow straightforwardly and need not be reproduced here [4].

The second example is the Kronig-Penney model [5], which, unlike Mitchell's model, admits the possibility of band structure. We assume that the single particle potential varies only in the x-direction and that its form is as shown in figure 1. (We eventually take the limit of $V_0\to\infty$, $b\to 0$ such that $(2mV_0b/\hbar^2)\to 2P/a$.) To be specific, the parameters of the model, P, a, and w_a, have been chosen to represent as nearly as possible the $\langle 111\rangle$ planes of Na: the model possesses the same spacing in the x-direction and has the same Fermi energy, first band gap, and photoelectric threshold. To limit the total current we introduce an effective depth into the matrix elements: this is purely *ad hoc* and is similar to the cut-off procedure used by Fan [6]. This limitation is based on the physical observation that photoelectrons never emerge from a depth greater than a micron. That such a cutoff is automatically present can in fact be derived from eq (8), as will be shown below. Some of the results for this model are shown in figure 2. We have plotted energy distribution curves for a photon energy of 4 eV (1.71 eV above threshold). The temperature is assumed to be 300 K and the curves are parametrized by L which is approximately the number of planes from which electrons are allowed to emerge. Both the conventional "surface" and "volume" effects are present. In fact the equations of the model explicitly show that these two effects may interfere with each other; i.e., the distributions are proportional to the

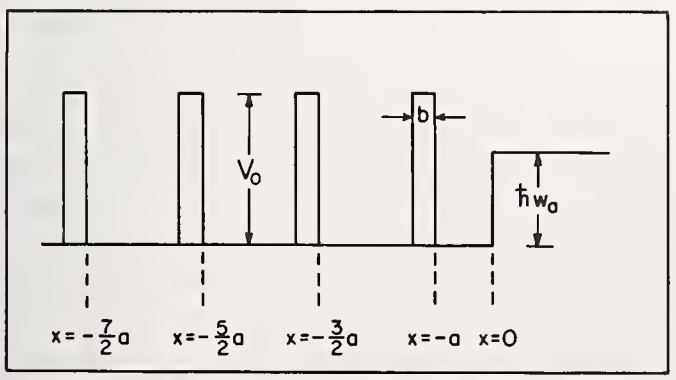

FIGURE 1. *Portion of modified Kronig-Penney potential.*
The metal is in the half space $x<0$ and the potential change at the surface is represented by a simple discontinuity.

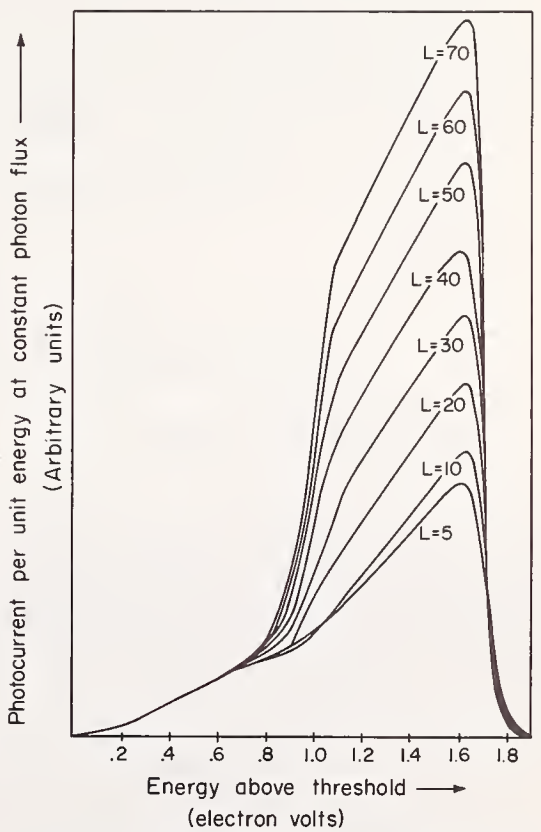

FIGURE 2. *Energy distribution curves for modified Kronig-Penney model (no scattering). (See text for an explanation of the parameters.)*

square of the sum of the two rather than to the sum of the squares. As the effective depth increases, the volume effect becomes dominant as expected.

On the basis of our experience with specific models, we shall now discuss for the general case (but still within the limitations of the independent particle model) what information concerning the electronic density of states we may expect to be determined from the spectral reduction of the photocurrent, which is essentially the expression in eq (10) but without the sum over the initial states $|n\rangle$. By limiting ourselves to the independent particle model, we are naturally assuming that at least the high energy part (say within 4 eV of the maximum) of the energy distribution curves is essentially unaffected by electron-electron scattering. This is consistent with phase space arguments about the degrading effect of electron-electron scattering and is the fundamental assumption used in the interpretation of the experimental energy distribution curves. Since we seek a density of states dependence we shall repeatedly use below the constant matrix element approximation.

In examining the photocurrent expressions we find that there need not be a simple dependence of its spectral reduction on the *joint* density of states. This lack of dependence arises essentially from the fact that our formulation is based on the explicit consideration of a surface; the evaluation of the formulae requires the determination of wavefunctions in the presence of the surface, hence **k**-vectors cannot serve to enumerate eigenstates, nor need crystal momentum be conserved. The addition of lifetime effects (see below) further strengthens this conclusion. Since the usual derivation of a dependence of $\langle J\rangle$ on the joint density of states requires (at the very least) both these properties, it is not clear whether such a dependence could ever result from an evaluation of eq (10). But, for the limiting case where volume (direct) transitions are dominant such a dependence on the density of states might be found (though to extract it from our formalism would appear to be arduous). For the general case, however, it is impossible (because of the presence of the surface) to extract a simple dependence of $\langle J\rangle$ on the joint bulk density of states.

4. Scattering Effects

For convenience we go now to zero temperature to consider the effects of Coulomb scattering among the electrons. Equation (8) for the current can be related to a time ordered product of three current operators. The result can be evaluated in the Hartree-Fock approximation which is a generalization of the independent particle model to include lifetime effects. We find

$$\langle J_\alpha(\mathbf{R},t)\rangle = \frac{1}{8c^2\hbar^2}\left(\frac{e\hbar}{2mi}\right)^3 \int d^3x_1 \int_{\cdot} d^3x_2 \sum_{\mu,\nu} A_\mu(\mathbf{x}_1)A_\nu(\mathbf{x}_2) \int \frac{dn}{2\pi}\int\frac{du}{2\pi}\int\frac{dv}{2\pi}$$

$$\lim_{\substack{\mathbf{x}_1'\to\mathbf{x}_1\\ \mathbf{R}'\to R\\ \mathbf{x}_2'\to\mathbf{x}_2}} (\nabla_\mu^{\mathbf{x}_1}-\nabla_\mu^{\mathbf{x}_1'})(\nabla_\alpha^{\mathbf{R}}-\nabla_\alpha^{\mathbf{R}_2'})(\alpha_\nu^{\mathbf{x}^\infty}-\nabla_\nu^{\mathbf{x}_2'})\cdot\left\{\left[\int_{-\infty}^{\infty} ds\ \ e^{-ins}\langle\psi^+(\mathbf{x}_1',s)\psi(\mathbf{x}_2,o)\rangle\right]\cdot\right.$$

$$\frac{1}{n+\Omega-u-i\delta}\left[\int_{-\infty}^{\infty} ds\ \ e^{ius}\langle\psi(\mathbf{x}_1,s)\psi^+(\mathbf{R}',0)\rangle\right]\frac{1}{n+\Omega-v+i\delta'}\cdot$$

$$\left.\left[\int_{-\infty}^{\infty} ds\ \ e^{-ivs}\langle\psi(\mathbf{R},0)\psi^+(\mathbf{x}_2',s)\rangle\right]+c.c.\right\} \qquad (11)$$

where; e.g., $\langle\psi^+(\mathbf{x}_1',s)\,\psi(\mathbf{x}_2,o)\rangle$ is the expectation value in the interacting ground state of the product of the Schrödinger operators $\psi^+(\mathbf{x}_1,s)$ and $\psi(\mathbf{x}_2,o)$ in the interaction representation:

$$\psi(\mathbf{x}_2,o) = \sum_u \langle\mathbf{x}_2|u\rangle c_u \qquad (12)$$

$$\psi^+(\mathbf{x}_1',s) = \sum_u \langle\mathbf{x}_1'|u\rangle e^{\frac{ihs}{\hbar}} c_u^+ e^{\frac{-ihs}{\hbar}} \qquad (13)$$

Here the c_u^+ and c_u are creation and annihilation operators for the single particle eigenstates, $|u\rangle$, associated with the Hamiltonian h. Note the similarity between eqs (10) and (11). The difference lies in the fact that eq (11) allows us to include the probability that an electron can propagate between any two points. Since an electron in the bulk material has a mean free path we now obtain a natural limitation of the volume effect, which in turn weakens the criterion of conservation of crystal momentum. We note, however, that within this approxi-

mation we have not obtained a damping of the incident electromagnetic wave and hence the analysis is only applicable to those materials whose electronic mean free paths (at the energy $\sim E_f + \hbar\Omega$) are less than their photon absorption lengths. Furthermore, we have lost a clear representation of the transition matrix elements which appear straightforwardly in eq (10).

We may reduce eq (11) to an expression similar to the result of Berglund and Spicer [7] for the current from those electrons which escape without scattering. To accomplish this we are forced to make some approximations whose physical interpretation and effect are difficult to estimate. Specifically we must assume that the energy integrals over u and v may be carried out as in the independent particle model with the resulting conservation of energy and that the effect of $\int_{-\infty}^{\infty} ds\, e^{-ins} \langle \psi^+(\mathbf{x}_1', s)\psi(\mathbf{x}_2, o)\rangle$ is to require the spatial arguments to be identical ($\mathbf{x}_2 = \mathbf{x}_1'$). Finally, we must assume that the two remaining expectation values can both be written as products of an excitation amplitude $J(\mathbf{x},n)$ (nonzero only for $\mathbf{x}$ inside the metal) and a transmission amplitude $T(\mathbf{x},\mathbf{R},n)$. We then find

$$\langle J_\alpha(\mathbf{R}, t)\rangle \approx \int dn \int_{\mathbf{r}\cdot\hat{x}<0} d\mathbf{r} |\mathbf{A}(\mathbf{r})\cdot\mathbf{J}(\mathbf{r}, n)|^2 |T(\mathbf{r}, \mathbf{R}, n)|^2 \tag{14}$$

which expresses the spectral reduction of the photocurrent as an integral over the product of an excitation probability and a transmission factor. The assumption of the existence of such a formula is the starting point of the analysis of Berglund and Spicer [7].

Finally we consider the effects of inelastic electron-electron scattering. A multitude of terms arise in the reduction of the time-ordered product whose interpretation is difficult. One of the main contributions, however, can be interpreted as the "once-scattered" term of Berglund and Spicer [7]. Explicitly it is

$$\langle J_\alpha(R, t)\rangle_{\text{scatt.}} = \frac{1}{4c^2}\int d^3x_1 \int d^3x_2 \sum_{\mu,\nu} A_\mu(\mathbf{x}_1)A_\nu(\mathbf{x}_2) \sum_{\substack{n,w,w'\\u,v\\s,t}} f^-(\epsilon_n)\langle n|j_\mu(\mathbf{x}_1)|w'\rangle \frac{f^+(\epsilon_{w'})}{\epsilon_n + \hbar\Omega - \epsilon_{w'}} \cdot$$

$$\left\langle w'\middle|\left\langle s\middle| \frac{c^2}{|r_i - r_j|}\middle|t\right\rangle\middle|u\right\rangle \frac{f^-(\epsilon_s)f^+(\epsilon_u)f^+(\epsilon_t)}{\epsilon_n + \hbar\Omega - (\epsilon_t - \epsilon_s) - \epsilon_u - i\eta''} \langle u|j_\alpha(\mathbf{R})|v\rangle \frac{f^+(\epsilon_v)f^+(\epsilon_t)f^-(\epsilon_s)}{\epsilon_n + \hbar\Omega - (\epsilon_t - \epsilon_s) - \epsilon_v + i\eta''} \cdot$$

$$\left\langle v\middle|\left\langle t\middle| \frac{e^2}{|r_i - r_j|}\middle|s\right\rangle\middle|w\right\rangle \frac{f^+(\epsilon_w)}{\epsilon_n + \hbar\Omega - \epsilon + i\eta} \langle w|j_\nu(\mathbf{x}_2)|n\rangle \tag{15}$$

where the $f^\pm$'s are evaluated at zero temperature and e.g.,

$$\left\langle v\middle|\left\langle t\middle| \frac{e^2}{|r_i - r_j|}\middle|s\right\rangle\middle|w\right\rangle = \int d\mathbf{r}_1 \int d\mathbf{r}_2 \langle v|\mathbf{r}_1\rangle\langle t|\mathbf{r}_2\rangle \frac{e^2}{|\mathbf{r}_1 - \mathbf{r}_2|}\langle \mathbf{r}_2|s\rangle\langle \mathbf{r}_1|w\rangle \tag{16}$$

As before $|n\rangle$, $|w\rangle$ . . . are all single particle eigenstates associated with h. An interesting consequence of this expression which seems to have escaped previous notice is that energy need not be conserved in the intermediate state. Only if the matrix elements involving $|w\rangle$ and $|w'\rangle$ are independent of the energy of $|w\rangle$ and $|w'\rangle$ will energy be conserved. This implies that there is a potentially much greater oscillator strength for excitations that simultaneously create a pair (or a plasmon) than for single particle excitations. It also unfortunately implies that the spectral reduction of the photocurrent due to *inelastically* scattered electrons (i.e., scattered by other electrons) will bear no simple relation to the underlying electronic band structure.

5. Concluding Remarks

We conclude by mentioning the extensions of this work that immediately suggest themselves, some of which we are currently investigating. It is quite clear that more of the contributions to the inelastic component of the photocurrent need to be classified, analyzed, and numerically estimated. It must be the case, for example, that a class of terms exist which represent the damping of the electromagnetic wave into the material. It is also of considerable interest to have an accurate description of the behavior of electrons as they approach the surface and to learn, in particular, how this can be related, if at all, to the properties of

bulk electrons. In this connection we make two observations. First, a soluble independent particle model somewhat more sophisticated than the Kronig-Penney model is evidently required. Second, we need an understanding more complete that we presently have, of the physics of an interacting electron gas in the presence of a potential discontinuity, a problem long familiar in the context of low energy electron diffraction. Finally, it is apparent that to facilitate direct comparison with experiment the analysis in its final form must be extended to nonzero temperatures.

6. References

[1] Elster and Geitel, Phys. Zeits. **14,** 741 (1913); **15,** 610 (1914); **17,** 268 (1916).

[2] To use simply $-iHt/\hbar$ is technically incorrect since H depends explicitly on time; however, the substitution obtained in eq (7) is correct to first order in the vector potential.

[3] Mitchell, K., Proc. Roy. Soc. **146A,** 442 (1934).

[4] This is true only to within a factor of two, by which Mitchell is in error. We agree with the correction of I. Adawi, Phys. Rev. **A134,** 788 (1964).

[5] Kronig, R. de L., and Penney, W. G., Proc. Roy. Soc. **A130,** 499 (1931).

[6] Fan, H. Y., Phys. Rev. **68,** 43 (1945).

[7] Berglund, C. N., and Spicer, W. E., Phys. Rev. **A136,** 1030 (1964).

[8] We limit this statement to those electrons which are inelastically scattered by other electrons. Since we are only considering the spectral reduction of the photocurrent with respect to energy (and not with respect to direction) the effects of inelastic phonon scattering are negligible.

Discussion on "Theory of the Photoelectric Effect and Its Relation to the Band Structure of Metals" by N. W. Ashcroft and W. L. Schaich (Cornell University)

W. E. Spicer *(Stanford Univ.):* The suggestion that a free electron final density of states rather than the band density of states should be used is quite interesting. This seems to agree with results in metals but not semiconductors.

PHOTOEMISSION

CHAIRMEN: E. T. Arakawa
C. J. Powell

RAPPORTEUR: S. B. M. Hagström

Optical Density of States Ultraviolet Photoelectric Spectroscopy*[1]

W. E. Spicer

Stanford Electronic Laboratory, Stanford University, Stanford, California 94305

The use of ultraviolet photoemission to determine the density of valence and conduction states is reviewed. Two approaches are recognized. In one, the photoemission as well as other studies are used to locate experimentally a limited number of features of the band structure. Once these are fixed, band structure calculations could be carried out throughout the zone and checked against other features of the photoemission data. If the agreement is sufficiently good, the density of states is then calculated from the band structure. The second method depends only on experimental data. Using this approach, features of the density of states are determined directly by the photoemission experiment without recourse to band calculations. In cases where bands are wide and **k** clearly provides an empirically important optical selection rule, this is possible only for portions of the bands which are relatively flat. Successful determinations of this type are cited for PbTe, and GaAs. In metals with narrow *d* bands such as Cu, it has been found empirically that one may explain fairly well the experimental energy distribution curves in terms of transitions between a density of initial and final states (the optical density of states, ODS) requiring only conservation of energy.

The ODS determined by such ultraviolet photoemission studies have more strong detailed structure than the density of states determined by any other experimental method. Studies on a large number of materials indicate that the position in energy of this structure correlates rather well with the position in energy of structure in the calculated density of states. It is suggested, following the very recent theoretical work of Doniach, that **k** conservation becomes less important (and nondirect transitions more important) as the mass of the hole becomes larger. This is due to the change in **k** of electrons in states near the Fermi level as they attempt to screen the hole left in the optical excitation process. These electrons take up the excess momentum. One would expect the **k** conservation selection rule to play an increasingly important role as the mass of the hole decreases. This is in agreement with experiment.

Key words: Copper; copper nickel alloys; density of states; GaAs; Ge; nondirect transitions; optical density of states; PbTe; ultraviolet photoemission.

1. Introduction

Photoemission can give a great deal of detailed information about the optically excited electronic spectra of solids. Adequate interpretation of photoemission data can produce detailed information on the electronic structure and, assuming that Koopmans' theorem [1] holds, on the ground state density of states.

The utility of photoemission lies in two factors: (1) The ability to determine the distribution in energy of electrons excited by monochromatic light, and (2) the ability to study the valence bands of solids over their entire widths. Difficulties arise in correcting for inelastic scattering and electron escape probability and in interpreting the data so corrected. Correction for scattering and escape probability seems to have been rather successfully done in a number of cases [2,3,4,5,6]. There are still detailed questions open in interpreting the data; however, as will be shown in this paper, it is clear that considerable information on the density of states can be obtained from photoemission data independent of these questions.

Let us look in more detail at the essence of optical excitation in solids and the photoemission experiment.

* An invited paper presented at the 3d Materials Research Symposium, *Electronic Density of States*, November 3-6, 1969, Gaithersburg, Md.

[1] Work supported by NASA, NSF, U.S. Army Night Vision Laboratories, U.S. Army—Durham, and the Advanced Research Projects Agency through the Center for Materials Research at Stanford University.

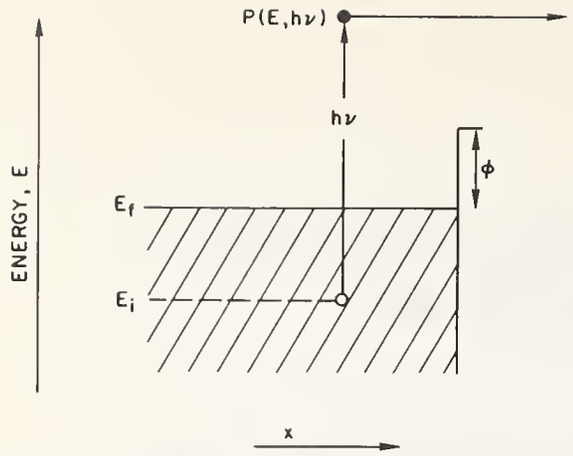

FIGURE 1. *Energy diagram for a metal.* P(E, hν) *is the probability of a photon of energy* hν *exciting an electron to final energy* E. ϕ *is the work function,* E_i *is the initial energy of the excited electron,* E_f *is the Fermi energy.*

Consider the probability, $P(E,h\nu)$, of a photon, of energy $h\nu$, exciting an electron to a final state of energy E (see fig. 1). The excitation spectrum in the solid is then given by the values of $P(E,h\nu)$ for all values of energy. The external photoemission energy distribution $N(E,h\nu)$ would correspond exactly to $P(E,h\nu)$ if all excited electrons escaped without inelastic scattering. Thus,

$$P(E,h\nu) \rightarrow N(E,h\nu). \tag{1}$$

In contrast, the optical constants $\omega\sigma$ or ϵ_2 (from which attempts are often made to determine the electronic structure) are related to the integral of $P(E,h\nu)$ over all possible final states

$$\epsilon_2 \rightarrow \int P(E,h\nu)dE. \tag{2}$$

ϵ_2 is the imaginary part of the frequency dependent dielectric constant and σ is the optical conductivity, $\sigma = \epsilon_{2/\omega}$. For the relations in eqs (1) and (2), it can be seen that photoemission contains much more detailed information than do the optical constants. This is illustrated by figure 2a, b, and c.

In figure 2a the imaginary part of the dielectric constant for Cu is plotted versus photon energy [7]. The arrows call attention to two values of photon energy, 5.0 and 10.2 eV. A maximum appears in ϵ_2 at $h\nu = 5.0$ eV. There has been considerable discussion [3,4,8,9,10] concerning the optical transition or transitions responsible for this peak. There is no measurable peak in ϵ_2 at 10.2 eV; rather, the curve is almost flat. In figure 2b and 2c, energy distribution curves, EDCs, are presented for $h\nu$ equal to 5.0 and 10.2 eV. The striking thing about these curves is the large amount of structure which is present in them. Whereas only one peak was present in the ϵ_2 curve near 5.0 eV and none was present near 10.2 eV, several pieces of structure are present in the EDCs for each value of $h\nu$.

From the energy at which the structure appears, the initial and final states involved in the optical transition can be quickly identified. In the present case, the electrons within 2 eV of the high energy cutoff, E_{max}, are excited from the almost free-electron-like conduction states lying within 2 eV of the Fermi level: whereas, the sharp structure lying more than 2 eV below E_{max} is due to excitation from the d states.

By noting the manner in which EDC structure moves with $h\nu$, the relative importance of initial and final states can be determined and information can be obtained about selection rules and/or matrix elements. For example, it was possible to determine that the peak in figure 2b at about 2.7 eV was due to a direct transition from states near the Fermi level with a threshold at about 4.4 eV [3]. Examination of band calculations showed that the transition must be centered near the L symmetry point. We will return later to the discussion of the interpretation of photoemission data. In fact, such discussion will provide the central theme for this paper; however, it is first useful to briefly review experimental techniques and the effects of scattering on photoemission data.

2. Experimental Techniques

As was suggested in the Introduction, a large amount of information can be obtained from the photoemission energy distribution curves. A second useful measurement is that of the spectral distribution of quantum yield. Let us briefly review the experimental methods for obtaining such data. In so doing, we will not attempt an exhaustive list of references, but rather will attempt to refer to recent articles representative of the various techniques. Because of his closeness to the work at Stanford, the author will draw particularly heavily on this work.

For many years EDCs were obtained by measuring an I-V curve and differentiating it by hand. The most important modern advancement was the replacement of this tedious and demanding practice by various schemes which yield EDCs directly from the experiment. Most popular are methods which add a small alternating voltage to the retarding voltage so that the derivative is taken electronically [11,12]. By slowly (typically 1 volt/minute) sweeping out the retarding voltage, a complete derivative curve can be obtained. Recently [13,14], measurements have been made at the second harmonic of the alternating voltage to obtain

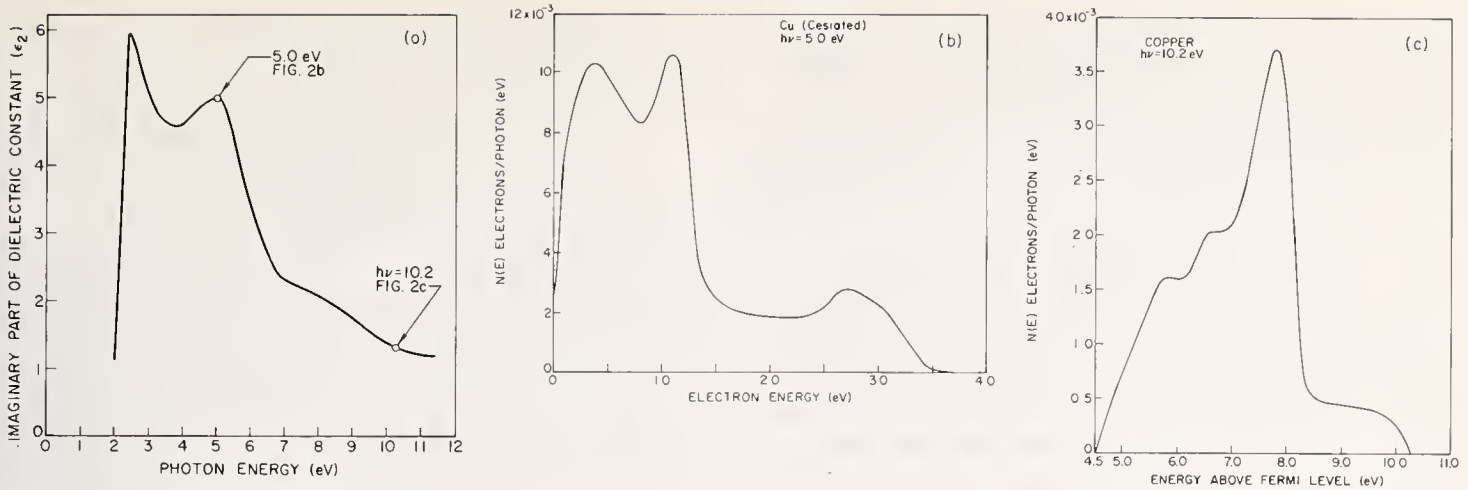

FIGURE 2. (a) ϵ_2 *for Cu.* (b) *EDC obtained from Cu with Cs on the surface for* $h\nu = 5$ *eV. Note that this curve has several pieces of structure in it, whereas the* ϵ_2 *curve had only one peak at 5 eV.* (c) *EDC for clean Cu.* $h\nu = 10.2$ *eV. Note that several pieces of structure occur in the EDC, whereas there is no strong structure near 10.2 eV in the EDC.*

the second derivative of the I-V curve. In this way weak structure in the EDCs can be detected and studied. A second approach is to take a I-V curve and then to either differentiate it electronically [15,16] or by means of a computer.

The geometry and other details of the energy analyzer are also of considerable importance. Because of ease of construction, wide use has been made of a cylindrical approximation [11] to the more ideal spherical geometry of the collector. This has given an energy resolution of between 0.1 and 0.3 eV, depending on the kinetic energy of the emitted electrons, the details of the emitter geometry, the uniformity of the collector work function, and other factors. Of particular importance for small electron kinetic energies are differences in work function between the face of the emitter and its sides. DiStefano and Pierce [17] have recently made an overall study of the factors limiting resolution. They conclude that a spherical collector with a spherical grid providing a field-free drift region should provide a significant increase in resolution provided that effects of the earth's magnetic field are properly minimized. Preliminary measurements with this geometry support these conclusions.

In principle, the measurement of the spectral distribution of quantum yield is much simpler than the energy distribution measurement. All that is needed is a standard detector of known response to which the emission of the sample under study can be compared. In the visible and near infrared spectral ranges, this is fairly easy to achieve because of the high light intensities available and the large number of suitable detectors. It is considerably more difficult in the ultraviolet where light intensity may be low and there are considerable problems with detectors [18]. Groups at the National Bureau of Standards, Stanford University, and other laboratories are cooperating in an attempt to establish good standards on a national-wide basis.

Another very necessary condition for successful photoemission experiments is the ability to provide emitter surfaces which are atomically clean. One must be able to provide such surfaces and insure that they do not contaminate in the course of study (pressures better than 10^{-8} or 10^{-9} Torr are usually necessary). Depending on the material, surfaces may be provided by cleaving [19], evaporation [4,6,20], heating [21], sputtering [22], or a combination of these methods. In covalent semiconductors such as Ge, it is well known that care must be taken to preserve crystalline perfection; however, in metals such considerations seem much less important. In fact, for Cu and Ni, which have been studied both as single crystals and evaporated films, the evaporated samples have given to date as good or better results than have sputtered and/or heat-cleaned samples [21,23]. This is despite the fact that some evaporated samples may have very small crystallite sizes (for example, about 100 Å in the case of Ni [6,20]). The insensitivity to crystallite size is due to the escape length for photoexcited electrons often being much less than 100 Å.

It is often useful to reduce the threshold for photoemission by placing a layer of cesium on the surface of a material. Ideally the cesium will only form a monatomic layer which reduces the work function without affecting any other properties of the solid. However, since Cs may chemically combine, amalgamate, or interact in other ways with the material under study, one must take care. The best procedure is to obtain EDCs from clean material over a photon energy range of several eV or more before placing the cesium on the

surface. Then, after the cesium is placed on the surface, EDCs should be obtained from the same photon energy range. By comparison of the two sets of EDCs, an estimate can be obtained of any extraneous changes produced by the cesium.

3. Electron Scattering Phenomena

As mentioned in the Introduction, one must understand the effects of electron scattering in order to properly interpret photoemission data. Two principal scattering mechanisms are electron-electron and electron-phonon scattering. In the first type of event, the scattered electron loses a large fraction of its original energy to a second electron, which is thus excited. The electron-electron event is characterized by a mean-free path which decreases rapidly as the primary electron energy is increased in the range $E < 12$ eV. The energy loss in the phonon-scattering event is much smaller than that in the electron-electron event and, since this energy loss varies roughly as the Debye temperature, it will be much smaller for the material containing heavier atoms than for those with lighter atoms. There is no evidence that the phonon mean-free path is highly dependent on electron energy as is the case for electron-electron scattering. Kane [24] has pointed out that the electron-phonon scattering will be enhanced for final states having low group velocity (*i.e.*, states associated with a high density of states). Eastman [25] has made the same observation for the electron-electron event. However, it does not appear that massive distortion of the energy distributions are produced by these effects.

There is a threshold for pair production in semiconductors and insulators of about the forbidden band gap energy (*i.e.*, the electron must be above the conduction band minimum by this amount before it can produce a secondary). Thus, only phonon scattering is possible below this threshold. In a metal there is no such threshold. However, as mentioned previously, in both semiconductors above threshold and in metals the electron-electron scattering length decreases quite fast with increasing electron energy. In figure 3 we present values [5,26,27,28] for Au obtained by several different methods. Note that the mean-free path drops by two orders of magnitude within a few eV. The electron-electron scattering effects have been taken into account quantitatively in interpreting photoemission data [3,4,6]. In fact, photoemission measurements can be used to determine the electron-electron mean-free path. The solid curve in figure 3 was deduced from such measurements by Krolikowski and Spicer [4].

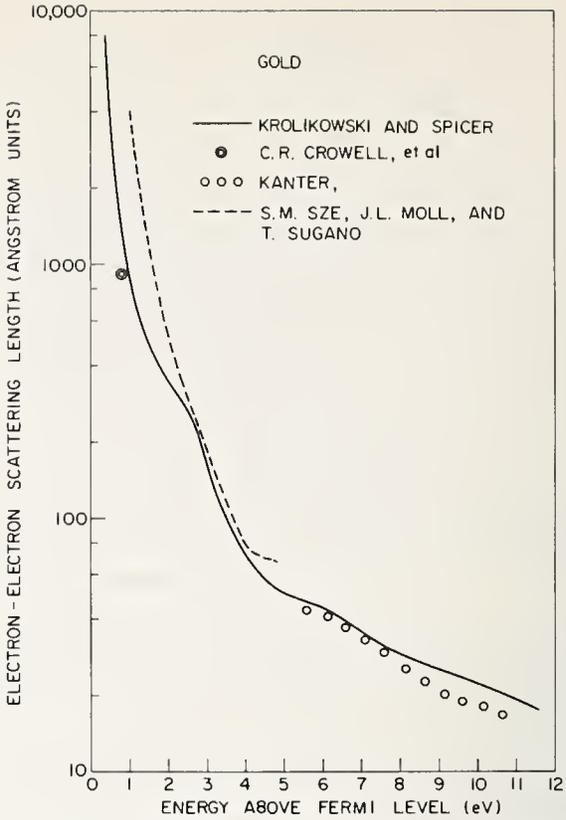

FIGURE 3. *Electron-electron scattering length for Au as obtained by several workers* [5,26,27,28].

More recently, Eastman [29] has developed a direct method for obtaining electron-electron mean-free paths from photoemission measurements. This is based on a variation of sample thickness.

For electron energies below the threshold for pair production in semiconductors, photoemission has been used extensively by James and Moll [30] to study the scattering of electrons by phonons in GaAs. This is of particular interest because of its importance in the Gunn effect. DiStefano and Spicer [31] have developed special photoemission techniques to study the scattering of hot electrons in alkali halides by phonons.

We give the examples listed above to illustrate the degree to which scattering of excited electrons in the photoemission experiment has been studied and is understood. This is not to say the processes are understood in all detail. This is not the case; however, a good, first-order understanding does seem to exist. There are other possible scattering phenomena which are less well understood. These include scattering from: (1) Bulk imperfections (such as grain boundaries), (2) the sample surface, and (3) scattering from oxide or other "crude" layers on the surface [19].

4. Interpretation of Photoemission Data: Direct and Nondirect Transitions

The present author and his coworkers have suggested [2,19,32] that, for excitation from *certain*

quantum states characterized by low mobility holes, conservation of **k** may not provide an important selection rule and that only conservation of energy need be considered in interpreting the photoemission data. Such transitions were called nondirect.

The suggestion of nondirect transitions was prompted by the character of the photoemission data obtained from states of this character. Based on this data, it was further suggested that a measure of the density of states could be obtained directly from analysis of the photoemission data. Of course, such a strong departure from accepted theory was met with considerable skepticism. Recently, band calculations [25,33,34,35], as well as new photoemission data (much of which will be reported at this meeting), have shown that there are certain strong similarities between the experimental EDCs interpreted as nondirect and the EDCs calculated using band structure results and **k** conservation when broadening effects were included in the calculation. However, other important systematic differences do remain, which may have considerable significance. In this paper, I will place particular emphasis on this discussion since it is central to the experimental determination of the density of states from uv photoemission.

Before proceeding further with this discussion, it should be recognized and emphasized that there were a number of materials in which direct transitions were clearly identified and many in which *only* direct transitions were seen; for example, the column IV and III-V semiconductors [36]. It should also be recognized that the criterion of peaks "moving with $h\nu$" (or the criteria of peaks which are stationary independent of $h\nu$) has been considered a necessary, but not sufficient, condition for identifying a nondirect transition [36,37,38]. In particular, abrupt appearance or disappearance or strong modulation of *peaks* has been taken as suggestive of direct transitions even when peaks "*move with* $h\nu$" [38]. PbTe [37], GaAs [36], CdTe, CdSe, and CdS [38] provide examples of this.

Another method for attempting to distinguish, experimentally, between direct and nondirect transitions is to examine the effects of reducing or destroying the periodicity of the lattice. Since **k** conservation is imposed by the periodicity of the lattice, destroying that periodicity should remove any importance of **k** conservation as an optical selection rule. Examples will be given of cases where periodicity is reduced or destroyed by alloying, melting, or forming an amorphous solid. Brust [39] has recently pointed out the possibility of explaining these changes by introducing an uncertainty in **k** rather than removing it completely as a selection rule.

Neville Smith has played a key role in the development of calculations of photoemission from *d* bands at Stanford [33]. A paper describing some of his work is included in this conference as is work on indium and aluminum by Koyama and Spicer [40]. The group of Janak, Eastman, and Williams [41] has also completed calculations assuming direct transitions for Pd which they will report at this meeting. I will not attempt to summarize these papers; but rather I will attempt to emphasize certain points.

The nondirect transition model was developed empirically since it appeared to give a good first approximation to the behavior of experimental photoemission data in a number of cases, including Cu. This model has been described in detail elsewhere [2,3]. The essence of it is that the optical transition probability, $P(E,h\nu)$, is given by the product of the optical densities of states (ODS) at energies E and $E-h\nu$:

$$P(E,h\nu) \rightarrow \eta(E)\eta(E-h\nu). \qquad (3)$$

Here $\eta(E)$ is the optical density of empty states at an energy, E; and $\eta(E-h\nu)$ is the filled ODS at an energy $h\nu$ below E. The term "optical density of states" is used since this density of states is obtained from the optical transitions as seen in photoemission. It is also appropriate since the optical density of states may be modified from the true density of states by optical matrix elements.

Let us examine direct and nondirect models for Cu as well as the experimental data used most recently. Copper is most appropriate for a number of reasons. First, its band structure seems to be as firmly established as any of the noble or transition metals. Second, it possesses relatively narrow *d* bands which might provide nondirect transitions; and third, experimentally Cu has been studied as thoroughly or more thoroughly than any of the other noble and transition metals so that the experimental data now seems to be on a very good footing.

Let us now examine photoemission from clean Cu for $6.0 \leqslant h\nu \leqslant 11.6$ eV. In figure 4 we present EDCs for Cu from the work of Krolikowski and Spicer [4]. More recently, Eastman [42] and Smith [43] have reproduced these curves; thus, the experimental data seems quite reliable. This data has all of the characteristics which lead to the assumption of nondirect transitions. For one thing, the peaks superimpose when they are plotted against $E-h\nu$, *i.e.*, against the *initial* state energy. Thus, it is apparent that the EDC struc-

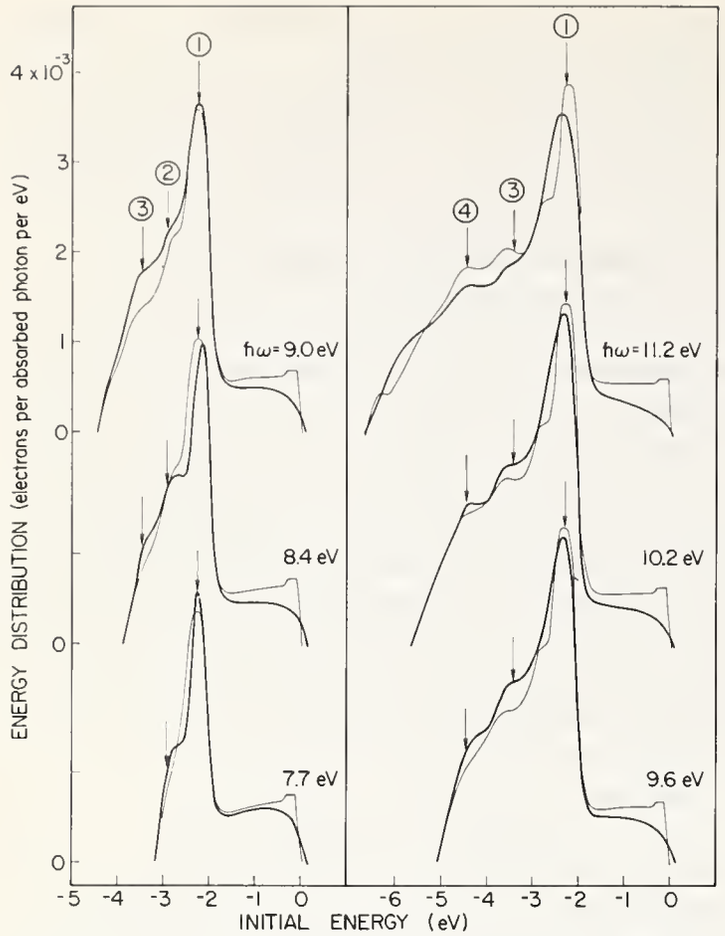

FIGURE 4. *EDCs for clean Cu plotted versus the initial energy. The solid curve indicates the experimental curve and the thin full curve gives the energy distribution calculated using the nondirect model for the values of photon energy indicated. The arrows indicate the position in energy of structure in the ODS.*

ture is due to the same structure in the initial ODS. Note also that the structure in the EDC varies very monatonically with photon energy. As we shall show later, a striking characteristic of the direct transitions calculations is the relatively larger amount of modulation which they predict in the peak strengths as a function of photon energy.

As described by Krolikowski and Spicer [4], the ODS was obtained from the photoemission and optical data. The ODS so obtained is presented in figure 5a and b. From this ODS, the thin full curves in figure 4 were obtained from this ODS using the nondirect, constant matrix element model. As can be seen, the agreement is rather good particularly since it is on an absolute basis. The notable difference is that the first peak broadens and the second peak appears to merge into it at higher photon energies.

In figure 5a and b, the ODS obtained from the photoemission studies is compared to the density of states from two band calculations [44,45]. As can be seen, rather good agreement is obtained between the locations of the major pieces of structure in the ODS and the calculated density of states. However, there is no such agreement between the relative strengths of the structure. This may be due to the effects of optical matrix elements, to difficulties in the band calculations (note the difference between the two calculated density of states), or to other effects.

In figure 6, the results [33] of calculations based on the direct-transition model for clean Cu are presented. These calculated curves have strong similarities to the experimental data. However, in order to obtain such agreement it was necessary to include a Lorentzian broadening of 0.4 eV for the calculated curve. Other calculations [34,35] use broadenings of between 0.3 and 0.7 eV. If the broadening is not used, much too much sharp structure appears in the calculated EDCs and this structure is modulated much too strongly and fast. The use of the broadening function finds partial justification in several factors—the instrumental and lifetime broadening, the finite lifetime of the excited carriers, and the inaccuracy in the band calculations. However, it is important that we keep the broadening in mind since it tends to make the direct and nondirect calculations more similar and also since it may provide an empirical method of making correction for many body effects. In the limit of flat initial bands, the direct and nondirect models would be identical. As the bands become less flat, increased broadening will still tend to keep the agreement between EDCs calculated on the direct and nondirect models.

Let us now examine the EDCs calculated by the direct method. In figure 6 we show the results of the calculations of Smith and Spicer and in figure 7 we compare the results of these calculations to experimental data. Again, the comparison is on an absolute basis. Several things are noteworthy about these results: (1) The position in energy of peaks in the direct calculations is constant on the $E-h\nu$ plot, (2) the position of structure corresponds rather well with the position observed experimentally (the numbered lines correspond to the position of structure found experimentally and in the ODS), and (3) the modulation of peak heights and widths is much stronger than anything seen experimentally. If, in fact, such strong modulation was observed experimentally, this would have been attributed to the effects of direct transitions or matrix elements effects despite the constant position in $(E-h\nu)$ of the peaks. Such identification was made, for example, in the II-VI compounds [38], GaAs [36] and PbTe [37] where strong modulation was observed experimentally.

The constant position in energy of the direct structure in figure 6 and its agreement with experiment is

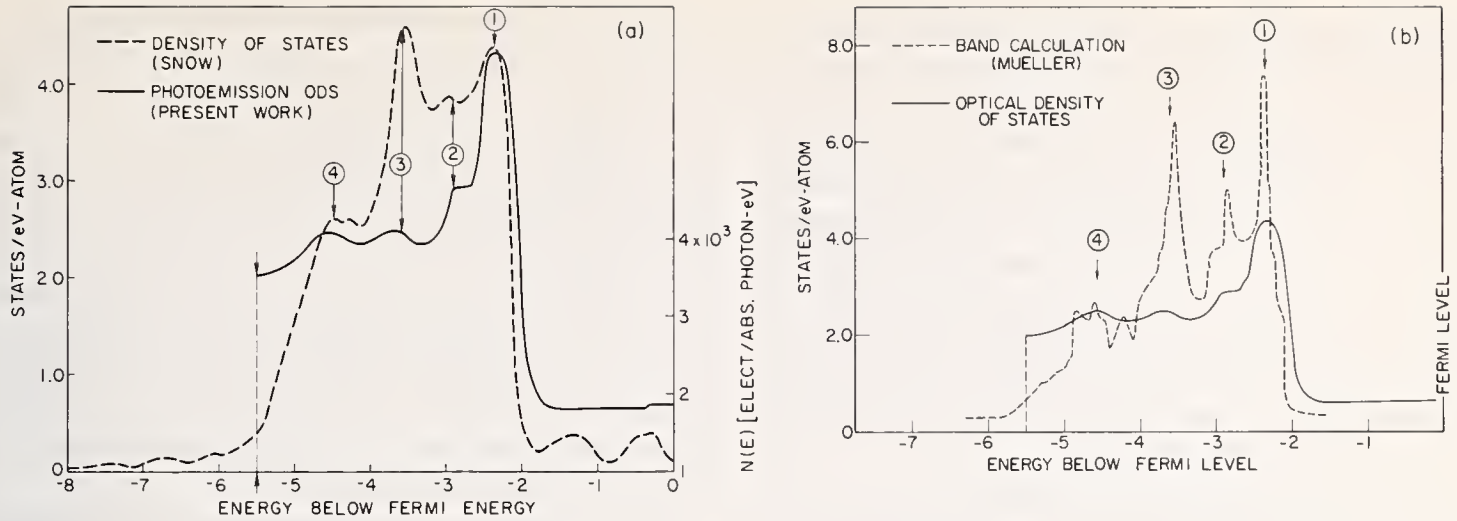

FIGURE 5. (a) *Comparison of the ODS with the density of states calculated by Snow [44] using an 5/6 $p^{1/3}$ exchange term. Snow's density of states have been shifted by 0.2 eV to place the Fermi level to d-band energy in exact agreement with experiment. The absolute scale was placed on the ODS by placing 11 electrons within 5.5 eV of the Fermi level. Note that the four pieces of numbered structure coincide rather well in energy. The numbered arrows correspond to those in figure 4.* (b) *Comparison of the ODS with the density of states calculated by Mueller [45].*

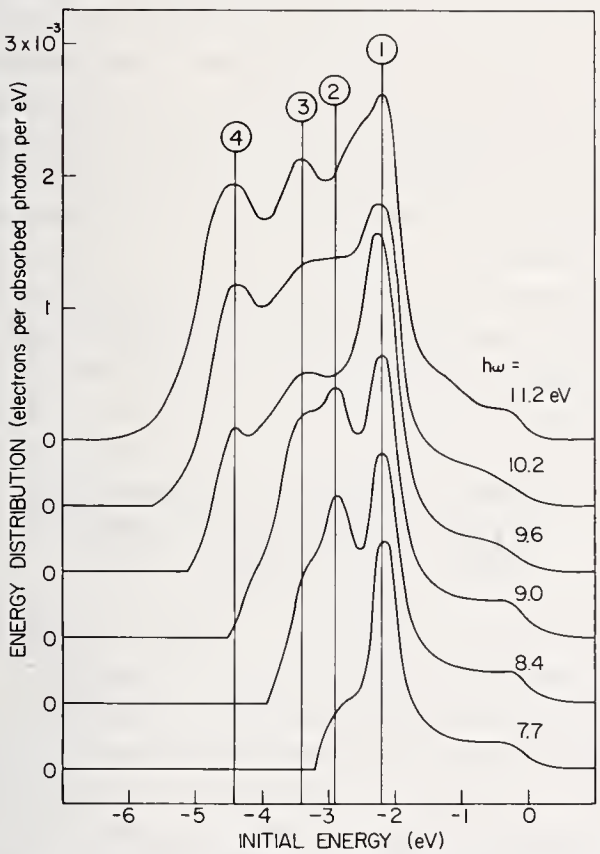

FIGURE 6. *The EDCs calculated for Cu by Smith and Spicer assuming direct transitions.*

not surprising in retrospect in view of the agreement between the ODS and band calculations shown in figure 5. It would appear, at least for the limited range of $h\nu$ covered by this study, that the Cu bands are sufficiently flat and that the broadening effects are sufficiently large so that the **k** conservation condition does not impose overwhelming constraints on the optical excitation process. The fact that the nondirect model gives better detailed agreement with the experimental data than the direct model, suggests that many body effects may still be important in bringing in a range of **k** rather than a delta function in the optical absorption process.

In another paper, presented at this meeting, Neville Smith [34] will show new experimental data which give

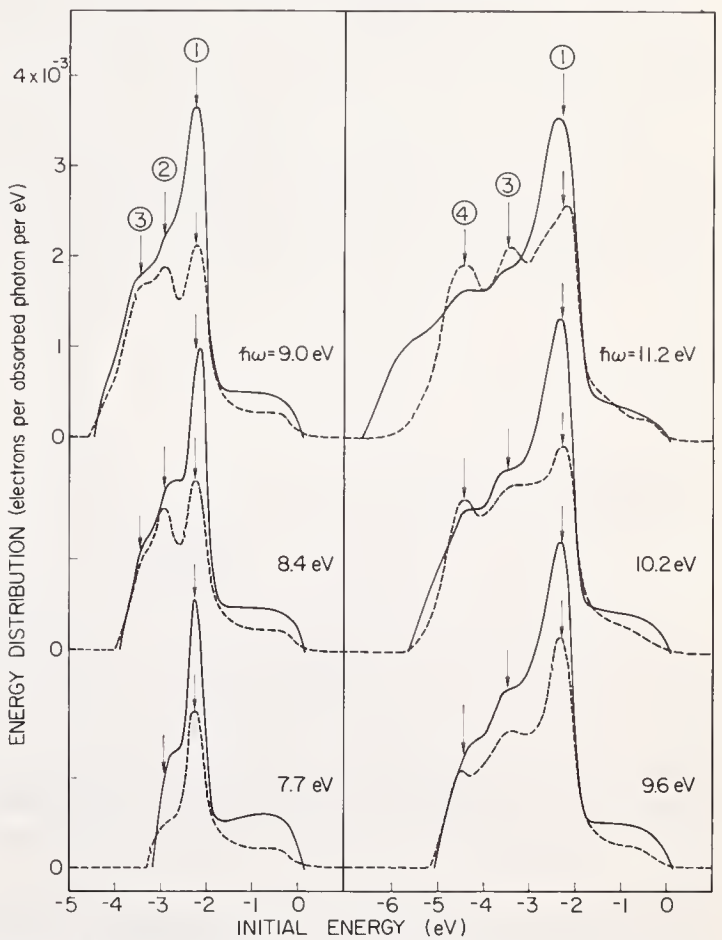

FIGURE 7. *Comparison of the EDCs calculated for Cu using the direct transition model with the experimental EDCs. The full line gives experimental and the dashed line calculated EDCs.*

417-156 O - 71 - 11

clear evidence of direct transitions in cesiated Cu. The transitions originate from states 2.8 to 3.8 eV below the Fermi level. It is in this region that the *d* bands have greatest curvature. Recognizing that this curvature should provide the most easily detectable evidence for direct transitions, Berglund and Spicer [3] looked especially for direct transitions in this region. Apparently poorer sample preparation conditions prevented them from seeing the transitions. The success of Smith is a tribute to him and to the advances in vacuum and preparation techniques made at Stanford and elsewhere in recent years.

Smith has also made direct transition calculations of the EDC for cesiated Cu. These show the effects found experimentally; however, despite the inclusion of a 0.3 eV broadening factor, the predicted modulation is considerably stronger than that observed experimentally.

There is perhaps a good analogy between the present situation in this matter and that with regard to x-ray emission spectroscopy for many years. The simple and popular view of the latter field was that one could always explain the x-ray emission spectra just in terms of single particle transitions so that the valence band density of states could be obtained directly from the emission spectra if "atomic-like" matrix elements were properly taken into account. With the simple metals fair agreement was obtained between experiment and theory on this model, although certain nagging inconsistencies remained. The situation has changed drastically in the last few years since theorists have had success in treating the many body effects of the hole in the core state. I will not attempt to review this work since it will be discussed in some detail at this conference. However, there may be a parallel with regard to the uv photoemission work.

At Stanford, Doniach [46] has been expanding his investigation of many body effects in the x-ray photoemission effect to include the many body effects associated with screening of the valence band hole in the uv optical excitation process [32]. Preliminary results suggest that such effects exist, producing a spread in possible **k** in the optical transitions, and increase in importance as the effective mass of the hole increases. Thus, the flatter the valence band is, the larger the effect. If one looks at the Cu results with this in mind, one notes that the flatter the bands, the better the nondirect model works.

In concluding this section, I would like to remark that the direct transition model is based on a rather idealistic assumption which applies best where the bands have good curvature; empirically, this model seems to work very well for a wide range of materials of this type. On the other hand, the nondirect, ODS, model should work best in materials with quite flat bands. It may never be completely correct (we must understand the physics better before it is possible to pass quantitative judgment); however, its great simplicity may make it a good first approximation when it can be successfully applied, *i.e.*, when the EDCs based on the ODS are in relatively good agreement with experiment. Certainly the success with Cu, Ni, and similar material, suggests that it may give us the best first approximation to the densities of states of these materials which can be obtained solely from experiment.

There may be an intermediate range of bands and materials in which neither the direct nor the nondirect model applies with great accuracy. In this case, detailed understanding can only be obtained when theories such as that of Doniach are fully developed. In the meantime, it is probably well to keep open the possibility of transitions occurring over a range of **k** and not just at a given value. It would be extremely nice if in the direct calculations, a broadening could be put in by a distribution in **k** before searching the zone rather than over energy after the vertical transitions have been tabulated.

Experimentally, it is important to obtain data over a wider range in energy to test the selection rules with more rigor. Eastman [29] has already begun to do this with very interesting results.

5. Effect of Reducing or Destroying Crystal Periodicity: Liquid In, Alloys, and Amorphous Ge

Another way of testing for the importance of **k** as an optical selection rule is to reduce or destroy the long-range order of a crystal. Clearly as the solid becomes increasingly disordered, any dependence of **k** must become less and less well defined, *i.e.*, a single value of **k** can no longer be used to define a quantum state. Rather, if a description in terms of **k** is used, it must contain a distribution of **k**; a single **k** will be insufficient. In the limit of complete disorder, **k** will lose meaning as a quantum number.

5.1. Indium

Indium has been studied experimentally by Koyama [18] in the crystalline, amorphous and liquid forms. Note that, since it contains no *d* electrons, In would not be expected to fall within the class of nondirect materials. In addition, Koyama has made calculations based

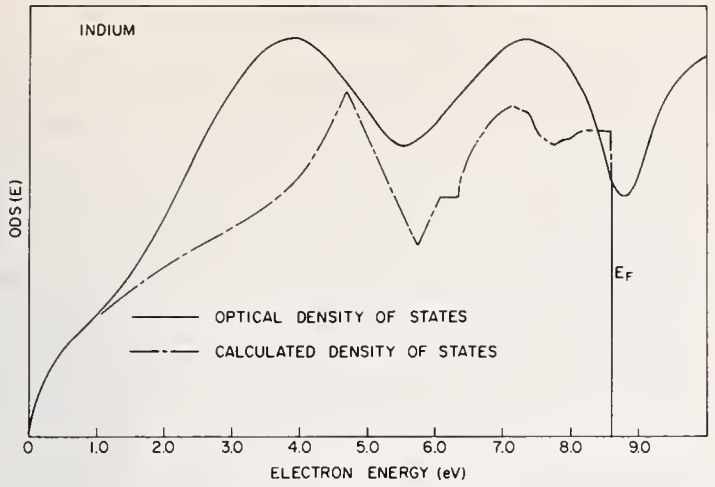

FIGURE 8. *Comparison of the ODS for In with the density of states obtained from band calculations [40].*

on direct as well as nondirect models. These calculations will be described in detail in a separate paper of this conference [40]. Koyama's findings for crystalline indium are quite interesting: (1) Both the direct and nondirect transition models fit the experimental data fairly well (as they do for Al), (2) the EDCs for In are characterized by two broad peaks separated by a minimum which correlates [47] well (in either model) with a large band gap in the band structure of Ashcroft and Lawrence [48] (see fig. 8), and (3) the principal features of the EDC (the two peaks) were seen to persist in liquid indium despite highly increased electron scattering. Since there seems, at least at present, to be less physical justification for the nondirect model in In than in Cu, it is tempting to assume for this material that direct transitions dominate in the crystalline material and that nondirect transitions occur in the liquid. Even then a question would arise as to why the density of states structure due to crystalline potentials persists into the liquid. (Shaw and Smith [49] have found theoretical evidence of such effects in Li.) Koyama [18] has suggested that this is due to the dominance of short-range interactions in determining the electronic structure and thus the density of states of both liquid and crystalline In. Clearly studies of In at higher resolution and for a wider range in $h\nu$ should prove very worthwhile.

In any case for both Al and In, the density of states obtained by the nondirect analysis seems to be in fair agreement with the results of band calculations. As the direct transition calculations show, this may be due to the large range in **k** space from which direct transitions can take place and thus not be a true indication that **k** vector is unimportant (although, again, some uncertainty in **k** is probably important in bringing the direct and nondirect models into agreement). The sensitivity of the calculated EDCs to the electronic structure is illustrated by the fact that, whereas Ashcroft and Lawrence's band structure for In agreed with experiment, other proposed band structures [49] did not give agreement with the ODS.

Mosteller, Huen and Wooten [50] have recently studied the photoemission from Zn as a function of temperature and found that the quantum yield decreased significantly on cooling the sample from room to liquid N_2 temperature. Based on this, they note the possibility that in Zn the ultraviolet optical transitions may be indirect, *i.e.*, phonons conserve **k**. Such temperature dependence has not been observed for other semiconductors and metals such as Cu, Gd [51] and Cr [52] which have been studied as a function of temperature. The Zn results are mentioned here because of the similarity between the In and Al band structure and that of Zn and because In and Al have not been measured below room temperature.

5.2. Amorphous and Crystalline Ge

In contrast to In, Ge provides a striking case of a material whose optical properties and uv EDCs change drastically when the long-range order is destroyed by forming amorphous Ge. Photoemission studies show clearly the direct nature of the transitions in crystalline Ge [36] in agreement with analysis of optical data [53]. Thus, differences between crystalline and amorphous Ge are of considerable importance.

Figure 9 indicates ϵ_2 for the amorphous and crystalline material [54,55] and figure 10 indicates EDCs for

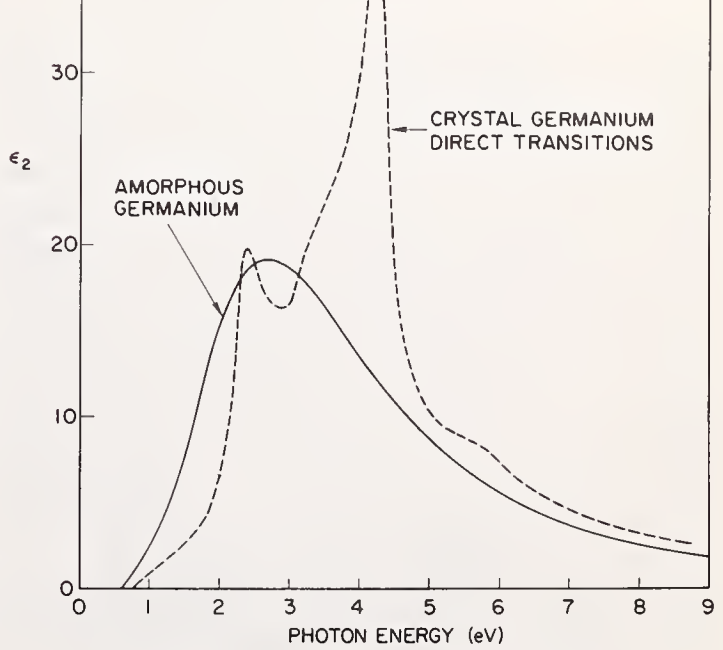

FIGURE 9. *ϵ_2 for amorphous and crystalline Ge.*

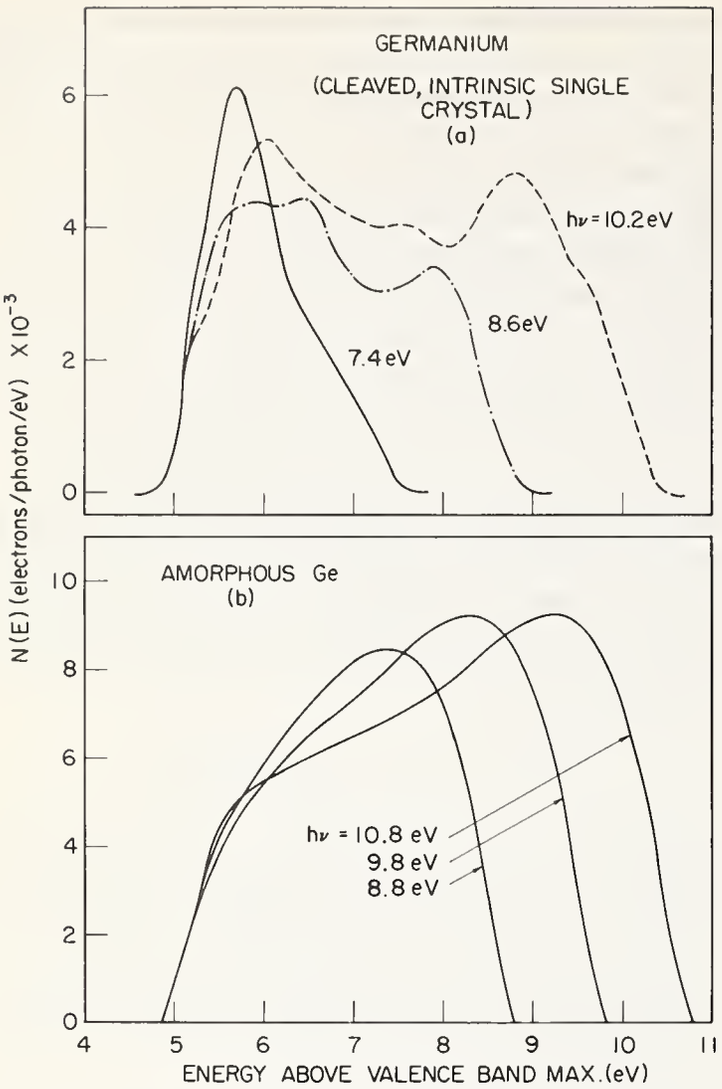

FIGURE 10. *Photoelectron energy distributions for Ge surfaces. (a) Cleaved, intrinsic, single crystal. (b) Amorphous film. The vertical axis gives the number of electrons per absorbed photon per eV. The horizontal axis gives the electron energy relative to the maximum in the valence band. The sharp structure in (a) is due to direct transitions in specific regions of the zone. The single broad peak in (b) is due to a peak in the valence-band optical density of states.*

crystalline and amorphous Ge [54,55,56,57]. As can be seen, the changes in ϵ_2 and the EDCs which accompany the change in form of Ge are first order. The loss of sharp structure is clearly due to the loss of long-range order. In their studies of amorphous Ge, Donovan and Spicer have used a nondirect analysis with considerable success to treat data from the amorphous material. In figure 11 the ODS obtained from these studies is compared to the density of states obtained from band calculations [58]. Brust is approaching the problem of amorphous Ge from calculated band structures by a method in which there is a spread in **k** associated with the optical transitions and thus is intermediate between the direct and nondirect models [59]. Because of its flexibility due to the possibility of assigning various values to the spread in **k**, this approach clearly has certain advantages over the pure nondirect approach.

5.3. Cu-Ni Alloys

A third example of the effect of disorder is in the alloys such as those between the noble and transition metals. Here the lattice periodicity is not destroyed. Rather, atoms with two different potentials are arranged at random, or almost at random (it appears that clustering effects are negligible [21]) within the periodic lattice. Since the potentials are quite different (for example the transition metal typically produces a virtual-bound state when dissolved in a noble metal), the effect on the periodicity should be considerable. Despite this, the effect on the ϵ_2 and on the EDCs of the host metal does not appear to be drastic. The principal effect is in the production of a virtual-bound state under the proper circumstances. Such states have been and are being qualitatively studied through the use of photoemission [21,23,60,61,62,63].

In figure 12, the optical parameter $\omega\sigma$ is presented for the Cu-Ni alloys studied by Seib and Spicer [21,23]. Except for $h\nu<2$ eV in the Cu-rich alloys where the change is due to the formation of a virtual-bound Ni state, the changes are much less than those found in the crystalline to amorphous transformation of Ge.

As outlined in the Introduction, photoemission can give a more detailed look at the optical transition than can the optical data. Examination of EDC data from the alloys shows that the direct transition from the *s-p*-derived bands near the Fermi surface at L is not detectable in the alloys [21]. However, the transitions from the d states are much less affected. In fact, the EDCs from Ni and Ni-Cu alloys with up to 19 percent

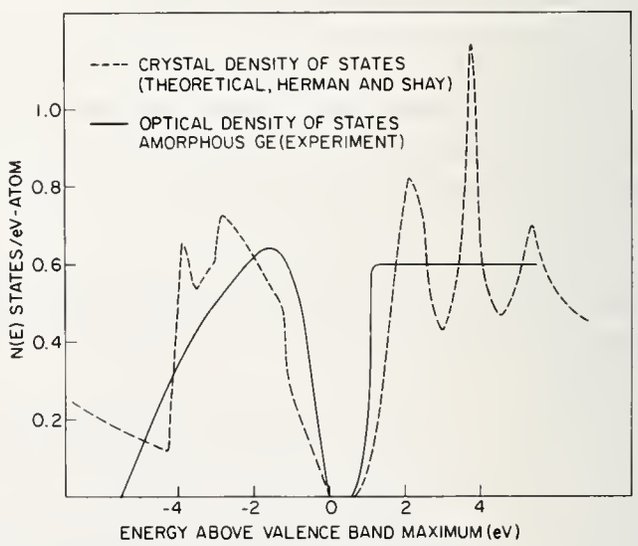

FIGURE 11. *Optical density of states for amorphous Ge as determined by photoemission compared with the electronic density of states for crystalline Ge calculated by Herman and Shay. The vertical axis is in units of states per eV per atom for the crystal density of states and in arbitrary units for the optical density of states. The energy zero in both cases is taken at the maximum of the valence band.*

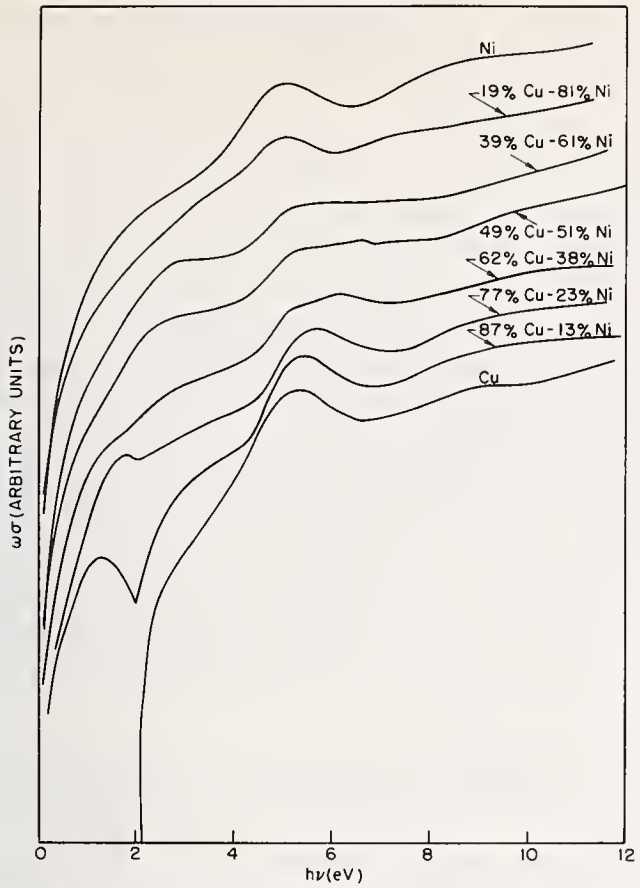

FIGURE 12. *The optical constant ωσ for pure Ni and Cu and a series of Ni-Cu alloys.*

Cu (atomic present) are almost indistinguishable except for effects due to the change in work function. This is shown by the data in figure 13. Even for 39 percent Cu, the position of the two strong peaks in the EDC were unchanged [23].

Let us next examine the Cu-rich alloys. In figure 14 we present data for pure Cu and Cu containing 13 and 23 percent Ni [21]. As can be seen, the Cu *d* edge is little changed and the position in energy of structure from the *d* bands is similar to that in the pure material; however, the relative strengths of the peaks are changed.

The contrast in optical properties and EDCs between these alloys and Ge in its crystalline and amorphous forms is striking. For the alloys, the changes are relatively small whereas, for Ge, they are much larger. **k** conservation clearly plays the dominant role in determining the optical transition probabilities in crystalline Ge; thus, destroying the long-range order completely changes the optical properties. The insensitivity of Cu and Ni to disruption of the long-range order suggests that the optical transitions from the *d* states of pure Cu and Ni are, on the average, much less strongly affected by the **k** conservation condition; however, the *L* transition from the *s*- and *p*-derived states is clearly a direct transition and this disappears in the alloys studied.

6. Methods of Determining the Density of States from Ultraviolet Photoemission Data

Two extreme approaches can be taken in using photoemission data to determine the density of states of solids. One is to use the photoemission results to provide input into band calculations. This approach is not necessary if first-principles band calculations give exact results. If this is not the case, the band calculations can be adjusted to give agreement with the experimental data. Such correction is often necessary and, in addition to overcoming uncertainty in the potential used in the band calculation, the empirical correction may correct for departures from Koopmans' theorem as, for example, suggested by Herman [66]. One approach is to parameterize the calculation and use experimental data. de Haas-van Alphen data or optical data could also be used for adjusting the band calculations. Since the de Haas-van Alphen data give experimental data only at the Fermi surface, it is not very sensitive to energy shifts from the Fermi level. Unambiguous interpretation of structure in the optical constants, such as ϵ_2, has proven very difficult. Piezoreflection has proven to be very powerful in Cu [10] but despite considerable effort, so far has not been successfully applied to Ni [67]. A difficulty in piezoreflection also lies in estimating the absolute or relative strength of optical transitions whose symmetry is determined by these measurements.

If first-principles band calculations were thought to be sufficiently good, the photoemission studies would

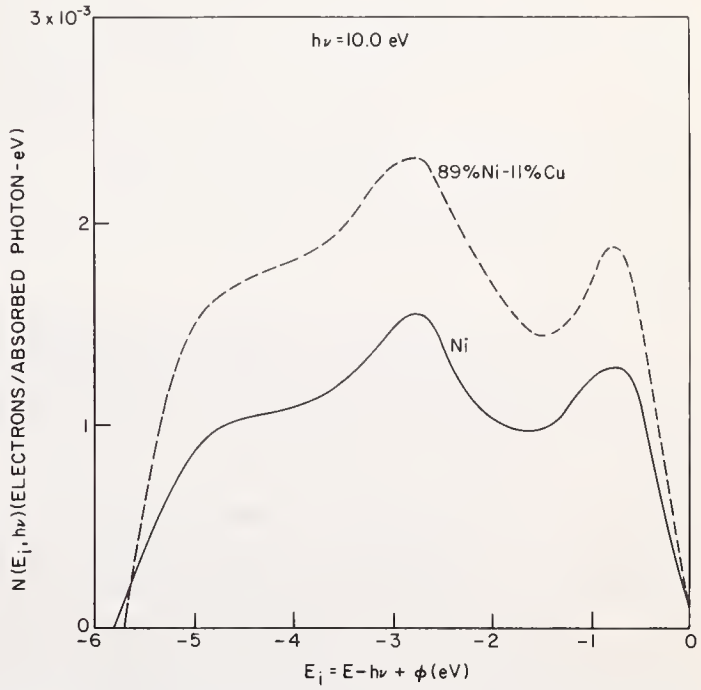

FIGURE 13. *The EDCs at* $h\nu = 10$ *eV obtained from pure Ni and a Cu-Ni alloy containing 11 atomic percent Ni.*

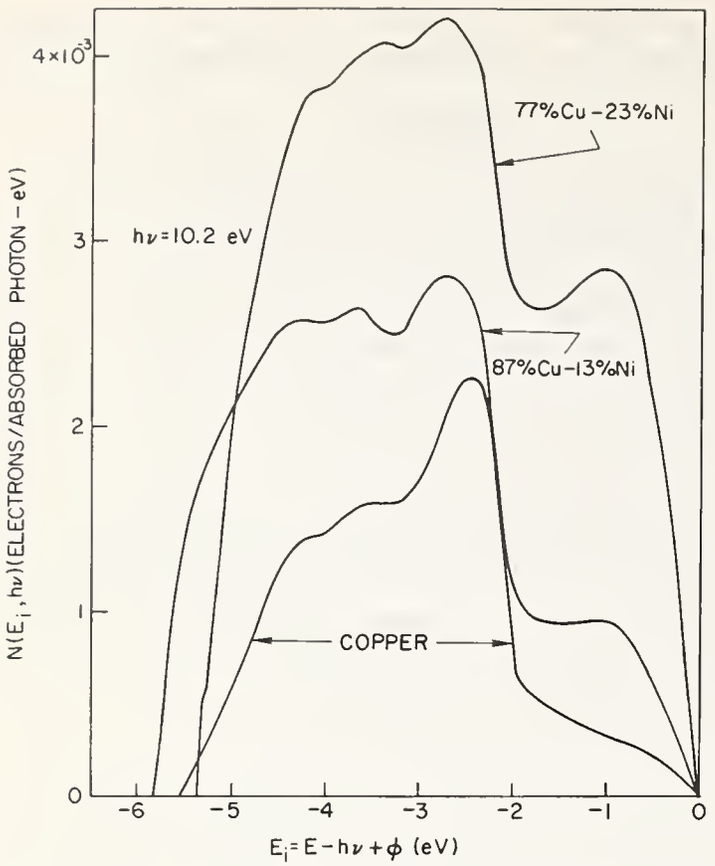

FIGURE 14. *EDCs from pure Cu and two different Cu-Ni alloys. Note that the Cu* d *edge and the position in energy of the* d *peaks is essentially unaffected by the alloy.*

simply serve as a check. For best results, this approach requires two conditions. First is a fairly accurate and well-advanced band theory. Without this, it is difficult to relate the photoemission data to the band structure in a meaningful way. Second is photoemission data which shows dramatic band structure effects such as the onset of the L transition in copper or the Γ transition in CdTe [38]. For materials like GaAs in which **k** conservation dominates the optical transition probability, Eden has developed a systematic method for comparing photoemission results and the results of band calculations. This will be reviewed briefly in the next section.

A second approach is to attempt to obtain density of states information directly from the photoemission data. The more apparent the connection between the photoemission data (*i.e.*, the optical transition probability) and the density of states, the more efficient is this approach. As we will see in the next section, it is very difficult to obtain density of states information from photoemission data for a material such as GaAs where **k** conservation provides a dominant optical selection rule; however, in a case such as copper where **k** conservation does not play such a dominant role, the nondirect method of analysis gives a good mechanism for obtaining the principal features of the density of states from experimental data.

The nondirect transition [3,4] model provides a simple way to analyse the photoemission data to obtain an ODS. Once this is done, EDCs can be calculated and compared with experiment. In this way, the consistency of the nondirect approach can be judged. Only where reasonable consistency is obtained can the nondirect approach be used in a meaningful way. However, even when clear evidence is obtained that some structure is due to direct transitions, useful density of states information can apparently be obtained from the nondirect approach when EDCs calculated using the ODS reproduce closely enough the major strengths in the experimental EDCs. (Cu [3,33,34] and Au [5] appear to be examples of this.) By major strengths, we mean attention should not be focused on relatively weak structure which is clearly direct, but on the overall amplitudes in the EDCs.

7. A Sampling of Experimental Data

Since this paper is already lengthy, we will not attempt a comprehensive survey of the photoemission literature: rather, we will attempt to present only a few representative results which have not been presented previously in this paper in order to illustrate and amplify the remarks made earlier.

Photoemission measurements and the nondirect analysis has been made on a fairly large number of transition and noble metals other than those mentioned earlier. Eastman, in particular, has obtained the ODS for a wide range of transition metals [6,20,29]. In figure 15 we present the ODS obtained by Eastman for ten metals [68]. For the sake of comparison, the density of states from band calculations are also given [68,69]. Although the agreement between experiment and calculation is not perfect, it is encouraging, particularly when one realizes that the band calculations were not highly refined and in some cases were just obtained from the calculation for a different material using a rigid-band approximation. The agreement obtained suggests that there is a meaningful relationship between the ODS and density of states obtained from band calculations, as does the agreement found for Cu [3,4], Ag [3,62,70], Ni and other transition [6,52] and rare earth metals [71].

In section 4, it was suggested that the narrower the bands the more valid the nondirect approach and thus the ODS of the correct density of states. If this is true, the situation within the transition metals should become less favorable as the atomic weight of the metal

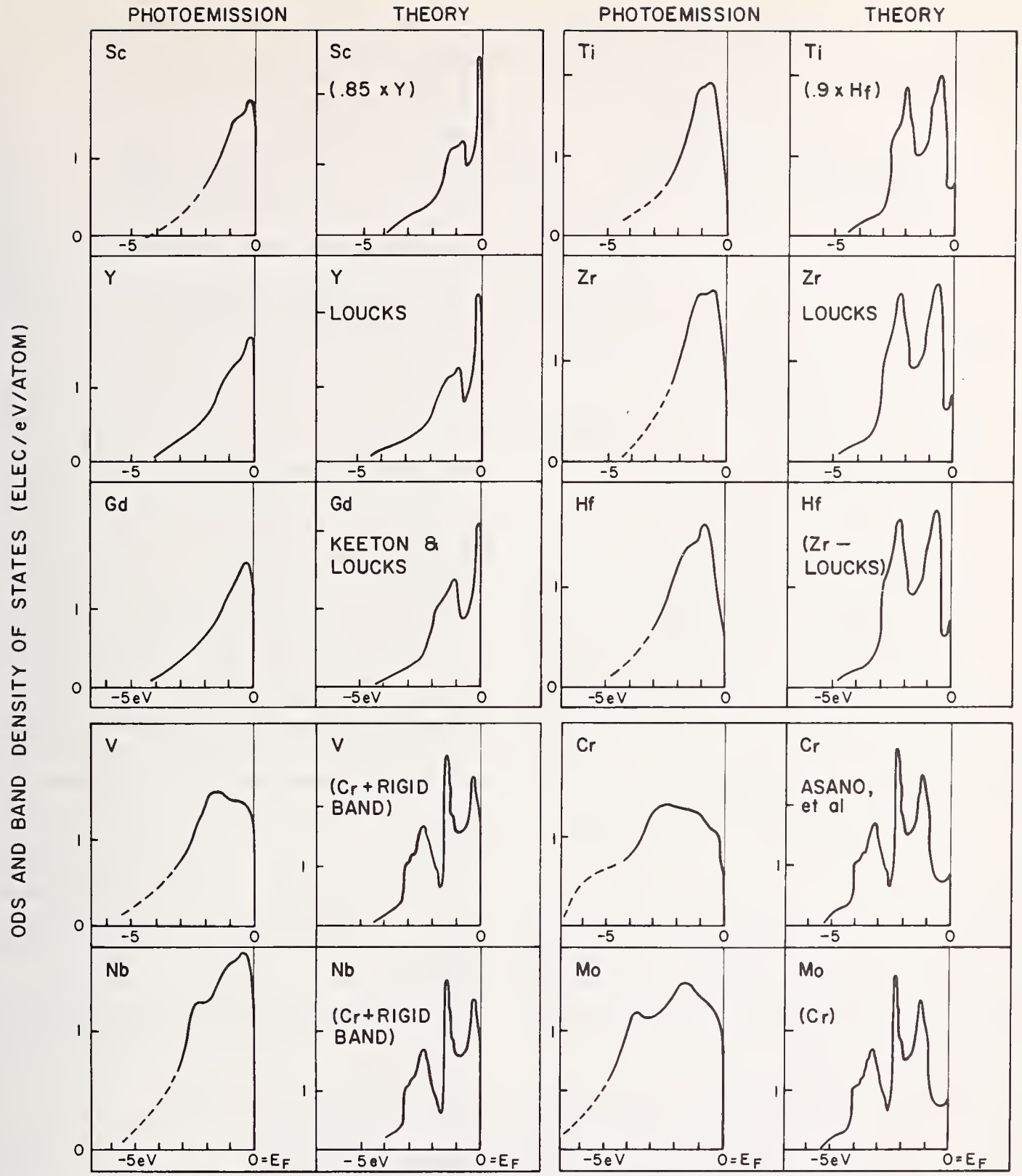

FIGURE 15. *Optical density of states obtained by Eastman as compared to the density of states obtained from band calculations. This figure is taken from ref. 68.*

increases since relativistic effects will broaden the bands. For example, the *d*-band width of Au is about twice that of Cu. Krolikowski and Spicer [5] have also studied clean Au in good vacuum for $5.4 \leq h\nu \leq 11.6$ eV and in poor vacuum for $h\nu$ values of 16.8 and 21.2 eV. From this work the ODS presented in figure 16 was obtained. As can be seen in figure 16, the ODS is in rather good agreement with the EDCs obtained from soft x-ray photoemission work [72]. The photoemission results also have been found by Ballinger and Marshall [73] to correlate rather well with their band calculations. On the other hand, work by Eastman at photon energies of 16.8 and 21.2 eV in good vacuum gives strong evidence that direct transitions are important in

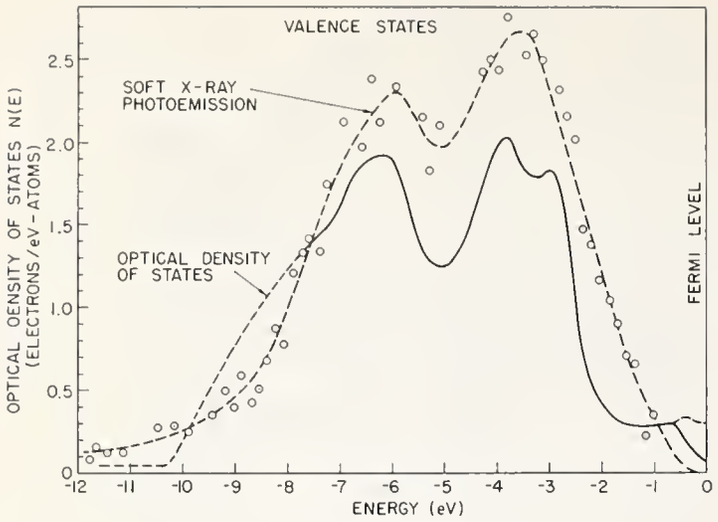

FIGURE 16. *Comparison of the ODS and the soft x-ray photoemission results of Siegbahn, et al. [72]. The x-ray results have been shifted to lower energy by 0.6 eV to obtain the best fit. (It is difficult to set the absolute zero of energy in the x-ray experiment.)*

Au. This series of results suggest that quite useful density of states information can be obtained from the relatively narrow bands of noble and transition metals by the ODS type of analysis even when direct transitions are important and that the broadening of the *d* band in going to Au does not make the ODS approach useless.

Up to this point we have concentrated to a large extent on materials for which the nondirect analysis can be used. In order to give perspective, let us now examine GaAs in which **k** conservation has been found to provide a dominant optical selection rule as it has been found for Ge, Si, and other III-V compounds [36]. If structure in the EDCs is due to peaks in the initial or final density of states, this can be detected by plotting the EDCs against initial energy ($E-h\nu$) or final energy (E) respectively. This argument holds even if the transitions are direct. The distinction between direct and nondirect transitions is made on the basis of modulation of the strengths of the peaks with particular attention being paid to evidence for them appearing or disappearing as photon energy is varied [36,37].

With this in mind, let us examine figure 17a and b where two typical EDCs for GaAs [36,74,75] are plotted versus final, figure 17a, and initial state energy, figure 17b. As can be seen, these EDCs are particularly strong in structure. Despite this, there is little tendency for the structure to fall at the same energy either on initial ($E-h\nu$) or final, energy plot. This shows clearly that **k** conservation provides an important selection rule. As a result, it is difficult to obtain density of states information directly from such plots. Eden [74] and Eden and Spicer [75] have derived a reasonable way of analyzing such data. This is done by making a plot of the final state energy of structure in the EDC, E, of structure versus the photon energy. Such a plot is shown in figure 18 for cesiated GaAs. One can obtain from band calculations theoretical plots of the same type for the symmetry directions of the crystal. By superimposing the two plots, it is possible to make identifications of the structure in the EDC. Such identification is indicated in figure 18. Further details are available elsewhere [36,74,75]. To obtain information on the density of states, it is sufficient to note two features: (1) A horizontal set of points for $E \approx 5$ eV labeled, "Final States Near L_3,W;" and (2) the 45° line between final state energies of about 4.5 and 8 eV labeled, "Transition II from Band 3 Minimum." Since (1) is a fixed, final state, it would suggest a peak in the final density of states at about 5 eV. In figure 19 we present a band structure for GaAs by Cohen and Bergstresser [76] along with the density of states calculated from it by Shay and Herman [77]. As can be seen, there is a very sharp peak in the final density of states at about 5 eV.

The 45° line in figure 18 indicates a transition from initial states at a fixed energy E_i since $E = E_i + h\nu$.

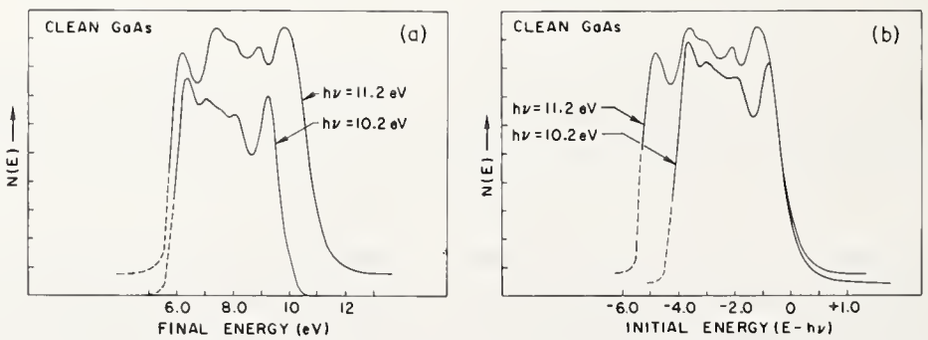

FIGURE 17. (a) *EDCs from GaAs for photon energies of 10.2 and 11.2 eV plotted as a function of final state energy.* (b) *EDCs for GaAs plotted vs* E − hν *to refer the energy distributions to the initial states. Note that the structure in the EDCs does not coincide on either a final energy plot (fig. 17a) or an initial energy plot as in this figure. This gives clear evidence that the transitions are direct.*

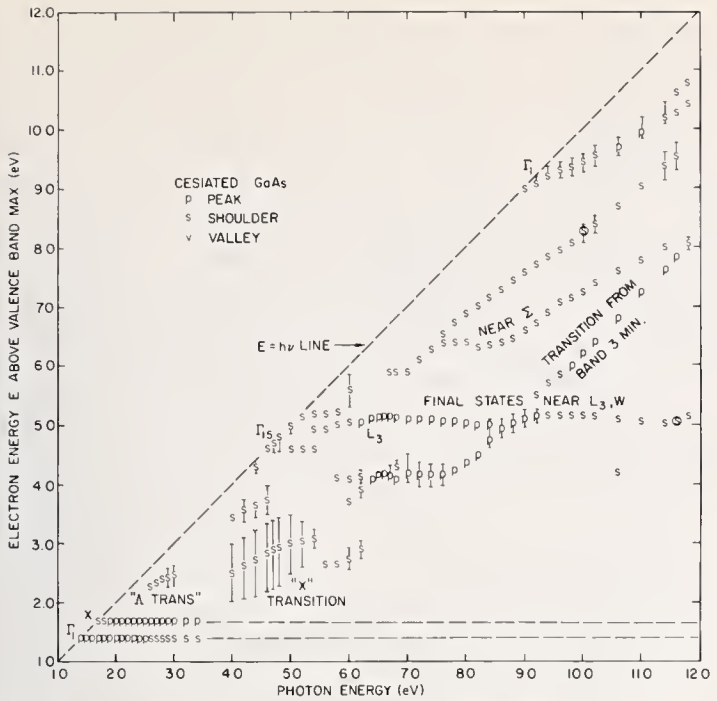

FIGURE 18. *A structure plot for the photoemission from cesiated GaAs. In such a plot the final energy of structure in the EDCs is plotted vs the photon energy. Such plots can be compared to predictions from band theories. They also provide at a glance certain information on the nature of the source of the structure in the EDCs, i.e., a horizontal line indicates transitions from flat portion of the valence band.*

Since the 45° line is located about 3.7 eV behind the $E = h\nu$ line, the initial states must be located this distance below the top of the valence band. As can be seen in the density of states plot of figure 19, there is a sharp density of states peak at just about this energy. Thus the two density of states peaks which are perhaps strongest and sharpest can be identified directly from the photoemission data; however, other strong structure which is not so narrow was not immediately detected from the photoemission data. This was because the curvatures were not sufficiently small so that a clear distinction could be made between the effects of initial and final density of states.

As is reported in a paper by Buss and Shirf [78] at this meeting, work by Spicer and Lapeyre [37] on PbTe seemed to have been successful in determining peaks in the density of states which correlate well with their band calculations. This occurred despite the fact that direct transitions are clearly important in these materials.

8. Comparison of Density of States Determinations Using Various Experimental Methods

In addition to uv photoemission spectroscopy, three other experimental techniques exist which can give direct information on the density of states of solids. In this section we will compare the density of states obtained by these methods for Cu with that obtained from our measurements.

8.1. Comparison with Results of Ion Neutralization Spectroscopy

In figure 20 the ODS for Cu is compared to the density of states obtained by Hagstrum [79] from Cu via the ion neutralization spectroscopy (INS) technique which he has developed. The peak between −2 and −4 eV is associated with the *d* states. As can be seen, the width of this peak is considerably greater than the *d* width indicated by the ODS or calculated band structure. In addition, there is no detailed structure in the ion neutralization results even though the instrumental resolution is sufficient to resolve structure such as that seen in the ODS or calculated density of states. Hagstrum has noted [80] that since his technique depends on electrons tunneling from the surface of the metal, it is sensitive to the electronic structure just at the surface and that for *d* electrons this structure may be different from that in the bulk of the material.

If it is suggested that a change of the electronic structure can take place at the surface, one must ask whether this can also affect photoemission studies. In principle, the photoemission is a bulk effect and thus would not be changed by variations in the electronic structure associated with the last atomic layer or so of the solid. However, the fast electron-energy dependency of the electron-electron scattering length (see fig. 3) and the low scattering length at high energies (as low as 10 Å in some materials) must be taken into account. Thus, as photon energy is increased up to 12 eV, the escaping electrons will come from regions closer and closer to the surface and it is possible that measurable changes in the EDCs might be due to changes in the electron structure at the surface. Comparison of the EDCs from cesiated [34] and uncesiated [4] Cu show that changes occur on cesiation in the relative strengths of the two leading *d* band peaks in Cu. Similar results are found in the Ni-Cu alloys [21]. These results are not understood, but are mentioned to indicate that the *d* band transitions appear to be sensitive to changes in the details of the conduction band electrons. If this is the case, changes of spatial distribution of conduction electrons at the surface might affect transitions from the *d* states. This could for example, contribute to the broadening of the first *d* peak from clean Cu which occurs as photon energy is increased (see fig. 4). The purpose of this discussion was to point out effects which might be important in photoemission but which have

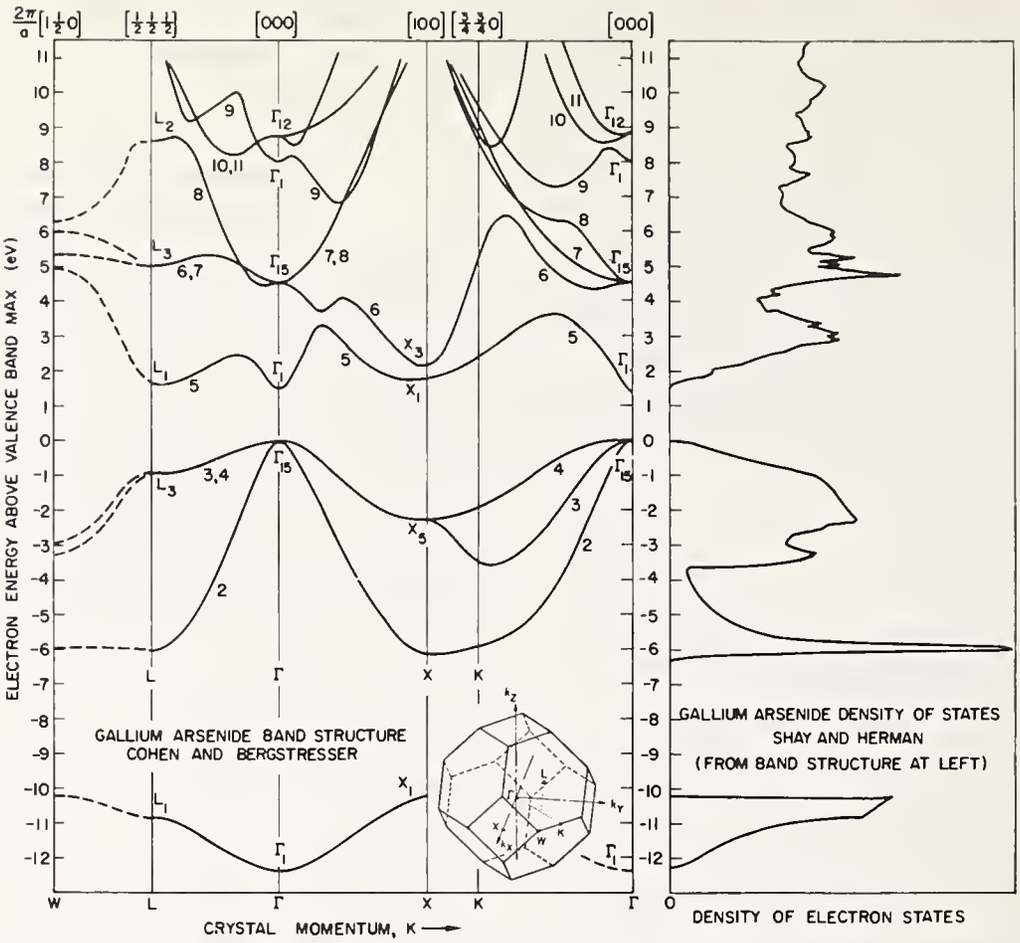

FIGURE 19. *The band structure of GaAs calculated by Cohen and Bergstresser* [76] *and the density of states calculated by Shay and Herman* [77].

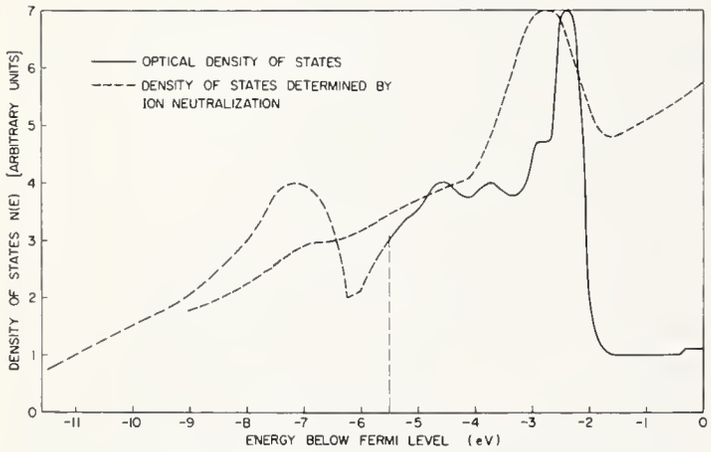

FIGURE 20. *Comparison between the ODS* [4] *and the results obtained by Hagstrum* [79] *through ion neutralization studies for Cu.*

not been established. If they do exist, it would appear that these effects are much smaller than the perturbation of the electron structure as seen at the surface in the INS experiments.

8.2. Comparison with Results of X-Ray Photoemission Spectroscopy

Let us next compare the ultraviolet photoemission work with the x-ray photoemission data. The ODS for Cu is compared in figure 21 with the results obtained by Fadley and Shirley [81] using the technique of x-ray photoemission spectroscopy (XPS). The XPS result is characterized by a single, almost symmetric, peak with a width at half maximum of about 3 eV. Since the total instrumental line width was about 1.0 eV, this width and lack of detailed structure does not appear to be instrumental. If we make the reasonable assumption that the broad peak is due to *d* electrons, it is also signifi-

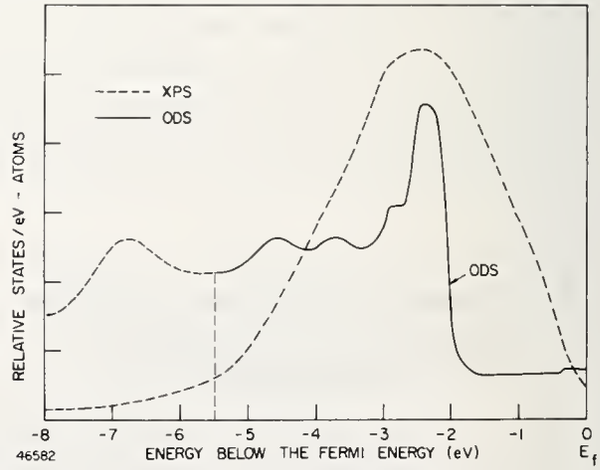

FIGURE 21. *Comparison between ODS* [4] *and results of the x-ray photoemission experiment of Fadley and Shirley* [81] *for Cu.*

cant that there is little evidence for the *s*- and *p*-derived states lying within 2 eV of the Fermi surface (see figure 5a and b). This effect can also be seen in the Au XPS data presented in figure 16. The *s*- and *p*-derived states can be clearly seen in the photoemission and INS work. The lack of any detailed structure in the excitation from the *d* states would also seem to be significant since such detailed structure does appear in the ODS as well as in the calculated band structure. However, it should be noted that substructure has been obtained in XPS results from Pt [81], Ag and Au [72] (see fig. 16) and that the position in energy of this structure is in reasonable agreement with structure in the ultraviolet photoemission work.

The reason for the lack of structure in the XPS for Cu is not clear at this time; however, it is interesting to note, as will be shown in the next section, that almost the same symmetric curve is obtained in soft x-ray emission spectroscopy as in the XPS results.

8.3. Comparison with Results of Soft X-Ray Emission Spectroscopy

A fourth experimental method used to investigate the filled states solids is that of soft x-ray emission spectroscopy (SXS). The results of such investigations [82,83] for Cu are compared in figure 22 with the ODS. As mentioned in the last section, the SXS curve is very similar to the XPS curve in that it contains a single almost symmetric peak and shows no evidence of the *s*- and *p*-derived states lying between the Fermi level and the top of the *d* band.

Cuthill, McAlister, Williams, and Watson [85] have reported structure in the SXS from Ni. However, it is not nearly as pronounced as that seen in the ODS of Eastman. There are some similarities between the ODS and the SXS results for Ni; however, the correlations do not seem to be strong.

Cu-Ni alloys have been studied both by SXS [86] and ultraviolet photoemission [21,23]. It is interesting to note that in the photoemission and optical work it has been possible to clearly identify a Ni virtual-bound state in the Cu-rich alloy and that these virtual-bound states are much different than Ni states in pure Ni. For example, their width at half maximum appears to be less than half of that of pure Ni for Ni concentrations up to about 25 atomic percent in Cu.

In contrast, in the x-ray work the spectrum obtained for Ni in Cu down to 10 percent concentrations was indistinguishable from that of pure Ni [86]. These results suggest that interactions with the deep hole override valence band structure in determining the SXS from

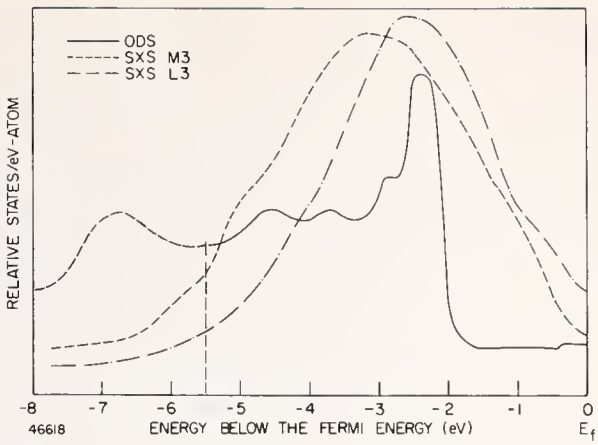

FIGURE 22. *Comparison between the ODS and results obtained from soft x-ray emission spectroscopy. The curve labeled* M3 *was obtained using* M_3 *radiation* [83] *and that labeled* L3 *using* L_3 *radiation* [84].

Ni; if this is so, the SXS would yield more information on the interaction between the deep hole and the valence electrons than on the valence band density of states.

9. Conclusions

The ultraviolet photoemission work done to date shows that density of states data can be obtained from such measurements. Because of the high resolution available in such measurements (0.05 to 0.3 eV), more detailed information can presently be obtained than by any other experimental method used to determine experimentally the density of states. In materials such as Cu where the most extensive work has been done, both experimentally and in theoretical calculations of the density of states, relatively good agreement is obtained between the position in energy of structure in the density of states. No other experimental method has given such clear-cut results or impressive agreement; however, good agreement is not obtained in the relative strengths of structure in the experimental and theoretical density of states. There are still fundamental questions which must be answered both with regard to the photoemission experiment and its interpretation and with regard to the band calculations and their relation to optical excitation spectra.

The photoemission data as well as calculations on Cu are probably the most complete available for any metal. The work of Smith [34] on Cu shows clear evidence of direct transitions from the regions of the *d* bands having large curvature. The calculations of Smith [34] and Smith and Spicer [33] show strong similarities between measurements and calculations based on direct transitions; however, the direct calculations predict much stronger modulation of the intensities of peaks than is seen experimentally. It should also be

noted that a broadening of 0.3 to 0.4 eV is used in the calculations to bring them into closer agreement with experiment. It is suggested that the experimental data is consistent with a model (suggested by Doniach's [46] theoretical work) which assumes that the delta function **k** selection rule be replaced by a selection distribution of **k**'s, with the width of the distribution increasing as the curvature of the bands decrease (*i.e.*, as the group velocity decreases). Thus, one would move in a continuous fashion from a completely direct transition model for a material with sufficiently wide bands to a non-direct-type of model for sufficiently narrow bands. The band widths at which such transitions take place would depend on the detailed characteristics of individual materials.

It appears that some density of states information can be obtained from photoemission data even when the transitions are completely direct. This can occur because peaks in the valence band density of states may produce EDC peaks which move with photon energy over a limited range of $h\nu$. Likewise, density of states peaks in the final states may produce peaks which fall at a constant energy over a limited range of $h\nu$. All of this is just a consequence of the fact that a large volume in **k** space must lie near a single energy to give a peak in the density of states. Such behavior has been pointed out at this meeting in, for example, GaAs and PbTe where the density of states peaks so identified have been found to correlate well with density of states peaks in the calculated band structure. However, other peaks in the density of states in GaAs were not identified. This may have been due to the fact that the $h\nu$ range used was not sufficiently large or that too crude a method is being used to identify density of states structure.

In a different type of approach, photoemission studies can also be used in direct collaboration with band calculations by providing empirical data on the band structure. This data can then be used to refine the band structure and the density of states can be calculated from the refined band structure.

10. Acknowledgment

It is a pleasure to acknowledge stimulating and fruitful conversations with Seth Doniach, Dean Eastman, Walter Harrison, Frank Herman, David Seib, Neville Smith and Leon Sutton as well as my other colleagues at Stanford University. I am particularly indebted to Seth Doniach, Dean Eastman, and Neville Smith for access to their work prior to publication.

11. References

[1] Koopmans' theorem states that the one-electron energy eigenvalue ϵ_j in the Foch equation for a solid is the negative of the energy to remove the electron in state ϕ_j from the solid. The proof of Koopmans' theorem depends on the spatial part of the wave function being of the Bloch type and on all other wave functions being unchanged when one electron is removed. If Koopmans' theorem holds, it follows that the photon energy necessary to excite an electron from state ϕ_j to state ϕ_k is just the difference between the one-electron energies of the two states. However, if the eigenfunctions of other states are modified in the excitation, Koopmans' theorem will not hold, and many-body effects must be taken into account. See also: F. Seitz, Modern Theory of Solids (McGraw-Hill Book Company, Inc., New York, 1940), p. 313; J. Callaway, Energy Band Theory (Academic Press, Inc., New York, 1964), p. 117; J. C. Phillips, Phys. Rev. **123,** 420 (1961); L. G. Parratt, Rev. Mod. Phys. **31,** 616 (1959).

[2] See, for example, refs. 3, 4, and 5.

[3] Berglund, C. N., and Spicer, W. E., Phys. Rev. **136,** A1030; **136,** A1044 (1964).

[4] Krolikowski, W. F., and Spicer, W. E., Phys. Rev., in press.

[5] Krolikowski, W. F., and Spicer, W. E., Phys. Rev., in press.

[6] Eastman, D. E., J. Appl. Phys. **40,** 1387 (1969).

[7] Beaglehole, D., Proc. Phys. Soc. (London) **85,** 1007 (1965).

[8] Ehrenreich, H., and Philipp, H. R., Phys. Rev. **128,** 1622 (1962).

[9] Mueller, F. M., and Phillips, J. C., Phys. Rev. **157,** 600 (1969).

[10] Gerhardt, U., Phys. Rev. **172,** 651 (1968).

[11] Spicer, W. E., and Berglund, C. N., Rev. Sci. Instr. **35,** 1665 (1964).

[12] Eden, R. C., Rev. Sci. Instr., in press.

[13] James, L. W., Moll, J. L., Spicer, W. E., and Eden, R. C., Phys. Rev. **174,** 909 (1968).

[14] James, L. W., Ph. D. Thesis, Stanford University (unpublished), 1969.

[15] Allen, F. G., and Gobeli, G. W., Phys. Rev. **144,** 558 (1966).

[16] Vehse, R. C., and Arakawa, E. T., Phys. Rev. **180,** 695 (1969).

[17] DiStefano, T. H., and Pierce, D. T., Rev. Sci. Instr., to be published.

[18] Koyama, R. Y., Ph. D. Thesis, Stanford University (unpublished), 1969.

[19] Spicer, W. E., Optical Properties and Electronic Structure of Metals and Alloys, F. Abelés, Editor (North-Holland Publishing Co., Amsterdam, 1965), p. 296.

[20] Eastman, D. E., and Krolikowski, W. F., Phys. Rev. Letters **21,** 623 (1968).

[21] Seib, D. H., and Spicer, W. E., Phys. Rev., to be published. (Cu-rich alloys)

[22] Calcott, T. A., and MacRae, A. U., Phys. Rev. **178,** 966 (1969).

[23] Seib, D. H., and Spicer, W. E., Phys. Rev., to be published. (Ni-rich alloys)

[24] Kane, E. O., Proc. Intern. Conf. Phys. Semiconductors, Kyoto, Japan, 1966, p. 37; Phys. Rev. **159,** 624 (1967).

[25] Eastman, D. E., private communication.

[26] Crowell, C. R., and Sze, S. M., Physics of Thin Films, G. Hass and R. E. Thun, Editors (Academic Press, 1967), Vol. 4.

[27] Kanter, H., to be published.

[28] Sze, S. M., Moll, J. L., and Sugano, T., Solid-State Elec. **7,** 509 (1964).

[29] Eastman, D. E., to be published.
[30] James, L. W., and Moll, J. L., Phys. Rev. **183**, 740 (1969).
[31] DiStefano, T. H., and Spicer, W. E., Bull. Amer. Phys. Soc. **13**, 403 (1968).
[32] Spicer, W. E., Phys. Rev. **154**, 385 (1967).
[33] Smith, N. V., and Spicer, W. E., Optics Comm., in press.
[34] Smith, N. V., Proc. of Electronic Density of States Symposium, Washington, D.C., November 3-6, 1969.
[35] Janak, J. F., Eastman, D. E., and Williams, A. R., Proc. of Electronic Density of States Symposium, Washington, D.C., November 3-6, 1969.
[36] Spicer, W. E., and Eden, R. C., Proc. of 9th Intern. Conf. on the Phys. of Semiconductors (Moscow, USSR), Vol. 2, p. 65 (1968).
[37] Spicer, W. E., and Lapeyre, J., Phys. Rev. **139**, A565 (1965).
[38] Shay, J. L., Proc. II-VI Conf., D. G. Thomas, Editor (Benjamin, Inc., New York, 1967), p. 651: Shay, J. L., Herman, F., and Spicer, W. E., Phys. Rev. Letters **18**, 649 (1967); Shay, J. L., and Spicer, W. E., Phys. Rev. **161**, 799 (1967); Shay, J. L., and Spicer, W. E., Phys. Rev. **169**, 650 (1968); and Phys. Rev. **175**, 741 (1968).
[39] Brust, D., to be published.
[40] Koyama, R. Y., and Spicer, W. E., Proc. of Electronic Density of States Symposium, Washington, D.C., November 3-6, 1969.
[41] Janak, J. F., Williams, A. R., and Eastman, D. E., to be published; Eastman, D. E., Janak, J. F., and Williams, A. R., to be published.
[42] Eastman, D. E., private communication.
[43] Smith, N. V., private communication.
[44] Snow, F. C., Phys. Rev. **171**, 785 (1968).
[45] Cohen, M. H., and Mueller, F. M., Atomic and Electric Structure of Metals (American Society of Metals, Metals Park, Ohio, 1967), p. 75.
[46] Doniach, S., private communication.
[47] Koyama, R. Y., Spicer, W. E., Ashcroft, N. W., and Lawrence, W. E., Phys. Rev. Letters **19**, 1284 (1967).
[48] Ashcroft, N. W., and Lawrence, W. E., Phys. Rev. **175**, 938 (1968).
[49] Shaw, R., and Smith, N., Phys. Rev. **178**, 985 (1969).
[50] Mosteller, L. P., Huen, T., and Wooten, F., Phys. Rev. **184**, 364 (1969).
[51] Blodgett, A., Spicer, W., and Yu, A., Optical Prop. and Electronic Structure of Metals and Alloys, F. Abelés, Editor (North-Holland Publishing Co., Amsterdam, 1965), p. 246.
[52] Lapeyre, G. J., and Kress, K. A., Phys. Rev. **166**, 589 (1968).
[53] Phillips, J. C., Solid-State Physics, F. Seitz and D. Turnbull, Editors (Academic Press, New York, 1966), Vol. 18, p. 55; Herman, F., Kortum, R. L., Kuglin, D. D., VanDyke, J. P., and Skillman, S., Methods of Computational Physics, B. Adler, S. Fernbach, and M. Rotenberg, Editors (Academic Press, New York, 1968), Vol. 8, p. 193.
[54] Donovan, T. M., Spicer, W. E., J. of Non-Crystalline Solids, in press.
[55] Donovan, T. M., Spicer, W. E., and Bennett, J., in preparation.
[56] Donovan, T., and Spicer, W. E., Phys. Rev. Letters **21**, 1572 (1968).
[57] Donovan, T., Ph. D. Thesis, Stanford University (unpublished), (1970).
[58] Herman, F., Kortum, R. L., Kuglin, C. D., and Shay, J. L., Proc. Intern. Conf. on II-VI Semiconductor Comp. (W. A. Benjamin, Inc., New York, 1967), p. 271.
[59] Brust, D., private communication.
[60] Seib, D. H., and Spicer, W. E., Phys. Rev. Letters **20**, 1441 (1968).
[61] Norris, C., and Nilsson, P. O., Solid State Comm. **6**, 649 (1968).
[62] Walldén, L., Solid State Comm., **1**, 593 (1969).
[63] Walldén, L., Seib, D., and Spicer, W., J. Appl. Phys. **40**, 1281 (1969).
[64] Smith, N. V., private communication.
[65] Herman, F., Kortum, R. L., Kuglin, C. D., and Short, R. A., Proc. Intern. Conf. Phys. Semiconductors, (Kyoto, Japan, 1966), p. 7.
[66] Herman, F., Intern. J. of Quantum Chem. **S**, in press.
[67] Gehardt, U., private communication.
[68] Eastman, D. E., Solid State Comm., in press.
[69] Loucks, T. L., Phys. Rev. **144**, 504 (1964); **159**, 544 (1967); Keeton, S. C., and Loucks, T. L., Phys. Rev. **168**, 672 (1968); Fleming, G. S., and Loucks, T. L., Phys. Rev. **173**, 685 (1968); Asono, S., and Yamashita, J., Phys. Soc. Japan **23**, 714 (1967).
[70] Snow, F. C., private communication.
[71] Yu, A., Blodgett, A., and Spicer, W. E., Proc. Intern. Colloquium Optical Properties and Electronic Structure of Metals and Alloys, F. Abelés, Editor (North-Holland Publishing Co., Amsterdam, 1966), p. 246.
[72] Siegbahn, K., Norling, C., Fahlman, A., Nordberg, R., Hamrin, K., Hedman, J., Johansson, G., Bergmark, T., Karlsson, S., Lindgren, I., Lindberg, B., ESCA Atomic, Molecular and Solid State Structure Studied by Means of Electron Spectroscopy (Almqvist and Wiksells Boktryckeri AB, Uppsala, 1967), Ser. IV, Vol. 20.
[73] Ballinger, R. A., and Marshall, C. A. W., to be published.
[74] Eden, R. C., Ph.D. Thesis, Stanford University (unpublished), (1968).
[75] Eden, R. C., Spicer, W. E., to be published.
[76] Cohen, M. L., and Bergstresser, T. K., Phys. Rev. **141**, 789 (1966).
[77] Shay, J. L., and Herman, F., private communication.
[78] Buss, D. D., and Shirf, V. E., Proc. of Electronic Density of States Symposium, Washington, D.C., November 3-6, 1969.
[79] Hagstrum, H. D., Phys. Rev. **150**, 495 (1966).
[80] Hagstrum, H. D., private communication.
[81] Fadley, C. S., and Shirley, D. A., Phys. Rev. Letters **21**, 980 (1968).
[82] Cauchois, Y., and Bonnelle, C., Proc. Intern. Colloquium Optical Properties and Electronic Structure of Metals and Alloys (North-Holland Publishing Co., Amsterdam, 1966), p. 83.
[83] Bedo, D. E., and Tomboulian, D. H., Phys. Rev. **113**, 464 (1959).
[84] Figure 40 has been taken from ref. 81.
[85] Cuthill, J. R., McAlister, A. J., Williams, M. L., and Watson, R. E., Phys. Rev. **164**, 1006 (1967).
[86] Clift, J., Curry, C., and Thompson, B. J., Phil. Mag. **8**, 593 (1963).

Discussion on "Optical Density of States Ultraviolet Photoelectric Spectroscopy" by W. E. Spicer (Stanford University)

J. Dow *(Princeton Univ.):* You mentioned that Doniach had done some calculations including the Mahan singularity in the photoemission. Are there measurements which indicate that this many-body effect is present?

W. E. Spicer *(Stanford Univ.):* The first place he looked for this was asymmetry in the x-ray line emission from a deep level. He has been examining experimental data and he is encouraged at the asymmetry that is seen although the resolution is still a problem.

H. Ehrenreich *(Harvard Univ.):* I just want to make a cautionary remark about the many-electron effects that have been discussed in connection with the x-ray emission and absorption problem by Mahan, Nozières, and Doniach recently. These effects are probably of importance only when the hole state is localized or when it occurs in a narrow band. Thus one might expect these effects to be of importance in transition metals as recently suggested by Doniach. They do not seem to be of importance in aluminum. Beeferman and I recently examined the many-electron contributions to the optical absorption in aluminum in considerable detail and found them to be unimportant. Here, of course, the bands in which the excited electron and hole find themselves are not flat. Therefore, our conclusions in no way contradict the proposal by Doniach.

The Density of States and Photoemission from Indium and Aluminum*

R. Y. Koyama and W. E. Spicer**

Stanford University, Stanford, California 93405

Experimental photoemission data from indium and aluminum are briefly described and can be understood in terms of a density of states model. In contrast to this, a direct transition model based on calculated band structures is found to yield photoelectron spectra which are fair reproductions of the density of states. This suggests that for these two metals, conclusions drawn concerning the density of states are independent of the model used to explain the photoemission data.

Key words: Aluminum (Al); direct and nondirect transitions; electronic density of states; indium (In); nondirect transitions; optical density-of-states; photoemission.

1. Introduction

Photoemission has become a powerful experimental tool for determining some features of the electronic states in a large spectrum of materials. In particular, by assuming a simple model, it is possible to deduce an "optical density of states" for some materials [1]. This model assumes that electronic transition probabilities are proportional to products of densities of states and that absorption occurs via "nondirect" transitions. In other materials [2], photoemission data has been used to document absorption processes which are due to "direct" transitions. In this paper results of recent work on experimental and model calculations for indium and aluminum are described. For these metals, it is found that either model gives a fair description of the photoemission properties. The data for indium is based on experiments performed by the authors [3]; the experimental data for aluminum is taken from the work of Wooten, Huen and Stuart [4].

2. Experimental Data

Figure 1 shows a partial set of electron energy distributions (normalized to the yield) for a sample of crystalline indium (single and polycrystalline samples had virtually identical spectra), plotted with the photon

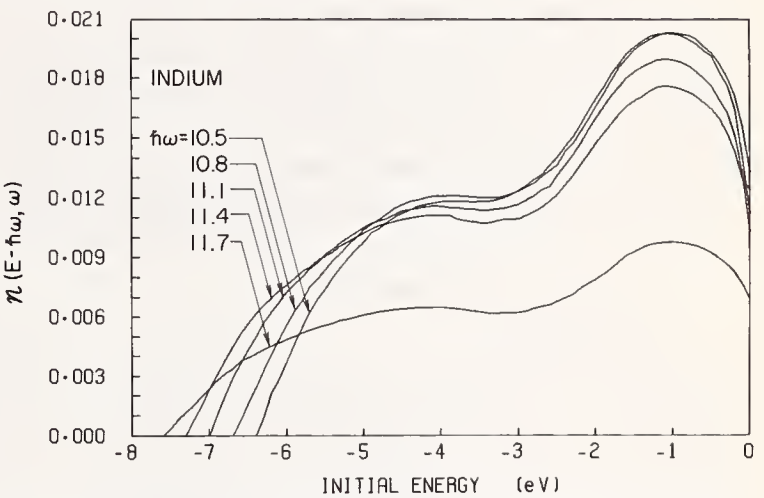

FIGURE 1. *A partial set of experimentol electron energy distributions referred to the initiol stotes (electrons/photon-eV).*

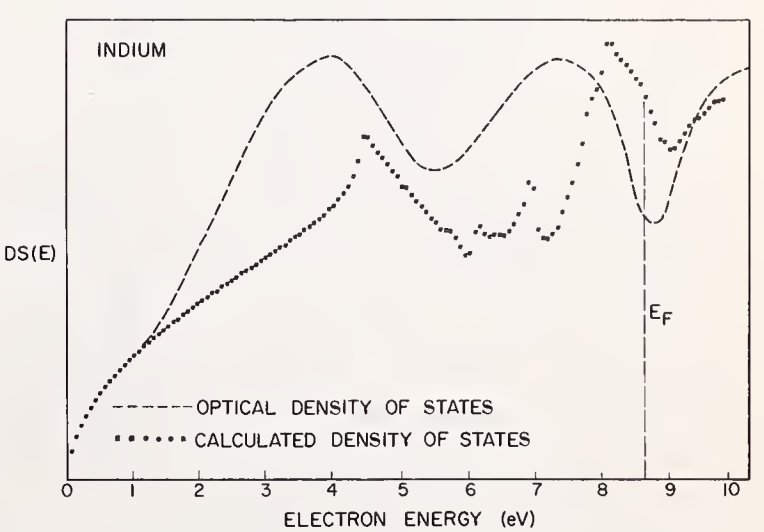

FIGURE 2. *The optical density of stotes function (deduced from the experimentol dota) and a calculated density of stotes for indium.*

*Work supported by U.S. Army Engineer Research and Development Laboratories, Fort Belvoir, Virginia, Contract No. DA-44-009-AMC 1474 (7); and the Advanced Research Projects Agency through the Center for Materials Research at Stanford University, Stanford, California.

**Present address: National Bureau of Standards, Washington, D.C. 20234.

energy as a parameter. These photoemission curves are plotted with respect to the initial energies of the electrons (the Fermi energy is the reference level). It is evident that there is high probability of exciting electrons from 1.2 and 4.2 eV below the Fermi energy. Based on the density of states model with nondirect transitions, these distributions reproduce structure in the "optical density of states" (ODS), which is shown as the dashed curve in figure 2 [3]. These experimental results would lead to the conclusion that indium can be characterized by nondirect transitions and an optical density of states.

Similar photoemission measurements have been made on evaporated films of aluminum by Wooten et al. [4]. Their data is reproduced in figure 3. These authors have concluded that the spectrum of emitted electrons is a good replica of the density of filled states. This again leads to the conclusion that aluminum too can be described by a density of states model deduced from empirical considerations.

3. Direct Transition Calculations

The previous section indicated that indium and aluminum can be characterized by a density of states model with nondirect transitions. They are typical of "nondirect" materials in that the photoemission spectra behave in a predictable and smooth fashion as the photon energy is changed. When compared with materials that display "direct" characteristics, the photoemission from these metals are rather featureless. Yet, it is a valid question to ask what the expected form of the photoemission would be if the transitions were direct.

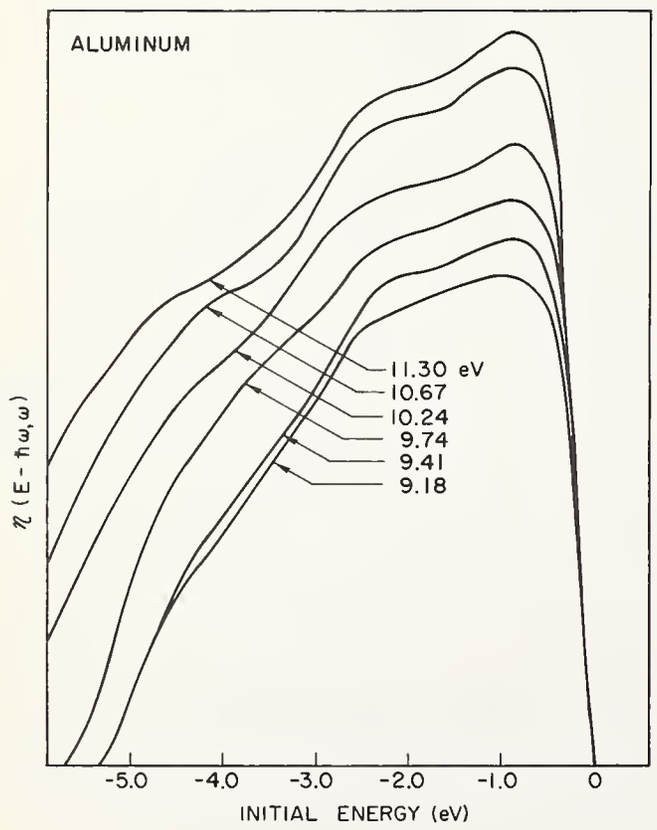

FIGURE 3. *Experimental electron energy distributions curves for aluminum* [4].

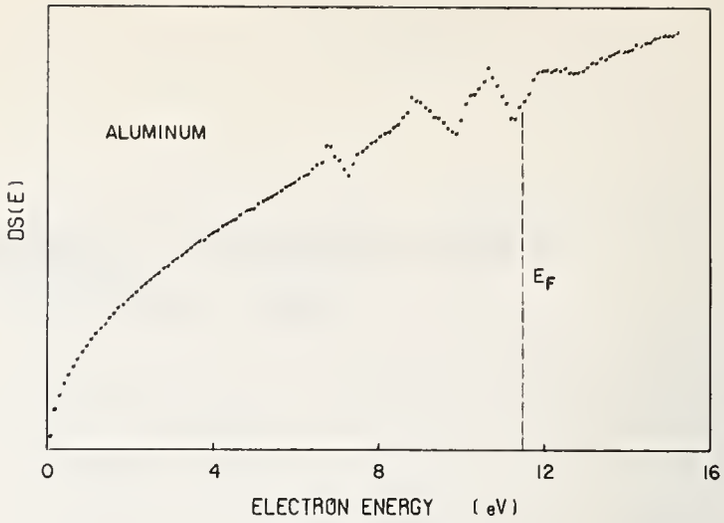

FIGURE 4. *The calculated density of states for aluminum.*

If the electron energy structure of a material is known, various electronic properties can be calculated. The two primary quantities of interest here are the electronic density of states and the photoelectron energy spectra. These have been calculated for indium [3] using the band structure of Ashcroft and Lawrence [5], and for aluminum [6] using Ashcroft's [7] band structure. Figures 2 and 4 show the results of the calculation for the density of states.

For indium, the experimentally deduced ODS (dashed curve of figure 2) does not show the sharp features of the calculated density of states (dotted curve of figure 2) (the sharp structure is caused by the interaction of the energy surfaces with the zone boundaries). However, the gross features such as the peak near the Fermi energy and the low energy bump are present in both curves. The symmetry of the indium lattice (BCT:$c/a = 1.53$ or pseudo-FCT:$c/a = 1.08$, as opposed to the higher fcc symmetry of the aluminum lattice) required some simplification to be made in the calculation of the eigenvalues [3]. Therefore, this calculated density of states can only be considered as an approximation.

The aluminum density of states shown in figure 4 is very nearly free electron like. There are only small deviations at energies near X, L, and W of the Brillouin zone. By comparison, it is evident that the bands in in-

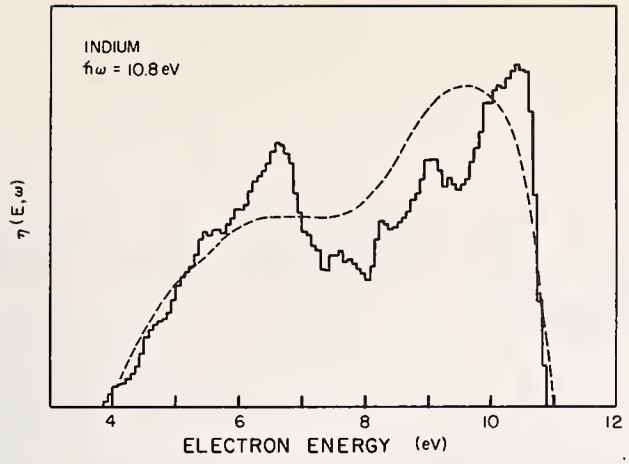

FIGURE 5. *A comparison of the calculated (direct transition) electron energy distribution to the experimental distribution for indium.*

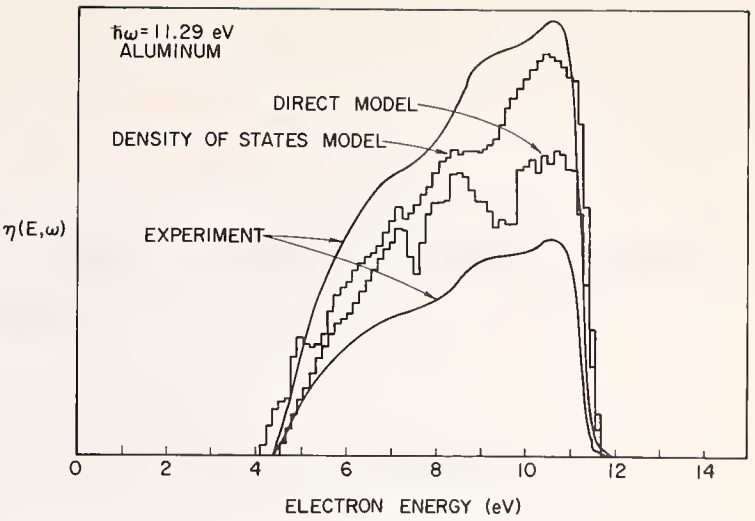

FIGURE 6. *A comparison of the calculated (direct and nondirect transition) electron energy distributions to the experimental distribution for aluminum.*

dium are perturbed significantly more than those for aluminum.

By assuming that the transitions are direct, the photoelectron energy distributions were calculated for the two band structures [3,6]. It was assumed that all transitions were equally probable (subject to the constraints on energy and momentum), and a simple escape function was used. Figures 5 and 6 display the calculated distributions at a single photon energy. For indium (fig. 5), there is a gross resemblance between the calculated and experimental distributions; there are two major groups of electrons in the distribution. It is of interest to note here that there is close replication of the structure in the calculated density of states (fig. 2) in the direct transition distribution of figure 5. For aluminum (fig. 6), the agreement between experiment and calculation is better. The calculated distribution shows stronger structure than the experiment, but all the structure is present. Also included in figure 6 is a calculated distribution based on figure 4 and the density of states model. Both of these calculated distributions (direct and nondirect transitions) reproduce structure in the density of states; the three bumps in the density of the states are clearly seen in the calculated distributions.

4. Conclusions

For the energy range where these photoemission experiments are done (4.0 to 11.6 eV), the empirical density of states model can be used to deduce information about the electronic density of states. By the same token, calculations of photoemission spectra due to direct transitions also reflect structure in the density of states. Therefore, it seems that either model can be used to describe the photoemission properties of these two metals in the photon energy range studied here. At higher photon energies where there is no experimental data, there are predictable differences which would distinguish the photoemission due to direct transitions and those due to nondirect transitions. Further experimental work at higher energy would be useful in determining which model is more applicable.

5. References

[1] Cu, Ag—Berglund, C. N., and Spicer, W. E., Phys. Rev. **136**, A1030 and A1044 (1964). Krolikowski, W. F., Ph. D. dissertation, Stanford University, 1967, unpublished. Co—Yu, A. Y-C., and Spicer, W. E., Phys. Rev. **167**, 674 (1968). Ni—Blodgett, A. J. and Spicer, W. E., Phys. Rev. **146**, 390 (1966). CdS—Shay, J. L., and Spicer, W. E., Phys. Rev. **169**, No. 3, 650 (1968).

[2] GaAs, GaP, Si—Eden, R. C., Ph. D. dissertation, Stanford University, 1967, unpublished. Ge—Donovan, T.M., and Spicer, W. E., Bull. Am. Phys. Soc. **13**, 1659 (1968). CdTe—Shay, J. L., and Spicer, W. E., Phys. Rev. **161**, No. 3, 799 (1967).

[3] Koyama, R. Y., and Spicer, W. E., to be published.

[4] Wooten, F., Huen, T., and Stuart, R., Optical Properties and Electronic Structure of Metals and Alloys. F. Abelés, Editor, (North-Holland Publishing Co., Amsterdam, 1966), p. 333.

[5] Ashcroft, N. W., and Lawrence, W. E., Phys. Rev. **175**, 938 (1968).

[6] Smith, N. V., Koyama, R. Y., and Spicer, W. E., to be published.

[7] Ashcroft, N. W., Phil. Mag. **8**, 2055 (1963).

417-156 O - 71 - 12

Electronic Densities of States from X-Ray Photoelectron Spectroscopy *[1]

C. S. Fadley and D. A. Shirley

Lawrence Radiation Laboratory, University of California, Berkeley, California 94720

In x-ray photoelectron spectroscopy (XPS), a sample is exposed to low energy x rays (approximately 1 keV), and the resultant photoelectrons are analyzed with high precision for kinetic energy. After correction for inelastic scattering, the measured photoelectron spectrum should reflect the valence band density of states, as well as the binding energies of several core electronic levels. All features in this spectrum will be modulated by appropriate photoelectric cross sections, and there are several types of final-state effects which could complicate the interpretation further.

In comparison with ultraviolet photoelectron spectroscopy (UPS), XPS has the following advantages: (1) the effects of inelastic scattering are less pronounced and can be corrected for by using a core reference level, (2) core levels can also be used to monitor the chemical state of the sample, (3) the free electron states in the photoemission process do not introduce significant distortion of the photoelectron spectrum, and (4) the surface condition of the sample does not appear to be as critical as in UPS. XPS seems to be capable of giving a very good description of the general shape of the density-of-states function. A decided advantage of UPS at the present time, however, is approximately a fourfold higher resolution.

We have used XPS to study the densities of states of the metals Fe, Co, Ni, Cu, Ru, Rh, Pd, Ag, Os, Ir, Pt, and Au, and also the compounds ZnS, $CdCl_2$, and HgO. The *d* bands of these solids are observed to have systematic behavior with changes in atomic number, and to agree qualitatively with the results of theory and other experiments. A rigid band model is found to work reasonably well for Ir, Pt and Au. The *d* bands of Ag, Ir, Pt, Au and HgO are found to have a similar two-component shape.

Key words: $CdCl_2$; density of states; HgO; noble metals; rigid band model; transition metals; x-ray photoemission; ZnS.

1. Introduction

The energy distribution of electronic states in the valence bands [1] of a solid is given by the density of states function, $\rho(E)$. There are several techniques for determining $\rho(E)$ at energies within $\sim kT$ of the Fermi energy, E_f, where relatively small perturbations can excite electrons to nearby unoccupied states. However, because of the nature of Fermi statistics, an electron at energy E, well below E_f (in the sense that $E_f - E \gg kT$), can respond only to excitations of energy $E_f - E$ or greater. Because the valence bands are typically several eV wide, a versatile, higher energy probe is required to study the full $\rho(E)$. The principal techniques presently being applied to metals are soft x-ray spectroscopy (SXS) [2,3] ion-neutralization spectroscopy (INS) [4], and photoelectron spectroscopy (by means of ultraviolet [5] or x-ray [6,7] excitation).

In each of these methods, either the initial or the final state involves a hole in the bands under study. Thus the measuring process is inherently disruptive. The actual initial and final states may not be simply related to the undisturbed ground state [8], and only for this ground state does $\rho(E)$ have precise meaning. Even if the deviations from a ground state description can be neglected, there are complications for each of the above techniques in relating measured quantities to $\rho(E)$ [2,3,4,5]. Nevertheless, all four have been applied with some success, and, where possible, experimental

* An invited paper presented at the 3d Materials Research Symposium, *Electronic Density of States*, November 3–6, 1969, Gaithersburg, Md.

[1] Work performed under the auspices of the U.S. Atomic Energy Commission.

results have been compared to the theoretical predictions of one-electron band theory.

In this paper, we outline the most recently developed of these techniques, x-ray photoelectron spectroscopy (XPS) [6,7], and apply it to several metallic and nonmetallic solids. In section 2, the principles of the technique are discussed from the point of view of relating measured quantities to a one-electron $\rho(E)$. In section 3, we present results for the twelve $3d$, $4d$, and $5d$ transition metals Fe, Co, Ni, Cu, Ru, Rh, Pd, Ag, Os, Ir, Pt, and Au, making comparisons with the results of other experimental techniques and theory where appropriate. In addition, results for nonmetallic solids containing the elements Zn, Cd and Hg are presented, to clarify certain trends observed as each d shell is filled. In section 4, we summarize our findings.

2. The XPS Method

The fundamental measurements in both ultraviolet photoelectron spectroscopy (UPS) and x-ray photoelectron spectroscopy (XPS) are identical and very simple. Photons of known energy impinge on a sample, expelling photoelectrons which are analyzed for kinetic energy in a spectrometer. In UPS [5], photon energies range from threshold to ~20 eV, whereas XPS utilizes primarily the $K\alpha$ x rays of Mg (1.25 keV) and Al (1.49 keV). For a given absolute energy resolution, an XPS spectrometer must thus be ~100 times higher in resolving power. We have used a double-focussing air-cored magnetic spectrometer [9], with an energy resolution of $\Delta\epsilon/\epsilon = 0.06$ percent. $\Delta\epsilon$ is defined to be the full width at half maximum intensity (FWHM) of the peak due to a flux of monoenergetic electrons of energy ϵ.

Conservation of energy requires that

$$h\nu = E^h - E^g + \epsilon + \phi_c. \tag{1}$$

where $h\nu$ is the photon energy, E^g the total energy of the initial ground state, E^h the total energy of the final hole state *as seen by the ejected photoelectron*, ϵ the electron kinetic energy, and ϕ_c the contact potential between the sample surface and the spectrometer. If E^h corresponds simply to a hole in some electronic level j, then the binding energy of an electron in level j is by definition $E_b^v = E^h - E^g$, where the superscript v denotes the vacuum level as a reference. The Fermi level can also be used as a reference and a simple transformation yields

$$h\nu = E_b^f + \epsilon + \phi_{sp} \equiv -E + \epsilon + \phi_{sp}, \tag{2}$$

where $E_b^f \equiv -E$ is the Fermi-referenced binding energy, and ϕ_{sp} is the work function of the spectrometer (a known constant). This transformation makes use of the relations $E_b^v = E_b^f +$ sample work function and $\phi_c = \phi_{sp} -$ sample work function. Positive charging of the sample due to electron emission can shift the kinetic energy spectrum to lower energies by as much as 1 eV for insulating samples but relative peak positions should remain the same. This effect is negligible for metals.

Returning to eq (1), we see that the fundamental XPS (or UPS) experiment measures the kinetic energy spectrum from which we attempt to deduce the final-state spectrum. This spectrum must then be related to $\rho(E)$, as discussed below.

In addition to $\rho(E)$ modulated by an appropriate transition probability, there will be six major contributors to lineshape in an XPS spectrum. Together with their approximate shapes and widths for the conditions of our experiments, these are:

1. Linewidth of exciting radiation—Lorentzian, ~0.8 eV FWHM for the unresolved Mg$K\alpha_{1,2}$ doublet used as "monochromatic" radiation in this study. The use of a bent-crystal monochromatic might permit narrowing this in future work [7].
2. Spectrometer resolution—slightly skew, with higher intensity on the low-kinetic-energy side, ~0.6 eV FWHM for 1 keV electrons analyzed with 0.06 percent resolution.
3. Hole lifetime in the sample—Lorentzian, ~0.1 to 1.0 eV for the cases studied here.
4. Thermal broadening of the ground state—roughly Gaussian, ~0.1 eV.
5. Inelastic scattering of escaping photoelectrons—all peaks have an inelastic "tail" on the low kinetic-energy side, which usually extends for 10 eV or more.
6. Various effects due to deviations of the final state from a simple one-electron-transition model.

Contributions analogous to (3), (4), and (6) will be common to all techniques used for studying $\rho(E)$. A UPS spectrum will exhibit analogous effects from all six causes. In XPS, there is thus a present lower limit of ~ 1.0 eV FWHM. Core levels with this width are well described by Lorentzian peaks with smoothly joining constant tails [10] (see fig. 1), verifying that the major contribution to linewidth is the exciting x ray. The corresponding lower limit for UPS appears to be 0.2 to 0.3 eV, so that XPS cannot at present be expected to give the same fine structure details as UPS.

The effects of scattering of escaping photoelectrons [(5) above] can be corrected for in both UPS [5] and

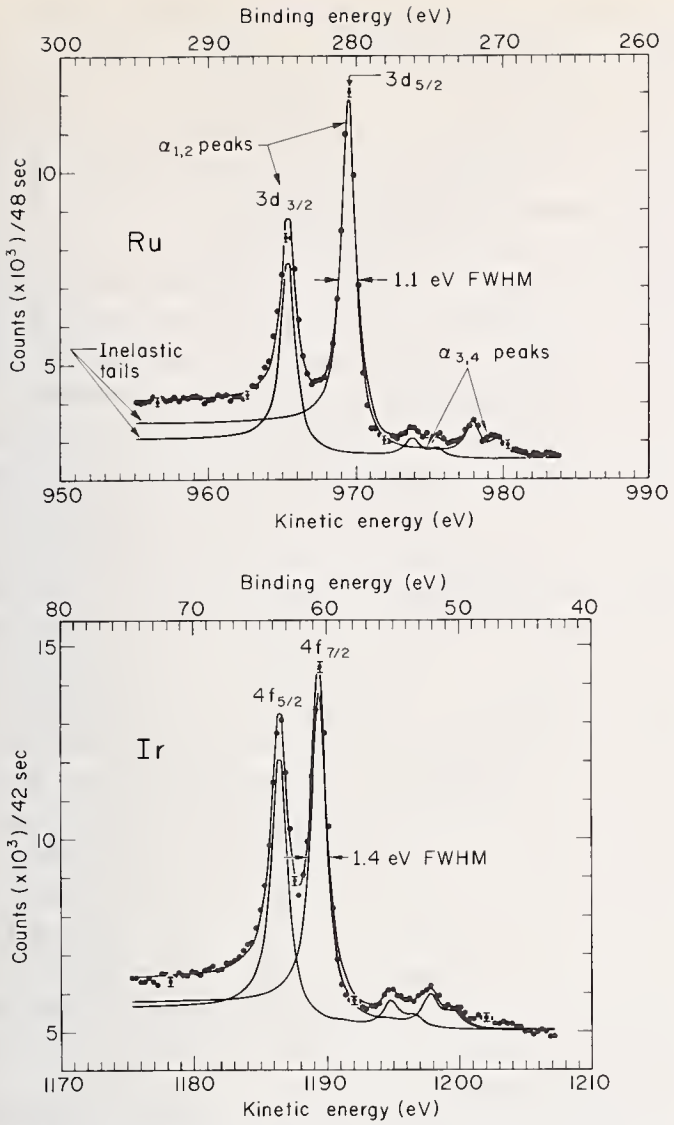

FIGURE 1. *Core level photoelectron spectra produced by exposure of Ru and Ir to Mg x-rays. The levels are Ru* $3d_{3/2}-3d_{5/2}$ *and Ir* $4f_{5/2}-4f_{7/2}$. *The peaks due to the Mg*$K\alpha_{1,2}$ *and Mg*$K\alpha_{3,4}$ *x rays ore noted, as well as the tail observed on each peak due to inelastic scattering. The analysis of these spectra into pairs of Lorentzian-based shapes is described in the text and reference 10.*

XPS [6]. This correction is particularly simple for XPS, however, because narrow core levels can be used to study the scattering mechanisms. As the kinetic energies of electrons expelled from core levels ~100 eV below the valence bands are very near to those of electrons expelled from the valence bands (*i.e*, 1150 eV versus 1250 eV), it is very probable that the scattering mechanisms for both cases are nearly identical.

Subject to this assumption [11], we can correct an observed valence band spectrum, $I_v(\epsilon)$, by using an appropriate core level spectrum, $I_c(\epsilon)$, as a reference [6,10]. If we construct a core level spectrum in the absence of scattering, $I_c'(\epsilon')$, from pure Lorentzian peak shapes, then $I_c(\epsilon)$ and $I_c'(\epsilon')$ can be connected by a response function, $R(\epsilon,\epsilon')$. Since XPS data is accumulated in discrete channels, $I_c(\epsilon)$ and $I_c'(\epsilon')$ can be treated as vectors with typically 100 elements and $R(\epsilon,\epsilon')$ as a 100×100 matrix, these quantities being related by

$$I_c(\epsilon)=R(\epsilon,\epsilon')I_c'(\epsilon'). \tag{3}$$

If we now make certain physically reasonable assumptions about the form of $R(\epsilon,\epsilon')$, the effective number of matrix elements to be computed can be reduced to $\leqslant 100$. This permits a direct calculation of $R(\epsilon,\epsilon')$. The next step is to apply $R^{-1}(\epsilon,\epsilon')$ to the observed valence band spectrum, $I_v(\epsilon)$, to yield the corrected spectrum, $I_v'(\epsilon')$. The Lorentzian widths in $I_c'(\epsilon')$ are selected to be 0.6 to 0.8 times the observed widths so that no appreciable resolution enhancement is accomplished by this correction. In addition to inelastic scattering, we can also easily allow for the extra peaks present in any XPS spectrum due to the satellite x-rays of the anode, the most intense of which are $K\alpha_{3,4}$. In XPS spectra produced by bombardment with magnesium x rays, these satellites produce a doublet approximately 10 eV above the main ($K\alpha_{1,2}$) peak and with about 10 percent of the intensity of the main peak (see fig. 1). The details of this correction procedure are discussed elsewhere [10].

The application of this procedure to data on the valence bands of copper is illustrated in figure 2. The strong similarity between corrected and observed spectra indicates the subtle nature of this correction: the essential shape and position of the *d*-band peak is obvious in the uncorrected spectrum. By comparison, this relatively high information content in raw data is not found in UPS [5] or ion-neutralization spectroscopy [4].

An additional advantage of XPS is that the chemical state of the sample can be monitored via observation of core level photoelectron peaks from the sample and possible contaminants [6]. In this way it is possible to detect chemical reactions occurring in the thin surface

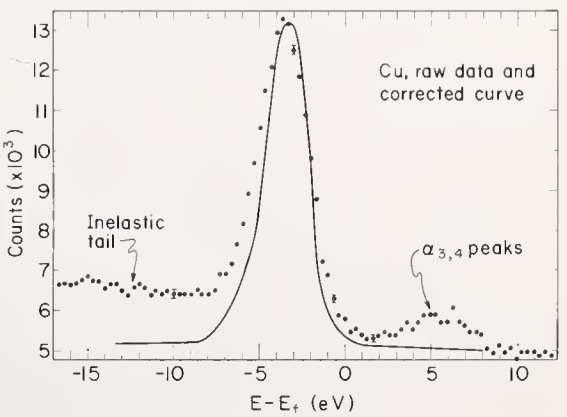

FIGURE 2. *Valence band photoelectron spectrum produced by exposure of Cu to Mg x-rays, together with the corrected spectrum obtained after allowance for the effects of inelastic scattering and Mg*$K\alpha_{3,4}$ *x-rays in the raw data. A peak due to the 3d bands of Cu is the dominant feature of these spectra.*

layer (~100 Å) responsible for the unscattered photoelectrons of primary interest. Furthermore, experimental results for Fe, Co, and Ni indicate that UPS is more sensitive to surface conditions [6,12].

The relationship of corrected XPS spectra to $\rho(E)$ can be considered in two steps: (1) a one-electron-transition model, in which the appropriate transition probability is expressed in terms of the photoelectric cross section, and (2) deviations from the one-electron-transition model.

The cross section for photoemission from a one-electron state j at energy E will be proportional to the square of the dipole matrix element between that state and the final continuum state,

$$\sigma_j(E) \propto |\langle \psi_j | \bar{r} | \psi(h\nu+E) \rangle|^2, \qquad (4)$$

where $\sigma_j(E)$ is the cross section and $\psi(h\nu + E)$ is the wave function of a continuum electron with energy $h\nu + E$. If there are no appreciable deviations of the final state from a one-electron transition model, the corrected kinetic energy spectrum will be related to $\rho(E)$ by

$$I'(h\nu+E-\phi_{sp}) \propto \int_{-\infty}^{\infty} \bar{\sigma}(E')\rho(E')\rho'(h\nu + E')F(E')L(E-E')dE', \qquad (5)$$

where $\bar{\sigma}(E')$ is an average cross section for all states j at E', $\rho'(h\nu + E')$ is the density of final continuum states, $F(E')$ is the Fermi function describing thermal excitation of electrons near the Fermi surface and $L(E - E')$ is the lineshape due to contributions (1), (2), (3), and (4) discussed above (essentially a Lorentzian).

The factor $\rho'(h\nu + E')$ can be considered constant over the energy range pertinent to the valence bands, as the final state electrons are ~1250 eV into the continuum and the lattice potential affects them very little [6,13]. Therefore, the appropriate final state density will be proportional simply to $\epsilon^{1/2}$. This function is only negligibly smaller for electrons ejected from the bottom of the valence bands ($\epsilon \cong 1240$ eV) than for those emitted from the top of these bands ($\epsilon \cong 1250$ eV). This constancy of $\rho'(h\nu+E')$ cannot be assumed in the analysis of UPS data, however [5].

Any changes in $\bar{\sigma}(E)$ from the top to the bottom of the bands will modulate the XPS spectrum in a way not simply connected to $\rho(E)$. From eq (4) it is apparent that these changes can be introduced by variations in either ψ_j or $\psi(h\nu + E)$ across the bands. The differences in ψ_j from the top to the bottom of the $3d$ band in transition metals have been discussed previously [2,14], but no accurate quantitative estimates of this effect on the appropriate dipole matrix elements have been made to date. It is thus possible that in both XPS and UPS, $\bar{\sigma}(E)$ varies substantially from the bottom to the top of the valence bands because of variation in the initial-state wave functions. This question deserves further study. In XPS, there should be little difference in the final-state wave function, $\psi(h\nu + E)$, between the top and bottom of a band, as a 1240 eV continuum state should look very much like a 1250 eV continuum state. The effects of changes in final state wave function on $\bar{\sigma}(E)$ need not be negligible in a UPS spectrum, however.

Our discussion up to this point has assumed that the photoemission process is strictly one-electron; *i.e.*, that we can describe the process by changing the occupation of only a single one-electron orbital with all other orbitals remaining frozen. This assumption permits the use of Koopmans' Theorem [15], which states that binding energies can be equated to the energy eigenvalues arising from a solution of Hartree-Fock equations. Or, with some admitted errors [16], the one-electron energies obtained from non-Hartree-Fock band structure calculations in which simplifying approximations have been made can be compared directly to a measured binding energy spectrum. We illustrate the use of Koopmans' Theorem in figure 3a, using a hypothetical level distribution for a $3d$ transition metal. There are, however, several types of potentially significant deviations from this one-electron model. We shall discuss these briefly.

The final-state effects leading to these deviations can be separated into several categories, although we note that there is considerable overlap. In a more rigorous treatment some of these separations might not be meaningful, but we retain them here for heuristic purposes. The effects are:

(1) Electrons in the sample may be polarized around a localized positive hole, thereby increasing the kinetic energy of the outgoing electron [8]. In this way, the entire $I(\epsilon)$ spectrum would be shifted toward higher kinetic energy. Polarization might also occur to a different extent for different core levels, for different energies within the valence bands, and for levels at the same energy in the valence bands, but with different wave vector. The latter two effects could act to broaden $I(\epsilon)$ relative to $\rho(E)$. These polarization effects are schematically illustrated in figure 3b. Polarizations will only affect $I(\epsilon)$ to the extent that the kinetic energy of the outgoing electron is altered, however (cf. eq (1)). Since both polarization and photoemission occur on a time scale

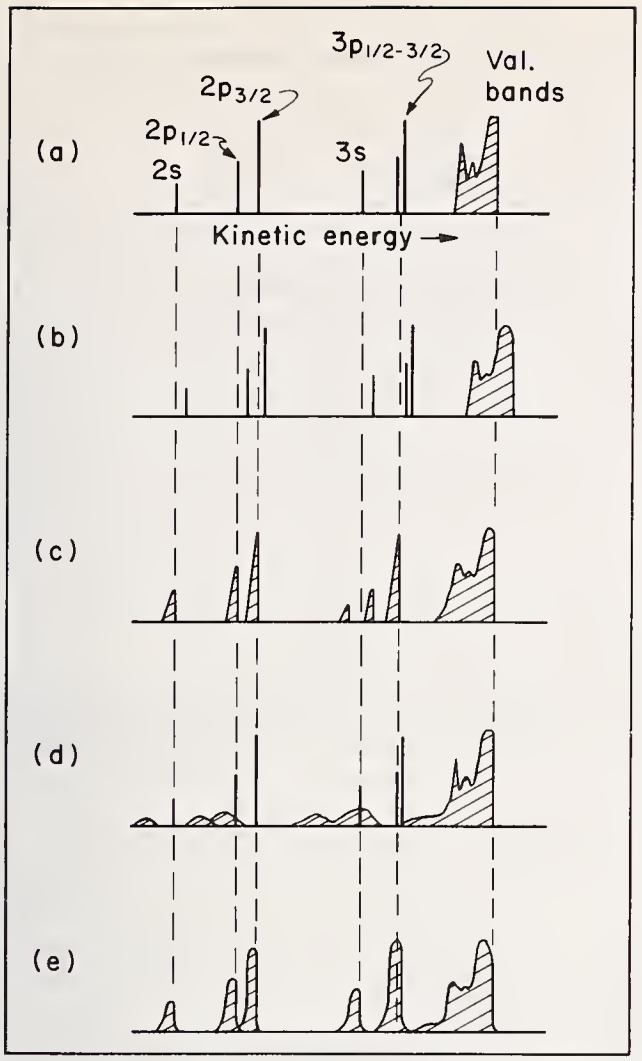

FIGURE 3. *Schematic illustration of various final-state effects on the photoelectron spectrum of a hypothetical 3*d *transition metal: (a) the Koopmans' Theorem spectrum, in which levels are positioned according to one-electron energies, with relative intensities determined by appropriate photoelectric cross sections; (b) the effect on spectrum (a) of polarization around a localized-hole final state; (c) the effect on spectrum (a) of strong coupling between a localized hole and the valence electrons (note the splitting of the 3*s *level); (d) the effect on spectrum (a) of two-electron excitation during photoemission; and (e) the effect on spectrum (a) of phonon excitation during photoemission.*

of $\sim 10^{-16}$ s, it is difficult to assess the importance of this effect. As the velocity of an XPS photoelectron is ~10 times that of a UPS photoelectron, the influence of polarization should be somewhat less on an XPS spectrum, however.

(2) In addition to a simple polarization, a localized hole can couple strongly with localized valence electrons [17] or with nonlocalized valence electrons [18]. In iron metal, for example, a 3*s* hole is found to couple in several ways with the localized *d* electron moment, giving rise to an approximately 4 eV "multiplet splitting" in the 3*s* photoelectron peak [17]. Also, it has been predicted that nonlocalized conduction electrons should couple with a localized core or valence hole yielding asymmetric line shapes in electron and x-ray emission [18]. Both of the above effects would act to broaden $I(\epsilon)$ spectra, with the former being more important for systems with a *d* or *f* shell approximately half-filled. These effects are indicated in figure 3c. It has also been predicted that the removal of a core or valence electron will be accompanied by strong coupling to plasma oscillations [19]. This coupling would lead to broad sidebands separated from the one-electron spectrum by as much as 20 eV [19].

(3) It is also possible that not just one electron is fundamentally affected in the photoemission process, but that other electrons or phonons are simultaneously excited [20]. Electrons may be excited to unoccupied bound states or they may be ejected from the sample, and this effect is indicated in figure 3d. The only direct observations of such electronic excitations during photoemission have been on monatomic gases, where two-electron processes are found with as high as 20 percent probability [21]. Vibrational excitations have a marked effect on the UPS spectra of light gaseous molecules [22], but it is difficult to estimate their importance in solids. A classical calculation indicates that for such heavy atoms as transition metals, the recoil energy available for such excitations in XPS is $\leq 10^{-2}$ eV [7]. Also, the observation of core reference levels with linewidths very close to the lower limit of the technique (see fig. 1) seems to indicate that vibrational excitation does not account for more than a few tenths eV broadening and shifting to lower kinetic energy of features observed in the valence-band region. This effect is schematically indicated in figure 3e.

For several reasons, then, XPS seems to be capable of giving more reliable information about the overall shape of $\rho(E)$ than does UPS. However, the present XPS linewidth limit of 1.0 eV precludes determination of anything beyond fairly gross structural features. With these observations in mind, we now turn to a detailed study of the XPS spectra for several solids. We note also that the XPS method is applied to $\rho(E)$ studies in two other papers of these proceedings [23,24].

3. Density-of-States Results for Several 3*d*, 4*d*, and 5*d* Series Metals

3.1. Introduction

Figure 4 shows the portion of the Periodic Table relevant to this work. The twelve elements Fe, Co, Ni, Cu, Ru, Rh, Pd, Ag, Os, Ir, Pt, and Au were studied as metals, while the three elements Zn, Cd, and Hg were studied in the compounds ZnS, $CdCl_2$, and HgO to illustrate the positions, widths, and shapes of filled core-like 3*d*, 4*d*, and 5*d* shells.

Ultra-high vacuum conditions were not attainable during our XPS measurements, as the base pressure in our spectrometer is approximately 10^{-5} torr. Surface contamination of samples is a potential problem, because the layer of the sample that is active in producing essentially inelastic photoelectrons extends only about 100 Å in from the surface [6,7]. This depth is not accurately known, however. Because the contamination consists of oxide formation as well as certain adsorption processes with lower bonding energy for the contaminant, all the metal samples were heated to high temperature (700 to 900 °C) in a hydrogen atmosphere (10^{-3} to 10^{-2} torr) *during* the XPS measurements [6]. These conditions were found to desorb weakly bound species, and to reduce any metal oxides present.

As mentioned previously, it is possible to do *in situ* chemical analyses of the sample by observing core-level photoelectron peaks from the metal and from all suspected contaminants [6]. For all metals, the most important contaminant was oxygen, which we monitored via the oxygen 1*s* peak. Because core electron binding energies are known to be sensitive to the chemical state of the atom [7,25], the observation of core peaks for metal and oxygen should indicate something about the surface chemistry of the sample. The intensities of contaminant peaks should also be a good indicator of the amounts present. Figure 5 shows such results for iron. At room temperature, the oxygen 1*s* peak is strong, and it possesses at least two components. The iron 3*p* peak is also complex and appears as a doublet due to oxidation of a thin surface layer of the sample. As the temperature is increased in the presence of hydrogen, the oxygen peak disappears (the right component disappearing first) and the left component of the iron peak also disappears, leaving a narrow peak characteristic of iron metal. Our interpretation of the disappearing components is that the left oxygen peak (higher electron binding energy) represents oxygen as oxide, the right oxygen peak (lower electron binding energy) represents oxygen present as more loosely bound adsorbed gases, and that the left iron peak (higher electron binding energy) represents oxidized iron [6,25]. Thus at the highest temperatures indicated in figure 5, we could be confident that we were studying iron metal. Similar checks were made on all the other metal samples and oxygen can be ruled out as a contaminant for every case except Pd. (We discuss Pd below.) For example, the core level peaks for Ru and Ir shown in figure 1 do not indicate any significant splitting or broadening due to chemical reaction. The results presented in table 1 indicate similar behavior for all metals studied. The carbon 1*s* peak was also observed and found to disappear for all cases at the temperature of our measurements.

26 $3d^6 4s^2$	27 $3d^7 4s^2$	28 $3d^8 4s^2$	29 $3d^{10} 4s^1$	30 $3d^{10} 4s^2$
Fe	Co	Ni	Cu	Zn
bcc	fcc	fcc	fcc	--
44 $4d^7 5s^1$	45 $4d^8 5s^1$	46 $4d^{10}$	47 $4d^{10} 5s^1$	48 $4d^{10} 5s^2$
Ru	Rh	Pd	Ag	Cd
hcp	fcc	fcc	fcc	--
76 $5d^6 6s^2$	77 $5d^9$	78 $5d^{10}$	79 $5d^{10} 6s^1$	80 $5d^{10} 6s^2$
Os	Ir	Pt	Au	Hg
hcp	fcc	fcc	fcc	--

FIGURE 4. *The portion of the periodic table studied in this work. The atomic number, free-atom electronic configuration, and metal crystal structures are given. Zn, Cd, and Hg were studied as compounds. The crystal structures are those appropriate at the temperatures of our metal experiments (700-900 °C).*

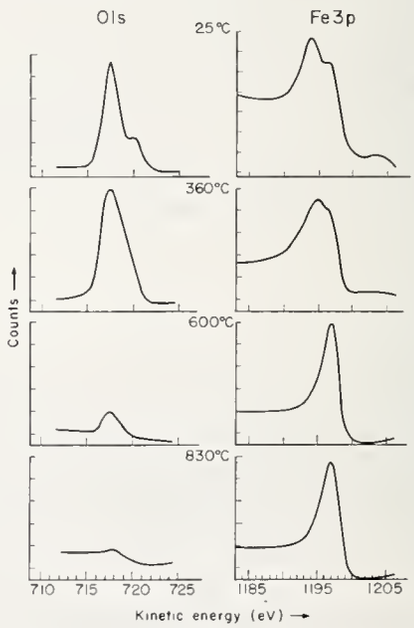

FIGURE 5. *Oxygen 1s and 3p photoelectron peaks from metallic iron at various temperatures in a hydrogen atmosphere. Note that the Fe 3p component at lower kinetic energy (an "oxide" peak) disappears at high temperature along with the 01s peaks. MgKα radiation was used for excitation throughout the work reported here.*

TABLE 1. *Summary of pertinent results for the fifteen solids studied.*

The reference core levels used for inelastic scattering correction are listed, along with their binding energies and widths. The widths of the *d*-band peaks are also given, along with the spacing of the two components in these peaks (if observed).

Solid	Reference core levels	Ref. core level binding energy [a] (eV)	FWHM of core levels [b] (eV)	FWHM of *d*-band peak (eV)	Separation of 2 components in *d*-band peak (eV)
Fe	$3p_{1/2-3/2}$ (unresolved) [c]	52	2.3	4.2	.....
Co	$3p_{1/2-3/2}$ (unresolved) [c]	57	2.5	4.0	.....
Ni	$3p_{1/2-3/2}$ (unresolved) [c]	66	3.4	3.0	.....
Cu	$3p_{1/2-3/2}$ (unresolved) [c]	75	4.2	3.0	.....
ZnS	$3p_{1/2-3/2}$ (unresolved) [c]	90	5.4	1.7	.....
Ru	$3d_{3/2-5/2}$	280	1.1	4.9	.....
Rh	$3d_{3/2-5/2}$	307	1.3	4.4	.....
Pd	$3d_{3/2-5/2}$	335	1.3	4.1	.....
Ag	$3d_{3/2-5/2}$	368	1.0	3.5	1.5–1.8
$CdCl_2$	$3d_{3/2-5/2}$	408	1.2	2.0	.....
Os	$4f_{5/2-7/2}$	50	1.3	6.5	.....
Ir	$4f_{5/2-7/2}$	60	1.4	6.3	3.3
Pt	$4f_{5/2-7/2}$	71	1.5	5.8	3.3
Au	$4f_{5/2-7/2}$	84	1.2	5.7	3.1
HgO	$4f_{5/2-7/2}$	103	1.5	3.8	1.8

[a] Binding energy of the $l + 1/2$ component, relative to the Fermi energy.
[b] Equal widths assumed for both components in the least-squares fits for $3d$ and $4f$ levels.
[c] The theoretical spin-orbit splitting for the $3p$ levels in this series range from 1.6 eV for Fe to 3.1 eV for Zn (Ref. 36). The partially resolved doublet in ZnS is found to have a separation of 2.8 eV, in good agreement.

All metals were studied as high purity polycrystalline foils, except for Ru and Os, which were studied as powders [10].

The nonmetallic samples (ZnS, $CdCl_2$, and HgO) were studied as powders at room temperature. Both considerations of chemical stability and observations of core levels indicated no significant surface contamination, although high purity for these cases was not of paramount importance.

The results reported here were obtained with 1.25 keV Mg$K\alpha$ radiation for excitation. However, no significant changes are introduced with Al$K\alpha$ radiation of 1.49 keV energy.

We present below our experimental results for these *d* group metals, as well as the results of other experiments and theory. Statistical error limits are shown on all XPS results. Throughout our discussion, we shall speak of "$\rho(E)$" as determined by a certain technique, bearing in mind that no experimental technique directly measures $\rho(E)$, but rather some distribution peculiar to the experiment (*e.g.*, the UPS "optical density of states" [5], or the INS "transition density function" [4]), which is related to $\rho(E)$ in some way (*e.g.*, by our eq (5)).

The location of the Fermi energy was determined by using eq (2). This determination was checked against photoelectron peaks from a Pt standard [10]. Our estimated overall accuracy in determining E_f is ± 0.5 eV, so that precise comparison of features in XPS spectra with features present in the results of other experiments (all of which have roughly the same E_f accuracy) is not always possible.

Finally, we note that the dominant feature in our results for all cases is a peak due to the bands derived from *d* atomic orbitals. The XPS method is not particularly sensitive to the very broad, flat, *s*- or *p*-like bands in metals, and such bands are seen with enhanced sensitivity only in studies using ion-neutralization spectroscopy [4].

3.2. The 3*d* Series: Fe, Co, Ni, Cu and Zn

Our results for Fe, Co, Ni, and Cu have been published elsewhere [6], but it is of interest to compare them with more recent results from theory and other experiments [3,12]. There are now enough data available that it is worthwhile to discuss and compare results for these iron group metals individually, as Eastman [12] has done.

a. Iron (bcc)

Hanzely and Liefeld [3] have studied Fe, Co, Ni, Cu, and Zn using soft x-ray spectroscopy (SXS). Their results for Fe, together with Eastman's UPS results [12] and our own, are plotted in figure 6a. In comparing the three $\rho(E)$ curves we note that their relative heights and areas have no significance: we have adjusted the heights to be roughly equal, in order to facilitate comparison. Also the UPS curve is terminated at E_f and is less reliable in the dashed portion, for $E < E_f - 4$ eV [12]. With these qualifications, the overall agreement

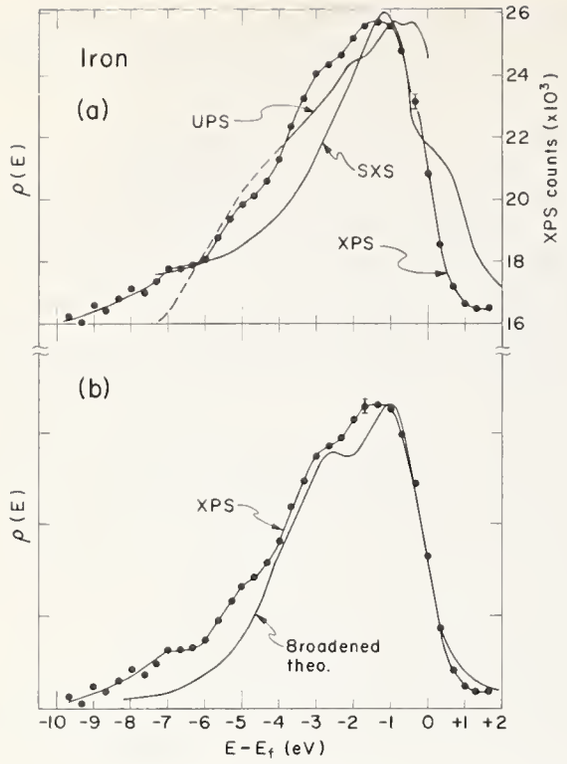

FIGURE 6. *Results for iron metal. The XPS data were obtained ot 780 °C and have been corrected for the effects of inelastic scattering and MgK$\alpha_{3,4}$ x-rays. In (a) the XPS dota ore compored with UPS (ref. 12) ond SXS (ref. 3) curves. In (b) the XPS dato ore shown together with a theoretical curve obtained by broadening the ferromagnetic density-of-states function of reference 26. Right ordinate is thousands of counts in the XPS dota*

among these results from three different experimental methods is really quite good. The function $\rho(E)$ appears to be essentially triangular, peaking just below E_f and dropping more or less linearly to zero at $E \sim E_f - 8$ eV.

Upon closer inspection however, the agreement is less impressive. The SXS results are somewhat narrower, but with more intensity *above* E_f, probably due to spurious effects [3]. There is little coincidence of structure, although the maxima for XPS and SXS coincide fairly well. A shift of ~1 eV of the XPS curve toward E_f or the UPS curve in the opposite direction would improve their agreement, but it is unlikely that the combined errors in the location of E_f location are that great.

In figure 6b, the XPS results are compared to the one-electron theoretical $\rho(E)$ calculated by Connolly [26] for ferromagnetic iron. The theoretical $\rho(E)$ has been smeared at the Fermi surface with a Fermi function corresponding to the temperature of our experiment (780 °C) and then broadened with a Lorentzian lineshape of 1.0 eV FWHM. It should thus represent a hypothetical "best-possible" XPS experiment in a one-electron model (*i.e.*, eq (5) with $\bar{\sigma}(E')$ and $\rho'(h\nu + E')$ constant). The agreement between theory and experiment is good, particularly above $E_f - 5$ eV. The XPS (or SXS) results give somewhat higher intensity below $E_f - 5$ eV than theory. We note that hybridization of the d bands can lead to significant broadening of the theoretical $\rho(E)$ of Ni [14]. A similar sensitivity of the iron $\rho(E)$ to the amount of hybridization could account for the discrepancy in width between XPS and theory.

Our reason for comparing experimental results to *ferro*magnetic instead of *para*magnetic theoretical predictions is as follows: In experiments on ferromagnetic metals, no significant differences are observed between XPS [6, 17] and INS [4] results obtained above and below the Curie temperature (T_c, where long-range ferromagnetic order should disappear). Furthermore, exchange-induced splittings of core electronic levels in iron are the same above and below T_c [17]. It thus appears that localized moments persist above T_c for times at least as long as the duration of the photoemission process. Local moments might be expected to affect the kinetic energy distributions of electrons ejected from valence bands and core levels [17] in much the same way, independent of the presence of long range order. Thus a comparison of experiment with a paramagnetic $\rho(E)$ may be *a priori* irrelevant, inasmuch as a ferromagnetic $\rho(E)$ takes these effects into account in an approximate way. Eastman [12] has also noted that UPS results for Fe, Co, and Ni *below* T_c are in general in better agreement with ferromagnetic theoretical $\rho(E)$'s than with similar paramagnetic theoretical results. Accordingly, we shall compare our results only with ferromagnetic theoretical curves for Ni and Co in the next sections.

b. Cobalt (fcc)

The experimental situation is illustrated by the three density-of-states curves in figure 7a. The comparison is quite similar to that for iron. Good overall agreement is apparent, with less agreement in detail. Eastman's UPS curves [12] in both cases show structure near the Fermi energy that is missing from the SXS [3] and XPS results, and at lower energies the UPS curve tends to be higher than the others, especially in the dashed portion where it is less reliable [12]. In this region the XPS curve lies between the other two for Co as well as for Fe. One index of agreement among the three curves in the full width at half-maximum height, which is about 3, 4, and 5 eV for SXS, XPS, and UPS, respectively.

In figure 7b, we compare our XPS results to a ferromagnetic theoretical curve of Wong, Wohlfarth, and Hum [27] for *hcp* Co (our experiments were done on *fcc* Co, for which no detailed theoretical results are available). The theoretical curve has been broadened in an analogous fashion to that for iron. The agreement

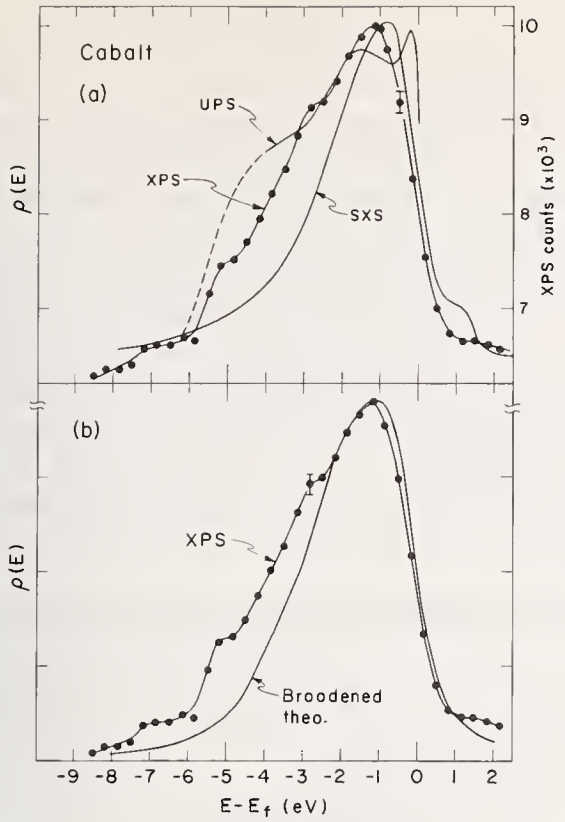

FIGURE 7. *Results for cobalt metal. The XPS data were taken at 925 °C and have been corrected for inelastic scattering and MgKα₃,₄ x-rays. In (a) these data are compared with UPS (ref. 12) and SXS (ref. 3) results. In (b) the comparison is with an appropriately broadened ferromagnetic theoretical curve from reference 27.*

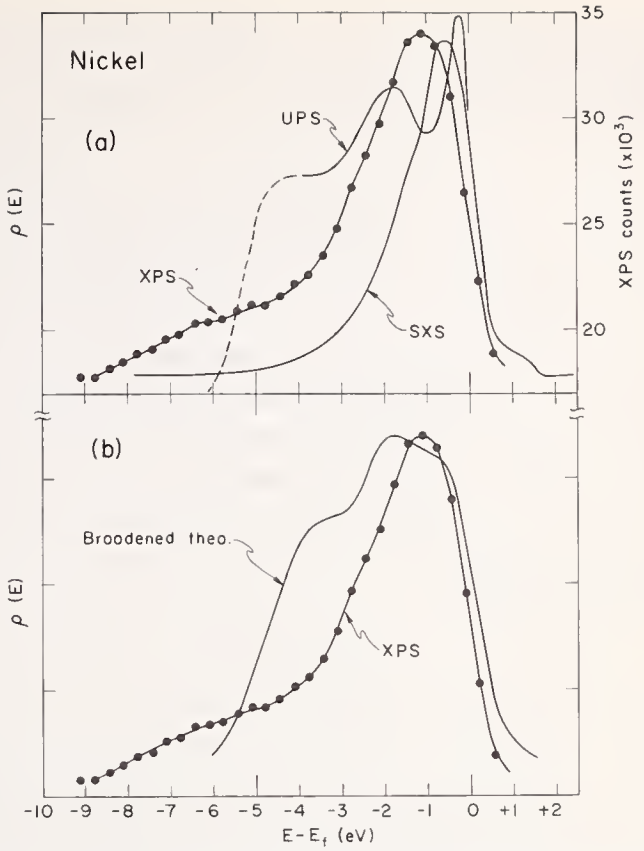

FIGURE 8. *Results for nickel metal. The corrected XPS data are based on measurements at 870 °C. In (a) they are compared with UPS (ref. 12) and SXS (ref. 3) curves. In (b) they are compared to the ferromagnetic theoretical density-of-states function from reference 14, which has been broadened.*

is good for E > E_f−3 eV, but the XPS results are somewhat high below that point. In fact, the overall agreement is probably best between theory and SXS (cf. fig. 7a).

c. Nickel (fcc)

Experimental results for Ni are presented in figure 8a [3,12]. We note a slight decrease in the XPS results in the region $E < E_f - 4$ eV relative to our earlier work [6]. This decrease is due to a more accurate allowance for a weak inelastic loss peak appearing at ~5 eV below the primary photoelectron peaks. The three sets of data show poor agreement, with the widths of the main peak decreasing in the order UPS, XPS, SXS. The SXS results are considerably narrower than the other two (FWHM ≈2 eV, 3 eV, and 5 eV for SXS, XPS, and UPS, respectively), but agree in overall shape with XPS. The SXS results in figure 8a were obtained from measurements of L x rays [3]. Similar work on M x rays (for which transition probability modulation may be a smaller effect [2]) shows somewhat more fine structure and a FWHM of ~3 eV [2], agreeing rather well with XPS. Nickel has also been investigated by INS [4] and a smooth peak of roughly the same position and width as the XPS peak is observed. Even with an allowance for the poorer resolution of XPS, the two peaks appearing in the UPS results are not consistent with the XPS curve.

The various theoretical $\rho(E)$ estimates for Ni have been discussed previously [2,12]. The FWHM of these estimates vary from ~3 to 4.5 eV, with the smallest width coming from an unhybridized calculation [14]. In figure 8b, we compare our XPS results to a hybridized, ferromagnetic $\rho(E)$ for Ni [14] which has been broadened in the same manner as those for Fe and Co. It is clear that the XPS results are too narrow (though they would agree in width with the unhybridized $\rho(E)$ [14]), and that, allowing for our broadening, the UPS results are in best agreement with theory. In view of the considerable discrepancies between UPS and XPS, SXS, or INS, however, we conclude that Ni does not represent a particularly well-understood case, in contrast with Eastman's conclusions [12].

d. Copper (fcc)

The experimental curves from UPS [12,28], SXS [3], and XPS are shown in figure 9a. There is agreement in that all curves show a peak between 2.3 and 3.3

eV below E_f, but with UPS showing more detailed structure and a somewhat uncertain overall width [12,28]. The widths and shapes of XPS and SXS are in good agreement though shifted relative to one another by ~1 eV. (A more accurate E_f location has shifted our XPS curve relative to our previous results [6].) In recent UPS work at higher photon energy ($h\nu = 21.2$ eV), Eastman [29] has obtained results with more intensity in the region 2.5 to 4.0 eV below E_f and which agree very well in shape and width with XPS and SXS. For this case it appears that even a slight increase in photon energy in the UPS measurement causes the results to look a great deal more like those of XPS. Copper has also been studied in INS [4] and the results for the d-band peak are in essential agreement with XPS and SXS.

In figure 9b, we compare a broadened version of the theoretical $\rho(E)$ due to Snow [30] with our XPS results. The agreement is excellent, and would also be so for SXS if we permit a shift of ~1 eV in E_f. The coincidence in energy of structure in the UPS curve with structure in the unbroadened theoretical $\rho(E)$ has been discussed previously [28], but we note that the relative intensities of the various features noted do not in fact coincide with theory.

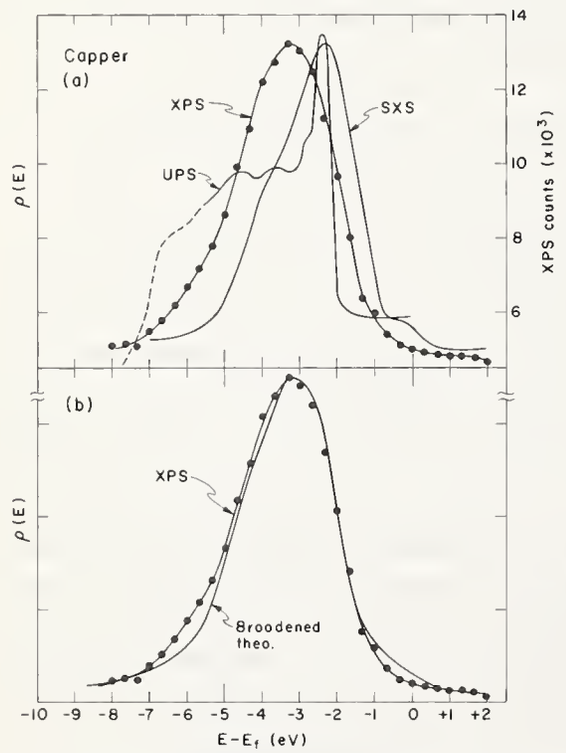

FIGURE 9. *Results for copper metal. The XPS data were obtained at 720 °C and have been corrected for inelastic scattering and* $MgK\alpha_{3,4}$ *x-rays. Curves from UPS (refs. 12 and 28) and SXS (ref. 3) are compared to the XPS results in (a). In (b) the XPS results are compared to a broadened theoretical curve based on reference 30.*

e. Zinc (as ZnS)

Zinc has been studied by XPS only in compounds, because of the difficulty of obtaining a clean metallic surface. We present results for ZnS in figure 10. The 3d electronic states show up as a narrow intense peak with a FWHM of 1.7 eV and located ~13 eV below E_f. (The separation of this peak from E_f may be too large, because of charging of the sample [25].) The valence bands are just above the d peak. The d states of metallic zinc have been studied also by SXS [3], and a peak of FWHM = 1.45 eV, at 8 eV below E_f, was obtained. Thus XPS and SXS are in good agreement on the width of these core-like 3d states, which are only about 10 eV below E_f.

3.3. The 4d Series: Ru, Rh, Pd, Ag and Cd

The corrected XPS spectra for the four metals Ru, Rh, Pd, and Ag are shown in figure 11. The metals are discussed separately below.

a. Ruthenium (hcp)

Our results for Ru are characterized by a single peak of ~4.9 eV FWHM. The high energy edge is quite sharp, reaching a maximum value at about $E_f - 1.7$ eV. The peak is rather flat, and there is some evidence for a shoulder at $E_f - 4.5$ eV. The peak falls off more slowly with energy on the low energy side than near E_f. The reference core level widths in Ru were quite narrow, as indicated in table 1, and spurious effects due to surface contamination are unlikely. There are no other experi-

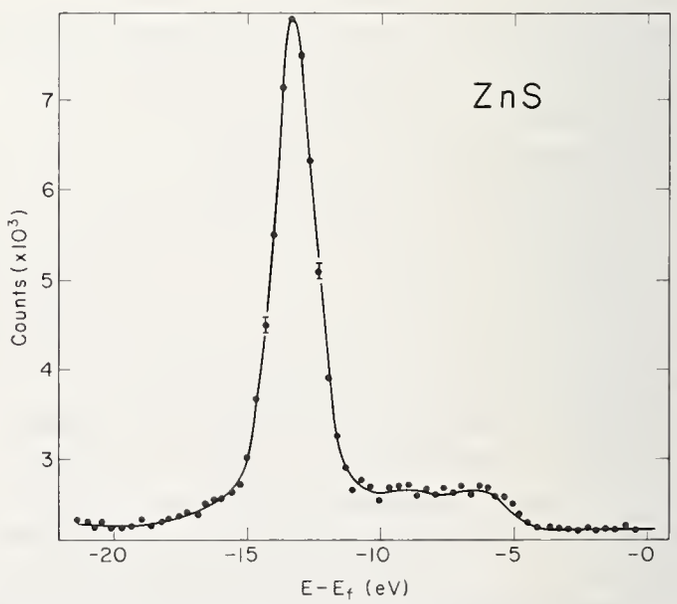

FIGURE 10. *Corrected XPS spectrum for ZnS, showing a narrow intense peak from the* 3d *levels, as well as the broad, flat valence bands.*

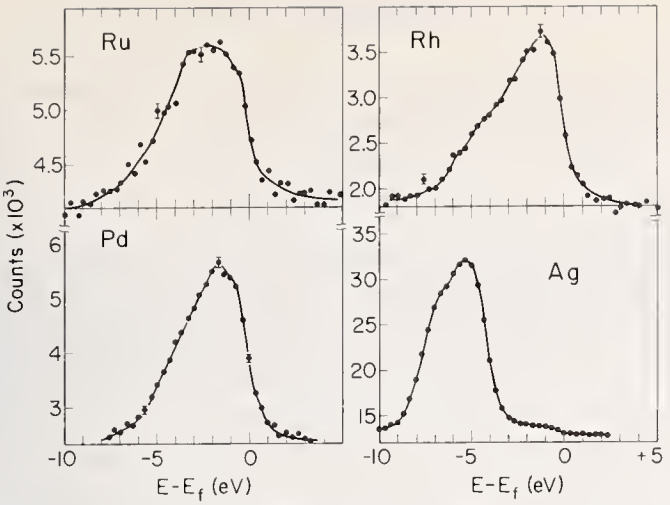

FIGURE 11. *Corrected XPS spectra for the 4d metals Ru, Rh, Pd, and Ag.*

mental or theoretical results on Ru presently available for comparison with our data.

b. Rhodium (fcc)

The XPS-derived $\rho(E)$ can be described by a single triangular peak, very steep on the high energy side, and reaching a maximum at $E_f - 1.3$ eV. There is little evidence for structure on the low energy side, which falls off monotonically. The peak FWHM of ~4.4 eV is slightly smaller than that for Ru. No other experimental or theoretical results on Rh are available for comparison.

c. Palladium (fcc)

Our corrected results for Pd have much the same appearance as those for Rh, but the Pd peak is slightly narrower with a FWHM of ~4.1 eV and the maximum occurs at $E_f - 1.7$ eV. The high-energy edge of the Pd peak is very steep, and most of the slope must be instrumental. Therefore, as expected, the true $\rho(E)$ for Pd is apparently very sharp at E_f.

The results presented in figure 11 have been corrected for a weak inelastic loss peak at 6 eV, and also for the presence of a small peak at $E_f - 10$ eV, arising from oxygen present as a surface contaminant. Samples of Pd were heated in hydrogen to approximately 700 °C and then studied at this temperature with either a hydrogen or argon atmosphere. It was not possible under these conditions (or even by heating to as high as 900 °C) to get rid of the oxygen 1s peak completely. Fortunately, the only effect of a slight oxygen contamination on the valence band XPS spectrum of certain metals appears to be a sharp peak at $E_f - 10$ eV (probably caused by photoemission from 2p-like oxygen levels). We have also observed this effect for slightly oxidized Cu. Thus we were able to correct our Pd results for this peak (which does not affect the region shown in fig. 11). A recently obtained uncorrected XPS spectrum for Pd is in good agreement with our results [31].

Palladium has also been studied by UPS [32,33], and the agreement with XPS is good in general outline. However, the precise shape of the UPS results below approximately $E_f - 3.5$ eV is uncertain [32,33].

In figure 12, we compare our results with the theoretical predictions of Freeman, Dimmock, and Furdyna [34]. The upper portion of the figure shows the fine structure of their $\rho(E)$ histogram and in the lower portion we compare our results to the broadened theoretical curve. The agreement between XPS and theory is good, although the shape of the peak is somewhat different.

d. Silver (fcc)

Our results for Ag also appear in figure 11. They differ in several respects from the Pd curve. The *d* bands are filled and below E_f, giving rise to a narrow peak (FWHM = 3.5 eV) with its most intense component at $E_f - 5.3$ eV. The edges of this peak are quite sharp, in view of the instrumental contributions of XPS.

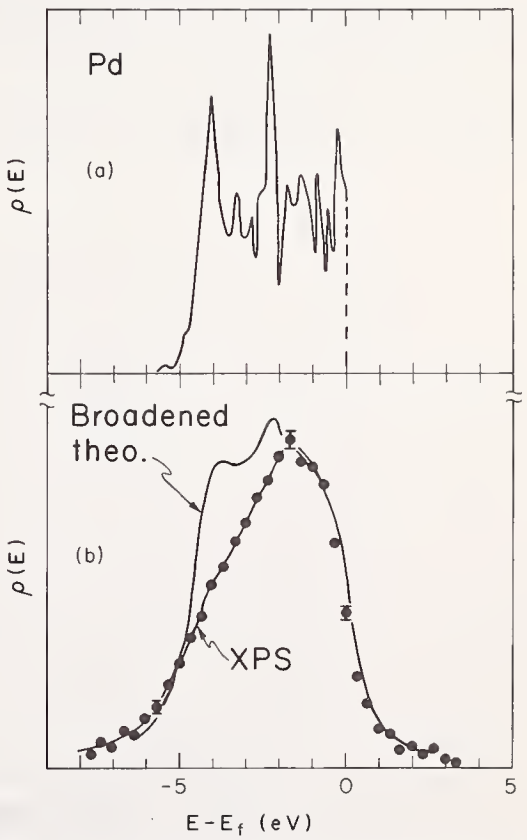

FIGURE 12. *Comparison of Pd XPS results with theory: (a) theoretical density-of-states function from reference 34, indicating the complexity of the one-electron* ρ(E), *(b) XPS results and a broadened theoretical curve.*

The $3d_{3/2}$ and $3d_{5/2}$ levels of Ag are also very narrow (see table 1), indicating no spurious linewidth contributions from instrumental or contamination effects. There is also strong evidence for a weaker component at $\sim E_f - 6.6$ eV. This two-component structure has also been verified by Siegbahn and co-workers in uncorrected XPS spectra [7,31]. Very similar structure appears in the d bands of several $5d$ metals and we discuss the possible significance of this below (sec. 3.5).

Silver has also been studied by means of UPS [5,29,35], using radiation up to 21.2 eV [29] in energy. The results of these studies (in particular those attained at 21.2 eV) are in essential agreement with our own, in that they show a peak of ~3 eV FWHM at $E_f - 5.0$ eV.

No theoretical $\rho(E)$ predictions for Ag are available at the present time.

e. Cadmium (as $CdCl_2$)

A corrected XPS-spectrum for $CdCl_2$ is shown in figure 13. The $4d$ peak appears at $\sim E_f - 14.5$ eV and the valence bands fall between roughly 5 and 10 eV below E_f. The $4d$ peak is very narrow (a FWHM of 1.7 eV, compared to 3.5 eV for Ag). As these d levels are quite strongly bound, we expect them to behave as core states, and perhaps to exhibit spin-orbit splitting (into $d_{3/2}$ and $d_{5/2}$ components). There is no evidence for splitting of this peak, but its shape is consistent with a theoretical free-atom prediction of only a 0.8 eV spin-orbit splitting [36]. The analogous $5d$-series levels in HgO do exhibit resolvable spin-orbit splitting, however (sec. 3.4.e).

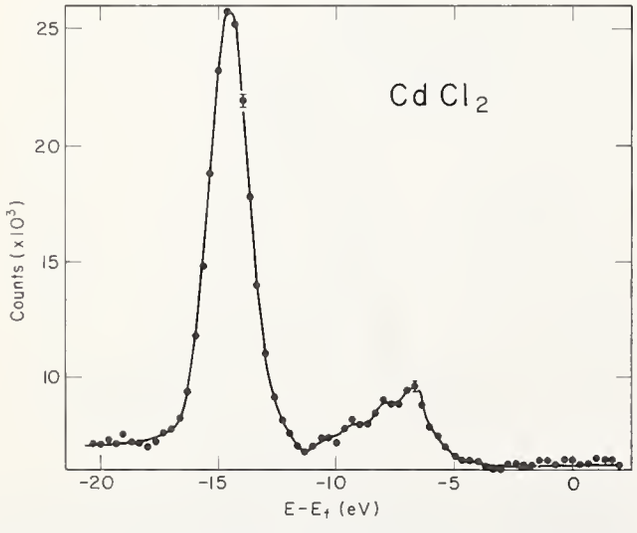

FIGURE 13. *Corrected XPS spectrum for $CdCl_2$. The filled 4d states appear at $E\text{-}E_f \approx -14.5$ eV. The broader peak at $E\text{-}E_f \approx -7$ eV represents valence bands.*

3.4. The $5d$ Series: Os, Ir, Pt, Au, and Hg

The corrected XPS spectra for the metals Os, Ir, Pt, and Au are shown in figure 14.

a. Osmium (hcp)

Hexagonal Os gives a valence band spectrum similar to that of hexagonal Ru. As in the Ru case, the Os peak rises sharply near E_f to a plateau beginning at $E_f - 1.7$ eV. The flat region of the Os peak extends over approximately 3 eV, and is broader than that for Ru. No comparisons with theory or other experiments are possible as yet.

The low energy tail of the Os peak does not fall to the base line primarily because of spurious photoelectron intensity in the valence band region due to the proximity of the very intense Os$4f$ levels in energy (see table 1). These core levels appear to interact with very weak Mg x rays whose energies are as high as ~1300 eV, giving rise to photoelectrons in the same kinetic energy region as valence bands interacting with the 1250 eV Mg$K\alpha_{1,2}$ x rays. Similar problems were encountered with Ir, but they do not affect our conclusions as to peak shapes and structure. An additional problem was encountered in correcting for the Mg$K\alpha_{3,4}$ x rays in both Os and Ir, as the low intensity $5p_{1/2}$ and $5p_{3/2}$ photoelectron peaks overlap the $\alpha_{3,4}$ regions of the reference $4f$ peaks. For example, this effect appears as a slight deviation of the data from the fitted function near a kinetic energy of 1202 eV in figure 1. However, the $\alpha_{3,4}$ correction is a small one and could nonetheless be made with sufficient accuracy not to affect our fundamental conclusions.

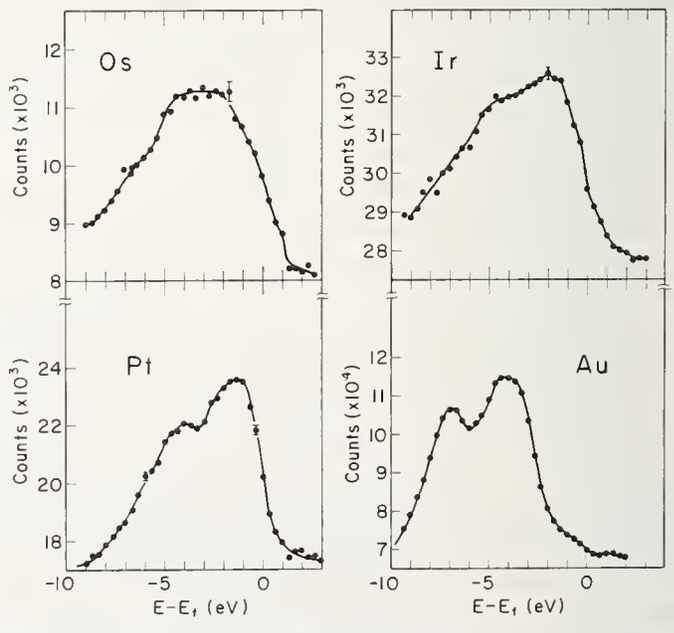

FIGURE 14. *Corrected XPS spectra for the 5d metals Os, Ir, Pt, and Au.*

b. Iridium (fcc)

The corrected XPS results for iridium are similar to those of Os in overall shape and width, but give evidence for two peaks, at approximately $E_f - 1.5$ eV and $E_f - 4.5$ eV. This two-peak structure is even clearer in the uncorrected XPS spectrum for Ir shown in figure 15. The higher-energy peak appears to be narrower, and, with allowance for this, we estimate the two peaks to be of roughly equal intensity.

c. Platinum (fcc)

Our corrected XPS results for Pt exhibit two partially-resolved peaks at $E_f - 1.6$ eV and $E_f - 4.0$ eV, with the more intense component lying nearer E_f. The steep slopes of our spectra for both Ir and Pt near E_f are consistent with the Fermi surface cutting through the d bands in a region of very high $\rho(E)$. The separations of the two components observed in the d bands are thus very nearly equal for Ir and Pt, but the relative intensities are different.

Theoretical results are available for Pt. The band-structure calculations of Mueller et al. [37] are shown in figure 16, together with our data. The theoretical $\rho(E)$ is also shown after broadening, to facilitate comparison. We note that both theory and experiment show roughly two major peaks but that the relative intensities are in poor agreement. The disagreement as to shape is the same as that observed for Pd in figure 12. (Relative intensities are arbitrary in both of these figures.) In addition, the band-structure calculations give a total width at half height of 8 eV, while the XPS data show a width of only 6 eV. Thus the overall agreement is only fair.

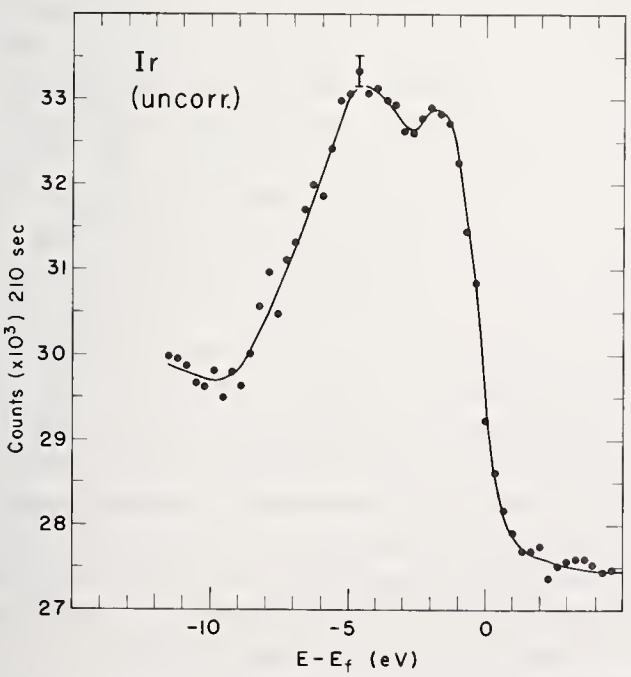

FIGURE 15. *Uncorrected XPS spectrum for Ir, in which the two-peak structure is clearly shown.*

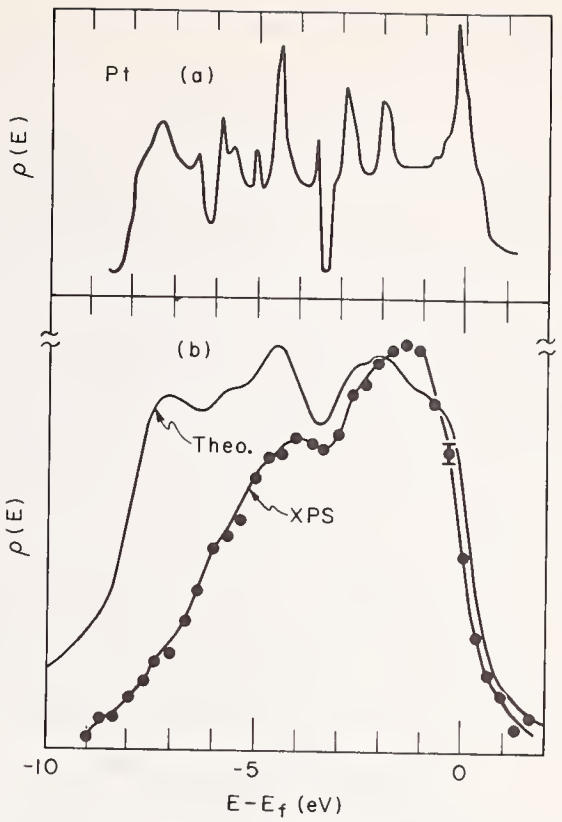

FIGURE 16. *Comparison of Pt XPS results with theory: (a) the theoretical density-of-states function of reference 37, (b) the broadened theoretical curve is compared to our XPS results.*

d. Gold (fcc)

The d bands of gold are filled and should lie several eV below E_f, as our results in figure 14 indicate. Two peaks are again evident in the corrected XPS results for gold, and these have been verified in uncorrected XPS spectra obtained by Siegbahn and co-workers [7,31]. The statistical accuracy of our data is quite good, and we can say that the lower intensity peak at $E_f - 6.8$ eV is narrower than the higher intensity peak at $E_f - 4.1$ eV. Apart from this, the shape of the d-band peak for Au is very similar to that for Pt.

Gold has also been studied by means of UPS [29,38]. In experiments at photon energies up to 21.2 eV [38], a two-peak structure is found, with components at $E_f - 3.4$ eV and $E_f - 6.1$ eV. The component at -3.4 eV is also observed to be split into a doublet [38], perhaps accounting for its extra width in the XPS results. Furthermore, a spectrum obtained with $h\nu = 26.9$ eV [29] (but not corrected for inelastic scattering) looks very much like our XPS results, again indicating that with increase in photon energy, UPS results converge rather quickly to those of XPS.

There are no theoretical $\rho(E)$ estimates at present available for Au.

e. Mercury (as HgO)

In HgO, the filled $5d$ levels should be tightly-bound and core-like. Figure 17 shows a corrected XPS spectrum for HgO, in which the $5d$ levels appear as a doublet whose components lie 13.6 and 12.0 eV below E_f. Valence bands overlap the high energy edge of the d peaks and extend to $E_f - 5$ eV. The intensity ratio of the two $5d$ peaks, as derived by least-squares fitting of Lorentzian curves to our data, is 1.4:1.0. The separation and intensity ratio are consistent with a $d_{3/2} - d_{5/2}$ spin-orbit doublet, as the free-atom theoretical prediction is for a 2.1 eV separation [36] and the intensity ratio should be given by the level multiplicities (*i.e.*, 6:4 = 1.5:1.0). (We have verified that the intensity ratios for the $3d_{3/2} - 3d_{5/2}$ core levels of the $4d$ metals in table 1 follow this rule to within experimental accuracy (± 0.1).) Thus the $5d$ levels of HgO appear to be very core-like. Furthermore, the relative intensity of the two components in the doublet is similar to those observed in Pt and Au. We discuss the possible implications of this similarity in the next section.

3.5. Discussion of Results

The XPS results for all 15 cases studied are presented in figure 18. In table 1 are given the binding energies and widths of the reference core levels used for correcting valence band spectra, as well as the width of the peak due to the d bands and (where observed) the separation of the two primary components in this peak.

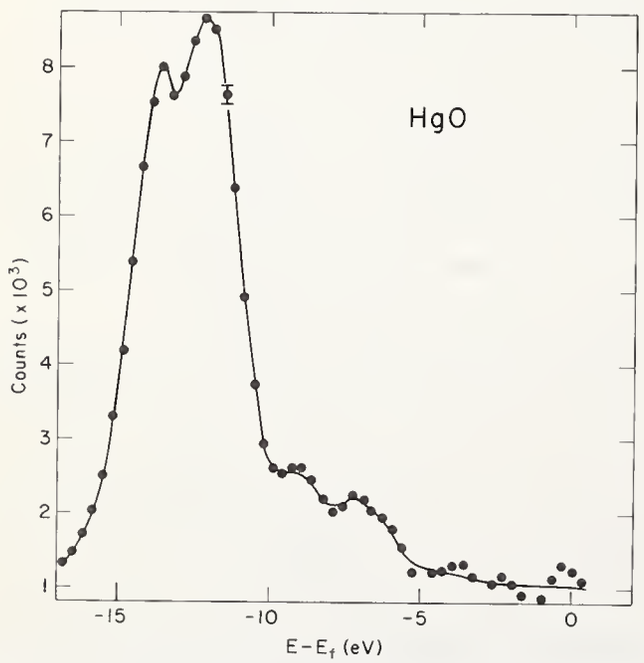

FIGURE 17. *Corrected XPS spectrum for HgO. The intense doublet at* $E\text{-}E_f \approx -12$ *eV is due to the core-like* $5d_{3/2}$ *and* $5d_{5/2}$ *states.*

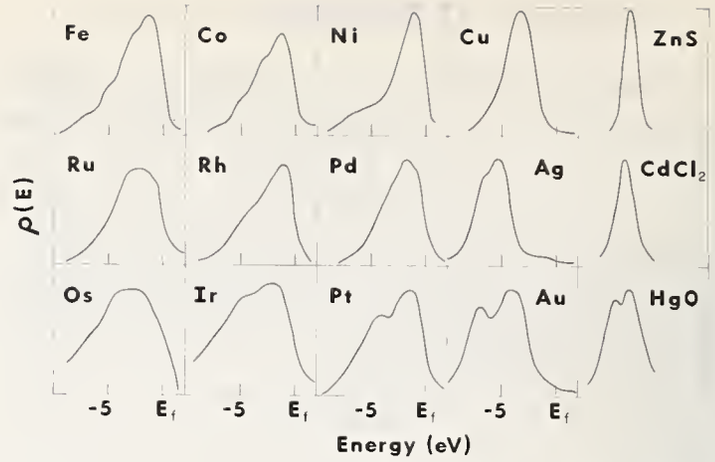

FIGURE 18. *Summary of the XPS results for the fifteen solids studied (cf. table 1). The peaks for ZnS,* $CdCl_2$*, and HgO lie at* $E\text{-}E_f \approx -13$ *eV,* -14 *eV, and* -12 *eV, respectively.*

Within a $3d$, $4d$, or 5d series, the XPS results show systematic variation, giving somewhat wider d bands for Fe, Ru, and Os than for Cu, Ag, and Au, respectively, and even narrower core-like states ~10 eV below E_f for ZnS, $CdCl_2$, and HgO. Much of this variation is no doubt connected with a one-electron $\rho(E)$, but we note also that experimental spectra obtained from metals with partially filled d bands might be broadened by the coupling of a localized hole to localized d electrons [17] (see fig. 3c and sec. 2). The $4d$ bands studied are only slightly wider than their $3d$ counterparts; the $5d$ bands are considerably wider and show gross structure.

Within two isomorphous series—Rh, Pd, Ag and Ir, Pt, Au, all members of which are face-centered cubic—there is sufficient similarity of the shapes of the d-band peaks to suggest a rigid-band model for $\rho(E)$. If $\rho(E)$ of Ag(Au) can be used to generate $\rho(E)$ of Rh and Pd (Ir and Pt) simply by lowering the Fermi energy to allow for partial filling of the d bands, then this model would apply. The peaks for Rh and Pd are too wide to be represented by a Ag $\rho(E)$, but the shapes of both could be very roughly approximated in this manner. The similarity of the two-peak structure for the three metals Ir, Pt, and Au gives more evidence for the utility of a rigid band model, especially as the uncorrected results for Ir (fig. 15) show a narrower peak near E_f (as though it were a broader peak cut off by the Fermi energy). The application of this model to the prediction of the experimental $\rho(E)$'s for Ir and Pt is shown in figure 19. The predictions are reasonably good. In our opinion, this limited success for Ir, Pt and Au probably indicates some similarity in the d bands in these metals, but we

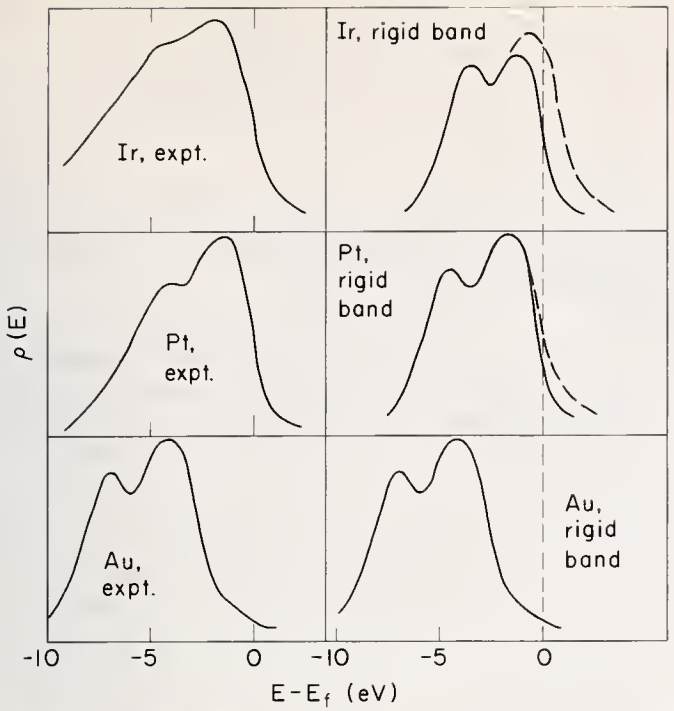

FIGURE 19. *An attempt to reproduce the shapes of the experimental XPS spectra for the 5d metals Ir, Pt, and Au from a Au-like rigid band density of states. Vertical scales are arbitrary. Note that the Ir experimental curve does not fall to as low a value as Pt or Au at low energy due to spurious sources of photoelectron intensity (see text).*

do not take it as a verification of the rigid band model *per se*.

The two-component structure observed in the *d*-band peaks of Pt and Au is very similar to the unresolved structure found in Ag. That is, a more intense component appears nearer E_f. To estimate the intensity ratios of these components more accurately, we have least-squares fitted two Gaussian peaks of equal width to our data for these three metals. The ratios and separations so derived are: Ag—1.51:1.00, 1.8 eV; Pt—1.60:1.00, 3.3 eV; and Au—1.48:1.00, 3.1 eV. As our accuracy in determining these ratios is $\sim \pm 0.1$, they could all be represented by a value of 1.50:1.00. A possible significance of this value is that it is the expected (and observed) intensity ratio for a spin-orbit split *d* level (e.g., the 5*d* levels of HgO). Thus, one might argue that as the 4*d* and 5*d* shells move nearer to the Fermi surface with decreasing Z, they must go continuously from core states to valence states, perhaps retaining some degree of simple spin-orbit character in the process. The observed separations are 1.5—2.5 times larger than free-atom theoretical spin-orbit splittings [36], but the various perturbations of the lattice might be responsible for this. Speaking against such a simple interpretation, however, is our observation (verified in UPS results [29,38]) that for Au the component nearer E_f is broader. In fact, the UPS results for $h\nu \leq 21.2$ eV show this component split into two peaks [29,32]. In view of this, our intensity ratio estimates based on two peaks of equal width may not have fundamental significance, and the agreement of these ratios, particularly between Ag and Pt or Au could be somewhat accidental. Nonetheless, the similarity in shape of our results for the *d* levels of Ag, Pt, Au, and Hg is rather striking.

We have noted that for Cu, Ag, and Au, the recent UPS work of Eastman [29] at higher photon energies (21.2 to 26.9 eV) is in much better agreement with XPS results than previous studies using a range of lower photon energies [28,35,38]. It thus appears that *as the photon energy is increased in a UPS experiment, the form of the energy distributions can be expected to approach rather quickly that observed in XPS work. We feel that photoelectron spectra for which XPS and UPS show agreement ought to be much more closely related to ρ(E).* Further UPS experiments at greater than 20 eV photon energies would thus be most interesting.

4. Concluding Remarks

We have discussed the use of x-ray photoelectron spectroscopy (XPS) in the determination of densities of states. The application of this technique to the *d* bands of 12 metals and 3 nonmetallic solids seems to indicate that reliable information about the overall shape of $\rho(E)$ can be obtained. The results show systematic behavior with changes in Z and crystal structure and agree qualitatively and in some cases quantitatively with theoretical predictions for both unfilled valence *d* levels and filled core-like *d* levels.

Throughout our discussion, we have placed special emphasis on comparison of XPS with the closely related ultraviolet photoelectron spectroscopy (UPS). It appears that UPS at the present time has an advantage in resolution, but that XPS results can be more easily corrected for inelastic scattering, are not significantly affected by final state density, and are less susceptible to the effects of surface contaminants. UPS results at photon energies $\geq$20 eV appear to be more reliable indicators of $\rho(E)$ in the sense that they agree better with the rough outline predicted by XPS. The need for further work at higher resolution and at all photon energies (including those in the relatively untouched range from 20 to 1250 eV) is evident.

5. Acknowledgments

The authors wish to thank W. E. Spicer, D. E. Eastman, S. Doniach, F. M. Mueller, A. J. Freeman and F. Herman for fruitful discussions relating to this work.

417-156 O - 71 - 13

6. References

[1] We shall use the term "valence bands" for those occupied electronic states that are derived principally from atomic valence shell orbitals.

[2] Cuthill, J. R., McAlister, A. J., Williams, M. L., and Watson, R. E., Phys. Rev. **164,** 1006 (1967).

[3] Hanzely, S., and Liefeld, R., this Symposium.

[4] Hagstrum, H. D., Phys. Rev. **150,** 495 (1966); Hagstrum, H. D., and Becker, G. E., Phys. Rev. **159,** 572 (1967); and Hagstrum, H. D., this Symposium.

[5] Berglund, C. N., and Spicer, W. E., Phys. Rev. **136,** A1030 and A1044 (1964); and Spicer, W. E., this Symposium.

[6] Fadley, C. S., and Shirley, D. A., Phys. Rev. Letters **21,** 980 (1968); and Fadley, C. S., and Shirley, D. A., J. Appl. Phys. **40,** 1395 (1969).

[7] Siegbahn, K. *et al.*, Electron Spectroscopy for Chemical Analysis, (Almqvist and Wiksells AB, Stockholm, Sweden, 1967).

[8] Spicer, W. E., Phys. Rev. **154,** 385 (1967).

[9] Siegbahn, K., Nordling, C., and Hollander, J. M., Lawrence Radiation Laboratory Report **UCRL-10023** (1962).

[10] Fadley, C. S., Ph. D. dissertation, University of California, Berkeley, 1970 (Lawrence Radiation Laboratory Report **UCRL-19535** (1970)).

[11] We note that such level-specific effects as two-electron transitions (see ref. 21) and core-electron binding energy splittings (see ref. 17) may render invalid the assumption that the tail behind a core level photoelectron peak is due entirely to inelastic scattering. However, if such effects are significant, they will generally result in noticeable peaks in the tail. The only peaks observed for the cases studied here were weak and can be explained as inelastic plasma losses. Therefore, we expect level-specific effects to have negligible influence on the results under discussion. They should be noted as a possible source of error in this correction procedure, however.

[12] Eastman, D. E., and Krolikowski, W. F., Phys. Rev. Letters **21,** 623 (1968); and Eastman, D. E., J. Appl. Phys. **40,** 1387 (1969).

[13] Baer, Y., Physik der Kondensierten Materie **9,** 367 (1969).

[14] Hodges, L., Ehrenreich, H., and Lang, N. D., Phys. Rev. **152,** 505 (1966).

[15] Callaway, J., Energy Band Theory (Academic Press Inc., New York, 1964), p. 117.

[16] Herman, F., Ortenburger, I. B., and Van Dyke, J. P., to appear in Intern. J. of Quant. Chem., **Vol. IIIS.**

[17] Fadley, C. S., Shirley, D. A., Freeman, A. J., Bagus, P. S., and Mallow, J. V., Phys. Rev. Letters **23,** 1397 (1969).

[18] Doniach, S., and Sŭnjić, to appear in J. Phys., and Doniach, S., to be published.

[19] Hedin, A. L., Lundqvist, B. I., and Lundqvist, S., Sol. State Comm. **5,** 237 (1967) and this Symposium.

[20] Nesbet, R. K., and Grant, P. M., Phys. Rev. Letters **19,** 222 (1967).

[21] Carlson, T. A., Phys. Rev. **156,** 142 (1967).

[22] Turner, D. W., Ch. 3 in Physical Methods in Advanced Inorganic Chemistry, M. A. O. Hill and D. Day, Editors, (Interscience Publishers, Inc., London, 1968).

[23] Broden, G., Heden, P. O., Hagström, S. B. M., and Norris, C., this Symposium.

[24] Chan, D., and Shirley, D. A., this Symposium.

[25] Fadley, C. S., Hagström, S. B. M., Klein, M. P., and Shirley, D. A., J. Chem. Phys. **48,** 3779 (1968).

[26] Connolly, J. W. D., this Symposium. (These results have also been presented in ref. 12.)

[27] Wong, K. C., Wohlfarth, E. P., and Hum, D. M., Phys. Letters **29A,** 452 (1969).

[28] Krolikowski, W. F., and Spicer, W. E., Phys. Rev. **185,** 882 (1969).

[29] Eastman, D. E., private communication, to be published.

[30] Snow, E. C., Phys. Rev. **171,** 785 (1968).

[31] Siegbahn, K., private communication.

[32] Yu, A. Y-C., and Spicer, W. E., Phys. Rev. **169,** 497 (1968).

[33] Janak, J. F., Eastman, D. E., and Williams, A. R., this Symposium.

[34] Freeman, A. J., Dimmock, J. O., and Furdyna, A. M., J. Appl. Phys. **37,** 1256 (1966) and private communication.

[35] Krolikowski, W. F., and Spicer, W. E., unpublished results.

[36] Herman, F., and Skillman, S., Atomic Structure Calculations (Prentice-Hall Inc., Engelwood Cliffs, New Jersey, 1963).

[37] Mueller, F. M., Garland, J. W., Cohen, M. H., and Benneman, K. H., to be published; and Mueller, F. M., this Symposium.

[38] Krolikowski, W. F., and Spicer, W. E., to be published.

Discussion on "Electronic Densities of States from X-Ray Photoelectron Spectroscopy" by C. S. Fadley and D. A. Shirley (University of California, Berkeley)

F. J. Blatt *(Michigan State Univ.):* Have you ever seen anything which resembles an Auger effect in photoemission?

D. A. Shirley *(Univ. of California):* We have seen Auger peaks. We can identify them by using exciting radiation of two different energies.

Direct-Transition Analysis of Photoemission from Palladium

J. F. Janak, D. E. Eastman, and A. R. Williams

IBM Thomas J. Watson Research Center, Yorktown Heights, New York 10598

The energy distribution of optically excited electrons in Pd arising from direct interband transitions has been calculated assuming constant momentum matrix elements. Principal features of new photoemission data (*d*-band structure with four peaks at 0.15, 1.2, 2.2, and 3.5 eV below the Fermi level and a *d*-band width of ~3.8 eV) are successfully explained by these calculations. The data can be analyzed with comparable success using the nondirect-transition model, but only by assuming a free-electron density of unoccupied states, which is shown to be unjustified for Pd. In addition to the photoemission spectra and the density of states, the imaginary part of the dielectric constant is computed and compared with experiment.

Key words: Copper; dielectric constant; direct interband transitions; electronic density of states; interband transition; Korringa-Kohn-Rostoker (KKR); "muffin-tin" potential; palladium (Pd); photoemission; plasmon; secondary emission; silver (Ag).

1. Introduction

Subsequent to the interpretation of the optical properties of Cu and Ag by Ehrenreich and Phillip [1] in terms of direct, or **k**-conserving, interband transitions a controversy has arisen over the applicability of the direct transition model to photoemission data. Although there had been no reflectance data which contradicted the model, the failure of early attempts to account for the characteristic behavior of photoemission data (the linear shift of structure with photon energy) led Spicer and others [2–4] to postulate an alternative model based on nondirect (**k** not conserved) transitions. While photoemission data for several transition metals have been successfully fit using this model [5], it has proven very difficult to account theoretically for the postulated nondirect transitions.

We show, via a first-principles calculation of the optically excited electron spectra in Pd, that the direct-transition model is capable of explaining the dominant features (viz, structure in the energy distribution, and the frequency dependence of the quantum yield) of new photoemission results for Pd. Similar results obtained by Smith and Spicer for Cu [6] (using a histogram technique employed earlier by Brust [7]) and recent data for Au [8], suggest that the optical excitations involved in photoemission from metals are due to direct transitions, at least in the transition and noble metals. The nondirect transition model shows comparable success in fitting the experimental data, but only if a smooth unoccupied density of states is postulated; the latter assumption is inconsistent with the calculated density of states in palladium (see fig. 1). Both analyses

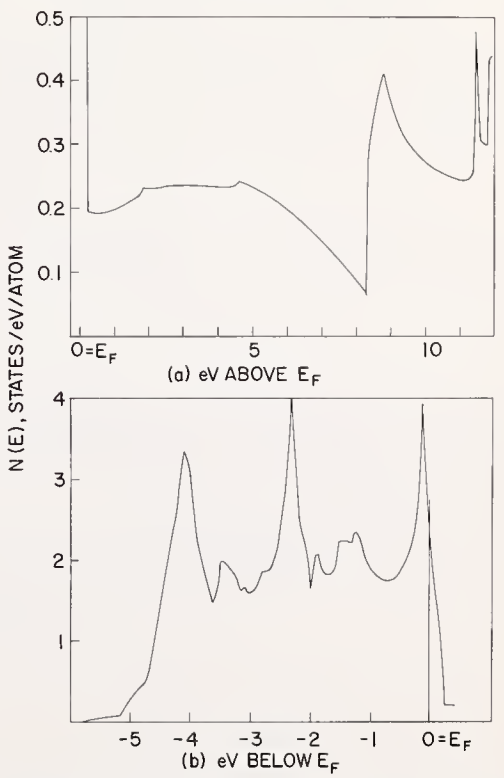

FIGURE 1. *Density of states (both spins) of* Pd *(a) above, and (b) below the Fermi level* [$N(E_f)=2.28$ *states/eV/atom*].

indicate a d-band width of ~3.8 eV for Pd, with four peaks in the density of ~0.15, 1.2, 2.2, and 3.5 eV below the Fermi level.

The quantities considered in this paper are the density of states $N(E)$, the optical absorption $\epsilon_2(\omega)$, and the photoemission energy distribution. The density of states is given by

$$N(E) = \frac{1}{4\pi^3} \sum_n \int d^3k \delta(E - E_n(\mathbf{k})) = \frac{1}{4\pi^3} \sum_n \int_{E-E_n(k)} \frac{dS_n}{|\nabla_k E_n|} \tag{1}$$

and, except for a constant factor,

$$\omega^2 \epsilon_2(\omega) = \sum_{nn'} \int d^3k f_n (1 - f_{n'}) |\langle n\mathbf{k}|\mathbf{p}|n'\mathbf{k}\rangle|^2 \delta(E_{n'}(\mathbf{k}) - E_n(\mathbf{k}) - \hbar\omega), \tag{2}$$

where f_n is the Fermi function, $E_n(\mathbf{k})$ the energy at $\mathbf{k}$ in band n, and $\hbar\omega$ the photon energy. We shall assume that the momentum matrix element $|\langle n\mathbf{k}|\mathbf{p}|n'\mathbf{k}\rangle|^2$ is a constant independent of n, n', and $\mathbf{k}$.

Our direct-transition photoemission analysis assumes a three-step process [2] consisting of (1) excitation via direct interband transitions; (2) hot-electron transport to the surface; and (3) escape into vacuum. The first step is described by the energy distribution $D(E,\omega)$ of optically excited electrons arising from direct interband transitions:

$$D(E, \omega) = \sum_{nn'} \int d^3k f_n (1 - f_{n'}) |\langle n\mathbf{k}|\mathbf{p}|n'\mathbf{k}\langle|^2 \delta(E - E_{n'}(\mathbf{k})) \delta(E - \hbar\omega - E_n(\mathbf{k})), \tag{3}$$

where E is the energy of the excited electron. In this equation, the first δ-function ensures that only final states of energy E are considered, while the second δ-function expresses conservation of energy for the excitation process; the Fermi functions guarantee that the initial state $|n\mathbf{k}\rangle$ is filled and the final state $|n'\mathbf{k}\rangle$ is empty. Note that $D(E,\omega)$ is a density function for the optical absorption:

$$\omega^2 \epsilon_2(\omega) = \int_{E_f}^{\infty} D(E, \omega) dE \tag{4}$$

The second and third steps in the photoemission process have been analyzed using the assumptions described by Berglund and Spicer [2], which include isotropic scattering of the hot electrons, and a free-electron surface escape probability (momentum escape cone). According to this model the transport and escape processes factorize into a hot-electron transport factor $T(\mathbf{k},E,\omega)$ (which describes the $\mathbf{k}$-dependence of the group velocity) and an energy-dependent surface escape probability. Integration over the $\mathbf{k}$-dependence of the excitation and transport processes leads to the energy distribution $D'(E,\omega)$ of the fraction of optically excited electrons per absorbed photon which reach the crystal surface:

$$D'(E, \omega) = \left\{ \int_{E_f}^{\infty} D(E', \omega) dE' \right\}^{-1} \sum_{nn'} \int d^3k f_n (1 - f_{n'}) |\langle n\mathbf{k}|\mathbf{p}|n'\mathbf{k}\rangle|^2 \delta(E - E_{n'}(\mathbf{k})) \delta(E - \hbar\omega - E_n(\mathbf{k})) T(\mathbf{k}, E, \omega) \tag{5}$$

The first factor in cq (5) normalizes $D'(E,\omega)$ to a single absorbed photon and the hot-electron transport factor T is defined in eq (12). The emission intensity $N(E,\omega)$, including once-scattered electrons, is then given by

$$N(E, \omega) = T_f (1 - T_f) \left\{ \tilde{D}'(E, \omega) + \int_E^{\hbar\omega + E_f} S_{ee}(E', E) \tilde{D}'(E', \omega) dE' \right\} \tag{6}$$

Here

$$T_f = \frac{1}{2} \left[1 - \left(\frac{\phi - E_f}{E - E_f} \right)^{1/2} \right] \qquad (E > \phi) \tag{7}$$

is the surface escape probability for free electrons (ϕ is the work function), $\tilde{D}'(E,\omega)$ is the lifetime-broadened D', and $S_{ee}(E',E)$ is the probability distribution for secondary internal electrons of energy E produced by a primary electron at energy E' (eq (38) in [2] and eq (17) in [9]). The energy distributions $D'(E,\omega)$ are convolved with lifetime-broadening Lorentzians to account for many-electron interactions. The first and second terms in eq (6) correspond respectively to the emission of primary electrons and secondary electrons arising from a single pair-creation process [2]. The quantity $N(E,\omega)$ is the photoemission energy distribution to be compared with experiment.

Our method of computing D and D' is described in section 2; the remaining steps in the analysis are described in section 3. Our results are described in section 3 and conclusions are summarized in section 4.

2. Computational Details

The energy distribution $D(E,\omega)$ of optically excited electrons is given in eq (3).

Each of the δ-functions in this equation defines an energy surface, and the integral can thus be rewritten as a line integral along the curve of intersection of these two surfaces:

$$D(E,\omega)=\sum_{nn'}\int dl\,\frac{|\langle n\mathbf{k}|p|n'\mathbf{k}\rangle|^2}{|\nabla_k E_n x\nabla_k E_{n'}|} \tag{8}$$

$$(E_{n'}(\mathbf{k})=E>E_f,\ E_n(\mathbf{k})=E-\hbar\omega\leq E_f)$$

Our method of computing this integral is an extension of the Gilat-Raubenheimer [10] procedure of replacing an integral over a single δ-function (as in the density of states) by a sum over small cubes in each of which an energy surface like $E_n(\mathbf{k})=E$ is approximated by a plane:

$$E=E_n(\mathbf{k}_0)+(\mathbf{k}-\mathbf{k}_0)\cdot\nabla_k E_n(\mathbf{k}_0),$$

where k_0 is the cube center. The density of states at energy E, for example, becomes the sum over cubes of the areas of the plane within each cube divided by $|\nabla_k E_n(\mathbf{k}_0)|$. Given accurate values of the energies and gradients at each cube center, it is found that 10,100 cubes in 1/48 of the fcc Brillouin zone are necessary to give the density of states over a range of energies with an rms error of less than 1 percent, although the relative error could be larger for a particular energy where the surfaces are small or highly curved. (It should be noted that the problem of loss of relative accuracy of volume integrals which are numerically small because the contributing subvolume is small is not unique to the Gilat-Raubenheimer procedure or our generalization of it. It can be avoided only by holding the number of mesh points roughly constant in the contributing volume, whatever its size. Thus, for example, histogram techniques also have this problem.)

Our generalization of this procedure to integrals containing two δ-functions, such as that in eq (3), consists of approximating both energy surfaces in a given cube by planes and computing the integral along the straight line of their intersection. The integral in eq (3) thus becomes the sum over cubes of the length of the line of intersection in each cube weighted by $|\nabla_k E_n x\nabla_k E_{n'}|^{-1}$ evaluated at the cube center.

This procedure depends on having a formula for the length of an arbitrary line within a cube, which is obtained as follows: let the line be given by

$$\mathbf{k}=\mathbf{d}+\mathbf{v}t,\ (\mathbf{d}\cdot\mathbf{v}=0) \tag{9}$$

with respect to the cube center ($\mathbf{v}$ is a unit vector along the line, and $\mathbf{d}$ is the shortest vector from the cube center to the line). If the cube edge is 2b, a portion of the line will lie within the cube if and only if there is a range of values of t for which the three inequalities

$$-b\leq d_i+v_i t\leq b,\ i=1,2,3 \tag{10}$$

are simultaneously satisfied. Each inequality defines a lower limit l_i and an upper limit u_i on t. If

$$t_1=\min\ (u_1,u_2,u_3),\ t_2=\max\ (l_1,l_2,l_3), \tag{11}$$

a portion of the line lies in the cube if, and only if, $t_1>t_2$, and the length of this portion is simply t_1-t_2. Thus eqs (10) and (11), along with the geometry required to find $\mathbf{d}$ and $\mathbf{v}$ in terms of the equations for the planes, furnish a method of computing the integral in eq (3).

The method replaces a smooth curve by a number of straight-line segments, and the cubes must be chosen small enough to ensure that each curve of intersection is replaced by enough segments. For cubes of a given size, the error is largest where the curvature is largest; just as in the density of states, this will usually occur for energies where a contribution from a particular band pair has just begun to appear or is about to disappear, i.e., for those cases where the length of the entire curve of intersection becomes comparable to the cube size. The largest relative errors produced by the method will therefore occur where the contribution to $D(E,\omega)$ is small. This is illustrated in figure 2, which compares the exact $D(E,\omega)$ to the computed $D(E,\omega)$ for the test case ($\mathbf{k}$ in units of $2\pi/a$)

$$E_1(k)=2k_xk_y+k_z^2;$$

$$E_2(k)=2k_x'k_y'+k_z'^2$$

$$k_i'=1-k_i$$

$$\omega=1.5\,Ry,\ E_f=0.7\,Ry.$$

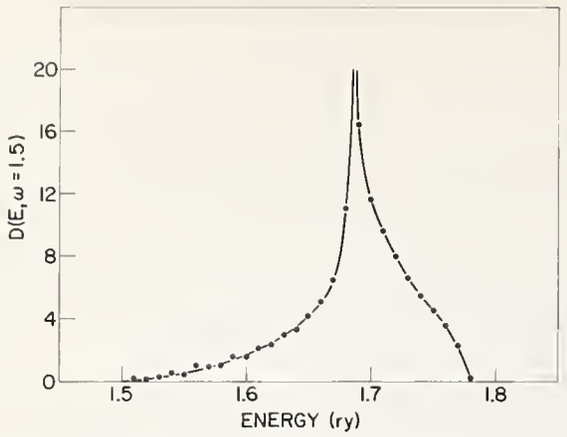

FIGURE 2. *Test of integration procedure for saddle-point singularity.*
Solid curve is analytic result; points are computed using the algorithm described in the text.

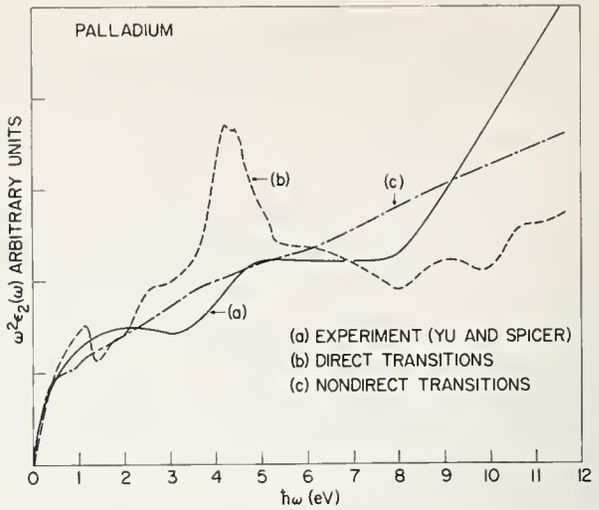

FIGURE 3. *Comparison of $\omega^2\epsilon_2(\omega)$ for direct transitions (b) and nondirect transitions (c) with experiment (a)[16].*
The ordinate is given in arbitrary units for both calculated curves.

This pair of bands has no physical significance; it simply forms a convenient test. For this case, for which $D(E,\omega)$ can be worked out analytically, a saddle-point (logarithmic) [11] singularity occurs at $E = 1.6875$ Ry. The only appreciable errors in the computations occur for the lower energies, where the curve of intersection passes through just a few cubes. In practice, it appears that 10,100 cubes in 1/48 of the fcc Brillouin zone (48 cubes along $\Gamma - X$) are adequate to give the line integral within an error of about 5% which is sufficiently accurate for our purposes.

The energies and gradients required by the method were obtained by first computing the energies of 3345 points in 1/48 of the Brillouin zone using the $4d^{10}$ — configuration Hartree-Fock-Slater potential [12] for atomic Pd, and the nonrelativistic KKR method of band calculation (a summary of computation times is given in table 1). The energies and gradients on the finer mesh were then obtained by 27-point Lagrangian interpolation [13]. The large number of KKR points is required to get good interpolated energies and gradients for palladium (the rms interpolation error in energy is $\sim 5 \times 10^{-4}$ Ry, the maximum interpolation error in energy is $\sim 5 \times 10^{-3}$ Ry, and the rms interpolation error in the gradient is $\sim 1 \times 10^{-3}$ Ry/$(2\pi/a)$). The maximum error in the interpolated energies increases rapidly as the number of KKR points is decreased (for example, the energies interpolated from 3345 KKR points differ by as much as 0.05 Ry from those interpolated from 89 KKR points in palladium).

TABLE 1. *CPU times on the IBM System/360 Model 91*

1. 3345 KKR energies for 9 bands.....30 min
2. Interpolation to 10,100 energies and gradients.....30 s
3. Density of states, 20 V energy range in steps of 0.068 V (9 bands).....30 s
4. Photoemission EDC's, 12 V energy range in steps of 0.05 V (9 bands).....3 s/value of ω
5. Construction of first 12 difference bands (from tape created in step 2).....20 s
6. Evaluation of $\epsilon_2(\omega)$: 8 V range in steps of 0.136 V (12 bands).....20 s

The density of states of palladium, computed using existing Gilat-Raubenheimer programs [14], is shown in figure 1. The most surprising feature of this density of states is the rather large amount of structure for energies about E_f, particularly the pronounced dip at 8.3 eV above E_f. Thus, the density of excited one-electron states in Pd is by no means free-electron-like.

We have also computed $\epsilon_2(\omega)$, the imaginary part of the dielectric constant, assuming direct transitions and constant matrix elements of momentum. This quantity, which is shown in figure 3, was obtained by forming the difference in energies and gradients for various band pairs, and then computing the density of states of the difference bands. Because interpolation errors are magnified in taking differences, this calculation is less accurate than the ordinary density of states.

To construct theoretical EDC's for photoemission, we need not only the energy distribution of optically excited electrons, but also the fraction of these per absorbed photons which reach the crystal surface. $D'(E,\omega)$, as defined in eq (5), includes the hot-electron transport factor [2]

$$T(\mathbf{k}, E, \omega) = \hbar^{-1}\alpha(\omega)\tau(E)\,|\nabla_k E_{n'}|\,\{1+\hbar^{-1}\alpha(\omega)\tau(E)\,|\nabla_k E_{n'}|\}^{-1} \tag{12}$$

which takes into account the photon absorption depth and the mean free path of the excited electron. The

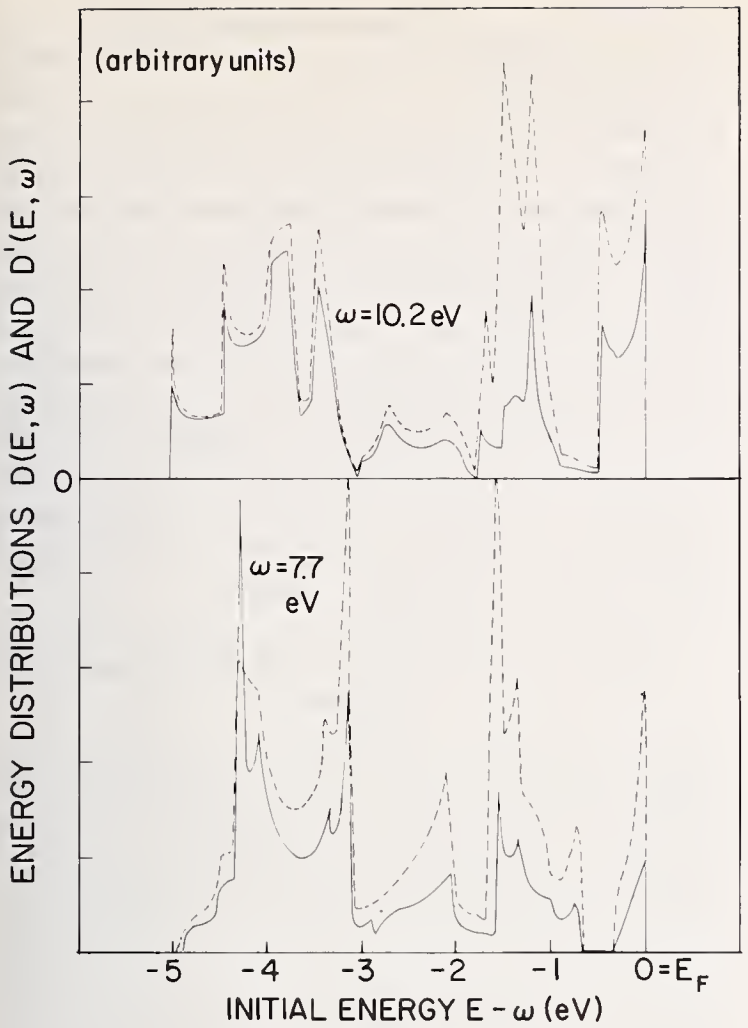

FIGURE 4. D(E, ω) *(broken curves) and* D'(E, ω) *(solid curves) for* Pd, *plotted versus initial energy* E-ħω.
Solid and broken curves are on different scales.

quantities $\alpha^{-1}(\omega)$, $\tau(E)$, and $\hbar\nabla_k^{-1}E_n(\mathbf{k})$ are, respectively, the optical absorption depth, and the lifetime and group velocity of the excited electron. Under the frequently-used assumption [2,4,5] that $E_{n'}(\mathbf{k})$ is free-electron-like, $|\nabla_k E_{n'}|$ becomes proportional to $E^{1/2}$; T is then independent of $\mathbf{k}$, and may be taken out of the integral. The density of states given in figure 1 shows, however, that this assumption is untenable for Pd.

The factor $|\nabla_k E_{n'}|$ in T enters the integrand in eq (5) almost linearly (for Pd, $T \sim 0.1$), and this tends to reduce the effect on $D'(E,\omega)$ of structure in the unoccupied density of states [15] (which involves $|\nabla_k E_{n'}|^{-1}$). Figure 4, which shows both $D(E,\omega)$ and $D'(E,\omega)$ for two values of ω, gives some indication of the effects of the transport factor. Note that $D'(E,\omega)$ is the "bare" distribution; to compare with experiment, the curves must be convolved with Lorentzians to take account of many-electron lifetime broadening, they must be multiplied by an energy-dependent surface escape function, and the distribution of secondary electrons must be included, as in eq (6). These calculations, and further

TABLE 2. k-*space locations and variances of contributions to photoemission energy distribution. Last column is the integrated contribution of the band to the photoemission* [*see eq* (4)].

Band	**k** (Units of $2\pi/a$)	σ (Units of $2\pi/a$)	Contribution to $\epsilon_2(\omega)$
	$\hbar\omega = 7.7$ eV		
1	(0.66, 0.39, 0.20)	0.18	22.21
2	(0.70, 0.37, 0.14)	0.18	17.16
3	(0.78, 0.40, 0.13)	0.17	15.50
4	(0.82, 0.42, 0.14)	0.17	15.52
5	(0.85, 0.48, 0.12)	0.17	6.02
6			0.0
	$\hbar\omega = 9.9$ eV		
1	(0.81, 0.35, 0.11)	0.20	10.12
2	(0.84, 0.37, 0.12)	0.19	10.24
3	(0.85, 0.48, 0.09)	0.15	5.19
4	(0.73, 0.50, 0.21)	0.24	8.31
5	(0.70, 0.44, 0.19)	0.18	11.74
6			0.0
	$\hbar\omega = 11.6$ eV		
1	(0.89, 0.40, 0.11)	0.16	4.72
2	(0.74, 0.46, 0.25)	0.21	11.80
3	(0.75, 0.43, 0.18)	0.22	12.21
4	(0.76, 0.39, 0.15)	0.21	10.66
5	(0.63, 0.40, 0.15)	0.16	5.32
6	(0.39, 0.36, 0.33)	0.02	0.05

details on the choice of $\tau(E)$ are described below.

The most important feature of the energy distributions in figure 4 is that they show structure which (1) shifts approximately linearly with photon energy and (2) reflects the *d*-band density of states. The first of these explains the central feature of photoemission data which provided the original motivation for the non-direct transition model [2-4]. This behavior occurs in Pd because the contributing transitions are restricted to a relatively small region in **k**-space near the point $(2\pi/a)(3/4,1/2,1/4)$ which is midway along the line Q from L to W on the (111) zone face (this was determined by computing the average of the cube center locations, weighted by the contribution to $D(E,\omega)$. Details for several values of ω are given in table 2). The standard deviation, $\sim 0.2(2\pi/a)$, is a measure of the localization. In this region each *d*-band is almost flat, leading to linearly shifting structure via the second delta function in eqs (3) and (5). The excited band $E_{n'}(\mathbf{k})$, on the other

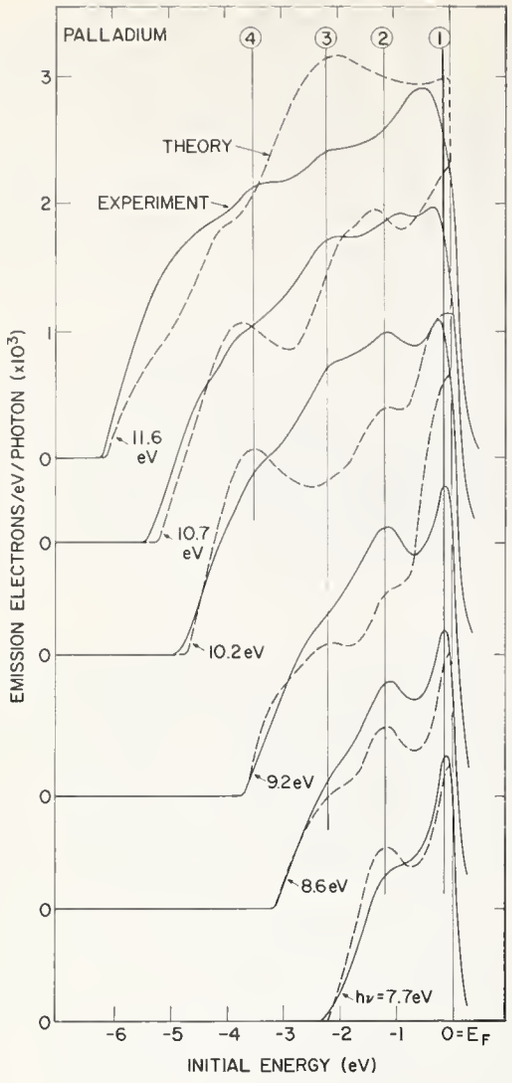

FIGURE 5. *Experimental energy distributions (solid curves) and theoretical energy distributions (for direct transitions) for* Pd, *plotted versus initial energy.*
All curves are normalized to the measured and calculated quantum yields, respectively.

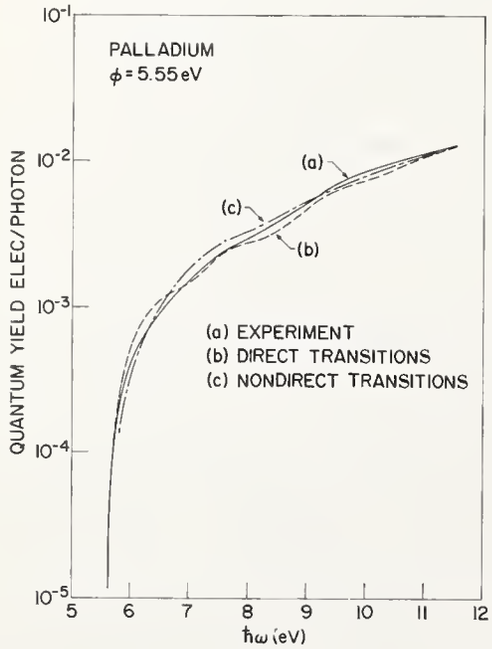

FIGURE 6. *Quantum yield (per absorbed photon) for* Pd.
Curves (a), (b) and (c) respectively give the measured results and calculated results for direct and nondirect transitions (see text).

hand, changes by ~3 eV in this region, thereby preventing severe modulation of the structure (with ω) by the other delta function.

While this localization in **k**-space explains the linear shift of structure with ω, it throws doubt upon any direct relationship between photoemission data and the d-band density of states. The localization implies that, at best, photoemission measures the d-band density of states in a small fraction of the Brillouin zone; the similarity in structure between this partial density of states and the total density of states in Pd appears to be coincidental. The localization also justifies our neglect of the **k** dependence of $|\langle n\mathbf{k}|\mathbf{p}|n'\mathbf{k}\rangle|^2$. Thus, the inclusion of matrix elements should affect only the relative amplitudes of the peaks in figure 4 and not their position in energy or their movement with ω.

3. Experimental Results and Comparison with Theory

Photoemission spectroscopy measurements were made in the energy range $5.5 < \hbar\omega < 11.6$ eV on evaporated polycrystalline Pd films (see 7. app.). Normalized energy distribution curves (EDC's) are shown in figure 5 (solid lines). The experimental quantum yield $Y(\omega)$ (number of emitted electrons per absorbed photon) is shown in figure 6 (solid line). The work function $\phi = 5.55 \pm 0.1$ eV was determined from the usual Fowler plot of $(Y(\omega))^{1/2}$ vs $\hbar\omega$ as $\hbar\omega \to \phi$. The experimental EDC's show 4 peaks (labeled (1), (2), (3) and (4)) at ~ 0.15, 1.2, 2.2, and 3.5 eV below E_f; this structure is stationary in initial energy, with the exception that the first two peaks merge for $\hbar\omega \gtrsim 11$ eV [16,17].

Before describing analyses of the data, we note that the leading edges of the EDC's are sharper (~ 0.2 to 0.25 eV from 10 to 90% points) than the theoretical energy uncertainty $\tau^{-1}(E)$ determined by normalizing to the quantum yield. Our conclusion is that the broadening is one-sided below the Einstein cutoff ($\hbar\omega$ above E_f) due to overall energy conservation for the photoelectric process. There is no obvious mechanism for imparting extra energy (of order $\tau^{-1} \simeq 0.5$ eV) in addition to $\hbar\omega$ to the photoelectron during the excitation and transport process. Thus the observed broadening of the leading edge is due to thermal smearing (~ 0.1 eV at 300 K), the electron spectrometer resolution, work function inhomogeneity, etc.

Direct transition analysis. Theoretical EDC's based upon direct interband transitions (secs. 1 and 2) are compared with experiment in figure 5. The theoretical EDC's show 4 peaks at ~ 0.1, 1.2, 2.2, and 4 eV below E_f, with the second (−1.2 eV) peak disappearing for $\hbar\omega \gtrsim 11$ eV. The theoretical EDC's show good agree-

ment with experiment, especially in the energy locations of observed structure. Identifying the lowest theoretical EDC structure (at -4 eV) with the lowest observed structure (at -3.5 eV) indicates that our calculated d-bands are ≈ 0.5 eV too wide. This difference is well within the uncertainties in the band energies due to uncertainties in the muffin-tin potential. A central feature of the theoretical EDC's is that structure remains essentially stationary in initial-state energy.

The theoretical EDC's in figure 5 were computed using eq (6) as follows. The required quantities include: the band density of states $N(E)$ in figure 1 for the occupied and unoccupied bands within $\hbar\omega_{max}$ of E_F, the optical absorption coefficient $\alpha(\omega)$ [16], the energy dependent lifetime $\tau(E)$, the work function ($\phi = 5.55$ eV), and the band energies $E_n(\mathbf{k})$ and energy gradients $\nabla_k E_n(\mathbf{k})$ which enter the computation of $D(E,\omega)$ and $D'(E,\omega)$ (see sec. 2).

The lifetime $\tau(E)$ has been computed in the random $-\mathbf{k}$ approximation (with constant Coulomb matrix elements) [9] and depends only on energy. Evaluation of the energy-dependence of $\tau(E)$, using the band density of states for Pd (fig. 1) and normalizing $\tau(E)$ to the measured quantum yield (total number of emitted electrons per absorbed photon) at $\hbar\omega \simeq 10$ eV, yields $\tau(E) = 28\ (E - E_f)^{-1.15}$ eV^{-1} for $5 < E < 12$ eV, e.g. the lifetime is $\tau \simeq 1.7$ eV^{-1} at 10 eV. The transport factor $T(\mathbf{k},E,\omega)$ is of order 0.1 for Pd; i.e., the average value of the mean free path $l(E_{n'},\mathbf{k}) \equiv \tau\ v_g$ is estimated to decrease from ~ 25 Å to ~ 10 Å in the 5 to 12 eV range [18].

Lifetime effects on the energy distributions have been treated in an ad hoc way by convolving the calculated sharp distributions with an energy-dependent Lorentzian lifetime function. Here we have used the above-mentioned $\tau(E)$ determined from the quantum yield, i.e., $\tilde{D}'(E,\omega)$ is $D'(E,\omega)$ convolved over E with a Lorentzian of halfwidth $\hbar/\tau(\omega)$. This broadening (with $0.4\ \text{eV} < \tau^{-1} < 0.6$ eV for energies from 7 to 12 eV) results in theoretical EDC's with resolution comparable to that of the experimental EDC's (changing this broadening does not affect the energy positions of dominant structure). We have folded back the smeared energy distributions ($\tilde{D}'$) about $E_f + \hbar\omega$ so as to conserve the number of excited states while maintaining overall energy conservation [9]. (This procedure produces no new structure in the final EDC's).

In summary, all quantities involved in the theoretical emission spectra (the energy bands, density of states, $S_{ee}(E,' E)$, v_g, etc.) are specified in terms of a small number of quantities: the one-electron muffin-tin potential, the measured work function ϕ, the measured optical absorption coefficient $\alpha(\omega)$ [16] and the lifetime normalization constant. Therefore, within the model, structure in the EDC's is directly related to the one-electron potential.

In the theoretical EDC's shown in figure 5, secondary emission contributes less than 25% of the total emission and does not lead to any observable peaks; thus peak locations and, to a large extent, amplitudes of the theoretical EDC's are not sensitive to our treatment of secondary emission. Comparison of the theoretical EDC structure with the d-band density of states (fig. 1) shows correlation, i.e., peaks in the EDC's tend to occur near energies corresponding to peaks in the density of states.

We have also studied the sensitivity of the theoretical EDC's by altering the muffin-tin potential so as to narrow the d-bands by ~ 0.5 eV. The principal effect of this change was to shift the locations of the dominant EDC peaks into better agreement with experiment; however, amplitude agreement was not improved. The relative peak amplitudes of the theoretical EDC's in figure 5 show more variation with photon energy than is observed. This behavior might be due to the assumption of constant matrix elements in the present analysis.

The quantum yield for $\phi < \hbar\omega < 11.6$ eV has been evaluated for the direct transition model (dashed line in fig. 6) and shows very good agreement with experiment. This agreement is a measure of the adequacy of the approximations of a free-electron escape probability and energy-dependent lifetime, both of which significantly influence the quantum yield.

The dielectric constant $\epsilon_2(\omega)$ has been calculated assuming direct transitions with constant matrix elements. Comparison with experiment (solid curve in fig. 3) shows some correlation (e.g., the structure at ~ 4 eV and minimum near 8 eV); however, overall agreement is mediocre. The increase in absorption observed experimentally for $\hbar\omega \gtrsim 8$ eV is likely to be due in part to plasmon excitations (the imaginary part of ϵ^{-1} shows a peak at ~ 7.5 eV [16]. Inclusion of momentum matrix elements is necessary for a more detailed comparison with the experimental $\epsilon_2(\omega)$, especially for $\hbar\omega \lesssim 4$ eV.

Nondirect transition analyses. An analysis of the experimental data has been made assuming nondirect transitions (with constant matrix elements) for two cases. First, a best fit to the experimental EDC's was made using the empirical occupied optical density of states [5] and the unoccupied conduction band density of states shown in figure 7. This ODS describes the energy positions and amplitudes of observed structure (except for the merging of the upper two peaks for $\hbar\omega \gtrsim 11$ eV).

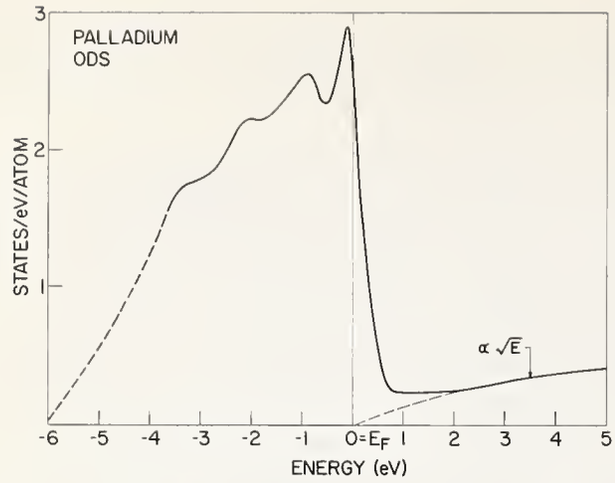

FIGURE 7. *The optical density of states (ODS) for* Pd *determined from a best fit to the experimental EDC's.*

The nondirect transition analysis closely follows the work of Berglund and Spicer [2]; the emission $N(E,\omega)$ is approximately given by eq (6) with the energy distribution $D'(E,\omega)$ given by

$$D'_{ND}(E,\omega)=\left(\frac{\rho_v(E-\hbar\omega)\rho_c(E)}{\int_{E_f}^{E_f+\hbar\omega}\rho_v(E-\hbar\omega)\rho_c(E)\,dE}\right)\cdot T(E,\omega) \tag{13}$$

with $T(E,\omega)=\alpha(\omega)l(E)(1+\alpha l)^{-1}$

$$l(E)=\tau(E)\sqrt{\frac{2E}{m}}$$

Here ρ_v and ρ_c are the occupied and unoccupied optical densities of states (fig. 7). The energy dependence of the inelastic mean free path $l(E)=\tau v_g$, with $v_g\propto\sqrt{E}$, was determined in the random-**k** approximation [9] using the ODS in figure 7. The mean free path was set equal to 15 Å at 8 eV in order to give a best fit to the quantum yield $Y(\omega)$. The resulting quantum yield (broken line in fig. 6) shows very good agreement with experiment.

The dielectric constant $\epsilon_2(\omega)$ has been calculated using the nondirect transition model with the ODS of figure 7 (see curve (c) in fig. 3) and shows much less structure than is observed experimentally. As with the direct transition analysis, the nondirect transition analysis (with constant matrix elements) fails to explain the observed increase in $\epsilon_2(\omega)$ for $\hbar\omega\gtrsim 8$ eV; this increase is likely to be due in part to plasmon excitations.

A nondirect transition analysis was also made using the theoretical band density of states (fig. 1) for both the occupied and unoccupied bands [19]. It is logical to describe both the unoccupied states and occupied states by band states if either are to be so-described. The resulting EDC's also exhibited stationary structure similar to that of the direct transition analysis in figure 4, but gave poorer agreement with experiment because of the strong structure in the unoccupied density of states at $\simeq 8.3$ eV above E_f. Nondirect-transition (and direct transition) analyses are compared with experiment in figure 8; curve (c) clearly illustrates the effect of the conduction band structure at ~8 eV in $N(E)$ (i.e., sharp dip at ~ -2.5 eV).

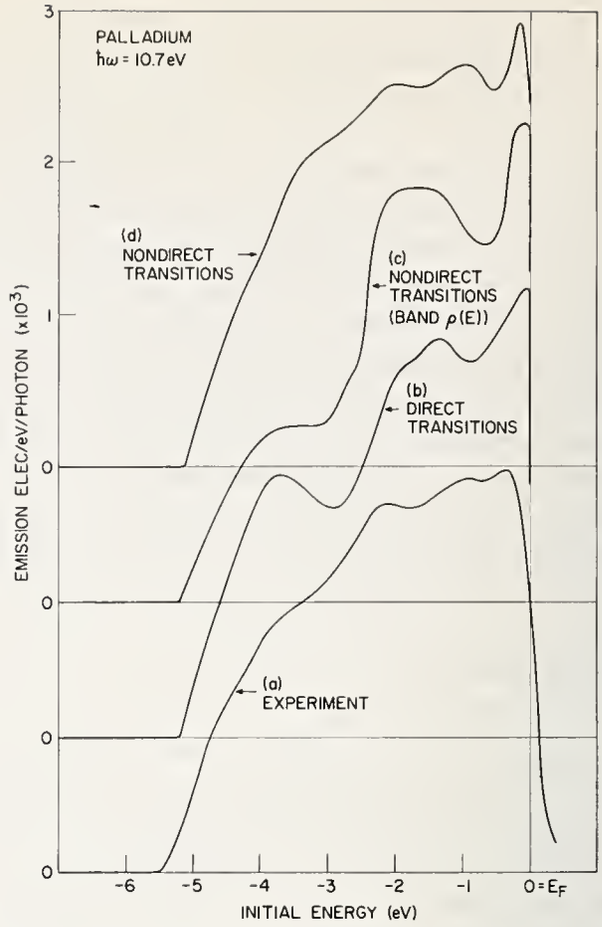

FIGURE 8. *Comparison of the experimental EDC (a) at* $\hbar\omega=10.7$ *eV with calculated curves for (b) direct transitions, (c) nondirect transitions using the band density of states (fig. 2), and (d) nondirect transitions using the ODS of figure 7.*

This result raises an interesting point concerning nondirect transitions—any reasonable muffin-tin potential for Pd would appear to lead to strong conduction band structure, which should be observable in nondirect transitions between band states are dominant. This is not observed in practice. Of course it is possible (but unlikely) that the escape process can suppress the effect of such structure. (Direct calculation has shown that inclusion of the transport factor using the **k**-dependent band group velocity diminishes only slightly the effect of structure in the unoccupied density of states on the nondirect-transition EDC's.) Thus, an optimal fit with the nondirect transition model requires the additional assumption (unjustified for Pd) of a smooth unoccupied density of states.

4. Conclusions

The photoemission energy distributions of palladium calculated using the direct-transition model (constant matrix elements) and the nondirect-transition model (with a free-electron unoccupied density of states), show about equal agreement with experiment. While we are therefore unable to offer conclusive proof of either model we have added two new elements to the controversy. First, the original motivation for the nondirect transition model has been removed by showing that the direct transition model does in fact predict structure which shifts linearly with photon energy over the limited range $\Phi < \hbar\omega < 11.6$ eV [6]. Second, we have shown that the success of the nondirect transition model depends on the unjustifiable assumption of a free-electron unoccupied density of states which is at best inconsistent with the identification of the optical density of states with the band density of states. Nonetheless, we are struck, particularly in view of these developments, by the apparent success of the nondirect transition model for many metals [5]. We are hopeful that experimental data over a broader range of photon energies will unequivocally establish one or the other model [8].

The discrepancy between theoretical and experimental $\epsilon_2(\omega)$ curves above 8 eV can possibly be attributed in part to the observed plasma edge at 7.5 eV [16]. The remaining discrepancies between theoretical and experimental $\epsilon_2(\omega)$ are most likely due to our assumption of constant momentum matrix elements. Presumably, the plasmons will also affect the photoemission spectra. We have not taken them into account in our direct-transition photoemission analysis.

5. Acknowledgments

The authors gratefully acknowledge the technical assistance of J. Donelon with the measurements.

6. References

[1] Ehrenreich, H., and Philipp, H. R., Phys. Rev. **128**, 1622 (1962).
[2] Berglund, C. N., and Spicer, W. E., Phys. Rev. **136**, A1030 (1964).
[3] Spicer, W. E., Phys. Rev. **154**, 385 (1967).
[4] Seib, D. H., and Spicer, W. E., Phys. Rev. Letters **22**, 711 (1969).
[5] Eastman, D. E., J. Appl. Phys. **40**, 1387 (1969).
[6] Smith, N. V., and Spicer, W. E., Optics Comm. **1**, 157 (1969). We were motivated to perform the present calculations by an early communication of their work, for which we are indebted.
[7] Brust, D., Phys. Rev. **139**, A489 (1965).
[8] Photoemission data for Au (D. E. Eastman) at 16.8 and 21.2 eV shows structure which contradicts the nondirect transition model. It remains to be seen if direct transitions can explain these Au data.
[9] Kane, E. O., Phys. Rev. **159**, 624 (1967).
[10] Gilat, G., and Raubenheimer, L. P., Phys. Rev. **144**, 390 (1966).
[11] Kane, E. O., Phys. Rev. **175**, 1039 (1968).
[12] Dimmock, J. O., and Freeman, A. J., private communication.
[13] Steffenson, J. F., Interpolation, Chelsea Publishing Co., New York, 1950.
[14] Janak, J. F., Phys. Letters **28A**, 570 (1969).
[15] Kane, E. O., Proc. Int. Conf. Semiconductor Physics, J. Phys. Soc. Japan Suppl. **21**, 37 (1966).
[16] Yu, A. Y. C., and Spicer, W. E., Phys. Rev. **169**, 497 (1968).
[17] Previous photoemission studies of Pd [16] have shown that the first two peaks below E_F for low energies ($\hbar\omega < 9$ eV), but did not clearly resolve structure at higher energies.
[18] We have ignored the **k**-dependence of the mean free path of once-scattered electrons in eq (6). This has no significant effect on our results for Pd since secondary emission is estimated to be $< 25\%$ for $\hbar\omega < 11.6$ eV and its energy distribution is smoother than that of the primaries.
[19] The occupied and unoccupied band densities of states were convolved with lifetime functions $\simeq\tau^{-1}(E)$.
[20] Blodgett, A. J., Jr., and Spicer, W. E., Phys. Rev. **146**, 390 (1966).

7. Appendix. Experimental Conditions

Photoemission EDC's and quantum yields were measured in the 5.5 to 11.6 eV range using experimental techniques similar to those described by Spicer and coworkers [20]. An ac synchronous detection system with a 2−1/2 inch diameter gold-plated spherical mesh collector was used (the mesh has 70 lines/inch and is ~85% transparent). An ac capacitance bridge was used to cancel stray capacitance to $\lesssim$.05 pf; with a $10^9\Omega$ sensing resistor (Keithley Model 601 electrometer) and 1 second integrating time constant, the input noise was typically $\sim 1 \times 10^{-14}$ amperes. The quantum yield was measured using a calibrated CsSb photodiode (with a LiF window) which is traceable to Prof. W. E. Spicer's laboratory calibration.

Palladium films ($\sim 1-2\times 10^3$ Å thick) were prepared by evaporation onto smooth Cr-plated 5/8 inch diameter quartz discs using an electron-beam gun in an ion-pumped ultra-high-vacuum system. The pressure (mainly hydrogen) rose from a base of $\sim 7 \times 10^{-11}$ torr to $\sim 1 \times 10^{-8}$ torr during evaporation (at ~2 Å/sec) and then rapidly fell to $\lesssim 4 \times 10^{-10}$ torr within 10 minutes after evaporation.

Discussion on "Direct-Transition Analysis of Photoemission from Palladium" by J. F. Janak, D. E. Eastman, and A. R. Williams (IBM Thomas J. Watson Research Center)

W. E. Spicer *(Stanford Univ.):* Historically, when we saw peaks moving with $h\nu$ until they disappeared, we interpreted this structure in terms of direct transitions. The examination of modulation is very important in choosing between direct and nondirect models. Secondly, I guess I would have to comment that it seems to me the agreement between your calculated transitions and the experimental data does not seem to be quite as strong as the abstract indicates. Would you comment on this?

J. F. Janak *(IBM):* Well, as I said, I think the agreement on the slide we showed is within about 20-40%. We never claimed in the abstract that the agreement was perfect. But inasmuch as we have assumed that the matrix elements are constant, and we have heard today how much they can vary, I think that 30%, assuming constant momentum matrix elements, is really pretty good.

J. T. Waber *(Northwestern Univ.):* I would like to reinforce what you have said about the need of very large number of points in **k** space to achieve accuracy in determining the Fermi energy. A more detailed statement of the reliability of density of states curves is appended as a short post-deadline paper [1]. The graphs shown there are for a pure parabolic band, $E = \mathbf{k}^2$, with **k** evaluated at points on a regular grid in the Brillouin zone. The QUAD scheme of Mueller et al. [2] was used to obtain additional points in the zone. The first graph is for 5000 points and the relative deviation from the parabola is 9.8%. It is necessary to go to 100,000 points to achieve a relative precision of 3.6%.

M. S. Dresselhaus *(MIT):* Since you deal with a range of **k** values wouldn't it be possible to include the **k** dependence of the momentum matrix elements without too much trouble? I am referring here to the method whereby the momentum matrix elements are computed from derivatives of the Hamiltonian.

J. F. Janak *(IBM):* Well, we have been trying. That is the next step in the analysis. I should point out that since the region is so small that the **k**-dependence is not really the important thing, the main thing is the band-to-band variation. In fact, the transitions occur in a region with a standard deviation or radius essentially 0.2 (in units of $2\pi/a$) around a point halfway between L and W on the (111) zone face. That actually covers about 20% of the zone, I think, when you use all the symmetry. But 20% of the total volume of a sphere is a pretty small shell on the outside. In that kind of a shell we would want the **k**-dependence of the matrix elements.

[1] Kennard, E. B., Koskimaki, D., Waber, J. T., and Mueller, F. M., these Proceedings, p. 795.
[2] Mueller, F. M., these Proceedings, p. 17.

Photoemission Determination of the Energy Distribution of the Joint Density of States in Copper*

N. V. Smith

Bell Telephone Laboratories, Murray Hill, New Jersey 07974

Measurements have been made of the photoemission properties of cesiated copper, with improved sample preparation over the previous work by Berglund and Spicer. The energy distribution curves (EDCs) of photoemitted electrons show structure in the region associated with the copper *d* bands which was not seen in the previous data. The behavior in the photon energy range 6 to 8 eV is particularly interesting in that some of these new peaks in the EDCs are observed to move, appear and disappear in a manner characteristic of direct transitions.

Parallel calculations have been performed of the energy distribution of the joint density of states (EDJDOS) similar to those reported recently by Smith and Spicer. The band structure used was the interpolation scheme of Hodges, Ehrenreich, and Lang fitted to the APW calculation of Burdick. In a constant matrix element approximation, the EDJDOS represents the energy distribution of photo*excited* electrons. This was converted to an energy distribution of photo*emitted* electrons by introducing appropriate threshold and escape factors. The overall agreement with experiment is good. In particular, some of the peaks in the theoretical EDCs are predicted to disappear and reappear on varying the photon energy, and there are strong similarities with the changes observed experimentally.

It is found, therefore, that the optical transitions from parts of the copper *d* bands can be identified as direct. Theoretical calculations based on the EDJDOS work quite well for these and other transitions. Photoemission provides a very sensitive tool for verifying and even determining the EDJDOS. Burdick's bands for copper appear to be essentially correct over a wide range of energies including the whole of the *d*-band region, although minor modifications of a few tenths of an eV would improve agreement. It is found that the most persistent peaks in the calculated EDJDOS tend to coincide with the peaks in the calculated true density of states. This indicates that when a phenomenological "optical density of states" can be obtained, it may well be a good approximation to the true density of states even if transitions are direct.

Key words: Aluminum-insulator-palladium (Al-Pd); augmented plane wave method (APW); cesium; copper; direct transitions; electronic density of states; joint density of states; nondirect transitions; optical density of states; optical properties; photoemission.

1. Introduction

One of the major landmarks in the photoemission investigation of metals was the observation of the *d* bands in Cu and Ag by Berglund and Spicer [1]. Their work has stimulated much of the subsequent effort in this area and it is now fair to say that photoemission is one of our most powerful tools for probing band structure. The measurements by Berglund and Spicer were performed on samples whose surfaces were covered with a thin layer of cesium in order to lower the work function. More recent work by Krolikowski and Spicer [2] on clean Cu has revealed more structure in the energy distribution curves (EDCs) of photoemitted electrons than was seen on cesiated Cu. However, the work function of clean Cu is almost 3 eV greater, so that this structure could be observed only over a more limited energy range.

So far, the photoemission data on Cu and other noble and transition metals [3,4] has been interpreted in terms of a predominantly nondirect model. The importance of the direct (i.e., **k**-conserving) nature of the optical transitions from the Cu *d* bands did not manifest itself in any noticeable way, although the direct nature of the transitions in the vicinity of $L_2' \rightarrow L_1$ was clearly

*The experimental part of this work was performed while the author was on assignment at Stanford University from Bell Telephone Laboratories. The facilities used at Stanford are supported in part by the Advanced Research Projects Agency through the center for Materials Research at Stanford University and by the National Science Foundation.

recognizable. Energy conservation appeared to be the main factor in determining the behavior of the d band structure in the EDCs. In fact, it was possible to unfold the EDCs and extract an "optical density of states" which bore a strong resemblance to the calculated band structure density of states [2].

The author has attempted to assess the merits of a purely direct transition model by performing band calculations of the energy distribution of the joint density of states (EDJDOS). A comparison of these calculations with the photoemission data on clean Cu has been reported by Smith and Spicer [5]. In performing the calculations, it became clear that the most interesting behavior characteristic of direct transitions would occur, if at all, at energies below the vacuum level for clean Cu. It was decided, therefore, to reinvestigate the photoemission properties of cesiated Cu. Since vacuum and sample preparation techniques had improved over the intervening years, there was hope that it might be possible to resolve more structure in the EDCs than had been seen by Berglund and Spicer. A selection of the results of these experiments is presented below, and it will be seen that this hope was indeed realized.

2. Photoemission and Direct Transitions

In the conventional theory of optical absorption by solids, transitions are allowed only between states which lie at the same point in $\mathbf{k}$-space in the reduced zone; i.e., the transitions must be direct. If $\epsilon_i(\mathbf{k})$ and $\epsilon_f(\mathbf{k})$ denote the energies in an initial band i and a final band f, optical transitions at photon energy $\hbar\omega$ are restricted to the surface in $\mathbf{k}$-space given by

$$\Omega_{fi}(\mathbf{k}) = \epsilon_f(\mathbf{k}) - \epsilon_i(\mathbf{k}) - \hbar\omega = 0. \tag{1}$$

The total number of direct transitions at this photon energy is represented by the well-known joint density of states given by

$$\mathscr{J}(\hbar\omega) = (2\pi)^{-3} \sum_{i,f} \int' d^3k \delta(\Omega_{fi}(\mathbf{k})). \tag{2}$$

The prime on the integral denotes that the integration is to be performed only over those portions of $\mathbf{k}$-space for which $\epsilon_i < E_F < \epsilon_f$ where E_F is the Fermi energy.

In photoemission experiments, we are interested in not just the total number of transitions, but also the energies at which the excited electrons emerge from the metal. A more relevant quantity for our purposes is what we call the *energy distribution of the joint density of states* (EDJDOS) defined by

$$\mathscr{D}(\epsilon, \hbar\omega) = (2\pi)^{-3} \sum_{i,f} \int' d^3k \delta(\Omega_{fi}(\mathbf{k})) \delta(\epsilon - \epsilon_i(\mathbf{k})). \tag{3}$$

The additional δ function picks out those transitions whose initial energy equals ϵ. In a constant matrix element approximation, $\mathscr{D}(\epsilon,\hbar\omega)$ represents the energy distribution of photoexcited electrons referred to initial states. Strictly speaking, we should weight each transition with the square of an appropriate momentum matrix element. This refinement has not been attempted so far, and for the remainder of the paper we will remain within the constant matrix element approximation. This has the advantage of making the calculation of the EDCs extremely straightforward, since $\mathscr{D}(\epsilon,\hbar\omega)$ is a property solely of the ϵ,$\mathbf{k}$-dispersion curves.

The EDJDOS of Cu has been evaluated numerically from eq (3). The band structure used was the interpolation scheme of Hodges, Ehrenreich, and Lang [6] with its parameters fitted to the APW calculation by Burdick [7]. A computer was programmed to sample the energy eigenvalues at more than 10^5 points in the primitive 1/48 of the zone, deduce the permitted transitions, and to keep running scores of these transitions catalogued according to photon energy and initial energy. Calculations of this kind were first performed by Brust on silicon [8].

The EDJDOS at a given $\hbar\omega$ obtained in this way still represents the energy distribution of photo*excited* electrons. This was converted to an energy distribution of photo*emitted* electrons (i.e., an EDC) by multiplying by an appropriate threshold function [1]. To take account of electron loss by inelastic scattering, this threshold function contains a factor $\alpha\ell/(1+\alpha\ell)$, where α is the optical absorption coefficient and ℓ is the electron mean free path. The details of the threshold function do not affect the qualitative features of the results, such as the shape of the EDCs. They do, however, determine the total photoelectric yield and therefore the normalization of the absolute magnitude of the EDCs. In these calculations, α was taken to be constant at $7.2 \times 10^{-5}\cdot\text{cm}^{-1}$ over the whole frequency range. The energy dependence of the mean free path ℓ was assumed to be given by $C(E - E_F)^{-2} v_g$, where E is the energy at which the electron emerges from the metal (i.e., final state energy), and v_g is a free electron group velocity for an electron of this energy inside the metal. C is a constant determined by insisting that ℓ should be 22 Å for $E = E_F + 8.6$ eV; this value was found by Krolikowski [2] in his nondirect analysis. The imaginary part of the dielectric constant was calculated from the joint density of states making the same matrix element approximation. This enabled the EDCs to be normalized to the yield per absorbed photon. Finally, some broadening was introduced into the curves by convolv-

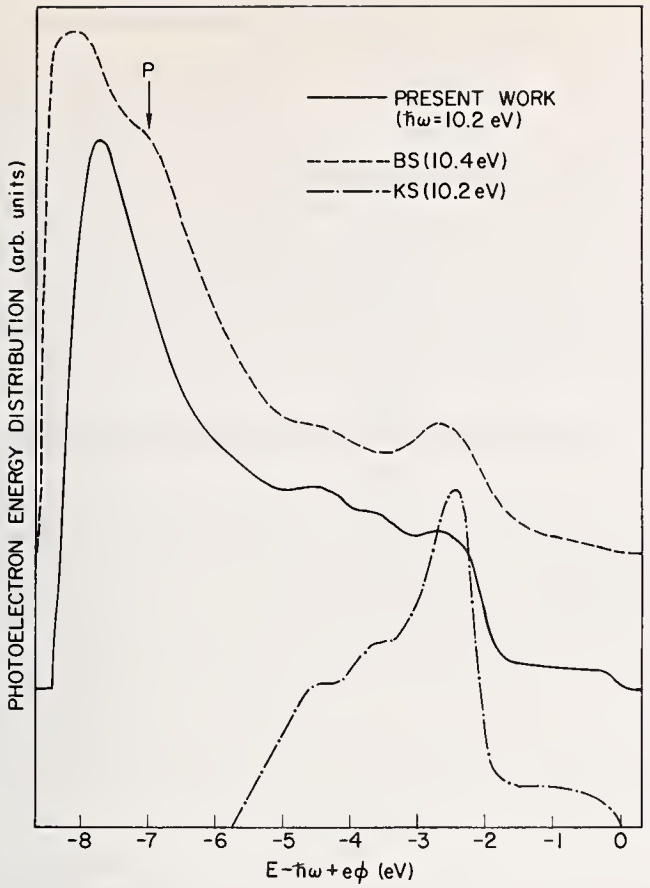

FIGURE 1. *Photoelectron energy distribution curves for* Cu *referred to initial state energy.*

The upper two curves were taken on cesiated copper; the full curve is the present work ($\hbar\omega = 10.2$ eV) and the dashed curve is from Berglund and Spicer ($\hbar\omega = 10.4$ eV). The lower curve was taken on clean Cu by Krolikowski and Spicer ($\hbar\omega = 10.2$ eV).

ing them with a Lorentzian function whose width at half maximum was 0.3 eV. The results of these calculations will be compared with experiment in section 4 below.

3. Experimental Details

The Cu sample was prepared by evaporation in a stainless steel vacuum system for which the base pressures were on the 10^{-11} torr scale. During the evaporation of the Cu, the pressure rose to 5×10^{-10} torr but quickly dropped to 1.5×10^{-10} torr after the evaporation. It was found that photoemission measurements performed on this clean Cu sample reproduced the previous results of Krolikowski and Spicer [2]. The sample was then cesiated. The cesium was contained in a glass ampule which had been broken open in the vacuum chamber at an earlier stage [9]. The cesiation was performed by gently heating the ampule and then exposing the Cu sample to the cesium beam for a few minutes. The EDCs were measured by the conventional a.c.-modulated-retarding potential technique [10].

The Cu samples used by Berglund and Spicer were prepared in glass vacuum systems operating at base pressures of around 10^{-8} torr. Their cesiation procedure was also rather different, but it is believed

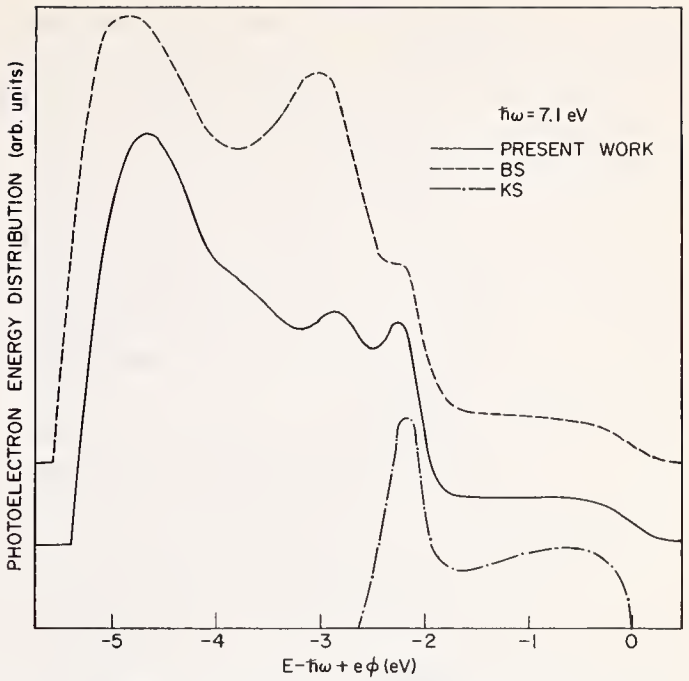

FIGURE 2. *Photoelectron energy distribution curves for* Cu *at* $\hbar\omega = 7.1$ *eV referred to initial state energy.*

The upper two curves were taken on cesiated copper; the full curve is the present work and the dashed curve is from Berglund and Spicer. The lower curve was taken on clean Cu by Krolikowski and Spicer.

that the differences in the data are due primarily to differences in the overall vacuum conditions under which the experiments were performed.

In figure 1 we compare the EDC obtained at $\hbar\omega = 10.2$ eV in the present work with that obtained at 10.2 eV by Krolikowski on clean Cu and that obtained at 10.4 eV by Berglund and Spicer. The EDCs have been plotted against $E - \hbar\omega + e\phi$, where E is the electron kinetic energy in vacuum, and $e\phi$ is the work function. This choice of scale refers the photoelectrons to their initial states and places the zero of energy at the Fermi level. It is seen that the structure associated with the Cu d bands is much more blurred in the data of Berglund and Spicer. Also, the piece of structure labelled P observed earlier at about 7 eV below the Fermi level is absent in the present data. One possible explanation for this structure proposed by Berglund and Spicer was that it was due to a low energy peak in the density of states unanticipated by band calculations. The same structure finds its way into Krolikowski's more refined optical density of states [2]. The present work, however, indicates that its existence is questionable. A parallel may be drawn here with a similar situation in nickel. Early work on Ni [3] indicated the existence of a low energy peak in the density of states. However, when samples were prepared under better vacuum conditions by Eastman [4], it was found that this peak was much reduced. The effects of cesium, or any surface contaminants for that matter, are still very imperfectly understood.

417-156 O - 71 - 14

Ideally, the only effect of cesium on the surface should be to lower the work function. If this were the case in practice, we would expect a detailed correspondence between the pieces of structure seen in the EDCs on cesiated Cu and those seen in clean Cu. It can be seen in figure 1 that the present results satisfy this requirement better than the data of Berglund and Spicer. This observation holds true at other photon energies. We will therefore proceed on the assumption that the present measurements are more representative of the properties of pure Cu.

The corresponding curves for $\hbar\omega = 7.1$ eV are shown in figure 2. In all the curves, a peak due to electrons from the uppermost d band can be clearly seen at about -2.3 eV. The energies below this peak were inaccessible in the clean Cu experiments, but are quite accessible in the cesiated experiments due to the lower work functions. In the range -2.6 to -4.0 eV, there is a marked discrepancy between the earlier data and the present data. Berglund and Spicer observed a single large piece of structure in this range which changed little with photon energy. The present work reveals two pieces of structure in this range and the profile is found to change on varying the photon energy. Indeed, this is the most interesting feature of the present work from the point of view of the direct versus nondirect interpretation, and it will be explored in more detail in the next section. The origin of the differences between the present results and those of Berglund and Spicer is not clear, although we have associated it with vacuum conditions during sample preparation and cesiation. Another indication that the surfaces are physically different is that the work function in the present experiments was 1.75 eV which is 0.2 eV higher than that of Berglund and Spicer.

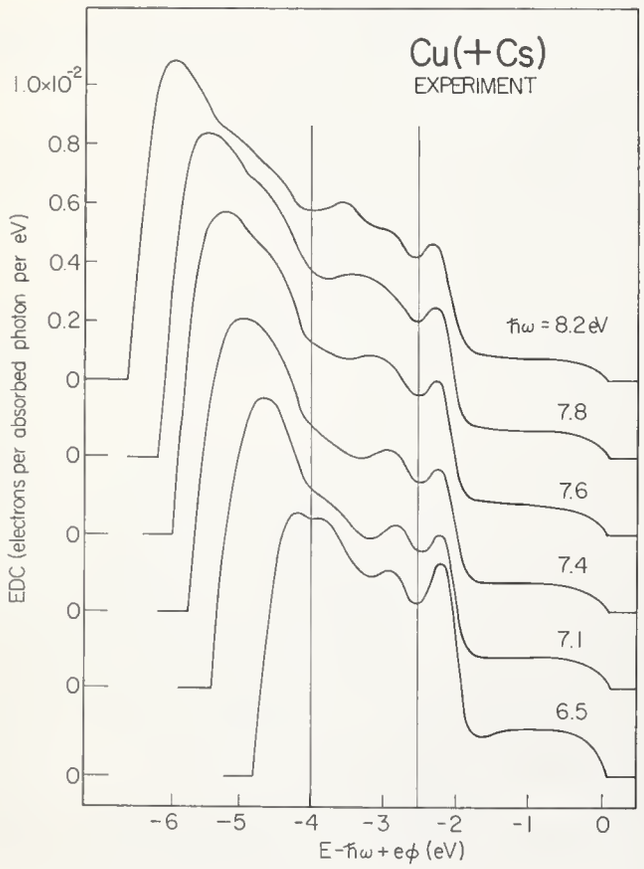

FIGURE 3. *Experimental EDC's from cesiated* Cu *between* $\hbar\omega = 6.5$ *and 8.2 eV.*

The curves are referred to initial state energy, and the zero of energy is placed at the Fermi level.

4. Comparison of Theory and Experiment

We confine ourselves here to a very limited selection of the experimental data. Roughly speaking, the EDCs at high photon energies ($\hbar\omega \gtrsim 9$ eV) are in fair accord with Krolikowski and Spicer's data on clean Cu. At low photon energies ($\hbar\omega \lesssim 5$ eV) the new data agrees well with that of Berglund and Spicer. It is in the photon energy range 6.5 eV $\leq \hbar\omega \leq$ 8.2 eV that the new and most noteworthy information has been obtained and so we will concentrate on this region.

The EDCs for photon energies in the range 6.5 to 8.2 eV are shown in figure 3. As before, we plot the EDC against the quantity $E - \hbar\omega + e\phi$ which places the zero of energy at the Fermi level. Let us focus attention on the behavior of the d-band structure in the energy range -2.6 to -4.0 eV indicated by the vertical lines. At $\hbar\omega = 6.5$ eV, we have two pieces of structure in this range. At $\hbar\omega = 8.2$ eV, we once again have a doublet, but for photon energies in between there is a continual change in the profile of the EDC. As the photon energy is increased, we find that the peak on the left fades away. While this is happening, the peak on the right expands by moving its low energy edge to lower energies, until at $\hbar\omega = 7.8$ eV there is one broad piece of structure filling the whole range. On increasing the photon energy further, this broad peak splits into a doublet. Such behavior is difficult to explain on a nondirect model, and is more characteristic of direct transitions.

The theoretical EDCs calculated according to the prescription outlined in section 2 are shown in figure 4 for the same photon energies. Let us once again focus attention on the behavior in the energy range -2.6 to -4.0 eV, indicated as before by the two vertical lines. At $\hbar\omega = 6.5$ eV, there are two peaks within this region. On increasing $\hbar\omega$, the left-hand peak fades away and then returns. At $\hbar\omega = 7.8$ eV we have a single broad piece of structure filling the whole range which then splits into a doublet on going to $\hbar\omega = 8.2$ eV. The similarity between these trends and those shown by the experimental data in figure 3 is very striking, and would

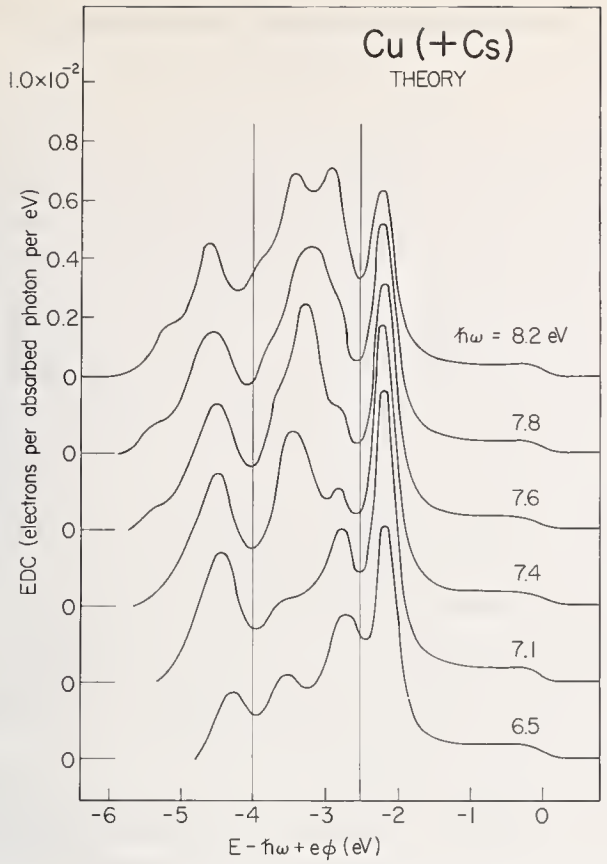

FIGURE 4. *Theoretically calculated EDCs from cesiated* Cu *between* $\hbar\omega = 6.5$ *and* 8.2 *eV.*

The curves are referred to initial state energy, and the zero of energy is placed at the Fermi level.

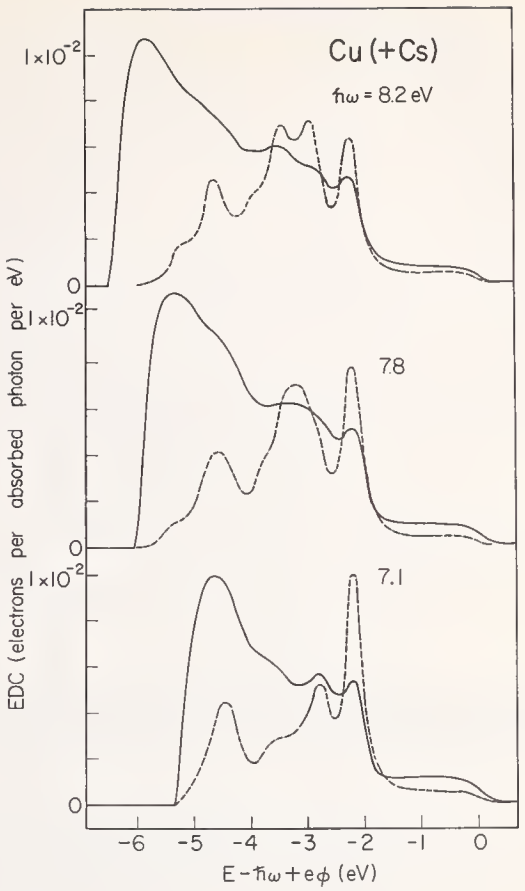

FIGURE 5. *Comparison of the theoretical and experimental EDCs from cesiated* Cu *for three representative photon energies.*

The full curves are experimental; the dashed curves are calculated theoretically assuming direct transitions.

seem to support the direct transition interpretation.

Theory and experiment are shown together for three photon energies in figure 5. The experimental EDCs all show a large contribution at the low energy end. This is due to electrons which have suffered an inelastic scattering but are still sufficiently energetic to escape from the metal. These have not been included in the theory which considers only those electrons which escape without scattering. It is seen that the calculations based on the EDJDOS are quite successful in predicting the energy location of structure in the EDCs. No great reliance can be attached to the relative peak heights in the theoretical curves in view of the crudity of the constant matrix element approximation; but even so, the agreement is encouraging. The peaks in the theoretical curves are much more pronounced than in experiment in spite of the 0.3 eV broadening we have introduced. Note, incidentally, that theory and experiment are plotted on the same absolute scale, all curves having been normalized to the yield per absorbed photon.

Let us very briefly consider the behavior at other photon energies. Figure 6 shows a comparison of the theoretical and experimental EDCs at 10.2 eV. These are typical of the high photon energy behavior. The relative number of slow scattered electrons is higher than at the lower photon energies shown in figure 3.

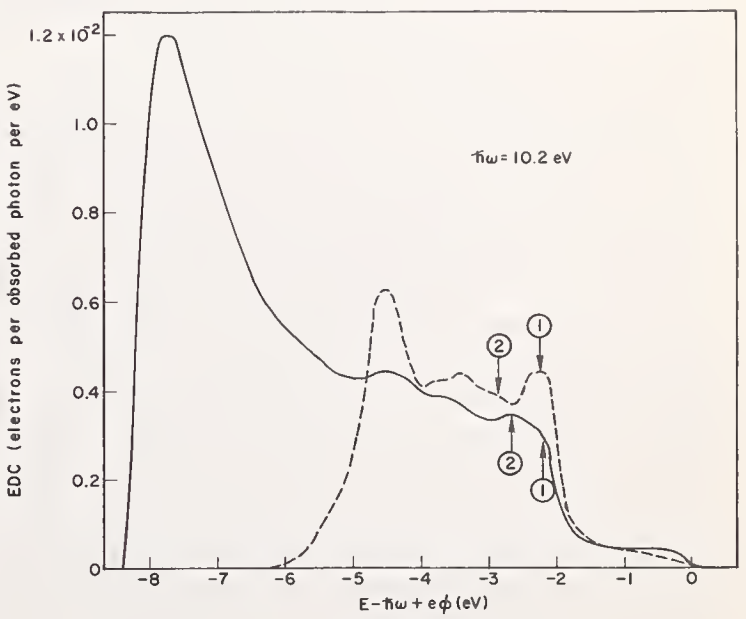

FIGURE 6. *Comparison of the theoretical EDC (dashed curve) and the experimental EDC (full curve) on cesiated* Cu *at* $\hbar\omega = 10.2$ *eV.*

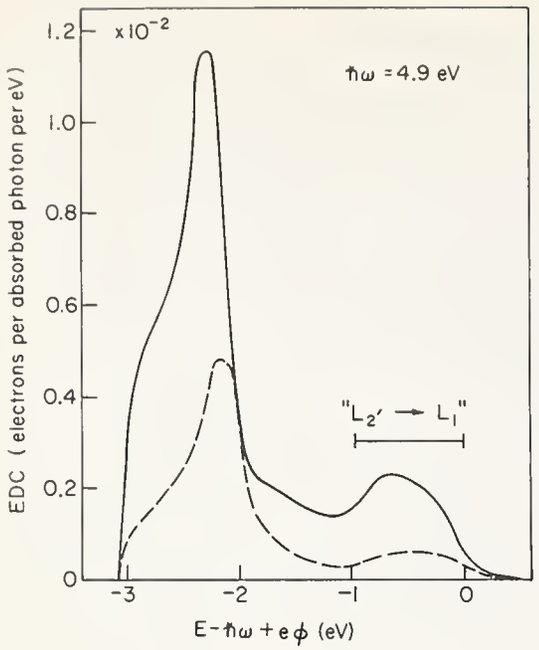

FIGURE 7. *Comparison of the theoretical EDC (dashed curve) and the experimental EDC (full curve) on cesiated* Cu *at* $\hbar\omega = 4.9$ *eV.* The structure at the high energy end is due to direct transitions in the vicinity of $L_{2'} \rightarrow L_1$.

The structure predicted in the theoretical EDC agrees well for the lower d bands, but not so well for the uppermost d bands. The uppermost d-band peak in the experimental curve is a composite of two peaks labelled 1 and 2 which merge at about this photon energy. The two uppermost pieces of structure in the theoretical curve are again labelled 1 and 2. It is seen that the theory places peak 2 a couple of tenths of an eV too low. A similar discrepancy can be discerned at $\hbar\omega = 8.2$ eV in figure 5. It may be necessary to make some empirical adjustment to Burdick's bands to remove this discrepancy. However, it should also be borne in mind that the interpolation scheme is likely to go astray for final states so far removed from the Fermi energy.

The typical behavior at lower photon energies is represented by the $\hbar\omega = 4.9$ eV curve shown in figure 7. The d-band-to-conduction-band transitions are now distinct from the conduction-band-to-conduction-band transitions. The latter occur in the vicinity of $L_{2'} \rightarrow L_1$ and give rise to the rectangular shaped contribution at the high energy end of the EDC. At even lower photon energies, the EDCs are very similar to those of Berglund and Spicer. In particular, it is found that at photon energies below the $L_{2'} \rightarrow L_1$ threshold, there is still a large contribution to the EDCs all the way up to the high energy cut-off determined by the Fermi energy. Our calculations confirm that there are no direct transitions in bulk Cu which could account for these photoelectrons. By definition, these transitions must be categorized as nondirect, and their origin would be worthy of further study.

5. Conclusions Concerning the Density of States

It has been found in new photoemission experiments that some of the optical transitions from the Cu d bands can be identified as direct. Theoretical calculations of the EDCs based on direct transitions work reasonably well for these and other transitions. If a direct model is more appropriate than a nondirect model, then photoemission EDCs measure the *energy distribution of the joint density of states* rather than the density of states itself. (The relative heights of peaks in the EDC may, of course, differ from those in the EDJDOS because of optical matrix element variations which have been ignored here.) To determine the density of states in such circumstances, the procedure must be to find a band structure whose EDJDOS is consistent with the photoemission EDCs: the density of states is then simply calculated from the band structure. The availability of high speed interpolation schemes is therefore of great importance here.

The currently available interpolation schemes [5.11] are very versatile in that the band structures of many noble and transition metals can be simulated by adjustments of only a dozen or so disposable parameters. The photoemission EDCs are rich in structure, so that to obtain the kind of agreement shown in figures 3—7 imposes very strong constraints on the permitted band structures. This holds out the exciting prospect that it may be possible, armed only with an interpolation scheme and the photoemission data, to arrive at an almost purely experimental determination of the E,k curves for any arbitrary d-band metal!

How similar is the EDJDOS to the density of states? Figure 8(b) shows the *calculated* EDCs for cesiated Cu based on direct transitions at three widely spaced photon energies. Figure 8(a) shows the histogram of the density of occupied states calculated from the same band structure. Certain similarities are evident. Prominent peaks in the EDC quite often coincide in energy location with peaks in the density of states. This is merely a consequence of the fact that in order to have initial states for optical transitions one must first of all have states. In other words, it is possible for the density of states to impose itself on the EDJDOS and, in certain cases (such as flat bands) to become the dominant consideration. Noting that the structure in the experimental EDCs is more blurred than in theory, only the strongest and most persistent peaks will survive. This may go some way towards explaining the success of the nondirect approach, and the similarity of the empirically derived optical densities of states to the band structure densities of states.

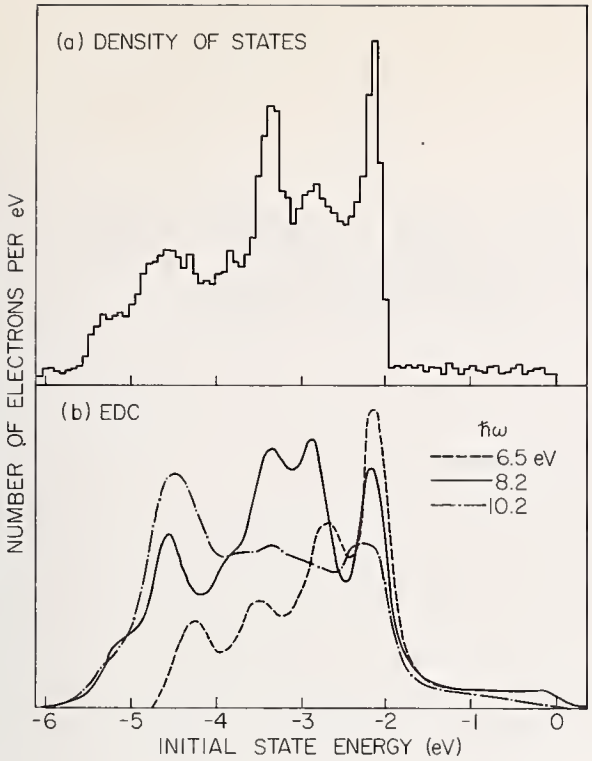

FIGURE 8. *Density of filled states for* Cu *is compared with the theoretical EDCs for* $\hbar\omega = 6.5$, *8.2 and 10.2 eV calculated on the basis of direct transitions.*

The zero of energy corresponds to the Fermi level.

6. Acknowledgments

I would like to thank Professor W. E. Spicer for placing the facilities of his laboratory at my disposal and for his interest. Useful conversations with Dr. L. F. Mattheiss and Dr. C. N. Berglund are also gratefully acknowledged.

7. References

[1] Berglund, C. N., and Spicer, W. E., Phys. Rev. **136**, A1030, A1044 (1964).
[2] Krolikowski, W. F., and Spicer, W. E., Phys. Rev., in press.
[3] Blodgett, A. J., Jr., and Spicer, W. E., Phys. Rev. **146**, 390 (1966), and **158**, 514 (1967); Yu, A. Y-C., and Spicer, W. E., Phys. Rev. **167**, 674 (1968).
[4] Eastman, D. E., J. Appl. Phys. **40**, 1387 (1969).
[5] Smith, N. V., and Spicer, W. E., Optics Communications **1**, 157 (1969).
[6] Hodges, L., Ehrenreich, H., and Lang, N. D., Phys. Rev. **152**, 505 (1966).
[7] Burdick, G. A., Phys. Rev. **129**, 138 (1963).
[8] Brust, D., Phys. Rev. **139**, A489 (1965). A more sophisticated method of performing this kind of calculation is outlined by J. F. Janak, D. E. Eastman, A. R. Williams, these Proceedings, p. 181.
[9] Further details of this equipment are given by N. V. Smith and W. E. Spicer, Phys. Rev., in press.
[10] Spicer, W. E., and Berglund, C. N., Rev. Sci. Instr. **35**, 1665 (1964); and Eden, R. C. (to be published).
[11] Mueller, F. M., Phys. Rev. **153**, 659 (1967).

The Band Structure of Tungsten as Determined by Ultraviolet Photoelectric Spectroscopy

C. R. Zeisse*

Naval Electronics Laboratory Center, San Diego, California 92152

The technique of photoelectron spectroscopy has been used to probe the band structure of tungsten in the energy region where the 5*d* bands are most prominent. The work function of the clean sample, a 25 micron thick polycrystalline foil, was found to be 4.36 ± 0.02 eV, and the yield rose by three orders of magnitude from 5.0 to 11.3 eV without showing prominent structure of any other sort. The electron energy spectra, on the other hand, contain two pieces of reliable structure which are found to increase in energy at the same rate as the exciting photon energy. A simple analysis of the data gives evidence that the density of *d* states in tungsten consists of a shoulder just below the Fermi level, a peak located about 1.5 eV below the shoulder, and a broad peak which extends at least 7 eV below the Fermi level.

Key words: Carbon contamination; electronic density of states; photoemission; tungsten (W); UV photoemission; work function.

1. Introduction

It is expected that the 5*d* electrons, often cited as the cause for the high resistivity of transition metals, will produce the most prominent structure in the density of states in tungsten. Each of the two tungsten band structure calculations, W_1 and W_2, which have been done by Mattheiss [1] show three peaks below the Fermi surface.

Experimentally, the density of states for tungsten is well known near the Fermi level, but not at other energies, and the object of this work is to present experimental photoemission data confirming the existence of this structure in the density of states below the Fermi energy.

2. Apparatus and Procedure

Particular attention has been paid to cleanliness and carbon contamination, known to have caused difficulties in photoemission, ion neutralization, and electron diffraction work on transition metals [2]. The standard ac technique of Spicer and Berglund [3] has been used with a spherical, gold plated collector and a LiF window. The incident light intensity was measured outside the window with a sodium salicylate wavelength convertor and photomultiplier tube. The maximum photon energy used was 11.2 eV, and the total resolution in the worst possible case of highest photon energy and highest retarding potential was 1.5 eV. The samples were 25 micron thick rolled tungsten foils [4], initially cleaned ultrasonically in detergent and methyl alcohol and then processed in a continuously pumped ultrahigh vacuum in the following manner: The sample was clamped between heating bars and flashed to high temperatures by passing a high ac current through it for about 10 seconds. The pressure rose as the gases were desorbed from its surface, but returned to the base pressure of $1\text{-}2 \times 10^{-11}$ torr within 1/2 minute. The maximum pressure during the flash depended linearly on the time spent by the cold sample between flashes and was typically 3×10^{-10} torr for each intervening minute. Assuming a sticking coefficient of unity, this figure is just what would be expected from complete vaporization of all gases which could collect on the sample surface during the intervening time interval at the base pressure. The flashing temperature was 2100 K, chosen because the use of higher temperatures up to 2500 K produced no change in any of the energy spectra. An energy spectrum could be started within 1 minute of the flash and was usually finished within 4 minutes. Carbon was removed by heating for at least one diffusion time constant (11.4 hours at 2200 K for a 25 micron thick sample) in an atmosphere of 5×10^{-7} torr oxygen [5].

*Mailing address: Code S350.2, NELC, San Diego, California 92152.

Unfortunately, a measurement could never be repeated exactly because of small but systematic changes in both the energy spectra and yield with the time from flash. These changes were on the order of a 1% increase in the area of a spectrum in 4 minutes and as much as a 50% decrease within 15 minutes in the yield near threshold. After several days in the vacuum the energy spectra showed increasing numbers of electrons at all kinetic energies, a factor of 2 increase in area being commonly observed. Upon flashing again the entire process could be repeated. The increase in area after long exposures is similar to that observed by Waclawski et al. [6] during yield measurements from a polycrystalline tungsten ribbon exposed to various gases, but the behavior immediately after the flash is more difficult to explain as a contamination effect since only about 1/2% of a monolayer can collect in 4 minutes at 1×10^{-11} torr. Furthermore, the process did not depend on total pressure or light exposure in any systematic way, so that it seems most likely that some change is occurring in the sample due to the recent flash. In short, the phenomenon is complicated and not understood but was taken into account wherever necessary by extrapolating the data back to the time of the flash.

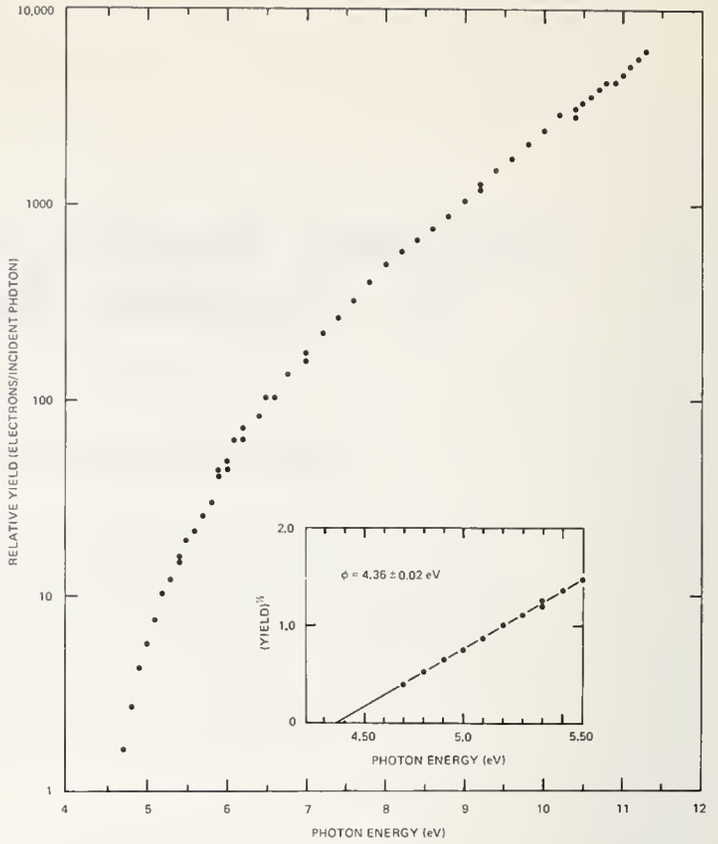

FIGURE 1. *The relative yield of Sample II, uncorrected for reflectivity.* The insert shows a Fowler plot of the data near threshold. The inclusion of data from Sample I would increase the scatter by a factor of 2.

3. Data and Discussion

The relative yield is shown in figure 1, uncorrected for reflectivity but corrected for the transmission of the LiF window. A Fowler plot, used to determine the work function, is shown in the inset. The sodium salicylate was at most 2 weeks old for this sample, but was several months old for Sample I, and since it was exposed to the diffusion oil environment of the monochromator its response probably is only flat to within 25% [7], which is considered to be the accuracy of the measurement. At any rate, there is no fine structure to the curve at this precision, but the continued rise in yield at high energies is interesting. The yield of chromium, for example, rises by a factor of about 2.5 in the energy

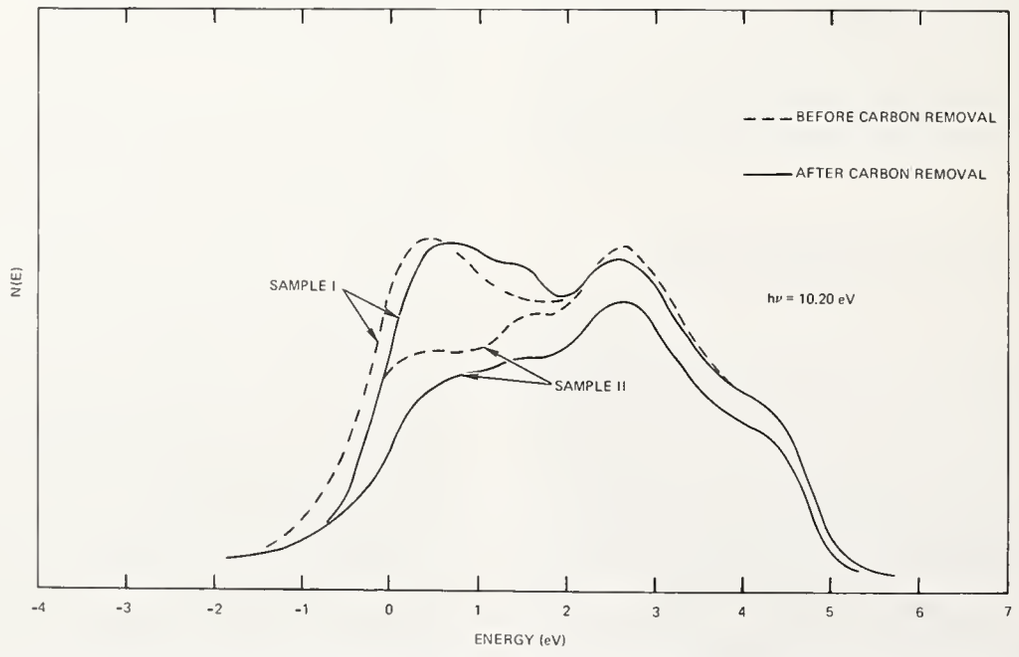

FIGURE 2. *A comparison of the electron energy spectra for the two samples before and after carbon removal.* The curves are unnormalized and have been shifted in energy to make the structure coincide.

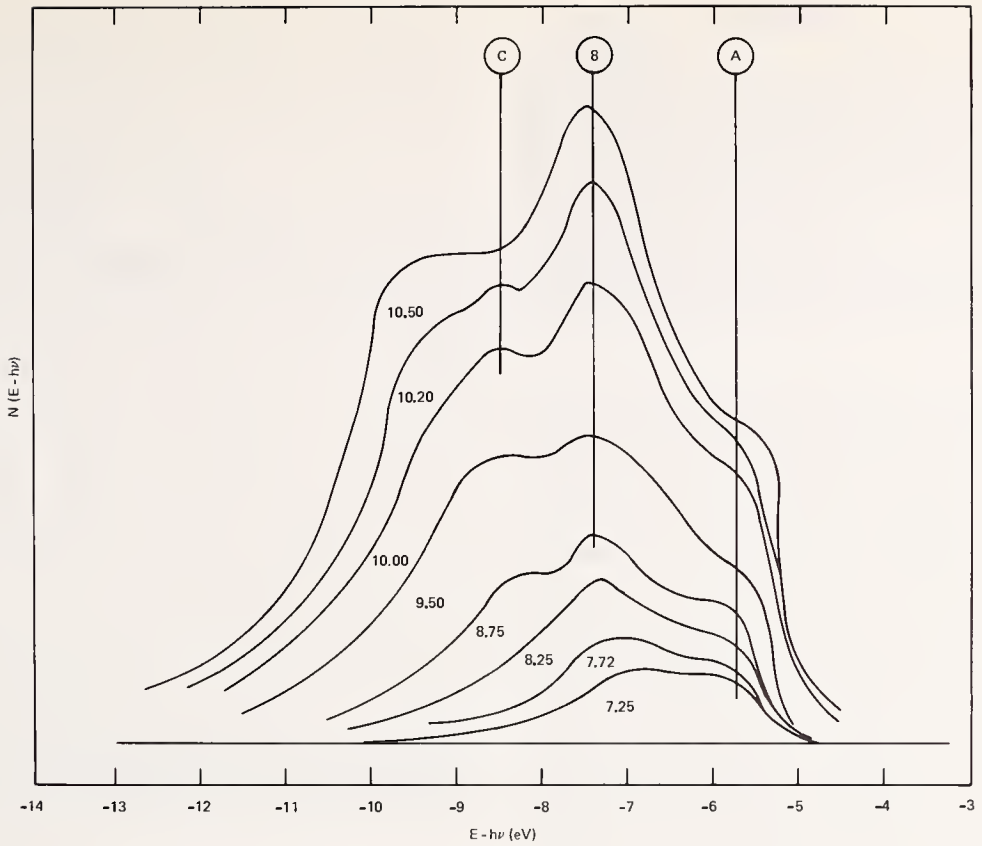

FIGURE 3. *Normalized energy spectra for Sample II, referred to initial energy states and labeled with the value of the exciting photon energy in eV.*

The Fermi energy occurs at about −5 eV on this plot, but its exact location is obscured by the high energy tail caused by scattered light.

range from 8 to 11 eV [8], whereas the yield for tungsten, two elements below chromium in that column of the periodic table, rises by a factor of 10 in this same energy region. The following argument implies an appreciably strong density of states in tungsten 11 eV below the vacuum level: According to Spicer [9], the yield far from threshold is proportional to A/(A+B), where A is a factor due to transitions from filled states to empty states above the vacuum level and B is a factor due to transitions from filled states to empty states between the Fermi and vacuum levels. An immediate consequence of this relation is that the yield is constant for all energies where B remains zero. Neglecting processes such as the creation of two electrons from a single photon or energetic electron (i.e., pair production and scattering effects), B will be zero for photon energies larger than the separation between the bottom of the *d* band and the vacuum level. Taking the bottom of the *d* band as the energy of the point H_{12} in the Mattheiss calculation and using the experimentally determined value of the work function, this energy turns out to be 10.5 eV for W_1 and 12.1 eV for W_2. Since there is no indication of a plateau in the yield up to 11.3 eV, and since the *s* electron contribution to the density of states is negligibly small compared to the *d* electron contribution, the yield results indicate a *d* bandwidth at least as great as 11.3 eV, tending to favor the W_2 calculation.

Figure 2 shows the energy spectra from the two tungsten foils, both before and after carbon removal. The shoulder and high energy peak are considered to be reliable structures, whereas the small hump at 1.5 eV was on the order of the noise in the trace and was not present in Sample I before carbon removal. The lowest energy peak in the first sample is attributed to scattering, since its amplitude increased but its position remained constant in energy as $h\nu$ was increased. This interpretation is supported by the fact that the shoulder smeared out in Sample I for energies larger than 10.5 eV, whereas it was still present at 11.2 eV in Sample II. The rounding of the high and low cut-offs due to scattered light is particularly conspicuous at zero energy in Sample II after carbon removal.

The energy spectra for Sample II are shown in figure 3. These curves have been normalized by dividing each by the incident light intensity and the transmission of the LiF window. For each curve the retarding potential E has been shifted down by $h\nu$ in order to emphasize structure which "moves with $h\nu$." It can be seen that the shoulder and high energy peak, labeled A and B in figure 3, line up nicely after this procedure, a characteristic feature of transitions from *d* states which have

been observed in other photoemission studies [10]. As mentioned above, the existence of the small peak labeled C is dubious experimentally. Examination of other spectra in the vicinity of 10.2 eV shows that it comes out of the threshold at 10.1 eV and disappears into the noise at 10.4 eV. Although this behavior is characteristic of a direct (i.e., **k**-conserving) transition [11], a search of the calculated band structures failed to reveal any direct transition to which this peak could be attributed.

Photoemission studies in which the structure moves with $h\nu$ have customarily been interpreted on the basis of a nondirect (i.e., non **k**-conserving) model, but a recent calculation in copper assuming direct transitions and using the full interpolated band structure has also been successful in predicting much of the data experimentally found in the *d* band [12]. This tends to blur the distinction between direct and nondirect models of the photoemission process, although the ability of both models to successfully predict the structure in the case of copper may merely be due to the flat E versus **k** behavior of the *d* states in that metal. In any case, a detailed analysis has not been made here, the major point being that the shoulder and high energy peak are somehow related to the density of *d* states in tungsten. The main point in favor of this interpretation is the coincidence of structure when plotted in terms of initial energy.

In figure 4 the 10.20 eV spectrum is compared with the W_1 density of states below the Fermi level. The main difference in the calculation of W_1 and W_2 is that the exchange potential in W_1 is 30% less than in W_2. This results in the W_2 density of states having a slightly larger separation between the two high energy peaks (about 1.7 eV) and a broader peak at low energy (a full width at half-maximum of about 1.7 eV). The energy spectra provide a slightly better fit to the W_1 calculation, although the yield data favor the deeper reach of the *d* band indicated by the W_2 calculation. Unfortunately, the energy spectra do not give a good indication of the total *d* bandwidth because the threshold function cuts off the low energy portion of the spectrum even at 11.2 eV.

4. Conclusion

Photoemission spectroscopy of two tungsten foils gives evidence of a shoulder just below the Fermi level and a peak about 1.5 eV below the shoulder. A broad peak occurs at lower energies. The evidence for the highest energy structure comes primarily from the electron energy spectra, which display these structures moving with the exciting photon energy and thereby due to initial states in the *d* band. The evidence for the broad low energy peak comes from the continued rapid increase of the tungsten yield between 8 and 11.3 eV. Comparison with the band structure calculation of Mattheiss provides no convincing reason for choosing his potential W_1 over W_2, but does confirm the existence of three peaks in the density of states below the Fermi level.

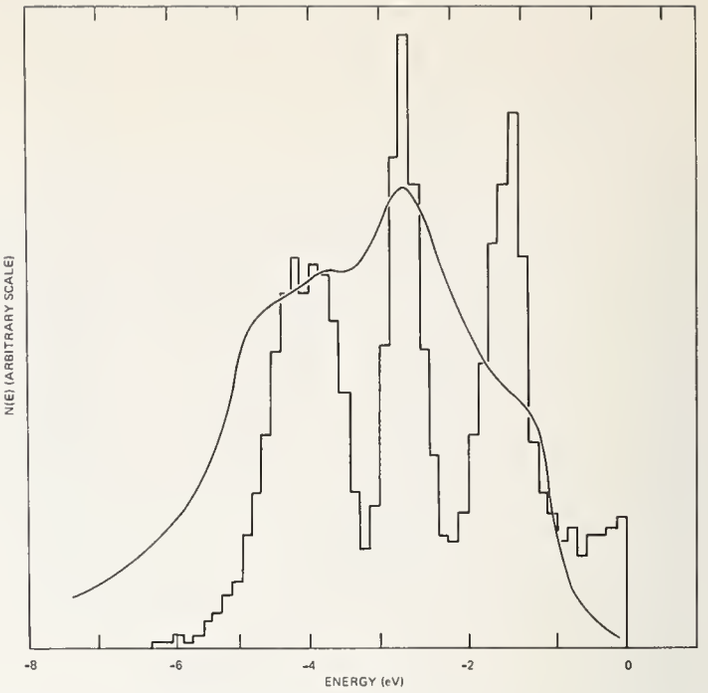

FIGURE 4. *A comparison of the 10.20 eV energy spectrum from Sample II and the* W_1 *density of states calculated by Mattheiss.*
The zero of energy is taken at the Fermi level, and the position of the experimental curve has been shifted to give the best agreement with the calculated structure.

5. Acknowledgments

The author acknowledges fruitful discussions with Dan Pierce, Neville V. Smith, and William E. Spicer, and the expert help of George Van Vleck in managing the ultrahigh vacuum system.

6. References

[1] Mattheiss, L. F., Phys. Rev. **139,** A1893 (1965).
[2] For example, see D. E. Eastman and W. F. Krowlikowski, Phys. Rev. Letters **21,** 623 (1968); D. W. Vance, Phys. Rev. **164,** 372 (1967); and P. J. Estrup and J. Anderson, J. Chem. Phys. **46,** 567 (1967).
[3] Spicer, W. E., and Berglund, C. N., Rev. Sci. Instr. **35,** 1665 (1964).
[4] Sample I was obtained from Materials Research Corporation and was stated to have less than 250 ppm total impurities including 20 ppm carbon. Sample II was obtained from the Rembar Company, Inc. and was listed as 99.99% pure.

[5] Becker, J. A., Becker, E. J., and Brandes, R. G., J. Appl. Phys. **32,** 411 (1961). One annoying aspect of oxygen processing was that the long times spent at high temperature caused the foils to become very bumpy, scattering light onto the collector and causing a reverse photocurrent which contributed unwanted high and low energy tails to the spectra.
[6] Waclawski, B. J., Hughey, L. R., and Madden, R. P., private communication.
[7] Samson, J. A. R., J. Opt. Soc. Am. **54,** 6 (1964), and Allison, R., Burns, J., and Tuzzolino, A. J., J. Opt. Soc. Am. **54,** 1381 (1964).
[8] Lapeyre, G. J., and Kress, K. A., Phys. Rev. **166,** 589 (1968).
[9] Spicer, W. E., Phys. Rev. **112,** 114 (1958), and Spicer, W. E., Phys. Chem. Solids **22,** 365 (1961).
[10] Spicer, W. E., Phys. Rev. **154,** 385 (1967).
[11] Berglund, C. N., and Spicer, W. E., Phys. Rev. **136,** A1030 (1964).
[12] Smith, N. V., and Spicer, W. E., private communication.

Photoemission Studies of Scandium, Titanium, and Zirconium

D. E. Eastman

IBM Thomas J. Watson Research Center, Yorktown Heights, New York 10598

Photoemission spectroscopy studies of the hexagonal metals Sc, Ti and Zr in the 4 to 11.6 eV range have resolved *d*-band structure and have determined occupied *d*-band widths (at 1/2 maximum) of 1.6, 2.0 and 2.3 eV respectively. Resolved structure for all three metals correlates with structure in energy band density of states: however, the observed band widths for Ti and Zr are much narrower than previously calculated band widths. The relation of the data to the controversy concerning the nature of optical excitations in transition and noble metals (direct *vs* nondirect transitions) is discussed.

Key words: Copper; direct versus nondirect transitions; electronic density of states; gold (Au); nondirect transitions; optical density-of-states; photoemission; scandium (Sc); silver (Ag); titanium (Ti); zirconium (Zr).

1. Introduction

Photoemission spectroscopy (PES) studies have been made on Sc, Ti and Zr in the 4 to 11.6 eV range. Energy distribution curves (EDCs), quantum yields, and workfunctions are reported. The data show narrow occupied *d*-bands with structure that correlates with structure in energy band densities of states. For example, the EDCs of Sc show a peak at the Fermi energy E_F, while the EDCs of Ti and Zr show a low intensity shoulder at E_F; this behavior is consistent with specific heat measurements and APW band calculations, both of which show a large density of states at E_F for Sc and much smaller densities of states for Ti and Zr.

The experimental data are summarized via the photoemission optical density of states (ODS), which has been determined using the nondirect transition model (with crystal momentum **k** not conserved in the excitation process) [1, 2]. In this case the ODS is a density of states function (weighted by transition probabilities) which describes the energy locations and amplitudes of observed structure, and which is expected to correspond to the occupied band density of states.

Currently, it is not clear that optical excitations in transition metals are due to nondirect transitions; in fact, there is evidence that direct (**k**-conserving) interband transitions [3] can account for observed photoemission structure. If the excitations are due to direct transitions, the ODS describes the energy locations and amplitudes of structure in the measured EDCs. In this case, the ODS only coincidently reflects structure in the total band density of states since only a small fraction of the occupied electron states are excited. Recent PES evidence for direct transitions is discussed in section 3.

2. Experimental Results

Photoemission measurements were performed on evaporated polycrystalline films of Sc, Ti and Zr. Experimental techniques are described elsewhere [4].

Scandium. Normalized energy distributions (EDCs) are shown in figure 1 and the quantum yield (electrons emitted per incident photon [5]) is shown in figure 2. The workfunction was determined as $\phi = 3.5 \pm 0.15$

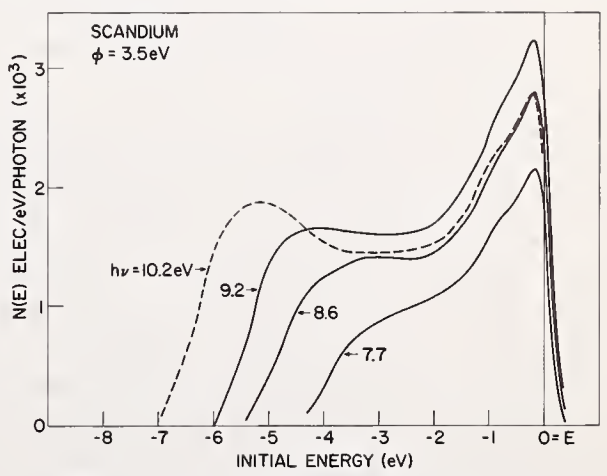

FIGURE 1. *Energy distributions (EDC's) for* Sc.
The EDC's are plotted versus the initial energy $E_i = E - h\nu + \phi$, with the Fermi level E_F set equal to zero.

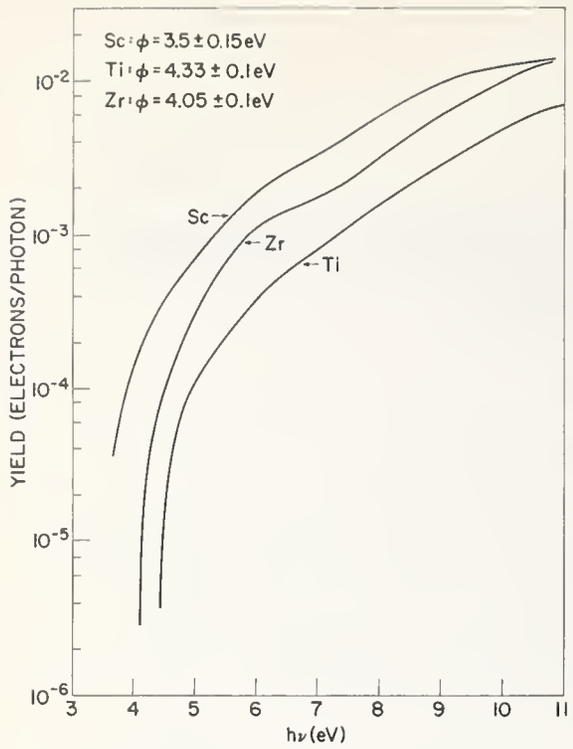

FIGURE 2. *The quantum yield (per incident photon) for* Sc, Ti *and* Zr.

eV. For Sc, maximum emission occurs from energy states within ~2 eV of E_F for all photon energies; these states are identified as the occupied d states. A stationary peak near E_F and a shoulder at ~ -0.9 eV are observed in all EDCs.

The low quantum yield ($Y \simeq 10^{-2}$ at 10 eV) is characteristic of the typically short hot electron mean free paths (~ 10 Å at 10 eV above E_F) in transition metals [6]. An analysis of secondary electron emission due to electron-electron scattering [1,6] for Sc indicate that this mechanism accounts for most of the observed slow electron emission (with energies less than −2 eV in fig. 1): our analysis assumed the usual optical absorption depth of ~100-150 Å. A fraction of the slow electron emission $\lesssim 2$ eV above the kinetic energy threshold which is observed for $h\nu \geq 10$ eV (at ~ -5 eV for $h\nu =$ 10.2 eV in fig. 1) is believed to be due to surface impurities (similar comments apply for Ti and Zr).

The ODS for the occupied d bands of Sc is compared with a theoretical band density of states in figure 3. The ODS was determined using the nondirect transition model with a smooth unoccupied conduction band [7]. The band density of states shown for Sc in figure 3 is the density of states calculated for Y by Loucks [8], which has been scaled in energy by 0.85 to account for the ~ 15% narrower d bands in Sc [9]. This approximation is expected to adequately represent the band width and major structure for Sc [9]. Agreement between the ODS and band density of states is excellent. The band widths agree, and the observed peak at E_F and shoulder at −0.9 eV agree with the principal structure in the band density of states.

Titanium. Energy distributions (EDCs) are shown in figure 4 and the quantum yield is shown in figure 2. The workfunction was determined as $\phi = 4.33 \pm 0.1$ eV using the usual Fowler plot. Emission from d states within ~2 eV of E_F dominates the EDCs for all photon energies. A low amplitude shoulder is observed at E_F, with two peaks at ~ -0.7 and −1.2 eV. Transition probability effects are observed for Ti which cannot be simply fitted using an ODS with constant matrix elements: the structure at −0.7 eV, which is a shoulder for low energies ($h\nu \simeq 8$ eV), increases in relative amplitude until it equals the amplitude of the −1.2 eV peak at $h\nu \simeq 10$ eV, and then decreases (and washes out) at still higher energies. This observed behavior contributes to the increasing evidence against the nondirect transition model (see sec. 3).

As with Sc, most of the slow electron emission (energies < -2 eV in fig. 4) is attributed to secondary electrons created by inelastic electron-electron scattering. The slow electron peak at $\simeq -5$ eV which increases for $h\nu \gtrsim 10$ eV is believed to be due in part to surface impurities.

An ODS is shown for Ti in figure 5 which describes the energy locations of observed structure, and the amplitudes for $h\nu \simeq 10$ eV [10]. The existence of a low amplitude shoulder at E_F and 2 peaks at lower energies (at ~ -0.7 eV and −1.2 eV) correlates with the major structure in the band density of states (fig. 5), however, the ODS band width (2 eV) is significantly narrower than the theoretical band width (2.8 eV) [11].

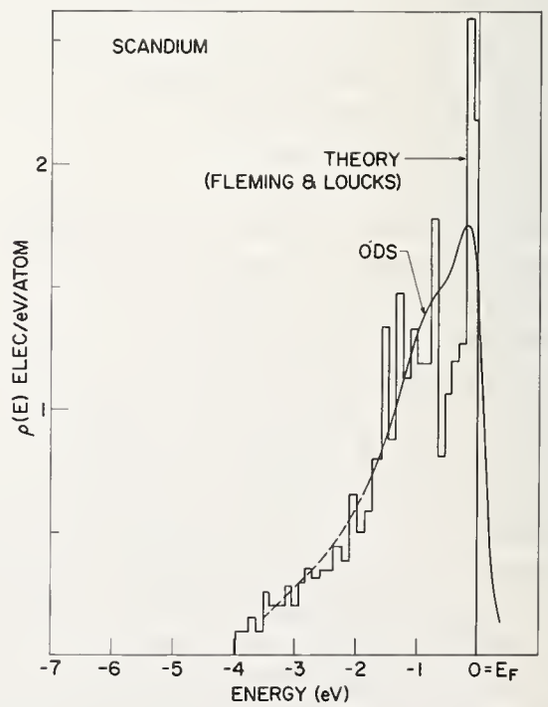

FIGURE 3. *ODS and theoretical density of states for* Sc.

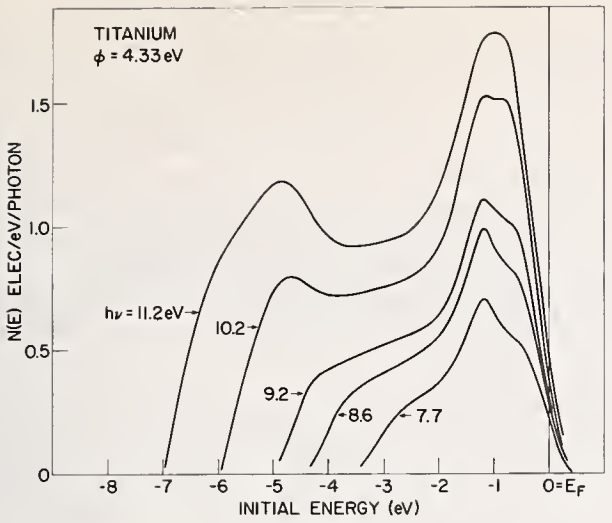

FIGURE 4. *Energy distributions (EDC's) for* Ti.

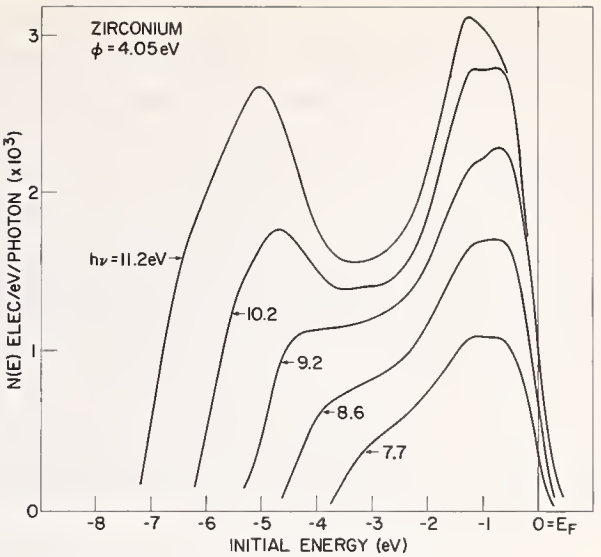

FIGURE 6. *Energy distributions (EDC's) for* Zr.

The ODS's of Ti and Sc show a rigid band relation; if the Fermi level of the ODS for Ti is lowered by ~0.7 eV to account for 3 rather than 4 valence electrons, the resulting ODS closely resembles that determined for Sc.

Zirconium. Energy distributions (EDCs) are shown in figure 6 and the quantum yield is shown in figure 2. The measured workfunction is $\phi = 4.05 \pm 0.1$ eV. The EDCs show structure and amplitude effects which are very similar to those described for Ti. An ODS for Zr is shown in figure 7 which summarizes the observed *d*-state structure and occupied band width (~ 2.3 eV). The band density of states for Zr calculated by Loucks [12] using the APW method is also shown in figure 7. The observed band width (~ 2.3 eV) is narrower than the calculated band width (~ 3 eV).

3. Discussion

Photoemission energy distributions for Sc, Ti and Zr show *d*-state structure (which is stationary in initial-state energy) which indicates narrow (~ 1.5-2.3 eV) occupied *d* bands. Observed structure tends to correlate with structure in theoretical densities of states. However, amplitude effects are observed for Ti and Zr which cannot be simply described using the nondirect transition model [1]. This result adds to recent developments which cast doubt upon nondirect transitions in transition and noble metals.

Two other papers (for Cu [13] and Pd [14]) presented at this conference show that the observation of stationary *d*-band structure (which has been assumed to imply nondirect transitions [1,2]) is con-

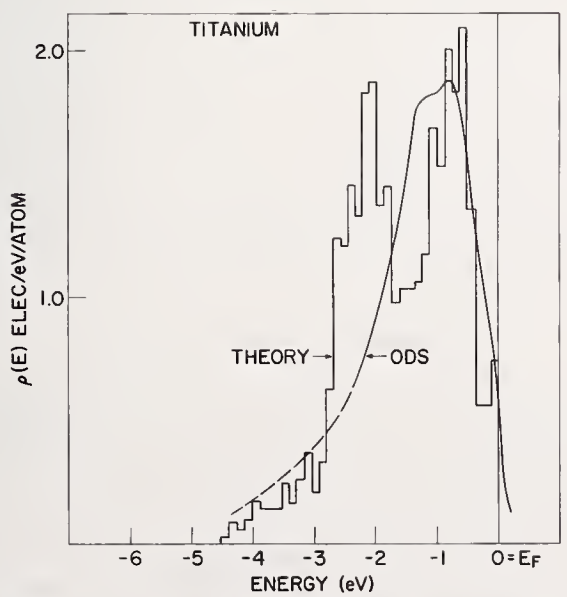

FIGURE 5. *ODS and theoretical density of states for* Ti.

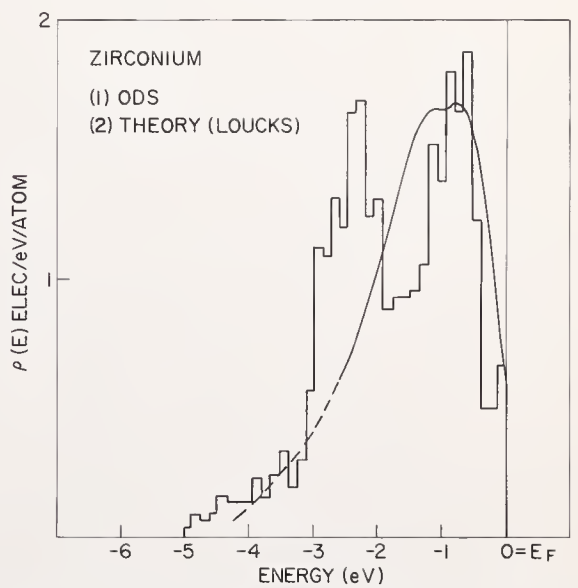

FIGURE 7. *ODS and theoretical density of states for* Zr.

sistent with direct interband transitions. This stationary structure results from the relative flatness of the *d*-bands (~ 3 eV) compared to the broad unoccupied bands (~ 40 eV), coupled with the limited range of photon energies usually accessible ($\phi < h\nu < 11.6$ eV). Further evidence which casts doubt upon nondirect transitions is given by recent high resolution photoemission measurements [15] on Au, Ag and Cu at 16.8 eV and 21.2 eV. These data show structure which is quite different from that observed at energies below LiF window cutoff (11.6 eV) and cannot be explained using the nondirect transition model [15]. It remains to be seen if direct transitions can explain this high energy data.

4. Acknowledgment

The technical assistance of J. Donelon is gratefully acknowledged.

5. References

[1] Berglund, C. N., and Spicer, W. E., Phys. Rev. **136**, A1030 (1964).

[2] Spicer, W. E., Phys. Rev. **154**, 385 (1967).

[3] Ehrenreich, H., and Philipp, H. R., Phys. Rev. **128**, 1622 (1962).

[4] See Janak, J. F., Eastman, D. E., and Williams, A. R., Proceedings of this conference (appendix). Sample chamber pressures rose to ~2 to 5×10^{-8} torr during evaporation (at ~2-5 Å/sec) and then rapidly fell to $\lesssim 2\times10^{-9}$ torr within 3 minutes after evaporation. All three metals are very reactive and require careful surface preparation.

[5] The yield $Y(\omega)$ is expressed in electrons per incident photon (rather than per absorbed photon) since the reflectance has not been measured.

[6] Eastman, D. E., to be published.

[7] The estimated accuracy in the determination of E_F is ±0.1 eV.

[8] Loucks, T. L., Phys. Rev. **144**, 504 (1964).

[9] Fleming, G. S., and Loucks, T. L., Phys. Rev. **173**, 685 (1968).

[10] This ODS doesn't represent the observed amplitudes for $h\nu \lesssim$ 9 eV and thus is not a unique ODS.

[11] The band density of states shown for Ti is the density of states calculated for Zr by Loucks [12] with the *d* band narrowed by ~ 10% to agree with the band width calculated for Ti by L. M. Mattheiss (Phys. Rev. **134**, 192 (1964)).

[12] Loucks, T. L., Phys. Rev. **159**, 544 (1967).

[13] Smith, N. V., these Proceedings, p. 191.

[14] Janak, J. F., Eastman, D. E., and Williams, A. R., these Proceedings, p. 181.

[15] Eastman, D. E., to be published.

Photoemission and Reflectance Studies of the Electronic Structure of Molybdenum*

K. A. Kress** and G. J. Lapeyre

Department of Physics, Montana State University, Bozeman, Montana 59715

Normalized energy distributions of photoemitted electrons for $4.3 < h\nu < 11.8$ eV (threshold is 4.3 eV) and near normal reflectance for $0.5 < h\nu < 11.8$ eV are measured for molybdenum films prepared with ultra high vacuum. The nondirect transition model with constant matrix elements is found to be consistent with the photoemission data. The above model, in conjunction with calculations for the emission of scattered electrons, is used to obtain the optical density of states (ODS) for the occupied states. Three peaks due to d-electrons are observed at $E - E_F = -0.5$, -1.6, and -3.9 eV where E_F is the Fermi energy. No structure is observed for $E - E_F > 4.3$ eV. The imaginary part of the dielectric constant, ϵ_2, is obtained by Kramers-Kronig analysis, and the occupied ODS are used to obtain the ODS for $0 < E - E_F < 4.3$ eV. The latter analysis is done by writing the finite difference approximation for the integral expression of ϵ_2 and solving for the empty ODS. The ODS is compared to the band calculations of Mattheiss where a molybdenum density of states is obtained by scaling his tungsten (W) results. Both the measured and calculated occupied densities of states have three peaks and both empty states have one dominant peak. The calculations predict a low density of states for $-1 < E - E_F < 0$ eV which is not observed in the data. The absorption coefficient has a minimum at 11.3 eV which correlates with a dip in the quantum yield. The energy distributions of the photoemitted electrons show small structural changes above the spectral range of the peak in the energy loss function at 10.8 eV. The relation of these data to the explanations based on the electron density of states for the anomalous isotopic mass dependence of the superconducting transition temperature is discussed.

Key words: Dielectric constant; electronic density of states; molybdenum (Mo); optical density of states; optical properties; photoemission; reflectivity; tungsten (W); zinc (Zn).

1. Introduction

Photoemission and optical measurements were used to study the electronic structure of the 4d metal molybdenum. The photoemission data were found to be consistent with the nondirect model with one possible exception. Because of the essentially nondirect character of the photoemission data, an optical density of states (ODS) graph was constructed. The results are compared with band calculation of molybdenum's 5d counterpart tungsten and its 3d counterpart chromium.

2. Experimental Procedures

The photoemission and optical data were taken from vapor deposited films of Mo. The measurements were made with the base pressure of the ion-pumped-vacuum system in the 10^{-10} torr range and the films were vapor deposited with an electron beam evaporator in the 10^{-9} torr range.

The photoemission and optical data were obtained by techniques reported elsewhere [1,2] with the exception of the quantum yield measurement. The spectral yield per incident photon was obtained directly by electronic division of the simultaneous measurement of the photoelectron current and the light flux incident on the photocathode. The yield per absorbed photon was obtained from the above data and the reflectance data. The signal proportional to the incident light flux was obtained by using sodium salicylate inside the high vacuum chamber to detect a small fraction of the incident radiation which passed through a small hole in the photocathode. The sodium salicylate was coated on the inside of a glass window and its fluorescence was measured by an external photomultiplier tube. The procedure produced a measurement of the quantum yield of gold that compared well with that measured by others [3,4]. In addition these studies showed that

*Research sponsored by the Air Force Office of Scientific Research, Office of Aerospace Research, United States Air Force, under AFOSR contract/grant number AF-AFOSR-838-65 and 68-1450. Based on a thesis submitted by Kenneth A. Kress to Montana State University in partial fulfillment of the requirements of the Ph. D. degree.

**Supported in part by the National Aeronautics and Space Administration Traineeship.

417-156 O - 71 - 15

sodium salicylate had stable fluorescent properties in ultra high vacuum for several weeks if it was maintained at room temperature. This latter observation is in agreement with other observations [5]. The above technique does not depend on the optical transmission of the LiF window used on the experimental vacuum chamber. Since the window transmission was found to change with time, this technique gave improved reproducibility of the measured quantum yield.

3. Optical Studies

The results of the optical studies that are used in the photoemission analysis are reported here. Complete discussion of the optical studies are reported elsewhere [3,6]. The reflectance of Mo films at near normal incidence is presented in figure 1. The reflectance of Mo falls rapidly as the photon energy increases in the near infrared spectral region indicating the onset of numerous optical excitations at small energies. The reflectance obtained in this study is smaller in magnitude for 2 eV $\leq h\nu \leq$ 6 eV than that reported by earlier investigators but is consistent in structure [7]. The magnitude is consistent, however, with the reported reflectance of Mo's 5*d* counterpart tungsten [7].

The optical constants were obtained by Kramers-Kronig analysis. Detailed discussion of the analysis is given elsewhere [3,6]. The reflectance was measured between 0.5 eV $\leq h\nu \leq$ 11.0 eV under ultra high vacuum conditions. The spectral range of the reflectance used in the analysis was extended by several techniques. The reflectance for $h\nu < 0.5$ eV was obtained from the Hagen-Ruben formula. It was extended to 14 eV by measurements on polished samples and to 23 eV by data obtained from the literature [7]. The magnitude of the latter data was adjusted to fit the present measurement at 14 eV and is represented by the dotted line in figure 1. In the Kramers-Kronig analysis the reflectance was extrapolated by an inverse power function for $h\nu > 23.0$ eV.

The imaginary part of the dielectric constant ϵ_2 of Mo is shown in figure 1. Shoulders are observed in ϵ_2 centered at 1.8 eV, 3.8 eV, and 7.4 eV and are consistent with structure observed in the photoemission data. The optical functions $(h\nu)^2\epsilon_2(h\nu)$ and $h\nu n(h\nu)$ which are useful in studying the photoemission data are shown in figure 2. A peak in the energy loss function, $Im(1/\epsilon)$, is observed at 10.8 eV and a relative minimum in the absorption coefficient, $\alpha(h\nu)$, is observed at 11.3 eV.

4. Photoemission Measurements

The quantum yield of Mo is shown in figure 3 along with the plot of the square root of the quantum yield used to determine the value of 4.3 eV for the photoelectric work function ϕ [2,8]. The value obtained for the work function agrees with those reported in the literature [9]. This value for ϕ was reproducible from all films deposited at $\leq 1 \times 10^{-8}$ torr with a base pressure of 6×10^{-10} torr achieved a few minutes after the deposition. The work function of films deposited at higher pressure varied from 4.4 to 4.7 eV. For films prepared at the lowest pressure, 7×10^{-9} torr, the value of ϕ increased a few tenths of an eV in eight hours with little change in the EDC's except for a decrease in width. A significant drop in the yield is centered at approximately 11.0 eV. This drop is interpreted as an optical effect. The maximum value of the quantum yield is less than 2% indicating that few of the excited electrons escape the metal even for the highest photon energies.

A representative set of the energy distribution curves (EDC's) is shown in figure 4. The EDC's are plotted as

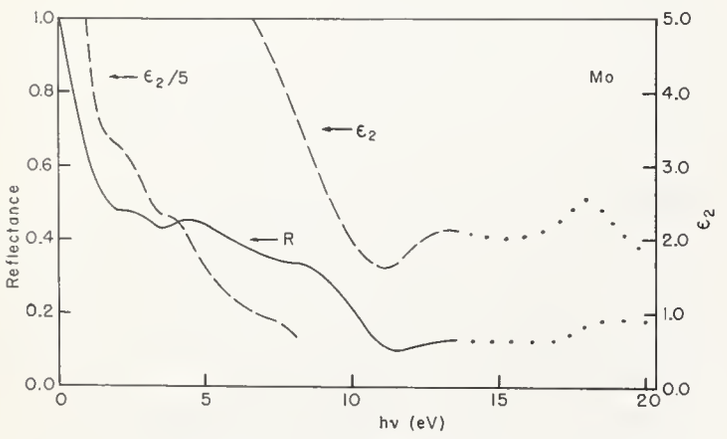

FIGURE 1. *The reflectance and imaginary part of the dielectric constant of molybdenum.*

The dotted portion represents the shape of the high energy reflectance reported in the literature (ref. [6]).

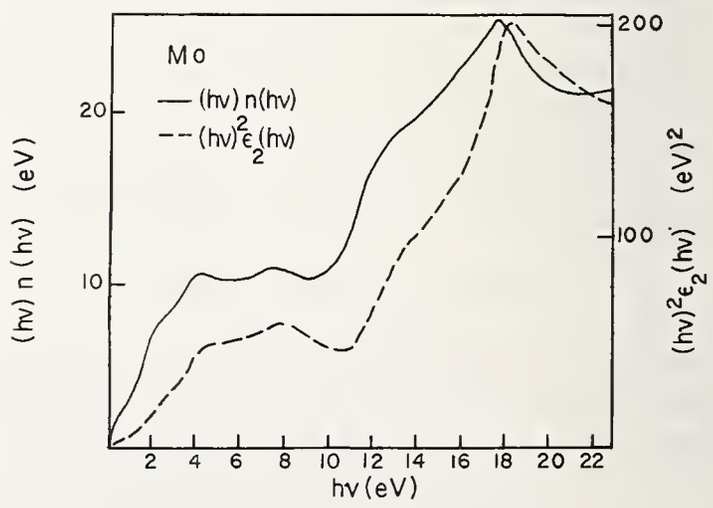

FIGURE 2. *The optical functions* hνn(hν) *and* $(h\nu)^2\epsilon_2(h\nu)$ *of molybdenum.*

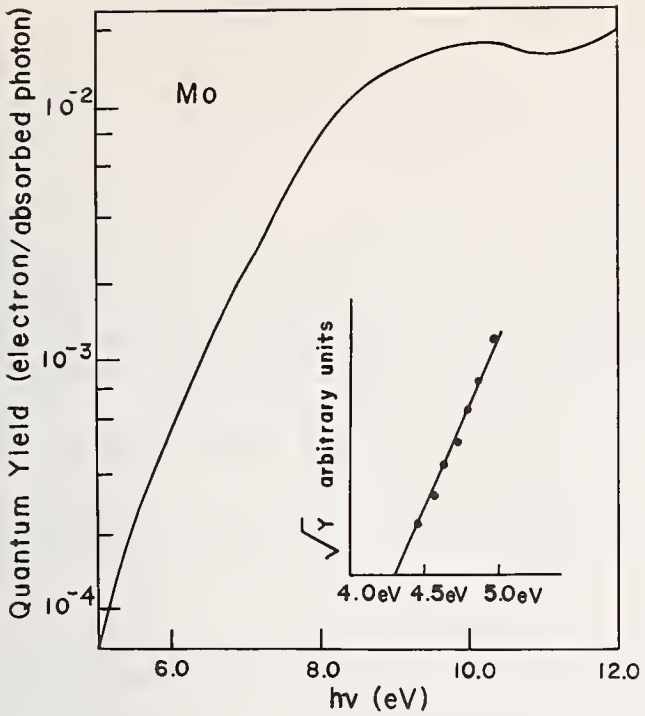

FIGURE 3. *Quantum yield of molybdenum.*

a function of the kinetic energy, $E - \phi$, and normalized to the quantum yield. The energy E is referred to the Fermi energy. The data from all other films studied were essentially identical with those shown in figure 4. Even the EDC's from film deposited at higher pressures differed only by a small attenuation of the population of high kinetic energy electrons and a small increase in the work function. Inspection of the EDC's in figure 4 reveals no structure with fixed kinetic energy and all structures move to higher kinetic energy as the photon energy is increased.

As shown in figure 5, the structures in the EDC's have fixed positions when plotted as functions of $(E - h\nu)$. Three structures are observed over the entire spectral range studied. The energies of the structures obey the equal increment rule, $E_{structure} = \Delta(h\nu)$ and are due to initial state structure at -0.5, -1.6, and -3.9 eV. The peak labeled (1) has a marked change in relative amplitude as the photon energy is increased from 10.0 to 11.0 eV. The analysis of this property is complicated by the existence of a peak in the energy loss function (10.8 eV) and a relative minimum in the absorption coefficient (11.3 eV) in this same spectral region. A definite shoulder appears at $E - h\nu = -5.0$ eV on the low kinetic energy edge of the EDC's for $h\nu > 10.0$ eV (see figs. 4 and 5). This shoulder persists and moves toward higher energy with increasing photon energy and is taken to indicate the bottom of the $4d$ bands of Mo.

5. Optical Density of States Analysis

The characteristics of the structure in the EDC's which are described in the last section indicate that the data are consistent with the nondirect transition model

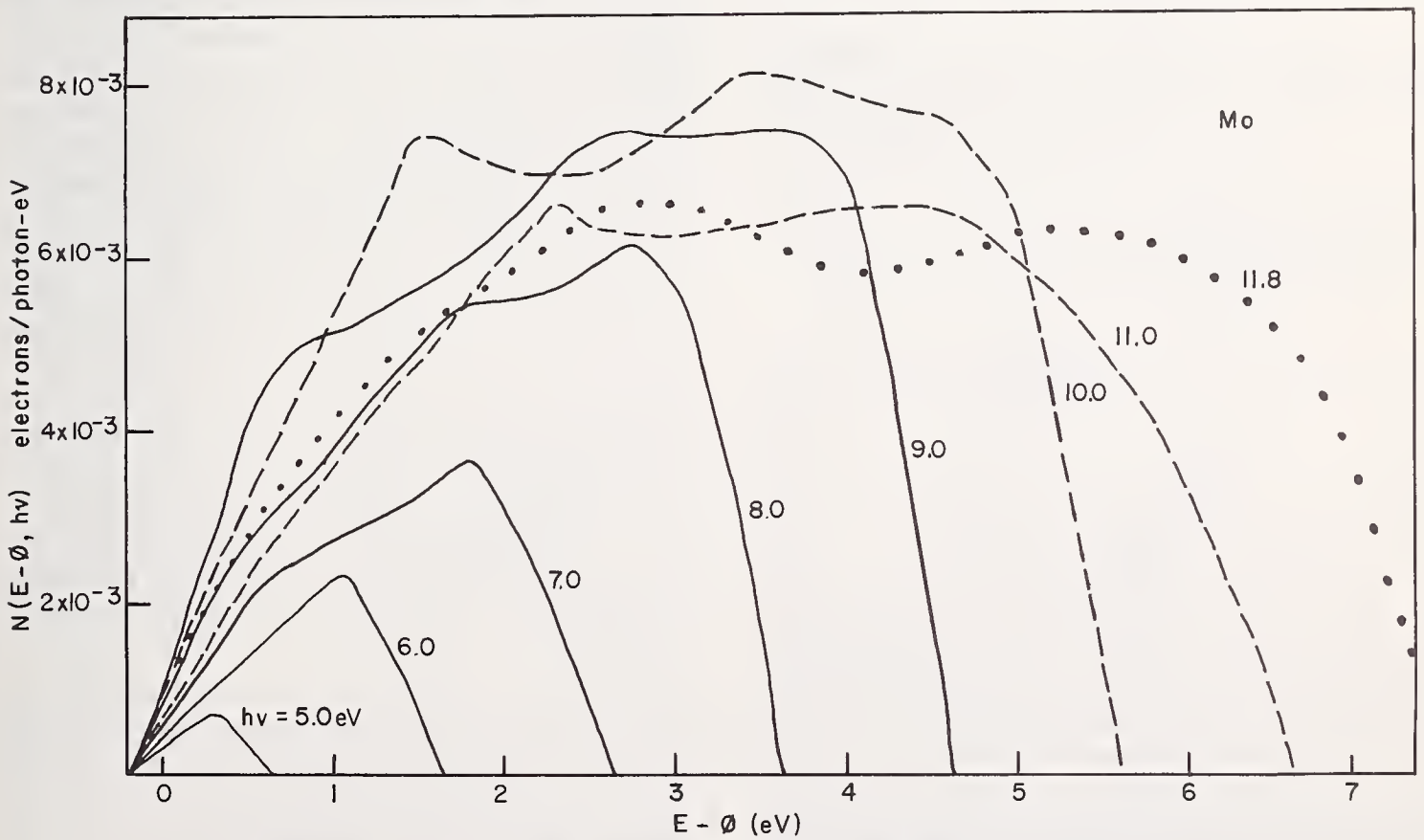

FIGURE 4. *Normalized energy distribution curves of molybdenum versus kinetic energy.*

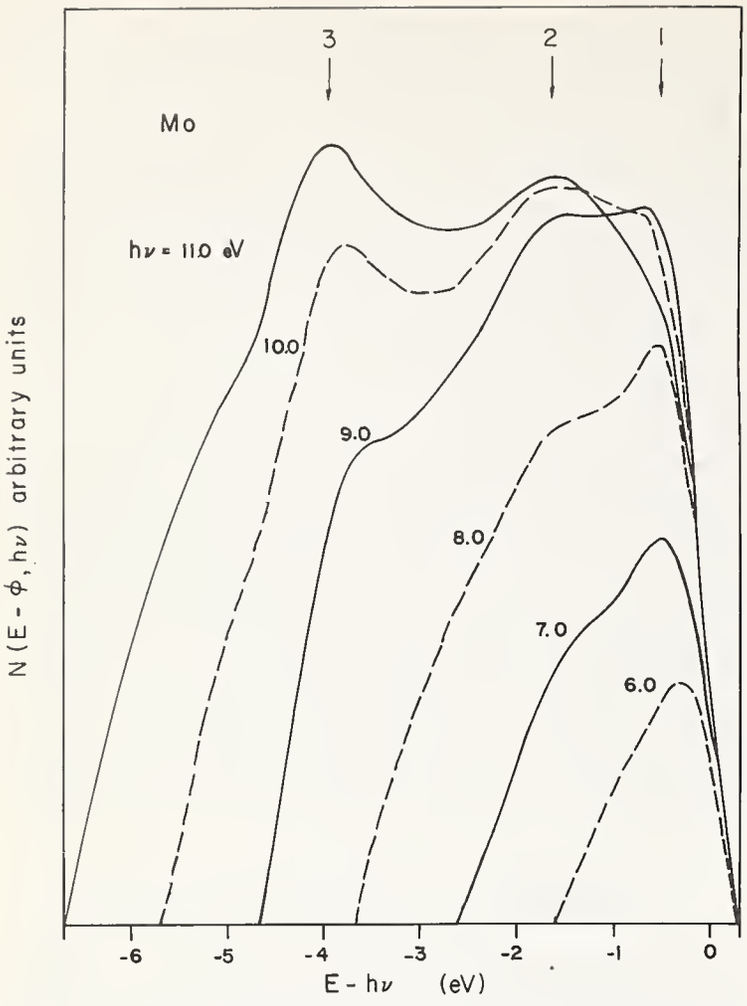

FIGURE 5. *Arbitrarily normalized energy distribution curves of molybdenum versus* E-hν.

with the possible exception of the structure labeled (1) in the 10.0 to 11.0 eV spectral range. The optical excitations in the nondirect model are proportional to the product of the density of initial and final states. The energy distribution of emitted electrons in the limit that the absorption depth is much greater than the electron-electron scattering length $L(E)$ is given by [10-12]

$$N(E-\phi, h\nu)=\frac{BN_i^{\mathrm{opt}}(E-h\nu)N_f^{\mathrm{eff}}(E)[1+S_i(E, h\nu)]}{h\nu n(h\nu)} \tag{1}$$

where

$$N_f^{\mathrm{eff}}(E)=T(E)L(E)N_f^{\mathrm{opt}}(E). \tag{2}$$

The real part of the index of refraction, the escape function and the scattering function is given by $n(h\nu)$, $T(E)$, and $S_i(E,h\nu)$ respectively. The optical density of initial and final states are respectively $N_i^{opt}(E-h\nu)$ and $N_f^{opt}(E)$ [11,12]. Any (E) or $(E-h\nu)$ functional dependence in the matrix elements is indistinguishable from the optical density of final and initial states respectively. Therefore such effects will be contained in the ODS and any other matrix elemcnts effects are taken to be constant in eq (1) [12].

For this model the imaginary part of the dielectric constant is given by [10]

$$(h\nu)^2\epsilon_2(h\nu)=A\int_0^{h\nu}N_i^{\mathrm{opt}}(E-h\nu)N_f^{\mathrm{opt}}(E)\,dE. \tag{3}$$

Given the function N_i^{opt} and $\epsilon_2(h\nu)$ one can numerically determine N_f^{opt}. Writing eq (3) in the finite difference approximation and rearranging terms eq (3) becomes,

$$N_f^{\mathrm{opt}}[(m-1)\Delta E]\simeq\frac{1}{AN_F\Delta E}\Bigg((m\Delta E)^2\epsilon_2(m\Delta E) - A\Delta E\sum_{L=1}^{m-1}N_i^{\mathrm{opt}}[(L-m-1)\Delta E]N_f^{\mathrm{opt}}[(L-1)\Delta E]\Bigg). \tag{4}$$

where $N_f^{opt}(0)=N_i^{opt}(0)=N_F=$DS at the Fermi energy. The energy scale is divided into equal increments and the increments are counted with the index m. Because ϵ_2 was not measured for small spectral values, eq (4) was not used to obtain the value of A. The constant A was adjusted to give six empty states per atom for $0<E<6.0$ eV.

The ODS calculation proceeded in two parts [3]. *First*, the effect of scattered electrons, S_i, was neglected in eq (1). Equation (1) was used to determine an approximate initial ODS which was then divided into the set of EDC's to obtain a set of approximate functions for $N_f^{eff}(E)$. Since the latter set was equivalent (within 5%) for all the EDC's, the initial ODS was assumed to be a reasonable approximation and provides additional evidence that the nondirect model is consistent with the data. The approximate initial density of states and measured ϵ_2 were used in eq (4) to obtain an approximate final density of states. With the above functions available, the *second* part of the analysis was to repeat the calculations including the effects of scattering, represented by the function $S_i(E,h\nu)$ in eq (1). $S_i(E,h\nu)$ was computed by the once scattered model of Berglund and Spicer [10] in the limit when the inelastic scattering length is much smaller than the mean optical absorption depth and when it is much smaller than the elastic scattering length. The scattering corrections were insensitive to the details of the ODS. The results of the scattering correction on a typical EDC are shown in figure 6.

The ODS obtained by the above method is shown in figure 7. Because of the spectral limit imposed by the LiF window, the states for $|E|\gtrsim 5.0$ eV cannot be studied in detail. These less reliable regions are indicated by dots in figure 7. Since the numerical inversion for N_f^{opt} was done in 0.2 eV increments, the resolution

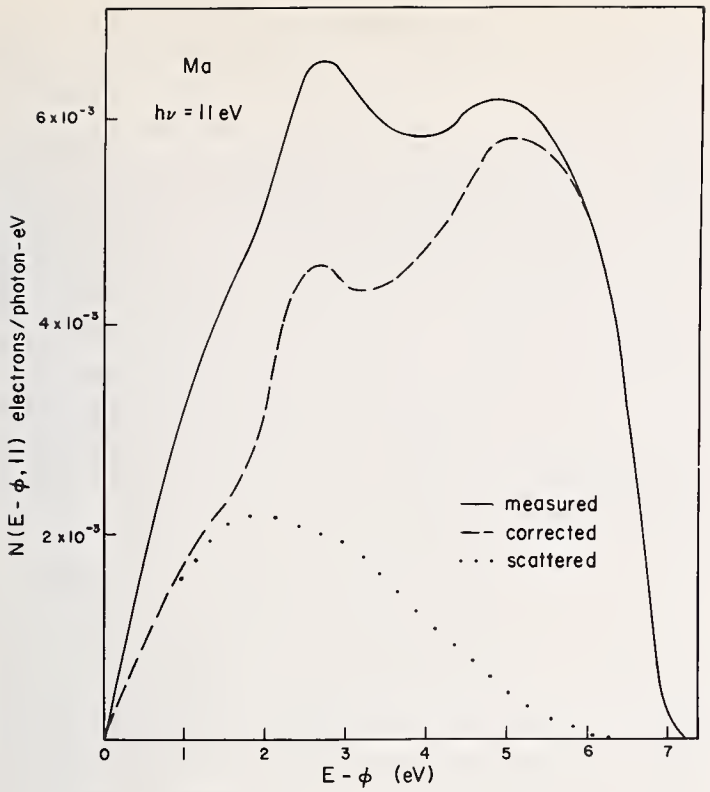

FIGURE 6. *Measured, corrected and scattered energy distribution curves of photoemitted electrons from molybdenum at* $h\nu = 11.0$ *eV.*

could not be better than this. If, in addition, the density of initial states used in the inversion for the density of final states already contains significant broadening, the details of the density of final states will be distorted. These effects combine to lessen the significance of the fine structure displayed in the density of final states seen in figure 7. The dashed, average curve for N_f^{opt} is possibly a better estimate of the density of final states even though it will not permit as accurate a recalculation of the imaginary part of the dielectric constant.

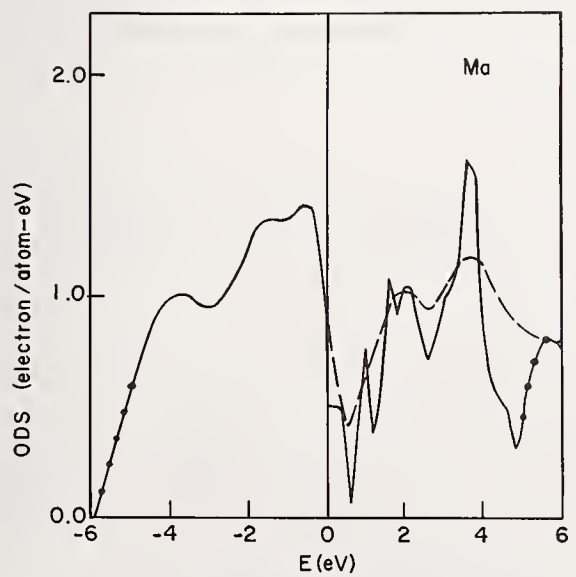

FIGURE 7. *Optical density of states of molybdenum.*

6. Discussion

The ODS is compared to a band calculation density of states (DS) in figure 8. The DS was obtained from Mattheiss' calculations for W with potential "one" [13]. Since Mo and W have the same crystal structure, bcc, and similar atomic electron configurations the band structures are expected to be essentially the same within an energy scale factor. The energy axis for the DS was rescaled by using Mattheiss' estimate of the relative d-band widths of Mo and W_I. There are three peaks below the Fermi energy in the experimental ODS (1, 2, and 3) and in the calculated DS (a, b, and c) although the energy position and amplitude of the peaks do not agree in detail. Above the Fermi energy there is one major peak in the ODS with several minor peaks at smaller energies. The calculated DS also has one large peak and two smaller ones above the Fermi energy. As with the structures observed below the Fermi energy the energy positions and amplitudes do not agree with those in the ODS. The most serious discrepancy noted between the ODS and the DS is in the region near the Fermi energy (-1 eV $\lesssim E \lesssim 0$ eV). The calculated DS has a deep and wide (~ 1 eV) valley at the Fermi energy with a small number of electron states per atom. In contrast, the ODS has a peak centered at $E = -0.5$ eV and a larger number of states per atom at the Fermi energy.

The expected essential difference between the band structure for Mo and paramagnetic Cr is an energy scale factor since they have the same atomic structure and crystal structure. In figure 9 the experimental ODS

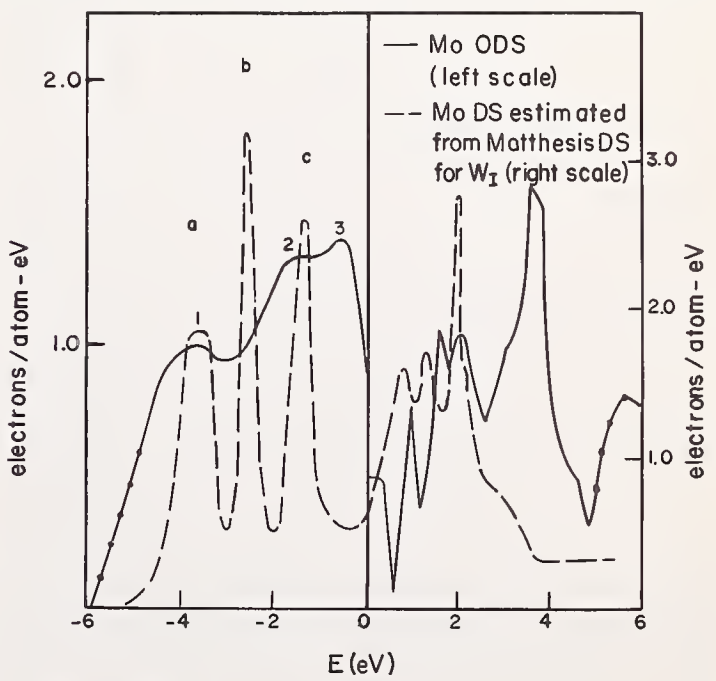

FIGURE 8. *The optical density of states of molybdenum (dotted line) is compared with the density of states estimated from Mattheiss' tungsten* (W_1) *band structure calculation (ref.* [13]).

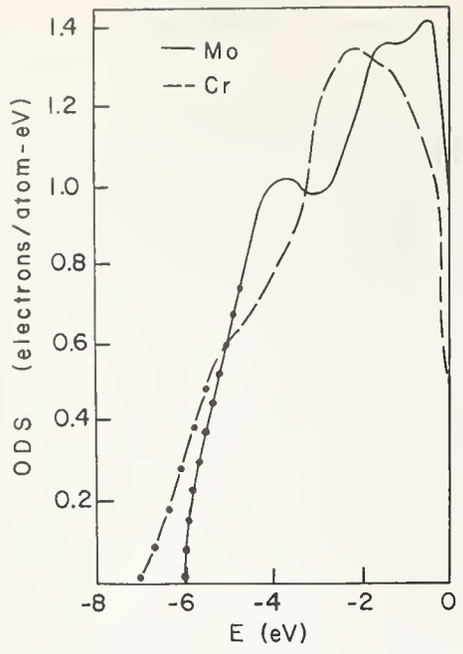

FIGURE 9. *Comparison of the optical density of states of molybdenum (present study) and chromium obtained by Eastman (ref.* [14]).

of Mo is compared to Eastman's ODS for Cr [14] which is similar to that obtained by Lapeyre and Kress [15]. There are three structure points in both Mo and Cr, but the relative amplitudes are different. The energy values of the structures are compared in table 1. Mattheiss' estimate of the *d*-band width of Cr gives a scale factor of 0.75 with respect to Mo whereas that obtained from the data is approximately 0.6.

The comparison of the ODS of Mo with the estimated DS from W and the ODS of Cr indicates that the number of structure points both above and below the Fermi energy are in reasonable agreement. The comparison also indicates that the details such as the energy position and amplitude are not in such good agreement. It may be that the ODS is simply not a good replica of the unperturbed ground state density of states due to systematic variation of the transition probability matrix elements with the initial state energy $E - h\nu$ [14]. Variations of the matrix elements with the initial energy cannot be distinguished from the initial density of states effects in the photoemission data.

Some of the difficulties in the above comparison may be due to an overly simplified model used to interpret the photoemission data. There is some theoretical evidence that the detailed predictions of the nondirect and direct transition model for photoemission processes in copper are not easily distinguished over a limited spectral range [16]. In addition to these recent calculations there is possible experimental evidence for direct transition character in the Mo photoemission data. In particular, note that the high energy peak of the EDC's in figure 5 is attenuated suddenly between $h\nu = 10.0$ eV and 11.0 eV. The sudden appearance and disappearance of structure is consistent with the direct transition model and is not consistent with the nondirect model.

The above discussion indicating the possibility of direct transitions must be considered tentative as there are other possible explanations for the deterioration of the high kinetic energy edge of the EDC's between 10.0 eV and 11.0 eV. For example, since the energy loss function has a peak at 10.8 eV, the photoexcited electrons with $E \gtrsim 10.8$ eV could interact inelastically and lose 10.8 eV. With such a large energy loss, these electrons could not escape the metal and would be missing from the EDC's. This phenomenon has been observed in photoemission studies on Zn [17].

The relative minimum in the quantum yield at approximately 11.0 eV is interpreted as an optical constant effect. This interpretation is supported by the observation that the amplitude of the EDC's and consequently the yield, is dependent on the factor $h\nu n(h\nu)$ [cf. eq (1)] which has a relative minimum at 11.3 eV. Furthermore, the effect of the minimum in the yield is compensated by the minimum in the optical function $h\nu n(h\nu)$ in just the manner necessary to produce a self-consistent ODS without appealing to $h\nu$ dependent matrix elements.

A narrow peak just below the Fermi energy in the DS has been proposed to explain the quenched isotopic mass dependence in Mo's superconducting transition temperature [18]. Although the optical studies of this particular work were not extended below 0.5 eV, the photoemission data does probe this region. Within the resolution of the photoemission experiment, ~0.1 eV, no large amplitude, narrow structure was observed near the Fermi energy. This observation is in agreement with a more recent treatment of the isotopic mass effect which accounts for the quenched isotope effect without any anomalous condition being imposed on the density of states [19].

TABLE 1. *Energies of the structure in the optical density of states for* Cr *and* Mo

Structure	Mo	Cr[a]	Cr[b]
1.....	−0.5 eV	−0.2 eV (shoulder)	−0.4 eV (shoulder)
2.....	−1.6 eV	−1.1 eV	−1.2 eV
3.....	−3.9 eV	−2.2 eV	−2.3 eV

[a] G. J. Lapeyre and K. A. Kress, Phys. Rev. **166**, 589 (1968).
[b] D. E. Eastman, J. Appl. Phys. **40**, 1371 (1968).

7. Summary

Photoemission measurements were used to study the electronic structure of Mo. The data show the filled d-band to be approximately 5.0 eV wide with three peaks at $E - E_F = -0.5$, -1.6, and -3.9 eV. The data show no strong electronic final-state structure for $E - E_F > 5.0$ eV. The above observations are independent of the nondirect model.

The nondirect model was used to obtain an ODS for Mo. The model was used in conjunction with ϵ_2 to infer an ODS above the Fermi energy. The ODS was compared to a band calculation and to measurements on Cr. The comparisons showed poor agreement except for the correlation in the number of peaks.

8. Acknowledgments

The contributions of Mr. C. Badgley and Mr. F. Blankenburg to the mechanical design, electrical design, and construction of part of the apparatus used in this investigation was certainly appreciated. Discussions with Dr. A. J. M. Johnson are acknowledged.

9. References

[1] Kress, K. A., and Lapeyre, G. J., Rev. Sci. Instr. **40**, 74 (1969).
[2] Berglund, C. N., and Spicer, W. E., Rev. Sci. Instr. **35**, 1665 (1964).
[3] Kress, K. A., Ph. D. Dissertation, Montana State University (1969).
[4] Krolikowski, W. F., Ph. D. Dissertation, Stanford University (1967).
[5] Allison, R., Burnes, J., and Tuzzolino, A. J., J. Opt. Soc. Am. **54**, 1381 (1964).
[6] Kress, K. A., and Lapeyre, G. J., to be published.
[7] Juenker, D. W., Leblanc, L. J., and Martin, C. R., J. Opt. Soc. Am. **58**, 164 (1968).
[8] Fowler, R. H., Phys. Rev. **38**, 45 (1931).
[9] Vance, D. W., Phys. Rev. **164**, 372 (1967).
[10] Berglund, C. N., and Spicer, W. E., Phys. Rev. **136**, A1030 (1964).
[11] Spicer, W. E., Phys. Rev. **154**, 385 (1967).
[12] Schechtman, B. H., Ph. D. Dissertation, Stanford University (1968).
[13] Mattheiss, L. F., Phys. Rev. **40**, 1371 (1968).
[14] Eastman, D. C., J. Appl. Phys. **40**, 1371 (1968).
[15] Lapeyre, G. J., and Kress, K. A., Phys. Rev. **166**, 589 (1968).
[16] Smith, N., and Spicer, W. E., to be published.
[17] Mosteller, L. P., Huen, T., and Wooten, F., to be published.
[18] Garland, J. W., Phys. Rev. **129**, 111 (1963).
[19] McMillan, W. L., Phys. Rev. **167**, 331 (1968).

Ultraviolet and X-Ray Photoemission from Europium and Barium

G. Brodén, S. B. M. Hagström, P. O. Hedén, and C. Norris

Department of Physics, Chalmers University of Technology, Göteborg, Sweden

Europium and barium are predicted to have very similar outer electronic structures with the exception that europium has a partially filled $4f$ shell. Measurements are reported on photoemission from thin films excited with both vacuum ultraviolet and soft x-ray radiation. The results obtained using the low energy excitation indicate the similarity of the materials. Both show structure close to the leading edge in agreement with band structure calculations which indicate an increase in the density of states immediately below the Fermi level. Only a very small feature is observed with europium films which can be associated with the $4f$ electrons. On the other hand using soft x-ray excitation a large peak corresponding to $4f$ states lying 2.5 eV below the Fermi level is observed. The difference in the magnitudes is attributed to the size of the matrix elements involved.

Key words: Barium (Ba); β-tungsten compounds; effects of oxidation; electronic density of states; europium (Eu); lanthanides; matrix elements; photoemission; rare-earth metals; UV and x-ray photoemission; x-ray photoemission.

1. Introduction

Recent band structure calculations [1-3] of the isoelectronic metals Eu ($4f^7 6s^2$) and Ba ($6s^2$) have shown that their respective conduction bands are closely related. Both are characterized by a $6sp$ band hybridized with a $5d$ band which extends slightly below the Fermi surface. Eu differs from Ba in that it possesses, in common with other rare-earth metals, a partially occupied $4f$ state. The $4f$ electrons are shielded by the closed $5s$ and $5p$ shells and behave in many ways as core states. This is illustrated by the chemical similarity of the rare earths. The $4f$'s are, however, important in connection with the complex magnetic structures of the lanthanide metals. Although band structure calculations [2,4] have been successful in correlating these structures with details of the Fermi surface, they are not able to accurately locate the energy position of the $4f$ state, due to the sensitivity of this energy to the exact form of the exchange. We have measured photoelectron spectra induced by both UV light and by soft x rays in order to investigate the band structure of Eu and Ba, and in particular to determine the position of the $4f$ level in Eu. This work is part of a wider study of the lanthanides now in progress.

X-ray photoemission (XPS) and UV photoemission (UPS) are two important techniques currently employed in the study of the electron density of states of solids. Their relative merits are a consequence of the very different photon energies involved, rather than competing, the two methods complement each other. With soft x rays one can probe deeper below the Fermi level and can also study core levels. This is useful in that it allows the purity of the sample to be monitored, and from a measurement of the chemical shift of the core levels, information can be gained concerning the nature of the valence states [5]. The more energetic electrons produced in ESCA have, moreover, a longer scattering length (typically 100 Å) compared to the low energy UV induced photoelectrons (typically 20 Å). Greater surface purity is thus required with UPS. On the other hand, although UPS is limited to investigating states near the Fermi level, it is at present capable of considerably better resolution.

2. Experimental

Both sets of measurements were made using films evaporated from tungsten filaments. The metals were obtained with a purity of 99.5 percent (Ba) and 99.7 percent (Eu). Both Eu and Ba are very reactive and it was inevitable that some oxidation occurred during mounting. The working pressures were 7×10^{-11} torr (UPS) and 5×10^{-7} torr (XPS). This was found sufficient to

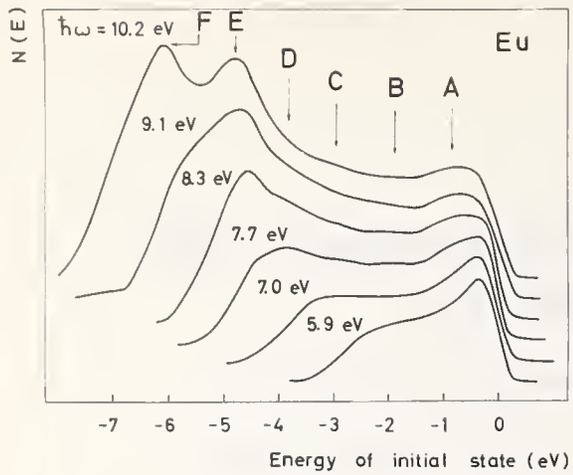

FIGURE 1. *Electron energy distribution curves of a europium film for different photon energies.*

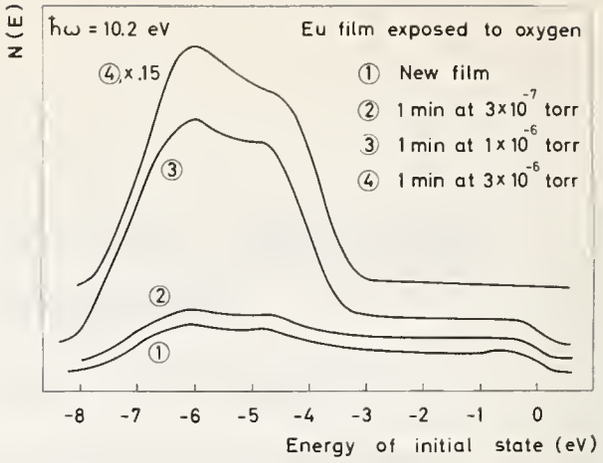

FIGURE 2. *Influence on the EDC curve for europium of exposure to oxygen.*

allow measurements for one to two hours without appreciable distortion of the spectra.

The UV photoemission spectra were obtained with light from an H_2 discharge lamp, dispersed by a McPherson monochromator. The monochromator was coupled to the measuring chamber via a LiF window. The photoelectrons were collected with a silver coated collector by applying a retarding field between the sample and the collector and using the A.C. modulation technique [6]. With this method an electron energy resolution of approximately 0.3 eV could be achieved.

For the ESCA measurements the exciting radiation was obtained from an x-ray source employing an aluminum anode, separated from the sample by a 1.5μ thick aluminum window. The photoemitted electrons were analyzed with a spherical electrostatic analyzer with a radius of curvature of 36 cm. They were recorded with standard counting techniques. The resolution obtained was of the order of 1.5 eV of which part (0.8 eV) was due to the natural line width of the incident x-radiation (Al K_α) and the rest came from instrumental broadening.

3. Results

Figure 1 shows a set of electron distribution curves (EDC's) obtained from a freshly evaporated film of Eu for different incident UV photon energies. The results are referred to the energy of the initial states by plotting them against $E - \hbar\omega + \phi$, where E is the measured energy, $\hbar\omega$ the photon energy, and ϕ the work function of the collector. The zero on this scale corresponds to the Fermi level. A number of peaks, some of them rather weak are observed and for reference are labelled A to F. For all photon energies the curves are characterized by a relatively high number of emitted electrons near the leading edge. At the higher photon energies two large peaks E and F appear. F remains at a fixed kinetic energy for increasing photon energy and probably corresponds to inelastically scattered electrons. Electron-electron scattering is an important process for both Eu and Ba as, according to the band structure, they are electronically similar to the transition metals with a high density of states near the Fermi level.

To determine whether or not any features of the photoemission spectra were associated with the presence of oxygen, a freshly prepared film was exposed to oxygen at various pressures for a given length of time. The EDC's obtained for $\hbar\omega = 10.2$ eV are shown in figure 2. Apart from the increased scattering peak which is characteristic of a contaminated surface, there is a large increase in peak E suggesting that it arises from the oxidized state. This assignment is confirmed by recent measurements on EuO [7] in which a strong peak attributed to p-states was observed at the same position (−4.6 eV).

Very similar results to those of Eu have been obtained for Ba. EDC's corresponding to $\hbar\omega = 7.7$ eV are shown in figure 3 for both metals. The evident similarity of the curves reflects the closeness of the valence band structure for the two metals. With the exception

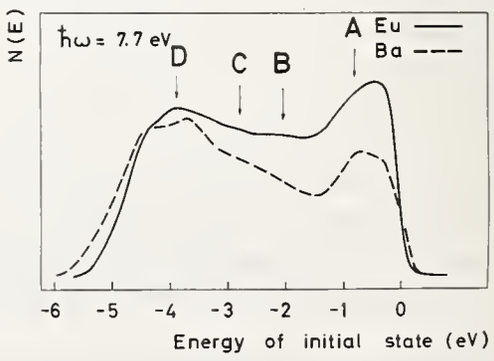

FIGURE 3. *Comparison of the EDC curves for barium and europium.*

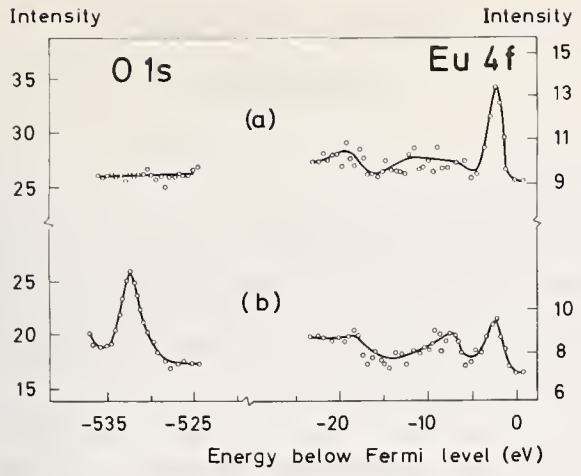

FIGURE 4. *Photo-electron spectrum obtained with* Al Kα *excitation of the* Eu 4f *band and* 0 1s *level immediately after evaporation (a) and after oxidation (b).*

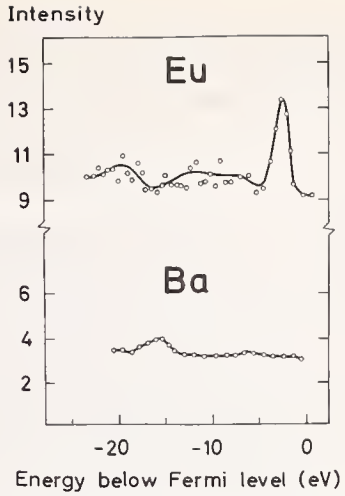

FIGURE 5. *Photo electron spectrum close to the Fermi level of europium and barium obtained with* AlKα *excitation.*
The intensities are normalized relative to the 4*d* core levels.

of the region between -1.5 and -3.2 eV the features observed in one curve can be recognized in the other.

Figure 4 shows photoelectron spectra obtained from a Eu film using soft x-ray excitation. As in the previous figures the energy scale corresponds to the binding energy with the Fermi level located at zero. The upper Eu curve is dominated by a peak at -2.5 ± 0.5 eV which we believe is due to the 4*f* state. It is likely that the feature at -5 to -10 eV is associated with scattering mechanisms as a similar feature was observed adjacent to the photoelectron peak corresponding to the $3d_{5/2}$ level. The peak near -20 eV is due to the Eu 5*p* level. In order to check the contamination of the sample surface the oxygen 1*s* line was monitored and is shown by the side of the corresponding Eu signal. The lower set of results were obtained after exposing the film briefly to the atmosphere. The intensity of the 4*f* line decreased and structure at lower energies appeared. A strong oxygen signal was also observed. Comparing the two sets of curves it is evident that oxygen had a little influence on the films studied immediately after evaporation, and we therefore feel that we are justified in regarding them as typical of pure Eu. XPS measurements of the outer electrons for bulk Eu samples have recently been reported [8]. The results which correspond to samples mounted in air are similar to the lower Eu curve shown in figure 4.

As a further check that the peak in figure 4 corresponds to the 4*f* state it is compared in figure 5 with the corresponding result for a Ba film. Clearly nothing as strong as the -2.5 eV peak in Eu is seen for Ba. The small peak at -6 eV corresponds to the oxygen 2*p* level. The one at -16 eV is due to the barium 5*p* level.

4. Discussion

From figure 1 it is seen that the structure in the Eu EDC's remains at constant energy (on the reduced scale) for increasing photon energy. Similar behavior was found for the Ba films. This indicates that the structure is associated with features in the initial density of states. Furthermore either the initial states have low dispersion in **k**-space or the transitions are non-direct (i.e., transitions in which the electron momentum vector **k** is not conserved).

Comparison with the calculated band structures of Eu and Ba suggests that the hump in the EDC's extending to -1.5 eV is associated with the filled part of the 5*d* band. The broad feature between -1.5 and -3.5 eV in the Ba EDC (fig. 3) would appear to be due to the 6*sp* conduction band. It is difficult to explain the feature which occurs in both EDC's in figure 3 near -4 eV. According to the calculations no states exist in this region. One possibility is that the peaks are associated with inelastically scattered electrons. In this connection we note that in a recent work [9] peaks observed in alkali metals have been attributed to scattering via the creation of surface plasmons.

From the differences in the two EDC's shown in figure 3 we believe that the 4*f* level is associated with the structure lying between -1.5 and -3.5 eV; that is with either of the features B or C. This conclusion is supported by the occurrence at -2.5 eV of the strong x-ray induced photoemission peak in figures 4 and 5. The weakness of the 4*f* structure in the EDC's of the UPS measurements, compared to the XPS measurements, is presumably due to the magnitude of the matrix elements involved. For 7 eV $< \hbar\omega <$ 11 eV the 4*f* level is coupled with empty 6*sp* states, transitions between which are not allowed by electric dipole selection rules. Transitions from the occupied 5*d* and 6*sp* bands will be allowed however. This explains the similarity of the Eu and Ba EDC's. On the other hand using soft x-ray excitation all initial states will be

coupled to plane wave states, approximately 1500 eV above the Fermi level. Thus in the case where there are important matrix element effects involved, soft x-ray induced photoemission spectra will reproduce more exactly the density of states than will measurements employing UV light.

Electric dipole selection rules will not, however, explain the optical properties of Ba and Eu [10]. The reflection curves for Ba and Eu were found to be very similar, suggesting that the $4f$ electrons are not excited for $\hbar\omega < 5.0$ eV. The band structure calculations and the present work suggest, however, that there is a high density of d states at the Fermi level. Transitions to these states from the $4f$ level are allowed and would be expected to give rise to an absorption edge in Eu but not in Ba. The nonappearance of this edge is possibly due to the core-like nature of the $4f$ states. The matrix element between the $4f$ and $5d$ states would in consequence be small. The conclusion is also in agreement with recent calculations on free atoms [11].

5. References

[1] Freeman, A. J., and Dimmock, J. O., Bull. Am. Phys. Soc. **11**, 216 (1966).

[2] Andersen, O. K., and Loucks, T. L., Phys. Rev. **167**, 551 (1968).

[3] Johansen, G., Solid State Communications **7**, 731 (1969).

[4] Keeton, S. C., and Loucks, T. L., Phys. Rev. **168**, 672 (1968).

[5] Fadley, C. S., Hagström, S., Klein, M., and Shirley, D. A., J. Chem. Phys. **48**, 3779 (1968).

[6] Spicer, W. E., and Berglund, C. N., Rev. Sci. Instr. **35**, 1664 (1964).

[7] Eastman, D. E., Holtzberg, F., and Methfessel, S., Phys. Rev. Letters **23**, 226 (1969).

[8] Nilsson, Ö., Nordberg, C. H., Bergmark, J. E., Fahlman, A., Nordling, C., and Siegbahn, K., Helvetica Physica Acta **41**, 1064 (1968).

[9] Smith, N. V., and Spicer, W. E., Phys. Rev. Letters **23**, 769 (1969); Phys. Rev. in press.

[10] Müller, W. E., Phys. Kondens. Materie **6**, 243 (1967).

[11] Fano, U., Cooper, J. W., Rev. Mod. Phys. **40**, 441 (1968).

Discussion on "Ultraviolet and X-Ray Photoemission from Europium and Barium" by G. Brodén, S. B. M. Hagström, P. O. Hedén, and C. Norris (Chalmers University of Technology)

S. J. Cho *(National Res. Council):* I have one comment about this interesting experiment on Eu. A few years ago Blodgett and Spicer (refer to my paper in this conference) had also obtained in gadolinium with uv photoemission studies a small peak at about 2.8 eV below the Fermi level, which is about the same position as you have obtained. I strongly feel right now that this small peak in Gd is the f band position. Do you have any idea about this f band width in Eu? Is your f band width due to the F_j multiplets?

D. E. Eastman *(IBM):* I have looked at gadolinium again since the earlier work several years ago by Dr. Spicer and co-workers [1] and I do not see any perceptible $4f$-state structure down to seven volts below the Fermi level that is bigger than 1% in amplitude. In the cases of europium, Dr. Hagstrom has reported on x-ray photoemission measurements.

S. J. Cho *(National Res. Council):* There is a very small peak over there in the early UPS works mentioned above. I do not have any detailed information about your recent experimental works. However, I do expect that the $4f$ band position in Gd with respect to the Fermi level should be almost the same as those in Eu.

D. E. Eastman *(IBM):* In uv photoemission, no $4f$-state peak is observed in gadolinium within 6 or 7 volts of the Fermi level.

S. J. Cho *(National Res. Council):* The reason for the large f band width of about 2.0 eV observed in Eu and Yb is still not clear. According to your XPS work, the f band positions for both Eu and Yb are practically the same. My own feeling is that the $4f$ band position in Yb could be somewhat (0.5 eV) lower than that in Eu.

A. R. Mackintosh *(Lab. for Electrophysics, Tech. Univ.):* We have recently performed some band calculations on ytterbium which may throw some light upon this question [2]. Although the position of the $4f$ bands is very uncertain in these calculations, due to their extreme sensitivity to the approximation used for exchange, we find that they are situated near the bottom of the conduction band, about 4 eV below the Fermi level, if Slater exchange is used. This is in reasonable agreement with the x-ray photoemission results. Spin-orbit coupling splits the bands into two sets, corresponding to $j = 7/2$ and $5/2$, separated by about 1.5 eV. The individual bands have a width of less than 0.05 eV, because the centrifugal barrier makes the f resonance extremely narrow. Perhaps the spin-orbit splitting could be seen in a high resolution experiment.

S. J. Cho *(National Res. Council):* I have made extensive studies on the f band problem by using a parameterized Slater $\rho^{1/3}$ exchange potential for the Eu-chalcogenides, which are magnetic semiconductors. Not only the $4f$ band positions, but also the total $4f$ band widths are fairly sensitive to the exchange potential used. It would be a difficult problem theoretically to find the proper $4f$ band positions for the case of metals. In spite of such uncertainty they can explain fairly well the Fermi surface topology, because the localized $4f$ bands are located a few electron volts below the Fermi energy for Eu, Gd, and Yb metals, and do not influence the Fermi surfaces much. For other rare earth metals the $4f$ bands can cross the Fermi energy. However, it could be difficult to measure the $4f$ Fermi surfaces due to the heavy effective masses. In the case of the semiconductors we can adjust a reduced exchange parameter to produce the right energy gap. It turned out that the $4f(\uparrow)$ bands become the highest occupied bands with correct energy gaps for all the Eu-chalcogenides with a fixed value (3/4) of the reduced exchange parameter. In these studies the $f(\uparrow)$ band positions are reliable, but there is no reliable experimental data available to justify the maximum f^7 band width of about 0.5 eV obtained from my work.

W. E. Spicer *(Stanford Univ.):* In general, I think in looking at photoemission from something like an f state one has to take into account not only the ground state splitting but (I think Dr. Cho was thinking of this) also the various spin states that can be left after the excitation. I believe that in the d-band of NiO these effects can give a width of about 2 eV. I don't know what it can give here, but I suspect it is large. I think it does have to be taken into account.

J. T. Waber *(Northwestern Univ.):* I would like to make two observations about papers which have just

been discussed. The comparative plot of the atom eigenvalues for the 3*d* and 4*d* transitions series shows in figure 1 that the 4*d* bands should fall more rapidly with atomic numbers than the 3*d* bands do. This difference is borne out by comparing the self-consistent band calculations of Snow on silver [3], and of Snow and Waber on copper [4]. Also, I think the relative position of the *d*-bands accounts for the difference in color of these two metals. In figure 2, I have compared the 3 density of states curves which have been obtained in conjunction with my colleagues at Los Alamos [5]. Titanium is compared with zirconium, vanadium with niobium and chromium with molybdenum. All six graphs are for the bcc phase. One striking feature is that in contrast to the well known two peak structure of the density of states curves for the 3*d* transition elements, the equivalent curves for the 4*d* transition series show three peaks. This result is consistent with Eastman's experimental observations on vanadium and

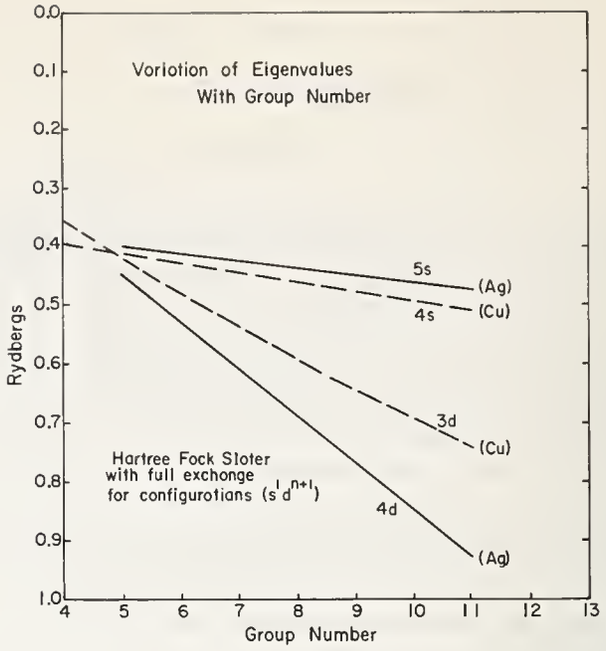

FIGURE 1. *Comparison of atomic energy levels for the* 3d *and* 4d *transition series.*

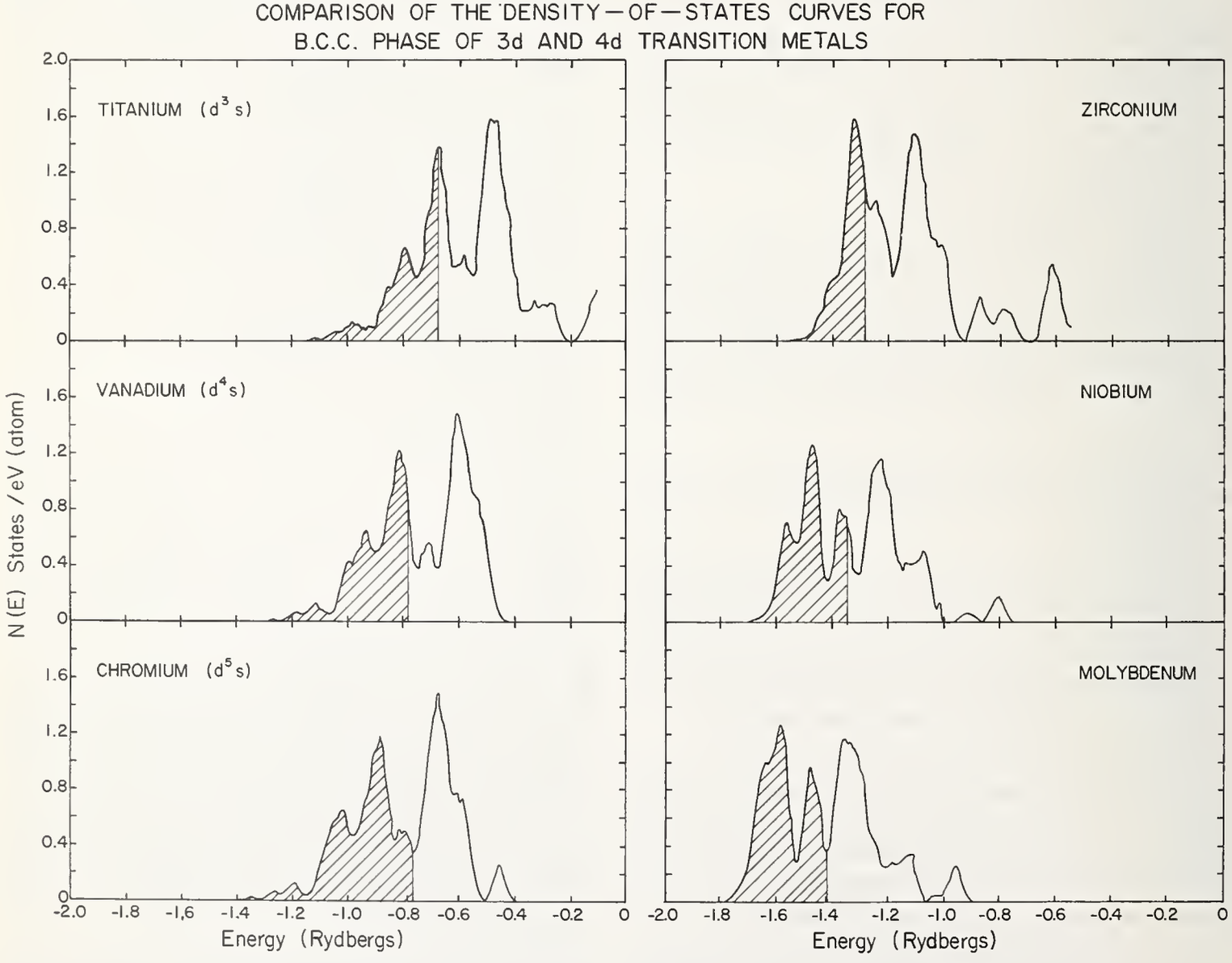

FIGURE 2. *Density of states curves for the bcc phases of* $3d^4$ *and* $4d^5$ *transition metals.*

niobium. Since the HCP forms of titanium and zirconium were used experimentally in place of the bcc form, which we have studied, agreement with the number of peaks in the $N(E)$ curves is not anticipated theoretically. The final point is that these six $N(E)$ curves are not very similar. This raises question about the validity of the rigid band model for the transition metals. I would like to make a final point. It relates to the very interesting paper by Collings and Ho. The calculated dependence of $N(E_F)$ on alloy composition shown in figure 3 was obtained from a very simple model of alloying which a graduate student, David Koskimaki, is currently working on.

We hope to report on this model in the very near future. By oversight the curve for $N(E_F)$ for Ti-Mo alloys was not supplied to Dr. Collings. This graph is similar to the one for Ti-V-Cr alloys. The shape is similar but the discrepancy remains between the numerical experimental and theoretical values.

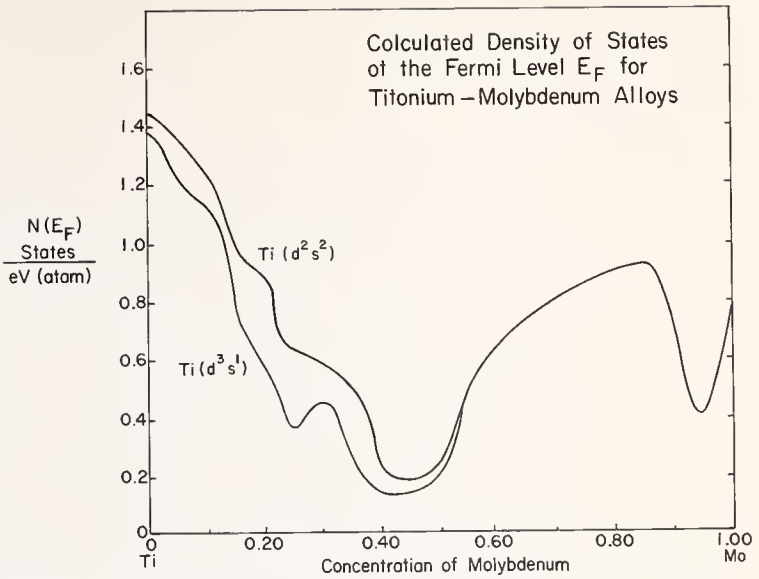

FIGURE 3. *Calculated variation of the state density at the Fermi level for Ti-Mo alloys (Waber and Koskimaki, unpublished).*

[1] Optical Properties and Electronic Structure of Metals and Alloys, F. Abeles, Editor (North-Holland Publishing Co., Amsterdam, 1965) p. 246.

[2] Johansen, G., and Mackintosh, A. R., to be published in Solid State Communications.

[3] Snow, E. C., "Self-Consistent APW Bands of Silver," Phys. Rev.

[4] Snow, E. C., and Waber, J. T., Phys. Rev. **157**, 570 (1967).

[5] Prince, M. Y., and Waber, J. T. (in press).

MANY-BODY EFFECTS

CHAIRMEN: L. N. Cooper
J. W. Cooper

417-156 O - 71 - 16

What is a Quasi-Particle?*[1]

J. R. Schrieffer

Department of Physics, University of Pennsylvania, Philadelphia, Pennsylvania

The concept of a quasi-particle excitation in an interacting many-body system will be discussed from both the physical and the mathematical points of view. The physical origin of mass enhancement, wave function renormalization, interactions between quasi-particles, *etc.* will be presented. Landau's Fermi liquid theory, including the quasi-particle kinetic equation, will be reviewed. Finally, the domain of validity of the quasi-particle approximation will be discussed.

Key words: Density of states; Green's function; mass enhancement; quasi-particle; superconductors.

1. Introduction

Since the early work of Drude and of Sommerfeld [1], it has been clear that an independent-particle picture represents in a qualitatively correct manner the electronic properties of a metal. The electronic specific heat, the transport properties, the magnetic susceptibility, *etc.* are all roughly accounted for by elementary band theory, without recourse to explicit many-body effects. Exceptions to the rule are the plasma modes observed in the energy loss of fast charged particles, as well as cooperative phenomena such as superconductivity ferromagnetism, antiferromagnetism, *etc.*

The success of the independent-particle approximation (IPA) is particularly striking in view of the large ratio of interelectronic Coulomb energy to kinetic energy experienced by electrons in metals. A measure of this ratio is the electron density parameter r_s defined essentially as the mean spacing between electrons, measured in units of the Bohr radius. For $r_s \ll 1$, the Coulomb interactions between electrons are weak compared to the kinetic energy effects, while if $r_s \gg 1$ the potential effects dominate the kinetic effects. For simple metals, r_s is typically between two and six. Thus, one might expect qualitative changes in the properties of metals relative to the IPA since this approximation includes only the *average* Coulomb interaction between electrons. The "correlation energy" neglected by the IPA is of order 1 to 2 eV per electron and is by no means trivial.

The qualitative reason that the IPA works so well is that typical measurements made on metals at normal temperatures ($T \ll T_F \sim 10^5$ K, where T_F is the Fermi temperature) involve only the low lying excited states of the metal. There is good theoretical (and experimental) evidence that these many-body states are well characterized in terms of a set of elementary excitations, called quasi-particles, which for the interacting system play the same role as the excited electrons (above the Fermi surface) and the excited holes (below the Fermi surface) in the IPA. As for electrons and holes, these quasi-particles are labelled by a wave vector $\mathbf{k}$ and a spin orientation $s = \pm 1/2$. It is assumed that there is a sharp Fermi surface in the actual system as $T \to 0$, although its shape may depend on the many-body interactions. By convention, one measures the quasi-particle energies $\epsilon_{\mathbf{k}}$ relative to their (common) value on the Fermi surface so that $\epsilon_{\mathbf{k}F} = 0$, where $\mathbf{k}_F$ is a wave vector on the Fermi surface.

At sufficiently low temperature, few quasi-particles are excited and therefore this dilute quasi-particle gas is nearly a "perfect" gas, in the sense that the quasi-particles rarely collide. Furthermore, at low temperature only low energy quasi-particles are excited. Since their intrinsic decay rate varies as $\epsilon_{\mathbf{k}}^2$, they constitute long lived, weakly interacting excitations, thereby justi-

*An invited paper presented at the 3d Materials Research Symposium, *Electronic Density of States*, November 3–6, 1969, Gaithersburg, Md.

[1] This work was supported in part by the National Science Foundation.

fying their use as the building blocks for the low lying excitation spectrum.

There is no need in principle for the effective mass of the quasi-particles (q.p.) to be simply related to the free electron (or band structure) mass. For simple metals, it turns out that the q.p. mass m^* is of the order of the free electron mass m_e, differing from it in most cases by a factor of less than two. The main source of the deviation of m^* from m_e (aside from band structure) is the electron-phonon interaction, which in general leads to an increase of m^*.

Unfortunately, there is at present no truly first principles proof of the above statements, *i.e.* the 1:1 correspondence of the low lying excited states of the noninteracting and interacting systems, a simple effective mass spectrum, long lifetimes of the quasi-particles, *etc.*, although one has a proof that these statements are true to *all* orders in perturbation theory starting from the noninteracting states [2]. This lack of a rigorous foundation for the theory is not merely a mathematical nicety, since we know of many systems (*e.g.* the superconducting phase) which are not connected perturbatively with the noninteracting system; nevertheless, quasi-particles are still of use even in this case. One assumes that in normal systems (absence of cooperative effects) perturbation theory (or alternatively, adiabatic switching on of the interactions) gives the correct physics of the interacting system despite subtle nonanalytic effects which are likely present even in normal systems.

Thus far we have discussed only the excitation spectrum and not the many-body wave functions. Response functions (*e.g.* transport phenomena) require information about both quantities. The remarkable fact is that a suitably defined kinetic (or Boltzmann-like) equation for the *quasi-particle* distribution function gives an accurate account of the response of the system to long wavelength, low frequency perturbations such as electric and magnetic fields. This second property of quasi-particles is the heart of why the Drude-Sommerfeld scheme works well for nonequilibrium as well as equilibrium phenomena.

There is not time here to go into the details of the Landau theory of Fermi liquids, upon which the present theory of quasi-particles in metals is based. The excellent books of Pines and Nozieres [3] and of Nozieres [4] deal in depth with this topic. We would like, however, to give a brief sketch of the theory and to make a few comments about it.

2. The Landau Picture of Fermi Liquids

In the Landau picture one assumes that the low energy excited states of the interacting system have energies well approximated by the form

$$E(\delta n_{\mathbf{k}s}) = \sum_{\mathbf{k}s} \epsilon_{\mathbf{k}s} \delta n_{\mathbf{k}s} + \frac{1}{2} \sum_{\mathbf{k}s\mathbf{k}'s'} f^{ss'}_{\mathbf{k}\mathbf{k}'} \delta n_{\mathbf{k}s} \delta n_{\mathbf{k}'s'}. \quad (2.1)$$

Here $\delta n_{\mathbf{k}s}$ is a measure of the quasi-particle (q.p.) occupation numbers. Assuming there is a well defined Fermi surface S_F at zero temperature described by the wave vectors $\mathbf{k}_F$, one has

$$\delta n_{\mathbf{k}s} = \begin{cases} +1, \ \mathbf{k}s \text{ outside } S_F \text{ and occupied by a quasi-electron} \\ -1, \ \mathbf{k}s \text{ inside } S_F \text{ and occupied by a quasi-hole} \\ 0, \text{ otherwise.} \end{cases}$$

The zero-order q.p. energy $\epsilon_{\mathbf{k}s}$ is measured relative to the chemical potential μ so that $\epsilon_{\mathbf{k}_F s} = 0$. One assumes that $\epsilon_{\mathbf{k}s}$ and its derivatives are continuous across S_F and one makes the effective mass approximation

$$\mathbf{v}_{\mathbf{k}s} = \frac{1}{\hbar} \nabla \epsilon_{\mathbf{k}s} = \frac{\hbar \mathbf{k}}{m^*}, \quad (2.2)$$

The approximation (2.2) often suffices, since one is usually interested in q.p. states $\mathbf{k}s$ in the immediate vicinity of S_F (since $T \ll T_F$). The term involving $f^{ss'}_{\mathbf{k}\mathbf{k}'}$ represents the energy of interaction between quasi-particles. This function and m^* are considered to be parameters to be determined from experiment or to be *roughly* estimated from a more fundamental theory.

Landau argued that if one views the quasi-particles as being described by wave packets whose extent is large compared to the wavelength of a q.p. at the Fermi surface ($\lambda_F \sim 2\pi/k_F \sim 10^{-8}$ cm in metals) then one can define a distribution function $\delta n_{\mathbf{k}s}(\mathbf{r}, t)$for q.p.'s which plays the role of the single particle distribution function $f(\mathbf{r},\mathbf{p},t)$ in kinetic theory. This concept is reasonable as long as $\delta n_{\mathbf{k}s}(\mathbf{r},t)$ varies slowly in space (compared to λ_F) and in time (compared to $\hbar/\mu$). By the usual arguments of kinetic theory one can write down a kinetic (Landau-Boltzmann) equation for δn.

$$\frac{\partial \delta n_{\mathbf{k}s}(\mathbf{r},t)}{\partial t} + \mathbf{v}_{\mathbf{k}} \cdot \nabla_{\mathbf{r}} \delta \bar{n}_{\mathbf{k}s}(\mathbf{r}, t) - \mathscr{F}_{\mathbf{k}} \cdot \mathbf{v}_{\mathbf{k}} \delta(\epsilon_{\mathbf{k}s}) = I(\delta n_{\mathbf{k}s}). \quad (2.3)$$

$\mathscr{F}_{\mathbf{k}}$ and $I(\delta n_{\mathbf{k}s})$ are the external force acting on the q.p. and the collision integral respectively, while $\nabla_{\mathbf{r}} \delta \bar{n}_{\mathbf{k}s}$ is defined by

$$\nabla_{\mathbf{r}} \delta \bar{n}_{\mathbf{k}s}(\mathbf{r}, t) = \nabla_{\mathbf{r}} \delta n_{\mathbf{k}s}(\mathbf{r}, t) + \delta(\epsilon_{\mathbf{k}s}) \sum_{\mathbf{k}'s'} f^{ss'}_{\mathbf{k}\mathbf{k}'} \nabla_{\mathbf{r}} \delta n_{\mathbf{k}'s'}(\mathbf{r}, t). \quad (2.4)$$

The term $\nabla_r \delta n_{\mathbf{k}s}$ in (2.4) describes the conventional streaming flow of q.p.'s familiar from kinetic theory. The other term, arising from the interactions, may be viewed as a dragging along of the ground state particles by the inhomogeneous distribution of quasi-particles, each q.p. dragging along its own cloud.

Naively, one might guess that the particle current density $\mathbf{J}(\mathbf{r},t)$ at point $\mathbf{r}$ may be expressed as $\sum_{\mathbf{k}s} \mathbf{v}_{\mathbf{k}s} \delta n_{\mathbf{k}s}(\mathbf{r},t)$. This is *not* true, but rather

$$\mathbf{J}(\mathbf{r},t) = \sum_{\mathbf{k}s} \mathbf{v}_{\mathbf{k}s} \delta \bar{n}_{\mathbf{k}s}(\mathbf{r},t)$$
$$= \sum_{\mathbf{k}s} \left[\mathbf{v}_{\mathbf{k}s} + \sum_{\mathbf{k}'s'} f_{\mathbf{k}\mathbf{k}'}^{ss'} \mathbf{v}_{\mathbf{k}'s'} \delta(\epsilon_{\mathbf{k}'s'}) \right] \delta n_{\mathbf{k}s}(\mathbf{r},t). \qquad (2.5)$$

The $\mathbf{v}\delta n$ term represents the current of the quasi-particle, while the term involving f represents the current of the ground state particles being "dragged along" with the q.p. It is clear from the kinetic equation (2.3) that this definition is correct since the continuity equation

$$\frac{\partial \rho}{\partial t} + \nabla \cdot \mathbf{J} = 0 \qquad (2.6)$$

is satisfied by $\mathbf{J}$ if we use the fact that

$$\rho = \rho_0 + \sum_{\mathbf{k}s} \delta n_{\mathbf{k}s}(\mathbf{r},t). \qquad (2.7)$$

Roughly speaking $f_{\mathbf{k}\mathbf{k}'}^{ss'}$ behaves like a velocity dependent potential acting on particles in $\mathbf{k}$ and $\mathbf{k}'$. A change in $\delta n_{\mathbf{k}s}$ acts on the particle in $\mathbf{k}'s'$ like a vector potential would, and induces a current even though the $\mathbf{k}'$ *wavefunction* does not change, like the Meissner effect in a superconductor.

3. Quasi-Particles in Metals

The above picture is suitable for a system like He^3 which is translationally invariant in its ground state and has only the Fermion degrees of freedom. Metals are clearly different: they are invariant only under the translation group of the crystal lattice and have lattice vibrations as well as electronic degrees of freedom. How much of the Landau picture survives? The "non-interacting system" is presumably now the IPA in which the Coulomb interactions between electrons are treated in the mean field approximation. In this case the one particle states are labelled by a wave vector $\mathbf{k}$ (restricted to the first Brillouin zone), a band index n and the spin s. We lump n and $\mathbf{k}$ together for now. There is a sharp Fermi surface at $T = 0$ and excited states are given by the usual electron and hole excitations. Since the Coulomb interaction has full translation invariance, $\mathbf{k}$ remains a good quantum number to describe the quasi-particles, although the ground state of the actual system may be the transform of some excited state of the IPA system, due to changes in shape of the Fermi surface. Luttinger and Nozieres [2] have shown to all orders in perturbation theory that the *volume* of $\mathbf{k}$ space inside S_F remains fixed, as it must for the Landau picture to make sense. The energy expression (2.1) still holds but $f_{\mathbf{k}\mathbf{k}'}^{ss'}$ is in general a function having only the symmetry of the crystal, rather than full the rotational symmetry present for say He^3. The effective mass expression for $\mathbf{v}_{\mathbf{k}}$ still holds except $1/m^*$ is in general a second rank tensor having only the symmetry of the crystal. If the crystalline anisotropy of m^* and f are very weak (as for Na) then the identity

$$\frac{m^*}{m} = \frac{1 + F_1^s}{3} \qquad (3.1)$$

relating the effective mass ratio and the spin symmetric $l = 1$ term F_1^s in a Legendre polynomial expansion of $f_{\mathbf{k}\mathbf{k}'}^{ss'}$ for a true Fermi liquid is valid. Here, if $N(0)$ is the density of single particle states of one spin orientation at the Fermi surface, then

$$F_1^s = N(0)\left[f_1^{\uparrow\uparrow} + f_1^{\uparrow\downarrow}\right] \qquad (3.2)$$

and

$$f_{\mathbf{k}\mathbf{k}'}^{ss'} = \sum_{l=0}^{\infty} f_l^{ss'} P_l(\cos \hat{\mathbf{k}}\mathbf{k}'). \qquad (3.3)$$

Thus, for nearly free electron metals the low temperature electronic specific heat, *i.e.* m^*/m, determines F_1. Other pieces of information about $f_{\mathbf{k}\mathbf{k}'}^{ss'}$ can be extracted from other experiments such as the anomalous skin effect, Azbel-Kaner cyclotron resonance, de Haas van Alphen effect, dynamic magnetic susceptibility, *etc.* Presumably the f_l drop off rapidly with increasing l so only $l = 0$, 1 and perhaps 2 need be retained. For non-free electron metals, it appears that the anisotropy of f is so large that unravelling this function will be quite involved. However, we know that the transport and the *dHvA* measurements have already given us a great deal of information about $1/m^*$ in complex metals. When combined with band structure calculations these measurements give information on the many-body effects in these systems. As we mentioned earlier, most of the m^*/m effect is due to the phonons, for which a reasonably good first principles calculation is becoming possible, in many metals. A careful comparison here would provide an important check on the approximation of band theory and of the approximate methods presently used in many-body theory.

Another problem is that the phonons complicate the kinetic equation and the current density expression, since the phonons carry momentum and energy. The necessary generalizations of the Landau theory have been worked by Prange and Kadanoff [5], although we do not have time to discuss these questions here.

4. Green's Function Picture of Quasi-Particle

An alternative way of viewing quasi-particles, which is more general than the Landau theory, is through the Green's function scheme of many-body theory [3,4,6,7]. Suppose that an interacting system of N electrons is initially prepared to be in its exact ground state, $|0, N\rangle$. If $c_{\mathbf{k}s}^{+}$ creates a (bare) Bloch electron in state $\mathbf{k}s$, then we desire the probability distribution $P_{\mathbf{k}s}(E)$ of the energy for the $N+1$ particle state $\Phi_{\mathbf{k}s}^{N+1}+1$ defined by

$$|\Phi_{\mathbf{k}s}^{N+1}\rangle = c_{\mathbf{k}s}^{+}|0, N\rangle. \tag{4.1}$$

In general, Φ is not an eigenstate of the full Hamiltonian so that Φ does not have a sharply defined energy, *i.e.* $P_{\mathbf{k}s}(E)$ is not a delta function. The rules of quantum mechanics tell us that if the states $|n, N+1\rangle$ are the exact energy eigenstates of the $N+1$ particle problem then

$$P_{\mathbf{k}s}(E) = \sum_n |\langle n, N+1 | c_{\mathbf{k}s}^{+} | 0, N\rangle|^2 \delta(E - [E_n^{N+1} - E_0^N] + \mu) \tag{4.2}$$

$$= \sum_n |\langle n, N+1 | \Phi_{\mathbf{k}s}^{N+1}\rangle|^2 \delta(E - [E_n^{N+1} - E_0^N] + \mu),$$

where the E_n^{N+1} are the energy eigenvalues of the many-body system. Within the IPA, $P_{\mathbf{k}s}(E)$ is a delta function, since $c_{\mathbf{k}s}^{+}$ creates a Bloch state electron, which by definition is an exact single particle eigenstate of energy $\epsilon_{\mathbf{k}s}$. Thus, for the independent particle approximation (IPA)

$$P_{\mathbf{k}s}^{\mathrm{IPA}}(E) = \begin{cases} \delta(E - \epsilon_{\mathbf{k}s}) & \epsilon_{\mathbf{k}s} > 0 \\ 0 & \epsilon_{\mathbf{k}s} < 0. \end{cases} \tag{4.3}$$

Clearly, according to the Pauli Principle P is zero if one tries to add a particle to an already filled state, $\epsilon_{\mathbf{k}s} < 0$. For the interacting system, P will be a complicated (positive) function of E in general, whose shape depends on the value of $\mathbf{k}s$. The essential point is that if $\mathbf{k}$ is slightly above the Fermi surface, $P_{\mathbf{k}s}(E)$ will consist of a narrow high peak centered about a "quasi-particle energy,"

$$E = \tilde{\epsilon}_{\mathbf{k}s}, \frac{1}{\hbar}\nabla_{\mathbf{k}}\tilde{\epsilon}_{\mathbf{k}s} \cong \frac{\hbar\mathbf{k}}{m^*}, \tag{4.4}$$

plus a background continuum which in general has a rather smooth behavior, as sketched in figure 1 for $\mathbf{k}$ just above the Fermi surface. The half-width of the peak $\Gamma_{\mathbf{k}s}$, gives the intrinsic decay rate of the quasi-particle according to $1/\tau_{\mathbf{k}s} = 2\Gamma_{\mathbf{k}s}/\hbar$. Perturbation theoretic arguments show that Γ goes to zero as $\epsilon_{\mathbf{k}s}^2$ for $\epsilon_{\mathbf{k}s} \ll \mu$ so that the fractional width (or the reciprocal "Q" of the particle) varies as $\tilde{\epsilon}_{\mathbf{k}s}$, showing the quasi-particle to be a well defined excitation near the Fermi surface. To complete the story, one considers hole states defined by

$$|\bar{\Phi}_{\mathbf{k}s}^{N-1}\rangle = C_{\mathbf{k}s}|0, N\rangle, \tag{4.5}$$

Like $\Phi_{\mathbf{k}s}^{N+1}$, $\Phi_{\mathbf{k}s}^{N-1}$ is not an eigenstate of energy for the interacting system. Thus, the probability distribution of E for the hole state, which is defined by

$$\bar{P}_{\mathbf{k}s}(E) = \sum_n |\langle n, N-1 | \bar{\Phi}_{\mathbf{k}s}^{N-1}\rangle|^2 \delta(E + [E_n^{N-1} - E_0^N] + \mu)$$

$$= \sum_n |\langle n, N-1 | c_{\mathbf{k}s} | 0, N\rangle|^2 \delta(E + [E_n^{N-1} - E_0^N] + \mu) \tag{4.6}$$

is not a delta function in general. Note the change of sign of the excitation energy term in the delta functions appearing in (4.2) and (4.6). This ensures that at zero temperature the holes have negative energy and electrons have positive energy. Within the IPA, $\bar{\Phi}_{\mathbf{k}s}^{N-1}$ is an eigenstate of H and $\bar{P}_{\mathbf{k}s}^{IPA}(E)$ given by

$$\bar{P}_{\mathbf{k}s}^{\mathrm{IPA}}(E) = \begin{cases} 0 & \epsilon_{ks} > 0 \\ \delta(E - \epsilon_{\mathbf{k}s}) & \epsilon_{\mathbf{k}s} < 0. \end{cases} \tag{4.7}$$

For the interacting system, if $\mathbf{k}s$ is just below the Fermi surface, a narrow, high "quasi-hole" peak centered about $\tilde{\epsilon}_{\mathbf{k}s}$ appears in $\bar{P}_{\mathbf{k}s}(E)$, with a continuum background again occurring as sketched in figure 2. The quasi-hole and quasi-electron energies presumably

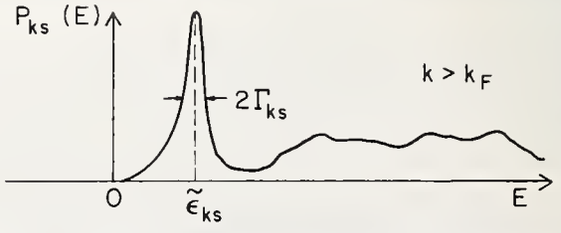

FIGURE 1. *Probability distribution* $P_{ks}(E)$ *for a "quasi-particle" corresponding to a bare Bloch state* ks *for* $k > k_F$.

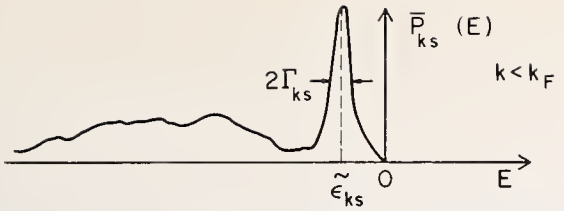

FIGURE 2. *Probability distribution* $P_{ks}(E)$ *for a "quasi-hole" state with* $k < k_F$.

join on smoothly at the Fermi surface so that m^* is continuous across S_F.

At nonzero temperature, one makes a statistically weighted average over initial states, rather than considering only the ground state $|0, N\rangle$. In this case the electron and hole probability distributions overlap, in that they are both nonzero for $E > 0$ and for $E < 0$. The overlapping corresponds to creating or destroying thermally excited quasi-particles, amongst other things. From the Fermi statistics of electrons, there follows the rigorous sum rule

$$\int_{-\infty}^{\infty} [P_{ks}(E) + \bar{P}_{ks}(E)]\,dE = 1. \tag{4.8}$$

One advantage of the Green's function description is that it allows the concept of quasi-particles to be usefully extended to systems which are not related by an adiabatic transform or by perturbation theory to the noninteracting states. For example, in a superconductor, $P_{ks}(E)$ shows at low temperature a sharp peak at the "quasi-particle" energy

$$E = E_{ks} \equiv \sqrt{\epsilon_{ks}^2 + \Delta_k^2}, \tag{4.9}$$

while $\bar{P}_{ks}(E)$ shows a sharp peak at $E = -E_{ks}$ as sketched in figure 3. In addition, P and $\bar{P}$ show background continua like in the normal metal. Note however that as **k** approaches the Fermi surface there is an energy gap between the quasi-hole and quasi-electron peaks, the gap being $2\Delta_{k_F}$, as is well known from the pairing theory. Thus a minimum energy $2\Delta_{k_F}$ is required to make a single-particle excitation in a superconductor (*i.e.* creation of a quasi electron-hole pair).

We should mention that the "background continuum" mentioned above corresponds physically to the creation of more complicated excitations, such as a quasi-particle plus electron-hole pairs, phonons, plasmons, *etc.* Generally these extra excitations are not strongly coupled together and therefore an incoherent (smooth) continuum appears. In special cases, however, resonant scatterings states of the excitations can appear, an example being the quasi-bound state of a hole and a plasmon, as Hedin *et al.* [8] have discussed.

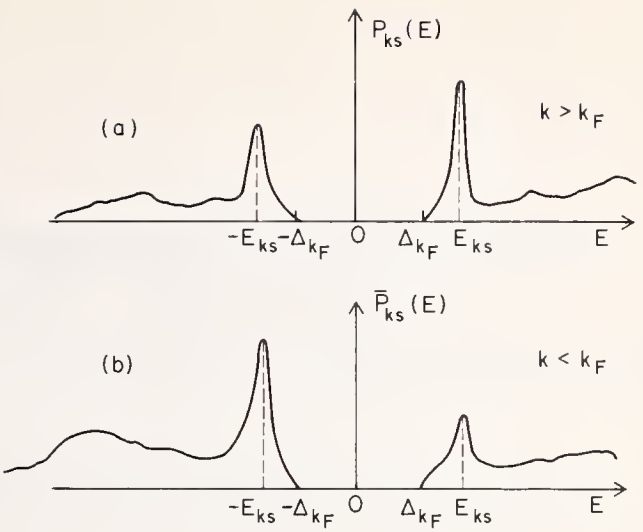

FIGURE 3. $P_{ks}(E)$ *and* $\bar{P}_{ks}(E)$ *for a superconductor showing (a) sharp peak at* $E = E_{ks}$ *in* $P_{ks}(E)$ *and (b) peak in* $\bar{P}_{ks}(E)$ *at* $E = -E_{ks}$.

There is a great deal more one should say about quasi-particles. The interested reader can follow the story further in the books mentioned above and the references contained therein. It is the present author's view that a clearer physical picture of such questions as "drag currents," "back flow," "screening," quasi-particle interactions (both forward and nonforward scattering amplitudes), particularly in real metals, deserve careful attention in the future.

5. References

[1] See C. Kittel, Introduction to Solid State Physics, Chapter 10, J. Wiley & Sons, Inc., New York, and J. Ziman, Principles of the Theory of Solids, Cambridge U. Press (1964).

[2] Luttinger, J. M., and Nozieres, P., Phys. Rev. **127**, 1423, 1431 (1962).

[3] Pines, D., and Nozieres, P., The Theory of Quantum Liquids, **Vol. I**, W. A. Benjamin, Inc., New York (1966).

[4] Nozieres, P., Interacting Fermi Systems, W. A. Benjamin, Inc., New York (1964).

[5] Prange, R. E., and Kadanoff, L. P., Phys. Rev. **134**, A566 (1964).

[6] Abrikosov, A. A., Gorkov, L. P., and Dzysloshinskii, I. E., Methods of Quantum Field Theory in Statistical Physics, Prentice-Hall, Inc. (1963).

[7] Schrieffer, J. R., Theory of Superconductivity, W. A. Benjamin, Inc., New York (1964).

[8] Hedin, L., Lundqvist, B. I., and Lundqvist, S., this Symposium.

Discussion on "What is a Quasi-Particle?" by J. R. Schrieffer (University of Pennsylvania)

H. Ehrenreich *(Harvard):* I was wondering just how far above the Fermi surface one can go before things really go bad?

J. R. Schrieffer *(Univ. of Pennsylvania):* I believe that the perturbation theory shows that, depending on the density of the particles, one can get high up into the spectrum and still have reasonably well defined quasi-particles. Calculations have been made, for example, for a free electron gas, of the damping as a function of the excitation energy. While the pair production cross-section starts up as the square of the excitation energy for a very fast particle there is a very different form for the level width, and depending upon the density, it can be that you never get into the region where the quasi-particle width is broader than the actual excitation energy.

L. N. Cooper *(Brown Univ.):* Assuming that the excitations of the Fermi level are in one-to-one correspondence with free particle excitations, what kind of experimental result could be said to contradict (or not be explainable) by the Landau theory?

J. R. Schrieffer *(Univ. of Pennsylvania):* If the low temperature specific heat turned out not to go linearly with temperature, but rather had a form T log T, for example.

L. N. Cooper *(Brown Univ.):* That would mean that the excitations were not in one-to-one correspondence with independent particles. Presumably it has to be something in the interaction term that goes wrong. I was just wondering what kind of a result would force you to the conclusion that you couldn't find an interaction which was consistent with observations.

J. R. Schrieffer *(Univ. of Pennsylvania):* The reason I had pulled in the T log T is that it is one deviation. Presumably, if the collision cross-section or damping rate did not vary at low energy according to ϵ^2, which is a rigorous prediction based on the Landau concepts, let's say it varied in a more singular way, e.g., as $\epsilon^2 \log \epsilon$, for example, then that would violate the Landau theory.

Beyond the One-Electron Approximation: Density of States for Interacting Electrons*

L. Hedin, B. I. Lundqvist, and S. Lundqvist

Chalmers University of Technology, Göteborg, Sweden

The concept "density of states" can be given many different meanings when we go beyond the one-electron approximation. In this survey we concentrate on the definition tied to excitation processes, where one electron is added or removed from the solid. We discuss the one-particle spectral function for conduction and core electrons in metals, how it can be approximately calculated, and how it can be related to different types of experiments like x-ray photoemission, x-ray emission and absorption, photoemission and optical absorption in the ultraviolet, and the Compton effect. We also discuss the form of the exchange-correlation potential for use in band structure calculations.

Key words: Density of states; interacting electrons; one-particle Green function; oscillator strengths; quasi particle density of states; x-ray emission and absorption.

1. Introduction

In the one-electron approximation the concept "electronic density of states" is unique and simple and is defined by the formula

$$N_1(\omega) = \sum_i \delta(\omega - \epsilon_i), \tag{1}$$

where ϵ_i denotes the single-particle energies. Similarly the optical density of states is given by the joint density of state for electrons and holes, thus

$$N_2(\omega) = \sum_i \delta(\omega - \epsilon_i^p + \epsilon_i^h). \tag{2}$$

These functions only describe the cruder aspects of experiments such as soft x-ray emission or optical absorption. They must be augmented with the proper *oscillator strengths*, which provide important selection rules and as well give rise to deviations from the density of state curves.

When one goes beyond the one-electron approximation and considers interactions not included in a self-consistent field theory the situation becomes non-trivial and one encounters a wide variety of density of states functions. The quantity which is most easy to define is the true density of states of the fully interacting systems

$$N(\omega) = \sum_n \delta(\omega - E_n), \tag{3}$$

where E_n are the energy levels of the system. Although being a key quantity in thermodynamics it is of no use for the description for *e.g.* optical, x-ray or energy loss spectra. We rather need the proper extensions of eqs (1) and (2) to describe one- and two-electron properties of the system. A particularly simple case is that of particles having a Lorentzian energy distribution

$$A_k(\omega) = \frac{1}{\pi} \frac{\Gamma_k}{(\omega - \epsilon_k)^2 + \Gamma_k} \cdot \tag{4}$$

The density of states is then given by

$$N_1(\omega) = \sum_k A_k(\omega). \tag{5}$$

In cases where the line width Γ_k is small compared with the width of the band, the formulas (5) and (1) obviously will give similar results.

The simple case just mentioned does not really carry us beyond the one-electron theory. We have in the general case to abandon a concept based on single-particle levels and instead use distribution functions or

* An invited paper presented at the 3d Materials Research Symposium, *Electronic Density of States*, November 3-6, 1969, Gaithersburg, Md.

spectral densities of which the function $A_k(\omega)$ given above is a simple and almost trivial case. Such distribution functions include the proper oscillator strengths, and they refer to formally exact many-electron states, properly weighted according to the physical process considered. They are closely related to correlation functions and Green functions. An example is the density-density correlation function $\langle \rho(\mathbf{r}t)\rho(\mathbf{r}'t')\rangle$, which correlates density fluctuations at different times and different positions. This function is of basic importance for describing optical experiments and energy loss spectra. Unfortunately it is very difficult to analyze its structure and we will here instead concentrate on a simpler entity, the one-particle Green function and its associated spectral function [1].

The one-particle spectral function is a generalization of the usual density of states $N_1(\omega)$. It gives an asymptotically exact description of x-ray photoemission, is connected with x-ray emission and absorption and also has some relevance for uv photoemission and absorption.

It is, however, not capable to describe edge effects in general, and does not at all account for final state or particle-hole interactions. Such effects, which in their simplest form are described by $N_2(\omega)$ or generalizations therefrom provide intricate problems upon which we shall only briefly touch here. These questions will be taken up in detail in the lecture by Mahan.

It has recently been noticed that the one-electron spectral function should exhibit some marked and strong structure. This structure is primarily associated with the interaction between the electron and plasmon excitations. It should be quite important in x-ray photoemission, influencing the line shape of the core electron peak and giving low energy satellites both to the core electron and conduction band structures. It is important in x-ray emission and absorption spectra showing up at the threshold, and giving rise to satellite structures. Its effect may also be noticeable in uv photoemission and optical absorption spectra.

We should also mention the structure in the one-electron spectrum caused by coupling to phonons. This structure is limited to a region of the order of the Debye energy around the Fermi level, but in that region it is quite pronounced, causing *e.g.* the well-known enhancement of the quasi particle density of states.

In the next section we will discuss the connections between the one-electron spectrum and x-ray photoemission, and with x-ray emission and absorption. In section 3 we discuss the spectrum of the conduction electrons from calculations to lowest order in the dynamic interaction between the electrons and between the electrons and phonons.

In section 4 we take up the core electron spectrum and discuss calculations to first order in the dynamic interaction with the valence electrons. We also survey the recent work by Langreth who obtained the exact solution to an important model problem. In section 5 we give a qualitative discussion of some experimental results for photon absorption and emission, photoemission and Compton scattering. In section 6 finally we give some concluding remarks.

2. The One-Electron Density of States in an Interacting System and its Connection with X-Ray Photoemission and with X-Ray Emission and Absorption

In this section we introduce some theoretical technicalities, which however seem unavoidable in order to establish a firm connection between theory and experiment.

The one-electron spectral weight function is defined as

$$A(\mathbf{x}, \mathbf{x}'; \omega) = \sum_s f_s(\mathbf{x}) f_s^*(\mathbf{x}') \delta(\omega - \epsilon_s). \qquad (6)$$

In the independent-particle approximation the quantities f_s and ϵ_s are the one-electron wave functions and energies. In an interacting system the oscillator strength function f_s is defined as

$$f_s(\mathbf{x}) = \langle N-1, s|\psi(\mathbf{x})|N\rangle, \qquad (7)$$

where $\psi(\mathbf{x})$ is the electron field operator. It gives the probability amplitude for reaching an excited state $|N-1, s\rangle$, when an electron is suddenly removed from the ground state $|N\rangle$. The quantity ϵ_s is the excitation energy

$$\epsilon_s = E(N) - E(N-1, s). \qquad (8)$$

These definitions apply for ω in eq (6) smaller than the chemical potential μ. For ω larger than μ, states with $N+1$ particles are involved.

In applications of the theory it is often practical to represent the spectral function as a matrix in a space spanned by some suitable complete orthonormal set of single-particle states $\mu_k(\mathbf{x})$, thus

$$A_{kk'}(\omega) = \int u_k^*(\mathbf{x}) A(\mathbf{x}, \mathbf{x}'; \omega) u_{k'}(\mathbf{x}') d\mathbf{x} d\mathbf{x}'$$
$$= \sum_s \langle N|a_k^+|N-1, s\rangle \langle N - 1, s|a_k|N\rangle \delta(\omega - \epsilon_s). \qquad (9)$$

The spectral weight function is the general distribution function describing one-electron properties, and is a generalization of the one-electron density matrix, which is obtained after an integration over the frequencies. Distributions with respect to a single variable are in the usual way obtained by summation over all other variables. Thus, the *one-electron density of states* is defined as

$$N(\omega) = \mathrm{Tr}\, A(\omega) = \int A(\mathbf{x}, \mathbf{x}; \omega) d\mathbf{x} = \sum_k A_{kk}(\omega). \quad (10)$$

As indicated, the definition is independent of the choice of matrix basis.

The spectral weight function is a key quantity in the Green function formulation of the many-electron problem. A more detailed account is given in many texts, *e.g.* in sections 9 and 10 of ref. [1].

We next discuss the particular cases of x-ray photoemission and soft x-ray emission, where approximate reductions to the one-electron spectrum can be made.

In the x-ray photoemission experiment (XPS), an energetic photon of energy ω is absorbed, exciting a photoelectron which leaves the system. If the electron has a large enough energy we can write the final state as

$$|\Psi_f\rangle = a_\kappa^+ |N-1, s\rangle, \quad (11)$$

where $\boldsymbol{\kappa}$ refers to a Bloch wave function of energy $\epsilon_\kappa \approx \hbar^2\mathbf{k}^2/(2m)$, describing the photoelectron. The probability of this event is, by the Golden rule,

$$W \sim \sum_f |\langle \Psi_f | \mathbf{P} | \Psi_i \rangle|^2 \delta(\omega - E_f + E_i)$$

$$= \sum_{\kappa, s} |\langle N-1, s | a_\kappa \sum_{k,k'} p_{k'k} \alpha_{k'}^+ a_k | N \rangle|^2 \delta(\omega - \epsilon_\kappa + \epsilon_s), \quad (12)$$

where $\mathbf{P}$ is the total momentum and $p_{kk'}$ the momentum matrix element. For a fast electron, which is outside the region of ground state fluctuations, $a_\kappa|N\rangle = 0$, and the expression for W reduces to

$$W \sim \sum_{\kappa, s} |\langle N-1, s | \sum_k p_{\kappa k}\, a_k | N \rangle|^2 \delta(\omega - \epsilon_\kappa + \epsilon_s)$$

$$= \sum_\kappa \sum_{k,k'} A_{kk'}(\epsilon_\kappa - \omega) p_{\kappa k}^* p_{\kappa k}, \quad (13)$$

The energy distribution of photoelectrons is hence given by

$$I(\epsilon) \sim \sqrt{\epsilon} \sum_{k,k'} A_{kk'}(\epsilon - \omega) p_{\kappa k}^*\ p_{\kappa k'}, \quad (14)$$

taking $e_\kappa = \epsilon$. Using an average momentum matrix element and neglecting nondiagonal terms in A we obtain the simple result

$$I(\epsilon) \sim \sqrt{\epsilon} p_{eff}^2 N(\epsilon - \omega). \quad (15)$$

The neglect of nondiagonal terms should be a good approximation if the one-electron functions are carefully chosen Bloch functions and core-electron functions. We note that if the electron is ejected from a core level and if we neglect excitations of the core electron system, the operator a_k in eq (13) must destroy a core electron ($a_k = a_c$), giving

$$W \sim \sum_{\kappa, s} |\langle N_v^*, s | N_v \rangle p_{\kappa c}\ |^2 \delta(\omega - \epsilon_\kappa + \epsilon_s). \quad (16)$$

Here $|N_v\rangle$ denotes the ground state of the valence electron system, and $|N_v^*, s\rangle$ are excited states in the presence of the core hole. We recognize eq (16) as the result in the sudden approximation.

We next turn to soft x-ray emission. In this case we may write the initial state as [2]

$$|\Psi_i\rangle = a_c |N^*\rangle \quad (17)$$

where the star on N indicates that the valence electron system is relaxed towards the core hole. Applying the Golden rule again we have for the x-ray intensity

$$I(\omega) \sim \omega \sum_f |\ \langle\ \Psi_f | \sum_{kk'} p_{k'k} a_{k'}^+ a_k a_c | N^*\ \rangle\ |^2 .$$

$$\delta(\omega - E_i + E_f)$$

$$= \omega \sum_s |\ \langle\ N_v - 1, s | \sum_k p_{ck} a_k | N_v^*\ \rangle\ |^2 \delta(\omega + \epsilon_c - \epsilon_s). \quad (18)$$

If we could neglect the relaxation effects in the initial state and replace $|N_v^*\rangle$ by $|N_v\rangle$, we would again have the spectral function A involved. The relaxation effects can be accounted for in an approximate way by only considering particle-hole excitations, thus

$$|N_v^*\ \rangle = (\alpha + \sum_{h,p} \alpha_h^p a_p^+ a_h) |N_v\ \rangle . \quad (19)$$

Insertion of this expression in eq (18) leads after some further approximations to a very simple expression

$$I(\omega) \sim \omega \sum_k |p_{ck}^{\mathrm{eff}}|^2 A_{kk}(\omega + \epsilon_c), \quad (20)$$

where p^{eff} involves the coefficients α and is ω-dependent. Such an approximation is however invalid at the Fermi edge, where, as Anderson [3] has pointed out, we need an infinite number of particle-hole pairs to represent $|N_v^*\rangle$.

The edge problem has recently been treated by several people [4–6]. We choose here to give a brief account of Langreth's version [6] of Nozieres; and de Dominicis' (ND) treatment of the problem in order to show how the one-electron spectrum enters the problem. The basic quantity needed for the evaluation of eq (18) is the correlation function

$$F_{kk'}(t) = \langle N^* | T(a_k(t) a_{k'}^+ a_c(t) a_c^+) | N^* \rangle . \quad (21)$$

To evaluate that function ND study the multiple time function

$$F_{kk'}(\tau, \tau'; t, t') = \langle N^* | T(a_k(\tau) a_{k'}^+(\tau') a_c(t) a_c^+(t') | N^* \rangle . \quad (22)$$

The simple way, in which the core state operator enters their model Hamiltonian, causes the equation of motion for F to close onto itself and allows a solution as a product,

$$F_{kk'}(\tau,\tau';t,t') = \phi_{kk'}(\tau,\tau';t,t')\, G_c(t,t') \quad (23)$$

where G_c is the core electron Green function,

$$G_c(t, t') = \langle N^* | T(a_c(t) a_c^+(t')) | N^* \rangle \quad (24)$$

and ϕ a valence electron Green function which obeys an equation with a transient potential from the core hole. The x-ray spectrum is given by a convolution of the core and valence electron spectra. Both spectra are singular at the edge as a power law and so is also the resulting convolution.

The point in keeping the operator a_c in eq (22) is that the time dependence of $a_k(t)$ then can be given by the same Hamiltonian as that used for $|N^*\rangle$, while when studying $\langle N_v^* | T(a_k(t) a_{k'}^+) | N_v^* \rangle$, the time evolution of $a_k(t)$ is given by a Hamiltonian that does not include the potential from the core hole, and thus the usual many-body techniques do not apply. X-ray absorption can be described in an analogous manner by the function F, only replacing $|N^*\rangle$ by $|N\rangle$.

It should be mentioned that the ND treatment is based on a model Hamiltonian that does not include interactions between the conduction electrons. This is quite appropriate for their purposes of treating the edge problem but is not sufficient for the spectrum far away from the edge. It is not clear if their treatment can be extended to the more general case. We then have to resort to other methods, such as the approximation in eq (19) or to a frontal attack on the dielectric function itself [7].

We have in this section given a definition of the one-electron density of states and have indicated its relation to some measurable quantities. We conclude from this that a theoretical investigation of this kind of experiments can not avoid the calculation of the one-electron density of states of interacting electrons, but at the same time due to a variety of effects there may be essential modifications of the density of states as it appears in the actual experiment. Explicit results from approximate calculations of the spectral function A and the density of states $N(\omega)$ are discussed in sections 3 and 4, and the actual comparison with experiment is made in section 5.

3. One-Electron Spectrum of Conduction Electrons

The common picture of the one-electron spectra of solids is obtained from energy band calculations, in which the Schrödinger equation of independent electrons in a periodic potential is solved. For the different bands one obtains the electron energy as a function of wave-vector, $\epsilon(\mathbf{k})$. The main contribution to the potential seen by an electron is the average electrostatic field or the Hartree field. When going beyond the one-electron approximation the next step would be to include dynamical effects of the interaction as well as exchange effects. Such effects can not be described by an ordinary local potential. A generalized "potential," non-local in space and time, must be introduced.

Let us for simplicity study the case, where specific effects of the periodicity are of minor importance, and assume the distribution of conduction electrons to be uniform. Due to the non-locality of the generalized "potential," its Fourier transform to momentum-energy space will show a dependence on both wave-vector $\mathbf{k}$ and energy ϵ, $\Sigma(\mathbf{k}, \epsilon)$. The quantity Σ is called the *self-energy* of the electron.

Adding the self-energy to the average potential, we have to solve the equation

$$\epsilon = \epsilon(\mathbf{k}) + \Sigma(\mathbf{k},\epsilon). \quad (25)$$

The self-energy includes all the interactions between the electron state considered and the system. This necessarily includes dissipative effects, which lead to the decay of the state. Consequently the self-energy must be a complex quantity, thus

$$\Sigma(\mathbf{k},\epsilon) = \Sigma_R(\mathbf{k},\epsilon) + i\Sigma_I(\mathbf{k},\epsilon). \quad (26)$$

The spectral weight function defined in section 2 is related to the self-energy according to the formula 1, sec-

tion 1

$$A(\mathbf{k},\epsilon)=\frac{1}{\pi}\frac{\left|\sum_I(\mathbf{k},\epsilon)\right|}{(\epsilon-\epsilon(\mathbf{k})-\sum_R(\mathbf{k},\epsilon))^2+\left(\sum_I(\mathbf{k},\epsilon)\right)^2}. \tag{27}$$

In the simple case that the self-energy Σ is independent of energy, the spectral function for fixed k will have a Lorentzian shape and Σ_I determines the width of the line. When Σ depends on energy there are no a priori restrictions on the shape of the spectrum.

Most of our present knowledge about the self-energy has been based on calculations, where vertex corrections have been neglected, *i.e.* using the formulae [9–13]

$$\sum(\mathbf{k},\omega)=\frac{i}{(2\pi)^4}\int e^{i\omega\delta}v(\mathbf{k}')\,\epsilon^{-1}(\mathbf{k}',\omega')G_0(\mathbf{k}+\mathbf{k}',\omega+\omega')d\mathbf{k}'d\omega', \tag{28}$$

where

$$G_o(\mathbf{k},\omega)=(\omega-\epsilon(\mathbf{k})+i\delta\ \text{sign}\ (k-k_p))^{-1} \tag{29}$$

is the propagator for a non-interacting electron, and

$$v(\mathbf{k})=4\pi e^2/\mathbf{k}^2 \tag{30}$$

is the bare Coulomb potential. The constant k_F means the Fermi momentum, and δ is a positive infinitesimal.

To make connection with another approximation, we note that the Hartree-Fock approximation corresponds to the choice $\epsilon=1$ in eq (28). As it stands, eq (28) expresses the lowest order coupling to the density fluctuations of the conduction electrons, described by the wave-vector- and frequency-dependent *dielectric function* $\epsilon(\mathbf{k},\omega)$. This function contains information about the static screening, given by $\epsilon(\mathbf{k},0)$, but also important effects of the dynamic behavior of the density fluctuations. The typical small-k-behavior of the spectral function for this kind of excitations, $-\text{Im}\ \epsilon^{-1}(\mathbf{k},\omega)$, is indicated in figure 1. The clearcut classification of the excitations into electron-hole pairs and plasmons is characteristic for the Linearized Time dependent Hartree (LTH) or Random Phase Approximation [14]. For small wave-lengths the electron-hole pair excitations become of increasing importance, while in the $k\to 0$-limit the plasmon exhausts completely the sum rule for Im ϵ^{-1}, *i.e.* it is the only excitation. The latter property follows from general arguments about charge conservation and translation invariance [8, p. 288], and should be valid for any useful approximation for $\epsilon(\mathbf{k},\omega)$. In the

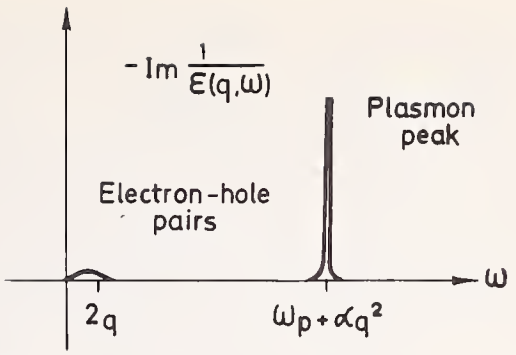

FIGURE 1. *Qualitative behavior of Im* $\epsilon^{-1}(q,\omega)$ *for small* q.

LTH approximation the plasmon is undamped for wave-numbers smaller than a critical value k_c, which at metallic densities is of the same order of magnitude as k_F.

A great part of the literature about the electron gas is devoted to the search for an improved dielectric function [15–20], particularly because of the failure of the LTH formula to describe interaction effects at short distances. The last word remains to be said in this question, but it is interesting to note the relative insensibility of the self-energy to the choice of dielectric function [11,12,21]. An approximation, which has proved to be most useful, is to take a plasmon-like sharp absorption for all $\mathbf{k}$ according to the formula

$$\epsilon^{-1}(\mathbf{k},\omega)=1.+\frac{\omega_p^2}{\omega^2-\omega^2(\mathbf{k})} \tag{31}$$

where ω_p is the classical plasma frequency and $\omega(\mathbf{k})$ the resonance frequency at wave number $\mathbf{k}$. The frequency $\omega(\mathbf{k})$ reduces to ω_p when $|\mathbf{k}|\to 0$ and is proportional to $|\mathbf{k}|^2$ for large $|\mathbf{k}|$. This formula correctly represents the small and large ω-limits and gives a quite reasonable interpolation for intermediate ω values [1, 1]. With this choice one can perform the frequency integration in eq (28) and obtain

$$\sum(\mathbf{k},\omega)=-\frac{1}{(2\pi)^3}\int d^3q\frac{v(q)n_0(\mathbf{k}+\mathbf{q})}{\epsilon(\mathbf{q},\epsilon(\mathbf{u}+q)-\omega)}+\frac{\omega p^2}{(2\pi)^3}\int d^3q\frac{v(\mathbf{q})}{2\omega(\mathbf{q})}\frac{1}{\omega-\epsilon(\mathbf{h}+\mathbf{q})-\omega(\mathbf{q})} \tag{32}$$

The first term in eq (32) is a *screened exchange potential*, $n_o(\mathbf{k})$ being the momentum distribution for independent electrons, and the second term describes the *correlation hole* around the electron [12,22].

Because of the plasma resonance in the dielectric function there will be a rapid variation in the real part

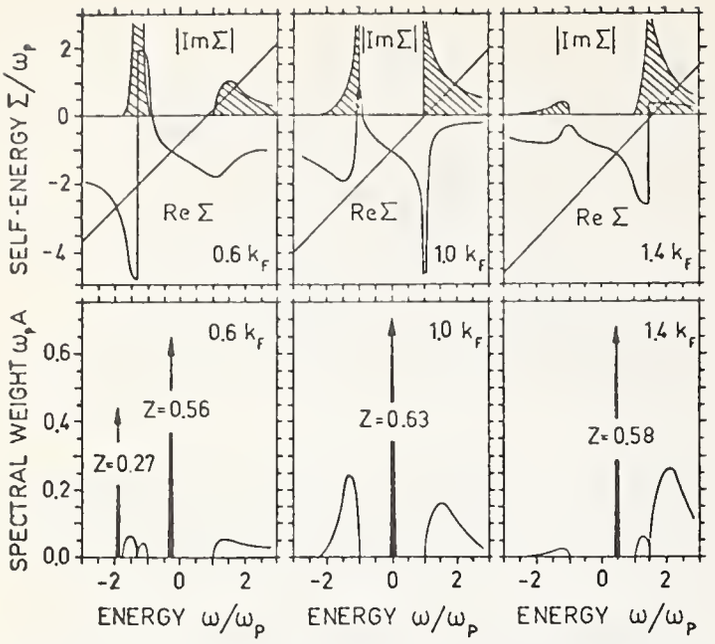

FIGURE 2. *The self-energy* Σ *and the corresponding spectral function* A *for* $r_s = 5$ [21]. *The crossings between the* Re Σ *curves and the straight lines give the solutions to the Dyson equation. The numbers at the peaks indicate the strengths of the lines.*

of Σ at the frequency $\omega = \epsilon(\mathbf{k}) + \omega_p$ for electrons and at $\omega = \epsilon(\mathbf{k}) - \omega_p$ for holes. This behavior of the electron gas seems to have been first noticed and discussed by Hedin *et al.* [23] and has been studied in great detail by Lundqvist [13,21]. Typical curves for Σ obtained with this dielectric function are shown in the upper half of figure 2. In the lower part of figure 2 we have given the results for $A(\mathbf{k},\omega)$ calculated from eq (27).

For $k = k_F$ there is only one strong peak in the spectral function, corresponding to the usual quasi particle. For the other k-values in the figure, we find three solutions of the Dyson equation

$$\omega = \epsilon(\mathbf{k}) + \Sigma_R(\mathbf{k},\omega). \tag{33}$$

One of them, however, falls at $\omega = \epsilon(\mathbf{k}) \pm \omega_p$, where the damping is very strong, and therefore this solution is effectively suppressed. Of the two remaining solutions, one corresponds to the usual quasi particle, *i.e.* a bare electron surrounded by a cloud of virtual plasmons and electron-hole excitations. For hole states, *i.e.* for $k < k_F$, a new state appears which has an energy lower than that corresponding to a hole plus a plasmon, *i.e.* $\epsilon(\mathbf{k}) - \omega_p$. This result from a low order treatment corresponds to a coherent state of hole-plasmon pairs, and may be thought of as holes coupled to *real* plasmons. This coupled state, which has been called a *plasmaron*, has a large oscillator strength, and thus gives an essential contribution to the sum rule for the one-electron spectrum. For electron states, $k > k_F$, there is no sharp state but a broad resonance with a sharp onset at $\omega = \epsilon(\mathbf{k}) + \omega_p$.

Figure 3 illustrates how the parabolic quasi particle dispersion law is accompanied by a second branch of the spectrum, the plasmaron. In figure 4 the momentum distribution function for the interacting electrons is given.

The characteristic structure due to plasmon effects will modify the density of states. This is demonstrated schematically in figure 5. The conduction band will retain approximately its parabolic shape. At an energy ω_p below the Fermi edge there is the onset of the second band due to the plasmaron states. This band is terminated at low energies with a rather distinct edge. For unoccupied states there is an extra contribution to the density of states starting at an energy ω_p above the Fermi level. Figure 6 gives a survey of the density of state curves at four different values of the electron gas parameter r_s ($r_s = 2$ corresponding roughly to the electron density of Al, and $r_s = 4$ to that of Na).

So far we have discussed the gross effects due to the coupling between electrons and plasmons. These are quite well represented by the plasmon-pole approximation for the dielectric function in eq (31). Electron-hole pair excitations are however not included, to represent

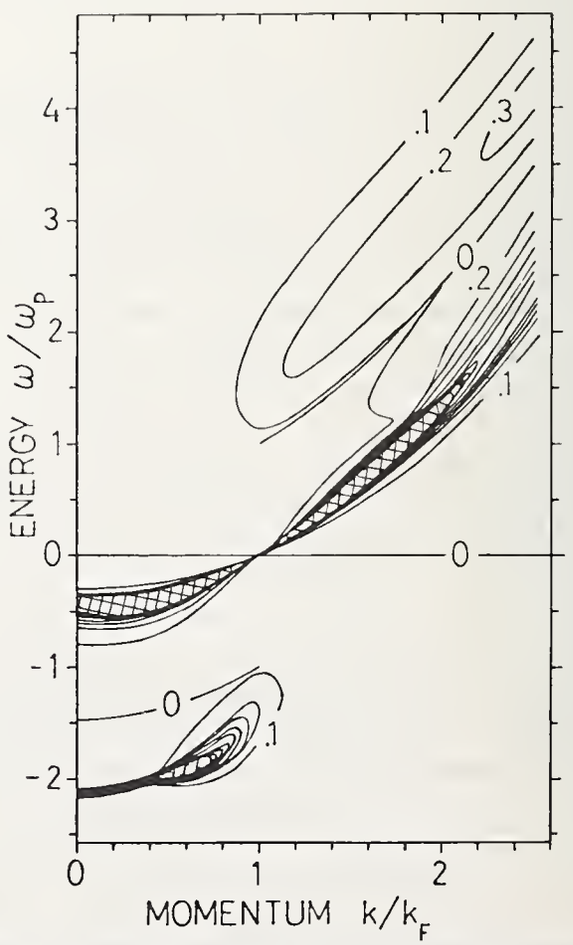

FIGURE 3. *The spectral weight function* A(k,ω) *given by level curves indicating the value of* $\hbar\omega_p$A, *at* $r_s = 4$ ($\hbar\omega_p = 0.435$ *Ry*) [13].

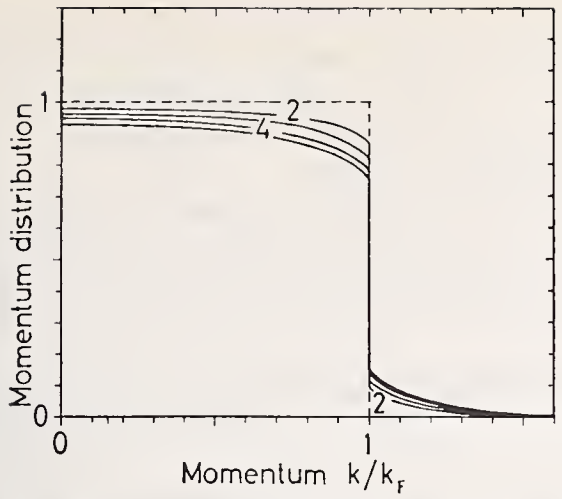

FIGURE 4. *The momentum distribution function* n(k) *at* $r_s = 2, 3, 4$ *and* 5 [13].

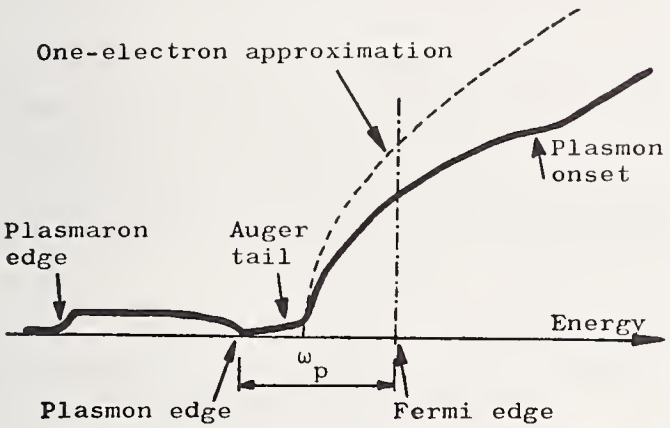

FIGURE 5. *Density of states for conduction electrons.*

them we must turn to the LTH dielectric function or higher approximations. These excitations are responsible for the broadening of the quasi particle peak and the Auger tail at the bottom of the main band in figures 5 and 6 as well as the broad spectral weight contours in figure 3.

Figure 7 shows $\Sigma_I(\mathbf{k},\epsilon(\mathbf{k}))$ calculated from eq (28) and is an indication of the high damping rate for quasi particles with k greater than $k_F + k_c$, *i.e.*, in the region where they can decay into plasmons [10,24]. However, as illustrated by the typical spectral forms for the quasi particle peak in figure 8, the quasi particle peak is always distinguishable from the spectral background, its width $\Gamma(\mathbf{k})$ is smaller than its excitation energy $E(\mathbf{k}) - \mu$.

From eq (28) one can also draw information about the exchange and correlation "potential" for the quasi particles. The inadequacy of the Hartree-Fock approximation in a metal is well-known, and in band calculations the effects of exchange and correlation are commonly simulated by using a local potential, such as the Slater [25] or the Gáspár [26,27] expressions. After solving the Dyson equation one can write the resulting quasi-particle energy in the form

$$E(\mathbf{k}) = \epsilon(\mathbf{k}) + V(\mathbf{k}), \tag{34}$$

where $V(\mathbf{k})$ can be interpreted as an effective exchange and correlation potential. In figure 9 such a potential is shown. It has a remarkably weak k-dependence for moderate wave vectors, its value lying roughly halfway between the Slater [25] and "2/3 Slater" values [26,27].

One of the shortcomings of the Hartree-Fock approximation is its prediction of a large bandwidth. The width of the occupied part of the main band deduced from eq (28) is practically the same as the Hartree value $\epsilon(k_F)$, a result which is in accord with the experimental findings.

For large momenta ($k \gtrsim k_F + k_c$) there is a characteristic k-dependence of $V(\mathbf{k})$, which might influence properties of electrons involved in photoemission and

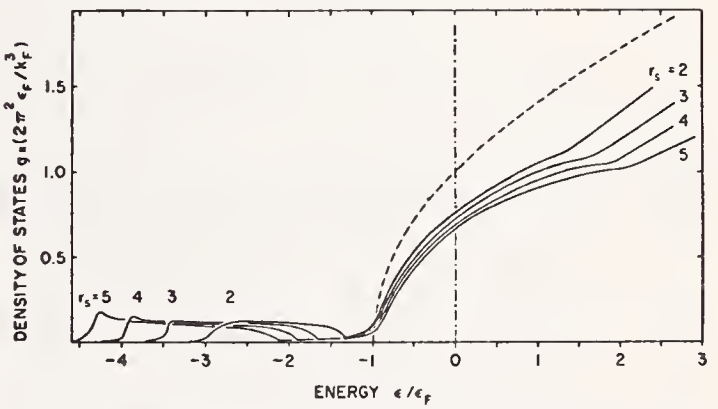

FIGURE 6. *The density of states for the values of the electron gas parameter* $r_s = 2, 3, 4, 5$. *The dashed curve is the result of the one-electron theory, and the vertical broken line indicates the Fermi level* [13].

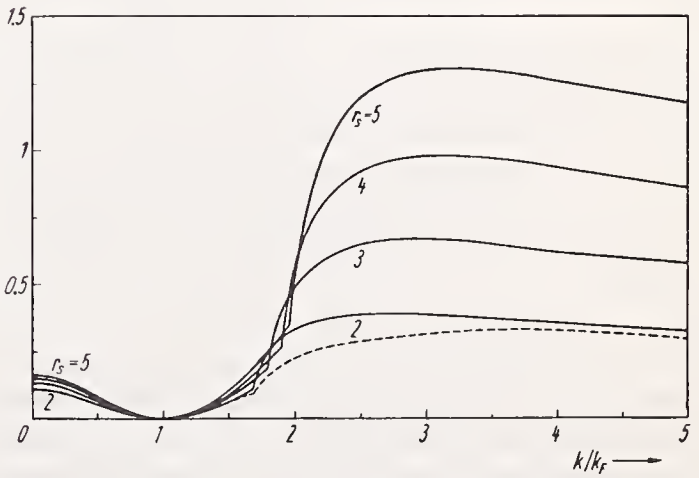

FIGURE 7. *The imaginary part of the quasi-particle self-energy Im* $\Sigma(k,\epsilon(k))/E_F$ *as a function of the momentum* k *of the electron at different metallic densities* ($E_F = 0.921, 0.409, 0.230$, *and* 0.147 *Ry at* $r_s = 2, 3, 4$ *and* 5, *respectively*). *The dashed curve is Quinn's result at* $r_s = 2$ [10,13].

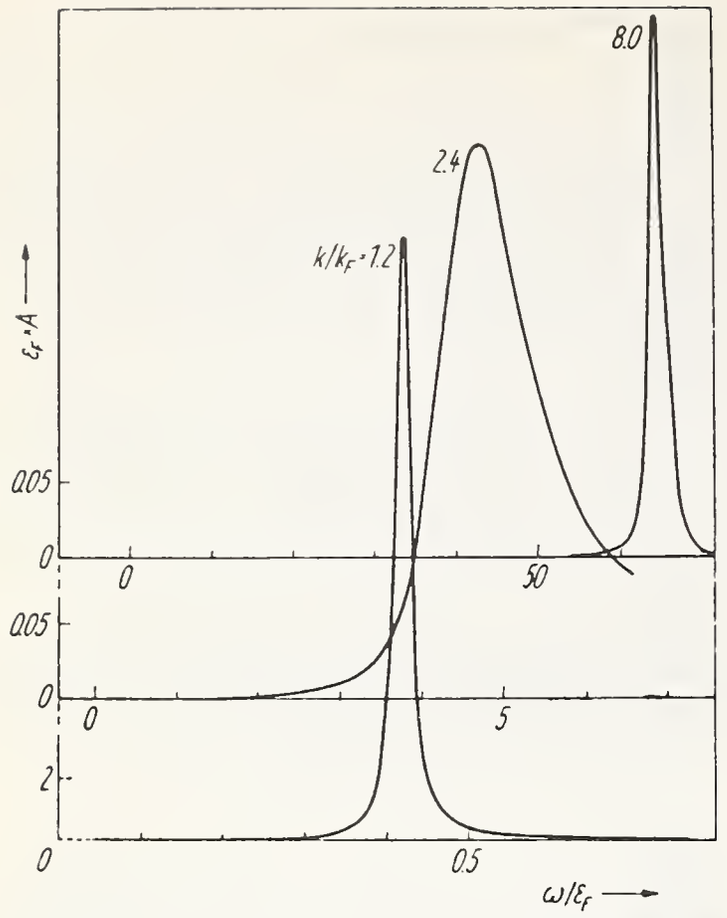

FIGURE 8. *Typical spectral forms for the quasi-particle peak of the spectral weight function in different momentum regions. The scales are different for the three curves, the energy ω is measured from the Fermi level μ, and the curves are drawn for* $r_s = 4$ [24].

LEED experiments. It is not clear, however, how much of this structure that may be observed due to the short-lifetime of the electrons at these energies.

We want to stress again that the discussion we have given of the one-electron spectrum is based on the assumption that vertex corrections are small. As discussed in the next section recent work by Langreth [29] shows that vertex corrections in the core electron problem can have a quite large effect on the form of satellite structures, while their effect on the quasi particle properties seems to be small. Preliminary investigations by one of us (L.H.) show similar strong vertex effects on the conduction band satellite. The details of the plasmaron structure should thus not be taken very seriously.

The quasi particle states close to the Fermi surface are of particular interest due to their importance for thermal and transport properties [30]. To study these problems the quasi particle density of states or density of levels rather than the one-electron density of states is of importance. Because of interactions the quasi-particle dispersion law is distorted, corresponding to the well-known mass enhancement at the Fermi surface. The corrections to the free-electron mass m due to the electron-electron interaction, as derived from eq (28), are small [11,12], *e.g.* $\delta m_e/m \approx -.01$ for Al and $\delta m_e/m \approx .06$ for Na, and the properties of the quasi particles close to the Fermi surface are dominated by the electron-phonon interaction.

The effects of the electron-phonon interaction on the quasi-particle dispersion law follow in a straightforward way using perturbation theory in the Brillouin-Wigner form, thus

$$E(\mathbf{k}) = \epsilon(\mathbf{k}) + \sum_{\mathbf{p}} |g_{\mathbf{k}-\mathbf{p}}|^{\epsilon} \left[\frac{1 - f_{\mathbf{p}}}{E(\mathbf{k}) - \epsilon(\mathbf{p}) - \omega(\mathbf{k}-\mathbf{p})} + \frac{f_{\mathbf{p}}}{E(\mathbf{k}) - \epsilon(\mathbf{p}) + \omega(\mathbf{k}-\mathbf{p})} \right]. \quad (35)$$

In this equation g_{k-p} is the matrix element for the electron-phonon coupling and $\omega(\mathbf{k}-\mathbf{p})$ the phonon frequency.

The qualitative effect of the phonons is to flatten out the dispersion curve in the immediate neighborhood of the Fermi surface, and this gives rise to the enhancement of the density of states (fig. 10), or, equivalently, of the *thermal effective mass* and one obtains from eq (35)

$$m_{ph} = m\ (1+\lambda) = N_0(E_F) \int \frac{d\Omega_{\mathbf{p}-\mathbf{k}}}{4\pi} \frac{|g_{\mathbf{p}-\mathbf{k}}|^2}{\omega(\mathbf{p}-\mathbf{k})}, \quad (36)$$

where $N_o(E_F)$ is the density of states without electron-phonon interaction, $|\mathbf{p}| = |\mathbf{k}| = k_F$ and the integration extends over the full solid angle.

Ashcroft and Wilkins [32] first calculated the corrections for Na, Al and Pb using eq (36), and several similar calculations have been published over the last

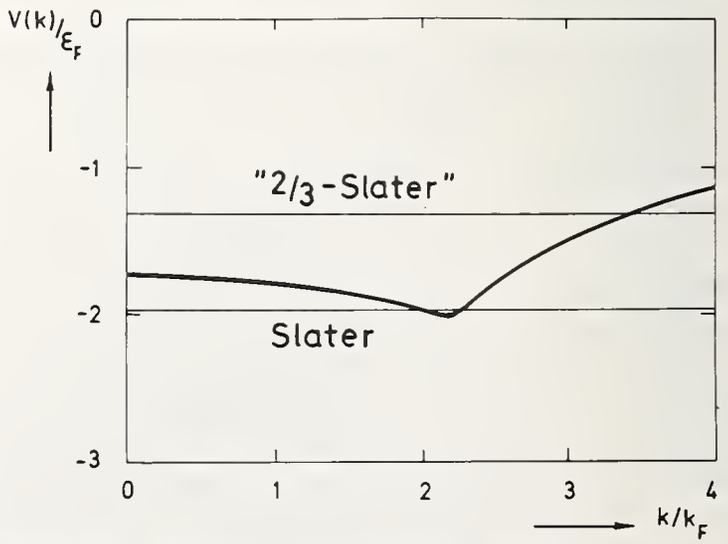

FIGURE 9. *Exchange-correlation potential for an electron gas at* $r_s = 4$ *compared with the Slater and the Gáspár (2/3 Slater) approximations* [28].

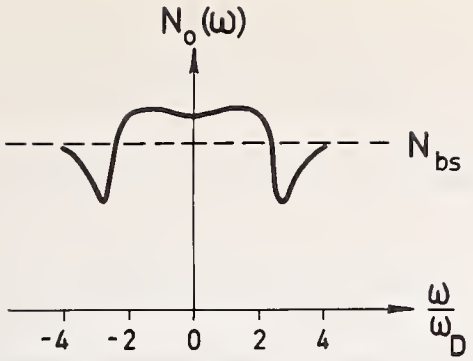

FIGURE 10. *Density of quasi-particle levels for Na at* T = 0°K [31].

few years. The most accurate values of λ are those deduced from tunneling data by McMillan and Rowell [33]. For example, the two methods give the values λ = 0.49 and 0.38, respectively, for Al; λ = 1.05 and 1.3, respectively, for Pb.

It is obvious that the enhancement varies with temperature and that no enhancement is left at high temperatures, where the phonon system behaves like a fluctuating classical medium.

Similarly to the case of electron-electron interaction the electron-phonon interaction gives a characteristic structure to the spectral function. Engelsberg and Schrieffer [34] pointed out that in the neighborhood of the Fermi surface the quasi particle picture will no longer apply. They calculated the spectral function for an Einstein model and for a Debye spectrum and obtained a spectral function with a very complex structure in the region close to the Fermi surface. For sodium no dramatic effects occur because of the rather weak electron-phonon interaction [31].

We conclude this section by noting that inclusion of dynamical and exchange effects, in particular consideration of the electron-electron interaction tells us why the one-electron theory works so well in explaining many gross features of metals and what limitations it has. However, at least in a low-order treatment there are also new structures introduced by the interaction, schematically characterized as due to the resonant coupling between electrons and plasmons. In section 5 we will discuss possibilities to observe this structure.

4. One-Electron Spectrum of Core Electrons

The preceding discussion has emphasized the strong effects of the electron-plasmon coupling on the spectrum of conduction electrons. Similar strong effects occur in the spectra of core electrons. For simplicity we limit the discussion to simple metals with small cores, so that the core electrons can be physically distinguished from the valence electrons and be well localized to a particular ion. The wave function of a core electron depends only weakly on the state of the outer electrons. The energy levels on the other hand are shifted by an appreciable amount compared to the corresponding atomic levels, typically of the order of 5 to 10 eV, which is large on the scale of valence electron energies but is a small *relative* change in the energy of a core electron. The core shifts can be measured accurately by the method of x-ray photoemission spectroscopy as well as by x-ray absorption and inelastic scattering of fast electrons.

The shift of the quasi particle energy of a core electron comes partly from changes in the average Coulomb field, partly from polarization effects. The *Coulomb shift* is due to the different valence charge distribution relative to that in a free atom. It generally results in a decrease of the binding energy. The *polarization shift* comes from the relaxation of the valence charge distribution around the hole created when we remove the electron. The valence electrons are drawn in towards the positive hole in the ion. This effect decreases the binding energy by half of the change in the Coulomb potential calculated at the core site, *i.e.* precisely the amount obtained if we calculate the self-energy of the hole using electrostatics. The shift in the core energy thus contains information about the valence electron distribution and polarizability, measured with the core electron as a probe. Theoretical calculations for simple metals (Li, Na, K, Al) are in very good agreement with the experimentally observed peaks in the XPS spectra [35].

In analogy with the strong effects of the interaction between particles and plasmons previously discussed, there is a corresponding coupling between a hole in the core and the density fluctuations of the conduction electrons. This leads to a strong structure in the core electron spectrum [36].

We assume for simplicity that we can neglect the spatial extension of the core electron wave function. Calculation of the self-energy to lowest order in the screened interaction gives the formula

$$\sum(\epsilon) = -\frac{i}{(2\pi)^4}\int d^3q\,d\omega\,v(q)\,[\epsilon^{-1}(q,\omega)-1]\,\frac{1}{\omega-\epsilon+\epsilon_n+i\delta}, \qquad (37)$$

where ϵ_n is the core quasi-particle energy. Remembering that $\epsilon^{-1}(q,\omega)$ has a strong resonance in the plasmon regime, we see that after integration over the frequency, the self-energy will show a resonance behavior in the energy region $\epsilon \simeq \epsilon_n - \omega_p$. This rapid variation will give rise to two solutions of the Dyson equation. The

417-156 O - 71 - 17

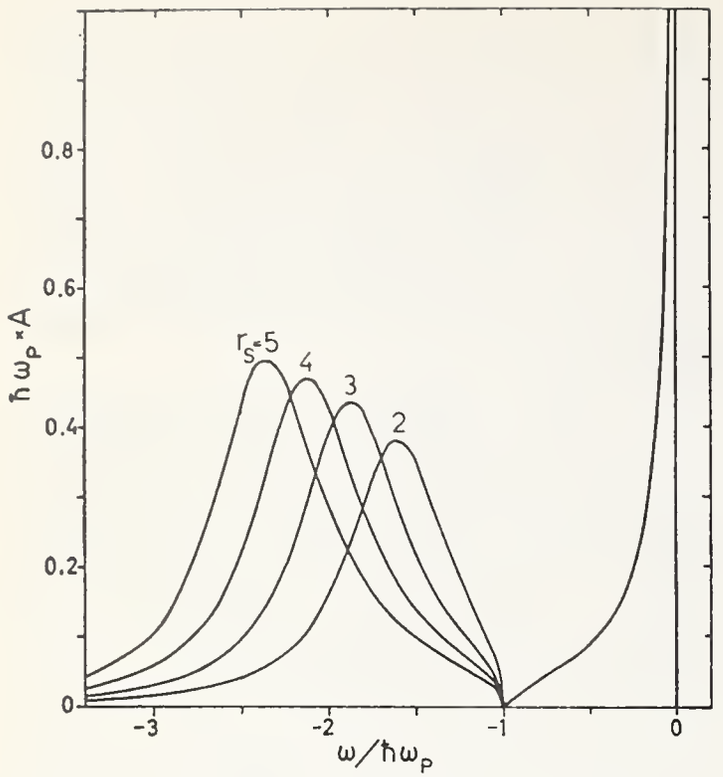

FIGURE 11. *Quasi-particle peak in the spectral function for a core electron and the associate plasmon satellite structure for different densities of the conduction electrons, measured by the electron gas parameter* r_s [36].

second solution, however, gives a quite broad peak in the spectral function. The results for different densities of the electron gas are illustrated in figure 11. The spectrum is measured from the shifted quasi particle energy, *i.e.* the zero of energy corresponds to complete relaxation of the electrons around the hole.

We summarize the characteristic features of the core spectrum

a. A large polarization shift of the core quasi particle level.
b. The shape of the spectrum is independent of the core level considered. This results from neglecting the actual size of the core wave function.
c. A pronounced satellite structure, which starts at $\omega = -\omega_p$ and has a broad peak.
d. An extended tail on the low energy side of the quasi-particle peak. This tail is due to the coupling between the hole and screened electron-hole pair excitations, and corresponds to states of the whole system involving two holes, one in the core and one in the conduction band plus one excited electron above the Fermi sea.
e. There is an appreciable reduction of the spectral strength of the quasi particle. Approximately half of the spectral strength corresponds to excitations close to the quasi particle state and approximatcly the same strength corresponds to high excitations of the conduction electrons as described by the broad satellite structure.

As discussed in section 2 the spectral function has the form (cf. eq (16))

$$A_c(\omega) = \sum_s |\langle N_v^*, s|N_v\rangle|^2 \delta(\omega - \epsilon_s) \qquad (38)$$

and shows a powerlaw singularity at the Fermi edge. The first order theory correctly predicts a singularity but of a somewhat different form, namely $(\omega \ln^2 \omega)^{-1}$.

The core electron spectrum can be obtained exactly if we use a simple model Hamiltonian

$$H = \epsilon a^+ a + a a^+ \sum_q g_q (b_q + b_{-q}^+) + \sum_q \omega_q b_q^+ b_q, \qquad (39)$$

Here a^+ is the creation operator for a core electron of energy ϵ and b_q^+ the creation operator for a plasmon of energy ω_q. The exact solution of this problem has been given by Langreth [29], and we now give a brief account of his work, which also shows the close resemblance of the problem to the Mössbauer or the impurity-phonon problem.

The self-energy Σ in this model is given by the sum of all diagrams where the core electron is dressed with plasmons (fig. 12). For the true Hamiltonian including all electron-electron interactions we have the same set of diagrams, where the plasmon propagator is replaced by a screened interaction $v(q)\ \epsilon^{-1}\ (q,\omega)$. Except for the first diagram the bare Coulomb potential gives no contribution (the hole propagates in only one direction) and we can thus replace ϵ^{-1} by $(\epsilon^{-1} - 1)$. By choosing the dielectric function in eq (31) and the coupling

$$g_q^2 = v(q)\omega_p^2/(2\omega_q), \qquad (40)$$

the plasmon diagrams and the screened interaction diagrams become the same. The core Green function

$$G_c(t) = -i\langle T(a(t)a^+(0))\rangle \qquad (41)$$

can be written as (cf. eq (38))

$$G_c(t) = i\langle 0|e^{i\tilde{H}t}|0\rangle e^{-i\epsilon t}\theta(-t) \qquad (42)$$

where $|0\rangle$ is the plasmon vacuum state and $\tilde{H}$ is the Hamiltonian for the plasmon in the presence of the core

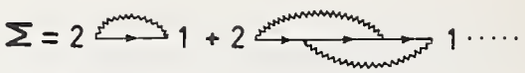

FIGURE 12. *Diagrams for the core electron self-energy.*

hole,

$$\tilde{H} = \sum_q g_q(b_q + b_{-q}^+) + \sum_q \omega_q b_q^+ b_q \qquad (43)$$

A canonical transformation shifts the zero point of the plasmon vibrations, thus

$$e^A \tilde{H} e^{-A} = H_0 - \Delta\epsilon, \qquad (44)$$

where

$$A = \sum_q f_q(b_q^+ - b_q);\ f_q = g_q/\omega_q;\ H_0 = \sum_q \omega_q b_q^+ b_q;$$

$$\Delta\epsilon = \sum_q \omega_q f_q^2. \qquad (45)$$

We may hence write

$$\langle 0|e^{i\tilde{H}t}|0\rangle = \langle 0|e^{-A}e^{iH_0 t}e^{A}|0\rangle e^{-i\Delta\epsilon t} = \langle 0|e^{-A(0)}e^{A(\epsilon)}|0\rangle e^{-i\Delta\epsilon t}, \qquad (46)$$

where

$$A(t) = e^{iH_0 t}Ae^{-iH_0 t} = \sum_q f_q(b_q^+ e^{i\omega q^t} - b_q e^{-i\omega q^t}). \qquad (47)$$

By applying the well-known formula

$$e^{A+B} = e^A\, e^B\, e^{-1/2[A,B]} \qquad (48)$$

repeated times the exact solution follows,

$$\langle 0|e^{i\tilde{H}t}|0\rangle = \exp(-\Delta\epsilon t)\exp\left(-\sum_q f_q^2\right)\exp\left(\sum_q f_q^2 e^{i\omega q^t}\right). \qquad (49)$$

This gives for the spectral function

$$A_c(\omega) = \frac{1}{\pi}\,\mathrm{Im}\,G_c(\omega) = \frac{1}{2\pi}\int_{-\infty}^{\infty} e^{i(\omega-\epsilon)t}\langle 0|e^{i\tilde{H}t}|0\rangle dt$$

$$= e^{-\sum_q f_q^2}\left\{\delta(\omega-\epsilon-\Delta\epsilon) + \sum_q f_q^2\delta(\omega-\epsilon-\Delta\epsilon+\omega_q) + \frac{1}{2?}\sum_{qq'} f_q^2 f_{q'}^2\delta(\omega-\epsilon-\Delta\epsilon+\omega_q+\omega_{q'}) + \ldots\right\} \qquad (50)$$

To compare the first order results (the first diagram in fig. 12) with the exact solution we have used the simple dispersion law $\omega_q = \omega_p + q^2$ (in units of the Fermi energy and the Fermi momentum), which allows an analytic solution. The result for the electron density of sodium metal ($r_s = 4$) is given in figure 13.

Since the dielectric function in eq (31) contains no particle-hole pairs, the quasi particle peak is a δ-function. A more realistic shape of the peak is indicated in the figure. The exact solution has structure also at $-3\omega_p$, $-4\omega_p$, *etc.*, which is not shown in the figure. This structure, however, has weak edges and carries only a few percent of the oscillator strength.

Comparing the results of the first order calculation and the exact solution we note:

1. The energy shift $\Delta\epsilon$ is exactly the same.

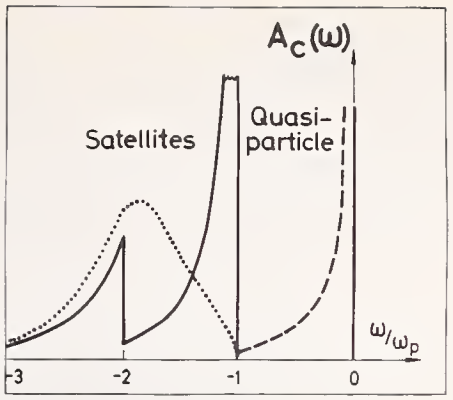

FIGURE 13. *Comparison of the first order (dotted line) and the exact result (full curve) for the core spectral function from the model Hamiltonian in eq (39). In this model the quasi-particle peak is a δ-function. The dashed curve indicates a more realistic form of that peak. The results are for* $r_s = 4$.

2. The oscillator strengths in the satellites are closely the same.
3. In the exact solution the satellite has two marked peaks instead of one, and the peaks are sharper.

The large difference between the first order result and the exact solution for this model case should be a warning against taking the details of a low order calculation too seriously. Knowing the importance of the higher order diagrams in this case one may ask if not other higher order diagrams, like those of the paramagnon problem, may play a role also for the core spectrum. Finally, it should be stressed that while the satellite structure may be poorly accounted for in the first order theory, the position and singular nature of the quasi particle are quite well represented.

5. Qualitative Discussion of Some Experiments

We shall discuss some different types of experiments utilizing the connections with the one-electron spectrum discussed in section 2 and the results from the approximate calculations reported in sections 3 and 4. We can really not put forward much more than guesses about where many-body effects may possibly occur. The difficulty is that the predictions by the one-electron approximation have seldom been worked out in enough detail to give reliable level densities and matrix elements, and this knowledge is required both to evaluate the many-body effects per se as well as to find out how much of the experimental structure that is accounted for by the one-electron approximation. Also the experimental data are sometimes not as accurate and reliable as one would need. Thus surface conditions are often not under good enough control, background effects are

poorly known and disturbing secondary effects are not carefully analyzed and subtracted.

The discussion will neglect the effects of final state interactions between the electron and hole. This means that the treatment is a simple extension of the usual theory for interband transitions in which the density of states for electrons and holes in band theory is replaced by the corresponding quantities including many-electron interactions as illustrated in figures 6, 11, and 13. Although certainly of restricted validity it seems that the predictions of such an approach are worthwhile to summarize.

5.1. X-Ray Photoemission (XPS)

This experiment has a fairly clearcut relation to the one-electron spectrum. Ideally the energy distribution of photoelectrons will be given by eq (15). However, this equation is valid only if the photoelectrons leave the solid without being scattered. Structure due to satellites in the density of states will thus be mixed with structure due to energy losses.

The losses to volume excitations are proportional to the sample thickness, while the intensity of the satellite structure in the one-electron spectrum has a definite relation to the intensity of the quasi particle peak. Thus by varying the sample thickness one should be able to separate the two kinds of processes.

Theory predicts an asymmetric form of the core-quasi particle peak [4,5,6,29,36,37] and satellite structure starting at ω_p below the main peak. According to the Langreth model solution there should be two satellites also with an asymmetric line shape (cf. fig. 13), while the first order theory predicts the satellite in figure 11. There should be a satellite structure in the conduction band, as well. Even if the exact shape of this structure might differ from the results of the low-order theory discussed in section 3, the total intensity of the satellite band should be appreciable.

An experimental verification of the many-body structure would be of great aid for the further development of the theory. As regards the position of the core levels there seems to be a good agreement between theory and experiments but further experimental and theoretical work on this problem would help to clarify how point defects polarize and distort their surroundings.

5.2. Soft X-Ray Emission

We consider only the simplest possible case where we can assume complete relaxation of the Fermi gas around the hole before the emission takes place. This limits the approximate validity to the light metallic elements such as Li, Be, Na, Mg, Al and K and excludes *e.g.* all transition metals.

Through the recent work by Nozières and de Dominicis and others [4-6] the possibility of a singular structure at the Fermi edge seems to be well established. The magnitude of this Fermi edge peak and the influence of this effect on the intensity at energies outside the immediate vicinity of the edge is however so far unsettled, although important progress has been made [38]. As regards the main band it is clear that the presence of the core hole will give an enhancement of the intensity [1]. The actual magnitude of this enhancement factor and its variation over the main band is so far not well-known. To obtain the one-electron density of states in the main band from experiments seems to require both careful calculations of dipole matrix elements and better estimates of the enhancement factor.

Below the main band the edge for plasmon production is well established experimentally [1,39]. The intensity of the satellite structure is strongly affected by intricate cancellation mechanisms due to the presence of the core hole and the theoretical predictions are uncertain. The plasmaron edge (cf. figs. 5 and 6) has been searched for in Al, but the experiment was not conclusive [40]. As discussed in section 3, it is not clear whether this edge is a feature of an exact solution of the problem or just a result of the low order treatment. A clear experimental confirmation or dismissal would be of great aid for the further study of these many-body effects.

5.3. X-Ray Absorption

Consideration of these experiments requires a treatment of final state interactions but in the absence of a detailed theory for these we shall here take a simple point of view and treat the structure in the one-electron spectra as additional levels or groups of levels in a one-electron scheme. A similar discussion of plasmon effects in x-ray absorption in metals was given by Ferrell [41]. Due to the presence of satellite structure in both core and conduction band spectra there should be a characteristic structure above the threshold [36].

Accurate x-ray absorption spectra for simple metals have recently [42] been obtained, which show an edge anomaly very similar to what one may expect from the Mahan exciton effect [4-6]. The fine structure of the absorption coefficient for the $L_{II,III}$ transition in magnesium is shown in figure 14 [43]. Immediately above the edge there is more detailed structure which

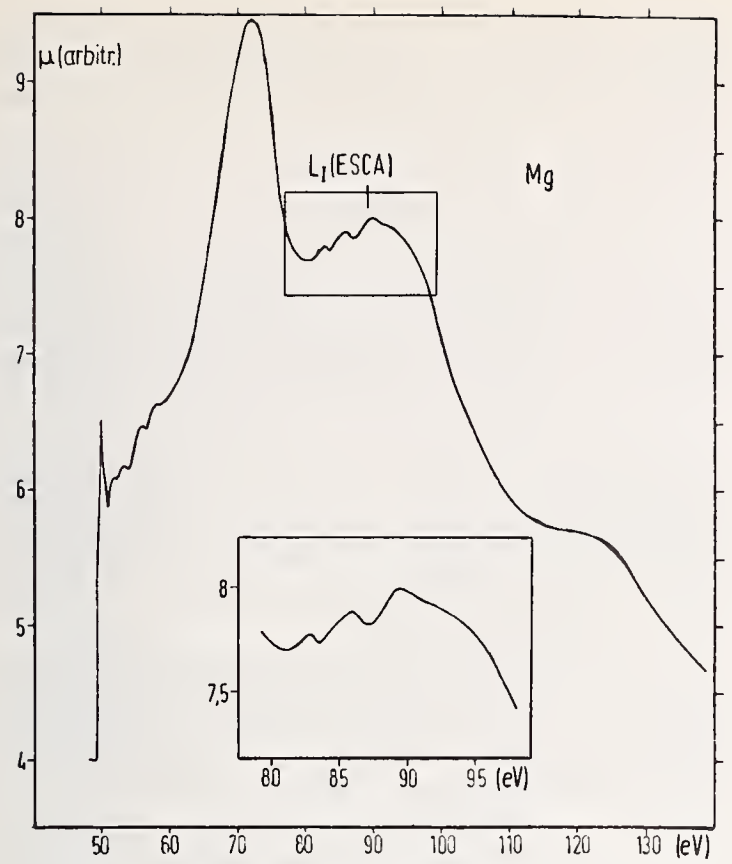

FIGURE 14. *The fine structure of the absorption coefficient for the* $L_{II,III}$ *transition in magnesium* [43].

possibly could be due to ordinary band structure effects in the final state.

At still higher energies comes a strong peak [43-45]. We will argue that this peak may be a many-body effect. In table 1 we give results for the positions of the peaks measured from the threshold [43], and compare with the position of the core plasmaron peak discussed in section 3 (cf. fig. 11). There is good agreement for aluminum but not for the other metals.

The important point, however, is that ϵ_{peak}/ω_p is a very smooth function of the electron density. Actually its value is closely 0.8 r_s in all cases. This indicates that the peak is associated with properties of the electron gas rather than being due to oscillator strength effects. The latter would be connected with the properties of the ion core and there is then no obvious reason to expect a regular variation with the conduction electron density. The position of the plasmaron peak should be given better at higher densities and the discrepancy with experiment at lower densities is in no way alarming. More serious is the fact that Langreth's calculation has shown the higher order effects to be strong. The strong peak could of course also be due to many-body effects involving final-state interactions.

TABLE 1. *Position of the strong peak in soft x-ray absorption and comparison with the location of the satellite peak* (ϵ_{pm}) *in figure 11.*

Element	r_s	ϵ_{peak}, eV	ϵ_{peak}/ω_p	ϵ_{pm}/ω_p
Al.....	2.07	24	1.6	1.7
Mg.....	2.66	22	2.1	1.8
Na.....	4.00	18	3.2	2.1

5.4. Photoemission in the Ultraviolet

The basic mechanisms of the photoemission process are still not well understood. It may be regarded in one extreme as a pure surface effect and in another as a pure volume effect. In the latter case we have to account for the very important inelastic scattering effects of the outgoing photoelectrons. If the surface effects are not too strong, and if we can sort out the inelastically scattered electrons, the photoemission results in the ultraviolet should reflect structure due to the satellite band of the conduction electrons. There is some hint of such a structure in the recent results for cesium [46] (fig. 15) at an energy of about 4 eV below the Fermi edge. However, the structure could also be due to a loss of two surface plasmons [46].

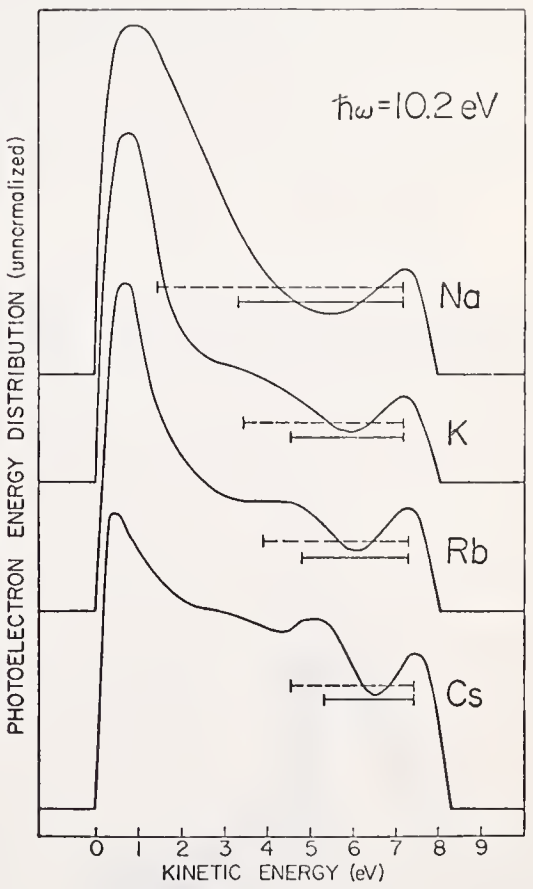

FIGURE 15. *Photoelectron energy distribution curves at* $\hbar\omega = 10.2$ *eV for Na, K, Rb and Cs* [46]. The horizontal bars indicate the values of the surface (full curve) and volume (dashed) plasmons.

5.5. Optical Absorption in the Ultraviolet

The description of optical properties of metals in terms of Drude (see *e.g.* refs 47,48) and interband contributions is often in qualitative agreement with experiment. To go beyond that description we need to know the dielectric function including final state interactions. The many-body effects may show up as changes in intensity and as new structures. Attempts to account for the former have been made *e.g.* by Mahan [49], who considered the contributions from virtually exchanged plasmons. Absorption caused by electron gas effects has been considered by Hopfield [50]. He observed that while the electron gas by itself cannot absorb radiation the effect of a weak perturbing potential from phonons or disorder is enough to provide the necessary momentum conservation for the absorption process and thus allow the plasmon resonances of the electron gas to show up.

A straightforward way to extend the one-electron joint density of states expression is to make a convolution of the spectral weights of occupied and unoccupied states. This has been done for semiconductors by Bardasis and Hone [51] who in addition considered vertex corrections. They obtained improved agreement with experiment. Calculations for metals by the convolution approximation indicate the existence of a plasmon-induced structure at photon energies above $E_g + \omega_p$ [52], where E_g is the interband threshold energy. There are some experimental indications of structure beyond the ordinary interband absorption in this energy region.

5.6. The Compton Effect

X-ray scattering from an electron gas in the regime of large momentum transfer is a direct measure of the one-dimensional momentum distribution [53]. From recent measurements of the Compton profiles of Li, Na and Al the linear momentum distribution has been derived [54]. The result for Li is shown in figure 16.

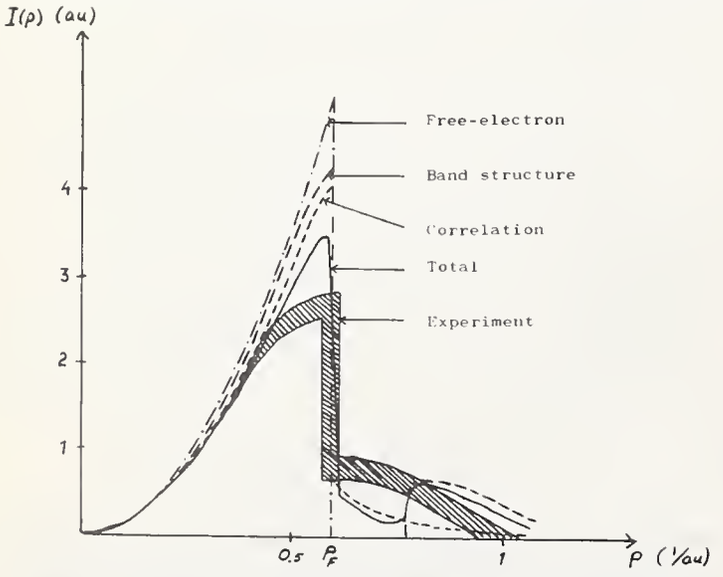

FIGURE 16. *The linear momentum distribution for Li* [54,55].

In section 3 approximate values of the momentum distribution for an electron gas have been shown (fig. 4). The corresponding linear momentum distribution shows a too small reduction compared to the free-electron case to reproduce the experimental results for Li (fig. 16) and Al, while for Na the electron gas curve falls almost entirely within the experimental region.

As band structure effects could be expected to be more important in Li and Al than in Na, this kind of correction has also been calculated using the OPW method [55]. As shown in figure 16 these effects reduce the discrepancy, even if a quantitative agreement has not been obtained.

This kind of experiment provides a way of illuminating another aspect of the distribution of electrons in metals and provides a useful way of checking theoretical models including many-body interactions.

6. Concluding Remarks

This paper has presented a discussion of the possible nature of many-electron effects on the density of states. It is based on a study of the one-electron spectrum including interactions and points out the existence of characteristic satellite structure in the density of states of electrons and holes in simple metals. Considering the joint density of states of electrons and holes as in the theory of interband transitions certain predictions about possible effects in x-ray and optical spectra can be made. All this material is however only qualitative and tentative. The structure in the one-particle spectrum has been calculated in low order and considerable changes may result by including higher-order effects. Further, the convolution of the electron and hole spectrum implies neglecting the final state interaction between the electron and the hole. The final state interactions may partly cancel out the structure in the electron and hole spectrum, and it leads to characteristic new effects such as edge singularities, and of course also gives an overall distortion of the spectrum. With all these reservations, however, the discussion points out the existence of a number of possible interesting effects which offer a challenge for further study. In assessing the possibility of pursuing this approach to obtain quantitative theoretical results one has to consider critically the present state of the art with regard to ordinary band theory. Indeed, rather little has yet been done in a quantitative way to calculate spectra

especially with regard to oscillator strengths. Such more detailed knowledge from energy band calculations also forms a necessary prerequisite for making quantitative statements about many-electron effects.

7. References

[1] For a general review, see L. Hedin and S. Lundqvist, Solid State Physics **23,** (F. Seitz, D. Turnbull and H. Ehrenreich, Editors (Academic Press, New York, 1969).

[2] Hedin, L., in "Soft X-Ray Spectra and the Electronic Structure of Metals and Materials," D. Fabian, Editor (Academic Press, New York, 1968).

[3] Anderson, P. W., Phys. Rev. Letters **18,** 1049 (1967).

[4] *e.g.*, Mahan, G. D., Phys. Rev. **163,** 612 (1967); Bergersen, B., and Brouers, F., J. Phys. Chem. **2,** 651 (1969); Mizuno, Y., and Ishikawa, K., J. Phys. Soc. Japan **25,** 627 (1968).

[5] Nozières, P., and de Dominicis, C. J., Phys. Rev. **178,** 1097 (1969).

[6] Langreth, D. C., Phys. Rev. **182,** 973 (1969).

[7] Longe, P., and Glick, A. J., Phys. Rev. **177,** 526 (1969).

[8] Nozières, P., Theory of Interacting Fermi Systems (W. A. Benjamin, Inc., New York, 1964).

[9] Quinn, J. J., and Ferrell, R. A., Phys. Rev. **112,** 812 (1958).

[10] Quinn, J. J., Phys. Rev. **126,** 1453 (1962).

[11] Rice, T. M., Ann. Phys. (N.Y.) **31,** 100 (1965).

[12] Hedin, L., Phys. Rev. **139,** A796 (1965).

[13] Lundqvist, B. I., Phys. Kondens. Materie **7,** 117 (1968).

[14] Lindhard, J., Dan. Math. Phys. Medd. **28,** No. 8 (1954).

[15] Hubbard, J., Proc. Roy. Soc. **A243,** 336 (1957).

[16] Glick, A. J., Phys. Rev. **129,** 1399 (1963).

[17] Geldart, D. J. W., and Vasko, S. H., Can. J. Phys. **44,** 2137 (1966).

[18] Singwi, K. S., Tosi, M. P., Land, R. H., and Sjölander, A., Phys. Rev. **176,** 589 (1968).

[19] Kleinman, L., Phys. Rev. **172,** 383 (1968).

[20] Langreth, D. C., Phys. Rev. **181,** 753 (1969).

[21] Lundqvist, B. I., Phys. Kondens. Materie **6,** 193 (1967); **6,** 206 (1967).

[22] Hedin, L., Lundqvist, B. I., and Lundqvist, S., Intern. J. Quantum Chem. **IS** (1967) 791.

[23] Hedin, L., Lundqvist, B. I., and Lundqvist, S., Solid State Comm. **5,** 237 (1967).

[24] Lundqvist, B. I., Phys. Stat. Sol. **32,** 273 (1969).

[25] Slater, J. C., Phys. Rev. **81,** 385 (1951).

[26] Gáspár, R., Acta Phys. Hung. **3,** 263 (1954).

[27] Kohn, W., and Sham, L. J., Phys. Rev. **140,** A1133 (1965).

[28] Hedin, L., Lundqvist, B. I., and Lundqvist, S. (to be published).

[29] Langreth, D. C. (to be published).

[30] *e.g.*, Pines, D., and Nozières, P., "The Theory of Quantum Liquids," **Vol. I,** (Benjamin, New York, 1966).

[31] Grimvall, G., J. Phys. Chem. Solids **29,** 1221 (1968); Phys. Kondens. Materie **6,** 15 (1967).

[32] Ashcroft, N. W., and Wilkins, J. W., Phys. Letters **14,** 285 (1965).

[33] McMillan, W. L., and Rowell, J. M., in "Superconductivity," R. D. Parks, Editor (Dekker, Inc., New York, 1969).

[34] Engelsberg, S., and Schrieffer, J. R., Phys. Rev. **131,** 993 (1963).

[35] Hedin, L., Ark. Fys. **30,** 231 (1965).

[36] Lundqvist, B. I., Phys. Kondens. Materie **9,** 236 (1969).

[37] Doniach, S., and Sunjić, M. (to be published).

[38] Ausman, G. A., Jr., and Glick, A. (to be published).

[39] Rooke, G. A., Phys. Letters **3,** 234 (1963).

[40] Cuthill, J. R., Dobbyn, R. C., McAlister, A. J., and Williams, M. L., Phys. Rev. **174,** 515 (1968).

[41] Ferrell, R. A., Rev. Mod. Phys. **28,** 308 (1956).

[42] Haensel, R., Keitel, G., Schreiber, P., Sonntag, B., and Kunz, C. (to be published).

[43] Haensel, R., and Kunz, C. (private communication).

[44] Fomichev, V. A., and Lukirskii, A. P., Soviet Physics—Solid State **8,** 1674 (1967); Sagawa, T., Iguchi, Y., Sasanuma, M., Ejiri, A., Fujiwara, S., Yokota, M., Yamaguchi, S., Nakamura, M., Sasaki, T., and Oshio, T., J. Phys. Soc. Japan **21,** 2602 (1966); Codling, K., and Madden, R. P., Phys. Rev. **167,** 587 (1968).

[45] Watanabe, H., J. Appl. Phys. **3,** 804 (1964); Swanson, N., and Powell, C. J., Phys. Rev. **167,** 592 (1968).

[46] Smith, N. V., and Spicer, W. E., Phys. Rev. Letters **23,** 769 (1969).

[47] Nettel, S. J., Phys. Rev. **150,** 421 (1966); Miskovsky, N. M., and Cutler, P. H., Solid State Comm. 7, 253 (1969).

[48] Haga, E., and Aisaka, T., J. Phys. Soc. Japan **22,** 987 (1967).

[49] Mahan, G. D., Phys. Letters **24A,** 708 (1967).

[50] Hopfield, J. J., Phys. Rev. **139,** A419 (1965).

[51] Bardasis, A., and Hone, D., Phys. Rev. **153,** 849 (1967); see also Brust, D., and Kane, E. O., Phys. Rev. **176,** 894 (1968).

[52] Lundqvist, B. I., and Lydén, C. (to be published).

[53] Platzman, P. M., and Tzoar, N., Phys. Rev. **139,** A410 (1965).

[54] Phillips, W. C., and Weiss, R. J., Phys. Rev. **171,** 790 (1968).

[55] Lundqvist, B. I., and Lydén, C. (to be published).

Discussion on "Beyond the One-Electron Approximation: Density of States for Interacting Electrons" by L. Hedin, B. Lundqvist, and S. Lundqvist (Chalmers University)

W. Kohn *(Univ. of California):* Dr. Lundqvist unfortunately brought in the Slater and the 2/3 exchange correction. Dr. Lundqvist had his own interpretation—he had a plot there and said that the reason why these corrections work is that they include things which the authors do not know they include. The corrections do not include anything except exchange. The literature shows very clearly and gives explicit formulas for how to include correlations in the locally uniform electron gas model. The question of whether you use 2/3 or 1 or an intermediate value in the exchange correction has a unique answer in every particular problem. For years now there has been a certain lack of rationalism here, although there is in every case, a clear, unique choice of how to treat exchange and how to treat correlation within the locally uniform electron gas model. All of these considerations are, of course, confined to that model and if that is not good enough, you have to go beyond it. Nevertheless, there is around an impression that there is a controversy about the exchange potential. I just want to say there is no controversy.

S. Lundqvist *(Chalmers Univ.):* I agree on the whole with this point of view.

K. H. Johnson *(MIT):* The electron gas has very little to do with real solids. The successful implementation of energy band theory on real materials has depended rather critically on the adoption of approximate exchange potentials based on *local* electronic charge density (e.g., Slater, Kohn-Sham, etc.). Would it not be worthwhile to explore the possibilities of developing *local* approximations to the true nonlocal self-energy or mass operator, which would attempt to get at the effects of electron-electron correlation on the band structures and densities of states of *real* solids?

S. Lundqvist *(Chalmers Univ.):* Professor Kohn and Dr. Sham have done considerable work on this problem and suggested precisely this procedure. They start from the energy dependent and non-local self-energy and convert this into a kind of consistent local approximation. We have also developed a similar approach, but in order to avoid the problems connected with large density gradients, we apply this procedure to the valence electrons only and described the ions in the ordinary way, whereas my impressions from the papers by Kohn and Sham is that they intended to use a local density approximation for the total electron density. Maybe Professor Kohn would like to add something?

W. Kohn *(Univ. of California):* I have very little to add to what you said. I am in general agreement with your point of view.

K. H. Johnson *(MIT):* Yes, but I think the nature of the proof is such that it breaks down if the density changes are too severe, i.e., if the system is too inhomogeneous. Is that correct?

W. Kohn *(Univ. of California):* Yes, that is correct, if you have extreme inhomogeneous systems, and by the way, we just completed some work on an example of such a system, namely on a metal surface. The assumptions of the proof are a formal matter. In reality, the results hold remarkably well, even for rather rapid density changes. I had a discussion with Dr. Hedin yesterday about how to treat the core electrons and we have been concerned with that and I would say, if I understand you correctly, I am again in general agreement with Dr. Lundqvist that the core electrons are sufficiently different from an electron gas that they must, in effect, be handled differently. Finally, concerning inhomogeneities, I don't know if Dr. Herman is in the audience now, but I suggest that perhaps he would like to add some comments. He is very much concerned with this.

F. Herman *(IBM):* I would just like to ask Professor Lundqvist what his conclusions would be if you did the same problem and included some inhomogeneities?

S. Lundqvist *(Chalmers Univ.):* This would in effect amount to a full self-energy calculation including Bloch electron states and all that. That has not been done.

M. Harrison *(Michigan State Univ.):* Are there any expected effects of the electron-plasmon interaction on bound states about a charged impurity center, or perhaps on scattering processes, either on level shifts or on level broadening, particularly on materials with large r_s?

S. Lundqvist *(Chalmers Univ.):* Yes, we believe that this effect would occur.

J. R. Schrieffer *(Univ. of Pennsylvania):* Back to this exchange question—if one takes the calculation that you are speaking about for the exchange and includes correlation effects which keep electrons apart then would the effective exchange be reduced towards 2/3 or even to 1/2 or 1/4?

S. Lundqvist *(Chalmers Univ.):* The answer is that the sum of these two effects appears in the curve I was showing. If you look at the contribution of these combined effects to the self energy, you find that it would correspond more to a classic correlation hole which is actually more important that the screened exchange. Screening of the exchange introduces correlations, that is true, but the correlation hole around a particle is a major contribution.

J. R. Schrieffer *(Univ. of Pennsylvania):* I am afraid I did not explain myself very carefully. There is a question of a screened U and then a correlated screened U. If you think of a low density gas, for example, you can have two different physical effects. One is to screen the effective interaction. That reduces the strength by the usual dielectric effects. With the screened interaction, one can calculate an interaction between say a pair of particles. If you go to the Born approximation, that is the screened exchange. If you go beyond the Born approximation, that is scattering, and one gets a new effective interaction. The new interaction for the low density Fermi gas, for example, as in nickel, we know is less than U and it is limited in strength by the relative bandwidth. Therefore, the effective exchange is reduced for two reasons: one is screening and the other is correlation. Would you expect the correlation effect on the exchange to be appreciable?

S. Lundqvist *(Chalmers Univ.):* I would not dare to guess what happens at very low densities. I have had too little experience with that problem.

L. N. Cooper *(Brown Univ.):* Perhaps Walter Kohn would dare to guess.

W. Kohn *(Univ. of California):* I want to point out just one little thing and not try to answer your question completely, but one thing is evident. The correlation correction has a completely different density dependence, and the rational way to handle it is to do it right. In the very high density limit it becomes negligible compared to the exchange. It does not go with the same power of the density, and so certainly the way not to handle it is to just put a constant in front and say it is somewhere between 2/3 and 1.

EXCITONS; SOFT X-RAY I

CHAIRMEN: R. A. Farrell
C. S. Koonce

RAPPORTEUR: L. Hedin

Excitonic Effects in X-Ray Transitions in Metals*

G. D. Mahan [1]

Institute of Theoretical Science and Department of Physics, University of Oregon, Eugene, Oregon 94703 [2]

and

General Electric Research and Development Center, Schenectady, New York 12301

In the study of soft x-ray transitions in solids, there has always been some hope that the results provide a direct measure of the density of states. This assumes that (a) matrix element variations over the band and (b) final state interactions are small. Both of these assumptions are now known to be incorrect. To illustrate the possible strength of these effects, two approximate calculations are presented: the one electron oscillator strength of a simple bcc metal as a function of energy; and the strength of the Nozieres—DeDominicis singularity at threshold, with phase shifts estimated from an assumed Yukawa interaction between conduction electrons and core hole.

Key words: Density of states; exciton; many body effects; phase shifts; soft x-ray; transition probability.

I. Introduction

The absorption of a photon can cause an electron to change its state. The traditional viewpoint of this transition assumes that if one knew the electrons initial ψ_i and final ψ_f state, then the oscillator strength was simply proportional to the square of the momentum matrix element.

$$p_{if} = \int d^3r \psi_f^* p \psi_i \qquad (1.1)$$

This simple viewpoint is now known to be incorrect. The proper picture is that the optical transition creates an electron and hole, and these two excitations interact with each other, and each separately with their environment. The coulomb scattering between the electron and hole is called the exciton effect, named after the first known example of Frankel excitons in solids. The electron and hole can also emit phonons, suffer electron-electron collisions, *etc.* The sum of all of these processes are called final-state interactions. The rate of optical absorption is affected by these subsequent interactions of the electron and hole.

Upon reviewing our present understanding of the optical properties of solids, one finds that some solids are well understood while others are not. We classify as understood the semiconductors Si and Ge, [1] and simple metals like aluminum [2,3]. It is noteworthy that in these materials the final-state interactions are small: they are small in semiconductors because the large dielectric constant suppresses the exciton effect. Ehrenreich and his co-workers have shown that many body effects are small in aluminum. In these solids the simple one-electron picture implied in (1.1) seems to work quite well.

We classify wide band gap insulators [4], and metals such as copper [5], as solids whose optical properties are not well understood. There is not yet good agreement between theory and experiment in these materials. The dominant optical transitions in these materials create hole states which are heavy, and which are subject to significant final state interactions [3]. We speculate that final state interactions are important in these materials, and explain the difference between theory and experiments.

In the study of x-ray transition in solids, there has always been some hope that the results provide a direct

*An invited paper presented at the 3d Materials Research Symposium, *Electronic Density of States*, November 3-6, 1969, Gaithersburg, Md.

[1] Alfred P. Sloan—Research Fellow.

[2] Research Supported by National Science Foundation Grant.

measure of the density of states [6]. This presumes that (a) matrix element variations over the band are small, and (b) final state interactions are small. Both of these assumptions are now known to be incorrect [7,8,9].

The importance of exciton effects in x-ray transitions was reported in an earlier reference [10]. The effects are large if the hole is highly localized, and if the conduction band of the electron is isotropic. Because the coulomb scattering between the electron and hole occurs in an electron gas, the electron can only scatter into states not already occupied. This Fermi-Dirac exclusion, as well as the exchange interaction among the electrons, causes the problem to resemble the Kondo effect more than the Wannier-exciton case. The hole also has a large interaction with the entire electron gas—this leads to a renormalization effect which inhibits the x-ray transition near threshold [11]. Nozieres and DeDominicis [12] have shown that the exciton and renormalization effects combine to give a threshold behavior for $\epsilon_2(\omega)$

$$\epsilon_2(\omega) \sim \frac{1}{\omega^2}\left(\frac{\xi_0}{\omega-\omega_T}\right)^{\alpha_l}\theta(\omega-\omega_T) \qquad (1.2)$$

where ω_T is the absorption threshold frequency, $\xi_0 \sim E_F$ is a characteristic band energy, and α_l is a function of the phase shifts δ_l of electrons at the Fermi energy scattering from the static potential of the hole.

$$\alpha_l = \frac{2\delta_l}{\pi} - 2\sum_{l=0}^{\infty}(2l+1)\left(\frac{\delta_l}{\pi}\right)^2 \qquad (1.3)$$

The term $2\delta_l/\pi$ is the exciton part which tends to make the threshold singular, while the second term in (1.3) arises from renormalization. The angular momentum l is that of the conduction electron [13]. If the x-ray hole has s-symmetry, the conduction electron must have p-symmetry ($l=1$). If the hole has p-symmetry, the conduction electron can have either s- or d-symmetry; in this case (1.2) has a separate term for each symmetry type.

The x-ray spectra can only be unravelled with a knowledge of the phase shifts δ_l—these are the phase shifts for simple electron-hole scattering. These have been calculated for a free electron gas by Ausman and Glick [13]. They find $\alpha_0 > 0$, and $\alpha_l < 0$ for $l \geq 1$ so that singularities only occur for the $l=0$ case (p-state hole). These results qualitatively agree with the experimental results.

We have independently calculated the phase shifts, and we describe our result in section II. We have concluded that these phase shifts are qualitatively correct but for the wrong reasons. The wrong potential is used in the calculation, but it does not seem to make much difference in this case.

II. Phase Shifts

The present calculations have been performed by assuming that the screened electron-hole interaction has the Yukawa form

$$V(r) = -\frac{e^2}{r}\exp(-k_s r)$$

where the Fermi-Thomas screening length is

$$k_s^2 = 6\pi e^2 n_0/E_f$$

for an electron gas of density n_0 and Fermi energy E_f. This is only a crude approximation to the actual potential the electron feels when scattering from the hole. For example, studies of a point charge impurity in an electron gas show that its potential differs from a Yukawa at long range where Friedel oscillations occur, and at short range where its potential is less steep [14]. In addition, because the hole is part of an atom, there are term due to the exchange and orthogonality with the atomic wave functions [7,8]. In a pseudo-potential formalism these latter effects contribute a short-range repulsive term to the interaction. In spite of these shortcomings of the Yukawa potential, we believe that it predicts phase shifts which are qualitatively correct. The reasons for this will be presented below.

The phase shifts are defined in terms of the eigenvalues E_k and eigen functions $\psi_k(r)$ of the electron in the region of the potential.

$$\left(-\frac{\nabla^2}{2m} + V(r) - E_k\right)\psi_k(r) = 0 \qquad (2.1)$$

The wave is decomposed into spherical harmonics

$$\psi_k(r) = \sum_{l=0}^{\infty}(2l+1)i^l P_l(\hat{k}\cdot\hat{r})\phi_l(k,r) \qquad (2.2)$$

In solving for the eigen functions in (2.1), one has the choice of specifying the boundary conditions for states which are plane wave-like outside of the potential region. By choosing standing wave conditions, one is solving for a reaction matrix $K_l(k,k')$ and the phase shifts are defined in terms of the diagonal $k=k'$ component [15].

$$\tan\delta_l(k) = -2mkK_l(k,k)$$
$$= -2mk\int_0^{\infty} r^2 dr j_l(kr)V(r)\phi_l(k,r) \qquad (2.3)$$

Similarly, if one chooses outgoing wave conditions, then one is solving for a T-matrix $t_l(k,k')$ whose diagonal components give the phase shift [15].

$$\sin \delta_l e^{i\delta_l} = -2mkt_l(k,k)$$
$$= -2mk \int_0^\infty r^2 dr j_l(kr) V(r) \phi_l(k,r) \qquad (2.4)$$

We have chosen to use the reaction-matrix formalism (2.3), mostly because it is a real function and this simplifies computation.

The phase shifts $\delta_l(k)$ go to zero as $k \to \infty$. Let us now examine their behavior as $k \to 0$. From (2.3) we have $j_l(kr) \sim (kr)^l$, so

$$\tan \delta_l(k) \sim k^{l+1} \int_0^\infty r^{l+2} dr V(r) \phi_l(0,r) \qquad (2.5)$$

From Levinson's Theorem we know that

$$\delta_l(0) = \pi M_l$$

where M_l is the number of bound states of (2.1) with angular momentum l. For example, if $M_l = 0$ we get $\delta_l \sim k^{l+1}$. Whereas if $M_l = 1$ we get $\delta_l = \pi + ck^{l+1}$ (where c is some constant) for small k. A typical case is shown in figure 1, where $M_0 = 1$, and $M_l = 0$ for $l \geq 1$. So the s-wave phase shift comes into π with a linear slope, while all other $\delta_l \sim k^{l+1}$ at small k.

So in calculating phase shifts, the first thing to decide is the number of bound states M_l. This is determined by examining the radial part of Schrödinger's equation (2.1) which we put into dimensionless form

$$\left[-\frac{\partial^2}{\partial \rho^2} + \frac{l(l+1)}{\rho^2} - \lambda \frac{e^{-\rho}}{p} - \mathscr{E} \right] r\phi_l = 0 \qquad (2.6)$$

$$\rho = k_s r$$
$$\lambda = \frac{2me^2}{\hbar^2 k_s} = \left(\frac{2\pi}{3}\right)^{1/3} \sqrt{r_s}$$
$$\mathscr{E} = 2mE/\hbar^2 k_s^2 \qquad (2.7)$$

The parameter λ determines the strength of the potential. Shey and Schwartz [16] have computed the number of bound states which exist for each value of λ and l. For s-waves ($l = 0$), they find no bound states exist for $\lambda < 1.68$, one bound state for $1.68 < \lambda < 6.45$, two bound states for $6.45 < \lambda < 14.3$, *etc*. For p-waves ($l = 1$) bound states only exist for $\lambda > 9.08$, and d-wave bound states exist for $\lambda > 21.8$.

In (2.7) we have written λ in terms of the density parameter r_s for an electron gas. Since metallic densities vary between $2 < r_s < 6$, then the range of λ values in metals is $1.8 < \lambda < 3.1$. For an electron gas of metallic density, there is one bound state for s-states, and no bound states for any other value of angular momentum l.

These are the predictions of the Yukawa potential. We must decide whether these are reasonable conclusions for the problem of interest. For an actual point charge in an electron gas, *e.g.*, a proton, there is probably a bound state. For an impurity in a host metal, *e.g.*, Al atoms in Mg, there is probably not a real bound state. This is because the atomic core of the impurity cuts off the attractive potential in the region where it is the strongest; for example, see Ashcroft's remarks about the cancellation influence of the atomic cores [8].

In the x-ray problem there is certainly an atomic core. Yet there is also certainly a bound state in the potential. This bound state is the x-ray level itself. That is, if an electron scattering from the potential of the hole did not think a bound state existed in the potential, then it would have no inclination to recombine with the hole in the final emission process. Since the emission can occur, a bound state does exist which must be reflected on the phase shifts.

The cancellation of the potential in atomic core is caused by the necessity of the conduction electron wave function to be orthogonal to all of the core states. In the x-ray problem, one core electron is absent so that the cancellation requirements are less stringent.

The foregoing discussion shows that any phase shifts calculated from a simple Yukawa potential are only going to be qualitatively correct. Yet there is some interest in what this simple model predicts. Our method of calculation proceeds by solving directly the scattering equation for the reaction matrix.

$$K_l(k_1, k_2) = V_l(k_1, k_2)$$
$$+ \frac{4m}{\pi} \int_0^\infty k_3^2 dk_3 \frac{V_l(k_1, k_3) K_l(k_3, k_2)}{k_2^2 - k_3^2} \qquad (2.8)$$

where the l^{th} component of the potential V_l is obtained from the Fourier transform $V(\mathbf{k}_1 - \mathbf{k}_2)$ of $V(r)$

$$V_l(k_1, k_2) = \frac{1}{2} \int_0^\pi d\theta \sin\theta P_l(\cos\theta) V(\mathbf{k}_1 - \mathbf{k}_2)$$
$$= \frac{e^2}{2k_1 k_2} Q_l((k_1^2 + k_2^2 + k_s^2)/2k_1 k_2) \qquad (2.9)$$

when cos θ is the angle between $\mathbf{k}_1$ and $\mathbf{k}_2$, and Q_l is a Legendre function. We will abbreviate the argument of the Legendre function to write it as $Q_l(k_1, k_2)$. Noyes' method is used to evaluate (2.8). We find

$$K_l(k, k) = V_l(k, k)/(1 - \Lambda_l(k)) \tag{2.10}$$

$$\Lambda_l(k) = \frac{-4m}{\pi V_l(k, k)} \int_0^\infty \frac{p^2 dp}{p^2 - k^2} V_l(k, p) f_l(k, p) \tag{2.11}$$

$$f_l(k, p) = V_l(k, p) + \frac{4m}{\pi V_l(k, k)} \int_0^\infty \frac{p'^2 dp' f_l(k, p')}{p'^2 - k^2} [V_l(p, k) V_l(k, p') - V_l(p, p') V_l(k, k)] \tag{2.12}$$

One obtains $f_l(k,p)$ from (2.12), perhaps by iterating this equation. This is used in (2.11) to obtain $\Lambda_l(k)$, and thus one has the reaction matrix in (2.10). This is an exact result if $f_l(k,p)$ is found exactly. The Born Approximation result is obtained by setting $K_l(k, k) = V_l(k, k)$.

Note that it is natural to write $\Lambda_l(k)$ as a power series in the interaction strength $\lambda = 2/k_s a_B$ in (2.7)

$$\Lambda_l(k) = \sum_{m=1}^{\infty} \lambda^m g_l^{(m)}(k/k_s) \tag{2.13}$$

Each successive power of λ corresponds to another iteration of the equation (2.12) which determines $f_l(k,p)$. For example, the first term is

$$g_l^{(1)}(k) = \frac{k_s}{\pi Q_l(k,k)} \int_0^\infty \frac{dp}{p^2 - k^2} Q_l(k,p)^2 \tag{2.14}$$

For $l = 0$ we can evaluate the integral and express the integral as a summation.

$$g_0^{(1)}(k) = \frac{k_s}{2kQ_0(k,k)} \sum_{l=1}^{\infty} \frac{(-)^l}{l^2} [2\rho^l \sin(\varphi l) - \sin(2l\varphi)]$$

$$\rho = [1 + 4k^2/k_s^2]^{-1/2} \tag{2.15}$$

$$\varphi = \tan^{-1}(2k/k_s)$$

$$Q_0(k,k) = \tfrac{1}{2} \ln (1 + 4k^2/k_s^2)$$

This form is convenient for numerical computation. In figure 1 is shown the s-wave phase shift calculated by approximating Λ_0 by the first term in (2.13)

$$\tan \delta_0(k) = \frac{Q_0(k,k)}{ka_B[1 - \lambda g_0^{(1)}(k)]}$$

Also shown in figure 1 are the phase shifts δ_1 and δ_2. We also calculated the first correction term $g_1^{(1)}(k)$ to the p-wave phase shift, and this correction has been added into the calculation of the curve labeled δ_1. This only changes the Born Approximation result by 10 percent. The $l = 2$ phase shift is the Born Approximation result. The multiple scattering terms are small except for the s-wave.

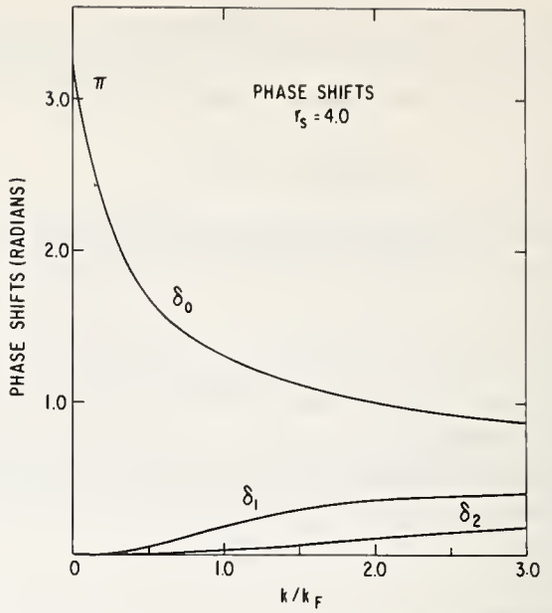

FIGURE 1. *The phase shifts δ_l calculated by a Yukawa potential. This potential represents a coulomb interaction of unit charge, with Fermi-Thomas screening. The phase shift δ_2 is calculated in the Born Approximation, while δ_0 and δ_1 have corrections for multiple scattering.*

In the x-ray transition, the singular effects occur at the Fermi surface, so we are interested in the phase shifts evaluated at k_f. Figure 2 shows the critical ex-

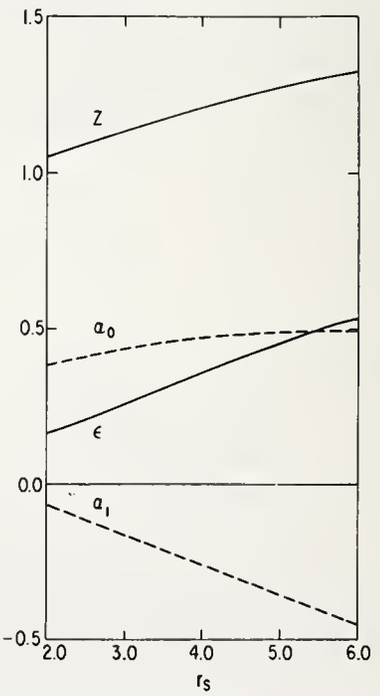

FIGURE 2. *The variation with electron density r_s of the exponents α_0 and α_1. These depend upon the phase shifts evaluated at the Fermi surface. Also shown is the renormalization parameter ϵ and the Friedel sum rate result Z. The value of Z is rigorously unity, and our deviations from that value indicate the errors in the calculation.*

ponents α_0 and α_1, in (1.3) plotted versus electron density r_s. Values of α_l for $l \geq 2$ are essentially equal to $-\epsilon$. Also shown are the values of the Friedel sum Z and the Anderson exponent ϵ, where

$$Z = 2 \sum_{l=0}^{\infty} (2l+1)(\delta_l/\pi)$$

$$\epsilon = 2 \sum_{l=0}^{\infty} (2l+1)(\delta_l/\pi)^2$$

The Friedel sum rule should rigorously be given by $z = 1$. Our deviation ~20 percent from the exact result of $z = 1$ provides an estimate of the error in the calculation.

Another estimate of the accuracy and convergence of the calculational method is obtained by seeing how well it estimates the position of bound states. As $k \to 0$ we get

$$\lim_{k \to 0} \delta_0(k) = \tan^{-1}\left(\frac{2k/ks}{1-\Lambda_0(0)}\right)$$

A bound state is predicted if $\Lambda_0 > 1$. We find that

$$g_0^{(1)}(0) = 1/2$$

$$g_0^{(2)}(0) = \ln\,(4/3) - 1/4$$

If we just use the first term in the expansion (2.13) so $\Lambda_0(0) = \lambda/2$ then the criteria $\Lambda_0(0) > 1$ means $\lambda > 2$. This is an error of 16 percent from the actual criteria $\lambda > 1.68$. But using two terms gives $\lambda/2 + \lambda^2(\ln 4/3 - 1/4) > 1$ or $\lambda > 1.765$. So a considerable improvement in accuracy is obtained by including the second term in (2.13). So we conclude that the series (2.13) converges rapidly for the range of λ values of interest.

III. Matrix Elements

The change of the matrix element with energy has been discussed before and is known to be a large effect [7,8,9]. We have calculated the change in matrix element near the first critical point in a bcc solid for an x-ray transition from a 1s core level. We used a simple two band model in each 1/12 of the Brillouin Zone [17], so that the energies and eigenstates are

$$E_k^{\pm} = \frac{1}{2}(\mathscr{E}_k + \mathscr{E}_{\mathbf{k}-\mathbf{G}}) \pm \left[\frac{1}{4}(\mathscr{E}_k - \mathscr{E}_{\mathbf{k}-\mathbf{G}})^2 + V_G^2\right]^{1/2}$$

$$\psi_k^{\pm}(r) = N_k \left\{ |\mathscr{E}_k - E_k^{\mp}|^{1/2} e^{i\mathbf{k}\cdot\mathbf{r}} \pm \frac{V_G}{|V_G|} |\mathscr{E}_k - E_k^{\pm}|^{1/2} e^{ir\cdot(\mathbf{k}-\mathbf{G})} \right\}$$

$$N_k = \frac{1}{2}\left[\frac{1}{4}(\mathscr{E}_k - \mathscr{E}_{\mathbf{k}-\mathbf{G}})^2 + V_G^2\right]^{-1/2}$$

The matrix elements were calculated assuming that the core was a delta function, and no attempt was made to orthogonalize the conduction states to the core. Thus, after averaging over polarizations, the matrix elements are

$$\langle p_k^2 \rangle^{\pm} = \tfrac{1}{3} N_k^2 \{ k^2 | \mathscr{E}_k - E_k^{\mp}| + (\mathbf{k}-\mathbf{G})^2 | \mathscr{E}_k - E_k^{\pm}| \pm 2\mathbf{k}\cdot(\mathbf{k}-\mathbf{G}) V_G \}$$

In figure 3 we show the density of states $\rho(E)$, and also the absorption strength

$$A(E) = \int \frac{d^3k}{(2\pi)^3} \{ \langle p_k^2 \rangle^{+} \delta(E - E_k^{+}) + \langle p_k^2 \rangle^{-} \delta(E - E_k^{-}) \}$$

In this figure, energy has been normalized to $E_0 = \hbar^2 G^2/8m$ so that $\mathscr{E} = E/E_0$ and $\nu = V_G/E_0$. The choice $\nu = 0.2$ is close to Ham's value for Li ($\nu = 0.23$). Indeed, the present calculation was done with Li in mind, since the lack of core orthogonalization should not matter here.

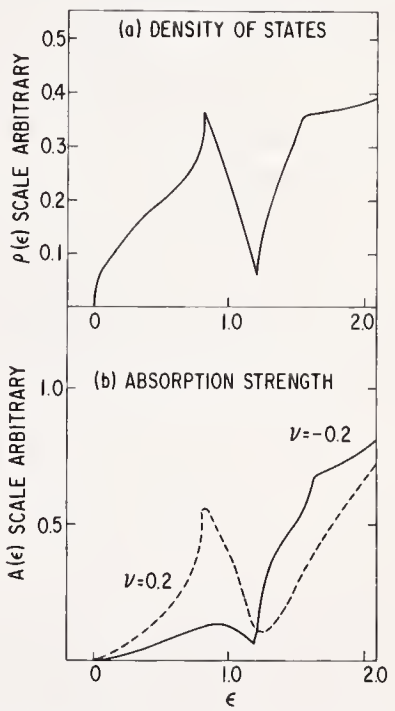

FIGURE 3. *The density of states $\rho(\epsilon)$ and absorption strength $A(\epsilon)$ for a bcc solid such as Li. The energy scale is listed in units $E_0 = \hbar^2 G^2_{110}/8m$, and $\nu = V_{110}/E_0$. The absorption strength $A(\epsilon)$ is defined as the integral of the x-ray matrix element $<p^2>$ averaged over the energy band.*

The curve for $\nu = 0.2$ in figure 3(b) has the expected shape for Li [18]. Because the wave function is p-like at the lower critical point $\mathscr{E} = 0.8$, the transition is allowed and the absorption strength has the same shape as the density of states in figure 3a. The density of states structure at $\mathscr{E} = 1.2$ is washed out in $A(\mathscr{E})$ because at the critical point the transition is s-like and largely

417-156 O - 71 - 18

forbidden. The curve for $\nu = -0.2$ has the same density of states, but now the upper critical point is p-like and $A(\mathscr{E})$ has the same structure as $\rho(\mathscr{E})$ near 1.2. Neither the curve $\nu = 0.2$ nor $\nu = -0.2$ has any striking resemblance to the density of states [18].

IV. Discussion

Exciton effects should influence nearly all parts of the absorption spectra. The singular behavior at the absorption or emission edge is just one prominent feature. Another result of final state interactions is that oscillator strength is moved from one frequency range to another. Often these shifts are small and can be neglected. Yet in most cases the true magnitude of these effects are unknown, because the relevant theoretical calculations are too complicated to do realistically.

The calculation of exciton effects is a formidable task which has not been performed properly. Of course Wannier excitons have been studied in detail. Some model calculations exist near critical point edges—the hyperbolic excitons [19,20,21]. But the main optical absorption strength comes from states throughout the Brillouin Zone [5], and all of these states are included in the final state interactions.

So before x-ray absorption and emission measurements can be used to provide information on the density of states, two sizable corrections need to be made. One of these is the exciton effect, and the other is the change in the matrix element with energy.

V. Acknowledgments

I wish to thank N. Ashcroft, L. Parrott, and M. Stoneham for informative discussions.

VI. References

[1] Dresselhaus, G., and Dresselhaus, M. S., Phys. Rev. **160**, 649 (1967).
[2] Ehrenreich, H., and Beeferman, L., (private communcation).
[3] Spicer, W. E., Phys. Rev. **154**, 385 (1967).
[4] Fong, C. Y., Saslow, W., and Cohen, M. L., Phys. Rev. **168**, 992 (1968); Park, K., and Stafford, R. G., Phys. Rev. Letters **22**, 1426 (1969).
[5] Dresselhaus, G., Sol. State Comm. **7**, 419 (1969); Mueller, F. M., and Phillips, J. C., Phys. Rev. **157**, 600 (1967).
[6] Tomboulian, D. H., Handbuch der Physik, **Vol. 30**, (Springer-Verlag, Berlin, 1957), 246-304.
[7] Harrison, W. A., Soft X-Ray Band Spectra, edited by D. J. Fabin (Academic Press, New York, 1968), p. 227.
[8] Ashcroft, N. W., ibid, p. 249.
[9] Rooke, G. A., ibid, p. 3.
[10] Mahan, G. D., Phys. Rev. **163**, 612 (1967).
[11] Anderson, P. W., Phys. Rev. Letters **18**, 1049 (1967).
[12] Nozieres, P., and DeDominicis, C. T., Phys. Rev. **178**, 1097 (1969).
[13] Ausman, G. A., and Glick, A., Phys. Rev.
[14] Langer, J. S., and Vosko, S. H., J. Phys. Chem. Solids **12**, 196 (1960).
[15] Goldberger, M. L., and Watson, K. M., Collision Theory (J. Wiley and Sons, New York, 1964), p. 232.
[16] Schey, H. M., and Schwartz, J. L., Phys. Rev. **139**, Bi428 (1965).
[17] Foo, E-Ni, and Hopfield, J. J., Phys. Rev. **173**, 635 (1968).
[18] Shaw, R. W., Smith, K., and Smith, N. V., Phys. Rev. **178**, 985 (1969).
[19] Duke, C. B., and Segall, B., Phys. Rev. Letters **17**, 19 (1966).
[20] Hermanson, J., Phys. Rev. Letters **18**, 170 (1967).
[21] Kane, E. O., Phys. Rev. **180**, 852 (1969).

Discussion on "Excitonic Effects in X-Ray Transitions in Metals" by G. D. Mahan (University of Oregon)

J. D. Dow *(Princeton Univ.):* I would like to make a comment about many-body effects *vs* one-electron effects in this problem. While I believe that Professor Mahan's mechanism greatly increases our understanding of the optical properties of metals, I am not convinced that many-body effects are the sole source of anomalies in the x-ray spectra. In particular, I believe that a major portion of the broadening of the image of the lithium Fermi surface is due to gigantic phonon-induced core-shifts—a local lattice distortion squeezes the 2*s* electron, changing the 2*s* wave function at the nucleus, the effective nuclear charge, and the binding energy of the 1*s* state. This electron-phonon mechanism is similar to one proposed by Drs. Overhauser and McAlister and is consistent with the x-ray data of Li, Be, and Na (but does not explain the many-body peak in Na). It is also consistent with Knight shift data, and can explain why the x-ray data shows Li to have a broad Fermi surface image, while Na is sharp. Conclusive evidence about the relative importance of such electron-phonon and many-electron effects could be provided by differential studies of the x-ray spectra, using temperature or pressure modulation.

G. D. Mahan *(Univ. of Oregon):* I would like to make a comment on that. I don't mean to say that all the threshold effects are due to excitons. I think this is particularly true in lithium and also in beryllium. When the x-ray emission spectra bends over in a very round way at threshold some of those effects are probably due to things not involved with the excitons, like band structure effects. Unfortunately, everybody who calculates it, calculates it a different way and gets perfect agreement with experiment when they put in band structure effects or electron-electron effects. So I think that I agree with you in that. I think it is worthwhile to try to do the experiment that would test some of these ideas.

W. Kohn *(Univ. of California):* Toward the end of your talk you discussed the question of the adequacy of the Yukawa approximation. It occurred to me that when you knock out an electron from one of the low-lying states, you are starting out with a closed shell and after you have knocked out the electron, that shell, for example, the L electrons, now constitutes really a degenerate level. The hole has an angular momentum associated with it and so there are several degenerate states. In other words, the situation that you now have (when you consider the interaction of the other electrons with this core) is quite similar to the Kondo effect situation. Is there in fact *any* simple potential that properly represents the interaction of the conduction electrons with the missing charge, or could the degeneracy play an important role?

G. D. Mahan *(Univ. of Oregon):* I would guess that spin flip processes, as you suggest, are probably small. It seems to me that this exchange between a deep core and a conduction electron would be rather small. Is that a reasonable statement to make?

W. Kohn *(Univ. of California):* I don't see why it is.

R. A. Ferrell *(Univ. of Maryland):* But is he referring only to spin flip? Couldn't there be some angular, some orbital-angular momentum exchange? That could be a stronger coupling, couldn't it?

P. M. Platzman *(Bell Telephone Labs.):* You treat the emission and absorption problems on the same footing. I do not understand this. The transition takes place in a time $T \sim \hbar/E$ where $T \ll \hbar/\omega p$, the time for the electron gas to adjust. Thus, in absorption the appropriate final state, (a sort of Frank Condon argument tells us) is to be calculated in the *absence* of the hole. In emission the hole is there for a long time and then vanishes suddenly so that the appropriate wave functions are those in the presence of the hole. Could you amplify on this point?

G. D. Mahan *(Univ. of Oregon):* I don't agree. I think that in the absorption, the wave functions would adjust and in the emission that they have adjusted already.

P. M. Platzman *(Bell Telephone Labs.):* I don't understand. It obviously takes time of the order of $\tau \sim 1/\omega p$ for the electrons to adjust in the presence of a hole. The time of transition for absorption is much shorter than that. The energy involved is 50 to 100 volts. I don't understand how the electrons readjust. It must be some kind of Frank-Condon principle where you make transitions to the states that correspond to the

electron gas before you make the hole, not after you make the hole.

R. A. Ferrell *(Univ. of Maryland):* Is the implication that the kind of potential one should use is different from the usual static screened potential if one wants to talk about the effect of the core on the conduction electrons?

G. D. Mahan *(Univ. of Oregon):* You're asserting that the renormalization term shouldn't be there?

R. A. Ferrell *(Univ. of Maryland):* Would that mean that the Friedel sum rule should not actually be obeyed by the potential which would more realistically describe the potential acting on the conduction electrons? In other words, there isn't time for static screening to set in?

G. D. Mahan *(Univ. of Oregon):* Yes.

J. R. Schrieffer *(Univ. of Pennsylvania):* I would like to return to the question Prof. Kohn brought up for I have a closely related question here. If you are making a p-state hole, the potential is not spherically symmetric, and therefore you have an electron scattering off an asymmetric potential. One question is: To what extent is a phase shift analysis an appropriate language in which to discuss this scattering? Secondly, in addition to the static asymmetry of the potential there is a dynamic aspect of sharing of the hole in different magnetic quantum states in a given atom. The third question: What is the effect of the wandering of the hole from atom to atom?

G. D. Mahan *(Univ. of Oregon):* The last answer is easy. I don't think the hole wanders. The first question is, what about using phase shifts? If you take a simple model where the p state is reasonably tightly bound and try to calculate what the potential is, it comes out spherically symmetric.

J. R. Schrieffer *(Univ. of Pennsylvania):* Are you suggesting that there is a motional averaging to remove the asymmetry corresponding to an electron in a given magnetic substate.

R. A. Ferrell *(Univ. of Maryland):* The question is, should you average or should you consider the potential set up by a certain core state in a certain magnetic substate?

G. D. Mahan *(Univ. of Oregon):* I agree. If you don't average, then you are going to get a definite lobe in your potential in some directions.

W. Kohn *(Univ. of California):* As Bob said, that is very much part of the same question that I asked. Since the potential in a given magnetic state (let's talk about angular momentum rather than spin for a moment), would not be spherically symmetric, therefore when an s-like electron interacts with it, it might very well go into a d-state. There will be, let us say, an s-d coupling. Then to conserve angular momentum, that core would in general make a transition to another state.

R. A. Ferrell *(Univ. of Maryland):* You probably agree that this is something to look at. It might turn out to be a small effect.

A. J. Freeman *(Northwestern Univ.):* Dave Shirley spoke yesterday about some x-ray emission experiments that he and Chuck Fadley did at Berkeley. He did not have time to talk about some recent experiments in which they were able to measure the splitting of the binding energy of core s and p electrons. The splittings of the $3p$ binding energy appear to reflect the multiplet structure of the final possible states of the system with a hole in the $3p$ level. This multiplet splitting gives experimental evidence for the importance of taking a degeneracy effect into account, as just stated by Schrieffer and Kohn.

F. Brouers *(Univ. Liege):* There are two problems if you calculate this exciton effect for the whole band. You can only find an exact solution at the Fermi edge; when you try to calculate the band, the terms which give this spike have too big an effect in a first order approximation in the electron-hole effective potential. The problem is to see if electron-electron interactions which are missed in the Nozières and di Dominicis paper, for instance, can reproduce something which is like a free-electron band between the high and low energy features which one can presently deal with. But if you introduce electron-electron interactions, you have troubles because the theorem of linked cancellation is not correct in this particular case. You have terms which are divergent in a first order theory throughout the band. So one of the points is to use some tricks from nonlinear oscillation theory to sum up all these secular terms and to put them in the exponential. You then have just a shift in the energy scale which has no physical importance. The problem with this method is to see if the addition of electron-electron correlations to the contribution which gives this singular spike can reproduce something which is very like a one-electron theory over the main band.

R. A. Ferrell *(Univ. of Maryland):* Thank you. I think it would take us too far afield to go into the details of this interesting question, but I believe it is apparent that it is in the direction of Platzman's question of making a more realistic treatment of the potential and its time dependence.

Vibronic Exciton Density of States in Some Molecular Crystals

R. Kopelman and J. C. Laufer

Department of Chemistry, University of Michigan, Ann Arbor, Michigan 48104

Excited states of molecular crystals, which happen to be the majority of known crystals, are almost always classified as excitonic. The largest class of well studied systems are very closely described by the Frenkel model, and a majority of these systems can actually be described by a special case of the Frenkel model, one with steeply falling-off intersite (intermolecular) interactions. In this specific model the expression for the band structure depends only on the interchange symmetry of the crystal, with a small number of intersite parameters. Examples are given for some aromatic crystals, comparing band structures derived from theoretically calculated parameters, experimentally derived parameters, and completely experimentally derived band structure.

Key words: Anthracene; aromatic crystals; benzene; excitonic density of states; molecular crystals; naphthalene.

1. Theory

Molecular crystals are characterized by intermolecular ground state energies which are much smaller than the intramolecular energies within the molecules themselves. The intermolecular forces in these crystals are considered to be weak and of short range. Consequently, it is not surprising that many exciton states in molecular crystals are best described by the Frenkel model rather than the Wannier one [1].

The crystal exciton function in the Frenkel model is constructed as a linear combination of the wavefunctions called "one-site excitons" which are equal in number to the number of molecules per primitive unit cell. For each "one-site exciton," the excitation formally resides on one sublattice only, and all the sublattices are of the same type if there exist symmetry operations of the crystal which operate on one of these sublattices and generate the others. These operations have been designated interchange operations and they can be formed into groups, called interchange groups [2]. Interchange groups are basic to the symmetry of crystals. For example, the unit cell group of a crystal is the direct product or union of the site group (of the molecules in the crystal) and an interchange group [2].

One-site Frenkel exciton functions ϕ^f_{nq} are constructed [3] from a tentative wavefunction which is the product of a crystal function χ^f_{nq}, representing a localized electronic, vibrational, or vibronic excitation f of a molecule located on the q^{th} site of the n^{th} primitive cell, and the other unexcited site functions of the crystal, $\chi^0_{n'q}$,

$$\phi^f_{nq} = A\chi^f_{nq} \prod_{n' \neq n}^{N/h} \chi^0_{n'q}. \tag{1}$$

In the above equation A is an antisymmetrizing operator, N is the number of molecules in the crystal, and h is the number of sublattices which also is the order of the interchange group. From ϕ^f_{nq} the one-site exciton functions in the Bloch representation can be formed,

$$\Phi^f_q(\mathbf{k}) = (N/h)^{-1/2} \sum_{n=1}^{N/h} \exp\,(i\mathbf{k}\cdot\mathbf{R}_{nq})\,\phi^f_{nq}, \tag{2}$$

where $\mathbf{k}$ is the reduced wave vector, and $\mathbf{R}_{nq}$ denotes the position of q^{th} site in the n^{th} primitive cell with respect to a common crystal origin. $\mathbf{R}_{nq}$ can be written as

$$\mathbf{R}_{nq} = \mathbf{r}_n + \boldsymbol{\tau}_{nq}, \tag{3}$$

where $\mathbf{r}_n$ is a vector from the crystal origin to the origin of the n^{th} primitive cell and $\boldsymbol{\tau}_{nq}$ is a vector from the n^{th} primitive cell origin to its q^{th} site.

In our model the crystal Hamiltonian H is the sum of a site-adapted-molecular Hamiltonian H° and an intersite Hamiltonian H':

$$H^0 = \sum_{n=1}^{N/h} \sum_{q=1}^{h} H^0(nq) \tag{4}$$

$$H' = \frac{1}{2} \sum_{n=1}^{N/h} \sum_{q=1}^{h} \sum_{n'=1}^{N/h} \sum_{q'=1}^{h} (1 - \delta_{nn'}\delta_{qq'}) H'(nq, n'q'). \quad (5)$$

For the case of a *single* nondegenerate excited state f, the $N \times N$ Hamiltonian matrix is blocked off along the main diagonal into N/h $h \times h$ Hermitian submatrices, each submatrix being characterized by a value of $\mathbf{k}$. The off-diagonal elements $\mathscr{L}^f_{qq}(\mathbf{k})$ in each submatrix are due to the interactions between the h sublattices. They are the sum over the entire lattice of interaction terms between molecules on sites of type q and q', modified by phase factors. The diagonal elements $\mathscr{L}^f_{qq'}(\mathbf{k})\ \delta_{qq'}$ have $\mathbf{k}$-independent terms which arise from the matrix elements in which simultaneously $q = q'$ and $n = n'$, and $\mathbf{k}$-dependent terms which solely arise from the pairwise interactions of the molecules. The general matrix element is $\langle \Phi^f_q(\mathbf{k}) | H | \Phi^f_{q'}(\mathbf{k}) \rangle$ which we have designated $\mathscr{L}^f_{qq'}(\mathbf{k})$. All matrix elements between states of different $\mathbf{k}$ vanish by symmetry. Expanding $\mathscr{L}^f_{qq'}(\mathbf{k})$, we write

$$\mathscr{L}^f_{qq'}(\mathbf{k}) = \sum_{n'=1}^{N/h} [\exp\ (i\mathbf{k}) \cdot (\boldsymbol{\tau}_{q'} - \boldsymbol{\tau}_q)] \, [\exp\ (i\mathbf{k}) \cdot (\mathbf{r}_{n'} - \mathbf{r}_n)] \int \phi^f_{nq} H \phi^f_{n'q'} dR. \quad (6)$$

Separating the $\mathbf{k}$-dependent terms $\mathscr{L}^f_{qq'}(\mathbf{k})$ from the $\mathbf{k}$-independent terms, we write

$$\mathscr{L}^f_{qq'}(\mathbf{k}) = (\mathscr{E}^f + D^f)\delta_{qq'} + L^f_{qq'}(\mathbf{k}) \quad (7)$$

where

$$\mathscr{E}^f = \int \phi^{f*}_{nq} H^0 \phi^f_{nq}\, \phi R \quad (8)$$

and

$$D^f = \int \phi^{f*}_{nq} H' \phi^f_{nq} dR. \quad (9)$$

D^f is a term representing a "Van der Waals-type interaction" between sites, and is the energy required to excite a single molecular site locally in the presence of the rest of the crystal. It shifts the exciton band energy from $\mathscr{E}^f$, the energy of the molecular *site* functions. Usually the major Van der Waals energy shift is $\mathscr{E}^f - \mathscr{E}^{of}$, where $\mathscr{E}^{of}$ is the free molecular excitation energy. $\mathscr{E}^f$, the "ideal mixed crystal level," can be derived from mixed crystal data [3].

The expression for a diagonal element $L^f_{qq}(\mathbf{k})$ written out fully is

$$\mathscr{L}^f_{qq}(\mathbf{k}) = \mathscr{E}^f + D^f + \sum_R e^{i\mathbf{K}\cdot\mathbf{R}} [2\delta_m (\chi^f_c \chi^0_R | H' | \chi^0_0 \chi^f_R) - (\chi^f_0 \chi^0_R | H' | \chi^f_R \chi^0_0)], \quad (10)$$

where $\delta_m = 1$ for a singlet state and $\delta_m = 0$ for a triplet or other multiplet state. $\mathbf{R}$ is $\mathbf{R}_{nq}$; χ^f_o is χ^f_{oq}, where the subscript of oq indicates the origin of sublattice q, and χ^f_R is χ^f_{Rq}, where the subscript $\mathbf{R}_q$ indicates the site at distance $\mathbf{R}_{nq}$ from the origin [4]. The off-diagonal elements $L^f_{qq}(\mathbf{k})$ are all $\mathbf{k}$-dependent and are conveniently expressed at this point as

$$L^f_{qq'}(\mathbf{k}) = \sum_{n'=1}^{N/h} \exp\ [i\mathbf{k} \cdot (\boldsymbol{\tau}_{q'} - \boldsymbol{\tau}_q)] \exp\ [i\mathbf{k} \cdot (\mathbf{r}_{n'} - \mathbf{r}_n)] \times \int \phi^{f*}_{nq} H' \phi^f_{n'q'} \phi R (1 - \delta_{qq'}). \quad (11)$$

In general, in order to find the eigenvalues for a particular $\mathbf{k}$, it would be necessary to solve an $h \times h$ secular equation. The expression for the eigenvalues would be a function of all the elements of the secular determinant. Such an expression for a system where $h = 2$ is given by Knox [4]:

$$E(\mathbf{k})^{\pm} = \tfrac{1}{2}[\mathscr{L}^f_{\mathrm{II}}(\mathbf{k}) + \mathscr{L}^f_{\mathrm{II\,II}}(\mathbf{k})] \pm \{\tfrac{1}{4}[\mathscr{L}^f_{\mathrm{II}}(\mathbf{k}) - \mathscr{L}^f_{\mathrm{II\,II}}(\mathbf{k})]^2 + |\mathscr{L}^f_{\mathrm{I\,II}}(\mathbf{k})|^2\}^{1/2}, \quad (12)$$

where the two eigenvalues are E^+ and E^-, and the two sublattices are labelled I and II. Although sublattices I and II are spacially equivalent, $\mathscr{L}^f_{II}(\mathbf{k})$ and $\mathscr{L}^f_{II\,II}(\mathbf{k})$ are not generally equal because they are $\mathbf{k}$-dependent. The reduced wavevector $\mathbf{k}$ designates a phase factor relationship with the vectors $\mathbf{R}$ which has a spacial orientation that is usually not isotropic with respect to the sublattices I and II. In certain cases, such as when $\mathbf{k} = 0$, $\mathscr{L}^f_{II}(\mathbf{k})$ equals $\mathscr{L}^f_{II\,II}(\mathbf{k})$. Equation (12) can then be written:

$$E^f(\mathbf{k})^{\pm} = \mathscr{L}^f_{\mathrm{II}}(\mathbf{k}) \pm \mathscr{L}^f_{\mathrm{I\,II}}(\mathbf{k}). \quad (13)$$

The eigenfunctions for the two states then become simply

$$\Psi^f(\mathbf{k})^{\pm} = \frac{1}{\sqrt{2}} [\Phi^f_{\mathrm{I}}(\mathbf{k}) \pm \Phi^f_{\mathrm{II}}(\mathbf{k})], \quad (14)$$

The above example is for a system of two interchange equivalent sublattices. For a system having an interchange group G of order h, there will be h interchange equivalent sublattices. *If* $\mathscr{L}^f_{qq}(\mathbf{k})$ is equal to $\mathscr{L}^f_{q'q'}(\mathbf{k})$ for all q', an eq (14) analog for the general case can be constructed group theoretically from the interchange group to give:

$$\psi^{f\alpha}(\mathbf{k})_j = \frac{1}{\sqrt{h}} \sum_{q=1}^{h} a^{\alpha}_q \Phi^f_q(\mathbf{k}), \quad (15)$$

where a_q^α's are coefficients corresponding to the α^{th} irreducible representation of G. The corresponding eigenvalues then become

$$E^{f\alpha}(\mathbf{k}) = \sum_{q=1}^{h} a_q^\alpha \mathscr{L}^f_{1q}(\mathbf{k}). \tag{16}$$

Equations (15) and (16) can be obtained [5] for any $\mathbf{k}$ if certain integrals are excluded from the summation in eq (10). Consider the effect of an interchange operation A on sublattice q. Every site in q will be mapped into an interchange equivalent site in sublattice q'. In other words, A operating on q generates q'. Equation (10) for $\mathscr{L}^f_{q'q'}(\mathbf{k})$ will be identical to that for $\mathscr{L}^f_{qq}(\mathbf{k})$ in E^f, D^f, and all corresponding terms within the brackets. But AR generates R' in q' and

$$A\mathbf{R} = \mathbf{R} \neq \mathbf{R} \qquad \text{for general } \mathbf{R} \tag{17}$$

and

$$\mathbf{k}\cdot\mathbf{R} \neq \mathbf{k}\cdot\mathbf{R}' \qquad \text{for general } \mathbf{k} \tag{18}$$

becomes $\mathbf{k}$ is a vector in the reciprocal lattice and is not operated on by A. However, for those $\mathbf{R}$ which are left invariant (to within a translation) by A, $\mathbf{R}$ is equal to $\mathbf{R}'$, and corresponding terms in the summations of $\mathscr{L}^f_{qq}(\mathbf{k})$ and $\mathscr{L}^f_{q'q'}(\mathbf{k})$ are equal. The sublattice q' may also be generated by another interchange operation B, which will fix other $\mathbf{R}$'s such that

$$\mathbf{R} = B\mathbf{R} = \mathbf{R}' \tag{19}$$

The terms in $L^f_{qq}(\mathbf{k})$ and $L^f_{q'q'}(\mathbf{k})$ associated with these $\mathbf{R}$ are also equal. By using all the interchange operations in the crystal and collecting only those terms in $\mathscr{L}^f_{qq}(\mathbf{k})$ and $\mathscr{L}^f_{q'q'}(\mathbf{k})$ which are equal, we can obtain the eqs (15) and (16) for any arbitrary $\mathbf{k}$, provided that the rest of the terms are negligible.

By the same procedure we can obtain the restrictions on $\mathbf{k}$ that lead to eqs (15) and (16) for any arbitrary $\mathbf{R}$. For an interchange operation A which generates sublattice q' from q, there must be a corresponding symmetry operation in the reciprocal lattice which will leave some $\mathbf{k}$ invariant. For this $\mathbf{k}$ eq (10) will not change in value as A changes $\mathscr{L}^f_{qq}(\mathbf{k})$ to $\mathscr{L}^f_{q'q'}(\mathbf{k})$. Repeating this procedure for all interchange operations, we find all $\mathbf{k}$ which satisfy eqs (15) and (16) for general $\mathbf{R}$. All such $\mathbf{k}$ have the property that the group of $\mathbf{k}$ contains at least one interchange group.

An examination of the terms which are retained in $\mathscr{L}^f_{qq}(\mathbf{k})$ *for general* $\mathbf{k}$ shows that they include the nearest translationally equivalent neighbors about the origin of the sublattice. Since vibronic interactions in molecular crystals are often extremely short-range, next-nearest translationally equivalent neighbors may be dropped from the summation as they make only a negligible contribution to $\mathscr{L}^f_{qq}(\mathbf{k})$. Equations (15) and (16) are therefore believed to be valid expressions for many physically real cases of excitions in molecular crystals.

For Frenkel excitons the crystal transition dipole operator M is the sum of the dipole operators on all the crystal sites. The evaluation of the transition moment matrix element

$$\langle \Psi^{f''\alpha''}(K'') | M | \Psi^{f\alpha}(\mathbf{k}) \rangle$$

by use of eq (15) shows it to be nonvanishing only under certain conditions. The first of these is the usual crystal selection rule, $\Delta\mathbf{k} = 0$. As long as eq (15) is applicable the transition moment becomes $\mathbf{k}$-independent [5]. An important consequence of this requirement is that every nonvanishing transition moment in a transition between two exciton bands will have the same intensity; the band profile of such a transition will be dependent only on the density-of-states functions of the two exciton bands. The second selection rule for the nonvanishing of the transition matrix element is that the direct product

$$\alpha'' \times \alpha_r \times \alpha',$$

where α_r is the interchange group representation of the electric dipole moment, must contain the totally symmetric representation. The combined selection rules, for *all* $\mathbf{k}$, are thus those of the interchange group. Actually they turn out [5] to be those of the factor group.

It follows from the above development that the band profiles of transitions between two exciton bands can be computed from the density-of-states functions of the two bands. If the low energy band is narrow ($\sim$10 cm^{-1}) and the upper band is an order of magnitude broader, then to a good approximation the experimentally observed band profile for such a transition will be just the density-of-states function for the upper band [6]. This function can be calculated directly from eq (16) if the values of the excitation exchange integrals

$$\int \phi^{f*}_{nq} H \phi^f_{n'q'} \, dR$$

are known. Theoretical calculations of these integrals using molecular wavefunctions have been made, and various experimental techniques have also been used to obtain values for these integrals. The best of these values have been obtained from Davydov splittings [7], mixed crystal data [8], and exciton diffusion measurements [9].

The crystals of naphthalene [10] and anthracene [11] both have C_{2h}^5 space groups with two molecules per primitive cell occupying sites of C_i symmetry. By using a C_2 interchange group, eq (16) can be written as

$$E^f(\mathbf{k})^{\pm} = 2M_a \cos(K_a a) + 2M_b \cos(K_b b) + 2M_c \cos(K_c c)$$
$$+ 2M_{(a+c)} \cos(K_a a) \cos(K_c c) - 2M_{(a+c)} \sin(K_a a) \sin(K_c c)$$
$$\pm 4M_{\mathrm{I\,II}} \cos(K_a \tfrac{1}{2} a) \cos(K_b \tfrac{1}{2} b) \pm 4M_{\mathrm{I\,II'}} \cos(K_c c) \cos(K_a \tfrac{1}{2} a)$$
$$\times \cos(K_b \tfrac{1}{2} b) \mp 4M_{\mathrm{I\,II'}} \sin(K_c c) \sin(K_a \tfrac{1}{2} a) \cos(K_b \tfrac{1}{2} b). \quad (20)$$

where the summation has been truncated after summing out to and including the two translationally equivalent neighbors at lattice positions (101) and $(\bar{1}0\bar{1})$ In eq (20)

$$K_a a = \mathbf{k} \cdot \mathbf{a}, \qquad K_b b = \mathbf{k} \cdot \mathbf{b}, \qquad K_c c = \mathbf{k} \cdot \mathbf{c}, \quad (21)$$

where **a**, **b**, and **c** are primitive lattice translations in the monoclinic system. M_a, M_b, M_c and $M_{(a+c)}$ are the excitation exchange interactions between the site-adapted molecule at the origin and the translationally equivalent molecules at positions (100), (010), (001), and (101) respectively; and $M_{I\,II}$ and $M_{I\,II'}$ are the interactions between the molecule at the origin and the interchange equivalent molecules at ($\frac{1}{2}$ $\frac{1}{2}$ 0) and ($\frac{1}{2}$ $\frac{1}{2}$ 1) respectively.

2. Calculations

We have used eq (20) to compute the exciton band profiles of the lowest $^3B_{2u}$ states of anthracene and naphthalene. The calculations were performed by computer, with each band profile being composed of about 200,000 states. When these states were collected in energy increments of 1 cm^{-1}, our density-of-states function was obtained. The band shape was determined solely by the values selected for the M's of eq (20), the excitation exchange interactions. A similar equation was used to compute the band profile of the lowest $^3B_{1u}$ electronic state of benzene. Benzene crystallizes [12] in an orthorhombic lattice of space group D_{2h}^{15} (P_{bca}), and has four molecules per primitive cell. We chose a D_2 interchange group to construct eigenvalues from eq (16). The benzene calculation involved the generation of about 800,000 states. They were collected in energy increments of 0.3 cm^{-1} to obtain the density-of-states function, which is plotted in figure 5. The $^3B_{2u}$ band profiles of naphthalene and anthracene, calculated from M values obtained theoretically from molecular orbital calculations by Rice and co-workers [13], are shown in figures 1 and 3, respectively. The corresponding band profiles for M values obtained from experimental data are shown in figures 2 and 4.

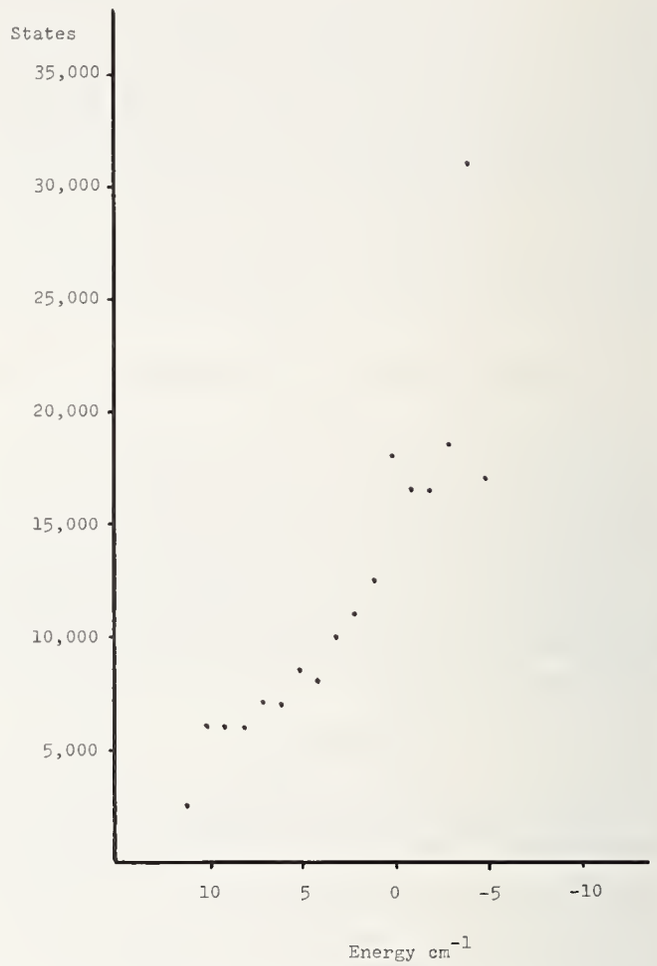

FIGURE 1. $^3B_{2u}$ *Exciton band of naphthalene calculated from theoretical parameters (see ref. [13]).*
$M_a = 0.0$, $M_b = 2.4$, $M_c = 0.0$, $M_{(a+c)} = 0.0$, $M_{\mathrm{I\,II}} = -1.4$ $M_{\mathrm{I\,II'}} = 0.0$.

The value of M_{12} used for the naphthalene calculation in figure 2 was taken from the Davydov splitting observed by Hochstrasser and Clarke [14]. Hanson and Robinson [15] have shown that the mean of the $^3B_{2u}$ Davydov components is shifted down by about 1 cm^{-1} from the mixed crystal $^3B_{2u}$ energy [15]. We have attributed this "translational shift" [3] to the interaction between molecules at (000) and (010). M_b thus becomes 0.5 cm^{-1}. However, the band profile would be the same if it were attributed to either M_a or M_c. The anthracene calculation in figure 4 was based on the constants derived from two experiments: the Davydov splitting in

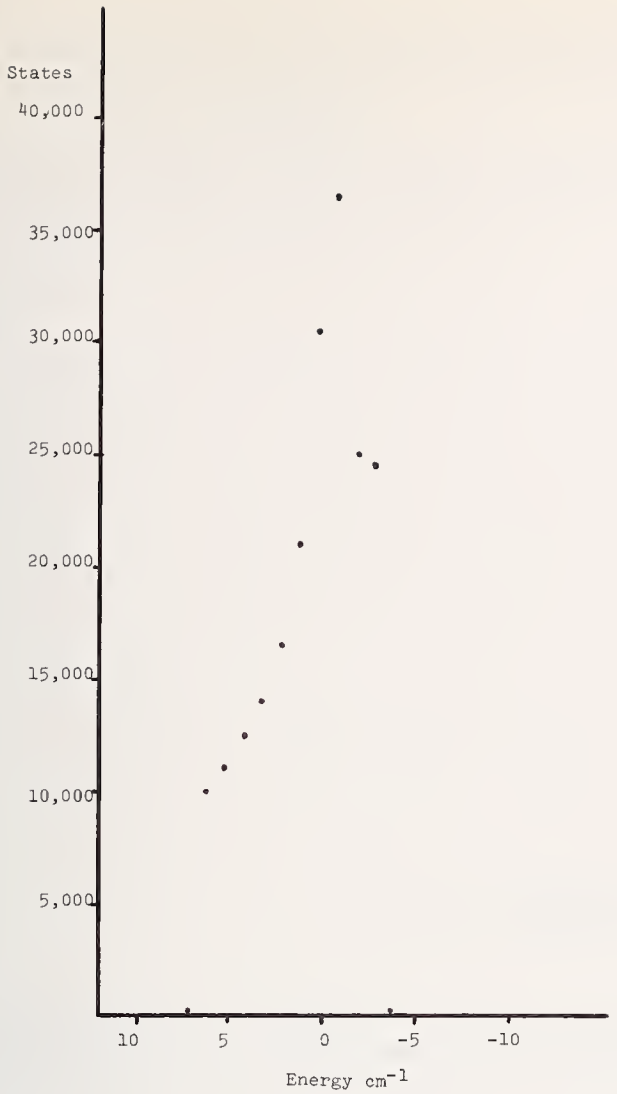

FIGURE 2. $^3B_{2u}$ *Exciton band of naphthalene calculated from experimental parameters (see refs. [14 & 15]).*
$M_a=0.0$, $M_b=0.5$, $M_c=0.0$, $M_{(a+c)}=0.0$, $M_{I\,II}=1.25$, $M_{I\,II'}=0.0$.

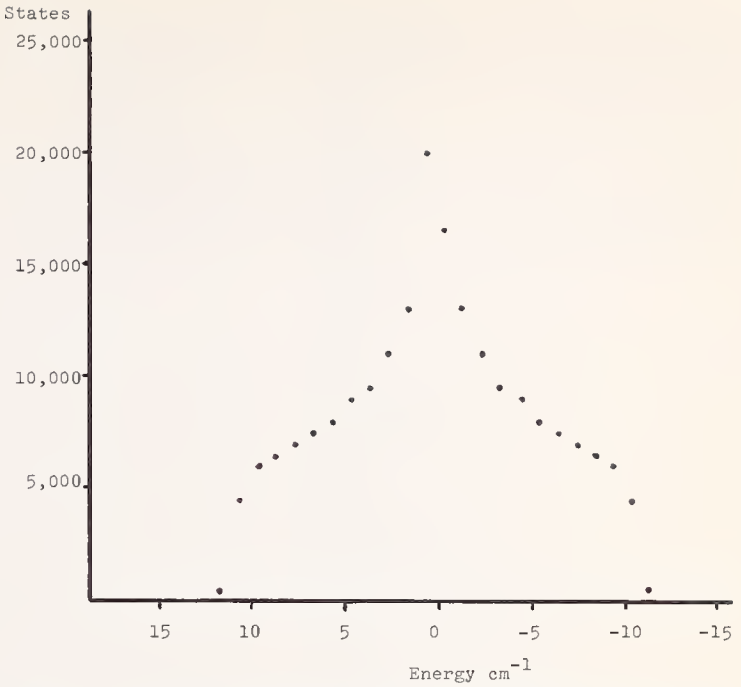

FIGURE 4. $^3B_{2u}$ *Exciton band of anthracene calculated from experimental parameters (see refs. [9 & 16]).*
$M_a=0.0$, $M_b=0.0$, $M_c=0.0$, $M_{(a+c)}=0.0$, $M_{I\,II}=2.5$, $M_{I\,II'}=0.30$.

the anthracene triplet as observed by Clarke and Hochstrasser [16] through the electronic Zeeman effect, and the anisotropy of triplet exciton diffusion as measured by Ern [9]. Only the absolute value of the ratio of $M_{I\,II'}$ to $M_{I\,II}$ can be obtained from Ern's work, but the band profile is not significantly affected by the choice of sign. It is interesting to note the difference in band shape between those profiles calculated from theoretical data and those calculated from experimen-

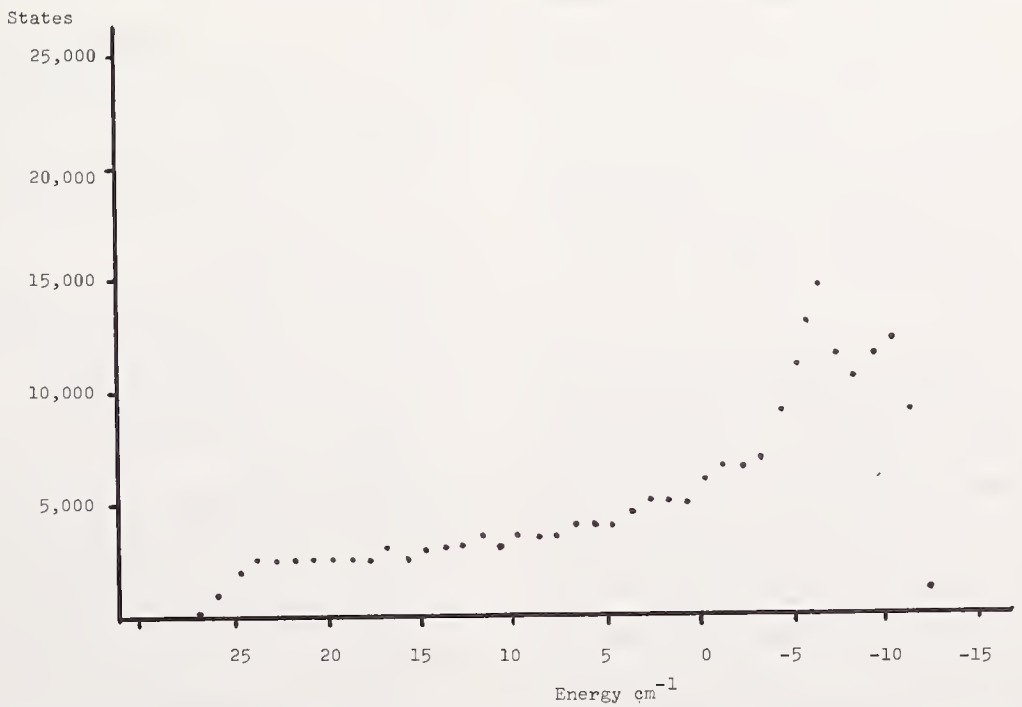

FIGURE 3. $^3B_{2u}$ *Exciton band of anthracene calculated from theoretical parameters (see ref. [13]).*
$M_a=0.0$, $M_b=3.6$, $M_c=0.0$, $M_{(a+c)}=0.0$, $M_{I\,II}=-4.7$, $M_{I\,II'}=0.21$.

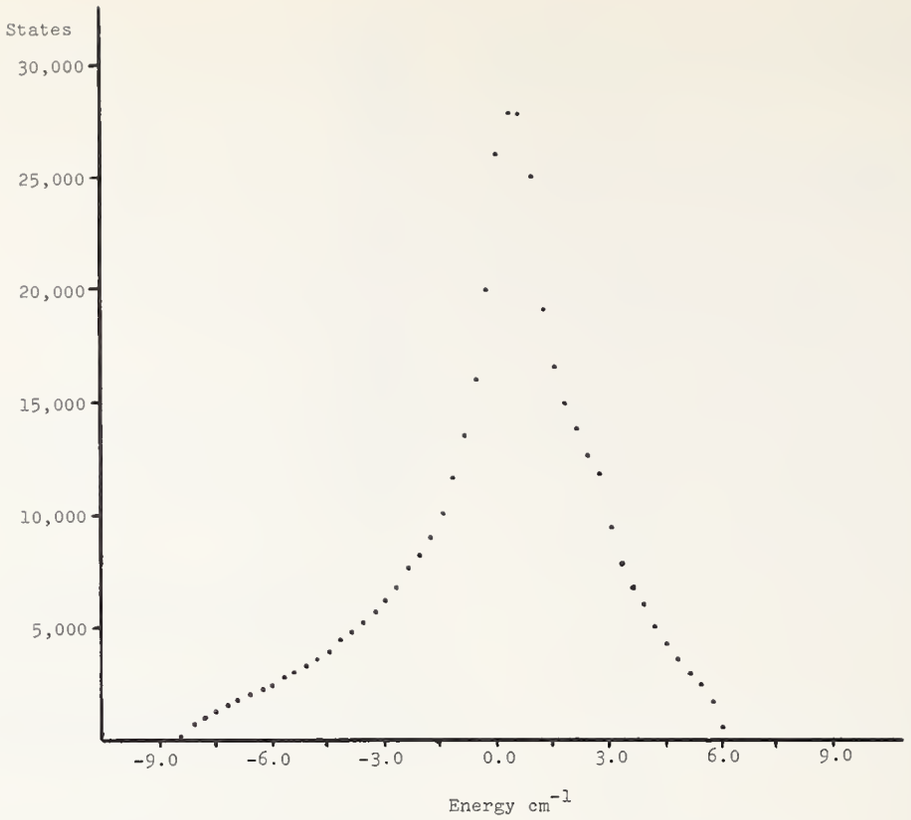

FIGURE 5. $^3B_{1u}$ *Exciton band of benzene calculated from experimental parameters (see ref. [17]).*
$M_a=0.0$, $M_b=0.0$, $M_c=0.0$, $M_{1\,II}=1.1$, $M_{1\,III}=0.7$, $M_{1\,IV}=-0.3$.

tal data. While the theoretical parameters account fairly well for the observed Davydov splittings and diffusion constants, they seem to fail the test of a more sensitive criterion—the band profile.

The benzene band was computed from M values derived from Davydov splittings observed in a triplet state [17]. Here it is possible to obtain three values to be assigned to $M_{I\,II}$, $M_{I\,III}$, and $M_{I\,IV}$. The individual factor group components were not classified as to symmetry; thus a set of $M_{I\,II}$, $M_{I\,III}$, and $M_{I\,IV}$ can be determined only to within a permutation. Fortunately, the symmetry of the density-of-states function is such that it is invariant to permutations of values of the interchange-equivalent M's.

There has not yet been any direct observation of any triplet band of any molecular crystal, so it is not possible to conclude which of our calculated bands, if any, are accurate in shape. However, the entire $^1B_{2u}$ exciton band of naphthalene has been observed [6]. The agreement between this band profile and the profile calculated for the $^1B_{2u}$ state from Davydov splittings and mixed crystal data is very good [6,8]. Such agreement is supporting evidence that eqs (15) and (16) are substantially correct for narrow molecular crystal exciton bands, and that the assumptions in the Frenkel theory which were used to derive them are valid. In fact, the agreement for the triplet bands is expected to be even better than for the singlet bands, as the former are narrower and in addition cannot have even small contributions from long-range interactions (e.g. dipole-dipole) in view of the fact [7] that $\delta_m = 0$ in eq (10).

3. References

[1] Knox, R. S., Theory of Excitons (Academic Press Inc., New York, 1963), Chap. II.

[2] Kopelman, R., J. Chem. Phys. **47**, 2631 (1967).

[3] Berstein, E. R., Colson, S. D., Kopelman, R., and Robinson, G. W., J. Chem. Phys. **48**, 5596 (1968).

[4] Knox, R. S., ibid., p. 31.

[5] Colson, S. D., Kopelman, R., and Robinson, G. W., J. Chem. Phys. **47**, 27 (1967) and J. Chem. Phys. **47**, 5462 (1967).

[6] Colson, S. D., Hanson, D. M., Kopelman, R., and Robinson, G. W., J. Chem. Phys. **48**, 2215 (1968).

[7] Craig, D. P., and Walmsley, S. H., Excitons in Molecular Crystals, (W. A. Benjamin Inc., New York, 1968). See also references 1 and 3.

[8] Hanson, D. M., Kopelman, R., and Robinson, G. W., J. Chem. Phys. **51**, 212 (1969) and unpublished work.

[9] Levine, M., Jortner, J., and Szöke, J. Chem. Phys. **45**, 1591 (1966); Ern, V., Phys. Rev. Letters **22**, 343 (1969); Durocher, G., and Williams, D. F., J. Chem. Phys. **51**, 1675 (1969).

[10] Robertson, J. M., and White, J. G., J. Chem. Soc. **18**, 358 (1947); Abrahams, S. C., Robertson, J. M., and White, J. G., Acta Cryst. **2**, 238 (1949).

[11] Mason, R., Acta Cryst. **17**, 547 (1964).

[12] Cox, E. G., Rev. Mod. Phys. **30**, 159 (1958); Cox, E. G., Cruickshank, D. W. J., and Smith, J. A. S., Proc. Roy. Soc. (London) **A247**, 1 (1958); Bacon, G. E., Curry, N. A., and Wilson, C. A., ibid., **A279**, 98 (1964).

[13] Jortner, J., Rice, S. A., Katz, J. L., and Choi, S. I., J. Chem. Phys. **42**, 309 (1965); Levine, M., Jortner, J., and Szöke, A., J. Chem. Phys. **45**, 1591 (1966).

[14] Clarke, R. H., and Hochstrasser, R. M., J. Chem. Phys. **49**, 3313 (1968).

[15] Hanson, D. M., and Robinson, G. W., J. Chem. Phys. **43**, 4174 (1965).

[16] Clarke, R. H., and Hochstrasser, R. M., J. Chem. Phys. **46**, 4532 (1967).

[17] Burland, D. M., and Castro, G., J. Chem. Phys. **50**, 4107 (1969).

Effect of the Core Hole on Soft X-Ray Emission in Metals

L. Hedin and R. Sjöström

Chalmers University of Technology, Göteborg, Sweden

We report a simple type of calculation to estimate the enhancement factor on the intensity of soft x-ray emission in free-electron like metals due to the effect of the core hole. We consider an electron gas in the presence of a perturbing potential and calculate the x-ray intensity assuming the dipole matrix elements to be constant. The calculation is based on a simple type of trial function for the initial state of the valence electron system and the coefficients are determined from the variation principle. The calculation does not give the Fermi edge singularity, which has recently aroused such a large interest, but instead aims at giving the gross effects for the whole spectrum. The results indicate an increase in the intensity by 25 to 50% at metallic densities. The enhancement factor is found to vary roughly linearly over the main band, increasing about 50% in going from the bottom of the band to the Fermi edge.

Key words: Aluminum; core hole; electronic density of states; Fermi edge singularity; pseudopotential; sodium (Na); soft x-ray emission.

1. Calculations

We consider the Hamiltonian

$$H=\sum_k \epsilon_k a_k^+ a_k+\frac{1}{2}\sum_{kk'q} v(q)a_{k'q}^+ a_{k'-q}^+ a_{k'}a_k$$

$$-\sum_{kq} v(q)F(q)a_{k'+q}^+ a_k, \quad (1)$$

where $F(q)$ is a form factor, taken as cos qR and as (sin qR)/qR. The initial state is represented as [1]

$$|N^+\rangle=\left(\alpha+\sum_{pq}\alpha_p^q a_q^+ a_p\right)|N\rangle, \quad (2)$$

where $|N\rangle$ is a Slater determinant of plane wavefunctions. Restricting the coefficients α_p^q to have the form

$$\alpha_p^q=g(q-p)\ (1-n_q)n_p, \quad (3)$$

the energy is minimized, neglecting some small exchange terms. The x-ray intensity is then calculated taking the dipole matrix elements as constants. We obtain [1] for the intensity $I(\omega)$

$$I(\omega)\sim\sum_k^{\text{occ}}|\alpha+\sum_q^{\text{unocc}} g(q-k)|^2\,\delta(\omega-\epsilon_k)$$

$$+\frac{1}{2}\sum_k^{\text{unocc}}\sum_{k_1k_2}^{\text{occ}}|g(k-k_1)-g(k-k_2)|^2\delta(\omega+\epsilon_k-\epsilon_{k_1}-\epsilon_{k_2}). \quad (4)$$

The function $g(q)$ is singular as q^{-1} for small q. The coefficient determines the magnitude of the polarization charge [2]. The variational calculation gives a polarization charge of $2\alpha^2$. We can easily obtain a charge of 1 by using a subsidiary condition in the variation, but the significance of this is not clear.

2. Results

Calculations were made for different r_s-values, with and without form factors. We find that the first term in eq (4) gives the dominant contribution in the main band while the multiple excitation term contributes to the Auger tail. The results are summarized in tables 1, 2 and 3. The total increase in intensity is proportional to the increase in charge density $\rho(0)/\rho_0$ at the center of the perturbing potential. The energy difference

TABLE 1. *Results without form factor*

r_s	$\rho(0)/\rho_0$	α^2	ϵ_0/ϵ_F	Mult. exc. %
2	3.7	0.81	0.88	5
3	4.8	0.78	1.44	4
4	5.9	0.76	2.03	4

TABLE 2. *Results with form factor* F(q)=*sin* (qR)/(qr)

	r_s	R^1	$\rho(0)/\rho_0$	α^2	ϵ_0/ϵ_F	Mult. exc. %	Increase of enhancement factor %
Al.....	2	2.15	1.25	0.86	0.59	12	40
Na.....	4	3.26	1.49	0.81	1.42	14	50

[1] Values for R are taken from R. W. Shaw, Jr., Phys. Rev. **174**, 769 (1968).

TABLE 3. *Results with form factor* F(q)= *cos* qR

	r_s	R^1	$\rho(0)/\rho_0$	α^2	ϵ_0/ϵ_F	Mult. exc. %
Li.....	3.26	1.06	1.41	0.80	1.30	16
Na.....	4.00	1.67	1.01	0.81	1.52	24
Al.....	2.07	1.12	0.90	0.86	0.66	19

[1] Values for R are taken from N. W. Ashcroft and D. C. Langreth, Phys. Rev. **155**, 682 (1967).

between the states $|N\rangle$ and $|N^*\rangle$ is denoted by ϵ_0. The increase in charge density $\rho(0)/\rho_0$ agrees very well with the positron annihilation rates at higher electron densities. We do not give the intensity function $I(\omega)$ explicitly since the enhancement factor $I(\omega)/\sqrt{\omega}$ is closely linear. Instead we give the increase in percent of the enhancement factor from $\omega=0$ to $\omega=\epsilon_F$ and the total enhancement which is proportional to $\rho(0)/\rho_0$. The column "multiple excitation" gives the integrated intensity of the last term in eq (4) in percent of the integrated intensity of the first term.

The results we have obtained give only a very crude picture of the magnitude of the effect from the core hole. In particular we see that use of different form factors give quite different results. We believe the results in table 2, to best represent the actual conditions. The reason is that the charge enhancement at $r=R$ rather than at $r=0$ should be taken as a measure of the intensity increase since it is at roughly that point where the pseudowavefunction should be matched to the correct Bloch function. With the Ashcroft pseudopotential, which in real space is zero for $r<R$, the charge density has a minimum at $r=0$ while with the Shaw pseudopotential, which in real space is constant for $r<R$ and joins continuously to the outer $(-1/r)$-part, the charge density has a maximum at $r=0$ and probably does not vary much out to $r=R$. The results in table 2 should thus represent an overestimate of the enhancement effects. Another reason for believing the results to be too large is that the total screening charge, $2\alpha^2$, is larger than unity. Calculations with a subsidiary condition to give a screening charge of unity indeed cuts down the enhancement but not however, by the full $2\alpha^2$-factor.

Neglecting the last term in eq (4), that is, the multiple excitation term, we see that the intensity has the form

$$I(\omega)=\sqrt{\omega}\ \rho_{\text{eff}}^2, \tag{5}$$

where the effective matrix element is

$$\rho_{\text{eff}}=\alpha+\beta(\omega). \tag{6}$$

The results for $\beta(\omega)$ at the Fermi surface obtained with the Shaw pseudopotential are 0.21 and 0.33 for Al and Na, respectively. Even if these values are somewhat too large they indicate that the mixing in of matrix elements from states above the Fermi surface can have a significant influence if there is a strong variation in matrix elements and density of states at the Fermi surface.

The contribution to the intensity from the multiple excitation term is zero at the Fermi edge, rises quadratically and reaches a maximum in the bottom of the main band. The tail intensity is down to $1/e$ of the maximum intensity at about $2\epsilon_F$ below the Fermi edge.

Our results essentially confirm the conclusion by Stott and March [3] that the shape of the intensity curve in general should not be very much affected by the core hole, and our results also indicate that the total intensity enhancement is quite small, contrary to the results by Glick, Longe and Bose [4].

It should be emphasized that the present calculation does not take the edge effects, just discussed by Dr. Mahan, into account. Actually if we consider the Anderson orthogonality catastrophe [5], the coefficient α in eq (2) should be equal to zero. If, however, the edge effects are restricted to a narrow energy region, as indicated by the experimental data, the approximations employed here should not be serious.

3. References

[1] Hedin, L., Sol. State Comm. **5**, 451 (1967).

[2] Hedin, L., in Soft X-Ray Band Spectra, D. Fabian, Editor, (Academic Press, New York, 1968).

[3] Stott, M. J., March, N. H., in Soft X-Ray Band Spectra, D. Fabian, Editor, (Academic Press, New York, 1968).

[4] Glick, A. J., Longe, P., and Bose, S. M., in Soft X-Ray Band Spectra, D. Fabian, Editor, (Academic Press, New York, 1968).

[5] Anderson, P. W., Phys. Rev. Letters **18**, 1049 (1967).

Discussion on "Effect of the Core Hole on Soft X-Ray Emission in Metals" by L. Hedin and R. Sjöström (Chalmers University, Sweden)

B. Mozer *(NBS):* I am a little confused about the Anderson catastrophe. I agree that if you have a polarized state it might well be orthogonal to the pure state you started with before the interaction was turned on. But are you not really interested in the dipole matrix element, or interaction Hamilton matrix elements between N* and N?

L. Hedin *(Chalmers Univ.):* Yes, but since the states are orthogonal, then independently of the matrix elements, you actually have the result, according to Anderson's theorem, that the intensity vanishes at the edge. This is, however, not the full story as just discussed by Mahan, in the *vicinity* of the edge the intensity has a power law behavior and may show a singularity.

B. Mozer *(NBS):* I think you have a problem. You have a problem that there are bound states. You get into the time dependence of the way things go. I forgot to say that the N* state is orthogonal to N. That is quite true, but you are interested in a matrix element that carries you from a case where you have no radiation in emission to a final state where you have a built-up hole in the core and a gamma ray floating around.

R. A. Ferrell *(Univ. of Maryland):* As a many-body system, suppose we have N + 1 electrons; we calculate the dipole moment for the (N+1)th electron but the contributions from the remaining N electrons are in terms of their overlap from their initial to final states. Anderson pointed out that that vanishes. It is a many-body effect. In other words, if one electron makes a transition you also have to consider what happens to all the others. Here you just have to calculate the overlap and that vanishes when you suddenly change the potential. I think you would agree with that, Dr. Hedin.

L. Hedin *(Chalmers Univ.):* Yes.

B. Mozer *(NBS):* I am surprised at that. Hartree-Fock method wave functions you would still get some overlap that is non-vanishing.

R. A. Ferrell *(Univ. of Maryland):* It is a characteristically many-body effect. Every overlap factor is finite, but the product of an infinite number of such factors, each less than unity, vanishes in the limit. One can look at it various ways.

B. Mozer *(NBS):* Most of the Hartree-Fock wave functions away from the impurity are equal to the original wave functions times the phase factor. Consequently, the overlap factor is unity and the product of the infinite number of such factor is unity times the phase factor. The problem is how you handle the region around the impurity and whether or not you have localized impurity states.

Cancellation Effects in the Emission and Absorption Spectra of Light Metals

B. Bergersen

Institute for Theoretical Physics, Göteborg, Sweden

F. Brouers

H. H. Wills Physics Laboratory, Bristol, England

Key words: Electronic density of states; light metals; many-body effects; plasmon satellite; soft x-ray.

1. Summary

The influence of the many-body effects and of the presence of a deep localized hole on the shape of soft x-ray spectra in light metals has been widely discussed recently.

Two observed features of x-ray spectra which cannot be explained by a one electron theory have particularly been emphasized.

(1) The first feature is the low energy tailing of the emission bands superposed by a weak plasmon satellite band. To obtain the correct order of magnitude, Brouers [1] and Longe and Glick [2] have shown that it is essential to take account of strong cancellations due to destructive interferences of the charge clouds surrounding the core hole and the electron performing the transition.

(2) It is now well established theoretically and experimentally that the effect of the core hole sudden switching causes an anomalous behavior near the emission and absorption Fermi edges. If effects causing the width of the core state are neglected together with many-body effects, Nozières and de Dominicis [3] have shown that there will be a power law singularity near the threshold. Independently, we have shown [4], that this result is expected already from simple positive definiteness arguments.

In spite of the success of the theory to explain the low and high energy features of the band, there is not until now a complete theory satisfactory for the whole spectrum. One difficulty in applying conventional many-body theory to x-ray spectra is the occurrence of diagrams diverging throughout the parent band in the first order theory [2]. If, on the other hand, a renormalized theory is formulated to get rid of these divergences, one has no information on the relative areas of the singular and nonsingular part of the spectrum. Nozières and de Dominicis have computed an exact solution only at the Fermi edge and with a rough potential.

We have obtained a number of formal and numerical results which fill a part of the gap between previous treatments and a good and complete theory for the whole band.

Since a first order theory is useful for gaining insight into the structure of the theory and the physical processes which contribute to the emission, we have shown that the divergences of the first order theory can be eliminated. This can be done if certain energy shifts are extracted in a consistent fashion and if one realizes that there is not an exact cancellation of unlinked diagrams between numerator and denominator in the intensity function. It has been shown [5] that this noncancellation is due to the sudden change of the potential when the electromagnetic transition occurs.

In the satellite and tailing region, this divergence free theory coincides with the previous first order theory. In the main band, the effect of electron-electron correlations neglected in the Nozières model and the one-body effect of the core hole can be separated. Contrary to what happens in the satellite region, there is no cancellation effect and it is obvious from the results that

417-156 O - 71 - 19

many-body and one-body effects cannot be treated on the same foot. The electron-electron effects give a correction of the order of 10% to the one-electron Sommerfeld theory [6] but to obtain the correct contribution of the electron-core hole transient potential one has to evaluate a vertex correction which is equivalent to introduce ladder type diagrams as this is done in the positron annihilation theory.

2. References

[1] Brouers, F., Phys. Stat. Sol. **22**, 213 (1967).
[2] Longe, P., and Glick, A. J., Phys. Rev. **177**, 526 (1969).
[3] Nozières, P., and de Dominicis, C., Phys. Rev. **178**, 1097 (1969).
[4] Bergersen, B., and Brouers, F., J. Phys. Chem. **2**, 651 (1969).
[5] Bergersen, B., and Brouers, F., Proc. of the Conf. on X-Ray Spectroscopy, Kiev (1969).
[6] Bergersen, B., Brouers, F., and Longe, P., to be published.

Photoabsorption Measurement of Li, Be, Na, Mg, and Al in the Vicinity of K and $L_{II, III}$ Edges

C. Kunz,* R. Haensel, G. Keitel, P. Schreiber, and B. Sonntag

Deutsches Elektronen-Synchrotron, Hamburg, Germany and Physikalisches Staatsinstitut, II. Institut für Experimentalphysik der Universität Hamburg, Hamburg, Germany

The absorption structure of five light metals has been measured in the vicinity of the onset of K shell respectively $L_{II,III}$ shell absorption. In accord with recent theoretical investigations a peaking of the cross section at the edge is observed for the $L_{II,III}$ edges of Na, Mg, and less pronounced for Al. There is structure of a different type at the K edges of Li and Be.

Key words: Aluminum (Al); beryllium (Be); electronic density of states; electron synchrotron light; K spectra; light metals; lithium (Li); L spectra; magnesium (Mg); photoabsorption; sodium (Na); transmission measurements.

Recent theoretical investigations [1-10] have shed new light on the old problem of the absorption and emission structure near the onset of inner shell transitions in simple metals. As the results are completely symmetric for emission and absorption we shall discuss here only the absorption behavior. The essential improvement of these theories is that they include the influence of the deep level hole potential on the electron states near the Fermi surface. As the charge of this hole is shielded by the conduction electrons the potential is confined to a small region around the excited atom. This implies that mainly the final states of s symmetry are influenced by this potential. As a consequence, the onset of p-electron transitions (e.g., $L_{II,III}$ edges) is expected to show up as an infinite singularity instead of a simple discontinuity. The result is [1-10]

$$\mu \propto \frac{1}{\Delta E^{\alpha}} \tag{1}$$

in the region immediately following the onset. ΔE is the distance from the onset and α a positive exponent approximately equal to 1/2 [9]. (Actually a prominent peak rather than a singularity is expected due to Auger and temperature broadening.) On the other hand no singularity should occur at the onset of s-electron transitions since for them α is expected to be negative and small. More details on the theoretical background of these anomalies are given in other papers at this conference.

Optical absorption at the $L_{II,III}$ edges of Na, Mg, Al, and at the K edges of Li, Be has been investigated for several decades. Because of the inherent experimental difficulties in the XUV range, many of these results are in disagreement with each other. As the situation has improved with the availability of electron synchrotrons as intense continuous light sources, it appeared desirable to investigate these materials in the light of recent theoretical interest. Our experiments were performed at the 7.5 GeV electron synchrotron DESY [11,12]. The results reported were obtained by means of transmission measurements on thin evaporated films. Details of the experimental procedure will be given elsewhere.

Figures 1 to 3 show the absorption coefficient of Na, Mg and Al near the $L_{II,III}$ edges. The spectra of Na [13] and Mg are very similar in shape. A peaking toward the edge, as postulated by the theory, is clearly recognized for both metals. The peaking is less pronounced for Al. The spectra, as shown, were taken with the samples at 77 K. The structure is complicated, due to the spin orbit splitting of the ground state. It should be noted that the intensity ratio of L_{III}:L_{II} is not 2:1 as expected from simple statistics but 3.1:1 for Na, 2.8:1 for Mg, and 2.5:1 for Al.

As present theories give no prediction about how the singularity of eq (1) should merge into the normal absorption behavior for large values of ΔE, we have tried to fit our results to a tentative law:

$$\mu = \mu_0 + \frac{a}{\Delta E^{1/2}} \tag{2}$$

*Present address: Department of Physics and Astronomy, University of Maryland, College Park, Maryland 20742.

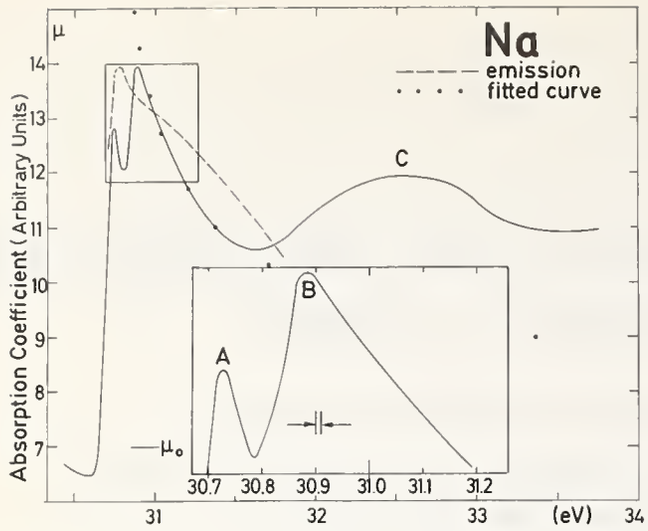

FIGURE 1. *Photoabsorption of* Na *in the neighborhood of the* $L_{II, III}$ *edge.*

Included is the emission curve given by Crisp and Williams [14]. The dots show the best fit of the experimental data by a function given by eq (2).

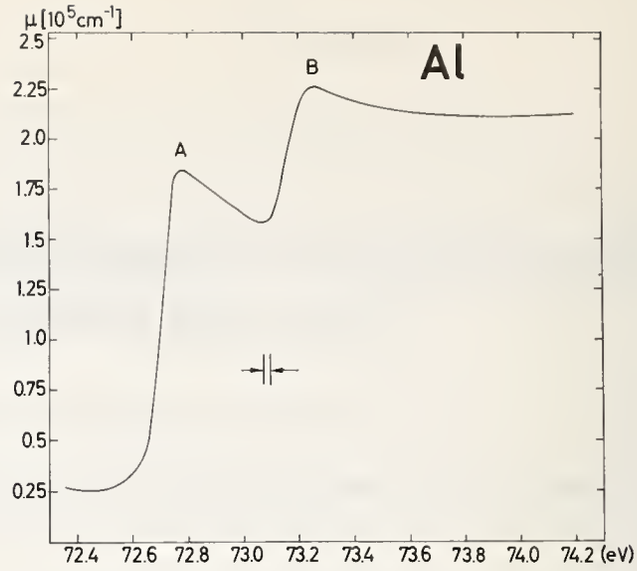

FIGURE 3. *Photoabsorption of* Al *in the neighborhood of the* $L_{II, III}$ *edge.*

for Na and Mg. The best fit is indicated in figures 1 and 2 by dots together with the level of μ_0.

In order to compare our results with emission data we have reflected the energy axis in these data and brought the L_{III} edges into coincidence for Na [14] and Mg [15]. Peaks are seen also in emission, but they are less pronounced.

In the results of earlier absorption measurements on Na [16] and Mg [17] the peak at the edge can be seen, but no special attention has been attributed to it. For Al only the plate density curve of Codling and Madden [18] shows a faint peak at the edge.

The absorption curves near the K edges of Li and Be are shown in figures 4 and 5. The samples were cooled to 77 K. Beryllium shows a peak which is clearly separated from the onset of absorption. Therefore it cannot be attributed to the type of singularity given by eq (1). This peak, which has been found previously by other authors [19,20], may be associated with a density of states maximum above the Fermi surface as shows up in band calculations [21,22].

The spectrum of Li also shows a peak above the edge. Band calculations indicate [23] that it could be caused by a singular point above the Fermi surface. In comparison to the Be spectrum, no shoulder can be seen; the edge appears to be very broad. We do not think that we can count the smooth rise of the edge as evidence for a negative value of α in eq (1). This is because of the fact that at least part of the width may be due to Auger broadening as we have found similar widths for exciton peaks at the K edge of Li halides

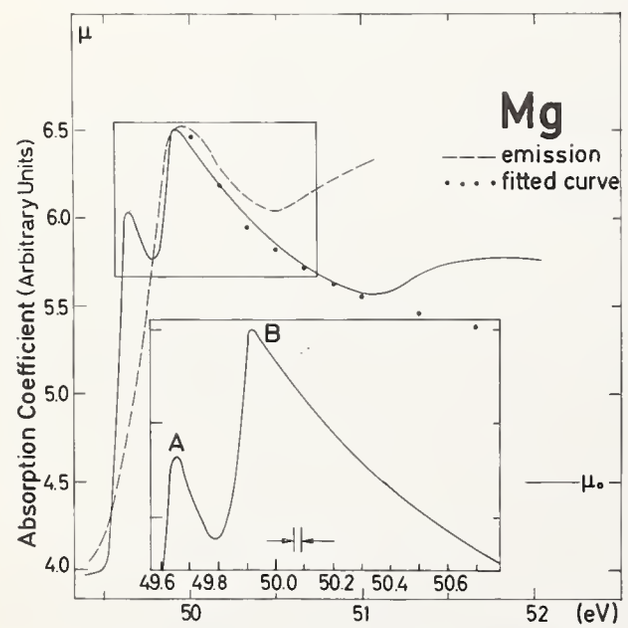

FIGURE 2. *Photoabsorption of* Mg *in the neighborhood of the* $L_{II, III}$ *edge.*

Included is the emission curve given by Watson et al. [15]. The dots show the best fit of the experimental data by a function given by eq (2).

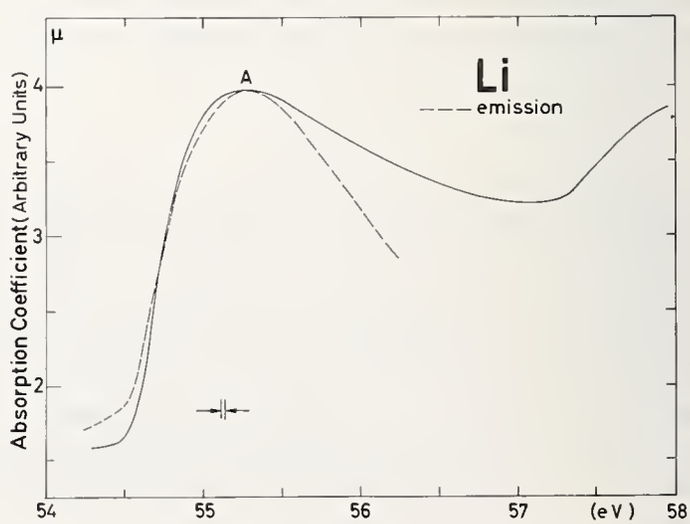

FIGURE 4. *Photoabsorption of* Li *in the neighborhood of the* K *edge.*

Included is the emission curve given by Aita and Sagawa [25].

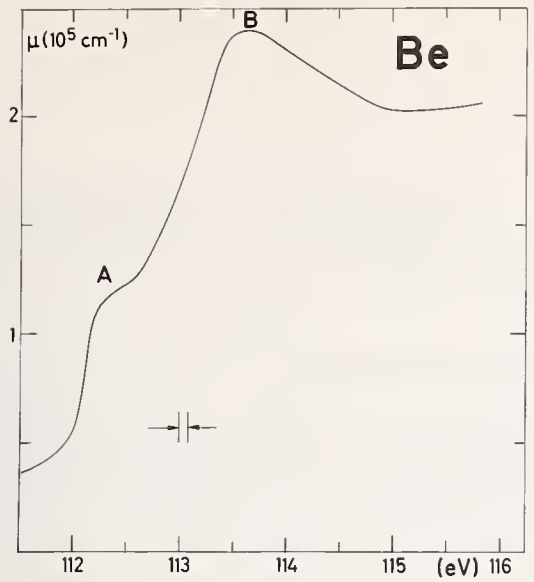

FIGURE 5. *Photoabsorption of* Be *in the neighborhood of the* K *edge.*

[24]. Here again the comparison with emission data [25] has been performed in figure 4. These show, quite similarily, a smooth behavior at the edge.

Acknowledgments

We wish to thank the directors of the Deutsches Elektronen-Synchroton and the Physikalisches Staatsinstitut, especially Professor P. Stähelin, for their interest in this work and for valuable support of the synchrotron radiation group. Thanks are also due to the Deutsche Forschungsgemeinschaft for financial support.

References

[1] Mahan, G. D., Phys. Rev. **163**, 612 (1967).
[2] Mizuno, Y., and Ishikawa, K., J. Phys. Soc. Japan **25**, 627 (1968).
[3] Roulet, B., Gavoret, J., and Nozières, P., Phys. Rev. **178**, 1072 (1969).
[4] Nozières, P., Gavoret, J., and Roulet, B., Phys. Rev. **178**, 1084 (1969).
[5] Nozières, P., and De Dominicis, C. T., Phys. Rev. **178**, 1097 (1969).
[6] Bergersen, B., and Brouers, F., J. Phys. Chem. Ser. 2, **Vol. 2**, 651 (1969).
[7] Friedel, J., Comments on Solid State Physics **2**, 21 (1969).
[8] Schotte, K. D., and Schotte, U., Phys. Rev. **182**, 479 (1969); also private communication.
[9] Glick, A. J., and Ausmann, G., Phys. Rev., to be published.
[10] Hopfield, J. J., Comments on Solid State Physics **2**, 40 (1969).
[11] Haensel, R., and Kunz, C., Z. Angew. Phys. **37**, 3449 (1966).
[12] Godwin, R. P., in Springer Tracts in Modern Physics, **Vol. 51**, G. Höhler, Editor, (Springer, Heidelberg, 1969).
[13] See also: Haensel, R., Keitel, G., Schreiber, P., Sonntag, B., and Kunz, C., Phys. Rev. Letters **23**, 528 (1969).
[14] Crisp, R. S., and Williams, S. E., Phil. Mag. **6**, 365 (1961).
[15] Watson, L. M., Dimond, R. K., and Fabian, D. J., in Soft X-Ray Band Spectra, D. J. Fabian, Editor, (Academic Press, 1968).
[16] O'Bryan, H. M., Phys. Rev. **57**, 995 (1940).
[17] Skinner, H. W. B., and Johnston, J. E., Proc. Roy. Soc. **A161**, 420 (1937).
[18] Codling, K., and Madden, R. P., Phys. Rev. **167**, 587 (1968).
[19] Sagawa, T., et al., J. Phys. Soc., Japan **21**, 2602 (1966).
[20] Swanson, N., and Codling, K., JOSA **58**, 1192 (1968).
[21] Loucks, T. L., and Cutler, P. M., Phys. Rev. **133**, A819 (1964).
[22] Terrell, J. H., Phys. Rev. **149**, 526 (1966).
[23] Rudge, W. E., Phys. Rev. **181**, 1024 (1969).
[24] Haensel, R., Kunz, C., and Sonntag, B., Phys. Rev. Letters **20**, 262 (1968).
[25] Aita, O., and Sagawa, J. Phys. Soc. Japan **27**, 164 (1969).

Optical Absorption of Solid Krypton and Xenon in the Far Ultraviolet

C. Kunz,* R. Haensel, G. Keitel, and P. Schreiber

Deutsches Elektronen-Synchrotron, and Physikalisches Staatsinstitut, II. Institut für Experimentalphysik der Universität Hamburg, Hamburg, Germany

Key words: Electronic density of states; electron synchrotron light; krypton; optical absorption; xenon.

We have performed an experimental comparison of the absorption behavior of both solid and gaseous krypton and xenon in the far ultraviolet using the 7.5 GeV electron synchrotron DESY as light source. We have measured Kr from the onset of $3d$ electron transitions ($\sim$ 90 eV) to 128 eV and Xe from the onset of $4d$ electron transitions ($\sim$ 60 eV) to 155 eV. The most remarkable feature in the gas absorption of Xe the broad hump [1] at 100 eV, where most of the oscillator strength is concentrated, is virtually pertained in the solid. This maximum has previously been attributed [2] to the delayed d to f transitions which are suppressed at the onset due to a centrifugal barrier in the atom. Our result gives an experimental justification for the application of atomic calculations to a solid in the region far above the onset.

Part of the fine-structure which is superimposed onto the low energy rise of this hump has been identified for Xe gas as double excitations [3]. It coincides with structures in the solid in energy position but not in shape. Most of the structure near the onset does not agree in gas and solid, but the first prominent lines almost coincide for both Kr and Xe. This leads to the identification of Frenkel type excitons in the solid. Also Wannier exciton aspects are recognized in the spectra. Other members of a series show up especially clearly in Kr. An analysis made with the help of Fowler's band calculation [4] has led us to the conclusion that they are members of a second class exciton series ("forbidden excitons" according to Elliot [5]). Details of this work are to be published in the Physical Review.

*Present address: Department of Physics and Astronomy, University of Maryland, College Park, Maryland 20742.

References

[1] Ederer, D. L., Phys. Rev. Letters **13**, 760 (1964).
[2] Cooper, J. W., Phys. Rev. Letters **13**, 762 (1964).
[3] Codling, K., and Madden, R. P., Appl. Opt. **4**, 1431 (1965).
[4] Fowler, W. B., Phys. Rev. **132**, 1591 (1963).
[5] Elliot, R. J., Phys. Rev. **108**, 1384 (1957).

The Piezo Soft X-Ray Effect

R. H. Willens

Bell Telephone Laboratories, Incorporated, Murray Hill, New Jersey 07974

In principle the soft x-ray emission spectrum should reveal the electronic structure of a material below the Fermi surface. In general, but for a few exceptions, the beginning and termination of the band structure are masked by low and high energy tails. The Van Hove singularities and critical points are unresolved due to effects such as Auger, lifetime and instrumental broadening.

The modulation of the L_{III} emission band of polycrystalline copper by an alternating elastic strain has recently been measured. Two effects are observed. First, there is an overall band shift which gives a measure of the deformation potentials. The band shift is not uniform as different sub-bands can shift varying degrees. For an applied load of 12,000 psi in uniaxial tension, the shift of the high energy side of the band is 0.015 eV and the low energy side is 0.010 eV. Because of the preferred orientation and polycrystalline nature of the sample, the exact microscopic sample is isotropic with a Young's modulus of 20×10^6 psi, the average deformation potential is 25 eV at the top of the band and 17 eV at the bottom of the band. Secondly, superimposed on this band shift is structure which is unresolved in the normal emission spectrum. The origin of this structure is presumed to be from positions in the electronic structure which are extra sensitive to strain as far as altering the x-ray emission. This would be at Van Hove singularities or critical points where a high degree of degeneracy and wave function mixing is prevalent which can be changed by the symmetry alteration of the lattice due to strain. Comparison between the theoretical band structure calculations of copper and the emission structure due to strain modulation show several similarities.

The application of this technique to alloys should be useful for studying their electronic structure.

Key words: Copper; electronic density of states; mechanical strain; modulation technique; nickel; soft x-ray.

1. Introduction

X-ray emission, at first glance, seems to be a simple and easily interpretable technique to probe the energy band structure of solids below the Fermi energy. The states involved in the emission process are fairly well defined, one of them being a core level. Surface preparation and contamination should not be as critical as that required for low energy optical and photoemission studies as the active volume can extend several microns into the material. However, on closer investigation, the interpretation of the emission spectra is not as simple as might be inferred from the one-electron description of a solid. The shape of the emission spectrum is not a good representation of the density of states due to such effects as variation of the transition probability within the band, life time broadening distortions mainly due to Auger transitions, and many body effects [1]. Peaks in the density of states which would correspond to Van Hove singularities in the electronic structure are usually unresolved. Also, except for a few simple metals like aluminum and magnesium, the beginning and terminus of the band are masked by the low and high energy tails.

Within the past five years, derivative techniques, which are the result of modulating a measured property by an external parameter, have come into prominence because of the enhanced structure which can be obtained. These modulation experiments have been applied mostly to optical studies like electroreflectance [2], thermoreflectance [3], and piezoreflectance [4]. The piezo soft x-ray effect is in the category of modulation experiments. It corresponds to the modulation of the emission spectrum due to an alternating mechanical strain. The intent is to reveal structure which is unresolved in the normal emission spectrum which can be correlated with Van Hove singularities or critical points and the Fermi energy. When a mechanical strain is applied to a material the sub-bands shift in energy as a consequence of the deformation potentials. The shifts are not uniform and depend both upon the band position and the strain conditions. Also, the strain alters the

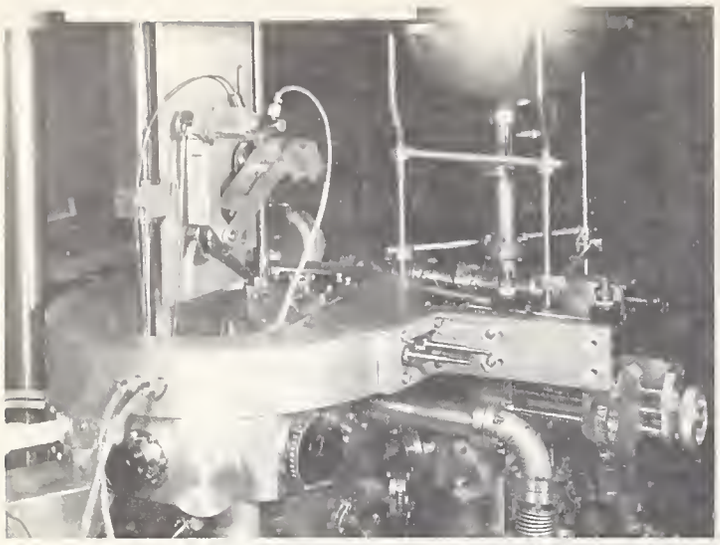

FIGURE 1. *Piezo soft x-ray spectrometer.*

symmetry of the lattice and may split formerly degenerate levels which would be most prevalent at Van Hove singularities or critical points. This could be in the form of either orbital of k-space degeneracy. Extra sensitivity of these locations as far as altering the x-ray emission due to strain could be attributed to either greater displacement with strain than adjacent energy levels or altering of the matrix element of the x-ray transition due to changing symmetry of wave function mixing of degenerate levels. Strain effects such as these were first observed accidentally in optical studies of the excitonic absorption in germanium [5,6] and the principle has been subsequently applied to numerous optical experiments [4,7]. The experiments reported here, which are very encouraging, are still in the early stages of interpretation and future experiments will disclose the usefulness of this technique to reveal the energy band description of metals and alloys.

2. Experimental Apparatus

Several experimental requirements must be satisfied in order to observe the piezo soft x-ray effect. First, the order of magnitude of the effect (between one part in a thousand to one part in ten thousand) requires the emission spectrum be excited to a high counting rate in order to perform the experiment in a reasonable time. This means that direct excitation by electrons is preferable. Secondly, a single scan of an emission band needs several days so the rate of contamination build-up on the specimen surface must be reduced to a minimum and finally, care must be taken to minimize any distortion strains transmitted to the spectrometer by the specimen stressing device.

The spectrometer is shown in figure 1 and schematically in figure 2. The spectrometer radius is 6 inches and the analyzing crystal is bent to the approximate focusing radius of 12 inches. The sample remains stationary and the analyzing crystal mount moves in a linear motion with the current angular motions transmitted to crystal and detector to maintain the focusing conditions. The specimen is excited directly by electrons at an incidence angle of about 75 to 80° with the specimen surface. The detector is a flow proportional counter with a stretched polypropolene window. The counter tube gas is usually P-10 maintained at a reduced pressure. The detector and analyzing crystal are located in a low vacuum chamber, the order of 10 microns pressure. The sample chamber box is isolated from the low vacuum chamber and pumped to a vacuum of 10^{-9} mm by ion and titanium sublimation pumps. The x rays from the sample pass through a stretched polypropolene window which separates the two vacuum systems. A liquid nitrogen cold finger in the proximity of the sample was necessary to reduce the contamination rate. Typically, there is less than 4% change in the intensity over the period of one week for the emission spectrum reported here. The sample is stressed by the force from a hydraulic cylinder which is actuated with a high speed solenoid valve. The loading system can apply a maximum stress of 40,000 psi (the specimen cross section is $1/8'' \times 1/4''$). The time required to load or unload the sample is about 15 msec. The loading of the sample is done in a coaxial manner, so that negligible distortion strains are transmitted to

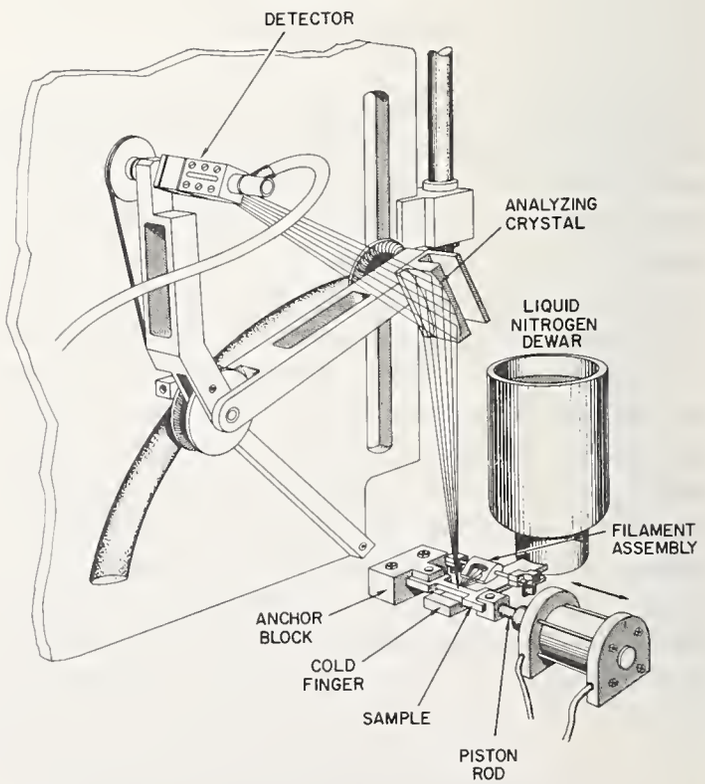

FIGURE 2. *Schematic of piezo soft x-ray spectrometer.*

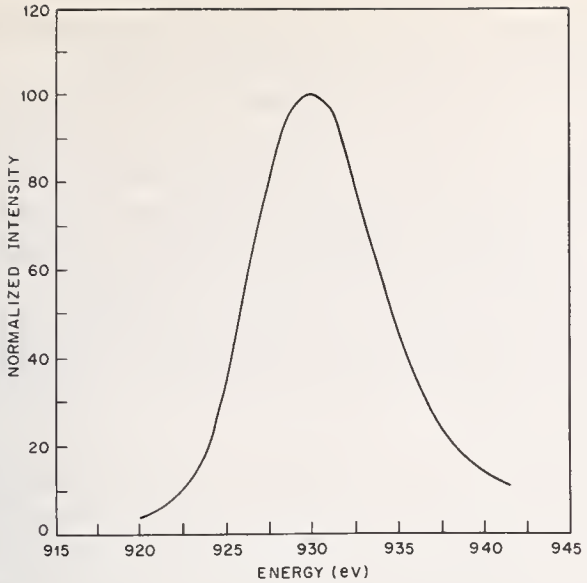

FIGURE 3. *Copper L_{III} emission band.*

the spectrometer which might introduce spurious emission intensity changes.

3. Experimental Results

The first experiments were performed on polycrystalline copper [8]. The L_{III} emission band, which has a maximum intensity at 930.1 eV [9], and corresponds to transitions between the $3d$-$4s$ levels to the $2p_{3/2}$ level, was step scanned in wavelength increments of 0.002 Å.

The analyzing crystal was KAP ($2d = 26.8$ Å). At each position the sample was alternately loaded, to a stress of 12,000 psi in tension, and unloaded 100 times at 10 sec intervals. The difference between the intensity under the strained and unstrained state was determined by subtracting the averaged corresponding readings. The magnitude of the strain effect required between 10^7 to 10^8 counts to be accumulated at each step position to assure statistical significance.

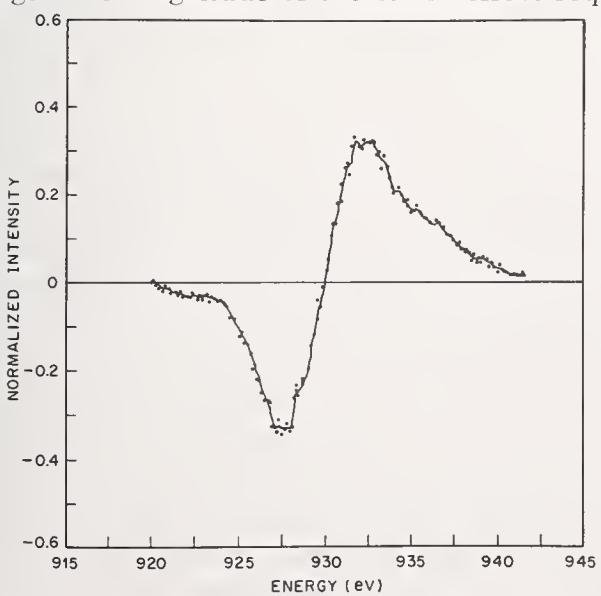

FIGURE 4. *Modulation of L_{III} emission band of copper due to an alternating strain.*

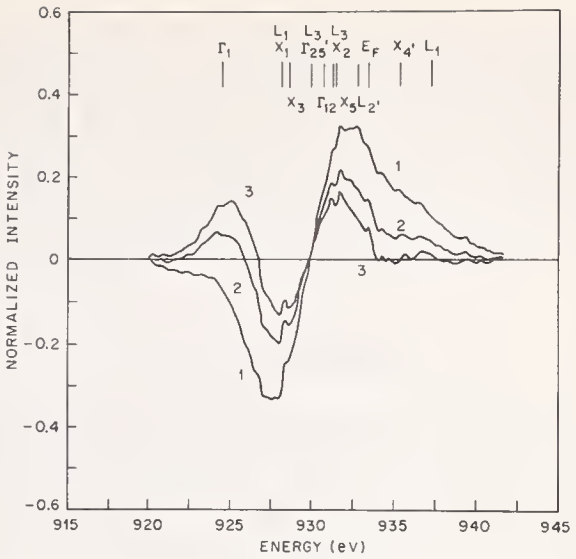

FIGURE 5. *Subtraction of derivative of emission band from modulation curve.*

Curve 1 is original curve. Curves 2 and 3 are resultant subtractions assuming shifts of 0.010 and 0.015 eV, respectively. Location of Fermi energy and Van Hove singularities are from Burdick's calculation (ref. [11]).

Figure 3 shows the observed emission spectrum normalized to a peak value of 100. It is completely structureless without any indication of the location of the Fermi energy which should be located somewhere in the region of 932 to 934 eV as determined by x-ray absorption measurements [10]. The lack of any indication of the Fermi energy is probably masked by satellite emissions or many body effects. There should only be natural lifetime and instrumental broadening at this energy as Auger processes would not contribute to the lifetime broadening. Figure 4 shows the change of the emission intensity which results when the copper specimen is stressed in tension. The modulation curve appears to be fairly representative of the derivative of the emission peak. There is also apparently additional structure present. One prominent feature, besides the small wiggles and peaks, is the abrupt change in slope that occurs at about 934 eV. For the same copper sample this curve reproduces itself when rescanned, including the fine structure. Additional copper samples show different modulation curves. The gross shape remains the same and an apparent sudden change of slope at about 934 eV is evident, but there is significant modification in fine structure and intensity. This is attributed to the difference in crystallographic texture between specimens.

If the modulation curve was the result of a rigid shift of the emission band, then the curve should exactly be the derivative of the emission band. To check this possibility, the product of the derivative of the emission

band and a suitable constant, which would correspond to the energy shift of the band, are subtracted from the modulation curve in an attempt to produce a null curve. Figure 5 shows the attempt to carry out this nulling procedure. Curve 1 is the original curve and curves 2 and 3 are the resultant subtraction curves assuming shifts of 0.010 and 0.015 eV, respectively. It is apparent that no appropriate uniform or smoothly varying band shift can account for the total modulation curve. The energy shift which reduces most of the effect to zero is 0.010 and 0.015 eV at the bottom and top of the band, respectively. Since the sample is polycrystalline, has preferred orientation, and elastically anisotropic, the microscopic strain conditions are not known. Assuming the sample is isotropic with a modulus of 1.38×10^{11} dynes/cm^2, the average deformation potential is 25 eV at the top of the band and 17 eV at the bottom. These numbers can only be considered approximate until experiments with single crystals are performed.

The remaining portion of the modulation curve which cannot be nulled by the derivative subtraction technique must be associated with regions in the band which are extra sensitive to strain as regards altering the x-ray emission intensity. This could be at the Fermi energy and Van Hove singularities or critical points. There is some arbitrariness between the energy scale as measured by x-ray emission and the scales used in the theoretical band structure calculations. Burdick [11] has correlated his energy scale to the x-ray emission scale by matching the peak in the density of states with the peak in the emission band. Burdick's calculated values for the Fermi energy and Van Hove singularities are indicated in figure 5. The abrupt slope change at 933.8 matches the Fermi energy and much of the fine structure matches with the Van Hove singularities. Whether or not this is the correct match should be revealed by investigations of single crystals.

The L_{III} emission spectrum of nickel is shown in figure 6. It is quite similar to the copper emission spectrum except there is a noticeable satellite on the high energy tail. The origin of this satellite is presumably due to multiple ionizations produced by Auger transitions from the initial L_I and L_{II} ionizations [12]. The peak in the emission band occurs at 14.561 Å or 851.5 eV [13]. X-ray absorption measurements [14] indicate that the Fermi energy is close to the emission peak (within 1 eV).

The piezo soft x-ray effect in nickel is quite different than that observed for copper. Generally, two different types of results are seen depending upon the initial condition of the nickel sample. Figure 7 shows the modulation curve for a nickel sample which was heavily cold worked by rolling and measured using the same experimental conditions as previously mentioned for copper. Figure 8 shows the modulation curve when the nickel specimen is not subject to the same degree of cold work. As can be seen from the figures, there are two modulation peaks. The magnitude of the effect increases about 7 fold for the sample which is not heavily cold worked and the fine structure which is present on figure 6 is unresolved. Why there is such a difference between the two specimens will be discussed later. It is quite evident that the strain must be altering the matrix element for the x-ray transition since the total emitted intensity is greater when the specimen is under tension (in compression the modulation curve is negative). The high energy modulation peak evidently corresponds to the satellite emission of nickel and the low energy peak to the normal $3d$-$4s$ to $2p_{3/2}$ transition. The

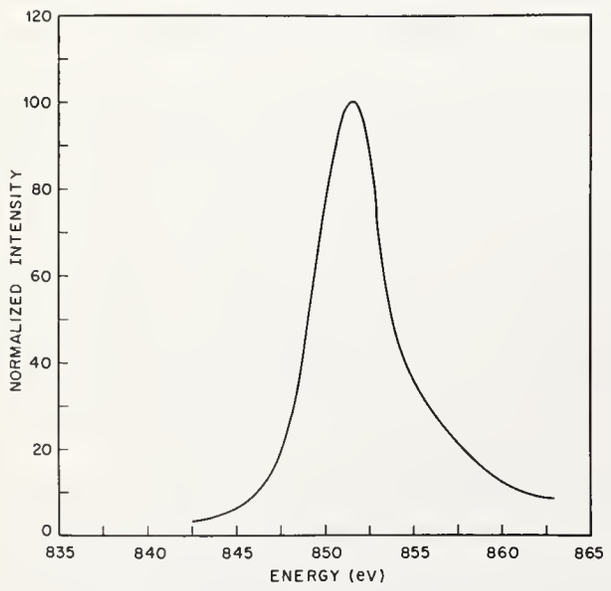

FIGURE 6. *Nickel L_{III} emission band.*

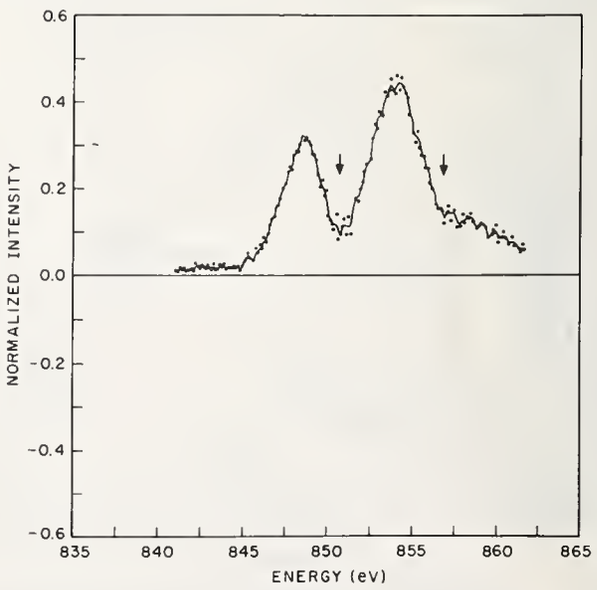

FIGURE 7. *Modulation of emission band for heavily cold-worked nickel.*

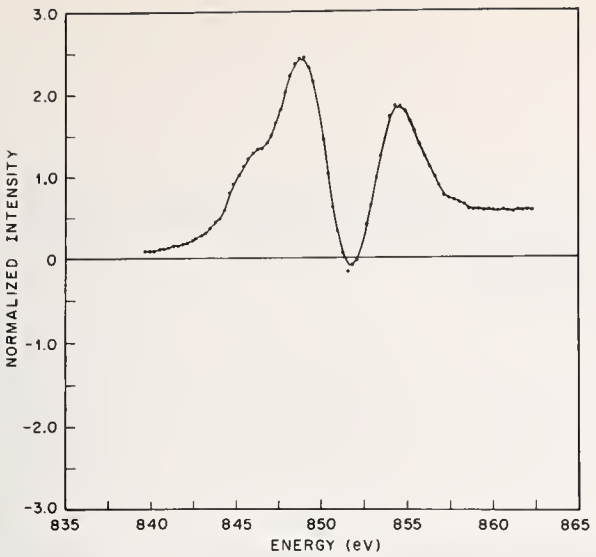

FIGURE 8. *Modulation of emission band for annealed nickel.*

separation of these two peaks is about 6 eV and the relative intensities of the two vary from sample to sample, probably dependent on the preferred crystallographic orientation.

First, refer to figure 7, which corresponds to the heavily cold worked sample. This sample is mostly exhibiting fine structure mostly associated with mechanical strain. The high energy modulation peak has a break at 856.9 eV and another at about 851 eV which is indicated by the arrow on the figure. This feature is also present on the high energy side of the low energy modulation peak. Assuming that this feature is the spin exchange splitting, the measured value, from extrapolations of the modulation curve, is 0.6 ± 0.05 eV. This agrees very well with the theoretical values of 0.4 or 0.6 eV [15]. The same kind of derivative analysis as that used for copper cannot be used for nickel because the gross shape of the curve is not representative of the derivative. However, one can attempt to null portions of the modulation curve by the derivative scheme assuming that the high and low energy parts of the emission curve shift in opposite directions with strain. By doing this, it becomes evident no simple shifts can null the modulation curve. The fine structure which can be readily seen on the modulation curve becomes enhanced as well as the abrupt changes in slope which occur on the high energy side of each modulation peak. The high energy modulation peak has its abrupt increase of intensity at 856.9 eV.

The mechanism for the increased piezo effect for the nickel sample not subject to the heavier cold work has been discussed in detail elsewhere [16]. Apparently, rather than mechanical strain being the dominant mechanism for producing the modulation, the magnetization of the sample rotates. This alters the spin-orbit splitting of the sub-bands and displaces the total band structure to a much greater extent than could be produced by mechanical strain, resulting in changes in x-ray emission throughout the total band. This explanation is tentative at this time and further investigation is required by doing solely a magnetic modulation experiment.

4. Conclusions

A new experimental technique has been developed to probe the energy band structure of solids. Although the interpretation of the results are still in a primitive state, it is evident that this method can be a useful means for studying the electronic structure of metals and alloys. One of the notable features of these experiments is that we have transformed a structureless emission spectrum to a modulation curve which contains considerable structure and awaits theoretical interpretation.

5. Acknowledgments

I wish to express my appreciation to H. Schreiber, E. Buehler, and D. Brasen for experimental assistance and J. H. Wernick and C. Herring for encouragement and helpful discussions.

6. References

[1] Rooke, G. A., J. Phys. C: Phys. Soc. (London) Proc. **1**, 767 (1968).
[2] Seraphin, B. O., and Hess, R. B., Phys. Rev. Letters **14**, 138 (1965).
[3] Batz, B., Solid State Commun. **4**, 241 (1965).
[4] Gerhardt, U., Phys. Letters **9**, 117 (1964).
[5] Zwerdling, S., Lax, B., Roth, L. M., and Button, K. J., Phys. Rev. **114**, 80 (1959).
[6] Macfarland, G. G., McLean, T. P., Quarrington, J. E., and Roberts, V., Phys. Rev. Letters **2**, 252 (1959).
[7] Gobeli, G. W., and Kane, E. O., Phys. Rev. Letters **15**, 142 (1965).
[8] Willens, R. H., Schreiber, H., Buehler, E., and Brasen, D., Phys. Rev. Letters **23**, 413 (1969).
[9] Sandström, A. E., Handbook der Physik, edited by S. Flügge (Springer-Verlag, Berlin, Germany, 1957), **Vol. 30**, pp. 186-187; Fisher, D. W., J. Appl. Phys. **36**, 2048 (1965).
[10] Cauchois, Y., Phil. Mag. **44**, 173 (1953).
[11] Burdick, G. A., Phys. Rev. **129**, 138 (1963).
[12] Liefield, R. J., Soft X-Ray Band Spectra, edited by D. J. Fabian (Academic Press, New York, 1968), p. 133.
[13] Bearden, J. A., Rev. Mod. Phys. **39**, 78 (1967).
[14] Cauchois, Y., and Bonnelle, C., Comptes Rendus Acad. Sci. Paris **245**, 1230 (1957).
[15] Zornberg, E. I., Phys. Rev. **B1**, 244 (1970).
[16] Willens, R. H., to be published.

Soft X-Ray Band Spectra and Their Relationship to the Density of States *

G. A. Rooke

Metallurgy Department, University of Strathclyde, Glasgow[1]

The paper concentrates on the similarities and differences between the one-electron spectrum and the density of states; many-body effects, although important, are listed but they are not considered in detail. It is shown that the only reliable information about the density of states that can be obtained from soft x-ray spectroscopy are the energies of the Fermi surface and the van-Hove singularities, although the shape of the density of states can be derived indirectly from the energies of the van-Hove singularities.

It is the differences between the density of states and the one-electron spectra that may prove to be most important. These differences can give information about the symmetry and the local nature of the screening electrons. This is particularly interesting when studying alloys.

The Li K, the Al L_{23} and the Zn L_3 spectra are given as examples which illustrate the above arguments. Finally, a brief discussion on the soft x-ray spectra from the Al-Mg system show how the results may be used to study alloys.

Key words: Alloys; auger transitions; density of states; many-body interactions; plasmons; singularities; soft x rays.

1. Introduction

Before commencing my discussion, I would like to state our objectives in attempting to measure the density of states: they are

(a) to compare experiments that are in some way related to the density of states;

(b) to derive some information about concepts of a more fundamental nature, the band structure, the effective potential, *etc.*, and

(c) to attempt to predict the properties of other metals and alloys.

It is important to bear these in mind, as sometimes our objectives can be achieved more directly by not making use of the density of states.

It will be remembered that when transitions involving atomic core states occur, x-rays may be emitted or absorbed. The x-rays have an energy equal to the energy difference between the two states involved in the transition. If one of the states lies in the valence band or the conduction band, a band spectrum is produced (see fig. 1). Experimentally, better energy resolution is obtained from the band spectra with lower energies; these are called soft x-ray band spectra. Although this paper specifically discusses soft x-ray spectra, the concepts are applicable to all band spectra.

For an introductory review of soft x-ray band emission spectroscopy, I recommend either Skinner [1] or Tomboulian [2]. An excellent bibliography of Yakowitz and Cuthill [3] reviews the literature up to 1961. Some of the most recent work in the field is described in a conference proceedings edited by Fabian [4]. All of these omit very interesting Russian work for which no comprehensive review is known to me.

2. Many-Body Interactions

The many-body interactions are treated in this paper as uninteresting complications that tend to hide the information we are seeking. Each interaction is considered as a perturbation on the one-electron spectrum.

The interactions between individual electrons create two types of perturbations on the spectra, the excited initial and final states, which directly affect the spectra, and exchange and correlation, which affect the spectra

*An invited paper presented at the 3d Materials Research Symposium, *Electronic Density of States*, November 3-6, 1969, Gaithersburg, Md.

[1] Present address: Ferranti Ltd., Western Road, Bracknell, Berks, U.K.

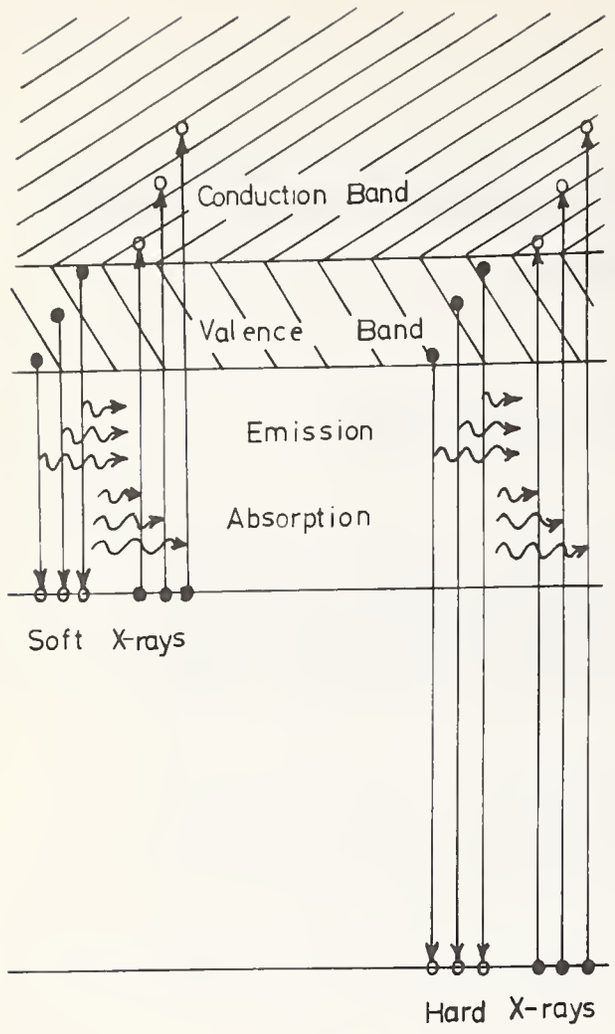

FIGURE 1. *One-electron energy-level diagram showing x-ray transitions.*

through their effects on the band structure. The exchange and correlation only cause trouble when comparing uncorrected one-electron band-structures with experimental results [5]. They are normally allowed for by theoreticians and are only important to experimentalists when they are measuring many-body effects or when they are trying to derive the uncorrected band-structures.

Excited states occur whenever electron transitions occur. For *all* radiating transitions, two single-particle excitations are involved; in emission processes both the initial and the final states are normally excited while in absorption processes the initial state is normally unexcited and the final state contains two single-particle excitations. Each excitation affects the spectrum through its lifetime and through its perturbing effects on the unexcited one-electron spectrum. Three types of one-electron excitation can occur and their effects on the spectra are discussed separately.

First, the hole in the core state perturbs the valence electrons, so that the intensity at the Fermi surface is reduced for K spectra (transitions to 1s-states) and enhanced for L_{23} spectra (transition to 2p-states) [6]. The lifetime of the hole in the core state causes the spectrum to be broadened because of the uncertainty in its energy. If this lifetime is known, it is possible to correct for this broadening [7]. The hole in the core state can only affect spectra that involve x-rays.

Second, a hole in the valence band can be filled by an electron in the same band, provided another valence-band electron is excited into the conduction band, thereby conserving energy; this interaction is called the Auger process. Because of this, there are both holes and excited electrons with energies close to the Fermi energy and this raises the possibility of excitons occurring in the metal. Also, Auger processes shorten the lifetime of the hole and this broadens the spectra considerably. Because many more electrons are capable of filling holes near the bottom of the band than those near the top of the band, the lifetime of a hole near the bottom of the band is shorter and the spectrum is broadened more near the bottom of the band than near the top. It has not yet proved possible to remove the Auger broadening from spectra, because the broadening is not constant throughout the band. Auger broadening is important to any spectroscopy involving the absorption of the ultraviolet light, to x-ray emission spectroscopy and to ion-neutralization spectroscopy.

Third, the scattering of electrons excited into the conduction band is important to any process involving the absorption of radiation. This scattering is very similar to the Auger process; an excited electron falls to an energy level closer to the Fermi energy, giving its energy to another electron which is excited out of the valence band and into the conduction band. The remaining holes and the scattered electrons could form excitons. For any electron emission spectroscopy the scattered electrons can contribute to the spectra and they enhance the spectra near the Fermi edge. In general, the lifetime of the excited states decreases as their energy increases, so that the resultant broadening is not constant throughout the band and is exceedingly difficult to remove.

For each type of optical spectroscopy discussed at this conference, two of these three types of one-electron excitations are involved and for ion-neutralization spectroscopy, four excitations occur.

The first two types of excitations are involved in soft x-ray band emission spectroscopy. The perturbations of the valence band, near the Fermi edge, by the hole in the core state is possibly the cause of the drop in intensity near the Fermi edge in the lithium K spectrum and the cause of the small pip near the Fermi edge in the sodium L_{23} spectrum [6]. It probably contributes more

to the shape of all light metal spectra than to the heavy metal spectra, because the hole represents a larger proportion of the core electrons in the light metals. The core broadening prevents the detection of spectra resulting from transitions to 2s, 3s, *etc.* core states and it also is important in changing the shape of the spectra from heavy metals; the lifetime of the excited state is considerably reduced because of competing non-radiative transitions. Auger broadening is responsible for the low-energy tails in the spectra from metals and this introduces uncertainty into the measurement of the bandwidths.

For other spectroscopic techniques, these excitations are also highly important, their importance depending on both the technique used and the metal examined.

Besides exciting a single electron state, it is also possible to excite the electrons collectively into plasma oscillations. When this occurs, together with the emission of an x-ray photon, the photon loses enough energy to create the plasmon and a satellite spectrum is formed at lower energies [8,9]. Interactions between individual electrons and the plasmons, which are called plasmarons [10], have a measurable effect on the plasmon satellite [11] but not on the parent band.

3. The Density of States and Band Spectra

In order to discuss the relationship between the density of states and the spectra, it is assumed in the remainder of this paper that the effects of the many-body interactions can be corrected for. The word "spectrum" then implies "one-electron spectrum that would result if such corrections were made"; this spectrum has the same width as the valence band, its shape is related to the density of states but it is affected by the transition probabilities.

The similarities between the density of states, N(E), and the one-electron spectrum divided by the cube of the radiation frequency, $\frac{I(E)}{\nu^3}$, are seen by comparing the following equations:

$$N(E) \propto \int_s d^2\mathbf{k} \frac{1}{\nabla_{\mathbf{k}} E} \tag{1}$$

$$I(E)/\nu^3 \propto \int_s d^2\mathbf{k} \frac{1}{\nabla_{\mathbf{k}} E} \left| \int \psi_{\mathbf{k}} \nabla_x \psi_f d\tau \right|^2 \tag{2}$$

where E is the energy of the state with wave vector **k** and the integral is taken over the surface, s, of constant energy, E. For the density of occupied states and for the emission spectrum, the integral is taken over the region of **k** space that lies inside the Fermi surface, while, for the density of unoccupied states and for the absorption spectrum, the integral is taken over the region of **k** space that lies outside the Fermi surface. The square of the modulus of the matrix element, $\int \psi_{\mathbf{k}} \nabla_x \psi_f d\tau$, is the transition probability, whose properties determine the difference between the two functions; the dipole approximation has been assumed.

A striking similarity between the two functions occurs because the integrations are terminated at the Fermi surface; this produces the Fermi edges in the functions. Unfortunately, for some heavy metals, the core-state broadening and the transition probabilities combine to make the Fermi edge almost impossible to measure.

The Brillouin zone effects are also common to both functions; at certain points of high symmetry on the Brillouin zone boundaries, the gradient, $\nabla_{\mathbf{k}} E$, is zero and van-Hove singularities exist at corresponding points in the two functions. Certain van-Hove singularities are of particular interest; in particular the energy of the bottom of the band can be used to estimate the bandwidth and the energy of the top and bottom of the d-band give the width of this band and its relation to the Fermi energy, both of which are of considerable theoretical interest.

Because the matrix element is **k**-dependent, it is not possible to remove the transition probabilities from inside the integral in eq (2). Hence, it is not possible to write the intensity as a product of the density of states and the average transition probability and, even if the transition probabilities are fully known, it is not possible to remove their effects from the spectra. Rooke [12] has shown that the **k**-dependence of the matrix element is large, sometimes changing it from nearly 1 to nearly 0 on the same constant energy curve, so that errors created by removing the matrix element from the integral can be serious.

From the above considerations it can be seen that the detailed density of states cannot be directly derived by using soft x-ray spectroscopy; or by using any form of spectroscopy, for that matter. Sometimes a spectrum and the density of states will have similar shapes and they will certainly have the Fermi edge and some van-Hove singularities in common. If the spectrum changes under different experimental conditions, such as heat or pressure, it may be possible to assume that the changes will be entirely due to the density of states and to obtain a little more information about the density of states in this way. This technique has been used to find the effect of the Fermi-Dirac statistics on the density of states, by heating the target (1) and to find the effect of

417-156 O - 71 - 20

alloying on the density of states. A more sophisticated version of this approach has just been developed by J. H. Willens in Bell Laboratories [13]. In another method for obtaining more information about the density of states, one derives a band structure that fits the measured van-Hove singularities and then uses this to calculate the density of states. However, as Fermi surface techniques are capable of making fine distinctions between band structures, they can also be used to obtain densities of states which are often more accurate than those obtained from soft x-ray spectroscopy. Even though it is only possible to obtain limited information about the density of states, this information is often very interesting. However, it is often even more interesting to examine the information that can be derived by studying the effect of the transition probabilities on the spectra. This information is discussed in the next section.

4. The Transition Probability and the Band Spectra

The differences between the functions defined in eqs (1) and (2) are determined by the matrix element

$$\int \psi_{\mathbf{k}} \nabla_x \psi_f d\tau$$

The integration is taken over all real space and ∇_x is the component of the real-space gradient-operator in the **x** direction.

ψ_f is the wavefunction of the core state and, because of its high symmetry, it is a good approximation to express it as

$$\psi_f(r, \theta, \phi) = R_{n'}(r) Y_{l'}(\theta)\ e^{im'\phi} \tag{3}$$

where $R_{n'}$ (r) is a radical function, $Y_{l'}(\theta)$ is a Legendre polynomial and n′, l′ and m′ are the usual quantum numbers. The radial function has appreciable magnitude only near the center of the atom and the state is localized. Because only one Legendre polynomial is involved, the state can be labeled by atomic notation; 1s, 2p, 3d, *etc.*

$\psi_{\mathbf{k}}$ is the wavefunction of a valence state and it may be expanded as a series of spherical harmonies

$$\psi_{\mathbf{k}} = \sum_{l,\,m} C_l(\mathbf{k})\, a_{l,\mathbf{k}}(r)\ Y_l(\theta)\, e^{im\phi} \tag{4}$$

Normally, only the first three values of l are important. The radial terms are roughly constant throughout real space so that the state is shared by all atoms and is not localized like the core states.

Substituting these expansions of the wavefunctions into the matrix elements gives

$$\int \psi_{\mathbf{k}} \nabla_x \psi_f d\tau \propto \sum_{l,\,m} C_l(\mathbf{k}) \times \int R_{n'}(r) a_{l,\mathbf{k}}(r)\, r^3 dr \times \int Y_{l'}(\theta)\ Y_l(\theta)\ f\binom{\sin}{\cos}\theta\, d\theta \times \int e^{i(m-m')\phi}\, g\binom{\sin}{\cos}\phi\, d\phi \tag{5}$$

where f and g are functions whose form depends on the polarization. Each of these four terms contributes a distinct characteristic to the transition probability. The **k**-dependence of the first two terms, as shown in the last section, prevents the direct derivation of the density of states from the spectra.

The third term is zero unless

$$l = l' \pm 1 \tag{6}$$

This selection rule is particularly important for x-ray transitions, because the core state involved has a well defined symmetry described by a single spherical harmonic. If the core state is an s-state, only p-like states can make the transition to it. Similarly, only s-like and d-like states can make the transition to a p-state.

This selection rule enables us to describe states in terms of partial densities of states; the density of s-states, the density of p-states and the density of d-states. K spectra (transitions to the s-state) give approximate estimates of the density of p-states, while L_{23} or M_{23} spectra (transitions to the 2p or 3p states respectively) give approximate estimates of the density of s and d states.

Because these partial densities of states only approximate to the shape of the spectra, it is not possible to add them and to derive a meaningful density of states. However, this symmetry dependence of x-ray band spectra makes them unique in the information that they can reveal. This is particularly interesting in the case of alloys, for which this characteristic of x-ray spectra should be fully exploited to determine the nature of the screening charges. Further, it is the authors unsubstantiated view, that the extended fine-structure occurring in absorption spectra can also be attributed to this selection rule.

Besides creating gross features in the spectra, this selection rule modifies the magnitudes of the van-Hove singularities. The symmetry of the crystal dictates that the states associated with points of high symmetry in the Brillouin zone will have high symmetry themselves. Thus, some of these states are almost entirely p-like while others are s-like or s and d like. If a state is entirely s-like, it will not contribute to a K spectrum and, if it

is associated with a van-Hove singularity, that singularity will not be seen in the K spectrum. Similarly, as most states contain a mixture of symmetries, van-Hove singularities associated with states that are entirely p-like will be exaggerated in the K spectra. The reverse situation occurs for L_{23} or M_{23} spectra, for which p-like singularities will not be observed and s and d like singularities will be exaggerated.

The last term in eq (5) is dependent on the polarization of the radiation and it is non-zero if $m = m' \pm 1$, but if the polarization is suitable it may also be non-zero if $m = m'$. We therefore write the second selection rule as

$$m = m' = \pm 1 \text{ or } 0 \tag{7}$$

This rule implies that not all the transitions described in the second last paragraph are allowed. For any one type of transition, say s to p, only a fraction of transitions are allowed and this fraction may vary throughout the band, thereby distorting the spectrum. However, this distortion may not be serious, as the fraction may be nearly constant throughout the band. Of course, the constant fraction for d to p type transitions will be different from that for s to p type transitions and, in fact, the fraction for these transitions can be shown to be about 2/5 of that for the s to p transitions. This means that the L_{23} or M_{23} spectra give an approximate measure of the density of s-states plus 2/5 density of d-states. This is one reason why the L_{23} and K spectra, when added together, do not give the full density of states.

The second term in eq (5) provides the spectra with some very interesting properties. The integral effectively takes a weighted average of a(r), using a weighting factor of $rR_{n'}(r)$. Because of the localized nature of $R_{n'}(r)$, this integral can be considered to take an average of a(r) in the region near the core state of the emitting atom. This is exceedingly interesting when studying alloys, as the spectra from each component metal will sample the wavefunction in the region of that type of atom. These local properties are of great interest and are only obtainable by the spectroscopies involving x-rays.

Finally, the degree of approximation involved in assuming that spectra are similar to the partial densities of states is discussed. Consider the case of the K spectrum, which samples p-states. Because the wavefunctions are normalized, the term $\int \psi_k{}^2 \, d\tau$ may be inserted into eq (1) without changing it. This term may be written as

$$\sum_l (2l+1)^2 \, C_l^2(\mathbf{k}) \int a_{l,k}^2 \, (r) \, r^2 \, dr$$

and the density of p-states may be defined as

$$N_p(E) \propto \int_s d^2\mathbf{k} \, \frac{1}{\nabla_{\mathbf{k}} E} \, C_l^2(\mathbf{k}) \int a_{l,k}^2(r) \, r^2 \, dr \tag{8}$$

By replacing the last two terms in eq (5) by non-zero constants and restricting the summation to $l = 1$, eq (2) may then be written as

$$I_k(E)/v^3 \propto \int d^2\mathbf{k} \, \frac{1}{\nabla_{\mathbf{k}} E} \, C_l^2(\mathbf{k}) \left| \int_0 a_{l,k}(r) r^2 \, dr \right|^2 \tag{9}$$

where the zero on the radial integral indicates that it is now restricted to the region of the core state of the emitting atom. The final terms in these equations differ, one being the average of the square of a(r) and the other being the square of a local average of a(r). For the densities of s-states and of d-states and the corresponding spectra, the situation is complicated by the factor of 2/5 and by cross terms, but the differences arise in the same way.

5. The Spectra from Pure Metals

It is shown above, that x-ray spectra sample only those wavefunctions that have specific symmetries and that lie near the core of the emitting atom. Apart from these restrictions, they tend to show some of the behavior of the density of states, particularly the Fermi edge and the van-Hove singularities. The spectra are broadened by the experimental resolution and by many-body effects and it is possible that these many-body effects also change the shape of the spectra near the Fermi edge. These ideas are now illustrated by three pure metal spectra; the Li K, the Al L_{23} and the Zn L_3 emission spectra.

The Li K emission spectrum [14] is shown in figure 2. The Auger tail is immediately obvious but the Fermi

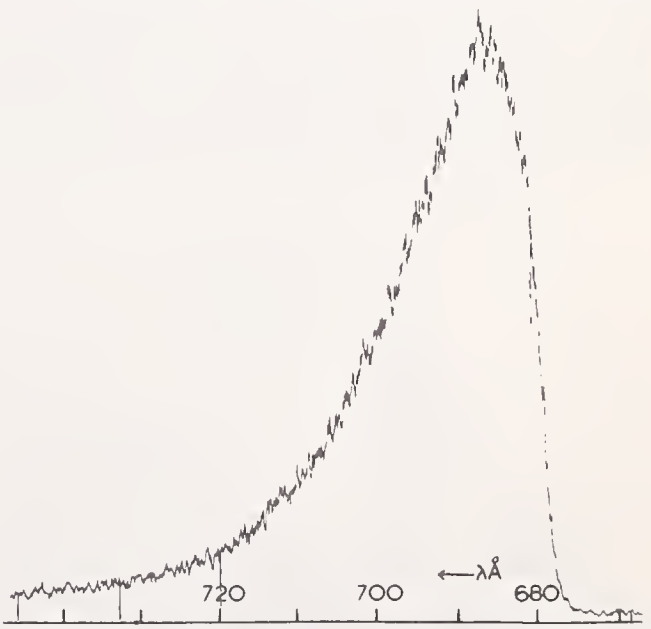

FIGURE 2. *Lithium K emission spectrum. Reproduced from Crisp and Williams [14].*

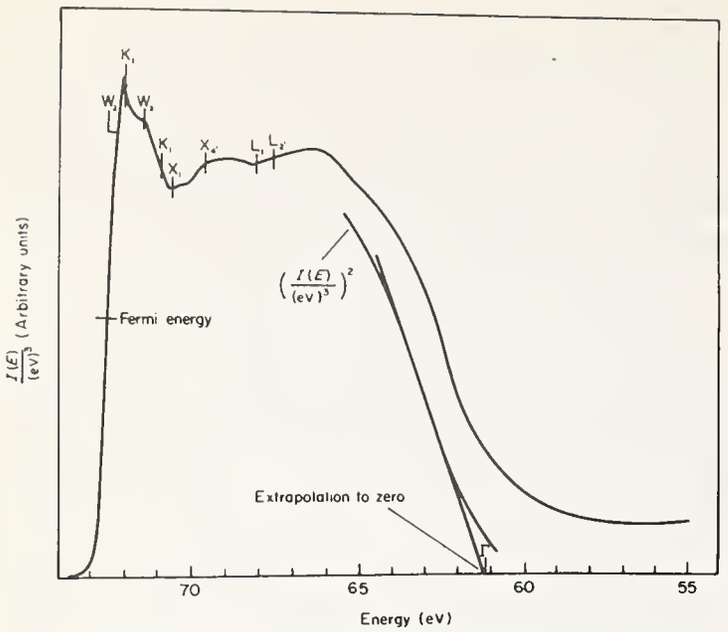

FIGURE 3. *Aluminum L_{23} emission spectrum. Reproduced from Rooke [15].*

edge at eV is not so obvious because of the fall in intensity towards the edge; this fall in intensity is attributed to the effect of the hole in the core state. Because of the low bandwidth, no van-Hove singularities occur below the Fermi edge. The shape of the density of states is almost certainly close to parabolic, but, because of the lack of p-like states near the bottom of the band, the spectrum does not reflect this; its intensity is considerably reduced near the bottom of the band.

The Al L_{23} emission spectrum [15] is shown in figure 3. The Fermi edge and the Auger tail are particularly obvious and the van-Hove singularities appear as discontinuities in the top half of the band. It is seen that the p-like van-Hove singularities, $X_{4'}$ and $L_{2'}$, are much less obvious than the s-like singularities, X_1 and L_1. The bottom of the band rises sharply to a broad hump at about 66 eV; this reflects the parabolic rise of the density of states and the fact that the states near the bottom of the band are nearly all observed because they are mostly s-like. From 66 eV to about 70 eV, the intensity

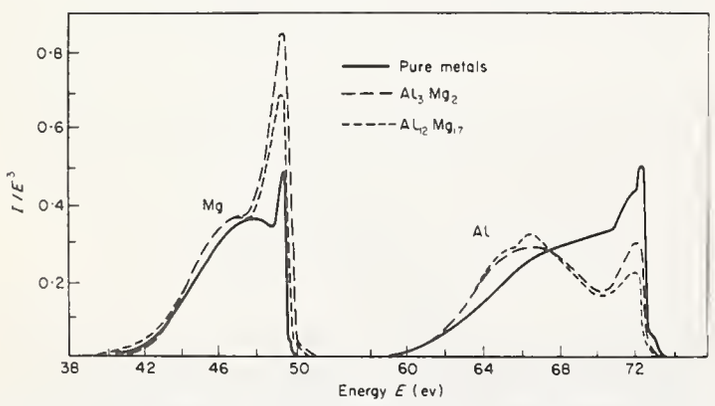

FIGURE 5. *Magnesium L_{23} and Aluminum L_{23} emission spectra from Al-Mg alloys. Reproduced from [17].*

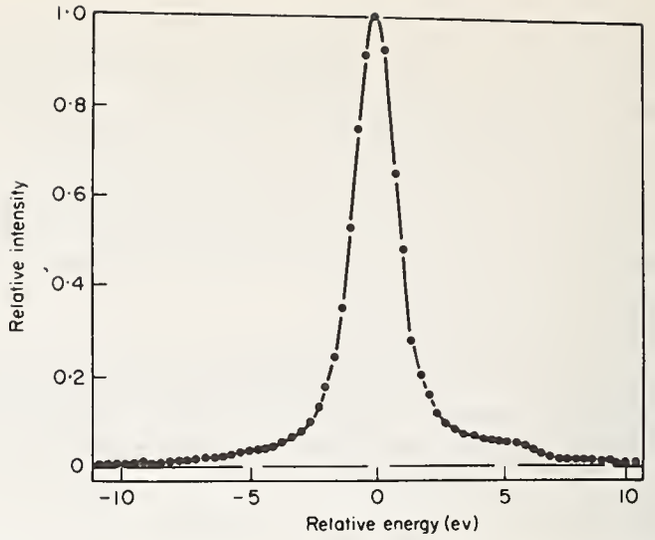

FIGURE 4. *Zinc L_{23} emission spectrum. Reproduced from Liefeld [16].*

falls but then it rises again towards the Fermi edge. This occurs because the states change from being mostly s-like at the bottom of the band to being mostly p-like near the center of the band and then to having both s and d character near the top of the band.

The Zn L_3 emission spectrum [16] is shown in figure 4. This spectrum has been obtained after considerable effort in allowing for the various experimental errors that occur. The tall peak at the center of the spectrum is possibly the d-band while the sharp fall in intensity at about + 7 eV may be the Fermi edge.

6. The Spectra from Alloys

Soft x-ray spectra are proving to be of considerable value for studying alloys and it is for this purpose that soft x-ray spectroscopy will be developed in the next few years. An excellent review of the work done in the West has been given by Curry [17], but the Russians have also done some interesting work, particularly on alloys containing d-band metals.

As an example the very interesting results from the Al-Mg system are discussed. The Mg L_{23} and Al L_{23} emission spectra from two alloys are shown together with the pure metal spectra in figure 5. At first sight, it is seen that the apparent bandwidths of the alloy spectra are not greatly different from those of the pure metal spectra. On alloying, the intensity of the Mg spectrum is relatively enhanced at the top of the band while the intensity of the bottom of the Al spectrum is relatively enhanced. The spectra have been carefully and independently checked by Dimond [18] and it is felt that the results are not due to clustering.

The following analysis produces some very interesting information. First, the width of the density of states must be at least as wide as the bandwidth of the Al spectrum; this fact is in contradiction with most theo-

ries of alloys. Second, either the states at the bottom of the band must be highly localized around the aluminum atoms or they must have mostly s-symmetry in the region of the aluminum ions and mostly p-symmetry in the magnesium ions; the former alternative is the most likely. It is possible that the states are tunneling through a potential barrier in the region of the magnesium ions and can only contribute to the spectra when they are in the vicinity of the aluminum ions. Third, states that are localized near the aluminum ions tend to be relatively more s-like than the states at the same energy in the pure metal. For magnesium, the states near the bottom of the spectrum tend to be relatively more p-like, reflecting the fact that they are now not near the bottom of the band.

This example shows how useful it can be to sample electrons locally and with selected symmetries. Another example involving d-band metals is given later in the conference by Lindsay, Watson and Fabian.

7. Acknowledgments

The author wishes to acknowledge Dr. L. M. Watson, C. A. W. Marshall, and R. K. Dimond for their discussions and help in preparing this paper and also Dr. D. J. Fabian and the Science Research Council for a Research Associateship (at the University of Strathclyde).

8. References

[1] Skinner, H. W. B., Phil. Trans. Roy. Soc. **A239**, 95 (1940).
[2] Tomboulian, D. H., Handbuch der Physik, **XXX**, 246 (1957).
[3] Yakowitz, H. and Cuthill, J. R., National Bureau of Standards (U.S.A.), Monograph **52**, (1962).
[4] Soft X-ray Band Spectra and the Electronic Structure of Metals and Alloys, D. J. Fabian, ed., Academic Press, London (1968).
[5] Pines, D., Solid State Physics **1**, 367 (1955).
[6] Mizuno, Y. and Ishikawa, K., J. Phys. Soc. Japan **25**, 627 (1968).
[7] Liefeld, R. J., p. 133 in [4].
[8] Rooke, G. A., p. 3 in [4].
[9] See part 4 in [4].
[10] Hedin, L., p. 337 in [4].
[11] Cuthill, J. R., McAlister, A. J., Williams, M. L. and Dobbyn, R. C., p. 158 in [4].
[12] Rooke, G. A., J. Phys. Chem. **1**, 767 (1968).
[13] Willens, J. H., Schreiber, H., Buehler, E., and Brasen, D., Phys. Rev. Letters **23**, 413 (1969).
[14] Crisp, R. S. and Williams, S. E., Phil. Mag. (8) **5**, 525 (1960).
[15] Rooke, G. A., J. Phys. Chem. **1**, 776 (1968).
[16] Liefeld, R., p. 149 in [4].
[17] Curry, C., p. 173 in [4].
[18] Dimond, R. K., Ph.D. Thesis, to be submitted to University of Western Australia, (1970).

SOFT X-RAY II; DISTRIBUTIONS IN MOMENTUM SPACE

CHAIRMEN: F. M. Mueller
A. J. McAlister

RAPPORTEUR: D. J. Fabian

Orbital Symmetry Contributions to Electronic Density of States of AuAl*

A. C. Switendick

Sandia Laboratories, Albuquerque, New Mexico 97115

From an augmented plane wave calculation of the valence and conduction bands of $AuAl_2$ we have constructed density of states histograms. From further calculations of the wave functions, one can attribute atomic-like character of the band states, e.g., Au 5*d*-bands, Al 3*s*-band. Al 3*p*-band. One can then partition the total density of states into atomic-like components according to the fractional atomic-like character of each state.

From the total density of states an electronic specific heat coefficient of 2.81 mJ/mole K^2 was calculated compared with the experimental value 3.03. The aluminum 3*s* density of states is compared with the aluminum $L_{2,3}$ soft x-ray emission spectra. Excellent agreement with experiment is obtained for the absolute location, and location relative to the Fermi energy, of the low energy peak. About half the calculated peak is attributable to tails of wave functions associated with the gold *d*-bands. Additional structure in the experimental curve is quite well reproduced in the calculation. This we take to be confirmation of the overall correctness of our bands.

Key words: Augmented plane wave method (APW); electronic density of states; electronic specific heat; gold aluminide ($AuAl_2$); "muffin-tin" potential; orbital density of states; soft x-ray emission.

1. Introduction

Augmented plane wave (APW) energy band calculations for $AuAl_2$ [1] have been extended to nineteen inequivalent points in $1/48^{th}$ of the Brillouin zone for the energy range −0.20 to 1.15 Ry. This gives a total of 256 points in the full Brillouin zone and includes bands derived from the aluminum 3*s*- and 3*p*-states and the gold 3*d*-states. Two sets of bands fall in the energy range −0.2 to 0.1 Ry. The lowest one from −0.2 to 0.1 Ry can best be described as the aluminum 3*s*-bonding band derived from the 3*s* atomic states of the two aluminum atoms in the unit cell. The narrow set of bands from −0.05 to 0.05 Ry are the gold *d*-bands. These bands are filled and contain twelve of the seventeen valence electrons per unit cell and are about 0.5 Ry below the Fermi energy. From .1 Ry to slightly above the Fermi energy (0.56 Ry) lies a partially filled aluminum 3*s*-antibonding band. A complex of bonding and antibonding bands formed from the aluminum 3*p*-levels extends from 0.3 to 1.2 Ry. The Fermi level falls in the region of aluminum 3*s*-antibonding and aluminum 3*p*-bonding and -antibonding levels. The interpretation of these bands in terms of their atomic geneses is confirmed by charge density calculations which were also made in this energy region. The APW method gives a very convenient description of the charge density, i.e., atomic-like near the nuclei and plane-wave-like in the exterior "muffin tin" region. We shall utilize this description to compare calculated values of the density of states and orbital densities with experimental values for the electronic specific heat and aluminum soft x-ray $L_{2,3}$ emission spectra, respectively. We shall be quite explicit in describing the numerical procedures and approximations which we have made, given the band eigenvalues and wave functions, leaving details of the band calculation for a more appropriate publication.

2. Fermi Energy

The Fermi energy is determined by the relationship

$$N = \frac{2V}{(2\pi)^3} \int_{E(k) \leq E_F} d^3k \qquad (1)$$

where N is the total number of electrons, the factor $V/(2\pi)^3$ represents the density of spin states in $\mathbf{k}$ space,

*This work was supported by the U.S. Atomic Energy Commission.

and the factor 2 the fact that we can put two electrons in each spin state, one up and one down. We shall endeavor to explicitly display this factor whenever it occurs. If we divide both sides by V and multiply by Ω, the unit cell volume, and subtract the electrons in filled core bonds then we have

$$Z = \frac{2\Omega}{(2\pi)^3} \int_{E_C < E_1(k) < E_F} d^3k \tag{2}$$

where Z is the number of valence electrons in the unit cell and the integral excludes core states. The number of cases for which the integral can be done analytically are few and we will always have to resort to numerical techniques. From the definition of the integral

$$Z = \frac{2\Omega}{(2\pi)^3} \int_{E_C < E(k) \leq E_F} d^3k = \frac{2\Omega}{(2\pi)^3} \lim_{n\to\infty} \sum_{\substack{i \\ E_C < E(k_i) \leq E_F}} \Delta^3 k_i \tag{3a}$$

where $\Delta^3 k_i$ is the i^{th} subvolume of the division of the Brillouin zone into n parts. For our calculation we choose $\Delta^3 k_i$ to be of equal size with the volume centered on k_i. This gives

$$Z \cong 2\frac{1}{n} \sum_{\substack{i \\ E_C < E(k_i) < E_F}} 1 \tag{3b}$$

By increasing n and varying the subinterval shape we can investigate the accuracy of this approximation as shown in table 1. The asymmetry in the table between

TABLE 1. *Convergence of sum determining Fermi energy,* E_F, *as a function of number of points,* n, *in* k-*space eq 3b*

n	$E_< < E_F \leq E_\leqslant$		$z(E(k_i) < E_F)$	$z(E(k_i) \leqslant E_F)$
32	0.5442	0.5620	16.75	17.125
64	.5442	.5620	16.875	17.0625
128	.5442	.5480	16.75	17.125
256	.5480	.5620	16.97	17.02

greater than and less than or equal to reflects the fact that many k_i's (up to 48 for cubic symmetry) all have the same energy so the sum rarely comes out exactly Z as the last column indicates. The statements [2,3] that both the state No. $Zn/2$ and the state No. $(Zn/2)-1$ have the same energy which is thus the Fermi energy we believe to be misleading. The second and third columns represent more accurately the precision with which the Fermi energy is determined. Although the results indicate a value closer to .560 Ry, the results for 128 points indicate a value below .550 Ry. In what follows we shall quote values of results as $X(y,z)$ where X is the value which seems most reasonable, y the increment gained by choosing the higher Fermi energy, and z the increment gained by choosing the lower one. The value X is the one one might see in less candid treatments. This presumes the correct solution of some *ad hoc* potential and reflects only the inaccuracy of our sampling and ignores any further inaccuracy due to the inadequate physical relevance of the potential used. Thus we quote a Fermi energy of .557 (+ .005, − .009) Ry.

3. Total Density of States

If one replaces E_F by E in eq (2) and considers Z as a function of E then the number of valence electrons states per unit cells between E and E and dE is given by

$$dZ(E) = \frac{2\Omega}{(2\pi)^3} \frac{d}{dE} \left[\int_{E_C < E_1(k) \leq E} d^3k \right] dE \tag{4}$$

or the number per unit energy range

$$z(E) = \frac{2\Omega}{(2\pi)^3} \frac{d}{dE} \int_{E_C < E_1(k) \leq E} d^3k \tag{5a}$$

Again, of course, we must resort to finite techniques and our result is

$$z(E_q) \cong \frac{2}{n} \frac{1}{\Delta E} \sum 1,$$

$$\left(E_q - \frac{\Delta E}{2} < E(k_i) \leq E_q + \frac{\Delta E}{2} \right) \tag{5b}$$

If we let ΔE go to zero in eq (5b) then our approximate density of states becomes just a series of delta functions located at $E(k_i)$ and is of no use to us. We therefore choose some mesh of energy $E_q = E_o + q\Delta E$ with finite ΔE and hope eq (5b) represents some average density of states over this interval. If we choose ΔE too large then our curve will be structureless and again of no use to us. Again we look for some sort of convergent procedure, decreasing ΔE until the resulting curve has stability of structure yet not so small to lose this stability. When we do this, we find minor variations as a state goes from one ΔE to the next higher. These minor variations become major ones if ΔE is too small and the curve reverts to regions of no states and delta-function-like square spikes. These minor variations of shifting states from one subinterval to another, similarly de-

pend on E_o, where we start our finite partition. Comparison of averaging over various starting points as done by Snow and Waber [4] with more sophisticated calculations [5] employing the same data indicate that where the number of states is large (d-bands), credible structure develops: but where the number is small, structure develops which may or may not be believable. All of which is to say they could have chosen a smaller ΔE in the region of the d-bands and probably should have chosen a larger one in the region of the s-bands. Since we have about twice as many states per unit energy range as Snow and Waber, and shall choose a larger ΔE, we shall tend to believe any structure which develops. We have then

$$\bar{z}(\xi_p) \cong \frac{1}{m}\frac{2}{n}\frac{1}{\Delta E}\sum_{j=0}^{m-1} z\left(E_q + \frac{j\Delta E}{m}\right),$$

$$\left(E_0 + \frac{(2p-1)\Delta E}{2m} < \xi_p \leq E_0 + \frac{(2p+1)\Delta E}{2m}\right) \qquad (6)$$

The integer p gives the region of interest, where E_o is the arbitrary starting point, ΔE is the sampling width and we are averaging over m histograms starting at E_o, $E_o + \Delta E/m, \ldots, E_o + (m-1)\Delta E/m$.

Using this procedure with $E_o = -0.281625$ Ry $\Delta E + 0.03675$ Ry, and $m = 5$ the histogram shown in figure 1 shows $\bar{z}/2$ for $AuAl_2$. The large peak near .5 eV is the d-band which has been spread out somewhat by our averaging procedure. The Fermi energy falls in a region of rising density of states. The value of the density of states at the Fermi energy which we calculate is 1.19 (+.05, −.14) electrons/(eV-unit cell). This gives us a value for the electronic specific heat coefficient $\gamma = C_e/T$ of 2.81 (+.12, −.33) mJ/mole K² compared with the experimental value of 3.03.

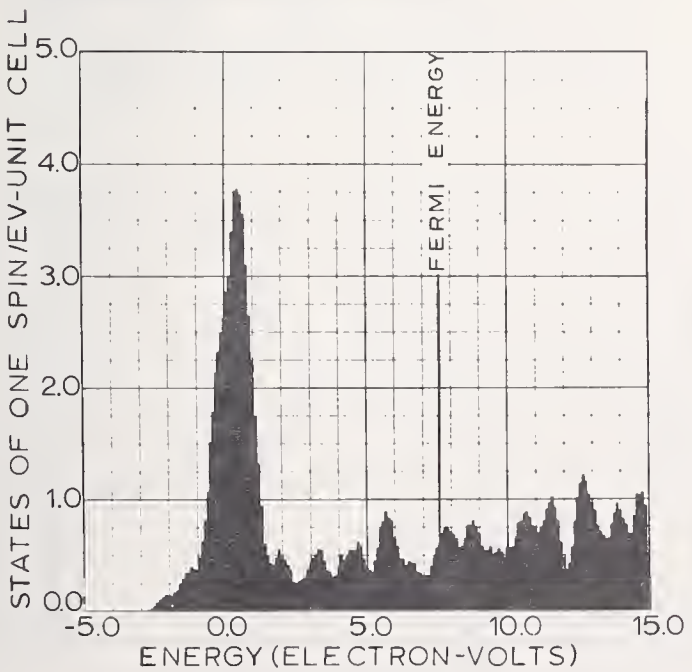

FIGURE 1. *Density of states for* $AuAl_2$ *constructed following the procedure outlined in Section III, factor of two in eq 6 has been omitted.*

4. Orbital Density of State and Soft X-Ray Spectra

The intensity of soft x-ray emission spectra can be written as

$$I(\omega) \propto \omega^3 \int |H_{fi}|^2 \qquad \delta(E_i(k) - \hbar\omega - E_f(k))\, d^3k \qquad (7)$$

where H_{fi} is the transition matrix element between the initial and final state. For x-ray emission E_f is a low lying core state and its **k**-dependence may be neglected. If we make the dipole approximation and use the APW expansion of the wave function inside the n^{th} sphere

$$\psi_{k_i}(\mathbf{r}_n) = \sum_{l,\,m} C^i_{lm} \frac{P^i_l(r_n)}{r_n} Y^m_l(\theta, \phi) \qquad (8)$$

we obtain

$$I(\omega) \propto \omega^3 \int \left| \int P^f_l C^i_{l\pm1} P^i_{l\pm1} r^3 dr \right|^2 \delta(E_i(k) - \hbar\omega)\, d^3k \qquad (9)$$

Specializing further to the $L_{2,3}$ emission spectra in $AuAl_2$ the final state is aluminum $2p$ and only the aluminum s- or d-like components of the wave function contribute to eq (9). If we assume that the radial wave function $P_l^i(r)$ is a slowly varying function of energy and can be written

$$P^i_l(r) = P^0_l(r) f^i_l(r) \qquad (10)$$

where $P_l^0(r)$ is some average radial function and $f_l^i(r)$ is smooth and in our approximation = 1. The only **k**-dependence is now in the C^i's and we can write

$$I(\omega)/\omega^3 \propto \int \{(C^i_s)^2 R^2_{ps} + (C^i_d)^2 R^2_{pd}\} \delta(E_i(k) - \hbar\omega)\, d^3k \qquad (11a)$$

where

$$R_{pl} = \int P^f_p(r) P^0_l(r) r dr \qquad (12)$$

with discrete representation (taking out a proportionality factor R_{ps}^2)

$$I(\xi_\nu)/\xi_\nu^3 \cong \sum_i [(C_s^i)^2 + (C_d^i)^2 R_{pd}^2/R_{ps}^2] \qquad (11b)$$

Defining

$$Q_l^i = \int_{\substack{\text{aluminum} \\ \text{spheres}}} (C_l^i)^2 (P_l^i(r))^2 dr \qquad (13)$$

The amount of l-like charge in the aluminum spheres for the i^{th} state, and an aluminum l-like density of spin states $N_l^{Al}(\xi)$

$$2N_l^{Al}(\xi) = \frac{1}{m}\frac{2}{n}\frac{1}{\Delta E}\sum_i Q_l^i \qquad (14)$$

Again approximating $P_l^i(r)$ by $P_l^0(r)$

$$Q_l^i \cong (C_l^i)^2 \int (P_l^0(r))^2 dr\,. \qquad (15)$$

dropping all irrelevant factors of proportionality we get

$$I(\zeta)/\zeta^3 \propto N_s^{Al}(\zeta) + CN_d^{Al}(\zeta) \qquad (16)$$

where $C \approx 1$. Plots of the orbital densities of states are shown in figures 2 and 3. The aluminum d-contribution is small and will be disregarded. The s curve fairly well replicates the total density of states in figure 1 with the exception that the low energy peak is shifted about a volt lower and the structure on the low side is more pronounced. This low energy peak corresponds to the aluminum 3s-bonding band although about half of its magnitude is attributable to tails of the gold d-band wave functions overlapping the aluminum sites.

This figure should be compared with the experimental results of Williams, et al. [6] reported in these proceedings as shown in figure 4 graciously supplied by Dr. A. J. McAlister. We see that their peak $\simeq$8 eV below the Fermi energy is well reproduced in our figure 2. This we take to be partial confirmation as to the location of the gold d-bands. Also the structure on the low energy side seems to be present in our calculations. Structure between the peak and the Fermi energy seems to be present in both curves although our values seem about 1 eV too high. We have calculated alu-

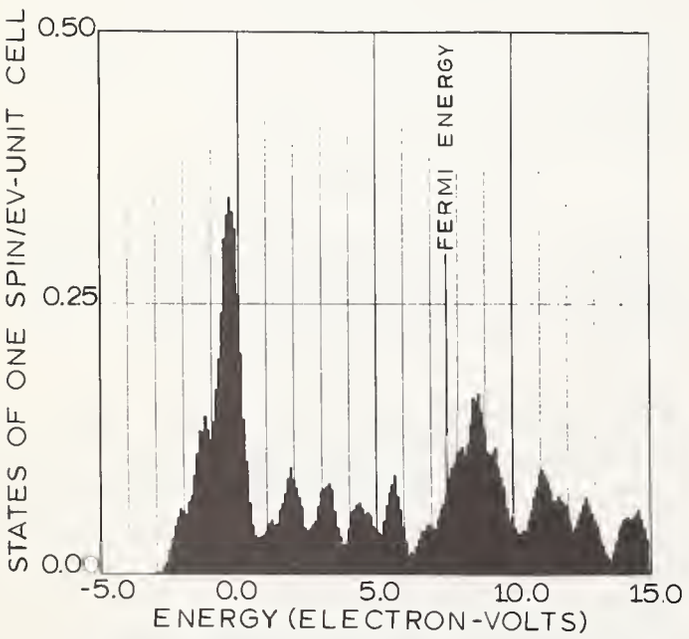

FIGURE 2. *Density of aluminum* 3s*-like-states*, N_s^{Al}.

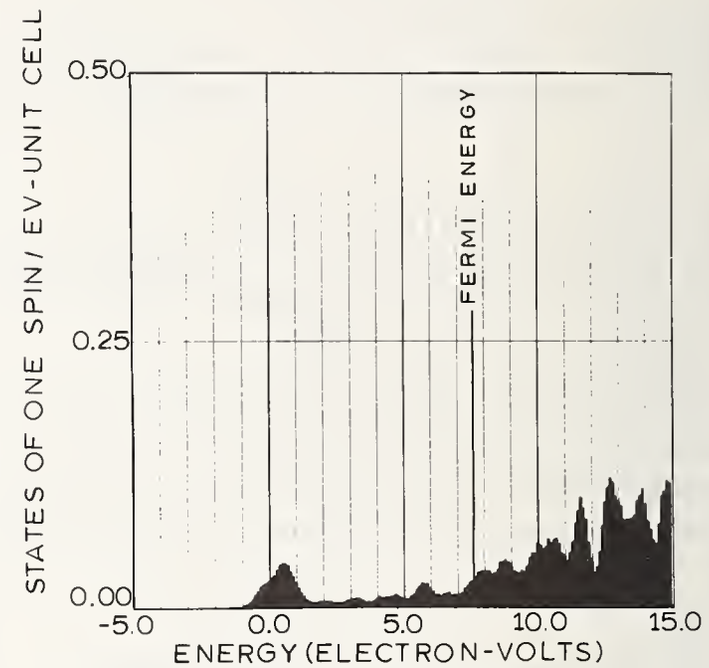

FIGURE 3. *Density of aluminum* 3d*-like states*, N_d^{Al}.

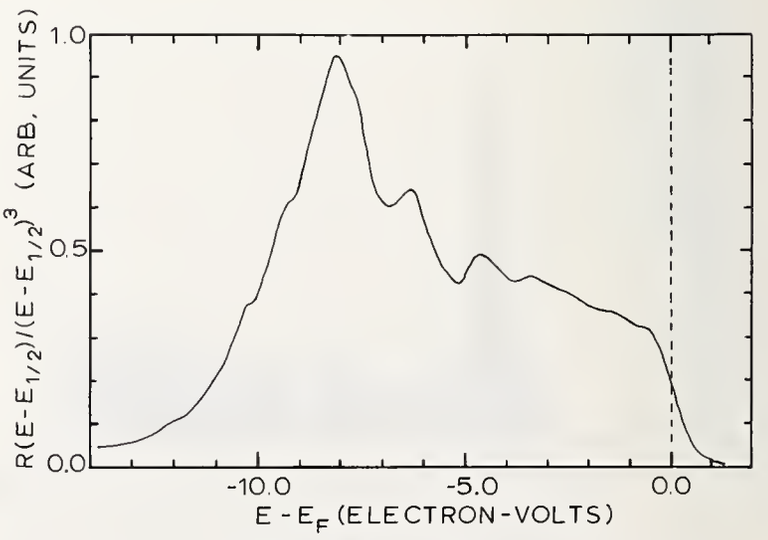

FIGURE 4. *Relative Intensity/*ω^3 *of aluminum* $L_{2,3}$ *soft x-ray spectra (courtesy of A. J. McAlister).*

minum $2p$-core bands and find them 73.8 ± 0.1 eV below the Fermi energy compared with the experimental value of 73.5 ± 0.5. This band is less than .02 eV wide and every state is 99.97% aluminum $2p$-like. This confirms our neglect of final state energy.

In table 2 we give the ratio

$$g(r) = \frac{[C_s^{\Gamma 1}]^2 [f_s^{\Gamma 1}(r)]^2}{[C_s^{\Gamma 2'}]^2 [f_s^{\Gamma 2'}(r)]^2} = \frac{[C_s^{\Gamma 1} P_s^{\Gamma 1}(r)]^2}{[C_s^{\Gamma 2'} P_s^{\Gamma 2'}(r)]2} \quad (17)$$

for the states $\Gamma 1 = -.194$ Ry and $\Gamma 2' = .625$ Ry, the bottom and top of the aluminum $3s$-bands, respectively. Although this varies by a factor greater than three from the origin to the sphere radius, in the region of overlap with the $2p$ peak it varies by less than 10% (discounting the value for $r = .8660$ which is small because it is near a node of $[P^{\Gamma 1}(r)]^2$). To the extent we can neglect the variation of the radial function with energy and define $P_s^0(r)$ and $f_s^1(r)$, the ratio given in eq (17) should be equal to a constant, $Q_s^{\Gamma 1}/Q_s^{\Gamma 2'}$, which is .5114 compared to a variation of from 0.33 to 1.25 within the sphere. Thus we may have overestimated low energy C^2's by 25% and underestimated the high energy C^2's by 25% at most. The extra factor or r in eq (9) would tend to prejudice the integral towards larger r values, reducing these errors to about $\pm 10\%$. In any case one could calculate the corrections throughout the band if more accurate results were needed.

In summary we conclude that our band structure calculation reproduces density of states information over an energy range of 10 eV with reasonable accuracy.

TABLE 2. *Variation in P_{3s} radial wave function from bottom to top of band*

r (a.u.)	$[f_s^{\Gamma 1}(r)]^2/[f_s^{\Gamma 2' 2'}(r)]^2$	$[P_{2p}]^2$
0.0019	0.3301	
.0188	.3302	
.0377	.3303	
.0754	.3310	$2p$ Peak/5.
.1130	.3330	
.1883	.3209	
.2636	.3281	
.4142	.3371	$2p$ Peak.
.5697	.3617	
.8660	.1977	
1.1672	.3013	
1.7697	.4469	$2p$ Peak/10.
2.3721	1.0410	
2.4549	1.2495	Sphere radius.

5. References

[1] Switendick, A. C., and Narath, A., Phys. Rev. Letters **22**, 1423 (1969): see figure 1 for a picture of these bands.

[2] Burdick, G. A., Phys. Rev. **129**, 168 (1963).

[3] Bhatnager, S., Phys. Rev. **183**, 657 (1969).

[4] Snow, E. C., and Waber, J. T., Phys. Rev. **157**, 570 (1969).

[5] Janak, J. F., Physics Letters **28A**, 570 (1969).

[6] Williams, M. L., Dobbyn, R. C., Cuthill, J. R., and McAlister, A. J., these Proceedings, p. 303.

Discussion on "Orbital Symmetry Contributions to Electronic Density of States of $AuAl_2$" by A. C. Switendick (Sandia Laboratories)

F. M. Mueller *(Argonne National Labs.):* Since you have the wave functions point by point in the zone separated into *s*, *p*, and *d* characters, do you have any plans to calculate dipole matrix elements as a function of position in the Brillouin zone itself? Presumably you could do this, but it would be rather difficult perhaps?

A. C. Switendick *(Sandia Labs.):* I think it would be fairly easy. I think the essential variation is in how much *s*, *p*, and *d* character there is in the wave function, but one certainly could do it quite easily with the wave functions we have.

Soft X-Ray Emission Spectrum of Al in $AuAl_2$

M. L. Williams, R. C. Dobbyn, J. R. Cuthill, and A. J. McAlister

Institute for Materials Research, National Bureau of Standards, Washington, D.C. 20234

Recently, Switendick and Narath have reported results of a systematic calculation of the electronic band structure of the compound series AuX_2(X = Al,Ga,In). We have measured the $L_{2,3}$ soft x-ray emission spectrum of Al in $AuAl_2$ and from it, estimated the Al L_3 emission profile. We compare the latter to the distribution in energy of *s*-like charge at Al sites, estimated by Switendick from his band calculation. This *s* density is the dominant factor in a one-electron estimate of the soft x-ray emission rate. Quite good agreement is found, lending strong support to the calculations for $AuAl_2$. This result also supports interpretation of a recently observed low energy peak in the $L_{2,3}$ emission spectrum of Al in Ag-Al alloys in terms of Ag *d* and Al *s-p* hybridization.

Key words: Electron density of states; gold aluminide ($AuAl_2$); gold-gallium ($AuGa_2$); gold-indium ($AuIn_2$); intermetallic compounds CsCl structure; L spectra; silver-aluminum alloys (AgAl); soft x-ray emission; *s*-orbital density of states.

1. Introduction

The series of intermetallic compounds, AuX_2(X = Al,Ga,In), is of considerable current interest, largely because of the unusual behavior of the magnetic susceptibility and Ga Knight shift in $AuGa_2$. Specific heat [1] and de Haas-van Alphen Fermi surface studies [2] indicate that these materials are fairly well described by the nearly free electron model, and reveal no strong differences between them. Yet while the Al and In Knight shifts are positive and essentially temperature independent, the Ga Knight shift displays a large and unusual temperature dependence, ranging from −0.13% at 4 K to +0.45% at 230 K [2]. The magnetic susceptibilities of $AuAl_2$ and $AuIn_2$ are temperature independent, but $AuGa_2$ displays a temperature dependence [2]. Switendick and Narath [3] have recently reported a systematic calculation of the electronic band structure of this compound series, and from it, suggest an interpretation of the Fermi surface and Knight shift data. A somewhat surprising feature of their results is the location of the *d* bands at 7 to 8 eV below the Fermi level. This is in sharp contrast to the 2 eV or so suggested by interpretation of the optical properties of these unusually colored materials via *d* band to Fermi level optical transitions [4]. While not giving a detailed analysis of the optical properties, Switendick and Narath suggest that the *d* bands are not necessary to an explanation of the optical properties, since the calculation predicts a large number of *s*- and *p*-like states both above and below the Fermi level.

We report here a measurement of the $L_{2,3}$ emission spectrum of Al in $AuAl_2$. From it, we estimate the Al L_3 emission profile, and compare it to the *s*-orbital state density at Al sites (the leading term in a one-electron calculation of the L spectrum) estimated by Switendick from his band calculation, and reported elsewhere at this conference [5]. Good agreement is found, lending strong support to the validity of the $AuAl_2$ band calculation. Analogies between the present work and the recent observation of a low energy peak in the $L_{2,3}$ emission spectrum of Al in Ag-Al alloys [6] support interpretation of the latter in terms of Ag *d* and Al *s-p* hybridization.

2. Experimental Details

Measurements were made in a previously described [7] glass grating, vacuum spectrometer using photoelectric detection. The spectrum was scanned continuously, total counts being recorded over successive short time intervals. Successive runs were summed to enhance signal to noise ratio. The relative counting error in the raw data, $(N)^{-1/2}$, where N is the accumulated count per channel, ranged from 1.8 to 0.8% This degree of statistical assurance was achieved at the expense of instrumental resolution, which we estimate to be 0.35 eV at the Al emission edge. Mea-

surements were made at an average pressure of 7×10^{-8} Torr, at approximately 500 °C. Electron beam excitation was used, at an energy of 2.5 keV. The sample was a polycrystalline rod, lightly machined and washed in acetone and absolute alcohol before mounting in the instrument. It was prepared from 99.999% pure Au and Al starting materials, by first adding Au in stoichiometric proportion to Al induction melted in an alumina boat under vacuum, then drawing the final melt into a graphite lined quartz tube. Optical metallographic examination of the sample showed that toward the center, the last part to freeze in this preparation technique, traces of free Al (much less than 1%) occurred at the grain boundaries. None was observed at the surface. Such Al contamination as might occur at the surface should not noticeably affect the results. A practical check of this is possible. The pure Al profile differs strongly from that of Al in the compound, and any significant distortion from this source would have been evident.

A further complicating factor is the Au $O_{2,3}$ spectrum which overlaps the Al $L_{2,3}$. Supplementary measurements on Au, not reported here, show the $O_{2,3}$ band to be very weak in the pure metal. If we make the reasonable assumption [8] that the Au $O_{2,3}$ and $N_{6,7}$ bands in the alloy have the same relative intensity as in the pure metal (Au $N_{6,7}$ does not overlap Al $L_{2,3}$), then we can assign a maximum peak intensity to Au $O_{2,3}$ in the alloy of no more than 2% of the Al $L_{2,3}$ maximum. Since an oil diffusion pump was used to evacuate the instrument, the fourth order of the C K band might also be expected to distort the observed spectrum. However, scans of the first and second order C K bands show them to be quite weak, and past experience indicates that C K lies very near or beyond the fourth order cutoff of our instrument. In view of the weakness of these distorting factors, we make no attempt to correct for them, and in treating the data, ignore their presence.

3. Comparison with Calculated *s*-Density

The upper curve of figure 1 is our corrected experimental estimate of the L_3 emission profile of Al in $AuAl_2$. The following procedure was used to construct it. First, a curve was drawn through the raw data in a manner consistent with the standard counting error. The background continuum was estimated according to a prescription given elsewhere [7], and subtracted off. The spectrum was then corrected for the presence of the L_2 band, using pure Al values of the L_2/L_3 intensity ratio (0.21) and spin orbit splitting (0.4 eV) determined from inspection of the pure Al emission edge in second order. Next, a first order correction was applied for the changing energy resolution of our spectrometer [7]. Finally, the spectrum was divided by the cube of the photon energy to reduce it as far as possible to a representation of the *s*-orbital density. The ordinate of the plot is arbitrary.

In the one-electron approximation, the soft x-ray L_3 emission rate per unit energy from the ith component of a compound may be written

$$R_i(\hbar\omega) \propto (E(\vec{k}) - E_c)^3 \sum_{\vec{k},n} |<2p \mid \vec{r} \mid \vec{k}>|^2 \delta(\hbar\omega - E(\vec{k}) + E_c)$$

The matrix element is evaluated at the site of the ith-type ion from normalized band wave functions $|\mathbf{k}\rangle$, of energy $E(\mathbf{k})$. $|2p\rangle$ is the core wave function and E_c its energy. $\hbar\omega = E(\mathbf{k}) - E_c$ is the photon energy. n is a band index. The sum extends over the Brillouin zone and all bands. Within the framework of an augmented plane wave (APW) calculation, one can estimate for a given state $|\mathbf{k}\rangle$ the fraction of the total charge within a unit cell which resides in the plane wave region, w_{pw}, and in the various orbital components within APW spheres of a given ion type, w_l^i. These orbital weights can be introduced into a sum over states to yield orbital state densities, $n_l^i(E)$. If the inner level wave function is well localized in the APW spheres (this is the usual case), then it is a straightforward, although tedious, task to show that the L_3 emission rate may be written

$$R_i(\hbar\omega) \propto (E - E_c)^3 \left[M^2_{\frac{1}{2}p,0}(E) n_0^i(E) + \frac{2}{5} M^2_{\frac{3}{2}p,2}(E) n_2^i(E) \right].$$

where

$$M_{2p,l} = \int_0^{A_i} dr\, r^3\, R_{2p}^i(r) R_l^i(r, E)$$

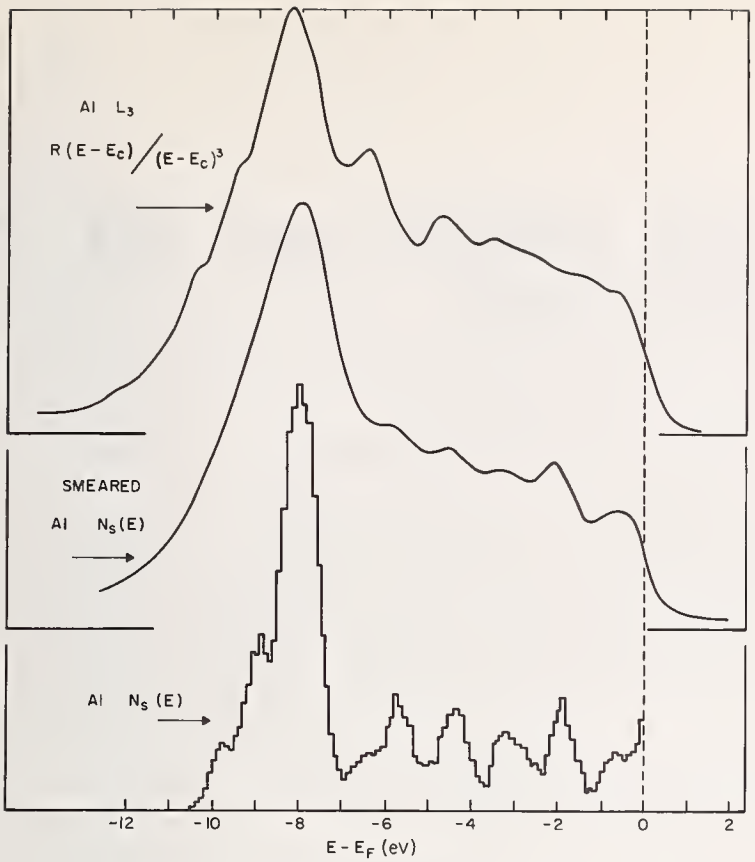

FIGURE 1. *The lower curve is the* s*-orbital state density at* Al *sites in* $AuAl_2$ *estimated by Switendick* [4].

The middle curve illustrates, in a rough approximation, the effects of spectrometer, inner level lifetime, and final state lifetime smearing on the calculated curve. The upper curve is the measured Al L_3 emission profile from $AuAl_2$, corrected as described in the text.

depends only on energy. The R's are radial wave functions, R_l^i being normalized over the APW sphere of radius A_i. For Al in $AuAl_2$, we anticipate negligible d contributions, on the basis of the nature of the potential within the Al spheres and symmetry considerations. The integral $M_{2p,o}$ is smoothly varying and will not affect structure in $n_o^{Al}(E)$, the quantity estimated by Switendick [5] from his band calculation and shown as the bottom curve of figure 1. In the middle curve, we have attempted to illustrate the effects of spectrometer, inner level lifetime, and final state lifetime smearing on the spectrum by folding into Switendick's curve a Lorentzian smearing function of energy dependent width. The width $\gamma(E)$ is the sum of two parts

$$\gamma(E) = \gamma_0 + \gamma_f(E)$$

The constant γ_o was taken as 0.5 eV, to represent the effects of the spectrometer and the inner level. The energy dependent part varies from 0 at the Fermi level to 2.0 eV at the bottom of the band, and has been taken to be proportional to the total fraction of s-charge lying above the level in question. It is intended only as a rough approximation to the many body final state level broadening which occurs in an interacting electron gas [9].

The general agreement between the calculated s density and the measured Al L_3 profile is quite striking. There is in fact, a one to one correlation of structural features, marred only by the slightly greater overall width of the measured spectrum, slight displacements of the peaks, and certain not too gross amplitude discrepancies. In all, the validity of the $AuAl_2$ band calculation is strongly confirmed by this comparison.

The large calculated peak at about −8.0 eV is of particular interest. The band calculation [4] indicates that about half its intensity arises from a high density of states which are d-like on Au sites and strongly localized there, but have roughly 5% of their total charge in s-like orbitals at Al sites. The occurrence of similar sharply peaked structure at −8.3 eV in the Al L_3 profile from the compound is consistent with this predicted location of the d bands. We further note that this behavior is strongly reminiscent of the distinct peak at 7.5 eV below E_F recently observed by Marshall et al. [5] in the $L_{2,3}$ emission spectrum of Al from alloys of up to 20 atomic percent of Ag in Al. It suggests that their interpretation in terms of Ag d and Al s-p hybridization in the alloy is correct.

4. Acknowledgments

We are most grateful to Dr. A. C. Switendick for communication of his results prior to publication. We also thank Dr. L. H. Bennett for introducing us to this problem and for many helpful discussions, Dr. R. E. Watson for instructive discussions, and Mr. D. P. Fickle for preparing the sample.

5. References

[1] Rayne, J. A., Phys. Letters **7**, 114 (1963).
[2] Jaccarino, V., Weber, M., Wernick, J. H., and Menth, A., Phys. Rev. Letters **21**, 1811 (1968).
[3] Switendick, A. C., and Narath, A., Phys. Rev. Letters **22**, 1423 (1969).
[4] Optical measurements have been reported by S. S. Vishnubhlata and J.-P. Jan, Phil. Mag. **16**, 45 (1967). Interpretation in terms of d band to Fermi level optical transitions has been suggested by J. H. Wernick, A. Menth, T. H. Geballe, G. Hull, and J. P. Maita, J. Phys. Chem. Solids **30**, 1949 (1969).
[5] Switendick, A. C., these Proceedings, p. 297.
[6] Marshall, C. A. W., Watson, L. M., Lindsay, G. M., Rooke, G. A., and Fabian, D. J., Phys. Letters **28A**, 579 (1969).
[7] Cuthill, J. R., McAlister, A. J., Williams, M. L., and Watson, R. E., Phys. Rev. **164**, 1006 (1967); Cuthill, J. R., Rev. Sci. Inst., **41**, 422 (1970).
[8] Cuthill, J. R., McAlister, A. J., and Williams, M. L., J. Appl. Phys. **39**, 2204 (1968).
[9] Landsberg, P. T., Proc. Phys. Soc. (London) **A62**, 806 (1949); Longe, P., and Glick, A. J., Phys. Rev. **177**, 526 (1969).

417-156 O - 71 - 21

Soft X-Ray Emission from Alloys of Aluminum with Silver, Copper, and Zinc

D. J. Fabian,* G. Mc D. Lindsay, and L. M. Watson

Department of Metallurgy, University of Strathclyde, Glasgow, Scotland

Measurements of the soft x-ray emission from the alloys Al-Ag, Al-Cu and Al-Zn are reported, and the effect of the *d*-bands of the metals Ag, Cu and Zn on the Al $L_{2,3}$-emission for these alloys is examined. For Al-Ag and Al-Cu alloys, sharp resonance peaks are observed in the Al $L_{2,3}$-spectra and are attributed to transitions from states in the hybridized silver and copper *d*-bands to core states of the aluminums atoms. The observations agree with the general theoretical considerations discussed by Harrison [7] for a simple metal alloyed with a noble metal. For the Al-Zn alloys the *d*-bands of Zn do not contribute to the Al $L_{2,3}$-emission.

Key words: Aluminum-copper alloys (AlCu); aluminum-zinc alloys (Al-Zn); electron density of states; silver aluminum alloys (Ag-Al); soft x-ray emission.

1. Introduction

Soft x-ray emission investigations for studying electronic structure have been steadily gaining the attention of physicists and metallurgists interested in the theory of alloys, despite the well established problems of interpreting the spectra of pure metals. Curry [1] usefully summarizes the experimental findings for many of the alloy systems examined to date. With alloys the problems of interpretation are further complicated by the absence of a fully satisfactory theory that explains the electronic behavior of a metal when it is alloyed with a second metal.

Theoretical work in this field is continually developing, and among the models that have been proposed for alloys are: the rigid-band model, first described by Jones in 1934 [2]; an "impurity" model that assumes restricted sharing of the valence electrons of the components, with consequent localized screening effects, developed chiefly by Friedel in 1952 [3]; and the two-band model successfully used by Varley in 1954 [4] to correlate thermodynamic heats of formation of binary alloys. The degree to which these models assume distinct valence bands for the two components of the alloy increases in the order listed.

At the one extreme, the rigid-band model assumes a common band of valence electrons, for which any incoherent scattering due to the additional random "impurity" potential, superposed on the basic periodic potential of the lattice, is negligible. Appleton [4] discusses this effect in relation to soft x-ray emission and also extends, qualitatively, the restricted-sharing approach used by Friedel to alloys with concentrations of solute that are greater than generally regarded as impurities, and to alloys of higher valence components.

At the other extreme we have the two-band model in which the valence electrons for a binary alloy are assumed to exist in two sets of energy states each associated with the potential fields of the ions of one component; this model is a consequence of the changes that arise in Wigner-Seitz boundary conditions for the valence electrons when the pure-metal atoms are randomly mixed.

Basically, both extremes recognize a valence band that is common to the alloy. Rooke [5] lends support to the two-band approach, pointing out that the pseudo-atom model, Ziman [6], will require local electron densities to remain unaffected on going from the pure metal to the alloy, provided that predominantly the electronic density for the pseudo-atom lies close to the ionic core; while Harrison [7], with a slightly different approach using pseudopotential theory, supports the view—for the simple metals—that the alloy components exhibit a common band structure.

In the case of a simple metal alloyed with a noble or transition metal, characterized by a narrow *d*-band,

*Present address: Visiting Professor at the Laboratory for Solid State Physics, Swiss Federal Institute of Technology, Zürich, Switzerland.

Harrison considers that this d-band for the transition metal will tend to retain its structure and carry over to the alloy; so that, if this is the "solute" metal, each solute atom will produce a strongly localized set of states at an energy that corresponds to the narrow d-band for the pure solute metal.

We describe here measurements of the soft x-ray emission from alloys of aluminum with, respectively, the metals silver, copper and zinc, and we examine the effect of the d-bands of these solute metals on the Al $L_{2,3}$-emission from the alloy.

2. Experimental, and Specimen Preparation

The spectrometer used in these investigations, and the method employed for processing the emission spectra, are fully described elsewhere; see Watson, Dimond and Fabian [8,9]. For the examination of alloys additional difficulties arise associated with preparation and homogeneity and with precise determination of structure during the excitation of soft x-ray emission. Where possible single-phase solid solutions were investigated for the measurements described here; for the Al-Ag and Al-Zn systems this necessitates quenching the alloy from the equilibrium temperature for the appropriate single phase. The Al-Cu alloys were mostly two-phase but were heat-treated in the same manner.

The alloys were prepared from high-purity component metals by melting and casting in a reducing atmosphere. Selected small ingots, free from imperfection, were homogenized for 7 days in evacuated capsules at a temperature chosen according to the equilibrium phase diagram for the system and then rapidly quenched. Specimens in the form of thin slabs 10 mm × 5 mm, and ~1 mm thickness, were obtained from the homogenized ingots by hot or cold rolling according to the physical properties of the alloy, one surface was ground flat and polished, and the slab then subjected to further annealing and quenching. Structure was checked metallographically before and after examination in the spectrometer.

All spectra reported here were recorded using a platinum coated, 1-meter radius, blazed grating with 600 lines/mm. The alloy specimens during measurement were supported on, and in good thermal contact with (using conducting cement), a water-cooled stainless steel target anode. Vacuum of $\sim 1 \times 10^{-6}$ Torr was established in the target chamber, after considerable out-gassing of the alloy, and spectra were recorded using 3 kV and 5 mA respectively for target voltage and current. For each alloy investigated, spectra were summed, in the manner previously described [8,9], until the total count obtained at a given wavelength position of the spectrum, was sufficient to reduce statistical uncertainty to $<1\%$.

The spectra are corrected for background (chiefly Bremsstrahlung) and for the intensity fall-off during a scan due to contamination of the specimen surface. The background is assumed to be linear with wavelength, and the contamination linear with time after an initial rapid fall-off which avoided by delaying the start of a scan. The specimen surface is scraped clean, under vacuum, between scans.

3. Results and Discussion

The Al $L_{2,3}$-emission spectra obtained for a series of aluminum-silver alloys, of varying silver content, are shown in figure 1. The spectra are plotted in terms of I/ν^5 (in arbitrary units) as a function of energy (in eV). The division of the emission intensity by the fifth power of the frequency takes account firstly of ν^2 in the relation

$$I(\lambda)d\lambda \propto \frac{1}{\nu^2} I(\nu)d\nu \qquad (1)$$

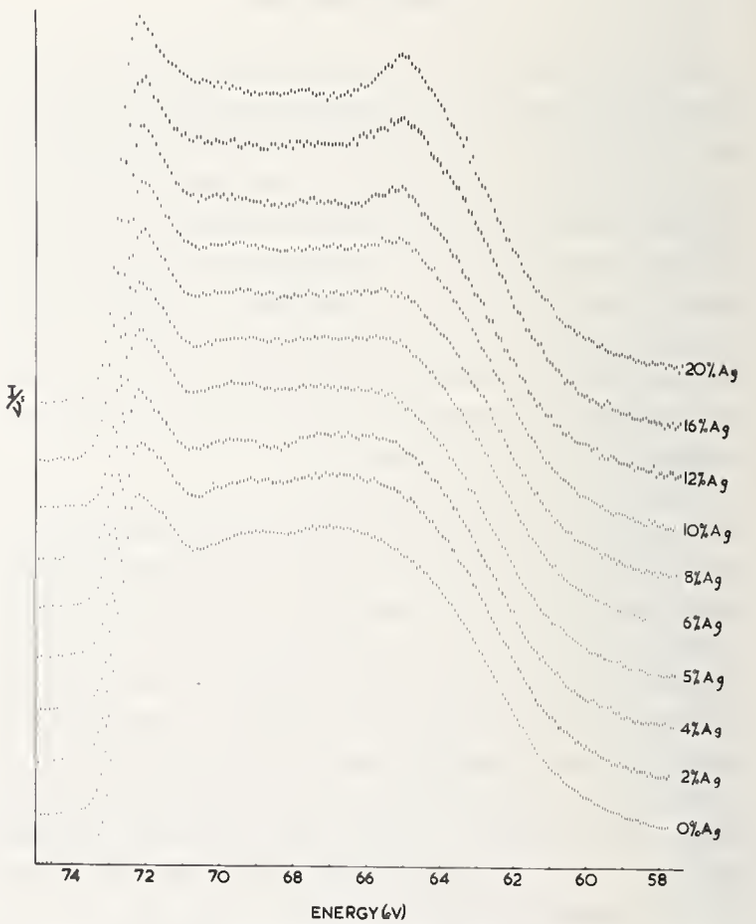

FIGURE 1. Al $L_{2,3}$-*emission from quenched* Al-Ag *alloys of compositions 0–20 atomic percent* Ag.

All are single-phase fcc solid solutions. The spectra, shown as I/ν^5 in arbitrary units versus energy in eV, are compared by normalizing to equal peak maximum. Each spectrum is the sum of 20 to 50 scans. Vertical bars indicate the statistical uncertainty in count rate, calculated from the total count.

which converts intensity at wavelength λ to intensity at frequency ν, and secondly of ν^3 in the relation

$$I^{\prime}(E) \propto \nu^3 \left| \int \psi_1 \sum r \psi_2 \, d\tau \right|^2 \qquad (2)$$

which gives the transition probability for the transition from initial state 1 to final state 2. Because an accurate knowledge of the initial-state and final-state wavefunctions is required, and is impossible to determine, no attempt is made to account for the matrix elements in this correction for transition probability, and the curves obtained—I/ν^5 vs E—are regarded as only approximately but usefully related to the density of valence-band states for the alloy.

With Al $L_{2,3}$-emission these will be the valence-band states as seen by aluminum atoms in the alloy. On comparing the emission spectra for Al-Ag alloys (fig. 1) for varying silver concentration, clearly the most important feature to emerge is the peak, at ~65.5 eV, that first appears at ~10 at. % Ag and rises sharply in intensity as the silver concentration is increased to 20 at. %. Over the whole of the composition range investigated these alloys form single-phase solid solutions at the temperatures selected for annealing, and the alloys were quenched from this temperature to retain the α-phase structure. The specimens showed, metallographically, no observable segregation before or after examination. The quenched alloys are known [10,11] to exhibit clustering of silver, but this we do not expect to observe in simple metallography.

We attribute this peak, in the Al $L_{2,3}$-emission from the alloys, to transitions from the lower part of the hybridized d-bands of silver to vacant aluminum core states. A preliminary comparison by Marshall et al. [12], of the emission spectrum for the 20 at. % Ag alloy with the band structure for silver metal (fig. 2), drew attention to the close correspondence of this peak with the energy at which the d-bands of silver are expected to hybridize with the s,p-band. This hybridization is of course common with d-bands, but for silver the hybridized states lie in a narrow band right at the bottom of the silver valence band, giving rise to a low grad $\mathbf{k}E$ and consequently a high density of s- and d-states. This will occur at ~ 7.2 eV (5.3 Ry, fig. 2) below the Fermi-energy and agrees well with the peak observed in the Al $L_{2,3}$-emission from Ag-Al alloys which appears at ~ 7.5 eV below the emission edge.

Our interpretation requires that the states in the upper regions of the hybridized d-bands contribute less strongly to the Al $L_{2,3}$-emission, and this is probably so because these states will tend more to hybridize with p-states which do not contribute to L spectra. The interpretation further requires that the d-bands for silver will remain, for the alloy, at much the same energy at which they occur for pure silver metal. This assumption may not be unreasonable, particularly in view of the clustering or coherent precipitation of silver that is known to occur to some extent for these quenched alloys.

The bandwidths observed appear to remain constant with varying silver concentration and this result lends no support to the rigid-band model for these alloys. An attempt was made to measure the Ag $N_{2,3}$-emission but the intensity was too low to permit this emission band to be detected above the background. However, our results for the Al $L_{2,3}$-emission support the conclusions reached by Harrison [7] that the d-bands of the solute metal will carry over to the alloy; we find that they contribute to the valence band and are "seen" by the solvent atoms.

The results can also be explained, although less neatly, using the approach developed by Friedel [3]. Restricted sharing of valence electrons between component atoms will lead to local screening of the higher positive charge on the aluminum ions and cause the electron wavefunctions to increase near these ions. This will result in a relative increase in intensity of emission at the bottom of the valence band since the electrons in the higher energy states will be more involved in sharing with other atoms in the alloy.

Our measurements of the Al $L_{2,3}$-emission from aluminum-copper alloys show a similar peak, first appearing for approximately 10 at. % Cu and increasing sharply with additional Cu concentration. For the 20 at. % Cu alloy which is a two-phase structure of fcc α-Al and tetragonal θ-Al_2Cu, the general shape of the spectrum, shown in figure 3, agrees well with that obtained by Curry [1] for Al_2Cu; the same intense peak is observed at ~66 eV. The Cu $M_{2,3}$-emission overlaps the Al $L_{2,3}$, but its intensity for the 20 at. % Cu alloy was too low to have any significant effect. The energy at which the hybridized d-bands for copper, figure 2, can be expected to contribute to transitions to Al core states does not in this case correspond as closely with the observed peak in the Al $L_{2,3}$-emission as for Al-Ag. The peak occurs at ~6.0 eV below the emission-edge, and the bottom of the hybridized copper d-bands at ~5.0 eV below the Fermi energy. However, the emission in the case of this alloy will come largely from the Al_2Cu phase which tends to order, and the emission from the α-Cu phase will be affected also by the coherent precipitation of ordered Al_2Cu that occurs for this quenched alloy [13]; if the transitions that give rise to the observed peak are assumed to be transitions from d-bands of ordered

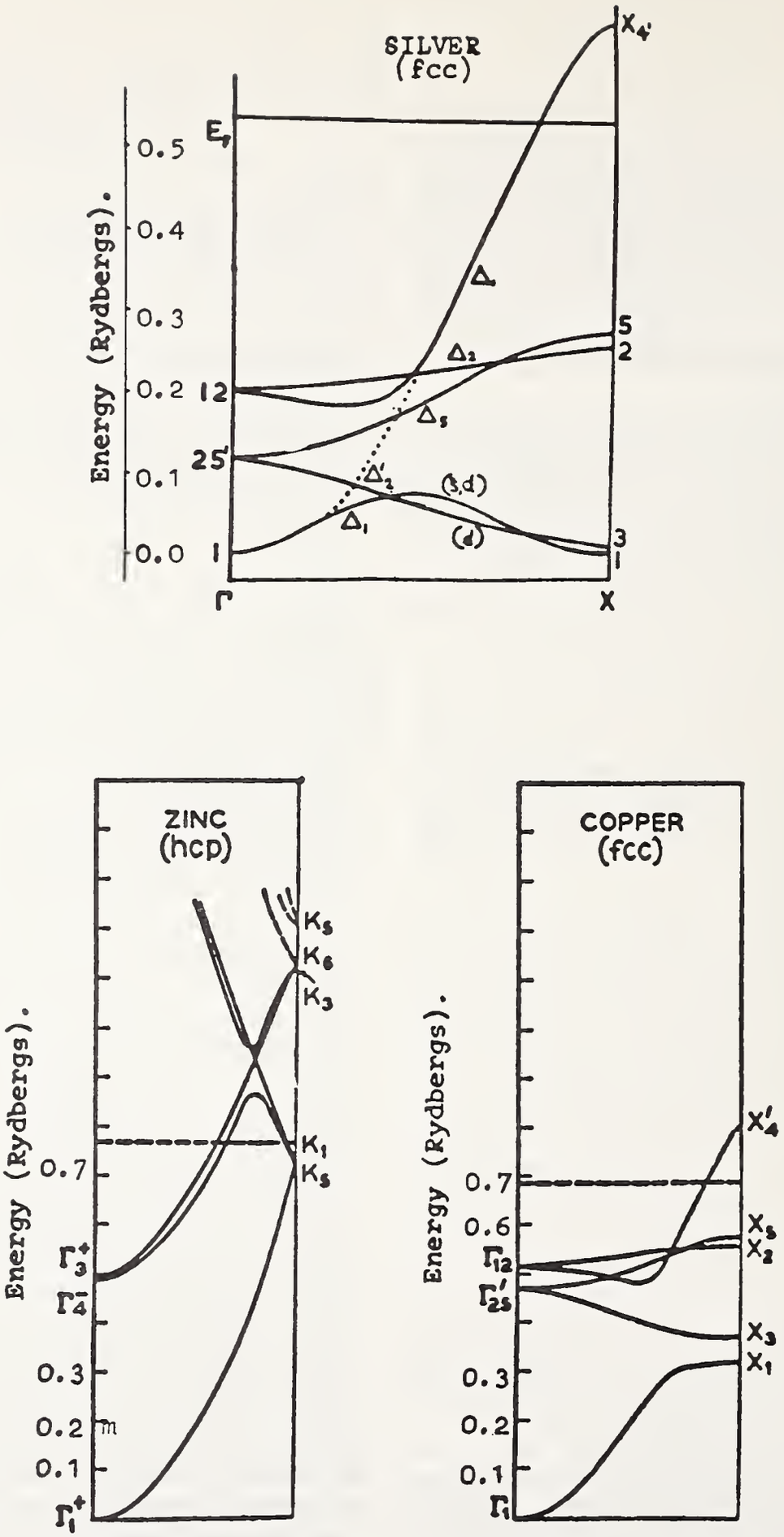

FIGURE 2. *Band structures for the pure metals* Ag, Cu, *and* Zn.
Silver; calculations of Ballinger and Marshall [17]. Copper and Zinc; calculations of Mattheiss [18].

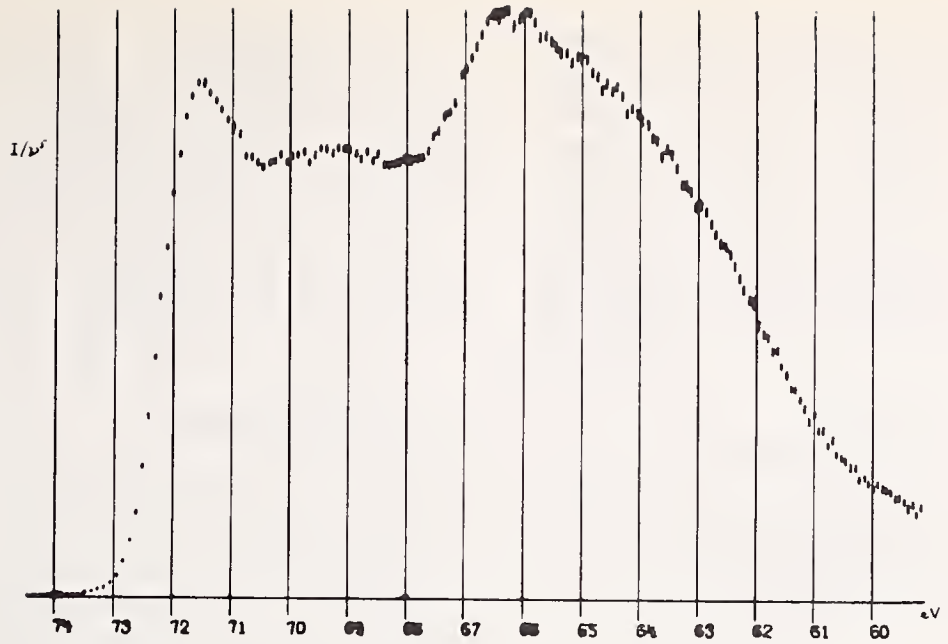

FIGURE 3. Al $L_{2,3}$-*emission from quenched* Al-Cu *alloy containing 20 atomic percent* Cu.

Two-phase alloy, α-Al (fcc) plus β-Al_2Cu (tetragonal). The spectrum is the sum of 25 scans; vertical bars indicate statistical uncertainty in count rate.

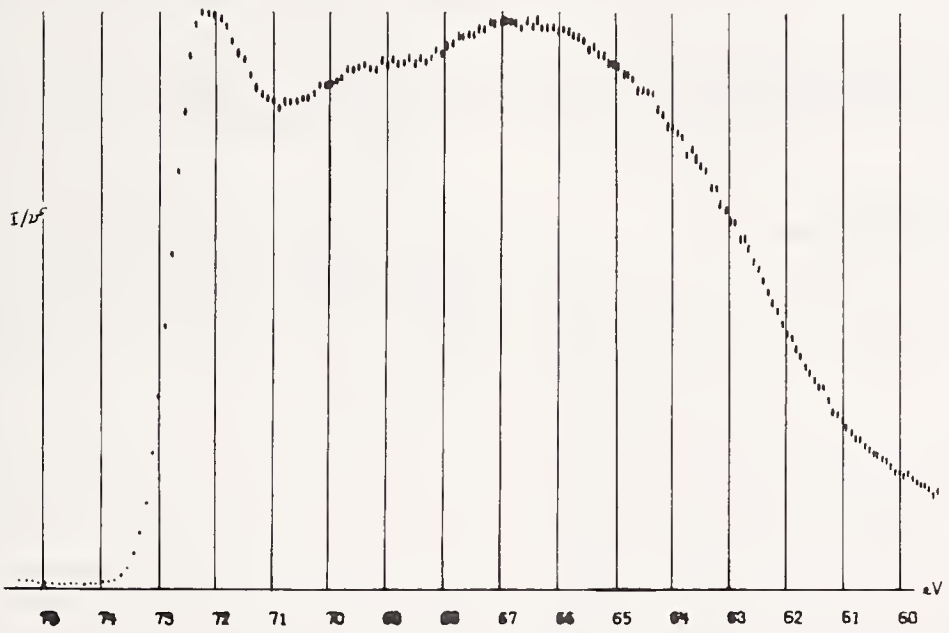

FIGURE 4. Al $L_{2,3}$-*emission from quenched* Al-Zn *alloy containing 55 atomic percent* Zn.

Single-phase alloy, cph. Spectrum is the sum of 30 scans; vertical bars indicate statistical uncertainty in count rate.

Al_2Cu to Al core states, we can explain the energy shift in terms of the lowering in energy of the Cu *d*-bands that must occur when Cu atoms form a locally ordered structure with Al atoms.

This is again the *d*-band structure of the solute metal carrying over to the alloy and being "seen" by the solvent atoms. The strong intensity of the observed peak must be attributed either to a high narrow density of these *d*-band states or to a matrix-element effect for these transitions.

In the case of Al-Zn alloys we find no contribution to the Al $L_{2,3}$-emission from the *d*-bands of Zn. This is entirely what we should expect from the band structure of zinc (fig. 2) where the *d*-bands do not appear because they are much lower than for Ag or Cu and are found below the 4*s*, so that little or no hybridization with *s*-states occurs. Our result for the Al $L_{2,3}$-emission from the 55 at. % Zn alloy is shown in figure 4. The bandwidth for these alloys remains constant and nearly equal to that for pure aluminum, indicating again that

the rigid-band model does not apply to these alloys. A small relative increase in intensity in the lower-energy part of the emission band does occur and is probably due to the localized screening of aluminum ions due to the restricted electron sharing discussed by Friedel, but no peak is observed such as that found for Al-Ag or Al-Cu. Clustering of Zn in the quenched alloys is also known to occur in this system [14], and clearly in itself does not affect the emission spectra. This suggests that for Al-Ag and Al-Cu, clustering cannot alone explain the features of the Al $L_{2,3}$-emission.

The results observed for the $L_{2,3}$-emission from Al-Ag and Al-Cu alloys show marked similarities to the effects observed in the K-emission spectra for these alloys by Baun and Fischer [15], and for the K-emission from Al-Ag by Nemnonov [16]. We believe that the same interpretation can be applied to the K-emission results.

4. Acknowledgments

This work was supported by a grant from the Science Research Council. The authors wish also to thank C. A. W. Marshall, G. A. Rooke, and Dr. Si Yuan for helpful discussion, Professor E. C. Ellwood for encouragement and support, and Professor G. Busch for his interest.

5. References

[1] Curry, C., in Soft X-Ray Band Spectra and Electronic Structure of Metals and Materials, D. J. Fabian, Editor (Academic Press, London, 1968), p. 173.
[2] Jones, H., Proc. Roy. Soc. **A144**, 255 (1934).
[3] Friedel, J., Phil. Mag. **43**, 153 (1952).
[4] Varley, J. H. O., Phil. Mag. **45**, 887 (1954).
[5] Rooke, G. A., in Soft X-Ray Band Spectra and Electronic Structure, D. J. Fabian, Editor (Academic Press, London, 1968), p. 185.
[6] Ziman, J. M., Proc. Phys. Soc. **91**, 701 (1967).
[7] Harrison, W. A., in Soft X-Ray Band Spectra and Electronic Structure, D. J. Fabian, Editor (Academic Press, London, 1968), p. 238.
[8] Watson, L. M., Dimond, R. K., and Fabian, D. J., J. Sci. Instru. **44**, 506 (1967).
[9] Watson, L. M., Dimond, R. K., and Fabian, D. J., in Soft X-Ray Band Spectra and Electronic Structure, (Academic Press, London, 1968), p. 45.
[10] Guinier, A., J. Phys. Radium **8**, 124 (1942).
[11] Simerska, M., Czech. Jnl. Phys. **B12**, 54 (1962).
[12] Marshall, C. A. W., Watson, L. M., Lindsay, G. M., Rooke, G. A., and Fabian, D. J., Phys. Letters **28A**, 579 (1969); and Fabian, D. J., Ellwood, E. C., Lindsay, G. M., Watson, L. M., and Marshall, C. A. W., in Proceedings X-Ray Spectra and Electronic Structure of Matter, Institute of Metal Physics, Ukr. Academy of Sciences, 1969, p. 26.
[13] Turnball, D., in Impurities and Imperfections, Amer. Soc. Metals, 1955, p. 121.
[14] Rudman, P. S., and Averbach, B. L., Acta Met. **2**, 576 (1954).
[15] Baun, W. L., and Fischer, D. W., International Res. Rep. **(AFML-TR-66-191)**, Air Force Materials Laboratory, Ohio, 1966.
[16] Nemnonov, S. A., private communication, to be published.
[17] Ballinger, R. A., and Marshall, C. A. W., J. Phys. Chem. (Proc. Roy. Soc.) **2**, 1822 (1969).
[18] Mattheiss, L. F., Phys. Rev. **134** (4A), 970 (1964).

Soft X-Ray Emission Spectra of Al-Mg Alloys

H. Neddermeyer

Sektion Physik der Universität München, München, Germany

In recent years the interpretation of soft x-ray emission band spectra has made good progress. With a detailed knowledge of the electronic band structure, of transition probabilities, and of lifetime broadening effects, it has been possible to calculate the shape of emission band spectra of a few pure elements [1,2]. However, the situation is much more complicated in the case of alloys where the problems are far from being solved. The different shapes of emission band spectra of the components of an alloy make the applicability of the usual model to alloy spectra doubtful.

As a contribution to these problems we have remeasured the soft x-ray emission band spectra of Al-Mg alloys using improved experimental techniques. The Al $L_{2,3}$- and Mg $L_{2,3}$-emission spectra lying in the same wavelength region can be studied in the same spectrometer. Since the spectra of the pure metals have characteristic details and the energy resolution in this wavelength region is good, shapes and changes of shape can be registered very precisely.

Key words: Aluminum (Al); aluminum-magnesium alloys (Al-Mg); charging effect; electronic density of states; emission spectra; magnesium (Mg); rigid-band approximation; soft x-ray emission.

1. Theory

For electronic transitions from occupied valence states to empty core states, causing a soft x-ray emission band spectrum, the basic formula for the intensity distribution of the spectrum can be written as [3]:

$$I_{c,v}(\omega) = A \int \frac{dk}{8\pi^3} |e \cdot M_{c,v}|^2 \cdot \delta(E_v - E_c - \hbar\omega) \qquad (1)$$

$I_{c,v}(\omega)$ means the number of transitions of energy $\hbar\omega$ per unit time, A is a constant, $|e \cdot M_{c,v}|$ the matrix element for the transition probability, and E_v, E_c the energies of the valence and core states. The integration has to be carried out over all possible wave vectors $\mathbf{k}$. Using the property of the δ-function the integration can be performed and we obtain

$$I_{c,v}(\omega) = A \int_s \frac{dS}{8\pi^3} \cdot \frac{|e \cdot M_{c,v}|^2}{|\nabla_{\mathbf{k}}(E_v - E_c)|}_{E_v - E_c = \hbar\omega} \qquad (2)$$

where dS represents an element of a surface in the $\mathbf{k}$-space defined by the equation

$$E_v(\mathbf{k}) - E_c(\mathbf{k}) = \hbar\omega. \qquad (3)$$

Usually one assumes $E_c(\mathbf{k})$= const for all $\mathbf{k}$, thus implying that the inner level is sharp, and one obtains the well known formula

$$I_{c,v}(\omega) = A \int_s \frac{dS}{8\pi^3} \frac{|e \cdot M_{c,v}|^2}{|\nabla \mathbf{k} E_v|}_{E_v - E_c = \hbar\omega} \qquad (4)$$

In simple cases this integral can be split into a product of two factors, namely the transition probability and the density of states.

In the case of alloys the difficulty arises that we know neither the transition probability, nor the density of states nor $E(\mathbf{k})$-curves. In the case of a well defined single-phase Al-Mg alloy one would first apply the concept of the rigid-band model. This would mean that the valence electrons of the Al and Mg atoms constitute a single valence band. The validity of the rigid-band model for dilute Al-Mg alloys has indeed been proved by measurements of the Fermi surface [4]. Thus one should expect similar Al and Mg spectra. The fact that the two spectra are different [5-7] can be explained by a charging effect of Al atoms having a higher valence than the Mg atoms [8]. Charging leads to a nonuniformity of the valence electron distribution within the crystal, i.e., the electron density near the Al atoms is higher than near the Mg atoms.

2. Experimental

The Al $L_{2,3}$- and Mg $L_{2,3}$-emission spectra of the alloys and of the pure metals have been obtained using a

concave grating spectrometer with ultrahigh vacuum conditions [9]. The x rays were excited directly by bombardment voltages of 2 kV and emission currents of 1 to 3 mA. The spectra were recorded either continuously with a strip-chart recorder or stepwise using digital equipment. The influence of contamination and self-absorption could be neglected. The spectra were corrected for the known reflectivity of the grating. The influence of the quantum efficiency of the multiplier photocathode seemed to be small.

Besides the pure metals Al and Mg, the following Al-Mg alloys were investigated: Al_5Mg_{95}, $Al_{10}Mg_{90}$, $Al_{30}Mg_{70}$, $Al_{12}Mg_{17}$, Al_3Mg_2, and Al_2Mg. Microscopic and x-ray diffractometer studies were made to check the crystallographic order. According to the phase diagram [10] $Al_{12}Mg_{17}$ and Al_3Mg_2 are single phase alloys. The dilute alloys Al_5Mg_{95} and $Al_{10}Mg_{90}$ are single phases at 430 °C; at room temperature these alloys decompose slowly into binary phases. During the spectroscopic studies this decomposition could be recognized slightly in the case of $Al_{10}Mg_{90}$. $Al_{30}Mg_{70}$ and Al_2Mg are binary phases.

3. Results: Dilute Alloys

The Mg $L_{2,3}$-spectra of Al_5Mg_{95} and $Al_{10}Mg_{90}$ agree with the Mg $L_{2,3}$-spectrum of pure Mg (fig. 2) within the limits of statistical error, of less than 3%. Also the positions of the emission edges agree within ± 0.01 eV with the emission edge of the pure metal. On the other hand, the shapes of the Al $L_{2,3}$-spectra of these alloys (fig. 1), which are in agreement with measurements reported earlier [5], differ markedly from the Mg $L_{2,3}$-spectra.

So one has to conclude that the rigid-band model is not applicable to these alloys. The differences between the Mg and Al spectra can hardly be explained by even a considerable influence of the unknown transition probability. As a possible explanation one would rather assume the existence of clusters and localized bound states. A further argument for this assumption is the good agreement between the Al $L_{2,3}$-spectra of Al_5Mg_{95} and $Al_{10}Mg_{90}$.

4. Nondilute Alloys

The Mg $L_{2,3}$-emission spectra of the nondilute alloys are shown in figure 2. In figure 3 the emission edges of these spectra are drawn in an enlarged energy scale. The Al $L_{2,3}$-emission spectra of these alloys are presented in figure 4, and the emission edges on an enlarged scale in figure 5. The exact positions of the edges and peaks and the widths of the edges are listed in table 1. The spectra of $Al_{12}Mg_{17}$ and Al_3Mg_2 are in rough agreement with those published by Appleton and Curry [7], but some fine structure features have not been reported previously.

The statements of Appleton and Curry concerning the general behavior of the spectra of metals on alloying are verified to a certain extent by the present measurements, but there are also some essential deviations. An increasing concentration of one alloy component does not always affect continuous variations of the shape of the emission bands. So the Mg $L_{2,3}$-emission spectra of Al_3Mg_2 and Al_2Mg are in good agreement with each other, and the Al $L_{2,3}$-emission bands of the dilute alloys Al_5Mg_{95} and $Al_{10}Mg_{90}$ also agree with the emission band of $Al_{30}Mg_{70}$.

Appleton and Curry further state that the widths of the emission bands of Al-Mg alloys are equal to those of

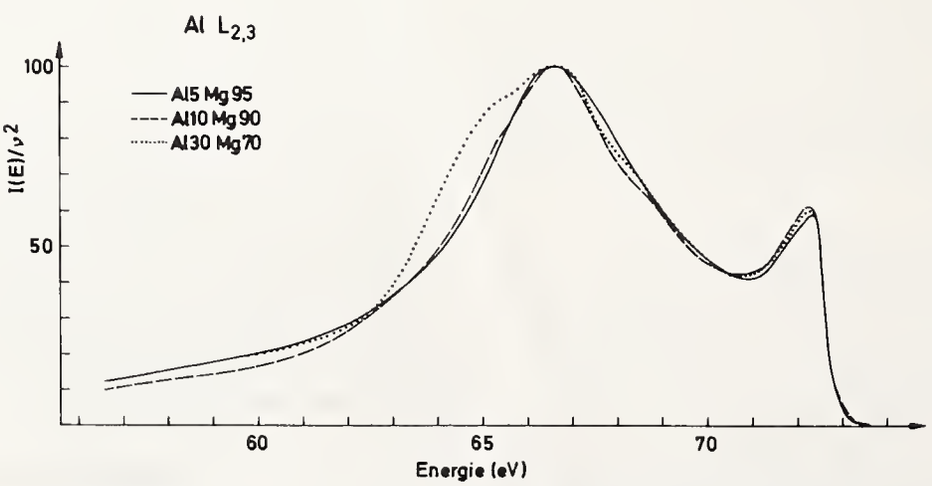

FIGURE 1. Al $L_{2,3}$-*emission spectra of* Al_5Mg_{95}, $Al_{10}Mg_{90}$, *and* $Al_{30}Mg_{70}$.
The spectra have been normalized.

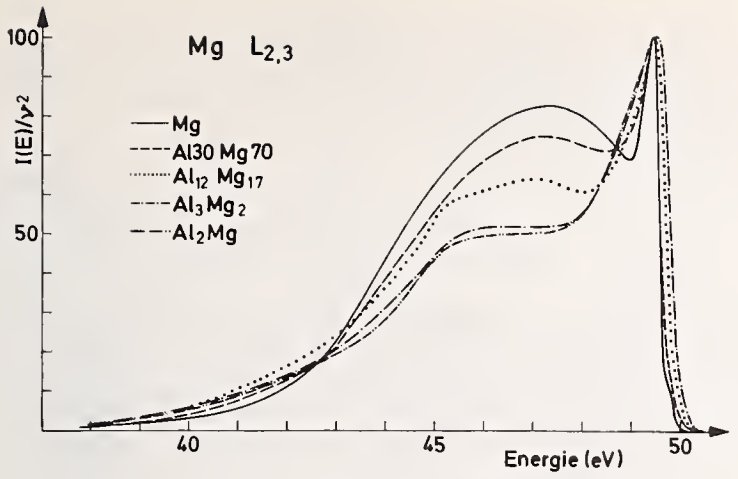

FIGURE 2. Mg $L_{2,3}$-*emission spectra of* Mg *and nondilute* Al-Mg-*alloys.*
The spectra have been normalized.

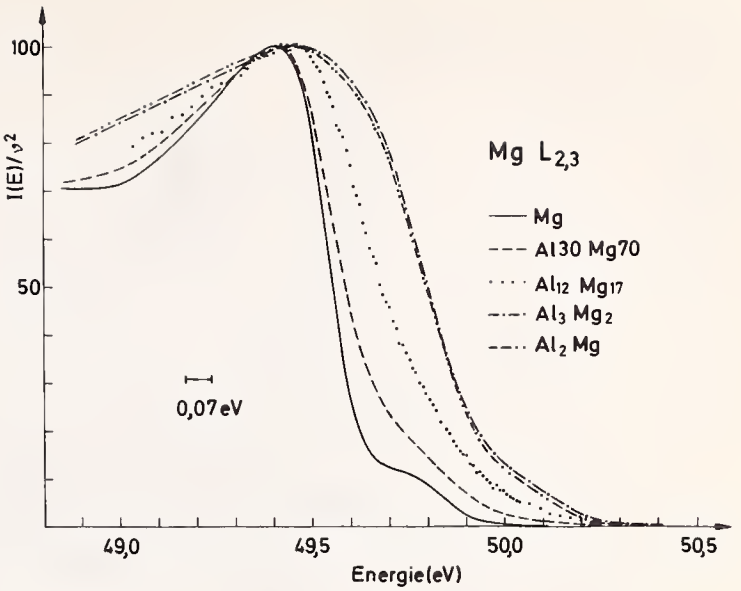

FIGURE 3. Mg $L_{2,3}$-*emission edges of* Mg *and nondilute* Al-Mg-*alloys.*
The theoretical resolving power in this wavelength region amounts to 0.07 eV [9].

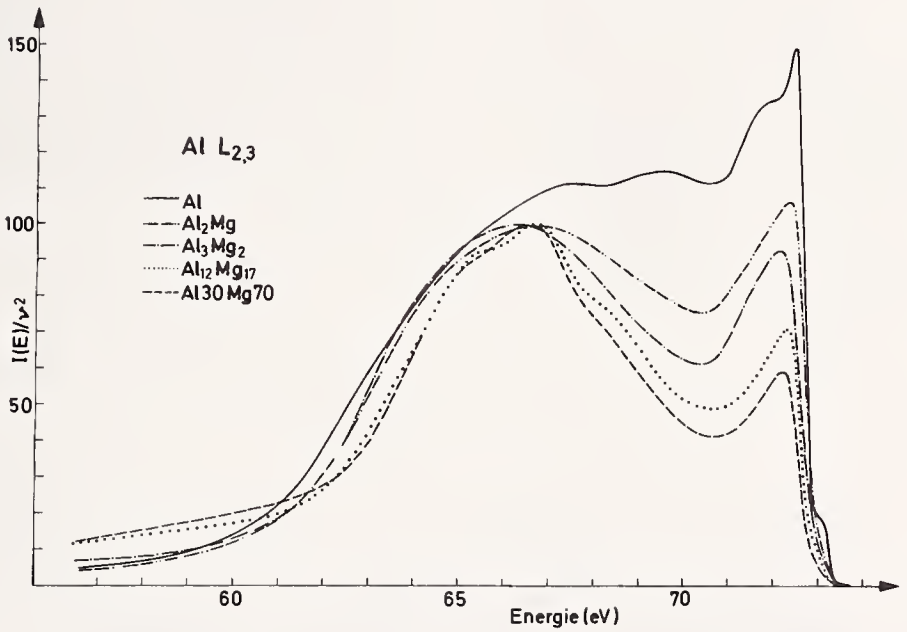

FIGURE 4. Al $L_{2,3}$-*emission spectra of* Al *and nondilute* Al-Mg-*alloys.*
The spectra of the alloys have been normalized at the broad maxima. The spectrum of pure Al has been adjusted to the low energy side.

the pure elements within 0.5 eV. Our measurements show that the usual parabolic extrapolation of the low-energy side of the band is not possible since the bands always have a concave shape. Therefore it can not be concluded from the experimental data that the Al and Mg atoms have valence bands of different widths.

On the other hand, if the Al $L_{2,3}$- and Mg $L_{2,3}$-spectra of the single phase alloys $Al_{12}Mg_{17}$ and Al_3Mg_2 are fitted to each other at the emission edge, one sees a similarity which is most pronounced in the high energy region (figs. 6 and 7): (1) the emission edges have the same width if the broadening by the spectral window function is taken into account;(2) the widths of the peaks agree rather well; (3) the characters and shapes of the emission bands are similar; both spectra of Al_3Mg_2 being smooth whereas the Al as well as the Mg spectrum of $Al_{12}Mg_{17}$ has a fine structure.

These similarities indicate a common valence band and support the views expressed by Harrison [11]. The differences of the spectra in the low energy region seem to be connected with the fact that the Al atoms with its higher valence are screened by the nearly free valence

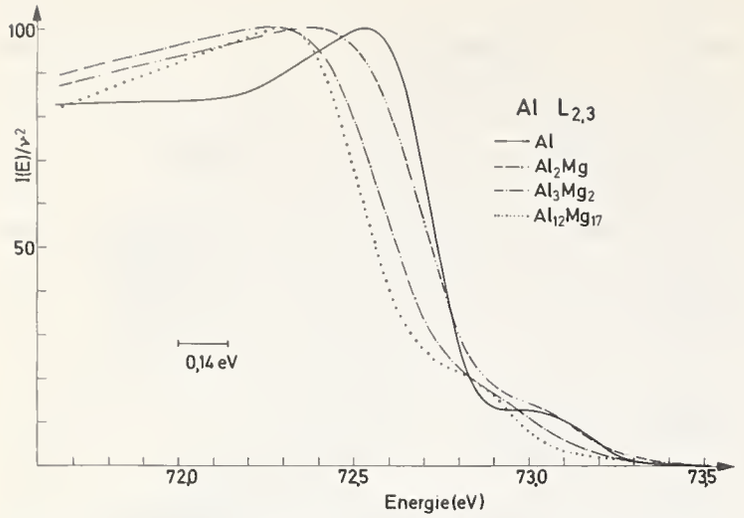

FIGURE 5. Al $L_{2,3}$-*emission edges of* Al *and nondilute* Al-Mg-*alloys.*
The theoretical resolving power in this wavelength region amounts to 0.14 eV.

TABLE 1. Al-Mg-*alloys and the pure metals* Al *and* Mg: *Positions of the* L_3-*peaks (maxima),* L_3-*edges (50% points on the* L_3-*edges). Widths of the emission edges (twice the difference between 50 and 90% points on the* L_3-*edges). Data in eV. No correction for instrumental line width has been made.*

		L_3-peak	L_3-edge	L_3-width
Mg $L_{2,3}$	Mg	49.40 ± 0.04	49.55 ± 0.03	0.14 ± 0.02
	Al_5Mg_{95}	49.40 ± 0.04	49.55 ± 0.03	.16 ± 0.02
	$Al_{10}Mg_{90}$	49.40 ± 0.04	49.56 ± 0.03	.16 ± 0.02
	$Al_{30}Mg_{70}$	49.41 ± 0.04	49.58 ± 0.03	.20 ± 0.02
	$Al_{12}Mg_{17}$	49.44 ± 0.04	49.67 ± 0.03	.28 ± 0.03
	Al_3Mg_2	49.45 ± 0.06	49.79 ± 0.03	.34 ± 0.04
	Al_2Mg	49.44 ± 0.06	49.79 ± 0.03	.36 ± 0.05
Al $L_{2,3}$	Al	72.53 ± 0.05	72.74 ± 0.05	0.22 ± 0.02
	Al_2Mg	72.39 ± 0.08	72.72 ± 0.05	.34 ± 0.03
	Al_3Mg_2	72.28 ± 0.08	72.62 ± 0.05	.36 ± 0.04
	$Al_{12}Mg_{17}$	72.30 ± 0.06	72.57 ± 0.05	.30 ± 0.04
	$Al_{30}Mg_{70}$		72.57 ± 0.05	
	$Al_{10}Mg_{90}$		72.59 ± 0.06	
	Al_5Mg_{95}		72.61 ± 0.06	

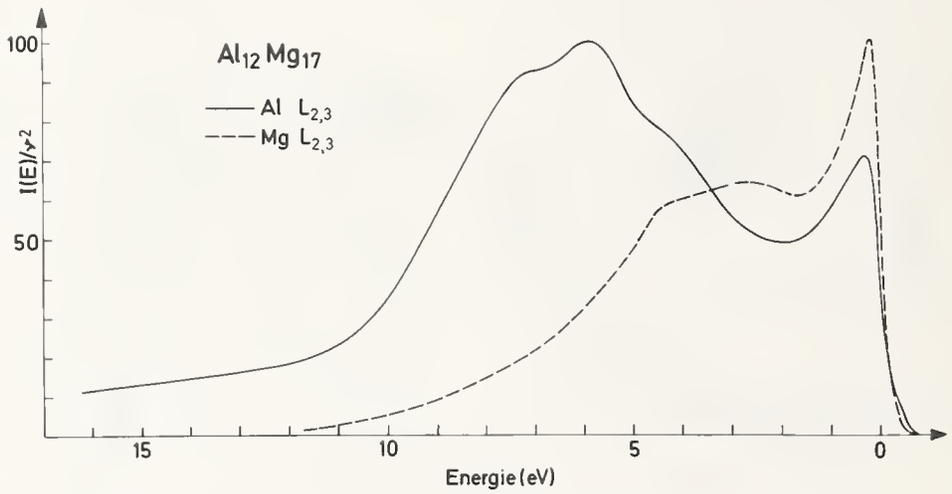

FIGURE 6. Al $L_{2,3}$ *and* Mg $L_{2,3}$-*emission spectra of single phase alloy* $Al_{12}Mg_{17}$.
The spectra have been adjusted to the emission edges.

electrons. Thus in the crystal the valence electrons are not distributed uniformly. This has an influence on the matrix element occurring in eq (1). The screening part of the valence electrons mainly will make transitions to the core states of the Al atoms because of the strong overlapping effects. These electrons are absent in the corresponding Mg spectra the intensity of which is lowered at the low energy side.

The differences of the emission spectra of well defined, homogeneous phases of binary alloys therefore would be a consequence of different transition probabilities. The knowledge of the transition probabilities is thus an essential prerequisite for statements on the density of states, and this holds especially in the case of alloys. It is clear that the emission spectra of all alloy components must also be taken into account.

The situation is more complicated in the case of two-phase alloys like $Al_{30}Mg_{70}$ and Al_2Mg. It appears that the emission spectra of the pure phases do not superpose corresponding to their quantity ratio. The experimental and theoretical investigations should therefore be restricted at first to monophase systems.

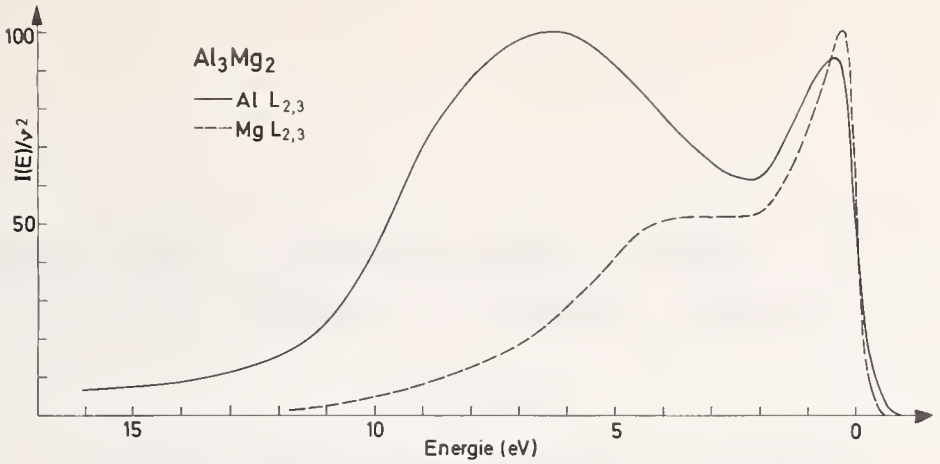

FIGURE 7. Al $L_{2,3}$ *and* Mg $L_{2,3}$*-emission spectra of single phase alloy* Al_3Mg_2.

The spectra have been adjusted to the emission edges.

5. References

[1] Rooke, G. A., Thesis, University of Western Australia (1967); Rooke, G. A., J. Phys. **2**, 767 and 776 (1968).

[2] Klima, J., to be puhlished.

[3] Bassani, G. F., The Optical Properties of Solids, J. Tauc, Editor (Academic Press, New York and London, 1966), p. 33.

[4] Ketterson, J. B., and Stark, R. W., Phys. Rev. **156**, 748 (1967).

[5] Gale, B., and Trotter, J., Phil. Mag. **1**, 759 (1956).

[6] Das Gupta, K., and Wood, E., Phil. Mag. **46**, 77 (1955).

[7] Appleton, A., and Curry, C., Phil. Mag. **12**, 245 (1965).

[8] Stern, E. A., Phys. Rev. **144**, 545 (1966).

[9] Wiech, G., Dissertation, University München (1964); Wiech, G., Z. Physik **193**, 490 (1966).

[10] Eickhoff, K., and Vosskühler, H., Z. Metallkunde **44**, 223 (1953); Samson, S., Acta Cryst. **19**, 401 (1965).

[11] Harrison, W. A., in Soft X-Ray Band Spectra and Electronic Structure, D. J. Ruhin, Editor (Academic Press, London, 1968), p. 238.

An L-Series X-Ray Spectroscopic Study of the Valence Bands in Iron, Cobalt, Nickel, Copper, and Zinc

S. Hanzely

Youngstown State University, Youngstown, Ohio 44503

R. J. Liefeld

New Mexico State University, University Park, New Mexico 88001

This paper presents the results of an attempt to evaluate the merits of the soft x-ray spectroscopic method by examining a group of neighboring elements possessing a variety of valence band properties. The emission lines studied were the threshold level L_α (valence $\rightarrow$ L_{III} shell) lines obtained from high purity, polycrystalline bulk samples under bombardment by a nearly monoenergetic ($\Delta E \sim 1$ eV) electron beam. The associated L_{III} absorption spectra were obtained in this work as self-absorption curves from the same anode samples. Experimental and instrumental distortions were either eliminated, minimized or explicitly corrected for. The results indicate the presence of some anomalous emissions on the high energy side of the L_α line in elements possessing a large density of unfilled valence levels just above the Fermi energy. The valence band emission line shape for these elements (iron, cobalt, and nickel) is found to be strongly dependent on the incident electron beam energy even for near-threshold-level excitations. Analysis of the emission and self-absorption curves demonstrates that the x-ray spectroscopic method is capable of exposing meaningful differences among the valence band energy structures of the solids examined here.

Key words: Cobalt; copper; electronic density of states; iron; nickel; satellite emissions; self absorption; soft x-ray emission; x-ray spectroscopy; zinc (Zn).

1. Introduction

It has been the purpose of this work to record L series valence band spectra of some first transition group metals, correct these for a number of experimental and instrumental distortions, and use the results to assess the utility of the x-ray spectroscopic method for the study of valence band energy structures in these solids.

1.1. The State of the Problem

X-ray spectroscopy has long been acclaimed to yield accurate and useful information about valence band densities of states in solids. An x-ray valence band emission line spectrum and the associated photon absorption spectrum are said to represent, in principle, the electronic densities of states (times appropriate transition probabilities) in the filled and empty portions of the valence band, respectively. This interpretation has been questioned on theoretical grounds [1]. Furthermore, the recorded data are unavoidably distorted by effects inherent in their acquisition [2,3]. Compensation of the observed spectra for such afflictions has largely been neglected in the past. Finally, although the last decade has brought forth experimental results and theoretical predictions that are in better general agreement [4], much discrepancy still remains between calculated band shapes and x-ray spectroscopic results that purport to show the densities of states in these bands.

There exists, therefore, a need to acquire statistically accurate raw data, obtained under desirable operating conditions, and to remove the distortions implicitly involved in their accumulation. Such corrected results would facilitate their own interpretations and the evaluation of the x-ray spectroscopic method for revealing significant features in the valence band characteristics of the source materials.

1.2. Materials

The materials chosen for this study offer a unique opportunity for accomplishing the above objectives.

Among them one finds a variety of crystal structures, associated band shapes and band positions, two different states of magnetization, filled and unfilled 3*d*- and 4*s*-type valence orbitals. They are available in a homogeneous and chemically stable form of high purity and do not change their physical characteristics either in a prolonged ultrahigh vacuum environment or under the high (less than sublimation) temperature operation caused by incident electron beam bombardment. Finally, selection rule-allowed valence band transitions occur in regions of the x-ray spectrum which are accessible to high resolution instruments.

1.3. Methods

Of the three series of x-ray spectra which exist for these materials, the K spectrum contains no selection rule allowed transitions involving the valence electrons. It is, therefore, of no relevance here. Although the $M_{II,III}$ spectra possess the desired valence band information, the recording of the corresponding $L_{II,III}$ valence band spectra appears to be a better choice. For one thing, the small M_{II}-M_{III} separation, being about one tenth the corresponding L_{II}-L_{III} separation of ~13 eV for Fe to ~23 eV for Zn, causes an undesirable overlapping of the M_{II} and M_{III} bands. For another, the probability for radiative de-excitation of the initial x-ray state decreases rapidly toward the ultrasoft x-ray region. Experimental factors such as vacuum conditions and clean sample surfaces become particularly important during the production and detection of the relatively low energy M x rays.

Considerable disagreement is apparent in previously published results on the L series valence band spectra of first transition metal elements [3,5,6]. The major source of these discrepancies can be attributed not to differences in instrumentation, but rather to the nature of the incident electron beam that was used to generate these spectra. Depending on the incident electron energy, line shape distortions can be grouped into three more or less distinct categories.

a. The Self-Absorption Region

When the energy of the incident electrons exceeds about three or four times the L_{III}-state threshold energy, one observes line shape changes and peak position shifts which are attributed to x-ray photon self-absorption in the source material. The phenomenon has been documented for some time [7], but its effects on valence band line shapes have only recently been demonstrated [3,8,9].

b. The Satellite Region

When the incident electrons possess energies in the range between the L_{II}-state threshold and about three times that amount, the high energy side of the diagram lines becomes distorted by the progressive development of satellite emissions from multiply ionized atoms.

c. The Threshold Level Region

When the incident electrons possess sub-L_{II} (but above-L_{III}) state excitation energies, multiple vacancy satellite emissions can be largely eliminated and, together with a normal electron incidence-normal x-ray take-off tube geometry, self-absorption effects become negligible.

The threshold level mode of excitation is admittedly the least desirable for intensity considerations. It is evident, however, that with the expenditure of additional time to accumulate statistically accurate data, this method permits the recording of valence band spectra which are free of the significant distortions mentioned above.

2. Apparatus and Techniques

The equipment used to produce and detect the spectra discussed here consisted basically of an ultrahigh vacuum demountable x-ray tube, an externally manipulated two-crystal vacuum spectrometer using potassium acid phthalate (KAP) crystals and a flowing gas (P-10) proportional counter. A detailed description of the instrument can be found elsewhere [10].

The x rays were generated by about a 100 mA beam of nearly monoenergetic ($\Delta E \sim 1$ eV) electrons emitted from directly heated, thoria coated iridium filament strips and accelerated to the target anodes by the interelectrode potential. The accelerating potential was monitored with a volt box-potentiometer arrangement. Positioning the filament strips "edge-on" with respect to the anode allowed the x rays to pass between them, through a thin x-ray transparent Formwar window, into the spectrometer. The Formwar window, mounted in a self-supporting fashion, was used to separate the ultrahigh x-ray tube vacuum from the moderate spectrometer vacuum ($\sim 10^{-3}$ torr). The anode-filament geometry permitted the electrons to strike the target at normal incidence and the x rays to "take-off" at 90° with respect to the spectrometer.

The x-ray tube vacuum was achieved by initially pumping the system with a mechanical forepump and an oil diffusion pump, both liquid nitrogen trapped. This was followed by a 3 to 5 hour bakeout period at

about 100 °C during which the target and the filament strips were outgassed at progressively higher temperatures. After isolating the system from the oil diffusion pump, the vacuum was improved to the eventual 10^{-9} torr operating level and maintained there by a titanium sublimation-ion pump combination. The x-ray tube components thus became immune to the effects of oil backstreaming and the resulting deposition of carbonaceous materials on the anode surface.

Prior to introducing the high purity (99+%) polycrystalline bulk samples into the x-ray tube, the sample surfaces were first mechanically polished and then electropolished. During actual experiments the anodes (except zinc) were generally kept red hot under about 100 watts of input power provided by the incident electron beam.The zinc anode was prepared by melting a layer of pure zinc onto a water cooled copper anode. The practice of enclosing the carefully cleaned, high purity samples in an ultrahigh vacuum environment and the subsequent operation at elevated temperatures was regarded as essential in minimizing contamination of the sample surfaces being studied.

3. Correction Procedures

The experimental curves used here as raw data represent intensity values accumulated at a series of regularly spaced Bragg-angle settings for preset counting times during which the bombarding electron energy was held constant. The spectrum constructed of such individual data points is affected first by contributions from extraneous atomic phenomena occurring simultaneously with the production of the x rays of interest and second by changes in the response of the instrumental components when they interact with photons of different energies. An enumeration of the relevant distortions and the procedure for their removal follows.

(1) The "x rays off" or detector background was found to be a constant 25 counts per 100 seconds of counting time and was simply subtracted from the observed data.

(2) The detector signals, after being preamplified, were stored in a multichannel analyzer. The dead time of the multichannel analyzer in the multichannel scaler mode was measured and found to be between 3 and 4 microseconds. With the counting rates afforded by the threshold level excitations used here ($\sim$ 100 cts/sec at the line peaks) dead time losses became negligible.

(3) The spectrometer Bragg-angle scale was converted to a linear energy scale according to

$$E=\frac{hc}{(2d)_{\mathrm{KAP}}\sin\theta_B} \tag{1}$$

where $(2d)_{KAP}=26.6$ Å and where h and c have their usual significance.

(4) Corrections for response variations of the KAP crystals and of the proportional counter with photon energy have been discussed elsewhere [10]. Such an operation was based on data (counter pressure, active counter path length, entrance window thickness, etc.) that is probably unique to our instrumentation and, therefore, of little or no use to any other system.

(5) Removal of the continuous spectrum background intensities was accomplished on the basis of a method developed by Liefeld [3]. The sensitivity of the spectrometer permitted the recording of the continuous spectrum alone (using an incident electron beam energy slightly below the L_{III}-state excitation threshold) with intensities at least ten times that of the "x rays off" background. The continuous spectrum was then displaced with respect to the L_α line + continuous spectrum and subtracted from it. The amount of shift was equivalent to the difference in incident electron beam energy between the two curves.

(6) The true spectrum $T(E)$ and the observed spectrum $O(E')$ are related by

$$0(E')=\int_{-\infty}^{+\infty} T(E)\times S(E-E')\,dE \tag{2}$$

where $S(E-E')$ is the instrumental smearing function and is proportional to the $(1,+1)$ position diffraction pattern for a two-crystal spectrometer. Until recently [11], measurement of the dispersive position diffraction pattern has been difficult at best in the absence of adequately intense monochromatic x-ray sources. Liefeld, using the relatively narrow $1s$-$3p$ resonance absorption line of neon as a spectral resolution probe, estimated that for KAP crystals the $(1,+1)$ position spectral window is about 0.7 eV wide at half maximum and not grossly asymmetric [12]. Coupled with the result that the widths of the $(1,+1)$ and $(1,-1)$ position patterns are roughly the same [7], the customary [13] procedure of approximating the former by the nearly Lorentzian shape and width of the measured $(1,-1)$ position

417-156 O - 71 - 22

rocking curve has been adopted here. The smearing function $S(E - E')$ was formed from the product of a Lorentzian with a 0.63 eV width at half maximum and the recorded triangular transmission function of the spectrometer. Solution of eq (2), based on a method described by Schnopper [14], was carried out by electronic computers. The computer was programmed to generate, from a smoothed curve of original data points, a curve which when smeared with $S(E - E')$ yielded the observed spectrum. The results converged to the extent that the change in the peak value between the last two iterations was of the order of 1%. Figure 1 illustrates the impact of the procedure on an iron self-absorption curve and on a threshold level iron L_α emission profile which were introduced into the computer as "original" data. (Except for the presence of the continuous spectrum background in the self-absorption spectra, such "original" data have previously been adjusted for the foregoing distortions (1) thru (5).) The comparison shows that removal of the spectral window smearing introduces no new structures but merely narrows and refines the original features.

Additional distortions such as Auger electron induced satellite emissions and anode self-absorption were minimized or eliminated by using threshold level excitations and by carefully selecting the anode to filament geometry. The remaining experimental affliction is that due to the finite width of the high energy inner state. The L_{III} states for these elements are judged to be Lorentzian in shape and possessing widths at half maximum of about 0.5 eV [2], although there is a marked variation among the values reported in the literature. Moreover, the correction for the inner state smearing presupposes the existence of very precise original data and accurate knowledge about the shape and width of the core state [2]. Because of the above difficulties and because such correction was not regarded as imperative for present interpretation, none of the spectra presented here have been adjusted for the L_{III}-state width.

4. Results and Discussion

The corrected, threshold level L_α valence band emission line shapes for bulk iron, cobalt, nickel, copper, and zinc are presented in figures 1 through 5. The statistical precision of the original data from which these curves were derived was 1% or better at the line peak.

A portion of the associated self-absorption spectra, obtained with the same anode samples, are also included in these figures. They were constructed by taking point by point ratios of two emission curves, one of which was negligibly distorted by self-absorption while the other was seriously altered by it. The statistical accuracy of the emission data was better than 1% in regions of significant self-absorption curve structure.

Figure 6 offers a direct comparison of the corrected, threshold level L_α emission line shapes. The curves are

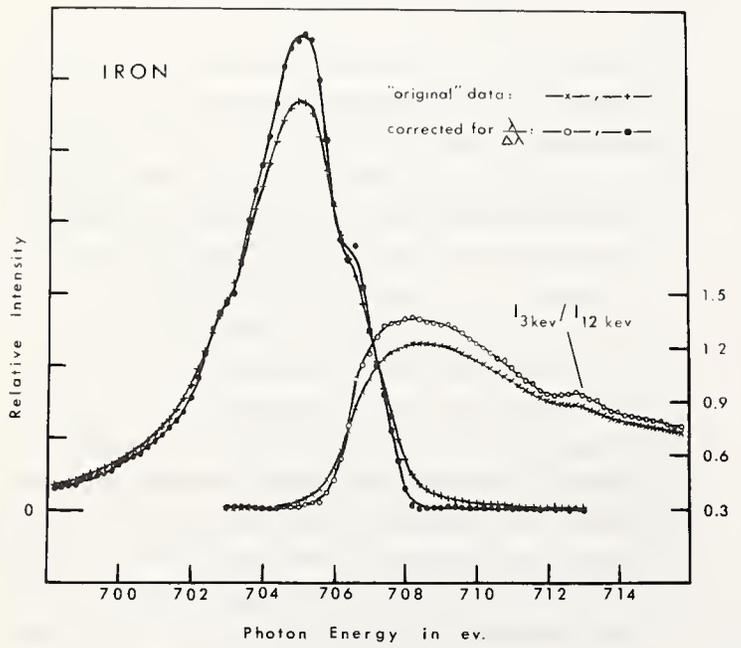

FIGURE 1. *The effect of "spectral window" smearing on a threshold level iron L_α-line shape and on an iron self-absorption spectrum.*

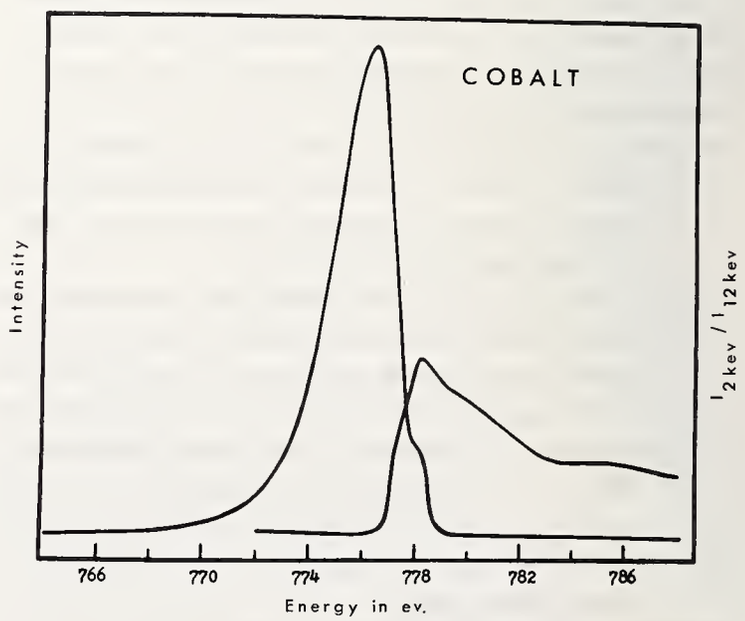

FIGURE 2. *The threshold level cobalt L_α-line shape and a self-absorption spectrum.*

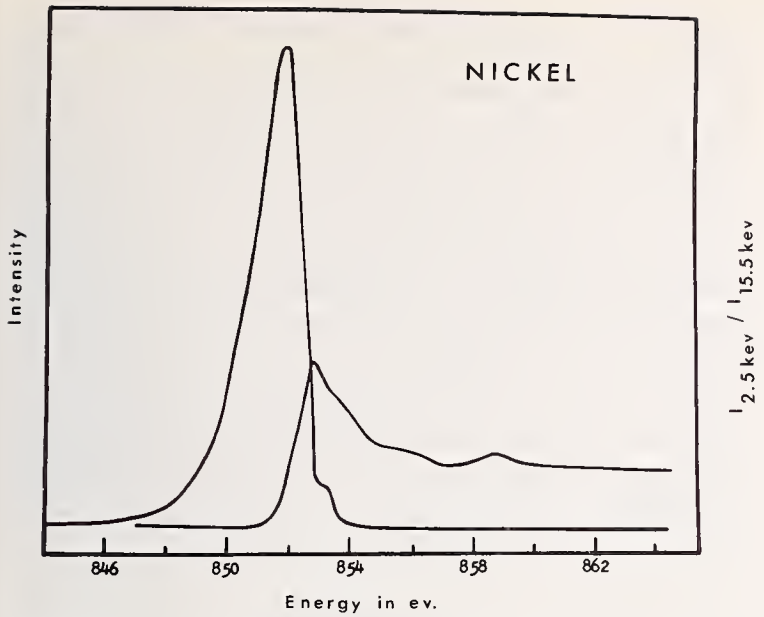

FIGURE 3. *The threshold level nickel* L_α*-line shape and a self-absorption spectrum.*

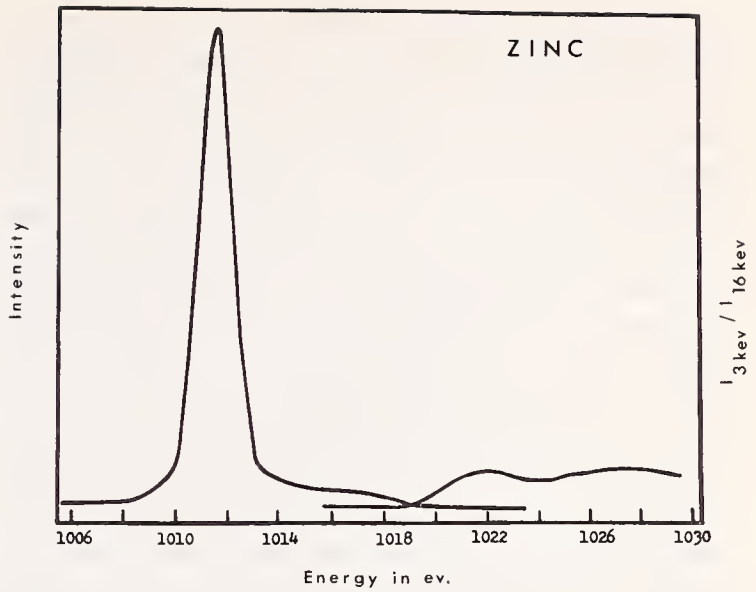

FIGURE 5. *The threshold level zinc* L_α*-line shape and a self absorption spectrum.*

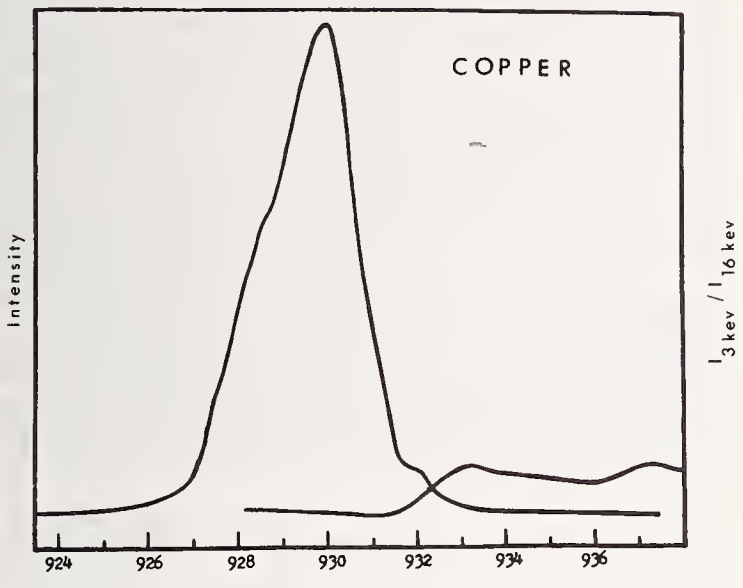

FIGURE 4. *The threshold level copper* L_α*-line shape and a self-absorption spectrum.*

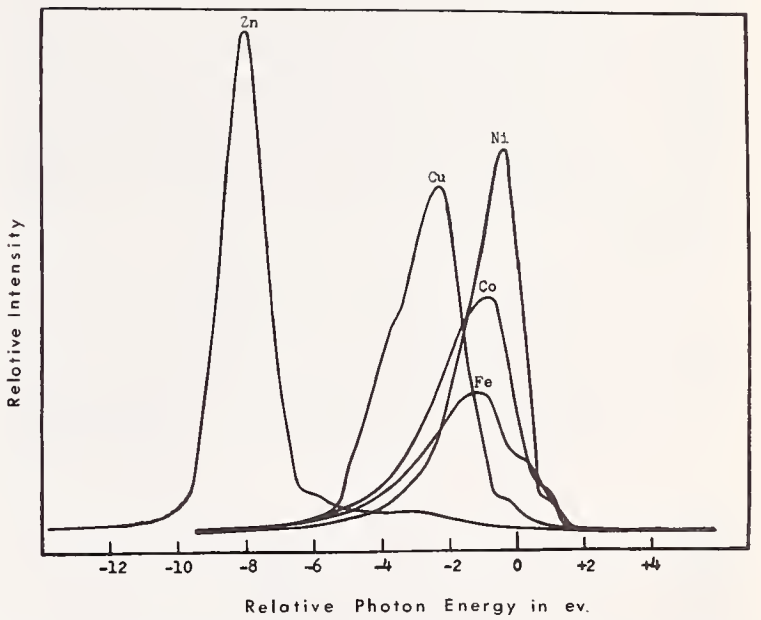

FIGURE 6. *Comparison of the threshold level iron, cobalt, nickel, copper and zinc* L_α*-line shapes matched at their estimated Fermi energies.*

matched at their estimated Fermi energies (taken as the position of the first inflection point of the relevant self-absorption curve) and their areas are proportional to the number of valence electrons possessed by each, i.e., Zn:Cu:Ni:Co:Fe = 12:11:10:9:8.

4.1. General Remarks

It is well known that the recorded intensity in an x-ray valence band emission (or absorption) spectrum is proportional to the product of the density of filled (or unfilled) valence states and the probability of transition $P(E)$ between the initial and final states. X-ray valence band spectra, therefore, cannot yield *direct* information about the distribution of valence states. Neither can they be used to determine the behavior of $P(E)$ over the domain of the band as such information must come from theory. Inasmuch as even crude calculations of the pertinent transition probabilities are scarce, the oft-enmade first approximation that $P(E)$ is relatively constant over the extent of the band will be invoked here. It is further proposed that the intense, narrow features in the emission spectrum represent contributions from valence states of $3d$-type symmetry. Although both $3d$ and $4s$ electrons can (and apparently do) contribute to

the observed L_α-line intensity, the former will presumably dominate since they are more abundant.

Analysis of the data shows that, except for Cu, the width of the prominent $3d$ band decreases as the shell gets filled in progressing from iron to zinc. In going from Ni to Cu, the orderly filling of the $3d$ band is interrupted. The configuration of valence electrons changes from $3d^8 4s^2$ for Ni to $3d^{10} 4s^1$ for Cu. The two additional electrons that are added to the Cu $3d$ band complete it and the larger than Ni bandwidth is exhibited in the resultant Cu L_α emission spectrum. The broad, low intensity structures in the Zn and Cu L_α-line spectra suggest the presence of the overlapping $4s$ band. Theoretically, the Fermi level in Zn is predicted to be in the region where the $4s$ and $4p$ bands begin to overlap, but since p to p type transitions are selection rule forbidden, our measurements should not display any $4p$ band contributions in the observed intensity. The density of filled valence states at E_F is seen to increase gradually from Fe through and then abruptly decrease in Cu and Zn. This behavior is strongly confirmed by Slater's [15] results deduced from specific heat measurements. Table 1 summarizes the valence band structure measurements made from the above figures. The listed base widths include some allowance for inner state smearing.

TABLE 1. *Valence band energy measurements in eV*

Material	L_α peak to L_{III} edge separation	Estimated base width of principal feature	
Iron	1.2	$3d$: 6	$4s$: —
Cobalt	0.8	5	—
Nickel	0.4	3—3.5	—
Copper	2.2	4	—
Zinc	8.4	2.5	12

The associated self-absorption curves have been included here because of their demonstrated similarity to conventional photon absorption spectra [3] and because of the consequent parallels in their interpretation. The self-absorption curves are purported here to give some indication of the distribution of available, localized $3d$ orbitals above E_F, with the assumption again that transition probability variations are negligible over the region of interest.

The above results are not at variance with existing knowledge regarding the valence bands of these metals. Band calculations for Cu [4,16] and Ni [17], for instance, correspond well to the values presented here. Where comparison is permitted, our emission line shapes are in remarkable agreement with the x-ray photoelectron spectroscopic results of Fadley and Shirley [18], although their Cu curve lacks any structure analogous to what has here been interpreted as the $4s$ band. In contrast to earlier photoemission spectroscopic studies on Cu [19] and Ni [20], the results of Eastman and Krolikowski [21] show improved accord with our valence band structure measurements. Finally, and perhaps most significantly, the results demonstrate that the x-ray spectroscopic method yields information which does not merely reflect the nature of a localized high energy inner state but is capable of exposing meaningful differences in the valence band energy structures among the solids examined here.

4.2. Iron Data

Figure 7 presents at iron L_α-line excitation curve obtained with a primary electron beam of $\Delta E \sim 0.2$ eV. Such contours are recorded by setting the spectrometer at the Bragg-angle position corresponding to the peak of the L_α line and by observing the emitted photon intensity at a series of incident electron energies. The excitation curves are used to determine the interelectrode potential in the L_{II}-L_{III} region which will yield the maximum L_α-line intensity. A study of their respective L_α-line excitation curves [10] indicates that for Cu and Zn the condition for maximum L_α-line intensity exists when using just-less-than L_{II}-state threshold energy electrons. Figure 7 shows, however, that for Fe maximum emission, intensity is gleaned by using just above L_{III}-state energy electrons to excite the iron L_α line.

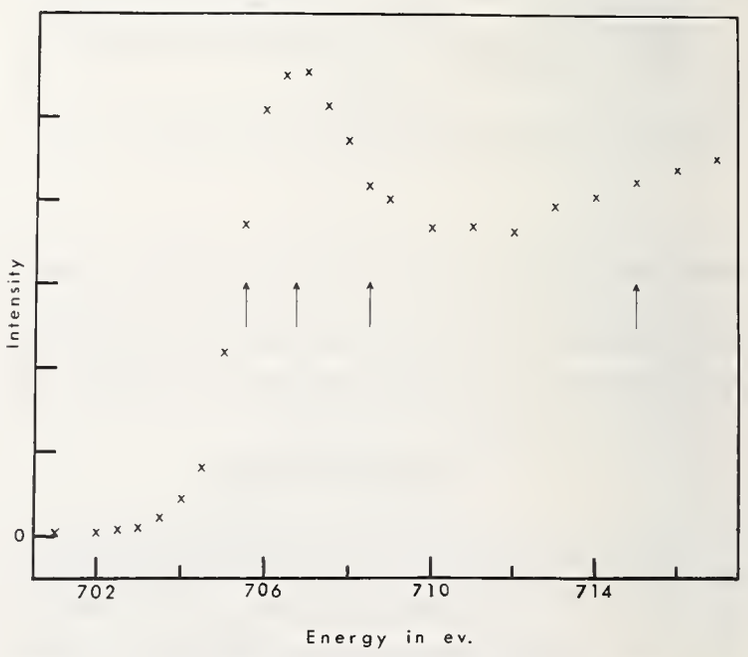

FIGURE 7. *The iron L_α-line excitation curve.*

When the Fe L_α line was recorded under such excitation conditions and the continuous spectrum removed, some anomalous emissions were found to distort the resultant line shape. Similar results have subsequently been observed for Co and Ni. The extraneous intensity structures possess the following properties: (1) They appear only on the high energy side of the L_α line. (2) Their intensities *and* their positions with respect to the L_α line are functions of the incident electron energy in contrast with conventional Auger electron induced satellites. Figure 8 compares four corrected Fe L_α-line shapes, plotted to the same peak intensity, which were generated with incident electrons whose energies relative to the iron Fermi level are indicated by the arrows and whose values are represented by the arrows in figure 7. (3) Such structures seem to be particularly accentuated in the materials which are known to possess large densities of empty, localized 3*d* orbitals just above E_F, although the distortions become progressively less pronounced with the filling of the 3*d* band. Zn and Cu both have the maximum allowable number of 3*d* electrons, their self-absorption curves suggest the presence of a relatively low density of available states just above E_F and as a result their valence band emission spectra are not expected to display such afflictions. (The broad and feeble features in these two metals have been interpreted here to represent contributions from the 4*s* band.)

Our present interpretation of these results suggests that the anomalous intensity structures represent radiative transitions from resonantly excited, bound-electron orbitals. Such emissions have not been reported before; the production of such bound-ejected-electron (BEE) excitation states, in fact, is thought to be unlikely when using electrons as the excitation source [2].

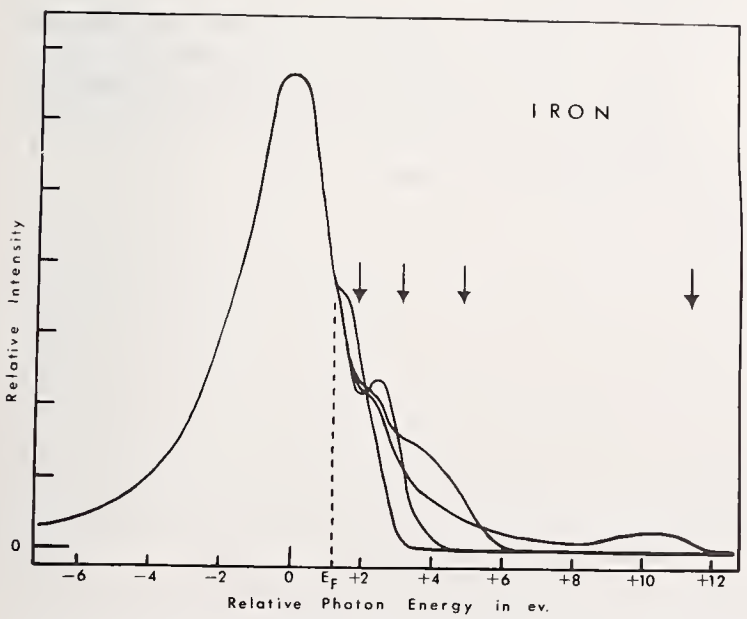

FIGURE 8. *Shape of the threshold level iron* L_α *line as a function of the incident electron energies indicated by the arrows.*

Friedel [22,23] claims that the valence electrons will respond to the presence of the inner shell vacancy by occupying discrete, bound electronic screening levels which possess the symmetry (or symmetries) of the valence electrons. His analysis shows that radiative transitions between these orbitals and the initial state vacancy can occur only if the position of the final state vacancy is at the top of the Fermi distribution, i.e., at E_F. As a result, the emission line shape should be distorted near the emission edge. (Skinner et al. [24] proposed that if such structures exist, they should be apparent in the vicinity of both emission and absorption edges. While the distortions are obvious in emission, a definite change in slope is also discernible in the leading edge of the Fe, Co, and Ni self-absorption curves.) Friedel's approach then apparently accounts for the experimentally observed excess intensity on the high energy side of the L_α line, but it fails to explain either the incident electron energy dependence of these excitation satellites or the fact that they seem to appear only in the elements possessing large densities of unfilled states just above E_F. There is some reason to believe that two different phenomena are contributing to the line shape distortion. A closer examination of figure 8 reveals a relatively stationary structure about 2 eV above the Fermi level in all but the very-near-threshold curve (perhaps because the electron energy was insufficient to excite it in this case), while the extraordinary emissions are seen to respond to changes in incident electron energy.

Holliday [25] and Bonnelle [6] have also reported some structure on the high energy side of the iron L_α line. Neither of these observations, however, appears to be the excitation satellites discussed here as both investigators employed incident electron energies well in excess of the L_{II}-state threshold. Holliday reports a "double peak" near the maximum of the emission profile, but it is too far removed from the emission edge to correspond to our results. Bonnelle's iron curve was apparently recorded under rather poor vacuum conditions ($\sim 10^{-5}$ torr). Considering further the fact that iron is a relatively reactive metal and that previously published results on Fe_2O_3 [26] match Bonnelle's iron curve in every important detail, it appears that she was examining a somewhat oxidized iron sample.

A final note of caution is perhaps in order. In spite of the careful anode preparation techniques employed here and the operation of the target at elevated temperatures in an ultrahigh vacuum environment, it is still

possible that a thin layer of oxide persisted on the anode surface. The possibility exists that the radiating source was characterized by a metal and metal oxide system, each exhibiting its own spectrum. This may be especially true for iron which is found to be very difficult to separate from its oxide. It does not appear likely, however, that such an oxide film was *accumulated* during actual experimentation, because the L_α-line peak intensity remained within statistical limits over extended periods (typically two weeks) of observation.

5. Summary

It has been the object of this investigation to extract, from corrected threshold level L_α-line shapes, incident electron energy independent emission contours and use these for further analysis regarding the distribution of valence states in the relevant solids. Such expectations have been thwarted in three of the elements studied here by extraordinary emissions that distort the resultant line shape and may thus prevent the observation of sharp emission edges in these metals. Such results, however, clearly support the contention that the x-ray spectroscopic method is capable, when carefully executed, of exhibiting significant differences among the valence band characteristics of the materials analyzed.

6. Acknowledgments

The authors gratefully acknowledge the support received from the New Mexico State University Physics Department and the National Aeronautics and Space Administration during this investigation.

7. References

[1] Parratt, L. G., and Jossem, E. L., Pjys. Rev. **97,** 916 (1955).
[2] Parratt, L. G., Revs. Mod. Phys. **31,** 616 (1959).
[3] Liefeld, R. J., "Soft X-Ray Emission Spectra at Threshold Excitation" in Soft X-Ray Band Spectra and the Electronic Structure of Metals and Materials, D. J. Fabian, Editor (Academic Press, New York, 1968), pp. 133-149.
[4] Burdick, G. A., Phys. Rev. **129,** 139 (1963).
[5] Van den Berg, C. B., Ph. D. Dissertation, University of Gröningen (1957).
[6] Bonnelle, C., Ann. Phys. **1,** 439 (1966).
[7] Compton, A. H., and Allison, S. K., X-Rays in Theory and Experiment (D. Van Nostrand Co., Inc., New York, 1935).
[8] Hanson, H. P., and Herrera, J., Phys. Rev. **105,** 1483 (1957).
[9] Liefeld, R. J., and Chopra, D., Bull. Am. Phys. Soc. **9,** 404 (1964).
[10] Hanzely, S., Ph. D. Dissertation, New Mexico State University (1968).
[11] Bearden, J. A., Marzolf, J. G., and Thomsen, J. S., Acta Cryst. **A24,** 295 (1968).
[12] Liefeld, R. J., App. Phys. Letters **7,** 276 (1965).
[13] Porteus, J. O., J. Appl. Phys. **33,** 700 (1962).
[14] Schnopper, H. W., Ph. D. Dissertation, Cornell University (1962).
[15] Slater, J. C., "The Electronic Structure of Solids" in Handbuch der Physik, S. Flügge, Editor (Springer-Verlag, Berlin, 1956), **Vol. 19,** pp. 1-137.
[16] Segall, D., Phys. Rev. **125,** 109 (1962).
[17] Connolly, J. W. D., Phys. Rev. **159,** 415 (1967).
[18] Fadley, C. S., and Shirley, D. A., Phys. Rev. Letters **21,** 980 (1968).
[19] Berglund, C. N., and Spicer, W. E., Phys. Rev. **136,** A1044 (1964).
[20] Blodgett, A. J., and Spicer, W. E., Phys. Rev. **146,** 390 (1966).
[21] Eastman, D. E., and Krolikowski, W. F., Phys. Rev. Letters **21,** 623 (1968).
[22] Friedel, J., Phil. Mag. **43,** 153 (1952).
[23] Friedel, J., Advances in Physics **3,** 446 (1954).
[24] Skinner, H. W. B., Bullen, T. G., and Johnston, J. E., Phil. Mag. **45,** 1070 (1954).
[25] Holliday, J. E., "Soft X-Ray Emission Bands and Bonding for Transition Metals, Solutions, and Compounds" in Soft X-Ray Band Spectra and the Electronic Structure of Metals and Materials, D. J. Fabian, Editor (Academic Press, New York, 1968), pp. 101-132.
[26] Gwinner, E., Z. Physik **108,** 523 (1938).

Discussion on "An L-Series X-Ray Spectroscopic Study of the Valence Bands in Iron, Cobalt, Nickel, Copper, and Zinc" by S. Hanzely (Youngstown University) and R. J. Liefeld (Los Alamos Scientific Lab)

K. J. Duff *(Ford Motor Co.):* For the magnetic materials is there any hope that the experimental results can be analyzed into separate contributions for majority spin and minority spins?

S. Hanzely *(Youngstown Univ.):* Let me say that we have done the following. The threshold level emission spectra, say in particular for the ferromagnetic materials, were taken with the anodes in the paramagnetic state. In other words, the anode temperatures were somewhat above the Curie point. However, when the self-absorption spectra were constructed, one of the two curves from which such self-absorption spectra were constructed was taken with the anode in the ferromagnetic state and it appears that there is no noticeable experimental evidence for any shift in the prominent structure whether the anode is in the paramagnetic or the ferromagnetic state.

W. Spicer *(Stanford Univ.):* There was mention of orbital states which appeared to lie above the Fermi energies if I read the diagram right. I don't understand these. Could you say something about them?

S. Hanzely *(Youngstown Univ.):* Your question is that you would like to know more about the origin of these transitions. It appears that they are particularly prominent in materials which have a high density of vacant states just above the Fermi level. These include iron, cobalt, and nickel in that order. The density of vacant states above the iron Fermi level is very large. It is still large but not as large in cobalt and somewhat smaller yet in nickel. If you analyze the copper and zinc graphs carefully, in those two metals the d shells are full and it turns out that the density of vacant levels above the Fermi level is very small. Structures on the low energy side of the Fermi level in these elements have been interpreted to indicate the presence of the underlying $4s$ band rather than $3d$ band.

The Electronic Properties of Titanium Interstitial and Intermetallic Compounds from Soft X-Ray Spectroscopy

J. E. Holliday

Edgar C. Bain Laboratory for Fundamental Research, United States Steel Corporation, Research Center, Monroeville, Pennsylvania 15146

The $TiL_{II,III}$ emission bands ($3d + 4s \rightarrow 2p$ transition) have been obtained from $TiC_{0.95}$ and TiN_x ($x = 0.2$ to 0.8) interstitial compounds and $TiCr_2$, TiCo, TiNi and intermetallic compounds. Additional peaks on the low energy side of the TiL_{III} band from TiC and TiN_x appear to be cross transitions from the $2s$ and $2p$ bands of the nonmetal to the $2p$ level of titanium. Agreement was found between the soft x-ray band spectra and the band calculations of Ern and Switendick on TiC and TiN. The soft x-ray emission spectra from TiC indicated strong admixture of the titanium $3d$ and carbon $2p$ bands which is in disagreement with LCAO band calculations of Lye and Logothetis. However, the $2p$ band of nitrogen was shown to be below the Ti $3d$ band indicating a localized state and a possible transfer of electrons from titanium to nitrogen.

The $TiL_{II,III}$ bands from $TiCr_2$, TiCo and TiNi show a progressive change with increasing electronegativity difference between titanium and the combining element indicating possible ionic character to the bond. No peaks were observed on the low energy side of the TiL_{III} bands, but a distinct splitting was observed in the peak of the TiL_{III} band from TiNi.

Key words: Electron concentration; electronic density of states; localized states; soft x ray; titanium compounds.

1. Introduction

The electronic structure of the first series transition metal interstitial compounds, especially the borides, carbides, and nitrides, are of particular interest because of their mechanical, electrical, and thermal properties. Two electronic structure models have been proposed for these materials. Utilizing LCAO (Linear Combination of Atomic Orbitals) type of band calculations, Lye and Logothetis [1] have calculated energy bands for TiC and preliminary calculations on TiN. Their band calculations are semiempirical and show localized states in the bands. In order to be consistent with the Madelung displacement of the energy levels and their own observed optical properties, they applied an electrostatic correction to their band calculation which resulted in the carbon $2p$ band being separated and lying above the titanium $3d$ band. As a result of this separation and from the filled portion of their density of states histogram they predicted that $1-1/4$ electrons would be transferred from the carbon $2p$ band to the titanium $3d$ band for TiC. In the other model Ern and Switendick [2] using the APW (Augmented Plane Wave) method showed no separation in the carbon $2p$ and titanium $3d$ bands and thus no electron transfer. For TiN they showed the nitrogen $2p$ band at the bottom of the titanium $3d$ band. These two band pictures have generated considerable controversy over the past several years. Lye and Logothetis [1] state that the key to solving the problem is to locate the position of the carbon $2p$ and titanium $3d$ bands experimentally. Ern and Switendick stated the L spectra from TiC and TiN would be an aid in understanding the electronic structure of these compounds. As a result of these comments the soft x-ray L emission spectra from TiC and TiN was measured to determine the relative location of the $2p$ and $3d$ bands, the degree of localization in the band and if there is some ionic character in the bond of these compounds.

Localized states may also be important in the band structure of alloys as demonstrated in recent soft x-ray measurements by Curry et al. [3]. Similarly, in a paper presented at the Density of States Conference, Rooke [4] suggested localized states around the aluminum

atom to explain some of the soft x-ray measurements on Al-Mg alloys. Since a localized band picture and ionic character in the bond would be more pronounced in intermetallic compounds than in alloys, the soft x-ray emission bands were measured for a series of titanium intermetallic compounds to determine if localized states and ionic character were present. The compounds were selected so there would be a progressive increase in the electronegativity difference between the titanium and the combining element.

2. Experimental Results

The soft x-ray emission bands were measured with a grazing incidence grating spectrometer. The grating used is a 1 meter radius 3600 groove/mm with a platinum surface and a 1° blaze. The target potential was 4 kV, and the beam current was 1.5 mA. Since the spectrometer has been thoroughly described in other publications [5], the details will not be presented here. The TiC and TiN_x targets were made from compressed powders of the compounds,[1] and the titanium intermetallic compounds were made by levitation melting of stoichiometric mixtures of the elements. The composition of these intermetallic compounds, determined by chemical analysis after the formation of the compound, is shown in table 1.

TABLE 1. *Composition of Intermetallic Compounds*

(Wt. Percent of Element)

	Cr	Fe	Co	Ni
$TiCr_2$	67			
TiFe		52.8		
TiCo			55.2	
Ti_2Ni				38.0
TiNi				55.4
$TiNi_3$				77.6

The $TiL_{II,III}$ emission band from TiC is shown in figure 1. The peak A, approximately 7.5 eV on the low energy side of the TiL_{III} band ($3d + 4s \rightarrow 2p$ transition), is not observed for the pure metal. In addition, the TiL_{II}/L_{III} intensity ratio for TiC has been reduced relative to metallic titanium, and the peak of the TiL_{III} band has shifted toward lower energy. Changes in the TiL_{II}/L_{III} intensity ratio have been shown previously by both Holliday [6] and Fischer and Baun [7] to be due to changes in self absorption.

[1] Prepared by Cerac, Inc., Butler, Wisconsin.

The $TiL_{II,III}$ emission bands from TiN_x nitrides where x is varied from 0.2 to 0.8 is shown in figure 2.

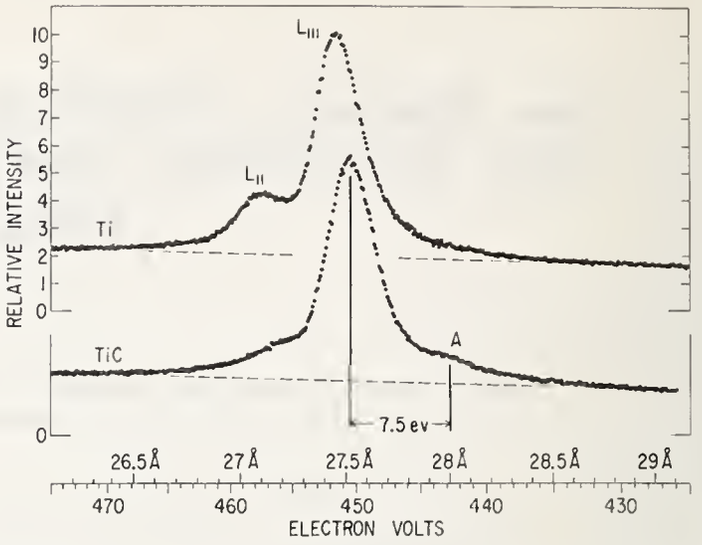

FIGURE 1. *The* $TiL_{II,III}$ *emission bands from* Ti *and* TiC; *target voltage was 4 kV.*

The Peak A', on the low energy side of the TiL_{III} band, is seen to increase in intensity relative to the TiL_{III} band with increasing x. There is also a shift in the TiL_{III} band toward higher energy, with x (fig. 3). A slight increase is observed in the TiL_{II}/L_{III} intensity ratio with x, but there is less of a change for a given range of x than that reported for TiO_x oxides [6]. In general, the changes in the $TiL_{II,III}$ emission bands from TiN_x nitrides are the same as those observed for TiO_x oxides but are somewhat less pronounced.

The $TiL_{II,III}$ emission bands for the titanium intermetallic compounds are shown in figure 4. These reveal an increase in the TiL_{II}/L_{III} intensity ratio, and a slight shift of the $TiL_{II,III}$ bands toward higher energy with increasing electronegativity difference between the Ti and combining atom. These changes are similar to that observed for the $TiL_{II,III}$ band from TiN_x with increasing x. The $TiL_{II,III}$ emission band from TiNi shows a split in the TiL_{III} peak which was not observed for the TiL_{III} bands from the other compounds. The separation of the peaks is approximately 1.5 eV which is the same as the separation of the two peaks in the $NiM_{II,III}$ bands from TiNi reported by Cuthill et al. [8].

3. Discussion of Results

As indicated in the introduction, the degree of localization and the amount and direction of electron transfer in TiC and TiN will depend on the amount of separation and position of the nonmetal $2p$ bands rela-

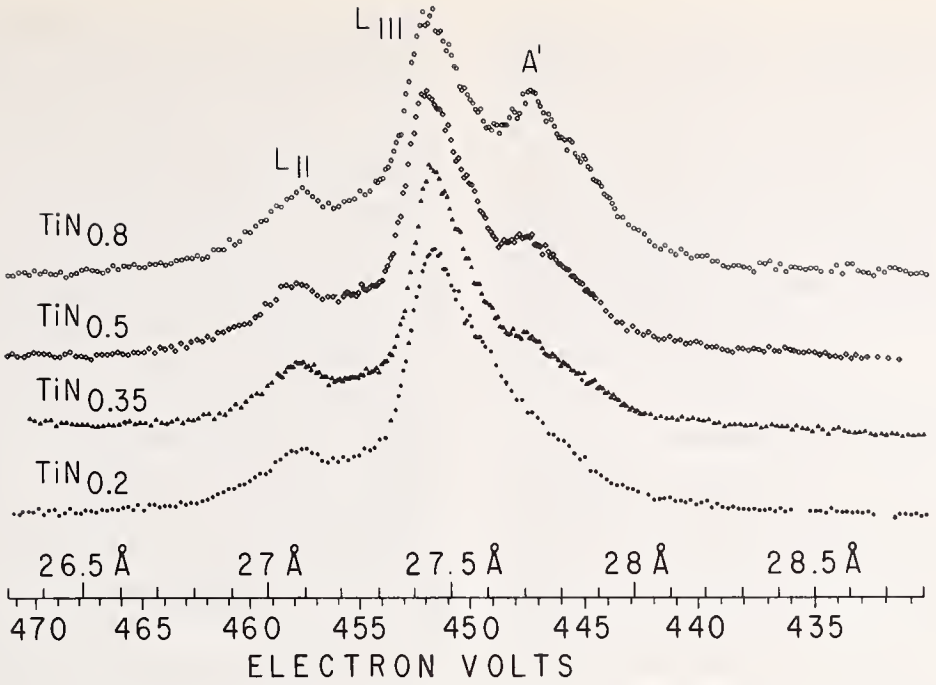

FIGURE 2. *The* $TiL_{II,III}$ *emission bands from* TiN_x *nitrides where* x *varies from 0.2 to 0.8.*
The target voltage was 4 kV.

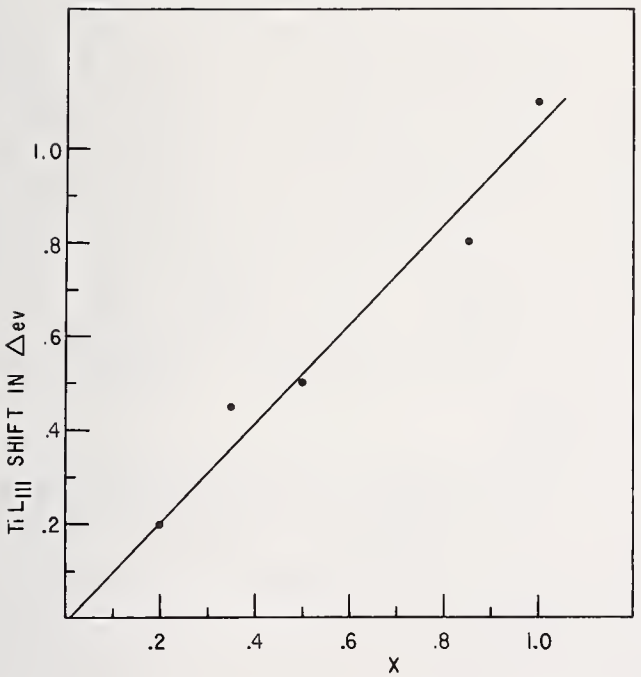

FIGURE 3. *The shift in the* TiL_{III} *band relative to pure* Ti *for* TiN_x *nitrides as a function of* x.

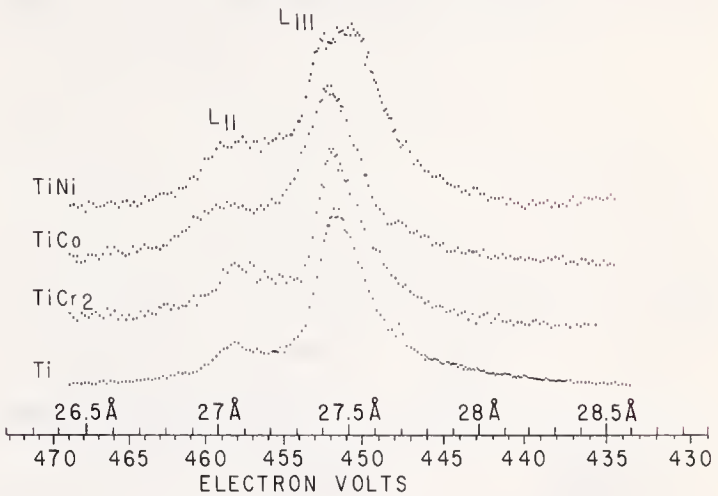

FIGURE 4. *The* $TiL_{II,III}$ *emission bands from* Ti *and* $TiCr_2$, TiCo *and* TiNi *intermetallic compounds; target voltage was 4 kV.*

tive to the Ti 3*d*. Of particular interest in this regard are peaks A and A′ in figures 1 and 2. The fact that peak A′ increases in intensity relative to the TiL_{III} peak with increasing N/Ti atom ratio indicates that the peak is associated with the amount of nitrogen in TiN. A peak also appears on the low energy side of the TiL_{III} band from TiO_x oxides, whose intensity increases with an increase in the O/Ti atom ratio [6]. Fischer [9] has presented arguments that this peak is a cross transition between the O 2*p* band and the Ti 2*p* level, and has correlated his TiO_x spectra with Ern and Switendick's band calculations on TiO. Zhorakovskii and Vainshlein [10] and Blochin and Shuvaev [11] have established justification for believing that the Kβ'' peak which appears on the low energy side of the Kβ_5 ($3d + 4s \rightarrow 1s$ quadrupole transition) emission bands of TiX compounds, where X is a 2nd period element, represents a cross transition between the 2*s* bands of the nonmetal and the 1*s* level (quadrupole transition) of titanium.

From the above discussion there appears to be sufficient justification to call peak A′ in figure 2 a cross

transition from the nitrogen valence band to the titanium $2p$ level. Ern and Switendick [2] have compared the energy separation between the $K\beta_5$ band and the $K\beta''$ cross transition from ($N2s \rightarrow Ti\ 1s$) which is 11 eV [11], with their calculated separation of 10.7 eV between the $2s$ and $3d+2p$ bands (fig. 5), the separation between the peak of the TiL_{III} band ($3d+4s \rightarrow 2p$) and peak A′ in figure 2 is 4.2 eV. Since the peak of the $2s$ band is approximately 11 eV from the peak of the $3d$ band, then peak A′ appears to be a cross transition from the nitrogen $2p$ band to the $2p$ level of titanium and any electron transfer would be from titanium to nitrogen. This indicates that there is a greater separation between the $2p$ and $3d$ bands than Ern and Switendick's [2] calculations show. However, Ern and Switendick state that the discrepancy between the initial and derived charges in the nitrogen sphere show that they should have assumed a greater separation in the $2p$ and $3d$ bands. Also, the experimental shifts of the $K\beta''$ and $K\beta_5$ bands of TiN relative to TiO when compared to Ern and Switendick's computer density of states show that TiN band picture is closer to TiO than that predicted by Ern and Switendick. The idea of electron transfer and ionic character in the bond for TiN is also shown by the increasing shift of the TiL_{III} band toward higher energy with x in figure 3. Shifts in the kinetic energy for the nitrogen $1s$ and titanium $2p_{3/2}$ levels from ESCA (Electron Spectroscopy for Chemical Analysis) by Ramquist et al. [12] shows that the electron transfer is from titanium to nitrogen.

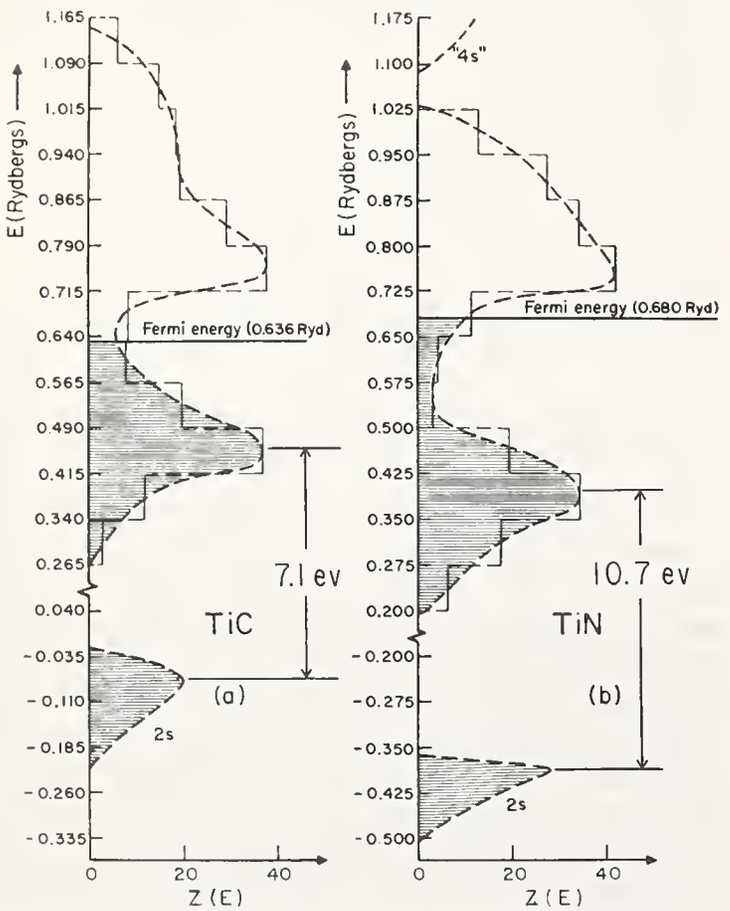

FIGURE 5. *Density of states histogram for* TiC *and* TiN *calculated by Ern and Switendick using the APW method.*
(Reprinted by permission—V. Ern and A. C. Switendick, Phys. Rev. **137A**, 1927 (1965).

In the case of TiC, peak A (fig. 1) is approximately 7.5 eV from the peak of the TiL_{III} band. Ern and Switendick calculate that the $2s$ and the $3d+2p$ bands of TiC are separated by 7.1 eV as shown in figure 5. Blochin and Shuvaev [11] show a separation in the $K\beta_5$ band ($3d+4s \rightarrow 1s$) and the $K\beta''$ (carbon $2s \rightarrow$ titanium $1s$) of 7.0 eV. It would thus appear that peak A is a cross transition from the carbon $2s$ band to the titanium $2p$ level. Although Lye and Logothetis [1] do not give a value for the separation in the maximum of the $2s$ and $3d$ bands in TiC the maximum in the $2s$ band is about 2 eV below the maximum of the $3d$ band. Thus the soft x-ray L emission spectra from TiC supports the band calculations of Ern and Switendick. It would appear that there is complete admixture of the carbon $2s$ and the titanium $3d$ bands because no peak was observed in the TiL spectra from TiC corresponding to the $2p$ band. This would indicate equal sharing of electrons. However, Ramquist et al. [13,14] have performed a number of ESCA and K x-ray measurements on the shifts of the $1s$ level of carbon, the $K\beta_{13}$, K_{α_1}, x-ray lines, and L_{III} and M_{III} levels of titanium from TiC relative to the pure element. From these measurements they conclude that electrons are being transferred from titanium to carbon which is opposite to that predicted by Lye and Logothetis. Holliday [15] has reported shifts in the Ti L_{III} peak which indicates the possibility of electron transfer in TiC.

The above experimental measurements on TiC show that Lye and Logothetis are incorrect in placing the $2p$ band of carbon higher than the $3d$ band of titanium. The degree of localization of the bands is somewhat uncertain. More theoretical work is required to fully understand the meaning of shifts in the inner atomic levels of the atoms relative to the uncombined atom in relation to electron transfer and ionic character of the bond for TiC. In the case of TiN the experiments and the calculations of Ern and Switendick show the $2p$ band below the $3d$ band with electron transfer from titanium to nitrogen. Although Lye and Logothetis did not publish any band calculations on TiN they state that the $2p$ band would lie closer to the $3d$ than in TiC. This is not in agreement with the above measurement on the TiL emission spectra from TiC which shows a wider separation in the $2p$ and $3d$ bands in TiN and none for TiC.

The observed progressive change in the wavelength and the intensity distribution of the TiL_{III} band from $TiCr_2$, TiCo and TiNi with increasing electronegativity difference between Ti and the combining element (fig. 4) suggests an increase in ionic bonding with increasing atomic number of the combining element. This interpretation is further substantiated by the fact that preliminary measurements of the $L_{II,III}$ bands from Cr, Co, and Ni do not have the same intensity distribution as the TiL_{III} bands. This is similar to the results reported by Neddermeyer [16] on Al-Mg alloys where large differences were noted between the bottom of the Al and $MgL_{II,III}$ bands. Neddermeyer attributed these changes to clusters and localized bound states at the bottom of the valence band which resulted in the density of states having a different distribution when in the vicinity of a given atom.

Since detailed band calculations have not been carried out for these intermetallic compounds, it is of interest to compare the present results for the TiL_{III} bands (fig. 4) with the $3dN(E)$ curve obtained by Cheng et al. [17] from specific heat measurements for bcc 1st series transition metals. Cheng deals in valence electron concentration rather than electron volts, and the approximate values for $TiCr_2$, TiCo and TiNi are 5.3, 6.5, and 7, respectively. Even though TiNi is a CsCl type structure, its soft x-ray band spectra shows a double peak in the $3d$ band which is also predicted from the $N(E)$ curve of Cheng et al. for an alloy with a valence electron concentration of 7. However, bcc and TiCo does not have a double peak even though the $N(E)$ curve of Cheng et al. predicts that a bcc alloy with a valence electron concentration of 6.5 should have a double peak. These results appear to add further experimental support to the fact that the rigid band model is a poor approximation to the density of states. However, before a complete interpretation of the results on the intermetallic compounds can be made, an understanding of the degree of oxidation of titanium in the alloy relative to uncombined titanium must be obtained.

4. Conclusion

The foregoing results on the L emission spectra from TiC and TiN support the band calculations of Ern and Switendick. Localized states and ionic character in the bond appear to be a part of the electronic structure of TiN but is somewhat uncertain in TiC. In addition the soft x-ray measurements on titanium intermetallic compounds have shown that the concepts of localized states, ionic character, and electronegativity appear to play a more important role in the electronic structure of metallic compounds than had been supposed previously. In his summarizing comments before the Electronic Density of States Conference, Ehrenreich [18] has emphasized that the idea of localized states should be given more consideration when considering the electronic structure of alloys.

5. Acknowledgments

The author wishes to acknowledge the help of the following members of this laboratory: W. A. Hester for assistance with the experiments, L. Zwell for the x-ray diffraction work, and C. Sharp for the chemical analysis.

6. References

[1] Lye, R. G., and Logothetis, E. M., Phys. Rev. **147**, 622 (1966).
[2] Ern, V., and Switendick, A. C., Phys. Rev. **137A**, 1927 (1965).
[3] Curry, C., in Soft X-Ray Band Spectra of Metal and Materials, D. J. Fabian, Editor (Academic Press, New York and London, 1968), pp. 173-184.
[4] Rooke, G. A., NBS J. Res. **74A2**, 273 (1970).
[5] Holliday, J. E., in The Handbook of X-Rays, E. F. Kaelbe, Editor (McGraw-Hill Book Co., New York, 1968), Chapter 38, pp. 38-1 to 38-42.
[6] Holliday, J. E., in Soft X-Ray Band Spectra and the Electronic Structure of Metals and Materials, D. J. Fabian, Editor (Academic Press, New York and London, 1968), pp. 101-132.
[7] Fischer, D. W., and Baun, W. L., J. Appl. Phys. **39**, 4757 (1968).
[8] Cuthill, J. R., McAlister, A. J., and Williams, M. L., J. Appl. Phys. **39**, 2204 (1968).
[9] Fischer, D. W., in Advances in X-Ray Analysis, B. L. Henke, J. B. Newkirk, and G. R. Mallett, Editors (Plenum Press, New York, 1970) **Vol. 13**, p. 168.
[10] Zhurakovskii, E. A., and Vainshlein, E. E., Dokl. Akad. Nauk. U.S.S.R. **129**, 1269 (1959). [English Transl: Soviet Phys. Doklady] **4**, 1308 (1960).
[11] Blochin, M. A., and Shuvaev, A. J., Bull. Acad. Sci. USSR Phys. Ser. **24**, 429 (1962).
[12] Ramquist, L., Hamrin, K., Johansson, G., Fahlman, A., and Nordling, C., J. Phys. Chem. **30**, 1835 (1969).
[13] Ramquist, L., Ekstig, B., Källne, E., Noreland, E., and Manne, R., J. Phys. Chem. Solids **30**, 1849 (1969).
[14] Ramquist, L., Jernkontorets Annaler **153**, 159 (1969).
[15] Holliday, J. E., J. Appl. Phys. **37**, 4720 (1967).
[16] Neddermeyer, H., Dissertation zur Erlangung der Doktorwüde, der Ludwig-Maximilians Universität München, May 1969.
[17] Cheng, C. H., Gupta, K. P., van Reuth, E. C., and Beck, P. A., Phys. Rev. **126**, 2030 (1962).
[18] Ehrenreich, H., NBS J. Res. **74A2**, 293 (1970).

Discussion on "The Electronic Properties of Titanium Interstitial and Intermetallic Compounds from Soft X-Ray Spectroscopy" by J. E. Holliday (U.S. Steel)

F. M. Mueller *(Argonne National Labs.):* I have one brief question for Dr. Holliday. I noticed in the curves for titanium and for titanium nitride you had an L_2 emission spectra and this was absent in the carbide. Is there a simple explanation for this?

J. E. Holliday *(U.S. Steel):* Even though the TiL_2/L_3 intensity is greatly reduced for TiC relative to Ti, the TiL_2 band from TiL is still observed. I have shown in other publications that the TiL_2/L_3 intensity ratio is strongly influenced by changes in self absorption.

Soft X-Ray Emission Spectrum and Valence-Band Structure of Silicon, and Emission-Band Studies of Germanium

G. Wiech and E. Zöpf

Sektion Physik der Universität München, München, Germany

With a photon-counting concave grating spectrometer the $L_{2,3}$-emission band of silicon and the energy range of the $M_{2,3}$-emission band of germanium were investigated. The Si L spectrum shows new structural details. The measured intensity distribution for both the K- and L-emission bands of silicon are compared with recent calculations of the K- and L-emission spectra and with the density-of-states curve.

Key words: Carbon; diamond; electronic density of states; germanium; kp method; orthogonalized plane wave (OPW) method; silicon; soft x-ray emission.

1. Introduction

X-ray spectroscopy has proved to be a valuable method for obtaining information about the electronic structure of solids. The x-ray emission bands resulting from valence electron transitions to excited core states allow the study of the whole energy range of the valence band. According to the selection rules, K-emission bands give information about the *p* electrons, $L_{2,3}$-emission bands about the *s* and *d* electrons in the valence band.

This paper deals with the elements carbon (diamond), silicon, and germanium which are of special theoretical and practical interest. Because they have the same crystal structure (diamond type) the energy band structure of these elements is very similar. Therefore their x-ray emission bands are expected to show a similar intensity distribution.

To date, theoretical work was limited to calculations of the band structure and the density-of-states. Recently the intensity distribution for the $L_{2,3}$- and the Kβ-emission bands of silicon, and for the K-, L-, and M-emission bands of germanium have been calculated. In the case of silicon the agreement between the results of the calculated and observed bands is very good; the Si Kβ band was observed in our laboratory by Läuger [1], the Si $L_{2,3}$ band was measured recently by the present authors.

2. Experimental

The concave grating spectrometer used for the measurements of the Si $L_{2,3}$ and C K band has been described elsewhere [22]. The Rowland circle radius is 1 m. A 600 grooves/mm grating with aluminum surface, and a 2400 grooves/mm grating with gold surface and blaze angles of 1°31′ and 1°0′ respectively were used. The slit width was 30 μ. The x-ray tube was operated at a pressure of about 10^{-8} Torr to keep target contamination by carbon low. The tube voltage was 2.5 kV, the beam current 0.6 to 3.2 mA. All measurements were performed with an open magnetic electron multiplier with a tungsten photocathode.

3. Results

3.1. Silicon

The Si $L_{2,3}$-emission band (and the C K-emission band of diamond) were measured stepwise. In order to obtain high accuracy about 4×10^4 pulses were taken for each point. Special care was taken of the influence of the 3rd order C K emission which is superimposed on the Si $L_{2,3}$-emission band, the peak intensity of the former being less than 1% of the latter. This means that in the region of 95 eV the intensity of the Si $L_{2,3}$-emission band is influenced by carbon only to an extent of 0.5%.

The measured band, expressed in terms of $I(E)/\nu^2$, is presented in figure 1c. There are two pronounced peaks at 89.55 and 92.05 eV. The high energy part of the band shows more details than have been observed in earlier investigations [3-5]: a small dip between 94 and 95 eV, a peak at about 95.2 eV and a sudden change in the slope at 97.5 eV. The dip is about 1% of the peak intensity.

The intensity obtained using the grating with 2400 grooves/mm was much less than that using the 600 grooves/mm grating, but the resulting intensity distributions agree within statistical uncertainty. No corrections have been applied for the instrumental distortion or for self absorption, because they have only little influence on the following discussion.

The theoretical curves for the intensity distribution of the x-ray emission bands, shown in figures 1b and 1d, have been calculated by Klima [6] according to the formula

$$\bar{I}(\nu) \sim \int_{E=h\nu} \frac{\sum_{\alpha} |\langle u_{\mathbf{k}}^{\text{core}} | P_{\alpha} | u_{\mathbf{k}}^{\text{valence}} \rangle|^2}{|\text{grad}_{\mathbf{k}} E|} d|S,$$

$$E = E_{\mathbf{k}}^{\text{core}} \quad E_{\mathbf{k}}^{\text{valence}}.$$

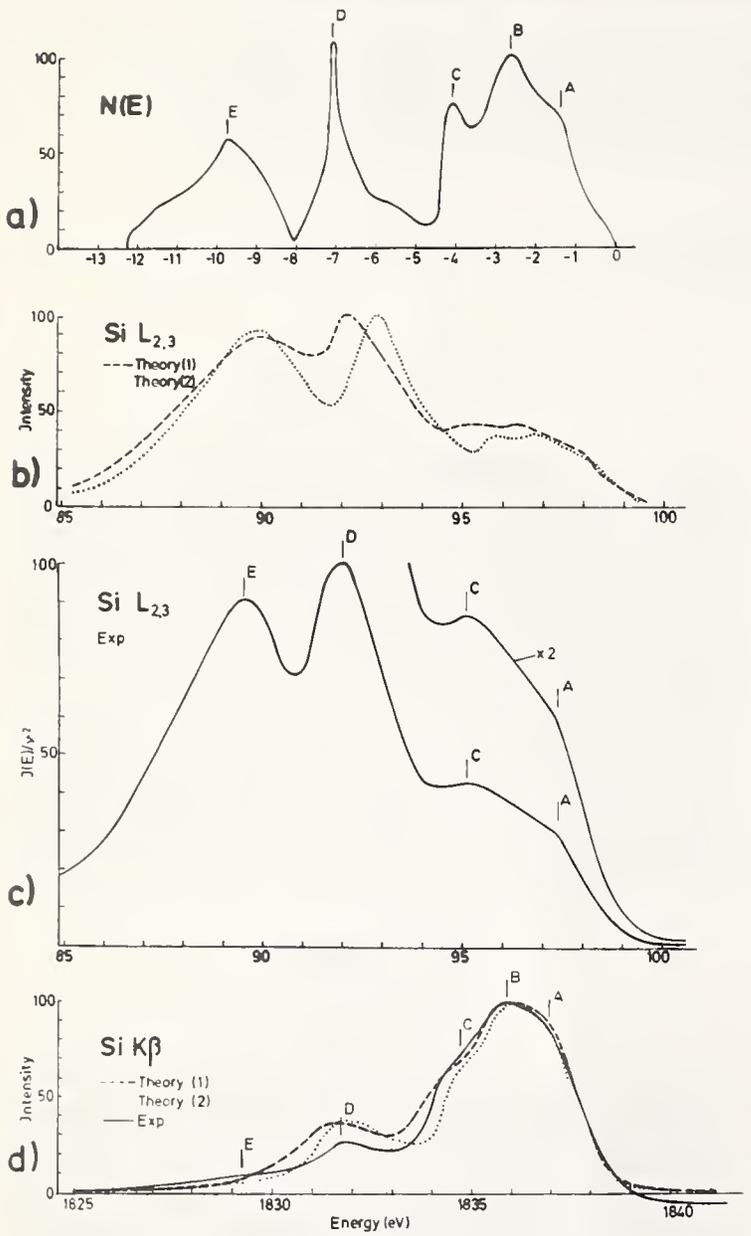

FIGURE 1. *Valence-band structure of Silicon.*

(a) Density of states (Kane [9]).

(b) Calculations of the Si $L_{2,3}$ emission band (Klima [6]).

(c) Experimental Si $L_{2,3}$ emission band, and

(d) Calculation of the Si Kβ emission-band (Klima [6]) and experimental curve (Läuger [1]).

For the computation of the curves labelled (1) in figures 1 and 1d he used the energy bands as given by Cardona and Pollak [7] (kp-method). The energy bands on which the curves labelled (2) are based were recalculated by Klima using the kp-OPW method. Spin-orbit splitting of the core state has been neglected, because its influence is small. The curves are corrected for broadening effects due to the lifetime of core states and valence states (Auger effect). The agreement between both the calculated curves and the measured curve (Läuger [1]) is quite good for the Kβ-emission band, while in the case of the L-emission band the calculated curve (1) is in better agreement with our experimental curve (fig. 1c) than curve (2). The reason probably, is that more experimental data have been introduced into the calculations of Cardona and Pollak than in Klima's kp-OPW calculations. A comparison of the experimental K and L bands shows that both curves have characteristic features indicated by A, ... E, and in both curves these characteristics have nearly the same relative energy with regard to the top of the valence band. The energy scales of the K and L bands have been correlated by the energy of the Kα_1 line (1739.66 eV: Kern [8]).

In the density-of-states curve (fig. 1a) calculated by Kane [9] the same characteristics A, . . ., E are observed. The energy position of these points relative to the top of the valence band depends on the particular energy band structure used for the calculation of the density-of-states.

A more detailed analysis shows that due to the transition probability observed emission band is considerably different from the *N(E)* curve, but the energy position of the characteristic features will be changed very little. As expected the K band of diamond (fig. 2) agrees qualitatively with that Kβ band of Si. In both cases we have electron transitions from the valence band into an *s* state.

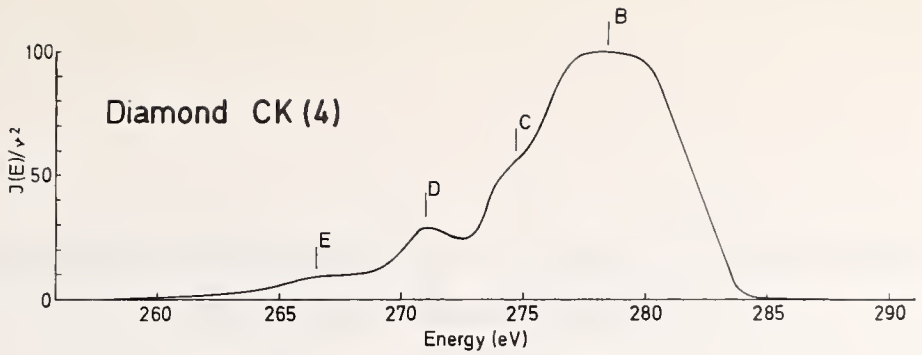

FIGURE 2. *K-emission band of diamond (4th order).*

3.2. Germanium

The calculated $M_{2,3}$ bands of germanium look similar to the $L_{2,3}$ bands of silicon. These calculated bands of Ge disagree with the experimental results of Tomboulian [10] which are to date the only measurements of the Ge $M_{2,3}$ bands available. To clear up this discrepancy the energy range of the Ge $M_{2,3}$ band was investigated.

Using the crystal powder, and a thin plate of a single crystal with a target input of 2.5 kV, 3 mA, only two relatively weak lines could be observed (of intensity 1200 and 1700 counts/min). The characteristics of these two lines are presented in table 1. In the energy range of the Ge $M_{2,3}$-emission band the intensity was only about 400 counts/min higher than the background intensity (about 400 counts/min), and no reproducible fine structure could be observed. The Ge $M_{2,3}$ emission is therefore of very low intensity; the same was found for the L emission by Deslattes [12].

The two weak lines observed may be interpreted as due to the intraband transitions $M_{4,5} - M_2$ and $M_{4,5} - M_3$ (table 1). A surprising observation is the big difference between the energy splitting of $M_2 - M_3$ as tabulated by Bearden and Burr [11] (7.16 eV) and found in our measurements (3.5 eV).

On the basis of these new theoretical and experimental data Tomboulian's interpretation of his results seems unlikely.

TABLE 1. *Characteristics of the intraband transitions* $M_{4,5}-M_2$ *and* $M_{4,5}-N_3$.

	Bearden and Burr [11]		Tomboulian [10]	Present authors			
	λ(Å)	*E*(eV)	*E*(eV)	λ(Å)	*E*(eV)	Half-width (eV)	Intensity
$M_{4,5}-M_2$	124.94	99.24	.....	129.3	95.9	1.7	1
$M_{4,5}-M_3$	134.65	92.08	.....	134.2	92.4	3.1	2
M_2-M_3	.....	7.16	2.0	.....	3.5	...	...

4. References

[1] Läuger, K., Thesis, University München (1968).
[2] Wiech, G., Z. Physik **193**, 490 (1966).
[3] Crisp, R. S., and Williams, S. E., Phil. Mag. **5**, 1205 (1960).
[4] Wiech, G., Z. Physik **207**, 428 (1967).
[5] Ershov, O. A., and Lukirskii, A. P., Soviet Physics-Solid State **8**, 1699 (1967).
[6] Klima, J., preprint sent for publication.
[7] Cardona, M., and Pollak, F. H., Phys. Rev. **142**, 530 (1966).
[8] Kern, B., Z. Physik **159**, 178 (1960).
[9] Kane, E. O., Phys. Rev. **146**, 558 (1966).
[10] Tomboulian, D. H., and Bedo, D. E., Phys. Rev. **104**, 590 (1956).
[11] Bearden, J. A., and Burr, A. F., Atomic Energy Levels (U.S. Atomic Energy Commission, Oak Ridge, Tennessee, 1965).
[12] Deslattes, R. D., Phys. Rev. **172**, 625 (1968).

417-156 O - 71 - 23

Density of States in α and β Brass by Positron Annihilation

W. Triftshäuser and A. T. Stewart

Queen's University, Kingston, Ontario

Positron annihilation experiments using a long slit angular correlation apparatus have been performed to investigate the momentum distribution of photons resulting from positron annihilating with electrons in brass. Single crystals of α and β brass which had been oriented along the 100, 110 and 111 directions respectively, were used for the measurements. The counter slits subtended an angle of 0.32 mrad at the sample. Thus, keeping the samples at liquid nitrogen temperature to reduce the positron motion, a total resolution of 0.42 mrad was achieved. The results show clearly deviations from a spherical Fermi surface. The observed anisotropies are found to agree very well with the theoretical predictions based on cross-sectional areas of the Fermi surface.

Key words: Angular correlation; brass; electronic density of states; positron annihilation.

1. Introduction

Positron annihilation experiments yield directly the density of states of electrons in k-space and the results are approximately independent of the electron mean free path. Thus, it can be used to examine the electron structure of alloys which, because of electron scattering, cannot be easily examined by the more usual transport techniques.

The principles of the positron annihilation technique are simple to describe. A positron from a radioactive decay is shot into a metal specimen and loses energy very rapidly, arriving at about thermal energy in a time somewhat less than the average lifetime which is of order 10^{-10} sec. Then the positron annihilates with one particular electron. The usual annihilation process results in the emission of two photons. These two photons have a total energy of $2h\nu = 2mc^2$ and are emitted at exactly 180° to each other to conserve momentum. In the laboratory a slight departure from 180° can be observed and, since the positron is thermalized, it is a direct measure of the transverse (to the photon direction) component of the electron's momentum. Using independent particle language, the wave function product $\psi_+(\mathbf{r})\psi_K(\mathbf{r})$ of the annihilating pair acts like the wave function of the center of mass and thus also of the gamma rays. The Fourier transform of this wave function product is then the momentum amplitude function, the square of which is the observable distribution $\rho(\mathbf{k})$.

Of course the positron and electron are not independent. The positron always surrounds itself with a polarization cloud of negative charge and annihilates with these electrons and not with the unperturbed electrons. The momentum distribution of electrons in this cloud—really of one electron and the positron—has been calculated for two extreme situations: (a) the electron gas, and (b) electrons in closed atomic shells. In both cases the distribution in momentum of the annihilation photons resembles quite closely that of the unperturbed electrons of the particular system being considered. In particular a sharp cutoff at the Fermi surface is both expected and indeed observed. Thus while the effect of the positron on the electrons in brass is not yet known, we have good reason to expect experimental results for momentum distributions of annihilation photons to resemble closely the momentum distributions of the electrons in the alloy.

The possibility of measuring momentum anisotropies in oriented single crystals has been first shown by Berko and Plaskett [1] for copper and aluminum. Measurements on other metals have been reported by other authors [2,3]. In this paper we present observations on single crystals of β and α brass, in order to examine how well this technique can be used in the determination of the electron states in alloys and especially in disordered alloys. Properties of ordered alloys, particularly the shape of the Fermi surface, can be obtained through de Haas-van Alphen measurements more accu-

rately than by the positron annihilation technique. We chose ordered β brass as a "test alloy" because the Fermi surface of this metal is very well known. We then used α brass to explore the possibilities of this technique. We shall discuss in this paper to what extent our results can be analyzed directly in terms of electron momentum distribution and cross-sectional areas of the Fermi surface.

2. Experimental Arrangement and Procedure

Let $\rho(\mathbf{k})d\mathbf{k}$ be the probability that a positron annihilates with an electron emitting two photons having total momentum between $\mathbf{k}$ and $\mathbf{k}+d\mathbf{k}$ in the laboratory system. The conventional long-slit apparatus then measures the coincidence counting rate $N(k_z)$, where

$$N(k_z)=\int_{-\infty}^{\infty}\int_{-\infty}^{\infty}\rho(\mathbf{k})dk_x dk_y \qquad (1)$$

The integral is taken over the plane of constant k_z. In the independent particle approximation $\rho(\mathbf{k})$ is given by

$$\rho(\mathbf{k})=\text{Const.}\ \sum\left|\int\psi_+(\mathbf{r})\psi_{\mathbf{K}1}(\mathbf{r})e^{-i\mathbf{k}\cdot\mathbf{r}}{}_{d\mathbf{r}}\right|^2 \qquad (2)$$

where $\psi_+(\mathbf{r})$ is the positron ground state wave function, and $\psi_{\mathbf{K}1}(\mathbf{r})$ is the electron wave function with wave number $\mathbf{K}$ and band index 1. The summation is over all the occupied states. In the lowest approximation of free electrons and a zero momentum positron, $N(k_z)$ is directly proportional to the cross-sectional areas of the Fermi surface in the extended zone scheme. For a less simplified situation, the importance and influence of the positron wave function, the higher momentum components of the electron wave functions, and the core electrons has been discussed already by De Benedetti et al. [4].

We present data both in the form of momentum distribution, that is $N(k_z)$, and also as the derivative of $N(k_z)$ with respect to k_z.

The derivative presentation of the data shows more sensitively the effects of changing Fermi surface topology and occupation probability.

In the experimental arrangement we used the long-slit geometry having 30 cm long NaI detectors, with slits subtending 0.3 mrad at the specimen. The brass single crystals had been oriented by x rays and were spark cut to rectangular solids of $6\times6\times12$ mm. After cutting, the surface of the specimens was carefully etched to remove possible distortions due to spark machining. As a positron source we used approximately 180 mCi of Co^{58} diffused into a very thin Cu foil. The radioactive area was sealed by an 0.005 mm thick stainless steel window to avoid contamination. All experiments were performed with the specimen at 78 K in order to reduce the thermal motion of the positrons and its broadening influence on the instrumental resolution [5]. The coincidence data were taken automatically and corrected for source decay.

3. Results and Discussion

The results for β brass are shown in figure 1. The three curves represent the angular distributions for [100], [110] and [111] directions (k_z was parallel to these directions) normalized to equal areas using the best visual fit through the data points. The statistical accuracy at $k_z=0$ was about 0.65%. In order to evaluate the part due to conduction electrons we subtracted the higher momentum tail from the angular distribution by fitting a Gaussian function in the region from about 7 to 14 mrad. From the resultant curve, we calculated the derivative by taking the difference of adjacent measured points. This is shown in figure 2 for the three crystal directions. The solid lines drawn through the points represent the momentum distributions obtained from calculations by Taylor who fitted the de Haas-van

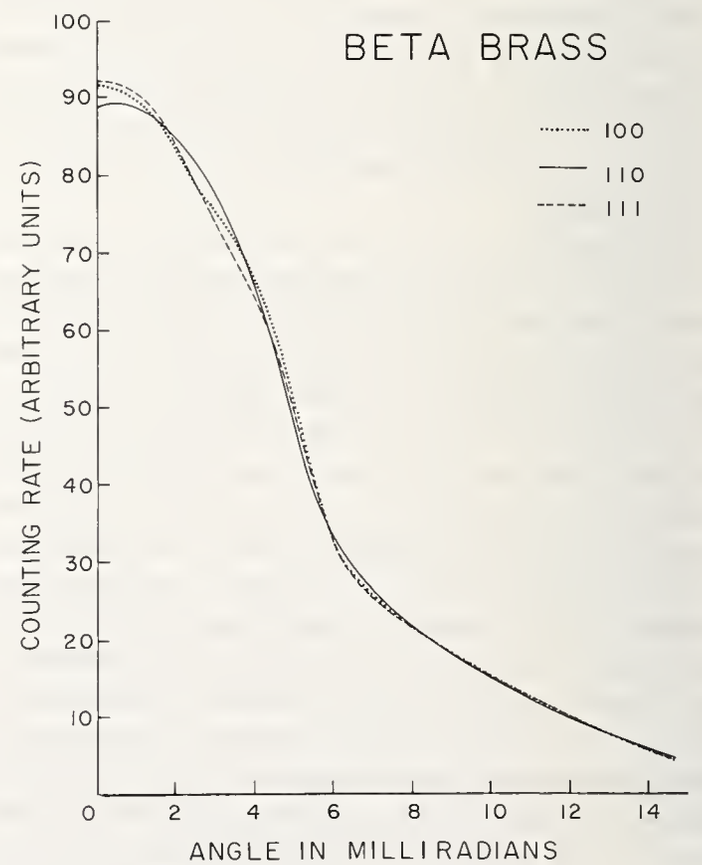

FIGURE 1. *Experimental angular distribution curves for [100], [110], and [111] directions in β CuZn at liquid nitrogen temperature.*
The curves are normalized to equal areas. The statistical accuracy of the data points at the peak is 0.65 percent.

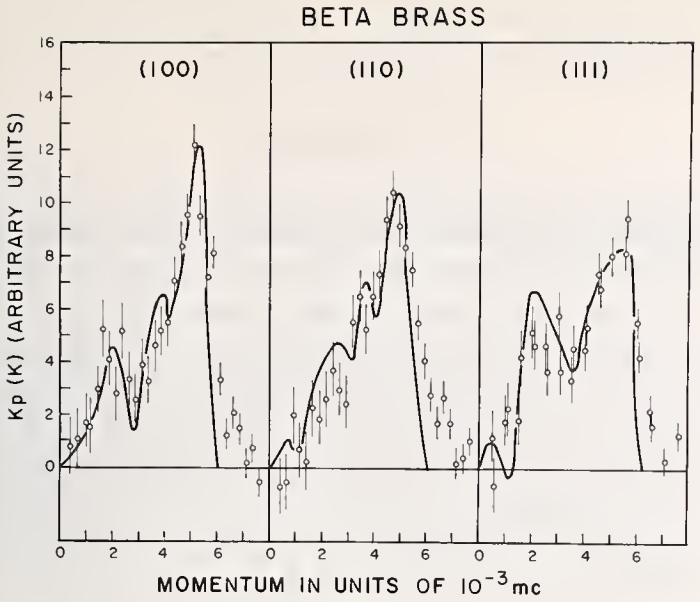

FIGURE 2. *Electron momentum distributions in* β CuZn.
These data are obtained from figure 1 by differentiating as discussed in the text. The theoretical difference curves were obtained from cross-sectional areas calculated by R. Taylor [6]. The Fermi surface was confined to the first two zones.

Alphen data to a six parameter description of the Fermi surface of ordered β brass using nonlocal pseudopotentials [6]. This calculated result shows the differences of adjacent cross-sectional areas of the Fermi surface. Higher momentum components are not included in this calculation. The agreement with the experimental data is remarkably good considering this approximation. The electron momentum distribution is quite different along the main cyrstallographic directions and deviates clearly from that of free electrons. The [110] necks and the [111] holes, lying at different positions for each of the three orientations are mainly responsible for the detailed structure in these momentum distributions.

Under the same experimental conditions the measurements on single crystals of α brass were performed. We used a specimen with 22% Zn and 78% Cu. This alloy has a face centered cubic lattice structure like pure copper. The angular distribution for the [100], [110] and [111] directions normalized to equal areas are shown in figure 3. The statistical accuracy at the peak was again about 0.65%. The angular distribution for the three orientations is different up to about the free electron momentum of 5.5 mrad. The higher momentum part of the curves is identical and was again fitted by a Gaussian distribution and subtracted. By this technique we hope to eliminate the momentum distribution due to core annihilations. It should be noted that this broad component is higher for α brass than for β brass because of the higher copper concentration. The differentiated data are shown in figure 4 for these three orientations. As in the case of β brass the devia-

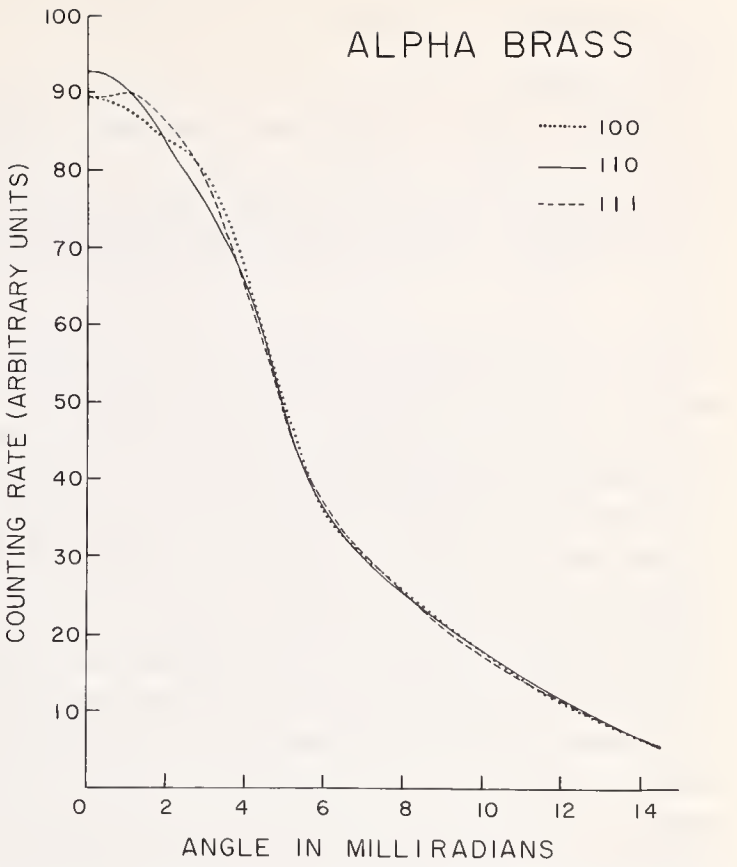

FIGURE 3. *Experimental angular distribution curves for* [100], [110], *and* [111] *directions in* α CuZn *at liquid nitrogen temperature.*
The curves are normalized to equal areas. The statistical accuracy of the data points at the peak is 0.65 percent.

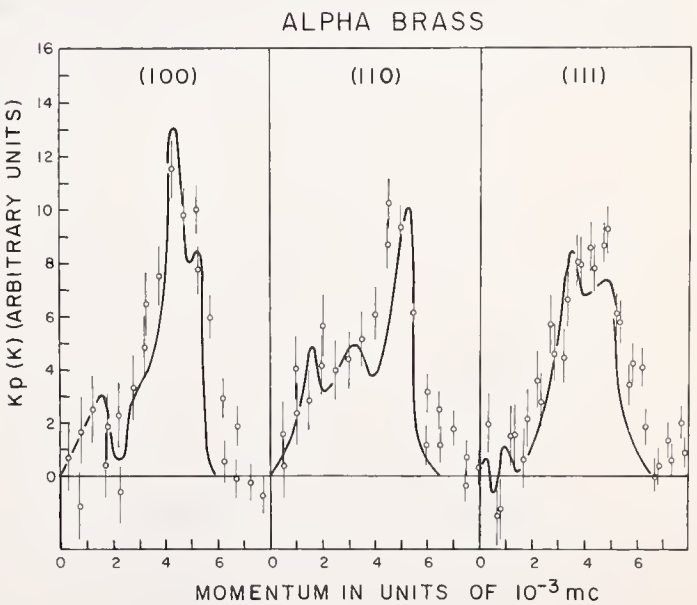

FIGURE 4. *Electron momentum distributions in* α CuZn.
These data are obtained from figure 3 by differentiating as discussed in the text. The theoretical difference curves were obtained from cross-sectional areas calculated using free electron approximation and an empirical Fermi surface configuration with a [111] neck radius of $(0.29 \pm 0.02)k_F$.

tion from a free electron momentum distribution is obvious.

The solid line is the result of a calculation using nearly free electron theory [7] and an empirical model derived from the known Fermi surface of copper [8]. We assumed the [111] necks expand and that the total sphere expands such that the volume remains the proper volume for the number of free electrons one would anticipate in copper and zinc. We joined the necks to the sphere by a smooth curve and tested various neck diameters in our model. Using the band gap energies given by Segall [9] and Burdick [10] we observed that the higher momentum states are important. We then calculated the expected momentum distribution taking into account the higher momentum components in an approximate way. The derivative of this calculation is shown as the full line in figure 4. The particular curves we have drawn here correspond to a neck radius of 0.29 ± 0.02 (units of k_F). For pure copper the neck radius is 0.20 in these units. This indicates an increase in neck size of almost 50% compared with copper.

In the case of β brass as well as in the α brass data, these theoretical calculations agree remarkably well with the experiment in overall shape but they exhibit differences in detail in certain regions. Even folding these calculations with the experimental resolution will not completely smooth out these differences. Possible explanations for these small discrepancies can be found in effects not considered in the approximations used, e.g. (1) anisotropy of the ground state positron wave function; (2) a more accurate consideration of the higher momentum components of the electron wave function; and (3) many-body correlation effects leading to a k-dependent annihilation probability [11,12].

4. Conclusions

In this paper, we have shown that the positron annihilation technique can be used to yield information about the occupation in k-space of electrons in alloys. This preliminary analysis has shown surprising sensitivity to small details of the topology of the Fermi surface and of the occupation of higher momentum components. In particular this preliminary analysis shows for this particular α brass specimen a neck size approximately 50% greater than that of copper. We anticipate that future calculations and experiments will yield much more detailed information.

5. References

[1] Berko, S., and Plaskett, J. S., Phys. Rev. **112,** 1877 (1958).
[2] Stewart, A. T., Shand, J. B., Donaghy, J. J., and Kusmiss, J. H., Phys. Rev. **128,** 118 (1962).
[3] Lang, L. G., and Hein, H. C., Bull. Am. Phys. Soc. **2,** 173 (1957).
[4] de Benedetti, S., Cowan, C. E., Konnecker, W. R., and Primakoff, H., Phys. Rev. **77,** 205 (1950).
[5] Stewart, A. T., Shand, J. B., and Kim, S. M., Proc. Phys. Soc. (London) **88,** 1001 (1966).
[6] Taylor, R., private communication. We are indebted to Dr. Taylor for these results in advance of publication.
[7] Mott, N. F., and Jones, H., Properties of Metals and Alloys, (Clarendon Press, Oxford, 1936).
[8] Roaf, D. J., Phil. Trans. Roy. Soc. (London) **A255,** 135 (1962).
[9] Segall, B., Phys. Rev. **125,** 109 (1962).
[10] Burdick, G. A., Phys. Rev. **129,** 138 (1963).
[11] Kahana, S., Phys. Rev. **129,** 1622 (1963).
[12] Carbotte, J. P., Phys. Rev. **155,** 197 (1967).

Discussion on "Density of States in α and β Brass by Positron Annihilation" by W. Triftshäuser and A. T. Stewart (Queens University)

P. Platzman *(Bell Telephone Labs.):* I would like to correct the impression given here that the positron annihilation unambiguously measures the momentum distribution. It measures the momentum distribution of the electrons in the metal in the presence of the positron, not in the absence of the positron. It may be true, under certain situations, that the momentum distribution is not significantly distorted by the presence of the positron but this is not obvious. Only if one assumes that the positron does not interact with the electron gas does one get an unambiguous connection between the annihilation spectrum and the momentum distribution of the host metal. I think that in some cases you may push things too far in trying to sort out certain small details of momentum distribution of the metal and not keep in mind that the positron is really distorting that distribution.

W. Triftshäuser *(Queens Univ.):* Now in one way you are right since there are certainly some effects that we are neglecting in this calculation. But as it comes out its effects are very small and therefore we have proceeded in first approximation by neglecting these effects, because it seems to be impossible at the moment to obtain a better calculation of the distortion of the electron momentum distribution by the positron than that of Carbotte and Kahana. This calculation shows that the distortion is surprisingly very small. Therefore, we are confident that the observed small details of the momentum distribution are real, which is proved also by the good agreement of the theoretical calculated cross-sectional areas of the Fermi surface with the experimental results. Thus it is reasonable to neglect these effects until better calculations are available.

A. T. Stewart *(Queens Univ.):* It is true that not enough is known about the effects of the positron in anything but simple situations. However, the **k**-dependence of the perturbation is probably not great and probably smooth. Thus the fine structure seen in these data for brass can probably yield fairly reliable conclusions about occupation in **k**-space, F. S. topology, etc.

Since the authors (Triftshäuser and Stewart) cannot answer this question, I (Stewart) wish to put it to the audience. The question is this: Why cannot the perturbing effect of the positron upon the electrons be handled in a way that is easy to understand and use? Since the results of these quite complicated calculations are usually simple, there should be a simpler way to look at the problem. It has long been known that in an electron gas the polarization cloud around the positron, although an order of magnitude more dense than the charge density in the metal, has a momentum distribution that is much like a Sommerfeld gas. The electrons from the Fermi surface are relatively 30% more dense in the polarization cloud than they are in the rest of the metal. And this is the most perturbable of electron systems! In an atom, recent work of Drachman, and of Salvadori shows that while the "enhancement" at the positron may be a factor of four, the momentum distribution in this polarization cloud is almost the same as that of the outer electrons of the above.

The need for a simpler outlook is especially important in interpreting the increasingly accurate data from positron annihilation experiments. Consider a Fermi surface touching a zone boundary as in figure 1. Along a direction like OA it is reasonable to use the usual enhancement as in figure 2. However, along the direction OB might we not find electrons less perturbable so that the enhancement function might look like figure 3?

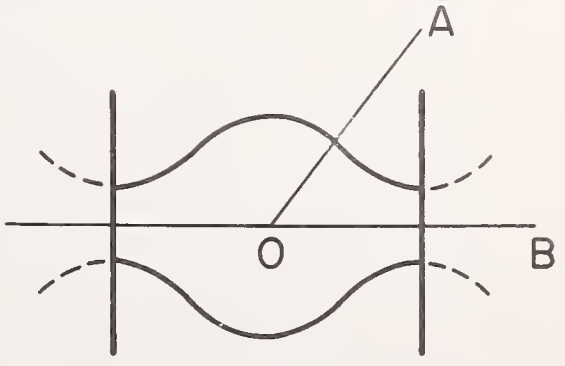

FIGURE 1. *A Fermi surface contacting the zone face.*

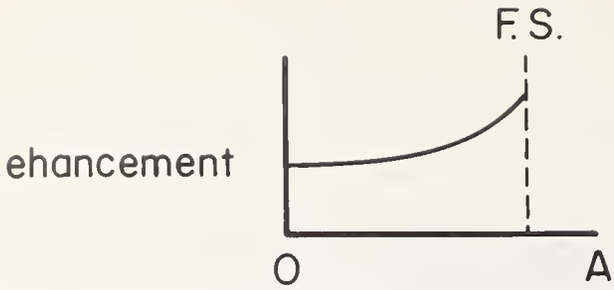

FIGURE 2. *The sort of momentum distribution enhancement usually assumed along* **k***-directions intersecting the Fermi surface.*

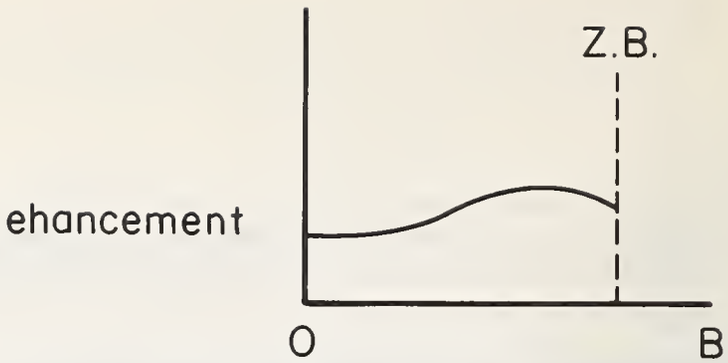

FIGURE 3. *A suggested enhancement for a* **k***-direction not intersecting the Fermi surface.*

Compton Scattering from Lithium and Sodium

P. Eisenberger and P. H. Schmidt

Bell Telephone Laboratories, Incorporated, Murray Hill, New Jersey 07974

Key words: Compton scattering; electronic linear momentum distribution function; lithium; potassium; sodium.

Recently Phillips and Weiss [1] have shown the experimental possibility of using the Compton effect to measure the gound state electronic linear momentum distribution function. In this work will be reported experimental results on single crystals of Li and Na.

The results on single crystals of Li reveal for the first time the true anisotropic ground state electronic linear momentum distribution function of the conduction electrons. As expected it is in the [110] directions that the major distortion from spherical symmetry occurs. However, the band structure distortion has secondary effects due to electron-electron interactions. These effects arise because the distortion of band near the [110] direction changes the ratio of the potential energy to kinetic energy for those states and thus the discontinuity at the Fermi surface and the high momentum tail of the momentum distribution are affected. These effects are not observable by positron annihilation experiments because they are relatively insensitive to electron-electron interactions [2].

The effects of band structure distortions on the electron-electron interactions are further stressed when the Li results are compared with those of Na. As expected Na is isotropic and thus the discontinuity at the Fermi surface and the high momentum tail are, except for small electron phonons effects, basically determined by the electron-electron interactions. The results for Na will be compared with the existing calculations [3] for the ground state momentum distribution function in which electron-electron interactions have been included.

In addition to the above completed work, experiments are already in progress on He, H_2, and K. The He experiments will provide a good test of the accuracy of Compton scattering for measuring linear momentum distributions since the helium distribution is fairly well known. It will enable one to make more quantitative statements about Compton scattering results. The experiments on H_2 will illustrate the power of the technique in studying molecular systems in which bonding considerations are important. Finally, the experiments on potassium should provide a further test of the electron gas calculations when electron-electron interactions are considered.

References

[1] Phillips, W. C., Weiss, R. J., Phys. Rev. **171**, 790 (1968).
[2] Donaghy, J. J., Stewart, A. T., Phys. Rev. **164**, 391 (1967).
[3] Goldhart, D. J. W., Houghton, A., Vosko, S. H., Canad. J. of Phys. **42**, 1938 (1964).

Discussion on "Compton Scattering from Lithium and Sodium" by P. Eisenberger and P. H. Schmidt (Bell Telephone Laboratories)

M. Dresselhaus *(MIT):* At one time I thought there was some controversy as to whether there was contact made by lithium's Fermi surface with the Brillouin zone boundary. Have you concluded from your work that there definitely is no such contact?

P. Eisenberger *(Bell Telephone Labs.):* No, as a matter of fact, one of the critical features in determining whether there is contact will be that the nature of the electron core contributions or the crystal field contributions will vary greatly if there is in fact contact at the surface. In other words, one will get a completely different spectrum. Before I can answer the question, I have to be sure what the relative magnitudes are. If they are actually touched, then one could expect the same sort of general shape for the tail as electron-electron interactions would predict. If they did not touch, then one would expect gaps. So one really has to do a calculation of all three effects before one can really single out and say anything about any one of them. By going to sodium where there definitely is no contact, we hope to be able to show what the nature of the electron-electron interaction is by itself.

L. Muldawer *(Temple Univ.):* Is your method similar to that of Weiss [1] at Watertown?

P. Eisenberger *(Bell Telephone Labs.):* Definitely.

L. Muldawer *(Temple Univ.):* Have you gotten similar type results?

P. Eisenberger *(Bell Telephone Labs.):* Weiss did not do the experiments in helium at all. He did the experiments in lithium and saw no single crystal effects. I think Dr. Weiss deserves great credit for pioneering this field experimentally. But I think that there is a phase shift between the experimental results and the theory as far as lithium is concerned.

S. Hanzely *(Youngstown Univ.):* You mentioned that you were using monochromatic x rays at different wavelengths. I would like to know just how monochromatic the x rays were and how you achieved the different wavelengths.

P. Eisenberger *(Bell Telephone Labs.):* By your standards, they are not monochromatic. They have a spread in energy of roughly 2 to 3 eV.

S. Hanzely *(Youngstown Univ.):* I presume then that your technique is not too sensitive to the fact that it is not monochromatic.

P. Eisenberger *(Bell Telephone Labs.):* No, at the moment I am not even limited by that width. I should have pointed out that in the Doppler shifting technique at x-ray frequencies, one has a built-in amplifying factor in the wavelength shifts one is talking about, because it is the product of the electron's momentum and the photon's momentum. The photon is at very high energy so you get a very spreadout spectrum. For a Fermi momentum of 4 eV one is actually talking about a couple hundred eV energy shift at x-ray wavelengths. So one does not need that good a resolution as one might if one were directly measuring the Fermi surface as one does in soft x ray, for example.

[1] Weiss, R. J., and Phillips, W. C., Phys. Rev. **171**, 790 (1968) and **176**, 900 (1968).

ION-NEUTRALIZATION; SURFACES; CRITICAL POINTS; ETC.

CHAIRMEN: E. Callen
R. R. Stromberg

RAPPORTEURS: D. E. Aspnes
B. Lax

Ion-Neutralization Spectroscopy*

H. D. Hagstrum

Bell Telephone Laboratories, Murray Hill, New Jersey 07974

The ion-neutralization spectroscopy (INS) is discussed in comparison with other spectroscopies of solids. It is shown that INS probes the local density of states of the solid at or just outside the solid surface. It is believed that this accounts for the clear-cut differences between INS results and those of other spectroscopies. Because of its unique specificity to the surface region INS is particularly useful in studying the surface electronic structures of atomically clean surfaces and of surfaces having ordered arrays of known atoms adsorbed upon them. In the latter case INS determines a portion of the molecular orbital spectrum of surface molecules formed from the adsorbed foreign atom and surface atoms of the bulk crystal. Such spectra provide information on local bonding symmetry and structure and electrical charging within the surface molecule which is as yet unavailable by any other method. INS is the first attempt to base a spectroscopy of electronic states on a two-electron process. More recent work on experimental and mathematical problems which such a spectroscopy entails are also briefly mentioned in this paper.

Key words: Auger processes; autoionization; density of states; ion-neutralization; transition probability.

1. Introduction

In general, spectroscopies of electronic states have been based on the absorption or emission of electromagnetic radiation when the system under observation is excited or de-excited. In absorption spectroscopies one can observe the absorption of the photon or observe the electrons emitted when the photon is absorbed as in photoelectron spectroscopy. All of these spectroscopies are based on one-electron transition processes. The ion-neutralization spectroscopy (INS), on the other hand, is the first, but not the only spectroscopy, to be based on a two-electron process in which a band transition density function is obtained. It is like the photoelectron spectroscopies in that the spectroscopic information is obtained by measurement of the kinetic energy distribution of electrons ejected in the process. However, because INS employs a two-electron process, the kinetic energy distribution contains the "spectroscopic function" in folded or convolved form, making data reduction somewhat more involved than for a spectroscopy based on a one-electron process.

INS is a relatively new spectroscopy of solids having its own unique set of characteristics, advantages, and limitations. It is the purpose of this paper to review these properties in comparison with other spectroscopies. We discuss the method and what it measures, its resolving power and operational limitations, and its unique contributions to our knowledge of electronic state densities.

2. The Nature and Method of INS

When an excited and/or ionized atom is projected at a solid surface, an excited solid-atom system is formed. The ion-neutralization process upon which INS is based is one of the processes of auto-ionization by which such an excited solid-atom system de-excites itself. Not all such processes are appropriate to INS, however. The autoionization processes can be divided into two principal classes depending upon whether unfilled electronic levels in the atom do or do not lie opposite filled electronic levels in the solid. These are in-

* An invited paper presented at the 3d Materials Research Symposium, *Electronic Density of States*, November 3-6, 1969, Gaithersburg, Md.

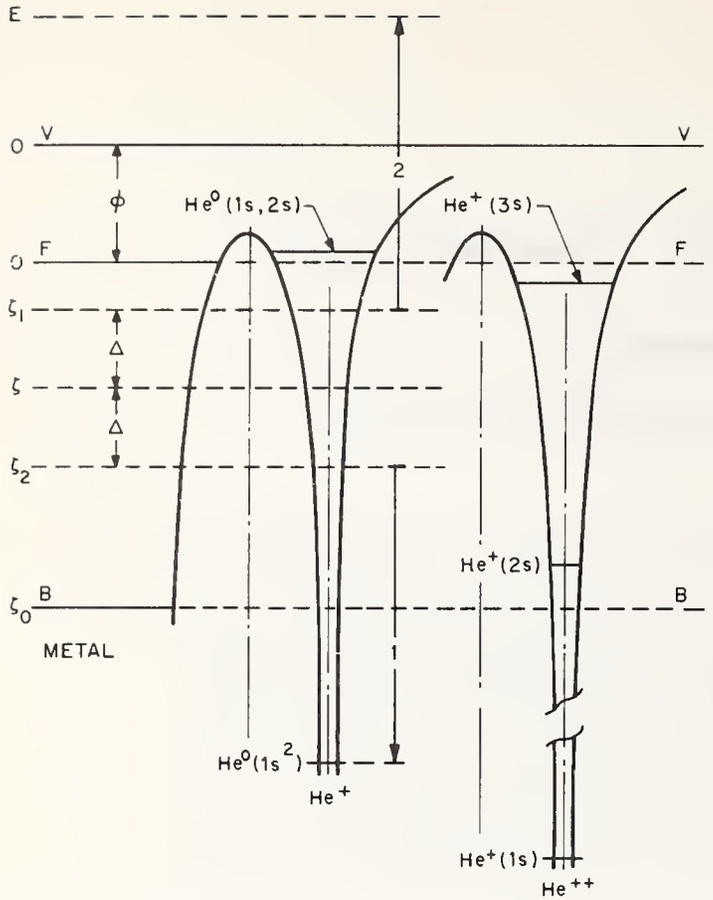

FIGURE 1. *Electron energy diagram showing metal at left and two atomic wells for He^+ and He^{++} cores.* V *is the vacuum level,* F *the Fermi level and* B *the bottom of the filled band. Transitions 1 and 2 are those of the ion-neutralization process.*

dicated schematically in figure 1. Here we show the electronic energy level diagram of a metal to the left and two atomic wells outside. One atomic well is that of the $He^+(1s)$ core in which the levels are those of He^0. The second well is that of the He^{++} core in which the energy levels are appropriate to He^+. We see that the two wells differ in that one (He^{++}) has two states [$He^+(2s)$ and $He^+(3s)$] lying in the energy range of the filled band of the metal, whereas the other (He^+) has no states in this energy range.

We expect that atomic levels lying in the range of allowed levels of the solid will become resonances or virtual bound states and that of these allowed levels, those lying in the range of the filled band will fill. Thus the atomic levels should control the autoionization process in some energy ranges when they can fill by tunneling. Preliminary experiments with doubly-charged He^{++} ions and with metastably-excited $He^+(2s)$ ions appear to bear this out. Thus if we want the autoionization process to be dominated by initial state electrons whose state density is determined by the solid or its surface there should be no atomic levels lying in the energy range of the filled band as is the case in figure 1 for He^+. This is a fundamental restriction on the ion-solid systems to which INS can be applied. For He^+ ions the solid band should lie within the energy range from ~4.5 eV to ~22.5 eV below the vacuum level. Earlier work has shown that the effective ionization energy of He is about two eV less than its 24.5 eV free-space value [1].

The transitions (1 and 2) of the two-electron, Auger-type, ion-neutralization process are also shown in figure 1. Since ζ_1 and ζ_2 may vary over the entire filled band we expect the ejected electrons to have energies lying in a broad band. Experimentally the kinetic energy distributions are measured by regarding potential means using apparatus we shall not describe here [2,3]. Examples of recorder plots of several kinetic energy distributions, $X(E)$, are shown in figure 2. It is clear that the X distribution is sensitive to the nature of the solid and the preparation of its surface. The spectroscopic information obtained by INS resides in these distributions. In order to extract it we must understand the structure of these distributions in detail.

The distribution functions which we need to understand the ion-neutralization process are shown for an atomically clean copper face in figure 3. Suppose we start with the simplification of constant transition probability independent of the initial energy ζ. Then it

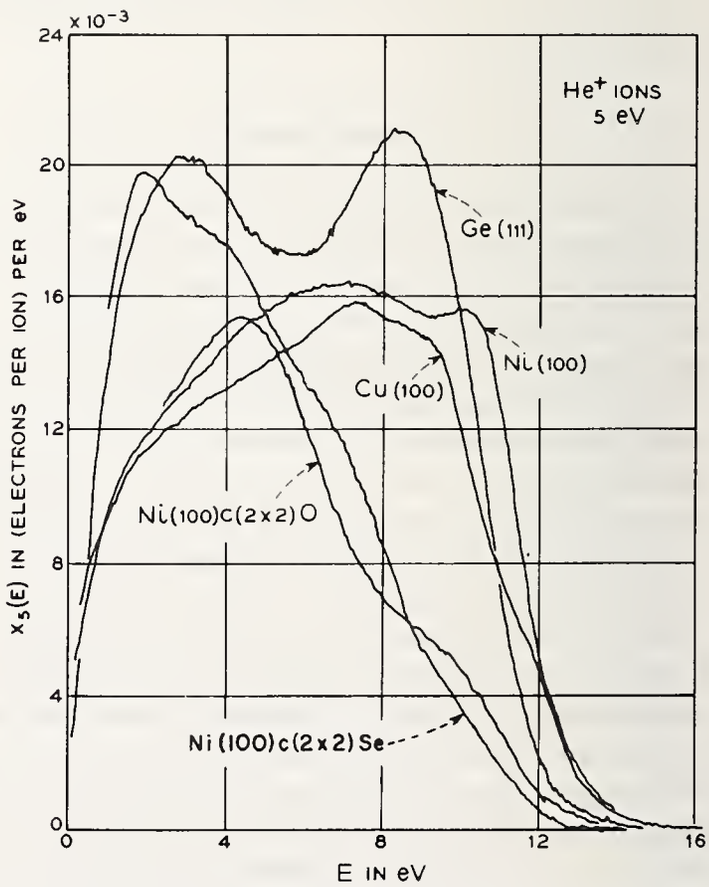

FIGURE 2. *Kinetic energy distribution of electrons ejected by 5 eV He^+ ions from atomically clean surfaces of Ge(100), Ni(100), and Cu(100) and from Ni(100) surfaces having ordered c(2×2)O and c(2×2)Se structures upon them.*

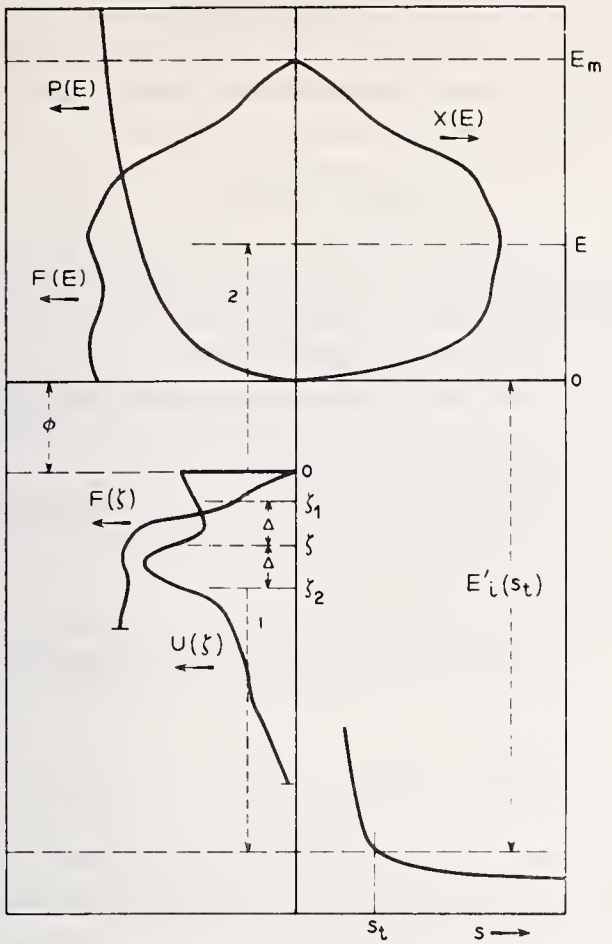

FIGURE 3. *Electron energy diagram showing distribution functions appropriate to copper. The arrows under the functional labels indicate the direction in which the function is plotted. Shown also is the variation of ground state position* $E_i'(s)$ *in the lower right-hand quadrant of the figure.*

is clear that the probability of the elemental process involving valence band electrons initially at ζ_1 and ζ_2 is $N(\zeta_1)N(\zeta_2)$ where $N(\zeta)$ is the appropriate state density of the combined metal-atom system. If we ask the relative probability of producing excited electrons in dE at E we see that all elemental processes contribute in which the electrons are symmetrically disposed on either side of the level ζ which lies halfway between the level E and the ground level of the atom at $-E_i'(s_t)$. Thus we must integrate over Δ obtaining the restricted pair distribution function $F_c(\zeta)$ appropriate to the assumption of constant transition probability:

$$F_c(\zeta) = \int_{-\zeta}^{\zeta} N(\zeta-\Delta)N(\zeta+\Delta)d\Delta. \qquad (1)$$

Relaxation of the restriction on transition probability to obtain a general $F(\zeta)$ function requires introduction into eq (1) of a factor proportional to the square of the matrix element. Thus:

$$F(\zeta) \propto \int_{-\zeta}^{\zeta} |H_{fi}|^2 N(\zeta-\Delta)N(\zeta+\Delta)d\Delta. \qquad (2)$$

We shall sidestep questions of antisymmetrization of wave functions discussed elsewhere [4] and discuss only the one elemental matrix element:

$$H' = \iint u_g^*(1)u_v'(1)(e^2/r_{12})u_e^*(2)u_v''(2)d\tau_1 d\tau_2 \qquad (3)$$

in which u_v' and u_v'' are initial state functions in the band, u_g is the atomic ground state function, and u_e is the function for the excited electron. In eq (3) terms have been rearranged so that functions of the variables of the same electron are brought together.

We see that the matrix element may be viewed as a Coulomb interaction integral between two electron clouds of spatial extent $u_g u_v'$ and $u_e u_v''$. Since u_g is limited to the general vicinity of the atom the term $u_g u_v'$ varies in magnitude with u_v'. Thus the "down" electron makes a contribution to H' which varies with energy as $[u_v'(\zeta-\Delta)]_A$, the u_v' function evaluated near the atom position. If the "up" electron were also restricted to the vicinity of the atom we could make a similar argument relating to the energy variation of the contribution of the up election to H' to the magnitude of $[u_v''(\zeta+\Delta)]_A$. This requires in addition that u_e' vary little and smoothly with energy as appears reasonable.

Several reasons can be adduced for believing that the up electron is excited near the atom position. These are listed here without really adequate discussion:

(1) Experimentally the prominence of the molecular orbital peaks in the results for surface molecules indicates that the wave function magnitudes in the surface region are controlling.

(2) Dominance of atomic level resonances in the results for ions in which atomic levels fill also points to the dominance of wave function magnitude at the atom in governing the autoionization process.

(3) The difference between INS and photoelectric results for atomically clean surfaces can be understood only if INS is surface dominated.

(4) Energy broadening in the $X(E)$ distribution is reduced by a factor 10 when an ordered monolayer of O, S, or Se is formed on the surface of Ni(100). This must be the result of reduction of the density of states just above the Fermi level. Since this reduction can occur only in and outside the monolayer we have evidence in this result that the INS process occurs predominantly in this region.

(5) There appear to be many fewer inelastically scattered electrons in INS than for equivalent photon energy in photoelectric emission, again

suggesting a surface source of excited electrons.

(6) Theoretical considerations by Heine [5] and Wenaas and Howsmon [6] lead to the conclusion that the up electron is excited predominantly outside and in the first layer of the solid.

(7) Large momentum transfer between the two participating electrons means a close collision near the atom where we know the down electron is concentrated. Also viewing the Auger process as photoemission by the down electron followed by photoabsorption by the up electron points to the conclusion that the up electron is most likely excited in the rapidly-decaying near field of the dipole of the down electron transition.

(8) If the up and down electrons made very different contributions to H_{fi} we could not conclude that F is the convolution square U^*U but must be the convolution product V^*W of two dissimilar factors. When V^*W is inverted as though it were a convolution square it can be shown that spurious features will be introduced into $U(\zeta)$ unless $V \cong W$. These are not found.

We are thus led to the general conclusion that:

$$H_{fi} \approx [u_v'(\zeta-\Delta)]_A [u_v''(\zeta+\Delta)]_A, \tag{4}$$

from which eq (2) becomes:

$$F(\zeta) \propto \int_{-\zeta}^{\zeta} [u_v'(\zeta-\Delta)]_A^2 N(\zeta-\Delta)\,[u_v''(\zeta+\Delta)]_A^2 N(\zeta+\Delta)\,d\Delta. \tag{5}$$

eq (5) may be written as:

$$F(\zeta) = \int_{-\zeta}^{\zeta} U(\zeta-\Delta)U(\zeta+\Delta)\,d\Delta = U*U, \tag{6}$$

defining the transition density function $U(\zeta)$ which thus includes both state density and transition probability factors. We see also from eqs (5) and (6) that $U(\zeta)$ is essentially the so-called local density of states in the vicinity of the atom, *i.e.*, the actual state density weighted by the local wave function magnitude at the atom position. This wave function magnitude must, of course, include the effect of the presence of the atom itself in this vicinity.

The pair distribution function $F(\zeta)$ of eq (6) becomes the distribution in energy of excited electrons, $F(E)$, when band variable ζ is replaced by the outside energy variable E according to the relation:

$$E = E_i'(s_t) - 2(\zeta+\varphi). \tag{7}$$

This equation is obtained by equating magnitudes of the energy transitions 1 and 2 in figures 1 or 3. The externally observed electron energy distribution $X(E)$ is related to $F(E)$ by the equation:

$$X(E) = F(E)P(E), \tag{8}$$

where $P(E)$ is the probability of escape over the surface barrier and includes any other dependences on E such as variation in density of final states.

The method of INS consists in reversing the above development to obtain $U(\zeta)$ from measured $X(E)$. It proceeds in the following steps:

(1) Experimental determination of two $X_K(E)$ at ion energies $K = K_1$ and K_2. Usually $K_1 = 5$ eV and $K_2 = 10$ eV.

(2) Linear extrapolation of X_{K_1} and X_{K_2} to X_0 to reduce the natural broadenings present in the X_K distributions. This is done by use of the relation:

$$X_0(E) = X_{K_1}(E) + R[X_{K_1}(E) - X_{K_2}(E)]. \tag{9}$$

Since it has been shown that broadening varies with ion velocity, it is possible to write $R_{K_1K_2}$ as

$$R_{K_1K_2} = (K_2/K_1)^{1/2} - 1. \tag{10}$$

(3) Division of $X_0(E)$ by a $P(E)$ function, reversing eq (8), to obtain $F(E)$. This step is really not necessary since replacement of $P(E)$ by a constant merely changes the intensity level of $U(\zeta)$ progressively as ζ increases without disturbing the structure. However, we have usually divided by a parametric $P(E)$ whose parameters are chosen so that the pieces of $F(\zeta)$ obtained by He^+, Ne^+, and Ar^+ ions are essentially coincident.

(4) After change of variable, $F(\zeta)$ is inverted by a sequential deconvolution procedure. The formulas used are:

$$U_0 = (F_1/2\Delta\zeta)^{1/2},$$

$$U_2 = (1/U_0)\,(F_2/2\Delta\zeta),$$

$$U_{2n-2} = (1/2U_0)\,[(F_n/2\Delta\zeta) - \Sigma_{p=1,\,n-2}\, U_{2n-2p-2}U_{2p}],\ n \geq 2, \tag{11}$$

in which F and U are digitalized as $F_n = F(n\Delta\zeta)$, $n = 1,m$; $U_{2n-2} = U[(2n\text{-}2)\Delta\zeta]$, $n = 1,m$.

(5) Tests of the mathematical uniqueness of $U(\zeta)$ by variation of its origin and by comparison with $F'(\zeta)$, the derivative of the fold function. These steps cannot be discussed in this paper

but will be discussed extensively in a forthcoming publication [7]. Suffice it to say that, although deconvolution is in general a difficult procedure, the sequential unfold works extremely well for the general class of $F(\zeta)$ functions we have for which $F(0)=0$, $F'(0)=k$, and $F(\zeta)$ does not depart drastically from $F(\zeta)=k\zeta$.

The procedure we now use is essentially that given when the INS method was first discussed [4]. However, in the interim we have learned a good deal about the mathematical side of the data reduction, particularly the unfolding procedure. We have derived all possible digital sequential unfold formulations which invert directly or with the independent calculation of no more than the first data point U_0. We have also studied the noise characteristics and shown that the step-midpoint formulation given above in eq (11) not only is the only one which inverts directly without independent calculation of the first point but also has by far the best stability characteristics with respect to noise in the data. We have also faced up to the problems involved in the possibility that we are inverting as a convolution square (U^*U) a function which is in reality a convolution product (V^*W) and have devised tests to determine if any spurious structure could possibly be introduced in this way. The data reduction procedures, although more complicated than for a one-electron spectroscopy, proceed smoothly on the digital computer and produce unique and correct answers. We shall discuss further some of the properties and limitations of INS in section 4.

3. Examples of INS Results

We turn now to the presentation of INS results. These are in two categories: (1) results for atomically clean surfaces of the transition metals Cu and Ni [8], and (2) results for the Ni(100) surface with ordered monolayers of O, S, and Se adsorbed upon it [9]. Some unpublished results for Si and Ge will be mentioned in the discussion of item (1).

In figure 4 we reproduce figure 6 of reference 8 showing $F(\zeta)$ and $U(\zeta)$ for Cu(111). Also shown in the correct relative position is the $P(E)$ function used, indicating how flat it is over the energy range of the data. The average $U(\zeta)$ function for (100), (110), and (111) faces of Cu (fig. 15 of ref. 8) is compared in figure 5 here with the optical density of states curve (ODS) of Krolikowski and Spicer [10]. In figure 6 the $U(\zeta)$ curve for atomically clean Ni(100) from INS is shown and compared with Eastman's ODS curve for a nickel film obtained by photoemission [11].

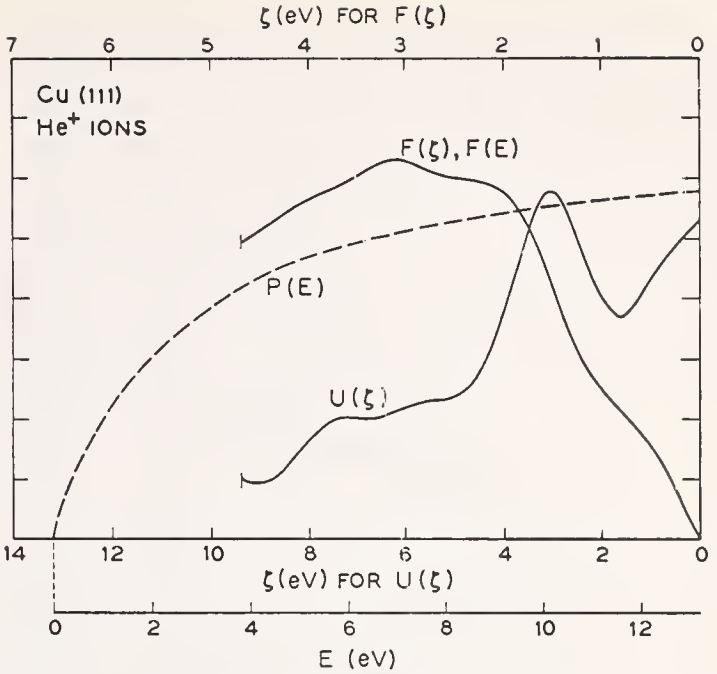

FIGURE 4. *F and U functions for atomically clean Cu(111) and He+ ions [fig. 6 of ref. 8]. The probability of electron escape used in the data processing is also shown.*

First, it is evident that the INS results show a peak in the general vicinity of the bulk *d*-band in both Cu and Ni. However, it is equally evident that this peak does not have the shape or width to be expected from band theory or measured by ultraviolet photoelectron spectroscopy (UPS). A strong case can be made that the differences evident in figures 5 and 6 are due to the fact that the two spectroscopic methods are sensitive to different things. Although the energy resolving power of INS is somewhat poorer than that of UPS, one cannot by any stretch of the imagination consider the INS $U(\zeta)$ curve as a smeared out version of the ODS curves. In reducing the Ni data of figure 6 very little digital

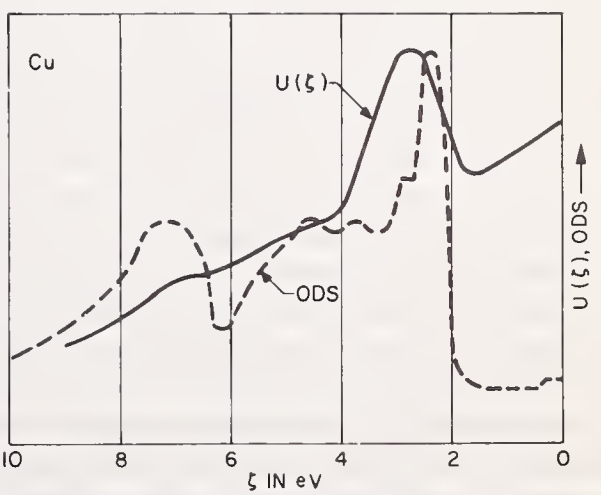

FIGURE 5. *Comparison of the average U(ζ) function for (100), (110), and (111) faces of Cu [fig. 15 of ref. 8] compared with the optical density of states curve (ODS) of Krolikowski and Spicer (ref. 10) obtained by photoelectron spectroscopy.*

417-156 O - 71 - 24

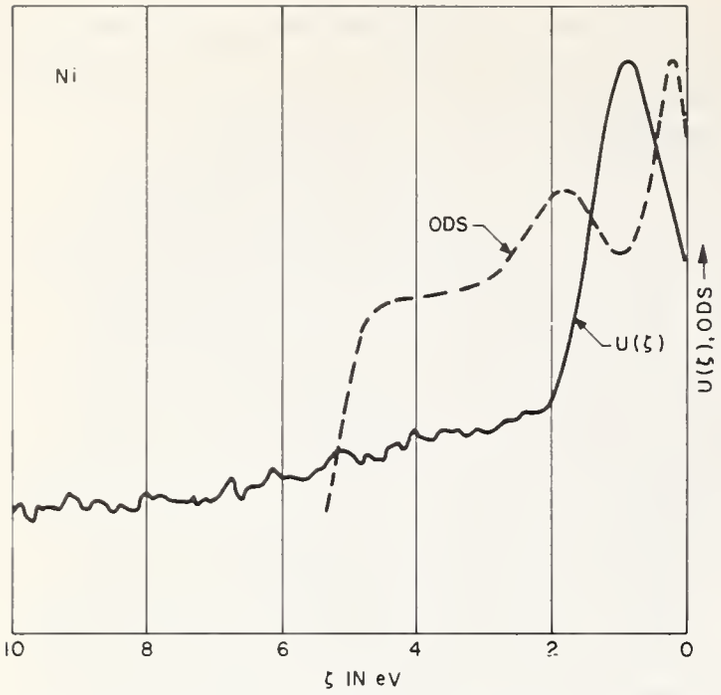

FIGURE 6. U(ζ) *for Ni(100) compared with the ODS curve of Eastman (ref. 11) also obtained by photoelectron spectroscopy. The amount of smoothing used in the INS data reduction was deliberately reduced to the point of leaving in the data the noise seen in an attempt to demonstrate the best resolving power of the INS method.*

smoothing of the data was used in an attempt to increase the resolving power at the expense of letting through low-frequency noise. Some increase in resolving power (about 20%) is evident when comparison with similar curves in reference 9 are made. The sharpness of the peak in $U(\zeta)$ at $\zeta = 1$ eV is an indication of the INS resolving power. In view of the characteristics of INS discussed above it is believed that the $U(\zeta)$ curve is in fact the local density of states at or just outside the surface whereas the UPS results are characteristic of the bulk.

Why the local density of states for *d* bands of transition metals outside the surface differs from the bulk band is an interesting question in surface physics. The reduction in number of nearest neighbors as well as a probable small dilatation of the lattice at the surface could narrow the tight-binding *d* band and make it more like an atomic level. Tight-binding bands are particularly vulnerable to such modification in the surface region. Unpublished work on Si and Ge appears to indicate that the INS results will much more closely mirror what is expected from bulk theory [12]. This is probably attributed to the fact that the *s* and *p* wave functions of the semiconductor valence bands overlap more strongly at the surface even though the surface atoms may be displaced from their "bulk positions" by larger amounts than are surface atoms of the transition metals. Another interesting suggestion to account for the INS results in Cu and Ni arises in the work of Pendry and Forstmann [13] who predict that on some faces of transition metal crystals a new type of surface state appears which should clearly modify the surface local density of states from the bulk density.

The second category of INS experimental result to be mentioned in this paper is found for metal surfaces upon which ordered monolayers of adsorbed atoms are present. In figure 7 is reproduced the $U(\zeta)$ functions from reference 9. Here in curve 1 is repeated the transition density for atomically clean Ni(100). Curves 2, 3, 4 are for $c(2\times2)$ structures of O, S, Se. respectively, and curves 2′, 3′, and 4′ are for $p(2\times2)$ structures involving these same adsorbed atoms, respectively. We note a very interesting increase in complexity of the *U* functions for the covered surfaces. These appear now

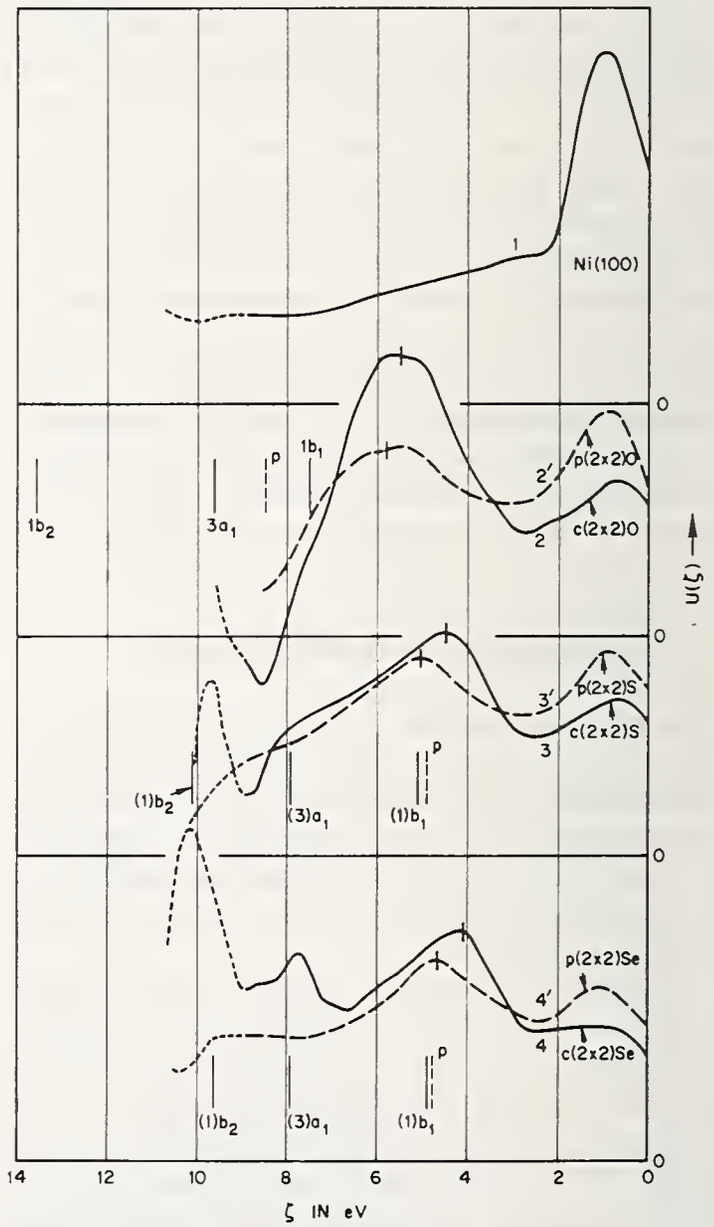

FIGURE 7. *Transition density functions,* U(ζ) *for atomically clean Ni(100) (curve 1) and for the surface with c(2×2) structures of O, S, Se (curves 2, 3, 4, respectively) and with* p*(2×2) structures of O, S, Se (curves 2′. 3′. 4′. respectively). Energies labelled* p, $1b_1$, $3a_1$, *and* $1b_2$ *are identified in the text.*

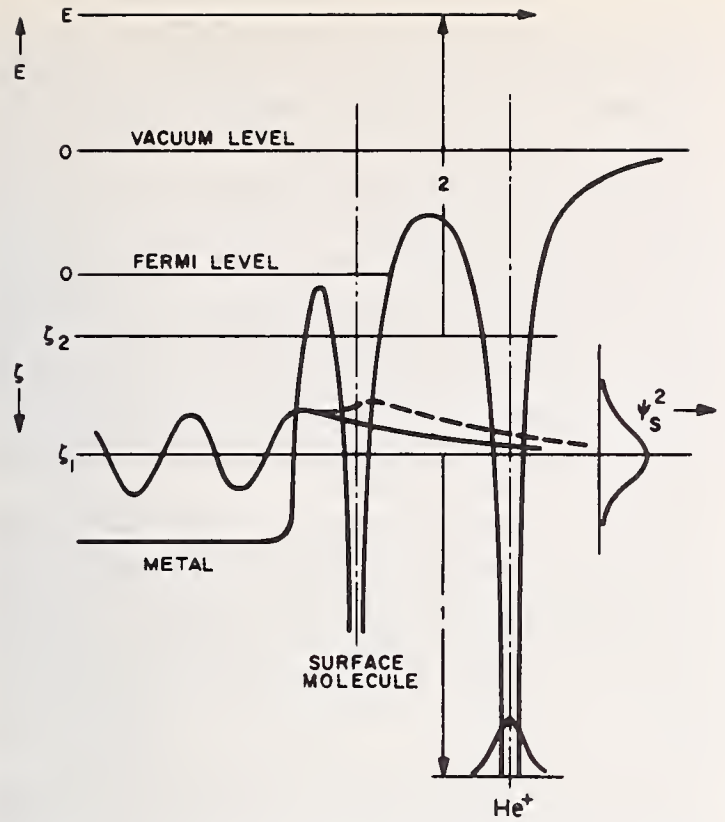

FIGURE 8. *Electron energy diagram illustrating the effect on INS of a resonance or virtual bound state of a surface molecule formed on a metal surface. The bond resonance in the surface molecule is assumed to lie at ζ_1 (which is also the initial energy of the down electron) and to increase the magnitude of the surface wave function ψ_s over a broadened energy range as indicated on the right-hand side of the diagram. The increase in wave function outside the solid in this energy region is indicated by the dashed-line modification of the electronic wave function at ζ_1.*

to indicate the energy spectra of electronic orbitals of electrons in the bonds of so-called "surface molecules" formed from the adsorbed atom and atoms of the substrate.

The electronic states to be associated with bond orbitals in surface molecules form resonances or virtual bound states. These will evidence themselves in the transition density for reasons we attempt to make clear by figure 8. The presence of the electronic orbital at the surface will increase the wave-function magnitude in the vicinity of the surface molecule as indicated by ψ_s^2 in the figure. This will in turn increase the tunneling probability for band electrons into the He^+ well. The dashed line indicates how a band wave function in the absence of the surface molecule (full line) is increased in the presence of the surface molecule (dashed line). These wave function increases in the He^+ well will result in peaks in the local density of states and hence the $U(\zeta)$ transition density function observed by INS.

This paper is not the place to discuss the results in figure 7 in any great detail. A preliminary discussion is to be found in the original publication [9] and an extensive paper is in preparation [7]. However, it is essential to an understanding of the scope of INS as a spectroscopy of electronic states to mention briefly the principal results for these cases of chemisorption. Several energies are indicated in figure 7. These are the levels of the atomic p orbitals in free O, S, and Se, labelled p in the figure. In the figure the second, third, and fourth panels from the top refer to adsorbates O, S, and Se respectively. The lines labelled $1b_1$, $3a_1$, and $1b_2$ are molecular orbital energies in the free molecules H_2X where X is O, S, or Se in the second, third, or fourth panels of the figure, respectively.

Three types of molecular orbital spectrum are to be found among the six curves for adsorbed species in figure 7. Curves 3 and 4 are the most complex spectra having peaks near the orbitals indicated for the free H_2X molecule. These have been attributed to the bridge-type bonding illustrated in figure 9(a) and (b). Relatively small negative charging of the $X = S,Se$ end of the surface molecule is indicated by the fact that the lone-pair orbital peak near $(1)b_1$ also lies near the atomic p orbital energy as for free H_2X.

When the structure is changed from the $c(2 \times 2)$ [fig. 9(b) to the $p(2 \times 2)$ [fig. 9(d)] by removal of half of the adsorbate we see that the molecular orbital spectra change completely to those of curves 3 and 4 in which there is a single peak below the Ni d-band peak indicating a change in the local bonding structure. The only other reasonable alternative is the π-type symmetrical bonding as shown in figure 9(c) and (d) for which we expect a nonbonding orbital in this energy range. Removal of the "center atom" in the $c(2\times2)$ structure removes the agent which distorts the square of Ni atoms of C_{4v} symmetry below each X atom into a rhombus of C_{2v} symmetry. C_{2v} symmetry is essential if the molecular structure is to resemble H_2X. Reversion to C_{4v} symmetry when the center atom is removed demands change of the molecular structure and spectrum as is indeed found.

Finally, both $c(2\times2)$O (curve 2) and $p(2\times2)$O (curve 2′) show a single peak shifted by a much larger amount toward the Fermi level from the atomic p level than is the case for either S or Se. This orbital spectrum (single peak in the available energy range) and larger negative charge (orbital energy shift) together with small work function change on adsorption can be shown to be consistent with a reconstructed surface in which the adsorbed atom is incorporated into the top layer of substrate atoms where relatively large charge will not result in large work function change. Although the above account of the data in figure 7 is admittedly

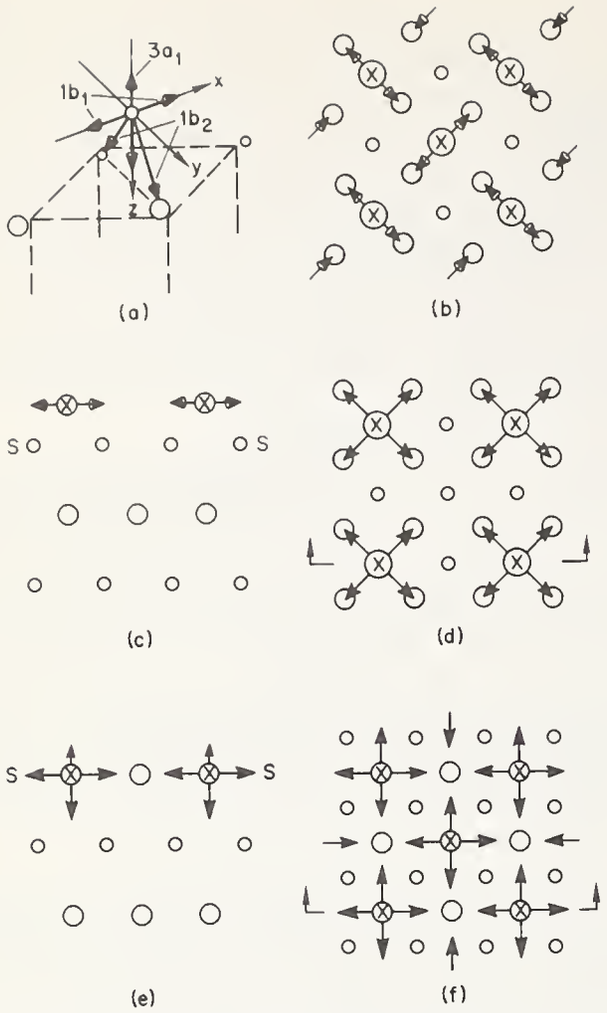

FIGURE 9. *Surface structures suggested (ref. 9) to account for the molecular orbital spectra of figure 7. (a) and (b) are for a bridge-type Ni_2X-type structure repeating over the surface in a c(2×2) pattern to account for curves 3 and 4 of figure 7. (c) and (d) illustrate a* p(2×2) *structure adequate to account for curves 3′ and 4′ of figure 7. (e) and (f) illustrate a reconstructed* c(2×2) *structure to account for curve 2 of figure 7. Simple removal of the "center atom" in (f) without other change produces the* p(2×2) *reconstructed surface thought to account for curve 2′ of figure 7. In these figures bond orbitals are indicated by the heavy arrows with conical arrowheads.*

sketchy, it does indicate how INS determines a portion of the molecular orbital spectrum of a surface molecule and the power such information has in elucidating symmetry and bonding character.

4. Comparative Critique of INS

A comparative critique of INS is perhaps best carried out by listing its characteristics and attempting to assess them as advantages or disadvantages in comparison with other spectroscopies of solids. The other spectroscopies are the two forms of photoelectron spectroscopy, ultraviolet photoelectron spectroscopy UPS [10,11] and x-ray photoelectron spectroscopy XPS [14]; soft x-ray spectroscopy SXS [15], and the surface Auger spectroscopy SAS [16].

In the first place INS is a two-electron spectroscopy as is SAS whereas UPS, XPS, and SXS are one-electron spectroscopies. SAS is based on a two-electron Auger process similar to that underlying INS except that the vacant ground level in the excited system is an inner level of a surface atom rather than the ground level of the parent atom of an incoming atomic ion. The SAS process has been used extensively in the identification of surface impurities but Amelio and Scheibner [16] were the first to attempt to separate the Auger distribution from the large background of secondary electrons and to unfold it to obtain spectroscopic information as has been done in INS.

The fact that INS, like SAS, is a two-electron spectroscopy must in itself be considered a drawback since it necessitates unfolding of the data. However, in INS the data are of such quality that unfolding now offers no significant problem. We have learned much about unfolding methods and possible errors since the last discussion of these matters in the literature [4].

A second characteristic of INS is its surface specificity and hence surface sensitivity. This means, as we have seen, that INS results can be compared with the results of bulk spectroscopies only in special cases. However, INS gives us a tool to study variation of electronic band structure from bulk to surface, to study surface states on both metals and semiconductors, and, perhaps most importantly, to measure molecular orbital spectra of surface molecules formed in chemisorption. Some recent UPS work [17] with 21.2 eV radiation and grazing incidence has shown the possibility of detection of large molecules adsorbed on surfaces. Whether surface molecules of the type discussed here can be observed in this manner has yet to be demonstrated.

The transition probability factors of INS arise from its surface specificity and the tunneling character of the electronic transitions. Four types can be listed: (1) a tunneling factor which decreases with depth in the band, (2) a symmetry factor arising from extent of the surface wave function which decreases as the character proceeds from s to p to d, *etc.*, (3) a second tunneling factor which favors bulk states whose k vector is normal to the crystal face used, and (4) the enhancement in certain energy ranges caused by the surface resonances of adsorbed atoms. Although they are distinctive, there appears to be no particular disadvantage associated with these transition probability factors. It is the last one which makes possible the study of surface molecules and this must be listed as an advantage.

The energy range which can be explored in the solid is $E_i' - 2\varphi$ where E_i' is the effective neutralization ener-

gy of the incident ion near the surface (effective ionization energy of the parent atom) and φ is the work function of the solid. This means that INS is the equivalent of a photoelectric process for which $h\nu = E_i' - \varphi$. For He, $E_i' \sim 22.5$ eV and for a representative solid $\varphi \sim 4.5$ eV. Thus $E_i - \varphi \sim 18$ eV. To equal this range with UPS one must use the 21.2 eV He resonance radiation. XPS, SXS, and SAS, on the other hand, have essentially no energy range limitation with respect to the valence bands of solids. Like UPS, INS is limited by vacuum level cutoff making it difficult to extract data near the vacuum level because of the rapid variation of escape probability there.

Energy resolving power of INS is undoubtedly somewhat less than that of UPS but as figure 6 indicates not greatly less. It is in all probability better than that of SXS, XPS, or SAS since each of these involve the relatively broad inner level of an atom at one point or other.

Finally, we shall mention a series of side effects which must be considered in evaluating any spectroscopy. There appear to be fewer inelastically scattered electrons to contend with in INS than in UPS at higher energies. SAS has a serious background problem unknown to INS. Plasma losses, which can be a complicating interpretive factor, apparently play no role in INS results. SXS has a serious spectral superposition problem unknown to INS. The signal intensity in INS is adequate which sometimes cannot be said for SXS or SAS. INS has the possibility of variation of natural broadenings by variation of a controllable experimental parameter, namely incident ion velocity, making it possible to extrapolate out broadenings admittedly greater than those of UPS.

In conclusion it is possible to state that ion-neutralization spectroscopy is a viable spectroscopy of solids having its own peculiar set of characteristics. It appears that its most important area of application at present is to the study of the molecular orbital spectra of surface molecules formed in chemisorption. Here it holds promise of extending our knowledge of surface structure beyond what low-energy electron diffraction (LEED) now can do. LEED tells us how a given adsorption or bonding structure repeats itself over the surface. INS yields information about bonding symmetry, orbital energy-levels, and electric charging within the surface molecular structure, which in many cases, using LEED and work function data, will permit the specification of bonding structure. Surface state and surface modifications of band structure also promise to be interesting fields in which INS can make a contribution.

5. References

[1] Hagstrum, H. D., Phys. Rev. **96**, 336 (1954).
[2] Hagstrum, H. D., Rev. Sci. Instr. **24**, 1122 (1953).
[3] Hagstrum, H. D., Pretzer, D. D., and Takeishi, Y., Rev. Sci. Instr. **36**, 1183 (1965).
[4] Hagstrum, H. D., Phys. Rev. **150**, 495 (1966).
[5] Heine, V., Phys. Rev. **151**, 561 (1966).
[6] Wenaas, E. P., and Howsmon, A., private communication and Proc. 4th Int'l Materials Symp. on the Structure & Chemistry of Solid Surfaces, 6/19-21/68. Univ. of California, Berkeley.
[7] Hagstrum, H. D., and Becker, G. E., to be published.
[8] Hagstrum, H. D., and Becker, G. E., Phys. Rev. **159**, 572 (1967).
[9] Hagstrum, H. D., and Becker, G. E., Phys. Rev. Letters **22**, 1054 (1969).
[10] Krolikowski, W. F., and Spicer, W. E., Phys. Rev., to be published.
[11] Eastman, D. E., and Krolikowski, W. F., Phys. Rev. Letters **21**, 623 (1968); Eastman, D. E., J. Appl. Phys. **40**, 1387 (1969).
[12] Hagstrum, H. D., and Becker, G. E., to be published.
[13] Pendry, J., and Forstmann, F., private communication.
[14] Fadley, C. S., and Shirley, D. A., Phys. Rev. Letters **21**, 980 (1968).
[15] Cuthill, J. R., McAlister, A. J., Williams, M. L., and Watson, R. E., Phys. Rev. **164**, 1006 (1967).
[16] Amelio, G. F., and Scheibner, E. J., Surface Science **11**, 242 (1968). Other forthcoming papers by these authors will give results for Si and discuss the experimental and mathematical methods in greater detail.
[17] Bordass, W. T., and Linnett, J. W., Nature **220**, 660 (1969).

Discussion on "Ion-Neutralization Spectroscopy" by H. D. Hagstrum (Bell Telephone Laboratories)

W. Plummer *(NBS):* I am very much concerned that you interpret the low energy structure as due to density of states when, in fact, you have assumed a constant escape probability, before and after adsorption of these gases. It is a well known fact, both experimentally [1] and theoretically [2], that adsorption will cause coverage dependent structure in the reflection which should be related to your escape probability. If you do not accept any structure, say for 4 eV above the vacuum level, then basically you have only two kinds of structure in all your curves. All of them would then have one broad hump with only the $p(2\times2)$ structure of Se having an extra peak. I understand from your 1966 paper that when you parameterized the escape probability, you could not explain satisfactorily the low energy escape probability for the various ions used, i.e., from 2 to 4 eV above the vacuum level. It is very important to your interpretation that some of the gases have three humps while others have only one or two.

H. G. Hagstrum *(Bell Telephone Labs.):* Dr. Plummer is certainly correct that one should consider seriously the effect of the results of Madey and Yates for escape probability of the ion-neutralization process. If the lowest energy structure observed with He^+ ions were to be due to a variation of escape probability with energy, this structure would have to appear at the same energy above the vacuum level in the results for Ne^+ ions. We have looked again at our results for Ne^+ ions and find that they give the same spectrum as we observed for He^+ from the Fermi level down to that energy below the Fermi level to which the Ne^+ ion-neutralization energy enables us to eject electrons. From this it does not appear that the structure in either of the electron distributions for He^+ and Ne^+ ions results from the variations observed by Madey and Yates in a different system. I would suggest that the reason for this is that the electrons we observe in the ion-neutralization process are electrons which are in the main excited outside the solid surface and, therefore, do not interact nearly as intensely with the surface barrier as do the electrons in the experiment of Madey and Yates. I would also suggest that our result which shows that the lowest energy peak disappears in going from the $c(2\times2)$ Se to the $p(2\times2)$ Se structure is quite strong evidence that the peaks in the spectrum are of molecular orbital origin and not due to variation of the escape probability. Dr. Plummer has alluded to the discussion in my 1966 paper concerning the difficulty of obtaining reliable data in the range 0 to 4 eV above vacuum level. Since the 1966 paper was published, we have worked very hard to improve our data in this region. In the retarding potential configuration we have been using, this problem relates to the difficulty in keeping the ion beam well focused at the lowest kinetic energy. We have been able to improve our situation since that time to the point where we believe that the presence or absence of a peak in the range 2 to 4 eV above the vacuum level is no longer in doubt although we cannot, with that experimental configuration, claim to know the peak position or width with the same accuracy that we know these data for other peaks at higher energies. During the last year we have rebuilt our apparatus so as to eliminate the effect of the electron retardation upon the incoming ion beam. With this apparatus we have been able to reproduce very well the results of the earlier apparatus, thus bolstering our confidence in the results in this energy range.

[1] Madey, T. E., and Yates, J. J., Supp. Nuovo Cimento, **Vol. 5,** Ser. 1, p. 483.
[2] Gadzuk, J. W., to be published in Surface Science.

Potential and Charge Density Near the Interface of a Transition Metal*

E. Kennard** and J. T. Waber

Northwestern University, Materials Science Department, Evanston, Illinois 60201

The early literature on methods of calculating surface energy and charge density and of dealing with potential barriers at an interface are reviewed.

The three dimensional potentials and charge densities were obtained by superimposing the relevant atomic information which had been obtained from Dirac-Slater self-consistent field calculations on free atoms.

The total charge density at each point P was found by summing the contributions from atoms located within a sphere of radius R centered at P. The local exchange potential was estimated at P by means of Slater's $\rho^{1/3}$ method. This was included with the overlapped atomic Coulomb potentials to obtain the crystal potential near the surface.

Key words: Absorption potential; charge density; metal-vacuum interface; platinum; surface energy.

1. Introduction

The theoretical investigation of the surface energy of metals has received considerable attention in the last few years. This trend has been stimulated by a large amount of excellent experimental data which has been appearing in the literature.

The first theoretical attempts to explain experimental values of surface energy were made in the late 1930's; the nearly free electron theory of metals was used. This is quite a reasonable approach for the alkali metals. The results were on the whole in reasonably good agreement with the experimetal data. But, as in all such studies, the results were strongly influenced by the model chosen. It is the aim of this paper to examine some of these models and then to discuss the calculation of more realistic models.

In reality, all metal specimens are finite and are bounded by surfaces. However, theoretical calculations of electronic structure can be simplified by assuming an infinite solid. When there is a regular arrangement of ion cores in a metal, calculations need only be carried out over one unit cell. That is, the infinite solid possesses a very high degree of translation symmetry.

At this conference on the electronic structure of metals and semiconductors, it is appropriate to consider the special quantum mechanical problems which occur when a surface intrudes into an infinite solid. There is a reduction in the symmetry; translational invariance is lost along some directions $[h\ k\ l]$ which is perpendicular to the free surface and in general certain planes which were mirror planes are no longer effective in "mapping" the crystal lattice onto itself. In general, Bloch's theorem will hold for translations having their components strictly parallel to the free surface, but not for translations with a component perpendicular to the surface.

For a realistic model of a solid, there will be a nonvanishing probability of finding electrons in a region slightly beyond the last row of ion-cores, and the average charge densities will decrease in a more or less exponential way toward zero over a region of several interatomic distances.

Surface studies are pertinent to the theme of this conference because certain experimental methods for determining $N(E)$ curves, such as photoemission and ion-neutralization spectroscopy, involve electrons passing through or coming from the surface regions of a metal. More understanding of the effects of crystallographic orientation on surface potentials would enhance our knowledge of the processes which occur at surfaces; in addition, it would increase our

*Research supported by the National Aeronautics and Space Agency, Washington, and by the Advanced Research Project Agency of the Department of Defense through the Materials Research Center at Northwestern University.

**Submitted in partial fulfillment of the requirements for the degree of Doctor of Philosphy, Northwestern University, Evanston, Illinois.

knowledge of the bulk electronic structure of metals and semiconductors.

2. Review of Pertinent Studies

To illustrate the problems associated with making realistic calculations of surface potentials and surface energy, we will review some of the early studies which utilized primarily the methods for studying the bulk density of states. Certain earlier studies of surfaces used the nearly free electron model of metals; these are related to the use of the "jellium" model. The several researchers in this field have assumed an infinite potential wall at the surface of the metal. Later, the effects of a finite barrier and the penetration of that barrier by electrons were considered. Although the "geometric" surface can be defined as the plane containing the last row of ion cores, those properties directly connected with the electron distribution cannot be considered to change abruptly from one side of this plane to the other. Instead, one should consider a surface region surrounding the last plane of ion cores and in that the properties of the finite solid may be different in this narrow region from those of the bulk.

The boundary-layer region and the charge density variations in this region have been treated in recent studies. Let us begin by defining the increase in energy associated with "cutting" a metal and forming an interface.

3. Surface Energy

The surface energy of a solid may be defined as the difference in energy between that of a given volume of metal contained in an infinite solid and the energy of an equivalent volume of metal removed from the metal and placed in vacuum—it is the energy increase which results from the presence of one or more surfaces. For ionic or covalent solids, one might reasonably consider surface energy in terms of broken bonds or dangling bonds.

The relatively free electrons and the ion cores are the ingredients of a metal; the mutual interactions between the many electrons and the many cores can lead to an increase in energy. Thus, the surface energy must be related to a change in the local concentration and kinetic energy of electrons. The redistribution of the ion cores which apparently occurs may be another contributing factor near the "surface." The attendant change in potential alters the local concentrations of electrons. If one thinks of a metal as a collection of plane waves (electrons being scattered about in a metal by the ion cores), it becomes very likely that standing waves will occur near the interface due to reflection at the interface.

4. Treatment of the Electronic Problem

Brager and Schuchowitzky [1] considered that the extra energy arose from the fact that the presence of a surface serves to define the position of the metallic electrons more exactly, i.e., it partially "localizes" them, and hence leads to an increase in their energy by the Heisenberg principle. These researchers did not clearly indicate whether the increase in surface energy would be confined to a surface region or whether it might lead to a general increase in energy of all the electrons.

Because of the penetration of the electrons beyond the geometric surface, a "double layer" is formed with a net positive charge inside and a negative charge outside. The energy of the dipole layer is also associated with surface energy. Early workers [2,3] attributed all of the surface energy to the potential energy which comes from separating the electrons from their ion cores, i.e., with the energy of the double layer. Subsequent calculations have shown that this contribution is negligible in comparison with the local change in kinetic energy [4,5].

5. Nearly Free Electron Model

In 1946, Brager and Schuchowitzky [1] assumed that the electrons move in a cubic box with side L and that the potential field becomes infinite at the walls of the box. The appropriate wave functions are of the form:

$$\psi(\mathbf{r}) = A \sin (nk_x x) \sin (mk_y y) \sin (lk_z z). \qquad (1)$$

Each such state is represented by a point in **k** space, i.e., reciprocal space which lies on a grid of spacing $(n\pi/L, m\pi/L, l\pi/L)$. In the usual way, one finds that the density of states at the Fermi level is:

$$\frac{dN}{dk} = \frac{\pi}{2} k_{\max} \left(\frac{L}{\pi}\right)^3 \qquad (2)$$

where k_{max} is the radius of the Fermi sphere. The total kinetic energy of these states is given by:

$$E_{\text{tot}} = \frac{h^2 k_{\max}^5 \Omega}{10\pi^2 m^*} \qquad (3)$$

where Ω is the (cell) volume and m^* is the effective electronic mass.

The number of states has been over-counted in this Sommerfeld model because the particular boundary conditions require that the functions vanish on the walls or limiting planes of the octant in **k** space, i.e., that states where n, m, or $l = 0$ are inadmissible. Brager

and Schuchowitzky obtained the number of reciprocal lattice points contained in the sphere of radius K and excluded those on the walls of the octant, using a formula given by Vinogradov [6], namely:

$$N=\frac{\pi}{6}K^3-\frac{3\pi}{8}K^2+O(K^{1.4}) \tag{4}$$

where O indicates the number of magnitude of the correction term. This correction arises from approximating a sphere by a collection of equal volume boxes centered on a lattice of points.[1] It leads to a total energy of

$$E=\frac{h^2k_{\max}^5\Omega}{10\pi^2m}+\frac{3\pi h^2}{32m}\left(\frac{L}{\pi}\right)^2k_{\max}^4+O(L^{1.4})\,. \tag{5}$$

The energy of such a bounded metal is made up of a term dependent on L^3 and a term dependent on L^2 plus correction term of order $L^{1.4}$. The surface energy in (eV/cm^2) (namely, the excess energy over the energy in the volume L^3 when divided by the surface area) becomes:

$$E_{\text{surface}}=\frac{h^2k_{\max}^4}{32\pi m}+O(L^{-0.6}). \tag{6}$$

When $L \gg a_0$, the latter term relates to surface irregularities and can be neglected. Sugiyama [7] proved that the same result held for any shaped metallic mass.

Brager and Schuchowitzky [1] showed that the surface energy is primarily dependent on the electronic charge density in the bulk of the metal. Figure 1 is a log-log plot of the experimental values of the surface tension of liquid metals against (ρ/A) where ρ is the density of the metal in gm/cm^2 and A is the atomic weight. Conversion of eq (6) indicates a slope of 4/3; the slope found is 1.2. Another result is that the second term, E_2, in eq (5) is one-fourth of the energy of a two-dimensional Fermi gas located on the surface.

The common model potentials have some form of a step at the geometric interface. When one uses an infinite, three-dimensional potential step, as several workers have done, the values of $\psi(r)\rightarrow 0$ on this boundary. Sugiyama [7] illustrated the spatial dependence $\rho(y)$ of the electron gas when an infinite barrier is erected at a geometric surface. There is a surface thickness which is the region in which the electrons are excluded. As a consequence of the barrier, the charge density must increase in other regions. This is illustrated in figure 2. Charge oscillations are also shown.

If it is assumed that the interior charge density remote from the surface is not altered by the presence of the surface and further, that k_{max} is not altered from its bulk value, then it can be shown [5,7] that the charge may be conserved by displacing the infinite

[1] In principle, a similar correction might be used to take account of the asphericity of the Fermi surface, but Brager and Schuchowitzky were content to use m^* for that purpose.

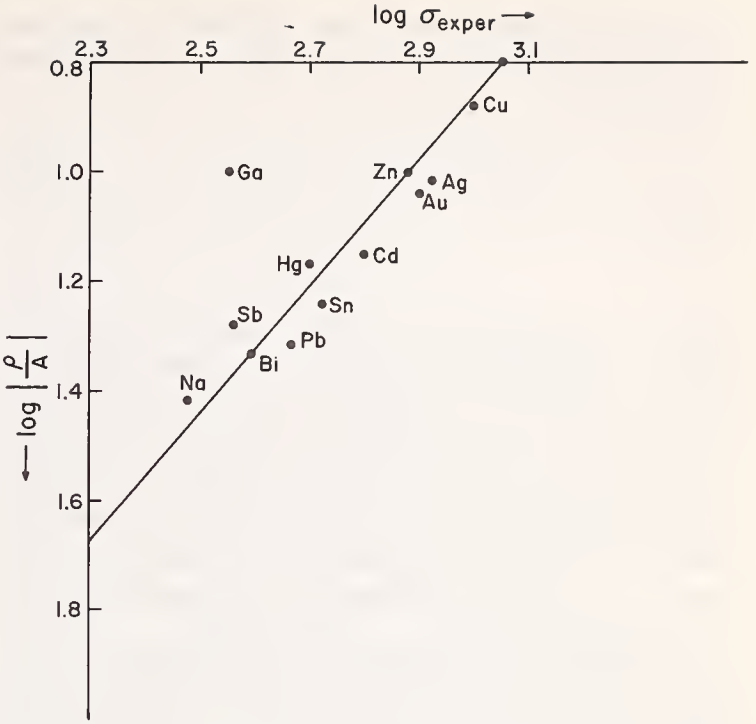

FIGURE 1. *Variation of the logarithm of the experimental values of the surface tension (σ) against the logarithm of the approximate electron density (ρ/A).*

The slope of the line is 1.2.

potential barrier outward from the geometric surface, by a length of the order of a lattice parameter. However, an imaginary node then occurs at $y = a$, a little way beyond the geometric surface.

The **k** vector is inversely proportional to the distance between nodes of $\psi(\mathbf{r})$; thus $k_y = m\pi/L - \delta/L$ where the "phase shift" δ due to barrier penetration can be defined by:

$$\tan\delta=\frac{k_y}{(2m\rho/\hbar^2-k_y^2)^{1/2}} \tag{7}$$

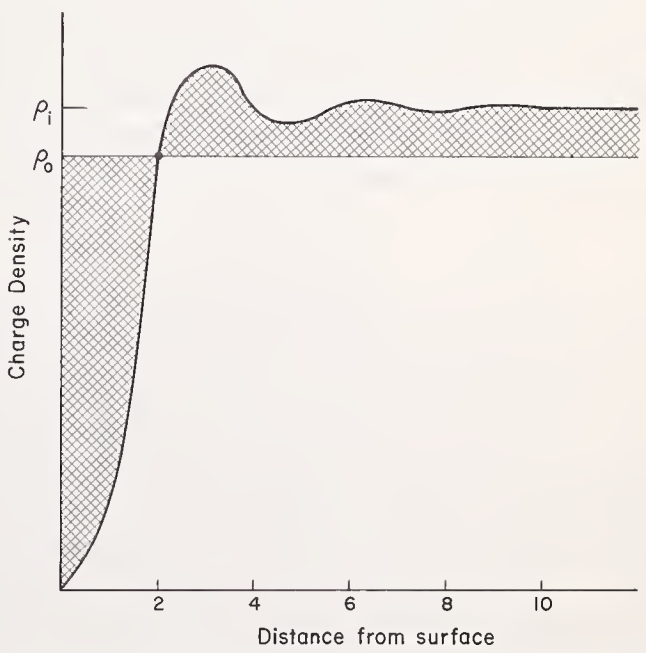

FIGURE 2. *Local variation of the charge density of free electron gas caused by an infinite potential wall placed at the geometric surface.*

ρ_i exceeds ρ_0 when the infinite step is at $y = 0$.

where ϕ is not the work function but the inner potential observed in LEED experiments. One notes for the wave vectors, that

$$k_y = \frac{n\pi}{2(L_y + a)} = \frac{\delta}{(L_y + a)}. \tag{8}$$

The term a is of the order of an interatomic distance. The surface energy computed with this model contains a term which is similar to the one in eq (6). A negative correction term σ_2 arises due to the reduction of each component of $\mathbf{k}$ by δ/L. Thus:

$$\delta_2 = \frac{p_{\max}^4}{16mh^2} [3(2-\lambda)(\lambda-1)^{1/2} + (3\lambda^2 - 8\lambda + 8) \text{ arc sin } (\lambda^{-1/2})] \tag{9}$$

where the parameter $\lambda = \phi/E_F$ is greater than unity. Huang and Wyllie [4] were apparently the first researchers to use a realistic finite step at the surface. The height of the barrier ϕ was estimated from the Fermi energy E_F and experimental values of the cohesive energy W. With such a finite potential barrier, the wave function $\psi(r)$ is not forced to approach zero at the barrier step. Instead it undergoes a change in phase as electrons penetrate into vacuum and $\mathbf{k}$ has an imaginary component. This will be discussed below. The calculations of Huang and Wyllie give better agreement with experimental data than those of Brager and Schuchowitzky. The results are compared in table 1.

However, it was pointed out by Stratton [5], Sugiyama [7], and Huntington [8], that such realistic potential barriers do not necessarily conserve charge. Even a finite potential step cannot be placed at the position $y = L$, because such a step leads to an excess of charge in the interior. Thus, the position must be altered so that charge is conserved. Sugiyama [7] showed that the Brager and Schuchowitzky energy E_S was in fact a poor approximation. He obtained a surface energy one fifth as large.

Stratton [5] similarly used a finite step function located at $y = +a$, that is, one somewhat in front of the geometric surface. The Stratton charge density is similar to that of Sugiyama [7], except that the effect of penetration of a finite barrier is more explicitly indicated. For a finite step the relation which will conserve charges requires that

$$a = a_\infty - \frac{3}{4k_{\max}} [(\lambda-1)^{1/2} + (2-\lambda) \text{ arc sin } (\sqrt{\lambda})] \tag{10}$$

where a_∞ is the value for an infinite step, i.e., when $\mu \to \infty$ and λ is defined to be (μ^2/k^2_{max}). The quantity a_∞ becomes $3\pi/8k_{max}$. This idea leads to a surface energy of

$$\sigma = \frac{\hbar^2 k_{\max}^2}{160\pi m^*} - \frac{\hbar^2 k_{\max}^4}{160\pi m^*}$$
$$[(14-15\lambda)\sqrt{1-\lambda} + (8-24\lambda+15\lambda^2) \text{ arc sin } (\sqrt{\lambda})] \tag{11}$$

agreeing with Sugiyama's calculation for $\phi \to \infty$. However, Stratton's values of the surface energy tend to be smaller than those given by Huang and Wyllie. Stratton [5] found that the contributions to the surface energy are confined to a narrow region which contained a lattice boundary or edge. Some of his results are also compared in table 1. A similar calculation was carried out by Huntington [8]. His value of σ for sodium was very close to that obtained by Stratton.

Huntington [8] also calculated the surface energy of sodium using the self-consistent image barrier worked out by Bardeen [9]. Huntington's values appear to be approximately 40 percent of the experimental values.

The probable cause for the substantial reduction of the surface energy can be illustrated in the following manner. In figure 3, the density of states for the bulk metal is drawn as a full curve. When the infinite barrier is located at one-half an interatomic distance beyond the last layer of atoms, those states are excluded for which one or more components of vector $\mathbf{k}$ are zero. The formula for the density of states remains the same. The number of disallowed states per unit energy is constant; because E is proportional k^2 and the number of points lying inside circles on the three orthogonal (Cartesian) planes inscribed by the Fermi sphere are also proportional to k^2. The excluded states which are

TABLE 1. *Surface energy σ due to the change in the kinetic energy of the electrons*

Metal	Surface energy (ergs/cm²)			
	B&S	H&W	Stratton	Exp
Lithium	.....	960	350	398
Sodium	777	470	165	190
Potassium	333	208	68	101
Copper	3720	2180	800	1103
Silver	2170	1400	490	800
Gold	2120	1490	500	580
Zinc	2330	.....	.....	743
Cadmium	1670	.....	.....	630
Mercury	1550	.....	341	465

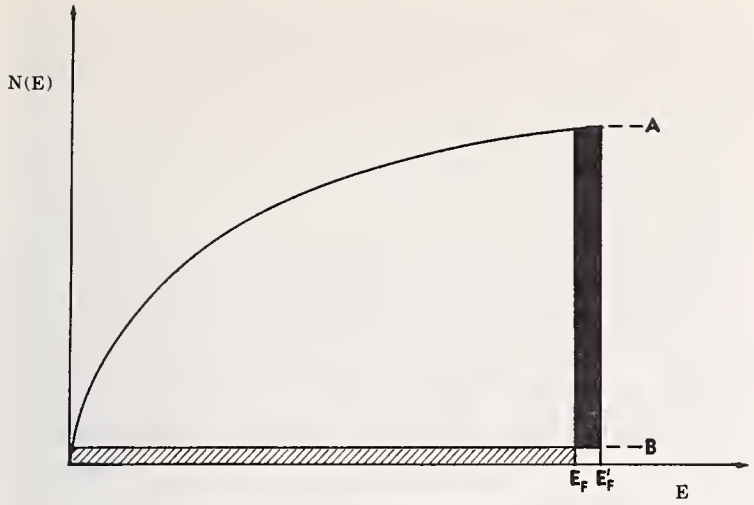

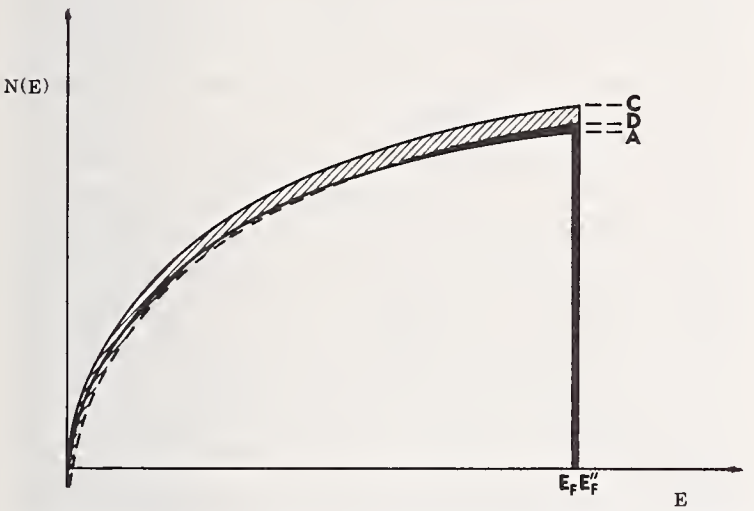

FIGURE 3a. *Curve A is for Density of States Curve for a infinite metal assuming nearly free electrons.*

The excluded states on the walls of the *XY*, *YZ*, and *XZ* planes in the Fermi sphere are indicated by curve B. The net effect is to increase the Fermi level at 0 K to E'_F.

FIGURE 3b. *The dotted curve C is the* N(E) *curve obtained by approximating barrier penetration by relocating the effective infinite barrier at* a *and thus increasing the constant of the parabola.*

The net density of states curve D (crosshatched) is obtained by subtracting B from C. The net effect of the increased number of occupied states is that $E''_F - E_F$ is smaller.

shown as shaded area must be added to the top of the band thus increasing k_{max}. The dashed curve represents the situation with an infinite barrier.

Alternatively, the electrons could be accommodated by altering the spacing of the states in **k**-space and keeping k_{max} a constant. The alteration of the spacing of allowable states in **k**-space is accomplished by increasing the distance between nodes of the wave function in real space, i.e., by moving the position of the potential barrier.

Due to barrier penetration the effective node lies at $L'=L+a$. The consequence of the analysis is that each new k'_y is reduced by $(a/\pi L)$. The lowest state which is now included is somewhat lower than in the case of an infinite barrier as indicated on the lower portion of figure 3. However, the density of states is increased because L' exceeds L and hence the density of excluded states remains the same, being constant for all E. In the analysis of Sugiyama, the Fermi level E_F is barely shifted and the unoccupied states are accommodated by the enhanced "width" of the $N(E)$ curve. It is reasonable that the additional energy in the lower portion of figure 3 may be less than on the left-hand side.

Huntington [8] in his paper showed that, providing the barrier was consistent at least with regard to charge conversation, i.e., that the height and position of the barrier were such as to conserve charge, then the surface energy varied by little more than 10 percent considering a wide range of possible values of height and position. Any barrier which conserves charge gives a good approximation to the surface energy.

6. Electrostatic Energy of the Double Layer

A double layer is formed near the interface of a metal because the electrons will penetrate into the "forbidden" region if the potential is finite at the edge or boundary. Because of the distribution of electrons beyond the boundary, a local depletion of electrons will occur just inside the boundary. Thus, a dipole layer will be set up with the negative side outside the boundary, i.e., outside the metal.

One may calculate formally the energy of this electrostatic double layer inside and beyond the lattice surface by means of the following integral:

$$\sigma_3 = -\pi \int_{-\infty}^{\infty} \int_{-\infty}^{\infty} \rho(y_1)\rho(y_2)|y_1 - y_2|^{-1} dy_1 dy_2 \qquad (12)$$

where y is the coordinate perpendicular to the surface and ρ is the local charge density. Evaluation of this integral requires a detailed knowledge of ρ.

Stratton [5] used free electron wave functions and found that

$$\sigma_3 = vNe^2 \qquad (13)$$

where v is a universal constant, 5×10^{-3}, for all metals. His values for σ_3 amount to a small increase in kinetic energy, namely, to approximately 10 to 20 percent of the major contribution to the surface energy.

The small contribution to the surface energy from the double layer at the surface is in agreement with the observation by Bardeen [9] that the surface barrier is due primarily to exchange and correlation forces. Juretschke [10], using Slater's method for the potential [11], was able to calculate the variation of the exchange potential along a line perpendicular to the surface. His results showed good agreement with those of Bardeen.

If one were to bring a test charge up to the vicinity of the lattice boundary, then its potential will cause an additional redistribution of electrons in the metal, i.e., it will cause local polarization. The effect would be equivalent to that of a classical image force with essentially an electron hole distributed over a region several Angstroms in extent. This, of course, is a further contribution to the apparent dipole moment at the interface.

The photoemission of an electron causes the kind of a localized redistribution of charges which is associated with an exciton. However, the statistical approximation possibly is inadequate beyond the surface because this is a region of low density or of rapidly varying density.

Loucks and Cutler [12] calculated the effect of using a screened exchange energy in the Bohm-Pines formalism. They obtained exchange potentials whose shape was very similar to that of Juretschke but whose magnitude varied with the screening parameter. These authors also included a long range correlation term which was independent of position. The exact form of the surface potential has been further investigated and applied by Davies [13] and Gadzuk [14]. At the present, it appears that these calculations of surface potential of a free electron metal are as exact as necessary. Gadzuk [14] remarks ". . . unfortunately there is very little experimental data which can be used to evaluate the exact shape and magnitude of the surface barrier."

7. Metallic Interfaces

Recently, a number of pertinent studies have appeared in the literature. Stern [15] discussed the problem of surface states in terms of scattering of nearly-free electron waves. He suggested that surface effects might extend into the metal to a depth approaching 50 lattice parameters and that such a skin effect should influence the optical properties of the metal since the penetration depth of electromagnetic waves in the visible range of wavelengths is comparable to this figure.

Bennett and Duke [16] studied the interface formed between two metals. This problem has many formal similarities to the problem of a metal-vacuum interface and the analogy grows in accuracy when the electron density in one metal is significantly lower than that in the other. This case has been subsequently studied by many investigators [17-20]. Tunneling from the high into the low density region occurs but there are generally no surface states of either the Tamm or the Shockley type. The "localized" states which Bennett and Duke [17] found on the high density side of the interface in the early stages of the calculations tended to disappear during successive iterations and were not found at the stage of achieving self consistency.

They observed that there are oscillations in the charge density near the interface which are similar to Friedel oscillations [21]. Such oscillations are to be contrasted with the simpler dipole layer which occurs near a metal-vacuum interface. In a subsequent paper, Bennett and Duke [22] studied the general effect of including the spatial dependence of the total exchange and correlation terms in the potential (rather than the bulk values as in their earlier paper) was to increase the size of the depletion region in the low density region. Since these effects arise from the evanescent waves and the tunneling into the low density metallic region, similar effects are to be anticipated for the metal-vacuum case. The depletion region and the charge oscillations were stabilized by exchange-correlation forces and did not disappear on subsequent iterations.

Surface states associated with a metal are similar to those one encounters with semiconductors. In the latter case, the levels typically lie in the energy gap of the semiconductors. The metallic surface states will be mixed with the Bloch states in the conduction band. The evanescent charge contributions are the electron-gas analogues of Heine's "virtual surface states," for metal-semiconductor interfaces [23]. Metal surface states have recently been predicted and observed experimentally [24-26]. Davison and his collaborators Stęślicka, Koutécky, and Cheng [27, 28], at the University of Waterloo have studied most of the cases of surface and impurity states which are tractable to analytic methods. In general, either a tight binding approach or a molecular orbital approach was used. The effects of deforming a surface layer and the correlation between electrons were also incorporated. Stęślicka [28] has added the additional complication of the relativistic wave functions in the crystal. That is, the typical free electron wave function $A_n \exp(ik_n x)$ is replaced by its four component, relativistic counterpart. Additional states were found by her.

The principal limitation in these researches is that a one-dimensional or linear crystal was assumed. Their concern was in proving the existence of solutions to the problems posed by the interruption of the full translational symmetry of the lattice by either changing (a) the spacing between atoms, (b) the nature of certain atoms, and (c) by truncating the crystal. Beyond the formal approach, they have not attempted to include interelectronic effects; however, because of their work, the reduction of the problem to numerical solutions and the

efforts to obtain self-consistency in the charge redistribution and surface potential will be simplified and facilitated. Sharma and Shrenk [29] recently studied analytically, the emission of electrons from a potential distribution modeled to stimulate the crystal structure of a metal.

There are two further simple approaches to calculating surface energy properties. We will take up these before proceeding to discuss the present analysis on potentials and other surface effects. The first involves a modification of the tight-binding method used to calculate energy bands; the second, the Lennard-Jones potential.

8. Tight-Binding Method

Cyrot-Lackmann [30] has used the tight-binding method to calculate several moments of density of states.

$$M_n = \int E^n N(E) dE \tag{14}$$

and expressed M_n in terms of the nearest neighbor resonance (overlap) integrals. For a simple nondegenerate band, the moments are easily calculated from the resonance integrals and a permutation operator representing the number of ways the nearest-neighbor interactions can be counted. The surface is then readily introduced by its effect on the permutations which can be made. In this way, the density of states with and without a surface can be calculated, and from this the surface energy is obtained. This model is interesting in that it is dependent on the geometry of the ions at the surface and thus enables a comparison of the surface energy of different crystallographic faces to be carried out. Although absolute values of surface energy for different faces of a solid metal are difficult to obtain experimentally, it is possible to obtain the ratios of surface energy of different crystallographic faces. Cyrot-Lackmann has shown her calculations to give good agreement with experimental ratios.

An atomic approach to adsorption properties was used by Neustadter and Bacigalupi [31] who assumed that the binding energy of the metal adsorbate was given by a Lennard-Jones 6-12 potential

$$V_i(r) = -\frac{a}{r^6} + \frac{b}{r^{12}} \tag{15}$$

at a given site and then summed over the lattice. Their values of absorption energy and surface diffusion activation energy agreed very well with values obtained experimentally. These authors showed that binding was greatest at certain sites where it would be expected that the maximum numbers of substrate atoms would interact with the outermost electrons of the adsorbed atom (or ion). Thus, although these workers did not include any electronic effects and did not investigate the actual nature of the interaction, they were able to estimate those properties arising from the "granular" geometric structure of the surface. It might be noted that Plummer and Rhodin [32] have presented experimental and analytic results for the adsorption of transition metal atoms on transition metal substrates which suggest that nearest neighbor arguments are inadequate. That is, they were unable to find a consistent set of a and b values for different crystallographic faces of the substrate.

9. Treatment of the Crystal Potential

It has been convenient in the past to deal with a crystal potential and the surface barrier in a very simplistic way. Basically two types of model potential have been in vogue: the one-dimensional Kronig-Penney model where one replaces the atom potentials by delta functions and secondly, where the atoms are represented by sinusoidal functions. There are evident advantages to such simple potentials; namely, (a) they lend themselves to analytic solutions, (b) they illustrate many of the features such as surface states, etc., which should also emerge from a full scale calculation, and (c) they do not involve extensive use of computers. Some surface properties, such as the average surface energy, are not so sensitive to the exact geometric structure of the surface and have been treated fairly successfully using a simple model of a surface potential as shown in figure 2. Levine [33] has made an interesting comparative analysis of various simple models and studied the accuracy of using a one-dimensional rather than a three-dimensional model.

As the greater complexities of a realistic crystal potential are incorporated into the model, the analytic solutions become less tractable. A numerical evaluation must be sought. Thus, a more realistic treatment of the potentials near the surface of a metal will be taken up below. Models of surface potential which do not consider the atomic structure at the surface, cannot be expected to give good information relating to effects such as surface diffusion and adsorption which are dependent on the arrangement of atoms at the surface. Figure 4 represents the potential along a line perpendicular to a metal surface. In region I we have the repeated atomic potentials of the bulk material, and in region III a zero potential corresponding to free space outside the metal. Region II is the surface region in

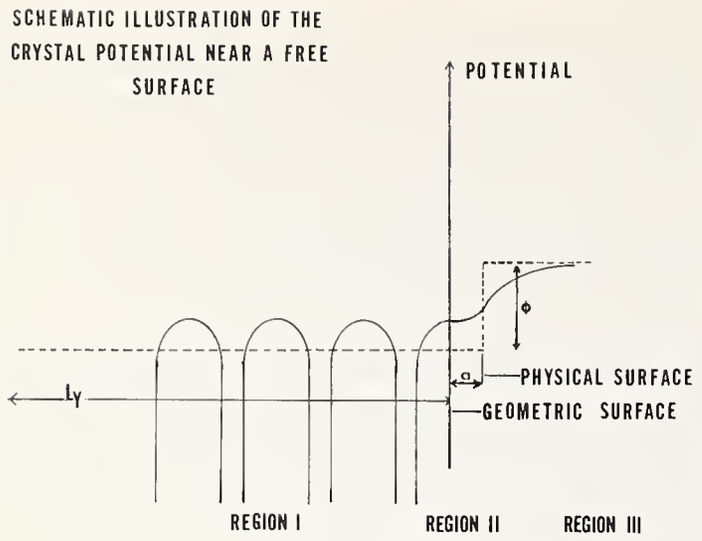

FIGURE 4. *A representation of surface potentials of a truncated crystal.*

The finite step associated with a "jellium" model is shown as a dotted line. Potential variations near the center of each atom are indicated by the full line. They are included in this schematic drawing for comparison with the model potentials previously used. The excess distance a needed to conserve charge in the interior of the metal is indicated beyond the last row of atoms.

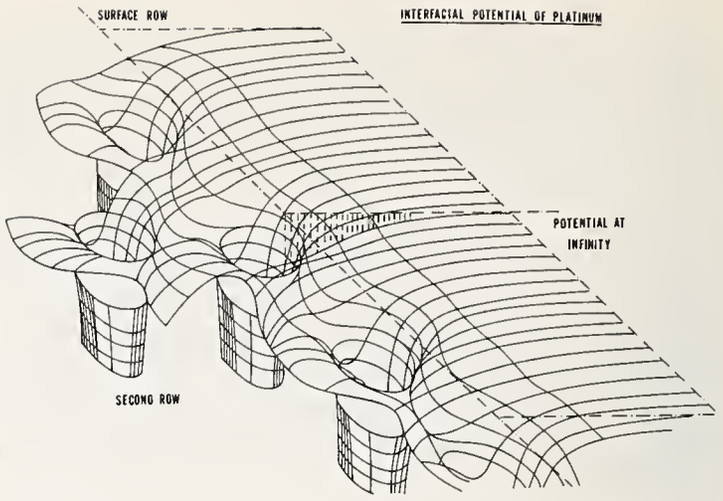

FIGURE 5. *Three dimensional representation of one-electron potential variation near the Metal-Vacuum Interface of Platinum.*

The center line of the last row of atoms is indicated by a dot-dash line. Only one atom of second row of this face-centered cubic metal is indicated. Method of computing of potential is discussed below in the text.

which both the potential and the electronic properties are changing from those of the bulk material to those of the free space region, i.e., are approaching zero. The calculated properties will be highly dependent on the exact model which is chosen to represent region II. The potential behavior pictured in figure 4 is, of course, very simplified. Even for the (100) surfaces of a face-centered cubic metal-like platinum, the potential surface resembles an egg carton. Neustadter and Bacigalupi had presented potential surfaces for various crystallographic orientations of the surface. In effect, the potential barrier shown in figure 5 will be different in shape and magnitude for each point on the surface. Added to this is the fact that LEED studies have shown that there may be a contraction or expansion of lattice spacing in a direction perpendicular to the surface, and they have also suggested that reconstruction of the surface layers possibly occurs.

10. Present Model

The model used to calculate the potential and charge density at a free surface assumes that the lattice consists of free atoms brought together and that the potential at any point is obtained by summing the (overlapping) potential contributions from the surrounding lattice sites. Using this model, a free surface is represented by removing the contributions from atoms located at lattice sites which lie outside any chosen crystallographic plane.

The starting data for these calculations has been the atomic charge densities obtained by Waber using a relativistic Dirac-Slater calculation [34]. The atomic potentials were obtained by numerical integration of Poisson's equation using a Simpson integration routine. As the summation procedure is essentially the same for potential and charge density, the description given below applies equally to either.

A face-centered cubic lattice with a cell side of 2 units was considered; its origin was at the center of a unit cell. The positions of the atoms on this lattice are given by the position vectors ($l\mathbf{x}$, $m\mathbf{y}$, $n\mathbf{z}$) where ($\mathbf{x},\mathbf{y},\mathbf{z}$) are unit vectors along the cube axes and the integers l,m,n satisfy the conditions:

$$l+m+n=(2N+1) \qquad N \text{ an integer.} \qquad (16)$$

It was decided to limit the summation of the potential to contributions from those sites located within a fixed sphere of radius R from the point under consideration. Convergence of the summation is discussed.

The unit cell was divided into 8000 points (a,b,c) at which calculations would be made. We used 20 points/cell edge. As a preliminary calculation, the atoms within a distance of 5 units from each point (a,b,c) were listed together with the distance r_{lmn}. However, of course, due to the symmetry of the cubic lattice, only points lying within the basic 1/48 of the unit cell were considered. This leads to a total number of 286 points. Thus from the set these 286 points (l,m,n), we select those atoms which will contribute to the potential at (a,b,c), and calculate the distance to these atoms.

Now consider a face-centered cubic lattice with cell edges parallel to coordinate axes, X, Y and Z. We assume that the lattice exists only for $Y \leq 0$ and that there

is free space in the positive y region. The XZ plane thus represents a (010) surface.

Consider a new unit cell inbedded in the lattice. Let the distance between the two origins be equal to d units on the Y axis, where d is a negative integer and $|d| > R + 1$ units. This new unit cell may be considered to be unaffected by the surface in that for all points within the unit cell, the sphere of radius R falls completely within the lattice side of the surface and all atoms contributing to the potential are present. Next consider some other particular point (e,f,g) which is nearer the surface, partially together with its sphere of radius R. At some such point, the sphere will lie outside the surface and as d becomes more positive, some lattice sites within the sphere will be empty. The potential at the point (e,f,g) will thus be increased. When one continues to increase the Y coordinate at some point (j,k,l) the sphere will be completely empty, i.e., this is a point in free space.

This is the way in which the summation is carried out by the computer. The $X\ Y\ Z$ coordinates are arranged so that the XY planes contain the origin of a unit cell. At the start $|d|$ is set equal to $R+1$. A point (xyz) in the initial unit cell, together with its set of vectors $\{l,m,n\}$ to atomic sites, and the set of distances $\{r\}$ are read. The distance r_{lmn} is multiplied by the lattice parameter and the potential contribution at that point V_{lmn} is calculated by interpolation of the values of atomic potential. The charge density ρ_{lmn} is also calculated. This procedure is repeated for all (lmn) values and the potential and charge density contribution are separately summed, giving the Coulomb potential V^0_{xyz} at that point and the total charge density ρ^0_{xyz} at that point. A table of values of $l,m,n,r,V_{lmn},\rho_{lmn}$ is maintained. The exchange potential contribution is then evaluated using Slater's original free electron approximation [11],

$$V_{ex}(r) = -6\left(\frac{3}{8\pi}\rho(r)\right)^{1/3} \tag{17}$$

giving the total potential V_{xyz} at this point. The value of d is then changed to $d'=d+2$, which is equivalent to moving to the next unit cell. At this position, the list of m's is scanned for those values for which $m > +d$. These represent empty lattice sites and the potential contribution $V_{l,m,n}$ is subtracted from V^o_{xyz} [also, ρ_{lmn} is subtracted from ρ^0_{xyz}]. When all m values have been tested, the remaining potential $V^0_{xyz}(d')$ is added to the new exchange potential obtained from $\rho^0(d')$ to give $V_{xyz}(d')$, the potential of the point (xyz) in the unit cell where the origin is at a distance d' from the surface. This process is repeated until $d'=(R+1)$, i.e., we include the potential outside the last row of ion cores for a distance equivalent to that inside. For unit cells which have lost potential contributions due to the surface, the potential distribution no longer has full cubic symmetry and thus the potential at the point (xyz) will no longer be equal to the potential at the 48 equivalent points. Thus corresponding to each point (xyz) the potential must be calculated separately for those equivalent points which are not produced by a rotation around Y. The procedure is thus to calculate V_{xyz} for each value of d and then repeat this for each equivalent position before proceeding to the next (xyz) value.

11. Convergence of Potential Summation

As was discussed in the method section, the radius R of the sphere which contains atoms contributing potential to any point was arbitrarily given some value and the infinite summation truncated after the same term at any point (xyz). In order to do this, we must determine whether the infinite summation converges rapidly or slowly and if so what error is to be expected by stopping the summation at any given point or R value.

Let us consider a sphere of radius R (as before we assume the side of our cell equal to 2 units) and calculate the number of lattice points n contained within it:

$$n(r) = \frac{4\pi}{3}R^3\left(\frac{4}{8}\right) = \frac{2\pi}{3}R^3 \qquad \text{for a FCC lattice} \tag{18}$$

then

$$\frac{dn(R)}{dR} = 2\pi R^2 \tag{19}$$

If the potential at a distance R due to a single atom is $V(R)$, then the total potential

$$V \simeq \int_0^\infty (2\pi R^2)V(R)\,dR. \tag{20}$$

In order for this integral to be finite, the potential $V(R)$ must decrease at a rate faster than R^{-4}. Figure 6 shows that the atomic potential $V(R)$ for platinum for high

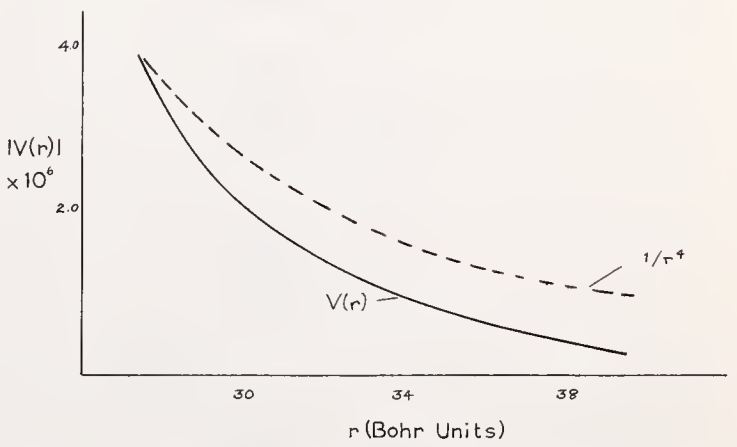

FIGURE 6. *Variation of atomic potential for platinum at distances far from the nucleus.*

TABLE 2. *Convergence of the summation* V(xyz) *for a sphere lying entirely in the lattice*

Sphere radius	No. of atoms within sphere	Potential	Potential increment % from $R=5$
5	286	−2.26849	.....
7	736	−2.28695	0.815
9	1566	−2.28879	.895
11	2796	−2.28941	.92

values of R. It can be seen that the potential is decaying at a rate much faster than R^{-4} and, therefore, it may be assumed that the potential summation is bounded. In order to determine the error introduced by truncation the summation at some arbitrary value of R, the value of the potential at one point in the unit cell of platinum was calculated using different values of R. The point at which the potential was calculated was in the center of the fcc unit cell where the nearest neighbor atoms contribute most to the potential and where the error introduced by series truncation would be expected to have the highest relative value. The results of the calculations are presented in table 2.

The question of whether there were sufficient points in the sphere of radius R to assure convergence of the potential was investigated for a point d_i well beyond the surface, that is, where $d_i > R$ units. The filled lattice sites will lie only in a "cap" of the sphere. The data in table 3 illustrates the effect of increasing R the number of units of $a_0/2$. The number of atoms counted with $R=5$ were 155, 74, 17, and 0 when d_i was 0, 2, 4, and 6 respectively. These values are underlined. The other entries in column three of table 3 are the number of additional points counted when R was increased from 5 to 8. For $d_i=0$, the potential $V(d_i)$ was multipled by 10, for $d_i=2$, by 10^4, for $d_i=4$, by 10^7 and for $d_i=6$ by 10^9. It will be seen that for $d_i<4$, the percentage changes are small. Although a large percentage change is obtained for a point at $d_i=6(a_0/2)$, the magnitude of the change is trivially small.

It is considered that the level of accuracy gained by using $R=5$ was sufficient at least as a starting point. From the point of view of the computer calculations, the time used for calculating a potential increases with the number of neighboring atoms considered, i.e., increases as R^3. Thus, from this standpoint very little increase in accuracy is gained by increasing R and a good deal of computer time is consumed.

TABLE 3. *Effect of Increasing Radius* R *on the Summation of the Potential* $V(d_i)$

Distance from surface d_i units of $a_0/2$	Radius R in units of $a_0/2$	Number of atoms counted	Potential (no exchange contribution) $V(y)$	Multiplier
0	5	155	−2.805371	10^1
0	6	104	−2.805371	
0	7	149	−2.805371	
0	8	164	−2.805371	
2	5	74	−9.398146	10^4
2	6	76	−9.398379	
2	7	109	−9.398419	
2	8	120	−9.398427	
4	5	17	−2.362965	10^7
4	6	36	−2.467100	
4	7	61	−2.491470	
4	8	88	−2.498100	
6	5	0	0	10^9
6	6	0	0	
6	7	25	−1.024532	
6	8	40	−1.323857	

12. Variation of the Potential Perpendicular to the Surface

Figures 7, 8, and 9 show the calculated potential distribution along lines perpendicular to a (010) surface of platinum. The cross section of the unit cell drawn on each figure shows the position of each line with respect to the surface atoms. The great variation of the shape

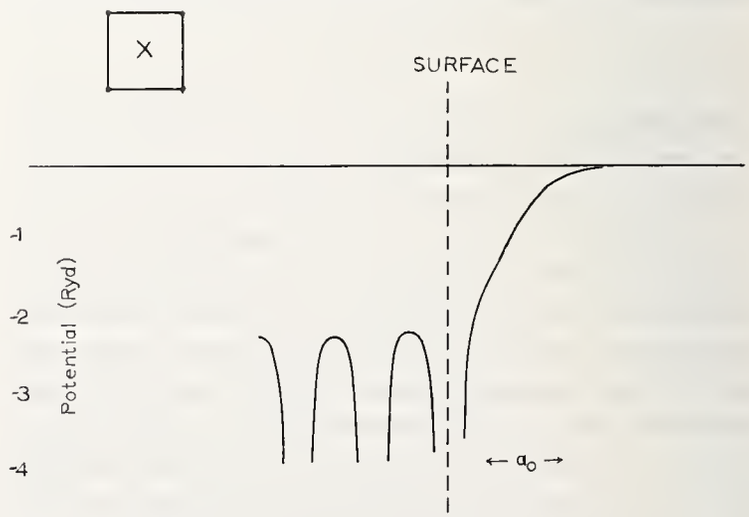

FIGURE 7. *The potential distribution along a line perpendicular to a [010] surface of platinum.*
The line passes through atom centers.

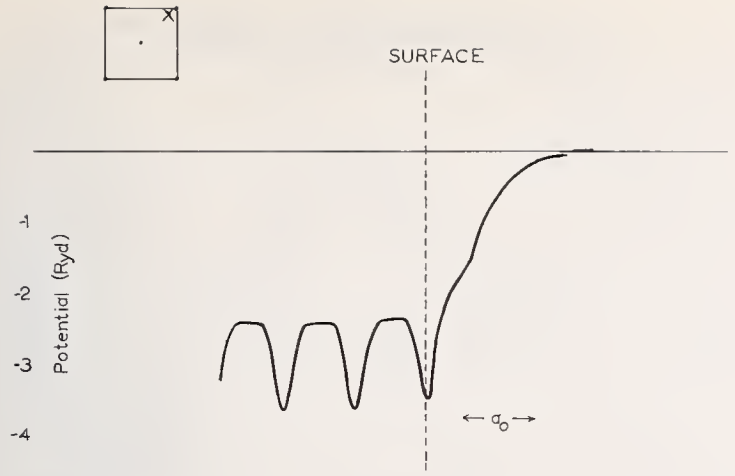

FIGURE 8. *Potential along a line perpendicular to a (010) surface of platinum.*
The line passes near to the atom centers.

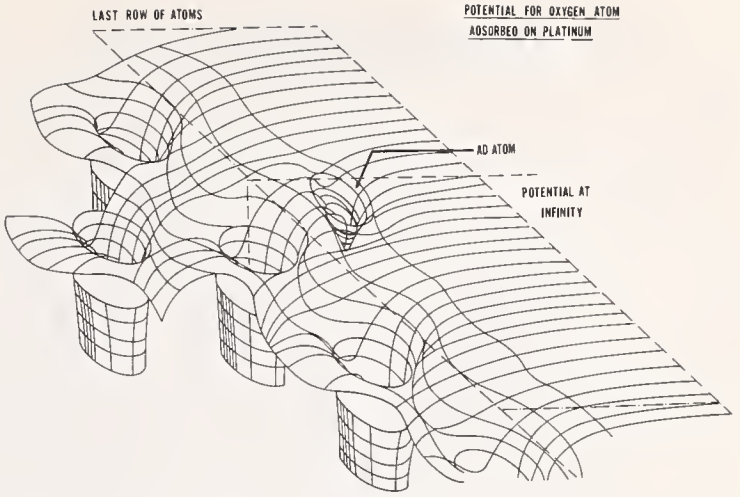

FIGURE 10. *Three dimensional plot of the potential variation on a (001) plane through the centers of atoms.*
The local depression near the oxygen atom would facilitate electron tunneling.

of the potential along different lines is apparent. Figure 7 shows the potential on a line passing through atom centers which shows the periodic behavior expected. Figure 8 is along a line which passes close to but not through the nucleus (atom centers). Here the periodic behavior can be seen. The fact that the potential far from the atom centers is very nearly flat can also be seen very clearly. In figure 9 the potential along a [010] ray in between atomic centers is illustrated. There is a small ripple about the mean "muffin-tin" potential V_m as each atom is "sliced." The muffin-tin value is independent of the distance from the surface. The "step" due to charge overlap and penetration which was indicated in the schematic drawing of figure 4 is seen in the curves of figures 7, 8, and 9, which were redrawn from the computer generated curves. The 3-dimensional drawing in figure 5 was obtained by combining a number of figures such as these last three figures.

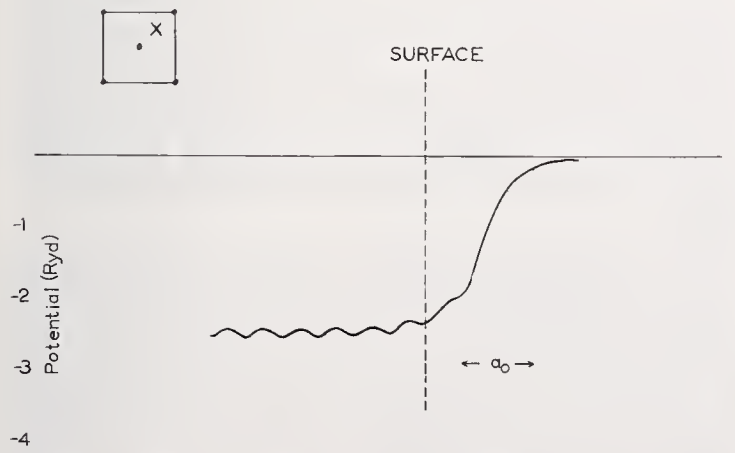

FIGURE 9. *Potential along a line perpendicular to a (010) surface of platinum.*
Line does not pass near to the atom centers.

13. Calculation for an Adsorbable Atom

The previous section described a method for determining the potential distribution at a perfect crystallographic surface. This method can easily be adapted to determine the potential distribution around a surface defect. Once the perfect surface potential distribution has been calculated and stored, the effect of a defect such as, for example, a vacancy in the surface layer, can be determined by subtracting the potential contribution due to this atom (or ion) from our crystal potential distribution. The effect of a foreign ion or atom on or above the surface can similarly be determined by adding the additional contributions to the existing potential. The results are shown in figure 10 for an oxygen atom approaching the (010) surface of platinum.

14. Surface Vacancies and Migration

Figure 11 shows equipotential contours on a (100) surface for platinum for the viewing plane cutting through the centers of the ion cores in the last plane. One atom has been removed from its position in this plane and the resulting distortion of the potential can be seen. It should be noted that the equipotential lines around the vacancy and the ions reflect the four-fold rotational symmetry of the lattice in this plane. Figure 12 shows the same surface but constructed by removing two adjacent atoms removed and replacing one atom in saddle point halfway between the two vacancies. This is a crucial stage during vacancy migration.

The results obtained for the potential distributions along lines perpendicular to a (100) surface are interesting in that they point out the great difference in poten-

417-156 O - 71 - 25

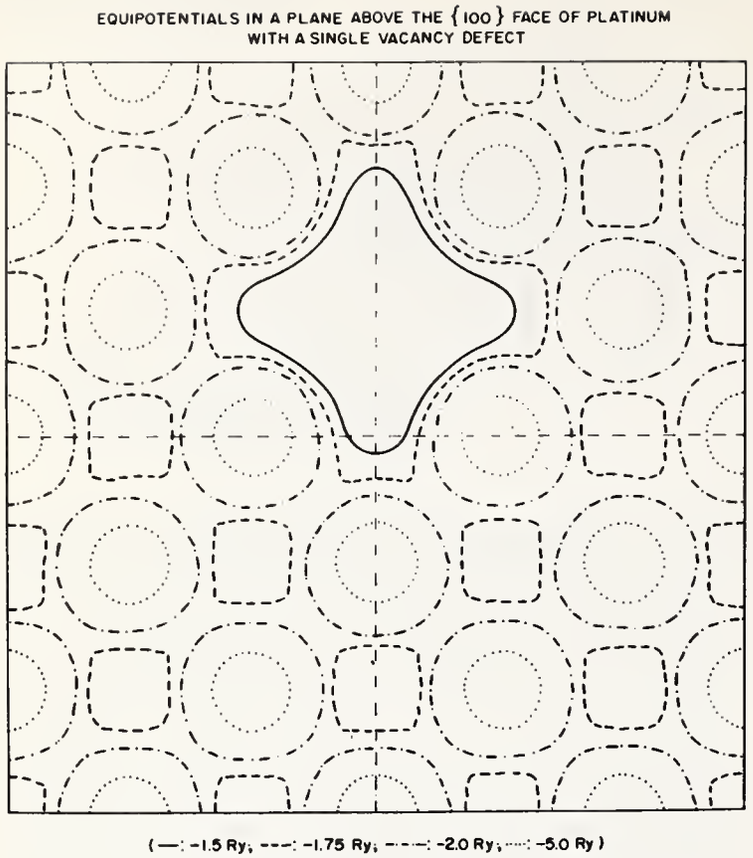

FIGURE 11. *Equipotential lines on a (010) face of platinum with a single vacancy defect.*

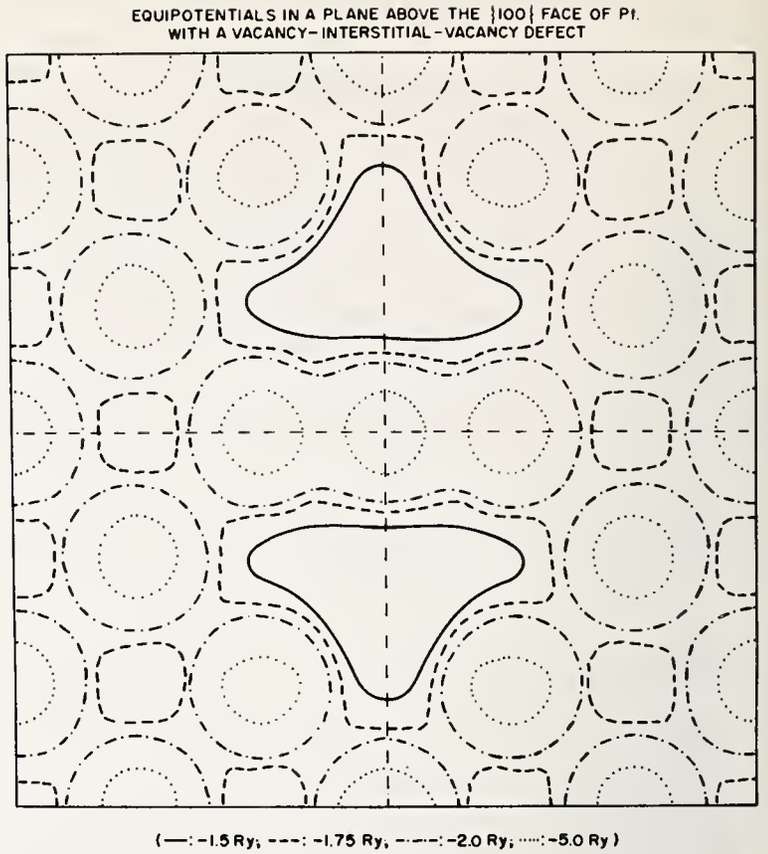

FIGURE 12. *Equipotential lines for a (010) face of platinum.* Two neighboring atoms have been removed and one atom replaced at the saddle point between the two sites, to simulate surface migration.

tial along different lines. In particular, along lines which do not pass close to the atom centers there is only a small oscillation in the potential. Thus the potential along such a ray is similar to that employed in the free electron models of surface behavior.

15. Previous Treatments of Adsorption Potentials

The various approaches described above all had the goal of predicting the properties of a clean metal surface in contact with vacuum. Other theoretical work has been concerned with the investigation of the effects of a foreign ion or atom approaching the surface and being adsorbed. Bennett and Falicov [35] and Gadzuk [36] have examined the problem of an alkali atom interacting with the surface of a free electron metal, using perturbation techniques. The effect of the interaction is to shift the level of the outer electron of the alkali metal.

Grimley [37] has shown that the charge density in the metal is disturbed in a long range oscillatory fashion by the presence of the adsorbate atom. The analysis he used was similar to that which leads to the Friedel oscillations. These three references are illustrative but do not represent the large number of approximate studies made in the past.

16. Variation of Total Charge Density

Figure 13 shows the electronic charge distribution for Pt, obtained by summation of charge contributions from neighboring atoms within a sphere of radius 5/2 a_0. The density (full line) is plotted along a line in the [100] direction connecting two atoms in the lattice. For comparison, the face atom charge density is also plotted. Close to an atom site the metal charge density is very little different from the free atom charge density, the overwhelming contribution coming from the atom at the site. However, as we move away from the actual lattice sites the contribution of the neighboring atoms become more and more important. It can be seen that for distances greater than ~1 Bohr unit (B.U.) from any lattice site there is an increasing discrepancy between the crystal atom and that of the free atom densities.

Note that the plot is made on semilogarithmic scale and the overlapped charge density at the midpoint between atom centers is 6 times as large as the free atom value. This position has an octahedral arrangement of atoms surrounding it. The accumulation of charge on the surface beyond the last atom is due to the Coulomb tails of the free atom. That is no redistribution of charge due to the presence of this metal-vacuum has been taken into account.

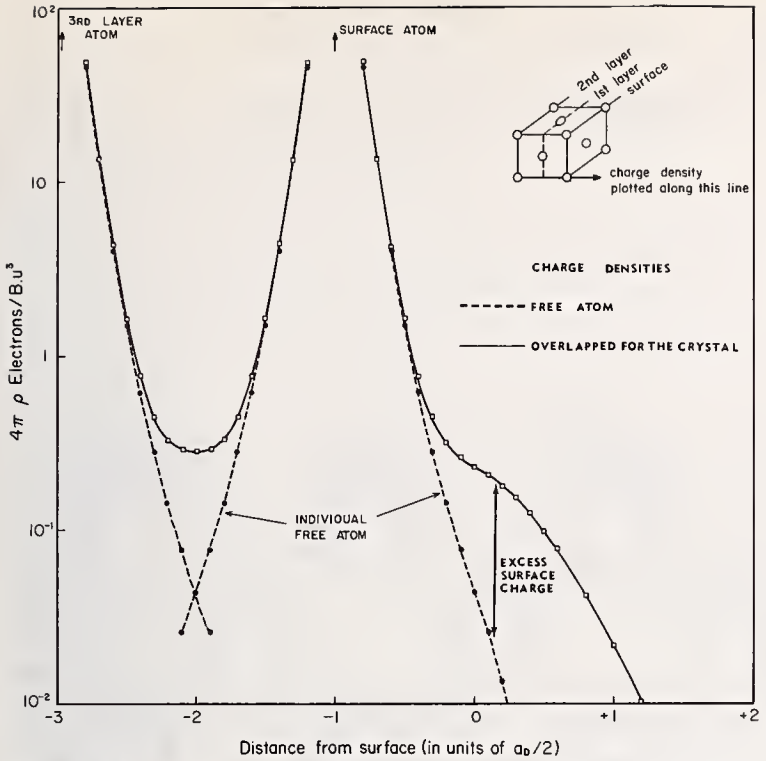

FIGURE 13. *Variation of the local charge density along a [010] as indicated in the inset.*

The excess surface charge due to the overlapping of the Coulomb tails of the atoms near the surface is indicated.

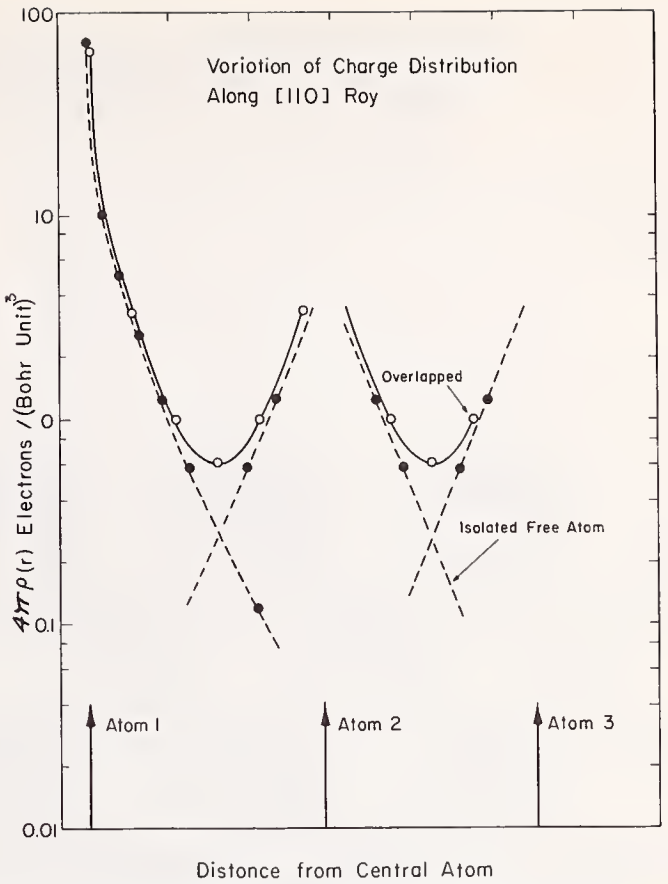

FIGURE 14. *Variation of charge distribution for platinum along a [110] direction passing through atom centers.*

In figure 14, which is similar to figure 13, is a plot of the charge density along a ray parallel to the [011] direction which is the close packed direction in *fcc* metals. At the midpoint between atoms the summed charge density is only 4 times as high as the value for the free atom but it is somewhat larger than the midpoint value in figure 13. The point (0,1/2,1/2) has a tetrahedral arrangement of neighboring atoms, but its distance from the center of an atom is smaller. The fact that $\rho(r)$ is larger leads to the higher value of the crystal charge density $\rho(xyz)$.

These last two figures illustrate the point made by Herring [38]; namely, that some of the electrons will be found in free space beyond the last row of atoms, just due to the overlap of Coulomb tails. Relatively little attention has been paid to this point in recent years. There is a figure in the book by Mueller and Tsong [39] which illustrates the probable redistribution of electronic charge and partial neutralization along the surface. This apparently has not been investigated to date. The present figures appear to be first quantitative presentations which have been made for a finite solid. These are not based on the assumption of penetration of the electrons into the "forbidden" region beyond a finite step but result from the process which Smoluchowski qualitatively discussed [40].

17. Remarks

The model used here, namely, of superimposing atomic potentials and then of superimposing atomic charge densities so as to calculate local exchange potential has one or two deficiencies in addition to its clear effectiveness.

This resulting potential is a one-electron potential which would be the input to a band-structure calculation when one uses either the KKR or APW methods or even to the simpler tight-binding method. The accuracy and limitation of the muffin-tin potential is directly indicated in accompanying figures. Sometime ago this approximation might have presented a stumbling block. But now both the KKR [41] and the APW [42] methods have been modified to permit angular variation $V(r,\theta)$ in the "muffin-tin" region, namely $R_s \leq r \leqslant R_{ws}$ where R_s is the contact radius and R_{ws} is the Wigner-Seitz radii.

Band structure calculations permit one to calculate the range of energies $E(k)$ associated with each valence and conduction band. These band energies lie above the potential calculated by the present method. Thus, although the values in table 2 are approximately -2 Ry, the lowest energy state is approximately 0.5 Ry above this and the band width of approximately 1 Ry for

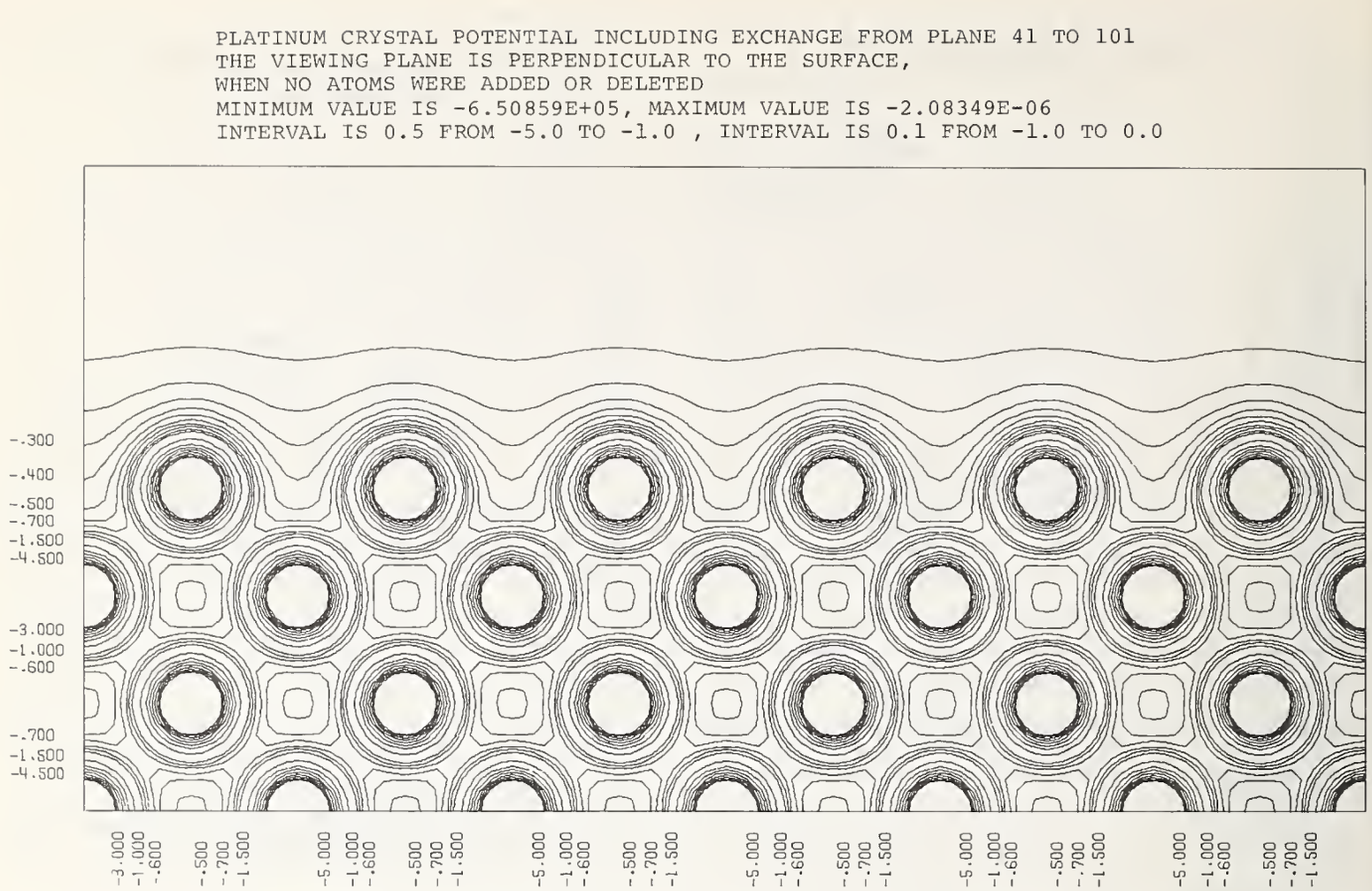

FIGURE 15: *Isopotential plots on a plane perpendicular to the (100) surface of platinum.*

platinum leads to a Fermi energy perhaps 0.5 to 0.75 Ry below vacuum level. This is, of course, consistent with experimental values of work functions. In short, the superimposed potential in the region between atoms may be very negative, but when the energy of the electrons is taken into account, what appears to be a significant error in the present calculation, would be substantially reduced. Nevertheless, the potential values reported here do not yet include these terms; they will be the subject of a subsequent report.

A more serious drawback is that the variations in the potential and charge density which arise from the reflection of the electrons near the surface and which cause Friedel-like oscillations (such as are indicated in fig. 2) are not incorporated into the present model. Bennett and Duke [16,22] have shown these oscillations to be substantial in a free-electron gas. Without first calculating these local variations, it is relatively pointless to include detailed exchange and correlation corrections. For any serious, self-consistent calculation of the potential in a solid which contains either lattice defects or a free surface, these important corrections must be included. The present study of the initial potential is the first step, but not the last one, toward obtaining realistic potentials near an interface.

18. Summary

The background information associated with the behavior of nearly free electrons has been reviewed as well as the possibility of computing surface energies from such simplified model. Typical potential plots have been calculated to illustrate the variation along various rays parallel to the [010] direction of platinum. The granular nature of the surface and crystal potentials have been illustrated for an element of high atomic number. The local variation of charge density along rays parallel [010] and [011] directions drawn through the centers of atoms has also been computed.

NOTE ADDED IN PROOF:

Recently a numerical multiplicative error was found in the calculations on platinum reported in this paper. The potential (see fig. 15) in the flat square region is approximately -0.5 Ry, a value more consonant with experimental values of the inner potential. The variation along a [110] ray would be seen to be relatively small.

19. References

[1] Brager, A., and Schuchowitzky, A., Acta Physicochimica (USSR) **21**, 13 (1946); **71**, 1001 (1946). See also Brager, A., J. Phys. Chem. (USSR) **21**, 623 (1947).

[2] Frenkel, J., Phil. Mag. **33**, 297 (1917).

[3] Dorfman, Y. G., and Kikoin, I. K., The Physics of Metals, State Technical and Theoretical Publishing House, Moscow, 1933.

[4] Huang, K., and Wyllie, G., Proc. Phys. Soc. **A62**, 180 (1949).

[5] Stratton, R., Phil. Mag. **44**, 1236 (1953).

[6] Vinogradov, I. M., Trans. Math. Inst., Akad. Nauk. (USSR) **9**, 17 (1935).

[7] Sugiyama, A., Jour. Phys. Soc. Japan **15**, 965 (1960).

[8] Huntington, H. B., Phys. Rev. **81**, 1035 (1951).

[9] Bardeen, J., Phys. Rev. **49**, 653 (1936).

[10] Juretschke, H. J., Phys. Rev. **92**, 1140 (1953).

[11] Slater, J. C., Phys. Rev. **81**, 385 (1951).

[12] Loucks, F. L., and Cutler, P. H., J. Phys. Chem. Solids **25**, 105 (1964).

[13] Davies, R. W., Surface Science **11**, 419 (1968).

[14] Gadzuk, J. W., Surface Science **11**, 465 (1968).

[15] Stern, E., Phys. Rev. **162**, 565 (1967).

[16] Bennett, A. J., and Duke, C. B., Phys. Rev. **160**, 541 (1967).

[17] Bennett, A. J., and Duke, C. B., "The Structure and Chemistry of Solid Surfaces," G. A. Somorjai, Editor (John Wiley & Sons, Inc., New York, 1969).

[18] Smith, J. R., Phys. Rev. **181**, 522 (1969).

[19] Lang, N. D., Solid State Comm. **7**, 1047 (1969).

[20] Lang, N. D., and Kohn, W., Phys. Rev. **B1**, 4555 (1970), and Phys. Rev. B (in press).

[21] Friedel, J., Adv. Phys. **3**, 446 (1954).

[22] Bennett, A. J., and Duke, C. B., Phys. Rev. **162**, 578 (1967).

[23] Heine, V., Phys. Rev. **138**, A1689 (1965).

[24] Forstman, M., and Heine, V., Phys. Rev. Letters **24**, No. 25, 1419 (1910).

[25] Forstmann, F., Z. Physik **235**, 69 (1970). See also Forstmann, F., and Pendry, J. B., Z. Physik **235**, 75 (1970).

[26] Plummer, E. W., and Gadzuk, J. W., Phys. Rev. Letters **25**, 1493 (1970).

[27] Davison, S. G., Intern. J. Quantum Chem. Suppl. II (1968) p. 297. See also Davison, S. G., and Cheng, Y. G., ibid., pp. 303, 312; Davison, S. G., and Koutécky, Proc. Phys. Soc. (London) **89**, 237 (1966); Stęślicka, M., Acta Phys. Polon. **30**, 883 (1966); ibid., **33**, 981 (1966), and **34**, 875 (1968); Davison, S. G., and Ho, H. T., Trans. Farad. Soc. **63**, 812 (1967).

[28] Stęślicka, M., Conference on Electronic Density of States, these Proceedings, p. 477. See also Stęślicka, M., Davison, S. G., and Brown, A. G., J. Chem. Phys. (1969) in press.

[29] Sharma, S. P., and Schrenk, G. L., (1970) in press.

[30] Cyrot-Łackmann, F., Surface Science **15**, 535 (1969). See also J. Phys. Chem. Solids **29**, No. 7, 1234 (1968).

[31] Neustadter, H. E., and Bacigalupi, R. J., Surface Science **6**, 247 (1967).

[32] Plummer, E. W., and Rhodin, T. N., J. Chem. Phys. **49**, 3479 (1968).

[33] Levine, J. D., and Mark, P., Phys. Rev. **182**, 181 (1969).

[34] Liberman, D. A., Waber, J. T., and Cromer, D. T., Phys. Rev. **137**, A27 (1965).

[35] Bennett, A. J., and Falicov, L. M., Phys. Rev. **151**, 512 (1966).

[36] Gadzuk, J. W., Surface Science **6**, 133 (1967).

[37] Grimley, T. B., Proc. Phys. Soc. **92**, 776 (1967).

[38] Herring, C., Metal Interfaces, Amer. Soc. for Metals, Cleveland (1952) p. 1.

[39] Müller, E. W., and Tsong, T. T., Field Ion Microscopy—Principles and Applications, (Elsevier, New York, 1969) p. 191.

[40] Smoluchowski, R., Phys. Rev. **60**, 661 (1941).

[41] Sommers, C. E., private communication (1970).

[42] Koelling, D. D., Phys. Rev. **188**, 1049 (1969). See also Koelling, D. D., Freeman, A. J., and Mueller, F. M., Phys. Rev. **1B**, 1318 (1970).

Discussion on "Potential and Charge Density Near the Interface of a Transition Metal" by E. Kennard and J. T. Waber (Northwestern University)

J. W. Gadzuk *(NBS):* It is usual to believe that far from a surface (far being several Fermi wavelengths), the exchange and correlation effects which dominate the surface forces result in an apparent image potential. This is of a long range nature, varying inversely with distance. How do you reconcile your very short range potential with the idea of the long range image potential?

J. T. Waber *(Northwestern Univ.):* Well, I think the dipole force which is the type of thing that you are talking about, comes about from the oscillating charge built up in the vicinity, i.e., local charge depletion, of the surface. What I've shown you here today was the static potentials. We have not yet described properly the response of the electrons to this potential. To consider your question we must do the job self-consistently. Finally, I think the point you raise is quite relevant and important.

E. Callen *(American Univ.):* But isn't it true that the correlation field seen by an electron outside the surface in a P_z level will be different from that seen by one in a P_x or P_y level and that this would alter, and, in fact, might even reverse your crystal field ordering?

J. T. Waber *(Northwestern Univ.):* I do not feel competent to answer your question directly. We are trying to do this splitting of levels in an inhomogeneous field to illustrate a basic point. When we have gained a deeper understanding I hope we will be able to answer your question. I agree that such points as you raise are significant and merit our further attention.

Virtual Impurity Level Density of States as Investigated by Resonance Tunneling

J. W. Gadzuk, E. W. Plummer, H. E. Clark, and R. D. Young

National Bureau of Standards, Washington, D.C. 20234

The analogy between a virtual electronic state of an atom adsorbed on a metal surface and an Anderson type magnetic impurity state is pointed out. The density of states of the impurity can be characterized through a knowledge of the host induced shift and broadening of the atomic state. This density of states can be related to the current-voltage characteristics in a field-emission resonance tunneling experiment in the same manner as Appelbaum has done for describing spin flip Kondo type resonance tunneling in junctions.

Experimental current-voltage (field-emission total energy distribution) characteristics for single zirconium, barium, and calcium atoms on atomically perfect tungsten surfaces are analyzed in terms of the resonance tunneling theory described here and the virtual impurity level density of states is thus determined. Preliminary results for a metal-thin semiconductor-vacuum junction are also discussed.

Key words: Anderson Hamiltonian; barium (Ba); calcium; chemisorption; electron density of states; field-emission resonance tunneling; germanium; tunneling; tungsten (W); zirconium.

1. Introduction

The chemisorption of single atoms on metal surfaces is now recognized as being nothing more than an impurity problem and thus a solvable impurity theory should provide us with an equally solvable chemisorption theory. The "solvable" impurity theories we have in mind are those which have evolved in the theory of localized magnetic moments [1-4]. The key result of these theories, as relevant to surface impurities (chemisorption), is that the level associated with a valence orbital of the impurity will either be pulled away from the conduction band of the host, thus forming a true impurity state in the Koster-Slater sense [5] or a virtual state within the conduction band will be formed. The interesting case for present purposes is the virtual state. The spin up and down levels are split by an amount dependent upon the intra-atomic Coulomb integral and also upon the energy of the level relative to the occupied portion of the conduction band. If one level lies above the Fermi energy and the other below, then a localized moment is formed. To solve the problem within the context of the Anderson Hamiltonian [2], various approximations for achieving self-consistent solutions have been put forth. In all cases it is recognized that due to the coupling of the impurity orbital with the continuum of metal states, the impurity level is broadened into a band of energies. Thus the impurity theories could be discussed in terms of a virtual impurity level density of states. The usual picture of a magnetic impurity density of states illustrating the manner in which localized magnetic moments of nonintegral Bohr magnetons are formed is shown in figure 1a.

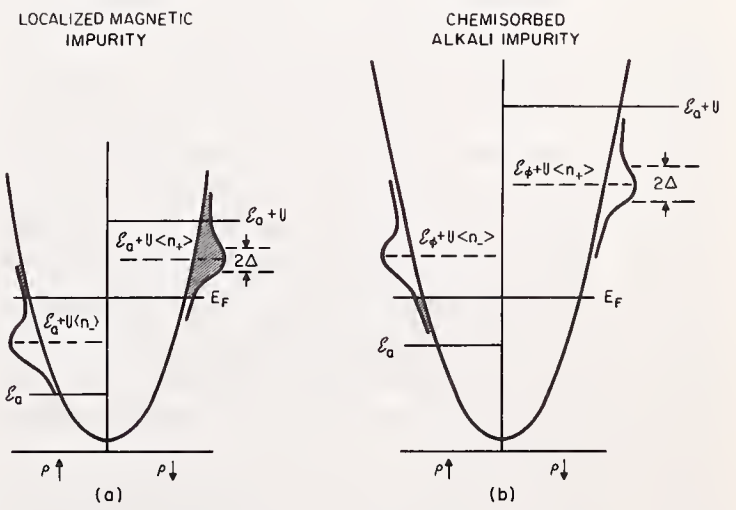

FIGURE 1*a*. *Density of state distributions for a magnetic impurity. The monotonic parabolic curve is a free electron metal density of states. b. Density of states for an electropositive adsorbate. The area in the cross hatched area is the amount of electron charge on the adsorbate.*

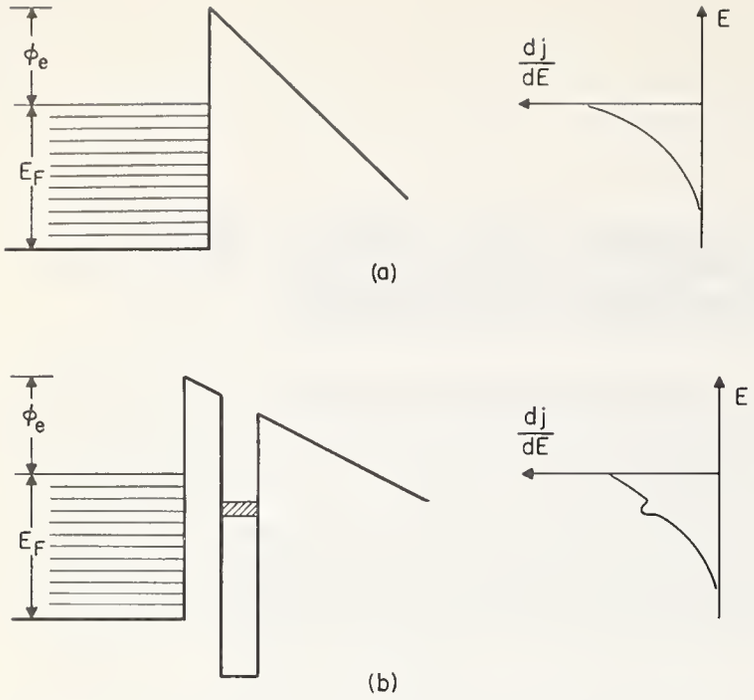

FIGURE 2*a*. *Model potential and total energy distribution for field emission from a metal. b. Model potential and total energy distribution for resonance tunneling field emission from a metal with a narrow band adsorbate.*

A similar picture has been adopted for describing the chemisorption of electropositive atoms on metal surfaces [6-12]. Obviously each theoretical approach has its own set of approximations to achieve a (hopefully) self-consistent solution to a model problem. Of particular interest have been the instances when the surface impurity was either an alkali or alkaline earth atom. In these instances, the ionization potential of the atom is sufficiently small so that both the spin up and down levels lie above the Fermi energy as shown in figure 1b. The occupation of the lower lying spin level n_+, (where $n_+ > n_-$) is small enough so that the question of the magnetic state of the impurity determined by n_+-n_- has not been considered at very great length. In a similar manner to the nonintegral Bohr magnetons, we see how it is possible to have a fractionally charged ion for the surface impurity. Obviously if we know the virtual surface impurity density of states, then the charge on the impurity, among other things, would be immediately deduced. Knowledge of the density of states would then permit theoretical calculations of the dipole moment associated with the metal-impurity complex (and thus work function changes) [8] and chemisorption or binding energies [8,11,12].

Duke and Alferieff have shown, through model calculations, how the presence of a potential well (impurity) could give rise to altered current-voltage characteristics in field-emission resonance tunneling experiments [13]. In the language of field-emission workers, the analog of conductance versus voltage curves in junction tunneling is called the total energy distribution (TED) [14,15]. The measured quantity is the incremental change in current per change in energy and is shown in figure 2a. As Duke and Alferieff pointed out, a potential well can give rise to resonance effects which manifest themselves as structure in the TED as shown in figure 2b. We have presented an alternate theory and experimental evidence of resonance tunneling in which the virtual impurity level density of states is of key importance in our interpretation [16-18]. It turns out that the resonance aspect of the theory is equivalent to Appelbaum's spin flip tunneling theory [19,20].

The structure of the paper is as follows. In section 2, the main equations in the theory of surface impurities and resonance tunneling are established. It is shown how experimentally determined TED's are related to the impurity density of states. Experimental results for Zr, Ba, Ca, and Ge on a tungsten host are presented in section 3 and the impurity density of states is thus determined.

2. Theory

The Anderson Hamiltonian describing the coupling of a surface impurity single electron orbital to the continuum of conduction band states is

$$H=\sum_{ks}\epsilon_{ks}n_{ks}+\sum_{s}\epsilon_{as}n_{as}+\sum_{ks}(V_{ak}c_{ks}^{\dagger}c_{as}+\text{H.C.})+U_{\text{eff}}n_{a+}n_{a-} \qquad (1)$$

where we have adopted the usual notation [2-4,11]. The atom-metal hopping integral V_{ak} has been discussed in detail for particular model surface potentials by several people [6-12]. We write the intra-atomic Coulomb integral $U \rightarrow U_{eff}$ to note that when dealing with alkali impurities or alkaline earth impurities in the single electron approximation [18], we should really be working in the low density approximation of Schrieffer and Mattis [3] in which U is replaced by some U_{eff} [3]. In fact, in the present analysis of a low density impurity, since both n_{a+} and n_{a-} are much less than unity, $U_{eff}\, n_{a+}\, n_{a-}$ is neglected here relative to the other terms with the subsidiary provision that the resulting single electron impurity density of states, integrated over all energies, contains only one electron. With this approximation, eq (1) can be subjected to a standard Green's function analysis in which the virtual impurity Green's function is

$$G_{aa}(\epsilon)=\left[\epsilon-\epsilon_{\phi}^{a}-\sum_{k}\frac{|V_{ak}|^2}{\epsilon-\epsilon_k+i\delta}\right]^{-1}=[\epsilon-\epsilon_{\phi}+i\Delta\,\text{sgn}\epsilon]^{-1} \qquad (2)$$

with $\Delta = \pi \sum_k \delta(\epsilon - \epsilon_k)|V_{ak}|^2$ and $\epsilon_\phi = \epsilon_a + \Delta\epsilon$ where $\Delta\epsilon$ is whatever shift the real part of the impurity energy level experiences [8,18]. An impurity density of states is identified as

$$\rho_{aa}(\epsilon) = \frac{1}{\pi} \operatorname{Im} G_{aa}(\epsilon) = \frac{1}{\pi} \frac{\Delta}{(\epsilon - \epsilon_\phi)^2 + \Delta^2} \tag{3}$$

Note that the total electronic charge on the impurity is

$$\langle n_a \rangle = \int_{-\infty}^{0} \rho_{aa}(\epsilon)\, d\epsilon = \frac{1}{\pi} \cot^{-1}\left(\frac{\epsilon_\phi}{\Delta}\right)$$

Here ϵ_ϕ is measured from a zero at the Fermi level and is given by $\phi_e - V_i + \Delta E$ with ϕ_e = metal work function and V_i the first ionization potential of the isolated impurity atom. Typically for alkali and alkaline earth atoms $\epsilon_\phi > \Delta$ so $\langle n_a \rangle < .25$ and the low density approximation seems valid. We will now see how ϵ_ϕ and Δ, and consequently the impurity density of states, are determined from resonance tunneling measurements.

We have noted that the TED in field emission is the analog of a conductance versus voltage measurement in junction tunneling. The TED is given by

$$j_0' = \frac{dj_0}{d\epsilon} = \frac{J_0}{d} f(\epsilon) e^{\epsilon/d}$$

with J_0 and d some constants depending upon system parameters and applied field but not energy and $f(\epsilon)$ the Fermi function [14,15]. The idealized TED is shown in figure 2a for zero temperature. Usually $.1 \lesssim d \lesssim .2$ eV in field emission experiments so the width of the TED is restricted by the exponential decay to something less than 1 eV due to instrumental limitations of presently existing energy analyzers [17,22]. Since we are dealing with a tunneling problem, in the transfer Hamiltonian formulation, j_0' is also proportional to the square of an appropriate tunneling matrix element $\equiv T^0_{m-f}$ [15,21].

If an impurity is on the surface, the TED is altered as shown in figure 2b. Duke and Alferieff chose to characterize this enhanced tunneling by a factor multiplying the original TED [13]. Thus in the presence of an impurity $j'(\epsilon) = R(\epsilon) j_0'(\epsilon)$ hereby defining $R(\epsilon)$ the enhancement factor. As with $j_0'(\epsilon)$, $j'(\epsilon)$ is proportional to the square of a resonance tunneling matrix element T_{m-f} so $R(\epsilon) = |T_{m-f}|^2 / |T^0_{m-f}|^2$. A simple perturbation expansion allowing for the possibility of an intermediate virtual impurity state for the tunneling electron is

$$T_{m-f} = T^0_{m-f} + T_{m-a} G_{aa} T_{a-f}$$

where T_{m-a} is the tunneling amplitude for going from the metal to the atom, T_{a-f} is the amplitude to go from the atom to free space and G_{aa} is the impurity Green's function given by eq (2). If all the amplitudes are real, then

$$R(\epsilon) = 1 + \left(\frac{T_{ma} T_{af}}{T^0_{mf}}\right)^2 (G_{aa}(\epsilon) \times G^*_{aa}(\epsilon)) + \frac{T_{ma} T_{af}}{T^0_{mf}} (G_{aa}(\epsilon) + G^*_{aa}(\epsilon)). \tag{4}$$

Since the presence of the atom effectively cuts a hole out of the tunneling barrier, the tunneling amplitude through the atom $T_{ma}\, T_{af}$ should be greater than the direct channel amplitude T^0_{mf}. In fact we have shown that the quantity

$$T(\epsilon) \equiv \frac{T_{ma} T_{af}}{T^0_{mf}} \simeq \frac{g(\epsilon)}{4} \frac{\hbar^2}{2m} \frac{k}{w} e^{kw} \tag{5}$$

with $k \approx (2m/\hbar^2(\phi_e - \epsilon))^{1/2}$ and w an effective well radius for the model atom potential. The function $g(\epsilon) = 1$ if the intermediate state is an s state whereas $g(\epsilon) < 1$ for intermediate d states due to the spatial contraction and thus reduced tunneling probabilities for d states degenerate with s states [18,23]. We also should note that eq (4) is identical with Appelbaum's expansion although he implicitly drops the second term on the right hand side, the direct resonance channel and concentrates on the interference channel, the third term [19]. As he was investigating a Kondo type mechanism this was the appropriate procedure. On the other hand, for our purposes the "uninteresting" direct term is the most significant. If we neglect the unity term on the right in eq (4) and combine eqs (2-5), the enhancement factor is then

$$R(\epsilon) \simeq \rho_{aa}(\epsilon;\, F) \left[\frac{\pi T(\epsilon)^2}{\Delta} + \frac{2\pi(\epsilon - \epsilon_\phi) T(\epsilon)}{\Delta}\right]. \tag{6}$$

Thus we see how an experimental determination of R can be used to obtain the virtual impurity state density of states. The situation is slightly more complicated when there is the possibility of observing excited states also. This has been discussed at some length together with methods for approximately treating two electron states [17,18]. Note that we have written ρ_{aa} also as a function of F, the applied electric field. The field shifts the impurity level downward such that ϵ_ϕ is replaced by $\epsilon_\phi - eFs$ with s the distance of the impurity center from the surface. The field thus brings the virtual levels below the Fermi level and consequently allows these levels to be observed in a resonance tunneling experiment. However, all results will be extrapolated back to the zero field limit.

Finally we note that the decomposition of the enhancement factor into a product of a density of states times another function of energy, $R(\epsilon) = \rho_{aa}(\epsilon) G(\epsilon)$ as we have done in eq (6), is useful for the following reason.

Any sharp structure in $R(\epsilon)$ will appear through the density of states factor. The factor in brackets in eq (6), $G(\epsilon)$, is a smoothly varying monotonic structure. Thus an interpretation of the structure in an enhancement factor is almost identical with determining the impurity density of states.

3. Results

It is our feeling that junction and field-emission tunneling measurements can and should serve to complement each other as each technique has strengths where the other technique is weak. In particular the advantage of field-emission measurements is that one is dealing with atomically perfect surfaces. It is possible to look at emission from a patch of say 25 atoms and then add a single impurity atom and monitor the changes in the TED due to the presence of *one* impurity. The experimental procedure has been outlined in great depth elsewhere [17,24].

3.1. Zirconium

The ionization potential of an isolated zirconium atom in the $5s^2$ ground state is 6.84 eV. It is expected that such a level would shift upwards 1 to 2 eV when interacting with a tungsten surface [8,18]. Analyzing the experimental enhancement factors in terms of eq (6), it is found that the energy parameters in the virtual $5s^2$ density of states are $\Delta E \approx 1.6$ eV and $\Delta \sim 1.0$ eV, in agreement with expectations. No excited states were observed.

3.2. Barium

The $6s^2$ ground state of free barium lies 5.2 eV below the vacuum level. Triplet $6s5d$ ^{3}D excited states lie between -4.03 and -4.1 eV and a singlet $6s5d$ ^{1}D lies at -3.8 eV. With the applied field, the $6s5d$ states should be pulled below the tungsten Fermi level and thus be observable. We would expect the width of the $6s5d$ state to be about 1/10 of the $6s^2$ state and the shift ΔE to be smaller [18]. An expression for the enhancement factor for two electron excited states, similar in principle to eq (6), has been derived [18]. A comparison between a typical experimental R factor and the theoretical curve is shown in figure 3. The energy zero is taken with respect to the vacuum. As can be seen, structure related to excited states is both observable and predictable. The spectroscopic findings for use in the density of states are: $\Delta E^{6s} = .95$ eV, $\Delta_{6s} = .75$ eV and $\Delta E^{3D} = \Delta E^{1D} \approx 0$, $\Delta_{3D} = \Delta_{1D} = .1$ eV; again in agreement with expectations.

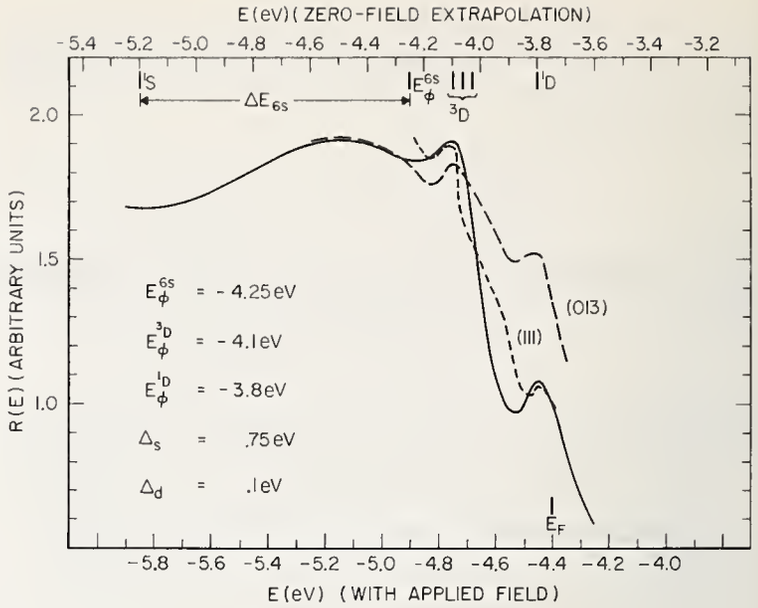

FIGURE 3. *Theoretical and experimental values of the enhancement factor and virtual energy level spectrum for barium on tungsten.*

The magnitude of R is left arbitrary due to experimental uncertainties but would generally fall in the range $10 \lesssim R_{max} \lesssim 10^3$. The scale on the bottom is that used in the experiment. The scale on the top is that resulting from an extrapolation to the zero field limit. In both cases the zero of energy is at the vacuum level. Note the positions of the unperturbed atomic levels and the position of E_F relative to the maximum in R. The theoretical curve is solid and the experimental one dashed.

3.3. Calcium

The $4s^2$ ground state of calcium lies at 6.1 eV below the vacuum level. We suspected that with the applied field this state would lie too far below the Fermi level to see with the present equipment. This was confirmed in the experiment. A $4s4p$ excited state exists at -4.25 eV which would be pulled below the Fermi level at -4.4 eV with the applied field. Because on parity selection rules involved in a partial wave analysis of the level width Δ, we felt that the $4s4p$ level would lie somewhere between the narrow d levels in barium and the wide s levels. Analysis of the data in terms of eq (6) and its two electron counterpart shows that $\Delta E_{4p} \approx .4$ eV and $\Delta_{4p} \approx .3$ eV as expected.

In figure 4 is shown a schematic energy level diagram for barium and calcium which depicts how the levels we have observed vary as a function of distance from the surface. The distance scale is arbitrary as are the relative heights of the density of states for each level. On the other hand the position of the structure is not arbitrary as it has been both observed and predicted.

3.4. Germanium

Using the techniques of resonance tunneling, a detailed study of the electronic states in "amorphous" germanium formed on a tungsten substrate, progressing from a single atom to several hundred layers is underway. Preliminary studies have been re-

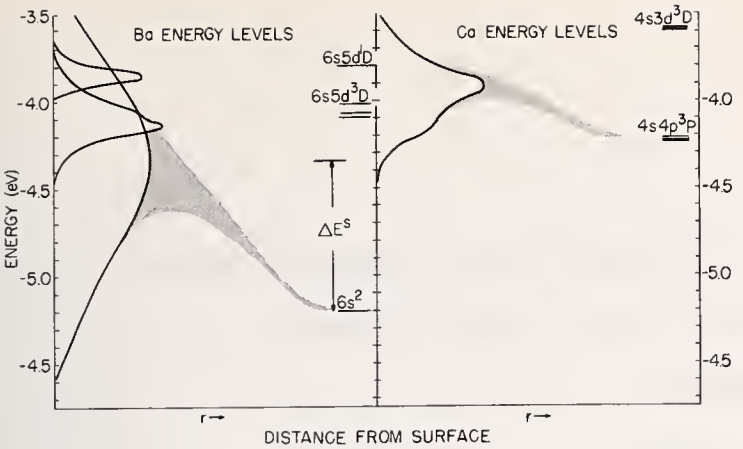

FIGURE 4. *Pictorial representation of the broadening and shifting of the energy levels of* Ba *and* Ca *as they interact with the surface.*
The shapes and position of the virtual levels at the surface are taken from the data on the low work function planes of tungsten.

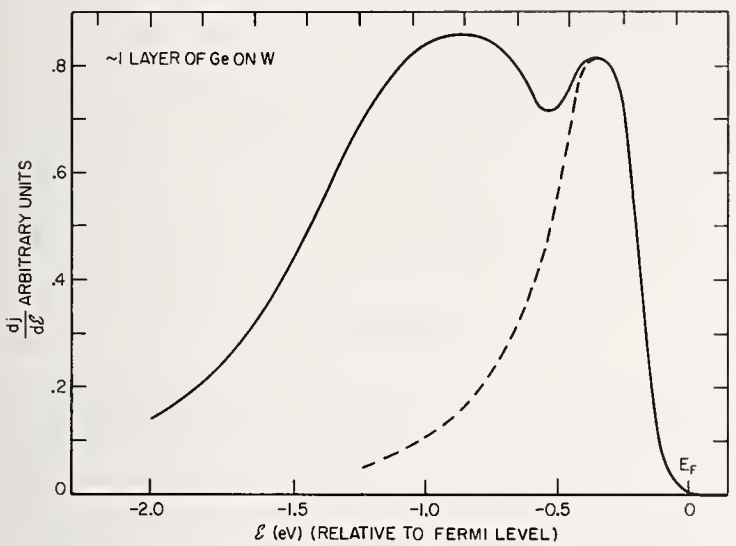

FIGURE 5. *Experimental total energy distribution of a system consisting of approximately one monolayer of germanium deposited on tungsten.*

ported on resonance tunneling through Ge films from a fraction of a monolayer up to tens of layers thick [25]. A characteristic TED for an approximately monolayer film is shown in figure 5. The peak near the Fermi level is associated with pseudo-clean tungsten as the continuation shown by the dashed line suggests. The interesting feature is the lower lying peak. We believe that this peak may be related to tunneling through the $4s^24p^2$ "level" which ultimately would become the valence "band" in amorphous or crystalline Ge. We would expect the peak height to lie somewhere between the 7.88 eV ionization potential of the isolated atom and the 4.76 eV work function or position of the top of the valence band of solid Ge which it does. If the TED in figure 5 is decomposed into an R factor, the full width at half-maximum of R is ~1.5 eV, a not unreasonable value. Since the theory of dense, interacting impurities on the surface is incomplete at this time, it is not possible to precisely analyze these monolayer results in terms of a density of states as in eq (6) and thus this width is not to be identified with Δ, the single impurity width. Further studies have been made in which the layers are thicker, hopefully approaching the stage where the properties of the film can be discussed in terms of bulk "amorphous" germanium. The evolution of the Ge peak in figure 5, as the thickness increases, is not inconsistent with the interpretation given here in which we claim to see early stages of a rudimentary valence band. These studies will be reported on in more detail in the future.

4. References

[1] Friedel, J., J. Phys. Radium **19,** 573 (1958); Suppl. Nuovo Cimento **VII,** 287 (1958).
[2] Anderson, P. W., Phys. Rev. **124,** 41 (1961); in Many-Body Physics, C. DeWitt and R. Balian, Editors (Gordon and Breach Publishers, New York, 1969).
[3] Schrieffer, J. R., and Mattis, D. C., Phys. Rev. **140,** A1412 (1965).
[4] Kjöllerström, B., Scalapino, D. J., and Schrieffer, J. R., Phys. Rev. **148,** 665 (1966).
[5] Koster, G. F., and Slater, J. C., Phys. Rev. **95,** 1167 (1954); **96,** 1208 (1954).
[6] Gomer, R., and Swanson, L. W., J. Chem. Phys. **38,** 1613 (1963).
[7] Bennett, A. J., and Falicov, L. M., Phys. Rev. **151,** 512 (1966).
[8] Gadzuk, J. W., Surface Sci. **6,** 133 (1967); **6,** 159 (1967); Proceedings Fourth International Materials Symposium, The Structure and Chemistry of Solid Surfaces, (J. Wiley Publishing Co., New York, 1969); J. Phys. Chem. Solids **30,** 2307 (1969).
[9] Schmidt, L., and Gomer, R., J. Chem. Phys. **45,** 1605 (1966).
[10] Grimley, T. B., and Walker, S. M., Surface Sci. **14,** 395 (1969).
[11] Newns, D. M., Phys. Rev. **178,** 1123 (1969).
[12] Gadzuk, J. W., Hartman, K., and Rhodin, T. N. (in preparation).
[13] Duke, C. B., and Alferieff, M. E., J. Chem. Phys. **46,** 923 (1967).
[14] Young, R. D., Phys. Rev. **113,** 110 (1959).
[15] Gadzuk, J. W., Surface Sci. **15,** 466 (1969).
[16] Plummer, E. W., Gadzuk, J. W., and Young, R. D., Solid State Comm. **7,** 487 (1969).
[17] Plummer, E. W., and Young, R. D., Phys. Rev. (in press).
[18] Gadzuk, J. W., Phys. Rev. (in press).
[19] Appelbaum, J., Phys. Rev. Letters **17,** 91 (1966); Phys. Rev. **154,** 633 (1967).
[20] Anderson, P. W., Phys. Rev. Letters **17,** 95 (1966).
[21] Duke, C. B., Tunneling in Solids, (Academic Press, New York, 1969).
[22] Young, R. D., and Kuyatt, C. E., Rev. Sci. Instr. **39,** 1477 (1968).
[23] Gadzuk, J. W., Phys. Rev. **182,** 416 (1969).
[24] Clark, H. E., and Young, R. D., Surface Sci. **12,** 385 (1968).
[25] Clark, H. E., and Plummer, E. W., 16th Field Emission Symposium, Pittsburgh, Pennsylvania, September 1969.

What Properties Should the Density of States Have in Order That the System Undergoes a Phase Transition?

P. H. E. Meijer

National Bureau of Standards, Washington, D.C. 20234 and The Catholic University of America, Washington, D.C. 20017

We have solved nothing that needs to be solved regarding the density of states problem in a system that undergoes a phase transition. We, however, raise the question of what conditions the density of state function of the total system (*not* the temperature dependent quasiparticle spectrum) should have in order that we are observing a phase transition. In general, one needs an extremely strong increase in the density—how strong can only be illustrated by using models. From these models we tried to obtain the density of states using the inverse Laplace transform. The results reveal that a vertical slope seems to be a necessary condition. There are reasons to believe that the condition is not sufficient.

Key words: Density of states; Ising model; Onsager model; partition function; phase transition; Weiss model.

1. Introduction

In order to obtain the physical properties of a large system, one has to calculate the partition function and this is in general preceded by the determination of the density of states. Let us take a discrete system: the density of states is a weight factor $w(E)$ indicating how many ways an energy E can be realized. If this factor is known, the partition function is found by summation over the values of E:

$$Z(\beta) = \sum_E w(E) \exp(-\beta E) \tag{1.1}$$

where $\beta = 1/kT$ [1]. Although such a summation may not be feasible analytically, this obstacle is much less of a stumbling block than the first requirement, the determination of $w(E)$.

It is of course possible to evaluate the general expression for the partition function directly. One sums over the microscopic variables, such as the spin variable(s) of each individual spin and calculates the value of E for each set of values of the spin variables. Since each value of E carries a different Boltzmann factor, this introduces a constraint on the summation. If one tries to eliminate this restriction by introducing a delta function or similar device, one arrives again at the density of states:

$$w(E_0) = \sum_{s_1} \cdots \sum_{s_n} \delta(E(s_1 \ldots s_n) - E_0) \tag{1.2}$$

as an intermediate step to obtain the partition function.

For the sake of completeness, we give also the continuous description. The partition function can be written as:

$$Z(\beta) = \int \exp[-\beta E(p, q)]\, dp\, dq \tag{1.3}$$

or as

$$Z(\beta) = \int_0^\infty \exp(-\beta E)\rho(E)\, dE \tag{1.4}$$

Here p,q stands for $p_1 \ldots p_{3N}$, $q_1 \ldots q_{3N}$ and $\rho(E)$ for the density of states. One can consider $\rho(E)$ also as a Jacobian, the variables p,q are replaced by $\alpha_1 \ldots \alpha_{6N}$, where $\alpha_1 = E$ and all other α's arbitrary but independent. The density of states is given by

$$\rho(E) = \int J(p, q; \alpha_1 \ldots \alpha_N)\, d\alpha_2 \ldots d\alpha_{6N},$$

or one can introduce the accumulated density of states $\Omega(E)$, also called "volume in phase space," given by

$$\Omega(E) = \int_0^E dp \ldots dq$$

which leads direetly to the density

$$\frac{d\Omega}{dE} = \rho(E)$$

The function $\Omega(E)$ is, in the discrete language, the total number of states with energies less than a given value.

The phase volume integral ean be written with a step function

$$\Omega(E_0) = \int_0^\infty \theta(E(p \cdot q) - E_0)\, dp\, dq$$

and the density funetion in a similar way

$$\rho(E_0) = \int_0^\infty \delta(E(p \cdot q) - E_0)\, dp\, dq$$

Sueh an artifaet is useless in itself, but one may introduee transforms of these funetions. The main question is, what properties should $\rho(E)$ have so that the system undergoes a phase transition?

Since it is impossible to obtain $\rho(E)$ for almost any N-body system, we try to extraet same information from the $Z(\beta)$, whieh is in some eases approximately known. We observe that eq (1.4) ean be eonsidered as a Laplaee transform exeeuted on $\rho(E)$. Henee we ean obtain $\rho(E)$ from $Z(\beta)$ by an inverse Laplace transform

$$\rho(E) = \int_{-i\infty+\gamma}^{i\infty+\gamma} Z(\beta) e^{\beta E} d\beta \tag{1.5}$$

This idea is not new. The use of the partition funetion to reeonstruct the density of states was used as early as 1911 [2].

2. Quasiparticle Description, the Three Level Model

In the quasipartiele deseription, the individual spins are deseribed by a density of states that depends on the temperature $w_i(E,\beta)$. The subseript i stands for the site,

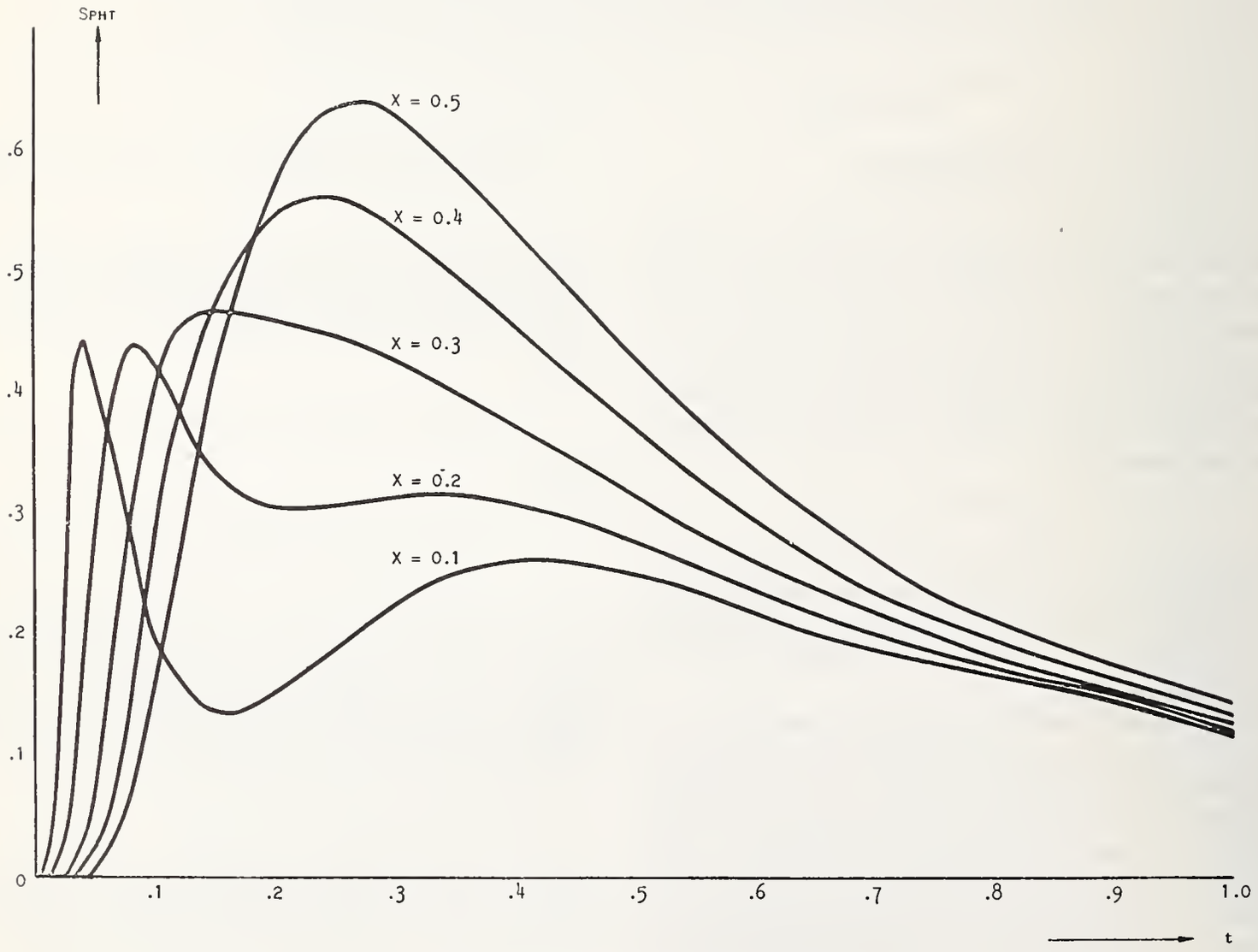

FIGURE 1. *Specific heat of a three level system.*
The temperature is measured in units $\Delta E = E_3 - E_1 : t = kT/\Delta E$. The relative location of the middle level E_2 is given by $X = (E_2 - E_1)/\Delta E$.

or if the system is homogeneous, for "individual." For a spin 1/2 system there are only one or two values of E for which this quantity is non-zero. In the first case, the Weiss theory above the critical temperature, we have $w_i = 2$ and the system shows no spontaneous magnetization; in the second case, the Weiss theory below the critical temperature, each $w_i = 1$ and the system is ordered. At the critical temperature, the levels move apart and this causes a peak in the specific heat. This motion of the level or levels with the temperature is a highly unsatisfactory description since the level structure should be given once and for all, independent of the temperature. Moreover, a very fine splitting between two levels does not give rise to a specific heat peak unless the level is situated at the bottom of the spectrum. This can be easily illustrated by a three level scheme.

If three levels are given by $E_1 = 0$, $E_2 = X\,\Delta E$ and $E_3 = \Delta E$, $(0 \leq X \leq 1)$, then for $X \approx 0$ one has a peak and a Schottky curve, for $X \approx 0.1$ two maxima and for all other values a single Schottky-like curve. The case $X \approx 1$ does not give a peak (fig. 1).

Hence the quasiparticle level structure is of no use to find out what is the typical behavior of $\rho(E)$.

3. Density Structure from the Accepted Theories

Assuming the generally accepted form of singularity [3] in Cv

$$C_v/k = \frac{A}{\left|\frac{T-T_c}{T_c}\right|^{\alpha}} + f(T)$$

one can try to deduce the behavior of the density of states. A is the amplitude or residue of the singularity and $f(T)$ is a regular function. Using

$$C_v/k = \beta^2 \frac{\partial}{\partial \beta^2} \ln Z$$

We try to determine $ln\ Z$ by twice integrating the specific heat

$$\frac{\partial}{\partial K} \ln Z = -\int_0^K \left(\frac{A}{k^2 |k - k_c|^{\alpha}} + k^{-2} f(k) \right) dk.$$

where $K = \beta J$, is a dimensionless inverted temperature. We know that $U(K = 0)$ is regular, hence the singular behavior near $K = 0$ in the first and the second term must cancel. Around K_c we can replace the integral by

$$-\frac{\partial \ln Z}{\partial K} = \int_0^K \left(\frac{A}{k_c^2 (k - k_c)^{\alpha}} + \hat{f}(k) \right)$$

where $\hat{f}(K)$ is $K^{-2} f(K)$ minus the singularity at $K = 0$.

$$\frac{\partial \ln Z}{\partial K} = \frac{1}{\alpha} \frac{A}{K_c^2} |K - K_c|^{-\alpha+1} - \int \hat{f}(k)\, dk \ln Z$$

$$= \frac{1}{\alpha(\alpha-1)} \frac{A}{K_c^2} |K - K_c|^{-\alpha+2} + g(K)$$

$$Z = \exp\left(\frac{1}{\alpha(\alpha-1)} \frac{A}{K_c^2} |K - K_c|^{-\alpha+2} \right) \cdot \exp\,[g(K)]$$

Compare this with eq (1.5), it leads to the inverse Laplace transform

$$\rho(\epsilon) = \int_{-i\infty+\gamma}^{i\infty+\gamma} \exp\left[\frac{1}{\alpha(\alpha-1)} \frac{A}{K_c^2} |K - K_c|^{-\alpha+2} + g(K) + K\epsilon \right] dK \quad (\epsilon = E/J)$$

This integral cannot be accomplished with the undetermined function $g(K)$, since the integrand is only known near K_c. In order to perform the line integral the value of the integrand must be known at some line or curve parallel to the imaginary K-axis. There is an additional handicap. The previous integrations assumed that the first and second integrals were continuous function in the point T_c, which does not have to be the case. Hence this approach is not leading to much information about the characteristic properties of the density of states.

4. Density of States of the Solvable Models

The One Dimensional Ising Model. The density of states is

$$\rho(E) = \left((1-E)^{1/2+2E} (1+E)^{1/2-2E} \right)^N$$

where E is in units $N\epsilon$ and ranges from -1 to $+1$. The curve has a peak for $E = 0$, which becomes more pronounced for larger N.

A similar calculation can be made for $H \neq 0$.

For the Weiss Model we find

$$(\rho(E))^{2/N} = e^{2 \ln 2} (1 + \sqrt{E^1})^{-(1+\sqrt{E^1})} (1 - \sqrt{E^1})^{-(1-\sqrt{E^1})}$$

where $E^1 = 1 - 2E$. E is in units Nez, where z is the number of nearest neighbors and ϵ the absolute value of the negative interaction energy. E is measured from the ground state. For $E = 0$ the degeneracy is 1, it goes up to 2^N at $E = 1$. The slope at $E = 0$ is infinite and at $E = 1$ is zero, using the quantity $\rho^{2/N}$ as vertical axis (fig.

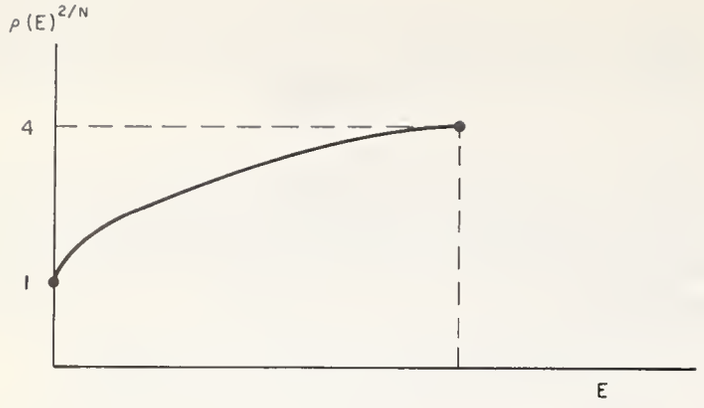

FIGURE 2. *Effective density of states for the Weiss model.*

2). If one plots ρ it is "infinite" everywhere. There is not such a thing as a steep increase in the density of states for $E \sim T_c$.

For the Onsager Model. In order to obtain a solution we use the method of steepest descent. This can be done easiest in thermodynamic terms

$$\int e^{-\beta F(\beta)+\beta E} d\beta \approx e^{-\beta_s F(\beta_s)-\beta_s E_I}$$

where I is a Gaussian integral in terms of $(\beta_s - \beta)^2$. The value of β_s is determined by

$$E = U(\beta_s)$$

Hence the integral is proportional to the exp (NS/k) and

$$\rho(E) = e^{NS/k}$$

To find $\rho(E)$ one has to convert $S(T)$ into $S(E)$. This needs the inversion $E = E(T)$ into $T = T(E)$. Since the first goes like $x\ lnx$, the second cannot be found. Hence the conclusion is that although the density undergoes a very sharp (vertical) increase near E_c, the value at this point cannot be determined. It is possible that one finds superposed on the sharp increase a delta-function-like spike.

5. First Order Phase Transitions

We like to consider briefly the first order transitions. Characteristic for a first order transition is the presence of another parameter X, such as the chemical potential or the external field. The density of states will depend on this parameter: $\rho = \rho(E,X)$. The entropy undergoes a jump when X is varied at a temperature below the critical temperature. This discontinuity can be calculated from the Clausius Clapeyron equations:

$$\frac{dP}{dT} = \frac{\Delta S}{\Delta X}$$

6. Summary

In this note we raise the question as to what the conditions are to obtain a system with a phase transition on the density of states. A phase transition is observed by a singularity in the specific heat or by the appearance of a magnetization (or a similar form of condensation) in the absence of a field (or similar order-inducing thermodynamic variable).

Although it is easy to trace in a quasiparticle description how such a singularity comes about, the general features are much harder to establish in terms of the proper many-body theory. An attempt is made to see what is at least required, using the general features of the scaling laws and the well known models that can be calculated. The basis of the consideration stems from the almost obvious relation between the underlying density of states on one hand and the Laplace transform on the other hand.

7. References

[1] Tolman, R. C., The Principles of Statistical Mechanics, Oxford (1963).

[2] See P. Ehrenfest, Ann. D. Phys., **36,** 91 (1911). The problem was independently considered by H. Poincare, J. de Physique **2,** 1 (1912). He first used a Laplace transform. He was criticized by Fowler, Proc. Roy. Soc. London **A99,** 462 (1921), for applying the transform to a discrete spectrum. All three papers deal with the density of states underlying the black body radiation.

[3] The scaling laws are reviewed by L. P. Kaganoff, et al., Rev. Mod. Phys. **39,** 395 (1967).

[4] All models (1. 2 Dim. Ising, Weiss and Bethe) can be found in K. Huang, Statistical Mechanics, Wiley.

[5] Glass, S. J., and Klein, M. J., Investigations on the Third Law of Thermodynamics, Case Institute of Technology, AEC Technical Report No. **2** (August 1958).

On Deriving Density of States Information from Chemical Bond Considerations

F. L. Carter

U.S. Naval Research Laboratory, Washington, D.C. 20390

The chemical picture of bond formation between neighboring atoms in crystalline solids can give valuable electronic density of states information including the rough shape and relative filling of bands. In addition, from the representation of the chemical bond in momentum space one can readily predict the distortion of the Fermi surface from sphericity. This latter approach appears to provide an alternate explanation of the apparent attraction of the Fermi surface to the Brillouin zone faces.

The first relationship is best demonstrated in cases where relatively unique schemes of bond formation can be devised. This is possible in many intermetallic compounds having high coordination by the use of orthogonal sets of bidirectional orbitals; their use leads to multicenter bonds or cycles which are approximately orthogonal. Via the Fourier transform, the series of Slater determinants (representing the multicenter bond) can be transformed into momentum p space and then related to the usual band picture. The occupation or filling of bands can be estimated from bond orders of the associated bonds and obtained from known interatomic distances by using Pauling's metallic radii. Bond hybridization is obtained from orthogonality requirements and bond angle considerations characteristic of valence bond theory. These ideas can be applied to FCC and HCP transition metals. For copper one would expect a sharp peak in the density of states corresponding to two unshared filled local d orbitals. In addition there would be a broad bonding band filled with electrons (6 per atom) containing large amounts of p character; and a half-filled s band. As one moves downward through the periodic table to iron while maintaining either FCC or HCP structures the high melting points of the elements involved indicate that the broad bonding band remains relatively unchanged (filled) while the number of electrons in the narrow d band is steadily decreased.

In the rare earth cubic Laves phases of composition AB_2, this relatively simple chemical approach suggests the presence of four bands. The two more important bands are: (1) a large narrow-width density of states band associated with two unshared local d orbitals per B atoms, and (2) a band which is generally more than half-filled associated with all the transition metal B—B as well as the A—B bonds. The other bands include an s band associated with the B atoms which is less than half-filled due to the transfer of electrons from the hyper-electronic B atom, and a band of unusually high d character associated with the A—A bonds and probably not occupied for the lighter rare earth compounds.

From the study of simple σ bonds, Coulson has shown that the momentum distribution function is compressed in the direction of the internuclear axis. By using this idea in conjunction with the Fourier transform of hydrogenic atomic orbitals it is comparatively easy to show that for a CCP* transition metal like copper the momentum distribution function has its principal projections in the ⟨111⟩ directions while the BCC transition metals should have projections in the ⟨110⟩ directions. Projections in more complicated structures can be obtained from considerations of bond hybridization and bond order. In summary, we see that the valence bond concepts of bond hybridization and bond order coupled with known structures and bond distances can be used to suggest band shapes, filling, and hybridization. It is apparent that the increased use of chemical concepts in the interpretation of information concerning the electronic density of states is an area of promise.

Key words: Aromatic compounds; chemical bond; electronic density of states; Fermi surface; Pauling radii; transition metals; rare earth intermetallic compounds.

*The abbreviation of CCP (cubic close packed) is preferable to the usual FCC (face centered cubic) terminology as many structures are FCC without being CCP.

417-156 O - 71 - 26

1. Introduction

The chemical concept of bond formation between adjacent atoms can be used to obtain density of states information such as the approximate shape and the relative filling of bands for many crystalline materials. Such qualitative information should be particularly useful in interpreting trends of density of states in related series of compounds and in making rough predictions about compounds having new structures. Moreover, from the representation of the chemical bond in momentum space, one can readily predict the distortion of the Fermi surface from sphericity. We intend to show that this representation provides an alternative explanation of the apparent attraction of the Fermi surface to the Brillouin zone faces.

As indicated above, the paper is in two parts. Some of the older chemical concepts of the valence bond approach are applied to a new set of hybrid orbitals in a discussion of transition metal compounds. The application of these concepts plus structural data leads to density of states information via the following logic: (a) Bond distances are used to indicate the number of electrons involved in a given bond; (b) A modified valence bond formulation is developed for the new bidirectional orbitals that permits the association of particular sets of bonds into bands which are orthogonal in both real and momentum p space; (c) The relative filling of the bands is estimated from the bonding model and the number of electrons in the associated bonds. Examples are given for several compounds and some differences in the treatment of these compounds by the chemists and physicists are discussed.

In the second part of the paper the density of states is approached from the point of view of the distribution of the bonding electron in momentum p space: Successive portions of the paper deal with: (a) The effect of bond formation and orbital hybridization on the momentum distribution function; (b) The qualitative similarity between the shapes of the Fermi surface and the total momentum distribution function for the outer electrons; (c) The application of a simple model predicting the Fermi surface for several examples; and (d) Generalization of these considerations to density of states information.

The desired starting point for the applications of chemical concepts is a reasonably accurate structure determination of the compound of interest. The interatomic distances accurate to $\simeq$0.002 Å provides one with an estimate of the number of electrons of each atom involved in bond formation. In addition, the angular aspects of each atom's coordination suggests possible hybridizations (i.e., LCAO) of the bonding orbitals which could give a fair amount of overlap with its near neighbors. While other types of data, such as estimates of interatomic force constants, magnetic data, conductivity type, etc., are useful for refining the bonding model or choosing between models, the structural information is essential.

The derivation of density of states information is best demonstrated in cases where relatively unique schemes of bond formation can be devised. This is possible in many intermetallic compounds having high coordination by the use of orthogonal sets of bidirectional orbitals. Since this approach, which we might term the bidirectional orbital approximation (BOA), makes use of s, p, and d orbital hybridization, we will generally confine our attention to transition metal compounds of high coordination. Prior to the consideration of particular compounds it will be useful to define some terms as well as to indicate what is involved in the BOA scheme of bond formation.

1.1. Definition of Terms

Although the "valence" of an atom initially referred to as the "degree of its combining power," the term "valence electrons" has widely different meanings for the physicist, the modern chemist, and those scientists preferring the purely ionic representation. To avoid confusion we will adopt the term, "valence electrons," to indicate the number of electrons of an atom outside its largest complete rare gas shell and coin the term "covalency" or "covalent electrons" to indicate the number of electrons used by an atom in the formation of covalent bonds (i.e., shared electron bonds). The "bond order," n_{ij}, of a bond (covalent) between atom i and atom j indicates the number of electrons contributed to that bond by each atom. Thus, the carbon–carbon single bond C–C has a bond order of $n_{ij} = 1.0$ indicating each carbon atom contributed one electron to the bond. Similarly, the carbon–carbon double bond C=C has a bond order $n_{ij} = 2.0$, in which each atom contributed two electrons. In the overwhelming majority of transition metal compounds the bond orders of all bonds are $n_{ij} \cong 0.5$ or less (exception Nb–Nb bonds in Nb_3Sn). In general the bond order is inversely related to the interatomic distances. When the atomic distances are such as to give a bond order $n_{ij} \lesssim 0.05$ the atoms are not considered to be bonding; in many transition metal compounds this distance is about 3.8 Å. All the electrons involved in covalent bonds are considered to be paired even though the bond order is less than 0.5.

The covalency V_i, of the atom i is just the sum of the bond orders n_{ij} over all the bonding neighboring atoms j, thus:

$$V_i = \sum_j n_{ij} \tag{1}$$

Pauling [1] has developed a semi-empirical equation for the calculation of n_{ij} from the known interatomic distance d_{ij}. It is as follows:

$$0.600 \log n_{ij} = R_1(i) + R_1(j) - d_{ij} \tag{2}$$

where $R_1(i)$ and $R_1(j)$ are single bond radii for atoms i and j, respectively. These metallic radii, R_1, may be calculated from equations given by Pauling knowing the average bond hybridization and number of valence electrons, z. For example, for the iron transition elements

$$R_1(sp^3, \delta) = 2.001 - 0.043z - (1.627 - 0.100z)\delta \tag{3}$$

where δ is the average d character and the s to p hybridization ratio is 1 to 3. On the plus side of this empirical approach we note that eq (3) is suitable for calculating the single bond metallic radii for ≈16 elements with other very similar equations for most of the remaining elements of the periodic table.

The average d character, δ, for the covalent electrons is taken by Pauling to be a smooth function of position in the periodic table and attains a value as high as 50% ($\delta = 0.5$) for some of the transition elements (e.g., Ru, Rh, Os) [2]. Although a table of R_1 has been given for the elements [1, p. 403], in their application to various compounds the author has found it necessary to use such values as a starting point in a reiterative calculation where a measure of self-consistency is sought among (i) the equations, (ii) the assumed and calculated values of the covalency V_i, and (iii) in the amount of charge transferred between atoms. To the potential user it is further suggested that this approach is most suitable in discussing trends in series of related compounds (i.e., differences of covalencies, etc., between similar compounds is to be taken as more meaningful than the values themselves for any isolated compound).

By using Pauling's metallic radii, as above, one can obtain estimates of (1) the number of electrons involved in bond formation, (2) the number of unshared electrons or localized electrons per atom, and (3) the relative occupancy or hybridization of atomic orbitals for each type of electron. In order to estimate from chemical considerations the distribution of the covalent electrons among bands, a model of bond formation between atoms is required.

2. The Bidirectional Orbital Approximation

In the usual valence bond treatment the angular parts of s, p, and d orbitals are superimposed to make a hybrid orbital which concentrates electron density in one major lobe toward a single neighbor. Such hybrid orbitals are of proven utility for elements of the first two rows (especially) but can give difficulties in their application to the transition elements. In those cases the bidirectional orbitals appear useful, where bidirectional orbitals are hybrid orbitals in which electron density is concentrated in two major directions. Equations between the coefficients of the nine atomic orbitals are obtained from the following restrictions: (1) All near neighbors are simultaneously bound: (2) lobes of equivalent orbitals are directed toward equivalent neighbors; and (3) all bidirectional orbitals are mutually orthogonal and orthogonal to the remaining orbitals. In structures with high coordination this approach has two advantages with respect to the usual valence bond treatment: (1) The high formal charges associated with either the ionic or single lobe valence bond treatment are avoided; and (2) the method usually results in a finite number of bonding descriptions that can be useful for either simple considerations or could be readily subjected to formal and extensive calculations. In contrast, full valence bond calculations for a solid, with or without ionic contributions, are extremely difficult and have not recently been attempted to the author's knowledge.

Rundle [3] used the simplest of bidirectional orbitals (the carbon p orbital) in his discussion of the transition metal carbides, and Ganzhorn [4] obtained orthogonal bidirectional orbitals of the general form as

$$+ \sqrt{(a^2-1)}\, d_{z^2}$$

for the octahedral and body-centered coordinations. By generalizing these orbitals into a C-type of p_y plus d_{xy} character and a G-type having s, d_{z^2}, and p_x character, it is possible to discuss the bonding in a wide variety of metallic and semiconducting transition metal compounds (e.g., those having the Th_3P_4, CCP, HCP, NiAs, WC, and Laves phase structures [5-8]).

In figure 1 the general shapes of the C and G orbitals and phase relationships between their lobes are indicated. In the process of maximizing the angular part of the two main lobes of a bidirectional orbital in the direction of two near neighbors one obtains, in general, three categories of orbitals. These are: (i) the bonding bidirectional orbitals of C- and G-type, suitable for the shared covalent electrons; (ii) local orbitals whose an-

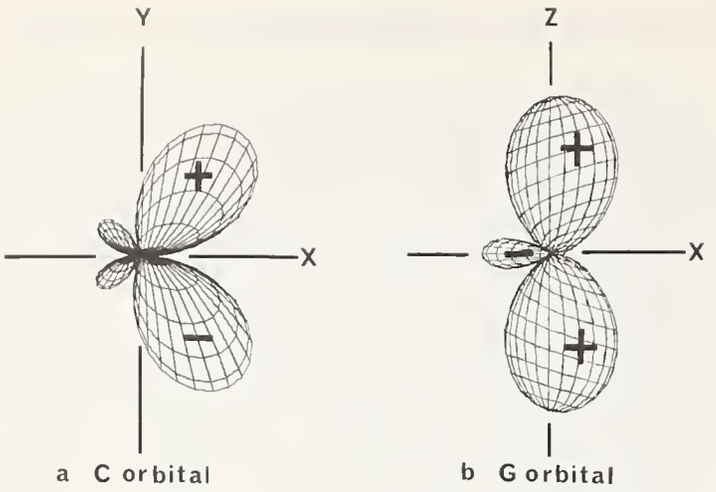

FIGURE 1. *The concentration of electron density into two major lobes is illustrated by the angular portions of the bidirectional orbitals.*

The included angle between the atoms to be bonded is much larger for the G-type (b) than for the C-type (a) to the left.

gular lobes are either small or not directed toward nearby atoms, suitable for unshared electrons (paired or unpaired); and (iii) an orbital of primarily *s* character, suitable for a simple band treatment. Later we will associate respectively with these orbital types; (i) a bonding or covalent band, (ii) a band of localized electrons, and (iii) a free-electron like band. Finally we point out that in structures of high symmetry the use of the bidirectional orbitals usually does *not* result in the atom of interest having the full symmetry of its atomic position in the structure. This is to be achieved at a later stage, in terms of multi-electron wave functions, by forming linear combinations which include the necessary other sets of bidirectional orbitals. These sets, ϕ_i^ν, are related to the original set ϕ_i by the missing symmetry elements corresponding to the operators S_ν by the eq (4).

$$\phi_i^\nu = S_\nu \phi_i \tag{4}$$

Bond formation between two adjacent atoms can result if the overlap integral between their orbitals is positive. This can usually be achieved by matching the phases (or signs) of the angular parts of their bonding orbitals. With bidirectional orbitals this leads very naturally to the formation of cycles which, for one electron per orbital, are closely related to the cycles of early valence bond treatments. Cycles then consist of linear arrays of bidirectional orbitals on adjacent atoms, forming either rings or infinite chains. Figure 2 (top) suggests an infinite periodic cycle of *C*- and *G*-type orbitals in the cubic Laves phase of composition AB_2. In figure 3 are seen cycles of four *C*-type orbitals in the (100) plane of a CCP structure.

By a phase structure (Ω) we refer to that set of cycles in a crystal such that all bonding orbitals are linked in cycles involving more than one orbital. A phase structure may be considered "good" if overlap between orbitals is high in terms of both phase matching and the directional properties of the orbital lobes. In MO terms the "good" criterion merely says that if a molecular orbital configuration contributes significantly to the ground state, the lowest electron level, at least, should be bonding.

Cycles within a phase structure are mutually orthogonal (approximately). This results from the mu-

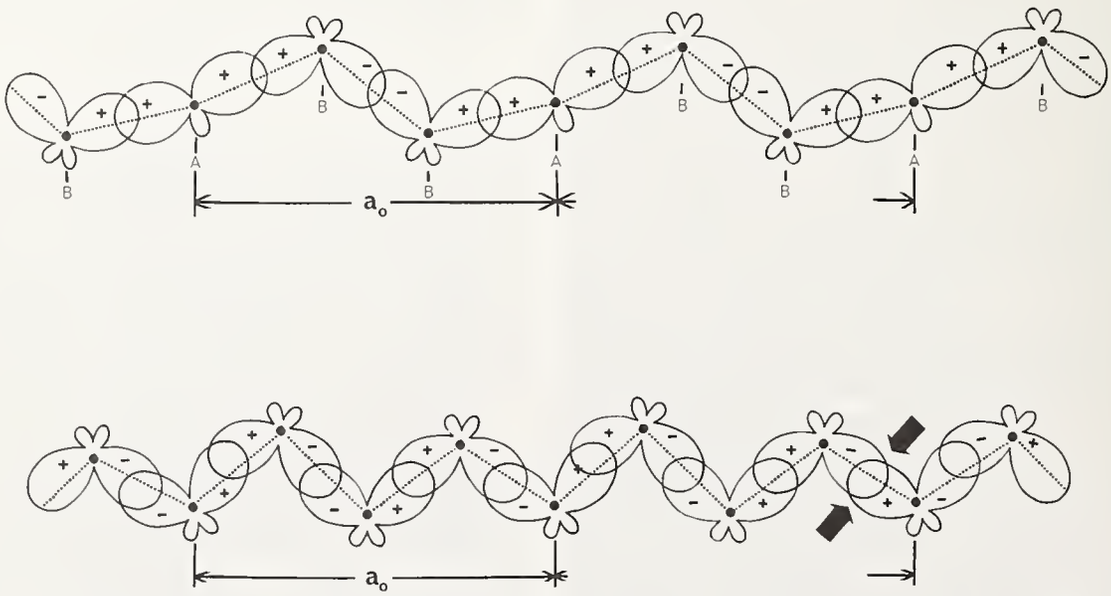

FIGURE 2. *Top—A linear periodic cycle is shown for the A-B band in the Laves phase* AB_2. *The phases of the* G *orbitals* (A *atom*) *and* C *orbitals* (B *atoms*) *are all matched to give good overlap. Bottom—In this cycle for the* A-A *band the use of* C *orbitals is symbolically illustrated. The arrows to the right denote an anti-bonding overlap which would become increasingly prevalent with high* k *values in the Bloch wave functions.*

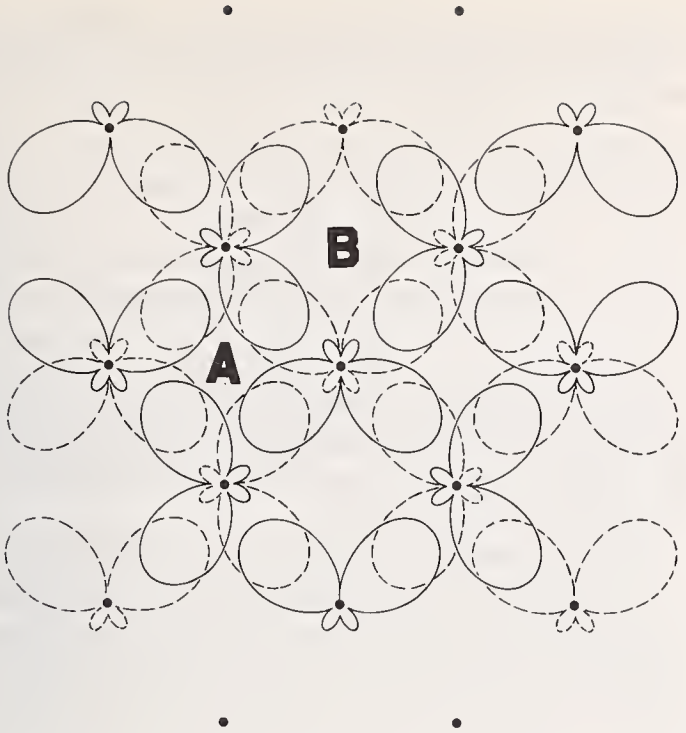

FIGURE 3. *The relative orientation of the C orbitals in a good phase structure for a (001) plane of a cubic close packed structure is shown.*

The C orbital with a dotted outline is orthogonal to the C orbital with a solid outline based at the same atom (black dot). Around the B position is a cycle of four C orbitals. This cycle is approximately orthogonal to all the other cycles of the phase structure. To restore the full symmetry to the lattice an equal amount of a phase structure corresponding to a reversal of A and B must be included in the n electron wave function.

tual orthogonality of bidirectional orbitals located on the same atom and the fact that the nodal planes of the bidirectional orbitals usually pass near or through neighboring atoms which are not being bonded by its lobes. A phase structure $\Omega(r_n)$ of n electrons with coordinates r_n can then be expressed as a product function of its cycles Γ_i

$$\Omega(r_n)=\prod_i \Gamma_i \tag{5}$$

where Γ_i is a Slater determinant of n_i electrons involving the appropriate C- and G-type spin orbitals ϕ_j

$$\Gamma_i=\begin{vmatrix} \phi_1(1)\ldots\ldots\ldots\ldots\phi_1(n_i) \\ \phi_2(1)\ldots\ldots\ldots\ldots\phi_2(n_i) \\ \vdots \qquad\qquad\qquad\quad \vdots \\ \phi_{n_i}(1)\ldots\ldots\ldots\ldots\phi_{n_i}(n_i) \end{vmatrix} \tag{6}$$

The full symmetry of the structure may be restored by forming a wave function from a linear combination of phase structures which include the different symmetry related bidirectional orbital sets, ϕ_i^ν, as obtained by eq (4).

It is of considerable interest that for many structures the ϕ_i of different ν and i (but the same atom) are orthogonal. For these crystals, partial phase structures can be written in terms of bands[1] such that the total wave function for N electrons can be equated to a product of the phase structures for the bands γ.

$$\Psi(r_N)=\Pi_\gamma \Omega(r_n,\gamma) \tag{7}$$

where

$$N=\Sigma n_\gamma \tag{8}$$

and bands of local orbitals[2] are included. Alternately $\Psi(r_N)$ can be considered as a Slater-like determinant of band phase structures $\Omega(r_n,\gamma)$ for diagonal blocks and zero off-diagonal blocks. The band phase structures, however, are linear combinations of phase structures $\Omega_{i,\gamma}$ associated with the band γ, and symmetry operations

$$\Omega_\gamma(r_n)=\sum_i a(i,\nu,\gamma)\Omega_{i,\gamma}(r_n) \tag{9}$$

where the individual phase structures $\Omega_{i,\gamma}$ of the same band are not necessarily orthogonal. Various symmetries about the site are possible by a suitable combination of the coefficients $a(i,\nu,\gamma)$.

If $X_i(p)$ is the Fourier inversion of the orbital $\phi_i(r)$ according to eq (10)

$$X_i(p)=\frac{1}{2\pi}\int \phi_i(r)e^{-ip\cdot r}d\tau_r \tag{10}$$

with p as the conjugate momentum of r then it may be shown [9] that the Fourier transform of a Slater determinant of ψ_i results in a Slater determinant of X_i in momentum space and is obtained by simply replacing $\phi_i(r_j)$ with $X_i(p_j)$. It follows that the Fourier transform of a sum of Slater determinants in real space results in a sum of Slater determinants in coordinate momentum space with the same coefficients. Accordingly we may associate with the phase structure, Ω_γ, of the γ band, a $3n_\gamma$ conjugate p space.

In a valence bond treatment of a solid there is no obvious need for the phase structures, Ω_γ to be periodic, except for reasons for organization. However, for the later discussions relating bonding to the density of

[1] The term "bands" used in this somewhat different sense refers to group-symmetry restricted n electron functions which may be associated with several of the usual one electron bands of band theory as below

$$\Omega_k(r_n,\gamma)=\sum_m A_m(k,\gamma)G_m$$

Here G_m is a Slater determinant of n (or less) electrons involving the customary band wave functions $\Phi_k(r,\alpha)$ with various combinations of the α bands.

[2] For some bands of local orbitals and for a band of "free" electrons of primarily s character it is probably adequate to take $\Omega_k(r,\gamma)$ the same as the customary band wave functions, $\Phi_k(r,\alpha)$, with $\gamma=\alpha$.

states and the Fermi surface, we remark that for a Bloch representation for n electrons of the form eq (11)

$$\psi(r_1, \ldots, r_n) = e^{i\sum_{j=1}^{n} kr_j} u_k(r_1, \ldots, r_n) \qquad (11)$$

the phase structures Ω_γ, may be identified with the periodic part $u_k(r_1, \ldots r_n)$ of ψ. For $k=0$ and one electron the phase structure is one associated with good bonding like figure 2 (top), while for $k \neq 0$ antibonding states as in figure 2 (bottom) may play an important role. For the one-electron case a clear distinction must be made between k space and the momentum (p) space. The former space is a space of good quantum numbers which can be considered to have the dimensions of momentum, whereas the momentum p is not a good quantum number for any nonconstant crystal potential.

3. Bonding in Some Transition Metals

At this stage it is appropriate to assess our position and to indicate the forthcoming directions. Having equipped ourselves with some chemical nomenclature and concepts and a bonding model appropriate to transition metal compounds we will now apply these to some close packed metal structures, the Laves phases of composition AB_2, and the NiAs structure. In doing so we will obtain coarse grain density of states information such as the number of bands (at least those partly filled), their rough shape, relative position, and percent filling. Important differences between the chemical and physical viewpoints will be discussed and a possible approach to the resolution of some of these differences will be suggested. In following sections the influence of bond formation in momentum p space will be indicated and the relation between the momentum distribution function and surfaces of constant energy will be suggested with examples referencing the Fermi surface.

In the following simple applications of the BOA picture we hope to clarify some of the BOA formalism above. Among transition metal compounds the coordination number of 12 is one of the most common, including the icosahedral coordination and the close packed structures. Even the sixteen coordination of the A atom in the Laves phases can be separated into one of 12 B atoms and 4 A atoms. A coordination of 12 can be sought through the use of bidirectional orbitals by generating a set of orbitals ϕ_i from one of the form eq (12)

$$\phi_1 = As + Bp_x + Cp_y + Dp_z + Ed_{xy} + Fd_{xz} + Gd_{yz} + HD_{x^2-y^2} + Id_{z^2} \qquad (12)$$

by the use of a twofold axis in the z direction and threefold axis in the [111] direction. The six orthonormality conditions are:

$$1/2 = A^2 + D^2 + E^2 + H^2 + I^2 = B^2 + C^2 + F^2 + G^2 \qquad (13)$$

$$2A^2 = H^2 + I^2 \qquad (14)$$

$$0 = BC + GF = CD + EF = BD + EG \qquad (15)$$

The requirement that equivalent atoms be bonded in an equivalent manner suggests that with respect to a 180° rotation about the x axis ϕ_i should be either symmetrical or antisymmetrical.

The antisymmetrical case leads to two different sets of six C-type orbitals. Each set would give good bonding for an icosahedral coordination of 12. The two different icosahedra are related by a diagonal minor plane, S_d. The two C-type orbitals, eqs (16a,16b),

$$\phi_1 = C_{yx} = (p_x + d_{xy})/\sqrt{2} \qquad (16a)$$

$$\phi_1^d = C_{yx} = (p_y + d_{xy})/\sqrt{2} \qquad (16b)$$

are representatives of the two different sets ϕ_i and ϕ_i^d, which are related by the mirror plane operator S_d as in eq (17).

$$S_d\phi_i = \phi_i^d \qquad (17)$$

In the formation of the six C-type orbitals (of each set) the three p and the d_{xy}, d_{xz}, and d_{yz} atomic orbitals are completely used. For each set (ϕ_i and $\phi_i{}^d$) the s, $d_{x^2-y^2}$, and d_{z^2} orbitals are mutually orthogonal and orthogonal to the bonding C orbitals.

The coordination of the twelve near neighbors in the CCP structures can be readily taken as the average of the two icosahedra just discussed, so the rehybridization of the atomic orbitals to form bonding hybrids is the same as for the icosahedron. By alternating the hybridization of the atoms in the (001) plane between the ϕ_i and $\phi_i{}^d$ sets it is possible to form good phase structures. In figure 3, showing the xy plane of a CCP structure, it is clear that such an alternation results in a phase structure, $\Omega_C{}^1$, of the C band (covalent) in which cycles, Γ_i, are rings of four C-type orbitals, two of the ϕ_i set and two of the $\phi_i{}^d$ set. If the phase structure, $\Omega_C{}^2$, represents the exchange of the ϕ_i sets with the $\phi_i{}^d$ sets, then the sum of these two-phase structures restores the full symmetry of the lattice. Other phase structures, $\Omega_C{}^{j+2}$, composed of various arrangements among the atoms of the ϕ_i and $\phi_i{}^d$ sets may be expected

to contribute to the phase structure, Ω_C, for the covalent band although the orbital overlap will not be as good on the average as in $\Omega_C{}^1$ and $\Omega_C{}^2$.

Two additional bands, Ω_L and Ω_S, can be constructed from the remaining atomic orbitals of the sets ϕ_i and $\phi_i{}^d$. The phase structures Ω_L, of the L band (L for local) is clearly constructed of atomic $d_{x^2-y^2}$ and d_{z^2} orbitals. These orbitals have lobes which are not directed towards any near neighbors and are accordingly suitable for unshared electrons, up to four electrons per atom. The phase structure, Ω_S, is clearly associated with the atomic s orbital and for our current purpose we will identify it with a free-electron type band. In accordance with our earlier discussion (see eq (7)) we note that all the $\Omega_C{}^j$ are orthogonal to both Ω_L and Ω_S.

A very similar distribution of hybrid orbitals obtains if the BOA method is employed in the HCP structures [6]. If the c/a ratio for the structure is $\simeq$1.63 six C-type orbitals of $\simeq$50% d character are employed to bond the twelve near neighbors, leaving two local d orbitals and an s orbital to form the Ω_L and Ω_S phase structures and bands. Changes in the c/a ratio result in d_{z^2} character in the s-type orbitals as well as changes in the d to p ratio in the C-type orbitals.

Now let us distribute valence electrons among the various bands starting with copper and working our way to manganese through the 12 coordination structures, including only CCP, HCP, and icosahedral coordinations. Correlating the high melting point of these elements and their compounds with a high valence, let us, in an attitude of willing disregard of prior commitments, associate with each C orbital one electron for bonding purposes. Of the eleven valence electrons of copper, five electrons remain; four of these can be placed in the two local d orbitals, leaving one electron per atom for the S band. If one electron per bidirectional orbital (the half-bond mentioned earlier) gives rise to a filled band, then we see that this naive picture results in a diamagnetic copper having a half-filled S band and good electron mobility. The latter is related to the nondirectional character of the s orbital[3] plus poor interband electron scattering associated with the existence of an energy gap in the C band at the Fermi level. This gap is between a bonding C band and a C band with appreciable antibonding character. Questions concerning the band gap, the high covalency (6 + 1), and the high percentage participation of d character in the C orbitals will be considered after the discussion of the NiAs structure.

TABLE 1. *Idealized distribution of electrons of some metals having HCP and CCP structures*

State	Idealized distribution of electrons			Unpaired electrons		Ref
	C band	S band	L band	Ideal	Obs	
Cu element	6	1	4	0	0	10
Ni element	6	1	3	1	0.55	10
Co element	6	1	2	2	1.60	10
Fe:*						
Element, γ-phase high temp	6	1	1	1	0.57	11
Element precipitated from Cu, pseudo single crystal**	6	1	1	1	0.78	12
Alloy, Fe in Cu	6	1	1	1	1	13
Mn:*						
In element and alloys (icosahedral position in phases)	6	1	0	0	$\simeq 0$	14

*We note that the magnetic behavior of the solute atoms in the dilute alloys of Mn in Cu [12] and Fe in Pd [15] are well known to be of a different type than Fe in Cu [12] and do not fit in this table.

**Neutron diffraction determination.

Applying this naive approach to the series Cu, Ni, Co, Fe, and Mn with these elements in the close packed or icosahedral coordinations leads to fair agreement (table 1) as regards to their observed magnetic properties. Excellent agreement can be obtained for Ni and Co with regard to both the number of conduction electrons in the S band and the magnetic moment by shifting $\simeq$0.4 electrons from the S bands to the local d orbitals (or the Ω_L-type bands). Good agreement is obtained for iron in its CCP forms and for Mn in the icosahedral coordinations in the σ phases. Unfortunately in the σ phases disorder is common among the sites and bond distances are only poorly known so that the effective covalency is uncertain.

The density of states picture is then composed of three bands. A medium broad C band with a capacity of about six electrons. This covalent band is generally filled and responsible for the cohesiveness and high melting point of the element. In the case of an incom-

[3] Due to the non-directionality of the s orbital the S band of a CCP metal is not associated with strongly directional bonds. As indicated in the latter part of the paper the S band is then expected to have a low density of states; accordingly, the associated curvature is small and the mobility high.

plete filling, hole character associated with low mobility is expected for this band. The L band has a high narrow density of states and is responsible for the magnetic character of the metals. Finally we have the broad half-filled (or less) S band associated with high mobility and low cohesiveness. Accordingly, for these structures, we see the splitting of the d orbitals into a broad hybrid band associated with bond formation and a narrow band; the latter fills up as copper is approached.

4. The Laves Phases

In the transition metal Laves phase compounds, AB_2, one finds four orthogonal phase structures corresponding to different bands, two of which are interpenetrating covalent phase structures. The B atom has a slightly distorted icosahedral coordination consisting of six A neighbors and six B neighbors. The bidirectional C orbitals as discussed above will be used for the B atom.

The larger A atom has a coordination of 12 B neighbors in a reduced Friauf configuration (see fig. 4) and four A neighbors tetrahedrally distributed along the threefold axes. (For a more complete discussion of these interesting structures see [8] as well as standard texts.) Whereas the antisymmetric solution (C orbital) was sought to the eqs (13,14,15) which link the hybridization coefficients for the icosahedron, the symmetric alternative is required for the Friauf polyhedron. By rotating a G-type orbital of the form eq (18)

$$G = as + bp_x + id_{z^2} \tag{18}$$

clockwise about the x-axis, solution of eqs (13,14,15) may be obtained as a function of the angle of rotation, α [8]. When $\alpha \cong 18°$ the lobes of the G orbital (fig. 1b) are then well directed to form bonds with B atoms at position 1 and 1′ of figure 4. A 180° rotation of this orbital about the z-axis will permit it to bond atoms at the 2 and 2′ positions while a 120° rotation about the [111] direction will give it good position with respect to the 3 and 3′ atoms.

Accordingly, six orbitals (G_i) can be obtained which are suitable for bond formation with the 12 B atoms of the reduced Friauf polyhedron. An alternate set G_i^d can be obtained by reflecting them through the diagonal mirror plane (S_d) at $x = y$. The sum of the square of the angular parts of these 12 orbitals is seen in figure 5 to reproduce the full symmetry of the site.

Of the nine original atomic orbitals three remain to form the four A—A bonds. These three orbitals, of p and d character only, can be hybridized to give two C-type orbitals whose lobes project through the faces of

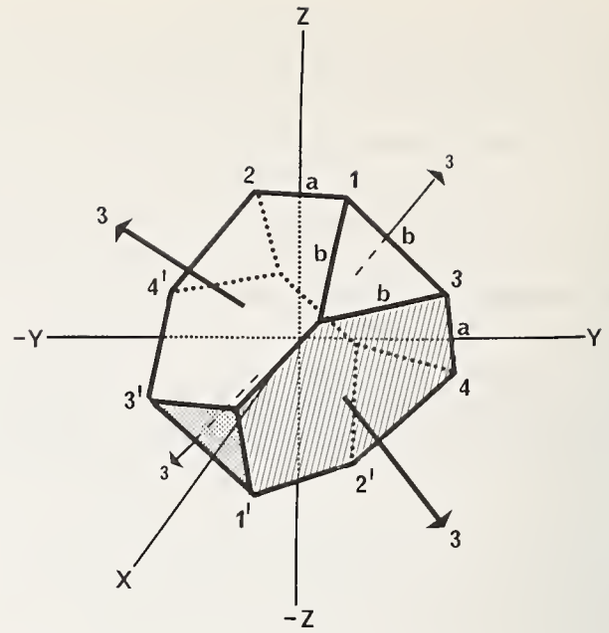

FIGURE 4. *The coordination of the 12* B *atoms about the* A *atom is illustrated for a reduced Friauf polyhedron.*

Four more atoms (A) are coordinated through the centers of the four hexagons. Six G type orbitals are used by the central A atom to bond pairs of B atoms at positions like 1 and 1′.

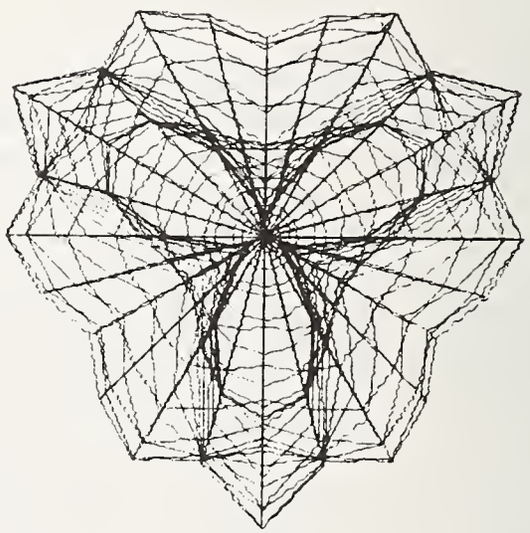

FIGURE 5. *This computer drawing illustrates the symmetry of total bonding for the G-type orbitals of the Friauf polyhedron.*

The viewer is looking down the threefold axis at a hexagonal face.

the hexagons of B atoms toward the four tetrahedrally distributed A atoms. The remaining orbital has no large lobes. It is important to note that three orthogonal orbitals (two C-type and one local) can be formed in three ways; in each case mutual orthogonality exists between them and the G-type orbitals (as well as their mirror images). That these C orbitals can give good bonding is suggested in figure 6. We note that in both figures 5 and 6 the direction of view is down the threefold axis of figure 4 and that the angular projections are exaggerated somewhat to resemble the orbital distortion due to bond formation.

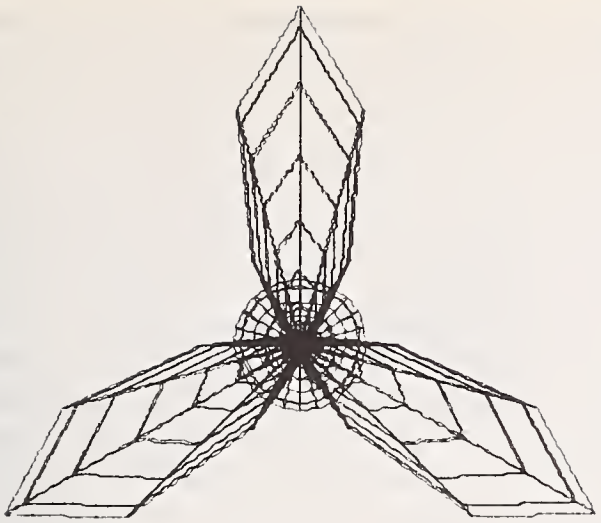

FIGURE 6. *In this figure the tetrahedral bonding of the C-type orbitals is shown.*

These have the same angle α (22.5°) and relative orientation as the G orbitals in figure 5.

A number of transition Laves phase compounds have such short A—A distances that they are considered [16] to be in a state of compression (up to 11%) when compared to the A—B distances (which appear normal). In terms of an average single bond metallic radius these contacts can be so short that the covalency of La in $LaNi_2$ is an impossible sixteen [17] compared to a maximum possible of four (for lanthanum with a formal charge of -1).

A solution to this dilemma may be sought in terms of the above bidirectional orbital discussion. While the G-type orbitals used in the A—B bonds have a normal d character that varies with the angle α from 42% to about 48%, the C-type orbital d character is much higher (about 75%). In terms of Pauling's metallic radii, the effect of increasing the d character of an orbital from 45% to 75% would result in a decrease of 0.32 Å in the single bond radius of a trivalent Pt transition element (as in eq (3)). This dramatic decrease, however, would be partially nullified by an increase of 0.11 Å due to the absence of s character in the C-type orbital. The net change for an A—A bond, 0.44 Å would reduce a ridiculous bond order of 7.2 to reasonable 0.5 or a bond order of 0.5 to one of 0.11. In other words, due to the difference in hybridization of the G- and C-type orbitals, there is a good reason for *not* expecting the hard sphere model or an *average* single bond radius to be applicable for elements with the Friauf coordination. In a later section we note that the correctness of this approach can be tested by Fermiology or density of states studies.

Cycles of the two orthogonal covalent phase structures Ω_{A-B} and Ω_{A-A} are illustrated symbolically in figure 2, top and botton, respectively. These are shown as periodic except for an anti-bond phase relation to the left in figure 2 (bottom). The phase structure Ω_{A-B} corresponds to the important A—B bonds as well as B—B bonds in the ratio suggested in figure 2 (top). Here the G-type orbital is used by the A atom. However, in the A—A bond only C orbitals of the A atom are employed (fig. 2, bottom). The two remaining bands, L and S, are like those in the close packed structures and may be expressed as Slater determinants involving the $d_{x^2-y^2}$ and d_{z^2} orbitals (L band) and the s orbital (S band) of the B atoms *only*. The A atom contributes nothing to the S band because its s orbital is completely used in forming six orthogonal G orbitals. Further, its only "local" orbital a (p-d hybrid) is deeply involved in the "resonating" C orbitals of the A—A bond, and hence is not suitable for unshared electrons.

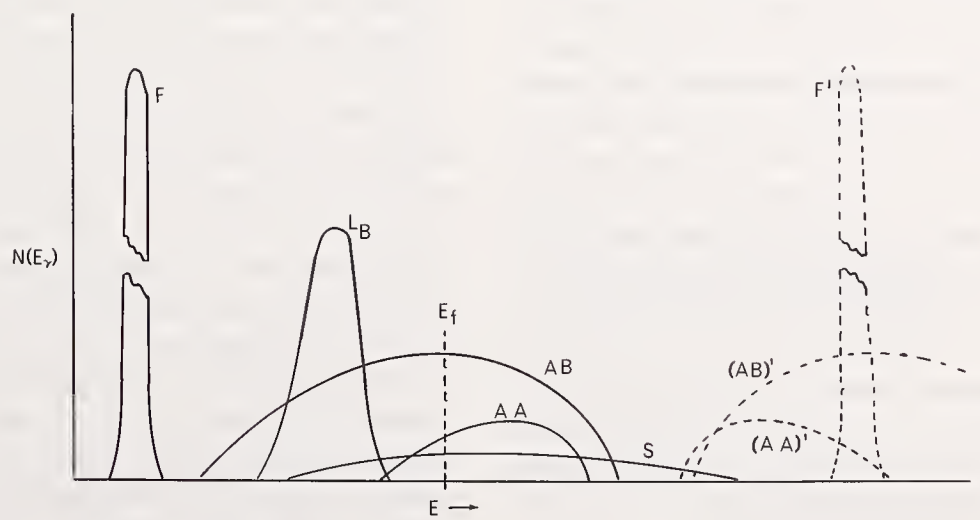

FIGURE 7. *Density of state curves are illustrated for the various bands of a hypothetical cubic rare earth Laves phase,* AB_2.

The solid lines indicate bands at least partly occupied, the unfilled (AB)' and (AA)' bands contain appreciable antibonding character. The separation and location of the filled (F) and unfilled (F') f orbitals of the A atoms are considered to be very sensitive to the number of occupied states. The band volumes per AB_2 are: AB, (AB)' bands—18 states; AA, (AA)' bands—4 states, L(B) band—8 states, L(F + F') band—14 states, S band—8 states.

Applying the above description to the rare earth compounds having the cubic Laves phase we obtain a density of states curve associated with five bands (fig. 7). The first, previously unmentioned, would be a very sharp band associated with the highly localized f electrons of the rare earth A atom. The less sharp L band is associated with the two local d orbitals on the B atom with much the same properties as the same band in the close packed structures. The number of electrons in these orbitals (and hence the magnetic moment) is dependent on the number of its valence electrons minus its covalence, V, and minus the electrons (up to about 1) transferred from it to the hypo-electronic A atoms [1, see p. 431]. Polarization of the A−B bonds towards the more electronegative A atom may be expected to largely neutralize the resultant formal charge. In these compounds an S band is not likely to be of major importance for three reasons: (1) The s character in the A atoms will not contribute since they are totally used ($A^2 = 1/6$) in the formation of the six G-type orbitals. (2) The next nearest neighbors of the B atoms are much more distant than those, say, of the close packed structures and accordingly will not help to stabilize the S band. (3) If electron transfer takes place from the hyper-electronic element (the B atoms), then the likely source will be the B atom s electron (i.e., the S band). Correspondingly the S band should have only a fraction of an electron per B atom and should be associated with a poor mobility (compared to copper) of n type. A calculation of bond orders for the A−B and B−B bonds ($n_{AB} \cong 1/3$) suggests that the A−B band is generally more than half filled (compared to one electron per bidirectional orbital) and so may be considered as p-type conductivity of low mobility.

The fifth band (A−A)—associated with just the A atoms and their tetrahedral C orbitals—is probably unoccupied for the Laves phases of the lightest rare earths but becomes increasingly important as the d character of the A atom increases with atomic number. The high d character of these orbitals is taken to be energetically unfavorable for the lighter elements which presumably use their available d character in the formation of the A−B bonds. The radius contraction for the A−A bond due to the high d character of these C-type orbitals also suggests low bond orders (hence, occupation) for this band (n-type). Finally, we note that these same considerations carry over to the hexagonal Laves phases, with due allowance for unit cell changes.

5. The NiAs Structure

Among the compounds having the NiAs structure one finds semiconducting as well as semi-metallic members. Although this difference is often discussed [18] in terms of the internuclear distance between the Ni-type atoms along the c_0 axis, the use of the BOA method suggests that the c/a ratio for these compounds can have an important effect independent of the internuclear distance. In addition we will note that semiconductivity can be associated with the half-bond (i.e., where $n_{ij} = 0.5$) between the Ni- and As-type atoms.

In the NiAs structure both components have six near neighbors arranged in a trigonal prism (As site) or trigonal antiprism (Ni site) coordination. In addition the metal atom has two metal neighbors in the antiprism directly above and below. Both G- and C-type bidirectional orbitals can be used in a description of bond formation in these coordinations. Using the C orbitals one can obtain three orthogonal orbitals suitable for the formation of six half-bonds in the general twisted trigonal prismatic coordination. The first is obtained by rotating the C orbital about the x axis by an angle γ; the other two by rotating the resultant orbital by angles of 120 and 240 degrees, respectively, about the z axis. Orthogonality relations [5] result in eq (19)

$$3a^2 \sin^2 \gamma = 1 \tag{19}$$

where a^2 is the p character of the orbital. This representation includes the pure p-state octahedral coordination, the 50% p octahedral coordination and trigonal prismatic coordinations at $\gamma = 90°$ and $\gamma = 37°$. About 8% d character is associated with this latter value of γ. For the As-site element in the prismatic position, this orbital with its high p character and low d character is probably suitable. On the basis of symmetry alone it is not possible to select a unique set of bidirectional orbitals which are appropriate for the transition metal in its distorted octahedral site (assuming $c/a \cong 1.63$). As indicated earlier, octahedral symmetry can be achieved by C orbitals of pure p character and 50% p character as well as by G orbitals of sd^2 hybridization. Let us assume for the moment that the latter hybridization is most nearly correct for a particular transition metal. Since this assumption is equivalent to assuming that the p orbitals are too high in energy for consideration we must look to a pure G-type orbital in the z direction to account for bonding between the metal atoms along the c axis. When the c/a ratio is 1.63 then the G_z orbital is pure d_{z^2}, however as the c/a ratio is decreased the orthonormality conditions require that s character is increased in such a way that overlap with the metal atoms along the z axis is increased. In figure 8 we see such an orbital with 25% s character corresponding to $c/a = 1.22$. (The four G orbitals are then also appropriate for

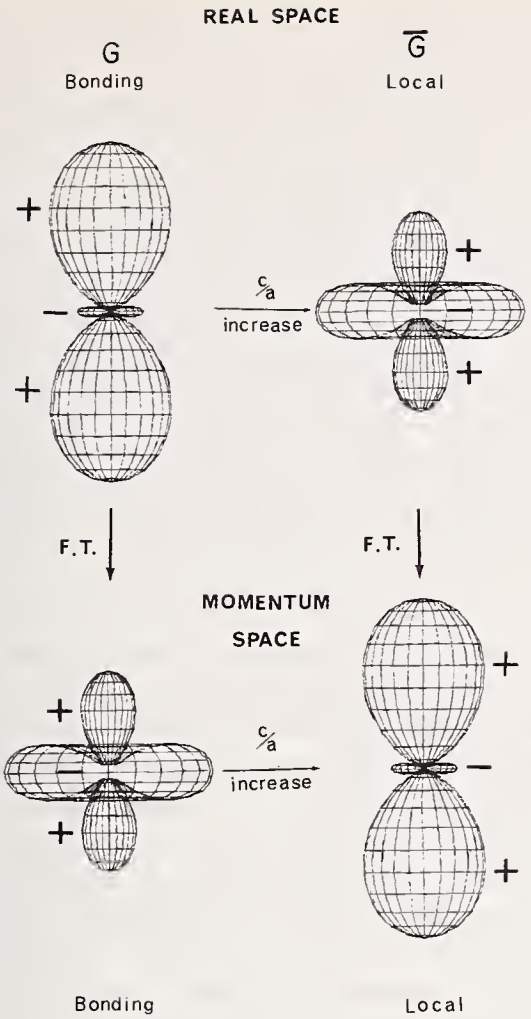

FIGURE 8. *For a hypothetical bonding scheme in the* NiAs *structure the angular parts of the bonding* G_z *orbital are shown for 25 percent* s *character with a* c/a *ratio of 1.22.*

As the *c/a* increases to 1.63 and beyond the *s* character first goes to zero and then is added with a negative sign to give a local $\bar{G}$ orbital of 25 percent *s* character. The effect in momentum *p* space is also illustrated.

bonding in a body centered cubic site with the body diagonal along the *c*-axis). Similarly, as the *c/a* ratio is increased beyond 1.63 an orbital (local) not suitable for bonding develops. Such an orbital is labeled *G* in figure 8 and is appropriate for unshared electrons. It is not surprising then that for prediction of metallic character in NiAs-type compounds, attention must be directed not only to interatomic distances but also to *c/a* ratios, as has been mentioned [18].

For an example relating the half-bond to semiconductivity we will briefly consider CrSe which has the NiAs structure. By transferring one electron from Se to Cr, Se^+ can form six half-bonds and still satisfy the octet rule. The negative chromium ion can use three of its seven electrons in half-bond formation with Se^+ using the octahedral *C*-type orbitals. The remaining four electrons can be localized in hybrid orbitals which consist primarily of d_{xy}-type orbitals plus a localized s-d_{z^2} hybrid. This is in agreement with the use of Pauling's metallic radii which suggests that metal-metal bonding is not appreciable. Accordingly, CrSe is expected to be semiconducting (observed) with a high effective moment (4.9 compared with 4.7μ. obs.). From electronegativity considerations we may expect the half-bonds to be polarized in such a way that the formal charges are essentially neutralized. Under compression in the *c* direction one predicts the appearance of electrical conductivity and a reduction in the effective moment.

For the typical NiAs structure, in the bidirectional orbital approximation, the density of states curve would be a composite of four bands. Of least interest would be a narrow band filled with the two *s* valence electrons of the As-type atom. The second is a filled band corresponding to three electrons per atom per unit cell (or to one electron for each of three bidirectional orbitals per atom). This band is responsible primarily for the cohesive properties of the solid and would correspond to largely *p* but some *d* character of the As-type atom and a poorly definable hybridization for the unspecified metal atom. The third band, an *L* band, is composed of the localized orbitals on the metal atom and in general will be partly unfilled and narrow. The size of this band, as well as its filling, will be dependent on the fourth band which corresponds to the metal-metal bonds along the *c* axis. If the fourth band is of high energy and unfilled the third band (*L*) will contain the $\bar{G}$ localized states of the fourth band. On the other hand, occupation of the fourth band suggests the $\bar{G}$ states are of high energy and unoccupied. Perhaps the more correct approach is to consider that the third band *(L)* contains only three orbitals per metal atom (filled at six electrons per atom) and that the nature of the fourth band changes dramatically from a localized state to a bonding state depending upon a cooperative phenomena governed by the number of electrons involved, the *c/a* ratio and the intermetallic distance. In the bonding state the fourth band is generally unfilled and conducting of *n* type.

6. On Some Significant Differences Between the Chemists' and Physicists' Approach to Solids

The differences in approach between the chemists and the physicists are more than just semantic. One of the most important of these is the restraint shown by the physicist in hybridization of orbitals compared to the apparent wild abandon of the chemists, as exemplified by this article. In band calculations of "hybridization" by physicists the primary energy values

are those of the free atom (used as an approximation) and the primary mechanisms are those from spin-orbit coupling, relativistic effects, and continuity restrictions on the wave function at special points, lines, and surfaces. However for atoms at sites of high symmetry this latter mechanism often gives no hybridization in the chemists' sense. The calculation scheme used is generally a first order independent particle, molecular orbital approach which yields the properties of the electron near the Fermi surface in fair agreement with experiment.

In partial contrast the chemist, in small molecule calculations, employs outer electron orbitals which are "quenched" of angular momentum and which contain scale parameters for total energy minimization. The interaction mechanism is bond formation leading to the best ground state. Although simple MO treatments give good energies for a one electron bond, the addition of a second electron to the same orbital almost totally destroys the formation of the bond, even with shifts in parameter values. This effect is due to failure of the simple MO treatments to properly account for the correlation of the bonding electrons and has been known for more than 35 years, since the work of James and Coolidge [19].

Of critical importance in the thinking of the chemists is the tetravalency and tetrahedral character of carbon in the millions of its organic compounds. Free carbon has a $2s^2 2p^2$ ground state while tetravalent carbon has a $2s2p^3$ valence state. The associated promotion energy as calculated by Slater is 9.05 eV. On the other hand the promotion energy for iron from a free atom state ($3d^6 4s^2$) to a covalency of six ($3d^5 sp^2$) with a hybridization of d^3sp^2 is 4 eV [20].

Accordingly, the chemists' query for the physicist is "If carbon employs an sp^3 valence state with a promotion energy of 9 eV to an appreciable extent in the coumpounds of carbon, one of the best understood elements, is it improper to form hexacovalent iron orbitals using s, p, and d orbitals having a promotion energy of only 4 eV?" One thing is certain: for accurate ground state energies (and hence bond energies) it is extremely important to take proper account of electron correlation and nature's result is still only very poorly approximated, with or without the super-computing systems of IBM and CDC.

In the simple application of BOA to copper, as in table 1, it would appear that the covalency is seven, corresponding to one electron in the S band and six in the C band. The corresponding atomic (bonding) configuration we will denote as sC^6. This valence is even higher than that used by Pauling (5.56) in his metallic radii table [1, p. 403] and differs considerably from that suggested by Brewer (2 to 3) on the basis of bond energies [21]. If the requirement that all near neighbors are simultaneously bonded is adhered to, then one must suggest that the C orbitals are not very good for simultaneously forming twelve half-bonds in copper due to the small radial extent of the d_{xy}-type orbitals. The correct explanation is probably that the configuration d^4sC^6 is as wrong as $d^{10}s$ and that phase structures involving symmetric combinations of d^8sC^2 and d^6sC^4 should be included as main contributing terms in the wave functions. However, if the argument (BOA) must be modified for copper, the bidirectional orbital approximation would appear to be a reasonable starting point for the other transition elements of Groups IIIb to VIII.

An oversimplified treatment of binding might lead one to expect spherical electron distributions for both carbon with its sp^3 hybridization and for the copper d shell with the full occupancy of its d orbitals by shared and unshared electron pairs. However, the sphericity required by Unsold's theory for atomic carbon with sp^3 hybridization is destroyed in the tetravalent bonding state because some of the electron density shifts into the bonding regions between atoms. If d character is employed in bond formation in copper, as in the C band of the BOA picture, then some d_{xy}, d_{xz}, and d_{yz} character is involved in the unoccupied antibonding orbitals of the C band. This then will also disturb the sphericity of the 10 d orbitals since the $d_{x^2-y^2}$ and d_{z^2} orbitals are occupied by unshared electron pairs.

Now we would like to adduce a few arguments supporting the assumption that one may associate a filled band with the concentration of one electron per bidirectional orbital (half-bond). In MO theory, the band associated with a chain of linear atoms has its greatest density of states at an electron concentration of one electron per orbital. However, in the BOA approach one generally is concerned with the interaction of chains (cycles) which involve two or three dimensional arrays of atoms. Accordingly, while a single partial phase structure $\Omega_{\gamma,i}$ associated with a band γ may not have a density of states depression at one electron per bidirectional orbital, it is anticipated that the interaction of different partial phase structures of the same band will give such a depression. This is because cycles from different phase structures are not orthogonal. If this is correct then, when the metal-metal bond in an NiAs compound can be ascribed to a single phase structure with one infinite cycle of G orbitals (as in the above example), one would not expect a band depression at one electron per orbital.

Considerable precedence in chemistry exists for associating special stability with one electron per orbital. Depending on the number of neighbors this electron concentration can lead to fractional bond orders. Pauling has called attention to this [1, p. 420] and, using his metallic radii, has noted the abundance of such cases among transition metal compounds while Rundle [22] has emphasized the importance of half-bonds. We would like to point out here, that since Pauling used the elemental bond distances as reference points, a "proof" that the number of covalent electrons used by copper is 5.56 by means of his metallic radii would be highly circular. Nevertheless, his formulae, such as eq (3), are firmly related to bond distances and covalencies about which no controversy exists. Accordingly his observations of fractional bond orders merit more than just passing attention.

In organic chemistry, the aromatic compounds play a special role because of their unusual stability. These are planar compounds consisting of fused benzene-like rings (hexagonal) to give what looks like sections of hexagonal bathroom tile. The p_z carbon orbitals are perpendicular to the plane containing the σ-bond structure and are occupied by one electron each. In valence bond theory the special stability of these compounds is attributed to the resonance (interaction) of the two Kekule structures (phase structures). These compounds form a continuous series starting with benzene having one ring and six p_z electrons through a long sequence of compounds involving many rings (e.g., 8 rings and 30 electrons) to a graphite sheet. In graphite we will see later that the bond order associated with the p_z electron is 1/3 and that the related band is described as filled with a zero band gap [23, 24]. Currently this represents the strongest argument that semiconductivity can be related to the half-bond ($n_{ij} = 1/2$). However in practice, semiconductivity can be readily predicted, as in the $C_2S_3 - C_3S_4$ series and FeS_2, etc. [5,7], by associating a band gap with the half-bond.

In returning to the primary difference between the chemists' and physicists' approach to transition metal compounds, i.e., the amount of d character involvement in bonding electrons, we will recall the suggestion that this may critically depend on the correctness with which electron correlation is handled. However, even within the band scheme a partial resolution of the difference in d character use may be sought by the use of scale factors in the radial part of the wave function. It would be of particular interest to associate a different scale factor with different symmetry related d orbitals, for example, one scale factor for the d_{xy} type orbitals in CCP copper and another scale factor for the $d_{x^2-y^2}$ and d_{z^2} orbitals. In such a case the scale factors are parameters which could be adjusted for energy minimization for each value of k. If the execution of this suggestion is exceedingly difficult (as the author is aware) the task posed below for the solid state chemist is no less possible.

Two methods of treating the correlation of bonding electrons are currently being tested on small molecules. The first of these, the alternate molecular orbital (AMO) approach, is being actively pursued by Pauncz [25] and involves the alternation of electrons of different spin on a linear chain or ring of orbitals. Energy is minimized as a function of the λ_i, which are related to the relative separations or phases between electrons of different spin. The second method is primarily due to Linnett [26, 27] and is termed the nonpaired spatial orbital (N.P.S.O.) treatment. For a cycle of four orbitals, C_1, C_2, C_3, and C_4 as in figure 3, new orbitals would be formed as below:

$$C_1 + KC_2,\ C_2 + KC_3,\ C_3 + KC_4,\ C_4 + KC_1$$

Symmetry must be restored to the wave function in both cases and in the N.P.S.O. method would involve inclusion of orbitals of the form $KC_1 + C_2$, etc. By employing either the AMO or the N.P.S.O. method in conjunction with bidirectional orbitals one has an approach which contains relatively few adjustable parameters with the inclusion of electron correlation. By varying these parameters (plus scale factors) as a function of k space it may be possible to achieve a partial resolution of the differences relating to d hybridization.

7. The Chemical Bond in Momentum Space

In this section we would like to consider three effects in momentum p space. The first is the effect of formation of the simple chemical bond, as between 1s electrons in molecular hydrogen. The second to be considered is the effect of bond hybridization. In the case of strong bond formation these two effects reinforce one another although they appear to be largely independent. Finally, we note that the effects of different bonds are essentially additive in momentum p space in terms of probability density just as they are in real space.

Although Podolsky and Pauling [28] had obtained the hydrogenic momentum distribution functions in 1929 and Hicks [29] had considered the effect of the momentum distribution of molecular hydrogen on Compton scattering, it remained for Coulson in 1940 to initiate a series of papers [30-34] specifically considering the effect of chemical bond formation in p space. His results for the homopolar and heteropolar bond

were essentially the same whether he used the molecular orbital (one electron) or valence bond method (two electrons). Coulson showed that contours of constant momentum density were very appreciably extended in the directions perpendicular to the internuclear axis of the bonding atoms. For the one electron momentum function he obtained eq (20)

$$X(p)X^*(p) = \frac{1 \pm \cos p \cdot (r_a - r_b)}{1 \pm S_{ab}} A(p)A^*(p) \qquad (20)$$

where r and p are vector coordinates in real and momentum space, respectively, r_a-r_b is the internuclear distance vector, and $A(p)$ is the Fourier transform of the atomic orbital $\Psi_a(r)$ on atom a. In the bonding case (+ signs) with $\Psi_a(r)$ (and $A_a(p)$) spherically symmetric we see that the momentum distribution function is a maximum when the vector momentum p is perpendicular to the internuclear direction (r_a-r_b). In the case of the antibonding state (− signs, eq (20)) for molecular hydrogen the signs of the 1s orbitals are different on atom a and atom b; this gives a nodal plane between the two atoms and corresponds to the exclusion of considerable electron density from the volume between the atoms. This phase reversal between atoms a and b now results in a maximum density when p is parallel to the internuclear axis. The situation is the same for the two electron bond.

The hybridization effect is readily seen from the hydrogenic wave functions in momentum p space obtained by Pauling and Podolsky [28]. In the traditional valence bond method, we noted earlier that in the process of maximization of overlap, primary attention was paid to the angular parts of the orbitals. In following the same procedure we recall [28] that the Fourier transform of an atomic orbital Ψ_{nlm} has the same angular functions in terms of spherical coordinates in momentum p space[4] as Ψ_{nlm} has in real space, except for $a(-i)^l$ factor.

The angular part of a hybrid orbital, $\Psi_{ang.}$, based on atom a, can be maximized in the direction of atom b by varying the coefficients C_i in the following equation (assuming normalization).

$$\Psi_{\text{ang.}} = C_s s + C_p p + C_d d$$

The corresponding momentum hybrid is given below.

$$X_{\text{ang.}} = C_s \tilde{s} - iC_p \cdot \tilde{p} - C_d \cdot \tilde{d}$$

Here s, p, and d refer to the angular parts of the orbitals in real space and $\tilde{s}$, $\tilde{p}$, and $\tilde{d}$ refer to the angular parts in momentum space. The results are most graphic for a bonding G-type orbital. If s character is added to a d_{z^2} orbital to obtain extension in real space along the + and − z axes (fig. 8, left) then the effect in momentum space is a contraction along the + and − p_z axes and extension in the $p_x p_y$ plane. The effect on a localized $\bar{G}$-type orbital is just the opposite (fig. 8, right). For bonding electrons and orbitals the effect of hybridization is clearly in addition to the effect of bond formation as between 1s orbitals in H_2.

If the eigenfunction, Ψ, for an n electron problem is expressed as a Slater determinant of ϕ_i, where ϕ_i represent the orthogonal one electron solutions, then the one electron density function, $\rho(r)$, is obtained by integrating $\Psi\Psi^*$ over $n-1$ electron configuration space.

$$\rho(r) = \sum_{i=1}^{n} \phi_i(r)\phi_i^*(r) \qquad (21)$$

We see that the result is simply the sum of the electron density probability functions of the individual occupied states ϕ_i. Since the corresponding expression for Ψ in momentum space is also a Slater determinant, we see that the total bonding electron density in momentum p space is simply the sum of the individual bonding covalent electron momentum densities.

8. That the Fermi Surface Mimics the Momentum Distribution Function of the Bonding Electrons

In this section we intend to show by a simple and heuristic argument that the Fermi surface in a sense copies the momentum distribution function associated with the outer electrons. Although the above title emphasizes the bonding electrons, there is no reason to exclude localized electrons if these energies are near the Fermi surface. While the subsequent discussions and applications will assume the Fermi surface to be in the unreduced form this will cause no distress to those familiar with such reductions to a single Brillouin zone. Finally no special attention is paid to energy gaps at Brillouin zone faces at such gaps are more closely related to crystal symmetry elements than to the effects of bond formation.

The argument to be given below involves the application of the Virial theorem which states that the average kinetic energy $\bar{T}$ is related to the average potential energy, $\bar{V}$, of a stationary state according to eq (22),

$$\bar{T} = \frac{s}{2}\bar{V} \qquad (22)$$

[4] Accordingly, for a p_z electron we see that it is extended in the same direction (z axis) in both real and momentum space, in apparent violation of the naive application of the Heisenberg uncertainty principle.

where the potential V is a homogeneous function of degree s of the coordinates.

Neglecting magnetic forces, the potential V for an electron is just the sum of all the coulombic potentials due to the nuclei and the other electrons; accordingly $s = -1$ and $\bar{V} = -2\bar{T}$. Inserting this relation into eq (23) for the average particle energy $\bar{E}$, we obtain $\bar{E} = -\bar{T}$.

$$\bar{E} = \bar{T} + \bar{V} = -\bar{T} \tag{23}$$

The derivation of the Virial theorm may be found in most standard quantum mechanics texts; its derivation as indicated above is due to a method of Foch and is given with applications to small molecules by Kauzmann [19]. The validity of eq (23), relating the average energy of a particle to the negative of its kinetic energy, will be illustrated for the hydrogenic atom. From the corresponding momentum eigenfunctions Podolsky and Pauling obtained eq (24)

$$\overline{p_n^2} = p_n^2 = \left(\frac{2\pi m e^2 z}{nh}\right)^2 \tag{24}$$

for the average momentum squared of an electron of mass m having a principle quantum number n. Inserting this in eq (23) we obtain

$$\bar{E} = -\bar{T} = \frac{-p_n^2}{2m} = \frac{-2\pi^2 z^2 e^4 m}{n^2 h^2} \tag{25}$$

which, of course, is the familiar atomic formula. Here the lowest, most stable energy state is associated with the highest average momentum squared, a typical molecular result.

For the free electron-like model, where the electron momentum is identified with the **k**-vector the Virial theorem as in eq (22) must be modified to include constant volume effects (i.e., the Virial associated with restraint of atomic nuclei); the net result for the energy $E_{k\gamma}$ of the γ band may be written as in eq (26).

$$E_{k\gamma} = \frac{\bar{p}^2}{2m} - E_{0\gamma} = \frac{k^2}{2m} - E_{0\gamma} \tag{26}$$

Here we see that the sign associated with the momentum term is just reversed.

The above considerations are now extended to the more general independent particle band picture. To satisfy the Bloch conditions we write eq (27) for the γ band

$$\psi_{k\gamma}(r) = e^{ik\cdot r} u_{k\gamma}(r) \tag{27}$$

where $u_{k\gamma}(r)$ is that real coordinate part of the eigenfunction which has a periodicity identical to that of the lattice. If $U_{k\gamma}(p)$ is the Fourier transform of the $u_{k\gamma}$ for a *single cell*[5] in real space then the momentum eigenfunction $X_{k\gamma}(p)$ corresponding to $\Psi_{k\gamma}(r)$ is simply eq (28).

$$X_{k\gamma}(p) = U_{k\gamma}(p - k) \tag{28}$$

The average value of momentum squared of the electron associated with the crystal momentum k of the γ band is

$$\overline{p_{el}^2} = \int U_{k\gamma}(p-k)\, p \cdot p U_{k\gamma}^*(p-k)\, d\tau_p \tag{29}$$

Substituting ω for $p - k$ we obtain

$$\begin{aligned}\overline{p_{el}^2} &= \int U_{k\gamma}(\omega)\,(k+\omega)\cdot(k+\omega) U_{k\gamma}^*(\omega)\, d\omega \\ &= k^2 + 2k\cdot\bar{\omega}_{k\gamma} + \overline{\omega_{k\gamma}^2}\end{aligned} \tag{30}$$

where we identify $\overline{\omega_{k\gamma}^2}$ as the average squared-momentum of the electron (k, γ) in a single unit cell. Thus $\overline{\omega_{k\gamma}^2}$ has a "molecular" character. Similarly $\bar{\omega}_{k\gamma}$ is identified with the single cell average momentum corresponding to $u_{k\gamma}(r)$, which for $k = 0$ and for a centrosymmetric cell, must be zero but may be expected to be non-zero otherwise. We now assert that the energy $E_{k\gamma}$ increases for k and decreases with $\overline{\omega_{k\gamma}^2}$ according to eq (31) below, essentially as suggested by a combination of eqs (25) and (26) above.

$$E_{k\gamma} = \frac{k^2}{2m} - \frac{\overline{\omega_{k\gamma}^2}}{2m} - V_{k\gamma} + \text{neglected terms} + \text{constant} \tag{31}$$

The potential energy term, $V_{k\gamma}$, is given by eq (32),

$$V_{k\gamma} = \sum_m^N \int u_{k\gamma} u_{k\gamma}^* Z_m \left[\frac{1}{r_{km}} + \frac{x_k}{r_{km}^2}\right] d\tau \tag{32}$$

where x_k is the coordinate of the k electron separated from N nuclei of charge Z_m by the distance r_{km}. For a centrosymmetric structure both $\overline{\omega_{k\gamma}^2}$ and $V_{k\gamma}$ are positive and change in a parallel fashion. Accordingly, only the variation of $E_{k\gamma}$ with $\overline{\omega_{k\gamma}^2}$ is considered. Further, since the derivation of eqs (31) and (32) are indicated in appendix A, here we add only that m is the real mass of the electron and that the neglected terms of possible interest involve derivatives of $\bar{\omega}_{k\gamma}$ and $\overline{\omega_{k\gamma}^2}$ with respect to the lattice parameters.

The shape of Fermi surface is contained in eq (31). For the γ band it is clear that for constant energy (i.e.,

[5] A single cell is used to achieve analogy of ω with p of the atomic or molecular case. $X(p)$ is usually expressed as the Fourier series having coefficients $U_{k\gamma}$ sampled at reciprocal lattice points.

$E_{k\gamma}=E_{k'\gamma}$), the absolute value of k will be greater than k' when

$$\overline{\omega^2_{k\gamma}} > \overline{\omega^2_{k'\gamma}}.$$

Accordingly, a Fermi surface for the γ band closely follows the variations in $\overline{\omega^2_{k\gamma}}$. Prior to discussing the expected variations of $\overline{\omega^2_{k\gamma}}$ for the bonding electrons we will first consider the cases for deep core electrons and highly excited states.

For K-shell electrons of a heavy metal we would expect that the depth of the γ band below the energy zero is determined essentially by eq (33), that is, eq (25) with the sum taken over equivalent atoms in the unit cell and with n referencing the principle quantum number. We may expect that

$$\overline{\omega^2_{\vec{0}\gamma}} = \sum \overline{p^2_{\vec{n}}} = \sum p^2_{\vec{n}} \cong \overline{\omega^2_{k\gamma}} \tag{33}$$

$\overline{\omega^2_{k\gamma}}$ is practically independent of k even though $p^2_{\vec{n}}$ is very large. In the highly excited electron case $\overline{\omega^2_{k\gamma}}$ should be quite small, with variations of $\overline{\omega^2_{k\gamma}}$ with k even smaller. Accordingly, in both of these cases the simpler band arguments should apply; for example, the free electron approximation for the excited electron should be reasonably correct.

Expectations of the variations of $\overline{\omega^2_{k\gamma}}$ for bonding electrons are most simply argued from a highly anisotropic example. Consider the case of a crystal composed of linear chains of atoms bonded along the [001] direction with distances between chains corresponding to van der Waals' contacts. In terms of bidirectional orbitals $\overline{\omega^2_{k\gamma}}$ would correspond to the "phase structure" of a single cell in which all the phases match so that overlap of the orbitals on adjacent atoms in the chain is high (e.g., see fig. 2, top). Now as k increases in the [001] direction, the value of $\overline{\omega^2_{k\gamma}}$ is expected to decrease corresponding to the increasing frequency of antibonding contributions (i.e., nodal planes between atoms as in fig. 2, bottom). However, as k increases in the $[k_x\ k_y\ 0]$ direction the value of $\overline{\omega^2_{k\gamma}}$ should be much less dependent on k because antibonding phase relations between non-bonded adjacent chains are of negligible importance. The result for a surface of constant E_γ is that the surface extends further from the origin in the plane perpendicular to the bond direction than along the bond direction, i.e., [001]. This, however, is similar to the shape of the momentum distribution, $X(p)\ X^*(p)$, for the bond formation in the [001] direction and supports the suggestion that the Fermi surface mimics the momentum distribution function for the bonding electrons. The generalization to include several bands of comparable energy is obvious.

It remains to point out that as more and more electrons are added to the system there is a reversal in the trend in variations of $\overline{\omega^2_{k\gamma}}$ with direction such that the Fermi surface becomes less spherically distorted. For example, as more electrons go into antibonding orbitals, $\overline{\omega^2_{k\gamma}}$ in the [001] direction can sustain only small variations (further decreases) because it already is small. However, in the $[k_x\ k_y\ 0]$ directions much larger variations will occur; with the result that the Fermi surface in the [001] direction will "catch up" with the Fermi surface in the $k_x\ k_y$ plane as more electrons occupy the antibonding, higher energy, levels.

In the next section a simple physical model will be described that is useful for estimating the distortion of the Fermi surface from a knowledge of the structure in real space. After a few examples the approach is generalized for a discussion of density of states functions.

9. Application with Examples

By extending the above considerations to all the bands of similar energies it is possible to make qualitative estimates of the unreduced shapes of the Fermi surface, or other surfaces of constant energy, from a simple knowledge of the structure in real space. In making the application the primary considerations are (1) number of bonds in a given direction; (2) their bond orders, n_{ij}, and (3) the hybridizations of bonds, if known. The latter point is relevant in that the presence of nodal planes in $X(p)$ can give reduced sensitivity of $\overline{\omega^2_{k\gamma}}$ with k in those planes and a similar effect on the Fermi surface of the γ band.

A simple and qualitative method of estimating the distortion of the Fermi surface from sphericity is to mark (e.g., with narrow tape) those great circles of a sphere[6] which are perpendicular to the bond directions. The effectiveness of a given circle in distorting the Fermi surface radially outward is taken to be proportional to the sum of the bond orders, n_{ij}, of those bonds perpendicular to the given circle. The directions of maximum distortion are taken to be at the intersections of the great circles, weighted by the number of circles involved and their associated bond orders. Of course the volume enclosed by the distorted surface must remain a constant.

As the first example we will consider the BOA picture of Cu in the CCP structure. Using C-type orbitals one obtains good Cu—Cu bonds in the ⟨110⟩

[6] True to his profession the author recommends a round bottom distillation flask as a transparent sphere.

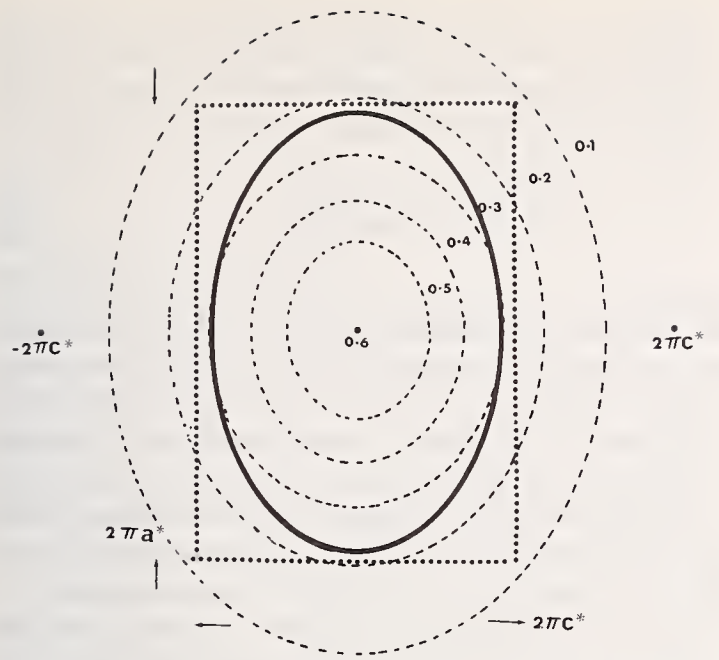

FIGURE 9. *The solid line gives the hypothetical elipsoidal Fermi surface of a tetragonal crystal of* H_2^+ *ions with unit cell edges of* $a_0=2.4$, $c_0=3.46$A.

The dashed contour lines are for constant momentum density and were calculated by Coulson [30] for the H_2^+ ion. The dotted rectangle represents the boundaries of the first Brillouin zone.

directions. The above rule of thumb gives rise to the intersections of three circles in the ⟨111⟩ directions (toward the L point) and intersections of two circles in the ⟨100⟩ directions (toward the X point). However, the effect of the latter two circles should be less than 2/3 the former due to the presence of nodal planes (containing the [100] direction) in the C-type orbitals associated with those circles. The result is in good agreement with the current picture of copper [35] in which the Fermi surface is strongly attracted to the large hexagonal Brillouin zone faces and less strongly attracted the smaller square faces.

By way of contrast we have shown in figure 9 that the hypothetical oblate spheroidal Fermi surface for an imaginary crystal of H_2^+ ions mimics the contours of constant momentum and appears primarily attracted to the smaller [100] zone face. The molecules are assumed to be packed with their bond directions parallel to the c axis with a van der Waals' separation of 2.4 Å between nuclei of different molecules.

For the alkali metals with the BCC structure it is doubtful that bonding effects would be the major cause of distortions in the Fermi surface since the bond order is no larger than 1/8. However, with the VB and VIB groups of the periodic table, distortions of Fermi surface can be estimated even though a unique bonding picture cannot be given at this time. For these transition elements (e.g., V, Cr) the most important bonds (8 nearest neighbors in the ⟨111⟩ directions) probably have a bond order of about 0.5. Using the above method one finds that the corresponding circles cross at the twelve ⟨110⟩ directions. This distortion is in agreement with the opinion that the Fermi surface is attracted to the centers of the rhombic faces of the BCC Brillouin zone. However, the effect of bond formation of an atom with its six next-nearest neighbors is to distort the Fermi surface toward the furthest point, H, from the center of the zone, that is, in the ⟨100⟩ directions. In going from V to Cr this distortion should show a slight increase as the additional electron is expected to participate most strongly in the next nearest neighbor bonding. To suggest this in another way, assume the bond order of the bond with the nearest neighbors remains constant at ≈0.5. Using Pauling's metallic single bond radius R_1, the nearest neighbor distance, d, is then

$$d=\frac{\sqrt{3}}{2}a_0=2R_1+0.18 \tag{34}$$

where a_0 is the cubic cell edge. However, a_0 is also the next neighbor distance so that eq (35) holds.

$$a_0-2R_1=-0.60\log n \tag{35}$$

where n is the corresponding bond order. Eliminating $2R_1$ from the equations we obtain

$$a_0\left(1-\frac{\sqrt{3}}{2}\right)+0.18=-0.60\log n \tag{36}$$

eq (36) which suggests that the observed decrease in lattice parameters with atomic number leads to an increase in the bonding order of the next-nearest neighbors and a corresponding greater distortion (small) in the ⟨100⟩ directions.

An extreme example among the non-cubic structures is to be found in graphite. In this hexagonal layer structure all the strong bonds are within the layers in the ⟨10$\bar{1}$0⟩ directions, whereas bonding between layers is very weak, i.e., van der Waals' contacts. The bond order between carbons is 1 1/3 corresponding to whole σ bonds (sp^2) and 1/3 of a π bond (using p_z orbitals). All of these bonds correspond to an unusually strong distortion of the Fermi surface in the [0001] direction. This distortion is shown very clearly in the surfaces of constant energy calculated by Wallace [23]. In the unfilled zone (corresponding to the π electrons) beyond the filled σ-electron zone, the above model suggests that the Fermi surface should be distorted in the ⟨11$\bar{2}l$⟩ directions where l is not necessarily integer.

417-156 O - 71 - 27

In the NiAs structures the onset of electrical conduction due to bond formation along the c axis should be accompanied (using the BOA picture, fig. 8) by the outward movement of the Fermi surface in the basal plane to give the greatest projection of the Fermi surface in the $\langle 21\bar{3}0\rangle$ directions. Appreciably weaker distortions occur in the $\langle 21\bar{3}l\rangle$ and $\langle 11\bar{2}l'\rangle$ directions where l and l' are non-integers dependent on the c_0/a_0 ratio.

In some of the cubic Laves phases we indicated earlier that simple bond distance considerations suggested that the A—A distances corresponded to an unusual state of compression and a large bond order ($n_{A-A} > 1$). However, the BOA picture suggested that the C-type orbitals had an unusually large d character. This would make the effective single bond radius, R_1(Å—A), so small that the A atoms were practically non-bonded. The decision between these choices could be made on the basis of Fermiological studies principally involving the projection of the Fermi surface in the $\langle 110\rangle$ directions. The simple model relating bond formation to Fermi surface projection is employed.

The B atoms form interconnected linear arrays of bonds in the $\langle 110\rangle$ directions among themselves. As in the simpler CCP transition metals this should give a pronounced projection of the Fermi surface in the $\langle 111\rangle$ directions. The A—B bonds, however, are in the $\langle 113\rangle$ directions and are not expected to result in pronounced distortions due to the diffusion of the intersections of their great circles.

The A—A bonds are in the $\langle 111\rangle$ directions and would contribute to a projection in the $\langle 110\rangle$ directions, where weak projections exist due to the intersection of a B—B circle with two A—B circles. A study of the extent of the $\langle 110\rangle$ projections as a function of the "compression" of the A—A bond for different compounds would make a valuable contribution to the chemical understanding of these compounds.

10. Density of States, General Remarks

The preceding discussion concerning the Fermi surface is, of course, generally applicable to any surface of constant energy in k space. On this basis a few concluding remarks can be made relating the density of states function, $N(E_\gamma)$, to the few chemical concepts of which use has been made in this article. If $|\delta E_\gamma/\delta k_n|$ is the length of the normal derivative of the constant energy surface, S, for a single band then the related density of states may be calculated from eq (37)

$$N(E_\gamma) = (\mathrm{Vol}/8\pi^3) \int\int |\delta E/\delta k_n|^{-1} dS \qquad (37)$$

where Vol is the volume of the crystal [36]. The manner in which the length $|\delta E_\gamma/\delta k_n|$ varies may be estimated from eq (38), which is for a spherical surface in polar coordinates, where m^* is an effective mass.

$$\frac{\delta E_\gamma}{\delta k_n} = \frac{k}{m} - \frac{1}{2m}\frac{\delta_{\omega\gamma}\overline{2}_k}{\delta k_n} = \frac{k}{m^*} \qquad (38)$$

The density of states is essentially then the integral of the surface area weighted by m^*/k. Therefore it is apparent that the distortion of the surface $S(E_\gamma)$ from sphericity gives rise to a high density of states, $N(E_\gamma)$. Furthermore the bottom of the band, $E_{0\gamma}$, is largely determined by $\overline{\omega_{0\gamma}^2}$ according to eq (31). In the examples using the BOA treatment, we also saw that particular sets of chemical bonds could be associated with a particular band (or set of symmetry related bands).

The use of chemical concepts would then suggest that for a high total density of states $N(E)$, with a constant number of bands, one should have chemical bonds of high bond order, n_{ij}, (or strength) with relatively few important bond directions. It appears reasonable that the relative positions of peaks in the density of states might be correlated with bonding and hybridization through the use of the different $\overline{\omega_{0\gamma}^2}$. For example, in the isostructural metal acetylides CaC_2, SrC_2, BaC_2, LaC_2, etc. a strong peak may be related to the carbon triple bond in $(C \equiv C)^{-2}$ radical, while the bottom (and the shape) of the partly filled conduction band may vary in a predictable manner with the metal atom. By way of contrast one would expect a comparatively flat band, neglecting local states, for a material with numerous weak bonds in a great variety of directions. Such a compound which was crystalline but whose unit cell contents had an amorphous-like structure (but repeated periodically) could be expected to have a spherical Fermi surface, not because the free electron approximation was realistic but because

$$\sum_\gamma \overline{\omega_{k\gamma}^2}$$

was not a strong function of the spherical coordinate angles ϕ_k, θ_k in k space.

11. Summary

By way of conclusion it will be useful to both summarize the current results and to attempt to forecast the benefits of further interaction between chemical concepts and those of solid state physics. For the application of the chemical approach an accurate structure determination is the essential input. If a reasonable bonding description for the compound can be devised then we have seen that in a variety of transition metal compounds the number, character, and relative filling

of bands can be readily estimated. Further, the distortion of Fermi surface from sphericity can be qualitatively estimated. Such information is of obvious importance in guiding the experimentalist studying the extended zone Fermi surface topology of a new structure. On the other hand we have pointed out, that in the Laves phases the aid of the physicist would be useful in refining the chemical concepts.

The value of the chemical approach may also be felt in the area of compounds of large unit cell size. For example, the cubic Laves phase of 24 atoms per unit cell is probably near the limit which can be accurately treated in band calculations with the larger computers. However, reasonably accurate structure determinations involving several hundreds of atoms are now possible. If the coordinations of the elements in such structures permit unique bonding descriptions then it may be feasible using BOA, coupled with group theory and standard k-space arguments, to develop useful band models for comparison with experimental density of states data. As an example, it may be possible to treat some of the metallurgically important sigma- and chi-phases of the iron transition metals. Band calculations are not feasible for such materials, nor are they likely to be in the near future.

The application of valence bond theory with the bidirectional orbital approximation to the Group IV and III-IV type compounds is less certain because cycles in the BOA sense lose some definition so that the distinction between "good" or "bad" (poor overlap) phase structures diminishes. The net result is a severe orthogonality problem which is likely to be a major obstacle in the treatment of related amorphous materials. It is interesting to note, however, that for such elements bidirectional orbitals of the G- and C-type can be employed to give tetrahedral coordination (see fig. 6).

Concerning the relationship between the Fermi surface and momentum distribution function it is also desirable not to paint too cheering a picture. The above interpretation of $\overline{\omega^2_{k\gamma}}$ and its variation with k is barely in its infancy and requires considerable refinement before it can be applied with confidence. For example, the simple model given in this article using the sphere and marking tape to indicate distortions of the Fermi surface suggests that the Fermi surface of two compounds would be identical if only the unit cell sizes were the same and if the same number of bonds ($\times n_{ij}$) were in the same directions. Since such limited information is insufficient to define a unique structure it is unlikely that the Fermi surface is as unique as the simple model suggests.

Nevertheless, it would appear that the use of these chemical concepts, as well as others, should play an increasingly important role in providing information to experimentalists and theorists, not only about the density of states, but about the Fermi surface topology and the spectral density as well.

12. Acknowledgments

The author wishes to indicate his appreciation of the continuing interest shown by Dr. L. H. Bennett of NBS in the chemical approach to solid phenomena and to thank Dr. J. Feldman of NRL for pointing out that the constant volume effect must be included in the application of the virial theorem. Thanks are due also to Mr. W. C. Sadler and Miss M. O'Hara both of NRL for technical assistance. Finally, it is with abiding pleasure that the author acknowledges innumerable discussions of the relations between chemical bond and the Fermi surface with Dr. G. C. Carter of NBS.

Appendix A

The intent of appendix A is to show the correctness of eq (31), that is, that the energy $E_{k\gamma}$ of the k state in the γ band can be expressed as below,

$$E_{k\gamma}=\frac{k^2}{2m}-\frac{\overline{\omega^2_{k\gamma}}}{2m}-V_{k\gamma}+\text{neglected terms} \qquad (31)$$

where m is the electron mass, $V_{k\gamma}$ is a potential term, and $\overline{\omega^2_{k\gamma}}$ is defined by eq (30). While use will be made of eq (1A), the generalized Hellmann-Feynman Theorem [37], the kinetic energy terms for the electrons of the γ band will be brought outside the integral

$$\frac{\partial E}{\partial \lambda}=\frac{\overline{\partial H}}{\partial \lambda}=\int \psi^* \frac{\partial H}{\partial \lambda}\psi d\tau \qquad (1A)$$

by use of eq (30)

$$\overline{p^2_{k\gamma}}=k^2+2k\cdot\overline{\omega_{k\gamma}}+\overline{\omega^2_{k\gamma}} \qquad (30)$$

In eq (1A) we note that H is an explicit function of the variable λ, which in our case will prove to be the unit cell edges.

The Hamiltonian H is taken as a sum of the Hamiltonians for the electrons in the γ band, H_γ, plus the interband electronic and internuclear repulsive potentials, $V_{\gamma\gamma'}$ and V_R, respectively.

$$H=H_\gamma+V_{\gamma\gamma'}+V_R \qquad (2A)$$

$$H=H_\gamma+\sum_k\sum_{k'}\frac{1}{r_{kk'}}+\sum_1^N\sum_{m>1}^N\frac{z_l\cdot z_m}{R_{lm}} \qquad (3A)$$

In eq (3A) only the filled k states are included; here $r_{kk'}$ represents the interelectronic distance between electrons of different bands and R_{lm} in the V_R term corresponds to the distance between the lth nucleus of charge z_l and mth nucleus of charge z_m. For the γ band we have eq (4A)

$$H_\gamma = \sum T_{k\gamma} - \sum_k \sum_m^N \frac{z_m}{r_{km}} + \sum_{i=1}^{k} \sum_{j>i}^{k} \frac{1}{r_{ij}} \tag{4A}$$

where r_{km} is the separation between the kth electron and the mth nucleus and $T_{k\gamma}$ is the kinetic energy term for the electron. Using eq (30) one obtains eq (5A) for T_k.

$$T_{k\gamma} = \frac{\overline{p_k^2}}{2m} = \frac{k^2}{2m} + \frac{k \cdot \overline{\omega}_{k\gamma}}{m} + \frac{\overline{\omega_{k\gamma}^2}}{2m} \tag{5A}$$

For the nuclei constrained by external forces to remain at fixed positions, the Virial theorem for the k electron can be written as eq (6A), where

$$\overline{E}_{k\gamma} = -\overline{T}_{k\gamma} - \sum_i^3 a_i \frac{\partial E_k}{\partial a_i} \tag{6A}$$

the a_i refer to the unit cell edges of the crystal. It is clear from the preceding equations (eqs (2A) through (5A)) that the "external forces" at constant volume for the $k\gamma$ electron are primarily those due to electronic and nuclear interactions within the crystal rather than just forces external to the crystal.

Of particular interest is the evaluation of the sum $\sum a_i \, (\partial k/\partial a_i)$ where k is expressed as eq (7A)

$$k = 2\pi \sum_i^3 \frac{n_i}{N_i} a_i^* \tag{7A}$$

with N_i indicating the number of unit cells of the crystal in the a_i direction and with n_i and N_i integers. For a triclinic unit cell [38] the reciprocal cell edges a_i^* may be expressed in terms of the unit cell angles, α_i, and edges as eq (8A) where S is given by eq (9A).

$$a_i^* = \frac{1}{a_i} \frac{\sin \alpha_1}{S} \tag{8A}$$

$$S = \left[1 + 2 \prod_i^3 \cos \alpha_i - \sum_i^3 \cos^2 \alpha_i\right]^{1/2} \tag{9A}$$

accordingly k can be written simply as

$$k = \sum_i^3 K_i / a_i \tag{10A}$$

where

$$K_i = 2\pi \frac{n_i \sin \alpha_i}{N_i S} \tag{11A}$$

The sum of interest is then eq (12A).

$$\sum_i^3 a_i \frac{\partial k}{\partial a_i} = -\sum a_i \frac{K_i}{a_i^2} = -\sum \frac{K_i}{a_i} = -k \tag{12A}$$

If we accept for the moment the potential energy term in $\sum a_i (\partial E_{k\gamma}/\partial a_i)$ as $-V_{k\gamma}$, then eq (6A) may be written

$$E_{k\gamma} = -\frac{k^2}{2m} - \frac{k \cdot \overline{\omega_{k\gamma}}}{m} - \frac{\overline{\omega^2}_{k\gamma}}{2m} + \frac{k^2}{m} + \frac{k \cdot \overline{\omega}_{k\gamma}}{m} - \sum_i \left[\frac{k a_i}{m} \cdot \frac{\overline{\partial \omega_{k\gamma}}}{\partial a_i} + \frac{1}{2m} \frac{\overline{a_i \partial \omega_{k\gamma}^2}}{\partial a_i}\right] - V_{k\gamma}$$

$$= \frac{k^2}{2m} - \frac{\overline{\omega_{k\gamma}^2}}{2m} - \sum_i \left[\frac{k a_i}{m} \cdot \frac{\overline{\partial \omega}_{k\gamma}}{\partial a_i} + \frac{1}{2m} \frac{a_i \overline{\partial \omega_{k\gamma}^2}}{\partial a_i}\right] - V_{k\gamma} \tag{13A}$$

as eq (13A) by making use of eq (12A). By neglecting the term involving $(\partial \overline{\omega}_{k\gamma}/\partial a_i)$ and $(\partial \overline{\omega_{k\gamma}^2}/\partial a_i)$ we obtain eq (31), the desired result. While $(\partial \overline{\omega}_{k\gamma}/\partial a_i)$ may be negligible for a centrosymmetric structure the variation of $\overline{\omega_{k\gamma}^2}$ with the unit cell lengths requires more careful consideration than we will give it here. We do note however that its variation in the direction of strong bonds may be appreciable and sensitive to k when k is parallel to the bond directions.

In considering the variation of the potential energy with respect to the a_i we note that these must be zero for the intraband and interband electronic terms since the l/r_{ij} do not explicitly contain the a_i. However, the electron-nuclear terms contain a_i in the form eq (14A),

$$r_{km} = x_k + x_m = x_k + \sum_i^3 a_i L_i \tag{14A}$$

where x refers to position of the kth electron and the mth nucleus and the L_i are integers only if the nuclei are exclusively at the lattice points. The variation of the potential terms for the γ band then gives

$$V_{k\gamma} = \sum_m^N \int u_{k\gamma} u_{k\gamma}^* z_m \left[\frac{1}{r_{km}} + \frac{x_k}{r_{km}^2}\right] d\tau \tag{15A}$$

Under equilibrium conditions the total potential is at a minimum with respect to the variations of a_i. This per-

mits the sum over all the bands to be equated to the internuclear repulsive potential. The constant term in eq (31) is then some appropriate fraction of this sum.

13. References

[1] Pauling, L., Nature of the Chemical Bond. 3rd ed. (Cornell University Press, Ithaca, New York, 1960).

[2] Pauling, L., Proc. Roy Soc. **196A**, 23 (1949).

[3] Rundle, R. E., Acta Cryst. **1**, 180 (1948).

[4] Ganzhorn, K., Z. Naturforschg. **7A**, 291 (1952); **8A**, 330 (1953).

[5] Carter, F. L., Rare Earth Research III, L. Eyring, Editor (Gordon and Breach, New York, 1965), p. 495.

[6] Carter, F. L., Fifth Rare Earth Research Conference, held at Iowa State University, Ames, Iowa, Aug. 1965 (preprint).

[7] Carter, F. L., Second International Conference on Solid Compounds of Transition Elements, held at Tech. University of Twente, Enschede, The Netherlands, June 1967.

[8] Carter, F. L., Proceedings of the Seventh Rare Earth Research Conference, held at Coronado, California, Oct. 28-30. 1968 (preprint), p. 283.

[9] Sneddon, I. N., Fourier Transforms, (McGraw-Hill, New York, 1951), lst ed., p. 368.

[10] Crangle, J., Electronic Structure and Alloy Chemistry of the Transition Elements, P. A. Beck, Editor (Interscience Publishers, New York, 1963), p. 51ff.

[11] Weiss, R. J., and Tauer, K. J., Phys. Rev. **102**, 1490 (1956).

[12] Abrahams, S. C., Guttman, L., and Kasper, J. S., Phys. Rev. **127**, 2052 (1962).

[13] Franck, J. P., Manchester, F. D., Martin, D. L., Proc. Roy. Soc. (London) **263A**, 494 (1961).

[14] Kasper, J. S., Theory of Alloy Phases, (American Society for Metals, Cleveland, Ohio, 1956), p. 264.

[15] Clogston, A. M., Matthias, B. T., Peters, M., Williams, H. J., Corenzwit, E., and Sherwood, R. C., Phys. Rev. **125**, 541 (1962).

[16] Pearson, W. B., Acta Cryst. **B24**, 7 (1968).

[17] Laves, F., Theory of Alloy Phases, (American Society for Metals, Cleveland, Ohio, 1956), p. 124.

[18] Kjekshus, A., and Pearson, W. B., Progress in Solid State Chemistry **1**, 160f, H. Reiss, Editor (Macmillan Co., New York, 1964).

[19] Kauzmann, W., Quantum Chemistry, (Academic Press Inc., New York, 1957).

[20] Pauling, L., Theory of Alloy Phases, (American Society for Metals, Cleveland, Ohio, 1956), p. 220.

[21] Brewer, L., Electronic Structure and Alloy Chemistry of the Transition Elements, P. A. Beck, Editor (Interscience Publishers, New York, 1963), p. 221.

[22] Rundle, R. E., J.A.C.S. **69**, 1327 (1947); J. Chem. Phys. **17**, 671 (1949).

[23] Wallace, P. R., Phys. Rev. **71**, 622 (1947).

[24] Slonczewski, J. C., and Weiss, P. R., Phys. Rev. **109**, 272 (1958).

[25] Pauncz, R., Alternate Molecular Orbital Method, (W. B. Saunders Co., Philadelphia, 1967).

[26] Hirst, R. M., and Linnett, J. W., J. Chem. Soc. **1035**, 3844 (1962).

[27] Empedocles, P. B., and Linnett, J. W., Proc. Roy. Soc. (London) **A282**, 166 (1964); Trans. Faraday Soc. **62**, 2004 (1966).

[28] Podolsky, B., and Pauling, L., Phys. Rev. **34**, 109 (1929).

[29] Hicks, B., Phys. Rev. **52**, 436 (1937).

[30] Coulson, C. A., Proc. Cambridge Phil. Soc. **37**, 55 (1941).

[31] Coulson, C. A., and Duncanson, W. E., *ibid*, **37**, 67 (1941).

[32] Coulson, C. A., *ibid*, **37**, 47 (1941).

[33] Duncanson, W. E., *ibid*, **37**, 397 (1941).

[34] Duncanson, W. E., and Coulson, C. A., *ibid* **37**, 406 (1941).

[35] Callaway, J., Energy Band Theory, (Academic Press Inc., New York, 1964), p. 184.

[36] Smith, R. A., Wave Mechanics of Crystalline Solids, (John Dickens and Company, Ltd., Northampton, Great Britain, 1963), p. 307.

[37] Frost, A. A., and Lykos, P. G., J. Chem. Phys. **25**, 1299 (1956).

[38] International Tables for X-Ray Crystallography **1**, 13 (Kynock Press, Birmingham, England, 1952).

Electroreflectance Observation of Band Population Effects in InSb

R. Glosser,* B. O. Seraphin, and J. E. Fischer**

Michelson Laboratory, China Lake, California 93555

It is found that bias changes applied to *n*-InSb produce shifts in portions of the electroreflectance spectra. We attribute this to changes in the conduction band population produced as the separation between the Fermi level and the bottom of the conduction band is varied. Spectra which displays red, blue, or no shift correlates to electronic transitions starting from, ending at, or bridging the Fermi level. These observations permit a band structure identification of the shifting spectra and optical monitoring of the surface potential.

Key words: Band population effects; electroreflectance; Fermi level shifts; indium antimonide (InSb); optical transitions; surface potential.

It has long been known that the Fermi level in *n*-type InSb can easily be moved into and up the conduction band by increasing the bulk concentration of donors. This rise of the Fermi level is responsible for the blue shift of the absorption edge as was first explained by Burstein [1] and Moss [2]. In contrast to shifts produced by changing the bulk doping of *n*-type InSb, we have found that the position of the Fermi level can similarly be changed in the surface with respect to the conduction band by varying the surface potential with bias. Such effects have been postulated earlier [3]. This observation is made by monitoring the direction of shift of certain parts of the electroreflectance spectra which permits the classification of the observed structure into three categories: spectra displaying red, blue, or no shift which correlate to transitions starting from, ending at, or bridging the Fermi level. This aids in their band structure identification. The results establish band population effects as an additional modulation mechanism in electroreflectance. It also permits optical monitoring of the surface potential and possible determination of the effective mass of otherwise inaccessible bands near $K = 0$.

The manner in which this effect comes about is shown in figure 1. Consider a degenerate *n*-type crystal with a *p*-type surface. As it is biased positively, the bands move downward and the conduction band drops further below the Fermi level. According to this model, for transitions ending at the Fermi level, the threshold

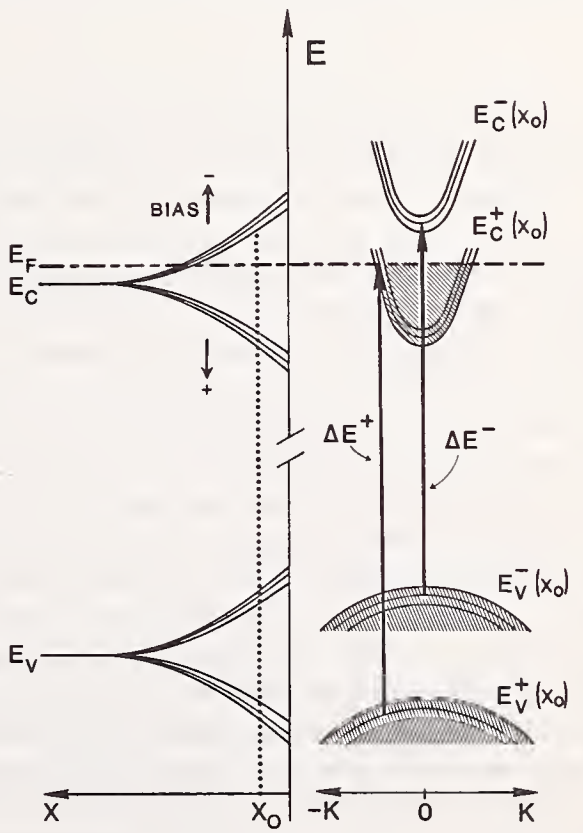

FIGURE 1. *Schematic showing the shift of the threshold energy* ΔE *at absolute zero for an optical transition as the bands of degenerate* n*-type* InSb *are shifted with respect to the Fermi level* E_F *by an applied bias.*

A valence band E_v and a conduction band E_c are shown as a function of depth X from the surface (left) and as a function of momentum K for an arbitrary depth X_0 about Γ point (right). Modulation around a given bias is represented by the band edge wobble. The symbols − and + represent the bias direction for a *p*- and *n*-type surface, respectively.

*Present address: Physics Department, University of California, Santa Barbara, California 93106.

**Present address: Physics Institute I, Technical University of Denmark, Lyngby/Denmark.

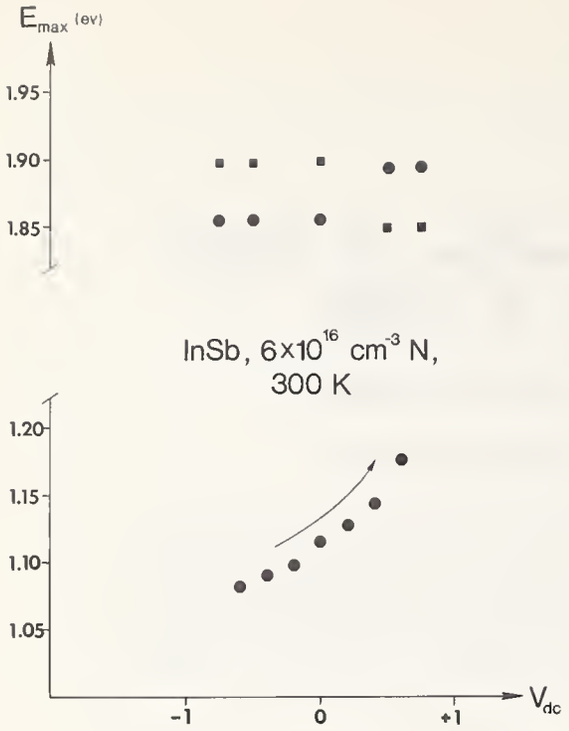

FIGURE 2. *Spectral shift with bias of structure associated with a transition ending at the Fermi level (lower half), as compared to reference structure associated with a transition bridging the Fermi level (upper half).*

Circles represent positive and squares negative extrema of the response. Arrows point in the direction of increasing peak magnitude. All data are taken in the MIS configuration. Modulation is ±300 mV.

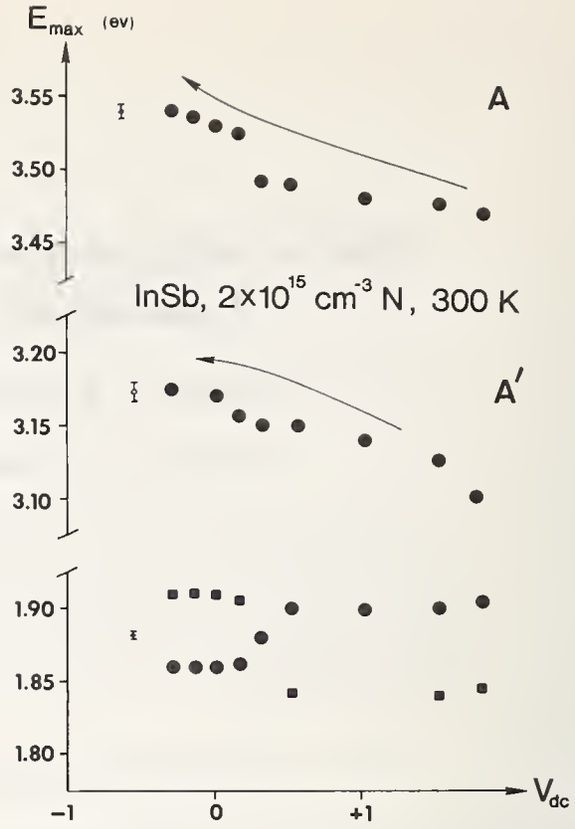

FIGURE 3. *Spectral shift with bias of structure associated with transitions starting from the Fermi level (upper two plots), as compared to reference structure associated with a transition bridging the Fermi level (lower plot).*

Circles represent positive and squares negative extrema of the response. Arrows point in the direction of increasing peak magnitude. All data are taken by the electrolyte technique. Modulation is ±60 mV.

energy is shifted towards the blue. Transitions starting from the Fermi level should show a red shift for these same conditions. Those transitions not involving the Fermi level should yield electroreflectance signals which show little shift with bias and change sign upon changing the polarity of the surface potential [4].

We have observed all three of these effects in the electroreflectance spectra of InSb. The geometry and apparatus have been described earlier [5]. Samples were prepared in both the MIS [6] (metal-insulator-semiconductor) and electrolyte configurations [7].

Figure 2 brings out the contrast between a transition ending at the Fermi level and one which bridges it. The structure at 1.1 eV has previously been identified as originating from the spin-orbit split valence to conduction band (Γ_{7v} to Γ_{6c}) [8]. A blue shift with bulk doping has been seen in the corresponding transition in GaAs [9]. Here we see a blue shift of about 95 MeV with applied bias which should be compared to the structure at 1.9 eV where over the same range of bias practically no shift is observed. This latter spectra is well identified as originating from the $\Lambda_4 + \Lambda_5$ to Λ_6 transition and consequently bridges the Fermi level. The blue shift at 1.1 compares very well with transmission measurements where the bulk doping is varied [10] if one equates a strongly p-type surface with intrinsic InSb (conduction band depopulated) and equates the flat band position (+0.25 V as observed by the polarity reversal of the 1.9 eV structure) with the bulk doping of 6×10^{16} cm^{-3}.

A complementary red shift with bias application is found at 3.1 and 3.5 eV which we label A-A′. This is shown in figure 3. We again use the $\Lambda_4 + \Lambda_5$ to Λ_6 transition as a comparison. In the MIS configuration, internal photoemission [11], above 2.8 eV at room temperature, tends to keep the surface p-type by populating trapping states. In order to overcome this problem, the data was taken using the electrolyte technique [7].

Over the bias range used, we see that the Λ calibration structure shifts at most 20 MeV which is in marked contrast to the 80 MeV shift of the A-A′ doublet. At room temperature, no other structure was seen in the 3 to 4 eV range with the electrolyte technique. Each member of the doublet exhibits only one peak at 300 K.

At liquid nitrogen temperatures in the MIS structure, the A-A′ doublet is now complemented by weaker structures at 3.4 and 3.8 eV, labeled B-B′. The spectra

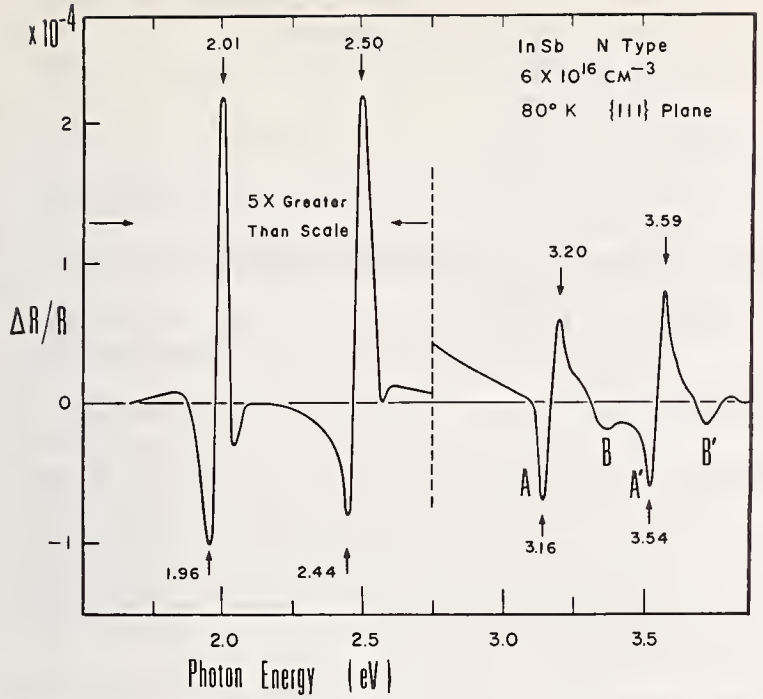

FIGURE 4. *Electroreflectance spectrum of an* InSb MIS-*sample at liquid-nitrogen temperature.*
The doublets A-A and B-B are discussed in the text.

are shown in figure 4. Because of the internal photoemission problem, no meaningful bias effects could be made in this temperature and energy range.

With our observation of the bias produced red shift of A-A′ and the weak structure at 3.4 and 3.8 eV and comparing this with recent band structure calculations for InSb we draw the following conclusions.

The A-A′ pair on the one hand and B-B′ on the other are mated pairs in the sense of components of a spin-orbit split doublet. The peaks A and A′ correlated to transitions starting from the Fermi level in the lowest conduction band and ending in higher conduction bands [12] (Γ_{6c} to Γ_{7c} and Γ_{6c} to Γ_{8c}). The B-B′ doublet probably ends in the same set of conduction bands but starts from the top of the valence band.

Further support for the interpretation of the A-A′ structure is obtained by comparing our results and the electroreflectance spectra of Shaklee et al. [13] and Cardona et al. [9] with the thermoreflectance spectra reported by Matatagui and co-workers [14].

Electroreflectance spectra for *n*-type InSb always shows structure at 3.1 and 3.5 eV but weak or no structure at 3.4 and 3.8 eV. Thermoreflectance in contrast, shows no structure at the former doublet but response for the latter. The spectra yielded elsewhere by the two types of modulated reflectance spectra are entirely comparable, in particular, the structural features near 2 and 4 eV. This is in line with our assignment of A-A′ structure to transitions starting from the lowest conduction band. Thermal modulation should only weakly affect a transition that starts above the band minimum at the Fermi level, in contrast to electric field modulation operating at such a transition through band population effects.

As a further test of our interpretation of these results, we observed the electroreflectance spectra of a *p*-type sample carrying a *p*-type surface. As expected, the A-A′ structure is practically absent except for a very small residual structure probably caused by the incident light and/or the electric field in the surface. Biasing towards the flat-band condition causes the structure to grow in agreement with the idea that conduction band population is being increased.

These results and their interpretation can be compared with the results of Bloom and Bergstresser [15]. The observed separation of the A-A′ doublet is in excellent agreement with their prediction of a splitting of Γ_{7c} and Γ_{8c} by 0.38 eV. The separation of A and B on the one hand and A′ and B′ on the other is 0.21 eV which is close to the fundamental gap of InSb at liquid nitrogen temperature as required by our assignment.

Aspnes [16] has pointed out that either of the A-A′ structure represents the first hope of observing an M_3 critical point. The structure observed evidently stems from a superposition of the singularity at the Fermi level with that at the bottom of the conduction band. An experiment at liquid He temperature with a more highly doped sample (and an *n*-type surface) would be necessary to clearly separate the spectra due to the two singularities.

As for the assignment of the weak B-B′ doublet, two possibilities are available. They most probably represent transitions at the Γ point from the top of the valence band to the higher conduction bands, but they can represent transition from the split valence band near Γ in the Δ direction to the second lowest conduction band. The splitting predicted by Bloom and Bergstresser is 0.42 eV which is sufficiently close to our observed value that this possibility must also be considered. Further work is necessary to conclusively decide the assignment of B-B′.

Regardless of which of the possibilities explains the exact origin of the weak doublet, we determine the separation of the conduction band at Γ_{7c} from the top of the valence to be 3.4 eV as compared to the calculated value of 3.6 eV [15].

In addition to the usefulness of band population effects for band structure identification, it appears that the spectral shifts could be used to determine the effective mass of the higher conduction and the split off valence band. A straightforward derivation using the

optical gap relation given in reference 1 yields, for example, the effective mass of the spin orbit split valence band

$$m_p(S0) = C \cdot m_p(FE) \cdot m_n(FE) \cdot [m_p(FE)(1-C) + m_n(FE)]^{-1}$$

where $C = \delta\Delta E(FE)/\delta\Delta E(SO)$ is the ratio of the observed spectral shifts for a given change in surface potential and $m_n(FE)$ and $m_p(FE)$ are the known effective masses at the fundamental edge. Because the fundamental edge was not accessible with our equipment, we could not determine $m_p(SO)$.

References

[1] Burstein, E., Phys. Rev. **93,** 632 (1954).

[2] Moss, T. S., Proc. Phys. Soc. (London) **B76,** 775 (1954).

[3] Aspnes, D. E., and Cardona, M., Bull. Am. Phys. Soc. **13,** 27 (1968); Seraphin, B. O., J. Physique **29,** C4-96 (1968).

[4] Seraphin, B. O., Hess, R. B., and Bottka, N., J. Appl. Phys. **36,** 2242 (1965).

[5] Seraphin, B. O., J. Appl. Phys. **37,** 721 (1966).

[6] Pidgeon, C. R., Groves, S. H., and Feinleib, J., Solid State Commun. **5,** 677 (1967); Ludeke, R., and Paul. W., in II-VI Semiconducting Compounds, D. G. Thomas, Editor (W. A. Benjamin Inc., New York, 1967) p. 123; Fischer, J. E., Bottka, N., and Seraphin, B. O., to be published.

[7] Shaklee, K. L., Pollak, F. H., and Cardona, M., Phys. Rev. Letters **15,** 883 (1965).

[8] Groves, S. H., Pidgeon, C. R., and Feinleib, J., Phys. Rev. Letters **17,** 643 (1966).

[9] Cardona, M., Shaklee, K. L., and Pollak, F. H., Phys. Rev. **154,** 696 (1967).

[10] Kosogov, O. V., and Maramzina, M. A., Sov. Phys.-Semiconductors **2,** 854 (1969).

[11] Mueller, R. K., and Jacobson, R. F., J. Appl. Phys. **35,** 1524 (1964); Glosser, R., and Seraphin, B. O., Z. Naturforsch. **24a,** 1320 (1969).

[12] Interconduction band transitions have previously been observed in transmission measurements in other materials. Zallen and Paul found this to occur in *n*-GaP at the X point [Zallen, R., and Paul. W., Phys. Rev. **134,** A1628 (1964)]. The recent work by Patrick and Choyke clearly shows interconduction band transitions in cubic *n*-SiC to occur also at the X point [Lyle Patrick and W. J. Choyke, Phys. Rev. (to be published)]. Other observations are discussed in these references.

[13] Shaklee, K. L., Cardona, M., and Pollak, F. H., Phys. Rev. Letters **16,** 48 (1966).

[14] Matatagui, E., Thompson, A. G., and Cardona, M., Phys. Rev. **176,** 950 (1968).

[15] Bloom, S., and Bergstresser, T. K., Solid State Commun. **6,** 465 (1968).

[16] Aspnes, D. E., private communication and this conference.

Spin-Orbit Effects in the Electroreflectance Spectra of Semiconductors

B. J. Parsons and H. Piller*

Michelson Laboratory, China Lake, California 93555

Measurements have been made of the electroreflectance spectra of germanium, gallium arsenide and gallium antimonide in the range of photon energies from 0.6 to 6.7 eV. Special attention has been paid to the resolution of multiplicity within the E_0' and E_1' structures. The identification of these structures in terms of critical point interband transitions involving the second conduction band has an important bearing on the hand structure of these materials. The data is discussed in terms of the possible identification, within these higher energy multiplets, of spin-orbit splittings associated with the valence band states at Γ and L.

Key words: Critical points; diamond semiconductors; electroreflectance; gallium antimonide (GaSb); gallium arsenide (GaAs); germanium; semiconductors, diamond; semiconductors, zinc blende; spin-orbit splittings.

1. Introduction

The interpretation of electroreflectance spectra in terms of critical point interband transitions relies heavily on direct comparison between experimental data and calculated band structure. The high resolution of electroreflectance, however, permits the direct observation, in many cases of interest of spin-orbit effects, which, at low energies, are interpretable with little ambiguity. In diamond and zinc blende semiconductors, for example, the spin-orbit splitting at Γ and along Λ (Δ_0 and Δ_1, [1] respectively) are easily identified within the E_0 and E_1 structures [2] and a wealth of information is available to substantiate these assignments. At higher energies the number of critical points increases and even tentative assignments become difficult in those not infrequent cases where the complexity of the observed structure suggests the near degeneracy of several critical points.

Transitions from the valence band to the second conduction band are expected to exhibit a multiplet structure since each band has two spin-orbit components. The degree of multiplicity observed experimentally will depend on the absolute and relative magnitudes of the spin-orbit splittings and on the selection rules. Some guidance in the assignment of certain of these higher energy structures is, in principle therefore, to be expected from the recurrence within this multiplet structure, of splittings characteristic of the initial valence band states. The Δ_0 and Δ_1 splittings, for example, might be expected to recur within the E_0' and E_1' structures, respectively, these structures having been associated in the past with transitions at Γ and L [2]. These expectations depend crucially on the assumption that the transitions involved occur at the same point in **k**-space. Thus, the Δ_0 splitting will recur exactly within the E_0' structure only if both the E_0 and E_0' transitions occur at Γ. In the case of the E_1 and E_1' transitions these almost certainly do not occur at the same point along the Λ direction. There is evidence to suggest, however, that the Δ_1 splitting of the $\Lambda_{4,5v}$ and Λ_{6v} bands is relatively constant over an extended region of **k**-space which includes the Λ and L critical points. This is a controversial point, but for the present we take the observed doublet nature of the E_1 structure [3] as justification for this assumption.

The range of photon energies beyond 4.5 eV has been investigated less extensively than the lower energy region and, because of the lack of a convenient and intense light source in this region of the spectrum, the available data is generally inferior to that obtained at lower energies. The E_1' structure observed in this region in a number of semiconductors has thus received only cursory attention in the past. We have used experi-

*Present address: Department of Physics and Astronomy, Louisiana State University, Baton Rouge, Louisiana.

mental techniques which have permitted a more detailed study of this region and have resolved the multiplicity in the E_1' structure in a number of semiconductors. The purpose of this paper is to report data for germanium, gallium arsenide and gallium antimonide which extends to 6.7 eV and to discuss the results in terms of the possible identification of recurrent valence band spin-orbit effects.

2. Experimental Details

Two reflectometers were used to obtain the present data. The first, based on a single pass prism monochromator (Perkin-Elmer model 98) has been described elsewhere [4]. The second is based on a 0.3 meter grating monochromator (McPherson model 218) and utilizes a modular electronic signal processing system (PAR). The light source used in the 4.5-6.7 eV range was a deuterium discharge lamp fitted with a suprasil window.

The sample geometry used was the so-called dry sandwich configuration [5]. Polished and etched samples were coated with a thin, 200 Å, film of aluminum oxide, and a thin semitransparent conducting film of nickel completed the thin film capacitor arrangement. Electric fields well in excess of 10^6 V/cm are readily attained using this technique. This sample geometry has a number of advantages over other more popular configurations, not the least of which for the present work is the ability to cover a wide range of photon energies using cooled samples.

3. Results and Discussion

3.1. Germanium

Germanium has been widely investigated and data on the electroreflectance spectrum for this diamond group semiconductor is well documented in the literature [2,6-8]. For reasons not fully understood at the present, the recurrence of the 300 mV Δ_0 spin-orbit splitting within the E_0' structure has not been established. Since the E_0' structure is relatively narrow and well separated from adjacent structures this is somewhat surprising. There is evidence, however, for the near degeneracy in this region of the spectrum of several critical point contributions to the optical properties, some of which may well be associated with off-center critical points.

The E_1' structure for germanium appears as a shoulder in the reflectance spectrum [9] and weak structure in the electroreflectance spectrum has been observed [2,8] at corresponding energies. This structure has generally been associated with the $L_3'-L_3$ quadruplet. In germanium the splitting of the L_{6c}^+ and $L_{4,5c}^+$ levels of the second conduction band is expected to be smaller than the valence band splitting at L ($\Delta_1 =$ 200 mV) and we expect to be able to identify the recurrence of this 200 mV effect. The spectrum obtained at 300 K in this region of the spectrum for a 0.3 ohm-cm p-type sample is shown in figure 1. The single peak at 5.75 eV has a half-width of only 100 mV suggesting that this peak is not associated with the L multiplet. Weak structure on the low energy side of this peak is barely resolved into a doublet with close to the correct splitting. No significant improvement is gained over this spectrum on cooling the sample to liquid nitrogen temperatures (80 K). It is noteworthy that we find no structure in the 4.65-5.1 eV region where structure has been observed in photoemission [10]. We conclude that the associated peak in the density of states is not a critical point effect.

3.2. Gallium Arsenide

The lack of inversion symmetry in the III-V compounds causes degeneracies in the valence and conduction bands at X to be lifted. The resulting multiplicity of the X transitions complicates the E_2 structure for these materials and makes the identification of structure in this region more difficult. The spectrum for n-type gallium arsenide between 3.6 and 6.7 eV is shown in figure 2. The peaks at 4.45 and 5.02 eV (300 K data) are well established [2] and have previously been labeled E_0' and E_2, respectively. It is clear that considerable overlap exists between satellites and components of these two structures. An edge between the two main peaks is resolved at 80 K. The observation of a small peak at 3.95 eV, which we interpret as an interconduction band

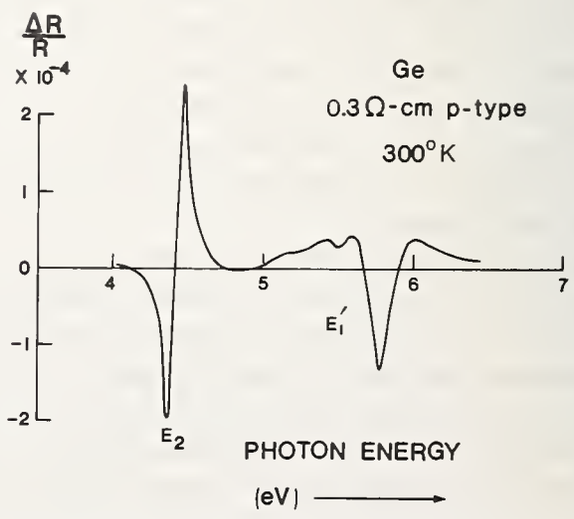

FIGURE 1. *Electroreflectance spectrum for p-type germanium at 300 K in the region of the E_1' structure.*

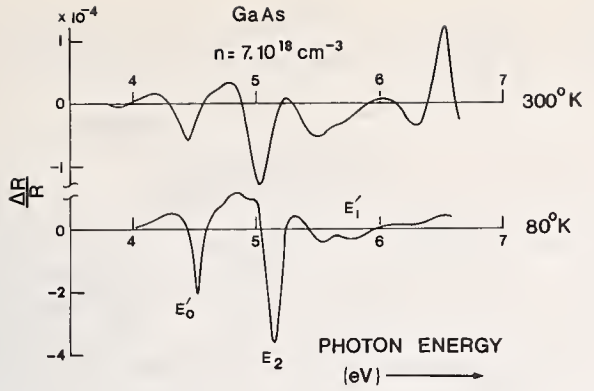

FIGURE 2. *Electroreflectance spectrum for n-type gallium arsenide in the region of the* E_0' E_2, *and* E_1' *structures at 300 and 80 K.*

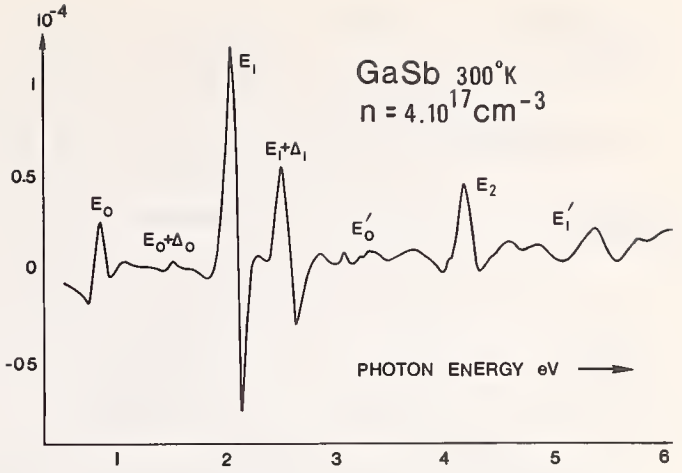

FIGURE 3. *Electroreflectance for n-type gallium antimonide at 300 K.*

transition [11,12] is close to small structure which has been reported in the reflectance [13]. This suggests that the peak at 5.50 eV is a component of the E_0' structure.

At high energies, peaks are observed at 5.70 and 6.55 eV (300 K data). The 6.55 eV peak corresponds to a shoulder in the reflectance [14] at the same energy which has been associated with the $L_3' - L_3$ transitions. The observed structure is clearly incomplete in our data and confirmation of this assignment will await an extension of the electroreflectance spectrum to higher energies. The two peaks at 5.50 and 5.70 eV do have the correct 200 mV separation to be associated with the recurring splitting, but in view of the expected multiplicity and overlap of the E_0' and E_2 structures in this region this is probably accidental.

3.3. Gallium Antimonide

The electroreflectance spectrum of *n*-type gallium antimonide at 300 K is shown in figure 3. The Δ_0 and Δ_1 splittings (730 mV and 440 mV, respectively) are larger than in germanium or gallium arsenide and the E_0' and E_1' structures are correspondingly broader and more detailed. The band structure of gallium antimonide, according to a recent calculation by Zhang and Callaway [15], yields values for the important energy level separations given in table 1 which also lists the observed electroreflectance peak energies. Data at the fundamental edge shows a pronounced dependence on bulk doping and the quoted energies for the $\Gamma_{8v} - \Gamma_{6c}$ and $\Gamma_{7v} - \Gamma_{6c}$ doublet are probably high. The spectrum for *p*-type material suggests that light and heavy hole transitions play an important role at low temperatures. We find no evidence for more than two peaks in the region of the E_1 structure. The single peak at 1.50 eV is almost certainly associated with the $\Gamma_{7v} - \Gamma_{6c}$ transitions.

TABLE 1. *Calculated energies of important interband transitions in gallium antimonide according to Zhang and Callaway [15] and the experimental peak energies observed in electroreflectance. Note that the* $\Gamma_{7v} - \Gamma_{7c}$ *transition is not allowed in the unperturbed crystal.*

Structure	Transition	Calculated energy (eV)	Experimental peak energy (eV)	
			300 K	80 K
E_0	$\Gamma_{8v} - \Gamma_{6c}$	0.81	0.78	0.89
	$\Gamma_{7v} - \Gamma_{6c}$	1.59	1.50	1.60
E_1	$L_{4,5v} - L_{6c}$	1.98	2.04	2.13
	$\Lambda_{4,5v} - \Lambda_{6c}$	2.10		
	$L_{6v} - L_{6c}$	2.42	2.48	2.59
	$\Lambda_{6v} - \Lambda_{6c}$	2.60		
E_0' and E_2	$\Gamma_{6c} - \Gamma_{7c}$	3.01		2.94
	$\Gamma_{6c} - \Gamma_{8c}$	3.45	3.11	3.20
	$\Gamma_{8v} - \Gamma_{7c}$	3.82	3.31	3.34
	$X_{7v} - X_{6c}$	4.26	3.38	3.41
	$\Gamma_{8v} - \Gamma_{8c}$	4.26	3.68	3.75
	$X_{6v} - X_{6c}$	4.29	4.03	4.13
	$X_{7v} - X_{7c}$	4.64	4.16	4.34
	$X_{6v} - X_{7c}$	4.67	4.62	4.57
	$\Gamma_{7v} - \Gamma_{8c}$	5.04		4.72
E_1'	$L_{4,5v} - L_{6c}$	5.48	4.95	5.11
	$L_{4,5v} - L_{4,5c}$	5.71	5.48	5.62
	$L_{6v} - L_{6c}$	5.92	5.94	5.98
	$L_{6v} - L_{4,5c}$	6.15		

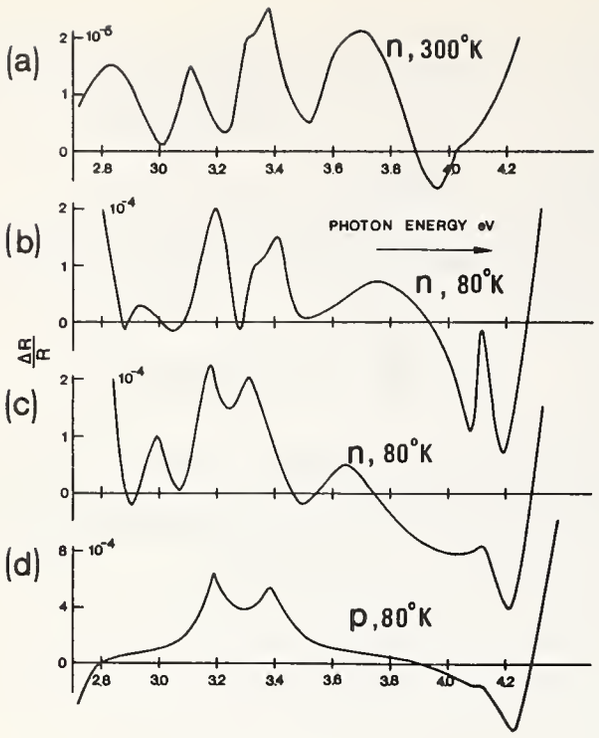

FIGURE 4. *Detailed behavior of the electroreflectance of gallium antimonide in the region of the* E_0' *structure: (a) for an* n*-type sample at 300 K, (b) for the same* n*-type sample at 80 K,* (c) *for a second* n*-type sample at 80 K, and (d) for a* p*-type sample at 80 K.*

The very detailed spectrum between 2.8 and 4.2 eV is shown in figure 4 (a) for an *n*-type sample at 300 K, (b) for the same sample at 80 K, (c) for a second *n*-type sample at 80 K, and (d) for a *p*-type sample at 80 K. The behavior in this region is considerably more complex than previously reported [2,16,17]. Peaks at 3.2 and 4.13 eV are present in all the 80 K spectra, other peaks at 2.94, 3.34, 3.41 eV and the broad peak at 3.75 eV are all dependent in some way on the bulk doping and/or the surface preparation. Further studies of the behavior of these peaks will be necessary before a satisfactory interpretation of this data can be proposed. The clear doping dependence of the lower energy members of this group indicates, however, that interconduction band transitions are important in this region. Similar behavior has been reported in indium antimonide [11,12]. Other structure in the same energy range is probably associated with critical points close to Γ along the Δ direction and correlated to the behavior of the $\Delta_{5c}^{(2)}$ band. On this basis the valence band to conduction band transitions at Γ should occur at energies close to the E_2 multiplet and considerable unresolved overlap is thus expected in this region. The small peaks at 4.57 and 4.72 eV are also probable members of one or other of these two groups of structure (see fig. 5).

The spectrum between 4.0 and 6.7 eV is shown for an *n*-type sample in figure 5. At 80 K the E_1' structure is

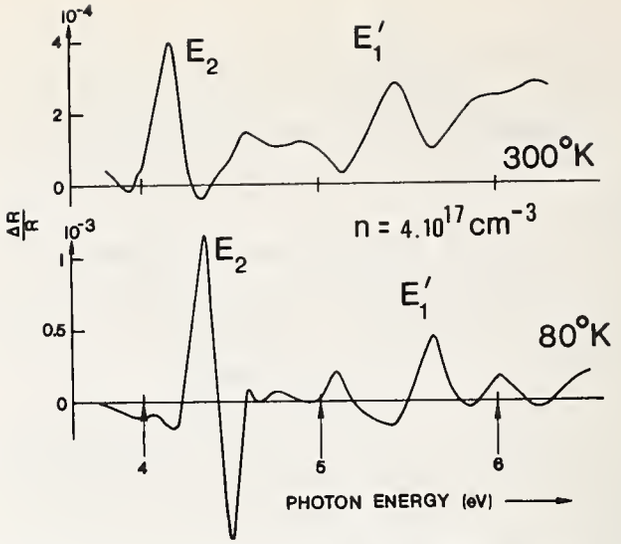

FIGURE 5. *Electroreflectance of gallium antimonide in the region of the* E_1' *structure.*

resolved into a triplet at 5.11, 5.62, and 5.98 eV. Since it might not be possible, if the $L_{4,5v} - L_{6v}$ and $L_{4,5c} - L_{6c}$ spin-orbit splittings are of the same magnitude, to resolve the $L_{4,5v} - L_{4,5c}$ and $L_{6v} - L_{6c}$ transitions, the association of this triplet with the $L_3' - L_3$ quadruplet is not unreasonable. According to this assignment the 5.11 eV peak is attributable to $L_{4,5v} - L_{6c}$, and the 5.98 eV peak to $L_{6v} - L_{4,5c}$ transitions. The 510 mV separation of the 5.11 and 5.62 eV peaks is not, in view of the unresolved doublet nature of the 5.62 eV peak, inconsistent with the measured 460 mV separation of the E_1 peaks.

4. Summary

We have measured the electroreflectance spectra for germanium, gallium arsenide and gallium antimonide over a wide range of photon energies and concentrated our attention on those regions of the spectrum where the Δ_0 and Δ_1 spin-orbit effects are expected to recur. The E_0' and E_2 structures are found to overlap considerably in the two III-V compounds investigated and a dependence on bulk doping of certain peaks comprising the E_0' structure, particularly in gallium antimonide, suggests that interconduction band transitions are of importance. The spectrum for gallium antimonide is considerably more detailed than earlier reported data indicated. Much of the data in the region of the E_1' structure for all three materials has not been reported previously. This structure has been resolved and evidence found in the spectra for germanium and gallium antimonide for the recurrence of the valence band spin-orbit splitting. As expected, the electroreflectance spectra in this region is considerably more detailed than reflectance data and there is evidence in the spec-

trum for germanium for contributions to the optical properties in addition to those associated with the L transitions.

5. References

[1] The notation used here is that originally introduced by Cardona and co-workers (M. Cardona, ref. 2).

[2] Cardona, M., Shaklee, K. L., and Pollak, F. H., Phys. Rev. **154**, 696 (1967).

[3] Fischer, J. E., Kyser, D. S., and Bottka, N., to be published in Solid State Communications.

[4] Seraphin, B. O., Phys. Rev. **140**, A1716 (1965).

[5] Ludeke, R., and Paul, W., in Proceedings International Conference II-VI Compounds, Providence, 1967 (Benjamin, New York, 1967); Pidgeon, C. R., and Groves, S. H., ibid.

[6] Seraphin, B. O., and Hess, R. B., Phys. Rev. Letters **14**, 138 (1965).

[7] Ghosh, A. K., Solid State Comm. **4**, 565 (1966).

[8] Ghosh, A. K., Phys. Rev. **165**, 888 (1968).

[9] Donovan, T. M., and Ashley, E. J., JOSA **54**, 1141 (1963).

[10] Donovan, T. M., private communication.

[11] Glosser, R., Fischer, J. E., and Seraphin, B. O., to be published.

[12] Glosser, R., Seraphin, B. O., and Fischer, J. E., this Symposium.

[13] Wooley, J. C., Thompson, A. G., and Rubenstein, M., Phys. Rev. Letters **15**, 670 (1965).

[14] Cardona, M., Proceedings of the Seventh International Conference on the Physics of Semiconductors, Paris, 1964, M. Hulin, Editor (Dunod).

[15] Zhang, H. I., and Callaway, J., Phys. Rev. **181**, 1163 (1969).

[16] Lukes, F., and Schmidt, E., Phys. Letters **23**, 413 (1966).

[17] Bordure, G., Phys. Stat. Sol. **31**, 673 (1969).

Experimental Verification of the Predictions of the Franz-Keldysh Theory as Shown by the Interference of Light and Heavy Hole Contributions to the Electroreflectance Spectrum of Germanium*

P. Handler, S. Jasperson, and S. Koeppen

Physics Department and Materials Research Laboratory, University of Illinois, Urbana, Illinois 61801

By the use of improved experimental techniques and samples of particular impurity concentration, we have been able to observe as many as eleven half oscillations in electroreflectance spectra of germanium at the direct edge ($\Gamma_8^+ \rightarrow \Gamma_7^-$) at room temperature. In addition, near the experimental sixth half oscillation where the light and heavy hole contributions are of opposite signs, we observe destructive interference which greatly modifies the signal lineshape in that region. The unique characteristics of the resultant lineshape allow the determination of the relative magnitudes of the dipole matrix elements and reduced masses for the two bands in a region of k-space somewhat removed from the Γ-point. The experimental results also demonstrate that neither thermal broadening nor field inhomogeneity need be a problem in electroreflectance measurements.

Key words: Electro-absorption techniques; electroreflectance; Franz-Keldysh theory; germanium; oscillatory dielectric function.

The predictions of the effect of an electric field on the band structure of solids show that the dielectric function becomes oscillatory as a function of the energy in the vicinity of critical points in the joint density of states of the valence-conduction bands. Therefore both the electro-absorption (EA) and the electroreflectance (ER) techniques should show a large number of oscillations with a very slowly decreasing envelope [1]. Unfortunately, in both EA and ER only four or five half oscillations have been observed for most materials studied [2-5]. In addition, the lineshapes that were observed were not in good agreement with the one-electron theory for a number of reasons.

In EA the discrepancy between theory and experiment arose because the Coulomb interaction had not been taken into account. In ER a number of serious problems were present in addition to the neglect of the Coulomb interaction. For example, in many experiments no effort was made to modulate from the flat band condition, although the theory was presented in those terms. Thermal broadening was incorporated in the theory at an early date and produced lineshapes which were in better qualitative agreement with experiment; however, it is now evident that broadening was being forced to account for other additional factors, and hence the broadening parameters so obtained were excessively large.

The problem of electric field variation over the penetration depth of the light was anticipated at an equally early date [5] but was not adequately treated until recently by Aspnes and Frova [6], who found that a significant field variation within one reciprocal wave vector of the surface would mix the real and imaginary parts of the dielectric function, giving rise to peculiar lineshapes. Both Frova and Aspnes [7] and Seraphin and Bottka [8] have shown good experimental verification of this point at the direct edge in Ge. The publication of these results seemed to indicate that it would be very difficult to obtain easily interpretable lineshapes except at very small fields in intrinsic material. Since then, however, Koeppen and Handler [9] have shown that, although intrinsic material is best for small fields, doped material is much superior for higher fields. Figure 1 (taken from ref. 9) shows graphs of R_1, the

*Supported by the Advanced Projects Agency under Contract No. SD-131 and the U.S. Army Research Office (Durham) under Contract No. DA-HC04-67-C-0025.

417-156 O - 71 - 28

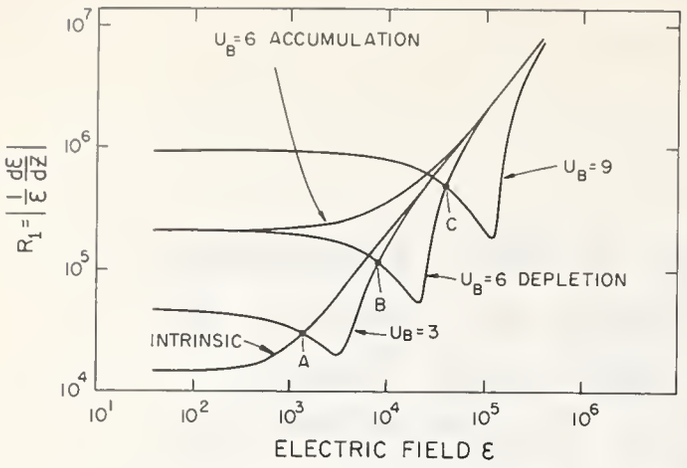

FIGURE 1. R_1 *versus magnitude of surface electric field* ϵ *for four values of impurity concentration for Ge at 300 K.*

Except for the $u_B = 6$ curve, only the depletion region is shown. The curves can be used for *n*- or *p*-type material. The points A, B, and C indicate the fields above which it is better to use a sample with the next higher doping level shown.

logarithmic derivative of the surface electric field with respect to distance, plotted versus the magnitude of the surface electric field under equilibrium conditions for several different impurity concentrations. The smaller R_1 is at any given field, the less important the problem of field nonuniformity will be. The smallest value of R_1 for each value of the field corresponds to a different u_B. Thus, for a peak surface field of $2 \cdot 10^4$ V/cm, a sample of $u_B \simeq 6$ will be optimum. Furthermore, the results so obtained should exhibit no more mixing than results obtained at $\epsilon = 3 \cdot 10^3$ V/cm with intrinsic Ge. In comparison, Frova and Aspnes found measurable mixing effects in intrinsic Ge lineshapes for $\epsilon > 10^4$ V/cm.

Using Ge samples doped in accordance with figure 1, we have obtained results in the high field limit which are in excellent agreement with simple one-electron theory. The data include both the direct edge ($\Gamma_8^+ \rightarrow \Gamma_7^-$) and spin orbit split ($\Gamma_7^+ \rightarrow \Gamma_7^-$) structures and show a number of effects not previously observed. These new results further suggest that it may become possible to determine the source in **k**-space of other ER signals.

The standard electrolyte electroreflectance technique was used in obtaining the present data. Except for the following two modifications, the experimental system was the same in most respects as that described by Hamakawa et al. [10]. First, the optical method for determining flat band described in that reference has since been improved so that it is now possible to monitor the proximity of the bands to the flat band condition every alternate half cycle while the experiment is in progress. Details of this will be presented in another paper published elsewhere. Secondly, potentiostatic control of the modulation and bias voltages is now employed for greater stability of conditions in the sample cell, and voltages quoted below were measured via a salt bridge located adjacent to the surface of the grounded Ge sample. The surface potential was square wave modulated at 310 Hz between flat band and arbitrary band bendings. The energy bands were always modulated in the depletion direction for greater field uniformity in the space charge region as suggested above. Under certain dynamic conditions it was even possible to reduce R_1 below the equilibrium values shown in figure 1.

The sample was a 0.13 Ω cm *n*-type wafer of Ge at room temperature (u_B=6.2) with a (1$\bar{1}$0) reflecting face. A Polaroid Corporation type HR sheet polarizer was used to polarize the light either along the [110] or [001] axis of the reflecting surface.

Several graphs of $\Delta R/R$ are plotted in figure 2 versus a common energy scale which extends from 0.7 to 1.2 eV. Experimental lineshapes are drawn as solid curves, and all were obtained with a peak-to-peak modulation voltage of 0.7 V from the flat band condition. Because the values of $\Delta R/R$ range over three decades, the data for the [110] and [001] polarizations are displayed semi-logarithmically in figures 2b and 2c, respectively. For comparison, the [110] data are also plotted versus the more customary linear scale (with one scale change) in figure 2a. Of immediate interest is the large number of half oscillations present in the $\Gamma_8^+ \rightarrow \Gamma_7^-$ structure: the oscillations extend nearly 0.2 eV above the gap energy where they finally disappear in the rising exponential tail of the spin orbit split structure. A comparable number of half oscillations has only been observed in the EA spectrum of the indirect edge of Si [11], shown in figure 3. This graph serves to demon-

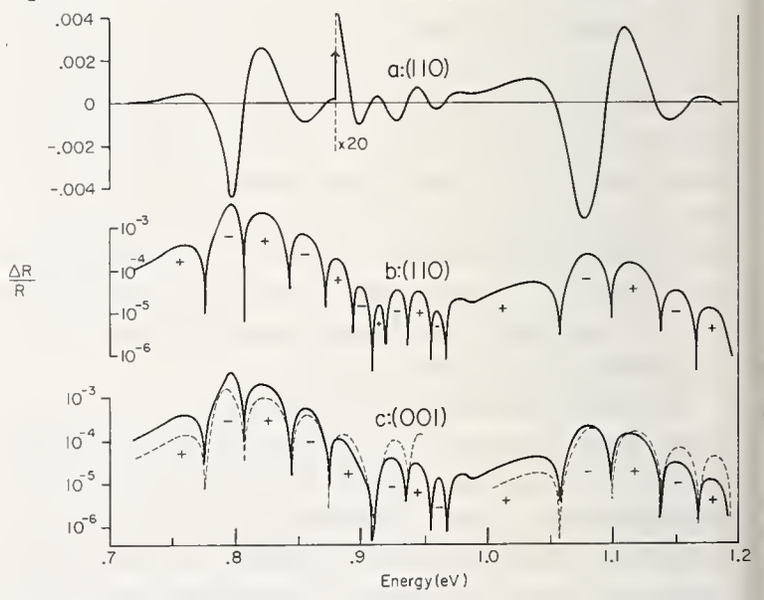

FIGURE 2. *Electroreflectance spectra between* 0.7 *and* 1.2 eV *for light polarized as indicated (note that the* $\Gamma_7^+ \rightarrow \Gamma_7^-$ *structure exhibits no polarization dependence).*

Curve (a) is plotted linearly with one scale change; curves (b) and (c) are plotted semi-logarithmically. Solid curves are experimental; the dashed line in (c) is a least-squares computer fit using one-electron theory. The rms noise magnitude during this work was approximately $2 \cdot 10^{-5}$.

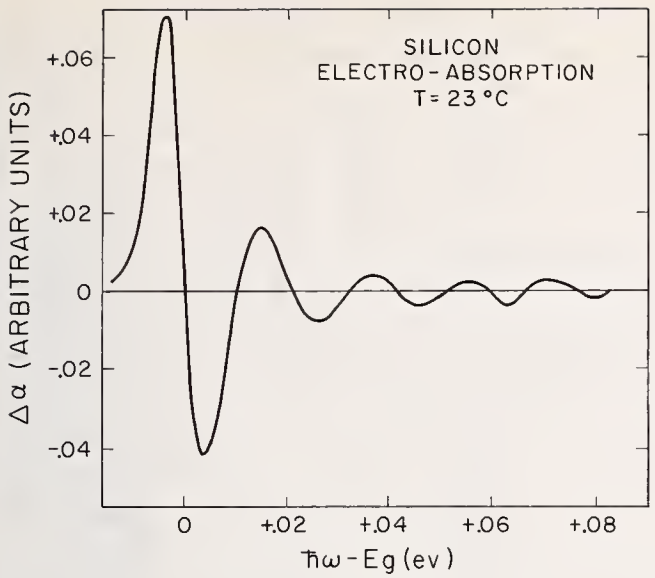

FIGURE 3. *Electro-absorption data of Frova et al., Phys. Rev.* **145**, *575 (1966).*

This curve, obtained with an electric field of $1.4 \cdot 10^4$ V/cm, shows ten half oscillations.

strate that junction EA measurements did not suffer from the severe field inhomogeneities encountered in ER.

Returning to figure 2, two conclusions can be reached on the basis of the large number of oscillations. First, the effect of electric field nonuniformity in the space charge region is small, since significant field variation over a distance equal to one reciprocal wave vector would cause oscillations above the gap to be smeared out [6,7]. This is further substantiated by the fact that the first positive peak is six times smaller than the second positive peak, in approximate agreement with simple Franz-Keldysh theory [1]. Frova, Aspnes [6,7], Seraphin and Bottka [8], have demonstrated that the magnitude of the positive peak below the gap becomes comparable or larger than that of the second positive peak when the nonuniformity becomes important. Secondly, the amount of thermal broadening cannot be as great as 30 MeV as previously thought [2,3], since that amount of broadening would similarly wash out the oscillations farthest from the gap and would require that the first negative peak be relatively much wider and more symmetric than is observed in figure 2. It will be demonstrated shortly that the broadening parameter compatible with the above data is 3 (0.11 kT) and 9 meV (0.35 kT) for the $\Gamma_8^+ \rightarrow \Gamma_7^-$ and $\Gamma_7^+ \rightarrow \Gamma_7^-$ structures, respectively. Our experience with thermal broadening precludes the possibility of values significantly greater than these for this energy range at room temperature.

Another striking feature of the lower energy structure is the collapse of the oscillation envelope and a brief irregularity in the oscillatory nature of the lineshapes just after the 5th (3rd positive) experimental

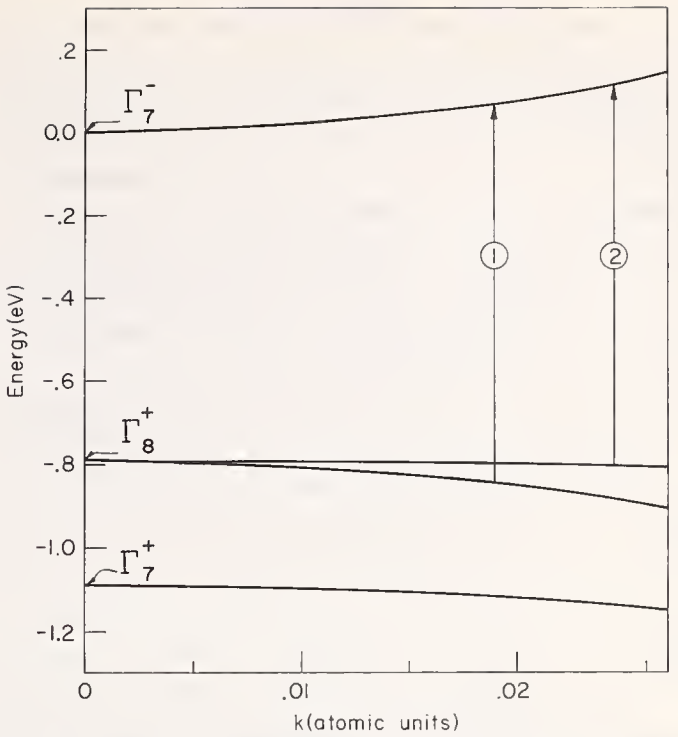

FIGURE 4. *Energy band diagram of the bands contributing to the structures shown in figure 1.*

Arrows 1 and 2 represent equal energy transitions of 0.91 eV, the central energy of the region of destructive interference. This figure is only schematic, since it neglects changes in curvature and anisotropy of the bands, as discussed in the text.

peak at approximately 0.9 eV. This effect is caused by the mutual cancellation of the light and heavy hole contributions to the resultant lineshapes. The period of oscillation of the electro-optic function is inversely proportional to the cube root of the reduced mass of the bands involved, and thus the difference in effective masses of the degenerate valence bands (see fig. 4) causes a periodic beating of contributions from equal-energy transitions, such as those indicated by arrows 1 and 2, centered at different points in **k**-space for the light and heavy hole bands. Since the contributions from the two bands are comparable in amplitude but opposite in sign, the resultant lineshape is a sensitive function of both the precise ratio of signal amplitudes and the ratio of reduced masses. The ratio of the reduced masses parallel to the electric field determines how far above the gap the cancellation will occur, and the ratio of oscillator strengths determines the exact lineshape in the beat region.

Blossey [12] has defined a parameter F (electric field strength in units of effective Rydbergs per Bohr radius) which is a measure of the electric field strength relative to that of the Coulomb interaction. He shows that for $F > 20$, the electroreflectance spectra at the direct edge energy will not be greatly altered by the presence of the Coulomb interaction. For the data shown in figure 2, $F = 174$ and $F = 61$ for the light and heavy holes, respectively. In addition, since the region of destructive interference occurs ~0.1 eV (57 to 96 ef-

fective mass Rydbergs) above the gap, the electron-hole pairs can certainly be thought of as nearly free particles. We shall compare the observed spectra with simple one-electron theory using Lorentzian-broadened electro-optic functions $G(\eta,\gamma)$ defined by Aspnes [13]. Furthermore, we shall assume that the complex $\Gamma_8^+ \rightarrow \Gamma_7^-$ structure can be represented by the algebraic sum of two G-functions, although in the immediate vicinity of the direct gap the degeneracy at $\mathbf{k}=0$ and the Coulomb interaction should make the fit less exact.

The dashed curves in figure 2c are the result of a least-squares computer fit of the following functions to the low and high energy structures, respectively:

$$\left.\frac{\Delta R}{R}\right|_{(\Gamma_8^+\rightarrow\Gamma_7^-)} = \frac{A}{(\hbar\omega)^2}\left[BG(\eta_l,\gamma)+G(\eta_h,\gamma)\right] \tag{1}$$

$$\left.\frac{\Delta R}{R}\right|_{(\Gamma_7^+\rightarrow\Gamma_7^-)} = \frac{A'}{(\hbar\omega)^2}G(\eta_{so},\gamma') \tag{2}$$

In the above, A and A' are amplitude factors, $\hbar\omega$ is the photon energy, B is the ratio of light to heavy hole contributions, γ and γ' are the broadening parameters, and the η's are defined as

$$\eta_i = \frac{E_i-\hbar\omega}{\left[\dfrac{(e\hbar\epsilon)^2}{2\mu_i}\right]^{1/3}} = \frac{E_i-\hbar\omega}{\hbar\theta_i} \tag{3}$$

where ϵ is the peak effective electric field at the Ge surface, and E_i, $\hbar\theta_i$ and μ_i are respectively, the effective energy gap, the electro-optic energy, and reduced mass associated with transitions from the ith hole band, $i = \ell$ (light), h (heavy), or so (spin orbit split) to the conduction band. Figure 5 shows an expanded view of the beat region for both polarizations, the solid curves representing the experimental data, the dashed lines the computer fit of eq (1).

The fit between theory and experiment for both polarizations is remarkably good; the only serious discrepancy is the too-rapid diminution of the envelope of the experimental structure with increasing energy. We expect that even this difference would disappear if the Coulomb interaction and a slight amount of electric field inhomogeneity were taken into account. These results of simple superposition of the light and heavy hole bands are also in agreement with the calculations of Enderlein et al. [16].

Table 1 lists the values of the various parameters obtained from the computer fit: only μ_{so} was assumed given; all other quantities were derived relative to it. To elaborate, the electron and hole masses for the $\Gamma_7^+ \rightarrow \Gamma_7^-$ structure were taken to be .036 m_o [14] and .077 m_o [15], respectively. The fit of eq (2) then uniquely

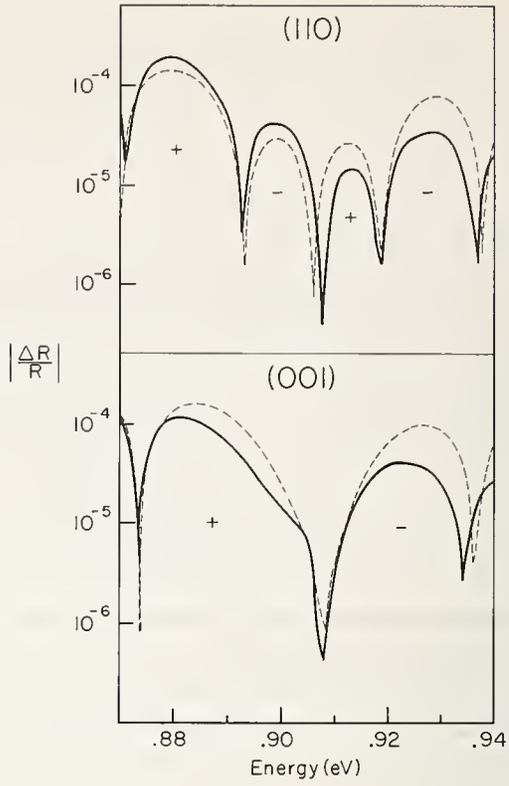

FIGURE 5. *Expanded view of the heat region of the* $\Gamma_8^+ \rightarrow \Gamma_7^-$ *structure for both polarizations.*
Solid curves are experimental; dashed lines are the theoretical predictions of eq (1).

specified $\hbar\theta_{so}$, γ', E_{so}, and the electric field ϵ. The parameters pertaining to the $\Gamma_8^+ \rightarrow \Gamma_7^-$ structure were subsequently derived by using the value of the field ϵ obtained above.

The reduced masses measured by this technique are average values since the effect of the electric field is to mix states in $\mathbf{k}$-space, especially those within one unit of η (25-30 meV) of the point under consideration. Nonetheless, two points can be made on the basis of these data. First, μ_h has a magnitude greater than the electron mass at the Γ-point, indicating the probability that both the electron and heavy hole band have undergone a significant change in curvature within .025 atomic units of $\mathbf{k} = 0$ (see fig. 4). Secondly, the

TABLE 1. *Summary of experimental parameters*

$\Gamma_7^+ \rightarrow \Gamma_7^-$	$\Gamma_8^+ \rightarrow \Gamma_7^-$
$\mu_{so} =$ 0.0245 m_0[14, 15]	$\mu_l =$ 0.022 m_0 (.0195 m_0 at $\mathbf{k}=0$)
	$\mu_h =$ .038 m_0 (.033 m_0 at $\mathbf{k}=0$)
$\epsilon =$ $4.2\cdot10^4$ V/cm	$\epsilon =$ $4.2\cdot10^4$ V/cm
$\hbar\theta_{so} = 30.3$ meV	$\hbar\theta_l = 31.5$ meV
	$\hbar\theta_h = 26.1$ meV
$\gamma' =$ 9 meV	$\gamma =$ 3 meV
$E_{so} =$ 1.08 eV	$E_{l,h} =$ .79 eV
	$B_{110} =$ .71 (110 polarization)
	$B_{001} =$ 1.16 (001 polarization)

anisotropy of the heavy hole band is clearly indicated by the polarization dependence of the lineshape in the beat region. Since B depends only on the ratio of the dipole matrix elements for the two transitions, which in turn can be shown to be functions of the effective masses evaluated along the polarization direction [17], the difference between B_{110} and B_{001} is an indication of the difference between corresponding components of the heavy hole mass tensor in these two directions. In fitting the data many small effects have been neglected such as the mass dependence upon the direction and magnitude of $\mathbf{k}$, the energy dependence of the broadening parameter and the Coulomb interaction. In fact it is quite surprising that the fit is as good as it is.

In conclusion we have shown that reliable ER data can be obtained when the energy bands are modulated from flat band and the sample is doped so that the variation of the electric field with distance is not important. We anticipate that it will now be possible to separate exciton effects from one-electron behavior at the direct edge in Ge since mixing can be made negligible in both high and low field regions where the respective effects dominate. Furthermore, by use of these techniques at higher photon energies, it should be possible to obtain lineshapes which are sufficiently good so as to permit the unambiguous identification of critical points which gave rise to those structures.

References

[1] Aspnes, D. E., Phys. Rev. **147**, 554 (1966); **153**, 972 (1967).

[2] Seraphin, B. O., Modulated Reflectance, (to be published in Optical Properties of Solids, F. Abeles, Editor, North Holland Publishing Co.).

[3] Seraphin, B. O., Electroreflectance (to be published in Semiconductors and Semimetals, K. Willardson and A. Beer, Editors, **Vol. VI**, Academic Press, New York).

[4] Cardona, M., Modulation Spectroscopy, Supplement 11 to Solid State Physics, F. Seitz, D. Turnbull and H. Ehrenreich, Editors (Academic Press, New York, 1969).

[5] Cardona, M., Shaklee, K. L., and Pollack, F. H., Phys. Rev. **154**, 696 (1967).

[6] Aspnes, D. E., Frova, A., Sol. State Comm. **7**, 155 (1969).

[7] Frova, A., and Aspnes, D. E., Phys. Rev. **182**, 795 (1969).

[8] Seraphin, B. O., and Bottka, N., Sol. State Comm. **7**, 497 (1969).

[9] Koeppen, S., and Handler, P., Phys. Rev., to be published.

[10] Hamakawa, Y., Handler, P., and Germano, F., Phys. Rev. **167**, 709 (1968).

[11] Frova, A., Handler, P., Germano, F. A., and Aspnes, D. E., Phys. Rev. **145**, 575 (1966).

[12] Blossy, D. F., Ph. D. thesis, University of Illinois (1969).

[13] See reference 1; also, at the direct edge, $\Delta R/R \simeq \Delta\epsilon_1 \sim G(\eta,\gamma)$.

[14] Zwerdling, S., Lax, B., and Roth, L. M., Phys. Rev. **108**, 1402 (1957).

[15] Smith, R. A., Semiconductors (Cambridge University Press, New York, 1961), p. 350.

[16] Enderlein, R., Keiper, R., and Tausenfreund, W., Phys. Stat. Sol. **33**, 69 (1969).

[17] Smith, R. A., Wave Mechanics of Crystalline Solids (John Wiley and Sons Inc., New York, 1961), pp. 464-466.

Variations of Infrared Cyclotron Resonance and the Density of States Near the Conduction Band Edge of InSb*

E. J. Johnson and D. H. Dickey

Lincoln Laboratory, Massachusetts Institute of Technology, Lexington, Massachusetts 02139

The electronic density of states near the conduction band edge of InSb with and without a magnetic field is obtained from dispersion relations based upon $k \cdot p$ interactions with nearby bands and parameters determined and confirmed by several intraband experiments including fundamental cyclotron resonance, spin resonance, spin-flip cyclotron resonance, phonon assisted cyclotron resonance and harmonics of cyclotron resonance. The density of states displays effects due to nearby band interactions and due to electron-phonon interaction.

Key words: Cyclotron resonance; electronic density of states; electron-phonon interaction; InSb; interband transitions; Landau levels.

1. Introduction

The electronic density of states can be obtained in a straightforward manner, once one has an electron energy dispersion relation in which one has some confidence, and if one has negligible broadening of the energy levels. We have determined the experimental parameters for such a dispersion relation for states near the bottom of the conduction band of InSb [1] by obtaining experimental data that is more precise and covers a wider range of conduction band energies than previous data. Our analysis takes into account interactions not previously recognized and reconciles various interband optical experiments for the first time. In this paper we summarize this work and apply it in determining the density of states both with and without a magnetic field. A variety of experiments involving intraband optical transitions confirm the dispersion relation for energies to ~80 meV above the band edge.

The density of states near the bottom of the conduction band of InSb can be expected to depart from simple parabolic band behavior, principally due to interactions between the conduction band and other nearby bands. These interactions for InSb have been treated theoretically by Kane [2]. The effects on the magnetic energy levels have been treated by Lax et al. [3] and by Bowers and Yafet [4]. When the cyclotron energy is comparable to an LO phonon energy an additional effect on the density of states occurs due to a polaron self-energy effect [5]. In InSb this effect occurs in a narrow energy range and can be easily accounted for in fitting the nonparabolic band theory to the experimental results [6].

The experimental results were obtained by observing the infrared transmission of InSb samples versus magnetic field for fixed photon energies from 4.5 to 50 meV. Absorption peaks were observed which can be identified with a variety of intraband transitions involving Landau levels. The fundamental cyclotron resonance absorption occurs as a triplet, and is used to determine the band edge effective mass. A combination resonance transition is observed which involves a spin flip, in addition to a fundamental cyclotron resonance transition, and is used together with spin resonance results of Isaacson [7] to determine the band edge effective g-factor. Using these band edge parameters energies for transitions involving cyclotron resonance harmonics, phonon assisted cyclotron resonance, and the variation of spin resonance energy with carrier concentration are calculated and are found to agree well with observed transition energies. The consistency among the various intraband transitions provides con-

*This work was sponsored by the Department of the Air Force.

fidence in the nonparabolic band theory and the values of the band paramcters determined from the earlier experiments. The density of states is calculated from the corresponding dispersion relations.

2. Dispersion Relations

The wave functions for the energy levels near the bottom of the conduction band of InSb have s-like symmetry near $k = 0$ and the energy surfaces are nearly spherical. The energy levels are given in Wigner-Brillouin perturbation theory by

$$E_c(k) = \frac{\hbar^2 k^2}{2m^*} \tag{1}$$

where m^* is an energy dependent effective mass given by

$$\frac{m}{m^*} = 1 + \frac{1}{m} \sum_{l \neq c} \frac{|p_{cl}^x|^2}{E_c(k) - E_l(0)} \tag{2}$$

where the summation is taken over all energy levels l with energy at $k = 0$ of $E_l(0)$, and where p_{cl}^{η} is the η component of the momentum matrix element between bands c and l at $k = 0$. To a good approximation we can neglect the energy dependence involving energy bands more remote than the three (six) valence bands and can write (2) in the form

$$\frac{m}{m^*} \approx 1 + \frac{m}{m_{rb}} + \frac{2}{m} \sum_{\substack{\text{valence} \\ \text{bands}}} \frac{|p_{cl}^x|^2}{E_c(k) - E_l(0)}. \tag{3}$$

This gives a cubic equation for the energy, $E_c(k)$. The solution relevant to the conduction band can be written

$$E_c(k) = -\frac{E_g}{2} + \frac{\hbar^2 k^2}{2} \left(\frac{1}{m} + \frac{1}{m_{rb}} \right) + \frac{E_g}{2} \left[1 + 4 \frac{\hbar^2 k^2}{2 m_c} \frac{f_1(E_c)}{E_g} \right]^{1/2} \tag{4}$$

where m_c is defined at $k = 0$ and is given by

$$\frac{m}{m_c} = \frac{2}{m} |\langle s|p_z|z\rangle|^2 \frac{E_g + \frac{2}{3}\Delta}{E_g(E_g + \Delta)}. \tag{5}$$

where Δ is the spin-orbit splitting of the valence band. The function $f_1(E_c)$ is equal to unity at $k = 0$ and is weakly energy dependent

$$f_1 = \frac{E_g + \Delta}{E_g + \frac{2}{3}\Delta} \frac{E_c(k) + E_g + \frac{2}{3}\Delta}{E_c(k) + E_g + \Delta}. \tag{6}$$

The density of states is obtained from (4) in the usual way for spherical energy surfaces

$$\rho(E) = \frac{1}{\pi^2} \int_0^{\infty} k^2 A(E, k)\, dk \tag{7}$$

where $A(E,k)$ gives the distribution in energy of the level of wave vector k. If the energy levels have negligible broadening, $E(k)$ is single valued: $A(E,k) = \delta(E - E(k))$ and (7) becomes

$$\rho(E) = \frac{1}{\pi^2} k^2 \left(\frac{dE}{dk} \right)^{-1} \tag{8}$$

To obtain the energy levels in a magnetic field we have to solve the effective mass equation

$$\left[\frac{\left(\mathbf{p} + \frac{e}{c}\mathbf{A}\right)^2}{2m^*} \mathbf{I} + \beta g^* \mathbf{S} \cdot \mathbf{H} - E_{c,j} \mathbf{I} \right] \begin{pmatrix} f_{cj}^{\uparrow} \\ f_{cj}^{\downarrow} \end{pmatrix} = 0 \tag{9}$$

where $\mathbf{A} = (1/2)\mathbf{H} \times \mathbf{r}$ and β is the Bohr magneton.

The effective g-factor, g^*, is energy dependent and given by

$$g^*(E_{c,j}) = 2 + g_{rb} - \frac{2}{mi} \sum_{\substack{\text{valence} \\ \text{bands}}} \frac{p_{cl}^x p_{lc}^y - p_{cl}^y p_{lc}^x}{E_{c,j} - E_l(0)} \tag{10}$$

where the contribution due to interactions with remote bands is concentrated in the constant term g_{rb} and the last term involves interactions with the three valence bands. The solution relevant to the conduction band is given by

$$E_{n\pm} = -\frac{E_g}{2} + \frac{E_g}{2} \left\{ 1 + \frac{4 f_1}{E_g} \left[(2n+1) \frac{m}{m_c'} \beta H \pm \frac{1}{2} g' \beta H f_4 + \frac{\hbar^2 k_z^2}{2 m_c'} \right] \right\}^{1/2} \tag{11}$$

where

$$\frac{1}{m_c'} = \frac{1}{m} + \frac{1}{m_{rb}} + \frac{1}{m_c} \tag{12}$$

$$g' = 2 + g_{rb} - 2 \frac{m}{m_c} \frac{\Delta}{3E_g + 2\Delta} \tag{13}$$

$$f_4 = \frac{E_g + \frac{2}{3}\Delta}{E_{n\pm} + E_g + \frac{2}{3}\Delta}. \tag{14}$$

Equation (11) provides a dispersion relation from which one can calculate the density of states with applied magnetic field. The singularities which occur in the density of states at $k = 0$ provides for well defined optical absorption lines. Using such experiments one can determine the parameters precisely.

3. Determination of Parameters

In figure 1 we show experimental traces of sample transmission versus magnetic field at certain fixed photon energies below and above the reststrahl energy. These samples are ~20μ in thickness and reveal only the strong absorption near $\hbar\omega_c$. Near the region $\hbar\omega_{TO} < h\nu < \hbar\omega_{LO}$ the sample is opaque due to high reststrahl reflection. We see that the absorption in general involves three peaks whose relative strengths depend upon temperature. Simple arguments [1] show that the high energy peak is associated with impurity transitions, which we shall not discuss further here. The two lower energy peaks are associated with fundamental cyclotron resonance which is spin split due to nonparabolic band effects. For $\hbar\nu > \hbar\omega_{LO}$ large broadening occurs and the three peaks are not resolved. The observed cyclotron resonance energies are plotted versus magnetic field in figure 2. The solid lines are our best fit of the nonparabolic band theory to the experimental points. We found that we could obtain a good fit to the lower energy part of the data if we ignored the points above $h\nu \approx 18$ meV. A further indication of anomalous behavior in this region is shown by the discontinuity in the data on either side of the reststrahl region. This anomalous behavior is due to polaron self energy effects and have been discussed in detail previously [6]. The behavior has been shown in more detail in experiments involving interband transitions [8] and combination resonance [9].

In attempting a best fit to the data we found that the splitting between the cyclotron resonance lines is insensitive to the precise choice of the magnitude of g' between values of 40-70. This uncertainty in the value of g' results in only a slight uncertainty in the value of m_c' obtained from the fit. We obtain a value $m_c' = 0.0139\text{m} \pm .0001\text{m}$ for the band edge effective mass in InSb.

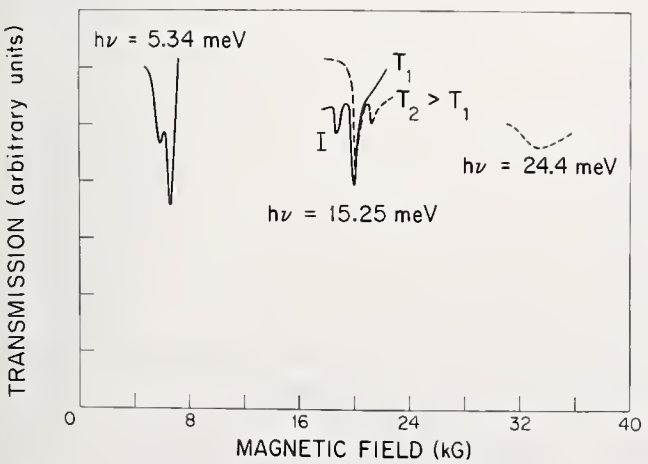

FIGURE 1. *Cyclotron resonance spectra observed in thin samples* ($t \approx 20\mu$) *at temperatures near liquid helium such that* $T_2 > T_1$.

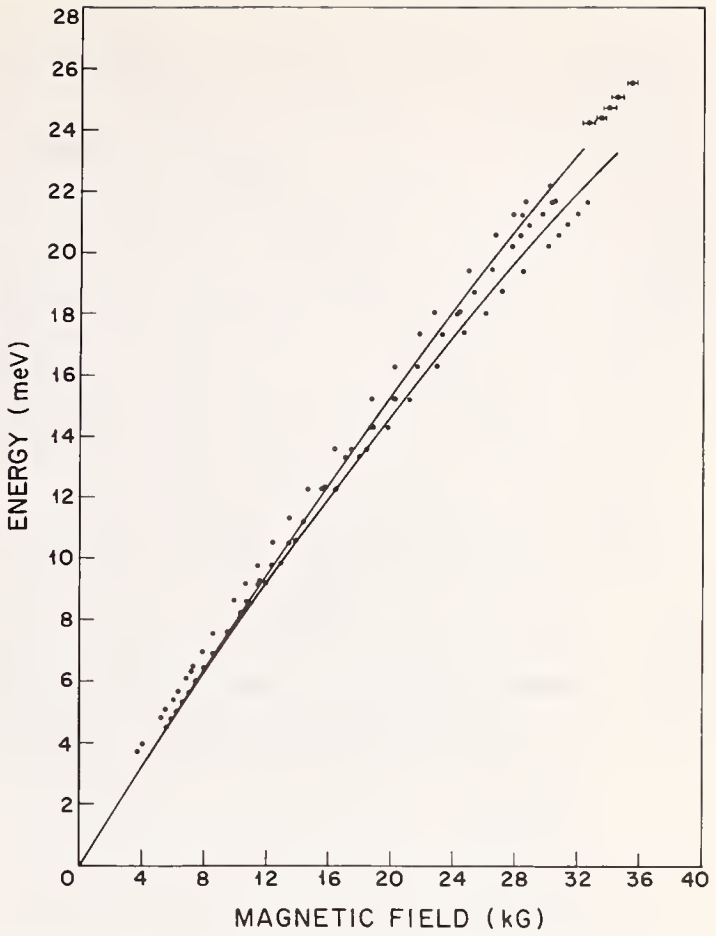

FIGURE 2. *Variation of cyclotron resonance absorption peaks with magnetic field.*

The solid lines give the theoretical predictions using $m_c' = 0.139$ and $g' = -51.3$.

Spin resonance experiments of Isaacson [7] for a sample with $n = 3.6 \times 10^{13}$ cm^{-3} and $H \sim 0.5$ kG yield an experimental g-factor of $\pm 51.3 \pm 0.1$. Such a sample would have a Fermi level $\zeta \sim 0.3$ meV above the band edge and should yield a value of g-factor very close to the band edge value. To check this value of band edge g-factor and to check the variation of spin energy with magnetic field, we have observed and analyzed combination resonance transitions which involve the transition E_{0+} to E_{1-} (i.e., a cyclotron resonance transition plus a spin flip). The shift of the resonance peaks with magnetic field is shown in figure 3 and compared to calculations of the energy $E_{1-} - E_{0+}$ according to eq (11). Excellent agreement between experiment and theory is obtained for magnetic fields less than ~27 kG. We conclude that the value of -51.3 for the band edge factor is a good one and that eq (11) faithfully predicts the spin energy for fields up to 27 kG. The discrepancy above 27 kG is easily attributed to polaron self-energy effects.

4. Further Tests

Having determined the parameters m_c', and g' we are in a position to calculate the density of states. However,

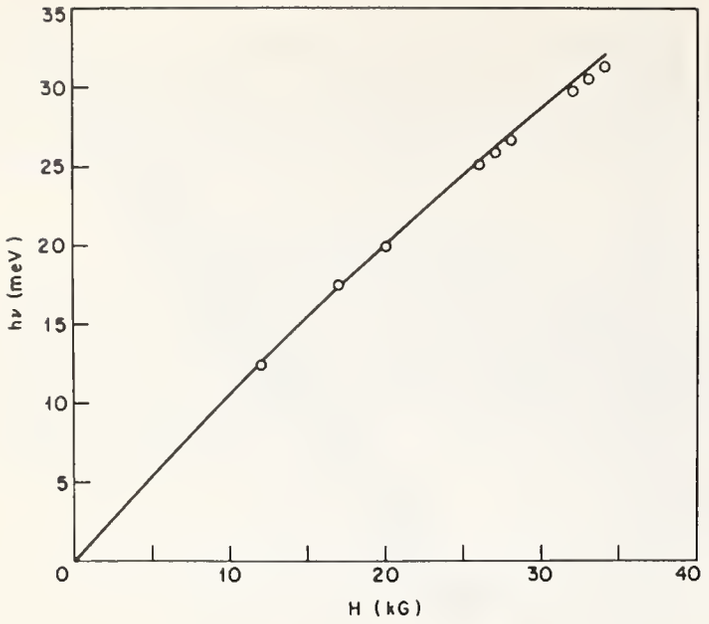

FIGURE 3. *Variation of combination resonance peaks with magnetic field.*
The solid line gives the theoretical prediction.

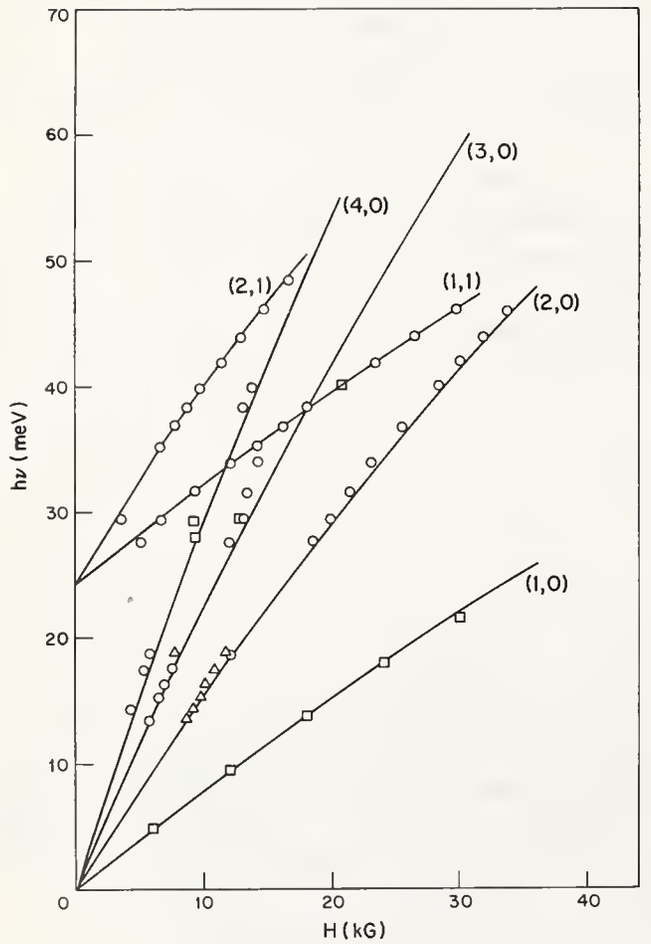

FIGURE 4. *Shift with magnetic field of the absorption peaks involving cyclotron resonance harmonics and phonon assisted transitions.*
The designations describe the excited states (Landau quantum number, number of photons). The solid lines give the theoretical predictions.

we first apply some further checks on the values obtained.

Experimental results using a thick sample $t \approx 2$mm and $n \approx 1.4 \times 10^{15}$ cm^{-3} have also been obtained. This sample thickness permits the observation of weak absorption on the high energy side of the fundamental cyclotron resonance. For $h\nu = 18.75$ meV the observed absorption peaks are spaced approximately equal in $1/H$. In figure 4 we see that the peaks observed at 18.75 meV converge to $h\nu = 0$ at $H = 0$. These peaks involved transitions from the same ground state to higher and higher Landau levels (i.e., cyclotron resonance harmonics). Additional peaks are seen which converge at $H = 0$ to an energy about 24 meV, which is close to the known value of the LO phonon energy. These transitions apparently involve the emission of an optical phonon. The transition energies for several of the cyclotron resonance harmonics have been calculated using eq (11) and the band parameters determined in section 3. These results are shown as the solid lines in figure 4. Also shown are the calculated cyclotron resonance harmonics shifted by 24.4 meV. A good agreement between experiment and theory is obtained. The identification of the transitions involved is confirmed and the fit to the data gives a value of 24.4 ± 0.3 meV for the longitudinal optical phonon energy. The agreement between the experimental cyclotron resonance harmonic transition energies and the calculated values supports the use of eq (11), and the parameters previously obtained to calculate the magnetic energy levels to energies ~80 meV above the band edge.

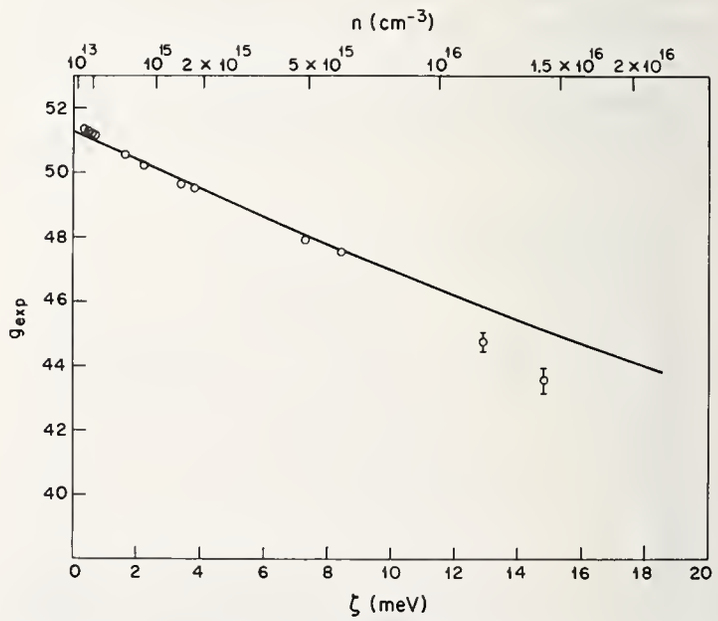

FIGURE 5. *Comparison of experiment and theory for variation of spin resonance with Fermi level for* InSb.
The experimental points are the data of Isaacson [7] for H ~ 125 and ~ 500 G. The solid line is a composite for the theoretical predictions at 0.125, 0.500, 3 and 20 kG.

According to eq (11) the spin energy depends upon Landau quantum number. In a spin resonance experiment one can select the Landau levels whose splitting is observed by doping the sample and moving the Fermi level through the Landau levels. Such a spin resonance experiment has been performed by Isaacson [7]. His data are reproduced in figure 6 where the Fermi energy has been calculated from the carrier concentration with the help of eq (11). The spin energies are expressed in terms of g_{exp} which is defined at resonance as

$$g_{\exp} = h\nu_{SR/\beta H}$$

where $h\nu_{SR}$ is the photon energy used in the experiment. The solid line in figure 5 is our prediction of the variation of g_{exp} with Fermi level. Excellent agreement is obtained for $\zeta \lesssim 8.5$ meV, which confirms the ability of (11) to predicts the spin energy. A discrepancy of $\sim 5\%$ occurs at $\zeta \approx 14$ meV, but this may be an impurity effect.

5. Density of States

The dispersion relation for the conduction band deduced from these experiments is shown in figure 6. The dashed curve is the result for a parabolic band with an effective mass equal to the InSb band edge mass. The corresponding density of states curve is given in figure 7, where again the dashed curve is the result for a parabolic band. The InSb density of states increases more rapidly than for a parabolic band and shows a marked departure for energies greater than ~3 meV above the band edge. In figure 8 we show the density of states for InSb in a magnetic field of 20 kG. The dashed curve gives the results for a simple parabolic band. At higher energies the peaks in the density of states crowd together and increase in magnitude due to the increase in effective mass and decrease in effective g-factor.

For a parabolic band the cyclotron resonance joint density of states has a singularity at the cyclotron energy $\hbar\omega_c$, and is zero elsewhere. For a nonparabolic band this behavior is modified as can be demonstrated qualitatively using eq (11). For these purposes we simplify (11) by setting $f_1 = f_4 = 1$ and neglect spin by setting $g' = 0$. The cyclotron resonance energy ($h\nu$) is then given by

$$\frac{2h\nu}{E_g} = \left\{1 + \frac{4}{E_g}\left[3\frac{m}{m_c'}\beta H + \frac{\hbar^2 k_z^2}{2m_c'}\right]\right\}^{1/2} - \left\{1 + \frac{4}{E_g}\left[\frac{m}{m_c'}\beta H + \frac{\hbar^2 k_z^2}{2m_c'}\right]\right\}^{1/2} \qquad (15)$$

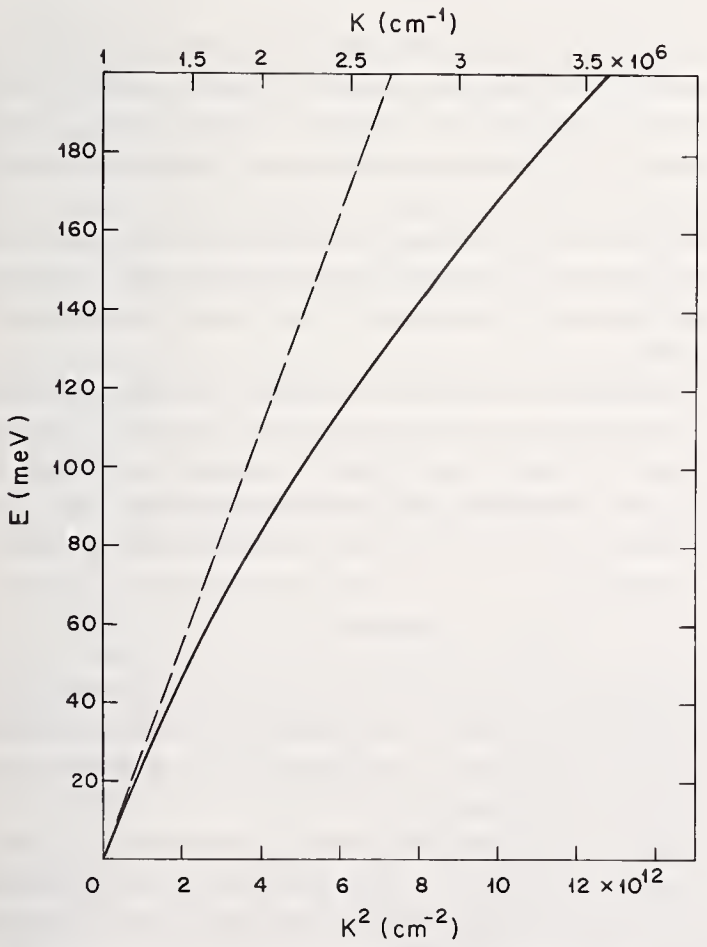

FIGURE 6. *The conduction band dispersion relation deduced from these experiments.*
The dashed line gives the parabolic band result using band edge value of effective mass.

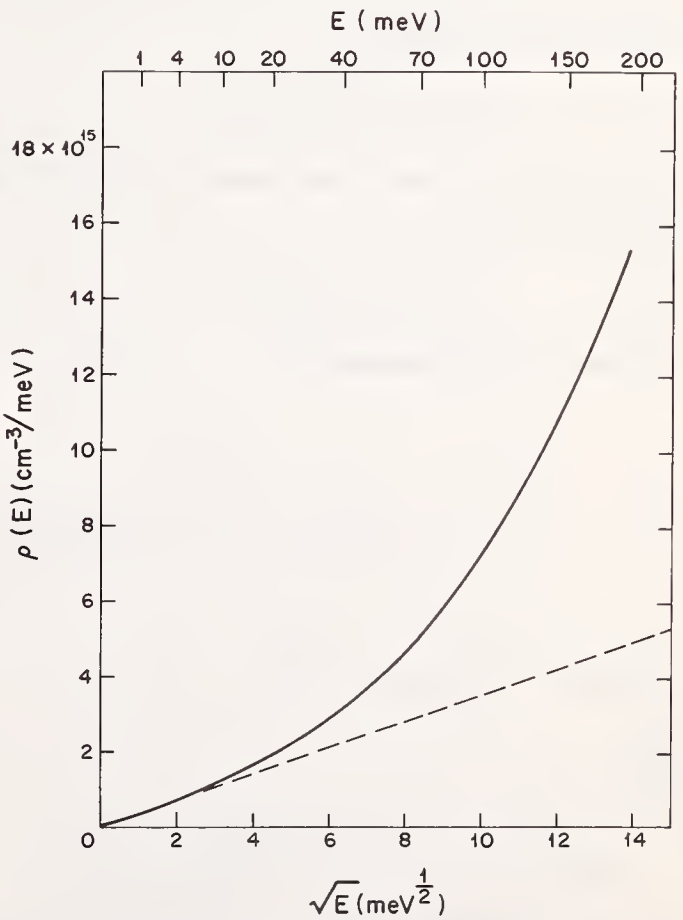

FIGURE 7. *Density of states versus energy.*
The dashed line gives the parabolic band result.

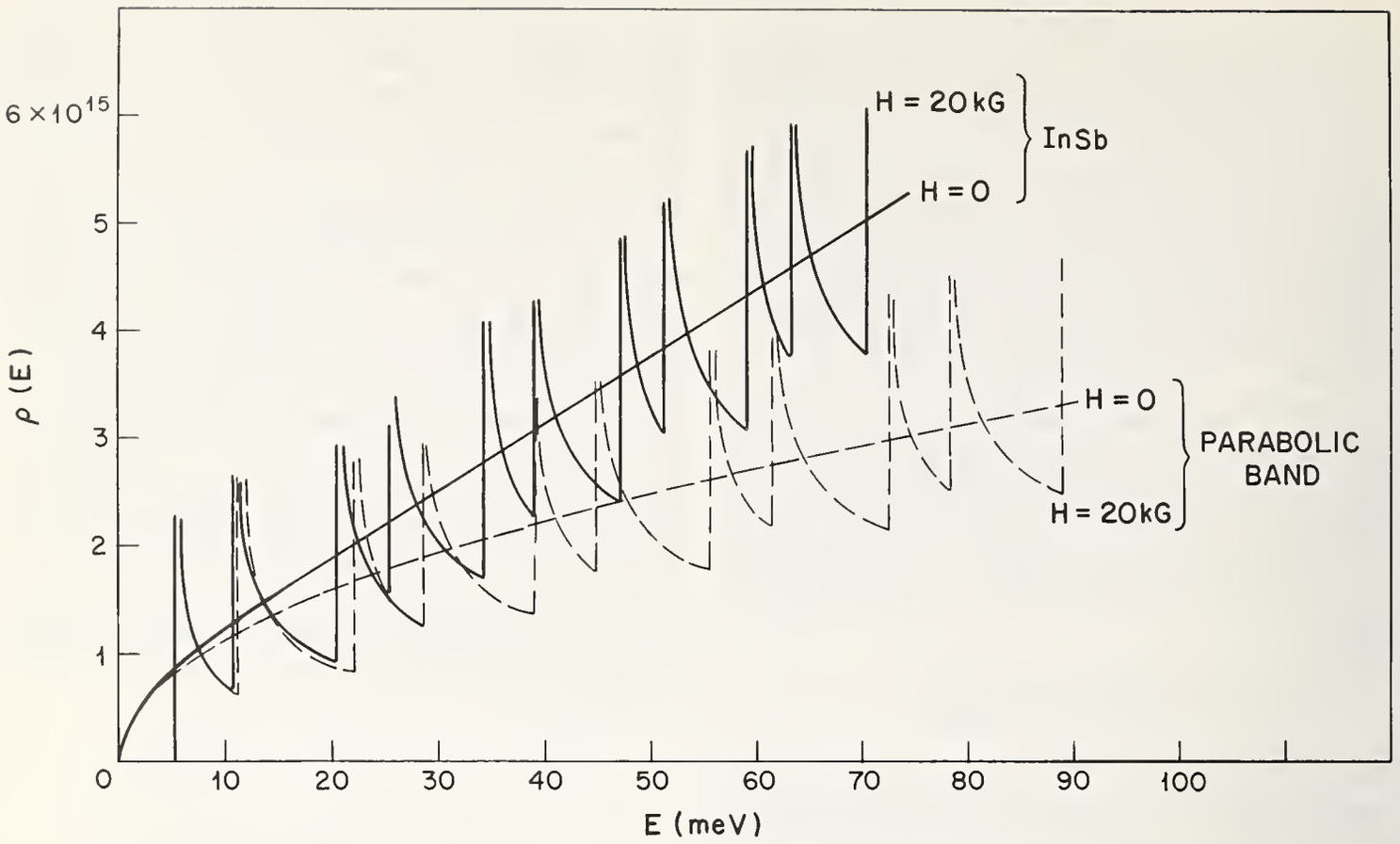

FIGURE 8. *Density of states in a magnetic field of 20 kG for* InSb.
The density of states is also shown for a parabolic band and for H=0.

From (15) one obtains the cyclotron resonance joint density of states as given by

$$\rho_j(h\nu) = \frac{N_\rho}{4\pi^3}\left(\frac{dh\nu}{dk_z}\right)^{-1} \tag{16}$$

where N_ρ is the Landau level degeneracy, which is independent of energy.

If

$$\frac{\hbar^2 k_z^2}{2m_c'} \ll \frac{E_g}{4} + \frac{m}{m_c'}\beta H,$$

eq (15) can be approximated by

$$h\nu(k_z) \approx h\nu(0)\left[1 - \frac{\frac{2}{E_g}\frac{\hbar^2 k_z^2}{2m_c'}}{\left\{1+\frac{12}{E_g}\frac{m}{m_c'}\beta H\right\}\left\{1+\frac{4}{E_g}\frac{m}{m_c'}\beta H\right\}}\right] \tag{17}$$

The derivative is given by

$$\frac{dh\nu(k_z)}{dk_z} = -\frac{\left[h\nu(0)\,\frac{1}{E_g}\frac{\hbar^2}{m_c'}\right]^{1/2}}{\left[\left\{1+\frac{12}{E_g}\frac{m}{m_c'}\beta H\right\}\left\{1+\frac{4}{E_g}\frac{m}{m_c'}\beta H\right\}\right]^{1/4}} \frac{}{[h\nu(0)-h\nu(k_z)]^{1/2}} \tag{18}$$

The variation in the joint density of states with energy is given principally by the factor $[h\nu(0)=h\nu(k_z)]^{1/2}$. The derivative goes to zero at $h\nu(k_z)=h\nu(0)$ giving a singularity in the joint density of states. Therefore, the peak observed in cyclotron resonance absorption corresponds to the Landau level separation at $k_z=0$. In addition, the joint density of states is nonzero for energies less than $h\nu(0)$, in contrast to the case with a parabolic band.

In figure 9 we show a computer calculation of the joint density of states for InSb, at H — 20 kG. This calculation is based upon eq (11) without simplification using the experimentally determined parameters. The calculation displays the expected qualitative behavior. A singularity occurs at $h\nu = h\nu(0)$ and the density at states is nonzero for lower energies. A second singularity occurs corresponding to $k_z = 0$ for the higher energy spin state as seen in the experiments. Indeed, additional singularities corresponding to higher Landau quantum numbers for the ground state occur at lower energies than these shown.

The infrared absorption is proportional to the density of states multiplied by a factor involving the population of the energy levels as given in the lower part of figure 9. In the computer calculation, the Fermi level is adjusted to give the correct carrier concentration for the given magnetic field and temperature.

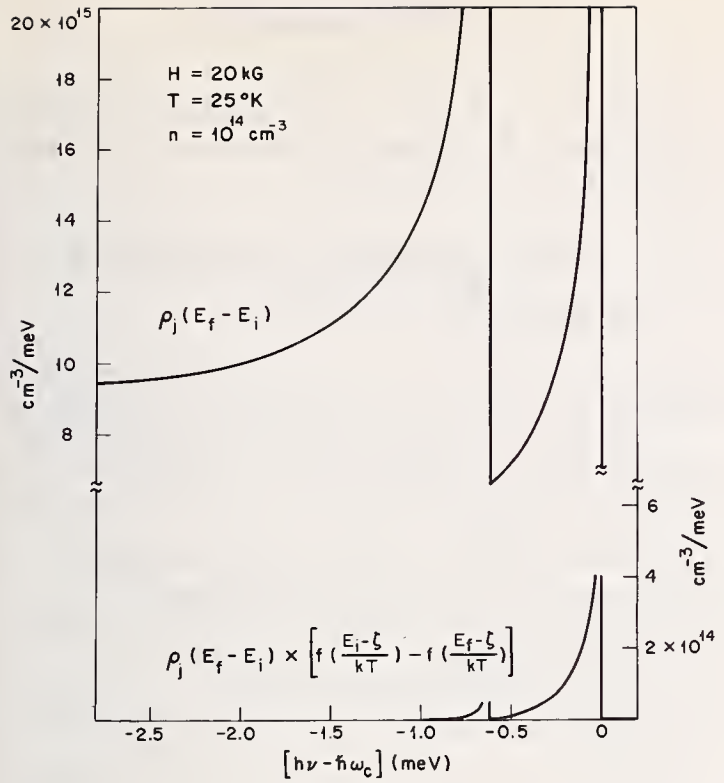

FIGURE 9. InSb *cyclotron resonance joint density of states computed using eq (11) and the experimental parameters.*

It is to be noted in figure 1 that the experimental absorption at 20 kG is asymmetric being sharper on the low magnetic field side which is consistent with the nonparabolic density of states. From figure 9 we obtain a half width for the absorption at 25 K of about 0.1 meV. This corresponds to an experimental half width of ~0.3 meV deduced from figures 1 and 2. Therefore, it is apparent that additional broadening mechanisms are present. The techniques for taking the broadening mechanisms into account is discussed in the accompanying paper by B. Sacks and B. Lax. The broadening mechanisms remove the singularity in the joint density of states, but a peak still should occur at $k_z = 0$, as indicated by the behavior of the single particle density of states calculated by Kubo [13].

6. Discussion

The density of states near the conduction band edge of InSb, both with and without a magnetic field, have been obtained from dispersion relations. These dispersion relations are based on a nonparabolic band theory and the values of band parameters m_c' and g' determined by several intraband experiments. These dispersion relations are found to hold to within 5% for conduction band energies to ~80 meV above the band edge. Presumably, the corresponding density of states are also good to this accuracy.

It is interesting to inquire whether the remote band terms $1/m_{rb}$ and g_{rb} in eqs (12) and (13) are necessary to explain the experimental data. An examination of the equations shows that the m_c' and g' are not independent parameters in the absence of the remote band terms. We have, however, experimentally determined m_c' and g. essentially independent of each other. We find that equations (12) and (13) can be reconciled with the experimental results only if we assume $g_{rb} \approx 0.1g'$ and $(m_{rb})^{-1} = 0$ or $(m_{rb})^{-1} \approx -.1(m_c')^{-1}$ and $g_{rb} = 0$, or some combination of nonzero values of these. Therefore, the remote band interactions are significant.

We have shown that the various *intraband* experiments are consistent with one another. The transition energies calculated from a single dispersion relation agree well with experiments. This consistency does not appear to apply to *intraband* versus *interband* transitions. Pidgeon and Brown [10] type of analysis of interband absorption [11] gives a value of m_c' that is 7% higher than the *intraband* value. The source of this discrepancy is currently under investigation.

A simple theory of the *intraband* absorption in a magnetic field would predict a single absorption line at the cyclotron resonance frequency. Most of the additional transitions we observe can be explained in terms of various band interactions. However, there is currently no explanation which is consistent with experiment for the cyclotron resonance harmonics.

In calculating the density of states from the dispersion relation we neglect energy level broadening. For $H = 0$ the effect of energy level broadening on the density of states would be most serious at the band edge where a tail on the density of states can be expected that extends into the energy gap. The nature of this tail has been the subject of much theoretical work, but definitive experiments are very difficult [12].

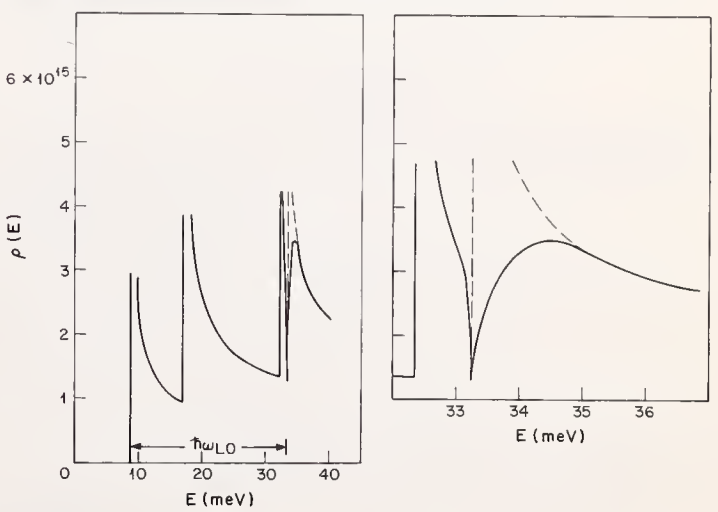

FIGURE 10. *Magnetic density of states for* $\hbar\omega_c = \hbar\omega_{LO}$.
The dashed curve gives the unperturbed result. The solid curve shows the modification in the density of states by electron-phonon interaction predicted by Nakayama [5].

In the presence of a magnetic field, collision broadening can be expected to smooth out the sharp structure in the magnetic density of states shown in figure 10. The problem of energy level broadening of Landau levels has been treated theoretically by Kubo et al. [13] who find significant departures from a theory based upon a simple Lorentzian broadening of each level associated with a value of k_z. Collision broadening of Landau levels is also discussed in the accompanying paper by Sacks and Lax.

The experiments indicate the presence of an anomaly in the density of states when $\hbar\omega_c \approx \hbar\omega_{LO}$. In figure 10 we show how the density of states obtained from the dispersion relation is expected to be modified by the electron-phonon interaction. The dashed curve is the result of the same calculation used in figure 8 for lower magnetic field. The solid curve gives the modification of the density of states predicted by the theory of Nakayama [5]. The $n = 1$ Landau level is split and a zero occurs in the density of states at an energy corresponding to $\hbar\omega_{LO}$ above the lowest Landau level. The splitting in the density of states has been seen in interband absorption [8] and combination resonance [9] and is consistent with the fundamental cyclotron resonance results. However, it remains a challenge to experimentally observe the detailed structure in the density of states shown in figure 10.

7. Acknowledgments

The authors would like to express their appreciation for discussions concerning the cyclotron resonance joint density of states with B. Lax.

8. References

[1] Johnson, E. J., and Dickey, D. H., Phys. Rev. (to be published).
[2] Kane, E. O., J. Phys. Chem. Solids **1**, 249 (1957): also Semiconductors and Semimetals, R. K. Willardson and A. C. Beer, eds., **Vol. 1**, (Academic Press, New York, 1966) p. 75.
[3] Lax, B., Mavroides, J. G., Zeiger, H. J., and Keyes, R. J., Phys. Rev. **122**, 31 (1961).
[4] Bowers, R., and Yafet, Y., Phys. Rev. **115**, 1165 (1959).
[5] Nakayama, M., J. Phys. Soc. Japan **27**, 636 (1969).
[6] Dickey, D. H., Johnson, E. J., and Larsen, D. M., Phys. Rev. Letters **18**, 599 (1967).
[7] Isaacson, R. A., Phys. Rev. **169**, 312 (1968).
[8] Johnson, E. J., and Larsen, D. M., Phys. Rev. Letters **16**, 655 (1966).
[9] Dickey, D. H., and Larsen, D. M., Phys. Rev. Letters **20**, 65 (1968).
[10] Pidgeon, C. R., and Brown, R. N., Phys. Rev. **146**, 575 (1966).
[11] Pidgeon, C. R., and Groves, S. H., Phys. Rev. (to be published).
[12] Johnson, E. J., Semiconductors and Semimetals, R. K. Willardson and A. C. Beer, eds., **Vol. 3**, (Academic Press, New York, 1967) p. 249.
[13] Kubo, R., Miyake, S. J., and Hashitsume, N., Solid State Phys. **17**, 269 (1965).

Cyclotron Resonances of Holes in Ge at Noncentral Magnetic Critical Points

J. C. Hensel and K. Suzuki

Bell Telephone Laboratories, Incorporated, Murray Hill, New Jersey 07974

The anomalous, "quantum" cyclotron resonance spectrum of holes in the degenerate valence bands of Ge is analyzed utilizing the concept of a critical point in the magnetic joint density of states. Contrary to previous work done for $k_H = 0$ (where k_H is the hole wave vector along the magnetic field) our results indicate that cyclotron resonance lines originating at critical points away from $k_H = 0$ are responsible for most of the prominent features of the observed quantum spectrum in Ge.

Key words: Cyclotron resonances; germanium; joint density of states; Landau levels; magnetic; magnetic critical points.

1. Introduction

At low temperatures and high magnetic fields (i.e., $\hbar\omega/kT \gtrsim 1$ where $\omega = eH_0/mc$) cyclotron resonances of holes in the degenerate valence bands of Ge exhibit a complex "quantum" spectrum, observed first by Fletcher [1]. According to Luttinger and Kohn [2,3] this anomalous behavior results from the deviations in spacing between the valence band Landau levels bearing low quantum numbers from the uniform intervals characteristic of the higher "classical" levels. The exceptional complexity of the resultant spectra observed presents a formidable challenge in their interpretation. Earlier attempts [4,5] to analyze the hole quantum spectra in Ge have achieved only limited success.

In the present work we have made a detailed analysis of the quantum spectra in Ge utilizing the concept of a critical point in the magnetic joint density of states. This may be understood as follows.

A cyclotron resonance absorption line due to transitions between two Landau states n and n' can be interpreted in terms of a critical point in the one-dimensional joint density of states $(\partial\epsilon_{nn'}/\partial k_H)^{-1}$ where $\epsilon_{nn'}$ is the energy between Landau states and k_H is the wave vector along the direction of the magnetic field. This quantity plays, by analogy, the role of the three-dimensional joint density of states of the interband optical transitions but with two (transverse) degrees of freedom quantized by the magnetic field. This analogy for magnetic transitions has no particular utility for simple bands; however, in more complex situations such as the degenerate valence bands where the Landau states depend upon k_H in a complicated way, the concept of a critical point becomes a highly useful one. Here the existence of a critical point and, hence, a peak in the spectrum at points away from $k_H = 0$ becomes possible. An investigation of the behavior of $\epsilon_{nn'}$ as a function of k_H locates the critical points as well as predicts the cyclotron resonance line shape from the nature of the critical point. Contrary to previous analyses [4] done for $k_H = 0$, our results show that cyclotron resonance lines originating away from $k_H = 0$ are responsible for most of the prominent features of the observed quantum spectra in Ge.

We illustrate these concepts by way of an example using the quantum spectrum in Ge for $\mathbf{H}_0 \| [111]$.

2. Energy Levels

The Landau states for a hole in the degenerate Γ_8^+ valence band of Ge are given by the Luttinger effective mass Hamiltonian [3],

$$\mathscr{H}_k = -\frac{\hbar^2}{m}\left\{\gamma_1\frac{k^2}{2} - \gamma_2\left[\left(J_x^2 - \frac{1}{3}J^2\right)k_x^2 + cp\right]\right.$$
$$-2\gamma_3(\{J_xJ_y\}\{k_xk_y\} + cp)$$
$$\left.+\frac{e}{\hbar c}k\mathbf{J}\cdot\mathbf{H}_0 + \frac{e}{\hbar c}q(J_x^3H_{0x} + cp)\right\} \quad (1)$$

where

$$\mathbf{k} = \frac{1}{i}\nabla + \frac{e}{c}\mathbf{A}. \quad (2)$$

Here, J_x, J_y, and J_z are the components of the angular momentum operator $\mathbf{J}(J = 3/2)$ referred to the cubic axes: "cp" denotes cyclic permutation; the quantities $\{J_xJ_y\}$, etc. represent the symmetrized products, i.e., $\{J_xJ_y\} = 1/2(J_xJ_y + J_yJ_x)$; and $\mathbf{A}$ is the vector potential of the external magnetic field $\mathbf{H}_0$.

For simplicity we represent the hole Landau levels by a conventional energy level diagram at $k_H = 0$; this is shown in figure 1 for the low-lying Landau states obtained by diagonalizing eq (1) for $\mathbf{H}_0 \| [111]$. (It should be emphasized that in the analysis of the experimental spectra the assumption $k_H = 0$ is *not* made.) The values of the parameters used are: $\gamma_1 = 13.38$, $\gamma_2 = 4.24$, $\gamma_3 = 5.69$, $\kappa = 3.41$, and $q = 0.06$. The inverse mass parameters γ_1', γ_2, and γ_3 have been obtained from precision cyclotron resonance experiments [6] in uniaxially stressed Ge; and the parameters κ and q, which are related to the hole g-factor, are derived from combined resonance experiments [7]. Throughout the present work these values will be taken as "fixed"; therefore, the theoretical analysis in section 4 will involve no adjustable parameters.

In figure 1 we classify the Landau levels (at $k_H = 0$) by the scheme [8] (N_n, K^π). Two quantum numbers are necessary to uniquely identify each eigenstate: N, the Landau quantum number for the envelope function, and its subscript n, which is required to differentiate among the four states of the same N. The quantum number K ($K = 0, \ldots \nu - 1$) embodies the ν-fold rotational symmetry of the crystal about the direction of $\mathbf{H}_0$ ($\nu = 3$ for $\mathbf{H}_0 \| [111]$). π is the parity of the envelope function.

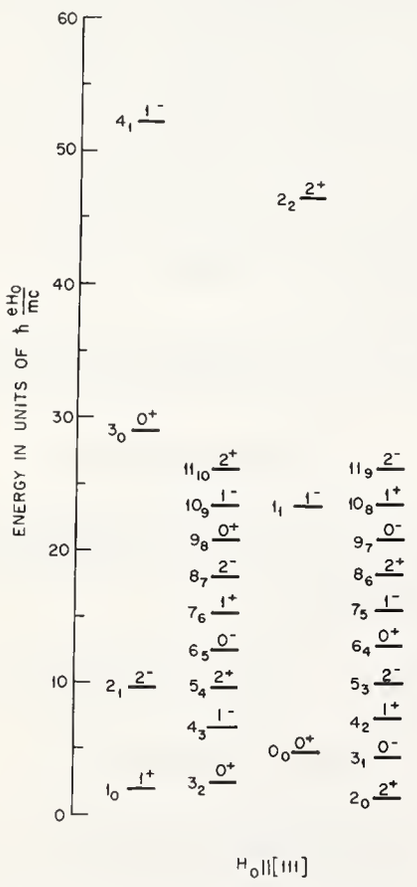

FIGURE 1. *Valence band Landau levels in* Ge *at* $k_H = 0$ *for* $\mathbf{H}_0 \| [111]$ *calculated from the Hamiltonian in Eq. (1).*

As customary, the sign of the energy is inverted so that the levels are plotted in an "electron" sense. The energy levels are labeled by the scheme (N_n, K^π) discussed in the text.

Using the quantum numbers (N_n, K^π) it is possible to express the cyclotron resonance selection rules [9] for $\boldsymbol{\epsilon}_1 \perp \mathbf{H}_0$, where $\boldsymbol{\epsilon}_1$ is the microwave electric field. If we symbolically categorize the successive symmetry breaking interactions

$$\mathscr{H}_0 + \mathscr{H}_1 + \mathscr{H}_2 + \mathscr{H}_3$$

where $\mathscr{H}_0$ is the axial Hamiltonian; $\mathscr{H}_1$ represents the k_H terms; $\mathscr{H}_2$ contains "warping" terms proportional to $\gamma_2 - \gamma_3$ (or q); and $\mathscr{H}_3$ combines warping and k_H interaction — we get a hierarchy of selection rules for a linear polarization of $\boldsymbol{\epsilon}_1$ as follows:

$\mathscr{H}_0$	$\Delta N = \pm 1$,	$\Delta\pi =$ yes,	$\Delta K = \pm 1$
$\mathscr{H}_1$	$\Delta N = \pm 1$		$\Delta K = \pm 1$
$\mathscr{H}_2$		$\Delta\pi =$ yes,	$\Delta K = \pm 1$
$\mathscr{H}_3$			$\Delta K = \pm 1$

In general the selection rule $\Delta K = \pm 1$ [understood to mean $\Delta K = \pm 1 \pmod{\nu}$] is the only strictly rigorous selection rule; the extent of the violation of the other selection rules depends upon the magnitudes of the symmetry breaking terms in the Hamiltonian, i.e., the magnitudes of $\gamma_2 - \gamma_3$ and k_H.

3. Experimental Details and Results

The cyclotron resonance experiments were done under "quantum" conditions at 54,000 Mc/s and at both 4.2 and 1.2 K on ultrapure samples of Ge. The above temperatures were strictly maintained by immersing the samples directly in the liquid He bath. The cavity spectrometer (TE_{101} rectangular mode) which employs a superheterodyne detection scheme was operated at very low power levels, 10^{-8} to 10^{-9} watts, to avoid cyclotron resonance line saturation. Also, for this same reason the samples were mounted in the cavity in a region of low microwave electric field. Carriers, both holes and electrons, were generated in the Ge sample by illumination with white light. To minimize line broadening from high carrier densities the light intensity was deliberately reduced by neutral density filters. The magnetic field was measured using field markers from proton NMR signals.

The complexity of the hole quantum spectrum is evident from the top two traces (a) of figure 2. These cyclotron resonance spectra were taken for $\mathbf{H}_0 \| [111]$ with linear microwave electric field polarization $\epsilon_1 \perp \mathbf{H}_0$. The positions of the hole lines are indicated by their effective mass values. (In taking the spectra in figure 2(a) an integration time constant of 0.1 sec was employed; at higher gain and with longer time constants many of the weaker lines can be more clearly discerned.) At 1.2 K only a vestige of the classical hole lines at $m^*/m = 0.0421$ and 0.374 remains; instead the cyclotron resonance intensity is redistributed among the twenty or more quantum transitions shown. As expected, the hole spectrum displays a marked dependence on temperature. The increase in intensity of some lines upon going to 1.2 K identifies them as originating from the lowest-lying Landau states.

In contrast to the electron lines, which have a simple Lorentzian shape characteristic of broadening by a relaxation time process, the hole lines are frequently asymmetric and of varied widths as expected for k_H-broadening. In a few cases the shapes of the hole lines, in particular the line at $m^*/m = 0.250$, display strain broadening and therefore, depend to some degree on the choice of sample. For certain samples a line at $m^*/m = 0.264$ appears as a partially resolved shoulder.

4. Comparison of Experimental Results and Theory

The analysis of the experimental spectra was accomplished by computer diagonalization of the effective mass Hamiltonian in eq (1) using the values of the parameters given in section 2. The infinite secular determinants generated by the Luttinger Hamiltonian with "warping" (terms proportional to $\gamma_2 - \gamma_3$) and k_H terms simultaneously present were truncated at a total dimension of 69×69 (i.e., 3 dets. of 23×23), the smallest size which gave satisfactory convergence of the eigenvalues for all relevant eigenstates. The intensities of all possible transitions were calculated by computer and integrated over k_H to yield synthesized quantum spectra. The k_H-broadened resonances were assumed to be composed of Lorentzian component lines having a width defined by the scattering time $\tau = 2.7 \times 10^{-10}$ sec [10]. The results calculated for T=4.0 K and $\mathbf{H}_0 \| [111]$ are shown in figure 2(b).

The salient features of these spectra can be interpreted by using the aforementioned principle that maximum stationary contributions to the integration occur at critical points in the magnetic joint density of states. This may be seen by referring to figure 2(c) which shows m^*/m for each transition plotted versus $\zeta = k_h/\sqrt{eH_0}/hc$, a dimensionless form for k_H. (The transitions in figure 2(c) are labelled with reference to the energy levels at $k_H = 0$ given in fig. 1.) The "magnetic" critical points for the transition curves in figure 2(c) are the points of zero slope

$$\frac{\partial(m^*/m)}{\partial\zeta} = 0. \tag{3}$$

We can categorize critical points as being either "strong" or "weak" depending upon the curvature of $m^*(\zeta)/m$ at the critical point. Nearly singular critical points of sharp curvature have a low density of states and contribute little to the integrated intensity. Conversely, more or less "flat" critical points, which have a high density of states, give strong resonances (all other factors being equal). In passing we note that for an isolated resonance the sign of the curvature dictates on which side of the asymmetric k_H-line the tail will fall.

Critical points must necessarily occur by symmetry at $\zeta = 0$ for every allowed transition; but many such transitions in Ge exhibit "cusp-like" behavior at $\zeta = 0$ and do not give lines in the integrated spectra even though their "differential" intensity at $\zeta = 0$ may be appreciable. We note in figure 2(c) several clear-cut examples of isolated transitions having cusp-like $\zeta = 0$ critical points—$1_0 \rightarrow 2_1$, $3_2 \rightarrow 2_1$, and $0_0 \rightarrow 2_1$—none of which show up as resonances in figure 2(b) [nor in the experimental spectra in figure 2(a)]. Transitions $2_0 \rightarrow 3_1$, $3_1 \rightarrow 4_2$, $4_3 \rightarrow 5_4$, $5_4 \rightarrow 6_5$, and $0_0 \rightarrow 4_3$ are of a similar kind and, likewise, give insignificant contributions to the integrated spectra. It would seem then that a substantial fraction of the lowest "quantum" transitions anticipated at $\zeta = 0$ do not materialize in the spectra.

On the other hand, numerous critical points off $\zeta = 0$, the noncentral critical points, give strong peaks in the line shape. In particular we note the secondary critical point for $3_2 \rightarrow 4_3$, as well as critical points for many transitions forbidden by parity at $\zeta = 0$, $2_0 \rightarrow 0_0$, $2_1 \rightarrow 6_5$, $5_4 \rightarrow 6_4$, $2_1 \rightarrow 4_3$, $4_2 \rightarrow 5_4$, and $0_0 \rightarrow 4_2$, all of which contribute strongly to the spectrum in the heavy mass region ($m^*/m > 0.2$). In the intermediate mass region ($0.1 < m^*/m < 0.2$) in figure 2(b) nearly all features result from noncentral critical points. We should point out that the line at $m^*/m = 0.125$, the most prominent experimental feature in this region at 1.2 K, comes from the noncentral transition $1_0 \rightarrow 5_4$ (forbidden at $\zeta = 0$). Numerous other critical points for $\zeta \neq 0$ contribute many weak lines in this region. [The "background" absorption beginning at $m^*/m > 0.15$ stems from contributions from the two series of transitions labelled $0 \rightarrow 1$, $0' \rightarrow 1'$, etc. throughout the range $\zeta = 2$ to 5 (the upper

417-156 O - 71 - 29

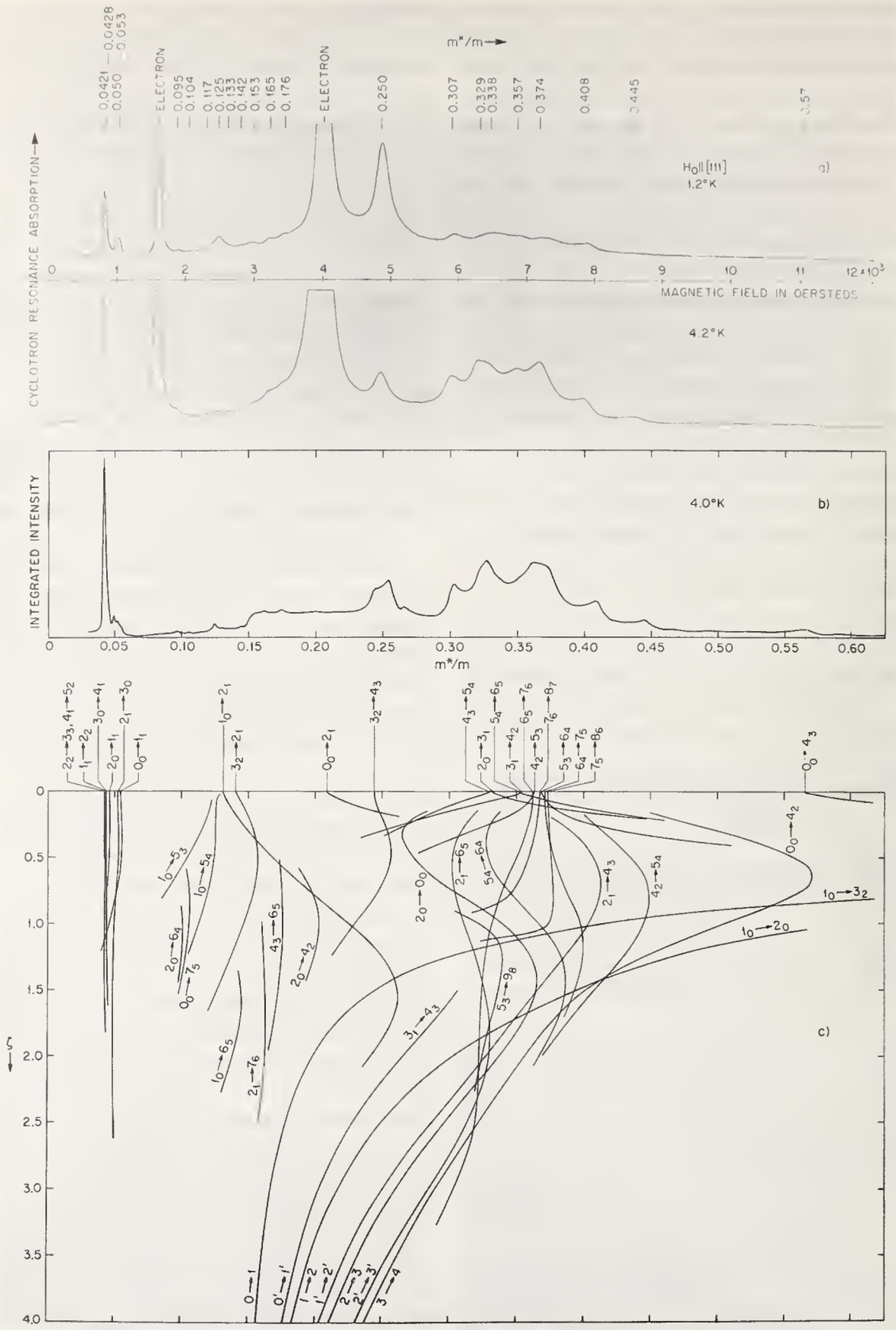

FIGURE 2. *Critical point analysis of the quantum cyclotron resonance absorption spectrum of holes in* Ge *for* $\mathbf{H}_0 \| [111]$.

Figure 2(a) shows the experimental traces for 1.2 K and 4.2 K taken at 54,496 Mc/s. In figure 2(b) we show the integrated intensity of the synthesized quantum spectrum calculated for 4.0 K. Figure 2(c) gives the position of each quantum transition as a function of ζ, a dimensionless form for k_H. The transitions are labeled with reference to the energy levels at $k_H = 0$ given in figure 1. At large ζ the labeling shifts to the simple scheme l and l' as the bands decouple and the levels of the two heavy hole Landau ladders approach equal spacing.

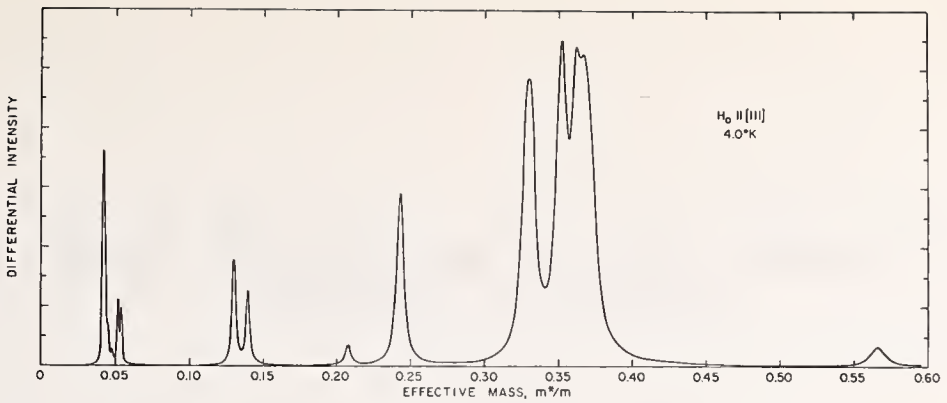

FIGURE 3. *The* $k_H = 0$ *"differential" cyclotron resonance spectrum computed for 4.0 K.*

limit of integration). As a point of interest, we estimate that at 4.2 K, contributions from transition $0 \rightarrow 1$ appear in the spectrum up to $\zeta \approx 6$ which corresponds to a value of $k_H \sim 1.5$ percent of the distance of the [111] zone boundary.] From the foregoing we conclude that the overall character of the spectrum is to a great extent dominated by the k_H-lines.

This point is further emphasized if we look at the "differential" spectrum calculated for $\zeta = 0$ which is shown in figure 3. Aside from the unrealistic Lorentzian line shapes, this spectrum (with the possible exception of the "light" holes) does not bear even qualitative resemblance to the experimental spectrum in figure 2(a). The observed structure of the absorption in the intermediate mass region is almost totally missing in figure 3; on the other hand the two strong peaks in the differential spectrum at $m^*/m = 0.130$ and 0.140 are either absent or extremely weak in both the integrated and observed spectra. In the same way, the differential lines at $m^*/m = 0.33$, 0.35 and 0.57 are "washed" out by integration. Their near coincidence with experimental lines is quite fortuitous as the noncentral critical points actually turn out to be responsible for the observed resonances. Finally, in the differential spectrum there is no hint of the prominent experimental lines at $m^*/m = 0.307$, 0.408, and 0.445 which are clearly portrayed in the integrated spectrum.

Some of the line assignments proposed here may be convincingly verified by experiments [6] utilizing small uniaxial stresses (along [111]) which gently decouple the valence band and shift the quantum lines in a measured fashion. We briefly mention two results. First, the resonance at $m^*/m = 0.250$ (whose sensitivity to strain broadening has been previously noted) is split into a resolved triplet of lines by uniaxial stress in accordance with the structure suggested in figure 2(b). Second, by observing the behavior of the lines $m^*/m = 0.125$ and 0.133 in figure 2(a) under uniaxial stress we confirm their assignments $1_0 \rightarrow 5_4$ and $1_0 \rightarrow 2_1$, respectively. Careful comparison of the experimental and calculated spectra, furthermore, strongly suggests that the third member $1_0 \rightarrow 5_3$ of the "fundamental" triplet is the weak line observed at $m^*/m = 0.117$.

In conclusion, we add that analyses similar to that above have been completed for $\mathbf{H}_0$ along the [001] and [110] crystal axes [11]. In both of these cases, just as we have seen for $\mathbf{H}_0 \| [111]$, the synthesized spectra faithfully reproduce nearly all significant features of the experimental spectra in regard to position, intensity, and line shape and further corroborate that the dominant contributions to the cyclotron resonance quantum structure stem from the noncentral critical points.

5. References

[1] Fletcher, R. C., Yager, W. A., and Merritt, F. R., Phys. Rev. **100**, 747 (1955).

[2] Luttinger, J. M., and Kohn, W., Phys. Rev. **97**, 869 (1955).

[3] Luttinger, J. M., Phys. Rev. **102**, 1030 (1956).

[4] Goodman, R. R., Ph. D. dissertation, University of Michigan, Ann Arbor, Michigan, 1958 (unpublished) and Phys. Rev. **122**, 397 (1961). Hensel, J. C., Proceedings of the International Conference on the Physics of Semiconductors, Exeter, 1962 (The Institute of Physics and the Physical Society, London, 1962), p. 281; Stickler, J. J., Zeiger, H. J., and Heller, G. S., Phys. Rev. **127**, 1077 (1962); Mercouroff, W., Physica Status Solidi **2**, 282 (1962).

[5] The possibility of k_H-lines was first pointed out by R. F. Wallis and H. J. Bowlden, Phys. Rev. **118**, 456 (1960) who considered only the spherical case ($\gamma_2 = \gamma_3$). Subsequent calculations which included k_H-effects were made by V. Evtuhov, Phys. Rev. **125**, 1869 (1962), and Okazaki, M., J. Phys. Soc. of Japan **17**, 1865 (1962).

[6] Hensel, J. C., and Suzuki, K. (to be published).

[7] Hensel, J. C., Phys. Rev. Lett. **21**, 983 (1968), and Hensel, J. C., and Suzuki, K., Phys. Rev. Lett. **22**, 838 (1969).

[8] We depart from the conventional Luttinger scheme for $\mathbf{H}_0 \|$ [111] (see ref. 3) so frequently used, because it does not admit to generalization either for other directions of $\mathbf{H}_0$ or for the case of $k_H \neq 0$ which is germane to the present work.

[9] Suzuki, K., and Hensel, J. C. (to be published).

[10] This scattering time is taken from an earlier experiment (ref. 6).

[11] Hensel, J. C., and Suzuki, K. (to be published).

Landau Level Broadening in the Magneto-Optical Density of States*

B. H. Sacks**

**Department of Electrical Engineering and Computer Sciences and the Electronics Research Laboratory
University of California, Berkeley, California 94720**

B. Lax

**Francis Bitter National Magnet Laboratory and the Department of Physics, M.I.T.
Cambridge, Massachusetts 02139**

In this paper we derive a convolution integral expression of the optical density of states for **k**-conserving transitions between broadened Landau levels in crystalline solids. The convolution is between single Landau level densities of states expressed in a form derived by Kubo. The expression includes as parameters the reduced mass, magnetic field strength, and the strength of the broadening mechanism. We present the results of numerical evaluation of this expression for various values of the parameters.

Our consideration is directed to dipolar transitions between the $n = 0$ Landau levels of the valence and conduction bands, and we assume that the dominant broadening effects are intraband scattering processes. This assumption is reasonable in view of the comparative intraband and interband lifetimes.

The resulting optical density of states function has an appearance identical to that of the single band function, but with the frequency measured from the gap energy replacing the energy measured from the band edge, the reduced mass replacing the single band mass, and a reduced broadening parameter replacing the single band parameter. Our expression for this last parameter is shown to be a consequence of a mutual consistency requirement between the single band and optical densities of states, and this same requirement also leads to the reduced lifetime expression encountered in the more conventional Lorentzian formulation.

Key words: Delta-function formulation of density of states; Green effect; **k**-conserving transitions; Landau levels; laser semiconductor; magneto-optical density of states; optical density of states; semiconductor laser.

1. Introduction

In this paper we derive a convolution integral expression of the optical density of states for **k**-conserving transitions between broadened Landau levels in crystalline solids. The expression includes as parameters the reduced mass, magnetic field strength, and the strength of the broadening mechanism. We present the results of numerical evaluation of this expression for various values of the parameters.

Our consideration is directed to dipolar transitions between the $n = 0$ Landau levels of the valence and conduction bands, and we assume that the dominant broadening effects are intraband scattering processes. This assumption is reasonable in view of the relative intraband and interband lifetimes.

*Research supported by the Air Force Office of Scientific Research to the Francis Bitter National Magnet Laboratory, M.I.T. and the Joint Services Electronics Program, grant AFOSR-68-1488 to the University of California, Berkeley 94720.

**Formally with the Francis Bitter National Magnet Laboratory, M.I.T., Cambridge, Massachusetts.

2. Single Landau Level Density of States

2.1. Density of States in Delta-Function Formulation

We begin by observing that in general terms a density of energy states for a quantum-mechanical system can be expressed by the operator relation

$$\rho(E) = \mathrm{tr}\ \delta(\mathscr{H} - E) \tag{1}$$

where $\mathscr{H}$ is the appropriate Hamiltonian. This notation, of course, implies a complete set of states between

which the operator on the right side is sandwiched, and the trace "sweeps" over this set. Equation (1) represents a "counting" process.

The simplest demonstration of this formulation can be carried out when the set of states used is the collection of eigenstates of the Hamiltonian in the operator. In the case of simple parabolic energy bands, the electronic eigenstates in the presence of a magnetic field are the familiar Landau functions,

$$\psi_L = K^{1/2} e^{ik_y y} e^{ik_z z} \phi_n(x - x_0(k_y)) u_0(\mathbf{r}) \tag{2}$$

where $K^{1/2}$ is a normalizing constant whose magnitude depends upon the magnetic field strength, ϕ_n is the nth harmonic oscillator wave function, and $u_0(\mathbf{r})$ is the cell-periodic part of the Bloch wave function associated with the band edge. (This form is not unique, but rather is the result of the choice of the unsymmetrical Landau gauge $\mathbf{A} = (0, Hx, 0)$ to express the vector potential of the magnetic field. We will use this gauge and its resulting wave functions throughout this work. All physical results, of course, turn out to be gauge independent.)

The energies associated with these Landau levels are given by

$$E_{cn} = (n + 1/2)\hbar\omega_c + \frac{\hbar^2 k_z^2}{2m_c} \tag{3.a}$$

$$E_{vn} = -E_g^{(0)} - (n + 1/2)\hbar\omega_c - \frac{\hbar^2 k_z^2}{2m_v} \qquad (n = 0, 1, 2, \ldots) \tag{3.b}$$

for levels originating in the conduction and valence bands, respectively, with the zero of energy taken at the zero-field conduction band edge.

For the $n = 0$ Landau level of the conduction band, the eigenvalues are expressed in terms of k_z, and the traces are readily converted to integrals over k_y and k_z, leading to the well-known result

$$\rho(E) = \mathrm{tr}\ \delta(\mathscr{H} - E)$$

$$= \int_{k_y=0}^{\frac{L_x}{l^2}} \int_{-\infty}^{\infty} \frac{dk_y}{(2\pi/L_y)} \frac{dk_z}{(2\pi/L_z)} \delta\left(\frac{\hbar^2 k_z^2}{2m^*} + \frac{1}{2}\hbar\omega_c - E\right) \cdot$$

$$= \frac{V}{4\pi^2 l^2} \left(\frac{2m^*}{\hbar^2}\right)^{1/2} \frac{1}{\sqrt{E - 1/2\hbar\omega_c}} \tag{4}$$

where $l^2 = (eH/\hbar c)^{-1}$ is the square of the cyclotron orbit radius.

It should be remarked that if the delta functions in energy are replaced by Lorentzian distributions of constant width $\hbar/\tau$

$$\delta(\mathscr{H} - E) \longrightarrow \frac{1}{\pi} \frac{\hbar/\tau}{(\mathscr{H} - E)^2 + \hbar^2/\tau^2} \tag{5}$$

which, we note, can also be written as

$$\frac{1}{\pi} \frac{\hbar/\tau}{(\mathscr{H} - E)^2 + \hbar^2/\tau^2} = \frac{1}{\pi} \mathrm{Im}\ \frac{1}{(\mathscr{H} - E) - i\hbar/\tau} \tag{6}$$

then the density of states at any given energy E is given by the expression

$$\rho(E) = \frac{1}{\pi} \mathrm{tr}\ \mathrm{Im}\ \frac{1}{(\mathscr{H} - E) - i\hbar/\tau} = \mathrm{Re}\ \frac{1}{4\pi^2 l^2} \frac{\left(\frac{2m^*}{\hbar^2}\right)^{1/2}}{\sqrt{E - (1/2)\hbar\omega_c - i\hbar/\tau}} \tag{7}$$

The trace sums over the quantum numbers k_y and k_z of the Landau states. Thus the term "Lorentzian broadening" indicates that the density of states is the sum of contributions *at a given energy* from the tails of Lorentzians whose centers are distributed over the whole energy range.

To give this result a physical interpretation, we can consider that the perfect periodicity of the lattice is slightly perturbed by the broadening mechanism, and hence k_z is no longer a good quantum number for states at a single energy. In other words, eqs (3a,b) no longer hold, and states with any given value of k_z are spread over the entire energy range in a Lorentzian distribution centered at the original value. Equivalently, we can say that an approximation to the wave function at any given energy is a linear combination of states of all values of k_z, with coefficients deduced from the Lorentzian formula. For the density of states at the energy of interest, we then count all the states that enter the linear combination, weighted by their Lorentzian coefficients. Summations of a related sort will appear in subsequent sections of this paper. In appendix A the optical density of states is derived for transitions between such Lorentzian-broadened sets of initial and final states.

2.2. Expressions in Terms of the Resolvent Operator

In order to treat the effects of scattering processes more rigorously, we must include in the Hamiltonian the scattering potential, written in general as V. However, since the trace is invariant under the similarity transformation that takes the eigenstates of the unperturbed Hamiltonian into those of the complete Hamil-

tonian, we will continue to use the complete set of unperturbed Landau state functions in the calculations that follow.

With the notation just introduced, the density of states is written

$$\rho(E) = \text{tr } \delta(\mathscr{H}_0 + V - E) \tag{8}$$

We now wish to take advantage of the well-known identity

$$\lim_{\epsilon \to 0} \frac{1}{x + i\epsilon} = \frac{P}{x} + i\pi\delta(x) \tag{9}$$

as a means of expressing the δ-function in eq (8). Hence

$$\rho(E) = \text{tr Im} \lim_{\epsilon \to 0} \frac{1/\pi}{\mathscr{H}_0 + V - E + i\epsilon} \tag{10}$$

This in turn bears a close resemblance to an operator called the Resolvent, used by Hugenholtz [1] and by van Hove [2] in connection with nuclear many-body theory, and introduced into semiconductor galvanomagnetic theory by Kubo [3]. The resolvent of a complex number, s, is defined by

$$R(s) = \frac{1}{\mathscr{H} - s} \tag{11}$$

so that our density of states function can be written

$$\rho(E) = \text{tr Im} \lim_{\epsilon \to 0} \frac{1}{\pi} R(E + i\epsilon) \tag{12}$$

The properties of the resolvent have been studied in detail and are discussed in several places in the literature [4,5], so we will merely present the results relevant to our needs and omit their rather complicated derivation. Because we calculate the trace, we are concerned only with the diagonal elements of the resolvent. Specifically, the diagonal part of the operator $R(s)$ is designated by $D(s)$ and is given by

$$D(s) = \frac{1}{\mathscr{H}_0 + G(s) - s} \tag{13}$$

in the representation of which $\mathscr{H}_0$ is diagonal. The effect of the perturbation is contained in the diagonal operator $G(s)$, given by a series expansion in powers of the perturbation:

$$G(s) = \{V\}_d - \{VD(s)V\}_d + \text{higher order terms} \tag{14}$$

where $\{\}_d$ indicates the diagonal part of the operator in brackets in the same representation in which $\mathscr{H}_0$ and $D(s)$ are diagonal. Following Kubo, we make the approximation of discarding the higher order terms, and we then relocate the zero of energy so that $\{V\}_d = 0$. Then eq (13) is inserted into the right hand side of eq (14) to yield an implicit equation for G in terms only of the unperturbed Hamiltonian and the perturbation V:

$$G(E + i\epsilon) = -V \left[\frac{1}{\mathscr{H}^0 + G - (E + i\epsilon)} \right] V \tag{15}$$

The solutions of this equation, i.e., the diagonal matrix elements of G in terms of E and the quantum numbers of the states involved, can be inserted back into eq (13) to yield the matrix elements of $D(E + i\epsilon)$, also in terms of E and the quantum numbers of the same set of states. The fact that $D(s)$ is diagonal removes one of the two summations over intermediate states involved in taking matrix elements of eq (15), and we are left with

$$\langle n, k_y, k_z | G(E + i\epsilon) | n, k_y, k_z \rangle = \sum_{n', x_0', k_z'} \frac{|\langle n, k_y, k_z | V | n', k_y', k_z' \rangle|^2}{E_0(n', k_y', k_z') + \langle n', k_y', k_z' | G(E + i\epsilon) | n' k_y', k_z' \rangle - (E + i\epsilon)} \tag{16}$$

A simple solution of eq (16) for $G(E + i\epsilon)$ can be obtained in cases where the perturbations V are of the following three types: the first and simplest one is the delta function potential, which corresponds physically to a highly localized or short range force acting to scatter the carriers. We will assume their distribution to be random throughout the sample. The second perturbation is the deformation potential as related in particular to the acoustic phonon density—it is an important source of scattering at moderate and higher temperatures. The final type of perturbation to be treated is an example of a long range force, namely the attractive screened Coulomb potential. This is an approximate representation of the effect of a charged or polarized impurity site on an electron in the conduction band or hole in the valence band. We limit ourselves at this point to describing the method of solution and proceeding with the results—the actual calculations for the three cases are carried out in appendix B.

The squared matrix element for each of the three potentials mentioned above is shown in the appendix to be independent of k_z and k_z' and to depend upon k_y and k_y' only in the combination $(k_y' - k_y)$. The energy of the unperturbed Landau levels, E_0, depends only on n' and

k_z', but not on k_y'; and because of the $(k_y' - k_y)$ dependence in the numerator, eq (16) has a solution for G which is independent of k_y. Therefore, eq (16) can be rewritten as

$$\langle n|G(E+i\epsilon)|n\rangle = \frac{L_y L_z}{4\pi^2}\int_{-\infty}^{\infty} dk_z' \frac{1}{E_0(k_z', n') + G_{n',k_z'}(E+i\epsilon) - (E+i\epsilon)} \cdot \int_0^{\frac{L_x}{l^2}} dk_y' f(k_y' - k_y) \tag{17}$$

where the k_y' integral contains the specific information about the potential responsible for the scattering. From the results given in the appendix, we see that the k_y' integral can be expressed as

$$\int dk_y' f(k_y' - k_y) = \frac{1}{2\pi l^2} W \tag{18}$$

where W is a scattering constant with dimensions of (energy)^2 × (volume) and l is the cyclotron orbit radius. Using eq (3a) or eq (3b) to express $E_0(k_z', n)$, the k_z' integral is elementary and yields the result

$$G_n(s) = \frac{W}{4\pi^2 l^2}\sum_{n'} \frac{\left(\frac{2m^*}{\hbar^2}\right)^{1/2}}{[(n'+\frac{1}{2})\hbar\omega_c + G_{n'}(s) - s]^{1/2}}. \tag{19}$$

A final simplification, based on the assumption that the dominant scattering processes occur between states within a single Landau level, allows us to suppress the summation over n'. We focus our attention on the $n = 0$ level; and to complete the solution for G and for the density of states, we adopt the following notation:

$$\epsilon \equiv \begin{cases} s - 1/2\ \hbar\omega_c & \text{conduction band} \quad (20.a) \\ s - (-E_y^0 - 1/2\ \hbar\omega_c) & \text{valence band} \quad (20.b) \end{cases}$$

$$\beta_\mu \equiv \frac{1}{4\pi^2 l^2}\left(\frac{2m_\mu}{\hbar^2}\right)^{1/2} \qquad \mu \equiv c, v \tag{21}$$

$$\zeta \equiv \beta W$$

In each case the quantity ϵ denotes the energy of interest as measured from the appropriate Landau level edge. With this notation, the equation for G, (19), reduces to

$$G = -\zeta[G - \epsilon]^{-1/2} \tag{22}$$

from which follows that

$$G^3 - \epsilon G^2 - \zeta^2 = 0. \tag{23}$$

Solution of this cubic equation is straightforward, and G has the following three possible values:

$$G_1(\epsilon, \zeta) = \frac{\epsilon}{3} + \sqrt[3]{\frac{\epsilon^3}{27} + \frac{\zeta^2}{2} + \zeta\sqrt{\frac{\epsilon^3}{27} + \frac{\zeta^2}{4}}} + \sqrt[3]{\frac{\epsilon^3}{27} + \frac{\zeta^2}{2} - \zeta\sqrt{\frac{\epsilon^3}{27} + \frac{\zeta^2}{4}}} \tag{24}$$

$$G_{2,3}(\epsilon, \zeta) = \frac{\epsilon}{3} - \frac{1}{2}\left[\sqrt[3]{\frac{\epsilon^3}{27} + \frac{\zeta^2}{2} + \zeta\sqrt{\frac{\epsilon^3}{27} + \frac{\zeta^2}{4}}} + \sqrt[3]{\frac{\epsilon^3}{27} + \frac{\zeta^2}{2} - \zeta\sqrt{\frac{\epsilon^3}{27} + \frac{\zeta^2}{4}}}\right]$$
$$\pm \frac{i\sqrt{3}}{2}\left[\sqrt[3]{\frac{\epsilon^3}{27} + \frac{\zeta^2}{2} + \zeta\sqrt{\frac{\epsilon^3}{27} + \frac{\zeta^2}{4}}} - \sqrt[3]{\frac{\epsilon^3}{27} + \frac{\zeta^2}{2} - \zeta\sqrt{\frac{\epsilon^3}{27} + \frac{\zeta^2}{4}}}\right] \tag{25}$$

In order to choose the correct solution, we impose the following two conditions: G must approach zero as ζ approaches zero, since the density of states must approach the unperturbed form under that condition; G must be a solution of (22), the equation from which the cubic equation was obtained. The first condition eliminates $G_1(\epsilon,\zeta)$. The second condition, which can be re-expressed as the requirement of a positive density of states, eliminates G_3, the complex solution with negative imaginary part.

Finally, in order to obtain the expression for the density of states function, we return to our original form, eqs (12) and (13):

$$\rho(E) = \text{Im tr} \lim_{\epsilon\to 0} \frac{1}{\pi} R(E+i\epsilon) \tag{12}$$

$$= \text{Im} \lim_{\epsilon\to 0} \sum \frac{1/\pi}{\mathscr{H}_0 + G(E+i\epsilon) - (E+i\epsilon)}$$

As long as the summations can be carried out under the condition that $G(s)$ does not depend upon either k_y or k_z, the result is directly obtained from two elementary integrals as

$$\rho(\epsilon) = \mathrm{Im} \lim_{\epsilon \to 0} \frac{1}{\pi} \frac{1}{4\pi l^2} \left(\frac{2m^*}{\hbar^2}\right)^{1/2} \frac{1}{\sqrt{-\epsilon + G}} = \mathrm{Im} \lim_{\epsilon \to 0} \frac{1}{\pi} \beta \frac{1}{\sqrt{G - \epsilon}} \tag{26}$$

On the other hand, the equation for G itself, eq (22), is

$$G(\epsilon) = -\lim_{\epsilon \to 0} \beta W \frac{1}{\sqrt{G - \epsilon}} \tag{22}$$

Hence

$$\rho(\epsilon) = -\frac{1}{\pi} \frac{1}{W} \mathrm{Im}\ G(\epsilon) \tag{27}$$

The interesting form of the result is a direct consequence of the approximations made in neglecting the higher order terms in the original equation for G and of keeping only the scattering terms within a single Landau level. The function $\rho(\epsilon)$ is graphed in figure 1. Also, we call attention to the summation process indicated in eq (17); in form it is very much like the one in eq (7), except that instead of summing over tails of Lorentzian functions of energy, this summation takes place over the tails of more complicated functions of energy determined by the imaginary part of $G(E)$. These functions, shown in figure 2, indicate the manner in which states of a given k_z value are distributed in energy by the scattering process. This is an important consideration when k_z conservation is required in the transitions, and it is discussed in the next section, where our method of calculating the optical density of states is presented.

We would like to restate the results of this section in terms of two functions whose definitions will be useful in the subsequent section. The first one, a density of states in ϵ and k_z, is given by

$$\rho(\epsilon, k_z) = \frac{1}{8\pi^2 l^2} \mathrm{Im} \left[\frac{1}{E_0(k_z) + G - \epsilon}\right] \tag{28}$$

so that

$$\int \rho(\epsilon, k_z) dk_z = \rho(\epsilon). \tag{29}$$

And the second function, a density of states in ϵ, k_z, and k_y, is given by

$$\rho(\epsilon, k_z, k_y) = \frac{1}{4\pi} \frac{1}{E_0(k_z) + G - \epsilon} \tag{30}$$

so that

$$\rho(\epsilon, k_z, k_y) dy = \rho(\epsilon, k_z). \tag{31}$$

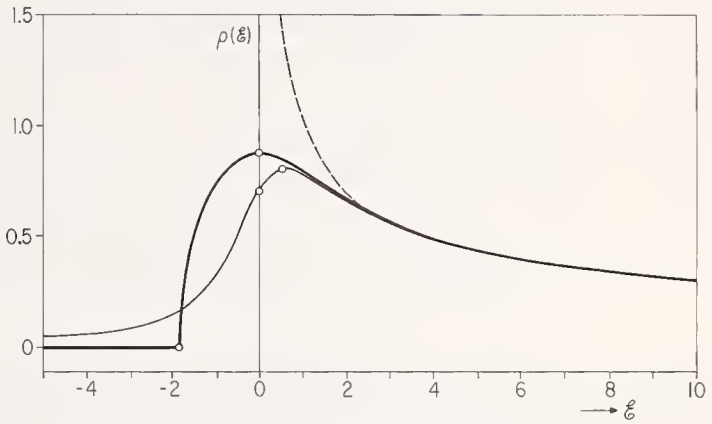

FIGURE 1. *Density of States functions.*
The dotted line indicates the unbroadened case; the thin line indicates the Lorentzian broadened case, and the thick line indicates the case considered in this paper. The energy scale is in units of $\zeta^{2/3}$.

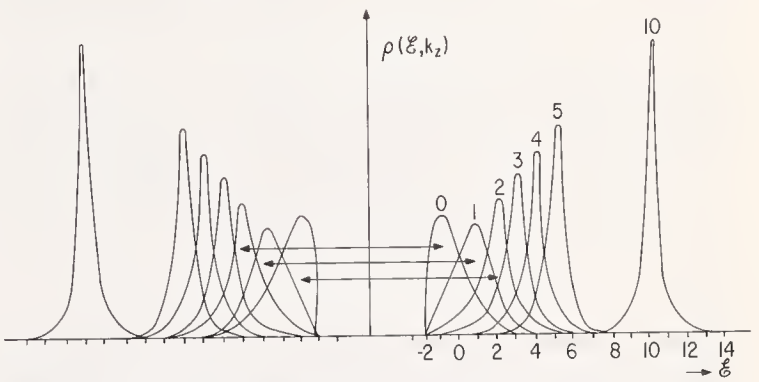

FIGURE 2. *Energy-Dependent Distributions of* k_z *states.*
The numbers atop the peaks stand for normalized values of k_z^2. The arrows represent photon energies.

Before going on to develop the optical density of states integral, we would like to examine briefly some of the properties of this single Landau level density of states.

2.3. The Density of States Function: Characteristics and Approximation

To begin with, we write out the function explicitly, using the result given in eq (25),

$$\rho(\epsilon) = \frac{1}{\pi} \frac{1}{W} \mathrm{Im} \lim_{\epsilon \to 0} G(s) = \frac{1}{\pi} \frac{1}{W} \left(\frac{\sqrt{3}}{2}\right) \sqrt[3]{\left(\frac{\epsilon^3}{27} + \frac{\zeta^2}{2}\right) + \zeta \sqrt{\frac{\epsilon^3}{27} + \frac{\zeta^2}{4}}} - \sqrt[3]{\left(\frac{\epsilon^3}{27} + \frac{\zeta^2}{2}\right) - \zeta \sqrt{\frac{\epsilon^3}{27} + \frac{\zeta^2}{4}}}. \tag{32}$$

It is shown as a function of the normalized variable, $\epsilon/\zeta^{2/3}$, in figure 1. The dependence of the value of this function on magnetic field, contained in the parameter ζ, is quite complicated; and unlike the Lorentzian-broadened case, it varies over the range of ϵ. We will show the explicit dependence on H in three regions shortly—here we remark only that the dependence is weaker on the low energy side and grows stronger with increasing energy.

Unlike the Lorentzian-broadened density of states, whose peak is shifted, this function peaks at exactly the value of the energy variable ϵ at which the unbroadened functions become singular, i.e., at $\epsilon = 0$. This can be readily established by differentiation. The value of the function on resonance can immediately be calculated from the above equation, by letting $\epsilon = 0$, and the result is

$$\rho(0) = \frac{1}{\pi}\frac{1}{W}\frac{\sqrt{3}}{2}\zeta^{2/3} = \frac{\sqrt{3}}{2\pi}\frac{\beta^{2/3}}{W^{1/3}} \tag{33}$$

We call attention to the dependence of the *peak* height on magnetic field. In this region of ϵ, the height goes as $H^{2/3}$, since β is linearly proportional to H.

We next examine the high energy side of the function, in the region where $\epsilon \gg \zeta^{2/3}$. It is convenient to rewrite eq (32) as follows, in terms of ϵ and the small dimensionless quantity $\zeta/\epsilon^{3/2}$:

$$\rho(\epsilon) = \frac{1}{\pi}\frac{1}{W}\frac{\sqrt{3}}{2}\frac{\epsilon}{3}\left[\sqrt[3]{1+\frac{1}{2}\left(\frac{\zeta}{\epsilon^{3/2}}\right)^2+\frac{\zeta\sqrt{27}}{\epsilon^{3/2}}\sqrt{1+\frac{1}{4}\left(\frac{\zeta}{\epsilon^{3/2}}\right)^2}}-\sqrt[3]{1+\frac{1}{2}\left(\frac{\zeta}{\epsilon^{3/2}}\right)^2-\frac{\zeta\sqrt{27}}{\epsilon^{3/2}}\sqrt{1+\frac{1}{4}\left(\frac{\zeta}{\epsilon^{3/2}}\right)^2}}\right] \tag{34}$$

If only the terms under the radical sign up to first order in this dimensionless quantity are retained, the equation is simplified to

$$\rho(\epsilon) \approx \frac{1}{\pi}\frac{1}{W}\frac{\sqrt{3}}{2}\frac{\epsilon}{3}\left[\sqrt[3]{1+\frac{\zeta\sqrt{27}}{\epsilon^{3/2}}}-\sqrt[3]{1-\frac{\zeta\sqrt{27}}{\epsilon^{3/2}}}\right] \tag{35}$$

and the cube roots can be expanded to yield the final expression

$$\rho(\epsilon) \approx \frac{1}{\pi}\frac{1}{W}\frac{\sqrt{3}}{2}\frac{\epsilon}{3}\left[\left(1+\frac{\zeta\sqrt{27}}{3\epsilon^{3/2}}\right)-\left(1-\frac{\zeta\sqrt{27}}{3\epsilon^{3/2}}\right)\right] = \frac{1}{\pi}\frac{1}{W}\frac{\sqrt{3}}{2}\frac{\epsilon}{3}\left[\frac{2\zeta\sqrt{27}}{3\epsilon^{3/2}}\right] = \frac{1}{\pi}\beta\frac{1}{\epsilon^{1/2}} \tag{36}$$

where we have used the relation $\zeta = \beta W$ to obtain the final line. This result is exactly the same as eq (4) for the unbroadened density of states. Thus, in the limits of very high energy or of vanishingly small broadening parameter, the broadening density of states equation we have presented in this chapter approaches the unbroadened result, as does the Lorentzian-broadened case we have also considered. At these values of ϵ, the function is linearly proportional to H.

However, it is on the low energy side of the peak that the distinguishing features of this form appear. First, as shown in the figure, the function vanishes for values of energy less than or equal to $\epsilon = (-3/\sqrt[3]{4}\,\zeta^{2/3})$. To show this from the equation, we note first that the terms of $G_2(\epsilon)$ (eq (25)) not multiplied by i must be real for all positive and negative real values of ϵ. This is true since whenever the square root under the cube root sign introduces an imaginary part, the complex terms are the *sum* of a number and its complex conjugate. Then, in the terms multiplied by $(i\sqrt{3/2})$, as soon as ϵ becomes equal to or less than $(-3/\sqrt[3]{4}\zeta^{2/3})$, these terms become the *difference* between a number and its complex conjugate, hence imaginary. And, multiplied by $(i\sqrt{3/2})$, they also give a real result so

$$\text{Im } G(\epsilon) = 0$$

for

$$\epsilon \leqslant \epsilon_0 = \frac{-3}{\sqrt[3]{4}}\zeta^{2/3} \tag{37}$$

Let us now examine the function in the vicinity of $\epsilon = \epsilon_0$. It turns out to be convenient, again for purposes of expansion, to rewrite the density of states equation in somewhat different form. By recognizing that the expressions under the cube root signs are perfect

squares, we can rewrite $\rho(\epsilon)$ as

$$\rho(\epsilon)=\frac{\sqrt{3}}{2}\frac{1}{\pi}\frac{1}{W}\left(\frac{\zeta}{2}\right)^{2/3}\left[\left(1+\sqrt{\frac{4\epsilon^2}{27\zeta^2}+1}\right)^{2/3}-\left(1+\sqrt{\frac{4\epsilon^2}{27\zeta^2}+1}\right)^{2/3}\right]. \tag{38}$$

When $\epsilon \approx \epsilon_0$, the quantity in the square root is small compared to unity and the above equation can be approximated by

$$\rho(\epsilon)\approx\left(\frac{\sqrt{3}}{2}\frac{1}{\pi}\frac{1}{W}\frac{\zeta^{2/3}}{2^{2/3}}\right)\left[\frac{4}{3}\sqrt{\frac{4\epsilon^2}{27\zeta^2}+1}\right] \tag{39}$$

This equation is to be expanded around $\epsilon=\epsilon_0$. Defining

$$\Delta\epsilon=\epsilon-\sqrt[3]{\frac{-27\zeta^2}{4}} \tag{40}$$

and inserting the resulting expression for ϵ into the previous equation, we obtain the result

$$\rho(\epsilon)\approx\left(\frac{\sqrt{3}}{2\pi}\frac{1}{W}\frac{\zeta^{2/3}}{2^{2/3}}\right)\frac{4}{3}\sqrt{\frac{4}{27\zeta^2}\left[\Delta\epsilon+\sqrt{\frac{-27\zeta^2}{4}}\right]^3+1}; \tag{41}$$

and if we cube the quantity in square brackets and keep only the lowest order term in the small quantity $\Delta\epsilon$, the final result for the approximate density of states in the vicinity of ϵ_0 is

$$\rho(\epsilon)\approx\left(\frac{\sqrt{3}}{2\pi}\frac{1}{W}\frac{\zeta^{2/3}}{2^{2/3}}\right)\frac{4}{3}\sqrt{\frac{4^{1/3}}{\zeta^{2/3}}\Delta\epsilon}=\frac{1}{\pi}\frac{2^{2/3}}{\sqrt{3}}\frac{\zeta^{1/3}}{W}\sqrt{\Delta\epsilon}\;\rho(\epsilon)=\frac{1}{\pi}\frac{2^{2/3}}{\sqrt{3}}\frac{\beta^{1/3}}{W^{2/3}}\sqrt{\Delta\epsilon}. \tag{42}$$

Thus the density of states at the bottom of the Landau level has exactly the same energy dependence as an ordinary parabolic band in the absence of a magnetic field, but with a coefficient that is many times larger and depends not only on the effective mass but also on the magnetic field and the broadening parameter. In this region the magnetic field dependence is weaker than in either the peak region or the higher energy region, being proportional here to $H^{1/3}$. However, a numerical computation shows that with typical values of W and β, this parabolic form is a very good approximation to the complete expression all the way from the bottom of the Landau level at $\epsilon=\epsilon_0$ to the peak at $\epsilon=0$. This interesting result enables one to use many of the available computational techniques for dealing with carriers in parabolic bands.

3. The Optical Density of States

3.1. Formulation of the Convolution Integral

An optical (or "joint") density of states can be defined as the number of pairs of quantum states separated by a given energy difference $\hbar\omega$ and joined by a given selection rule. A count of these pairs is obtained as the product of the density of initial states times the density of final states to which transitions are allowed by the selection rules. For the Landau states expressed by eq (2), the appropriate quantum numbers are k_y, k_z, and ϵ. It is important to reiterate here that, because of the broadening, there is no longer a one-to-one correspondence between k_z values and energy values. In counting pairs of states we must therefore sum over energy *and* momentum variables. Nonetheless, we can consider interband transitions that conserve momentum and energy simultaneously, and the optical density of states for these transitions is expressed in the following manner:

$$\rho(\hbar\omega)=\int\int\int\int\int\int \rho_u(E_u,k_{zu},k_{yu})\rho_l(E_l,k_{zl},k_{yl})\times\delta(E_u-E_l-\hbar\omega)\delta(k_{yu}-k_{yl})\delta(k_{zu}-k_{zl})\times d\epsilon_u d\epsilon_l dk_{yu}dk_{yl}dk_{zu}dk_{zl} \tag{43}$$

where the subscripts u and l stand for "upper" and "lower," respectively.[1] The delta functions assure energy conservation and momentum conservation; the latter arise from the dipole matrix element between the Landau wave functions.

We can begin to simplify this expression by performing the integrations over k_{yu} and k_{yl}, which removes one delta function and then yields a coefficient proportional to magnetic field in front of the remaining integrals.

[1] The subscripts u and l can be considered interchangeable with c and v, for "conduction" and "valence," respectively.

Further simplification is then affected by integrations over k_{zl} and ϵ_l, to remove the remaining two delta functions. The result of these operations is the expression

$$\rho(\hbar\omega) = \frac{1}{4\pi^2 l^2} \int\int \rho_u(E_u, k_z)\rho_l (E_u - \hbar\omega, k_z) dE_u dk_z \qquad (44)$$

The form of eq (44) can be recognized as that of a convolution. And indeed an optical density of states signifies precisely that, namely, the convolution of a final density of states with an initial density of states, for a given value of separation $\hbar\omega$ between the two energy arguments.

We are now ready to insert the actual expressions derived in section 2 for the initial and final density functions into eq (44) and carry out the remaining integrations. Expressing the complex function $G(\epsilon)$ as $\Lambda(\epsilon) + i\Gamma(\epsilon)$, and explicitly taking the imaginary part indicated in eq (28), we write

$$\rho(\hbar\omega) = \frac{1}{4\pi^2 l^2} \int\int dk\, d\epsilon_u \frac{\Gamma(\epsilon_u)}{\left(\frac{\hbar^2 k^2}{2m_u} + \Lambda(\epsilon_u) - \epsilon_u\right)^2 + \Gamma^2(\epsilon_u)} \cdot \frac{\Gamma(\epsilon_l)}{\left(\frac{\hbar^2 k^2}{2m_l} + \Lambda(\epsilon_l) - \epsilon_l\right)^2 + \Gamma^2(\epsilon_l)} \qquad (45)$$

where ϵ_l and ϵ_u must be measured from the respective unbroadened band edges in order to correctly evaluate the factors in the integral.

Before going further in the mathematical development, we would like to consider the physical meaning of this integration. This is best done by reference to figure 2. There it can be seen how the k_z states of both the conduction and valence bands are spread into distributions over energy. Unlike the Lorentzian case, the distribution function itself varies with energy, and two important features are clearly evident. First, since the numerator of the function, $Im\ G(\epsilon) \equiv \Gamma(\epsilon)$, goes to zero at $\epsilon = \epsilon_0$, all the distributions vanish at ϵ_0; this affects low energy distributions quite strongly. The second feature is that for high energies, where $G(\epsilon)$ is rather slowly varying, the distributions again appear Lorentzian, but the peak heights are proportional to $[\Gamma(\epsilon)]^{-1}$, so they gradually increase with increasing ϵ, at a rate of $(\epsilon)^{+1/2}$.

We have drawn several arrows of equal length to indicate direct transitions absorbing or emitting photons of equal energy, but having different initial and final energies from one another. The double integral represents the summation for a given "arrow length" of all values of k_z at a particular upper energy and then the sum over all allowed upper energies. The range of allowed upper energies is determined at the low end of the scale by the cutoff energy ϵ_{0u}, and at the high end by the cutoff occurring in the other band. In other words, for a given value of $\hbar\omega$ imagine the arrow to slide on the energy diagram from where one arrowhead touches one cutoff energy to where the other head touches the other cutoff energy. In this manner, the upper and lower limits on the E_u integral are determined. The limits on the k-integral are taken as $-\infty$ to $+\infty$.

3.2. Evaluation of the Integral and Relation to Single-Band Density of States

For generality and convenience of application, we have chosen to evaluate the integral in terms of the dimensionless quantity obtained by normalizing all energies to the upper cutoff energy ϵ_{0u}. Thus $\rho(\hbar\omega)$ is rewritten

$$\rho(\hbar\omega) = \left[\frac{1}{4\pi l^2}\sqrt{\frac{2m_u}{\hbar^2}}\frac{1}{\sqrt{\epsilon_{0u}}}\right] R_M^{\frac{1}{2}} R_E^{-1} \cdot \int\int dy\, dE_u \frac{\Gamma(E_u)}{(y^2 + \Lambda(E_u) - E_u)^2 + \Gamma^2(E_u)} \cdot \frac{\Gamma(E_l)}{\left(y^2 + \frac{\Lambda(E_l)}{\alpha} - \frac{E_l}{\alpha}\right)^2 + \frac{\Gamma^2(E_l)}{\alpha^2}} \qquad (46)$$

where:

$$R_M \equiv \frac{m_u}{m_l}$$

$$R_E \equiv \frac{\epsilon_{0u}}{\epsilon_{0l}}$$

$$E_u \equiv \frac{\epsilon_u}{\zeta_u^{2/3}}$$

$$E_l \equiv \frac{\hbar\omega - Eg - \epsilon_u}{\zeta_u^{2/3}} \cdot R_E$$

$$\alpha \equiv R_M \cdot R_E \qquad (47)$$

and where the gap energy, Eg, has the magnetically expanded value $Eg^{(0)} + \hbar\omega_c + \hbar\omega_v$.

The integration over k can be carried out analytically and is most easily affected by contour integration. The pole pattern in the complex plane exhibits quadrantial symmetry, with the poles occurring at

$$\begin{aligned} k_1 &= \pm\sqrt{\Lambda(E_u) + E_u + i\Gamma(E_u)} \\ k_2 &= \pm\sqrt{\Lambda(E_u) + E_u - i\Gamma(E_u)} \\ k_3 &= \pm\sqrt{\frac{\Lambda(E_l) + E_l + i\Gamma(E_l)}{\alpha}} \\ k_4 &= \pm\sqrt{\frac{\Lambda(E_l) + E_l - i\Gamma(E_l)}{\alpha}}. \end{aligned} \tag{48}$$

Our computer program began by reading in values of R_M, R_E, and $\hbar\omega$ and evaluating the residues at the four poles in the upper half plane. It then integrated the residues over E_u between the appropriate limits, as discussed above. In terms of our normalized energies, the limits on E_u run from $-3/\sqrt[3]{4}$ up to $3/\sqrt[3]{4} \cdot \mathrm{R}_E^{-1} + (\hbar\omega - Eg)/\zeta^{2/3}$. The result, as a function of $\hbar\omega$, is in each case a curve having the form shown in figure 1. The general characteristics are the following: (1) The function vanishes at a value of $\hbar\omega$ given by

$$\hbar\omega - Eg = -\epsilon_{0u}\left(1 + \frac{1}{R_E}\right) \tag{49}$$

(2) The function reaches a peak at $\hbar\omega - Eg = 0$. Thus, unlike the Lorentzian case, this peak occurs at exactly the value of energy where the singularity occurs for the unbroadened optical density of states. The height at the peak is discussed below; (3) On the high energy side of the peak, the curve diminishes and approaches the unbroadened form proportional to $(\hbar\omega - Eg)^{-1/2}$.

Since the appearance of the optical density of states function is identical to that of the single band function, we are led to ask if we can define an appropriate reduced broadening parameter analogous to the reduced lifetime for the Lorentzian case discussed in appendix A. This is indeed possible, and in fact turns out to be a direct consequence of the mutual consistency among the single band densities of states and the optical density of states. Essentially the condition for consistency can be stated as the requirement that the zero of the optical density of states, which defines the absorption or emission edge, occur at an energy equal to the separation of the individual band edges, and similarly, that the peak of the optical density of states occur at an energy equal to the separation of the individual peaks. We will show that a certain relationship must exist among the density of states parameters, the β's and W's, in order to fulfill these requirements.

The consistency condition is expressed as follows:

$$\epsilon_{0r} = \epsilon_{0c} + \epsilon_{0v} \tag{50}$$

where the subscripts r, c, and v refer respectively to reduced, conduction, and valence. Equation (37) allows us to write this directly as

$$(\beta_r W_r)^{2/3} = (\beta_c W_c)^{2/3} + (\beta_v W_v)^{2/3}. \tag{51}$$

Also, we recall from eq (33) that at the peak the density of states is given by

$$\rho_\mu(\text{peak}) = \frac{\sqrt{3}}{2\pi}\frac{\beta_\mu^{2/3}}{W_\mu^{1/3}} \quad (\mu \equiv c,\ v,\ \text{or}\ r) \tag{52}$$

On the other hand, in terms of the familiar phenomenological parameter τ, the peak height of a Lorentzian-broadened density of states is given by the expression

$$\rho_{\mu(\text{Lor})}(\text{peak}) = \frac{\beta_\mu}{\pi}\sqrt{\frac{\tau_\mu}{\hbar}}\left(\frac{3}{4}\right)^{3/4} \tag{53}$$

Experimental observation shows that the magnitude of τ is somewhat magnetic field dependent, decreasing with increasing field. If we now equate the two expressions for the peak height, we obtain the equation

$$\beta_\mu^{1/3} W_\mu^{1/3} = \frac{\sqrt{3}}{2}\frac{4^{3/4}}{3}\frac{\hbar}{\tau_\mu} \tag{54}$$

and squaring it yields the very interesting result that

$$\beta_\mu^{2/3} W_\mu^{2/3} = \frac{2}{\sqrt{3}}\frac{\hbar}{\tau_\mu}. \tag{55}$$

In other words, $\epsilon_{0\mu} \propto h/\tau_\mu$, and substituting this result into eq (51), we obtain the condition

$$\frac{1}{\tau_r} = \frac{1}{\tau_c} + \frac{1}{\tau_v}. \tag{56}$$

This result, which holds at any value of magnetic field, restates our condition for mutual consistency among the set of broadened densities as the usual expression for the interband (reduced) phenomenological collision time in terms of the single band times. In addition, eq (55) above would predict, at least qualitatively, the kind of variation in the value of τ_μ with variation in magnetic field that has been observed experimentally.

A reduced broadening parameter, W_r, can now be defined directly from the consistency condition, as follows: Inserting

$$\beta_r \equiv \frac{1}{4\pi l^2}\left(\frac{2m_r^*}{\hbar^2}\right)^{1/2} \tag{57}$$

into eq (51) and doing some algebraic manipulation, we find

$$W_r^{2/3} = (1 + R_M)^{1/3} W_c^{2/3} + \left(1 + \frac{1}{R_M}\right)^{1/3} W_v^{2/3} \quad (58)$$

Hence W_r depends only upon the individual W's and the mass ratio, and is independent of magnetic field.

And when W_c and W_r are replaced by their expressions in terms of β_c, β_r, ϵ_{0c} and ϵ_{0v}, and the entire right hand side inserted into eq (52) for the peak value of $\rho(\hbar\omega)$, we obtain

$$\rho(\text{peak}) = \frac{\sqrt{3}}{2\pi} \frac{\beta_r^{2/3}}{W_r^{1/3}} = \frac{\sqrt{3}}{2\pi} \left[\frac{1}{4\pi l^2} \left(\frac{2m_u}{\hbar^2}\right)^{1/2} \left(\frac{1}{\epsilon_{0u}}\right)^{1/2}\right] \frac{R_E^{1/2}}{(1 + R_M)^{1/2}(1 + R_E)^{1/2}} \quad (59)$$

Note that the factor in square brackets is the same as that in eq (46). To confirm the hypothesis that the optical density of states is formally identical to the single band function, we should be able to equate eq (59) above to eq (46) with the integral evaluated for $\hbar\omega = Eg$, for any chosen pair of values of R_M and R_E. This has been verified by our numerical integration, using values of R_M and R_E ranging from 1 to 20. Therefore, the properties of the function, as developed in section 2, apply equally well to the optical function considered in this section.

4. Conclusions

From the single Landau level densities of states in the presence of energy dependent broadening, we have developed a convolution integral to express the optical density of states for transitions between Landau levels across the energy gap. The form is identical to that of the single band function; but with the frequency measured from the gap energy replacing the energy measured from the band edge, the reduced mass replacing the single band mass, and a reduced broadening parameter replacing the single band parameter. This last parameter was shown to be a consequence of a mutual consistency requirement, and this same requirement also leads to the reduced lifetime expression encountered in the more conventional Lorentzian formulation.

The most striking contrast of these results with the Lorentzian expressions lies in the vanishing of the functions near the band edges. In this region, a parabolic approximation turns out to be valid, and this behavior enables us to explain the functioning of the semiconductor laser in the presence of a magnetic field. Further applications of this formulation to other electron transition processes are currently being studied, notably the Gunn effect.

5. Acknowledgments

The authors wish to express their appreciation to Mr. James Raphel and Mr. James Spoerl for programming assistance, and their gratitude for the services of the University of California Computation Center. Special thanks go to Mrs. Teddi Herron for preparation of the manuscript.

Appendix A

In this appendix we outline the calculation of the optical density of states for transitions between Lorentzian broadened sets of initial and final states. Inserting Lorentzian functions centered around the energies given by eqs (3a,b) into the integral expression (44), we can write

$$\rho(\hbar\omega) = \int\int\int\int\int\int \left(\frac{\Gamma_u}{\left(\frac{E_u - \hbar^2 k_u^2}{2m_u}\right)^2 + \Gamma_u^2}\right)\left(\frac{\Gamma_l}{\left(E_l + Eg + \frac{\hbar^2 k_l^2}{2m_l}\right)^2 + \Gamma_l^2}\right)$$
$$\times \delta(E_u - E_l - \hbar\omega)\delta(k_{yu} - k_{yl})\delta(k_{zu} - k_{zl}) \times dk_{yu}dk_{yl}dk_{zu}dk_{zl}dE_u dE_l \quad (A.1)$$

where Γ_u and Γ_l are constants.

As in section 3, this expression is greatly simplified by carrying out the integrals over E_l, k_{yl}, k_{zl}, and k_{yu} in order to remove the three delta functions and to yield a coefficient proportional to magnetic field. Thus

$$\rho(\hbar\omega) = \frac{V}{8\pi^3 l^2} \int_{-\infty}^{\infty} dk \int_{-\infty}^{\infty} dE_u \left(\frac{\Gamma_u}{\left(E_u - \frac{\hbar^2 k^2}{2m_u}\right)^2 + \Gamma_u^2}\right) \times \left(\frac{\Gamma_l}{\left(E_u - \hbar\omega + E_g + \frac{\hbar^2 k^2}{2m_l}\right)^2 + \Gamma_l^2}\right) \quad (A.2)$$

This double integral is most easily accomplished by contour integration. Defining new variables

$$y \equiv E_u - \frac{\hbar^2 k^2}{2m_u} \tag{A.3}$$

$$\epsilon \equiv \frac{\hbar^2 k^2}{2m_r} - \hbar + Eg \tag{A.4}$$

where m_r is the reduced mass, we find poles in the upper half plane at

$$y = i\Gamma_u \qquad \text{and} \qquad y = -\epsilon + i\Gamma_l, \tag{A.5}$$

so the remaining integral becomes

$$\rho(\hbar\omega) = \frac{V}{4\pi^2 l^2}\int_{-\infty}^{\infty} dk\, \frac{(\Gamma_u + \Gamma_l)}{\epsilon^2(k) + (\Gamma_u + \Gamma_l)^2}$$

$$= \frac{V}{4\pi^2 l^2}\int_{-\infty}^{\infty} dk\, \frac{(\Gamma_u + \Gamma_l)}{\left(\frac{\hbar^2 k^2}{2m_r} - \hbar\omega + Eg\right)^2 + (\Gamma_u + \Gamma_l)^2}$$

$$= \frac{V}{4\pi^2 l^2}\sqrt{\frac{2m_r}{\hbar^2}}\,\mathrm{Re}\,\frac{1}{\sqrt{\hbar\omega - Eg - i\Gamma_r}}. \tag{A.6}$$

It is interesting to note that the sum over Lorentzians in eq (A.6) is formally identical to the sum encountered in the single Landau level density of states, eq (7). Also, the resulting optical density of states is formally identical to the single level density, but with the energy measured from the band edge replaced by the photon energy measured from the band gap, the single band mass replaced by the reduced mass, and the single band broadening parameter Γ replaced by the joint broadening parameter $\Gamma_u + \Gamma_l$. This last replacement is equivalent to the replacement of the lifetime τ by a reduced lifetime τ_r given by

$$\frac{1}{\tau_r} = \frac{1}{\tau_u} + \frac{1}{\tau_l}. \tag{A.7}$$

Appendix B

In this appendix we will evaluate the matrix element in the numerator of the right hand side of eq (16) for each of the three scattering potential functions mentioned.

B.1. Scattering by Low Energy Acoustic Phonons

In examining the effect of lattice vibrations as the source of perturbation, we take advantage of the mutual independence of the various normal modes of the lattice. We assume that the electrons couple to the various modes separately and do not serve as a source of mode mixing. Hence, we will treat the interaction between the electrons and a particular phonon mode of wave vector $\mathbf{q}$ and then sum over all the $\mathbf{q}$'s to obtain the final result. Following Ziman [6] we indicate the matrix element of the perturbation by

$$\langle |v| \rangle = \langle n_{\mathbf{q}}, \Psi | H_{ep} | n'_{\mathbf{q}}, \Psi' \rangle \tag{B.1}$$

where $\mathscr{H}_{ep}$, the electron-phonon interaction operator, is given by

$$\mathscr{H}_{ep} = \left(\frac{\hbar}{2\rho V_c \nu_q}\right)^{1/2} V_d (n_{\mathbf{q}}^{1/2} a_{\mathbf{q}} e^{-i\mathbf{q}\cdot\mathbf{r}} + (n+1)^{1/2} a_{\mathbf{q}}^{+} e^{-i\mathbf{q}\cdot\mathbf{r}}) \tag{B.2}$$

where a_q^+ and a_q are creation and annihilation operators, respectively, of phonons with wave vector $\mathbf{q}$, and V_d is the deformation potential operator on the electronic wave functions, n_q is the phonon density, $\nu_{\mathbf{q}}$ their frequency and ρ is the mass density of the crystal lattice.

It is clear that n_q' must be equal to $(n_q + 1)$ or $(n_q - 1)$ for this operator to have nonvanishing matrix elements; to be specific, let us carry out the calculation for $n_q' = n_q - 1$, and then add the obvious extension to the other case. Letting the phonon operators act on the phonon density part of the state, we obtain

$$\langle |v| \rangle = \left(\frac{\hbar n_q}{2\rho V_c \nu_q}\right)^{1/2} \int e^{i\mathbf{q}\cdot\mathbf{r}} \Psi^* V_d \Psi' d^3 r \tag{B.3}$$

and then invoking the slow variation of the envelope functions F and F' and the factor $e^{\mathbf{q}\cdot\mathbf{r}}$ compared to that of the cell-periodic part of the Bloch function, we effect the usual separation of the integral into a product of two integrals. One is treated by deformation potential theory [6] and leads to q times a constant, usually called the deformation potential parameter and denoted by E_d. The other integral is separable into product of factors along the three cartestian coordinates, with the two in the y and z directions resulting in δ-functions that insure momentum conservation. Hence

$$\langle |v| \rangle = \left(\frac{\hbar n_q}{2\rho V_c \nu_q}\right)^{1/2} qE_d \delta(k_y' - k_y - q_y)\, \delta(k_z' - k_z - q_z) J n n'(k_y, q_x, k_y') \tag{B.4}$$

where we have used the notation $J_{nn'}(k_y,q_x,k_y')$ introduced by Argyres [7] and now used by other authors [8,9] to indicate the integral along the x-coordinate:

$$J_{nn'}(k_y, q_x, k_y') \equiv \int dx \psi_n(x - l^2 k_y) e^{iq_x x} \psi_{n'}(x - l^2 k_y'). \tag{B.5}$$

The matrix element corresponding to an initial state $n_q' = (n_q + 1)$ would then have $(n_q + 1)$ in the coefficient where the one just calculated has n_q.

We will make the further assumption of restricting our attention to the case of low energy acoustical phonon scattering. (This is of particular interest, and is certainly justified, for the moderate temperatures and narrow range of kinetic energies of the quasi-equilibrium carriers involved in the lasing process.)

Because these are low energy phonons, they are numerous enough so that $n_q \approx n_q + 1$, which is consistent with rewriting n_q, a Bose-Einstein factor, as follows:

$$n_q = \frac{1}{\dfrac{h\nu_q}{e^{kT} - 1}} \approx \frac{kT}{h\nu_q} \approx \frac{kT}{\hbar v_s q} \tag{B.6}$$

where v_s is the sound velocity in the semiconductor.

Thus the form of the matrix element for a single phonon mode to be used in eq (14) is

$$\langle |v| \rangle = \left(\frac{kTE_d^2}{2\rho V_c v_s^2} \right)^{1/2} \delta(k_y' - k_z - q_z) \delta(k_z' - k_z - q_z) Jnn'(k_y, q_x, k_y') \tag{B.7}$$

and the equation itself is written

$$G(s) = \sum_{n', k_y', k_z'} \sum_{\mathbf{q}} \frac{kTE_d^2}{\rho V_c v_s^2} \times \frac{\delta(k_y' - k_y - q_y) \delta(k_z' - k_z - q_z) |J_{nn'}(k_y, q_x, k_y')|^2}{E^0_{n', k_z'} + G - s} \tag{B.8}$$

where the coefficient has been multiplied by 2 to account for both the processes of absorption and emission of phonons. The summation over $\mathbf{q}$ brings in the effects of all the phonon modes. As discussed by Callaway [10], no difficulty is introduced by squaring a matrix element containing momentum-conserving delta functions.

We now proceed with the summation in order to obtain the expression for G: first the two delta functions are eliminated by integration over q_z and k_y', leaving

$$G = \sum_{n', k_z'} \sum_{q_x, q_y} \frac{kTE_d^2}{\rho V_c v_s^2} \frac{|J_{nn'}(k_y, q_x, k_y + q_y)|^2}{E^0_{n', k_z} + G_{n', k_z + q_y, k_z} - s} \tag{B.9}$$

Since $|J_{nn'}|^2$ depends upon k_y only in the combination $x - x_0(k_y)$, it is possible to have a solution for G which is independent of k_y; hence G in the denominator of the right hand side is independent of $k_y' = k_y + q_y$, and the summation over q_y need only involve the numerator. A theorem due to Argyres [7],

$$\int\int dq_x dq_y J_{nn'} J^*_{mm'}(k_y, q_x, k_y + q_y) = \frac{2\pi}{l^2} \delta_{nn'} \delta_{mm'} \tag{B.10}$$

allows the result to be written immediately as

$$G = \sum_{n_j' k_z'} \left(\frac{kTE_d^2}{\rho v_s^2 L_z} \right) \frac{1}{2\pi l^2} \frac{1}{E^0_{n', k_z} + G(s) - s} \tag{B.11}$$

and a simple linear transformation of variable will now lead directly to the form of the k_y integral mentioned in section 2. The factor in parentheses is a specific expression for the factor we called $W/2\pi l^2$.

B.2. A Random Distribution of Scattering Potentials

To insert a random distribution of scatterers into the formalism we have been using, it proves most convenient to deal with the Fourier transform of the poten-

tial in computing its matrix element. Thus, at any point $\mathbf{r}$, the potential $V(\mathbf{r})$ due to the N_s scatterers distributed throughout the crystal at locations R_j is

$$V(r)=\sum_{j=1}^{N_s} v(\mathbf{r}-\mathbf{R}_j) \tag{B.12}$$

and its Fourier transform is given by

$$\tilde{V}(\mathbf{q})=\frac{1}{V_c}\int e^{i\mathbf{q}\cdot\mathbf{r}}V(\mathbf{r})d^3r \tag{B.13}$$

from which an elementary transformation of variable leads to

$$V(\mathbf{q})=\frac{1}{V_c}\sum_{j=1}^{N_s} e^{-i\mathbf{q}\cdot\mathbf{R}_j}\tilde{v}(\mathbf{q}) \tag{B.14}$$

where V_c is the crystal volume and $v(q)$ is the Fourier transform of the single scatterer's potential. The matrix element which appears in the numerator of the right hand side of eq (14) has the following form:

$$\langle V(r)\rangle=\sum_{\mathbf{q}}\tilde{V}(\mathbf{q})\int\int e^{(k'_y-k_y+q_y)y}\times e^{i(k'_z-k_z+q_z)z}\psi_n(x-k_yl^2)\times e^{iq_xx}\psi'_n(x-k'_yl^2)d^3r$$

$$=\sum_{\mathbf{q}}\tilde{V}(\mathbf{q})\delta_{k'_y,\,k_y+q_y}\,\delta_{k'_z,\,k_z+q_z}\,J_{nn'}(k_y,\,q_x,\,k'_y) \tag{B.15}$$

Before putting the specific expression for $V(q)$ and proceeding to evaluate the right hand side of eq (16), let us square eq (16) and average over the spatial distribution of scatterers

$$\langle|\langle V(r)\rangle|^2\rangle_s=\sum_{\mathbf{q},\,q'}\langle\tilde{V}(\mathbf{q})\tilde{V}^*(\mathbf{q}')\rangle_s\,\delta_{k'_y,\,k_y+q_y}\delta_{k'_z,\,k_z+q_z}$$

$$\times\delta_{k'_y,\,k_y+q'_y}\delta_{k'_z,\,k_z+q'_z}\times J_{nn'}(k_y,\,q_x,\,k'_y)J^*_{nn'}(k_y,\,q'_x,\,k'_y) \tag{B.16}$$

It is evident that only the product of $V(q)$'s has explicit dependence upon the distribution of scattering centers; hence that is the only part included in the brackets $\langle\rangle_s$ that indicate spatial average. Using eq (B.14) and taking account of the random distribution of the R_j's, it immediately follows that

$$\langle\tilde{V}(\mathbf{q})\tilde{V}^*(\mathbf{q}')\rangle_s=\frac{N_s}{V_c^2}\,\delta_{\mathbf{q},\mathbf{q}'}\,|\,\tilde{v}\,(\mathbf{q})|^2 \tag{B.17}$$

and the average of the squared matrix element simplifies to

$$\langle|\langle V(r)\rangle|^2\rangle_s=\sum_{\mathbf{q}}\frac{N_s}{V_c^2}\,|\tilde{v}(\mathbf{q})|^2\delta_{k'_y,\,k_y+q_y}\delta_{k'_z,\,k_z+q_z}|J_{nn'}(k_y,\,q_x,\,k'_y)|^2 \tag{B.18}$$

which we proceed to insert into eq (14):

$$G(s)=-\sum_{n',\,k'_y,k'_z}\sum_{\mathbf{q}}\frac{N_s}{V_c^2}\frac{|v(\mathbf{q})|^2|J_{nn'}(k_y,\,q_x,\,k'_y)|^2}{E^0_{n',k'_z}+G(s)-s}\delta_{k'_y,\,k_y+q_y}\delta_{k'_z,\,k_z+q_z} \tag{B.19}$$

The two delta functions are then eliminated by summations over q_z and k_y', where the latter is carried out as in the two previous cases, under the condition that G is independent of k_y. The result is the following expression:

$$G(s)=-\sum_{n',\,k'_z}\sum_{q_x,\,q_y}\frac{N_s}{V_c^2}\frac{|\tilde{v}(\mathbf{q})|^2|J_{nn'}(k_y,\,q_x,\,k_y+q_y)|^2}{E^0_{n',\,k'_z}+G(s)-s} \tag{B.20}$$

Before continuing, we would like to remark that up to this point no properties of the particular scattering centers have been invoked. The result has only required that the distribution be random to allow the

417-156 O - 71 - 30

averaging to yield the $\delta_{q,q'}$ in eq (B.17). If the scattering centers were delta-function potentials of amplitude $\hbar^2\sigma^{1/2}/\pi m$, the Fourier transform $\tilde{V}(q)$ would be a constant, and eq (B.20) above would be identical to eq (B.9), but with $W/2\pi l^2$ given by $(n_s/4\pi l^2\ \hbar^4\sigma/m^2)$. The delta function can be considered a good approximation wherever the force range of the potential is considerably smaller than the cyclotron orbit radius of the electrons being scattered.

On the other hand, the scattering source to be considered is that of the attractive screened Coulomb potential; we write:

$$v(\mathbf{r}) = \frac{Ae^{-q_s r}}{r} \tag{B.21}$$

where A is the amplitude and $(q_s)^{-1}$ the screening length. The screening length determines the force range of the potential, and unlike that of the delta-function potential just treated, the validity of our approximation in this case depends upon this force range being *large* compared to the cyclotron orbit radius. The Fourier transform of this potential is given by

$$\tilde{v}(\mathbf{q}) = \frac{A}{q^2 + q_s^2} \tag{B.22}$$

where, because of the δ function involving q_z,

$$\mathbf{q} = (q_x,\ q_y,\ k_z' - k_z); \tag{B.23}$$

and since we are restricting our attention to elastic collisions with attractive potentials only, $k_z' = +k_z$. Furthermore, we retain the assumption that only scattering within the $n = 0$ Landau level is important so we can write $|J_{00}|^2$ explicitly in simple form. Thus

$$G(s) = -\frac{A^2 n_s}{l^2} \sum_{k_z'} \iint dq_x dq_y \frac{e^{-\frac{l^2}{2}(q_z^2 + q_y^2)}}{(q_s^2 + q_x^2 + q_y^2)^2 (E^0_{k_z'} + G(s) - s)} = -\frac{A^2 n_s}{l^2} \sum_{k_z'} \frac{1}{E^0_{k_z'} + G - s} \int_0^\infty dq_\perp^2 \frac{e^{-\frac{l^2 q_\perp^2}{2}}}{q_\perp^2 + q_s^2} \tag{B.24}$$

A change of variable, $t \equiv q_s^2 + q^2/2q_s^2$ enables the above equation to be rewritten as

$$G(s) = \frac{A^2 n_s}{l^2} \sum_{k_z'} \frac{1}{E^0_{k_z'} + G - s}\ e^{+\frac{l^2 q_z^2}{2}} \int \frac{e^{-l^2 t q_s^2}}{t}\, dt. \tag{B.25}$$

Performing the sum over k_z' and also recognizing the exponential integral leads to the following expression for G:

$$G(s) = +\frac{A^2 n_s}{4\pi^2 l^2} \left(\frac{2m^*}{\hbar^2}\right)^{1/2} \frac{e^{\frac{l^2 q_z^2}{2}}}{\sqrt{1/2\hbar\omega_c + G(s) - s}} (\gamma + \ln\ q_s^2 l^2 - q_s^4 l^4\ \ldots)$$

$$\approx \frac{1}{4\pi^2 l^2} \left(\frac{2m^*}{\hbar^2}\right)^{1/2} \frac{A^2 n_s \ln\ q_s^2 l^2}{\sqrt{1/2\hbar\omega_c + G(s) - s}} \tag{B.26}$$

where γ, the Euler-Mascheroni constant, is approximately equal to 1/2, and our assumption that $q_s^2 l^2 \ll 1$ allows us to replace the exponential by unity and to ignore γ and the higher powers of $q_s^2 l^2$.

Again we arrive at an equation for G whose form is identical to eq (19) and (B.11), and therefore the same procedure would be used in finding the density of states, with $A^2 n_s / \ln q_s^2 l^2$ as the factor we labelled W. We point out in passing that this form of W, unlike the previous two forms, has an explicit dependence on magnetic field.

6. References

[1] Hugenholtz, N. M., Physics **23**, 481 (1957).

[2] Van Hove, L., in Quantum Theory of Many-Particle Systems (Benjamin Press, New York, 1961), p. 1.

[3] Kubo, R., Miyake, S., and Hashitsume, N., in Solid State Physics, Seitz and Turnbull, Editors, **17**, 269 (1965).

[4] Kumar, K., Perturbation Theory and the Nuclear Many Body Problem (North Holland Publishing Co., Amsterdam, 1962).

[5] Roman, P., Advanced Quantum Theory (Addison-Wesley Publishing Co., Reading, Mass., 1965).

[6] Ziman, J. M., Electrons and Phonons (Oxford University Press, London, 1960).

[7] Argyres, P., Phy. Rev. **109**, 1115 (1958).

[8] Korovin, L., and Kharitonov, E., Sov. Phys. Sol. St. **7**, No. 7, p. 1740 (January 1966).

[9] Roth, L., and Argyres, P., Magnetic Quantum Effects, in Physics of III-V Compounds, Willardson and Beer, Editors (Academic Press, New York, 1966).

[10] Callaway, J., Energy Band Theory, Chapter 4 (Academic Press, New York, 1964).

DISORDERED SYSTEMS I

CHAIRMEN: L. F. Mattheiss
A. Kahn

The Electronic Structure of Disordered Alloys*

J. L. Beeby

Theoretical Physics Division, Atomic Energy Research Establishment, Harwell, Didcot, Berks., England

The problem of calculating the electronic density of states in an alloy is considered from first principles. Choosing a suitably simplified model potential a diagrammatic expansion is discussed within which the various existing theories can be compared. Some comments are made on the comparison with experiment.

Key words: Density of states; disordered alloys; one-electron propagator; perturbation expansion; sum rule.

1. Introduction

It has long been appreciated that the information obtainable from experiments on alloys provides a useful supplement to one's knowledge of the pure materials. Much of this information, such as the Hume-Rothery rules, was obtained using binary alloys with similar non-transition-metal constituents. In such an alloy the electron mean free path is long and the alloy can often be regarded as homogeneous. The problem which will be discussed in this paper concerns how to calculate the properties of an alloy in which the constituents are very different. For such an alloy there arises, besides the routine difficulty of choosing an appropriate potential, a major problem involving the order. Perfectly ordered alloys can be handled just as for pure materials, but disordered alloys with strong scattering potentials have needed the development of new theoretical techniques. These methods will be discussed below via a diagrammatic expansion which appears to give improved insight into the whole problem of disorder. No attempt will be made to formally review the literature and no claim is made to completeness. Rather, it is hoped, readers will be better able to judge for themselves the contents of papers in the field.

The paper will begin with a derivation of the alloy potential. The intention here is to clarify, for those not already familiar with the field, what disorder is and how the theorist can describe it by an averaging process. While concepts of this type are already common, as in statistical mechanics for example, it is clear from the current literature that many authors still misunderstand them in the alloy context. The derivation of the potential is then completed by briefly listing the assumptions required with a few comments on their validity. The potential used is of muffin-tin type with invariant potentials for each constituent. The brevity of this section should not be regarded as indicative of the trivial nature of obtaining the potential, which in itself forms a most interesting and difficult task. The heart of the paper is contained in sections 4-6 where the density of states is obtained by considering the imaginary part of the T-matrix for the alloy. The T-matrix can be expanded in a series involving the individual scattering centers (the muffin tins) in the usual way. The procedure adopted in section 5 concerns the way in which the series is to be averaged term by term. Each term requires the knowledge of a probability function and it is these probability functions which must be approximated if the series is to be resumed. A diagrammatic expansion is given which, it is argued, formally converges like Z^{-1} where Z is the number of nearest neighbors. In practice, however, it is the degree of fluctuation which determines the convergence which is anyhow at best asymptotic. Section 6 illustrates these remarks by looking at numerical solutions for different approximations. In the final sections a few examples will be cited of the interrelation between this work and experiment. These are mainly concerned with the transition metals to which the formalism is most appropriate.

*An invited paper presented at the 3d Materials Research Symposium, *Electronic Density of States*, November 3–6, 1969, Gaithersburg, Md.

2. The Meaning of Disorder

When an alloy sample is made there is much information which is available in principle yet is not available in practice. It is normally possible to determine the content of each constituent, the structure and certain ordering parameters. But it is plainly absurd to expect to know the *actual* positions of all the atoms in a disordered sample. Thus while an experiment is performed on a particular sample whose atomic positions may be regarded as fixed during the experiment, a theoretical calculation for this sample must proceed in ignorance of the actual positions. The formal device used to offset this ignorance consists of an averaging procedure about which one might make the following comments.

(i) It is expected that all macroscopically *identically produced* samples will have (within experimental error) identical properties. Systems with large fluctuations in their properties due to unavoidable variations in production need a different approach. Such fluctuations are usually due to variations in some macroscopic parameter not yet controlled in the production process.

(ii) The detailed microscopic order is therefore only important to the extent that certain macroscopic properties (*e.g.*, order parameters) are satisfied.

(iii) Naturally the theoretician is, in these circumstances, at liberty to choose any one microscopic distribution which satisfies the macroscopic restraints. However, since all such distributions are equivalent, it is easier to average over them with a probability function specifying the chance that they occur.

(iv) Such an approach is well known in Statistical Mechanics and works for the same reason: the number of particles involved in the average is very large.

It is most important that any such averaging is made only over observable properties of the sample. As an example consider the density of states which for a given sample might be written $n(E, q_1, q_2, \ldots q_n)$ depending on certain parameters of the sample. If these parameters have a probability of occurence $P(q_1 \ldots q_n)$ within the constraints of the sample production then the *average* density of states is $\int n(E, q_1 \ldots q_n)\, P(q_1 \ldots q_n)\, dq_1 \ldots dq_n$. If the job has been done properly this average value should differ from a typical single alloy value only to the order (1/N) where N is the number of atoms.

Averaging in this way makes things a little simpler algebraically because, like the experimenter, the theorist can ignore all except the macroscopic features of the sample. There are some conceptual difficulties, however, which are worth briefly illustrating. Take first a perfect lattice of one type of atom. Figure 1a shows for a finite number of atoms the energy levels of the system and the singularities which will occur in the complex E-plane for a single particle Green function. A pole will correspond to each energy level. When N becomes infinite the energy levels pack together and can be described by a density of states n(E) as in figure 1b. At

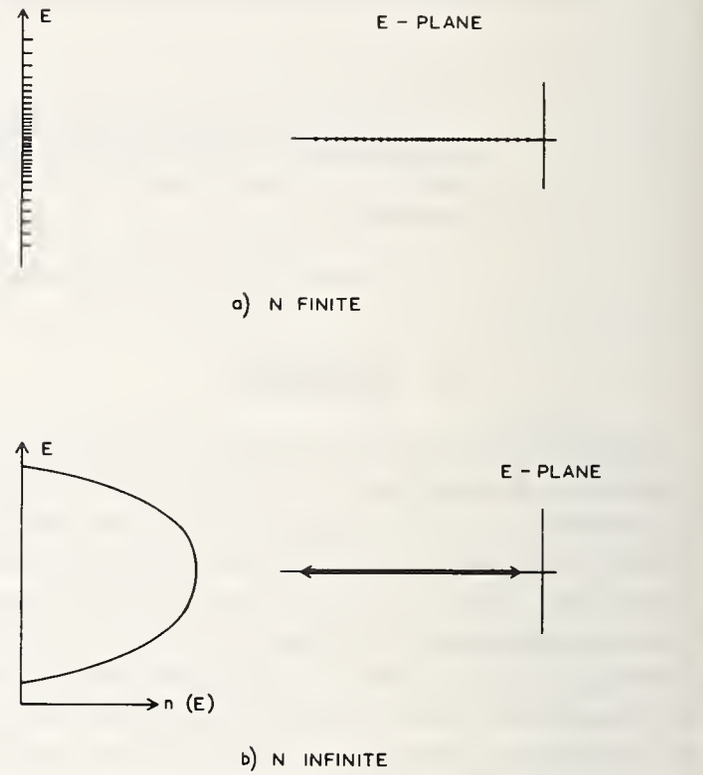

FIGURE 1. *The energy levels and complex plane singularities for (a) a finite, (b) an infinite ordered system.*

the same time the poles merge together to form a branch cut along a portion of the real axis. For an imperfect arrangement the finite system again has poles on the real axis which will turn into branch cuts upon averaging. When approximations are made in the averaging these branch cuts may have been replaced by poles *off* the real axis; the importance of remembering that this is a consequence of the approximations has been particularly stressed by S. F. Edwards. A related point concerns the limit $N \to \infty$. In the perfect lattice case periodic boundary conditions can be used and no difficulty arises. In the disordered case the limit can only be taken *after* the averaging procedure. To see this consider a group of N atoms which is infinitely extended by repetition. The resultant crystal then has N atoms/unit cell and this is well known to yield a band structure with N-1 band gaps in general. As N is increased the band gaps become more numerous and narrower, showing that this is not a sensible treatment.

3. The Alloy Potential

A correct procedure for obtaining an alloy potential would be as follows.

(i) The positions of the nuclei and core electrons are considered known. (But will in practice be supposed to lie on a perfect lattice).

(ii) The potential throughout the entire lattice is guessed.

(iii) The density of electrons in the system is then obtained.

(iv) A new estimate of the potential is made.

Such an "in principle" self-consistent calculation must be made for a single unaveraged alloy and is plainly an impossible task. Some part of this self-consistency can be achieved in special cases, *e.g.*, where the Friedel sum rule can be used in dilute alloys. Step (iii) to (iv) is, of course, similar to the same step in the perfect lattice except for the lack of order, but even in the perfect lattice case is far from easy to carry out properly. The novelty of alloy theory lies in steps (ii) to (iii), describing the electron density once the potential is known. Since this step is the primary interest of this paper the discussion can be greatly clarified by choosing a suitably simple form for the potential. Only the one-electron approximation will be considered.

For a dilute alloy the best potential to use is the perfect lattice (host) potential with an additional potential at each impurity site representing the difference between the impurity and host potentials. This potential can then be used in perturbation theory or even in more sophisticated schemes. A modified version of this approach will also work quite well for concentrated nearly-free-electron alloys.

For the case where at least one constituent of the alloy has a strong scattering potential with just-bound or nearly-bound states the muffin-tin approximation is best. The muffin-tin assumption is worse in an alloy than in a pure material because the local interstitial energy may vary from place to place through the alloy. It is hard to see how one can readily estimate the effects of such variation. It is customary to make the additional assumption that the muffin-tin potentials for each constituent are independent of the environment. This is not generally correct; there is a spill over of the impurity potential onto neighboring sites. Unfortunately neglecting this change is inevitable at this stage in the development of the theory and, it will be noticed, resembles neglect of positional relaxation about the impurity site in defect calculations. It should be borne in mind, however, that the level of the theory at which such effects would enter is well beyond anything that will be discussed in this paper. Since it is clear that particular features of the band structure may depend critically upon such local effects, the most obvious example being bound states localized near an impurity atom, the defect type theories plainly have important applications here.

The virtue of the nonoverlapping muffin-tin form of the potential is that in the potential free region between the spheres electrons move as in free space. The motion of an electron can thus be seen as a series of scatterings from individual sites with free electron propagation in between. It is this separation of the scattering events which is so important to what follows.

If the alloy constituents are at sites R_i, i = 1, . . . N then the potential just discussed may be written for a particular alloy

$$V(\mathbf{r}) = \sum_i \nu_{\mu_i}(\mathbf{r} - \mathbf{R}_\nu)$$

where μ_i is the type of atom at site R_i and $v_\mu(r)$ is the potential of the μ'th atom type. The nonoverlapping restriction is that

$$\nu_\mu(\mathbf{r}) = 0 \qquad r > r_o$$

where r_o is half the near neighbor distance. There is actually no restriction that $v(r)$ be spherically symmetric though this is often quoted as necessary. With this greatly simplified form for the potential it is possible to proceed with the formal theory of disordered alloys.

4. The T-Matrix

In the discussion of the density of states in an alloy it is necessary to appeal to the concept of a T-matrix and it is therefore worthwhile to demonstrate that it is actually a simple concept. Indeed, while much of the algebra is rather involved, the use of the T-matrix allows almost classical mental pictures to be used and the algebra very largely suppressed.

Consider then a single scattering center of potential V(*r*) with particles incident upon it. It is well known that this problem can be solved in integral equation form as

$$\psi(\mathbf{r}) = \phi(\mathbf{r}) - \frac{1}{4\pi}\int \frac{e^{ik|\,\mathbf{r}-\mathbf{r}'|}}{|\mathbf{r}-\mathbf{r}'|} V(\mathbf{r}')\psi(\mathbf{r}')d\mathbf{r}'$$

where $\phi(r)$ is the incident beam and the second term gives the wave scattered from the potential. Note that the complete wave function $\psi(r')$ appears in this latter term; if $\phi(r)$ were inserted here the scattering would be given in Born approximation. The T-matrix is formally defined by

$$V(r')\psi(\mathbf{r}') = \int T(\mathbf{r}', \mathbf{r}'')\phi(\mathbf{r}'')d\mathbf{r}''$$

but is best understood in terms of the physical description. The point is that it is very convenient to describe a potential by the scattering it induces among a set of states defined outside the potential and this is what the T-matrix describes. In the crystal these states will be spherical harmonics centered on the atomic position in question. The T-matrix for the potential describes the scattering from one (ingoing) spherical state to another (outgoing) such state.

The infinite crystal potential leads to a T-matrix of different interest. The feature dominant here is that the scattering cross section is infinite for electrons incident on a potential well at an energy at which that well has a bound state. Using this in reverse one may look for the energy levels of the crystal by seeking the poles (or branch cuts) of the T-matrix. Actually the density of states is directly proportional to the imaginary part of the T-matrix and this is the link which will be adopted below. One can now utilize the fact that the total alloy potential is made up of individual scattering sites with their own T-matrices t_i. All scattering processes from the alloy can be described in terms of the sequence of scatterings from these sites. Thus

$$T=\sum_i t_i+\sum_{i\neq j} t_iG_{ij}t_j+\ldots \qquad (1)$$

where the nth term describes those scatterings from the alloy in which n individual site scatterings occur. G_{ij} describes formally the way in which the electron moves between the scatterings at i and j and it is to be noted that two consecutive scatterings cannot be from the same site.

5. The Alloy Formalism

The aim of this section is to introduce a diagrammatic technique which carries considerable insight into the nature of the disorder problem. The algebra required to set up the diagrams is given mainly because of its intrinsic interest. This algebra may otherwise largely be skipped since the meaning of the diagrams is fairly readily understood.

For a single alloy the series (1) can be cast in an entirely real form and the imaginary part corresponding to the density of states ($n(E)\sim\Sigma\delta(E-E_i)$ for this alloy) will only emerge after the infinite series has been summed. In other words the bound states occur at the points where the series diverges. Since the averaging plainly cannot be carried out on the summed T-matrix it is necessary to resort to a term by term averaging followed by the infinite summation. To be specific consider a binary alloy specified by writing at the site i

$$t_i=\sum_{\nu=\alpha,\,\beta} t_\nu c_i^\nu$$

where t_α, t_β are the t-matrices for potential wells of type A and B respectively. Also the c_i^ν are defined by

$$\begin{aligned} c_i^\alpha &= 1 && \text{if the atom at site } i \text{ is of type A}\\ &= 0 && \text{otherwise}\\ c_i^\beta &= 1-c_i^\alpha=1 && \text{if the atom at site } i \text{ is of type B}\\ &= 0 && \text{otherwise}\end{aligned}$$

In the average system these c_i^ν are given by certain distribution functions appropriate to the alloy composition in question. It is convenient to introduce dummy variables c^ν, $c^\nu=0,\ 1$ so that $c_i^\nu=\sum_{c^\nu} c^\nu\delta_{c^\nu,\,c_i^\nu}$. Then the T-matrix becomes

$$T=\sum_{i,\,c^\nu\nu} t_\nu c^\nu\delta_{c^\nu,\,c_i^\nu}+\sum_{\substack{i\neq j\\ c^\nu,\,c^\mu\\ \nu,\,\mu}} t_\mu c^\mu G_{ij}t_\nu c^\nu\delta_{c^\mu,\,c_i^\mu}\delta_{c^\nu,\,c_j^\nu}+\ldots \qquad (2)$$

and the averaging which must be performed has been entirely concentrated into the Kronecker-delta functions.

Consider these averages. What one requires to know are probability distributions such as

$$P\begin{pmatrix}c^1, & c^2, & c^3, & c^4\\ i & j & k & l\end{pmatrix}=\langle\,\delta_{c^1,\,c_i^\mu}\,\delta_{c^2,\,c_j^\nu}\,,\,\delta_{c^3,\,c_k^\eta}\,,\,\delta_{c^4,\,c_l^\lambda}\,\rangle \qquad (3)$$

For example, take a completely disordered binary system in which the concentration of the constituent A is c. Then the probability distribution of the c_i^ν's is

$$\prod_{\text{all sites}}\{c\delta_{c_i^\mu,\,c_i^\alpha}+(1-c)\delta_{c_i^\mu,\,c_i^\beta}\} \qquad (4)$$

Since the probability of finding atom A is independently c on every site. When this probability function is used to evaluate the average on the right-hand side of (3) the factor in braces in (4) only occurs once for each independent site in (3). This means there is not necessarily one such factor for each Kronecker delta in (3) but rather only one for each independent site. Thus one obtains

$$P\begin{pmatrix}c^1, & c^2, & c^3, & c^4\\ i & j & k & l\end{pmatrix}=\sum_{c_i^\mu,\,c_j^\nu\,\text{etc.}}{}'\{c\delta_{c_i^\mu,\,c_i^\alpha}+(1-c)\delta_{c_i^\mu,\,c_i^\beta}\}$$

$$\delta_{c^1,\,c_i^\mu}\ \ldots\ \delta_{c_,\,c_l^\lambda} \qquad (5)$$

where the prime on the product denotes the restriction that *only independent sites* among the i, j, k, l are included. It is this restriction which is at the heart of the disordered alloy problem. It states that when the same atom appears more than once in a term of the series (2) the average cannot be taken as though each appearance is independent of the others. It is to be

emphasized that this restriction is geometrical; it is a sort of counting problem. Obviously the magnitude of any counting error will depend on the relative size of the various terms and the precise determination of the physical parameters determining these sizes is the essential problem to be faced. The partial progress in this direction will later be illustrated by example but much remains to be done.

A common first step in dealing with a restriction is to first ignore it and then make successively more accurate corrections. This procedure is readily adopted here. Consider the product over independent sites of some factor f_i:

$$\prod_{\substack{\text{indep.}\\ \text{sites}}} f_i = \prod_{\substack{\text{indep.}\\ \text{sites}}} f_i \prod_{\substack{\text{other}\\ \text{sites}}} [f_i + 1 - f_i]$$

$$= \prod_{\substack{\text{all}\\ \text{sites}}} f_i \{1 + \sum_{\substack{\text{other}\\ \text{sites}}} \frac{(1-f_i)}{f_i} + \sum_{\substack{\text{two other}\\ \text{sites}}} \frac{(1-f_i)}{f_i}\frac{(1-f_j)}{f_j} + \ldots\} \qquad (6)$$

where the last line is obtained by expanding the second product. Clearly the correct result will only be regained after all the terms in the sum have been included. This formula allows a simple diagrammatic representation in which all the sites appearing in a term are given as dots on a line as in figure 2a. The dots themselves represent the t-matrices and the lines between the dots represent the propagators G_{ij}. In this series of scatterings the repetition of a given scattering center can be treated by the device of eq (6). The first term in the sum in (6) corresponds to ignoring the restriction in which case the probability distribution will be given by

$$P\begin{pmatrix} c^1 & c^2 & c^3 \\ i, & j, & k, \ldots \end{pmatrix} \simeq P\begin{pmatrix} c^1 \\ i \end{pmatrix} P\begin{pmatrix} c^2 \\ j \end{pmatrix} P\begin{pmatrix} c^3 \\ k \end{pmatrix} \ldots$$

where

$$P\begin{pmatrix} c^1 \\ i \end{pmatrix} = \sum_{c_i^\mu} \delta_{c^1, c_i^\mu} \{c\delta_{c_i^\mu, c_i^\alpha} + (1-c)\delta_{c_i^\mu, c_i^\beta}\}$$

This gives at once

$$\sum_{c^\mu, \mu} t_\mu c^\mu P\begin{pmatrix} c^\mu \\ i \end{pmatrix} = ct_\alpha + (1-c)t_\beta = \bar{t} \qquad (7)$$

The independent averaging of a point can be denoted by a cross as in figure 2b. The next term in the sum (6) connects each repeat site with the *previous* occasion on which the site appeared and can be represented by a dotted line as in figure 2c. The third term contains

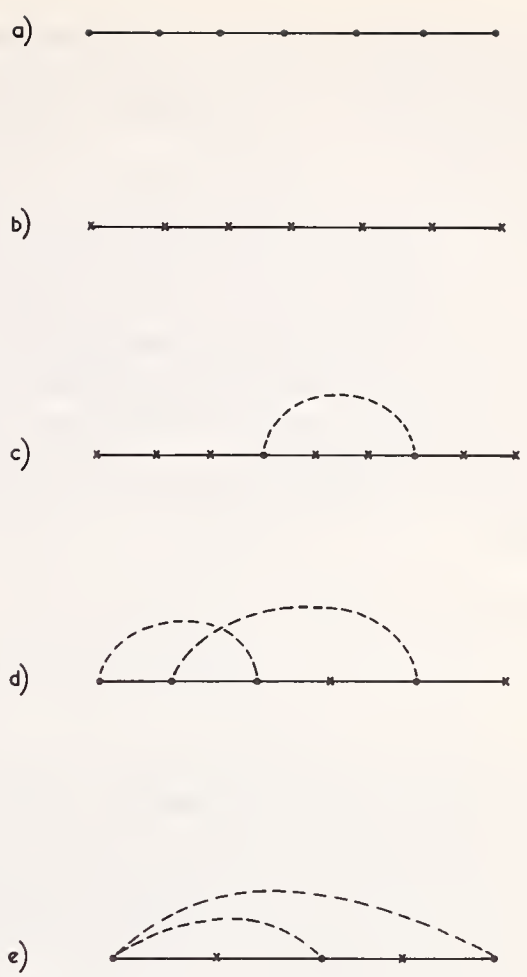

FIGURE 2. *The diagrammatic expansion for the T-matrix showing (a) an unaveraged line, (b) the lowest order approximation, (c) a typical lowest order correction term, (d) a second order correction term, and (e) a forbidden graph.*

two repeats *i.e.* two dashed lines and so on. Indeed, the entire series (2) may be given by the diagrammatic expansion satisfying four simple rules. For each value of n, n = 1, 2, 3, . . . draw all possible diagrams having the following properties

(i) There are n points on a straight line.

(ii) Pairs of these points (but not a consecutive pair) are joined by dashed lines.

(iii) No two dashed lines leave a point in the same direction.

(iv) All points not touched by a dashed line have crosses on them.

The meaning of these diagrams can be readily put into words. For example figure 2c corresponds to a term in which the electron first scatters from 6 different sites then scatters again at the fourth one and finally scatters at two more different sites. Figure 2d represents the electron returning to the first and second sites for its third and fifth scatterings. All such scattering topologies must be drawn and included in the series though it is important to note that diagrams of the type of figure 2e are forbidden by rule (iii). Finally, the dashed line does not represent the actual value of the process it

describes but the *correction* to the related process in which the restriction is ignored and the two ends of the dashed line replaced by crosses. This is illustrated in the example below.

The evaluation of the contribution of a diagram is complicated by the two separate features involved. First there is the t-average which is given by the procedure outlined between eqs (3) and (6). Secondly the propagator sum must be evaluated for each diagram; it is this which is the limiting difficulty as the diagram becomes more and more complicated. Consider any diagram of the type 2c *i.e.* with only one dashed line. The average corresponding to the dashed line may be written

$$\sum_{c^\mu,\, c^\nu} t_\mu t_\nu \delta_{c^\mu,\, c_i^\mu} \delta_{c^\nu,\, c_i^\nu} \{c\delta_{c_j^\mu,\, c_j^\alpha} + (1-c)\,\delta_{c_j^\mu,\, c_j^\beta}\} \times [\delta_{ij} - \{c\delta_{c_j^\nu,\, c_j^\alpha} + (1-c)\,\delta_{c_j^\nu,\, c_j^\beta}\}] = ct_\alpha^2 + (1-c)t_\beta^2 - \bar{t}^2 \tag{8}$$

δ_{ij} is written here as a reminder that j is exactly the same as i and was only introduced as a dummy variable. This is plainly of the form of the exact term less the zeroth approximation to it. Each cross on the line is replaced by $\bar{t}$ as in eq (7). Propagator lines which do not appear inside the dashed curve occur in the combination $\sum_{j(\neq i)} G_{ij} = G$. (In practice the sum is k-dependent;

$$G(\mathbf{k}) = \sum_{j(\neq i)} G(\mathbf{R}_i - \mathbf{R}_j) e^{i\mathbf{k}(\mathbf{R}_i - \mathbf{R}_j)}.$$

Between the ends of the dashed line the propagator must trace a scattering path beginning and ending at the same point so that the sum involved is

$$S = \sum_{j(\neq i),\, k(\neq j)\ \text{etc.}} G_{ij} G_{jk} \ \ldots\ G_{mn} \delta_{ni}.$$

There is an additional restriction that no intermediate site can be that of the end point, otherwise rule (iii) will be violated and the correction terms overcounted. This sum is readily completed by Fourier transformation giving

$$S = I/(1+tI)$$

where

$$I = \tau \int d\mathbf{k} G^2(\mathbf{k}) \bar{t} [1 - \tau \bar{t} G(\mathbf{k})]^{-1}. \tag{9}$$

Here the appropriate number of $\bar{t}$ factors has been introduced and the integral in (9) is over the Brillouin zone of volume τ.

The formal derivation above yields a diagrammatic expansion of a very familiar sort on which the usual tricks can be pulled. These will be discussed in the next section but it is appropriate that some feeling for the meaning of the diagrams be obtained. It will readily be seen that the expansion is not necessarily in powers of any small parameter of a physical nature (it might be *e.g.* if t were very small) but is more precisely viewed as an expansion in the disorder of the system. One way of looking at this is to consider the sequence of neighboring sites, i,j,k. Of the possible values of k, one will be i and therefore (1/number of values of k) of the terms will require corrections as discussed above. If G_{ij} is short ranged, as is the tight-binding case, this means that the proportion of correction terms is 1/Z (where Z is the number of near-neighbors) for each dashed line. An alternative is to regard the series as an expansion in the fluctuations of the system. While 1/Z appears to be small the number of terms with n dashed lines inceases something like n! as n becomes large so that the series is at least asymptotically convergent. This is well known to occur in certain statistical mechanical expansions to which the above procedure is naturally related.

6. The Simplest Approximations

It is now possible to classify most of the theories of disordered alloys according to which diagrams they retain. This is useful in two ways. It gives information about the nature of the various approximations and it helps one to understand some of the physical parameters determining the convergence of the resummations. Begin with the simplest possible terms.

6.1. The average t-matrix approximation [1]

Ignoring all the diagrams with dashed curves gives at once the result

$$\langle T(\mathbf{k}) \rangle = \frac{N\bar{t}}{1 - \bar{t}G(\mathbf{k})} = \frac{N}{\bar{t}^{-1} - G(\mathbf{k})}$$

in which the alloy is represented by a perfect lattice with identical scatterers having the average scattering of the alloy constituents. The density of states given by this approximation for a binary tight-binding alloy is shown in figure 3. The tightly bound energy levels are E_A and E_B and the various cases are found by comparing $|E_A - E_B|$ with the bandwidth. While the gap between

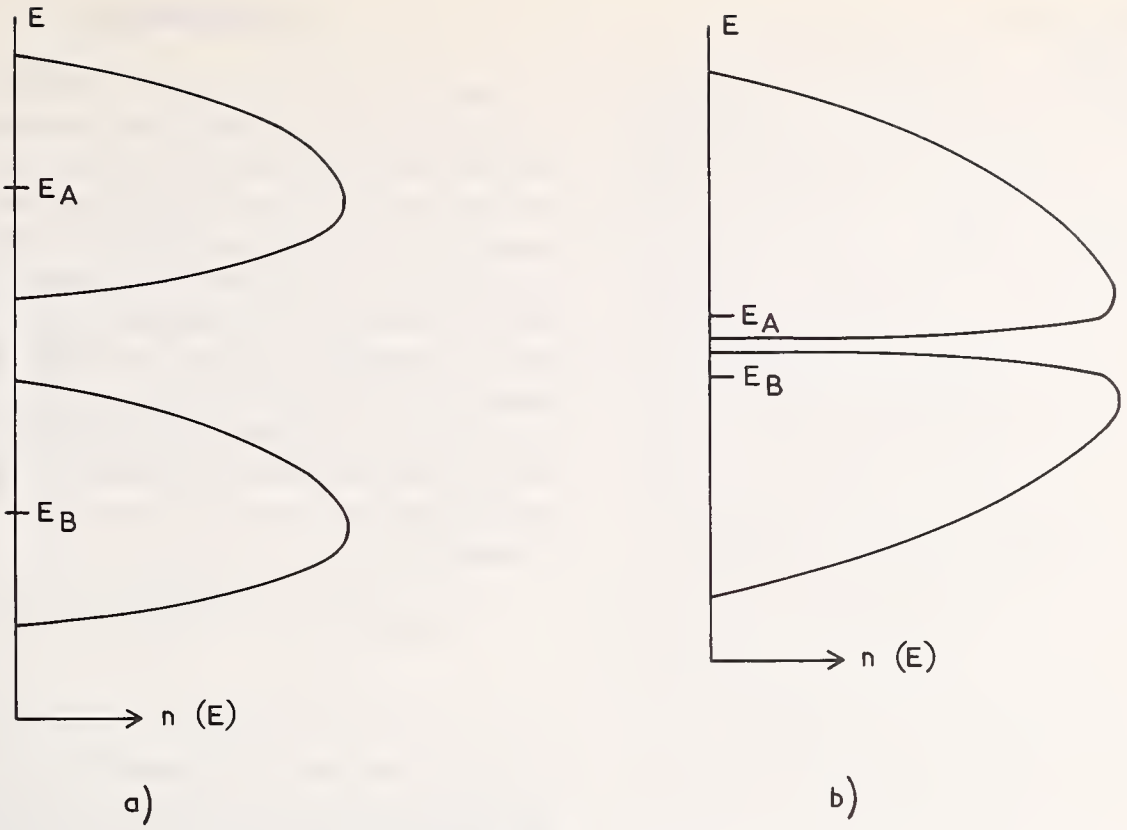

FIGURE 3. *The density of states in the average t-matrix approximation. (a) when* $|E_A\text{-}E_B| >> $ *bandwidth, (b) when* $|E_A\text{-}E_B| << $ *bandwidth.*

the band halves is reasonable when the bandwidth is much less than the energy splitting (fig. 3a), this approximation incorrectly predicts the gap even when the bandwidth is very large (fig. 3b). At the same time the rest of the band is moderately well described showing that the accuracy of the approximation for a given energy depends on the position of that energy within the band.

6.2. First order approximation

Under the assumption that the 1/Z series converges one might next evaluate the contribution of the terms of the type shown in figure 2c. This contribution must include all possible numbers of intermediate scatterings both inside and outside the dashed loop. But now consider the diagrams in figure 4a. These each have an intermediate denominator which we expect to be nearly singular and all this sequence must be included too. This is simply the usual manipulation to give a self-energy rather than a t-matrix which is absolutely necessary in this context. Now

$$T = \frac{N}{(\bar{t} + \Sigma)^{-1} - G}$$

where Σ is given by the diagram of figure 4b, with all possible numbers of intermediate states and can be evaluated from eqs (8) and (9). The inclusion of this term is an improvement over the average t-matrix approximation but does not resolve all the difficulties.

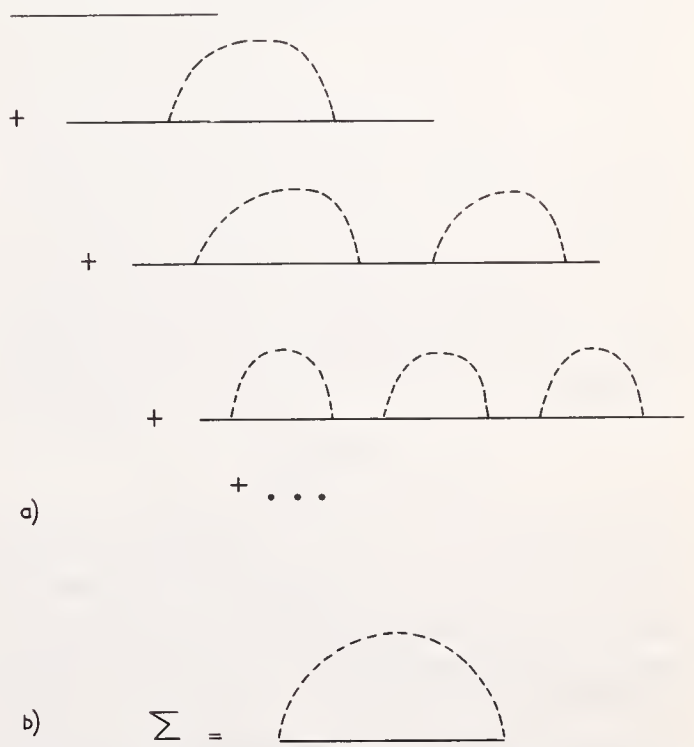

FIGURE 4. *(a) the diagrams summed to give the self energy form, (b) the definition of* Σ.

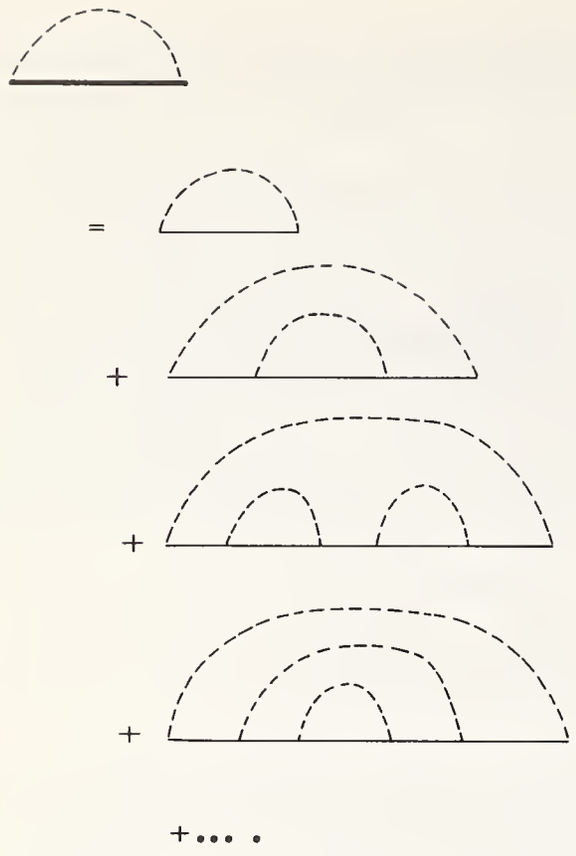

FIGURE 5. *The diagrams summed to give the self-consistent propagator inside the dashed line.*

6.3. Self-consistency

It has long been known that using the unperturbed propagator in the expression for the self-energy is not the best that can be done. The same is true here, where the motion of the electron between successive scatterings can readily be included as if it were being scattered by $(\bar{t}+\Sigma)$ scatterers. This corresponds to including the infinite series of diagrams seen in figure 5. This step is necessary because one really wants to allow scattering of the electron into the *true*, not the unperturbed, density of states. Once this has been done the self-consistent equations obtained can be solved when the unperturbed density of states is given by the expression [2]

$$n_o(E) = \frac{4}{\pi\Delta}\sqrt{1-\left(\frac{E-T_o}{\frac{1}{2}\Delta}\right)^2} \text{ if } |E-T_o| < \tfrac{1}{2}\Delta$$

$$= 0 \quad \text{otherwise.}$$

This self-consistency calculation is an immediate improvement in the sense that the band gap now closes as the splitting $|E_A\text{-}E_B|$ becomes smaller than the bandwidth. Figures 6 and 7 show the alloy density of states in

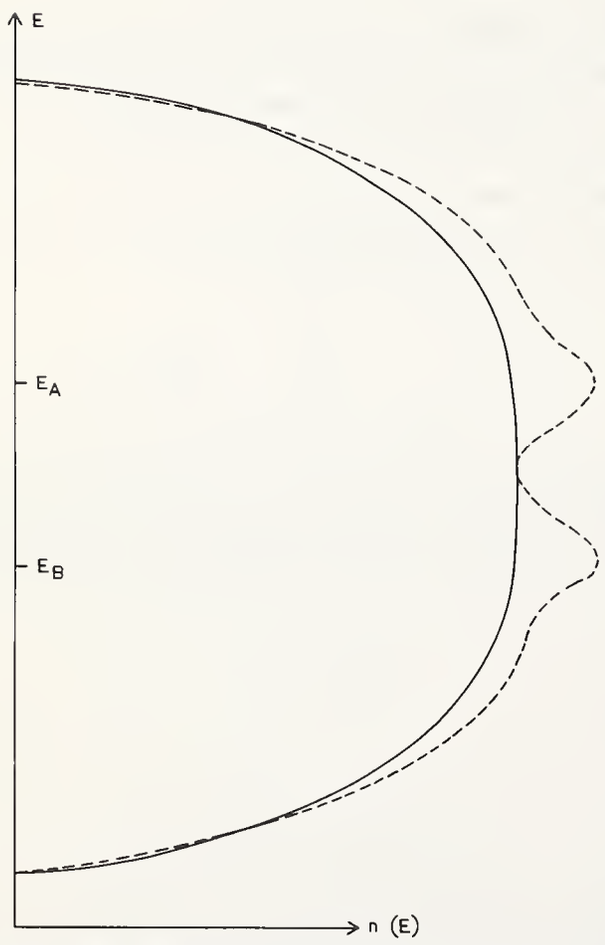

FIGURE 6. *Some density of states curves showing approximations (iii) dashed lines and (iv) full lines for* $c = 0.5$ and $|E_A\text{-}E_B| = \Delta/3.9$.

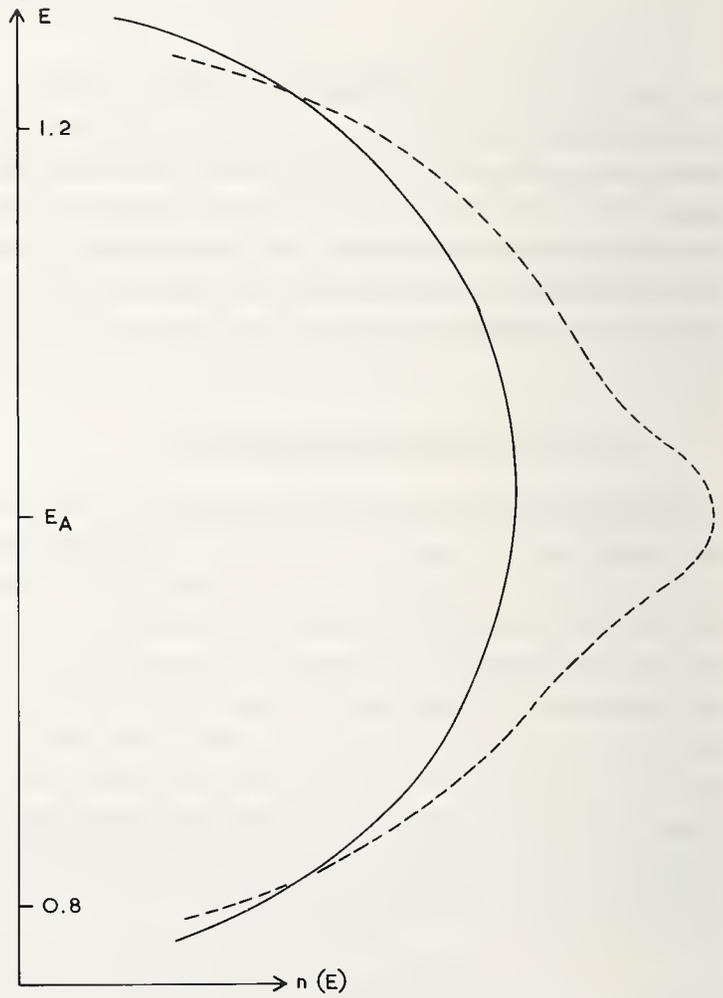

FIGURE 7. *The density of states curves for* $c=0.5$ *and* $|E_A\text{-}E_B|=\Delta/0.7$. *The scale here is such that* $E_A=+1, E_B=-1.0$.

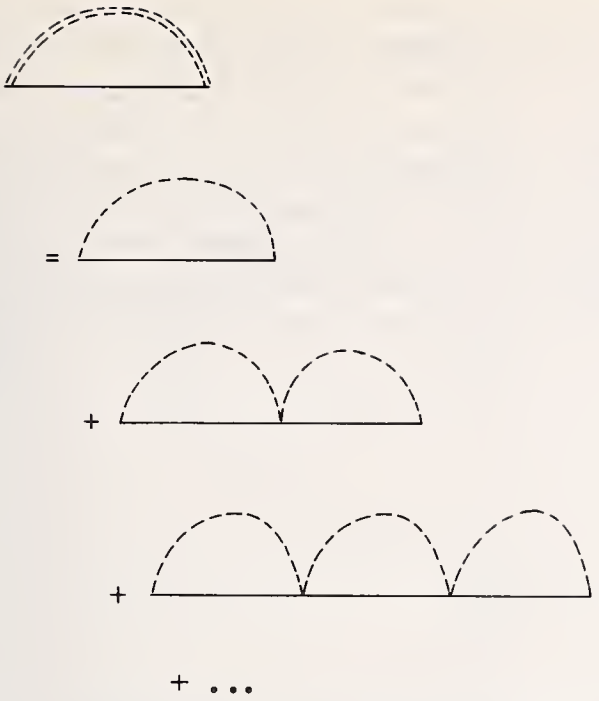

FIGURE 8. *The self-energy graphs required to renormalize the scattering energy levels.*

the approximation as a dashed line. One major error of such a density of states is that it does not satisfy the sum rule on the density of states, a difficulty that can be overcome by a further resummation.

6.4. The renormalized energy levels

The work of Hubbard [2] and later workers [3,4] overcomes the sum rule problem by extending the scattering from any single site to include all possible processes involving only that site. These are the diagrams of figure 8. This has the effect of renormalizing the energy levels and gives the full line density of states in figures 6 and 7. It will also be noticed that the bump in n(E) near E_A and E_B has flattened out. Thus overall this more sophisticated summation gives a smoother density of states. It is interesting to observe that neither the value of the gap width nor the critical ratio $\left|\frac{E_A - E_B}{\Delta}\right|$ at which the gap closes is affected by this last improvement. Within the numerical error approximations (6.3) and (6.4) are identical in this respect.

This last approximation has allowed several alloy density of states calculations to be carried through [3,4] and is probably the best that can be done at the moment. It is rather difficult to see what to do next. There is no general rule for selecting sets of diagrams obeying the density of states sum rule and one has no insight into which of the higher order terms are the most important. Indeed different sets will probably be important in different regions of the energy spectrum.

7. Dimensions and Fluctuations

This section is intended to draw attention to a few of the difficulties associated with the alloy theories just outlined. Rather than dealing directly with the alloy case it is preferable to simplify to the vacancy problem. Here the second alloy species is replaced by vacancies so that only a proportion c of the perfect lattice sites are occupied by type A atoms. In the formalism of the preceding sections it is only necessary to put $t_\beta \equiv 0$.

The illustrative value of the number of dimensions in this argument arises because the formed procedure just outlined is independent of the dimensionality for fixed unperturbed n(E). The physical nature of the problem, however, depends extremely strongly on the dimension principally through the importance of fluctuations. Obviously the fluctuations in one dimension are very large compared to those in three dimensions since the number of neighbors is so much less. This is reflected in the fact that in one dimension the density of states for the alloy problem has a strongly peaked structure, the peaks being identifiable as local groupings of a few atoms as was first remarked upon by Borland [5]. In particular, for the vacancy tight binding cases, the probability of finding a line of n occupied sites with a vacancy on either end is $c^n(1\text{-}c)^2$ and the density of states for such a group is $\sum_{i=1}^{n} \delta(E\text{-}E_i)$. The total density of states is then effectively a weighted sum over δ-functions and is not continuous. Obviously in two and three dimensions the same is true for sufficiently small concentrations but not in general. Plainly when fluctuations are this important there is no chance that the theory described previously can hold.

Another point which can be readily demonstrated is that in such a vacancy case there exist states outside the bands calculated by any of the models just discussed. Consider a simple square lattice in two dimensions. This has coordination 4. A square of side n fully occupied by atoms will have a mean coordination number

$$\frac{4n^2 - 4n}{4n^2} = 1 - \frac{1}{n}$$

since atoms at the sides only have coordination 3. In a tight binding model the mean coordination number is a least estimate for the bandwidth of a group of atoms compared to that for the full lattice. This can be readily seen by a variational calculation with trial function $\Psi = \sum_{i=1}^{n^2} \Psi_i/n$. Now the theories described above give a bandwidth $\propto$ (approx. (6.1)) or $\sqrt{c}$ (approx. (6.4)) so for

the latter case there is a probability $c^{n^2} \simeq c^{(1-\sqrt{c})-2}$ of groups of atoms with energy levels outside the calculated band. Such states of course tail off rapidly but nevertheless exist with positive density of states right out to the full perfect lattice bandwidth. The same applies in three dimensions where the tail is smaller but still there. Figure 9 illustrates this point. Obviously such states are very difficult to spot in the type of theory discussed earlier. They certainly exist at the outside edges of the alloy bands but whether or not they exist inside the band gap is a more difficult question which will undoubtedly be the object of more study.

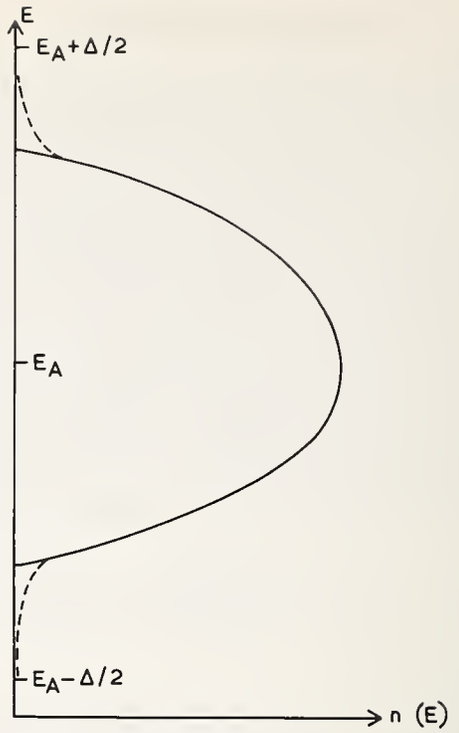

FIGURE 9. *Density of states in the vacancy case showing the limits of the perfect band and the tails extending to those limits.*

9. The Experimental Comparison

It is natural enough that when developing a theory of alloys one begins with the simpler, one-body quantities such as the density of states. Other properties, such as conductivity, Hall effect, *etc.* really require more sophisticated theoretical treatments. The relevant experiments are well dealt with elsewhere in the symposium and so will not be discussed in detail here, but it would be wrong to completely omit commentary on them.

Calculations of the density of states yield a function of energy and a proper experimental comparison would require that function to be observed. Only in the optical type measurements, particularly photoemission and soft x-ray work, is this possible even in principle. In practice there is a good deal of ambiguity in separating out the n(E) curves from other energy dependent variations typically in the matrix elements and many-electron effects. It is clear that for a general comparison with experiment the theoretical work must be pushed to the point of predicting directly the observed data. This is a step which at the moment looks to be just about possible though complicated by the need to take into account local effects through the matrix elements.

Those experiments which measure densities of states at the Fermi surface are complicated by many-body features which, for example, can cause the density of states to be enhanced by quite large factors (~ 1.5 or more). There is the additional difficulty that the pure transition metal band structures lead to density of states curves with a good deal of structure on them so that detailed comparison with experiment requires precise knowledge of potentials and the Fermi energy. Beck and coworkers [6] have overcome some of these objections by using transition metal alloys which seem to conform very closely to the rigid band model and in which the parameters vary only with electron concentration. It is still questionable whether theory can yet predict those cases where Beck's attack will work and in particular where and why it breaks down in the transition metal alloys.

The need for an indirect step in all these experimental analyses has hitherto prevented a satisfactory comparison between the calculated and the measured density of states. It now seems possible that since sophisticated yet fast band structure calculations have been developed and better theoretical understanding of the alloy problem is being rapidly gained the time should soon come when the comparison will become direct.

Finally one might expect some rewards by looking for the gap predicted by the theories when the energy levels are well split as in figure 3a. However, this particular gap is strongly reminiscent of those predicted in the more general disordered system theories and still argued about at length. It is very difficult to observe the difference between a gap and a very low flat minimum even though the distinction is theoretically very important. Perhaps the tunnelling experiments can help here.

10. Conclusions

The theory of disordered alloys is at last coming to the point where it can truly be regarded as a theory rather than being a collection of ad hoc methods. The

problem of a disordered alloy can thus be treated in a parallel fashion to many-body theories and in consequence considerable experience taken over from the many-body theorists. At the same time there remains a real difficulty in producing a satisfactory dialogue with the relevant experiment work. Overall, however, the picture is one holding promise of good developments in the near future which may have a catalyzing effect on the theoretical understanding of disordered systems.

11. References

[1] Beeby, J. L., Phys. Rev. **135**, A130 (1964).

[2] Hubbard, J., Proc. Roy. Soc. **A281**, 401 (1964).

[3] Soven, P., Phys. Rev. **156**, 809 (1967); Onodera, Y. and Toyozawa, Y., J. Phys. Soc. Japan **24**, 341 (1968).

[4] Velicky, B., Kirkpatrick, S., and Ehrenreich, H., Phys. Rev. **175**, 747 (1968).

[5] Borland, R. E. and Agacy, R. L., Proc. Phys. Soc. **84**, 1017 (1964).

[6] See for example, Cheng, C. H., Gupta, K. P., van Reuth, E. C., and Beck, P. A., Phys. Rev. **126**, 2030 (1962).

Local Theory of Disordered Systems*[1]

W. H. Butler[2] and W. Kohn

Department of Physics, University of California, San Diego, La Jolla, California

The most striking characteristic of crystalline solids is their periodicity. As a result of this feature, theoretical descriptions of physical phenomena in such systems are usually given in wave number or *momentum* space. The reciprocal lattice of a crystal and the Fermi surface of a metal are examples. In a disordered system, on the other hand, there is no such periodicity and momentum space descriptions are much less natural. However, in such systems, physical conditions near a point $\mathbf{r}$, in *coordinate* space, become independent of the conditions at a distant point $\mathbf{r}'$, provided that $|\mathbf{r}'-\mathbf{r}|$ is large compared to either a characteristic mean free path or some other appropriate length. This suggests that one can analyze a macroscopic disordered system by averaging over the properties of microscopic neighborhoods.

In the present paper we report some details of such a program. Although the point of view is of quite general applicability we have, for the sake of definiteness, studied so far only one type of system: Noninteracting electrons moving in the field of interacting, disordered scattering centers. We have focused especially on the electronic density of states. The macroscopic system is represented by an average over small neighborhoods. If one did not take special precautions, one would encounter one class of errors of the order of d/L where L is a characteristic dimension of the neighborhood, and d is a characteristic atomic dimension; and another class of errors of the order of $1/N$ where N is the number of ions. Both are too large to be tolerable for practical purposes. However, by an appropriate treatment of the statistical mechanics of the scatterers and by periodic repetition of the small neighborhoods, these errors can be avoided. The remaining errors are exponentially small in the ratio $\gamma(L/R)$ where γ is of order unity and R is the smaller of the electronic mean free path or the deBroglie wavelength of the electrons. This exponential convergence of the small neighborhood theory promises to make it a useful practical method for the study of disordered systems, especially very highly disordered ones.

Numerical examples are presented and discussed.

Key words: Binary alloys; density of states; disordered systems; periodically continued neighborhood.

1. Introduction

The physical properties of strongly interacting disordered systems are in general difficult to calculate since simplifying symmetries, present in crystalline materials, are not present. In this paper we present and develop to some small extent a viewpoint which appears to provide a useful line of attack on the theory of disordered systems.

We shall demonstrate and utilize the rather plausible fact that in a disordered system the physical characteristics at a point $\mathbf{r}$ depend significantly only on conditions inside a rather small neighborhood $|\mathbf{r}'-\mathbf{r}|<R$, where R is of the order of a mean free path l or a characteristic thermal deBroglie wavelength, Λ_t. The effects of the more distant environment fall off exponentially with distance. This suggests that the properties of an infinite disordered system could be accurately calculated by suitable averaging over an ensemble of small neighborhoods. This scheme, furthermore, should be most successful for strongly disordered systems in which the mean free path is short.

In the following sections we sketch an application of these ideas to the much-studied problem of the density

* An invited paper presented at the 3d Materials Research Symposium, *Electronic Density of States*, November 3-6, 1969, Gaithersburg, Md.

[1] Supported in part by the Office of Naval Research and the National Science Foundation.

[2] Present address: Department of Physics, Auburn University, Auburn, Alabama.

417-156 O - 71 - 31

of states of noninteracting electrons moving in the static potential of disordered scattering centers.[3]

2. Demonstration of the Locality Principle

In this section we shall sketch the demonstration that the physical properties near a point $\mathbf{r}$ of a system of noninteracting electrons moving in a disordered external potential are nearly independent of the circumstances outside a characteristic range R. More specifically, the effect of a perturbation at a distant point $\mathbf{r}'$ on physical properties at $\mathbf{r}$ falls off exponentially, on a scale given by a range of influence, R, which is of the order of either the mean free path or, at high temperatures, the thermal wavelength of the electrons, whichever is the smaller.

We consider a very large system of volume Ω described by the Hamiltonian

$$H=H_0+V+v; \tag{2.1}$$

here H_0 is a periodic Hamiltonian, which for simplicity we take to be the kinetic energy

$$H_0=\mathbf{p}^2; \tag{2.2}$$

V is a potential produced by disordered scattering centers, located at the points $\mathbf{r}_\alpha$,

$$V=\sum_\alpha V_\alpha(\mathbf{r}-\mathbf{r}_\alpha); \tag{2.3}$$

and v is an additional small perturbation localized at a point $\mathbf{r}'$. We shall study the effect of v on physical conditions at the point $\mathbf{r}$.

First, we shall consider the one particle Green's function

$$G(\mathbf{r}, \mathbf{r}'; E)=\left(\mathbf{r}\left|\frac{1}{E-H}\right|\mathbf{r}'\right). \tag{2.4}$$

In terms of the eigenfunctions ψ_n of H, and the eigenvalues E_n,

$$G(\mathbf{r}, \mathbf{r}'; E)=\sum_n \frac{\psi_n^*(\mathbf{r})\psi_n(\mathbf{r}')}{E-E_n}. \tag{2.5}$$

Of special interest is the contracted function $G(\mathbf{r}, \mathbf{r}; E)$ which determines the density of states by means of the following relation,

$$n(E)=-\frac{1}{\pi}\,\mathrm{Im}\int d\mathbf{r} G(\mathbf{r}, \mathbf{r}; E+i0). \tag{2.6}$$

We see that we may regard the unintegrated quantity

$$n(\mathbf{r}, E)\equiv-\frac{1}{\pi}\,\mathrm{Im}\,G(\mathbf{r}, \mathbf{r}; E+i0) \tag{2.7}$$

as the local density of states density.

We would like to estimate the effect of introducing the weak additional potential v, at the point $\mathbf{r}'$, on $n(\mathbf{r}, E)$ at the point $\mathbf{r}$. The quantity of physical interest is then

$$\left\langle \frac{\delta}{\delta v(\mathbf{r}')} G(\mathbf{r}, \mathbf{r}; E+i0)\right\rangle = \langle G(\mathbf{r}, \mathbf{r}'; E+i0)G(\mathbf{r}', \mathbf{r}; E+i0)\rangle_{v=0} \tag{2.8}$$

where the brackets $\langle\rangle$ denote configuration average. The equation (2.9) follows directly from the equation of motion of G.

Now it is well known that, for weak random potentials V_α,

$$\langle G(\mathbf{r}, \mathbf{r}'; E+i0)\rangle \approx \frac{1}{4\pi|\mathbf{r}-\mathbf{r}'|} e^{i\sqrt{E}|r-r'|} e^{-|\mathbf{r}-\mathbf{r}'|/2l(E)}, \tag{2.9}$$

where $l(E)$ is the mean free path of an electron of energy E. Similarly, one can show from (2.8) that for large $|\mathbf{r}\text{-}\mathbf{r}'|$

$$\left|\left\langle \frac{\delta}{\delta v(\mathbf{r}')} G(\mathbf{r}, \mathbf{r}; E+i0)\right\rangle\right| \sim e^{-|\mathbf{r}-\mathbf{r}'|/l(E)} \tag{2.10}$$

Thus we see that when $|\mathbf{r}'\text{-}\mathbf{r}| \gg l(E)$, a change of potential at $\mathbf{r}'$ has a negligible effect on the quantity $n(\mathbf{r}, E)$.

Next we show a similar locality effect, this time not due to a finite mean free path but due to elevated temperature. We consider a system of independent electrons and use Boltzmann statistics for simplicity. We take as Hamiltonian

$$H=H_0+v, \tag{2.11}$$

where, in comparison with (2.1), we have eliminated the disordered scattering potentials. We write the partition function as

$$Z=\int d\mathbf{r}\, Z(\mathbf{r}), \tag{2.12}$$

where

$$Z(\mathbf{r})\equiv(\mathbf{r}|e^{-\beta H}|\mathbf{r}). \tag{2.13}$$

Our interest now is in the influence of a small perturbation v at $\mathbf{r}'$ on $Z(\mathbf{r})$. By standard perturbation theory one can show that, for large $|r'-r|$,

$$\frac{\delta Z(\mathbf{r})}{\delta v(r')} \sim -\frac{\pi^{5/2}}{16\beta^{3/2}|\mathbf{r}-\mathbf{r}'|} e^{-|\mathbf{r}-\mathbf{r}'|^2/\Lambda_t^2}, \tag{2.14}$$

[3] Among fairly recent papers we mention the following: H. Schmidt, *Phys. Rev.* **105**, 425 (1957); S. F. Edwards, *Phil. Mag.* **3**, 1020 (1958); ibid. **6**, 617 (1961); *Proc. Roy. Soc.* **A267**, 518 (1962); J. L. Beeby, *Proc. Roy. Soc.*, **A279**, 82 (1964); *Phys. Rev.* **135A**, 130 (1966); P. Soven, *Phys. Rev.* **151**, 539 (1966); ibid., **156**, 809 (1967).

where Λ_t is the thermal wavelength

$$\Lambda_t \equiv \beta^{1/2} (= \hbar/(2m\,kT)^{1/2}). \tag{2.15}$$

Of course at high temperature *and* with disorder, the characteristic "range of influence" R will be either a representative mean free path $\bar{l}$, or Λ_t, whichever is the smaller.

3. The Periodically Continued Neighborhood

We shall now develop a concrete method of calculation, based on the locality principle of the previous section. We shall concentrate on the density of states $n(E)$.

The most straightforward way would be as follows. We imagine the large disordered system as given. We choose at random a large number of points $\mathbf{R}_l$ and surround them by spheres of radius ρ considerably larger than the "range of influence" R, but not too large. Each sphere is surrounded by an infinite wall (see fig. 1). The electronic Hamiltonian for each sphere is given by

$$H = H_0 + V \tag{3.1}$$

where

$$V = \begin{cases} \Sigma V_\alpha(\mathbf{r} - \mathbf{r}_\alpha) & |\,\mathbf{r} - \mathbf{R}_l\,| \leqslant \rho \\ +\infty & r > \rho \end{cases} \tag{3.2}$$

We then calculate for each sphere the density of states density at its center, $n(\mathbf{R}_l,E)$. Because of the relatively small size of the neighborhood this is a much more manageable problem than $n(E)$ for the macroscopic disordered system. In view of the locality principle, $n(\mathbf{R}_l,E)$ is only insignificantly affected by the presence of the infinite wall. Hence, the density of states for the macroscopic system is given by

$$n(E) \approx \Omega \overline{n(\mathbf{R}_l,E)}, \tag{3.3}$$

where the bar denotes an average over many R_l.[4]

The praetical drawbacks, for finite ρ/R_0, are two: (1) The replacement, in the outside region, of the actual potential, $\Sigma\, V_\alpha$, by an infinite repulsive barrier is a quite drastic change and unless ρ/R is very large, will cause sizeable errors. (2) This method does of course not lead to the exact results in the special case of a vanishing or periodic potential.

These drawbacks can be largely overcome by using, instead of a finite and bounded neighborhood, as in figure 1, a periodically continued finite neighborhood as indicated in figure 2. We choose a fundamental cell, say the cube, of volume $\Omega_L \equiv L^3$,

$$|x|,\ |y|,\ |z| \leqslant \frac{L}{2}$$

$$L \gg 2R \tag{3.4}$$

and construct the space-lattice generated by it. Let us call $\boldsymbol{\tau}^{(\nu)}$ the lattice translation vectors. Then we place any number of scatterers in some definite configuration c in the fundamental cell and populate the other cells in the identical way (see fig. 2). The electrons now move in a periodic cubic lattice. Their energy eigenvalues

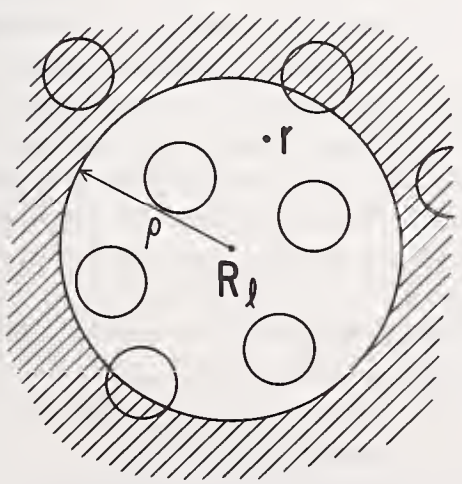

FIGURE 1. *Spherical neighborhood centered at* $\mathbf{R}_l$.

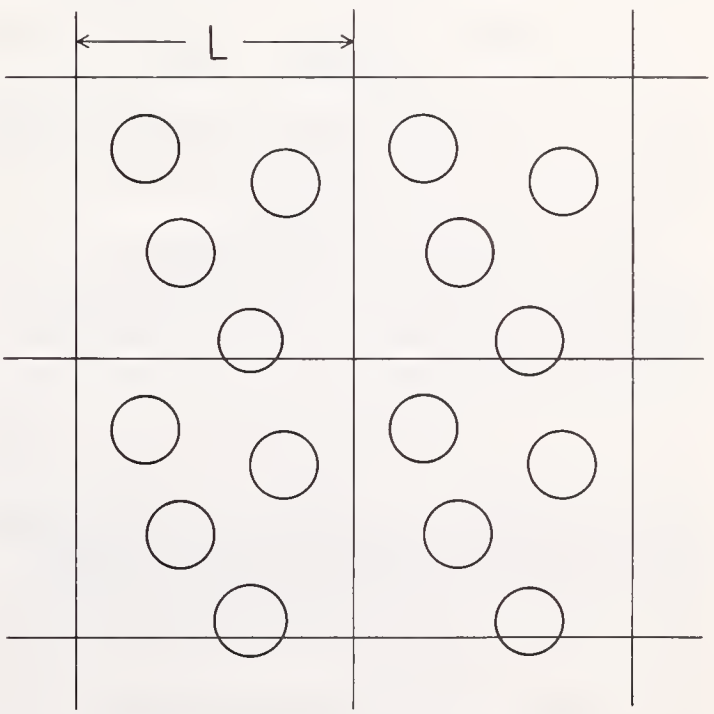

FIGURE 2. *Periodically continued neighborhood.*

[4] If we would use the total densities of states of the spherical neighborhoods, rather than the quantities $n(\mathbf{R}_l,E)$ computed at their centers, we would incur large errors behaving as L^{-1}, due to the presence of the infinite wall boundaries.

are, because of the relatively small size of the unit cell, much more amenable to calculation than the eigenvalues of the macroscopic disordered system. Let us call the density of states, corresponding to the configuration c and total volume Ω, $n_c(E)$. Then our approximation for the density of states of the actual macroscopic system will be

$$n(E) \approx \sum_c w_c n_c(E). \tag{3.5}$$

where w_c are weights, which we shall presently discuss, and the approximate equality, $\approx$, will signify accuracy to within terms exponentially small in $L/2R$.[5]

We shall now describe a suitable choice of w_c and later demonstrate that it leads to the claimed accuracy. Let us suppose that in the actual, macroscopic system under consideration there are given two-body forces between the scatterers,

$$\varphi_{\alpha\beta} = \varphi_{\alpha\beta}(\mathbf{r}_\alpha - \mathbf{r}_\beta), \tag{3.6}$$

which vanish beyond a range a which is much smaller than L. Let us suppose further than the scatterers obey classical statistics. Thus, in the macroscopic system the probability of a given configuration $c = (\mathbf{r}_1, \mathbf{r}_2, \ldots)$ is given by the grand canonical weight function,

$$w_c^{(\infty)} = A^{(\infty)} \exp\left\{-\beta\left[\frac{1}{2}\sum_{\alpha\neq\beta}\varphi_{\alpha\beta} - \sum_j \mu_j N_j\right.\right. \tag{3.7}$$

where $A^{(\infty)}$ is the normalization constant, μ_j is the chemical potential of scatterer of type j, and N_j is the total number of scatterers of this type.[6]

A suitable choice of w_c, for the periodically continued neighborhood, is obtained as follows. We take the unit cell and associate with each original position vector $\mathbf{r}$, the infinite set of vectors

$$\mathbf{r}^{(\nu)} \equiv \mathbf{r} + \boldsymbol{\tau}^{(\nu)} \tag{3.8}$$

This corresponds to the topology of a three dimensional torus and is illustrated in figure 3 in one dimension.

The weight w_c is then determined by the equation

$$w_c = A \exp\left\{-\beta\left[\frac{1}{2}\sum_{\alpha\beta}\varphi_{\alpha\beta}(\tilde{\mathbf{r}}_{\alpha\beta}) - \sum \mu_j N_j\right]\right\} \tag{3.9}$$

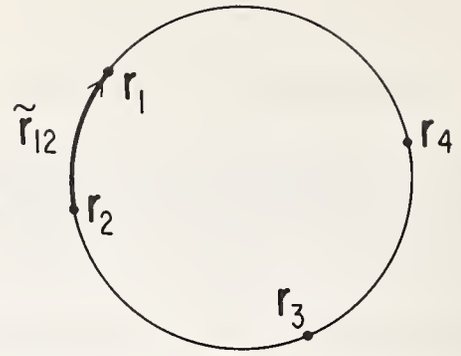

FIGURE 3. *Schematic representation of the toroidal topology. The circumference is* L.

where $\mathbf{r}_{\alpha\beta}$ is the shortest vector contained in the set $\mathbf{r}_\alpha^{(\mu)} - \mathbf{r}_\beta^{(\mu)}$. For example, $\mathbf{r}_{12}$ is shown schematically in figure 3. The normalization constant A is chosen so that

$$\sum_c w_c = 1, \tag{3.10}$$

where the sum goes over all configurations, including all possible numbers of the scatterers.

It can be shown that, with the choice (3.10), the correlation functions, $n_s(\mathbf{r}_1 \ldots \mathbf{r}_s|L)$, in the finite toroidal system, differ negligibly from those of the infinite system, $n_s(\mathbf{r}_1, \ldots \mathbf{r}_s|\infty)$, for values of $|\mathbf{r}_\alpha - \mathbf{r}_\beta| \leq L/2$ and s up to $s \leq L/a$. The error of a given correlation function behaves as $\exp[-\alpha_s L/a]$, where α_s is of order unity. This fact assures that, if $L \gg a$, the statistical distributions of the ions in any neighborhood of size $< L/2$ are practically identical in the ensemble of periodically continued neighborhoods and in the macroscopic system. Hence, in view of the locality principle demonstrated in section 2, the density of states $n(E)$ of the infinite system may be determined, via eq (3.5), from the density of states in the periodically continued neighborhoods. The error will be exponentially small in the quantity L/R or L/a, whichever is the smaller. Typically both a and R are of the order of 1 Å, so that one must work with neighborhoods of dimensions of several in order to obtain quantitatively useful results.

It is evident that this method will give exact results for perfectly periodic systems. Since it is also very accurate for highly disordered systems (small R), it should give good answers for most intermediate situations.

The ensemble of systems defined by eq (3.9) is a grand canonical ensemble in which the volume $\Omega_L (= L^3)$ is fixed while the numbers of particles N_j assumes all possible values. For a single species of atoms it has been found practically preferable to work with a periodically continued isothermal-isobaric ensemble, in which N is fixed but the volume Ω_L is variable. Here

[5] Provided the forces between the scatterers are sufficiently short range.

[6] For the macroscopic system, one could of course equally well use a canonical distribution. However, in our local neighborhood theory, this would lead to unacceptable errors of order $1/N$, where N is a mean number of scatterers in Ω_L.

a unit cell of volume Ω_L, with the N atoms in a configuration c must be given the weight

$$w_{\Omega_L,c}=\frac{A}{\Omega_L}\exp\left\{-\beta\left[\frac{1}{2}\sum_{\alpha,\beta}\varphi_{\alpha\beta}(\bar{\mathbf{r}}_{\alpha\beta})-R\Omega_L\right]\right\} \quad (3.11)$$

where P is the pressure. The density of states of the actual macroscopic system is approximated by

$$n(E)\approx\int d\Omega_L\sum_c w_{\Omega_L,c}n(E;\Omega_L;c) \quad (3.12)$$

where $n(E;\Omega_L;c)$ is the density of states, per unit cell Ω_L, in the periodically continued neighborhoods. The normalization A of $w_{\Omega_L,c}$

$$\int d\Omega_L\sum_c w_{\Omega_L,c}=N_{\text{tot}}/N \quad (3.13)$$

where N_{tot} is the total number of scatterers in the macroscopic system. Again the convergence of (3.13) to the exact result is exponential, as for the case of the grand canonical ensemble.

4. Numerical Illustration

To illustrate the theory of the previous sections we have numerically studied the following model of a one-dimensional alloy:

$$H=-\frac{d^2}{dx^2}+\sum_\alpha\lambda_\alpha\delta(x-\alpha d) \quad (4.1)$$

where the distance between potentials, d, was taken as 1, and λ_α was taken, with equal probability, as -2 and -4. (This corresponds to a high temperature limit for the two different kinds of scatterers, an idealized model for crystalline Cu Au well above the ordering temperature.) Here the grand canonical method was appropriate. Two calculations were performed, with $L=6$ and $L=10$. Let us take the case $L=6$. A typical, periodically continued neighborhood is shown schematically in figure 4. Each configuration of potentials in the fundamental interval $0<x\leqslant 6$ has the same weight, 2^{-6}.

In this simple example all correlation functions are evidently exact, as long as the crystal sites considered are all contained in a single unit cell.

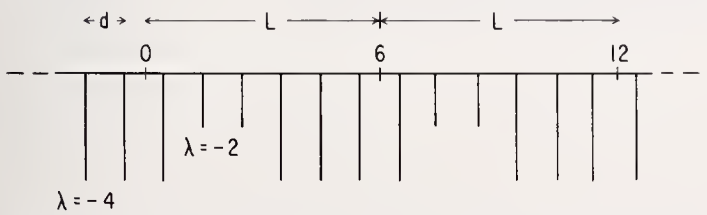

FIGURE 4. *A typical periodically continued neighborhood of the illustrative model.*

The density of states curves was calculated for each of the 2^6 configurations and then averaged. For $L=10$ a sampling procedure was used. The results are shown in figure 5, together with the exact result obtained for the infinite system using the Schmidt method.[3] Our approximation reproduces quite accurately all the details of the density of states structure, even for $L=6$. To obtain similar accuracy from a single randomly populated chain would require a length of the order of $L\approx 10^3$.

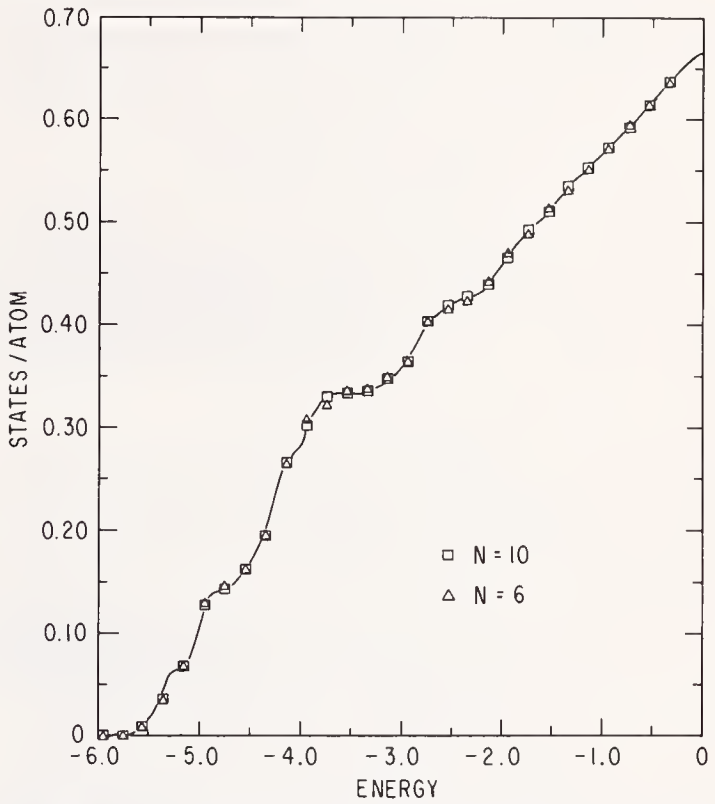

FIGURE 5. *Integrated density of states for binary alloy. The solid line is the exact result.*

5. Concluding Remarks

It is commonplace to emphasize the theoretical difficulties caused by disorder. In the present paper we draw attention to a favorable feature: For a highly disordered system the physical properties near a given point depend only on circumstances in a small neighborhood, whose dimension is of the order a mean free path. Consequently, a macro-system may be treated, so to speak, neighborhood by neighborhood and the macro-problem can be reduced to an ensemble of micro-problems. We have shown that the errors of such a procedure can be made to vanish exponentially with the size of the neighborhood. A numerical model calculation bears out these considerations.

A more complete account of this program will be published elsewhere.

Discussion on "Local Theory of Disordered Systems" by W. H. Butler and W. Kohn (University of California)

D. Redfield *(RCA Labs.):* In a system with local variations in densities of states, it would seem there should be local variations in the mean free path. Does this treatment imply that the assumed smallness of this path makes these variations unimportant?

W. Kohn *(Univ. of California):* Qualitatively speaking yes. Having established this general locality principle in which a representative mean free path appears just guides one in one's further thinking. One does not actually introduce a mean free path into the calculation. I am not sure we are in communication.

J. Tauc *(Bell Telephone Labs.):* It seems to me that this locality principle, if it is applied in the sense that you first mentioned, is different from what you were speaking about later. If you say that it is only the environment of an atom which is important, then, of course, considering only a few atoms, you get a discrete energy spectrum; the energy spectrum for the whole body would be continuous by averaging. But an electron at a certain place would have a discrete spectrum, and this would have very important consequences for the conductivity and optical properties. Do you think that an electron at a certain place sees a discrete spectrum, or rather a continuous density of states?

W. Kohn *(Univ. of Calif.):* The locality principle holds only for the statistical average. Your question is an interesting one because it brings out this point. Let me answer this in two ways. First of all, in terms of the first rudimentary model, which actually we are not following, but I think it is perhaps best for answering your question. That is the model where we simply surround the four or five scattering centers by an infinite wall. And now we put the electrons in there. Obviously the energy levels are discrete. Now imagine that this sphere is rather large so that the spacing between the discrete states becomes small. Now average over all positions of the scatterers. Then for each configuration you get a discrete spectrum. When you average over all you get a very large number of discrete spectra which in fact results in a continuous spectrum. And it is that average continuous spectrum whose density relates to the density of the infinite system. I think I did forget a point in discussing my viewgraph. You notice that there are these brackets here; I apologize, I did not speak about them—these are configuration averages. And the locality principle holds for the average quantities. Now what you are interested in finally for the alloy is the density of states of an infinite system that is equivalent to averaging within the individual small cells over all possible configurations. In this way you do in fact end up with a continuous spectrum. In the second method that we use, and which is much better from a quantitative standpoint, namely extending the individual cell periodically, then obviously we get a continuous spectrum even for an individual configuration.

A. Williams *(IBM):* It seems to me, if I understand correctly what is being suggested, that the proposed method holds a great deal in the way of computational promise. It seems to me that you are suggesting that we can do several band calculations for a lattice with a basis. The question then becomes how many members shall we have in the basis and over what statistical ensemble of bases must we average, but nontheless the fundamental calculation is something we have learned to do quite well for a very realistic system.

W. Kohn *(Univ. of Calif.):* Yes, I agree fully with that, and just to go out on a limb I would say there will be quite a few systems where you could expect an accuracy of 2% by working with a basis in three dimensions with as few as 2, 3, or 4 scatterers.

DISORDERED SYSTEMS II

CHAIRMEN: L. M. Roth
H. P. R. Frederikse

RAPPORTEUR: M. H. Cohen

Density of Electron Levels for Small Particles*

L. N. Cooper and S. Hu**

Physics Department, Brown University, Providence, Rhode Island 02912

The density of electronic levels for small particles is calculated. This differs from the usual expression which is valid as the volume of the sample becomes very large. The leading term of the correction is proportional to the surface/volume of the sample. Depending on the environment the density of electronic levels may be increased or decreased.

Key words: Diffusion equation; electronic density of states; "muffin-tin" potential; small particles; two dimensional classical membrane.

1. Introduction

The commonly employed formula for the number of levels of a quantum system in the momentum range d^3p

$$dN = \Omega \frac{d^3p}{\hbar^3}$$

comes from an expression derived by H. Weyl which is valid asymptotically (as the volume of the sample becomes very large). For small samples this is modified. The leading additional term can be expressed as a surface/volume correction.

Recently Kac [1] has written down the first few terms for the density of levels for a two dimensional classical membrane, asking "Can One Hear the Shape of a Drum?" We have generalized Kac's result for the leading correction term to three dimensional specimens for two boundary conditions: for the first the wavefunction is zero at the boundary while for the second the derivative of the wavefunction is zero at the boundary. In the latter case the density of electron levels is increased.

2. Development

In this section we outline, very briefly, a method for obtaining the density of states developed by Kac. The expression

$$\sum_{m=1}^{\infty} e^{-\lambda_m t} |\psi_m(r)|^2 \tag{1}$$

gives the number of eigenfunctions in some range of λ using

$$\int d\tau \sum_{m=1}^{\infty} e^{-\lambda_m t} |\psi_m(r)|^2$$

$$\sum_{m=1}^{\infty} e^{-\lambda_m t} = \int_0^{\infty} N(\lambda) e^{-\lambda t} d\lambda \tag{2}$$

where $N(\lambda)$ is number of levels per unit interval of λ. This is related to the usual expression by

$$N(E) = \frac{d\lambda}{dE} N(\lambda) \tag{3}$$

where $\lambda = mE/\hbar^2$.

Kac observes that

$$\sum_{m=1}^{\infty} e^{-\lambda_m t} \psi_m^*(r_0) \psi_m(r) \tag{4}$$

is a solution of the classical diffusion equation

$$\frac{\partial U(r, t)}{\partial t} - \frac{1}{2} \nabla^2 U(r, t) = 0 \tag{5}$$

with the initial condition

$$U(r, t=0) = \delta(r - r_0) \tag{6}$$

if

$$\frac{1}{2} \nabla^2 \psi_m = -\lambda_m \psi_m. \tag{7}$$

But the solution for the classical diffusion equation far from any boundary should be the same as the solution

*Supported in part by ARPA and the National Science Foundation.

**Present address: Northeastern University, Boston, Massachusetts.

in an infinite volume; this can be obtained by assuming periodic boundary conditions and in two dimensions has the following well known form:

$$U_0(r, t) = \frac{1}{2\pi t} \exp\left[-\frac{|\mathbf{r}-\mathbf{r}_0|^2}{2t}\right] \tag{8}$$

Evaluated at $\mathbf{r}=\mathbf{r}_0$ this gives

$$\sum_{m=1}^{\infty} e^{-\lambda_m t}|\psi_m(\mathbf{r})|^2 = \frac{1}{2\pi t} \tag{9}$$

which when integrated over the area yields

$$\sum_{m=1}^{\infty} e^{-\lambda_m t} = \frac{\text{area}}{2\pi t} \tag{10}$$

This argument is obviously equally valid for any number of dimensions. In particular for a three dimensional sample one obtains:

$$\sum_{m=1}^{\infty} e^{-\lambda_m t} = \frac{\Omega}{(2\pi t)^{3/2}} \tag{11}$$

where Ω is the volume of the sample. This using (2) yields

$$N(\lambda) = \frac{\Omega}{\pi^2}\left(\frac{\lambda}{2}\right)^{1/2}$$

or

$$N(E) = \frac{4\pi\Omega}{h^3} m(2mE)^{1/2} \tag{12}$$

which is the usual expression.

To take account of a boundary Kac rederives the solution of the classical diffusion equation, approximately, in the following way. If one is close enough to the boundary, to the first approximation the boundary will appear as a line. As he says "for small t, the particle has not had time to feel the curvature of the boundary." He then writes down what is the solution of the classical diffusion equation with the initial condition (6) and with the boundary condition that the solution go to zero at the boundary and obtains for $\mathbf{r}=\mathbf{r}_0$

$$U_1(\mathbf{r}=\mathbf{r}_0, t) = \frac{1-e^{-2\delta^2/t}}{2\pi t} \tag{13}$$

where δ is the distance of the point $\mathbf{r}$ from the boundary.

This result can easily be generalized to any number of dimensions and for the opposed boundary condition, that in which the derivative of the solution is zero at the boundary. One then obtains for a three dimensional specimen

$$U_1(\mathbf{r}=\mathbf{r}_0, t) = \frac{1 \mp e^{-2\delta^2/t}}{(2\pi t)^{3/2}} \tag{14}$$

where the $\mp$ signs correspond to the wavefunction or its derivative going to zero at the boundary.

When (14) is integrated over the volume of the sample, one obtains for a three dimensional particle

$$\sum_{m=1}^{\infty} e^{-\lambda_m t} = \frac{\Omega}{(2\pi t)^{3/2}} \mp \frac{\Sigma}{(2\pi t)^{3/2}} \frac{\sqrt{2\pi t}}{4} + \cdots \tag{15}$$

where Ω and Σ are respectively the volume and surface of sample.

3. Conclusions

Using (2) the above expression yields the following density of electronic levels for a three dimensional sample:

$$N(E) = N_0(E)\left(1 \mp \frac{\Sigma}{\Omega}\frac{\pi\hbar}{4}\frac{1}{\sqrt{2mE}} + \ldots\right) \tag{16}$$

where $N_0(E)$ is the usual density of levels as given by the Weyl asymptotic formula and Σ/Ω is the ratio of the surface area to the volume of the sample. The two signs correspond to the boundary conditions:

$$\psi = 0 \text{ at boundary} \longleftrightarrow \text{minus}$$

$$\psi' = 0 \text{ at boundary} \longleftrightarrow \text{plus}$$

[The next term in the expansion which is related to the curvature of the surface bounding the sample has been evaluated by Kac for various special two dimensional closed curves but has not been generalized to higher dimensions. For a two dimensional circular sample of radius R evaluated near the Fermi level, one obtains for $\psi=0$ at the boundary:

$$N(E_F) = N_0(E_F)\left(1 - (k_F R)^{-1} + \tfrac{2}{3}(k_F R)^{-2} + \ldots\right).$$

Thus it is reasonable to expect that for most samples this next term would be much smaller than the second.]

Near the modified Fermi surface (16) becomes

$$N(E_F) = N_0(E_{F0})\left(1 \mp \frac{\Sigma}{\Omega}\frac{\pi}{8k_{F0}} + \ldots\right) \tag{17}$$

Referring the ratio of surface to volume to that for a sphere we have

$$N(E_F) = N_0(E_{F0})\left(1 \mp 3\pi/8(k_{F0}R)^{-1}\frac{(\Sigma/\Omega)}{(\Sigma/\Omega)_{\text{sphere}}} + \ldots\right) \tag{18}$$

For an irregular metallic sample we might guess that Σ/Ω could be an order of magnitude larger than that for a sphere so that one could expect the second term to be

as large as 10% of the first for particles of the order of 10^{-6} cm in radius. For a smaller sample or for a material like a semiconductor with smaller k_F the effect would of course be larger.

Such an alteration in the density of electronic levels would be expected to produce dramatic effects in the various density dependent physical quantities. Unfortunately under ordinary conditions it will very likely be obscured because the physical boundary condition will fall between the two extremes above ($\psi = 0$ and $\psi' = 0$ at the boundary) diminishing the effect of the second term. In a properly arranged environment, however—for example, one might consider a metal-vacuum boundary to simulate $\psi = 0$ at boundary, or a metal-other material boundary to simulate $\psi' = 0$ at the boundary—the effect might become visible and possibly important.

4. References

[1] Kac, M., American Math. Monthly **73**, No. 1, Part II, p. 1 (1966).

Discussion on "Density of Electron Levels for Small Particles" by L. N. Cooper and S. Hu (Brown University)

A. Yelon *(Yale Univ.):* For a linear combination boundary condition, does the effect tend to disappear?

L. N. Cooper *(Brown Univ.):* Yes, it may well be that one does not see the effect normally. It may add to confusion in work with small particles if one is comparing results in one environment with results in another environment and having changes in the density of states due to that.

H. H. Soonpaa *(Univ. of North Dakota):* The effect described in this paper has been observed. We have measured an increase (by 2.3 eV) in the contact potential of 40 Å thick semimetal film as compared to the bulk material. A similar effect was observed by Batt and Mee [1]. They observed a decrease in the work function by about 0.2 eV when an Al film used in their photoemission work was made thinner than about 50 Å. These changes are related to the Fermi energy, which increases with decreasing thickness, as predicted by the equations derived for size effect quantization.

[1] Batt and Mee, Journal of Vacuum Science and Technology **6**, 737 (1969).

One-Dimensional Relativistic Theory of Impurity States*

M. Stęślicka, S. G. Davison, and A. G. Brown*****

Quantum Theory Group, Departments of Applied Mathematics and Physics, University of Waterloo, Ontario, Canada

The one-dimensional Dirac equation is solved for the Kronig-Penney model containing a δ-potential impurity. Depending on certain existence conditions, the impurity states can be classified into two types called relativistic and Dirac impurity states. In the nonrelativistic limit, the Dirac states disappear and the relativistic ones become the ordinary impurity states. A detailed discussion is given of the complete energy spectrum.

Key words: Impurity states: Kronig-Penney model: one-dimensional Dirac equation.

1. Introduction

An important problem in the electronic theory of semiconductors is that of impurity doping. Up to now, only nonrelativistic (NR) investigations [1-4] have been carried out on the effect of substitutional impurities on the electronic properties of crystals. During the last few years, however, a relativistic theory of heavy atomic solids has been developed. Most of the calculations have involved the solution of the Dirac equation for the "muffin-tin" potential [5]. In order to study localized states, within the framework of the relativistic theory, the simpler Kronig-Penney (KP) potential [6] has been employed [7-10]. In this paper, the behavior of relativistic electrons in the region of an impurity is examined, by means of the Seitz model [11]. Comparisons are made with the NR results in the final section.

2. Plane Wave Solution of the Dirac Equation

For the k-region of constant potential V_k, the 2-component form of the Dirac equation is [12]

$$i\hbar c\,\boldsymbol{\sigma}_x\nabla_x\boldsymbol{\phi}_2=-(\epsilon-V_k)\boldsymbol{\phi}_1, \qquad \epsilon=E-m_0c^2, \quad (1)$$

$$i\hbar c\,\boldsymbol{\sigma}_x\nabla_x\boldsymbol{\phi}_1=-(\epsilon-V_k+2m_0c^2)\,\boldsymbol{\phi}_2, \quad (2)$$

where

$$\phi_1=\begin{pmatrix}\psi_1\\ \psi_2\end{pmatrix}, \qquad \boldsymbol{\phi}_2=\begin{pmatrix}\psi_3\\ \psi_4\end{pmatrix}, \qquad \boldsymbol{\sigma}_x=\begin{pmatrix}0 & 1\\ 1 & 0\end{pmatrix}. \quad (3)$$

Decoupling these equations yields

$$\nabla_x^2\boldsymbol{\phi}_j=-\rho_k^2\boldsymbol{\phi}_j; \qquad j=1 \text{ or } 2, \quad (4)$$

in which

$$\rho_k^2=(\epsilon-V_k)(\epsilon-V_k+2m_0c^2)/\hbar^2c^2. \quad (5)$$

The general solution of (4) is

$$\boldsymbol{\phi}_j=\mathbf{A}_je^{i\rho_kx}+\mathbf{B}_je^{-i\rho_kx}. \quad (6)$$

$\mathbf{A}_j$ and $\mathbf{B}_j$ being 2×1 matrices. From (1) and (6), it follows that

$$\mathbf{A}_1=\gamma\boldsymbol{\sigma}_x\mathbf{A}_2, \qquad \mathbf{B}_1=-\gamma\boldsymbol{\sigma}_x\mathbf{B}_2, \quad (7)$$

with

$$\gamma=(\epsilon-V_k)/\hbar c\rho_k. \quad (8)$$

Thus, the 4-component plane wave solution to the Dirac equation can be written as

$$\boldsymbol{\phi}(x)=\begin{pmatrix}\boldsymbol{\phi}_1\\ \boldsymbol{\phi}_2\end{pmatrix}=\begin{pmatrix}\gamma\boldsymbol{\sigma}_x\\ \mathbf{I}\end{pmatrix}\mathbf{A}_2e^{i\rho_kx}+\begin{pmatrix}-\gamma\boldsymbol{\sigma}_x\\ \mathbf{I}\end{pmatrix}\mathbf{B}_2e^{-i\rho_kx}, \quad (9)$$

where $\mathbf{I}$ is the 2×2 unit matrix.

*QTG article: S-156

**Permanent address: Department of Experimental Physics, University of Wroclaw, Poland

***Work supported by the National Research Council of Canada and the University of Waterloo Research Committee

3. Relativistic Crystals States

The simplest relativistic theory of solids is based on the KP model in a δ-function limit. Initially, the volume [7] and surface [8] states of such heavy atomic systems were analyzed by adopting a continuity condition in which only the 2-component spinors were matched across potential discontinuities. However, the choice of this continuity condition means that there is a nonmatching of the component slopes. Furthermore, the resulting mathematics are somewhat complicated. Since electron velocities in solids are not extremely high, the contribution of the small component ϕ_1 is not as significant as that of the large component ϕ_2. Thus, another set of suitable continuity conditions is the equating of the large component and its derivative across the potential discontinuities. This, of course, implies a nonmatching of the small component and its derivative. The problem of boundary conditions has been discussed at length in a recent paper [9].

The latter type of continuity condition is adopted here, because it not only leads to a simplification of the subsequent mathematical analysis but also is a very good approximation, as was shown in [9]. In this approach, the relativistic Kronig-Penney (RKP) relation in δ-function limit takes the form [9]

$$\cos \mu a = \cos \rho_2 a + p_R \frac{\sin \rho_2 a}{\rho_2 a}, \tag{10}$$

where

$$\rho_2^2 = \epsilon(\epsilon + 2m_0c^2)/\hbar^2c^2 \tag{11}$$

and

$$-p_R = \lim_{\substack{b \to 0 \\ \rho_3 \to \infty}} \tfrac{1}{2} \rho_3^2 ab, \tag{12}$$

(b is the width of the potential wall), while the bulk large component wave function in the unit cell $a/2 \leqslant x \leqslant 3a/2$ is given by [9]

$$\phi_2 = \alpha_2 [e^{i\rho_2(x-a/2)} + \lambda_R e^{-i\rho_2(x-a/2)}], \tag{13}$$

where

$$\lambda_R = (1 - e^{-i(\mu-\rho_2)a})/(e^{-i(\mu+\rho_2)a} - 1). \tag{14}$$

The subscripts 2 and 3 refer to the two regions II and III of different constant potential in the KP model.

4. Relativistic Seitz Model

4.1. Impurity Energy Expression

The potential field in the vicinity of an impurity atom in a linear crystal is represented schematically in figure 1 [2,11]. The procedure for analyzing the problem of impurity states is to match the wave function in the unperturbed periodic part of the crystal to that in the perturbed region near the impurity atom. With the system being symmetrical about $x = 0$, it is sufficient to perform the matching process at the potential discontinuity at $x = a/2$ only. In region I, the solution to the Dirac equation is even or odd, i.e.,

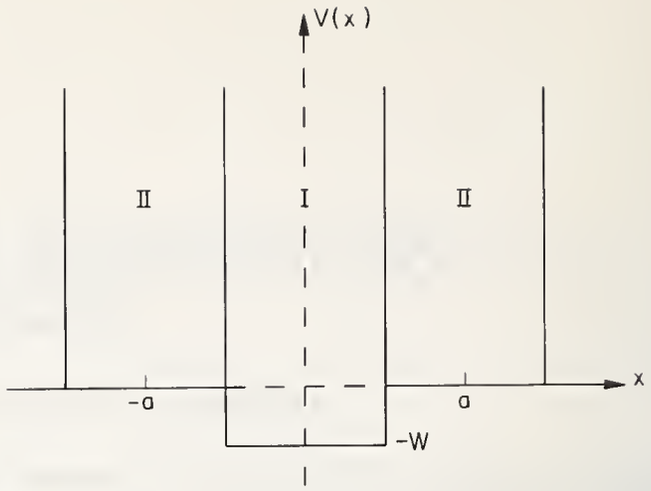

FIGURE 1. *δ—Barrier representation of the potential field in a linear crystal (II) containing an impurity atom (I).*
The difference between the crystal and impurity potential strengths is − W.

$$\phi_1^{\pm} = \alpha_1^{\pm} (e^{i\rho_1 x} \pm e^{-i\rho_1 x}), \tag{15}$$

ρ_1 being defined in (5), where V_1 is the strength of the impurity potential.

Matching the wave functions (13) and (15), and their derivatives, at $x = a/2$, leads to a determinantal equation in $\alpha_1^{\pm}$ and α_2. Setting the determinant equal to zero gives

$$(1 + \lambda_R)/(1 - \lambda_R) = -\rho_1\tau^{\pm}/i\rho_2, \tag{16}$$

where

$$\tau^+ = -\tan \tfrac{1}{2} \rho_1 a, \tag{17}$$

$$\tau^- = \cot \tfrac{1}{2} \rho_1 a. \tag{18}$$

After some simple rearranging, (14) and (16) give

$$e^{i\mu a} = \cos \rho_2 a + (\rho_1\tau^{\pm}/\rho_2) \sin \rho_2 a. \tag{19}$$

For localized states to occur, μ has to be complex [1,11], that is, of the form

$$\mu = n\pi/a + i\zeta, \qquad \zeta \text{ real} > 0. \tag{20}$$

With the aid of (20), combining (10) and (19) yields

$$\cot \rho_2 a = \rho_2 a [1 + (\tau^2\rho_1^2 a - 2p_R\tau\rho_1)/\rho_2^2 a]/2p_R, \tag{21}$$

where, for convenience the superscript $\pm$ has been omitted from τ. Equation (21) gives the relativistic impurity state energy (via ρ_2) in terms of the impurity strength (ρ_1) and the crystal potential (p_R). It should be noted that for τ^+ or τ^- eq (21) has solutions in alternant bands only, thus, to obtain the complete energy spectrum it is necessary to include both the even and odd solutions.

4.2. Existence Condition

Subtracting (19) from (10) using (20) gives

$$(-1)^n \sinh \zeta a = [(p_R - \tau\rho_1 a) \sin \rho_2 a]/\rho_2 a. \tag{22}$$

For the $(n+1)th$ forbidden energy gap (FEG), which lies in the range $n\pi < (n+1)\pi$, the RKP relation (10) shows that

$$\operatorname{sign}\left(\frac{\sin \rho_2 a}{\rho_2 a}\right) = (-1)^n. \tag{23}$$

Thus, since $\zeta > 0$, it follows from (22) that

$$p_R > \tau\rho_1 a, \tag{24}$$

which is a *necessary* condition for the impurity states to exist (i.e., *existence condition*). This inequality imposes a restriction on the values of the parameters for which the solutions of (21) correspond to the impurity state energies.

5. Analysis of Relativistic Effects

5.1. Energy Correction

The NR analog of (21) is obtained by taking $c \to \infty$ to give

$$\cot \rho_2^0 a = [\rho_2^0 a + \tau^0\rho_1^0(\tau^0\rho_1^0 a - 2p^0)/\rho_2^0]/2p^0, \tag{25}$$

where the zero superscript denotes the NR limiting value of the corresponding parameters. Solving (21) and (25) numerically, enables the impurity state energies ρ_2 and ρ_2^0 to be determined, respectively. The effect of the relativistic corrections on the energy is shown graphically in figure 2, where $\Delta\rho$ $(= \rho_2^0 - \rho_2)$ is plotted against n, the band number. At low energies, the relativistic shift in the impurity level is sufficiently small to be ignored. However, for high energies, the shift becomes of the order of the FEG and, therefore, cannot be neglected.

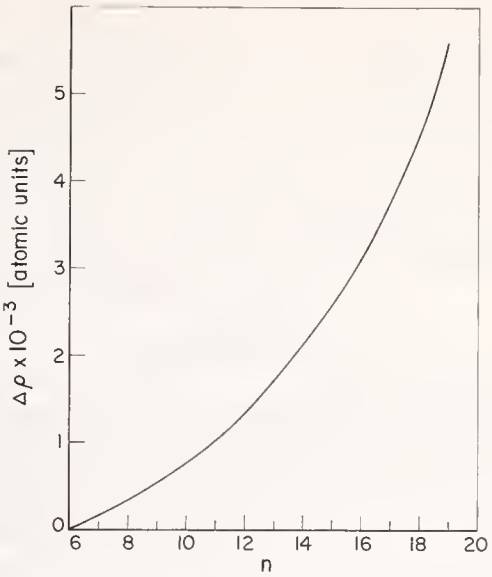

FIGURE 2. *Variation of relativistic energy correction* $(\Delta\rho)$ *with band number* (n) *for* $p_R = p^\circ = 0.25$, $a = 6 (\simeq 3\text{A})$ *and* $V_1 = \pm p^\circ/2$.

5.2. Classification of Impurity States

The NR counterpart of (24) is

$$p^0 > \tau^0\rho_1^0 a. \tag{26}$$

It is convenient to introduce the relations

$$p_R = \eta p^0, \qquad \tau = \nu\tau^0, \qquad \rho_1 = \kappa\rho_1^0. \tag{27}$$

where η, ν and κ are positive and equal to unity in the NR limit. Inserting (27) in (24) leads to

$$p^0 + R > \tau^0\rho_1^0 a \tag{28}$$

where the relativistic correction term

$$R = (1 - \nu\kappa/\eta)\tau^0\rho_1^0 a \tag{29}$$

can be positive or negative, depending on the particular band being considered, and the values of the parameters ν, κ, η. If (28) is always valid, then

$$p^0 \gtrless \tau^0\rho_1^0 a \tag{30}$$

depending on the sign and magnitude of R.

Comparing (30) with (26), shows that the upper (lower) inequality is identical (opposite) to the NR situation. Thus, the impurity states satisfying the upper inequality are called *relativistic impurity states* (RIS), since they become the usual impurity states in the NR limit. However, the states for which the lower inequality holds violate the NR existence condition (i.e., disappear altogether in the NR limit). Hence, these states

arise solely because of the Dirac formulation and, for this reason, are known as *Dirac impurity states* (DIS). It is worth noting that, near a band edge, if $R > 0$ ($R < 0$) in the existence condition (28), then the presence of this relativistic correction term enhances (hinders) the possibility of an impurity state occurring compared with the NR case.

6. Conclusions

A relativistic investigation of the impurity states of heavy atomic crystals has been made, using a simple model, which was proposed initially by Seitz [11]. In deriving the expression relating the impurity energy and strength, only the so-called *large component* was taken to represent the relativistic wave function in the crystal lattice. The *form* of the energy relation is identical to that of the Schroedinger approach. The subsequent analysis showed that both the existence and location of the impurity states in the energy spectrum are sensitive to the relativistic correction terms, especially at high energies. The impurity states appear in two categories, namely, relativistic and Dirac states. In the NR limit, the former become the ordinary impurity states, while the latter have no analog.

7. References

[1] Saxon, D. S., and Hutner, R. A., Philips Res. Rep. **4**, 81 (1949).
[2] Friedel, J., Advs. Phys. **3**, 445 (1954).
[3] Koster, G. F., and Slater, J. C., Phys. Rev. **95**, 1167 (1954).
[4] Breitenecker, M., Sexl, R., and Thirring, W., Z. Phys. **182**, 123 (1964).
[5] Loucks, T. L., Augmented Plane Wave Method (W. A. Benjamin, New York and Amsterdam, 1967), for literature survey and collection of relevant reprints.
[6] Kronig, R. de L., and Penney, W.G., Proc. Roy. Soc. **A130**, 499 (1931).
[7] Glasser, M. L., and Davison, S. G., Intern. J. Quantum Chem., in press (1969).
[8] Davison, S. G., and Steslicka, M., J. Phys. C. (Proc. Phys. Soc.) **2**, 1802 (1969).
[9] Steslicka, M., and Davison, S. G. (to be published).
[10] Davison, S. G., and Levine, J. D., in Solid State Physics, F. Seitz, D. Turnbull and H. Ehrenreich, Editors (Academic Press, New York, in press).
[11] Seitz, F., The Modern Theory of Solids (McGraw-Hill, New York and London, 1940), p. 325.
[12] Davydov, A. S., Quantum Mechanics (Pergamon Press, Oxford, 1965), p. 222.

Discussion on "One-Dimensional Relativistic Theory of Impurity States" by M. Stęślicka, S. G. Davison, and A. G. Brown (University of Waterloo)

L. Roth *(General Electric):* (1) How does the relativistic impurity energy shift compare with the shift of the edge of the forbidden energy gap? (2) How many bound states are there in the forbidden gap?

M. Stęślicka *(Univ. of Waterloo):* (1) We have calculated only the difference between the relativistic as compared with the non-relativistic effect. We did not calculate how it is related to band edges. (2) In one gap at most one level (zero or one).

417-156 O - 71 - 32

The Influence of Generalized Order-Disorder on the Electron States in Five Classes of Compound-Forming Binary Alloy Systems

E. W. Collings, J. E. Enderby,* and J. C. Ho

Metal Science Group, Physics Department, Battelle Memorial Institute, Columbus Laboratories
Columbus, Ohio 43201

The influence of generalized order-disorder (including solid-state order-disorder, and melting) on electronic structures will be discussed for various types of binary intermetallic compounds which, for the purposes of discussion, will be arbitrarily subdivided into five classes. Classes A and B exhibit solid-state order-disorder (O-D) reactions. In the first of these the atomic potentials are sufficiently similar that the use of low-order perturbation theory at all concentrations is valid. The effect of O-D on such alloys will be described in relationship to the density-of-states, as measured by low-temperature specific heat and magnetic susceptibility, and to the electrical transport properties, particularly the conductivity and Hall coefficient. We then consider from the same standpoint a second type of system in which the potentials are sufficiently different as to produce bound states which appear in the *ordered* form. The disappearance of these bound states when the alloy disorders gives rise to characteristic electronic behavior.

The effect of O-D on the experimental parameters referred to above will be compared for the two types of systems. In particular, published data for Cu-Au, as a representative example of the first type of system, will be contrasted with new electronic property data for Ti-Al, and compared with recent experimental results for Pt-Cu, which occupies an intermediate position. In class C, which is metallic in the solid, and in classes D and E which are semiconducting in the solid, structural order persists up to the melting point. For D the liquid is metallic, and data are presented for Bi_2Te_3, a typical system of this class. The conditions for the existence of intermetallics of class E are extreme, and give rise to nonmetallic behavior in the liquid.

These various systems will be discussed in terms of differences in atomic potentials. The major problems involved in giving precise estimates of the required differences will be outlined and a critical account of the use of concepts like the electronegativity parameter will be presented.

Key words: Binary alloys; Bi_2Te_3; CdSb; copper-gold (Cu-Au); Cu_3Au; CuPt; Cu_3Pt; ductility; electrical resistivity; Hall effect; magnesium bismide (Mg_3Bi_2); mechanical behavior; melting; model potential of Heine and Abarenkov; nickel aluminide; order-disorder; Peierls barriers; Pt-Cu; silver$_2$ tellurium (Ag_2Te); Ti-Al; TiCo; TiFe; TiNi; Tl_2Te.

1. Introduction

It is reasonably well established that when one element is dissolved in another of sufficiently similar atomic potential, relatively minor perturbation of the electronic states occurs, even at high concentrations [1,2]. In terms of a screening model, the ions are screened independently or linearly. Provided that the atomic potential differences and the atomic size differences are favorable, pairs of elements will exhibit unlimited mutual disordered solid solubility, and the electronic structures of the alloys will tend to follow the rigid-band prescription. Examples are consecutive pairs of transition elements near the middle of the 4*d* and 5*d* series, respectively.

Within the low-perturbation region, increasing deviations from ideality will manifest themselves near the stoichiometric compositions, by the occurrence first of all of short-range order, and eventually of long-range order. However, in the linear screening model, changes of structure brought about by order-disorder (O-D) or even melting will produce only small electronic effects.

*On leave from the University of Sheffield. Present address: Physics Department, The University, Leicester, England.

TABLE 1. *Five distinct classes of intermetallic compounds*

Class	Representative compound	Solid state order-disorder	Major changes in electronic properties with order-disorder	Type of electrical conductivity		Major changes in electronic properties with melting
				Solid	Liquid	
A	Cu_3Au	Yes	No			
B	Ti_3Al	Yes	Yes			
C	NiAl Ti_3Sn	No		Metallic	Metallic	Yes*
D	Bi_2Te_3	No		Semiconducting	Metallic	Yes
E	Mg_3Bi_2 Tl_2Te Ag_2Te	No		Semiconducting	Semiconducting	No

*Measurements through the melting point have not been made on these systems, but it is expected that these compounds will be more nearly free-electron-like in the liquid than in the solid.

On the other hand, as the atomic potentials of the two species become increasingly different, the electronic properties become increasingly structure sensitive as the linear screening approximation breaks down.

This effect is discussed with respect to long-range ordering systems, commencing with Cu_3Au as the representative member of our first class of compound (class A, table 1). In Cu_3Au the atomic potentials of Cu and Au are sufficiently similar that Cu_3Au undergoes O-D with practically no change of density-of-states.

In contrast to this are compounds of elements of sufficiently different atomic potentials that significant changes of electronic structure take place during solid state O-D. For example in Ti-Al, near the composition Ti_3Al, experiments in which the degrees of order were controlled by suitable heat treatments, demonstrated that for Ti_3Al, $n(E_F)_{disord.}/n(E_F)_{ord.} \sim 2$. Frequently, however, it is observed that intermetallic compounds, which may be either metallic or semiconducting in the solid, are structurally stable up to the melting point and therefore do not undergo O-D prior to melting. To discuss the effect of structure on electronic properties of this type of material we must therefore consider the solid-liquid transition. *Metallic* intermetallic compounds invariably behave when molten like conventional liquid metals. In *semiconducting* intermetallics, on the other hand, two types of melting behavior can be distinguished. In most cases a metallic description of the electron states in the liquid is appropriate; but a few intermetallic semiconductors are characterized by nonmetallic behavior when in the liquid phase.

We will set out to show that the wide variety of behaviors exhibited by intermetallic compounds can be correlated through an appropriate electronic screening model.

2. Experimental Results

Described below are a representative selection of experimental results based on measurements which we and other authors have carried out on the five classes of intermetallic compounds, the properties of which are summarized in table 1.

2.1. Class A Intermetallic Compounds

The low temperature specific heat of Cu_3Au, the representative class A compound, has been measured for both the ordered and disordered states by Rayne [3] and Martin [4] who agree that the change in electronic specific heat coefficient (γ) accompanying O-D is extremely small. According to Martin $\gamma_{disord.}/\gamma_{ord.} = 1.04$.[1] The results of measurements of total magnetic susceptibility [5], taken in conjunction with the density-of-states data outlined above, indicate a small change of electronic *diamagnetism* with O-D. Recognizing that the interband diamagnetism [6,7] usually makes a significant contribution to the susceptibility of a nontransitional metal or alloy, the magnetic results suggest again that relatively small changes in the elec-

[1] γ is proportional to the density-of-states at the Fermi level, $n(E_F)$, according to the relation $n(E_F) \propto \gamma[1+V_n(E_F)]^{-1}$; where $V\ n(E_F)$, a correction term for electron-phonon effective mass enhancement, is small for a nonsuperconductor. This results in an approximately second-order correction to the density-of-states *ratio*.

tronic states accompany O-D in Cu_3Au. The Hall coefficient changes from R_H(disord.) $= -0.64 \times 10^{-12}$ Ω-cm/oe to R_H(ord.) $= +0.17 \times 10^{-12}$ Ω-cm/oe: both values being well within the range normally associated with good metals.[2] (This change in Hall coefficient is small compared to that encountered in class B compounds (fig. 5)). In contrast to the behavior of γ and R_H, the residual resistivity of Cu_3Au is extremely sensitive to O-D, responding to the change in structure-factor which controls the scattering [9].

Cu-Pt may be regarded as transitional between class A systems typified by Cu_3Au above and the subsequent classification. The low temperature specific heats of ordered and disordered CuPt have been measured by Roessler and Rayne [10]. At the time, the possibility of a magnetic transition seemed to obscure the interpretation. However, recent magnetic measurements in this laboratory have confirmed the absence of a transition to a cooperative magnetic state on ordering, permitting the results of the above authors, viz $\gamma_{disord.}/\gamma_{ord.} = 1.5_6$, to be interpreted as indicating simply a density-of-states change of that ratio. We have also measured the low temperature specific heat of the O-D compound Cu_3Pt and studied the electrical resistivities and Hall coefficients of a series of Cu-Pt alloys. The calorimetric results are summarized here for the first time. For Cu_3Pt, $\gamma_{disord.}/\gamma_{ord.} = 1.1_5$. The results of measurements of the room temperature resistivities of disordered[3] Cu-Pt alloys as a function of composition were in satisfactory agreement with those of Schneider and Esch [11] after extrapolation from the high-temperature disordered region. As expected the resistivities of the ordered compounds Cu_3Pt and CuPt were found to have dropped to relatively low values. The results of the electrical resistivity and R_H measurements are summarized in figure 1. The measured Hall coefficient corresponds to an effective change in carrier concentration of $0.5 - 1.0 \times 10^{23}$ electron/cc; although it is expected that at least a two-band model would be required to describe this system. The ordering reactions of both Cu_3Pt and CuPt are accompanied by small positive-going increments in R_H. It is clear that this system exhibits no wide departures from good metallic behavior. These results will be discussed later in the context of class A and class B intermetallic compounds.

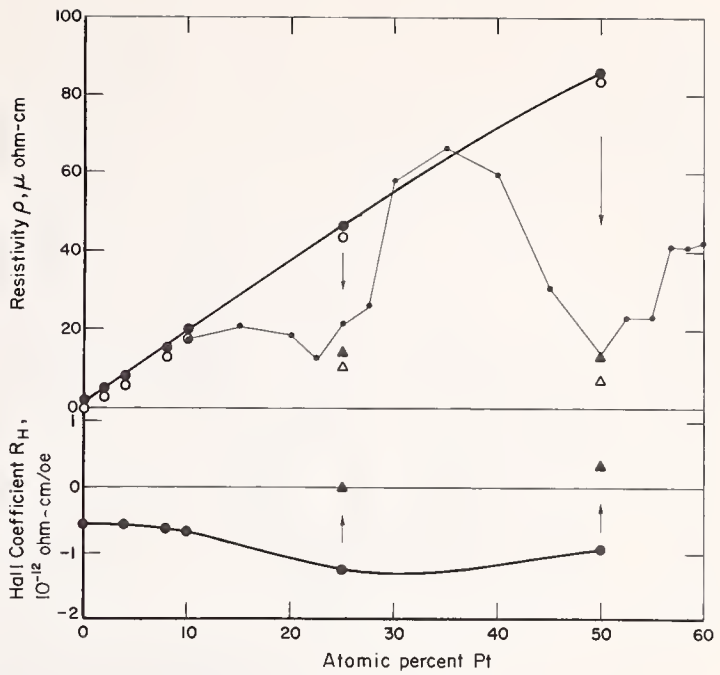

FIGURE 1. *Resistivity and Hall coefficient for* Cu-Pt *alloys.*
Filled points—room temperature; open points—4.2 K. ○●—"disordered" (cold-rolled from arc-melted buttons). △▲—after a long ordering heat treatment (Cu_3Pt—step-cooled from 500 °C over a period of 2 weeks; CuPt—step-cooled from 850 °C during 18 days). Analyzed compositions of the compounds were respectively, 25.7 at.% and 50.5 at.% Pt. Broken line refers to the room-temperature "ordered" alloy resistivity data of reference [11]. Arrows indicate the response to ordering heat treatment which, as the resistivity data shows, is still not complete.

2.2. Class B Intermetallic Compounds

Systems of this type, in which major changes in electronic properties accompany solid-state O-D, although not common, are of considerable importance both practically and from the standpoint of this discussion. Ti_3Al is taken as an example, and some new experimental results are presented below. Figure 2 shows the results of room-temperature magnetic susceptibility measurements. Using Blackburn's [13] *equilibrium* phase diagram as a guide (see inset to fig. 2) the degrees of long-range order present in the small (~150 mg) susceptibility specimens were controlled over wide ranges[4] by suitable heat treatments followed by rapid quenching into iced brine. The chief components of susceptibility in a transition-metal alloy are χ_{spin}, the spin paramagnetism which is approximately proportional to $n(E_F)$, and χ_{orb}, the orbital paramagnetism [14]. Clearly figure 2 demonstrates that major changes in electronic structure accompany O-D in the Ti-Al system and particularly in Ti_3Al itself. The electronic specific heat results are shown in figure 3. Because of their bulk (30-40 g) the specific heat specimens were not able to be quenched as rapidly as were those used for magnetic susceptibility measurements. For example, the Ti-Al (28 at. %) specific heat specimen could not be retained in the disordered form. However, the results of figure 2 help to validate the extrapolation procedures used in figure 3 for estimating $\gamma_{disord.}$ For Ti_3Al it follows that $n(E_F)_{disord.}/n(E_F)_{ord.} \cong 2.1$. Some of the results of elec-

[2] For example, R_H (Cu, experimental) $= -0.55 \times 10^{-12}$ Ω-cm/oe; and R_H (Cu, free electron model) $= -0.74 \times 10^{-12}$ Ω-cm/oe.

[3] Rolled strips from arc-melted buttons were measured in the unannealed condition to avoid the possibility of short-range ordering, as discussed by Kim and Flanagan [12].

[4] An exception is Ti_3Al itself, in which the ordering reaction is so rapid that it proceeds almost to saturation, with respect to density-of-states properties, during ice-brine quenching.

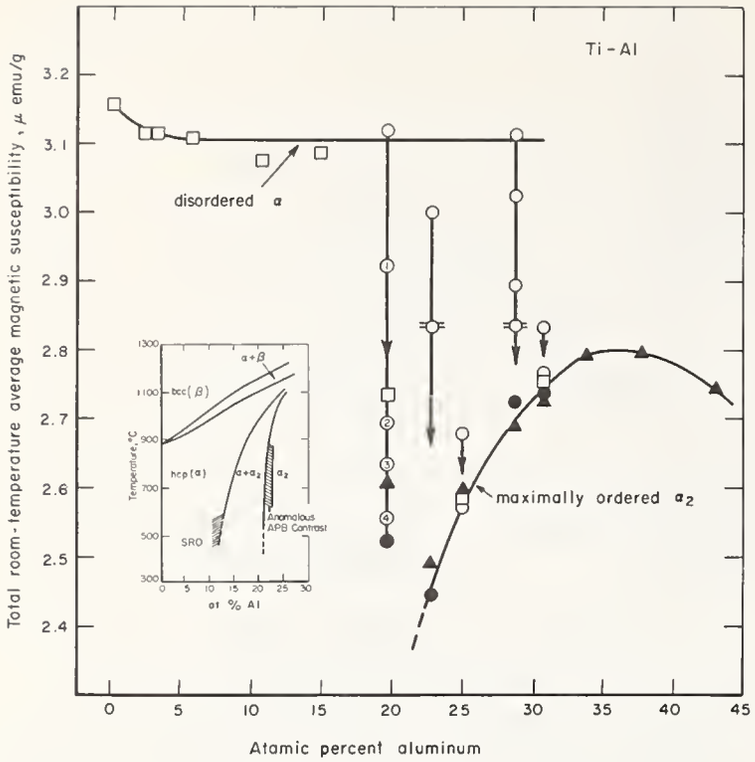

FIGURE 2. *Average room-temperature magnetic susceptibility* ($\chi_{av.}$) *of* Ti-Al *alloys.*

$\chi_{av} = 1/3(\chi_x + \chi_y + \chi_z)$. Inset is the equilibrium phase diagram (0–25 at.% Al) due to Blackburn [13]. The arrows indicate the effect of improving the degree of long-range order. □—annealed at 50 °C below $\alpha/(\alpha+\beta)$ and quenched, except for Ti-Al (30) which was heat treated as for Ti-Al (20). ○—quenched into iced brine from bcc field. ① to ④—quenched from 1260, 1,000, 800, and 700 °C, respectively. ⊃—quenched from 1100 °C. ▲—as cast. ●—long step-cooling anneal to promote maximal long-range ordering.

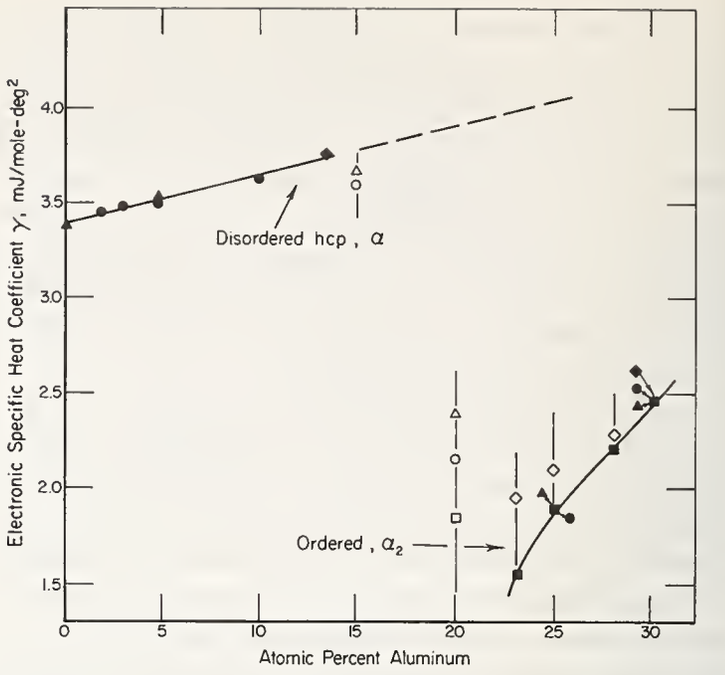

FIGURE 3. *Low-temperature specific heat of disordered and ordered* Ti-Al.

Filled symbols represent single-phase (α or α_2) material, while open symbols represent alloys which are known or suspected to be two-phase ($\alpha+\alpha_2$) (see inset to fig. 2). Circles: as cast; Triangles: quenched from 50 °C below $\alpha/(\alpha+\beta)$ transus; Squares: prolonged low-temperature anneal; Diamonds: quenched from β field.

trical resistivity measurements on Ti-Al are shown in figure 4. This type of measurement, and particularly residual resistance ratio, is well known[5] to be much more responsive to the degree of long-range order than are $n(E_f)$-sensitive measurements such as specific heat and magnetic susceptibility. Although Ti_3Al in the as-cast condition may from the point of view of $n(E_F)$, and for most practical purposes, be regarded as fully ordered, the antiphase domain size is still sufficiently small [13] that grain boundaries make a significant contribution to the electron scattering. As a consequence, the resistivity-concentration curve for as-cast Ti-Al shows only a dip at 25 at.% Al characteristic of partial ordering (fig. 4 cf., also [15]) instead of the otherwise expected sharp drop to the baseline. The results of the present Hall coefficient study are summarized in figure 5 (cf., [16]). Considerable scatter of the data was encountered for alloys of compositions close to 25 at. % Al. This was attributable to microcracking, which always occurred even when special preparation procedures were followed.[6]

Of crucial importance for an interpretation of the electronic property data presented above are the results of x-ray structural measurements by Gehlen [17] of a maximally-ordered single crystal of Ti-Al (26.7 at. %). The results of that work, whose physical significance has been the subject of a preliminary note [18] are best described with reference to figure 6. Gehlen's work has demonstrated that Ti_3Al possesses a hexagonal DO_{19} structure, but with the Ti atoms slightly displaced "inwardly," within the basal planes, toward a hexad axis passing through the Al atoms. This results in the formation of the chains of—Al-Ti_3—tetrahedra delineated in figure 6.

The spatial arrangement of ordered Ti_3Al, in conjunction with the electronic property evidence as a function of O-D, suggests (a) that part of the bonding in ordered Ti_3Al is covalent in type with some fraction of the total number of otherwise-available conduction electrons removed from conducting states: and (b) that such an electronic arrangement, favored by the structural long-range order, becomes smeared out in the disordered lattice. In terms of our model we would say that the ordered state is characterized by nonlinear screening, which requires a self-consistent readjustment in response to a change of structure.

2.3. Class C Intermetallic Compounds

This is a large class of compounds. Members of this category (table 1) may exist within a finite compositional range about stoichiometry and are generally suf-

[5] For example, relatively large changes of residual resistance ratio brought about by cold work or very dilute alloying are frequently accompanied by negligible changes in γ or χ.

[6] The end of a suspended "finger-ingot" of Ti_3Al was remelted by r.f. induction heating in a gettered argon atmosphere, and cooled to room temperature in about 8 hours.

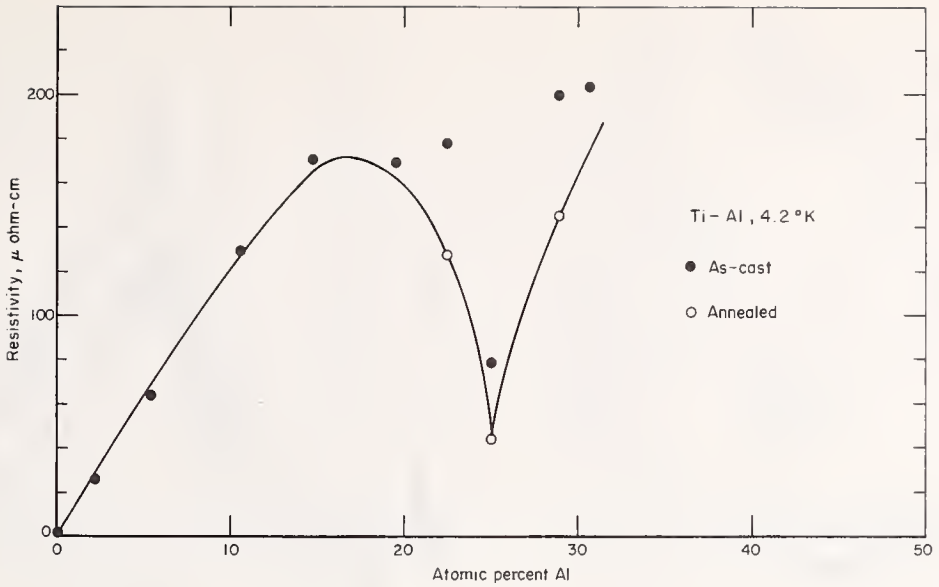

FIGURE 4. *Electrical resistivity of* Ti-Al *at* 4.2 K: ●—*as cast;* ○—*annealed for 14 days at* 900 °C *and furnace-cooled.*

A comparison of the magnetic susceptibility and specific heat data for Ti_3Al with the resistivity data presented here shows that, while the density-of-states is practically unaffected by annealing (figs. 2 and 3), the improvement in the degree of long-range-order has a profound effect on the electron scattering.

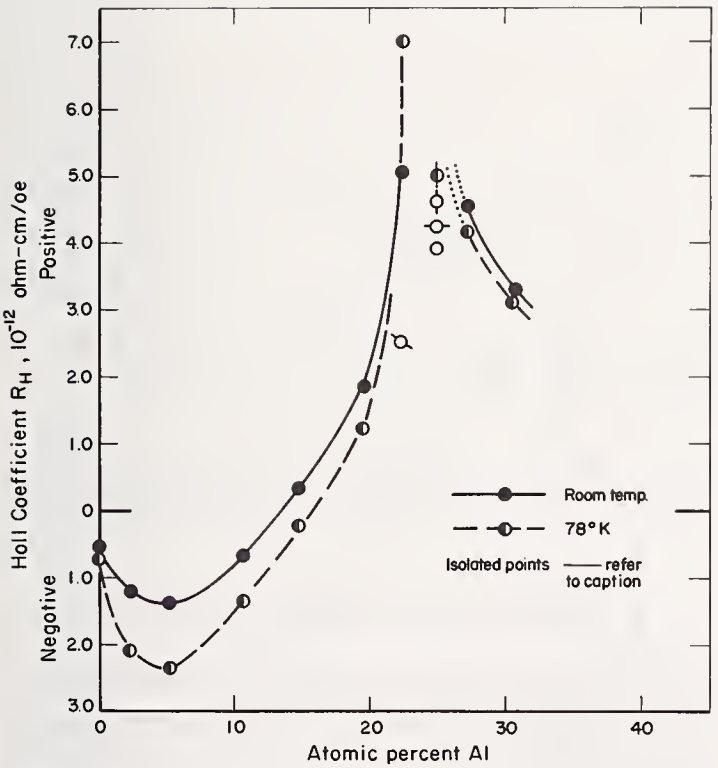

FIGURE 5. *Hall coefficient of* Ti-Al *at room temperature* (-●-) *and 78 K* (-◐-).

The isolated points refer to specimens which were more or less imperfect through cracking; ○—Ti-Al (22.3 at.%) (RT); ○, -○-, ○—Ti_3Al specimens 1, 2, and 3 resp. (*RT*); ◐—Ti_3Al specimen 3 (78 K). Microcracking in Ti_3Al was unavoidable. The data for Ti-Al (22.3 at.%) indicates that the presence of cracks drastically lowers R_H. This fact, together with the behavior of the surrounding data, suggests that R_H (Ti_3Al) should, in a perfect specimen, be much higher than the measured values. The data compares favorably with that of reference [16].

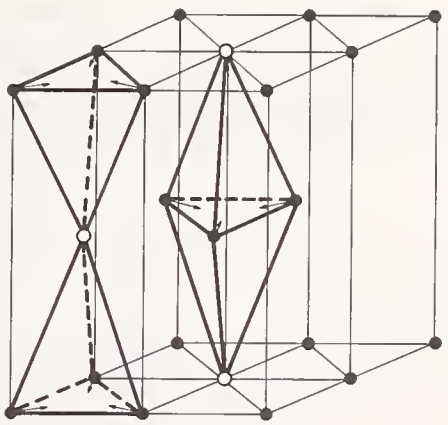

FIGURE 6. *Regular hexagonal* DO_{19} *structure.*

In Ti_3Al the Ti atoms (●) are displaced, in the directions indicated by the arrows, towards an axis passing through the Al (○) atoms. The resulting chains of tetrahedra are indicated by the heavy lines.

ficiently stable to resist disorder prior to melting. In regard to both electronic and mechanical properties they are metallic solids; and of course are metallic when liquid (disordered). The ductility of class C intermetallic compounds is poor at temperatures low compared to the Debye temperature, but improves at higher temperatures. An example is β-NiAl for which a considerable amount of published data are available.[7] Figures 7 and 8 summarize the results of recent measurements by Yamaguchi et al. [19,20] and Jacobi et al. [21] of the electrical resistivities and Hall coefficients of Ni-Al and related systems.

The resistivity curves exhibit sharp minima at the stoichiometric composition, characteristic of metallic

[7] Paraphrasing [21], β-NiAl has a homogeneity range of approximately 40-55 at. % Al at room temperature, and on the basis of x-ray measurements it probably remains ordered up to the melting point. The aluminum-rich compound is a (Ni) vacancy structure.

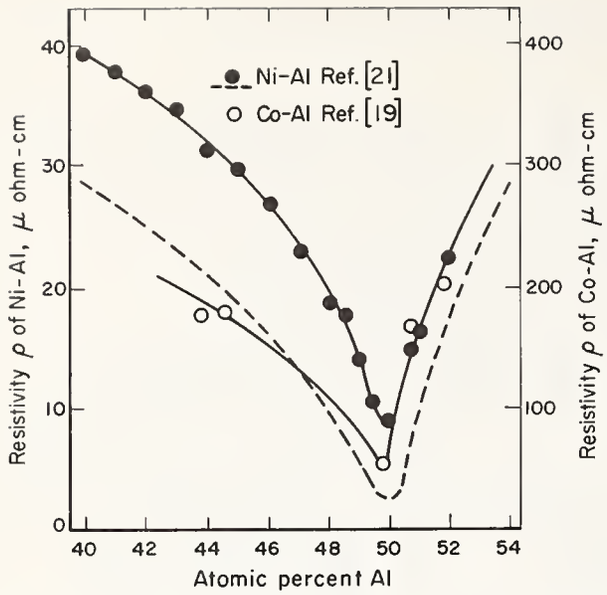

FIGURE 7. *Electrical resistivity of* Ni-Al [21] *and* Co-Al [19].
(○● — room temperature; ···77 K).

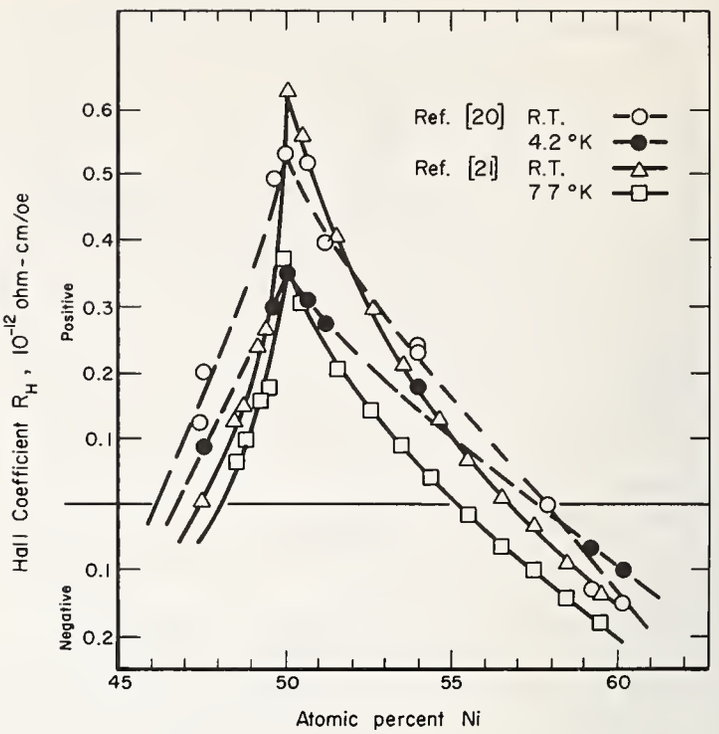

FIGURE 8. *Hall coefficients of* Ni-Al.
Data points are from references [20] and [21] (excepting that data from [21] has been shifted slightly in composition, bringing the peak to 50 at. % Ni).

conduction in a long-range ordered structure. The depth of a residual resistivity minimum is a measure of the degree of ordering, which is controlled mainly by the precision with which exact stoichiometry can be achieved. The Hall coefficient rises sharply to a positive value at the composition NiAl, the effective charge-carrier concentration still appearing to remain well within the metallic regime. Recent measurements in this laboratory have shown the R_H versus composition curve for Ti-Sn to be comparable to that of Ti-Al (fig. 5) but of the opposite sign in the vicinity of the first intermetallic compound.

The electrical and magnetic properties of TiFe, TiCo, and TiNi have been discussed by Allgaier [22] and Butler et al. [23], but because of their complicated and uncertain metallurgical properties, these compounds cannot be unequivocally placed in the simplified classification scheme described here.

2.4. Class D Intermetallic Compounds

This is a relatively populous class. Here we refer to intermetallic compounds, semiconducting in the crystalline state, which revert to metallic behavior when molten. Some of the many semiconducting compounds which exhibit this behavior (e.g., CdSb, ZnSb, Bi_2Te_3, and Sb_2Te_3) have been discussed elsewhere [24,25].

We offer here, as an example of class D, the compound Bi_2Te_3 and the results of some new measurements of R_H through the melting point (fig. 9), which demonstrate the transition from the semiconducting to the metallic state on melting.

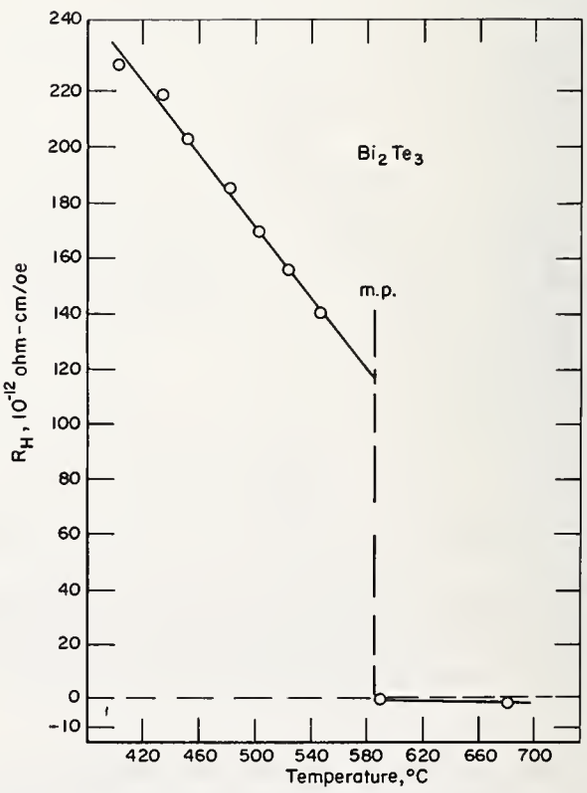

FIGURE 9. *Hall coefficient of* Bi_2Te_3 *showing the transition to the metallic state on melting.*

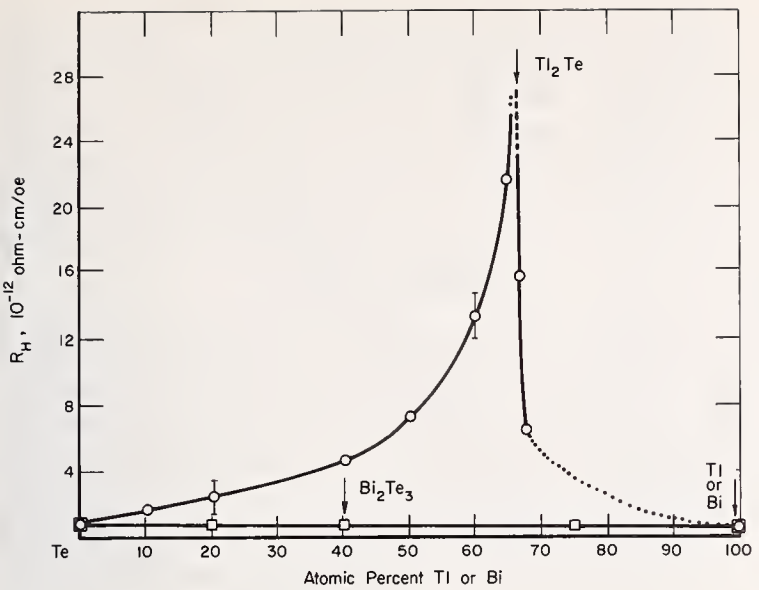

FIGURE 10. *Hall coefficient as a function of composition for liquid* Te-Tl *showing a singularity at the composition of the liquid semiconductor* Tl_2Te.

The dotted portion of the curve for Te-Tl refers to the two-phase region. The Hall coefficient of liquid Te-Bi, which is metallic at all compositions, is shown for comparison (after reference [25]).

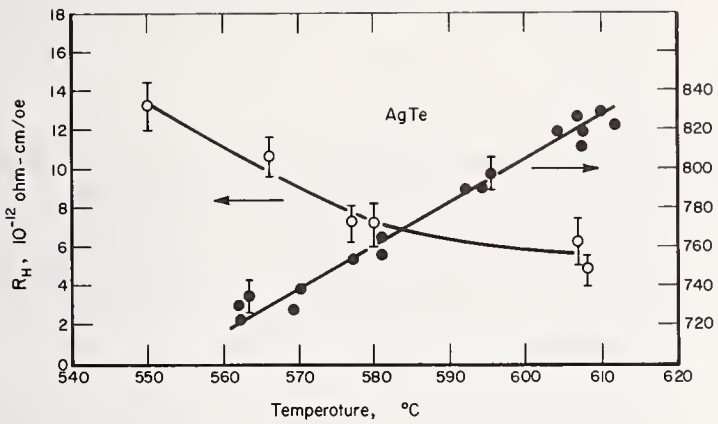

FIGURE 11. *Transport properties,* R_H *and* σ, *of the liquid semiconductor* AgTe *as functions of temperature (after reference* [25]).

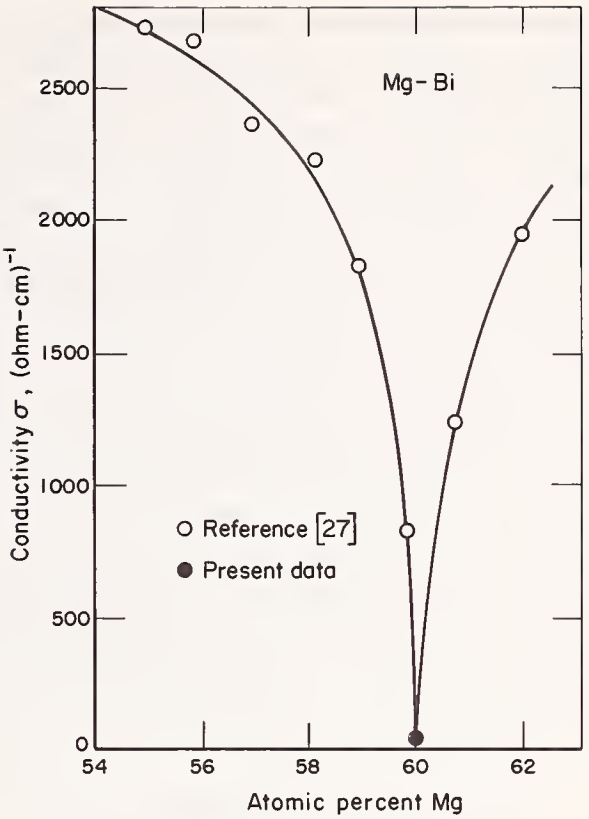

FIGURE 12. *Electrical conductivity of liquid* Bi-Mg *near the composition of the liquid semiconductor* Mg_3Bi_2.

Open circles are data from reference [27]. Filled circle represents the minimal conductivity obtained in the present experiment [26] after enriching the alloy Bi-Mg (63 at.%) with Bi (through evaporation of Mg, and by direct addition of Bi).

2.5. Class E Intermetallic Compounds

Compounds in this class are not common. They possess an extreme type of behavior in which their nonmetallic character in the crystalline state persists into the liquid. We cite as examples Tl_2Te and Ag_2Te which have been discussed in the recent paper of Enderby and Simmons [25]. Again the Hall coefficient is quoted as a useful measure of the degree to which a given material can be characterized as nonmetallic. Figure 10 shows R_H for liquid Tl-Te rising to a singularity at the composition Tl_2Te. Figure 11 reproduces the results of transport property measurements on AgTe. Both R_H and σ are out of the range of values usually associated with metallic conduction. As a final example we quote Mg_3Bi_2 currently under investigation in this laboratory [26]. Figure 12, most of the data for which are due to Ilschner and Wagner [27], shows the conductivity of the liquid alloy dropping to less than 60 $(\Omega\text{-cm})^{-1}$ near what must be assumed to be the stoichiometric composition.

3. Discussion

In the data presented above an overall pattern can be discerned in the properties of intermetallic compounds. The chief features of this pattern have been summarized in table 1. In proceeding further it is of considerable heuristic value to focus attention on the *cohesive energy* and note how this quantity varies as we proceed from A to E. We introduce the partial cohesive energies [28] such that $\mathscr{E}_{coh} = \sum_{i=1}^{\infty} \mathscr{E}_i$. For weak pseudopotential metals only $\mathscr{E}_1$ (the structure-independent term) and $\mathscr{E}_2$ (the term depending on pair potentials) are important. Under this condition rearrangement of the atoms at constant volume will not significantly change $\mathscr{E}_{coh}$. If the pseudopotential is weak the ions may be screened separately. Movement of such ions, with self-consistent adjustment of the screening results effec-

tively in a screening charge that accompanies the ions (or neutral pseudo-atoms as they may then be called [29]). That is, in the linear screening regime of weak pseudopotentials, the electron states are approximately independent of structural order. This situation obtains for (a) pure metals with weak local pseudopotentials, and (b) alloys of metals whose differences in atomic potentials (to be defined) are small (cf., Stern [1,2]). As the differences in pseudopotentials become larger, a new aspect enters the problem. There are many equivalent mathematical descriptions of this. For example, the concept of nonlinear screening on one hand, as discussed by Phillips [30], or the breakdown of perturbation theory on the other (cf., Stern [1], Beeby [31]). In terms of our basic approach it means that $\mathscr{E}_i$ $(i > 3)$ become of increasing importance, i.e., the ionic screening becomes increasingly nonlinear.[8] Although no single piece of evidence is conclusive, the trends in the data discussed above are unmistakable and are outlined as follows:

3.1. Mechanical Behavior

A loss of ductility occurs as we proceed from class A to class E intermetallic compounds. This is associated with a high resistance to shear (i.e., high Peierls barriers) brought about by noncentral forces. For example, Cu_3Au is ductile but, as expected, is easily work-hardenable [4]; whereas the class C compound β-NiAl is already extremely brittle [21].

3.2. Hall Effect

It is not possible to calculate from first principles the Hall coefficient of solid-solution alloys. Conversely it is usually difficult to make a satisfactory detailed physical interpretation of an experimentally-measured value of R_H. If, however, during alloying charge carriers became immobilized, as bound states begin to form, a significant increase in $|R_H|$ may occur. We see this just beginning to take effect in class B compounds (fig. 5); whereas class E compounds are characterized by singularities in $|R_H|$ at stoichiometry indicative of a nonmetallic state (fig. 10).

However, in multiband conduction, the possibility of which must be considered in any intermetallic compound, positive and negative components of R_H may partially cancel. Poor metallic characteristics in a solid intermetallic compound are therefore necessary, but not sufficient, conditions for appearance of a large value of $|R_H|$. Such measurements in the solid must therefore be reinforced by other electronic property measurements when studying the bonding behavior of alloys. With liquids (in which only negative Hall coefficients have been observed experimentally) the interpretation seems more straightforward.

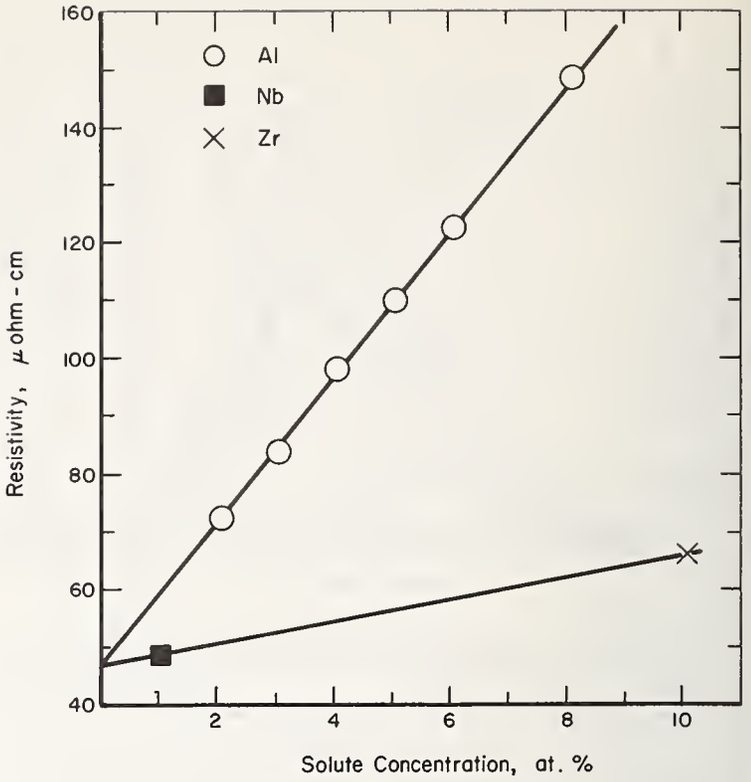

FIGURE 13. *Influence of small additions of* (*a*) Al, (*b*) Nb, *and* Zr, *on the resistivity of* Ti—*after Ames and McQuillan, Acta Met.* **4**, *619 (1956).*

The scattering cross-section of an "adjacent" transition element is seen to be relatively small.

3.3. Electrical Resistivity for Low Solute Concentrations

A marked increase is observed in the resistivities of dilute alloys (per atomic percent solute concentration) as the atomic potential difference between solute and solvent increases. This is illustrated in figure 13 in which the resistivities of dilute Ti-Zr and Ti-Al alloys are compared. Ti-Zr may be regarded as an "ideal" solid solution alloy while Ti-Al leads eventually to a class B intermetallic compound.

3.4. Electrical Resistivity near Stoichiometry

In classes A and B compounds, disordering can be achieved either by heat treatment or by varying the stoichiometry; while in classes C through E compounds, only the latter technique is available in the solid state. Bearing this in mind we make the general observation that in classes A, B, and C the resistivity decreases on ordering through structural considera-

[8] In an alloy it is useful to regard this as a description of incipient bound state formation.

tions in spite of a lowering electron density (brought about by the bound state formation which may produce an increase in $|R_H|$). On the other hand in classes D and E the bound state effect dominates, and both the resistivities and Hall coefficients have maximal values at the stoichiometric compositions.

3.5. X-Ray Studies

Direct crystallographic evidence also reinforces the above picture. As has been pointed out in detail in section 2.2 the results of x-ray structural studies on Ti_3Al attest to the existence of noncentral bonding forces. Similarly electronic density contours, such as those derived from CoAl and NiAl by Cooper [32] demonstrate graphically the existence of directional charge distributions in class C intermetallic compounds.

4. Conclusions

Given a binary alloy how can we determine *ab initio* which of these categories represents an appropriate description? Clearly the gross features can be determined simply by looking at the periodic table. The further apart the elements are, the more the alloys or compounds tend to E-type behavior. The next degree of sophistication is to use the concept of electronegativity in either its traditional [33] or its modern [34] form. The estimates that these give of the differences in potentials sometimes fail in detail; for example, they would predict that the class D compound Au_2Te falls in class E. The reason for this is that such methods do not take into account the self-consistency of the conduction electron screening. However, the Pauling electronegativity approach to bonding [33] and the theories of structural stability propounded by Brewer and his collaborators [35] are linked by considerations relating to the gaseous atomic energy levels. However, these levels form the basic input data for calculations of pseudopotentials of the type described by Heine and co-workers. Such potentials are known to be useful for a variety of applications. In our view the successes of both the electronegativity concept and the approaches used by Brewer, which at first sight seem highly empirical, can be fully understood from this point of view.

The pseudopotential in its **k**-space form is not well suited to this present discussion since it relates to the first few lattice vectors in reciprocal space, whereas to discuss bound state formation and the localization of electrons we need to consider the first few atomic spacings in *real* space. The pseudopotential in **k**-space deals with the long range part of this potential (i.e., screening) in a satisfactory way, but the influence of the core is distributed through **k**-space and is not accessible. The Engel-Brewer theory emphasizes the importance of the core but does not take sufficient account of screening and the requirement of self-consistency that the screening imposes on the problem. What we seek is a synthesis of these two points of view, and our starting point is the model potential of Heine and Abarenkov [36]. This potential in real space has the correct asymptotic behavior, and though ill-defined near R_M, the core radius, is fixed inside the core by terms from the spectroscopic data.

Table 2 lists the energy parameters of the Heine-Abarenkov model potential. It is apparent that large dif-

TABLE 2. *Selected parameters for the screened model potential of Heine and Abarenkov* [36]*

	A_0**	A_1	A_2
Li^+	0.336	0.504	0.455
Na^+	.305	.339	.402
K^+	.240	.256	.368
Rb^+	.224	.226	.384
Cs^+	.205	.207	.366
Be^{2+}	1.01	1.22	1.48
Mg^{2+}	0.78	0.88	0.99
Ca^{2+}	.54	.50	1.49
Ba^{2+}	.45	.34	1.07
Zn^{2+}	.99	1.14	0.98
Cd^{2+}	.88	0.98	1.78
Hg^{2+}	.97	1.11	0.85
Al^{3+}	1.38	1.64	1.92
Ga^{3+}	1.44	1.58	1.41
In^{3+}	1.32	1.46	1.10
Tl^{3+}	1.44	1.51	0.98
Si^{4+}	2.08	2.39	2.44
Ge^{4+}	2.10	2.34	2.09
Sn^{4+}	1.84	2.04	1.62
Pb^{4+}	1.92	***(2.00)	0.90
As^{5+}	2.71	(3.08)	(2.0)
Sb^{5+}	2.42	2.66	(1.8)
Bi^{5+}	2.38	2.58	0.25
Se^{6+}	3.42	(3.77)	(3.0)
Te^{6+}	3.04	3.32	(2.80)

*After A.O.E. Animalu and V. Heine, Phil. Mag. **12**, 1249 (1965).

**The A_l (which are defined in the above-mentioned references) are in atomic-energy units; 1 atomic unit=2 Ry.

***The numbers in parentheses are obtained by "extrapolation" from one point.

ferences can exist between the A_0 energy parameters for pairs of metals. For example A_0(Sb)-A_0(Mg) is fairly extreme on the scale of atomic potential differences. Accordingly Mg_3Sb_2 is a class E compound. On the other hand CdSb is in class D. This example demonstrates that, contrary to some previous suggestions, *valence difference* alone is insufficient to describe the effect but that the type of bonding depends in detail on the core energy levels. When comparisons between the data of table 2 and experiment are possible the correct trends are observed.

One outstanding problem is the proper way of describing the core states in *transition metals*. The evidence that we have from this work (see also [28]) is that they can be treated on roughly the same footing as normal metals. But we know that a simple model like that of Heine and Abarenkov would be completely inappropriate. For transition metals even the published electronegativity values are of little help since they do not show sufficient variation. The recent theoretical work by Harrison [37] might form the basis of an attempt to resolve this difficulty. On the experimental side, in view of the results already obtained for liquids of class E, it is clear that useful information on the relative potentials of metals can be obtained from suitably designed experiments on molten alloys and that this type of work should be extended to include transition metals.

5. Acknowedgments

We wish to acknowledge Messrs. R. D. Smith and G. W. Waters for technical assistance, and the following two agencies for financial assistance: The Air Force Materials Laboratory, Wright-Patterson Air Force Base, Ohio; and the Division of Research (Metallurgy and Materials) U.S. Atomic Energy Commission. J. E. Enderby wishes to acknowledge Battelle Memorial Institute for the award of a Battelle Institute Fellowship, during the tenure of which some of the ideas submitted here were developed.

6. References

[1] Stern, E. A., Physics **1**, 255 (1965).
[2] Stern, E. A., Phys. Rev. **144**, 545 (1966).
[3] Rayne, J. A., Phys. Rev. **108**, 649 (1957).
[4] Martin, D. L., Can. J. Phys. **46**, 923 (1963).
[5] Airoldi, G., and Drosi, M., Phil. Mag. **19**, 349 (1969).
[6] Verkin, B. I., Svechkarev, I. V., and Kuźmicheva, L. B., Soviet Physics, JETP **23**, 944 (1966).
[7] Misra, P. K., and Roth, L. M., Phys. Rev. **177**, 1089 (1969).
[8] Komar, A., and Sidorov, S., J. Tech. Phys. (USSR) **11**, 711 (1941); J. Phys. (USSR) **4**, 552 (1941).
[9] Ziman, J. M., Electrons and Phonons, (Oxford 1960).
[10] Roessler, B., and Rayne, J. A., Phys. Rev. **136**, A1380 (1964).
[11] Schneider, A., and Esch, U., Zeits. Elektrochem. **50**, 290 (1944).
[12] Kim, M. J., and Flanagan, W. F., Acta Met. **15**, 735 (1964).
[13] Blackburn, M. J., Trans. AIME **239**, 1200 (1967).
[14] Kubo, R., and Obata, Y., J. Phys. Soc. Japan **11**, 547 (1956).
[15] Kornilov, I. I., Pylaeva, E. N., and Volkova, M. A., in Titanium and its Alloys, Publication No. 10, Israel Program for Scientific Translations, Jerusalem (1966) p. 76.
[16] Grum-Grzhimailo, N. V., Kornilov, I. I., Pylaeva, E. N., and Volkova, M. A., Dokl. Akad. Nauk, SSR **137**, 599 (1961).
[17] Gehlen, P. C., Proc. Intern. Conf. on Titanium (London, 1968) to be published by Pergamon Press (1970).
[18] Ho, J. C., Gehlen, P. C., and Collings, E. W., Solid State Communications **7**, 511 (1969).
[19] Yamaguchi, Y., Kiewit, D. A., Aoki, T., and Brittain, J. O., J. Appl. Phys. **39**, 231 (1968).
[20] Yamaguchi, Y., and Brittain, J. O., Phys. Rev. Letters **21**, 1447 (1968).
[21] Jacobi, H., Vassos, B., and Engell, H. J., J. Phys. Chem. Solids **30**, 1261 (1969).
[22] Allgaier, R. S., J. Phys. Chem. Solids **28**, 1293 (1967).
[23] Butler, S. R., Hanlon, J. E., and Wasilewski, R. J., J. Phys. Chem. Solids **30**, 281 (1969).
[24] Enderby, J. E., and Walsh, L., Phil. Mag. **14**, 991 (1966).
[25] Enderby, J. E., and Simmons, C. J., Phil. Mag. **20**, 125 (1969).
[26] Enderby, J. E., and Collings, E. W., Proc. Intern. Conf. on Amorphous and Liquid Semiconductors, to be published in J. Non-Crystalline Solids.
[27] Ilschner, B. R., and Wagner, C., Acta Met. **6**, 712 (1958).
[28] Collings, E. W., and Enderby, J. E., in preparation.
[29] Ziman, J. M., Advances in Physics **13**, 89 (1964).
[30] Phillips, J. C., Phys. Rev. **166**, 832 (1968); **168**, 905 (1968); **168**, 912 (1968).
[31] Beeby, J. L., Phys. Rev. **135**, A130 (1964).
[32] Cooper, M. J., Phil. Mag. **8**, 811 (1963).
[33] Pauling, L., The Nature of the Chemical Bond (3rd edition), (Cornell University Press, Ithaca, N.Y., 1960).
[34] Phillips, J. C., Phys. Rev. Letters **22**, 645 (1969).
[35] Brewer, L., in Phase Stability in Metals and Alloys, P. S. Rudman, J. Stringer, and R. I. Jaffee, Editors, (McGraw-Hill 1967), p. 39.
[36] Heine, V. and Abarenkov, I., Phil. Mag. **9**, 451 (1964).
[37] Harrison, W. A., Phys. Rev. **181**, 1036 (1969).

Localized States in Narrow Band and Amorphous Semiconductors

D. Adler* and J. Feinleib**

Lincoln Laboratory, Massachusetts Institute of Technology, Lexington, Massachusetts 02139

The electronic density-of-states is discussed in situations where some of the states near the Fermi energy are localized, due to either intraionic Coulomb repulsion or disorder. When localized states are present, the Franck-Condon principle necessitates separate electrical and optical densities-of-states. In the case of ionic Mott insulators, it is shown that doping or nonstoichiometry drastically affects the energy-band structure. For the particular example of NiO, introduction of Li^+ impurities or excess oxygen leads to a large upward displacement of the $2p$ band associated with the oxygen ions, moving it sufficiently near the Fermi level that hole conduction in the $2p$ band predominates above 200 K, in agreement with the available experimental data. In the case of amorphous semiconductors, it is shown that introduction of electron-electron and electron-phonon interactions results in a shift of the relative position of the localized parts of the valence and conduction bands, as well as shifts of the localized states relative to the itinerant states. However, the qualitative features of the model of Cohen et al. are preserved.

Key words: Amorphous semiconductors; Anderson transition; augmented plane wave method (APW); chalcogenide glasses; electronic density of states; Franck-Condon principle; localized states; Mott insulator; NiO; optical density-of-states; photoconductivity; photoemission; polaron.

1. Introduction

The existence of localized electronic states in a crystalline solid has been recognized for many years, and methods have been developed for representing these states on an effective one-electron density-of-states diagram. In particular, donor, acceptor, and exciton states in ordinary semiconductors are familiar. These states are represented in such a way that the energy to excite an electron, a hole, or an electron-hole pair, either optically or thermally, is the correct value. Since the states are localized, certain additional rules must be borne in mind, in order to use the resulting density-of-states diagrams. In particular, these states generally do not contribute to electrical conductivity, and the simultaneous presence of both a spin-up and a spin-down electron in such a state results in a large Coulomb repulsion, and this possibility must be excluded from consideration. These rules significantly affect the statistics, and consequently modify the temperature dependence of the conductivity.

It is also clear that many other localized electronic states exist in crystalline materials. The core electrons are much more reasonably treated in a Heitler-London approximation, as always moving with their corresponding nucleus, than as itinerant Bloch electrons moving in the periodic potential of all the nuclei. However, it can be shown, for closed-shell configurations, the two opposing treatments give identical results [1]. The fact that this is not the case for partially-filled shells was first emphasized by Mott [2,3], who showed that electronic interactions in narrow energy bands could lead to the localization of outer electrons. It is now recognized that many transition-metal and rare-earth compounds are Mott insulators, nonconducting because electronic correlations localize their outer electrons. A quantitative version of Mott's model has been presented by Hubbard [5-7]. Hubbard introduced the effects of correlations into ordinary band theory by adding a term to the Bloch Hamiltonian which increased the energy of the system by a constant, U, whenever two electrons were simultaneously present

*Dept. of Electrical Engineering and Center for Materials Science and Engineering, M.I.T., Cambridge, Mass. 01239. Research sponsored by the Advanced Research Projects Agency.

**Research sponsored by the Department of the Air Force.

on a particular ion core. U represents the intraionic Coulomb repulsion between two electrons, and can be estimated in the atomic limit, or limit of infinite lattice parameter, as the difference between the ionization potential and the electron affinity of the atom. In a real solid, the value of U is much smaller than in the atomic limit, due to the effects of screening. However, in many crystals, such as NiO, this screening does not appear to be very large [8]. The result found by Hubbard [7], for the case of a half filled s band, is that the solid will be a Mott insulator provided

$$U > 0.87\,\Delta, \tag{1}$$

where Δ is the electronic bandwidth. If the condition (1) is not fulfilled, the material is metallic. For degenerate bands, Δ must be replaced in (1) by $12J$, where J is the relevant overlap integral.

Mott [9,10] has recently called attention to the localizing effects of lattice disorder. A quantitative treatment of an analogous problem was performed by Anderson [11], who considered the diffusion of a single electron out of a state in one of a series of equally-spaced potential wells of random strengths distributed over an energy range V. Anderson found that if

$$V > 5\,\Delta \tag{2}$$

the electron would not diffuse away. This result indicates the occurrence of an "Anderson transition" in which localization of an electron can be brought about by sufficient disorder. Mott [10] has suggested that a disordered lattice has energy bands whose states are itinerant if the density-of-states, $g(E)$, is greater than a critical value, but are localized if $g(E)$ is smaller than this value. This proposal has obtained some quantitative confirmation from the calculations of Ziman [12], Edwards [13], and Neustadter and Coopersmith [14]. The sharp edge between itinerant and localized states has been termed a "mobility edge" by Cohen et al. [15].

It seems clear that in situations in which both the energy spread due to disorder, V, and the intraionic Coulomb repulsion, U, are important, a condition analogous to (1) and (2), such as

$$[U^2 + 0.03\,V^2]^{1/2} > 0.87\,\Delta \tag{3}$$

will result in localization. This combination of correlation energy and disorder are most likely responsible for the suppression of metallic conductivity in the high temperature phase of Cr-doped V_2O_3 found by MacMillan [16] and by McWhan et al. [17].

These effects are complicated in ionic materials by the strong coupling between the electrons and the longitudinal optical phonons, which leads to polaron formation. It is a reasonable assumption that in the itinerant states the overlap integral is sufficiently large that large polarons will form. However, in the localized states the overlap is sharply reduced by the localization, leading to the likelihood of small-polaron formation. In nonpolar substances, the possibility of a Jahn-Teller stabilization of degenerate localized states must not be overlooked.

Finally, the Franck-Condon principle suggests that ionic rearrangements do not occur at optical frequencies. This does not affect the effective density-of-states to be used in analyzing the results of transport experiments, but has important consequences as far as the optical density-of-states is concerned.

In this paper, we shall be concerned with localized states in crystalline Mott insulators, such as NiO, and in amorphous semiconductors, such as chalcogenide glasses. In section 2, we discuss the optical density-of-states of pure and doped Mott insulators. In section 3, we analyze the electrical density-of-states of the same materials, pointing out the drastic effects that doping or nonstoichiometry can have on the mechanisms for electrical conductivity in transition-metal compounds. In section 4, we discuss the electrical and optical density-of-states in amorphous semiconductors in terms of the theory developed in the previous two sections. The conclusions are summarized in section 5.

2. Optical Density-of-States of Crystalline Mott Insulators

For simplicity, we begin with a discussion of the optical properties of pure, stoichiometric single crystals. We assume that the Franck-Condon principle applies, and that no ionic motion accompanies an optical transition. We restrict ourselves to photon energies of 20 eV or less.

It is convenient to illustrate our major points by a concrete discussion of a single material. We shall use NiO as the prototype Mott insulator, primarily because more experimental data exist for NiO than for any other transition-metal or rare-earth compounds. However, all our conclusions and techniques can be applied equally well to any other Mott insulator. Restricting ourselves to energies within 20 eV of the Fermi energy, we need consider only the $2p$ band associated with the oxygen ions, and the $3d$ and $4s$ bands associated with the nickel ions. Since the covalency parameters of NiO have been shown to be less than 4% [18], a good starting point for determination of the band structure is the energy levels of the fully-ionized atoms, Ni^{2+} and O^{2-}, in the limit of infinite separation. We then must take into account the

stabilizations and destabilizations due to the Madelung potential, the crystalline field potential, large-polaron formation, and various many-body effects such as electronic screening of the electrostatic Coulomb interaction and induced ionic polarization.

The evidence is now quite convincing [4,19] that the $2p$ and $4s$ bands in NiO are made up of itinerant states, and thus $\Delta/U \gg 1$. On the other hand there is much evidence that the $3d$ band is very near the atomic limit, in which $\Delta/U \ll 1$ [19]. Thus the $3d$ states are very localized, and NiO, with 8 $3d$ electrons per Ni^{2+} ion, is a Mott insulator.

The possible transitions which we must treat in detail are:

$$3d^8 \rightarrow 3d^{8*} \tag{4}$$

$$3d^8 + 3d^8 \rightarrow 3d^7 + 3d^9 \tag{5a}$$

$$3d^8 + 3d^8 \rightarrow 3d^7 + 3d^{9*} \tag{5b}$$

$$3d^8 + 3d^8 \rightarrow 3d^{7*} + 3d^9 \tag{5c}$$

$$3d^8 + 3d^8 \rightarrow 3d^{7*} + 3d^{9*} \tag{5d}$$

$$3d^8 \rightarrow 3d^7 + (\text{electron in } 4s \text{ band}) \tag{6a}$$

$$3d^8 \rightarrow 3d^{7*} + (\text{electron in } 4s \text{ band}) \tag{6b}$$

$$3d^8 + (\text{electron in } 2p \text{ band}) \rightarrow 3d^9 \tag{7a}$$

$$3d^8 + (\text{electron in } 2p \text{ band}) \rightarrow 3d^{9*} \tag{7b}$$

$$(\text{electron in } 2p \text{ band}) \rightarrow (\text{electron in } 4s \text{ band}) \tag{8}$$

Reaction (4) is just a localized excitation on a particular Ni^{2+} ion, the notation $3d^{8*}$ indicating an excited crystalline-field or multiplet split $3d^8$ configuration. Reactions (5a-d) represent transitions between localized states, with two Ni^{2+} ions being excited into a $Ni^+ - Ni^{3+}$ pair in their ground or excited states. Reactions (6a, b) represent the excitation of a localized electron on a Ni^{2+} ion into the $4s$ band, leaving behind a ground-state or excited Ni^{3+} ion. Reactions (7a, b) indicate the possibility of exciting an itinerant electron in the $2p$ band into a localized state on a nickel ion, leading to the formation of a Ni^+ ion in its ground state or an excited state, and leaving a hole in the $2p$ band. Finally, reaction (8) represents the usual interband excitations between itinerant one-electron states.

The crystalline-field and multiplet splittings of Ni^{2+} states in NiO can be determined either experimentally [20] or theoretically [21], and are in good agreement. They lead to a series of optical absorption peaks in the 1-4 eV range.

The energy range of reaction (5a) can be estimated from the difference between the ionization potential and the electron affinity of Ni^{2+} as requiring 18.6 eV [22]. This figure, however, takes no account of any screening of the intraionic Coulomb repulsion. This screening could result from either polarization of the surrounding O^{2-} ions and covalency effects, or it could be caused by the presence of other $3d$ and core electrons on the Ni^{2+} ions themselves. The latter effect is one which must occur in free Ni^{2+} ions, and can be estimated from the fact that the experimental Slater-Condon parameters are about 15% smaller than those calculated from Hartree-Fock wave functions [23]. The effects of polarization and covalency can be estimated from the reduction in the multiplet splittings of Ni^{2+} in MgO compared to those in free Ni^{2+} ions, an effect which amounts to approximately 20% [24]. Finally, we should also expect some screening from overlap between $3d$ electrons on nearest-neighbor Ni^{2+} ions. This can be estimated from the experiments of Reinen [20], who found that the Racah parameter, B, which is a measure of intraionic electronic repulsion, decreases 7% from dilute solutions of Ni^{2+} in MgO to pure NiO. Taking into account all of these screening effects, we find that the intraionic Coulomb repulsion for the $3d$ electrons in NiO is reduced from 18.6 eV to approximately 12 eV.

We still must take into account the differences in crystalline-field stabilizations of 2 Ni^{2+} ions as compared to one Ni^+ and one Ni^{3+} ion. It is likely that Ni^{3+} is in a high-spin state in NiO [19]. Assuming this to be the case, and using the estimated values [25] of the crystalline-field parameter, Dq, we can conclude that reaction (5a) requires approximately 13 eV. This is the effective value of U which should be used in condition (1) to determine whether or not the $3d$ electrons in NiO are localized. Since the $3d$ bandwidth in NiO can be estimated as being of the order of 0.3 eV [26] or considerably less [19], there is little question that condition (1) is fulfilled, and the $3d$ electrons are extremely localized.

Assuming the same values of Dq for Ni^{3+} and Ni^+ as used in estimating the crystalline-field stabilizations, we find that the d^7 excited states extend over a 5 eV range, while the d^9 configuration is 1 eV wide. Thus, reactions (5a-d) should contribute to optical absorption in the 13-20 eV range.

In order to estimate the energies of reactions (6-8), we must take into account the finite bandwidths of the $2p$ and $4s$ bands. We expect both bands to be in the Bloch limit, with effective values of U small compared to the bandwidths. It is a reasonable approximation that

the APW calculations should be quite good in determining the bandwidths and relative separations of these bands. Despite the differences in assumed potential, both the APW results of Switendick [27] and Wilson [28] are in agreement that the $2p$ band of NiO is 4 eV wide, while the $4s$ band is 6 eV wide. Furthermore the bottom of the $4s$ band is about 5.5 eV above the top of the $2p$ band. There is a small band measuring due to large-polaron formation [19]. Assuming that these values are good approximations, the $2p$-$4s$ transitions, reaction (8), should contribute interband optical absorption between 5.5 and 16 eV.

We can estimate the energy range for reaction (6) by noting that the free-ion process, $3d^8 \rightarrow 3d^7\ 4s$, takes 7 eV in Ni^{2+} [29]. Assuming that the effective value of U is negligible in the $4s$ band, we can conclude that in the NiO crystal, the 6 eV wide band spreads symmetrically around the free-ion $4s$ level. This reaction (6a) should contribute to the optical absorption in the 4-10 eV range. Since the $3d^7$ configuration is 6 eV wide, reaction (6b) extends the energy range of this $d \rightarrow s$ absorption up to 16 eV.

Finally, the energy range of reaction (7) involves electron transfer from the oxygen to the nickel ions. The free-ion process, $Ni^{2+} + O^{2-} \rightarrow Ni^{+} + O^{-}$, is extremely exothermic, since Ni^{2+} has an electron affinity of 17.5 eV and O^- has a negative electron affinity of 9 eV [22]. Thus, as free ions, the process would release 26.5 eV of energy. However, in an NiO crystal, the Madelung potential, which is 24.0 eV [22], stabilizes both the Ni^{2+} and the O^{2-} ions relative to Ni^+ and O^-. Thus the net stabilization of the free Ni^{2+} and O^{2-} ions in NiO is 22 eV. Assuming the same screening and crystalline-field stabilizations as used previously, we can estimate the average energy of the process which creates a $Ni^+ - O^-$ pair as 16 eV. Since the $2p$ orbitals can be assumed to spread into a band 4 eV wide, with an effective value of U small compared to the bandwidth, reaction (7a) should contribute to optical absorption in the 14-18 eV range. Reaction (7b) should give a further contribution between 15 and 19 eV.

We have not yet considered the excitonic contributions to the optical absorption. The most significant of these should be the Mott-type excitons representing $Ni^+ - Ni^{3+}$ bounded pairs, or the excitons in which a hole in the $2p$ band is bound to a Ni^+ ion. Estimates of the excitonic binding energies give maximum values of 0.8 eV in the former case and 1.1 eV in the latter case [19]. Thus, we might expect one exciton peak in the vicinity of 12 eV and another near 13 eV.

Reactions (4) and (5) are d-d transitions which should be somewhat suppressed by the parity selection rules. However, the crystalline-field splittings, (4), represent the only contributions to absorption on the 1-4 eV range, and thus should be quite observable. Reaction (6) requires a change of 2 in the orbital angular momentum quantum number, and also would be strongly suppressed, were it not for hybridization between $2p$ and $3d$ orbitals, which is very significant in NiO [27]. Reaction (7) represents an itinerant-localized allowed transition, and should give an important contribution to absorption. Finally, reaction (8) is an allowed interband transition and should produce the most effective photon absorption of all. A sketch of the expected optical absorption as a function of photon energy is shown in figure 1. The antiferromagnetic peak at 0.24 eV which appears below the Neel temperature [30] is indicated in the sketch. The experimental absorption below 4 eV [30] is shown in figure 2, and the absorption above 4 eV, as determined from reflectivity measurements [25], is shown in figure 3. Our interpretation is that the edge at 4 eV is the onset of reaction (6a), and the strong absorption above 12 eV represents the combined effects of (5), (7), and (8). The large peak at 17.6 eV thus represents the maximum contribution of the allowed absorptions, reaction (7), estimated as in the 14-19 eV range. The peak at 13.8 eV is most easily interpreted as due to $Ni^+ - (2p$ hole) bound excitons. The shoulder at 13.0 eV can be associated with the $Ni^+ - Ni^{3+}$ bound exciton. Our interpretation of the optical results is also consistent with the observed photoconductivity [31], since the lowest energy excitation to a conducting state is the 4 eV edge of reaction (6a).

Figure 1 represents the possible optical transitions in pure stoichiometric NiO. However, it is not an effective single particle density-of-states diagram in the usual manner. We have previously suggested a method for such a representation when localized states are present [19,32]. The basic idea is to employ a split density-of-states plot, with itinerant states drawn to the left and localized states drawn to the right. The left-hand side can thus be treated as ordinary one-electron band states, and free carriers on the left contribute to conductivity in the normal manner. However, states on the right-hand side are not one-electron states and can be treated as such only if certain rules are borne in mind. The positions and number of states on the right must vary with the occupation numbers, and partially-filled bands contribute to conduction only by means of thermally-activated hopping. Furthermore, it is necessary to set the energy of one of the states on the right relative to that of one of the ones on the left. Exactly how this is done should depend on the experiment being interpreted.

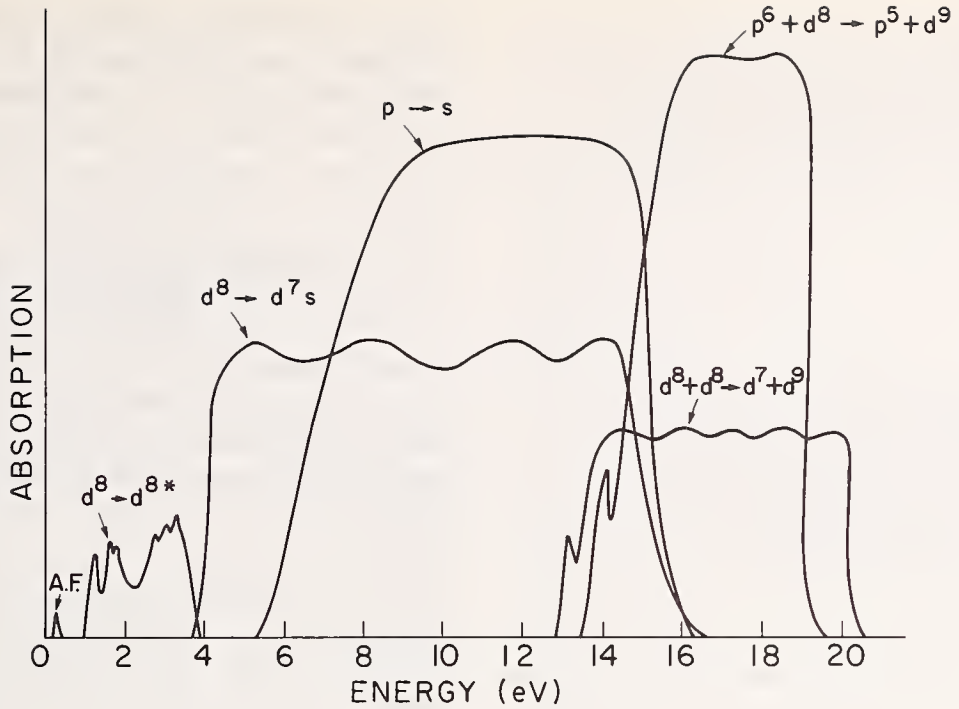

FIGURE 1. *Sketch of the predicted optical absorption of pure, stoichiometric* NiO *as a function of photon energy.*

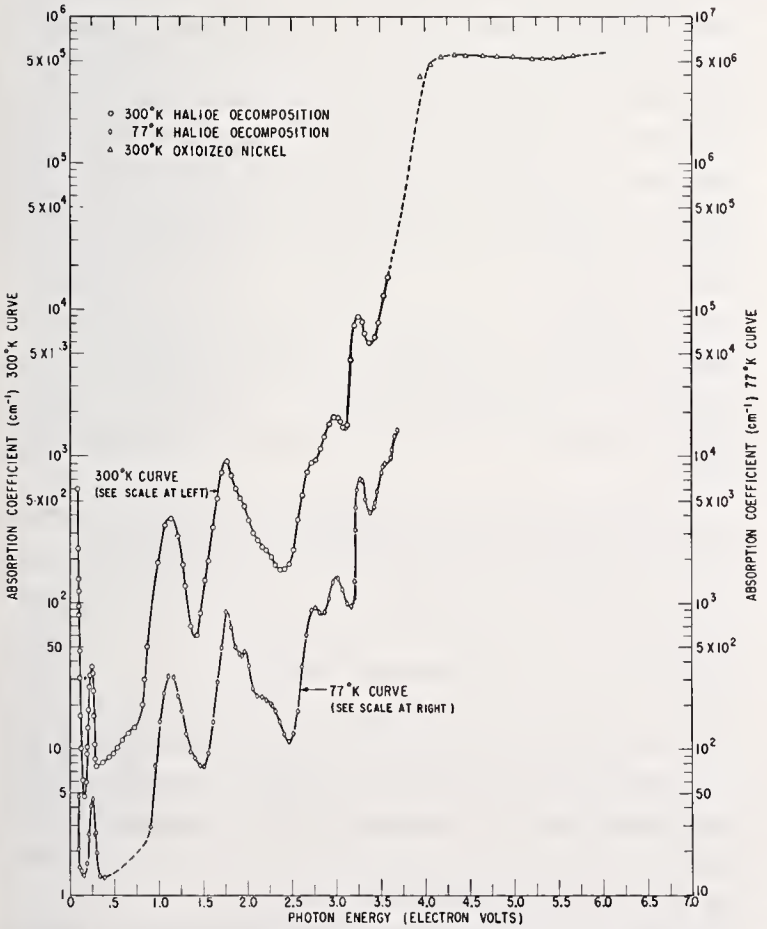

FIGURE 2. *Experimental optical absorption of* NiO *crystals below 6 eV (data of Newman and Chrenko [30]).*

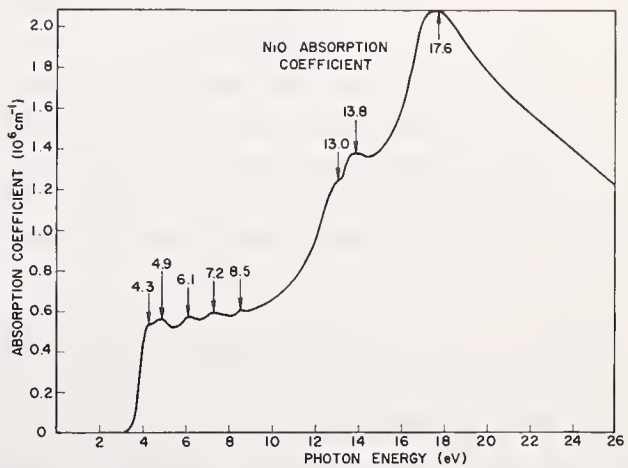

FIGURE 3. *Experimental optical absorption of an* NiO *crystals above 4 eV, as determined from reflectivity measurements (data of Powell [25]).*

417-156 O - 71 - 33

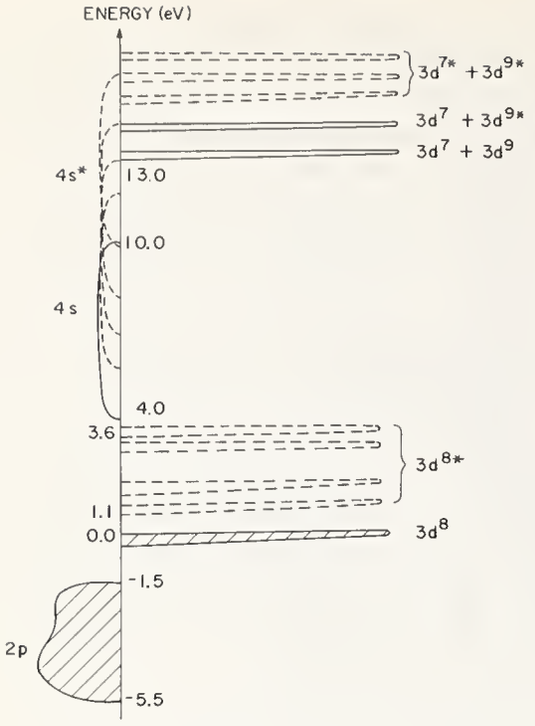

FIGURE 4. *Optical density-of-states of pure, stoichiometric* NiO.
Itinerant states are drawn to the left, localized states to the right. States which are filled at $T=0$ are shaded.

For photoemission experiments, the work function of the material is a convenient reference point for all states. Electrical conductivity is most easily analyzed if the Fermi energy is fixed on both sides. In this section we are concerned with optical absorption measurements. The most convenient choice would appear to be one which sets correctly the energy of the lowest-energy optical transition between a localized and an itinerant state. This is just the technique used in handling donor, acceptor, and exciton states in a conventional semiconductor.

Such an effective density-of-states diagram is given for pure, stoichiometric NiO in figure 4. The zero of energy has been taken to be the energy for the uppermost state which is occupied at $T=0$, a localized $3d^8$ state of the Ni^{2+} ion. States on the right and left are connected by setting the minimum energy of reaction (6a), $3d^8 \rightarrow 3d^7 +$ (electron in the 4*s* band), correctly. All other transitions across the center line are then approximations. However, in the case of NiO, the only other low-energy set of transitions between localized and itinerant states, reaction (7), is correct to within 0.5 eV.

As figure 4 is presented, only one special rule need be introduced. We must require that states drawn with a dotted line be available for transitions only from filled states on the right. Thus the crystalline-field split states, $3d^{8*}$, can only be excited from the $3d^8$ ground states. The excited transitions given by reaction (6b) can then be easily handled by introducing a multiplicity of dotted 4*s* bands, labeled $4s^*$ in the diagram. This is to be interpreted as the excitations of electrons from the $3d^8$ ground state to the 4*s* band which leave excited $3d^{7*}$ states of the nickel ion. With this rule in mind, figure 4 can be used to obtain an excellent approximation of the optical absorption spectrum of pure, stoichiometric NiO, figure 1.

Extension of this discussion of the optical properties to impure or nonstoichiometric NiO is straightforward. In fact, the optical absorption spectrum above 1 eV need not be modified at all, since the strong absorption continuously present in the 1-20 eV range will mask any effects of doping and vacancy concentrates up to a few percent.

The most common dopants in NiO are monovalent ions, such as Li^+. Li^+ enters the NiO lattice substitutionally for Ni^{2+}, and in order to preserve charge neutrality in the crystal, a Ni^{3+} ion is formed for each Li^+ ion in the material. The lowest-energy state of the doped material clearly is that in which all Li^+ ions have a nearest-neighbor Ni^{3+} ion, forming an effective "electron-hole" bound state, similar to an exciton. The maximum binding energy of this pair can be estimated as 0.4 eV [19]. A series of optical transitions are possible in the doped material which were not present in pure crystals. These represent excitation of an electron from any of the Ni^{2+} ions to the bound Ni^{3+} ion. The dominant optical transitions of this type are from Ni^{2+} ions far removed from the Li^+ center, and can be looked as a photon-assisted freeing of the hole (Ni^{3+} ion) which was bound to the Li^+ center. This transition should thus require about 0.4 eV. The other transitions, to more weakly-bound $Li^+ - Ni^{3+}$ states, where the Ni^{3+} is located farther from the Li^+ center than the nearest-neighbor Ni^{2+} sites should give weak absorption in the 0.2-0.4 eV range. Clear evidence for such Li^+-induced optical absorption has been found with a peak at 0.43 eV [33].

Another possible absorption in Li^+-doped, but not in pure, NiO can be represented by the reactions

$$3d^7 + (\text{electron in } 2p \text{ band}) \rightarrow 3d^8 \qquad (9a)$$

$$3d^7 + (\text{electron in } 2p \text{ band}) \rightarrow 3d^{8*} \qquad (9b)$$

This additional absorption can occur because of the presence of bound Ni^{3+} ($3d^7$) ions in the doped material. Assuming that the vast majority of Ni^{3+} ions are bound to Li^+ centers, reaction (9) can be shown to lead to absorption between 0.7 and 4.7 eV [19]. There is evidence for a Li^+-induced background absorption which increases from 0.2 eV through at least 2 eV, with

a peak at about 1.0 eV [34,35], which may well be a combination of excitations from both bound and free Ni^{3+} ions of type (9). The peak at 1.0 eV, if real, alternatively could represent the lowest crystalline-field peak of the Ni^{3+} ion.

3. Electrical Density-of-States of Crystalline Mott Insulators

As pointed out in the Introduction, when localized states are present, we cannot use the same density-of-states diagram for analyzing the electrical properties as we did for the optical absorption. This is because transport of electrons through the lattice occurs at times sufficiently long for the ions to relax around the new charge distribution, and thus ionic motion can no longer be neglected. We must thus take into account small-polaron formation and perhaps Jahn-Teller distortions in the localized states.

We can, however, use the optical density-of-states as a starting point for the analysis of electrical transport. As in section 2, we shall confine our remarks to NiO, whose optical density-of-states is shown in figure 4. The lowest energy excitations are the $3d^8 \rightarrow 3d^{8*}$ transitions, which are completely localized and do not contribute to conduction. The lowest energy excitations which do produce intrinsic conductivity are those given by reaction (6), which creates an itinerant electron in the 4*s* band and leaves a localized hole in the $3d^8$ band. Optically, this transition requires about 4 eV. The corresponding electronic transition will require somewhat smaller energy, since a lattice distortion will be induced around the $3d^7$ (Ni^{3+}) ion, lowering the energy of the final state.

As discussed in section 2, the 3*d* electrons in NiO are very near the atomic limit, and the corresponding electronic bandwidth, Δ, is expected to be negligibly small [19]. It is thus clear that the effects of the electron-photon interaction on the 3*d* electrons must be analyzed by nonadiabatic small-polaron theory [36]. Using the value for the strength of the electron-phonon interaction which gives a formal equivalence with large-polaron theory [37], and the parameters appropriate to NiO, we can show that the small-polaron binding energy is then of the order of 0.01 eV [19]. In this case, the transition temperature above which conduction by thermally activated hopping of small polarons dominates polaronic band conductions is small compared to the Debye temperature [19]. It is clear that the band like conductivity of the electron excited into the itinerant 4*s* band dominates the phonon-assisted hopping of the 3*d* hole at all temperatures. Using large-polaron theory [38] for the 4*s* band, we can estimate the polaron binding energy as 0.2 eV. Thus the intrinsic thermal energy gap should be about 0.2 eV lower than the intrinsic optical gap. The intrinsic conductivity must be *n*-type, and requires an activation energy near 2 eV. Thus intrinsic conduction should be observable only at extremely high temperatures and only in either extremely pure or highly compensated samples. There is some experimental evidence for this intrinsic process. In one relatively pure crystal of NiO, an activation energy of 1.9 eV was found between 700 and 1200 K at atmospheric pressure [31]. In a number of highly compensated polycrystalline samples, activation energies equal to approximately 1.8 eV have been measured [39].

In section 2, we showed that neither doping nor nonstoichiometry results in a major modification of the optical absorption spectrum of NiO. On the other hand, neither has a profound influence on the electrical properties.

Once again, let us first consider the effects of doping with Li^+ impurities. As discussed in section 2, this will lead to the formation of Ni^{3+} ions. A Ni^{3+} site is much like a hole on a Ni^{2+} ion, and this hole can move through the lattice by hopping to adjacent Ni^{2+} sites. The narrow bandwidth of these hole states allows for a localized deformation of the lattice around the hole, and thus the formation of a small polaron. The polaron initially will be electrostatically bound to the Li^+ centers. Theoretically and experimentally, this binding energy can be estimated as 0.4 eV. Once thermally freed from the Li^+ center, the small polaron will conduct by means of thermally activated hopping, but because of the small value of the polaron binding energy, the mobility will be only weakly dependent on temperature. Thus this process should contribute a term to the conductivity equal to

$$\sigma = N_A e \mu_0 e^{-(0.2eV)/kT} \tag{10}$$

where N_A is the density of Li^+ centers and μ_0 is the mobility of the hopping process.

In the view of normal band theory, the holes just described would be simply empty states in the $3d^8$ band of figure 4. But in the present context of localized states, we must take into account the fact that the separation between the 2*p* band and the $3d^8$ states is determinded by the energy to add an electron to the $3d^8$ states. This results in it being much easier to excite a 2*p* hole in the Li^+-doped material than in the pure material. The reason for this is that doping with Li^+ *automatically* results in the presence of Ni^3 ions. Since the electron affinity of Ni^{3+} is 18.6 eV greater than that

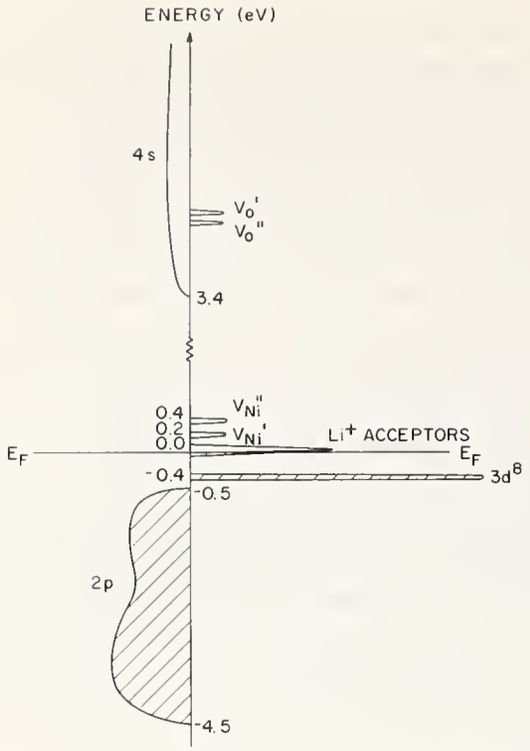

FIGURE 5. *Electrical density-of-states of* Li^+ *doped* NiO.
Itinerant states are drawn to the left, localized states to the right. States which are filled at $T=0$ are shaded. V_A' and V_A'' refer to singly and doubly ionized A-vacancy levels, respectively.

of Ni^{2+}, reaction (9a) takes much less energy than the analogous intrinsic process, reaction (7a). The significance of this point with respect to the density of states is that Li^+ doping raises the $2p$ band up to the vicinity of the Fermi energy. Because of this, conduction by means of free holes in the $2p$ band cannot be neglected. This process, which can be represented by reaction (9), was shown to require a minimum photon energy of 0.7 eV. However, thermally, this minimum energy is significantly reduced by large polaron formation about the $2p$ hole. This reduction in energy can be estimated as 0.25 eV [19], leaving a thermal activation energy of the order of 0.45 eV. This value depends critically on differences between large numbers, such as the Madelung potential and the ionic energies, and should not be expected to be very accurate. However, the important point is that it is comparable in magnitude to the activation energy for conduction by hopping in the $3d^8$ band.

Since the Fermi energy is of major importance in determining transport properties, an electrical density-of-states diagram should refer all states, both localized and itinerant, to E_F. Such a diagram is constructed for primarily Li^+ doped NiO in figure 5. The acceptor levels corresponding to singly and doubly ionized nickel and oxygen vacancies are also shown. There is much evidence for partial self-compensation in Li^+ doped NiO [4,40,41], and this is indicated in the diagram by the presence of the Fermi energy in the Li^+ acceptor band. The compensating donors appear to be oxygen vacancies [19]. At low temperatures, when the free hole concentration is small compared to the donor concentration N_D, $2p$ hole transport will contribute a term to the conductivity equal to [19]

$$\sigma = N_v e \mu_0 \frac{N_A - N_D}{N_D} e^{-(0.3eV/kT)} \tag{11}$$

where $N_v = 2(m^* kT/2\pi h^2)^{3/2}$, $\mu_0 = 0.3$ cm^2/V-sec, and m^* is the large polaron effective mass, which can be estimated as 6 free electron masses for the $2p$ band of NiO. It was assumed that optical phonon scattering dominates the mobility in this temperature range. The activation energy is affected by interactions between the Li impurities. At temperatures sufficiently high that the free hole concentration is large compared to N_D, the contribution of $2p$ hole conduction becomes

$$\sigma = N_v \tfrac{1}{2} N_A \tfrac{1}{2} e \mu_0 e^{-(0.13eV/kT)}. \tag{12}$$

It can be shown that the observed conductivity of Li^+ doped NiO is given by eq (11) from 200 to 500 K, and by eq (12) from 500 to 1000 K in well characterized samples [19]. We can conclude that conduction in Li^+ doped NiO is dominated by the transport of free holes in the $2p$ band above 200 K.

It might be expected that small-polaron hopping conduction will dominate at sufficiently low temperatures, because of the somewhat smaller energy necessary to create a free $3d^8$ hole than a free $2p$ hole. However, there is much evidence for the predominance of impurity conduction in the Li^+ acceptor band below 150 K [33,40,41]. Thus, it appears that small-polaron hopping is unobservable in NiO in dc measurements. Bound small-polaron hopping has been observed in ac conductivity experiments [42,43], and is in agreement with the calculation presented here [19].

4. Density-of-States of Amorphous Semiconductors

Mott [2,3] and Cohen et al. [15] have presented qualitative band models which have had great success in accounting for experimental data on covalent amorphous semiconductors, such as the chalcogenide glasses. At first, this appears to be surprising, since electron-electron interactions and electron-phonon interactions, which should be of the utmost importance in these systems, are completely neglected. An essential feature of the model of Cohen et al. [15] is a broad tailing of localized states up from the valence band and down from the conduction band into the energy gap. In

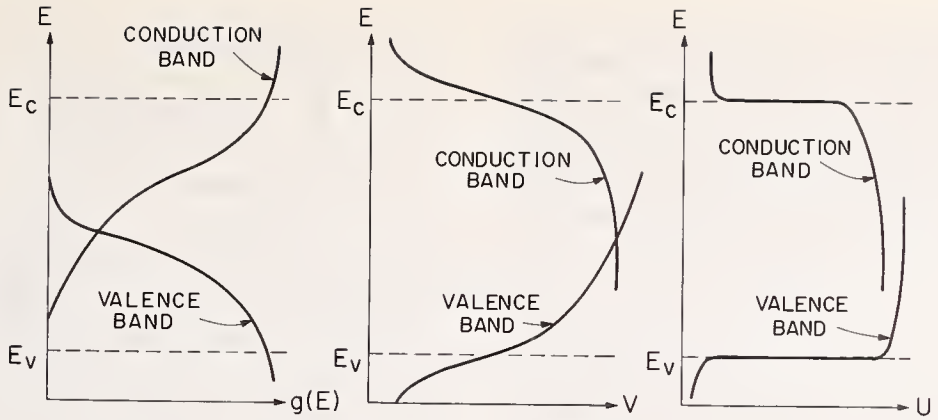

FIGURE 6. *Density of states, g(E), disorder potential, V, and intra-atomic Coulomb repulsion, U, as functions of energy for a covalent amorphous semiconductor.*

the chalcogenide glasses, it is assumed that the combination of positional and compositional disorder creates such a large density of these localized states that the valence and conduction band tails cross somewhere in the middle of the original gap. Thus there is no gap in the density-of-states of these materials. However, as discussed in the Introduction, a "mobility gap" exists between the itinerant states in the two bands.

Since this model is based on a one-electron approximation, electronic correlations are ignored completely. However, they can be introduced into the model in the same approximation used by Hubbard [5-7], and discussed in the Introduction. We consider only correlations between electrons located on the same atom, and introduce the intra-atomic Coulomb repulsion, U. Since it is known that the crystalline phases of most elemental and covalent amorphous semiconductors are wide-band materials, U is not expected to be an important quantity in the itinerant states. Let us consider the valence and conduction band densities-of-states shown in the left third of figure 6. As we move out in energy from the main part of each band into the tail, the associated disorder, V, defined in the Introduction, increases. This is shown in the center of figure 6. When V becomes sufficiently large that the Anderson condition, (2), is satisfied, all states further out in the tail become localized. At this point, the mobility edge, the effective difference in ionization potential and electron affinity U, suddenly becomes significant. Thus U must behave qualitatively as in the right third of figure 6. It is V and not U which is responsible for the localization, but once this Anderson transition takes place, U stabilizes this localization considerably. This is a reasonable explanation for the sharpness of the mobility drop at the edge.

If the valence and conduction band tails overlap, some states in the unoccupied conduction band have lower energy than states in the occupied valence band. It has consequently been suggested [15] that the material will reduce its ground state energy by undergoing a redistribution of electrons in these states, creating equal numbers of positively and negatively charged localized states deep in the gap. However, this suggestion fails to take into account the strong dependence of localized states on occupation numbers, due to the finite value of U. The redistribution of electrons can be represented by the process

$$X + Y \rightarrow X^+ + Y^-, \tag{13}$$

in which an electron is transferred from a state localized on atom Z to one on atom Y. If there is a large difference in the ionization potential of atom X and the electron affinity of atom Y, reaction (13) can be highly endothermic, even if the one-electron state corresponding to an electron on X is much higher than that corresponding to a hole on Y. The effective difference between the ionization potential of X and the electron affinity of Y is just equal to U. If the difference in one-electron energies were smaller than U, the redistribution would increase rather than decrease the total energy of the system, and thus would not occur spontaneously.

However, we have still ignored the electron-phonon interaction. Reaction (13) can be thought of as the creation of a localized electron-hole pair. The redistribution of electronic charge density which accompanies this process couples strongly to the longitudinal optical phonons, and can lead to lattice distortions in the vicinities of both atoms X and Y. Since the states under discussion are localized, the effective overlap integral is small, and we would expect small polarons to form.

If the binding energy of these small polarons is sufficiently large, reaction (13) could well be stabilized, despite a large U. Another possible stabilizing force could be the reduction in energy around X^+ and Y^- brought about by a Jahn-Teller distortion of the surroundings of the ions. The condition for the spontaneous occurrence of the redistribution is thus

$$\Delta > U - 2E_{JT} - 2E_{SP}. \tag{14}$$

where Δ is the difference in one-electron energies of X and Y^-. E_{JT} is the Jahn-Teller stabilization energy, E_{SP} is the small polaron binding energy, and U is the effective value of the difference between ionization potential and electron affinity, in which the effects of electronic screening are taken into account.

In elemental and simple compound amorphous semiconductors, such as Ge, Si, and As_2Se_3, there does not appear to be qualitative differences between the band structures of the amorphous materials and the corresponding crystalline materials, except for a smearing out of the bands brought about by the positional disorder [44]. For these materials, the right-hand side of (14) can be approximated from the experimentally known differences in the first and second ionization energies of multivalent donors in the corresponding crystal. This is a reasonable estimate because the same effects enter when a donor is doubly ionized as when a redistribution such as (13) takes place. The difference between ionization potential and electron affinity of the singly-ionized donor atom is analogous to U, and small-polaron formation (important only if the crystal is partially ionic) and Jahn-Teller distortions can stabilize the doubly-ionized donor in the same way that it can stabilize the redistribution, (13). For example, the difference in the first and second donor ionization energies of Au in Ge is 0.2 eV [45]. Using this as an estimate for $U - E_{JT} - E_{SP}$, we can conclude from (14) that a redistribution such as

$$Ge(1) + Ge(2) \rightarrow Ge^+(1) + Ge^-(2) \tag{15}$$

will take place spontaneously at $T=0$ only if the one-electron energy of the filled state localized on Ge(1) exceeds the one-electron energy of the empty state localized on Ge(2) by at least 0.2 eV. For a material such as amorphous Ge, in which only positional disorder is present, it is extremely doubtful that the valence and conduction band tails overlap by 0.2 eV. Thus, we should not expect any charged traps to be present at $T=0$ in an equilibrium. On the other hand, the positional and compositional disorder present in the chalcogenide glasses makes an overlap of this magnitude quite possible. Thus, the major features of the model

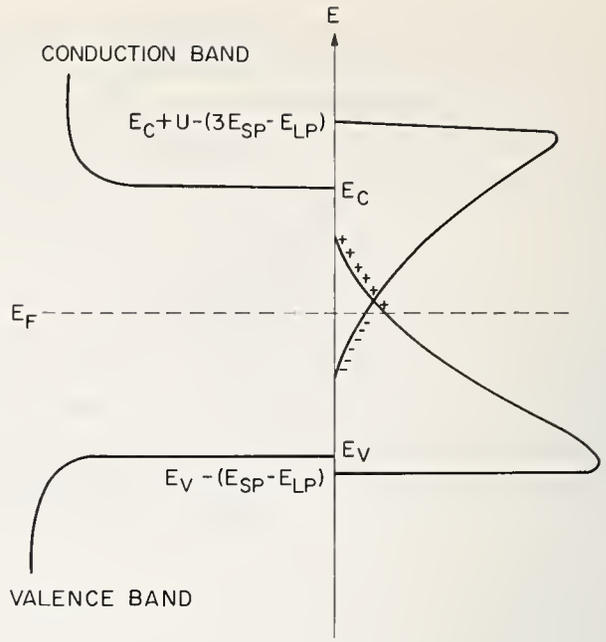

FIGURE 7. *Electrical density-of-states for a covalent amorphous semiconductor.*

Itinerant states are drawn to the left, localized states to the right. E_{SP} is the sum of the small polaron binding energy and the Jahn-Teller stabilization energy.

of Cohen et al. [15] are preserved when electronic correlations and electron-phonon interactions are included in this manner.

The question remains whether or not this modified model can be represented by an effective one-electron density-of-states diagram. This can be done, in much the same way as was discussed for the case of NiO in sections 2 and 3. Once again, the Franck-Condon principle forces us to draw separate diagrams for interpreting the optical properties and the electrical properties. Figure 7 shows a plot of the electrical density-of-states for a glass with positional and compositional disorder. As in figure 5, itinerant states are drawn to the left and localized states to the right. The possibility of large-polaron formation in the itinerant states is taken into account by a downward shift of these states relative to the Fermi energy. The small-polaron binding energies and Jahn-Teller stabilization energies result in downward displacements of the localized states. The finite value of the correlation energy, U, in the localized states must be represented by a relative separation of the localized parts of the valence and conduction bands.

5. Conclusions

We wish to emphasize the following conclusions: (1) When localized states are present and the electron-phonon interaction is important, the Franck-Condon principle forces us to use different density-of-states diagrams for interpreting electrical and optical properties;

(2) When localized states are present, the intra-atomic Coulomb repulsion, U, cannot be neglected. This makes it convenient to separate localized from itinerant states on a density-of-states plot; (3) In the case of ionic transition-metal or rare-earth compounds, doping with an ion of different valency or preparation of non-stoichiometric material leads to the formation of minority valence states of the transition metal or rare-earth ion. If these materials are Mott insulators, the vastly different ionization potentials of the majority and minority valence states can drastically change the relative positions of the energy bands. In particular, in NiO, creation of a significant density of Ni^{3+} ions, either by Li^{+} doping or introduction of excess oxygen, results in a large upward displacement of the oxygen $2p$ band relative to the localized levels. The $2p$ band moves sufficiently close to the Fermi energy so that $2p$ hole conduction dominates the dc conductivity from 200 to 1000 K; (4) The different relative positions of the bands in pure, stoichiometric crystals and in doped or non-stoichiometric material necessitates the use of at least *four* density-of-states diagrams, rather than the two indicated by the Franck-Condon principle; and (5) In amorphous semiconductors, electronic correlations and electron-phonon coupling lead to changes in the relative positions of the localized and itinerant parts of the valence and conduction bands. However, provided the overlap of the band tails is sufficiently large, the essential features of the model of Cohen et al. [15] for the chalcogenide glasses are preserved.

6. Acknowledgments

We should like to thank N. F. Mott, M. H. Cohen, and F. S. Ham for the valuable discussions.

7. References

[1] Wannier, G. H., Elements of Solid State Theory, (Cambridge U. Press, 1959) pp. 161-162.
[2] Mott, N. F., Proc. Phys. Soc. **A62**, 416 (1949).
[3] Mott, N. F., Phil. Mag. **6**, 287 (1961).
[4] See, for example, D. Adler, Solid State Phys. **21**, 1 (1968); F. J. Morin, Bell Syst. Tech. J. **37**, 1047 (1958).
[5] Hubbard, J., Proc. Roy. Soc. **A276**, 238 (1963).
[6] Hubbard, J., Proc. Roy. Soc. **A276**, 237 (1964).
[7] Hubbard, J., Proc. Roy. Soc. **A281**, 401 (1964).
[8] Adler, D., and Feinleib, J., J. Appl. Phys. **40**, 1486 (1969).
[9] Mott, N. F., Phil. Mag. **17**, 1259 (1968).
[10] Mott, N. F., Festkorperprobleme **9**, 22 (1969).
[11] Anderson, P. W., Phys. Rev. **109**, 1492 (1958).
[12] Ziman, J. M., J. Phys. C **2**, 1230 (1969).
[13] Edwards, S. F., J. Non-Cryst. Solids, to be published.
[14] Neustadter, H. E., and Coopersmith, M. H., Phys. Rev. Letters **23**, 585 (1969).
[15] Cohen, M. H., Fritzsche, H., and Ovshinsky, S. R., Phys. Rev. Letters **22**, 1065 (1969).
[16] MacMillan, A. J., Tech. Rept. No. 172, Lab. Insulation Res., M.I.T. 1962 (unpublished).
[17] McWhan, D. B., Rice, T. M., and Remeika, J. P., to be published.
[18] Fender, B. E. F., Jacobson, A. J., and Wedgewood, F. A., J. Chem. Phys. **48**, 990 (1968).
[19] Adler, D., and Feinleib, J., to be published.
[20] Reinen, D., Ber. Bunsenges. Physik. Chem. **69**, 82 (1965).
[21] Orgel, L. E., J. Chem. Phys. **23**, 1819 (1955).
[22] Kroger, F. A., J. Phys. Chem. Solids **29**, 1889 (1968).
[23] Watson, R. E., Phys. Rev. **118**, 1036 (1960).
[24] Low, W., Phys. Rev. **109**, 247 (1958).
[25] Powell, R. J., Stanford Electronics Laboratory Technical Report No. 5220-1, 1968 (unpublished).
[26] Austin, I. G., and Mott, N. F., Adv. Phys. **18**, 41 (1969).
[27] Switendick, A. C., Quart. Progr. Rept. No. 49, Solid State and Molecular Theory Group, M.I.T., 1963, p. 41 (unpublished).
[28] Wilson, T. M., Res. Note No. 1, Quant. Theoret. Res. Group, Oklahoma State U., 1969 (unpublished).
[29] Moore, C. E., Atomic Energy Levels, NBS Circular 467, **Vol. II** (1952).
[30] Newman, R., and Chrenko, R. M., Phys. Rev. **114**, 1507 (1958).
[31] Ksendzov, Ya. M., and Drabkin, I. A., Soviet Phys. Solid State **7**, 1519 (1965).
[32] Feinleib, J., and Adler, D., Phys. Rev. Letters **21**, 1010 (1968).
[33] Ksendzov, Ya. M., Avdeenko, B. K., and Makorov, V. V., Soviet Pbys. Solid State **9**, 828 (1967).
[34] Austin, I. G., Clay, B. D., Turner, C. E., and Springthorpe, A. J., Solid State Commun. **6**, 53 (1968).
[35] Austin, I. G., Clay, B. D., and Turner, C. E., J. Phys. C **1**, 1418 (1968).
[36] Holstein, T., Ann. Phys. (NY) **8**, 343 (1959).
[37] Holstein, T., Ann. Phys. (NY) **8**, 325 (1959).
[38] Allcock, G. R., Adv. Phys. **5**, 412 (1956).
[39] Pizzini, S., and Morlotti, R., J. Electrochem. Soc. **114**, 1179 (1967).
[40] Bosman, A. J., and Crevecoeur, C., Phys. Rev. **144**, 763 (1966).
[41] Austin, I. G., Springthorpe, A. J., Smith, B. A., and Turner, C. E., Proc. Phys. Soc. (London) **90**, 157 (1967).
[42] Snowden, D. P., and Saltzburg, H., Phys. Rev. Letters **14**, 497 (1965).
[43] Kabashima, S., Kawakubo, T., J. Phys. Soc. Japan **24**, 493 (1968).
[44] Stucke, J., Festkorperprobleme **9**, 46 (1969).
[45] Woodbury, H. H., and Tyler, W. W., Phys. Rev. **105**, 84 (1957).

Discussion on "Localized States in Narrow Band and Amorphous Semiconductors" by D. Adler and J. Feinleib (MIT)

H. P. R. Frederikse *(NBS):* You left out the anti-ferromagnetism of NiO. Is that not important? Switendick had to invoke the anti-ferromagnetism in order to obtain an insulator rather than a metal.

D. Adler *(MIT):* In our model, NiO is an insulator rather than a metal because of the intraionic Coulomb repulsion, independent of the anti-ferromagnetic ordering. Anti-ferromagnetism should modify the densities of states presented here by energies of the order of kT_N, or 0.04 eV for NiO. There is an optical absorption in the i.r., at 0.24 eV, apparently due to the magnetic ordering, which can be included on our optical density of states diagram above the $3d^8$ ground-state band. Since it refers to a localized excitation, it does not contribute to the electrical conductivity.

D. F. Barbe *(Westinghouse Aerospace Div.):* What would you expect to happen to the energy bands in say NiO as positional disorder is introduced?

D. Adler *(MIT):* Positional disorder always introduces a tailing of the itinerant energy bands, and an Anderson localization of some of the state in the tails. Consequently, in amorphous NiO, the $2p$ and $4s$ bands would tail into the energy gap, and some of these states would be localized. On the other hand, the $3d$ electrons are already localized because of correlation effects, and positional disorder is largely irrelevant. The crystalline-field and multiplet $3d$ levels are insensitive to positional disorder, since they are near the ionic limit. A slight broadening of these narrow $3d$ bands should take place, but since no significant mobility changes are induced by positional disorder, this broadening could not be expected to be observable experimentally. The major measurable effect should be the broadening of the optical $2p \rightarrow 4s$ absorptions.

A Cluster Theory of the Electronic Structure of Disordered Systems *

K. F. Freed and M. H. Cohen**

James Franck Institute, University of Chicago, Chicago, Illinois 60637

The equation of motion for the averaged Green's function in an alloy couples the latter to the Green's function for which the average is restricted so that the composition of one atom is held fixed. The average Green's function may be regarded as the Green's function for a zero-atom cluster, and it is coupled to the Green's function for a one-atom cluster. There is thus an infinite hierarchy of equations of motion in which the n-atom functions are coupled to the $(n+1)$-atom functions. The coherent potential approximation of Soven corresponds to truncation in the equation of motion of the one-atom function. We have generalized the coherent potential theory to a theory the n-atom functions with truncation in the equation of motion of the $(n+1)$-atom function. The formalism is developed and a few of the results obtained thus far are presented in this paper.

Key words: Amorphous semiconductors; band tail of localized states; cluster theory; coherent potential approximation; disorder systems; electronic structure; Neel temperature.

Apart from strongly ionic or molecular materials or from simple metals, our present knowledge of the electronic structures of condensed materials is rudimentary except for crystals. There, structural periodicity leads to the remarkable simplicity of the electronic wave functions expressed in the Bloch-Floquet theorem and to the existence of energy bands. Our present concern is with the corresponding universal features of the electronic structures of disordered materials. Soven and others [1] have developed the coherent potential approximation (CPA) into a quantitative tool for the study of the electronic structures of simple alloys. It yields, however, only bands of extended states with sharp edges and shows signs of inaccuracy at the band edges. In amorphous semiconductors, the band edges must play a central role in determining the electronic properties. Moreover, on both theoretical and empirical grounds it seems highly plausible that the electronic structure of disordered materials consists of bands of extended states with tails of localized states which may, in fact, overlap [2]. The character of the wave functions changes from extended to localized at an energy E_c near each band edge, where the carrier mobility drops abruptly. One of the central tasks of the electron theory of disordered materials is to substantiate or correct these models. Accordingly, we have addressed ourselves to improving the CPA to the point where it can conceivably contain such features as tails of localized states and mobility edges [3].

The localized states appear to be associated with fluctuations (in composition, local order, etc.), whereas the CPA averages over all such configurations. It is necessary to solve for the electronic structure before carrying out the averaging over the configurations important to the formation of localized states. The equation of motion for the one-electron Green's function is

$$(E - H_0 - V)\mathcal{G}(E) = 1, \tag{1}$$

where H_0 is a simple reference Hamiltonian, free-particle for a liquid or amorphous material, or crystal for an alloy, and V is a random potential. We suppose V can be decomposed into a sum of contributions from each site α, V_α, in a crystalline alloy or from each atom α in a liquid or amorphous material,

$$V = \sum_\alpha V_\alpha \tag{2}$$

The CPA concerns itself only with the average Green's function

$$G_0(E) = \langle \mathcal{G}(E) \rangle \tag{3}$$

where the brackets indicate an average over the random potential V. We examine here Green's functions in

*Supported by ARO(D), NASA, and ARPA.

**Alfred P. Sloan Foundation Fellow.

which the averaging is incomplete, a cluster of $\mathbf{n}$ of atoms being fixed either in composition and/or in position.

The potential V can be decomposed into a contribution from the cluster $V_{\mathbf{n}}$ and one from the remaining atoms $V_{N-\mathbf{n}}$,

$$V = V_{\mathbf{n}} + V_{N-\mathbf{n}}. \tag{4}$$

Let $\langle\ \rangle^{\mathbf{m}}$ imply an average only over the set of atoms $\mathbf{m}$ and $\langle\ \rangle_{\mathbf{l}}$ one over all atoms excluding the cluster $\mathbf{l}$ so that

$$\langle\rangle_{\mathbf{l}} = \langle\rangle^{N-\mathbf{l}} \tag{5}$$

The cluster Green's function is then defined as

$$G_{\mathbf{n}} = \langle\, \mathcal{G}\,\rangle_{\mathbf{n}} \equiv \langle\, \mathcal{G}\,\rangle^{N-\mathbf{n}} \tag{6}$$

$G_{\mathbf{0}}$ now appears as the lowest member of a hierarchy of cluster Green's functions. By averaging eq (1) we obtain the corresponding hierarchy of equations of motion.

$$(E - H_0 - V_{\mathbf{n}})\ G_{\mathbf{n}} - \sum_{\alpha \notin \mathbf{n}} \langle\, V_\alpha G_{\mathbf{n}\alpha}\,\rangle = 1. \tag{7}$$

Here $\mathbf{n}\alpha$ is that cluster $\mathbf{n}+\mathbf{1}$ composed of the cluster $\mathbf{n}$ and the atom α. It is convenient to rewrite (7) in terms of the proper self energy $\sigma_{\mathbf{n}}(E)$,

$$(E - H_0 - V_{\mathbf{n}} - \sigma_{\mathbf{n}})\ G_{\mathbf{n}} = 1, \tag{8}$$

and to define the T-matrix $T^{\alpha}_{\mathbf{n}}$ for the scattering of an electron by the specified atom α in the presence of a specified cluster $\mathbf{n}$ by

$$G_{\mathbf{n}\alpha} = G_{\mathbf{n}} + G_{\mathbf{n}} T^{\alpha}_{\mathbf{n}} G_{\mathbf{n}}. \tag{9}$$

From (7), (8), and (9) it follows that

$$\sigma_{\mathbf{n}} = \sum_{\alpha \notin \mathbf{n}} \sigma^{(\alpha)}_{\mathbf{n}}, \tag{10}$$

$$\sigma^{(\alpha)}_{\mathbf{n}} = \langle\, V_\alpha + V_\alpha G_n T^{\alpha}_{n}\,\rangle^{\alpha}, \tag{11}$$

$$T^{\alpha}_{\mathbf{n}} = U^{\alpha}_{\mathbf{n}}\,[1 - G_{\mathbf{n}} U^{\alpha}_{\mathbf{n}}]^{-1}, \tag{12}$$

$$U^{\alpha}_{\mathbf{n}} = V_\alpha + \sigma_{\mathbf{n}\alpha} - \sigma_{\mathbf{n}}. \tag{13}$$

Truncation of the hierarchy can be affected by a relationship between $\sigma_{\mathbf{n}\alpha}$ and $\sigma_{\mathbf{n}}$, leading to $T^{\alpha}_{\mathbf{n}}$ being a functional of $\sigma_{\mathbf{n}}$ via (12) and (13) and hence to closure via (10) and (11). Equivalently, we may observe that

$$G_{\mathbf{n}} \equiv \langle\, G_{\mathbf{n}\alpha}\,\rangle^{\alpha} \tag{14}$$

which, from (9), requires that

$$\langle\, T^{\alpha}_{\mathbf{n}}\,\rangle^{\alpha} = 0, \text{ all } \mathbf{n} \text{ and } \alpha \not\in \mathbf{n}. \tag{15}$$

The coherent potential approximation follows from (15) for $\mathbf{n}=0$ together with the truncation condition

$$\sigma^{(\beta)}_{\alpha} = \sigma^{(\beta)}_{\mathbf{0}}, \text{ all } \beta \neq \alpha, \tag{16}$$

i.e., $\sigma_{\mathbf{n}}$ for $\mathbf{n}=1$ is related to $\sigma_{\mathbf{n}}$ for $\mathbf{n}=0$. We can immediately generalize the CPA so that the truncation occurs for an n*th* instead of for a zero order cluster,

$$\sigma^{(\beta)}_{\mathbf{n}\alpha} = \sigma^{(\beta)}_{\mathbf{n}}, \text{ all } \beta \not\in \mathbf{n}\alpha, \tag{17}$$

and consequently

$$U^{\alpha} = V_\alpha - \sigma^{(\alpha)}_{\mathbf{n}}. \tag{18}$$

Inserting (18) into (12) and (12) into (15) gives us an equation which can be solved selfconsistently together with (8) for $\sigma_{\mathbf{n}}$ and $G_{\mathbf{n}}$

The CP$\mathbf{n}$ approximation has a number of important properties, among which are:

(1) Consistency for clusters of lower order.

$$\langle\, T^{\alpha}_{\mathbf{m}}\,\rangle = 0,\ 0 \leq m \leq n, \text{ all } \mathbf{m} \not\in \mathbf{n}. \tag{19}$$

(2) Locality of $\sigma^{(\alpha)}_{\mathbf{n}}$ and $T^{\alpha}_{\mathbf{n}}$.

If V_α is local in the sense that it is site diagonal,

$$\langle \beta | V_\alpha | \gamma \rangle = V_\alpha \delta_{\beta\alpha} \delta_{\alpha\gamma}, \tag{20}$$

then so are $\sigma^{(\alpha)}_{\mathbf{n}}$ and $T^{\alpha}_{\mathbf{n}}$.

(3) Asymptotic limits of $G_{\mathbf{m}}$ and $\sigma^{(\alpha)}_{\mathbf{m}}$.

If we assume that all of the eigenstates of $H_0 + V$ are either extended with a short phase coherence length or localized, as in the simple models, then $G_{\mathbf{m}}$, $(m \leq n+1)$ must have a finite range R in the sense that

$$\langle\, \alpha | G_{\mathbf{m}} | \beta\,\rangle \to 0,\ |\mathbf{r}_\alpha - \mathbf{r}_\beta| > R. \tag{21}$$

This implies that

$$\langle\, \gamma | G_{\mathbf{m}} | \delta\,\rangle \to \langle\, \gamma | G_{\mathbf{o}} | \delta\,\rangle \tag{22}$$

for $|r_\gamma - r_\beta| \rangle R$ or $|r_\delta - r_\beta| \rangle R$, where $\beta \epsilon \mathbf{m}$. Similarly, we have

$$\langle\, \beta | G_{\mathbf{n}\alpha} | \gamma\,\rangle \to \langle\, \beta | G_\alpha | \gamma\,\rangle \tag{23}$$

$$|r_{\beta,\gamma} - r_\delta| \rangle R,\ \delta \epsilon \mathbf{n},$$

and

$$\sigma^{(\alpha)}_{\mathbf{n}} \to \sigma^{(\alpha)}_{A} \text{ independent of } (\alpha) \tag{24}$$

$$|r_\alpha - r_\delta| \rangle R, \qquad \delta \epsilon \mathbf{n}.$$

(4) Bound states occur in $G_{\mathbf{n}}$ provided $\sigma_{\mathbf{n}}(E)$ is real outside a finite arc of the real E axis and the statistical fluctuations in V_α are large enough.

(5) For sufficiently disordered systems, convergence in G_0 obtained by averaging down from successively higher $G_{\mathbf{n}}$ may occur at values of $\mathbf{n}$ which are tractable for numerical calculations. Even for G obtained by averaging down G_1 derived from the CP**1** approximation, the proper self energy is nonlocal and in that sense a significant improvement over the CPA.

(6) Our final approximation to $\langle \mathscr{G} \rangle$ would then be obtained by averaging down a $G_{\mathbf{n}}$ from the CP$\mathbf{n}$ is

$$\bar{G} = \sum_{\mathbf{n}} P_{\mathbf{n}} G_{\mathbf{n}} \tag{25}$$

where the sum on $\mathbf{n}$ is over all possible clusters $\mathbf{n}$, each having the probability of occurrence $P_{\mathbf{n}}$.

References

[1] Soven, P., Phys. Rev. **156**, 809 (1967); Velický, B., Kirkpatrick, S., and Ehrenreich, H., Phys. Rev. **175**, 747 (1968); Soven, P., Phys. Rev. **178**, 1136 (1969); Velický, B., Phys. Rev. (to be published).

[2] Mott, N. F., Adv. Phys. **16**, 49 (1967); Cohen, M. H., Fritzsche, H., and Ovshinsky, S. R., Phys. Rev. Letters **22**, 1065 (1969).

[3] Cohen, M. H., J. Non Cryst. Solids (to appear).

Discussion on "A Cluster Theory of the Electronic Structure of Disordered Systems" by K. F. Freed and M. H. Cohen (University of Chicago)

J. L. Beeby *(Atomic Energy Res. Establishment):* Can it be proved that the density of states sum rule is satisfied in your proeedure?

M. H. Cohen *(Univ. of Chicago):* It is satisfied automatically at each stage in the approximation.

R. M. More *(Univ. of Pittsburgh):* If V is not site diagonal, can $\langle T_{K,K'} \rangle = 0$ be satisfied even off-shell?

M. H. Cohen *(Univ. of Chicago):* You just have an additional series of equations to take care of the additional set of variables in the proper self energy. It is possible in principle. One can say the following: if one does not have a site diagonal potential but a potential of finite range, then the T-matrix will have a range which is some compromise between the range of the potential and the range of the Green's function itself. It is influenced by both. So the T-matrix itself has finite range and all the asymptotic theorems still go through. The overall structure remains the same; the difficulty then is in satisfying the condition of the average T-matrix which must be 0. You have both the diagonal elements of that equation then the off-diagonal elements of that equation and this gives you an additional set of conditions which are satisfied by varying instead of just the *diagonal* elements of the proper self energy now varying the *off-diagonal* elements as well.

T Matrix Theory of Density of States in Disordered Alloys—Application to Beta Brass

M. M. Pant and S. K. Joshi

Physics Department, University of Roorkee, Roorkee, India

The T matrix theory of electronic states in disordered systems, has been used to determine the spectral density for states of various symmetries, for binary alloys. Soven's averaged t matrix procedure is improved by retaining the distinction between the t matrices of the constituents, and introducing partial Greenians of the Pant-Joshi theory. Information about the pair-correlation function obtained by critical neutron scattering method is used to evaluate the partial Greenians, as well as the crystalline potentials for the constituents. In order to facilitate computation of the t matrices, these potentials have been replaced by energy-dependent model potentials. The parameters of the model potentials are determined by the requirement that they yield logarithmic derivatives (of the radial wave function at the muffin-tin spheres) identical with those generated by the real potentials. The scheme has been applied to disordered beta-brass. The separation in energy of the peaks of the spectral density of states at the high symmetry points of the Brillouin zone, are compared with experimental results, and with the results obtained by the virtual crystal approximation.

Key words: Alloys; brass; delta-function potential; disordered systems; Green's functions; Korringa-Kohn Rostoker (KKR); "muffin-tin" potential; short-range-order parameters; spectral density of states; t-matrices.

1. Introduction

The object of this paper is to outline a t matrix approach to determine the spectral density for states $\rho(E,\mathbf{k})$ in disordered alloys, and apply it to the disordered substitutional binary alloy β-brass. For the case of a perfect lattice, $\rho(E,\mathbf{k})$ plotted against E, has δ-function peaks at the band energies. The presence of disorder results in the broadening of these peaks and their widths give an indication of the departure of the alloy wave function from Bloch-like character. An investigation which bears on this aspect is that of Soven [1], who determined the spectral density for some states in α-brass, by employing the averaged t matrix approximation. This approximation consists in placing at every site of the alloy lattice, a scatterer whose t matrix is the average of the t matrices of the constituents. The averaged t matrix method yields spurious band gaps in the case of one-dimensional alloys [2]. The approach presented in this paper retains the distinction between the constituents of the alloy. The method relies heavily on the work of Beeby [3], and the calculation utilizes the model δ-function potentials of Soven [1] and the incomplete Green's functions of Pant and Joshi [4]. Any short-range order present in the alloy is accounted for, by the occurrence of the short-range-order parameters in the expressions for the potentials as well as the incomplete Green's functions. There are two basic approximations in the theory. The first is the approximation of the actual potential around a lattice site, by a potential of the muffin-tin form. The other is the geometric approximation introduced by Beeby [3] to enable a summation of the infinite series expressing the T matrix of the system in terms of the t matrices for the individual scatterers. For an ordered alloy, this approximation gives the exact result.

The method has been applied to the disordered β-brass to determine the spectral density for states of various symmetries. The results of the experimental measurements of the short-range-order diffuse scattering are available for this alloy [5]. The band structures of the constituents are well understood and an attempt at studying the electronic structure of β-brass has been made within the framework of the virtual crystal approximation [6]. These considerations prompted us to study the spectral density of states for disordered β-brass at a few symmetry points.

2. Formalism

The spectral density of states for noninteracting electrons in the presence of a system of potentials U_α is given by

$$\rho(E, \mathbf{k}) = -\frac{1}{(E-k^2)^2 \pi\Omega} \operatorname{Im} \langle \int T(\mathbf{x}, \mathbf{x}') \exp[-i\mathbf{k}\cdot(\mathbf{x}-\mathbf{x}')] d\mathbf{x} d\mathbf{x}' \rangle,$$

which we write as

$$\rho(E, \mathbf{k}) = -\frac{1}{(E-k^2)^2 \pi\Omega} \operatorname{Im} \langle T(\mathbf{k}) \rangle. \tag{1}$$

In these expressions, Ω is the volume of the assembly, the angular brackets denote an average over the disordered system of potentials and Im indicates the imaginary part of the expression that follows it. The T function for the assembly is given by the series

$$T = \sum_\alpha t_\alpha + \sum_{\alpha\neq\beta} t_\alpha \mathcal{G}_0 t_\beta + \sum_{\substack{\alpha\neq\beta \\ \beta\neq\gamma}} t_\alpha \mathcal{G}_0 t_\beta \mathcal{G}_0 t_\gamma + \ldots \tag{2}$$

where t_α is the t function corresponding to the potential U_α at the αth site and is defined by

$$t_\alpha(\mathbf{x}, \mathbf{y}) = U_\alpha(\mathbf{x})\delta(\mathbf{x}-\mathbf{y}) + \int U_\alpha(\mathbf{x}) \mathcal{G}_0(\mathbf{x}-\mathbf{z}) t_\alpha(\mathbf{z}, \mathbf{y}) d\mathbf{z}.$$

$\mathcal{G}_0(\mathbf{x}-\mathbf{z})$ is the free particle propagator. In order to obtain a matrix representation, we make angular momentum expansions of the t functions. It is convenient to use the real spherical harmonics $Y_L(\hat{\mathbf{x}})$ of the angles of $\hat{\mathbf{x}}$, where L is a compound subscript denoting both l and m, so that

$$t(\mathbf{x}, \mathbf{y}) = \sum_L t_l(x, y) Y_L(\hat{\mathbf{x}}) Y_L(\hat{\mathbf{y}}). \tag{3}$$

In the case of a disordered binary alloy, any site may be occupied by either of the two types of atoms. We use the superscripts 1 and 2 to denote the two types of atoms. The T matrix series may then be split into four parts, such that

$$T = \sum_{\substack{s=1,2 \\ s'=1,2}} T^{ss'}. \tag{4}$$

We have

$$\begin{aligned}
T^{11} &= \sum_\alpha t_\alpha^1 + \sum_{\alpha\neq\beta} t_\alpha^1 \mathcal{G}_0 t_\beta^1 + \sum_{\substack{\alpha\neq\beta \\ \beta\neq\gamma}} t_\alpha^1 \mathcal{G}_0 t_\beta \mathcal{G}_0 t_\gamma^1 + \ldots \\
T^{12} &= \sum_{\alpha\neq\beta} t_\alpha^1 \mathcal{G}_0 t_\beta^2 + \sum_{\substack{\alpha\neq\beta \\ \beta\neq\gamma}} t_\alpha^1 \mathcal{G}_0 t_\beta \mathcal{G}_0 t_\gamma^2 + \ldots \\
T^{21} &= \sum_{\alpha\neq\beta} t_\alpha^2 \mathcal{G}_0 t_\beta^1 + \sum_{\substack{\alpha\neq\beta \\ \beta\neq\gamma}} t_\alpha^2 \mathcal{G}_0 t_\beta \mathcal{G}_0 t_\gamma^1 + \ldots \\
T^{22} &= \sum_\alpha t_\alpha^2 + \sum_{\alpha\neq\beta} t_\alpha^2 \mathcal{G}_0 t_\beta^2 + \sum_{\substack{\alpha\neq\beta \\ \beta\neq\gamma}} t_\alpha^2 \mathcal{G}_0 t_\beta \mathcal{G}_0 t_\gamma^2 + \ldots
\end{aligned} \tag{5}$$

Here t_α^s is the t function corresponding to the potential U^s at α. $T^{ss'}$ corresponds to that part of the total T function in which the electron scatters firstly off an atom of the sth type and lastly off one of the s'th type. The intermediate scatterers may be of either type and are represented by t's without any superscript in the above series.

The Fourier transformation $T(\mathbf{k})$ implied in eq (1) may now be carried out separately for each term of the series (5). The first term of T^{11} or T^{22} gives

$$\int \exp[-i\mathbf{k}\cdot(\mathbf{x}-\mathbf{y})] \sum_\alpha t_\alpha^s(\mathbf{x}, \mathbf{y}) d\mathbf{x} d\mathbf{y} = (4\pi)^2 N_s \sum_L \int j_l(kx) j_l(ky) t_l^s(x, y) x^2 dx\, y^2 dy\, Y_L(\hat{\mathbf{k}}) Y_L(\hat{\mathbf{k}}), \tag{6}$$

where N_s is the number of potentials of the type s. The calculation of a general term involves angular integrations of the type

$$(S_{\alpha\beta}^{ss'})_{LL'} = i^{l'-l} \int Y_L(\hat{\mathbf{y}}) \mathcal{G}_0(\mathbf{y}-\mathbf{z}+\mathbf{R}_\alpha-\mathbf{R}_\beta) \exp[-i\mathbf{k}\cdot(\mathbf{R}_\alpha-\mathbf{R}_\beta)] Y_{L'}(\hat{\mathbf{z}}) d\Omega_y d\Omega_z, \tag{7}$$

besides the radial integrals involved in t_l and a summation over L. R_α, R_β, etc. denote the positions of the α, β, and other sites. A typical term in series of eq (5) therefore contains products of the form

$$\left[\sum_{\beta\neq\alpha} S_{\alpha\beta}^{ss'} \sum_{\gamma\neq\beta} S_{\beta\gamma}^{s's''} \ldots \sum_{\omega\neq\psi} S_{\psi\omega}^{s'''s''''} \ldots \right]_{LL'},$$

where the superscripts on S take the values 1 and 2 depending on the type of atoms at locations specified by the subscripts. The problem is to sum an infinite series with terms of this nature, and then to average such sums over all configurations. The simplest way to manipulate this is to replace $S_\psi^{ss'} = \sum_{\omega\neq\psi} S_{\psi\omega}^{ss'}$ by some $S^{ss'}$

which does not depend on ψ. This is the "geometric approximation" and may be seen to be exactly true for a perfectly ordered alloy. We then have

$$[S^{ss'}]_{LL'}=\frac{1}{N_{s'}}\sum_{\beta\neq\alpha}[S^{ss'}_{\alpha\beta}]_{LL'}=\frac{1}{N_s}\sum_{\beta\neq\alpha}\int i^{l'-l}Y_l(\hat{\mathbf{y}})\mathscr{G}_0(\mathbf{y}-\mathbf{z}+\mathbf{R}_\alpha-\mathbf{R}_\beta)\exp[-i\mathbf{k}\cdot(\mathbf{R}_\alpha-\mathbf{R}_\beta)]Y_{l'}(\hat{\mathbf{z}})d\mathbf{\Omega}_y d\mathbf{\Omega}_z. \tag{8}$$

We can now identify $\sum_{\beta\neq\alpha}\mathscr{G}_0(\mathbf{y}-\mathbf{z}+\mathbf{R}_\alpha-\mathbf{R}_\beta)\exp[-i\mathbf{k}\cdot(\mathbf{R}_\alpha-\mathbf{R}_\beta)]$ as the incomplete Green's function of reference 4, with the $\alpha=\beta$ term omitted. This may therefore be expanded in terms of the spherical Bessel functions j_l as done in eq (16) of reference 4.

$$\sum_{\beta\neq\alpha}\mathscr{G}_0(\mathbf{y}-\mathbf{z}+\mathbf{R}_\alpha-\mathbf{R}_\beta)\exp[-i\mathbf{k}\cdot(\mathbf{R}_\alpha-\mathbf{R}_\beta)]=\sum_{LL'}i^{l'-l}G^{ss'}_{LL'}j_l(\kappa y)j_{l'}(\kappa z)Y_L(\hat{\mathbf{y}})Y_{L'}(\hat{\mathbf{z}}).$$

Therefore,

$$[S^{ss}_{ll'}]_{LL'}=G^{ss'}_{LL'}j_l(\kappa y)j_{l'}(\kappa z), \tag{9}$$

where $\kappa=\sqrt{E}$ if $E>0$ and $i\sqrt{-E}$ if $E<0$, and $G^{ss'}_{LL'}$ are related to the $B^{ss'}_{LL'}$ of reference 4. The $G^{ss'}_{LL'}$ are independent of y and z and will be collectively denoted by $G^{ss'}$. The radial y and z integrals now involve only Bessel functions and the radial t_l functions. Their most general form is

$$t^s_l(p,q)=\int j_l(px)t^s_l(x,y)j_l(qy)x^2dx\,y^2dy, \tag{10}$$

with p and q taking values of k or κ. We use τ^s to denote $t^s_l(\kappa,\kappa)$. In this notation, we have for the series of eq (5)

$$T^{11}=(4\pi)^2N_1\sum_{LL'}Y_L(\hat{\mathbf{k}})Y_{L'}(\hat{\mathbf{k}})\Big\{t^1_l(k,k)\delta_{LL'}+\Big[t^1(k,\kappa)\Big\{G^{11}+\sum_{s=1,2}G^{1s}\tau^sG^{s1}+\sum_{\substack{s=1,2\\s'=1,2}}G^{1s}\tau^sG^{ss'}\tau^{s'}G^{s'1}+\dots\Big\}t^1(\kappa,k)\Big]_{ll'}\Big\},$$

$$T^{12}=(4\pi)^2N_1\sum_{LL'}Y_L(\hat{\mathbf{k}})Y_{L'}(\hat{\mathbf{k}})\Big[t^1(k,\kappa)\Big\{G^{12}+\sum_{s=1,2}G^{1s}\tau^sG^{s2}+\sum_{\substack{s=1,2\\s'=1,2}}G^{1s}\tau^sG^{ss'}\tau^{s'}G^{s'2}+\dots\Big\}t^2(\kappa,k)\Big]_{ll'} \tag{11}$$

with similar expressions for T^{21} and T^{22}. On performing the summations, we arrive at

$$T^{11}=(4\pi)^2N_1\sum_{LL'}Y_L(\hat{\mathbf{k}})Y_{L'}(\hat{\mathbf{k}})\{t^1_l(k,k)\delta_{LL'}+\Big[t^1(k,\kappa)M_1^{-1}\times\{G^{21}+(1-G^{22}\tau^2)(G^{12}\tau^2)^{-1}G^{11}\}t^1(\kappa,k)\Big]_{ll'}\},$$

$$T^{12}=(4\pi)^2N_1\sum_{LL'}Y_L(\hat{\mathbf{k}})Y_{L'}(\hat{\mathbf{k}})\Big[t^1(k,\kappa)M_1^{-1}\{G^{22}+(1-G^{22}\tau^2)(G^{12}\tau^2)^{-1}G^{12}\}t^2(\kappa,k)\Big]_{ll'}. \tag{12}$$

T^{22} and T^{21} are obtained by interchanging the superscripts 1 and 2 in the above expressions. M_1 and M_2 are defined by the following expressions

$$M_1=(1-G^{22}\tau^2)(G^{12}\tau^2)^{-1}(1-G^{11}\tau^1)-G^{21}\tau^1.$$
$$M_2=(1-G^{11}\tau^1)(G^{21}\tau^1)^{-1}(1-G^{22}\tau^2)-G^{12}\tau^2. \tag{13}$$

The above set of eqs (10), (12), and (13) enable us to determine the spectral density of states. The only problems we face at this stage are the calculations of the matrix elements of $G^{ss'}$ and of the evaluation of the t matrices. It is clear that the calculations of $G^{ss'}$ require a detailed knowledge regarding the relative

positions of the atoms. In the case of a disordered alloy, the short-range-order parameters may be used to estimate an average distribution pattern of the constituents, thus enabling us to calculate the $G^{ss'}$. A complete discussion of the use of the short-range-order parameters to determine the matrix elements of $G^{ss'}$ has been given in reference 4. The approximation introduced in order to calculate these, is that the short-range-order extends only up to a certain neighborhood, beyond which the occupation probabilities are those of a randomly occupied lattice. If σ is the *order of significant neighborhood* we have for the matrix elements of $G^{ss'}$

$$G^{ss'}_{LL'} = 4\pi \sum_{L''} D^{ss'}_{L''} C_{LL'L''}. \tag{14}$$

Here $C_{LL'L''}$ are related to the Clebsch-Gordon coefficients and

$$D^{ss'}_{L} = m_{s'} D_L + \frac{i\kappa}{\sqrt{4\pi}} m_{s'} \delta_{LL'} + \kappa i^{-l} \sum_{\gamma<\sigma}{}' \exp(i\mathbf{k}\cdot\mathbf{R}_\gamma) \times [n_l(\kappa R\gamma) - i j_l(\kappa R\gamma)] Y_L(\hat{\mathbf{R}}\gamma) [P^{ss'}(\mathbf{R}\gamma) - m_{s'}]. \tag{15}$$

In this expression, $m_{s'}$ is the atomic concentration of atoms of s'th type and the D_L without superscripts are the familiar structure constants of the ordered crystal which occur in the Kohn-Rostoker method. n_l is the spherical Neumann function. $P^{ss'}(\mathbf{R}_\gamma)$ denotes the probability of finding an atom of the s'th type at a position $\mathbf{R}_\gamma$ with respect to an atom of the sth type. This probability can be expressed in terms of the short-range-order parameters as discussed in reference 4. The summation in eq (15) runs through a neighborhood in the direct space, and the prime on the summation indicates that the term with $\gamma = 0$ is to be omitted. The $\delta_{LL'}$ term is introduced to compensate for the fact that the calculation of D_L for the perfect lattice does not exclude this term. The matrix elements of $G^{ss'}$ are then directly obtained from eqs (14) and (15). We discuss the calculation of the t matrix in the following section.

3. Potentials and Evaluation of the t Matrix

The type of crystal potential which has been found to be most successful in describing the band structures of noble and transition metals is obtained from a superposition of atomic potentials on neighboring sites [7]. This is the Mattheiss prescription [8]. It seems reasonable therefore to construct the muffin-tin potentials for the constituents of the alloy, along the lines of the Mattheiss prescription. The difference from the procedure for pure metals is that the overlap contribution from the γth neighboring Cu (or Zn) atom has to be multiplied by the probability of its occurrence. This probability may be determined from a knowledge of the short-range-order parameters [9].

In order to facilitate the calculation of the t matrix, Soven [1] suggested the replacement of the muffin-tin potentials by δ-function potentials of the form

$$V^s(\mathbf{x}, \mathbf{x}') = \sum_L Y_L(\hat{\mathbf{x}}) \frac{\delta(x - r_{mt})}{r^2_{mt}} v^s_l(E) \frac{\delta(x' - r_{mt})}{r^2_{mt}} Y_L(\hat{\mathbf{x}}'), \tag{16}$$

where r_{mt} is the radius of the muffin-tin-sphere and $v^s_l(E)$ are energy-dependent potential amplitudes. The $v^s_l(E)$ are chosen to yield the same logarithmic derivative of the radial wave function as generated by the actual potential. We then have

$$v^s_l(E) = r^2_{mt}[\gamma^s_l(E) - \kappa j'_l(\kappa r_{mt})/j_l(\kappa r_{mt})], \tag{17}$$

where j'_l is the derivative of Bessel function and $\gamma^s_l(E)$ is the logarithmic derivative of the radial wave function (for angular momentum l and energy E) at the sphere radius r_{mt}. With this form of the potential, the angular momentum components of the t matrix can then be written as

$$t_l(x, x') = t_l \frac{\delta(x - r_{mt})}{r^2_{mt}} \frac{\delta(x' - r_{mt})}{r^2_{mt}}, \tag{18}$$

so that

$$t_l = v_l[1 - v_l g_l]^{-1}, \tag{19}$$

where $g_l = G_l(r_{mt}, r_{mt})$ is the lth component in the angular momentum representation of $G(x - x)$. We then arrive at the following simple expression for the matrix elements in eq (10) of t

$$t_l(p, q) = t_l j_l(pr_{mt}) j_l(qr_{mt}). \tag{20}$$

The eqs (17-20) completely define $T^{ss'}(\mathbf{k})$ in terms of $G^{ss'}$ and the logarithmic derivatives of the radial functions at the muffin-tin radius. The spectral density of states is then obtained from

$$\rho(E, \mathbf{k}) = -\frac{1}{(E - k^2)^2 \pi \Omega} \operatorname{Im} \sum_{\substack{s=1,2 \\ s'=1,2}} T^{ss'}(\mathbf{k}). \tag{21}$$

Soven [1] has shown that the use of energy-dependent model potentials necessitates the use of the correction factor $\left|1 - \sum_{s=1,2} m_s \frac{dv^s_l(E)}{dE}\right|$ with eq (12). Our calcula-

tions showed no significant difference in the peak positions due to this term. However, all the results presented or discussed in the following are for $\rho(E, \mathbf{k})$ calculated with the correction term included in eq (12).

4. Application to β-Brass

Walker and Keating [5] found that it was not possible to assign unique values to the short-range-order parameters in β-brass, because of the long-range nature of the short-range order. But the short-range-order parameters could be fitted to a Zernike type expression $|\alpha(r)| = 0.540 \exp(-0.400r')/r'$, where $r' = 2r/a$ and a is the lattice constant. We have used this expression to calculate the short-range-order parameters employed in the calculation of the muffin-tin potentials and $G^{ss'}$. Although the disordered β-phase is found for a range of zinc concentrations in the vicinity of 50-50 stoichiometry, we have chosen the concentrations of the Cu and Zn atoms to be equal. The relevant parameters regarding the calculation are shown in table 1.

TABLE 1. *Parameters for β-brass calculation*

Lattice parameter, a	= 5.6521 a.u.
Radius of inscribed sphere	= 2.4472 a.u.
Radius of muffin-tin sphere for both copper and zinc, r_{mt}	= 2.4148 a.u.
Constant part of muffin-tin potential U_c	= −0.9152 Ry,
Order of significant neighborhood, σ	= 10

We have carried out numerical calculations for the points Γ, H, P and N to determine what Soven calls the reduced spectral density

$$\tilde{\rho}(E, \mathbf{k}) = \sum_{\mathbf{K}} \rho(E, \mathbf{k} + \mathbf{K}),$$

Where $\mathbf{K}$ is a reciprocal-lattice vector and $\mathbf{k}$ is confined to the first Brillouin zone. The curves for the reduced spectral density $\tilde{\rho}(E, \mathbf{k})$ plotted against E for some of the states are displayed in figures 1 to 3 and the peak positions in $\tilde{\rho}(E, \mathbf{k})$ for all states at the symmetry points Γ, H, P and N are tabulated in table 2.

5. Discussion

In this section we compare our results with experimental data for β-brass. In the case of disordered alloys, electronic states are probed rather indirectly, through analysis of the optical measurements, positron annihilation and short-range-order diffuse scattering. Moss [10] has conjectured that nonspherical pieces of the Fermi surface may give rise to a detectable singu-

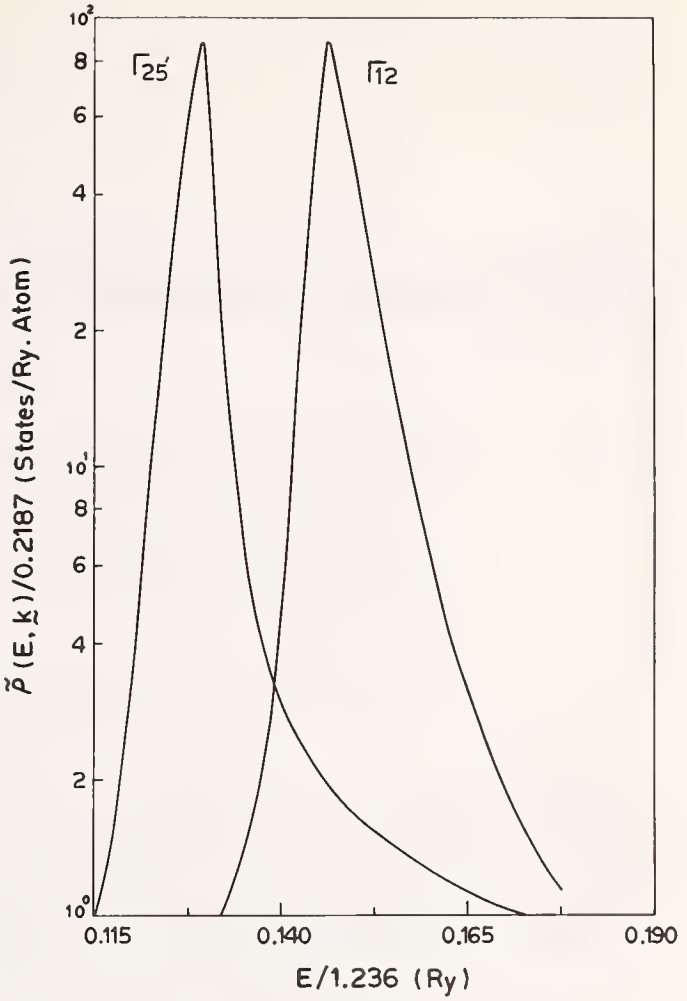

FIGURE 1. *The spectral density of states for* Γ'_{25} and Γ_{12} (d-*like*) *states in β-brass, plotted as a function of energy.*

TABLE 2. *Positions of peaks in* $\tilde{\rho}(E, \mathbf{k})$ *versus* E *curves for states of various symmetries in β-brass. All energies are in Ry and relative to the muffin-tin zero,* $U_c = -0.9152$ *Ry.*

State	Energy	State	Energy
Γ_1	0.018	P_4	0.158
$\Gamma_{25'}$	.160	P_3	.162
Γ_{12}	.180	P_4	.896
H_{12}	.124	P_1	.985
$H_{25'}$	.198	N_1	.120
H_{15}	1.051	N_2	.141
H_{12}	1.333	N_1	.165
H_1	1.693	N_4	.183
E_F(Cohen-Heine method)	0.511	N_3	.204
		$N_{1'}$	.404
		N_1	.571

417-156 O - 71 - 34

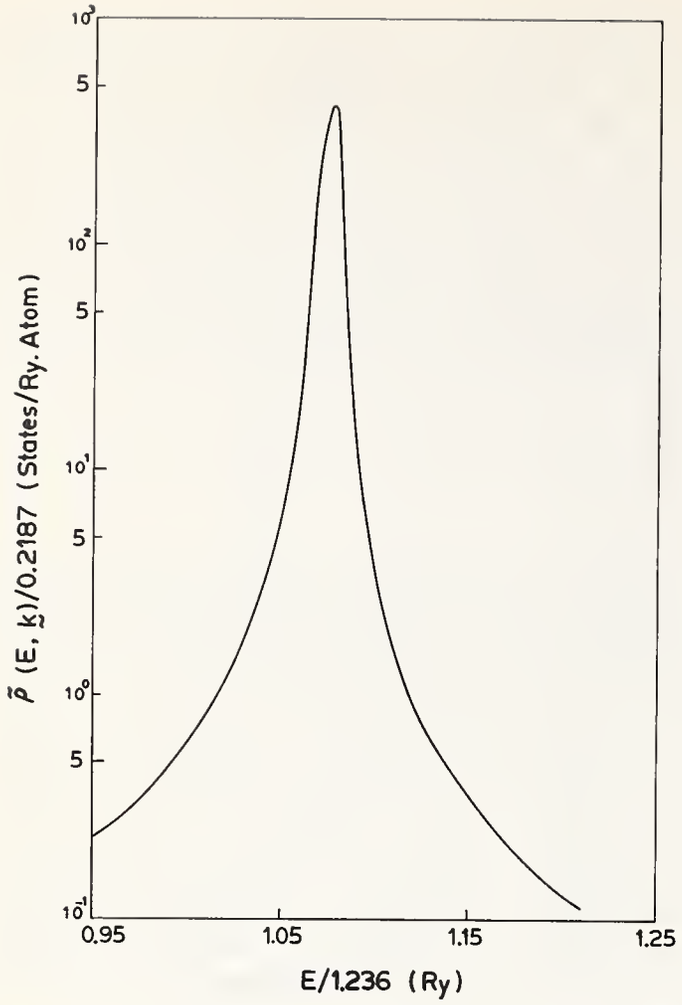

FIGURE 2. *The spectral density of states for* H_{12} (d-*like*) state in β-*brass, plotted as a function of energy.*

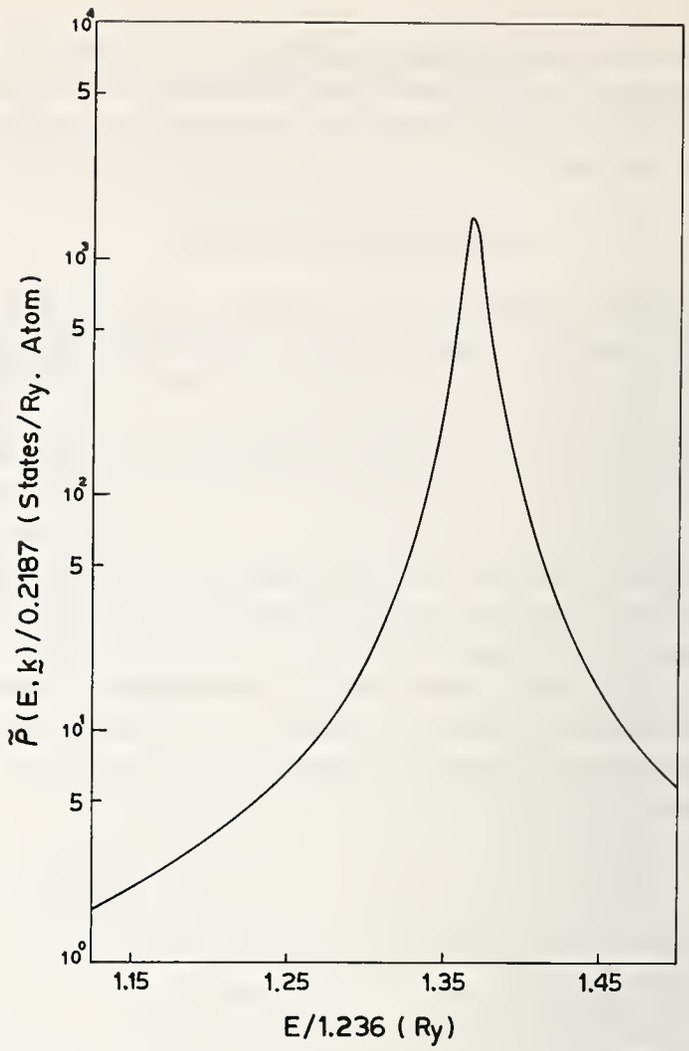

FIGURE 3. *The spectral density of states for* P_1 (s-*like*) *state in* β-*brass, plotted as a function of energy.*

larity in the intensity of diffusely scattered x rays, electrons or neutrons. He applied the idea to the neutron-scattering curves for β-brass, measured by Walker and Keating, and concluded that along ⟨111⟩, $k_F = 0.74$ of the $\Gamma - P$ distance. The free-electron value for this ratio is 0.82, and our calculations (using the Cohen-Heine [11] approach) give 0.75 compared to Amar and Johnson's virtual crystal approximation [6] result of 0.78. The flatness calculated by us compares well with Moss's speculative analysis of the neutron scattering data. If we compare the separation in peak positions for the spectral density for N_1 and $N_{1'}$ states we find the $N_{1'} - N_1$ gap to be 2.2 eV whereas Amar and Johnson's value for this gap is 1.5 eV. Both these results imply that the Fermi surface for β-brass shows greater departure from sphericity than that given by the virtual crystal approximation.

6. References

[1] Soven, P., Phys. Rev. **151**, 539 (1966).
[2] Soven, P., Phys. Rev. **156**, 809 (1967).
[3] Beeby, J. L., Phys. Rev. **135**, A130 (1964).
[4] Pant, M. M., and Joshi, S. K., Phys. Rev. **184 (1969).**
[5] Walker, C. B., and Keating, D. T., Phys. Rev. **130**, 1726 (1963).
[6] Amar, H., Johnson, K. H., and Wang, K. P., Phys. Rev. **148**, 672 (1966).
[7] Pant, M. M., and Joshi, S. K., Phys. Rev. **183** (1969).
[8] Mattheiss, L. F., Phys. Rev. **133**, A1399 (1964).
[9] Klein, M. J., Am. J. Phys. **19**, 153 (1951).
[10] Moss, S. C., Phys. Rev. Letters **22**, 1108 (1969).
[11] Cohen, M. H., and Heine, V., Adv. in Phys. **7**, 395 (1961).

On the Terms Excluded in the Multiple-Scattering Series*

R. M. More

Department of Physics, University of Pittsburgh, Pittsburgh, Pennsylvania 15213

We have evaluated certain of the excluded terms in the multiple-scattering series for a simple soluble potential. We discuss three aspects of the result: first, the reduction to "on-shell" quantities; second, the numerical contribution of the excluded terms; and third, the analytic properties of these terms.

Key words: Delta-function potential; excluded terms; Green's functions; multiple-scattering series; rigid-band approximation; scattering phase-shifts; t-matrices.

We have been interested in the multiple-scattering series for an electron in the presence of several potentials, i.e., "impurities" [1-4]. There exist many methods for processing the terms of this series, in order to obtain approximate formulas for the change in density of states caused by the impurities. One common procedure is a relaxation of the strict exclusion of terms in the series in which two t-matrices for the same impurity appear adjacent. In the present note we examine such "excluded" terms in an effort to assess the seriousness of the errors introduced when they are included. We have chosen the simplest sensible example for our evaluations, the case of a zero-range (delta-function) potential in a band of finite width [4]. However, because of the simple form of the results, we were led to a quite general formula appropriate to a general potential in an arbitrary band. We only quote that result in this note, and supply the proof elsewhere.

We have deferred the usual average over impurity positions, in the interests of effecting a reduction to "on-shell" quantities, i.e., to scattering phase-shifts. This is possible for all the "included" terms for well-separated impurities. We feel that it is also desirable, because there is a powerful parameterization of the energy dependence of the phase-shifts in the effective-range theory [5]. However, as we shall show, the excluded terms cannot (strictly speaking) be reduced to "on-shell" quantities for the potential in question. Thus theories which include the excluded terms have a spacious dependence on the off-shell amplitudes. This is a first important point about the inclusion of excluded terms. A second logical question is that of their numerical size: Do they yield contributions to the density of states which are comparable to those of the various included terms? And finally, a more subtle question is whether their inclusion alters the analytic properties of the density of states.

In the multiple-scattering theory, one computes the change of the density of states of a noninteracting electron gas due to the presence of impurities through a formula

$$\delta\rho(E) = -\frac{1}{\pi}\,\mathrm{Im\ Tr}\,[G(E+i\eta) - G_0(E+i\eta)] \tag{1}$$

where $G(z)$ and $G_0(z)$ are the exact and unperturbed Green's functions, respectively. They are defined by the formal equations

$$G(z) \equiv \frac{1}{z-H} \qquad G_0(z) \equiv \frac{1}{z-H_0} \tag{2}$$

For each impurity potential V_n we may define a scattering amplitude $T_n(z)$ by a Lippmann-Schwinger equation:

$$H = H_0 + \sum_n Vn$$

$$T_n(z) = V_n + V_n G_0(z) T_n \tag{3}$$

and then the exact Green's function if formally given by the expansion

$$G = G_0 + \sum_n G_0 T_n G_0 + \sum_n \sum_{m\,(m\neq n)} G_0 T_n G_0 T_m G_0 + \ldots \tag{4}$$

*This work was supported in part by the Air Force Office of Scientific Research under Contract AFOSR-69-1678.

It would be a counting error to include in the series (4) such terms as

$$G_0 T_n G_0 T_n G_0$$

and we refer to any term with T's for the same impurity adjacent as an "excluded" term. We are going to consider terms associated with one (particular) impurity only, and therefore we drop the impurity subscript on T_n. The simplest class of excluded terms would lead to the following contribution to the density of states, were they included:

$$\delta\rho^{(k)}(E) = -\frac{1}{\pi} \text{Im Tr } [(G_0 T)^k G_0] \tag{5}$$

In order to determine the general trace of this form we consider a generating function

$$P(\xi;\ E) \equiv \sum_{k=1}^{\infty} \xi^k \delta\rho^{(k)}(E) \tag{6}$$

and direct our attention to its evaluation.

By formal manipulations of the Lippmann-Schwinger equation, one can establish the general result:

$$P(\xi;\ E) = \frac{\xi}{\pi(1+\xi)} \sum_{l=0}^{\infty} (2l+1) \frac{d}{dE} \delta_l(1+\xi;\ E) \tag{7}$$

where $\delta_l(\lambda;\ E)$ is the ℓth partial-wave phase shift associated with the potential $\lambda V(r)$, where λ is a dimensionless numerical multiplier. In formula (7) we have shown how the excluded terms may be reduced to quantities (phase-shifts) related to the on-shell scattering amplitude *for a different potential* (λV) from the actual one. There is not, in general, any reduction to the strictly on-shell values for the actual potential.

For the specific model which we discuss below, formulas for $\delta\rho^{(k)}$ may easily be obtained by direct k-space evaluation of the traces. The results are in agreement with the general formal evaluation (7).

The simple model which we consider is defined by the Green's function

$$(k|G_0(z)|k') \equiv \frac{\delta k,\ k'}{z - \epsilon_k} \tag{8}$$

and the factorable potential

$$V_{kk'} \equiv v_0 \tag{9}$$

If the states $|k\rangle$ are thought of as plane-wave states, then (9) is produced by a zero-range potential (a delta-function in position space). This scheme is pathological for the usual free-electron case $\epsilon_k = k^2$, but it is entirely sensible for a band of finite width. We consider a special band-shape defined by the density of states [4]

$$\rho(E) = \sqrt{1 - E^2} \tag{10}$$

for which the required integrals are easily evaluated. There is no mathematical difference (only slight interpretive differences) between this model and the Slater-Koster model [6]. The required integral is the function we shall call $F(z)$:

$$F(z) \equiv \text{Tr } G_0(z) = \int \frac{\rho(E)\,dE}{z - E} = \pi z - i\pi\rho(z) \tag{11}$$

The T-matrix for the potential (9) is simply

$$T_{kk'}(z) = \frac{v_0}{1 - v_0 F(z)} \tag{12}$$

Because of the k-independence of this, there is no difficulty carrying out the k-space evaluation of the traces indicated in eq (5). In addition, we are able to compare the exact evaluation with what seems to be an erroneous procedure advanced by Edwards and Beeby [2]. This latter method is discussed in the appendix. The simplest of the traces (5) is the actual one-impurity contribution to the density of states; it is of course an "included" term. It is

$$\delta\rho^{(1)}(E) = \frac{v_0}{\rho(E)} \frac{E - \pi v_0}{1 + \pi^2 v_0^2 - 2\pi v_0 E} \tag{13}$$

This term has the form derived by Friedel [1],

$$\delta\rho^{(1)}(E) = \frac{1}{\pi} \frac{d}{dE} \delta_0(E)$$

where the s-wave phase-shift $\delta_0(E)$ is determined by

$$\tan \delta_0(E) = \frac{-\pi v_0 \rho(E)}{1 - \pi v_0 E}$$

The first excluded term is

$$\delta\rho^{(2)}(E) = -\frac{1}{\pi} \text{Im Tr } [G_0 T G_0 T G_0]$$

performing the trace we obtain

$$\delta\rho^{(2)}(E) = -\frac{\pi v_0^2}{\rho(E)} \frac{1 - \pi^2 v_0^2 + 2\pi v_0 E - 2E^2}{1 + \pi^2 v_0^2 - 2\pi v_0 E} \tag{14}$$

and the general result is easily found

$$P(\xi;\ E) = \frac{\xi v_0}{\rho(E)} \frac{E - (1+\xi)\pi v_0}{1 + \pi^2 v_0^2 (1+\xi)^2 - 2\pi v_0 (1+\xi) E} \tag{15}$$

To estimate the numerical importance of these terms, we evaluate them at the midpoint of the band (i.e., at $E=0$).

$$\delta\rho^{(1)}(0)=-\frac{\pi v_0^2}{1+\pi^2 v_0^2}$$

$$\delta\rho^{(2)}(0)=(1-\pi^2 v_0^2)\delta\rho^{(1)}(0) \tag{16}$$

$$\sum_{k=2}^{\infty}\delta\rho^{(k)}(0)=\frac{1-2\pi^2 v_0^2}{1+4\pi^2 v_0^2}\,\delta\rho^{(1)}(0)$$

From these results we conclude that inclusion of "excluded" terms will produce an appreciable numerical error whenever the Born approximation is not justified, i.e., whenever πv_0 is not much smaller than unity. This conclusion is scarcely surprising, because it is precisely an erroneous counting of the high powers of V that is made when an excluded term is included.

Perhaps the most dramatic analytic property of the density of states change $\delta\rho^{(1)}$ is its singularity at the threshold, indicated in the proportionality to $1/\rho(E)$ for each term of (15). This feature appears in all straightforward evaluations of (1). For example, in the case of the scattering of free electrons with the free-space dispersion relation $\epsilon_k=k^2$, the Friedel formula

$$\delta\rho^{(1)}(E)=\frac{1}{\pi}\frac{d}{dE}\,\delta_0(E)+\ \ldots$$

leads to a $1/k$ singularity at $k=0$ because of the universally true scattering length approximation [5]:

$$k\cot\delta_0(k)=-\frac{1}{a_0}+0(k^2)+\ \ldots$$

We think that any mathematically correct processing of the multiple-scattering series must exhibit this singularity, but of course a physically correct discussion will not predict an infinite density of states. A very common, but perhaps not altogether satisfactory resolution of this singularity is that it is to be associated with a "rigid band theorem" shift in the location of the threshold. We note that the Edwards-Beeby evaluation described in the appendix erroneously omits the quantity which gives rise to this singularity.

The formulas given above in (15), or more generally in (7) show that the excluded terms have the same threshold singularity as the one-impurity terms (13). Thus we may conclude that approximations which include the excluded terms make serious numerical errors but no analytic error, in general.

From (13), (14), and (15) we may extract the coefficients of the singular terms at the lower threshold:

$$\lim_{E\to -1}\rho(E)\delta\rho^{(1)}(E)=-\frac{v_0}{1+\pi v_0}$$

$$\lim_{E\to -1}\rho(E)\delta\rho^{(2)}(E)=\pi v_0^2 \tag{17}$$

$$\lim_{E\to -1}\rho(E)\sum_{k=2}^{\infty}\delta\rho^{(k)}(E)=\frac{\pi v_0^2}{(1+\pi v_0)(1+2\pi v_0)}$$

One final comment may be interesting. One often likes to contemplate the possibility that, while V is so large that the Born approximation is unjustified, T may be still quite small. This is a rather generalized expression of the "pseudopotential" idea. Even if this were true, we would expect such fortuitous cancellation of large terms to occur only for a limited range of values of V. Therefore, reasoning from formula (7), inclusion of "excluded" terms appears to be especially dangerous in such a situation.

Appendix

Edwards and Beeby [2] evaluate $\delta\rho^{(1)}$ by first computing the quantity

$$\delta\rho(k;E)\equiv-\frac{1}{\pi}\,\mathrm{Im}\,G_0^2(k;E)T_{kk}(E)$$

They urge that, except on a set of measure zero, one has

$$\delta\rho(k;E)=-\frac{1}{\pi}\,G_0^2(k;E)\,\mathrm{Im}\,T_{kk}(E)$$

However, the contribution from the set of measure zero is proportional to a delta function, and their procedure leads to an erroneous result. From formula (12) we see

$$\frac{1}{\pi}\,\mathrm{Im}\,T_{kk}(E)=\frac{v_0^2\rho(E)}{1+\pi^2 v_0^2-2\pi v_0 E}$$

which is independent of k. Interpreting the square of G_0 as *real*, we have

$$\int G_0^2(k;E)d^3k=p\int\frac{d^3k}{(E-\epsilon_k)^2}=-\pi$$

and therefore

$$\delta\rho_{\mathrm{Beeby}}(E)=-\frac{\pi v_0^2\rho(E)}{1+\pi^2 v_0^2-2\pi v_0 E}$$

This disagrees with the result (13) above. In particular, it has the wrong analytic behavior; it misses the

threshold singularity. It is unhappy to have to complain that a nondivergent answer is wrong, however! We think that this error is actually related to a famous error in the application of the multiple scattering series to nuclear many-body theory [5,7]. The result we have labelled $\delta\rho_{Beeby}$ is not compatible with the Friedel sum rule, whereas (13) above is.

References

[1] Anderson and MacMillan, in Theory of Magnetism in Transition Metals, Proceedings of International School of Physics "Enrico Fermi," Course XXXVII.

[2] Beeby and Edwards, Proc. Roy. Soc. (London) **A247**, 395 (1962). Beeby, in Lectures on the Many-Body Problem, **Vol. 2**, Edited by Cainiello (Academic Press, 1964).

[3] Soven, P., Phys. Rev. **156**, 809 (1967).

[4] Velický, Kirkpatrick and Ehrenreich, Phys. Rev. **175**, 747 (1968).

[5] Goldberger and Watson, Collision Theory, (Wiley, 1964).

[6] Slater and Koster, Phys. Rev. **96**, 1208 (1954).

[7] Reisenfeld and Watson, Phys. Rev. **104**, 492 (1956; DeWitt, B., Phys. Rev. **103**, 1565 (1956); Fukuda and Newton, Phys. Rev. **103**, 1558 (1956).

Discussion on "On the Terms Excluded in the Multiple-Scattering Series" by R. M. More (University of Pittsburgh)

J. L. Beeby *(Atomic Energy Res. Establishment):* The expression for the density of states derived by Beeby and Edwards is specifically for a dense array of scatterers in which the band structure is not markedly shifted from free electron form. The remarks of More in his appendix concern a single scatterer problem and hence the criticism of the Beeby and Edwards' paper is incorrect.

On Non-Localization at the Centre of a Disordered Bound Band

F. Brouers*

H. H. Wills Physics Laboratory, Royal Fort, Bristol

It is shown for a three dimensional model of tightly bound electrons with cellular disorder that the electronic states at the middle of a continuous band cannot be strictly localized. This conclusion is just the opposite of what has often been suggested.

Nevertheless, an approximate calculation of the electron localization "life-time" suggests that with increasing disorder the localized character of the electron states become more and more pronounced.

It is argued that in such a system there is no sharp transition between localized and non-localized regions of the energy spectrum.

Key words: Cellular disorder; disordered systems; electronic density of states; localization life-time; quasi-localized state; tight-binding.

1. Introduction

In a number of papers (for references see the review papers of Mott [1] 1967 and Halperin [2] 1967), it has been suggested that under certain circumstances the solutions of the Schröedinger equation are localized for an electron moving in a non-periodic field. If the Fermi level lies in a region of the density of states where the states are localized, the dc conductivity is supposed to vanish at $T=0$. This result has application in the theory of liquids, amorphous semiconductors, impurity bands, alloys, etc.

This assumption is generally discussed in terms of the wavefunction of the "disordered electron," a concept which is questionable when one is concerned with macroscopic quantities such as the density of states, the electrical conductivity or the optical properties which have to be averaged over all possible values of a random field.

If in doped and compensated semiconductors, one can admit intuitively that the electrons can be localized at low impurity concentrations, in the case of liquid metals, amorphous and liquid semiconductors and disordered alloys, the statement that some regions of the *continuous* density of states correspond to localized states is much less obvious.

Several authors (Taylor [3] 1965, Bonch-Bruevitch [4] 1968) have questioned the validity of the various arguments and concepts used in the theory of electronic states in disordered systems. This paper is a contribution to this discussion.

Ten years ago, Anderson [5] (1958) applied to the discussion of impurity conduction a formalism set up to investigate the absence of diffusion when the atomic potentials vary randomly. So far this model is the only one which can be treated qualitatively in three dimensions. Anderson's theorem is that at sufficiently low densities transport does not take place and that the exact wavefunctions are localized in a small region of space.

These conclusions have been extended to the case where there is a random potential on each site of a regular lattice (cellular disorder). This model is supposed to yield some insight into the behaviour of electrons in a tightly bound band of an amorphous system or a liquid. In that case the generalization of Anderson's theorem leads to the following statement: If we consider a uniform distribution with width W, the whole spectrum becomes localized when the energy of the individual atomic states varies randomly over a range which is somewhat greater than the width of the band that would be produced by their overlap.

Ziman [6] (1969) has written a clear and simplified version of Anderson's arguments and formalism applied to this problem in a critical review of various approaches used in this field. We refer to this paper and to the references quoted in it for a discussion of the physical interest and limitation of this model.

*Royal Society E. P. Research Fellow 1968-1969. Permanent address: The Institute of Physics of the University of Liège (Belgium).

On the other hand, very recently Lloyd [7] (1969) has shown that if we choose for the random electrostatic potential a Lorentzian distribution, this model can be solved exactly and a theorem is derived proving that localization is never possible.

Lloyd was chiefly concerned with the discussion of localization in the tail of the density of states. In this paper, attention is concentrated upon the situation considered in the paper of Ziman, states at the centre of the band and a bounded flat random distribution.

Our conclusion is that the Anderson theorem which must be valid at sufficiently low concentration of impurities cannot be generalized to the continuous disordered tightly bound band of an amorphous or liquid semiconductor. It is shown, however, that when the width of the distribution increases, the electron gets more and more localized but no sharp transition between localized and non-localized states appears in the theory.

2. The Model

We use the model of cellular disorder in a tightly bound band. It is assumed that in a three dimensional regular lattice, each site ℓ is occupied by an atom with a single tightly bound state $|\ell\rangle$. The energy eigenvalue ϵ_ℓ is supposed to be a stochastic variable with a probability distribution $P(\epsilon)$ characterized by a width W. The atomic states interact through a potential $V_{\ell\ell'}$. This interaction may itself be a statistical variable but here is supposed constant and equal to V when ℓ and ℓ' are nearest neighbors and zero otherwise. Coulomb and statistical correlations, though probably important in disordered systems, are ignored.

The Hamiltonian can be written in the base of the set of localized atomic orbitals $|\ell\rangle$ (single site representation)

$$H = H_1 + H_0 = \sum \epsilon_\ell a_\ell^\dagger a_\ell + \sum_{\ell\ell'} V_{\ell\ell'} a_\ell^\dagger a_\ell \qquad (1)$$

where a_ℓ and $a_\ell^\dagger$ are respectively the annihilation and creation operator for an electron localized at site ℓ and obey the usual anticommutation rules.

In the ordered system, all energies ϵ_ℓ can be put equal to zero and the first term drops out, the Hamiltonian H_0 is then a quadratic form and can be diagonalized in the reciprocal space:

$$H_0 = \sum_{\mathbf{k}} V_{\mathbf{k}} A_{\mathbf{k}}^\dagger A_{\mathbf{k}} \qquad (2)$$

with

$$A_{\mathbf{k}}^\dagger = \sum_{\ell} \exp(i\mathbf{k}\ell) a_\ell^\dagger \qquad (3)$$

[1] Note that $a_\ell(t)$ is not the probability amplitude for the physical diffusion process; for this quantity one must take account of the Pauli exclusion principle.

The eigenvalues of H_0 give rise to a band

$$V_{\mathbf{k}} = ZVs(\mathbf{k}) \qquad (4)$$

where Z is the number of next nearest neighbors. The function $s(\mathbf{k})$ is defined in the first Brillouin zone. It depends on the symmetry of the crystal and for cubic lattices is such that $\max.s(\mathbf{k}) = 1$ and $\min.s(\mathbf{k}) = -1$ (Mott and Jones [8] 1936). The width of the ordered band is thus $B = 2ZV$.

In the disordered system described by H, because of the lack of translation invariance, there is no dispersion relation similar to (4). If we are interested in the energy spectrum and more precisely in the density of states, the averages over Green functions are made (Matsubara and Kaneyoshi [9] 1966, and Ziman 1969).

3. Conditions for Localization

Now following Anderson, we ask how fast, if at all, does an electron put onto a site ℓ diffuse away from this site?

The probability amplitude $\mathscr{A}_\ell(t)$ is simply defined by

$$\mathscr{A}_\ell(t) = i\langle 0|a_l(t)a_l^\dagger(0)|0\rangle = iG_\ell(t) \qquad \text{for } t > 0 \qquad (5)$$

The state $|0\rangle$ is the true vacuum and we are concerned with non-interacting electrons.[1] The time dependent Green function $G_\ell(t)$ is the Fourier transform of:

$$G_\ell(t) = \int_{-\infty}^{+\infty} G_l^+(E) e^{-iEt} dE \qquad (6)$$

where $G_\ell(t)$ is the diagonal part of the Green function in the single site representation. It satisfies the equation

$$G_{\ell\ell'}(E) = \frac{\delta_{ll'}}{E - \epsilon_l} + \frac{1}{E - \epsilon_l} \sum_{\ell'' \neq l} V_{\ell\ell''} G_{\ell''\ell'} \qquad (7)$$

The retarded form $G^+(E)$ means that we have to add to E a small imaginary part $i\delta$ in order to fulfill causality requirement.

Equation (7) can be solved by successive iterations for the diagonal part $G_\ell(E)$ and one obtains:

$$G_\ell(E) = \frac{1}{E - \epsilon_l - \Delta_l(E)} \qquad (8)$$

where $E = E_1 + iE_2$ is a complex variable and the self-energy is given by a Brillouin-Wigner expansion:

$$\Delta_\ell(E) = \sum_{l' \neq l} \frac{V_{\ell\ell'} V_{\ell'\ell}}{E - \epsilon_{l'}} + \sum_{\substack{l', l'' \\ \neq l}} \frac{V_{\ell\ell'} V_{\ell'\ell''} V_{\ell''\ell}}{(E - \epsilon_{l'})(E - \epsilon_{l''})} + \cdots \qquad (9)$$

The terms in the series represent all possible successive virtual transitions which start out from the site ℓ

and propagate throughout the disordered system until the electron returns to the initial state.

The condition for the amplitude to be finite when $t \to \infty$ (see condition for non-transport in Van Hove [10] 1957) is that $G_l(E)$ should have a pole on the real axis. Thus the conditions for having a localized state with energy E_1 are simply:

$$\text{Im } \Delta_l(E_1) = 0 \tag{10}$$

and

$$-\epsilon_l + E_1 - \text{Re } \Delta_l(E_1) = 0 \tag{11}$$

If Im $\Delta_l(E_1)$ is different from zero, its value gives the decay rate of the state and we can define a lifetime for the electron state.

In the case of an ordered lattice:

$$\Delta_l^0(E) = \sum_{l' \neq l} \frac{V_{ll'}V_{l'l}}{E} + \sum_{\substack{l',l'' \\ \neq l}} \frac{V_{ll'}V_{l'l''}V_{l''l}}{E^2} + \ldots \tag{12}$$

is equal to

$$\Delta_l^0(E) = E - (G_l^0(E))^{-1} \tag{13}$$

where $G_l^0(E)$ is the Green function of the ordered band. This function can be expanded along the same lines as $\Delta_l^0(E)$. In the **k** representation it can be written in the form:

$$G_l^0(E) = \frac{1}{N} \sum_k \frac{1}{E - V_k} \tag{14}$$

For a tightly bound band, this function is well described by a model function (Hubbard [11] 1964):

$$G_M^0(E) = 2[E - \sqrt{E^2 - 1}] \tag{15}$$

if $B/2$ is the energy unit.

In the disordered case, the quantity $\Delta_l(E)$ has to be averaged over all the random configurations of the disordered system. The difficulty arises from the stochastic nature of the function $\Delta_l(E)$. In eq (9) we have to average products of site locators

$$\langle S_{\ell'} S_{\ell''} S_{\ell'''} \ldots \rangle$$

with

$$S_\ell(E) = \frac{1}{E - \epsilon_\ell}$$

The averaged Green function

$$\tilde{G}_\ell(E) = \frac{1}{E - \epsilon_\ell - \langle \Delta_\ell(E) \rangle} \tag{16}$$

must be considered as a conditional averaged since the energy of state $|l\rangle$ is fixed and equal to ϵ_ℓ. The function $\tilde{G}_l(E)$ is different from the ensemble averaged Green function:

$$\langle G_\ell(E) \rangle = \left\langle \frac{1}{E - \epsilon_\ell - \Delta_\ell(E)} \right\rangle \tag{17}$$

which must be used to calculate the density of states, for instance.

It has been shown by Lloyd (1969), that the conditional average Green function $\tilde{G}_\ell(E)$ can be calculated directly without involving any series expansion if the distribution is a Lorentzian one:

$$P(\epsilon) = \frac{1}{\pi} \frac{\Gamma}{\epsilon^2 + \Gamma^2} \tag{18}$$

This is due to the fact that for such a distribution, the averaged product $\langle S_{\ell_1} S_{\ell_2} \ldots S_{\ell_n} \rangle$ is exactly equal to

$$\langle S_\ell(E) \rangle^n = \left(\frac{1}{E + i\Gamma} \right)^n \tag{19}$$

One can see that all the cumulants (Kubo [12] 1962) except the first are zero and the average can be performed for each S_ℓ independently. Physically this means that there is no correlation between different site locators. For the particular distribution (18), the self-energy is given by:

$$\Delta_\ell^{\mathscr{L}}(E)$$

$$= \sum_{l' \neq l} \frac{V_{ll'}V_{l'l}}{E + i\Gamma} + \sum_{\substack{l',l'' \\ \neq l}} \frac{V_{ll'}V_{l'l''}V_{l''l}}{(E + i\Gamma)^2} + \ldots = \Delta_\ell^0(E + i\Gamma) \tag{20}$$

the density of states

$$\rho^{\mathscr{L}}(E) = -\frac{1}{\pi} \text{Im } G^0(E + i\Gamma)$$

$$= -\frac{2}{\pi}\Gamma + \frac{2}{\pi} \text{Im } \sqrt{(E + i\Gamma)^2 - 1} \tag{21}$$

and

$$\tilde{G}_\ell^{\mathscr{L}}(E) = \frac{1}{E - \epsilon_\ell - \Delta_\ell^0(E + i\Gamma)} \tag{22}$$

which must be used to calculate (6). This expression is equivalent to eq (39) of Lloyd's paper, if use is made of relation (13).

We can see immediately from (13) and (15) that Im $\Delta_l^0(E + i\Gamma) \neq 0$. This gives the theorem proved in a more complicated way by Lloyd (1969). For any value of E and Γ no localized state can occur.

In particular, if we are interested in states at the middle of the band, one has

$$\mathrm{Im}\,\Delta^0(i\Gamma)=\Delta^0(i\Gamma)\neq 0 \tag{23}$$

4. Non-Localization at the Centre of the Band

We turn now to the case considered by Anderson (1958): a rectangular distribution with width W. Ziman (1969) reproducing Anderson's arguments and conclusions has assumed in the discussion of the convergence of (9) that:

$$\begin{aligned}&\langle S_{\ell_1}S_{\ell_2}\ \ldots\ S_{\ell_n}\rangle\\&=\exp\left[\log\langle S_{\ell_1}\ \ldots\ S_{\ell_n}\rangle\right]=\exp\left[n\langle\log S_\ell\rangle\right]\end{aligned} \tag{24}$$

This approximation means that all the cumulants except the first are zero or that the site locators are uncorrelated. It is equivalent to assume that:

$$\langle S_{\ell_1}\ \ldots\ S_{\ell_2}\rangle=\langle S_\ell\rangle^n \tag{25}$$

The full argument of Anderson's paper is more complicated. Correlations are included in the theory by replacing ϵ_l in the locators by a renormalized energy but qualitatively Anderson's conclusion on localization at the centre of the band is not very dependent on this refinement. For a uniform distribution of width W, one has

$$\langle S_W^+(E)\rangle=\frac{1}{W}\log\left|\frac{E-W/2}{E+W/2}\right|-\frac{i\pi}{W}\,\eta\left(\frac{W}{2}-|E|\right) \tag{26}$$

where $\eta(x)$ is the usual step function.

Though in this approximation, the ensemble averaged $\langle G^W(E)\rangle$ is simply $G^0(1/\langle S_\ell\rangle)$, it does not seem possible to find a simple expression for the conditionally averaged $\tilde{G}^W(E)$ in terms of $\langle S_\ell\rangle$ because of the restricted summation in (9). But for $E=0$, i.e., in the middle of the band, the result is simply:

$$\tilde{G}_\ell^W(0)=-\frac{1}{\Delta^0\left(\dfrac{iW}{\pi}\right)}, \tag{27}$$

and one necessary condition for localization is that $\Delta^0(iW/\pi)$ should be equal to zero.

It is the same condition as for a Lorentzian distribution (eq 22) except that we replace Γ by W/π. This result is physically meaningful. If we neglect correlations, the electronic states at the center of the band are not very dependent on the form of the random distribution of individual site potentials.

We conclude that for states at the middle of the band and in the case of statistically independent site locators, a situation described in Ziman's paper (1969), no state can be strictly localized in Anderson's sense.

5. Localization Life-Time

We can now, using (13) and (15) evaluate the value of the imaginary part of the self-energy at the centre of the band:

$$\mathrm{Im}\,\langle\Delta(0)\rangle=\Delta^0(i\Gamma)=\Gamma-\frac{1}{2(\sqrt{\Gamma^2+1}-\Gamma)} \tag{28}$$

and the localization "life-time":

$$\tau(\Gamma)=-\hbar/\gamma \tag{29}$$

with

$$\gamma=\frac{\Delta_0(i\Gamma)}{\left\{1-\left(\dfrac{\partial\ \mathrm{Re}\ \Delta^0(E+i\Gamma)}{\partial E}\right)_{E=0}\right\}} \tag{30}$$

and

$$\left[1-\left(\frac{\partial\ \mathrm{Re}\ \Delta^\circ(E+i\Gamma)}{\partial E}\right)_{E=0}\right]=\frac{1}{2}\,\frac{1}{\sqrt{1+\Gamma^2}[\sqrt{1+\Gamma^2}-\Gamma]} \tag{31}$$

In the limit $\Gamma=0$, i.e., in the case of the ordered band, the life-time is two times the inverse of the ordered band width. If Γ or (W/π) is increased, the function (28) decreases and tends to zero as $\Gamma\to\infty$. But for any finite Γ, no state can be strictly localized. This result is in agreement with Lloyd's theorem.

In figure 1, we have plotted the localization life-time defined by (29) with respect to (or W/π). For every value, we can give a measure of the electron localization at the middle of the band. For instance for $\Gamma=5$ (in $B/2$ units), the localization corresponds to that of an electron in an ordered band of width $B/20$.

It is also possible to obtain directly a closed formula for the self-energy (9) by using the Matsubara and Kaneyoshi (1966) technique, if we neglect the restriction $(l', l'', \ldots \neq l)$ in the summation. In this case, one has:

$$\langle\Delta_M(E)\rangle=\frac{1}{N}\sum_{\mathbf{k}}\Delta_{\mathbf{k}}(E) \tag{32}$$

with

$$\Delta_{\mathbf{k}}(E)=V_k^2\langle G_{\mathbf{kk}}(E)\rangle \tag{33}$$

where V_k and $G_{kk'}$ are the Fourier transform of the overlap integral $V_{\ell\ell'}$, and the disordered Green function.

If we discard correlations between site locators, it can be shown easily that

$$\langle \Delta_M(E) \rangle = -\frac{1}{\langle S_{\ell}(E) \rangle} + \frac{1}{\langle S_{\ell(E)} \rangle^2} G_0\left(\frac{1}{\langle S_{\ell(E)} \rangle}\right) \tag{34}$$

The expressions corresponding to (28) and (31) are then written as

$$\mathrm{Im}\,\langle \Delta_M(0) \rangle = -\Gamma(1+2\Gamma^2) + 2\Gamma^2\sqrt{\Gamma^2+1} \tag{35}$$

$$\left[1-\left(\frac{\partial\, Re\,\Delta\,(E)}{\partial E}\right)_{E=0}\right]$$

$$= 2+2\Gamma^2\left[\frac{\sqrt{1+\Gamma^2}-\Gamma}{\sqrt{1+\Gamma^2}}\right] + 4\Gamma[\Gamma - \sqrt{\Gamma^2+1} \tag{36}$$

It is interesting to note that this expression almost coincides with (28) for $\Gamma > 0.5$. But for $\Gamma < 0.5$, the lifetime increases and is infinite for $\Gamma = 0$. In the vicinity of $\Gamma = 0$, the present discussion is not quite valid because the decay in the ordered band is an algebraic decay due to a cut in the ordered Green function.

6. Discussion

There is a discrepancy between these conclusions and the statement on localization in disordered tightly bound band reproduced in review papers by Mott (1967) and Ziman (1969).

In the discussion of the self-energy expansion convergence, Anderson eliminated singular factors in averaging the terms of the series for $\langle \Delta(E) \rangle$. In this case, to have a localized state $Re\langle \Delta_l(E) \rangle$ must converge and this convergence is a criterion for localization.

The same procedure would give a non-continuous disordered density of states and can be justified when the concentration of impurity is so low that there is no banding effect (Miller and Abrahams 1960 [13]). But in the model of a disordered tightly bound band when the distribution of random potentials is continuous, the consideration of the singularities in the expansion of $\langle \Delta(E) \rangle$ when the average is performed is essential to rediscover the exact result of Lloyd in the case of a Lorentzian distribution and to find a continuous density of states (eq 21). It turns out that when the terms of the series are summed, the small imaginary part of the locators gives rise to a finite imaginary contribution for $\langle \Delta \rangle$. We have shown that the condition $\mathrm{Im}\,\langle \Delta \rangle (0) \rangle = 0$ is never fulfilled in the model considered in this paper. Moreover it is possible to define a closed form for $Re\langle \Delta(E) \rangle$ at the centre of the band.

The conclusion of this paper is that it is impossible with conditions (10) and (11) to define regions in a *continuous* disordered tightly bound band where electronic states are strictly localized. This conclusion is thus in agreement with a general theorem of Bonch-

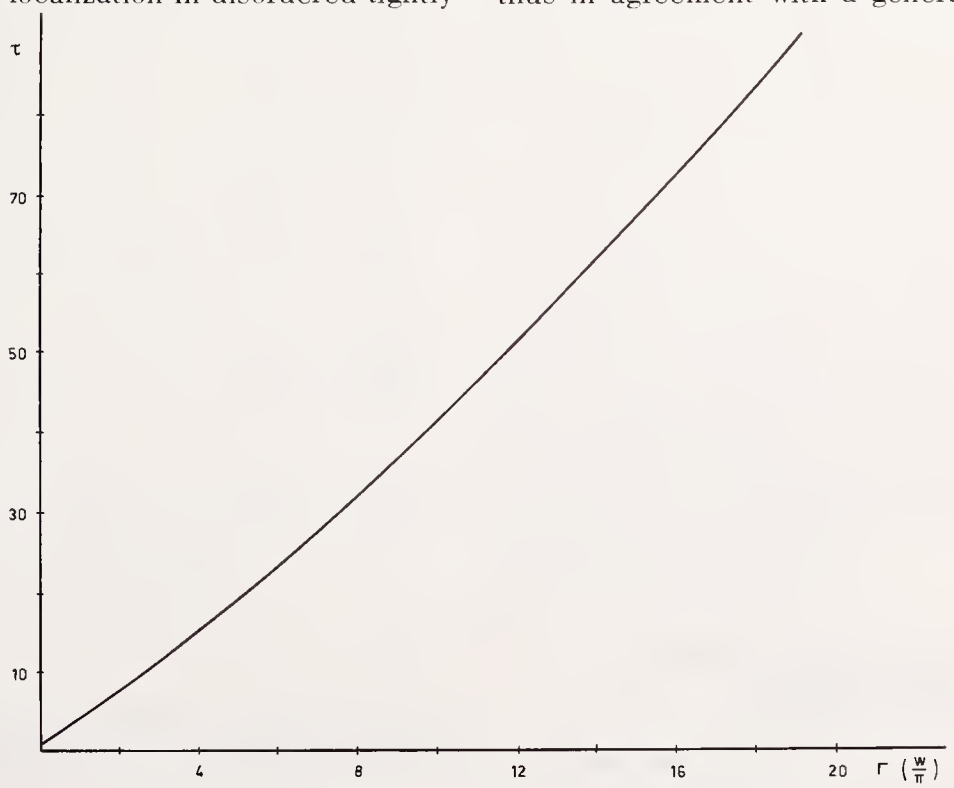

FIGURE 1. *Localization "life-time" (eq 29) as a function of the width of the random distribution of random atomic potentials.*
The units are $B/2$ for Γ and $(2/B)\,\hbar$ for τ.

Bruevitch (1968) on conductivity stating that the electrical conductivity of the macroscopically homogeneous system at zero temperature is non-zero if and only if the Fermi level lies in the region where the density of states is non-zero and continuous.

This conclusion is also consistent with the results of Nakai and Flawiter (1968) [14]. These authors show using a quite different approach in a model where the randomness is included in the hopping distances that localization for an impurity band appears when the spectrum becomes discrete and dispersed in a wide region.

Nevertheless, as was suggested by a rough calculation of the localized electron lifetime in section 5, when the width W of the random distribution increases, the localized character of the electron state becomes more and more pronounced.

This discussion suggests, however, that if in a continuous band some states are more localized than others, it is hard to imagine a sharp transition between them.

A relevant theoretical problem would be to try to define this concept of "quasi-localized state" on a more rigorous basis. The lifetime of this quasi-particle should be calculated for all the energy spectrum and compared with other characteristic lifetimes of the system. Without this knowledge, it seems difficult to reach definite conclusions concerning the behavior of the electrical conductivity when the Fermi level varies across the density of states distribution.

7. Acknowledgments

I am grateful to Professor Ziman for suggesting this problem. He is acknowledged as well as Drs. B. Bergersen, D. Herbert, P. Lloyd and K. Thornber for informative and stimulating discussions.

8. References

[1] Mott, N. F., Adv. Phys. **16**, 49 (1967).
[2] Halperin, B. I., Advances in Chemical Physics **13**, 123 (1967).
[3] Taylor, P. L., Phys. Lett. **18**, 13 (1965).
[4] Bonch-Bruevitch, V. L., The theory of condensed matter, Inter Atomic Energy, p. 989 (Vienna, 1968).
[5] Anderson, P. W., Phys. Rev. **109**, 1492 (1958).
[6] Ziman, J. M., J. Phys. Chem. **2**, 1230 (1969).
[7] Lloyd, P., J. Phys. Chem. **2**, 1717 (1969).
[8] Mott, N. F., and Jones, H., The theory of the properties of metals and alloys (1936).
[9] Matsubara, T., and Kaneyoshi, T., Progr. Theor. Phys. **36**, 695 (1966).
[10] Van Hove, L., Physica **23**, 441 (1957).
[11] Hubbard, J., Proc. Roy. Soc. **A281**, 401 (1964).
[12] Kubo, R., J. Phys. Soc. Japan **17**, 1100 (1962).
[13] Miller, A., and Abrahams, E., Phys. Rev. **120**, 745 (1960).
[14] Nakai, S., and Flawiter, W. F., Phys. Lett. **27A**, 393 (1968).

The Half-Filled Narrow Energy Band *

L. G. Caron ** and G. Kemeny ***

Department of Electrical Engineering, Massachusetts Institute of Technology, Cambridge, Massachusetts 02139

The antiferromagnetic and paramagnetic states of a half-filled narrow energy band are investigated using a t-matrix approach. This method is justified despite the high particle density in the system. A phase diagram including the Mott state is given. Employing the gap of the antiferromagnetic insulator as a variational parameter, it is shown that the increase of the band width potential energy ratio leads to a first order phase transition into the paramagnetic metal state, nearly where Mott has estimated it to occur.

Key words: Antiferromagnetic insulator; first order phase transition; half-filled narrow energy band; Mott state; paramagnetic metal; t-matrix.

1. Introduction

The Mott insulator [1] on the Hubbard model [2] has been the subject of investigation in two papers by the authors [3,4]. In the paper presented at the first International Conference on the Metal-Nonmetal Transition [4] some of this research was reviewed. Parts of this paper and the discussion that followed were devoted to the paramagnetic and antiferromagnetic ranges of the half-filled narrow band, and to the competition of the long range antiferromagnetic order with the short range Mott order. We have outlined the physical motivation and mathematical methods we felt were necessary to treat these problems. In this paper we present the solutions of these problems. The results indicate that the problem is not as complex as we have anticipated and the self-consistent pair correlation method is unnecessary except in the Mott insulator range. Other than that our physical expectations seem to be justified by the results.

Apart from the Mott insulator we consider two possible physical states of the half-filled narrow energy band, with the Hubbard Hamiltonian [3]

$$H = \sum_{ij\sigma} T_{ij} c_{i\sigma}^{\dagger} c_{j\sigma} + J \sum_{i} n_{i+} n_{i-}. \tag{1.1}$$

These are the paramagnetic and the antiferromagnetic states. In the paramagnetic state the electrons scatter on each other. This will be handled by a t-matrix approximation. As we have argued in [4] an expansion in powers of the t-matrix could handle the scattering problems. Our results indicate that already the first term should be a good approximation. If the interaction is strong enough the antiferromagnetic state becomes stable. Part of the effect of the interaction is the establishment of the long range order. The rest of the effect is taken care of by the same t-matrix calculation but now the zero order wave functions are antiferromagnetic rather than paramagnetic.

The stability of the paramagnetic versus antiferromagnetic states is decided by the minimization of the total energy in the t-matrix approximation with the antiferromagnetic gap as a variational parameter. When the gap so determined turns out to be zero the paramagnetic state is stable. A semiquantitative argument is used for the competition of the antiferromagnetic and Mott insulator states near the atomic limit. We shall use Martin-Schwinger [5] Green's functions in a manner similar to Reynolds and Puff [6]. The general formulas are evaluated for a simple cubic lattice in the tight-binding approximation.

2. Paramagnetic State: Hartree Approximation

In the limit of small intra-atomic interaction, $J \to 0$, one would expect the correlation effects to be small. One might even be tempted to neglect them completely. The energy would then be approximated by first-order stationary perturbation theory on the noninteract-

*Supported in part by the Office of Naval Research, Contract No. 78721 and by the Canadian National Research Council.

**Permanent address; Department of Physics, University of Sherbrooke, Quebec.

***Permanent address; Department of Metallurgy, Mechanics and Materials Science, Michigan State University, East Lansing, Michigan 48823.

ing electron system. This is the Hartree approximation. It is best worked out by first Fourier transforming the Hubbard Hamiltonian in the reciprocal space of the crystal structure. This diagonalizes the motional part of the Hamiltonian eq (1.1). With

$$c_{i\sigma} = N^{-1/2} \sum_{\mathbf{k}} e^{i\mathbf{k}\cdot\mathbf{R}_i} c_{\mathbf{k}\sigma} \tag{2.1}$$

one finds

$$H = \sum_{\mathbf{k}} \sum_{\sigma} \epsilon(\mathbf{k}) n_{\mathbf{k}\sigma} + JN^{-1} \sum_{\mathbf{k}_1\mathbf{k}_2\mathbf{k}_3\mathbf{k}_4} \delta(\mathbf{k}_1 + \mathbf{k}_2 - \mathbf{k}_3 - \mathbf{k}_4) c^+_{\mathbf{k}_{1+}} c^+_{\mathbf{k}_{1-}} c_{\mathbf{k}_{4+}} c_{\mathbf{k}_{2-}} \tag{2.2}$$

where

$$\epsilon(\mathbf{k}) = \sum_{\mathbf{l}} T_{0\mathbf{l}} e^{i\mathbf{k}\cdot\mathbf{R}_{\mathbf{l}}}. \tag{2.3}$$

The unperturbed ground state of the half-filled band is obtained by filling all $\mathbf{k}$ states for which $\epsilon(\mathbf{k}) < 0$. This makes up the Fermi sea whose surface is defined by $\epsilon(\mathbf{k}) = 0$. The Hartree energy is then simply

$$\begin{aligned} \langle H \rangle &= 2 \sum_{\mathbf{k}<\mathbf{k}_F} \epsilon(\mathbf{k}) + JN^{-1} \sum_{\mathbf{k}_1\mathbf{k}_2<\mathbf{k}_F} n_{\mathbf{k}_{1-}} n_{\mathbf{k}_{2-}} \\ &= 2 \sum_{\mathbf{k}<\mathbf{k}_F} \epsilon(\mathbf{k}) + NJ/4. \end{aligned} \tag{2.4}$$

3. Paramagnetic State: Reaction Matrix Approximation

We wish to study the behavior of the Hubbard model as a function of the strength of the interaction. It is obvious that correlation effects will be of importance for larger values of J. One might try adding a few more terms in the perturbation series expansion of the energy. The danger is that this series diverges over a paramagnetic ground state as J becomes large. So, *a priori* it seems to be necessary to get rid of this pending divergence by summing up judiciously chosen terms to all orders. It is known from the Breuckner-Goldstone work [7] that those terms which involve only two electrons—the reaction matrix expansion—are easily summed. This means the binary collision problem is solved exactly and this in turn leads to a well behaved treatment of the short-range intra-atomic interaction.

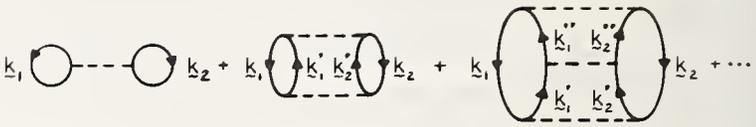

FIGURE 1. *Reaction matrix correction to the noninteracting energy in the paramagnetic system.*

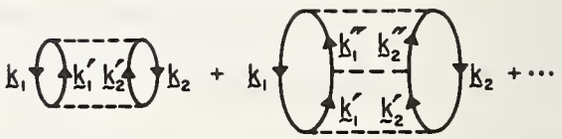

FIGURE 2. *Reaction matrix correction to the Hartree energy in the paramagnetic system and to the Matsubara energy in the antiferromagnetic system.*

Using time dependent perturbation theory and the adiabatic approximation it is possible to deduce a diagram representation equipotent to the perturbation series expansion [7]. In this diagram representation, the reaction matrix correction to the noninteracting electron energy is given in figure 1. In these processes, any two opposite-spin electrons of the Fermi sea $\mathbf{k}_1$,$\mathbf{k}_2$ undergo all possible scatterings on one another. The exclusion principle is partly taken into account by restricting the scattered electrons above the Fermi sea. If we wish to compare the final energy to the Hartree energy we are left with figure 2 where the first term is missing because it is already included in the Hartree energy.

Following Day [7], we write down the wavevector for two such electrons in momentum space as:

$$|\Psi(\mathbf{k}_1\mathbf{k}_2)> = |\phi(\mathbf{k}_1)\phi(\mathbf{k}_2)> - Q/ev|\Psi(\mathbf{k}_1\mathbf{k}_2)> = |\phi(\mathbf{k}_1)\phi(\mathbf{k}_2)$$

$$> - \sum_{\mathbf{k}_1'\mathbf{k}_2'>\mathbf{k}_F} \frac{|\phi(\mathbf{k}_1')\phi(\mathbf{k}_2')><\phi(\mathbf{k}_1')\phi(\mathbf{k}_2')|v|\Psi(\mathbf{k}_1\mathbf{k}_2)>.}{\epsilon(\mathbf{k}_1') + \epsilon(\mathbf{k}_2') - \epsilon(\mathbf{k}_1) - \epsilon(\mathbf{k}_2)} \tag{3.1}$$

where $|\phi(\mathbf{k})\rangle$ is the one-electron wavevector, v is the inter-electron interaction, Q restricts the scattered states above the Fermi level, and e is the energy difference between the final and the initial states.

The correction to the Hartree energy is then

$$\Delta E = \sum_{\mathbf{k}_1\mathbf{k}_2<\mathbf{k}_F} [<\Psi(\mathbf{k}_1\mathbf{k}_2)|v|\phi(\mathbf{k}_1)\phi(\mathbf{k}_2) > - <\phi(\mathbf{k}_1)\phi(\mathbf{k}_2)|v|\phi(\mathbf{k}_1)\phi(\mathbf{k}_2)>]. \tag{3.2}$$

Translating this into configuration space

$$\Psi_{\mathbf{k}_1\mathbf{k}_2}(\mathbf{R}_1\mathbf{R}_2) = \phi_{\mathbf{k}_1}(\mathbf{R}_1)\phi_{\mathbf{k}_2}(\mathbf{R}_2) - \sum_{\mathbf{k}_1'\mathbf{k}_2'>\mathbf{k}_F} \frac{\phi_{\mathbf{k}_1'}(\mathbf{R}_1)\phi_{\mathbf{k}_2'}(R_2)}{[\epsilon(\mathbf{k}_1') + \epsilon(\mathbf{k}_2') - \epsilon(\mathbf{k}_1) - \epsilon(\mathbf{k}_2)]} \times \sum_{\mathbf{R}_1'\mathbf{R}_2'} \phi^*_{\mathbf{k}_1'}(\mathbf{R}_1')\phi^*_{\mathbf{k}_2'}(\mathbf{R}_2')v(\mathbf{R}_1'\mathbf{R}_2')\Psi_{\mathbf{k}_1\mathbf{k}_2}(\mathbf{R}_1'\mathbf{R}_2') \tag{3.3}$$

and

$$\Delta E = \sum_{\mathbf{k}_1\mathbf{k}_2<\mathbf{k}_F} \sum_{\mathbf{R}_1\mathbf{R}_2} [\Psi^*_{\mathbf{k}_1\mathbf{k}_2}(\mathbf{R}_1\mathbf{R}_2)v(\mathbf{R}_1\mathbf{R}_2)\phi_{\mathbf{k}_1}(\mathbf{R}_1)\phi_{\mathbf{k}_2}(\mathbf{R}_2) - \phi^*_{\mathbf{k}_1}(\mathbf{R}_1)\phi^*_{\mathbf{k}_2}(\mathbf{R}_2) \times v(\mathbf{R}_1\mathbf{R}_2)\phi_{\mathbf{k}_1}(\mathbf{R}_1)\phi_{\mathbf{k}_2}(\mathbf{R}_2)]. \tag{3.4}$$

Since $\epsilon(\mathbf{k}) = -\epsilon(\pi \pm \mathbf{k})$, we can transform the summation above the Fermi sea to one below, by changing the sign of the corresponding energies. Substituting

$$v(\mathbf{R}_1\mathbf{R}_2) = J\delta_{\mathbf{R}_1\mathbf{R}_2} \tag{3.5}$$

and

$$\phi_{\mathbf{k}}(\mathbf{R}) = N^{-1/2}e^{i\mathbf{k}\cdot\mathbf{R}}, \tag{3.6}$$

into eq (3.3) we find

$$\Psi_{\mathbf{k}_1\mathbf{k}_2}(\mathbf{R}_1\mathbf{R}_2) = N^{-1}e^{i(\mathbf{k}_1\cdot\mathbf{R}_1 + \mathbf{k}_2\cdot\mathbf{R}_2)} + J\sum_{\mathbf{k}_1'\mathbf{k}_2'<\mathbf{k}_F} \times \frac{N^{-1}e^{i(\mathbf{k}_1'\cdot\mathbf{R}_1 + \mathbf{k}_2'\cdot\mathbf{R}_2)}}{[\epsilon(\mathbf{k}_1') + \epsilon(\mathbf{k}_2') + \epsilon(\mathbf{k}_1) + \epsilon(\mathbf{k}_2)]} \times N^{-1}\sum_{\mathbf{R}_1'} e^{-i(\mathbf{k}_1' + \mathbf{k}_2')\cdot\mathbf{R}_1'} \times \Psi_{\mathbf{k}_1\mathbf{k}_2}(\mathbf{R}_1'\mathbf{R}_1') \tag{3.7}$$

from which

$$\Psi_{\mathbf{k}_1\mathbf{k}_2}(\mathbf{R}_1\mathbf{R}_1) = \frac{e^{i(\mathbf{k}_1+\mathbf{k}_2)\cdot\mathbf{R}_1}}{1 - JN^{-1}\sum_{\mathbf{k}_1'\mathbf{k}_2'<\mathbf{k}_F} \frac{\delta(\mathbf{k}_1 + \mathbf{k}_2 - \mathbf{k}_1' - \mathbf{k}_2')}{[\epsilon(\mathbf{k}_1') + \epsilon(\mathbf{k}_2') + \epsilon(\mathbf{k}_1) + \epsilon(\mathbf{k}_2)]}} \tag{3.8}$$

is obtained. The reaction matrix energy correction is then

$$\Delta E = \sum_{\mathbf{k}_1\mathbf{k}_2<\mathbf{k}_F} \frac{J}{\left[1 - JN^{-1}\sum_{\mathbf{k}_1'\mathbf{k}_2'<\mathbf{k}_F} \frac{\delta(\mathbf{k}_1 + \mathbf{k}_2 - \mathbf{k}_1' - \mathbf{k}_2')}{[\epsilon(\mathbf{k}_1') + \epsilon(\mathbf{k}_2') + \epsilon(\mathbf{k}_1) + \epsilon(\mathbf{k}_2)]}\right]} - \frac{J}{4} \tag{3.9}$$

4. Antiferromagnetic State: Hartree Approximation

As the interaction becomes very large one would expect the electrons to avoid one another very effectively. The band being half filled this can be best achieved either by a parallel alignment of the electron spins or by an antiferromagnetic one. In both cases there is a spreading out of the electrons throughout all states in the Brillouin zone. In this limit the paramagnetic state is a bad trial state on which to build the perturbation expansion since it confines the electrons below the Fermi level. A ferromagnetic or antiferromagnetic trial state would be better suited to a perturbation treatment. It is known the half-filled band in the Hubbard model cannot be ferromagnetic [8,9]. We then look at the antiferromagnetic state in the large J limit. A band theory of antiferromagnetism was discussed by Matsubara and

417-156 O - 71 - 35

Yokota [10]. They reduced the inter-electron interaction to a single particle spin symmetry breaking potential

$$\sum_i \sum_\sigma \Delta_{i\sigma} n_{i\sigma}$$

in which $\Delta_{i\sigma}$ is self-consistently defined as the Hartree potential seen by an electron

$$\Delta_{i\sigma} = J n_{i-\sigma}. \tag{4.1}$$

This potential has one value on one sublattice and another one on the other. The Hubbard Hamiltonian in the Matsubara approximation is then

$$H_M = \sum_{ij} \sum_\sigma T_{ij} c^+_{i\sigma} c_{j\sigma} + \sum_i \sum_\sigma \Delta_{i\sigma} n_{i\sigma}. \tag{4.2}$$

Transforming into momentum coordinates

$$H_M = \sum_{\mathbf{k}} \sum_\sigma \left(\epsilon(\mathbf{k}) + \frac{J}{2}\right) n_{\mathbf{k}\sigma} + \sum_{\mathbf{k}} \sum_\sigma \frac{\Delta_\sigma}{2} (c^+_{\mathbf{k}\sigma} c_{\mathbf{k}+\pi\sigma} + c^+_{\mathbf{k}+\pi\sigma} c_{\mathbf{k}\sigma}) \tag{4.3}$$

where

$$\Delta_\sigma = \begin{cases} \Delta_{0+} - \frac{J}{2} = +\Delta \text{ for up spins} \\ \Delta_{0-} - \frac{J}{2} = -\Delta \text{ for down spins} \end{cases} \tag{4.4}$$

each $\mathbf{k}$ state is seen to be coupled to a $\mathbf{k}+\boldsymbol{\pi}$ state. The eigenstates of this Hamiltonian are going to be linear superpositions of states below and above the Fermi level of the noninteracting system. The electrons will then be spread out throughout the Brillouin zone as wished.

The Matsubara Hamiltonian is diagonalized by the following canonical transformation:

$$\begin{aligned} \epsilon_{\mathbf{k}\sigma} &= A_{\mathbf{k}} b_{1\mathbf{k}\sigma} \pm B_{\mathbf{k}} b_{2\mathbf{k}\sigma} \\ \epsilon_{\mathbf{k}+\pi\sigma} &= \mp B_{\mathbf{k}} b_{1\mathbf{k}\sigma} + A_{\mathbf{k}} b_{2\mathbf{k}\sigma} \end{aligned} \tag{4.5}$$

the upper sign being for up spins and the lower for down spins, and where

$$\begin{aligned} A_{\mathbf{k}} &= \sqrt{\left(1 - \frac{\epsilon(\mathbf{k})}{\sqrt{\Delta^2 + \epsilon(\mathbf{k})^2}}\right)/2} \\ B_{\mathbf{k}} &= \sqrt{\left(1 + \frac{\epsilon(\mathbf{k})}{\sqrt{\Delta^2 + \epsilon(\mathbf{k})^2}}\right)/2}. \end{aligned} \tag{4.6}$$

Since there are two solutions for each spin σ, we labeled them with the same value of $\mathbf{k}$ chosen in the noninteracting Fermi sea, differentiating them with a second quantum number taking on two possible values 1 and 2 for the lower and higher energy solutions, respectively.

The eigenfunctions and eigenvalues are:

$$\phi_{1\mathbf{k}\pm}(\mathbf{R}) = N^{-1/2} e^{i\mathbf{k}\cdot\mathbf{R}} (A_{\mathbf{k}} \mp B_{\mathbf{k}} e^{i\pi\cdot\mathbf{R}}) \tag{4.7}$$

$$E_1(\mathbf{k}) = -\sqrt{\Delta^2 + \epsilon(\mathbf{k})^2} + \frac{J}{2} \tag{4.8}$$

$$\phi_{2\mathbf{k}\pm}(\mathbf{R}) = N^{-1/2} e^{i\mathbf{k}\cdot\mathbf{R}} (B_{\mathbf{k}} \pm A_{\mathbf{k}} e^{i\pi\cdot\mathbf{R}}) \tag{4.9}$$

$$E_2(\mathbf{k}) = \sqrt{\Delta^2 + \epsilon(\mathbf{k})^2} + \frac{J}{2}. \tag{4.10}$$

In the half filled band case, the lower energy band is filled and the higher energy one empty.

The self-consistency condition is then

$$\pm\Delta + \frac{J}{2} = J \sum_{\mathbf{k} < \mathbf{k}_F} |\phi_{1\mathbf{k}\mp}(0)|^2 \tag{4.11}$$

or

$$\Delta = J\Delta \sum_{\mathbf{k} < \mathbf{k}_F} \frac{1}{\sqrt{\Delta^2 + \epsilon(\mathbf{k})^2}} \tag{4.12}$$

There are two possible solutions to this self-consistency equation. The first one is trivial:

$$\Delta = 0. \tag{4.13}$$

This is the paramagnetic Hartree solution already studied. The second one is the Matsubara condition for an antiferromagnet:

$$J \sum_{\mathbf{k} < \mathbf{k}_F} \frac{1}{\sqrt{\Delta^2 + \epsilon(\mathbf{k})^2}} = 1. \tag{4.14}$$

The energy of the Matsubara state is

$$\langle H \rangle = \sum_{\mathbf{k} < \mathbf{k}_F} \sum_\sigma \sum_{ij} T_{ij} \phi^*_{1\mathbf{k}\sigma}(\mathbf{R}_i) \phi_{1\mathbf{k}\sigma}(\mathbf{R}_j) + J \sum_{\mathbf{k} < \mathbf{k}_F} \sum_i |\phi^*_{1\mathbf{k}+}(\mathbf{R}_i)|^2 \times |\phi_{1\mathbf{k}-}(\mathbf{R}_i)|^2. \tag{4.15}$$

In the tight binding approximation this becomes

$$\langle H \rangle = 2 \sum_{\mathbf{k} < \mathbf{k}_F} (A^2_{\mathbf{k}} - B^2_{\mathbf{k}}) \epsilon(\mathbf{k}) + J \sum_{\mathbf{k} < \mathbf{k}_F} (1 - 4A^2_{\mathbf{k}} B^2_{\mathbf{k}}). \tag{4.16}$$

5. Antiferromagnetic State: Reaction Matrix Approximation

The Matsubara approximation is surely very decent in the $J \to \infty$ limit. For not so large J's one could again

attempt a perturbation series expansion, this time using the Matsubara states as single electron eigenstates. This series would not diverge since opposite spin electrons already undergo minimal interaction in the Matsubara approximation. But in order to treat the antiferromagnetic solution on equal footing with the paramagnetic one, we will again perform a reaction matrix analysis. We add an extra degree of freedom to the approximation by leaving the degree of polarization of the wavefunctions as a parameter with which to minimize the total energy.

The logic behind such an expansion on long-range ordered wavefunctions can be understood using thermodynamic Green's function theory. This requires the addition of a chemical potential term

$$-\frac{J}{2}\sum_i\sum_\sigma n_{i\sigma}$$

to the Hamiltonian in order to be consistent with the grand canonical ensemble involved in Green's functions. Let us also add and subtract a Matsubara potential. We can then subdivide the Hamiltonian into a one-electron part and an interacting part:

$$H' = H - \frac{J}{2}\sum_i\sum_\sigma n_{i\sigma} = H_1 + H_I \tag{5.1}$$

$$H_1 = \sum_{ij} T_{ij} c^+_{i\sigma} c_{j\sigma} + \sum_i\sum_\sigma \left(\Delta_{i\sigma} - \frac{J}{2}\right) n_{i\sigma} \tag{5.2}$$

$$H_I = J\sum_i n_{i+} n_{i-} - \sum_i\sum_\sigma \Delta_{i\sigma} n_{i\sigma}. \tag{5.3}$$

The one-electron propagator's time evolution is then controlled by H_1 in which the Matsubara part of the interaction is already included. Its equation of motion is:

$$\left(i\frac{\partial}{\partial t} - h_{1\sigma}\right) G_1^m(1_\sigma; 1'_\sigma) = \delta(1-1') \tag{5.4}$$

where

$$h_{1\sigma} G_1^m(1_\sigma; 1'_\sigma) = \left(\Delta_{1\sigma} - \frac{J}{2}\right) G_1^m(1_\sigma; 1'_\sigma) + \sum_j T_{1j} G_1^m(1+j_\sigma; 1'_\sigma). \tag{5.5}$$

Following Martin and Schwinger [5] we define

$$\left(i\frac{\partial}{\partial t_1} - h_{1\sigma}\right) = G_1^m(1_\sigma)^{-1} \tag{5.6}$$

The equation of motion for the two particle Green's function is then

$$\begin{aligned} &G_1^m(1_+)^{-1} G_1^m(2_-)^{-1}\{G_2(1_+2_-; 1'_+2'_-) - G_1^m(1_+; 1'_+) G_1^m(2; 2'_-)\} - G_1^m(1_+; 1'_+)[\Delta_{2-} G_1(2_-; 2'_-) + iJG_2(2_-2_+; 2'_-2^+_+)] \\ &\quad - G_1^m(2_-; 2'_-) \times [\Delta_{1+} G_1(1_+; 1'_+) + iJG_2(1_+1_-; 1'_+1^+_-)]\} = \Delta_{1+}\Delta_{2-} G_2(1_+2_-; 1'_+2'_-) + i\Delta_{1+} JG_3(1_+2_-2_+; 1'_+2'_-2^+_+) \\ &\quad + i\Delta_{2-} JG_3(1_+1_-2_-; 1'_+1^+_-2'_-) - J^2 G_4(1_+1_-2_-2_+; 1'_+1^+_-2'_-2^+_+) + iJG_2(1_+2_-; 1'_+2'_-)\delta(1-2). \end{aligned} \tag{5.7}$$

If a Hartree approximation is made

$$iJG_2(2_-2_+; 2'_-2^+_+) = -\Delta_{2-} G_1(2_-; 2'_-) \tag{5.8}$$

$$iJG_2(1_+1_-; 1'_+1^+_-) = -\Delta_{1+} G_1(1_+; 1'_+) \tag{5.9}$$

$$iJG_3(1_+2_-2_+; 1'_+2'_-2^+_+) = -\Delta_{2-} G_2(1_+2_-; 1'_+2'_-) \tag{5.10}$$

$$iJG_3(1_+1_-2_-; 1'_+1^+_-2'_-) = -\Delta_{1+} G_2(1_+2_-; 1'_+2'_-) \tag{5.11}$$

$$J^2 G_4(1_+1_-2_-2_+; 1'_+1^+_-2'_-2^+_+) = J^2 G_2(1_+2_-; 1'_+2'_-) \times G_2(1_-2_+; 1^+_-2^+_+) \tag{5.12}$$

$$= -G_2(1_+2_-; 1'_+2'_-)\Delta_{1+}\Delta_{2-} \tag{5.13}$$

we get

$$G_1^m(1_+)^{-1} G_1^m(2_-)^{-1}[G_2(1_+2_-; 1'_+2'_-) - G_1^m(1_+; 1'_+) G_1^m(2_-; 2'_-)] = iJG_2(1_+2_-; 1'_+2'_+)\delta(1-2). \tag{5.14}$$

FIGURE 3. *Power series expansion in* J.
The first hole-hole scattering diagram is of third order in J.

This is similar to the Ω approximation on a long-range ordered state. $\Delta_{i\sigma}$ now serves as a variational parameter with which to minimize the energy. The reaction matrix is that part of the Ω matrix which includes only electron-electron interaction. Since it involves lower order terms to the energy correction than any hole-hole scattering—as shown in figure 3—this equation also serves as justification for the reaction matrix approximation. It is interesting to note that neglecting the right hand side of this equation one gets back the Matsubara result since it is for $\Delta_{i\sigma}=Jn_{i-\sigma}$ that the energy is minimized.

In the diagram representation, the reaction matrix correction to the Matsubara energy would be as given in figure 2. The first diagram of figure 1 is here again missing since it is already included in the Matsubara energy. This is in analogy with the paramagnetic case. The difference is in the electron propagators which can here be adjusted variationally to yield the minimum energy.

As in the paramagnetic case, we write down a wavefunction for any two opposite-spin electrons:

$$\Psi_{\mathbf{k}_1\mathbf{k}_2}(\mathbf{R}_1\mathbf{R}_2)=\phi_{1\mathbf{k}_{1+}}(\mathbf{R}_1)\phi_{1\mathbf{k}_{2-}}(\mathbf{R}_2)-J\sum_{\mathbf{k}_1'\mathbf{k}_2'<\mathbf{k}_F}\frac{\phi_{2\mathbf{k}_{1+}'}(\mathbf{R}_1)\phi_{2\mathbf{k}_{2-}'}(\mathbf{R}_2)}{[E_2(\mathbf{k}_1')+E_2(\mathbf{k}_2')-E(\mathbf{k}_1)-E_1(\mathbf{k}_2)]}$$
$$\times\sum_{\mathbf{R}}\phi^*_{2\mathbf{k}_{1+}'}(\mathbf{R})\phi^*_{2\mathbf{k}_{2-}'}(\mathbf{R})\Psi_{\mathbf{k}_1\mathbf{k}_2}(\mathbf{RR}). \tag{5.15}$$

The energy correction to the Matsubara energy as given in eq (4.16) with $\Delta_{i\sigma}$ as a variational parameter is:

$$\Delta E=J\sum_{\mathbf{k}_1\mathbf{k}_2<\mathbf{k}_F}\sum_{\mathbf{R}}[\Psi^*_{\mathbf{k}_1\mathbf{k}_2}(\mathbf{RR})\phi_{1\mathbf{k}_{1+}}(R)\phi_{1\mathbf{k}_{2-}}(\mathbf{R})-\phi^*_{1\mathbf{k}_{1+}}(\mathbf{R})\phi^*_{1\mathbf{k}_{2-}}(\mathbf{R})\times\phi_{1\mathbf{k}_{1+}}(\mathbf{R})\phi_{1\mathbf{k}_{2-}}(\mathbf{R})]. \tag{5.16}$$

Since the wavefunction amplitude must be antiferromagnetically modulated, we can write

$$\Psi_{\mathbf{k}_1\mathbf{k}_2}(\mathbf{R}_1\mathbf{R}_2)=\Psi_{1\mathbf{k}_1\mathbf{k}_2}(\mathbf{R}_1-\mathbf{R}_2)+e^{i\boldsymbol{\pi}\cdot\mathbf{R}_1}\Psi_{2\mathbf{k}_1\mathbf{k}_2}(\mathbf{R}_1-\mathbf{R}_2) \tag{5.17}$$

Substituting into eq (5.15) the expressions for the wavefunctions in eqs (4.7) and (4.9) it can be deduced that

$$\Psi_{1\mathbf{k}_1\mathbf{k}_2}(0)=\frac{[A_{\mathbf{k}_1}A_{\mathbf{k}_2}-B_{\mathbf{k}_1}B_{\mathbf{k}_2}]}{[1+P_{\mathbf{k}_1\mathbf{k}_20}+Q_{\mathbf{k}_1\mathbf{k}_2\boldsymbol{\pi}}+Q_{\mathbf{k}_1\mathbf{k}_2-\boldsymbol{\pi}}]} \tag{5.18}$$

$$\Psi_{2\mathbf{k}_1\mathbf{k}_2}(0)=\frac{[A_{\mathbf{k}_1}B_{\mathbf{k}_2}-B_{\mathbf{k}_1}A_{\mathbf{k}_2}]}{[1+Q_{\mathbf{k}_1\mathbf{k}_20}+P_{\mathbf{k}_1\mathbf{k}_2\boldsymbol{\pi}}+P_{\mathbf{k}_1\mathbf{k}_2-\boldsymbol{\pi}}]} \tag{5.19}$$

with

$$P_{\mathbf{k}_1\mathbf{k}_2\mathbf{k}_3}=N^{-1}J\sum_{\mathbf{k}_1\mathbf{k}_2<\mathbf{k}_F}\frac{\delta(\mathbf{k}_1+\mathbf{k}_2+\mathbf{k}_3-\mathbf{k}_1'-\mathbf{k}_2')\,[B_{\mathbf{k}_1}B_{\mathbf{k}_2}-A_{\mathbf{k}_1}A_{\mathbf{k}_2}]^2}{[E_2(\mathbf{k}_1')+E_2(\mathbf{k}_2')-E_1(\mathbf{k}_1)-E_1)\mathbf{k}_2)]} \tag{5.20}$$

$$Q_{\mathbf{k}_1\mathbf{k}_2\mathbf{k}_3}=N^{-1}J\sum_{\mathbf{k}_1'\mathbf{k}_2'<\mathbf{k}_F}\frac{\delta(\mathbf{k}_1+\mathbf{k}_2+\mathbf{k}_3-\mathbf{k}_1'-\mathbf{k}_2')\,[A_{\mathbf{k}_1}B_{\mathbf{k}_2}-B_{\mathbf{k}_1}A_{\mathbf{k}_2}]^2}{[E_2(\mathbf{k}_1')+E_2(\mathbf{k}_2')-E_1(\mathbf{k}_1)-E_1(\mathbf{k}_2)]} \tag{5.21}$$

The energy correction will then become:

$$\Delta E=J\sum_{\mathbf{k}_1\mathbf{k}_2<\mathbf{k}_F}\{\Psi_{1\mathbf{k}_1\mathbf{k}_2}(0)\,[A_{\mathbf{k}_1}A_{\mathbf{k}_2}-B_{\mathbf{k}_1}B_{\mathbf{k}_2}]+\Psi_{2\mathbf{k}_1\mathbf{k}_2}(0)\,[A_{\mathbf{k}_1}B_{\mathbf{k}_2}-B_{\mathbf{k}_1}A_{\mathbf{k}_2}]-[A_{\mathbf{k}_1}A_{\mathbf{k}_2}-B_{\mathbf{k}_1}B_{\mathbf{k}_2}]^2-[A_{\mathbf{k}_1}B_{\mathbf{k}_2}-B_{\mathbf{k}_1}A_{\mathbf{k}_2}]^2\} \tag{5.22}$$

6. Density of States

The electron transport properties are governed by the density of states at the Fermi level. It would surely be of interest to calculate this quantity for the Hubbard model within our reaction matrix approximation. The electron density of states can be related to the spectral representation of the single-electron Green's function

$$\rho(E)=\pi^{-1}\lim_{\epsilon\to 0+}\operatorname{Im}\,[G_1(\mathbf{1}_+;\,\mathbf{1}_-|\nu)]_{\pi\nu/\tau=E-i\epsilon} \tag{6.1}$$

where the zero of energy is at the chemical potential. Because of the energy gap occurring in the antiferromagnetic state, its density of states at the chemical potential will surely be zero. We then need only concentrate on the paramagnetic case. The equation of motion for the one-particle Green's function in the paramagnetic state using the Hamiltonian in eqs (5.1), (5.2), and (5.3) with $\Delta_{1+}=\Delta_{2-}=J/2$ is:

$$G_1^0(1_+)^{-1}G_1(1_+;\,1'_+)=\delta(1-1')-iJG_2(1_+1_-;\,1'_+1'_-)-J/2G_1(1_+;\,1'_+) \tag{6.2}$$

from which we deduce

$$G_1(1_+;\,1'_+)=G_1^0(1_+;\,1'_+)-iJ\int d\bar{1}G_1^0(1_+;\,\bar{1}_+)[G_2(\bar{1}_+\bar{1}_-;\,1'_+\bar{1}_-)-G_1(\bar{1}_+;\,1'_+)G_1(\bar{1}_-;\,\bar{1}_-^+)]. \tag{6.3}$$

The knowledge of the two-particle Green's function is required. This we get from the Ω approximation. Since the density of states requires a better approximation than the energy we use the more accurate form [5]:

$$G_2(1_+2_-;\,1'_+2'_-)=G_1(1_+;\,1'_+)G_1(2_-;\,2'_-)+iJ\int d\bar{1}G_1^0(1_+;\,\bar{1}_+)G_1^0(2_-;\,\bar{1}_-)G_2(\bar{1}_+\bar{1}_-;\,1'_+2'_-). \tag{6.4}$$

We define the Ω matrix by the following equation:

$$JG_2(1_+1_-;\,1'_+2'_-)=\int d\bar{1}\Omega(1;\,\bar{1})G_1(\bar{1}_+;\,1'_+)G_1(\bar{1}_-;\,2'_-) \tag{6.5}$$

which with eq (6.4) leads to

$$\Omega(1;\,1')=J\delta(1-1')+iJ\int d\bar{1}G_1^0(1_+;\,\bar{1}_+)G_1^0(1_-;\,\bar{1}_-)\Omega(\bar{1};\,1') \tag{6.6}$$

If we now Fourier transform the space and time variables into the momentum and frequency domain, with

$$G_1(1_+;\,1'_+)=1/N\tau\sum_{\mathbf{k}}\sum_{\nu}^{\text{odd}}e^{i\mathbf{k}\cdot(\mathbf{R}_1-\mathbf{R}'_1)}e^{-i(\pi\nu/\tau)(t-t')}G_1(\mathbf{k}\nu) \tag{6.7}$$

and

$$G_1^0(\mathbf{k}\nu)=\frac{1}{\pi\nu/\tau-\epsilon(\mathbf{k})} \tag{6.8}$$

and also

$$\Omega(1;\,1')=1/N\tau\sum_{\nu}^{\text{even}}\sum_{\mathbf{k}}e^{i\mathbf{k}\cdot(\mathbf{R}_1-\mathbf{R}_1)}\,e^{-i(\pi\nu/\tau)(t-t')}\Omega\,(\mathbf{k}\nu). \tag{6.9}$$

we get the following equation for the Ω matrix

$$\Omega(\mathbf{k}\nu)=J+i(J/N\tau)\sum_{\nu_1}^{\text{odd}}\sum_{\mathbf{k}_1\mathbf{k}_2}\frac{\delta(\mathbf{k}-\mathbf{k}_1-\mathbf{k}_2)}{[\pi\nu_1/\tau-\epsilon(\mathbf{k}_1)][\pi(\nu-\nu_1)/\tau-\epsilon(\mathbf{k}_2)]}\Omega(\mathbf{k}\nu). \tag{6.10}$$

But then, from the Poisson sum rule, the summation over ν_1 yields

$$\Omega(\mathbf{k}\nu) = J - JN^{-1} \sum_{\mathbf{k}_1\mathbf{k}_2} \frac{\delta(\mathbf{k}-\mathbf{k}_1-\mathbf{k}_2)}{[\pi\nu/\tau - \epsilon(\mathbf{k}_1) - \epsilon(\mathbf{k}_2)]} \left[\frac{1}{1+e^{\beta\epsilon(\mathbf{k}_1)}} - \frac{1}{1+e^{-\beta\epsilon(\mathbf{k}_2)}} \right] \times \Omega(\mathbf{k}\nu) \tag{6.11}$$

At zero temperature, $\beta \to \infty$, and the term in brackets is either $+1$ or -1 depending on whether $\mathbf{k}_1$ and $\mathbf{k}_2$ both are below or above the Fermi surface, respectively. Since we are restricting ourselves to the reaction matrix approximation where only electrons interact, this implies we must restrict the scattered electrons above the Fermi sea. This brings us to a reaction or t-matrix whose equation is

$$T(\mathbf{k}\nu) = J + JN^{-1} \sum_{\mathbf{k}_1\mathbf{k}_2 > k_F} \frac{\delta(\mathbf{k}-\mathbf{k}_1-\mathbf{k}_2)}{[\pi\nu/\tau - \epsilon(\mathbf{k}_1) - \epsilon(\mathbf{k}_2)]} T(\mathbf{k}\nu) \tag{6.12}$$

that is

$$T(\mathbf{k}\nu) = \frac{J}{\left\{ 1 - J/N \sum_{\mathbf{k}_1\mathbf{k}_2 > k_F} \frac{\delta(\mathbf{k}-\mathbf{k}_1-\mathbf{k}_2)}{[\pi\nu/\tau - \epsilon(\mathbf{k}_1) - \epsilon(\mathbf{k}_2)]} \right\}} \tag{6.13}$$

We can now substitute this value for the t-matrix into eq (6.3) for G_1 and get:

$$G_1(\mathbf{k}\nu) = G_1^0(\mathbf{k}\nu) - i/N\tau \sum_{\nu'}^{\text{odd}} \sum_{k'} e^{i(\pi\nu'/\tau)0+} G_1^0(\mathbf{k}\nu) G_1(\mathbf{k}\nu) \times T(\mathbf{k}+\mathbf{k}',\ \nu+\nu') G_1(\mathbf{k}'\nu') - (J/2) G_1(\mathbf{k}\nu) G_1^0(\mathbf{k}\nu). \tag{6.14}$$

In order to perform the summation over ν', we must transform the t-matrix into its spectral representation:

$$T(\mathbf{k}\nu) = S_0(\mathbf{k}) + \int d\omega \, \frac{S_1(\mathbf{k}\omega)}{(\pi\nu/\tau - \omega)} \tag{6.15}$$

where

$$S_0(\mathbf{k}) = J \tag{6.16}$$

$$S_1(\mathbf{k}\nu) = 1/\pi \lim_{\epsilon \to 0+} \operatorname{Im}[T(\mathbf{k}\nu)]_{\pi\nu/\tau = \omega - i\epsilon} \tag{6.17}$$

$$\frac{J^2 N^{-1} \sum_{\mathbf{k}_1\mathbf{k}_2 > \mathbf{k}_F} \delta(\mathbf{k}-\mathbf{k}_1-\mathbf{k}_2)\delta(\omega - \epsilon(\mathbf{k}_1) - \epsilon(\mathbf{k}_2))}{\left\{ \left[1 - JN^{-1}P \sum_{\mathbf{k}_3\mathbf{k}_4 > \mathbf{k}_F} \frac{\delta(\mathbf{k}-\mathbf{k}_3-\mathbf{k}_4)}{(\omega - \epsilon(\mathbf{k}_3) - \epsilon(\mathbf{k}_4))} \right]^2 + \pi^2 \left[N^{-1} \sum_{\mathbf{k}_3\mathbf{k}_4 > \mathbf{k}_F} \delta(\mathbf{k}-\mathbf{k}_3-\mathbf{k}_4)\delta(\omega - \epsilon(\mathbf{k}_3) - \epsilon(\mathbf{k}_4)) \right] \right\}} \tag{6.18}$$

It is seen from eq (6.18) the t-matrix has a branch cut in the positive real axis of the complex frequency plane. If we now perform the summation over ν' using the spectral representation and approximating $G_1(\mathbf{k}', \nu')$ by $G_1^0(\mathbf{k}', \nu')$:

$$1/N\tau \sum_{\mathbf{k}} \sum_{\nu'}^{\text{odd}} T(\mathbf{k}+\mathbf{k}', \nu+\nu') G_1^0(\mathbf{k}'\nu') e^{i(\pi\nu'/\tau)0+}$$

$$= 1/N\tau \sum_{\nu'}^{\text{odd}} \sum_{\mathbf{k}} \left\{ J + \int_0^\infty d\omega \, \frac{S_1(\mathbf{k}+\mathbf{k}', \omega)}{[\pi(\nu+\nu')/\tau - \omega]} \, \frac{e^{i(\pi\nu'/\tau)0+}}{[\pi\nu'/\tau - \epsilon(\mathbf{k}')]} \right\} \tag{6.19}$$

$$= iJ/2 + i/N \sum_{\mathbf{k}' < \mathbf{k}_F} \int_0^\infty d\omega \, \frac{S_1(\mathbf{k}+\mathbf{k}', \omega)}{[\pi\nu/\tau - \omega + \epsilon(\mathbf{k}')]} \tag{6.20}$$

$$= -iJ/2 + i/N \sum_{\mathbf{k}' < \mathbf{k}_F} [T(\mathbf{k}+\mathbf{k}', \nu'')]_{\pi\nu''/\tau = \pi\nu/\tau + \epsilon(\mathbf{k}')} \tag{6.21}$$

we then get

$$G_1(\mathbf{k}\nu) = G_1^0(\mathbf{k}\nu) + \sum_{\mathbf{k}' < \mathbf{k}_F} \frac{J G_1^0(\mathbf{k}\nu) G_1(\mathbf{k}\nu)}{1 - J \sum_{\mathbf{k}_1 \mathbf{k}_2 > \mathbf{k}_F} \frac{\delta(\mathbf{k}+\mathbf{k}'-\mathbf{k}_1-\mathbf{k}_2)}{[\pi\nu/\tau + \epsilon(\mathbf{k}') - \epsilon(\mathbf{k}_1) - \epsilon(\mathbf{k}_2)]}}$$

$$- J G_1(\mathbf{k}\nu) G_1^0(\mathbf{k}\nu) \tag{6.22}$$

Before pursuing the calculation further, one notices the energy spectrum for G_1 is not symmetric with respect to electrons and holes, i.e. $G_1(k,\nu) \neq -G_1(\pi - \mathbf{k}, -\nu)$. This was to be expected since only electron-electron pair scattering has been considered. One would have to include hole-hole scattering to restore electron-hole symmetry. Since the hole-hole contribution to the energy occurs only in higher order terms as shown in figure 3, and since convergence of the perturbation expansion is rather rapid in the paramagnetic domain, we can safely restore electron-hole symmetry without upsetting the reaction-matrix approximation. We then define a hole reaction matrix which is the result of all possible sequential hole-hole scattering within the Fermi sea. From eq (6.11) its Fourier transform is:

$$\Omega(\mathbf{k}\nu) = J - JN^{-1} \sum_{\mathbf{k}_1 \mathbf{k}_2 < \mathbf{k}_F} \frac{\delta(\mathbf{k}-\mathbf{k}_1-\mathbf{k}_2)}{[\pi\nu/\tau - \epsilon(\mathbf{k}_1) - \epsilon(\mathbf{k}_2)]} \tag{6.23}$$

Going through a similar analysis as with the electron reaction matrix we would arrive at the final expression for G_1:

$$G_1(\mathbf{k}\nu) = \left\{ \pi\nu/\tau - \epsilon(\mathbf{k}) - \sum_{\mathbf{k}' < \mathbf{k}_F} \frac{J}{\left[1 - JN^{-1} \sum_{\mathbf{k}_1 \mathbf{k}_2 > \mathbf{k}_F} \frac{\delta(\mathbf{k}+\mathbf{k}'-\mathbf{k}_1-\mathbf{k}_2)}{(\pi\nu/\tau + \epsilon(\mathbf{k}') - \epsilon(\mathbf{k}_1) - \epsilon(\mathbf{k}_2))}\right]} \right.$$

$$\left. + \sum_{\mathbf{k} > \mathbf{k}_F} \frac{J}{\left[1 + JN^{-1}_{\mathbf{k}_1 \mathbf{k}_2 < \mathbf{k}_F} \frac{\delta(\mathbf{k}+\mathbf{k}'-\mathbf{k}_1-\mathbf{k}_2)}{(\pi\nu/\tau + \epsilon(\mathbf{k}') - \epsilon(\mathbf{k}_1) - \epsilon(\mathbf{k}_2)}\right]} \right\}^{-1} \tag{6.24}$$

From eqs (6.1) and (6.24) the density of states at the Fermi level can be shown to be:

$$\rho(E_F) - \sum_{\mathbf{k}_i}\sum_{i}\delta(E_i)\left\{1 + J^2\sum_{\mathbf{k}_2<\mathbf{k}_F}\frac{\sum_{\mathbf{k}_3\mathbf{k}_4>\mathbf{k}_F}\frac{\delta(\mathbf{k}_1+\mathbf{k}_2-\mathbf{k}_3-\mathbf{k}_4)}{(\epsilon(\mathbf{k}_2)-\epsilon(\mathbf{k}_3)-\epsilon(\mathbf{k}_4))^2}}{\left[1 - J\sum_{\mathbf{k}_5\mathbf{k}_6>\mathbf{k}_F}\frac{\delta(\mathbf{k}_1+\mathbf{k}_2-\mathbf{k}_5-\mathbf{k}_6)}{(\epsilon(\mathbf{k}_2)-\epsilon(\mathbf{k}_5)-\epsilon(\mathbf{k}_6))}\right]^2} + J^2\sum_{\mathbf{k}_2<\mathbf{k}_F}\frac{\sum_{\mathbf{k}_3\mathbf{k}_4<\mathbf{k}_F}\frac{(\delta(\mathbf{k}_1)+\mathbf{k}_2-\mathbf{k}_3-\mathbf{k}_4)}{(\epsilon(k_2)-\epsilon(k_3)-\epsilon(k_4))^2}}{\left[1 + J\sum_{\mathbf{k}_5\mathbf{k}_6<\mathbf{k}_F}\frac{\delta(\mathbf{k}_1\pm\mathbf{k}_2-\mathbf{k}_5-\mathbf{k}_6)}{(\epsilon(\mathbf{k}_2)-\epsilon(\mathbf{k}_5)-\epsilon(\mathbf{k}_6))}\right]^2}\right\} - 1 \qquad (6.25)$$

where

$$E_i - \epsilon(\mathbf{k}_1) - \sum_{\mathbf{k}_2<\mathbf{k}_F}\frac{J}{\left[1 - J\sum_{\mathbf{k}_3\mathbf{k}_4>\mathbf{k}_F}\frac{\delta(\mathbf{k}_1+\mathbf{k}_2-\mathbf{k}_3-\mathbf{k}_4)}{(E_i+\epsilon(\mathbf{k}_2)-\epsilon(\mathbf{k}_3)-\epsilon(\mathbf{k}_4))}\right]} + \sum_{k_2>k_F}\frac{J}{\left[1 + J\sum_{\mathbf{k}_3\mathbf{k}_4<\mathbf{k}_F}\frac{\delta(\mathbf{k}_1+\mathbf{k}_2-\mathbf{k}_3-\mathbf{k}_4)}{(E_i+\epsilon(\mathbf{k}_2)-\epsilon(\mathbf{k}_3)-\epsilon(\mathbf{k}_4))}\right]} = 0 \qquad (6.26)$$

7. Results

In this section we present the results of the above quantitative analysis together with some semiquantitative and qualitative arguments to round out our considerations. Figure 4 shows the energy of the four states in question as a function of c which is defined by

$$c = 4T/J \qquad (7.1)$$

In these units the width of the tight binding band for a simple cubic lattice is $12T$. We see that the t-matrix energy is always lower than the corresponding Hartree and Matsubara energies. The calculations of previous authors [10-12] generate only the two latter curves which never intersect. The antiferromagnetic state always has lower energy than the paramagnetic one in this approximation. The t-matrix approximation gives a different result. The corresponding energy curves intersect at about $c = 1.4$. For lesser c, i.e. nearer the atomic limit, the antiferromagnetic state has lower energy. For larger c, i.e. nearer the band limit, the paramagnetic state has lower energy. We see then that the short range correlations introduced by the t-matrix not only lower the energies of the respective zero order states but also change the predictions for the ground state of the system. Figure 5 exhibits the energy gap in the Matsubara and the variational

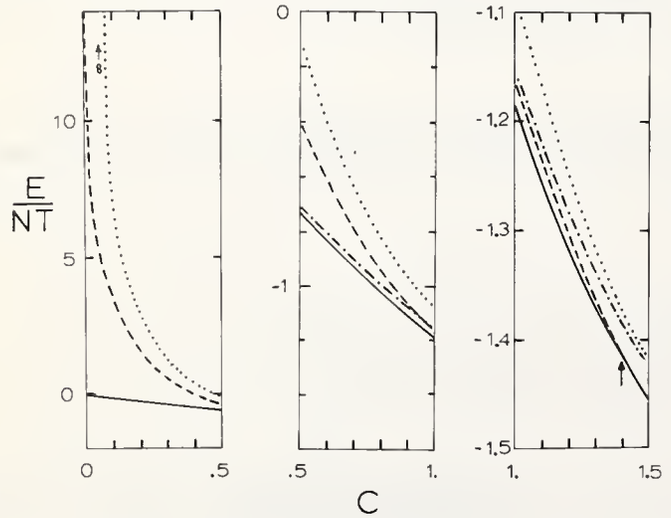

FIGURE 4. *Energy per electron in units of* T *in the . . paramagnetic Hartree - - - - paramagnetic* t*-matrix —·—· antiferromagnetic Matsubara and antiferromagnetic variation* t*-matrix states.*

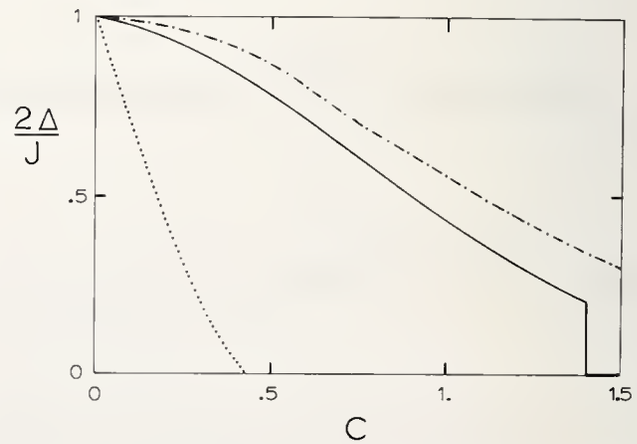

FIGURE 5. *Energy gap* 2Δ *in units of* J *in the —·—· antiferromagnetic Matsubara _____ antiferromagnetic variational* t*-matrix and . . . . Mott insulator states.*

t-matrix approximations for the antiferromagnetic states. The variational t-matrix gap is smaller than the Matsubara gap. Apparently it is energetically worthwhile to exchange some long range correlations for short range correlations. We see that at $c = 1.4$ the antiferromagnetic t-matrix gap and the sublattice magnetization, which are related by

$$\Delta/J = n - 1/2 \tag{7.2}$$

and where Δ is half the gap energy. collapse into the paramagnetic t-matrix state. Since the order changes discontinuously, this is a first order phase transition. Thus the density of states in the gap is suddenly raised to a finite value, which is shown in figure 6. This conclusion agrees with that of Edwards [11], who found that the density of states across an energy gap lifts at once if the long range order fails. The phase diagram is shown in figure 7. We have now two solutions in the range $c < 0.42$. They are the Mott insulator and the long range antiferromagnetic solutions. The question is which one is more stable or does one possibly have to consider some combination of these two states. For the latter case the system would possess both short and long range order. Our considerations are only qualitative because we do not produce the combined state, neither do we know how to calculate the Mott insulator at elevated temperatures. It is known that the long range antiferromagnetic order and the energy gap decrease with increasing temperature and they both disappear at a second order phase transition into the paramagnetic state [10]. But this can happen only if the paramagnetic state is stable. For $c < 0.42$ probably the Mott insulator is stable as we shall see below. Thus in this range one expects the gap to decrease from its value at zero temperature to the Mott value at the Néel temperature, while the long range order diminishes and the short range order increases. At the Néel temperature the long range order completely disappears. The system is an insulator both below and above the Néel temperature and the phase transition manifests itself only in the disappearance of long range order. Thus one expects a second order phase transition from the mixed insulator state to the Mott insulator state. If the temperature decreases to zero in the mixed insulating state the long range order will not become perfect except at the atomic limit $c = 0$. Thus the short range order shall have room to operate and lower the energy. Therefore we expect the phase transition line between the mixed and antiferromagnetic insulators not to cut the c axis somewhere at $c < 0.42$. It is possible that the axis should be cut at $0.42 < c < 1.4$ because we cannot exclude the possibility that the antiferromagnetic insulator retains some short range order for a range of c values at which the bound states of the Mott insulator do not exist. We have to realize that the short range order in the mixed insulator does not necessarily exist in the form of bound states. Above the Néel temperature the paramagnetic state provides the correct noninteracting one particle Green's functions. If $c < 0.42$ and the temperature is zero the Mott insulator is stable with respect to the paramagnetic metal. The question is, will the elevated temperature disrupt the Mott state and cause transition to a metal? We do not believe this will happen near the Néel temperature. Since the Mott state requires only short range order the increasing temperature will not affect it as drastically as it affects the antiferromagnetic state. If a given atom is principally occupied by an up spin electron and down spin hole, the nearest neighbor atoms are most likely occupied by pairs of opposite spin. Thus some short range antiferromagnetic order prevails. Increasing temperature can take its toll on this short range order. Note, however, that this is not just a local effect, since each pair is spread over the entire crystal. Thus probably the average binding energy per pair would decrease with

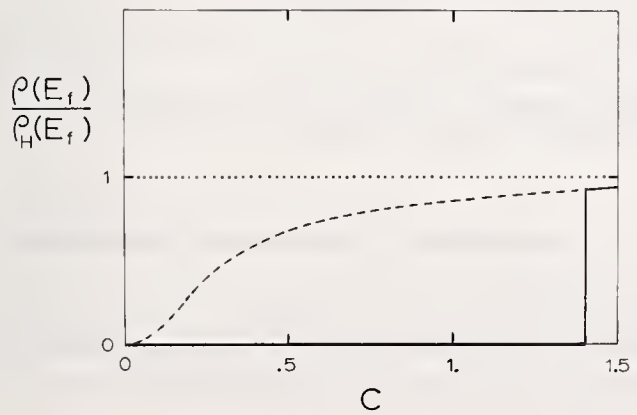

FIGURE 6. *Electronic density of states at the Fermi level for the . . . . paramagnetic Hartree - - - - paramagnetic t-matrix and ——— antiferromagnetic variational t-matrix states.*

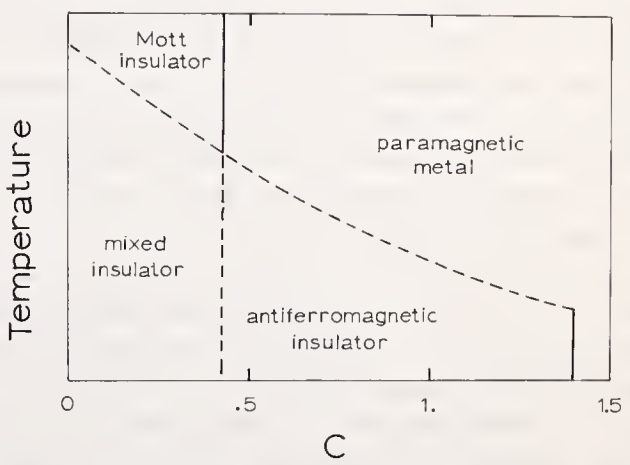

FIGURE 7. *Phase diagram.*
Solid lines: first order phase transitions. Broken lines: second order phase transitions.

increasing temperature. In addition to this, free pairs will also be created at elevated temperatures. Experience with the density of states at the antiferromagnet-paramagnet transition indicates that the Mott insulator paramagnetic-paramagnet transition will also be first order as a function of c. Mott's original discussions of this subject matter did include both the bound-pair insulator free-pair and antiferromagnetic insulator-paramagnetic metal transitions, although it was not made clear that these are two different transitions. Mott estimated [1] that in a hydrogen lattice the transition from antiferromagnet to paramagnet occurs at an interatomic distance of 4.5 Bohr radii. The other transition was not calculated. On the basis of Slater's [12] solution of the hydrogen 1s integrals, we can evaluate the intra-atomic interaction strength as

$$J \approx 1.25 \text{ Rydbergs}$$

and the hopping integral, as a function of the interatomic distance R, as

$$T \int a(\mathbf{r})(-\nabla_1^2 - 2/r_{1a} - 2/r_{1b})b(\mathbf{r})d_{\mathbf{r}} = -e^{-R}(3 + 3R + R^2/3) \text{ Rydbergs} \tag{7.3}$$

where $a(r)$, $b(r)$ are 1s hydrogen orbitals centered on nearest neighbor atoms, and where electron-electron interaction two center integrals in the Hartree-Fock approximation have been neglected as by Mott. Our estimate of the interaction is then

$$R = 3.8 \text{ Bohr radii}$$

which is close to the estimate of Mott.

8. Discussion

One may object to using a t-matrix approach in a high density system without going to higher orders in the expansion. The results indicate that the higher order terms are not necessary. Starting with the paramagnetic state as the ground state near $J=0$, a phase transition into the antiferromagnetic state occurs before the interaction could have drastic effects within the paramagnetic state. When the interaction could have drastic effects in the antiferromagnetic state the system is so close to the atomic limit that additional correlations have no room left to operate in. Thus it seems likely that once the correct zero order paramagnetic or antiferromagnetic wavefunctions have been chosen, the additional correlation effects could be handled by a power series expansion in J, i.e., by ordinary perturbation theory. Since we have not anticipated such simple results we did not use this approach. There is one more merit to the t-matrix method. It is necessary in the low density system where even with strong interactions phase transtitions are hard to achieve. This is duc to the fact that in a low density system particles can keep out of each other's way most of the time and a collective state does not easily form. Thus the zero order wavefunctions are not so sensitive so the strength of the interaction has to be handled with the t-matrix. Thus our present results will join better with the low density calculations we plan to perform if the same method is used.

9. Acknowledgments

The authors are indebted to Professor G. W. Pratt, Jr., for the hospitality extended to them at the Massachusetts Institute of Technology. The initial stages of this work were performed at Ledgemont Laboratory, Kennecott Copper Corporation, Lexington, Massachusetts. The numerical calculations were performed at the University of Sherbrooke Computation Center.

10. References

[1] Mott, N. F., Proc. Phys. Soc. (London) **62**, 416 (1949); Canadian J. Phys. **34**, 1356 (1956); Nuovo Cimento Supp. **7**, 312 (1958); Rev. Mod. Phys. **40**, 677 (1968).
[2] Hubbard, J., Proc. Roy. Soc. (London) **A276**, 238 (1961); **A281**, 401 (1964).
[3] Kemeny, G., and Caron, L. G., Phys. Rev. **159**, 687 (1967).
[4] Kemeny, G., and Caron, L. G., Rev. Mod. Phys. **40**, 790 (1968).
[5] Martin, P. C., and Schwinger, J., Phys. Rev. **115**, 1342 (1959).
[6] Reynolds, J. C., and Puff, R. D., Phys. Rev. **130**, 1877 (1963).
[7] Day, B. D., Rev. Mod. Phys. **39**, 719 (1967).
[8] Slater, J. C., Phys. Rev. **52**, 198 (1937).
[9] Kemeny, G., Phys. Letters **25a**, 307 (1967).
[10] Matsubara, T., and Yokota, T., Proc. Int. Conf. Theor. Phys. Kyoto and Tokyo, p. 693 (1953).
[11] Edwards, S. F., Phil. Mag. **6**, 617 (1961).
[12] Slater, J. C., Quantum Theory of Molecules and Solids, **Vol. I** (McGraw Hill, New York, 1963).
[13] des Cloizeaux, J., J. Phys. Rad. **20**, 606, 751 (1959).
[14] Penn, D. R., Phys. Rev. **142**, 350 (1966).

11. Appendix A: Numerical Technique

The various expressions for the energy we have derived for the Hubbard model all have in common the following typical summation in momentum space:

$$X = N^{-1} \sum_{\mathbf{k}_1 \mathbf{k}_2 < \mathbf{k}_F} \delta(\mathbf{k} - \mathbf{k}_1 - \mathbf{k}_2) f(\epsilon(\mathbf{k}_1); \epsilon(\mathbf{k}_2)) \tag{A.1}$$

To evaluate such a summation we went over to the continuum representation and calculated a density of states $\rho_{\mathbf{k}}(E_1E_2)$ such that:

$$N^{-1}\sum_{\mathbf{k}_1\mathbf{k}_2<\mathbf{k}_F}\delta(\mathbf{k}-\mathbf{k}_1-\mathbf{k}_2)\Longleftrightarrow\int_{-\infty}^{0}dE_1dE_2\rho_{\mathbf{k}}(E_1E_2) \tag{A.2}$$

Thus

$$X=\int_{-\infty}^{0}dE_1dE_2\rho_{\mathbf{k}}(E_1E_2)f(E_1;\,E_2) \tag{A.3}$$

The two energy variables in this density of states were subdivided into 50 intervals each. There were 64000 values chosen for the relative momentum in the Brillouin zone and 75 values of the total momentum $\mathbf{k}$ chosen in the S.C. symmetry element. In order to further smooth out fluctuations in the density of states the spread of the energies around each value of $\mathbf{k}$ was estimated using the first derivative of these energies. The paramagnetic Hartree energy then becomes:

$$\langle H\rangle=2N\int_{-\infty}^{0}dE_1dE_2\rho_0(E_1E_2)E_1+NJ/4 \tag{A.4}$$

while the t-matrix correction to this is:

$$\Delta E=J\sum_{\mathbf{k}}\int_{-\infty}^{0}\frac{dE_1dE_2\rho_{\mathbf{k}}(E_1E_2)}{\left\{1-J\int_{-\infty}^{0}\frac{dE_1'dE_2'\rho_{\mathbf{k}}(E_1'E_2')}{(E_1+E_2+E_1'+E_2')}\right\}}-NJ/4 \tag{A.5}$$

On the other hand, the Matsubara energy is:

$$\langle H\rangle=2N\int_{-\infty}^{0}dE_1dE_2E_1[A(E_1)^2-B(E_1)^2]+JN\int_{-\infty}^{0}dE_1dE_2\rho_0(E_1E_2)\times[1-4A(E_1)^2B(E_1)^2] \tag{A.6}$$

where

$$A(E)^2=\frac{1-E/\sqrt{\Delta^2+E^2}}{2} \tag{A.7}$$

$$B(E)^2=\frac{1-E/\sqrt{\Delta^2+E^2}}{2} \tag{A.8}$$

The correction to this energy from the t-matrix is:

$$\begin{aligned}\Delta E=J\sum_{\mathbf{k}}\int_{-\infty}^{0}dE_1dE_2\rho_{\mathbf{k}}(E_1E_2)\{&\Psi_{1\mathbf{k}}(E_1E_2)[A(E_1)A(E_2)-B(E_1)B(E_2)]\\&+\Psi_{2\mathbf{k}}(E_1E_2)[A(E_1)B(E_2)-B(E_1)A(E_2)]-[A(E_1)A(E_2)-B(E_1)B(E_2)]^2\\&-[A(E_1)B(E_2)-B(E_1)A(E_2)]^2\}\end{aligned} \tag{A.9}$$

with

$$\Psi_{1\mathbf{k}}(E_1E_2)=\frac{A(E_1)A(E_2)-B(E_1)B(E_2)}{1+P_{\mathbf{k}}(E_1E_2)+Q_{\mathbf{k}+\pi}(E_1E_2)+Q_{\mathbf{k}-\pi}(E_1E_2)} \tag{A.10}$$

$$\Psi_{2\mathbf{k}}(E_1E_2)=\frac{A(E_1)B(E_2)-B(E_1)A(E_2)}{1+Q_{\mathbf{k}}(E_1E_2)+P_{\mathbf{k}+\pi}(E_1E_2)+P_{\mathbf{k}-\pi}(E_1E_2)} \tag{A.11}$$

and

$$P_{\mathbf{k}}(E_1E_2)=J\int_{-\infty}^{0}\frac{dE_1'dE_2'\rho_{\mathbf{k}}(E_1'E_2')[A(E_1')A(E_2')-B(E_1')B(E_2')]^2}{(\sqrt{\Delta^2+E_1^2}+\sqrt{\Delta^2+E_2^2}+\sqrt{\Delta^2+E_1'^2}+\sqrt{\Delta^2+E_2'^2})} \tag{A.12}$$

$$Q_{\mathbf{k}}(E_1E_2)=J\int_{-\infty}^{0}\frac{dE_1'dE_2'\rho_{\mathbf{k}}(E_1'E_2')[A(E_1')B(E_2')-B(E_1')A(E_2')]^2}{(\sqrt{\Delta^2+E_1^2}+\sqrt{\Delta^2+E_2^2}+\sqrt{\Delta^2+E_1'^2}+\sqrt{\Delta^2+E_2'^2})} \tag{A.13}$$

The overall accuracy of this scheme was estimated at three significant digits for the Hartree and Matsubara energies and two significant digits for their t-matrix corrections. The resulting accuracy on the position of the energy crossover is somewhat poor because of the small energy differences involved. The critical value of c could possible by off by as much as 20%. But knowledge of the exact value of c at the crossover from the antiferromagnetic state to the paramagnetic state is not too critical, its existence being of primary importance.

12. Appendix B: $c \to \infty$ Limit

We will show that in the limit of very large c's, i.e., $J \to 0$, the paramagnetic state has lower energy than the antiferromagnetic state.

In this limit, the self-consistent value of the gap should be very small. As a matter of fact, in the Matsubara state

$$\lim_{c\to\infty} \Delta = 0 \text{ and } \lim_{c\to\infty} \Delta/J = 0 \tag{B.1}$$

This parameter Δ could then serve as an expansion parameter for the energy. The expression for the energy of the antiferromagnetic t-matrix approximation as a function of Δ is:

$$\epsilon(\Delta) = \sum_{\mathbf{k}} \int_{-\infty}^{0} dE_1 dE_2 \rho_{\mathbf{k}}(E_1E_2) \left\{ -2E_1^2/\epsilon_1 + J\left[\frac{(1-\Delta^2/\epsilon_1\epsilon_2 + E_1E_2/\epsilon_1\epsilon_2)}{2(1+P_{\mathbf{k}}(E_1E_2)+Q_{\mathbf{k}+\pi}(E_1E_2)+Q_{\mathbf{k}-\pi}(E_1E_2))} + \frac{(1-\Delta^2/\epsilon_1\epsilon_2 - E_1E_2/\epsilon_1\epsilon_2)}{2(1+Q_{\mathbf{k}}(E_1E_2)+P_{\mathbf{k}+\pi}(E_1E_2)+P_{\mathbf{k}-\pi}(E_1E_2))} \right] \right\} \tag{B.2}$$

with

$$P_{\mathbf{k}}(E_1E_2) \approx J/2 \int_{-\infty}^{0} \frac{dE_1' dE_2' \rho_{\mathbf{k}}(E_1'E_2')}{(\epsilon_1+\epsilon_2+\epsilon_1'+\epsilon_2')} \left(1 - \frac{\Delta^2}{\epsilon_1'\epsilon_2'} + \frac{E_1'E_2'}{\epsilon_1'\epsilon_2'}\right) \tag{B.3}$$

$$Q_{\mathbf{k}}(E_1E_2) \approx J/2 \int_{-\infty}^{0} \frac{dE_1' dE_2' \rho_{\mathbf{k}}(E_1'E_2')}{(\epsilon_1+\epsilon_2+\epsilon_1'+\epsilon_2')} \left(1 - \frac{\Delta^2}{\epsilon_1'\epsilon_2'} - \frac{E_1'E_2'}{\epsilon_1'\epsilon_2'}\right) \tag{B.4}$$

and

$$\epsilon = \sqrt{\Delta^2 + E^2}$$

As $J \to 0$ we can approximate

$$\frac{1}{1+P_{\mathbf{k}}(E_1E_2)+Q_{\mathbf{k}+\pi}(E_1E_2)+Q_{\mathbf{k}-\pi}(E_1E_2)} \approx 1 - P_{\mathbf{k}}(E_1E_2) - Q_{\mathbf{k}+\pi}(E_1E_2) - Q_{\mathbf{k}-\pi}(E_1E_2) \tag{B.5}$$

Taking the derivative of the energy with respect to Δ we get to first order in Δ' with $(E/\epsilon \approx 1)$:

$$\lim_{c\to\infty} \frac{\partial\epsilon(\Delta)}{\partial\Delta} \approx \Delta \sum_{\mathbf{k}} \int_{-\infty}^{0} dE_1 dE_2 \rho_k(E_1E_2) \left\{ 2/\epsilon_1 - \frac{2J}{\epsilon_1\epsilon_2} + \frac{2J}{\epsilon_1\epsilon_2} \times [P_{\mathbf{k}}^0(E_1E_2) + P_{\mathbf{k}-\pi}^0(E_1E_2) + P_{\mathbf{k}-\pi}^0(E_1E_2)] \right.$$
$$\left. + J(1/\epsilon_1^2 + 1/\epsilon_2^2)[P_{\kappa}^0(E_1E_2) - P_{\mathbf{k}+\pi}^0(E_1E_2) - P_{\mathbf{k}-\pi}^0(E_1E_2)] - JP_{\mathbf{k}}'(E_1E_2) \right\} \tag{B.6}$$

where

$$P_{\mathbf{k}}^0(E_1E_2) = J \int_{-\infty}^{0} \frac{dE_1' dE_2' \rho_{\mathbf{k}}(E_1'E_2')}{(\epsilon_1+\epsilon_2+\epsilon_1'+\epsilon_2')} \tag{B.7}$$

$$P_{\mathbf{k}}'(E_1E_2) = -J \int_{-\infty}^{0} \frac{dE_1' dE_2' \rho_{\mathbf{k}}(E_1'E_2')}{(\epsilon_1+\epsilon_2+\epsilon_1'+\epsilon_2')^2} [1/\epsilon_1' + 1/\epsilon_2' + 1/\epsilon_1 + 1/\epsilon_2) \tag{B.8}$$

Since it is those integrals containing the factor $1/\epsilon_1^2$ or $1/\epsilon_2^2$ which will dominate as $\Delta \to 0$, we conclude:

$$\lim_{c\to\infty} \frac{\partial \epsilon(\Delta)}{\partial \Delta} \approx 2J\Delta \sum_{\mathbf{k}} \int_{-\infty}^{0} \frac{dE_1 dE_2}{\epsilon_1^2} \rho_{\mathbf{k}}(E_1 E_2)[P_{\mathbf{k}}^0(E_1 E_2) - P_{\mathbf{k}+\pi}^0(E_1 E_2) - P_{\mathbf{k}-\pi}^0(E_1 E_2)] \tag{B.9}$$

But since

$$\lim_{\Delta\to 0+} \frac{\Delta}{\epsilon_1^2} = \lim_{\Delta\to 0+} \frac{\Delta}{\Delta^2 + E_1^2} = \pi\delta(E_1) \tag{B.10}$$

we finally get:

$$\lim_{c\to\infty} \frac{\partial \epsilon(\Delta)}{\partial \Delta} \approx \pi J \sum_{\mathbf{k}} \int_{-\infty}^{0} dE_2 \rho_{\mathbf{k}}(0, E_2) \times [P_{\mathbf{k}}^0(0, E_2) - P_{\mathbf{k}+\pi}^0(0, E_2) - P_{\mathbf{k}-\pi}^0(0, E_2)] \tag{B.11}$$

This integral was evaluated numerically and it is found that:

$$\lim_{c\to\infty} \frac{\partial \epsilon(\Delta)}{\partial \Delta} \approx \frac{0.04\pi}{c^2} > 0. \tag{B.12}$$

The energy then increases for $\Delta > 0$ which implies any antiferromagnetic state has larger energy than the paramagnetic one $\Delta = 0$.

ALLOYS; ELECTRONIC SPECIFIC HEAT I

CHAIRMEN: J. R. Anderson
J. H. Schooley

Electronic Structure of Gold and Its Changes on Alloying

E. Erlbach*

City College of CUNY, New York, New York 10032

D. Beaglehole

University of Maryland, College Park, Maryland 20740

We have measured the changes in reflectivity upon alloying small amounts of Ag, Cu and Fe into Au. By means of a Kramers-Kronig analysis, we have deduced the changes in ϵ_2 produced by this alloying. We relate these changes to shifts in the position and character of the electron energy bands in gold.

Key words: Electronic constant; electronic density of states; gold (Au); gold-copper alloys (Au-Cu); gold-iron alloys (Au-Fe); gold-silver alloys (Au-Ag); optical constants; reflectivity.

The optical constants of gold have been measured by several methods [1,2] and feature an edge at 2.5 eV followed by a second peak which starts at 3.5 eV (fig. 1). The first edge has been identified as being due to transitions from the top of the *d*-bands to the Fermi surface. The second edge has recently [3,4] been associated with transitions from the Fermi surface to the upper conduction band ($L_2' \rightarrow L_1$). This identification is supported by its similarity to the second edge in copper, where this identification has been verified by piezoreflectance measurements [5]. Additional structure is seen at 4.5 eV which has been assigned [2] to transitions from the *d*-band to the Fermi surface at $X(X_5 \rightarrow X_4')$ and another peak in ϵ_2 is seen around 7.5 eV.

Upon alloying Ag, Cu and Fe into Au, we see structure at all the above energies, and also at some additional energies (figs. 2-4). The experimental method has

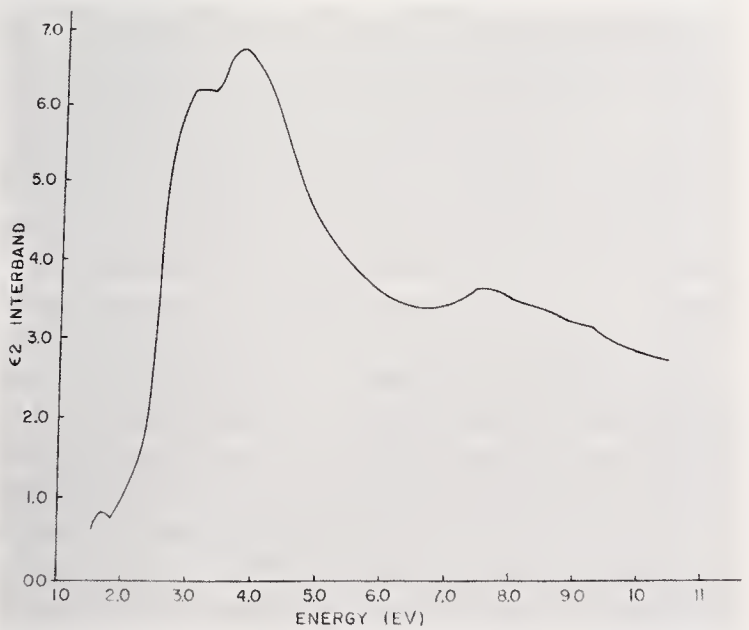

FIGURE 1. *The real part of the dielectric constant, ϵ_2, for pure gold.*

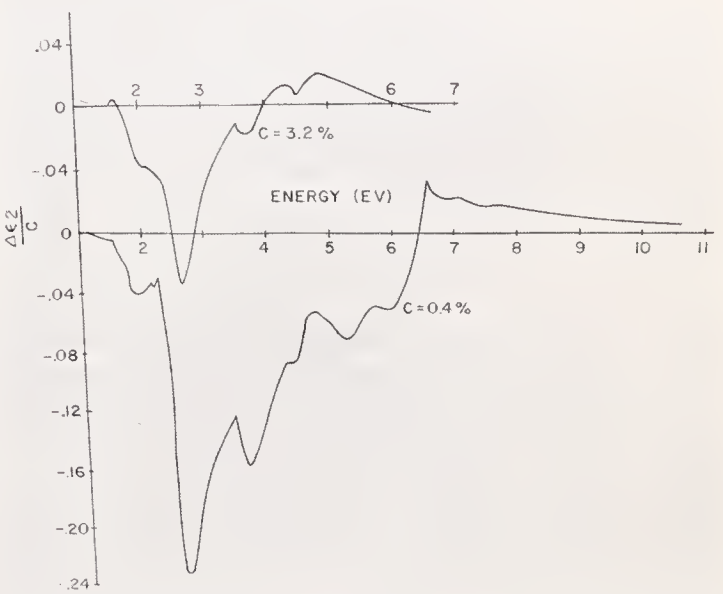

FIGURE 2. *The normalized changes in ϵ_2 for two* Au-Ag *alloys.* The concentration of Ag are as indicated.

*Work performed while on a Sabbatical at the University of Maryland.

417-156 O - 71 - 36

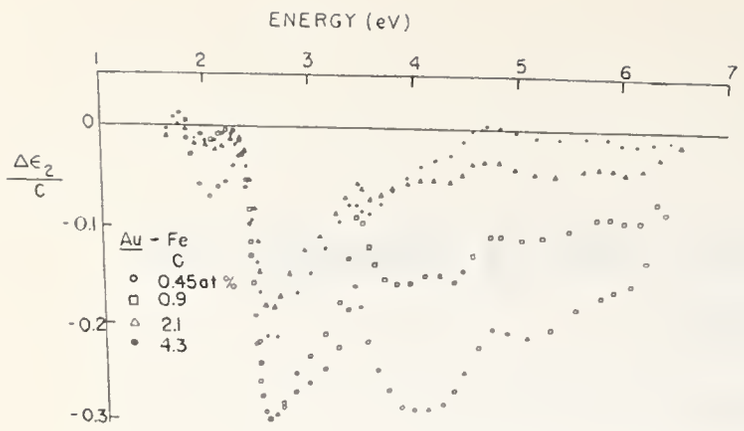

FIGURE 3. *The normalized changes in* ϵ_2 *for four* Au-Fe *alloys.* This data is taken from Phys. Rev. Letters **22**, 133 (1969). The concentrations of Fe are as indicated.

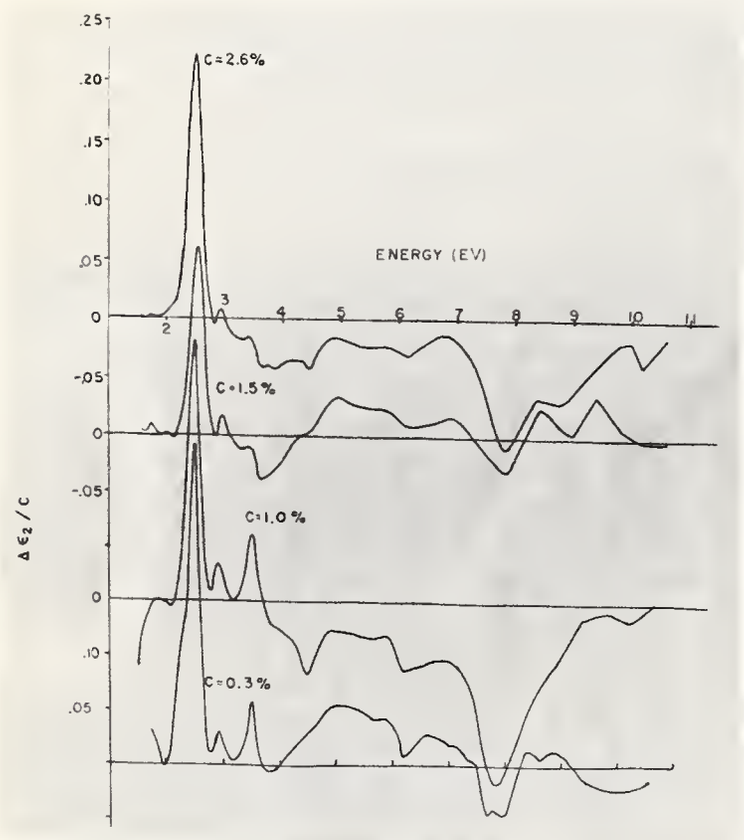

FIGURE 4. *The normalized changes in* ϵ_2 *for four* Au-Cu *alloys.* The concentrations of Cu are as indicated.

been partly published already [3,4], and a more detailed account will be published in the future. Briefly, we evaporate, simultaneously two films, one of pure gold and one containing the desired impurity, and then we measure the difference in reflectivity of the two films. A Kramers-Kronig analysis is used to convert these reflectivity differences into changes in ϵ_2 which are then normalized to 1 at. % concentration by dividing by the impurity concentration and plotted as a function of incident photon energy. Structure referred to in the following refers to these $\Delta\epsilon_2/c$ curves.

If alloying causes a shift of a band edge to higher energy, then the curves of $\Delta\epsilon_2/c$ will be proportional to $-d\epsilon_2/dE$ of the pure material, and a peak will be found at the point of maximum slope of ϵ_2. If alloying causes a broadening of a peak, then $\Delta\epsilon_2/c$ will exhibit a dispersive-resonance-like shape, going through zero at the peak of $d\epsilon_2/dE$.

Referring to our experimental curves in figures 2, 3 and 4, we find peaks in $\Delta\epsilon_2/c$ at 2.5 eV, which we have associated with a shift of the band edge upon alloying. The edge moves to higher energies for Ag [4,6] or Fe [3] alloys and to lower energies for the Cu [4] alloys. In the Ag and Cu alloys, the shifts have been explained as due to smooth changes in the relative energies of the d-bands and Fermi surface as one moves from Au to the other noble metals. These shifts are determined by two effects, perturbations in the average potential caused by the impurity atoms, and by changes in lattice constants [4].

We have found an additional sharp structure in $\Delta\epsilon_2$ for Au-Cu alloys at an energy of 2.9 eV (fig. 4); the peak at about 2.9 eV is evident in the curves for all four concentrations of copper. When one subtracts the background, one finds that the amplitude of the peak of $\Delta\epsilon_2/c$, when plotted vs. the concentration, c, decreases roughly linearly with c, being approximately given by

$$\Delta\epsilon_2/c = 0.039 - 0.009c \qquad (c \text{ in atomic percent}) \qquad (1)$$

A larger concentration is relatively less effective in increasing ϵ_2 in this region than a smaller concentration. A possible explanation for this will be given later.

If the curves for $\Delta\epsilon_2/c$ for Au-Ag and Au-Fe alloys (figs. 2 and 3) are examined closely near 2.9 eV, one notices a change in slope occurring at this energy. Furthermore, this change of slope can be seen in the curve of the derivative of ϵ_2 with energy. It is likely that both this change in slope and the peak in the Au-Cu curves have the same origin. Thus we believe the evidence indicates that the peak in gold at 2.5 eV actually consists of two peaks, which are not resolved in the ϵ_2 curve for pure gold nor in the $\Delta\epsilon_2$ curves for Au-Fe and Au-Ag. The fact that the edge in gold is not as sharp as the equivalent edge in copper would tend to corroborate this interpretation. The addition of copper to gold enhances the peak near 2.9 eV more than the peak at 2.5 eV, thus allowing it to be resolved from the main peak.

The reason for the particular effectiveness of copper in enhancing this peak may be the following. One can

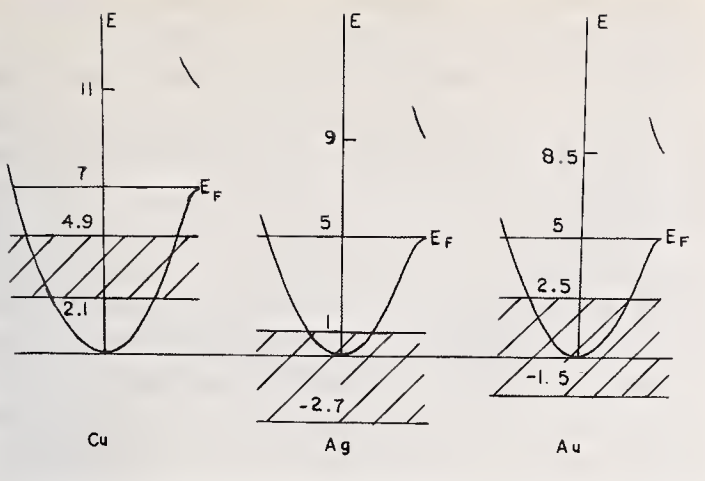

FIGURE 5. *Schematic diagrams of the band structure of gold, silver and copper.*

plot the bands of the noble metals schematically as in figure 5. The Fermi levels have been placed at their free electron values, and the top of the *d*-bands at an energy E_1 below, where E_1 is the energy of the first absorption edge for the pure metals. The widths of the *d*-bands have been taken as 2.8 eV for copper (from piezoreflectance measurements [5]), as 4 eV for gold (from our results) and 3.7 eV for silver (estimated by Lewis and Lee [7]). If one alloys copper into gold, one expects a mixing of the *d*-levels since they overlap, and the greatest perturbation is expected initially in the region of overlap. Since the bottom of the *d*-band of copper fails at an energy of 0.4 eV below the top of the gold *d*-band, one would initially expect the greatest perturbation near this energy. This is just the energy needed to affect the level responsible for ϵ_2 at 2.9 eV in gold since this is 0.4 eV below the absorption edge of 2.5 eV in gold. Thus, the addition of copper would be expected to greatly affect the 2.9 eV level and we see that this is indeed the case. As one increases the concentration of copper, one expects the perturbation to spread more evenly through the *d*-bands of gold and the enhancement per unit concentration of the 2.9 eV level should decrease with *c*. This may be the reason for the linear decrease in the peak mentioned previously. The addition of silver to gold would not be expected to single out the level at 2.9 eV more than the 2.5 eV level since the overlap is mainly with the lower part of the gold *d*-band. This would explain the absence of a large effect in Au-Ag at 2.9 eV.

While the existence of the double edge seems to be established, the nature of the splitting is not determined. Since gold is expected to have a spin-orbit splitting at the edge of the zone, and the order of magnitude of this splitting would not be inconsistent with a value of 0.4 eV the doubling of the edge may well be due to this splitting. Recently, Jacobs [8] has calculated the band structure of gold and suggests that the first edge of gold is shifted by 0.5 eV if spin-orbit coupling is included. This is close to our measured value. Other experiments and calculations are needed to confirm this identification.

We now turn our attention to the structure at 3.5 eV. We see that for the Au-Cu alloys, for the two lowest concentrations there exists a peak in $\Delta\epsilon_2$ at 3.5 eV. Since $d\epsilon_2/dE$ has a peak at this same energy, we associate the structure in the alloy data with a shift of the edge to lower energies. This shift seems to be linear at these low concentrations, but changes drastically when *c* is greater than 1.0 at. %. Above this concentration, there is still a small peak which has moved to a slightly lower energy but since the peak in $d\epsilon_2/dE$ occurs on the descending edge of the structure, it is probably now better to consider it as a dispersive resonance. This suggests that at higher concentrations the edge is broadened by alloying rather than shifted. The rate of shift at low concentrations is about -0.03 eV/at. %.

If one now examines the data for Au-Ag alloys one notices a pronounced *peak* at 3.5 eV and a *dip* at 3.65 eV in the low concentration sample, both becoming smaller for the higher concentration sample. One notes that the structure in $d\epsilon_2/dE$ peaks at 3.5 eV thus indicating that the addition of Ag to Au causes a shift of the edge to lower energies. The rate of shift is approximately $-.023$ eV/at. % for the lower concentration sample and $-.007$ eV/at. % for the higher concentration samples. The presence of the dip at 3.65 eV, however, makes it difficult to be certain that this interpretation is correct, and further study is required.

As outlined above, we also found nonlinearity of the 3.5 eV structure for the Au-Cu system, and the previously reported data [3] for Au-Fe is also nonlinear in this region (fig. 3). In the Au-Fe alloy system a sharp peak is clearly seen at 3.5 eV for the lowest concentrations, and this peak decreases in size for higher concentrations. Thus, all three alloy systems exhibit this characteristic behavior, i.e., a reduction or even disappearance in the shift of the edge per unit concentration as the concentration increases.

The interpretation of this variation is not clear. The 3.5 eV edge has been attributed to transitions at L from the region of the Fermi surface to the higher lying L_1 state. The equivalent edge occurs at 4.3 eV in Cu and at 4.1 eV in Ag. Thus, the simplest guess one would make for the motion of this edge is that it moves to higher energy for both Au-Ag and Au-Cu alloys. The average shift would be expected to be .006 eV/at. % for Ag and .008 eV/at. % for Cu. In both silver and copper,

however, the experimental shift is in the opposite direction. Furthermore, effect of a lattice constant change which explained the anomalous variation of the 2.5 eV edge in Au-Cu is also in the wrong direction. This can be estimated as follows. Since piezoreflectance measurements have not been made on single crystals of gold, we must use the piezoreflectance measurements on unoriented films [9]. The results for gold and copper are very similar, except that the magnitude of $\Delta\epsilon_2$ is about a factor of two lower in Cu compared with Au. We thus assume that we can use the single crystal results for copper, with a reduction by a factor of two for gold. This predicts a shift of +.01 eV/at. % of Cu for the 3.5 eV edge of Au using the published lattice constant parameters [10]. The experimental shift to lower energies is thus inconsistent both with the stress produced shifts and with the expected smooth shift of the same edge from its position in gold to its position in copper.

When one notes that (1) all the alloys exhibit the same type of nonlinearity for low concentrations, and that (2) the edge at 3.5 eV seems to be most affected, one concludes that the energy levels associated with this transition are particularly sensitive to small amounts of impurities. Since these effects do not occur for the level at 2.5 eV, which also involves the Fermi surface, it is likely that the L_1^u conduction band level is the one which is being perturbed nonlinearly. This level is the one which is split from the L_2' level primarily by *s-d* interaction with the L_1^l level at the bottom of the *d*-band (see fig. 2 of ref. 13, p. 662) [5,11-13]. One might expect that this splitting, which can be affected by changes in any of the other levels via changes in matrix elements or by changes in hybridization through orthogonalization, could be nonlinear with impurity concentration. One would then also expect that an edge caused by transitions from the lower L_1^l level to the Fermi surface would also be nonlinear with concentration. This edge should occur around 6.5 eV if the *d*-band is 4 eV wide. Examining the data near this energy, one sees in the Au-Cu alloys that one does indeed have nonlinear structure near 6.1 eV. This structure is strong for the low concentrations and much weaker for the higher concentration. It thus appears that the $L_1^l \rightarrow$ F. S. edge occurs at 6.1 eV. The $L_1^l - L_3^u$ separation—the width of the *d*-band at L—is thus 3.6 eV.

Our conclusion is thus that the nonlinearities in the edges at 3.5 and 6.1 eV are due to changes in the splitting of the two L_1 levels which are very sensitive to changes in potentials. A detailed calculation of the effect of impurities on the $L_1^u - L_1^l$ splitting would be most interesting.

The structure around 4.5 eV is more difficult to analyze. The data for ϵ_2 for pure gold shows only a slight shoulder at this energy: $d\epsilon_2/dE$ showing an asymmetric dip. The added absorption in this region has been attributed to $X_5 \rightarrow X_4'$ transitions [2] but the peak expected from this is obviously somewhat obscured by the background absorption from other points in the zone. The most prominent feature of the curves for $\Delta\epsilon_2/c$ for all gold alloys is a sharp rise beginning at 4.5 eV. This rise is also seen in $d\epsilon_2/dE$ and indicates that $\Delta\epsilon_2$ caused by alloying is roughly proportional to $d\epsilon_2/dE$ in this region. The data thus indicate a shift to lower energies for the states responsible for this transition. Since it is difficult to separate out the part of $d\epsilon_2/dE$ contributed by this edge alone, we have not estimated the rate of shift of this edge. In pure copper the $X_5 - X_4'$ edge is at 3.9 eV [5], while in pure silver, the edge is at 5.4 eV [7]. Thus adding copper to gold shifts the $X_5 - X_4'$ edge toward the copper value, while adding silver to gold shifts it away from the silver value. Once again, hybridization effects must subtly determine the way these energy levels vary.

Additional structure is seen in the form of a large dip in $\Delta\epsilon_2$ for the Au-Cu alloys at 8 eV. The curve of ϵ_2 for pure gold also has structure near this energy, resulting in a small negative dip in $d\epsilon_2/dE$ around this energy. The alloys data is not as reliable in this region as it is below 6 eV, because of experimental difficulties in the vacuum ultraviolet and because of uncertainties in the Kramers-Kronig analysis near the limit of the available data. But, within experimental error, we do not find any nonlinearities in the dip in this region. Further, the dip is a relatively large one, and it is not found in the Au-Ag alloys. The structure is thus particularly strongly perturbed by copper impurities, which move the edge to lower energies at a fairly high rate.

If one examines the band structure calculations for copper and gold, the only critical points which seem

TABLE 1

Levels	Separation in eV
$FS - L_1^u$	3.5 eV
L_1^l – F.S.	6.1 eV
$L_1^l - L_1^u$	9.6 eV
L_3^u – F.S.	2.5 eV
$L_1^l - L_3^u$	3.6 eV (*d*-band width at L)
$X_5 - X_4'$	4.5 eV
$X_1 - X_4'$	8 eV
$X_1 - X_5$	3.5 eV (*d*-band width at X)

capable of producing an edge near 8 eV are $X_1 \rightarrow X_4'$. (We are grateful to J. C. Phillips for this suggestion.) If this identification is correct then we can calculate the width of the *d*-band at X, i.e., $X_1 - X_5$, using the previously established value of 4.5 eV for $X_5 \rightarrow X_4'$. We thus get $X_1 - X_5$ as 3.5 eV, nearly the same width as we found at L. These energy levels are summarized in table 1.

We gratefully acknowledge conversations with N. F. Berk, J. C. Phillips and T. J. Hendrickson: This work was supported by ARPA and the NSF.

References

[1] Cooper, B. R., Ehrenreich, H., and Philipp, H. R., Phys. Rev. **138**, A494 (1965); Hodgson, J. Phys. Chem. Solids **29**, 2175 (1968); Theye, M. L., Proc. Colloquium on Thin Films, Budapest, 1965, p. 251 (1966); Canfield, L. R., Hass, A., and Hunter, W. R., J. Phys. (Paris) **25**, 124, (1964); Beaglehole, D., Proc. Phys. Soc. (London) **85**, 1007 (1965).

[2] Pells, G. P., and Shiga, M., to be published.

[3] Beaglehole, D., and Hendrickson, T. J., Phys. Rev. Letters **22**, 133 (1969).

[4] Erlbach, E., and Beaglehole, D., Bull. Am. Phys. Soc. II, **14**, 322 (1969); Beaglehole, D., and Erlbach, E., U. of Md. technical report No. 1000, to be published.

[5] Gerhardt, U., Beaglehole, D., and Sandrock, R., Phys. Rev. Letters **19**, 309 (1967); Gerhardt, U., Phys. Rev. **172**, 651 (1968).

[6] Wessel, P. R., Phys. Rev. **132**, 2062 (1963); Fukutani, H., and Sueka, O., in Optical Properties and Electronic Structure of Metals and Alloys, F. Abeles, Editor (North Holland Publishing Company, Amsterdam, 1966).

[7] Lewis, P. E., and Lee, P. M., Phys. Rev. **175**, 795 (1968).

[8] Jacobs, R. L., J. Phys. **C1**, 1296 (1968).

[9] Garfinkel, M., Tiemann, J. J., and Engeler, W. E., Phys. Rev. **148**, 695 (1966).

[10] Pearson, W. B., Handbook of Lattice Spacings and Structures of Metals, (Pergamon Press, New York, 1958).

[11] Mueller, F. M., and Phillips, J. C., Phys. Rev. **157**, 600 (1967).

[12] Dresselhaus, G. D., Solid State Comm. **7**, 419 (1969).

[13] Mueller, F. M., Phys. Rev. **153**, 662 (1967).

Discussion on "Electronic Structure of Gold and Its Changes on Alloying" by E. Erlbach (City College of CUNY) and D. Beaglehole (University of Maryland)

W. E. Spicer *(Stanford Univ.):* We have a measurement of the *d*-band width from photoemission data and it appears fairly definitely to be 5 to 5 1/2 volts wide, which I think is in fair agreement with the calculations.

E. Erlbach *(City College of CUNY):* Well it is unlikely that I'd get 5 electron volts even when one understands that the energy of the maximum at L and the maximum at X don't have to be the same. And therefore it's entirely possible you would get 4.6 possibly 5. You would be unlikely to get the 5 1/2 that you apparently get from your photoemission measurements, but it's possible also that the minimum does not occur at X or L. It could occur somewhere else. I do not know. It does seem that the widths at the X and L are smaller than the total widths of the *d*-bands in any case. I don't know if our results are inconsistent with yours although they don't seem consistent automatically.

W. E. Spicer *(Stanford Univ.):* But the widths you give there can be so much smaller than the density of states widths.

E. Erlbach *(City College of CUNY):* That's also right.

Density of States of AgAu, AgPd, and AgIn Alloys Studied by Means of the Photoemission Technique

P. O. Nilsson

Chalmers University of Technology, Göteborg, Sweden

The density of states of AgAu, AgPd, and AgIn alloys have been studied by means of the photoemission technique. General trends of the results are compared with the predictions from simple models of alloys. The rigid-band or virtual-crystal approximation cannot explain the results, while model calculations in the coherent potential approximation reproduces the observed density of states. The Friedel screening theory explains the shift of the Fermi level on alloying.

Key words: Coherent potential approximation; electronic density of states; Friedel screening theory; photoemission; silver-gold alloys (AgAu); silver-indium alloys (AgIn); silver-palladium alloys (AgPd); virtual crystal approximation.

1. Introduction

One of the earliest theories of the electronic properties of disordered alloys was the rigid-band approximation, which was introduced by Mott and Jones [1]. This first order perturbation theory predicts that the shape of the density of state curve does not change on alloying but is only rigidly shifted. Similar results are obtained in the so called virtual-crystal approximation in which the crystal has a periodic, concentration weighted mean potential. Although these theories have been widely used to interpret experimental results they do not in general describe the properties of disordered alloys correctly. For large band separations the theories are of course not valid at all: separated bands are formed which may be treated individually. More refined theories have to be used to describe intermediate cases. Korringa [2] and Beeby [3] used a multiple scattering description [4] to derive a t-matrix approximation. This theory was an important contribution but gave even for small band separations a spurious band gap. This is not present in the coherent potential approximation (CPA) introduced by Soven [5]. The free electron Green's function is here modified to contain an energy dependent self energy, which is self-consistently chosen so that the perturbation potentials do not contribute further to the scattering on the average. Velický et al. [6] showed that the CPA properly interpolates between the extreme limits of small and large band separations. Model calculations in three dimensions were also performed, to which we will return below.

We have studied by means of the photoemission technique three silver based alloys: AgAu, AgPd, and AgIn. These alloys have overlapping, slightly overlapping, and separated d-bands, respectively, and constitute suitable testing cases for alloy theories. A more extensive report on these measurements will appear elsewhere [8,9].

2. Results and Discussion

When one substance is dissolved in another the new density of states can be said to depend on three factors, namely the atomic potentials, the atom valence, and the lattice spacing. Both Ag and Au have almost the same lattice constant, 4.07 Å and 4.08 Å respectively, and the same valency, +1, so we have the largest contribution from potential effects. Figure 1 shows a summary of the photoemission results for this alloy system. Here the electron energy distribution curves are shown for the highest available photon energies, approximately 10 eV. Except for the cut-off at low electron energies, due to the so called escape function, the spectra are supposed to be a picture of the optical density of states below the Fermi level. We shall not discuss for the time

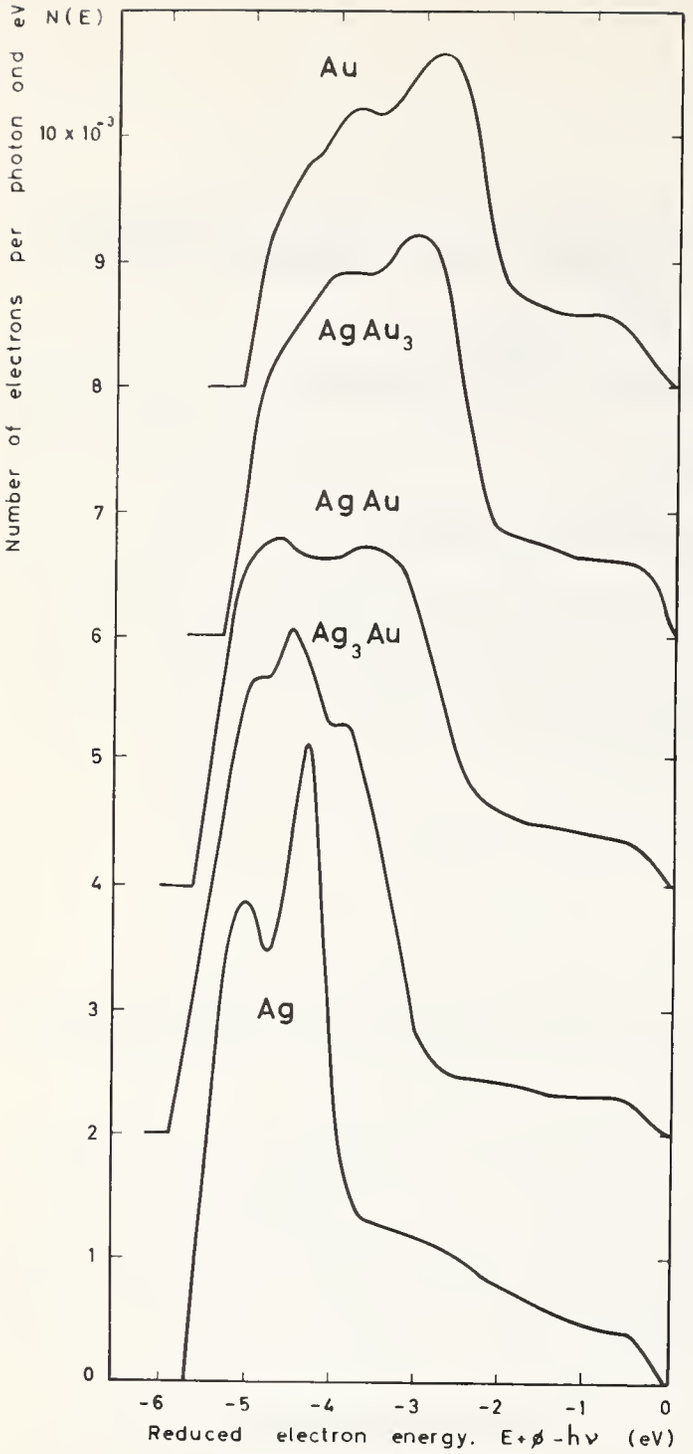

FIGURE 1. *Electron distributions obtained from photoemission experiments on* AgAu *alloys.*

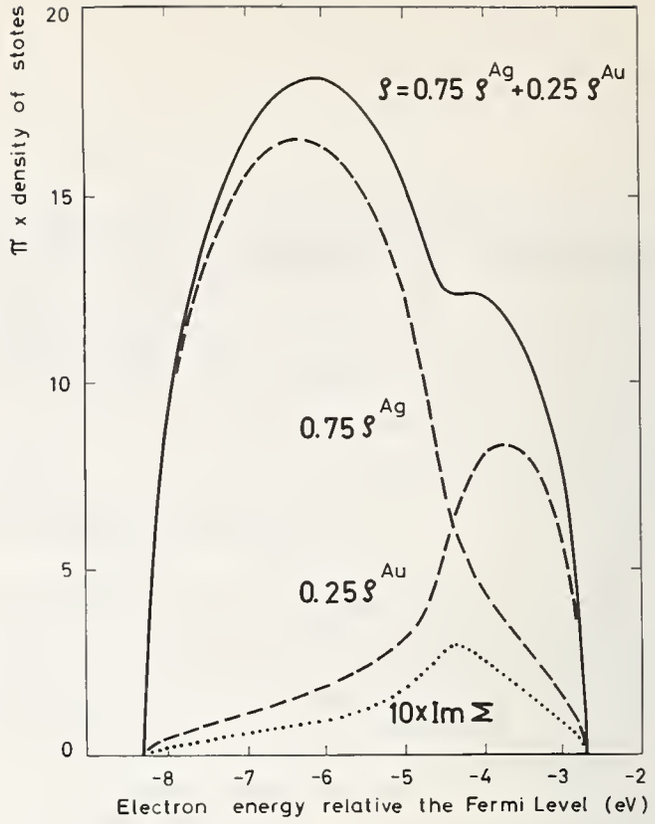

FIGURE 2. *Model calculation of the density of states in a 75–25 percent alloy.*

The equations derived in CPA by Velicky et al. [6] were used ($\delta = 0.70$). ρ^{Ag} and ρ^{Au} is the component density of states and Σ the self-energy.

being the relative importance of nondirect versus direct optical transitions [10]. It suffices to say that because of the low dispersion of the *d*-bands this question is not of importance when studying the main behavior of the bands on alloying. We observe in figure 1 that when Au is dissolved in Ag (the Ag_3Au-alloy) the Ag *d*-band is largely unaffected while the gold electrons seem to set up a band which extends above the Ag band. This is in contradiction to the rigid-band and virtual-crystal approximations. To study the predictions of the CPA we use the equations derived by Velický et al. in their model calculations [6] and calculate the alloy component density of states with appropriate parameters. Of course such a comparison is very crude (a single band Hamiltonian is used, in which all elements are independent of alloy composition. Thus we cannot take the real band structure into account). In the comparison we also disregard interference from conduction electrons. However, the results, presented in figure 2 tell us that in fact a Au band is expected at the top of the Ag band, where it was observed experimentally. In the decomposition of the electron densities we observe that the Au states in reality extend down to the bottom of the Ag band and vice versa. The electrons at the bottom of the Ag band can still be described by quasiparticles. At the top of the Ag band and in the impurity band the spectral density, however, will have a certain non-negligible width. The imaginary part of the self energy in figure 2 tells us that we have a damping of up to 0.6 eV halfwidth. The spectral density is found to be large over a range of *k*-values which means that the Au-state is "half-localized." On increasing the Au content (in the AgAu alloy), the Au band increases further in strength and width, again in agreement with CPA. As regards the $Ag\,Au_3$ alloy, the pure Au-spectrum is observed at the high energy part of the *d*-band. This is the same behavior as for the Ag_3Au alloy but with the con-

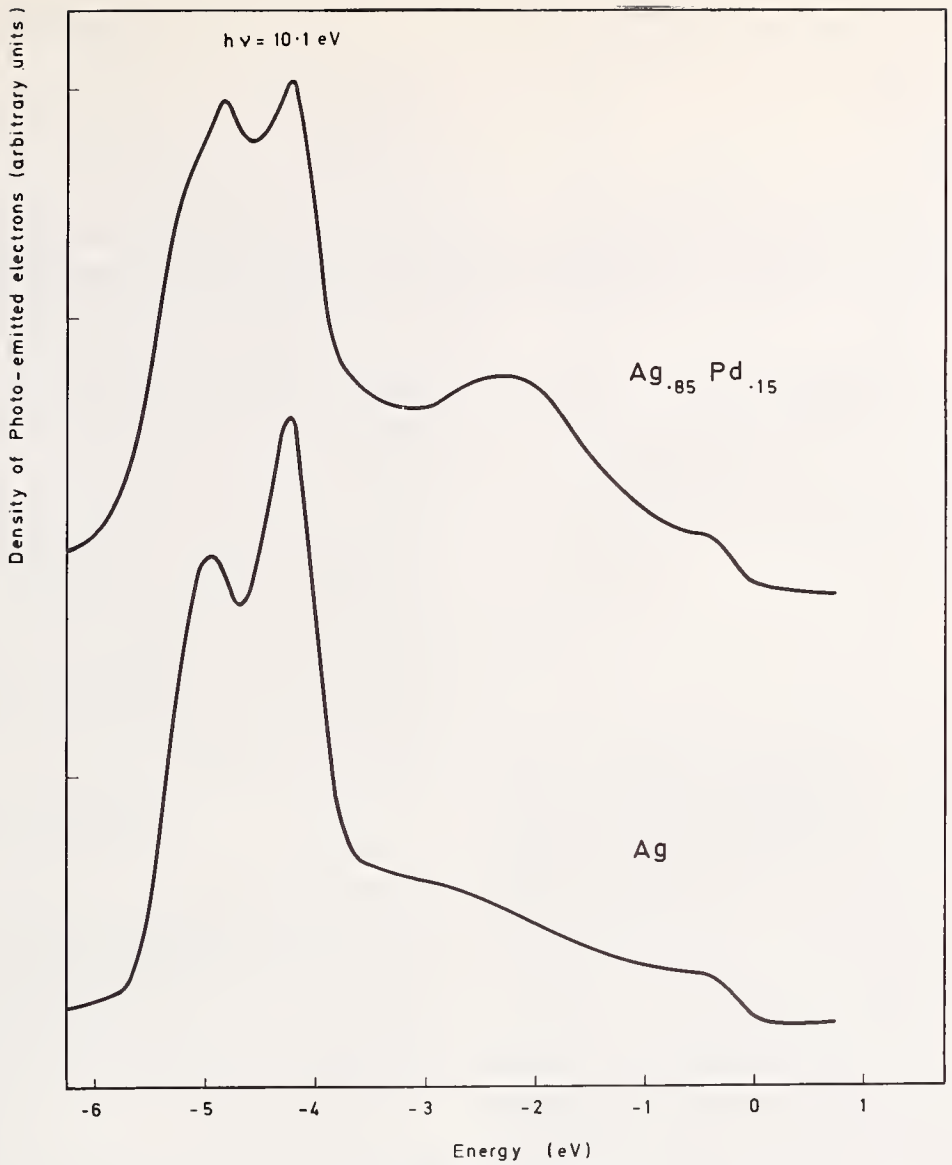

FIGURE 3. *Photoelectron distributions from* Ag *and* $Ag_{85}Pd_{15}$.

stituents exchanged. Influence of the Ag-atoms at the bottom of the band is not observed in our experiment because of masking by the escape function.

Turning to the AgPd alloys, we expect, according to the CPA, a gap in the density of states for low Pd-content because of the relative large band separation. In figure 3 is shown the photoemission spectra for pure Ag and for $Ag_{0.85}In_{0.15}$ [11]. As seen, the qualitative prediction is borne out. By choosing appropriate parameters in the model calculation it is also possible even for this alloy system to obtain quantitative agreement. The decomposition of the density of states shows that even for split bands we have a contribution from one kind of atom in the band of the other kind of atom. This can be viewed in the following way. Electrons scattered from, for instance the Pd atoms, will propagate through the lattice and resonate strongly with other Pd atoms. Because of the fact that the Ag atoms have a potential not differing too much from that of the Pd atoms they also contribute to the scattering in the Pd band but not, however, with the same strength. (A ratio 1:6 is obtained for $\rho^{Ag}:\rho^{Pd}$ in the Pd band). We also know that the band gap introduces strong fluctuations in the real part of the self energy, $Re\Sigma$. (In fact, a pole is present if the band gap is large but we cannot with certainty say if this is the case here.) Because of this, $Im\Sigma$ will have appreciable strength at Pd energies (2.5 eV at the bottom and 0.5 eV at the middle of the band), causing strong damping and a deviation of the spectral density from Lorentzian form. The energy versus k curve is flat and extends over all k values showing the strong localization of the d electrons. For a more complete description of the Pd states the interaction with the conduction electrons must be considered. The electron states are then said to be virtual bound [12]. Increasing the Pd content the band gap disappears at about 30 at. % Pd again at least qualitatively in agreement with the CPA.

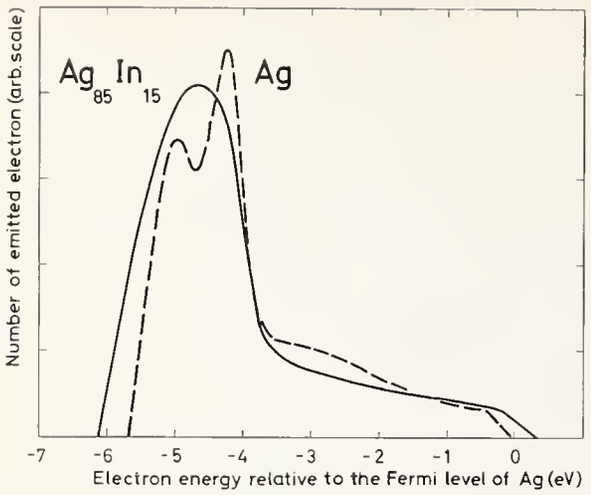

FIGURE 4. *Photoelectron distributions from* Ag *and* $Ag_{85}In_{15}$.

Finally we consider the AgIn alloys. The *d*-band of In is about 10 eV below that of Ag and the interaction is expected to be small. As seen in figure 4 the main effect on alloying is a smearing out of the fine structure. We assume that the upper part of the *d*-band does not shift very much. This is a reasonable assumption because the effect of decreasing bandwidth and the repulsion effect between the two *d*-bands is small and of opposite sign. We then note a shift of the Fermi level of about 0.3 eV. A pure filling of the conduction band gives a shift of the Fermi level of 1.6 eV if we assume a density of states at the Fermi level of 0.275 eV^{-1} $atom^{-1}$ [13]. However, taking the effect of screening of the In atoms into account [14] gives a shift of 0.27 eV in good agreement with the present experimental result. For the $Ag_{0.85}Pd_{0.15}$ alloy a downward shift of the Fermi level of 0.14 eV is calculated while no change is observed in separation between the *d*-band and the Fermi level. This may be due to the fact that the decreased bandwidth and the downward repulsion effect of the Ag *d*-band now sum up and contribute just as much as the Fermi level is shifted.

3. Conclusions

The theories for the electronic structure of disordered alloys give different predictions about the general shape of the alloy density of states. Among the theories the CPA seems to be the most general and applicable one. It gives the right predictions about the general shape of the density of states for the three alloy systems we have studied, while other theories fail. By using model calculations in the CPA even finer details in the density of states can be studied and interpreted.

We have found that for the AgAu alloys contributions from the two kinds of atoms can be followed through the alloy compositions although the density of states is strongly overlapping. For the $Ag_{0.85}Pd_{0.15}$ alloy the two constituents form two split bands with a contribution one in the other of about 15%. The $Ag_{0.85}In_{0.15}$ alloy has small interaction between the *d*-bands and it is possible to determine the shift of the Fermi level approximately. The observed value of 0.3 eV is in agreement with the screening theory by Friedel.

4. References

[1] Mott, N. F., and Jones, H., Theory of the Properties of Metals and Alloys (Dover Publication, Inc., New York, 1958).
[2] Korringa, J., J. Phys. Chem. Solids **7**, 252 (1958).
[3] Beeby, J. L., Phys. Rev. **135**, A130 (1964).
[4] Lax, M., Rev. Mod. Phys. **23**, 287 (1951).
[5] Soven, P., Phys. Rev. **156**, 809 (1967).
[6] Velický, B., Kirkpatrick, S., and Ehrenreich, H., Phys. Rev. **175**, 747 (1968).
[7] Soven, P., Phys. Rev. **178**, 1136 (1969).
[8] AgAu, AgIn: Nilsson, P. O., to be published.
[9] AgPd: Norris, C., to be published.
[10] Nilsson, P. O., Norris, C., and Wallten, L., Solid State Comm., in print.
[11] Norris, C., and Nilsson, P. O., Solid State Comm. 649 (1968).
[12] See e.g. Friedel, J., Nuovo Cim. Suppl. **7**, 287 (1958) and Myers, H. P., Proc. of the Chania Conference on Magnetism, June, 1959, and references therein.
[13] Kittel, C., Introduction to Solid State Physics (John Wiley & Sons, 1956).
[14] Friedel, J., in Advances in Physics, N. F. Mott, Editor (Taylor and Francis, Ltd., London, 1954) **Vol. 3**, p. 461.

Discussion on "Density of States of AgAu, AgPd, and AgIn Alloys Studied by means of the Photoemission Technique" by P. O. Nilsson (Chalmers University, Göteborg, Sweden)

H. Ehrenreich *(Harvard Univ.):* I would like to point out that largely as result of the work by Kirkpatrick and Velický that we've been able to extend the coherent potential approximation calculations to systems having degenerate bands and *s-d* hybridization effects such as in those described in the last two papers. We have applied this only to copper-nickel so far, but it's quite clear that the rigid band model does break down. These kinds of calculations are actually done fairly easily and I would hope that more people will undertake them. There is just one other point I wanted to make. The *d*-band width in the various noble metals can be quite different. For example, the gold *d*-band may be as much as 2-3 volts wider than that of Cu. Accordingly, the models involving overlapping or non-overlapping *d*-bands discussed in the preceding paper may be somewhat over-simplified until one knows more about what the widths really are.

A. Williams *(IBM):* Can the data be analyzed with comparable success by simply averaging the EDC's for the pure materials?

P. O. Nilsson *(Chalmers Univ.):* The experimental results cannot be obtained by taking the concentration weighted sum of the density of states of the constituents. Consider, e.g, the Ag-Au alloys. In pure Ag and Au the *d*-bands begin at about 4 and 2 eV, respectively, below the Fermi level. In, e.g., the Ag_3Au alloy, however, the *d*-band begins at 3 eV; that is, 1 eV lower than the value one would expect for an averaged density of states.

H. Ehrenreich *(Harvard Univ.):* Our calculations also indicate the failure of simple averaging.

W. E. Spicer *(Stanford Univ.):* I would just like to reinforce that. Seib has just completed a very detailed photoemission study where he looked in detail at this type of analysis. You just cannot add copper and nickel data of pure materials and get the photoemission results actually obtained from the alloys. It's a very interesting thing because there is a paper in the literature on soft x-ray emission where the authors stated that they were able to use successfully such an analysis—add copper and nickel and get the soft x-ray result of the alloy. That would indicate that there is a basic difference between the sort of information you get out of the two measurements.

Density of States Information from Low Temperature Specific Heat Measurements*

P. A. Beck and H. Claus

University of Illinois, Urbana

The calculation of one-electron density of state values from the coefficient γ of the term of the low temperature specific heat linear in temperature is complicated by many-body effects. In particular, the electron-phonon interaction may enhance the measured γ as much as twofold. The enhancement factor can be evaluated in the case of superconducting metals and alloys. In the presence of magnetic moments, additional complications arise. A magnetic contribution to the measured γ was identified in the case of dilute alloys and also of concentrated alloys where parasitic antiferromagnetism is superimposed on an over-all ferromagnetic order. No method has as yet been devised to evaluate this magnetic part of γ. The separation of the temperature-linear term of the specific heat may itself be complicated by the appearance of a specific heat anomaly due to magnetic clusters in superparamagnetic or weakly ferromagnetic alloys.

Key words: Alloys; density of states; low temperature specific heat; magnetic specific heat; many-body effects; superconductivity.

1. Introduction

In the Sommerfeld-Bethe theory of metals the electronic specific heat at low temperatures is linear in temperature in first order approximation. The lattice specific heat in the low temperature approximation is proportional to T^3 so that, in the absence of other contributions, the total specific heat

$$C=\gamma T+\beta T^3 \tag{1}$$

If C is known as a function of T, the two terms can be separated by making use of the linear variation of C/T with T^2 and by extrapolating to $T=0$. The intercept of the extrapolated line with the ordinate axis gives the temperature coefficient of the electronic specific heat γ. In the simplest case, γ is proportional to the electronic density of states at the Fermi surface, $N(E_F)$:

$$\gamma=(1/3)\pi^2\alpha k^2 N(E_F) \tag{2}$$

where k is the Boltzman constant and α is a numerical factor determined by the units used for γ, $N(E_F)$ and k.

Unfortunately, in a very large majority of cases, the simple procedure just described cannot be used, or at least it does not give reliable results. Many-body effects and, in some alloys, magnetic effects may make the determination of $N(E_F)$ from low temperature specific heat data more complicated than implied by eqs (1) and (2), or even impossible at the present state of the art.

2. Many-body Effects

In recent years it has become known that many-body effects, in particular the electron-phonon interaction, require renormalization of the effective mass of the electrons at the Fermi surface. This increases the measured electronic specific heat coefficient over the one-electron "band structure" value by the enhancement factor $(1+\lambda)$. For Na, Al and Pb, it was possible to determine the value of this factor [1], by comparing the "band structure electronic specific heat," calculated from the known band structure and the topography of the Fermi surface, with the measured electronic specific heat. These values: 1.25, 1.45 and 2.00, respectively, were found to agree quite well with the enhance-

*An invited paper presented at the 3rd Materials Research Symposium, *Electronic Density of States*, November 3-6, 1969, Gaithersburg, Md.

ment factors calculated from band structure, Fermi surface topography and phonon dispersion curves, on the basis of the electron-phonon interaction [1]. Unfortunately, for most other metals calculations of this sort cannot be made at present since at least some of the required data are not yet available. For superconducting metals the electron-phonon coupling constant λ has been recently calculated by McMillan [2], using the following equation which he derived from the strong coupling theory:

$$T_C = \frac{\theta}{1.45} \exp - \left[\frac{1.04(1+\lambda)}{\lambda - \mu^*(1+0.62\lambda)} \right], \qquad (3)$$

where T_C is the superconducting transition temperature and θ is the Debye temperature. The electron-electron interaction constant μ^* was assumed to have a value of 0.13 for all transition metals. The values of λ calculated by McMillan [2] for superconducting metals are given in table I.

TABLE I. *The Electron-Phonon Interaction Coefficient* λ *and "Band Structure" Density of States* $N(E_F)$ *for Superconducting Metals.*[2]

Element	T_c °K	Θ °K	λ	$N(E_F)$ $eV^{-1}atom^{-1}$
Be	.026	1390	.23	.032
Al	1.16	428	.38	.208
Zn	.85	309	.38	.098
Ga	1.08	325	.40	.091
Cd	.52	209	.38	.106
In	3.40	112	.69	.212
Sn	3.72	200	.60	.238
Hg	4.16	72	1.00	.146
Tl	2.38	79	.71	.182
Pb	7.19	105	1.12	.276
Ti	.39	425	.38	.51
V	5.30	399	.60	1.31
Zr	.55	290	.41	.42
Nb	9.22	277	.82	.91
Mo	.92	460	.41	.28
Ru	.49	550	.38	.46
Hf	.09	252	.34	.34
Ta	4.48	258	.65	.77
W	.012	390	.28	.15
Re	1.69	415	.46	.33
Os	.65	500	.39	.35
Ir	.14	420	.34	.51

It is now clear that the enhancement factor $(1+\lambda)$ of the electronic specific heat due to the electron-phonon interaction can be as high as 2, or more. This interaction affects only the electrons whose kinetic energy is close to the Fermi energy. The density of states at lower levels, that is for most of the electrons in the metallic band, may be assumed to correspond to the one-electron "band structure" situation. Hence, the lower, "band structure density of states" values must be used in determining the band width, for instance, rather than the density of states enhanced by electron-phonon interaction, as obtained from low temperature specific heat measurements. Using the electron-phonon coupling constant λ, for instance the values given in table I, the "band structure density of states" at the Fermi level $N(E_F)$ can be calculated from the experimentally determined value of the low temperature specific heat coefficient γ' as follows:

$$N(E_F) = \frac{3}{\pi^2 k^2 \alpha (1+\lambda)} \gamma' \qquad (4)$$

For most of the nonsuperconducting metals and alloys the value of λ is at present unknown and, as a result, the "band structure density of states" cannot be calculated from the low temperature specific heat.

As seen in figure 1, the experimental electronic specific heat coefficient γ' for the b.c.c. 3*d*-transition metals and their alloys as a function of electron concentration [3] shows prominent maxima and minima in the range of *e/a* from 4 to 9. Since in the region of the minima and of the second maximum the alloys are not superconducting, the "band structure density of states" cannot be calculated at present. Thus, the interesting question whether the prominent features of these curves are due to changes in the electron-phonon enhancement factor upon alloying, or indeed these features are characteristic of the electronic band structure of the transition metals concerned, cannot be answered

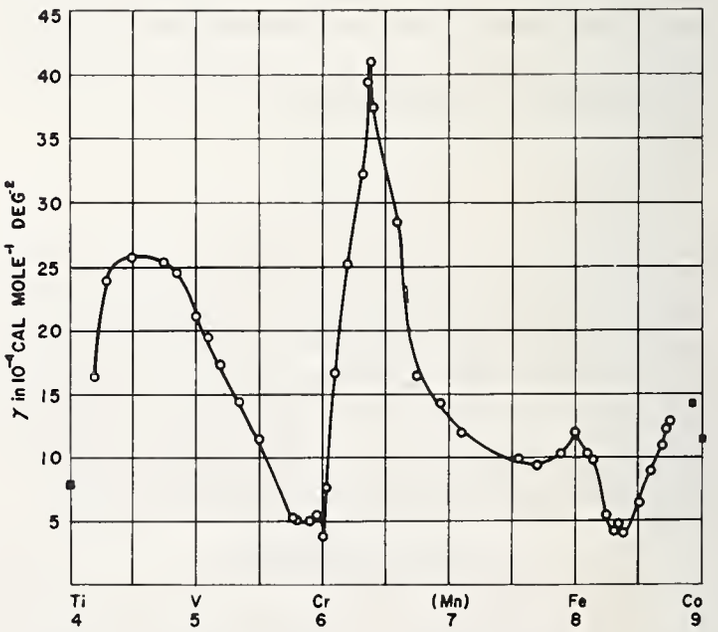

FIGURE 1. *Coefficient* γ' *or* γ'' *of the low temperature specific heat term linear in temperature vs electron concentration* e/a *for b.c.c. alloys of* 3d *transition metals* [3]. *Points marked by filled squares represent data for close-packed structures.*

with certainty. However, the work of McMillan [2] allows the conclusion that the electron-phonon coupling constant (and, thus, the enhancement factor) depends primarily on the phonon frequencies, rather than on the electronic properties. Since the elastic constants and, therefore, the phonon frequencies are not known to undergo drastic changes with the composition in such solid solution alloys composed of metals near one another in the same row of the periodic table, it may be concluded with a reasonable degree of probability that the prominent features mentioned of the γ' versus e/a curve of figure 1 are in fact resulting from corresponding variations in the "band structure density of states," even though the relative magnitude of the various minima and maxima may be appreciably altered by the gradual changes in the coupling constant with composition.

3. Magnetic Effects

Considerable difficulties are often encountered in determining the value of γ' for solid solution alloys of ferromagnetic with antiferromagnetic or nonmagnetic metals. For instance, it was found [4] for the random solid solution alloys Mn-Ni that, in addition to the electronic specific heat coefficient γ', the measured coefficient γ'' of the term of the low temperature specific heat linear in temperature includes also a magnetic contribution γ_m:

$$\gamma'' = \gamma' + \gamma_m. \tag{5}$$

The alloy $MnNi_3$ can be ordered by thermal treatment and, in the well-ordered condition, the coefficient of the linear term of the low temperature specific heat is approximately half that for the disordered alloy of the same composition. This lower value is substantially free of the magnetic contribution γ_m and it may be considered as approximately equal to the real experimental electronic specific heat γ' of the alloy. On the other hand, the larger γ'' value for the disordered alloy includes γ_m. Similar magnetic contributions to γ'' were identified in a number of other f.c.c. solid solution alloy systems [4] and in b.c.c. Fe-Al alloys [5]. It is significant that in the same alloy systems, and at similar compositions, magnetic measurements by Kouvel [6,7] detected the appearance of an asymmetrical hysteresis loop after cooling in a magnetic field through the Curie temperature ("exchange anisotropy"). In addition to this effect of field cooling on the magnetic properties, in several instances an effect of field cooling on γ_m was also detected [4,8], figure 2.

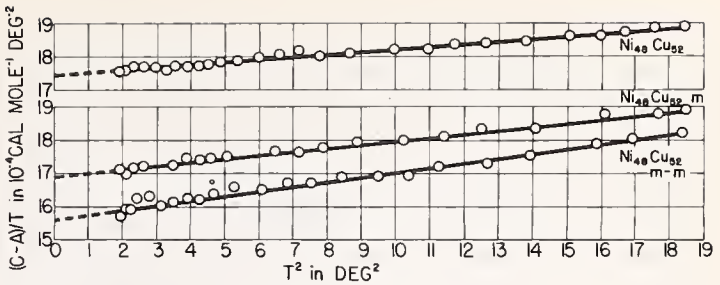

FIGURE 2. (C-A)/T *vs* T^2 *(where* C-A *is low temperature specific heat less magnetic cluster contribution, see eq (5)) for alloy* $Ni_{0.48}$ $Cu_{0.52}$ *cooled without a magnetic field (top graph), cooled in 14 kOe field from 300 to 4.2 K with the field turned off during the measurements (graph* m*) and field-cooled with the field on during measurements (graph* m − m*)* [8].

The occurrence in the same alloys of "exchange anisotropy" and of a magnetic contribution to the low temperature specific heat term linear in temperature suggests that these two phenomena may be associated with the same structural condition. This expectation is further supported by the fact that γ_m is normally also affected by field cooling. According to Kouvel's highly successful model [7], the structural condition responsible for "exchange anisotropy" is a spatially inhomogeneous magnetic state, *e.g.*, the superposition of local "parasitic antiferromagnetism" on net overall ferromagnetism. Overhauser [9] and Marshall [10] connected the magnetic contribution to the linear term of the low temperature specific heat with the location of a sufficient number of spins in a near-zero field. In Overhauser's theory this condition arises at the nodes of the static spin density waves of an antiferromagnet. Marshall pointed out that the required condition may arise in dilute spin systems, where the average distance between neighboring spins is sufficiently large, so as to make the interactions weak, as in dilute Cu-Mn alloys. The alloys considered above are neither antiferromagnetic nor dilute. However, because of the peculiar, complicated spin arrangement, resulting from the superposition of local parasitic antiferromagnetism on net overall ferromagnetism, it may be expected that many spins are located in small regions where ferromagnetic and antiferromagnetic exchange interactions nearly cancel each other locally, so that the average field in such regions is near zero [4]. In accordance with this "local field-cancellation" model, the effect of field cooling on γ_m may come about if the application of an external magnetic field during cooling through the Curie temperature increases or decreases the number of spins located in near-zero field. Both increase and decrease [($MnNi_3$ [4], $Ni_{0.48}Cu_{0.52}$ [8])] were in fact observed. It is easy to visualize that the change in γ_m as a result of field cooling may also happen to be negligibly

small, even though the value of the magnetic contribution γ_m itself is large. Thus, while the occurrence of a measurable effect of field cooling on the temperature-linear term of the low temperature specific heat may be considered as a proof for the existence of a magnetic contribution to this term, the absence of such an effect does *not* prove that γ_m is zero, or that it arises through a mechanism different from the "local field cancellation."

If the experimentally determined coefficient of the temperature-linear term of the low temperature specific heat includes a magnetic contribution, it is at present not possible to derive from such a γ'' value the "experimental electronic specific heat coefficient" γ', which is free from γ_m. This is well illustrated by the Ni-Cu alloys, for which the coefficient of the linear term has a maximum around the composition $Ni_{0.48}Cu_{0.52}$ [8]. A detailed study of the properties of these f.c.c. solid solutions at compositions in the vicinity of the maximum [11] shows that the experimental values of the coefficient do in fact include a magnetic contribution. It is, therefore, not possible to tell whether the maximum is entirely due to γ_m, or whether γ' itself has a maximum, which is merely increased by the addition of γ_m. A maximum in γ' has been expected on theoretical grounds [12] because of enhancement due to the electron-paramagnon interaction [13,14]. The theory

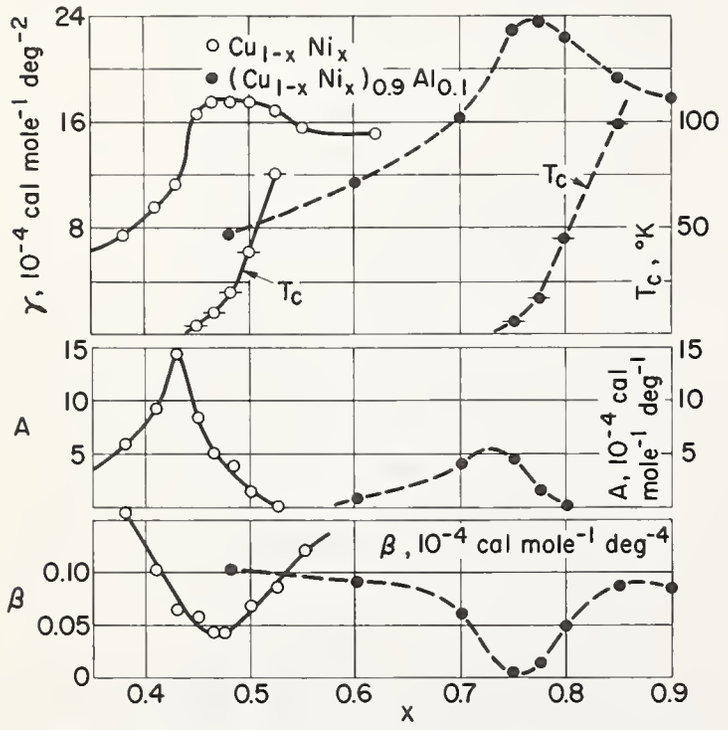

FIGURE 3. *Coefficient γ'' of the temperature-linear low temperature specific heat term, Curie temperature T_C, temperature independent specific heat term A and coefficient β of the T^3 term, obtained by least squares fitting to eq (5), for $Cu_{1-x}Ni_x$ (solid lines) and for $(Cu_{1-x}Ni_x)_{0.9}Al_{0.1}$ (dashed lines) alloys vs x [11,22,24].*

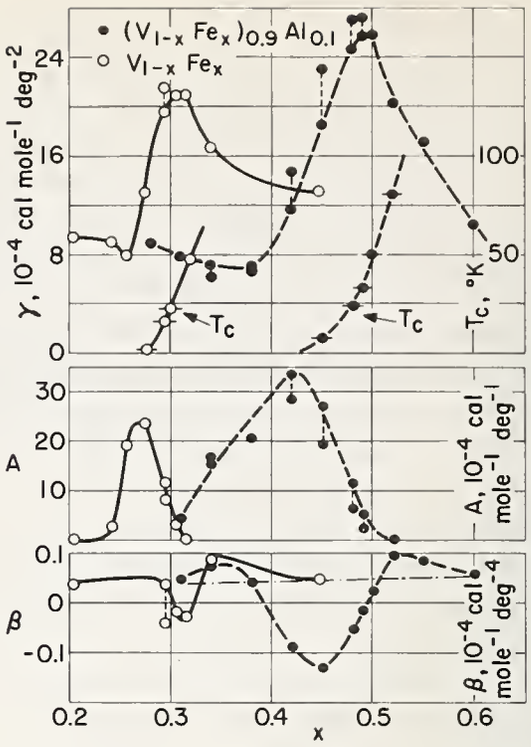

FIGURE 4. *Low temperature specific heat and Curie temperature data, as in figure 3, for $V_{1-x}Fe_x$ (solid lines) and $(V_{1-x}Fe_x)_{0.9}Al_{0.1}$ (dashed lines), alloys [3,23,24].*

would require the maximum of γ' to occur at the critical composition, where ferromagnetism just begins to set in at 0 K. Detailed study of the magnetic properties showed [11] that the critical composition is at approximately 57 percent Cu, where γ'' already decreased to a value far below its maximum. Figure 3 gives γ'' for the Ni-Cu solid solutions, together with Curie temperature data, which define the critical composition. One may conclude that the maximum in γ'' is largely, or entirely, due to γ_m, rather than to γ'. That the maximum in γ_m should occur in the weakly ferromagnetic region is entirely consistent with the "local field cancellation" model discussed above. It is quite likely that the maximum in the coefficient of the linear term for the f.c.c. Rh-Ni solid solutions, which apparently also occurs off the critical composition on the ferromagnetic side [15,16], is also due to a magnetic contribution γ_m. In fact, several solid solution alloy systems are now known to exhibit similar conditions. Figure 3 shows this for a series of Ni-Cu-Al ternary alloys with a constant Al-content of 10 percent. It is seen that the Al addition shifts the critical composition to a higher Ni/Cu ratio, that the maximum in γ'' (which is here even higher than for the binary alloys) is also shifted, and that it again appears away from the critical composition, on the ferromagnetic side. Further examples are given in figure 4, which shows similar data for b.c.c. V-Fe binary and V-Fe-Al ternary solid solutions with a constant Al-content of 10 percent.

As yet there appears to be no experimental evidence for the theoretically predicted [14] peak in γ' in alloys at the critical composition, resulting from the electron-paramagnon interaction.

Figures 3 and 4 illustrate also a complication, which arises quite frequently in extracting the coefficient of the temperature-linear term from low temperature specific heat data for weakly ferromagnetic and almost ferromagnetic alloys. In many alloy systems in a certain region around the critical composition an anomaly in the measured low temperature specific heat is observed, so that C is no longer given by eq (1). This anomaly is conspicuously evident in the usual C/T versus T^2 graph. Instead of being a straight line, this graph becomes a curve, extending upward at low temperatures. It was shown by Schroeder [16] that, in such cases, eq (1) can be usually replaced by

$$C = A + \gamma T + \beta T^3. \tag{6}$$

Schroeder found that the addition of a temperature-independent term A to the low temperature specific heat results from the thermal excitation of magnetic clusters present in many nearly ferromagnetic and weakly ferromagnetic alloys. The presence of magnetic clusters in Ni-Cu alloys in the composition range 50-56 percent Cu has been recently beautifully documented by Hicks, Rainford, Kouvel, Low and Comley [17] by means of neutron magnetic diffuse scattering. In Schroeder's theory the magnetic clusters, which interact with a weak crystal field, are thermally excited and they contribute an Einstein specific heat, which is temperature-independent above the Einstein temperature. The temperature range of 1.4 to 4.2 K, frequently used in low temperature specific heat measurements, appears to be above the Einstein temperature in most such systems. Investigations by Scurlock [18] show a decrease at lower temperatures of the anomalous specific heat from its constant value above 1.4 K, suggesting that the Einstein temperature is near 1.4 K. Since A includes an equal contribution of k for each cluster, regardless of the cluster moment [16], the low temperature specific heat data, from which the value of A can be extracted by least squares fitting to eq (6), give reliable information as to the number of thermally excited magnetic clusters. The correlation of the number of clusters for Ni-Cu alloys by specific heat measurements [11] with the number of clusters derived from neutron scattering [17] is given in figure 5. It is seen that the low temperature specific heat data for the superparamagnetic alloys (Cu-content larger than 57%) are quite consistent with the neutron scattering data. For the weakly ferromagnetic alloys the number of thermally excitable clusters rapidly decreases with increasing Curie temperature (decreasing Cu-content). In this composition range most of the magnetic clusters interact with one another and become part of the ferromagnetic system. As seen in figures 3 and 4 the maximum of A corresponds well with the critical composition for all four alloy systems considered. Figures 3 and 4 also show the anomalous behavior of the parameter β, obtained by least squares fitting to eq (6). The anomalous variation of β with composition occurs in all four alloy systems in the vicinity of the critical composition, and it is clearly magnetic in origin [5].

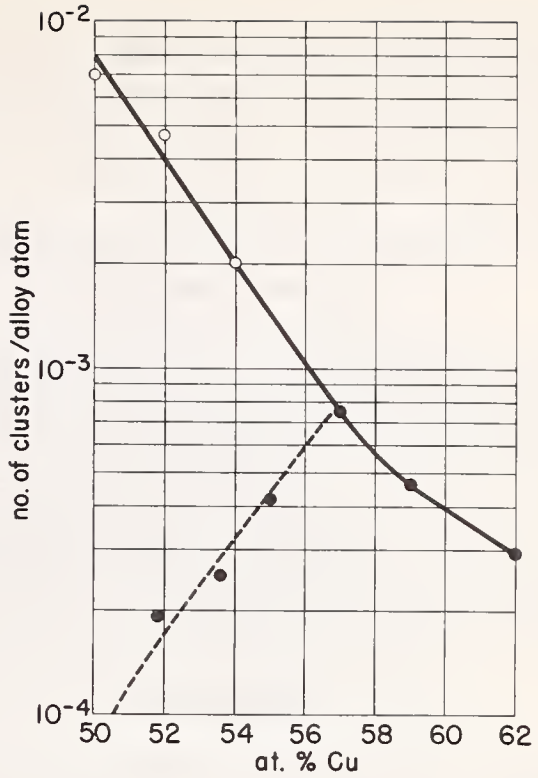

FIGURE 5. *Concentration of magnetic clusters in Ni-Cu alloys vs composition* [22]. *Filled circles represent cluster concentrations calculated from specific heat data. Empty circles give magnetic cluster concentrations derived from neutron magnetic diffuse scattering* [17].

4. Nuclear Specific Heat Effects

It was shown by Marshall [19] that the hyperfine interaction between the dipole moments associated with certain nuclides and the effective field H_{eff} at these nuclei, resulting from electronic spin moments, gives rise to a contribution to the low temperature specific heat. This contribution decreases rapidly with increasing temperature; in the 1.4 to 4.2 K range it is proportional to T^{-2} ("high temperature" approximation). Consequently, the nuclear magnetic specific heat term can

417-156 O - 71 - 37

be separated easily from the electronic specific heat term γT in that temperature range. The nuclear quadrupole specific heat recently reported by Phillips [20] and by Martin [21] is also proportional to T^{-2} and, thus, poses no problem in determining the electronic specific heat.

5. Acknowledgments

This work was supported in part by grants from the United States Army Research Office, Durham, and by the National Science Foundation. Most of the heretofore unpublished low temperature specific heat data for Ni-Cu-Al alloys were measured by C. G. Robbins. One of the alloys in this series was measured by R. Viswanathan. T. J. Rowland's help in reviewing the manuscript is much appreciated.

6. References

[1] Ashcroft, N. W., and Wilkins, J. W., Phys. Letters **14,** 285 (1965).
[2] McMillan, W. L., Phys. Rev. **167,** 331 (1968).
[3] Cheng, C. H., Wei, C. T., and Beck, P. A., Phys. Rev. **120,** 426 (1960); and Cheng, C. H., Gupta, K. P., Van Reuth, E. C., and Beck, P. A., Phys. Rev. **126,** 2030 (1962).
[4] Gupta, K. P., Cheng, C. H., and Beck, P. A., J. Phys. Chem. Solids **25,** 73 (1964).
[5] Cheng, C. H., Gupta, K. P., Wei, C. T., and Beck, P. A., J. Phys. Chem. Solids **25,** 759 (1964).
[6] Kouvel, J. S., and Graham, C. D., J. Phys. Chem. Solids **11,** 220 (1959).
[7] Kouvel, J. S., J. Appl. Phys. **30,** 313S (1959) and **31,** 142S (1960).
[8] Gupta, K. P., Cheng, C. H., and Beck, P. A., Phys. Rev. **133,** A203 (1964).
[9] Overhauser, A. W., J. Phys. Chem. Solids **13,** 71 (1960).
[10] Marshall, W., Phys. Rev. **118,** 1519 (1960).
[11] Robbins, C. G., Claus, H., and Beck, P. A., J. Appl. Phys. **40,** 2269 (1969).
[12] Bennemann, K. H., Phys. Rev. **167,** 564 (1968).
[13] Berk, N. F., and Schrieffer, J. R., Phys. Rev. Letters **17,** 433 (1966).
[14] Doniach, S., and Engelsberg, S., Phys. Rev. Letters **17,** 750 (1966).
[15] This is suggested by the data in the following papers, although their authors did not reach this conclusion: Bucher, E., Brinkman, W. F., Maita, J. P., and Williams, H. J., Phys. Rev. Letters **18,** 1125 (1967); and Brinkman, W. F., Bucher, E., Williams, H. J., and Maita, J. P., J. Appl. Phys. **39,** 547 (1968).
[16] Schroder, K., J. Appl. Phys. **32,** 880 (1961).
[17] Hicks, T. J., Rainford, B., Kouvel, J. S., Low, G. G., and Comly, J. B., J. Appl. Phys. **40,** 1107 (1969).
[18] Scurlock, R. G., and Wray, E. M., Phys. Letters **6,** 28 (1963); and Proctor, W., and Scurlock, R. G., Proc. 11th Conf. Low Temp. Phys. (St. Andrews, 1969), p. 1320.
[19] Marshall, W., Phys. Rev. **110,** 1280 (1958).
[20] Phillips, N. E., Phys. Rev. **118,** 644 (1960).
[21] Martin, D. L., Phys. Rev. Letters **18,** 839 (1967).
[22] Robbins, C. G., University of Illinois Thesis, (1969).
[23] Pessall, N., Gupta, K. P., Cheng, C. H., and Beck, P. A., J. Phys. Chem. Solids **25,** 993 (1964).
[24] New measurements by H. Claus, to be reported in detail elsewhere.

Discussion on "Density of States Information from Low Temperature Specific Heat Measurements" by P. A. Beck and H. Claus (University of Illinois)

M. Dresselhaus *(MIT):* I would like to ask a question about electron-phonon enhancement not necessarily of the speaker, but perhaps of a many-body theorist in the audience. It has been found experimentally in the group V semimetals that the cyclotron effective mass m_c^* is the same whether measured statically or at frequencies high compared with the Debye frequency ω_D. Because of the electron-phonon interaction, it would seem that m_c^* should be different if measured at low frequencies $\omega \ll \omega_D$ (as by the temperature dependence of the de Haas-van Alphen effect or by a microwave cyclotron resonance experiment) or at high frequencies $\omega \gg \omega_D$ (as by interband Landau level transitions). In both types of experiments, m_c^* can be measured accurately. No electron-phonon enhancement has been observed in m_c^* for certain carriers in bismuth and arsenic.

A. Baratoff *(Brown Univ.):* Well, I would expect that in bismuth, which is a semimetal, where there are comparatively few electrons, the electron-phonon enhancement would be rather small and maybe you would not notice it at all.

J. Schooley *(NBS):* The same sort of thing occurs also in aluminum.

J. Callaway *(Louisiana State Univ.):* When you analyze the specific heat of a ferromagnetic metal, do you make allowance for the contribution of the spin waves to the specific heat?

P. Beck *(Univ. of Illinois):* In these measurements, no such analysis has been made. For iron this was done by Rayne and Chandrasekhar [1] by using their own elastic constant measurements and our specific heat data. They found very little effect on the electronic specific heat. Most of the spin wave contribution appears in the "lattice specific heat."

F. J. Blatt *(Michigan State Univ.):* I should like to ask if, possibly, you had extended your measurements to sufficiently low temperatures so that you could estimate the Einstein temperature for what obviously cannot really be a constant contribution to the specific heat?

P. Beck *(Univ. of Illinois):* Yes, magnetic cluster contribution is indeed not constant. It is only nearly constant in the temperature range from 1.4 to 4.2 K. We did not make measurements at lower temperatures, but Scurlock [2] did and he found a decrease starting just below the range at which we are measuring. He made measurements down to about 0.3 K, and he found values quite compatible with an Einstein function. The Einstein temperature appears to be somewhere usually around 1 K.

N. M. Wolcott *(NBS):* With regard to the comment of Prof. Blatt, we have measured the specific heat of a Cu-Ni 60-40 at. % alloy down to He^3 temperatures and have observed the decline in the constant term in the specific heat. Fitting our results to an Einstein function gives a value of $\theta_E \sim 1.5$ K.

[1] Rayne, J. A., and Chandrasekhar, B. S., Phys. Rev. **122**, 1714 (1961).

[2] Scurlock, R. G., and Wray, E. M., Phys. Letters **6**, 28 (1963); and Proctor, W., and Scurlock, R. G., Proc. 11th Conf. Low Temp. Phys. (St. Andrews) 1969, p. 1320.

Electronic Density of States Determined by Electronic Specific Heat Measurements

T. Mamiya and Y. Masuda

Department of Physics, Nagoya University, Chikusa-ku, Nagoya, Japan

The superconducting transition temperatures, electronic specific heats, and Debye temperatures have been recently measured by us for 5*d* transition-metal alloy series Ta-Re. By making use of these data and the theoretical predictions by McMillan, we have deduced the electron-phonon coupling constant and bare electronic density of states. The density of states is compared with the theoretical one derived from band-structure calculations of Ta using the augmented-plane-wave (APW) method by Mattheiss.

Key words: Augmented plane wave method (APW); Debye temperatures; electronic density of states; electron-phonon coupling constant; electronic specific heat; superconducting transition temperatures; tantalum (Ta); tantalum-rhenium (Ta-Re) alloys; Ta-Re alloys.

1. Introduction

McMillan has recently calculated the superconducting transition temperature, using the strong-coupling theory assuming the appropriate phonon spectrum of density of states, as a function of the coupling constants for the electron-phonon and Coulomb interaction [1]. Our recent experiments provide detailed information about the superconducting transition temperature T_c, the Debye temperature Θ, and the electronic heat capacity coefficient γ for the *bcc* 5*d* transition metal alloys of Ta-Re [2]. By making use of McMillan's theoretical predictions and our experimental data, we can find empirical values of electron-phonon coupling constant and the band-structure density of states in the 5*d* band. The theoretical density of states of Ta was calculated by Mattheiss using the augmented plane wave (APW) method [3]. Our empirical values of the band-structure density of states of Ta-Re alloys were compared with the theoretical ones.

2. Experimental Procedures and Results

The detailed descriptions of the experimental equipments and procedures will appear elsewhere [2]. Our new data for the alloy series Ta-Re are reproduced in table 1 and figure 1, in which the superconducting transition temperature T_c, Debye temperature Θ, and electronic heat capacity coefficient γ are listed as a function of the number of electrons per atom n. The detailed measurements on the superconducting properties of Ta-Re alloys, especially the temperature dependences of the critical field show that they are the weak or intermediate-coupled superconductors, depending on Re concentration.

In the light of McMillan's theoretical model, we calculate the electron-phonon coupling constant λ and the bare density of states $N_0(0)$, from experimental values of T_c, Θ, and γ in the alloy series Ta-Re. The method of obtaining the values of Coulomb coupling constant μ^* will be mentioned below.

TABLE 1. *Superconducting transition temperature* T_c, *Debye temperature* Θ, *and electronic specific heat* γ *of bcc* 5d *transition metal alloys of* Ta-Re *series.*

Sample	% Second metal	n $\left(\frac{\text{electrons}}{\text{atom}}\right)$	T_c (K)	Θ (K)	γ (mJ/mole K^2)
Ta		5.0	4.463	250	6.15
TaRe	2.5	5.05	3.458	261	5.70
	5.0	5.1	2.77	277	5.12
	7.5	5.15	2.08	285	5.05
	10	5.2	1.49	296	4.10
	15	5.3	0.75	307	3.75
	20	5.4	.21	317	3.00
	25	5.5	<.06	330	2.42
	30	5.6	<.06	345	1.90
	40	5.8	<.06	361	1.0

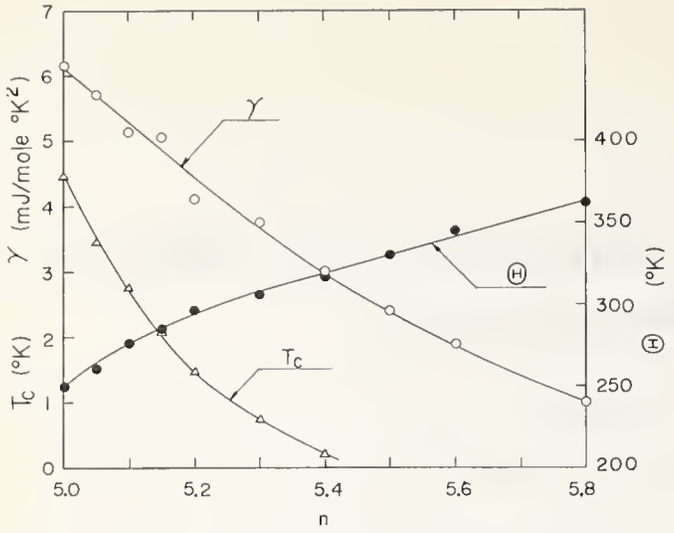

FIGURE 1. *The superconducting transition temperature* T_c, *the Debye temperature* Θ, *and the electronic specific heat coefficient* γ, *versus the number of valence electrons per atom* n, *for* Ta-Re *alloy series.*

According to McMillan [1], T_c was given as functions of the electron-phonon coupling constant λ and Coulomb coupling constant μ^*:

$$T_0=\frac{\Theta}{1.45}\exp\left[-\frac{1.04(1+\lambda)}{\lambda-\mu^*(1+0.62\lambda)}\right]. \tag{1}$$

This equation holds well not only for strong-coupled superconductors but for the intermediate coupling ones in question. It is well known that the electronic specific heat γ is enhanced by electron-phonon interactions. γ is therefore written in terms of the bare density of states $N_0(0)$:

$$\gamma=\frac{2\pi^2k^2}{3}N_0(0)(1+\lambda). \tag{2}$$

If we want to find $N_0(0)$, it is necessary to know the values of λ and γ. The empirical values of μ^* can be found from the superconducting isotope effect. McMillan has determined empirically the average value of $\mu^*=0.13$ for the transition metals. However, the isotope shift can be measured in only a few metals. In the case of superconductors for which the isotope effect was not determined, we can derive μ^* from the measured electronic specific heat by making use of the expression of Morel and Anderson [4],

$$\mu^*=\frac{\mu}{1+\nu\ \ln\ (E_B/\omega_0)}, \tag{3}$$

where E_B is the electronic band width and ω_0 is the maximum phonon frequency. Using a Fermi-Thomas model, μ was given by

$$\mu=\frac{1}{2}a^2\ln\left(1+\frac{1}{a^2}\right),$$

$$a^2=\frac{3e^2\hbar^2\gamma}{4\pi k^2m^*E_F}. \tag{4}$$

where E_F is the Fermi energy and m^* is the effective mass of the electron which is given by $m^*=(1+\lambda)m_0$. For Ta-Re alloy series, E_F ranges from 6.8 to 7.4 eV, which were derived from the theoretical band structure for W obtained by Mattheiss [3]. In order to obtain μ^* for Ta-Re alloys, we must determine μ^* first, using λ which was obtained from McMillan's value $\mu^*=0.13$ as a first approximation. Substituting this m^*, the measured value of γ, and E_F into eqs (2), (3), and (4), the new value of μ^* for Ta was determined to be 0.111. As the Re concentration increases, the value of μ^* decreases very slightly and becomes to 0.107 for $Ta_{0.8}Re_{0.2}$. Accordingly, μ^* was taken to be 0.11 through the whole Ta-Re alloy series. Substituting the value of $\mu^*=0.11$, the experimental value of T_c, and the Debye temperature Θ into eq (1), one can obtain the phonon coupling constant λ. Using eq (2) together with the values γ and λ, the bare density of states $N_0(0)$ thus can de derived. The values of λ and $N_0(0)$ determined are summarized in table 2 and plotted as a function of the electrons per atom ratio in figures 2 and 3, together with the other data on *bcc* 5*d* transition alloys [5].

To determine the values of λ for alloys which do not show any superconducting behavior in the temperature range examined, we assumed the linear relation between λ and $N_0(0)$ and calculated the values of λ from

TABLE 2. *Electron phonon coupling constant* λ *and bare density of states at the Fermi energy* $N_0(0)$ *of bcc* 5d *transition metal alloys of* Ta-Re *series. Coulomb interaction parameter* μ^* *was assumed to be 0.11.*

Sample	% Second metal	n	$\mu^*=0.11$	
			λ	$N_0(0)\left(\frac{\text{states}}{\text{eV}\cdot\text{atom}}\right)$
Ta		5.0	0.62	0.80
TaRe	2.5	5.05	.56	.77
	5.0	5.1	.52	.72
	7.5	5.15	.48	.72
	10	5.2	.45	.60
	15	5.3	.39	.57
	20	5.4	.34	.48
	25	5.5	(.29)	(.40)
	30	5.6	(.23)	(.32)
	40	5.8	(.13)	(.19)

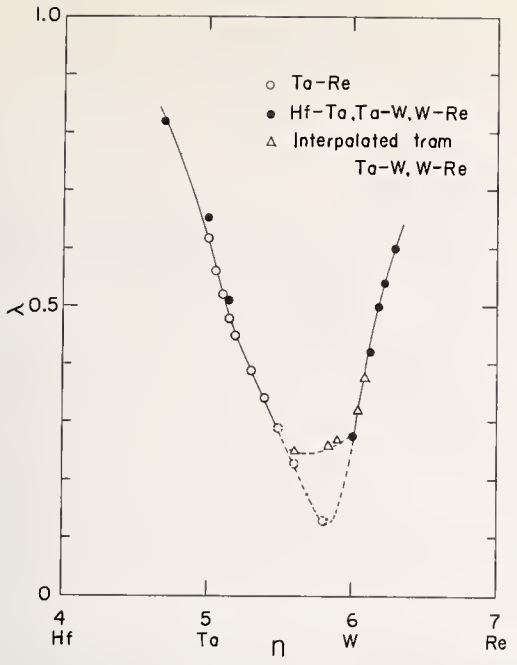

FIGURE 2. *The electron-phonon coupling constant* λ *versus the number of electrons per atom* n, *for a* Ta-Re *alloy series.*

Open circles shown by dotted line show the estimated values for which the interpolated value of T_c was used.

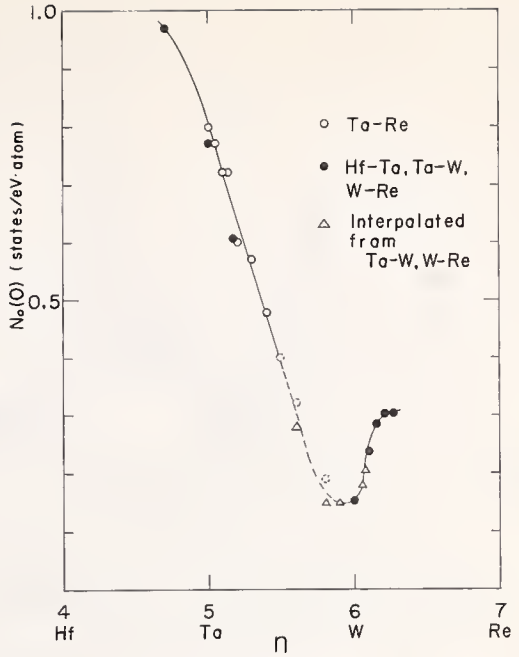

FIGURE 3. *The bare density of states* N_0 (0) *versus the number of electrons per atom* n, *for a* Ta-Re *alloy series.*

The dotted circles have the same meaning as in figure 2.

the measured values of γ. This relation holds well in alloys in the concentration between pure Ta and $Ta_{0.8}Re_{0.2}$, for which we can easily measure T_c. These values of λ and $N_0(0)$ are shown by the dotted circles in figures 2 and 3. The corresponding values of T_c which are obtained using these procedures are extremely low compared with the transition temperatures for 4*d* series Nb-Mo alloys [6]. The reason for the extremely low transition temperature may be that at small λ values, $N_0(0)$ is not always proportional to λ and also Coulomb interaction parameter μ^* can not be taken to be 0.11.

3. Discussion

Mattheiss [3] has calculated the band structures of Ta and W using the augmented plane wave (APW) method. Relativistic effects have been included in Ta but not W calculation. The potentials he used were derived from superposed atomic charge densities which were determined from self-consistent calculations involving a $(5d)^3(6s)^2$ atomic configuration for Ta and $(5d)^5(6s)^1$ for W, respectively. The energy bands were determined at a total of 1024 uniformly distributed points in the *bcc* Brillouin zones. These results were converted to the density of states by a method of weighted average of the APW eigenvalues or an interpolation scheme. The theoretical density of states for electrons has been compared by McMillan [1] with the experimental density of states for *bcc* 5*d* transition metal alloys. However, the experimental density of states he used is not complete enough but includes the interpolated plots for several alloys of *bcc* transition metals (Ta-W and W-Re), whose superconductivity was not detected.

The theoretical densities of states for Ta and W which were calculated by Mattheiss and the experimental result of Ta-Re alloys are shown in figures 4 and 5 together with other data of Hf-Ta, Ta-W, and W-Re alloys. The agreement of the theoretical density of states for Ta metal and experimental one for Ta-Re alloys (Ta rich side) is spectacular, but those for W and W-Re alloy (W-rich side) are less exact. On the other hand, the experimental density of states for Ta-Re alloys is 10 to 20% larger than the theoretical one calculated for W, but the experimental data for W and W-Re alloys are in good agreement. It is therefore concluded that the experimental data for Ta rich alloys agree well with the band calculation for Ta, and data for W rich alloys show good agreement with the theoretical prediction for W. As described by Mattheiss, the interpolation scheme yields crude density of states because the number of points in the Brillouin zone are limited and therefore some of the peaks in the density of states may be overlooked. Meanwhile, more accurate values of the Fermi energy and the density at the Fermi energy can be obtained in such a way that the square of the wave vector is expanded in lattice harmonics. As Mattheiss also points out, the accurate density of states for Ta, 0.65 states/eV·atom does not agree well with the experimental data of 0.77, but the crude estimate of about 0.80 states/eV·atom agrees much better. It is interesting to note that the experimental data for not only Ta but also

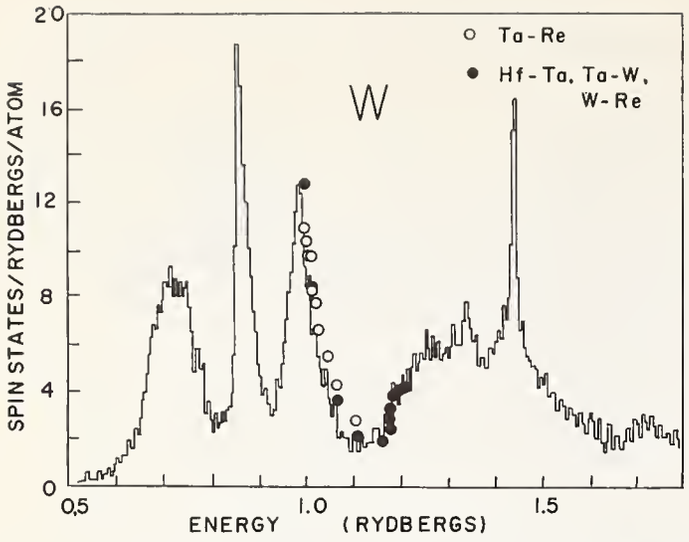

FIGURE 4. *The theoretical bare density of states for* W *by Mattheiss and the experimental data for a* Ta-Re *alloy series.*

Ta-Re alloy series are in good agreement with the crude density of states.

4. Acknowledgment

It is a pleasure to thank L. F. Mattheiss for his permission to use figures 4 and 5, and for communication of his results prior to publication.

5. References

[1] McMillan, W. L., Phys. Rev. **167**, 331 (1968).
[2] Mamiya, T., Nomura, K., and Masuda, Y., J. Phys. Soc. Japan (to be published).
[3] Mattheiss, L. F., Phys. Rev. **139**, A1893 (1965) and ibid. (to be published).

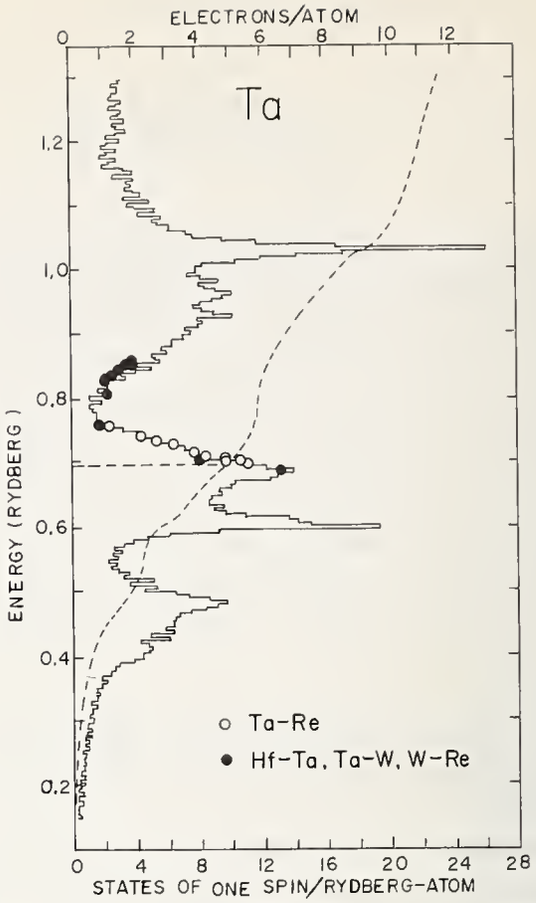

FIGURE 5. *The theoretical bare density of states for* Ta *by Mattheiss and the experimental data for a* Ta-Re *alloy series.*

[4] Morel, P., and Anderson, P. W., Phys. Rev. **125**, 1263 (1962).
[5] Morin, F. J., Maita, J. P., Phys. Rev. **129**, 1115 (1963).
[6] Veal, B. W., Hulm, J. K., Blaugher, R. D., Ann. Acad. Sci. Fennicae **A210**, 108 (1966).

ELECTRONIC SPECIFIC HEAT II; KNIGHT SHIFT; SUSCEPTIBILITY

CHAIRMEN: A. Narath
H. C. Burnett

RAPPORTEURS: J. Rayne
I. D. Weisman

Low-Temperature Specific Heats of Hexagonal Close-Packed Erbium-Thulium Alloys

A. V. S. Satya* and C. T. Wei

Michigan State University, East Lansing, Michigan 48823

The specific heats of hexgonal close-packed erbium and thulium metals, and three of their isostructural alloys were measured in the liquid-helium temperature range between 1.3 and 4.2 K for examining the validity of the localized 4*f*-band model, on which the current theories of the rare-earth metals are based. Barring possible uncertainties in the magnetic properties of the samples and their impurity contents, the coefficients of the specific-heat component linear in temperature calculated from the present data range in values approximately two to twenty times the constant electronic specific-heat coefficient predicted by the above model for all the hexagonal close-packed rare-earth lanthanides. Possible explanations for such discrepancies are discussed. An itinerant 4*f*-band model based on the one-electron-band model suggested by Mott is proposed for the lanthanides as an alternative to the localized 4*f*-band model.

Key words: Anti-ferromagnet; anti-phase domain; augmented plane wave method (APW); Curie temperature; electronic density of states; enhancement factors; erbium; erbium-thulium alloys; ferro-magnetic spiral structure; gadolinium; itinerant 4*f*-band model; lanthanides; low-temperature specific heat; rare-earth lanthanides; specific heats; spin-wave theory; thulium.

1. Introduction

The rare-earth lanthanides, characterized by their incomplete 4*f* shells in the atomic state, have been traditionally viewed as consisting of trivalent atomic cores including the partially-filled and localized 4*f* shells, with three $5d^1 \cdot 6s^2$ electrons per atom forming nearly-free-electron type conduction bands [1-5]. Recent band calculations [6-10] show, however, that the Fermi surfaces of the rare earths are considerably different from those predicted by the nearly-free-electron model.

Dimmock and Freeman [6] calculated the band structure of gadolinium using the nonrelativistic augmented-plane-wave (APW) approximation, and obtained a very narrow (0.05 eV wide) 4*f* band about 10.9 eV below the bottom of the 5*d*-6*s* conduction bands. Their results also indicate that the 5*d* band has a width of about 6.8 eV, and that it resembles the *d* band in the transition metals. Extending the APW calculations, Freeman et al. [7] computed the Fermi surface for thulium as being largely determined by the 5*d* electrons. The position of the 4*f* band was found to be strongly dependent on the crystal potential assumed. Herring [11] has some doubts about the reliability of the values of the widths and positions of the 4*f* bands predicted by the one-electron calculations. He believes that there is a narrow group of 4*f*-like bands in the lanthanides appreciably hybridized with the *s*-*p*-*d* bands.

Based on the Hall-coefficient data and a room-temperature specific-heat analysis, Gschneidner [12] concluded that the 4*f* electrons occupy either discrete energy levels, or very narrow one-electron bands as proposed by Mott [13]. Where the overlap between atomic orbitals is small, as is probably the case for the 4*f* inner-shells in the lanthanides, Mott [13] suggested that an inner band would split into sub-bands of energy levels containing only one electron per each atom.

Lounasmaa [14-20] measured the low-temperature specific heats of all the lanthanides except Pm and Er. Parks [21] determined the specific heats of Dy and Er. In evaluating the various contributions to the specific heats, they both used a more or less constant electronic specific-heat coefficient based on the localized 4*f*-band model for all the hexagonal close-packed lanthanides. Similar measurements were reported by Dreyfus et al. [22] in a summary form for Pr, Sm, Tb, Ho, and Er, but

*Present address: IBM Components Division, East Fishkill, N.Y.

without using the above model in their analysis. While the seven localized $4f$ electrons per atom in Gd appear to account for the major part of the 7.5 μ_B saturation magnetic moment observed in this metal, [23] the electronic specific heat predicted by Dimmock et al. [6] for Gd is only 40% of the value measured by Lounasmaa [15]. This discrepancy has been attributed to an electron-phonon enhancement in the metal.

The concept that the $4f$ shells are partially filled in the lanthanides and yet the $4f$ electrons contribute neither to the conduction band nor to the low-temperature specific heats, referred to above as the localized $4f$-band model, is similar to that proposed by Mott and Stevens [24] for the transition metals in which the d electrons would be localized. Based primarily on the results of the low-temperature specific-heat work of Beck and co-workers [25], this localized d-electron model was corrected by Mott [26]. If the localized f-electron model for the rare earths is vindicated, it would be a unique case in all metals.

If the $4f$ electrons are indeed localized, and hence do not contribute to the Fermi surface, then isostructural alloys of the Er-Tm, Tm-Yb, and Tm-Lu systems (for example) should have similar Fermi surfaces as it was assumed by Dimmock et al. [6,7] and Lounasmaa [14-20]. All such alloys should show a constant electronic specific-heat coefficient. On the other hand, if the $4f$ electrons do form a band in the usual sense, and hence do contribute to the Fermi surface, then alloying thulium with erbium, which have complete solid-solubility in each other, should gradually increase the number of f electrons in the conduction band. The alloys should then show variations in the electronic specific-heat coefficients. The only alloy system of the lanthanides that has been investigated with the low-temperature specific-heat method is the Gd-Pr system by Dreyfus et al. [27]. They did not try to establish the localized $4f$-band model, but used such a model to evaluate the hyperfine coupling constants for the alloys. The purpose of this work is to test the validity of the localized $4f$-electron model for the lanthanides by measuring the specific heats of hexagonal close-packed Er-Tm alloys at liquid helium temperatures.

2. Experimental Details

Erbium and thulium metals of 99.9% purity were obtained from Messrs. Gallard Schlesinger Chemical Manufacturing Corporation. Pure erbium metal of approximately one-fifth of a mole was arc melted under a helium atmosphere in a water-cooled copper crucible. Due to the high vapor pressure of thulium at elevated temperatures, the Er-Tm alloys and the thulium metal were induction melted in tungsten crucibles under a purified argon atmosphere. The analyses of these samples are listed in table 1 as measured by Messrs. Atomergic Chemetals Inc. using the mass-spectrographic method. The heat capacities of the samples were measured in the liquid-helium^{IV} temperature range in an experimental set-up only slightly modified from that described by one of the authors [28]. The temperature of the specimen was monitored by means of a carbon resistor embedded in the specimen assembly. The carbon thermometer was calibrated against the liquid-helium vapor pressure prior to each heat-capacity measurement. The resistance R of the thermometer and the corresponding temperature of the specimen T were found to satisfy the Keesom-Pearlman relation [29]

$$(\log R/T)^{1/2} = \sum_{n=0}^{N} C_{n+1} (\log R)^n \qquad (1)$$

with $N=1$, with a scatter of less than 10 milli-degrees in all the experiments. Figures 1 through 3 show the specific-heat data plotted against temperature for the Er and Tm metals and three of their alloys with 25, 50, and 75 wt. % Tm. The accuracy of the present set-up was discussed by Tsang [30]; and an overall accuracy of $\pm 2\%$ can be expected in the specific-heat measurement.

TABLE 1. *Some impurity analyses of the samples in ppm by weight*

Element	Er	$Er_{0.75}Tm_{0.25}$	$Er_{0.5}Tm_{0.5}$	$Er_{0.25}Tm_{0.75}$	Tm
Ca	18	550	93	260	170
Fe	400	19	30	43	31
Na	13	3800	10	29	510
Nd	110	390	580	940	2000
Ni	3	35	46	98	600
W	140	700	500	620	750
Y	1100	520	400	150	20
C	86	36	140	200	850
F	6300	8600	4500	3800	320
N	1300	54	21	7	1100
O	120	470	240	490	1400

3. Analysis of Results

The specific heat of the rare-earth metals and their alloys can be expressed as

$$C_p = C_v + C_d = C_E + C_L + C_M + C_N + C_d \qquad (2)$$

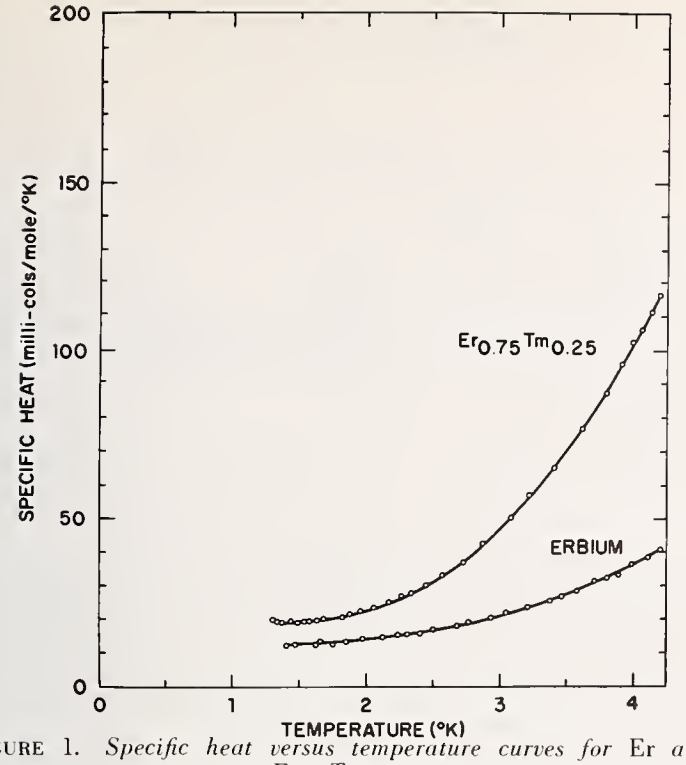

FIGURE 1. *Specific heat versus temperature curves for* Er *and* $Er_{0.75}Tm_{0.25}$.

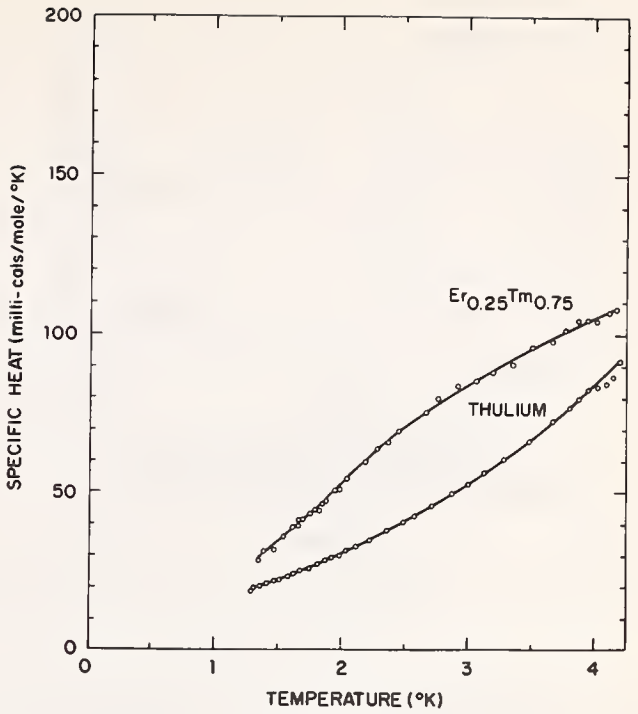

FIGURE 3. *Specific heat versus temperature curves for* $Er_{0.25}Tm_{0.75}$

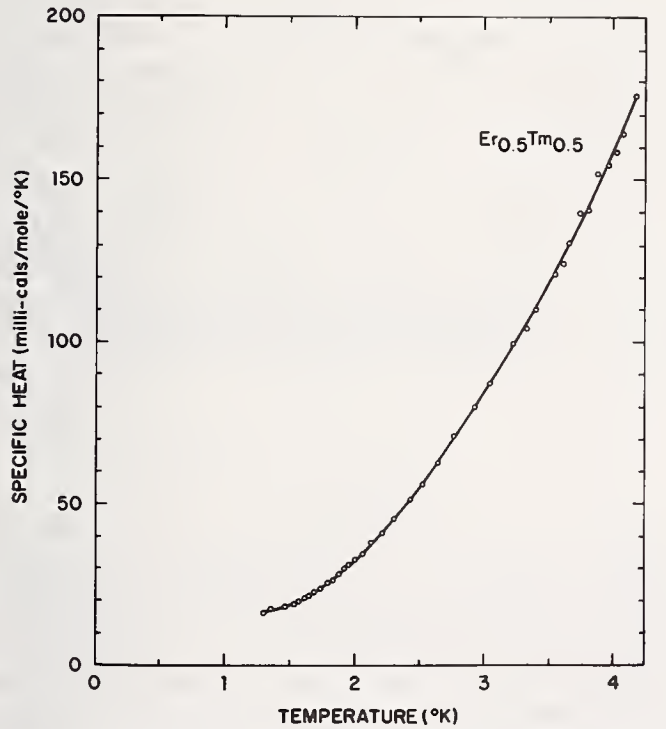

FIGURE 2. *Specific heat versus temperature curve for* $Er_{0.5}Tm_{0.5}$.

where C_p and C_v are the specific heats at constant pressure and volume, respectively, separated by the dilatation term C_d (negligible at low temperatures), $C_E = \gamma T$ is the electronic specific heat, $C_L = \alpha T^3$, the lattice specific heat, C_M, the magnetic specific heat, and $C_N = \nu T^{-2}$, the hyperfine contribution to the specific heat. A proper analysis of the specific-heat data for the separation of the various specific-heat contributions depends on the magnetic specific-heat contributions as dictated by the magnetic properties of the samples.

Koehler and co-workers [31-33] found that erbium transforms into a ferromagnetic spiral structure below its Curie temperature of 19.6 K and that thulium adopts an anti-phase domain-type structure below 40 K. Lounasmaa [19,20] reported that the magnetic specific heats of thulium are 1.5 $T^{2.5}$ and 1.98 $T^{2.3}$ millicals/mole/K in the 0.4 to 4.0 and 3.0 to 25.0 K temperature ranges, respectively, in contrast to the $T^{1.5}$ dependence predicted by the spin-wave theory [34,35] for the ferri- and ferro-magnetic materials, and the T^3 dependence for the antiferromagnets. It may be noted that the experimentally determined magnetic specific-heat values are close to that predicted by the spin-wave theory for the antiferromagnetic materials. In the case of holmium metal, which has a ferromagnetic spiral type of structure similar to erbium below 20 K, Lounasmaa [14,20] obtained $C_M = 0.3\ T^{3.2}$ millicals/mole/K in the 3.0 to 25.0 K range and a T^3 dependence for C_M in the 0.4 to 4.2 K range. Kaplan [36] suggested a linear dispersion relation between $\omega(\mathbf{q})$ and $\mathbf{q}$ for small values of the wave vector $\mathbf{q}$ in the ferromagnetic spiral case, and treated it as being similar to that of an anti-ferromagnet. Bozorth and Gambino [37] found that the Curie temperature decreased in the Er-Tm system up to 12% Tm, and after a discontinuous rise, the thulium-type Curie temperature followed a slowly declining

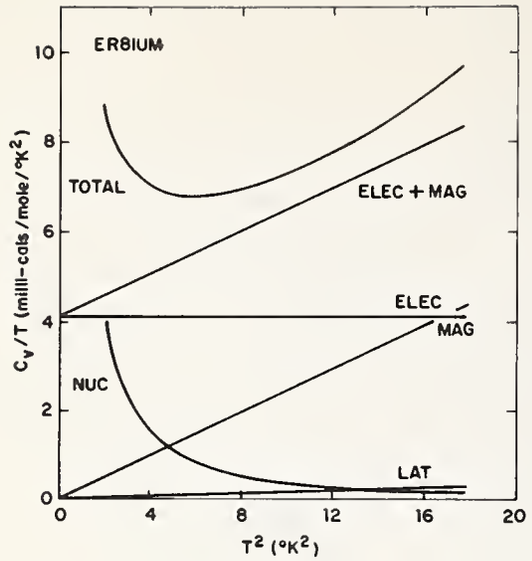

FIGURE 4. C_v/T *versus* T^2 *curve and analyses for* Er.

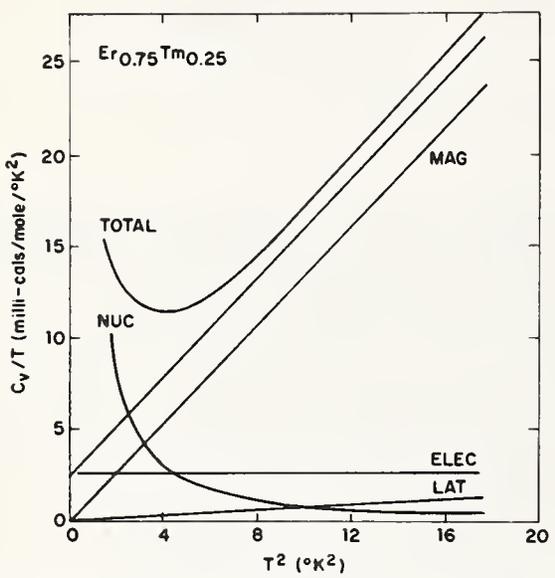

FIGURE 5. C_v/T *versus* T^2 *curve and analyses for* $Er_{0.75}Tm_{0.75}$.

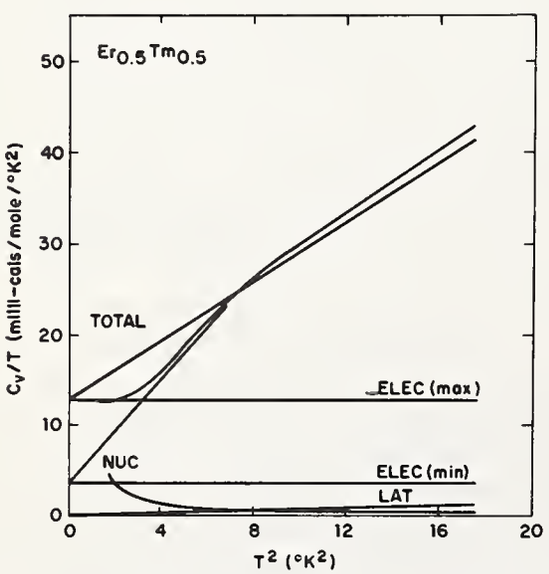

FIGURE 6. C_v/T *versus* T^2 *curve and analyses for* $Er_{0.5}Tm_{0.5}$.

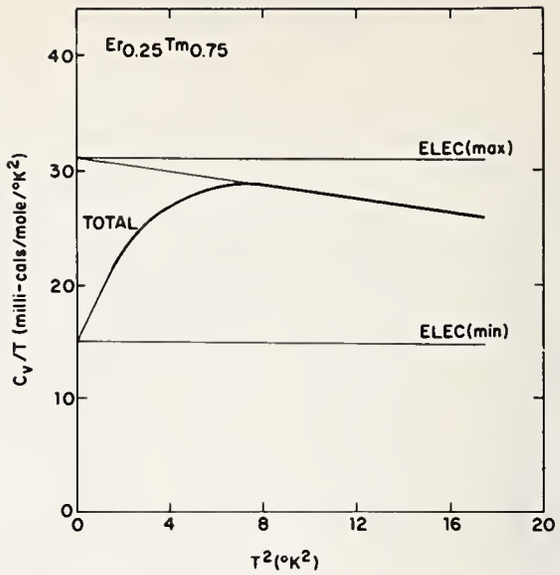

FIGURE 7. C_v/T *versus* T^2 *curve and analyses for* $Er_{0.25}Tm_{0.75}$.

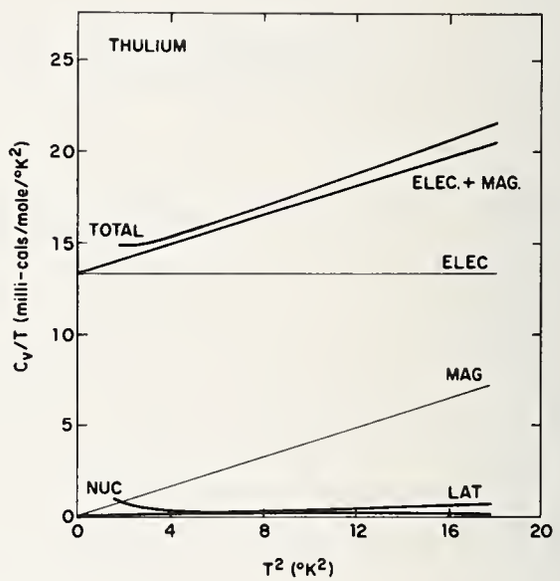

FIGURE 8. C_v/T *versus* T^2 *curve and analyses for* Tm.

trend again with increasing Tm content. One may, therefore, expect a T^3 dependence of the magnetic specific heat for all the present samples.

The specific-heat data obtained with Er, Tm and their three alloy samples were analyzed by a least-squares fit to

$$C_v/T = \gamma + (\alpha + \mu)T^2 + \nu T^{-3}, \tag{3}$$

where γ, α, μ, and ν are respectively the electronic, lattice, magnetic and the nuclear specific-heat coefficients, with no assumption made on the nature of the $4f$ band. The analysis was straightforward for Er, $Er_{0.75}Tm_{0.25}$, and the Tm samples as shown in figures 4, 5, and 8.

The C_v/T versus T^2 curves for the $Er_{0.5}Tm_{0.5}$ and $Er_{0.25}Tm_{0.75}$ samples, shown in figures 6 and 7, appear

TABLE 2. *Specific-heat contributions of the present samples in milli-cal/mole/K*

Sample	Electronic	Lattice*	Magnetic	Nuclear
Er	$4.1T$	$0.063T^3$	$1.23T^3$	$11.73T^{-2}$
$Er_{0.75}Tm_{0.25}$	$2.5T$	$0.0615T^3$	$1.47T^3$	$23.9T^{-2}$
$Er_{0.5}Tm_{0.5}$	$8.7\pm5.3T$	$0.060T^3$	$2.4\pm0.8T^3$	$9.29T^{-2}$
$Er_{0.25}Tm_{0.75}$	$23.3\pm7.9T$	$0.059T^3$	.....	.....
Tm	$13.3T$	$0.058T^3$	$0.42T^3$	$1.76T^{-2}$

*Computed from the Debye temperatures taken from Lounasmaa's work [14, 20].

to concave downward in the middle, similar to that observed in $Gd_{0.23}Pr_{0.77}$ by Dreyfus et al. [27]. None of the known theories seem to be able to account for such a feature. In order to obtain an upper and a lower limit of the electronic specific-heat coefficient, the C_v/T data of the $Er_{0.5}Tm_{0.5}$ sample was analyzed by first fitting the values below 2.5 K to evaluate the nuclear contribution, which was then subtracted from the C_v/T values for the entire temperature range. The remainder, consisting of only the linear and the T^3 terms in C_v, was then analyzed by treating separately the data below and above 2.8 K for obtaining γ_{min} and γ_{max}, respectively. The true electronic specific-heat coefficient would probably lie between these two values. For the $Er_{0.25}Im_{0.75}$ sample, γ_{min} and γ_{max} were obtained by extrapolating the two branches of the C_v/T curve to 0 K. The various specific-heat contributions thus obtained are listed in table 2. The electronic specific-heat coefficients are plotted against the composition as shown in figure 9.

4. Discussion

The results indicate that the γ values of the samples range from 2.5 to 23 ± 8 millicals/mole/K². The constant values of 1.0 and 2.5 millicals/mole/K² respectively predicted by the APW calculations [6], and assumed by Lounasmaa [14-20] based on the localized 4*f*-band model, are also shown in figure 9 for comparison. Differences between theoretically predicted and experimentally determined values of the electronic specific heat have long been observed in the rare-earth metals [14-20,22], but the magnitude of the discrepancies observed in the present alloys is astonishing. The discrepancies have been so far attributed to the electron-electron enhancement [9], the electron-phonon and electron-magnon enhancements [5], and the impurity contents of the samples the different workers [10] used.

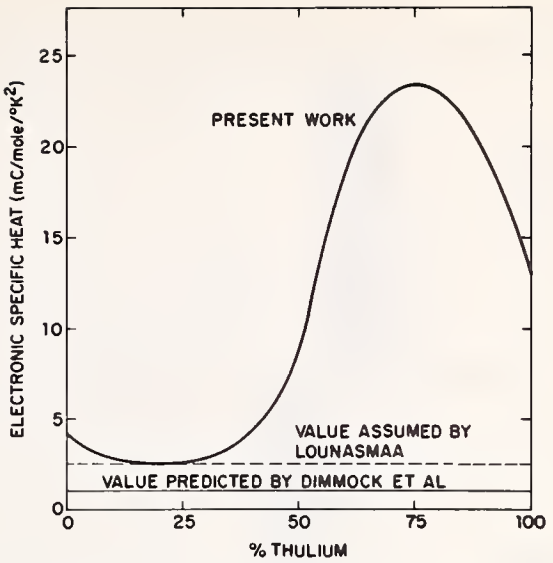

FIGURE 9. *Electronic specific-heat coefficient versus weight percent thulium.*

Kasuya [5] estimated that for Gd the electron-phonon enhancement may amount to 30%, and the electron-magnon enhancement, 20% of its γ value. Such enhancements can account for at most a factor of two in the electronic specific heats.

Lounasmaa [19] pointed out that the discrepancies in the low-temperature specific-heat data of the different workers are not uncommon for the rare-earth metals below 4.0 K, possibly due to the differences in the impurity contents in the samples. Crane [38] reported an increase in the specific heats of Gd by as much as a factor of two due to the presence of 0.1% oxygen by weight. If similar impurity effects are present in the Er-Tm system, a factor as great as four can be included in all the corrections. This is still insufficient to bring down the γ values of the Tm, $Er_{0.5}Tm_{0.5}$ and $Er_{0.25}Tm_{0.75}$ samples to the 1 millical/mole/K² range predicted by the localized 4*f*-band model.

If the localized 4*f*-band model were valid, the 5*d*-band should be the major contributor to the Fermi surfaces in the rare earths, and to their electronic specific heats. The 5*d* band, having a width of 6.8 eV [6], is comparable to the 3*d* band of a width of 5 eV, as calculated by Belding [39] for *bcc* paramagnetic Cr using the tight-binding approximation. A close resemblance can be noted between Belding's result and the experimentally determined 3*d* energy band of Beck and co-workers [25]. On the other hand, all the experimental evidence from the present work as well as the results of Lounasmaa [14-20] and Dreyfus et al. [22] indicate much larger γ values than what might be predicted by the localized 4*f*-band model.

A localized 4*f*-band model is not necessarily needed to explain the low-temperature magnetic structures in

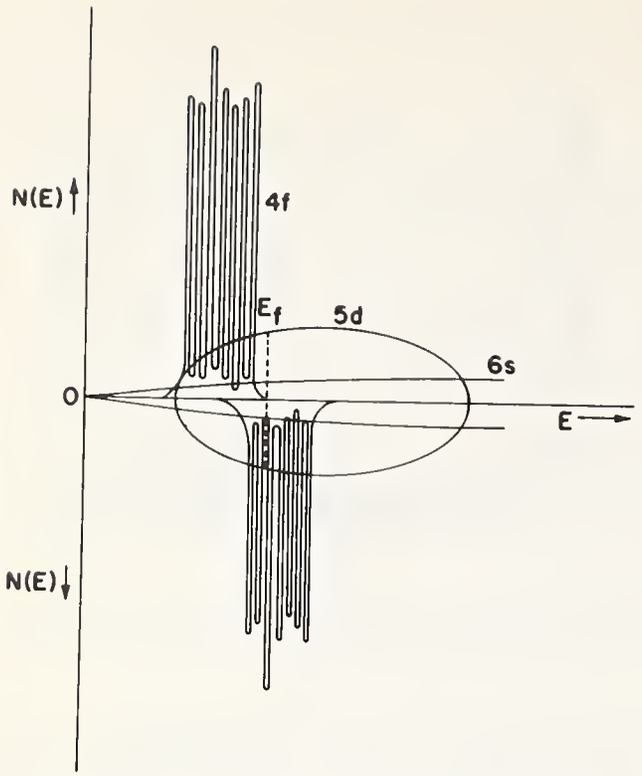

FIGURE 10. *A schematic itinerant* 4f*-band model.*

the rare-earth metals any more than a localized 3*d*-band model is required to explain the magnetic properties of the transition metals. Instead, it is possible that a narrow 4*f* band could split into an up-spin and a down-spin half-bands, which may or may not overlap. The relative positions of the two half-bands with respect to the Fermi surface may vary from one rare-earth metal to another depending upon such factors as the crystal structure, the number of 4*f* electrons per atom, and the exchange interaction between the electrons. One may modify Mott's one-electron band model [13] so that each half-band, not necessarily localized, is built of seven overlapping one-electron bands. The density of states of each of these half bands may contain peaks and valleys. When there is an integral number of 4*f* electrons as in a metal, the Fermi surface is most likely to be near a valley. Such a model would explain the nearly uniform electronic specific-heat coefficients of the pure rare-earth metals as well as the large variations in the γ values of the alloys observed in the present work. A schematic diagram of such an itinerant 4*f*-band model is shown in figure 10.

Further work such as the room-temperature specific-heat measurements of the isostructural rare-earth alloys may help to confirm the proposed model. Should this itinerant 4*f*-band model be established, then it would not be necessary to resort to using the electron-phonon type enhancements in explaining the discrepancies between the theoretically predicted and the experimentally obtained electronic specific heats of the rare-earth lanthanides.

5. Acknowledgment

Thanks are due to the National Science Foundation for making this work possible with its grant #GK-2224.

6. References

[1] Kasuya, T., Prog. Theor. Phys. (Kyoto) **16**, 38, 45 (1956).
[2] Kasuya, T., Prog. Theor. Phys. (Kyoto) **22**, 227 (1959).
[3] Yosida, K., and Watabe, A., Prog. Theor. Phys. (Kyoto) **28**, 361 (1962).
[4] Elliott, R. J., and Wedgewood, F. A., Proc. Phys. Soc. (London) **81**, 846 (1963).
[5] Kasuya, T., Magnetism, **IIB**, 215, Edited by Rado and Suhl (Acad. Press, N.Y., 1966).
[6] Dimmock, J. O., and Freeman, A. J., Phys. Rev. Letters **13**, 199 (1964).
[7] Freeman, A. J., Dimmock, J. O., and Watson, R. E., Phys. Rev. Letters **16**, 94 (1966).
[8] Watson, R. E., Freeman, A. J., and Dimmock, J. O., Phys. Rev. **167**, 497 (1968).
[9] Kim, D. J., Phys. Rev. **167**, 545 (1968).
[10] Andersen, O. K., and Loucks, T. L., Phys. Rev. **167**, 551 (1968).
[11] Herring, C., Magnetism, **IV** (Acad. Press, N.Y., 1966).
[12] Gschneidner, K. A., Jr., Rare Earth Research, **II**, 153, Edited by Eyring (Gordon and Breach Inc., N.Y., 1965).
[13] Mott, N. F., Phil. Mag. **6**, 306 (1961).
[14] Lounasmaa, O. V., (Ho:) Phys. Rev. **128**, 1136 (1962).
[15] Lounasmaa, O. V., (Gd,Yb:) Phys. Rev. **129**, 2460 (1963).
[16] Lounasmaa, O. V., (Pr,Nd:) Phys. Rev. **133**, A211 (1964).
[17] Lounasmaa, O. V., (Lu:) Phys. Rev. **133**, A219 (1964).
[18] Lounasmaa, O. V., (Ce,Eu:) Phys. Rev. **133**, A502 (1964).
[19] Lounasmaa, O. V., (Tm:) Phys. Rev. **134**, A1620 (1964).
[20] Lounasmaa, O. V., and Sundstrom, L. J., (Gd,Tb,Dy,Ho,Tm:) Phys. Rev. **150**, 399 (1966).
[21] Parks, R. D., Rare Earth Research, Edited by Nachman and Lundin (Gordon and Breach, N.Y., 1962), p. 225.
[22] Dreyfus, B., Cunningham, B. B., Lacaze, A., and Trolhet, G., Compte Rendu (Acad. des Sciences, 1964), p. 1764.
[23] Nigh, H., Legvold, S., and Spedding, F. H., Phys. Rev. **132**, 1092 (1963).
[24] Mott, N. F., and Stevens, K. W. H., Phil. Mag. **2**, 1364 (1957).
[25] Cheng, C. H., Wei, C. T., and Beck, P. A., Phys. Rev. **120**, 246 (1960).
[26] Mott, N. F., Adv. Phys. **13**, 325 (1964).
[27] Dreyfus, B., Michel, J. C., and Combiende, A., Prox. IX Intl. Conf. Low Temp. Phys. (Plenum Press, N.Y., 1965), p. 1054.
[28] Wei, C. T., Ph. D. Thesis, Univ. of Illinois, 1960.
[29] Keesom, P. H., and Pearlman, N., Encyclopaedia of Phys. **14**, 297, Edited by S. Fluge (1956).
[30] Tsang, P. J., Ph. D. Thesis, Michigan State University, 1968.
[31] Koehler, W. C., Child, H. R., Wollan, E. O., and Cable, J. C., J. Appl. Phys. **S32**, 48 (1961).
[32] Koehler, W. C., Phys. Rev. **126**, 1672 (1962).
[33] Koehler, W. C., Child, H. R., Wollan, E. O., and Cable, J. C., J. Appl. Phys. **S34**, 1335 (1963).

[34] Kronendonk, J. V., and van Vleck, J. H., Rev. Mod. Phys. **30**, 1 (1958).
[35] Gopal, E. S. R., Specific Heats at Low Temperatures, (Plenum Press, N.Y., 1966).
[36] Kaplan, T. A., Phys. Rev. **124**, 329 (1961).
[37] Bozorth, R. M., and Gambino, R. J., Phys. Rev. **147**, 487 (1966).
[38] Crane, L. T., J. Chem. Phys. **36**, 10 (1962).
[39] Belding, E. I., Phil. Mag. **4**, 1145 (1959).

417-156 O - 71 - 38

Low-Temperature Specific Heats of Face-Centered Cubic Ru-Rh and Rh-Pd Alloys*

P. J. M. Tsang and C. T. Wei**

Department of Metallurgy, Mechanics and Materials Science, Michigan State University, East Lansing, Michigan 48823

The specific heats of Rh, Pd, and a number of face-centered cubic Ru-Rh and Rh-Pd alloys were determined between approximately 1.4 and 4.2 K. Whereas the C/T vs. T^2 plots for the Ru-Rh alloys show a straight-line behavior, a low temperature anomaly is observed in similar plots for Pd and the Rh-Pd alloys below 2.2 K. This low temperature anomaly appears to be most pronounced in the alloy $Rh_{0.78}Pd_{0.22}$, and diminishes with increasing Rh or Pd. The electronic specific heats of these alloys are generally high with a minimum occurring at $Ru_{0.30}Rh_{0.70}$. A portion of the total density-of-states curve for the outer electronics in face-centered cubic transition metals is derived numerically from the present results and those available in the literature as a first approximation. Such a curve shows qualitative agreement with the first peak below Fermi level of the theoretical total *s-d* energy band of Pd calculated by Janak et al.

Key words: Electronic density of states; electronic specific heat; palladium (Pd); Rh; Rh-Pd alloys; Ru-Rh alloys; specific heat; tight-binding approximation.

1. Introduction

The electronic structure of a metal is of importance in understanding the physical properties of the metal and its alloying behavior. Significant progress has been made in recent years in both the theoretical calculation of the electron energy bands and the experimental investigation of the Fermi surfaces in metals. However, an accurate experimental method for determining the detailed structure of the electron energy bands in a metal is still lacking, and low-temperature specific heat measurement remains to be a useful method by which some knowledge of the electron energy bands in metals can be obtained.

The low-temperature specific heat of a metal has two main contributions: the electronic contribution which is linear in T, and the lattice contribution which is proportional to T^3.

$$C=\gamma T+\beta T^3 \tag{1}$$

The coefficient γ of the electronic specific heat is, according to Sommerfeld's theory [1], proportional to the density of states $N(E_F)$ at the Fermi surface.

$$\gamma=\frac{2}{3}\pi^2k^2N(E_F) \tag{2}$$

The coefficient β of the lattice specific heat is related to the Debye characteristic temperature Θ [2].

$$\beta=\frac{12}{5}\pi^4K\Theta^{-3} \tag{3}$$

By measuring the specific heats of a number of isostructural alloys of neighboring elements in the periodic table it is in principle that a plot of γ vs. the number of outer electrons per atom would reveal the qualitative nature of the electron energy bands in the metals. Such a plot can be converted to an $N(E)$ vs E curve numerically by using a rigid-band model as a first approximation, and compared with the results of band calculations for any agreement, or the lack of it.

Keesom and Kurrelmeyer [3] first made a systematic investigation of the specific heats of a number of face-centered cubic Fe-Ni and Ni-Cu alloys of the 3*d* transition series. Further work has been carried out since with fcc Pd-Ag alloys by Hoare and Yates [4], and by Montgomery [5]. Their results are in agreement with one another. The specific heats of fcc Rh-Pd alloys were determined from pure Pd to $Rh_{0.5}Pd_{0.5}$ by Budworth et al. [6]. Perhaps the most extensive investigation has been that of Beck and co-workers [7] carried

*This paper is from part of a thesis presented by P. J. M. Tsang to the graduate school of Michigan State University, East Lansing, Michigan, in partial fulfillment of the requirements for the degree of Doctor of Philosophy in Metallurgy.

**Now at IBM, Hopewell Junction, New York 12533.

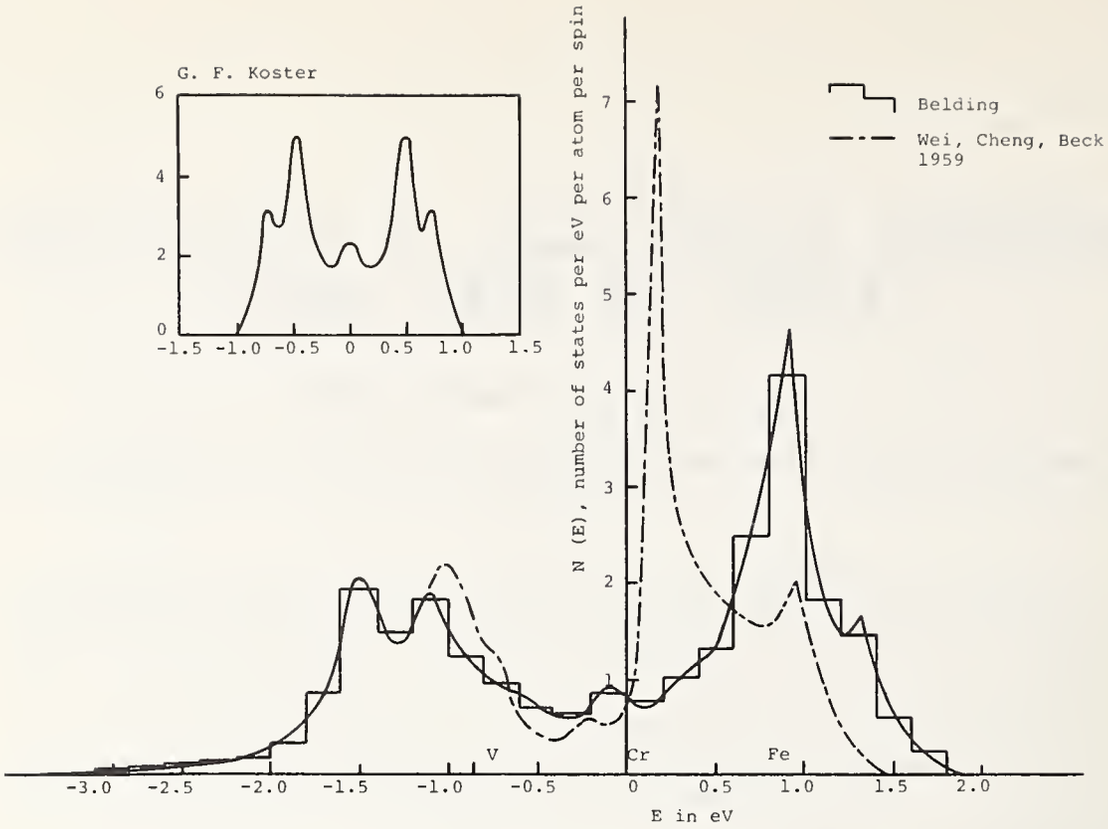

FIGURE 1. *Density of states of the* 3d *bands in the transition metals for the body-centered cubic structure.*

out with alloys of the transition elements of various combinations and crystal structures. Figure 1 shows the total density-of-states curve derived from the specific heat data of Beck et al. [7] for the 3*d* bands in the body-centered cubic structure as compared with Koster's calculation [8] using the tight-binding approximation (inset). Belding [9] modified Koster's calculation by taking into consideration the second nearest neighbors, and obtained the stepped curve. A smooth curve drawn through Belding's curve is in qualitative agreement with the experimentally derived one as it is clearly indicated.

Pessall et al. [10] repeated the measurements with bcc alloys of the 3*d* transition elements except with the addition of 10% Al. Their results confirmed those obtained originally by Cheng et al. [7]. The investigation has since been extended to alloys of the 4*d* and 5*d* series and reviewed by Bucher et al. [11]. The parallelism in the γ vs. the number-of-outer-electrons curves for the three transition series suggests that the 4*d* and 5*d* bands are similar to the 3*d* bands in the transition metals for the bcc structure, and a somewhat rigid-band behavior in these metals.

For the fcc structure, the results of Hoare and Yates [4] with Pd-Ag alloys and that of Budworth et al. [6] with Rh-Pd alloys show characteristic variations in the γ vs electron concentration plot that a high peak occurs at $Rh_{0.05}Pd_{0.95}$, and the γ value decreases sharply on both sides of this peak when more Rh or Ag is added to Pd. These features have been confirmed by Montgomery [5], and are believed to be characteristic of the tail portion of the 4*d* bands in the fcc structure. The results of Keesom and Kurrelmeyer [3] obtained with fcc Fe-Ni alloys and those obtained by Walling and Bunn [12], and by Gupta et al. with fcc Co-Ni alloys show variations parallel to each other and to the results of Budworth et al. [6] between the outer-electron-concentration range from 9 to 10 per atom. However, between the electron-concentration range from 8 to 9 the results of Gupta et al. obtained with fcc alloys of Fe-Ni, Mn-Fe, and Mn-Ni show disparities which are attributed by these authors to a possible ordering and complications of a magnetic nature.

The purpose of this work is to extend the measurement of the low-temperature specific heats of fcc alloys of the second long period transition elements to the extent of the electron concentration range in which such alloys exist for furthering the understanding of the nature of the *d* bands in the transition metals.

2. Experimental Procedure

The specimens used in this work were melted in an inert mixture of argon and nitrogen using Ru, Rh, and

TABLE 1. *Spectroscopical analyses of the* Ru, Rh, *and* Pd *metals used for making the alloy specimens and that of a typical specimen with the nominal composition* $Rh_{0.7}Pd_{0.3}$ *(weight percent)*

Element	Ru	Rh	Pd	$Rh_{0.7}Pd_{0.3}$
Ag	0.001	0.001	0.02	0.0005
Al	0.001	.001	.003	.0005
Au			.001	
B			.001	
Cu	.005	.001	.01	.0002
Fe	.01	.01	.05	.02
Ir		.02		.005
Mg	.001	.0002	.001	.0005
Mn		.001	.001	.001
Mo			.001	
Ni			.005	
Pd	.005	.005	balance	28.0
Pt		.001	.02	0.03
Rh	.003	balance	.003	71.9
Ru	balance			
Si		0.001	.1	0.005
W				.04

Pd metals of 99.8+% purity obtained from Gallard-Schlesinger Chemical Manufacturing Corporation. Each specimen was made into two halves with each half melted at least three times to insure the homogeneity of the alloy. The total weight of each specimen was approximately one fourth of a gram-mole. The compositions of the alloys were controlled by their weights before and after the melting. It was found that the maximum loss in the weight of a specimen due to evaporation and sputtering during the melting operation was less than 2%, with a more or less even evaporation rate for all three metals. Thus the uncertainty in the composition of each alloy was less than 2%. The alloys were sealed in vacuum in quartz tubes, and each was annealed at 1,080 °C for at least 24 hours and then water quenched. The results of spectroscopical analyses of the metals as received and a typical alloy sample are shown in table 1.

The complete equilibrium diagram of neither Ru-Rh nor Rh-Pd system has been reported. Rh and Pd are both fcc and completely intersoluble at high temperatures [13]. Below 845 °C a concentrated alloy may separate into a phase mixture of Rh and Pd rich solid solutions. This transition is very sluggish, and can be suppressed by quenching from the single-phase region [14]. Five Rh rich Rh-Pd specimens together with one for each of pure Rh and Pd were prepared. The alloys were examined metallographically and with x rays after heat treating and found to be single-phase fcc alloys. Ru has a hexagonal close-packed structure. Its solubility in fcc Rh has not been established exactly. It was found that the alloys $Ru_{0.40}Rh_{0.60}$ was a single fcc phase, and the alloy $Ru_{0.42}Rh_{0.58}$ was a mixture of two phases. Thus, seven Rh-rich fcc Ru-Rh specimens were made with Ru less than 40 at. %.

The specific heats of the fourteen specimens were determined at liquid helium temperatures between approximately 1.4 and 4.2 K using a calorimetric method described by Corak et al. [15]. A heater-thermometer assembly, consisted of a carbon resistor embedded in a copper disk to serve as the thermometer and a heating coil of approximately 300 ohms, was sandwiched between the two halves of a specimen. The carbon thermometer was calibrated against the vapor pressure of the liquid helium bath during the cooling cycle of each experiment. The heat input was determined by measuring the heating current, the resistant of the heating coil at the particular temperature, and the heating time. The corresponding temperature change was recorded in terms of the resistance change of the thermometer. The resistance R of the thermometer as a function of temperature was found to agree well with the equation

$$\sqrt{\log R/T} = A + B \log R \tag{4}$$

suggested by Keesom and Pearlman [16]. The parameters A and B in the equation were determined by a least-squares fit of eq (4) to the experimental data. The overall design of the cryostat and the instrumentation were similar to those used before by one of the authors [7]. The detailed experimental procedure and a discussion of the experimental accuracy were described in reference 7. The probable error in the measured electronic specific heat coefficient is estimated to be approximately $\pm 2\%$.

3. Results

Figures 2 to 5 show the C/T vs. T^2 plots for the fourteen specimens measured. The curves for the Ru-Rh alloys and the pure Rh specimen show a normal straight-line behavior with well defined γ and β values according to eq (1). The γ and Θ values are listed in table 2. All the Rh-Pd alloys and the pure Pd specimen show a low-temperature anamoly below approximately 2.2 K. Several of these Rh-Pd alloys were measured more than once, and the results were found to be reproducible within the experimental accuracy. It appears than an additional low-temperature contribution to the specific heat other than those described by eq (1) is present. This anamoly is most pronounced in the alloy $Rh_{0.78}Pd_{0.22}$, and diminishes toward Rh and Pd.

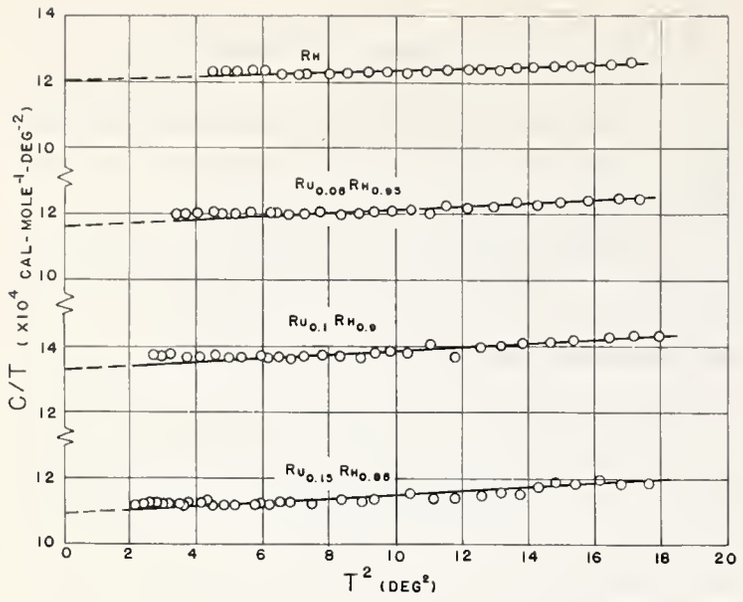

FIGURE 2. *Low-temperature specific heats of face-centered cubic* Rh *and* Ru-Rh *alloys.*

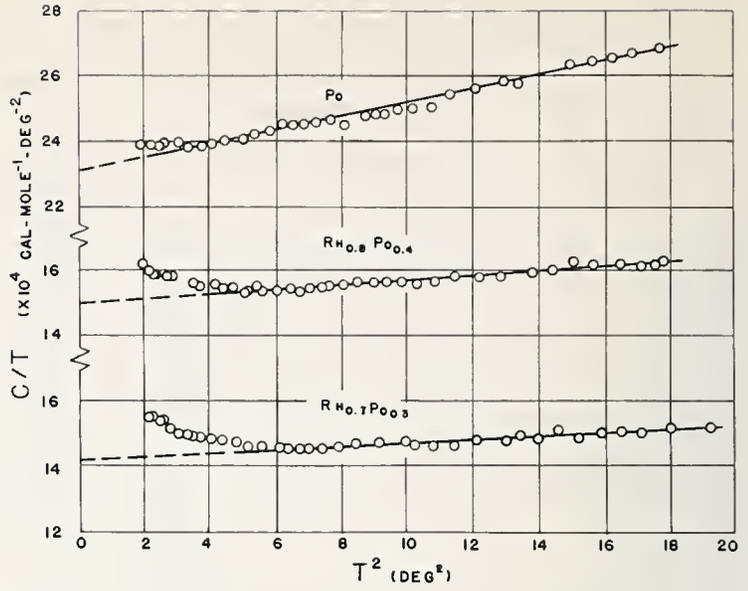

FIGURE 4. *Low-temperature specific heats of face-centered cubic* Pd *and* Rh-Pd *alloys.*

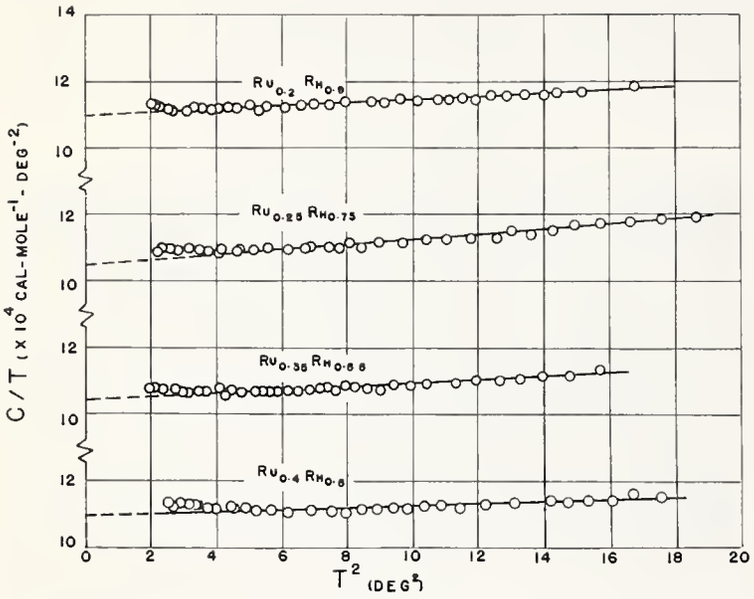

FIGURE 3. *Low-temperature specific heats of face-centered cubic* Ru-Rh *alloys.*

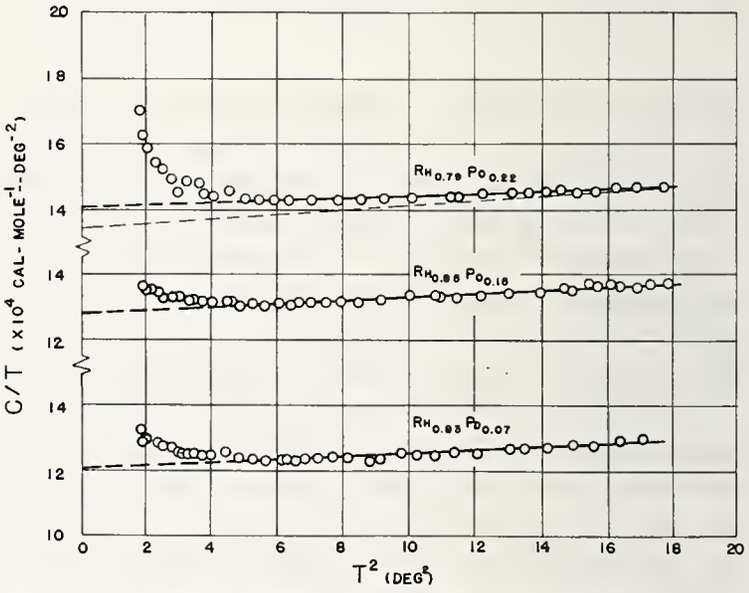

FIGURE 5. *Low-temperature specific heats of face-centered cubic* Rh-Pd *alloys.*

4. Discussion

The presence of the low-temperature anomaly in the Rh-Pd alloys would cause some uncertainty in the evaluation of the electronic specific-heat coefficient and the lattice specific heat, unless the nature of the extra contribution to the total specific heat is determined. Some of the solid-state phenomena that may happen at such low temperatures and affect the measured specific heats are associated either with superconductivity, ferro- or antiferro-magnetic transitions, hyperfine interaction, magnetic clustering, or martensitic transformation. Both Rh and Pd are known to be nonsuperconducting at the lowest temperature ever tested. It is unlikely that the Rh-Pd alloys would be superconducting above 1.3 K. A martensitic transformation usually gives rise to a surface relief which was not observed in any of the specimens.

Pd is often considered as super-paramagnetic. The presence of a few parts per million of ferromagnetic impurities such as Fe in Pd is known to cause Pd to become ferromagnetic. The chemical analyses show that the Pd metal used in making the specimens contained 0.05% Fe. It is thus possible that the low-temperature anomaly is mainly caused by the Fe impurity in the specimens.

TABLE 2. *Results of least-squares fit of the low-temperature specific heat data of face-centered cubic* Ru-Rh *and* Rh-Pd *alloys to:*

(1) $C_v/T=\gamma+\beta T^2$

Alloy composition	$\gamma\times10^4$ (cal/mol-deg^2)	Debye temperature Θ (K)
$Ru_{0.4}Rh_{0.6}$	11.00	527.9
$Ru_{0.35}Rh_{0.65}$	10.40	444.3
$Ru_{0.25}Rh_{0.75}$	10.48	396.9
$Ru_{0.2}Rh_{0.8}$	10.97	454.7
$Ru_{0.15}Rh_{0.85}$	10.89	427.5
$Ru_{0.1}Rh_{0.9}$	11.29	429.8
$Ru_{0.05}Rh_{0.95}$	11.65	456.6
Rh (Present work)	12.03	528.6
(Budworth et al.)	11.56 ± 0.07	512.0 ± 17.0
$Rh_{0.93}Pd_{0.07}$	12.01	451.9
$Rh_{0.85}Pd_{0.15}$	12.81	453.1
$Rh_{0.78}Pd_{0.22}$	13.99	498.4
$Rh_{0.7}Pd_{0.3}$	14.17	447.5
$Rh_{0.6}Pd_{0.4}$	14.94	397.5
Pd (Present work)	23.01	278.3
(Budworth et al.)	25.6 ± 1.3	274.0 ± 3.0

(2) $C_v/T=\alpha T^{-3}+\gamma+\beta T^2$

Alloy composition	$\alpha\times10^4$ (cal-deg/mol)	$\gamma\times10^4$ (cal/mol-deg^2)	Debye temperature Θ (K)
$Rh_{0.93}Pd_{0.07}$	3.61	11.86	406.8
$Rh_{0.85}Pd_{0.15}$	2.69	12.53	413.5
$Rh_{0.78}Pd_{0.22}$	6.75	13.44	412.8
$Rh_{0.7}Pd_{0.3}$	5.62	13.76	401.5
$Rh_{0.6}Pd_{0.4}$	4.35	14.56	366.2

(3) $C_v/T=A/T+\gamma+\beta T^2$

Alloy composition	$A\times10^4$ (cal/mol-deg)	$\gamma\times10^4$ (cal/mol-deg^2)	Debye temperature Θ (K)
$Rh_{0.93}Pd_{0.07}$	3.63	10.22	349.6
$Rh_{0.85}Pd_{0.15}$	2.59	11.51	370.0
$Rh_{0.78}Pd_{0.22}$	6.47	10.91	328.7
$Rh_{0.7}Pd_{0.3}$	4.84	11.95	343.4
$Rh_{0.4}Pd_{0.6}$	4.09	12.96	324.6

Schroeder and Cheng [17] suggest that the ferromagnetic impurities may form clusters which would contribute a constant term in the total specific heat.

$$C=A+\gamma T+\beta T^3 \tag{5}$$

The similar anomaly observed in Pd-Ag alloys by Montgomery et al. [15] is attributed to such a ferromagnetic clustering effect.

Another possible cause of the anomaly is perhaps the hyperfine interaction. Pd^{105}, whose relative abundance is 22.2% of the total, has a nuclear magnetic moment of -0.57 Bohr magneton. Natural Rh is almost entirely Rh^{103} which has a small nuclear moment of -0.0885 Bohr magneton. Should an effective magnetic field exist at any of these nuclei there would be a hyperfine contribution to the specific heat proportional to T^{-2} as suggested by Marshall [18].

$$C=\alpha T^{-2}+\gamma T+\beta T^3 \tag{6}$$

To evaluate the electronic specific heat coefficients of the Rh-Pd alloys each set of the experimental data was analyzed in three different ways: (1) Assuming the anomaly to be only a low-temperature effect which exists below 2.2 K, the linear portion of each of the C/T vs. T^2 curves above 2.2 K was fittbd with eq (1) for the best γ and β values. This would probably give the higher limit of γ. (2) Assuming there was a hyperfine contribution, each set of data was fitted with eq (6) for evaluating α, γ, and β. (3) Assuming that there were magnetic clusters, each set of data was fitted with eq (5) for evaluating A, γ and β. This would probably give the lower limit of γ. The results of these analyses are listed in table 2. Listed in table 2 are also the γ and Θ values for Rh and Pd determined by Budworth et al. [6] for comparison. The present γ value for Rh is 4% higher than that determined by Budworth et al., but the rest of the quantities agree with one another well. Figure 5 shows a plot of the γ values obtaincd in this work together with those available in the literature [4-6] as a function of alloy composition. The portion of the curve corresponding to the Rh-Pd alloys is drawn between the γ values obtained by analyses (1) and (2) to join smoothly with the rest of the curve. The results of analysis (3) show irregular variations in γ which may not be realistic. A general feature, which seems to be true regardless of the methods of fitting, is that the electronic specific heat coefficient γ decreases with decreasing number of outer electrons per atom in the present alloys, reaches a minimum at approximately $Ru_{0.30}Rh_{0.70}$, and then increases again.

The Debye temperatures of these alloys show irregular variations in all the three analyses as can be seen in table 2. This type of nonsystematic variations was also observed in bcc alloy of the first-long-period transition metals by Cheng et al. [7]. Stoner [19] studied the electronic specific heat of a metal with an arbitrarily shaped energy band and found that a term proportional to T^3 of a power series in T depending upon both the slope and the curvature of the density-of-states curve at the Fermi surface might arise. Such a term will not

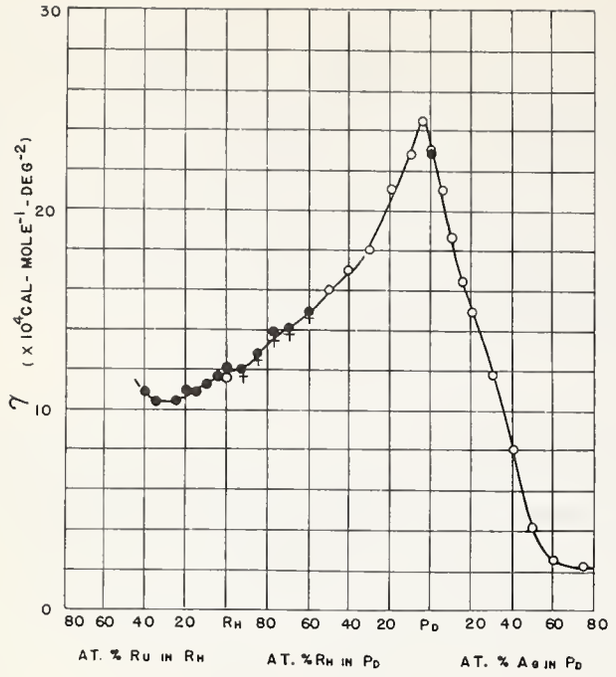

FIGURE 6. *Electronic specific heat coefficient* γ *versus composition curve for face-centered cubic* Ru-Rh, Rh-Pd, *and* Pd-Ag *alloys; present results obtained by fitting the experimental data to* $C=\gamma T+\beta T^3$, +, *by fitting to* $C=dT^{-2}+\gamma T+\beta T^3$, ●, *and* 0, *data available in literature.*

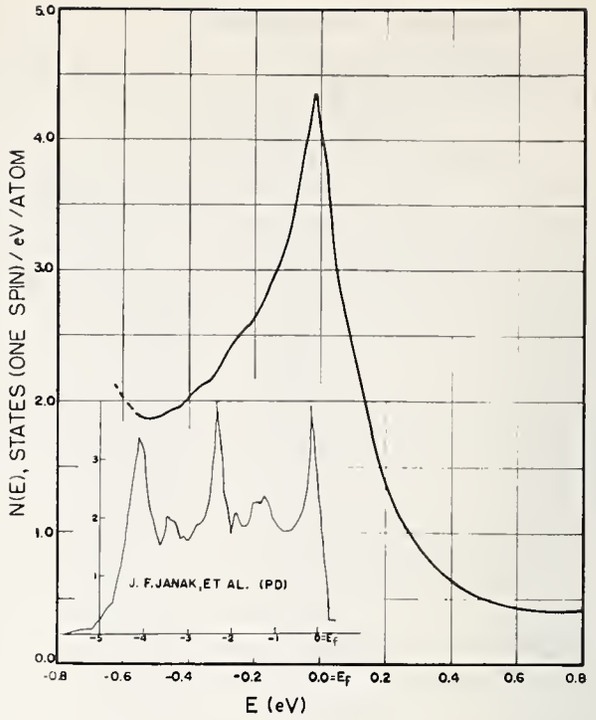

FIGURE 7. *Density of states of the* d *bands in the transition metals for the face-centered cubic structure.*

be separable from the lattice specific heat since both are T^3 dependent. The electronic specific heats of the alloys of the transition elements vary much more drastically with composition as compared with alloys of the noble metals. Stoner's theory may explain the irregularity observed in the apparent Debye temperatures of the alloys of the transition metals. Although this complication will affect the accuracy in the evaluation of the Debye temperature, it would not affect the evaluation of the density of states from the coefficient γ of the term which is linear in T.

The abscissa in figure 6 is proportional to the number of outer electrons per atom, and the ordinate, the density of states at the Fermi surface of the corresponding alloy. If a small increment Δc is taken near a particular composition, the corresponding increment in energy ΔE can be found by dividing Δc with the density of states $N(E)$ at that composition. Thus the curve can be converted to an $N(E)$ vs. E curve numerically. Figure 7 shows the results of such a numerical calculation. To a first approximation this curve can be taken as the combined total density-of-states curve for the 4*d* and 5*s* bands in fcc transition metals. In doing so a rigid band model is implied, although the applicability of which has often been questioned. Such is one of the drawbacks of the specific-heat method for investigating the energy bands in metals.

Tight-binding approximation (TBA) is generally used to calculate *d* bands. Using TBA methods, 3*d* bands of paramagnetic Ni was calculated by Koster [8] and 4*d* bands of Pd by Lenglart et al. [21]. Recently, a hybridized *s-d* band was thought to be more truthful describing the energy bands of transition metals [25]. In these calculations, [20,22-24], the TBA was used as a base to treat *d* electrons whereas APW or OPW method was used to treat *s* electrons and the *s-d* hybridization was achieved by certain interpolation scheme. The effect of *s-d* hybridization on 3*d* bands was that the location of the lower peaks (in reference to E_f) of the band were altered and their magnitudes reduced, as in the case of Ni calculated by Hodges et al. [20] and by Mueller [22]. On the other hand, as shown in the total *s-d* band of palladium calculated by Janak et al. [23], *s-d* hybridization strongly enhanced the middle peak of the 4*d*-bands. However, there is a common feature of the 3*d* and 4*d* bands that was not altered too much by *s-d* hybridization, namely, the strong peak in the vicinity of Fermi level which spans about 1.0 to 1.5 eV and can accommodate about two electrons per atom. And, due to the solubility limit of Ru in Rh or of Ru in Pd, this is the portion of 4*d* bands that can be investigated by electronic-specific measurements. In figure 7, the total energy band of Pd calculated by Janak et al. [23] was inserted for comparison. As can be seen, very good qualitative agreement was indeed found between present experimental $N(E)$ vs. E curve

and the first peak of the theoretical 4*d* bands. Good agreement was also found between present experimental *N(E)* vs. *E* curve and the 4*d* bands of Pd calculated by Mueller [24]. The energy band calculations in the present stage of sophistication are a close approximation to a true description of the electron energy states in the transition metals. We observed that the low-temperature-specific-heat method for investigating the energy bands in the transition metals may have some validity when suitable alloys are available.

5. Conclusions

(1) The specific heats of Rh, Pd and twelve face-centered cubic Ru-Rh and Rd-Pd alloys were determined between 1.4 and 4.2 K. The C/T vs. T^2 curves show a straight-line behavior for all Ru-Rh alloys, but show a low temperature anomaly for Pd and Pd alloys below 2.2 K.

(2) Aside from some uncertainty in the evaluation of the electronic specific heat coefficients of the Rd-Pd alloys due to this anomaly, a plot of γ vs. alloy concentration together with the data available in the literature can be converted numerically to a density-of-state curve as a first approximation. The resulting curve is in agreement with recent band calculations using the tight-binding approximation for treating the *d* electrons in the transition metals.

(3) The present results and those reviewed in this paper seem to indicate that for the fcc crystal structure, a strong peak in the vicinity of Fermi level exists in both 3*d* and 4*d* bands and that the tight-binding approximation is essentially the correct approach in treating the *d* electrons in the transition metals.

6. Acknowledgments

The authors wish to thank Professor F. Seitz, President of Rockefeller University for his interests in this work and his help. They are also grateful to the Division of Engineering Research and its Director, Mr. J. W. Hoffman, for their continuous support in this work. Thanks are also due to Drs. A. R. Williams, J. F. Janak, D. E. Eastman, and F. M. Mueller for their kind permission of quoting their data prior to publication. This work was supported financially in part by National Science Foundation through the grant NSG GK (475).

7. References

[1] Sommerfeld, A., Ann. Physik **28**, 1 (1937).
[2] Debye, P., Ann. Physik **39**, 789 (1912).
[3] Keesom, W. H., and Kurrelmeyer, B., Physica **7**, 1003 (1940).
[4] Hoare, F. E., and Yates, B., Proc. Roy. Soc. (London), **A240**, 42 (1957).
[5] Montgomery, H., unpublished, see article by F. E. Hoare in Electronic Structure and Alloy Chemistry of the Transition Elements, edited by P. A. Beck (John Wiley & Sons, New York, 1963).
[6] Budworth, D. W., Hoare, F. E., and Preston, J., Proc. Roy. Soc. (London), **A257**, 250 (1960).
[7] Cheng, C. H., Wei, C. T., and Beck, P. A., Phys. Rev., **120**, 426 (1960); Cheng, C. H., Gupta, K. P., VanReuth, E. C., and Beck, P. A., Phys. Rev. **126**, 2030 (1962). See also review by K. P. Gupta, C. H. Cheng, and P. A. Beck, Journal de Physique et le Radium **23**, 721 (1962).
[8] Koster, G. F., Phys. Rev. **98**, 901 (1955).
[9] Belding, E. F., Phil. Mag. **4**, 1145 (1959).
[10] Pessall, N., Gupta, K. P., Cheng, C. H., and Beck, P. A., J. Phys. Chem. Solids **25**, 993 (1964).
[11] Bucher, E., Heiniger, F., and Muller, J., article in Low Temperature Physics, edited by J. G. Daunt et al. (Plenum Press, New York 1965).
[12] Walling, J. C., and Bunn, P. B., Proc. Phys. Soc. **74**, 417 (1959).
[13] Raub, E., J. Less Common Metals **1**, 3 (1959).
[14] Raub, E., Beeskow, H., and Manzel, D., Z. Metallkunde **50**, 428 (1959).
[15] Corak, W. S., Garfunkel, M. P., Satterthwaite, C. B., and Wexler, A., Phys. Rev. **98**, 1699 (1955).
[16] Keesom, P. H., and Pearlman, N., in Encyclopedia of Physics, **Vol. 14**, edited by S. Fluegge (Springer-Verlag, Berlin 1956) p. 297.
[17] Schroeder, K., and Cheng, C. H., J. Appl. Phys. **31**, 2154 (1960).
[18] Marshall, W., Phys. Rev. **110**, 1280 (1958).
[19] Stoner, E. C., Proc. Roy. Soc. (London), **A154**, 656 (1936).
[20] Hodges, L., Ehrenreich, H., and Lang, N. D., Phys. Rev. **152**, 505 (1966).
[21] Lenglart, P., Lemam, G., and Lelieur, J. P., J. Phys. Chem. Solids **27**, 377 (1966).
[22] Mueller, F. M., Phys. Rev. **153**, 659 (1967).
[23] Janak, J. R., Eastman, D. E., and Williams, A. R., these Proceedings, p. 181.
[24] Mueller, F. M., these Proceedings, p. 17.
[25] Heine, V., Phys. Rev. **153**, 673 (1967).

Density of States of Transition Metal Binary Alloys in the Electron-to-Atom Ratio Range 4.0 to 6.0

E. W. Collings and J. C. Ho

Battelle Memorial Institute, Columbus Laboratories, 505 King Avenue, Columbus, Ohio 43201

Using Ti-Mo as a prototype of binary bcc transition metal alloys for $4 < e/a < 6$, densities-of-states at the Fermi level, $n(E_F)$, have been studied using low-temperature specific heat augmented by magnetic susceptibility (χ) measurements. A survey of the literature has revealed that the principal descriptors of density of states, γ (the electronic specific heat coefficient), and T_c (the superconducting critical temperature), generally decrease as e/a decreases below about $e/a \sim 4.3$ to 4.5. The maxima in γ and T_c so induced have usually been interpreted as indicating the existence of maxima in $n(E_F)$ near $e/a \cong 4.5$ for bcc alloys. But since the region $e/a \lesssim 4.5$ also corresponds to that in which a submicroscopic hexagonal-structured precipitate (ω-phase) always appears in quenched alloys, a detailed study of microstructure was undertaken in conjunction with the electronic property measurements. It was concluded that a steadily increasing abundance of an ω-phase precipitate was responsible for the observed drops in γ, T_c, and χ below $e/a \cong 4.5$. Because of the fineness of the precipitate (70-330 Å) the physical property results themselves are indistinguishable from those usually associated with single-phase materials. Using magnetic susceptibility at elevated temperatures, where the prototype Ti-Mo alloy is known to be single phase bcc, it has been shown that $n(E_F)_{bcc}$ increases monotonically as e/a is reduced from 6 to 4, in agreement with deductions based on the results of recent band-structure calculations on bcc 3*d* transition metals.

Key words: Alloys; bcc transition metal alloys; charging effect; electronic density of states; G. P. zone; Ginzburg-Landau coherence length; Hf-Ta; low-temperature specific heat; magnetic susceptibility; omega phase; rigid-band approximation; superconducting transition temperatures; tantalum-tungsten (Ta-W); Ti-Mo; titanium-molybdenum (Ti-Mo) alloy; tungsten (W); W-Re.

1. Introduction

Important theoretical contributions to our understanding of the conditions for validity of, and the limitations of, the rigid-band approximation have been made by Beeby [1] and Stern [2,3]. According to the latter [3] perturbation theory is appropriate when the difference between the atomic potentials of the participating atoms is sufficiently small, regardless of solute concentration. Conversely, large differences in atomic potentials result in what is effectively a transfer of screening charge from one kind of atom to the other, accompanied by a breakdown of perturbation theory. The so-called charging effect can be parameterized by means of the quantity $\langle |V_{12}| \rangle_{av}/\Delta$, where V_{12} is a measure of the difference between the atomic potentials of the two types of atom, and Δ is the zero-order energy band-width. Stern's theory of charging thus provides a unifying interpretation of alloy behavior in terms of differences in atomic potentials. Accordingly "similar" atoms tend to form solid-solution alloys over a wide composition range, while the binary phase diagrams for pairs of atoms widely separated in the periodic table usually exhibit a plurality of intermetallic compounds. A survey of the physical and electronic properties of pure transition metals and their binary alloys leads to the conclusion that pairs of transition metal atoms chosen from adjacent columns in the periodic table probably provide optimal conditions for the validity of the rigid-band model. It follows that it should be possible to transcribe the curve of γ vs. e/a,[1] in the range

[1] γ is the low-temperature electronic specific heat coefficient, and (e/a) is the ratio of the total number of valence $(s+d)$ electrons to the number of atoms. For a free electron gas $\gamma^0 (2/3)\pi^2 k^2 n(E_F)$, where $n(E_F)$ refers to the density of states at the Fermi level E_F for a single spin direction (i.e., one-half of the *total* density of states). If the units of γ are mJ/mole-deg^2, and those of $n(E_F)$ are states/eV-atom, then $\gamma^0 = n(E_F)/0.212$.

(i − 1 to i + 1), into a reasonable experimental representation of the density-of-states curve, for a transition metal of the ith group of the periodic table, over a small energy interval about the Fermi energy. Near the middle of a transition series, where the greatest number of electrons are available for screening we expect to see the closest conformity to the rigid-band model [4]. Indeed, as McMillan has shown [5], there is remarkable agreement between the experimental rigid-band "density-of-states curve" derived from specific heat data for bcc binary Hf-Ta-W-Re alloys, and the results of band structure calculations for W by Matthies [6]. Implicit throughout this discussion is that some degree of similarity should exist between the density-of-states curves for transition metals of adjacent groups. The recent work of Snow and Waber [7] has enabled, for the first time, such a comparison to be made. Their calculated $n(E)$[2] curves for the bcc phases of the 3d transition series exhibit a gradual change of profile on proceeding from Ti to Fe. Some similarity between the hcp $n(E)$ curves for Sc and Ti has also been noted by Altmann and Bradley [8].

The extensive literature relating to calorimetric measurements on cubic phase (bcc and fcc) transition metal binary alloys has been reviewed by Heiniger, Bucher, and Muller [9]. Low temperature specific heat has not succeeded in extending the bcc γ curve to $e/a = 4$ since the bcc phases of Ti, Zr, and Hf (and the dilute alloys of slightly higher e/a) are not stable except at elevated temperatures. However, the limited amount of calorimetric work that has been carried out on alloys in the range $e/a \lesssim 5$ has always suggested the existence of a maximum in $n(E_F)$ near $e/a \cong 4.5$ (or a maximum in $n(E)$ near the appropriate value of E, if rigid-band conditions are fulfilled). Low temperature specific heat data in the range $4 < e/a < 6$ are reviewed in figure 1. In agreement with these are the results of earlier studies of the superconducting transition temperatures (T_c) of transition-metal binary alloys. Maxima in T_c have frequently been noted in Ti-base alloys near $e/a \cong 4.5$ [10]; and for Ti-Mo in particular, Blaugher et al. [11] have suggested that the turning point observed in T_c might be connected with a corresponding maximum in $n(E_F)$ for that alloy system. In addition the nuclear spin relaxation data of Masuda et al. [12] in the form $(T_1T)^{-1/2}$ vs. e/a exhibited a rather flat maximum, located near $e/a \sim 4.5$, which was correlated with a maximum in $n(E_F)$ based on calorimetric evidence such as that of figure 1.

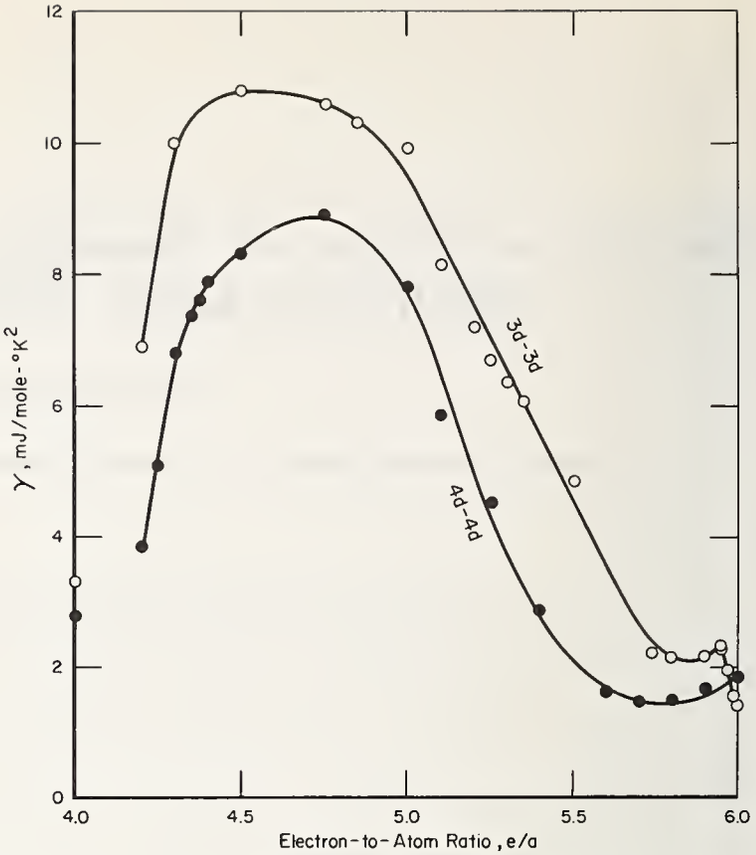

FIGURE 1. *Plot of electronic specific heat coefficient* γ *versus valence electron* (s + d) *to atom ratio*, e/a *for pure transition metals and binary alloys of the* 3d *and* 4d *series.*

Sources of data for the (3d-3d)4 series are: (i) Ti-V [20-85 at.% (e/a=4.20-4.85)]-ref. (a); (ii) V-Cr [10-35 at.% (e/a=5.10-5.35)]-refs. (b) and (c); (iii) V-Cr [50-95 at.% (e/a=5.50-5.95)]-ref. (d); (iv) V-Cr [95-99 at.% (e/a=5.95-5.99)]-ref. (e).

Sources of data for the (4d-4d) series are: (i) Zr-Rh [4-8 at.% (e/a=4.20-4.40)]-ref. (f); (ii) Zr-Nb [50-75 at.% (e/a=4.50-4.75)]-ref. (e); (iii) Nb-Mo [10-25 at.% (e/a=5.10-5.25)]-ref. (g); (iv) Nb-Mo [40–90 at.% (e/a=5.40–5.90)]-ref. (h)

(a) Cheng, C. H., et al., Phys. Rev. **126**, 2030 (1962).
(b) Gupta, K. P., et al., J. Phys. Radium **23**, 721 (1962).
(c) Srinivasan, T. M., and Beck, P. A., Ann. Acad. Sci. Fennicae A **VI 210**, 163 (1966).
(d) Cheng, C. H., et al., Phys. Rev. **120**, 426 (1960).
(e) Heiniger, G., Phys. kondens. Materie **5**, 243 (1966).
(f) Dummer, G., Z. Phys. **186**, 249 (1965).
(g) Morin, F. J., and Maita, J. P., Phys. Rev. **129**, 1115 (1963).
(h) Veal, B. W., et al., Ann. Acad. Sci. Fennicae A **VI 210**, 108 (1966).

One of the aims of the present research was to determine experimentally whether the inferred density of states maximum at $e/a \sim 4.5$ was in fact a property of single-phase bcc alloys (i.e., a property of the rigid-band bcc density of states curve). The alloy system chosen for this study was Ti-Mo, which exhibits continuous uninterrupted solid solubility in the bcc field from pure Ti to pure Mo.

2. Experimental

Ti-Mo alloys of nominal composition 1, 2, 3, 3.5, 4, 4.5, 5, 7, 8.5, 10, 15, 20, 25, 40, and 70 at. % Mo were prepared by arc-melting high-purity ingredients, the actual compositions subsequently being accurately established by chemical analysis. The ingots were an-

[2] $n(E_i)$ is the density of states at energy E_i. Many authors, including Snow and Waber [7] consider *both* electron spin directions when calculating $n(E_F)$. Others consider only a single spin direction resulting in an "$n(E_F)$ for *one* spin directi n" which is one-half of the other value. We are arbitrarily following the latter convention, cf., our figure 12 with the figure 6 of reference [7].

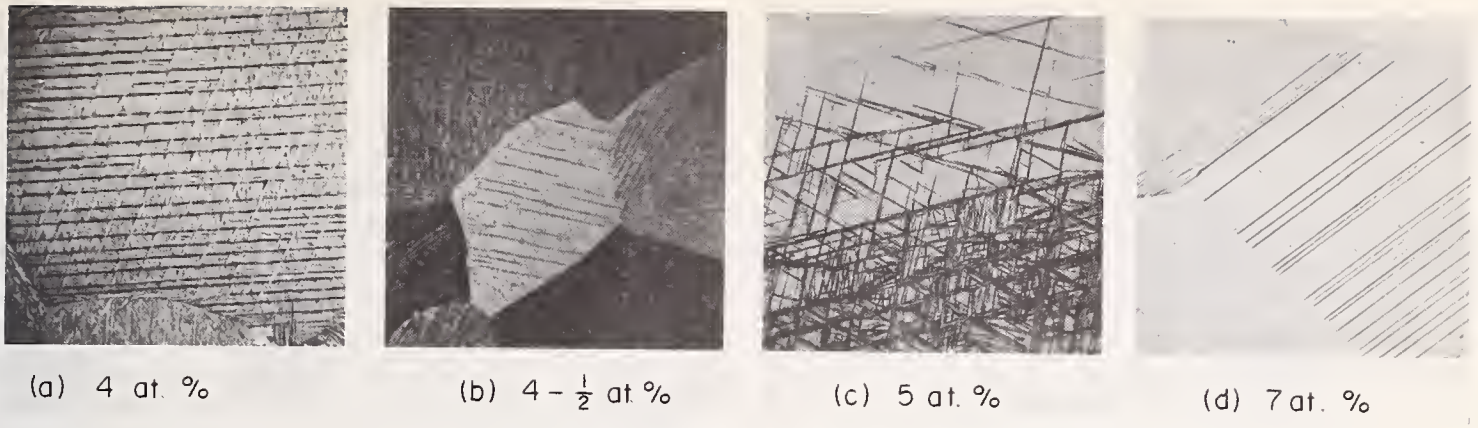

FIGURE 2. *Representative optical microstructures of quenched (from 1300 °C)* Ti-Mo *alloys.*

A dense martensitic structure is apparent in (a) and (b), with (c) representing the end of the field. Some twinning is visible in (d) but no second phase *appears* to be present at this magnification. Magnification of the original photographs—50X.

nealed for eight hours at 1300 °C in a titanium-gettered argon environment and rapidly quenched into iced brine. Specimens of 4 through 7 at. % Mo were examined by conventional optical metallography (fig. 2). The quenched alloys of up to and including 4.5 at. % Mo were apparently almost completely martensitic in structure. The martensitic field seems to terminate at approximately 5 at. % Mo; and the micrograph of the 7 at. % alloy is clear except for some slight twinning. Ti-Mo alloys in the composition range above 6 or 7 at. % used in previously-reported physical property studies have generally been assumed to be single-phase bcc. In a search for the presence of an expected second-phase precipitate in the "clear," apparently single-phase, regions (cf., fig. 2) of the present alloys, specimens of 5, 7, and 10 at. % Mo were examined by electron diffraction and electron microscopy. The results of these observations will be discussed later.

The principal technique used in this investigation was conventional low temperature calorimetry (1.5-6 K) which in general yields the electronic specific heat coefficient γ and the Debye temperature, θ_D. In addition for Ti-Mo a superconducting transition was observable for Mo concentrations greater than 5 at. %. Low temperature calorimetry also shows clearly the degree of sharpness of a superconducting transition, and through the relative height of the specific heat jump, the approximate abundance of the superconducting component in a mixture. As a result of the metallurgical studies we were able to show that of the quenched alloys only those of concentrations greater than about 20 at. % Mo could be regarded as completely single phase bcc. In the low concentrated alloys, in which the bcc phase is stable only at elevated temperatures, density-of-states was gauged by magnetic susceptibility (up to 1140 °C), after having established that for this alloy system at least magnetic susceptibility was, under the circumstances, a reasonably reliable substitute.

3. Results and Discussion

3.1. Low-Temperature Specific Heat

The low-temperature specific heat data are summarized in figure 3 where they are compared with the results of previously-published calorimetric measure-

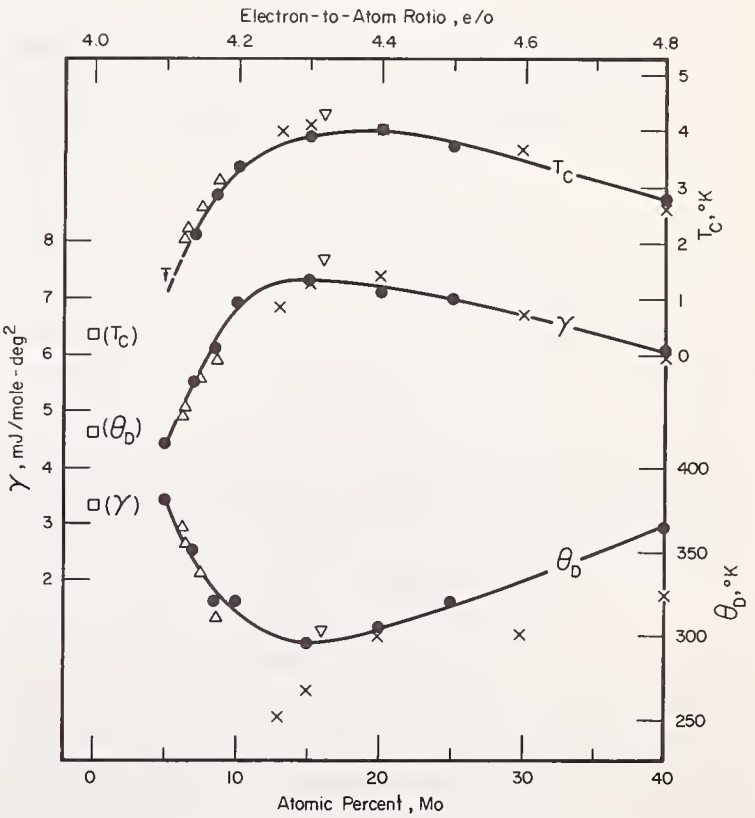

FIGURE 3. *Low-temperature specific heat data for bcc- and (bcc + ω)-phase* Ti-Mo *alloys.*

●—this work; △—ref. [13]; ▽—ref. [14]; ×—ref. [15]. The open squares refer to pure hcp Ti, the data being obtained in the present experiments excepting for T_c, which is due to R. H. Batt [Ph.D. Thesis, University of California, Berkeley (1964)].

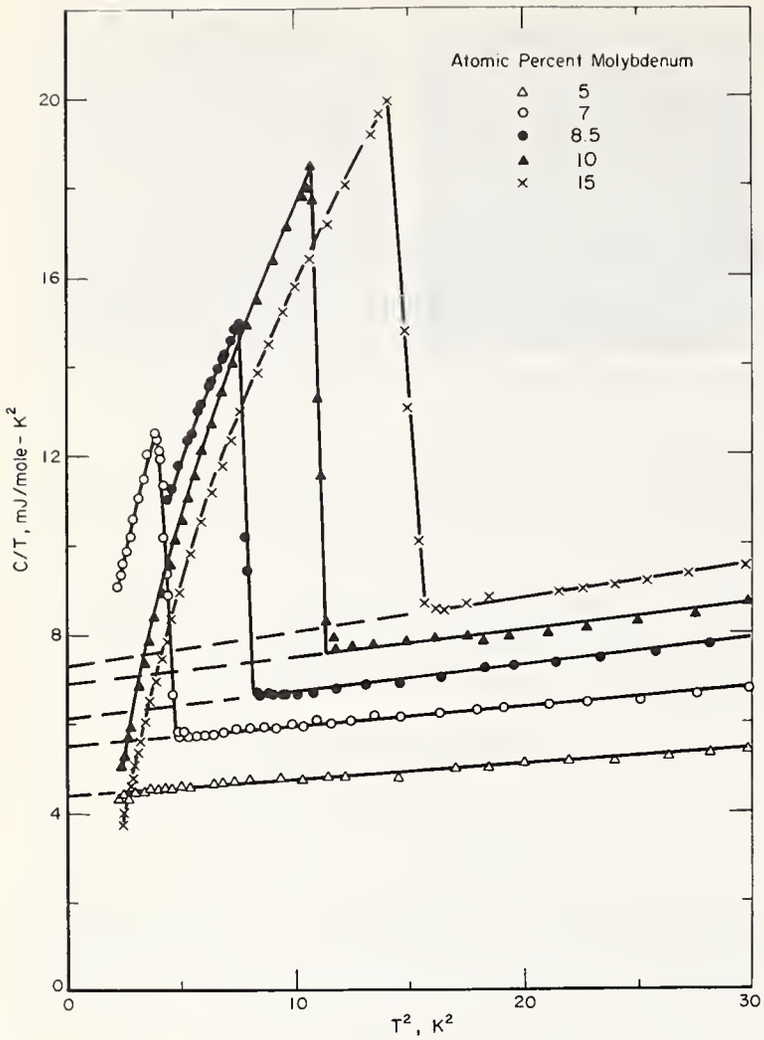

FIGURE 4. *Low temperature specific heat data for* Ti-Mo *alloys plotted in the usual format,* C/T *versus* T².

A sharp superconducting transition was found in all the alloys of concentrations greater than 7 at.% Mo. This is exemplified in the figure for Ti-Mo (7-15 at.%).

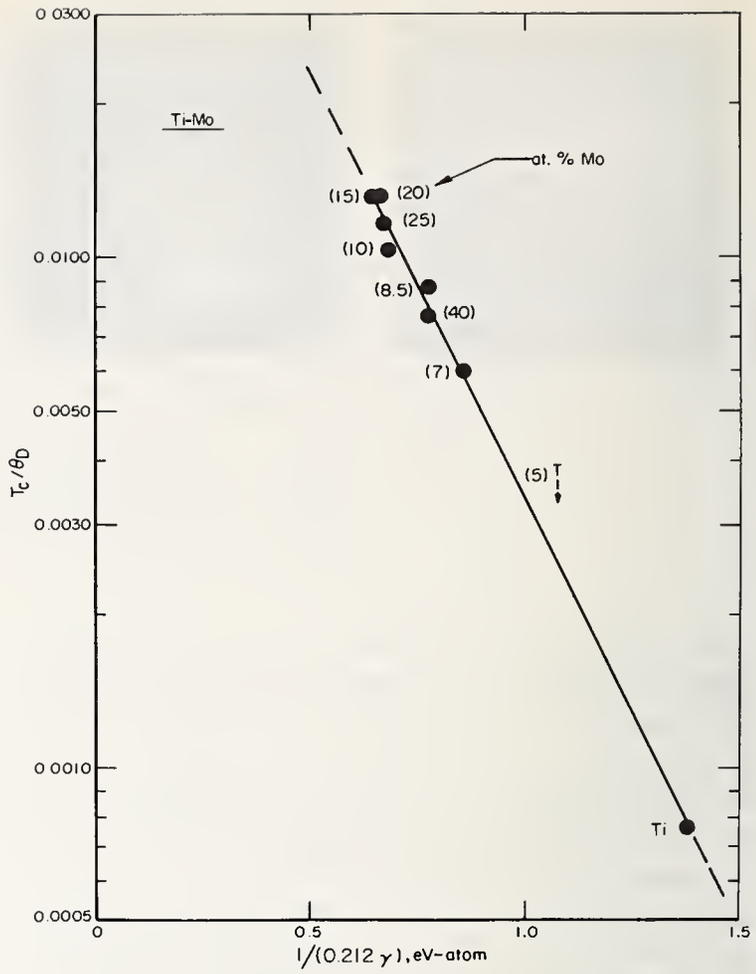

FIGURE 5. *Plot of log* (T_c/θ_D) *versus* $(0.212\ \gamma)^{-1}$ *the slope of which according to eq* (2) *yields* $V_{app.}$, *an apparent electron-pairing potential; which is directly usable in the electron-phonon enhancement factor* $(1 + 0.212\ \gamma\ V_{app.})$ *of eq* (7).

ments [13-15]. There is fortunately no serious numerical disagreement between the present results and those of previous authors. Figure 3 shows that the behaviors of the three properties T_c, γ, and θ_D are, in the absence of further evidence to the contrary, entirely consistent with a bcc density of states which rises to a rather flat maximum at about $e/a \sim 4.5$. T_c and γ are seen to have their characteristically similar trends, a property which follows from the BCS-Morel [16] relationship:

$$T_c/\theta_D \propto \exp\{-1/n(E_F)V\}, \qquad (1)$$

where V is the electron pairing potential. In addition γ and θ_D have their frequently-observed [9] inverse relationship, as do T_c and θ_D.[3] Another property usually associated with homogeneous alloys is a sharp superconducting transition. Figure 4 shows T_c to remain sharp throughout the entire concentration range 7-15 at. % Mo.

In the presence of electron-phonon interactions the measured γ is enhanced, beyond what would be expected for a free electron gas of density $n(E_F)$, by a factor $(1+\lambda)$ in which it is usual to assume $\lambda \cong n(E_F)\ V$. Equation (1) may therefore be re-written:

$$T_c/\theta_D \propto \exp\{-1/0.212\ \gamma_{\text{app.}}\}, \qquad (2)$$

where $V_{app.} = V/(1+\lambda)$. It follows that a plot of log (T_c/θ_D) vs. $(0.212\ \gamma)^{-1}$ should be linear for any alloy system in which $V_{app.}$ is constant. As figure 5 shows such a linearity is exhibited by the entire alloy series from hcp Ti through Ti-Mo (40 at. %) with an apparent electron interaction potential, $V_{app.}$, equal to 0.26 eV-atom.

To summarize, on the basis of all the low-temperature physical properties described above it would appear that the structures of quenched Ti-Mo ($\gtrsim$ 7 at. %) are not disturbed by the presence of a second phase,

[3] In other words, as pointed out by McMillan [5] there is a variation of coupling constant with $n(E_F)$ through a relationship between density-of-states and elastic stiffness.

and that the rigid-band bcc density of states curve does in fact possess a maximum at $e/a \sim 4.5$.

3.2. Microstructure Studies

By now a considerable bulk of metallurgical evidence points to the conclusion that *submicroscopic* precipitation does occur within the bcc regions of quenched Ti-M and Zr-M alloys (where M represents a transition element from groups V to VIII) in the composition range corresponding to $e/a \lesssim 4.5$. The occurrence of this so-called ω-phase precipitate in Ti-base alloys has been discussed and reviewed in recent papers by Blackburn and Williams [17] and Hickman [18]. Although the detailed mechanism of its formation from the bcc matrix is not yet clear, it has been pointed out by Boyd [19] that the transformation kinetics are analogous to G. P. zone formation; i.e., below some sharp solvus temperature the second phase forms rapidly as a high density of precipitates. The ω-phase has a complex hexagonal structure which exhibits partial coherency with the parent bcc lattice. According to Hickman [18] it is possible for the ω-phase to be of the same composition as the matrix, in which case its rate of formation is too rapid to be suppressed even by quenching from the bcc field.

In quenched alloys the precipitated particles should increase in abundance as the solute concentration is reduced below the formation threshold, which for Ti-Mo alloys seems to be in the vicinity of 15 at. % of Mo. A correlation therefore exists between the drop in density of states (as gauged by T_c and γ) and the expected fraction of precipitated ω-phase. To substantiate the correlation, it remains to demonstrate the presence of ω-phase in the specific heat specimens themselves.

Electron microscope observations were made on samples taken from quenched specific heat ingots of compositions 4.5, 5, 7, and 10 at. % Mo. Typical results, those for Ti-Mo (5 and 10 at. %) are presented in figures 6, 7, and 8. Figure 6 is an electron diffraction photograph from Ti-Mo (5 at. %). Two bright spot patterns are superimposed: a rectangular arrangement of round spots from the bcc matrix; and groups of elongated spots[4] originating from the ω precipitate. The precipitate itself[5] may be selectively photographed against a dark background by forming an image from one of the ω-phase diffraction spots. Dense precipitation is seen in both the 5 at. % (fig. 7) and 10 at. % (fig. 8) alloys, the particles becoming smaller in size but more densely packed as the Mo concentration is reduced. Measurements taken from figures 7 and 8 showed the particle diameters to vary from 70-130 Å (5 at. % Mo) to 170-330 Å (10 at. % Mo).

The structural studies have demonstrated that as e/a decreases below about 4.5 the decreases in the quantities T_c and γ correlate with an increasing proportion of ω-phase observed to be present in the same specific heat specimens.

3.3. Magnetic Susceptibility

Magnetic susceptibility measurements on pure Ti have shown that the transformation from hcp to bcc at 883 °C is accompanied by a relatively large increase in total magnetic susceptibility [20] and presumably $n(E_F)$. It was, therefore, postulated that $n(E_F)$ for Ti-Mo alloys lay on an extrapolation of the data for the region $e/a \geq 4.5$; and that the observed maximum near $e/a \sim 4.5$ was *induced* by the presence of ω-phase in the lower concentration alloys. If this were so, removal of the ω-phase should restore $n(E_F)$ to its expected extrapolated value. Since the formation of the precipitate cannot be suppressed by quenching, the experiments on single-phase bcc alloys would need to be performed at elevated temperatures, which eliminates low-temperature calorimetry as a technique. However, this region can be explored using magnetic susceptibility. But in order to be able to employ this technique as a valid substitute for calorimetry, it is first of all necessary to establish a suitable relationship between susceptibility and specific heat for a series of the quenched alloys.

3.4. Magnetic Susceptibility and Specific Heat

For free electrons it is well known that

$$\chi_{\text{spin}} \propto 2\mu_B^2 n(E_F), \tag{3}$$

where μ_B is the magnetic moment per spin (Bohr magneton); $n(E_F)$ is our conventional Fermi density-of-states referring to a single spin direction; and the constant of proportionality depends on the units employed. We have already shown that for free electrons:

$$n(E_F) = 0.212\,\gamma^0. \tag{4}$$

It follows that

$$\chi_{\text{spin}} = 13.71\,\gamma^0, \tag{5}$$

in which, if γ^0 is expressed as mJ/mol-deg^2, χ_{spin} appears as μ emu/mole. γ^0 may be derived from the experimentally-obtained γ, by allowing for electron-

[4] According to Blackburn and Williams [17] the spot elongation is evidence of a hexagonal atomic structure and an ellipsoidal precipitate morphology.

[5] Actually only one-quarter of the precipitate can be visualized, at one time, by this technique.

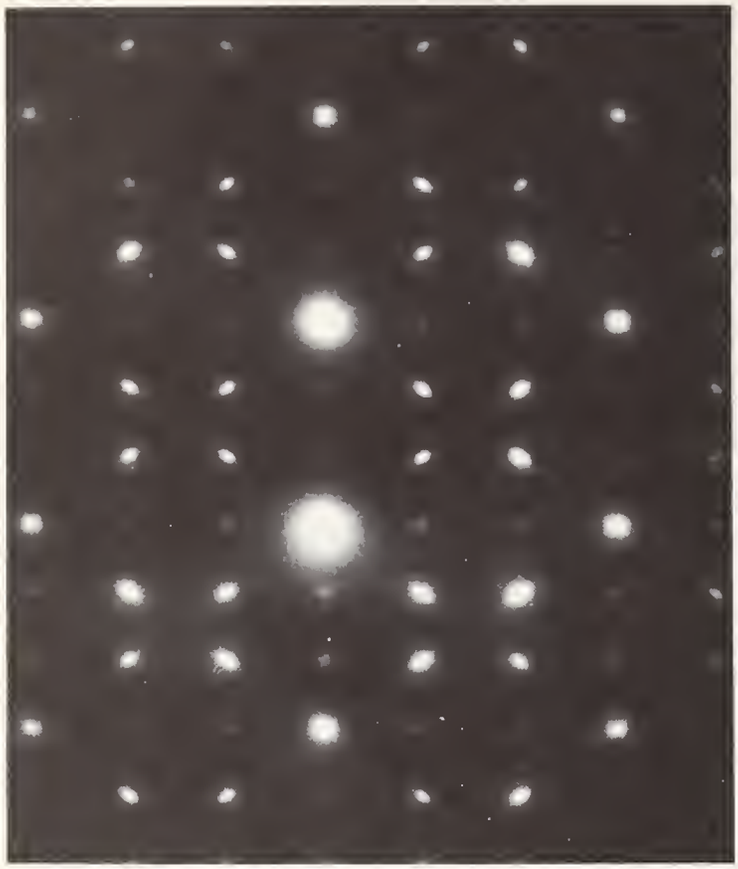

FIGURE 6. *Electron diffraction pattern from* Ti-Mo (5 *at.%*).

Two principal types of spot patterns are superimposed: a rectangular arrangement of (twelve) bright round spots; and groupings of elongated spots originating from the ω-phase precipitate. The rectangular pattern of faint round spots is due to a different orientation of the ω-phase.

FIGURE 7. *Dark field electron micrograph showing* ω*-phase in* Ti-Mo (5 *at.%*).

Inset is the preliminary electron diffraction pattern (shown enlarged in fig. 6), with the originating ω-spot indicated by the arrow. By this technique the bright patches of the photograph are specific to ω-phase; however, only one-quarter of the precipitate is visualized at one time.

phonon enhancement $(1+\lambda)$ present in a real crystal, in the following way:

$$\gamma^0 = \gamma/(1+\lambda), \tag{6}$$

where

$$\lambda \cong n(E_F)\ V.$$

Using (4) and re-applying (6),

$$\lambda \cong 0.212\ \gamma\ V/(1+\lambda)$$

$$= 0.212\ \gamma\ V_{\text{app.}}\ \text{[c.f., (2)]}.$$

The required experimental γ^0 is therefore

$$\gamma^0 \cong \gamma/(1+0.212\ \gamma\ V_{\text{app.}}),$$

with (7)

$$V_{\text{app.}} = 0.26\ eV - \text{atom}.$$

The density-of-states may then be obtained by using eq (4).

The chief components of the measured total magnetic susceptibility are given by $\chi_{total} \cong \chi_{spin} + \chi_{orb.}$, where $\chi_{orb.}$, the orbital paramagnetism, has been discussed by Clogston et al. [21], and others. In the present work, $\chi_{orb.}$ was derived *experimentally* by comparing χ_{total} (room temperature) with χ_{spin} [calculated from the measured γ using eqs (5) and (7)] for single-phase bcc alloys (100-20 at. % Mo) and then extrapolating into the two phase region.[6] Figure 9 compares γ^0 with χ_{spin} for quenched Ti-Mo alloys. Agreement between the curves has of course been forced in the single-phase bcc field between 100 and 20 at. % Mo as described above. But *below* 20 at. % Mo there is a simultaneous drop in both γ^0 and χ_{spin}, which in this range is taken to be given by χ_{total} (measured)-$\chi_{orb.}$. The continued agreement in this latter region is sufficiently convincing to suggest that χ_{spin} may be used, with a reasonable degree of confidence, as a substitute for γ^0 in the high temperature measurements to be described.

Magnetic susceptibility measurements were made at temperatures of up to 1140 °C. After reaching struc-

[6] This extrapolation was practically horizontal yielding for bcc Ti-Mo (0-20 at. %) $\chi_{orb.} = 132\ \mu$ emu/mole. This compares favorably with $\chi_{orb.} \cong 150\mu$ emu/mole for bcc Ti-V alloys containing less than 70 at. % V (and including, we assume, bcc Ti) according to N. Mori [J. Phys. Soc. Japan **20**, 1383 (1965)].

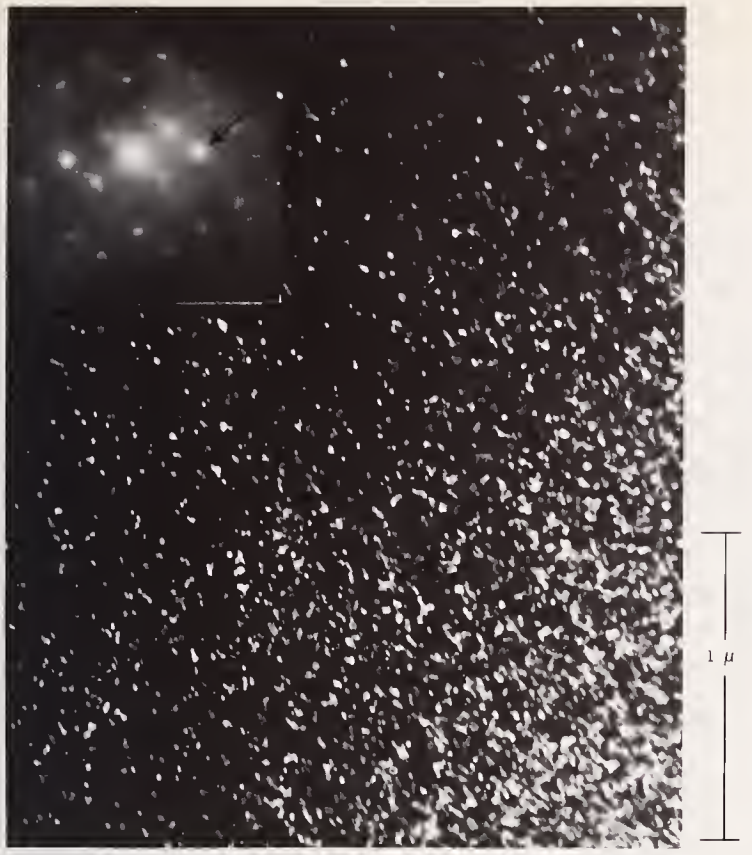

FIGURE 8. *Dark-field electron micrograph showing ω-phase in* Ti-Mo (*10 at.%*).

Inset is the preliminary electron diffraction pattern, with the originating ω-spot indicated by the arrow.

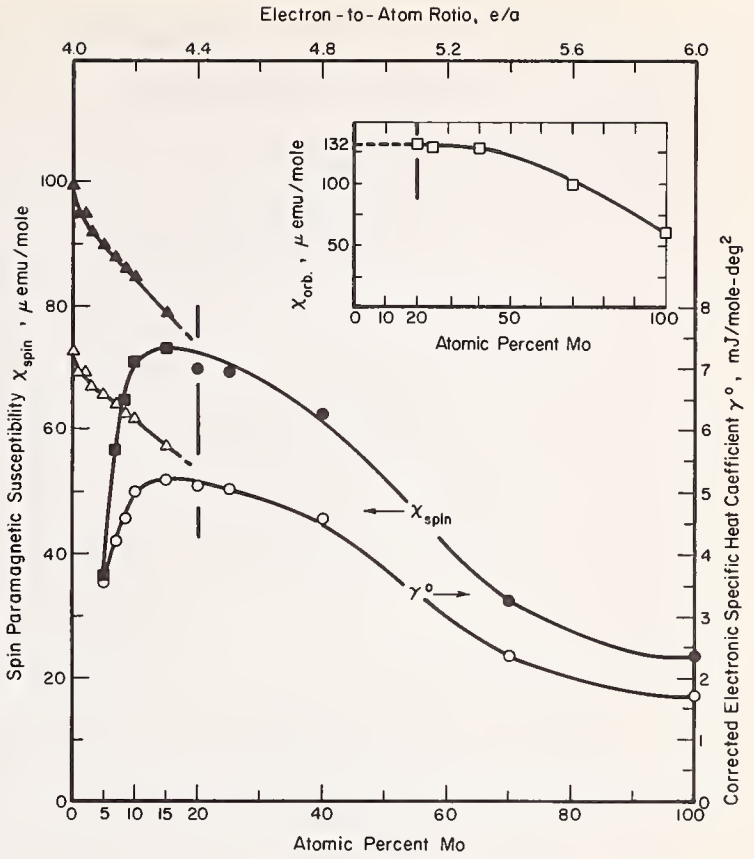

FIGURE 9. *Reduced magnetic susceptibility and specific heat data for bcc and (bcc + ω) Ti-Mo alloys.*

○ – reduced experimental data $\gamma^0 = \gamma/(1+\lambda)$; ● – χ_{spin}, calculated from γ^0 in the range 100-20 at.% Mo; □ (inset) – $\chi_{orb.}$ calculated from $(\chi_{total} - \chi_{spin})$ in the range 100-20 at.% Mo, and extrapolated; ■ – $(\chi_{total} - \chi_{orb.})$ for (bcc + ω) alloys (note the un-forced agreement of the ■ and ○ data below 20 at.% Mo); ▲, △ – χ_{spin} and γ^0 for single-phase bcc, respectively.

tural equilibrium in the bcc region the alloys exhibited almost temperature independent susceptibility as shown in figure 10. Figure 11 compares the extrapolated room temperature total susceptibilities of single-phase bcc Ti-Mo alloys with those in which ω-phase precipitation has occurred. Clearly, as e/a decreases below about 4.5, χ_{total} (bcc) continues to increase monotonically on an extrapolation of the curve for $4.5 \lesssim e/a < 6$; whereas the curve for χ_{total} (bcc + ω) turns over and proceeds downwards as the proportion of ω-phase increases.

It is concluded as a direct result of the susceptibility work that the turning points at $e/a \cong 4.5$ which appear in the χ, γ, and T_c curves for quenched alloys are induced by the formation of an ω-phase precipitate.

3.5. Analysis of the Experimental Data

The essential semi-quantitative features of the experimental results are immediately obvious from an inspection of figure 11 followed by a visual extrapolation of the γ^0 curve of figure 9. However, in order to make the best possible quantitative comparisons between the experimental χ and γ results and theoretical predictions, our data has been analyzed in a manner which is best described with reference to the appropriate row numbers of table 1.

From the low-temperature specific heat results, γ^0 may first be calculated using eq (7). This is plotted (0-100 at. % Mo) as the lower curve in figure 9 and is listed (bcc only, 20-100% Mo) in row 8. From γ^0, χ_{spin} may next be calculated [eq (5)] and is listed (20-100% Mo) in row 9. Using the measured χ_{total} for this concentration range, a $\chi_{orb.}$ may be derived (row 10) and extrapolated to lower concentrations (row 11). From the results presented in figure 10 a set of values of χ_{total} (bcc; 0-20 at. % Mo; 300 K) may be obtained by extrapolation. Using these values (row 5), and the extrapolated $\chi_{orb.}$ (row 11), the corresponding χ_{spin} is derived (row 12). These values are plotted to form the upper susceptibility branch in figure 9 and appear to fall more or less on a continuation of the curve for χ_{spin} (20-100 at. % Mo). γ^0 (0-20 at. % Mo) is next calculated from eq (5) and is listed in row 13. These values are also plotted in figure 9. Referring to the *single-phase* bcc data, the χ_{spin} and γ^0 curves of figure 9 *must* of course follow each other over the entire concentration range since they are connected throughout by eq (5). By this technique we now

417-156 O - 71 - 39

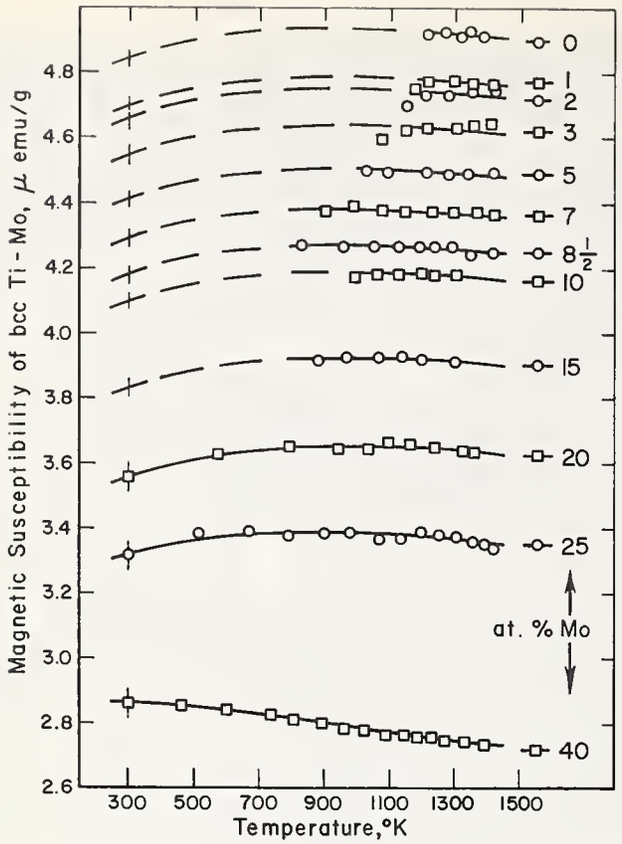

FIGURE 10. *Temperature dependences of susceptibility of single-phase bcc* Ti-Mo *alloys.*

Whereas the quenched 40, 25, and 20 at.% alloys are bcc at room temperature, the lower temperature limit for bcc Ti, for example, is 1156 K. Susceptibilities have been extrapolated back to 300 K by guessing that the temperature dependences are always similar to that for Ti-Mo (20 at.%).

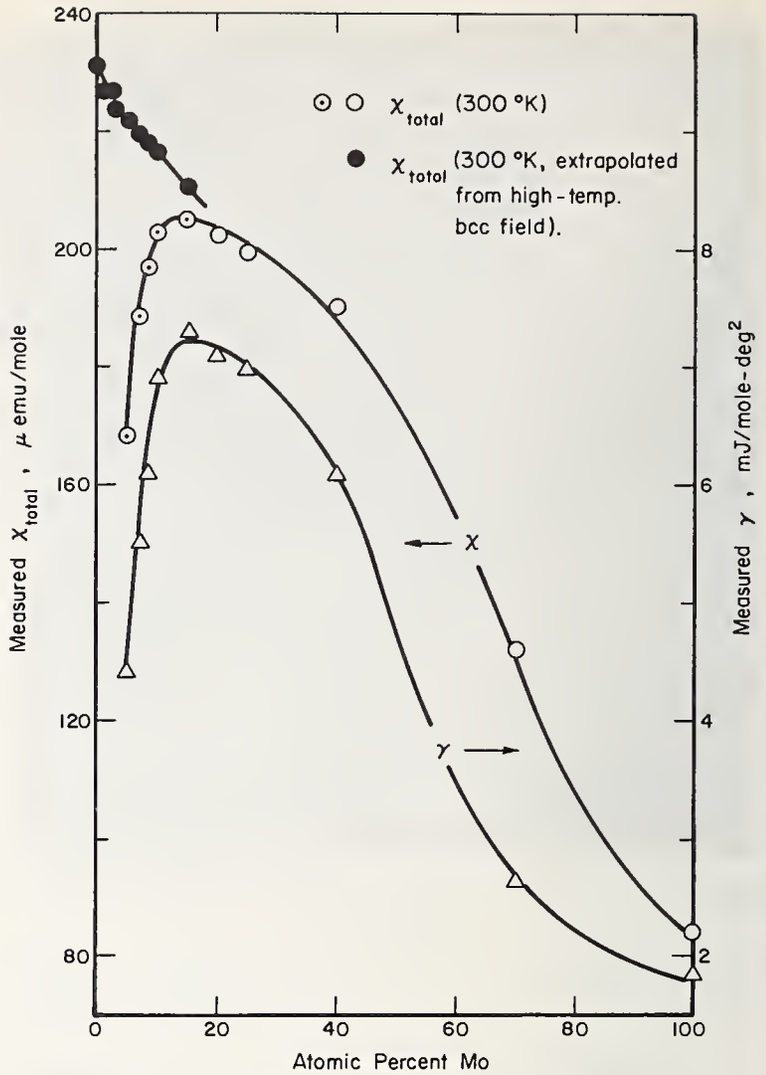

FIGURE 11. *Using the extrapolated data from figure 10, it is seen that* χ_{total} *(single-phase, bcc, < 20 at.% Mo)—●, fall on a monotonically-increasing continuation of the curve for* χ_{total} *(bcc, 100-20 at.% Mo)—○; whereas the presence of ω-phase (in* Ti-Mo *< 15 at.%* Mo*) depresses the susceptibility—⊙.*

Note the remarkable agreement between the total measured molar susceptibility (○⊙) and the measured (molar) electronic specific heat coefficient (△).

have a complete set of γ^0 data with which to compute $n(E_F)$ for single-phase bcc alloys using eq (4). The final results are listed in row 14 and plotted in figure 12.

4. Theoretical and Experimental $n(E_F)$ Values

4.1. $n(E_F)$ for bcc and hcp Pure Titanium

An immediate result of the above analysis is an experimental value for the Fermi density-of-states for bcc Ti, viz 1.54 (eV-atom)$^{-1}$. Again, applying eqs (7) and (4) respectively to the results of specific heat measurements on pure hcp, Ti yields $\gamma_{hcpTi}{}^0 = 2.84$ mJ/mole-deg^2: and $n(E_F)_{hcpTi} = 0.60$ (eV-atom)$^{-1}$. It follows that $[n(E_F)_{bcc}/n(E_F)_{hcp}]_{exp.} = 2.5_5$.

Band structure calculations have been carried out for both the hcp and the bcc phases of Ti by Altmann and Bradley [8] and Snow and Waber [7], respectively. The resulting density-of-states curves are juxtaposed in figure 13. A comparison of values at the Fermi level yields $[n(E_F)_{bcc}/n(E_F)_{hcp}]_{theo.} = 2.1$.

4.2. Theoretical and Experimental Rigid-Band Density-of-States Curves

An experimentally-derived curve of $n(E_F)$ vs. e/a ($4 < e/a < 6$) obtained from the single-phase bcc Ti-Mo data is presented in figure 12, for comparison with Snow and Waber's [7] "calculated" curve deduced from the calculated $n(E_F)$ values for Ti, V, Cr (and Mn). There is clearly a qualitative similarity between these "rigid-band density of states" curves. It may be possible at least to reduce the quantitative discrepancy between the experimental and calculated $n(E_F)$ curves by attacking some of the more obvious sources of error. For example on the experimental side, $n(E_F)$ for pure Mo (and possibly the Mo-rich alloys) may be too large through a possible underestimate of λ, which was derived by assuming $V_{app.} = \text{constant} = 0.26$ eV-atom for the entire Ti-Mo series. If instead we use for λ the value quoted by McMillan [5], the experimental value of $n(E_F)$ for pure Mo is reduced from 0.367 to 0.278 (eV-atom)$^{-1}$, which draws the curves closer together in the range 70-100 at. % Mo. On the other hand, in the Ti-

TABLE 1. ANALYSIS OF THE EXPERIMENTAL DATA FOR SINGLE-PHASE bcc Ti-Mo ALLOYS

1	Nominal At.%-Mo	100	70	40	25	20	15	10	8.5	7	5	3	2	1	0 (bcc)	0 (hcp)	Comments
2	Actual At.%-Mo	100	71.02	39.81	25.36	19.38	14.92	10.30	8.86	6.96	5.16	2.87	1.91	0.99	0	0	Chemical analysis
3	Molar wt. (g)	95.95	82.03	67.03	60.09	57.22	55.06	52.85	52.16	51.24	50.38	49.28	48.82	48.37	47.90	47.90	
4	$\chi^{300^\circ K}_{Total}$ (μ emu/mole)	84.41	132.2	190.4	199.7	202.8											Measured (300°K)
5	$\chi^{300^\circ K}_{Total}$ (μ emu/mole)						210.9	216.7	218.0	219.8	221.8	223.7	227.0	226.9	231.4	–	Extrapolated values from Figure 10
6	γ (mJ/mole-deg^2)	1.85	2.65	6.1	7.0	7.1										3.36	Measured (1.5-6°K)
7	λ	0.102	0.146	0.336	0.386	0.391										0.185	$\lambda = 0.212\,\gamma\,V_{app}$ $V_{app} = 0.26$ eV-atom
8	γ^0 (mJ/mole-deg^2)	1.68	2.31	4.66	5.05	5.10										2.84	$\gamma^0 = \gamma/(1+\lambda)$
9	χ_{spin} (μ emu/mole)	23.0	31.7	63.9	69.2	69.9											$\chi_{spin} = 13.71\,\gamma^0$
10	$\chi^{300^\circ K}_{orb}$ (μ emu/mole)	61.4	100.5	126.5	131.1	132.9											$\chi_{orb} = \chi_{Total} - \chi_{spin}$
11	$\chi^{300^\circ K}_{orb}$ (μ emu/mole)						132	132	132	132	132	132	132	132	132	–	Extrapolated values from Figure 9 (inset)
12	χ_{spin} (μ emu/mole)						78.9	84.7	86.0	87.8	89.8	91.7	95.0	94.9	99.4	–	$\chi_{spin} = \chi_{Total} - \chi_{orb}$
13	γ^0 (mJ/mole-deg^2)						5.75	6.18	6.27	6.40	6.55	6.69	6.93	6.92	7.25	–	$\gamma^0 = \chi_{spin}/13.71$
14	$n(E_F)$ (1/ev-atom)	0.36	0.49	0.99	1.07	1.08	1.22	1.31	1.33	1.36	1.39	1.42	1.47	1.47	1.54	0.60	$n(E_F) = 0.212\,\gamma^0$

rich region, the calculated $n(E_F)$ may be too small; for as Snow and Waber [7] have implied, excessively wide energy-intervals in a calculated energy histogram will reduce the apparent height of any sharp energy peak. Thus $n(E_F)$ for fcc Ti which does seem to be situated at such a peak, may be underestimated in the calculations.

5. Summary

In quenched single-phase bcc Ti-Mo alloys, as Ti is added to Mo, the various quantities that parameterize the density-of-states viz χ, γ, and T_c increase as e/a decreased from 6 to about 4.5. But, for $e/a \lesssim 4.5$ a second phase precipitate (ω-phase) inevitably appears in the quenched alloys. In this range $n(E_F)$ decreases as the proportion of ω-phase increases. That there is indeed a causative relationship between these effects has been verified experimentally with the aid of magnetic susceptibility measurements at temperatures sufficiently high to dissolve the precipitate. For the (bcc + ω) alloys the observed reduced values of γ would normally be interpreted as the weighted averages of γ_{bcc} for the matrix, and γ_ω for some macroscopic precipitate. But this does not satisfy the requirements imposed by the observed superconducting behavior. In the (bcc + ω) material the height and sharpness of each specific heat jump indicate that the superconducting transition is experienced uniformly by the *entire* specimen. Were it not for the fact that the ω-phase precipitate can be visualized and measured by means of electron diffraction and electron microscopy, macroscopic physical properties observations alone would lead to the conclusion that the (bcc + ω) material was single phase. This apparent paradox is undoubtedly related to the smallness of the precipitate size. Varying within the range of about 70-330 Å, the precipitate diameter is commensurate with a Ginzburg-Landau coherence length for Ti-Mo [14]. It is postulated that detailed microstructural investigations of other Ti-M and Zr-M alloys, which have been found to exhibit apparent $n(E_F)$ maxima near $e/a \sim 4.5$ would also reveal the presence of ω-phase below this composition. The curve of $n(E_F)$ vs. e/a for single-phase bcc Ti-Mo alloys

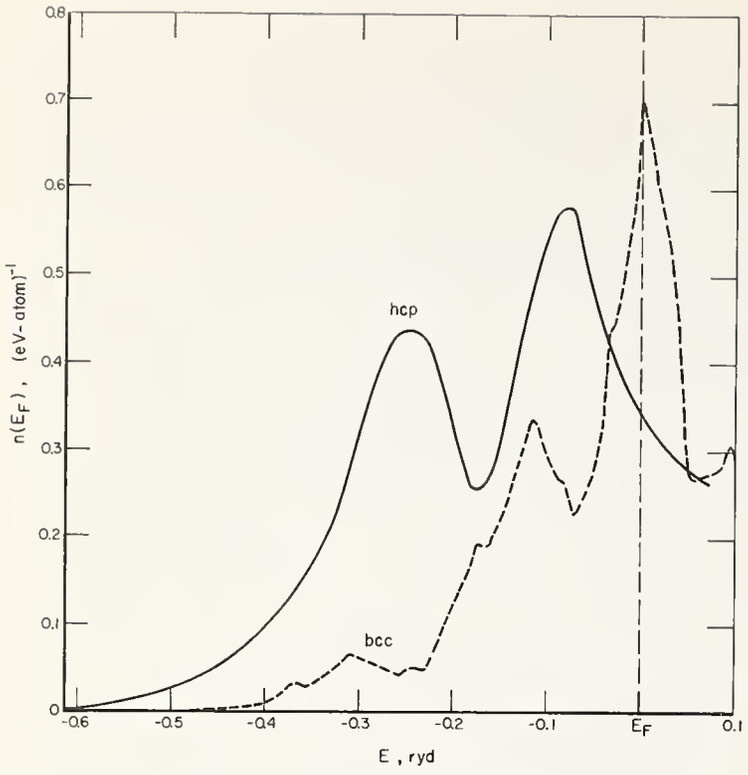

FIGURE 12. *Calculated density-of-states curves for bcc (broken line) and hcp (full line) Ti with energy referred to the Fermi level.*
The bcc curve is due to Snow and Waber [7] and the hcp curve to Altmann and Bradley [8]. Note that $n(E_F)$ in this paper arbitrarily referes to *one* spin direction ([7] and [8] use *both* spin directions).

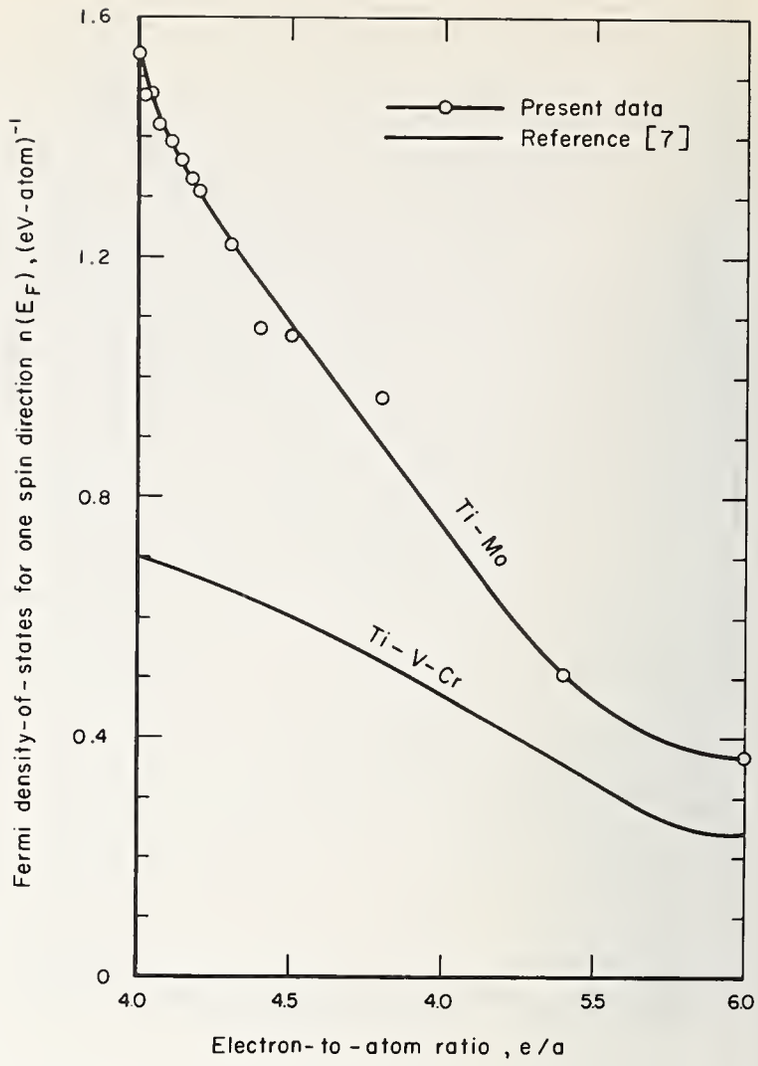

FIGURE 13. *"Rigid-band density-of-states curves" for 4 < e/a < 6.*
An "experimental" curve passes through the Fermi density-of-states data points for Ti-Mo alloys (table 1, row 14), for comparison with a "calculated" curve band on $n(E_F)$ values for $Ti_{bcc}-V-Cr-Mn$ (after [7]). [Note: $n(E_F)$ is the single-spin-direction density-of-states.]

increases monotonically as e/a proceeds from 6 to 4, as does a "calculated" curve based on $n(E_F)$ values for Cr, V, and bcc Ti. Comparing the experimentally-derived density-of-states values for the bcc and hcp allotropes of Ti we find that $[n(E_F)_{bcc}/n(E_F)_{hcp}]_{exp} = 2.5_5$, compared to a theoretical value of 2.1 based on the published results of band-structure calculations.

6. Acknowledgments

We wish to acknowledge Messrs. C. J. Martin, R. D. Smith, and G. W. Waters for expert technical assistance; Dr. J. E. Enderby for stimulating discussions, and Dr. J. D. Boyd for his generous help with the microstructural studies. For financial assistance, we wish to acknowledge the Air Force Materials Laboratory, Wright-Patterson Air Force Base; and Battelle-Columbus Laboratories.

7. References

[1] Beeby, J. L., Phys. Rev. **135**, A130 (1964).
[2] Stern, E. A., Physics **1**, 255 (1965).
[3] Stern, E. A., Phys. Rev. **144**, 545 (1966).
[4] Friedel, J., discussion in Phase Stability in Metals and Alloys, P. S. Rudman et al. Editors (McGraw-Hill, New York 1967), p. 162.
[5] McMillan, W. B., Phys. Rev. **167**, 331 (1968).
[6] Matthies, L. F., Phys. Rev. **139**, A 1893 (1965).
[7] Snow, E. C., and Waber, J. T., Acta Met. **17**, 623 (1969).
[8] Altmann, S. L., and Bradley, C. J., Proc. Phys. Soc. **92**, 764 (1967).
[9] Heiniger, F., Bucher, E., and Muller, J., Phys. kondens Materie **5**, 243 (1966).
[10] Matthais, B., Compton, V. B., Suhl, M., and Corenzwit, E., Phys. Rev. **115**, 1597 (1959).
[11] Blaugher, R. D., Chandrasekhar, B. S., Hulm, J. K., Corenzwit, E., and Matthais, B. T., J. Phys. Chem. Solids **21**, 2521 (1961).
[12] Masuda, Y., Nishioka, M., and Watanabe, N., J. Phys. Soc. Japan **22**, 238 (1967).
[13] Hake, R. R., Phys. Rev. **123**, 1986 (1961).
[14] Barnes, L. J., and Hake, R. R., Phys. Rev. **153**, 435 (1967).
[15] Sinha, A. K., J. Phys. Chem. Solids **29**, 749 (1968).
[16] Morel, P., J. Phys. Chem. Solids **10**, 277 (1959).
[17] Blackburn, M. J., and Williams, J. C., Trans. AIME **242**, 2461 (1968).
[18] Hickman, B. S., Trans. AIME **245**, 1329 (1969).
[19] Boyd, J. D., private communication.
[20] Kohlhaas, R., and Weiss, W. D., Z. Naturforschg. **20A**, 1227 (1965).
[21] Clogston, A. M., Gossard, A. C., Jaccarino, V., and Yafet, Y., Phys. Rev. Letters **9**, 262 (1962).

Specific Heat of Vanadium Carbide, 1-20 K

D. H. Lowndes, Jr., L. Finegold, and D. W. Bloom

Department of Physics and Astrophysics, University of Colorado, Boulder, Colorado 80302

R. G. Lye

Research Institute for Advanced Studies, Martin Marietta Corporation, Baltimore, Maryland 21227

Key words: Electronic density of states; specific heat; vanadium carbide.

The specific heat has been measured at low temperatures (~ 1 to 20 K) for four large crystals of VC_x, with results that indicate the presence of maxima near $x = 0.85$ in both the Debye characteristic temperature, θ_0, and the electronic density of states at the Fermi level $n_\gamma(\xi)$. The behavior of θ_0 suggests that the maximum melting temperature of VC_x occurs at a composition close to that of the ordered compound V_6V_5, rather than at the composition $VC_{0.75}$ proposed recently by Rudy. The variation of $N_\gamma(\xi)$ with x has been used to obtain an estimate for the density-of-states curve in the vicinity of the Fermi level. The result is discussed in terms of the behavior expected from elementary considerations of the electronic structure. Preliminary measurements show that the superconducting transition temperature of these crystals is lower than 50 mK. This work has been published in Phil. Mag. **21**, 245 (1970).

Discussion on "Specific Heat of Vanadium Carbide, 1-20 K" by D. H. Lowndes, Jr., L. Finegold, D.W. Bloom (University of Colorado), and R. G. Lye (RIAS, Martin-Marietta Corporation)

N. M. Wolcott *(NBS):* I would like to address a question to all the speakers of the group of papers dealing with low temperature specific heats and to the rapporteur (John Rayne). One usually makes comparisons of the electronic density of states in terms of the number of levels per atom per eV. And in many of these comparisons, particularly where the same electron-to-atom ratio is used, I wonder if it might not be more appropriate to use levels per unit volume (per cc), because, at least in the free electron model, it's the number of carriers per unit volume which determines the electronic specific heat. In many of these cases, the curve might look quite different if one included the volume change on alloying, particularly when there is a phase change in the alloy system.

A. Narath *(Sandia Labs.):* Would anyone care to respond to that comment? (No response).

J. E. Holliday *(U.S. Steel):* I would like to ask two questions. The first concerns the rigid band model. Our soft x-ray band spectra, the photoemission spectra presented at this conference, and the theoretical band calculations of Altman on Sc, Ti, Y and Zr show that the rigid band model is a very poor approximation. However, there has been a number of references to the rigid band model at this conference especially in the session on electronic specific heats. In light of these remarks I would like someone to comment on the rigid band model.

The second question concerns the APW calculations on TiC by Ern and Switendick and the LCAO band calculations on TiC by Lye and Logothetis. The APW calculations of Ern and Switendick show nearly complete admixture of the C-2p and the Ti-3d bands (possibly their C-2p band is at the bottom of the Ti-3d band), while the LCAO band calculations of Lye and Logothetis put the 2p band of carbon above the Ti-3d band which would result in a transfer of electrons from Ti to carbon. This direction of transfer was rather startling since it is opposite to the predictions of electronegativity and has been quite disturbing to chemists. The rapporteur implied that the discrepancy results from differences in the APW and LCAO methods of calculations. However, is it possible that the difference is due to the original assumptions. In other words, couldn't the APW method show a separation in the C-2p and Ti-3d bands with the proper assumptions. I believe that both Lye and Switendick are in the audience and possibly they would like to comment on this question.

Our soft x-ray band spectra, and the electron spectroscopy results at Uppsala, on TiC show a separation of the C-2p and Ti-3d bands with the C-2p band below the Ti-d band. This will result in a transfer of electrons from Ti to carbon which is opposite to that predicted by Lye and Logothetis.

J. T. Waber *(Northwestern Univ.):* I would like to respond to the question just raised about the validity of the rigid band model. Recently Snow and I [1] published a paper giving the band structures for the bcc and fcc forms of the 3d transition metals from titanium to copper. The trends in these $N(E)$ curves were compared with the trend of the energy eigenvalues of the 3d and 4s electrons in the isolated atoms.

One of the unexpected results of band calculations was that the Fermi level did not steadily increase with group number but was to the first approximation constant when it was compared with the vacuum level (namely, compared with the zero corresponding to separation of an electron from an isolated atom). Although, of course, the Fermi level did rise consistently with respect to X_1 (for fcc) or H_{12} (for bcc) the bottom of the d band. Note that this zero (vacuum level) can be retained when one superimposes the free atoms to form a solid. The set of fcc and bcc series of $N(E)$ curves are illustrated in figures 5 and 6 of reference 1. The two peak structure is discernible for the bcc metals—the structure of $N(E)$ for the fcc phases is harder to describe in a few words. However, it is clear that the bands are not rigid when such a series of elements is considered.

Because of the way that the Fermi level samples the $N(E)$ curve, one will find $N(E_F)$, i.e., the density of states at the Fermi level, does display the familiar 2-peak shape which we come to expect for 3d bcc alloys following the very significant deduction that Slater made thirty years ago. However, the deduction that the

N(E) curve is therefore fixed or universal is not correct. The distinction is that currently we believe the *d*-bands change both their position and shape as a function of atomic number, whereas in 1939 Slater had only one or two density-of-states curves available to him and could not be sure of a specific trend. He advanced this idea as a working hypothesis. The newer deduction has resulted from the advice and generosity of Prof. Slater, John Wood and A. C. Switendick who made their computer codes available to various research workers.

In a discussion I made yesterday, the *N(E)* curves of bcc titanium, vanadium, and chromium were compared with those for the bcc forms of zirconium, niobium and molybdenum. In that figure, a two peak structure can be seen for the three 3*d*-metals whereas the *N(E)* curves for the three equivalent 4*d*-transition metals show 3 peaks. Such results reinforce the opinion that the rigid band model is not appropriate for transition metals in general.

R. G. Lye *(RIAS, Martin Marietta Corp.):* I have two comments: (1) The rigid band model has severe limitations, which suggest the need for caution in its application to alloy systems in which the composition is varied over a wide range with resultant large changes in the position of the Fermi level. This limitation also poses problems in our study of VC. However, if the electronic structure near the Fermi level of VC is dominated by energy bands derived largely from *d*-states of the metal atom, as we believe, then our results suggest that changing the carbon concentration from $VC_{0.76}$ to $VC_{0.87}$ moves the Fermi level by only 0.1 eV relative to a prominent critical point in the band structure. Thus, we believe that the method we have used gives an approximate description of the electronic density-of-states curve near this critical point, but we do not specify how the energy of this critical point changes, nor how the band structure remote from the Fermi level changes as the carbon content is varied. These aspects of the electronic structure require separate consideration. (2) As Holliday mentioned, Ramqvist [2] has measured the binding energies of the carbon 1*s* levels in various materials and has determined that they are reduced in the carbides relative to carbon. Ramqvist infers from his studies that there is a net negative charge associated with the carbon atoms, and concludes that this contradicts our proposed band structure for TiC [3]. I believe, to the contrary, that his results provide additional support for certain features of our band structure. In particular, we found it necessary to raise the Herman and Skillman one-electron-energies of the carbon atom by 2.77 eV for the 2*p* state and by 4.15 eV for the 2*s*-state in order to make the empirical band structure agree with experimental data. This displacement is in the same direction and has approximately the same magnitude as that observed experimentally for the 1*s* state by Ramqvist ($\simeq$ 3.3 eV), so we agree to this extent. The magnitude of the displacement can be related to the charge on the atoms if the spatial distribution of the charge is known. Various assumptions regarding this distribution lead to a negative charge of approximately 0.2*e* to 0.4*e* on the carbon atoms.

It is important to distinguish this charge transfer from the transfer of electrons between states of different symmetry, even though the two are interdependent. In particular, because the 2*p*-states are elevated, electrons are transferred from them into lower-lying bands derived from the 3*d*-states of the metal atom. This transfer compensates for some of the negative charge that otherwise may have been associated with the carbon atoms. At equilibrium, a net negative charge (0.2*e* to 0.4*e*) remains on the carbon atoms, and some 2*p* electrons ($\simeq$ 1 1/4) have been transferred to 3*d*-states. This question will be discussed in more detail elsewhere.

A. Narath *(Sandia Labs.):* Would Dr. Switendick care to make a very brief comment?

A. C. Switendick *(Sandia Labs.):* I really wish we could straighten this out, because we both seem to find, no matter what the experiment is, that our results agree with them. Yet the models are vastly different in the physical interpretation of what is going on in these materials. I thought that the soft x-ray results, in which the non-metal *p* band seems to be well below the Fermi energy and moved down as a function to say carbon to nitrogen to oxygen in these transition metal compounds, showed that our results were a better model, but Bob Lye says he thinks he can get the same thing out of his model.

[1] Snow, E. C., and Waber, J. T., Acta Met. **17**, 623 (1969).
[2] Ramqvist, L., Jernkont. Ann., 153 (1969).
[3] Lye, R. G., and Logothetis, E. M., Phys. Rev. **147**, 622 (1966).

Relevance of Knight Shift Measurements to the Electronic Density of States*

L. H. Bennett

Institute for Materials Research, National Bureau of Standards, Washington, D.C. 20234

R. E. Watson[1]

Brookhaven National Laboratory[2]**, Upton, New York 11973**

G. C. Carter

Institute for Materials Research, National Bureau of Standards, Washington, D.C. 20234

The Knight shift, $\mathcal{K}$, measures the magnetic hyperfine field at the nucleus produced by the conduction electrons which are polarized in a magnetic field. Knight shifts are often dominated by the Pauli term and, in its most simple form, can be written as $\mathcal{K} = \langle a \rangle \chi_p$. Here χ_p is the conduction electron Pauli spin susceptibility which depends on the density of states at the Fermi level, $N(E_F)$, and $\langle a \rangle$ is an average magnetic hyperfine coupling constant associated with the wave function character at the nucleus, $|\psi_F(0)|^2$, for conduction electrons at the Fermi surface.

The Knight shift therefore provides, through $\langle a \rangle$, insight into the wave-function character associated with $N(E_F)$. Calculations of $\langle a \rangle$ involving an averaging over k-space have been attempted for a few simple metals up to the present time. For alloys and intermetallic compounds, rather different $\langle a \rangle$'s are experimentally observed for different local environments, indicating that $\mathcal{K}$ samples the variation in *local* wave-function character, or a variation in *local* density of states. There is no unique way of separating the local variation of $N(E_F)$ from $|\psi_F|(0)|^2$.

In this article the methods developed for relating $\mathcal{K}$ to the electronic properties for most of the types of cases encountered in the literature are reviewed. We discuss "simple" metals including problems of orbital magnetism and changes in $\mathcal{K}$ caused by electronic transitions such as melting. Knight shifts and their temperature dependence in metals and intermetallic compounds involving unfilled d shells, are discussed. We give estimates of atomic hyperfine fields due to single electrons, appropriate to those cases where problems due to electronic configurations do not make deductions from experiment too ambiguous. A density of states curve calculated for Cu is given, showing the relative importance of s-p, and d character for that metal. In a qualitative sense this Cu curve implies such information for other transition metals. We discuss alloy solid solutions for the cases where a "rigid" band model might be used to explain the results, and for cases where local effects have to be taken into account. The charge oscillation and RKKY approaches and their limitations are reviewed for cases of dilute nonmagnetic and d- or f-type impurities.

Key words: Electronic density of states; hyperfine fields; Knight shift; nuclear magnetic resonance; susceptibility; wave functions.

1. Introduction

Twenty years ago W. D. Knight [1][3] discovered that the nuclear magnetic resonance (NMR) of ^{63}Cu occurs at about a quarter percent higher frequency in metallic copper than in a salt, CuCl. Since then, there have been over 500 papers reported on the theory and observation of this effect, the "Knight shift," in a wide

*An invited paper presented at the 3d Materials Research Symposium, *Electronic Density of States*, November 3-6, 1969. Gaithersburg, Md.

[1] Also Consultant, National Bureau of Standards.

[2] Work supported by the U.S. Atomic Energy Commission.

[3] Figures in brackets indicate the literature references at the end of this paper.

variety of metals and alloys. The first observation of the Knight shift is shown in figure 1. This paramagnetic shift of the resonance between the diamagnetic salt, CuCl, and the diamagnetic metal, Cu, was attributed

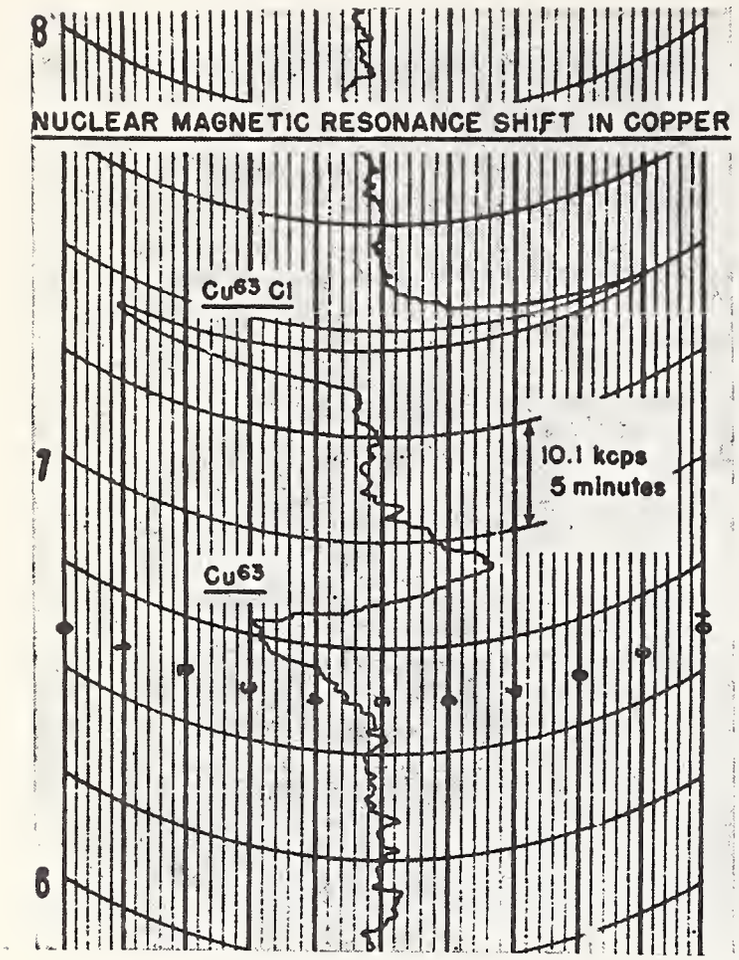

FIGURE 1. *The ^{63}Cu resonance in CuCl (upper resonance) and metallic copper (lower resonance), illustrating the Knight shift* [1].

[2] to the Pauli paramagnetism of the conduction electrons. The shift is much larger than could be explained by the average susceptibility of the conduction electrons. It was proposed [2] that the nuclei sampled a concentrated local susceptibility, arising from the fact that the conduction electrons in a metal have a very large probability density at the nucleus. In its simplest form, the Knight shift ($\mathcal{K}$) may be written

$$\mathcal{K} = \langle a \rangle \chi_p, \tag{1}$$

where $\langle a \rangle$ is an appropriate sampling of the hyperfine interaction of the conduction electrons at the Fermi surface.

For noninteracting electrons, χ_p is proportional to $N(E_F)$, the electronic density of states at the Fermi level,

$$\chi_p = \mu_B{}^2 N(E_F) \tag{2}$$

where μ_B is the Bohr magneton. Thus in this simple approximation, the Knight shift samples, via $\langle a \rangle$, local behavior of the density of states (at the Fermi level) at a particular atomic site.

In this article we will inspect in detail this relationship of $\mathcal{K}$ with the density of states, thereby omitting several important topics on other aspects of NMR in metals. Good review articles have appeared earlier on this broader topic [3-5].

Unfortunately, as with most of the methods for studying the electronic density of states discussed at this symposium, untangling the factors folded in with the density of states is not an easy task. Very often, the experimental Knight shift is used to measure the factor $\langle a \rangle$, χ_p having been obtained from other experiments such as electronic specific heat or bulk magnetic susceptibility. The Knight shift provides a particularly complicated weighted sampling of electronic character but with these complications comes the possibility of obtaining unique information which is otherwise experimentally inaccessible.

A more complete expression for the Knight shift would include other terms,

$$\mathcal{K} = \mathcal{K}_{\text{Pauli}} + \mathcal{K}_{\text{dia}} + \mathcal{K}_{\text{orb}} + \text{higher order terms}. \tag{3}$$

$\mathcal{K}_{\text{Pauli}}$, given by eq (1), includes isotropic and anisotropic effects, directly by contact and spin dipolar interactions, and indirectly via core polarization and polarization of conduction band electrons below the Fermi level. The orbital paramagnetic and diamagnetic terms, $\mathcal{K}_{\text{orb}}$ and $\mathcal{K}_{\text{dia}}$, are important at times. We will review in this paper the various contributions to $\mathcal{K}$, as summarized in eq (3), in the light of experimental observations, together with theoretical methods for relating these results to the electronic structure of metals.

2. General Observations

In NMR one looks at transitions of a nucleus (with spin states $m = I, I-1, I-2, \ldots 1-I, -I$) from spin state m to $m \pm 1$, by measuring the frequency, ν, of the photons involved in these transitions. The energy difference between the two states, $\Delta E_{m \to m-1} = h\nu$, is directly proportional to the applied magnetic field, H_{appl}. However, even for a given isotope, the proportionality constant is different for different solids because the electrons in the solid respond differently to H_{appl} (paramagnetically or diamagnetically) causing an additional (positive or negative) field at the resonating nucleus. This magnetization field, as seen by the nucleus, is often referred to as the "internal field," H_{int}.

The Knight shift, $\mathcal{K}$, measures the internal field at the nucleus produced by those electrons in metals which respond linearly (with one exception, noted in sec. 6) to an applied field. Thus $\mathcal{K} \equiv H_{\text{int}}/H_{\text{appl}}$. Specifically, this definition excludes materials with spontaneous magnetization.

For simple metals, the conduction electrons cover a broad band of energy states. Those electrons at the Fermi surface are aligned paramagnetically by an external applied magnetic field. The resulting polarization of these electrons causes large internal fields, via the Fermi contact interaction hamiltonian, $\mathcal{H}_F$,

$$\mathcal{H}_F = \frac{16\pi}{3}\mu_B\gamma\hbar\mathbf{I}\cdot\mathbf{S}(\mathbf{r})\delta(\mathbf{r}), \tag{4}$$

where γ is the nuclear gyromagnetic ratio, and $\mathbf{S}(\mathbf{r})$ is the electron spin as a function of its position vector $\mathbf{r}$ from the nucleus. The contact (or δ-function) interaction samples the probability density $|\psi_A(0)|^2 \equiv P_A$ at the nucleus, for an electron in the atom. It is related to the atomic hyperfine coupling constant, $a(s)$, by

$$a(s) = \frac{16\pi}{3}\gamma\hbar\mu_B P_A. \tag{5}$$

The $\delta(\mathbf{r})$ thus restricts this effect to s-electrons and to the minor components of relativistic p-electrons. The s-effects are large, while the p-terms are almost invariably small and will henceforth be neglected. This large hyperfine term is generally absent in nonmetallic materials, because for each s-electron of spin-up, there is an s-electron of spin-down, and these are not decoupled by the usual applied magnetic fields.

For monovalent metals, $a(s)$ is obtained with high accuracy from atomic beam experiments. Values of $a(s)$ for the alkali metals are shown in table 1. The quantity more important to Knight shift considerations, P_A, is also shown. Note that P_A increases monotonically with atomic number for a given group, whereas $a(s)$ is dominated by the nuclear moment and appears random. Except for a possible small hyperfine structure anomaly, P_A is the same for all isotopes of a given element, whereas $a(s)$ depends on the given isotope.

TABLE 1. *Comparison of different ways of expressing the hyperfine coupling of a single s-electron, for the alkali metals.*

	$a(s)$ (cm^{-1})	P_A (cm^{-3})	$H_{\text{eff}}^{\text{atom}}$ (kOe)
^{7}Li.....	0.0134	15.7×10^{23}	122
^{23}Na.....	.0296	50.2×10^{23}	390
^{39}K.....	.00770	74.6×10^{23}	580
^{87}Rb.....	.114	154×10^{23}	1200
^{133}Cs.....	.0766	257×10^{23}	2000

The data for $a(s)$ were derived from data given by P. Kusch and H. Taub. Phys. Rev. **75**, 1477 (1949); the other columns were calculated from these using eqs (5) and (12).

In a metal the appropriate probability density P_F is obtained by taking a suitable average over the Fermi surface, $P_F = \langle\psi(0)^2\rangle_{E_F}$. The Knight shift, eq (1), has shown [2] to be

$$\mathcal{K} = \frac{8\pi}{3}\chi_p P_F, \tag{6}$$

where χ_p is the Pauli spin susceptibility per atom. Sometimes an explicit volume or mass factor appears in the expression for $\mathcal{K}$, but this depends on the appropriate normalization of $\langle\psi^2(0)\rangle_{E_F}$ and on whether a mass, volume, atomic or molar susceptibility is used.

If we define

$$\langle a\rangle \equiv \frac{8\pi}{3}\langle\psi(0)^2\rangle_{E_F} = \frac{8\pi}{3}P_F, \tag{7}$$

then we obtain eq (1).

Alternately it is convenient to introduce the effective hyperfine field H_{eff}, which is the field measured directly in ferromagnetic materials by, for example, ferromagnetic NMR or by Mössbauer spectroscopy. Then

$$H_{\text{eff}} \equiv \mu_B\langle a\rangle = \frac{8\pi}{3}\mu_B P_F. \tag{8}$$

Hence

$$\mathcal{K} = \frac{1}{\mu_B}\chi_p H_{\text{eff}}. \tag{9}$$

It has been found useful to define a factor ξ, sometimes called Knight's ξ factor [3], as

$$\xi \equiv \frac{P_F}{P_A} \equiv \frac{H_{\text{eff}}^{\text{metal}}}{H_{\text{eff}}^{\text{atom}}}. \tag{10}$$

In the simplest cases, ξ has been said to express the fraction of s-character at the nucleus in the metal at E_F, but as we shall see, ξ is more complex in its meaning for less simple cases. The Knight shift then becomes

$$\mathcal{K} = \frac{1}{\mu_B}\chi_p\xi H_{\text{eff}}^{\text{atom}}, \tag{11}$$

where

$$H_{\text{eff}}^{\text{atom}} = 19.65\ a(s)\frac{I}{\mu_I}. \tag{12}$$

Here $a(s)$ is in cm^{-1}, $H_{\text{eff}}^{\text{atom}}$ in Oe, and μ_I is in nuclear magnetons. Values of $H_{\text{eff}}^{\text{atom}}$ are listed in table 1 for the alkali metals and in table 2 for some B-subgroup metals. The values for the monovalent metals are derived from atomic beam measurements. For polyvalent metals, Knight [3] has used measurements

on *excited ionic* states and then corrected for the degree of ionization. Knight estimated his resulting values of $a(s)$ to be accurate to perhaps 50 percent. Rowland and Borsa [6] avoided the problem of corrections by using measurements on *excited neutral* atom states. The values for the polyvalent metals in table 2 do not depend on *excited* state measurements, but instead were determined by scaling, based on atomic calculations, from the known monovalent values [7].

TABLE 2. H_{eff}^{atom} *values obtained by scaling from monovalent values* [7].

Group	*Atom*	H_{eff}^{atom} (kOe)
I	Cu	2,600
	Ag	5,000
	Au	20,600
II	Cd	7,000
	Hg	25,800
III	B	1,000
	Al	1,900
	Ga	6,200
	In	10,100
	Tl	34,000
IV	Sn	12,800
	Pb	41,400
V	N	3,300
	P	4,700
	As	8,900
	Sb	14,500
	Bi	49,000
VI	Te	17,200
X	Pt	20,000

The ξ factor accounts for any deviation in hyperfine coupling from free atom behavior. It may deviate from a value of one for a variety of reasons. For example, the average conduction electron density in a metal is greater than that in the free atom (*i.e.*, P_ψ is normalized to a Wigner-Seitz cell in the metal whereas the free atom P_ψ extends over a significantly larger volume). If no other factors were present, ξ would then be greater than unity. A Fermi surface orbital, ψ_F, has only partial s-character and this causes a reduction in ξ. In a "free electron metal," ψ_F is a plane wave ϕ_F (suitably orthogonalized to atomic core states) or a linear combination of plane waves. With increasing number of electrons in the bands the s-character of ψ_F decreases [8]. In a metal such as Tl, Pb, or liquid Bi, this reduction is quite substantial. In metals with one "free" conduction electron (*e.g.*, the alkali and noble metals), $\mathbf{k}_F$ is relatively small, and the reduction could be expected to be slight. Here, other orthogonalized plane waves, $\phi_{\mathbf{k}_F+\mathbf{Q}}$ (where $\mathbf{Q}$ is a reciprocal lattice vector) are mixed into ϕ_F and the normal *sign* of the mixing is such that interference causes $|\psi_F(0)|^2$ to be less than that predicted by $|\phi_F(0)|^2$ alone. This, as well as d-band hybridization and core-polarization factors which will be considered shortly, tend to predominate over the normalization effect reducing ξ to values typically between 0.1 and 0.8 in "simple" metals.

Experimental values for $\mathcal{K}$ are given in figures 2a and 2b. Using these measured values of $\mathcal{K}$, and obtaining χ_p as explained in the next section, the systematic trends for ξ seen in figure 3 are obtained.[4] In each period the largest ξ values are found for the monovalent metals, with ξ falling smoothly to lower values as the group valence increases, as would be expected from the wave function behavior just discussed. It is interesting that these results are obtained despite the changing crystal structures. About one-half the observed drop in ξ is expected from simple estimates [8] of the reduction in s-character with increasing $\mathbf{k}_F$; the increasing atomic volumes of the polyvalent over the monovalent metals further enhances the trend.

The induced conduction electron Pauli spin density may also contribute to the hyperfine coupling constant, $\langle a \rangle$, via the spin dipolar interaction

$$\mathcal{H}_{SD} = -2\mu_B \gamma N\hbar \mathbf{I} \cdot \left(\frac{\mathbf{S}}{r^3} - \frac{3\mathbf{r}(\mathbf{S}\cdot\mathbf{r})}{r^5} \right), \qquad (13)$$

where $\mathbf{r}$ is the vector from the nucleus to the electron. This interaction is anisotropic and contributes an orientation dependent Knight shift term, $\mathcal{K}_{anis}$, for nuclei at noncubic sites, and occasionally at cubic sites if spin-orbit coupling is present. In powders, this term results in structure and broadening of the NMR line.

The induced Pauli spin density interacts *directly* with the nucleus only via the contact and spin dipolar interactions but it may act *indirectly* as well. The spin density has a spin dependent exchange interaction associated with it, which arises from the Pauli exclusion principle. This may polarize the closed shells of an ion core and the paired electrons in the conduction bands *below* E_F, producing spin densities which will then interact with the nucleus via the contact (and for noncu-

[4] From figure 3, a ξ value for Zn between that of Cd and Hg can be extrapolated. From this $\mathcal{K}$ for Zn is predicted to be 0.20 percent. This is in complete agreement with a prediction [9] obtained from quite different considerations.

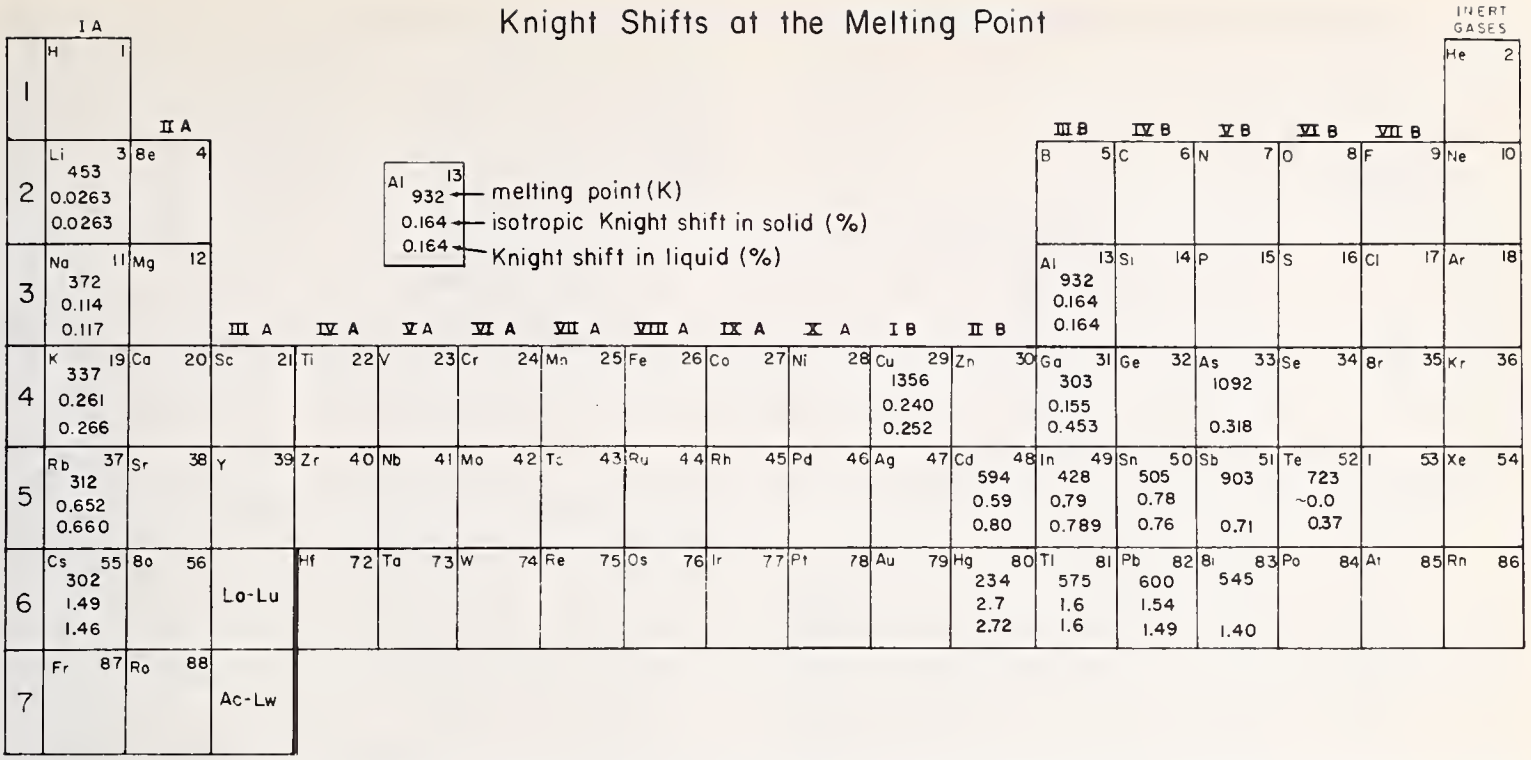

FIGURE 2a. *Knight shifts in metals as compiled at the Alloy Data Center (NBS). Note: Literature references available on request. (a) Knight shifts in the solid and liquid state at the melting point.*

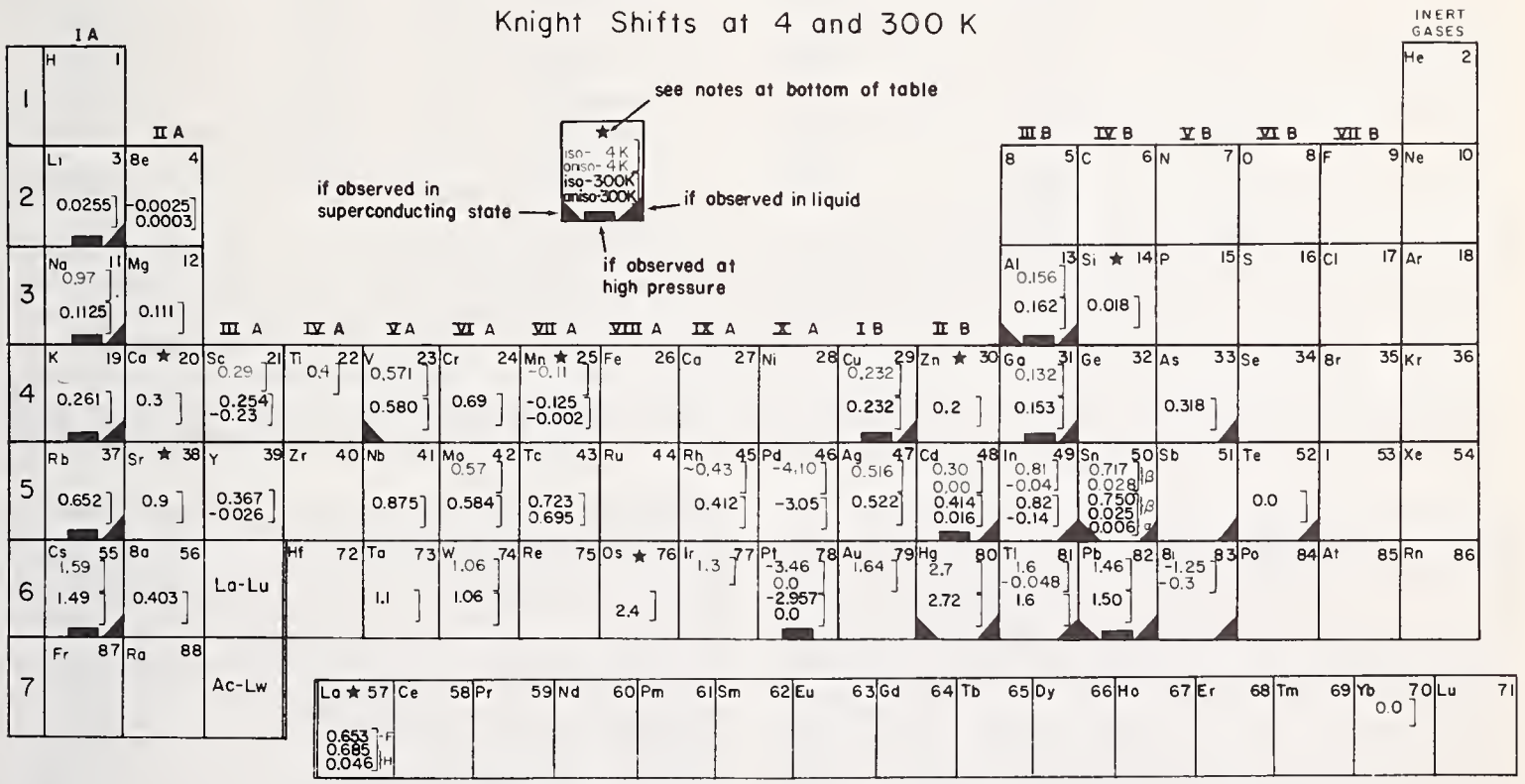

Element	No.	Notes
Si	14	Chemical shift
Co	20	Predicted value (1956)
Mn	25	All data are for β phase
Zn	30	Predicted value
Ga	31	Anisotropic shifts: $K(X) = 0.015(4)\%$; $K(Y) = -0.001(4)\%$; $K(Z) = -0.014(4)\%$; all independent of T to 4K
Sr	38	Predicted value (1956)
La	57	F = FCC, H = HCP
Os	76	Predicted value (1956)

FIGURE 2b. *Knight shifts in metals as compiled at the Alloy Data Center (NBS). Note: Literature references available on request. (b) Isotropic and anisotropic Knight shifts at room and liquid helium temperatures.*

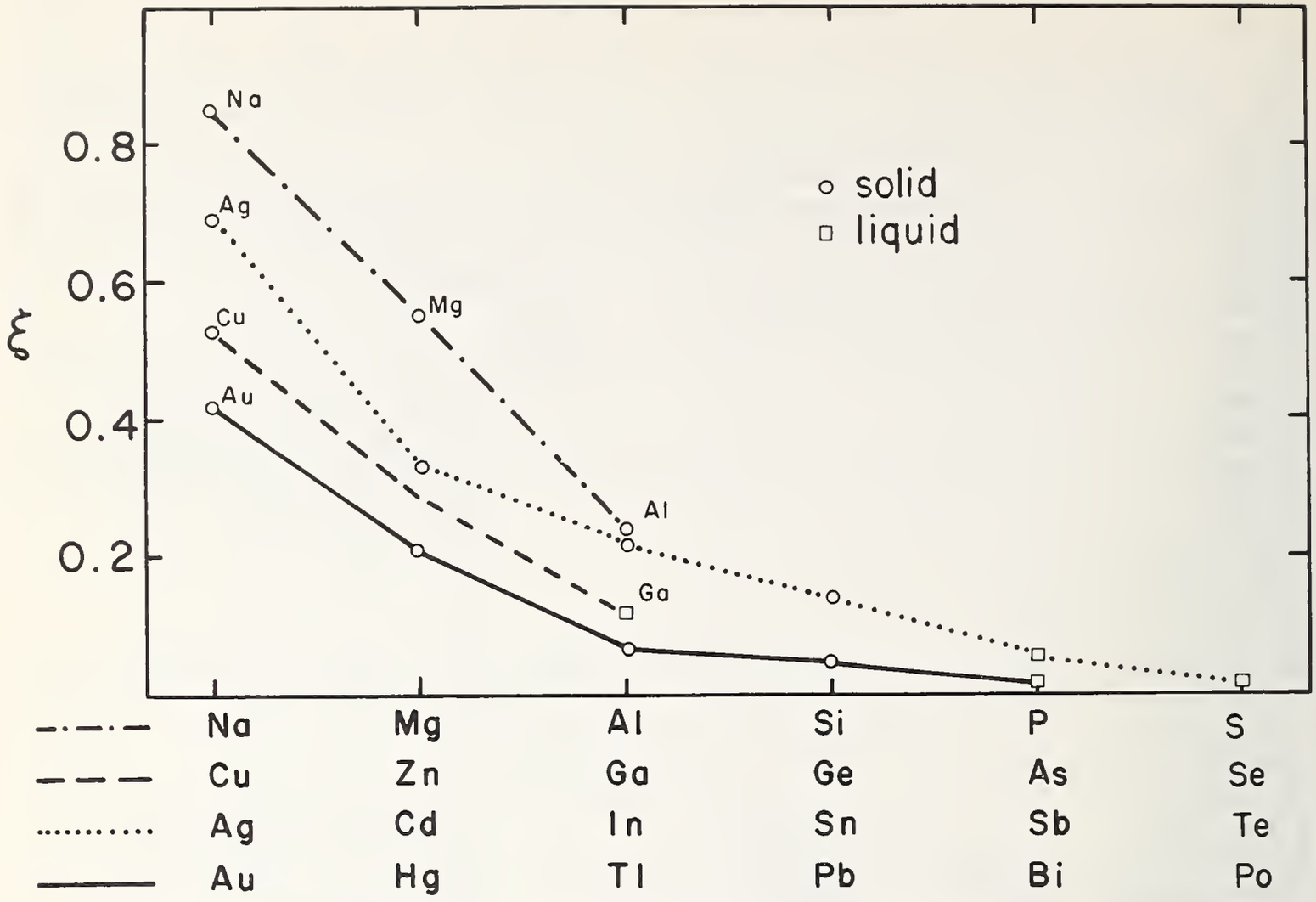

FIGURE 3. *Behavior of Knight's ξ values for metallic elements as a function of their position in the periodic table. The points for each row in the table are connected using the sumbols for lines as shown outside the left lower corner of the plot. Those points shown as circles are for the metals in the solid state and those shown as squares were calculated for the metals in the liquid phase. For the former points χ_p was calculated using γ_{el} values [37]; for the liquid metals χ_p was taken to be $3/2(\chi_{expt}-\chi_{dia}^{core})$ using χ_{expt} from the Landolt-Börnstein Tables and χ_{dia}^{core} from Hurd and Coodin [33]. The absolute values of ξ are affected by uncertainties in the estimates of χ_p and H_{eff} but the relative behavior (from element to element) along each row is probably realistic. Points for solid Ga and liquid As are omitted for lack of accurate values for $\mathcal{K}_{iso}$ and $\chi_p(liq)$, respectively. The plot provides an estimate for the Knight shift of Zn which has yet to be observed.*

bic sites, spin dipolar) interaction(s). These interactions arise from *differences* induced in the spatial behavior of spin up and spin down pairs of electrons with *zero net spin* induced in the electron pairs. Their existence has been established experimentally by the fact that half filled shell (p^3, d^5, and f^7) S-state atoms have nonzero hyperfine fields. While the exchange interaction is believed to be the origin of this spin polarization, correlation effects should, in principle, be important to its quantitative behavior. These interactions have been discussed extensively elsewhere [10].

For the moment we will limit our considerations to intra-atomic contributions to the contact interaction. This necessarily involves the spin polarization of closed s-shells of the core and of the s-character in the conduction bands below E_F, since only these will interact directly with the nucleus. Estimates of these core polarization effects from valence electrons in the various shells are summarized in table 3. These are based on experimental data and on exchange polarization calculations (*i.e.*, no correlation effects). Listed are the sign and magnitude characteristic of the core polarization response to a single unpaired s-, p-, d-, or f-valence electron characteristic of various rows of the periodic table. (In the case of the open p-shell atoms, the listed response includes that associated with the closed valence s-shell.) For comparison, the direct contact interaction appropriate to an unpaired atomic s-valence electron is shown in table 4, for the d- and f-shell atoms. The core polarization is negative for d- and f-shells, and for np-shells, where n, the principal quantum number, is 4 or greater. The negative sign implies a core spin density at the nucleus, whose orientation is *antiparallel* to the unpaired spin responsible for the

TABLE 3. *Rounded value for hyperfine fields due to the core polarization response to a* single *unpaired open valence shell electron.*

Open valence shell	Core polarization hyperfine field, H_{eff}, per unpaired valence electron, *kOe*	Comments on source(s) of core polarization values. (For further comments and details of most of the data see Ref. 10).
$2p$.....	+30	Experiment, appropriate to neutral N alone.
$3p$.....	+15	Experiment, appropriate to neutral P alone.
$4p$.....	−50	Experiment, (neutral As $4s^2 4p^3\ {}^4S$).
$5p$.....	−150	Experiment (neutral Sb $5s^2 5p^3\ {}^4S$).
$6p$.....	−300	Experiment (neutral Bi $6s^2 6p^3\ {}^4S$).
$3d$.....	−125	Calculation and experiment for $3d^n 4s^0$ ions.
$4d$.....	−350	Calculation and limited experiment for $4d^n\ 5s^0$ ions.
$5d$.....	−750	Calculation (J. V. Mallow, A. J. Freeman and P.S. Bagus, J. Appl. Phys., to be published).
	−600	Inferred from hyperfine anomaly, [G. J. Perlow, W. Henning, D. Olson and G. L. Goodman, Phys. Rev. Letters **23**, 680 (1969)].
$4f$.....	0 to −50	Calculation and limited experimental data.
ns.....	>0	Estimated by calculation to make a 10–50% enhancement of a ns shell's direct contact interaction.

TABLE 4. *Direct plus associated core polarization contact hyperfine fields due to a single unpaired valence* s*-electron for various rows in the periodic table.*

s shell	Atoms	s-contact hyperfine field, H_{eff}, kOe
$2s$.....	$2p^1$–$2p^3$ elements	1,000– 4,000
$3s$.....	$3p^1$–$3p^3$ elements	2,000– 5,000
$4s$.....	$3d$ transition metals	2,000– 3,000
$4s$.....	$4p^1$–$4p^3$ elements	4,000–10,000
$5s$.....	$4d$ transition metals	4,000– 5,000
$5s$.....	$5p^1$–$5p^3$ elements	7,000–15,000
$6s$.....	rare earths	9,000–15,000
$6s$.....	$5d$ transition metals	15,000–20,000
$6s$.....	$6p^1$–$6p^3$ elements	25,000–50,000

polarization. The core polarization response to an unpaired s-valence electron is positive and simply serves to enhance the contact interaction associated with the valence electron. [When using experimental atomic hyperfine data to evaluate P_A, this effect is already included.] The $3d$, and $4d$ (little is known yet for the $5d$) core polarization values appear to be quite stable for their respective rows in the periodic table. The quoted values hold to within twenty percent for any member of a row and it is believed that these values are appropriate to the core polarization response to a d-moment in a metal.

The situation is less certain and more complicated for the p-shell elements. Experimental data for which there are no competing orbital and spin dipolar terms exist only for the p^3 S-state atoms. It should be noted that these experimental values include the contribution coming from the polarization of the closed *valence* s-shells. In a metal this term is associated with the conduction band and not the core states. There is some uncertainity as to the sign and magnitude of this core plus valence s polarization term as one goes across the $2p$ and $3p$ rows. Recent spin polarized Hartree-Fock calculations of Bagus *et al.* [11] for these rows suggest that both the core and valence contributions are significant with the total becoming less positive (or more negative) as one goes to the lighter elements in the row. As with earlier efforts [10], these calculations do not satisfactorily reproduce the experimental data and must be used with caution, (*e.g.*, the wrong sign is predicted for atomic P). Bagus *et al.* also obtained results for the $4p$ row. Again the total becomes more negative by a factor of, say, two for the lighter elements but now the valence term dominates. This latter fact suggests that such atomic hyperfine constants will be of little quantitative utility when inspecting p-electron metals until one understands the polarization response of s-electron character deep in a conduction band. An example in the literature of the use of a p-core polarization term larger than that shown in table 3, is Ga in $AuGa_2$ [12], where a p-term of an order of magnitude larger than that of As (table 3) was used to explain the observed negative Knight shift.

One complication associated with extracting wave function and density of states information from Knight shift measurements is suggested by the numbers in table 3. Consider the $3d$- and $4d$-transition metals. As discussed in section 7, the Pauli Knight shift term almost invariably has the opposite sign of temperature dependence as the Pauli susceptibility [13]. This is consistent with having d-bands at E_F, with negative hyperfine constants of the sort seen in the table. Now, the s-contact densities are an order of magnitude larger than the corresponding d-core polarization hyperfine constants. Thus a few percent admixture of s-character into the Fermi surface d-states can violently affect $\langle a \rangle$.

While complicating matters, such interband hybridization is of considerable interest in itself and one can attempt to use Knight shift data to ascertain its nature and extent [14,15].

Relatively little is known of the intra-atomic hyperfine contribution arising from the exchange polarization of conduction band states below E_F, except that it probably makes a positive contribution to $\langle a \rangle$ for transition metals. Some measure of the effect can be obtained for the 3*d* metals by inspection of the spin polarization of the $4s^2$ shell in the neutral $3d^n4s^2$ atoms. Experiment and exchange polarized calculations indicate [10,16] a $4s^2$ hyperfine field of $\sim +100$ kOe per unpaired *d*-electron, a contribution which almost cancels the $1s^2 + 2s^2 + 3s^2$ core polarization. One expects a smaller effect in a metal since there are typically one, not two, electrons worth of "*s*" character below E_F. One might expect a further reduction, in view of the fact that ξ values defined for Fermi level states always lie below 1. Paired Block states near the bottom and throughout an occupied "conduction" band contribute to the exchange polarization. These states have stronger hyperfine coupling than those at E_F which contribute to the Knight shift, as is evidenced by internal conversion experiments [17]. It is probable that there is little or no reduction in this polarization term due to band effects.

There may be *inter*-atomic as well as *intra*-atomic contributions to $\langle a \rangle$, since an applied magnetic field induces spin moments on the neighboring atoms as well as the atom in question. The two contributions are indistinguishable for the pure monatomic metals, but there is indirect evidence, from alloying, that the interatomic term is quantitatively important in some transition metals. *Inter*-atomic contributions will be seen to be important in transition metal alloys and intermetallics. As with the concept of a *local* density of states, there will frequently be ambiguity when attempting to divide $\mathcal{K}$ into inter- and intra-atomic terms.

In addition to these contributions to the Knight shift coming from the Pauli paramagnetism of the conduction electrons, there is an important contribution, especially in transition metals, from the orbital magnetic moment of the conduction electrons induced by the applied magnetic field. We can write, in analogy with eq (1)

$$\mathcal{K}_{\text{orb}} = \langle b \rangle \chi_{\text{orb}} \tag{14}$$

where $\langle b \rangle$ is an appropriate orbital hyperfine coupling constant. In contrast to the Pauli contribution to the Knight shift, the orbital Knight shift is not proportional to $N(E_F)$.

The orbital Knight shift [18-20] involves the orbital moment induced in occupied conduction electron states by an applied magnetic field, **H**. It is a second order term of the form

$$\mathcal{K}_{\text{orb}} = \frac{2\mu_B^2}{IH} \sum_{\substack{i \\ E<E_F}} \sum_{\substack{f \\ E^{'}>E_F}} \frac{\langle i|\mathbf{H}\cdot\vec{\ell}|f\rangle \left\langle f \left| \frac{2\vec{\ell}\cdot\mathbf{I}}{r^3} \right| i \right\rangle \delta(\mathbf{k}_f - \mathbf{k}_i)}{E_i - E_f}$$

$$\equiv \langle b \rangle \chi_{\text{orb}} \equiv 2\chi_{\text{orb}} \langle r^{-3} \rangle. \tag{15}$$

Here the matrix elements are evaluated over a Wigner-Seitz cell. The occupied and unoccupied Bloch states, *i* and *f*, are admixed by the application of the field. The resulting admixture produces a moment which interacts with the nucleus. Except for pathological cases, where there are a substantial number of strongly admixed states within kT or E_F, there is little or no temperature dependence in this term, as is the case in the analogous Van Vleck temperature-independent paramagnetism in ionic salts. A rough estimate of the strength of the orbital Knight shift is given by [17].

$$\mathcal{K}_{\text{orb}} \approx \frac{n_i n_f \left\langle \frac{1}{r^3} \right\rangle}{\Delta}, \tag{16}$$

where n_i and n_f are the numbers of occupied and unoccupied Bloch states respectively and Δ is the conduction electron bandwidth. This equation suggests that particularly strong orbital effects are expected in roughly half-filled *d*-band transition metals. In half-filled bands the product $n_i n_f$ is a maximum, and in transition metals, Δ is small. Strong effects have indeed been found in W [21], Nb [20], V [19,20,22], Cr [23] and CrV alloys [24].

Although we have treated the Pauli and orbital hyperfine parameters, *a* and *b*, as multiplicative factors of the appropriate susceptibilities, it should be emphasized that $\langle a \rangle$ and $\langle b \rangle$ are not the simple averages customarily employed, but are more correctly the weighted averages

$$\langle a \rangle \equiv \frac{\langle a\chi_p \rangle}{\chi_p} \tag{17}$$

and, as is clear from eqs (14) and (15),

$$\langle b \rangle \equiv \frac{\langle b\chi_{\text{orb}} \rangle}{\chi_{\text{orb}}}. \tag{18}$$

The $\langle\,\rangle$ denote an average over all bands. For the Pauli term, the average is over segments of Fermi surface where the contribution of a segment to χ_p is multiplied

by the hyperfine constant, a, appropriate to that segment (*i.e.*, to its electron character). Equation 15 defines the average for the orbital term, where the induced orbital moments associated with initial and final states, i and f, are weighted by their hyperfine coupling constants. With this, the general expression for the Knight shift, eq (3), becomes

$$\mathcal{K} = \langle a\chi_p \rangle + \mathcal{K}_{\text{dia}} + \langle b\chi_{\text{orb}} \rangle + \text{higher order terms.} \quad (19)$$

The Knight shift provides samplings of wave function and, in some senses, density of states character different from that obtainable in other experiments. The Pauli term can in principle, and does occasionally in practice, yield considerable insight into the Fermi surface states contribution to $N(E_F)$. A particular case is that of alloys and intermetallic compounds with different $\langle a \rangle$'s at different atomic sites. This involves the variation in wave function character from site to site and, if you will, the variation in a *local* density of states. There is some arbitrariness as to whether one wishes to describe this in terms of $\langle a \rangle$ or a local χ_p.

A particularly clear example of this local nature is that of α-Mn. For this structure there are four crystallographically inequivalent sites. Above the Néel temperature of 95 K, four distinct resonances were observed [25,26]. Two of these had large negative shifts of -5.2 and -2.6 percent at room temperature [26], and were temperature dependent [25], with the former value increasing to -5.85 percent at 120 K, where χ shows a maximum. The nuclei at the other two crystallographically inequivalent sites showed much smaller, and temperature independent, Knight shifts (-0.45 and -0.15%).

A number of complications have been indicated in this section. There is more than one term in the Knight shift; also the hyperfine constants $\langle a \rangle$ and $\langle b \rangle$ are significantly affected by band character and hybridization. There will in general be *inter-* and *intra*-site contributions to $\langle a \rangle$. As will be seen, two important "tools" are available to aid in the identification of the different contributions to $\mathcal{K}$: the Korringa relation [27] relating Knight shifts to nuclear spin-lattice relaxation times, and the temperature dependence of both $\mathcal{K}$ and χ [13]. Finally one can sample Knight shift behavior at sites involving different atoms in an alloy or intermetallic compound. Matters such as these, while complicating Knight shift interpretations in terms of density of states, can supply insight into the electronic structure and local wave function character which cannot generally be obtained from other experiments.

3. Pauli Spin Susceptibility

The Knight shift samples the density of states via the Pauli spin susceptibility, χ_p. However, in pure metals, the density of states has usually been obtained in other ways and the Knight shift then used to explore the associated wave-function character. In this section, we will review some of these methods of obtaining χ_p, and their implications to our understanding of Knight shift behavior.

First let us note that the expression relating the Pauli susceptibility to the density of states given in eq (2) neglects correlation and exchange effects between conduction electrons. Electron gas estimates are frequently applied to "free" electron metals [28,29], and exchange enhancement theories to transition metals [30-32]. With a conduction-electron conduction-electron exchange interaction parameter $\mathcal{J}_{\text{eff}}$ defined in reciprocal space and taken to be constant, the random phase approximation yields [30-32] an exchange enhanced susceptibility

$$\chi_p = \frac{\chi_p^0}{1 - \mathcal{J}_{\text{eff}}\chi_p^0}, \quad (20)$$

where χ_p^0 is the unenhanced susceptibility of eq (2). The induced spin sets up an exchange field encouraging further polarization hence an enhanced χ_p. Similar looking expressions, with $N(E_F)$ appearing in numerator and denominator are obtained from correlated electron gas theory. These as well as interband effects obviously complicate the averages taken in eq (17). In general one is forced to neglect them in $\langle a \rangle$ and assume their presence in χ_p alone. Even with this simplification, there is no simple linear relation between an observed Knight shift and the density of states at the Fermi surface. As remarked earlier, this shortcoming is shared with the experimental data obtained by many of the other techniques reviewed in this symposium.

It might appear that an adequate value of χ_p could be obtained from direct measurements of magnetic susceptibilities, χ_{exp}, especially since these would already have the exchange enhancement included. We will return to the case of transition metals later, but in simple metals it turns out that bulk susceptibility results usually do not give reliable values of χ_p. Consider, for instance, the noble metals. The bulk susceptibilities (χ_{exp}) are each negative, *i.e.*, the metals are diamagnetic. The ion core diamagnetism ($\chi_{\text{dia}}^{\text{core}}$) plus conduction electron diamagnetism ($\chi_{\text{dia}}^{\text{cond}}$) is larger than χ_p. Hartree-Fock [7] and Hartree-Fock-Slater [33] calculations for $\chi_{\text{dia}}^{\text{core}}$ agree to within two percent. However these calculations are for singly ionized valence states

417-156 O - 71 - 40

which is not a totally satisfactory description in the metal. This, and interband mixing effects, raise the probable error in χ_{dia}^{core} considerably. By the same token, χ_{dia}^{cond} is poorly known due to electron-electron interactions. The net result is that χ_p obtained from χ_{exp} is probably good to no better than twenty percent for the noble metals. Various ξ values for the noble metals obtained by use of various schemes are shown in table 5. It can be seen that ξ values employing the traditionally quoted values for χ_{dia}^{core} are not consistent with those using more modern Hartree-Fock or Hartree-Fock-Slater estimates. The situation in the case of the alkali metals is not as bad for two reasons. First the theoretical evaluation of both the core- and conduction-electron diamagnetism is on firmer ground, especially for the free electron-like metal, Na. Secondly, χ_p has been obtained directly (*i.e.*, without the need for the troublesome diamagnetic corrections) using conduction electron spin resonance (CESR) for the alkali metals and for Be. Combined CESR-NMR has also been used in Na and Li [34-36] to obtain χ_p.

For many metals it has been customary to use electronic specific heat, γ, measurements for information about χ_p^0 using the one-electron relationship

$$\chi_p^0 = 3\left(\frac{\mu_B}{\pi k}\right)^2 \gamma, \tag{21}$$

where k is the Boltzmann constant. There are two difficulties here. One is that there may be many-body contributions to γ (such as electron-phonon or paramagnon enhancement). The other is that the exchange enhancement part of χ_p is missing here [see eq (20)]. The ξ values derived from γ, given in table 5, were obtained from eq (21) and experimental γ values [37], and therefore neglect these corrections for enhancement effects. It may be that in some cases these two factors approximately cancel one another. The ξ values plotted for the elements in figure 3 were obtained by use of uncorrected γ values [37]. The final set of ξ values in table 5 utilizes a set [38] of band theory predictions for χ_p^0. Cancellations of various enhancement factors do not occur. The resultant ξ values are therefore larger.

TABLE 5. *ξ values for Cu, Ag and Au using various available data for χ_p* (see text for details).

	Cu	Ag	Au
From $3/2(\chi_{exp} - \chi_{dia}^{core})$ Hartree-Fock core	.37	.50	.32
From $\chi_{exp} - \chi_{dia}^{core} - \chi_{dia}^{cond}$ Hartree-Fock core	.45	.45	.36
From $3/2(\chi_{exp} - \chi_{dia}^{core})$ Hartree-Fock-Slater core	.38	.52	.36
From $3/2\ (\chi_{exp} - \chi_{dia}^{core})$ traditional core	.45	.16	.08
From uncorrected electronic specific heat, γ	.53	.69	.42
From band calculations presented at this Symposium, χ_p^{bare} [38]	.57	.68	.56

It is instructive [39] to compare the value of χ_p^0 (obtained from γ) to the value of $\xi\chi_p$ obtained by dividing $\mathcal{K}$ by atomic H_{eff} values (tables 1 and 2). This is done in figure 4. The trend in our plot differs from that of Ziman [39] primarily due to our choice of atomic, rather than mass, units. The lightest alkali, Li, displays significantly less *s*-character than the other alkali metals [40-47]. The ξ values for the *B*-subgroup metals are all considerably lower, especially for the polyvalent elements; this might be expected, since the Fermi level lies higher in conduction bands, implying less *s*-character at E_F and hence a smaller contact term. The associated increase in *p*- and *d*-character will generally make a negative (core-polarization) contribution to $\mathcal{K}$, also lowering ξ.

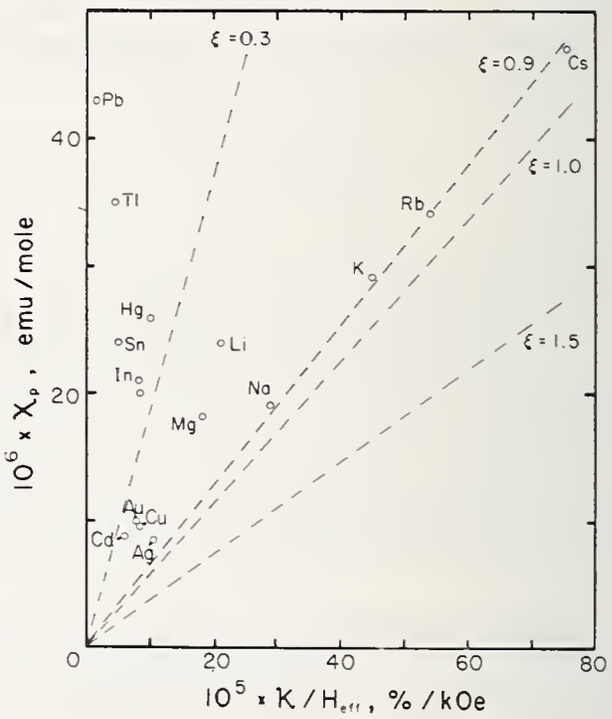

FIGURE 4. *χ_p versus $\mathcal{K}/H_{eff}$ for pure metals in customary units. Lines of constant ξ (dashed) are shown. Due to the small ξ values for the heavier metals most of the data points are bunched at the left hand side of the plot. The χ_p values were obtained from electronic specific heat data [37]. In the case of potassium a large uncertainty in the specific heat gives rise to an error of nearly half the size of the vertical dimension. The point shown for potassium represents the listed [37] γ value. Direct measurements [239, 240] yield ξ(Li)=0.44 and ξ(Na)=0.64, rather than the values, ξ(Li)=0.49 and ξ(Na)=0.89, used in this figure for the sake of consistency.*

We note an interesting correlation in figure 4 in that the alkali metals, except for Li, fall on a straight line near $\xi = 0.9$. That is to say, the *s*-density of states apparently increases proportionately to the total density of states at the Fermi level for Na, K, Rb and Cs. The

increase in χ_p from Na to Cs is attributable primarily to the large volume increase in this series. The constancy of ξ might seem to be surprising, since simple volume renormalization should effect ξ as well as χ_p. It is to be recalled, that volume renormalization of ξ depends on the atomic volume in the metal *relative* to that of the free ion. It would thus appear that the alkali metal lattice constants faithfully reflect the sizes of the free ions, and hence ξ is roughly constant implying that the amount of *s*-character is essentially constant for the alkali metals Na to Cs. This constancy was already noted by Pauling [47]. His calculations of *s-p* hybridization of bond orbitals indicated fractional *s*-characters of 0.72 to 0.74 for Na to Cs and a lower value (0.59) for Li, similar to the trend of figure 4.

Knight shift experiments on the pressure dependence, as well as alloying, show that the contact density in metals is not simply an inverse function of volume [7]. This is also illustrated by recent pressure dependence calculations [48] on monovalent metals. The wave function effects which depress ξ values below 1, suppress the dependence of ξ on volume.

In this section, we have seen the difficulty in obtaining a reliable value of χ_p for use in obtaining ξ values for simple metals. Nonetheless, even in these cases, the Knight shift provides a rather unique measure of the *s*-contribution to the density of states in "simple" metals.

4. "Simple" Metals

It is an interesting challenge to obtain the absolute value of the Knight shift, or its change with temperature or pressure, from band-theoretical calculations. A number of near *a priori* calculations have been made with varying degrees of semiquantitative success. For example, Das and coworkers, using the orthogonalized plane wave (OPW) method, have calculated wave functions and densities-of-state at various points on the Fermi surface for Al [49], Be [50-53] and In [54]. A few of these papers are of particular interest in that they represent efforts to use the weighted average form of $\langle a \rangle$ as given in eq (17). In the case of the divalent metals Be, Mg and Cd, the spin susceptibility has been extracted from Knight shift measurements by use of such estimates of $\langle a \rangle$ [55]. Comparison with theoretical values of their bare χ_p [*i.e.*, eq (2)] permitted estimates of the exchange enhancement to be made. This process resulted in a reduction in χ_p for Be; the authors concluded that this arose from inadequacies in the energy band estimate of χ_p^0 and $\langle a \rangle$.

The alkali metals, particularly Li and Na, have traditionally attracted theoretical attention, often giving relatively close agreement with experiment [40-42]. Even in these simplest "free electron" metals, corrections to the hyperfine coupling constant due to non-free electron-like band structure effects, can amount to 25 percent or more [45,56,57].

It should be stressed that for the heavier simple metals (*i.e.*, potassium and above) *d*-hybridization associated with *d*-bands above or below the conduction band affects the Knight shift and other properties at (and off) the Fermi level (see, for example, Kmetko [46]). In the case of Cu and Au these *d*-hybridization effects are large. Such effects do not arise in the Li row, but there may be abnormal "2*p*" effects due to the near degeneracy of atomic 2*s*- and 2*p*-levels [58-61]. In these "simple" metals, the change in Knight shift at the melting point [62] (fig. 2a) is usually not large, and its temperature dependence in the solid, slight (fig. 2b). As an example, consider Al. At the melting point, $\mathcal{K}$ has the same value for both liquid and solid. The temperature dependence in the solid is illustrated by the data of Feldman [63] (fig. 5). The change in Knight shift of Al is less than 2 percent of $\mathcal{K}$ over a temperature range from 4 to 300 K. The solid line in figure 5 represents a simple volume renormalization theory based on the thermal lattice expansion, which fits quite well at temperatures above the Debye temperature. No satisfactory explanation has been given for the deviation from this theory at low temperatures. Similar effects were observed in Na and Pb [63].

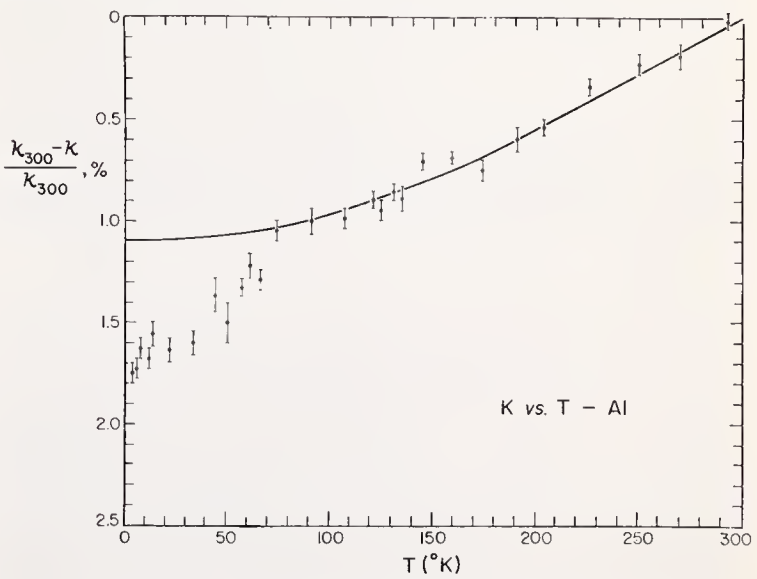

FIGURE 5. *Change in the aluminum Knight shift with temperature, as taken from Feldman [63]. The solid line is theoretical.*

A more unusual case is that of cadmium [64-70]. In the solid the Knight shift varies considerably. $\mathcal{K}$ increases ten times more rapidly in Cd than in Al, over the same temperature range (4-300 K). At 600 K, $\mathcal{K}$ in

Cd is about 70 percent larger than its value at 4 K. This change is seen in figure 6. An additional increase in $\mathcal{K}$ ($\sim 33\%$ of $\mathcal{K}$) is observed upon melting (see sec. 5). The anisotropic Knight shift, $\mathcal{K}_{\text{anis}}$, [see eq (13)] also increases with temperature. Cd exhibits a large change

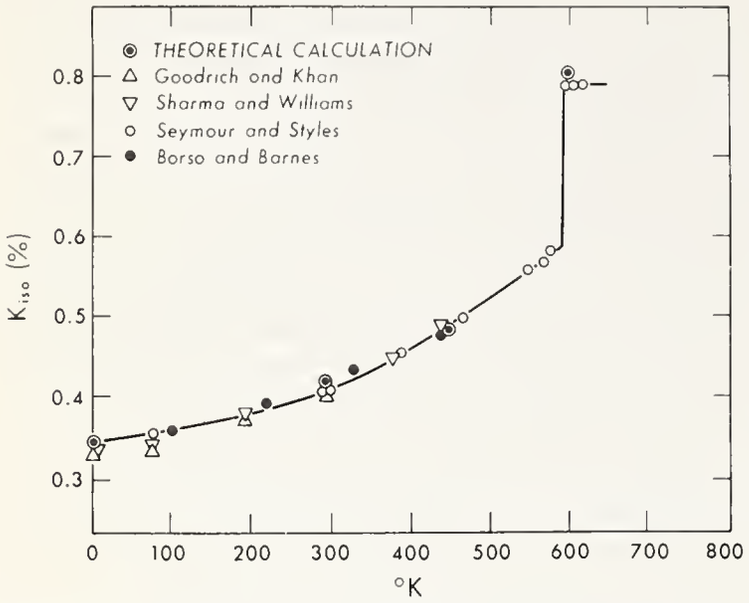

FIGURE 6. *Change in the cadmium Knight shift with temperature, as taken from Kasowski and Falicov* [68].

in the shape (c/a ratio) and volume of the unit cell with temperature and it had been suspected that the changes with temperature of $\mathcal{K}_{\text{iso}}$ and $\mathcal{K}_{\text{anis}}$ could somehow be correlated with these cell dimensions. Kasowski and Falicov [68] have explained the behavior with a different scheme: in the solid the lattice vibrations cause an increase in both χ_p and in the s-character as the temperature is raised, thereby increasing $\mathcal{K}_{\text{iso}}$. On the other hand, $\mathcal{K}_{\text{anis}}$ arises from the non-s part of the wave-function, which of course is decreasing as the s-part is increasing. However, again invoking eq (17), we require not the average hyperfine coupling associated with the non-s part, but the appropriate average over the Fermi surface. Cancellation occurs in this average at low temperatures. The reduction in the cancellation at higher temperatures more than compensates for the increase in s-character, thereby providing an increase in $\mathcal{K}_{\text{anis}}$. On the other hand, pressure dependence measurements of $\mathcal{K}_{\text{anis}}$ for Sn [71] was interpreted as due to charge redistribution rather than a change in the s-p character of the wave-function.

Other data further indicate the complexity of the behavior of the Knight shift in solid Cd. Borsa and Barnes [65] note that alloying Mg (in quantities of $\sim 1\%$) with Cd will cause substantial changes in cell size and shape without affecting the Knight shift. Kushida and Rimai [72] have separated the implicit and explicit contributions to the temperature dependence of $\mathcal{K}$ by their measurements of the pressure dependence in Cd. Volume renormalization was found inadequate to explain the observed pressure dependence [72].[5]

5. Sudden Changes in $\mathcal{K}$

The abrupt change in $\mathcal{K}$ of Cd upon melting was presumed by Ziman [39] to indicate an abrupt change in $N(E_F)$ associated with solid and liquid Cd. This conclusion was examined in two different calculations, each employing nonlocal pseudopotentials [68,70], resulting in opposite conclusions. Shaw's calculated [70] values for $N(E)$ per unit volume for solid and liquid Cd are shown in figure 7. $N(E_F)$ is found to be 0.7 percent *lower* in the liquid than in the solid. Shaw concludes that "Ziman's assertion that the strong change in the Knight shift of cadmium is a density-of-states effect is not borne out by our detailed calculations." In contrast Kasowski and Falicov [68] assume that Cd is free-electron-like in the liquid and finds that most of the change in $\mathcal{K}$(Cd) upon melting is due to an increase in $N(E_F)$. They note that "this agrees with Ziman's hypothesis and confirms it quantitatively." Although these two calculations [68,70] resulted in opposite conclusions, in part due to choice of different model-potentials, there is an abrupt increase in $N(E_F)$ in Shaw's calculations if solid Cd is compared with the free electron value, as indicated in figure 7.

An interesting example of an even more abrupt increase in $\mathcal{K}$ upon melting is found in the behavior of the III-V compound InSb [73]. In the semiconducting solid the Knight shift of either the In or Sb in InSb is zero, but in the metallic liquid state, the Knight shifts have normal metallic magnitudes. Another example is Bi [62], in which $\mathcal{K}$ has the opposite sign in the liquid from the solid.

There are various cases besides melting where a sudden change in $\mathcal{K}$ occurs. In an alloy system, $\mathcal{K}$ usually changes smoothly with composition within a particular phase, but shows a jump across a phase boundary. An example of this is shown for the AgCd system in figure 8, taken from Drain [74]. By correlating $\mathcal{K}$ and γ across a phase boundary, Drain showed that in this case the abrupt change is associated in part with changes in densities of states.

[5] There are other examples of an observation concerning the volume dependence of $\mathcal{K}$. As noted earlier, in our discussion of figure 4, simple volume renormalization is not often useful in explaining Knight shift results. See also [7] for a discussion of this point.

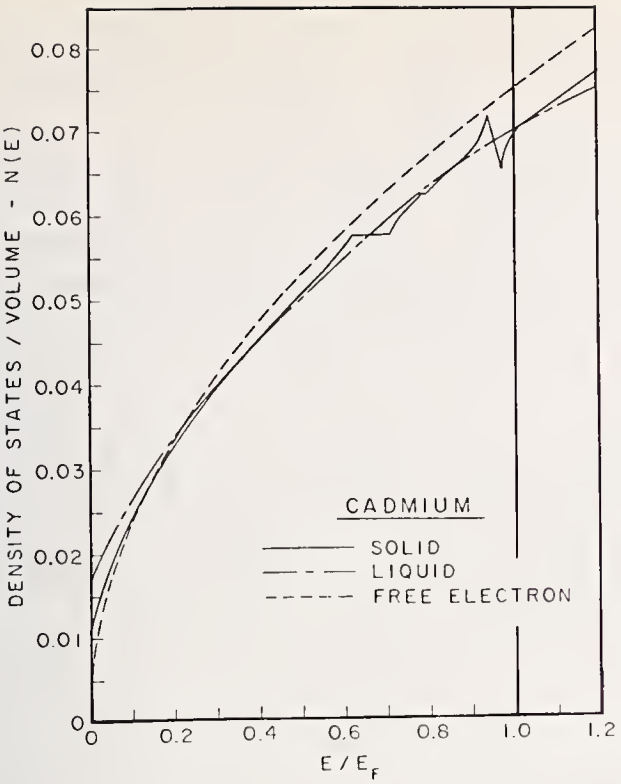

FIGURE 7. *Calculated values of* N(E) *for Cd, as taken from Shaw and Smith* [70].

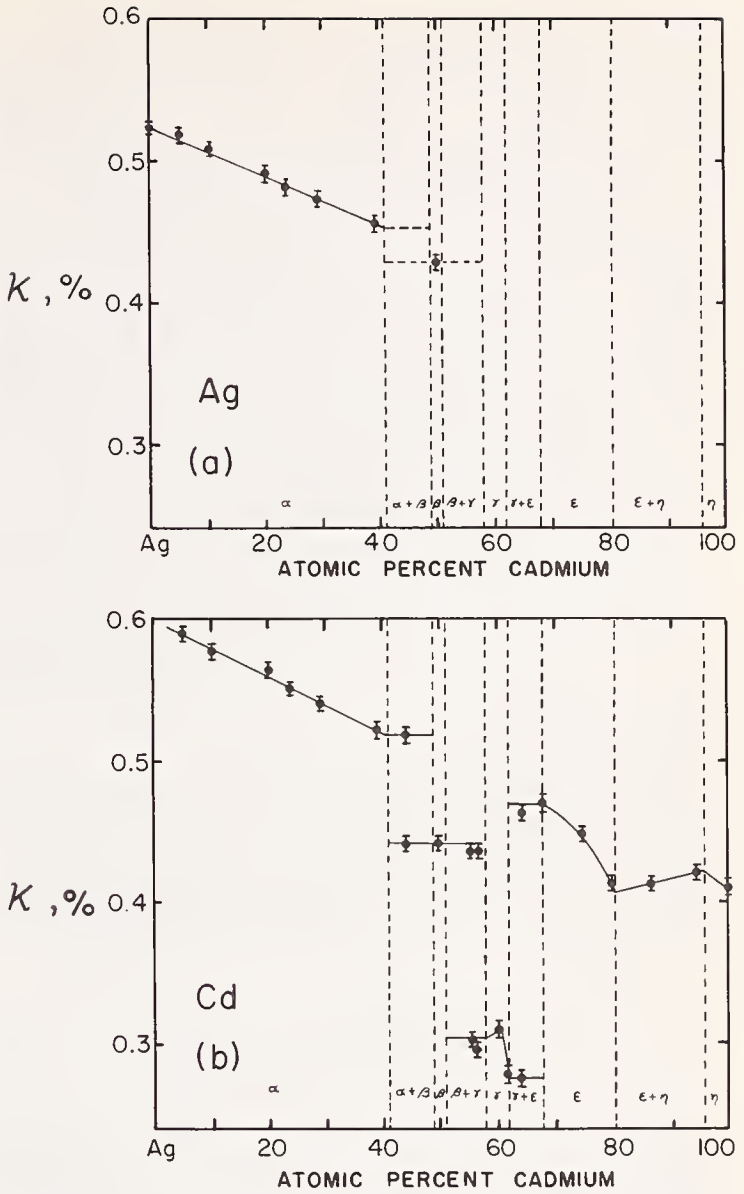

FIGURE 8. *Knight shifts in AgCd for (a) the Ag resonance and (b) the Cd resonance, as taken from Drain* [74]. *In the two phase regions, Cd resonances for both phases are simultaneously seen, due to the rather different* $\mathcal{K}$*'s for the different phases. For ranges of solid solubility* $\mathcal{K}$ *changes smoothly.*

The semiconductor-(or insulator-) to-metal transition, whether or not a Mott transition, offers a number of examples in which the Knight shift changes more or less suddenly. For example, when tin changes from its metallic to its semiconducting phase, $\mathcal{K}$ changes from 0.75 percent to near zero (see fig. 2b). Also consider VO_2 which is metallic above and semiconducting below a crystal structure change occurring at $T_c = 68$ °C [75,76]. The Knight shift is ~ -0.4 percent at 100 °C and $\sim +0.2$ percent below. The negative shift above T_c is attributed to a metallic d-band.

A case where there is an electronic transition without further structural changes is that of phosphorous-doped silicon [77-79]. At donor concentrations (n_d) greater than 2×10^{19} cm^{-3}, the material appears to be a metal, the Knight shift is proportional to $n_d^{1/3}$, and the Korringa relation holds. Below this critical concentration, $\mathcal{K}$ drops sharply. In the transition range, $3 \times 10^{18} < n_d < 2 \times 10^{19}$, there is a measurable $\mathcal{K}$, but the Korringa relation no longer holds. The electrons are "delocalized" in some type of impurity "band."

Other systems exhibiting nonmetal-to-metal transitions are the alkali-ammonia solutions. As the metal to ammonia ratio is increased, the liquid becomes gradually metallic, and the conductivity as well as the Knight shift increases substantially [80-83].

6. Orbital Magnetism in Simple Metals

The Bardeen, Cooper and Schrieffer theory of superconductivity [84] predicts that, as a result of spin pairing, χ_p vanishes at $T = 0$. Hence it was expected [85] that $\mathcal{K} \to 0$ as $T \to 0$ for superconductors. This expectation often is not borne out. It seems certain that the residual Knight shift is predominantly of orbital origin for transition metals such as V and Nb [22]. Ferrell [86] and Anderson [87] proposed that spin-reversal scattering due to spin-orbit coupling is another possible mechanism for obtaining a residual Knight shift. This mechanism requires that $\mathcal{K}$ be a function of mean free path, *i.e.*, particle size and impurity scattering. This

spin-orbit term has been shown by Wright [88] to be important in Sn. Wright also reviews earlier experiments on other metals. He concludes that although spin-orbit coupling is dominant in some cases, two types of orbital magnetism cannot be ruled out in simple metals. These are the Van Vleck orbital paramagnetism [18-22] and a higher order mechanism introduced by Appel [89]. Similar higher order mechanisms were discussed earlier by Clogston *et al.* [20]. We have already discussed the Van Vleck term and will note its importance in the transition metals and alloys to be discussed later. The Appel mechanism involves spin-orbit and $\vec{\ell}\cdot\vec{\mathbf{H}}$ coupling to an intermediate excited conduction electron state, which contributes to the Knight shift through the contact interaction. It is of the order of $\lambda/\Delta E$ times the contact Knight shift, where λ is the spin-orbit interaction energy, and ΔE is the energy between states connected by λ. The sign of the Appel contribution to the Knight shift may be either positive or negative.

Another important orbital effect is the Landau-Peierls diamagnetism [90]. The magnitude of this term is not easy to predict. In the simplest (and greatly oversimplified) free electron approximation the Knight shift, $\mathcal{K}_{dia}$ arising from Landau-Peierls diamagnetism, is

$$\mathcal{K}_{\text{dia}} = -\frac{8\pi}{3}\left(\frac{1}{3}\chi_p\right)\left\langle\frac{m}{m^*}\right\rangle^2, \qquad (22)$$

where m^* is an appropriate electron effective mass. This term has been proposed to explain a number of negative, or near zero, Knight shifts in nontransition metals. In transition metals, *d*-core polarization (see table 3) gives an important negative contribution to $\mathcal{K}$, through the Pauli paramagnetism of the *d*-band. In nontransition elements *p*-core polarization has often been proposed as an alternate to $\mathcal{K}_{\text{dia}}$ as a negative contribution to $\mathcal{K}$ (see table 3). For example Das and Sondheimer [90] first suggested the importance of the Landau term to the negative Knight shift in Be. In later papers, Das and coworkers [50-52] performed detailed calculations for the contact and the *p*-core polarization terms in this metal. A reluctance to believe that the diamagnetic shift is as large as was originally suggested [90] is evident from these papers [50-52]. Although they do not give further quantitative estimates for $\mathcal{K}_{\text{dia}}$ in this later work, in each case they are forced [52] to the same conclusion that the remaining negative shift is of diamagnetic origin. Using eq (22), available m^* values can, in fact, give a $\mathcal{K}_{\text{dia}}$ of -0.003% [52,53].

Yafet [91] considered the importance of $\mathcal{K}_{\text{dia}}$ for Bi, but Williams and Hewitt [92] proposed *p*-core polarization as the origin of the quite substantial negative Knight shift in Bi of -1.25%. It is interesting to note that if χ_p is estimated from the electronic specific heat [37], using eq (21), and if there is no *s* contact contribution to $\mathcal{K}$, the *p*-core polarization necessary to explain a shift of -1.25% is 800 times larger than the experimental value [93] for atomic Bi (table 3). The presence of an *s* term will increase this estimate of 800. Note that the experimental atomic "core" polarization term includes the polarization of the 6*s-valence* electrons which are part of the conduction bands in the metal. This atomic value therefore provides an estimate of the *s* polarization in the core *and* throughout the occupied conduction band: the applicability of this value to the metal depends on the distribution of *s*-character in the occupied bands (as compared with the free atom). Granted the uncertainty in χ_p and the question of relevance of the atomic hyperfine constant to this metal it would still appear that *p*-core polarization is at least one hundred times too small to account for the experimental Knight shift. On the other hand, Bi has m/m^* ratios which, using eq (22), are large enough to suggest a Landau diamagnetic shift that can approach magnitudes of the order of the observed $\mathcal{K}$ value.

Other examples of negative shifts in diamagnetic, non-*d* materials are Tl in NaTl [9,94-96] and In in BiIn at 77 K [97]. For these cases the situation is much less clear due to the lack of data for χ_p, m^*, and γ. In addition we do not have free atom experimental values for *p*-core polarization for Tl and In. Using some upper estimates for the unknown quantities, it is evident that either *p*-core polarization or Landau diamagnetism is hard pressed to reproduce the observed shifts. A discussion of diamagnetic Knight shifts and *p*-core polarization effects in these materials will be given elsewhere [98].

Das and Sondheimer [90] also indicated that oscillations would be present in the diamagnetic term. These would be periodic in $1/H$, similar to de Haas-van Alphen oscillations. However, when this effect was first observed by Reynolds *et al.* [99,100], the amplitude of the oscillations was considerably larger than that expected from the diamagnetic term [101-106]. Glasser [107] explained this by proposing that the Fermi surface wave functions also change with $1/H$, and that this introduces oscillations into the Pauli term which dominate over the diamagnetic oscillations. Goodrich *et al.* also observed Knight shift oscillations in Cd [108]. Their data are shown in figure 9.

The importance of observing oscillations in $\mathcal{K}$ is that it is possible to obtain the Knight shift over a segment of the Fermi surface. Thus the Knight shift has become

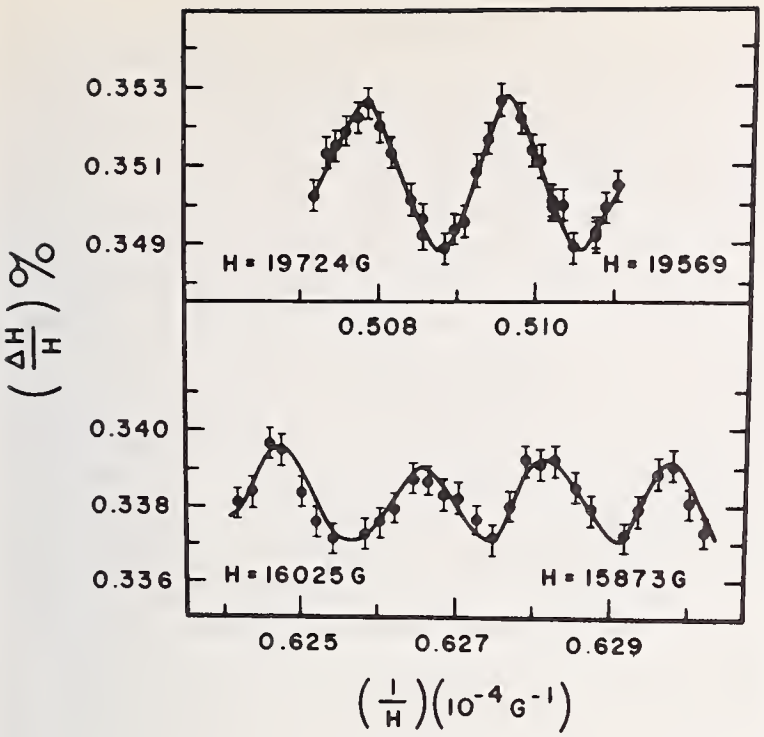

FIGURE 9. *Knight shift in Cd, illustrating oscillations in $\mathcal{K}$ with* 1/H, *as taken from Goodrich, Khan and Reynolds* [*108*].

a potentially important tool for examining the wavefunction character associated with $N(E_F)$ not only in the average sense of eq (19), but also in finer detail over Fermi surface segments.

7. Transition Metals

The simple metals considered in the preceding sections display, in the main, only weak orbital Knight shifts and temperature independent, usually positive, Pauli terms. Transition and noble metals with their *d*-bands tend to have a negative Pauli term arising from *d*-core polarization (see table 3). Narrow *d*-bands, with many states close in energy to E_F, often have substantial orbital effects [see eq (15)]. Structure and curvature in $N(E_F)$ contribute a temperature dependence to the Pauli term. Given the presence of *d*- and non-*d*, or "conduction" band character, it has been normal to describe the paramagnetic transition metals in terms of a "two band" model involving discrete "*s*" and "*d*" bands. We follow common nomenclature in designating the conduction band as an *s*-band. (The *d*-bands, of course, also contribute to conduction.) The orbital Knight shift is associated with the *d*-band; the average taken in the Pauli term is rewritten

$$\langle a\rangle\chi_p = \langle a_s\rangle\chi_p^s + \langle a_d\rangle\chi_p^d(T), \qquad (23)$$

where the "*s*" or conduction band is assumed to contribute a positive, temperature independent term, and the *d*-bands, a negative temperature dependent term. The latter dominates since $N(E_F)^d$, hence χ_p^d, is much larger than its *s*-band counterpart. It is assumed in eq (23) that the temperature dependence of $\mathcal{K}$ is entirely associated with the susceptibility and not with any variation in the hyperfine coupling constants [13]. The fact that the slope, $d\mathcal{K}/d\chi$, is a constant for these metals offers some experimental justification for this assumption. An example of this is seen [109] in figure 10, where $\mathcal{K}$ is plotted versus χ_{tot}, with temperature the implicit variable, for Pd. In this case $\chi(T)$ goes through an extremum with increasing T, but is faithfully tracked by $\mathcal{K}(T)$. Pd displays the largest temperature variation in χ among the paramagnetic metallic elements. As is discussed in Mott and Jones [110], such a temperature dependence arises from sampling by the Fermi function of structure and curvature in the density of states in the vicinity of E_F.

While the two band model has proven most useful when discussing Knight shifts and other experimental data, there is, in fact, strong hybridization of *s*- and *d*-band character and a transition metal is not constituted of discrete *d* and "*s*" bands. Some measure of this is given in figure 11, which displays the density of states obtained[6] for fcc Cu.

The results can be taken as characteristic of all transition metals. The density of states behavior is similar to that reported by Mueller for Fe [115], and to that obtained by Goodings and Harris [116], and by Cuthill *et al.* [117] in their estimates of soft x-ray spectra for Cu. The density of states has been plotted separately for the first, second and sixth bands while that for the third, fourth and fifth has been added together for the sake of legibility. In figure 11, the Cu Fermi energy is designated by E_F and that appropriate to Ni by E(Ni). The high density of states peak, intersected by E(Ni), is due to the fifth band. Details of this band and of its Fermi surface are essential to the differ-

[6] These results [111] involve a sampling of $\sim 1.5\times10^6$ points in 1/48th of the Brillouin zone. The sampling employed a quadratic fit to a set of pseudopotential bands by Ehrenreich *et al.* [112, 113] involving a mesh of 28 intervals from Γ-X in the zone. The pseudopotential bands were obtained from an adjusted analytic fit of some new APW calculations for Cu [114]. Spin-orbit coupling effects, though slight, have been included. The Fermi surface is in better agreement with experiment than is usual for calculations. Details of the density of states and grosser features of the wavefunction analysis are, of course, dependent on the use of a pseudopotential band description (which assumes tight binding *d*-bands and a set of four orthogonalized plane waves for the non-*d* part). These results can be considered analogous to the OPW results, obtained by Das and coworkers [49-52, 55] for the Knight shift in various "simple" metals.

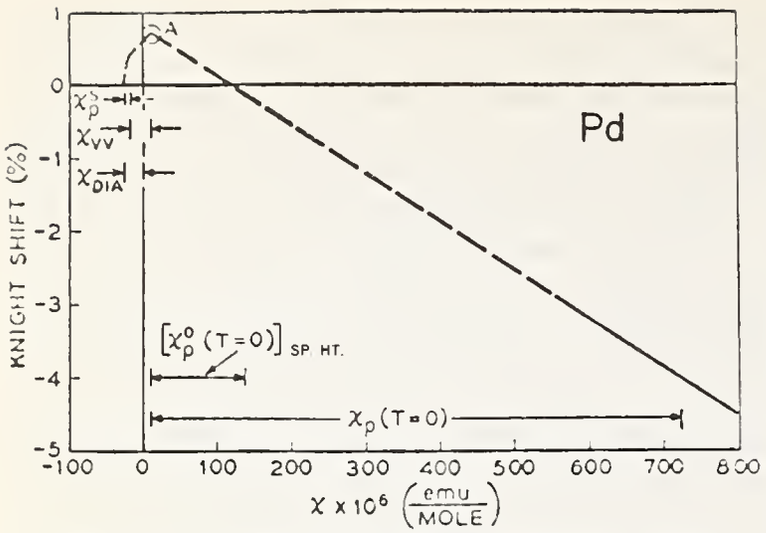

FIGURE 10. *$\mathcal{K}$(T) versus χ(T) plot for Pd, as taken from Seitchik, Gossard and Jaccarino [109].*

ing magnetic behavior of Ni, Pd, and Pt. The Cu Fermi level intersects the sixth band, often named the "free electron" band, which lies above the five "*d*" bands.

The density of states associated with non-*d* electron character; $N(E)_{\text{non-}d}$, is also shown in figure 11. It must be emphasized that details of these results depend on the scheme used to describe the bands (in this case a pseudopotential description [111] with tight binding *d*-functions). Hybridization effects cause a build up of non-*d* character at the bottom and a depletion in the middle and just above the bulk of the *d*-bands (*i.e.*, in the range $-0.35 \leq E \leq -0.15$ Ry). The peak seen at ~ -0.4 Ry can be important to optical and soft x-ray properties. The sixth band is predominantly of *d*-character at the bottom and remains almost thirty percent *d* at the Fermi level. This particular set of results [111] yields 9.8 electrons worth of *d*-character out of a total of eleven electrons, in the bands below E_F. [A free electron parabola, holding the remaining 1.2 electrons, and with an effective mass chosen so that its Fermi level matches E_F, has been drawn for comparison with the actual non-*d* density of states.] The lowest band is strongly free-electron like up to $E \sim -0.45$ Ry and 0.61 of the two electrons residing in the band are of non-*d* character. Roughly 0.35 of the remaining 0.6 non-*d*-

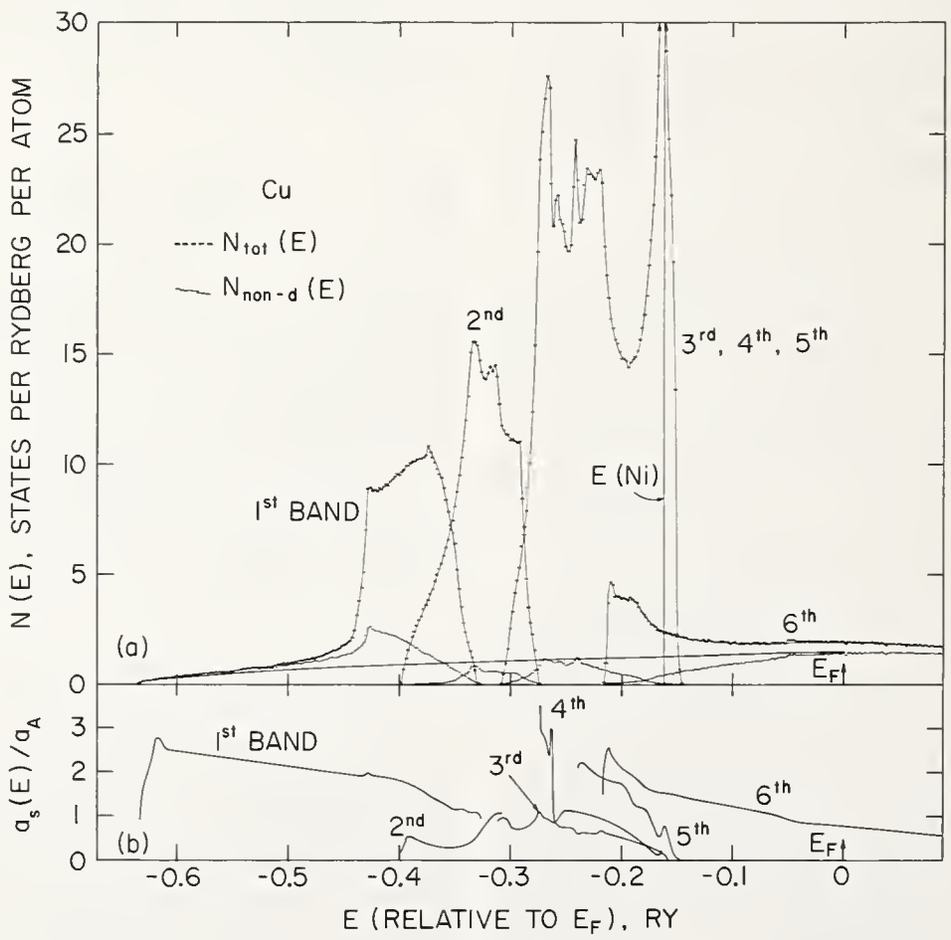

FIGURE 11. *(a) Total density of states and non-d density of states for the 1st, 2nd and 6th bands of Cu separately, and for the 3rd, 4th and 5th summed. The smooth, flat band is the free electron parabola containing 1.21 "conduction" electrons, as discussed in the text. This is shown for comparison with the $N_{\text{non-}d}(E)$ results. (b) Ratio of band to atomic hyperfine constants as defined by eqs (24a) and (24b).*

electron character is associated with the one electron in the sixth band.

The 3*d*-electron character can be expected to interact with the nucleus via a core polarization term of ~ -125 kOe per μ_B throughout the bands. The non-*d* character is expected to interact predominantly via the direct contact term. Its behavior is shown at the bottom of figure 11 in the form of the ratio

$$\frac{a_s(E)}{a_A} \equiv \frac{\langle a(E) N_{\text{TOT}}(E) \rangle}{a_A N_{\text{non-}d}(E)} \tag{24a}$$

with respect to the non-*d* electron density of states at E, *i.e.*, the contact interaction normalized with respect to the non-*d* electron density at E, and to an atomic 4*s* hyperfine constant.[7] Omitting all core polarization contributions to $\mathcal{K}$, this ratio is then related to ξ by

$$\frac{a_s(E)}{a_A} = \xi(E) \frac{N_{\text{TOT}}(E)}{N_{\text{non-}d}(E)}. \tag{24b}$$

A ratio of 2 to 2.5 occurs at the bottom of the bands reflecting the volume normalization enhancement of ξ discussed previously in connection with figure 4. Values closer to one are appropriate to the non-*d* character hybridized into the second, third, fourth and top of the first bands. This suggests that an $a_s(E)$ set equal to a_A can be used as a first approximation when estimating the effect of hybridization on reducing a *d*-band a_d from a pure *d*-core polarization value. The ratio is higher in the fifth band but here hybridization is almost zero. The ratio tends to fall with increasing E, as is seen in the lower part of the first and in the sixth bands. This is associated with the decrease in *s*-character in OPW's of increasing **k**. The ratio has dropped to a value of 0.78 at the Cu Fermi level. Here $\xi(E_F)$, defined in the manner of eq (24b), has the value of 0.57. If one adds the negative core-polarization contribution which can be attributed to the twenty-eight percent *d*-character in the bands at E_F, $\xi(E_F)$ becomes 0.55.

The above $\xi(E_F)$ values agree with the upper end of the range estimated as the experimental ξ for Cu in table 5. Davis [118] has obtained[8] $\xi(E_F) = 0.67$ employing the method of Korringa-Kohn-Rostoker. Comparison with the experimental data may not be meaningful because core polarization terms, arising from "conduction band" spin character, have been omitted in the $\xi(E_F)$ estimates while being present in the quantities of tables 2 and 5. It is thus proper to make the comparison only if core polarization affects the numerator and denominator so as to leave the ratio constant. This seems unlikely since *s and p* character terms will contribute to the conduction electron core polarization.

These two band calculations yield $N(E_F)$ values which are in good numerical agreement with the electronic specific heat for Cu. Both calculations suggest that *d*-hybridization is a significant factor in reducing ξ. This is one reason for the tendency noted earlier for Ag to have a larger ξ than Cu or Au. The *d* bands are twice as far below E_F in Ag, and weaker *d* hybridization ($\sim 10\%$) occurs at the Fermi level of Ag.

Noting that the atomic *s*-contact interaction is typically ten times larger than, and opposite in sign to, *d*-core polarization, figure 11 suggests that hybridization is important throughout the transition metals. Consider the case of Ni. The Fermi level intersects the high peak of the fifth band. This band has almost no hybridization, as is shown in figure 11, which was obtained with Cu bands. The sixth band has an $N(E_F)$ value which is better than an order of magnitude smaller than the fifth band at E(Ni). However the sixth band has twenty percent *s*-admixture at E(Ni) causing a large, positive a_d, which compensates for this. Neglecting exchange enhancement of the susceptibility, the sixth band contribution can then cancel approximately one third of the Knight shift term, a_d, associated with the fifth band alone. Exchange enhancement is important and an estimate of the exact role of the sixth band requires opinions of interband exchange effects. Scanning the lower energy parts of the plot, it appears that hybridization may affect the a_d values for the lighter transition metals more severely. This hybridization trend should hold although changes occur in the crystal structures.

Despite the complexities just discussed, the two band model of the Knight shift has frequently proven fruitful, with hybridization absorbed in the a_d term. The various Knight shift contributions are normally disentangled in two ways. First, comparisons can be made between the relaxation time, T_1, and Knight shift results which weight the various terms differently. The Korringa relation [27] provides a test for the *s*-contact contribution. Secondly, one can employ the graphical technique of figure 10. This scheme, applied to Pt [20]

[7] An a_A of 1600 kOe/μ_B, omitting core polarization contributions, was used, since core polarization effects were omitted in the evaluation of $\langle a(E) N_{TOT}(E) \rangle$. With core polarization, correlation and relativistic effects present, the (experimental) a_A is ~ 2600 kOe/μ_B. For discussion of this see [7].

[8] Actually Davis [118] chose to quote a ξ-ratio by dividing his computed hyperfine term *without* core polarization by an atomic a_A *with* core polarization. This yields a smaller numerical value than we quote here.

appears in figure 12. The experimental data are plotted for $\mathcal{K}$ versus χ_{tot} with temperature the implicit parameter and, following eq (23), it is assumed that

$$\chi_{tot} = \chi_{dia} + \chi_{orb} + \chi_p^s + \chi_p^d \tag{25a}$$

and

$$\mathcal{K} = \langle b \rangle \chi_{orb} + \langle a_s \rangle \chi_p^s + \langle a_d \rangle \chi_p^d(T). \tag{25b}$$

The slope of the experimental data yields an empirical value for $\langle a_d \rangle$. The diamagnetic susceptibility is estimated and subtracted out, shifting the origin of the plot to point A. An estimate is then made of χ_p^s (usually with the free electron approximation) and of a_s and the s-band contributions are subtracted out shifting the origin, with respect to orbital and d-band Pauli terms, to point B. Finally, $\langle b \rangle$ is estimated, defining the slope of $\mathcal{K}_{orb}$ versus the χ_{orb} line, which is drawn until it intercepts the experimental $\mathcal{K}$ versus χ_{tot} curve (at point C). The intercept defines the relative roles of orbital and d-band Pauli terms. In this case, the d-band Pauli term dominates.

A value for the *unenhanced* χ_p^0, estimated from specific heat data is shown in figure 12. The larger value, deduced from the Knight shift, provides a measure of the effect of exchange enhancement. While

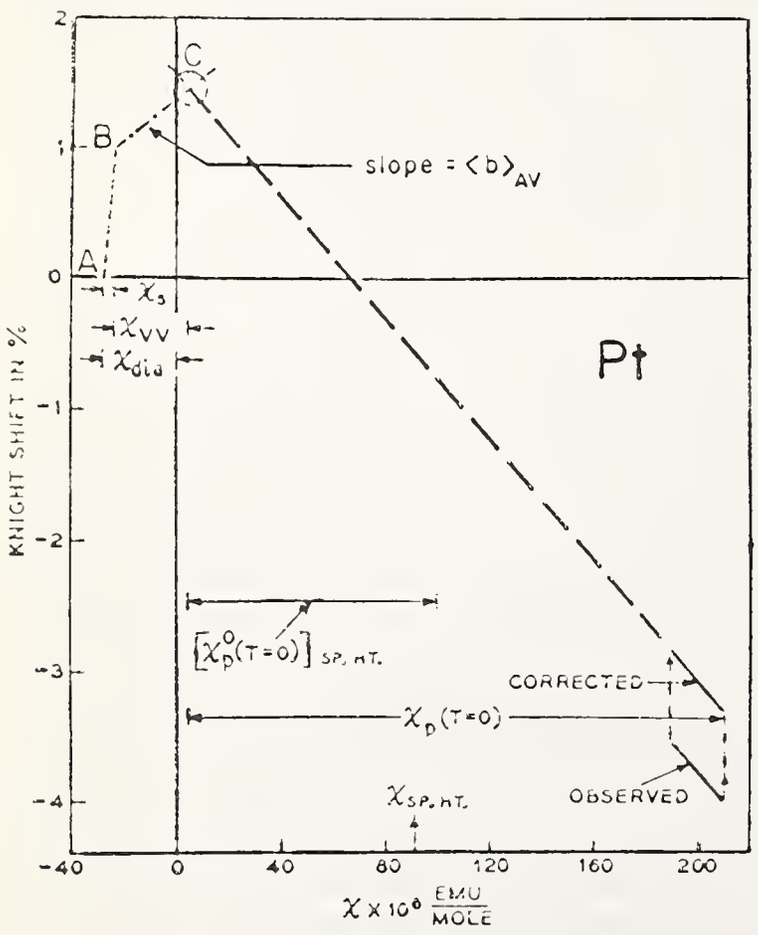

FIGURE 12. $\mathcal{K}$(T) *versus* χ(T) *for Pt, as taken from Clogston, Jaccarino and Yafet* [20].

quantitative results depend on the detailed choice of χ_{dia}, χ_p^s, $\langle a_s \rangle$ and $\langle b \rangle$, the qualitative conclusion does not. Changing the hyperfine constants by reasonable amounts or omitting the s band term altogether does not change the basic result. Analyses which compare T_1 and $\mathcal{K}$ data also rely on estimates of hyperfine constants. Results indicate that the d-band term also dominates in Pd (see fig. 10) and Rh [119]. Note that figures 10 and 12 indicate a greater exchange enhancement in Pd (5 to 6) than in Pt ($\sim$ 2). The enhancement in Pt is as expected, whereas the factor of 5 to 6 for Pd is somewhat smaller than is currently fashionable to believe. The orbital term dominates in V [19,20,22], Cr-rich Cr-V alloys [24], W [21] and Nb [22]. This is not surprising since these metals have roughly half-filled d-bands, encouraging orbital effects, whereas Pt, Pd, and Rh have almost filled d-bands. Equation (16) predicts the difference in magnitude of ortibal effects for these two groups of metals to within the uncertainty in the appropriate band occupation (n) factors appearing in that equation.

The slopes of the $\mathcal{K}$ versus χ plots for Pd, Rh and Pt yield a_d values of -345, -162 and -1180 kOe/μ_B respectively. The Pd result is in good agreement with the 4d-core polarization value quoted in table 3 while that for Rh is half that value. It is believed [10] that core polarization is almost constant across the 4d-row, implying that the variation in a_d arises from other sources. Two suggest themselves. First, different amounts of s character may be hybridized into the d bands at the Fermi surface: increased s-d hybridization in Rh would produce a less negative a_d. Figure 11 suggests that there is a distinct probability that this occurs. Secondly, there may be different *intersite* contributions to a_d. The Pauli term spin density induced on neighboring sites will, after all, make some contribution to the hyperfine coupling constants. These two contributions are expected to be present in Pt as well, and may contribute to the fact that the experimental a_d is not in numerical agreement with table 3. (Some uncertainty must be attached to the theoretical estimate quoted there.)

Intersite effects, s-hybridization and d-core polarization cannot be separated by inspection of a_d for a pure metal alone, but some insight can be gained by studying alloys. NMR results have been obtained for Cu in the Cu-Pd system [120] and Ag in AgPd [121]. The data for dilute Cu or Ag in Pd suggest that these atoms go in the lattice with filled d shells and with relatively little perturbation on the surrounding Pd matrix. Negative solute Knight shifts are obtained, in contrast with the positive ones appropriate to pure Cu and Ag. Using Ag

site T_1 data to estimate an $a_s\chi_p^s$ term, Narath obtained [121] an intersite hyperfine field of -140 kOe/μ_B for dilute Ag in Pd. (The susceptibility is essentially that of the host, measured in μ_B units.) He noted that this term is approximately twice the value obtained for dilute Cu in Pd, *i.e.*, that

$$\mathcal{K}_{\text{intersite}}^{\text{solute}} \propto \chi_p^{\text{host}} a_{\text{solute}} \tag{26}$$

where a_{solute} is the atomic valence s-electron hyperfine coupling constant appropriate to the solute (see table 4). Now the intersite term sampled by Pd in Pd can be quite different from that sampled by either Ag or Cu which are charge impurities but the above results suggest that approximately one third of the a_d value in Pd arises from intersite effects and that the numerical agreement with the 4*d* core polarization value was fortuitous. The presence of an intersite contribution of between -100 and -150 kOe/μ_B then implies an equal but positive contribution from *s* hybridization, or from polarization of the paired *s* character in the occupied conduction bands (*e.g.*, see sec. 2). A two or three percent admixture of *s* character in the *d* bands at E_F would produce such an effect (see table 4). The variation in a_d between Pd and Rh is within the realm of reasonable change in hybridization, though intersite effects can be expected to vary.

Negative shifts of the Cu resonance are also observed [122] for dilute Cu in Pt. Inspection of the results is again troubled by the question of perturbations on the host lattice (which are thought to be slight) and second order quadrupole shifts (which are estimated). The result is [122] an intersite term of somewhat less than -100 kOe/μ_B in agreement with Cu-Pd. There also exist results for the Pt Knight shift in Cu-Pt[122] and Au-Pt[123] alloys. A similar tendency, of negative shifts in pure Pt and positive shifts in the noble metal-rich alloys, arises. This is in qualitative agreement with the above observations concerning a negative intersite term in Pt. Questions concerning the perturbation on the solvent's local susceptibility, due to the presence of an atom such as Pt (or Pd) in a noble metal, makes quantitative estimates of an intersite hyperfine constant from the dilute Pt data less plausible.

Experience with solute hyperfine fields [124,125] for impurities in Fe, Co and Ni, and the above observations for noble metal alloys, suggest that substantial intersite effects arise in the heavy 3*d*, 4*d* and 5*d* metals. These are expected to be of the order of -100 kOe/μ_B (the moment being that characteristic of the solvent susceptibility). There is some suggestion of weaker intersite effects in the lighter elements of the various transition metal rows. The changes in crystal structure from fcc to bcc, and the associated decrease in the number of nearest neighbors to any one site may be a factor contributing to this.

8. Alloys and Local Effects

The introduction of a foreign atom in a pure metal has several effects. First, if the atom has a different number of valence electrons than the host, its insertion will change the number of conduction electrons per atom (the e/a ratio) in the metal. Neglecting other effects of the insertion, this acts to shift the Fermi level in the bands. The bands will, of course, be perturbed by the addition of impurities. If the perturbation is gradual, and relatively weak, it is often useful to scan alloy data as if the Fermi level shifts (as a function of e/a) over a set of "rigid" bands. This is a rigid band picture which may (or may not) bear some resemblance to the host metal conduction bands off their Fermi energy [126], but this picture properly describes the alloy system at E_F. Such a rigid band scheme has little or no relevance to some alloy systems (*e.g.*, Cu-Pd) while displaying striking trends between alloys of common e/a (*e.g.*, $Cr_{1-x}V_x$ versus $TiFe_yCo_{1-y}$) elsewhere. Some examples will be considered in the next section.

Any impurity in a metal will produce a charge disturbance. Atomic size and electronegativity effects cause this to be true, to a limited extent, even in the case when the valence of the host and that of the impurity is identical. The conduction electrons act to screen the charge difference associated with the impurity as is indicated schematically in figure 13. There will be a build up (as in fig. 13) or dilation in the total conduction electron charge in the vicinity of the impurity, depending on the sign of the difference[9]. There is a highly local "main peak" with the familiar Friedel oscillations to the outside. These arise from the presence of a conduction electron Fermi surface and have a period which is inversely proportional to $2k_F$, *i.e.*, the extremal caliper of the Fermi surface in the direction in question [127].

[9] The conduction electron distribution is distorted by the Coulomb perturbation in a very similar manner to the core polarization effects discussed earlier, the latter case being an exchange polarization and the spin difference resulting from it, the present case involving the sum of charge terms. Both may be viewed as involving the admixture of excited orbital character into the originally unperturbed occupied one-electron states.

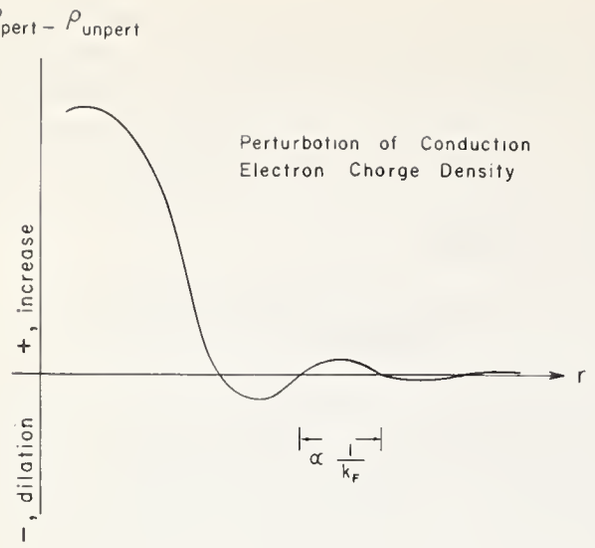

FIGURE 13. *Schematic illustration of conduction electron charge screening induced in a metal host by a single impurity at* R=0. *The half-period of the Friedel oscillations, which is proportional to* $1/k_F$, *is indicated.*

Solvent atoms can make various differently weighted samplings of this charge distribution, for example, by quadrupole interactions [128-133] and by isomer shifts.

The presence of an impurity also affects the solvent Knight shift. Only the perturbation of the Fermi surface electrons is important here, as it is these electrons which are involved in the Pauli term. The Fermi surface electrons undergo a redistribution [127,134] which is similar to the total charge screening in character and which can be sampled as a distribution through their $\langle a \rangle$ values appropriate to the different solvent sites in the lattice. This, and the bulk charge disturbance, are usually described in terms of free electron or simple OPW bands employing pseudopotential or phase shift scattering analyses of the perturbation. Due to the complex nature of the problem, neither scheme usually supplied quantitatively satisfying *a priori* predictions of experiment and, in the few cases where they have, there arise questions of the uniqueness of the result. In terms of the phase shift analysis, the change in Knight shift at a nucleus some distance R from the impurity is given [134] by

$$\frac{1}{\mathcal{K}}\frac{\Delta\mathcal{K}(R)}{\Delta c} = \sum_{\ell} \{\alpha_{\ell}(R) \sin^2 \eta_{\ell} + \beta_{\ell}(R) \sin 2\eta_{\ell}\}, \quad (27)$$

where

$$\alpha_{\ell}(R) \equiv (2\ell+1) \sum_{R} \{n_{\ell}^2(k_F R) - j_{\ell}^2(k_F R)\}, \quad (28)$$

and

$$\beta_{\ell}(R) \equiv -(2\ell+1) \sum_{R} j_{\ell}(k_F R) n_{\ell}(k_F R). \quad (29)$$

The ℓ^{th} term in the sum is associated with the ℓ^{th} partial wave, η_{ℓ} is the phase shift of the ℓ^{th} component, and j_{ℓ} and n_{ℓ} are spherical Bessel and Neumann functions respectively. To obtain the effect on a solvent metal Knight shift, the α_{ℓ} and β_{ℓ} must be suitably averaged over R. For "simple" solvent metals and "simple" solutes the effect is presumed to be dominated by s- and p-wave scattering. Changes in the relative roles of s- and p-wave scattering are important in rationalizing the variation in $\Delta\mathcal{K}/\mathcal{K}$ with varying valence of the solvent, or varying valence of a solute, relative to the solvent.

There is traditionally some question of how large an effect can be associated with pure s-screening. From a strictly atomic viewpoint, one might expect it to be limited to two electrons worth of charge. The recent investigations of Slichter *et al.* [135,136] conclude that higher ℓ scattering is very important to the screening when solute-solvent valence differences exceed two.

A local spin moment will produce a spin disturbance similar to that seen in figure 13. Such a spin disturbance is obviously important to magnetically ordered metals[10] but it also produces the dominant Knight shift term at some sites in certain paramagnetic alloys (see sec. 12). Consider the Knight shift of a nonmagnetic site in a paramagnetic rare-earth alloy. The principal term in the Pauli susceptibility, *i.e.*, in the spin induced by the magnetic field, is that of the open $4f$-shells, and this spin will contribute to the nonmagnetic site $\langle a \rangle$ behavior via conduction electron polarization. The susceptibility associated with the moment would obey a Curie-Weiss law. Examples of this are the above mentioned rare earths with their open $4f$-shells, and $3d$ alloys, such as Fe in Cu. Sometimes the moment may arise from band-paramagnetism involving localized d levels which are too weakly coupled by *intra-atomic* exchange to produce a true local paramagnetic moment. Curie-Weiss behavior is then not followed. The $3d$ elements as impurities in Ag, or dilute Ni in Cu are examples of such band paramagnetism.

Given an induced local spin monent of either of the above types, there will inevitably be a spin disturbance in the solvent conduction bands producing, in turn, a Knight shift term. There will be a variety of contributions to this. First, and most obviously, the exchange field due to the local moment will produce a spin dependent scattering of conduction electrons. As described

[10] We should note that in a magnetically aligned metal, cross terms will cause a magnetic imputiry to contrihute a charge disturbance, and a charge impurity to contribute a magnetic disturbance (the charge impurity Knight shift contribution can be considered a special example of this).

by Ruderman, Kittel, Kasuya and Yosida (RKKY) [137-141], the Pauli response of the conduction electrons to the diagonal exchange term, $\mathcal{J}(k_F,k_F)$, contributes a net spin density which is then piled up in a screening distribution of the sort plotted in figure 13. Formally the theory is almost identical to the charge screening case. Exchange, rather than electrostatic Coulomb, terms are responsible for the disturbance, and details of the shape of the main peak and of the behavior of the phase and amplitude (relative to the main peak) of the Friedel oscillations should differ from the charge scattering distribution. The $\ell = 0$ and 1 partial waves will again tend to predominate. Details [141] of the intra-atomic term in the electrostatic exchange, $\mathcal{J}_{el}$, are such that if the local moment is of odd (or even) ℓ character, partial wave scattering of odd (or even) ℓ' is enhanced (*i.e.*, *s*-wave scattering is of increased importance with *d*-moments present while *p*-wave effects are amplified in 4*f*-moment scattering). Only *s*-wave spin density is nonzero at the solute's nucleus. In the scattering picture, it describes the intra-atomic conduction electron exchange polarization term discussed in section 2.

If the value of electrostatic exchange were somehow zero, the presence of a local spin moment would still cause a spin disturbance in the conduction bands [142-144]. Resonant scattering of spin-up and spin-down conduction electrons will occur at different energies as the result of the splitting of the local virtual (or real) bound state to form the local magnetic moment. One reason the scattering differs is the different occupation of spin up and spin down orbitals on the local moment site. Consider some partial wave component, with quantum members ℓ and m_ℓ of a scattered conduction electron at the local moment site. If the local moment had an occupied component of the same ℓ, m_ℓ and spin, the conduction electron component would be unaffected (except for any nonorthogonality effects which might arise); if there were a hole in that local moment orbital component, the orbital could be admixed into the conduction electron function to the extent it is energetically favorable. The existence of a net spin residing in the local moment implies a difference in hybridization (and orthogonalization) effects in conduction electron states of the same **k** and differing spin. This results in a spin density distribution similar to the core polarization effects discussed earlier. There is no net spin in the disturbance; instead there are regions of spin parallel and antiparallel to the local moment. In their original inspection of such hybridization effects, Anderson and Clogston concluded [142] that this disturbance would fall off as $1/r^4$; subsequent numerical estimates of their model [145] are consistent with this observation. It would seem that the effect is largely concentrated at the local moment site. An *effective* exchange interaction arises when the next order in hybridization effects is taken [142,143]. Consider the energy shift of a Fermi surface electron. The mixing of local moment *hole* components into the wave function will lower the state's energy whereas orthogonality with occupied components can only raise its energy. Hybridization thus stabilizes the energy of Bloch states with spin moment antiparallel to the local moment whereas those with spin moment parallel are less favored since they undergo orthogonalization and *decreased* hybridization. This produces [142-144] a *negative* interband exchange constant $\mathcal{J}_{ib}(k_F,k_F)$ in contrast with $\mathcal{J}_{el}(k_F,k_F)$ which is always positive.[11] A negative value implies a conduction electron Pauli spin density term of spin moment antiparallel to the local moment. Such situations occur experimentally, implying that "interband" hybridization (and higher order effects) do, on occasion, predominate over electrostatic exchange, which can only produce a net spin moment parallel to the local moments. (These effects are obviously intimately related to the Kondo effect.) The earliest evidence for negative exchange constants was obtained by nuclear magnetic resonance and electron paramagnetic resonance measurements for rare earths in several host metals [146-149] such as Pd. This has subsequently been borne out by magnetization and neutron diffraction studies.

Interband hybridization exchange also differs from electrostatic exchange in that hybridization will only be strong between band and local moment components of common ℓ. The summing over individual Bloch state contributions to the spin disturbance yields partial wave scattering only from those same ℓ components directly involved in the mixing. Thus, unlike electrostatic exchange, hybridization effects with their predominant *d*- or *f*-scattering, will not contribute an $\ell = 0$ contact spin density term to the hyperfine field at the scattering site, unless higher order (*i.e.*, double, triple, *etc.*) scattering processes are significant.

A disturbance of the type plotted in figure 13 produces a distribution in solvent site $\langle a \rangle$'s causing a broadening of the solvent Knight shift line. The distribution in $\langle a \rangle$ will not necessarily provide a detailed, accurate mapping of the bulk conduction electron disturbance. This is due to interference effects arising from orthogonalization of the conduction electron wave functions with the solvent site ion cores which are

[11] Schrieffer and Wolff [143] have explored the circumstances for which $\mathcal{J}_{ib}$ can be properly defined.

penetrated. This interference is important in that it affects the apparent shape of the disturbance at sites near the impurity, while providing little more than scaling to the result for sites at asymptotically large R.

The sampling of the disturbance will inevitably cause the average solvent site $\langle a \rangle$ to increase or decrease with respect to the pure solvent value, thus causing a shift $\delta\mathcal{K}$, of the resonance line. Some sites will have values of $\langle a \rangle$ so different from the average that they will not contribute to the main resonance line, but satellites outside instead. This will cause a decrease in line intensity, *i.e.*, wipe-out, upon alloying. Blandin and Daniel's estimate [134] of one such distribution in $\langle a \rangle$ is seen in figure 14. The theoretical estimate is drawn to the same scale as an experimental [150] NMR derivative in Ag containing a small quantity of Sn. The

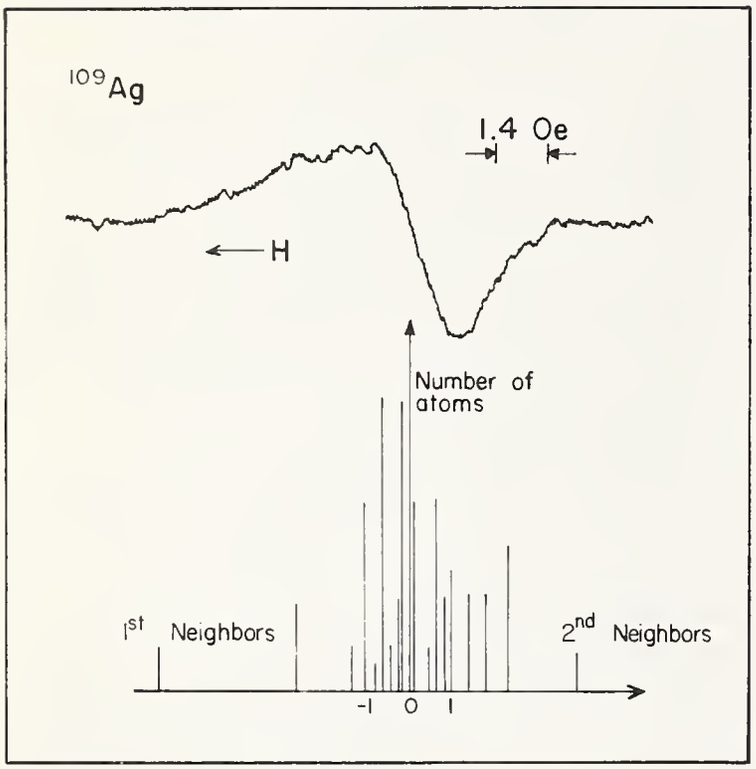

FIGURE 14. *(Above). Rowlond's experimentol [150] NMR absorption derivative curve in an alloy with 1 percent Sn in Ag. (Below). Blandin ond Doniel's calculated [134] positions and relative contributions to silver Knight shifts ot silver sites in near neighbor, next neor neighbor, etc. . . positions with repsect to on Sn impurity in Ag. This is plotted on the same horizontol scole as the experimentol curve.*

near and next near neighbor $\langle a \rangle$'s in Ag(Sn) may well be responsible for the partially resolved satellites. Another experimental example [151] of satellite structure is shown in figure 15 for Pt containing small quantities of Mo. Here three satellites are clearly resolved.

Details of the effect of alloying will depend on such

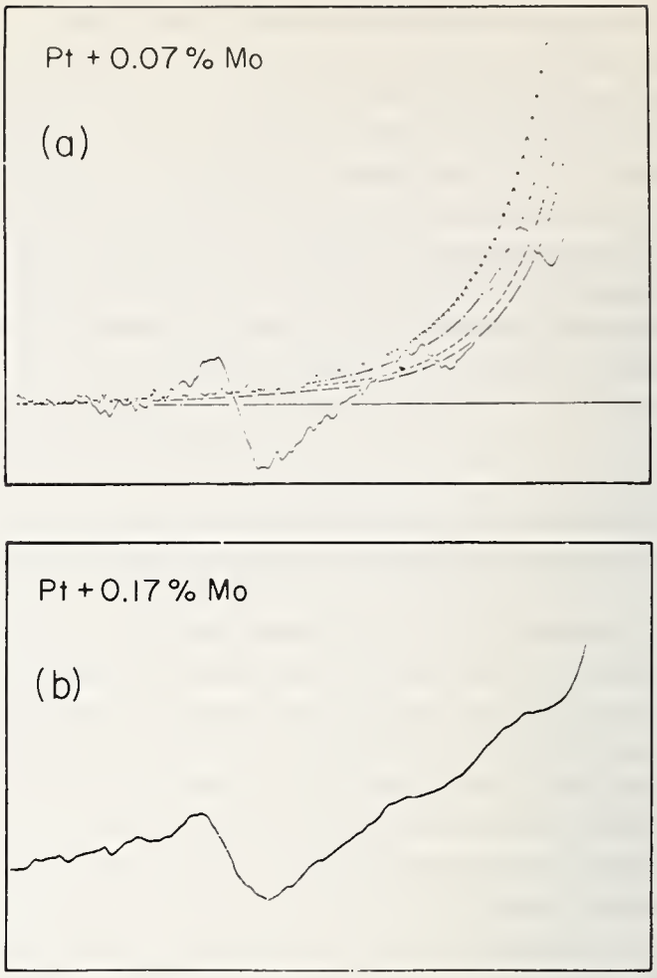

FIGURE 15. *Experimental NMR absorption derivotive curve in Pt-Mo alloys as taken from Weisman and Knight [151]. The resonance in (a) shows several distinct satellites ond thot in (b) shows satellites in the same positions but those near the central resonance begin to merge with the centrol line, thus cousing resononce broodening for increosed alloy concentrations.*

factors as whether or not the main peak of the disturbance extends out and encompasses any neighboring nuclear sites. Little is known experimentally, and less from accurate calculation, concerning main peak behavior. (Most theoretical work makes the doubtful, but computationally necessary, use of asymptotic estimates for the entire disturbance.) It is generally thought that the main peak of the Coulomb screening is largely localized at the impurity site while the spin density peak is of longer range. For Fe in Pd the latter is known to cover many lattice sites. This is due to a large $1/2k_F$ value (which affects the main peak as well as the Friedel oscillations) and to the substantial conduction-electron conduction-electron enhancement of χ_p [152-154].

It has been seen that solvent data are largely limited to shifts of the main resonance line and this does not provide a unique test for any given detailed model of

alloy effects. Although such experiments are difficult, further observations of solvent satellite resonances in very dilute alloys would be invaluable for this purpose. Satellite lines would arise from near neighbor region $\langle a \rangle$'s and, providing they can be disentangled, would provide a severe test for any theory.

The interpretation of the alloy Knight shift data depends somewhat on the nature of the material in question. The change of $\mathcal{K}$, $\Delta\mathcal{K}$, upon introducing a second component into a metal, will cause a change in $\langle a \rangle \chi_p$. Whether one interprets $\Delta\mathcal{K}$ as a change in χ_p or in $\langle a \rangle$ [recall the latter is an average involving the product of a's and χ's, over all points of the Fermi surface; see eq (17)] depends upon one's preference for the particular case at hand.

In a simple form one may write, in analogy with eq (1),

$$\mathcal{K}_{\text{alloy}} = \langle a \rangle_{\text{alloy}} \chi_p^{\text{alloy}}. \tag{30}$$

Permitting both $\langle a \rangle$ and χ_p to vary, as in eq (30), is not as practical a viewpoint for scanning alloy data, as is holding one of the two quantities constant and attributing the trend in $\Delta\mathcal{K}$ to a variation in the other. For instance, in the case of the transition metal alloys such as the Ti-V-Cr series, the vanadium Knight shift change may be most conveniently discussed in terms of a change in density of states (*i.e.*, χ_p). We will discuss this case in more detail later and see that for this case such a description is a useful one. On the other hand, in dilute alloys, where the Friedel oscillation description may be used, the change in $\mathcal{K}$ is better described by considering the different $\langle a \rangle$ values as appropriate to the different environmental conditions of the host atoms, keeping χ_p constant.

A general version of eq (30), sampling the Knight shift behavior of the two types of atoms *(A,B)* in a binary alloy is

$$\chi_p = (1-c)\frac{\langle a\chi \rangle^A_{\text{alloy}}}{\langle a \rangle_{A \text{ in alloy}}} + \frac{c\langle a\chi \rangle^B_{\text{alloy}}}{\langle a \rangle_{B \text{ in alloy}}} \tag{31}$$

$$= (1-c)\frac{\mathcal{K}^A_{\text{alloy}}}{\langle a \rangle_{A \text{ in alloy}}} + \frac{c\mathcal{K}^B_{\text{alloy}}}{\langle a \rangle_{B \text{ in alloy}}}, \tag{32}$$

where $\mathcal{K}^A$ and $\langle a \rangle_A$, are the shift and averaged hyperfine constant of atom A in the alloy. χ_p is defined as the susceptibility per atom and c the concentration of B type atoms. Making the nontrivial assumptions that $\langle a \rangle_{\text{alloy}}$ is equal to its value in the pure metal *(A* or *B)*, and that there is no significant exchange enhancement of χ, this equation may be rewritten (using eq 17) in the form given by Drain [74],

$$N(E_F)_{\text{alloy}} = (1-c)N_A(E_F)\frac{\mathcal{K}^A_{\text{alloy}}}{\mathcal{K}^A_{\text{metal}}} + cN_B(E_F)\frac{\mathcal{K}^B_{\text{alloy}}}{\mathcal{K}^B_{\text{metal}}}. \tag{33}$$

Thus

$$N(E_F)_{\text{alloy}} \equiv (1-c)N_A(E_F)^{\text{alloy}} + cN_B(E_F)^{\text{alloy}}, \tag{34}$$

which defines *local* densities of states $N_A(E_F)^{\text{alloy}}$ and $N_B(E_F)^{\text{alloy}}$. The assumption of setting $\langle a \rangle$ in the alloy equal to $\langle a \rangle$ in the metal forces the whole effect of alloying to be described in terms of these local densities of states. At times this proves useful. Drain [74] has used eq (33) and the data of figure 8 to scan the AgCd alloy system. The results are in agreement with general trends seen within and between phases obtained in a "rigid band" scan of electronic specific heat data. However, using eq (33), such a scan should not *rigorously* reflect the variation in the density of states of Ag at and above E_F for a number of reasons. These include charge screening (for discussion see ref. 8) and the fact that the hyperfine constants are held fixed.

Local effects in covalent compounds, such as chalcogenides and SiC can also be examined using eq (31). Consideration of these materials is aided by the fact that the energy bands are often more well-known in these than in intermetallic compounds. An example is n-doped silicon carbide [78,155]. The ^{29}Si Knight shift is near zero whereas a substantial Knight shift is measured for ^{13}C. This information, together with T_1 data for both sites, permitted Alexander and Holcomb [78,155] to infer important wave function symmetries. It was concluded that a zero Knight shift implied a zero wave function density at Si but that symmetry allowed a substantial shift at the carbon site.

Lead telluride is another case where local effects are important and where a significant amount of experimental and theoretical information is available on the energy band structure. Although the results are affected by sample preparation, for the better samples the ^{207}Pb Knight shift in n-type PbTe was found [156] to be temperature independent, and relatively small and positive with respect to undoped PbTe. On the other hand in p-type, PbTe $\mathcal{K}$(Pb) was found to be large, negative and temperature dependent. This was interpreted [156] in terms of a band structure model in which the valence band possesses substantial *s*-

character with respect to the Pb atoms, whereas the conduction band lacks *s*-character at Pb. The small positive shifts in *n*-type material were assumed to be of orbital origin. The negative contact interaction is ascribed to a negative *g*-value for the *L*-point valence band states. The same band model was used to explain the ^{125}Te Knight shift results in these materials.

9. Correlations of $\mathcal{K}$, χ and γ with Electron Concentration in Transition Metal Alloys

There are many cases in the literature where the Knight shift has been observed to vary smoothly with composition in alloy systems. Where γ values are available from specific heat data, or other $N(E_F)$ information is known, a direct correlation between these quantities and $\mathcal{K}$ can sometimes be found. Usually the complex nature of $\mathcal{K}$ (eq 19) causes the correlation to be somewhat obscured, and the fact that $\mathcal{K}$ does not follow the $N(E_F)$ curve is not necessarily an indication of nonrigid band behavior. Examples are shown in figure 16a. Looking first at the 3*d*-alloys, there is a gradual increase in $\mathcal{K}$ with *e*/*a*, with a peak at about 5.6 electrons per atom. Between $e/a = 5.6$ to 6, there is a gradual decrease in $\mathcal{K}$. This decrease is steepest for V-Fe alloys. The vanadium hydride results follow those of V-Cr extremely closely, as if the electron of the hydrogen is absorbed in the common conduction band, filling the band in the same manner that Cr does. Recent data by Rohy and Cotts [169,170] on V-Cr hydrides (not shown) fall on the same line. The other data, including those for the 4*d* alloys, all are similar to the V-Cr curve in that they show a peak in $\mathcal{K}$ at about $e/a = 5.6$. The Nb-Tc alloy data shown in figure 16a deviate from the general trend. The reason for discrepancy in the case of $\mathcal{K}$ measurements may be a result of a difference in $N(E_F)$, but again may be due to local effects so that no direct conclusion can be drawn from the $\mathcal{K}$ versus *e*/*a* results alone.

To give a further picture of the shape of the density of states curves for these alloys we show the total susceptibility data in figure 16b. Both for the 3*d* and 4*d* series, there is a possible cusp at $e/a = 5$. Both χ curves have quite similar behavior. The V-Tc(3*d*-4*d*) alloy system also follows this trend. From this picture we get a different impression of the density of states curve than from the curves obtained from γ data as shown in figure 16c. Here there is no cusp at $e/a = 5$ and a major peak occurs between $e/a = 4$ and 5. Thus there is a discrepancy between the γ curves on one hand, and the χ curves on the other. Depending on which curves are used, the Knight shift data may be interpreted in a

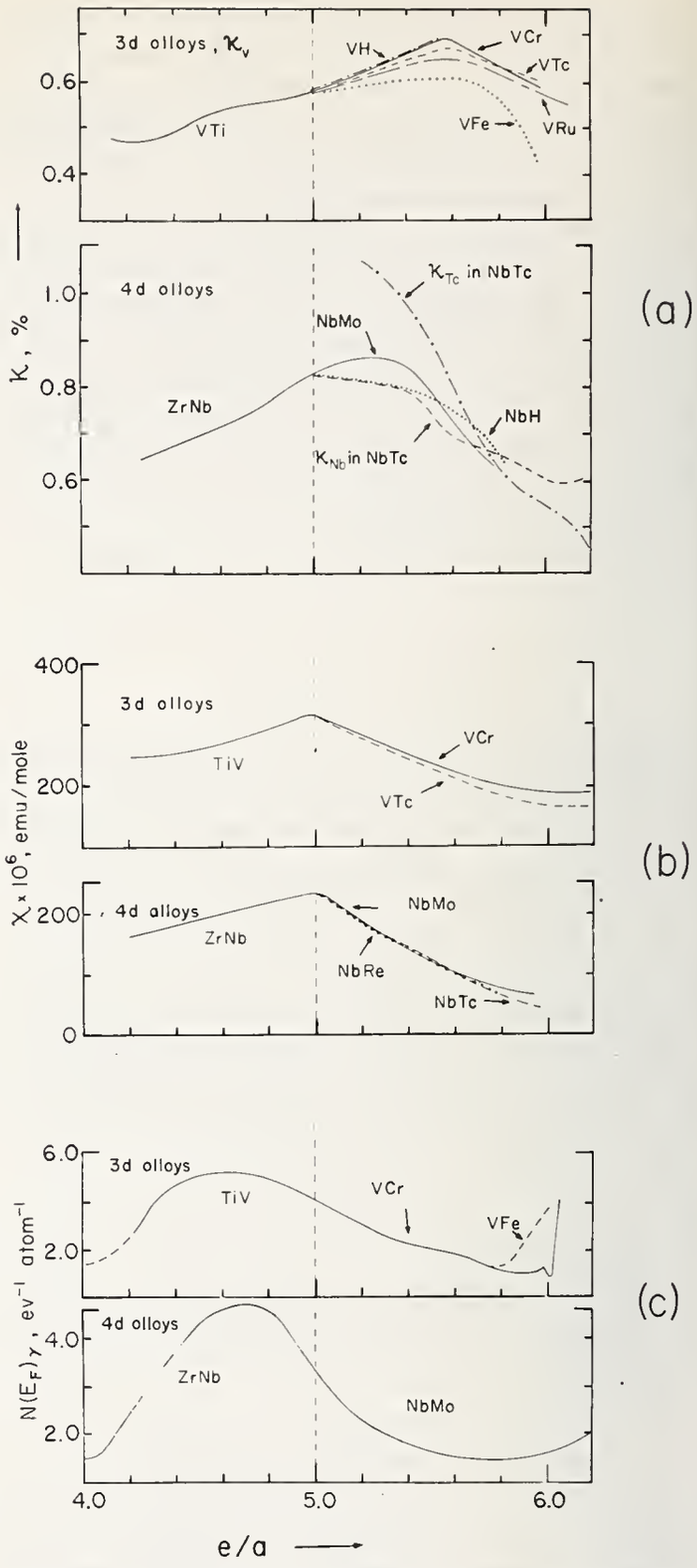

FIGURE 16. *Variation of (a) Knight shift, (b) susceptibility and (c) density of states as measured by electronic specific heat, with e/a ratio for the b.c.c. transition metals of the 3d and 4d rows. While for $\mathcal{K}$ and χ there are substantial ranges where χ and $\mathcal{K}$ track one another, the $N(E_F)_\gamma$ curves show less similarity. The data were taken from the following sources: (a) Ti-V [157], V-Cr [157,158], V-Tc [157], V-Fe [159], V-Ru [160], V-H [161], Nb-H [162], Nb-Tc [163], Zr-Nb and Nb-Mo [164]. (b) Ti-V [165], V-Cr [157,165], V-Tc [157], Zr-Nb [164], Nb-Mo [163,164], Nb-Re and Nb-Tc [163]. (c) Ti-V and V-Cr [164,166,167], V-Fe [164], Zr-Nb and Nb-Mo [168].*

quite different manner. In either case there is no direct correlation between $\mathscr{K}$ and the other data, and there must be an interplay of several terms as a function of e/a. A number of attempts have been made using γ, χ, $\mathscr{K}$, as well as T_1 data and the Korringa relation [27], to derive the various contributions to $\mathscr{K}$. For example, the results of figure 16 have been rationalized [24,163,164] by using a two-band model for the Pauli term, as in eq (23), and estimates of the Van Vleck orbital effects. Although these do explain the results, the description is not unique. An alternative explanation in terms of varying *s-d* admixture in a single band has been offered [171, 172] to explain the maximum in $\mathscr{K}$ at $e/a \approx 5.6$. In the region above 5.6 both γ and χ are decreasing. Within this model, the decrease in $\mathscr{K}$ arises from a Pauli contribution which becomes less negative, and, in fact, positive with increasing e/a. Only 10 to 15 percent *s*-character in the *d*-band is required to balance or overtake the negative *d*-core polarization term. Changes in *s*-character of only a few percent can produce the observed variations in $\mathscr{K}$. As noted earlier for Cu (see fig. 10), admixture and variations of admixture of this magnitude are not unreasonable. This model is more obviously appropriate to the $TiFe_{1-x}Co_x$ alloys, with e/a from 6 to 6.5 [172], where the slope of the $\mathscr{K}(^{59}Co)$ versus χ plot reverses sign across the alloy sequence. If the hybridization model is proven valid, the Knight shift can provide a useful probe of the variation of the density of *s*-states in "*d*"-bands.

An example of a different type of application of a rigid band model is the proposed band structure in the lanthanum-hydrogen system by Bos and Gutowsky [173]. Lanthanum is a metal and upon adding hydrogen up to 67 percent (LaH_2) the material remains metallic. At LaH_3, however, the material becomes an insulator. This, together with $\mathscr{K}$ and χ information, was then used [173] to propose the density of states shown in figure 17. These measurements lead to the conclusion that adding hydrogen means *lowering* the e/a ratio, which can be considered equivalent to the hydrogen absorbing an electron. This is in contrast to the other model in which hydrogen in the alloy gives up an electron to the conduction band and remains in the lattice as a proton. This latter model has been used, for example, to describe the V-H and Nb-H results shown in figure 16a, and for the compounds ScH_2 and YH_2 [174]. An interstitial proton is expected to be a larger perturbation in the La matrix and it may bind two 1*s* electron states to it (as in fig. 17) whereas such electrons might not be bound in the other systems where the perturbation is weaker. Such behavior can be anticipated from *s*-wave impurity scattering theory.

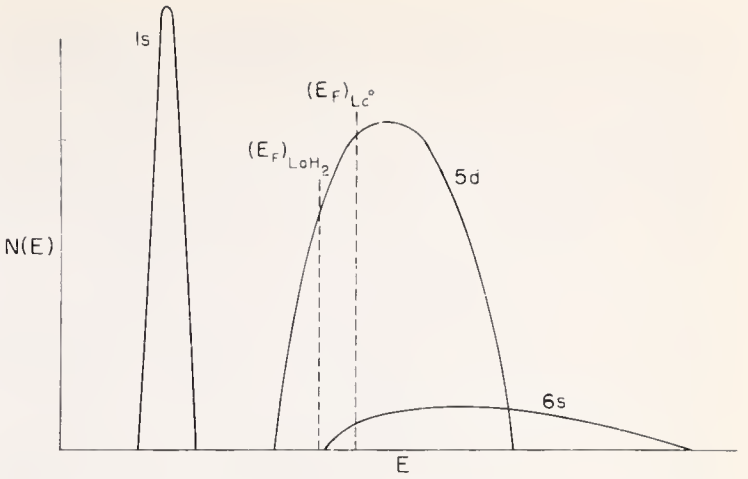

FIGURE 17. *Proposed band structure for lanthanum dihydride [173]. For each hydrogen atom entering the metallic lattice, two electrons are assumed to be transferred to localized hydrogen 1s orbitals. Formation of LaH_3 would correspond to complete emptying of the conduction band.*

10. Solvent Knight Shifts

Confidence that the Friedel oscillations (fig. 13) can be observed was given by Rowland's quadrupole wipeout data in Cu alloys [129], and reinforced by his solvent Knight shift results [150]. Rowland measured the change of the Knight shift upon alloying, $\Delta\mathscr{K}$, for a large number of *B*-subgroup solutes in Ag. From these, he obtained values for Γ ($\Gamma \equiv \mathscr{K}^{-1}\Delta\mathscr{K}/\Delta c$, where c is the fractional impurity concentration). These Γ data are plotted in figure 18. While there is a general tendency

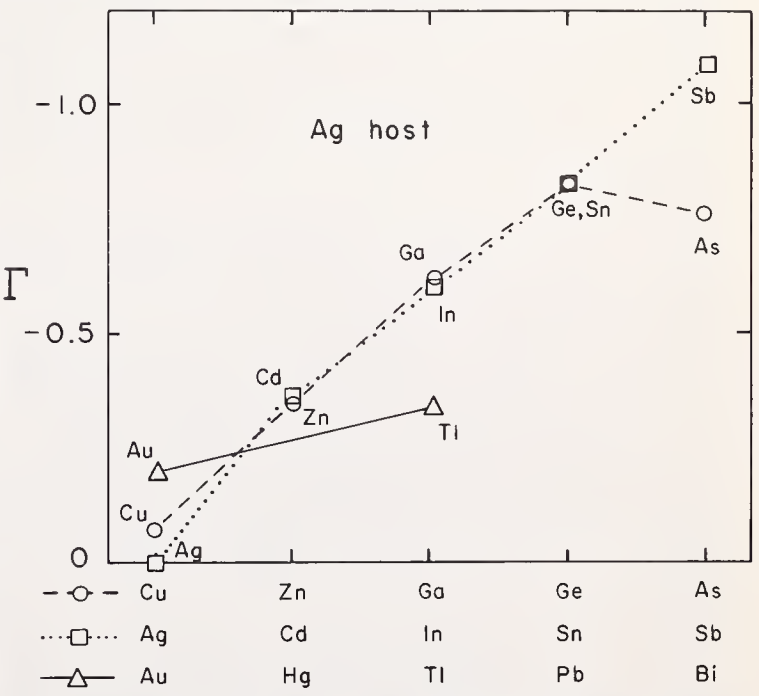

FIGURE 18. *$\Gamma = 1/\mathscr{K} \cdot \Delta\mathscr{K}/\Delta c$ values for impurities in a Ag host versus position of the impurity in the periodic table. The dashed, dotted and solid lines connect points for impurities occurring in the Cu, Ag and Au rows, respectively. These data are taken from Rowland [150], from his table 1. As pointed out by Rowland, the Γ values are dependent on the range of data employed.*

417-156 O - 71 - 41

for Γ to increase with solute valence, there is a slight turn back (*i.e.*, decrease in magnitude) of Γ from Ag-Ge to Ag-As. For the silver row (namely Cd, In, Sn, and Sb), there is no such turn back. In figure 19a we have chosen two sets of Rowland's $\Delta\mathscr{K}$ data, for pairs of impurities of common valence, which clearly display the valence effect seen in figure 18. Rowland [150] noted that curved lines could be drawn to fit the datum points, as we have done for some of the data in figure 19b. Rowland points out that due to lineshape effects (for example, see fig. 14), the uncertainty of the individual points is such that his representation by a straight line is all that is quantitatively reasonable. Granted this uncertainty, the possibility of nonlinearity in these plots of $\mathscr{K}$ versus c may be real, as was noted by Rowland. Using Rowland's raw data, a Γ defined for low concentrations is smaller than that defined by fitting out to larger concentrations. This fact was used by Alfred and Van Ostenburg [175] in *their* version of the Γ plot which differs from figure 18, for the Sb in Ag point. By using low concentration data, this Γ point was reduced from the value given by Rowland, bringing it into line with their [175] predicted turn back. If the same treatment over the same concentration range is used for *all* of Rowland's datum points, then all the Γ points in figure 18 will tend to be somewhat lower but the general picture will remain as shown in our figure 18. Alfred and Van Ostenburg neither used Rowland's choice for Γ, nor treated the data for all the alloys equivalently. If all of the Γ values are obtained consistently, their phase shift analysis yields neither better, nor worse, agreement with experiment than the earlier phase shift estimates of Kohn and Vosko [176], and of Blatt [177].

Similar valence effects have been seen for *B*-subgroup solutes in liquid copper alloys [178] and, as seen in figure 20a, in solid lead alloys [179]. The liquid copper results of Odle and Flynn [178] also display the high valence turn back. This result is more evident than in the solid Ag case, the $\mathscr{K}$ versus c plots being more linear and the turn back in Γ being larger, although errors for the points of most interest are somewhat large. Odle and Flynn [178], utilized the phase shifts of Blatt [176] and Kohn and Vosko [177] to discuss their results.

In the solid Pb case, the Γ values are largest for the smallest valence (Hg), but a reduced effect of valence difference (*i.e.*, the beginning of a turn back) is also evident. The raw data in figure 20a also reveal curvature in $\mathscr{K}$(Pb) versus concentration for solid PbTl [179], similar to the Ag data in figure 19b. This curvature is not evident for the other Pb alloys. In liquid lead alloys, as seen in figure 20b, taken from Heighway and

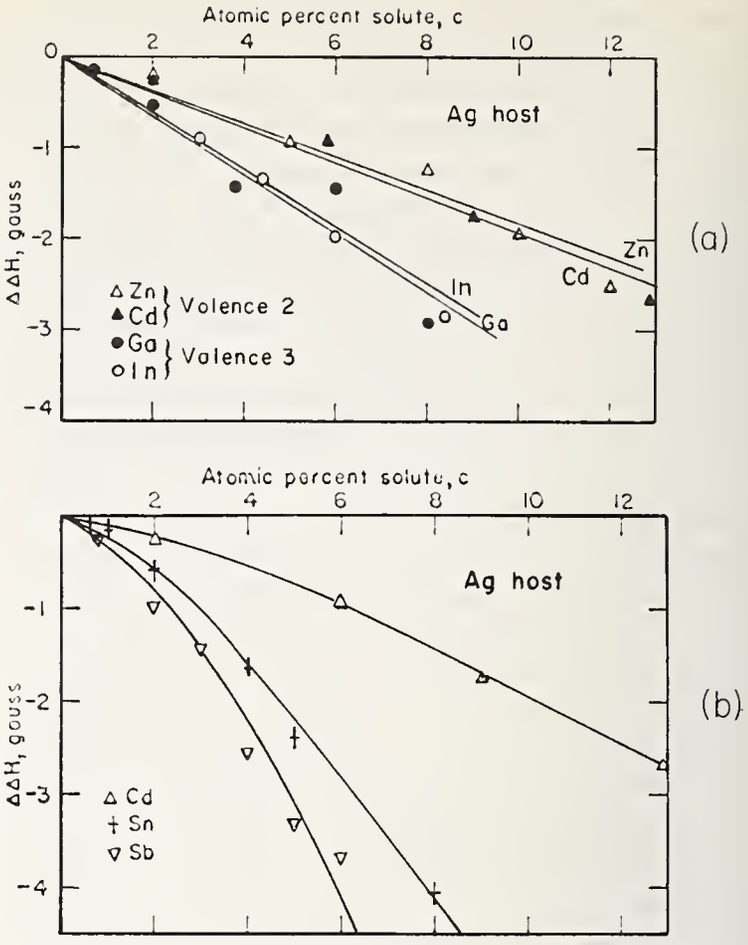

FIGURE 19. *(a) Silver solvent Knight shift datum points with straight lines, as chosen by Rowland [150]. (b) Silver solvent Knight shift datum points [150], indicating smooth curves through these points, without the assumption of linearity.*

Seymour [180], there are some cases of linearity and others of nonlinearity. A very interesting fact here is that, in the solid, Γ has the opposite sign to Γ in the liquid for many of these alloys. This result was verified [180] by following the resonance in Pb-Bi from the liquid to the solid state.

In figure 21a and *c*, $\mathscr{K}$ versus c plots for solid InPb and InSn alloys [123] are shown. These are examples where there is a tremendous dip in $\mathscr{K}$ versus c, before a more linear behavior is achieved. This dip falls within a 1% impurity concentration in one case, and 2% in the other. The magnitude of these dips is up to 10% of the total Knight shift. For comparison, data for these alloys in the liquid state [181] are shown in figure 21b and d on the same vertical scale as the solid data [182]. Dips may also exist in the liquid state, but, if so, were missed due to the coarse grain scans over the dilute range of alloying. On the other hand the dip may be peculiar to these alloys in the solid state only.

The linearity of $\mathscr{K}$, bearing in mind the coarse composition mesh studied, is striking for the liquid alloys displayed in figure 21 b and d. This linearity is characteristic of many, though by no means all alloy systems.

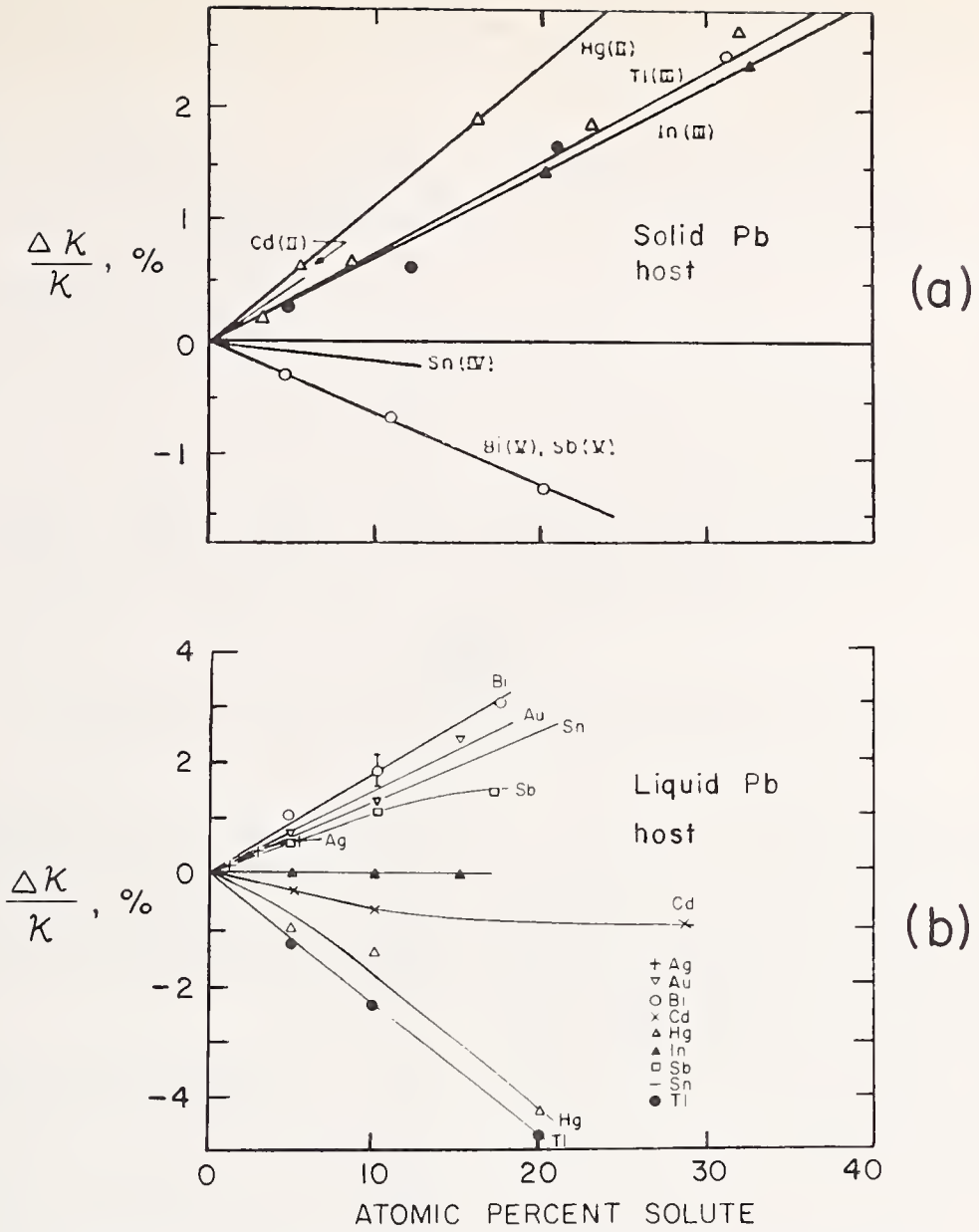

FIGURE 20. *(a) Pb solvent Knight shifts upon alloying in solid alloys, as taken from Snodgrass and Bennett [179]. (b) Pb solvent Knight shifts upon alloying in liquid alloys, as taken from Heighway and Seymour [180].*

Several other examples of linear behavior have been observed [183-188]. In these papers some cases of nonlinear behavior are also encountered. The linearity, even at higher concentrations, may be relevant to some suitable phase shift description. However, it should be recalled that in its formulation the traditional phase shift analysis was developed for infinite dilution only.

A dip in $\mathscr{K}$ versus c is also suggested by the solid Cd-In data [189] shown in figure 22. In this case we have drawn a straight line through the higher concentration data points merely to show a very general trend for the alloys. Although the scatter is large, it is again clear that the data are not best represented by a single straight line from the origin.

The complexity of the various terms contributing to $\mathscr{K}$, and the local nature of $\mathscr{K}$, is such that the observation of nonlinearities should not be surprising. These nonlinearities are not amenable to simple phase shift analyses, although the turn back in Γ is.

For the liquid alkali alloys a form of the single scattering model was employed by van Hemmen *et al.* [190]. Agreement with experiment was obtained by including volume renormalization, without considering the details of the charge oscillations. The phase shift description used by Odle and Flynn [178] for liquid Cu alloys, and similar attempts by Rigney and Flynn [191] using newly derived phase shifts, as well as pseudopotential methods as employed by Moulson and Seymour [192] have been partially successful in describing $\mathscr{K}$ versus c behavior in liquid alloys.

The observed behavior of $\mathscr{K}$ upon alloying should be described by a "nondilute" scattering model coupled

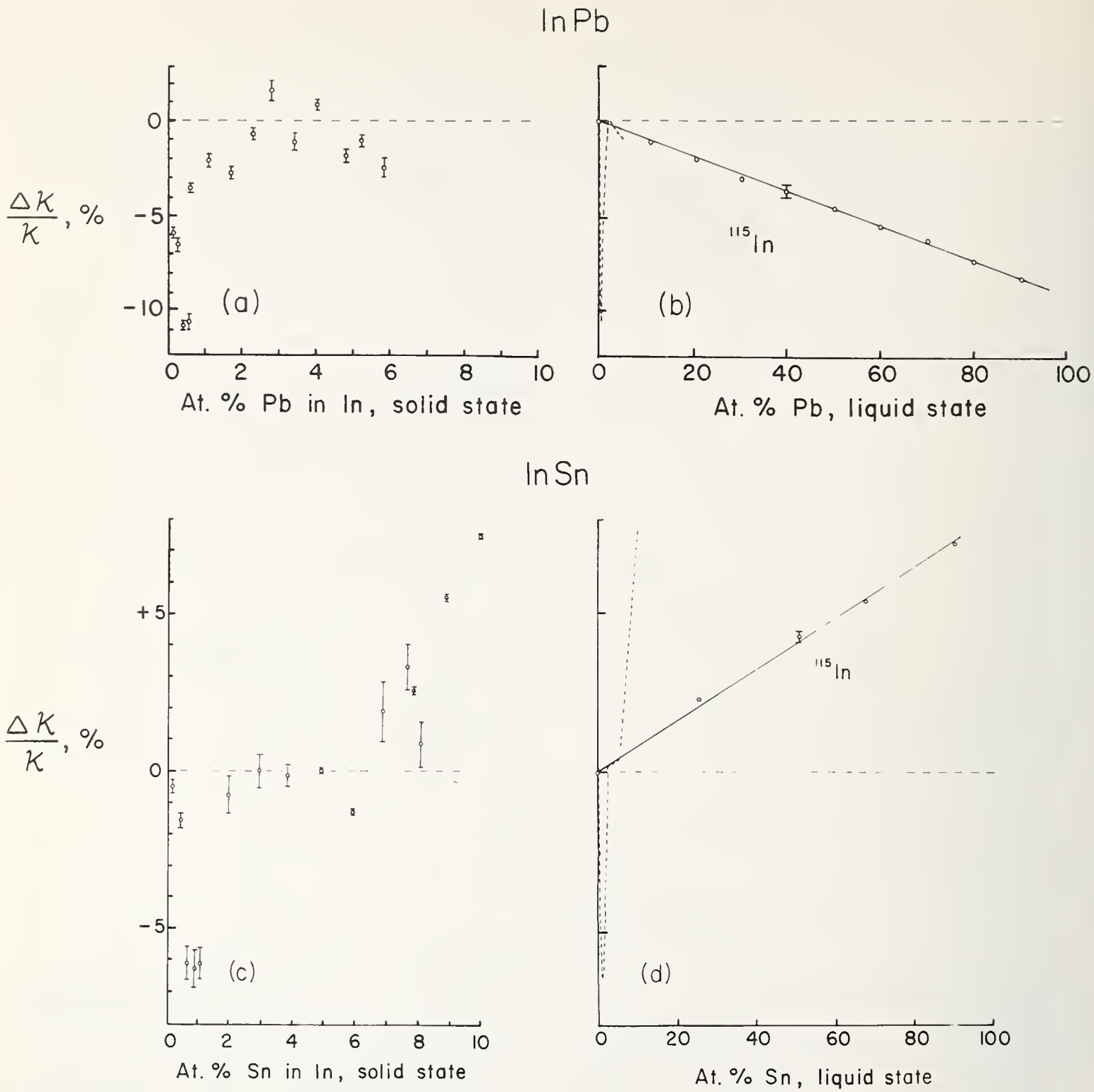

FIGURE 21. *Solvent Knight shifts for two alloy systems in the solid and the liquid state. The indium shift is shown for InPb alloys in (a) and (b), and for InSn alloys, in (c) and (d). In the left hand picture, (a) and (c), data are shown for solid alloys of up to ten percent impurity taken from Anderson, Thatcher and Hewitt [182]. On the right, (b) and (d), data for these same alloys in the liquid state by Seymour and Styles [181] are shown on the same vertical scale over the full range of alloy composition. All the reported alloy datum points are shown. (Note that there is no overlap of the data in the dilute region. We have merely transferred the solid data as dashed lines, onto the liquid curves for ease of comparison.) Lacking data there may or may not be strong structure in these liquid alloys in the dilute region.*

with some accounting of "rigid band" effects [8], in addition to other possible mechanics. Such a combined theory is not yet available.

{**Note added in proof:** An interesting proposal to explain the low composition dip was given by R. A. Craig. (We thank the author for sending us a preprint of his manuscript, to be published in the Journal of Physics and Chemistry of Solids.) Anisotropic many-body effects were found to give a contribution to $\mathcal{K}$ in a pure metal. According to Craig, the contribution

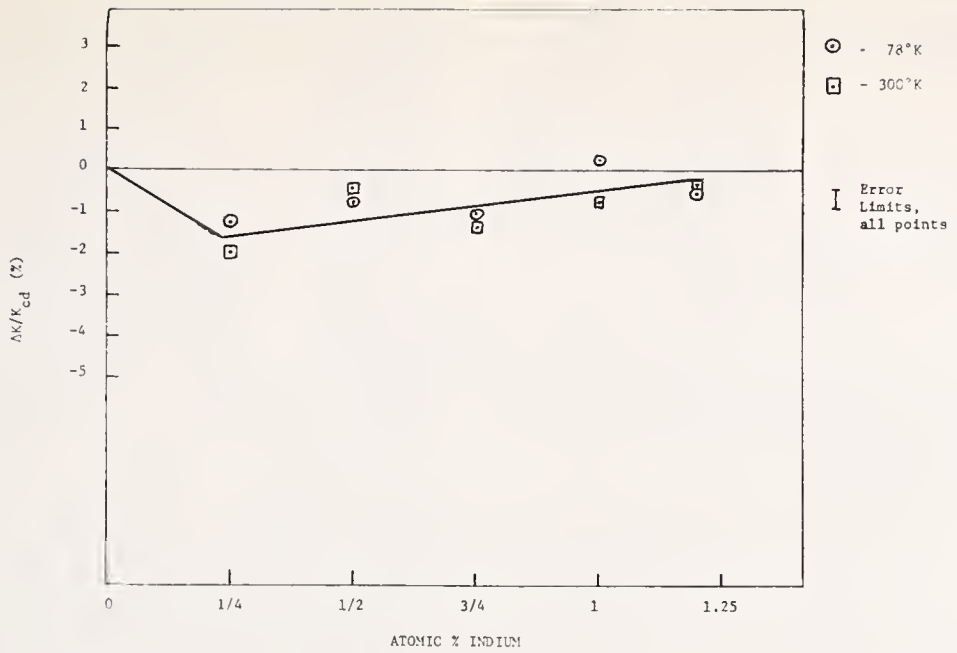

FIGURE 22. *Change of the cadmium Knight shift in CdIn alloys, as taken from Slocum [189]. The indicated straight line through these points has been drawn to demonstrate that these points are clearly nonlinear with respect to the origin.*

is expected to become unimportant upon introducing impurities and at high temperatures (e.g. absent in the liquid), because impurity scattering of the quasiparticles will cause a loss of memory of the angular correlations between the quasiparticle-quasiparticle collisions.}

11. Solute Knight Shifts

When a foreign atom is substituted in a lattice, it causes a certain amount of screening about it, and long range charge oscillations, as discussed in previous paragraphs. Let us now look at what this impurity atom sees as situated in a foreign host. The Knight shift will respond to such a situation in the same way noted above, namely by an $\langle a \rangle$ of the impurity (be it altered somewhat by its environment) and a χ_p of the host, which may also be changed by the introduced impurity. Again it is a matter of how Knight's ξ factor is used as to whether we use χ_p to mean the measured average derived from χ_{expt}, or whether to ascribe a local χ nature to the immediate environment as the impurity sees it. To make this situation more clear we rewrite eq (11) for the Knight shift of an impurity, B, in a given host, A, as

$$\mathcal{K}_{B \text{ in } A} = \frac{1}{\mu_B} \chi_p^A \xi H_{\text{eff}}^B. \tag{35}$$

This definition then uses ξ to absorb solute site changes in both $\langle a \rangle$ and χ_p from the free atom and pure solvent behavior, respectively.

It is useful to explore eq (35) for a sequence of alloys, varying either impurity or host. One might follow the quantity $\mathcal{K}_{B \text{ in } A}$, or $\mathcal{K}_{B \text{ in } A}/\chi_p{}^A$, for a specific impurity through a series of host metals. For example, we have done this for charge impurities in the sequence Cu, Ag, Au. A similar type of scan is often done for Mössbauer hyperfine data across rows in the periodic table.

Alternatively, one can dissolve a series of impurities in a particular host. The observed trends are less difficult to interpret as we have the advantage of remaining within one crystal structure. Such solute studies have been done for example for Cu and Ag [6], for lead [193], and for Au [7,194] based alloys. Taking these data, we have plotted the quantity $\mathcal{K}_{B \text{ in } A}/H_{\text{eff}}{}^B$ in figures 23 and 24. We have connected points of impurities belonging in the same row of the periodic table, and dissolved in the same host metal. We see a general downward trend as we go to higher valence for three of the four host materials, but for gold there is a definite reversal of trend. If we now assume an experimental $\chi_p{}^A$ of the pure host material, A, then this behavior reflects directly the nature of ξ, or $\langle a \rangle$, in Au versus that in Cu, Ag and Pb. In other words, the gold host causes the details of the wave function at the impurity site to change quite differently from the other three hosts. This could, of course, involve local density of states effects as well. We believe [7] that strong *s-d* hybridization, arising from the proximity of the *d* band to the Fermi level, is important to the Au behavior. Unfortunately, auxiliary specific heat, susceptibility, and other experimental data which might help resolve this

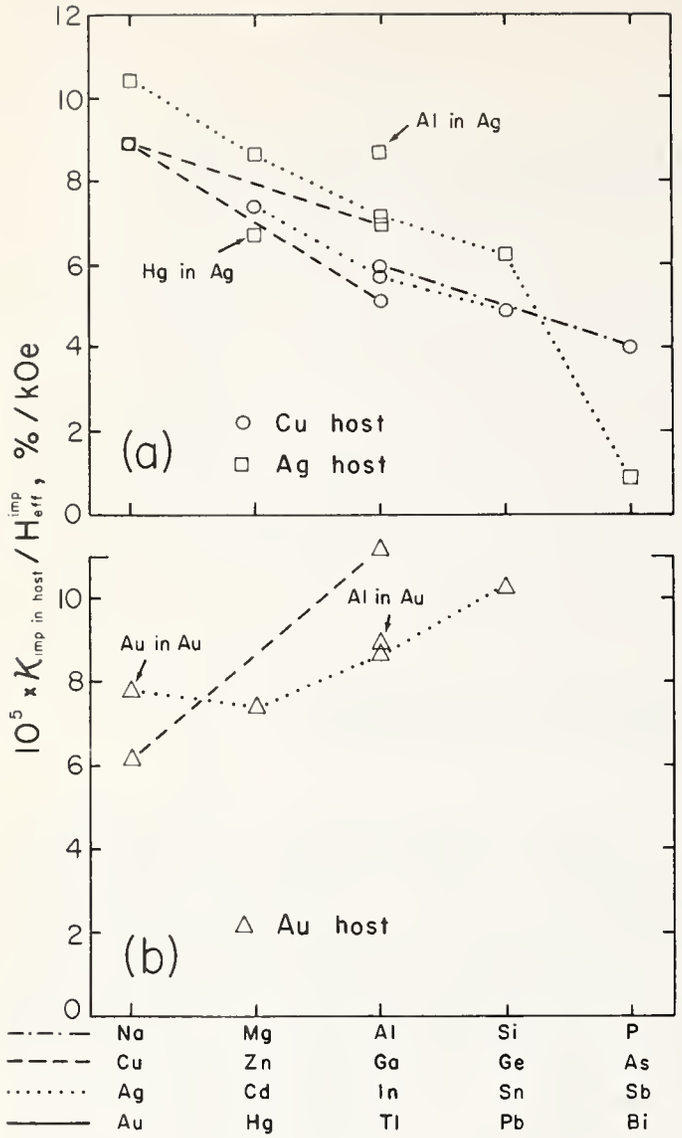

FIGURE 23. *Impurity Knight shifts in Cu, Ag and Au hosts. Atomic effects due to the hyperfine coupling constants are divided out, using our* H_{eff} *values for the impurities, listed in table 2. The resulting trends are opposite for a gold host than for copper and silver hosts. (Data for boron in gold [195] of* 15×10^{-5}% *per kOe agrees with the upward trend for the gold host. The uncertainty in this value is greater than that of the points given in the plot.) Points for impurities occurring in the same row of the periodic table are connected with the line symbols indicated in the lower left hand corner (e.g., the dotted line connecting the square datum points is for Ag, Cd, In, Sn, and Sb in a silver host). The Cu and Ag data were taken primarily from Rowland and Borsa [6]; the Au data from Bennett* et al. *[7]. This latter paper gives in its table 1 further references to the literature for several of the shown points. The Sb in Ag point was taken from Matzkanin* et al. *[194].*

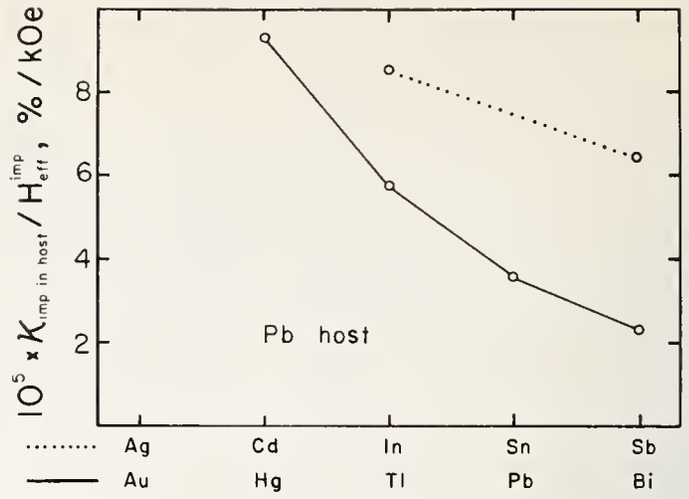

FIGURE 24. *Impurity (B) Knight shifts in a lead host divided by the impurity hyperfine fields,* H_{eff}^{B}. *Data taken from Bennett* et al. *[193]. The dotted line connects points for impurity atoms belonging to the Ag row of the periodic table and the solid line connects those for impurity atoms belonging to the Au row. The trend is similar to that for Cu and Ag hosts and opposite that for an Au host.*

matter is not readily available for the Au alloys. More data of this type would be worth obtaining.

12. Magnetic Disturbances

The effects of a charge impurity in a metal have been described above (sections 8, 10, 11). When a *magnetic* impurity is introduced into the metal, a similar response occurs: spin density oscillations (rather than, or in addition to, charge oscillations) are set up around the impurity, as discussed in section 8. The behavior is similar to the oscillations shown in figure 13. The unbalanced spin at a neighboring site interacts with that nucleus via a spin-dependent interaction. Generally this interaction is rather strong compared to charge effects causing correspondingly larger variations in the Knight shift and thus larger values of Γ.

Gardner and Flynn [196] have reported susceptibility and solvent Knight shift results for transition element (3*d*) impurities in liquid Cu. The dominant Knight shift term in these cases is associated with the 3*d*-magnetic moment aligned at impurity sites by the magnetic field. The susceptibilities of alloys with Cr, Mn, Fe, and Co as impurities obey the Curie-Weiss law implying the existence of local paramagnetic *d*-moments at impurity sites. The moment values, μ, inferred from the susceptibilities are plotted in figure 25. Sc, Ti and Ni alloys do not follow a Curie-Weiss law, suggesting that local virtual *d*-level *band* paramagnetism dominates.[12] The Mn, Fe, and Co moments plotted in figure 25 are of some interest if one assumes that they are entirely associated with impurity site *d*-character, *i.e.*, little or no moment either residing on the host lattice, or in conduction band character at an impurity site. The moments then equal the number of holes in the *d*-bands and the quantity (10-μ) provides an estimate of the number of *d*-electrons at a local site.

[12] The detailed susceptibility behavior of the Cr, Mn, Fe and Co alloys suggests the presence of a small term, of perhaps this sort, in addition to local moment paramagnetism.

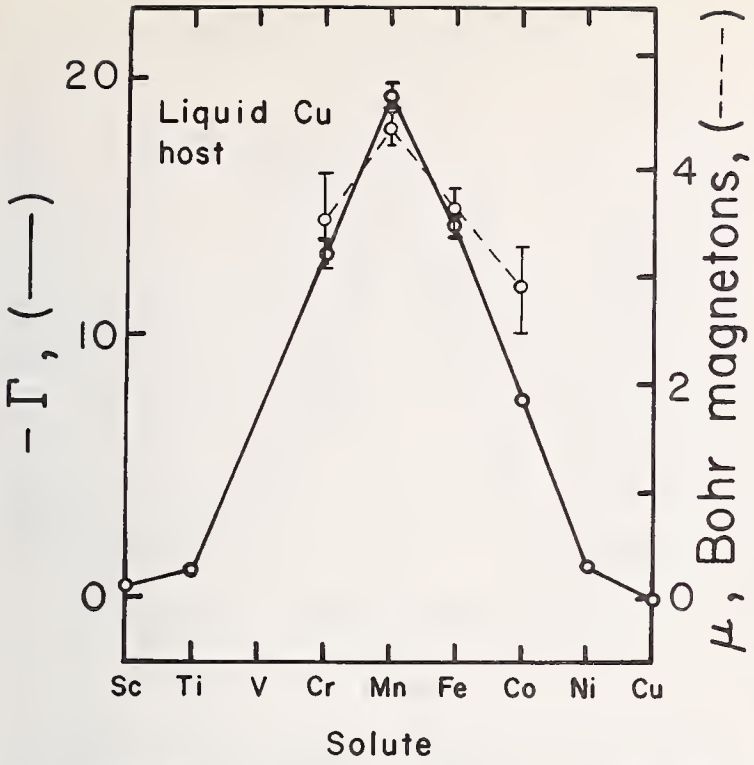

FIGURE 25. $\Gamma = 1/\mathcal{K} \cdot \Delta\mathcal{K}/\Delta c$ *values for 3*d *transition metal impurities in liquid copper (solid line) and effective magnetic moment,* μ*, (dashed line) plotted versus position in the periodic table. Both sets of data are taken from Gardner and Flynn [196]. The vertical scale of the* μ *plot was arbitrarily chosen so that the height of the* Γ *and* μ *peaks are nearly equal.*

Gardner and Flynn [196] obtained values of 7.1, 6.4, and 5 for the number of Co, Fe and Mn respectively. These numbers are 0.5 to 1.0 electrons smaller than the *d*-electron counts believed appropriate to the pure solute transition metals and, if real, this trend offers valuable evidence as to the electronic character of these impurities. The estimate, of course, relies strongly on the assumption that the moments are entirely of impurity site *d*-character with no hybridization with the conduction bands. Electron count estimates for lighter 3*d*-element impurities, such as Cr, are further hampered by the question of whether or not there is any occupied *d*-character of spin antiparallel to the net spin of the moment. The density of states with and without such behavior is shown schematically in figure 26. It is probably reasonable to assume that a strong paramagnetic moment such as Cr in Cu has little or no *d*-spin moment component antiparallel to the net local moment.

The Γ values appropriate to the various 3*d*-Cu alloys are also plotted in figure 25. These roughly follow the moment behavior, are negative, and are large when compared with the charge perturbation Γ's of, for example, figure 17. They are large because a local 3*d*-susceptibility, and its associated spin density disturbance, contributes a larger Knight shift effect

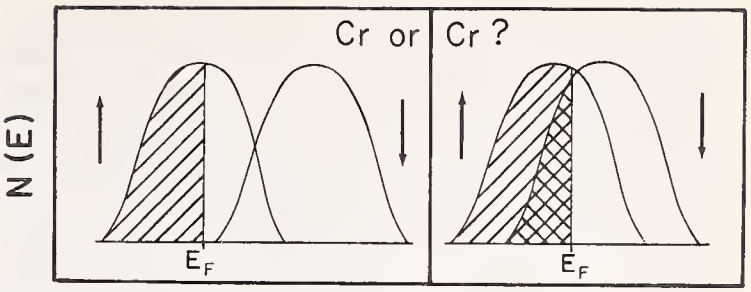

FIGURE 26. *Schematic density of states as a function of energy for Cr metal. In the first case the spin up (* $\uparrow$ *) band and spin down (* $\downarrow$ *) band do not overlap at the Fermi surface; in the second case both spin up, and spin down bands are partially filled.*

than the weak perturbation of charge impurities. Charge effects are undoubtedly also present in the vicinity of 3*d*-impurity sites, but these appear to be insignificant if a local paramagnetic moment is formed. The strength of the magnetic term, relative to other effects, is a prime reason for the observed linearity in $\mathcal{K}$ versus impurity concentration. (This assumes that the magnetic term above tends to be linear.) The negative sign of the Γ's might imply that the main peak of the conduction electron spin disturbance (see fig. 13) has its moment antiparallel to the local moment. This negative sign is reminiscent of charge impurity effects and might instead indicate, as in the charge case, that the main peak either fails to overlap solvent nuclear sites or, if it does overlap, contributes satellite lines which are shifted out of the main resonance (*e.g.*, see fig. 14). While the latter would be consistent with charge impurity experience, most workers believe that the main peak is sampled by the main resonance line, and that a negative Γ indicates spin moment antiparallel to the local moment. This in turn implies that hybridization and higher order effects predominate over electrostatic exchange scattering. Combined hybridization and electrostatic exchange terms will provide an *effective* exchange coupling which is *not* constant as one traverses the 3*d*-elements. One thus expects a crude but *by no means linear* relation between Γ and μ. This is seen to be the case in figure 25. Gardner and Flynn showed that a partial wave description involving *d*-wave scattering crudely reproduces the trend and magnitude of the Γ's.

Flynn and coworkers have also obtained [197] results for 3*d*-impurities in liquid Al and these are summarized in figure 27. Since band, rather than local moment, paramagnetism prevails for all impurities, the added susceptibilities per mole of solute have been plotted (rather than local moment μ values). The Γ values, except for Sc and Ti, are smaller than those obtained in the Cu alloys. This is largely accounted for by

the smaller susceptibilities (per added solute atom) in the Al alloys.

The Cu and Al hyperfine fields, per effective spin moment induced on solute sites, are of the order of −100 kOe for impurities in the middle of the 3*d*-series. The hyperfine fields obtained (and the ξ's derived from them) for the Cu alloys are plotted in figure 28. (A similar plot for 3*d*-impurities in liquid Al alloys results in much larger uncertainties.) One might expect a somewhat smaller value of H_{eff} for Al relative to that of Cu, since the free atom *s*-contact interaction of Al is approximately half that of Cu. The fact that it has a similar value suggests that the magnetic response in the Al matrix, due to a given moment on the impurities, is slightly larger[13] than in Cu.

If one attributes H_{eff} on an average solvent site to an *s*-moment, with its associated atomic $\langle a \rangle$, the results correspond to antiparallel spin moments of 0.05 to 0.08 μ_B for Al and up to 0.05 μ_B for Cu for every Bohr magneton of moment aligned at solute sites and in the solvent matrix. The moment at any given solvent site is small but the total moment residing in the solvent lattice can become a significant fraction of that residing on the solutes thus affecting the arithmetic average of *d*-electron population estimates from susceptibility data.

A comparison of the Γ behavior and the susceptibilities for the Al alloys (fig. 27) shows Γ tracking χ more poorly than was the case in the Cu alloys (fig. 25). When making such a comparison it should be noted that the Γ for Sc, Co, Ni and Cu are of the order of charge impurity Γ's. Thus, charge as well as magnetic effects, may be contributing to Γ. As we have discussed, the negative sign of the Γ's in figures 25 and 27 would seem to indicate that hybridization exchange scattering predominates over direct exchange effects (see sec. 8). There is no reason why such hybridization effects should be constant across the 3*d* row and the deviation in Γ from the χ curve in figure 27 is of a magnitude appropriate to such a variation in hybridization effects. Flynn and coworkers explain the trend with a particular version of such higher order effects, in which the exchange enhancement of the virtual *d*-level susceptibility (see eq. 20) plays an important role. The fact that Γ lies higher for the lighter 3*d* impurities could be due to charge effects but it would seem to imply that hybridization effects are stronger (and/or coulomb exchange weaker) for the lighter elements in Al. The peaking of Γ at Cr or Mn seen in figures 25 and 27 is characteristic of the 3*d* elements. Quite different behavior is seen for the rare earths (*e.g.*, see fig. 29).

As already noted, the variation in Knight shift with impurity concentration is strikingly linear in both the Al and Cu alloys over the ranges of concentration studied.

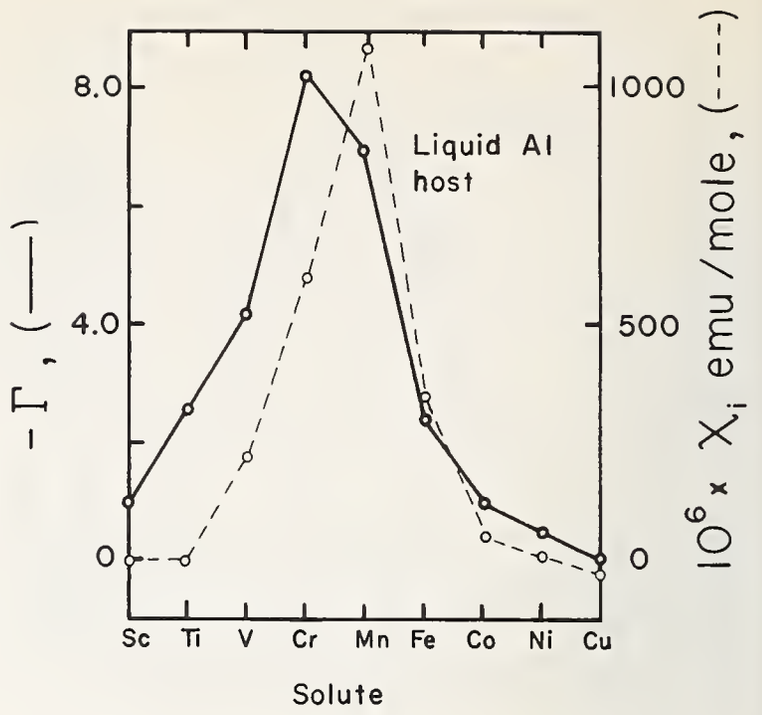

FIGURE 27. *$\Gamma = 1/\mathcal{K}\ \Delta\mathcal{K}/\Delta c$ values for 3d transition metal impurities in liquid aluminum (solid line) and χ_i, the susceptibilities per mole of solute plotted versus position in the periodic table. Both sets of data are taken from Flynn* et al. *[197].*

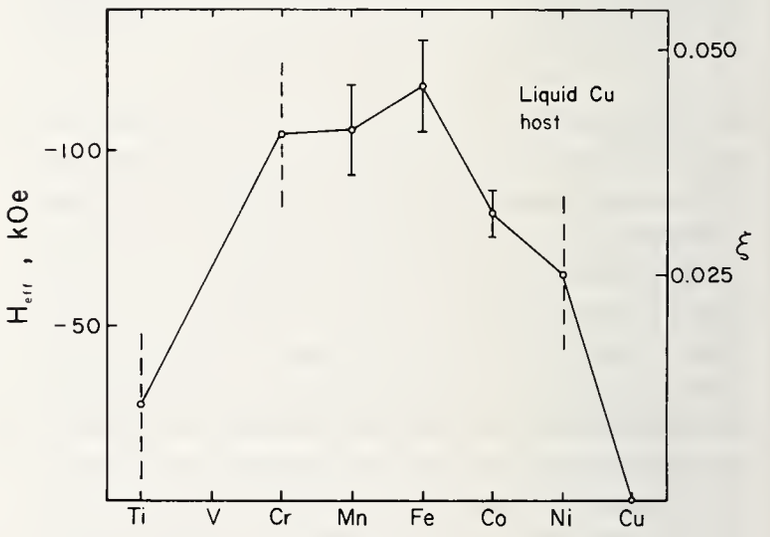

FIGURE 28. *Hyperfine fields and effective ξ values for liquid copper sampling the effects produced by liquid transition metal impurities. Unlike the normal definition of such quantities these are defined with respect to the impurity susceptibility. This is accomplished by using composition, rather than temperature, as the implicit parameter in a $\mathcal{K}$ versus χ plot.*

[13] One might be tempted to attribute this to band effects associated with the band paramagetism of the impurities in Al versus the local moment paramagnetism of Cr, Mn, Fe and Co in Cu, but note the small effective fields for the band paramagnetic impurities of V and Ni in Cu.

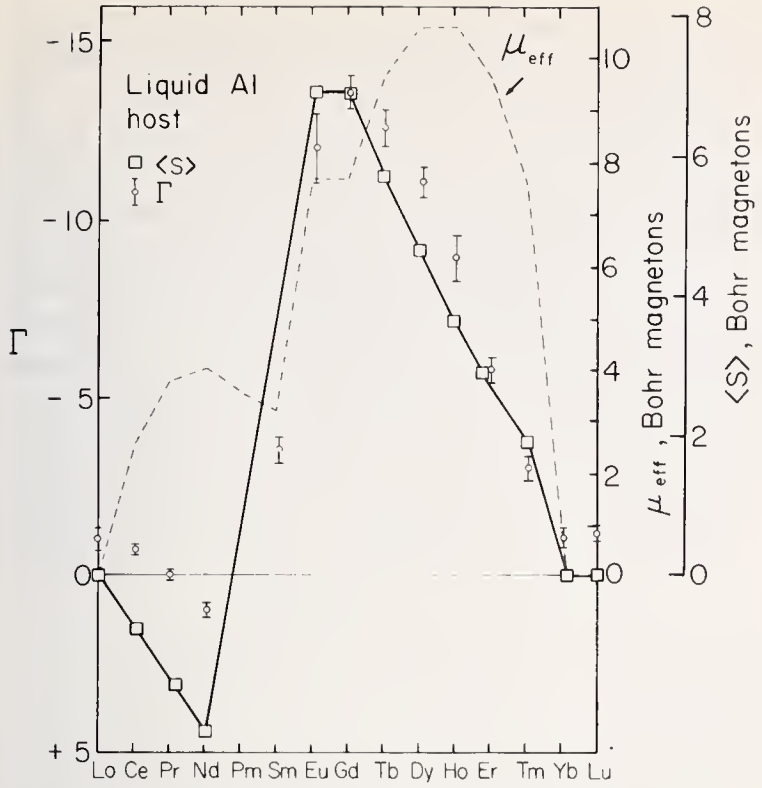

FIGURE 29. *$\Gamma = 1/|\mathscr{K} \cdot \Delta\mathscr{K}|/\Delta c$ for rare earth metal impurities in liquid aluminum (circles with error bars) and μ_{eff}, the effective total magnetic moment (dashed line) plotted versus position in the periodic table. Both sets of data are taken from Stupian and Flynn [200]. Also plotted is the effective spin moment $\langle S \rangle$, as discussed in the text (solid lines with squares).*

In some cases these extended up to five and six percent. These are concentrations at which one magnetic impurity would have another magnetic impurity as a near neighbor roughly half the time. At such concentrations it is doubtful that a Friedel or RKKY type of theory should be expected to work, for they assume noninteracting impurities which are dilute enough that there are no saturation effects in the solvent. Any effective local-moment local-moment exchange coupling is reduced due to the fact that the experiments were done at high temperature (above 1000 K). This may serve to reduce apparent nonadditive effects. It may be that averaged multimoment effects are contributing to the Γ's. Extremely dilute alloys were not examined; with one exception the lower ranges of alloy concentrations were one-half to one percent.

Knight shift data in alloys have also been obtained by γ-γ, perturbed angular correlation experiments [198]. In such an experiment, a nucleus is observed which has emitted a gamma ray in some particular direction. Thus defining the nuclear orientation, one then observes that nucleus as it emits a second gamma ray in some characteristic multipole distribution. Application of an applied magnetic field produces a Larmor precession of the nucleus between the emission of the first and second gamma ray. The precession rate, with its associated Knight shift term, can be deduced from its effect on the second gamma ray distribution. Rao *et al.* [198] have recently used the technique to obtain the Knight shift of very dilute Rh in Pd over a temperature range of 4.2 to 1053 K. They then used existing susceptibility data, extrapolated to infinite Rh dilution, to obtain a $\mathscr{K}$ versus impurity site χ plot, which was not linear. The $\mathscr{K}$ versus χ slope appropriate to particular temperature regimes are uncertain due to questions concerning scatter in the Knight shift data and the purity of the samples used in two different sets of susceptibility measurements. (These are strongly paramagnetic alloys and any magnetic impurities will strongly perturb the magnetic response.) The results yield a large negative $\mathscr{K}$ versus χ slope at high temperatures, which is of the order of 4*d*-core polarization effects, but a much smaller slope at low temperatures. This is consistent with a picture where the impurity contribution to the susceptibility at high temperatures is almost entirely associated with Rh sites, but, due to exchange enhancement effects involves the entire Rh-Pd matrix at low temperatures. The low temperature $\mathscr{K}$ versus χ slope is consistent with an effective magnetic moment of $\sim 10\mu_B$ residing largely on the solvent matrix. Such a moment was *independently* deduced [199] from Curie-Weiss fits for these alloys at low temperatures.

Stupian and Flynn [200] studied the effect of adding rare earth impurities to liquid Al. The susceptibilities were consistent with local moments as predicted by Van Vleck [201]. With the exception of Sm($4f$)^5 where there is strong multiplet mixing, the moments are approximately

$$\mu_{\text{eff}} = [J(J+1)]^{1/2} g\mu_B \equiv \frac{\mathbf{L}\cdot\mathbf{J} + 2\mathbf{S}\cdot\mathbf{J}}{[J(J+1)]^{1/2}}\mu_B, \qquad (36)$$

where the Landé *g*-factor has been written out. Very substantial orbital terms contribute to μ and therefore the Γ's should not, and do not, track μ. The Γ's are compared with $\langle S \rangle$ in figure 29 where $\langle S \rangle$ is the spin component along **J**, *i.e.*

$$\langle S \rangle \equiv \frac{2\mathbf{S}\cdot\mathbf{J}}{[J(J+1)]^{1/2}} = \mu_{\text{eff}}\left(\frac{2\mathbf{S}\cdot\mathbf{J}}{\mathbf{L}\cdot\mathbf{J} + 2\mathbf{S}\cdot\mathbf{J}}\right) = 2\mu_{\text{eff}}\left(\frac{g_j - 1}{g_J}\right) \qquad (37)$$

is a measure of the spin component (in μ_B) parallel to the aligned **J**. This provides a crude first order measure of effective exchange perturbations. **S** is antiparallel to **J** in the first half of the rare earth row and parallel in the second, hence the sign reversal in $\langle S \rangle$. The Γ's dis-

play a weaker reversal which is, in part, associated with uncertainties such as the *natural* zero line for magnetic contributions to Γ. [Note that La, Yb and Lu impurities have zero-valued magnetic moments yet their Γ's lie above the zero line.] The differences between Γ and $\langle S \rangle$ are on a similar scale to the effects seen in figure 27. Otherwise there are fundamental differences in Γ behavior as one transverses the rare earths in contrast to the 3*d*'s. Negative Γ's prevail suggesting a tendency for the conduction electron spin disturbance to be antiparallel to the spin of the rare earth moment. This is consistent with almost all experience with rare earth elements in alloys or intermetallics. This sign was also observed for rare earths as impurities in Pd [202-204], at Al sites in $REAl_2$ intermetallic compounds [146], and for ^{31}P, ^{75}As and ^{121}Sb in PrP, PrAs, TmP, TmAs and TmSb[14] [206]. There is general agreement that hybridization effects are responsible for these results.[15]

The situation with magnetic alloys is seen to be similar to the charge impurity case. Both can be described with models of the perturbations which reproduce the experimental behavior, usually crudely, although occasionally in detail. The magnetic alloy problem is complicated by the presence of several scattering mechanisms and by the fact that a magnetic impurity is also a charge impurity. Solvent Knight shift experiments provide unique data for testing alloy models in both magnetic and charge difference systems, but as yet they have provided little *unique* insight into alloy behavior. Further studies of very dilute systems and of satellite lines outside the main resonance peak should prove invaluable for this purpose.

13. Intermetallic Compounds

Relating the Knight shift to the electronic density of states in ordered alloys or intermetallic compounds presents some problems which we have tacitly ignored when considering disordered systems. Let us review the analysis of the Knight shift results [22,207,208] for the technologically important V_3X compounds [X = As, Au, Ga, Ge, Pt, Sb, Si or Sn]. It was in their now classic investigation of these intermetallic compounds that Jaccarino and Clogston developed the graphic $\mathcal{K}$ versus χ analysis described earlier [13]. $\mathcal{K}$ versus χ plots (with temperature an implicit parameter) are shown in figure 30 for V and Ga in V_3Ga. The temperature variation in χ is huge. The variation in χ *per* V atom

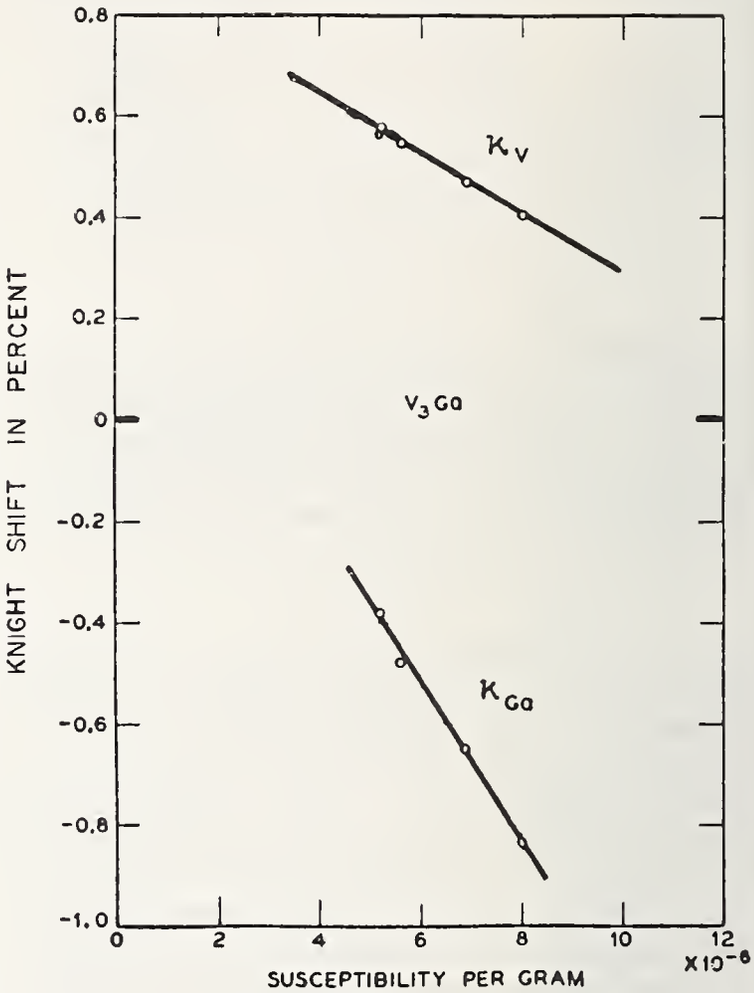

FIGURE 30. *Knight shift versus susceptibility for V and Ga in V_3Ga, as taken from Clogston and Jaccarino [13].*

as a function of temperature in V_3Ga is somewhat larger than that per Pd atom in Pd metal. This strong variation requires significant structure in the density of states (*e.g.*, see [110]) within kT of the Fermi energy. To investigate possible sources of density of states structure, Weger [209] considered the role of the linear chains of V atoms which occur on the cube faces in the V_3X structure. These chains impose anisotropic electronic properties which, in turn, could produce strong structure in $N(E)$ near E_F. Gossard [210] has studied Knight shift and quadrupole effect changes in V_3Si across the low temperature cubic-to-tetragonal phase

[14] Jones [205] also succeeded in observing the ^{141}Pr and ^{169}Tm Knight shifts in these paramagnetic compounds. Shifts as large as 8,900 percent were observed. Jones showed that this is consistent with theory and is due to large orbital hyperfine effects associated with the 4*f*-moments. He also noted that the temperature dependence of the rare earth and of the nonmagnetic site Knight shifts tracked each other quite faithfully.

[15] But other effects may also play a role. For example, direct electrostatic exchange scattering was not added to hybridization effects in Stupian and Flynn's consideration of the rare earth-Al alloys. Reasonable estimates of the appropriate exchange integrals suggest contributions to Γ of the order of (and opposite sign to) the observed Γ behavior. Inclusion of the effect would have overburdened the model with too many disposable parameters.

transition. He interpreted the transformation in terms of such a linear chain model. Labbé and Friedel [211] presented an alternative linear chain model which also is in accord with the experimental situation.

Strong negative $\mathcal{K}$ versus χ slopes are seen in figure 30. The slope for Ga is twice as steep as that for V. The χ=0 intercepts of $\mathcal{K}$ are positive and were attributed to a temperature independent Pauli term arising from a broad conduction band with *s*-like wave function character at both Ga and V sites. (There is probably also a significant orbital Knight shift term contributing to the V site intercept.) The temperature dependent Knight shift was attributed to a narrow V 3*d*-band into which Ga 4*p*-character is hybridized, contributing shifts of the form

$$\mathcal{K}_V(T) = w_V \langle a \rangle_V \chi_p$$
$$\mathcal{K}_{Ga}(T) = w_{Ga} \langle a \rangle_{Ga} \chi_p \qquad (38)$$

where χ_p is the *d*-band Pauli susceptibility per formula unit. The w_i are weights *per atom* of V and Ga character in a formula unit in the band. They *also* account for any deviation in the hyperfine constants from the chosen values. With correct $\langle a \rangle$'s chosen, then the w_i are simply weights and subject to the normalization requirement[16]

$$3\, w_V + w_{Ga} = 1. \qquad (39)$$

The $\langle a \rangle$'s were assumed to arise from V 3*d* and Ga 4*p* core polarization. The free atom values of -117 and -44 kOe/μ_B (consistent with table 3) were used, respectively. Given these $\langle a \rangle$'s, the slopes of the $\mathcal{K}$ versus χ plots yield $w_V = 0.13$, and $w_{Ga} = 0.92$. The greater w_{Ga} value is in large part due to the steeper slope of the Ga plot. Testing the normalization condition yields

$$3\, w_V + w_{Ga} = 1.31, \qquad (40)$$

a sum remarkably close to one. This might suggest that the *w*'s are essentially measures of wave function weight. Clogston and Jaccarino observed trends in Knight shift behavior of various V_3X compounds which further suggest this. If the *w*'s are real weights, their values are surprising, for they would indicate that Ga *p*-character, rather than transition metal *d*-character, dominates at the Fermi surface. Subsequent band calculations by Mattheiss [212], yield $2 \leq w_v/w_{Ga} \leq 3$ unlike a value of 1/7 obtained from $\mathcal{K}$ versus χ plots. The V_3X compounds have large $N(E_F)$'s and their susceptibilities are strongly temperature dependent. Such behavior is characteristic of a *d*-band metal. This would suggest that the ratio obtained by Mattheiss is reasonable, and thus, that the w_i's obtained from the Knight shifts are largely a measure of hyperfine field behavior. Assuming a value for the weight ratio, the Knight shift slopes can be used to estimate experimental $\langle a \rangle$ values for this compound. A ratio of 2 yields values of -53 and -283 kOe/μ_B for V and Ga respectively. The reduced $\langle a \rangle_V$ could be caused by interatomic effects, by intrasite *s*-band polarization, or by *s*-*d* hybridization. Three percent *s*-character admixture into the *d*-band at E_F will account for the reduction. Large negative intra-atomic effects, over and above the core polarization term, are unknown. The value for the core polarization term, shown in table 3, includes the polarization of the closed valence *s*-shell. Wave function changes on going from a neutral atom to the metal might effect this core polarization term by a factor of two or three but not likely by an order of magnitude. Thus the enhanced $\langle a \rangle_{Ga}$ is most likely due to interatomic effects [$\langle a \rangle_{Ga}$ goes to -400 kOe/μ_B if w_V/w_{Ga} is taken equal to 3]. A similar situation occurs in V_3Si. The $\langle a \rangle_{Si}$ is observed to be negative yet the core polarization hyperfine field appropriate to atomic P, and thus presumably Si, is positive. The P atomic behavior might be irrelevant to Si but the result again suggests the presence of substantial negative interatomic terms at X sites in the V_3X compounds. An X-site in these compounds has twelve nearest V neighbors. This implies the presence of a nearest neighbor spin moment which is 20 to 40 times that induced at the X site itself by the magnetic field. Conduction electron polarization effects of the order of those encountered for transition metals in either liquid Cu or Al can, given such a large neighboring moment, account for the value of $\langle a \rangle_{Ga}$ as well as the apparent sign reversal in $\langle a \rangle_{Si}$. With such a large *near neighbor* moment, it is also possible that there is a substantial contribution to $\langle a \rangle$ via direct exchange polarization of the X-site ion core. Knight shift data [213,214] suggest that similar effects occur at Sn sites in the isostructural system Nb_3Sn.

Subsequent investigations of rare earth and transition metal intermetallic compounds have often relied on $\mathcal{K}$ versus χ plots to disentangle terms. Most of the data are associated with nonmagnetic atomic sites and band hybridization. Interatomic effects are featured heavily when rationalizing the behavior of the hyperfine constants. Interatomic effects are normally interpreted

[16] Noting that the molar susceptibility appears in eq (38) and an atomic χ_p in eqs (31) and (32), eqs (38) and (39) are equivalent to, and can be used to derive, eqs (31) and (32).

in terms of an RKKY type of spin distribution induced by the aligned spin moments on the magnetic ion sites. A variant of the two-band description of the nonmagnetic site Pauli shift has frequently proved useful, namely

$$\mathcal{K}(T)=\mathcal{K}_0+\mathcal{K}_{loc}(T), \tag{41}$$

where $\mathcal{K}_0$ is the Knight shift associated with the conduction band Pauli term and $\mathcal{K}_{loc}$ is the shift arising from the interatomic response to the aligned spin moment on the magnetic atom site. $\mathcal{K}_{loc}$, which is presumably responsible for the temperature dependence of $\mathcal{K}$, has the form

$$\mathcal{K}_{loc}(T)=\frac{2(g_J-1)}{g_J}H'_{eff}\chi_{loc}(T)/N\mu_B. \tag{42}$$

Here χ_{loc} is the Pauli susceptibility of either the local moment or band type associated with the moment induced on the local moment site. The $2(g_J-1)/g_J$ factor is included in anticipation of the rare earths, so that H'_{eff} is the hyperfine field at the nonmagnetic site per local *spin* moment (per molecule) at the magnetic site. The details of the conduction electron distribution arise in the sampling

$$H'_{eff}\sim\sum_R\rho(R), \tag{43}$$

where we have assumed that H'_{eff} arises from the contact interaction and the sum spans all interatomic radii, R, connecting all magnetic sites with a nonmagnetic atom. Efforts [215, 216] have been made to relate such a sum to $\mathcal{K}$ values. These have been hampered by inadequate knowledge of $\rho(R)$. Asymptotic RKKY distributions were of necessity used, although it is the near R (nonasymptotic) region which is most important to H'_{eff}. More often the alternate approach of assuming that H'_{eff} effectively samples the *average* ρ, *i.e.*, the Pauli or Zener response to the local moment exchange field is used. Then

$$H'_{eff}=\mathcal{K}_\alpha\mathcal{J}/2\mu_B, \tag{44}$$

where $\mathcal{J}/2\mu_B$ is the exchange coupling per unit local moment between the local moment and the Fermi surface conduction electrons. $\mathcal{K}_\alpha$ is the Pauli response of the conduction electrons to this exchange field. If one assumes that the *average* hyperfine coupling in the RKKY disturbance equals that associated with Fermi surface states alone, then $\mathcal{K}_\alpha=\mathcal{K}_0$ and

$$\mathcal{K}(T)=\mathcal{K}_0[1+(g_J-1)\mathcal{J}\chi_{loc}(T)/g_JN\mu_B^2]. \tag{45}$$

Knowing $\mathcal{K}_0$ from an isostructural nonmagnetic compound, $\mathcal{J}$ can be estimated. Physically reasonable numbers for the exchange constants normally result. Even assuming that the average spin moment sampled is equal to the Pauli term in the RKKY response, it is not inevitable that $\mathcal{K}_\alpha$ should equal $\mathcal{K}_0$. The spin response involves states off E_F and the hyperfine coupling for these states can vary radically from that at E_F, as is indicated for the case of Cu in figure 11. Another possible shortcoming of the scheme is that the entire resonant scattering disturbance is not necessarily describable in terms of an effective exchange scattering. Although $\mathcal{J}$ can be numerically affected by factors other than exchange coupling, tabulation of shift results in this form can prove useful when comparing results in a sequence of intermetallic compounds. For example, Jones [205] has tabulated the nonmagnetic site Knight shift results of rare earth intermetallic compounds in terms of $\mathcal{J}$. The same results [146,217-229] are plotted in a different form in figure 31, namely in terms of $\xi\equiv H'_{eff}/H^{At}_{eff}$. Atomic hyperfine behavior is thus normalized out, providing a crude estimate, in μ_B, of the spin moment residing at a nonmagnetic site due to the local moment disturbance. The resulting ξ's are an order of magnitude smaller than those appropriate to the transition metal alloys (compare with figure 28) implying much weaker magnetic perturbations in rare earth compounds.[17] The ξ's appear to be in three distinct groups; the Al compounds, the P, As and Sb compounds, and those involving elements in the 6*s*-6*p*-5*d* row of the periodic table. (Data also exist for two hexaborides yielding ξ's of ~ -0.005.) We presume the grouping is associated with band and wave function character specific to the various sets of compounds. More interesting than the grouping is the variation in ξ across the rare earth row; ξ is largest at the Ce end, falling and becoming relatively constant for the heavy rare earths. The trend is very different than that seen for 3*d*-moments in figure 28 and appears characteristic of rare earth 4*f*-moment effects. This trend was first observed in electron spin and nuclear resonance of the $REAl_2$ compounds [202, 146] and subsequently in ESR of rare earth impurities in Pd [203]. The negative sign of ξ suggests that hybridization polarization effects dominate. One contributing factor to the large ξ at the Ce end is the well-known tendency for the occupied 4*f* levels to be close to E_F. The resulting small energy

[17] This comparison underestimates the drop in polarization because the ξ values natural to ordered intermetallic compounds are intrinsically larger than those in alloys by the nature of the differing definition of these two ξ factors. For example, the ξ appropriate to the intermetallic compounds $REAl_2$ and $REAl_3$ (see fig. 31) are larger than those for the RE-Al alloys.

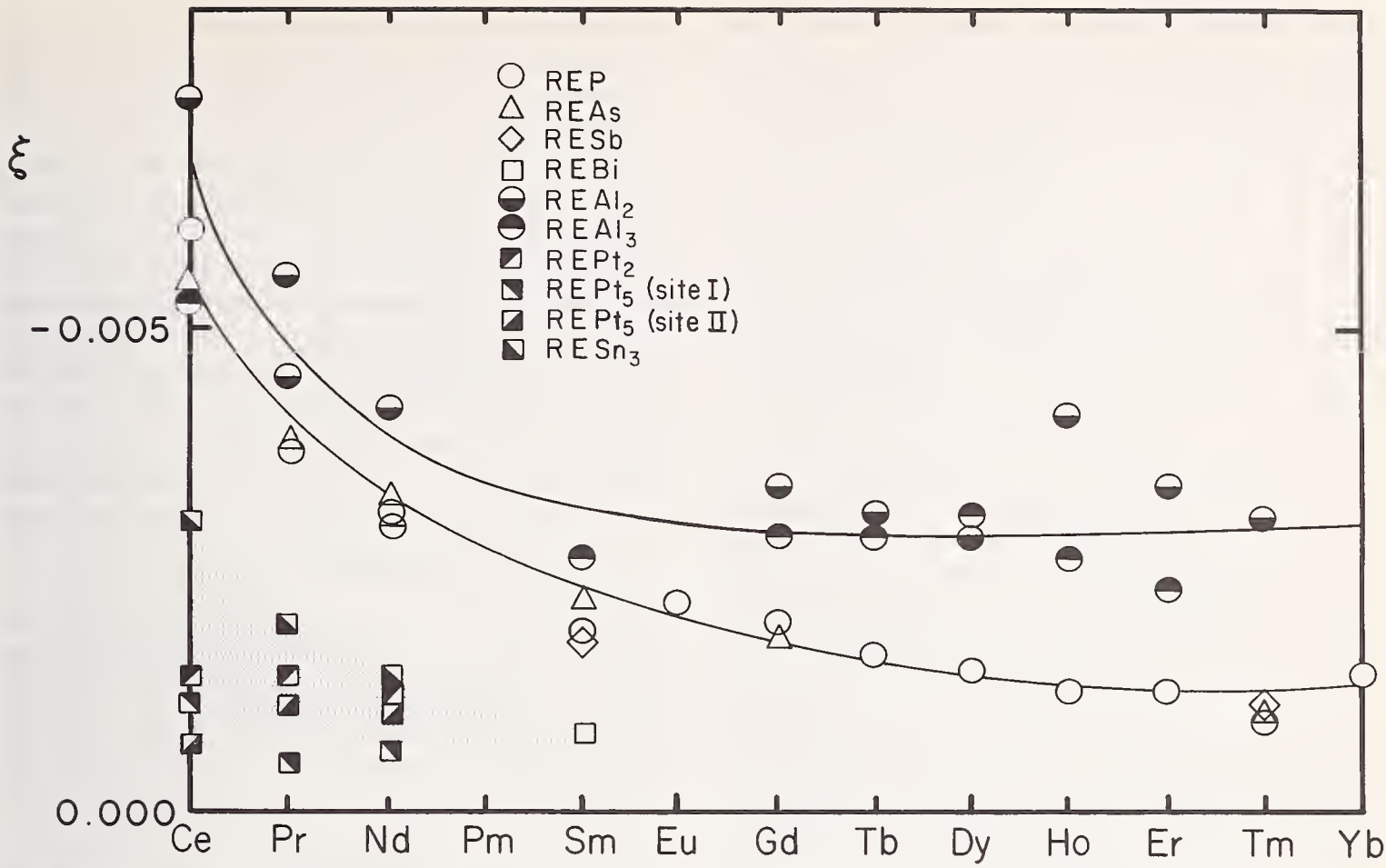

FIGURE 31. *Behavior of Knight's ξ factor as defined in the text, for the light metal site in rare earth intermetallic compounds. The data are from a number of sources [205,217-229], as collected in tabular form by Jones [206].*

denominators tend to enhance hybridization, and hence ξ. An example of this $4f$ behavior is that a phase transition occurs in metallic Ce, one phase involving no $4f$ electrons, and the other, one.

Positive, strongly temperature dependent $\mathcal{K}$'s have been observed for nonmagnetic sites in UAl_2 [215] and USn_3 [230]. The susceptibility behavior suggests the presence of $5f$ band paramagnetism, rather than local moment paramagnetism. The resulting ξ's (~ 0.1 to 0.3) for the two compounds are opposite in sign and substantially larger than the values appropriate to the isostructural rare earth compounds (fig. 31). The authors [215,230] pointed out that the results could arise from several percent Al (or Sn) valence s-orbital hybridization into the $5f$ bands at E_F and/or from RKKY polarization with quite reasonable $\mathcal{J}$ values. The positive sign of the ξ's implies that electrostatic exchange then dominates. The $\mathcal{K}$ versus χ plots for the two compounds also indicated the presence of a strong χ_{orb} term associated with $5f$ character at the U sites, which makes no contribution to the Al (or Sn) site $\mathcal{K}$.

Abundant data exist for a variety of transition metal compounds. In some of the more magnetic systems the results are strongly dependent on metallurgical details of the samples. For example, NiAl, CoAl and FeAl have been studied by West [231,232] and by Seitchik and Walmsley [216,233] at and off stoichiometry. West found that the Co susceptibility results in CoAl are very sensitive to the thermal history. These results suggested nonequilibrium magnetic clustering. The effects of thermal history on the Knight shift are less important, because the number of atoms near clusters is small and do not contribute sensibly to the observed resonance. Despite these difficulties there are several distinct features of the results which give insight into the character of these compounds. First, the Al shift in FeAl is negative and temperature dependent, suggesting the existence of intersite effects of the sort encountered in the Al alloys and the V_3X compounds. Second, while the Co shift can be strongly temperature dependent (depending on Co concentration), the Al shift in CoAl is small and is effectively independent of temperature (not depending on Co concentration). From this it was concluded that there is little Al s-character in the Fermi surface states of CoAl. The slope of a $\mathcal{K}$(Co) versus χ plot, using composition as the intrinsic parameter, is negative at room temperature and positive at low temperature. Thus there are at least two par-

tially cancelling temperature dependent mechanisms operative at the Co site in this system. West attributed the positive slope to a temperature dependent orbital term. Finally in NiAl, the Al shift, the Al relaxation time, and the susceptibility are characteristic of an *s*-band metal, suggesting that Al electrons "fill" the Ni 3*d* band. This does not imply that there are ten 3*d*-electrons at a Ni site in NiAl, just as there aren't at a Cu site in pure Cu (see discussion of fig. 11). Instead, charge effects have so affected the bands that there is no substantial *d*-band character at or within kT of E_F. A similar situation appears to occur in dilute alloys of Ni in Cu [234].

Knight shift results have been obtained for both transition metal sites and nonmagnetic sites in itinerant ferromagnets [235,236,14] such as $ZrZn_2$. These systems are characterized by having ferromagnetic saturation moments, q_s, which are small compared with *effective* moments, q_c, associated with the paramagnetic susceptibility. This implies a band rather than local Heisenberg type of ferromagnetism. A plot of the q_c/q_s ratio for a variety of compounds is shown in figure 32. These were obtained with the Rhodes-Wohlfarth "intermediate model" [238]. There has been some uncertainty as to whether magnetic impurities drive some of the "itinerant" systems ferromagnetic. In cases,

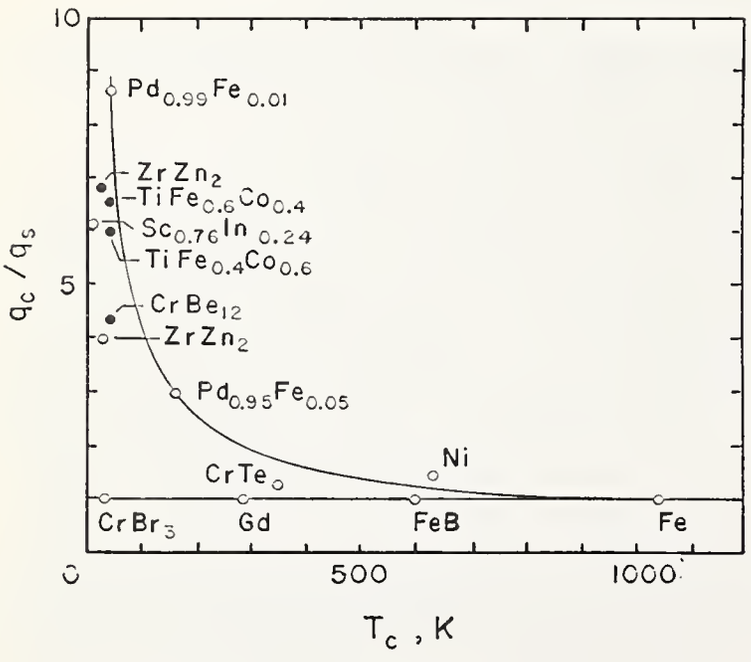

FIGURE 32. *The ratio q_c/q_s of the number of magnetic carriers deduced from the paramagnetic Curie-Weiss constant to the number deduced from the saturation magnetization. Datum points are identified by Rhodes and Wohlfarth [237] and Swartz* et al. *[15].*

such as $CrBe_{12}$ [236], the NMR lines are sharp and the hyperfine fields track the magnetization, indicating that the ferromagnetism is a bulk effect, whether or not triggered by impurities. The slopes of the $\mathcal{K}$ versus χ plots for hyperfine fields associated with magnetic atom sites, such as Zr in $ZrZn_2$, or Fe or Co in $TiFe_xCo_{1-x}$, are generally small, ranging between 0 and ± 100 kOe/μ_B. Similar small fields occur for Ti in paramagnetic $TiBe_2$, and V in the V_3X compounds, suggesting the presence of band effects such as *s-d* hybridization. Weaker hyperfine constants occur at nontransition metal sites in the itinerant ferromagnets, implying that only weak intersite effects are present in this class of compounds. This contrasts with the X site behavior of the localized paramagnetic V_3X systems which we believe is due, in large part, to substantial intersite effects.

There are a number of examples where $\mathcal{K}$ versus χ plots, with $\langle a \rangle$ assumed constant, have proven to be very useful. This is not always the case. For example, the Ga resonance in $AuGa_2$ is temperature dependent [12] and while $\mathcal{K}$ follows χ quite faithfully, T_1 data indicate a substantial variation with temperature in the contact *s* contribution to $\langle a \rangle$. This has led to a model of thermal population of an *s* band [238], which, however, does not explain the susceptibility behavior. As of yet, this system is not completely understood.

14. Summary

In this paper, we have dealt with the Knight shift and its interpretation in terms of various models of the electronic behavior in metals, emphasizing recent developments. It is apparent that the relation of the Knight shift to the density of states is complicated, but there are compensations in that a large amount of closely related and more intricate information may be deduced from Knight shift studies in metals, compounds and alloy systems. Information may be obtained concerning the wave functions of the electrons at the Fermi surface as probed at the resonating nuclei. Contributions to $\mathcal{K}$ can be separated into terms arising from *s*-electron and *d*-electron character, and in some instances there are indications of contributions due to *p*-character. In addition, orbital and diamagnetic contributions can be deduced at times. We have discussed most of the methods with which one obtains wavefunction insight from Knight shifts. This wavefunction information is related directly to $N(E)$ and is needed in the evaluation of $\langle a \rangle$. The relations between $\mathcal{K}$, $\langle a \rangle$, and the density of states are shown quantitatively in several equations throughout the text.

These same equations display the unique relation of $\mathcal{K}$ with a *local* density of states due to the weighted averaging associated with $\langle a \rangle$. This becomes useful particularly in the case of intermetallic compounds and

less so for alloys where atoms occupy positions with a random arrangement. Often it is preferable to absorb this randomness into $\langle a \rangle$. In intermetallic compounds, the Knight shift behavior definitely suggests a description in terms of wavefunctions *and* densities of states that are different for inequivalent sites. In such a situation the magnetic response of one site to another is of concern. In other words now there are *inter-* as well as *intra*-atomic effects. In the case of pure metals this complication also arises but is hidden in $\langle a \rangle$.

In this Symposium, a number of advanced theoretical and experimental techniques for studying the electron density of states have been discussed. It is to be hoped that fruitful correlations between these methods and Knight shifts will be obtained in the future.

15. Acknowledgments

Valuable assistance with the bibliographical aspects and preparation of the Knight shift tables, by D. J. Kahan of the Alloy Data Center (part of the National Standard Reference Data System) is gratefully acknowledged. Useful suggestions and comments by T. J. Rowland, M. N. Alexander, A. T. Fromhold and I. D. Weisman have aided in preparation of this manuscript. We wish to thank J. A. Hofmann for making a draft of his work [156] available to us prior to publication.

16. References

[1] Knight, W. D., Phys. Rev. **76,** 1259 (1949).
[2] Townes, C. H., Herring, C., and Knight, W. D., Phys. Rev. **77,** 852 (1950).
[3] Knight, W. D., Solid State Phys. **2,** 93 (1956).
[4] Rowland, T. J., Prog. Materials Sci. **9,** 1 (1961).
[5] Drain, L. E., Metallurgical Rev. **119,** 195 (1967).
[6] Rowland, T. J., and Borsa, R., Phys. Rev. **134,** A743 (1964).
[7] Bennett, L. H., Mebs, R. W., and Watson, R. E., Phys. Rev. **171,** 611 (1968).
[8] Watson, R. E., Bennett, L. H., and Freeman, A. J., Phys. Rev. Letters **20,** 653 (1968); ibid. **20,** 1221 (1968); Phys. Rev. **179,** 590 (1969).
[9] Bennett, L. H., Phys. Rev. **150,** 418 (1966).
[10] Watson, R. E., and Freeman, A. J., in Hyperfine Interactions, A. J. Freeman and R. B. Frankel, Editors (Academic Press, N.Y. 1967) p. 53.
[11] Bagus, P. S., Liu, B., and Schaefer, H. F., III, Phys. Rev. **A** (to be published Sept. 1970).
[12] Jaccarino, V., Weger, M., Wernick, J. H., and Menth, A., Phys. Rev. Letters **21,** 1811 (1968).
[13] Clogston, A. M., and Jaccarino, V., Phys. Rev. **121,** 1357 (1961).
[14] Bennett, L. H., Swartzendruber, L. J., and Watson, R. E., Phys. Rev. **165,** 500 (1968).
[15] Swartz, J. C., Bennett, L. H., Swartzendruber, L. J., and Watson, R. E., Phys. Rev. **B1,** 146 (1970).
[16] Winkler, R., Phys. Letters **23,** 301 (1966).
[17] Pleiter, F., (private communication).
[18] Kubo, R., and Obata, Y., J. Phys. Soc. Japan **11,** 547 (1956).
[19] Orgel, L. E., J. Phys. Chem. Solids **21,** 123 (1961).
[20] Clogston, A. M., Jaccarino, V., and Yafet, Y., Phys. Rev. **134,** A650 (1964); Clogston, A. M., Gossard, A. C., Jaccarino, V., and Yafet, Y., Phys. Rev. Letters **9,** 262 (1962); Jaccarino, V., Proc. Col. Ampère **13,** 22 (1964).
[21] Narath, A., and Fromhold, A. T., Jr., Phys. Rev. **139,** A794 (1965).
[22] Clogston, A. M., Gossard, A. C., Jaccarino, V., and Yafet, Y., Rev. Mod. Phys. **36,** 170 (1964).
[23] Barnes, R. G., and Graham, T. P., Phys. Rev. Letters **8,** 248 (1962); Denbigh, J. S., and Lomer, W. M., Proc. Phys. Soc. (London) **82,** 156 (1963).
[24] Butterworth, J., Proc. Phys. Soc. (London) **83,** 71 (1964); Erratum, *ibid.* **83,** 893 (1964).
[25] Seitchik, J., Jaccarino, V., and Wernick, J. H., Bull. Am. Phys. Soc. **10,** 317 (1965).
[26] Andersson, L. O., Phys. Letters **26A,** 279 (1968).
[27] Korringa, J., Physica **16,** 601 (1950).
[28] Herring, C., in Magnetism, G. T. Rado and H. Suhl, Editors (Academic Press, N.Y. 1966) **Vol. IV,** Section III.
[29] Silverstein, S. D., Phys. Rev. **128,** 631 (1962); and Silverstein, S. D., Phys. Rev. **130,** 912 (1963).
[30] Wolff, P. A., Phys. Rev. **120,** 814 (1960).
[31] Wolff, P. A., Phys. Rev. **129,** 84 (1963).
[32] Herring, C., in Magnetism, G. T. Rado and H. Suhl, Editors (Academic Press, N.Y. 1966) **Vol. IV,** Sections X and XII.
[33] Hurd, C. M., and Coodin, P., J. Phys. Chem. Solids 28, 523 (1967).
[34] Schumacher, R. T., and Slichter, C. P., Phys. Rev. **101,** 58 (1956).
[35] Schumacher, R. T., and Vehse, W. E., J. Phys. Chem. Solids **24,** 297 (1963).
[36] Schumacher, R. T., and Vander Ven, N. S., Phys. Rev. **144,** 357 (1966).
[37] Hultgren, R. R., Orr, R. L., Anderson, P. D., and Kelley, K. K., Selected Values of Thermodynamic Properties of Metals and Alloys (John Wiley & Sons, Inc., N.Y. 1963) and Addenda (unpublished).
[38] O'Sullivan, W. J., Switendick, A. C., and Schirber, J. E., this Symposium.
[39] Ziman, J. M., Advances in Phys. **16,** 421 (1967).
[40] Kohn, W., Phys. Rev. **96,** 590 (1954).
[41] Kjeldaas, T., Jr., and Kohn, W., Phys. Rev. **101,** 66 (1956).
[42] Cohen, M. H., Goodings, D. A., and Heine, V., Proc. Phys. Soc. (London) **73,** 811 (1959).
[43] Jones, H., and Schiff, B., Proc. Phys. Soc. (London) **67A,** 217 (1954).
[44] Holland, B. W., Phys. Stat. Solidi **28,** 121 (1968).
[45] Micah, E. T., Stocks, G. M., and Young, W. H., J. Phys. C (Solid St. Phys.) **2,** 1653 (1969); Meyer, A., Stocks, G. M., and Young, W. H., this Symposium.
[46] Kmetko, E. A., this Symposium.
[47] Pauling, L., Proc. Roy. Soc. **196A,** 343 (1949).
[48] Micah, E. T., Stocks, G. M., and Young, W. H., J. Phys. C (Solid St. Phys.) **2,** 1661 (1969).
[49] Shyu, Wei-Mei, Das, T. P., and Gaspari, G. D., Phys. Rev. **152,** 270 (1966).
[50] Pomerantz, M. and Das, T. P., Phys. Rev. **119,** 70 (1960).
[51] Shyu, Wei-Mei, Gaspari, G. D., and Das, T. P., Phys. Rev. **141,** 603 (1966).
[52] Jena, P., Mahanti, S. D., and Das, T. P., Phys. Rev. Letters **20,** 544 (1968); ibid. **20,** 977 (1968).

[53] Gerstner, J., and Cutler, P. H., Phys. Letters **30A**, 368 (1969), and this Symposium.
[54] Gaspari, G. D., and Das, T. P., Phys. Rev. **167**, 660 (1968).
[55] Jena, P., Das, T. P., Mahanti, S. D., and Gaspari, G. D., this Symposium.
[56] Moore, R. A., and Vosko, S. H., Canadian J. Phys. **46**, 1425 (1968).
[57] Moore, R. A., and Vosko, S. H., Canadian J. Phys. **47**, 1331 (1969).
[58] Hartree, D. R., Hartree, W., and Swirles, B., Phil. Trans. Royal Soc. (London) **A238**, 229 (1939).
[59] Kabartas, Z. V., Kavetskis, V. I., and Yutsis, A. P., JETP **2**, 481 (1956).
[60] Linderberg, J., and Shull, H., J. Mol. Spectros. **5**, 1 (1960).
[61] Watson, R. E., Ann. Phys. **13**, 250 (1961).
[62] Knight, W. D., Berger, A. G., and Heine, V., Ann. Phys. (N.Y.) **8**, 173 (1959).
[63] Feldman, D., Ph. D. Thesis, University of California, Berkeley, (1959).
[64] Seymour, E. F. W., and Styles, G. A., Phys. Letters **10**, 269 (1964).
[65] Borsa, F., and Barnes, R. G., J. Phys. Chem. Solids **27**, 567 (1966).
[66] Sharma, S. N., and Williams, D. L., Colloque Ampère **XIV**, 480 (1967).
[67] Dickson, E. M., Phys. Rev. **184**, 294 (1969).
[68] Kasowski, R. V., and Falicov, L. M., Phys. Rev. Letters **22**, 1001 (1969).
[69] Schone, H. E., Phys. Rev. Letters **13**, 12 (1964).
[70] Shaw, R. W., and Smith, N. V., Phys. Rev. **178**, 985 (1969).
[71] Matzkanin, G. A., and Scott, T. A., Phys. Rev. **151**, 360 (1966).
[72] Kushida, T., and Rimai, L., Phys. Rev. **143**, 157 (1966).
[73] Allen, P. S., and Seymour, E. F. W., Proc. Phys. Soc. (London) **85**, 509 (1965); Warren, W. W., Jr., and Clark, W. G., Phys. Rev. **177**, 600 (1969).
[74] Drain, L. E., Phil. Mag. **4**, 484 (1959).
[75] Umeda, J., Kusumoto, H., Narita, K., and Yamada, E., J. Chem. Phys. **42**, 1458 (1965).
[76] Adler, D., Solid State Physics **21**, 1 (1968).
[77] Sundfors, R. K., and Holcomb, D. F., Phys. Rev. **136**, A810 (1964).
[78] Alexander, M. N., and Holcomb, D. F., Revs. Mod. Phys. **40**, 815 (1968).
[79] Alexander, M. N., and Holcomb, D. F., Solid State Communications **6**, 355 (1968).
[80] O'Reilly, D. E., J. Chem. Phys. **41**, 3729 (1964).
[81] Acrivos, J. V., and Pitzer, K. S., J. Phys. Chem. **66**, 1693 (1962).
[82] McConnell, H. M., and Holm, C. H., J. Chem. Phys. **26**, 1517 (1957).
[83] Hughes, T. R., Jr., J. Chem. Phys. **38**, 202 (1963).
[84] Bardeen, J., Cooper, L. J., and Schrieffer, J. R., Phys. Rev. **106**, 162 (1951); **108**, 1175 (1957).
[85] Yosida, K., Phys. Rev. **110**, 769 (1958).
[86] Ferrell, R. A., Phys. Rev. Letters **3**, 262 (1959).
[87] Anderson, P. W., Phys. Rev. Letters **3**, 325 (1959).
[88] Wright, F., Jr., Phys. Rev. **163**, 420 (1967).
[89] Appel, J., Phys. Rev. **139**, A1536 (1965).
[90] Das, T. P., and Sondheimer, E. H., Phil. Mag. **5**, 529 (1960).
[91] Yafet, Y., J. Phys. Chem. Solids **21**, 99 (1961).
[92] Williams, B. F., and Hewitt, R. R., Phys. Rev. **146**, 286 (1966).
[93] Christensen, R. L., Hamilton, D. R., Bennewitz, H. G., Reynolds, J. B., and Stroke, H. H., Phys. Rev. **122**, 1302 (1961).
[94] Bloembergen, N., and Rowland, T. J., Acta. Met. **1**, 731 (1953).
[95] Schone, H. E., and Knight, W. D., Acta. Met. **11**, 179 (1963).
[96] Bennett, L. H., Acta Met. **14**, 997 (1966).
[97] Setty, D. L. Radhakrishna, and Mungurwadi, B. D., Phys. Rev. **183**, 387 (1969).
[98] Watson, R. E., Bennett, L. H., Weisman, I. D., and Carter, G. C. (to be published).
[99] Reynolds, J. M., Goodrich, R. G., and Khan, S. A., Phys. Rev. Letters **16**, 609 (1966).
[100] Khan, S. A., Reynolds, J. M., and Goodrich, R. G., Phys. Rev. **163**, 579 (1967).
[101] Kaplan, J. I., J. Phys. Chem. Solids **23**, 826 (1962).
[102] Stephen, M., Phys. Rev. **123**, 126 (1961).
[103] Dolgopolov, D. G., and Bystrik, P. S., Sov. Phys. JETP **19**, 404 (1964).
[104] Dolgopolov, D. G., Phys. Metal Metaloved **22(3)**, 6 (1967).
[105] Hebborn, J. E., Proc. Phys. Soc. (London) **80**, 1237 (1962).
[106] Hebborn, J. E., and Stephen, M. J., Proc. Phys. Soc. (London) **80**, 991 (1962).
[107] Glasser, M. L., Phys. Rev. **150**, 234 (1966).
[108] Goodrich, R. G., Khan, S. A., and Reynolds, J. M., Phys. Rev. Letters **23**, 767 (1969).
[109] Seitchik, J. A., Gossard, A. C., and Jaccarino, V., Phys. Rev. **136**, A1119 (1964).
[110] Mott, N. F., and Jones, H., The Theory of the Properties of Metals and Alloys, (Clarendon Press, N.Y. 1936).
[111] Misetich, A., Hodges, L., and Watson, R. E. (unpublished).
[112] Hodges, L., Ehrenreich, H., and Lang, N. D., Phys. Rev. **152**, 505 (1966).
[113] Ehrenreich, H., and Hodges, L., Methods in Comp. Physics **8**, 149 (1968).
[114] Watson, R. E., Ehrenreich, H., and Hodges, L., Phys. Rev. Letters **24**, 829 (1970).
[115] Mueller, F. M., this Symposium.
[116] Goodings, D. A., and Harris, R., Phys. Rev. **178**, 1189 (1969), and J. Phys. C. **2**, 1808 (1969).
[117] Dobbyn, R. C., Williams, M. W., Cuthill, J. R., and McAlister, A. J., Phys. Rev. **2B** (to be published).
[118] Davis, H., Phys. Letters **28A**, 85 (1968).
[119] Seitchik, J., Jaccarino, V., and Wernick, J. H., Phys. Rev. **138**, A148 (1965).
[120] Kobayashi, S., Asayama, K., and Itoh, J., J. Phys. Soc. (Japan) **18**, 1735 (1963).
[121] Narath, A., J. Appl. Phys. **39**, 553 (1968).
[122] Itoh, J., Asayama, K., and Kobayashi, S., Proc. Col. Ampère **13**, 162 (1964).
[123] Froidevaux, C., Gautier, F., and Weisman, I., Proc. Col. Ampère **13**, 114 (1964).
[124] Balabanov, A., and Delyagin, N., Soviet Phys. JETP 27, 752 (1968).
[125] Shirley, D. A., and Westenbarger, G. A., Phys. Rev. **138**, A170 (1965).
[126] Stern, E. A., Phys. Rev. **157**, 544 (1967) and in Energy Bands in Metals and Alloys, L. H. Bennett and J. T. Waber, Editors (Gordon and Breach, 1968) p. 151.
[127] Watson, R. E., in Hyperfine Interactions, A. J. Freeman and R. B. Frankel, Editors (Academic Press, N.Y., 1967) p. 413.
[128] Kohn, W., and Vosko, S. H., Phys. Rev. **119**, 912 (1960).
[129] Rowland, T. J., Phys. Rev. **119**, 900 (1960).
[130] Drain, L. E., J. Phys. C. **1**, 1690 (1968).

[131] Redfield, A. G., Phys. Rev. **130**, 589 (1963).
[132] Fernelius, N. C., Thesis, University of Illinois (1966); Proc. Colloque Ampère **14**, 497 (1967); ibid. **15**, 347 (1968).
[133] Minier, M., Phys. Letters **26A**, 548 (1968); Minier, M., and Berthier, Cl., Proc. Colloque Ampère **15**, 368 (1968); Minier, M., Phys. Rev. **182**, 437 (1969).
[134] Blandin, A., and Daniel, E., J. Phys. Chem. Solids **10**, 126 (1959).
[135] Asik, J. R., Ball, M. A., and Slichter, C. P., Phys. Rev. **181**, 645 (1969).
[136] Ball, M. A., Asik, J. R., and Slichter, C. P., Phys. Rev. **181**, 662 (1969).
[137] Vonsovski, S., JETP **16**, 981 (1946); ibid. **24**, 419 (1953).
[138] Ruderman, M. A., and Kittel, C., Phys. Rev. **96**, 99 (1954); Mitchell, A. H., Phys. Rev. **105**, 1439 (1957).
[139] Kasuya, T., Prog. Theoret. Phys. **16**, 45 (1956).
[140] Yosida, K., Phys. Rev. **106**, 893 (1957).
[141] Condon, E. U., and Shortley, G. H., The Theory of Atomic Spectra (University Press, Cambridge, 1964).
[142] Anderson, P. W., and Clogston, A. M., Bull. Am. Phys. Soc. **6**, 124 (1961).
[143] Schrieffer, J. R., and Wolff, P. A., Phys. Rev. **149**, 491 (1966).
[144] Watson, R. E., Koide, S., Peter, M., and Freeman, A. J., Phys. Rev. **139**, A167 (1965).
[145] Watson, R. E., and Freeman, A. J., J. Appl. Phys. **37**, 1444 (1966).
[146] Jaccarino, V., Matthias, B. T., Peter, M., Suhl, H., and Wernick, J. H., Phys. Rev. Letters **5**, 251 (1960).
[147] Peter, M., J. Appl. Phys. **32**, 338S (1961).
[148] Peter, M. Shaltiel, D., Wernick, J. H., Williams, H. J., Mock, J. B., and Sherwood, R. C., Phys. Rev. **126**, 1395 (1962).
[149] Shaltiel, D., Wernick, J. H., Williams, H. J., and Peter, M., Phys. Rev. **135**, A1346 (1964).
[150] Rowland, T. J., Phys. Rev. **125**, 459 (1962).
[151] Weisman, I. D., and Knight, W. D., Phys. Rev. **169**, 373 (1968).
[152] Wolff, P. A., Phys. Rev. **120**, 814 (1960).
[153] Wolff, P. A., Phys. Rev. **129**, 84 (1963).
[154] Giovannini, B., Peter, M., Schrieffer, J. R., Phys. Rev. Letters **12**, 736 (1964).
[155] Alexander, M. N., Phys. Rev. **172**, 331 (1968).
[156] Senturia, S. D., Smith, A. C., Hewes, C. R., Hofmann, J. A., and Sagalyn, P. L., Phys. Rev. B, **Vol. 1**, 40–45 (1970).
[157] Van Ostenburg, D. O., Lam, D. J., Trapp, H. D., and MacLeod, D. E., Phys. Rev. **128**, 1550 (1962).
[158] Drain, L. E., J. Phys. Radium **23**, 745 (1962).
[159] Lam, D. J., Van Ostenburg, D. O., Nevitt, M. W., Trapp, H. D., and Pracht, D. W., Phys. Rev. **131**, 1428 (1963); ibid. **133I**, 1 (1964).
[160] Bernasson, M., Descouts, P., Donzé, P., and Treyvaud, A., J. Phys. Chem. Solids **30**, 2453 (1969).
[161] Betsuyaku, H., Takagi, Y., and Betsuyaku, Y., J. Phys. Soc. Japan **19**, 1089 (1964).
[162] Zamir, D., Phys. Rev. **140**, A271 (1965).
[163] Van Ostenburg, D. O., Lam, D. J., Shimizu, M., and Katsuki, A., J. Phys. Soc. Japan **18**, 1744 (1963).
[164] Masuda, Y., Nishioka, M., and Watanabe, J. Phys. Soc. Japan **22**, 238 (1967).
[165] Taniguchi, S., Tebble, R. S., and Williams, D. E. G., Proc. Roy. Soc. **265A**, 502 (1962).
[166] Cheng, C. H., Gupta, K. P., Van Reuth, E. C., and Beck, P. A., Phys. Rev. **126**, 2030 (1962).
[167] Gupta, K. P., Cheng, C. H., and Beck, P. A., Metallic Solid Solutions, J. Friedel and A. Guinier, Editors, (W. A. Benjamin, Inc., N.Y., 1963) chapter 25.
[168] Morin, F. J., and Maita, J. P., Phys. Rev. **129**, 1115 (1963).
[169] Rohy, D., and Cotts, R. M., Phys. Rev. **1B**, 2070 (1970).
[170] Rohy, D., and Cotts, R. M., Phys. Rev. **1B**, 2484 (1970).
[171] Swartz, J. C., Swartzendruber, L. J., Bennett, L. H., and Watson, R. E., Phys. Rev. **B1**, 146 (1970).
[172] Bennett, L. H., Swartzendruber, L. J., and Watson, R. E., Phys. Rev. **165**, 500 (1968).
[173] Bos, W. G., and Gutowsky, H. S., O.N.R. Tech. Rept. No. 93, (available as AD-640514) (1966).
[174] Schreiber, D. S., Phys. Rev. **137**, A860 (1965).
[175] Alfred, L. C. R., and Van Ostenburg, D. O., Phys. Rev. **161**, 569 (1967).
[176] Kohn, W., and Vosko, S. H., Phys. Rev. **119**, 912 (1960).
[177] Blatt, F. J., Phys. Rev. **108**, 285 (1957).
[178] Odle, R. L., and Flynn, C. P., Phil. Mag. **13**, 699 (1966).
[179] Snodgrass, R. J., and Bennett, L. H., Phys. Rev. **134**, A1294 (1964).
[180] Heighway, J., and Seymour, E. F. W., Phys. Letters **29A**, 282 (1969).
[181] Seymour, E. F. W., and Styles, G. A., Proc. Phys. Soc. (London) **87**, 473 (1966).
[182] Anderson, W. T., Jr., Thatcher, F. C., and Hewitt, R. R., Phys. Rev. **171**, 541 (1968).
[183] Kaeck, J. A., Ph. D. Thesis University of Cornell, N.Y. (1968).
[184] Van der Molen, S. B., Van der Lugt, W., Draisma, G. G., and Smit, W., Physica **38**, 275 (1968).
[185] Van der Molen, S. B., Van der Lugt, W., Draisma, G. G., and Smit, W., Physica **40**, 1 (1968).
[186] Van der Lugt, W., and Van der Molen, S. B., Phys. Stat. Solid **19**, 327 (1967).
[187] Seymour, E. F. W., Styles, G. A., and Taylor, B., Proc. Col. Ampère **11**, 612 (1962).
[188] Seymour, E. F. W., and Styles, G. A., Proc. Phys. Soc. (London) **87**, 473 (1966).
[189] Slocum, R. R., Ph. D. Thesis, College of William and Mary, Virginia (1969).
[190] Van Hemmen, J. L., Caspers, W. J., Van der Molen, S. B., Van der Lugt, W., and Van de Braak, H. P., Z Physik **222**, 253 (1969).
[191] Rigney, D. A., and Flynn, C. P., Phil. Mag. **15**, 1213 (1967).
[192] Moulson, D. J., and Seymour, E. F. W., Advan. Phys. **16**, 449 (1967).
[193] Bennett, L. H., Cotts, R. M., and Snodgrass, R. J., Proc. Colloque Ampère **13**, 171 (1965).
[194] Matzkanin, G. A., Spokas, J. J., Sowers, C. H., Van Ostenburg, D. O., and Hoeve, H. C., Phys. Rev. **181**, 559 (1969).
[195] Wells, J. C., Jr., Williams, R. L., Jr., Pfeiffer, L., and Madansky, L., Phys. Letters **27B**, 448 (1968).
[196] Gardner, J. A., and Flynn, C. P., Phil. Mag. **15**, 1233 (1967).
[197] Flynn, C. P., Rigney, D. A., and Gardner, J. A., Phil. Mag. **15**, 1255 (1967).
[198] Rao, G. N., Matthias, E., and Shirley, D. A., Phys. Rev. **184**, 325 (1969).
[199] Clogston, A. M., Matthias, B. T., Peter, M., Williams, H. J., Corenzwit, E., and Sherwood, R. C., Phys. Rev. **125**, 541 (1962).
[200] Stupian, G. W., and Flynn, C. P., Phil. Mag. **17**, 295 (1968).
[201] Van Vleck, J. H., Theory of Electric and Magnetic Susceptibilities, (Oxford University Press, 1932).

417-156 O - 71 - 42

[202] Peter, M., Shaltiel, D., Wernick, J. H., Williams, H. J., Mock, J. B., and Sherwood, R. C., Phys. Rev. **126**, 1395 (1962).
[203] Shaltiel, D., Wernick, J. H., Williams, H. J., and Peter, M., Phys. Rev. **135**, A1346 (1964).
[204] Cragle, J., Phys. Rev. Letters **13**, 569 (1964).
[205] Jones, E. D., Phys. Rev. **180**, 455 (1968).
[206] Jones, E. D., Phys. Rev. Letters **19**, 432 (1967).
[207] Shulman, R. G., Wyluda, B. J., and Matthias, B. T., Phys. Rev. Letters **1**, 278 (1958).
[208] Blumberg, W. E., Eisinger, J., Jaccarino, V., and Matthias, B. T., Phys. Rev. Letters **5**, 149 (1960).
[209] Weger, M., (to be published).
[210] Gossard, A. C., Phys. Rev. **149**, 246 (1966); Errata, ibid. **164**, 878 (1967) and **185**, 862 (1969).
[211] Labbé, J., and Friedel, J., J. Physique **27**, 153 (1966).
[212] Mattheiss, L. F., Phys. Rev. **138**, A112 (1965).
[213] Shulman, R. G., Wyluda, B. J., and Matthias, B. T., Phys. Rev. Letters **1**, 278 (1958).
[214] Lütgemeier, H., Z. Naturforsch. **20A**, 246 (1965).
[215] Gossard, A. C., Jaccarino, V., and Wernick, J. H., Phys. Rev. **128**, 1038 (1962).
[216] Seitchik, J. A., and Walmsley, R. H., Phys. Rev. **137**, A143 (1965).
[217] Cooper, B. R., Phys. Letters **22**, 244 (1966).
[218] Jaccarino, V., J. Appl. Phys. **32S**, 102 (1961).
[219] Jones, E. D., and Budnick, J. I., J. Appl. Phys. **37**, 1250 (1966).
[220] Barnes, R. G., and Jones, E. D., Solid State Comm. **5**, 285 (1967).
[221] de Wijn, H. W., van Diepen, A. M., and Buschow, K. H. J., Phys. Rev. **161**, 253 (1967).
[222] van Diepen, A. M., de Wijn, H. W., and Buschow, K. H. J., J. Chem. Phys. **46**, 3489 (1967).
[223] Buschow, K. H. J., van Diepen, A. M., and de Wijn, H. W., Phys. Letters **24A**, 536 (1967).
[224] van Diepen, A. M., de Wijn, H. W., and Buschow, K. H. J., Phys. Letters **26A**, 340 (1968).
[225] Gossard, A. C., and Jaccarino, V., Proc. Phys. Soc. (London) **80**, 877 (1962).
[226] Vijayaraghavan, R., Malik, S. K., and Rao, V. U. S., Phys. Rev. Letters **20**, 106 (1968).
[227] Barnes, R. G., Borsa, F., and Peterson, D., J. Appl. Phys. **36**, 940 (1965).
[228] Rao, V., U. S., and Vijayaraghavan, R., Phys. Letters **19**, 168 (1965).
[229] Borsa, F., Barnes, R. G., and Reese, R. A., Phys. Status Solidi **19**, 359 (1967).
[230] Rao, V. U. S., and Vijayaraghavan, R., J. Phys. Chem. Sol. **29**, 123 (1968).
[231] West, G., Phil. Mag. **9**, 979 (1964).
[232] West, G., Phil. Mag. **15**, 855 (1967).
[233] Seitchik, J., and Walmsley, R. H., Phys. Rev. **131**, 1473 (1963).
[234] Asayama, K., J. Phys. Soc. Japan **18**, 1727 (1963).
[235] Yamadaya, T., and Asanuma, M., Phys. Rev. Letters **15**, 695 (1965).
[236] Wolcott, N. M., Falge, R. L., Jr., Bennett, L. H., and Watson, R. E., Phys. Rev. Letters **21**, 546 (1968).
[237] Rhodes, P., and Wohlfarth, E. P., Proc. Roy. Soc. (London) **273A**, 247 (1963).
[238] Switendick, A. C., and Narath, A., Phys. Rev. Letters **22**, 1423 (1969).
[239] Ryter, C., Phys. Rev. Letters **5**, 10 (1960).
[240] Ryter, C., Phys. Letters, 69 (1963).

Discussion on "Relevance of Knight Shift Measurements to the Electronic Density of States" by L. H. Bennett (NBS), R. E. Watson (Brookhaven National Laboratory), and G. C. Carter (NBS)

R. V. Kasowski *(DuPont and Co.):* The density of states for Cd as calculated by Shaw at the Fermi surface does not agree with superconductivity data as is shown in the W. L. McMillan paper (Phys. Rev. **167**, 331 (1968)). We have calculated [1] the density of states at the Fermi surface and find exact agreement with McMillan's superconductivity data and specific heat.

[1] Allen, P. B., Cohen, M. L., Falicov, L. M., and Kasowski, R. V., Phys. Rev. Letters **21**, 1794 (1968).

Pauli Paramagnetism in Metals with High Densities of States*[1]

S. Foner

Francis Bitter National Magnet Laboratory, Massachusetts Institute of Technology, Cambridge, Massachusetts 02139

Because the Pauli paramagnetic susceptibility of a free electron gas, χ_p^0 is proportional to the density of states $N(0)$ at the Fermi energy, it is expected that measurements of χ_p^0 of metals and alloys can yield a reasonable measure of $N(0)$. If χ_p^0 can be measured directly, then $N(0)$ can be determined with high accuracy. The major obstacle to this procedure is that the measured static susceptibility $\chi_p = \chi_p^0/(1-N(0)V) = \chi_p^0 D$ (for the Stoner model) where V is a measure of the electron-electron interaction potential. Unfortunately, V is not easily determined experimentally, or theoretically, so that measurements of χ_p do not yield accurate measures of $N(0)$. More detailed (realistic) models involve additional parameters which are also not accurately determined. Thus direct measurements of χ_p can yield a measure of $N(0)$, but these values of $N(0)$ are subject to the uncertainties of various parameters in the theories. In this talk we discuss the present status of experiments and theories of χ_p in metals and alloys with low $N(0)$ where D is generally near unity, and high $N(0)$ where D is expected to be large. Comparisons with independent low-temperature electronic specific heat measurements are discussed and attempts to derive $N(0)$ from both susceptibility and specific heat are reviewed.

Many recent investigations of metals and alloys with high densities of states have been of great interest because such systems start to approach ferromagnetic order. The properties of Pd have been investigated extensively and very detailed band calculations now exist. The large exchange enhancements in this metal and its alloys have permitted considerable progress to be made. The properties of these systems are reviewed and estimates of $N(0)$ and V are examined. Here qualitative and quantitative comparisons of various experiments can be made. The possibilities of applying large magnetic fields and thereby independently measuring $N(0)$ and small changes of $N(0)$ near the Fermi energy by such studies are discussed. Recent theories which examine the changes of χ_p with alloying are also compared with experimental results.

A few useful references for relevant recent papers concerning the susceptibility of nearly ferromagnetic metals and alloys are tabulated in references 1 to 4. Recent detailed band calculations in Pd have been reported in references 5 to 8. Several papers at this conference also deal with high densities of states materials.

References

[1] Foner, S., Freeman, A. J., Blum, N., Frankel, R. B., McNiff, E. J., Jr., and Praddaude, H., Phys. Rev. **181**, 863 (1969).
[2] Foner, S., and McNiff, E. J., Jr., Phys. Rev. Letters **19**, 1438 (1967).
[3] Foner, S., and McNiff, E. J., Jr., Phys. Letters **29A**, 28 (1969).
[4] Doclo, R., Foner, S., and Narath, A., J. Appl. Phys. **40**, 1206 (1969).
[5] Mueller, F. M., Freeman, A. J., Dimmock, J. O., and Furdyna, A. (to be published).
[6] Hodges, L., Ehrenreich, H., and Lang, N. D., Phys. Rev. **152**, 505 (1966).
[7] Anderson, O. K., and Mackintosh, A. R., Solid State Comm. **6**, 285 (1968).
[8] Misetich, A. A., and Watson, R. E., J. Appl. Phys. **40**, 1211 (1969).

*An invited paper presented at the 3d Materials Research Symposium, *Electronic Density of States*, November 3–6, 1969, Gaithersburg, Md.

[1] Supported by the U.S. Air Force Office of Scientific Research.

Discussion on "Pauli Paramagnetism in Metals with High Densities of States" by S. Foner (Massachusetts Institute of Technology)

F. Ajami *(Univ. of Pennsylvania):* Would you care to comment on the temperature dependence of the various contributions to the susceptibility?

S. Foner *(MIT):* Most of the contributions to the total susceptibility, χ_{TOTAL}, where $\chi_{TOTAL} = \chi_{dia} + \chi_{s,p} + \chi_{vv} + \chi_d + (\chi_{imp} + \chi_{sw}) + \ldots$ are not strongly temperature dependent. This includes χ_{dia} (diamagnetic core), $\chi_{s,p}$ (of the s,p bands) and χ_{vv} (the orbital or Van Vleck susceptibility). For the strongly paramagnetic exchange enhanced metal or alloy (which is the main topic of this talk) the largest contribution comes from χ_d (the enhanced Pauli paramagnetism of the relevant d bands in say Pd) and this can be strongly temperature dependent. The terms in the ( ), χ_{imp} (impurity) and χ_{sw} (spin-wave contributions of ferromagnetic systems) can often be suppressed at low temperatures with a sufficiently high magnetic field. If we can use the band calculations we can in principle take into account the smearing of the Fermi distribution as we increase the temperature and hope to be able to calculate the temperature dependent susceptibility. There have been numerous attempts of this in the literature; qualitatively, they will give good results, but quantitatively, I am not sure that one can really believe them.

O. K. Andersen *(Univ. of Pennsylvania):* About the band structure calculations, I think perhaps you have been a bit unfair to them, because I think all three or at least the two—the Mueller, Freeman et al. and the Mackintosh and Andersen agree. The Watson-Misetich-Lang results differ somewhat. The two first mentioned calculations are essentially first principles calculations, either fitted to a first principle APW calculation as closely as possible or done entirely with the first principles relativistic APW method.

The discrepancy between different band structures calculated for the same transition metal is mainly a discrepancy in the width and the position of the d-bands relatively to the sp-band. Therefore, for such parts of a d-band where hybridization with the sp-band is unimportant, the results of different calculations only differ in the energy-scale; the shape of this part of the band, which is a structural property, is unique. Now, in that narrow energy range around the Fermi level, which is relevant for the high field susceptibility of Pd, the dominant contribution to the density of states comes from such a purely d-like part of the bands. If, therefore, the density of states were calculated with infinitely high resolution for each of the three above mentioned Pd-bands, the derived deviations from linearity of the curve magnetic field versus magnetization would in each case have the same shape, but would differ by the scale of the d-bandwidth; If the position of the Fermi level within the d-band was the same for all those calculations then they would, for instance, all predict the existence of a van Hove singularity in the magnetization curve for Pd at a magnetization of about 0.06 Bohr magnetons per atom, but the estimates for the corresponding magnetic field would scale with the d-bandwidths.

Finally, let me mention that from our relativistic APW bands we have dared to derive the band structure contribution to the deviation from linearity of the magnetization curve for Pd and, using the dubious rigid band model, for dilute RhPd alloys. Our results seem to agree with the measurements of Foner and McNiff, but comparison is difficult, since the effect is of the same order of magnitude as the experimental uncertainty. We will report on these results at the coming conference for Magnetism and Magnetic Materials.

R. E. Watson *(Brookhaven National Lab.):* It might be best if I first reviewed the origin of the three sets of band structure results. The Andersen-Mackintosh result relied on a relativistic APW calculation: In a narrow range around the Fermi energy the details in the density of states were calculated by tracing of constant energy surfaces and by fitting the calculated volumes to a power expansion in energy, which includes the characteristic 3/2-power van Hove term. The Freeman-Mueller, et al. results involved nonrelativistic APW bands which were then fitted with Mueller's d tight binding-OPW interpolation scheme and spin orbit effects were added. The resulting band structure was then sampled with a quadratic interpolation scheme when estimating $N(E)$. The results of Misetich, Lange and myself involved a fit, with the Hodges, Ehrenreich and Lange tight binding-OPW scheme, to one set of the Freeman, Dimmock, Furdyna nonrelativistic APW

results. A spin orbit constant was chosen (different from that of Mueller et al.) and the interpolation scheme parameters were further adjusted to improve agreement with the experimental Fermi surface areas. The final set of parameters was by no means unique. There are obvious dangers in such adjustments to the prediction of other quantities such as $N(E_F)$. The bands were then sampled with a quadratic scheme to construct a histogram. Dr. Foner mentioned "high resolution calculations." The three sets of results are "high resolution" in only one sense: Given particular band structures, careful samplings were taken when constructing density of states histograms. The Andersen result is, in principle, to be preferred since it did not utilize an intermediate tight binding-OPW description of the bands with attendant questions, such as those concerning subtle features of the d bands which are not reproduced by the near neighbor tight binding scheme. I would suggest that the three sets of results are in essential agreement, though perhaps not for Dr. Foner's purposes. Our experience with other transition metals shows it is difficult to nail down such factors as d bandwidth to the accuracy important to our estimates of $N(E_F)$ here. There may be serious shortcomings in the potentials employed to date in the "a priori" calculations for the transition metals. Good predicted Fermi surfaces are inadequate tests of band results; the band structure results of Misetich, Lange, and myself are probably the poorest of the three sets due to improving the Fermi surface fit.

J. Callaway *(Louisiana State Univ.):* It was evident from Professor Ziman's lecture earlier in the week that d bands may be sensitive to the crystal potential in the region between atomic spheres. One should therefore be cautious in considering the APW results as valid without independent confirmation. Specifically, the density of states at the top of the d band will depend sensitively on the relative positions of the X_5 and the X_2 levels. These have different symmetry, and are split by crystal field effects. The relation of those levels will be affected by the non-spherical components of the crystal potential and by the potential in the interstitial region. It is thus possible that these levels may not be correctly located by APW calculations which use a spherical "muffin tin" potential. These considerations emphasize the need for self-consistency.

A. J. Freeman *(Northwestern Univ.):* Let me point out that the calculations originally done by myself, John Dimmock and Anna Furdyna, a number of years ago, were first principles APW calculations. We considered a number of potentials; we did not just take the first potential off the shelf. These calculations are, I think, important for the following reasons: Palladium has now become perhaps the best studied metal; all these various APW calculations agree very well with each other and with experiment.

I do not understand why the interpolation used by Misetich, Lange, and Watson of the bands that were calculated by the Furdyna, Dimmock, Freeman group give such different results, because in fact, the agreement of the relativistic calculations of Andersen and Mackintosh with our calculations is remarkable (as you saw and heard). Now as far as the question of sensitivity and so forth of those levels near the point X, well, you are right, there is great sensitivity. It turns out that despite this sensitivity, we do not find differences in the results despite the differences expected, due to the use of essentially different techniques. Andersen-Mackintosh solved the Dirac equation. We solved the nonrelativistic Schrödinger form. Finally, let me say that we have here a wealth of material to discuss, argue about, and try to understand. I think that is what Si was trying to do for us. At the moment, I would say that the two of the three groups agree—the burden of proof is on the third group, to ascertain why their results disagree.

A. R. Mackintosh *(Lab. for Electrophysics, Tech. Univ., Denmark):* I just wanted to make a suggestion. Could you not improve the accuracy of your experimental measurements by using field modulation and measuring the gradient of the susceptibility? I believe that this is the direction in which improvement is to be sought, rather than in attempting further refinements of the calculations which, after all, already make much more precise predictions than the experiments can test.

S. Foner *(MIT):* The modulation technique is probably *not* the way to go. Estimates show that this approach lacks about a factor of 100 in sensitivity over our present magnetic moment measurements in high dc fields (see S. Foner and E. J. McNiff, Jr., Rev. Sci. Instr. **39,** 171 (1968)). The major limitations are the background noise in the high field magnets—even 0.01% peak to peak noise at 150 kG is a large flux change. We wish to detect a change of 0.1% in the moment of Pd at 200 kG corresponding to a change of about 0.01G at this field. As improvement of a factor of 10 in the signal-to-noise is needed in order to reexamine the field dependence of χ for pure Pd, where we have high resolution band calculations. I want to make another comment. One susceptibility measurement which I have not discussed is the dHvA experiments which have been carried out so well by the Argonne group who are just starting to see parts of the pipes. If they can get more information on these major pieces of Fermi surface we would have much more confidence in

the various Pd band calculations. Perhaps Windmiller might want to say something about this.

L. Windmiller *(Argonne National Labs.):* We are trying to press our measurements further. We have seen some more of those pieces. The only other comment I wanted to make was about the g-factor. It is anisotropic and deviates from 2. When we reported measurements before, we only found the g-factor being different from 2 on the Γ-centered surface. Since then, in both Pd and Pt we have seen spin-splitting zeroes for the large d-like surface and in both of these the deviations from 2 are even greater on the open hole surface than they are on the Γ-centered surface. The relation of the susceptibility to the density of states thus seems to be a question. I think we should start pushing the band structure people to see what they can do. Also, questions concerning how the g-factor varies with the Fermi surface as we start alloying things and putting in different materials so that you keep the Fermi level fixed are moot points. We just don't know what happens right now.

Calculation of the Knight Shift in Beryllium*

J. Gerstner and P. H. Cutler

Department of Physics, The Pennsylvania State University, University Park, Pennsylvania 16802

Key words: Beryllium; Knight shift; orthogonalized plane wave (OPW); pseudopotential.

A nonlocal pseudopotential theory has been used to calculate the contributions to the Knight shift in beryllium. For the first time, the computed value has both the correct sign and numerical agreement with recent experiments. This work has been published in Physics Letters **30A**, 368 (1969) with the exception of the following changes:

$$\left(\frac{\Delta H}{H}\right)_{\text{diam}} = -0.00514\%$$

$$\left(\frac{\Delta H}{H}\right)_{\text{calc}} = -0.00410\%$$

*Research sponsored in part by the Air Force Office of Scientific Research, United States Air Force, Grants No. 213-66 and 69-1704.

Discussion on "Calculation of the Knight Shift in Beryllium" by J. Gerstner and P. H. Cutler (Pennsylvania State University)

P. L. Sagalyn *(Army Matls. & Mech. Res. Cent., Mass.):* I would like to ask Dr. Gerstner whether he has or possibly could, calculate the contribution of the diamagnetic field to the spin-lattice relaxation time?

J. Gerstner *(Operations Res. Inc.):* The answer is no and no. We have essentially stopped this calculation for a lack of funds and time. So I consider it a closed subject. I would be glad to discuss it with you on the side though and see what could be done.

Knight Shifts of the Alkali Metals

A. Meyer

Northern Illinois University, DeKalb, Illinois 60115

G. M. Stocks* and W. H. Young

University of Sheffield, Sheffield, England

K, Rb and Cs, being leading members of transition series, have pseudoatoms with virtual bound d states; Li has a somewhat analogous p state. By contrast, Na has no such states. Evidence is offered of how the associated scattering accounts for the following observed electron transport properties: (a) Under pressure, the resistance of Li rises and, eventually, so do those of Cs, Rb and K, (b) the thermopower of Li is anomalous (positive) and stays so under pressure while that for Cs very quickly becomes positive when pressure is applied.

The same features can now be used in the theory of Knight shifts to explain the following observations. (c) The conduction electron susceptibility for Li is enhanced very significantly above that for free (and even interacting) electrons, (d) the nuclear contact density in Li is much lower than that predicted by one-OPW theory, (e) the Knight shifts of Li and Na decrease and those for Rb and Cs increase when pressure is applied, (f) the Knight shift for a given ion increases when it is successively resonated in Na, K, Rb, and Cs matrices. The key to the interpretation of (e) and (f) is the variation in the density of states (and therefore susceptibility) under conditions of pressure change and alloying.

Key words: Alkali metals; alloys; cesium; Knight shift; lithium; potassium; pressure dependences; pseudopotential; resistivity ratios; rubidium; sodium; thermoelement power.

1. Introduction

This paper is concerned with interpreting the absolute Knight shifts of the alkalis, their variations with pressure and the absolute Knight shifts in binary alkali systems. While based on precise and detailed calculations [1-3], for the present conference it seems to us desirable to give an overall (and less formal) perspective to the work, to highlight the main features and show how the basic underlying explanation of these is the same as for the electronic transport properties.

We will use for the Knight shift, K, the basic formula [4]

$$K = [8\pi/3)\chi\Omega P_F \tag{1}$$

where Ω is the total volume of the metal, P_F is the (average) density of valence electrons evaluated at the resonant nuclear site and at the Fermi level, and χ is the magnetic susceptibility per unit volume of the valence electrons. In section 2 we indicate the development of a simple formalism that enables one to calculate both χ and ΩP_F in a mutually consistent manner.

Guided by the Ziman [5] pseudoatom concept, the problem is reduced to the solution of radial Schrödinger equations. ΩP_F is given, after renormalization, by the nuclear contact part, the latter being very conveniently summarized by a simple formula, as we shall see. At large distances the solutions are characterized by phase shifts, these describing χ and the renormalization factors indicated above, as well as the transport properties. The phase shifts have been tabulated [6] and are not so conveniently summarized. Nevertheless, each metal has its own characteristic behavior which can be qualitatively illustrated by its transport properties. It seems better to do this (as we do in sec. 3) than quote a lot of already available numbers.

Turning to the Knight shift applications, in section 4, we consider the absolute Knight shifts, including those under pressure [7] and in section 5 we present an interpretation of recent work on alloys [8,9]. Finally, in section 6, there is a summary.

*Present address: Metals and Ceramics Division, Oak Ridge National Laboratory, Tennessee.

2. Formalism

We consider an electron with Hamiltonian

$$H = T + \sum_{\mathbf{R}} U(\mathbf{r}-\mathbf{R}) \tag{2}$$

where the U's describe the screened ion fields. (For the moment we consider a pure metal where all the U's are the same; the generalization to alloys is straightforward and will be affected later.) Then we postulate the wave function

$$\psi_{\mathbf{k}} \propto e^{i\mathbf{k}\cdot\mathbf{r}} + \sum_{\mathbf{R}} e^{i\mathbf{k}\cdot\mathbf{R}}\ \phi_{\mathbf{k}}(\mathbf{r}-\mathbf{R}) \tag{3}$$

which is written so as to show a plane wave together with the scattered waves ϕ emanating from the various ions. The latter interpretation is formalized by computing the expectation value of (2) with respect to (3), discarding multi-center terms and using the ϕ's as variable functions. The result is

$$(T+U(r))\ \xi_{\mathbf{k}}(\mathbf{r}) = (\hbar^2k^2/2m)\ \xi_{\mathbf{k}}(\mathbf{r}) \tag{4}$$

where

$$\xi_{\mathbf{k}}(\mathbf{r}) = e^{i\mathbf{k}\cdot\mathbf{r}} + \phi_{\mathbf{k}}(\mathbf{r}) \tag{5}$$

In a similar approximation we find a mean contact density of

$$P \equiv \langle N^{-1} \sum_{\mathbf{R}} |\psi_{\mathbf{k}}(\mathbf{R})|^2 \rangle = \frac{|\xi_{\mathbf{k}}(0)|^2}{\Omega + N\int\{\ |\xi_{\mathbf{k}}(\mathbf{r})|^2 - 1\}\, dr} \tag{6}$$

The interpretation of this is clear. If the integral were not present in the denominator, the result would correspond to (4), i.e., one center in an otherwise featureless medium. The renormalizing term consists of equal contributions from each of the N sites and is an expression of electron-ion affinity.

The solutions (5) of (4) lead to phase shift $\eta_l(k)$, from which, when small (modulo π), the energy can be obtained by first order perturbation theory. From

$$mE/\hbar^2 = \frac{1}{2}\, k^2 - 2\pi(N/\Omega)\Sigma(2l+1)\eta_l/k, \tag{7}$$

one computes an effective mass at the Fermi level given by

$$m/m^* = 1 + s - \sigma, \tag{8}$$

where

$$s = (2/3\pi)\Sigma(2l+1)\eta_l(k_F) \tag{9}$$

and

$$\sigma = (2/3\pi)\Sigma(2l+1)\,(k\partial\eta_l/\partial k)_F \tag{10}$$

and a susceptibility can then be computed from $(m^*/m)\chi_f$ where χ_f is the free-electron value. One must also incorporate an important valence electron correlation correction [10-12], but the essential features seem already to be present in the above analysis.

The phase shift gradients which occur in (10) are also the parameters needed to evaluate the denominator of (6). In fact (Kittel [13]), on the mean,

$$\int\{|\xi_{\mathbf{k}}(\mathbf{r})|^2 - 1\}\, d\tau = (2\pi/k^3)\Sigma(2l+1)\,(k\partial\eta_l/\partial k) \tag{11}$$

Thus we need to compute $\xi(0)$'s for (6), and η's and $\partial\eta/\partial k$'s for (6) and (8); this can be done straightforwardly from (4) once U is specified.

As developed above, the theory does not distinguish between solids and liquids (except by the small density change involved) and this is in agreement with experiment [14]. In fact the applications to pure metals under pressure given in section 4 are for solids, while those to the alloys in section 5 are for liquids.

The choice of U faces us with a difficult problem. In the past, the present authors have used truncated ion potentials and guided by pseudopotential theory [5], have required (cf. (9) above) that $s = 1/3$ governs the choice of cut-off. On the other hand, recently, it has been suggested [15,16] that $s \approx 0$ (corresponding to muffin tins; see below) might be better. Indeed Lee [17] has fitted the observed Fermi surface anisotropies in the solid alkalis to phase shifts which roughly satisfy this criterion.

It seems to us [18] that the resolution of this difficulty lies in remembering that pseudopotentials overlap somewhat and are rigidly located on the various ions. Thus, as the ions move about, fluctuations in the net potential in the interstitial regions are described [19]. This physical aspect of the pseudopotentials is missed by the muffin tins which correspond only to the *mean* minimal nonoverlapping potential. If fluctuations are unimportant, then the use of $s = 0$ should be better for formulas derived on the basis of perturbation theory, since the corresponding phase shifts are smaller. On the evidence of computations, fluctuations *are* important in electron transport theory for which $s = 1/3$ seems more appropriate. (Computations based on the latter criterion are fairly successful [20-24]; similar calculations using a mean muffin tin are not.)

It may well be that $s = 0$ is more appropriate for calculating m^* via (8). Certainly, in the low temperature

solids, fluctuations should be negligible; also the experimental evidence [25] suggests that χ for Li is little changed across the melting point. However, at the present time, we have not made enough systematic calculations to report here fully in this approximation, though it does appear that both criteria lead to the same general conclusions, both explaining semi-quantitatively the broad features of the Knight shifts in the alkalis and their alloys.

Below, then, we rely on pseudopotential screening. Ion core potentials are truncated to form $U(r)$ and solutions of (4) are found with the large r behavior $(kr)^{-1} \sin (kr - 1/2\, l\pi + \eta_l(k))$. In general, those phase shifts for $k = k_F$ will not satisfy $s = 1/3$, but the cut-off radius in $U(r)$ is adjusted until the criterion is satisfied. Once $U(r)$ is fixed, $\eta_l(k)$ can be found for any k. Phase shifts found in this way have been successful in explaining the electron transport properties [20-24].

On evaluating the s-wave functions at the origin, we obtain values of the contact term. On analyzing these, we find they are all well represented by the formula

$$|\xi_{kF}(0)|^2 = 5.3Z(k_F a_0)^{-1.45} a_0^{-3} \tag{12}$$

when Z is the atomic number and $a_0 = \hbar^2/me^2$, the first Bohr radius.

3. Phase Shifts and Electron Transport

For very general reasons [26], the low energy phase shifts for a screened ion are described by

$$\eta_l \propto k^{2l+1};\ k\partial\eta_l/\partial k = (2l+1)\eta_l \tag{13}$$

and, in fact, this is quite a reasonable representation of the situation up to quite near the Fermi level (fig. 1). The higher energy behavior then depends on the specific ion. Most stay small over the ranges of energy of interest, but certain exceptional η's (two of which are shown in fig. 1) grow large.

The latter behavior may be interpreted using the concept of the virtual bound state [27]. The lowest unoccupied energy level of the Cs atom is the 5d level. When the atoms join to form the metal, this level is not lost, though it is no longer sharply defined. It may be detected by the strong scattering it produces on electrons of appropriate energy. Thus η_2 for Cs rises to high values characteristic of resonant scattering ($\eta_2 \sim \pi/2$ for maximum cross section; $\partial^2\eta_2/\partial k^2 = 0$ for maximum delay time [26]). Similar behavior is found in the d waves of Rb and K, though the onset of resonance occurs at higher energies than for Cs. In Li, the 2p level plays a role somewhat akin to the 5d level in Cs,

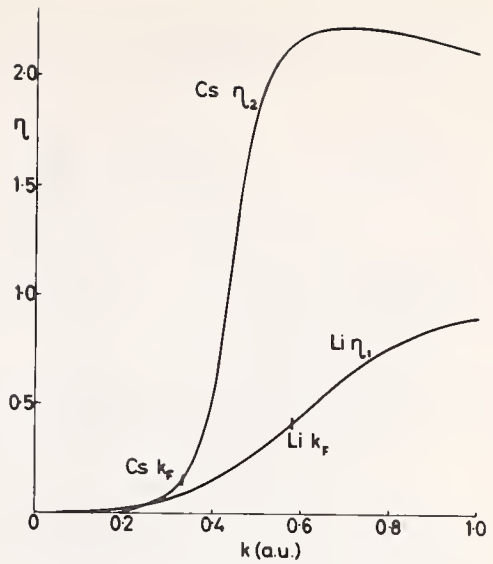

FIGURE 1. *Energy dependence of two pseudoatom phase shifts (η_2 for Cs and ν_1 for Li).*

Rb and K have similar η's to Cs, though the resonance occurs at higher energies. All other phase shifts for the alkalis are small over the energy range indicated. This seems to be the common feature correlating the experimental results of figures 2–5 and of table 1.

though, as is usual for a p level, the curve is much broader.

If we squeeze or alloy a metal, the scattering characteristics of the ions have to be worked out afresh. However it is a useful first approximation (and excellent for illustrative purposes) to think of such curves as those shown in figure 1 to stay the same, with only the Fermi level moving.

To indicate that we have a basically correct picture we quote a number of pieces of experimental evidence and we emphasize that out comments on them have been backed up by detailed computations [20-24].

Resistance measurements are, of course, good for revealing strong scattering at the Fermi level; the stronger the scattering, the higher the resistance. Figure 2 shows the variation of the resistivities of the alkalis under pressure [28,22]. Normally, the resistance of a metal drops under pressure, the explanation being [29] that the stiffer lattice is more favorable for coherent diffraction by conduction electrons. Figure 2 indicates, however, that under pressure all the alkalis behave abnormally; to explain this, we turn to the other effect involved, namely, the strength of conduction electron scattering at single sites.

Returning to figure 1, we see that for Li, even at zero pressure, the Fermi level occurs well up the η_1 curve, the application of pressure causing it to move further up. The scattering is thus increased in intensity and this is reflected in the *increased* resistance. In Cs, the stiffening of the lattice wins to begin with, but very soon the growing d-wave scattering dominates and one ob-

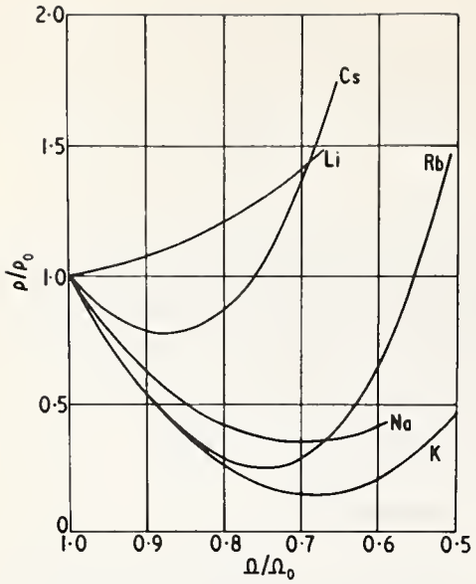

FIGURE 2. *Experimental resistivity ratios versus fractional volume changes* [28].

The rising curve for Li reflects k_F in figure 1 rising up the η_1 curve. The subsequent rise in Cs is due to the same effect for the η_2 curve in figure 1.

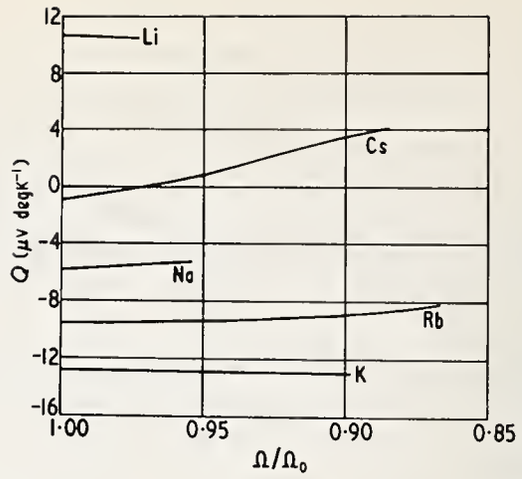

FIGURE 3. *Experimental thermoelectric powers versus fractional volume changes* [30].

The positive and constant value for Li arises from the shape of η_1 in figure 1, while the shape of η_2 explains the positive value for Cs under pressure.

tains a sharp increase in resistance. To a much lesser extent, Rb and K exhibit the same characteristics as Cs, the resistivity increases being more delayed in these cases because of the higher-energy positions of the virtual bound states.

This picture is corroborated by the thermopower measurements [30]. The thermoelectric power of a metal depends on the change in the cross section experienced by electrons as the Fermi level is traversed. Clearly the presence of a virtual bound state not far above the Fermi level gives rise to a rapidly increasing cross section at the Fermi level. The (positive) thermopower thus produced is anomalous in that, contrary to the simplest free-electron arguments, electrons diffuse from cold to hot regions in the metal. Figure 3 shows the experimental situation. Li already shows an anomalous thermopower, even at zero pressure, indicating the already dominant η_1, while the thermopower of Cs becomes positive on applying only modest pressures. That for Rb is beginning to turn in the expected direction and at higher pressures the same should happen to K. (Note that the compression range is smaller in fig. 3 than in fig. 2.)

With the above general picture in mind, we now turn to the Knight shifts.

4. Knight Shifts in Pure Metals

4.1. Absolute Knight Shifts in Li and Na

Usually, susceptibility measurements refer to a sample as a whole. Actually, only for Li [31] and for Na [32] has χ for the conduction electrons alone been observed (conduction electron spin resonance being the technique used). Since the Knight shifts are also known [7,14], then, assuming (1), both χ and ΩP_F are known independently for these metals. The experimental situation and our computed numbers are shown in table 1.

To understand the experimental effective masses, we need, first, to remember that valence electron correlation plays an important role [10-12]. In fact, this effect can be "subtracted out" and, according to Rice's calculations [12] one needs an m^*/m, from eq (8), slightly greater than unity for Na but considerably greater for Li (see table 1).

Such behavior is easily explained by the present approach. Na has no nearby virtual bound state (cf. fig. 2). All its phase shifts are rather small and also (cf. eq (13))

TABLE 1. *Susceptibility and nuclear contact data*

Metal	m^*/m [1] (expt.)	Target m^*/m [1]	m^*/m [1] (calculated)	ΩP_F (expt.)	ΩP_F (calculated)	ΩP_F (OPW)
Li	2.6	1.6	1.8	15	21	54
Na	1.7	1.1−1.2	1.0	119	120	176

[1] m^*/m (expt.) is the ratio of the observed to the free-electron susceptibilities. According to theory [10–12], this contains a substantial contribution from conduction electron correlation effects; when these are removed, one obtains a target m^*/m which a one-electron theory must aim at for eventual agreement with experiment. (There is a little uncertainty here due to our imprecise knowledge of the susceptibility of an interacting electron gas. The numbers quoted rely on the calculations due to Rice, the lower value for Na arising from the Hubbard and the higher from the Silverstein interpolation formula. Both schemes give the same number, to the accuracy shown, for Li). The target m^*/m's may thus be compared with those calculated from eq (8). The experimental ΩP_F's are obtained from eq (1) using the observed K's and χ's and directly following them are the values obtained by the present techniques. The one-OPW results quoted in the final column give a measure of the improvement wrought by the present method of calculation.

so are its phase shift gradients. It follows, therefore, that m^*/m, as given by eq (8) will be near to unity. But for Li, the dominant η_1 corresponds (cf. eq (13) and fig. 1) to an even more dominant gradient and so eq (8) leads to an elevated value of m^*/m (table 1).

Turning to the contact term, we see that the present approach improves on the single-OPW method, especially for Li (table 1). To explain the numbers, note that eq (6) gives 35 and 170 for Li and Na respectively and in fact the corresponding OPW numerators [33] are not radically different from these. The difference occurs in the denominator of eq (6). In the OPW approximation this is always less than Ω [33] (corresponding to a displacement of the free electrons into the interstitial regions) and is responsible for the enhanced OPW results shown in table 1. But remembering the dominant p wave in Li, on the basis of eq (11) we expect, and find, a renormalized volume considerably in excess of Ω in eq (6). This leads to the substantially reduced (and very satisfactory) calculated value shown in table 1. The strong p character lowers the contact density which, of course, represents the s-wave component only. The result for Na, though less drastically affected, is in the same direction and agrees well with experiment.

4.2. Volume Dependence of Knight Shifts

We now provide an explanation of the experimental results of Benedek and Kushida [7] shown in figure 4. From (6), (8), (10) and (11), we may write (1) in the form

$$K=\frac{8\pi}{3}\cdot\frac{\chi_f}{1+s-\sigma}\cdot\frac{|\xi_{kF}(0)|^2}{1+\sigma} \qquad (14)$$

This omits the important effect of correlation on the absolute magnitude of χ (cf. 4.1. above) but is quite adequate for explaining the qualitative *variations* of K exhibited in figure 4. In view of (14), one might consider as normal those cases where the volume dependence is adequately described by $\chi_f|\xi_{kF}(0)|^2$. Recalling (12) and remembering that $\chi_f \propto k_F$, we see that normal behavior (as thus defined) corresponds to a slight decrease of Knight shift with increasing pressure.

To understand departures from this behavior, one must examine the two denominators of (14) which, unlike the numerators, are peculiar to the metal under consideration. The important variable is σ for, in the present pseudopotential screening approximation, $s=$ 1/3 and even for muffin tins eq (13) applies.

As has been emphasized, all phase shifts and gradients for Na remain small, even under pressure (fig. 2). It follows, therefore, that Na will be normal as indeed it is (fig. 4). Our calculations indicate that a

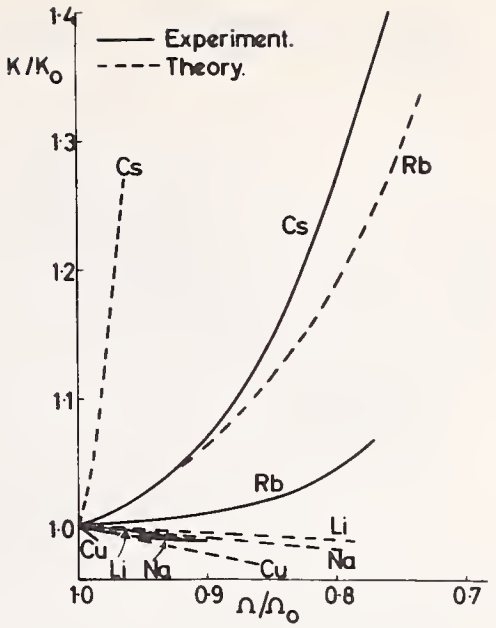

FIGURE 4. *Knight shift ratio versus fractional volume changes.*
The experimental values are taken from ref. [7]; the theoretical values are computed using eq (12) and the data of ref. [6]. The use of muffin tins (cf. sec. II) should improve agreement with experiment. The rise shown for Cs and the fall shown for Li are explained by the curves of figure 1.

similar explanation seems appropriate for Cu (eq (12) being an adequate, if rather less accurate, representation of the contact term in this metal). The normal behavior of Li follows since, while η_1 is significant at the Fermi level (and therefore giving, for example, as we saw in 4.1., an enhanced m^*), its gradient (cf. fig. 1) is rather constant. There is a complete parallel with the thermopower situation (fig. 3). The high value of the gradient gives the anomalous negative result, while the insignificant variation with pressure of the gradient implies the constant thermopower shown.

Finally, to explain the observed abnormal response of Rb and Cs we note the nearby virtual bound states in these metals (figs. 1-3), these giving rise to sharply increasing σ's when pressure is applied. The variation of $1+s-\sigma$ in (14) is more important than that of $1+\sigma$ since the effect of the zero in the former (or, cf. (14), the pole in χ) can be felt even at the densities of interest. (The eventual divergence in χ is, of course, a purely mathematical consequence of the terminated perturbation expansion (7); physically a greatly enhanced value should be anticipated.) Thus, one concludes that the rising Knight shifts shown in figure 4 primarily arise from the sharply increasing effective masses. Consistent with figures 2 and 3, the curve for Cs rises more rapidly than that for Rb.

5. Knight Shifts in Alloys

The observed Knight shifts of binary alkali systems vary quite linearly with concentration across the com-

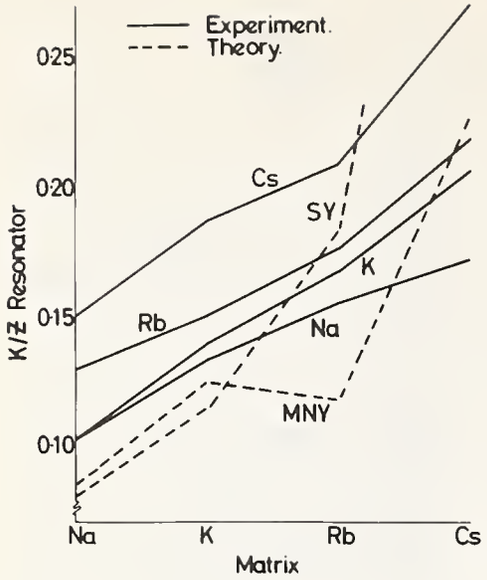

FIGURE 5. *Experimental Knight shift of a resonant ion, scaled by its atomic number for various matrices.*

The pure metal results are taken from Drain's review [14] and the alloy results from van der Molen et al. [8]. (There is little difference between the latter's results and those of Kaeck [9]). The present theory can explain (using figure 1; see also the caption) the trend from matrix to matrix, but not the variations for a given matrix. The theoretical results labelled MNY were computed using the data of ref. [6]. The results for Na, K, and Rb matrices include correlation in the calculation of χ but not that for Cs which would, in that case, be divergent (recall the limitations of eq (7) discussed in sec. II). We believe the slight drop thus calculated in moving from K to Rb matrices arises only from our inability to calculate with adequate precision. To illustrate this, we show also theoretical results (labeled SY) using the data of Stocks and Young [34] which are, in principle, an improvement on those of ref. [6].

position diagrams [8,9]. The experimental situation may, therefore, be summarized as in figure 5 where we have plotted the Knight shifts for very low concentration solute ions as well as those for the pure metals.

To explain figure 5 we need to generalize section 2 to the case of alloys. This is formally quite easy; one adds appropriate subscripts to the U's and ϕ's of eqs (2) and (3) and finds a Schrödinger equation of type (4) for each type of ion, the appropriate k_F being that of the alloy.

Specializing to the case of solute shifts, the numerator of (6), the unrenormalized contact density is for the solute since this is the resonant ion but this must be evaluated for k_F defined by the solvent. Also, since the denominator of (6) arises from the matrix ions (see the comment following that equation), this, like χ, will be given by the solvent. Thus, from (1), (6), (11) and (12), we have

$$K=\frac{8\pi}{3}\cdot\chi_{\text{matrix}}\frac{5.3Z_{\text{resonator}}\,(k_{F\,\text{matrix}}\,a_0)^{-1.45}a_0^{-3}}{1+\sigma_{\text{matrix}}} \qquad (15)$$

We can look upon (15) as a generalization of the pure metal formula, though in the latter case every ion is participating in the resonance and the signal is much stronger.

On scaling these Knight shifts by the atomic number on the resonant ion, we expect, therefore, a number depending only on the matrix. As figure 5 shows, this is a fair first approximation, though there are systematic trends for various ions in a given matrix which the present theory cannot account for. The increase as one moves to heavier matrices is, however, easily explained. Just as in section 4.2., the susceptibility dominates the renormalization term and, in view of figures 2-4, this should increase as one moves from Na to heavier matrices. This conclusion is consistent with the observed electronic specific heat data [35-37] though the correlation is not clear-cut because of the significant electron-phonon contributions to the effective masses in the latter cases [38]. The realization that the susceptibility dominates this problem was due to Kaeck [9].

Note that we have not discussed the rate of change of Knight shift as the alloy concentration is varied. This would have involved us in different and, as yet, unresolved problems [39,40].

6. Summary

The scale and shape of the calculated η_1 curve for Li shown in figure 1 are corroborated by (a) the *rise* in resistance with increasing pressure (fig. 2), and (b) the sign and lack of variation of thermopower with pressure (fig. 3). When applied to the theory of Knight shifts, it explains also (c) the enhanced susceptibility (table 1), (d) the failure of the single-OPW method to predict the contact term, and (e) the *fall* of Knight shift under pressure (fig. 4).

Similarly, the virtual bound state shown in the η_2 curve for Cs in figure 1 is corroborated by (a) the eventual rise in resistance shown in figure 2, and (b) the change of sign of the thermopower shown in figure 3. In the theory of Knight shifts, it explains also (c) the rise of Knight shift with increasing pressure (fig. 4) and (d) the enhanced Knight shifts exhibited by solute ions in a Cs matrix. Virtual bound states associated with Rb and K account for the corresponding properties of these metals in a similar way.

Na has no strong phase shifts and so has unremarkable transport properties: (a) a resistance which falls and stays small when pressure is applied (fig. 2), and (b) a negative thermopower which does not change much under pressure. In the theory of Knight shifts (c) its contact density and susceptibility can be understood by free-electron arguments (table 1) though preferably, in a correlated framework for χ, (d) it has a normal (cf. sec. 4.2.) falling shift (fig. 4) when pressurized, and (e) the decreased shifts exhibited by solute ions dissolved in Na is thus explained.

7. Acknowledgment

G. M. Stocks acknowledges a United Kingdom Science Research Council award.

8. References

[1] Micah, E. T., Stocks, G. M., and Young, W. H., J. Phys. C. **2**, 1653 (1969).
[2] Micah, E. T., Stocks, G. M., and Young, W. H., J. Phys. C. **2**, 1661 (1969).
[3] Stocks, G. M., Young, W. H., and Meyer, A., J. Phys. C. (to be published).
[4] Knight, W. D., Solid State Phys. **2**, edited by F. Seitz and D. Turnbull (Academic Press, New York, 1956), p. 93.
[5] Ziman, J. M., Advanc. Phys. **13**, 89 (1964).
[6] Meyer, A., Nestor, C. W., and Young, W. H., Proc. Phys. Soc. (London) **92**, 446 (1967).
[7] Benedek, G. B., and Kushida, T., J. Phys. Chem. Solids **5**, 241 (1958).
[8] vander Molen, S. B., vander Lugt, W., Draisma, G. G., and Smit, W., Physics **38**, 275 (1968); **40**, 1 (1968).
[9] Kaeck, J. A., Phys. Rev. **175**, 897 (1968).
[10] Pines, D., in Solid State Phys. **1**, edited by F. Seitz and D. Turnbull (Academic Press, New York, 1955), p. 367.
[11] Silverstein, S. D., Phys. Rev. **130**, 912 (1963).
[12] Rice, M., Ann. Phys. **31**, 100 (1965).
[13] Kittel, C., Quantum Theory of Solids, (John Wiley and Sons, New York, 1963).
[14] Drain, L. E., in Metallurgical Reviews **12**, edited by J. S. Bristow (Institute of Metals, London), p. 195.
[15] Ziman, J. M., Proc. Phys. Soc. (London) **91**, 701 (1967).
[16] Ball, M. A., J. Phys. C. **2**, 1248 (1969).
[17] Lee, M. J. G., Phys. Rev. **178**, 953 (1969).
[18] Meyer, A., and Young, W. H., Phys. Rev. Letters **23**, 973 (1969).
[19] Ziman, J. M., Proc. Phys. Soc. (London) **88**, 387 (1966).
[20] Young, W. H., Meyer, A., and Kilby, G. E., Phys. Rev. **160**, 482 (1967).
[21] Dickey, J. M., Meyer, A., and Young, W. H., Phys. Rev. **160**, 490 (1967).
[22] Dickey, J. M., Meyer, A., and Young, W. H., Proc. Phys. Soc. (London) **92**, 460 (1967).
[23] Thornton, D. E., Young, W. H., and Meyer, A., Phys. Rev. **166**, 746 (1968).
[24] Meyer, A., and Young, W. H., Phys. Rev. **184**, 1003 (1969).
[25] Hahn, C. E. W., and Enderly, J. E., Proc. Phys. Soc. (London) **92**, 418 (1967).
[26] Mott, N. F., and Massey, H. S. W., The Theory of Atomic Collisions (Clarendon Press, Oxford, 1965), 3rd ed.
[27] Friedel, J., Nuovo Cim. (Suppl.) **7**, 287 (1958).
[28] Dugdale, J. S., Science **134**, 77 (1961).
[29] Mott, N. F., and Jones, H., The Theory of the Properties of Metals and Alloys (Clarendon Press, Oxford, 1936).
[30] Dugdale, J. S., and Mundy, J. N., Phil. Mag. **6**, 1463 (1961).
[31] Schumacher, R. T., and Slichter, C. P., Phys. Rev. **101**, 58 (1956).
[32] Schumacher, R. T., and Vehse, W. E., J. Phys. Chem. Solids **24**, 297 (1963).
[33] Bennett, L. H., Mebs, R. W., and Watson, R. E., Phys. Rev. **171**, 611 (1968).
[34] Stocks, G. M., and Young, W. H., J. Phys. C. **2**, 680 (1969).
[35] Martin, D. L., Proc. Roy. Soc. (London) A **263**, 378 (1961); Phys. Rev. **124**, 438 (1961).
[36] Lien, W. H., and Phillips, N. E., Phys. Rev. A **133**, 1370 (1964).
[37] Martin, B. D., Zych, D. A., and Heer, C. V., Phys. Rev. A **135**, 671 (1964).
[38] Ashcroft, N. W., and Wilkins, J. W., Physics Letters **14**, 285 (1965).
[39] Watson, R. E., Bennett, L. H., and Freeman, A. J., Phys. Rev. Letters **20**, 653, 1221 (1968); Phys. Rev. **179**, 590 (1969).
[40] Van Ostenburg, D. O., and Alfred, L. C. R., Phys. Rev. **161**, 569 (1967); Phys. Rev. Letters **20**, 1484 (1968).

417-156 O - 71 - 43

Discussion on "Knight Shifts of the Alkali Metals" by A. Meyer (Northern Illinois University) and G. M. Stocks and W. H. Young (University of Sheffield, England)

M. Natapoff *(Newark College of Engineering):* Do the phase shifts mentioned here differ from those previously published by you?

A. Meyer *(Northern Illinois Univ.):* This is just the comment I would make. The original sets of phase shifts that were published were obtained using repulsive pseudopotentials. They are the ones that we primarily relied on. However, we indicated that we have others in which we do not use repulsive pseudopotentials but use instead the full atomic potential truncated to simulate screening. We simply subtract our multiples of π from the phase shifts so obtained and we get the phase shifts modulo π which are close to the original set, and are far easier to obtain. Presumably we would use this method in other cases for which doing a full pseudopotential treatment would be just too hard.

A. Narath *(Sandia Labs.):* I would like to apologize to the authors of the post deadline papers. In view of the hour, I think we should skip them and I therefore declare this session closed.

Role of Exchange Effects on the Relationship Between Spin Susceptibility and Density of States of Divalent Metals

P. Jena and T. P. Das

Department of Physics, University of Utah, Salt Lake City, Utah 84112

S. D. Mahanti

Bell Telephone Laboratories, Incorporated, Murray Hill, New Jersey 07974

G. D. Gaspari

Department of Physics, University of California, Santa Cruz, California 95060

The influence of exchange and correlation of conduction electrons on the spin susceptibility, χ_s, is well understood in alkali metals. There is reasonable agreement between theoretical and experimental results where the latter are available. No such comparison has been reported for the divalent metals, mainly because of a lack of experimental information. Only for Be is χ_s known (from spin resonance measurements). We have made semi-empirical estimates of χ_s for Mg and Cd by adjusting the measured Knight shifts with theoretical values of the core polarization and $\langle\psi^2(0)\rangle$. The values of χ_s so deduced are compared to theoretical estimates made by the method of Silverstein, who treated the exchange enhancement by an interpolation procedure analogous to that of Nozières and Pines for calculating correlation energies, and included the effects of band structure through the calculated thermal (band) effective mass. Agreement is good for Mg, which behaves more like a free electron metal, and poor for Be and Cd. Possible sources of the discrepancies are discussed.

Key words: Be; Cd; density of states; divalent metals; exchange enchancemnt; Mg; spin susceptibility.

1. Motivation for this Work

One of the major properties related to the density of states, $g(E_F)$ at the Fermi surface (F.S.) in a metal is the spin susceptibility, χ_s. In the one-electron approximation the relation between χ_s and $g(E_F)$ is well-known, [1] namely

$$\chi_s = \mu_B^2 g(E_F) \tag{1}$$

where μ_B is the Bohr magneton. However, when one includes the effects of exchange and correlation among electrons, the response of the electrons to the magnetic field is expected to alter in the direction of increased susceptibility. Theories developed for quantitative treatment of these effects are limited in applicability to free (uniform) electron systems [2,3] and only intuitive extensions [3] have been made to take into account the Bloch character of electrons in the metal. Such theories are therefore expected to be reasonably valid for alkali metals which are nearly free electron like in their properties and this is indeed found to be true [3] in the cases where χ_s has been obtained directly from electron spin resonance (esr) measurements. To subject the theory to a more severe test for Bloch electrons, we need to analyze the cases where there are strong departures from the free electron behavior. The divalent metals, beryllium, magnesium, zinc, and cadmium are particularly suitable examples in this respect. These metals have four electrons per unit cell which fill up a volume in k-space equal to two Brillouin Zones (B.Z.). As a consequence, there are substantial intersections between the Fermi surface and B.Z. boundary. The electrons on the Fermi surface are therefore expected

to depart rather markedly from free-electron character.

Among these metals, direct measurement of χ_s from esr experiment has been made only for beryllium [4]. However, one can extract experimental values of χ_s for the other metals through analysis of Knight shift (K_s) data from nuclear magnetic resonance (nmr) measurements. For this purpose, one needs to evaluate the conduction electron spin density at the nucleus and make use of the well known expression [5]

$$K_s=\frac{8\pi}{3}\chi_s\Omega\langle|\psi_{\mathbf{k}_F}(0)|^2\rangle_{\mathrm{av}} \qquad (2)$$

Ω being the volume of the unit cell over which the wave function, $\psi_{\mathbf{k}}(\mathbf{r})$ is normalized. The average in eq (2) is taken over the Fermi surface. Unfortunately, the Knight shift of zinc is not currently available due to difficulties in observing nmr signals in this metal. Careful determinations of the Knight shift have, however, been made in magnesium [6] and cadmium [7] and concurrently, band structure studies are available for these metals [8,9] to permit determination of the spin densities $\langle|\psi_{\mathbf{k}_F}(0)|^2\rangle_{\mathrm{av}}$. We have analyzed the direct and exchange core polarization (ECP) contributions to the spin density in both of these metals [10,12,14] in order to obtain χ_s and study the trend of the agreement between theory and experiment for χ_s in the series formed by these two metals and beryllium.

2. Extraction of Spin Susceptibility of Mg and Cd From Knight Shift Data

The direct spin density, $\langle|\psi_{\mathbf{k}_F}(0)|^2\rangle_{\mathrm{av}}$ requires a detailed scanning of $|\psi_{\mathbf{k}_F}(0)|^2$ over the F.S. with appropriate weighting according to the local density of states [10,15]. The ECP contribution was calculated using the moment perturbation (MP) procedure [16] which has been applied in the past to the study of this effect in several metals [17]. The averaging of the ECP effect was carried out in the same manner as for the direct effect.

In the case of magnesium, there are four segments of the F.S. [8] described respectively as lens, cigars, butterflies, and monster. Of these segments, the lens and the butterflies were found [10] to have predominantly s-character whiles the other two had substantial p-character. In reference 10, the spin densities and local density of states were calculated by using the orthogonalized plane wave [OPW] procedure and a potential constructed from first principle by Falicov [11]. A more extensive scanning [12] of the Fermi surface has been carried out using the nonlocal pseudopotential of Stark and Mueller [13] and the spin densities have been evaluated at 110 nonequivalent points on the Fermi surface. The results of this calculation indicate that the s-character of electrons occupying the cigar and the monster have been underestimated in the earlier OPW calculation [10]. This may be due to (1) inaccuracies in the potential, (2) use of pseudo-core wave functions instead of crystal-core functions for the purposes of orthogonalization, and (3) insufficient scanning of general points on the Fermi surface. Lens has the strongest s-character, but in view of the large surface areas associated with the butterflies and monster, the latter two make the dominating contribution to the spin density. The s-part of the ECP contribution from various segments was found to follow the same relative trend as the direct spin density. The p-type ECP effect was contributed to mainly by the monster. ECP contributions from higher l-components of the wave functions were found to be small. The s-type ECP contribution to the spin density was found to be positive and about 25% of the direct ECP effect. The p-type ECP contribution was also positive and about 13% of the direct. On including the small negative contributions to the spin density from higher l-components, the net ECP effect was found to be about 38% of the direct.

In cadmium, the F.S. has only two segments, lens and monster. Both of these segments were found to have substantial s-character, with the monster making the major contribution to the spin density both due to its larger s-character and larger surface area. The ECP contribution was a smaller fraction (9%) of the direct spin density. This smallness of the fractional ECP spin density was a consequence of two factors. First, the larger direct spin density compared to magnesium, and secondly, the reduced exchange interaction between the conduction electrons and s-cores due to the screening effect of the intervening 4d-core electrons. The p-type ECP effect was again found to be positive but much smaller in relative importance, namely 1.3% of the direct spin-density. Substituting the total calculated spin density including direct and ECP effects in eq (2) we have obtained the experimental χ_s listed in table 1.

TABLE 1. *Susceptibility enhancement factors and other pertinent parameters in* Be, Mg, *and* Cd
[Extrapolated to 0 K]

Metal	c/a	m_t/m	χ_s expt. (cgs. vol. units)	χ_s band. (cgs. vol. units)	$\eta^{\mathrm{expt.}}$	$\eta^{\mathrm{theo.}}$
Be.....	1.567	0.45	0.20×10^{-6}	0.64×10^{-6}	0.31	1.09
Mg.....	1.624	.95	1.14×10^{-6}	$.93\times10^{-6}$	1.23	1.32
Cd.....	1.862	.54	1.03×10^{-6}	$.54\times10^{-6}$	1.90	1.17

It is appropriate to remark here about the possible inaccuracies of these results for $\psi_s^{expt.}$ due to the neglect of the orbital contribution [18] to K_s. This latter effect (only Landau diamagnetism) was found to be of determining importance [19] in explaining the negative sign of K_s in beryllium. However, beryllium was somewhat special in that the p-type ECP effect was substantial and negative [15] and cancelled out the major part of the direct spin density contribution to K_s. In contrast, the p-type ECP effect in magnesium [10,12] and cadmium [14] is positive and the absolute values of the total spin densities are orders-of-magnitude larger, due to a larger fractional s-character. Thus, any contribution from either the Landau [20] or Van Vleck-Ramsey type orbital effect [21] to K_s is expected to be a small fraction of the spin-contribution to K_s.

3. Comparison of Theoretical and Experimental Spin-Susceptibilities — Discussion

The commonly used procedure for studying the exchange enhancement is the one based on the random phase approximation [22] (RPA) of many-body theory. This procedure involves a self-consistent treatment of the wave functions for the electron gas in a magnetic field. The difficulty with this procedure is that the RPA approximation is strictly valid for high densities, that is, for electron sphere radii r_s less than 1, and takes appropriate account of the long range interactions (small momentum transfer). Silverstein [3] has improved upon the RPA by utilizing a momentum transfer interpolation procedure analogous to that developed by Nozières and Pines [23] for correlation energy calculations. The interactions in the presence of a magnetic field involving small momentum transfers (long range effect) are handled by the RPA procedure while the large momentum encounters (short range effect) are handled by second-order perturbation theory, an interpolation procedure being applied for intermediate momentum transfers. Additionally, Silverstein [3] has attempted to include the effects of band structure through the thermal (band) mass, m_t related to the density of states by the relation

$$m_t/m_0 = g(E_F)/g_0(E_F) \tag{3}$$

where $g_0(E_F)$ is the density of states for free-electrons (mass m_o). Silverstein's expression may be expressed in the compact form

$$\eta = 1/\left[1 - \frac{\alpha - 1}{\alpha\beta}\right] \tag{4}$$

where

$$\beta = m_0/m_t$$
$$\alpha = \chi_s^*/\chi_s^{\text{free}} \tag{5}$$

χ_s^* being the susceptibility obtained by Silverstein in the absence of the band effect and

$$\eta = \chi_s/\chi_s^{\text{band}} \tag{6}$$

with χ_s^{band} given by eq (1).

In table 1 are listed the values of c/a, $1/\beta$, $\chi_s^{expt.}$, and $\eta^{theo.}$ from eq (4).

For beryllium [15] and cadmium [24], the density of states at the F.S. $g(E_F)$ has been calculated with great accuracy and we have used these values to calculate $1/\beta$. For magnesium, no such detailed calculation of $g(E_F)$ is available. We have therefore utilized [10] the density of state obtained from the specific heat measurement after making appropriate corrections for the phonon enhancement of $g(E_F)$. The results in the last two columns show that agreement between $\eta^{expt.}$ and $\eta^{theo.}$ for beryllium and cadmium is quite poor where as for magnesium, the agreement is reasonably good. Amongst the three, magnesium behaves more like a free electron system and it is not surprising that an effect mass approximation for treating the exchange enhancement of χ is reasonably good for this metal. The small theoretical value of η for cadmium is primarily due to the small value of m_t/m, which indicates that there are not enough electrons at the Fermi surface to take part in the exchange enhancement process. It should be pointed out that our derived experimental value of η for cadmium is 1.9 compared to 1.5 obtained by Kasowski and Falicov [24]. This discrepancy may be due to (1) the choice of Hartree-Fock-Slater core states in [24] and (2) the use of smaller number of OPW basis functions to construct the conduction electron wave function which overestimates the theoretical spin s_o density and hence underestimates $\eta^{expt.}$.

There seems to be an interesting trend in the value of $\eta^{expt.}$ in going from beryllium to cadmium, although there is no trend with respect to the parameter β. A part of the difference between experiment and theory could perhaps be due to the neglect of some additional contributions to Knight shift in deriving χ_s.

For beryllium, the theoretical situation is rather poor since η seems to have a de-enhancement from the band susceptibility while theory predicts the reverse. As a matter of fact, under no circumstances can eq (4) lead to $\eta^{theo.}$ less than unity.

While the Knight shift involves the susceptibility χ_s in a uniform field, the nuclear spin lattice relaxation

rate, T_1^{-1} requires an average [25,26] involving the momentum dependent susceptibility, $\chi_s(q)$ over the range $q = 0$ to $2k_F$. We have utilized the calculated direct and ECP spin densities for beryllium and cadmium to calculate T_1^{-1} in these two metals where $(T_1T)^{-1}$ has been studied experimentally [27,7]. In keeping with the trend for χ_s the theoretical $(T_1T)^{-1}$ in beryllium is found to require a de-enhancement factor of .60 to agree with the experiment [27] while cadmium requires an enhancement factor of 3.10.

Evidently, two types of improvements are necessary in the theory of the response of the electrons to a magnetic field. First one needs to handle actual electronic densities ($r_s > 1$) more rigorously and second, to incorporate Bloch effects which lead to nonuniformity in the electron density distribution. It appears that the latter is the more pressing problem for the case of divalent metals. It is hoped that present self-consistent procedures [2] for the free-electron gas can be extended without too much complexity to the study of Bloch electrons.

4. Acknowledgments

The portion of this investigation carried out at the University of Utah was supported by the National Science Foundation.

5. References

[1] Pauli, W., Z. Physik, **41**, 81 (1927).
[2] Hamann, D. R., and Overhauser, A. W., Phys. Rev. **143**, 183 (1966). Gell-Mann, M., and Brueckner, Phys. Rev. **106**, (1957).
[3] Silverstein, S. D., Phys. Rev. **130**, 912 (1963).
[4] Feher, G., and Kip, A. F., Phys. Rev. **98**, 337 (1955).
[5] Townes, C. H., Herring, C., and Knight, W. D., Phys. Rev. **77**, 852 (1950).
[6] Rowland, T. J., in Progress in Materials Science, Bruce Chalmers, ed. (Pergamon Press, New York) **Vol. IX**, p. 14, (1961). Dougan, P. C., Sharma, S. N., and Williams, D. L. (to be published in Canadian Journal of Physics).
[7] Seymour, E. F. W., and Styles, G. A., Phys. Letters **10**, 269 (1964). Borsa, F., and Barnes, R. G., J. Chem. Phys. Solids **27**, 567 (1966). Sharma, S. N., and Williams, D. L., Phys. Letters **25A**, 738 (1967). Dickson, E. M., Ph. D. Thesis (unpublished), University of California, Berkeley, California (1968).
[8] Falicov, L. M., Phil. Trans. Roy. Soc., **A255**, 55 (1962). Kimball, J. C., Stark, R. W., and Mueller, F. M., Phys. Rev. **162**, 600 (1967).
[9] Stark, R. W., and Falicov, L. M., Phys. Rev. Letters **19**, 795 (1967).
[10] Jena, P., Das, T. P., and Mahanti, S. D., Phys. Rev. (in press).
[11] Falicov, L. M., Ref. 8.
[12] Das, T. P., Jena, P., and Mahanti, S. D., Addendum to Ref. 10, (to be published).
[13] Kimball, J. C., Stark, R. W., and Mueller, F. M., Ref. 8.
[14] Jena, P., Das, T. P., Gaspari, G. D., and Mahanti, S. D., Phys. Rev. (in press).
[15] Jena, P., Mahanti, S. D., and Das, T. P., Phys. Rev. Letters **20**, 544 (1968), and Ref. 10.
[16] Gaspari, G. D., Shyu, W. M., and Das, T. P., Phys. Rev. **134**, A852 (1964).
[17] Shyu, W. M., Das, T. P., and Gaspari, G. D., Phys. Rev. **152**, 270 (1966). Also see Refs. 10, 11, and 12.
[18] Kubo, R., and Obata, Y., J. Phys. Soc. (Japan) **11**, 547 (1963); Obata, Y., J. Phys. Soc. (Japan) **18**, 1020 (1963).
[19] Gerstner, J., Ph. D. Thesis (unpublished), Pennsylvania State University, University Park, Pennsylvania (1969).
[20] Landau, L, Z. Physik **64**, 629 (1930).
[21] Ramsey, N. F., Phys. Rev. **78**, 699 (1950). Ibid., **86**, 243 (1952).
[22] Pines, D., Elementary Excitations in Solids, (W. A. Benjamin, Inc., New York, 1964).
[23] Nozières, P., and Pines, D., Phys. Rev. **109**, 762 (1958).
[24] Kasowski, P. V., and Falicov, L. M., Phys. Rev. Letters **22**, 1001 (1969).
[25] Moriya, T., J. Phys. Soc. (Japan) **18**, 516 (1963).
[26] Narath, A., and Weaver, H. T., Phys. Rev. **175**, 373 (1968); Mahanti, S. D., and Das, T. P., Phys. Rev. **183**, 674 (1969).
[27] Barnaal, D. E., Barnes, R. G., McCart, B. R., Mohn, L. W., and Torgeson, D. R., Phys. Rev. **157**, 510 (1967). T represents the absolute temperature.

Discussion on "Role of Exchange Effects on the Relationship Between Spin Susceptibility and Density of States of Divalent Metals" by P. Jena and T. P. Das (University of Utah), S. D. Mahanti (Bell Telephone Laboratories) and G. D. Gaspari (University of California, Santa Cruz)

R. V. Kasowski *(DuPont and Co.):* I have calculated the Knight shift in cadmium and also the spin-susceptibility. I find that the enhancement due to, say, many-body effects, is about .54 (this was published in Phys. Rev. Letters in March). I think in the units that the author, Professor Das, uses, it is about 1.54. So I would like to know what potential he used and how the density of states at the Fermi level was calculated? We used the potential that was fitted to data by Stark and Falicov and it has been quite successful in a number of Fermi surface properties for cadmium.

S. D. Mahanti *(Bell Telephone Labs.):* I believe that for cadmium, the value of the exchange enhancement factor for χ_s (the spin susceptibility) as calculated by Dr. Kasowski is 1.54 compared to our value of 1.90. The potential utilized in both the calculations are the same—that of Stark and Falicov. The density of states used in our band susceptibility was that of Kasowski and Falicov (your Phys. Rev. Letters paper of March 1969). However, the difference is in the calculated spin density at the nucleus. Two plausible reasons that come to mind are: (1) We have utilized Hartree-Fock cores for constructing the OPW functions whereas Dr. Kasowski uses Hartree-Fock-Slater cores. We have found that this may lead to 15-20% difference in the spin density. (2) The second reason is the difference in the number of OPW's utilized to construct the conduction electron wavefunction. We have utilized nearly 25 OPW's, and if Dr. Kasowski has utilized a fewer number of OPW's, then this may explain the differences in the calculated spin densities and the exchange enhancement factor.

Correlation of Changes in Knight Shift and Soft X-Ray Emission Edge Height Upon Alloying

L. H. Bennett, A. J. McAlister, J. R. Cuthill, and R. C. Dobbyn

Institute for Materials Research, National Bureau of Standards, Gaithersburg, Maryland 20760

In simple metals and alloys—those having no significant local d-character at or near the Fermi level—the Knight shift provides a measure of the local s-electron density of states. If the particular atom under study has a p-like core level, then soft x-ray emission arising from transitions of elcctrons at the Fermi level into p-like core vacancies should provide a similar measure. Using Al as the example, we compare results of these two techniques by studying fractional changes, relative to Al metal, of the Knight shift and $L_{2,3}$ soft x-ray emission edge height of Al in NiAl, $AuAl_2$, Mg_2Al_3, $Mg_{17}Al_{12}$, and Al_2O_3. A distinct correlation is observed.

Key words: Aluminum oxide (Al_2O_3); electronic density of states; gold aluminide ($AuAl_2$); Knight shift; magnesium-aluminum alloy phases; nickel aluminide (NiAl); soft x-ray emission.

1. Introduction

Among the various experimental techniques yielding information on the occupied density of electronic states in solids, we can distinguish two classes or families: the Fermi level probes (Knight shift, specific heat, susceptibility), and the deep band probes (photoemission, ion neutralization, soft x-ray emission). There have been many comparisons of results of techniqucs within a family. However, so far as we are aware, there has been no systematic attempt to correlate results of techniques belonging to different families. In this paper, we exhibit such a correlation, focusing attention on the Knight shift and soft x-ray emission.

Analysis, given in the next section, shows that such a correlation is predicted by the one electron model for simple materials—those having no significant local d-character at or near the Fermi level. An experimental search for the correlation can serve two useful purposes. If the one electron model is valid, these two techniques should serve as sensitive tests of band theory, particularly for alloys, since alone in each family, they are capable of yielding information on the contribution of a specific orbital component of the Bloch waves to the state density, at a specific ion site. On the other hand, if many body effects, such as exchange enhancement of the Knight shift [1] or resonant behavior of the soft x-ray emission rate at the Fermi level [2], are important, we would expect to observe systematic deviations from the predicted correlation.

As our example, we have chosen to study Al, in Al metal, in alloys with Au, Ni, and Mg, and in the oxide Al_2O_3. For the cases considered so far, a distinct correlation is observed. No systematic deviations are noted. Thus, many body effects are small, constant upon alloying, or compensating.

2. Analysis

In simple materials as defined above, the Knight shift provides some measure of the local density of s-electron states at the Fermi level. If the ion under study has a p-like core level, the soft x-ray emission arising from transitions of Fermi surface electrons into p-like core vacancies, should provide a similar measure.

For the Knight shift, we assume a simple contact interaction from which we write

$$\kappa \propto \sum_{\mathbf{k},\, n} |\psi_{\mathbf{k}}(0)|^2 \delta(E(\mathbf{k}) - E_F), \qquad (1)$$

which, aside from constants, is the first term in the usual expression,

$$\kappa = a_s n_s(E_F) + a_d n_d(E_F) + \ldots\ldots$$

The second term in the latter expression is an indirect contact term, arising from a net spin density at the nucleus produced by polarization of core s-levels via exchange interaction with unpaired d-states. The ratio of hyperfine coupling constants, a_d/a_s, is typically negative and of the order of 0.1. However, in our assumed simple materials, $n_d(E_F)$ is assumed to be negligible, and we omit this and higher terms from consideration.

For the soft x-ray emission process, the spontaneous L-emission rate from states near the Fermi level may be written

$$R_L(h\omega) \propto \sum_{\mathbf{k}, n} (E_F - E_c)^3 |<\psi_{2p}|\mathbf{r}|\psi_{\mathbf{k}}>|^2 \delta(h\omega - E_F + E_c) \tag{2}$$

Both sums are carried out over the Brillouin Zone. n is a band index, $\psi_{\mathbf{k}}$ is a band wave function; $\psi_{\mathbf{k}}(0)$ its value at the nuclear site. ψ_{2p} is the soft x-ray core state, and E_c its excitation energy.

The suggested correlation can be clearly exhibited by introducing orbital state weights, w_l^{ν}, which are conveniently defined for an augmented plane wave (APW) calculation employing a muffin tin potential by

$$\sum_{l,\nu} w_l^{\nu} + w_{pw} = \int_{\text{cell}} \psi^*(\mathbf{k}, E)\psi(\mathbf{k}, E)\, d^3X = 1$$

$$w_l^{\nu}(\mathbf{k}, E) =$$

$$4\pi(2l+1) \sum_{i,j} c_i c_j e^{i\mathbf{k}_{ij}\cdot\mathbf{r}_{\nu}} P_l(\cos\theta_{ij}) j_l(k_i A_{\nu}) j_l(k_j A_{\nu})$$

$$\times \int_0^{A_{\nu}} dr r^2 \left(\frac{R_l^{\nu}(r, E)}{R_l^{\nu}(A_{\nu}, E)}\right)^2 \tag{3}$$

$$w_{pw} = \sum_{i,j} c_i c_j \left(\Omega\delta_{ij} - 4\pi \sum_{\nu} A_{\nu}^2 e^{i\mathbf{k}_{ij}\cdot\mathbf{r}_{\nu}} \frac{j_1(k_{ij}A_{\nu})}{|k_{ij}|}\right)$$

Here ν denotes the ν^{th} ion in the unit cell. A_{ν} is the APW sphere radius for the ion under consideration. $\mathbf{g}_i$ is a reciprocal lattice vector, and $\mathbf{k}_i = \mathbf{k} + \mathbf{g}_i$. The c_i's are coefficients of the normalized band eigenfunction expanded in APW's. $j_l(k_iA)$ is an l^{th} order spherical Bessel function. $\mathbf{k}_{ij} = \mathbf{k}_i - \mathbf{k}_j$. θ_{ij} is the angle between two vectors $\mathbf{k}_i$ and $\mathbf{k}_j$. P_l is the l^{th} order Legendre polynomial. Ω is the primitive cell volume.

These weights can be introduced into a sum over states to yield local orbital state densities, $n_l^q(E)$, q denoting ion type. It is then tedious, but straightforward to show that the sums (1) and (2) may be rewritten

$$\kappa_q \propto \left(\frac{R_0^q(0, E_F)}{R_0^q(A, E_F)}\right)^2 \frac{n_0^q(E_F)}{I_{N0}^q} \tag{4}$$

and

$$R_L^q(h\omega) \propto \frac{(I_{2p,0}^q)^2}{I_{N0}^q} n_0^q(E_F) + \frac{2}{5} \frac{(I_{2p,2}^q)^2}{I_{N2}^q} n_2^q(E_F) \tag{5}$$

where

$$I_{Nl}^q = \int_0^{A^q} dr\, r^2 \left(\frac{R_l^q(r, E_F)}{R_l^q(A_q, E_F)}\right)^2$$

$$I_{2p,l}^q = \int_0^{A_q} dr\, r^3 R_{2p}^q(r) \left(\frac{R_l^q(r, E_F)}{R_l^q(A_q, E_F)}\right)$$

The R_l's in these expressions are the orbital components of the radial wave functions with the APW sphere.

For pure Al and the alloys under consideration, it is reasonable to assume that $n_2^{Al}(E_F)$ makes a negligible contribution to $R_L(h\omega_F)$ [3,4]. We may therefore rewrite eq (5) as

$$R_L^{Al}(h\omega_F) \propto \left(\frac{R_0^{Al}(0, E_F)}{R_0^{Al}(A, E_F)}\right)^2 \frac{n_0^{Al}(E_F)}{I_{N0}^{Al}} \int_0^{A_{Al}} dr\, r^3 R_{2p}^{Al}(r)$$

$$\left(\frac{R_0^{Al}(r, E_F)}{R_0^{Al}(0, E_F)}\right)^2 \tag{6}$$

Only slight variation upon alloying is anticipated for the integral on the right hand side of eq (6). Thus the essential difference in κ_{Al} and $R_L^{Al}(h\omega_F)$ should be only a constant. Both should yield measures of $n_0^{Al}(E_F)$. Further, a plot of R_{alloy}/R_{Al} versus $\kappa_{alloy}/\kappa_{Al}$ should yield a straight line of unit slope.

3. Corrections to Measured Soft X-Ray Emission Rate

Soft x-ray emission rates measured at constant voltage and current density differ from true emission rates, and must be corrected for differences in absorption coefficient, μ, and the density of radiating atoms, $\rho_L(\xi)$, as a function of depth ξ below the sample surface.

These quantities enter the emission rate through a factor

$$I=\int_0^{\xi_L} d\xi \rho_L(\xi)\ e^{-\mu\xi/\sin\psi}. \tag{7}$$

ξ_L is a maximum depth, beyond which excitation of L shell vacancies is no longer energetically possible. It is a function of tube voltage, angle of incidence of the electron beam, the rate of electron energy loss, and the probability of inner level excitation. ψ is the x-ray takeoff angle. These quantities are schematically illustrated in figure 1. By taking the measured emission rate, subtracting the background continuum from it, and then dividing the difference by a reasonable approximation to the factor I, an estimate of the true emission rate can be obtained.

We calculate I in the following approximate way. First, straight, average paths are assumed for the electrons in the exciting beam, with electron energy varying along the mean trajectory according to the prescription

$$V(\xi)=V_0-(\xi/\beta\sin\phi)^{1/\alpha} \tag{8}$$

This expression is consistent with Feldman's empirical range formula for 1 to 10 keV electrons in solids [5],

$$r=\beta V_0^{\alpha}.$$

V_0 is the initial electron energy in keV, and

$$\beta=250A/\rho Z^{\alpha/2},$$

$$\alpha=1.2/(1-0.29\log_{10}Z),$$

with A the atomic weight, Z the atomic number, and ρ the density. For alloys, appropriate averages of A and Z are used. We now write

$$\rho_L(\xi)=n_{\mathrm{Al}}P_L(\xi)$$

where n_{Al} is the density of Al sites in the material studied, and $P_L(\xi)$ is the probability of direct $2p$ shell ionization of an Al ion.

For the L shell ionization probability, we use Bethe's nonrelativistic expression, as modified by Worthington and Tomlin [6],

$$P_L(\xi)\propto \ln U/V_L^2U, \tag{9}$$

where $U=V(\xi)/V_L$, and V_L is the $2p$ excitation energy.

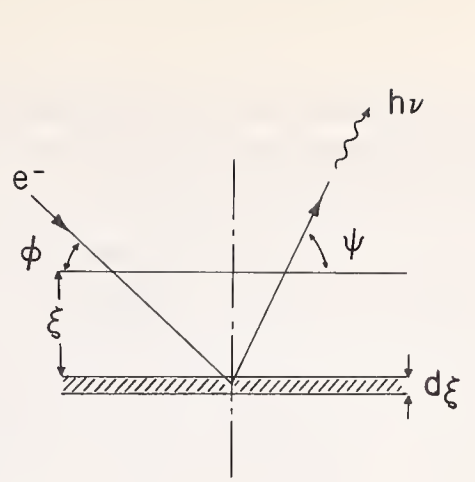

FIGURE 1. *The geometry of soft x-ray generation.*
Electrons incident at angle ϕ to the sample surface excite inner level vacancies at various depths, ξ, below the sample surface. To be collected by the spectrometer, an emitted photon must traverse a distance $\xi/\sin\psi$ of the sample, and may be absorbed along the way.

The absorption coefficients, $\mu(\hbar\omega)$, are not known for the alloys. We therefore make the estimate

$$\mu_{\mathrm{Al,B}}=\sigma_{\mathrm{Al}}n_{\mathrm{Al}}+\sigma_B n_B$$

from the absorption cross sections σ_i of the pure metals, and the appropriate ion densities in the solids. Table 1 lists our estimates of σ_i and the data from which they are evaluated.

TABLE 1. *Numerical values for atomic density, linear mass absorption coefficient, and absorption cross section*

Metal	Atoms per cm³ n_i	Mass absorption coefficient μ_i (cm⁻¹)	Absorption cross section $\sigma_i=\mu_i/n_i$ (cm²)
Al[16]	6.07×10^{22}	0.1×10^{5}	0.16×10^{-18}
Mg[17]	4.30	2.2	5.11
Au[18]	5.93	7.5	12.64
Ni[16]	9.17	8.6	9.37

From the expressions above, we write the factor I as

$$I=\frac{n_{\mathrm{Al}}}{V_L}\int_0^{\beta\sin\phi(V_0-V_L)^{\alpha}} d\xi\,\frac{\{\ln[V_0-(\xi/\beta\sin\phi)^{1/\alpha}]-\ln V_L\}}{\{V_0-(\xi/\beta\sin\phi)^{1/\alpha}\}}$$

$$\exp\left\{\frac{-\mu_{\mathrm{Al,B}}\xi}{\sin\psi}\right\} \tag{10}$$

and evaluate it numerically. Appropriate data and results are listed in table 2.

TABLE 2. *Numerical values for atomic densities, linear mass absorption coefficient, and excitation electron range parameters, α, β*

Alloy	Atoms per cm^3 n_{Al}	Atoms per cm^3 n_B	Mass absorption coefficient (cm^{-1})	α	β
Al	6.07×10^{22}	0×10^{22}	0.1×10^5	1.77	2.57×10^2
Al_3Mg_2	3.1	2.08	1.11	1.76	3.11
$Al_{12}Mg_{17}$	2.05	2.90	1.51	1.75	3.32
Al_2Au	3.70	1.85	2.40	2.17	0.85
AlNi	4.14	4.14	4.0	1.93	0.97

We have also estimated, by extrapolation of Green's [6a] experimental results, the change in backscatter loss on alloying. For the experimental conditions used in the NiAl and $AuAl_2$, we expect fractional losses relative to Al metal of .04 and .09 respectively. For the Mg alloys, the effect should be nil, owing to the negligible change in average atomic number.

While fairly realistic, these approximate values of I are generally overestimates, because of our straight electron path assumption [7]. A further complication, in the case of $AuAl_2$, is the possibility of enhancement of the Al L emission rate via fluorescent excitation of Al cores by Au $N_{4,5}$ radiation.

The experimental soft x-ray data employed here are from three sources. In our own laboratory, we have made measurements on Al, NiAl, and $AuAl_2$. The following experimental parameters were employed: $\psi=90°$ $\phi=20°$, $V_0=2.5$ keV. We have also included in this analysis the data of Appleton and Curry [8], who employed $\psi=90°$, $\phi=30°$, and applied a 4.0 keV peak sinusoidal voltage to their x-ray tube, and corrected the observed spectra for variations in n_{Al}. Since I is not a linear function of V, we have calculated a time average of it for application to their data. Also included in Fomichev's [9] measurement of the L-spectrum of Al in Al_2O_3.

There remains one important consideration in the reduction of the soft x-ray data. At what point along the emission edge should one choose an intensity value characteristic of emission at the Fermi energy? There is some arbitrariness involved in answering such a question. Aside from possible singular structure mentioned above, the emission edge is always broadened by the instrument, by the finite temperature at which measurements are made and by the finite lifetime of the initial state. All of these factors combine to render an exact answer an arduous, if not impossible, task. We therefore assume these factors constant with alloying and use the intensity, above background, of the first definite structural feature at or below the Fermi energy. The emission edge of aluminum, in the metal and in the alloys considered here, exhibits the sharp cut-off at the Fermi energy characteristic of free electron metals, and consequently, the location of this intensity value is unambiguous. The Al spectrum of the oxide shows no emission edge. The Fermi level falls within the band gap, and the Fermi level emission rate is zero.

The soft x-ray measurements made in our laboratory were performed on 99.999% pure aluminum and on the single-phase alloys $AuAl_2$ and NiAl. Details of sample characterization and instrumentation are reported elsewhere [4,10]. Results for Al_3Mg_2 and $Al_{12}Mg_{17}$ are based on measurements reported by Appleton and Curry, to which we have applied only the correction n_{Al}/I.

Knight shift measurements on pure aluminum [11], $AuAl_2$ [12], and NiAl [13] have been previously reported. Those on Al_3Mg_2 and $Al_{12}Mg_{17}$ were taken at both 77 K and room temperature, on powders crushed from arc-melted ingots. Measurements at 77 K indicate a 0.01% reduction in κ from room temperature values in each case. The diamagnetic reference is $AlCl_3$. X-ray diffraction and metallographic analyses showed them to be primarily single-phase alloys, with minute traces of second phase at the grain boundaries ($<1\%$). Table 3 (a,b) gives the measured mean values of emission rate

TABLE 3. *Numerical values of: measured* Al $L_{2,3}$ *emission edge heights, at constant voltage, per scan, per unit current density,* ΔR; *density of* Al *sites, per* $Å^3$, n_{Al}; *the partial range-absorption factor,* $I'=I/n_{Al}$; *fractional backscatter loss,* γ; *corrected emission edge height,* $R(\hbar\omega_F)$; Al *Knight shift,* κ; *and values relative to pure* Al *of emission edge height and Knight shift,* $R'=R_{alloy}/R_{Al}$ *and* $\kappa'=\kappa_{alloy}/\kappa_{Al}$.

Material	ΔR	n_{Al}	I'	γ	$R(\hbar\omega_F)$	κ	R'	κ'
Al	458.4	0.0606	1.000	0.00	7564.	0.164	1.00	1.00
NiAl	23.1	.0414	.311	.04	1866.	.061	.25	.38
$AuAl_2$	42.9	.0370	.391	.09	3232.	.061	.43	.38

Material	ΔR	I'	$R(\hbar\omega_F)$	κ	R'	κ'
Al.....	22.0	1.000	22.0	.164	1.00	1.00
Al_3Mg_2.....	13.3	.616	21.6	.135	.98	.82
$Al_{12}Mg_{17}$	9.7	.509	19.0	.138	.86	.84

above background, ΔR, the correction I and n_{Al}, and measured Knight shifts, κ. The data on Al_3Mg_2 and

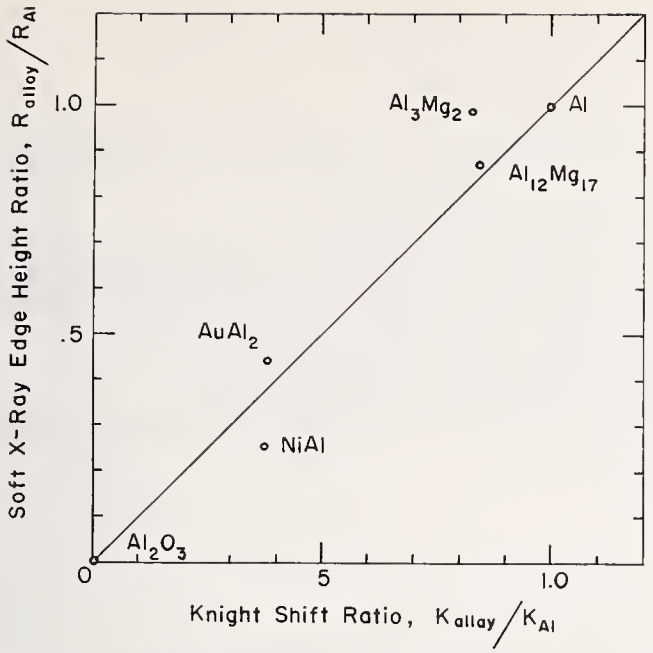

FIGURE 2. $L_{2,3}$ *soft x-ray emission edge height versus Knight shift of* Al *in a number of compounds.*

Each is expressed as a fraction of the pure metal value. The solid straight line of unit slope is the one electron prediction for simple materials.

$Al_{12}Mg_{17}$ are shown separately (table 3b) since changes in emission rate from these alloys are calculated with respect to the pure aluminum data of Appleton and Curry, and they have already been corrected for changes in n_{Al}. Also listed are the ratios R_{alloy}/R_{Al} and $\kappa_{alloy}/\kappa_{Al}$, plotted in figure 2.

4. Discussion

The correlation between the soft x-ray intensity at the Fermi edge and the Knight shift is illustrated in figure 2. The solid line of unit slope passing through the origin is the one electron prediction, and *not* an attempt to fit the data. The point for Al metal falls on the line by definition, and is not a verification of the correlation. The point for Al_2O_3 at the origin *is* a valid data point, and presumably is typical of nonmetallic compounds. Here the Knight shift is expected to be zero because there is no Pauli paramagnetism. All electrons are paired in spin. Actually, quadrupole effects have prevented a simple determination of a Knight shift. The soft x-ray emission edge height is zero because the Fermi level falls within the band gap, where the state density is zero. We would expect semi-metals to have near-zero Knight shifts and Fermi edge emission heights as well.

The principal uncertainty in the Knight shift involves such factors as chemical shifts, orbital shifts (paramagnetic or diamagnetic), p-electron core polarization. All must be considered carefully, or systems chosen in which they are known to be small. Uncertainty in the soft x-ray values comes mainly from our estimates of the factor I, defined above. The values of I used can reasonably be taken as upper limits. Thus, the points for NiAl, $AuAl_2$, Mg_2Al_3, and $Mg_{17}Al_{12}$ lie no higher on the plot than shown. The extreme, and definitely incorrect, procedure of correcting only for changes in the density of Al sites would reduce the corrected emission edge heights by factors ranging from .3 to .6, and move the points substantially below the line of unit slope. Thus, there exists the possibility of a systematic deviation from the expected correlation which, if real, could be interpreted as due either to enhanced Knight shifts or to reduced emission edge height enhancement in the alloys, with respect to Al metal. A more exact estimate of I can be made by replacing the assumption of average straight line electron trajectories with a diffuse scattering model. Considerably more labor would be involved. The calculations of I can be experimentally tested by studying emission edge height as a function of exciting potential at constant current density. We hope to make these better estimates in the future. However, our present feeling is that no gross error has been made, and that the indicated correlation is real.

Within the approximations and uncertainties outlined above, we have shown that Knight shift and soft x-ray estimates of local s-wave state densities are simply related. Although consideration has been given to Al alloys, we expect that other simple metal alloy systems will show similar correlation. We also expect that phenomena such as melting, which produce changes in the Knight shift in certain metals, will produce comparable changes in soft x-ray emission edge heights. Lastly, we would suggest that investigation of the soft x-ray emission edge heights can shed light on the question of whether the small Knight shifts observed in a number of metals and alloys [14] are due to dominant p-character (i.e., little s-character) at E_F or to cancellation of s-character by core polarization.

5. Acknowledgment

We thank R. L. Parke for his able technical assistance with the NMR measurements of the Al-Mg alloys.

6. References

[1] Pines, D., Solid State Physics, edited by F. Seitz and D. Turnbull (Academic Press, Inc., New York, 1955), **Vol. 1**; Narath, A., Phys. Rev. **163**, 232 (1967).

[2] Mahan, G. D., Phys. Rev. **163**, 612 (1967); Nozières, P., and DeDominicis, C. T., Phys. Rev. **178**, 1097 (1969); Ausman, G., and Glick, A. J., Phys. Rev. **183**, 687 (1969).
[3] Rooke, G. A., J. Phys. C**1**, 767 (1968).
[4] Williams, M. L., Dobbyn, R. C., Cuthill, J. R., and McAlister, A. J., these Proceedings, p. 303.
[5] Feldman, C., Phys. Rev. **117**, 455 (1960).
[6] Worthington, C. R., and Tomlin, S. G., Proc. Phys. Soc. **A69**, 401 (1956).
[6a] Green, M., Ph. D. Thesis, Univ. of Cambridge, 1962, unpublished.
[7] Archard, G. D., in X-Ray Microscopy and Microanalysis, edited by A. Engstrom, V. Coslett, and H. Pattee (Elsevier Publishing Company, New York, 1960) p. 331.
[8] Appleton, A., and Curry, C., Phil. Mag. **12**, 245 (1965).
[9] Fomichev, V. A., Soviet Physics, Solid State **8**, 2312 (1967).
[10] Cuthill, J. R., McAlister, A. J., and Williams, M. L., J. Appl. Phys. **39**, 2204 (1968).
[11] Knight, W. D., Solid State Physics, edited by F. Seitz and D. Turnbull (Academic Press, Inc., New York, 1956), **Vol. 2.**
[12] Jaccarino, V., Weger, W., Wernick, J. H., and Menth, A., Phys. Rev. Letters **21**, 1811 (1968).
[13] Miyatani, K., Ehara, S., Sato, T., and Tomono, Y., J. Phys. Soc. Japan **18**, 1345 (1963); West, G., Phil. Mag. **9**, 979 (1964).
[14] Schone, H. E., and Knight, W. D., Acta Met. **11**, 179 (1963); Bennett, L. H., Phys. Rev. **150**, 418 (1966).
[15] Haensel, R., private communication.
[16] Townsend, J. R., Phys. Rev. **92**, 556 (1953).
[17] Haensel, R., Kunz, C., and Sonntag, B., Phys. Letters **25A**, 205 (1967).

TUNNELING; SUPERCONDUCTORS; TRANSPORT PROPERTIES

CHAIRMEN: J. R. Leibowitz
J. W. Gadzuk

Tunneling Measurements of Superconducting Quasi-Particle Density of States and Calculation of Phonon Spectra*

J. M. Rowell

Bell Telephone Laboratories, Inc., Murray Hill, New Jersey

It is an unfortunate fact that the tunneling technique, which has proved incredibly successful in the study of superconductivity, has given little information about the normal state properties of metals and semiconductors. It will be shown that, in the determination of the superconducting quasi-particle density of states, it is the change in density induced by the onset of superconductivity which is measured rather than the total density.

Returning to the problem of normal materials, a review of the limited achievements and failures of tunneling will be presented. This will include the influence of band edges on tunneling in *p-n* diodes and metal-semiconductor contacts, the structures observed in tunneling into bismuth and the negative results obtained in nickel and palladium. The dominant effect of the change in barrier shape in most of these tunneling characteristics will be illustrated.

Key words: Density of states; phonons; semiconductors; superconductivity; tunneling.

Many of the talks heard this week have outlined experimental techniques which determine the density of electron states in metals and semiconductors over energy ranges which are typically 1-10 volts. I would like to discuss a technique which is much happier in the range of 1-10 millivolts, is the only method which can measure the change in density of electron states induced by superconductivity, but which to date must be classed as a failure in the determination of band properties of normal metals. For semiconductors and semimetals, because of smaller energies and larger fractional changes in electron density at band edges, the situation is a little better. Even in these materials, however, we can only say that density-of-states effects are observed and cannot generally deduce a density measurement from the experimental results.

After those opening remarks, it will be obvious that most of you attending this conference should not be familiar with the tunneling technique so I will briefly review the experimental method. Two structures are commonly used, the metal-insulator-metal (M-I-M) junction, which relies on the oxide of the first metal to form the insulator, and the metal-semiconductor (M-S) contact which uses the depletion layer (Schottky barrier) at the surface of the semiconductor. In the M-I-M case it is generally hard to prepare sufficiently smooth clean surfaces of bulk metal that oxidize in a controlled way so films have been used in all but a few cases. After evaporation of the first metal film (Al, Pb, Sn, Mg, for example), oxidation takes place by exposure to air, oxygen, or a glow discharge in oxygen, and the second film is then cross evaporated to complete the junction. Typical oxide thicknesses are 15–20 Å. To make the M-S contact a semiconductor is cleaved in vacuum and covered with the metal very rapidly. The barrier is lower and ~ 100 Å thick. In some materials, where a suitable Schottky barrier does not form at the surface (*e.g.* InAs), a M-I-S structure can be made by oxidizing the semiconductor before evaporation of the metal.

These three tunneling structures are shown in figure 1, with the circuit used to measure the current-voltage characteristic or, if greater detail is required, the

*An invited paper presented at the 3d Materials Research Symposium, *Electronic Density of States*, November 3–6, 1969, Gaithersburg, Md.

417-156 O - 71 - 44

dynamic resistance $(dV)/(dI)$ versus voltage. The figure also shows schematically the potential barrier (with typical energies indicated) which separates the electrodes.

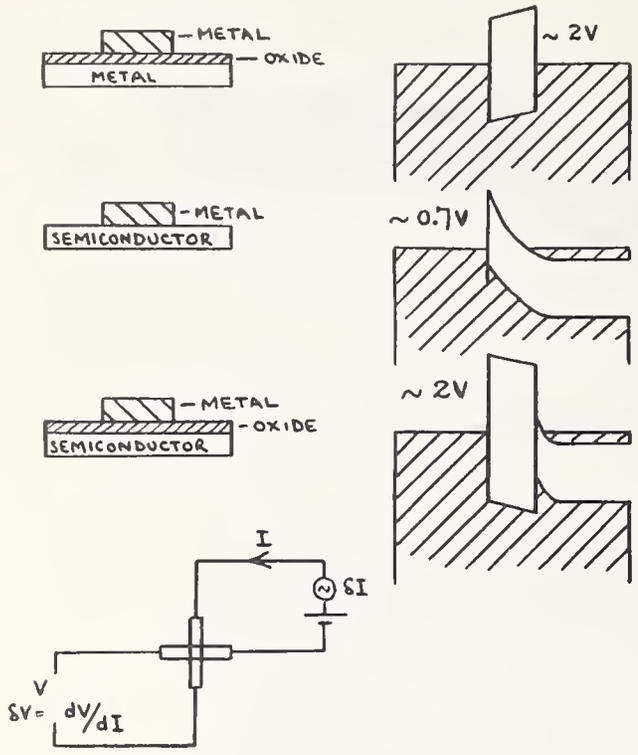

FIGURE 1. *Schematics of three widely studied tunneling structures and the circuit used to measure their I-V characteristics.*

Considering the M-I-M junction as the most favorable case for studying metals, I would like to make a number of points regarding the theoretical possibilities of observing band structure effects and the probable experimental difficulties.

The tunneling current through a barrier of the type shown in figure 2 is given by [1],

$$j=\frac{4\pi e}{\hbar}\sum_{k_t}\int_{-\infty}^{\infty} dE_x \rho_a(E)\rho_b(E)\,P(E_x)\,[f(E) - f(E-eV)], \qquad (1)$$

where $\rho_a(E)$ and $\rho_b(E)$ are the density of states for a given transverse momentum k_t and total energy E, $f(E)$ is the usual Fermi distribution and E_x the total electron energy perpendicular to the barrier. The tunneling probability $P(E_x)$ has the form

$$P(E_x)=A\exp\left\{-\frac{2}{\hbar}\int_0^d [2m(\phi(x,V)-E_x)]^{1/2}dx\right\} \qquad (2)$$

where d is the barrier thickness and $[\phi(x,V)\text{-}E_x]$ is the barrier potential at position x when a voltage V is applied. The pre-exponential factor A describes the frequency with which an electron arrives at the barrier interface and its exact form determines whether one expects to observe density of states effects at all. In the W.K.B. approximation, which makes the metal-barrier interface properties vary slowly compared to the electron wavelength [1], A is proportional to $1/[\rho_a(E)\rho_b(E)]$ so that the current in (1) is independent of electron density of states. The other extreme limit, with the metal-barrier interface absolutely sharp, gives a complicated prefactor A which does not exactly cancel the density terms in eq (1) [1,2] so some density of states effect in tunneling might be expected. However, as the interface properties can never be known in this detail, a serious interpretation of any such observation would be impossible. Rather than looking for results of the slow energy variation of $\rho(E)$ within a band, a more likely experiment is to look for effects of band edges, where the number of final available states for the tunneling electron changes more abruptly. It is generally felt that band edges can be observed in tunneling as long as an appreciable fractional change in total electron density is produced by the new band. As we will see later, this usually happens at convenient energies only in semiconductors. Duke [3] has also pointed out that an increased tunneling probability into the new band will enhance the magnitude of the current onset near the band edge.

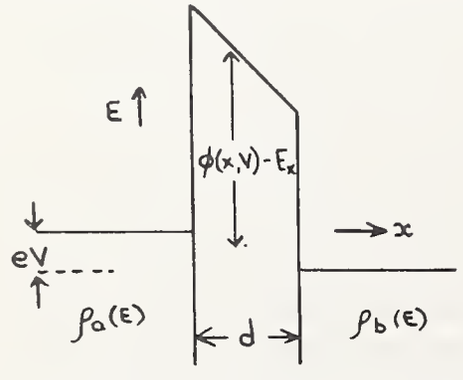

FIGURE 2. *The potential in an ideal trapezoidal barrier between metal electrodes.*

Apart from the theoretical question of the exact nature of the metal-insulator interface and its role in producing density of states effects, there are a number of serious experimental problems which lead me to question whether these effects could be observed in metals. These problems can be illustrated by reference to figure 3. First, typical barrier heights in oxides are ~ 2 volts, which is a small energy compared to interesting band structure in most metals. For an applied bias $> \phi_R$, electrons from the Fermi level (at A for example) tunnel into the conduction band of the insulator rather than into the second electrode. Second, the tunneling probability is much greater for electrons at B than for those at C, which enter the second metal just above the Fermi level. In figure 3b, for example, where

we assume $\phi_R = \phi_L = 2V$, the transmission probability at B is $\sim 10^{-9}$, whereas at C it is $\sim 10^{-16}$. Thus the chance of probing band edges far below the Fermi level in the left metal seems remote, as practically none of the

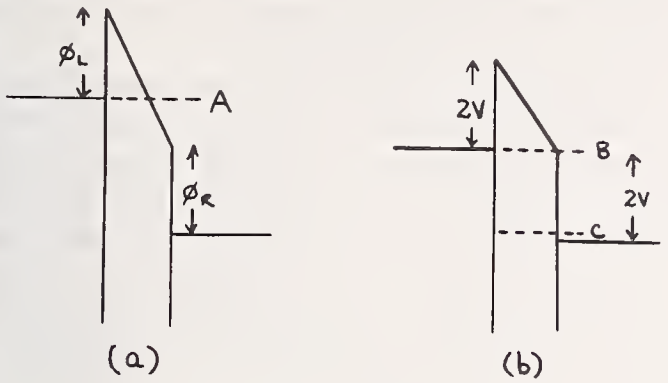

FIGURE 3. *Figure (a) shows the possible injection of electrons into the conduction band of the insulator (Fowler Nordheim tunneling). Figure (b) shows two possible tunneling paths into the second electrode.*

current, flows from these levels. The possibility of probing band edges above the Fermi level (at B in the right metal for example) raises the third problem, namely that the current-voltage characteristic of the junction is dominated very strongly by the changes in barrier shape. Typical results obtained by Fisher and Giaever [4] are shown in figure 4. At low voltages the junctions are ohmic (small deviations are observable only in detailed conductance plots) but from 0.2 to 1.4 V the current depends almost exponentially on voltage. This strong current dependence is purely the result of the barrier becoming lower (for electrons leaving the Fermi level) as the voltage increases. Thus any small changes in current (or conductance) due to band edges, superimposed on this exponential behavior, will be extremely hard to observe. There are also other difficulties which one has to consider in many tunneling experiments. If evaporated metal films are used it is unusual for these to have the properties of single crystals or even clean polycrystals. Even more critical are the surface properties of the films, as tunneling between normal metals is sensitive to the material only within a screening length of the surface. As this surface is in contact with (or diffused into) the insulating oxide the chance of it having bulk properties seems remote.

After this very pessimistic survey of why tunneling is not the right technique for the study of density of states effect in metals, let me review a number of experiments where band edges at least are observed, or affect the tunneling characteristic noticeably.

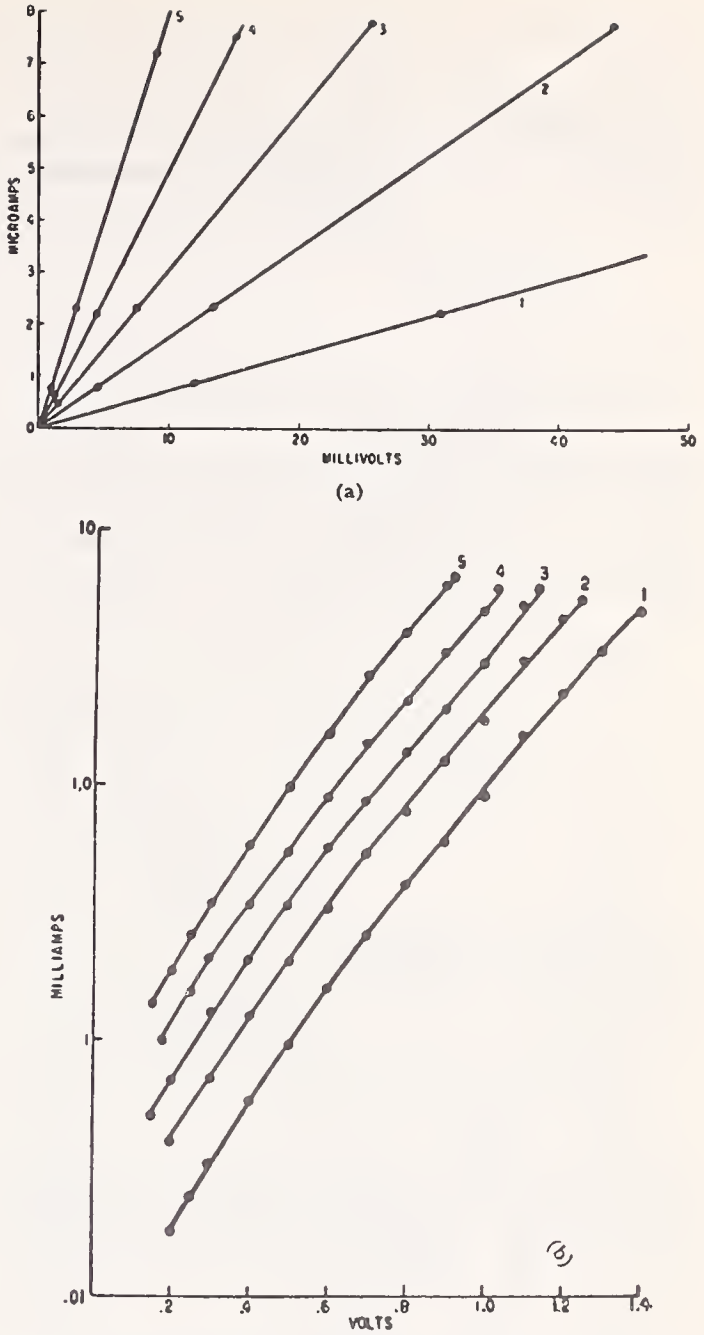

FIGURE 4. *I-V characteristics reported by Fisher and Giaever [4]. (a) At low voltages, the current through thin oxide films is proportional to voltage and to film area. Curves shown are for five films with areas in the proportions* 5:4:3:2:1 *as indicated. (b) At higher voltages, the current increases exponentially with voltage.*

1. Metal-Semiconductor Contacts

In a heavily doped n-type semiconductor the Fermi energy is relatively small (< 100 mV) and the depletion layer formed at the surface is thin enough to permit tunneling. Unfortunately the barrier height is rather low and barrier thickness varies with bias, leading to a strong dependence of conductance on voltage. Nevertheless, the calculation of Conley *et al.* [5] predicts that the minimum conductance occurs when the bottom of the band crosses the Fermi level of the metal (fig. 5). This has been observed in the experiments of

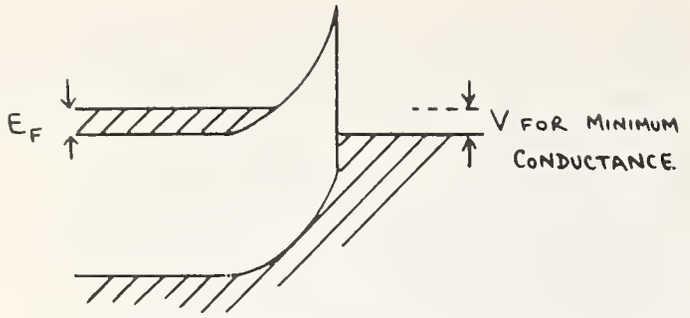

FIGURE 5. *Metal-semiconductor contact with bais applied to produce a minimum in conductance.*

Steinrisser *et al.* [6], as shown in figure 6. The barrier parameters were determined independently and the agreement between calculated and experimental conductances is orders of magnitude better than in most tunneling systems. The density of states in the semiconductor band was assumed constant in this calculation. The general aim of this type of experiment has been to obtain such a satisfactory agreement with the calculated conductance rather than to determine a density of states variation. Uncertainty in the energy dependence of the barrier parameters would make such a determination exceedingly difficult.

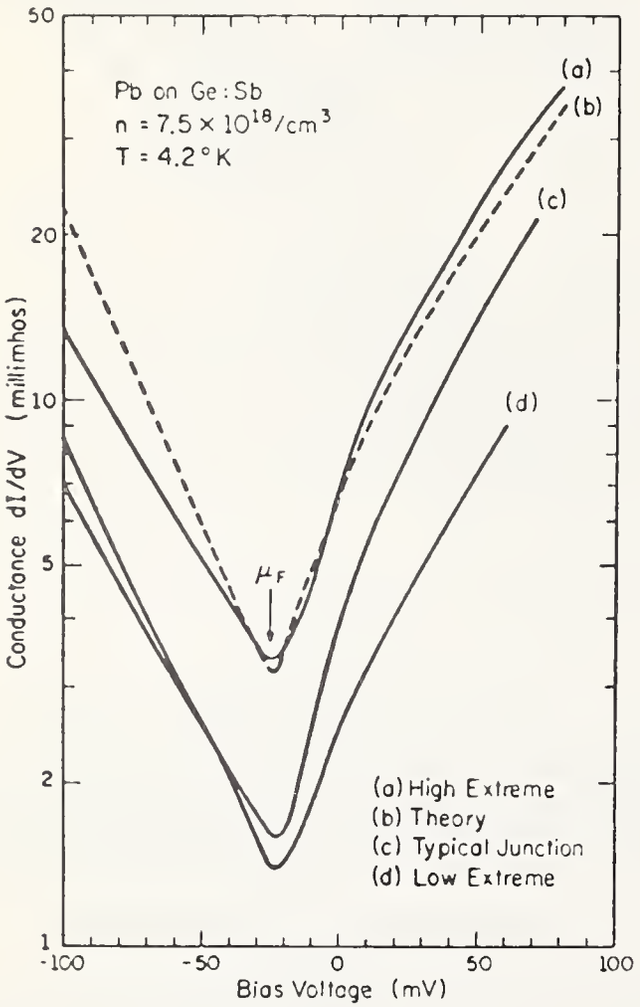

FIGURE 6. *Calculation and measurement of conductance in M-S contacts by Steinrisser et al. [6]. Comparison between three experimentally measured conductance curves on* $n = 7.5 \times 10^{18}/cm^3$ *Sb-doped Ge [solid lines (a), (c), and (d)] at 4.2 K and the calculated conductance [dashed line (b)] for a barrier height* $V_b = 0.63$ *eV obtained from capacitance measurements. The most commonly observed conductance curves were similar to (c), whereas (a) and (d) represent the high- and the low-conductance extremes. The contact metal is Pb and the contact area is* $2.5 \pm 0.5 \times 10^{-4}$ cm^2. *Structure associated with the superconducting energy gap has been omitted. The Fermi degeneracy* $\mu_F = 25$ *mV has been indicated.*

A second band structure effect, observed in Au-Ge surface barrier contacts by Conley and Tieman [7], is the onset of tunneling into the k=0 conduction band minimum, roughly 150 mV above the Fermi level. The influence of the band edge is rather dramatic in this case, as shown in figure 7, and a decrease of resistance by at least a factor of 10 is observed within ~ 10 mV of the edge. Note that the band edge is marked by a decrease in resistance, or increase in conductance.

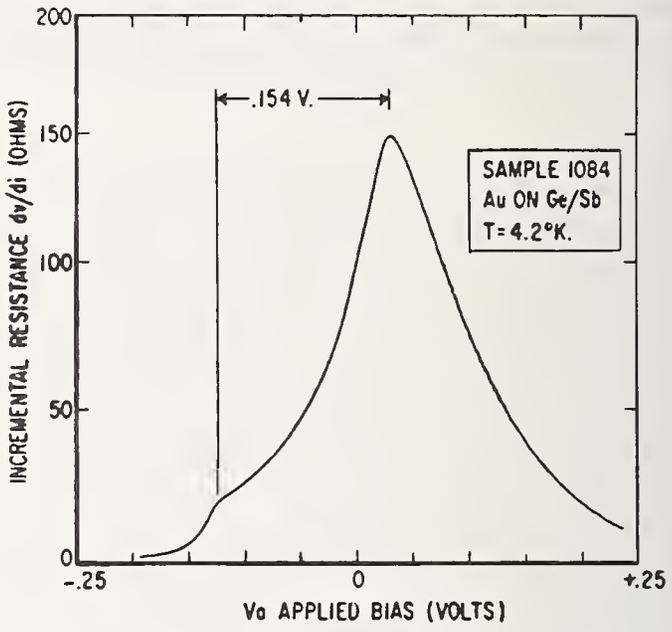

FIGURE 7. *Tunneling resistance of a Au-Ge surface barrier contact, measured by Conley and Tiemann [7]. The onset of transitions to the zone-centered* (Γ_2') *conduction band in Ge observed in the incremental resistance* dv/di *at an applied bias* $V_a = -0.124$ *V. Note that that threshold is* 0.154 *V from the maximum, a value which corresponds to the interband* $L - \Gamma_2'$ *separation.*

2. Metal-Insulator-Semiconductor Junctions

In order to investigate tunneling into semiconductors to higher voltages, or study those materials which do not form surface barrier contacts, an oxide can be grown on the surface before evaporation of the metal. Alternatively, for semiconductors which can be evaporated, junctions of the type aluminum-aluminum oxide-semiconductor have been fabricated. The current calculated by Chang *et al.* [8] for such a structure, on a degenerate *p*-type semiconductor, is shown in figure 8. The current is a maximum at the top of the valence

band and a minimum at the bottom of the conduction band. At higher voltages it is interesting to see that properties of the insulator, namely the increased tunneling probability at voltages corresponding to the heights ϕ_R and ϕ_L, dominate the characteristic. Experiments on a number of different III-V and II-VI semiconductors have confirmed this type of behavior except that the current minimum is not so sharp as the calculated one, as shown in figure 8 for SnTe.

The observation of interface states and impurity bands has also been reported from tunneling studies. The left-hand plots of figure 9 show the conductance results, obtained by Gray [9], for two M-I-S structures with different boron doping levels in silicon.

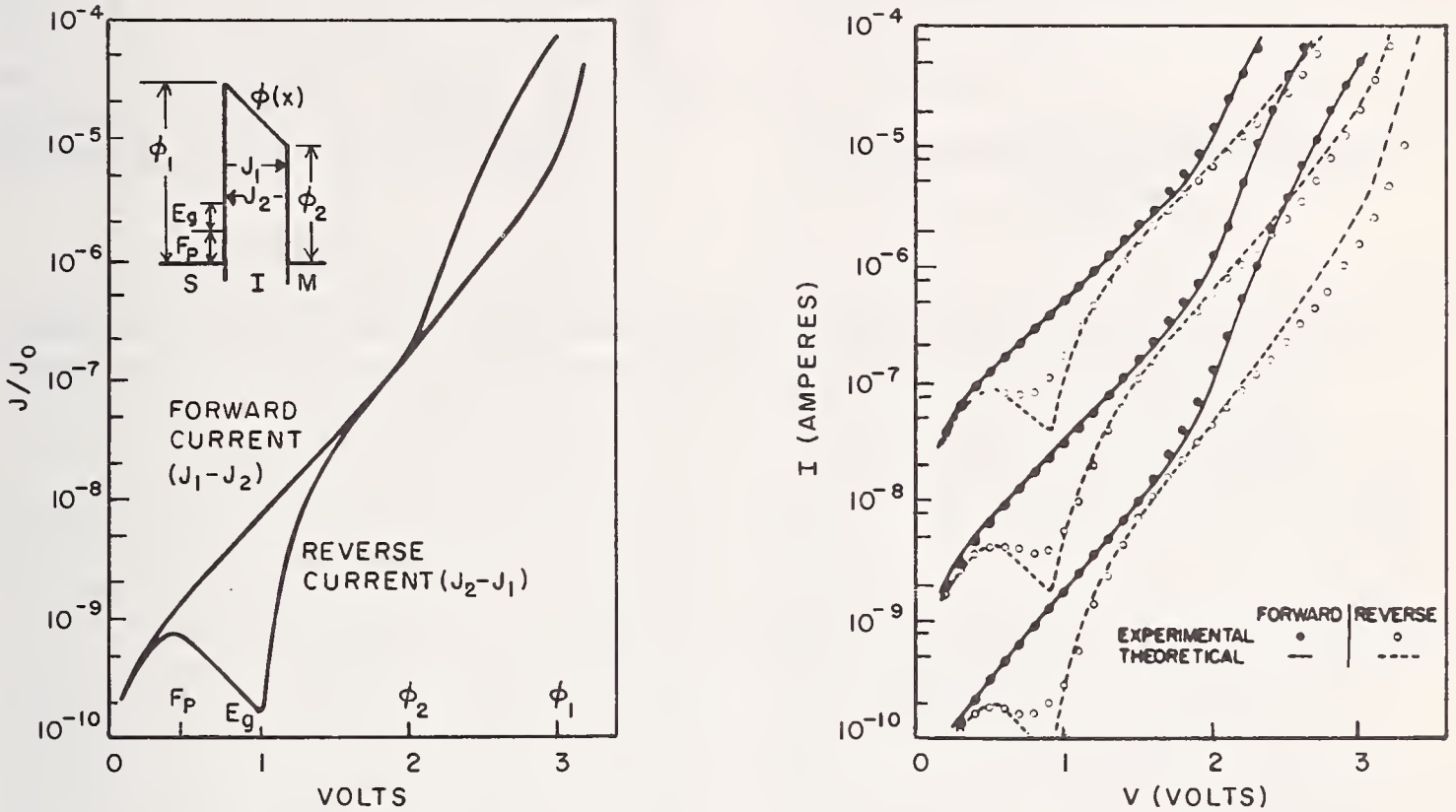

FIGURE 8. *Calculation and measurement of current in metal-insulator-semiconductor junctions by Chang et al. [8]. (a) Theoretical current-voltage characteristics for a M-I-S junction. The semiconductor is degenerate* p *type and the conduction band of the insulator provides the tunneling barrier. (b) Current-voltage characteristics for Al-Al_2O_3-SnTe junctions at 4.2 K. Three sets of curves are shown corresponding to samples with various oxide thickness.*

3. p-n Diodes

The I-V characteristic of the Esaki diode [10] is a clear observation of the influence of band edges on tunneling but recently this system has received little attention, probably because the barrier profile is difficult to measure. It is also difficult in this case to decide how much of the junction current is due to tunneling.

An interesting effect which has been observed in p-n diodes is the influence of Landau levels on the tunneling conductance. This was first reported by Chynoweth *et al.* [11] for InSb diodes and extensive studies of Ge diodes have been made by Bernard *et al.* [12]. Recently Landau levels in InAs have been measured by Tsui [13] in an M-I-S structure. Because only one electrode is a semiconductor the latter results are simpler to interpret.

4. Metal-Insulator-Metal Junctions

This type of tunneling structure is usually comprised of aluminum-aluminum oxide-second electrode of semimetal or metal. Considerable effort by various groups has gone into trying to observe the band edges in bismuth. Tunneling structures at low energies (<50 mV) have been reported by Esaki *et al.* [14] but these results have not been reproduced elsewhere [15]. At higher voltages the characteristics for polycrystalline films were first reported by Hauser and Testardi [16]. In figure 10 we show the good agreement between their results and those of Sawatari and Arai [17]. However, the exact position of the bands which give rise to this structure is difficult to determine from the tunneling characteristic.

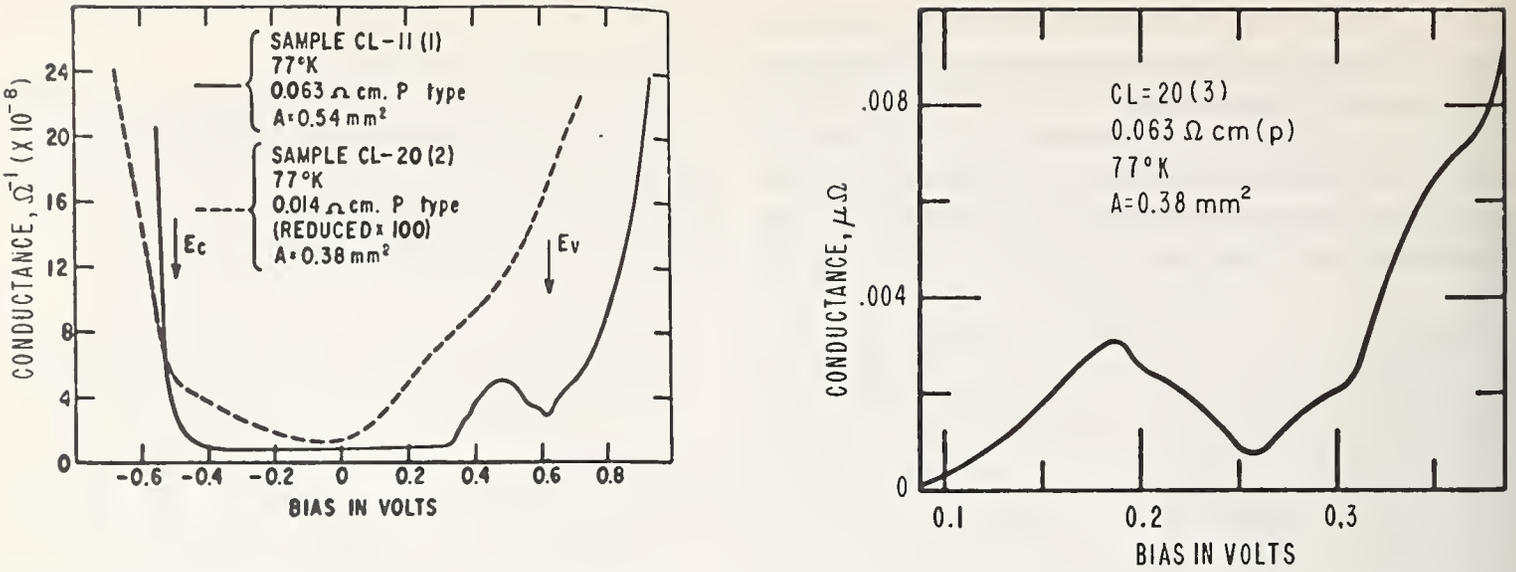

FIGURE 9. *Observation of impurity levels in tunneling by Gray* [9]. (*a*) dc *conductance versus bias showing the effect of a boron-impurity band at two different doping levels. The conductance of the more heavily doped sample is reduced* ×100 *for comparison.* (*b*) *Detailed* dc *conductance near an impurity band* (0.19 *V*). *This sample was cleaved in air before mounting in the vacuum jar.*

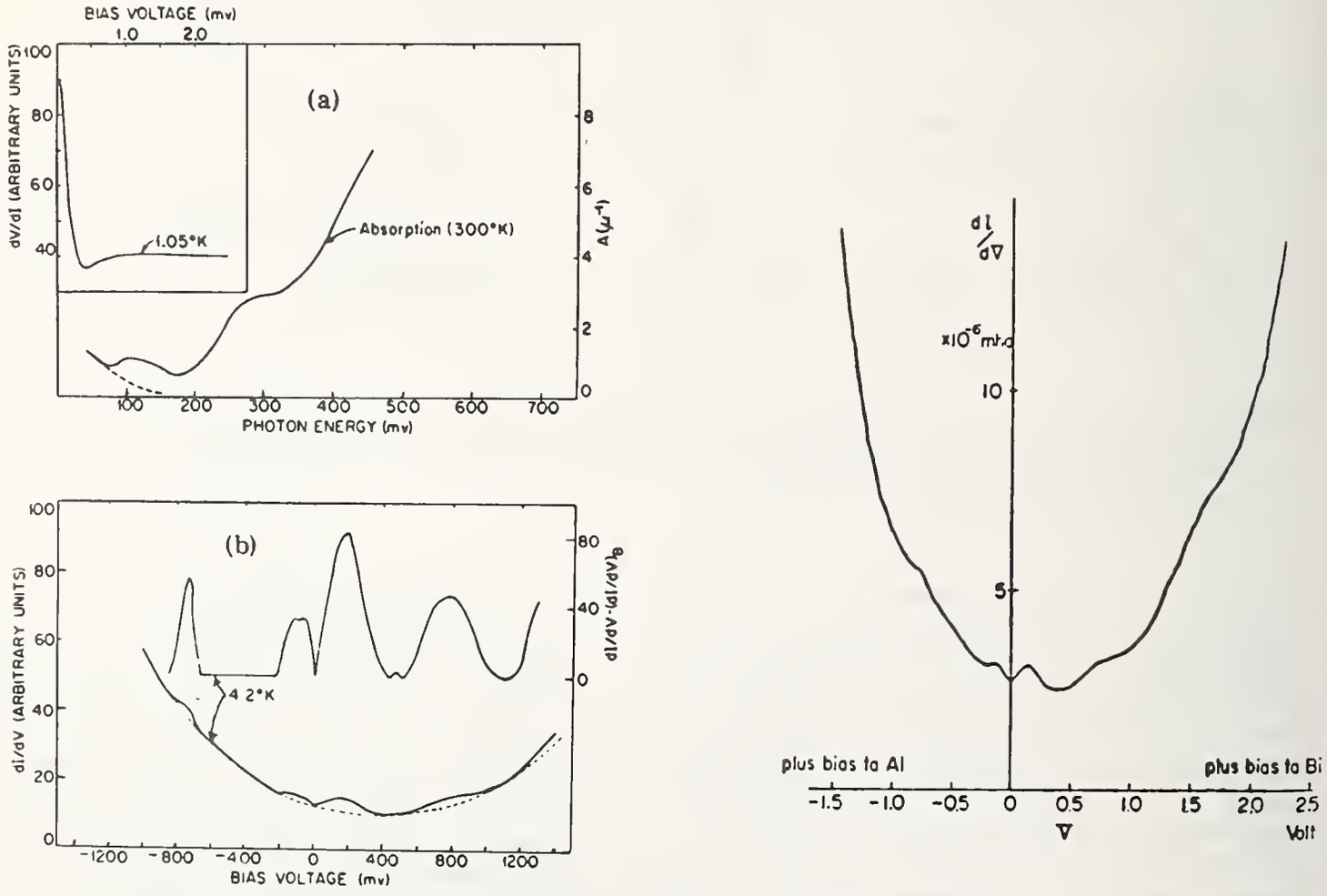

FIGURE 10. *Tunneling conductance for Al-I-polycrystalline Bi, as determined by Hauser and Testardi* [16] *(left figure) and Sawatari and Arai* [17] *(right figure). (a) Insert:* dV/dI *vs* V *for an Al-*Al_2O_3*-Bi junction. Bottom curve, adsorption as a function of energy. The dashed line shows the contribution from free carriers. (b)* dI/dV *vs* V *(solid line) and background curve (dashed line); curve of* $(dI/dV)/(dI/dV)_{bkg}$ *vs* V. (+V *corresponds to Bi positive.) (c) Conductance-voltage curve in the voltage range* $-1.4 \sim +2.3$ *V at 77 K. The sample is different from that of (a) and (b).*

The conductance characteristics of M-I-M junctions generally show considerable structure at voltages <1 volt, most of which is due to excitation processes in the insulator (oxide). These excitation interactions of the tunneling electron are with organic impurities in the oxide [18], phonons of the oxide [18,19] or phonons of the surfaces of the metal electrodes [19]. In a number of junctions, (Al-I-Ni, Al-I-NiPd alloys [20] and single crystal Cr-I-Pb [21]) there are additional effects which are not yet understood. However, it would be unwise to ascribe these to density of states variations without much more detailed experimental work as the barrier properties are, as usual, practically unknown.

5. Metal-Insulator-Superconductor

There are two main reasons why tunneling into superconductors has been so successful. First, the important parameter is the normalized density of states, which is the conductance versus voltage with the second electrode superconducting divided by the conductance with it normal. Thus it is not necessary to be able to calculate, or even understand, the normal state characteristic, as long as it is entirely due to tunneling. The barrier parameters, which are exceptionally difficult to determine, can remain as unknowns as long as they do not change when the electrode becomes superconducting. As far as we know, the only change might be in the position of the excitation processes, but these are fortunately weak compared with the superconducting effects. The second advantage of the superconducting measurement is that we can determine essentially bulk properties of the superconductor, whereas all normal state measurements probe the interface and surface properties of the normal electrode. As this technique has been discussed in numerous publications [22], no more detail will be given in this text.

6. References

[1] Harrison, W. A., Phys. Rev. **123**, 85 (1961).
[2] Davydov, A. S., "Quantum Mechanics," Fizmatgiz, Moscow 1963, English trans. Neo Press, Ann Arbor, 1966.
[3] Duke, C. B., "Tunneling in Solids," Academic Press, New York, 1969, page 55.
[4] Fisher, J. C., and Giaever, I., J. Appl. Phys. **32**, 172 (1961).
[5] Conley, J. W., Duke, C. B., Mahan, G. D., and Tiemann, J. J., Phys. Rev. **150**, 466 (1966).
[6] Stinrisser, F., Davis, L. C., and Duke, C. B., Phys. Rev. **176**, (1967).
[7] Conley, J. W., and Tiemann, J. J., J. Appl. Phys. **38**, 2880 (1967).
[8] Chang, L. L., Stiles, P. J., and Esaki, L., J. Appl. Phys. **38**, 4440 (1967).
[9] Gray, P. V., Phys. Rev. **140**, A179 (1965).
[10] Esaki, L., Phys. Rev. **109**, 603 (1958).
[11] Chynoweth, A. G., Logan, R. A., and Wolff, P. A., Phys. Rev. Letters **5**, 548 (1960).
[12] Bernard, W., Goldstein, S., Roth, H., Straub, W. D., and Mulhern, J. E., Jr., Phys. Rev. **166**, 785 (1968).
[13] Tsui, D. C., Phys. Rev. Letters **24**, 303 (1970).
[14] Esaki, L., and Stiles, P. J., Phys. Rev. Letters **14**, 902 (1965); Esaki, L., Chang, L. L., Stiles, P. J., O'Kane, D. F., and Wiser, N., Phys. Rev. **167**, 637 (1968).
[15] Giaever, I., Solid State Comm. **5**, X (1967) unpublished.
[16] Hauser, J. J., and Testardi, L. R., Phys. Rev. Letters **20**, 12 (1968).
[17] Sawatari, Y., Arai, M., Japan J. Appl. Phys. **7**, 791 (1968).
[18] Lambe, J., and Jaklevic, R. C., Phys. Rev. **165**, 821 (1968).
[19] Rowell, J. M., McMillan, W. L., and Feldmann, W. L., Phys. Rev. **180**, 658 (1969).
[20] Rowell, J. M., J. Appl. Phys. **40**, 1211 (1969).
[21] Shen, L. Y. L., J. Appl. Phys. (to be published).
[22] McMillan, W. L., and Rowell, J. M., Phys. Rev. Letters **14**, 108 (1965); Chapter 11 of "Superconductivity," R. Parks, Editor, Marcel Dekker, New York, 1969.; Rowell, J. M., "Tunneling Phenomena in Solids," S. Lundqvist and E. Burstein, Editors, Plenum Press, New York, 1969.

Discussion on "Tunneling Measurements of Superconducting Quasi-Particle Density of States and Calculation of Phonon Spectra" by J. M. Rowell (Bell Telephone Laboratories)

J. D. Penar *(Harry Diamond Labs.):* Do you know of any work that has been done to control substrate temperatures when the metal electrodes are deposited on the films? In particular, I was wondering what would be the effect of single crystal electrodes on the results that were found?

J. M. Rowell *(Bell Telephone Labs.):* The only example where you really see anything in the normal state is bismuth. And there I believe that the characteristic strength of those conductance structures changes somewhat with the annealing of the film. I think Hauser and Testardi [1] were typically evaporating bismuth films on a hot substrate; in fact as close to the melting point of bismuth as they could get. The bismuth effects apparently changed in magnitude with the annealing of the films.

J. D. Penar *(Harry Diamond Labs.):* Is this good or important when one is doing this?

J. M. Rowell *(Bell Telephone Labs.):* It made changes in the strength of the structure in this case. One would hope the annealed films were more representative of bulk material. It is the only example we can point to.

J. W. Gadzuk *(NBS):* Band edge effects in field emission tunneling have been observed along certain crystallographic directions in tungsten, molybdenum, and rhenium both by Swanson and coworkers and by Plummer and Young. Based upon the original observations and interpretation of the tungsten data, it was predicted that the band edges would be observed in molybdenum and rhenium. The experiments confirmed this. Furthermore, such edge effects have not appeared anomalously in materials or along crystallographic directions where they would not be expected.

J. M. Rowell *(Bell Telephone Labs.):* I would have thought that the energy distribution was so strongly peaked from the Fermi level of the metal that the chances of seeing any electrons coming from lower energies would be almost zero.

J. W. Gadzuk *(NBS):* The width of this peak is between .5 and 1 eV. If a band edge falls within this range of the Fermi level, enhanced emission is seen as structure upon the structure associated with the exponential tunneling probability drop off.

E. W. Plummer *(NBS):* All of the structure we have seen in field emission is very dependent upon the crystallographic direction of the exposed single crystal face and to the amount of contamination. All of the band edges which have been observed disappear when less than a monolayer of any kind of chemisorbed gas. It would seem that at a junction interface, any possible band edge structure might be suppressed for similar reasons.

[1] Hauser, J. J., and Testardi, L. R., Phys. Rev. Letters **20,** 12 (1968).

Density of States from Superconducting Critical Field Measurements*

G. Dummer and D. E. Mapother**

Department of Physics and Materials Research Laboratory, University of Illinois, Urbana, Illinois 61801

For a superconducting metal, the entropy difference, ΔS, between the normal and superconducting states is thermodynamically related to the critical field, H_c, by the equation

$$\Delta S = S_n - S_s = 1\ (VH_c/4\pi)\ (dH_c/dT),$$

where V is the molar volume and T is the absolute temperature. As the temperature approaches 0 K, it can be shown that ΔS is dominated by the normal electronic entropy, γT, where γ is the temperature coefficient of the normal electronic specific heat. This behavior has been known for a long time but its application has been largely confined to inferences based on conjectural extrapolations of H_c data measured about 1 K. In the limit of very low temperatures where $\Delta S = \gamma T$, it follows that

$$H_c^2(T) = H_0^2 - (4\pi\gamma/V)T^2,$$

where H_0 is the limiting value of H_c at 0 K. For most superconductors the range of validity of this expression lies below 1 K but new techniques have made this range relatively accessible in recent years. Within this range precise static measurements of H_c and T permit determination of the ratio, $\gamma^* = (\gamma/V)$, with a relative accuracy of about 1:3000. This is considerably better than the accuracies typically obtained in low temperature calorimetry. This method has been used to study the change in γ^* under hydryostatic pressures up to 1000 atm for In and Tl. Nonlinear changes in γ^* are clearly resolved for the first time, despite the relatively low values of applied pressure. For In the values of γ^* show a parabolic decrease with increasing pressure. The results for Tl show an initial increase in γ^* which reaches a maximum near $p = 500$ atm. For larger pressures the value of γ^* shows the normal decrease with increasing p.

Key words: Critical field; density of states; In; pressure dependence; superconductivity; Tl.

For a superconducting metal, the entropy difference $\Delta S(T)$, between the normal and superconducting states is thermodynamically related to the critical field, $H_c(T)$, by the equation

$$\Delta S(T) = S_n(T) - S_s(T) = -\ (VH_c/4\pi)\,(dH_c/dT) \qquad (1)$$

where V is the molar volume and T is the absolute temperature. The change in lattice entropy during the superconducting transition is negligibly small [1]. As a result, the entropy difference of (1) is essentially the difference between the electronic entropies, $S_{en}(T)$ and $S_{es}(T)$, in the normal and superconducting states [2].

It has long been recognized that, as $T \to 0$ K, $S_{en}(T)$ decreases linearly in T while $S_{es}(T)$ falls much more rapidly. As first noted by Daunt, Horseman, and Mendelssohn [3], the implication of this circumstance is that, for sufficiently low T,

$$\lim_{T\to 0} \Delta S(T) = \gamma T, \qquad (2)$$

where γ is the temperature coefficient of the normal electronic specific heat. Early efforts to apply (2) were limited by the technical difficulties of making measurements below 1 K and the resulting γ values were relatively imprecise [4].

The analytic form of $S_{es}(T)$ can be estimated using the BCS theory [5] from which it can be shown that S_{es}

*This work was supported in part by the Advanced Research Projects Agency under Contract No. SD-131.

**On leave from the Universität Karlsruhe, Karlsruhe, Germany.

becomes negligible for temperatures lower than about 0.25 T_c. For temperatures below this value it follows that the shape of the critical field curve is wholly determined by the normal electronic specific heat. Equating he right sides of (1) and (2) and integrating yields

$$H_c^2(T) = H_0^2 - (4\pi\gamma^*)T^2 \tag{3}$$

where $\gamma^* = \gamma/V$. It should be noted that this differs from the parabolic dependence of H_c on T which is commonly assumed.

Three considerations make (3) an especially useful and reliable means for the experimental determination of γ: (a) The validity of (3) is a general thermodynamic consequence of two well established experimental facts, the linear T dependence of S_{en}, and the fact that S_{es} vanishes more rapidly than S_{en} as T approaches 0 K. (b) The experimental parameters of (3) are quantities which can be measured under conditions of static equilibrium with very high precision. (c) The degree of linearity exhibited by experimental $H_c(T)$ data when plotted according to (3) provides a test of the validity of the analysis under the prevailing conditions of measurement. For sufficiently low temperatures, this linearity has been well confirmed by measurements on several different superconducting elements [2].

For most Type I superconductors the range of validity of (3) lies below 1 K, but new techniques have made temperatures down to about 0.03 K relatively accessible in recent years [6]. The experiment may be done as a difference measurement between the H_c values of two specimens held in isothermal equilibrium. This reduces the effect of experimental uncertainty in the absolute value of T and puts the main burden of accuracy on dc magnetic field measurements which can be made with high precision using conventional measuring methods. The resulting values of the ratio, $\gamma^* = (\gamma/V)$, from the present measurements have a relative accuracy of about 1:3000 which is substantially better than the typical precision of low temperature calorimetry.

The principles just described have been applied to study the change in γ^* under hydrostatic pressures up to 1000 atm for In and Tl. In each case the measurements consist of comparisons of $H_c(T,p)$ for pressurized and unpressurized specimens mounted in thermal equilibrium in a He^3 cryostat. The experimental details will be published separately but qualitatively similar techniques have already been reported [2,7].

The critical field is displaced by pressure and, using (3), the observed difference may be written as

$$\Delta H_c^2(T, p) = \Delta H_0^2(p) - 4\pi\Delta\gamma^*(p)T^2 \tag{4}$$

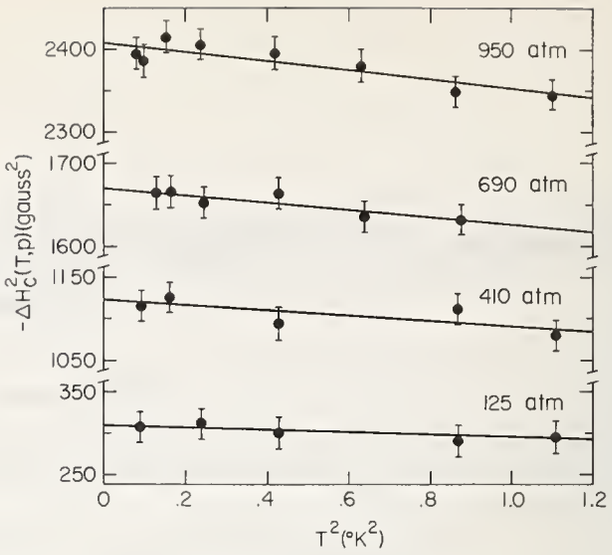

FIGURE 1. *Isobaric shifts in the critical field of* In *near 0 K plotted according to (4).*

where

$$\Delta H_c^2(T, p) = H_c^2(T, p) - H_c^2(T, 0),$$

$$\Delta H_0^2(p) = H_0^2(p) - H_0^2(0),$$

and

$$\Delta\gamma^*(p) = \gamma^*(p) - \gamma^*(0).$$

Data for In are plotted in figure 1 for measurements at four different pressures. The experimental points show a satisfactory linear dependence on T^2 as expected from (4) and the slope is directly proportional to the change in γ^* with pressure. The critical field constants for In are such that a change of 100 units on the ΔH_c^2 scale corresponds to a shift in H_c of approximately 0.18 G within the temperature range of figure 1.

The variation of γ^* calculated from the data of figure 1 is shown by the points in figure 2. The solid curve represents the parabolic relation

$$\Delta\gamma^*(p) = -6.5\times10^{-7}p + 2\times10^{-10}p^2.$$

Using the pressure dependent compressibility for In [8] yields

$$\gamma(p) = \gamma(0) - 1.4\times10^{-5}p + 3.4\times10^{-9}p^2 \tag{5}$$

where p is in atm and γ in mj/mol.deg.

For comparison with other measurements (5) may be used to calculate the logarithmic derivative, $d\ \ln\gamma/d\ \ln V$. the nonlinearity of $\gamma(p)$ results in substantial variation of $d\ \ln\gamma/d\ \ln V$ within the pressure range of the present work. Its value drops from 3.40 ± 0.1 at $p=0$ to 1.80 ± 0.05 at $p=1000$ atm [9].

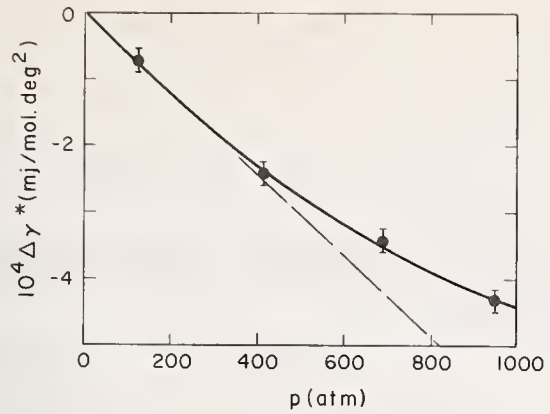

FIGURE 2. *Pressure induced shift in γ^* for* In.

Comparable values reported for this derivative at $p = 0$ are collected in table 1. Except for the low value obtained in experiments on the volume change during the superconducting transition, the values show a satisfactory consistency within the experimental error.

TABLE 1. *Experimental values of* (d *ln* γ/d *ln* V)$_{p=0}$ *for Indium*

$(d \ln \gamma / d \ln V)_{p=0}$	Method
3.40 ±0.1	Present work.
2.9 ±0.8	Thermal expansion.[a]
2.5 ±0.3	Pressure effect.[b]
1.0 ±0.5	Volume expansion at T_c.[c]

[a] J. G. Collins, J. A. Cowan, and G. K. White, Cryogenics 7, 219 (1967).
[b] See Reference 10.
[c] H. Rohrer, Helv. Phys. Acta 33, 675 (1960).

At pressures above zero, our results are qualitatively similar to those reported by Berman, Brandt, and Ginzburg [10] but the nonlinearity becomes apparent at lower pressure in our data. Part of this difference may be attributable to the smaller experimental scatter of the present work. However the analysis used by Berman et al. to derive the density of states, $N_0(p)$, involves two approximations which are inconsistent with the present results. The limiting form of $H_c(T)$ is assumed to follow a corrected parabolic law that is incompatible with (3) and leads to values of γ which are systematically too high by about 7%. Their analysis also involves the so-called "similarity principle" [11] which, according to our measurements, is not valid. These approximations have relatively little influence on $d \ln \gamma / d \ln V$ near $p = 0$ but they cause systematic errors at higher pressures.

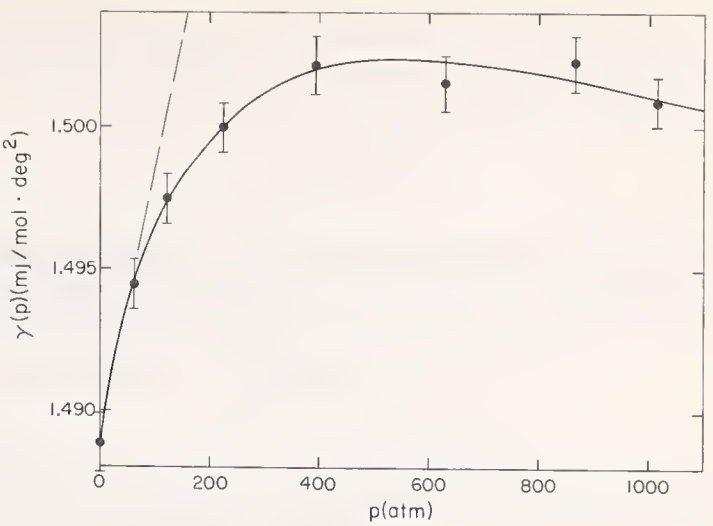

FIGURE 3. *Pressure induced shift in γ for* Tl.

The results of equivalent measurements on Tl are presented in figure 3 where $\gamma(p)$ is plotted vs. p. The values of γ are computed from observed values of γ^* using a molar volume 16.9 cm^3 and a compressibility of 2.64×10^{-6} atm^{-1} [12]. The observed value at $p = 0$, $\gamma(0) = 1.489$ mj/mol. deg.^{2}, is in excellent agreement with the values obtained by calorimetric measurement [13]. The initial increase in the density of states with pressure is very sharp, reaching a maximum near 600 atm. At $p = 0$, we find

$$d \ln \gamma / d \ln V = -26 \pm 2$$

which, in absolute terms, is the largest value of any material yet studied [11].

It should be noted that Tl is one of the few superconducting elements which shows an initial increase in critical temperature, T_c, with applied pressure. The shift of T_c with p is non-linear reaching a maximum value near 2000 atm [8]. This behavior and the present results for $\gamma(p)$ indicate that the Fermi surface for Tl lies near a critical energy value such that a small contraction in the lattice causes a relatively large change in the electronic density of states.

In this connection it is of interest to mention a recent brief report by Anderson, Schirber, and D. R. Stone [14]. Using measurements of the deHaas-van Alphen (dHvA) effect, these authors have studied pressure induced changes in the Fermi surface of Tl. They find that the logarithmic pressure derivatives of certain dHvA frequencies are as much as 9 times the value estimated from the known compressibility of Tl. This is about the same factor by which the present value of $d \ln \gamma / d \ln V$ for Tl exceeds that of the electronically similar element, In.

In the literature of experimental superconductivity it has been usual to calculate an "observed" density of states at the Fermi level, $N(0)$, from the relation

$$\gamma^* = \tfrac{2}{3}\pi^2 k_B^2 N(0)$$

where k_B is Boltzmann's constant. More recent theoretical arguments express the so-called "band structure" density of states, $N_{bs}(0)$, by the relation

$$N_{bs}(0) = N(0)/(1+\lambda)$$

where the "enhancement factor," $(1+\lambda)$, is determined by the electron-phonon coupling constant, λ. The calculation of λ has been described by McMillan [15] who gives numerical values for most of the superconducting elements. Both $N_{bs}(0)$ and λ are expected to change with volume.

Reliable experimental evidence on the volume dependence of λ is lacking, but, for In, it can be estimated that about 30-40% of the observed $d \ln \gamma / d \ln V$ is due to this contribution. The values of λ are identical for In and Tl. Thus it appears that the abnormally large value of $d \ln \gamma / d \ln V$ for Tl is dominated by the volume dependence of $N_{bs}(0)$.

References

[1] Welber, B., and Quimby, S. L., Acta Met. **6,** 351 (1958).

[2] Finnemore, D. K., and Mapother, D. E., Phys. Rev. **140,** A507 (1965).

[3] Daunt, J. G., Horseman, A., and Mendelssohn, K., Phil. Mag. **27,** 764 (1939).

[4] Daunt, J., Progress in Low Temperature Physics, D. J. Gorter, Editor, **1,** Ch. XI, p. 202 (North-Holland Publ. Co., Amsterdam, 1955).

[5] Mühlschlegel, B., Z. Physik **155,** 313 (1959).

[6] Wheatley, J. C., Vilches, O. E., and Abel, W. R., Physics **4,** 1 (1968).

[7] Harris, E. P., and Mapother, D. E., Phys. Rev. **165,** 522 (1968).

[8] Jennings, L. D., and Swenson, C. A., Phys. Rev. **112,** 31 (1958).

[9] The compressibility of 2.2×10^{-6} atm^{-1}, deduced from elastic constants by B. S. Chandrasekhar and J. A. Rayne, Phys. Rev. **124,** 1011 (1961), modifies the coefficients in (5). The resulting values of $d \ln \gamma / d \ln V$ become 3.7 at $p = 0$ and 1.9 at $p =$ 100 atm.

[10] Berman, I. V., Brandt, N. B., and Ginzburg, N. I., Sov. Phys. JETP **26,** 86 (1968). Recalculation of the graphical data of $N_o(p)$ given as figure 7 of this article and using the compressibility of reference 8 gives $d \ln \gamma / d \ln V = 3.3 \pm 0.3$ which is very close to our result.

[11] Boughton, R. I., Olsen, J. L., and Palmy, C., Progress in Low Temperature Physics, C. J. Gorter, Editor, **VI** (to be published).

[12] Ferris, R. W., Shepard, M. L., and Smith, J. F., J. Appl. Phys. **34,** 768 (1963).

[13] van der Hoeven, B. J. C., and Keesom, P. H., Phys. Rev. **135,** A631 (1964).

[14] Anderson, J. R., Schirber, J. E., and Stone, D. R., Abstract **B-II 3,** Colloque International du Centre National de la Recherche Scientifique sur les Propriétés Physiques des Solides sous Pression, Grenoble, 1969.

[15] McMillan, W. L., Phys. Rev. **167,** 331 (1968).

Temperature Dependence in Transport Phenomena and Electronic Density of States for Transition Metals

M. Shimizu

Department of Applied Physics, Nagoya University, Nagoya, Japan

The calculated results of the temperature variations of electronic specific heat and spin susceptibility and their comparison with the experimental results for various transition metals are briefly summarized. In these calculations the empirical densities of states, which were determined in the rigid band model from the experimental data of low temperature specific heat coefficient, were made use of. In a model similar to the Mott model of *s-d* scattering, the electrical resistivity, thermal conductivity, and thermoelectric power have been calculated at high temperatures for palladium, platinum, rhodium, iridium, molybdenum, and tungsten, by assuming appropriate electronic structures and making use of the same empirical densities of states. The calculated temperature dependences of electrical resistivity, thermal conductivity, and thermoelectric power and the sign of the thermoelectric power at high temperatures are found to be strongly dependent on the shape of the density of states and the position of the Fermi level. It is shown that all of these temperature dependences and the sign of the thermoelectric power are consistent with the experimental results. It is confirmed that there is a strong correlation between these temperature dependences and those of the electronic specific heat and spin susceptibility.

Key words: Chromium; electronic density of states; iridium; low-temperature specific heat; magnetic susceptibility: molybdenum; niobium; palladium (Pd); platinum; rhenium; rhodium; rigid band approximation; tantalum (Ta): thermal conductivity: thermoelectric power; transition metal; transport properties; tungsten (W).

1. Introduction

It has so far been shown [1] that electrical and thermal resistivities, R and $1/\kappa$, at high temperatures increase more rapidly than T for some transition metals, molybdenum, tungsten, rhodium, iridium, etc., and increase less rapidly than T for other metals, palladium, platinum, niobium, etc. Hereafter we call the former metals "plus group" and the latter ones "minus group," as defined before by us [2]. The fact that for palladium and platinum of the minus group the temperature coefficient R at high temperatures falls below the normal value was first explained by Mott [1], using the *s-d* scattering model. It was also suggested by Jones [3] that the temperature dependence of R of tungsten may be accounted for by occurrence of the Fermi level at 0 K, ϵ_F, near a minimum in the electronic density of states curve $\nu(\epsilon)$.

On the other hand, in the plus-group transition metals, e.g., chromium, molybdenum, tungsten, rhodium, etc., magnetic susceptibility χ at high temperatures increases with increasing temperatures, whereas in the minus group metals, e.g., palladium, platinum, niobium, tantalum, etc., it decreases. In general, the values of χ and the temperature coefficient γ of electronic specific heat, $C_E=\gamma T$, at low temperatures are small in the plus group and large in the minus group [4]. In the band model of *d*-electrons in transition metals, Stoner [4] showed that if the ϵ_F occurs near a minimum of the $\nu(\epsilon)$, the values of χ and γ at low temperatures are small and χ increases with increasing temperatures. It was also shown [2] that γ at lower temperatures, as well as the spin susceptibility χ_s, increases with increasing temperatures in the plus group metals and decreases in the minus group metals. Our calculated results [2,5] of the temperature variations of χ_s and γ for various paramagnetic transition metals and their comparison with the experimental results are briefly summarized in section 2. In these calculations the $\nu(\epsilon)$'s, which were determined in the rigid band

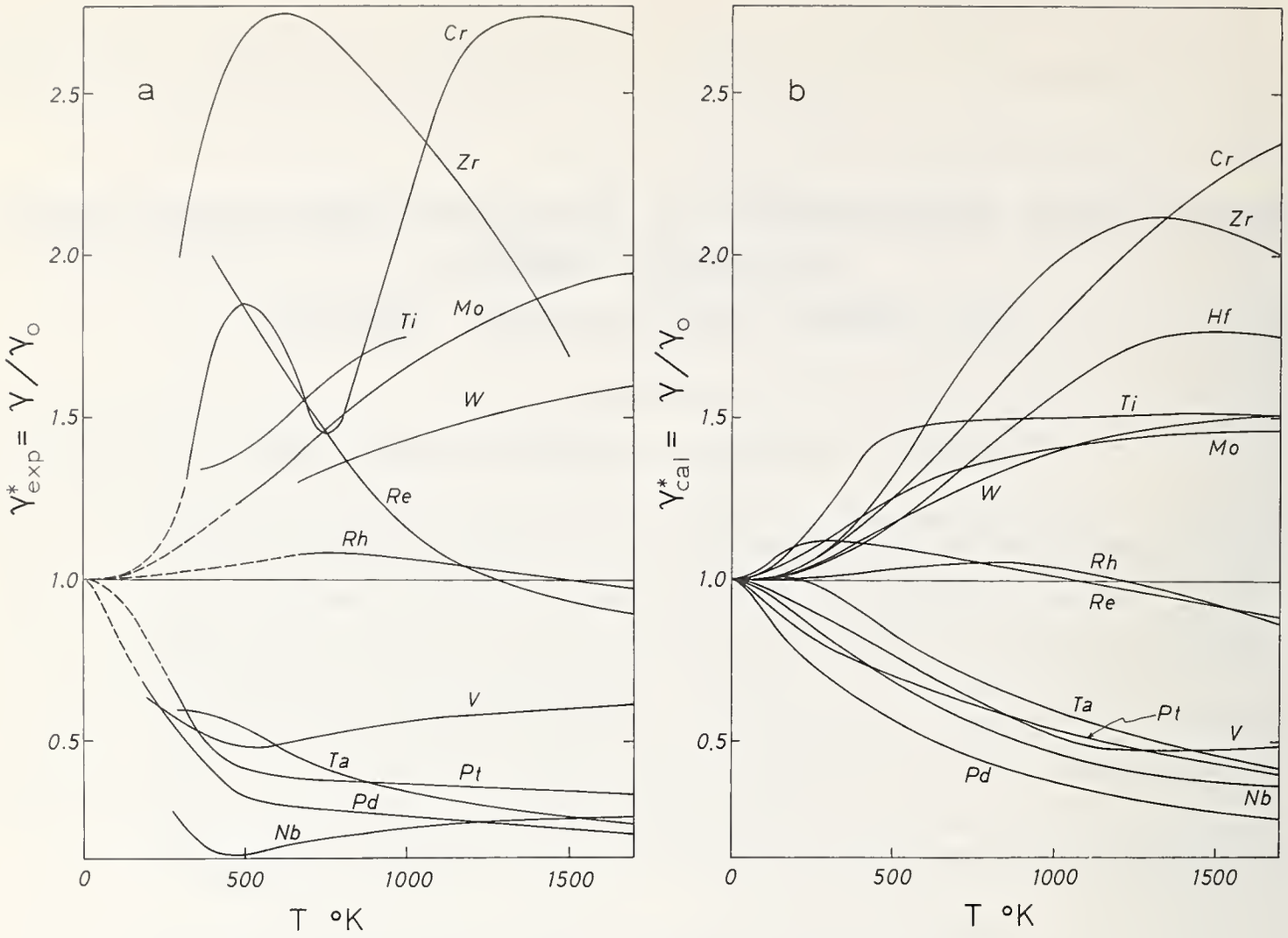

FIGURE 1. *(a) Experimental and (b) calculated results of the reduced electronic specific heat coefficient* $\gamma^* = \gamma/\gamma_0$.

model from the experimental data of the low temperature specific heat coefficient γ_0 without including corrections due to the many-body effects of electrons, phonons and paramagnons, were made use of.

From the experimental and calculated results of R, κ, γ and χ_s, it is easily seen that there are certain correlations among their temperature variations for paramagnetic transition metals. The object of this paper is to explain the correlations among the temperature dependences of thermoelectric power S, R, κ, γ and χ_s and the sign of S in connection with the shape of $\nu(\epsilon)$ and the position of ϵ_F for typical transition metals of the plus and minus groups.

Our recent calculated results [6] of the temperature variations of R, κ, and S at high temperatures for molybdenum, tungsten, rhodium, iridium, palladium and platinum metals by the usual theory of conduction in a model similar to the Mott model of *s-d* scattering [1] are shown in section 3. By using simple approximations R, κ and S are expressed in terms of $\nu(\epsilon)$ and parameters of electronic band structures. These calculated results are compared with the experimental ones. In section 4 it is concluded that the temperature variations of R, κ, and S and the sign of S at high temperatures are strongly dependent on the shape of $\nu(\epsilon)$ and the position of ϵ_F.

2. Temperature Dependences of Electronic Specific Heat and Magnetic Susceptibility

The part of the electronic specific heat $C_E = \gamma T$ is evaluated by subtracting the Debye specific heat and dilatation correction from the observed specific heat at constant pressure in the usual way [2]. The temperature variations of the ratio $\gamma_{exp}{}^* = \gamma/\gamma_0$ obtained from the experimental values of $\gamma = C_E/T$ and γ_0 and of the ratio of the observed value of χ at T to the one at 300 K, i.e., $\chi_{exp}{}^* = \chi/\chi_{300\,K}$, for various paramagnetic transition metals are shown in figures 1a and 2a, respectively (cf. the references 2 and 5 for details of the experimental data). From figures 1a and 2a, it is easily seen that for the plus group metals, where the ϵ_F occurs in the

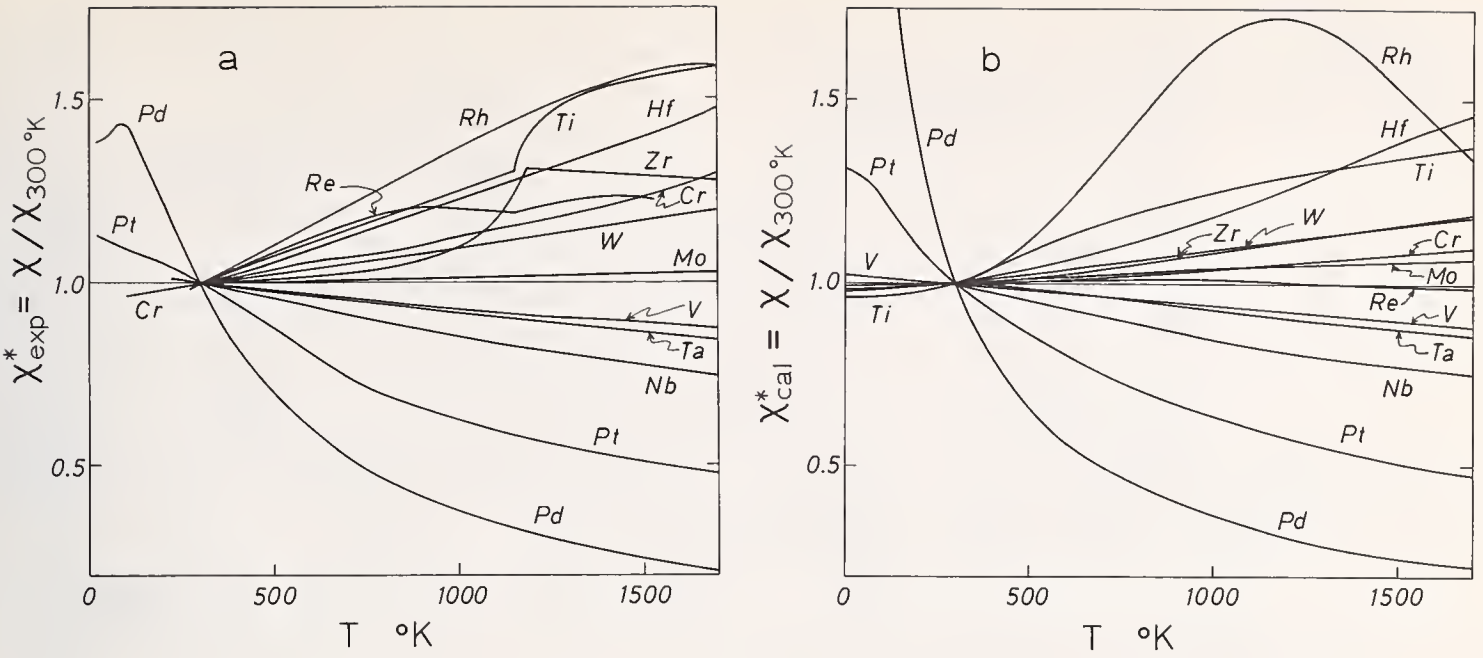

FIGURE 2. *(a) Experimental and (b) calculated results of the reduced susceptibility* $\chi^* = \chi/\chi_{300\,K}$.

TABLE 1. *Estimation of the molecular field coefficient* α and the constant part of the magnetic susceptibility χ_c

$\alpha(10^4$ mole/emu)						$\chi_c(10^{-4}$ emu/mole)					
Ti	V	Cr				Ti	V	Cr			
0.82	0	0				0.73	1.8	1.32			
Zr	Nb	Mo		Rh	Pd	Zr	Nb	Mo		Rh	Pd
0	0.24	0		1.33	0.72	0.83	0.82	0.55		−3.2	0
Hf	Ta	W	Re		Pt	Hf	Ta	W	Re		Pt
0.88	0	3.06	0		0.74	0.14	0.71	0.31	0.42		−0.15

neighborhood of a minimum of $\nu(\epsilon)$ and hence the values of γ_0 and χ_s are small, $\gamma_{exp}{}^*$ and $\chi_{exp}{}^*$ increase from one with increasing temperatures and for the minus group, where the ϵ_F occurs in the neighborhood of a maximum of $\nu(\epsilon)$ and hence the values of γ_0 and χ_s are large, they decrease from one with increasing temperatures. Rhodium and rhenium metals are intermediate between the plus and minus groups.

The C_E and χ_s can be calculated in the one-particle approximation by the usual electron theory of metals, if the shape of $\nu(\epsilon)$ is given. The curves of $\nu(\epsilon)$ for paramagnetic transition metals of 3*d*-, 4*d*- and 5*d*-groups with bcc and fcc crystal structures were obtained in the rigid band model from the experimental data of γ_0 for various metals and their alloys, as shown in figure 3, where the positions of ϵ_F for various metals are also shown. It is easily seen that the width of the 4*d*-band is broader than that of the 3*d*-band and narrower than that of the 5*d*-band.

From the $\nu(\epsilon)$'s shown in figure 3, the temperature variations of $\gamma = C_E/T$ and χ_s are calculated in the usual electron theory of metals. The total magnetic susceptibility χ is calculated from the calculated results of χ_s by using $\chi = \chi_s/(1 - \alpha\chi_s) + \chi_c$, where α is a molecular field coefficient and χ_c is the sum of the constant orbital-paramagnetic and core-diamagnetic susceptibilities, $\chi_c = \chi_{orb} + \chi_d$. The calculated results of the ratios, $\gamma_{cal}{}^* = \gamma/\gamma_0$ and $\chi_{cal}{}^* = \chi/\chi_{300\,K}$, are shown in figures 1b and 2b, respectively. The values of α and χ_c are determined so as to get the best fit of the calculated values of χ to the observed ones for respective metals. These values are shown in table 1. It seems that these values of α are reasonable except rhodium and tungsten metals, where the values of α are anomalously large, and the values of χ_c are consistent with the calculation of the χ_{orb} by Place and Rhodes [7], except rhodium metal. The agreement between the calculated and experimental values of γ^* in rhodium is very

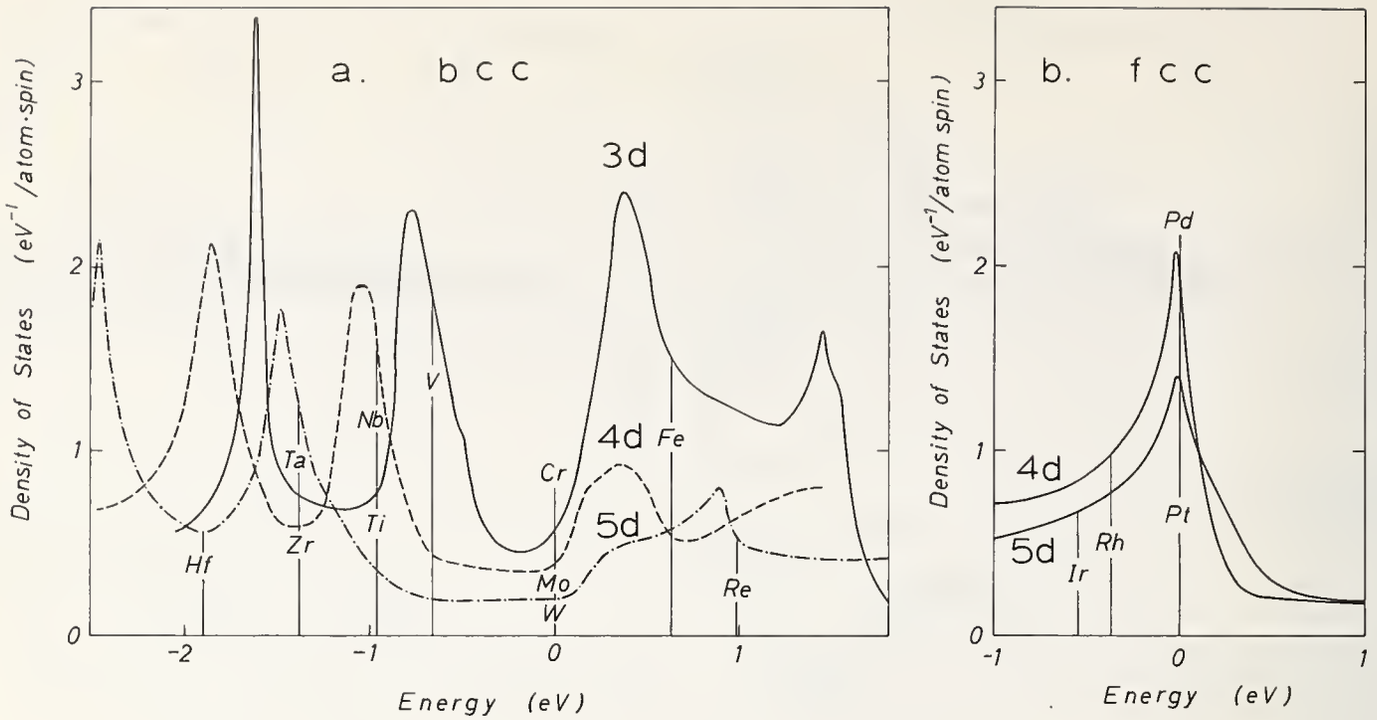

FIGURE 3. *(a) Electronic densities of states for transition metals of* 3d-, 4d-, *and* 5d-*groups with bcc structure and (b) those with fcc structure.*

satisfactory, nevertheless the variation of χ for this metal is very large and it is very difficult to explain the reason.

From figures 1 and 2 we can see that there are qualitative agreements between the calculated and experimental results of $\gamma = C_E/T$ and χ for various paramagnetic transition metals of the plus and minus groups.

3. Electrical Resistance, Thermal Conductivity and Thermoelectric Power

By using a model similar to the Mott model of *s-d* scattering [1] and by the usual theory of conduction [8], the temperature variations of R, κ and S at high temperatures are numerically calculated for molybdenum, rhodium, palladium, tungsten, iridium, and platinum metals. The main scattering of electrons at high temperatures is due to electron-phonon interactions, and for the sake of simplicity their matrix elements are averaged over the Fermi surfaces and assumed to be a constant denoted by ξ. Because of the approximation for the matrix elements of electron-phonon interactions and of the effective mass approximation in the simple model of electronic structure, R, κ and S can be expressed in terms of the $\nu(\epsilon)$ and the parameter of electronic band structures as follows;

$$R = (e^2 B \Theta_D^2/\xi)^{-1} (T/G_1), \tag{1}$$

$$\kappa = (B\Theta_D^2/\xi)(G_3 - G^2/G_1)/T^2, \tag{2}$$

$$S = -(G_2/G_1)/(eT), \tag{3}$$

$$G_n = -\int d\epsilon \frac{\partial f(\epsilon)}{\partial \epsilon} (\epsilon - \zeta)^{n-1} \nu(\epsilon)^{-1} \times \sum_i m_i^{1/2} E_i^{3/2}, \tag{4}$$

where B is a constant which depends on the lattice constant, density, etc., Θ_D the Debye temperature, $f(\epsilon)$ the Fermi-Dirac distribution function, ζ the chemical potential, and m_i the effective mass ratio of electrons in the i^{th} band. Further, E_i in (4) is given by $E_i = \epsilon - \epsilon_e$ or $\epsilon_h - \epsilon$ for an electron or hole band, where ϵ_e or ϵ_h is the energy at the bottom or top of the respective bands.

The values of the parameters of electronic structure m_i, ϵ_e and ϵ_h in (4) are determined in the following way. For palladium and platinum the two band model of *s*-electrons and *d*-holes, for rhodium and iridium the four band model of two hole surfaces around the X point and two electron surfaces around the Γ point, and for molybdenum and tungsten the four band model of two hole surfaces around the N and H points and two electron surfaces around the Γ point and centered on the Δ axis are made use of. These closed Fermi surfaces are replaced by spheres of equal volume so as to be consistent with the calculated results of electronic bands and the observed results of γ_0 and the de Haas-van Alphen oscillations.

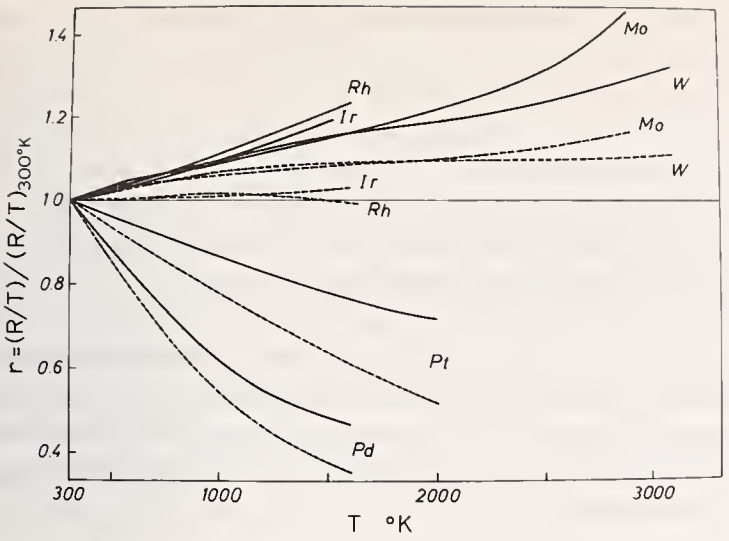

FIGURE 4. *Calculated results (solid curves) of the reduced electrical resistivity divided by* T.
Broken curves are obtained for constant Θ_D's.

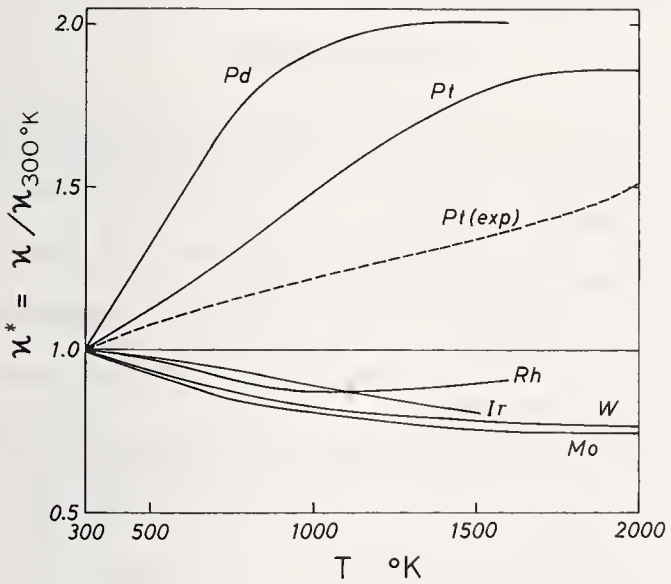

FIGURE 5. *Calculated (solid curves) and observed (broken curve [9]) results of reduced thermal conductivity* $\kappa^* = \kappa/\kappa_{300\,K}$.

By using the values of m_i, ϵ_h and ϵ_e determined in this way and the $\nu(\epsilon)$ shown in figure 3 and by taking account of the temperature variation of Θ_D due to the thermal expansion [1] in (1) and (2), the temperature variations of R, κ and S are calculated by (1-4). The value of ξ in (1) and (2) for each metal is determined in such a way that the calculated value of R agrees with its observed value at the highest temperature, and the values of ξ obtained are shown in table 2. It is noted that the values of ξ for superconducting metals are larger than those for normal metals.

The calculated results of R at high temperatures agree almost completely with the observed results [9]

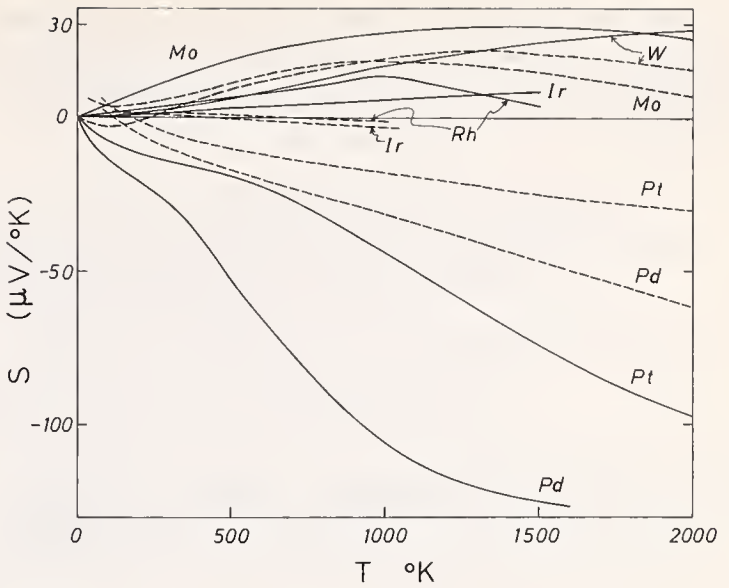

FIGURE 6. *Calculated (solid curves) and observed (broken curves [9]) results of thermoelectric power* S.

TABLE 2. *Values of electron-phonon coupling constant* ξ *in* $(eV)^2$

Metals	Mo	Rh	Pd	W	Ir	Pt
ξ.....	10.5	1.92	1.63	13.3	4.56	2.46

for all metals except palladium metal (cf. [6]). The calculated results of the ratio of R/T to its value at 300 K are shown by solid curves in figure 4, where the broken curves are obtained without taking account of the temperature variation of Θ_D. The calculated results of the ratio of κ to its value at 300 K and of S are shown in figures 5 and 6, respectively, where broken curves are the observed results [9]. It is seen that there are qualitative agreements between the calculated and observed results of κ and S.

4. Discussion and Conclusion

At lower temperatures, R, κ and S in (1-4) can be expanded as power series of T as [6]

$$(R/T)/(R/T)_{T=0} = 1 - \frac{1}{6}(\pi kT)^2(3\nu_1^2 - \nu_2), \qquad (5)$$

$$\kappa/(\kappa)_{T=0} = 1 + \frac{1}{6}(\pi kT)^2\left(\frac{37}{5}\nu_1^2 - \frac{21}{5}\nu_2\right), \qquad (6)$$

$$S = \frac{1}{3e}(\pi k)^2 T\nu_1\left\{1 + \frac{1}{6}(\pi kT)^2\left(\frac{37}{5}\nu_1^2 - \frac{42}{5}\nu_2 + \frac{7}{5}\frac{\nu_3}{\nu_1}\right)\right\}, \qquad (7)$$

417-156 O - 71 - 45

where $\nu_n = (d^n\nu(\epsilon_F)/d\epsilon_F{}^n)/\nu(\epsilon_F)$ and the contributions from E_i in (4) are all neglected. The expression (5) was given before by Jones [3]. The low temperature expansion for χ_s and γ were given by [4,2]

$$\chi_s = 2\mu_B^2\nu(\epsilon_F)\left\{1-\frac{1}{6}(\pi kT)^2(\nu_1^2-\nu_2)\right\}. \tag{8}$$

$$\gamma = \frac{2}{3}(\pi k)^2\nu(\epsilon_F)\left\{1-\frac{1}{6}(\pi kT)^2\left(3\nu_1^2-\frac{21}{5}\nu_2\right)\right\}. \tag{9}$$

From (5-9) it is expected that χ_s, γ, R/T, $1/\kappa$ and $T/|S|$ at lower temperatures increase with increasing temperatures for the plus group metals where ϵ_F occurs in the neighborhood of a minimum of $\nu(\epsilon)$ or $\nu_2 > \nu_1{}^2 \simeq 0$, and they decrease for the minus group metals where ϵ_F occurs in the neighborhood of a maximum of $\nu(\epsilon)$ or $\nu_2 < 0$. Moreover, from (5), (8) and (9), the temperature variations of R/T are expected to be smaller for the plus group metals and larger for the minus group metals, respectively, than those χ_s and γ. Accordingly, as shown by broken curves in figure 4, the deviations of the values of R/T from unity at high temperatures are relatively small for the plus group metals and large for the minus group metals, respectively. As the temperature variations of R/T are very small for rhodium and iridium of the plus group it seems that ν_2 is nearly equal to $3\nu_1{}^2$ in these metals. In the plus group metals the temperature variations of χ_s and γ show a maximum at a certain temperature because χ_s and γ become zero at infinite temperature. It has been shown [2,10,11] that even in the minus group metals, e.g., palladium, χ_s and hence γ may show a maximum if $\nu_1{}^2 - \nu_2 < 0$ as seen from (8) and (9). As the sign of S at low temperatures is determined by the sign of ν_1 as seen from (7), from the results in figure 6 it is concluded that the positions of ϵ_F in $\nu(\epsilon)$ shown in figure 3 are all consistent with the experimental results of S.

From the comparisons between the calculated and experimental results shown in figures 1, 2, 4, 5 and 6, it is concluded that the temperature variations of R, κ and S and the sign of S at high temperatures are strongly dependent on the shape of $\nu(\epsilon)$ and the positions of ϵ_F, and the Mott model for the *s-d* scattering is a satisfactory approximation to calculate the temperature variations of R, κ and S at high temperatures for paramagnetic transition metals. By our calculations of R, κ and S, it is confirmed that for the transition metals of the plus group, where the Fermi level occurs in the neighborhood of a minimum of the $\nu(\epsilon)$ curve and the values of γ_0 and χ_s are small, R/T and $1/\kappa$, as well as χ_s and γ, increase with increasing temperatures and for the minus group metals, where the Fermi level occurs in the neighborhood of a maximum of the $\nu(\epsilon)$ and the values of γ_0 and χ_s are large, they decrease with increasing temperatures.

5. Acknowledgments

The author wishes to thank T. Takahashi, A. Katsuki, H. Yamada, T. Aisaka and K. Ohmori for their cooperation and assistance.

6. References

[1] Mott, N. F., and Jones, H., The Theory of the Properties of Metals and Alloys (Oxford Univ. Press, London, 1936) p. 268; Mott, N. F., Advances in Phys. **13**, 325 (1964); Proc. Roy. Soc. **A153**, 699 (1936).

[2] Shimizu, M., Takahashi, T., and Katsuki, A., J. Phys. Soc. Japan **17**, 1740 (1962); **18**, 240 (1963).

[3] Jones, H., Encycl. of Physics, S. Flügge, Editor (Springer, Berlin, 1956) **XIX**, p.265.

[4] Stoner, E. C., Proc. Roy. Soc. **A154**, 656 (1936); Acta Metallurgica **2**, 259 (1954).

[5] Shimizu, M., and Katsuki, A., J. Phys. Soc. Japan **19**, 1135, 1856 (1964); Katsuki, A., and Shimizu, M., ibid. **21**, 279 (1966); Shimizu, M., Katsuki, A., and Ohmori, K., ibid. **21**, 1922 (1966).

[6] The details of this calculation will be published by T. Aisaka and M. Shimizu elsewhere.

[7] Place, C. M., and Rhodes, P., J. Appl. Phys. **39**, 1282 (1968).

[8] Wilson, A. H., The Theory of Metals, 2nd ed., (Cambridge Univ. Press, London, 1953) p. 193.

[9] Touloukin, Y. S., Thermophysical Properties of High Temperature Solid Materials **1** (Macmillan Co., New York, 1967).

[10] Elcock, E. W., Rhodes, P., and Teviotdale, A., Proc. Roy. Soc. **A221**, 53 (1954).

[11] Allan, G., Leman, G., and Lenglart, P., Journ. de Phys. **29**, 885 (1968).

Discussion on "Temperature Dependence in Transport Phenomena and Electronic Density of States for Transition Metals" by M. Shimizu (Nagoya University, Japan)

J. F. Goff *(NOL):* I have treated κ and ρ for chromium (which Prof. Shimizu does not treat) and find compatible results. I would recommend that people use this method of moments formulation due to Klemous for analysis. Since one would expect dense d-bands not to conduct, do your results for the elements to the right of the transition series imply the contrary?

M. Shimizu *(Nagoya University, Japan):* In our model of transition metals, both s- and d-electrons in the neighborhood of the Fermi level contribute to conduction.

Metal-Semiconductor Barrier Junction Tunneling Study of the Heavily Doped N-Type Silicon Density of States Function*

Y. Hsia and T. F. Tao**

University of California, Los Angeles, California 90024

Experimental and analytic techniques and procedure used in the study are described. Experimental data showing the dependency of the Fermi level on the dopant types of the heavily doped *n*-type silicon are reported. A dopant type dependent density of states effective mass is postulated to describe the effect of different dopants on the Fermi level. Tbe deviation of the experimental data curve from the calculated curve is ascribed to the effect of degenerate semiconductor band tailing. In addition, through interpretation of incremental conductance versus applied bias characteristic curves of the different tunnel junction evaluated, a consistent description of the density of states function of the heavily doped silicon is obtained. The density of states function, dependent on the dopant type and dopant concentration, is generally parabolic above the band edge, but towards the band edge, band tailing can be severe.

Key words: Antimony-doped silicon; arsenic-doped silicon (As doped Si); band absorption; band tailing; depletion layer barrier tunneling; electronic density of states; Esaki diode; gallium-arsenide (GaAs); heavy doping with As, Ga, P, Sb; luminescence experiments; P doped Si; Schottky-barrier; silicon; transport properties; tunneling.

1. Introduction

The study of the transport properties across a tunnel junction has been an active field of research for a decade. There are three types of tunnel junctions that have been studied in various degrees: (1) *p-n* junction, (2) insulated layer tunnel junction, and (3) depletion layer metal-semiconductor tunnel junction. In this paper, we are presenting some of our experimental results on the metal-semiconductor barrier junction tunneling study of the heavily doped *n*-type silicon density of states function.

It was Gechwend et al. [1] who first indicated the possibility of a metal-semiconductor depletion layer tunnel junction. Since then, Conley, Duke, Mahan, and Tiemann [2] calculated the tunneling current through the depletion layer in a metal to heavily doped semiconductor junction and found that dV/dI has a maximum at a bias potential equal to the Fermi degeneracy calculated by the parabolic band model. Conley and Tiemann [3] reported reasonable verifications of the calculations based on their measurements of metal to *n*-type Ge Schottky barrier diodes. Conley and Mahan [4,5], also studied *n*- and *p*-type GaAs. For *p*-GaAs, they found that the location of dV/dI maximum was affected by the band tailing in heavily doped semiconductor. For *n*-type GaAs, it occurred at a bias much smaller than the calculated Fermi degeneracy. The deviation was accounted for by the effect of band mixing in the forbidden gap. Using a thin oxide layer as a tunneling barrier, Chang, Esaki, and Jona [6] had earlier reported their tunneling study of metal to both *n*- and *p*-type InSb junctions, and suggested that the dI/dV minimum observed in the case of *p*-InSb occurred at Fermi degeneracy.

The depletion layer barrier tunneling appears to be an amenable tool for the study of the properties of heavily doped semiconductor near and about the band edge, including the determination of the Fermi degeneracy, the amount of band tailing, and generally the effect of impurity band on the overall band structure of the heavily doped semiconductor; because the tunnel current measurement is referenced to the zero bias which is located at the Fermi level. This is an im-

*This paper is based on part of a dissertation submitted by Y. Hsia in partial fulfillment of the requirements for a Ph. D. degree in the School of Engineering and Applied Science, University of California, Los Angeles, 1969.

**Mailing address: Litton Systems, Inc., Guidance and Control Division, Woodland Hills, California 91364.

provement over the band absorption [7-10] and the luminescence experiments [11-13] commonly used in the study of the heavily doped semiconductors. In all of these optical measurements, they are referenced to the energy band gap, whereas the band edge phenomena to be evaluated are only a small proportion of the reference energy level. In addition, when measurements are made as a function of dopant concentrations, for example, in the study of the Fermi degeneracy due to impurity dopant, data interpretation becomes extremely hazardous because of the existence of the band gap narrowing phenomenon introduced by heavy impurity doping [14-16].

2. Analyses of Tunneling Transport

2.1. Physical Model

When a metal-semiconductor junction is formed, there is an exchange of carriers, such that the Fermi level is continuous across the junction. In most of group IV (Si included) and zinc blende III-V semiconductors, Mead and Spitzer found that the Fermi level at the junction interface is fixed very close to one-third from the valence edge, and thus the potential barrier at the interface which results from the redistribution of charge depends not on the metallic element or the doping of the semiconductor [17]. The potential barrier is maintained by the electric dipole layer at the contact. The positive charge at the semiconductor side of the junction is resultant from the fixed ionized donors having a density much less than the ionized lattice metallic atoms in the metal. Therefore, the ionized donors at the semiconductor contribute a distributed charge layer near the junction interface, quite different from the surface charge layer at the metal element. The distributed charge layer in the semiconductor is commonly called the depletion region of the junction as the region has been depleted of charge carriers, leaving behind the fixed ionized impurities locked in the lattice. Figure 1 is a diagram showing the potential distribution at a metal-semiconductor junction.

The I-V characteristics of a metal-semiconductor tunnel junction is shown in figure 2. At zero bias, electrons tunneling through the depletion layer barrier from the metal to the n-semiconductor are in equilibrium with electrons tunneling in the reverse direction, and we have zero current flow. With forward bias, the electrons in the conduction band of the n-semiconductor are brought to opposite to the empty states above the Fermi level of the metal, thus increasing the tunnel current which is proportional to the joint probability of the occupancy of the conduction band of the n-semiconductor and the availability of empty states in the metal. At forward bias above V_p where

$$eV_p = E_F - E_C \tag{1}$$

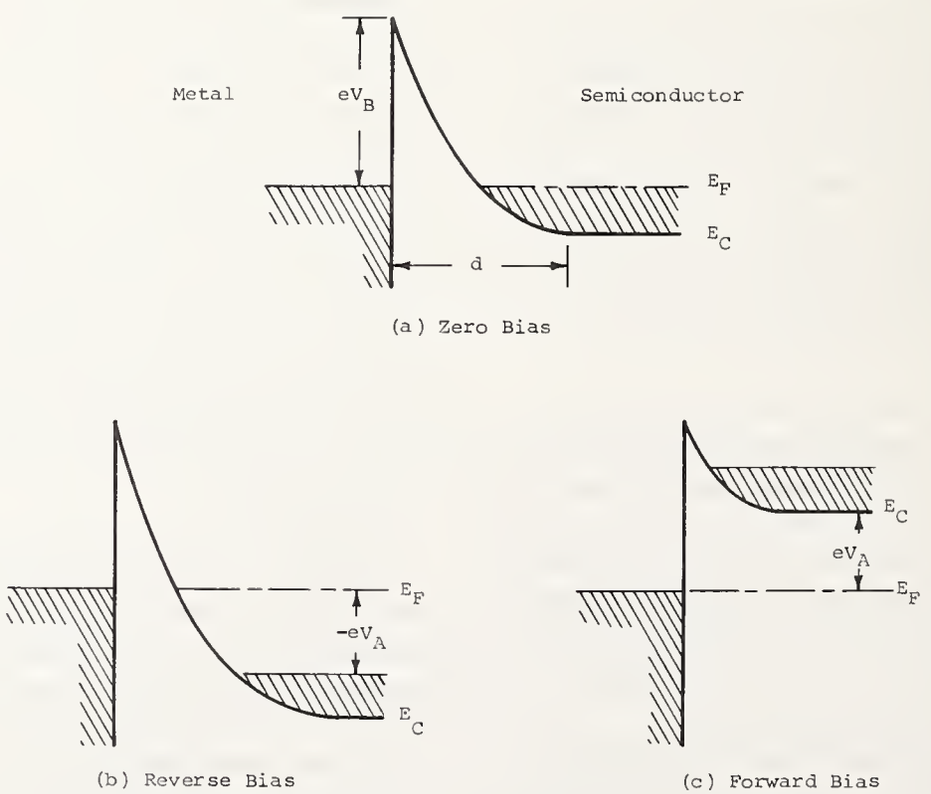

FIGURE 1. *The idealized metal-semiconductor tunnel junction.*

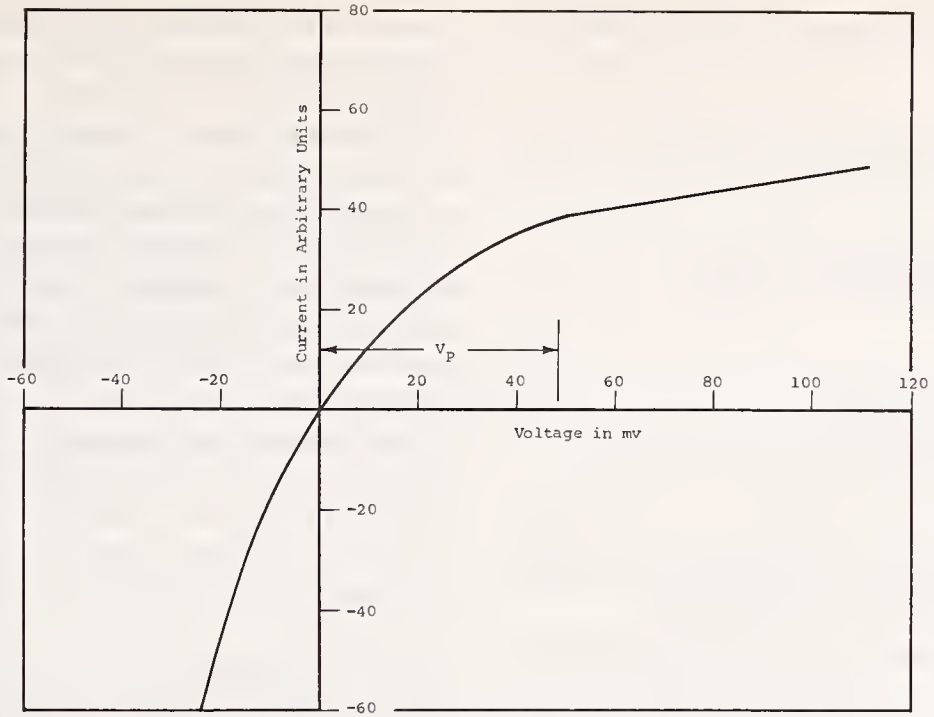

FIGURE 2. *The idealized I-V characteristics of a metal-semiconductor tunnel junction.*

no additional filled electron states in the *n*-semiconductor are brought to opposite empty states in the metal with increasing applied bias, and the tunnel current remains approximately constant. The slight increase in the tunneling current at bias above V_p is attributed to the modification of the barrier transparency by the applied bias field.

2.2. Mathematical Model

The generalized tunneling equation that we are using to study the analytic behavior of the metal-semiconductor barrier tunneling is

$$I = A \int [f_m(E) - f_s(E)] g_m(E) g_s(E) P(E) dE \quad (2)$$

where

$f_m(E)$ = the Fermi function describing the occupancy of the density of states function of the metal

$f_s(E)$ = the Fermi function describing the occupancy of the density of states function of the semiconductor

$g_m(E)$ = the density of states function of the metal/superconductor

$g_s(E)$ = the density of states function of the semiconductor

$P(E)$ = the tunneling probability

A = the constant of proportionality

This generalized tunneling equation is very similar to the original tunnel diode equation proposed by L. Esaki except that the tunneling probability is *P(E)* instead of an assumed constant [18]. It is also similar to the basic equation used in the interpretation of superconductor tunneling experiments [19]. Quantitative data on superconductivity based on the interpretations of the tunneling experiments have been obtained on the assumption of the tunneling current being directly proportional to the density of states of the quasi-particles in the superconductors [20,21].

To determine the metal-semiconductor barrier tunnel current according to the generalized eqs (2-48) we first derive the potential distribution of the tunnel barrier and then arrive at the tunneling probability function *P(E)* using the WKBS approximation solution of the Schrödinger's equation describing the electronic wave function across a barrier potential.

The potential distribution at the metal-semiconductor junction can be readily derived from Poisson's equation. The parabolic potential in the depletion region results from the assumption of uniform distribution of the impurity charge density N_0. The one-dimension Poisson's equation is given by

$$\frac{\partial^2}{\partial x^2} V(x) = \frac{qN_0}{\epsilon} \quad (3)$$

where

$V(x)$ = potential distribution as function of x

q = electronic charge

ϵ = dielectric constant of material

Assume width of depletion layer = d, then solution to eqs (3) is given by

$$V(x) = \frac{qN_0}{2\epsilon}(d-x)^2 + V_A - V_F \tag{4}$$

where

$$d = \left[\frac{2\epsilon}{qN_0}(V_B + V_F - V_A)\right]^{1/2} \tag{5}$$

and

V_A = applied voltage bias
V_F = Fermi voltage
V_B = barrier height of the junction in volts

For the Schottky barrier of heavily doped Si, in the voltage bias range of interest ($< |\pm 100|$ mv), the width of the depletion layer d is of the order of 100 Å.

Experiments to determine the barrier height of metal-semiconductor junctions were carried out by C. A. Mead and W. G. Spitzer on Si, Ge, and many group III-V compound semiconductors [17]. The barrier height was found to be nearly independent of the metallic element work function or the doping of the semiconductor. It was shown that one can estimate the barrier height to a fair degree of accuracy by

$$\psi_B = eV_B = \frac{2}{3}Eg \tag{6}$$

A detailed study of the interface surface states at the metal-semiconductor junction by J. Bardeen [22] and recently by V. Heine [23] led to the conclusion that the barrier height is independent of the metal used provided the density of surface states is sufficiently high ($\geq 10^{13}$ cm^{-2}), a condition adequately met for the group IV and III-V semiconductors.

In terms of our diode fabrication technique as will be described in a later section, it is expected that the description of the barrier height can be given by eq (6) [24].

In the development of the barrier potential function (eq (4)), we neglected the effect of the image force experienced by an electron when it approaches the metal. C. R. Crowell and S. M. Sze [25] have shown that even at room temperature, with low doping impurity materials and at large bias, i.e., high field, the effect of image force barrier potential lowering does not affect appreciably the current voltage characteristics of a Schottky barrier. Therefore, image force consideration is not included in our development of the barrier potential function.

Also assumed in deriving the barrier potential function is the uniform distribution of the doping impurities in the semiconductor. The effect of random distribution of impurities in the depletion region on the Schottky barrier potential function has been studied by J. W. Conley and G. D. Mahan [3]. They showed that inclusion of the fluctuation in barrier height due to nonuniform impurity doping distribution changes little the theoretical prediction of the tunneling current through the barrier potential. Therefore, the assumption of uniform distribution of impurity doping distribution in the development of the barrier potential function can be made.

The WKBJ approximation solution [26-28] of the Schrödinger's equation describing the electronic wave function across the depletion layer barrier potential

$$U(x) = eV(x) \tag{7}$$

yields the tunneling probability

$$P(E) = e^{-W(E,U)} \tag{8}$$

$$W(E, U) = 2\left|\int_a^b \left[\frac{2m}{\hbar^2}(E - U(x))\right]^{1/2} dx\right| \tag{9}$$

The integral function $W(E,U)$ is the WKBJ integral. We calculate the tunneling probability for the metal-semiconductor barrier by eq (8), with $W(E,U)$ obtained from eq (9) where $V(x)$ is as given in eq (4). Then

$$W(E, U(x)) = \frac{(2\kappa d + \beta)\sqrt{\alpha + \beta d + \kappa d^2}}{4\kappa} - \frac{\beta\sqrt{\alpha}}{4\kappa} + \frac{4\alpha\kappa - \beta^2}{8\kappa^{3/2}} \ln \frac{\sqrt{\alpha + \beta d + \kappa d^2} + d\sqrt{\kappa} + \dfrac{\beta}{2\sqrt{\kappa}}}{\sqrt{\alpha} + \dfrac{\beta}{2\sqrt{\kappa}}} \tag{10}$$

where

$$\alpha = \frac{qN_0}{2\epsilon} d^2 + V_A - V_F - q^{-1}E$$

$$\beta = \frac{qN_0}{\epsilon} d$$

$$\kappa = \frac{qN_0}{2\epsilon}$$

It is noted that the independent-particle theory of barrier tunneling using the WKBJ method [29] assumes a tunneling velocity in **k**-space and thus the tunnel velocity must be included in the integrand as $\mathbf{v}(k)$ in the generalized theory. And the general form for the tunneling current so obtained is independent of the density of states function because the tunneling velocity in the **k**-space is taken to be reciprocal of the density of states.

J. W. Conley et al. [2] have calculated an exact solution of the one-dimensional Schrödinger equation for a parabolic depletion layer potential and determined the transparency of the barrier in the generalized tunneling equation originally derived by Fredkin and Wannier [30].

$$j=-2e\int \frac{d^3\vec{k}_m}{(2\pi)^3}\, v_{SZ}|T_{m\to s}|^2[f_m(E)-f_s(E)] \quad (11)$$

The barrier transparency $|T_{m\to s}|$ is found to contain the factor $E^{1/2}$ describing the parabolic density of states function of the semiconductor. To obtain analytic and numerical correspondence between the exact barrier transparency calculation containing the density of states term $E^{1/2}$, represented to be P_{CDMT}, and the approximate transmission coefficient obtained from the independent-particle WKBJ tunneling calculation, P_{WKBJ}, J. W. Conley and G. D. Mahan arrived at the following expression [5]:

$$I=\beta\int_{E_1}^{E_2} dE E^{1/2} P_{WKBJ} \quad (12)$$

where

$$P_{WKBJ}=\exp\left[-2\int_{z'}^{z''} dz k(z,E)\right]$$

an expression equivalent to the generalized tunneling eq (2) we are using in this study. The validity of the eqs (2) or (13) are shown empirically with the study of Conley et al. on the Schottky barrier tunneling studies on GaAs [6,7].

Comparing eq (12) with (13), R. Stratton and F. A. Padovani [31] obtain:

$$P_{CDMT}=\frac{4}{\pi}\left[\frac{m_m E}{m_s(E_{Fm}-E_{Fs}+V+E)}\right]^{1/2} \times\frac{b_{m0}K_{mx}^2+\frac{1}{2}\exp(-b_{m0})}{\left[1+\frac{m_m b_{m0}E_{00}}{m_s(E_{Fm}-E_{Fs}+V+E)}\right]} \times\left[\Gamma^{-2}\left(\frac{1}{4}-\frac{1}{2}K_{mx}^2\right)+\frac{1}{2}K_{mx}^2\Gamma^{-2}\left(\frac{3}{4}-\frac{1}{2}K_{mx}^2\right)\right]^{-1}$$

where

$$b_{m0}=(E_B+E_{Fm}-V)/E_{00}$$

$$K_{mx}^2=E/2E_{00}$$

$$E_{00}=\tfrac{1}{2}qh(N/m_m\epsilon)^{1/2}$$

And the WKBJ approximation of P is determined to be

$$P_{WKBJ}=(b_{m0})^{K_{mx}^2}(e/K_{mx}^2\sqrt{2})^{K_{mx}^2}\exp(-b_{m0}) \quad (14)$$

assuming $E = E_F$, that is, all participating tunneling electrons are to originate at the Fermi level. Stratton and Padovani then determine from both the exact and approximate tunnel current calculations of incremental junction resistance, the occurrence of sharp peaks in p-type GaAs; n- and p-type Ge and Si are at the voltage corresponding to the semiconductor Fermi energy and in the case of n-type GaAs, at voltage lower than the corresponding Fermi energy. They also obtain very excellent agreement for the WKBJ calculations with the experimental incremental resistance data of the Ge Schottky barrier by Conley and Tiemann [3].

More recently, F. A. Padovani and R. Stratton [32] questioned the general applicability of the eqs (2) and (12) through their detailed numerical analysis on P_{CDMT} and on P_{WKBJ} derived with the same identical assumptions as those for the exact P_{CDMT}. The WKBJ expression is given as

$$P_{WKBJ}=\exp-\left\{b_{m0}\left[1-\frac{2K_{mx}^2}{b_{m0}}\right]^{1/2}-2K_{mx}^2\ln\left[\left[\frac{b_{m0}}{2K_{mx}^2}\right]^{1/2}\left[1+\left(1-\frac{2K_{mx}^2}{b_{m0}}\right)^{1/2}\right]\right]\right\} \quad (15)$$

Then, from (11) and (12), according to the development given by Mahan and Conley, the expression can be obtained:

$$P_{CDMT}\cong E^{1/2}P_{WKBJ} \quad (16)$$

And in the case of GaAs, through their numerical calculations, Padovani and Stratton show that expression 2 is valid to an accuracy of about 6 percent only if $E <$ 2.1 meV, a very narrow range.

Assuming a parabolic density of states function for the heavily doped semiconductor, the tunneling current of the metal-semiconductor is obtained as a function of the voltage bias with either the WKBJ in the exact method. Figure 3 compares the calculated 4.2 K tunnel

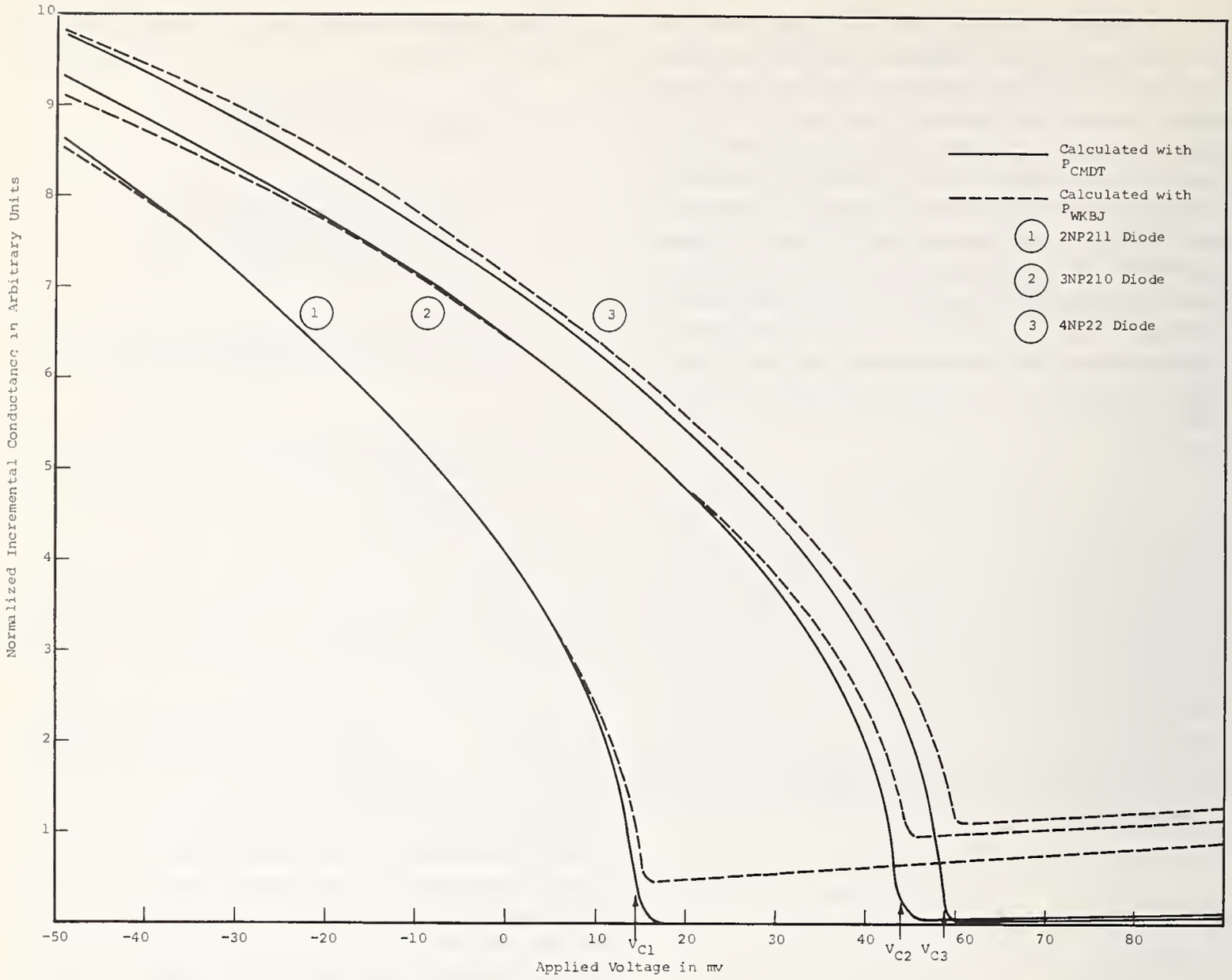

FIGURE 3. *Comparison of calculated tunnel junction incremental conductance characteristics, using* P_{WKBJ} *and* P_{CMDT}.

junction incremental conductance characteristics of several diodes using both methods. Both methods yield the same characteristic features, especially the existence of an incremental conductance minimum corresponding to the Fermi voltage of the semiconductor.

Figure 3 also reveals that the parabolic density of states function of the heavily doped semiconductor is reflected in the incremental conductance of the junction diode. Study of eqs (2) and (13) indicate that at helium temperatures. the equations can be approximated by the incremental tunneling conductance equation:

$$dI/dV \alpha P_{WKBS}(V) g_s(V) \tag{17}$$

giving a mathematical designation of the dependence of the incremental junction conductance of the semiconductor density of state function.

To assure that variations of barrier heights due to different surface properties on different samples, image force and nonuniformity of doping impurity distribution do not significantly alter the interpretability of the data generated by the tunneling current measurements, conductance curves of different barrier heights ($V_B = 1/2\ V_g$, $2/3\ V_g$, $3/4\ V_g$) are compared (fig. 4). It is noted that even though the absolute magnitude of the tunnel current differs almost in orders of magnitude with the different barrier height assumed, the normalized conductance curves do not differ widely with each other (less than $\pm$ 10 percent within the range of experimental interest).

With the validity and accuracy of the function *P(E)* and the mathematical model established, we can conclude that the calculated normalized conductance curves based on eq (2) and typified by those given in

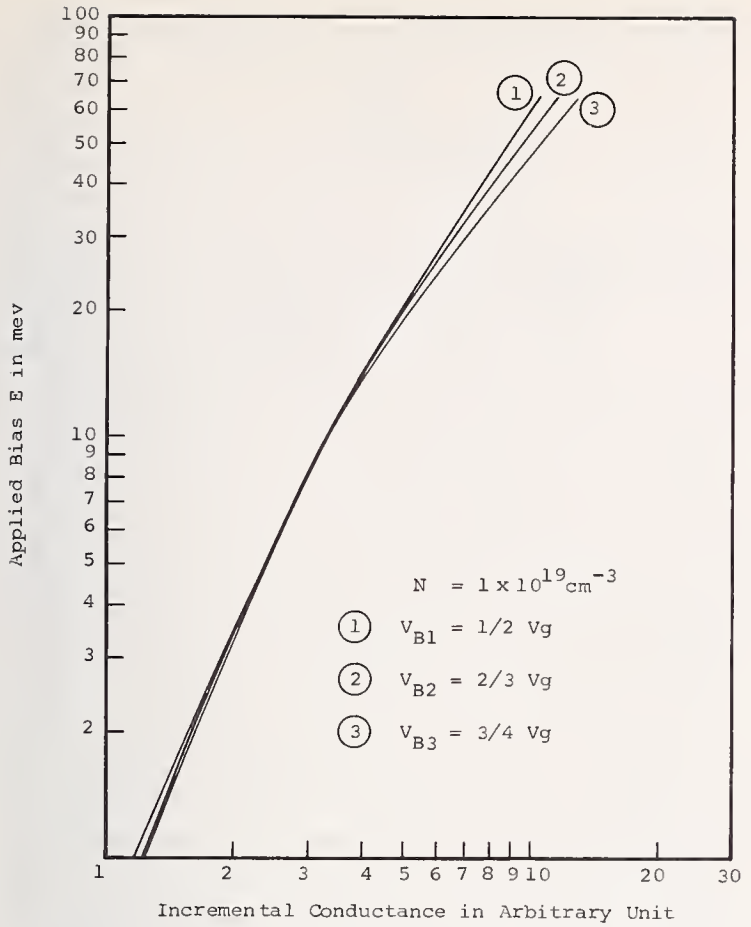

FIGURE 4. *Study of the effect of barrier height on incremental conductance.*

figure 5 can be utilized to evaluate the experimental tunneling curves with regard to the density of states function of the heavily doped semiconductor.

3. Experimental Techniques and Procedures

3.1. Diode Preparation

Silicon wafers heavily doped with different dopants and uncompensated, cut from an (111) pulled ingot are purchased from Wacker Chemical Corporation, Los Angeles, California. The dopant types chosen are As, P, and Sb for *n*-type Si and B for *p*-type Si, because of their relatively high solid solubility in Si so that heavy doping concentrations are more readily available for study. The highest concentration chosen for this study in each dopant type is more than an order of magnitude less than the maximum theoretical possible concentration so that we will not encounter experimental results complicated by precipitation effects in the extremely heavily doped materials [32]. These wafers are generally 3/4 inch to 1-1/4 inch in diameter, 10 to 15 mils thick, and mechanically lapped on both sides with all traces of saw marks removed. Resistivity measurements are made on the wafers with a four-point probe [33]. Several measurements are made on each wafer for a measure of the uniformity of electrical properties of the wafer. With few exceptions at extremely low resistivities, with measurements sensitive to electrical statics due to low output signal voltages, variations in resistivities measured for any wafer are within ± 10 percent. Resistivity variations for the majority of the wafers are within ± 5 percent. Carrier concentrations for the *n*-type materials are interpreted from the resistivity data interpreted from the published data by Irvin [34], Logan, Gilbert and Trumbore [35], and Furukawa [36].

One of the early procedures used was a mechanical polish step after completing the resistivity measurements. Starting with a large ($\sim$ 15 micron) particle size abrasive, and progressing downward to abrasive size of 0.3 micron, the wafers were mechanically polished to a mirror finish. This polishing step was eliminated after it was found that the chemical etch that followed was effective in etching down the wafer by a few mils and polished it to mirror finish at the same time.

The chemical etch used is a modified CP-4 solution [37], the etchant composition is 2 parts hydrofluoric acid, 9 parts nitric acid and 4 parts acetic acid. At room temperature, with a tumbling agitator, the etchant is effective in etching down uniformly the Si wafers to a depth of 2-5 mils in about 30 minutes while at the same time polishes the wafer to a mirror finish. The etch depth is more than sufficient to eliminate all surface damages introduced when the wafer is cut from the ingot [38]. If the surface damages are not removed from the wafer, dislocations in the damaged semiconductor crystal will distort the measured semiconductor density of states function significantly by contributing localized imperfection energy levels in the energy gap. The electrons no longer need to tunnel completely through the depletion layer barrier, but can make use of these localized levels as trapping centers resulting in a smearing of the tunneling current whereby the voltage bias can no longer be considered as a good measure of the energy of the electron involved in the current transport [39].

The etch polished wafer is then diced into small dice of 75 mils square with a string saw. The string saw is used so that saw damage to the die edges will be minimal. The dice are then mounted on a transistor TO-5 header by a Si-Au eutectic alloy technique to result in an ohmic contact.

We use a gold plated base TO-5 transistor header. A 98 percent Au-2 percent Si perform is placed between the die to be mounted and the transistor header. Using

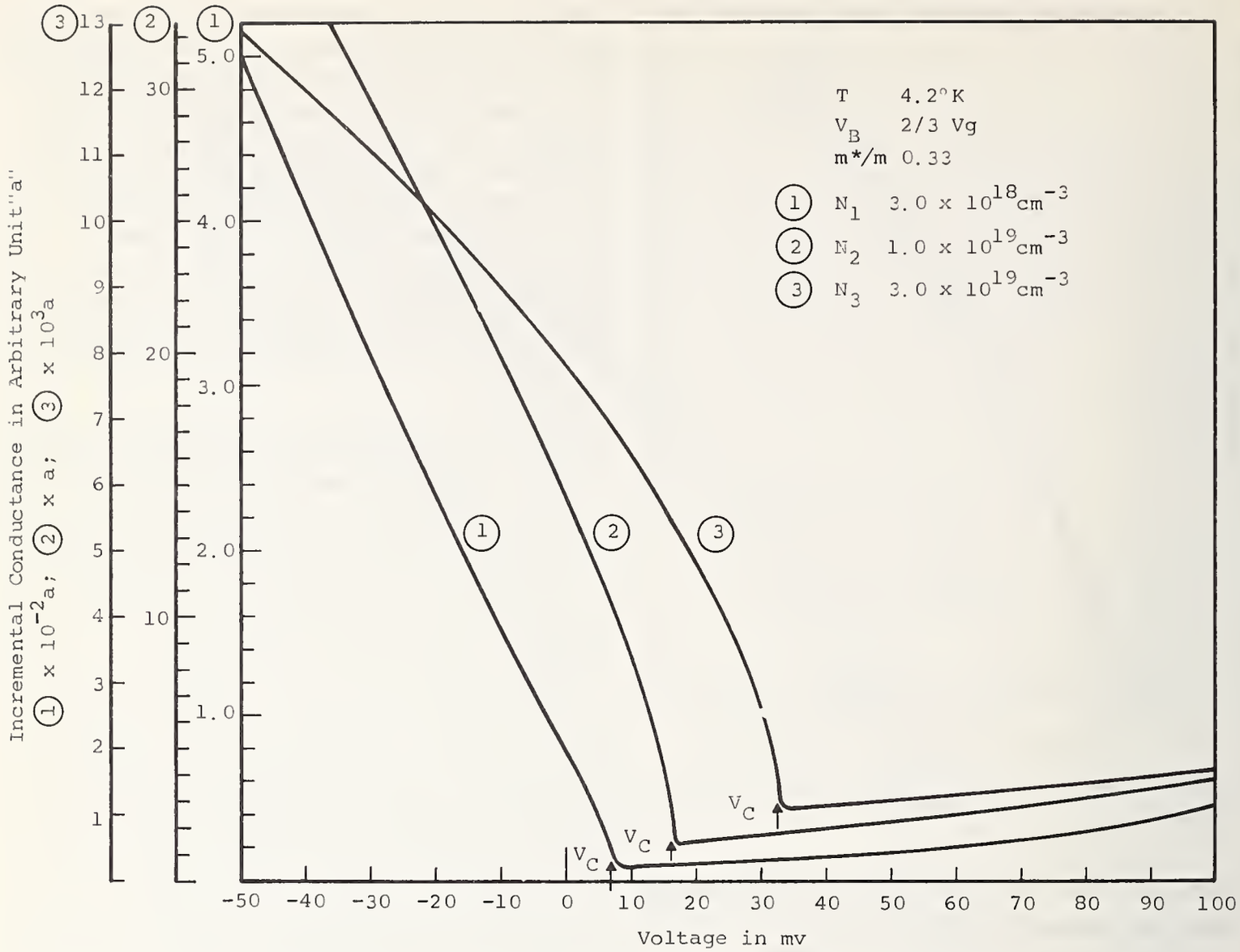

FIGURE 5. *Computed incremental conductance curves of metal-semiconductor tunnel junctions.*

a molybdenum strip heater set at 450 °C, with a slight pressure applied on the die to break the thin oxide layer on the underside of the die, the Si-Au eutectic bound can be obtained. The Si-Au eutectic is at 370 °C. The die mounting operation is performed under flowing nitrogen gas to minimize oxide formation on the top surface of the mounted die.

The mounted die is then subjected to ultrasonic cleaning. This cleaning serves two purposes. First, it provides a check on the die bounding process. If a Si-Au eutectic has not been obtained, the mechanical bound of the die to the header is weak and the die will break loose under ultrasonic vibration. Secondly, the cleaning solvent (deionized distilled water) and the ultrasonic action will remove the last traces of organic impurities on the Si surface that have not been burnt away in the die bounding process. After this cleaning process, it is assumed that the Si surface is entirely free of organic contaminants, residual abrasive particles and dust particles, etc. From this point onward, extreme care is taken to prevent introduction of contaminants on the Si surface. Between the processing steps to follow, the mounted dice are stored under deionized distilled water in chemically inert containers which have been carefully cleaned. To handle the transistor header on which the die is mounted, cleaned teflon-coated tweezers are used.

The Si die is then masked for evaporation of the metal-superconductor contact. The masking material used is the black wax which does not outgas in a vacuum. Enough area of the Si die is covered such that damaged areas on the edge of the die which resulted from the cutting action of the string saw during dicing of the wafer are masked and eliminated from the junc-

tion area of the tunnel barrier diode to be formed. The masking procedure is performed under flowing nitrogen gas on the molybdenum strip heater at the temperature under which the wax will have the right viscosity for ease of masking. This temperature is estimated to be less than 75 °C.

Immediately prior to metal evaporation, the Si die is etched in a solution of 1 part hydrofluoric acid and one part H_2O to remove the surface oxide formed during the different preceding preparation steps.

The evaporation is done in a bell jar vacuum system at 2×10^{-6}mm Hg and lower; the pressure is measured by an ion guage. The metal shots used for evaporation (Pb, Sn, and In) are guaranteed 99.9999 percent chemically pure. No attempt is made to pre-etch the metal shots before evaporation to remove the surface oxide. The various forms of the metallic oxides either dissociate before reaching the boiling point of the metal or sublime in vacuum at relatively low temperatures. Organic surface contaminants on the shots are burnt off at even lower temperatures. To prevent contamination of the junction surface, a shutter is used. The shutter is opened to permit evaporation onto the Si dice only during the mid-period of metal evaporation, preventing the deposition of low boiling impurities, as well as eliminating the possibility of the deposition of high boiling point impurities when the metal source is depleted. A very high rate of evaporation, approximately 1000 Å per minute, is used since it is found that it gives the best results in terms of good evaporated films of highly metallic appearance and subsequent good tunnel diodes. It is suspected that a slow evaporation rate may cause some oxidation of the evaporated films due to the prolonged thermal radiation from the tungsten boat, resulting in thin, dull appearance. The thickness of the films are monitored during the evaporation by a Sloan quartz crystal film thickness monitor. The film thickness is made to be at least 5000 Å, so that later on when measurements are made at temperatures below the superconductor transition temperature of the metal electrode, the superconductors will behave as a bulk superconductor, without the uncertainties introduced by thin film superconductor behavior [40-42].

After the metal contact electrode evaporation, the wax mask is cut to remove all electrical shorts produced by the evaporated film. Then the electrode is connected to the TO-5 header emitter binding post with a 2-mil gold wire. The electrode contact solder used is a liquid Hg-In-Tl alloy [43]. A liquid solder contact is used so that there will be eliminated the possibility of mechanical damages to the Si crystal or to the metal-semiconductor junction using the commonly available wire bounders. The liquid alloy is found to be the best among the several contact materials tried: the conductive paint has a tendency to open up when subject to thermal stress, and the different low melting indium alloy solders do not wet the metal surface as readily and are difficult to use with manual tools. However, because of the excellent wetting properties of the Hg-In-Tl alloy solder, care has been taken to avoid possibility of either destroying the evaporated film or forming complicated superconducting alloy films [44,45] right at the metal-semiconductor junction by applying the alloy solder contact to the evaporated film on top of the masking wax immediately adjacent to the junction area (fig. 6).

After completion of the liquid solder contact to the metal electrode, the diode fabrication is completed and the device is ready for study. Figure 7 is a schematic drawing of the metal-semiconductor barrier tunnel diode thus made.

Several of the P doped *n*-type Si dice are prepared slightly differently than reported above in that after chemical etch of the wafer, the wafer is processed by M. Weiss of TRW Semiconductors, into Si dice with steam grown Si dioxide mask ready for mounting, and metal electrode evaporation, after a ten second etch in a 10 percent HF solution for removal of surface oxide introduced in the junction area by transit and die mounting and with further black wax masking needed only for ease in the removal of electrical shorts caused by the evaporated films. Diodes made from the masked dice so obtained exhibit no difference in electronic properties when compared with the others, and are not treated separately.

3.2. Electronic Measurements

For each junction, two types of curves are obtained: the current versus voltage bias curve *(I-V)* and the incremental conductance versus voltage bias curve *(dI/dV-V)*. Two separate ranges of voltage bias are used for both types of curves: In the study of superconductivity structures about zero bias, a small voltage bias range centered at zero volts and extended in both forward and reverse bias directions over only a few millivolts is used. For the study of Fermi degeneracy in heavily doped Si, the voltage bias range used extends from approximately 80 mV negative to over 120 mV positive. To study the effects of superconductivity on the barrier junction, the *I-V* and *dI/dV-V* curves are evaluated over a temperature range extending from 4.2 to 1.1 K. In the case of Fermi degeneracy studies, the experiments are performed in liquid helium under atmospheric pressure (4.2 K).

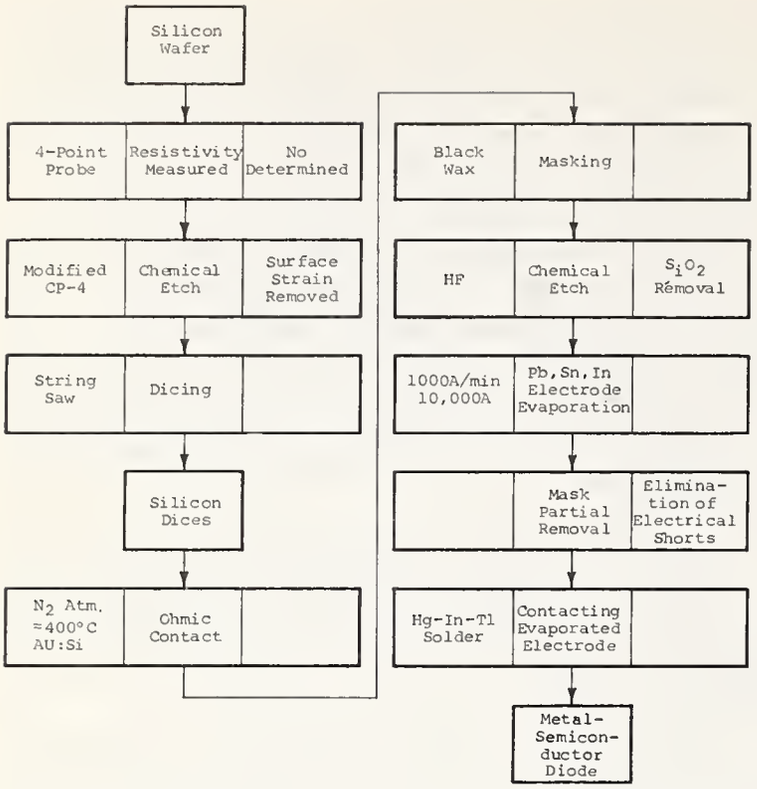

FIGURE 6. *Fabrication procedure of the metal-semiconductor tunnel diode.*

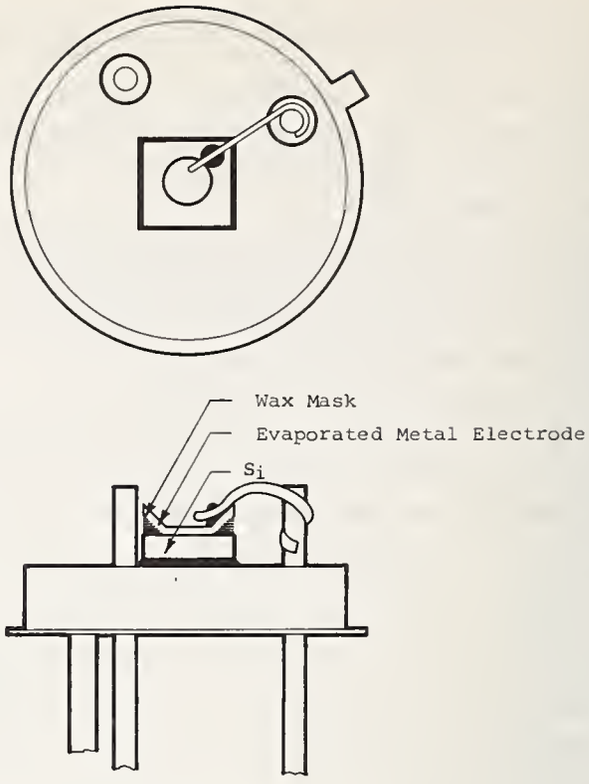

FIGURE 7. *Schematic of the metal-semiconductor tunnel diode.*

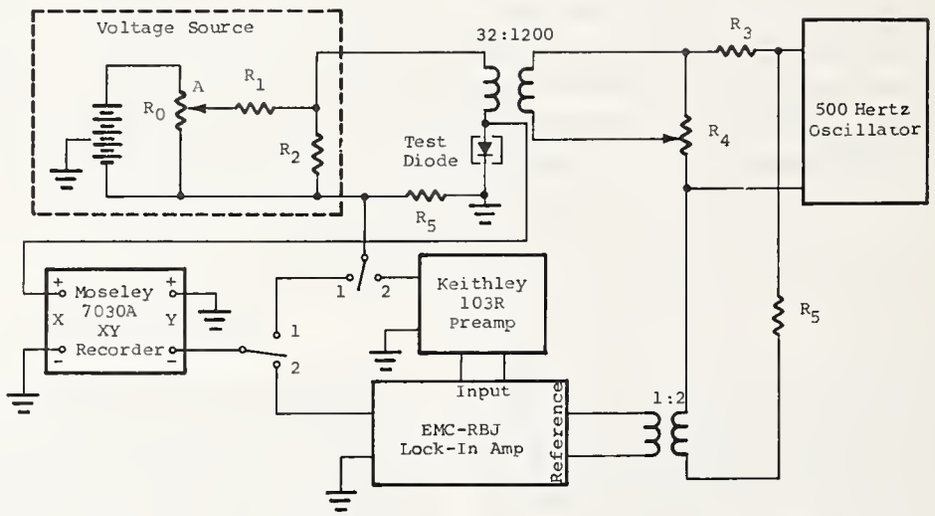

FIGURE 8. *Measurement circuits; position 1, current versus voltage, position 2, incremental conductance versus voltage.*

A schematic of the measuring electronics is shown in figure 8. The applied voltage bias is directly measured across the tunnel diode, the tunnel current is measured over a current sensing resistor. Using an X-Y recorder and a variable voltage supply which can be swept automatically with a timing motor drive, the measurements of the *I-V* characteristics of the tunnel diode are easily made. To avoid loading of the circuit, the input impedance of both the X and Y channels must be high with respect to the resistance of the diode and the current sensing resistor. The X-Y recorder used has input impedance $\gtrsim 1$ megohm, a value much higher than the usual kilo-ohm range of the diode, and the 1 to 100 ohm resistance value of the current sensing resistor.

To measure the incremental conductance of the tunnel diode, we bias the tunnel diode at the dc level about which the incremental value is to be measured, and obtain the incremental conductance by measuring the ac conductance of the diode under a small ac voltage signal. A 500 Hertz signal is introduced into the diode

circuit via an isolating, impedance matched transformer. The magnitude of the ac signal is adjustable via the voltage divider R_3R_4. For good definition of the zero bias tunneling structure, as well as the determination of the incremental conductance minimum, the ac signal is set to be $\lesssim 50\ \mu V$. The incremental conductance value is picked up by the current sensing resistor because the ac signal voltage is coupled into the diode circuit at a constant magnitude.

$$G_{ac}=\frac{i_{ac}}{v_{ac}} \tag{18}$$

$$i_{ac}=\frac{V_S}{R_S} \tag{19}$$

where

G_{ac} = the diode incremental conductance

V_S = signal voltage at R_S

The signal voltage is first amplified by the Keithley AC amplifier (model 104) which is an ultra-low noise preamplifier with high gain (100 to 1000) and high input impedance (100 megohm). In addition, it provides high and low frequency cut-off filter to reduce the effective band width and improve signal to noise ratio, a feature most suited for our application because our ac signal is narrow band (500 Hertz sinusoidal). The signal from the preamplifier is then further amplified and converted to a dc output which is proportional to the diode incremental conductance, using the EMC model RJB, Lock-In Amplifier employing the standard phase lock-in technique of derivative measurements [46,47]. The dc output from the Lock-In Amplifier can be applied directly to the Y input of the X-Y recorder for the mechanized plotting of the incremental conductance versus voltage bias curve of the tunnel diode.

It is important to note that the variable dc voltage bias source is in series with the tunnel diode in both the *I-V* and *dI/dV-V* measurements. In order that the observed bias dependent structures in the *I-V* and *dI/dV-V* measurements are solely the results of the bias dependent properties of the tunnel diode, the variable voltage source must be such that its internal impedance is independent of output voltage. In addition, its internal impedance must be low compared with the tunnel diode, otherwise the measured *I-V* characteristics reflect the internal impedance of the voltage source, with the tunnel diode providing a second order perturbation effect on the *I-V* curve. A detailed analysis of the measurement circuits shows that under no case will the voltage source constitute more than 0.5 percent error to the measured tunneling characteristics of the diode under study [48].

Finally, it should be noted that the ac signal pickup at the current sensing resistor R_s is of the order of one microvolt. Because of the low signal level, and the long lead length needed for diode measurements in the cryostat, ground shields and low noise shielded cables must be incorporated in the measurement set-up. Some basic considerations such as avoidance of ground loops, use of electrostatic shielding guards in the diode circuit, minimization of lead length, etc., are included in the packaging design of the measurement electronics and the sample holders for use in the low temperature cryostat and in the helium dewer for measurements at 4.2 K.

4. Experimental Data and Analyses

There are two independent variables that can be experimentally varied in the study and evaluation of heavily doped *n*-type Si. They are: (1) impurity dopant concentration and (2) the type of impurity dopant used, be it Sb, P, or As. We expect that the density of states function of the semiconductor will be modified to some extent according to the impurity doping concentration and to the type of dopant used, and this modification of the density of states function will show up in the measured tunneling current and more so in the measured incremental conductance of the depletion layer tunnel diode.

Figure 9 presents a current-voltage and incremental conductance-voltage x-y recorder plot of a typical metal-semiconductor tunnel diode. There is a zero bias conductance structure similar to many reported in literature. We found that by assuming the metal electrode is superconducting and using the BCS theory in describing the superconductivity, the zero bias conductance structure can be matched very accurately over the temperature range by the generalized tunneling eq (2) [48].

In addition to the zero bias features due to superconductor tunneling, we observe in the figure the presence of an incremental conductance minimum which occurs at a voltage V_{min} in the forward bias direction. According to the analytic study given earlier, the incremental conductance minimum is a result of the sharp change in the density of states function at the bottom of the conduction band, and qV_{min} is equivalent the Fermi energy of the semiconductor.

With increasing carrier concentration, the density of states function is occupied at higher and higher energy levels, hence a corresponding increase in the Fermi

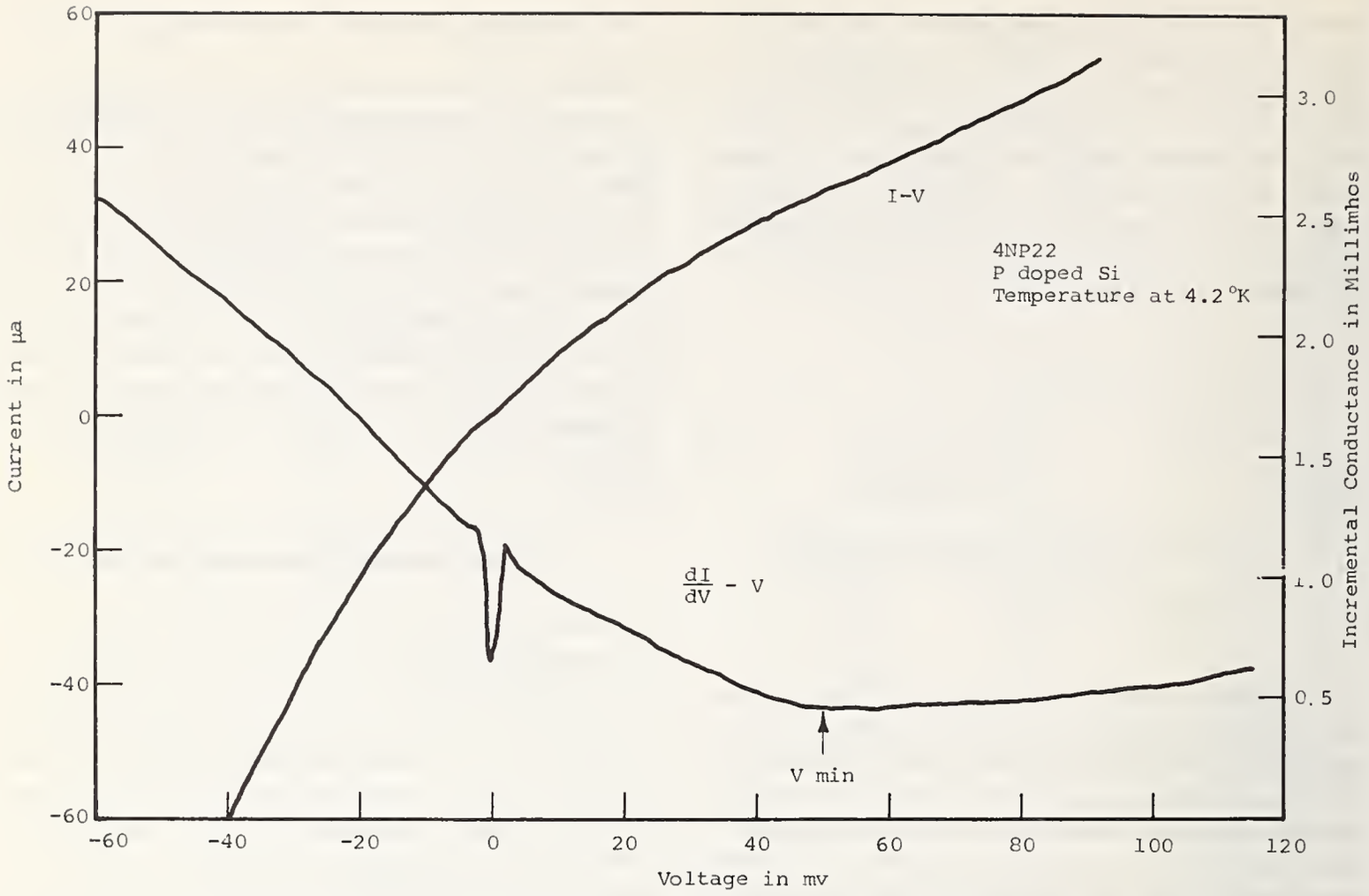

FIGURE 9. *Transport properties of a superconducting* Pb-Si *tunnel junction.*

energy of the semiconductor. Figure 10 compares the conductance curves of two diodes showing the shift of the conductance minimum with impurity dopant concentration. In addition to the dependence on concentration, the Fermi level is found to be strongly dependent on the type of impurity dopant in the semiconductor. Figure 11 is a log-log plot of E_F versus N_D showing the dependence of the Fermi level on impurity dopant concentration and on the type of impurity dopant. The boundary of the rectangle about each point is the estimate of possible error due to accuracy of measurements.

A brief study of the figure will reveal several important features: (1) the Fermi level of the heavily doped Si at an impurity concentration is strongly dependent on the type of impurity dopant in the semiconductor; (2) the variation of the Fermi level as a function of impurity dopant concentration approximates the same power dependence of E_F and N_D irrespective of the dopant type; (3) the separations in the E_F versus N_D curves for Sb, P, and As doped Si are more than that can be accounted for by the differences between their ionization energies in Si which are 39, 45, and 49 meV, respectively [49]. The separation increases with dopant concentration. For example, in the case of P doped Si versus As doped Si, it varies from 3 meV at the dopant concentration of 2×10^{18} cm^{-3} to 10 meV at 4×10 meV, compared to a difference of 6 meV between the ionization energies of P and As in Si.

It is noted that the E_F versus N_D curves for the three different types of dopants tend to approach the slope as given by the parabolic dependence of E_F and N_D. This observation is further explored in figure 12, where astride each of the E_F versus N_D experimental curve is an assumed curve which corresponds to the parabolic dependence of E_F and N_D. The offset of the three curves can be interpreted to be the result of the dopant type dependent density of states effective mass. A study of the experimental curve and its adjacent assumed parabolic curve reveals that they are actually separated approximately by a small constant δ throughout the entire range. That is

$$(E_F - \delta) \propto N_D^{2/3} \tag{20}$$

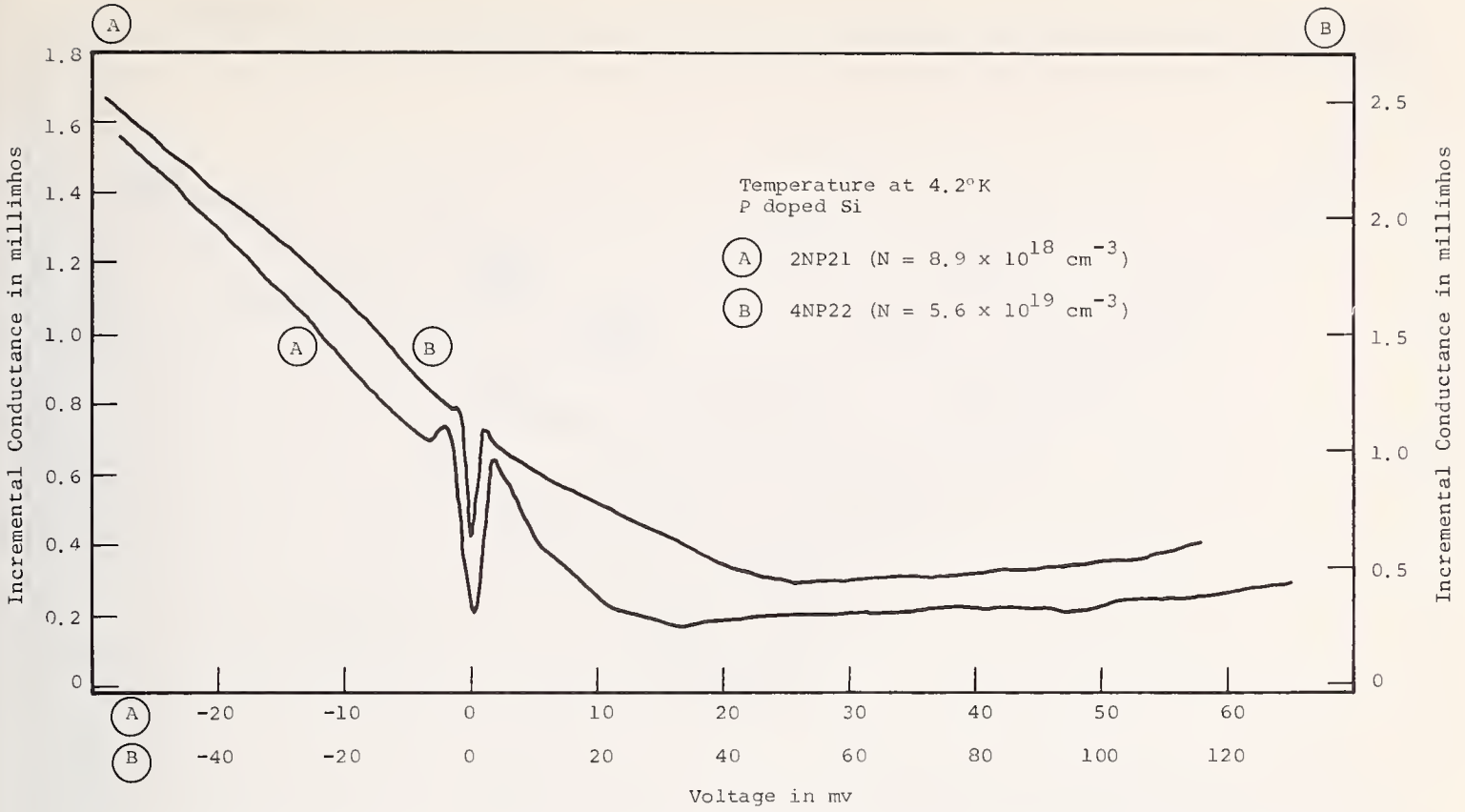

FIGURE 10. *The effect of dopant concentration in* Si *on the incremental conductance of the* Pb-Si *tunnel junction.*

where

$$\delta \approx 1 \text{ meV for P-doped Si}$$
$$1.6 \text{ meV for Sb-doped Si}$$
$$-1.5 \text{ meV for As-doped Si}$$

Therefore, according to the band-filling model of electron occupancy where the dependence of the Fermi level on the carrier concentration is taken to reflect directly the density of states function of the semiconductor, we can conclude from the empirical curves of the Fermi dependence on impurity dopant concentration that allowing for some deviations at the lower range of the density of states function, the parabolic model of the density of states function accurately describes the heavily doped Si, provided we can assume a density of states effective mass which is dependent on the impurity dopant type. At the lower energy range where E is of the same order of magnitude as δ, the parabolic model of the density of states function breaks down in that the 2/3 power dependence of E_F and N_D is no longer correct even in the sense of eq (20) because δ is only approximately a constant, as is shown in table 1.

Following the above discussion, according to eq (20), we can approximate the density of states function of the heavily doped semiconductor, in the region where $E > \delta$ as follows:

$$G(E) = 8\pi\sqrt{2}\left(\frac{m_0^{1/2}}{h}\right)^3\left(\frac{m^*}{m_0}\right)^{3/2}(E-\delta)^{1/2} \qquad (21)$$

in which m^* is the dopant type dependent density of states effective mass. It is 0.178 m_0, 0.330 m_0, and 0.418 m_0 for Sb, P, and As doped Si, respectively, according to our experimental data as given in figure 12. Reference can be made to figure 13 which summarizes the resistivity vs carrier density measurements of several investigators. The dopant-type dependence of the resistivity is studied as an impurity effect upon electron mobility in the heavily doped Si:

$$\sigma = \rho^{-1} = ne\mu \qquad (22)$$

TABLE 1. *Function Dependence of* δ *on* N

N, cm^{-3}	δ(Sb), meV	δ(P), meV	δ(As), meV
5×10^{18}	1.6	1.2	−1.6
3×10^{18}	1.6	1.1	−1.3
2×10^{18}	1.6	1.0	−1.1
1×10^{18}	1.4	0.7	.....

417-156 O - 71 - 46

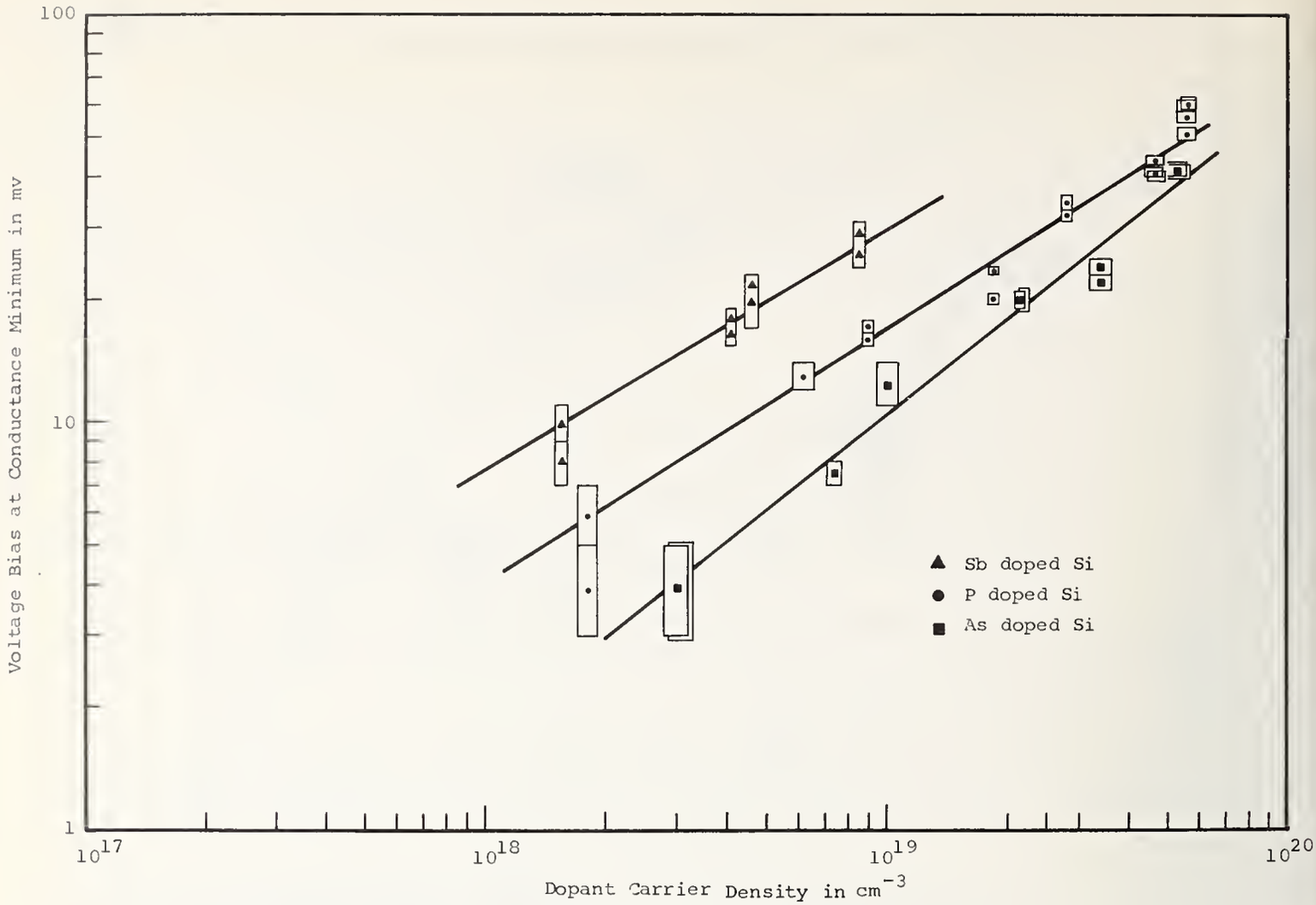

FIGURE 11. *Measured* V_{min} *Dependence on dopant type and on dopant carrier concentration.*

At a given carrier concentration n, the resistivity increases in the order $\rho(\mathrm{Sb}) < \rho(\mathrm{P}) < \rho(\mathrm{As})$, so that mobility decreases in the order $\mu(\mathrm{Sb}) > \mu(\mathrm{P}) > \mu(\mathrm{As})$. The mobility differences are not due to long range impurity scattering which considers the effect of the Coulombic forces acting at large distances proportional to the electronic charges involved and give rise to a mobility which depends only on the impurity dopant density. Instead, the mobility increases in the same order as the ionization energy decreases, suggesting that there exists a scattering mechanism which interacts at close range between the carrier electron and the impurity atom. Description of the scattering mechanism must take into account the nature of the potential well of the impurity atom in the semiconductor. The same considerations given for the differences in mobility of the differently doped Si can be given for the differences in the density of states functions as manifested in the inequality $m^*(\mathrm{Sb}) < m^*(\mathrm{P}) < m^*(\mathrm{As})$.

And, if we are to use the simple hydrogenic model to describe the ionization of the impurity atom in a semiconductor, we obtain for Si the following:

$$E_i = \frac{e^4 m^*}{2\epsilon^2 h^2} = 99.3 \left(\frac{m^*}{m_0}\right) \mathrm{meV} \qquad (23)$$

From which we can obtain the impurity dopant dependent effective mass which takes into account the effect of the close range interaction between the conduction electron and the impurity atom affecting its ionization energy. They are $m^*(\mathrm{Sb}) = 0.393\ m_o$, $m^*(\mathrm{P}) = 0.444\ m_o$ and $m^*(\mathrm{As}) = 0.494\ m_o$. The order and magnitude of the differences are in general agreement with that suggested for eq (21).

A detailed discussion on the significance of the dopant dependent density of states effective masses, and their correlation with other known experimental data available in literature will be presented elsewhere by the same authors.

Thus far we have directed our attention to the position of the incremental conductance minimum and its functional dependence on impurity dopant and dopant concentration. Additional qualitative and quantitative

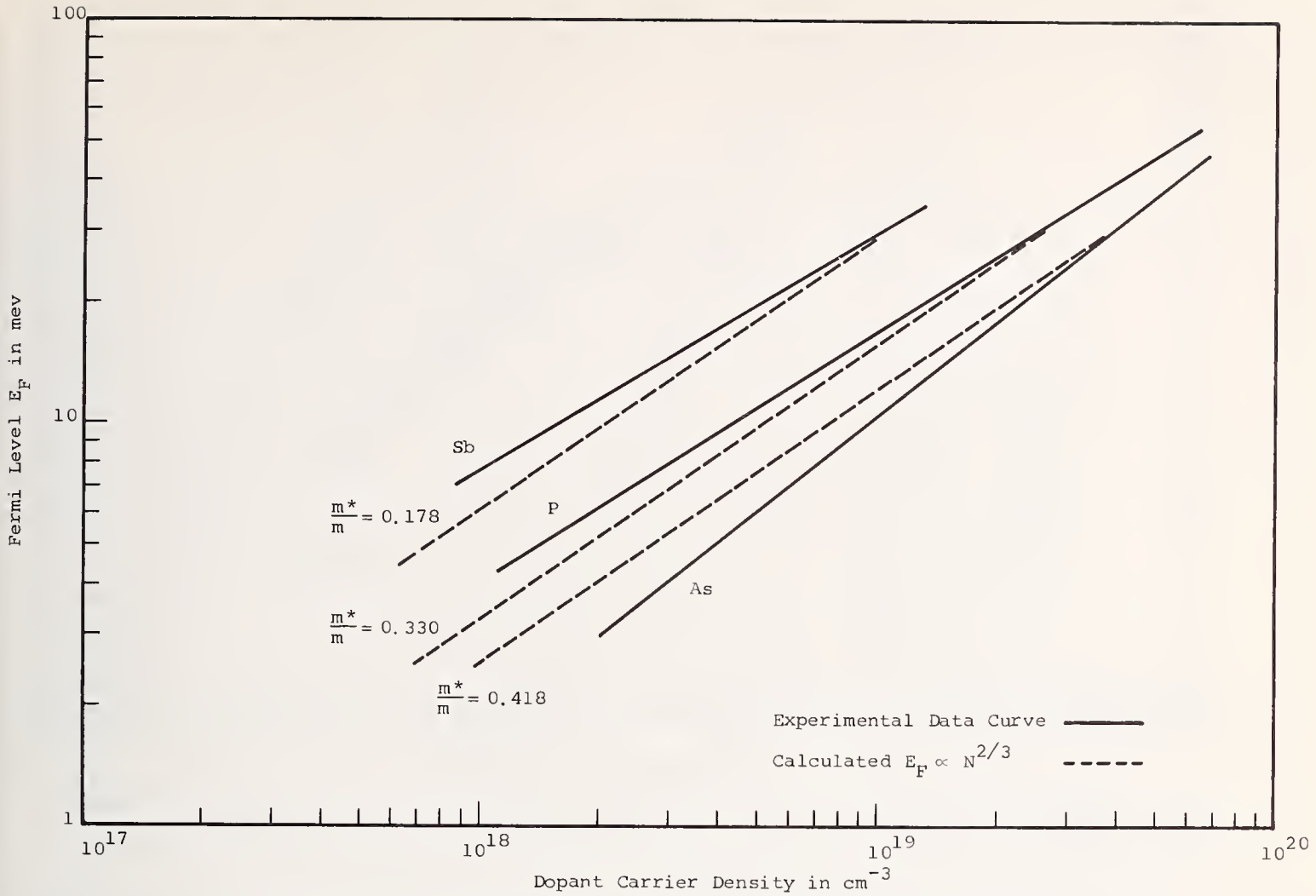

FIGURE 12. *Dopant dependency of fermi level location in heavily doped silicon.*

information on the properties of the heavily doped Si can be obtained from further analyses of the incremental conductance versus voltage bias curve based upon the analytic treatment given earlier.

In figure 14, we compare the experimental incremental conductance curves of P-doped Si with the normalized calculated incremental conductance curves based on P_{WKBJ} and P_{CMDT} and the corresponding tunneling equations, assuming for the heavily doped semiconductor, the parabolic density of states function.

Near the band edge, i.e., below approximately 12 meV, the experimental conductance curves drop off at a much lower rate than that predicted by the calculation using P_{WKBJ} or P_{CMDT}. Furthermore, the direction from the parabolic density of state function is observed to be less for the very heavily doped material. The density of states tail has been interpreted as the result of strong electron interaction with clustered impurity atoms, assuming no correlation in the distribution of the dopant impurity atoms. At high impurity concentrations, the distribution of the impurity atom is strongly correlated, resulting in minimizing the density of states tail. And, hence, less deviation from the parabolic density of states function at higher dopant concentration.

Above the band edge, the experimental curve follows closely the normalized calculated curve, demonstrating the applicability of the parabolic form of the density of states function for the heavily doped Si, in agreement with the physical model for heavily doped semiconductor [48,50,51].

At high energies the experimental curve increases more rapidly than the calculated curve, indicating the density of states function increases at a more rapid rate than parabolic. A review of the conduction band $E(k)$ function of Si shows that at the high energy range, using the band filling model, we may be into the double degeneracy at the X point (on the 100 axis of the diamond structure).

Reference can be made to figure 12 and the corresponding discussion on it, where we observe that the As doped Si is found to depart more from the parabolic dependence of E_F and N_D than P doped Si. From the

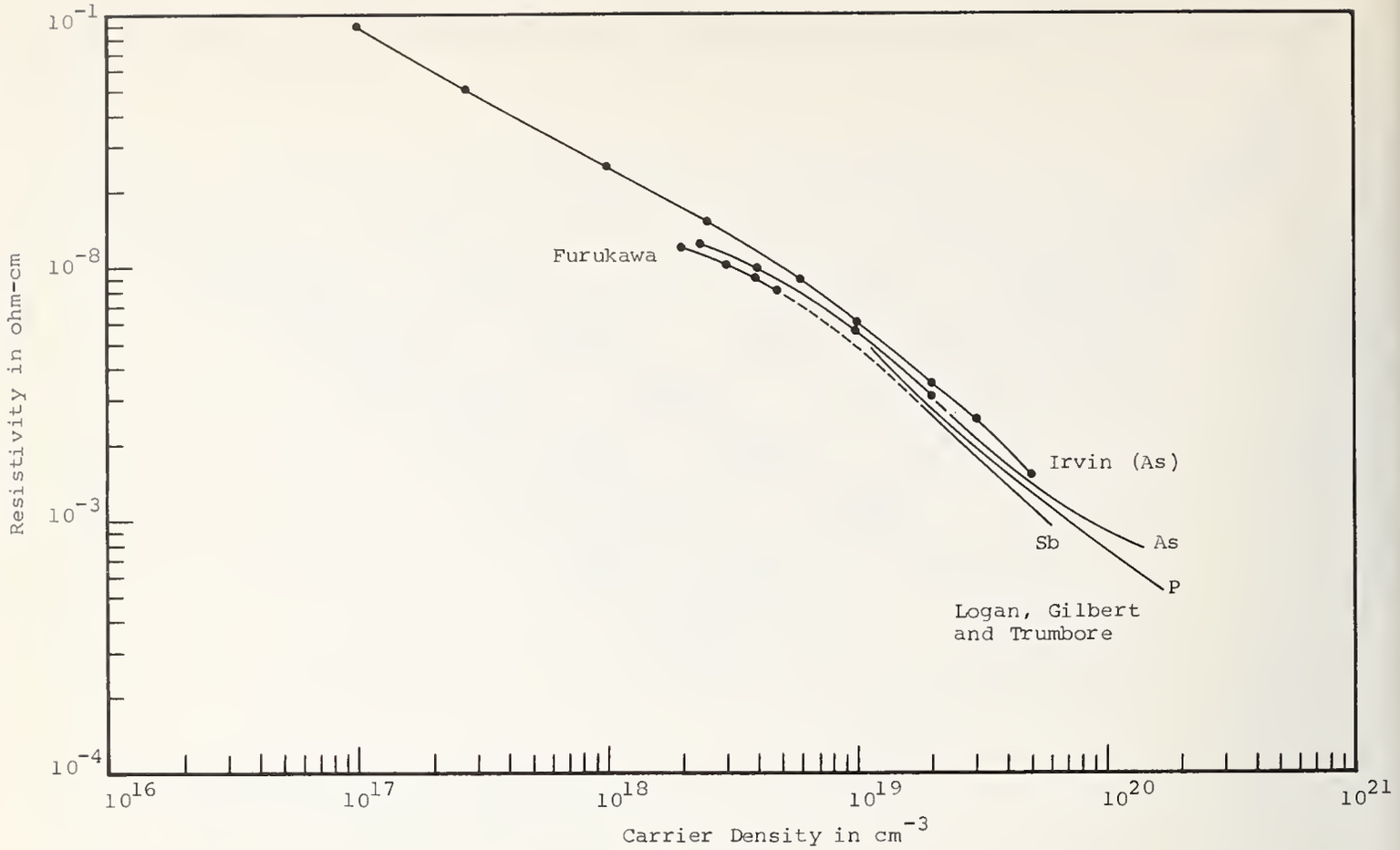

FIGURE 13. *Summary of resistivity versus carrier density data curves for heavily doped* n*-silicon.*

study of the incremental conductance curves, a similar difference between the P doped Si and the As doped Si is found. Figure 15 compares the experimental incremental conductance curves of the As doped Si with the corresponding calculated curve. In comparison with figure 14, it is seen that in the low energy range, band tailing is more severe in magnitude and extent in the case of As doped Si than P doped Si. And the energy range in which the density of states functions follows the parabolic form is relatively narrow in As doped Si. On the other hand, it appears that the X point double degeneracy for As doped Si occurs at a much higher energy level for the impurity dopant concentration.

The incremental conductance of the metal-semiconductor junctions is directly proportional to the products of the tunneling probability $P_{WKBJ}(E)$ and the density of states function $g_s(E)$ according to eq (17). In the log-log plot of the calculated incremental conductance curve, as in figures 14 and 15, we can determine the power dependence of $P_{WKBJ}(E)$ on E from the slope of the incremental conductance curve, given the parabolic density of states function assumed in the calculation of the incremental conductance. Then, with the power dependence of $P_{WKBJ}(E)$ on E known, we can determine the power dependence of $g_s(E)$ on E from the slopes of the experimental incremental conductance log-log plot for all E.

Based on the above procedure, we determine from figure 14, the power dependency of $g_s(E)$ on E for P doped Si at $E=5$ meV as follows:

$$N=8.9\times10^{18}\ \text{cm}^{-3}, \qquad g_s(E)\propto E^{-0.01}$$
$$N=4.7\times10^{19}\ \text{cm}^{-3}, \qquad g_s(E)\propto E^{0.48}$$
$$N=5.6\times10^{19}\ \text{cm}^{-3}, \qquad g_s(E)\propto E^{0.38}$$

We note from figure 14 that the slope of the log-log plot of the conductance curve is a monotonically decreasing function of E near the band edge. We observe also that V_{min} exists for $N = 8.9 \times 10^{18}\text{cm}^{-3}$ implying a sharp drop of the density of states tail at eV_{min}, even as the corresponding $g_s(E)$ for Si of this dopant concentration at 5 meV above the band edge has a negative power dependence on E, implying increasing magnitude of the density of states function at that energy level. Therefore, we conclude that near the band edge, for the less heavily doped Si, the impurity band produces a small hump on the density of states function of the semiconductor. At higher dopant concentrations,

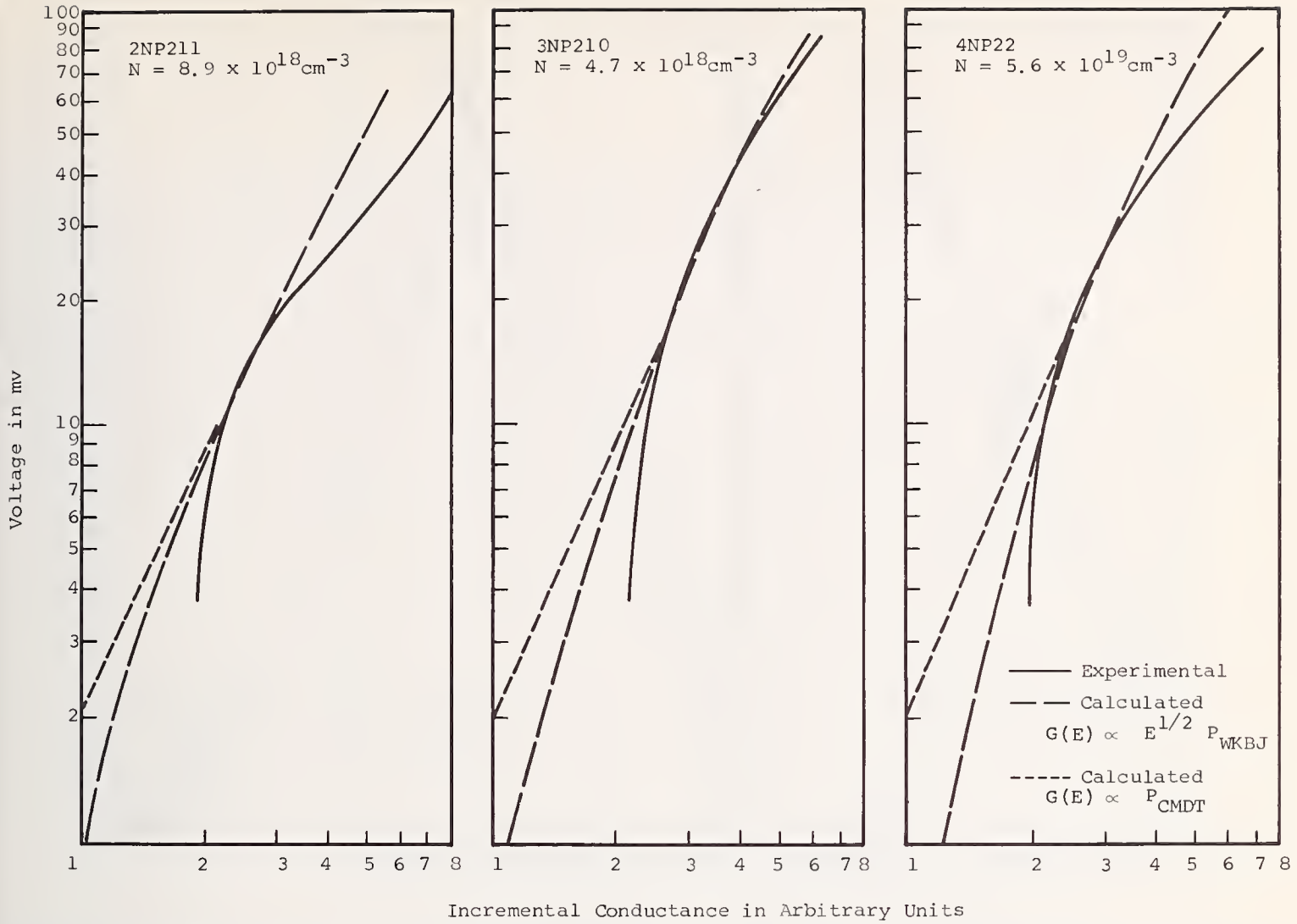

FIGURE 14. *The effect of the density of states band tail in* P *doped* Si *on the incremental conductance of the metal-semiconductor tunnel junction.*

by the evaluation of figure 14 and eq (21), based on similar analysis, it can be concluded that the impurity band near band edge becomes fully merged into the density of states function by its complete disappearance. Figure 16 summarizes the estimated density of states functions for different levels of dopant concentrations of P doped Si. Included in the figure is also the summary curves of the estimated density of states function of As doped Si based on similar analysis of the increment conductance curves of the corresponding metal-semiconductor junctions.

It is observed from the figure that for the As doped Si, the density of states function as well as the band tail near the bottom of the conduction band is distorted from the parabolic dependency on energy much more severely when compared with P doped Si, in agreement with earlier observations in the study of figures 12-15.

The hump in the Si density of states function due to the impurity band obtained experimentally by us is in general agreement with the work by G. D. Mahan and J. W. Conley [4] on their study of the heavily doped *p*-type GaAs density of states function, except that the Si impurity hump is confined to a narrower energy range near the bottom of the conduction band than that obtained for *p*-GaAs.

5. Conclusion

In this study, we have developed the necessary mathematical analyses of the metal-semiconductor junction for the evaluation of the experimental data. Both the WKBJ approximation and the exact transmission coefficient calculations of the tunnel diode equation were used. For the case of silicon diode, both methods yielded comparable solutions which predict the characteristic features of the metal-semiconductor tunneling current experimental curves.

Through the study of both the incremental resistance and conductance curves of the metal-semiconductor

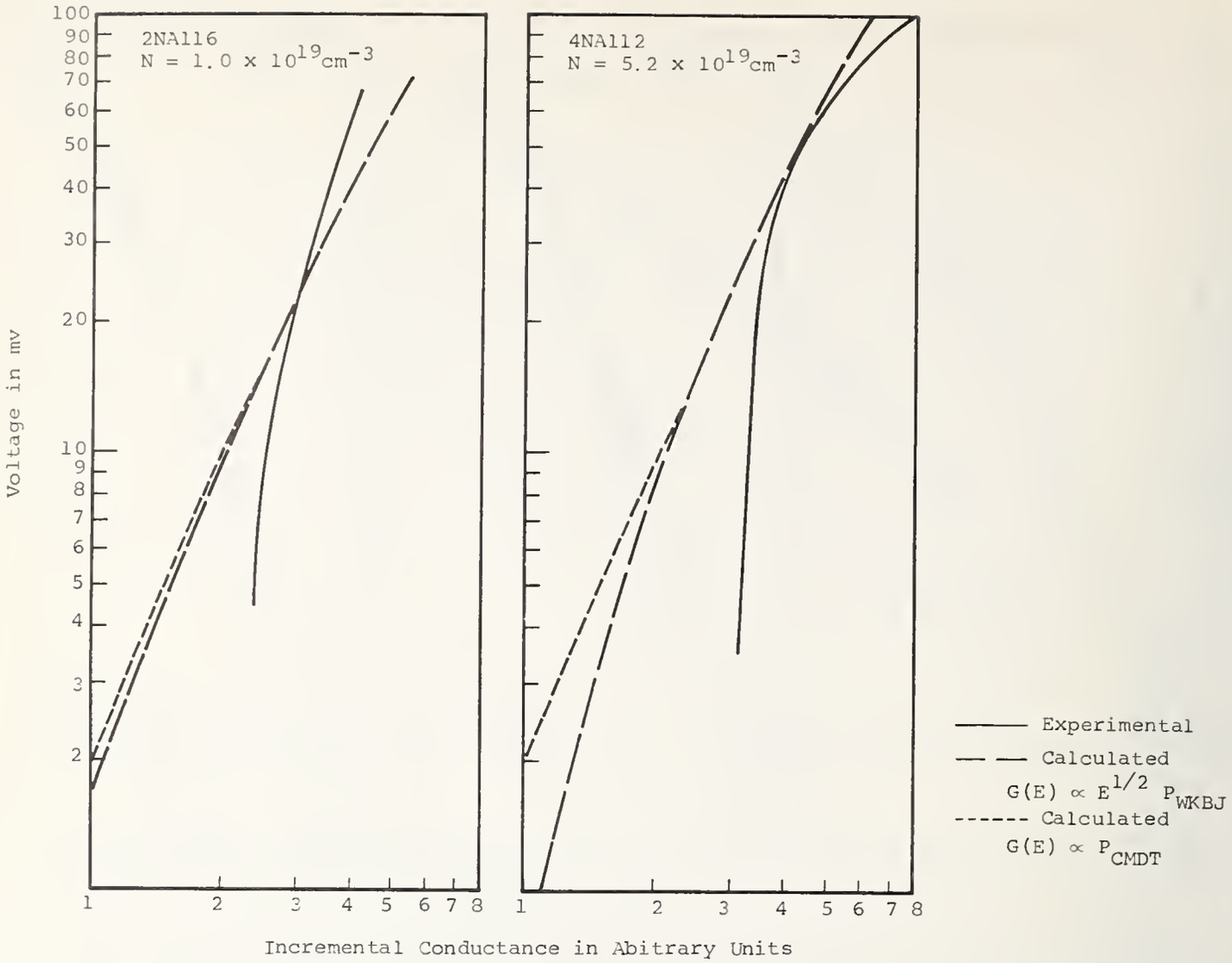

FIGURE 15. *The effect of the density of states band tail in* As *doped* Si *on the incremental conductance of the metal-semiconductor tunnel junction.*

diodes, it is concluded that the incremental conductance curve describes to a greater degree of clarity some of the important properties of the bulk material under study than that possible with the incremental conductance curve. Based on this evaluation, we measure directly the incremental conductance curves of the diodes under study. In addition, the measurement circuits have been analyzed to assure the accuracy of the measurements made, as well as to determine the magnitude of the inclusion of extraneous impedance effects from the measurement circuits in the diode conductance curves.

Our tunneling data are interpreted by two different procedures: (1) evaluation of the V_{min} versus N curves, the curves being the compilation of the most prominent features of all the diode conductance curves; (2) the evaluations of the individual diode conductance curve. Using the V_{min} curves, we discover the dopant type dependence of the Fermi level of the semiconductor, leading us to postulate a dopant type dependent density of states effective mass for Si. This density of states effective mass also can be considered to be a measure of the effect of different dopants on the density of states function of the heavily doped Si. Using the individual diode conductance curves, we can determine the overall characteristic features of the density of states function of the heavily doped Si at particular dopant concentrations and with specific dopants. And with either procedure, we arrive at the same consistent interpretation that the density of states of the heavily doped semiconductor is generally parabolic above the band edge, but near the band edge, band tailing can be severe, depending on the dopant type and on the dopant concentration.

Quantitative data on the density of states function of the heavily doped Si are obtained through the comparison between the calculated curves, using known functions for the density of the functions of the

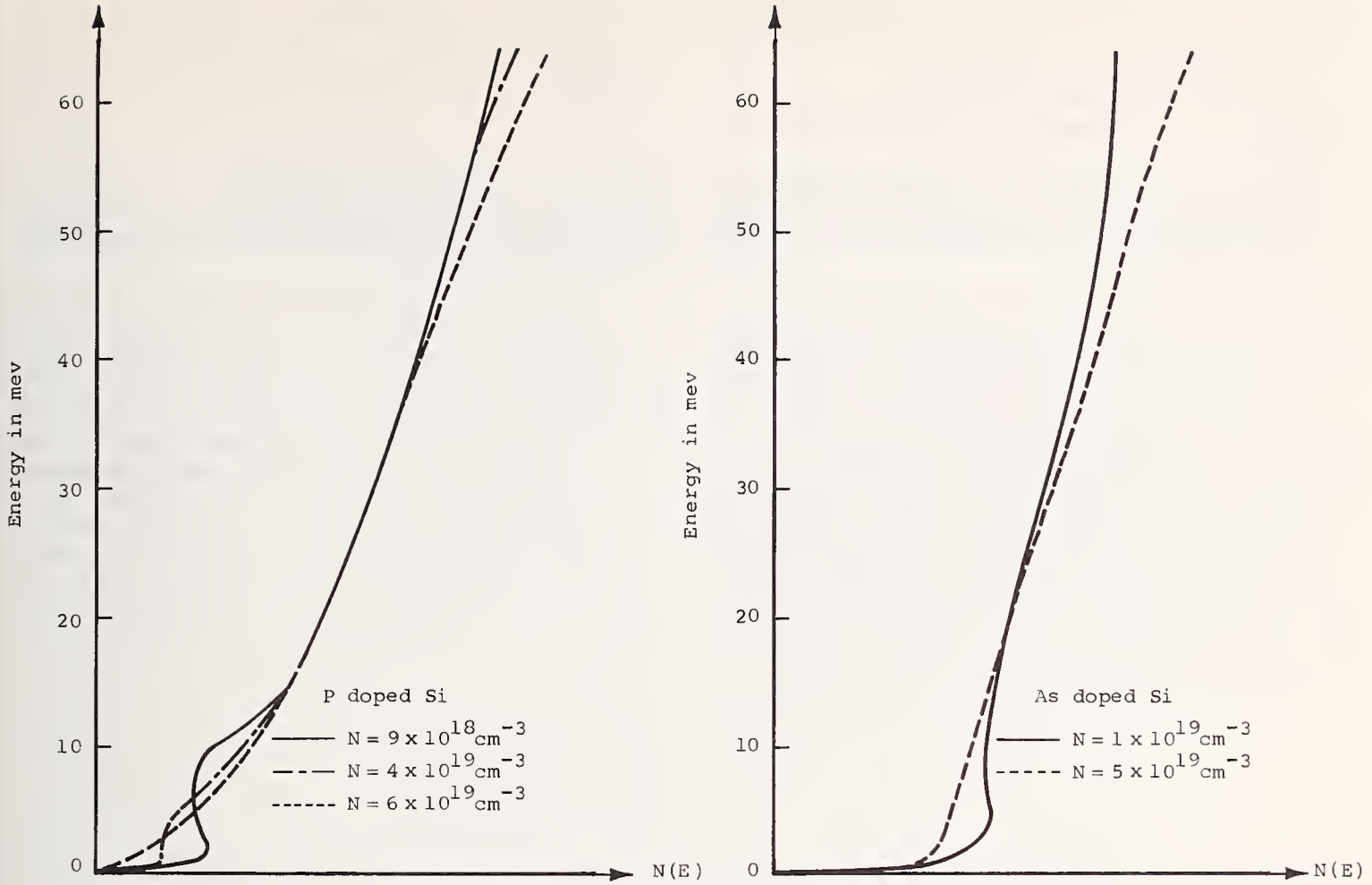

FIGURE 16. *Density of states of the heavily doped* n*-silicon.*

semiconductor, and the experimentally derived curves. The data so obtained include the dopant dependent density of states effective masses and the power dependence of the density of states functions on energy in the band tail region. Density of states functions of the heavily doped Si, at different dopant levels and different dopant types, can also be derived from the experimental conductance curves. It is hoped that our experimental data on heavily doped Si will be of interest to those active in the theoretical modeling of the heavily doped semiconductors.

6. References

[1] Gschwend, V. F., Kleinknecht, H. P., Neft, W., and Steiler, K., Z. für Naturforschung **18a**, 1366 (1963).

[2] Conley, J. W., Duke, C. B., Mahan, G. D., and Tiemann, J. J., Phys. Rev. **150**, 466 (1966).

[3] Conley, J. W., and Tiemann, J. J., J. Appl. Phys. **38**, 2880 (1967).

[4] Mahan, G. D., and Conley, J. W., Appl. Phys. Letters **11**, 29 (1967).

[5] Conley, J. W., and Mahan, G. D., Phys. Rev. **161**, 681 (1967).

[6] Chang, L. L., Esaki, L., and Jona, F., Appl. Phys. Letters **9**, 21 (1960).

[7] Burnstein, E., Phys. Rev. **93**, 632 (1954).

[8] Hill, D. E., Phys. Rev. **133**, A866 (1964).

[9] Lucovsky, G., Solid State Commun. **3**, 105 (1965).

[10] Pankove, J. I., Phys. Rev. **140**, A2059 (1965).

[11] Curie, D., Luminescence in Crystals (Wiley, New York, 1963).

[12] Lucovsky, G., Varga, A. J., and Schwarz, R. F., Solid State Commun. **3**, 9 (1965).

[13] Morgan, T. N., Phys. Rev. **139**, A343 (1965).

[14] Haas, C., Phys. Rev. **125**, 1965 (1962).

[15] Fowler, A. B., Howard, W. E., and Brock, G. E., Phys. Rev. **128**, 1664 (1962).

[16] Pankove, J. I., and Aigrain, P., Phys. Rev. **126**, 956 (1962).

[17] Mead, C. A., Spitzer, W. G., Phys. Rev. **134**, A713 (1964).

[18] Esaki, L., Phys. Rev. **190**, 603 (1958).

[19] Giaever, I., Phys. Rev. Letters **5**, 464 (1960).

[20] Giaever, I., and Megerle, K., Phys. Rev. **122**, 1101 (1961).

[21] Shapiro, S., Smith, P. H., Nicol, J., Miles, J. L., and Strong, P. F., IBM Journal **6**, 34 (1962).

[22] Bardeen, J., Phys. Rev. **71**, 717 (1947).

[23] Heine, V., Phys. Rev. **138**, A1689 (1965).

[24] Geppert, D. V., Cowley, A. M., and Dore, B. V., J. Appl. Phys. **37**, 2458 (1966).

[25] Crowell, C. R., and Sze, S. M., Solid State Electronics **9**, 1035 (1966).

[26] Mathews, J., and Walker, R. L., Mathematical Methods of Physics (W. A. Benjamin Inc., New York, 1964) pp. 26-37.

[27] Morse, P. M., and Feshbach, H., Methods of Theoretical Physics (McGraw-Hill, New York, 1953) pp. 1092-1106.

[28] Kohn, W., Shallow Impurity States in Silicon and Germanium, Solid State Physics **5**, F. Seitz and D. Turnbull, Editors (Academic Press Inc., New York, 1957).
[29] Harrison, W. A., Phys. Rev. **123**, 85 (1961).
[30] Fredkin, D. R., and Wanniev, G. H., Phys. Rev. **128**, 2054 (1962).
[31] Stratton, R., and Padowani, F. A., Solid State Electronics **10**, 813 (1967).
[32] Runyan, W. R., Silicon Semiconductor Technology (McGraw-Hill, New York, 1965).
[33] Buehler, M. G., and Pearson, G. L., Solid State Electronics **9**, 395 (1962).
[34] Irvin, J. C., The Bell System Technical Journal **41**, 387 (1962).
[35] Logan, R. A., Gilbert, T. F., and Trumbore, F. A., J. Appl. Phys. **32**, 131 (1961).
[36] Furukawa, Y., J. Phys. Society of Japan **16**, 577 (1961).
[37] Holmer, P. J., IEEE Proceedings **106**, B861 (1959).
[38] Gatos, H. C., and Lavine, M. C., Chemical Behavior of Semiconductors: Etching Characteristics, Progress in Semiconductors, A. F. Gibson and R. E. Burgess, Editors (Temple Press Books Ltd., London, 1965), pp. 1-45.
[39] Chynoweth, A. G., Feldmann, W. L., and Logan, R. A., Phys. Rev. **121**, 684 (1961).
[40] Vogel, H. E., and Garland, M. M., J. Appl. Phys. **38**, 5116 (1967).
[41] Vogel, H. E., Ph. D. Thesis, University of North Carolina (1962).
[42] Blumberg, R. H., and Seraphim, D. P., J. Appl. Phys. **33**, 163 (1962).
[43] King, V. J., Rev. Sci. Instr. **32**, 1407 (1961).
[44] Claeson, T., Phys. Rev. **147**, 340 (1966).
[45] Nemback, E., Phys. Rev. **172**, 425 (1968).
[46] Rowell, J. M., Anderson, R. W., and Thomas, D. E., Phys. Rev. Letters **10**, 334 (1963).
[47] Schrieffer, J. R., Scalapino, D. J., and Wilkins, J. W., Phys. Rev. Letters **10**, 336 (1963).
[48] Hsia, Y., Ph. D. Thesis, University of California, Los Angeles (1969).
[49] Tao, T. F., and Hsia, Y., Appl. Phys. Letters **13**, 291 (1968).
[50] Bonch-Bruyevich, V. L., The Electronic Theory of Heavily Doped Semiconductors (American Elsevier, New York, 1966).
[51] Bonch-Bruyevich, V. L., Effect of Heavily Doping on the Semiconductor Band Structure, Semiconductors and Semimetals, **Vol. 1**, R. K. Willardson and A. C. Beer, Editors (Academic Press, New York, 1966), pp. 101-142.

Discussion on "Metal-Semiconductor Barrier Junction Tunneling Study of the Heavily Doped N-Type Silicon Density of States Function" by Y. Hsia and T. F. Tao (University of California, Los Angeles)

G. D. Mahan *(Univ. of Oregon):* In silicon metal-semiconductor junctions it is very easy to get a significant oxide layer unless proper precautions are taken. This would seem to be the case here. Thus you should be cautious about over-interpreting your data.

Y. Hsia *(Litton Systems, Inc.):* There is probably a residual layer of oxide about 30 Å to 50 Å at the junction. The effect of the oxide on the tunnel current should be dopant independent. The main problem is its effect on the assumed tunnel barrier and consequently the theoretical calculation of the tunnel current. (Fig. 4 of the text compares the effect of the tunnel barrier variation on the normalized incremental conductance features which are utilized in comparison with our experimental data.) The determination of the Fermi level by interpreting V_{min} measurements on oxide junctions has been shown experimentally by the work of Esaki et al. [1] on many materials.

M. Cardona *(Brown Univ.):* Have you compared your results with those obtained from infrared reflectivity measurements?

Y. Hsia *(Litton Systems, Inc.):* The dopant dependence of the effective mass in heavily doped semiconductors has actually been previously obtained by Spitzer et al. [2] in their reflectivity measurements on As, P, and Sb doped Ge to determine carrier density dependent density of states effective mass (though interpretation of their data presented in fig. 8 of the cited reference). The dependence is similar but differs in having smaller differences of values. We are planning to do free carrier reflectivity measurements in the infrared region on the variously doped silicon to obtain density of states effective mass data for comparison with this tunneling work.

[1] Esaki, L., and Stiles, P. J., Phys. Rev. Letters **14**, 902 (1965); Esaki, L., and Stiles, P. J., Phys. Rev. Letters **16**, 574 (1966); Chang, L. L., Esaki, L., and Jona, F., Appl. Phys. Letters **9**, 21 (1966); Chang, L. L., Stiles, P. J., and Esaki, L., J. Appl. Phys. **38**, 4440 (1967).

[2] Spitzer, W. G., Trumbore, F. A., and Logan, R. A., J. Appl. Phys. **32**, 1822 (1961).

TRANSPORT PROPERTIES: APPLICATIONS

CHAIRMEN: A. I. Schindler
A. Feldman

RAPPORTEUR: R. J. Higgins

The Effect of Hydrostatic Pressure on the Galvano-Magnetic Properties of Graphite

I. L. Spain

Institute for Molecular Physics, University of Maryland, College Park, Maryland 20742

Measurements of the Hall Effect and magneto-resistance in crystals of graphite with current flow in the basal planes at high pressures are described. Galvanomagnetic measurements enable the magneto conductivity tensor components σ_{xx} and σ_{xy} to be obtained, and from them the electron and hole densities and mobilities. The results are compared with the band model for the semi-metal graphite proposed by Slonczewski and Weiss. Of particular interest at the present time is the information that these results give about the assignment of carriers at the symmetry point K in the Brillouin zone of graphite and the properties of mobile minority carriers.

Key words: Electronic density of states; galvano-magnetic properties; graphite; Hall Effect; magneto-resistance; pressure effects.

1. Introduction

The determination of the effect of pressure on the electronic properties of graphite is of interest for several reasons. The highest occupied valence band overlaps the lowest unoccupied conduction band by about 32 meV [1], so that graphite behaves like a semimetal when the current flows along the layer planes. As a result, changes in the lattice spacing induced by hydrostatic pressure are expected to produce quite large effects in the electronic properties. The large elastic anisotropy enables the change in lattice parameter in the plane (a_0) to be neglected compared to the change in c-axis spacing (c_0) ($(\Delta c/c_0) \sim 29(\Delta a/a_0)$) [2] so that changes in electronic properties are expected to originate from corresponding changes in the overlap integrals between planes.

The generalised band model proposed by Slonczewski and Weiss [3], with adjustable parameters related to overlap integrals, has been successful in interpreting many of the experiments on graphite, and some experiments have attempted to directly relate pressure effects to changes in these parameters [4-8]. However, recent studies of Schroeder, Dresselhaus, and Javan [9], have proposed several fundamental changes in the band structure that have important consequences on the interpretation of galvanomagnetic data.

A program to study the effect of pressure on the galvanomagnetic properties of graphite, with current flow both along and perpendicular to the planes, is being carried out. So-called "c-axis effects" are very interesting because of the possibility of observing the role of localised "electron-hole" or "exciton" states on the properties of solids [10] but this problem is not discussed here. Measurements of pressure on the Hall Effect and magneto-resistance of highly oriented graphite are reported at two temperatures and the information that they give about the band parameters and the density of states discussed.

2. The Band Model of Graphite

The Slonczewski-Weiss band model [3] concerns itself only with those states of interest to free-electron phenomena near the vertical Brillouin zone edges (HKH′). The variation of energy for electron states along (HKH′) is shown in figure 1a, being given by:

$$\epsilon_1 = \Delta + 2\gamma_1 \cos \phi$$

$$\epsilon_2 = \Delta - 2\gamma_1 \cos \phi$$

$$\epsilon_3 = 2\gamma_2 \cos^2 \phi$$

where

$$\phi = \frac{k_z C_0}{2}$$

and $\gamma_1 \gamma_2, \Delta$ are related to out-of-plane overlap integrals.

The theory obtains the energy of those states near the zone boundary by a perturbation calculation. In the event that the effect of (other overlap) parameters

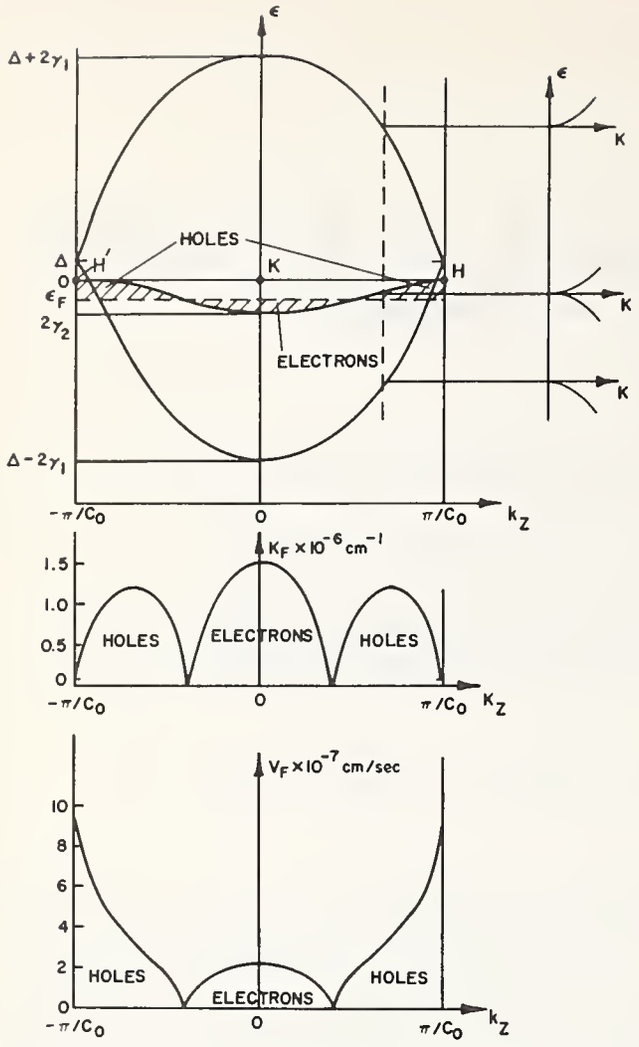

FIGURE 1(a). *Sketch of the variation of electron energy for states along the vertical zone edge HKH' of the Brillouin zone of graphite.* The assignment of electrons at point K is used in this diagram in agreement with the work of Dresselhaus et al. The variation of energy with wave-ratio component perpendicular to HKH' is indicated.

FIGURE 1(b). *Sketch of the variation of electron and hole wave-vector* K_F *along the Brillouin zone edge of graphite.*

FIGURE 1(c). *The basal velocity* (v_F) *of carriers with the Fermi energy.*

$\gamma_3, \gamma_4, \gamma_5$ appearing in the theory may be neglected (γ_3 accounts for trigonal warping effects), the dispersion relation may be written:

$$\epsilon = \frac{\epsilon_{1,2} + \epsilon_3}{2} + \left[\left(\frac{\epsilon_{1,2} - \epsilon_3}{2}\right) + \frac{3\gamma_0^2 a_0^2 \kappa^2}{4}\right]^{1/2}$$

where

$$\epsilon_{12} = \epsilon_1 \text{ or } \epsilon_2$$

a_0 is the lattice constant in the plane $= 2.46$ Å

γ_0 is an in-plane overlap integral

$$\kappa = (k_x^2 + k_y^2)^{1/2}$$

For the "four-parameter band model," the basal component of the effective mass tensor along the zone edge is given by $m_{xx}^*\ (k=0) = 4/3\hbar^2(\gamma_1 - \gamma_2)/3a_0^2\gamma_0^2 \sim 0.061\ m_0 \cos\phi$. The wave-vector K_F is plotted as a function of ϕ in figure 1b, and the basal velocity (V_F) for electrons on the Fermi surface in figure 1c. The following values of the band parameters were used [9,11]:

$$\gamma_0 = 3 \text{ eV}$$

$$\gamma_1 = 0.395 \text{ eV}$$

$$\gamma_2 = -0.016 \text{ eV}$$

$$\Delta = +0.02 \text{ eV}$$

$$\epsilon_F = -0.0208 \text{ eV at } T = 0 \text{ K}$$

Until recently, the value of γ_2 was taken to be positive, indicating that holes occupied that volume of the Brillouin zone around point K. From magneto-reflection data, Schroeder et al. [9] concluded that γ_2 was negative, implying electron occupancy at this point. The assignment is discussed later in relation to galvano-magnetic data.

Dresselhaus and Dresselhaus [12] also suggested that Δ was positive, implying that the tips of the hole regions of the Fermi surface protrude into the next zone. As a result of spin orbit splitting, a pocket of holes (with a positive value of γ_2, the pocket would be occupied by electrons) is located at the zone corner, having very small effective mass.

Dresselhaus has also suggested [13] that the value of γ_3 (~ 0.3 eV) is much larger than previously thought, so that a perturbation calculation of the electron energy for states near the zone edge is no longer applicable. A large value for γ_3 implies that the electron energy surfaces are trigonally warped, possibly to the extent of producing pockets of electrons split off from the main body.

3. Galvanomagnetic Effects

In the experiments to be described, measurements of the Hall Constant (R_H), zero field resistivity ρ_0 and resistivity in a magnetic field $\rho(H)$ are reported. In general it is convenient to compare theoretical models with the conductivity tensor components. In the case of current flow along the planes, magnetic field in the c-axis direction (H_z) and no preferred direction along the planes, the relationships between measured effects and conductivity components are [14]:

$$R_H = \frac{1}{H}\frac{\sigma_{xy}}{(\sigma_{xx}^2 + \sigma_{xy}^2)}$$

$$\rho = \frac{\sigma_{xx}}{(\sigma_{xx}^2 + \sigma_{xy}^2)}$$

with inverse relationships:

$$\sigma_{xx} = \frac{\sigma}{1 + (R_H \sigma H)^2}$$

$$\sigma_{xy} = \sigma_{xx} \ (R_H \sigma H)$$

$$\sigma = \rho^{-1} \equiv \text{measured conductivity}$$

The conductivity components may then be expressed as integrals over the volume of reciprocal space in the following way [15,16]:

$$\sigma_{xx}(H_z) = \frac{-e^2}{4\pi^3} \int \frac{v_x^2 \tau \ (k)}{(1 + \omega^2 \tau^2 (k))} \cdot \frac{\partial f_0}{\partial \epsilon} \, d^3k.$$

$$\sigma_{xy} \ (H_z) = \frac{-e \ H_z}{4\bar{u}^3 c} \int \frac{v_x^2 \tau^2 \ (k)}{m_{xx}^* \ (1 + \omega^2 \tau^2 \ (k))} \frac{\partial f_0}{\partial \epsilon} d^3k$$

where

$$\omega \equiv \frac{eH_z}{m_{xx}^* c}$$

and $\tau(k)$ = relation time for scattering electrons.

These equations hold to high magnetic fields in the approximtion that the basal plane effective mass tensor $m_{xx}^* = m_{yy}^*$ does not vary appreciably with energy in a plane in k-space perpendicular to k_z. The approximation is not strictly valid for graphite, since the dispersion relation in such a plane is hyperbolic, not parabolic. In addition, the strong variation of carrier properties along the zone edge make the conductivity integrals difficult to calculate. Even if the details of the bands are known, a detailed knowledge of the relaxation time as a function of wave vector is required. Since this is determined by the scattering of electrons by lattice imperfections it cannot be calculated precisely, and the fine details of the bands become hidden by gross assumptions made in the function $\tau(k)$.

A simple solution presents itself, since the condition of charge neutrality in the crystal implies an equal number of free carriers in the valence and conduction bands. Soule [14] then suggested the following multiband formula:

$$\sigma_{xx} = \sum_{i=1}^{N} \frac{\sigma_{0i}}{1 + (H/H_i)^2}$$

$$\frac{\sigma_{xy}}{H} = \sum_{i=1}^{N} \frac{\frac{n_i e_i c}{H_i^2}}{1 + (H/H_i)^2}$$

n_i = number of carriers per unit volume in band i
N = total number of bands
$e_i = + \mid e \mid$ for holes, $- \mid e \mid$ for electrons
σ_{0i} = measured conductivity of band i in zero magnetic field
H_i = characteristic field of carriers in band i
$= \dfrac{cm_i^*}{e\tau_i} = \dfrac{c}{\mu_i}$
μ_i = carrier mobility
$\sigma_{0i} = n_i e \mu_i$.

The underlying assumption in this theory is that the properties of the carriers can be approximated by averaging effects from groups of carriers with different properties as though they all had the same properties. In addition, the relaxation time appearing in the denominator of the integrals is assumed to be independent of energy.

Galvanomagnetic data has been fitted using these formulae by Soule for natural crystals and Spain, Ubbelohde and Young [17], for synthetic material. In both cases one majority band of holes and electrons was assumed, with a minority carrier to explain marked deviations from two-band behaviour in the Hall Constant at low fields.

In the approximation of two majority carriers a simplification may be made, enabling a mean mobility to be calculated.

If $a = \dfrac{n_2}{n_1} \sim 1$ suffix (1) refers to majority electrons

$b = \dfrac{\mu_1}{\mu_2} \sim 1$ suffix (2) refers to majority holes

$$\text{Then } \mu^2 \sim c^2 \left(\frac{\Delta \rho}{\rho_0 H^2} \right)$$

In summary, this simplified analysis enables the galvanomagnetic data to be fitted approximately with averaged parameters for the electron and hole bands, yielding values for the average mobility μ_i and number of carriers n_i. The method enables the properties of minority carriers to be explored from low-field Hall data. From the number of carriers of each type, a direct comparison may be made with the theoretical prediction:

$$n_i = \int_{\text{band } i} n(\epsilon) f_0(\epsilon) \ d\epsilon$$

It must be remembered, however, that the number of carriers calculated from galvanomagnetic data must first be corrected by a numerical factor ($\sim$ unity) which comes from the integration procedure.

The measurement of the effect of pressure on the galvanomagnetic coefficients gives information about the changes occurring in the constant energy surfaces brought about by changes in overlap parameters. This is reflected in the change in the number of carriers with pressure and in the mobility, since the relaxation time depends on the energy wave-vector relationship. In the case of scattering by lattice vibrations, the relaxation time is inversely proportional to the density of states into which scattering takes place [18], while for scattering at crystallite boundaries it is inversely proportional to the velocity of the carriers (i.e., proportional to $\epsilon^{-1/2}$ for both scattering mechanisms for ellipsoidal bands of standard form).

4. Experimental

Details of the experimental apparatus used for the present work are to be reported elsewhere. Using helium fluid as the pressure-transmitting medium, measurements could be made to 10 kbar in magnetic fields up to 15 kG, with the temperature controlled to ±0.02 °C. Conventional D.C. techniques were used to measure the galvanomagnetic coefficients.

Techniques for fabricating bridge specimens and attaching leads to them have been described elsewhere [17]. One unexpected problem was encountered that has still not been solved. After compression to above about 3 kbar, irreversible changes occurred in the measured galvanomagnetic coefficients. This probably arose from changes in the current and potential contacts to the specimen. With a normal isotropic metal or semiconductor, small changes in the probe configuration do not affect the isopotential lines in the body of the specimen, provided that the length to width or thickness ratio is greater than about 5. However, in graphite, the high anisotropy ratio ($> 10^3$) ensures that equal sharing of current between the planes is extremely difficult to achieve. Small changes in contacts could easily produce the changes observed. Experiments described in this paper are limited to the pressure range below about 3 kbar for this reason. Attempts are being made to improve contacts using different plating and soldering techniques.

Experimental results are presented for two specimens cut from different types of synthetic material. Material for specimen A-2 was obtained from Union Carbide Corporation, hot pressed at 2500 °C and annealed above 3000 °C. Stress recrystallised material was used for specimen A-6 obtained from Pennsylvania State University. Values of measured parameters for these specimens are given in table 1, comparison being made with data from Soule's crystal EP-14. It can be seen that A-6 compares quite closely with his crystal and probably has a grain size greater than 10 microns. A-2 is definitely an inferior specimen with a smaller grain size. For comparison purposes, data is also included from previous work on similar synthetic material [17], close similarities being observed between samples SA-20 [17] and A-2; and SA-26 [17] and A-6.

TABLE 1. *Galvanomagnetic coefficients of specimens A-2 and A-6 compared with data from other sources*

Sample	Ratio of resistance $\rho 295/77.5$ K	Mobility at* 77.5 K (cm^2/volt-s)	Value of Hall constant at maximum value	Room temperature resistivity
A-2†	1.30	4.87×10^4	-0.005 cm^3/C	3.54×10^{-5}
A-6†.....	1.59	5.3×10^4	$+0.060$ cm^3/C	4.12×10^{-5}
EP-14‡.....	~ 1.82	6.8×10^4	**$+0.18$ cm^3/C	4.42×10^{-5}
SA-20‡.....	1.41	4.85×10^4	-0.005 cm^3/C	4.42×10^{-5}
SA-26‡.....	1.74	5.75×10^4	.07 cm^3/C	4.43×10^{-5}

†Present measurements.
‡Soule, reference [14].
‡Spain, Ubbelohde and Young, reference [17].
*All data taken at 3.00 kG for exact comparison.
**A plateau rather than a maximum.

5. Experimental Results at Room Temperature

Graphs of the variation of the Hall Effect and magneto-resistance coefficient with pressure at room temperature are shown in figures 2 to 5. It can be seen that the trend in the Hall Constant is to more positive values ($dR_H/dp = 0.0025$ cm^3/C.kbar for A-2, $dR_H/dp = 0.0032$ cm^3/C.kbar for A-6). This trend is in agreement with the results of Arkhipov et al. [6], but in numerical disagreement. Their zero pressure value at 300 K at unspecified magnetic field being ~ -0.03 cm^3/C compared to ~ 0.05 cm^3/C for A-2 and A-6, while their value of $dR/dp \sim 0.001$ cm^3/C.kbar. This may be due in part to differences in specimen perfection, Arkhipov et al. [6], working with natural crystals of unspecified perfection.

The largest error in the measurements reported here arises from the c-axis dimension (S_z) of the crystals (± 5%). Assuming a correct value for S_z, the Hall Constant was then measured with a precision and reproducibility of $\sim \pm 0.0002$ cm^3/C at 15 kG, reducing to approximately ± 0.0005 cm^3/C at 1 kG.

The trend in the magneto-resistance coefficient ($\Delta\rho/\rho_{0H^2}$) is to lower values as the pressure increases, indicating that the average mobility ($\mu = (\Delta\rho/\rho_{0H^2})^{1/2} \times 10^8$ cm^2/volt-sec) also decreases. However μ^2 varies

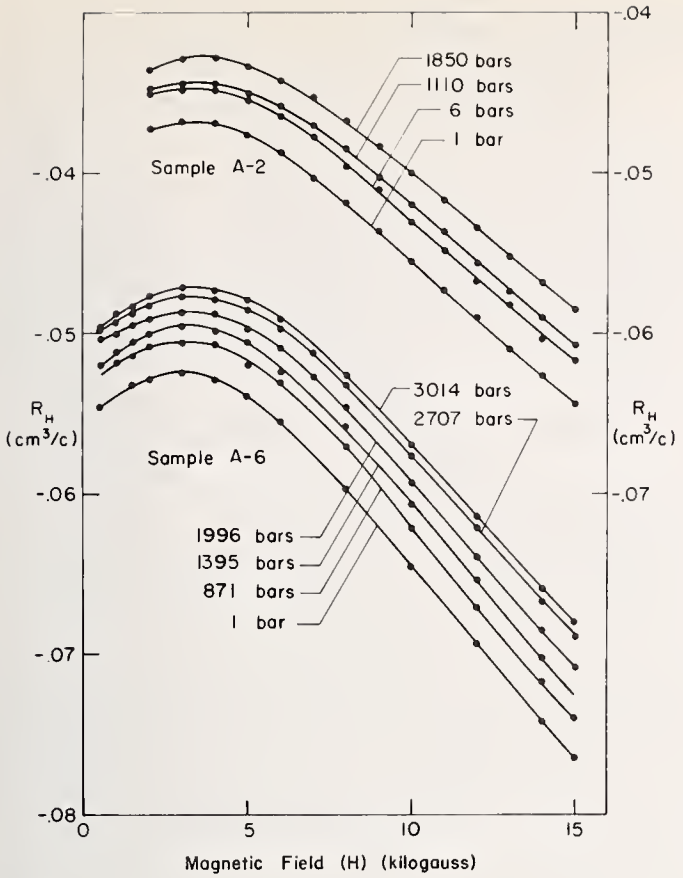

FIGURE 2. *The effect of pressure on the Hall Constant* (R_H) *plotted as a function of magnetic field for two samples at room temperature.*

Note that the ordinate corresponding to sample A-6 is on the left-hand side, that corresponding to A-2 on the right-hand side.

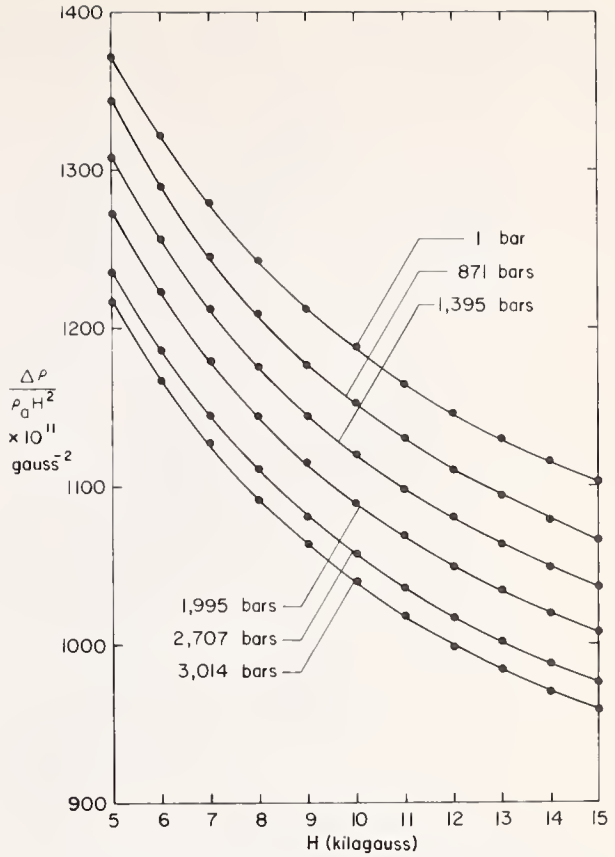

FIGURE 4. *The value of the magnetoresistance coefficient* ($\Delta\rho/\rho_0 H^2$) *for specimens A–2 and A–6 as a function of pressure at room temperature.*

linearly with pressure rather than μ^1. Values of μ were taken at 14 kG. Since the resistance does not vary as the square of the magnetic field, a consistent criteria for calculating μ is required. The magnetic field was correspondingly chosen to be that value for which $\Delta\rho/\rho_0 \sim 2.00$. At this condition, minority carrier effects should be unimportant, and the data susceptible to accurate analysis.

The change in basal plane resistance was extremely small [$(1/\rho_0 d\rho_0/dp \leq 10^{-3}$/kbar)] indicating that an increase in the number of carriers produced by swelling of the energy surfaces was compensated very closely by the decrease in mobility. This result agrees with that of Spain [19] and Yeoman and Young [20]. The large decrease in ($\Delta\rho/\rho_0 H^2$) with pressure reported here ($\sim -3.2\%$/kbar for A-2, -4.3%/kbar for A-6) is larger

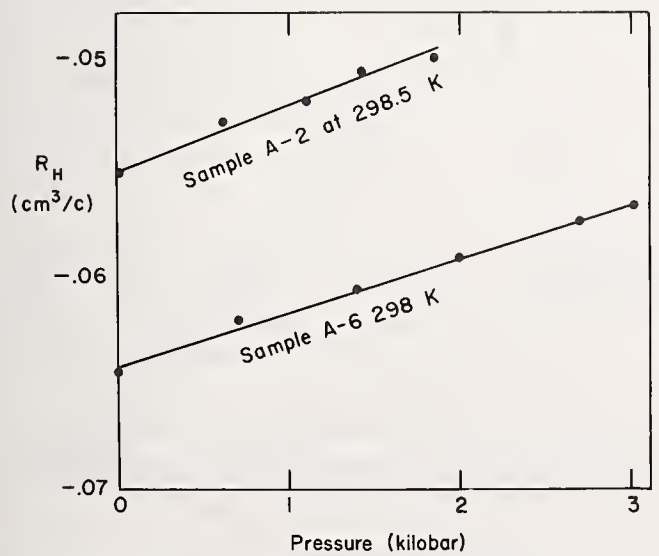

FIGURE 3. *The value of the Hall Constant at 10 kG for specimens A–2 and A–6 plotted as a function of pressure at room temperature.*

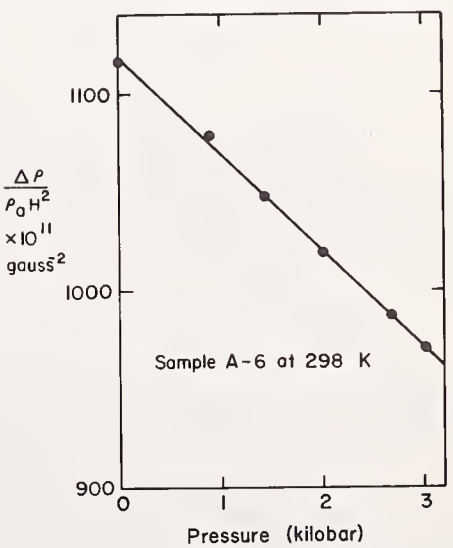

FIGURE 5. *The variation with pressure of the parameter* ($\Delta\rho/\rho_0 H^2$) *obtained for sample A–6 at 14 kG and 298 K.*

417-156 O - 71 - 47

TABLE 2. *Experimental coefficients for A-2 and A-6*

Temp. K	Parameter	A-2	A-6
298	$\mu=\left(\frac{\Delta\rho}{\rho_0 H^2}\right)^{1/2}\times 10^8$ (cm²/volt s)	$(0.90\pm0.01)\times10^4$	$(1.05\pm0.01)\times10^4$
	ρ_0 (Ωcm)	$(3.45\pm0.15)\times10^{-5}$	$(4.12\pm0.15)\times10^{-5}$
	n total $=\frac{\sigma_0}{e\mu}$ (cm^{-3})	$(17.8\pm0.8)\times10^{18}$	$(14.5\pm0.7)\times10^{18}$
	R_H at 10k.g. (cm³/C)	-0.0581 ± 0.0002	-0.0656 ± 0.0002
	$\frac{dR_H}{dp}$ (cm³/C.k.bar)	$+0.0025\pm0.0002$	$+0.0032\pm0.0002$
	$d\left(\log\left(\frac{\Delta\rho}{\rho_0 H^2}\right)\right)\Big/dp$ (k.bar^{-1})	-0.032 ± 0.003	-0.043 ± 0.003
	$d(\log\rho_0)/dp$ (k.bar^{-1})	$-(0.0004\pm0.0003)$	$-(0.0005\pm0.0003)$
77.5	$\mu=\left(\frac{\Delta\rho}{\rho_0 H^2}\right)^{1/2}\times 10^8$ (cm²/volt-s)	$(4.87\pm0.01)\times10^4$	$(5.35\pm0.01)\times10^4$
	ρ_0 (Ωcm)	$(2.72\pm0.10)\times10^{-5}$	$(2.61\pm0.10)\times10^{-5}$
	n total $=\frac{\sigma_0}{e\mu}$	$(4.7\pm0.25)\times10^{18}$	$(4.45\pm0.25)\times10^{18}$
	$a=\frac{n_2}{n_1}$	0.99 ± 0.005	0.99 ± 0.005*
	$b=\frac{\mu_1}{\mu_2}$	1.00 ± 0.01	0.91 ± 0.01*

*A three band model does not fit the data for SA-6 beyond about 8 k bar.

than that reported by Arkhipov et al. [16], ($\sim-1.8\%$/kbar) who also reported a linear variation of $(\Delta\rho/\rho_0 H^2)$ with pressure. Results are summarised in table 2.

Computing the value of the number of carriers in all bands from the simple formula:

$$n=\frac{\sigma}{e\mu}$$

gives the value $(17.8\pm0.8)\times10^{18}$ for A-2, $(14.5\pm0.7)\times10^{18}$ for A-6. This compares with the value computed for the four-parameter band model, with parameter values given earlier.

$$n=13.3\times10^{18}$$

6. Experimental Results at 77.5 K

The variation of Hall Constant with magnetic field for sample A-2 at 77.5 K is shown in figure 6. The curve at 1 atmosphere is typical for synthetic material, with a maximum (~-0.0050 cm³/c) at about 2 kG. Below this, the downward trend in the Hall Constant may be attributed to a minority electron, while at higher fields, the trend is produced through a small excess of majori-

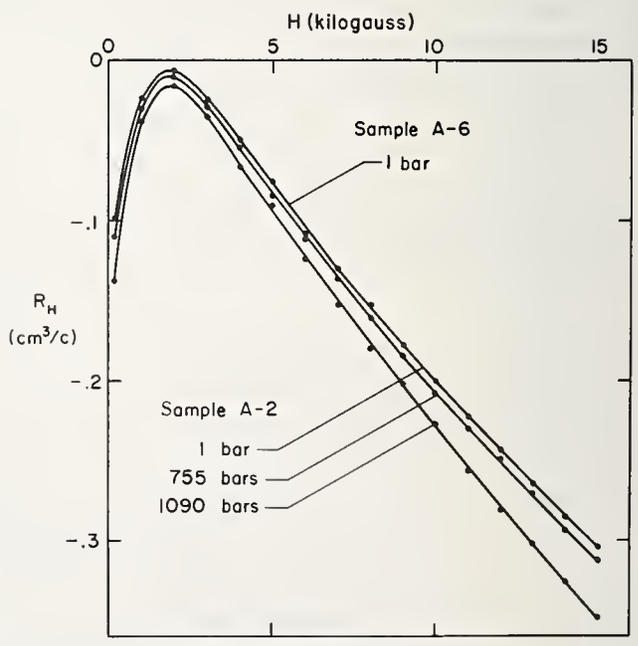

FIGURE 6. *The effect of pressure on the Hall Constant of Sample A-2 at 77.5 K.*

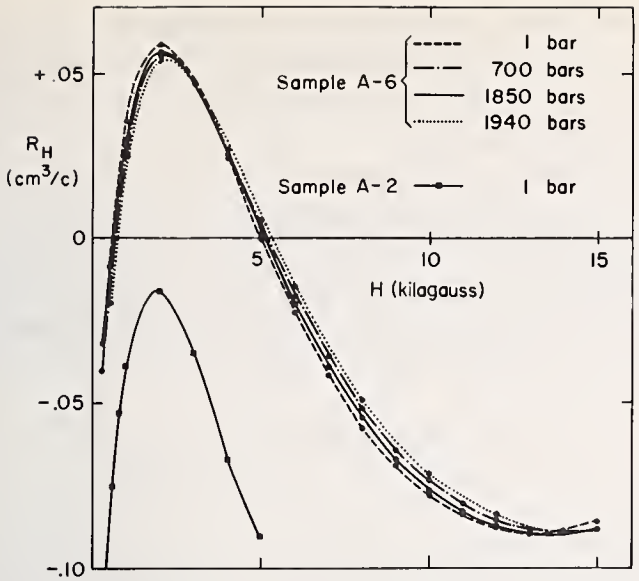

FIGURE 7. *The effect of pressure on the Hall Constant of sample A-6 at 77.5 K.*

ty electrons ($a \sim 0.99$). The effect of pressure is to move the curves to more negative values ($dR_H/dp \sim -.001$ cm³/C.kbar)—a smaller effect than at room temperature, and in the opposite direction.

The curve for specimen A-6 is shown in figures 7 and 8. Several different features are observed. Firstly, the maximum in the room pressure curve occurs at a positive value of the Hall Constant ($\sim +0.050$ cm³/c) indicating a smaller value for the ratio $b = \mu_1/\mu_2$ ($b \sim 0.91$ for A-6; $b \sim 1.00$ for A-2). Secondly, a minimum in the Hall curve at approximately 13 kG($R_H \sim -0.084$ cm³/c) can be seen—a feature not previously reported in the literature. The cause of the minimum is not known at present. This feature invalidates the simple three band model, and awaits detailed interpretation until measurements at high field are made. Thirdly, the Hall Constant does not change in a simple way with pressure, decreasing below about 3 kG and increasing between ~ 3kG—15kG.

For both specimens the small changes in Hall Constant and magneto-resistance coefficient (fig. 9) are to be noted, and were too small to effectively determine whether the pressure variation was linear or not.

The number of carriers calculated for this temperature is $(4.7 \pm 0.25) \times 10^{18}$ for A-2; $(4.45 \pm 0.25) \times 10^{18}$ for A-6. This compares with a value $n = 4.2 \times 10^{18}$ based on the four-parameter band model.

7. Galvanomagnetic Data and the Assignment of Holes at the Point K in the Brillouin Zone of Graphite

For the interpretation of any electronic property of graphite, the carrier assignment at point K is of the ut-

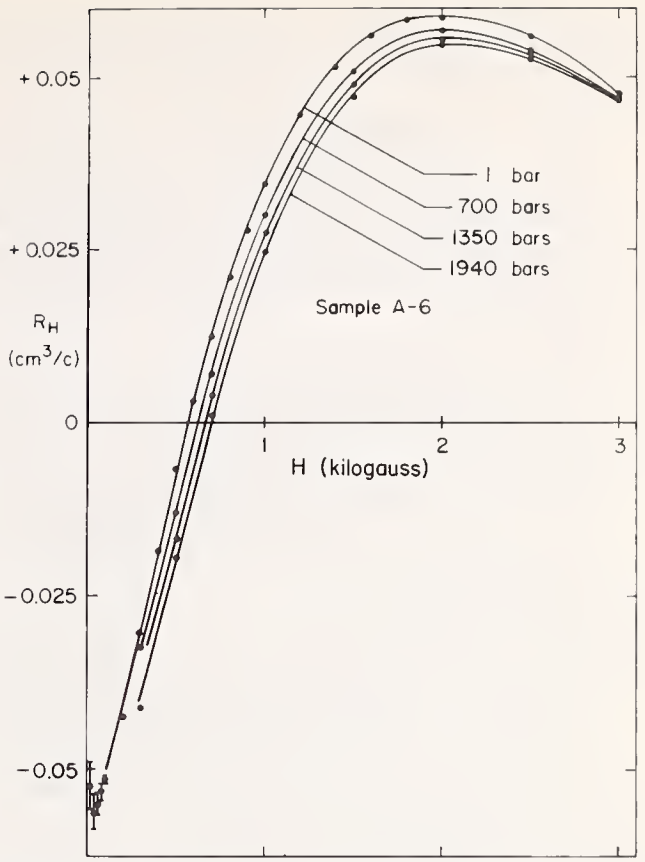

FIGURE 8. *The effect of pressure on the Hall Constant of sample A-6 at 77.5 K for low values of magnetic field only* (0–3 kG).

most importance. From galvanomagnetic data it is concluded that electrons are located at point K, in agree-

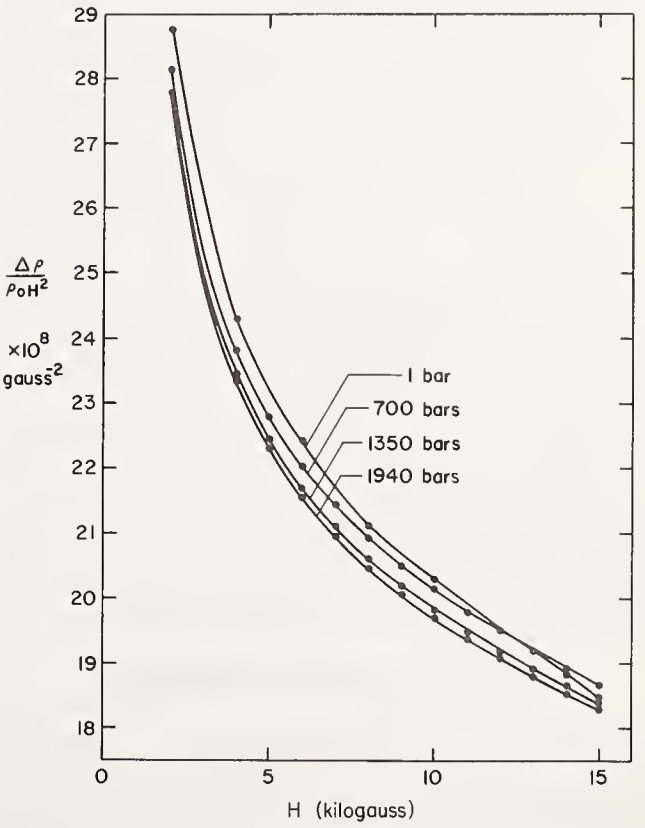

FIGURE 9. *The effect of pressure on the magnetoresistance coeffi-* ($\Delta\rho/\rho_0 H^2$) *for sample A-6 at 77.5 K.*

ment with the assignment of Schroeder et al. [9]. The strongest reasons for this are as follows:

(1) For the most perfect specimens, the ratio $b = \mu_1/\mu_2$ is less than unity for the temperature range ~ 50 to 200 K. Since the electrons are predominantly scattered by phonons in this temperature range, this fact is explained only by a heavier effective mass for electrons than holes.

(2) At a given temperature in the temperature range below about 150 K, increase of specimen perfection decreases the ratio b. For poorer specimens, boundary scattering is increased. If the average hole velocity is greater than that of electrons, then the observed behavior can be explained (see fig. 1c).

(3) As the temperature is reduced below about 50 K, the ratio b is observed to increase. This is consistent with an increase in the importance of boundary scattering as the phonon-electron scattering probability decreases, and is consistent with the new assignment.

Above about 200 K, the observed rise in the ratio b above unity for even the best specimens can be attributed to the following effects:

(1) A shift in the value of the mean chemical potential to more negative values (see fig. 1a) as the temperature is raised.

(2) Effects arising from the excitation of carriers to levels within about 2kT of the mean chemical potential, thereby averaging the properties of electrons and holes.

(3) The increased importance of intervalley scattering which acts to average the properties of the carriers.

(4) The change in overlap parameters arising from thermal expansion of the crystal.

This last effect may be estimated from the galvanomagnetic data reported here. A pressure of about 2kbar reduces the c-axis spacing by approximately the same amount that a 100 K change in temperature increases the spacing. Since the pressure coefficient of the Hall Effect is ~ 0.0025 cm^3/C.kbar, a temperature change from 200-300 K probably increases the ratio b by about 4%, through the expansion of the lattice only.

8. Minority Carrier Behaviour

With the new assignment of electrons at point K, and with a positive value of Δ demanded by de Haas-van Alphen measurements [21], the pocket of minority carriers at points H and H' can only contain holes. The Hall Constant at low fields for synthetic materials clearly indicates the presence of a mobile minority electron, since the sign of the contribution to the tensor component σ_{xy} is only determined by the sign of the charge of the carrier.

The de Haas-van Alphen period $\Delta(^1/H) = 2.24 \times 10^{-4}$ gauss^{-1} observed by Williamson et al. [21] corresponded to an extremal cross sectional area of minority carriers in the basal plane (S) equal to 4.25×10^{11} cm^{-2}. This compares with the value predicted by the Słonczewski Weiss model [3]:

$$S = \frac{3\pi\epsilon_F(\epsilon_F - \Delta)}{4a_0^2\gamma_0^2} = 2.16 \times 10^{11} \text{ cm}^{-2}$$

with parameters defined before.

A period anisotropy of only 1.9 in synthetic material corresponds to a spheroidal Fermi surface of the same axial ratio containing 3.2×10^{15} available electronic states per cm^3 of material. For the specimens used in the present measurements, the minority carrier density is ten times greater than this ($\sim 3 \times 10^{16}$ cm^{-3}). This points to the conclusion that the minority carriers observed in the de Haas-van Alphen effect (not identified as holes or electrons by this measurement) do not originate from the same volume of the Brillouin zone as the minority electrons observed in the Hall Effect.

An attempt was made to observe minority hold behavior in the Hall Effect. Assuming that the minority holes are more mobile than the observed minority electrons, an upward trend in the Hall Constant should be seen at very low magnetic fields. Data was obtained down to 10 gauss (fig. 8) where some indication was obtained for this effect. However, the Hall voltage was extremely small at this field (0.12μv) and even with repeated measurements and data averaging, the best that can be said at the moment is that the possibility of such minority hole behavior is not ruled out. Shortly, measurements will be made utilizing a two frequency Hall technique with a PAR Lock-In-Amplifier. With this system measurements can be made in principle to 0.1 gauss.

Another indication that the minority electrons do not originate from the corners of the Brillouin zone is given by the effect of pressure on the Hall Constant at low magnetic field values (fig. 8). Application of pressure does not distort the curves, but only moves them downwards. This implies that the number of minority carriers and their mean mobility does not change with pressure within the precision of the measurement. However, measurements by Anderson et al. [5] on the change of de Haas-van Alphen periods for minority electrons at point H indicate that the parameter Δ,

which largely controls the properties of these carriers, changes by approximately 9%/kbar.

The mobile minority electrons could originate in the feet of the energy surfaces, connecting electron-like with hole-like surfaces. Dresselhaus [22] has suggested that if the trigonal warping is large enough, arising from a value of $\gamma_3 \sim 0.3$ eV, outrigger electron surfaces may be formed there. Such electrons might have relatively low values of the effective mass, and have properties relatively independent of pressure.

9. Conclusions

Measurements of the Hall Effect and magnetoresonance are reported for two synthetic specimens of graphite at 298 and 77.5 K at hydrostatic pressures up to 3 kbar. The data supports the assignment of electrons at point K in the Brillouin zone of graphite as suggested by magneto-reflection experiments of Schroeder et al. [9]. Minority electron behavior observed in the Hall Effect at low fields at 77.5 K cannot be accounted for using the "four-parameter band model." When a calculation is made for the dispersion relation of electrons at points near the zone edges with $\gamma_3 \sim 0.3$ eV it is possible that pockets of electrons near the "feet" of the energy surfaces (outrigger pieces) may account for the observed properties. The number of carriers calculated from the four-parameter band model agrees quite well with the number obtained from the experiments.

10. Acknowledgments

The author wishes to thank the United States Atomic Energy Commission for a grant supporting this work, also, Dr. A. W. Moore of Union Carbide Corporation and Dr. C. Roscoe of Pennsylvania State University for supplying the graphite used in this work. Thanks are also due for technical and secretarial assistance in the Institute for Molecular Physics and to Mr. Raymond Crafton III for helping with numerical calculations.

11. References

[1] McClure, J. W., Phys. Rev. **108**, 612 (1957).
[2] Vereschagin, L. F., and Kabalkina, S. S., DAN SSR **131**, 300 (1960). English translation Doklady **5**, 373 (1960).
[3] Slonczewski, J. C., and Weiss, P. R., Phys. Rev. **109**, 272 (1958).
[4] Itskevich, F. S., and Fischer, L. M., JETP **5**, 141 (1967). English translation JETP Letters **5**, 114 (1967).
[5] Anderson, J. R., O'Sullivan, W. J., and Schirber, J. E., Phys. Rev. **164**, 1038 (1967).
[6] Arkhipov, R. G., Kechin, V. V., Likhter, A. I., and Pospelov, Yu. A., JETP **44**, 1964 (1963). English translation JETP **17**, 1321 (1964).
[7] Likhter, A. I., Kechin, V. V., Fizika Tverdoga Tela. **5**, 3066 (1963). English translation in Soviet Physics Solid State **5**, 2246 (1964).
[8] Kechin, V. V., Likhter, A. I., and Stepanov, G. N., Fizika Tverdoga Tela. **10**, 1242 (1968). English translation in Soviet Physics Solid State **10**, 987 (1968).
[9] Schroeder, P. R., Dresselhaus, M. S., and Javan, A., Phys. Rev. Letters **20**, 1292 (1968).
[10] Spain, I. L., reported at the Ninth Biennial Conference on Carbon, Boston (1969) to be submitted to J. Chem. Phys.
[11] Dresselhaus, M. S., and Mavroides, J. G., Carbon **3**, 465 (1966).
[12] Dresselhaus, G. and Dresselhaus, M. S., Phys. Rev. **140**, A401 (1965).
[13] Dresselhaus, M. S., reported at the Ninth Biennial Conference on Carbon, Boston (1969).
[14] Soule, D. E., Phys. Rev. **112**, 698 (1958).
[15] Blochinzev, D., and Nordheim, L., Z. Physik **84**, 168 (1933).
[16] Shibuya, M., Phys. Rev. **95**, 1385 (1954).
[17] Spain, I. L., Ubbelohde, A. R., and Young, D. A., Phil. Trans. Roy. Soc. **262**, 345 (1967).
[18] Radcliffe, J. M., Proc. Phys. Soc. **A68**, 675 (1955) see also F. J. Blatt "Theory of Mobility of Electrons in Solids," Solid State Physics, **Vol. 4**, F. Seitz and D. Turnbull, editors.
[19] Spain, I. L., Ph. D. Thesis, London University (1964).
[20] Yeoman, H. L., and Young, D. A., reported at the Ninth Biennial Conference on Carbon, Boston (1969).
[21] Williamson, S. J., Foner, S., and Dresselhaus, M. S., Phys. Rev. **140**, A1429 (1965) and Carbon **4**, 29 (1966).
[22] Dresselhaus, M. S., private communication, September (1969).

Electrical Resistivity as a Function of Hydrogen Concentration in a Series of Palladium-Gold Alloys

A. J. Maeland

Department of Chemistry, Worcester Polytechnic Institute, Worcester, Massachusetts 01609

The changes occurring in the electrical resistance of a series of gold-palladium alloys during hydrogen absorption have been measured. The results are presented for each alloy in the form of relative resistance, R/R_0 vs. hydrogen concentration H/M; R is the resistance of a particular gold-palladium alloy containing a certain amount of hydrogen, given by H/M, the atomic ratio of hydrogen to metal, and R_0 is the resistance of the same *hydrogen free* alloy. For pure palladium the relative resistance increases as a function of hydrogen concentration to a maximum value of ~ 1.80 at $H/M = 0.75$; further hydrogen absorption results in a decrease in R/R_0. Similar maxima are found in some gold-palladium alloys; however, the maxima occurs at decreasing R/R_0 values and also shifts to lower H/M values with increasing gold concentrations. At sufficiently high gold contents the maximum disappears and a continuous decrease in resistance with increasing hydrogen content occurs. The results are evaluated in terms of the band model.

Key words: Electron donation model; electronic density of states; gold-palladium alloys; hydrogen absorption; hydrogen in palladium-gold alloys; palladium-gold alloys; rigid-band approximation.

1. Introduction

The earliest application of the band theory of solids to a process of chemical interest [1] appears to be that of Mott and Jones [2] who proposed the electron donation model for hydrogen absorption by pure palladium. According to this model, hydrogen is considered to be absorbed as protons plus electrons. The electron from hydrogen is assumed to be donated primarily to the partially empty d band of palladium. The protons enter interstitial sites in the palladium lattice where d-band electrons pile up to screen them. Subsequent work has shown these sites to be the octahedral interstices in the face-centered cubic palladium lattice [3]. The behavior of the magnetic susceptibility of H-Pd alloys [4] is usually cited, perhaps unjustifiably so, as strong evidence in favor of a simple rigid-band model which indicates that pure palladium has roughly 0.6 holes per atom in the d band. However, recent work [5] on the band structure seems to point to a much smaller number, namely 0.36. Thus the rigid-band approximation appears to be invalid. The electron donation model, however, is not invalidated by these results. It has, in fact, been substantially strengthened by some very recent low-temperature electronic heat capacity measurements on the hydrogen-palladium system by Mackleit and Schindler [6] who obtained direct evidence that the density of states in the d band of palladium decreases with hydrogen absorption.

The utility of the electron donation model may be tested by applying it to alloys of palladium. Gold-palladium alloys are of particular interest in this respect because gold is believed to donate a 6s electron to the d band of palladium. Thus in the gold-palladium-hydrogen system both hydrogen and gold act as electron donors to the d band of palladium. We have previously reported x-ray and thermodynamic results on the gold-palladium-hydrogen system [7]. The data, we feel, was successfully interpreted in terms of this model, thus contributing further evidence in its favor. In the present experiments we have measured the electrical resistivity of a number of gold-palladium alloys as a function of hydrogen concentration. The results may be rationalized in terms of the electron donation model referred to above.

2. Experimental

The gold-palladium specimens were in the form of wires 0.012 and 0.025 cm in diameter and were supplied

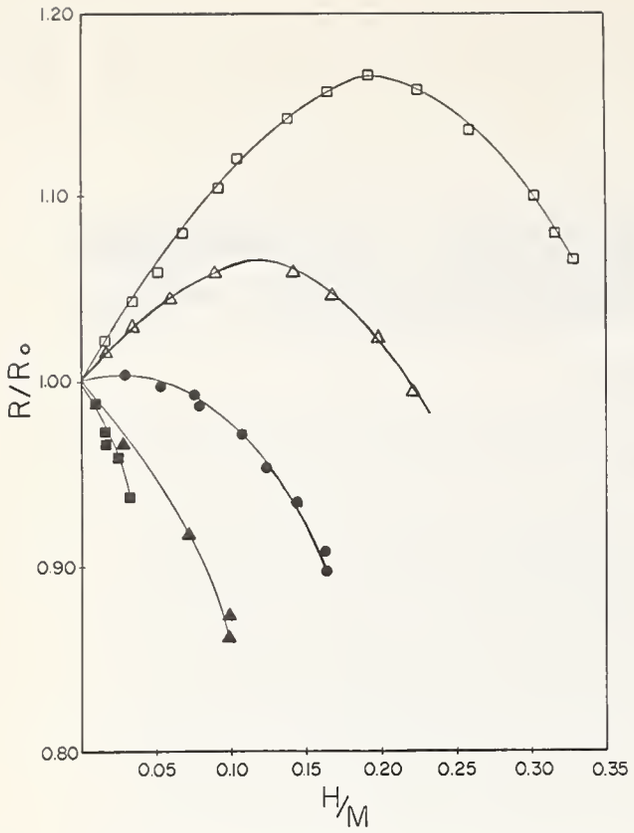

FIGURE 1. *Relationship between relative resistance and hydrogen content.*

□, 18.80 percent Au; △, 26.47 percent Au; ●, 35.07 percent Au; ▲, 44.76 percent Au; ■, 55.76 percent Au.

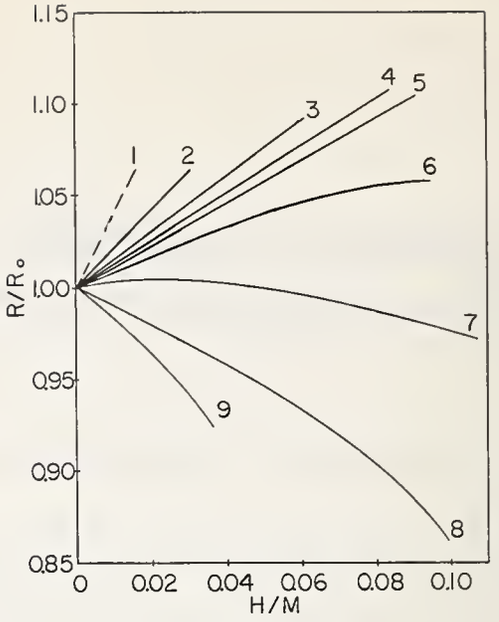

FIGURE 2. *Relationship between relative resistance and hydrogen content in the α-phase.*

1, Pure Pd; 2, 5.66 percent Au; 3, 11.90 percent Au; 4, 15.26 percent Au; 5, 18.80 percent Au; 6, 26.48 percent Au; 7, 35.07 percent Au; 8, 44.76 percent Au; 9, 55.77 percent Au.

by Engelhard Industries, Inc., who also performed the analysis. The samples had been prepared from 99.99% purity gold and palladium melted under argon. X-ray powder patterns revealed that the alloys were face-centered cubic and showed no evidence of long-range order. Hydrogen was introduced by direct absorption from hydrogen-stirred dilute HCl solutions (< 0.04 N) under slow absorption conditions; i.e., the hydrogen pressure was reduced to below 1 atm. by dilution with helium. Details of the technique as well as the sample holder are available in the literature [7,8]. The resistance was determined potentiometrically; the voltage across the specimen was matched with that across a standard resistor. All measurements were made at 25.0 ± 0.1 °C. Hydrogen contents were established by vacuum degassing in a calibrated volume apparatus. The procedure was to remove the specimen from the reaction vessel after charging it to a certain hydrogen concentration and submerging it in cold acetone containing sulfur (catalytic poison). The sample holder was then attached to the vacuum line which was subsequently evacuated. Degassing the sample was accomplished by passing a current directly through the specimen until it reached a dull red color. This heating was sufficient to remove all of the hydrogen from the specimens. Any loss of hydrogen occurring between the time of measuring the resistance and the time of degassing was shown to be minimal [9]. The two sizes of wires used gave essentially identical results indicating again no hydrogen loss during the transfer and evacuating stage. Any such loss would have affected the smaller diameter specimens proportionally more than the larger because hydrogen loss would be proportional to the surface/volume ratio.

3. Results and Discussion

The relative resistance, R/R_0, as a function of hydrogen content, H/M, was determined for a number of gold-palladium alloys. Some of the results are shown in figure 1; here only those gold-palladium-hydrogen alloys which exhibit one phase behavior of 25 °C are included; i.e., alloys having more than 17 atomic percent gold [7a]. Alloys having less than 17 atomic percent gold behave like the palladium-hydrogen system in the sense of having a two phase region at room temperature [7a]. The two phases are commonly referred to as α-phase (hydrogen poor) and β-phase (hydrogen rich). Figure 2 shows in detail the changes in resistance occurring at low hydrogen contents: here we have included some alloys which do have a two phase region (curves 1-4). As in the palladium-hydrogen system there is a discontinuous change in the slope, $d(R/R_0)/d(H/M)$, at the point where the second phase begins to form (not shown in fig. 2). The change in slope may, in fact, be used to determine the phase boundary [7a].

It may be noted that some of the curves in figure 1 show maxima in R/R_0 vs. H/M. A maximum has also been observed in the Pd-H system: this maximum occurs at $R/R_0 \sim 1.80$ and H/Pd $\simeq 0.75$ [10]. The maxima move toward lower values of R/R_0 and H/M with increasing gold content. At sufficiently high gold concentration the maximum disappears and a continuous decrease in resistance with increasing hydrogen content occurs (e.g., the 44.76% Au alloy).

A qualitative rationalization based on electron donation to the partially filled d band of palladium may be made as follows: The electrical resistance in transition metals is believed to be mainly due to scattering processes in which the electron makes a transition from the s to the d band; the current is carried by s electrons. The probability of an s-d transition is proportional to the density of states in the d band; the density of states is in turn proportional to the cube root of the number holes in the d band. Therefore the resistance, R, may be written [2]

$$R\alpha \frac{n_d^{1/3}}{n_s} \tag{1}$$

where n_d stands for the number of holes in the d band and n_s denotes the number of s electrons.

On one hand the introduction of hydrogen into the palladium lattice destroys the periodicity of the potential field of the lattice and leads to an increase in the resistance. Furthermore, the lattice expands causing additional increase in resistance [11] ($d \ln R/d \ln V = 4.0$ at room temperature for pure Pd). On the other hand, hydrogen reduces the s-d scattering if its electron enters the d band of palladium, thereby decreasing the number of holes in the band. This leads to a decrease in the resistance which can be estimated from (1).

$$\frac{dR}{dn_d} \alpha -\frac{1}{3n_s}\left(\frac{1}{n_d^{2/3}}\right) \tag{2}$$

We have assumed here than n_s is constant. This is approximately true since the density of states of the d band in pure palladium is about 10 times that of the s band. Consequently the electrons from hydrogen enter primarily the d band without increasing the number of s electrons appreciably. The first two effects initially dominate the resistance behavior as hydrogen is absorbed. However, as the d band gradually fills, the s-d scattering becomes less probable and the resistance begins to decrease. Furthermore, as the d band fills, its density of states in relation to the density of states of the s band decreases and the electrons begin to enter the s band, resulting in further decrease of the resistance.

The decrease in slope of R/R_0 vs. H/M, figure 2, with increasing gold content may be explained similarly. The addition of gold also decreases the number of holes in the d band of palladium. From eq (2) it can be seen that dR/dn_d decreases more as n_d becomes less (by addition of gold, e.g.). If the two other effects, i.e., the increase in resistance due to alteration of the periodicity of the lattice and volume increase, are assumed to be essentially independent of gold content, then the net effect should be a smaller increase in R/R_0 vs. H/M with increasing gold content. Also when a substantial portion of the d band holes in Pd has been filled by the addition of Au, dR/dn_d becomes large enough to dominate the resistance behavior. In addition relatively more electrons enter the s band providing more conduction electrons. As a result, when enough gold has been added, the addition of hydrogen causes a decrease in the resistance.

4. Acknowledgments

Financial support by U.S. Atomic Energy Commission is gratefully acknowledged. We wish to thank the Engelhard Industries Inc., for the gold-palladium alloys used in this work.

5. References

[1] Flanagan, T. B., Techn. Bull. Engelhard Ind. Inc. **7**, 9 (1966).
[2] Mott, N. F., and Jones, H., The Theory of Metals and Alloys, (Oxford Univ. Press, Oxford, 1936).
[3] Worsham, J. E., Jr., Wilkinson, M. K., and Schull, C. G., J. Phys. Chem. Solids **3**, 303 (1957); Maeland, A. J., Can. J. Phys. **46**, 121 (1968).
[4] Svensson, B., Ann. Physik **18**, 299 (1933); Biggs, H. F., Phil. Mag. **32**, 131 (1916).
[5] Vuillemin, J. J., and Priestly, M. G., Phys. Rev. Letters **14**, 307 (1965); Kimura, H., Katsuki, A., and Shimizu, M., J. Phys. Soc. (Japan) **21**, 307 (1966).
[6] Mackleit, C. A., and Schindler, A. J., Phys. Rev. **146**, A463 (1966).
[7] (a) Maeland, A. J., and Flanagan, T. B., J. Phys. Chem., **69**, 3575 (1965); (b) Allard, K., Maeland, A. J., Simons, J. W., and Flanagan, T. B., ibid., **72**, 136 (1968).
[8] Simons, J. W., and Flanagan, T. B., ibid., **69**, 3581 (1965).
[9] Simons, J. W., and Flanagan, T. B., J. Chem. Phys. **44**, 3486 (1966).
[10] Barton, J. C., and Lewis, F. A., Z. Physik. Chem., Nem Folge **33**, 99 (1962).
[11] Bridgmann, P. W., Proc. Acad. Sci. **79**, 125 (1951).

The Volume Dependence of the Electronic Density of States in Superconductors

R. I. Boughton,* J. L. Olsen, and C. Palmy

Laboratorium für Festokörperphysik, Swiss Federal Institute of Technology, Zürich, Switzerland

The volume dependence of the electronic specific heat coefficient γ can be obtained from measurements of the low temperature thermal expansion, from observations on the pressure dependence of the superconducting threshold curve, and from the volume change occurring at transition. We make use of recent theoretical results to obtain values of the change in the density of states with volume from the existing experimental data for a number of metals.

Key words: Aluminum (Al); electronic density of states; electronic specific heat; gallium; Gruneisen parameter, electronic; superconductivity; thermal expansion; thorium; volume dependence of density-of-states.

1. Introduction

The volume dependence of the electronic specific heat γ is of interest since it is a function of the volume dependence of the electronic density of states, and of the electron-phonon interaction and its volume dependence. It is a quantity that is difficult to measure directly, but a number of simple thermodynamic relationships exist which allow it to be determined indirectly by several methods. The logarithmic volume derivative of γ, commonly referred to as the electronic Gruneisen parameter Γ_e, can be obtained from the electronic thermal expansion coefficient, from a knowledge of the change of the superconducting critical field curve under pressure, and from measurements of the difference in volume between the normal and superconducting states.

It is the purpose of the present note to present data from measurements of the critical fields of aluminum, gallium, and thorium under pressure and to make a brief summary of available results on other superconductors.

2. Thermodynamic Expressions

The relations connecting the measured properties with the electronic Gruneisen parameter Γ_e in the three methods referred to above are the following:

Γ_e is related [1] to the electronic volume expansion β_e by

$$\Gamma_e = \frac{V}{\kappa\gamma T}\beta_e \tag{1}$$

where T is the absolute temperature, and κ is the isothermal compressibility. Due to the fact that this type of experiment is easily carried out only at zero pressure, it can only give the inital slope in the dependence of γ on volume. The second method, which is applicable only to superconductors, involves the measurement of the superconducting threshold curve as a function of pressure. In general, the threshold relation for any superconductor can be written

$$H_c = H_0 f(t) \tag{2}$$

where H_o is the critical field at 0 K; $t = T/T_c$ is the reduced temperature; and, $f(t)$ is the normalized threshold function. The electronic specific heat coefficient is related to the threshold parameters by the well-known relation [2]

$$\gamma = \frac{-V}{4\pi}\frac{H_0^2}{T_c^2} f''(0) \tag{3}$$

where $f''(0)$ is the second derivative of the threshold function at 0 K. Here, $\gamma(V)$ is determined directly from measurements of H_o and T_c as functions of the volume. The threshold function, $f(t)$, is usually assumed to be independent of pressure (the similarity principle) and most of the existing experimental evidence indicates that this is indeed so [3,4].

*Present address: Northeastern University, Department of Physics, Boston, Massachusetts 02115.

Finally, we arrive at the third method which involves the measurement of the change in volume at the normal-to-superconducting transition as a function of temperature. This quantity is related [5] to the derivative of the critical field with respect to pressure by the following equation

$$\frac{\Delta V}{V}=\frac{V_n-V_s}{V_s}=\frac{H_c}{4\pi}\left(\frac{\partial H_c}{\partial p}\right)_T. \tag{4}$$

The derivatives of H_c at $T=0$ K and $T=T_c$ can be related to Γ_e by making use of (2) and (3), and by assuming $f(t)$ to be unaffected by pressure. We find.[6]

$$\Gamma_e=\frac{-2}{\kappa H_0}\left\{\frac{1}{f'(1)}\left(\frac{\partial H_c}{\partial p}\right)_{T_c}+\frac{dH_0}{dp}\right\}+1 \tag{5}$$

where $f'(1)$ is the slope of the threshold function at $T=T_c$. The experimental techniques required to make such measurements are quite similar to those used in measuring thermal expansion, and unfortunately suffer from the same limitation, namely that only a zero pressure value of Γ_e can be obtained.

3. Theory

In order to relate the electronic specific heat coefficient to the band-structure density of states, it is necessary to include the effect of electron-phonon enhancement [7,8] to give

$$\gamma=\tfrac{1}{3}\pi^2 k_B^2 N(0)\,(1+\lambda) \tag{6}$$

where $\lambda=N(0)\ V_{ep}$, and V_{ep} is the electron-phonon interaction. From this expression it follows that the band-structure Gruneisen parameter Γ_N is given by

$$\Gamma_N\equiv\frac{\partial \ln N(0)}{\partial \ln V}=\Gamma_e-\frac{\lambda}{(1+\lambda)}\cdot\frac{\partial \ln \lambda}{\partial \ln V}. \tag{7}$$

The second term on the right-hand side is thus seen to have an influence which tends to reduce the total value of Γ_N below the observed Γ_e if $\partial \ln \lambda/\partial \ln V$ is a positive quantity as it usually is.

Several authors [9-13] have obtained expressions for λ which differ from each other somewhat. It has been demonstrated elsewhere [14] that by using an expression due to Baryakhtar and Makarov [12], a reasonably good fit to the existing data on the volume dependence of T_c is obtained for several elements. On this basis, the following expression results

$$\frac{\partial \ln \lambda}{\partial \ln V}=\left(2\Gamma_G-\Gamma_N-\frac{2}{3}\right)=(1+\lambda)\left(2\Gamma_G-\Gamma_e-\frac{2}{3}\right) \tag{8}$$

where Γ_G is the lattice Gruneisen parameter. Twice Γ_G is usually larger than $(\Gamma_e+2/3)$, and therefore λ is in general a decreasing function of pressure.

Substitution of (8) into (7) yields

$$\Gamma_N=\Gamma_e(1+\lambda)-\lambda(2\Gamma_G-\tfrac{2}{3}). \tag{9}$$

Although no theoretical calculations have yet been made to determine Γ_N for any real metals except copper, the nearly-free-electron (nfe) model predicts a value of 2/3 for an isotropic metal [15]. This is simply the result of the fact that in this approximation the Fermi surface scales with the reciprocal lattice as the volume is changed. Such a result would, of course, be most likely in the case of a cubic metal like aluminum under hydrostatic pressure. However, for an anisotropic material, an applied hydrostatic pressure gives rise to a nonuniform strain field and may change the band structure considerably, even in the nfe model. It is therefore reasonable to assume that somewhat different values of Γ_N will result from measurements on anisotropic metals. It should also be pointed out that measurements on anisotropic materials using uniaxial stress or change in length at transition should give a more detailed idea of how the band structure is affected.

4. Results

Experiments on the change in the superconducting threshold curves under pressure for aluminum, gallium, and thorium have been carried out and the results are presented in figure 1, where γ, as determined from (3), is plotted against the reduced volume, using published values of the volume dependence of the compressibility at room temperature [16]. It is apparent that within the present range of experimental accuracy

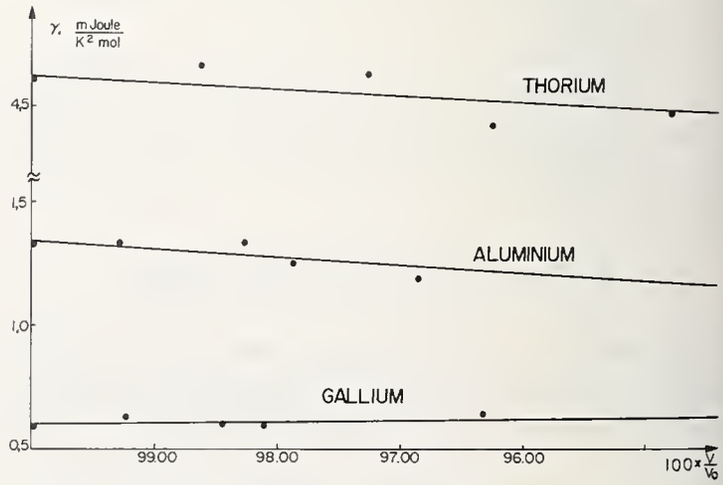

FIGURE 1. *Electronic specific heat as a function of relative change in volume for gallium, aluminum, and thorium.*

TABLE 1. *Experimental values of Γ_e at zero pressure and calculated values of Γ_N*

Element	Method*	$\Gamma_e(p=0)$	$\lambda_0 q$	$\Gamma_G p$	$\Gamma_N(p=0)$	Ref.
Al	Te	1.8 ± 0.1	0.38	2.18	1.1	(a)
	PE	1.9 ± 0.7			1.2	(b)
Cd	TE	0.7 ± 1.5	.38	2.30	-0.5	(c)
	PE	5.4 ± 2			6.0	(d)
Ga	PE	-0.8 ± 1	.40	1.45	-1.4	(b)
Hg α	PE	7.3 ± 0.3	1.0	3.00	9.3	(e)
	VC	10.2 ± 2			15.1	(f)
In	TE	3.2 ± 0.4	0.69	2.48	2.4	(g)
	PE	3.4 ± 0.1			2.8	(r)
	VC	1.0 ± 0.2			-1.3	(f)
Ir	TE	2.7 ± 0.3	.34	2.49	2.2	(h)
La	TE	-2.0 ± 0.2	.84	0.74	-4.4	(i)
	VC	-3.4 ± 1.0			-6.9	(f)
Mo	TE	1.6 ± 0.3	.41	1.65	1.2	(c)
Nb	TE	1.5 ± 0.2	.82	1.74	0.4	(a)
Pb	TE	1.7 ± 0.5	1.12	2.84	-2.0	(a)
	PE	6.0 ± 0.9			7.1	(j)
	VC	1.8 ± 0.4			-1.8	(f)
Re	TE	4.5 ± 0.5	0.46	2.66	4.4	(c)
Sn	TE	≈ 1.0	.60	2.27	-0.7	(k)
	PE	2.0 ± 0.3			0.9	(e)
	US	1.7 ± 0.3			0.4	(o)
Ta	TE	1.3 ± 0.1	.65	1.82	0.2	(a)
	PE	4.0 ± 0.5			4.7	(l)
Th	PE	0.6 ± 1	.53	1.41	-0.2	(b)
Ti	TE	≈ 2.0	.38	1.33	2.0	(m)
Tl	PE	-4.0 ± 1	.71	2.3	-9.6	(n)
V	TE	1.7 ± 0.1	.60	1.55	1.2	(a)
	VC	-0.8 ± 0.6			-2.7	(f)
Zn	PE	4.7 ± 2	.38	2.1	5.2	(d)
Zr	TE	0.0 ± 0.2	.41	0.82	0.4	(m)

*TE—Thermal expansion; PE—Pressure effect; VC—Volume change; US—Uniaxial stress.

[a] J. G. Collins and G. K. White, *Progress in Low Temp. Physics*, Vol. IV, Ed. C. J. Gorter (North Holland Publ. Co., Amsterdam, 1964).

[b] Present work.

[c] K. Andres, Phys. kondens. Mat. **2**, 294 (1964).

[d] I. V. Berman, N. B. Brandt and N. I. Ginzburg, Zh. Eksp. i Teor. Fiz. **53**, 124 (1967); Sov. Phys. JETP **26**, 86 (1968).

[e] J. E. Schirber and C. A. Swenson, Phys. Rev. **123**, 1115 (1961).

[f] H. Rohrer, Helv. Phys. Acta **33**, 675 (1960).

[g] J. G. Collins, J. A. Cowan and G. K. White, Cryogenics **7**, 219 (1967).

[h] E. Fawcett and G. K. White, Jour. Appl. Phys. **39**, 576 (1968).

[i] K. Andres, Phys. Rev. **168**, 708 (1968).

[j] M. Garfinkel and D. E. Mapother, Phys. Rev. **122**, 459 (1961).

[k] G. K. White, Phys. Letters **8**, 294 (1964).

[l] C. H. Hinrichs and C. A. Swenson, Phys. Rev. **123**, 1106 (1961).

[m] J. A. Cowan, A. T. Pawlowics and G. K. White, Cryogenics **8**, 155 (1968).

[n] M. D. Fiske, J. Phys. Chem. Solids **2**, 191 (1958).

[o] C. Grenier, Compt. Rend. **241**, 862 (1955).

[p] See Ref. 16.

[q] See Ref. 6.

[r] G. Dummer and D. E. Mapother, Proc. N.B.S. Electronic Density of States Symposium, Nov. 3–6, 1969.

no definite conclusions as to the detailed behavior of γ as a function of volume can be made, other than that the slope appears to be positive (γ decreases with decreasing volume) for Al and Th while being nearly zero for Ga.

Earlier pressure effect data on Al yielded values of Γ_e several times as large as those obtained from thermal expansion data. The present results show that the two methods are capable of yielding consistent results.

For Th and Ga our measurements provide only an order of magnitude estimate of the magnitude of the effect.

In order to summarize the present situation in this field, we compare the existing data for a number of elements in table 1. As is evident from the table, there appear to be rather large discrepancies between the superconducting and thermal expansion results for Γ_e. At present, this lack of agreement is still unexplained and will certainly require further experimental work to be resolved. The most reliable results appear to be those obtained from thermal expansion measurements, because of the small errors reported in most cases. In particular, the Γ_N values for the nontransition elements are of the predicted order of magnitude and, for example, the experimental value of 1.1 for Al is not very far from the nfe model's prediction.

5. Conclusion

It is readily apparent that more accurate techniques for the measurement of the threshold parameters are necessary to determine the volume dependence of $N(0)$ with any accuracy. The present experiments only serve to give an order of magnitude estimate of the effect and therefore any detailed comparison with theory cannot be attempted. It should be realized, however, that theoretical information will be required on both the band-structure density of states and on the volume dependence of the electron-phonon coupling in order to completely resolve the question.

6. References

[1] Collins, J. G., and White, G. K., Progress in Low Temp. Physics. **Vol. IV**, C. J. Gorter, Editor (North Holland Publ. Co., Amsterdam, 1964).

[2] Lynton, E. A., Superconductivity, (Methuen, London, 1962), p. 19 for example.

[3] Berman, I. V., Brandt, N. V., and Ginzburg, N. I., Zh. Eksp. i Teor. Fiz. **53**, 124 (1967); Sov. Phys. JETP **26**, 86 (1968).

[4] Harris, E. P., and Mapother, D. E., Phys. Rev. **165**, 522 (1968).
[5] Shoenberg, D., Superconductivity, (Cambridge Univ. Press., London, 1952), p. 74.
[6] Boughton, R. I., Olsen, J. L., and Palmy, C., Progress in Low Temp. Physics, **Vol. VI**, C. J. Gorter, Editor, in press.
[7] Buckingham, M. J., and Schafroth, M. R., Proc. Phys. Soc. **67A**, 828 (1954).
[8] Migdal, A. B., Zh. Eksp. i Teor. Fiz. **34**, 1438 (1958); Sov. Phys. JETP **7**, 996 (1958).
[9] Ziman, J. M., Phys. Rev. Letters **8**, 272 (1962).
[10] McMillan, W. L., Phys. Rev. **167**, 331 (1968).
[11] Seiden, P. E., Phys. Rev. **179**, 458 (1969).
[12] Baryakhtar, V. G., and Makarov, V. I., Zh. Eksp. i Teor. Fiz. **49**, 1934 (1965); Sov. Phys. JETP **22**, 1320 (1966).
[13] Fröhlich, H., and Mitra, T. K., Proc. Phys. Soc. **1**, 544 (1968).
[14] Boughton, R. I., Brändli, G., Olsen, J. L., and Palmy, C., Helv. Phys. Acta **42**, 587 (1969).
[15] Harrison, W. A., Physics of Solids at High Pressures, C. T. Tomizuka and R. M. Emrick, Editors (Academic Press, New York, 1965), p. 3ff.
[16] Gschneidner, K. A., Solid State Physics, **Vol. 16**, F. Seitz and D. Turnbull, Editors (Academic Press, New York, 1964).
[17] Ziman, J. M., Principles of the Theory of Solids (Cambridge Univ. Press, London, 1964), p. 116.

Alloy Fermi Surface Topology Information from Superconductivity Measurements*

H. D. Kaehn and R. J. Higgins

Department of Physics, University of Oregon, Eugene, Oregon 97403

Key words: Electronic density of states; Fermi surface; In-Cd alloys; pressure; strain; superconductivity.

A great deal of progress has been made recently in calculating the energy band structure of random alloys [1]. In searching for an experimental test of these theories, we have found that the rapid variation with concentration of the pressure and strain derivatives of the superconducting transition temperature (dT_c/dp and $dT_c/d\epsilon$) observed [2,3] in the In-Cd alloy system has a direct connection with the alloy density of states $n(E)$ at the Fermi level E_F. These measured derivatives are proportional to the energy derivative of $n(E)$ at E_F, hence show strong structure near van Hove singularities where the Fermi surface (FS) topology changes. The amount of broadening of the singularities is a measure of the Bloch state lifetime, and the sign and shape of the observed structure is a direct indicator of the type of FS topology change.

The basic formalism for the dT_c/dp calculation and its application to In-Cd has been presented elsewhere [4]. We shall concentrate here on important corrections to that calculation which were found in the course of interpreting the $dT_c/d\epsilon$ data on whiskers which has recently been reported [3]. Since pressure and uniaxial stress are just special cases of a generalized stress, the analysis is similar. As in [4] we take into account the rapid variation in $n(E)$ near a singular point E_c by separating $n(E)$ into a rapidly varying part $\delta n(E_F - E_c)$ plus a monotonic background $n_0(E_F)$. It follows that the varying part of the derivative may be written:

$$\frac{dT_c}{dX} = \frac{T_c}{2n_0(E_F)} \frac{dF}{d\eta} \frac{d\eta}{dX} \qquad X = p, \epsilon$$

where η is $(E_F - E_c)/\Gamma$, Γ is h/τ, and $F(\eta)$ is $\delta n(E_F - E_c, \Gamma)$ convoluted with a broadening function of width kT_c. The calculated impurity dependence of dT_c/dp is shown in figure 1 compared with experiment assuming electron saddle point and pocket singularities in $n(E)$ near 0.8% and 1.9% Cd, respectively. These features are consistent with available information on the pure In FS. It is convenient to compare the calculated ratio of the derivatives at the peak values

$$\frac{dT_c}{dp} \Big/ \frac{dT_c}{d\epsilon} = R$$

with the experimental value of -2×10^{-4} (% ϵ)/(kg/cm^2). We find that by neglecting the derivatives of E_c, as in [4], the calculated value is an order of magnitude too large. We associate E_c with a feature of the

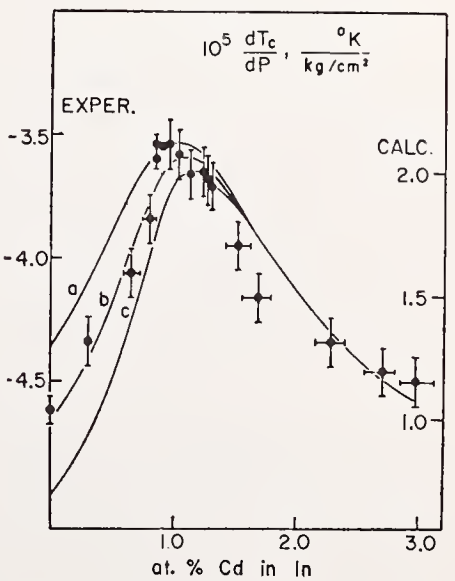

FIGURE 1. *Computed* dT_c/dp *for* In *doped with* Cd [4] *compared with experiment* [2].

*Research supported by the National Science Foundation. This is a portion of the Ph. D. thesis work of Mr. H. D. Kaehn, the full details of which will be published shortly elsewhere: H. D. Kaehn and R. J. Higgins (to be published).

third zone Fermi surface near the corners T of the Brillouin zone and write

$$E_c = E_T + E_{BS}$$

where E_{BS} is the band structure contribution to the free electron value of E_T for the bottom of the band near T. The calculation of R including the derivatives of E_T and E_{BS} leads to a value in good agreement with the experimental data. It is interesting to note, however, that the pressure derivative of E_T nearly cancels the pressure derivative of E_F so that the smaller term from E_{BS} is significant.

References

[1] e.g., Soven, P., Phys. Rev. **151**, 539 (1966).
[2] Makarov, V. I., and Volynskii, I. Ya., JETP Letters **4**, 249 (1966).
[3] Overcash, D. R., Skove, M. J., and Stillwell, E. P., Bull. Am. Phys. Soc. **14**, 129 (1969).
[4] Higgins, R. J., and Kaelin, H. D., Phys. Rev. **182** (1969).

Hydrogenation Effects on Palladium Tunnel Junctions

W. N. Grant, R. C. Barker, and A. Yelon

Yale University, New Haven, Connecticut 06520

The effects of hydrogenation on the electron tunneling characteristics of Al-oxide-Pd junctions have been investigated. It is found that the impedance of the junctions increases from 1 to 5 percent with increasing hydrogenation, with the greatest increase occurring at large positive bias on the Pd. We attribtue this effect to the introduction of electrons from hydrogen into the *d* bands of palladium.

Key words: Al-oxide-Pd; electronic density of states; hydrogen in palladium; rigid-band approximation; tunnel junctions.

1. Introduction

We have measured the tunneling characteristics of the Al-insulator-Pd junctions, ranging in zero-bias impedance from 50 to 12,000 ohms, at 4.2 and 120 K. The experiment was designed to investigate the effect of hydrogenation upon the level and shape of the differential impedance curves of the junctions.

Hydrogen dissolves in sizable quantities in palladium, and dissociates, leaving an increased number of electrons per Pd atom, plus interstitial protons [1,2,3]. Measurements with increasing hydrogen show a decrease in the specific heat [4], paramagnetic susceptibility [4], temperature dependent resistivity [5], and thermoelectric power [6]. All of these measurements, combined with de Haas-van Alphen experiments [7], galvanomagnetic experiments [8], and, more recently, band calculations [9] indicate that Pd has a closed electron Fermi surface, centered about the Γ point of the Brillouin zone, and two hole surfaces, one of which is open, and both of which are centered about the X point of the zone [7,9]. The Fermi level of Pd is near the top of the *d* band of the copper-like band structure, resulting in a rapidly varying density of states with sharp peaks in the vicinity of the Fermi surface. Hydrogenation of the Pd raises the Fermi level in the approximately rigid *d* band by filling some of the *d* states. This reduces the energy density of states at the Fermi surface, and moves the peaks with respect to it.

The tunneling current is given by a sum of the contributions from the portions of k-space falling within the bands in question. The energy density of states does not appear explicitly in these contributions. However, the departures from simple one-band spherical energy surfaces in k-space and the degeneracy of the bands, which account for the variations in the energy density of states, also determine the $E(k)$ relations in the integral and the limits of the integrals [10]. Thus, if any metal were to show any reflection of its electron structure in its tunneling behavior, Pd, with its rapidly varying density of states near the Fermi surface, might be expected to do so.

2. Experimental Results

Hydrogenation experiments have been performed with a large number of samples. On each substrate there are three similar junctions, 6.3×10^{-4} mm^2 in area, of Al-oxide-Pd, and a control junction with a counter electrode usually of Al, Pb, or Ag. The oxide is produced by glow discharge in dry oxygen, and all layers are formed before the evaporator is opened. Different junctions with the same counter electrode on the same substrate have zero-bias resistances typically within 20 percent of each other. However, their differential resistance curves normalized to the same zero-bias level are usually within 2 percent of each other over the range -0.5 to $+0.5$ volts. The resistance level for different junctions is determined by time in the glow discharge.

The maximum in the differential resistance of the Al-oxide-Pd junctions is shifted toward positive bias on the Pd, by about 100 mV. A similar shift occurs in junctions with control electrodes, and is characteristic of our method of oxidizing. It suggests a barrier height at the counter-electrode oxide interface about twice that at the Al-oxide interface [11].

417-156 O - 71 - 48

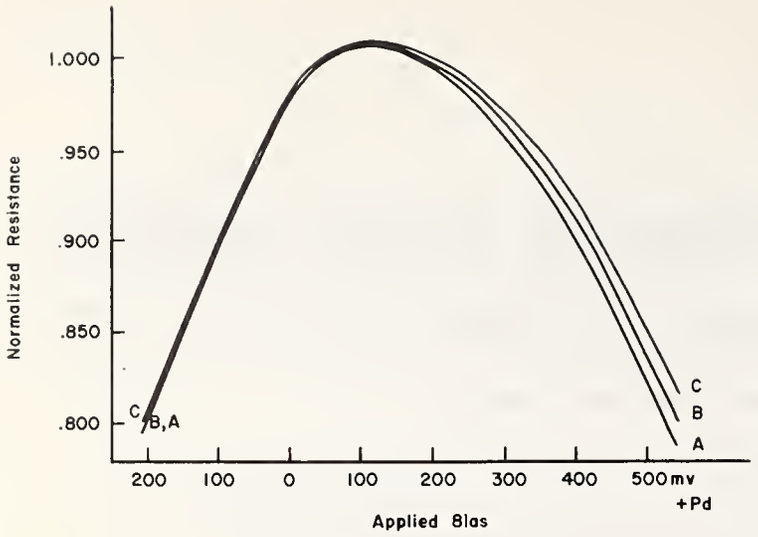

FIGURE 1. *Differential resistance versus voltage for an Al-oxide-Pd junction at 120 K for different levels of hydrogenation.*
A is the unhydrogenated sample. B and C have increasing levels of hydrogen.

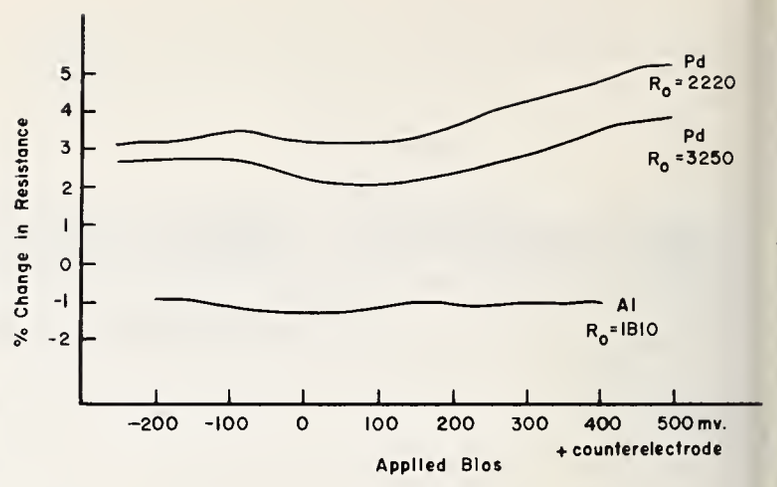

FIGURE 2. *Percent change in differential resistance versus voltage due to hydrogenation for* Al-*oxide*-Pd *and* Al-*oxide*-Al *junctions on the same substrate.*

An example of the effect of hydrogenation upon the differential resistance curves of Al-oxide-Pd junction is shown in figure 1. The junction was hydrogenated at 120 K, and measurements at this temperature are shown. The curves A, B, and C were taken before hydrogenation, after 1/2 hr. of hydrogenation, and after 4 1/2 hrs. of hydrogenation at 300μ pressure, respectively. The zero-bias differential resistances were 2220Ω, 2240Ω, and 2290Ω respectively. The curves have been normalized at zero-bias for comparison. After the completion of these measurements, the sample was brought to room temperature in dry nitrogen, to drive off the hydrogen. A fourth curve, which falls directly upon curve A, was then run at 120 K, indicating a reversible hydrogenation process, and reversible response in the tunneling resistance.

In order to clarify the shift of resistance with hydrogenation, we show in figure 2 the percentage change in resistance, ΔR, as a function of voltage for the sample of figure 1, for a second Al-oxide-Pd sample, and a control junction with an Al counter electrode, all on the same substrate. The zero bias differential resistance for each of the junctions is shown in the figure. The variation of R with V for the control is due to a combination of data plotting error and instrument zero shift totalling about 1/4 percent. The downward shift of 1 percent represents a reduction in R_0 from 1810Ω to 1795Ω upon hydrogenation. R_0 remained at 1795Ω after dehydrogenation. R_0 returned to its original value for both Pd junctions, when they were dehydrogenated and measured, 5 days after these experiments. In figure 2, we observe a minimum in the percent resistance rise at applied voltages close to the

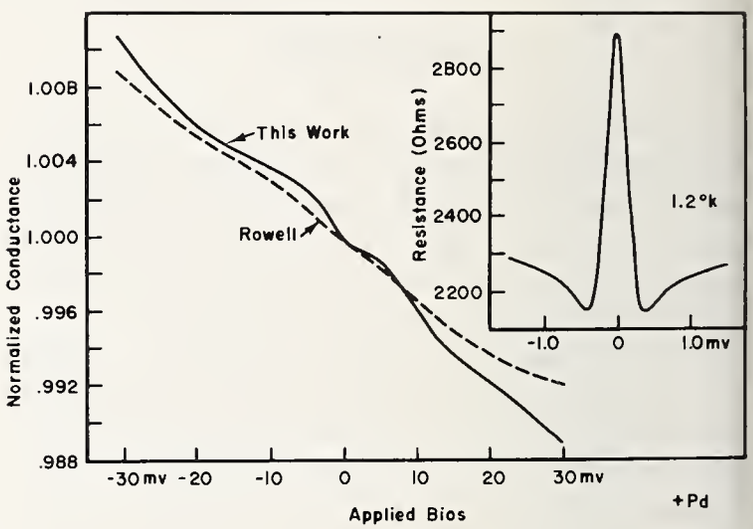

FIGURE 3. *Differential conductance near zero-bias at 4.2 K, for an* Al-I-Pd *junction, compared with data of Rowell [12], and resistance structure due to the superconducting energy gap of the aluminum electrode, at 1.2 K.*

resistance maximum at about 65 mV, followed by a general rise to the right, reaching 4 or 5 percent at +500 mV.

We have also performed such measurements at 4.2 K. For low-impedance junctions at the higher temperature, application of the relatively large biases in measurement warms the junction enough to drive out the hydrogen. The results of measurements at 4.2 K are not significantly different from those obtained at 120 K, but the use of the low temperature reduces the effects of heating.

As an indication that the observed effects are in fact due to tunneling, we show in figure 3 the zero-bias structure at 4.2 K, compared with the data of Rowell [12], and the aluminum gap at 1.2 K. Calculation from

this gap yields a transition temperature of 1.4 K for the aluminum.

3. Conclusions

We have found a reversible tunnel resistance increase of up to 5 percent at positive Pd bias, in Al-I-Pd junctions. This effect increases with increasing applied voltage with that polarity. No evidence for such an effect is found with Al, Pb, or Ag counter electrodes. The change in tunneling characteristics seems to be due to the introduction of electrons into the Pd electrode. It may arise directly from a change in density of tunneling states near the Fermi surface of the Pd, or from a change in the effective barrier height at the Pd-oxide interface, either one produced by the introduction of the electrons. We are conducting further studies, in order to clarify this point, and are also attempting to determine quantitatively by other measurements, the amount of hydrogen introduced into the samples.

4. References

[1] Ebisuzaki, Y., and O'Keefe, M., Progress in Solid State Chemistry **4**, (Pergamon Press, N.Y., 1967) p. 187.

[2] Mott, N. F., Advances in Phys. **13**, 325 (1964).

[3] Tsuchida, T., J. Phys. Soc. Japan **18**, 1016 (1963).

[4] Hoare, F. E., in Electronic Structure and Alloy Chemistry of the Transition Elements, P. A. Beck, ed. (Wiley, N.Y, 1963); Hoare, F. E., and Yates, B., Proc. Roy. Soc. **A240**, 42 (1957); Shimizu, M., Takahashi, T., and Katsuki, A., J. Phys. Soc. Japan **18**, 240 (1963); Froidevaux, C., Launois, H., and Gautier, F., J. Appl. Phys. **39**, 557 (1968).

[5] Coles, B. R., and Taylor, J. C., Proc. Roy. Soc. **A267**, 139 (1962); Burger, J. P., Am. Phys. (France) **9**, 345 (1964).

[6] Fletcher, R., and Greig, D., Phil. Mag. **17**, 21 (1968).

[7] Vuillemin, J. J., Phys. Rev. **144**, 396 (1966).

[8] Alekseevskii, N. E., Karstens, G. E., and Mozhaev, V. V., Soviet Phys. JETP **19**, 1333 (1963).

[9] Mueller, F. M., Freeman, A. J., Dimmock, J. O., and Furdyna, A. M., to be published.

[10] Duke, C. B., Tunneling in Solids **10**, (Academic Press, N.Y., 1969) p. 52; Friedkin, D. R., and Wannier, G. H., Phys. Rev. **128**, 2054 (1962).

[11] Barker, R. C., and Gruodis, A. J., to be published.

[12] Rowell, J. M., J. Appl. Phys. **40**, 1211 (1969).

Calculation of Thermodynamic Information Based on the Density of States Curves of Two Allotropes of Iron*

D. Koskimaki and J. T. Waber**

Northwestern University, Materials Science Department, Evanston, Illinois 60201

The use of density of states curves to obtain thermodynamic information associated with the allotropic phase transitions in iron is discussed. The density of states curves for both body-centered cubic and face-centered cubic iron are determined using a program which randomly interpolates between previously calculated eigenvalues to generate a large number of new energy solutions. These new eigenvalues enable a more accurate determination of density of states curves than is possible by plotting and averaging the original eigenvalues themselves. The density of states curves determined for each phase are used to obtain the energy sum of the eigenvalues of the valence electrons, the shift in the Fermi potential with temperature for the two curves, and the electronic specific heat versus temperature curves for both phases of iron over the temperature range from 0 K to the melting point.

Key words: Electronic density of states; iron; phase transitions; thermodynamic information.

1. Introduction

1.1. Phase Changes in Iron

Pure iron experiences two allotropic phase changes as it is heated from 0 K to its melting point. Iron is body-centered cubic (α-iron) from 0 to 1183 K, face-centered cubic (γ-iron) from 1183 to 1673 K, and once again body-centered cubic (δ-iron) from 1673 to 1812 K, the melting point. In addition, α-iron experiences a ferromagnetic Curie point at 1042 K. From a thermodynamic viewpoint, these phase changes have been explained from experimental specific heat and enthalpy values adjusted for thermodynamic consistency. Very little successful work has been done, however, to derive these thermodynamic relations entirely from the basic electronic structure of the phases, mostly because energy band calculations at least initially lacked the accuracy needed for these calculations. The present work is a calculation of the information which is directly obtainable from density of states curves for both crystal structures, that is, the summation of the energy eigenvalues of the valence electrons, and the electronic specific heat versus temperature curves for the entire temperature range of solid iron. To our knowledge, a true electronic specific heat versus temperature curve based on an actual density of states has never been calculated for any element.

1.2. Previous Work

In 1932, Austin [1] first discussed the allotropic phase changes in iron in light of the temperature dependence of the specific heats and free energies of both crystal structures. He indicated the necessary thermodynamic equations and used a mixture of observed and hypothetical specific heats and enthalpy differences to obtain a consistent set of free energies for the two phases. As Austin indicates, the most stable phase at any temperature must have the lowest value for the Gibbs free energy in relation to other possible phases at this temperature. The Gibbs free energy is given by

$$G = H - TS$$

or

$$G(T) = H_0 + \int_0^T C_p dT - T \int_0^T \frac{C_p}{T'} dT' \qquad (1)$$

where H_O is the enthalpy at zero degrees, and C_p is the specific heat at constant pressure for the phase. Since

*This research was supported by the Advanced Research Projects Agency of the Department of Defense, through the Northwestern University Materials Research Center.

**Graduate student and Professor, respectively, Department of Materials Science and Materials Research Center, The Technological Institute, Northwestern University, Evanston, Illinois 60201.

the entropy term or third term on the right side of eq (1) has a greater magnitude than the second term, the free energy will decrease with increasing temperature. The temperature T in front of the entropy term integral gives the term an increasingly large magnitude at higher temperatures, while the temperature T' in the denominator of the integrand causes the specific heat at higher temperatures to become increasingly less important in relation to the specific heat at lower temperatures. For this reason differences in the specific heat at low temperatures have a more profound effect on the free energy and hence the phase stability at higher temperatures than do the specific heat differences at these higher temperatures. Obviously, since the stable phase at zero degrees is body-centered cubic, the free energy at zero degrees is lower for the *bcc* phase than for the *fcc* phase. At low temperatures the specific heat of *fcc* iron must exceed the specific heat of *bcc* iron, if the free energy of *fcc* iron is to be lowered relative to *bcc* iron as the temperature is raised, causing the first phase transition. However, if the *bcc* phase is to reoccur above 1673 K, the specific heat versus temperature curves must intersect at some intermediate temperature far enough below 1673 K to allow the specific heat difference to have an appreciable effect in lowering the free energy of *bcc* iron relative to *fcc* iron as the temperature is raised. Obviously, to predict this behavior, one needs the specific heat curves for both phases at all temperatures between zero degrees and the melting point, along with the difference in enthalpies between the two phases at 0 K. Since each phase exists only in a certain range of temperatures, the specific heat curves and enthalpy difference at zero degrees must be derived theoretically for these phases outside their observed range of existence.

Austin obtained the specific heat relations for γ-iron in the temperature range from 0 to 1183 K by extrapolating the specific heat values for face-centered cubic iron alloys of 19.4 and 30% manganese content. Using these values for *fcc* iron and experimentally observed values for *bcc* iron, he obtained curves for the temperature dependence of the free energy. Then, by adjusting these curves to coincide at the first transition temperature, he found an enthalpy difference of 960 calories per gram-mole at 0 K.

In 1942, Seitz [2] showed that the necessary behavior of the specific heat versus temperature curves for the two crystal structures could be explained if *bcc* iron had a higher electronic specific heat, while *fcc* iron had a higher lattice specific heat in relation to the other phase. Since the electronic specific heat is a significant part of the total specific heat only at high and very low temperatures, the higher electronic specific heat of *bcc* iron would allow the total specific heat of this phase to exceed that for *fcc* iron at high temperatures, while the higher lattice specific heat of *fcc* iron would enable the total specific heat of this phase to dominate at lower temperatures. The total specific heat curves of the phases would then be consistent with the behavior necessary for the phase transitions as suggested by Austin.

In 1943, Manning [3] and Greene and Manning [4] calculated the electronic band structures of both *bcc* and *fcc* iron, using a Wigner-Seitz method. They were able to show that the electronic specific heat coefficient of *bcc* iron does indeed exceed the electronic specific heat for *fcc* iron. At low temperatures the electronic specific heat is proportional to the density of states at the Fermi level and can be found approximately by using a formula derived by E. C. Stoner [5]:

$$C_{el} \cong 0.209 \times 10^{-4}\, n(E_F)\, RT \qquad (2)$$

where $n(E_F)$ is the density of states at the Fermi level E_F in states/Rydberg K, and R is the gas constant. Manning and Greene obtained Fermi level density of states values of 17 and 11.4 states/atom Rydberg for *bcc* and *fcc* respectively. However, due to the approximate nature of their density of states curves, they did not attempt to derive any further thermodynamic information from these curves.

By extrapolating and adjusting existing specific heat curves to conform to the observed phase changes in iron, Johanson [6] and Darken and Smith [7] have obtained values for the total specific heat of both crystal structures of iron at temperatures outside the range of their observed existence.

Zener [8] and Weiss and Tauer [9] have divided the total specific heat of α-iron into magnetic and nonmagnetic contributions. Using their nonmagnetic specific heat curves and Manning and Greene's values for the electronic specific heat coefficients, Weiss and Tauer concluded that *fcc* iron has a Debye temperature of 335 K as compared to 420 K for *bcc* iron, and that *fcc* iron would be stable by 130 calories/mole at 0 K in the absence of magnetic effects.

Kaufman, Clougherty and Weiss [10] have analyzed thermal expansion data, the effects of pressure on electrical resistance, and extrapolated results from *fcc* alloys of iron to conclude that *fcc* iron has two spin states. At very low temperatures *fcc* iron is antiferromagnetic with a moment of less than one Bohr magneton, while at high temperatures it has a high moment, greater than two Bohr magnetons, and is not ferromag-

netic. As the temperature is raised, the transition from the low spin to the high spin state imparts an extra entropy to the *fcc* structure, lowering the free energy for *fcc* iron and causing the stabilization of this phase above 1183 K. As the temperature continues to rise the entropy resulting from the magnetic disordering above the Curie point for *bcc* iron is multiplied by an increasing value for temperature and eventually overrides the entropy of the *fcc* structure, causing the *bcc* phase to once more become stable above 1673 K. Based on their calculations, Kaufman and coworkers found that the values of the Debye temperature and the electronic specific heat coefficients are approximately the same for both phases ($\theta_D \approx 432$ K, $\gamma_{Fe} \approx 12 \times 10^{-4}$ cal/mole K).

In addition to the work of Manning and Greene, energy bands have been calculated by Wood [11], Stern [12], Abate and Asdente [13] and Snow and Waber [14]. The present work is based primarily on the calculations of Snow and Waber.

2. Theory

2.1. The Enthalpy Difference at 0 K

The electrons in a metal are generally divided into core electrons and valence electrons. In iron and other 3*d* transition elements, the core electrons exist in the argon configuration, that is, $1s^2 2s^2 2p^6 3s^2 3p^6$. Between two phases, the core electrons are altered only slightly and, as such, their effect on the enthalpy difference for two phases is ignored in this paper.

The enthalpy difference due to the valence electrons consists of a magnetic part and an electronic part. The magnetic enthalpy difference results from the ferromagnetic ordering of unpaired electron spins in adjacent atoms of *bcc* iron, which has been calculated by Weiss and Tauer [9] to lower the energy of *bcc* iron by approximately 2086 cal/mole at 0 K.

To calculate the electronic enthalpy difference, the eigenvalues of the energy band calculation are considered. In most calculations, the eigenvalues are given by

$$\epsilon_i = \langle T_i + V_i \rangle + \sum V_{ij} + \sum_j W_{ij} \tag{3}$$

where T_i is the kinetic energy of the ith electron with respect to the nucleus, V_i is the electrostatic potential of the ith electron with respect to the nucleus, V_{ij} is the electrostatic potential of the ith electron with respect to the jth electron, and W_{ij} is the exchange potential energy of the ith electron with respect to the jth electron. The summation j is over all the occupied orbitals including $j = i$. The total energy, which is used to find the electronic enthalpy difference, is given by

$$E_T = \sum_i \epsilon_i - \tfrac{1}{2} \sum_{ij} V_{ij} - \tfrac{1}{2} \sum_{ij} W_{ij} \tag{4}$$

where the second and third terms on the right side of the equation are correction terms due to the fact that each electron pair is counted twice in eq (3). The first term on the right is the sum of the eigenvalues, which is easily evaluated at 0 K by integrating the density of states times the energy, or

$$\epsilon_T = \sum_i \epsilon_i = \int_0^{E_F} E n(E)\, dE. \tag{5}$$

The electrostatic and exchange energy corrections can be approximated using an equation given by Snow, Canfield and Waber [15]:

$$\tfrac{1}{2} \sum_{ij} V_{ij} + \tfrac{1}{2} \sum_{ij} W_{ij} = \tfrac{1}{2} \int \rho\ (r) [V(r) + W(r)]\ d^3 r \tag{6}$$

where $\rho(r)$ is the charge density which is found by summing the square of the radial electron wave functions, or

$$\rho(r) = \sum_i \psi_i^*\ (r)\ \psi_i(r). \tag{7}$$

$V(r)$ is the self-consistent crystal potential used in the energy band calculation and $W(r)$ is the exchange potential which can be approximated using Slater's $\rho^{1/3}$ method [16]. Thus

$$W(r) = -6 \left(\frac{3\rho}{8\pi}\right)^{1/3} \tag{8}$$

where $W(r)$ is in Rydbergs when ρ is given in electrons/(atomic unit)^3.

2.2. The Shift in Fermi Potential with Temperature

At any temperature above zero degrees, eq (5) must include the Fermi-Dirac distribution, or

$$\epsilon_T = \int_{E_1}^{E_2} E f(E, T, \zeta) n(E)\, dE \tag{9}$$

where E_2 and E_1 are the upper and lower limits respectively of the density of states curve, and $f(E,T,\zeta)$ is the Fermi-Dirac distribution given by

$$f(E, T, \zeta) = \frac{1}{1 + \exp\left(\dfrac{E - \zeta\ (T)}{kT}\right)} \tag{10}$$

The function $f(E,T,\zeta)$ gives the probability that an electron will occupy a state at a given energy and temperature. The Fermi potential $\zeta(T)$, which is equal to the Fermi level E_F at absolute zero, is defined as the energy level at which the Fermi-Dirac function $f(E,T,\zeta)$ equals 1/2. The Fermi level E_F is defined as the energy at which the number of vacated levels below this level equals the number of excited electrons above. As the temperature is raised above 0 K, the Fermi potential shifts in energy from its value of E_F at 0 K, the Direction and magnitude of this shift depending upon the temperature and on the shape of the density of states curve near the Fermi level. This behavior can be understood by studying figure 1. At any temperature, the electron distribution is given by the product of the Fermi-Dirac distribution curve and the density of states curve, as shown in figure 1(c). However, if the Fermi potential is prevented from shifting, the number of states vacated from below the Fermi level will not necessarily equal the number of electrons excited to above the Fermi level, due to the asymmetry of the density of states curve about the Fermi level. In order that the number of valence electrons remain conserved as the temperature is raised, the Fermi potential must shift, as shown in figure 1(d). Mathematically, this shift can be understood from the following argument. The total number of valence electrons n is given by

$$n = \int_{E_1}^{E_2} n(E) f(E, T, \zeta)\, dE \tag{11}$$

At absolute zero the Fermi-Dirac distribution is unity for energies less than the Fermi level and zero above, as shown in figure 1(a). Therefore, at 0 K eq (11) can be reduced to

$$n = \int_{E_1}^{E_F} n(E)\, dE \tag{12}$$

At any temperature, the integral in eq (11) can also be split into two integrals at some constant energy which can be chosen as the Fermi level E_F,

$$n = \int_{E_1}^{E_F} n(E) f(E, T, \zeta)\, dE + \int_{E_F}^{E_2} n(E) f(E, T, \zeta)\, dE. \tag{13}$$

Substituting eq (12) for n, one obtains

$$\int_{E_1}^{E_F} n(E)\,[1 - f(E, T, \zeta)]\, dE = \int_{E_F}^{E_2} n(E) f(E, T, \zeta)\, dE. \tag{14}$$

The left side of this equation represents the number of empty states below the Fermi level E_F, as can be seen by the fact that if $f(E,T,\zeta)$ is the probability that a state at a certain energy and temperature is occupied, then $[1-f(E,T,\zeta)]$ is the probability that this state is unoccupied. The right side of the equation gives the number of electrons excited to states above the Fermi level. When a certain temperature and density of states curve are given, then eq (14) determines the position of the Fermi potential $\zeta(T)$, contained in the expression $f(E,T,\zeta)$, since the Fermi potential is the only quantity in this equation which remains a variable. It is important to note that at all temperatures the definite integrals of eq

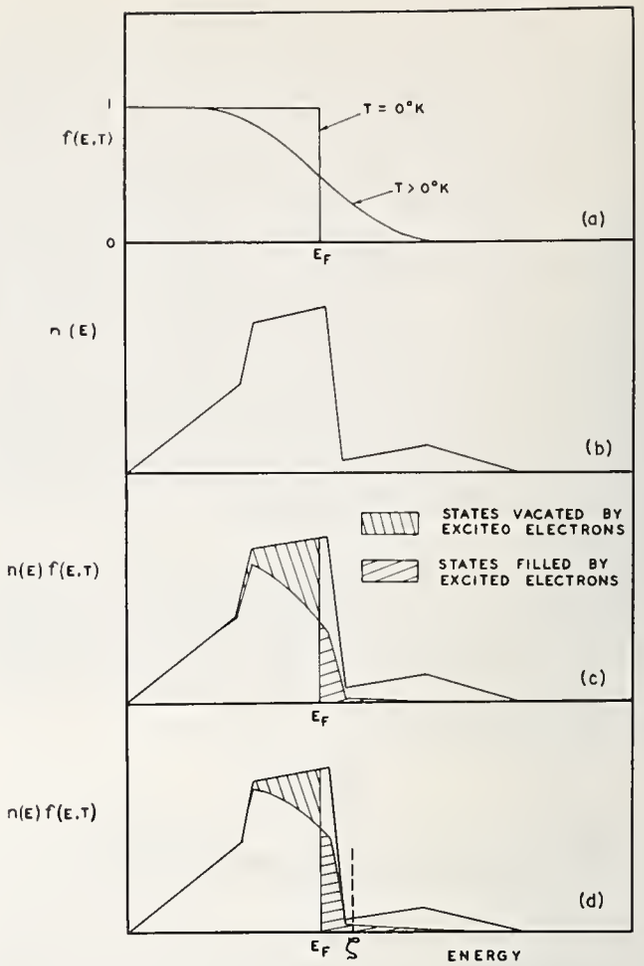

FIGURE 1a. *The Fermi-Dirac distribution, which gives the probability that a state will be occupied at a given energy and temperature.*

In this case, the Fermi potential is assumed to equal the Fermi level.

FIGURE 1b. *A hypothetical density of states curve.*

FIGURE 1c. *The Fermi-Dirac distribution for some temperature than zero multiplied by the density of states curve of figure 1(b) to give the distribution of electrons.*

The Fermi potential ζ is assumed equal to the Fermi level E_F. The cross-hatch regions represent states vacated by and filled by thermally excited electrons. Note that the area representing the states vacated by these electrons is unequal to the area of the states filled by these electrons, violating the fact that electrons must be conserved as the temperature is raised.

FIGURE 1d. *The Fermi-Dirac distribution for some temperature greater than zero multiplied by the density of states curve.*

In this case the correct Fermi potential is used, equating the areas representing states vacated and filled by thermally excited electrons.

(14) are integrated over the limits of E_1 to E_F and E_F to E_2 rather than from E_1 to $\zeta(T)$ and $\zeta(T)$ to E_2, as this condition is necessary to conserve the number of electrons occurring at 0 K. If the latter limits were taken, then eq (14) would no longer uniquely determine the position of $\zeta(T)$.

2.3. The Electronic Specific Heat

The electronic specific heat is found by taking the derivative with respect to temperature of the energy ϵ_T given by eq (9). Ideally, the derivative of the total electronic energy E_T given by eq (4) should be used instead, but the temperature dependence of the electrostatic and exchange potential energy corrections is assumed small enough to be neglected. Values for the electronic specific heat must be obtained numerically, since the energy integral of eq (9) must be obtained numerically. The Fermi potential shift with temperature complicates this energy integral even further.

Ziman [17] has given an expression for the electronic specific heat which is usually quite accurate at low temperatures:

$$C_{el}=\frac{\pi^2k^2}{3}Tn(E_F)+\zeta n(\zeta)\left[\frac{d\zeta}{dT}+\frac{\pi^2k^2T}{3n(E)}\frac{\partial n(E)}{\partial E}\right]_{E=\zeta}. \tag{15}$$

The second term accounts for the Fermi potential shift with temperature, which can be found using the approximate formula

$$\zeta(T)\approx E_F-\frac{\pi^2}{6}\frac{(kT)^2}{n(E_F)}\left[\frac{\partial n(E)}{\partial E}\right]_{E=E_F} \tag{16}$$

Eq (16) is only approximate since $\partial n(E_F)/\partial E$ gives the slope at the Fermi level, but other than this, no account is made of the shape of the density of states curve near the Fermi level.

3. Procedure

The starting point in the calculation was a set of eigenvalues for both *bcc* and *fcc* iron calculated by Snow and Waber using the augmented plane wave method. They used a reciprocal lattice grid spacing of $2\pi(m,n,p)/4a$ where a is the unit vector of the real lattice. For *bcc* and *fcc* lattices, this lattice spacing amounts to 128 and 256 points respectively, within the Brillouin zone of each structure.

Snow and Waber calculated these eigenvalues for two electron configurations, $3d^74s^1$ and $3d^64s^2$, and concluded on the basis of calculated occupancies for the bands, that $3d^74s^1$ is the preferred configuration for both phases. Stern [12] also found previously that the $3d^74s^1$ configuration was the most compatible with his self-consistent field calculations for *bcc* iron. Since there are substantial changes in charge distribution and energy with changes in configuration, the $3d^74s^1$ configuration is used for both phases, although we recognize that the Engel-Brewer theory [18] predicts the configuration of *fcc* iron to be $3d^54sp^2$.

Although the density of states curves calculated by Snow and Waber have a resolution of roughly 0.03 Rydbergs, which is better than any previously published curves for iron, this resolution is not small enough for an accurate calculation of the temperature dependence of the Fermi potential and the density of states at the Fermi potential. The energy range of the electrons affected by the Fermi-Dirac function is about 1 or 2 kT on each side of the Fermi level, and at 1000 K this energy span amounts to only 0.02 Rydberg. Thus, any fine peaks or other detailed structure in the density of states curve which might affect the Fermi-Dirac distribution, would be partially or wholly smoothed out if such detail occurred over a span less than the resolution of 0.03 Rydberg.

Fortunately, an ingenious program written by F. M. Mueller, et al. [18], was made available to the authors, which takes the set of original reciprocal lattice points and interpolates quadratically for points between them to obtain new eigenvalues. In order to prevent false structure in the density of states curve from the regular choice of these points, the new points are chosen randomly. In this way 20,000 new points and their eigenvalues were obtained on a CDC 6400 computer in just five minutes of machine time. The reliability of this QUAD method is discussed by Kennard et al. in another paper of this Conference (p. 795).

Using the density of states curves obtained in this way, the Fermi levels for both phases were found by using eq (12) to fill the density of states curves to contain eight electrons.

3.1. The Shift in Fermi Potential

The Fermi potential shift was found by solving eq (14) for the Fermi potential $\zeta(T)$. Since both sides of the equation had to be numerically integrated, the Fermi potential shift could not be obtained directly. Instead, a trial and error method was used in which the Fermi potential was first chosen randomly, and then interpolated between successive solutions for the right and left sides of the equation, until the two sides were equal.

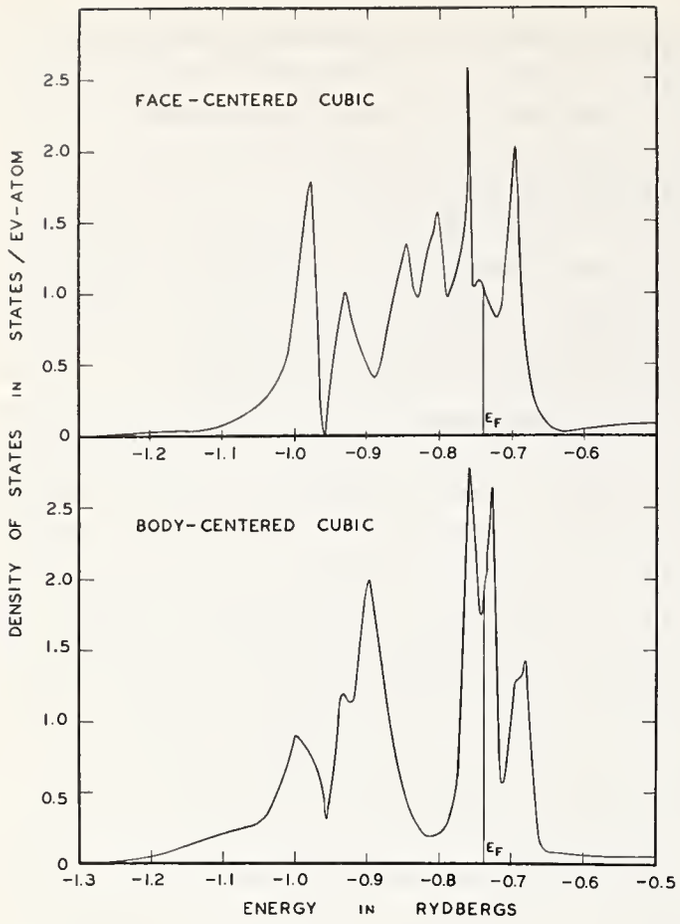

FIGURE 2. *The density of states curves for* $3d^7\,4s^1$ *iron.*

These curves were obtained by using eigenvalues calculated by Snow and Waber [14] as input for the QUAD interpolation program of Mueller et al. [19]. Twenty thousand points in the Brillouin zone were used.

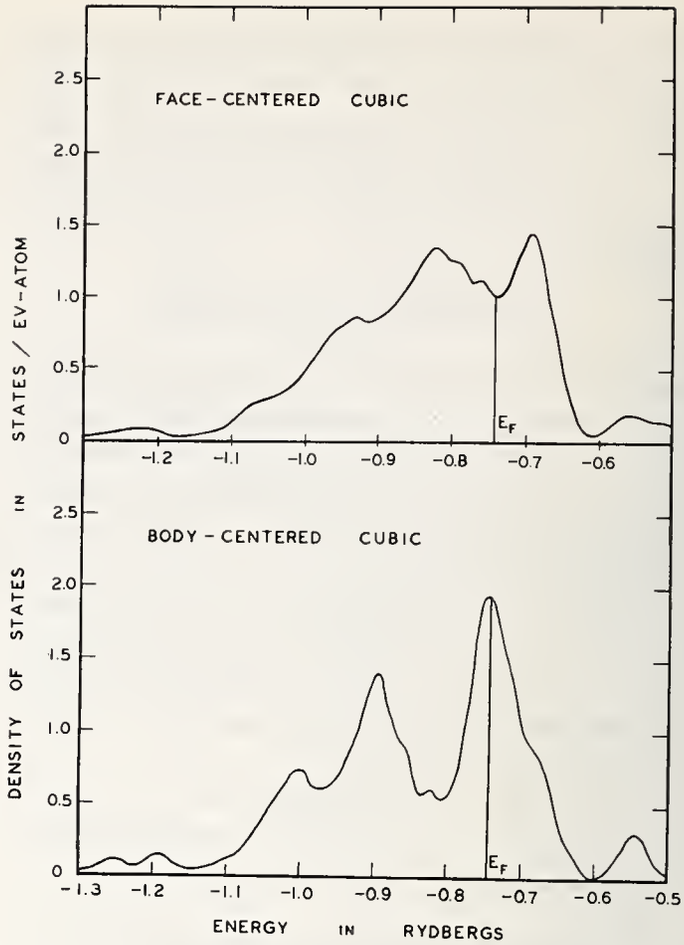

FIGURE 3. *The smoothed density of states curves for* $3d^7\,4s^1$ *iron as calculated by Snow and Waber.*

One hundred twenty-eight and 256 points in the Brillouin zone were used for body-centered cubic and face-centered cubic iron respectively. Note that these curves lack much of the structure of the curves of figure 2 which were obtained using the QUAD interpolation program.

For each temperature, eq (14) had to be solved for about five iterations to obtain a consistent value for $\zeta(T)$.

3.2. Total Energy and Specific Heat

The energy summation of the eigenvalues was found for a range of temperatures by using the shifted value for the Fermi potential and numerically integrating eq (9).

The electronic specific heat was found by plotting the energies obtained from eq (9) for a range of temperatures and determining the slope of this curve at each temperature. A smooth curve was constructed from these graphical values.

4. Results and Discussion

4.1. Density of States Curves

The density of states curves obtained for both crystal structures are presented in figure 2. The energy scale is chosen to give the same zero energy as that used in the self-consistent crystal potential of the APW calculation by Snow and Waber. This energy scale gives the energy of an electron state in the density of states curve relative to the energy of an electron just free of the solid. For the purposes of comparison, the density of states curves calculated by Snow and Waber are given in figure 3. The curves of the present calculation contain much more structure than the curves of Snow and Waber. However, one should note that the Fermi levels and the density of states at the Fermi levels agree surprisingly well.

4.2. The Summation of the Eigenvalues

At 0 K the summation of the energy eigenvalues was found to be −7.1868 Rydbergs/atom for *bcc* iron and −7.0257 Rydbergs for *fcc* iron. To obtain a value for the enthalpy difference of the valence electrons, these values must be corrected for the electrostatic and exchange potential energies given in eq (6). This calculation is presently being carried out by the authors. If one can assume that the largest term in the enthalpy difference between two phases is that given by the difference in the sum of the eigenvalue energies, then a

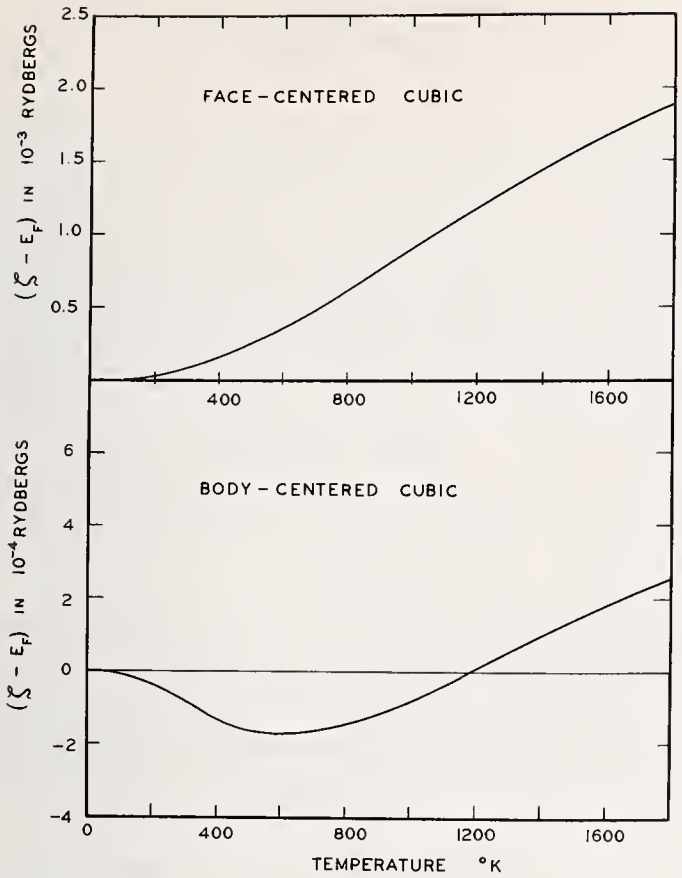

FIGURE 4. *The shift in the Fermi potential with temperature for both phases of iron.*

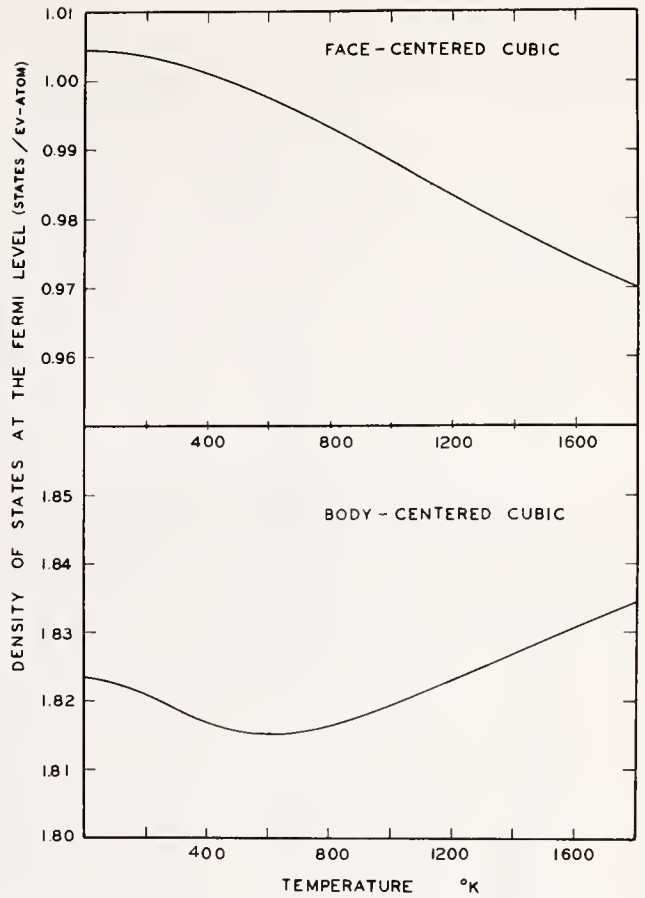

FIGURE 5. *The change in the density of states at the Fermi potential with temperature.*

rough indication of the stability of one phase with respect to another is possible by comparing these sums. As such, the difference in the eigenvalue sums for both phases is 0.1611 Rydberg/atom at 0 K with the b.c.c. phase having the lower energy. This value, about 50,400 cal/mole, is large compared to the approximately 1000 calories/mole accepted by most workers to be the enthalpy difference at 0 K. However, when compared to the sums of the eigenvalues for both phases, the value represents only about 2% of these sums.

4.3. Electronic Specific Heat

Figure 3 gives the result of calculating the Fermi potential shift with temperature for a range of temperatures from 0 to 2000 K. Figure 4 gives the corresponding change in the density of states curve at the Fermi potential. From figure 1, one could expect the Fermi potential to shift along the density of states curve from regions of higher density toward regions of lower density. As can be seen from figures 4 and 5, this is indeed the case. Face-centered cubic iron shifts down the density of states curve over the entire temperature range. Body-centered cubic iron shifts down the slope initially, but as the temperature is raised the direction of the shift is reversed. The reason is that the Fermi-Dirac function extends over an increased energy range to include the whole peak rather than just part of the double peak in the immediate vicinity of the Fermi level. At this higher temperature the tendency of the Fermi potential is to move away from the center of the entire double peak and to do this the Fermi potential must shift temporarily up the slope of one part of the double peak.

The density of states at the Fermi level obtained by various authors are compared with the present results in table 1. The experimental electronic specific heat coefficient of *bcc* iron is slightly higher than that predicted by eq (2), since the electron-phonon enhancement has not been included in the present work. On the basis of their energy band calculations, Snow and Waber have estimated this enhancement to increase the value of the electronic specific heat for $3d^74s^1$ iron by factors of 1.09 and 2.09 for *bcc* and *fcc* iron respectively.

The electronic specific heat versus temperature curves are presented in figure 6 with numerical values given in table 2. The values extrapolated from low temperature are plotted as dotted lines. It can be seen that

TABLE 1. *Density of states at the fermi level and electronic specific heats found by several authors*

	States/eV-atom		10^{-4}calories/mole K	
	$n(E_F)^\alpha$	$n(E_F)^\nu$	γ^α	γ^γ
Present work	1.823	1.005	10.3	5.7
Greene and Manning [3, 4]	1.25	0.85	7.1	4.8
Snow and Waber [14]	1.862	.978	10.5	5.5
Kaufman et al. [10]	.....	.....	12	12
Cheng, Wei, and Beck [26]	.....	.....	*11.9	.....
Deegan [27]	1.67	1.12	9.4	6.3

*Obtained experimentally.

TABLE 2. *The electronic specific heat and the electronic components of the Gibbs Free Energy for bcc and fcc iron between 0 K and 1812 K. Values for the specific heat are in calories/K mole and values for the free energy are in calories/mole.*

T, K	C_{el}^α	C_{el}^γ	$-(G_0-G_T)^\alpha$	$-(G_0-G_T)^\nu$	$G_T^\alpha-G_T^\gamma$
100	0.102	0.056	0	0	0
200	.208	.112	10.3	5.6	−4.7
300	.312	.169	30.9	16.9	−14.0
400	.421	.230	61.5	33.9	−27.6
500	.532	.295	103	56.4	−47
600	.645	.363	155	84.8	−70
700	.762	.433	218	122	−96
800	.865	.507	292	162	−130
900	.943	.586	376	208	−168
1000	.990	.664	471	262	−209
1100	1.024	.737	575	323	−252
1183	1.043	.800	668	380	−288
1200	1.045	.812	690	390	−300
1300	1.061	.890	812	463	−349
1400	1.071	.966	942	542	−400
1500	1.077	1.043	1082	631	−451
1600	1.085	1.112	1224	726	−498
1700	1.096	1.180	1376	822	−554
1800	1.102	1.240	1536	929	−607
1812	1.104	1.246	1555	942	−613

the electronic specific heat deviates substantially from the linear behavior usually assumed by most authors. With increasing temperature, the *bcc* curve deviates first positively and then negatively from linear behavior while the *fcc* curve deviates positively. This behavior can be only partly predicted by eqs (15) and (16). Calculations performed using these equations correctly give the initial change in Fermi potential along with the resulting change in the electronic specific heat. However, eq (16) is an approximation which gives the change in Fermi potential as a function of the slope of the density of states at the Fermi level. No provision is made for the fact that the slope of the density of states curve may change substantially on both sides of the Fermi level. Perhaps eq (16) could be improved using terms of a higher order with respect to T, but it would be simpler and more accurate to obtain the electronic

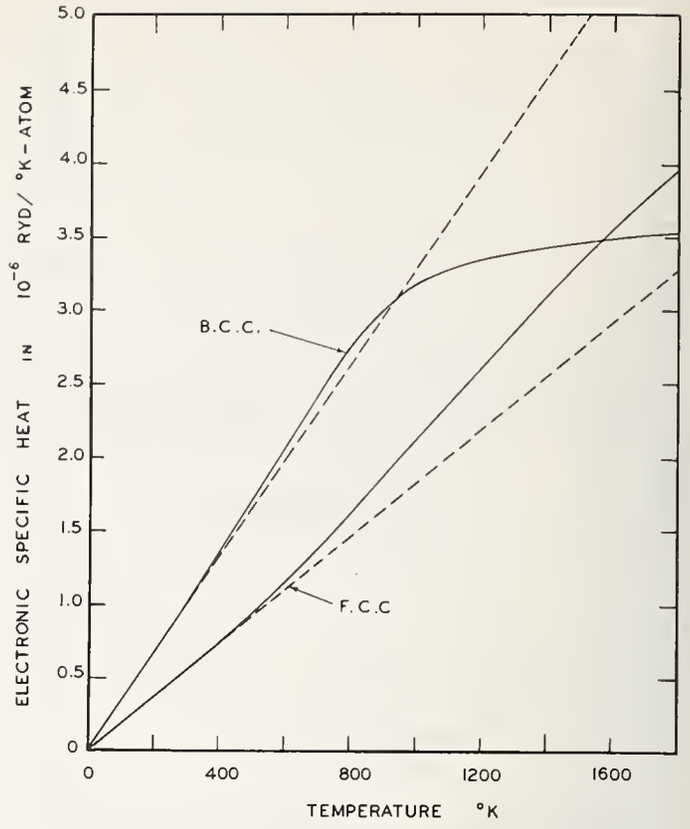

FIGURE 6. *The electronic specific heat versus temperature for both phases of iron.*

The dotted lines are extrapolated from the low temperature behavior. The two curves intersect at 1560 K.

specific heat directly by finding the change with respect to temperature of the energy given by eq (9).

The unusual behavior of the electronic specific heat of *bcc* iron is due to the fact that the Fermi level coincides with a large double peak in the density of states curve. The Fermi-Dirac function changes from 0.99 to 0.01 over an energy span of about 13 kT. The number of electrons which are thermally excited is a rough function of the average density of states in this energy span. At 1000 K this energy span amounts to about 0.08 Rydberg, while the total width of the double peak is only about 0.06 Rydberg. As the temperature is increased above 1000 K, the number of electrons thermally excited is a function of a decreasing average density of states, and this behavior is reflected by the decreasing slope in the electronic specific heat curve above 1000 K. Similarly, around 600 K the energy span of the major change in the Fermi-Dirac function occurs over about 0.05 Rydberg, which is less than the total width of the double peak. Since the Fermi level occurs in the dip between the peaks, the average density of states in this region is increased, causing the positive deviation from linear behavior of the electronic specific heat curve around 600 K.

The behavior of the electronic specific heat curve for *fcc* iron can be explained in a similar manner.

4.4. Comparison of the Contributions to the Total Specific Heat

To determine what effect the electronic specific heat has in relation to the phase transitions in iron, a rough calculation was performed to resolve the total specific heat for each phase into its various components. These are compared in tables 3 and 4. The free energy difference resulting from each of these components was then calculated using eq (1) and compared in table 5. This calculation is described in the following paragraphs.

The total specific heat is given by

$$C_p(T) = C_v\left(\frac{\theta_D}{T}\right)[1 + \alpha_v\gamma T] + C_{el}(T) + C_p^{\mu}(T), \quad (17)$$

where $C_v\,(\theta_D/T)$ is the lattice specific heat at constant volume; θ_D is the Debye temperature; α_v is the volume coefficient of thermal expansion; $C_{el}(T)$ is the electronic specific heat; and $C_p^{\mu}(T)$ is the magnetic specific heat. The Gruneisen constant is given by

$$\gamma = \frac{\alpha_v V}{C_v \beta} \quad (18)$$

where β is the compressibility or $-1/V(\partial V/\partial P)_T$. The first term, $C_v(\theta_D/T)\,[1 + \alpha_v\gamma T]$, is the lattice specific heat at constant pressure, C_p. When $T \ll \theta_D$, C_v is proportional to the cube of the temperature, and when $T \gg \theta_D$, C_v is approximately constant and equal to the Dulong-Petit value of 3R or 5.96 cal/K mole.

Basinsky, Sutton, and Hume-Rothery [19] have measured α_v in the range 300 K $\leq T \leq$ 1812 K, thus determining α_v for both crystal phases of iron. For α-iron, the value of the Gruneisen constant γ has been determined by Kittel [20] to be 1.6 and by Slater [21] to be 1.4, employing a correction to Slater's value given by Dugdale and MacDonald [22]. However, the present authors could not find an experimentally determined value for the Gruneisen constant for γ-iron, nor a value of the compressibility or bulk modulus of γ-iron measured at high temperatures. Referring to eq (18), one would expect the Gruneisen constant for γ-iron to be slightly higher than the constant for α-iron, since α_v is higher for γ-iron and β could be expected to be less for the more densely packed *fcc* structure. A rough estimate of the Gruneisen constant for *fcc* iron is possible from the temperature dependence of Young's modulus as determined by Koster [23]. Since Young's modulus is approximately equal to the bulk modulus (assuming Poisson's ratio ≈ 0.33), then the bulk modulus of *fcc* iron is about 12×10^5 Kg/cm^2 at 1200 K, giving a com-

TABLE 3. *Components of the Total Specific for bcc iron. All values are in calories/K mole. The electronic specific heat includes an electron-phonon enhancement factor of 1.15*

T, K	C_v	$C_p - C_v$	C_{el}	C_p magnetic	C_p unknown	C_p (total)
100	2.72	0.01	0.11	0.02	.....	2.86
200	4.77	.05	.24	.10	.....	5.06
300	5.38	.07	.36	.19	.....	6.00
400	5.63	.10	.48	.28	.....	6.49
500	5.76	.15	.61	.53	0.02	7.07
600	5.83	.20	.74	.79	.05	7.61
700	5.87	.25	.88	1.20	.10	8.30
800	5.88	.31	1.00	1.80	.22	9.21
900	5.89	.37	1.10	2.90	.32	10.58
1000	5.90	.43	1.14	5.70	.46	13.63
1100	5.91	.50	1.18	2.10	.73	10.42
1183	5.91	.56	1.20	0.90	.75	9.32
1200	5.92	.57	1.21	.80	.76	9.26
1300	5.92	.65	1.22	.45	.90	9.14
1400	5.92	.74	1.23	.25	1.06	9.20
1500	5.93	.83	1.24	.12	1.20	9.32
1600	5.93	.92	1.25	.06	1.37	9.53
1673	5.93	.99	1.26	.03	1.50	9.71
1700	5.93	1.02	1.26	.02	1.53	9.76
1800	5.94	1.12	1.27	.01	1.68	10.02
1812	5.94	1.13	1.27	.01	1.70	10.05

TABLE 4. *Components of the total specific heat for fcc iron. All values are in calories/K mole. The electronic specific heat includes an electron-phonon enhancement factor of 1.11*

T, K	C_v	$C_p - C_v$	C_{el}	C_p (total)
100	3.65	0.07	0.06	3.78
200	5.22	.20	.12	5.54
300	5.61	.32	.18	6.11
400	5.76	.44	.26	6.46
500	5.82	.54	.33	6.69
600	5.88	.65	.40	6.93
700	5.90	.75	.48	7.13
800	5.91	.85	.56	7.32
900	5.92	.96	.65	7.53
1000	5.92	1.06	.74	7.72
1100	5.93	1.16	.82	7.91
1183	5.93	1.24	.89	8.06
1200	5.93	1.26	.90	8.09
1300	5.94	1.36	.99	8.29
1400	5.94	1.46	1.07	8.47
1500	5.94	1.56	1.16	8.66
1600	5.95	1.65	1.24	8.84
1673	5.95	1.72	1.29	8.96
1700	5.96	1.74	1.31	9.00
1800	5.95	1.83	1.38	9.16
1812	5.95	1.84	1.38	9.17

TABLE 5. *Free energy differences between fcc and bcc iron due to the various components of the total specific heat for each phase. All values are in calories/mole. Note that the total free energy difference refers both phases to zero energy at 0 K. To get the actual free energy difference, 1131 calories/mole must be added to the free energy of the fcc phase*

T, K	$(G^{\nu}-G^{\alpha})$ due to ΔC_v	$(G^{\nu}-G^{\alpha})$ due to $\Delta(C_p-C_v)$	$(G^{\nu}-G^{\alpha})$ electronic	$-G^{\alpha}$ unknown	$-G^{\alpha}$ magnetic	$(G^{\nu}-G^{\alpha})$ total
100	−29	.....	.....	.....	.....	−29
200	−146	−6	5	.....	2	−145
300	−287	−20	15	.....	8	−284
400	−438	−41	31	.....	21	−427
500	−592	−71	53	.....	41	−569
600	−747	−108	81	.....	71	−703
700	−904	−153	114	2	113	−828
800	−1061	−205	152	4	165	−945
900	−1218	−265	187	10	242	−1043
1000	−1375	−330	247	18	350	−1090
1100	−1534	−403	300	32	481	−1124
1183	−1664	−467	347	49	604	−1131
1200	−1692	−481	356	52	626	−1139
1300	−1849	−565	415	79	778	−1146
1400	−2008	−665	475	112	942	−1144
1500	−2166	−749	538	153	1083	−1141
1600	−2324	−848	600	202	1235	−1135
1673	−2441	−924	646	243	1345	−1131
1700	−2483	−952	663	260	1388	−1124
1800	−2642	−1061	726	326	1539	−1112
1812	−2661	−1074	733	335	1557	−1110

pressibility of 8.33×10^{-7} cm²/Kg. Using this value and the value of α_v determined by Basinsky, et al., the Gruneisen constant of *fcc* iron was found to be 2.48.

Using the thermal expansion data of Basinsky, et al., and Gruneisen constants of 2.48 and 1.6 for *fcc* and *bcc* iron respectively, C_p-C_v was calculated for each phase. The lattice specific heat was calculated for each phase using Debye temperatures of 330 and 432 K for *fcc* and *bcc* iron respectively.

Assuming that there is no magnetic contribution to the specific heat for *fcc* iron, an experimental value for the electronic specific heat can be found by subtracting the calculated lattice specific heat C_p at constant pressure from the experimental specific heat measured for *fcc* iron over its stable range of temperature. Using the experimental results of Anderson and Hultgren [24], it was found that the electronic specific heat determined in the present investigation should be multiplied by an electron-phonon enhancement of approximately 1.11 to be consistent with experimental data. This valuc is very close to the electron-phonon enhancement of 1.15 which results for *bcc* iron when the low temperature experimental heat coefficient determined by Cheng, Wei and Beck [25] is compared with the results of this investigation.

The magnetic specific heat due to the second-order ferromagnetic transition in *bcc* iron was found graphically by assuming that this contribution is almost zero below 200 K and above 1700 K. The nonmagnetic specific heat was then interpolated between these temperatures and subtracted from the total specific heat, leaving the magnetic specific heat. It was found, however, that when the contributions from the lattice specific heat and the enhanced electronic specific heat are added and compared to the experimental specific heat above 1700 K, a large part of the total specific heat was unaccounted for. To account for this unknown contribution, which amounts to 1.7 cal/K mole at 1800 K, an electron-phonon enhancement of about 2.6 at 1800 K would be necessary for *bcc* iron, in contrast to the value of 1.15 at low temperatures. It was decided to treat this contribution as a separate component and simply call it C_p (unknown).

When the free energies resulting from each specific heat contribution are calculated and compared in table 5, it is apparent that the largest free energy differences are due to the ferromagnetism of *bcc* iron, and to the difference in C_v between *fcc* and *bcc* iron. Since all values in table 5 are determined by subtracting the free energy of *bcc* iron from the free energy of *fcc* iron, all negative values for the free energy difference tend to stabilize *fcc* iron and all positive values tend to stabilize *bcc* iron. Thus the negative values are responsible for the *bcc* ⇄ *fcc* transition at 1182 K, and the positive values are responsible for the *fcc* ⇄ *bcc* transition at 1673 K. It is apparent that the major cause of the first transition is the free energy difference due to the larger C_v for *fcc* iron, while a minor cause is the free energy difference due to the larger rate of thermal expansion for *fcc* iron, which is determined from $\Delta(C_P - C_v)$. The largest component responsible for the second phase transition is the magnetic free energy due to the ferromagnetic specific heat of *bcc* iron. The contribution to the free energy due to the larger electronic specific heat for *bcc* iron is about one-half the contribution from ferromagnetism.

In this calculation, any effect due to the low spin ⇄ high spin transition described by Kaufman et al., was ignored. This was done as a matter of convenience, as we were only interested in showing the effect of the electronic specific heat in relation to the phase transitions. Presumably, the free energy difference which

results from differences in C_v for the two phases could be accounted for instead by a low spin $\rightleftarrows$ high spin transition as Kaufman et al., have done. It should also be noted that Kaufman et al., assumed that $C_{el}^{\alpha} \approx C_{el}^{\gamma}$ and that $C_p^{\alpha} \approx C_p^{\gamma}$, in disagreement with the results of this investigation. However, when taken together, the contributions to the free energy difference due to ΔC_{el}, $\Delta(C_p - C_v)$ and C_p (unknown) approximately cancel each other out, unaffecting the rest of the investigation by Kaufman et al.

4.5. Factors Needed for a More Complete Analysis

The authors clearly recognize that a number of important factors have been neglected in this paper. These are briefly summarized here.

(a) As previously mentioned, the electrostatic and exchange potential corrections have not been taken into account to calculate the difference in enthalpy at zero degrees. The summation of the eigenvalues gives only a rough comparison as to which phase is stable at zero degrees.

(b) Although the core electrons can normally be neglected, for the purpose of calculating the enthalpy difference between two phases they must be taken into account. Since the enthalpy difference is a small quantity which is found by subtracting two comparatively large sums, any small factor such as the difference in energy of the core electrons may have a substantial effect on the total enthalpy difference.

(c) The effect of the thermal expansion of the lattices on the energy bands, and hence on the density of states curves has not been considered. In fact, the *fcc* lattice parameter used by Snow and Waber is for 910 °C and the *bcc* lattice parameter is for 25 °C. For this reason, the energy summation of the eigenvalues may be slightly in error, and there will be a change in this energy summation as the temperature is changed.

(d) The bands for up and down spins will be slightly different, giving a different density of states curve for each spin, with a slightly different density of states at the Fermi level for each spin.

5. Conclusion

The density of states for the $3d^7 4s^1$ configuration of both crystal structures of iron have been determined using a set of eigenvalues previously determined by Snow and Waber and an interpolation program which randomly generates new eigenvalues. The density of states curves established by these new eigenvalues were found to contain more sharp peaks and dips than the original density of states curves determined by Snow and Waber; however, the Fermi levels and density of states at the Fermi levels were very similar.

The density of states curves times the energy were integrated for both crystal structures to establish a rough indication of the enthalpy difference at 0 K and the phase stability. The difference in energy was found to be 50,400 calories with *bcc* iron having the lower energy. This is quite large when compared to the experimental enthalpy difference of approximately 1000 cal/mole. However, a large number of factors were neglected in the calculation, the most important of which are the electrostatic and exchange potential corrections.

The electronic specific heat versus temperature curves were determined for the two phases. These curves were found to deviate substantially from the linear behavior given by $C_{el} = \gamma_{el} T$ where γ_{el} is the electronic specific heat coefficient. Although at lower temperatures the electronic specific heat of *bcc* iron is greater than that for *fcc* iron, the two curves intersect at 1560 K.

When the values obtained for the electronic specific heat were added to calculated lattice specific heat values, an electron-phonon enhancement factor of 1.11 for *fcc* iron was needed to adjust the theoretical values to the observed values for the total specific heat curves. For *bcc* iron, the low temperature electron-phonon enhancement was found to be 1.15. At high temperatures, there is an increasingly large unknown component for the specific heat of *bcc* iron.

The high temperature phase transition at 1673 K is due to: (1) the magnetic specific heat resulting from the ferromagnetic phase transition in *bcc* iron; (2) the electronic specific heat difference due to the higher electronic specific heat for *bcc* iron; and (3) an unknown component in the specific heat of *bcc* iron.

The phase transition at 1182 K is due to: (1) either a low spin $\rightleftarrows$ high spin transition in *fcc* iron, or a difference in C_v for the two phases with $\Theta_D \approx 330$ K for *fcc* iron and $\Theta_D \approx 432$ K for *bcc* iron; and (2) a higher $(C_p - C_v)$ value for *fcc* iron.

6. Acknowledgments

The authors would like to take this opportunity to thank Dr. F. M. Mueller for making available his QUAD interpolation program, and Mrs. David Kennard for converting this program for use by the CDC 6400 computer.

7. References

[1] Austin, J. B., Ind. and Eng. Chem. **24,** 1225 (1932).
[2] Seitz, F., "The Modern Theory of Solids," (McGraw Hill, New York and London, 1940) p. 487.
[3] Manning, M. F., Phys. Rev. **63,** 190 (1943).
[4] Greene, J. B., and Manning, M. F., ibid, p. 203.
[5] Stoner, E. C., Proc. Roy. Soc. (London) **A154,** 656 (1936).
[6] Johanson, C. H., Arch. Eisenhuttenw. **11,** 241 (1937).
[7] Darken, L. S., and Smith, R. P., Ind. and Eng. Chem. **43,** 1815 (1951).
[8] Zener, C., Trans. AIME **167,** 513 (1946).
[9] Weiss, R. J., and Tauer, K. J., Phys. Rev. **102,** 1490 (1956).
[10] Kaufman, L., Clougherty, E. V., and Weiss, R. J., Acta Met. **11,** 323 (1963).
[11] Wood, J. H., Phys. Rev. **126,** 517 (1962).
[12] Stern, F., Phys. Rev. **116,** 1399 (1959).
[13] Abate, E., and Asdente, M., Phys. Rev. **140,** A1303 (1956).
[14] Snow, E. C., and Waber, J. T., Acta Met. **17,** 623 (1969).
[15] Snow, E. C., Canfield, J. M., and Waber, J. T., Phys. Rev. **135,** A969 (1964).
[16] Slater, J. C., Phys. Rev. **81,** 385 (1951).
[17] Ziman, J. M., "Principles of the Theory of Solids," (Cambridge University Press, London, 1964) p. 124.
[18] Hume-Rothery, W., Progress in Materials Science **13,** 229 (1967).
[19] Mueller, F. M., Cohen, N. H., Garland, J., and Bennemann, K., to be published.
[20] Basinski, Z. S., Hume-Rothery, W., and Sutton, A. L., Proc. Roy. Soc. (London) **A229,** 459 (1955).
[21] Kittel, C., "Introduction to Solid State Physics," 3rd ed., (John Wiley & Sons, New York and London, 1966) p. 184.
[22] Slater, J. C., Phys. Rev. **57,** 744 (1940).
[23] Dugdale, J. S., and MacDonald, D. K. C., Phys. Rev. **89,** 832 (1953).
[24] Koster, W., Z. Metallk. **39,** 1 (1948).
[25] Anderson, P. D., and Hutgren, R., Trans. AIME **224,** 842 (1962).
[26] Cheng, C. H., Wei, C. T., and Beck, P. A., Phys. Rev. **120,** 426 (1960).
[27] Deegan, R. A., submitted to J. Phys. Chem.

Discussion on "Calculation of Thermodynamic Information Based on the Density of States Curves of two Allotropes of Iron" by D. Koskimaki and J. T. Waber (Northwestern University)

O. K. Andersen *(Univ. of Pennsylvania):* In calculations like this, where you have calculated the shift in the Fermi energy as function of temperature, you seem only to be interested in a small energy region of about 10 mRy. Why do you in this case use a histogram technique which puts equal weight on every point in the Brillouin zone? Actually the information used is contained in a tiny fraction of the zone, and even your 20,000 points/zone probably does not give very good statistics. One would think that tracing of constant energy contours is a more appropriate technique, and it has the additional advantage of yielding the Van Hove singularities.

J. T. Waber *(Northwestern Univ.):* I think your point is well taken and we would be well-advised to look at the actual region of the Brillouin zone from which the electrons are thermally excited and into which they go. The nature of the electronic contributions to the specific heat would be revealed. We have not done that. But I think that spikes from electron-phonon interactions and Van Hove singularities might very well contribute more to the specific heat, etc., than has been incorporated in detail in either our work or literature on iron in the past. The point I wish to make is that we have established that it was not necessary to invoke a magnetic transformation to be able to get the BCC → FCC → BCC phase transformation in Fe. I will not go into the details here.

M. B. McNeil *(Mississippi State Univ.):* How does the ΔE calculated on Fe due to Fermi level shift compare, at high temperatures, to $T\Delta S$ due to differences in the lattice specific heats?

J. T. Waber *(Northwestern Univ.):* Considering just the body-centered cubic gamma phase at high temperatures, $T\Delta S$ due to lattice specific heat is approximately 20,000 cal/mole. This is offset by an enthalpy of about 10,000 calories/mole, to give a net change in free energy of around 10,000 calories/mole. The change in the electronic free energy is about 1,500 calories per mole, which is quite a bit smaller. When the two phases are compared, the free energy difference due to lattice specific heats is about 3,600 calories/mole and the free energy difference due to electronic specific heats is around 700 calories/mole.

It is important to realize that ΔE for the electronic energy is not due to the Fermi level shift, but is primarily due to the redistribution of the electrons having energies nearly equal to the Fermi level. The Fermi level shift results from this redistribution.

K. J. Duff *(Ford Motor Co.):* Just a comment to perhaps dampen your enthusiasm for the prospect of doing the calculation sufficiently well when magnetic interactions are included. I would refer you to a paper presented on Monday by Prof. Das and myself. It is our conclusion that the density of states at the Fermi surface is probably the least reliable number that can come out of even a careful band calculation. We found that satisfactory agreement with all other aspects could be obtained with a variation of that number by a factor of something like 4.

J. T. Waber *(Northwestern Univ.):* Of how much?

K. J. Duff *(Ford Motor Co.):* A factor of 4 would be the range of theoretical predictions of the density of states at the Fermi surface.

J. T. Waber *(Northwestern Univ.):* I believe that those properties which involve integration over the entire density of states, such as magnetism does, may be insensitive to $N(E_F)$. But when you attempt to calculate the temperature dependence of that property, the slope and height of the $N(E)$ curve, both above and below E_F, become significant. They sensitively influence the answer. Well, I will not try to quote numbers here about how reliable our density of state curves are, but will refer you to our post-deadline paper [1]. We are trying to make an effort to find better ways of obtaining reliable curves. We recognize that peaks may exist which lead to very high values of $N(E)$ which we might not observe or see in our "smoothing" method. It is less clear at this time, whether "false" peaks might be developed when using either the specific sampling method of Snow and Waber, or the QUAD interpolation scheme; I am inclined to think not. However, if there are large narrow peaks, then a small error in determining E_F could have a profound effect on the value of $N(E_F)$. The

417-156 O - 71 - 49

specific question of how well we can perform the integration of $N(E)$ to locate E_F precisely, has not been investigated in our post-deadline paper and will be a topic for future work. Nevertheless, it is clear that by increasing the number of $E(k)$ values which lie in each interval $E_i + \Delta E$, will improve our reliability of both the $N(E)$ curve and the Fermi level.

[1] Kennard, E. B., Koskimaki, D., Waber, J. T., and Mueller, F. M., these Proceedings, p. 795.

Potential-Independent Features of Crystal Band-Structure*

M. M. Saffren

Jet Propulsion Laboratory, California Institute of Technology, Pasadena, California 91103

Key words: Band structure; crystal potential; electronic density of states; pseudopotential.

Using theorems in addition to those previously developed [1] it has been shown that a portion of the band structure of a crystal is independent of crystal potential depending solely on the space-group to which the crystal belongs. As a result, the band structure of a crystal can be analyzed in terms of its potential-dependent and potential-independent parts. The latter, which we call the "invariant" band structure, is predicted as soon as the symmetry of a crystal is known.

The invariant band structure of the face-centered, body-centered, and tetragonal lattices have been deduced. One of the more interesting results is the invariant structure associated with the 3-*d*, and 4-*f* bands. This structure remains the same regardless of the width these bands may have.

*This paper presents the results of one phase of research carried out at the Jet Propulsion Laboratory, California Institute of Technology, under Contract No. NAS7-100, sponsored by the National Aeronautics and Space Administration.

The existence of an invariant band structure can be applied to the problem of the determination of crystal pseudopotentials. In fact, it can be shown that any local pseudopotential for a 3*d*-transition metal must nearly be as strong as the actual crystal-potential itself.

In subsequent work, it has been shown that the band structure of two or more phases of the same material can be precisely related. In particular the correlation between band structure of a material in its body-centered and face-centered phases have been deduced. The correlations then allow the band structure of one phase of a material to be deduced from that of any one of its other phases.

Reference

[1] Saffren, M. M., Phys. Rev. **165**, 870 (1968).

417-156 O - 71 - 50

Discussion on "Potential-Independent Features of Crystal Band Structure" by M. M. Saffren (California Institute of Technology)

J. F. Goff *(NOL):* In the first long period it is observed that the transport properties of the transition metals and their compounds show a remarkable similarity when they are compared in terms of their electron numbers [1]. It would seem that the potential independent portions of the Fermi surface must be responsible for these similarities. Thus, the transport properties of these solids can serve as a sort of test of the effect of core potential on the higher energy portions of the band structure.

M. M. Saffren *(California Inst. of Tech.):* I don't quite see the connection really.

J. F. Goff *(NOL):* You have the band structure as independent of the core potential essentially. And transport properties seem to be dependent upon that independent portion of the band structure. Did I understand you?

M. M. Saffren *(California Inst. of Tech.):* Well perhaps we can talk about it privately.

J. T. Waber *(Northwestern Univ.):* If I understood you correctly, you said that the *ns* level is always below *np* level. My recollection is that for heavy elements, where spin-orbit splitting is important, the order can be $2p\ 1/2 < 2s\ 1/2 < 2p\ 3/2$. Have you considered relativistic effects such as spin-orbit splitting and the relabelling of your states?

M. M. Saffren *(California Inst. of Tech.):* No I did not say that. In fact *np* and *ns* cannot be ordered independent of potential. As for relativistic levels, I have not found a way so far to order relativistic states. The results stand as results for non-relativistic bands.

[1] Goff, J. F., J. Appl. Phys. **39**, 2208 (1968).

Nonlinear Optical Susceptibility of Semiconductors with Zincblende Structure*

M. I. Bell**

Physics Department, Brown University, Providence, Rhode Island 02912

A simple model for the band structure and electronic density of states in zincblende semiconductors has been used to calculate the dispersion of the nonlinear susceptibility responsible for second-harmonic generation. The calculation requires no adjustable parameters, and results have been obtained for GaAs, InAs, ZnTe, and InSb in substantial agreement with experiment in the energy range 0-2.0 eV.

Key words: Electronic density of states; gallium arsenide (GaAs); indium antimony (InSb); indium arsenide (InAs); joint density of states; nonlinear optical susceptibility; optical properties; semiconductors; zincblende structure; ZnTe.

1. Introduction

The dispersion of the nonlinear optical susceptibility $\chi^{(2)}(\omega)$ which is responsible for the second harmonic generation of light (SHG) has been calculated for four semiconductors of the zincblende type (GaAs, InAs, InSb, and ZnTe) in the energy range 0-2 eV. A highly simplified band-structure model has been used, and assumptions introduced which reduce the calculation to a form similar to that of density-of-states calculations of the linear dielectric constant.

SHG is by now a well-known phenomenon, and its quantum-mechanical description has been developed fully, both for localized (atomic) systems [1] and in the context of band theory [2-6]. The process is described by a third-rank tensor $\chi^{(2)}$ which relates the applied macroscopic field ϵ to a polarization which is quadratic in the field:

$$P_i(2\omega) = \chi^{(2)}_{ijk}(\omega)\epsilon_j(\omega)\epsilon_k(\omega). \tag{1}$$

The profusion of variables and indices surrounding $\chi^{(2)}$ has led to a variety of conventions and notations, most of which are described by Robinson [7]. The definition of eq (1) will be used here.

2. Theory

2.1. General

In materials with zincblende structure (point group $\bar{4}3m$) the tensor $\chi^{(2)}$ is particularly simple. The only nonzero components $\chi_{ijk}{}^{(2)}$ are those in which no two of i, j, and k are equal. In addition, all such nonvanishing components are equal. Hence $\chi^{(2)}$ is completely specified by the single component $\chi_{123}{}^{(2)}$ which will be calculated here.

The results of Butcher and McLean [3], evaluated in the one-electron approximation, give for the susceptibility

$$\chi^{(2)}_{123}(\omega) = -\frac{i}{32\hbar^2}\left(\frac{e}{\pi m\omega}\right)^3 \sum_{rst}\int_{B.Z.} d^3\mathbf{k} f_{r\mathbf{k}}$$

$$\left\{\frac{P^1_{rs}(\mathbf{k})P^2_{st}(\mathbf{k})P^3_{tr}(\mathbf{k}) + P^1_{rs}(\mathbf{k})P^3_{st}(\mathbf{k})P^2_{tr}(\mathbf{k})}{[\omega_{rs}(\mathbf{k}) + 2\omega][\omega_{rt}(\mathbf{k}) + \omega]}\right.$$

$$+\frac{P^2_{rs}(\mathbf{k})P^1_{st}(\mathbf{k})P^3_{tr}(\mathbf{k}) + P^3_{rs}(\mathbf{k})P^1_{st}(\mathbf{k})P^2_{tr}(\mathbf{k})}{[\omega_{rs}(\mathbf{k}) - \omega][\omega_{rt}(\mathbf{k}) + \omega]}$$

$$\left.+\frac{P^2_{rs}(\mathbf{k})P^3_{st}(\mathbf{k})P^1_{tr}(\mathbf{k}) + P^3_{rs}(\mathbf{k})P^2_{st}(\mathbf{k})P^1_{tr}(\mathbf{k})}{[\omega_{rs}(\mathbf{k}) - \omega][\omega_{rt}(\mathbf{k}) - 2\omega]}\right\}. \tag{2}$$

Here the electrons are assumed to occupy Bloch states

$$\psi_{n\mathbf{k}}(\mathbf{r}) = u_{n\mathbf{k}}(\mathbf{r})e^{i\mathbf{k}\cdot\mathbf{r}}, \tag{3}$$

specified by the band label n and the wavevector $\mathbf{k}$. The frequencies are complex and restricted to the upper half-plane; $f_{r\mathbf{k}}$ is the Fermi-Dirac function for the state $\psi_{r\mathbf{k}}$; and $\mathbf{P}_{rs}(\mathbf{k})$ is the matrix element of the linear momentum operator between states $\psi_{r\mathbf{k}}$ and $\psi_{s\mathbf{k}}$.

Two useful observations can be made concerning eq (2). First, the result of applying the time reversal opera-

*Supported in part by ARPA contract SD 86.

**Corning Glass Works Foundation Fellow.

tor $T = -i\sigma_y K$ (where $\boldsymbol{\sigma}$ is the Pauli spin operator and K is the complex conjugation operator) to a Bloch function $\psi_{\mathbf{k}}$ is another Bloch function $\psi_{-\mathbf{k}}$ which is degenerate with and orthogonal to $\psi_{\mathbf{k}}$. Since $T\mathbf{P}T^{-1} = -\mathbf{P}$ one obtains

$$\langle r, \mathbf{k}|\mathbf{P}|s, \mathbf{k}\rangle = -\langle r, -\mathbf{k}|\mathbf{P}|s, -\mathbf{k}\rangle^*. \tag{4}$$

Thus in the integration over the Brillouin zone a product of the form $P_{rs}^{\alpha}(\mathbf{k})P_{st}^{\beta}(\mathbf{k}\ P_{tr}^{\gamma}(\mathbf{k})$ can be replaced by its imaginary part. This result is not altered when the spin-orbit interaction is taken into account, since this requires only that $\mathbf{P}$ be replaced [3] in eq (2) by

$$\mathbf{P}' = \mathbf{P} + \frac{\hbar}{4mc^2}\boldsymbol{\sigma} \times \nabla V(\mathbf{r}), \tag{5}$$

and $T\mathbf{P}'T^{-1} = -\mathbf{P}'$. The second observation is that if all the momentum matrix elements in (2) are replaced by components in the [111] direction

$$P_{ij}^{[111]} = \frac{1}{\sqrt{3}}\left(P_{ij}^{x} + P_{ij}^{y} + P_{ij}^{z}\right) \tag{6}$$

one obtains a quantity $\chi_{[111]}^{(2)}$ which is given by

$$\chi_{[111]}^{(2)} = \frac{2}{\sqrt{3}}\chi_{123}^{(2)} \tag{7}$$

Thus $\chi_{123}^{(2)}$ can be written in a form which depends only upon the [111] components on the momenta. Both of these results have been used elsewhere [8] to obtain simplified expressions equivalent to (2).

In the summation over bands in (2) three types of terms can be distinguished [5]. The labels r, s, t may refer to states in one, two, or three bands. In the first case it is easy to see (by writing (2) in terms of $P_{ij}^{[111]}$) that the contribution to $\chi_{123}^{(2)}$ vanishes. For two bands one may use the symmetry requirement $\chi_{123} = \chi_{213} = \chi_{312}$ and the first observation above to show that these contributions must also vanish. As Kelley [5] has pointed out, the two-band contributions may in general be nonzero; the present zero result is due to the particular point-group symmetry of the zincblende structure. Thus only three-band terms need be included in the summation in (2).

2.2. Three-Band Model

Even with these simplifications eq (2) is not amenable to direct calculation without some approximations for the matrix elements and energy denominators. It has been found that in general $|P_{rs}^{\alpha}(\mathbf{k})|$ is nearly constant across the Brillouin zone [9,10]. For the imaginary part of the linear dielectric constant ϵ_2, this approximation leads to the conclusion that the dispersion of ϵ_2 is governed by the behavior of the joint density of states for the various possible transitions [9]. The dispersion can then be obtained from consideration of critical points in the density of states [11]. The corresponding approximation for $P_{rs}^{\alpha}(\mathbf{k})P_{st}^{\beta}(\mathbf{k})P_{tr}^{\gamma}(\mathbf{k})$ can be justified only by a detailed examination of band structure calculations [8], but with the aid of eq (4) it can easily be shown that to third order in $\mathbf{k}$

$$T_{rst}(\mathbf{k}) = \mathrm{Im}\ [P_{rs}^{1}(k_i)P_{st}^{2}(k_i)P_{tr}^{3}(k_i)] = F + F'k_i^2 \tag{8}$$

Then the assumption that $|P_{rs}^{\alpha}(\mathbf{k})|$ is approximately constant leads to the conclusion that at worst $|F| \approx |F'|$. Thus treating $T_{rst}(\mathbf{k})$ as a constant is no less (or more) justified than the assumption usually made in density-of-states calculations that $|P_{rs}^{\alpha}(\mathbf{k})|$ is constant.

If the Fermi-Dirac function $f_{r\mathbf{k}}$ is approximated by 1 for valence bands and zero for conduction bands, the contribution to $\chi_{123}^{(2)}$ of a valence band $|1, \mathbf{k}\rangle$ and two other bands $|2, \mathbf{k}\rangle$, $|3, \mathbf{k}\rangle$ can be written

$$\Delta\chi_{123}^{(2)} = -\frac{iF}{16\hbar^2}\left(\frac{e}{\pi m\omega}\right)^3 \sum_{i=1}^{6}\int_{B.Z.} d^3\mathbf{k}\ \frac{s_i}{[\omega_{12}(\mathbf{k}) - n_i\omega][\omega_{13}(\mathbf{k}) - m_i\omega]} \tag{9}$$

where

$$F = \frac{\sqrt{3}}{2}P_{12}^{[111]}(0)P_{23}^{[111]}(0)P_{31}^{[111]}(0) = iT_{123}(0)$$

$$s_i = \begin{cases} 1, & i = 1, 3 \\ -1, & i = 4, 6 \end{cases} \tag{10}$$

$$n_i = -2, 1, 1, -1, -1, 2$$

$$m_i = -1, -1, 2, -2, 1, 1$$

Suitable approximations for the energy denominators in (9) are also needed. The upper valence and first two conduction bands of InAs are shown in figure 1 as calculated by the full-zone $\mathbf{k}\cdot\mathbf{p}$ method [12]. The main features of the band structure of other zincblende-type semiconductors have been found to be qualitatively similar [12-14]. The major contributions to $\epsilon_2(\omega)$ in the range 0-4 eV have been found [12] to come from transitions at $\Gamma(\mathbf{k} = 0)$ and along $\Lambda(\mathbf{k} = (k/\sqrt{3}))$ [111]. These transitions are $\Gamma_{8v} - \Gamma_{6c}$ (E_0); $\Gamma_{7v} - \Gamma_{6c}$ $(E_0 + \Delta_0)$; Λ_{4v}, $\Lambda_{5v} - \Lambda_{6c}$ (E_1); and $\Lambda_{6v} - \Lambda_{6c}$ $(E_1 + \Delta_1)$. The band structure model used was chosen to provide critical points of the proper type at the energies of these transitions,

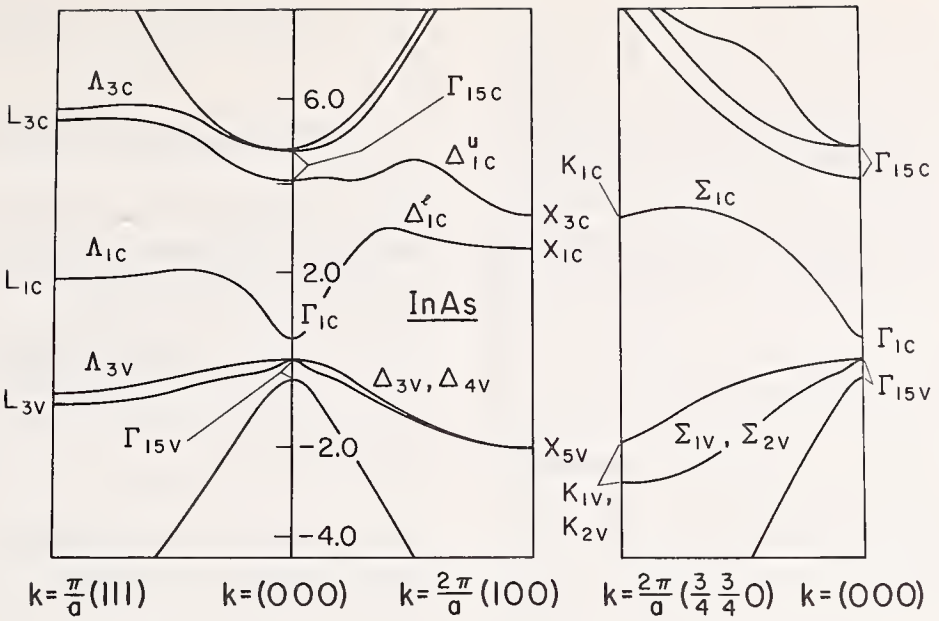

FIGURE 1. *Band structure of* InAs *as calculated by the full-zone* $\mathbf{k}\cdot\mathbf{p}$ *method.*

and includes a second conduction band in order to permit calculation of three-band terms. The transitions at Γ are described by parabolic bands extended to infinity:

$$\omega_{12}(\mathbf{k}) = -\omega_0 - \frac{k^2}{2m_{12}}$$
$$\omega_{13}(\mathbf{k}) = -\omega_0' - \frac{k^2}{2m_{13}} \tag{11}$$

The integrals in (9) then take the form

$$\int \frac{d^3k}{[\omega_{12}(\mathbf{k}) - n_i\omega][\omega_{13}(\mathbf{k}) - m_i\omega]} = 8m_{12}m_{13}\pi$$
$$\int_0^\infty \frac{\alpha^{1/2}d\alpha}{(2x_i+\alpha)(2x_i'+\alpha)} \tag{12}$$

where

$$\alpha = k^2$$
$$x_i = m_{12}(\omega_0 + n_i\omega)$$
$$x_i' = m_{13}(\omega_0' + m_i\omega). \tag{13}$$

A contour integration yields

$$\Delta\chi^{(2)}_{123} = \frac{-ie^3Fm_{12}m_{13}}{\sqrt{2}\pi\hbar^2m^3\omega^3} \sum_{i=1}^{6} \frac{s_i}{\sqrt{x_i} + \sqrt{x_i'}} \tag{14}$$

The exact locations in the Brillouin zone of the Λ critical points are difficult to determine, and in fact reference to figure 1 indicates that the upper valence and lowest conduction bands are very nearly parallel in the [111] direction for perhaps 2/3 of the zone. We can therefore approximate these critical points by 2-dimensional minima while retaining a parabolic second conduction band:

$$\omega_{12}(\mathbf{k}) = -\omega_1 - \frac{k_\perp^2}{2m_\perp}$$
$$\omega_{13}(\mathbf{k}) = -\omega_0' - \frac{k_\perp^2 + k_\parallel^2}{2m_{13}} \tag{15}$$

where the subscripts on $k_\perp$, $k_\parallel$, and $m_\perp$ refer to directions parallel and perpendicular to [111]. While this approximation is crude, it has been used, together with that of eq (11), to obtain a quite satisfactory description of the intrinsic piezobirefringence of Si, Ge, and GaAs [15]. For this case (9) becomes

$$\Delta\chi^{(2)}_{123} = -\frac{ie^3F}{\pi^2\hbar^2m^3\omega^3} m_\perp m_{13}k_L \sum_{i=1}^{6} \int_{-1}^{1} d\mu \frac{s_i}{x_i' - x_i'' + \frac{1}{2}k_L^2\mu^2} \log \frac{x_i' + \frac{1}{2}k_L^2\mu^2}{x_i''} \tag{16}$$

where

$$x_i'' = m_\perp(\omega_1 + n_i\omega)$$
$$\mu = \frac{k_\parallel}{k_L}$$

and $k_L = \pi\sqrt{3}/a$ is the magnitude of the wavevector at L. The integral in (16) cannot be evaluated in closed form, so a numerical integration is required. Before attempting to obtain numerical results from eqs (14) and (16) it is necessary to make an observation which will

lead to a rather extended digression. The results (14) and (16) have been derived from (2) and therefore describe the frequency dependence of the entire (complex) susceptibility—no attempt has been made to separate the real and imaginary parts. However, when an exactly analogous technique [15,16] is used to compute ϵ_1, the real part of the linear dielectric constant, it is found that a constant (frequency-independent) term must be added to the result in order to fit the experimental data. This term results from the neglect of the higher conduction bands which contribute to ϵ_2 at high frequencies and hence, through the dispersion (Kramers-Kronig) relations, to ϵ_1 at low frequencies. Since identical dispersion relations [16] apply to $\chi^{(2)}$ one would anticipate that the results (14) and (16) underestimate the real part of $\chi_{123}^{(2)}$. If the neglected conduction bands are assumed to lie high enough in energy that $\omega_{12}, \omega_{13} \gg \omega$ for ω in the region of interest then the contribution of these bands to Re $\chi_{123}^{(2)}$ can be regarded as a constant. The frequency dependence of $\chi_{123}^{(2)}$ is thus given by

$$\chi_{123}^{(2)}(\omega) = \Delta\chi_{123}^{(2)}(\omega) + \delta\chi_{123}^{(2)} \tag{17}$$

where $\Delta\chi_{123}^{(2)}(\omega)$ is computed from (14) and (16), and $\delta\chi_{123}^{(2)}$ is a real, frequency-independent correction given by

$$\delta\chi_{123}^{(2)} = \chi_{123}^{(2)}(0) - \Delta\chi_{123}^{(2)}(0) \tag{18}$$

(Here $\omega = 0$ must always be interpreted as referring to frequencies well below those of the electronic transitions but above the lattice resonances). While $\delta\chi_{123}^{(2)}$ could be treated as an adjustable parameter or inferred from infrared (10.6μ) measurements of $\chi_{123}^{(2)}$, it is more satisfying to obtain this quantity from a direct calculation of $\chi_{123}^{(2)}(0)$.

2.3. Low-Frequency Limit

A number of calculations of $\chi_{123}^{(2)}(0)$ have been made for various zincblende-type materials [18-20], based on an approach originated by Robinson [7]. The results of these calculations differ significantly, so it is worthwhile to attempt yet another calculation along these lines but employing the same model as will be used to compute $\Delta\chi_{123}^{(2)}(\omega)$. The basis for the calculation is provided by the relations

$$P_\alpha = \chi_{\alpha\beta}^{(1)}\epsilon_\beta + \chi_{\alpha\beta\gamma}^{(2)}\epsilon_\beta\epsilon_\gamma + \ldots \tag{19}$$

and

$$W = -\tfrac{1}{2}\chi_{\alpha\beta}^{(1)}\epsilon_\alpha\epsilon_\beta - \tfrac{1}{3}\chi_{\alpha\beta\gamma}^{(2)}\epsilon_\alpha\epsilon_\beta\epsilon_\gamma - \ldots \tag{20}$$

for the polarization $\mathbf{P}$ and total energy W of the system in an applied field $\boldsymbol{\epsilon}$ (in the zero-frequency limit). If the Hamiltonian is taken to be

$$H = H_0 + e\mathbf{x}\cdot\boldsymbol{\epsilon} \tag{21}$$

then for N unit cells per unit volume perturbation theory gives

$$W = NE_0 \tag{22}$$

where

$$E_0 = E_0^{(0)} + E_0^{(1)} + E_0^{(2)} + E_0^{(3)} + \ldots \tag{23}$$

$$H_0|m\ \rangle = E_m^{(0)}|\ m\rangle \tag{24}$$

$$E_0^{(1)} = e\epsilon_\alpha\langle 0|x_\alpha|0\rangle \equiv e\epsilon_\alpha\bar{x}_\alpha \tag{25}$$

$$E_0^{(2)} = -e^2\epsilon_\alpha\epsilon_\beta \sum_s{}' \frac{\langle 0|x_\alpha|s\rangle\langle x|x_\beta|0\rangle}{E_s^{(0)} - E_0^{(0)}} \tag{26}$$

$$E_0^3 = e^3\epsilon_\alpha\epsilon_\beta\epsilon_\gamma \sum_s{}' \sum_t{}' \frac{\langle 0|x_a|s\rangle\langle s|\bar{x}_\beta - \bar{x}_\beta|t\langle\rangle t|x_\gamma|0\rangle}{(E_s^{(0)} - E_0^{(0)})\ (E_t^{(0)} - E_0^{(0)})} \tag{27}$$

A comparison of (20) with (26) and (27) would permit evaluation of $\chi^{(1)}(0)$ and $\chi^{(2)}(0)$, given a method of performing the summations involved. Jha and Bloembergen [18] employ a single energy denominator and the closure property, while Flytzanis and Ducuing [19] use the method of Delgarno and Lewis in the form of a variational principle, and Phillips and Van Vechten [20] assume the existence of only two states. The method here will be to use the formalism of band theory and restrict the summations to states in the three bands described above. Since the lowest valence band lies well below any bands with which it can interact through the perturbation in (21), the perturbation energies (25) and (26) can be regarded as arising entirely from perturbation of states in the top valence band $|1\rangle$. Then (20), (26), and (27) give

$$\chi_{\alpha\alpha}^{(1)} = 2Ne^2 \int d^3\mathbf{k} \left[\frac{|\langle 1|x_a|2\rangle|^2}{E_{21}} + \frac{|\langle 1|x_\alpha|3\rangle|^2}{E_{31}} \right] \tag{28}$$

$$\chi^{(2)}_{\alpha\beta\gamma} = -3Ne^3 \int d^3\mathbf{k} \left[\frac{1}{E_{21}E_{31}} \left(\langle 1|x_\alpha|2\rangle\langle 2|x_\beta|3\rangle\langle 3|x_\gamma|1\rangle \right.\right.$$

$$+ \langle 1|x_\alpha|3\rangle\langle 3|x_\beta|2\rangle\langle 2|x_\gamma|1\rangle) + \frac{1}{E_{21}^2} \langle 1|x_\alpha|2\rangle\langle 2|x_\alpha|1\rangle$$

$$\left.\left. (\langle 2|x_\beta|2\rangle - \langle 1|x_\beta|1\rangle) + \frac{1}{E_{31}^2} \langle 1|x_\alpha|3\rangle\langle 3|x_\gamma|1\rangle (\langle 3|x_\beta|3\rangle - \langle 1x_\beta|1\rangle) \right] \right. \tag{29}$$

These results can be expressed in terms of the well-known relation for off-diagonal matrix elements of $\mathbf{P}$ and $\mathbf{x}$ [21]

$$\langle \alpha|\mathbf{P}|\beta\rangle = im\omega_{\alpha\beta}\langle \alpha|\mathbf{x}|\beta\rangle. \tag{30}$$

As before, $|P_{rs}{}^{\alpha}(\mathbf{k})|$ and $T_{rst}(\mathbf{k})$ will be approximated as constant throughout the Brillouin zone. These quantities will be evaluated at $\mathbf{k} = 0$, employing a model proposed by Cardona [22] in which the zincblende-type material is regarded as derived from a fictitious diamond-type material by the action of an antisymmetric potential V. In the diamond-structure materials the top valence and first two conduction bands at $\mathbf{k} = 0$ have the symmetries described by the representations Γ_{25}', Γ_2', and Γ_{15} of the full cubic group. If all other states are neglected, the effect of V is to mix the $\Gamma_{25'}$ and Γ_{15} states to produce two states belonging to the representation Γ_{15} of 43m. The Γ_{25}' state (now Γ_1) is unaffected, and the Hamiltonian for the Γ_{15} states (referred to Γ_{25}', Γ_{15} basis) is

$$H = \begin{pmatrix} E & V \\ V^* & 0 \end{pmatrix} \tag{31}$$

where $E(\Gamma_{25}')=0$, and $E(\Gamma_{15})=E$. This Hamiltonian has eigenvalues

$$\begin{aligned} E(\Gamma_{15c}) &= \tfrac{1}{2}\{E + [E^2 + (2V)^2]^{1/2}\} \\ E(\Gamma_{15v}) &= \tfrac{1}{2}\{E - [E^2 + (2V)^2]^{1/2}\} \end{aligned} \tag{32}$$

and eigenvectors

$$\begin{aligned} \psi_{15c} &= a\psi_{15} - b\psi_{25'} \\ \psi_{15v} &= b\psi_{15} + a\psi_{25'} \end{aligned} \tag{33}$$

where

$$\begin{aligned} a &= \frac{1}{\sqrt{2}} \left(\frac{E_{31}+E}{E_{31}} \right)^{1/2} \\ b &= \frac{1}{\sqrt{2}} \left(\frac{E_{31}-E}{E_{31}} \right)^{1/2} \end{aligned} \tag{34}$$

and

$$E_{31} = E(\Gamma_{15c}) - E(\Gamma_{15v}) = [E^2 + (2V)^2]^{1/2} \tag{35}$$

If $E_{31}{}^3 \gg E_{21}{}^3$ then in this model eqs (28) and (29) give

$$\chi^{(2)}_{123}(0) \approx \frac{3e\hbar}{m} \chi^{(1)}_{\alpha\alpha} \frac{QV}{(E_{31})^3} \tag{36}$$

where

$$i\langle \Gamma_{25}'|\mathbf{P}|\Gamma_{15}\rangle = Q. \tag{37}$$

While $\chi_{\alpha\alpha}{}^{(1)}$ can be determined experimentally, Q and V depend upon the fictitious diamond-structure material referred to above. Since E_{31} is known from experiment, V can be found from (35) if E is known. Figure 2 shows E and Q as a function of the lattice parameter a for Si, Ge, and α-Sn. The values for E are those of the

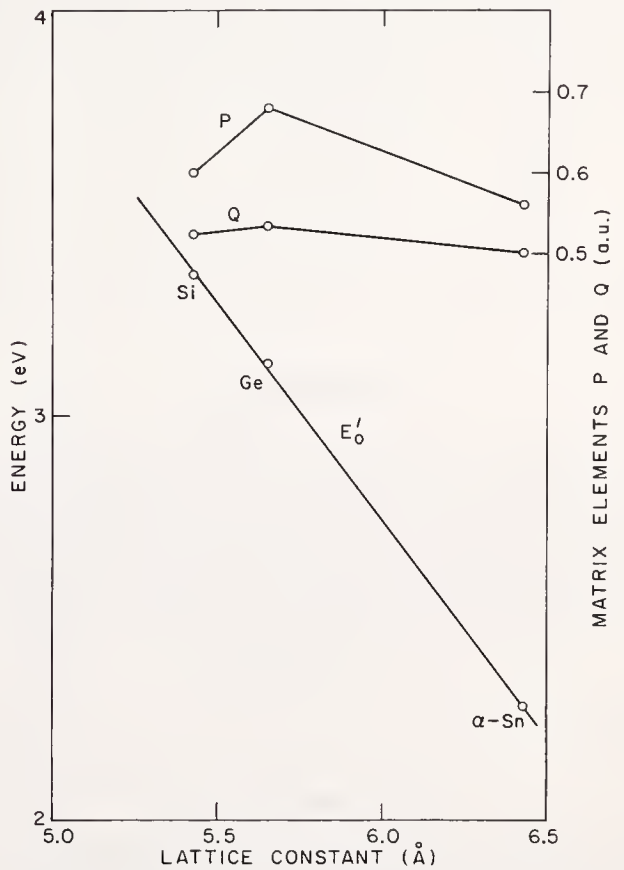

FIGURE 2. *Dependence on lattice constant of the* $\Gamma_{25}' - \Gamma_{15}(E_0')$ *gap and the matrix elements in diamond structure materials.*

E_0' peak in the electroreflectance spectra [23]. The matrix elements are determined from cyclotron resonance [24,25]. For a zincblende-type material of lattice constant a, figure 2 was used to determine the values of E and Q for a fictitious diamond-type material of the same lattice constant. Since E_0' varies in almost exactly linear fashion with the lattice constant from Si to α-Sn. E was obtained by linear interpolation. Since Q varies little (less than 8%) the method used to estimate it is not of great importance. Compounds of elements from the same row of the periodic table were assigned the value of Q belonging to the group IV material in that row. In general, compounds of elements from different rows were assigned the average of the values for the group IV materials in each row. The details of this procedure are given elsewhere [14]. The linear susceptibility $\chi^{(1)}_{\alpha\alpha}(0)$ was obtained from Phillips and Van Vechten [20], and E_{31} from electroreflectance data [22]. Table 1 lists all the necessary parameters and the results of eq (36) for 9 zincblende-type semiconductors.

TABLE 1. *Parameters used in the calculation and results for the low-frequency limit* $\chi^{(2)}_{123}(0)$

	a(Å)	E_{31}(eV)	E(eV)	$\chi^{(1)}$	Q (a.u.)	$2V$(eV)	$\chi^{(2)}$ (10^{-8} esu)
GaAs.....	5.62	4.44	3.15	0.79	0.535	3.12	97.7
GaSb.....	6.11	3.27	2.63	1.07	.518	1.94	199
InAs.....	6.05	4.44	2.69	0.90	.518	3.53	122
InSb.....	6.49	3.16	2.22	1.17	.501	2.25	271
GaP.....	5.45	4.78	3.34	0.65	.530	3.42	70.0
InP.....	5.87	4.72	2.89	.68	.535	3.73	83.7
AlSb.....	6.14	3.72	2.60	.73	.513	2.66	126
ZnTe.....	6.09	5.40	2.65	.50	.518	4.71	50.3
CdTe.....	6.48	5.30	2.23	.49	.501	4.81	51.4

2.4. Dispersion

The dispersion of $\chi^{(2)}_{123}(\omega)$ can now be obtained from eqs (14), (16), and (17). Since experimental data are available [8,26] only for GaAs, InAs, InSb, and ZnTe, discussion will be restricted to these four materials.

With the aid of eqs (33-35) we find that at $\mathbf{k}=0$

$$F = iP^2QV/E_{31} \tag{38}$$

where

$$i\langle \Gamma_{25}' | \mathbf{P} | \Gamma_2' \rangle = P. \tag{39}$$

Examinations of the matrix elements for the various possible transitions show that the spin-orbit splitting of the valence band at Γ may be taken into account by evaluating (14) with $\hbar\omega_0 = E_0$, $\hbar\omega_0' = E_0'$ (for the light-hole and heavy-hole bands) and with $\hbar\omega_0 = E_0 + \Delta_0$, $\hbar\omega_0' = E_0' + \Delta_0$ (for the split-off band). The spin-orbit splitting of the Γ_{15} conduction states has been neglected.

The valence band masses (m^*_{lh}, m^*_{hh}, and m^*_{sh} for the light-hole, heavy-hole and split-off hole bands, respectively) were obtained from the average masses [22].

$$\begin{aligned} \frac{m}{m^*_{lh}} &= -A - B\left(1 + \frac{C^2}{10B^2}\right) \\ \frac{m}{m^*_{hh}} &= -A + B\left(1 + \frac{C^2}{10B^2}\right) \\ \frac{m}{m^*_{sh}} &= -A' \end{aligned} \tag{40}$$

where A, B, and C are the inverse mass parameters of Dresselhaus, Kip, and Kittel [27], and A' is given by [22]

$$A' = \frac{1}{3}\left(\frac{E_0 F}{E_0 + \Delta_0} + 2G + 2M\right) + 1 \tag{41}$$

where

$$\begin{aligned} F &= -\frac{P^2(E_{31}+E)}{E_0 E_{31}} \\ G &= -0.8\,\frac{(E_{31}+E)}{E_{31}} \\ M &= -\frac{2Q^2}{E_{31}}\,. \end{aligned} \tag{42}$$

The assumption that the shape of the second conduction band near Γ is determined entirely by its interaction with the valence band leads (neglecting the spin-orbit interaction) to the result that the effective mass is approximately m^*_{hh}. In eq (16) the value $m_{13} = m^*_{hh}/2$ has been used.

The spin-orbit splitting along Λ can be treated in the same way as that at Γ, but the split-off valence band may be ignored. The interband mass $m_\perp$ is found by assuming that the shape of the valence band is determined by the $\Lambda_{3v} - \Lambda_{1c}$ interaction. Then $m_\perp = m^*_\perp (L_{1c})/2$.

Table 2 lists the values used in the calculation. The energies E_0, E_1, Δ_0, and Δ_1 were obtained from electroreflectance measurements [22,28], with the exceptions noted in table 2. The matrix element P was deter-

TABLE 2. *Parameters used in the calculation of* $\chi^{(2)}_{123}(\omega)$

	GaAs	InAs	InSb	ZnTe
P(a.u.)	0.68	0.62	0.56	0.62
E_0(eV)	1.43	[a].41	[b].17	2.25
E_1(eV)	3.12	2.50	1.88	3.61
Δ_0(eV)	0.34	[a]0.43	0.82	0.93
Δ_1(eV)	.23	.28	.50	.57
m^*_c	.067	.026	.0145	[c].180
$m^*_\perp$	.116	.132	.127	[c].199
A	−7.39	−17.1	−26.5	−4.0
B	−4.93	−14.9	−24.1	−2.3
$\|C\|$	5.06	10.9	13.9	2.0
A'	[c]−6.30	[c]−8.71	[c]−7.68	[c]−3.23

[a]F. Matossi and F. Stern, Phys. Rev 111, 472 (1958).
[b]O. Madelung, *Physics of III-V Compounds* (J. Wiley and Sons, Inc., New York, 1964), p. 53.
[c]Calculated as described in text.

mined by the method described above for Q. The inverse mass parameters for InSb and ZnTe are available from cyclotron resonance experiments [29,30]. Those for InAs and GaAs were obtained from the full-zone $\mathbf{k}\cdot\mathbf{p}$ band structure calculations [12,14], and the calculated values for InSb [14] were found to give slightly better results than the experimental ones.

The conduction band masses m^*_c (at Γ) were taken from magneto-optical absorption and Faraday rotation measurements [31-33], except in the case of ZnTe where no experimental data are available. In the three-band approximation this mass is given by [22]

$$\frac{m}{m^*_c}=1+\frac{P^2}{E_{31}}\left[\frac{E_{31}+E}{3}\left(\frac{2}{E_0}+\frac{1}{E_0+\Delta_0}\right)-\frac{E_{31}-E}{E_{31}-E_0}\right] \quad (43)$$

The results of (43) agree well with experiment (10% or better) in the three materials where m^*_c has been measured, so the use of this approximation for ZnTe is probably justified. Finally, $m^*_\perp(L_{1c})$ was obtained from the $\mathbf{k}\cdot\mathbf{p}$ calculations, again with the exception of ZnTe where (43) was used with E_0 and Δ_0 replaced by E_1 and Δ_1, E_{31} replaced by $E(L_{3c})-E(L_{3v})$, and E by the $L_{3c}-L_{3v}$ gap in the corresponding homopolar material (average of Ge and α-Sn)[22].

The frequencies appearing in (9) are complex; the real-frequency limit can be taken in the conventional way [3]. However, for the sake of comparison with observations at room temperature, thermal broadening has been included by using the complex frequency $\omega+i\eta$, with $\eta=0.05\ eV$ (≈ 2 kT).

Equation (17) was evaluated for energies from 0.05 to 2.0 eV at intervals of 0.05 eV by a computer program which required approximately 2 minutes per material on an IBM 360 Model 50 computer. (The integral in (16) was evaluated by a 6-point Gauss quadrature.) Figure 3 shows the real and imaginary parts of $\chi_{123}{}^{(2)}(\omega)$ for GaAs. The modulus of the susceptibility

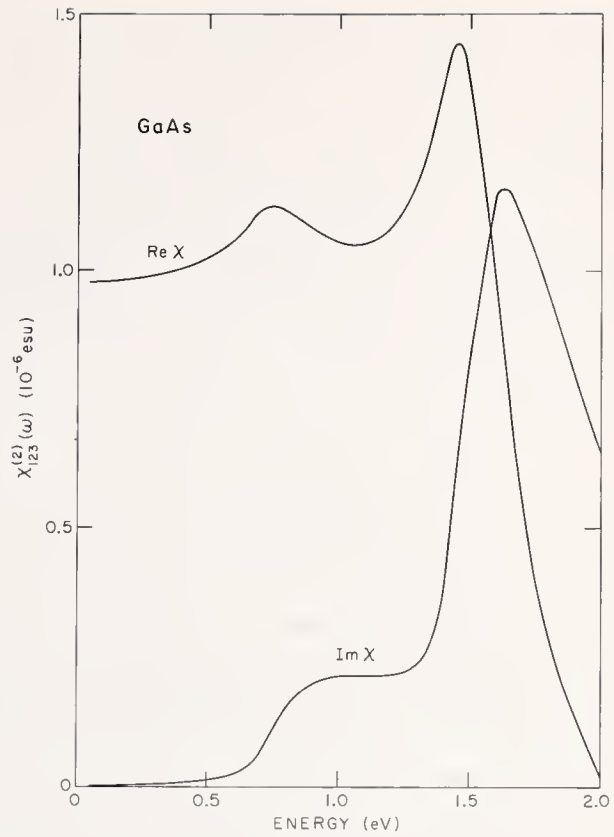

FIGURE 3. *Real and imaginary parts of* $\chi^{(2)}_{123}(\omega)$ *as calculated for* GaAs.

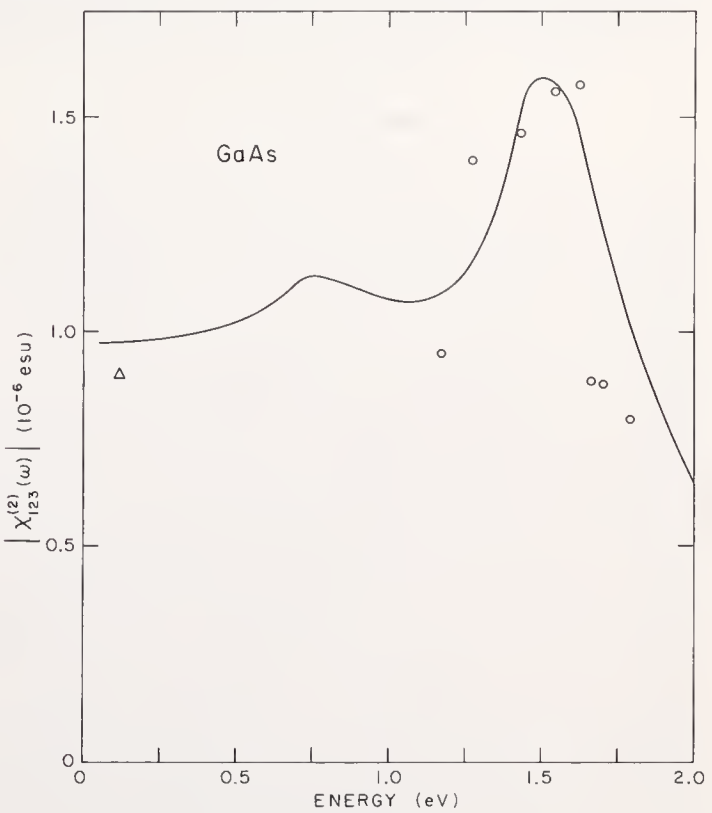

FIGURE 4. *The modulus* $|\chi^{(2)}_{123}(\omega)|$ *as calculated for* GaAs.

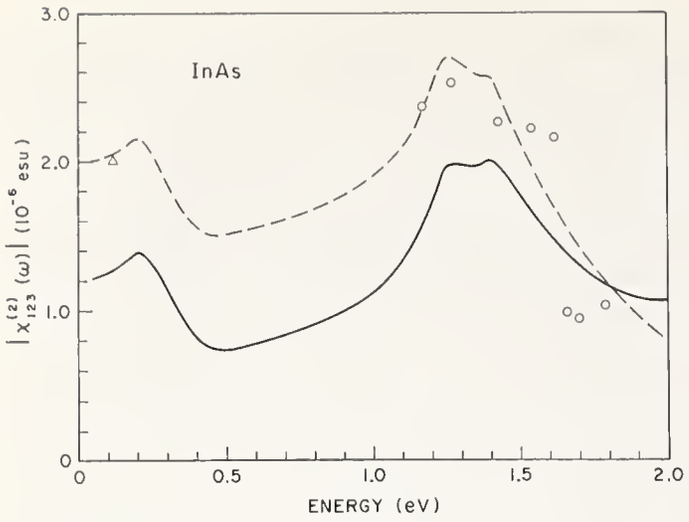

FIGURE 5. *The modulus* $|\chi^{(2)}_{123}(\omega)|$ *as calculated for* InAs.

$|\chi_{123}{}^{(2)}(\omega)|$ is given in figures 4-7, together with the available experimental data. The experiments of Chang, Ducuing, and Bloembergen [26] measured $|\chi_{123}{}^{(2)}(\omega)|$ relative to its value in KH_2PO_4 (KDP). The result of Bjorkholm [34] for KDP, $|\chi_{123}{}^{(2)}| = (1.6 \pm 0.4) \times 10^{-9}$esu, was used to convert these measurements to absolute values. The results, indicated by circles in figures 4-7, have a total uncertainty of about 30%, most of which is contributed by the 25% error in the measurement for KDP. The relative measurements for the semiconductors have an error of about 15%. Also shown (by triangles) are the results of absolute measurements at 10.6μ by Patel [35] and Wynne and Bloembergen [36]. These have uncertainties of the order of 30-50%.

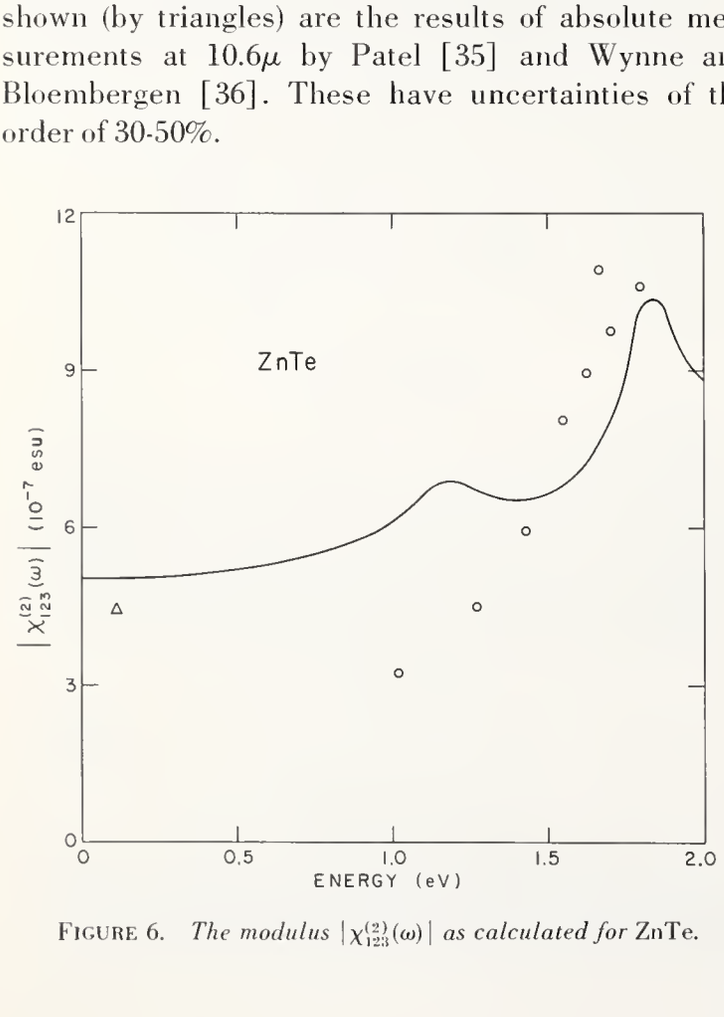

FIGURE 6. *The modulus* $|\chi^{(2)}_{123}(\omega)|$ *as calculated for* ZnTe.

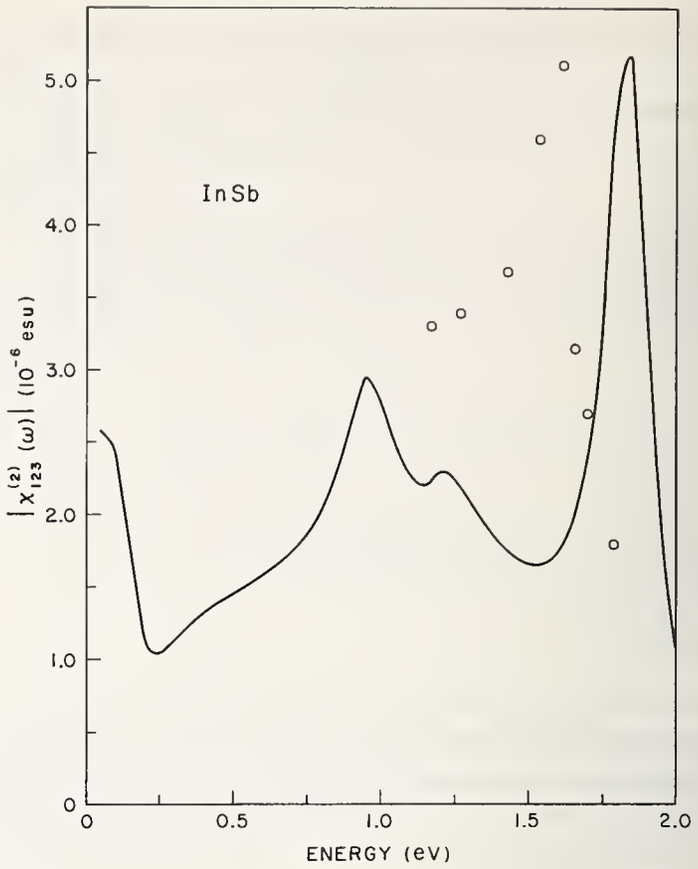

FIGURE 7. *The modulus* $|\chi^{(2)}_{123}(\omega)|$ *as calculated for* InSb.

3. Discussion

3.1. Low-Frequency Limit

Table 3 compares the results of the present calculation with those of Flytzanis and Ducuing [19] and Phil-

TABLE 3. *Comparison of the results for the low-frequency limit* $\chi^{(2)}_{123}(0)$ *with experiment and with the calculations of Flytzanis and Ducuing (F–D) [19] and Phillips and Van Vechten (P–VV) [20]. Values are in units of* 10^{-8} *esu.*

	F–D	P–VV		Present work	Expt.
		$\chi^{(2)}$	$f_c^2\chi^{(2)}$		
GaAs	190	256	122	97.7	[a] 90 ± 30
GaSb	160	433	236	199	[a] 302 ± 100
InAs	410	380	157	122	[a] [b] 200 ± 60
InSb	650	611	282	271	
GaP	140	186	85	70.0	[a] 52 ± 17
InP	280	269	106	83.7	
AlSb	70	337	111	126	
ZnTe		257	53	50.3	[b] 44 ± 16
CdTe		257	27	51.4	[b] 80 ± 30

[a] Ref. 36.
[b] Ref. 35.

lips and Van Vechten [20]. Two values of $\chi_{123}^{(2)}(0)$ are given for [20] since the authors argue that their results should be multiplied by a factor of f_c^2, where f_c is the fraction of covalent character in the crystal bonding [37]. It is interesting to note that in five of the seven cases treated by Flytzanis and Ducuing their results agree well with the uncorrected values of $\chi_{123}^{(2)}(0)$ obtained by Phillips and Van Vechten. The present results, however, are in general agreement with the corrected values $f_c^2\chi_{123}^2(0)$. Both of the calculations [19] and [20] employ pure sp^3 hybrid molecular orbitals, and Phillips and Van Vechten suggest that the correction f_c^2 may arise from the neglect of other electronic configurations. The use of a band-structure formalism and experimentally determined momentum matrix elements seems to avoid this difficulty.

3.2. Dispersion

The results for GaAs and InAs are qualitatively similar and will be discussed together. In each case the most notable feature in the dispersion is a peak in the vicinity of $E_1/2$ and $(E_1 + \Delta_1)/2$ which arises from the coincidence of the harmonic photon energy $2\hbar\omega$ with the energy of the $\Lambda_{3v} - \Lambda_{1c}$ transitions. The broken curve for InAs (fig. 5) was calculated by assuming the experimental value $\chi_{123}^{(2)}(0) = 2 \times 10^{-6}$esu [35] rather than $\chi_{123}^{(2)}(0) = 1.22 \times 10^{-6}$ as calculated above. The result indicates that the present calculation of the dispersion is consistent with the observed low-frequency value and that the result of part 2.3 is probably too small.

It has been suggested [26] that the sharp decrease in $\chi_{123}^{(2)}(\omega)$ observed between 1.62 and 1.66 eV in these two materials is due to the variation of $T(\mathbf{k})$ across the Brillouin zone, since no pronounced structure is observed in the linear dielectric constant $\epsilon(\omega)$ or $\epsilon(2\omega)$ at this energy. While it is likely that the wavevector dependence of T produces some structure in $\chi_{123}^{(2)}(\omega)$, the present calculation (which assumes T constant) reproduces the structure near 1.66 eV fairly well. As can be seen in figure 2 (for GaAs) the calculated decrease is caused primarily by a sharp drop in the real part of the susceptibility. The results are similar for InAs. It should be noted that it is possible for the nonlinear susceptibility to show rapid variations as a function of energy in regions where the linear susceptibility does not. While $\mathrm{Im}\chi^{(2)}$ will in general exhibit rapid variation only where $\mathrm{Im}\chi^{(1)}$ does also, the linear susceptibility is restricted by the requirement $\mathrm{Im}\chi_1 > 0$ [38] while no such restriction applies to the nonlinear susceptibility. Thus, contributions to $\mathrm{Im}\chi^{(2)}$ from different points in the Brillouin zone may be of opposite sign. In an energy region where $\mathrm{Im}\chi^{(1)}$ is (for example) increasing rapidly, $\mathrm{Im}\chi^{(2)}$ may decrease or even change sign. The real part of the susceptibility, which is related to the imaginary part by the Kramers-Kronig relations, may then behave quite differently in the linear and nonlinear cases. The fact that most experiments measure only the modulus $|\chi_{123}^{(2)}(\omega)|$ of the susceptibility further complicates the situation. While structure in $\chi^{(2)}(\omega)$ can be expected at energies where $\chi^{(1)}(\omega)$ or $\chi^{(1)}(2\omega)$ varies rapidly, $\chi^{(2)}$ does exhibit additional structure unrelated to the matrix element product $T(\mathbf{k})$.

In ZnTe (fig. 6) the main peak near 1.8 eV is also due to the coincidence of the harmonic photon energy $2\hbar\omega$ with that of the E_1 and $E_1 + \Delta_1$ transitions. The small peak near 1.15 eV is produced by transitions at Γ. The failure of this peak to appear experimentally casts some doubt on the accuracy of eq (14). Further experimental results in the 0.5-1.5 eV region for these materials would be needed to confirm (14).

The calculation for InSb is less satisfactory than the others. The experimentally observed peak near 1.6 eV has been attributed to the coincidence of the fundamental photon energy $\hbar\omega$ with the E_1 peak [8,26]. This structure appears in the calculation, but it occurs about 0.2 eV too high in energy. Band structure calculations [39] indicate that the critical point at E_1 may occur exactly at L. In that case the eqs (15) would not apply, and (16) would have to be modified to take into account the correct symmetry of the critical point.

4. Conclusion

A highly simplified band-structure model has been found to predict the dispersion of the nonlinear optical susceptibility of four zincblende-structure semiconductors with reasonable accuracy in the energy range 0-2 eV. Separate calculations were made of the low-frequency limit and of the contributions of critical points in the joint density of states for the top valence band and the first two conduction bands. The results for the low-frequency limit were found to agree well with the calculations of Phillips and Van Vechten [20], and the calculated dispersion is in substantial agreement with the experimental work of Chang, Ducuing and Bloembergen [26]. Variations in the susceptibility which had previously been regarded as arising from the wavevector dependence of interband momentum matrix elements are successfully predicted by the model in spite of the fact that the momenta are treated as constant throughout the Brillouin zone.

5. Acknowledgments

The author would like to express his gratitude to Professor H. J. Gerritsen who suggested this problem and to Professor M. Cardona who gave valuable guidance and encouragement. Professor F. H. Pollak and Dr. C. W. Higginbotham were generous with advice and helpful criticism. Dr. J. C. Phillips, Professor J. A. Van Vechten, Dr. J. J. Wynne, and Professor N. Bloembergen made available their results prior to publication.

6. References

[1] Armstrong, J. A., Bloembergen, N., Ducuing, J., and Pershan, P. S., Phys. Rev. **127**, 1918 (1962).
[2] Loudon, R., Proc. Phys. Soc. **80**, 952 (1962).
[3] Butcher, P. N., and McLean, T. P., Proc. Phys. Soc. **81**, 219 (1963); **83**, 579 (1964).
[4] Kelley, P. L., J. Phys. Chem. Solids **24**, 607 (1963).
[5] Kelley, P. L., J. Phys. Chem. Solids **24**, 1113 (1963).
[6] Cheng, H., and Miller, P. B., Phys. Rev. **134**, A683 (1964).
[7] Robinson, F. N. H., Bell System Tech. J. **46**, 913 (1967).
[8] Bloembergen, N., Chang, R. K., and Ducuing, J., in Physics of Quantum Electronics, P. L. Kelley, B. Lax, and P. E. Tannenwald, Editors (McGraw-Hill Book Co., New York, 1966), p. 67.
[9] Brust, D., Phys. Rev. **134**, A1337 (1964).
[10] Cardona, M., and Pollak, F. H., Phys. Rev. **142**, 350 (1966).
[11] Van Hove, L., Phys. Rev. **89**, 1189 (1953).
[12] Higginbotham, C. W., Pollak, F. H., and Cardona, M., Proc. IX Int. Conf. Phys. Semiconductors Moscow (Nauka, Leningrad, 1968).
[13] Pollak, F. H., and Cardona, M., J. Phys. Chem. Solids **27**, 423 (1966).
[14] Pollak, F. H., Higginbotham, C. W., and Cardona, M., J. Phys. Soc. Japan Supplement **21**, 20 (1966).
[15] Higginbotham, C. W., Cardona, M., and Pollak, F. H., Bull. Am. Phys. Soc. **14**, 416 (1969); Phys. Rev. **184**, 821 (1969).
[16] Cardona, M., in Solid State Physics, Nuclear Physics, and Particle Physics, I. Saaverdra, Editor (W. A. Benjamin, Inc., New York, 1968), p. 737.
[17] Kogan, Sh. M., Sov. Phys. JETP **16**, 217 (1963).
[18] Jha, S. S., and Bloembergen, N., Phys. Rev. **171**, 891 (1968).
[19] Flytzanis, C., and Ducuing, J., Phys. Rev. **178**, 1218 (1969).
[20] Phillips, J. C., and Van Vechten, J. A., Phys. Rev. **183**, 709 (1969).
[21] Schiff, L. I., Quantum Mechanics (McGraw-Hill Book Co., New York, 1968).
[22] Cardona, M., J. Phys. Chem. Solids **24**, 1543 (1963).
[23] Cardona, M., Shaklee, K. L., and Pollak, F. H., Phys. Rev. **154**, 696 (1967).
[24] Levinger, B. W., and Frankl, D. R., J. Phys. Chem. Solids **20**, 281 (1961).
[25] Hensel, J. C., and Feher, G., Phys. Rev. **129**, 1041 (1963).
[26] Chang, R. K., Ducuing, J., and Bloembergen, N., Phys. Rev. Letters **15**, 415 (1965).
[27] Dresselhaus, G., Kip, A. F., and Kittel, C., Phys. Rev. **98**, 368 (1955).
[28] Cardona, M., Shaklee, K. L., and Pollak, F. H., Phys. Rev. Letters **23**, 37 (1966).
[29] Bagguley, D. M. S., Robinson, M. L. A., and Stradling, R. S., Phys. Letters **6**, 143 (1963).
[30] Stradling, R. A., Solid State Comm. **6**, 665 (1968).
[31] Cardona, M., Phys. Rev. **121**, 752 (1961).
[32] Pidgeon, C. R., and Brown, R. N., Phys. Rev. **146**, 575 (1966).
[33] Vrehen, Q. H. F., J. Phys. Chem. Solids **29**, 129 (1968).
[34] Bjorkholm, J. E., IEEE J. Quant. Elec. **QE-4**, 970 (1968).
[35] Patel, C. K. N., Phys. Rev. Letters **16**, 613 (1966).
[36] Wynne, J. J., and Bloembergen, N., Bull. Am. Phys. Soc. **14**, 26 (1969); Phys. Rev., to be published.
[37] Phillips, J. C., Phys. Rev. Letters **22**, 645 (1969).
[38] Landau, L. D., and Lifshitz, E. M., Electrodynamics of Continuous Media (Addison-Wesley Pub. Co., Reading, Mass., 1960).
[39] Higginbotham, C. W., Ph. D. thesis, Brown University, 1969 (unpublished).

Model Density of States for High Transition Temperatures Beta-Tungsten Superconductors*

R. W. Cohen, G. D. Cody, and L. J. Vieland

RCA Laboratories, Princeton, New Jersey 08540

We have applied a simple density of states model to the problem of superconductivity in high T_c beta-tungsten superconductors. If we assume that the interaction responsible for superconductivity is predominately between d-band carriers and acoustic phonons via a deformation potential matrix element, simple analytic expressions for the effective electron-electron coupling constant λ and $T_c(\lambda)$ can be obtained. The quantities λ and T_c can then be estimated using parameters determined from an application of the density of states model to the cubic state elastic constants. We are able to establish the simple condition $\lambda > \lambda_{crit} \approx 0.7$ for the existence of a cubic-tetragonal lattice transformation in these materials. Using our result for T_c, we find $T_c \gtrsim 15$ K for all materials which exhibit a lattice transformation. Thus, we have established the relation between high T_c superconductivity and lattice transformation in the β-W compounds.

Key words: Beta-tungsten; lattice transformation; model electronic density of states; superconductivity.

1. Introduction

In the field of superconductivity, it is of prime importance to determine the cause(s) of the observed high transition temperatures in the β-tungsten compounds and to utilize this knowledge, if possible, to exceed the present maximum T_c of about 21 K. In approaching the problem of the transition temperature, it can be assumed that there is little hope unless an understanding is achieved of the anomalous normal state properties [1] of these materials with particular attention to the cubic-tetragonal lattice transformation [2,3]. Recently attention has been focused on a unique structure in the electronic density of states for these materials as the source of their unusual normal state properties, and models have been developed which permit the correlation of this structure with high T_c. The Labbé-Friedel-Barišić [4,5] model used a one dimensional (3 independent degenerate sub-bands) tight binding calculation to obtain a density of states in energy $N(E)$ for electrons with d-like character which has singularities at the band edges and a gradually decreasing $N(E)$ as one proceeds away from the band edge. This model can account for the tetragonal transformation in V_3Si and Nb_3Sn. The authors further proposed [5] that the high T_c's in these materials result from the same source, i.e., the placement of the Fermi level in a high density of states region near a band edge. It was later shown [6,7] that singularities in $N(E)$ are not necessary in order to explain the anomalous normal state properties, but that the idea of independent d-sub bands is essential.

It is possible to explain a wide variety of experimental results in both the high temperature cubic and low temperature tetragonal lattice phases using simple rectangular energy bands [6,7] with just three important band structure parameters obtained from experiment. The results of calculations using this simple model are often in simple analytic form and are surprisingly successful in quantitatively understanding the experimental data. Indeed the success of this model suggests its use in an attempt to calculate T_c from the basic parameters of the normal state.

The usual calculations of superconducting transition temperatures require detailed information about the phonon spectrum, the Fermi surface, and the electron-phonon coupling [8]. Such information is clearly not available for the high T_c β-tungsten superconductors, so that accurate calculations of T_c are not yet possible. However, as noted above, our analyses of the normal state properties of these materials has led to an experi-

*Work supported in part by the National Aeronautics and Space Administration under Contract No. NAS 8-21384.

mentally determined set of parameters that can be used in a first principles calculation of T_c. The primary assumption is that the predominant contribution to the electron-phonon interaction is between d-band particles and acoustic phonons via a simple deformation potential matrix element. With this assumption, simple analytic expressions for the effective electron-electron coupling constant λ and the transition temperature can be obtained. The quantities λ and T_c can then be computed using parameters determined only from an analysis of the temperature dependent elastic constants [6]. Although such an approach is, admittedly, over simplified, we believe that it contains the essential ingredients of the problem of superconductivity in these materials. It enables us to establish, in a simple way, the relation between high T_c superconductivity and the cubic-tetragonal lattice transformation.

In section 2, we sketch the important aspects of the electronic band structure model for β-W superconductors. In the next section we derive expressions for T_c and λ and relate the magnitude of λ to the condition for the existence of the lattice transformation from the high temperature cubic to the low temperature tetragonal phase. The effect of the tetragonal transformation on the T_c's of V_3Si and Nb_3Sn is discussed and compared to the results of previous work. In a final section, we enumerate our conclusions.

2. The Model Density of States

We present here the important aspects of the model electronic density of states. This model has been successful in explaining for Nb_3Sn and V_3Si (where data is available) [6,7,9,10] the behavior of the elastic constants and magnetic susceptibility in both the cubic and tetragonal lattice states, the magnitude of the tetragonal lattice distortion, the temperature dependence of the electrical resistivity, the acoustic attenuation, and the low temperature specific heat.

As is usual in the case of transition metals, the relevant electronic band structure is presumed to consist of a narrow high density of states d-band overlapping a wide, low density of states s-band. The additional assumption is made that the d-band is almost entirely empty (or filled) so that the Fermi level at $T=0$ K would occupy a position $E=E_F(0)=k_BT_o\sim 10^2$ K, very close to the d-band edge $E=0$. Over the energy range of interest ($<10^3$ K), the density of electronic states $N(E)$ is regarded as constant both above and below the d-band edge. For the purpose of calculating the superconducting transition temperature, we shall assume that only the d-band carriers contribute to superconductivity, so that we may ignore the s-band entirely. We consider, without loss of generality, the case of a nearly empty band. The density of electronic states for electrons of one spin in the cubic lattice state, including all interaction effects, is written in the form

$$N(E)=N_0,\ E>0 \qquad (2.1)$$
$$=0,\ E<0.$$

The density of states in the cubic state is shown in figure 1a. In order to deal with the effect of homogeneous uniaxial strains ϵ_{ii} directed along the crystallographic axes $i(i=1,2,3)$, we follow Labbé and Friedel [4] and assume that the d-band consists of three independent equal contributions (sub-bands) arising from the chains of the β-tungsten lattice. Because of the assumed independence of the sub-bands, under a uniaxial strain directed along a single transition metal chain, only the sub-band associated with that chain is perturbed. The shift of the sub-band i under the strain ϵ_{ii} is given by

$$\delta E_i=U\epsilon_{ii} \qquad (2.2)$$

where U is a deformation potential. Thus, in the tetragonal lattice state in which the spontaneous strains

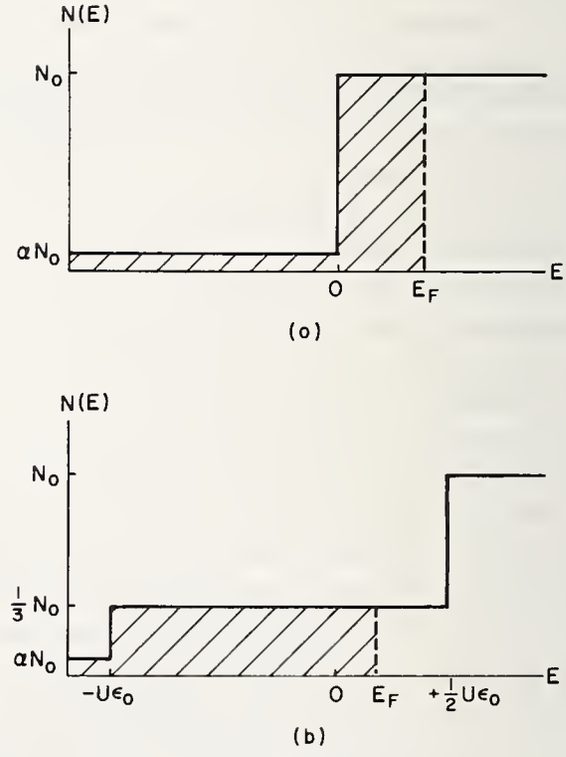

FIGURE 1. *The density of states configuration in (a) the cubic lattice state and (b) the tetragonal lattice phase with the sense of* ϵ_0 *corresponding to that for* Nb_3Sn.

At $T=0$ K, the Fermi energy $E_F=k_BT_0$ in the cubic state and $E_F=(-U\epsilon_0+3k_BT_0)$ in the tetragonal state. The sub-band displacement at $T=0$ K $U\epsilon_0/k_B=2T_0\,[1\text{-exp}\,(-T_0/T_m)]^{-1}$. For Nb_3Sn, $T_0=80$ K, $T_m=43$ K, and $U=4.1$ eV, so that $U\epsilon_0/k_B=190$ K and $\epsilon_0=4.0\times10^{-3}$.

are $\epsilon_{11} = -\epsilon_o(T)$ and $\epsilon_{22} = \epsilon_{33} = 1/2\ \epsilon_o(T)$, the positions of the sub-band edges are

$$\delta E_1 = -U\epsilon_0(T)$$
$$\delta E_2 = \delta E_3 = \tfrac{1}{2}\ U\epsilon_0(T). \tag{2.3}$$

The density of states in the tetragonal state is shown in figure 1b for the case $\epsilon_o(T) > 0$ (the case of Nb_3Sn).

The experimental quantities which will concern us in superconductivity calculations are the temperature dependent elastic constants $C_{11}(T)$ and $C_{12}(T)$ and the sub-band displacement $U\epsilon_o(T)$. These quantities have been calculated in previous work [6], and we merely state the results here. In the cubic lattice state, which exists above a lattice transformation temperature T_m, we have

$$C_{11}(T) - C_{12}(T) = -\tfrac{2}{3}\ N_0U^2[1 - \exp\ (-T_0/T)] + A_{11} - A_{12} \tag{2.4a}$$

$$C_{11}(T) = -\frac{4}{9}\ N_0U^2[1 - \exp\ (-T_0/T)] + A_{11}, \tag{2.4b}$$

where A_{11} and A_{12} are temperature independent core contributions to C_{11} and C_{12}, respectively. The quantities N_oU^2, A_{11}, A_{12} and T_o can be determined by fitting the above expressions to experimental data. As can be seen from eq (2.4a), the quantity $[C_{11}(T) - C_{12}(T)]$ decreases with decreasing temperature. If the condition

$$\tfrac{2}{3}\ N_0U^2 > (A_{11} - A_{12}) \tag{2.5}$$

is obeyed, the quantity $(C_{11} - C_{12})$, which represents the restoring force against a tetragonal transformation, will vanish at a finite temperature. The lattice then transforms to a stable tetragonal phase, the sense of the transformation (the sign of ϵ_o) being determined by the higher order elastic constants. The transformation is predicted to be first order, occurring at a temperature T_m which is slightly higher than the temperature at which $(C_{11} - C_{12})$ extrapolates to zero. We shall ignore this small temperature difference (about 2 K for Nb_3Sn [$T_m \approx 43$ K]) and define T_m by setting the right side of eq (2.4a) equal to zero:

$$1 - \exp\ (-T_0/T_m) = 3(A_{11} - A_{12})/2N_0U^2. \tag{2.6}$$

At temperatures below T_m, the spontaneous tetragonal distortion $\epsilon_o(T)$ grows rapidly, and the elastic constants C_{ij} are soon restored to their lattice values A_{ij} [7,10]. The values of the sub-band displacement at $T = 0$ K for $\epsilon_o > 0$ (Nb_3Sn) and $\epsilon_o < 0$ (V_3Si) are given by the expressions

$$U\epsilon_0(0) = 2k_BT_0\ [1 - \exp\ (-T_0/T_m)]^{-1}, \text{ (Nb}_3\text{Sn)} \tag{2.7a}$$
$$= -k_BT_0\ [1 - \exp\ (-T_0/T_m)]^{-1}. \text{ (V}_3\text{Si)} \tag{2.7b}$$

Even for fairly large reduced temperatures $T/T_m \lesssim 0.7$, the results (2.7) are good approximations for the spontaneous strains. Thus, given the expressions (2.3) for the various sub-band displacements and the result (2.7), we can determine the Fermi level position in relation to the various sub-band edges. This is shown in figure 1b. The various energies at $T = 0$ K are given in the figure caption. It is noteworthy that at sufficiently low temperatures the final density of states is $1/3\ N_o$ for Nb_3Sn ($2/3\ N_o$ for V_3Si).

3. Calculation of T_c for β-W Superconductors

3.1. Formalism and Assumptions

In order to treat superconductivity in these materials, we shall make certain reasonable simplifying assumptions that will allow us to give estimates of T_c from the elastic properties alone and to pinpoint the parameters which control T_c. First, we shall assume that the first order process for virtual phonon exchange is the essential interaction for superconductivity [11]. We shall also assume that the d-electrons are primarily responsible for superconductivity. The large penetration depths [12] and small coherence lengths [13] in these materials are justifications for this assumption. We treat each sub-band separately; each sub-band has its own energy gap parameter and density of states function. In the Nambu [14] formalism, the self energy Σ_i of an electron in sub-band i is

$$\sum_i (k) = -\int \frac{d\mathbf{k}'}{(2\pi)^3}\ T \sum_{n'} \tau_3 g_j(k')\tau_3 \sum_\lambda |M_{ij}(q, \lambda)|^2 d(q, \lambda) \tag{3.1}$$

In this equation, $g_j(k')$ is the temperature dependent propagator for quasi-particles of 4-momentum $k' = (k', i\omega')$ in sub-band j, and $d(q, \lambda)$ is the propagator for phonons of 4 momentum $q \equiv (Q, i\omega - i\omega')$. The summation convention has been employed for the index j. The matrix element $M_{ij}(q,\lambda)$ is the electron-phonon coupling

for transferring a quasi-particle from sub-band i to j using a phonon (q, λ). The τ_i are the Pauli spin matrices (with τ_o the unit matrix), and all frequencies have the discrete values $\omega = \pi T(2n+1)$ with n integral (we use units where $\hbar = k_B = 1$). We have, temporarily, ignored the Coulomb repulsion. Nambu's *ansatz* for the self energy is

$$\sum_i (k) = i\omega(1 - Z_i(k))\tau_0 + \chi_i(k)\tau_3 + \varphi_i(k)\tau_1. \tag{3.2}$$

Here $\chi_i(k)/Z_i(k)$ is the contribution of (3.1) to the quasi-particle energy and $\phi_i(k)/Z_i(k)$ is the energy gap parameter. The quasi-particle Green's function at T_c is given by

$$g_i(k) = \frac{i\omega Z_i(k)\tau_0 - \bar{\epsilon}_i(k)\tau_3 + \varphi_i(k)\tau_1}{(i\omega Z_i(k))2 - \bar{\epsilon}^2(k)}, \tag{3.3}$$

where the energy $\bar{\epsilon}_i(k)$ is written in the form

$$\bar{\epsilon}_i(k) = \epsilon(k) + \chi_i(k). \tag{3.4}$$

In eq (3.4), $\epsilon(k)$ is the quasi-particle energy without including renormalization effects, measured from the unrenormalized Fermi energy. For the phonon propagator, we use that of bare phonons of frequency ω_q:

$$d(q, \lambda) = \frac{2\omega_q}{(i\omega - i\omega')^2 - \omega_q^2}. \tag{3.5}$$

In order to evaluate the functions Z, χ and ϕ, we employ the method of Koonce and Cohen [15], valid for the case where the Fermi energy is larger or of the order of the important phonon energies. We first perform the sum on n' in eq (3.1) where the functions $Z_j(k')$, $\chi_j(k')$ and $\phi_j(k')$ are considered to be independent of ω'. Performing the sum using the Poisson summation formula and requiring the self-consistent condition that the τ_3 and τ_1 components of $\Sigma_i(k)$ be independent of ω and the τ_o component be proportional to ω [16], we find

$$1 - Z_i = \sum_\lambda \int \frac{d\mathbf{k}'}{(2\pi)^3} \frac{|M_{ij}(q, \lambda)|^2}{Z_j'} \operatorname{sgn} \xi_j' \frac{d}{d\xi_j'} \frac{1}{\omega_q + |\xi_j'|} \tag{3.6a}$$

$$\chi_i = -\sum_\lambda \int \frac{d\mathbf{k}'}{(2\pi)^3} \frac{|M_{ij}(q, \lambda)|^2}{Z_j'} \frac{\operatorname{sgn} \xi_j'}{\omega_q + |\xi_j'|} \tag{3.6b}$$

$$\Delta_i = (Z_i)^{-1} \sum_\lambda \int \frac{d\mathbf{k}'}{(2\pi)^3} \frac{|M_{ij}(q, \lambda)|^2}{Z_j'} \frac{\Delta_j'}{\xi_j'} \left\{ \frac{f(-\xi_j')}{\omega_q' + \xi_j'} - \frac{f(\xi_j')}{\omega_q - \xi_j'} \right\}. \tag{3.6c}$$

In eqs (3.6), $Z_i \equiv Z_i(k)$, $Z_j' \equiv Z_j(k')$, etc., $\Delta_i = \phi_i/Z_i$, $\beta_c = T_c^{-1}$, $f(\xi_j')$ is the Fermi function, and

$$\xi_j = \bar{\epsilon}_j/Z_j = E_j - E_F(T_c) \tag{3.7}$$

is the quasi-particle energy; the observed density of states refers to the energies E_j. Thus, the functions χ_i do not appear explicity in eqs (3.6a) and (3.6c) for Z_i and Δ_i, so that for the purposes of calculating T_c, it is not necessary to calculate the χ_i. In deriving eqs (3.6), we have ignored the effect of real phonons, which are not expected to be important at low temperatures $T_c \ll \omega_q$. We have also replaced Z_i and χ_i by their $T = 0$ K values since these quantities do not vary significantly in the temperature range $T \lesssim T_c$.

It is now necessary to make some statement about the matrix element $M_{ij}(q, \lambda)$. We shall employ a deformation potential matrix element for longitudinal phonons [17]:

$$|M_{ij}(q, \lambda)|^2 = q^2 U^2 / 2\rho\omega_{q\lambda} \text{ for longitudinal phonons}$$
$$= 0 \text{ for transverse phonons,} \tag{3.8}$$

where U is the deformation potential defined in section 2 and ρ is the atomic mass density. The actual matrix element is undoubtedly reduced by screening [17], but Umklapp processes and a nonspherical Fermi surface may bring in transverse phonons [17] and thereby increase the effective interaction. Therefore, the errors involved in using (3.8) tend to cancel and may permit (3.8) to give us a rough picture of the magnitude of the interaction. We shall also assume that this matrix element applies to both inter- and intra-sub-band transitions, a crucial assumption in considering the effect of

the lattice transformation on T_c. Next, for ω_{qL} we employ a Debye spectrum:

$$\omega_{qL} = s_L q, \tag{3.9}$$

where s_L is the longitudinal sound velocity which, at low temperatures, is given approximately by [7,10]

$$s_L = (A_{11}/\rho)^{1/2}. \tag{3.10}$$

Finally, we replace the factor $D = (\omega_q + |\xi_j'|)^{-1}$ in eqs (3.6) by the BCS-like model

$$\begin{aligned} D &= (\omega_{qL})^{-1} \quad \text{for } |\xi_j'| < \theta_D \\ &= 0 \qquad\quad \text{for } |\xi'| > \theta_D, \end{aligned} \tag{3.11}$$

where θ_D is the Debye temperature. The choice of θ_D as a cut-off energy is reasonable since θ_D is approximately equal to the average longitudinal phonon energy. Using eqs (3.8)-(3.11) in eqs (3.6a) and (3.6c) we find that Z_i and Δ_i are constant and are given by

$$Z_i = 1 + \tfrac{1}{2}\,(U^2/A_{11}) \int d\xi_j' N_b(\xi_j')\,[\delta(\xi_j' - \theta_D) + \delta(\xi_j' + \theta_D)] \tag{3.12a}$$

$$\Delta_i = (\Delta_j U^2/A_{11} Z_i) \int_{|\xi_j'| < \theta_D} d\xi_j' N_b(\xi_j')\,(1/2\xi_j')\tanh \tfrac{1}{2}\beta_c \xi_j'. \tag{3.12b}$$

Here $N_b(\xi_j)$ is the "bare" density of states of sub-band j. The renormalized density of states $N(\xi_j)$, which was given in section 2, is related to $N_b(\xi_j)$ through the formula

$$N(\xi_j) = Z_j N_b(\xi_j). \tag{3.13}$$

3.2. T_c in the Cubic State

We first solve eqs (3.12) for the cubic state which will exist at the lowest temperature if the inequality (2.5) does not hold. Here the Δ_i and $Z_i = Z$ are the same for all sub-bands, and we easily obtain

$$Z = 1 + \tfrac{1}{2}\lambda \tag{3.14}$$

$$T_c = 1.13\,(\theta_D T_0)^{1/2} \exp\left\{-\frac{1+\frac{1}{2}\lambda}{\lambda - \mu^*}\right\}, \tag{3.15}$$

where the effective electron-phonon coupling constant λ is given by

$$\lambda(1 + \tfrac{1}{2}\lambda) = N_0 U^2/A_{11}. \tag{3.16}$$

In eq (3.15), we have included the term μ^*, which represents the Coulomb repulsion [18]. In deriving eq (3.15) for T_c, we have assumed T_c is sufficiently low so that $E_F(T_c) \cong T_0 \gg T_c$.

Equations (3.14) and (3.15) are our equations for Z and T_c for high T_c β-W superconductors which are analogous to those of McMillan [19] for ordinary superconductors. The reduction of $(Z - 1)$ by a factor of two from the expression of McMillan results from the fact that the band edge cuts off phonon interactions at energies below the Fermi level. The factor $T_0^{1/2}$ in the pre-exponential in eq (3.15) results for the same reason. Note the predicted isotope effect $T_c \propto M^{-1/4}$ instead of the usual $M^{-1/2}$ dependence. Equations (3.14) and (3.15) would be of little use were it not for the fact that we can use eq (3.16) to estimate λ from quantities determined from the cubic state elastic constants (sec. 2). For example, if we apply our equations to transforming Nb_3Sn and V_3Si, we find, respectively [20], $\lambda = 0.92$, $T_c = 28$ K and $\lambda = 0.72$, $T_c = 21$ K. Our values of λ, calculated from eq (3.16) are quite close to those given by McMillan [19] from his equation for T_c. However, because of the difference between our eq (3.15) for T_c and that of McMillan, there is only an approximate relation between them. Our calculated value of T_c for V_3Si is close to the observed value of 17 K, whereas the computed value is about 10 K too large for Nb_3Sn. The significance of this discrepancy will be discussed below when we calculate T_c for the tetragonal lattice configuration.

3.3. Relation of λ to the Tetragonal Transformation

Using the foregoing results, we can easily relate the magnitude of the electron-phonon coupling λ to the condition for the existence of the cubic-tetragonal lattice transformation. From eqs (2.5) and (3.16), and noting the empirical relation [20] $A_{12} \cong 1/3\, A_{11}$ which holds for Nb_3Sn and V_3Si, we have immediately,

$$\lambda > 0.7, \tag{3.17}$$

for a tetragonal transformation. Equation (3.17) illustrates the intimate relation between high T_c's and the lattice transformation; large λ's favor high T_c's but lead to the lattice instabilities.

3.4. T_c in the Tetragonal State

Let us now solve eqs (3.12) for the tetragonal lattice state of V_3Si and Nb_3Sn and compare the results with those for the cubic state. For Nb_3Sn the relevant density of states configuration is shown in figure 1b. For our

purposes, the $T = 0$ K values of the various energies shown in the figure are sufficiently accurate. We find once again the result

$$Z = 1 + \tfrac{1}{2}\lambda$$

for all sub-bands. However, there are now two values of the energy gap, i.e., the gap Δ_1 for the single widened sub-band and the gap Δ_2 for the two narrowed sub-bands. Equation (3.12b) is then actually two coupled homogeneous algebraic equations for Δ_1 and Δ_2. The transition temperature is obtained by setting the determinant of the coefficients equal to zero. If the energy difference $(1/2\ \ U_{\epsilon 0} = E_F) = 3T_0\ \ (\exp(T_0/T_m) - 1)^{-1} \gg T_c$, we find

$$T_c = 1.13\ (\theta_D/3T_0)^{1/2}\ \theta_D[\exp\ (T_0/T_m) - 1]\ \exp\left\{-\frac{1 + \frac{1}{2}\lambda}{\frac{1}{3}\ (\lambda - \mu^*)}\right\}. \tag{3.18}$$

The factor 1/3 occurs in the denominator of the argument of the exponential in eq (3.18) because the final density of states in the tetragonal state of Nb_3Sn is reduced to 1/3 of the cubic state value. Note the large predicted isotope effect in the tetragonal state $T_c \propto M^{-3/4}$. Substituting our values of the parameters for Nb_3Sn, we compute $T_c = 8$ K, and the energy gap parameters Δ_1 and Δ_2 differ by less than 1%. A similar calculation for V_3Si yields $T_c = 20$K, close to the cubic state value. The small difference in the cubic and tegragonal T_c's for V_3Si results primarily from its low [2] $T_m \cong 22$K; at T_c, the effective density of states at the Fermi level is still large, so that the interaction extends over roughly the same energy range in all sub-bands as it would if the material were cubic.

Thus, we have the result that the approximations we have made work well for V_3Si; we calculate T_c's close to the observed value and predict little difference between the cubic and tetragonal T_c's. On the other hand, Nb_3Sn is predicted to have a high T_c (28 K) in the cubic state and a relatively low one (8 K) in the tetragonal state. This is suprising because we would expect our approximations to be either uniformly good or uniformly bad for these materials. We believe that we have considerably underestimated the tetragonal T_c for Nb_3Sn. Evidence for this exists in the low temperature susceptibility data which indicates a fall-off of the final density of states to about 0.5 N_0 rather than 1/3 N_0. The value 0.5 N_0 is very close to the value predicted from the band model if we employ the effective mass approximation [10] ($N(E) \propto E^{1/2}$) rather than rectangular energy bands. The final density of states is critical in determining T_c, since it occurs in the exponential, so that close agreement with the observed value of T_c is obtained if we employ this modification to our model. On the other hand, we believe that the figure of 28 K for cubic Nb_3Sn may actually represent the T_c that this compound would have if it did not first undergo a lattice transformation. There is some experimental [21] and other theoretical [22] evidence that Nb_3Sn ought to have a much higher T_c than the observed 18 K. If we are correct, it is then a simple matter to show by a calculation similar to that of McMillan [19] that the maximum T_c occurs for $\lambda \approx 4$ and is 45 K for Nb_3Sn and 40K for V_3Si. Thus, in contrast to McMillan, we find that Nb_3Sn has an intrinsically higher T_c than that of V_3Si. Of course, our result rests on the assumptions we have made in obtaining our equations for T_c and λ; of particular importance is the assumption of equal intra- and inter-sub-band coupling in our model, Labbé, Barišić, and Friedel [5] did not calculate the difference in T_c in the two lattice states but felt that the difference between them ought to be small because T_c in the cubic phase varies only slowly with N_o in their model. The experimental situation with regard to the effect of the lattice transformation on T_c is not clear. A Nb_3Sn crystal [1] which showed lattice softening [23] but did not transform according to x-ray measurements had a T_c only 0.2 K larger than that for a transforming crystal [3]. However, analysis of the elastic constants [24] to obtain the quantities in eqs (3.15) and (3.16) yields the smaller computed values of $\lambda = 0.78$ and $T_c = 20$ K, so that the failure to realize a significantly higher T_c in this particular nontransforming crystal is understood. The situation is further complicated by the fact that tetragonal crystals of Nb_3Sn are heavily twinned [25,26], and the effect of the attendant internal strains is not known.

4. Conclusion

The results presented here and in previous papers show that a simple electronic density of states model can account for many properties of the normal tetragonal and cubic phases and the high T_c's of these materials. Our approach to the density of states differs only in detail from that of Labbé-Friedel-Barišić [4,5], although our model gives better numerical agreement

[1] This crystal was found to contain 1.5% interstitial H.

with most of the experimental data [6]. The present treatment of superconductivity differs considerably from that of other authors [5,19,22] in that (a) we specifically treat the effect of the tetragonal transformation, and (b) attempt to estimate the magnitude of the electron-phonon interaction from the elastic properties of the material.

Despite the success of the model, certain important questions remain to be answered. First, and perhaps most important, is it true that transforming Nb_3Sn would have a T_c of substantially higher than 18 K were it not for the lattice transformation? This question can only be answered experimentally. The question which is most relevant to this conference is the relation of the model density of states to the actual band structure in the vicinity of the Fermi surface. This question is very difficult to answer because ordinary band calculations overlook structure on the energy scale that we have considered. If our success in explaining the properties of these materials has a physical basis, then the essential features of our model must result from a fundamental treatment of the β-W compounds. The early pioneering calculation of Mattheiss [27] and the insights of Weger [28] and the Orsay group [4,5] provide the foundation for such a study. The technical and theoretical importance of understanding the source of high T_c's should provide sufficient motivation.

5. Acknowledgments

The authors acknowledge Drs. J. Gittleman, G. Webb, and A. Rothwarf for many helpful discussions.

6. References

[1] A summary of extensive experimental work on Nb_3Sn can be found in RCA Rev. **25**, 333, F. D. Rosi, Editor (1964) (19 papers).

[2] Batterman, B. W., and Barrett, C. S., Phys. Rev. Letters **13**, 390 (1964); Phys. Rev. **145**, 296 (1966).

[3] Mailfert, R., Batterman, B. W., and Hanak, J. J., Phys. Letters **24A**, 315 (1967).

[4] Labbé, J., and Friedel, J., J. Phys. Radium **27**, 153, 303 (1966) (2 papers).

[5] Labbé, J., Barišić, S., and Friedel, J., Phys. Rev. Letters **19**, 1039 (1967).

[6] Cohen, R. W., Cody, G. D., and Halloran, J. J., Phys. Rev. Letters **19**, 840 (1967); Cody, G. D., Cohen, R. W., and Vieland, L. J., Proceedings of the 11th International Conference on Low Temperature Physics (St. Andrews University, 1968) p. 1009.

[7] Rehwald, W., Phys. Letters **27A**, 287 (1968).

[8] See for example Allen, P. B., Cohen, M. L., Falicov, L. M., and Kasowski, R. V., Phys. Rev. Letters **21**, 1794 (1968).

[9] Since Nb_3Al does not display the same kind of anomalous behavior as Nb_3Sn and V_3Si (Willens et al., Sol. State Comm. **7**, 837 (1969)), we do not believe the approach presented here applies to this material. On the other hand, since the magnetic susceptibility of V_3Ga is extremely temperature dependent (Clogston et al., Phys. Rev. Letters **9**, 262 (1962)), we have reason to believe that V_3Ga can be treated by the present theory.

[10] Cohen, R. W., Cody, G. D., Vieland, L. J., and Rehwald, W., to be published.

[11] If the effective Fermi energy T_o is actually of the order of or smaller than the important phonon energies, it is possible that the first order process may not be sufficiently accurate for strong coupling superconductors, Migdal, A. B., Sov. Phys. JETP **7**, 505 (1958)). However, it is possible to treat (R. W. Cohen, thesis (unpublished)) the effect of higher order processes involving strong attractive interactions whose range in momentum space is greater than the Fermi momentum. It is found that the effect of these processes, in the t matrix approximation, is only to renormalize the pre-exponential factor in the expression for T_c. We shall ignore this effect.

[12] Cody, G. D., RCA Rev. **25**, 414 (1964).

[13] The coherence length is estimated to be approximately 130 Å. This estimate is arrived at using the penetration depth given in Reference [12] and the Ginzburg-Landau parameter $K = 21.7$ (Vieland, L. J., and Wicklund, A., Phys. Rev. **166**, 424 (1968)).

[14] Nambu, Y., Phys. Rev. **117**, 648 (1960).

[15] Koonce, C. S., and Cohen, M. L., Phys. Rev. **177**, 707 (1969).

[16] Equations (3.6a) and (3.6c) for Z_i and Δ_i are similar to McMillan's (ref. 19) eqs. (2a) and (2b) in limit $\omega \rightarrow 0$ with the frequency ω' put on the energy shell $\omega' = \xi_j'$. Our result ignores real phonons ($\omega_q/T_c \gg 1$) and explicitly treats the self energies in each sub-band.

[17] See for example Ziman, J. M., Electrons and Phonons (Oxford University Press, London, England, 1962) Chapter V.

[18] Morel, P., and Anderson, P. W., Phys. Rev. **125**, 1263 (1962).

[19] McMillan, W. L., Phys. Rev. **167**, 331 (1968).

[20] For transforming Nb_3Sn, we use the value $\theta_D = 300$ K (Vieland, L. J., and Wicklund, A., Phys. Rev. **166**, 424 (1968)). The parameters obtained from elastic constant measurements [7,10] are $T_o = 80$ K, and, in units of 10^{12} erg-cm^{-3}, $N_oU^2 = 7.86$, $A_{11} = 2.94$ and $A_{12} = 0.84$. For transforming V_3Si, we use the values $\theta_D = 500$ K, $T_o = 75$ K, and, in units of 10^{12} erg-cm^{-3}, $N_oU^2 = 6.33$, $A_{11} = 3.22$ and $A_{12} = 1.05$. These parameters were obtained from an analysis of the elastic constant data of Testardi, L. R., and Bateman, T. B., Phys. Rev. **154**, 402 (1967). For both materials, we use the value $\mu^* = 0.13$ for the Coulomb pseudopotential (ref. 19).

[21] Cody, G. D., Hanak, J. J., McConville, G. T., and Rosi, F. D., RCA Rev. **25**, 338 (1964).

[22] Hopfield, J. J., Phys. Rev. (in press).

[23] Keller, K. R., and Hanak, J. J., Phys. Rev. **154**, 628 (1967).

[24] For this crystal, analysis of the elastic constants reported in reference 23 yields $T_o = 100$ K, and, in units of 10^{12} erg-cm^{-3}, $N_oU^2 = 6.46$, $A_{11} = 2.96$, and $A_{12} = 0.90$.

[25] Batterman, B. W., presented at the Eighth General Assembly and International Congress of the International Union of Crystallography, University of New York (Stony Brook), August 1969.

[26] McEvoy, J. P., presented at the International Conference on the Science of Superconductivity, Stanford University, August 1969; Conference proceedings, Physica (to be published).

[27] Mattheiss, L. F., Phys. Rev. **138**, A112 (1965).

[28] Weger, M., Rev. Mod. Phys. **36**, 175 (1964).

417-156 O - 71 - 51

Summary of the Conference on Electronic Density of States*[1]

H. Ehrenreich

Division of Engineering and Applied Physics, Harvard University, Cambridge, Massachusetts

It is very difficult to summarize a conference such as this, involving as it did a many splendored array of topics, both experimental and theoretical, expounded in no less than ninety papers. The organization of a conference of such size is ordinarily impossible without resort to simultaneous sessions. When there are simultaneous sessions, of course, it is easier for a single summarizer because he can only be at one place at one time and therefore can be excused for failing to do justice to half of the papers. It is also easier for the audience because if you permit people to resonate between sessions, you also allow them to become trapped in the halls, advertently or inadvertently as the case may be. However, through the devilish cleverness of the organizers of the present conference, a goodly fraction of the papers were delivered by a rapporteur. Accordingly, the entire audience, including the summarizer were exposed to everything during a period of three and a half hard-working and elaborately organized days. Furthermore, I lose my excuse for having overlooked, as I undoubtedly did, some of the important new developments presented or presaged here.

As it is, in the time of thirty-two minutes that have been allotted to me it is, of course, impossible to mention even a representative fraction of the contributions. Indeed, even the various areas discussed here can only be sketched in broad outlines. Fortunately my task is considerably eased by the various excellent review lectures and rapporteur summaries that punctuated the conference. In order to avoid the risk of offending a few, I have decided instead to offend everybody by not mentioning names in this talk, except when referring to work which was not explicitly reported at this conference which is appropriately referenced.

*An invited paper presented at the 3d Materials Research Symposium, *Electronic Density of States*, November 3–6, 1969, Gaithersburg, Md.

[1] Supported in part by Grant No. GP-8019 of the National Science Foundation and the Advanced Research Projects Agency.

At the outset, let me thank the organizers on behalf of everyone attending it for providing us with an outstanding scientific program that clearly focussed on the principal questions which those of us who are grappling with the electronic structure of condensed matter are facing. During the time when we were not riding buses or listening to papers, there was also a most pleasant social program, and mercifully, a few hours for sleep.

I would regard the title of the present symposium, "Electronic Density of States" a *leitmotif* rather than an *idée fixe* because the subject matter presented at the conference in fact was far more general than might be implied by the title. Since the density of states is very influential in the determination of many basic physical properties, it provides an excellent focal point for presenting some of the more recent developments in the electronic properties of condensed matter.

More importantly (and to my view this is one of the chief motivations of this conference) the density of states is a convenient central quantity for confronting theory and experiment even though, unfortunately, it never seems to be measured directly by *any* experiment. In the jargon of the modern theorist one might phrase this difficulty in the following way. The density of states is proportional to the imaginary part of the single particle Green's function, whereas many experiments determine a response function, which involves Green's functions of two or more particles. When suitable approximations are made, however, the state density enters in a fairly direct way into the theoretical interpretation of all of the various kinds of measurement described at this conference.

The list of techniques available to the solid state physicist, which was extensively sampled here, is truly impressive and stands in contrast to the much more limited variety available to our colleagues in the elementary particle field. We heard about optical absorp-

tion and reflectance, x-ray spectroscopy, photoemission, Fermi surface experiments, tunneling, measurements of the electronic specific heat, magnetic susceptibility, superconducting critical fields, and transport properties, positron annihilation, Compton scattering, ion neutralization spectroscopy among others, and how some of these are influenced by pressure, strain, and temperature.

The preceding list reflects the fact that photons continue to be one of the favorite probes for studying the microscopic properties of matter. It is therefore tempting to use the 1965 Conference in Paris on the Optical Properties and Electronic Structures of Metals and Alloys [1] which dealt with the same class of materials as the present conference and similar ideas concerning the interpretations of experiments as a fiducial mark to give us some indication of what we have learned about metals and alloys during the interim.

Pippard, in his summary of that conference, remarked on the extraordinary number of times the audience was shown the Cu band structure. Since then the variety of band calculations, and, in particular the kinds of materials considered has proliferated greatly. Pd has received a great deal of recent attention largely as a result of excellent high field susceptibility and photoemission measurements. Other examples discussed here involved more exotic materials such as $AuAl_2$, EuO and GeO_2. Evidently the machinery for doing such calculations on ordered alloys containing several atoms per unit cell, some of which are sufficiently heavy that relativistic effects become important, is now available at several laboratories in a readily usable form. However, as in all band calculations, even if one accepts the Hartree-Fock approximation, the result obtained is only as good as the potential that is used as input information. In metallic alloys one might expect some charge transfer among the atoms belonging to a single unit cell. In my view this possibility has not yet received adequate attention.

For example, $AuAl_2$ has the CaF_2 structures and is one of the few metals in which a Raman frequency has been observed [2]. Remarkably, its magnitude is similar to that of CaF_2. One might ask whether the very similar stiffness of the optical frequencies in these materials is purely an accident or whether there could be enough charge transfer among the atoms in the cell to result in appreciable ionic character. I realize that I am undoubtedly not saying anything that is not already familiar to band theorists. However, experimentalists should be warned that the construction of alloy potentials, even for ordered systems, is still a problem that requires attention.

Indeed, the simpler problem of calculating band structures for monatomic metals on the single particle picture is still controversial. As we saw in connection with several of the contributions and much of the spirited discussion that followed them, we still don't understand clearly how, when, or why to localize the exchange interaction. To date no sufficient theoretical reason has been advanced for preferring either the Slater or the Gaspar-Kohn-Sham versions of this potential. Proponents of either point of view, or those favoring intermediate values of the coefficients at present usually support their position by comparison with experiment rather than basic theoretical arguments.

In this same connection we might note the debate following the introductory lecture concerning the relative merits of first principles and pseudo- or model-potential band calculations. The essential point made in that lecture, in my view, is that "pseudism" is important because it provides elementary insight into the meaning of the results of the elaborate machine computations. The two approaches, in fact, are complementary and the proponents of each have a genuine need for, and indeed ideally should merge with the other.

There is no doubt whatsoever that band theory has done sufficiently well that it is worth using its results to calculate the density of states accurately. This is a difficult numerical problem, particularly if one resignedly accepts spending ceilings that curtail the amount of available computer time, for one needs to know the energy at many millions of points in the Brillouin zone in order to construct adequate histograms that yield all the fine detail in the density of states that is often necessary to interpret experimental information reliably. We saw several examples of advances in performing such calculations more economically at this conference. The QUAD scheme is one of these. Another, which I will call the IBM scheme, not after the machine but the workers, is similar to QUAD in its ability to generate very detailed E(k) curves, but it avoids the use of histograms. All these result in very finely grained structure in the state density.

In this same connection, I think the importance of learning how to sum functions of k over constant energy surfaces in the Brillouin zone efficiently and reliably needs emphasis. This is important not only for calculating the state density, but also for computing Green's functions that are central to the solution of alloy band problems, frequency dependent dielectric functions that can be compared with optical data, susceptibilities, and many other quantities. While many theorists may think such problems as insufficiently dignified, I would, nevertheless, stress that their solution is impor-

tant if one ever expects to confront theory and experiment realistically on a more complete basis for more complicated systems.

At the same time let me temper this call to computer and numerical analysis handbooks by reminding you of the obvious fact stressed by many speakers that band calculations are single particle descriptions involving electrons or holes as ideal quasi-particles which interact with a self-consistent field that is in practice determined more or less self-consistently. However, due to electron interactions including those involving phonons, real quasi-particles acquire finite lifetimes, except right at the Fermi surface. Some of the papers presented here reflected the fact that methods of taking quasi-particle effects into account more systematically in band calculations are now being developed. I would look towards greater exploitation of such techniques in the band calculations of the near future. It is important to remember that when we speak of dressing effects, say, due to electron-phonon interactions, we ought to be dressing the right bare object, namely the correctly calculated quasi-particle appropriate to the stationary lattice.

One should again be reminded of the fact that very few if any of the experiments discussed at this meeting correspond to creation of just one quasi-particle near the Fermi surface. This fact was also stressed already at the Paris Conference. Optical experiments, for example, correspond to the creation of two quasi-particles and ion neutralization measurements to three. These may interact with each other as well as with the other particles in the system. This was illustrated in the discussion of the various types of phenomena that can occur in x-ray emission, which lead to the conclusion that the observed spectrum of the valence band may bear less resemblance than one would hope to what is calculated from band theory. In addition to the long familiar Landsberg or Auger tails that smear out the lower valence band edge, there are recently predicted elementary excitations such as the plasmaron and other broad structures that also result from interactions with plasmons. Another effect that was reported on here results from exciton type interactions between electrons near the Fermi surface and the core holes with which they combine in an x-ray emission process. These may strongly affect the transition rate and lead to substantial enhancement or dimunition of the observed intensity near the Fermi surface. As has been pointed out to us, these effects must be quantitatively understood before information concerning band structure can be reliably extracted from such experiments. As a result of particle interaction effects, the information supplied, even what would in a simple minded view correspond to the same theoretical quantity, often differs from experiment to experiment. The Fermi surface effective mass determined from electronic specific heat and Pauli susceptibility measurements is an example of this.

Even within a single particle framework, the state density function is only characteristic of a particular type of experiment. For example, in x-ray emission experiments, optical selection rules pick out only those components of the valence band state density having appropriate symmetries with respect to the core hole. We saw that this fact has particular utility in providing insight into the character of the wave function overlap and hybridization among different components in both ordered and disordered alloys. Since the core hole is localized in a given atomic site, the study of say the Al-$L_{2,3}$ emission spectrum in systems such as $AuAl_2$ and others discussed here, provide an indication of the amount of d wave function in these systems located on the Al sites.

As another example, we might mention the k-conversation rule entering interband optical processes which implies that the state density appearing in theoretical expressions for the optical constants is the so-called "joint density of states." This seemingly innocuous fact has led to a spirited controversy in connection with the interpretation of photoemission experiments which was already in full bloom at the Paris Conference. As you all know by now, there are two schools of thought whose proponents we might call the k-conservationists and the k-nonconservationists. The latter group has maintained, on the basis of a considerable body of experimental evidence, that particularly in materials having narrow bands such as the noble and transition metals, the energy distribution of the photoemitted electrons should directly reflect the structure in the density of states pertaining to these bands. The k-conservationists on the other hand have asked, "Why should this conservation law be violated?" Indeed, one of the papers, which represents the first attempt at the formulation of a systematic theory of the photoelectric effect in solids, points to ways in which this might come about.

Several of the other contributions point to progress towards a reconciliation of these viewpoints. For example, we have heard in connection with Cu that a direct transitions analysis using constant matrix elements accounts quite well for the observed energy distribution. Similar conclusions have been reached on the basis of very detailed calculations for Pd. The essential point, which was emphasized by both camps, is that the strongest peak in the joint density of states coincide with

peaks in the calculated state density, particularly in the case of narrow valence bands.

While in many cases the photoemission technique is a very useful tool, this may not be the case universally. It was suggested, for example, that it is less successful in providing information concerning f states in the Eu chalcogenides and rare earth metals since these states are seen to give rise to abnormally low quantum yield relative to, for example, p states. It is also clear that the variation of optical matrix elements with energy and selection rules, which can also lead to structure in the observed spectra, needs further attention because in many calculations this matrix element is still regarded to be a constant.

Before leaving the subject of optical properties of crystal, two other points are worth making. Despite the fact that one learns only about the joint density of states in such experiments, it is, in fact, possible to derive the conventional state density from optical data by a more circuitous route. The usefulness of differential reflectance techniques is now well established and was illustrated in several of the contributions presented here which even extended to the x-ray case. Information from such measurements can be used as input for pseudopotential band calculations or those based on the $k \cdot p$ approximation. The problem of constructing potentials which plague first principle band calculations is thereby avoided. Since the secular equations for such problems are generally smaller, they can be solved at sufficiently large numbers of points in the Brillouin zone to obtain the state density.

The other point concerns another recent development. A fact that has been distressing to many theorists is that, while in semiconductor calculations of optical coefficients there was always good agreement between theory and experiment in regard to both the position and magnitude of the observed structure, this has not been the case in metals. For the case of Al we saw quite convincing evidence that such discrepancies are on the point of disappearing, largely as a result of better calculations which deal more adequately with the k-dependence of the momentum matrix element. Indeed, other recent investigations have shown that electron-electron scattering effects, which lead to vertex corrections that might be expected to be stronger in metals than semiconductors, are, in fact, very weak in this material [3]. Even though the so-called Mayer-El Naby resonance is probably no longer with us [4], our understanding of the alkali metals is unfortunately still not in as good a shape.

It is regrettable that relatively few papers presented at the conference attempted to provide a detailed comparison between the results obtained by different types of experiments. There was only one noteworthy exception, which was concerned with efforts to confront Knight shift data with those of soft x-ray emission experiments. There is a real need for more such detailed comparisons, even on the basis of band theory alone.

According to a paper count, superconductors and semiconductors received less attention than the simple, transition, and rare earth metals. However, there are good reasons for mentioning them even in this broad summary. As appropriate, superconductivity was not discussed as a phenomenon, but rather as a tool to extract information relevant to the state density. On the positive side, we heard how strong coupling theory can be used together with other measurements to obtain the electron-phonon coupling constants, and how measurements of the critical field at very low temperatures can be made to yield the electronic specific heat as a function of pressure with high accuracy. On the negative side, it was pointed out in connection with a general review of the information provided by tunneling experiments, that such measurements for superconductors do not really tell us all that much about the normal state properties of metals and semiconductors.

It is clear from the exquisitely detailed interpretable information being currently obtained from cyclotron resonance, magneto-optical, and even nonlinear optical data in simple semiconductors and semimetals, that our understanding of these materials is still in a somewhat more mature state than that of most metals. Of course this applies only to the classical and long studied materials like Ge and InSb and not to amorphous semiconductors which were discussed in only a single paper. However, the very beautiful interplay and agreement between theory and experiment must still be regarded as serving as a standard of excellence which solid state physics in general must continue to emulate.

Surfaces also were not discussed extensively here, largely, I think, because the theoretical ideas and techniques for dealing with such problems in realistic systems are only beginning to be developed. However, some very promising experimental techniques, notably ion neutralization spectroscopy and resonance tunneling which shed light on the nature of surfaces and important phenomena like chemisorption were described. This area will surely see a great deal of activity in the near future.

Since the discussion of a large variety of alloy systems occupied so much of the conference, let me conclude this summary with some remarks concerning this subject. We were exposed to a wide variety of data concerning many alloy systems, most of them involving

transition metals. Certainly there are many more than were considered at the Paris Conference. However, this comparison is somewhat unfair since even now, with one or two notable exceptions which were presented here, there is still a dearth of optical information concerning disordered alloys. This is to be contrasted with the situation involving specific heat and transport measurements about which we heard a great deal. Indeed, most of the papers dealing with the electronic specific heat were concerned with alloy systems. A most interesting effect that was described dealt with the recently discovered magnetic clusters in NiCu alloys which can make their own appreciable contribution to the specific heat. This conjecture is quite new and deserves detailed theoretical treatment. There was also an intriguing discussion concerning rare earth metals which raised the question as to whether the *f* electrons could possibly be at least partially itinerant in some of these systems.

One fairly obvious thing that needs emphasis in connection with these papers and that was stressed in a number of them is the need for data of single crystal specimens having known phases, and how crucial it is to avoid samples involving mixture of phases. Without these precautions, the overanxious theorists will, as they did in the case of the Mayer-El Naby anomalies, find themselves in the awkward position of explaining what Pippard already warned in 1965 might be nonfacts.

As we saw, many of the experimental techniques applicable to pure metals are relevant for disordered alloys as well. We have already mentioned optical and x-ray data in this connection. The fruitful and relatively easily interpretable Fermi surface experiments, alas, seem to be much more difficult for many alloy systems. However, measurements such as those involving positron annihilation which also probe the Fermi surface geometry are not restricted by such criteria. They have already been very successfully used to investigate detailed Fermi surface changes in Cu-Al [5] and as we heard here, to brass.

A great deal of progress in this area since the Paris Conference has come along the theoretical front. Until a few years ago the only theoretical models available for describing alloy behavior involved perturbation theory, the virtual crystal, or the rigid band models. However, recently a number of rather effective techniques based on scattering theory have been adapted to this problem and implemented by calculations for both model and realistic systems. These all transcend the earlier, more limited approaches. The first incisive contributions to electronic theory, made by Edwards and Beeby [6], involved the so-called average t-matrix approach which Soven [7] applied to brass. An extension of such calculations was discussed here. Subsequently, Soven [8] formulated a more general self-consistent effective field approach that he termed the coherent potential approximation which is more general than the other. While this was mentioned in several of the papers, it is perhaps worthy of some additional commentary because of its possible applicability to realistic alloy systems.

In this approximation the alloy is replaced by an effective medium described by a single particle non-Hermitian and complex Hamiltonian which, however, is still periodic in the case of substitutional alloys. The self-consistency condition determining this Hamiltonian is simply that an effective electron wave travelling through the crystal which impinges on an atomic site suffers no further scattering due to the random character of the crystal potential. Put another way, the effective wave, just like a Bloch wave in a crystal, is not scattered by the atoms. However, unlike the Bloch wave, the effective wave may be damped as it propagates through the crystal. The present limitation of this description is that it is only applicable to certain classes of Hamiltonians in which the random character is cell localized. The theory has the virtue of correctly reducing to the known results for small impurity concentrations and arbitrary scattering strengths on the one hand, and for arbitrarv concentrations but small scattering strengths on the other. It interpolates in a physically reasonable way between these limits, yielding results that are valid for arbitrary alloy concentrations and reasonably strong scattering strengths. It fails in predicting band tailing effects, experimental evidence for which we heard described here in connection with semiconductor tunneling experiments. Also, it does not yield strictly localized states except in the limit of very small impurity concentrations.

We should note parenthetically that while the existence of such states near band edges is generally believed, some questions were raised here as to whether or not such states can exist in the middle of a tight binding band and whether or not the frequently made hypothesis that there exists a sharp demarcation between localized and nonlocalized states is correct. As we were reminded, localized states such as those due to f-electrons, can exist even in periodic systems when the Coulomb interaction is sufficiently strong. As was shown, conventional band descriptions break down under these circumstances.

To obtain the effects omitted by the coherent potential description of disordered alloys it is necessary to

allow for the possibility of statistical clustering effects. This is a much more difficult problem. But as we heard in two of the papers presented here, some very promising progress is beginning to be made in these directions. Indeed, the early work of I. M. Lifshitz [9] has already given us an indication of the sorts of results to be expected.

Because of the previously stated limitations, the coherent potential theory in its present form is strictly speaking applicable only to isoelectronic alloys like GeSi, where the random part of the potential is substantially confined to the core region at each site, or to 3d transition-noble metal alloys in which the d-states that are most affected by the disorder are substantially localized.

To give these remarks a sharper focus, I should like to show you by means of one example the results of an application of this theory to CuNi alloys. Figure 1 exhibits S. Kirkpatrick's calculations [10] for the density of states of these alloys and also the results of photoemission experiments by Seib and Spicer [11], which, for reasons already mentioned, should only be compared qualitatively with the theoretical results. It should be emphasized that these calculations do involve approximations, most of them probably not too serious. Since it would be inappropriate to discuss these in the present context, I would like to confine my remarks to a few brief comments. The first is that the coherent potential approximation is evidently applicable to quite complicated density of states functions

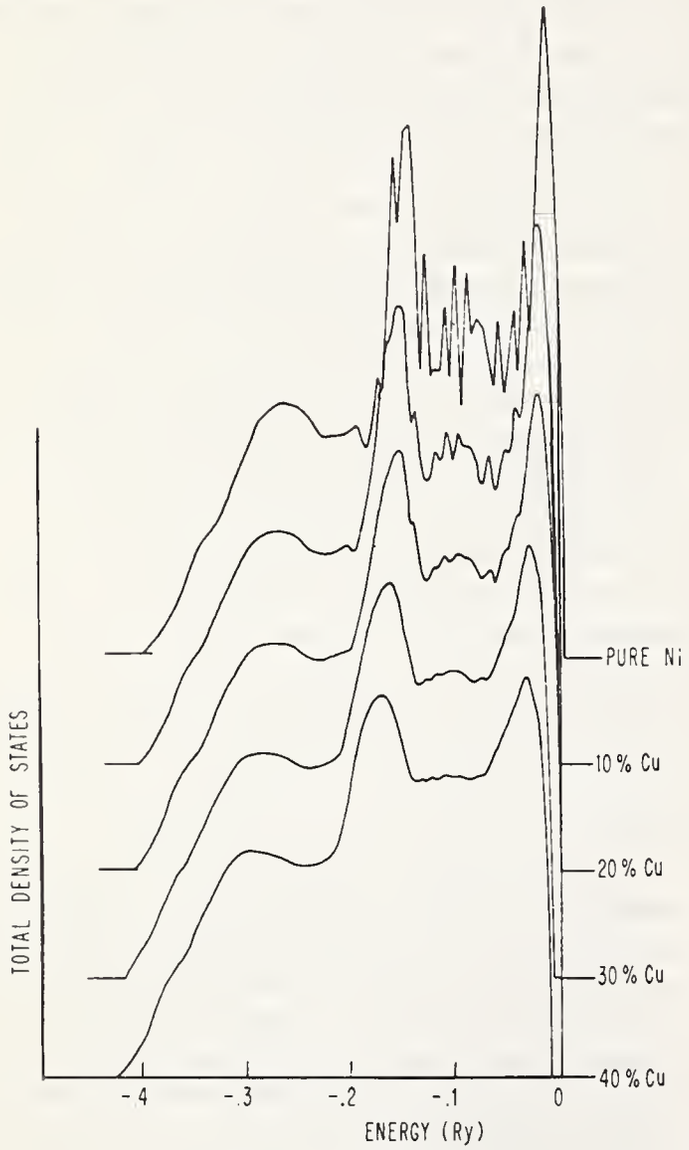

CPA CALCULATION
FOR NiCu

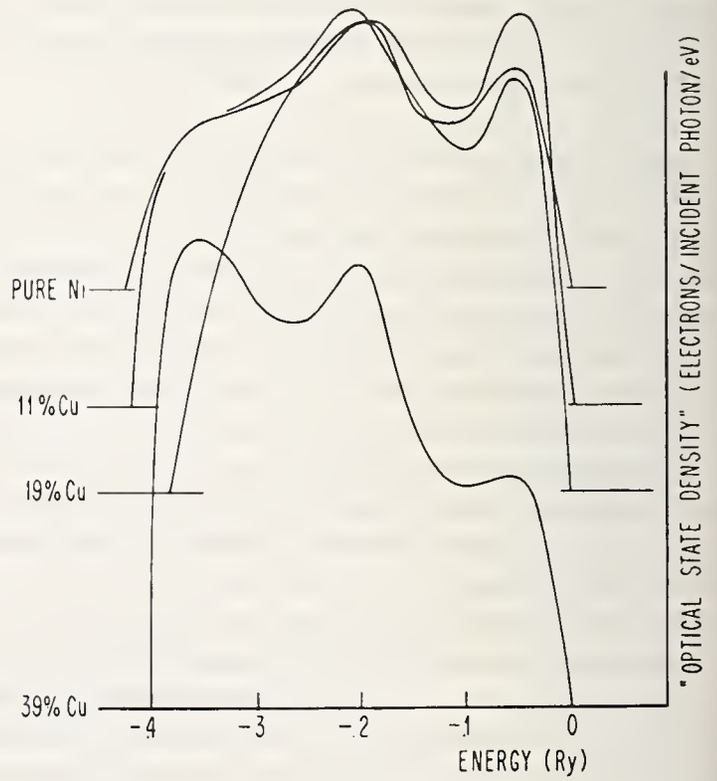

PHOTO EMISSION RESULTS FOR NiCu
(Seib and Spicer)

FIGURE 1. *The hybridized d state densities, calculated in the coherent potential approximation, are compared with the optical state density obtained from photoemission experiments [10, 11].*

which include degenerate d-bands and hybridization with conduction bands. Second, the only input information needed for nickel-rich alloys is the hybridized nickel state density, the positions of the resonant Ni and Cu d-levels which give rise to the d-bands, and the concentration. Third, the distortion in the state density curve with increased alloying shows the rigid band model, which has been particularly popular for this alloy system, does not really apply. This is seen even more clearly in the results of calculations of the magnetic properties [12]. Finally, the prominent calculated structures and their behavior is qualitatively in accord with the experimental observations. The principal peaks remain stationary, but they change in intensity and shape in both the calculations as well as the experiment. The contribution of copper to the state density turns out to be broad and relatively structureless and comes principally from the lower regions of the d-band.

While this kind of theory predicts a wealth of detail, its quantitative validity remains an open question that must be explored further. More important, some of its present limitations must be overcome to render it applicable to a wider class of alloys. However, given the improving theoretical and experimental situation that is clearly evidenced from this conference, it seems clear that at the next meeting of this type we will surely hear about further, more extensive developments which will place the theory of alloys on a firmer footing.

After these somewhat discursive concluding remarks, let me close the conference by once again thanking everyone; organizers, speakers, and rapporteurs, questioners, commenters, and listeners for having made it as stimulating as it turned out to be.

References

[1] The Proceedings of that Conference were edited by F. Abeles and published under that title by North-Holland Publishing Company (Amsterdam) in 1966.

[2] Feldman, D. W., Parker, J. H., and Ashkin, M., Phys. Rev. Letters **21**, 607 (1968).

[3] Beeferman, L., and Ehrenreich, H., (Phys. Rev., to be published).

[4] Mayer, H., and El Naby, M. H., Z. Physik **174**, 289 (1963); Smith, N. V., Phys. Rev. Letters **21**, 96 (1968).

[5] Fujiwara, K., Sueoka, O., and Imura, T., J. Phys. Soc. Japan **24**, 467 (1968).

[6] Beeby, J. L., Proc. Roy. Soc. (London) **A279**, 82 (1964) and cited papers.

[7] Soven, P., Phys. Rev. **151**, 539 (1966).

[8] Soven, P., Phys. Rev. **156**, 809 (1967).

[9] Lifshitz, I. M., Soviet Physics—Uspekhi **7**, 549 (1965).

[10] Kirkpatrick, S., Velicky, B., and Ehrenreich, H. (to be published).

[11] Seib, D. H., and Spicer, W. E., Phys. Rev. Letters **22**, 711 (1969).

[12] Kirkpatrick, S., Velicky, B., Lang, N. D., and Ehrenreich, H., J. Appl. Phys. **40**, 1283 (1969).

Thermal Electron Effective Mass of Rubidium and Cesium

D. L. Martin

Division of Physics, National Research Council of Canada, Ottawa, Canada

Key words: Cesium; effective mass; electronic density of states; rubidium; specific heat.

Specific heat measurements in the range 0.4 to 3.0 K on 99.99% pure rubidium give a thermal electron effective mass of 1.37 ± 0.01 and on 99.97% pure cesium give an effective mass of 1.80 ± 0.04. These results are much closer to the previous specific heat results of Lien and Phillips [1] than to those of Martin, Zych and Heer [2]. The result for rubidium is in good agreement with the theoretical results of Ashcroft [3] (1.38 ± 0.09) and Wasserman and deWitt [4] (1.36). The cesium result is in fair agreement with Wasserman and deWitt [4] (1.69) and Mahanti and Das [5] (1.63). This work has been published in Canadian Journal of Physics **48**, 1327 (1970).

References

[1] Lien, W. H., and Phillips, N. E., Phys. Rev. **133**, A1370 (1964).
[2] Martin, B. D., Zych, D. A., and Heer, C. V., Phys. Rev. **135**, A671 (1964).
[3] Ashcroft, N. W., Phys. Rev. **140**, A935 (1965).
[4] Wasserman, A., and deWitt, H. E., J. Phys. Chem. Solids **29**, 2113 (1968).
[5] Mahanti, S. D., and Das, T. P., Phys. Rev. **183**, 674 (1969).

Density of States and Numbers of Carriers from the dHvA Effect *

S. Hornfeldt, J. B. Ketterson, and L. R. Windmiller

Argonne National Laboratory, Argonne, Illinois 60439

With the dHvA effect, one can determine the angular dependence of the extremal area and effective mass over all sheets of the Fermi surface. Using recently developed techniques this data can be inverted and the angular dependence of the Fermi radius and Fermi velocity determined. Techniques have been developed to allow the inversion of both open and closed surfaces. For closed surfaces we use an expansion in symmetry adapted spherical harmonics (to order $l=60$) while for open surfaces a three-dimensional Fourier series representation is used. With this information one may determine, for a given sheet of the surface, the number of carriers $n(E_F)$ and density of states $N(E_F)$ by performing the appropriate integrations.

Key words: Electronic density of states; de Haas van Alphen effect; Fermi surface; Fermi velocity; Fourier series; spherical harmonics; symmetrized techniques.

1. Introduction

In this paper we will discuss methods for deducing the Fermi radius and Fermi velocity from measurements of the de Haas van Alphen (dHvA) effect. The period of the dHvA oscillations determines the extremal cross-sectional areas of the Fermi Surface (FS) $A(\theta,\varphi)$, where θ and φ are the polar angles of the magnetic field. In addition, dHvA measurements allow a determination of the associated cyclotron effective masses $m^*=1/2\pi\ \partial A(\theta,\varphi)/\partial E$. We will discuss the mathematical techniques that allow one to determine the Fermi radius and velocity from a knowledge of $A(\theta,\varphi)$ and $m^*(\theta,\varphi)$.

If we have the radius $k(\theta,\varphi)$ then by integration we can determine the number of carries, $n(E)$, contained within a given sheet of surface, i.e.:

$$n(E_F)=\frac{2}{3(2\pi)^3}\int k^3(\theta,\varphi)\sin\theta d\theta d\varphi. \tag{1}$$

Furthermore, a knowledge of $\dot{k}(\theta,\varphi)$ and $\mathbf{v}(\theta,\varphi)$ allows us to determine the density of states, $N(E)$, for each sheet of the surface, i.e.,

$$N(E_F)=\frac{2}{(2\pi)^3}\int\frac{k^2(\theta,\varphi)\sin\theta d\theta d\varphi}{v_k(\theta,\varphi)}. \tag{2}$$

It is well known that the inclusion of many-body effects decreases the magnitude of the Fermi velocity from the single particle value that would be deduced from a band structure calculation. As can be seen from eq (2), this results in an increase in $N(E_F)$. Such many-body effects include electron-electron and electron-phonon interactions. The paramagnon contribution, which is really a form of electron-electron interaction, has received considerable attention recently. According to the Landau's Fermi liquid theory, the density of states determined according to eq (2) (using techniques to be described here) should be identical to that determined in a heat capacity experiment, i.e., the quasi-particle density of states accounts for all of the density of states. Actually the Fermi velocity information should be regarded as potentially much more valuable than the density of states since there is probably a wealth of information in the anisotropy of the velocity reduction and its variation from sheet to sheet of the surface.

In order to accomplish this "inversion" it is useful to have a mathematical representation for the surface (or surfaces in cases where the FS consists of several sheets). Two cases arise quite naturally; either the surface is open or it is closed. For a closed surface our representation must be invariant to the operations of the point group of the surface. For an open surface the representation must be invariant under the operations of the space group of the crystal. We will discuss these two cases separately.

*Work performed under the auspices of the U.S. Atomic Energy Commission.

2. The Point Group Representation

Lifshitz and Pogorelov [1] have shown that closed surfaces containing a center of inversion symmetry are invertable providing the radious vector measured from this center is single valued. The theorem, in its original form, was awkward to apply and Mueller [2] has reformulated it in a manner which considerably simplifies its application. A comparison of the Lifshitz-Pogorelov and the Mueller formulation has been given by Foldy [3]. For the representation of the surface we use symmetry adapted spherical harmonics. Since the radius vector is a real quantity we deal with the real spherical harmonics.

$$C^g_{lm} = \frac{1}{\sqrt{2}} [Y_{l,m}(\theta,\varphi) + Y_{l,-m}(\theta,\varphi)] \tag{3a}$$

$$C^u_{lm} = \frac{1}{i\sqrt{2}} [Y_{l,m}(\theta,\varphi) - Y_{l,-m}(\theta,\varphi)] \tag{3b}$$

$$C_{l0} = Y_{l0}(\theta,\varphi) \tag{3c}$$

We expand the area $A(\theta,\varphi)$ and the square of the radius vector $k^2(\theta,\varphi)$ as follows:

$$k^2(\theta,\varphi) = \sum_{l,m} [\gamma^g_{l,m} C^g_{l,m}(\theta,\varphi) + \gamma^u_{l,m} C^u_{l,m}(\theta,\varphi)] \tag{4}$$

$$A(\theta,\varphi) = \sum_{l,m} [\beta^g_{l,m} C^g_{l,m}(\theta,\varphi) + \beta^u_{l,m} C^u_{l,m}(\theta,\varphi)]. \tag{5}$$

What Mueller showed was that

$$\beta_{l,m} = \pi P_l(0) \gamma_{l,m}, \tag{6}$$

where $P_l(0)$ is the Legendre function of order l. A unique connection between the radii and areas requires even l since $P_l(0) = 0$ for odd l. Even l is the same as requiring inversion symmetry since the parity of spherical harmonics is $(-1)^l$. Of the 32 crystal point groups 10 contain the inversion element, these being S_i, C_{2h}, D_{2h}, C_{4h}, D_{4h}, C_{3i}, D_{3d}, C_{6h}, D_{6h}, and O_h. The values of m to be summed over in eqs (4) and (5) depend on which of these 10 point groups the surface in question belongs [4]. The z-axis is chosen as the axis of highest symmetry. The inclusion of even (g) and uneven (u) coefficients are required when the z-axis does not lie in a mirror plane. If the z-axis does lie in a mirror plane, then the z-axis is also chosen to lie within the mirror plane and only even coefficients are required. All values of m ($0 - l$) are required for the group S_2 along with both even and odd coefficients. Only even coefficients are required for the groups D_{2h}, D_{4h}, D_{3d}, and D_{6h} and $m = 0 \pmod 2$, $m = 0 \pmod 4$, $m = 0 \pmod 3$, and $m = 0 \pmod 6$ respectively. Both even and odd coefficients are required, and the x-axis may be chosen arbitrarily, for the groups C_{2h}, C_{4h}, C_{3i}, and C_{6h} and $m = 0 \pmod 2$, $m = 0 \pmod 4$, $m = 0 \pmod 3$, and $m = 0 \pmod 6$ respectively. The group O_h requires special consideration [5]. The symmetrized harmonics $K_{l,i}(\theta,\varphi)$ which transform according to the cubic group are called Kubic harmonics. These harmonics are linear combinations of real even spherical harmonics.

$$K^i_l = \sum_m a^i_{l,m} C^g_{l,m}(\theta,\varphi). \tag{7}$$

The coefficients $a^i_{l,m}$ have been tabulated to order $l = 30$ by Mueller and Priestley [5] and to order $l = 60$ by Aurbach, Ketterson, Mueller, and Windmiller [6].

The actual inversion proceeds as follows. The coefficients β_{lm} are found by least squares fitting the available experimental areas to eq (5). The Fermi momentum then follows by combining eqs (4) and (6). It is necessary that the available experimental areas be measured over a wide range of angles, otherwise the number of coefficients which can be determined is limited [4,5].

Often one encounters surfaces which are nearly ellipsoidal in shape. This is particularly true in semi-metals. Equations (4) and (5) do not terminate for ellipsoids and converge slowly if the ellipsoid is quite elongated. For such surfaces it is convenient to perform a "spherical mapping" on the coordinates in order to map the "ellipsoid" into a "sphere" [4]. We do this by the following transformation

$$\begin{aligned} x' &= \alpha x \\ y' &= y \\ z' &= \gamma z. \end{aligned} \tag{8}$$

Let T represent this transformation, i.e., $T(x,y,z) = (x',y',z')$ or in polar coordinates $T(\gamma,\theta,\varphi) = (\gamma',\theta',\varphi')$. We will also need the inverse transformation $T^{-1}(x',y',z') = (x,y,z)$ or equivalently $T^{-1}(\gamma',\theta',\varphi') = (\gamma,\theta,\varphi)$. It is easy to show the following

$$r'^2(\theta',\varphi') = r^2(\theta,\varphi)[\sin^2\theta(\sin^2\varphi + \alpha^2\cos^2\varphi) + \gamma^2\cos^2\theta] \tag{9a}$$

$$\cos\varphi' = \frac{\alpha\cos\varphi}{(\sin^2\varphi + \alpha^2\cos^2\varphi)^{1/2}} \tag{9b}$$

$$\cos\theta' = \frac{\gamma\cos\theta}{[\sin^2\theta(\sin^2\varphi + \alpha^2\cos^2\varphi) + \gamma^2\cos^2\theta]^{1/2}}. \tag{9c}$$

The question arises as to what the relation is between the area in the transformed system and the untransformed system. It can be shown that [4]

$$A'(T^{-1}\theta, T^{-1}\varphi) = \alpha\gamma[\sin^2\theta(\sin^2\varphi + \alpha^{-2}\cos^2\varphi) + \gamma^{-2}\cos^2\theta]^{1/2} A(\theta, \varphi). \tag{10}$$

What one does in practice is map the areas measured in the untransformed to the transformed system using eq (10). The coefficients in eq (5) are then determined by the least squares procedure. The radii in the transformed system (which follow from eq (6)) are then mapped back to the untransformed system using eq (9a).

We now turn to the inversion of areas and effective masses into the Fermi velocity $\mathbf{v}_F(\theta,\varphi)$ [7]. The velocity is given by ($\hbar = 1$):

$$\mathbf{v}(\theta, \varphi) = \left(\frac{\partial E}{\partial k}\right)_{\theta,\varphi} \hat{k} + \frac{1}{k}\left(\frac{\partial E}{\partial \theta}\right)_{k,\varphi} \hat{\theta} + \frac{1}{k\sin\theta}\left(\frac{\partial E}{\partial \varphi}\right)_{k,\theta} \hat{\varphi} \tag{11}$$

We expand $\partial A(\theta,\varphi)/\partial E$ ($= 2\pi m^*(\theta,\varphi)$) in a series of the form given in eq (5)

$$\frac{\partial A(\theta, \varphi)}{\partial E} = \sum_{l,m} [\beta'^{g}_{l,m} C^{g}_{l,m}(\theta, \varphi) + \beta'^{u}_{l,m} C^{u}_{l,m}(\theta, \varphi)] \tag{12}$$

$$\frac{\partial k^2(\theta, \varphi)}{\partial E} = \sum_{l,m} [\gamma'^{g}_{l,m} C^{g}_{l,m}(\theta, \varphi) + \gamma'^{u}_{l,m} C^{u}_{l,m}(\theta, \varphi)]. \tag{13}$$

where $\beta'_{l,m} = \pi P_l(0)\gamma'_{l,m}$.

Since $\partial k^2(\theta,\varphi)/\partial E = 2k(\theta,\varphi)\,\partial k(\theta,\varphi)/\partial E = 2k(\theta,\varphi)/v_k(\theta,\varphi)$ we have immediately the $\hat{k}$ component of the velocity (since k is known from eq (4)), i.e.,

$$v_k = \frac{2\left\{\sum_{l,m} [\gamma^{g}_{l,m} C_{l,m}(\theta, \varphi) + \gamma^{u}_{l,m} C_{l,m}(\theta, \varphi)]\right\}^{1/2}}{\sum_{l,m} [\gamma'^{g}_{l,m} C^{g}_{l,m}(\theta, \varphi) + \gamma'^{u}_{l,m} C^{u}_{l,m}(\theta, \varphi)]}. \tag{14}$$

The other two components may easily be calculated using the laws for the differentiation of implicit functions, i.e.,

$$\left(\frac{\partial E}{\partial \theta}\right)_{k,\varphi} = -\left(\frac{\partial k}{\partial \theta}\right)_{E,\varphi} \Big/ \left(\frac{\partial k}{\partial E}\right)_{\varphi,\theta} \text{ and } \left(\frac{\partial E}{\partial \varphi}\right)_{k,\theta} = -\left(\frac{\partial k}{\partial \theta}\right)_{E,\theta} \Big/ \left(\frac{\partial k}{\partial E}\right)_{\varphi,\theta}.$$

$$v_\theta = -\frac{\dfrac{\partial}{\partial \theta}\sum_{l,m} [\gamma^{g}_{l,m} C^{g}_{l,m}(\theta, \varphi) + \gamma^{u}_{l,m} C^{u}_{l,m}(\theta, \varphi)]}{\left\{\sum_{l,m} [\gamma'^{g}_{l,m} C^{g}_{l,m}(\theta, \varphi) + \gamma'^{u}_{l,m} C^{u}_{l,m}(\theta, \varphi)]\right\}\left\{\sum_{l,m} [\gamma^{g}_{l,m} C^{g}_{l,m}(\theta, \varphi) + \gamma^{u}_{l,m} C^{u}_{l,m}(\theta, \varphi)]\right\}^{1/2}} \tag{15}$$

Thus we find:

$$v_\varphi = -\frac{(\sin\theta)^{-1}\dfrac{\partial}{\partial \varphi}\sum_{l,m} [\gamma^{g}_{l,m} C^{g}_{l,m}(\theta, \varphi) + \gamma^{u}_{l,m} C^{u}_{l,m}(\theta, \varphi)]}{\left\{\sum_{l,m} [\gamma'^{g}_{l,m} C^{g}_{l,m}(\theta, \varphi) + \gamma'^{u}_{l,m} C^{u}_{l,m}(\theta, \varphi)]\right\}\left\{\sum_{l,m} [\gamma^{g}_{l,m} C^{g}_{l,m}(\theta, \varphi) + \gamma^{u}_{l,m} C^{u}_{l,m}(\theta, \varphi)]\right\}^{1/2}}. \tag{16}$$

It is also possible to obtain similar formulas when using the spherical mapping procedure [6].

3. The Space Group Representation

A representation which is invariant under the operations of the space group is a three-dimensional Fourier series of the form:

$$F(\mathbf{k}) = \sum_{\mathbf{R}} C_{\mathbf{R}} e^{i\mathbf{k}\cdot\mathbf{R}} \tag{17}$$

where the $C_{\mathbf{R}}$ are the Fourier coefficients. This representation was used by Roaf [8] to construct the FS of Cu, Ag and Au from the dHvA data of Shoenberg [9]. The vectors $\mathbf{R}$ are the vectors of the real space lattice:

$$\mathbf{R}_{lmn} = l\mathbf{a} + m\mathbf{b} + n\mathbf{c} \tag{18}$$

where l, m, and n are integers and $\mathbf{a}$, $\mathbf{b}$, and $\mathbf{c}$ are the primitive translation vectors of the lattice. The vectors $\mathbf{R}_{lmn}$ may be factored into sets, which we will call stars, according to their length $|\mathbf{R}_{lmn}|$ [10]. Thus eq (17) may be written in the form

$$F(\mathbf{k}) = \sum_{j} C_j S_j(\mathbf{k}) \tag{19}$$

where the j number the stars of increasing length, and $S_j(\mathbf{k})$ is the sum of $e^{i\mathbf{k}\cdot\mathbf{R}}$ over all $\mathbf{R}$ in the jth star. In eqs (17) and (19) $F(\mathbf{k})$ is not necessarily identical to the band structure $E(\mathbf{k})$. If the coefficients are determined by fitting to a band structure calculation over some range of energy then $F(\mathbf{k})$ will approximate the band structure in that interval. In this case the Fermi velocity is given by

$$\mathbf{v} = i \sum_{\mathbf{R}} \mathbf{R} C_{\mathbf{R}} e^{i\mathbf{k}\cdot\mathbf{R}} \tag{20}$$

If on the other hand the C_j are determined only from information involving the shape of the FS (e.g. dHvA areas) then $F(k) = E_F$ is a number which may be chosen arbitrarily and the velocity is not given by eq (20). If, however, we have both area and effective mass data then we can construct both the Fermi radii and Fermi velocities.

We discuss first the inversion of areas to radii. The calculated area is given by

$$A^c = \frac{1}{2}\int_0^{2\pi} k_\perp^2(\psi)\, d\psi \tag{21}$$

where $k_\perp$ measures the component of the momentum in the plane of the orbit, and ψ measures the angle of $\mathbf{k}_\perp$ in the plane of the orbit. Since eq (19) is an implicit function of $\mathbf{k}$ we must solve using the Newtron-Raphson technique. Assume that we have a set of N areas A_i and an initial set of coefficents C_j. The problem is to vary the C_j until the areas calculated using eqs (19) and (21) minimizes the rms error Δ between the calculated and measured areas where Δ is given by:

$$\Delta^2(C_j) = \frac{1}{N}\sum_{i=1}^{N}\left(\frac{A_i^c - A_i}{A_i}\right)^2. \tag{22}$$

The amount δC_j by which we must correct C_j follows from minimizing eq (22), i.e.:

$$\frac{\partial \Delta^2}{\partial C_j} + \sum_{jl} \frac{\partial \Delta^2}{\partial C_j \partial C_l}\,\delta C_l = 0. \tag{23}$$

It can be shown that the vector and tensor coefficients in eq (23) are given by [11]:

$$\frac{\partial \Delta^2}{\partial C_j} = \frac{2}{N}\sum_{i=1}^{N}\frac{(A_i^c - A_i)}{A_i^2}\frac{\partial A_i^c}{\partial C_j} \tag{24}$$

and

$$\frac{\partial \Delta^2}{\partial C_j \partial C_l} = \frac{2}{N}\sum_{i=1}^{N}\left[\frac{\partial A_i^c}{\partial C_j}\frac{\partial A_i^c}{\partial C_l} + (A_i^c - A_i)\frac{\partial^2 A_i^c}{\partial C_j \partial C_l}\right]\cdot\frac{1}{A_i^2} \tag{25}$$

where

$$\frac{\partial A^c}{\partial C_j} = -\int_0^{2\pi}\frac{k_\perp^2}{\mathbf{k}_\perp\cdot\nabla F} S_j(\mathbf{k})\, d\psi \tag{26}$$

and

$$\frac{\partial^2 A^c}{\partial C_j \partial C_l} = \int_0^{2\pi}\left[k_\perp^2\frac{S_j(\mathbf{k})S_l(\mathbf{k})}{(\mathbf{k}_\perp\cdot\nabla F)^2} + k_\perp^2\frac{S_j(\mathbf{k})\mathbf{k}_\perp\cdot\nabla S_l(\mathbf{k}) + S_l(\mathbf{k})\mathbf{k}_\perp\cdot\nabla S_j(\mathbf{k})}{(\mathbf{k}_\perp\cdot\nabla F)^2} - k_\perp^2\frac{S_j(\mathbf{k})S_l(\mathbf{k})\mathbf{k}_\perp\cdot\nabla\nabla F\cdot\mathbf{k}_\perp}{(\mathbf{k}_\perp\cdot\nabla F)^3}\right] d\psi. \tag{27}$$

Using the above equations we can determine a set of C_j which fit the data and thus construct the shape of the surface. This technique is applicable to both open and closed surfaces.

We will now show how this technique can be extended to determining Fermi velocities from area and effective mass data. As mentioned previously ∇F will not yield the Fermi velocity when the C_j are determined using eqs (23) through (27). While it is possible to determine a set of coefficients C_j such that $\nabla E = \mathbf{v}_F$ it is simpler to introduce a new set of coefficients C_j'. We define these coefficients by writing the velocity in the following form

$$\mathbf{v} = -\frac{\nabla F(\mathbf{k})}{\sum_j C_j' S_j(\mathbf{k})}. \tag{28}$$

The effective mass follows from

$$m^* = \frac{1}{2\pi}\frac{\partial A}{\partial E} = \frac{1}{2\pi}\int_0^{2\pi} \frac{k_\perp^2}{\mathbf{k}_\perp \cdot \nabla E}\, d\psi$$

$$= -\frac{1}{2\pi}\sum_j \int_0^{2\pi} \frac{k_\perp^2 C_j' S_j(\mathbf{k})}{\mathbf{k}_\perp \cdot \nabla F}\, d\psi. \tag{29}$$

We assume that the C_j which yield $F(\mathbf{k})$ are already known and that we vary the C_j' until a best fit is achieved to the effective masses. We define a new function Δ' similar to eq (22) by

$$\Delta'(C_j') = \frac{1}{N'}\sum_{i=1}^{N'} \left(\frac{m_i^{*c} - m_i^*}{m_i^*}\right)^2 \tag{30}$$

which on minimizing leads to an equation similar to (23). Thus we need

$$\frac{\partial \Delta'^2}{\partial C_j'} = \frac{2}{N'}\sum_{i=1}^{N'} \frac{(m_i^{*c} - m_i^*)}{m_i^{*2}} \frac{\partial m_i^{*c}}{\partial C_j'} \tag{31}$$

and

$$\frac{\partial \Delta'^2}{\partial C_l' \partial C_j'} = \frac{2}{N'}\sum_{i=1}^{N'} \left[\left(\frac{\partial m_i^{*c}}{\partial C_j'}\right)\left(\frac{\partial m_i^{*c}}{\partial C_j'}\right) + (m_i^{*c} - m_i^*)\frac{\partial^2 m^*}{\partial C_j' \partial C_l'}\right]\frac{1}{m_i^{*2}}. \tag{32}$$

These derivatives follow immediately from eq (29) (recalling $k_\perp$ does not change on varying C_j')

$$\frac{\partial m_i^{*c}}{\partial C_j'} = -\frac{1}{2\pi}\int_0^{2\pi} \frac{k_\perp^2}{\mathbf{k}_\perp \cdot \nabla F} S_j(\mathbf{k})\, d\psi, \quad \frac{\partial^2 m^{*c}}{\partial C_j' \partial C_l'} = 0. \tag{33}$$

The important point is that $\int_0^{2\pi} \frac{k_\perp^2}{\mathbf{k}_\perp \cdot \nabla F} S_j(\mathbf{k})\, d\psi$ was already evaluated when doing the area to radii inversion. Thus it is only necessary to save these coefficients in order to perform the effective mass inversion.

To evaluate the number of carriers and density of states using the Fourier series representation it is convenient to evaluate the integrals differently than in eqs (1) and (2). We rewrite (1) and (2) in the following form:

$$n(E) = \frac{2}{(2\pi)^3}\int A(k_{||})\, dk_{||} \tag{34}$$

and

$$N(E) = \frac{2}{(2\pi)^3}\int 2\pi m^*(k_{||})\, dk_{||} \tag{35}$$

where $k_{||}$ is measured normal to the plane of the orbit. A problem arises when the surface is open in that the orbits can change from "hole like" to "electron like." This problem is solved by subtracting the area of the hole orbits from the corresponding area of the Brillouin zone, and selecting the direction of $\hat{k}_{||}$ such that no open orbits occur.

4. Applications

The techniques involving the symmetrized spherical harmonic representations have been applied to the Γ centered electron surfaces in Pt [7] and Pd [12]. For Pt the number of carriers in the 6th band electron surface is found to be $n(E_F) = 0.419$ electrons/atom while the corresponding density of states if $N(E_F) = 6.35$ electrons/atom Ry. The data are not yet sufficient to allow an inversion of the heavy "*d* like" open hole surface of Pt but should be in the near future. Fermi radii in Cu, Ag and Au were deduced by Roaf using the Fourier series approach [8]. This was extended by Halse to calculate the Fermi velocity in Cu and Ag [13]. The improved Fourier series techniques developed here will shortly be applied to recent dHvA data in Au [14]. An inversion of the As and Sb electron Fermi surface was reported recently using the symmetrized spherical harmonic approach [4].

5. References

[1] Lifshitz, I. M., and Pogorelov, A. V., Dokl. Akad. Nauk. SSSR **96**, 1143 (1954).

417-156 O - 71 - 52

[2] Mueller, F. M., Phys. Rev. **148,** 636 (1966).
[3] Foldy, L. L., Phys. Rev. **170,** 670 (1968).
[4] Ketterson, J. B., and Windmiller, L. R., to be published in Phys. Rev.
[5] Mueller, F. M., and Priestley, M. G., Phys. Rev. **148,** 638 (1966).
[6] Aurbach, R., Ketterson, J. B., Mueller, F. M., and Windmiller, L. R., Argonne National Laboratory report to be published.
[7] Ketterson, J. B., Windmiller, L. R., Hornfeldt, S., and Mueller, F. M., Solid State Communications **6,** 851 (1968).
[8] Roaf, D. J., Phil. Trans. Roy. Soc. (London) **A255,** 135 (1962).
[9] Shoenberg, D., Phil. Trans. Roy. Soc. (London) **A255,** 85 (1962).
[10] In the *fcc* lattice this test is insufficient. There are R_{lmn} whose lengths are the same which do not, however, transform into each other under the operations of the point group. Those are distinguished by comparing $|R_x|^3+|R_y|^3+|R_z|^3$.
[11] Ketterson, J. B., Mueller, F. M., Windmiller, L. R., to be published in Phys. Rev.
[12] Windmiller, L. R., Ketterson, J. B., and Hornfeldt, S., Journal of Applied Phys. **40,** 1291 (1969).
[13] Halse, M. R., to be published.
[14] Bosacchi, B., Ketterson, J. B., Shaw, J., and Windmiller, L. R., to be published.

A Note on the Position of the "Gold 5*d* Bands" in $AuAl_2$ and $AuGa_2$ *

P. D. Chan and D. A. Shirley

Department of Chemistry and Lawrence Radiation Laboratory, University of California, Berkeley, California 94720

Switendick and Narath [1] recently proposed a solution for the "$AuGa_2$ dilemma" pointed out by Jaccarino, et al. [2]. This solution was based on the results of band structure calculations [1]. The density of states for $AuAl_2$ derived from these band-structure calculations were presented at this conference [3]. A surprising result of this calculation was the position of the "gold *d*-band" states. These states were located at about −7 eV in $AuAl_2$ and at similar energies in $AuGa_2$ and $AuIn_2$ [1]. The interesting optical properties of gold intermetallic compounds (e.g., $AuAl_2$ is violet) are often attributed to the proximity of the gold *d*-bands to the Fermi energy, E_F. If these states really lay at E_F-7 eV, and were as flat (i.e., the $\rho(E)$ peak was as narrow) as the calculation indicated, then they could scarcely affect the compounds' optical properties [4]. To help resolve this "*d*-band dilemma," we undertook measurements of the valence-band spectra of $AuAl_2$ and $AuGa_2$ by x-ray photoelectron spectroscopy (XPS). This method has been described elsewhere [5]: accordingly we describe below only those experimental features of this work that were peculiar to the $AuAl_2$-$AuGa_2$ problem. The two compounds are first treated in separate sections. The results are then discussed in the final section.

Key words: Electronic density of states; gold aluminum two ($AuAl_2$); gold gallium two ($AuGa_2$); x-ray photoelectron spectroscopy.

1. $AuAl_2$

This compound was prepared by heating stoichiometric amounts of metallic Au and Al to ~ 1000 °C in an induction furnace which was flushed a few times with argon and then pumped down to 2×10^{-6}. One of the compounds (sample B.1) was further remelted at ~ 1000 °C in an arc furnace also flushed with argon and then pumped down to 10^{-6}. The resulting alloys were spark-cut and polished with size 600 sand paper and, in two cases, with one micron diamond paste and kerosene on a canvas wheel; but they were not etched. They were rinsed with absolute ethanol before mounting. A total of three samples were used to collect the data that were accepted for final analysis. The samples were studied in a H_2 atmosphere ($p \cong 0.01$ torr) at temperatures indicated in table 1. The signal-to-noise ratio for energies near E_F was unusually low, and it was not possible to make a detailed study of the density-of-states function $\rho_{AuAl2}(E)$. The Spectra showed one dominant peak at $E_F - 6$ eV, however. A least-squares analysis was made on each spectrum. The trial function consisted of a linear, sloping background plus a Gaussian with a constant tail on the low energy side. This combination usually fits XPS spectra quite well, and it did in this case. For some of the spectra the "*d*-band" peak appeared on visual inspection to be slightly asymmetric, and two-Gaussian fits were made. These fits give a very weak higher-energy peak of variable position and shifted the main peak only a few tenths eV. We therefore did not regard the experimental evidence for a second peak as being conclusive, and the question was of no particular interest, so only the one-Gaussian fits are presented in table 1.

One of the $AuAl_2$ spectra is shown in figure 1. Our final values for the position and width of the "*d*-band" peak are

$$E = E_F - (6.0 \pm 0.3) \text{ eV},$$

$$\Delta E = (4.1 \pm 0.5) \text{ eV FWHM}.$$

The Al 2*p* peak was found to be at

$$E = E_F - 75.05 \pm 0.20 \text{ eV}.$$

*Work performed under the auspices of the U.S. Atomic Energy Commission.

TABLE 1

$AuAl_2$ sample no.	T(°C)	Reference peak	$-E$ [a]	ΔE (FWHM)	$-E$ (5d-band)	ΔE (FWHM)
B.1	25	.....	.....	.....	5.99(14)	4.6(3)
B.2	25	Al 2p	75.0(2)	.....	5.71(19)	4.6(4)
B.3	600	Al 2p	75.2(2)	.....	6.42(14)	3.3(4)
Adopted values [b]	.....	.....	75.1(2)	.....	6.0(3)	4.1(5)
$AuGa_2$ sample no.:						
A.3	400	Ga 3d(1) [c]	20.1	[d] 1.8	5.62(21)	5.9(5)
		Ga 3d(2)	18.2	1.8		
A.4	400	Ga 3d(1)	20.8	1.95	5.81(14)	4.6(3)
		Ga 3d(2)	18.9	1.95		
A.5	375	Ga 3d(1)	20.5	2.0	5.90(8)	4.2(4)
		Ga 3d(2)	18.7	1.5		
Adopted values [b]	.....	.....	20.5(4)	1.9	5.8(2)	4.6(3)
			18.6(4)	1.8		

[a] All energies in eV, relative to the Fermi Energy. Errors in last place are indicated parenthetically.
[b] Adopted values and assigned errors reflect some systematic errors.
[c] The Ga 3d(2) peak was 0.4–0.6 times as intense as the Ga 3d(1) peak.
[d] For samples A.3 and A.4, peak widths were constrained to be equal.

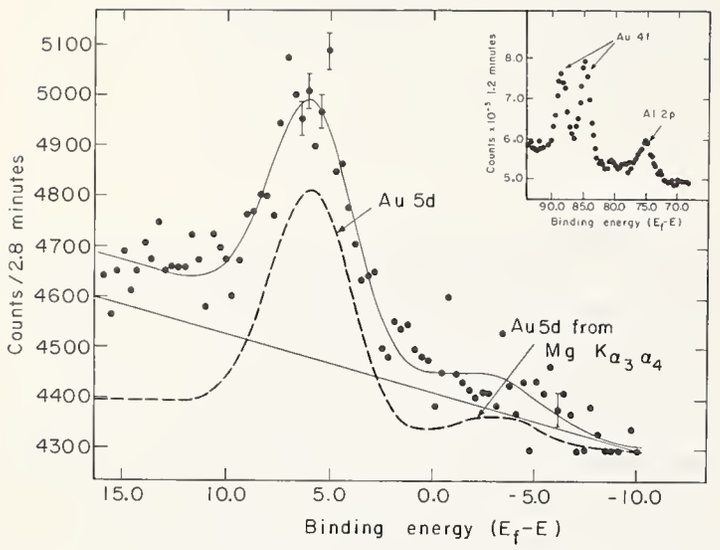

FIGURE 1. *Typical x-ray photoemission spectrum for* $AuAl_2$ *near the Fermi energy.*

Filled circles represent data points. Top solid curve was fitted to the data. It was composed of background, indicated by sloping solid line, plus a response curve indicated by dashed curve. The main peak of this dashed curve arises through photoemission from the "gold 5d" bands by $MgK\alpha_{12}$ radiation. Core-level peaks in inset indicate chemical purity of sample.

2. $AuGa_2$

Dr. Narath kindly provided one of our $AuGa_2$ samples: the other two were prepared in our laboratory as described above for $AuAl_2$. The experimental and data reduction procedures were also similar to those used for $AuAl_2$. Again a single Gaussian was fitted to the "d-band" peak; in this case the peak was quite symmetrical and no attempt was made to fit two Gaussians to it. The Ga 3d peak, which lay about 20 eV below E_F, was asymmetric, however. It appeared to consist of two peaks, each of width 2 eV FWHM, and spaced about 2 eV apart, with the higher-energy peak about 0.4 as intense as the lower-energy peak. We attributed the high-energy peak to free Ga, and auxiliary experiments on nonstoichiometric samples seemed to support our assignment, although we were not able to eliminate this peak. Further support is given by the Au $4f_{5/2}$, $4f_{7/2}$ doublet in $AuGa_2$, which showed no evidence of a second phase. It is also possible that the asymmetric 3d

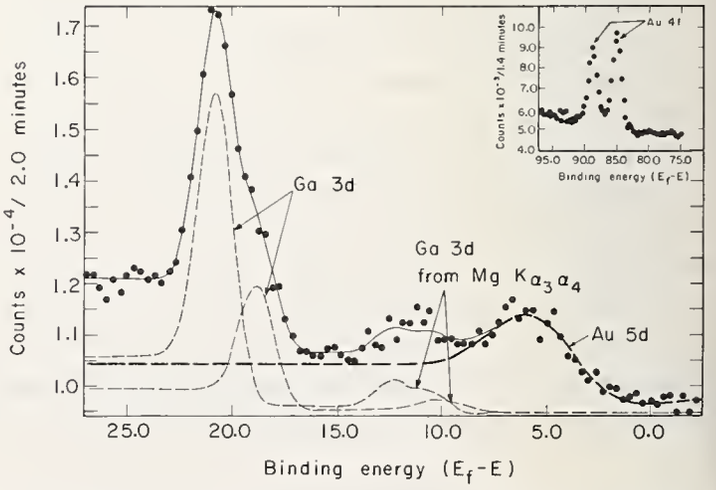

FIGURE 2. *Typical x-ray photoemission spectrum from* $AuGa_2$ *near the Fermi energy.*

peak shape reflects real broadening arising from its proximity to E_F.

A spectrum of $AuGa_2$ is shown in figure 2. Our final values for the "d-band" peak are

$$E = E_F - (5.8 \pm 0.2) \text{ eV},$$

$$\Delta E = (4.6 \pm 0.4) \text{ eV}.$$

3. Discussion

The peaks at $\sim E_f - 6$ eV in the photoemission spectra from $AuAl_2$ and $AuGa_2$ can be attributed to the "gold 5d bands" with considerable confidence. We interpret these spectra as giving strong support for Switendick's band structure calculations, in a qualitative way: the positions of these peaks are in good agreement with his predictions. On closer inspection, however, there are points of difference. The experimental peaks are not quite so deep ($E_F - 6$ eV) as the theoretical value ($E_F - 7$ eV), and the experimental linewidth (~ 4 eV) is about twice theoretical. In fact the combination of less depth and greater width for the experimental d bands somewhat weakens the conclusion that these bands are not important in optical phenomena.

Comparison with the Al($L_{2,3}$) soft x-ray emission spectrum from $AuAl_2$, reported by Williams, et al. [6], is interesting. These workers studied x-ray spectra from transitions in which holes in the 2p shell of Al were filled by electrons from s-like states at Al sites. States derived from Al 3s atomic states are of course s-like at Al sites, but so also are some states that are d-like on Au sites. Thus the strong peak that Williams et al., found at $E_F - 8$ eV could be attributed in part to the "gold 5d bands," and they took this as support of Switendick's calculation. Our results are basically in very good agreement with Switendick's band structure results and the x-ray spectra results of Williams et al., but the small differences are also of interest. The soft x-ray work shows a peak at $E_F - 8.3$ eV, while the XPS peak in the $AuAl_2$ is at $E_F - 6.0$ eV. We attribute this difference to the fact that XPS is most sensitive to d electrons and thus determines the position of the "gold 5d bands" directly, while the soft x-ray emission work is sensitive to bands with s-like symmetry at the Al sites. Switendick [3] has calculated, for $AuAl_2$, peak positions of $E_F - 8.0$ eV and $E_F - 7.1$ eV, respectively, for the peak in the Al 3s-like states and the peak in the total density of states. This would account for some, but not all, of the difference between the positions of the experimental peaks obtained by the two methods. Another more direct point of disagreement is the position of the Al 2p state. Switendick calculated $E = E_F - (73.8 \pm 0.1)$ eV for this state, and he quoted an experimental value of $E_F - (73.5 \pm 0.5)$ eV. Our XPS spectra showed this peak at $E_F - (75.1 \pm 0.2)$ eV. While these points of disagreement in detail are worth further study, it now seems clear that the three investigations mentioned here—Switendick's theoretical work, the x-ray emission work of Williams et al., and our XPS results—all concur on one major point: the gold 5d bands in the $AuAl_2$-type alloys lie 6-8 eV below the Fermi energy.

4. Acknowledgments

Several people contributed significantly to the success of this work, Dr. Albert Narath suggested the problem. Dr. Jack Hollander and Mr. Charles Fadley gave valuable advice during the experiments. Miss Carol Martinson assisted in preparing the alloys. Dr. A. C. Switendick elucidated the relationships among his work, that of Williams, et al., and ours. Dr. R. E. Watson and Dr. L. H. Bennett encouraged us to prepare this note for the Proceedings during a discussion of the $AuAl_2$ problem. Mr. Charlie Butler and Mr. Lee Johnson provided technical assistance in the preparation of the experiments.

5. References

[1] Switendick, A. C., and Narath, A., Phys. Rev. Letters **22**, 1423 (1969).

[2] Jaccarino, V., Weber, M., Wernick, J. H., and Menth, A., Phys. Rev. Letters **21**, 1811 (1968).

[3] Switendick, A. C., these Proceedings, p. 63.

[4] A wavelength of 3000 Å corresponds to an energy of 4.14 eV.

[5] The application of XPS to valence-band studies in metals is discussed by C. S. Fadley and D. A. Shirley, NBS J. Res. **74A**, 543 (1970) and these Proceedings, p. 163.

[6] Williams, M. L., Dobbyn, R. C., Cuthill, J. R., and McAlister, A. J., these Proceedings, p. 303.

The Reliability of Estimating Density of States Curves from Energy Band Calculations*

E. B. Kennard, D. Koskimaki, J. T. Waber,*** and F. M. Mueller****

Materials Science Department, Northwestern University, Evanston, Illinois 60201

The density of states curve for aluminum was calculated for different initial energy bands using the quadratic interpolation method (QUAD) developed by Mueller et al. In one case, a true parabolic energy band was used as input and in the second, the $E(\mathbf{k})$ values were those obtained for aluminum by Snow using the APW method. Deviations from the parabolic density of states curve were found to be inversely proportional to the number of $E(k)$ values per histogram box and hence inversely proportional to the square root of the number of random $\mathbf{k}$ points in the Brillouin zone. It was necessary to use 100,000 points to obtain a relative deviation of 0.3%. In the second case, the self consistent band calculations for 2048 points in the full Brillouin zone and for a subset of 256 of these were used as input data. The effect of increasing the number of input values was assessed for 25,000 random points in the Brillouin zone. The relative errors were 26 and 9 respectively for 256 and 2048 points.

The effects of "smoothing" as an alternative method of reducing statistical error in computing density of states curves are also discussed.

Key words: Aluminum; electronic density of states; free electron parabola; QUAD scheme; reliability of smoothing procedures.

It has been known by many workers in the field of energy bands that substantial statistical errors could occur in drawing the histograms for a density-of-states curve when a small set of $E(\mathbf{k})$ values was used. We can imagine a discrete spectrum of calculated $E(\mathbf{k})$ values falling randomly within the set of n boxes given by $E_{min} + n\Delta E$. Therefore, the relative errors would be dependent upon not only on the width of the energy intervals ΔE but also on their relative location. Waber and Snow [1] discussed a smoothing procedure in their paper on copper, in which several sets of $N(E)$ curves were computed. The value of E at the location of the first histogram was given by $E_{min} + (\Delta Ep/q)$ where q is an integer and $p = 1,2 \ldots (q\text{-}1)$. The resulting set of q density of states curves were than averaged at energy points which were separated by $\Delta E/q$. Despite this procedure, Snow [2] observed that the $N(E)$ curve for aluminum was very ragged when only 256 input $\mathbf{k}$ values were used. He observed that a smoother $N(E)$ curve resulted when he employed 2048 points in his study of the self-consistent APW bands. An $N(E)$ curve drawn from the data of Snow [2] using only 256 points is presented as figure 1; it may be compared with his published curve for 2048 points.

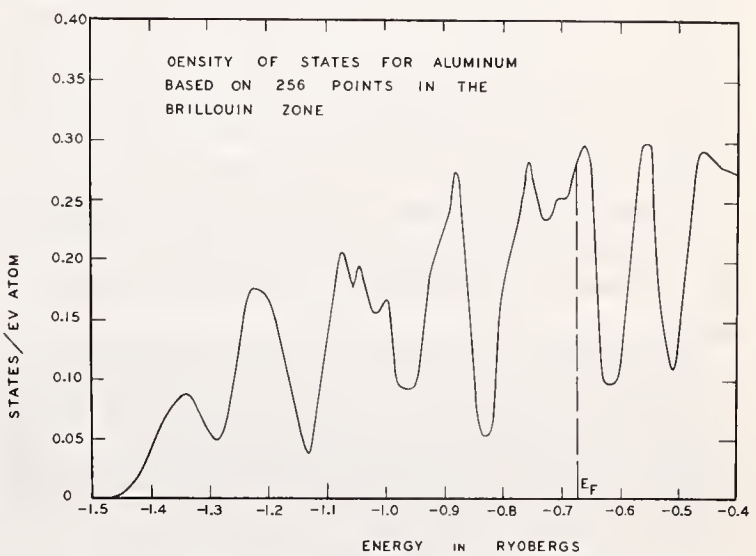

FIGURE 1. *Density of States curve drawn from the* E(**k**) *data which Snow* [2] *obtained in his self-consistent band study of aluminum.*
The subset with $f = 1$ was employed. The smoothing procedure of Snow and Waber [1] was employed with $q = 5$.

*Research supported by the Advanced Research Projects Agency of the Department of Defense through the Materials Research Center of Northwestern University.

**Work done in partial fulfillment of the requirements of the degree of Doctor of Philosophy. Materials Science Dept., Northwestern University, Evanston, Illinois 60201.

***Research Assistant and Professor, respectively, Materials Science Dept., Northwestern University, Evanston, Illinois 60201.

****Solid State Physics Division, Argonne National Laboratory, Argonne, Illinois 60439.

An idealized free-electron band in a body-centered cubic Brillouin zone was studied by Wood [3] to assess the efficacy of this technique. A fixed number of k points and three different widths of the histograms were employed. The strong dependence of the $N(E)$ on the number of values per box was demonstrated. A $N(E)$ curve which almost reproduced the parabola was found for the largest ΔE width. The difficulty is that although a smooth $N(E)$ could be obtained by increasing ΔE, one simultaneously becomes less able to estimate the value of E_F accurately. It would appear that the smoothing procedure would also tend to level peaks and valleys and thus eliminate some of the fine-structure in $N(E)$, which is legitimately there. Thus, one is lead to the necessity of using small energy intervals and many $E(k)$ values. Of course, it is impractical to carry out full scale band calculations for 100,000 points in the Brillouin zone in order to obtain more precise values for both the Fermi level E_F and the density-of-states at the Fermi level $N(E_F)$.

An alternative method of estimating $N(E)$ curves has been developed by Mueller et al. [4]. In this quadratic interpolation scheme (QUAD), the $E(\mathbf{k})$ surface is fitted locally by a quadratic expression to a set of input energies which have been calculated by any independent method for fixed values of $\mathbf{k}$. A Monte-Carlo method is used to generate a large number of random $\mathbf{k}$ points, the appropriate $E(\mathbf{k})$ values are found from the local fitting expression, and these are used to construct an improved density-of-states curve.

Because an energy surface is locally fitted to a given set of $E(\mathbf{k})$ values, the reliability of the curved surface directly depends on how accurately the actual set of $E(\mathbf{k})$ can represent the surface when the $\mathbf{k}$ points have high local symmetry and when therefore several sheets of the $E(\mathbf{k})$ surface intersect at $\mathbf{k}$ or nearby. This question is quite apart from the precision of the QUAD method. The interpolated values cannot be superior to the input information. One way to improve the accuracy of the density-of-states curve and hence, of information derived from it is to increase the number of members in the set of calculated $E(\mathbf{k})$ which are used as input.

To evaluate the effectiveness of the QUAD scheme in reducing statistical error, the input values of $E(k)$ were taken from an ideal parabolic band. As a further test, a set and a subset of $E(k)$ values obtained an actual band structure calculation were also used.

1. Methods

In the original QUAD method, the values of $E(\mathbf{k})$ were calculated in terms of a model Hamiltonian matrix of nine basis functions representing the interaction of s and d bands of a fcc transition metal. The method was adapted in the current study to permit one to use an input $E(\mathbf{k})$ values obtained in any separate independent manner.

For example, in the idealized parabolic band (using atomic units where $h = m = e = 1$) the energy $E(\mathbf{k}) = k^2/2$ Rydbergs. We used as the coordinates of $\mathbf{k}$ the set of evenly spaced points in the Brillouin zone which were given by $(m/2, n/2, p/2)\ \pi/a_0 f$. Herein a_0 is the lattice parameter of the direct lattice, f is an integer and the integers m, n, p individually range from 0 to 8. A unit value of f corresponds to 256 points in the Brillouin zone which is associated with a face centered cubic metal and $f = 2$ yields 2048 points. For the Brillouin zone associated with the body centered cubic metals, a unit value of f yields 128 and $f = 2$ yields 1024 k points.

The QUAD method was applied to free-electron $E(k)$ values with f set equal to unity and only a single $E(k)$ curve was used. Only those grid points were used for which k was less than or equal to the distance from Γ to X. In the study of the smoothing procedure, single energy band was used and f was set equal to 2.

For the input from an APW calculation, we employed 2048 points arranged in the coordinate grid given above as well as a subset of 256 of these. In order to shorten the machine time required, the random $\mathbf{k}$ values were obtained by a Monte-Carlo method in only 1/48 of the Brillouin zone. The remainder of the zone was "filled" by symmetry operations and the resulting $E(\mathbf{k})$ values were sorted into the energy "boxes."

In the case of aluminum, Snow [2] did not find the $E(\mathbf{k})$ roots for all of the 2048 k values where the energies were well above the Fermi level. Those needed to complete the four s plus p bands were obtained in two ways. In the first case, all the unknown $E(\mathbf{k})$ values were set equal to zero. This choice had a strong effect on the $N(E)$ curve at values near the Fermi level and produced an abnormally high spike at $E = 0$. In the second case, the unknown values were estimated by the formula

$$E(k) = E_0 + a\,(k - k_0)^2$$

where k_0 and E_0 correspond to values already found in a given band. This method was used for the construction of figure relating to the effect of the number of points used in the Brillouin zone.

2. Results

Three "smoothed" density-of-states curves obtained using the parabolic band are shown in figures 2a, 2b,

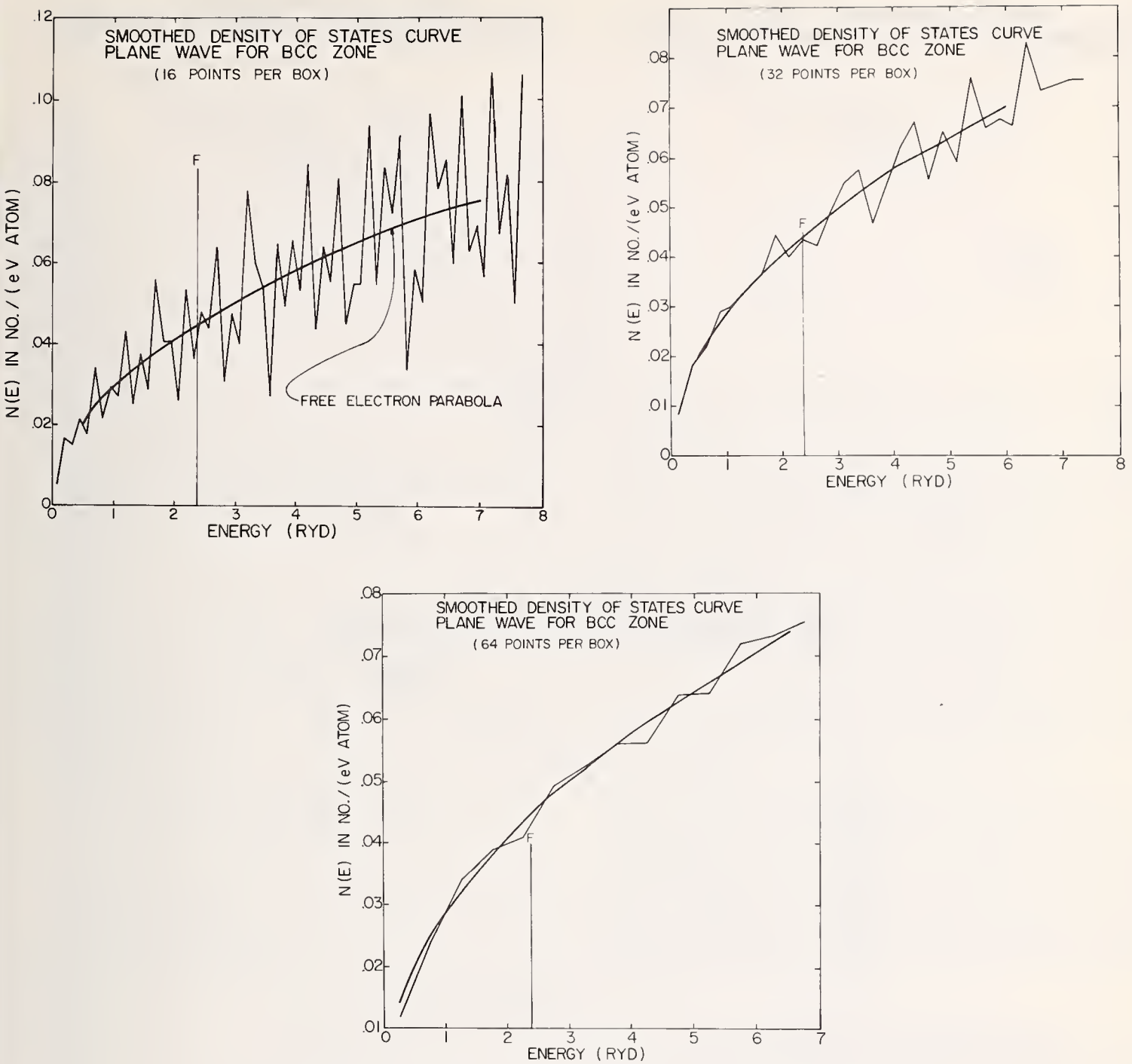

FIGURE 2. *Smoothed Density of States curve for a free electron parabola.*

The effect of increasing the energy interval for a fixed set of $E(\mathbf{k})$ values in a single band. (a) *For* $\Delta E = 0.125$, (b) *for* $\Delta E = 0.250$, (c) *for* $\Delta E = 0.500$.

and 2c. These pertain to using 1024 **k** values in the full Brillouin zone of a *bcc* metal and three energy intervals, $\Delta E = 0.125$, 0.25 and 0.5 Ryd. The smoothing integer q was set at 5. The mean number of points per interval was obtained by dividing the number of k values by the number of histogram intervals before smoothing. The results in terms of points per histogram box are presented in table 1. The precision, as indicated by the maximum $[N(E) - k^2]/k^2$, is clearly dependent on the number of values per "box."

In a rather similar way, the ability to reproduce the ideal free-electron parabola was investigated with the QUAD method. The results are presented in figures 3a, 3b, and 3c. The three graphs pertain to using ν equal to 5,000, 25,000, and 100,000 random k values in a cell which is 1/48 of the *fcc* Brillouin zone. The root mean square relative deviation, from the parabola, namely $(2\delta N(E)/k^2)$ were computed using all of the histograms. These results are given on these graphs. The ragged appearance of these curves is apparent. It is clear that

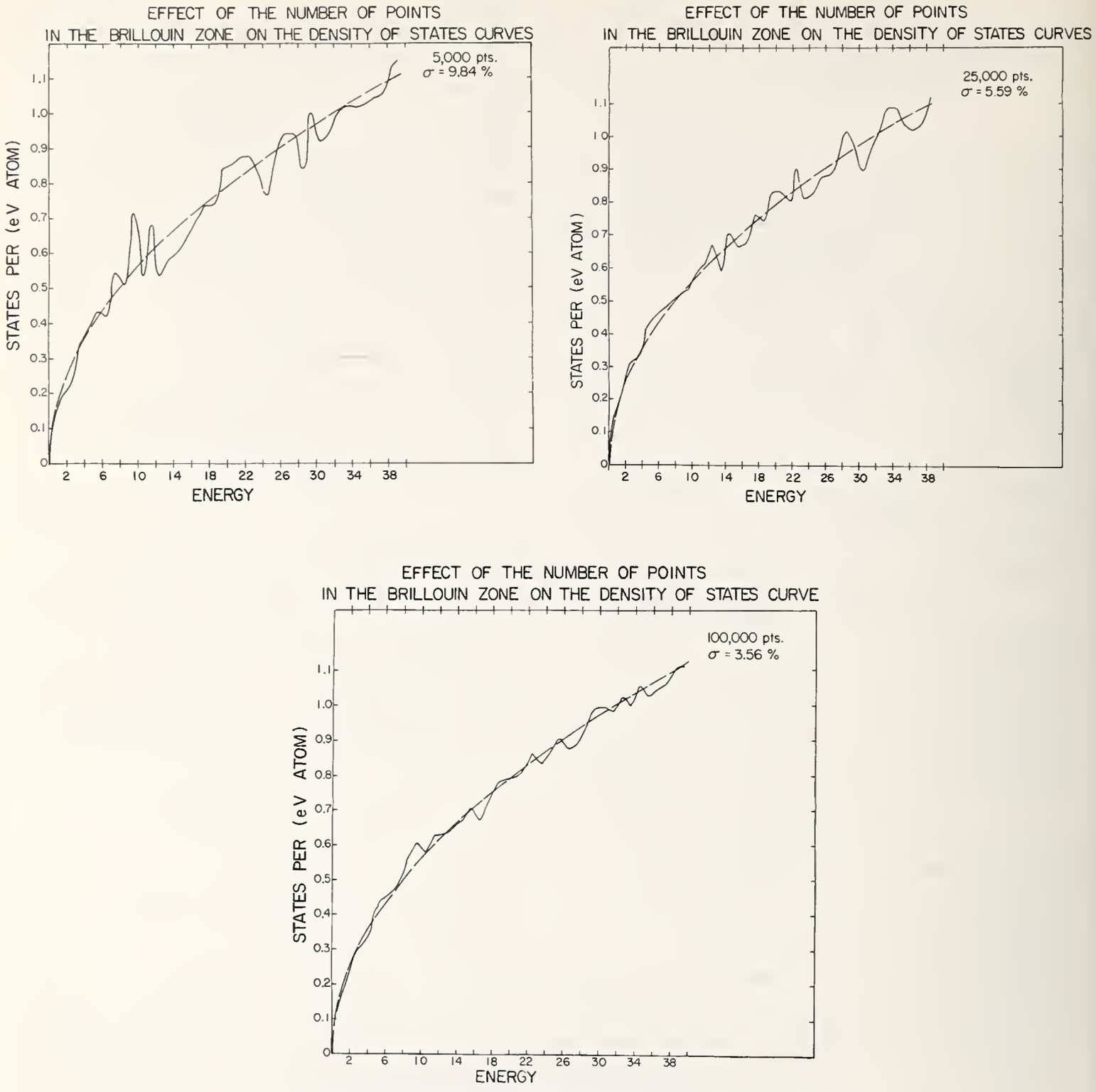

FIGURE 3. *Illustration of the effect of increasing the number of* $E(\mathbf{k})$ *values found by the QUAD procedure for a fixed number of input values.* (a) $\nu = 5{,}000$ *pts*, (b) $\nu = 25{,}000$ *pts*, (c) $\nu = 100{,}000$ *pts.*

one must employ a large number of random k values to obtain a smooth parabolic curve. The precision depends upon how many $E(\mathbf{k})$ values are found within each energy box of width ΔE. Table 2 presents the values found for the ideal parabolic band.

In figure 3, only the first band of a free electron metal was used. However, in a realistic solid, the $E(\mathbf{k})$ curves are disjoint and piecewise continuous—the separation being caused by the lattice potential. Thus, one would anticipate that when the wave vector $(\mathbf{k}+\mathbf{g})$ takes on critical values which correspond to touching the surface of the Brillouin zone, there would be large peaks in the $N(E)$ curve. The reason is that dE/dk becomes approximately equal to zero on "each side" of the critical k value. Thus, when one includes the four s plus p bands of a metal like aluminum several peaks in the

TABLE 1. *Deviation of the smoothed N(E) curve from the free electron parabolic curve (1024 k points)*

Energy interval (Ryd)	Mean points per histogram	Maximum deviation percent
0.125	16	50.5
.250	32	15.0
.500	64	8.8

TABLE 2. *Deviation of calculated density of states curve from a parabolic band (120 energy intervals)*

Total k points	Values per histogram	Standard deviation percent
5,000	42	9.84
25,000	210	5.59
100,000	840	3.56

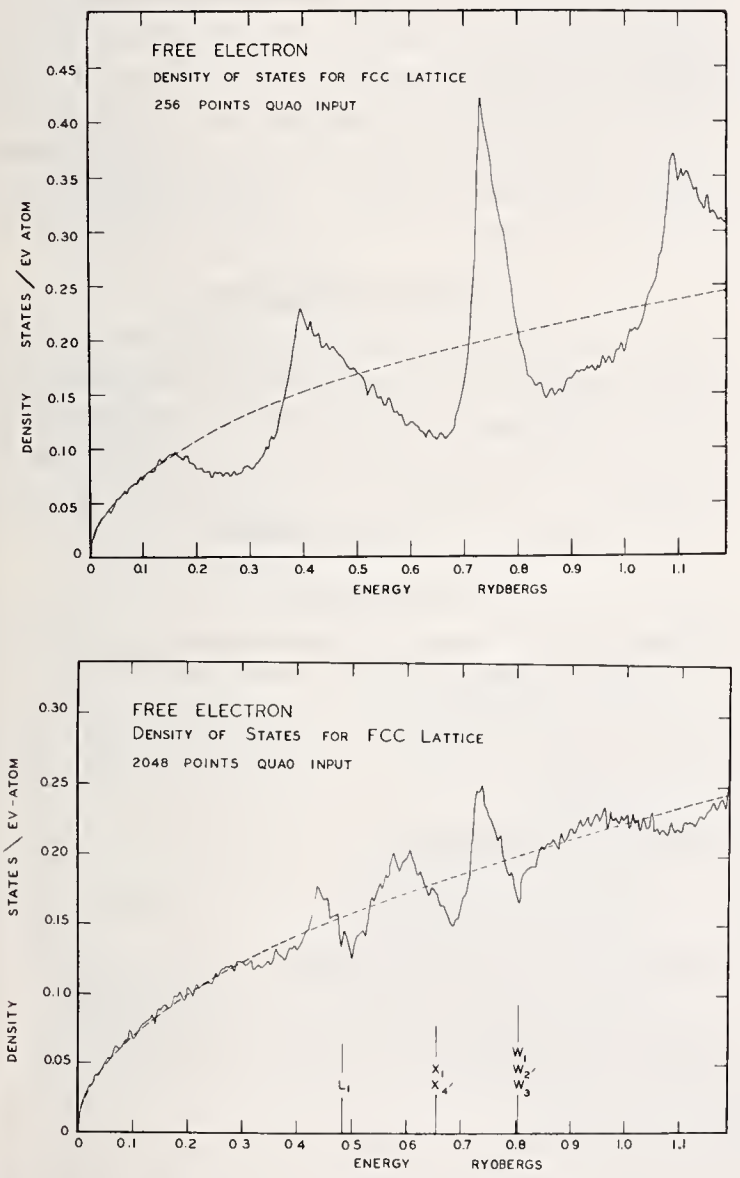

FIGURE 4. *Effect of increasing the number of input* k *values from 256 to 2048 on the standard deviations with a total of 25,000 points found by the QUAD scheme. For 4 bands if an FCC metal.* (a) *For subset with* f = *1,* (b) *fuller set with* f = *2.*

$N(E)$ curve would be observed even though the $N(E)$ curve would confirm to a parabola for small k values.

The effect of increasing the set of $E(k)$ values before using QUAD was investigated. In figure 4, the calculated $N(E)$ curves are presented for 256 and 2048 input values using the free-electron model for a *fcc* metal. The standard deviations are 26 and 9 percent respectively. This was done to make the fourth test more valid. The location of various states is also illustrated.

The fourth test made was of the ability of the QUAD scheme to reproduce not only an idealized parabola but also a real $N(E)$ with its peaks and valleys. Aluminum was chosen, since Snow [2] and Harrison [5] have shown it to approach very closely to being a free-electron metal. The close agreement with a parabola is seen at low energies.

In a similar test on aluminum, the $N(E)$ curves are presented for 2048 points and the subset of 256 of these. Both parts of figures 4 and 5 relate to extending the calculations to 25,000 points by the QUAD method. For comparison with figure 4, the location of specific states and their relation to the peaks in the $N(E)$ curve are indicated.

3. Discussion and Conclusions

As Mueller et al. [3] pointed out, when the mesh points of the Brillouin zone are a simple fraction of the distance from Γ to X, a number of peaks in the $N(E)$ curves will occur. This is illustrated for figures 4 and 5 drawn for face centered cubic metals. A large prime value of f would have been desirable in such an analysis, but suitable input values were not available. The use of the free electron curve for $N(E)$ forms a reliable test of the interpolation method since the correct answer for a single band is known *a priori;* procedures for choosing the number of $E(\mathbf{k})$ values are identical to those used in most band structure calculations. The present study emphasizes two points about reliability; there is a joint dependence on both the fineness of the

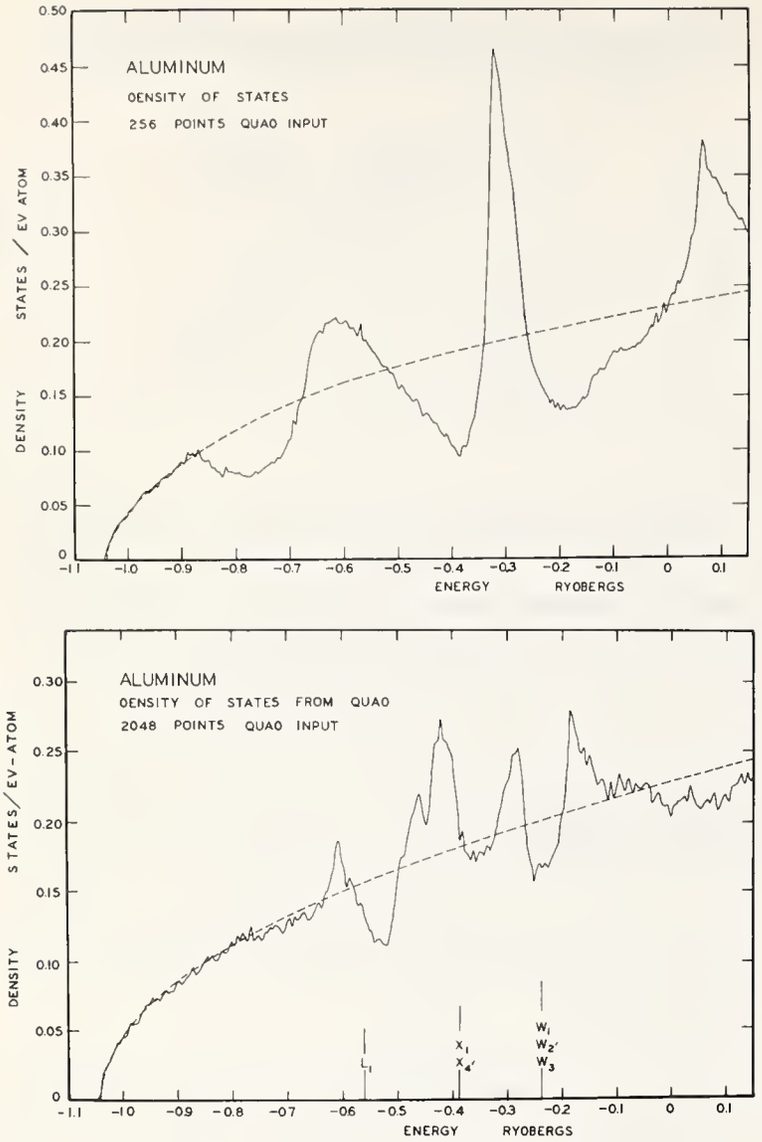

FIGURE 5. *A similar calculation for aluminum using the Snow's values of* E(**k**) *at 2048 vectors of the Brillouin Zones and completing the values for the 4 bands where necessary.* (a) *For subset of 256 points* (f = *1*), (b) *for 2048 points* (f = *2*).

mesh of points in the Brillouin zone and on number of values available per histogram interval. The first point is illustrated by the effect of the number of input values on either the smoothed curve from Snow's data or the subsequent tests in figures 4 and 5. The effect of the number of values per interval is shown in table 2. The two parameters are not wholly independent of each other but both are important if one wishes to know simultaneously the value of $N(E_F)$ and the location of E_F to better than 1 percent precision.

Wood [6] recently called our attention to the local gradient method of Gilot and Raubenheimer [7]. He reports that his study of this method by a scheme similar to that outlined herein indicates an equivalent (or superior) reliability can be achieved at a similar cost.

It has been shown that the reliability of estimating $N(E)$ curves from calculated data can be improved so that a precise measure of the error for each E can be given by increasing the number of points for which $E(k)$ values are obtained and by increasing the number of values per histogram box. A procedure such as the QUAD interpolation scheme can contribute significantly the reliability by gaining more $E(k)$ values for ΔE interval without incurring an excessive cost in machine time that would be necessary to solve the $\det|H-E(k)| = 0$ at many points.

4. Acknowledgments

The authors are indebted to Dr. John Wood who made his study of the smoothing method available to us prior to publishing. In addition, he offered valuable advice. We appreciate the cooperation of Dr. Edward Snow, also of Los Alamos Scientific Lab, who made detailed sets of $E(\mathbf{k})$ values available to us.

5. References

[1] Snow, E. C. and Waber, J. T., "Self Consistent Energy Bands of Metallic Copper by the Augmented Plane Wave Method," Phys. Rev. **157**, 570 (1967).

[2] Snow, E. C., "Self Consistent Energy Bonds of Metallic Copper by the Augmented Plane Wave Method," Phys. Rev. **158**, 683 (1967).

[3] Wood, J. W., unpublished work. Los Alamos Scientific Lab. Communicated June 1968.

[4] Mueller, F. M., Garland, J. W., Cohen, M. H., and Bennemann, K. H., submitted to Phys. Rev.

[5] Harrison, W. W., "Pseudopotentials in the Theory of Metals," Frontiers in Physics, (Benjamin Press, New York, 1966).

[6] Wood, J. W., private communication, December 1969.

[7] Gilat, H., and Raubenheimer, B., Phys. Rev. **144**, 390 (1966).

Appendix I

ELECTRONIC DENSITY OF STATES

SYMPOSIUM COMMITTEES

Elio Passaglia, General Chairman, Metallurgy Division
Harry C. Burnett, Committee Coordinator, Metallurgy Division

PROGRAM COMMITTEE

Lawrence H. Bennett, Chairman, Metallurgy Division

Russell C. Casella	Center for Radiation Research
John R. Cuthill	Metallurgy Division
Albert Feldman	Inorganic Materials Division
H. P. R. Frederikse	Inorganic Materials Division
John W. Gadzuk	Atomic and Molecular Physics Division
Arnold H. Kahn	Inorganic Materials Division
Calvin S. Koonce	Heat Division
Archie J. McAlister	Metallurgy Division
Elio Passaglia	Metallurgy Division
Cedric Powell	Atomic and Molecular Physics Division
James F. Schooley	Heat Division
John W. Cooper	Atomic and Molecular Physics Division

REGISTRATION COMMITTEE

Robert R. Stromberg, Chairman, Polymers Division

ARRANGEMENTS COMMITTEE

Robert T. Cook, Chairman, Office of Technical Information and Publications

SOCIAL COMMITTEE

Howard T. Yolken, Chairman, Institute for Materials Research

LADIES' HOSPITALITY COMMITTEE

Mrs. Evelyn Brady, Chairman
Mrs. Edna Passaglia, Vice Chairman
Mrs. Joan Yolken
Mrs. Alice Ambler
Mrs. Leatrice Gevantman

FINANCE COMMITTEE

Ronald B. Johnson, Chairman, Institute for Materials Research

Appendix II

Session Chairmen and Rapporteurs

BAND STRUCTURE I
Chairmen: A. J. Freeman, Northwestern University
E. Passaglia, NBS

BAND STRUCTURE II
Chairmen: F. Herman, IBM Research Center, San Jose
R. C. Casella, NBS
Rapporteur: R. E. Watson, Brookhaven National Laboratory

OPTICAL PROPERTIES, BAND STRUCTURE III
Chairmen: E. A. Stern, University of Washington
J. R. Cuthill, NBS
Rapporteur: G. W. Pratt, Jr., Massachusetts Institute of Technology

PHOTOEMISSION
Chairmen: E. T. Arakawa, Oak Ridge National Laboratory
C. J. Powell, NBS
Rapporteur: S. B. M. Hagström, Chalmers University, Göteborg, Sweden

MANY-BODY EFFECTS
Chairmen: L. N. Cooper, Brown University
J. W. Cooper, NBS

EXCITONS; SOFT X-RAY I
Chairmen: R. A. Farrell, University of Maryland
C. S. Koonce, NBS
Rapporteur: L. Hedin, Chalmers University, Göteborg, Sweden

SOFT X-RAY II; DISTRIBUTIONS IN MOMENTUM SPACE
Chairmen: F. M. Mueller, Argonne National Laboratory
A. J. McAlister, NBS
Rapporteur: D. J. Fabian, University of Strathclyde, Glasgow, Scotland

ION-NEUTRALIZATION; SURFACES; CRITICAL POINTS; ETC.
Chairmen: E. Callen, American University
R. R. Stromberg, NBS
Rapporteurs: D. E. Aspnes, Bell Telephone Laboratories
B. Lax, National Magnet Laboratory, Massachusetts Institute of Technology

DISORDERED SYSTEMS I
Chairmen: L. F. Mattheiss, Bell Telephone Laboratories
A. Kahn, NBS

DISORDERED SYSTEMS II

Chairmen: L. M. Roth, General Electric Research and Development Center
H. P. R. Frederikse, NBS
Rapporteur: M. H. Cohen, University of Chicago

ALLOYS; ELECTRONIC SPECIFIC HEAT I

Chairmen: J. R. Anderson, University of Maryland
J. H. Schooley, NBS

ELECTRONIC SPECIFIC HEAT II; KNIGHT SHIFT; SUSCEPTIBILITY

Chairmen: A. Narath, Sandia Laboratories
H. C. Burnett, NBS
Rapporteurs: J. Rayne, Carnegie-Mellon University
I. D. Weisman, NBS

TUNNELING; SUPERCONDUCTORS; TRANSPORT PROPERTIES

Chairmen: J. R. Leibowitz, Catholic University of America
J. W. Gadzuk, NBS

TRANSPORT PROPERTIES; APPLICATIONS

Chairmen: A. I. Schindler, Naval Research Laboratory
A. Feldman, NBS
Rapporteur: R. J. Higgins, University of Oregon

Appendix III

Registrants — Electronic Density of States Symposium
National Bureau of Standards
November 2–6, 1969

Ajami, F.
University of Pa.
Philadelphia, Pa. 19104

Albers, W. A.
General Motors Research Labs.
12 Mile & Mound Rds.
Warren, Mich. 48090

Albert, F.
Laboratoire de Phys. Solides
Giorsay, France

Alexander, M. N.
Materials Research Laboratory
Army Materials & Mechanical Research Center
Watertown, Mass. 02172

Amar, H.
Temple University
Philadelphia, Pa. 19102

Anderson, J. R.
Dept. Phys. & Astronomy
University of Maryland
College Park, Md. 20740

Anderson, O. K.
University of Pennsylvania
Philadelphia, Pa. 19104

Arakawa, E. T.
Oak Ridge National Lab.
Bldg. 4500–S, H–160
Oak Ridge, Tenn. 37830

Arlinghaus, F. J.
General Motors Research Labs.
Warren, Mich. 48090

Artman, G.
Northwestern University
Evanston, Ill. 60202

Ashcroft, N. W.
Laboratory of Atomic and Solid State Physics
Cornell University
Ithaca, N.Y. 14850

Aspnes, D. E.
Bell Telephone Labs.
Murray Hill, N.J. 07974

Ausman, G. A.
Harry Diamond Laboratories
Washington, D.C. 20438

Austin, R.
AFOSR
Wilson Blvd.
Arlington, Va. 22207

Azaroff, L. V.
University of Connecticut
Storrs, Conn. 06268

Baarle, C. V.
Kamerligh Onnes Labs.
Leiden, Netherlands

Bambakidis, G.
NASA, Lewis Research Center
Cleveland, Ohio 44135

Baratoff, A.
Brown University
Providence, R.I. 02912

Barbe, D. F.
Westinghouse Electric Corp.
Baltimore, Md. 21203

Barker, R. C.
Yale University
New Haven, Conn. 06520

Baumgardner, C. A.
University of Idaho
Moscow, Idaho 83843

Beck, Paul
University of Illinois
Metallurgy Department
Urbana, Ill. 61801

Beeby, John L.
Atomic Energy Research Establishment
Theoretical Physics Div. B.8.9
Harwell, Didcot, Berks
England

Bell, M. I.
Brown University
Physics Department
Providence, R.I. 02912

Bennett, H.
National Bureau of Standards
Washington, D.C. 20234

Bennett, L. H.
National Bureau of Standards
Washington, D.C. 20234

Blatt, F. J.
Michigan State University
Physics Department
East Lansing, Mich. 48823

Blewer, R. S.
Sandia Labs.
Albuquerque, N.M. 87106

Bohm, Horst
Owens-Illinois Tech. Cent.
Toledo, Ohio 43601

Boyle, John J.
Night Visions Lab.
Ft. Belvoir, Va. 22060

Bradley, D. C.
Queen Mary College
London, England

Brailsford, Alan D.
Ford Motor Co.
Science Lab.
Dearborn, Mich. 48121

Breedlove, H.
Ch. Tng. and Dev. Div. CPO
Ft. Belvoir, Va. 22060

Brodersen, Rohert W.
M.I.T.
Cambridge, Mass. 02139

Brouers, F.
Institut de Physique
Universite de Liege
Sart-Tilman, Liege 1
Belgium

Brown, J. S.
University of Vermont
Burlington, Vt. 05401

Burke, J. Richard
Naval Ordnance Lab.
Silver Spring, Md. 20910

Burnett, H. C.
National Bureau of Standards
Noordwijk, Holland
Washington, D.C. 20234

Butler, W. H.
Auburn University
Auburn, Ala. 36830

Butrymowicz, D. B.
National Bureau of Standards
Washington, D.C. 20234

Callaway, J.
Louisiana State University
Baton Rouge, La. 70803

Callen, E.
American University
Washington, D.C. 20016

Campbell, W. J.
U.S. Bureau of Mines
College Park, Md. 20740

Campi, Morris
Harry Diamond Labs.
Washington, D.C. 20438

Cardona, M.
Deutsches Elektronen-Synchrotran
(DESY) F 41
Notkestieg 1
Hamburg 52
German Federal Republic

Carlson, F.
Night Visions Lab.
Ft. Belvoir, Va. 22060

Caron, L. G.
Universite de Sherbrooke
Quebec, Canada

Carr, W. J.
Westinghouse Res. and Dev.
Pittsburgh, Pa. 15235

Carter, Forrest L.
Naval Research Labs.
Washington, D.C. 20390

Carter, G. C.
National Bureau of Standards
Washington, D.C. 20234

Casella, R. C.
National Bureau of Standards
Washington, D.C. 20234

Caskey, George R.
National Bureau of Standards
Washington, D.C. 20234

Cate, Robert
National Bureau of Standards
Washington, D.C. 20234

Chang, K.
Night Visions Lab.
Ft. Belvoir, Va. 22060

Chen, An-Bun
College of William & Mary
Williamsburg, Va. 23185

Cho, Sang-Jean
National Research Council
Ottawa, Ontario, Canada

Choyke, W. J.
Westinghouse Res. Labs.
Pittsburgh, Pa. 15235

Christman, J. Richard
Tufts University
Medford, Mass. 02155

Church, E. L.
Brookhaven National Labs.
Physics Department
Upton, N.Y. 11713

Clark, Howard
National Bureau of Standards
Washington, D.C. 20234

Clune, Lavern C.
Ohio University
Physics Department
Athens, Ohio 45701

Cohen, Morrel H.
University of Chicago
Chicago, Ill. 60637

Cohen, Roger W.
RCA Labs.
Princeton, N.J. 08540

Collings, E. W.
Battelle Memorial Inst.
Columbus Labs.
Columbus, Ohio 43201

Collins, Thomas C.
Aerospace Res. Labs.
Area B, Bldg 450
Wright Patterson Air Force Base, Ohio 45433

Colwell, J. H.
National Bureau of Standards
Washington, D.C. 20234

Conklin, James B.
University of Florida
Physics Dept., Williamson Hall
Gainesville, Fla. 32601

Connolly, John W. D.
Advanced Materials Research &
Development Laboratory
Pratt and Whitney Aircraft
Middletown, Conn. 06458

Cooper, J. W.
National Bureau of Standards
Washington, D.C. 20234

Cuthill, John R.
National Bureau of Standards
Washington, D.C. 20234

Cutler, Paul H.
Pennsylvania State University
101 Osmond Lab.
University Park, Pa. 16802

Damon, Dwight H.
Westinghouse Research Labs.
Beulah Road
Pittsburgh, Pa. 15235

Davis, H. L.
Oak Ridge National
Metals & Ceramics Div.
Oak Ridge, Tenn. 31830

Deegan, R. A.
University of Illinois
Urbana, Ill. 61801

DePorter, Gerald L.
Los Alamos Scientific Lab.
Los Alamos, N.M. 87544

Dobbyn, Ronald C.
National Bureau of Standards
Washington, D.C. 20234

Dow, John D.
Palmer Physical Lab.
Princeton University
Princeton, N.J. 08540

Dresselhaus, Mildred
M.I.T.
Cambridge, Mass. 02139

Driscoll, T. E.
U.S. Bureau of Mines
College Park, Md. 20740

Dryer, Joseph E.
Ohio State University
Res. Found.
Columbus, Ohio 43220

Duff, K. J.
Ford Motor Company
Dearborn, Mich. 48141

Eastman, Dean E.
IBM
Yorktown Heights, N.Y. 10598

Ehrenreich, Henry
Division of Pure & Applied Physics
Harvard University
Cambridge, Mass. 02138

Eisenberger, Peter
Bell Telephone Labs.
Murray Hill, N.J. 07974

Erlbach, E.
City College of CUNY
251 Ft. Washington Avenue
New York, N.Y. 10032

Esaki, L.
IBM, Thomas J. Watson Research Center
Yorktown Heights, N.Y. 10598

Eschenfelder, A. H.
IBM Res. Lab.
San Jose, Calif. 95114

Etzel, H.
National Science Foundation
Washington, D.C. 20550

Evenson, William E.
University of Pennsylvania
Philadelphia, Pa. 19104

Fabian, Derek J.
Laboratorium fur Festkorperphysik
Gloriastrasse 35
8006 Zurich, Switzerland

Falge, Raymond L.
National Bureau of Standards
Washington, D.C. 20234

Faulkner, J. S.
Oak Ridge National Lab.
Oak Ridge, Tenn. 37830

Fehrs, Delmer
NASA-ERC
Cambridge, Mass. 02139

Feldman, A.
National Bureau of Standards
Washington, D.C. 20234

417-156 O - 71 - 53

Ferris-Prabhu, A.
IBM, Dept. 392
Essex Junction, Vt. 05452

Fert, Albert
Laboratoire de Phys. Solides
Orsay, France

Finegold, L. X.
University of Colorado
Boulder, Colo. 80302

Fitton, B.
European Space Res. Organization
Noordwijk, Holland

Foner, Simon
M.I.T.
Francis Bitter Natl. Magnet Lab.
Cambridge, Mass. 02139

Forest, H.
Zenith Radio Corp.
Chicago, Ill. 60639

Forman, Richard A.
National Bureau of Standards
Washington, D.C. 20234

Frederikse, H. P. R.
National Bureau of Standards
Washington, D.C. 20234

Freeman, A. J.
Northwestern University
Evanston, Ill. 60201

Frolen, Lois J.
National Bureau of Standards
Washington, D.C. 20234

Fromhold, Al
National Bureau of Standards
Washington, D.C. 20234

Gadzuk, J. W.
National Bureau of Standards
Washington, D.C. 20234

Gerstner, J.
Operation Res. Inc.
State College, Pa. 16801

Goff, James F.
Naval Ordnance Lab.
Silver Spring, Md. 20910

Gordon, William L.
Case Western Reserve Univ.
Cleveland, Ohio 44106

Grabner, Ludwig H.
National Bureau of Standards
Washington, D.C. 20234

Grant, Wesley
Yale University
New Haven, Conn. 06520

Gray, A.
Watervliet Arsenal
Watervliet, N.Y. 12189

Gray, D. M.
Watervliet Arsenal
Watervliet, N.Y. 12189

Greenfield, Arthur J.
BAR-Ilan Univ.
Ramat-Gan, Israel

Greer, William
National Bureau of Standards
Washington, D.C. 20234

Grobman, Warren D.
IBM, Watson Research Center
Yorktown Heights, N.Y. 10598

Gross, Chris
NASA-Langley Res. Center
Hampton, Va. 23366

Hacker, K.
University of Pittsburgh
Pittsburgh, Pa. 15213

Haeringen, W. Van
Philips Res. Labs.
Eindhoven, Netherlands

Hagstrum, Homer D.
Bell Telephone Labs.
Mountain Avenue
Murray Hill, N.J. 07974

Hagstrom, S.
Chalmers University
Göteborg, Sweden

Halder, N.C.
State University of New York
Albany, N.Y. 12203

Hammond, Robert H.
University of California
Berkeley, Calif. 94720

Handler, Paul
University of Illinois
Urbana, Ill. 61801

Hanzely, Stephen
Youngstown State University
Department of Physics
410 Wick Avenue
Youngstown, Ohio 44503

Harrison, Michael J.
Michigan State University
East Lansing, Mich. 48823

Harvey, W. W.
Kennecott Copper Corp.
Lexington, Mass. 02173

Hayes, Timothy M.
Xerox Corp. Res. Labs.,
Rochester, N.Y. 14603

Hedin, L.
Chalmers University of Tech.
Göteborg, Sweden

Hensel, J. C.
Bell Telephone Labs.
Murray Hill, N.J. 07974

Herman, Frank
IBM Research Lab.
San Jose, Calif. 95114

Herzog, Donald C.
College of William & Mary
Williamsburg, Va. 23185

Hicks, Jay Charles
684 N.W. 18th
Corwallis, Oreg. 97330

Higgins, Richard J.
University of Oregon
Eugene, Oreg. 97403

Hindley, Norman K.
Corning Glass Works
Corning, N.Y. 14830

Hirst, Robert G.
General Electric Co.
Pittsfield, Mass. 01201

Ho, James C.
Battelle Memorial Institute
Columbus, Ohio 43201

Hofer, Alvin D.
TAM-National Lead Corp.
Niagara Falls, N.Y. 10013

Hoffman, Herbert J.
NASA-ERC
Cambridge, Mass. 02139

Holliday, Jerome E.
E. C. Bain Lab.
Fundamental Research
U.S. Steel Corp. Res. Cen.
Monroeville, Pa. 15146

Horowitz, Emanuel
National Bureau of Standards
Washington, D.C. 20234

Houston, Bland
U.S. Naval Ordnance Lab.
Silver Spring, Md. 20910

Hsia, Yukun
Litton Systems Inc.
Guidance and Control Systems Div.
5500 Canoga Avenue
Woodland Hills, Calif. 91364

Hyde, G. R.
U.S. Bureau of Mines
College Park, Md. 20740

Islar, William E.
Harry Diamond Labs.
Washington, D.C. 20438

Janak, James
IBM
Yorktown Heights, N.Y. 10598

Jan, Jean-Pierre
National Research Council
Ottawa, Ontario, Canada

Jarrett, Howard S.
DuPont and Co.
Wilmington, Del. 19898

Johnson, Keith H.
M.I.T.
Cambridge, Mass. 02139

Johnson, Ronald B.
National Bureau of Standards
Washington, D.C. 20234

Joshi, S. K.
University of Roorkee
Roorkee, India

Kahan, Daniel
National Bureau of Standards
Washington, D.C. 20234

Kahn, A. H.
National Bureau of Standards
Washington, D.C. 20234

Kane, Evan O.
Bell Telephone Labs.
Murray Hill, N.J. 07974

Karo, Arnold M.
Lawrence Radiation Lab.
Livermore, Calif. 94550

Kasowski, Robert V.
DuPont and Co.
Wilmington, Del. 19898

Kaufman, Larry A.
M.I.T.
National Magnet Labs.
Cambridge, Mass. 02139

Ketterson, John
Argonne National Labs.
Argonne, Ill. 60439

Keyes, Robert W.
IBM
Thom. J. Watson Res. Cent.
Yorktown Heights, N.Y. 10598

Kjeldaas, T.
Polytechnic Inst. of Brooklyn
Brooklyn, N.Y. 11201

Klein, Michael W.
Wesleyan University
Middletown, Conn. 06457

Klein, W.
Night Visions Lab.
Ft. Belvoir, Va. 22060

Kmetko, Edward A.
Los Alamos Sci. Lab.
University of California
Los Alamos, N.M. 87544

Kohn, Walter
University of California
La Jolla, Calif. 92037

Koonce, Calvin S.
National Bureau of Standards
Washington, D.C. 20234

Korringa, J.
Ohio State University
Columbus, Ohio 83210

Krieger, J. B.
Polytechnic Inst. of Brooklyn
Brooklyn, N.Y. 11201

Kunz, Christof
University of Maryland
College Park, Md. 20740

Kunzler, J. E.
Bell Telephone Labs.
Murray Hill, N.J. 07974

Kurrelmeyer, B.
Brooklyn College of CUNY
Brooklyn, N.Y. 11210

Lalevic, Bogoljub
Franklin Inst. Res. Lab.
Philadelphia, Pa. 19103

Langer, Dietrich W. J.
Aerospace Res. Labs.
Wright Patterson Air Force Base
Ohio 45433

Lapeyre, Gerald J.
Montana State University
Bozeman, Mont. 59715

Laufer, Jeffrey
University of Michigan
Department of Chemistry
Ann Arbor, Mich. 48104

Lax, Benjamin
M.I.T.
National Magnet Lab.
Cambridge, Mass. 02139

Libelo, Louis
U.S. Naval Ordnance Lab.
White Oak, Md. 20910

Long, Jerome R.
V.P.I.
Department of Physics
Blacksburg, Va. 24061

Lopez-Escobar, Albert H. M.
Goddard College
Plainfield, Vt. 05667

Lundqvist. Bengt I.
Chalmers Univ. of Tech.
Göteborg 5, Sweden

Lundqvist, Stig
Chalmers University
Institute of Physics
Göteborg, Sweden

Lye, Robert G.
Head, Metal Physics Group
Martin Marietta Corp.
1450 South Rolling Rd.
Baltimore, Md. 21227

Mackintosh, A. R.
Lab. for Electrophysics
Technol. Univ.
Lungby, Denmark

Maeland, Arnulf
Worcester Polytechnic Inst.
Worcester, Mass. 01609

Mahan, G. D.
Clare-Hall
Herschnell Road
Cambridge, CB39A1
England

Mapother, D. E.
University of Illinois
Physics Department
Urbana, Ill. 61801

Marcus, Paul M.
IBM Research Center
Yorktown Heights, N.Y. 10598

Martin, D. L.
National Research Council
Ottawa, Ontario, Canada

Martin, Richard M.
Bell Telephone Labs.
Murray Hill, N.J. 07974

Massey, Walter E.
University of Illinois
Department of Physics
Urbana, Ill. 61801

Masuda, Yoshika
Nagoya University
Department of Physics
Chikusa-Ku, Nagoya, Japan

Mattheiss, Leonard F.
Bell Telephone Labs.
Murray Hill, N.J. 07974

Mayroyannis, C.
National Research Council
Ottawa, Ontario, Canada

McAlister, Archie J.
National Bureau of Standards
Washington, D.C. 20234

McNeil, M. B.
Department of Materials Engineering
Mississippi State University
P.O. Drawer CM
State College, Miss. 39762

Mebs, R.
National Bureau of Standards
Washington, D.C. 20234

Menth, A.
Bell Telephone Labs.
Murray Hill. N.J. 07974

Meyer, Axel
N. Illinois University
Physics Department
DeKalb, Ill. 60115

Misetich, Antonio
National Magnet Lab.,
M.I.T.
Cambridge, Mass. 02139

Mitchell, Dean L.
Naval Research Labs.,
Washington, D.C. 20390

More, Richard M.
Department of Physics
Faculty of Arts and Sciences
University of Pittsburgh
Pittsburgh, Pa. 15213

Mozer, Bernard
National Bureau of Standards
Washington, D.C. 20234

Mueller, Fred M.
Argonne National Labs.
Argonne, Ill. 60439

Muldawer, Leonard
Temple University
Physics Department
Philadelphia, Pa. 19122

Mura, Toshio
National Bureau of Standards
Washington, D.C. 20234

Narath, A.
Sandia Labs.
Albuquerque, N.M. 87115

Narsing, G. R.
U.S. Bureau of Mines
College Park, Md. 20740

Natapoft, Marshall
Newark College of Eng.
Newark, N.J. 07102

Neddermeyer, H.
8035 Gauting, Waldpromenade 61
8 Munchen 22, Germany

Nedoluha, Alfred
NWC Corona Labs.
Corona, Calif. 91720

Neustadter, H.
NASA
Cleveland, Ohio 44135

Nilsson, Olof
Chalmers Univ. of Tech.
Physics Department
40220 Göteborg 5, Sweden

Novak, Robert L.
Westinghouse Astronuclear
Pittsburgh, Pa. 15228

Ortenburger, Irene B.
IBM Research Labs.
San Jose, Calif. 95114

Overhauser, A. W.
Ford Motor Co.
Dearborn, Mich. 48121

Parsons, Brian J.
Michelson Labs., N.W.C.
China Lake, Calif. 93555

Passaglia, Elio
National Bureau of Standards
Washington, D.C. 20234

Paul, William
Harvard University
Pierce Hall
Cambridge, Mass. 02138

Penchina, Claude
University of Massachusetts
Physics Department
Amherst, Mass. 01002

Petroff, Irene
University of California
Department of Electrical Sciences
Los Angeles, Calif. 90024

Piller, Herbert
Louisiana State University
Physics Department
Baton Rouge, La. 70803

Platzman, P. M.
Bell Telephone Labs.
Murray Hill, N.J. 07974

Plummer, Ward
National Bureau of Standards
Washington, D.C. 20234

Pollard, John
Night Visions Lab.
Ft. Belvoir, Va. 22060

Powell, Cedric
National Bureau of Standards
Washington, D.C. 20234

Praddaude, Hernan
M.I.T.
National Magnet Lab.
Cambridge, Mass. 02139

Price, Peter J.
IBM
Watson Lab.
New York, N.Y. 10025

Rayne, J. A.
University of Lancaster
England

Redfield, David
RCA Labs.
Princeton, N.J. 08540

Reilly, M. H.
U.S. Naval Res. Lab.
Washington, D.C. 20390

Richardson, P. E.
U.S. Bureau of Mines
College Park, Md. 20740

Rooke, G. A.
University of Strathclyde
Glasgow, Cl, Scotland

Ross, Gaylon S.
National Bureau of Standards
Washington, D.C. 20234

Ross, Marvin
University of California
Lawrence Radiation Lab.
Livermore, Calif. 94550

Roth, Laura M.
General Electric Corp.
P.O. Box 8
Schenectady, N.Y. 12301

Rothberg, Gerald M.
Stevens Inst. of Tech.
Hoboken, N.J. 07030

Rousseau, Cecil C.
Baylor University
Department of Physics
Waco, Tex. 76703

Rowe, J. E.
Bell Telephone Labs.
Murray Hill, N.J. 07974

Rowell, J. M.
Bell Telephone Labs.
Mountain Avenue
Murray Hill, N.J. 07974

Rowland, T. J.
University of Illinois
Metallurgy Department
Urbana, Ill. 61801

Rubin, Robert J.
National Bureau of Standards
Washington, D.C. 20234

Rudge, William E.
IBM Research
San Jose, Calif. 95114

Sacks, Barry H.
University of California
Berkeley, Calif. 94720

Saffren, M. M.
California Institute of Technology
Jet Prop. Lab.
Pasadena, Calif. 91103

Sagalyn, Paul L.
Army Materials & Mechanical Res. Center
Watertown, Mass. 02172

Sanford, Edward R.
Ohio University
Clippinger Research Labs.
Athens, Ohio 45701

Satya, A. V. S.
IBM
New York, N.Y. 12533

Savage, Howard T.
Naval Ordnance Labs.
Silver Spring, Md. 20910

Schaich, William
Cornell University
Clark Hall
Ithaca, N.Y. 14850

Schindler, A. I.
Naval Research Laboratory
Washington, D.C. 20390

Schirber, J. E.
Sandia Labs.
Albuquerque, N.M. 87115

Schone, Harlan E.
College of William & Mary
Physics Department
Williamsburg, Va. 23185

Schooley, James F.
National Bureau of Standards
Washington, D.C. 20234

Schrieffer, J. R.
University of Pennsylvania
Physics Department
Philadelphia, Pa. 19104

Schwartz, Lawrence
Harvard University
Cambridge, Mass. 62138

Shaw, R. F.
Energy Conver. Dev. Inc.
Troy, Mich. 48084

Shaw, Robert W.
Bell Telephone Labs.
Murray Hill, N.J. 07974

Sher, M. A.
College of William & Mary
Williamsburg, Va. 23185

Shimizu, Masao
Nagoya University
Department of Applied Physics
Nagoya, Japan

Shirley, David A.
University of California
Chemistry Department
Berkeley, Calif. 94720

Sievert, Paul R.
Battelle Memorial Inst.
Columbus, Ohio 43201

Simmons, John A.
National Bureau of Standards
Washington, D.C. 20234

Smith, John R.
NASA
Cleveland, Ohio 44135

Smith, Neville V.
Bell Telephone Labs.
Murray Hill, N.J. 07974

Sonntag, Bernd
Physikalisches Staatsinstitut
Hamberg, Bahrenfeld, Germany

Soonpaa, Henn H.
Department of Physics
The University of North Dakota
Grand Forks, N.D. 58201

Spain, Ian
Inst. for Mol. Phys.
University of Maryland
College Park, Md. 20740

Speiser, Rudolph
Ohio State University
Columbus, Ohio 43221

Spicer, William E.
Stanford University
Stanford, Calif. 93405

Stanley, D. A.
U.S. Bureau of Mines
College Park, Md. 20740

Stearns, Mary Beth
Ford Sci. Lab.
Dearborn, Mich. 48121

Stern, Edward A.
University of Washington
Physics Department
Seattle, Wash. 98105

Stern, Frank
IBM, Watson Res. Center
Yorktown Heights, N.Y. 10598

Steslicka, Maria
University of Waterloo
Department of Applied Math
Waterloo, Ontario, Canada

Stewart, A. T.
Queen's University
Physics Department
Kingston, Ontario, Canada

Stilwell, E. P.
Clemson University
Physics Department
Clemson, S.C. 29631

Stromberg, R. R.
National Bureau of Standards
Washington, D.C. 20234

Swartzendruber, Lydon J.
National Bureau of Standards
Washington, D.C. 20234

Swerdlow, Max
A. F. Office of Sci. Res.
Arlington, Va. 22209

Switendick, A. C.
Sandia Labs.
Albuquerque, N.M. 97115

Suzuki, K.
Bell Telephone Labs.
Murray Hill, N.J. 07974

Tahir-Kheli, R. A.
Temple University
Department of Physics
Philadelphia, Pa. 19122

Tauc, J.
Bell Telephone Labs.
Murray Hill, N.J. 07971

Teitler, Sidney
Naval Research Labs.
Washington, D.C. 20390

Thompson, James C.
Energy Conv. Dev. Inc.
Troy, Mich. 48084

Thornber, Karvel K.
Bell Telephone Labs.
Murray Hill, N.J. 07974

Torgesen, John L.
National Bureau of Standards
Washington, D.C. 20234

Toxen, A. M.
IBM
Yorktown Heights, N.Y. 10598

Triftshauser, Werner
Queen's University
Department of Physics
Kingston, Ontario, Canada

Tsang, Paul Sa-Min
IBM
Hopewell Junction, N.Y. 12533

Uriano, George A.
National Bureau of Standards
Washington, D.C. 20234

Vechten, James A. Van
Bell Telephone Labs.
Murray Hill, N.J. 07974

Violet, Charles E.
Lawrence Radiation Lab.
Livermore, Calif. 94550

Vosko, S. H.
Westinghouse Res. Labs.
Pittsburgh, Pa. 15235

Waber, James T.
Northwestern University
Materials Science Department
Evanston, Ill. 60201

Wachtman, J. B.
National Bureau of Standards
Washington, D.C. 20234

Walford, Lionel K.
McDonnel Douglas Corp.
St. Louis, Mo. 63166

Warren, William W.
Bell Telephone Labs.
Murray Hill, N.J. 07974

Watson, R. E.
Brookhaven National Lab.
Upton, N.Y. 11973

Weisman, Irwin D.
National Bureau of Standards
Washington, D.C. 20234

Weisz, Gideon
College of William & Mary
Williamsburg, Va. 23185

Welch, Gerhard
University of Utah
Physics Department
Salt Lake City, Utah 84112

Wei, C. T.
Michigan State University
East Lansing, Mich. 48823

Wiech, Gerhard
8000 Munchen Fl
Engadinerstr 34, Germany

Willens, R. H.
Bell Telephone Labs.
Murray Hill, N.J. 07974

Williams, A. R.
IBM
Yorktown Heights, N.Y. 12535

Williams, Morgan L.
National Bureau of Standards
Washington, D.C. 20234

Williams, Ronald W.
Oak Ridge National Labs.
Oak Ridge, Tenn. 37830

Windmiller, Lee
Argonne National Labs.
Argonne, Ill. 60439

Winogradoff, Nicholas
National Bureau of Standards
Washington, D.C. 20234

Wolcott, Norman M.
National Bureau of Standards
Washington, D.C. 20234

Wood, John K.
Utah State University
Physics Department
Logan, Utah 84321

Woods, Joseph F.
IBM, T. J. Watson Res. Cent.
Yorktown Heights, N.Y. 10598

Wooten, Frederick
Lawrence Radiation Lab.
Livermore, Calif. 94550

Yelon, Arthur
Yale University
10 Hillhouse Avenue
New Haven, Conn. 06520

Yolken, H. Thomas
National Bureau of Standards
Washington, D.C. 20234

Young, Russell
National Bureau of Standards
Washington, D.C. 20234

Zeisse, Carl R.
Naval Elec. Lab. Cent.
San Diego, Calif. 92152

Ziman, John M.
University of Bristol
Physics Laboratory
Bristol, England

Subject Index

Following each subject is the page number of the first page of the article in which the subject appears.

A

actinide metals—17
absorption—
—potential—359
—spectra—223, 253, 275, 319
alkali—
—ammonia solutions—601
—metal alloys—191
—metals—67, 103, 223, 253, 269, 275, 287, 359, 601, 651, 783
alloy phase—
—local density of states—307, 313
—stability—19
amorphous semiconductors—1, 493, 505, 521
Anderson transition—493
anthracene—261
anti-ferromagnetism—27, 493, 527, 557, 571, 741
anti-phase domain—571
aromatic crystals—261
Auger—
—effect—179
—transitions—281, 287
augmented plane wave method (APW)—1, 19, 53, 63, 67, 105, 111, 115, 191, 297, 493, 565

B

band—
—absorption—693
—population effects—407
—tail—493, 505, 579, 693
—transitions, direct-non-direct—159, 181, 191, 205, 217
benzene (C_6H_6)—261
bond, chemical—385
brass, βCu—Zn—339, 509

C

carbon contamination—199
cellular disorder—521
chalcogenide glasses—493
chalcogenides—601
charge density—359
charging effect—313, 587
chemisorption—375
cluster theory—505
coherent potential approximation—505, 551
compressibility—67, 731, 741
Compton scattering—233, 345
conduction electron spin resonance (CESR)—601
core hole—233, 269
core polarization—601, 649, 659
correlation—47, 233, 665
crystal potential—63, 755
Curie temperature—105, 557, 571
Curie-Weiss law—601
cyclotron resonance—423, 431, 757

D

Davydov splitting—261
Debye temperatures—139, 557, 565, 579, 597, 601, 685, 741, 767
de Haas-van Alphen effect—57, 339, 649, 673, 685, 717, 737, 785
—and the Knight shift—601
delta—
—function formulation of density of states—437
—function potential—509, 515
—potential impurity—473
depletion layer barrier tunneling—693
diamond—335
dielectric constant—33, 77, 111, 115, 125, 223, 757
diffusion equation—473
Dirac equation, one-dimensional—477
disordered—
—solid solution alloys—19
—systems—1, 453, 465, 505, 509, 521
Drude model—33
ductility—483

E

electroreflectance—407, 411, 417, 757
electron—
—donation model—727
—electron scattering—129, 139, 767, 785
—enhancement—571
—interaction—63, 233, 493
—phonon
—coupling constant—681, 731, 741, 767, 785
—enhancement—571
—interaction—63, 227, 233, 493, 565, 587, 685
—paramagnetic resonance—601
—synchrotron light—275
electronic specific heat—57, 63, 297, 565, 579, 651, 685, 731
electrons in a box—129
electrical resistivity—483, 665, 685, 737
—temperature dependent—737
energy distribution curves (EDC)—139
enhancement—
—electron-electron—571

enhancement—Continued
—electron-phonon—557, 571, 681
—exchange—601, 657, 665
Esaki diode—673, 693
exchange—43, 659, 665
exchange—
—Kohn-Sham—93
—Liberman—93
—Slater—19, 57, 93, 111, 359
exchange potential—105, 233, 741
excitons—253, 261, 717
excluded terms—515

F

f-bands—105
Fermi-Dirac—253, 287, 685, 741, 757
Fermi—
—edge singularity—269
—energy—53
—surface—39, 385, 735, 785
ferro-magnetic spiral structure—571
ferromagnetism—27, 47
field-emission resonance tunneling—375
Franck-Condon principle—493
Franz-Keldysh theory—93, 417
Friedel—
—oscillations—253, 359, 601
—screening theory—551

G

G. P. zone—587
galvanomagnetic—
—experiments—737
—properties—717
Ginzburg-Landau coherence length—587
glass—
—chalcogenide—493
—tetrahedral—1
graphite—717
Green's functions—1, 233, 465, 509, 515, 527, 551, 767
Gruniesen parameter, electronic—731, 741
Gunn effect—437

H

Hall effect—483, 717
Hamiltonian—
—Anderson—375
—Ashcroft—33
—Hubbard—527
Hartree-Fock method—67, 93, 233, 271, 527, 601
Hartree-Fock-Slater potential—63, 181, 601
Hellman-Feynman theorem—27
Hume-Rothery electron compound—19
hydrocarbons—13, 261
hydrogen—
—absorption—727
—in palladium—737
hyperfine fields—601, 649

I

indirect transition—111
interband transition—33, 39, 125, 181
intermetallic compounds, CsCl
structure—19, 303
interpolation method—27
itinerancy—47
ion-neutralization spectroscopy (INS)—163, 349
Ising model—381

J

joint density of states—19, 93, 129, 192, 209
—magnetic—431
Josephson tunnelling—1

K

k-conservation—19, 139, 181, 191, 199, 205, 437
Knight shift—303, 601, 649, 651, 659, 665
Korringa-Kohn-Rostoker method (KKR)—19, 57, 63, 181, 509
Kondo effect—1, 601
$k \cdot p$ method—115, 335, 757
Kronig-Penney model—129, 477

L

Landau levels—39, 431, 437, 673
Landau-Peierls diamagnetism—601
lanthanides—67, 217, 571
lasers—
—semiconductor—437
LCAO—19, 27, 115, 329
LEED spectra—1, 349
liquids—1
local—
—field cancellation—557
—density of states—465
localized states—493
low-temperature specific heat—57, 483, 571, 579, 587, 597, 681, 685, 767
luminescence experiments—693

M

magnetic—
—clusters—557
—critical points—431
—specific heats—571, 741
—susceptibility—483, 587, 601, 645, 649, 651, 685, 737, 767
magneto—
—optical density of states—437, 757
—reflection—39
—resistance—717
Matsubara approximation—527
mechanical behavior—483
melting—483
membrane, two dimensional
classical—473
metal—
—insulator-metal (MIM)—673
—insulator-semiconductor (MIS)—407, 673
—vacuum interface—359, 473

model—
— density of states—767
— potential of Heine and Abarenkov—483
modulation technique—281
molecular crystals—1, 261
Mott insulator—493, 527, 601
muffin-tin potential—1, 19, 57, 181, 297, 349, 453, 473, 509
multiple-scattering series—515

N

near-free electron model—359
nearly free electron approximation—19
naphthalene—261
Néel temperature—493, 527, 601
noble metal alloys—
— Ag—1, 303, 307, 483, 545, 551, 601
— Au—19, 303, 483, 493, 545, 601, 673, 727, 791
— Cu—139, 339, 385, 483, 509, 557, 601
noble metals—17, 19, 67, 105, 139, 163, 181, 191, 205, 253, 281, 303, 319, 349, 359, 545, 551, 597, 601, 651, 795
nonlinear optical susceptibility—757
nuclear magnetic resonance (NMR)—601, 659

O

omega phase—587
one-dimensional Dirac equation—477
Onsager model—381
optical—
— absorption—77, 111, 125, 233, 253, 279
— constants—545
— density-of-states—139, 159, 191, 205, 209, 437, 493
— properties—19, 33, 111, 115, 125, 191, 209, 233, 303, 758, 791
— reflection—47
order-disorder—483
orthogonalized plane wave (OPW)—27, 47, 53, 93, 335, 601, 649, 651, 659
oscillatory dielectric function—417

P

Pauli spin susceptibility—601, 645, 649, 737, 757
Pauling radii—385
Peierls barriers—483
phonon—673, 767
photoabsorption—275
photoconductivity—493
photo-electric effect—129
photoemission spectroscopy (PES)—27, 47, 53, 105, 159, 163, 181, 191, 199, 205, 209, 217, 493, 551, 597
piezo soft x-ray effect—281
plasmeron—233
plasmon—125, 181, 287
polaron—293
positron annihilation—269, 339, 345
potential—
— coherent approximation—505, 551
— deformation—767
— exchange—105, 233, 741
— model of Heine and Abarenkov—483
— muffin-tin—1, 19, 57, 181, 297, 453, 473, 509
pressure dependence of the—
— band structure—67, 77
— Knight shift—601, 651
— superconducting transition temperature—681, 731, 735
pressure effects—63, 717
pseudopotential—1, 33, 57, 93, 115, 125, 269, 483, 601, 649, 651, 659, 755

Q

QUAD scheme—17, 181, 741, 795
quasi—
— localized state—521
— particle—125, 227, 381

R

random phase approximation (RPA)—115, 233, 659
rare-earth metals—67, 217, 571
reflectivity—33, 39, 115, 209, 493, 545
resistivity ratios—651
rigid-band approximation—19, 53, 163, 313, 329, 515, 551, 587, 597, 601, 685, 727, 737

S

satellite—
— emissions—319
— structure—125
scattering phase shifts—515
Schottky barrier—693
Schrödinger equation—1, 253, 521, 651
secondary emission—181
self absorption—319
semiconductor laser—437
semiconductors—
— amorphous—1, 493, 505, 521
— compounds—135, 483
— diamond or zinc blende—93, 335, 411, 693, 757
short-range-order parameters—509
small particles—473
soft x-ray spectroscopy (SXS)—139, 163, 217, 233, 253, 269, 273, 275, 281, 287, 297, 303, 307, 313, 319, 327, 335, 555, 597, 601, 665, 791
specific heat—
— electronic—57, 63, 297, 565, 579, 651, 685, 731, 737
— low temperature—57, 483, 571, 579, 587, 597, 681, 767, 783
— magnetic—571, 741
spin—
— dipolar interactions—601
— orbit splittings—39, 67, 163, 221, 303, 411, 545, 717, 756, 757
— wave theory—571
strain dependence of superconducting transition temperature—731, 735
superconducting transition temperatures—557, 565, 587, 731, 735
superconductivity—565, 731, 735, 767
surface—
— Auger spectroscopy (SAS)—349
— energy—359
— potential—407
synchrotron light—279

T

temperature dependent resistivity—737
thermal—
— conductivity—685
— effective mass—233
— expansion, electronic—731
thermoelectric power—651, 685, 737

tight-binding approximation—27, 47, 115, 359, 453, 521, 527, 579, 601
tetrahedral—
—glass—1
—semiconductor—93, 335, 411, 693, 757
t-matrices—129, 253, 509, 527, 551
transition-metal behavior—57, 527
transition metals—17, 19, 163, 191, 349, 385, 483, 565, 756, 767
transport properties—651, 685, 693
tunnel junctions—737
tunneling—1, 375, 693

U

uv photoemission spectroscopy (UPS)—163, 199, 217, 233, 349

V

vacuum ultraviolet reflectance spectra—111
Van der Waals type interaction—261
Van Vleck temperature-independent paramagnetism—601
virtual crystal approximation—551
volume dependence of density-of-states—731

W

Weiss model—381
Wigner-Seitz cell—53, 67, 601, 741

X

x-ray—
—absorption—233
—emission—47
—photoemission spectroscopy (XPS)—163, 217, 233, 319, 349, 791

Z

zinc blende structure—163, 693, 757

Materials Index

Following each material is the page number of the first page of the article in which the material appears. All materials in the index are arranged alphabetically by their chemical symbols. Compounds (e.g., oxides, nitrides, etc.) are also listed alphabetically. Example: NaCl is listed under ClNa. A hyphen is used to indicate various compositions which may include compounds or solid solutions. Example: Al-Cu.

A

Actinide metals—17
Ag—63, 163, 181, 205, 551, 601
AgAl—303, 307
Ag-Al—303, 601
Ag-Au—1, 545, 551, 601
Ag-In—551
Ag-Pd—551, 601
Ag-Sb—601
Ag-Sn—601
Ag_2Te—483
alkali—
—ammonia solutions—601
—metal alloys—191
Al—33, 159, 233, 253, 269, 275, 287, 303, 313, 601, 673, 731, 795
Al-Al_2O_3-semiconductor—673
Al_2-Au—297, 303, 665, 791
Al_2Au-$AuGa_2$—791
$AlCl_3$—665
AlCo—19, 601
Al-Cu—307
Al-Cu-Ni—557
AlFe—601
Al-Fe—557
Al-Fe-V—557
Al-insulator-Ni—673
Al-insulator-NiPd—673
Al-Mg—287, 313, 329, 665
AlNi—19, 27, 483, 601, 665
Al-insulator-Pd—191, 737
Al_2O_3—665
AlP—93
AlSb—757
$AlTi_3$—483
Al-Ti—329, 483
Al_2U—601
Al-Zn—307
amorphous semiconductors—1, 493, 505, 521
anthracene—261
aromatic crystals—261
As—39
AsGa—77, 93, 139, 407, 411, 693, 757
AsIn—77, 673, 757
AsNi—385
As-Si (As doped)—693
Au—17, 63, 139, 163, 205, 303, 545, 551, 601
$AuCu_3$—483
Au-Cu—483, 545
AuFe—545
$AuGa_2$—303, 601, 791
AuGe—493
Au-Ge—673
$AuIn_2$—303, 791
Au-Pd—727
Au-Pd-H—727
AuZn—19

B

BTi—329
Ba—67, 217, 375
Be—233, 275, 601, 649, 659
benzene (C_6H_6)—261
Bi—601, 673
BiIn—601
Bi_2Mg_3—483
Bi_2Te_3—483
brass, βCu-Zn—339, 509

C

C—335, 597, 717
CTi—329, 598
CSi—601
CV—597
Ca—57, 67, 375
Cd—359, 659
$CdCl_2$—163
Cd-In (Cd dilute)—601, 735
CdS—139
CdSb—483
CdSe—139
CdTe—139, 757
Ce—67, 601
chalcogenides—
—glass—493
Co—105, 163, 319
CoTi—329, 483
Cr—27, 209, 221, 571, 587, 598, 685
Cr-Cu—601
Cr-insulator-Pb—673

Cr_2Ti—329
Cr-V—601
Cs—67, 233, 601, 651, 783
Cu—33, 63, 74, 105, 139, 163, 181, 191, 205, 253, 281, 319, 339, 349, 555, 598, 601, 651, 795
Cu (cesiated)—139, 191
Cu-Mn—385, 557
Cu-Ni—139, 557
Cu-Pd—601
CuPt—483
Cu-Pt—483
CuZn—339, 509

D

diamond—335
diamond semiconductors—335, 411

E

Er—571
Er-Tm—571
Eu—105, 217
Eu-chalcogenides—105, 221
EuO—105
EuO-EuSe—105
EuS—105
EuSe—105
EuS-EuSe—105

F

Fe—1, 17, 27, 47, 67, 105, 163, 319, 587, 641
Fe_2O_3—319
FeTi—483
Fe-V—557, 601

G

Ga—303, 601, 731
GaP—757
GaSb—411, 757
Gd—105, 221, 571
Gd-Pr—571
GdS—105
Ge—1, 33, 77, 93, 139, 253, 335, 349, 375, 411, 417, 431
GeO_2—111
graphite—717
glass
—chalcogenide—493
—tetrahedral—1

H

H_2 in Au-Pd—727
H_2La—601
H-Nb—601
H-Pd—727
H-Sc—601
H-V—601
H_2Y—601
Hf-Ta—565
hydrocarbons—13, 261
He—345, 349
Hg—359, 587
HgO—181
Ho—571

I

In—159, 601
InP—757
In-Pb—601
In-Pd—26
InSb—407, 693, 757
In-Sn—601
Ir—163, 685

K

K—103, 233, 287, 651
Kr—279

L

lanthanides—67, 217, 571
Li—67, 139, 253, 269, 275, 359, 493, 651

M

Mg—233, 253, 275, 313, 601, 659, 673
MgO—493
Mg_3Sb_2—483
Mn—587
Mn-Ni—557
Mo—53, 209, 221, 598, 673, 685
Mo-Ti—221, 587
molecular crystals—1, 261

N

Na—103, 125, 233, 269, 275, 359, 601, 651
naphthalene—261
Nb—221, 598, 685
Nb_3Sn—601, 767
Ne—358
NTi—329
Ni—17, 105, 139, 163, 281, 319, 349, 555, 601, 673
NiO—221, 493
NiTi—329, 483
noble metal alloys—
—Ag—1, 303, 307, 483, 545, 601
—Au—19, 303, 483, 493, 545, 601, 673, 727, 791
—Cu—139, 339, 385, 483, 509, 557, 601

O

O_3Re—27
OTi—329
Os—163

P

P-Si (P doped)—685
Pb—67, 233, 557, 601, 673

Pb chalcogenides—77
PbTe—77, 115, 139, 601
Pd—17, 91, 139, 163, 181, 571, 601, 645, 673, 685, 735, 737
Pd-Rh—579, 601
Pt—17, 163, 359, 601, 658, 685
Pu—67

R

rare-earth metals—67, 217, 571
Rb—601, 651, 783
Re—587, 685
Re-Ta—565
Re-W—565
Rh—163, 579, 685
Rh-Ru—579
Ru—163

S

SbZn—483
Sb-Si (Sb doped)—693
Sc—17, 57, 205, 587, 598
semiconductors—
—amorphous—1, 493, 505, 521
—compounds—135, 483
—diamond or zinc blende—93, 335, 411, 693, 757
SeZn—93
Si—1, 77, 93, 253, 335, 349, 693
Si (As, P, Sb, doped)—693
SiV_3—601, 767
Sn—673
Sn-Ti—483
Sn_3U—601
Sr—67

T

Ta—53, 565, 587, 685
TaW—565
$TeTl_2$—483
TeZn—757
Th—731
Ti—205, 221, 329, 587, 597
TiZr—483
Tl—601, 681
Tm—571
transition metals—17, 19, 163, 191, 349, 385, 483, 556, 565, 767

U

U—67

V

V—221, 587, 601

W

W—53, 67, 209, 375, 387, 685, 691
W (β-W compounds)—767

X

Xe—279

Y

Y—598
Yb—221

Z

Zn—163, 209, 287, 319, 359, 659
zincblende structure—163, 693, 757
Zn_2Zr—601
ZnTe—757
Zr—205, 375, 587, 598

FORM NBS-114A (1-71)

U.S. DEPT. OF COMM. BIBLIOGRAPHIC DATA SHEET	1. PUBLICATION OR REPORT NO. NBS-SP-323	2. Gov't Accession No.	3. Recipient's Accession No.

4. TITLE AND SUBTITLE

Electronic Density of States

5. Publication Date: December 1971

6. Performing Organization Code

7. AUTHOR(S)

Lawrence H. Bennett, Editor

8. Performing Organization

9. PERFORMING ORGANIZATION NAME AND ADDRESS

NATIONAL BUREAU OF STANDARDS
DEPARTMENT OF COMMERCE
WASHINGTON, D.C. 20234

10. Project/Task/Work Unit No.

11. Contract/Grant No.

12. Sponsoring Organization Name and Address

National Bureau of Standards

13. Type of Report & Period Covered: Final

14. Sponsoring Agency Code

15. SUPPLEMENTARY NOTES

16. ABSTRACT (A 200-word or less factual summary of most significant information. If document includes a significant bibliography or literature survey, mention it here.)

This volume is based on materials presented at the Third Materials Research Symposium of the National Bureau of Standards, held November 3-6, 1969. It provides a review of various experimental and theoretical techniques applied to the study of the electronic density of states in solids and liquids. The topics covered in a series of invited and contributed papers include theory of and experiments to obtain the one-electron density-of-states; many-body effects; optical properties; spectroscopic methods such as photoemission (x-ray and UV), ion neutralization, and soft x-ray; obtaining the density-of-states at the Fermi level by specific heat, magnetic susceptibility, and the Knight shift; the disordered systems of alloys, liquids, dirty semiconductors, and amorphous systems; and superconducting tunneling and the application of density of states to properties such as phase stability. An edited discussion follows many of the papers.

17. KEY WORDS (Alphabetical order, separated by semicolons) Band structure; disordered systems; electronic density of states; ion neutralization; Knight shift; magnetic susceptibility; many-body effects; optical properties; photoemission; soft x-ray; specific heat; superconductivity; transport properties; tunneling.

18. AVAILABILITY STATEMENT

[X] UNLIMITED.

[ ] FOR OFFICIAL DISTRIBUTION. DO NOT RELEASE TO NTIS.

19. SECURITY CLASS (THIS REPORT): X UNCLASSIFIED

21. NO. OF PAGES: 834

20. SECURITY CLASS (THIS PAGE): UNCLASSIFIED

22. Price: $7.75

U.S. GOVERNMENT PRINTING OFFICE 1971 OL—417-156

USCOMM-DC 66244-P71